Consortium for Small-Scale Modelling

Technical Report No. 42

A methodology towards the hierarchy of COSMO parameter calibration tests via the domain sensitivity over the Mediterranean area

April 2020

DOI: 10.5676/DWD_pub/nwv/cosmo-tr_42

Deutscher Wetterdienst
MeteoSwiss
Ufficio Generale Spazio Aereo e Meteorologia
ΕΘΝΙΚΗ ΜΕΤΕΩΡΟΛΟΓΙΚΗ ΥΠΗΡΕΣΙΑ
Instytucie Meteorogii i Gospodarki Wodnej
Administratia Nationala de Meteorologie
ROSHYDROMET
Agenzia Regionale Protezione Ambiente Piemonte
Agenzia Regionale Prevenzione Ambiente Energia Emilia Romagna
Centro Italiano Ricerche Aerospaziali
Amt für GeoInformationswesen der Bundeswehr
Israel Meteorological Service

www.cosmo-model.org

Editor: Massimo Milelli, ARPA Piemonte

A methodology towards the hierarchy of COSMO parameter calibration tests via the domain sensitivity over the Mediterranean area

E. Avgoustoglou[1], ***A. Voudouri***[1], ***I Carmona***[2],

E. Bucchignani[3], ***Y. Levy***[2], ***J. M. Bettems***[4]

[1]Hellenic National Meteorological Service

[2]Israel Meteorological Service

[3]CIRA -Centro Italiano Ricerche Aerospaziali

[4]MeteoSwiss

Contents

1 Abstract **3**

2 Introduction **3**

3 Model setup **4**

3.1 Configuration 4

3.2 Parameter selection and model tests 5

4 Methodology **7**

4.1 Elemental application over one meteorological field 7

4.2 Extension of the methodology over several meteorological fields 7

5 Discussion of the relative sensitivity of different domains **8**

6 Conclusions **11**

7 Acknowledgments **11**

8 References **11**

9 Appendix for Figs. 2 to 10 **14**

1 Abstract

The goal of this work is to estimate systematically the sensitivity of COSMO model over a large number of expected high impact parameters, using objective criteria for their selection. The proposed methodology is based on the relative average values of certain meteorological fields over a considered model domain and time period. Its main advantages are its economy as well as its flexibility, due to its *ab initio* character, as observations do not enter into the decision process. In this way, the calibration procedure is considered as a separate independent stage of the model optimization according to the computational resources available to the user and in reference to the available observations. Another important feature of the method deals with the selection of the proper domain in case of nesting by employing the similarities of the parameter sensitivities between the wider and the internal domain. Twelve parameters were examined over the wider Mediterranean area for a period of 62 dates from February, June, and December of 2013 and a horizontal grid of 0.0625° ($\sim 7\,Km$). The validity of the method is demonstrated via the resulting sensitivities of this domain compared with those of internal domains over the areas of Greece, Italy, Israel and Switzerland leading to a distinct hierarchy regarding the parameter choice as well as the dominant interaction terms of the parameter combinations.

2 Introduction

Numerical weather prediction (NWP) models are tools of exceptional complexity both from the computational perspective regarding the applied numerical schemes as well as the physical processes included along with their approximations. From the operational standpoint, the physical processes are implemented by means of parameters that are either user defined or hardcoded into the model software (default values herein). However, the optimization of the model performance depends significantly on these parameter values. The process of finding the default parameter values is generally addressed as model tuning (Skamarock 2004; Duan et al., 2006). The more physical processes are included in the NWP model, the larger is the number of parameters expected to be tuned to control and optimize its performance. This feature leads usually to a task of employing complicated methodologies of relatively high computational cost (Annan and Hargreaves 2007). This is also the case for COSMO, a state of the art non-hydrostatic local NWP model developed and supported by the synonymous COSMO consortium (COnsortium for Small-scale Modeling, www.cosmo-model.org) consisting of the national meteorological services of Germany, Greece, Israel, Italy, Poland, Romania, Russia and Switzerland. In our previous works (Khain et al., 2015, 2017; Voudouri et al., 2016, 2017, 2018, 2019), there have been performed extensive efforts to increase the performance of COSMO model over the area of Switzerland and Northern Italy through the choice of an optimum set of tunable model physics parameters. The optimization process was based on the use of an objective calibration procedure that has been applied for a regional climate model (RCM) (Bellprat et al., 2012a and 2012b). This calibration methodology relies on a meta-model (MM) that approximates the parameter space, using a multi-variate quadratic regression in an N-dimensional model (Neelin et al., 2010 and 2010a; Box and Behnken, 1960; Mayers et al., 2009) where the dimension N of the model is the number of the parameters that are chosen to be optimized. The number of simulations required to create the quadratic polynomial necessary to construct the MM for calibrating N parameters varies from a minimum of 2N+N(N-1)/2 to a maximum of 2N+2N(N-1) plus a simulation standing for the default parameter values combination. In principle, the first step is to perform the runs of COSMO model with the default parameter values for the time period and

domain under consideration and then repeat the process, first by changing one parameter at a time to its maximum and minimum limits values and then changing two parameters at a time to account for the interaction between these parameters. Although the approach is rather straightforward, its computational cost rises practically in analogy to N^2 providing significant constraints in its realization if the number of the parameters rises, especially when relatively large domains are considered along with fine grid spacing.

In the present approach, a strategy is developed on how to decrease the computational cost of the above process by providing realistic options towards the truncation both of the number N of the parameters chosen as well as the choice of the interaction terms. The key concept of this mechanism is the relative sensitivity of the minimum and maximum parameter values with respect to their default values in reference to certain meteorological fields that are considered as the most important ones from the operational perspective of the user (e.g. cloud cover, precipitation, 2m temperature etc.). In this work and in analogy to the work of Dierer et al (Dierer et al., 2009), this sensitivity is defined as the ratio of the difference of the average area values of the considered meteorological fields between their limit parameter values and their default ones over the total period of the model runs. A direct insight regarding the relative sensitivity among the parameters is visualized in the form of spider-graphs. Another feature of the methodology is the possibility to use the parameter sensitivities to relate meteorological similarities among internal domains in reference to the wider area of the model run and potentially attribute criteria for their optimum position and extent in case of the application of nesting techniques to further increase the local model performance. Towards this direction, the relative sensitivities of domains over the areas of Greece, Italy, Israel and Switzerland are presented in reference to the domain of the Mediterranean.

3 Model setup

3.1 Configuration

In this work. Version 5.0 of COSMO model was used that forms the reference version of the current operational applications of the model. Extensive physical parametrizations, as well as refined numerical schemes are induced in the model making it particularly applicable for the current study, since it is mainly designed to be applied operationally in the Meso-β and Meso-γ scales (Steppeler et al., 2003; Baldauf et al., 2011; Gebhardt et al., 2011; Schättler et al., 2013; Collaud Coen, 2014). The model runs were performed for 48hr periods starting at 00 UTC over the wider Mediterranean area (Fig. 1), the domain used operationally by the Hellenic National Meteorological Service (HNMS), on a 0.0625° ($\sim 7\,Km$) horizontal grid spacing, 649x393 grid points with 60 vertical levels and a 30 second integration time step.

This configuration has also been used for research purposes that highlight the value of the model towards the further understanding of storm surges (Calafat et al., 2014), cloud schemes (Avgoustoglou and Tzeferi, 2015), tornadoes (Avgoustoglou et al., 2018) and non-adiabatic atmospheric processes (Kouroutzoglou et al., 2018). The model was initialized from 6-hour analysis of the ECMWF operational model (www.ecmwf.int/en/forecasts/datasets/set-i) over a 0.150° ($\sim 15\,Km$) horizontal grid, while the outputs were produced in 3-hour time intervals. The model runs were performed at ECMWF's High Performance Computing Facility (www.ecmwf.int/en/computing/our-facilities/supercomputer) and are equivalent of approximately 6 years of model runs.

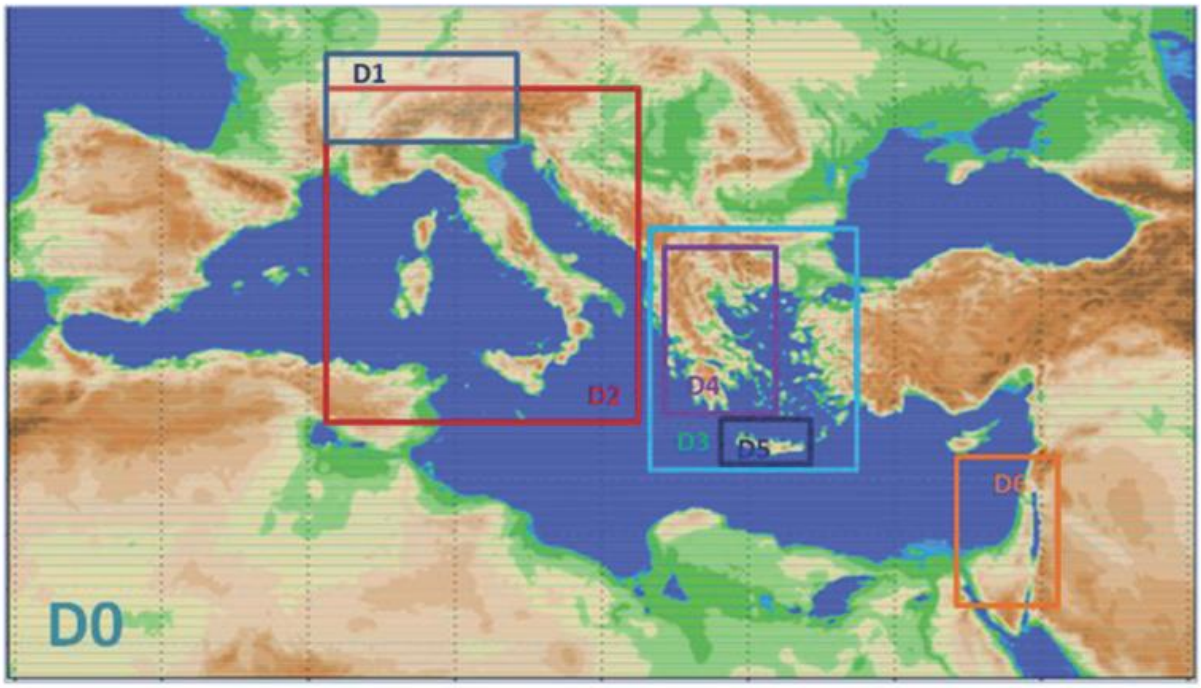


Figure 1: Domain of model runs over the wider Mediterranean area (D0) along with specific test domain for areas around: Switzerland (D1), Italy (D2), Greece (D3), Continental Greece (mainly) (D4), Crete (D5), and Israel (D6).

3.2 Parameter selection and model tests

A set of twelve parameters was selected (Table 1) that practically envelops the most significant physical processes of COSMO model over a general domain selection (Schättler et al 2013).

PARAMETER	INTERPRETATION	TEST VALUES
a_stab	stability correction factor of horizontal length scale	**0.0** , 0.5, 1.0
crsmin	minimum stomatal resistance	50, **150**, 300
c_soil	surface area index of evaporative soil	0, **1**, 2
entr_sc	mean entrainment rate for shallow convection	$5 \cdot 10^{-5}$, $\mathbf{3 \cdot 10^{-4}}$, $2 \cdot 10^{-3}$
mu_rain	shape parameter of the rain drop size distribution	0, **1**, 2
q_crit	critical value for normalized oversaturation	1.6, 2.8, **4.0**
rain_n0_factor	factor to reduce the evaporation of raindrops	0.02, **1.0**, 5.0
rat_sea	ratio of laminar scaling factors for heat over sea	1, **20**, 100
rlam_heat	scaling factor of the laminar boundary layer for heat	0.1, **1.0**, 2.0
tkmmin tkhmax	minimal value of diffusion coefficients for heat and momentum (kept equal)	0.1,**0.4**, 1.0
tur_len	asymptotic maximal turbulent length scale (m)	100, **150**, 1000
v0snow	factor in the terminal velocity for snow	10, **20**, 30

Table 1: List of the 12 parameters of tested sensitivity based on their code names (first column), interpretation (second column) and test values range (third column). The default values are denoted with bold italic characters.

However, the application of a MM for the calibration of COSMO model over such a large number of parameters is prohibitive, especially when a domain with the complexities and

size of the Mediterranean should be considered. In our previous works (Voudouri et al., 2017 and 2018), the reduction of the parameters was decided mainly on heuristic arguments based on the works of Bellprat et al (Bellprat et al. 2012a, Bellprat et al. 2012b) as well as the climatological and meteorological characteristics of the considered domain of Switzerland and Northern Italy. The choice of the parameters to be tuned was an essential task and a considerable effort was given regarding their selection since there are numerous parameters in COSMO model specifically related to sub-grid scale turbulence, surface layer parametrization, grid-scale clouds, precipitation, moist and shallow convection, radiation, the soil scheme etc. (Doms et al., 2011, Gebhardt et al., 2011).

Therefore, the consensus regarding the selection of parameters turns out to be the most crucial task to control the number of the model simulations and the consequent computational cost. In the present work and under this motivation, the domain parameter sensitivity (DPS) is introduced as the key term. DPS is considered that leads to the desired most convenient parameter choice in an objective manner via a consequent imposed hierarchy over the resulting DPS of the considered parameters.

For a model field F the domain parameter sensitivity DPS_F is defined as ,

$$DPS_F = \frac{< F >_{TEST} - < F >_{DEFAULT}}{< F >_{DEFAULT}} \cdot 100 \tag{1}$$

where $< F >_{DEFAULT}$ stands for the temporal domain areal average of F for the default parameter values, while $< F >_{TEST}$ stands for the test run where one of the parameters has been set equal to its limit values given in Table 1, while the other parameters are kept with their default values (Avgoustoglou et al., 2016). Although, there is no constraint on the model fields attributed for consideration, the applicability of the method is presented upon the choice of rather common meteorological features related with cloud cover,precipitation and temperature (Table 2).

0-24 hr period accumulated precipitation (kg m^{-2})	TOTPREC
0-24 hr periods accumulated grid-scale snow (kg m^{-2})	SNOW_GSP
Low cloud cover (%) average of 3hr time steps 03-24 hs	CLCL
Medium cloud cover (%) average of 3hr time steps 03-24 hs	CLCM
High cloud cover (%) average of 3hr time steps 03-24 hs	CLCH
Total cloud cover (%) average of 3hr time steps 03-24 hs	CLCT
Maximum 2m temperature (^oC) for 0-24 hr periods	TMAX2m
Minimum 2m (^oC) temperature 0-24 hr periods	TMIN2

Table 2: List of the examined meteorological fields. Their encoded names in COSMO model are given in the second column.

Regarding TMAX2m and TMIN2m the denominator of (1) changes very little relative to the absolute temperature and it was considered more convenient to define DPS simply as,

$$DPS_{\left[\begin{smallmatrix} TMIN2m \\ TMAX2m \end{smallmatrix}\right]} = \begin{bmatrix} TMIN2m \\ TMAX2m \end{bmatrix}_{TEST} - \begin{bmatrix} TMIN2m \\ TMAX2m \end{bmatrix}_{DEFAULT} \tag{2}$$

For the sake of seasonal coverage, the model tests were performed over a total of 62 days in continuous periods of 20, 20 and 22 days over February, June and December 2013 respectively. Periods from spring and autumn were not included in order to avoid any complexities due to the transitional nature of these seasons.

4 Methodology

4.1 Elemental application over one meteorological field

In order to present the essence of the method, we focus on a single meteorological field, the precipitation (TOTPREC) for the domain of the Mediterranean (D0). After completion of the tests, the resulting DPSs are presented in a standard column graph at the upper part of Fig. 2, from which it is obvious that for D0 the parameters are divided practically in three groups with respect to their sensitivities. According to the magnitude of the DPSs, the first group includes the two most sensitive parameters rat_sea and rlam_heat, the second group includes the five less sensitive parameters c_soil, entr_sc, v0_snow, rain_n0_factor and crsmin while in the third group the five least sensitive remaining parameters are included. Although this preponderance regarding the sensitivities of rat_sea and rlam_heat is directly visible from this graph, it has also been supported by previous works especially regarding rat_sea and rlam_heat parameters (Dierer et al., 2009; Kouroutzoglou et al., 2018) directly from physical arguments regarding mainly non adiabatic atmospheric processes. Of particular importance to our approach is the presentation of DPSs in the form of a spider-graph as given in the lower part of Fig. 2. In this graph the DPSs are given as bullets, the positive ones over and the negative ones under the red polygon of "no sensitivity". The line that connects the dots defines the domain parameter sensitivity polygon (DPSP). It is drawn to address visually a geometrical morphology to the DPSs that is considered to be important over the next stages of the procedure. The limit parameter values are given as the extensions of the parameter names addressed in the tables and figures of the present work. In case the goal is to optimize the model performance with respect to TOTPREC using a MM, there is also the demand to consider tests with pair parameter combinations (Voudouri et al., 2017 and 2018), an essential task that becomes more and more complicated as the number of sensitive parameters is rising. This requirement is accounted by the creation of the domain parameter sensitivity priority board (DPSPB) presented in Table 3 where the absolute differences of the different parameter pair limit values are given in descending order. It can be easily shown that for N parameters, the number of pairs is 2N(N-1). So in the present case (12 parameters) the number of pairs is 264. Due to the large number of parameter pairs, only the first 20 are given in Table 3. As also shown in Fig. 2, the largest differences correspond to the most sensitive parameters (shaded rows) while there are also large differences between these parameters and those of very low sensitivity. Additionally, in the third column of Table 3, the relative sensitivity of the pairs of the DPSs is addressed by attributing the value -1 if the sensitivities have opposite signs and 1 if the signs are the same. In principle, the couples of the parameters with the highest DPS differences and with opposite sign sensitivities should be considered as the most appropriate choices in the optimization process via the use of a MM (highlighted rows in Table 3). According to the above analysis, upon the application of a model optimization technique, the initial choice of 12 parameters regarding D0 can be truncated from two to seven most sensitive ones and in case of the use of a MM the dominant parameter pairs are the ones addressed with the highlighted rows in Table 3.

4.2 Extension of the methodology over several meteorological fields

Although the precipitation has a standalone value regarding the optimization of model performance (Dierer et al., 2009), in principle, it is necessary to account for the model calibration with respect to more meteorological fields. In that case the parameter selection method can be readily generalized. Under this requirement, the meteorological fields of gridpoint snow (SNOWGSP), minimum 2m temperature (TMIN2m), maximum 2m temperature

(TMAX2m), high, medium and low cloud cover (CLCH, CLCM, CLCL respectively) are also included modifying the method accordingly.

TOTPREC		
rat_sea_ 1 - rlam_ heat_0.1	28.389	-1
rat_sea_100 - rlam_heat_2.0	25.164	-1
c_soil_0 - rat_sea_100	25.023	-1
entr_sc_5E-5 - rat_sea_100	24.617	-1
c_soil_0 - rlam_heat_0.1	23.195	-1
entr_sc_5E - 5-rlam_heat_0.1	22.789	-1
rat_sea_100 - v0snow_10	22.743	-1
rlam_heat_0.1 - v0snow_10	20.915	-1
rain_n0_factor_5.0 - rat_sea_100	20.732	-1
crsmin_300 - rat_sea_100	20.686	-1
mu_rain_0 - rat_sea_100	20.029	-1
rat_sea_100 -tur_len_1000	19.872	-1
rat_sea_100 - tur_len_100	19.599	-1
rat_sea_100 - tkhmin_tkmmin_1	19.592	-1
a_stab_0.5 - rat_sea_100	18.910	1
rain_n0_factor_5.0 - rlam_heat_0.1	18.904	-1
a_stab_1.0 - rat_sea_100	18.862	1
crsmin_300 - rlam_heat_0.1	18.858	-1
rat_sea_100 - tkhmin_tkmmin_0.1	18.792	1
q_crit_2.8 - rat_sea_100	18.463	1
...	...	...

Table 3: DPSPB for TOTPREC, i.e. the absolute values, in descending order, of DPS differences of temporal area 24-hour means for pairs of different parameter combinations for precipitation (TOTPREC) over the wider Mediterranean area D0 and over the 62-day period. The highest 20 values of the total of 264 combinations are displayed (second column) along with the corresponding parameter pair (first) column and their relative sensitivity signs (third column) denoted with -1 if they are opposite and 1 they are the same.

The corresponding DPSs are given in Table 4 and are shown in Fig. 3 where the spider graphs are referenced with respect to TOTPREC as it is given in the lower part graph of Fig. 2 and placed again in the head of Fig. 3. From the DPSs given in Table 4, it can be noticed that the most sensitive parameters (in gray shade) are essentially the same with those assessed from Table 3 with the inclusion of the minimal value of diffusion coefficients for heat and momentum (tkhmin & tkmmin) which have a significant impact in middle and low cloud cover, a feature that was the central point of a previous work (Avgoustoglou and Tzeferi, 2015). Moreover, towards the selection of the dominant interaction terms, a compiled DPSPB for all the meteorological fields is given in Table 5 as an extension to Table 3 and in reference to Fig. 3. Although the content of this table is considerably broad, the hierarchical display of the DPSs differences for several meteorological fields in adjacent places provides the framework to place consistent quantitative criteria on the interaction terms that should be considered.

5 Discussion of the relative sensitivity of different domains

As a sequel to the previous analysis regarding the establishment of a parameter ranking for model tuning of a particular domain, there is the possibility to use the DPSs for inducing similarities among different internal areas of the wider domain. These similarities may provide a valuable insight regarding the application of nesting techniques. In Figs. 4-10 the

spider graphs for domains D0 to D6 are presented for the meteorological fields of precipitation (TOTPREC) (Fig. 4), grid-point snow (SNOWGSP) (Fig. 5), high, medium, low cloud cover (CLCH, CLCM, CLCL respectively) (Figs. 6, 7, 8), minimum (TMIN2m) (Fig. 9) and maximum 2m temperature (TMAX2m) (Fig. 10).

PARAM	TOTPREC	SNOW_GSP	CLCH	CLCM	CLCL	TMAX2m	TMIN2m
a_stab_0.5	0.1511	-0.2403	0.1904	0.3191	0.1767	0.0003	-0.0341
a_stab_1.0	0.1988	-0.4219	0.3066	0.3665	0.2914	-0.0022	-0.0853
crsmin_300	-16.255	0.0182	0.2097	0.6191	0.1221	0.0818	0.0014
crsmin_50	25.727	0.0595	0.3373	10.707	0.1045	-0.1294	-0.0046
c_soil_0	-59.616	-30.841	0.3787	55.408	0.1548	0.2641	0.0644
c_soil_2.0	3.05	15.448	0.2361	29.961	0.0753	-0.1242	-0.031
entr_sc_2E-3	23.585	0.9937	22.646	62.603	15.248	0.0027	0.0031
entr_sc_5E-5	-55.557	0.7613	87.764	14.055	4.354	-0.0242	0.0006
mu_rain_0	-0.9676	0.2466	0.0088	0.409	0.0441	-0.0036	-0.0017
mu_rain_2	0.6006	-0.0872	0.0074	0.2646	0.0282	0.0025	0.001
q_crit_1.6	1.144	-13.807	0.8898	12.745	0.5128	-0.0161	-0.0061
q_crit_2.8	0.5978	-0.5607	0.4207	0.4144	0.3494	-0.0088	-0.0035
rain_n0_factor_0.02	38.139	-0.7431	0.0045	14.879	0.1475	0.0176	0.0073
rain_n0_factor_5.0	-16.706	0.3933	0.0193	0.6899	0.0723	-0.0063	-0.0037
rat_sea_1	-111.563	0.0619	10.611	31.985	22.331	-0.1486	-0.1196
rat_sea_100	190.612	0.0206	16.945	31.229	2.493	0.1323	0.0923
rlam_heat_0.1	172.325	0.3037	15.349	31.584	23.333	0.1309	0.0633
rlam_heat_2.0	-61.031	-0.2522	0.5916	18.652	11.356	-0.076	-0.0264
tkhmin_tkmmin_0.1	0.2694	13.823	0.68	56.307	12.637	-0.0726	-0.0646
tkhmin_tkmmin_1.0	-0.5307	-21.134	10.701	95.062	21.172	0.133	0.129
tur_len_100	-0.5381	0.3148	0.4474	0.7197	1.178	0.0045	0.0069
tur_len_1000	-0.8106	-21.356	17.747	-2.316	12.931	0.1205	-0.0749
v0snow_10	-36.822	-27.122	0.4876	0.0536	10.252	0.0037	0.0023

Table 4: DPSs for min and max parameter values for precipitation (TOTPREC), grid-point snow (SNOWGSP), minimum 2m temperature (TMIN2m), maximum 2m temperature (TMAX2m), high, medium and low cloud cover (CLCH, CLCM, CLCL respectively) over the wider Mediterranean area D0 and over the 62-day period.

In addition to the wider area of the Mediterranean D0 where the corresponding spidergraph is placed on the top of the figures, D1 refers to an area around Switzerland; D2 refers to an area around Italy, D3 to an area around Greece, D4 to an area constrained mainly to continental Greece, D5 to the area of Crete and D6 to an area around Israel as shown in Fig. 1. All graphs are scaled with respect to the most sensitive parameter of the specific meteorological field and particular domain to provide a better perspective of the analogies and similarities of the DPSs among the domains. For TOTPREC all domains show comparable DPSs and similar corresponding polygons (DPDPs) with the exception of D1 that exhibits considerably lower DPSs from the other areas. In addition, the areas of Italy (D2) and Greece (D3, D4) are very close in DPSs. An interesting aspect with this analysis are the close similarities between D5 (Crete) and D6 (Israel) which most probably addresses climatic characteristics between the two areas directly from the model parameters. This is also highlighted in Fig. 5 regarding SNOWGSP although this parameter might have certain spurious features due to the small number of events for the particular time sampling of 62 days including 20 days in summer. The situation is similar with the rest of the meteorological fields although for low cloud-cover (CLCL) the domains associated with the areas of Greece (D3, D4, D5) and Israel D5 denote sensitivity for several parameters however in good analogy with the reference domain D0.

TOTPREC			SNOW_GSP			CLCL			CLCM			CLCH			TMAX2m			TMIN2M		
P08MIN-P09MIN	28.389	-1	P03MIN-P10MIN	4.466	-1	P04MAX-P10MAX	15.766	-1	P04MIN-P08MIN	6.587	-1	P04MIN-P10MAX	9.846	-1	P03MIN-P08MIN	0.413	-1	P08MIN-P10MAX	0.249	-1
P08MAX-P09MAX	25.164	-1	P03MAX-P12MIN	4.257	0	P09MIN-P10MAX	12.664	-1	P04MIN-P10MAX	6.471	-1	P04MIN-P08MIN	9.837	-1	P02MIN-P03MIN	0.393	-1	P01MAX-P10MAX	0.214	-1
P03MIN-P08MAX	25.023	-1	P10MIN-P12MIN	4.094	-1	P08MAX-P10MAX	12.629	-1	P04MIN-P11MAX	5.647	-1	P04MIN-P09MAX	9.368	-1	P03MIN-P09MAX	0.340	-1	P10MAX-P11MAX	0.204	-1
P04MIN-P08MAX	24.617	-1	P03MIN-P04MAX	4.078	-1	P03MAX-P10MAX	12.502	-1	P04MIN-P09MAX	5.490	-1	P04MIN-P11MIN	9.223	-1	P03MIN-P10MIN	0.337	-1	P03MIN-P08MIN	0.184	-1
P03MIN-P09MIN	23.195	-1	P03MIN-P04MIN	3.845	-1	P03MIN-P04MAX	11.801	-1	P04MIN-P06MIN	4.867	-1	P03MIN-P04MIN	9.155	-1	P03MIN-P04MIN	0.288	-1	P08MIN-P09MIN	0.183	-1
P04MIN-P09MIN	22.789	-1	P04MAX-P12MIN	3.706	-1	P03MIN-P10MIN	11.172	-1	P04MIN-P06MAX	4.703	-1	P02MAX-P04MIN	8.986	-1	P08MIN-P10MAX	0.282	-1	P01MAX-P08MAX	0.177	-1
P08MAX-P12MIN	22.743	-1	P03MAX-P11MAX	3.681	-1	P06MIN-P10MAX	10.780	-1	P04MIN-P12MAX	4.685	-1	P04MIN-P12MAX	8.859	-1	P08MIN-P09MIN	0.280	-1	P08MAX-P11MAX	0.167	-1
P09MIN-P12MIN	20.915	-1	P03MAX-P10MAX	3.658	-1	P02MIN-P10MAX	10.577	-1	P01MAX-P04MIN	4.645	-1	P04MIN-P07MAX	8.795	-1	P03MIN-P06MIN	0.280	-1	P01MIN-P10MAX	0.163	-1
P07MAX-P08MAX	20.732	-1	P10MIN-P11MAX	3.518	-1	P07MAX-P10MAX	10.196	-1	P08MAX-P10MAX	4.610	-1	P04MIN-P05MIN	8.785	-1	P03MIN-P06MAX	0.273	-1	P03MAX-P10MAX	0.160	-1
P02MAX-P08MAX	20.686	-1	P03MIN-P07MAX	3.477	-1	P06MAX-P10MAX	9.920	-1	P08MIN-P09MIN	4.566	-1	P04MIN-P05MAX	8.783	-1	P03MIN-P07MAX	0.270	-1	P08MAX-P10MIN	0.157	-1
P05MIN-P08MAX	20.029	-1	P04MIN-P12MIN	3.473	-1	P05MIN-P10MAX	9.915	-1	P01MIN-P04MIN	4.531	-1	P04MIN-P07MIN	8.772	1	P08MIN-P11MAX	0.269	-1	P09MAX-P10MAX	0.155	-1
P08MAX-P11MAX	19.872	-1	P03MIN-P11MIN	3.399	-1	P10MAX-P12MIN	9.560	-1	P03MIN-P04MIN	4.509	-1	P01MIN-P04MIN	8.586	1	P03MIN-P05MIN	0.268	-1	P01MAX-P03MIN	0.149	-1
P08MAX-P11MIN	19.599	-1	P03MIN-P09MIN	3.388	-1	P10MAX-P12MAX	9.477	1	P04MIN-P07MIN	4.501	-1	P03MAX-P04MIN	8.540	1	P03MIN-P12MAX	0.266	-1	P01MAX-P09MIN	0.148	-1
P08MAX-P10MAX	19.592	-1	P03MIN-P05MIN	3.331	-1	P04MAX-P08MIN	9.459	-1	P02MIN-P04MIN	4.458	-1	P01MAX-P04MIN	8.469	1	P01MAX-P03MIN	0.266	-1	P03MIN-P11MAX	0.139	-1
P01MIN-P08MAX	18.910	1	P03MIN-P08MIN	3.146	-1	P05MAX-P10MAX	9.241	1	P09MIN-P10MAX	4.450	-1	P02MIN-P04MIN	8.439	1	P01MIN-P03MIN	0.264	0	P09MIN-P11MAX	0.138	-1
P07MAX-P09MIN	18.904	-1	P02MIN-P03MIN	3.143	-1	P01MIN-P10MAX	9.187	1	P04MIN-P05MAX	4.382	-1	P04MIN-P06MAX	8.355	1	P02MIN-P10MAX	0.262	-1	P06MIN-P10MAX	0.135	-1
P01MAX-P08MAX	18.862	1	P04MAX-P11MAX	3.130	-1	P01MAX-P10MAX	9.140	1	P04MIN-P05MIN	4.310	1	P04MIN-P12MIN	8.288	1	P02MIN-P08MAX	0.261	-1	P02MIN-P10MAX	0.134	-1
P02MAX-P09MIN	18.858	-1	P04MAX-P10MAX	3.107	-1	P02MAX-P10MAX	8.887	1	P04MIN-P07MAX	4.282	1	P04MIN-P10MIN	8.096	1	P03MIN-P05MAX	0.261	1	P07MAX-P10MAX	0.133	-1
P08MAX-P10MIN	18.792	1	P07MAX-P12MIN	3.105	-1	P08MIN-P10MIN	8.830	-1	P03MAX-P04MIN	4.279	1	P04MIN-P06MIN	7.886	1	P03MIN-P04MAX	0.261	1	P06MAX-P10MAX	0.133	-1
P06MAX-P08MAX	18.463	1	P03MIN-P08MAX	3.105	-1	P10MAX-P11MIN	8.786	1	P02MAX-P04MIN	4.232	1	P04MIN-P09MIN	7.241	1	P02MIN-P09MIN	0.260	-1	P05MIN-P10MAX	0.131	-1
...	...	...	...	...	...	...	...	...	...	...	...	...	...	...	...	...	...	...	...	...

Table 5: Three-column groups of the DPS differences absolute values for different parameter pair combinations regarding precipitation (TOTPREC), grid-point snow (SNOWGSP), minimum 2m temperature (TMIN2m), maximum 2m temperature (TMAX2m), high, medium and low cloud cover (CLCH, CLCM, CLCL respectively) over the wider Mediterranean area D0. The highest 20 values of the total of the 264 combinations are displayed (second) column along with the corresponding parameter pair (first) column and their relative sensitivities (third column) denoted with -1 if it is of the opposite and 1 if it is of the same sign. Due to space constraints, we correspond, P01 → a_stab, P02 → crssmin, P03 → c_soil, P04 → entr_sc, P05 → mu_rain, P06 → q_crit, P07 → rain_n0_factor, P08 → rat_sea, P09 → rlam_heat, P10 → tkhmin (together with tkmmin), P11 → tur_len , P12 → v0snow.

6 Conclusions

In the present study, a method was given aimed to restrict consistently the number of parameters chosen for COSMO model optimization especially via the use of a MM. The criteria were based on parameter sensitivities with additional insight of their relative values via spider-graphs. The method was developed analytically for the meteorological field of precipitation and was generalized to more meteorological fields where an internal consistency regarding the parameter choice was displayed. A decision process with respect to the interaction terms was also provided based on the differences of parameter sensitivities as well as their relative sign via the domain sensitivity priority boards. Finally, it was shown that the domain sensitivity spider graphs provide an important direct visual insight to certain similarities among them. These similarities might turn out to be important on the domain choice for the application of nesting techniques. This methodology is currently utilized in the development of CALMO-MAX project of COSMO (http://www.cosmo-model.org/content/tasks/priorityProjects/calmoMax/).

7 Acknowledgments

The current study was realized using computational resources provided gratis by the Hellenic National Meteorological Service (HNMS) taken from the available allocation billing units at the European Center for Medium-Range Forecasts (ECMWF) supercomputer resources.

8 References

Annan JD, Hargreaves JC 2007. Efficient estimation and ensemble generation in climate modeling. *Philosophical Transactions of the Royal Society A-mathematical Physical and Engineering Sciences.* **365**, 2077–2088.

Avgoustoglou, E., Tzeferi, T., 2015. The effect of a sub-grid statistical cloud-cover scheme applied to the COSMO local numerical weather prediction model over the wider geographical domain of Greece. *Atm. Res.* **152**, 69–73.

Avgoustoglou E., Voudouri A., Khain P., Grazzini F., J.-M. Bettems, 2016. Design and Evaluation of Sensitivity Tests of COSMO Model over the Mediterranean Area. *Perspectives on Atmospheric Sciences*, pp 49-54, Springer Atmospheric Sciences.

Avgoustoglou, E., Matsangouras, I., Pytharoulis, I., Kamperakis, N., Mylonas, M., Nastos P., Bluestein, H., 2018. Numerical modeling analysis of the mesoscale environment conducive to two tornado events using the COSMO.Gr model over Greece. *Atm. Res.* **208**, pp 148-155, doi.org/10.1016/j.atmosres.2017.07.022.

Baldauf, M., Seifert, A., Förstner, J., Majewski, D., Raschendorfer, M., Reinhart, T., 2011. Operational Convective-Scale Numerical Weather Prediction with the COSMO Model: Description and Sensitivities.
Mon. Wea. Rev. **139**, pp 3887-3905, http://dx.doi.org/10.1175/MWR-D-10-05013.1

Bellprat, O., Kotlarski, S., Lüthi, D., Schär, C., 2012a. Objective calibration of regional climate models. *Journal of Geophysical Research* **117**, D23115.

Bellprat, O., Kotlarski, S., Lüthi, D., Schär, C., 2012b. Exploring perturbed physics ensembles in a regional climate model. *Journal of Climate* **25**, pp 4582-4599.

Box, G.E.P., Behnken, D.W., 1960. *Technometrics* **2**, pp 455-475.

Calafat, F. M., Avgoustoglou, E., Jordà, G., Flocas, H., Zodiatis, G., Tsimplis , M. N., Kouroutzoglou, J. 2014. The ability of a barotropic model to simulate sea level extremes of meteorological origin in the Mediterranean Sea including explosive cyclones. *Journal of Geophysical Research: Oceans* **119 (11)**, pp 7840-7853. doi. 10.1002/2014JC010360.

Doms, G., Förstner, J., Heise, E., Herzog, H-J., Mironov, D., Raschendorfer, M., Reinhardt, T., Ritter, B., Schrodin, R., Schultz, J.-P., Vogel, G., 2011. A description of the nonhydrostatic regional COSMO model. Part II: Physical Parameterization. Available at: http://www.cosmo-model.org

Dierer, S., Arpagaus, M., Seifert, A., Avgoustoglou E., Dumitrache R., Grazzini, F. Mercogliano, P., Milelli, M., Starosta, K., 2009. Deficiencies in quantitative precipitation forecasts: sensitivity studies using COSMO model. *Meteorologische Zeitschrift* **18**, pp 631-645.

Duan, Q., Di, Z., Quan, J., Wang, C., Gong, W., Gan, Y., Fan, S., 2016. Automatic model calibration - a new way to improve numerical weather forecasting. *Bulletin of the American Meteorological Society* https://doi.org/10.1175/BAMS-D-15-00104.1

Gebhardt, C., Theis, S.E., Paulat, M., Ben Bouallègue, Z., 2011. Uncertainties in COSMO-DE precipitation forecasts introduced by model perturbations and variation of lateral boundaries. *Atm. Res.* **100**, pp 168-177.

Mayers, R.H., Montgomery, Douglas C., Anderson-Cook, Christine M., 2009. Response Surface Methodology: Process and Product Optimization Using Designed Experiments. *Wiley Series in Probability and Statistics.*

Khain P., Carmona I., Voudouri A., Avgoustoglou E., Bettems J.-M. and Grazzini F., 2015:The Proof of the Parameters Calibration Method: CALMO Progress Report. *COSMO Technical Report* **25**, DOI: 10.5676/DWDpub/nwv/cosmo-tr_25. Available at: www.cosmo-model.org/content/model/documentation/techReports/docs/techReport25.pdf

Khain P., Carmona I., Voudouri A., Avgoustoglou E., Bettems J.-M., Grazzini F., Kaufmann P., 2017, CALMO - Progress Report, *COSMO Technical Report*, **31**, DOI: 10.5676/DWDpub/nwv/cosmo-tr_31. Available at: www.cosmo-model.org/content/model/documentation/techReports/docs/techReport31.pdf

Kouroutzoglou, J., Avgoustoglou, E., Flocas, H., Hatzaki, M., Skrimizeas, P., Keay, K., 2018. Assessment of the role of sea surface fluxes on eastern Mediterranean explosive cyclogenesis with the aid of the limited-area model COSMO.GR. *Atm. Res.* **208**, pp 132-147. doi.org/10.1016/j.atmosres.2017.10.005.

Neelin, J. D., Bracco, A., Luo, H., McWilliams, J.C., Meyerson, J.E., 2010. Considerations for parameter optimization and sensitivity in climate models. *Proc. of the National Academy of Sciences of the United States of America* **107**, pp 21349-21354.

Neelin, J. D., Bracco, A., Luo, H., McWilliams, J.C., Meyerson J. E., 2010a. Supporting information for:Considerations for parameter optimization and sensitivity in climate models.

www.pnas.org /content /suppl /2010 /11 /24 /1015473107. DCSupplemental/Appendix.pdf

Schättler U., Doms G., Schraff C., 2013. A Description of the Nonhydrostatic Regional COSMO-Model Part VII : User's Guide.
www.cosmo-model.org/content/model/documentation/core/cosmoUserGuide.pdf

Skamarock, W.C., 2004. Evaluating Mesoscale NWP Models Using Kinetic Energy Spectra. *Mon. Wea. Rev.* **132**, pp 3019-3032.

Steppeler, J., Doms, G., Schättler, U., Bitzer, H. W., Gassmann, A., Damrath, U., Gregoric, G., 2003. Meso-gamma scale forecasts using the nonhydrostatic model LM. *Meteor. Atmos. Phys.* **82**, pp 75–96.

A. Voudouri, E. Avgoustoglou, P. Kaufmann 2016. Impacts of observational data assimilation on operational forecasts/ *Perspectives on Atmospheric Sciences*, pp 143-150, Springer Atmospheric Sciences.

Voudouri, A., Khain, P., Carmona, I., Bellprat, O., Grazzini, F., Avgoustoglou, E., Bettems, J. M. and Kaufmann, P., 2017. Objective calibration of numerical weather prediction models. *Atm. Res.* **190**, pp 128-140. DOI: 10.1016/j.atmosres.2017.02.007

Voudouri, A., Khain, P., Carmona, I., Avgoustoglou E., Kaufmann, P., Grazzini, F. and Bettems, J.-M. 2017. Optimization of high resolution COSMO model performance over Switzerland and Northern Italy. *Atm. Res.* **213**, pp 70-85.
https://doi.org/10.1016/j.atmosres.2018.05.026

Voudouri A., Khain P., Carmona I., Avgoustoglou E., Bettems J.-M., Grazzini F., Bellprat O., Kaufmann P., Bucchignani E., 2017, Calibration of COSMO Model, Priority Project CALMO Final report, *COSMO Technical Report* **32**, DOI: 10.5676/DWDpub/nwv/cosmo-tr_32. Available at:
www.cosmo-model.org/content/model/documentation/techReports/docs/techReport32.pdf

Voudouri A., Carmona I., Avgoustoglou E., Levi Y. and Bettems J.-M., 2018. Optimization of COSMO model interannual variability. *14th International Conference on Meteorology, Climatology and Atmospheric Physics COMECAP, Conference Proceedings*, pp 294-299.

Voudouri A, Carmona I, Avgoustoglou, Levi Y, Bettems J.-M, E.Buchignani , 2019. Impacts on model performance score from CALMO and CALMO-MAX. *COSMO News Letter* **16**. pp 32-36, DOI: 10.5676/dwd_pub/nwv/cosmo-nl_19_05. Available at:
www.cosmo-model.org/content/model/documentation/newsLetters/newsLetter19/cnl19_05.pdf

9 Appendix for Figs. 2 to 10

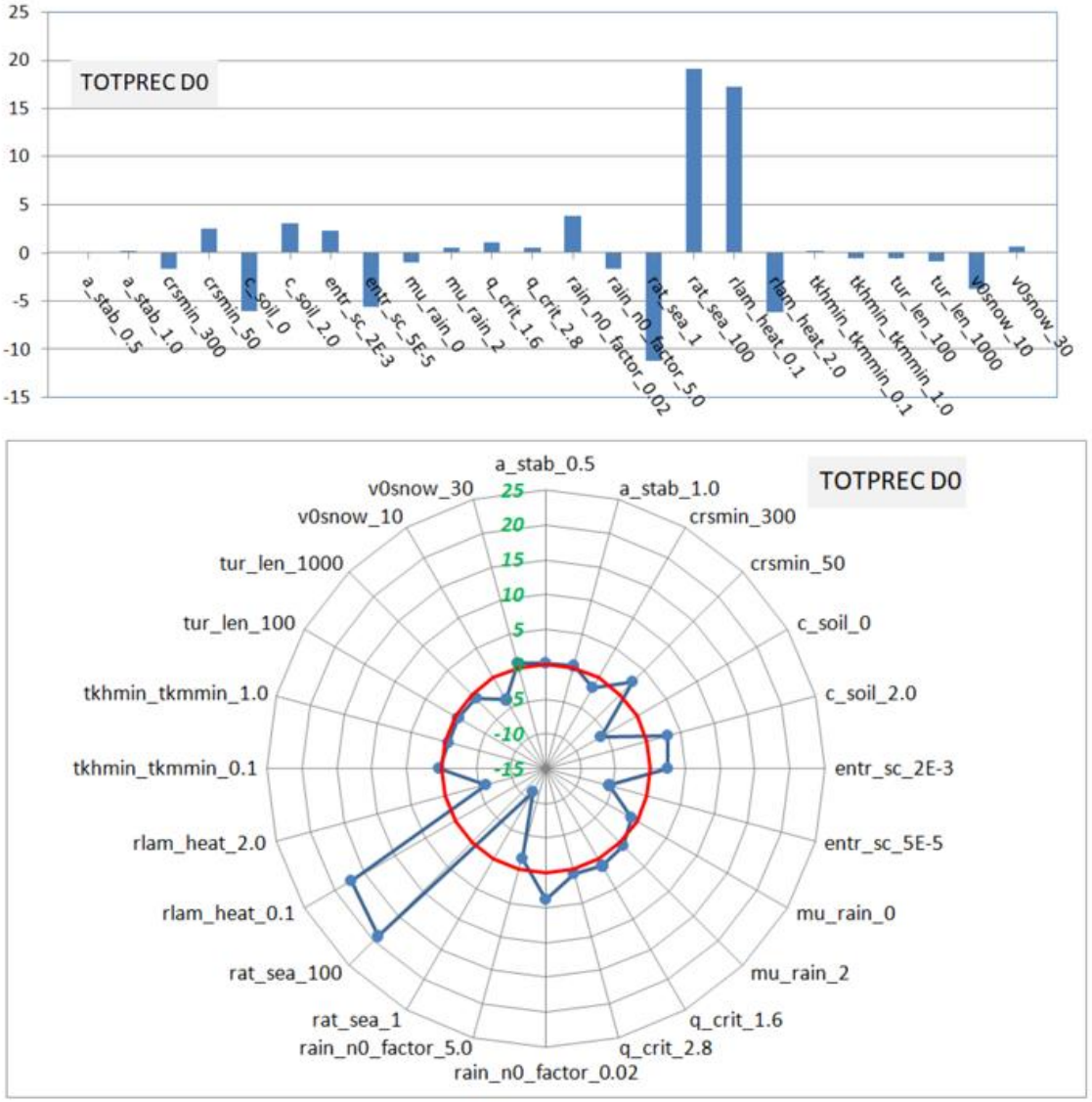


Figure 2: : DPSs for 24-hour precipitation (TOTPREC) over the wider Mediterranean area D0 in standard column form and in the form of spider-graph.

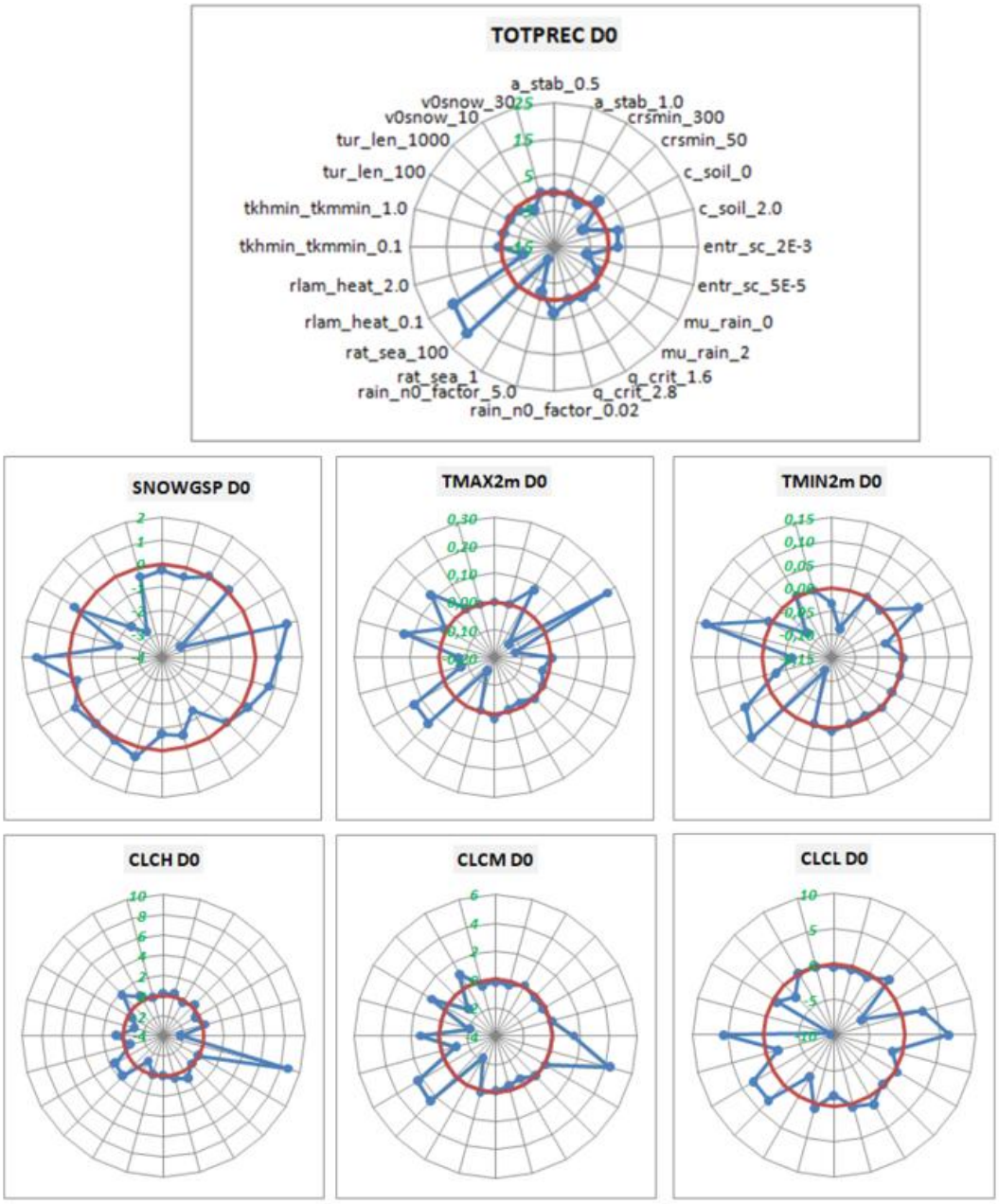


Figure 3: : DPS spider-graphs for temporal area 24-hour means of precipitation (TOTPREC), grid-point snow (SNOWGSP), minimum 2m temperature (TMIN2m), maximum 2m temperature (TMAX2m), high, medium and low cloud cover (CLCH, CLCM, CLCL respectively) over the wider Mediterranean area D0 and over the 62-day period.

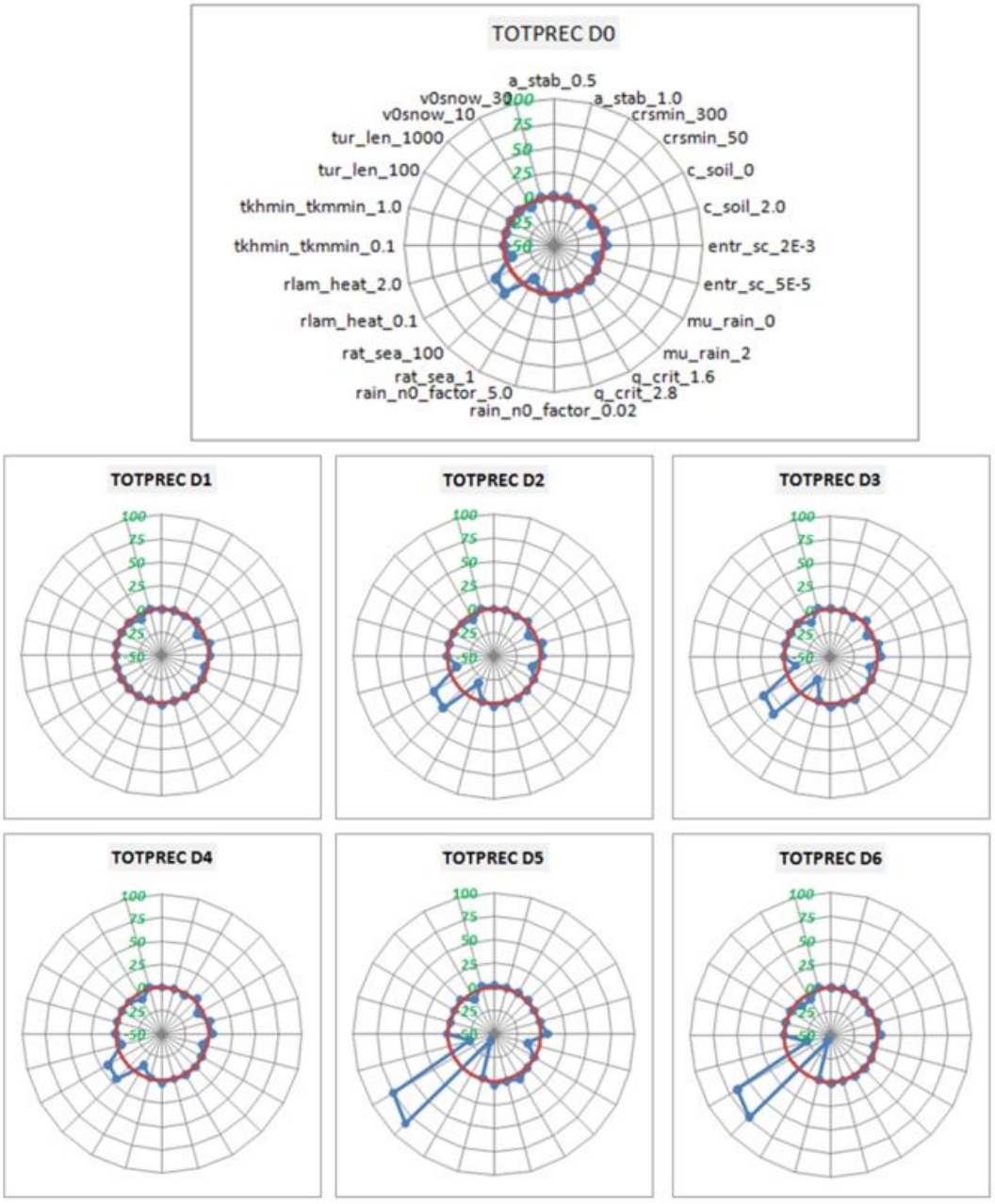


Figure 4: : DPS spider-graphs for temporal area 24-hour means of precipitation (TOTPREC), over the wider Mediterranean area D0, Switzerland (D1), Italy (D2), Greece (D3), Continental Greece (D4), Crete (D5) and Israel (D6) over the 62-day period.

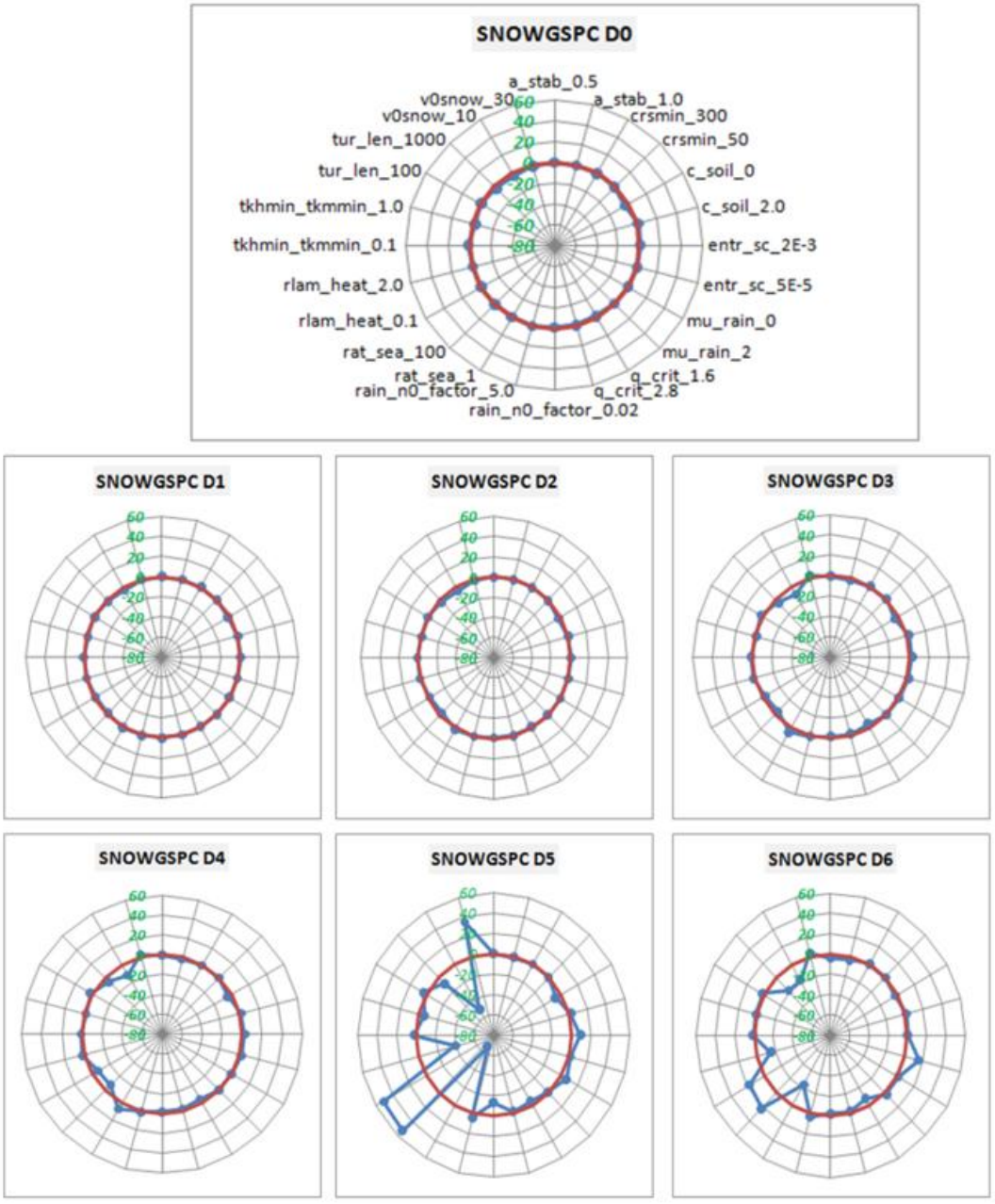


Figure 5: : DPS spider-graphs for temporal area 24-hour means of grid point snow(SNOWGSP), over the wider Mediterranean area (D0), Switzerland (D1), Italy (D2), Greece (D3), Continental Greece (D4), Crete (D5) and Israel (D6) over the 62-day period.

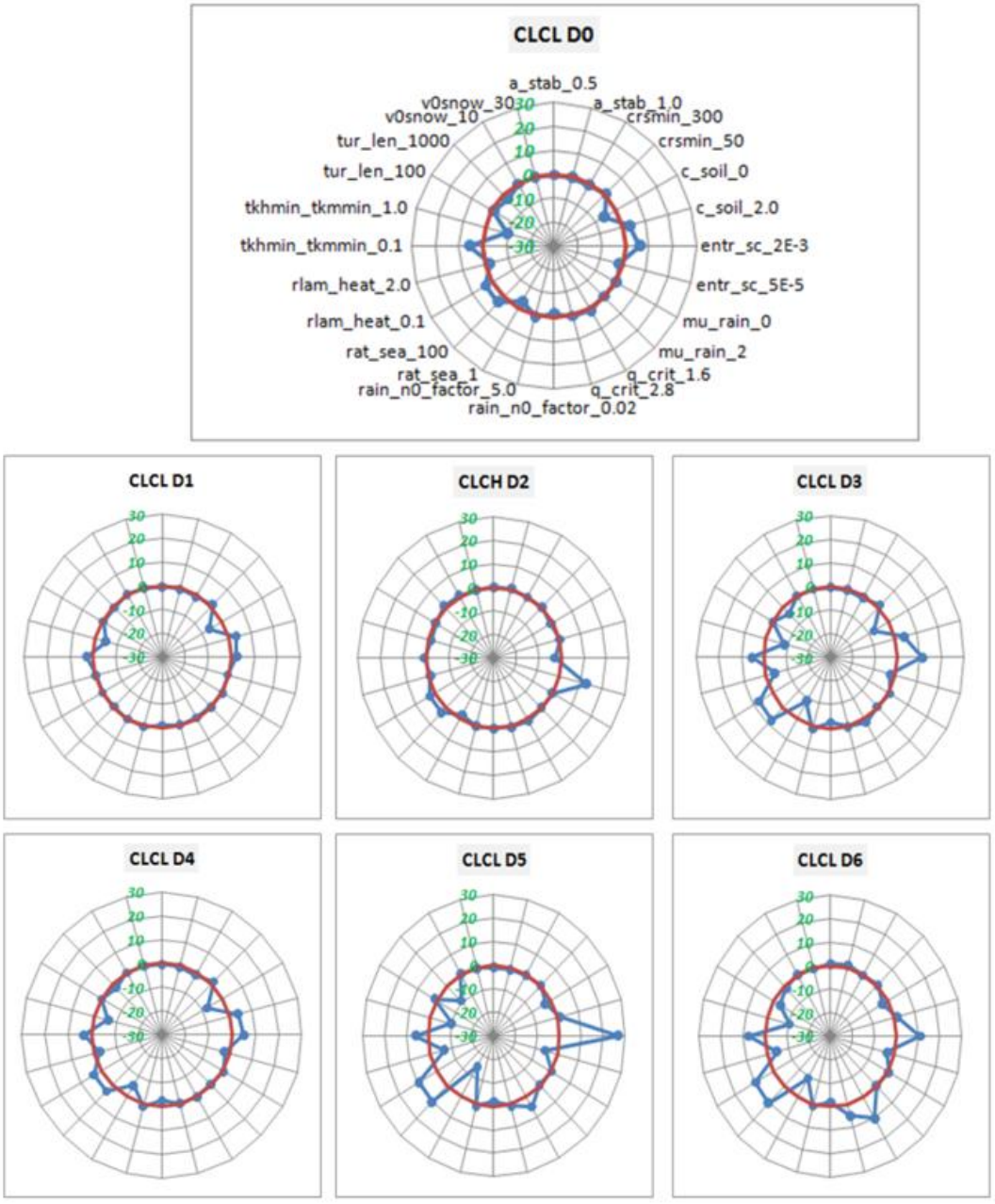


Figure 6: : DPS spider-graphs for temporal area 24-hour means, in 3-hour intervals, for low cloud cover (CLCL), over the wider Mediterranean area (D0), Switzerland (D1), Italy (D2), Greece (D3), Continental Greece (D4), Crete (D5) and Israel (D6) over the 62-day period.

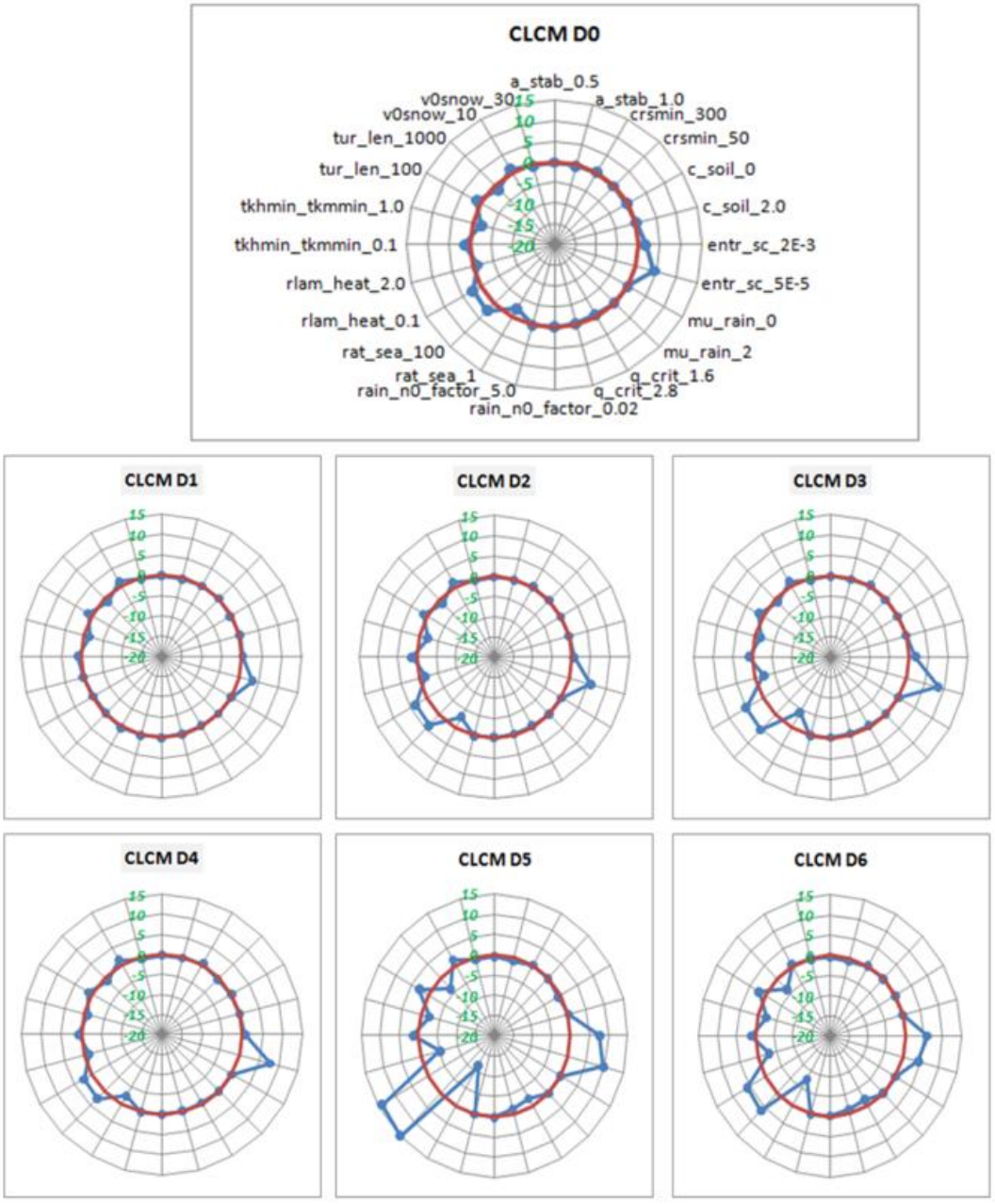


Figure 7: :DPS spider-graphs for temporal area 24-hour means, in 3-hour intervals, for medium cloud cover (CLCM), over the wider Mediterranean area (D0), Switzerland (D1), Italy (D2), Greece (D3), Continental Greece (D4), Crete (D5) and Israel (D6) over the 62-day period.

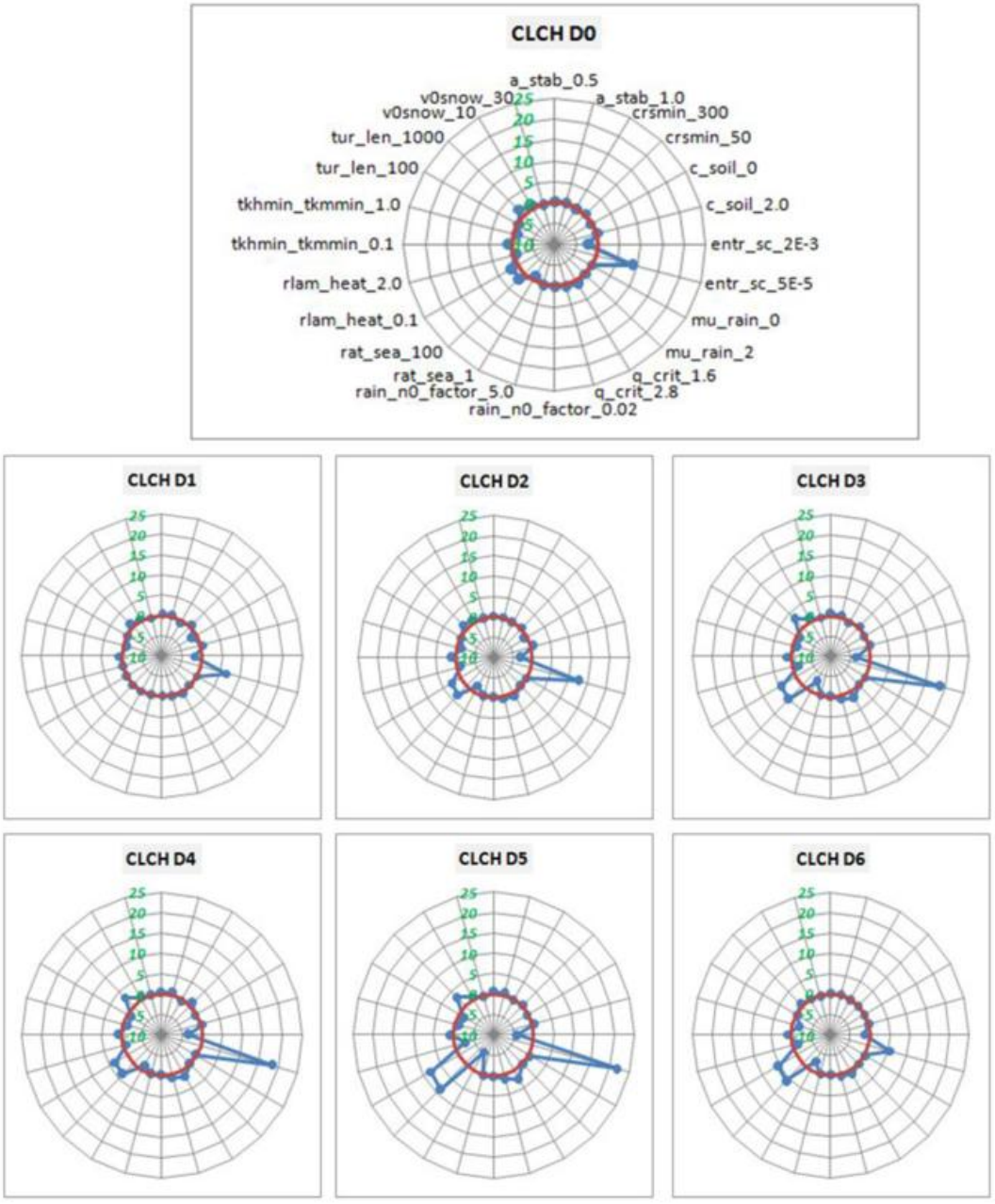


Figure 8: : DPS spider-graphs for temporal area 24-hour means, in 3-hour intervals, for high cloud cover (CLCM), over the wider Mediterranean area (D0), Switzerland (D1), Italy (D2), Greece (D3), Continental Greece (D4), Crete (D5) and Israel (D6) over the 62-day period.

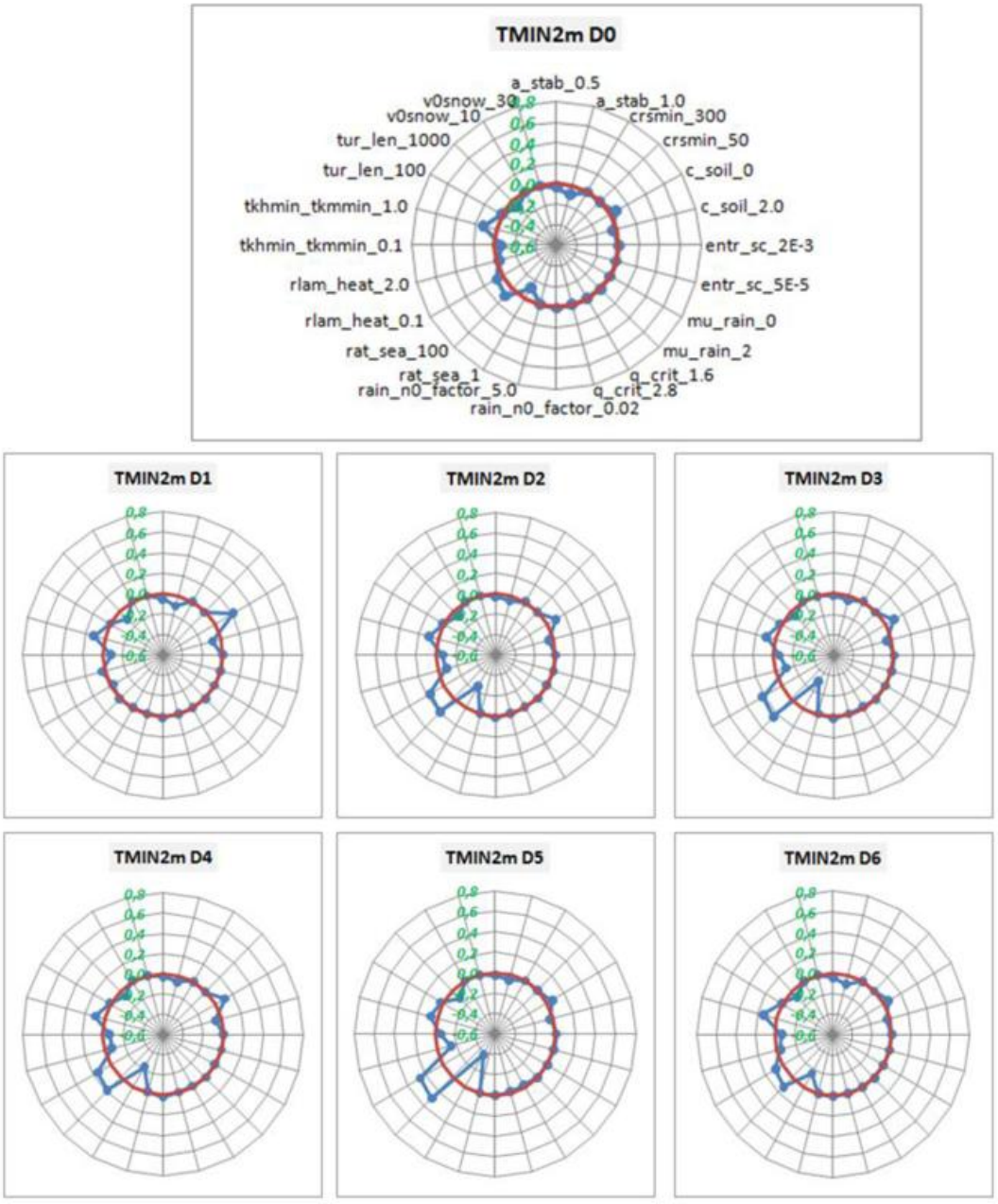


Figure 9: : DPS spider-graphs for temporal area 24-hour means, for minimum 2m-Temperature (Tmin2m), over the wider Mediterranean area (D0), Switzerland (D1), Italy (D2), Greece (D3), Continental Greece (D4), Crete (D5) and Israel (D6) over the 62-day period.

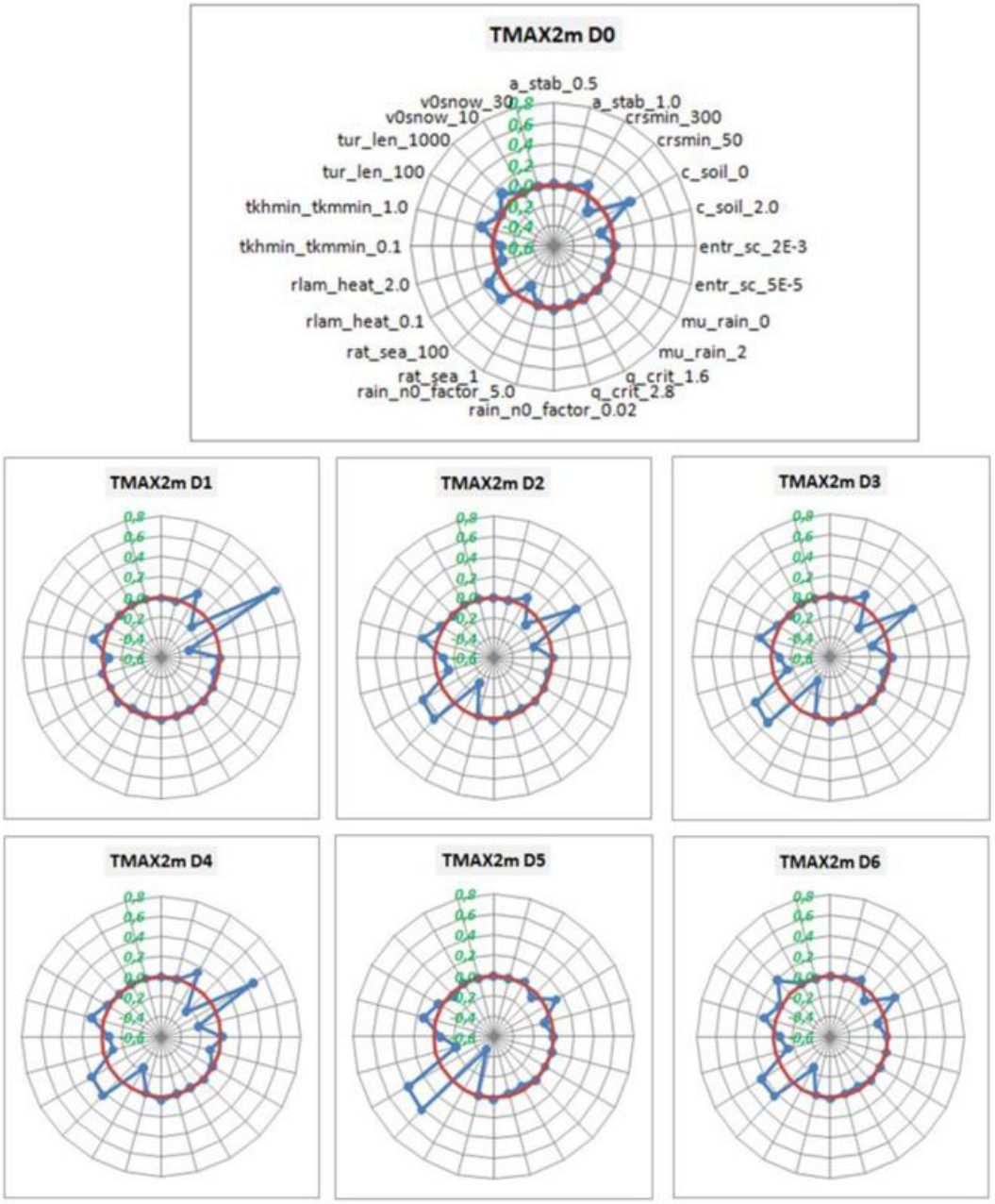


Figure 10: :DPS spider-graphs for temporal area 24-hour means, for minimum 2m-Temperature (Tmin2m), over the wider Mediterranean area (D0), Switzerland (D1), Italy (D2), Greece (D3), Continental Greece (D4), Crete (D5) and Israel (D6) over the 62-day period.

List of COSMO Newsletters and Technical Reports

(available for download from the COSMO Website: www.cosmo-model.org)

COSMO Newsletters

No. 1: February 2001.

No. 2: February 2002.

No. 3: February 2003.

No. 4: February 2004.

No. 5: April 2005.

No. 6: July 2006.

No. 7: April 2008; Proceedings from the 8th COSMO General Meeting in Bucharest, 2006.

No. 8: September 2008; Proceedings from the 9th COSMO General Meeting in Athens, 2007.

No. 9: December 2008.

No. 10: March 2010.

No. 11: April 2011.

No. 12: April 2012.

No. 13: April 2013.

No. 14: April 2014.

No. 15: July 2015.

No. 16: July 2016.

No. 17: July 2017.

No. 18: November 2018.

No. 19: October 2019.

COSMO Technical Reports

No. 1: Dmitrii Mironov and Matthias Raschendorfer (2001):
Evaluation of Empirical Parameters of the New LM Surface-Layer Parameterization Scheme. Results from Numerical Experiments Including the Soil Moisture Analysis.
DOI: 10.5676/DWD_pub/nwv/cosmo-tr_1

No. 2: Reinhold Schrodin and Erdmann Heise (2001):
The Multi-Layer Version of the DWD Soil Model TERRA_LM.
DOI: 10.5676/DWD_pub/nwv/cosmo-tr_2

No. 3: Günther Doms (2001):
A Scheme for Monotonic Numerical Diffusion in the LM.
DOI: 10.5676/DWD_pub/nwv/cosmo-tr_3

No. 4: Hans-Joachim Herzog, Ursula Schubert, Gerd Vogel, Adelheid Fiedler and Roswitha Kirchner (2002):
LLM ¯ the High-Resolving Nonhydrostatic Simulation Model in the DWD-Project LITFASS. Part I: Modelling Technique and Simulation Method.
DOI: 10.5676/DWD_pub/nwv/cosmo-tr_4

No. 5: Jean-Marie Bettems (2002):
EUCOS Impact Study Using the Limited-Area Non-Hydrostatic NWP Model in Operational Use at MeteoSwiss.
DOI: 10.5676/DWD_pub/nwv/cosmo-tr_5

No. 6: Heinz-Werner Bitzer and Jürgen Steppeler (2004):
Documentation of the Z-Coordinate Dynamical Core of LM.
DOI: 10.5676/DWD_pub/nwv/cosmo-tr_6

No. 7: Hans-Joachim Herzog, Almut Gassmann (2005):
Lorenz- and Charney-Phillips vertical grid experimentation using a compressible nonhydrostatic toy-model relevant to the fast-mode part of the 'Lokal-Modell'.
DOI: 10.5676/DWD_pub/nwv/cosmo-tr_7

No. 8: Chiara Marsigli, Andrea Montani, Tiziana Paccagnella, Davide Sacchetti, André Walser, Marco Arpagaus, Thomas Schumann (2005):
Evaluation of the Performance of the COSMO-LEPS System.
DOI: 10.5676/DWD_pub/nwv/cosmo-tr_8

No. 9: Erdmann Heise, Bodo Ritter, Reinhold Schrodin (2006):
Operational Implementation of the Multilayer Soil Model.
DOI: 10.5676/DWD_pub/nwv/cosmo-tr_9

No. 10: M.D. Tsyrulnikov (2007):
Is the particle filtering approach appropriate for meso-scale data assimilation ?
DOI: 10.5676/DWD_pub/nwv/cosmo-tr_10

No. 11: Dmitrii V. Mironov (2008):
Parameterization of Lakes in Numerical Weather Prediction. Description of a Lake Model.
DOI: 10.5676/DWD_pub/nwv/cosmo-tr_11

No. 12: Adriano Raspanti (2009):
COSMO Priority Project "VERification System Unified Survey" (VERSUS): Final Report.
DOI: 10.5676/DWD_pub/nwv/cosmo-tr_12

No. 13: Chiara Marsigli (2009):
COSMO Priority Project "Short Range Ensemble Prediction System" (SREPS): Final Report.
DOI: 10.5676/DWD_pub/nwv/cosmo-tr_13

No. 14: Michael Baldauf (2009):
COSMO Priority Project "Further Developments of the Runge-Kutta Time Integration Scheme" (RK): Final Report.
DOI: 10.5676/DWD_pub/nwv/cosmo-tr_14

No. 15: Silke Dierer (2009):
COSMO Priority Project "Tackle deficiencies in quantitative precipitation forecast" (QPF): Final Report.
DOI: 10.5676/DWD_pub/nwv/cosmo-tr_15

No. 16: Pierre Eckert (2009):
COSMO Priority Project "INTERP": Final Report.
DOI: 10.5676/DWD_pub/nwv/cosmo-tr_16

No. 17: D. Leuenberger, M. Stoll and A. Roches (2010):
Description of some convective indices implemented in the COSMO model.
DOI: 10.5676/DWD_pub/nwv/cosmo-tr_17

No. 18: Daniel Leuenberger (2010):
Statistical analysis of high-resolution COSMO Ensemble forecasts in view of Data Assimilation.
DOI: 10.5676/DWD_pub/nwv/cosmo-tr_18

No. 19: A. Montani, D. Cesari, C. Marsigli, T. Paccagnella (2010):
Seven years of activity in the field of mesoscale ensemble forecasting by the COSMO–LEPS system: main achievements and open challenges.
DOI: 10.5676/DWD_pub/nwv/cosmo-tr_19

No. 20: A. Roches, O. Fuhrer (2012):
Tracer module in the COSMO model.
DOI: 10.5676/DWD_pub/nwv/cosmo-tr_20

No. 21: Michael Baldauf (2013):
A new fast-waves solver for the Runge-Kutta dynamical core.
DOI: 10.5676/DWD_pub/nwv/cosmo-tr_21

No. 22: C. Marsigli, T. Diomede, A. Montani, T. Paccagnella, P. Louka, F. Gofa, A. Corigliano (2013):
The CONSENS Priority Project.
DOI: 10.5676/DWD_pub/nwv/cosmo-tr_22

No. 23: M. Baldauf, O. Fuhrer, M. J. Kurowski, G. de Morsier, M. Müllner, Z. P. Piotrowski, B. Rosa, P. L. Vitagliano, D. Wójcik, M. Ziemiański (2013):
The COSMO Priority Project 'Conservative Dynamical Core' Final Report.
DOI: 10.5676/DWD_pub/nwv/cosmo-tr_23

No. 24: A. K. Miltenberger, A. Roches, S. Pfahl, H. Wernli (2014):
Online Trajectory Module in COSMO: a short user guide.
DOI: 10.5676/DWD_pub/nwv/cosmo-tr_24

No. 25: P. Khain, I. Carmona, A. Voudouri, E. Avgoustoglou, J.-M. Bettems, F. Grazzini (2015):
The Proof of the Parameters Calibration Method: CALMO Progress Report.
DOI: 10.5676/DWD_pub/nwv/cosmo-tr_25

No. 26: D. Mironov, E. Machulskaya, B. Szintai, M. Raschendorfer, V. Perov, M. Chumakov, E. Avgoustoglou (2015):
The COSMO Priority Project 'UTCS' Final Report.
DOI: 10.5676/DWD_pub/nwv/cosmo-tr_26

No. 27: J-M. Bettems (2015):
The COSMO Priority Project 'COLOBOC': Final Report.
DOI: 10.5676/DWD_pub/nwv/cosmo-tr_27

No. 28: Ulrich Blahak (2016):
RADAR_MIE_LM and RADAR_MIELIB - Calculation of Radar Reflectivity from Model Output.
DOI: 10.5676/DWD_pub/nwv/cosmo-tr_28

No. 29: M. Tsyrulnikov and D. Gayfulin (2016):
A Stochastic Pattern Generator for ensemble applications.
DOI: 10.5676/DWD_pub/nwv/cosmo-tr_29

No. 30: D. Mironov and E. Machulskaya (2017):
A Turbulence Kinetic Energy – Scalar Variance Turbulence Parameterization Scheme.
DOI: 10.5676/DWD_pub/nwv/cosmo-tr_30

No. 31: P. Khain, I. Carmona, A. Voudouri, E. Avgoustoglou, J.-M. Bettems, F. Grazzini, P. Kaufmann (2017):
CALMO - Progress Report.
DOI: 10.5676/DWD_pub/nwv/cosmo-tr_31

No. 32: A. Voudouri, P. Khain, I. Carmona, E. Avgoustoglou, J.M. Bettems, F. Grazzini, O. Bellprat, P. Kaufmann and E. Bucchignani (2017):
Calibration of COSMO Model, Priority Project CALMO Final report.
DOI: 10.5676/DWD_pub/nwv/cosmo-tr_32

No. 33: N. Vela (2017):
VAST 2.0 - User Manual.
DOI: 10.5676/DWD_pub/nwv/cosmo-tr_33

No. 34: C. Marsigli, D. Alferov, M. Arpagaus, E. Astakhova, R. Bonanno, G. Duniec, C. Gebhardt, W. Interewicz, N. Loglisci, A. Mazur, V. Maurer, A. Montani, A. Walser (2018):
COsmo Towards Ensembles at the Km-scale IN Our countries" (COTEKINO), Priority Project final report.
DOI: 10.5676/DWD_pub/nwv/cosmo-tr_34

No. 35: G. Rivin, I. Rozinkina, E. Astakhova, A. Montani, D. Alferov, M. Arpagaus, D. Blinov, A. Bundel, M. Chumakov, P. Eckert, A. Euripides, J. Förstner, J. Helmert, E. Kazakova, A. Kirsanov, V. Kopeikin, E. Kukanova, D. Majewski, C. Marsigli, G. de Morsier, A. Muravev, T. Paccagnella, U. Schättler, C. Schraff, M. Shatunova, A. Shcherbakov, P. Steiner, M. Zaichenko (2018):
The COSMO Priority Project CORSO Final Report.
DOI: 10.5676/DWD_pub/nwv/cosmo-tr_35

No. 36: A. Raspanti, A. Celozzi, A. Troisi, A. Vocino, R. Bove, F. Batignani (2018):
The COSMO Priority Project VERSUS2 Final Report.
DOI: 10.5676/DWD_pub/nwv/cosmo-tr_36

No. 37: A. Bundel, F. Gofa, D. Alferov, E. Astakhova, P. Baumann, D. Boucouvala, U. Damrath, P. Eckert, A. Kirsanov, X. Lapillonne, J. Linkowska, C. Marsigli, A. Montani, A. Muraviev, E. Oberto, M.S. Tesini, N. Vela, A. Wyszogrodzki, M. Zaichenko, A. Walser (2019):
The COSMO Priority Project INSPECT Final Report.
DOI: 10.5676/DWD_pub/nwv/cosmo-tr_37

No. 38: G. Rivin, I. Rozinkina, E. Astakhova, A. Montani, J-M. Bettems, D. Alferov, D. Blinov, P. Eckert, A. Euripides, J. Helmert, M.Shatunova (2019):
The COSMO Priority Project CORSO-A Final Report.
DOI: 10.5676/DWD_pub/nwv/cosmo-tr_38

No. 39: C. Marsigli, D. Alferov, E. Astakhova, G. Duniec, D. Gayfulin, C. Gebhardt, W. Interewicz, N. Loglisci, F. Marcucci, A. Mazur, A. Montani, M. Tsyrulnikov, A. Walser (2019):
Studying perturbations for the representation of modeling uncertainties in Ensemble development (SPRED Priority Project): Final Report.
DOI: 10.5676/DWD_pub/nwv/cosmo-tr_39

No. 40: E. Bucchignani, P. Mercogliano, V. Garbero, M. Milelli, M. Varentsov, I. Rozinkina, G. Rivin, D. Blinov, A. Kirsanov, H. Wouters, J.-P. Schulz, U. Schättler (2019):
Analysis and Evaluation of TERRA_URB Scheme: PT AEVUS Final Report.
DOI: 10.5676/DWD_pub/nwv/cosmo-tr_40

No. 41: X. Lapillonne, O. Fuhrer (2020):
Performance On Massively Parallel Architectures (POMPA): Final report.
DOI: 10.5676/DWD_pub/nwv/cosmo-tr_41

COSMO Technical Reports

Issues of the COSMO Technical Reports series are published by the *COnsortium for Small-scale MOdelling* at non-regular intervals. COSMO is a European group for numerical weather prediction with participating meteorological services from Germany (DWD, AWGeophys), Greece (HNMS), Italy (ITAF-ReMet, ARPAE, ARPA Piemonte), Switzerland (MeteoSwiss), Poland (IMGW), Romania (NMA), Russia (RHM) and Israel (IMS). The general goal is to develop, improve and maintain a non-hydrostatic limited area modelling system to be used for both operational and research applications by the members of COSMO. This system is initially based on the COSMO-Model (previously known as LM) of DWD with its corresponding data assimilation system.

The Technical Reports are intended

- for scientific contributions and a documentation of research activities,
- to present and discuss results obtained from the model system,
- to present and discuss verification results and interpretation methods,
- for a documentation of technical changes to the model system,
- to give an overview of new components of the model system.

The purpose of these reports is to communicate results, changes and progress related to the LM model system relatively fast within the COSMO consortium, and also to inform other NWP groups on our current research activities. In this way the discussion on a specific topic can be stimulated at an early stage. In order to publish a report very soon after the completion of the manuscript, we have decided to omit a thorough reviewing procedure and only a rough check is done by the editors and a third reviewer. We apologize for typographical and other errors or inconsistencies which may still be present.

At present, the Technical Reports are available for download from the COSMO web site (www.cosmo-model.org). If required, the member meteorological centres can produce hard-copies by their own for distribution within their service. All members of the consortium will be informed about new issues by email.

For any comments and questions, please contact the editor:

Massimo Milelli
Massimo.Milelli@arpa.piemonte.it

Consortium for Small-Scale Modelling

Technical Report No. 21

A new fast-waves solver for the Runge-Kutta dynamical core

April 2013

DOI: 10.5676/DWD_pub/nwv/cosmo-tr_21

Deutscher Wetterdienst
MeteoSwiss
Ufficio Generale Spazio Aereo e Meteorologia
ΕΘΝΙΚΗ ΜΕΤΕΩΡΟΛΟΓΙΚΗ ΥΠΗΡΕΣΙΑ
Instytucie Meteorogii i Gospodarki Wodnej
Administratia Nationala de Meteorologie
ROSHYDROMET
Agenzia Regionale per la Protezione Ambientale del Piemonte
Agenzia Regionale per la Protezione Ambientale dell'Emilia-Romagna
Centro Italiano Ricerche Aerospaziali
Amt für GeoInformationswesen der Bundeswehr



www.cosmo-model.org

Editor: Massimo Milelli, ARPA Piemonte

A new fast-waves solver for the Runge-Kutta dynamical core

Michael Baldauf*

* Dr. Michael Baldauf
Deutscher Wetterdienst
Frankfurter Str. 135
63067 Offenbach am Main
Germany

Contents

1 Abstract **4**

2 Introduction **4**

3 The Euler equations **6**

4 Discretization **8**

4.1 Numerical operators for the spatial discretization 8

4.2 Discretization of the Euler equations 12

4.2.1 Discretization of the divergence 13

4.2.2 Mahrer discretization of the horizontal pressure gradients 14

5 Boundary conditions **14**

5.1 The free slip condition 14

5.2 Boundary treatments 15

5.2.1 The vertical pressure gradient in the horizontal equations of motion . 15

5.2.2 Boundary treatment of the divergence 16

6 The linear equation system for the vertical velocity **17**

6.1 Setup of the equation system 17

6.2 Solution of the tridiagonal equation system 19

7 Stability of the divergence damping in tilted terrain **22**

8 Discretization errors in a stretched grid **23**

8.1 General analysis procedure 23

8.1.1 Discretization error analysis - variant A 23

8.1.2 Discretization error analysis - variant B 24

8.2 Horizontal pressure gradient term in the u-equation 25

8.3 Buoyancy term in the w-equation 27

8.4 The divergence term 29

9 Idealized tests **30**

9.1 Linear gravity and sound wave expansion 30

9.2 2D linear flow over a series of hills 32

9.3 3D linear flow over a hill 34

9.4 2D flow over steep mountains 34
9.5 3D flow over steep mountains 36
9.6 Convective warm bubble test 36

10 Real cases **38**

11 Conclusions **39**

12 Acknowledgments **40**

1 Abstract

An essential part of the COSMO dynamical core is the fast waves solver. Here, the processes sound wave and gravity wave expansion are integrated and a stabilization of the whole time-splitting procedure by divergence damping is done. Sound and long gravity waves have high velocities and therefore are solved with a smaller time step (small compared to the larger time step of the advection process) and vertically implicit, to prevent from the strong time step reduction by flat grid elements in the vicinity of the ground.
This report describes a complete revision of the previously existing fast waves solver and incorporates several new aspects. First, all vertical discretizations are done with the proper distance weightings in the vertically stretched grid. Second, the so called strong conservation form of the divergence operator is used. Third, the possibility to use a fully 3D divergence damping should be possible. Fourth, the option to use a discretization of the horizontal pressure gradient, which promises to be more stable in steep terrain, should be implemented. Beyond these broader development goals several smaller improvements concerning e.g. the formulation of boundary conditions, the use of the reference state, more accurate formulation of the buoyancy term, or several other numerical operations have been done.
The report at first describes the discretization of the new fast waves solver to enable the model developer or user to understand the code structure. The second part motivates the chosen discretization by a truncation error analysis. Finally the third part assess the properties of the new solver against idealized test setups, where partially exact solutions are known.
This development is available since COSMO version 4.24 (together with INT2LM 1.20).

2 Introduction

This technical report describes a complete revision of the fast waves solver and thus the development of its new version. This new development is available since COSMO version 4.24 (available since July 2012).

The COSMO model was developed during the 1990's and at first went into operations at the end of 1999 at DWD (at this time named LM). Due to the planned usage of the COSMO model for convection-permitting resolutions, the decision to abandon the hydrostatic approximation was made from the beginning. The rising of massively parallel computers at this time further led to the decision not to use any anelastic approximation, but to use the fully compressible equation system. The latter equation system leads to a fast waves solver which is relatively easy to parallelize. G. Doms (?) developed the first fast waves solver for the LM, which mainly based on the solver of the MM5 (?, ?), and further using ideas of the leapfrog based split explicit solver by ? and ?. A. Gassmann abandoned the 3-time level leapfrog scheme and implemented a 2-time level Runge-Kutta scheme (? and ?). Additionally, she introduced e.g. the dynamical bottom boundary condition (?) in the fast waves solver. This at this time improved a lot the model behavior at the lower boundaries. J. Förstner implemented the Runge-Kutta scheme of ? into the COSMO model and introduced T' instead of T into the fast waves solver. This resulted in a reduced noise in the vertical velocity field, mainly due to the better behavior of the temperature advection. Later on, G. Zängl has demonstrated that the introduction of vertical weightings in some of the explicit terms of the fast waves solver largely improves the pressure bias. This was one of the prerequisites to be able to use the Runge-Kutta dynamical core for the 7 km COSMO applications at the different COSMO services (e.g. COSMO-EU at DWD).

The main goals of this development project are the following:

- The consideration of the vertical grid stretching by introduction of appropriate weightings in *all* vertical discretizations of the fast waves solver. In particular their use in the *implicit* terms in the discretization of the Euler equations requires a complete re-derivation of the tridiagonal equation system.

- The usage of the 'strong conservation form' for the divergence operator. Though mainly developed for finite volume schemes with conservation properties, there was the hope to gain advantages by a more direct discretization of the metric terms and by a better formulation of the lower boundary conditions.

- The option for a fully 3-dimensional (3D) isotropic divergence damping instead of the 'traditional' quasi-3D version should be available. ? have derived the dispersion relation of sound and gravity waves and have found a larger deviation from the correct one in the case of the quasi-3D version compared to the isotropic version.

- A further option should be the alternative discretization of the horizontal pressure gradients by the methodology of ?. This z-plane treatment should result in a more stable behavior in steep terrain.

These new features did not only require changes at almost every place in the fast waves code, but partially required a restructuring of the code logic, too. Together with the aim to introduce a bit more descriptive variable names, the decision was made, to reprogram the whole fast waves solver from scratch; a work which started at the end of 2010. This approach resulted in additional smaller improvements at other places, too, concerning e.g. the formulation of boundary conditions, the use of the reference state, a more accurate formulation of the buoyancy term, and others.

This report is subdivided into three parts. In the first part, sections 3-7, the discretization of the Euler equations, the setup and the solution of the vertically implicit tridiagonal equation for w is explained. To offer the reader an as much as possible consistent description, several repetitions of material presented in ? (or the revised version ?) have been unavoidable. But with this, the model developer (and model user) should be able to understand the code structure of the module `fast_waves_sc`.
To understand the embedding of the fast waves solver in the whole Runge-Kutta time integration framework, the reader should consult chapter 8 in ?. Also not contained here is the stability analysis of the COSMO dynamical core. For this we refer to ?. There, the reader will find reasons why the time integration scheme is done in the current manner.
In the second part (section 8), a motivation is given for one of the main development goals, namely the improved vertical discretization, by a truncation error analysis.
In the third part (9 and 10) a broad investigation of the properties of the new fast waves solver by idealized tests is performed. A few statements about model performance in real cases closes this part.

3 The Euler equations

The Euler equations in spherical, terrain following coordinates (λ, ϕ, ζ) with $\zeta = \zeta(\lambda, \phi, z)$, $r = r_{earth} + z$, can be written as

$$\frac{\partial u}{\partial t} = -\frac{1}{\rho}\frac{1}{r\cos\phi}\left(\frac{\partial p'}{\partial \lambda} + \frac{\partial \zeta}{\partial \lambda}\frac{\partial p'}{\partial \zeta}\right) + \frac{1}{\rho}\frac{1}{r\cos\phi}\left(\frac{\partial\, \alpha^h_{div}\,\rho\, D}{\partial \lambda} + \frac{\partial \zeta}{\partial \lambda}\frac{\partial\, \alpha^h_{div}\,\rho\, D}{\partial \zeta}\right) + \left.\frac{\partial u}{\partial t}\right|_{slow} \quad (1)$$

$$\frac{\partial v}{\partial t} = -\frac{1}{\rho}\frac{1}{r}\left(\frac{\partial p'}{\partial \phi} + \frac{\partial \zeta}{\partial \phi}\frac{\partial p'}{\partial \zeta}\right) + \frac{1}{\rho}\frac{1}{r}\left(\frac{\partial\, \alpha^h_{div}\,\rho\, D}{\partial \phi} + \frac{\partial \zeta}{\partial \phi}\frac{\partial\, \alpha^h_{div}\,\rho\, D}{\partial \zeta}\right) + \left.\frac{\partial v}{\partial t}\right|_{slow} \quad (2)$$

$$\frac{\partial w}{\partial t} = -\frac{1}{\rho}\frac{\partial \zeta}{\partial z}\frac{\partial p'}{\partial \zeta} + g\left(\frac{p_0}{p}\frac{T'}{T_0} - \frac{p'}{p} + \frac{p_0}{p}\frac{T}{T_0}q_x\right) + \frac{1}{\rho}\frac{\partial \zeta}{\partial z}\frac{\partial\, \alpha^v_{div}\,\rho\, D}{\partial \zeta} + \left.\frac{\partial w}{\partial t}\right|_{slow} \quad (3)$$

$$\frac{\partial p'}{\partial t} = -\frac{c_p}{c_V} p\, D + g\rho_0 w + \left.\frac{\partial p'}{\partial t}\right|_{slow} \quad (4)$$

$$\frac{\partial T'}{\partial t} = -\frac{R}{c_V} T\, D - \frac{\partial T_0}{\partial z} w + \left.\frac{\partial T'}{\partial t}\right|_{slow} \quad (5)$$

The denotations are the same as in **?**, in particular $T = T_0 + T'$ and $p = p_0 + p'$ are split into the stationary reference state and deviations. Here only the 'fast' processes are written down and grouped into sound (left group of terms on the rhs), buoyancy (middle group of terms in the w, p', and T'-equations) and artificial divergence damping (right group in the three momentum equations). $\left.\frac{\partial u}{\partial t}\right|_{slow}$, ..., $\left.\frac{\partial T'}{\partial t}\right|_{slow}$ denote the remaining ('slow') processes advection, Coriolis force and all physical parameterizations.

The occurring coordinate derivatives may be understood as

$$\frac{\partial \zeta}{\partial \lambda} \equiv \left.\frac{\partial \zeta}{\partial \lambda}\right|_z \equiv \frac{\partial \zeta(\lambda,\phi,z)}{\partial \lambda}, \quad \frac{\partial \zeta}{\partial \phi} \equiv \left.\frac{\partial \zeta}{\partial \phi}\right|_z \equiv \frac{\partial \zeta(\lambda,\phi,z)}{\partial \phi}, \quad \frac{\partial \zeta}{\partial z} \equiv \left.\frac{\partial \zeta}{\partial z}\right|_z \equiv \frac{\partial \zeta(\lambda,\phi,z)}{\partial z}.$$

We remind the abbreviations and relations valid for the COSMO coordinate transformation

$$\sqrt{g} := -\frac{\partial z}{\partial \zeta} = -\frac{1}{\frac{\partial \zeta}{\partial z}} \quad \Leftrightarrow \quad \frac{\partial \zeta}{\partial z} = -\frac{1}{\sqrt{g}}, \quad (6)$$

$$\left.\frac{\partial z}{\partial \lambda}\right|_\zeta = -\frac{\partial z}{\partial \zeta}\frac{\partial \zeta}{\partial \lambda} \quad \Leftrightarrow \quad \frac{\partial \zeta}{\partial \lambda} = \frac{1}{\sqrt{g}}\left.\frac{\partial z}{\partial \lambda}\right|_\zeta, \quad (7)$$

$$\left.\frac{\partial z}{\partial \phi}\right|_\zeta = -\frac{\partial z}{\partial \zeta}\frac{\partial \zeta}{\partial \phi} \quad \Leftrightarrow \quad \frac{\partial \zeta}{\partial \phi} = \frac{1}{\sqrt{g}}\left.\frac{\partial z}{\partial \phi}\right|_\zeta. \quad (8)$$

The divergence is denoted by $D = \operatorname{div}\mathbf{v}$. One difference to the former version of the fast-waves solver is the use of its so-called strong conservation form (**?**, eq. (3.122))

$$D \equiv \operatorname{div}\mathbf{v} = \frac{1}{r^2\cos\phi}\frac{1}{\sqrt{g}}\left[\frac{\partial}{\partial \lambda}(r\sqrt{g}\,u) + \frac{\partial}{\partial \phi}(r\cos\phi\sqrt{g}\,v) + \frac{\partial rZ}{\partial \zeta}\right] \quad (9)$$

with the definition

$$Z := r\cos\phi\,\sqrt{g}\,\dot{\zeta} = \frac{\partial z}{\partial \lambda}u + \frac{\partial z}{\partial \phi}\cos\phi\,v - r\cos\phi\,w. \quad (10)$$

Obviously, the divergence is expressed on one hand by derivatives in *terrain following* coordinates but on the other hand of the physical components u, v, w in *spherical* coordinates. Here one can cancel one factor r due to the shallow atmosphere approximation $r \approx r_{earth} = const.$, which is used throughout in the COSMO model

$$D = \frac{1}{r\cos\phi}\frac{1}{\sqrt{g}}\left[\frac{\partial}{\partial \lambda}(\sqrt{g}\,u) + \frac{\partial}{\partial \phi}(\cos\phi\sqrt{g}\,v) + \frac{\partial Z}{\partial \zeta}\right]. \quad (11)$$

It is advisable to introduce some other abbreviations

$$\tilde{d}_{hor} := \frac{\partial}{\partial\lambda}(\sqrt{g}\,u) + \frac{\partial}{\partial\phi}(\cos\phi\,\sqrt{g}\,v), \tag{12}$$

$$\tilde{d}_{vert} := \frac{\partial Z}{\partial\zeta}, \tag{13}$$

so we can write the divergence as

$$D = \frac{1}{r\cos\phi}\frac{1}{\sqrt{g}}\left[\tilde{d}_{hor} + \tilde{d}_{vert}\right]. \tag{14}$$

Furthermore we define

$$Z = Z_{hor} + Z_{vert} \tag{15}$$

with

$$Z_{hor} := Z_x + Z_y, \tag{16}$$

$$Z_x := \frac{\partial z}{\partial\lambda}\,u, \tag{17}$$

$$Z_y := \frac{\partial z}{\partial\phi}\cos\phi\,v, \tag{18}$$

$$Z_{vert} := -r\cos\phi\,w. \tag{19}$$

The artificial divergence damping has been written in a more efficient form - compared to the original idea of having a damping of the divergence[1] - analogous to ?. This form allows a common discretization of $\tilde{p} = p' - \alpha^h_{div}\rho D$ in the horizontal momentum equations. To indicate the optional divergence damping in the w-equation, the diffusion coefficient α^v_{div} carries an upper index 'v'.

The buoyancy term in the w-equation has a slightly different form than in the former COSMO versions. To derive it we use the ideal gas equation for moist air

$$p = \rho\,R_d\,(1 + q_x)\,T, \tag{23}$$

where

$$q_x := \left(\frac{R_v}{R_d} - 1\right)q_v - q_{cond}, \tag{24}$$

describes the so-called 'water loading' in the buoyancy term. From this we can derive the

[1] A more self-evident form of the divergence damping leads to the three momentum equations

$$\frac{\partial u}{\partial t} = -\frac{1}{\rho}\frac{1}{r\cos\phi}\left(\frac{\partial p'}{\partial\lambda} + \frac{\partial\zeta}{\partial\lambda}\frac{\partial p'}{\partial\zeta}\right) + \alpha^h_{div}\frac{1}{r\cos\phi}\left(\frac{\partial D}{\partial\lambda} + \frac{\partial\zeta}{\partial\lambda}\frac{\partial D}{\partial\zeta}\right) + \left.\frac{\partial u}{\partial t}\right|_{slow}, \tag{20}$$

$$\frac{\partial v}{\partial t} = -\frac{1}{\rho}\frac{1}{r}\left(\frac{\partial p'}{\partial\phi} + \frac{\partial\zeta}{\partial\phi}\frac{\partial p'}{\partial\zeta}\right) + \alpha^h_{div}\frac{1}{r}\left(\frac{\partial D}{\partial\phi} + \frac{\partial\zeta}{\partial\phi}\frac{\partial D}{\partial\zeta}\right) + \left.\frac{\partial v}{\partial t}\right|_{slow}, \tag{21}$$

$$\frac{\partial w}{\partial t} = -\frac{1}{\rho}\left(\frac{\partial\zeta}{\partial z}\frac{\partial p'}{\partial\zeta}\right) + g\left(\frac{p_0}{p}\frac{T'}{T_0} - \frac{p'}{p} + \frac{p_0}{p}\frac{T}{T_0}q_x\right) + \alpha^v_{div}\frac{\partial\zeta}{\partial z}\frac{\partial D}{\partial\zeta} + \left.\frac{\partial w}{\partial t}\right|_{slow}. \tag{22}$$

However the discretization of this form leads to much more inefficient code, because - in contrast to the above form - the divergence terms cannot be treated together with the pressure terms. Beyond this, both forms have the same slight tendency to instability in a Bretherton-transformed equation system (see (?, Appendix B)). Hence, there is no advantage in using this form.

buoyancy term, expressed by p' and T', without any approximation

$$\begin{aligned}
-g\frac{\rho'}{\rho} = -g\frac{1}{\rho}(\rho-\rho_0) &= -g\frac{1}{\rho}\left(\frac{p}{R_d(1+q_x)T}-\frac{p_0}{R_dT_0}\right)\\
&= -g\frac{\rho_0}{\rho}\left(\frac{T_0}{p_0}\frac{p}{(1+q_x)T}-1\right)\\
&= -g\frac{\rho_0}{\rho(1+q_x)}\left(\frac{T_0}{p_0}\frac{p'+p_0}{T}-(1+q_x)\right)\\
&= -g\frac{\rho_0}{\rho(1+q_x)}\left(\frac{T_0}{T}\frac{p'}{p_0}+\frac{T_0-T}{T}-q_x\right)\\
&= +g\frac{\rho_0}{\rho(1+q_x)}\left(-\frac{T_0}{T}\frac{p'}{p_0}+\frac{T'}{T}+q_x\right)
\end{aligned}$$

In former versions of the fast waves solver, $(1+q_x)$ was neglected in the denominator because q_x is at most about 1%. Nevertheless one can avoid this neglect by

$$-g\frac{\rho'}{\rho} = +g\frac{p_0}{T_0}\frac{T}{p}\left(-\frac{T_0}{T}\frac{p'}{p_0}+\frac{T'}{T}+q_x\right) = +g\left(-\frac{p'}{p}+\frac{p_0}{p}\frac{T'}{T_0}+\frac{p_0}{p}\frac{T}{T_0}q_x\right), \tag{25}$$

i.e. densities are expressed by pressure and temperature in an efficient manner. By the way, inserting $T' = T - T_0$ results in

$$-g\frac{\rho'}{\rho} = +g\left(-1+\frac{p_0}{p}\frac{T}{T_0}(1+q_x)\right). \tag{26}$$

This form is used for the 'dynamical bottom boundary condition' (section 5.2.1). The reason is, that for parallelization no boundary exchange of T' is needed; instead an estimation of T by the starting value is used.

4 Discretization

4.1 Numerical operators for the spatial discretization

To define the numerical operators for the *spatial* discretizations we have to remember the distinct grid positions, where the different variables are located in the COSMO model. The main grid positions with integer indices (i, j, k) are those, where the scalars p, T, ρ, p_0, T_0, ρ_0, p', T', q_v, q_c, ... and the divergence D are located. The velocity components u are defined at the staggered grid position $(i+\frac{1}{2}, j, k)$, v at $(i, j+\frac{1}{2}, k)$, and w at $(i, j, k-\frac{1}{2})$. In the following, we will keep the half indices for the staggered velocity positions for clarification. One should notice that in the *COSMO code* the staggered grid positions $(i+\frac{1}{2}, j, k)$, $(i, j+\frac{1}{2}, k)$, and $(i, j, k-\frac{1}{2})$ (minus sign!) are denoted as `(i,j,k)` (this is indicated by the gray connection lines in Figure 1).

For the grid position definition of the metric terms one has to notice that the half level positions $z^{(h)}$ (or 'hhl'), i.e. with the 'w'-position indices $(i, j, k-\frac{1}{2})$ are prescribed. Therefore, $\frac{\partial z}{\partial \zeta}$ and $\frac{\partial \zeta}{\partial z}$ or $\sqrt{g}$ and $1/\sqrt{g}$ are defined most naturally at the scalar ('s') position (i, j, k) (in this context it might by denoted equally as the 'ww'-position), $\frac{\partial z}{\partial \lambda}$ is defined most naturally at the 'uw'-position $(i+\frac{1}{2}, j, k-\frac{1}{2})$, and $\frac{\partial z}{\partial \phi}$ most naturally at the 'vw'-position $(i, j+\frac{1}{2}, k-\frac{1}{2})$.

For the spatial discretization we introduce the following 2-point operators, leading to at most second order formulas. The limitation to two point operators in the vertical stems from the fact, that only a tridiagonal implicit equation system should occur. For the horizontal

operations in principle higher order discretizations may be used (this is currently under investigation by A. Will and J. Ogaja at the University in Cottbus), but here only 2-point formulas are used, too.

We start with the spatial *averaging* operators. Horizontal averaging is done by

$$\overline{\psi}^{\lambda}\Big|_{i,j,k} \equiv A_\lambda \psi|_{i,j,k} := \frac{1}{2}(\psi_{i-\frac{1}{2},j,k} + \psi_{i+\frac{1}{2},j,k}), \tag{27}$$

$$\overline{\psi}^{\phi}\Big|_{i,j,k} \equiv A_\phi \psi|_{i,j,k} := \frac{1}{2}(\psi_{i,j-\frac{1}{2},k} + \psi_{i,j+\frac{1}{2},k}). \tag{28}$$

These are second order discretizations. In the following, the notation with an over-bar '$\overline{\psi}$' is mostly used for prefactors, whereas the operator notation '$A\psi$' is mostly used for the prognostic variables, for which an implicit equation system will be derived.

For the vertical averaging we have to keep in mind the special definition of the so called main levels (index k) and the half levels (index $k+\frac{1}{2}$). As stated above, in the COSMO model, the user can prescribe the grid positions of the half levels $z^{(h)}_{i,j,k-\frac{1}{2}}$. The height of the main levels is a simple arithmetic average

$$z^{(m)}_{i,j,k} := \frac{1}{2}\left(z^{(h)}_{i,j,k-\frac{1}{2}} + z^{(h)}_{i,j,k+\frac{1}{2}}\right). \tag{29}$$

Accordingly an averaging from half level variables (e.g. w) to the main level is done by arithmetic averaging:

$$\overline{\psi}^{\zeta}\Big|_{i,j,k} \equiv A_\zeta \psi|_{i,j,k} := \frac{1}{2}(\psi_{i,j,k-\frac{1}{2}} + \psi_{i,j,k+\frac{1}{2}}). \tag{30}$$

But averaging from main level variables (e.g. p', T', ...) to the half level position is done by a weighting

$$\overline{\psi}^{\zeta,N}\Big|_{i,j,k-\frac{1}{2}} \equiv A^N_\zeta \psi\big|_{i,j,k-\frac{1}{2}} := g_{i,j,k-\frac{1}{2}}\psi_{i,j,k} + (1 - g_{i,j,k-\frac{1}{2}})\psi_{i,j,k-1} \tag{31}$$

with

$$g_{i,j,k-\frac{1}{2}} := \frac{z^{(h)}_{i,j,k-\frac{1}{2}} - z^{(h)}_{i,j,k-\frac{3}{2}}}{z^{(h)}_{i,j,k+\frac{1}{2}} - z^{(h)}_{i,j,k-\frac{3}{2}}}. \tag{32}$$

To be complete, we also note the extrapolation formula

$$\psi_{i,j,k+\frac{1}{2}} = -(1 - g_{i,j,k-\frac{1}{2}})\ \psi_{i,j,k-1} + (2 - g_{i,j,k-\frac{1}{2}})\ \psi_{i,j,k}. \tag{33}$$

For vertical averages for u and v one has to use appropriate weights $g_{i+\frac{1}{2},j,k-\frac{1}{2}}$ or $g_{i,j+\frac{1}{2},k-\frac{1}{2}}$, respectively. The appropriate averaging operators are denoted by a bar above the N: $A^{\bar{N}}_\zeta$ (of course one should even distinguish between the u or v position; but this can be easily seen from the context).

In the program code the denotations $g_{i,j,k-\frac{1}{2}}$ = `wgtfac(i,j,k)` , $g_{i+\frac{1}{2},j,k-\frac{1}{2}}$ = `wgtfac_u(i,j,k)` and $g_{i,j+\frac{1}{2},k-\frac{1}{2}}$ = `wgtfac_v(i,j,k)` (introduced by G. Zängl) are used.

Now we turn to spatial *derivatives*. For horizontal derivatives we can simply use the standard centered difference formulas

$$\delta_\lambda \psi|_{i,j,k} := \frac{\psi_{i+\frac{1}{2},j,k} - \psi_{i-\frac{1}{2},j,k}}{\Delta\lambda}, \tag{34}$$

$$\delta_\phi \psi|_{i,j,k} := \frac{\psi_{i,j+\frac{1}{2},k} - \psi_{i,j-\frac{1}{2},k}}{\Delta\phi}, \tag{35}$$

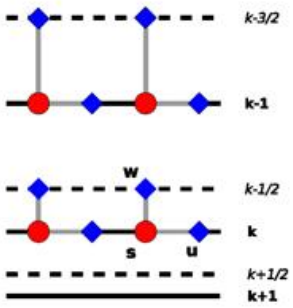


Figure 1: Denotation of the levels and the position of variables in the COSMO-model. Grey connection lines indicate staggered grid positions with the same indices in the COSMO program code.

and analogous for staggered variables.

In the case of vertical derivatives things become a little bit more complicated. Here one has to distinguish if the variable is defined on the half or the main level and if the target point is on a half or a main level.

The derivative of a half level variable at the position of the main level is obviously done by

$$\delta_\zeta \psi|_{i,j,k} := \frac{\psi_{i,j,k+\frac{1}{2}} - \psi_{i,j,k-\frac{1}{2}}}{\Delta\zeta}. \tag{36}$$

The derivative of a main level variable to the half level position could be done in the same way

$$\delta_\zeta^N \psi\big|_{i,j,k-\frac{1}{2}} := \frac{\psi_{i,j,k} - \psi_{i,j,k-1}}{\Delta\zeta} \tag{37}$$

with the argumentation, that from two points one can calculate a derivative only in one manner, independently from the position of the target point. But a second order formula can only be achieved if the target point is exactly in between the two main level points. For a decentered target point, the formula is only of first order accurate. Therefore, one should avoid this type of derivation operator, if possible.

Vertical derivative of a 'scalar variable to the u-Position':

$$\delta_\zeta^{(s,u)} \psi := A_\lambda \delta_\zeta A_\zeta^N \psi \tag{38}$$

An equally accurate discretization is

$$\delta_\zeta^{(s,u)} \psi := \delta_\zeta A_\zeta^{\bar{N}} A_\lambda \psi \tag{39}$$

For the vertical derivative 'u-Position to a scalar point' one can use

$$\delta_\zeta^{(u,s)} u := A_\lambda \delta_\zeta A_\zeta^{\bar{N}} u \tag{40}$$

analogous to eq. (38) or alternatively

$$\delta_\zeta^{(u,s)} u := \delta_\zeta A_\zeta^N A_\lambda u. \tag{41}$$

Vertical derivatives 'scalar to v-position' or 'v-position to scalar' are discretized analogously.

Now we define operators for combinations or products of vertical derivatives. Such larger stencils occur in particular in the metric correction terms.

- The following metric term occurring in the 'strong conservation'-form of the divergence is best discretized as

$$discr.^{(s)}\left[\frac{\partial z}{\partial \lambda}u\right] = \delta_\zeta\left(A_\lambda\left(\frac{\partial z}{\partial \lambda}A_\zeta^{\bar{N}}u\right)\right). \tag{42}$$

  Analogous for the y-direction.

- Metric terms of ∇p and ∇D

$$discr.^{(u)}\left[\frac{\partial \zeta}{\partial \lambda}\ \frac{\partial \psi}{\partial \zeta}\right] \tag{43}$$

  occur in the explicit integration of the horizontal momentum equations (hence, at the u- or v-position). The calculation of the metrical prefactor is done in any case by the partitioning

$$\frac{\partial \zeta}{\partial \lambda} = -\frac{\partial \zeta}{\partial z}\ \frac{\partial z}{\partial \lambda}. \tag{44}$$

  Here $\frac{\partial \zeta}{\partial z}$ is defined most naturally at the 's'-position and $\frac{\partial z}{\partial \lambda}$ most naturally at the 'uw'-position. Therefore

$$discr.\left[\frac{\partial \zeta}{\partial \lambda}\right] = -\left(A_\lambda\frac{\partial \zeta}{\partial z}\right)\cdot\left(A_\zeta\frac{\partial z}{\partial \lambda}\right). \tag{45}$$

  This results in

$$discr.^{(u)}\left[\frac{\partial \zeta}{\partial \lambda}\ \frac{\partial \psi}{\partial \zeta}\right] = -\left(A_\zeta\frac{\partial z}{\partial \lambda}\right)\cdot\left(A_\lambda\underbrace{\left(\frac{\partial \zeta}{\partial z}\delta_\zeta A_\zeta^N\psi\right)}_{=discr.^{(s)}\left[\frac{\partial \psi}{\partial z}\right]}\right). \tag{46}$$

  This means that a ζ-derivative can be expressed most naturally by a z-derivative. Analogous:

$$discr.^{(v)}\left[\frac{\partial \zeta}{\partial \phi}\ \frac{\partial \psi}{\partial \zeta}\right] = -\left(A_\zeta\frac{\partial z}{\partial \phi}\right)\cdot\left(A_\phi\underbrace{\left(\frac{\partial \zeta}{\partial z}\delta_\zeta A_\zeta^N\psi\right)}_{=discr.^{(s)}\left[\frac{\partial \psi}{\partial z}\right]}\right). \tag{47}$$

- For the z-derivative of a scalar variable at the s-position we use in the following

$$discr.^{(s)}\left[\frac{\partial \psi}{\partial z}\right] \equiv \delta_z^{(s,s)}\psi := \frac{\partial \zeta}{\partial z}\delta_\zeta A_\zeta^N\psi. \tag{48}$$

- We further remark that $\sqrt{g}$ at the 'w'-position can be better calculated directly by

$$\left.\frac{\partial z}{\partial \zeta}\right|_{k-\frac{1}{2}} = \frac{z_k^{(m)} - z_{k-1}^{(m)}}{1} = \frac{\frac{1}{2}\left(z_{k+\frac{1}{2}}^{(h)} + z_{k-\frac{1}{2}}^{(h)}\right) - \frac{1}{2}\left(z_{k-\frac{1}{2}}^{(h)} + z_{k-\frac{3}{2}}^{(h)}\right)}{1} = \frac{z_{k+\frac{1}{2}}^{(h)} - z_{k-\frac{3}{2}}^{(h)}}{2} \tag{49}$$

  instead of a weighted averaging, due to the special definition of the position of the main levels (hint by A. Will (personal communication)).

Some definitions of these operators may seem a bit ad hoc for the reader. A deeper reasoning for them is given in section 8, where truncation errors are calculated and those operators with the smallest error are chosen.

4.2 Discretization of the Euler equations

In the last section, spatial discretization operators have been defined, which are necessary for the numerical treatment of the Euler equations. The basic time integration idea behind the fast waves solver is the horizontally explicit-vertically implicit (HE-VI) scheme, where the horizontal integration is further done by a forward-backward scheme and the vertical implicit step is a general Crank-Nicholson scheme (?). It is therefore reasonable to define a general time averaging operator, here called a 'Crank-Nicholson time averaging operator', by

$$\hat{\beta}_i^{(a)}\phi := \beta_i^{(a)}\phi^{n+1} + \left(1-\beta_i^{(a)}\right)\phi^n. \tag{50}$$

The upper index (a) denotes a process, e.g. the terms for sound expansion (s), the lower index i simply enumerates terms. This nomenclature for the Crank-Nicholson weights is adopted from ?. To limit the number of weights $\beta_i^{(a)}$, not for every term an own Crank-Nicholson weighting parameter is introduced. u- and v-terms, which are analogous in a process, get the same weighting parameter, because the both horizontal directions have often quite equal rights in real model applications and their appropriate grid stretching in a limited area model are not so different.

Now, the discretized Euler equations are expressed by the formerly defined operators:

$$\begin{aligned}
\frac{u^{n+1}-u^n}{\Delta t} &= -\overline{\frac{1}{\rho}}^{\lambda}\,\overline{\frac{1}{r\cos\phi}}^{\lambda}\left(\hat{\beta}_1^s\delta_\lambda p' - \hat{\beta}_7^s\overline{\frac{\partial z}{\partial\lambda}}^{\zeta}\,A_\lambda\left(\delta_z^{(s,s)}p'\right)\right) + \\
&\quad +\overline{\frac{1}{\rho}}^{\lambda}\,\overline{\frac{1}{r\cos\phi}}^{\lambda}\left(\delta_\lambda(\alpha_{div}^h\rho D_{(uv)}) - \overline{\frac{\partial z}{\partial\lambda}}^{\zeta}\,A_\lambda\left(\delta_z^{(s,s)}(\alpha_{div}^h\rho D_{(uv)})\right)\right) + \left.\frac{\partial u}{\partial t}\right|_{slow} \qquad (51)\\
\frac{v^{n+1}-v^n}{\Delta t} &= -\overline{\frac{1}{\rho}}^{\phi}\,\overline{\frac{1}{r}}^{\phi}\left(\hat{\beta}_1^s\delta_\phi p' - \hat{\beta}_7^s\overline{\frac{\partial z}{\partial\phi}}^{\zeta}\,A_\phi\left(\delta_z^{(s,s)}p'\right)\right) + \\
&\quad +\overline{\frac{1}{\rho}}^{\phi}\,\overline{\frac{1}{r}}^{\phi}\left(\delta_\phi(\alpha_{div}^h\rho D_{(uv)}) - \overline{\frac{\partial z}{\partial\phi}}^{\zeta}\,A_\phi\left(\delta_z^{(s,s)}(\alpha_{div}^h\rho D_{(uv)})\right)\right) + \left.\frac{\partial v}{\partial t}\right|_{slow} \qquad (52)\\
\frac{w^{n+1}-w^n}{\Delta t} &= -\overline{\frac{1}{\rho}}^{\zeta,N}\left(\hat{\beta}_2^s\overline{\frac{\partial\zeta}{\partial z}}^{\zeta,N}\,\delta_\zeta^N p'\right) + \\
&\quad +g\left(\hat{\beta}_1^b\overline{\frac{p_0}{p}}^{\zeta,N}\,\overline{\frac{1}{T_0}}^{\zeta,N}\,A_\zeta^N T' - \hat{\beta}_2^b\overline{\frac{1}{p}}^{\zeta,N}\,A_\zeta^N p' + \overline{\frac{p_0}{p}}^{\zeta,N}\,\overline{\frac{T'}{T_0}}^{\zeta,N}\,\overline{q_x}^{\zeta,N}\right) + \\
&\quad +\overline{\frac{1}{\rho}}^{\zeta,N}\,\overline{\frac{\partial\zeta}{\partial z}}^{\zeta,N}\,\delta_\zeta^N(\alpha_{div}^v\rho D_{(w)}) + \left.\frac{\partial w}{\partial t}\right|_{slow} \qquad (53)\\
\frac{p'^{n+1}-p'^n}{\Delta t} &= -\frac{c_p}{c_V}pD_{(p)} + \hat{\beta}_3^b g\rho_0\,A_\zeta w + \left.\frac{\partial p'}{\partial t}\right|_{slow} \qquad (54)\\
\frac{T'^{n+1}-T'^n}{\Delta t} &= -\frac{R}{c_V}TD_{(T)} - \hat{\beta}_4^b\frac{\partial T_0}{\partial z}\,A_\zeta w + \left.\frac{\partial T'}{\partial t}\right|_{slow} \qquad (55)
\end{aligned}$$

Here, different divergences $D_{(p)}$, $D_{(T)}$, $D_{(uv)}$, $D_{(w)}$ have been introduced, because they can carry different Crank-Nicholson weights (see sections 4.2.1).

Be aware, that each variable has a distinct time index, too, by the Crank-Nicholson operators $\hat{\beta}$. Only the additional slow processes $\left.\frac{\partial u}{\partial t}\right|_{slow}, \ldots, \left.\frac{\partial T'}{\partial t}\right|_{slow}$ don't carry any time index: they are assumed to be constant during the small time step integration.

In deviation from the above defined operators, the following coefficient functions occurring

in the buoyancy terms are calculated by

$$\overline{\frac{1}{p}}^{\zeta,N} = \frac{1}{p_0(z_{k+1/2}) + A_\zeta^N p'}, \qquad \overline{\frac{p_0}{p}}^{\zeta,N} = \frac{1}{1 + \frac{A_\zeta^N p'}{p_0(z_{k+1/2})}}, \tag{56}$$

$$\overline{\frac{1}{T_0}}^{\zeta,N} = \frac{1}{T_0(z_{k+1/2})}, \qquad \overline{\frac{T}{T_0}}^{\zeta,N} = 1 + \frac{A_\zeta^N T'}{T_0(z_{k+1/2})}. \tag{57}$$

The writing for the reference state variables T_0 and p_0 indicates that they can be calculated *exactly* at their grid position[2] (proposal by A. Will (personal communication)). Analogous to that, $\overline{\frac{1}{\rho}}^{\zeta,N}$ in eq. (53) is calculated with the aid of the ideal gas equation by the values of $T_0(z_{k+1/2}) + A_\zeta^N T'$ and $p_0(z_{k+1/2}) + A_\zeta^N p'$. In particular $\overline{\frac{\partial \zeta}{\partial z}}^{\zeta,N}$ is calculated by (49).

4.2.1 Discretization of the divergence

The horizontal contributions of the divergence can be discretized by

$$\tilde{d}_{hor} := \delta_\lambda(\overline{\sqrt{g}}^{\lambda}\, u) + \delta_\phi(\overline{\cos\phi}^{\phi}\, \overline{\sqrt{g}}^{\phi}\, v). \tag{58}$$

For the vertical contribution

$$\tilde{d}_{vert} := \delta_\zeta Z, \tag{59}$$

Z, Z_x, Z_y, Z_{hor} and Z_{vert} are needed. They are most naturally defined at the w-position $(i, j, k - \frac{1}{2})$. However, one cannot directly use $\tilde{d}_{vert}$, because the implicit weighting must be considered.

Z_{hor} is calculated in the subroutine `calc_Z_horiz`, and discretized by

$$Z_{hor} = Z_x + Z_y, \tag{60}$$

$$Z_x = A_\lambda \left(\frac{\partial z}{\partial \lambda}\, A_\zeta^{\bar{N}}\, u \right), \tag{61}$$

$$Z_y = A_\phi \left(\frac{\partial z}{\partial \phi}\, \cos\phi\, A_\zeta^{\bar{N}}\, v \right). \tag{62}$$

In this manner Z_{hor} can be calculated for $k = 2, 3, ..., ke$. At $k = 1$ (upper boundary) one immediately gets $Z_{hor} = 0$ (due to $\frac{\partial z}{\partial \lambda} = 0$, ...). At $k = ke + 1$ (lower boundary) u and v must be extrapolated. In contrast

$$Z_{vert} := -r \cos\phi\, w \tag{63}$$

can be calculated at the boundaries, too.

The different divergence terms are:

$$D_{(p)} = \frac{1}{r\cos\phi}\, \frac{1}{\sqrt{g}} \left[\hat{\beta}_3^s\, \tilde{d}_{hor} + \hat{\beta}_8^s\, \delta_\zeta Z_{hor} + \hat{\beta}_4^s\, \delta_\zeta Z_{vert} \right]. \tag{64}$$

$$D_{(T)} = \frac{1}{r\cos\phi}\, \frac{1}{\sqrt{g}} \left[\hat{\beta}_5^s\, \tilde{d}_{hor} + \hat{\beta}_9^s\, \delta_\zeta Z_{hor} + \hat{\beta}_6^s\, \delta_\zeta Z_{vert} \right]. \tag{65}$$

[2]Therefore the reference state variables have to be calculated not only on the main levels but on the half level positions, too. This must be done in all modules, which calculate them. In particular in the interpolation program `int2lm` one has to set the namelist switch `lanalyt_calc_p0T0=.TRUE.`, if `irefatm=1` is still used.

$$D_{(uv)} = \frac{1}{r\cos\phi}\frac{1}{\sqrt{g}}\left[\hat{\beta}_1^d\,\tilde{d}_{hor} + \hat{\beta}_5^d\,\delta_\zeta Z_{hor} + \hat{\beta}_2^d\,\delta_\zeta Z_{vert}\right]. \tag{66}$$

$$D_{(w)} = \frac{1}{r\cos\phi}\frac{1}{\sqrt{g}}\left[\hat{\beta}_3^d\,\tilde{d}_{hor} + \hat{\beta}_6^d\,\delta_\zeta Z_{hor} + \hat{\beta}_4^d\,\delta_\zeta Z_{vert}\right]. \tag{67}$$

4.2.2 Mahrer discretization of the horizontal pressure gradients

The basic idea behind the discretization of the horizontal pressure gradient by ? consists in using the gradient $\frac{\partial p'(\lambda,z)}{\partial\lambda}$ on z-planes instead of the conventional form $\frac{\partial p'(\lambda,\zeta)}{\partial\lambda} + \frac{\partial\zeta}{\partial\lambda}\frac{\partial p'(\lambda,\zeta)}{\partial\zeta}$ (equivalently for the ϕ-direction). To this purpose p' is interpolated vertically on the left- and right hand side of the target u-position. This means, at both columns (i,j) and $(i+1,j)$ p' is interpolated at the height $z_{i+\frac{1}{2},j,k}$ from the vertically nearest p'-values (analogous to the λ-direction). In this manner, the nearest values of p' are used in steep terrain. In contrast, in the above mentioned 'conventional' discretization, it can happen, that $\frac{\partial p'(\lambda,\zeta)}{\partial\zeta}$ is estimated from p'-values, which are (vertically) quite far away. This bears the risk of an instability, which does not occur in the Mahrer-approach.

A crucial point in the Mahrer discretization lies in the fact, that in the vicinity of steep terrain, interpolation is not longer possible, when $z_{i+\frac{1}{2},j,k}$ lies under the orography at least on one side of the u-position. As pointed out by ?, the then required *extrapolation* of p' often leads to similar instabilities as the conventional discretization. ? describes a way, how to estimate the extrapolation by the hydrostatic approximation in the ICON dynamical core. Unfortunately, the need for a (quasi-)3-dimensional divergence damping necessary in the time-splitting approach (?, ?) does not allow to transfer this idea to the COSMO fast waves solver (there is no hydrostatic approximation for the divergence).

However, in the new fast waves solver, an also linear extrapolation is used if $z_{i,j,ke} > z_{i+\frac{1}{2},j,k}$ (similar for the other neighboring orography heights). This indeed can help to increase stability in steep terrain in idealized test scenarios (see sections 9.4 and 9.5). But in real case applications, this approach is not entirely satisfying. One reason could be the occurring of a mixed term in the Taylor expansion (section 8.2). Therefore, though the Mahrer discretization has proven as a stable method in several real case runs (mainly for COSMO-DE), the conventional discretization is still recommended.

5 Boundary conditions

5.1 The free slip condition

At the upper and lower boundaries the pure Euler equations (i.e. without friction/diffusion) possess only one physical boundary condition: the free slip condition, i.e. the velocity component perpendicular to the boundary must be zero

$$\dot{\zeta} = 0, \tag{68}$$

which is equivalent to

$$w = \frac{1}{r\cos\phi}\frac{\partial z}{\partial\lambda}u + \frac{1}{r}\frac{\partial z}{\partial\phi}v. \tag{69}$$

As mentioned above, the vertically implicit solver needs this boundary condition at time level $n+1$. This is not a problem, because u^{n+1} and v^{n+1} are already known by the forward step of the horizontal momentum equations.

At the top boundary we can simply prescribe

$$\dot{\zeta}_{i,j,k=\frac{1}{2}} = 0 \quad \Rightarrow \quad w^{n+1}_{i,j,\frac{1}{2}} = 0. \tag{70}$$

At the lower boundary the free slip condition reduces to

$$w^{n+1}_{i,j,ke+\frac{1}{2}} = \frac{1}{r\cos\phi}\left[A_\lambda\left(\frac{\partial z}{\partial \lambda}\, u^{n+1}_{(sfc)}\right) + A_\phi\left(\frac{\partial z}{\partial \phi}\cos\phi\, v^{n+1}_{(sfc)}\right)\right], \tag{71}$$

where the $\cos\phi$-terms are arranged analogous to the strong conservation form of the divergence. $u^{n+1}_{(sfc)}$ and $v^{n+1}_{(sfc)}$ must be known at $k = ke + \frac{1}{2}$, therefore they must be extrapolated.

5.2 Boundary treatments

The following considerations does not concern true physical boundary conditions, but *boundary treatments* in the sense that the appropriate terms cannot longer be calculated by centered differences but need a different numerical treatment.

5.2.1 The vertical pressure gradient in the horizontal equations of motion

In the both horizontal momentum equations there is a need to have a different discretization of $\partial p'/\partial z$ or alternatively of $\partial\left(p' - \alpha^h_{div}\rho D\right)/\partial z$.

At the bottom boundary there exist two options. Th first option is to use a one sided formula. Günther Zängl proposed to use a one sided derivative of *2nd order accuracy* (a first order formula is not accurate enough!) instead of the boundary treatment described in[3] (?, section 5.4).

For three arbitrarily prescribed points

$$z_1, \quad z_2 = z_1 + h_1, \quad z_3 = z_1 + h_2, \tag{72}$$

one can derive a one-sided derivative formula of 2nd order for a function $f(z)$ in z_1 by

$$af(z_1) + bf(z_2) + cf(z_3) = (a+b+c)f + (bh_1 + ch_2)f' + \left(b\frac{h_1^2}{2} + c\frac{h_2^2}{2}\right)f'' + \ldots. \tag{73}$$

This results in the weights

$$a = -(b+c), \tag{74}$$

$$b = \frac{1 - ch_2}{h_1}, \tag{75}$$

$$c = \frac{h_1}{h_2(h_1 - h_2)}. \tag{76}$$

This is active if the switch `ldyn_bbc=.FALSE.` is set. If it is set to `.TRUE.`, then the other possibility is used, the so called 'dynamical bottom boundary boundary' (?), described in the next section 5.2.1.

At the top boundary a one sided derivative formula of first order is sufficient.

[3]Therefore the switch `ldyn_bbc=.FALSE.` has a different meaning in the two fast waves solver versions.

Dynamic bottom boundary condition for the pressure In section 5.4 of ? the strong influence of the formulation of the lower boundary condition for the pressure p' was mentioned. Instead of a pressure extrapolation, ? proposed a so called 'dynamic bottom (or lower) boundary condition' for p'. The goal is to determine $\partial p'/\partial\zeta$ in a manner *consistent* to the free-slip condition $\dot{\zeta} = 0$. The starting point for the derivation is the bottom boundary condition $\dot{\zeta} = 0$ at the surface $z = h_s(\lambda, \phi)$, explicitly written

$$\dot{\zeta} = \frac{u}{r\cos\phi}\left.\frac{\partial\zeta}{\partial\lambda}\right|_z + \frac{v}{r}\left.\frac{\partial\zeta}{\partial\phi}\right|_z + w\frac{\partial\zeta}{\partial z} = 0. \tag{77}$$

The vertical pressure gradient occurs in the three momentum equations, therefore we differentiate by time to obtain

$$\frac{\partial\dot{\zeta}}{\partial t} = \frac{1}{r\cos\phi}\left.\frac{\partial\zeta}{\partial\lambda}\right|_z \frac{\partial u}{\partial t} + \frac{1}{r}\left.\frac{\partial\zeta}{\partial\phi}\right|_z \frac{\partial v}{\partial t} + \frac{\partial\zeta}{\partial z}\frac{\partial w}{\partial t} = 0. \tag{78}$$

Here we insert the momentum equations (1)-(3) in the form

$$\begin{aligned}
\frac{\partial u}{\partial t} &= F_u - \frac{1}{\rho}\frac{1}{r\cos\phi}\frac{\partial z}{\partial\lambda}\left(-\frac{\partial\zeta}{\partial z}\frac{\partial\tilde{p}}{\partial\zeta}\right), \\
\frac{\partial v}{\partial t} &= F_v - \frac{1}{\rho}\frac{1}{r}\frac{\partial z}{\partial\phi}\left(-\frac{\partial\zeta}{\partial z}\frac{\partial\tilde{p}}{\partial\zeta}\right), \\
\frac{\partial w}{\partial t} &= F_w - \frac{1}{\rho}\frac{\partial\zeta}{\partial z}\frac{\partial\tilde{p}}{\partial\zeta},
\end{aligned}$$

with $\tilde{p} = p' - \alpha^h_{div}\rho D$ and

$$F_u := -\frac{1}{\rho}\frac{1}{r\cos\phi}\frac{\partial\tilde{p}}{\partial\lambda} + \left.\frac{\partial u}{\partial t}\right|_{slow} \tag{79}$$

$$F_v := -\frac{1}{\rho}\frac{1}{r}\frac{\partial\tilde{p}}{\partial\phi} + \left.\frac{\partial v}{\partial t}\right|_{slow} \tag{80}$$

$$F_w := +g\left(-1 + \frac{p_0}{p}\frac{T}{T_0}(1+q_x)\right) + \frac{1}{\rho}\frac{\partial\zeta}{\partial z}\frac{\partial(\alpha^v_{div} - \alpha^h_{div})\rho D}{\partial\zeta} + \left.\frac{\partial w}{\partial t}\right|_{slow}. \tag{81}$$

In F_w the form (26) of the buoyancy term was used. Sorting by $\frac{\partial\zeta}{\partial z}\frac{\partial p'}{\partial\zeta}$ finally results in

$$\frac{\partial\zeta}{\partial z}\frac{\partial p'}{\partial\zeta}\frac{1}{\rho}\left[\left(\frac{1}{r\cos\phi}\frac{\partial z}{\partial\lambda}\right)^2 + \left(\frac{1}{r}\frac{\partial z}{\partial\phi}\right)^2 + 1\right] = -\frac{1}{r\cos\phi}\frac{\partial z}{\partial\lambda}F_u - \frac{1}{r}\frac{\partial z}{\partial\phi}F_v + F_w. \tag{82}$$

This delivers the needed value of $\frac{\partial\zeta}{\partial z}\frac{\partial p'}{\partial\zeta}$ at the lower boundary (for $k = ke$) in the u- and v-equation. The discretization of this expression and the averaging to the u and v position is straightforward. Nevertheless, several spatial interpolations with 4-point or even 8-point formulas are needed.

5.2.2 Boundary treatment of the divergence

In the 'strong conservation form' the horizontal derivatives may be calculated in every grid point by centered differences, even at the boundary points (see eq. (10)).

For the remaining vertical derivative $\frac{\partial Z}{\partial\zeta}$ one needs Z at the boundary, i.e. at $k = ke + 1/2$ and $k = 1/2$. For this two variants are possible. First it can be calculated by extrapolation; this is currently implemented.

Second, through the use of the *exact* boundary condition $Z = 0$. This is a theoretical advantage of the 'strong conservation form'. An important requirement for this is that the implicit weightings are chosen as

$$\beta_8^s = \beta_4^s, \quad \text{and} \quad \beta_9^s = \beta_6^s. \tag{83}$$

But nevertheless, there remains the problem that Z must be subdivided into horizontal and vertical parts, due to the vertically implicit solver. Therefore one cannot pose this exact boundary condition for the divergence itself. This probably is the reason, why this second boundary treatment does not work until now.

6 The linear equation system for the vertical velocity

6.1 Setup of the equation system

To get rid of the sound speed limitation, the Euler equations are solved vertically implicit. To derive the equation system we write the Euler equations in the following linear form

$$\mathbf{A} \begin{pmatrix} u^{n+1} \\ v^{n+1} \\ w^{n+1} \\ p'^{n+1} \\ T'^{n+1} \end{pmatrix} = \mathbf{b}^n$$

with

$$\mathbf{A} = \begin{pmatrix} \frac{1}{\Delta t}\mathbf{1} & 0 & 0 & \mathbf{A}_{up} & 0 \\ 0 & \frac{1}{\Delta t}\mathbf{1} & 0 & \mathbf{A}_{vp} & 0 \\ \mathbf{A}_{wu} & \mathbf{A}_{wv} & \mathbf{A}_{ww} & \mathbf{A}_{wp} & \mathbf{A}_{wT} \\ \mathbf{A}_{pu} & \mathbf{A}_{pv} & \mathbf{A}_{pw} & \frac{1}{\Delta t}\mathbf{1} & 0 \\ \mathbf{A}_{Tu} & \mathbf{A}_{Tv} & \mathbf{A}_{Tw} & 0 & \frac{1}{\Delta t}\mathbf{1} \end{pmatrix}, \tag{84}$$

and

$$\mathbf{b}^n = (b_u, b_v, b_w, b_p, b_T)^T. \tag{85}$$

Of course, nearly all the terms arising in the Euler equations are non-linear. But this non-linearity in the sound and buoyancy terms is small enough, that in every small time step, the coefficients can be considered as quasi constant. They can even be considered as constant through the whole fast waves integration procedure[4].

Here the following operators have been used for the horizontal momentum equations

$$\mathbf{A}_{up} = \overline{\frac{1}{\rho}}^{\lambda} \overline{\frac{1}{r\cos\phi}}^{\lambda} \left(\beta_1^s \, \delta_\lambda - \beta_7^s \overline{\frac{\partial z}{\partial \lambda}}^{\zeta} A_\lambda \delta_z^{(s,s)} \right), \tag{86}$$

$$\mathbf{A}_{vp} = \overline{\frac{1}{\rho}}^{\phi} \overline{\frac{1}{r}}^{\phi} \left(\beta_1^s \, \delta_\phi - \beta_7^s \overline{\frac{\partial z}{\partial \phi}}^{\zeta} A_\phi \delta_z^{(s,s)} \right), \tag{87}$$

In $\mathbf{A}$ we have already used the fact, that the artificial divergence damping in the u- and v-equation must be treated explicitly, i.e. $\beta_1^d = \beta_2^d = \beta_5^d = 0$, otherwise no tridiagonal

[4]There is an internal switch `l_small_pert_in_pT`. If it is set to `.TRUE.`, then the coefficients (i.e. the lhs) of this equation system is calculated only once per *large* time step. If it is set to `.FALSE.`, then they are set in every small time step. The latter setting may be an interesting, although efficiency reducing, option in heavy weather conditions, e.g. in the simulation of tornadoes.

system can be achieved. We will see below that the horizontal pressure gradient terms must be treated fully explicit, too; therefore, $\mathbf{A}_{up} = 0$ and $\mathbf{A}_{vp} = 0$.

For the vertical momentum equation we get

$$\mathbf{A}_{wu} = -\overline{\left(\frac{1}{\rho}\right)}^{\zeta,N} \overline{\frac{\partial\zeta}{\partial z}}^{\zeta,N} \delta_\zeta^N \left[\alpha_{div}^v \rho \frac{1}{r\cos\phi} \frac{1}{\sqrt{g}} \left(\beta_3^d \, \delta_\lambda(\overline{\sqrt{g}}^\lambda \cdot ...) + \beta_6^d \, \mathbf{B}_x\right)\right], \tag{88}$$

$$\mathbf{A}_{wv} = -\overline{\left(\frac{1}{\rho}\right)}^{\zeta,N} \overline{\frac{\partial\zeta}{\partial z}}^{\zeta,N} \delta_\zeta^N \left[\alpha_{div}^v \rho \frac{1}{r\cos\phi} \frac{1}{\sqrt{g}} \left(\beta_3^d \, \delta_\phi(\overline{\cos\phi\sqrt{g}}^\phi \cdot ...) + \beta_6^d \, \mathbf{B}_y\right)\right], \tag{89}$$

$$\mathbf{A}_{ww} = \frac{1}{\Delta t}\mathbf{1} + \overline{\left(\frac{1}{\rho}\right)}^{\zeta,N} \overline{\frac{\partial\zeta}{\partial z}}^{\zeta,N} \delta_\zeta^N \left[\alpha_{div}^v \rho \frac{1}{r\cos\phi} \frac{1}{\sqrt{g}} \beta_4^d \, \delta_\zeta(r\cos\phi \cdot ...)\right], \tag{90}$$

$$\mathbf{A}_{wp} = \overline{\left(\frac{1}{\rho}\right)}^{\zeta,N} \overline{\frac{\partial\zeta}{\partial z}}^{\zeta,N} \beta_2^s \, \delta_\zeta^N + g\beta_2^b \overline{\frac{1}{p}}^{\zeta,N} A_\zeta^N, \tag{91}$$

$$\mathbf{A}_{wT} = -g\beta_1^b \overline{\frac{p_0}{p}}^{\zeta,N} \overline{\frac{1}{T_0}}^{\zeta,N} A_\zeta^N, \tag{92}$$

for the pressure equation

$$\mathbf{A}_{pu} = +\frac{c_p}{c_v} p \frac{1}{r\cos\phi} \frac{1}{\sqrt{g}} \left[\beta_3^s \, \delta_\lambda \left(\overline{\sqrt{g}}^\lambda \cdot ...\right) + \beta_8^s \, \mathbf{B}_x,\right] \tag{93}$$

$$\mathbf{A}_{pv} = +\frac{c_p}{c_v} p \frac{1}{r\cos\phi} \frac{1}{\sqrt{g}} \left[\beta_3^s \, \delta_\phi \left(\overline{\cos\phi\sqrt{g}}^\phi \cdot ...\right) + \beta_8^s \, \mathbf{B}_y\right], \tag{94}$$

$$\mathbf{A}_{pw} = -\frac{c_p}{c_v} p \frac{1}{r\cos\phi} \frac{1}{\sqrt{g}} \beta_4^s \, \delta_\zeta(r\cos\phi \cdot ...) - \beta_3^b g\rho_0 A_\zeta, \tag{95}$$

and for the temperature equation

$$\mathbf{A}_{Tu} = +\frac{R}{c_v} T \frac{1}{r\cos\phi} \frac{1}{\sqrt{g}} \left[\beta_5^s \, \delta_\lambda \left(\overline{\sqrt{g}}^\lambda \cdot ...\right) + \beta_9^s \, \mathbf{B}_x\right], \tag{96}$$

$$\mathbf{A}_{Tv} = +\frac{R}{c_v} T \frac{1}{r\cos\phi} \frac{1}{\sqrt{g}} \left[\beta_5^s \, \delta_\phi \left(\overline{\cos\phi\sqrt{g}}^\phi \cdot ...\right) + \beta_9^s \, \mathbf{B}_y\right], \tag{97}$$

$$\mathbf{A}_{Tw} = -\frac{R}{c_v} T \frac{1}{r\cos\phi} \frac{1}{\sqrt{g}} \beta_6^s \, \delta_\zeta(r\cos\phi \cdot ...) + \beta_4^b \frac{\partial T_0}{\partial z} A_\zeta, \tag{98}$$

where operators for the calculation of $\delta_\zeta Z_{hor}$ have been introduced:

$$\mathbf{B}_x := \delta_\zeta \left(A_\lambda \left(\frac{\partial z}{\partial\lambda} \, A_\zeta^{\bar{N}} \, \ldots\right)\right), \tag{99}$$

$$\mathbf{B}_y := \delta_\zeta \left(A_\phi \left(\frac{\partial z}{\partial\phi} \, \cos\phi \, A_\zeta^{\bar{N}} \, \ldots\right)\right). \tag{100}$$

Using again the shallow atmosphere approximation ($r \approx r_{earth}$ in all the prefactors) we can cancel $r\cos\phi$ in $\mathbf{A}_{pw}$, $\mathbf{A}_{Tw}$, and $\mathbf{A}_{ww}$.

The right hand sides are

$$b^n_{(u)} = \frac{1}{\Delta t}u^n - \overline{\frac{1}{\rho}}^{\lambda}\overline{\frac{1}{r\cos\phi}}^{\lambda}\left((1-\beta^s_1)\delta_\lambda p'^n - (1-\beta^s_7)\overline{\frac{\partial z}{\partial\lambda}}^{\zeta} A_\lambda\left(\delta^{(s,s)}_z p'^n\right)\right) + \\ + \overline{\frac{1}{\rho}}^{\lambda}\overline{\frac{1}{r\cos\phi}}^{\lambda}\left(\delta_\lambda(\alpha^h_{div}\,\rho\,D^n_{(uv)}) - \overline{\frac{\partial z}{\partial\lambda}}^{\zeta} A_\lambda\left(\delta^{(s,s)}_z(\alpha^h_{div}\,\rho\,D^n_{(uv)})\right)\right) + \left.\frac{\partial u}{\partial t}\right|_{slow}, \quad (101)$$

$$b^n_{(v)} = \frac{1}{\Delta t}v^n - \overline{\frac{1}{\rho}}^{\phi}\overline{\frac{1}{r}}^{\phi}\left((1-\beta^s_1)\delta_\phi p'^n - (1-\beta^s_7)\overline{\frac{\partial z}{\partial\phi}}^{\zeta} A_\phi\left(\delta^{(s,s)}_z p'^n\right)\right) + \\ + \overline{\frac{1}{\rho}}^{\phi}\overline{\frac{1}{r}}^{\phi}\left(\delta_\phi(\alpha^h_{div}\,\rho\,D^n_{(uv)}) - \overline{\frac{\partial z}{\partial\phi}}^{\zeta} A_\phi\left(\delta^{(s,s)}_z(\alpha^h_{div}\,\rho\,D^n_{(uv)})\right)\right) + \left.\frac{\partial v}{\partial t}\right|_{slow}, \quad (102)$$

$$b^n_{(w)} = \frac{1}{\Delta t}w^n - \overline{\frac{1}{\rho}}^{\zeta,N}(1-\beta^s_2)\overline{\frac{\partial\zeta}{\partial z}}^{\zeta,N}\delta^N_\zeta p'^n + \\ + g\left((1-\beta^b_1)\overline{\frac{p_0}{p}}^{\zeta,N}\overline{\frac{1}{T_0}}^{\zeta,N} A^N_\zeta T' - (1-\beta^b_2)\overline{\frac{1}{p}}^{\zeta,N} A^N_\zeta p' + \overline{\frac{p_0}{p}}^{\zeta,N}\overline{\frac{T}{T_0}}^{\zeta,N}\overline{q_x}^{\zeta,N}\right) + \\ + \overline{\frac{1}{\rho}}^{\zeta,N}\overline{\frac{\partial\zeta}{\partial z}}^{\zeta,N}\delta^N_\zeta(\alpha^v_{div}\,\rho\,D^n_{(w)}) + \left.\frac{\partial w}{\partial t}\right|_{slow}, \quad (103)$$

$$b^n_{(p)} = \frac{1}{\Delta t}p'^n - \frac{c_p}{c_V}pD^n_{(p)} + (1-\beta^b_3)g\rho_0\,A_\zeta w^n + \left.\frac{\partial p'}{\partial t}\right|_{slow}, \quad (104)$$

$$b^n_{(T)} = \frac{1}{\Delta t}T'^n - \frac{R}{c_V}TD^n_{(T)} - (1-\beta^b_4)\frac{\partial T_0}{\partial z}A_\zeta w^n + \left.\frac{\partial T'}{\partial t}\right|_{slow}, \quad (105)$$

with the explicit divergence terms

$$D^n_{(p)} = \frac{1}{r\cos\phi}\frac{1}{\sqrt{g}}\left[(1-\beta^s_3)\,\tilde{d}^n_{hor} + (1-\beta^s_8)\,\delta_\zeta Z^n_{hor} + (1-\beta^s_4)\,\delta_\zeta Z^n_{vert}\right], \quad (106)$$

$$D^n_{(T)} = \frac{1}{r\cos\phi}\frac{1}{\sqrt{g}}\left[(1-\beta^s_5)\,\tilde{d}^n_{hor} + (1-\beta^s_9)\,\delta_\zeta Z^n_{hor} + (1-\beta^s_6)\,\delta_\zeta Z^n_{vert}\right], \quad (107)$$

$$D^n_{(uv)} = \frac{1}{r\cos\phi}\frac{1}{\sqrt{g}}\left[(1-\beta^d_1)\,\tilde{d}^n_{hor} + (1-\beta^d_5)\,\delta_\zeta Z^n_{hor} + (1-\beta^d_2)\,\delta_\zeta Z^n_{vert}\right], \quad (108)$$

$$D^n_{(w)} = \frac{1}{r\cos\phi}\frac{1}{\sqrt{g}}\left[(1-\beta^d_3)\,\tilde{d}^n_{hor} + (1-\beta^d_6)\,\delta_\zeta Z^n_{hor} + (1-\beta^d_4)\,\delta_\zeta Z^n_{vert}\right]. \quad (109)$$

Here $\tilde{d}^n_{hor}$ is calculated by eq. (58) and Z^n_{hor} by eq. (60)-(62) (in both cases with u^n and v^n, Z^n_{vert} analogous to eq. (63) with w^n).

6.2 Solution of the tridiagonal equation system

The solution of the tridiagonal equation system is a tedious, but straightforward work. First, one only ends up with a tridiagonal equation system, if the following requirements for the implicit weightings are fulfilled:

$$\beta^{(s)}_1 = 0, \quad \beta^{(s)}_7 = 0, \quad (110)$$

and

$$\beta^{(d)}_1 = 0, \quad \beta^{(d)}_2 = 0, \quad \beta^{(d)}_5 = 0, \quad \beta^{(d)}_7 = 0. \quad (111)$$

This simply means, that the equations for u and v must be solved explicitly, i.e. in a pure forward sense:

$$u^{n+1} = \Delta t\, b^n_{(u)}, \tag{112}$$
$$v^{n+1} = \Delta t\, b^n_{(v)}. \tag{113}$$

This can be done at the beginning of the small time step. As said above, the updated values u^{n+1}, v^{n+1} are already available to formulate the boundary condition for the implicit equation system for w^{n+1}. ? determines optimal values of the remaining off-centering weights by a stability analysis to

$$\beta_3^{(s)} = \beta_5^{(s)} = 1, \quad \beta_2^{(s)} = \beta_4^{(s)} = \beta_6^{(s)} = 0.7, \tag{114}$$
$$\beta_1^{(b)} = \beta_2^{(b)} = \beta_3^{(b)} = \beta_4^{(b)} = 0.7, \tag{115}$$
$$\beta_3^{(d)} = \beta_4^{(d)} = 1.0. \tag{116}$$

Further we use for the metric correction terms $\beta_8^{(s)} = \beta_4^{(s)}$, $\beta_9^{(s)} = \beta_6^{(s)}$, and $\beta_6^{(d)} = \beta_4^{(d)}$.

Finally the equation system can be formulated as a linear system of equations for w

$$A_{k-\frac{1}{2}} w_{k-\frac{3}{2}} + B_{k-\frac{1}{2}} w_{k-\frac{1}{2}} + C_{k-\frac{1}{2}} w_{k+\frac{1}{2}} = rhs_{k-\frac{1}{2}} \tag{117}$$

(A, B, C, rhs and w are further defined at (i, j)) with the coefficients

$$\begin{aligned}
A_{k-\frac{1}{2}} = \; & -a_{wp1\,|\,k-\frac{1}{2}} \cdot a_{pw1\,|\,k-1} \cdot r_c \\
& +a_{wp1\,|\,k-\frac{1}{2}} \cdot a_{pw2\,|\,k-1} \cdot \frac{1}{2} \\
& +a_{wp2\,|\,k-\frac{1}{2}} \cdot (1-g_{k-\frac{1}{2}}) \cdot a_{pw1\,|\,k-1} \cdot r_c \\
& -a_{wp2\,|\,k-\frac{1}{2}} \cdot (1-g_{k-\frac{1}{2}}) \cdot a_{pw2\,|\,k-1} \cdot \frac{1}{2} \\
& +a_{wT\,|\,k-\frac{1}{2}} \cdot (1-g_{k-\frac{1}{2}}) \cdot a_{Tw1\,|\,k-1} \cdot r_c \\
& -a_{wT\,|\,k-\frac{1}{2}} \cdot (1-g_{k-\frac{1}{2}}) \cdot a_{Tw2\,|\,k-1} \cdot \frac{1}{2} \\
& +\frac{1}{\Delta t}\, a_{ww1\,|\,k-\frac{1}{2}} \cdot a_{ww2\,|\,k-1} \cdot r_c
\end{aligned}$$

$$\begin{aligned}
B_{k-\frac{1}{2}} = \; & +a_{wp1\,|\,k-\frac{1}{2}} \cdot \left[a_{pw1\,|\,k} + a_{pw1\,|\,k-1}\right] \cdot r_c \\
& -a_{wp1\,|\,k-\frac{1}{2}} \cdot \left[a_{pw2\,|\,k} - a_{pw2\,|\,k-1}\right] \cdot \frac{1}{2} \\
& -a_{wp2\,|\,k-\frac{1}{2}} \cdot \left[-g_{k-\frac{1}{2}} \cdot a_{pw1\,|\,k} + (1-g_{k-\frac{1}{2}}) \cdot a_{pw1\,|\,k-1}\right] \cdot r_c \\
& -a_{wp2\,|\,k-\frac{1}{2}} \cdot \left[+g_{k-\frac{1}{2}} \cdot a_{pw2\,|\,k} + (1-g_{k-\frac{1}{2}}) \cdot a_{pw2\,|\,k-1}\right] \cdot \frac{1}{2} \\
& -a_{wT\,|\,k-\frac{1}{2}} \cdot \left[-g_{k-\frac{1}{2}} \cdot a_{Tw1\,|\,k} + (1-g_{k-\frac{1}{2}}) \cdot a_{Tw1\,|\,k-1}\right] \cdot r_c \\
& -a_{wT\,|\,k-\frac{1}{2}} \cdot \left[+g_{k-\frac{1}{2}} \cdot a_{Tw2\,|\,k} + (1-g_{k-\frac{1}{2}}) \cdot a_{Tw2\,|\,k-1}\right] \cdot \frac{1}{2} \\
& -\frac{1}{\Delta t}\, a_{ww1\,|\,k-\frac{1}{2}} \cdot \left[a_{ww2\,|\,k} + a_{ww2\,|\,k-1}\right] \cdot r_c \\
& +\frac{1}{\Delta t^2}
\end{aligned}$$

$$
\begin{aligned}
C_{k-\frac{1}{2}} \;=\; & -a_{wp1\,|\,k-\frac{1}{2}} \cdot a_{pw1\,|\,k} \cdot r_c \\
& -a_{wp1\,|\,k-\frac{1}{2}} \cdot a_{pw2\,|\,k} \cdot \frac{1}{2} \\
& -a_{wp2\,|\,k-\frac{1}{2}} \cdot g_{k-\frac{1}{2}} \cdot a_{pw1\,|\,k} \cdot r_c \\
& -a_{wp2\,|\,k-\frac{1}{2}} \cdot g_{k-\frac{1}{2}} \cdot a_{pw2\,|\,k} \cdot \frac{1}{2} \\
& -a_{wT\,|\,k-\frac{1}{2}} \cdot g_{k-\frac{1}{2}} \cdot a_{Tw1\,|\,k} \cdot r_c \\
& -a_{wT\,|\,k-\frac{1}{2}} \cdot g_{k-\frac{1}{2}} \cdot a_{Tw2\,|\,k} \cdot \frac{1}{2} \\
& +\frac{1}{\Delta t}\, a_{ww1\,|\,k-\frac{1}{2}} \cdot a_{ww2\,|\,k} \cdot r_c
\end{aligned}
$$

using the denotations

$$
a_{wp1} := \overline{\left(\frac{1}{\rho}\right)}^{\zeta,N} \overline{\frac{\partial\zeta}{\partial z}}^{\zeta,N} \beta_2^s, \qquad a_{wp2} := g\,\beta_2^b \overline{\left(\frac{1}{p}\right)}^{\zeta,N}, \tag{118}
$$

$$
a_{ww1} := \overline{\left(\frac{1}{\rho}\right)}^{\zeta,N} \overline{\frac{\partial\zeta}{\partial z}}^{\zeta,N}, \qquad a_{ww2} := \alpha_{div}^v\,\rho\,\frac{1}{r\cos\phi}\,\frac{1}{\sqrt{g}}\,\beta_4^d, \tag{119}
$$

$$
a_{wT} := -g\,\overline{\left(\frac{p_0}{p}\right)}^{\zeta,N} \overline{\left(\frac{1}{T_0}\right)}^{\zeta,N} \beta_1^b, \tag{120}
$$

$$
a_{pw1} := -\frac{c_p}{c_v}\,p\,\frac{1}{r\cos\phi}\,\frac{1}{\sqrt{g}}\,\beta_4^s, \qquad a_{pw2} := -\beta_3^b g\rho_0, \tag{121}
$$

$$
a_{Tw1} := -\frac{R}{c_v}\,T\,\frac{1}{r\cos\phi}\,\frac{1}{\sqrt{g}}\,\beta_6^s, \qquad a_{Tw2} := \beta_4^b \frac{\partial T_0}{\partial z}, \tag{122}
$$

and

$$
r_c := \overline{r\,\cos\phi}^{\zeta}. \tag{123}
$$

In a_{pw1}, a_{Tw1}, and a_{ww2} one can cancel $r\cos\phi$ terms by the shallow atmosphere approximation and may set $r_c = 1$. (By efficiency reasons the averaging factor $1/2$ is defined into a_{pw2} and a_{Tw2} in the program code.)

The right hand side of eq. (117) reads

$$
\begin{aligned}
rhs \;:=\; & -\mathbf{A}_{wp} \underbrace{\left[b_p^{(n)} - (\mathbf{A}_{pu}u^{n+1} + \mathbf{A}_{pv}v^{n+1})\right]}_{=:b_{4,p}} \\
& -\mathbf{A}_{wT}\left[b_T^{(n)} - (\mathbf{A}_{Tu}u^{n+1} + \mathbf{A}_{Tv}v^{n+1})\right] \\
& +\frac{1}{\Delta t}\left[b_w^{(n)} - (\mathbf{A}_{wu}u^{n+1} + \mathbf{A}_{wv}v^{n+1})\right].
\end{aligned} \tag{124}
$$

We express some of the needed terms more explicitly by

$$
\mathbf{A}_{pu}u^{n+1} + \mathbf{A}_{pv}v^{n+1} = \frac{c_p}{c_v}\,p\,\frac{1}{r\cos\phi}\,\frac{1}{\sqrt{g}}\left[\beta_3^s\,\tilde{d}_{hor}^{n+1} + \beta_8^s\,\delta_\zeta Z_{hor}^{n+1}\right], \tag{125}
$$

$$
\mathbf{A}_{Tu}u^{n+1} + \mathbf{A}_{Tv}v^{n+1} = \frac{R}{c_v}\,T\,\frac{1}{r\cos\phi}\,\frac{1}{\sqrt{g}}\left[\beta_5^s\,\tilde{d}_{hor}^{n+1} + \beta_9^s\,\delta_\zeta Z_{hor}^{n+1}\right], \tag{126}
$$

$$
\mathbf{A}_{wu}u^{n+1} + \mathbf{A}_{wv}v^{n+1} = -\overline{\left(\frac{1}{\rho}\right)}^{\zeta,N} \overline{\frac{\partial\zeta}{\partial z}}^{\zeta,N} \delta_\zeta^N \left[\frac{\alpha_{div}^v\,\rho}{r\cos\phi}\,\frac{1}{\sqrt{g}}\left(\beta_3^d\,\tilde{d}_{hor}^{n+1} + \beta_6^d\,\delta_\zeta Z_{hor}^{n+1}\right)\right] \tag{127}
$$

where $\tilde{d}_{hor}^{n+1}$ is calculated via (58) and Z_{hor}^{n+1} via (60) (both with u^{n+1} and v^{n+1}).

The explicit solution for p'^{n+1} reads

$$p'^{n+1} = \Delta t \left(b_{4,p} - \mathbf{A}_{pw} w^{n+1} \right) \tag{128}$$

(this can be calculated without any further boundary conditions/treatments).

The explicit equation for T'^{n+1} directly follows from eq. (55) using p'^{n+1} from eq. (128).

7 Stability of the divergence damping in tilted terrain

Though the divergence damping is in general necessary to stabilize the whole split-explicit time integration scheme, it can itself become unstable. Beyond the stability limitation $\alpha_{div}\Delta t/\Delta x^2 \leq 1/2$ (?), there is an additional constraint in tilted terrain.

To derive this constraint, one can start from the following 2D equations for the quasi-2D-divergence damping alone in terrain following coordinates

$$\frac{\partial u}{\partial t} = \alpha_{div}^h \left(\frac{\partial D}{\partial x} + \frac{\partial \zeta}{\partial x}\frac{\partial D}{\partial \zeta} \right), \tag{129}$$

$$\frac{\partial v}{\partial t} = \alpha_{div}^h \left(\frac{\partial D}{\partial y} + \frac{\partial \zeta}{\partial y}\frac{\partial D}{\partial \zeta} \right), \tag{130}$$

$$\frac{\partial w}{\partial t} = 0, \tag{131}$$

$$D = \frac{\partial u}{\partial x} + \frac{\partial \zeta}{\partial x}\frac{\partial u}{\partial \zeta} + \frac{\partial v}{\partial y} + \frac{\partial \zeta}{\partial y}\frac{\partial v}{\partial \zeta} + \frac{\partial \zeta}{\partial z}\frac{\partial w}{\partial \zeta}. \tag{132}$$

For an explicit discretization of these equations analogous to (51), a von-Neumann stability analysis is relatively straightforward and results in the sufficient condition

$$\alpha_{div}^h \, \Delta t \left\{ \frac{1}{\Delta x^2} \left(2 + \frac{\Delta x}{\Delta \zeta} \left| \frac{\partial \zeta}{\partial x} \right| \right)^2 + \frac{1}{\Delta y^2} \left(2 + \frac{\Delta y}{\Delta \zeta} \left| \frac{\partial \zeta}{\partial y} \right| \right)^2 \right\} \leq 2. \tag{133}$$

This can be reformulated by prescribing $\frac{\partial z}{\partial x}$ (at constant ζ). Due to the relations similar to (7) and (8) and the estimation $\Delta\zeta \approx \frac{\partial \zeta}{\partial z}\,\Delta z$, this can be written as

$$\alpha_{div}^h \, \Delta t \left\{ \frac{1}{\Delta x^2} \left(2 + \frac{\Delta x}{\Delta z} \left| \frac{\partial z}{\partial x} \right| \right)^2 + \frac{1}{\Delta y^2} \left(2 + \frac{\Delta y}{\Delta z} \left| \frac{\partial z}{\partial y} \right| \right)^2 \right\} \leq 2. \tag{134}$$

This is a quite general stability condition not only for the divergence damping but for explicit discretizations of the diffusion equation in general. Because $\Delta h := \frac{\partial z}{\partial x}\,\Delta x$ is just the height jump along a ζ-coordinate line, the expression

$$\frac{\Delta h}{\Delta z} \equiv \frac{\Delta x}{\Delta z}\frac{\partial z}{\partial x} \tag{135}$$

describes the ratio between the height change Δh of a coordinate plane over one grid mesh size Δx and the vertical thickness Δz of the grid box.

Near the ground, where small $\Delta z \sim 20$ m are common, the ratio $\Delta h/\Delta z$ can be quite large even for rather gentle slopes. Therefore, in steep terrain the dimensionless value $xkd := \alpha_{div}/(c_s^2 \Delta t)$ must be chosen much smaller than the recommended value of 0.1 by ? or even as the recommendation of 0.3 by ?. It is interesting that $\Delta h/\Delta z$ often achieves higher values for coarser resolutions, where the jumps from one grid box to another are larger than for

finer resolutions. Hence, the steeper slopes occurring in fine scale model applications are not the limiting factor in this case.

The good news is that in practice, the limitation (134) must not be strictly fulfilled. One reason is, that the forward-backward scheme of the fast waves solver rather adds the tendencies of sound, buoyancy and divergence damping instead of doing an operator splitting. Therefore, in the COSMO code a namelist variable `divdamp_slope` was introduced to weaken up the condition (134). The true value of α_{div}^h is determined by

$$\alpha_{div}^h = \min\left(\texttt{xkd} \cdot c_s^2\,\Delta t,\ \texttt{divdamp_slope} \cdot \alpha_{div,slope}\right),$$

where `xkd` is the namelist variable for divergence damping, and $\alpha_{div,slope}$ is the value determined by (134). Consequently, the divergence damping coefficient never exceeds the value given by `xkd`.

8 Discretization errors in a stretched grid

8.1 General analysis procedure

Now, in a certain sense we go back to section 4.1 and answer the question, why the vertical weighting is advantageous and why the chosen operators are to favor compared to other choices. To this purpose, a truncation error analysis is carried out. But first, we have to consider the following question: how can we determine the convergence order or the truncation error for discretizations on a *stretched* grid?

Hence, we consider a (vertical) interval $[0, L]$ which is discretized by $N+1$ grid points

$$z_{\frac{1}{2}}^{(h)} = L, \quad z_{1+\frac{1}{2}}^{(h)}, \quad \ldots, \quad z_{N-\frac{1}{2}}^{(h)}, \quad z_{N+\frac{1}{2}}^{(h)} = 0. \tag{136}$$

In COSMO the position of the half levels is prescribed, therefore we write half indices and add an upper index (h). The grid mesh size in a grid box is $\Delta z_k := z_{k-\frac{1}{2}}^{(h)} - z_{k+\frac{1}{2}}^{(h)}$, $k = 1, .., N$.

In contrast to an equidistant grid there exist arbitrary many different possibilities to perform a grid refinement. In the following, two variants of grid refinements are analyzed, that lead to different orders of the truncation error.

8.1.1 Discretization error analysis - variant A

In this first variant, the grid stretching is described by a *coordinate transformation* $z(\zeta)$. The transformed coordinate ζ generates an equidistant grid:

$$\zeta_{k+\frac{1}{2}} = \left(k + \frac{1}{2}\right) \cdot \Delta\zeta, \quad k = 0, \ldots, N. \tag{137}$$

With increasing grid refinement $\Delta\zeta \to 0$ all the grid mesh sizes $\Delta z_k \approx \left.\frac{\partial z}{\partial \zeta}\right|_{k+\frac{1}{2}} \cdot \Delta\zeta$ converge to 0, too. Hence, the convergence inspection takes place for $\Delta\zeta \to 0$.

With decreasing $\Delta\zeta$ the stretching function *locally* becomes increasingly linear. Consequently, with this approach to refine the grid one gets formally 2nd order truncation errors for all two-point discretizations.

In the following analysis one has to distinguish carefully between main and half levels; otherwise a restriction to 2-dimensional fields in (λ, z) is sufficient. The grid is horizontally defined by

$$\lambda_i = i \cdot \Delta\lambda \tag{138}$$

with $i = 0, 1, 2, \ldots$ (for scalar- or w-positions) or $i = 1/2, 3/2, 5/2, \ldots$ (for u-position), and vertically by the z-coordinates of the half levels

$$z^{(h)}_{i,k+\frac{1}{2}} = z\left(\lambda_i, \zeta_{k+\frac{1}{2}}\right) \tag{139}$$

(with the above mentioned stretching function) and the main levels

$$z^{(m)}_{i,k} = \frac{z^{(h)}_{i,k+\frac{1}{2}} + z^{(h)}_{i,k-\frac{1}{2}}}{2}. \tag{140}$$

Hence, the w-positions are in $(\lambda_i, z^{(h)}_{i,k+\frac{1}{2}})$, the scalars T, p are in $(\lambda_i, z^{(m)}_{i,k})$, and so on. In the following truncation error analysis these coordinates have to be inserted into the discretizations according to the grid positions of the variables. Then a Taylor expansion for $\Delta\lambda \to 0$ and $\Delta\zeta \to 0$ *around the position of the target point* (which itself can be a function of $\Delta\lambda$ and $\Delta\zeta$, too) must be carried out.

8.1.2 Discretization error analysis - variant B

To avoid the circumstance, that for increasing resolution $\Delta z_k \to 0$ the grid stretching becomes *locally* more and more linear, one can prescribe a constant grid stretching

$$\frac{\Delta z_k}{\Delta z_{k-1}} = s$$

instead. Without any loss of generality we can assume that $s > 1$, i.e. the grid becomes finer in the vicinity of $z^{(h)}_0 = 0$.

To this purpose we choose the grid points in

$$\begin{aligned}
z^{(h)}_{i,-1-\frac{1}{2}} &= h(\lambda_i) - \frac{1}{2}\Delta\zeta - \frac{1}{s}\Delta\zeta, \\
z^{(h)}_{i,-\frac{1}{2}} &= h(\lambda_i) - \frac{1}{2}\Delta\zeta, \\
z^{(h)}_{i,\frac{1}{2}} &= h(\lambda_i) + \frac{1}{2}\Delta\zeta, \\
z^{(h)}_{i,1+\frac{1}{2}} &= h(\lambda_i) + \frac{1}{2}\Delta\zeta + s\Delta\zeta,
\end{aligned} \tag{141}$$

Here the prescription of a slope by $h(x)$ is possible. The flattening of coordinate surfaces with increasing height is neglected. The position of the main levels again is defined by Eq. (140). The Taylor expansion is performed in analogy to variant A.

One has to note, that such a grid refinement does not converge *globally*! For the grid mesh size it follows by the geometric summation formula

$$\Delta z_k = \Delta z_1 \cdot s^{k-1} = \frac{L}{\sum_{l=0}^{N-1} s^l} \cdot s^{k-1} = \frac{L}{\frac{s^N-1}{s-1}} \cdot s^{k-1}. \tag{142}$$

In particular for the coarsest grid mesh size it follows

$$\Delta z_N = L\frac{s-1}{s-s^{1-N}} \overset{N\to\infty}{\to} L\frac{s-1}{s} \neq 0!$$

By this kind of grid refinement one inserts smaller and smaller grid boxes only on one end of the interval (at $z = 0$), without a significant refinement at the other end (at $z = L$) for the coarse grid boxes. This, of cause, is a bit odd situation for this variant of grid refinement.

8.2 Horizontal pressure gradient term in the u-equation

We inspect the discretization of the horizontal pressure gradient

$$\frac{\partial p(\lambda, z)}{\partial \lambda} = \frac{\partial p(\lambda, \zeta)}{\partial \lambda} + \frac{\partial \zeta}{\partial \lambda}\frac{\partial p}{\partial \zeta} = \frac{\partial p(\lambda, \zeta)}{\partial \lambda} - \frac{\partial z}{\partial \lambda}\frac{\partial p}{\partial z}.$$

Discretization error analysis - variant A

1. The discretization with weighted vertical interpolation delivers

$$\begin{aligned}\delta_\lambda p - \left(A_\zeta \frac{\partial z}{\partial \lambda}\right)\left(A_\lambda\left(\frac{\partial \zeta}{\partial z}\delta_\zeta A_\zeta^N p\right)\right) = \left.\frac{\partial p}{\partial \lambda}\right|_z + \\ + d\zeta^2\left[-\frac{1}{6}\frac{\partial z}{\partial \lambda}\left(\frac{\partial z}{\partial \zeta}\right)^2\frac{\partial^3 p}{\partial z^3} - \frac{1}{4}\frac{\partial z}{\partial \lambda}\frac{\partial^2 z}{\partial \zeta^2}\frac{\partial^2 p}{\partial z^2}\right] + \\ + d\lambda^2[\ldots] + d\zeta\, d\lambda \cdot 0 + O(d\zeta^4, d\zeta^2 d\lambda^2, d\lambda^4). \qquad (143)\end{aligned}$$

   The discretization operators are defined in section 4.1. For the 2nd order term $\sim \Delta\zeta^2$ one has either a contribution from the curvature of $p(z)$ (first term) or a stretching (=curvature) in the grid $z(\zeta)$ (second term).

2. The same discretization, but without weighted averages delivers

$$\begin{aligned}\delta_\lambda p - \left(A_\zeta \frac{\partial z}{\partial \lambda}\right)\left(A_\lambda\left(\frac{\partial \zeta}{\partial z}\delta_\zeta A_\zeta p\right)\right) = \left.\frac{\partial p}{\partial \lambda}\right|_z + \\ + d\zeta^2\left[-\frac{1}{6}\frac{\partial z}{\partial \lambda}\left(\frac{\partial z}{\partial \zeta}\right)^2\frac{\partial^3 p}{\partial z^3} - \frac{1}{2}\frac{\partial z}{\partial \lambda}\frac{\partial^2 z}{\partial \zeta^2}\frac{\partial^2 p}{\partial z^2}\right] + \\ + d\lambda^2[\ldots] + d\zeta\, d\lambda \cdot 0 + O(d\zeta^4, d\zeta^2 d\lambda^2, d\lambda^4). \qquad (144)\end{aligned}$$

   In the term $\sim \Delta\zeta^2$ the second term has a twice as large prefactor compared to the discretization above. The prefactor of the term $\sim d\lambda^2$ is the same as above, as expected.

3. One can think about a lot of other discretizations for the horizontal pressure gradient, for example with

$$\begin{aligned}\delta_\lambda p - \left(A_\lambda \frac{\partial \zeta}{\partial z}\right)\left(A_\zeta\left(\frac{\partial z}{\partial \lambda}A_\lambda \delta_\zeta p\right)\right) = \left.\frac{\partial p}{\partial \lambda}\right|_z + \\ + d\zeta^2\left[-\frac{1}{6}\frac{\partial z}{\partial \lambda}\left(\frac{\partial z}{\partial \zeta}\right)^2\frac{\partial^3 p}{\partial z^3} - \frac{1}{2}\frac{\partial z}{\partial \lambda}\frac{\partial^2 z}{\partial \zeta^2}\frac{\partial^2 p}{\partial z^2} - \frac{1}{4}\frac{\partial z}{\partial \zeta}\frac{\partial^2 z}{\partial \lambda \partial \zeta}\frac{\partial^2 p}{\partial z^2}\right. \\ \left. - \frac{1}{4}\frac{\frac{\partial^2 z}{\partial \lambda \partial \zeta}\frac{\partial^2 z}{\partial \zeta^2}}{\frac{\partial z}{\partial \zeta}}\frac{\partial p}{\partial z} - \frac{1}{4}\frac{\frac{\partial^3 z}{\partial \zeta^3}\frac{\partial z}{\partial \lambda}}{\frac{\partial z}{\partial \zeta}}\frac{\partial p}{\partial z}\right] + \\ + d\lambda^2[\ldots] + d\zeta\, d\lambda \cdot 0 + O(d\zeta^4, d\zeta^2 d\lambda^2, d\lambda^4). \qquad (145)\end{aligned}$$

   Obviously this is discretization generates larger errors.

4. The Mahrer (1984)-discretization can only be inspected for gentle slopes. In this case it follows

$$\frac{\partial p}{\partial \lambda} = \left.\frac{\partial p}{\partial \lambda}\right|_z + d\zeta^2 \left[-\frac{1}{24}\frac{\partial z}{\partial \lambda}\left(\frac{\partial z}{\partial \zeta}\right)^2 \frac{\partial^3 p}{\partial z^3}\right] + \\ + d\zeta\, d\lambda \left[\frac{1}{16}\frac{\partial^2 z}{\partial \lambda^2}\frac{\partial z}{\partial \zeta}\frac{\partial^2 p}{\partial z^2} + \ldots\right] + d\lambda^2 [\ldots] + \ldots \quad (146)$$

Though the term $\sim d\zeta^2$ is much smaller than in the above discretizations, another second order term arises which is proportional to $d\zeta\, d\lambda$. This could explain the slightly worse discretization properties in the vertical.

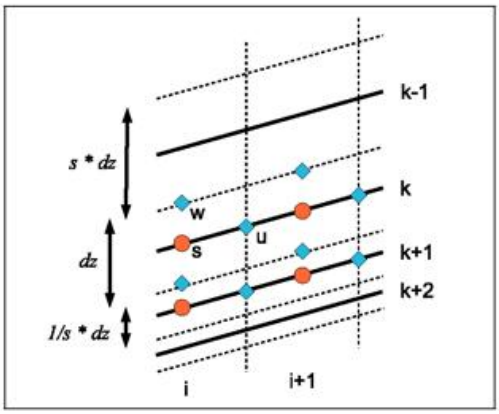


Figure 2: Grid positions and stretching in the 'discretization error analysis - variant B' for the horizontal pressure gradient $\partial p/\partial \lambda$.

Discretization error analysis - variant B

1. The discretization with weighted vertical interpolation delivers

$$\delta_\lambda p - \left(A_\zeta \frac{\partial z}{\partial \lambda}\right)\left(A_\lambda\left(\frac{\partial \zeta}{\partial z}\delta_\zeta A_\zeta^N p\right)\right) = \left.\frac{\partial p}{\partial \lambda}\right|_z + \\ + dz\left[\frac{1}{8}\frac{\partial h}{\partial \lambda}\left(\frac{1}{s} - s\right)\frac{\partial^2 p}{\partial z^2}\right] + \\ + d\lambda^2 [\ldots] + dz^2 [..] + O(dz^3, d\lambda^2\, dz, \ldots) \quad (147)$$

Now the leading truncation error is indeed of *first order* in dz.

2. The same discretization but without weighted averaging

$$\delta_\lambda p - \left(A_\zeta \frac{\partial z}{\partial \lambda}\right)\left(A_\lambda\left(\frac{\partial \zeta}{\partial z}\delta_\zeta A_\zeta p\right)\right) = \left.\frac{\partial p}{\partial \lambda}\right|_z + \\ + dz\left[\frac{1}{4}\frac{\partial h}{\partial \lambda}\left(\frac{1}{s} - s\right)\frac{\partial^2 p}{\partial z^2}\right] + \\ + d\lambda^2 [\ldots] + dz^2 [..] + \ldots \quad (148)$$

Again the truncation error structure is the same as above but now the prefactor is twice as large.

3. The inappropriate discretization from above delivers

$$\delta_\lambda p - \left(A_\lambda \frac{\partial \zeta}{\partial z}\right)\left(A_\zeta\left(\frac{\partial z}{\partial \lambda} A_\lambda \delta_\zeta p\right)\right) = \left.\frac{\partial p}{\partial \lambda}\right|_z + \frac{\partial p}{\partial \zeta}\frac{\partial h}{\partial \lambda}\left(\frac{1}{2} - \frac{1}{4}\left(\frac{1}{s} + s\right)\right) + \\ + dz\,[...] + d\lambda^2\,[...] + dz^2\,[..] + ... \tag{149}$$

   For $s \neq 1$ this don't even is a consistent discretization!

4. For the Mahrer (1984) discretization one gets:

$$\begin{aligned} \frac{\partial p}{\partial \lambda} &= \left.\frac{\partial p}{\partial \lambda}\right|_z + \\ &+ dz^2\left[-\frac{1}{24}\frac{\partial h}{\partial \lambda}\frac{\partial^3 p}{\partial z^3}\right] + \\ &+ d\lambda dz\,[...] + d\lambda^2\,[...] + dz^2\,[..] + ... \end{aligned} \tag{150}$$

   The interesting result is, that no terms $\sim dz$ or $\sim dz\ d\lambda$ occur. So it is indeed a second order discretization!

Summarizing the results, it is clear, that the discretization with vertical weightings (option 1) is the best one. Further one can see, that discretizations with slightly wider stencils (option 3) in general lead to worse truncation errors. For the Mahrer discretization, the decision is a bit more difficult. Whereas in analysis variant A there occurs a mixed second order term, which is probably detrimental, in analysis variant B this is the only discretization which is really of second order.

8.3 Buoyancy term in the w-equation

Terms of the form T'/T_0 (or $p'/p0$) occuring in the buoyancy term of the w-equation.

Discretization error analysis - variant A

1. The discretization in the new fast waves solver uses weighted vertical interpolations for T' and calculates T_0 exactly at the w-position.

$$\frac{1}{T_0} A_\zeta^N T' = \frac{T'}{T_0} + d\zeta^2 \frac{1}{T_0}\left[\frac{1}{8}\left(\frac{\partial z}{\partial \zeta}\right)^2 \frac{\partial^2 T'}{\partial z^2}\right] + O(d\zeta^4). \tag{151}$$

2. use no weighting for the vertical averaging and calculate T_0 exactly at the w-position

$$\frac{1}{T_0} A_\zeta T' = \frac{T'}{T_0} + d\zeta^2 \frac{1}{T_0}\left[\frac{1}{8}\left(\frac{\partial z}{\partial \zeta}\right)^2 \frac{\partial^2 T'}{\partial z^2} + \frac{1}{4}\frac{\partial^2 z}{\partial \zeta^2}\frac{\partial T'}{\partial z}\right] + O(d\zeta^4). \tag{152}$$

   Compared to the above truncation error an additional term occurs, which stems from the curvature of the coordinate transformation. Therefore the weighted average is the better discretization.

3. use weighted averages both for T_0 and T':

$$\frac{1}{A_\zeta^N T_0} A_\zeta^N T' = \frac{T'}{T_0} + d\zeta^2 \frac{1}{T_0}\left[\frac{1}{8}\left(\frac{\partial z}{\partial \zeta}\right)^2 \frac{\partial^2 T'}{\partial z^2} - \frac{1}{8}\frac{1}{T_0}\frac{\partial^2 T_0}{\partial z^2}\left(\frac{\partial z}{\partial \zeta}\right)^2 T'\right] + O(d\zeta^4) \tag{153}$$

As expected, an additional term occurs when the reference state temperature exhibits a curvature. Since no statement about the sign of this term can be made, it is in general better to have no such term at all, i.e. the direct calculation of T_0 at this position is the better solution here.

4. Previous version without weighted averages

$$A_\zeta^N \left(\frac{T'}{T_0}\right) = \frac{T'}{T_0} + d\zeta^2 \frac{1}{T_0}\left[\frac{1}{8}\left(\frac{\partial z}{\partial \zeta}\right)^2 \frac{\partial^2 T'}{\partial z^2} + \ldots\right] + O(d\zeta^4). \tag{154}$$

There arise several additional terms compared to the first version above.

Discretization error analysis - variant B Instead of (141) we use the following z-positions of the grid

$$\begin{aligned} z^{(h)}_{i,-1-\frac{1}{2}} &:= h(\lambda) - 2\frac{1}{s+1}dz, \\ z^{(h)}_{i,-\frac{1}{2}} &:= h(\lambda), \\ z^{(h)}_{i,+\frac{1}{2}} &:= h(\lambda) + 2\frac{s}{s+1}dz, \end{aligned} \tag{155}$$

with the (dimensionless) stretching factor s; this simply leads to more symmetric formula in s if applied to the w equation terms.

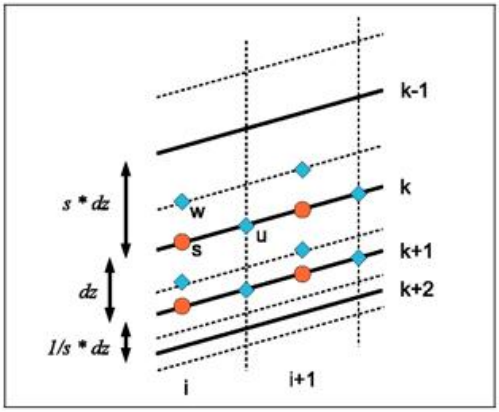


Figure 3: Grid positions and stretching in the 'discretization error analysis - variant B' for the buoyancy term in the w-equation.

1. use weighted vertical interpolations for T' and calculates T_0 exactly at the w-position

$$\frac{1}{T_0} A_\zeta^N T' = \frac{T'}{T_0} + dz \cdot 0 + dz^2 \left[\frac{1}{2}\frac{s}{(s+1)^2}\frac{1}{T_0}\frac{\partial^2 T'}{\partial z^2}\right] + O(dz^3). \tag{156}$$

Through the weighting this discretization is indeed of 2nd order in dz.

2. use no weighting for the vertical averaging and calculate T_0 exactly at the w-position

$$\frac{1}{T_0} A_\zeta T' = \frac{T'}{T_0} + dz\left[\frac{1}{2}\frac{s-1}{s+1}\frac{1}{T_0}\frac{\partial T'}{\partial z}\right] + dz^2\left[\frac{1}{4}\frac{s^2+1}{(s+1)^2}\frac{1}{T_0}\frac{\partial^2 T'}{\partial z^2}\right] + O(dz^3) \tag{157}$$

This is only of first order for all $s \neq 1$..

3. use weighted averages both for T_0 and T'

$$\frac{1}{A_\zeta^N T_0} A_\zeta^N T' = \frac{T'}{T_0} + dz^2 \frac{1}{2} \frac{s}{(s+1)^2} \left[\frac{1}{T_0} \frac{\partial^2 T'}{\partial z^2} - \frac{1}{T_0^2} \frac{\partial^2 T_0}{\partial z^2} T' \right] + O(dz^3). \quad (158)$$

   There arise additional terms.

4. Old version:

$$A_\zeta^N \left(\frac{T'}{T_0} \right) = \frac{T'}{T_0} + dz^2 \frac{1}{T_0} \left[\frac{1}{2} \frac{\partial^2 T'}{\partial z^2} \frac{s}{(s+1)^2} + \ldots \right] + O(dz^3). \quad (159)$$

   There arise additional terms.

As in the section before, both analysis variants qualitatively deliver the same picture: the use of vertical weightings delivers discretizations with the smallest errors. In particular for variant B, there is a difference between a true second order discretization (option 1 with weightings) and an only first order discretization (option 2, without weightings). Further, the use of the exact values of the reference atmosphere is favorable.

8.4 The divergence term

$$\operatorname{div} \mathbf{v} = \frac{1}{g} \left[\frac{\partial g u(x,\zeta)}{\partial x} + \frac{\partial}{\partial \zeta} \left(\frac{\partial z}{\partial x} u - w \right) \right] \quad (160)$$

Discretization error analysis - variant A

1. $\frac{\partial Z_x}{\partial \zeta}$ is discretized by a weighted vertical average

$$\begin{aligned} \operatorname{div} \mathbf{v} = \frac{\partial u(x,z)}{\partial x} + \frac{\partial w(x,z)}{\partial z} + d\zeta^2 \Bigg(& -\frac{1}{4} \frac{\partial^2 z}{\partial x \partial \zeta} \frac{\partial z}{\partial \zeta} \frac{\partial^2 u}{\partial z^2} - \frac{1}{4} \frac{\partial^2 z}{\partial \zeta^2} \frac{\partial z}{\partial x} \frac{\partial^2 u}{\partial z^2} \\ & - \frac{1}{6} \left(\frac{\partial z}{\partial \zeta} \right)^2 \frac{\partial z}{\partial x} \frac{\partial^3 u}{\partial z^3} + \frac{1}{24} \left(\frac{\partial z}{\partial \zeta} \right)^2 \frac{\partial^3 w}{\partial z^3} \Bigg) + dx^2 () + \ldots \end{aligned} \quad (161)$$

2. $\frac{\partial Z_x}{\partial \zeta}$ is averaged without weights:

$$\begin{aligned} \operatorname{div} \mathbf{v} = \frac{\partial u(x,z)}{\partial x} + \frac{\partial w(x,z)}{\partial z} + d\zeta^2 \Bigg(& -\frac{1}{4} \frac{\partial^2 z}{\partial x \partial \zeta} \frac{\partial z}{\partial \zeta} \frac{\partial^2 u}{\partial z^2} - \frac{1}{2} \frac{\partial^2 z}{\partial \zeta^2} \frac{\partial z}{\partial x} \frac{\partial^2 u}{\partial z^2} \\ & - \frac{1}{6} \left(\frac{\partial z}{\partial \zeta} \right)^2 \frac{\partial z}{\partial x} \frac{\partial^3 u}{\partial z^3} + \frac{1}{24} \left(\frac{\partial z}{\partial \zeta} \right)^2 \frac{\partial^3 w}{\partial z^3} \\ & - \frac{1}{4} \frac{\partial \zeta}{\partial z} \frac{\partial^2 z}{\partial x \partial \zeta} \frac{\partial^2 z}{\partial \zeta^2} \frac{\partial u}{\partial z} - \frac{1}{4} \frac{\partial \zeta}{\partial z} \frac{\partial^3 z}{\partial \zeta^3} \frac{\partial z}{\partial x} \frac{\partial u}{\partial z} \Bigg) + dx^2 () + \ldots \end{aligned} \quad (162)$$

   One of the terms has a twice as large prefactor and two additional terms occur.

Discretization error analysis - variant B

1. $\frac{\partial Z_x}{\partial \zeta}$ is discretized by a weighted vertical average

$$\operatorname{div} \mathbf{v} = \frac{\partial u(x,z)}{\partial x} + \frac{\partial w(x,z)}{\partial z} + dz \left(\frac{1}{8} \frac{\partial h}{\partial x} \frac{\partial^2 u}{\partial \zeta^2} \left(\frac{1}{s} - s \right) \right) + O(dz^2, dx^2) \quad (163)$$

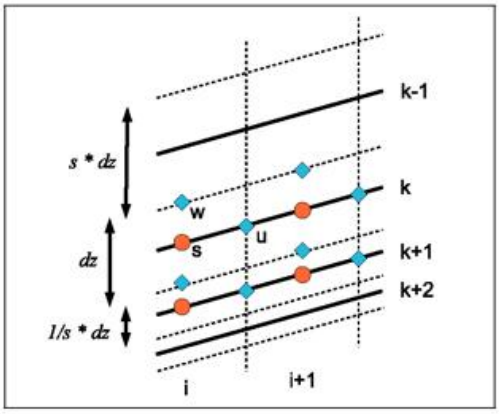


Figure 4: Grid positions and stretching in the 'discretization error analysis - variant B' for the divergence term in the scalar p'- or T'-equations.

2. $\frac{\partial Z_x}{\partial \zeta}$ is discretized without weightings

$$\begin{aligned} \operatorname{div} \mathbf{v} &= \frac{\partial u(x,z)}{\partial x} + \frac{\partial h}{\partial x}\frac{\partial u(x,z)}{\partial z}\left(\frac{1}{2} - \frac{1}{4}\left(s + \frac{1}{s}\right)\right) + \frac{\partial w(x,z)}{\partial z} + \\ &+ dz\left(\frac{1}{8}\frac{\partial h}{\partial x}\frac{\partial^2 u}{\partial \zeta^2}\left(\left(\frac{1}{s} - s\right) + \frac{1}{2}\left(\frac{1}{s^2} - s^2\right)\right)\right) + O(dz^2, dx^2) \end{aligned} \tag{164}$$

For a stretched grid ($s \neq 1$) this is not a consistent discretization at all!

9 Idealized tests

In this section, the properties of the new fast waves solver are inspected using several idealized test setups. All the following simulations are performed with COSMO version 4.26.2 (concerning the dynamics this is similar to the more official version 4.27). If not otherwise stated, the switches for the new fast waves solver are `itype_fast_waves=2`, `ldyn_bbc=.FALSE.`, and `itype_bbc_w=114`. These settings will be denoted as 'FW2' in the following. The namelist values for the simulations with the old fast waves solver are `1`, `.TRUE.`, and `2`, respectively. The old fast waves solver settings are denoted by 'FW1'.

9.1 Linear gravity and sound wave expansion

In ? (in the following abbreviated by BB13) an exact analytic solution for the expansion of linear gravity and sound waves for the compressible, non-hydrostatic Euler equations in an isothermal atmosphere was derived. This test case inspects almost all terms of the fast waves solver (with the exception of the 'horizontal' metric terms) together with the time integration scheme and the coupling with the advection process.

In the following simulations, the same setup as proposed for the small-scale test in BB13 is used. A weak warm bubble is set into a 10 km high and 300 km wide channel with periodic boundary conditions in the horizontal. The only difference is the definition of the grid. To demonstrate the benefit of the vertical weightings in the new fast waves solver a vertical grid stretching is introduced, with a grid stretching ratio of 1:10 between the finest vertical mesh size around $z = 5$ km and the coarsest mesh size around $z = 0$ and $z = 10$ km. Figures 5 show the grid for the first three chosen (horizontal) resolutions $\Delta x = 1000$ m, 500 m,

and 250 m with 300×20, 600×40, and 1200×80 grid points, respectively, and the initial temperature perturbation T' of the weak warm bubble at $t = 0$. The time steps for these simulations are 20 s, 10 s, and 5 s, respectively, and analogous for the finer resolutions. During the expansion of the waves a background velocity field with $u_0 = 20$ m/s advects the waves to the right. Figure 6 shows the solution for T' and w of FW2 after 30 min. together with the analytic solution.

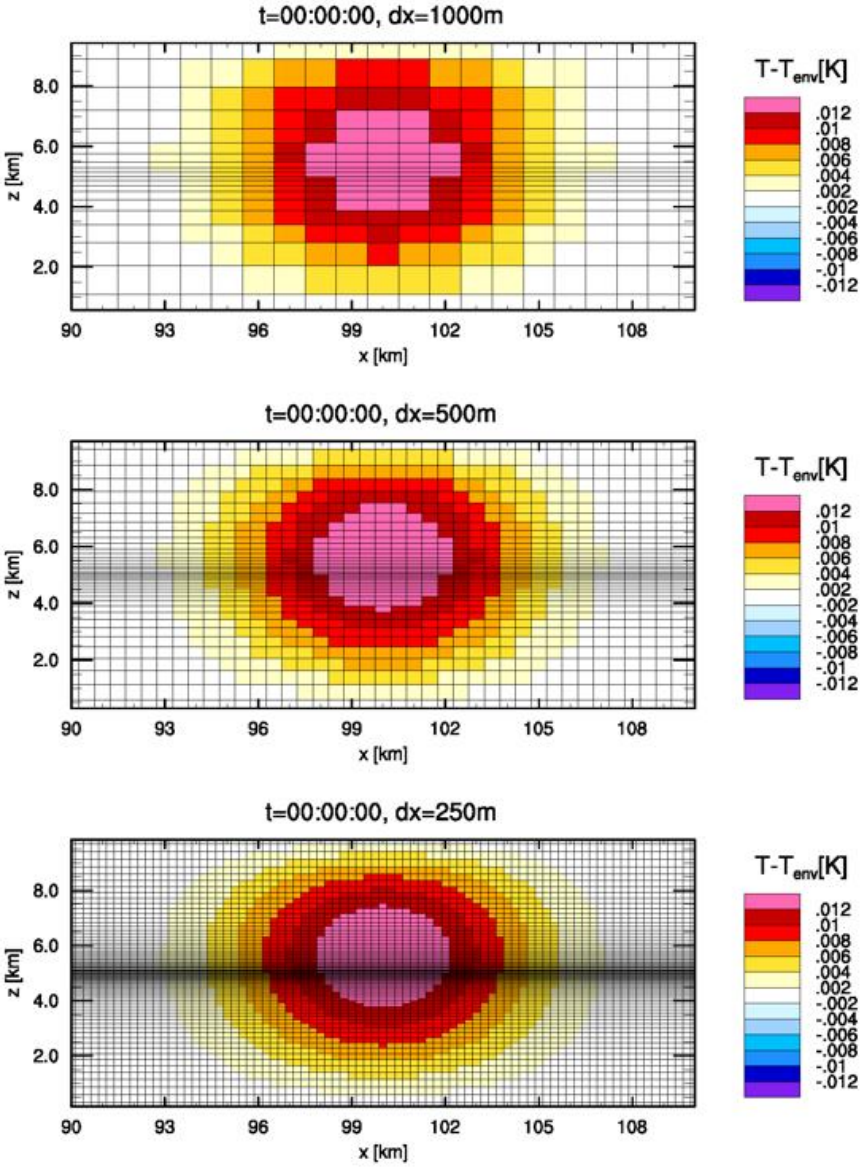


Figure 5: Grid and initial temperature perturbation $T'(t = 0)$ for the first three resolutions $\Delta x = 1000$ m, 500 m, and 250 m for the linear gravity/sound wave test.

The following results are obtained by COSMO 4.26.2 (with the additional implementation of the grid stretching in `src_artifdata.f90`). Figures 7 and 8 show the error norms of the simulated solution against the analytic solution after 30 min. The error norms

$$L_m(\psi) = \left(\frac{1}{N_x N_z} \sum_{i=1}^{N_x} \sum_{k=1}^{N_z} |\psi(x_i, z_k) - \psi_{\text{lin}}(x_i, z_k)|^m \right)^{1/m}, \quad m = 1, 2, \infty \tag{165}$$

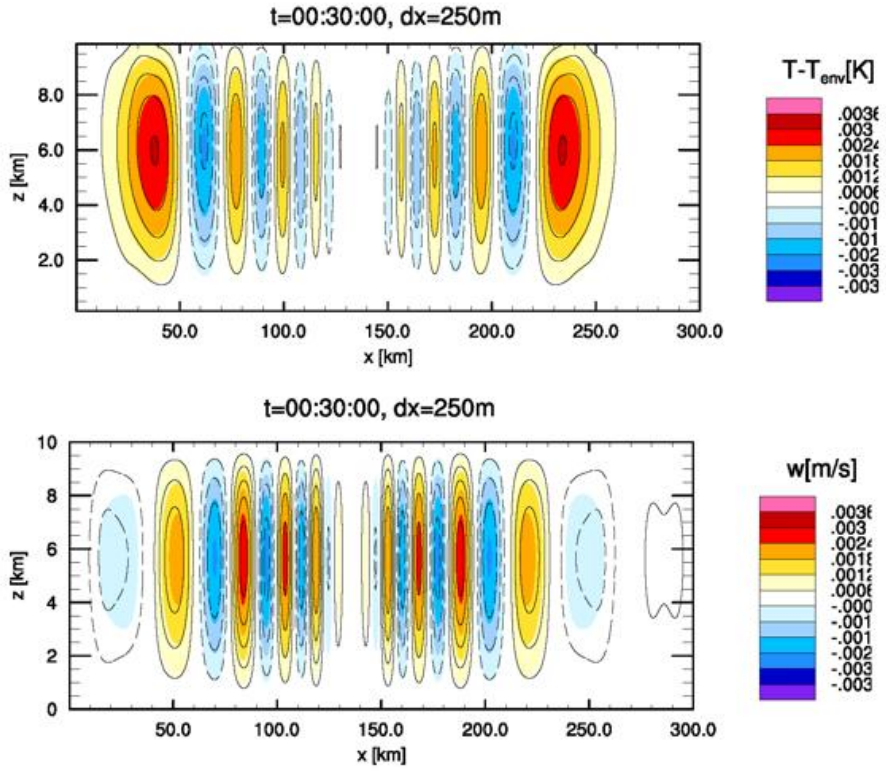


Figure 6: Temperature perturbation T' and vertical velocity w after 30 min. for $\Delta x = 250$ m horizontal resolution. Comparison between FW2-simulation (shaded) and analytic solution (lines).

for any field $\psi(x, z, t)$ are calculated as described in BB13 for the COSMO model; in particular the L_∞ norm is the usual maximum norm. In all cases, the errors of the new fast waves solver (FW2) are smaller compared to those of the old one (FW1). For the coarsest resolution the error of FW1 is nearly twice as large compared to FW2. One should notice that the more gentle slope for FW2 does not mean a smaller convergence rate. As one can see from the curvature of the lines, the simulation for the coarser resolutions is not yet in the convergence range. In contrast, these error norms show that the errors for not completely resolved structures are better with the vertical weightings in the new FW2. For very fine resolutions, at least for the L_∞-error of w, the error norms of FW1 and FW2 are nearly the same and result in a convergence rate of about 0.7 for T' and slightly higher for w. The reason for this behavior is, that for an increasing number of vertical grid points, the local grid stretching becomes increasingly linear. This can be seen in figures 5, too. Consequently, the importance of the weightings in the averages decreases.

9.2 2D linear flow over a series of hills

To test the proper inclusion of metric terms, 2-dimensional flow over a couple of hills is inspected. The test setup is chosen as in (?, section 5.b), but with a reduced mountain height of $h_{max} = 1$ m. This test combines hydrostatic and non-hydrostatic features of flow over mountains. An analytic solution for linear flow over hills for exactly the compressible, non-hydrostatic Euler equation system used in the COSMO model and in particular for this test setup is given in ?.

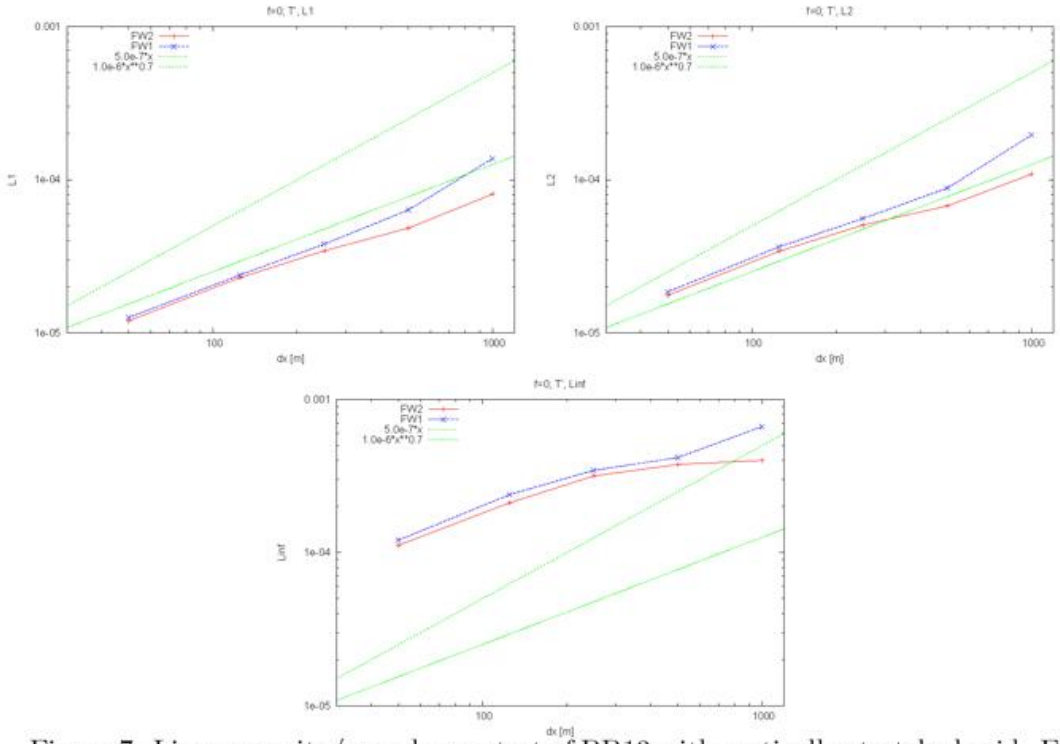


Figure 7: Linear gravity/sound wave test of BB13 with vertically stretched grid. Error norms of T' for the new fast waves solver (FW2, red) and the old one (FW1, blue) for different resolutions.

The vertical grid is stretched by a quadratic stretching function, i.e

$$z_k^{(h)} = H_{top} \cdot (\beta\eta^2 + (1-\beta)\eta), \qquad \eta = 1 - \frac{k-1}{ke}, \qquad k = 1, 2, \ldots, ke+1. \tag{166}$$

$(1+\beta)/(1-\beta)$ is roughly the ratio $\Delta z_{top}/\Delta z_{bottom}$. We choose $H_{top} = 25$ km and $\beta = 0.95$ and the following two resolutions:
1.) $\Delta x = 1000$ m and $ke = 50$ vertical levels,
2.) $\Delta x = 500$ m and $ke = 100$ vertical levels.
The tables 1 give an impression about the resulting vertical levels. All physical parameterizations, in particular the turbulence scheme, are switched off. Otherwise boundary layer effects would prevent from a correct comparison with the analytic solution.

The comparison for these two resolutions with the analytic solution is quite good (see figure 9). Both the hydrostatic pattern (higher above the hills) and the non-hydrostatic pattern (in the vicinity of the hills) is well represented by the simulation. The convergence to the correct solution can be seen also in the error measures between the simulations for the two different resolutions and the analytic solution (table 2). The integration area for the determination of the errors is chosen as far as possible away from the boundaries, therefore it was chosen horizontally in the range $[80, 120]$ km and vertically approximately in the range $[0.5, 7]$ km. The errors for the new fast waves solver are smaller compared to the old one. Again, as for the linear wave expansion in the section before, the differences become smaller, when the local grid stretching ratio becomes smaller. It is interesting, that the version with the isotropic 3D divergence damping is even better than with the quasi-3D version.

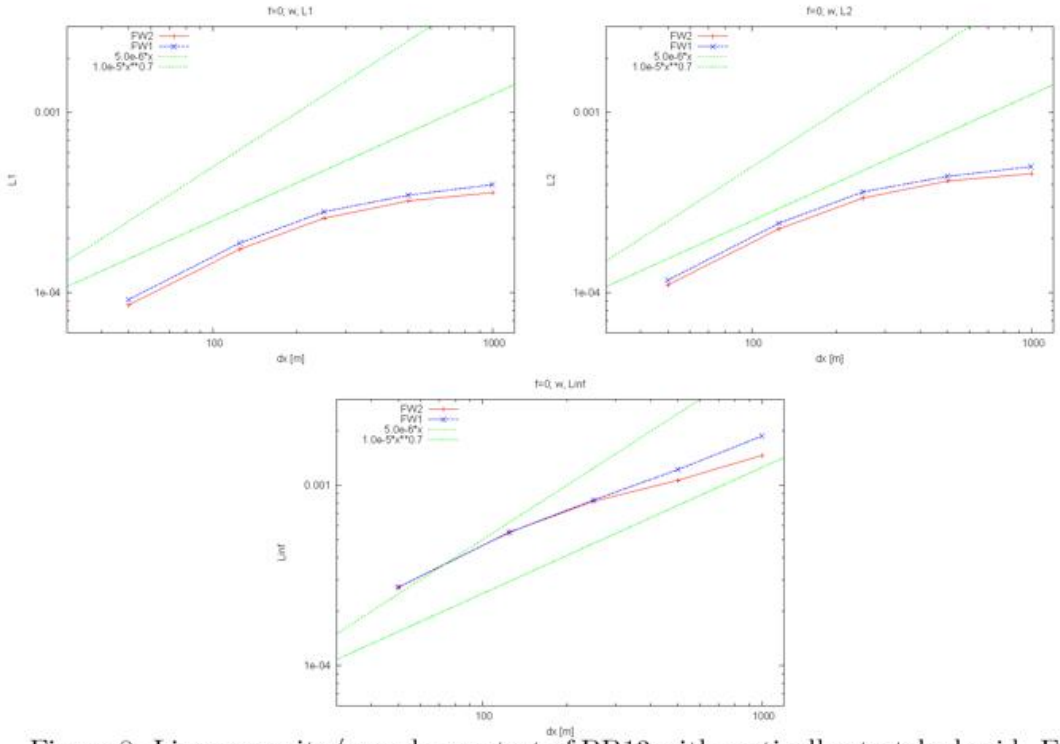


Figure 8: Linear gravity/sound wave test of BB13 with vertically stretched grid. Error norms of w for different resolutions.

9.3 3D linear flow over a hill

An analogous 3D test uses a single mountain with a rotational symmetric Gaussian shape

$$h(x) = h_{max} \cdot 2^{-\frac{x^2+y^2}{a^2}} \tag{167}$$

and a half width of $2a = 10000$ m. The hill is located exactly in the center of the simulation domain at the position $(100, 100)$ km.

Again the turbulence scheme and other parameterizations are switched off. The vertical stretching is done as in section 9.4. The inflow velocity is $u_0 = 20$ m/s, the atmospheric stratification $N = 0.01$ 1/s. The horizontal resolution is $\Delta x = \Delta y = 500$ m and a time step $\Delta t = 5$ s has been chosen.

Figure 10 shows horizontal cross sections of w after 24h simulation time. In this 3D test case the error norms of FW2 and FW1 (again against the analytic solution of ?) are almost the same, with an improvement of only about one percent for FW2.

9.4 2D flow over steep mountains

To inspect the ability to stably simulate flow over steep mountains, a single 2D mountain (i.e. a mountain ridge) with a Gaussian shape

$$h(x) = h_{max} \cdot 2^{-\left(\frac{x}{a}\right)^2} \tag{168}$$

and a half width of $2a = 6000$ m is used. A constant inflow velocity of $u_0 = 20$ m/s and a dry atmosphere with a stable stratification $N = 0.01$ 1/s are prescribed. In the following different values for the height h_{max} are tested.

k	VCOORD(k)
1	25000.0000
2	24034.5000
3	23088.0000
4	22160.5000
...	
45	492.0000
46	362.5000
47	252.0000
48	160.5000
49	88.0000
50	34.5000
51	0.0000

k	VCOORD(k)
1	25000.0000
2	24514.8750
3	24034.5000
4	23558.8750
...	
95	160.5000
96	121.8750
97	88.0000
98	58.8750
99	34.5000
100	14.8750
101	0.0000

Table 1: vertical levels for the 2D linear flow over hills generated by eq. (166) for $ke = 50$ (left) and $ke = 100$ (right).

Δx	FW	$L_1 \cdot 10^{-5}$	$L_2 \cdot 10^{-5}$	$L_\infty \cdot 10^{-5}$
1000	FW1	4.377	7.749	34.88
1000	FW2	3.357	5.898	26.91
1000	FW2, 3D div.damp.	3.007	5.183	28.92
500	FW1	2.112	3.191	15.23
500	FW2	1.940	2.890	12.89
500	FW2, 3D div.damp.	1.273	1.780	7.56

Table 2: 2D linear flow over flat mountains. Error measures for two different resolutions in a stretched grid.

The horizontal grid mesh size of the 2-dimensional simulations is $\Delta x = 1000$ m. Therefore a time step $\Delta t = 10$ s has been chosen. The vertical grid is stretched again by the quadratic stretching function (166). Here we choose $H_{top} = 25$ km, $ke = 65$, and $\beta = 0.95$, leading to $\Delta z_{bottom} = 24.9$ m and $\Delta z_{top} = 745$ m, which are quite realistic values for model applications. The simulations run with a turbulence scheme switched on, to prevent from unphysically strong wave breaking.

The simulation with FW1 remains stable until $h_{max} = 2100$ m, but becomes unstable for $h_{max} = 2200$ m. This latter mountain height corresponds to a maximum slope angle $\alpha \approx 27°$ and a maximum step size of the orography $\max_i |h_i - h_{i+1}| \approx 500$ m. The instability develops in the bottom grid boxes, where high vertical velocities occur (Fig. 11).

In contrast, the simulation with the new fast waves solver FW2 remains stable until $h_{max} = 3100$ m. This corresponds to a maximum slope angle $\alpha \approx 35°$ and a maximum step size of the orography $\max_i |h_i - h_{i+1}| \approx 710$ m (left panel in Fig. 12). The same height can be achieved both for the quasi-3D and for the full 3D-divergence damping.

Of course, one cannot expect a large increase in stability over steeper mountains, because the main time integration scheme is the same in the new and the old fast waves solver. In particular the treatment of the metric correction terms is nearly the same. But nevertheless, the better discretization of vertical operations seems to help a bit in stability.

The same simulation with Mahrer discretization (see section 4.2.2) allows even much higher mountains until $h_{max} = 4800$ m. This corresponds to a maximum slope angle $\alpha \approx 47°$ and

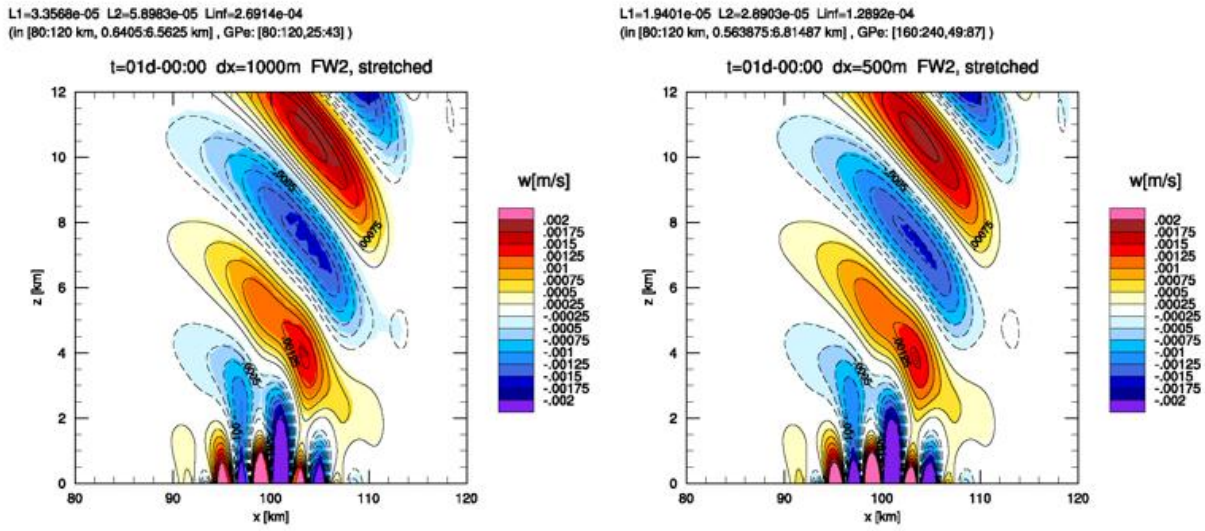


Figure 9: Linear flow over mountains (Schaer et al. 2002-setup) with vertical grid stretching by FW2. Vertical velocity w for $\Delta x = 1000$ m (left column) and $\Delta x = 500$ m (right column).

a maximum step size of the orography $\max_i |h_i - h_{i+1}| \approx 1100$ m (right panel in Fig. 12).

9.5 3D flow over steep mountains

To inspect stability over 3D steep mountains we use again a rotational symmetric Gaussian hill

$$h(x) = h_{max} \cdot 2^{-\frac{x^2+y^2}{a^2}} \tag{169}$$

with a half width of $2a = 6000$ m.

The horizontal resolution is $\Delta x = \Delta y = 1000$ m. Other model settings (vertical grid, time step, parameterizations, ...) are as in the section 9.4 before.

The simulation with FW1 is stable until a hill height of 1900 m (and becomes unstable for 2000 m). In contrast, the simulation with FW2 is stable until a hill height of 3000 m (and becomes unstable for 3100 m). Again much steeper slopes can be simulated with FW2 and the Mahrer discretization, here hill heights until 4600 m can be achieved (becomes unstable for 4700 m).

Compared to the values for the flow over 2D mountain ridges, all these maximum heights are a bit reduced for the 3D case. This indicates that more complex flows tend to reduce the maximum allowable slopes and orography steps.

9.6 Convective warm bubble test

The warm bubble test by ? is a standard test case to investigate the model behavior in strong convective situations.

An elliptic shaped 3D warm bubble with horizontal radius of $x_d = y_d = 10000$ m, a vertical radius of $z_d = 1400$ m and a maximum temperature increment of 2 K is set into a prescribed moist atmosphere (see figure 13). The atmosphere has a prescribed velocity profile with no velocity at the bottom and an increasing velocity with height until $u_{max} = 30$ m/s (this value is used here).

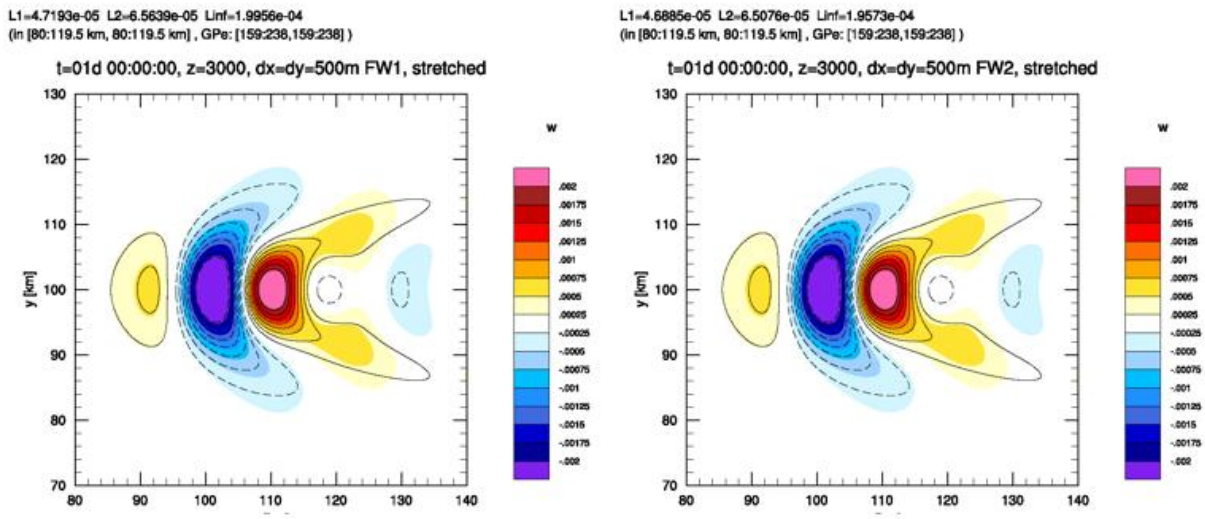


Figure 10: Vertical velocity w for linear Flow over a 3D Gaussian shaped mountain with height 1 m. Vertical velocity w simulated with the old (left) and new (right) fast waves solver (FW2) after 24 h. Cross section in $z = 3000$ m. Shaded: COSMO simulation, black lines: analytic solution

The COSMO setup has been chosen as close as possible to WK82; exceptions are a higher horizontal resolution of $\Delta x = \Delta y = 1000$ m, a time step of $\Delta t = 10$ sec., and the use of the 6-class graupel microphysics scheme (i.e. the prognostic variables q_v, q_c, q_i, q_r, q_s, q_g are used). The vertical grid points are prescribed again by (166) with $ke = 65$, $H_{top} = 22$ km, and $\beta = 0.95$. Figure 14 shows the specific mass concentrations after 30 min. and 1 h simulation time for three different model setups. The runs with FW1 generates higher maximum values of graupel and rain compared to the runs with FW2, whereas FW2 produces higher maxima of cloud ice and snow.

Figure 15 shows the time development of the maximum vertical velocity. The first cumulonimbus cloud with maximum updrafts develops after about 30 min. This structure then dissipates and generates new clouds later on. Generally these values are in a realistic range, nevertheless they are a bit higher than those of ?. But one should notice, that their simulations have been done with $\Delta x = \Delta y = 2000$ m, probably leading to more diffusion compared to the higher resolution used here. FW2 produces slightly higher values of $w_{max}(t)$ than FW1, in particular for later times.

The simulations with FW2 have been performed with 2 setups: one with the standard quasi-3D divergence damping (i.e. $\alpha^v_{div} = 0$) and one with the full 3D divergence damping (i.e. $\alpha^v_{div} = \alpha^h_{div}$). The differences between these two versions are quite small. Therefore the slightly unphysical modification of the dispersion relation for gravity waves by the quasi-3D divergence damping mentioned in ? seems to be not too strong in this case.

An interesting aspect in connection with divergence damping is the treatment of the first small time step. For the quasi-3D version it is absolutely necessary for real case simulations to perform *no* divergence damping in the first step; otherwise instabilities occur. These are obviously induced by complex terrain, because they haven't been neither seen in the stability analysis without orography (?) nor do they occur in idealized tests with simple orographies. In contrast to this, simulations with the full 3D divergence are independent from the treatment of the first small time step: they run stable, both if it is applied in the first step or not. [5]. In this respect, the full 3D divergence damping is also more satisfying

[5]To force the application of divergence damping also in the first small time step, one has to set the *internal*

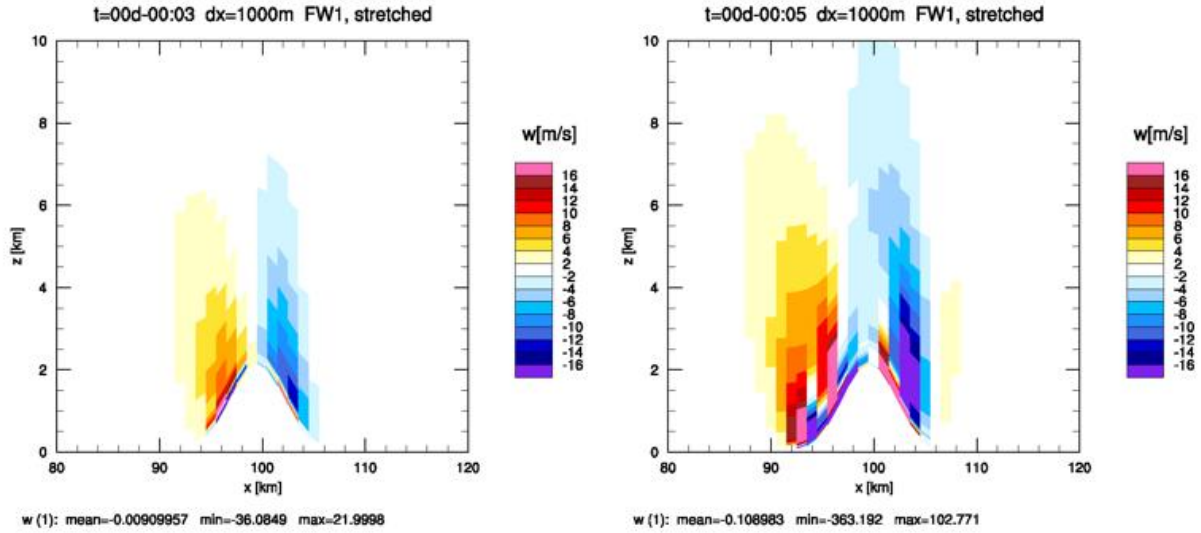


Figure 11: Flow over a 2D Gaussian shaped mountain with height 2200m. Vertical velocity w simulated with FW1 after 3 and 5 minutes. The run crashed only a few time steps later.

from a theoretical viewpoint than the quasi 3D version (the better dispersion properties of the full 3D version have been mentioned already in the introduction 2).

10 Real cases

The predominant feature of the new fast waves solver is its higher stability property. This has been demonstrated in the idealized tests in sections 9.4 and 9.5. There have been numerous examples of real case simulations which have been stabilized by using FW2. To list some of them:

The operational deterministic COSMO-DE and several COSMO-DE-EPS ensemble runs at '28.06.2011, 6 UTC' crashed by a shear instability after about 16 hours simulation time. Although this should be cured by a Smagorinsky diffusion, the runs with the new FW2 remained stable.

Another problem occurs, if the velocity fields near the ground become too noisy. This happened for the operational COSMO-DE run at '12.07.2011, 6 UTC', where q_r 'exploded' in the Alps. This could be cured by the more stable version of the tracer advection scheme, namely with the Strang-splitting variant of the Bott advection scheme. Otherwise, without this measure, the runs with the new FW2 remained stable, too.

Other examples were several experimental COSMO-DE runs with 65 levels which crashed during the summer 2012 period. (e.g. the '15.07.2011, 12 UTC' run crashed after only 215 time steps (i.e. after about 1.5 h)) FW2 experiments didn't show any crash during July and August 2012.

O. Fuhrer reported an operational COSMO-2 '16.06.2011, 0 UTC' run model crash after 1190 time steps (6.6 h). A. Seifert reported a model crash of an experimental COSMO-1 (resolution 0.01° (about 1.1km), 1700 * 1700 grid points) at the '24.08.2011 after only 10 time steps. Again these two runs have been stably simulated by FW2.

switch `l_no_div_damping_in_1st_step=.FALSE.` in module `fast_waves_sc`.
Attention: the runs with the 3D divergence damping *and* `l_no_div_damping_in_1st_step=.TRUE.` do *not work* in COSMO 4.27 due to a bug in the code. This will probably be fixed in version 4.28.

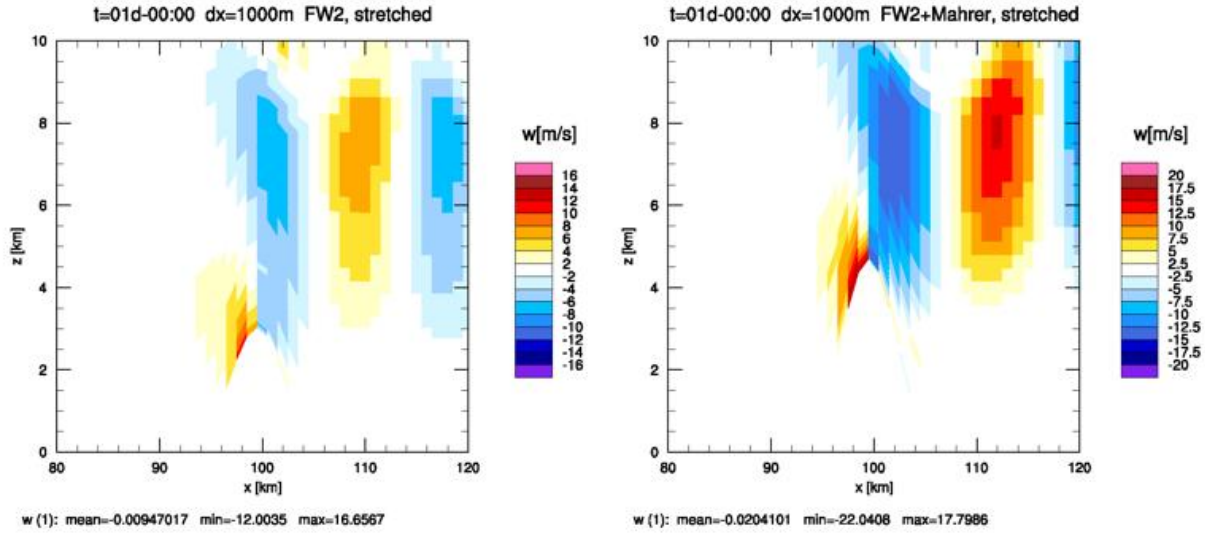


Figure 12: Flow over a 2D Gaussian shaped mountain. Vertical velocity w simulated with the new fast waves solver (FW2) after 24 h. Left: with conventional pressure discretization and a mountain height $h_{max} = 3100$ m. Right: with Mahrer (1984)-discretization and $h_{max} = 4800$ m.

Though a slightly higher accuracy of FW2 compared to FW1 has been shown in the idealized tests, the verification results for several periods at DWD didn't show larger deviations between these two versions. In particular during the winter period 2012/2013 there occured slight improvements in the pressure bias but a slight negative behavior in the cloud coverage. Nevertheless, the higher stability of the new fast waves solver led to the decision to introduce it both in COSMO-DE (2.8 km) and COSMO-EU (7 km) at 16 January 2013 after a 5 month testing period at DWD.

One should notice, that for a proper interpolation form driving initial and boundary data, the interpolation program INT2LM (since version 1.20) must use the same reference state as COSMO for the *half levels*, too. Therefore, the namelist switch `lanalyt_calc_T0p0` must be set to `.TRUE.` if `itype_fast_waves=2` is used (to be precise: this is only necessary, if the older reference atmosphere `irefatm=1` is used). The same holds for possible postprocessing programs, e.g. the `lmstat` feedback file generator.

11 Conclusions

The development of a new fast waves solver for the COSMO model has been described in this report. This new development is available since COSMO version 4.24 and should be used together with the interpolation program INT2LM since version 1.20. The slightly better accuracy properties and in particular the better stability properties in steeper terrain has been demonstrated. In the end, the new fast waves solver was introduced operationally at DWD for both model setups 2.8 km COSMO-DE (deterministic and ensemble mode) and 7 km COSMO-EU at 16 January 2013.

On the NEC SX9 (DWD) the new fast waves solver needs about 30 percent more computation time compared to the old one. This results in an increase of runtime of about 6 percent for the whole COSMO model. A certain increase in runtime is understandable due to the larger number of computations and storage loads by the additional vertical weightings. These values are also quite dependent from the computer architecture. On some Intel based computers

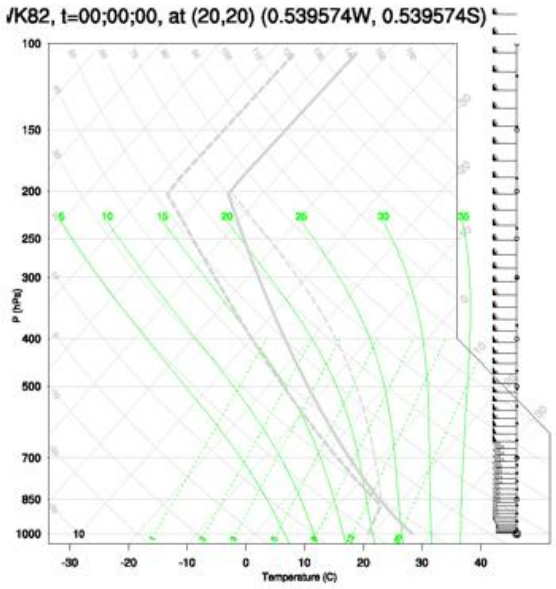


Figure 13: skew T - log p -digram for the environment atmosphere of the Weisman, Klemp (1982) test case.

these run times can be even higher, but a report from our Russian colleagues (running COSMO on an SGI ALTIX, built on Intel(R) Xeon(R) X5560 processors) indicates, that the runtime can even be much smaller with the new FW solver.

Of course, there is still enough work to be done. For example, until now it is not possible to use the exact boundary condition for Z and hence for the divergence, which is a bit unsatisfying. Though the Mahrer discretization (section 4.2.2) has been proven as advantageous in idealized steep mountain tests and as stable in many real case simulations, a detailed verification and assessment is still needed, possibly together with an improvement of the lower boundary treatment. Finally, the isotropic 3D divergence damping offers theoretical advantages and runs stable in several real test cases. Consequently, it should be further investigated. The full 3D divergence damping results in an about 10 percent longer runtime for the fast waves solver, resulting in an about 2 percent longer runtime for the whole COSMO model. Therefore, the question remains, if these additional computational costs justify its usage in operational applications.

The new solver was developed for the Runge-Kutta time integration scheme, which is now used by every NWP center of the COSMO consortium and by the most (if not all) climate runs of the climate CLM community. But in principle, there is no reason, why the new solver shouldn't be used for the 'old' leapfrog time integration scheme, too (a certain harmonization of other discretizations used in the leapfrog scheme and the vertical weightings introduced here is probably needed, before). Hence, there is a certain hope to replace the other fast waves solvers in future by this new development and therefore to reduce complexity and maintenance efforts in the COSMO code.

12 Acknowledgments

The author is grateful to Günther Zängl (Deutscher Wetterdienst), who initiated this project and helped a lot with many discussions about the topic. Many thanks also to Andreas Will

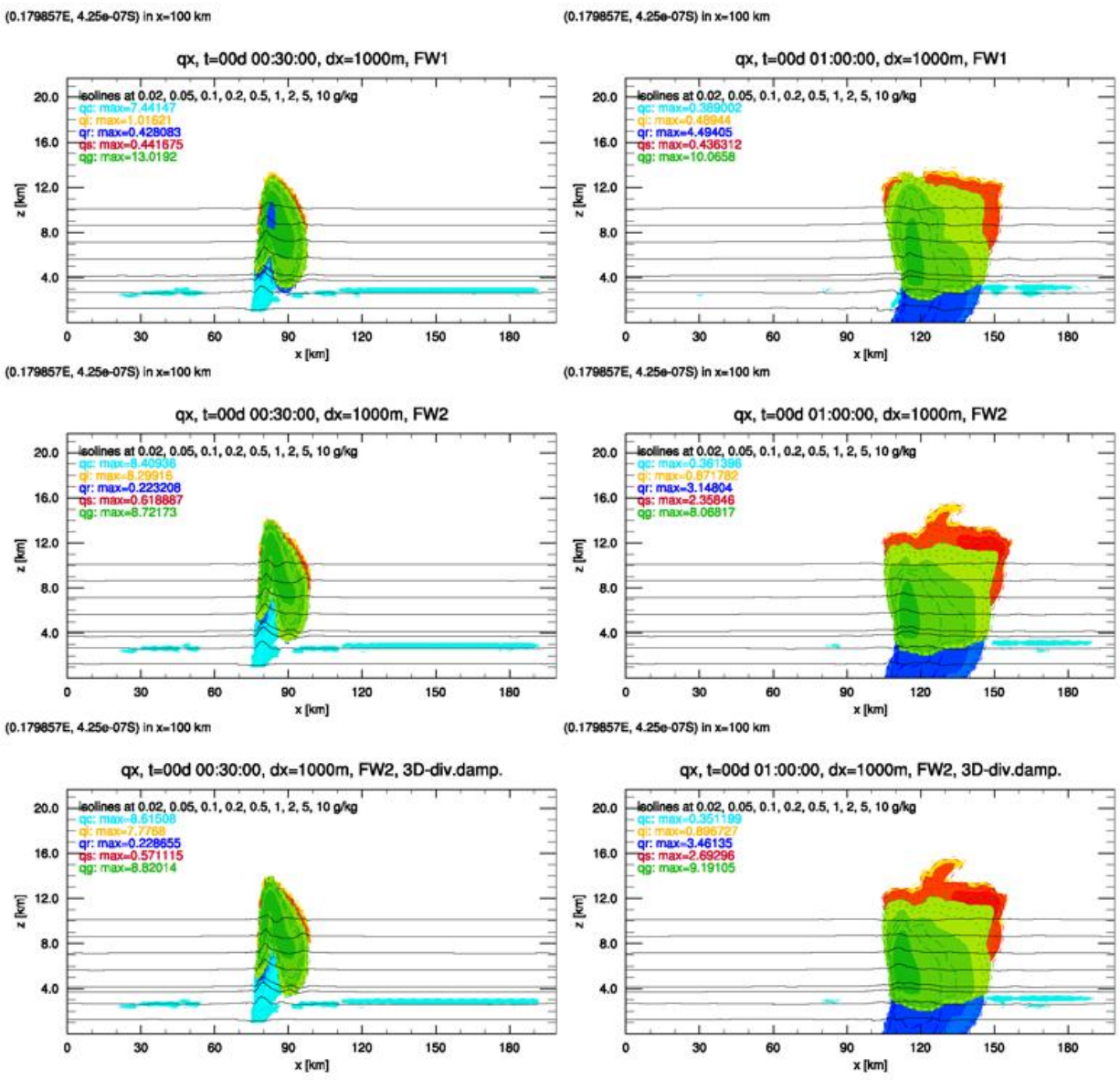


Figure 14: Weisman, Klemp (1982) test case with the 6-class graupel scheme. Specific masses of the microphysical constituents q_r, ... Left: after 30 min., Right: after 1 h. Top row: old FW1, middle row: new FW2, bottom row: new FW2 with 3D-divergence damping. Black lines: isolines of temperature; thick line is 0° C.

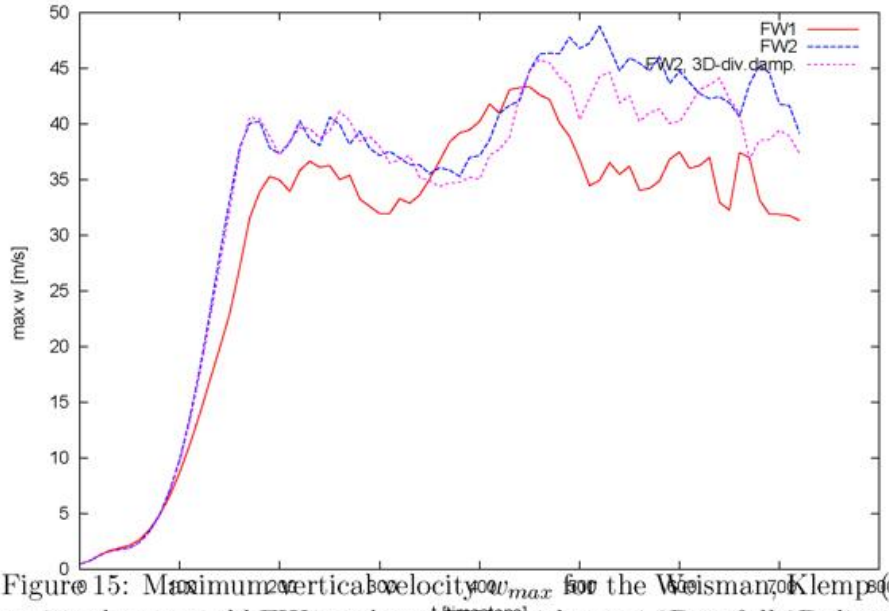


Figure 15: Maximum vertical velocity w_{max} for the Weisman, Klemp (1982) test case. Comparison between old FW1 and new FW2 with quasi-3D or full 3D divergence damping. Time step $\Delta t = 10$ sec.

(University of Cottbus) for many fruitful discussions and valuable hints. Further thanks go to Guy deMorsier and Oliver Fuhrer (MeteoSwiss), who helped a lot in testing the new fast waves solver for the COSMO-1 project. Many thanks also to Ulrich Schättler (Deutscher Wetterdienst), who has given many technical advices about the COSMO code.

List of COSMO Newsletters and Technical Reports

(available for download from the COSMO Website: www.cosmo-model.org)

COSMO Newsletters

No. 1: February 2001.

No. 2: February 2002.

No. 3: February 2003.

No. 4: February 2004.

No. 5: April 2005.

No. 6: July 2006.

No. 7: April 2008; Proceedings from the 8th COSMO General Meeting in Bucharest, 2006.

No. 8: September 2008; Proceedings from the 9th COSMO General Meeting in Athens, 2007.

No. 9: December 2008.

No. 10: March 2010.

No. 11: April 2011.

No. 12: April 2012.

No. 13: April 2013.

COSMO Technical Reports

No. 1: Dmitrii Mironov and Matthias Raschendorfer (2001):
Evaluation of Empirical Parameters of the New LM Surface-Layer Parameterization Scheme. Results from Numerical Experiments Including the Soil Moisture Analysis.

No. 2: Reinhold Schrodin and Erdmann Heise (2001):
The Multi-Layer Version of the DWD Soil Model TERRA_LM.

No. 3: Günther Doms (2001):
A Scheme for Monotonic Numerical Diffusion in the LM.

No. 4: Hans-Joachim Herzog, Ursula Schubert, Gerd Vogel, Adelheid Fiedler and Roswitha Kirchner (2002):
LLM ¯ the High-Resolving Nonhydrostatic Simulation Model in the DWD-Project LITFASS.
Part I: Modelling Technique and Simulation Method.

No. 5: Jean-Marie Bettems (2002):
EUCOS Impact Study Using the Limited-Area Non-Hydrostatic NWP Model in Operational Use at MeteoSwiss.

No. 6: Heinz-Werner Bitzer and Jürgen Steppeler (2004):
Documentation of the Z-Coordinate Dynamical Core of LM.

No. 7: Hans-Joachim Herzog, Almut Gassmann (2005):
Lorenz- and Charney-Phillips vertical grid experimentation using a compressible nonhydrostatic toy-model relevant to the fast-mode part of the 'Lokal-Modell'.

No. 8: Chiara Marsigli, Andrea Montani, Tiziana Paccagnella, Davide Sacchetti, André Walser, Marco Arpagaus, Thomas Schumann (2005):
Evaluation of the Performance of the COSMO-LEPS System.

No. 9: Erdmann Heise, Bodo Ritter, Reinhold Schrodin (2006):
Operational Implementation of the Multilayer Soil Model.

No. 10: M.D. Tsyrulnikov (2007):
Is the particle filtering approach appropriate for meso-scale data assimilation ?

No. 11: Dmitrii V. Mironov (2008):
Parameterization of Lakes in Numerical Weather Prediction. Description of a Lake Model.

No. 12: Adriano Raspanti (2009):
COSMO Priority Project "VERification System Unified Survey" (VERSUS): Final Report.

No. 13: Chiara Marsigli (2009):
COSMO Priority Project "Short Range Ensemble Prediction System" (SREPS): Final Report.

No. 14: Michael Baldauf (2009):
COSMO Priority Project "Further Developments of the Runge-Kutta Time Integration Scheme" (RK): Final Report.

No. 15: Silke Dierer (2009):
COSMO Priority Project "Tackle deficiencies in quantitative precipitation forecast" (QPF): Final Report.

No. 16: Pierre Eckert (2009):
COSMO Priority Project "INTERP": Final Report.

No. 17: D. Leuenberger, M. Stoll and A. Roches (2010):
Description of some convective indices implemented in the COSMO model.

No. 18: Daniel Leuenberger (2010):
Statistical analysis of high-resolution COSMO Ensemble forecasts in view of Data Assimilation.

No. 19: A. Montani, D. Cesari, C. Marsigli, T. Paccagnella (2010):
Seven years of activity in the field of mesoscale ensemble forecasting by the COSMO–LEPS system: main achievements and open challenges.

No. 20: A. Roches, O. Fuhrer (2012):
Tracer module in the COSMO model.

No. 21: M. Baldauf (2013):
A new fast-waves solver for the Runge-Kutta dynamical core.

COSMO Technical Reports

Issues of the COSMO Technical Reports series are published by the *COnsortium for Small-scale MOdelling* at non-regular intervals. COSMO is a European group for numerical weather prediction with participating meteorological services from Germany (DWD, AWGeophys), Greece (HNMS), Italy (USAM, ARPA-SIMC, ARPA Piemonte), Switzerland (MeteoSwiss), Poland (IMGW), Romania (NMA) and Russia (RHM). The general goal is to develop, improve and maintain a non-hydrostatic limited area modelling system to be used for both operational and research applications by the members of COSMO. This system is initially based on the COSMO-Model (previously known as LM) of DWD with its corresponding data assimilation system.

The Technical Reports are intended

- for scientific contributions and a documentation of research activities,
- to present and discuss results obtained from the model system,
- to present and discuss verification results and interpretation methods,
- for a documentation of technical changes to the model system,
- to give an overview of new components of the model system.

The purpose of these reports is to communicate results, changes and progress related to the LM model system relatively fast within the COSMO consortium, and also to inform other NWP groups on our current research activities. In this way the discussion on a specific topic can be stimulated at an early stage. In order to publish a report very soon after the completion of the manuscript, we have decided to omit a thorough reviewing procedure and only a rough check is done by the editors and a third reviewer. We apologize for typographical and other errors or inconsistencies which may still be present.

At present, the Technical Reports are available for download from the COSMO web site (www.cosmo-model.org). If required, the member meteorological centres can produce hard-copies by their own for distribution within their service. All members of the consortium will be informed about new issues by email.

For any comments and questions, please contact the editor:

Massimo Milelli
Massimo.Milelli@arpa.piemonte.it

Consortium

for

Small-Scale Modelling

Technical Report No. 3

A Scheme for Monotonic Numerical Diffusion in the LM

by

G. Doms

November 2001

DOI: 10.5676/DWD_pub/nwv/cosmo-tr_3

Deutscher Wetterdienst

MeteoSwiss

Ufficio Generale per la Meteorologia

Hellenic National Meteorological Service

Amt für Wehrgeophysik

Il Servicio Meteorologico Regionale di ARPA

www.cosmo-model.org

Editors: G. Doms and U. Schättler, Deutscher Wetterdienst, P.O. Box 100465, 63004 Offenbach, Germany
Printed at Deutscher Wetterdienst, Offenbach am Main

A Scheme for Monotonic Numerical Diffusion in the LM

Günther Doms

Deutscher Wetterdienst, Abteilung Meteorologische Analyse und Modellierung,
Frankfurter Str. 135, D-63067 Offenbach am Main, Germany
guenther.doms@dwd.de

1. Introduction

Numerical weather prediction (NWP) models as well as other simulation models of atmospheric flow often apply numerical or computational smoothing in order to control small scale noise at or near the two grid interval ($2\Delta x$) wavelength. As these scales cannot be resolved adequately by the discretized dynamics, they have to be damped since otherwise large errors in the numerical solution can arise.

Numerical noise of such type is continuously generated by numerical dispersion, especially within the Leapfrog time integration using centred difference operators for advection as, e.g., in the current operational version of the Lokal-Modell (LM). Also, weak nonlinear numerical instabilities resulting from aliasing can contribute to the generation of small-scale noise, and physical processes, which in general act discontinuous at single grid points, will always introduce noise at the $2\Delta x$-scale. The formation of non-resolvable small-scale structures will also arise from topographical forcing and from surface inhomogeneities.

High-order scale-selective spatial filters can be applied to remove small-scale noise from the numerical solution (Shapiro, 1975, and Raymond, 1988). But most NWP models use computationally more efficient high-order numerical diffusion schemes to provide a scale selective control of small-scale noise. These schemes, however, have unwanted side effects. First, they are in general not monotonic and thus can introduce negative values on fields that are positive definite as, e.g., the cloud water content or the specific humidity. Second, they introduce noise by themselves on the resolvable scales via the so-called Gibbs phenomenon.

Another problem of using high-order numerical diffusion schemes in NWP models arises from the fact that smoothing is usually applied as a horizontal diffusion, that is along terrain-following model layers and not explicitly in the vertical direction. A full 3-D formulation would have to take into account a large number of metric terms from the terrain-following coordinate transformation and thus is too expensive for an operational application. In case of high-resolution modelling with steep slopes of the model layers, however, a 2-D numerical diffusion along model layers will imply a large but unwanted vertical mixing (e.g. between mountain tops and narrow valleys), especially in an atmosphere with strong stratification of the thermodynamic variables. To tackle this problem, a simple orographic flux-limiter is proposed which reduces numerical diffusion with increasing steepness of the topography.

The formulation of a monotonic scheme for horizontal numerical diffusion in the LM is based on the work of Xue (2000), who proposed two types of schemes: one based on Zalesak-type flux-correction (Zalesak, 1979) using the combination of high- and low-order schemes, and the other based on a simple flux-limiter which ensures that the diffusive fluxes are downgradient. The latter formulation, however, was found to be not strictly monotonic when applied to real cases. Thus, a third scheme is formulated which is based on direct multi-dimensional flux-limiting.

Section 2 summarizes the basic features of high-order numerical diffusion, followed by a description of three monotonic schemes in Section 3. The application of these schemes to simple 1-D and 2-D square wave tests is described in Section 4. In Section 5, an additional flux-limiter related to the slope of the model layers is introduced. The application of the new scheme to simulation of real cases with the LM is discussed in Section 6, and results from parallel test suites at MeteoSwiss and at DWD are described in Section 7. Finally, an outline of the technical implementation is given in Section 8.

2. High-Order Numerical Smoothing

Computational diffusion is mostly realized by introducing an additional operator to the right hand side of the prognostic equations:

$$\frac{\partial \psi}{\partial t} = S(\psi) + (-1)^{m/2+1} \alpha_m \nabla^m \psi \,, \tag{1}$$

where ψ is one of the prognostic variables and S represents all physical and dynamical source terms for ψ. The last term in Eq.(1) is the added linear diffusion term where m ($m = 2, 4, 6, \cdots$) denotes the (even) order of computational diffusion and α_m is the corresponding diffusion coefficient of order m.

The higher the order of the diffusion operator, the more scale selectively wavelength components are damped. Figure 1 shows the amplification factor (here: damping factor) for a one dimensional version of Eq.(1) using a forward in time and centred in space finite difference scheme for integration, plotted against the normalized wavelength $k\Delta x$ where k is the wavenumber and Δx is the grid spacing. For each of the second, fourth and sixth order schemes the corresponding diffusion coefficient α_m is chosen so that the shortest waves representable on a discrete grid ($2\Delta x$, i.e. $k\Delta x = \pi$) are damped completely within one integration time step.

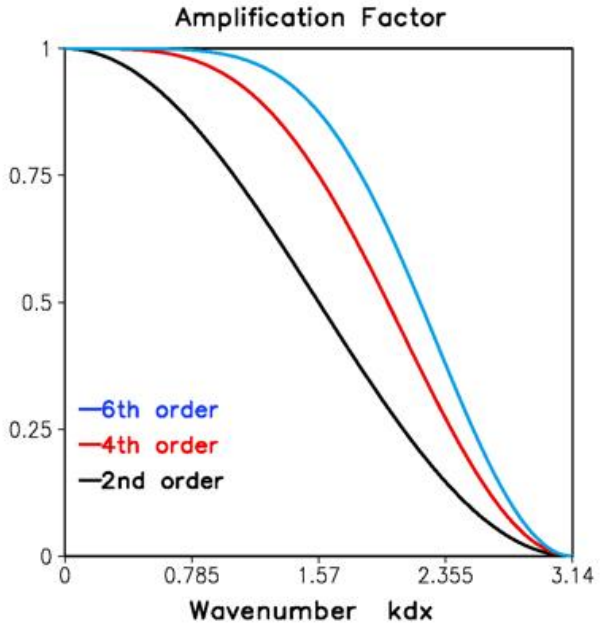


Figure 1: Amplification factor plotted against the normalized wavenumber

As can be seen from Fig. 1, all schemes damp not only the two grid interval wavelength, but also longer wave components in a wave spectrum. For example, the amplitude of a $4\Delta x$

wave is reduced by a factor of 0.5 in the second order scheme, and longer waves are also damped significantly. The fourth and sixth order scheme have much less damping for these longer waves, which contain physical meaningful information in a simulation and should not be affected by a numerical filter. Clearly, higher order schemes provide a more scale selective damping.

Many models use the 4th order linear computational diffusion scheme because of its relative computational efficiency compared to the 6th order scheme and of its superior damping properties compared to the second order scheme. Schemes of higher than 2nd order, however, have unwanted side effects. The 2nd order scheme has a Laplacian form and thus is always monotonic: by transferring higher values of the field into regions with smaller values no new minima or maxima can be created. This is not the case for the 4th, 6th and even higher order schemes, where spatial oscillations are introduced (Gibbs phenomenon), as can be seen in Fig. 2.

Figure 2 shows the one dimensional numerical solution of Eq.(1) (with $S = 0$) for 2nd, 4th and 6th order diffusion applied to an initial rectangular structure. The second order scheme (left) is strongly diffusive even for the large scale structure. At the end of the integration ($t = 100$) the amplitude of the entire square wave is significantly reduced. The 4th (middle) and 6th order (right) schemes retain the initial structure much better, and at the lateral edges, where short wavelengths components dominate, the sharp gradients are maintained in the solution (somewhat better by using the 6th order scheme).

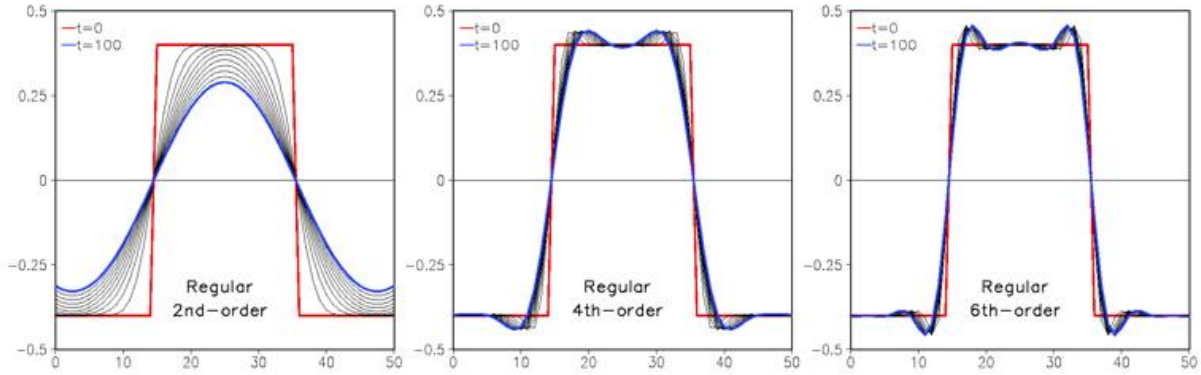


Figure 2: 1-D numerical solution of Eq.(1) for an initial square wave (red, $t = 0$) in case of 2nd (left), 4th (middle) and 6th order (right) linear diffusion. The domain has 51 grid points with a grid spacing of 1/50 m and the time step is 1 sec. The diffusion coefficients are chosen such that there is full damping of a $2\Delta x$ wave within one time step, i.e. $\alpha_m = (\Delta x/2)^m/\Delta t$. The solutions are plotted at 10 timestep intervals (thin lines).

However, over- and undershoots are generated by the numerical solution. The amplitude of these unphysical, both positive and negative spatial oscillations is increased by increasing the order of the diffusion operator. That is, going to higher than 4th order diffusion will not cure this side effect. Obviously, the $2\Delta x$ waves are removed from the solution, but at the cost of *introducing new noise on the resolvable scales.* In the context of a full simulation model these oscillations will interact nonlinearly with the physics as well as with the dynamics (as they are on the resolvable scales) and thus can result in unforeseeable effects. Moreover, negative oscillations are unacceptable for positive definite fields such as cloud water content or specific humidity.

3. Monotonic Diffusion Operators

This section describes three types of monotonic diffusion schemes. The first one is based on a Zalesak-type flux correction, similar to that used in many advection schemes. The second scheme is based on a simple flux limiter proposed by M. Xue (2000). And the third scheme uses a multidimensional flux limiter, where the formulation of the limiter factor closely follows the approach of Smolarkiewicz (1989).

The basic pre-requisite to apply these schemes is to rewrite the diffusion operator in Eq.(1) in a flux form. Omitting the source term S, the diffusive tendency then reads

$$\frac{\partial \psi}{\partial t} = (-1)^{m/2+1} \alpha_m \nabla^m \psi = -\nabla \cdot \mathbf{F}\,, \tag{2}$$

where $\mathbf{F}$ denotes the diffusive flux being defined by

$$\mathbf{F} \equiv (-1)^{m/2} \alpha_m \nabla (\nabla^{m-2} \psi)\,. \tag{3}$$

(a) Zalesak-type Flux Correction

Using the notations from Eqs.(2) and (3), the numerical scheme to integrate the 1-D version of the diffusion equation (the extension to more than one dimension is readily adopted) for a forward in time and centred in space scheme reads

$$\psi_i^{n+1} \;=\; \psi_i^n - (A_{i+1/2}^n - A_{i-1/2}^n), \tag{4}$$

where n denotes the time level, i is the gridpoint index and

$$A_{i+1/2}^n \equiv F_{i+1/2}^n \Delta t / \Delta x \tag{5}$$

denotes the normalized diffusive flux. Following the flux correction idea of Zalesak (1979), that was applied to the advection equation, Xue proposed a flux corrected scheme based on the combination of a low-order and a high-order diffusion scheme. Let A^L be the low-order diffusive flux, which is chosen to be of second order and thus will guarantee monotonicity, and A^H be a higher order diffusive flux, e.g. 4th or 6th order. Denoting the difference between the high-order diffusive flux A^H and the 2nd order one by

$$A^{HL} \;=\; A^H - A^L\,, \tag{6}$$

the Zalesak-type time integration scheme (4) can be written as

$$\begin{aligned} \psi_i^* &= \psi_i^n - (A_{i+1/2}^L - A_{i-1/2}^L)\,, \\ \psi_i^{n+1} &= \psi_i^* - (C_{i+1/2} A_{i+1/2}^{HL} - C_{i-1/2} A_{i-1/2}^{HL})\,. \end{aligned} \tag{7}$$

The factor C is called the flux correction coefficient or flux limiter, where $0 \leq C \leq 1$. When $C = 0$, the integration scheme (7) reduces to the 2nd order scheme, and when $C = 1$ it becomes purely high order. The idea is to use the high order scheme to the maximum extend possible, i.e. to reduce the fluxes by a factor C (to be determined for each grid interval interface) only when the monotonicity constraint is not met. As has been pointed out by Xue, the diffusion coefficients α_m of the low- and high-order schemes in the two step scheme (7) have to be chosen to be consistent with each other. To do so, it is required that two grid interval waves are damped by the same amount per time step. This means that different diffusion coefficients have to be used in the high-order flux A_H and in the low-order flux A_L. Longer waves, however, will be damped by a different amount.

Since the diffusion process should not generate new minima or maxima by stepping from the current time level n to the future time level $n+1$, the monotonicity constraint is chosen to be

$$\psi_i^{min} \leq \psi_i^{n+1} \leq \psi_i^{max}, \tag{8}$$

where ψ_i^{min} and ψ_i^{max} are the minimum and the maximum of ψ at the gridpoint and the adjacent points at the current time level n:

$$\psi_i^{min} = \min\left(\psi_{i-1}^n, \psi_i^n, \psi_{i+1}^n\right), \quad \psi_i^{max} = \max\left(\psi_{i-1}^n, \psi_i^n, \psi_{i+1}^n\right). \tag{9}$$

Following Zalesak, a flux limiter satisfying condition (8) can be defined as

$$C_{i+1/2} = \begin{cases} \min\left(1, R_{i+1}^+, R_i^-\right) & \text{if} \quad A_{i+1/2}^{HL} \geq 0\,, \\ \min\left(1, R_i^+, R_{i+1}^-\right) & \text{if} \quad A_{i+1/2}^{HL} < 0\,, \end{cases} \tag{10}$$

where

$$\begin{aligned} R_i^+ &= (\psi_i^{max} - \psi_i^*)/(A_i^{in} + \epsilon)\,, \\ R_i^- &= (\psi_i^{min} - \psi_i^*)/(A_i^{out} + \epsilon)\,. \end{aligned} \tag{11}$$

Here, ϵ is a small positive number to avoid division by zero. A_i^{in} and A_i^{out} are, respectively, the sum of all incoming and outgoing corrective fluxes A^{HL} of a grid box.

(b) The Xue Flux-Limiter

The monotonic scheme described above guarantees monotonicity, the computational costs, however, appear to be quite high. Xue pointed out that diffusive fluxes in high order schemes are not necessarily downgradient (as they are in the monotonic second order scheme) because they are no longer related to the local gradient of the diffused variable ψ. Upgradient fluxes can result in unphysical solutions and explain the over- and undershoots when applying high order schemes.

As a simple way to prevent upgradient fluxes to occur, Xue proposed to set the diffusive fluxes to zero whenever they have the same sign as the gradient of ψ. In the time integration scheme (4), the normalized fluxes A are thus replaced by

$$\tilde{A}_{i+1/2} = -A_{i+1/2} \min[0, \mathrm{sign}(A_{i+1/2}\delta_x\psi)]\,, \tag{12}$$

where the sign-function returns the sign of the argument. The application of this simple flux limiter in higher order diffusion schemes seems to prevent over- and undershoots in simple test cases. Obviously, the Xue-limiter (12) is far more efficient than the Zalesak-type flux corrected scheme since the extra computational costs are very small.

However, it cannot be shown analytically that the limiter will ensure strict monotonicity of the solution. Tests of the simple flux limiter (12) for the 4th order diffusion of real field distributions of cloud water and specific humidity have shown that over- and undershoots may still be present (see Section 4).

(c) Multidimensional Flux-Limiter

The multidimensional flux limiting scheme follows closely the ideas of the Zalesak-type flux correction scheme described above, but uses a direct limiter instead of the correction method based on antidiffusive fluxes. In this way, the two-step time integration scheme (7) as well as the problem of using consistent diffusion coefficients for low- and high-order fluxes is avoided. The construction of the limiter follows the approach of Smolarkiewicz (1989).

The numerical scheme for integrating the 2-D version of the diffusion equation using a forward in time and centred in space scheme reads

$$\psi_{i,j}^{n+1} = \psi_{i,j}^{n} - (A_{i+1/2,j}^{n} - A_{i-1/2,j}^{n} + A_{i,j+1/2}^{n} - A_{i,j-1/2}^{n}), \tag{13}$$

where n denotes the time level, (i,j) are the gridpoint indices with i counting in x-direction and j in y-direction, and

$$A_{\cdot,\cdot}^{n} \equiv F_{\cdot,\cdot}^{n} \Delta t / \Delta x \tag{14}$$

are the normalized $(m-1)$-th order diffusive fluxes at cell interfaces calculated from Eq. (3). The numerical scheme (14) can be rewritten as

$$\psi_{i,j}^{n+1} = \psi_{i,j}^{n} + A_{i,j}^{in} - A_{i,j}^{out}, \tag{15}$$

with $A_{i,j}^{in}$ denoting the sum of all fluxes into a grid cell and $A_{i,j}^{out}$ denoting the sum of all fluxes going out of a grid cell. Both the sum of the incoming and outgoing fluxes, $A_{i,j}^{in}$ and $A_{i,j}^{out}$, respectively, are defined to be positive. Using the notation

$$A_{\cdot,\cdot}^{+} = \max\left(A_{\cdot,\cdot}^{n}, 0\right), \quad A_{\cdot,\cdot}^{-} = \min\left(A_{\cdot,\cdot}^{n}, 0\right) \tag{16}$$

to indicate positive and negative fluxes at the cell interfaces, the sum of the incoming and outgoing fluxes is given by

$$\begin{aligned} A_{i,j}^{in} &= -A_{i+1/2,j}^{-} + A_{i-1/2,j}^{+} - A_{i,j+1/2}^{-} + A_{i,j-1/2}^{+}, \\ A_{i,j}^{out} &= +A_{i+1/2,j}^{+} - A_{i-1/2,j}^{-} + A_{i,j+1/2}^{+} - A_{i,j-1/2}^{-}. \end{aligned}$$

The difference $A_{i,j}^{in} - A_{i,j}^{out}$ is equivalent to the discretized total flux divergence. Since a monotonic numerical scheme shall not produce new minima or maxima within a time step, the monotonicity constraint is

$$\psi_{i,j}^{min} \leq \psi_{i,j}^{n+1} \leq \psi_{i,j}^{max}, \tag{17}$$

where $\psi_{i,j}^{min}$ is the minimum and $\psi_{i,j}^{max}$ is the maximum of the field variable ψ at the point (i,j) and the adjacent grid points at time level n:

$$\begin{aligned} \psi_{i,j}^{min} &= \min\left(\psi_{i,j}^{n}, \psi_{i+1,j}^{n}, \psi_{i-1,j}^{n}, \psi_{i,j+1}^{n}, \psi_{i,j-1}^{n}\right), \\ \psi_{i,j}^{max} &= \max\left(\psi_{i,j}^{n}, \psi_{i+1,j}^{n}, \psi_{i-1,j}^{n}, \psi_{i,j+1}^{n}, \psi_{i,j-1}^{n}\right). \end{aligned}$$

Using the monotonicity constraint (17) in the numerical scheme (15) yields

$$\psi_{i,j}^{min} \leq \psi_{i,j}^{n} + A_{i,j}^{in} - A_{i,j}^{out} \leq \psi_{i,j}^{max}. \tag{18}$$

Thus, the following conditions on the sum of the incoming and outgoing fluxes are sufficient to ensure monotonicity:

$$\begin{aligned} A_{i,j}^{in} &\leq \psi_{i,j}^{max} - \psi_{i,j}^{n}, \\ A_{i,j}^{out} &\leq \psi_{i,j}^{n} - \psi_{i,j}^{min}. \end{aligned}$$

With these conditions, the sum of all incoming fluxes cannot add more mass within one time step than that required to reach the maximum value $\psi_{i,j}^{max}$ and the sum of all outgoing fluxes cannot remove more mass than that to fall to the minimum value $\psi_{i,j}^{min}$. These conditions can be rewritten in the form of flux limiter ratios

$$\begin{aligned} \beta_{i,j}^{in} &= \frac{\psi_{i,j}^{max} - \psi_{i,j}^{n}}{A_{i,j}^{in} + \epsilon} \\ \beta_{i,j}^{out} &= \frac{\psi_{i,j}^{n} - \psi_{i,j}^{min}}{A_{i,j}^{out} + \epsilon}, \end{aligned} \tag{19}$$

where ϵ is a small number to avoid division by zero in the computer program. Whenever $\beta^{in}_{i,j} \geq 1$, the total incoming flux does not need to be modified. But if $\beta^{in}_{i,j} < 1$ the incoming fluxes are overestimated and the flux limiter has to be applied. Similar, if $\beta^{out}_{i,j} \geq 1$, the total outgoing fluxes will ensure monotonicity, but if $\beta^{out}_{i,j} < 1$, the outgoing fluxes are overestimated and have to be limited.

Since the total incoming and outgoing fluxes are additively composed of the fluxes at the cell interfaces, the limiter (19) is applied for each of these fluxes. And as the limiter for the incoming fluxes has been constructed independently of the limiter for the outgoing fluxes and because the outgoing flux at a cell interface is equivalent to the incoming flux at the adjacent cell, it is sufficient to simply take the minimum of both limiters. The application of the limiters (19) to the fluxes at the cell interfaces in the i- and j-direction can be written in a compact manner:

$$\begin{aligned} \tilde{A}^n_{i+1/2,j} &= \min\left(1, \beta^{out}_{i,j}, \beta^{in}_{i+1,j}\right) A^+_{i+1/2,j} + \min\left(1, \beta^{out}_{i+1,j}, \beta^{in}_{i,j}\right) A^-_{i+1/2,j}\,, \\ \tilde{A}^n_{i,j+1/2} &= \min\left(1, \beta^{out}_{i,j}, \beta^{in}_{i,j+1}\right) A^+_{i,j+1/2} + \min\left(1, \beta^{out}_{i,j+1}, \beta^{in}_{i,j}\right) A^-_{i,j+1/2}\,. \end{aligned} \tag{20}$$

For example, if the flux $A_{i+1/2,j}$ at the cell interface separating cell (i,j) and $(i+1,j)$ is positive, i.e. is an outgoing flux from cell (i,j) and thus an incoming flux for cell $(i+1,j)$, it will be limited with the minimum of the limiter $\beta^{out}_{i,j}$ of cell (i,j) and the limiter $\beta^{in}_{i+1,j}$ from cell $(i+1,j)$. By replacing the normalized fluxed A in the time integration scheme (13) with the limited normalized fluxes $\tilde{A}$ from Eq. (20), a monotonic diffusion scheme is finally obtained.

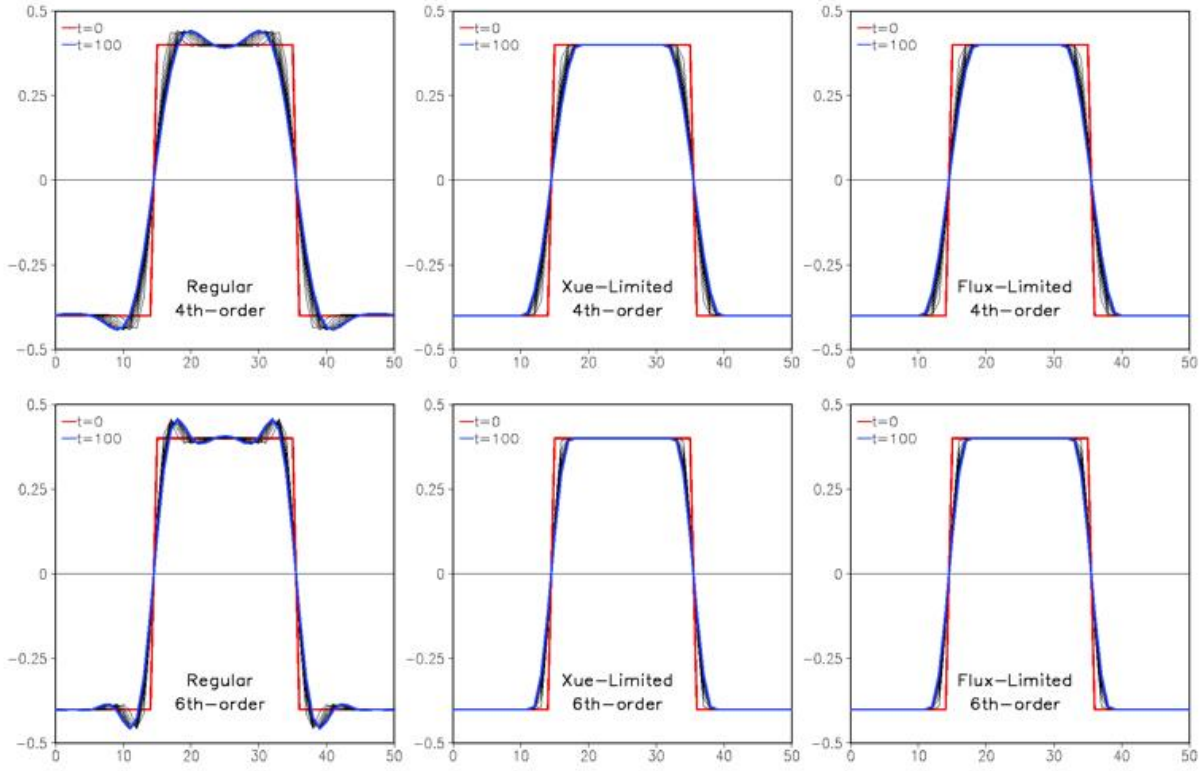


Figure 3: As in Fig. 2, but for 4th (upper panel) and 6th order (lower panel) linear diffusion. Left: Regular diffusion. Middle: Xue-limited diffusion. Right: Flux-limited diffusion.

4. Results from Simple Tests Cases

The solutions of the one-dimensional square waves test using 4th and 6th order regular diffusion as well as the monotonic scheme based on the Xue flux-limiter (12) and the scheme (20) based on direct flux limiting are shown in Figure 3.

Obviously, the unwanted numerical effects associated with the Gibbs phenomena are no longer present when using the simple Xue-limiter or the full flux limiter, but the smoothing characteristic is maintained in both schemes. The solution obtained with the Zalesak-type flux correction method (not shown) are very similar.

The extension of the monotonic schemes described in Section 3 to more than one dimension is straightforward. Fig. 4 shows the field distribution at initial time and the numerical solution obtained with 2nd-order diffusion after 100 time steps for the 2-D square wave test, where initially a block of 20 by 20 gridlines with a field value of 0.4 is placed in a background field having a value of -0.4. All parameters are the same as in the 1-D test, except that the diffusion coefficient for maximal damping has been adopted for the twodimensional case. Similar to the 1-D case, the initial distribution is significantly smoothed even at the larger scales. The peak value of 0.4 is reduced to 0.28 and the initial rectangular structure is no longer visible.

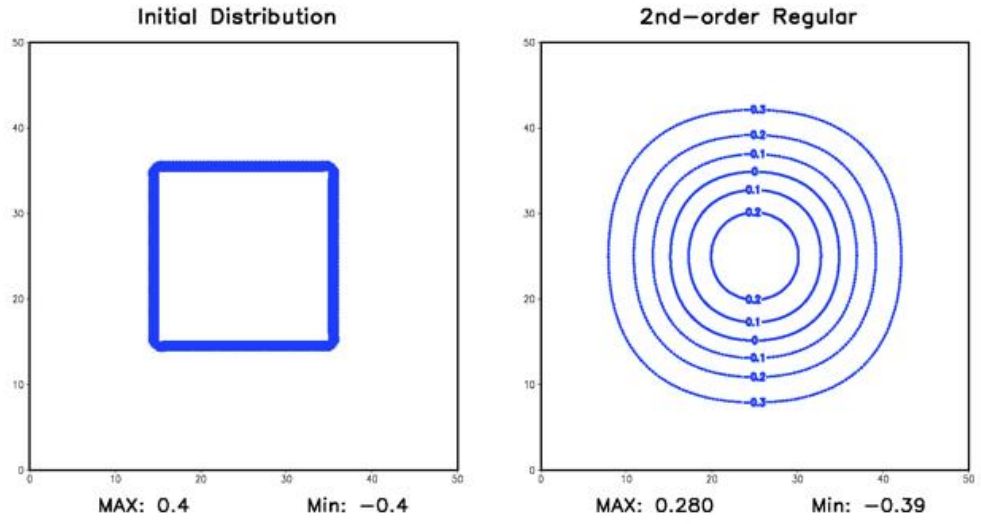


Figure 4: Contour maps of a field for the 2D square wave test. Left: Initial field distribution, where a block with field values with 0.4 is placed in a background field having the value of -0.4. Right: Solution of the 2nd-order regular diffusion after 100 time steps. The contour interval is 0.1

The results of the 4th-order regular linear diffusion and of the three alternative monotonic 4th-order schemes from Section 3 are shown in Fig. 5. When compared to the 2nd-order scheme, much sharper gradients at the lateral sides are retained by using the regular 4th-order diffusion scheme. Also, the large scale features of the initial field distribution are still visible. However, the 4th-order scheme suffers significantly from the Gibbs phenomenon, with severe overshoots of the order of 10% and undershoots of the order of 5% of the initial amplitude.

This effect is completely avoided by applying the Zalesak flux-correction scheme, the Xue-limiter or the multidimensional flux limiter. In all three schemes no over- or undershooting exists and the maxima and minima values of the field are exactly 0.4 and -0.4, respectively. Also, a slightly better gradient is maintained by the monotonic schemes compared to the solution from the regular 4th-order scheme and the rectangular shape of the contour lines

is retained somewhat better. The noisy appearance of the 0.4 and -0.4 contour line in the solution by the Zalesak scheme is due to roundoff errors which, however, have no detrimental impact.

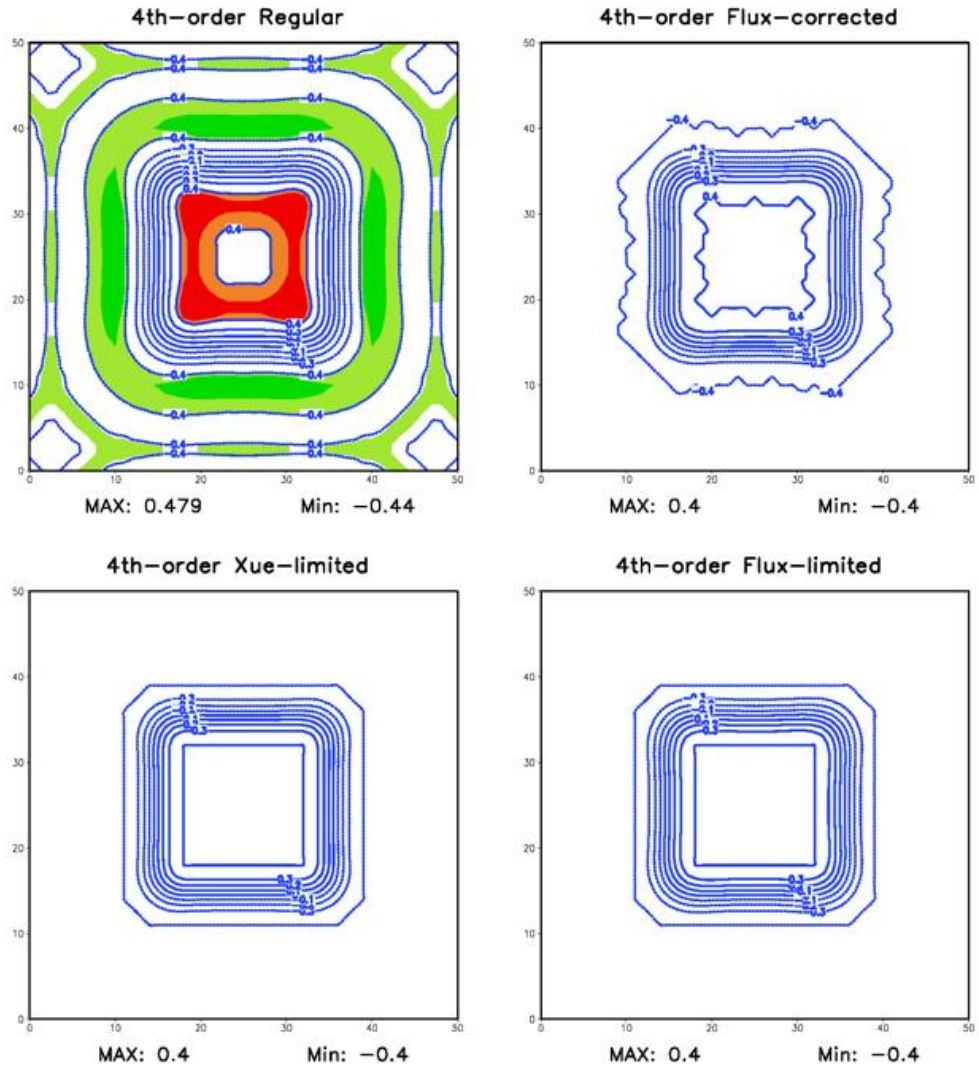


Figure 5: 2-D numerical solution of Eq.(1) for the square wave test after 100 time steps. Top left: 4th-order regular diffusion. Top right: 4th-order flux corrected. Bottom left: 4th-order Xue-limiter. Bottom right: 4th-order flux limited. Red shading indicates regions of overshoots, green shading regions of undershoots. The contour interval is 0.1.

All three schemes with monotonic limiters give very similar numerical solutions, but the simple Xue-limiter is the most efficient one as the additional computational costs are very small. Compared to the regular 4th-order diffusion, the computation time ratio of the Zalesak flux-correction scheme is 3.6, of the multidimensional flux-limiting scheme is 3.1, but is only 1.9 for the simple Xue-limiter (on an SGI Octane workstation).

Thus, from a practical point of view, the Xue-limiter seems to be the most efficient scheme to ensure monotonicity of high-order numerical diffusion. When applied to the cloud water field (a field with values varying within a few orders of magnitude) in simulations of real cases with the LM, however, this limiter was found to be not strictly monotonic. At a large number of gridpoints with a positive definite field distribution at the beginning of a time step, negative field values are observed after subjecting to 4th order diffusion with the Xue-limiter. To demonstrate this, a few gridpoint values (normalized by a factor) of a real

case simulation are chosen as initial condition for a 1-D numerical solution of the diffusion equation over 10 timesteps. In the beginning, a high value of water content is prescribed, with two much smaller side-maxima to the left and right, but separated by a zero value (see Fig.6). Structures like this are not too frequent but not unusual in simulations of real cases.

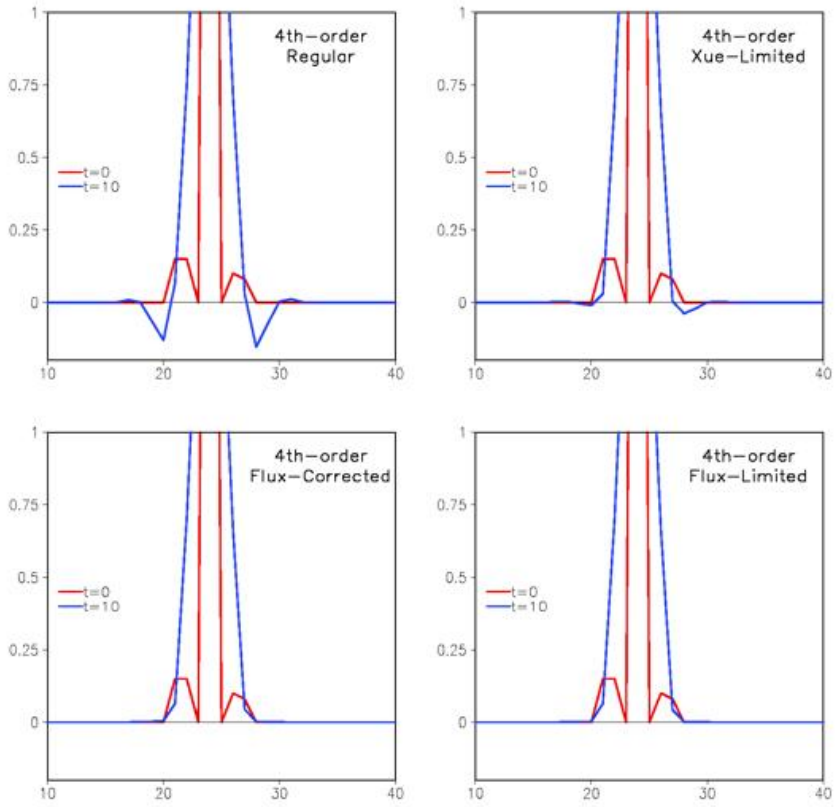


Figure 6: As in Fig. 2, but for a non-regular initial distribution (t=0, red) after 10 time steps (t=10, blue) for 4th-order diffusion. Top left: Regular. Top right: Xue-limiter. Bottom left: Flux-correction. Bottom right: Flux-limiting. The peak value of the initial distribution is 6.0.

The results of applying 4th-order numerical diffusion to this initial distribution using the regular scheme, the Xue-limiter, the Zalesak-limiter and the flux-limiter are shown in Fig. (6). Quite large undershoots with negative cloud water contents are generated by the regular scheme. This characteristic effect is drastically reduced by using the Xue-limiter, but is not cured completely: small negative values are still present in the solution. Both the flux-corrected and the flux-limited schemes guarantee a smooth and strictly monotonic solution.

Thus, the simple Xue flux-limiter seems not to be suited for application to the specific humidity and the specific water variables in a numerical prediction model, since spurious negative values of these variables may still be generated. For such fields, the schemes based on flux-correction or on flux-limiting should be used, where the multidimensional flux limiter is a little bit in favor because of its slightly better computational efficiency and a simpler formulation. For fields being not positive definite, as e.g. the velocity components, the Xue limiter is a viable and efficient alternative.

5. An Orographic Flux Limiter

Most mesoscale NWP models use a terrain-following sigma-type vertical coordinate and numerical smoothing is realized as horizontal diffusion, i.e. along quasi-horizontal surfaces of constant vertical coordinate. Over complex terrain, this may lead to systematic numerical biases which are induced by horizontal diffusion, as an unwanted vertical mixing in physical space will be implied. Clearly, the impact of this type of numerical error will increase with increasing steepness of the topography and is thus more noticeable in models with very high resolution.

For instance, if horizontal diffusion is applied directly to temperature in the prognostic equation for temperature, the smoothing will tend to cool the valleys and to heat the mountain tops in any stratification where the temperature decreases with height. Similarly, in an atmosphere with decreasing specific humidity with height, horizontal diffusion will dry the valley and moisten the mountains, which can have an unwanted positive feedback to precipitation formation over mountain tops.

Various modifications have been proposed to reduce the spurious biases resulting from quasi-horizontal mixing. Most models use a so-called slope correction for horizontal smoothing in the temperature equation, where instead of the actual temperature the difference of temperature and a reference profile is diffused. In LM, we use the model base state for this purpose. Errors from unwanted vertical mixing are then zero when the actual vertical temperature gradient is identical to the gradient of the base-state profile. However, when the profiles deviate from each other, large error may still be introduced (e.g. in very stable or unstable stratification). Slope corrections for other variables are normally not used.

Another popular method is the use of "true" horizontal diffusion, i.e. along surfaces of constant height or constant pressure (e.g. Zängl, 2000). Here, the values of the diffused variables at the adjacent gridpoints are interpolated to the height or pressure level of each gridpoint before diffusion is applied. Since the gridpoints usually have different heights, however, the diffusive fluxes at the cell interfaces will differ for neighboring gridpoints. Thus, mass conservation cannot be guaranteed with such a scheme. One could also try to locally reduce the value of the diffusion coefficient depending on the steepness of the orography (a commonly used measure is the Laplacian of topographical height). But here again the diffusive fluxes at the cell interface between two neighboring gridpoints will be different and mass can be artificially generated or lost.

Numerical smoothing schemes which introduce uncontrollable sources or sinks in momentum, heat or water mass are problematic, especially in an operational NWP model. With the flux-limited scheme discussed in the preceding Section, we have the opportunity to reduce the topography-induced biases without violating mass conservation: One can simply reduce the diffusive fluxes at the cell interfaces, depending on the steepness of the model surfaces. As the scheme is in flux-form, mass will be conserved automatically. And if the fluxes are artificially reduced before the monotonic flux limiters are applied, the monotonicity of the diffused field will also be guaranteed.

Two variants of this methods have been tested. The first is a non-continuous formulation, where the diffusive fluxes are simply set to zero whenever the height difference between two neighboring grid points exceeds a threshold value. Defining this height differences at cell interfaces and denoting them by

$$\Delta h_{i+1/2,j} = |h_{i+1,j} - h_{i,j}|\,, \quad \Delta h_{i,j+1/2} = |h_{i,j+1} - h_{i,j}|\,, \tag{21}$$

where $h_{i,j}$ is the geometrical height of a grid point at a surface of constant vertical coordinate,

the limiter function for the diffusive fluxes A in Eq. (13) can be written as

$$A_{i+1/2,j} = \begin{cases} F_{i+1/2,j}\frac{\Delta t}{\Delta x}, & \text{if} \quad \Delta h_{i+1/2,j} \leq H_{max}\,, \\ 0\,, & \text{if} \quad \Delta h_{i+1/2,j} > H_{max}\,, \end{cases}$$
$$A_{i,j+1/2} = \begin{cases} F_{i,j+1/2}\frac{\Delta t}{\Delta x}, & \text{if} \quad \Delta h_{i,j+1/2} \leq H_{max}\,, \\ 0\,, & \text{if} \quad \Delta h_{i,j+1/2} > H_{max}\,. \end{cases} \tag{22}$$

Here, H_{max} is a threshold value for the maximal height difference. Another approach is to gradually reduce the fluxes with increasing steepness. One can try various functional dependences, but to keep things simple we apply a simple quadratic form, where the fluxes become zero when the threshold value for the height difference is exceeded:

$$A_{i+1/2,j} = \max\{\,0\,, 1 - (\Delta h_{i+1/2,j}/H_{max})^2\} \cdot F_{i+1/2,j}\frac{\Delta t}{\Delta x}\,.$$
$$A_{i,j+1/2} = \max\{\,0\,, 1 - (\Delta h_{i,j+1/2}/H_{max})^2\} \cdot F_{i,j+1/2}\frac{\Delta t}{\Delta x}\,. \tag{23}$$

Tests of the application of the orographic flux limiters (22) and (23) are discussed in Section 6.2.

6. Results from Test Simulations with the LM

This Section describes some results from single test simulations of real cases using the current operational version of LM (lm_f90, V 2.6). The basic model setup is identical to the operational configuration (7km grid spacing, 40 sec timestep, full physics). First, the impact of monotonicity is discussed in Section 6.1. Second, the application of the orographic flux-limiters is described in Section 6.2.

6.1 The Impact of Monotonic Flux-Limiting

As a first test, the Xue limiter was applied to all prognostic variables for a randomly chosen real case from 18 September 2000. Figure 7 shows the vertically integrated cloud water content of a 12h-forecast starting at 00 UTC. Concerning the structure of the two cloud bands over Denmark and over the Northern Sea, no apparent differences between the reference run using regular 4th order diffusion and the model version with monotonic diffusion can be noticed. However, the area mean value of the integrated cloud water content is slightly reduced from 41 to 38 gm^{-2}.

This can also be noticed from the scatter diagram (Figure 7, right), where the gridpoint values of the integrated cloud water content of the reference run (y-axis) are plotted against those from the experiment (x-axis). Obviously, the values obtained from the reference are on average somewhat larger than those resulting from the run with monotonic diffusion. The same type of impact can also be noticed in the precipitation amount, which is slightly smaller in the experiment (not shown). One could attribute this to the removal of overshoots from the solution for the cloud water field. In a complex nonlinear model, however, such a clear assignment of cause and effect is not possible. Due to the noticeable effect on the cloud water content, a more thorough evaluation is necessary to assess the impact of the monotonic diffusion scheme on the cloud-radiation interactions.

6.2 The Impact of Orographic Flux-Limiting

First test integrations using the monotonic flux limiter (20) in connection with the orographic limiter (23) have been performed for a number of cases from the period October-November 2000. During this time, a synoptic-scale weather situation with southerly flow over the Alps

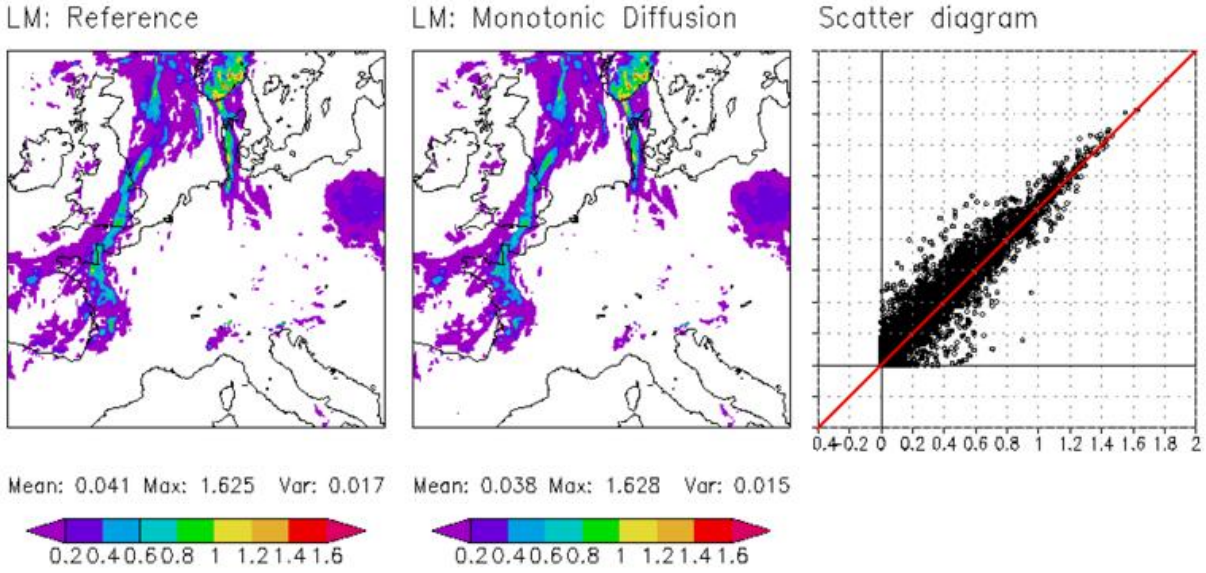


Figure 7: Vertically integrated cloud water (kg/m^2) content of a 12-h LM forecast starting at 18 September 2000 00 UTC. Left: reference solution with 4th oder regular diffusion; middle solution from a run with monotonic Xue limited diffusion; right: Scatter diagram of values from the reference (y-axis) viz. experiment (x-axis) runs.

prevailed, causing often a Föhn-effect in regions to the north of the Alps with blocking or weakening of cold fronts from the west. In the operational forecasts with the LM at DWD, however, the Föhn-effect was overestimated in most cases. This can be noticed when comparing the monthly mean precipitation from the forecasts and from a high resolution observation network for October 2000 in Fig. 8: The precipitation amount for southwestern Germany and for Bavaria is severely underpredicted due to a too frequent blocking or too strong weakening of fronts. A similar underprediction is noticed for the northern and western parts of Switzerland.

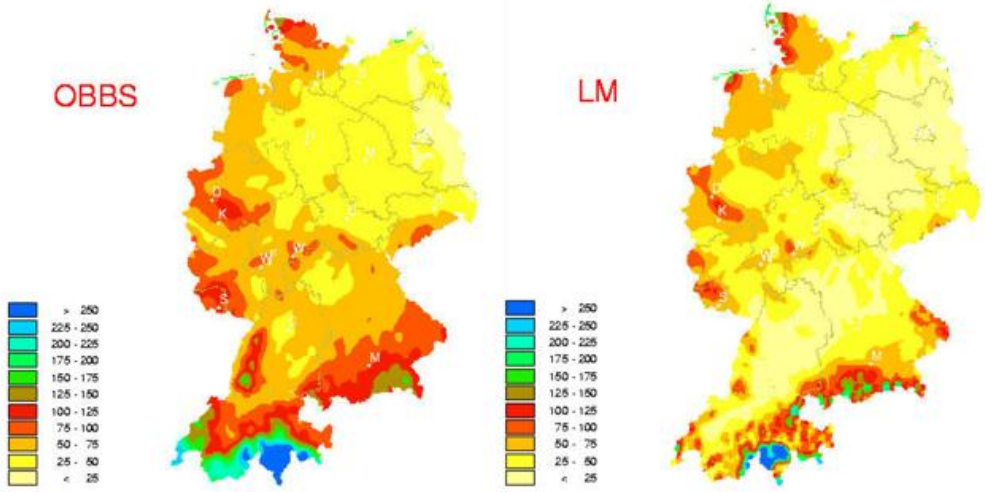


Figure 8: Monthly precipitation amount (mm) for October 2000 as observed (OBBS) by climate networks (max: 525 mm, mean: 63mm) and derived from 00 UTC LM forecasts (+30h - 06h) at DWD (max: 999 mm, mean: 69mm).

During a number of experimental studies related to the failure of the model forecasts for these Föhn situations, it was found that horizontal diffusion has an unexpected large dynamical

impact on the onset and strength of the Föhn flow. As an example, we choose here the forecast starting from 00 UTC at 11 October 2000. For experimentation, a somewhat smaller model domain (241x241 gridpoints) than the operational one (325x325 gridpoints) has been used. The initial and boundary conditions come from interpolated GME data.

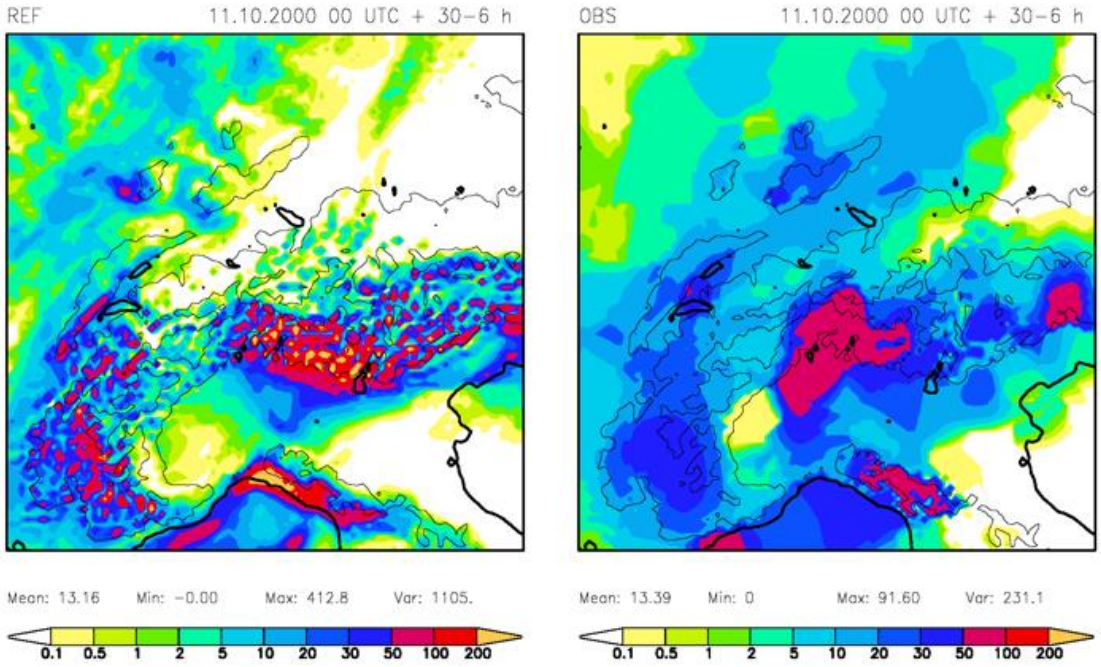


Figure 9: 24h accumulated precipitation (mm) for 11 October 2000 00 UTC +06h ...+30h. Left: Reference run. Right: Analysis based on Synop observation. The thick contour lines show the land-sea mask, the thin lines are the 700m and 2100m contour lines of orography

Fig. 9 compares the 24 h accumulated precipitation amount from the reference run (left) and from the Synop observations (right) on a model subdomain of about 700x700 km covering the Alpine region. As the observation come from the rather coarse SYNOP network, the structure of the precipitation field is only a first guess and many details may be lost. Nevertheless, the observation indicate a large region along the southern ridge of the Alps with precipitation amounts in the range 50 - 100 mm (which resulted in a severe flooding event in the Turin region). This is well captured by the model forecast, the centre is shifted somewhat to the east. The peak precipitation, however, is certainly overestimated by the model. Another region with high precipitation amounts is along the western ridge of the alps, but also here the peak values seem to be too high. In general, the forecasted precipitation field looks very noisy, with $2\Delta x$ structures located in regions of steep topography. This is not believed to be realistic.

The effect of a too strong blocking by southerly Föhn flow is obvious in the northern part of the Alps: whereas the observations indicate precipitation amounts in the range of 5 - 20 mm in a region extending from the Lake of Geneva over the Lake of Constance into the southwestern parts of Bavaria, the forecast gives almost no indication of precipitation at all, except for a spotty structure over northern Switzerland. Another typical feature of many LM precipitation forecasts can also be noticed: The valley of Valais, a steep valley extending southeast of the Lake of Geneva, remains almost dry, whereas a large amount of rain and snow falls over the mountain tops at the valley sides. The observations, however, indicate significant precipitation at the valley ground.

The impact of monotonic and orographic flux limiting for horizontal diffusion to the precipitation forecast is quite large. The left picture in Fig. 10 displays the result obtained with the quadratic form (23) of the orographic limiter with H_{max} set to 250 m. This limiter is only applied for temperature perturbation, specific humidity and cloud water content, whereas pressure perturbation and the wind components are treated with the computationally more efficient Xue limiter. Experiments have shown that the application of the flux-limiter scheme to the latter variables has not a significant impact to the forecasts. They are thus treated with the computationally more efficient Xue-scheme.

When compared to the reference run, the precipitation pattern looks less noisy than in the reference run and a part of the $2\Delta x$ structures are gone or their amplitude appears to be smaller: the field variance is reduced from 1105 mm down to 890 mm and the field maximum from 413 mm to 355 mm. Also, the southwest-northeast orientation of the small-scale precipitation bands over the western parts of the Alps has changed to a more northwest-southeast orientation. As a distinct feature of the new scheme, the "dry valley effect" seems to be cured: with flux-limited horizontal diffusion a significant precipitation amount is now predicted for the valley of Valais. Most interestingly, a coherent rainband extending from northern Switzerland to western Bavaria is now formed, with an eastern boundary close to the observed one. Clearly, a large part of precipitation is still missing to the west of this band, but this experiment indicates that a too strong horizontal diffusion over steep terrain can have significant effects to the fields far away.

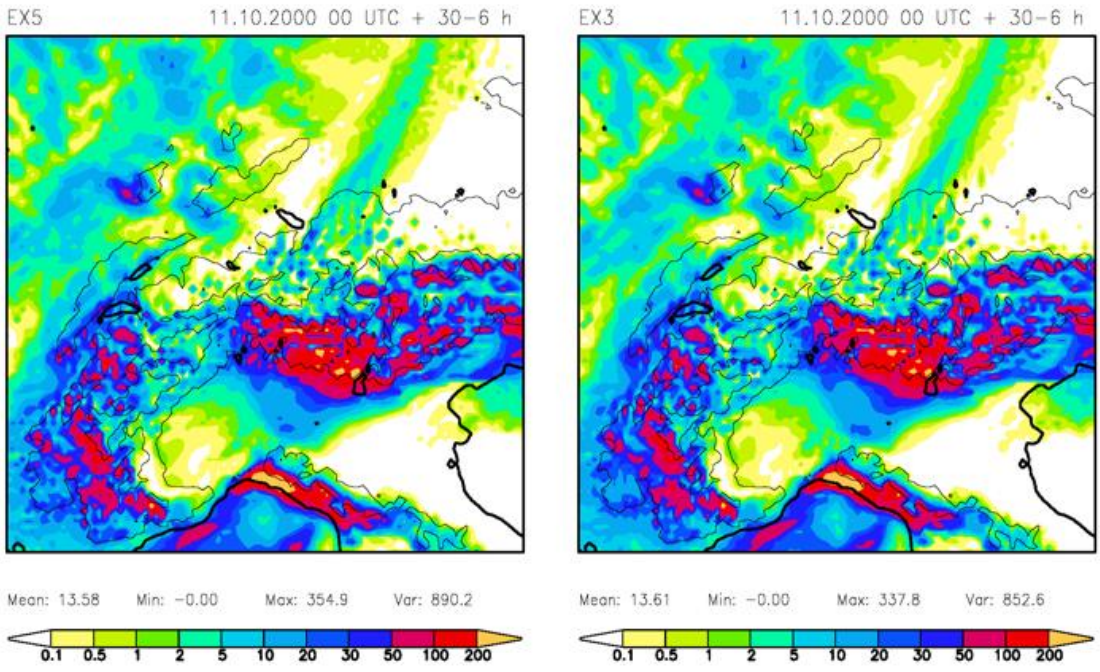


Figure 10: As in Fig. 9 but for the flux-limited diffusion scheme using the quadratic form (23) of the orographic flux limiter (left). Right: The same scheme, but with generally reduced diffusion coefficients for temperature and pressure perturbation (by a factor of 0.6) and for water vapour and cloud water (by a factor of 0.3).

Also, a number of test runs using generally reduced diffusion coefficients have been performed since overdamping over complex terrain was found to be crucial for the failure of the precipitation forecasts. The right picture in Fig. 10 shows the result from a run using a reduction factor of 0.6 and of 0.3 for the default diffusion coefficient for temperature and pressure perturbation and for water vapour and cloud water, respectively. There is not too much difference between the results, the run with reduced coefficients is slightly more smooth

and has a lower field maximum. This beneficial impact of smaller diffusion coefficients is lost with a further reduction, since a certain amount of damping is necessary to control small-scale noise. As a default for the reduction factors for the diffusion coefficients for heat and moistures, the values 0.75 and 0.5 have been implemented.

The stepwise form (22) of the orographic limiter behaves in general very similar to the continuous quadratic form (23). The latter version, however, gives a slightly more smooth solution and the extra computational costs are negligible. Thus, the limiter (23) was implemented. Additional sensitivity tests concerning the threshold value H_{max} for the maximum height difference between neighboring gridpoints in the limiter function (23) have been performed. For a very high value of H_{max} the results tend to become similar to the monotonic scheme using no orographic limiter, and for a very low value the scheme tends to produce an underdamped, i.e. very noisy solution. For values between 200 m and 300 m, the results are quite similar and thus $H_{max} = 250$ m has been implemented as a default. Clearly, this applies only for the current 7 km grid spacing, and a resonable value has to be set for other horizontal resolutions.

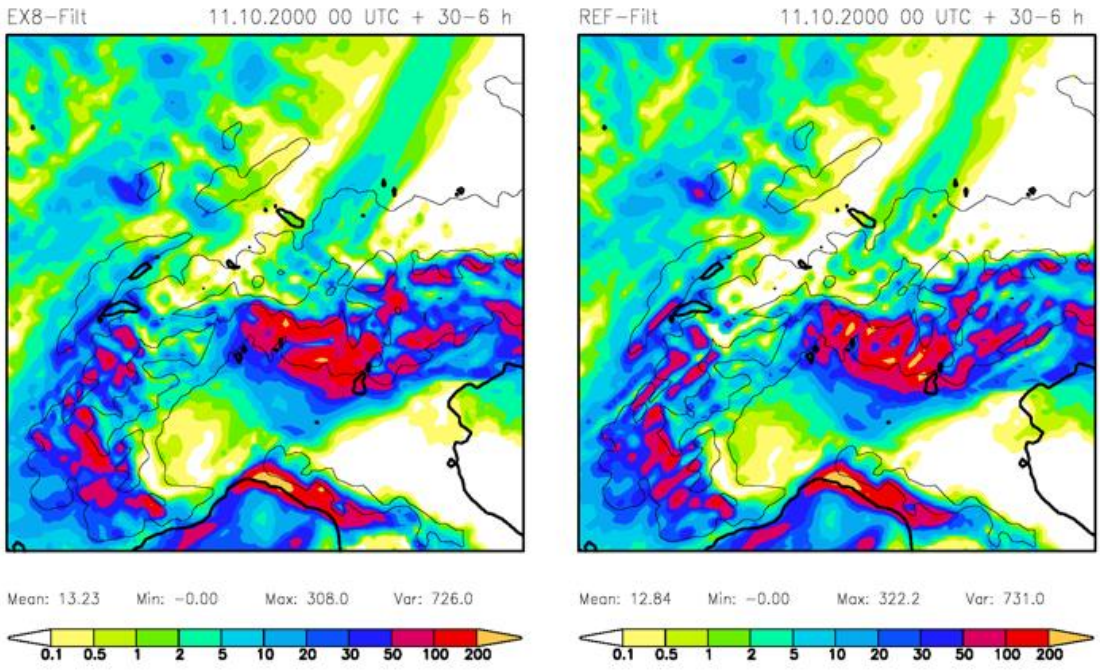


Figure 11: As in Fig. 9 but for the filtered topography. Left: Quadratic form (23) of the orographic flux limiter and with reduced diffusion coefficients for heat (factor 0.75) and moisture (factor 0.50) (left). Right: reference run.

All test runs described above have been done with the original mean topography at the grid scale. Using a mean topography, however, constantly forces the generation of $2\Delta x$-waves, which are represented hopelessly inaccurate in numerical models. Thus, a filtering of topography has been introduced in the operational applications of the LM in order to get a more correct interaction of dynamics with the surface. For this purpose, the Raymond (1988) filter is applied which removes $2\Delta x$ and $3\Delta x$ wave components from the mean orography (Gassmann, 2001).

Since the filtered orography is smoother and less steep, the errors from horizontal diffusion are expected to become smaller. And indeed, reruns of cases from the Föhn period during October-November 2000 showed a beneficial impact of topographical filtering to precipitation and 2m-temperature forecasts. The right hand picture in Fig. 11 displays the 24-h

precipitation amount for the 11 October case using the filtered topography and standard horizontal diffusion. When compared to the reference run using the mean topography (Fig. 9, left), the precipitation field has become much less noisy. Also, the blocking effect north of the Alps is reduced and a rainband in southern Germany appears. However, there is still a noticeable impact of using monotonic horizontal diffusion with the orographic limiter (Fig. 11, left): The rainband appears to be slightly broader and more intense, and the unrealistic southeast-northwest orientation of precipitation bands over the western part of the Alps is removed.

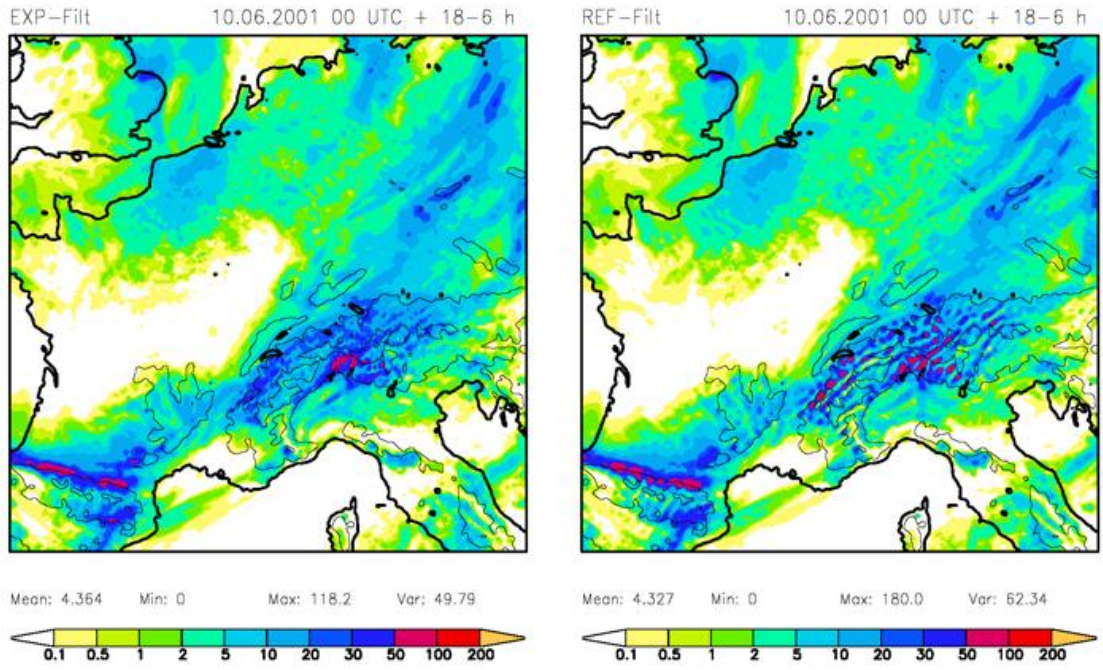


Figure 12: 24h accumulated precipitation (mm) for 10 June 2001 00 UTC +06h ...+18h. Left: Default version of the flux-limited scheme for horizontal diffusion. Right: Reference run. The thick contour lines show the land-sea mask, the thin lines are the 700m and 2100m contour lines of orography

The beneficial impact of the new diffusion scheme is noticeable also in cases other than Föhn flow. For instance, Fig. 12 compares the 12-h precipitation amount for 10 June 2001 as predicted with the standard scheme for horizontal diffusion (right) and with the default version of the flux-limited scheme (left), where in both runs the filtered topography is used. On this day, a frontal system moved slowly eastwards with only weak winds over the Alpine region. Most of the precipitation is stratiform since a stable thermodynamic stratification prevailed. In the reference run, the predicted precipitation is rather noisy with high peak values over the Alps and the Pyrenees. Also, there is an organization of the maxima along a southeast-northwest line in these areas, which is related to bands of positive and negative vertical velocity being formed perpendicular to the flow direction. These structures are not believed to be realistic but the mechanisms for their formation are not yet clear. In the run with the new diffusion scheme, the amplitude of these vertical velocity bands is strongly reduced, resulting in a much smoother precipitation field over the mountainous regions.

7. Results from Parallel Experiments

Tests experiments with the modified horizontal diffusion scheme have been conducted at MeteoSwiss and at DWD over longer time periods. At MeteoSwiss, the LM was rerun for November 2000 and compared with the operational implementation and with model versions

using topographical filtering. The stepwise form (22) of the orographic limiter was used. At DWD, the period from 31 July 2001 to 24 August 2001 was rerun using the continuous form (23) of the topographical limiter function. In this experiment, the full data assimilation cycle including the soil moisture analysis has been involved. Also, a weak filtering of topography is used as in the operational model version. For the impact of the filtering of LM-topography, see Gassmann (2001).

7.1 Parallel Runs at MeteoSwiss

The test experiment for November 2000 was evaluated using the standard Swiss verification package (F. Schubiger, pers. comm.) for surface parameters. The verification is against measurements taken by synoptical and automatic stations in Switzerland (the ANETZ).

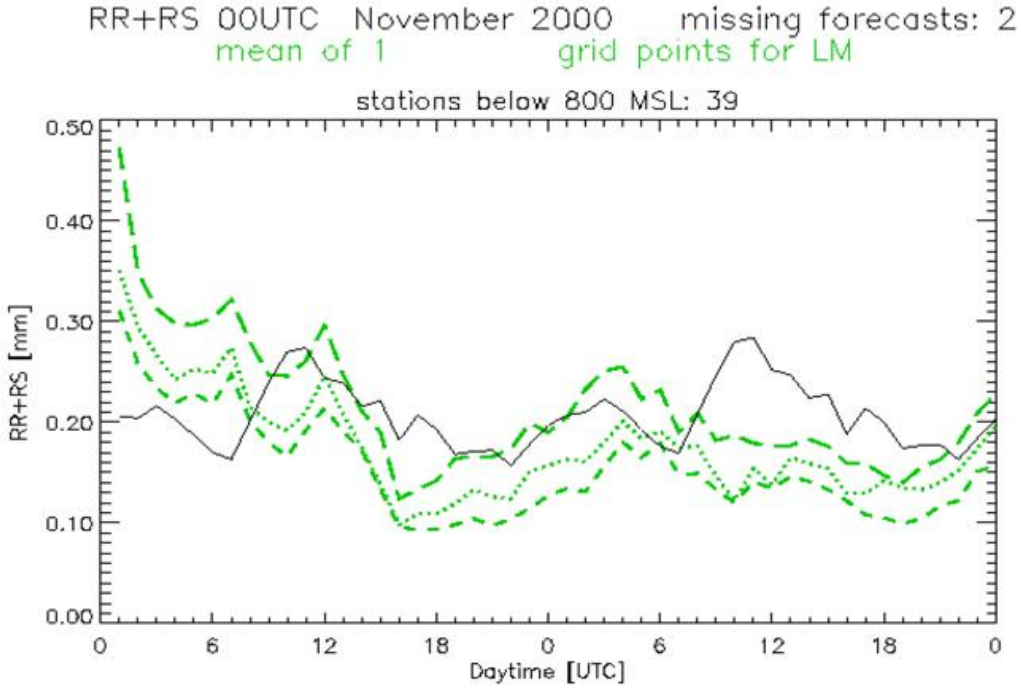


Figure 13: Monthly mean diurnal cycle of predicted and observed precipitation for November 2000 at ANETZ-stations in Switzerland. Full line: observations. Short-dashed line: model version with weak filtering of topography. Dotted line: model version with strong filtering of topography. Long-dashed line: model version with weak filtering and modified horizontal diffusion.

Figure (13) shows the monthly mean diurnal cycle of total precipitation for the 48-h forecast period of all 00 UTC runs compared to the observations. All three model versions overestimate the precipitation amount during the first 6 hours of simulation time because of the spin-up phenomenon (no data assimilation has been used). Later on, the forecasts using a weak topographical smoothing with a filter-parameter $\epsilon = 0.1$ underestimate the observed amount of rain and snow significantly, but less than the former operational version without filtering (not shown). A much stronger smoothing of the topography by using $\epsilon = 10.0$ results in slightly larger precipitation amounts which, however, are still below the level indicated by the observed data. The combination of the weakly filtered topography with the new scheme for horizontal diffusion fits more closely to the observations during most of the simulation time.

The verification shown in Fig. (13) used the nearest-gridpoint method, i.e. only one LM-gridpoint was used for the comparison with the observation. It is interesting to note that

the results depend on the method used for verification: If a horizontal average of 5 or 13 gridpoints is used (upscaling), then the predicted precipitation amounts for the model versions using a filtered orography increase slightly to compare more favorably with the observations. However, when the modified diffusion scheme is applied, then the results depend much less on the verification method. This indicates a much smaller spatial variability than when using a filtered topography only.

Table 1: Frequency bias of 00 UTC LM precipitation forecasts during November 2000 at ANETZ-stations in Switzerland (all 6-h intervals of 48hr forecasts).

Station Selection	Model Version	Threshold (mm/6h) at				
		0.1	2.0	10.0	30.0	50.0
Stations < 800 m	LM filt+hdiff	108	93	89	170	-
	LM at Met.Sw.	87	57	61	105	-
	LM at DWD	74	48	48	35	-
All stations	LM filt+hdiff	111	88	72	126	-
	LM at Met.Sw.	95	63	51	78	-
	LM at DWD	84	54	41	32	-

The frequency bias of the LM-forecasts for November 2000 at ANETZ-stations is shown in Table 1 for various threshold values, where all 6-h intervals of the 48-h forecasts have been considered. The upper part of the table gives the results for all stations with altitude below 800 m, i.e. mountain stations have been excluded. The operational LM-versions at MeteoSwiss and at DWD, which both were run without topographical filtering at that time, show a significant underestimation of precipitation, especially for precipitation amounts exceeding the 2mm/6h and 10mm/6h thresholds. This underestimation is more severe in the DWD model version (using a full data assimilation cycle). Note that the heavy precipitation class with a threshold of 30mm/6h is statistically not significant (only 0.3% of all cases) and thus is not considered here. By applying a weak topographical filtering and the new horizontal diffusion scheme (LM filt+hdiff), the higher precipitation amounts are much better represented in the model forecasts: there is still an underestimation, but it is much smaller than with the operational version. For smaller precipitation amounts with a threshold of 0.1 mm/6h, however, a slight overprediction can be noticed.

The impact of the new scheme for horizontal diffusion is much smaller for surface parameters other than precipitation. Figure (14) displays the mean diurnal cycle of 2m-temperature (top) and 2m-dewpoint depression (bottom) for November 2000 over Switzerland. The model version without filtering of topography underestimates the extrema of the 2m-temperature, but more severe the nighttime minimum, resulting in a too large amplitude of the 2m-temperature (5.7 K compared to the observed 3.6 K on day 2). The model version with filtered topography reduces this amplitude error by about 50 %, the amplitude is only 4.9 K in this case. An additional inclusion of the new horizontal diffusion scheme has only a slight impact with a further reduction of the amplitude to 4.7 K. The 2m-dewpoint depression appears to be too large in the standard model runs, i.e. the surface layer is too dry over the Alpine area. By using a filtered topography, this type of error is significantly reduced, especially during nighttime. At noon, the model is now simulating a slightly too moist surface layer. An additional moistening effect can be noticed from applying the new horizontal diffusion scheme.

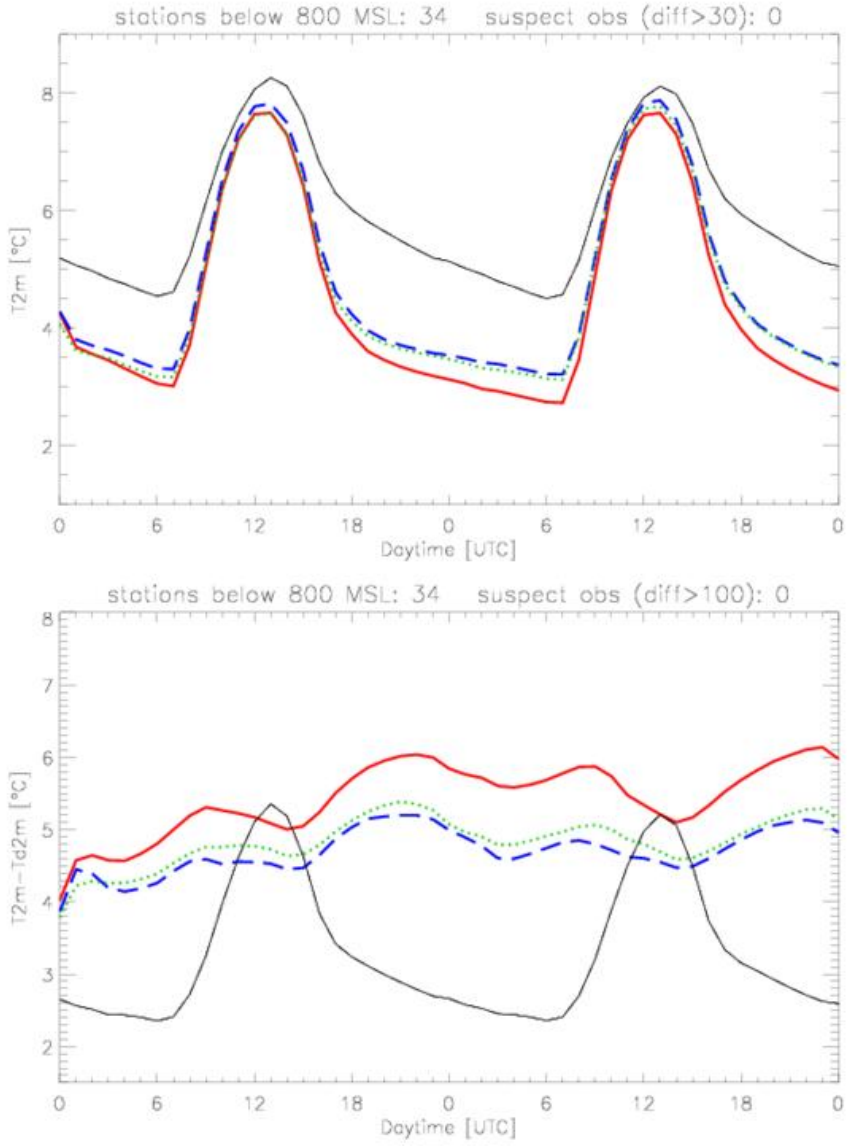


Figure 14: Monthly mean diurnal cycle of predicted and observed 2m-temperature (top) and 2m-dewpoint depression (bottom) for November 2000 at ANETZ-stations below 800m altitude in Switzerland. Full black line: observations. Full red line: former operational version without filtering of topography. Dotted green line: model version with weak filtering of topography. Dashed blue line: model version with weak filtering and modified horizontal diffusion.

7.2 Parallel Runs at DWD

The parallel test experiment at DWD for the August 2001 period was evaluated using the standard verification package for surface weather parameters (U. Damrath, pers. comm.). The verification is against observations from Synop Stations in the integration domain of LM at DWD, and the only difference between the operational and the experimental runs is the inclusion of the new horizontal diffusion scheme.

Fig. (15) shows mean verification scores of various surface parameters as a function of forecast time for all weather stations in the domain. The root mean square errors of 10m-wind, surface pressure, 2m-temperature and 2m-dewpoint depression, as well as the percent-correct score for cloud cover, are practically the same for the experimental and operational runs. A slight improvement with the new version of LM can be noticed for precipitation, especially for

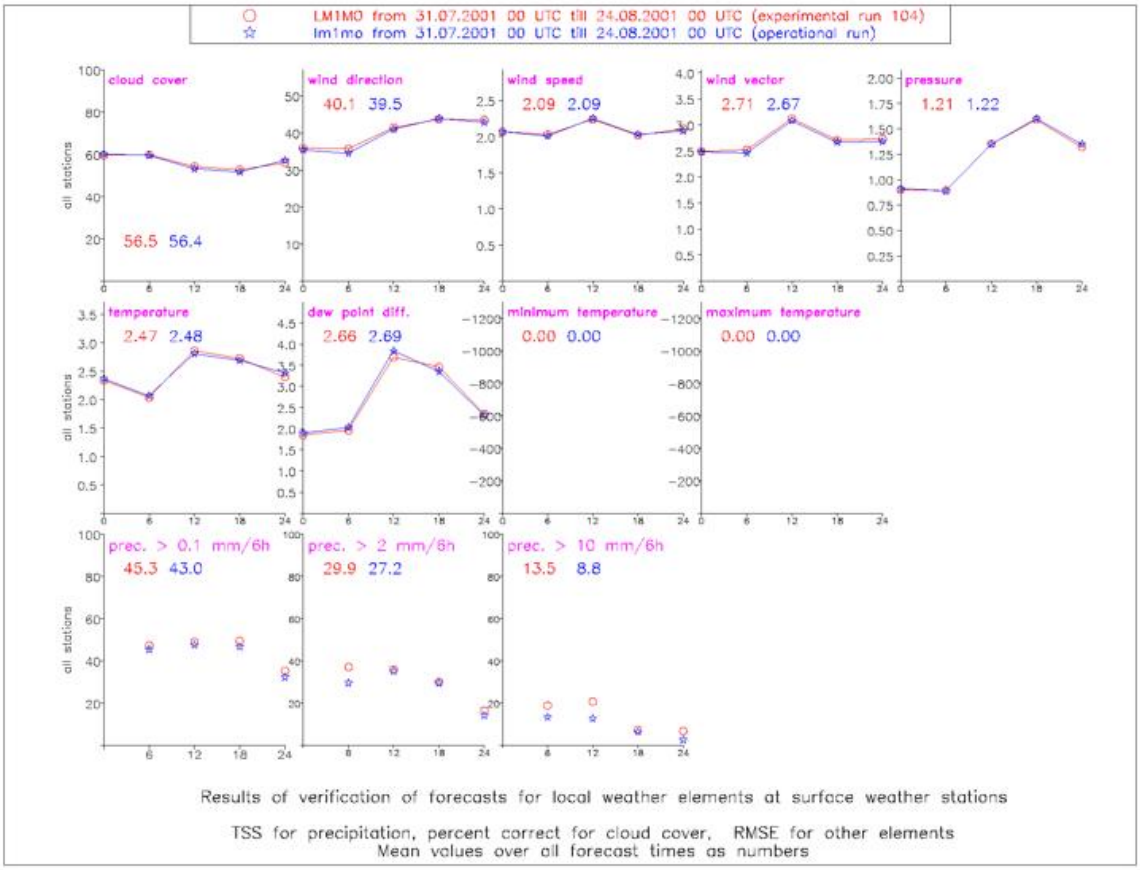


Figure 15: Mean verification scores at all Synop Stations in the LM integration domain for the period 31 July to 24 August 2001 as a function of forecast time (00, 06, 12, 18, 24 h). Verification time is 00 UTC. Red – experimental run exp_104, blue – operational run. Root-mean-square error for all elements except for cloud cover (percent correct) and precipitation (TSS); numbers are mean values over all forecast times. Top (from left to right): cloud cover, wind direction, wind speed, wind vector and surface pressure. Middle (from left to right): temperature, dew point difference, minimum and maximum temperature. Bottom: TSS of 6 h precipitation amounts (prec) for the three indicated threshold values.

higher precipitation amounts. For a threshold value of 10mm/6h the TSS score increases from 8.8 to 13.4, indicating a more reliable prediction of heavy precipitation events.

When considering mean verification scores of all stations in the domain, there will be a large contribution of stations in non-mountainous areas. Fig. (16) displays the mean verification scores for Synop Stations with an altitude between 300m and 800m above sea-level. These stations are representative for mountainous areas in the vicinity of steep terrain, where the impact of the orographical limiter in the diffusion scheme is expected to be more noticeable. As in case of all stations, the scores for the 10m-wind and surface pressure are indifferent to the change in the horizontal diffusion scheme. However, there is a marginal improvement of cloud cover, and the rmse-errors for the 2m-dewpoint depression are slightly smaller, whereas the rmse-errors of the 2m-temperature remain practically the same. This indicates – similar to the verification results in Fig. (14) for the diurnal cycle of 2m-temperature and dewpoint over Switzerland – that the near-surface moisture is affected by the orographically limited diffusion to a larger extend than temperature. The quality of the precipitation forecasts increases significantly for all threshold values, as seen in the lower panel of Fig. (16).

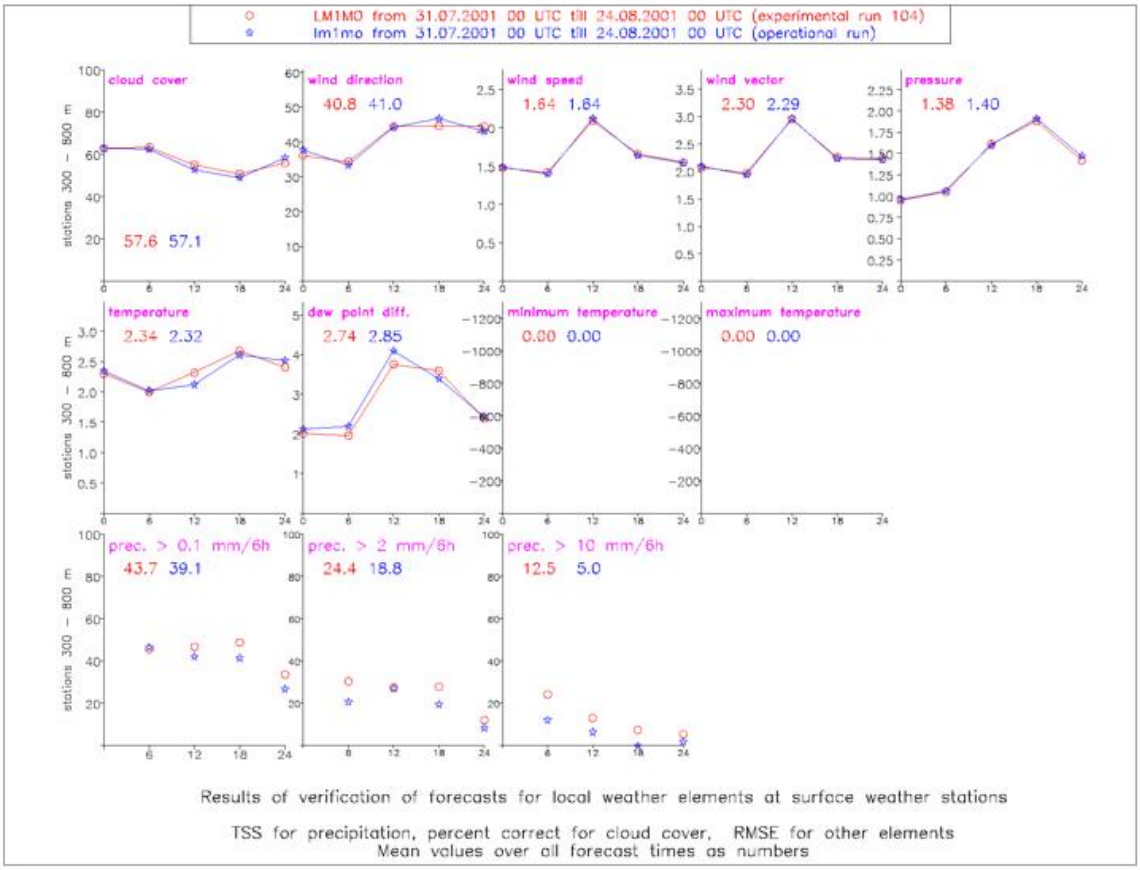


Figure 16: As in Figure 15 except for all Synop Stations with an altitude between 300m and 800m above sea-level.

8. Implementation of the Scheme

The new scheme for monotonic numerical diffusion including orographic flux limiting has been implemented as an option in model version `lm_f90 V 2.9`. It can be switched on by setting the parameter `itype_hdiff = 2` in the NAMELIST-Input list `INPUT_DYN`. Orographic limiting is done for temperature, specific humidity and specific cloud water content only. All other prognostic variables, i.e the three wind components and the perturbation pressure, are treated with the quasi-monotonic Xue limiter. Three additional control parameters have been introduced in this NAMELIST-Input group. Table 2 summarizes the new input parameters.

Table 2: New control parameters in the NAMELIST-Input group `INPUT_DYN`.

Parameter	Definition / Purpose	Default value
`itype_hdiff`	a switch to select a scheme for horizontal diffusion =1: regular 4th-order linear horizontal diffusion =2: new monotonic 4th-order scheme	`itype_hdiff = 2`
`hd_max:`	the threshold value H_{max} in the quadratic form (23) of the orographic flux limiter in m.	`hd_max = 250`
`hd_cor_t:`	a factor by which the standard coefficient for numerical diffusion is reduced in case of temperature and pressure smoothing.	`hd_cor_t = 0.75`
`hd_cor_q:`	a factor by which the standard coefficient for numerical diffusion is reduced in case of humidity and cloud water smoothing.	`hd_cor_q = 0.50`

9. Summary

Most NWP models require numerical smoothing to damp small-scale (2 grid interval) noise being related to stepwise or singular signals which are permanently generated in a nonlinear model. Regular high order linear diffusion, however, tends to introduce unphysical solutions and thus new noise on the resolvable scales. In order to achieve monotonic and mass-conserving numerical diffusion, a new scheme based on direct multi-dimensional flux-limiting has been constructed.

Tests with 1-D and 2-D idealized cases show the beneficial impact of the new scheme. All over- and undershoots are removed from the solution. In contrast to a simple version using the Xue-limiter, the scheme with a direct flux-limiter guarantees a strictly monotonic solution. In LM simulations of real cases considered so far, there is only a relatively small impact from using monotonic 4th order diffusion with a tendency for lower vertically integrated cloud water and smaller peak precipitation amounts.

Numerical smoothing is often realized as horizontal diffusion, i.e. along surfaces of constant vertical coordinate. As most NWP models use a terrain-following vertical coordinate, this will result in systematic numerical biases, as an unwanted vertical mixing in physical space is implied. This type of numerical error will increase with increasing steepness of the topography, and thus poses a severe problem in high-resolution regional models. Current remedies, such as doing diffusion on z- or p-surfaces or applying a local reduction of the diffusion coefficients, are not mass-conserving and will thus introduce other errors. With the new smoothing scheme, the topography-induced biases can be reduced without violating mass conservation while still maintaining monotonicity by simply applying an orographic limiter to the diffusive fluxes at cell interfaces.

LM test simulations with the orographical limiter in cases of southerly Föhn flow over the Alps showed a noticeable improvement of the predicted precipitation field. The spatial distribution of rain over mountainous areas appears to be much less noisy and the peak values over mountain tops are significantly reduced compared to the reference runs with standard 4th-order horizontal diffusion. Also, the dry valley effect is removed and the model's tendency for blocking frontal precipitation north of the Alps is weakened.

Parallel test experiments with the modified horizontal diffusion scheme have been conducted at MeteoSwiss and at DWD for longer time periods. The statistical evaluation against observed surface weather parameters revealed a neutral impact of the new smoothing scheme to most parameters, but a beneficial impact to the predicted precipitation, especially in mountainous areas.

Acknowledgements

Thanks to all colleagues who contributed to this work: J.-M Bettems implemented and supported the test suite at MetoSwiss, F. Schubiger did the statistical evaluation at MeteoSwiss, T. Hanisch supported the experimental test suite at DWD and U. Damrath did the statistical evaluation at DWD. Special thanks to A. Gassmann and D. Majewski for discussions and helpful suggestions.

References

Gassmann, A., 2001: Filtering of LM-Orography. *COSMO Newsletter*, No.1, 71-78.

Raymond, W.H., 1988: High-order low-pass implicit tangent filters for use in finite area calculations. *Mon. Wea. Rev.*, **116**, 2132-2141.

Shapiro, R., 1975: Linear filtering. *Math. Comp.*, **29**, 1094-1097.

Smolarkiewicz, P.K., 1989: Comment on "A positive definite advection scheme obtained by nonlinear renormalization of the advective fluxes". *Mon. Wea. Rev.*, **117**, 2626-2632.

Xue, M., 2000: High-Order Monotonic Numerical Diffusion and Smoothing. *Mon. Wea. Rev.*, **128**, 2853-2864.

Zalesak, S.T.,1979: Fully multidimensional flux-corrected transport algorithms for fluids. *J. Comp. Phys.*, **31**, 335-362.

Zängl, G., 2000: A modified temperature diffusion scheme for simulations over complex terrain and its application to idealized Foehn simulations. *MAP Newsletter*, No. 13.

List of COSMO Newsletters and Technical Reports

(available for download from the COSMO Website: www.cosmo-model.org)

COSMO Newsletters

Newsletter No.1, February 2001.

COSMO Technical Reports

No. 1, Dmitrii Mironov and Matthias Raschendorfer (2001): *Evaluation of Empirical Parameters of the New LM Surface-Layer Parameterization Scheme. Results from Numerical Experiments Including the Soil Moisture Analysis.*

No. 2, Reinhold Schrodin and Erdmann Heise (2001): *The Multi-Layer Version of the DWD Soil Model TERRA_LM.*

No. 3, Günther Doms (2001): *A Scheme for Monotonic Numerical Diffusion in the LM.*

COSMO Technical Reports

Issues of the COSMO Technical Reports series are published by the *Consortium for Small-Scale Modelling* at non-regular intervals. COSMO is a European group for numerical weather prediction with participating meteorological services from Germany (DWD, AWGeophys), Greece (HNMS), Italy (UGM, ARPA-SMR) and Switzerland (MeteoSwiss). The general goal is to develop, improve and maintain a non-hydrostatic limited area modelling system to be used for both operational and research applications by the members of COSMO. This system is initially based on the Lokal-Modell (LM) of DWD with its corresponding data assimilation system.

The Technical Reports are intended

- for scientific contributions and a documentation of research activities,
- to present and discuss results obtained from the model system,
- to present and discuss verification results and interpretation methods,
- for a documentation of technical changes to the model system,
- to give an overview of new components of the model system.

The purpose of these reports is to communicate results, changes and progress related to the LM model system relatively fast within the COSMO consortium, and also to inform other NWP groups on our current research activities. In this way the discussion on a specific topic can be stimulated at an early stage. In order to publish a report very soon after the completition of the manuscript, we have decided to omit a thorough reviewing procedure and only a rough check is done by the editors and a third reviewer. We apologize for typographical and other errors or inconsistencies which may still be present.

At present, the Technical Reports are available for download from the COSMO web site (www.cosmo-model.org). If required, the member meteorological centres can produce hard-copies by their own for distribution within their service. All members of the consortium will be informed about new issues by email.

For any comments and questions, please contact the editors:

Günther Doms
guenther.doms@dwd.de

Ulrich Schättler
ulrich.schaettler@dwd.de

Consortium for Small-Scale Modelling

Technical Report No. 29

A Stochastic Pattern Generator for ensemble applications

July 2016

DOI: 10.5676/DWD_pub/nwv/cosmo-tr_29

Deutscher Wetterdienst
MeteoSwiss
Ufficio Generale Spazio Aereo e Meteorologia
ΕΘΝΙΚΗ ΜΕΤΕΩΡΟΛΟΓΙΚΗ ΥΠΗΡΕΣΙΑ
Instytucie Meteorogii i Gospodarki Wodnej
Administratia Nationala de Meteorologie
ROSHYDROMET
Agenzia Regionale per la Protezione Ambientale del Piemonte
Agenzia Regionale per la Protezione Ambientale dell'Emilia-Romagna
Centro Italiano Ricerche Aerospaziali
Amt für GeoInformationswesen der Bundeswehr



www.cosmo-model.org

Editor: Massimo Milelli, ARPA Piemonte

A Stochastic Pattern Generator

for ensemble applications

M. Tsyrulnikov and D. Gayfulin

Hydrometeorological Center of Russia
11-13 B. Predtechensky Lane
123242 Moscow
Russia

Contents

1 Abstract **5**

2 Introduction **5**

2.1 Stochastic dynamic prediction 5

2.2 Model errors 5

2.3 Ensemble prediction 6

2.4 Practical model error modeling 6

3 SPG: Requirements **8**

4 The proposed solution **8**

5 Tentative first-order SPG model **9**

5.1 Physical-space model 9

5.2 Spectral-space model 9

5.3 Stationary spectral-space statistics 10

5.4 Physical-space statistics 11

5.5 Imposing the SPG requirements 12

5.5.1 "Proportionality of scales" implies that $q = \frac{1}{2}$ 12

5.5.2 For $\mathsf{Var}\,\xi(t, \mathbf{s})$ to be finite, $\alpha(t, \mathbf{s})$ needs to be a red noise in space . . . 13

5.5.3 Implications for the SPG design 13

6 Higher-order in time model **13**

6.1 Motivation and formulation 13

6.2 Stationary spectral-space statistics 14

6.3 Finite-variance criterion 15

6.4 Isotropy in space-time 15

6.4.1 Spatial isotropy 15

6.4.2 Spatio-temporal spectra 16

6.4.3 Continuity of realizations of ξ in space-time 17

6.5 Spatio-temporal covariances: the Matérn class 17

6.5.1 Spatial correlation functions 18

6.5.2 Temporal correlation functions 18

6.5.3 Spatio-temporal correlations 19

6.6 The final formulation of the SPG model 19

7 Time discrete solver for the third-order in time SPG model 21

7.1 The spectral solver 21

7.2 Correction of spectral variances 21

7.3 "Warm start": ensuring stationarity from the beginning of time integration . 22

7.4 Computational efficiency 22

7.4.1 Making the time step Δt dependent on the spatial wavenumber k . . . 22

7.4.2 Introduction of a coarse grid in spectral space 23

7.4.3 Numerical acceleration: results 24

7.5 Examples of the SPG fields 25

8 Application to the COSMO model 25

9 Discussion 28

9.1 Physical-space or spectral-space SPG solver? 28

9.2 Extensions of the SPG 28

10 Conclusions 29

10.1 Summary 29

10.2 Applications 30

Appendix A Illustration of the "proportionality of scales" property 31

Appendix B Spatio-temporal structure of the driving 4-D noise 33

B.1 White noise 33

B.2 Spectrum of the white noise on $\mathbb{T}^d$ 33

B.3 Space-integrated spatio-temporal white noise on $\mathbb{T}^d \times \mathbb{R}$ 34

B.4 Spatial spectrum of a spatio-temporal white noise 34

B.5 Spectral decomposition of a white in time and colored in space noise 35

B.6 Discretization of the spectral processes $\tilde{\alpha}_{\mathbf{k}}(t)$ in time 35

Appendix C Physical-space approximation of the operator $\sqrt{1-\lambda^2\Delta}$ 36

Appendix D Stationary statistics of a higher-order OSDE 39

Appendix E Smoothness of sample paths of the spatial Matérn random field for different ν 41

Appendix F Stationary statistics of a time discrete higher-order OSDE 43

F.1 First-order numerical scheme 43

F.2 Third-order numerical scheme 43

1 Abstract

A generator of spatio-temporal pseudo-random Gaussian fields that satisfy the "proportionality of scales" property (Tsyroulnikov 2001) is presented. The generator is based on a third-order in time stochastic differential equation with a pseudo-differential spatial operator defined on a limited area 2D or 3D domain in the Cartesian coordinate system. The generated pseudo-random fields are homogeneous and isotropic in space-time. The correlation functions in any spatio-temporal direction belong to the Matérn class. The spatio-temporal correlations are non-separable. A spectral-space numerical solver is implemented and accelerated exploiting properties of real-world geophysical fields, in particular, smoothness of their spatial spectra. The generator is designed to simulate additive or multiplicative, or other spatio-temporal perturbations that represent uncertainties in numerical prediction models in geophysics. The generator is tested with the COSMO model as a source of additive spatio-temporal perturbations to the forecast model fields.

2 Introduction

2.1 Stochastic dynamic prediction

Since the works of [1] and [2], we know that accounting for the uncertainty in the initial forecast fields can improve weather (and other geophysical) predictions. Assigning a probability distribution for the truth at the start of the forecast (instead of using deterministic initial data) and attempting to advance this distribution in time according to the dynamic (forecast) model is called stochastic dynamic prediction.

The advantage of the stochastic dynamic prediction paradigm is twofold. First, the resulting forecast probability distribution provides a valuable measure of the *uncertainty* in the prediction, leading to probabilistic forecasting and flow-dependent background-error statistics in data assimilation. Second, for a nonlinear physical model, switching from the deterministic forecast to the mean of the forecast probability distribution improves the mean-square accuracy of the prediction, i.e. can improve the deterministic forecasting.

2.2 Model errors

Since [3], we realize that not only uncertainties in the initial data (analysis errors) matter, forecast model (including boundary conditions) imperfections also play an important role. Simulation of model errors is the subject of this study, so we define them now. Let the forecast model be of the form

$$\frac{\mathrm{d}\mathbf{x}}{\mathrm{d}t} = \mathbf{F}(\mathbf{x}), \tag{1}$$

where t is time, $\mathbf{x}$ is the vector that represents the (discretized) state of the system, and $\mathbf{F}$ is the model (forecast) operator. The imperfection of the model Eq.(1) means that the (appropriately discretized) truth does *not* exactly satisfy this equation. The discrepancy is called the model error [e.g. 4]:

$$\boldsymbol{\xi}^t = \mathbf{F}(\mathbf{x}^t) - \frac{\mathrm{d}\mathbf{x}^t}{\mathrm{d}t}. \tag{2}$$

The true model error $\boldsymbol{\xi}^t$ is normally unknown. In order to include model errors in the stochastic dynamic prediction paradigm, one *models* $\boldsymbol{\xi}^t(t)$ as a *random process*, $\boldsymbol{\xi}(t)$, or, in

other words, as a spatio-temporal random field $\xi(t, \mathbf{s})$ (where $\mathbf{s}$ is the spatial vector). The probability distribution of $\boldsymbol{\xi}(t)$ is assumed to be known.

Rearranging the terms in Eq.(2), and replacing the unknown $\boldsymbol{\xi}^t$ with its stochastic counterpart $\boldsymbol{\xi}$, we realize that the resulting model of truth is the stochastic dynamic equation

$$\frac{\mathrm{d}\mathbf{x}}{\mathrm{d}t} = \mathbf{F}(\mathbf{x}) - \boldsymbol{\xi}. \tag{3}$$

Thus, the extended stochastic dynamic prediction (or modeling) paradigm requires two input probability distributions (that of initial errors and that of model errors) and aims to transform them to the output (forecast) probability distribution.

2.3 Ensemble prediction

Stochastic dynamic modeling of complex geophysical systems is hampered by their high dimensionality and non-linearity. The output probability distribution appears to be in most cases analytically intractable. An affordable approximate solution is provided by the Monte-Carlo method called in geophysics *ensemble prediction*.

In ensemble prediction, the input uncertainties (i.e. initial and model errors) are represented by simulated *pseudo-random draws* from the respective probability distributions. A relatively small affordable number of these draws are fed to the forecast model giving rise to an *ensemble* of predictions (forecasts). Members of this ensemble (called ensemble forecasts) are solutions to Eq.(3) with $\boldsymbol{\xi}$ replaced with simulated pseudo-random draws from the model-error probability distribution. The ensemble forecasts start from the initial data perturbed according to the probability distribution of initial errors.

If initial and model errors are sampled from the correct respective distributions, then the forecast ensemble members are draws from the correct probability distribution of the truth given all available external data (initial and boundary conditions). This mathematically justifies the ensemble prediction principle. From the practical perspective, members of the forecast ensemble can be interpreted as "potential truths" consistent with all available information.

In what follows, we concentrate on the model error field $\xi(t, \mathbf{s})$. We briefly review existing models for $\xi(t, \mathbf{s})$ and then present our stochastic pattern generator, whose goal is to simulate pseudo-random draws of $\xi(t, \mathbf{s})$ from a meaningful and flexible distribution.

2.4 Practical model error modeling

In meteorology, our knowledge of the actual model error probability distribution is scarce. Justified stochastic model-error models are still to be devised and verified. In the authors' opinion, the best way to stochastically represent spatio-temporal forecast-model-error fields is to treat each error source separately, so that, say, each physical parametrization is accompanied with a spatio-temporal stochastic model of its uncertainty. Or, even better, to completely switch from deterministic physical parameterizations to stochastic ones. There is a growing number of such developments [see 5, for a review], but the problem is so complex that we cannot expect it to be solved in the near future. Its solution is further hampered by the fact that the existing meteorological observations are too scarce and too inaccurate for model errors to be objectively identified by comparison with measurement data with satisfactory accuracy [6].

As a result, in meteorology *ad-hoc* model-error models are in wide use. The existing approaches include generating pseudo-random additive or multiplicative perturbations of the right-hand sides of the model equations [e.g. 7, 8] in the course of forecast. These two model-error modeling techniques as well as Stochastic Kinetic Energy Backscatter schemes [9] require a pseudo-random spatio-temporal field as a stochastic input. Stochastic parameterization schemes can also demand such fields [see e.g. 10].

The simplest non-constant pseudo-random field is the white noise, i.e. the uncorrelated in space and time random field. The white noise is the default forcing in stochastic differential equations [e.g. 11, 12]. Its advantage is the complete absence of any spatio-temporal structure, it is a pristine source of stochasticity. But in model-error modeling, this lack of structure precludes its direct use as an additive or multiplicative perturbation field because model errors are related to the weather pattern and so should be correlated (dependent) both in space and time. Tsyrulnikov [13] showed in a simulation study that model errors can exhibit complicated spatio-temporal behavior.

A correlated pseudo-random spatio-temporal field can be easily computed by generating independent random numbers at points of a *coarse* spatio-temporal grid and then assigning each of them to all model grid points within the respective coarse-grid cell [8]. As a result, the model-grid field becomes correlated in space and time. The decorrelation space and time scales are, obviously, defined by the respective coarse-grid spacings. This determines the choice of the coarse grid, e.g. in [8] the spatial grid spacing was about 1000 km and the temporal one 6 hours). This technique is extremely simple but it suffers from two flaws.

First, the resulting model-grid field appears to be discontinuous and inhomogeneous. Second, the spatio-temporal structure of the field is not scale dependent, that is, the resulting temporal length scales do not depend on the respective spatial scales. In reality, longer spatial scales "live longer" than shorter spatial scales, which "die out" quicker. This 'proportionality of scales' is widespread in geophysical fields [see 14, and references therein] and other media, [e.g. 15, p.129], so we believe this property should be represented by model-error models. Note also that the "proportionality of scales" is a special case of the *non-separability* of spatio-temporal covariances. For a critique of simplistic separable space-time covariance models, see [16, 17, 18] and Appendix A in this report.

Another popular pseudo-random field generation technique in space and time employs a spectral transform in space and then imposes independent temporal auto-regressions for the coefficients of the spectral expansion [19, 9, 20, 21, 22]. This technique is more general and produces homogeneous fields, but the above implementations use *the same time scale* for all spatial wavenumbers so that there are still no space-time interactions in the generated spatio-temporal fields.

In this report, we propose and test a spatio-temporal Stochastic (pseudo-random) Pattern Generator (SPG) that accounts for the above "proportionality of scales" and imposes meaningful space-time interactions. The SPG operates on a limited-area domain. It is based on a (spectral-space) solution to a stochastic partial differential equation, more precisely, to a stochastic differential equation in time with a pseudo-differential spatial operator. In what follows, we present the technique, examine properties of the resulting spatio-temporal fields in 2D and 3D spatial domains, and describe the numerical scheme. We start with a first-order in time SPG model. Then we show that this model needs to be modified in order to meet all the criteria we impose. Eventually, we end up with a third-order in time model. The technique is implemented as a Fortran program freely available from https://github.com/gayfulin/SPG.

3 SPG: Requirements

The general requirements are:

- The SPG should produce stationary in time and homogeneous and isotropic in space Gaussian pseudo-random fields $\xi(t, \mathbf{s})$ in 3D and 2D spatial domains.
- The SPG should be fast enough so that it does not significantly slow down the forecast model computations.
- Variance as well as spatial and temporal length scales of $\xi(t, \mathbf{s})$ are to be tunable.

We also impose more specific requirements:

1. The random field $\xi(t, \mathbf{s})$ should have finite variance and continuous realizations (sample paths).
2. The spatio-temporal covariances should obey the "proportionality of scales" principle: larger (shorter) spatial scales should be associated with larger (shorter) temporal scales [14].
3. The SPG *ansatz* should be flexible enough to allow for practicable solutions in both physical space and spectral space.

4 The proposed solution

We select the general class of *linear evolutionary stochastic partial differential equations* (SPDE) as a starting point in the development of the SPG. This choice is motivated by the flexibility of this class of spatio-temporal models [e.g. 23]. In particular, for an SPDE, it is relatively easy to introduce inhomogeneity in space and time as well as local anisotropy—either by changing coefficients of the spatial operator or by changing local properties of the driving noise. One can also produce non-Gaussian fields by making the random forcing non-Gaussian [e.g. 24, 25]. Physical-space discretizations of SPDEs lead to *sparse* matrices, which give rise to fast numerical algorithms. If an SPDE has constant coefficients, then it can be efficiently solved using spatial spectral-space expansions.

In this study, we develop the SPG that relies on a spatio-temporal stochastic model with *constant coefficients* so that both physical-space and spectral-space solvers can be employed. To facilitate the spectral-space solution, the general strategy is to define the SPG model on a standardized spatial domain. The operational pseudo-random fields are then produced by mapping the generated fields from the standardized domain to the forecast-model domain. In 3D, the standardized spatial domain is chosen to be triply periodic: the three-dimensional (3D) unit torus. In 2D, the standardized domain is the 2D unit torus. The 3D and 2D cases are distinguished by the dimensionality $d = 2$ or $d = 3$ in what follows. To simplify the presentation, the default dimensionality will be $d = 3$.

5 Tentative first-order SPG model

5.1 Physical-space model

The random field in question $\xi(t, \mathbf{s})$ is a function of the time coordinate t and the space vector $\mathbf{s} := (x, y, z)$, where (x, y, z) are the three spatial coordinates. Each of the spatial coordinates belongs to the the unit circle $\mathbb{S}^1$, so that $\mathbf{s}$ is on the unit torus $\mathbb{T}^3 \equiv \mathbb{S}^1 \times \mathbb{S}^1 \times \mathbb{S}^1$ ($\mathbb{T}^2$ in the 2D case).

We start with the simplest general form of a first-order Markov model:

$$\frac{\partial \xi(t, \mathbf{s})}{\partial t} + A\,\xi(t, \mathbf{s}) = \alpha(t, \mathbf{s}), \tag{4}$$

where A is the spatial linear operator to be specified and α is the driving noise postulated to be homogeneous in space and white in time.

The SPG is required to be fast, so we choose A to be a *differential* operator (because, as we noted, in this case a physical-space discretization of A gives rise to a very sparse matrix).

Further, since we wish $\xi(t, \mathbf{s})$ to be homogeneous and isotropic in space, we define A to be a polynomial of the negated spatial Laplacian:

$$A := P(-\Delta) := \sum_{j=0}^{q} c_j (-\Delta)^j, \tag{5}$$

where $P(x)$ is the polynomial and q its degree (a positive integer). We will refer to q as the spatial order of the SPG model. Note that the negation of the Laplacian is convenient because $(-\Delta)$ is a non-negative definite operator.

The coefficients c_j are selected to ensure that the spatial operator $\sum c_j(-\Delta)^j$ has only positive eigen-values not close enough to 0, which can be achieved if all $c_j \geq 0$ and $c_0 > 0$; this guarantees *stability* of the SPG.

The model Eq.(5) appears to be too rich for the purposes of the SPG at the moment, so in what follows we employ an even more reduced (but still quite flexible) form

$$A = P(-\Delta) := \mu(1 - \lambda^2 \Delta)^q, \tag{6}$$

where μ and λ are positive real parameters.

So, we start with the following SPG equation:

$$\frac{\partial \xi(t, \mathbf{s})}{\partial t} + \mu(1 - \lambda^2 \Delta)^q\, \xi(t, \mathbf{s}) = \alpha(t, \mathbf{s}). \tag{7}$$

5.2 Spectral-space model

On the torus $\mathbb{T}^d$, a Fourier series is an expansion in the basis functions $\mathrm{e}^{\mathrm{i}(\mathbf{k},\mathbf{s})} \equiv \mathrm{e}^{\mathrm{i}(\mathrm{mx}+\mathrm{ny}+\mathrm{lz})}$, where the wavevector $\mathbf{k}$ is the triple of integer wavenumbers, $\mathbf{k} := (m, n, l)$. We perform the Fourier decomposition for both $\alpha(t, \mathbf{s})$ and $\xi(t, \mathbf{s})$,

$$\alpha(t, \mathbf{s}) = \sum_{\mathbf{k} \in \mathbb{Z}^d} \tilde{\alpha}_{\mathbf{k}}(t) \mathrm{e}^{\mathrm{i}(\mathbf{k},\mathbf{s})} \tag{8}$$

and

$$\xi(t,\mathbf{s}) = \sum_{\mathbf{k}\in\mathbb{Z}^d} \tilde{\xi}_{\mathbf{k}}(t)\mathrm{e}^{\mathrm{i}(\mathbf{k},\mathbf{s})} \tag{9}$$

(where $\mathbb{Z}$ denotes the set of integer numbers) and substitute these expansions into Eq.(7). Noting that the application of $P(-\Delta)$ to $\mathrm{e}^{\mathrm{i}(\mathbf{k},\mathbf{s})}$ returns $P(\mathbf{k}^2)\,\mathrm{e}^{\mathrm{i}(\mathbf{k},\mathbf{s})}$, recalling that $P(-\Delta)$ is defined by Eq.(6), and using orthogonality of the basis functions, we obtain that Eq.(7) decouples into the set of ordinary stochastic differential equations [OSDE, e.g. 11, 12] in time:

$$\frac{\mathrm{d}\tilde{\xi}_{\mathbf{k}}}{\mathrm{d}t} + a_{\mathbf{k}}\,\tilde{\xi}_{\mathbf{k}}(t) = \tilde{\alpha}_{\mathbf{k}}(t), \tag{10}$$

where

$$a_{\mathbf{k}} := \mu(1+\lambda^2\mathbf{k}^2)^q. \tag{11}$$

From the postulated homogeneity of α in space, its spectral-space coefficients $\tilde{\alpha}_{\mathbf{k}}(t)$ are mutually independent. This is well known for random fields on $\mathbb{R}^d$ (where spectra are continuous), see e.g. Chapter 2 in [26] or section 8 in [27], and can be directly verified in our case of the fields on the torus (where spectra are discrete). Therefore, for different wavevectors $\mathbf{k}$, the resulting spectral-space equations, Eqs.(10)–(11), are probabilistically completely *independent* from each other. This greatly simplifies the solution of the SPG equations because instead of handling the complicated SPDE Eq.(7) we have to solve a number of independent simple OSDEs Eq.(10).

Further, from the postulated whiteness of α in time, all $\tilde{\alpha}_{\mathbf{k}}(t)$ are white in time random processes (see Appendix B.4). So, we may write

$$\tilde{\alpha}_{\mathbf{k}}(t) = \sigma_{\mathbf{k}}\,\Omega_{\mathbf{k}}(t), \tag{12}$$

where $\Omega_{\mathbf{k}}(t)$ are independent *standard* white noises, i.e. derivatives of independent standard Wiener processes $W_{\mathbf{k}}(t)$ such that

$$\Omega_{\mathbf{k}}(t)\mathrm{d}t = \mathrm{d}W_{\mathbf{k}}(t) \tag{13}$$

and $\sigma_{\mathbf{k}}$ are *intensities* of the white-noise processes. In space, $\sigma_{\mathbf{k}}^2$ is proportional to the spatial spectrum of the driving noise $\alpha(t,\mathbf{s})$, see Eq.(8), Eq.(12), and Appendix B. If $\sigma_{\mathbf{k}} = \mathsf{const}$, then $\alpha(t,\mathbf{s})$ is white both in space and time, otherwise $\alpha(t,\mathbf{s})$ is a colored in space and white in time noise.

Thus, the first-order SPG model reduces to a series of OSDEs

$$\mathrm{d}\tilde{\xi}_{\mathbf{k}} + \mu(1+\lambda^2\mathbf{k}^2)^q\,\tilde{\xi}_{\mathbf{k}}\,\mathrm{d}t = \sigma_{\mathbf{k}}\,\mathrm{d}W_{\mathbf{k}}. \tag{14}$$

For practical purposes the series is truncated, so that $\mathbf{k} \equiv (m,n,l)$ is limited: $|m| < m_{max}$, $|n| < n_{max}$, and $|l| < l_{max}$, where m_{max}, n_{max}, and l_{max} are the truncation limits. If not otherwise stated, all the truncation limits are the same and denoted by n_{max}.

5.3 Stationary spectral-space statistics

Equation (14) is a first-order OSDE with constant coefficients sometimes called the Langevin equation, see e.g. [12] or Example 4.12 in [11]. Its generic form is

$$\mathrm{d}\eta + a\eta\,\mathrm{d}t = \sigma\mathrm{d}W, \tag{15}$$

where $\eta(t)$ is the random process in question, a and σ are constants, and $W(t)$ is the standard Wiener process. The solution to Eq.(15) is known as the Ornstein-Uhlenbeck random process, whose stationary (steady-state) temporal covariance function is

$$B_\eta(t) = \frac{\sigma^2}{2a}\,\mathrm{e}^{-\mathrm{a}|\mathrm{t}|} \tag{16}$$

[e.g. 11, Example 4.12]. From Eq.(16), it is clear that a has the meaning of the inverse temporal length scale $\tau := 1/a$.

Now, consider the stationary covariance function of the elementary random process $\tilde{\xi}_{\mathbf{k}}(t)$,

$$\mathsf{E}\,\tilde{\xi}_{\mathbf{k}}(t_0) \cdot \overline{\tilde{\xi}_{\mathbf{k}}(t_0 + t)} = b_{\mathbf{k}} \cdot C_{\mathbf{k}}(t), \tag{17}$$

where $b_{\mathbf{k}}$ is the variance and $C_{\mathbf{k}}(t)$ the correlation function. According to Eq.(9), $\tilde{\xi}_{\mathbf{k}}$ is the spatial spectral component of the random field in question $\xi(t, \mathbf{s})$. Therefore $b_{\mathbf{k}} = \mathsf{Var}\,\tilde{\xi}_{\mathbf{k}}$ is called the *spatial spectrum* of $\xi(t, \mathbf{s})$. From Eqs.(14) and (16), we have

$$b_{\mathbf{k}} = \frac{\sigma_{\mathbf{k}}^2}{2\mu(1 + \lambda^2\mathbf{k}^2)^q} \tag{18}$$

and

$$C_{\mathbf{k}}(t) = \mathrm{e}^{-\frac{|\mathrm{t}|}{\tau_{\mathbf{k}}}}, \tag{19}$$

where

$$\tau_{\mathbf{k}} := \frac{1}{a_{\mathbf{k}}} = \frac{1}{\mu(1 + \lambda^2\mathbf{k}^2)^q} \tag{20}$$

is the temporal length scale associated with the spatial wavevector $\mathbf{k}$.

Note that by the spectrum (e.g. $b_{\mathbf{k}}$), we always mean the *modal* spectrum, i.e. the variance associated with a single basis function (a single wavevector $\mathbf{k}$); the modal spectrum is not to be confused with the variance (or energy) spectrum.

5.4 Physical-space statistics

In the stationary regime (i.e. after an initial transient period has passed), the above independence of the spectral random processes $\tilde{\xi}_{\mathbf{k}}(t)$ (see section 5.2) implies that the random field $\xi(t, \mathbf{s})$ is spatio-temporally *homogeneous*, i.e. invariant under shifts in space and time:

$$\mathsf{E}\,\xi(t, \mathbf{s}) \cdot \overline{\xi(t + \Delta t, \mathbf{s} + \Delta\mathbf{s})} = B(\Delta t, \Delta\mathbf{s}), \tag{21}$$

where

$$B(t, \mathbf{s}) = \sum_{\mathbf{k}} b_{\mathbf{k}}\, C_{\mathbf{k}}(t)\, \mathrm{e}^{\mathrm{i}(\mathbf{k},\mathbf{s})}. \tag{22}$$

In particular, the spatial covariance function is

$$B(\mathbf{s}) = B(t = 0, \mathbf{s}) = \sum_{\mathbf{k}} b_{\mathbf{k}}\, \mathrm{e}^{\mathrm{i}(\mathbf{k},\mathbf{s})}, \tag{23}$$

where it is seen that the spatial spectrum $b_{\mathbf{k}}$ is the Fourier transform of the spatial covariance function $B(\mathbf{s})$. Finally, the variance is

$$\mathsf{Var}\,\xi = B(t = 0, \mathbf{s} = \mathbf{0}) = \sum_{\mathbf{k}} b_{\mathbf{k}}. \tag{24}$$

5.5 Imposing the SPG requirements

In section 3, we have formulated requirements 1–3 the SPG model should satisfy. In more specific terms, they imply the following three conditions.

Requirement 1 states, in particular, that

$$\mathsf{Var}\,\xi < \infty. \tag{25}$$

Next, the more precise formulation of requirement 2 states that that for large k, the temporal length scale $\tau_{\mathbf{k}}$ should be inversely proportional to k:

$$\tau_{\mathbf{k}} \sim \frac{1}{k} \quad \text{as} \quad k \to \infty. \tag{26}$$

Finally, requirement 3 entails that the driving noise $\alpha(t, \mathbf{s})$ should be white not only in time but also in space:

$$\sigma_{\mathbf{k}} = \sigma = \mathsf{const}. \tag{27}$$

This is because the physical-space simulation of the discretized white noise is cheap (since its grid-point values are just independent zero-mean Gaussian pseudo-random variables), whereas to simulate a non-white noise requires building a model for the noise and solving its equations, which is normally expensive (and complicates the design of the SPG).

In the rest of this section we show that these three conditions cannot be simultaneously satisfied for the first-order SPG model Eq.(7).

5.5.1 "Proportionality of scales" implies that $q = \frac{1}{2}$

We start with condition Eq.(26). Substituting Eq.(20) into Eq.(26) yields

$$(1 + \lambda^2 k^2)^q \sim k \quad \text{as k} \to \infty \quad \Leftrightarrow \quad \boxed{q = \frac{1}{2}}. \tag{28}$$

Note that here and elsewhere, boxed equations are the ones that present the key aspects of our final SPG model.

With $q = \frac{1}{2}$, the model's spatial operator A becomes (see Eq.(6))

$$\boxed{A = \mu(1 - \lambda^2 \Delta)^{\frac{1}{2}} \equiv \mu\sqrt{1 - \lambda^2 \Delta}}. \tag{29}$$

This is a pseudo-differential operator [e.g. 28] with the *symbol*

$$\boxed{a(k) := \mu\sqrt{1 + \lambda^2 k^2}}, \tag{30}$$

so that the action of A on the test function $\varphi(\mathbf{s})$ is defined as follows. First, we Fourier transform $\varphi(\mathbf{s})$ getting $\{\tilde{\varphi}_{\mathbf{k}}\}$. Then, $\forall \mathbf{k} \in \mathbb{Z}^d$, we multiply $\tilde{\varphi}_{\mathbf{k}}$ by the symbol $a(k)$. Finally, we perform the backward Fourier transform of $\{a(k)\tilde{\varphi}_k\}$ retrieving the result, the function $(A\varphi)(\mathbf{s})$.

Obviously, there is no problem with the above fractional negated and shifted Laplacian in spectral space (as its action on test functions is well defined, see the previous paragraph). Importantly, the pseudo-differential operator A appears to have nice properties in physical space, too. Specifically, A can be approximated by a discrete-in-space operator which is

a *very sparse matrix*, see Appendix C. So, in both spectral space and physical space, the resulting operator A with the fractional degree $q = \frac{1}{2}$ is numerically tractable.

The spectral-space SPG model Eq.(14) becomes

$$\mathrm{d}\tilde{\xi}_{\mathbf{k}} + \mu\sqrt{1+\lambda^2\mathbf{k}^2}\,\tilde{\xi}_{\mathbf{k}}\,\mathrm{d}t = \sigma_{\mathbf{k}}\,\mathrm{d}W_{\mathbf{k}}. \tag{31}$$

The resulting spatial spectrum is

$$b_k = \frac{\sigma_{\mathbf{k}}^2}{2\mu\sqrt{1+\lambda^2 k^2}}. \tag{32}$$

The SPG model becomes

$$\frac{\partial\xi(t,\mathbf{s})}{\partial t} + \mu\sqrt{1-\lambda^2\Delta}\cdot\xi(t,\mathbf{s}) = \alpha(t,\mathbf{s}). \tag{33}$$

Below, we will see that the choice $q = \frac{1}{2}$ implies that besides the "proportionality of scales", the generated spatio-temporal field has other nice properties.

5.5.2 For $\mathsf{Var}\,\xi(t,\mathbf{s})$ to be finite, $\alpha(t,\mathbf{s})$ needs to be a red noise in space

Next, we turn to condition Eq.(25) in section 5.5. Substituting Eq.(32) into Eq.(24) yields

$$\mathsf{Var}\,\xi = \frac{1}{2\mu}\sum\frac{\sigma_k^2}{\sqrt{1+\lambda^2k^2}}. \tag{34}$$

Assuming that σ_k is smoothly varying, we may approximate the sum in this equation with the integral (where $\sigma(k) = \sigma(\mathbf{k})$ for integer wavenumbers), getting

$$\mathsf{Var}\,\xi \approx \int_{\mathbb{R}^d}\frac{\sigma_k^2}{\sqrt{1+\lambda^2k^2}}\,\mathrm{d}\mathbf{k} \propto \int_{\mathbb{R}}\frac{\sigma_k^2}{\sqrt{1+\lambda^2k^2}}\,k^{d-1}\,\mathrm{d}k. \tag{35}$$

To check the convergence of the integral in Eq.(35), we examine the $k\to\infty$ limit (where $\sqrt{1+\lambda^2k^2}\sim k$). As we know, the integral of this kind converges if the integrand decays faster than $\frac{1}{k^{1+\epsilon}}$ with some $\epsilon > 0$. This is the case whenever

$$\sigma_k^2 \sim \frac{1}{k^{d-1+\epsilon}} \quad \text{as} \quad k\to\infty. \tag{36}$$

So, to satisfy the requirement $\mathsf{Var}\,\xi < \infty$, the spectrum σ_k^2 needs to be a *decaying* function of its argument k. This clearly contradicts to white-in-space-driving-noise condition Eq.(27).

5.5.3 Implications for the SPG design

As we have just seen, the conditions Eqs.(25)–(27) cannot be met by the first-order SPG model. So, the model Eq.(7) is to be somehow changed. The solution is to increase the temporal order of the stochastic model.

6 Higher-order in time model

6.1 Motivation and formulation

Equation (36) shows that with the first order SPG model, we could met both the the finite-variance condition Eq.(25) and the proportionality-of-scales condition Eq.(26) if we specified

a *red* in space (i.e. with the decaying spectrum) driving noise α. The red noise can be obtained by the application of a linear integral operator *with the decaying symbol* to the white noise. The problem here is that with the quite rapidly decaying red-noise spectrum Eq.(36), the support of the physical-space integral operator will be rather large, resulting in a computationally expensive numerical scheme.

The idea is, instead of introducing of an expensive *integral* operator with a decaying symbol to the *right-hand side* of the model, Eqs.(4) or (7) or (33), to introduce a *differential* operator (with a growing symbol) to the *left-hand side* of the SPG equation. The simplest way of doing so is to raise the operator $\partial/\partial t + A$, which already acts in our model on ξ in the l.h.s. of Eq.(4), to a power. This implies that the *temporal order* of the SPG model increases:

$$\boxed{\left(\frac{\partial}{\partial t} + \mu\sqrt{1-\lambda^2\Delta}\right)^p \xi(t,\mathbf{s}) = \alpha(t,\mathbf{s})}, \tag{37}$$

where p is the temporal order of the modified SPG model (a positive integer) and α is white both in time and in space. In spectral space, the model Eq.(37) becomes, obviously,

$$\boxed{\left(\frac{\mathrm{d}}{\mathrm{d}t} + \mu\sqrt{1+\lambda^2 k^2}\right)^p \tilde{\xi}_{\mathbf{k}}(t) = \sigma\,\Omega_{\mathbf{k}}(t)}, \tag{38}$$

where, we recall, $\Omega_{\mathbf{k}}(t)$ are mutually independent standard white noises.

The resulting higher-order SPG model satisfies condition Eq.(27) by construction. Now, we show that the model Eq.(37) can be defined to satisfy the two remaining conditions, Eqs.(25)–(26).

6.2 Stationary spectral-space statistics

For each $\mathbf{k}$, Eq.(38) is a pth-order in time OSDE. In Appendix D, we examine properties the generic pth-order OSDE, specifically, the steady-state statistics of its solution. Using Table 2 in Appendix D, we can write down the stationary variance $b_{\mathbf{k}}$ and the temporal correlation function $C_{\mathbf{k}}(t)$ of the solution to Eq.(38), the process $\tilde{\xi}_{\mathbf{k}}(t)$:

$$b_{\mathbf{k}} \propto \frac{\sigma^2}{\mu^{2p-1}(1+\lambda^2 k^2)^{p-\frac{1}{2}}} \tag{39}$$

and

$$C_{\mathbf{k}}(t) = \left(1 + \frac{|t|}{\tau_{\mathbf{k}}} + r_2\frac{|t|^2}{\tau_{\mathbf{k}}^2} + \cdots + r_{p-1}\frac{|t|^{p-1}}{\tau_{\mathbf{k}}^{p-1}}\right)\mathrm{e}^{-\frac{|t|}{\tau_{\mathbf{k}}}}. \tag{40}$$

Here $r_2, \ldots, r_{p-1}$ are real numbers (given for $p = 1, 2, 3$ in Table 2) and $\tau_{\mathbf{k}}$ is the temporal length scale associated with the spatial wavevector $\mathbf{k}$:

$$\boxed{\tau_{\mathbf{k}} = \frac{1}{\mu\sqrt{1+\lambda^2 k^2}}}. \tag{41}$$

Specifically, for the temporal order $p = 2$, we have

$$b_{\mathbf{k}}|_{p=2} = \frac{\sigma^2}{4\mu^3(1+\lambda^2 k^2)^{\frac{3}{2}}} \tag{42}$$

and

$$C_{\mathbf{k}}(t)|_{p=2} = \left(1 + \frac{|t|}{\tau_{\mathbf{k}}}\right)\mathrm{e}^{-\frac{|t|}{\tau_{\mathbf{k}}}}. \tag{43}$$

For the temporal order $p = 3$, we have

$$\boxed{b_{\mathbf{k}}|_{p=3} = \frac{3\sigma^2}{16\mu^5(1+\lambda^2 k^2)^{\frac{5}{2}}}} \tag{44}$$

and

$$\boxed{C_{\mathbf{k}}(t)|_{p=3} = \left(1 + \frac{|t|}{\tau_{\mathbf{k}}} + \frac{1}{3}\frac{|t|^2}{\tau_{\mathbf{k}}^2}\right) \mathrm{e}^{-\frac{|t|}{\tau_{\mathbf{k}}}}.} \tag{45}$$

From Eq.(41), it is seen that the "proportionality of scales" condition Eq.(26) is indeed satisfied because $\tau_{\mathbf{k}}$ is indeed inversely proportional to k for large k. In order to achieve the desired dependency of $\tau_{\mathbf{k}}$ not only on k (which we already have from Eq.(41)), but also on λ (the greater is λ the greater should be $\tau_{\mathbf{k}}$), we parameterize μ as

$$\mu = \frac{U}{\lambda}, \tag{46}$$

where $U > 0$ is the velocity-dimensioned tuning parameter. With this parameterization, λ affects both the spatial length scale of ξ (due to Eq.(39)) and the temporal length scale (thanks to Eq.(41)). In contrast, U affects only the temporal length scale.

6.3 Finite-variance criterion

Substituting b_k from Eq.(39) into Eq.(24), approximating the sum over the wavevectors by the integral (as in Eq.(35)), and exploiting the isotropy of the integrand yields

$$\mathsf{Var}\,\xi \approx \mathsf{const} \cdot \int_0^\infty \frac{\sigma^2}{(1+\lambda^2 k^2)^{p-\frac{1}{2}}} k^{d-1}\,\mathrm{d}k, \tag{47}$$

so that $\mathsf{Var}\,\xi < \infty$, i.e. the finite-variance condition Eq.(25) is met, whenever

$$\boxed{p > \frac{d+1}{2}}. \tag{48}$$

Thus, in the higher-order-in-time model Eq.(37) we can rely on the white in space and time driving noise $\alpha(t, \mathbf{s})$ *provided that the temporal order is large enough*: in 2D, it is required that $p \geq 2$ whilst in 3D, we have to set up $p \geq 3$.

6.4 Isotropy in space-time

In this subsection, we show that, remarkably, $q = \frac{1}{2}$ is the unique spatial order for which the field $\xi(t, \mathbf{s})$ appears to be isotropic is space-time. In particular, the shape of the correlation function is the same in any spatial or temporal or any other direction in the spatio-temporal domain $\mathbb{T}^d \times \mathbb{R}$.

6.4.1 Spatial isotropy

First, we note that spatial isotropy of the random field ξ is invariance of its covariance function $B(\mathbf{s})$ under rotations. If we were in $\mathbb{R}^d$ rather than on $\mathbb{T}^d$, isotropy of $B(\mathbf{s}) = B(s)$, where $s := |\mathbf{s}|$, would be equivalent to isotropy of its Fourier transform (spectrum) $b(\mathbf{k})$, so that the latter would be dependent only on the modulus of the wavevector $\mathbf{k}$, i.e. the

total wavenumber $k := |\mathbf{k}| = \sqrt{m^2 + n^2 + l^2}$. On the torus, spectra are discrete, i.e. m, n, l take only *integer* values, so, strictly speaking, $b(\mathbf{k})$ cannot be isotropic there. To avoid this technical difficulty, we resort to the device used in sections 5.5.2 and 6.3, the approximation of a sum over the wavevectors by the integral.

Specifically, we assume that $b(\mathbf{k})$ is smooth enough (which is tantamount to the assumption that $B(\mathbf{s})$ decays on length scales much smaller than the domain's extents) for the validity of the approximation

$$B(\mathbf{s}) = \sum_{\mathbf{k}\in\mathbb{Z}^\mathrm{d}} b_\mathbf{k}\, \mathrm{e}^{\mathrm{i}(\mathbf{k},\mathbf{s})} \approx \int_{\mathbb{R}^\mathrm{d}} \mathrm{b}(\mathbf{k})\, \mathrm{e}^{\mathrm{i}(\mathbf{k},\mathbf{s})} \mathrm{d}\mathbf{k}, \tag{49}$$

where $b(\mathbf{k})$ is a smooth function of the real vector argument $\mathbf{k}$ such that $\forall \mathbf{k} \in \mathbb{Z}^\mathbf{d}, \mathbf{b}(\mathbf{k}) = \mathbf{b_k}$. From Eq.(49), it is obvious that $B(\mathbf{s})$ is indeed approximately invariant under rotations because so is $b(\mathbf{k})$, see Eq.(39).

In the theoretical analysis in this section, we will rely on the approximation Eq.(49) and thus assume that the "spectral grid" is dense enough for the spatial spectra to be treated as continuous ones.

6.4.2 Spatio-temporal spectra

Consider the OSDE Eq.(38) in the stationary regime. Following [27, section 8], the stationary random process can be spectrally represented as the stochastic integral

$$\tilde{\xi}_\mathbf{k}(t) = \int_{\mathbb{R}} \mathrm{e}^{\mathrm{i}\omega t}\, \mathrm{Z}_\mathbf{k}(\mathrm{d}\omega), \tag{50}$$

where ω is the angular frequency (temporal wavenumber) and Z is the orthogonal stochastic measure such that

$$\mathsf{E}\,|Z_\mathbf{k}(\mathrm{d}\omega)|^2 = b_\mathbf{k}(\omega)\,\mathrm{d}\omega, \tag{51}$$

where $b_\mathbf{k}(\omega)$ is the spectral density of the process $\tilde{\xi}_\mathbf{k}(t)$ and, at the same time, the spatio-temporal spectrum of the field ξ. In the spectral expansion of the driving white noise $\Omega_\mathbf{k}(t)$ (see Eq.(38)),

$$\Omega_\mathbf{k}(t) = \int_{\mathbb{R}} \mathrm{e}^{\mathrm{i}\omega t}\, \mathrm{Z}_{\Omega_\mathbf{k}}(\mathrm{d}\omega), \tag{52}$$

we have $\mathsf{E}\,|Z_{\Omega_\mathbf{k}}(\mathrm{d}\omega)|^2 = \mathsf{const}\cdot\mathrm{d}\omega$ because the white noise has constant spectral density. Next, we substitute Eqs.(50) and (52) into Eq.(38), getting

$$(\mathrm{i}\omega + \mu\sqrt{1+\lambda^2 k^2})^p Z_\mathbf{k}(\mathrm{d}\omega) = Z_{\Omega_\mathbf{k}}(\mathrm{d}\omega). \tag{53}$$

In this equation, taking expectation of the squared modulus of both sides yields

$$[(\omega^2 + \mu^2(1+\lambda^2 k^2)]^p\, b_\mathbf{k}(\omega) = \mathsf{const}, \tag{54}$$

whence, recalling that $\mu = U/\lambda$ and introducing the scaled angular frequency $\omega' := \omega/U$, we finally obtain

$$b_\mathbf{k}(\omega') \equiv b_\mathbf{K} \propto \frac{1}{(\lambda^{-2} + (\omega')^2 + k^2)^p} = \frac{1}{(\lambda^{-2} + \mathbf{K}^2)^p}, \tag{55}$$

where

$$\mathbf{K} = (\,\frac{\omega}{U}, \mathbf{k}) \equiv (\frac{\omega}{U}, m, n, l) \tag{56}$$

is the spatio-temporal wavevector.

From Eq.(55), one can see that with the scaled frequency (note that the change $\omega \to \omega/U$ corresponds to the change of the time coordinate $t \to t \cdot U$), the spatio-temporal spectrum $b_{\mathbf{k}}(\omega') = b_{\mathbf{K}}$ becomes *isotropic in space-time*. This implies that the correlation function of ξ in isotropic in space-time as well (with the scaled time coordinate). Note that this remarkable property can be achieved only with the spatial order $q = \frac{1}{2}$.

6.4.3 Continuity of realizations of ξ in space-time

The functional form of the spatio-temporal spectrum Eq.(55) together with the constraint Eq.(48) imply that the conditions of Theorem 3.4.3 in [26] are satisfied, so that spatio-temporal sample paths of the random field ξ are almost surely continuous, as we demanded in section 3, see requirement 1.

6.5 Spatio-temporal covariances: the Matérn class

The spatio-temporal field satisfying the p-th order SPG model Eq.(37) has the spatio-temporal correlation function belonging to the so-called *Matérn* class of covariance functions [e.g. 29, 30]. To see this, we denote

$$\nu := p - \frac{d+1}{2} > 0, \tag{57}$$

where positivity follows from Eq.(48). Then Eq.(55) rewrites as

$$b_{\mathbf{K}} \propto \frac{1}{(\lambda^{-2} + \mathbf{K}^2)^{\nu + \frac{d+1}{2}}}. \tag{58}$$

Note that here $d+1$ is the dimensionality of space-time. Equation (58) indeed presents the spectrum of the Matérn family of correlation functions, see e.g. Eq.(32) in [29]. The respective isotropic correlation function is given by the equation that precedes Eq.(32) in [29] or by Eq.(1) in [30]:

$$B(r) \propto (r/\lambda)^{\nu} K_{\nu}(r/\lambda), \tag{59}$$

where r is the distance (in our case, the spatio-temporal distance $r = \sqrt{(Ut)^2 + s^2}$, with s being the spatial distance) and K_{ν} is the MacDonald function (the modified Bessel function of the second kind).

The Matérn family is often recommended for use in spatial analysis due to its notable flexibility with only two free parameters: ν and λ, see e.g. [29] and [30]. Specifically, λ controls the length scale, whereas $\nu > 0$ determines the degree of smoothness (the higher ν the smoother sample paths of the random field, for illustration see Appendix E).

Table 1 lists the resulting spatial correlation functions for several combinations of d and p [see 30, for details].

With the fixed d, the larger p corresponds, according to Eq.(57), to the larger ν and so to the smoother in space and time field ξ. This allows us to change the degree of smoothness of the generated field by changing the temporal order of the SPG model.

From the constraint Eq.(48), the minimal temporal order p that can be used in both 2D and 3D is equal to 3. This value $\boxed{p = 3}$ will be used by default in what follows and in the current SPG computer program.

Table 1: **The spatial correlation functions $B(s)$ for some plausible combinations of the dimensionality d and the temporal order p**

d	p	$\nu = p - \frac{d+1}{2}$	$B(s)$
2	2	$\frac{1}{2}$	$\mathrm{e}^{-\frac{s}{\lambda}}$
2	3	$\frac{3}{2}$	$(1+\frac{s}{\lambda})\,\mathrm{e}^{-\frac{s}{\lambda}}$
2	4	$\frac{5}{2}$	$(1+\frac{s}{\lambda}+\frac{1}{3}\left(\frac{s}{\lambda}\right)^2)\,\mathrm{e}^{-\frac{s}{\lambda}}$
3	3	1	$\frac{s}{\lambda}K_1(\frac{s}{\lambda})$

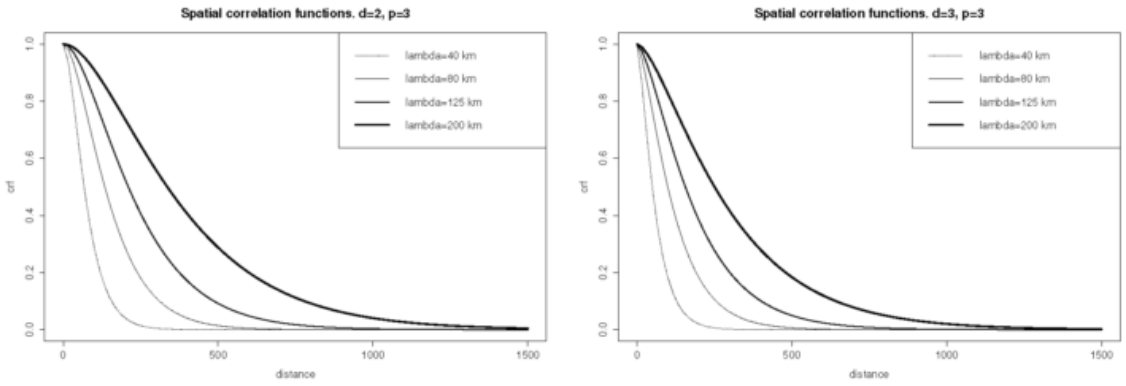


Figure 1: The spatial correlation functions for $p = 3$ in 2D (the left panel) and 3D (the right panel)—for four spatial length scales indicated in the legend.

6.5.1 Spatial correlation functions

The above spatio-temporal isotropy (see section 6.4.2 and Eq.(59)) means, in particular, that the spatial correlations are also isotropic. Figure 1 presents the *spatial* correlation functions calculated for different length scales in 2D and 3D following Eq.(59). To make the plots more accessible, it is arbitrarily assumed that the extent of the standardized spatial domain (the torus) in each dimension equals 3000 km, so that the distance is measured in kilometers. From Fig.1, one can notice, first, that the actual length scale is indeed well controlled by the parameter λ. Second, it is seen that in 2D (the left panel), where, according to Eq.(57), $\nu = \frac{3}{2}$, the correlation functions are somewhat *smoother* at the origin than in 3D (the right panel), where $\nu = 1$. This is consistent with the above statement that the greater ν the smoother the field. But in general, the 2D and 3D spatial correlation functions are quite similar.

6.5.2 Temporal correlation functions

Equation (59) shows that the spatial and temporal correlations have the same *shape*. The latter feature is very nice because atmospheric spectra are known to be similar in the spatial and in the temporal domain, e.g. the well-known "-5/3" spectral slope law is observed both in space and time, see e.g. [31, section 23]. So, our SPG does reproduce this observed in the nature similarity of spatial and temporal correlations.

Figure 2 shows the temporal correlation functions for the truncated (with $n_{max} = 90$) spatial spectral series Eq.(22). It is evident that the temporal length scale is well controlled by

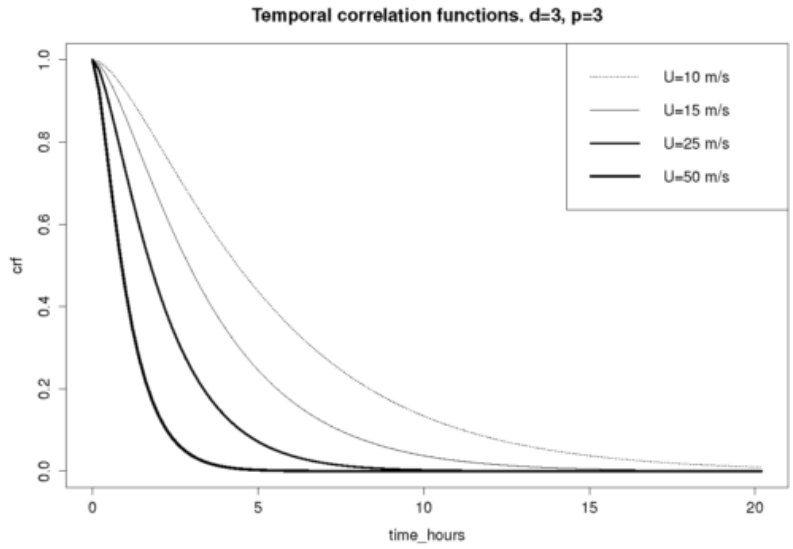


Figure 2: The temporal correlation functions in 3D for the four values of U indicated in the legend and $\lambda = 125$ km.

the parameter U. Comparing Fig.2 with Fig.1(right), one can observe that the spatial and temporal correlations indeed have the same shape; the effect of the spatial spectral truncation, which can cause a difference in the shapes, is barely visible.

6.5.3 Spatio-temporal correlations

Here, we explore the 3D spatio-temporal correlations calculated using Eq.(22) with the maximal wavenumbers in all three dimensions equal to $n_{max} = 90$, $\lambda = 125$ km, and $U = 20$ m/s. Figure 3 presents the spatial correlation functions for four time lags. Figure 4 displays the spatio-temporal correlation function.

From both Fig.3 and Fig.4, one can see the noticeable *non-separability* of the spatio-temporal covariances. The larger the time lag, the broader the spatial correlations. Note that this is consistent with the behavior of the spatio-temporal covariances found by [their Fig.8 16] in real-world wind speed data.

6.6 The final formulation of the SPG model

1. The temporal order of the SPG model is $\boxed{p = 3}$.
2. The driving noise $\alpha(t, \mathbf{s})$ is white both in time and space, so that the intensities of the spectral-space driving noises $\tilde{\alpha}_{\mathbf{k}}(t)$ are constant (and equal to σ). The intensity of the spatio-temporal white noise α is $(2\pi)^{d/2}\,\sigma$.

The resulting SPG model is

$$\boxed{\left(\frac{\partial}{\partial t} + \frac{U}{\lambda}\sqrt{1 - \lambda^2\Delta}\right)^3 \xi(t, \mathbf{s}) = \alpha(t, \mathbf{s})}. \tag{60}$$

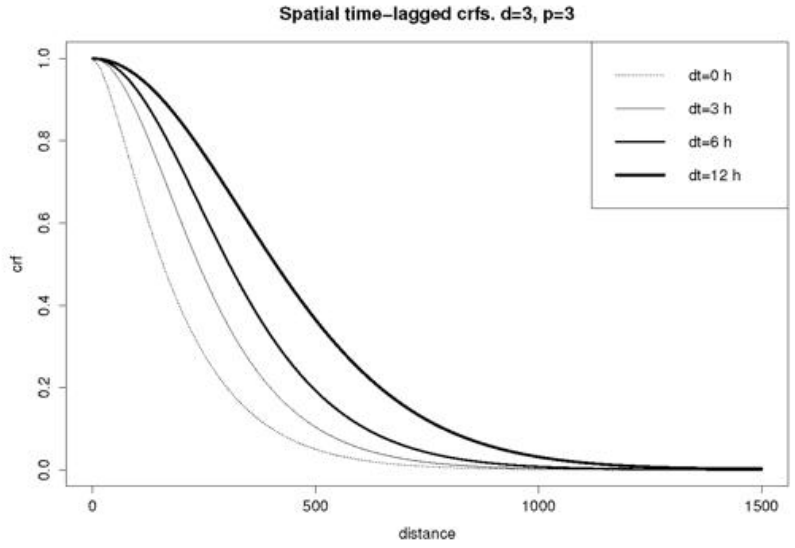


Figure 3: The spatial correlations in 3D for the four time lags indicated in the legend and $U = 20$ m/s.

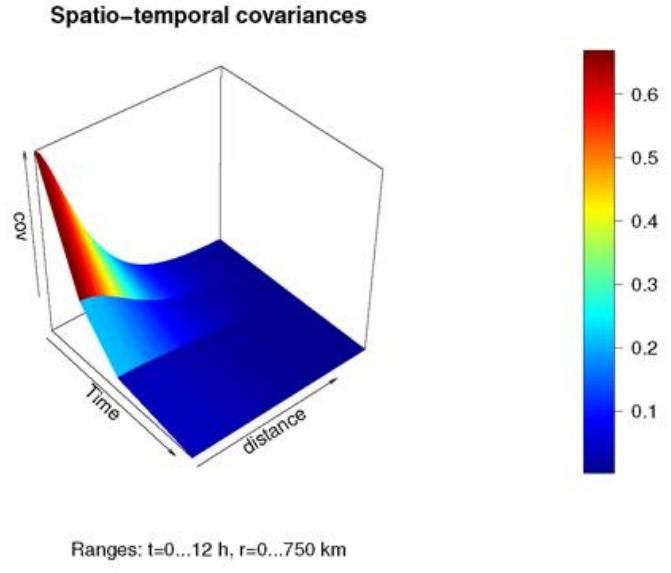


Figure 4: The spatio-temporal covariances.

In spectral space, each spectral coefficient $\tilde{\xi}_{\mathbf{k}}(t)$ satisfies the equation

$$\boxed{\left(\frac{\mathrm{d}}{\mathrm{d}t}+\frac{U}{\lambda}\sqrt{1+\lambda^2 k^2}\right)^3 \tilde{\xi}_{\mathbf{k}}(t)=\tilde{\alpha}_{\mathbf{k}}(t)=\sigma\,\Omega_{\mathbf{k}}(t)}, \tag{61}$$

where $\Omega_{\mathbf{k}}(t)$ are mutually independent complex standard white noise processes.

7 Time discrete solver for the third-order in time SPG model

In *physical space*, our final evolutionary model Eq.(60) can be discretized using the approximation of the operator $\sqrt{1-\lambda^2\Delta}$ proposed in Appendix C. The respective physical-space solver looks feasible but we do *not* examine it in this study. Below, we present our basic *spectral-space* technique. From this point on, we will consider only the *spectral* SPG.

7.1 The spectral solver

To numerically integrate the SPG model equations in spectral space, we discretize Eq.(61) using an implicit scheme. The model operator $(\frac{\mathrm{d}}{\mathrm{d}t}+a_{\mathbf{k}})^3$ (where, we recall, $a_{\mathbf{k}}:=\frac{U}{\lambda}\sqrt{1+\lambda^2k^2}$) is discretized by replacing the time derivative $\frac{\mathrm{d}}{\mathrm{d}t}$ with the backward finite difference $\frac{\mathcal{I}-\mathcal{B}}{\Delta t}$, where Δt is the time step, $\mathcal{I}$ is the identity operator, and $\mathcal{B}$ is the backshift operator. The r.h.s. of Eq.(61) (the white noise) is discretized following Appendix B, Eq.(89). As a result, we obtain the time discrete evolution equation

$$\hat{\xi}_{\mathbf{k}}(i)=\frac{1}{\varkappa^3}\left[3\varkappa^2\hat{\xi}_{\mathbf{k}}(i-1)-3\varkappa\hat{\xi}_{\mathbf{k}}(i-2)+\hat{\xi}_{\mathbf{k}}(i-3)+\sigma\Delta t^{\frac{5}{2}}\zeta_{\mathbf{k}t}\right], \tag{62}$$

where $i=0,1,2,\ldots$ denotes the discrete time instance, $\varkappa:=1+a_{\mathbf{k}}\Delta t$, and $\zeta_{\mathbf{k}t}\sim CN(0,1)$ are independent complex standard Gaussian pseudo-random variables (for their definition, see Appendix B.6). Note that the solution of the time-discrete Eq.(62) is denoted by the hat, $\hat{\xi}_{\mathbf{k}}(i)$, in order to distinguish it from the solution of the time-continuous Eq.(61), which is denoted by the tilde, $\tilde{\xi}_{\mathbf{k}}(t)$.

It can be shown that the numerical stability of the scheme Eq.(62) is guaranteed whenever $\varkappa>1$, which is always the case because $a_{\mathbf{k}}>0$, see Eq.(11).

Note that the derivation of the numerical scheme for a higher-order (i.e. with $p>3$) SPG model is straightforward: one should just raise the difference operator $\frac{\mathcal{I}-\mathcal{B}}{\Delta t}$ to a power higher than 3.

7.2 Correction of spectral variances

Because of discretization errors, the time discrete scheme Eq.(62) gives rise to the steady-state spectral variances $\hat{b}_{\mathbf{k}}:=\mathsf{Var}\,\hat{\xi}_{\mathbf{k}}(i)$, which are different from the "theoretical" ones, $b_{\mathbf{k}}$, given in Eq.(42) or Eq.(44). The idea is to correct $\hat{\xi}_{\mathbf{k}}(i)$ so that their steady-state variances coincide with $b_{\mathbf{k}}$. To this end, we derive $\hat{b}_{\mathbf{k}}$ from Eq.(62), see Eq.(104) in Appendix F, and then, knowing the "theoretical" $b_{\mathbf{k}}$, we introduce the correction coefficients, $\sqrt{b_{\mathbf{k}}/\hat{b}_{\mathbf{k}}}$, to be applied to $\hat{\xi}_{\mathbf{k}}(i)$. As a result of this correction, $\mathsf{Var}\,\hat{\xi}_{\mathbf{k}}(i)$ becomes, obviously, equal to the desired spectral variances $b_{\mathbf{k}}$. This simple device ensures that for any time step, the spatial spectrum and thus the *spatial* covariances are perfect. But the *temporal* correlations do depend on the time step, this aspect is discussed below in section 7.4.1.

7.3 "Warm start": ensuring stationarity from the beginning of time integration

To start the numerical integration of the third-order scheme Eq.(62) (for any wavevector $\mathbf{k}$), we obviously need three initial conditions. If the integration is the continuation of a previous run, then we just take values of $\hat{\xi}_{\mathbf{k}}(i)$ at the three last time instances i from that previous run; this ensures "continuity" of the resulting trajectory. If we start a new integration, we have to somehow generate values of $\hat{\xi}_{\mathbf{k}}(i)$ at $i = 1, 2, 3$, let us denote them here as the vector $\boldsymbol{\xi}^{ini} := (\hat{\xi}_{\mathbf{k}}(1), \hat{\xi}_{\mathbf{k}}(2), \hat{\xi}_{\mathbf{k}}(3))^{\top}$. Simplistic choices like specifying zero initial conditions give rise to a substantial initial transient period, which distorts the statistics of the generated field in the short time range.

In order to have the steady-state regime right from the beginning of the time integration and thus avoid the initial transient period altogether, we simulate $\boldsymbol{\xi}^{ini}$ as a pseudo-random draw from the multivariate Gaussian distribution with zero mean and the steady-state covariance matrix of $\hat{\xi}_{\mathbf{k}}(i)$. In Appendix F, we derive the components of this 3×3 matrix, namely, its diagonal elements (all equal to the steady-state variance), see Eq.(104), and the lag-1 and lag-2 covariances, see Eq.(105).

7.4 Computational efficiency

In this subsection, we describe two techniques that allow us to significantly decrease the computational cost of running the spectral SPG.

7.4.1 Making the time step Δt dependent on the spatial wavenumber k

For an ordinary differential equation, the accuracy of a finite-difference scheme depends on the time step. More precisely, it depends on the ratio of the time step Δt to the temporal length scale τ of the process in question. For high accuracy, $\Delta t \ll \tau$ is needed.

In our problem, $\tau_{\mathbf{k}}$ decays with the total wavenumber k, see Eq.(41). This implies that for higher k, smaller time steps are needed. To maintain the accuracy across the wavenumber spectrum, we choose the time step to be a portion of the time scale:

$$(\Delta t)_k := \gamma \tau_k. \tag{63}$$

The less γ, the more accurate and, at the same time, more time consuming the numerical integration scheme.

We note that in the atmospheric spectra, small scales have, normally, much less variance (energy) than large scales. But with the constant γ, the computational time would be, on the contrary, spent predominantly on high wavenumbers (because the latter require a smaller time step on the one hand and are much more abundant in 3D or 2D on the other hand). So, to save computer time whilst ensuring reasonable overall (i.e. for the whole range of wavenumbers) accuracy, we specify γ to be wavenumber dependent (growing with the wavenumber) in the following ad-hoc way:

$$\gamma_k := \gamma_{min} + (\gamma_{max} - \gamma_{min}) \left(\frac{k}{k_{max}} \right)^2, \tag{64}$$

where γ_{min} and γ_{max} are tunable parameters, $k = \sqrt{m^2 + n^2 + l^2}$, and $k_{max} := \max k$.

Note that the choice of γ depends on the shape of the temporal correlation function. For an OSDE of the type defined by Eq.(91) and τ defined to be equal to a^{-1}, the higher is the order p, the slower is the decay of the temporal correlation function for the same τ and thus the larger is to be γ.

The choice of the "optimal" γ_{min} and γ_{max} is discussed just below in section 7.4.2.

7.4.2 Introduction of a coarse grid in spectral space

Here we propose another technique to reduce the computational cost of the spectral solver. The technique exploits the *smoothness* of the SPG spectrum $b_{\mathbf{k}}$ Eq.(44). This smoothness allows us to introduce a *coarse grid in spectral space* and perform the integration of the time discrete spectral OSDEs Eq.(62) only for those wavevectors that belong to the coarse grid. The spectral coefficients $\hat{\xi}_{\mathbf{k}}(i)$ are then interpolated from the coarse grid to the dense (full) grid in spectral space.

The latter interpolation would introduce correlations between different spectral coefficients $\hat{\xi}_{\mathbf{k}}(i)$, which would destroy the spatial homogeneity. In order to avoid this, we employ a device used to generate so-called surrogate time series [32, section 2.4.1]. At each t, we multiply the interpolated $\hat{\xi}_{\mathbf{k}}(i)$ by $\mathrm{e}^{i\theta_{\mathbf{k}}}$, where $\theta_{\mathbf{k}}$ are independent *random phases*, i.e. independent for different $\mathbf{k}$ random variables uniformly distributed on the segment $[0, 2\pi]$. It can be easily seen that this multiplication removes any correlation between the spectral coefficients.

Note also that the random phase rotation does not destroy the Gaussianity because $\hat{\xi}_{\mathbf{k}}(i)$ are complex circularly-symmetric random variables with uniformly distributed and independent of $|\hat{\xi}_{\mathbf{k}}(i)|$ arguments (phases), see e.g. [33, section A.1.3].

To preserve the temporal correlations of the field $\xi(t, \mathbf{s})$, we keep the set of $\theta_{\mathbf{k}}$ constant during the SPG-model time integration.

The exact spectrum $b_{\mathbf{k}}$ after the trilinear (bilinear in 2D) interpolation of $\hat{\xi}_{\mathbf{k}}(i)$ from the coarse to the full spectral grid is imposed in a way similar to that described in section 7.2 as follows. At any time instance when we wish to compute the physical space field, for each $\mathbf{k}$ on the full spectral grid, the linearly interpolated value $\check{\xi}_{\mathbf{k}}$ is a linear combination of the closest coarse-grid points $\mathbf{k}_j$:

$$\check{\xi}_{\mathbf{k}} = \sum_{j=1}^{2^d} w_j \, \hat{\xi}_{\mathbf{k}_j} \tag{65}$$

where $\check{}$ denotes the interpolated value and w_j is the interpolation weight (note that the set of the closest coarse-grid points $\mathbf{k}_j$ depends, obviously, on $\mathbf{k}$). In Eq.(65), the coarse-grid variances $\mathsf{Var}\,\hat{\xi}_{\mathbf{k}_j} = b_{\mathbf{k}_j}$ are known for all $\mathbf{k}_j$ from the spectrum $\{b_{\mathbf{k}}\}$, see Eqs.(42) or (44). Therefore, we can find $\mathsf{Var}\,\check{\xi}_{\mathbf{k}} = \sum_j w_j^2 \, b_{\mathbf{k}_j}$. Besides, we know which variance $\check{\xi}_{\mathbf{k}}$ *should* have on the fine grid, namely $b_{\mathbf{k}}$. So, we normalize $\check{\xi}_{\mathbf{k}}$ by multiplying it by $\sqrt{b_{\mathbf{k}}/(\mathsf{Var}\,\check{\xi}_{\mathbf{k}})}$, thus imposing the exact spatial spectrum for all $\mathbf{k}$.

Technically, the 3D coarse spectral grid is the direct product of three 1D grids. Any of the (non-uniform) 1D coarse grids is specified as follows. The jth coarse grid point is located at the fine-grid wavenumber n_j, which equals j for $|j| \le n_0$ (where n_0 is an integer) and the closest integer to $n_0(1+\varepsilon)^{|n|-n_0}$ for $|j| > n_0$. Here, ε is a tunable small positive number. In the below numerical experiments, the coarse-grid parameters were $n_0 = 20$ and $\varepsilon = 0.2$, which resulted in the following positive 1D coarse-grid points: 1 2 3 ... 19 20 24 29 35 42 50 60 72 86 103 124 150 (if not otherwise stated, the 1D grid extent was 300 points and, correspondingly, the maximal wavenumber was 150).

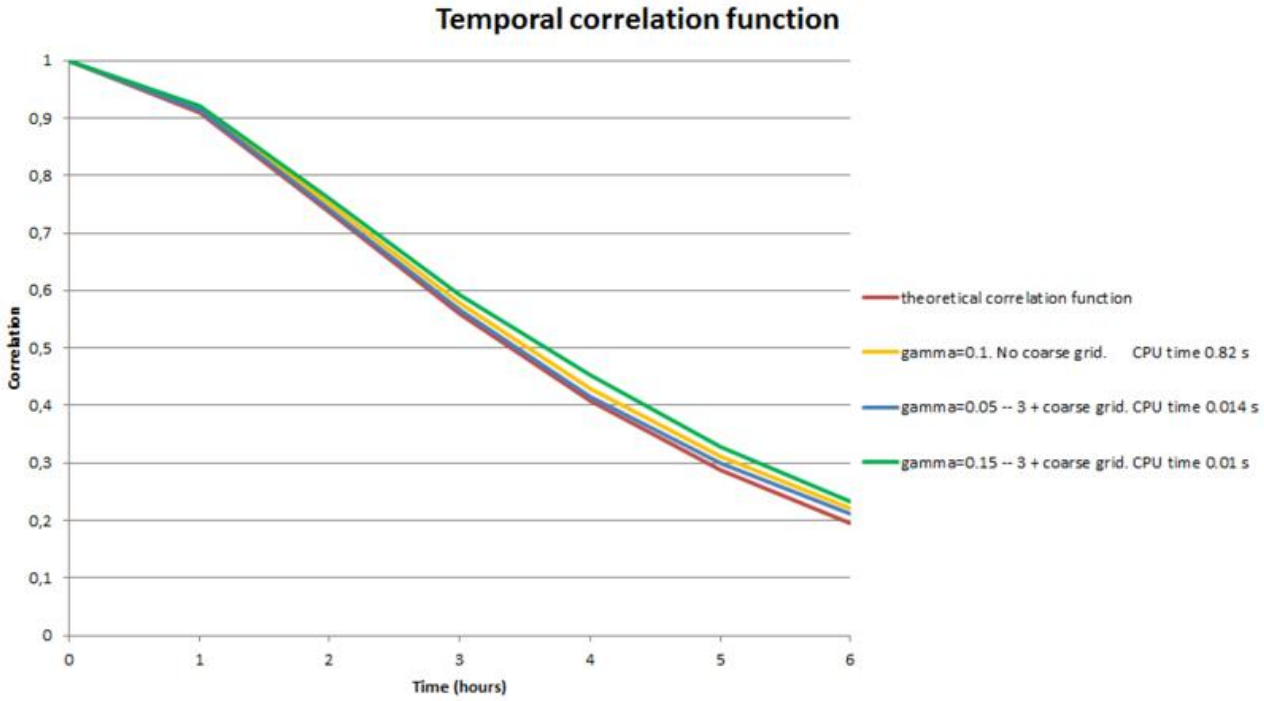


Figure 5: The theoretical and estimated temporal correlations and CPU times for the 2D SPG. The legend indicates the range γ_{min}–γ_{max} and whether the coarse grid was used. The respective spectral-space computation time (per one hour of time integration on one CPU) is also indicated in the legend. The SPG setup: $\lambda = 85$ km, $U = 12$ m/s.

7.4.3 Numerical acceleration: results

As the two above acceleration techniques guarantee that the *spatial* spectrum is always precise, we test how these techniques impact the *temporal* correlations (and what is the speedup).

In the numerical experiments, the introduction of the coarse spectral grid impacted the temporal correlations to a lesser extent than an increase in the time-step parameter γ. So, we examined the role of the two parameters γ_{min} and γ_{max} of the acceleration technique described in section 7.4.1, and the impact of the presence or absence of the coarse spectral grid introduced in section 7.4.2.

Figure 5 shows the temporal correlations functions for the different setups (indicated in the legend) of the 2D SPG. The respective CPU times for the spectral-space computations (on one CPU per one hour of model integration) are also shown in the legend. The discrete backward Fourier transforms were performed every hour of lead time.

From Fig.5, one can see that the combined effect of both numerical acceleration techniques (the green curve) was dramatic: the speedup was about 80 times as compared to the non-accelerated scheme (i.e. without the coarse grid and with constant $\gamma = 0.1$, the yellowish curve). The contributions of the two above numerical acceleration techniques to this speedup were comparable in magnitude (not shown). Most importantly, this big speedup was achieved at the very little cost: the temporal correlation length scale was distorted, as a result of approximations caused by the two acceleration techniques, by only some 5 percent w.r.t. the non-accelerated scheme and some 10 percent w.r.t. the theoretical model (the red curve).

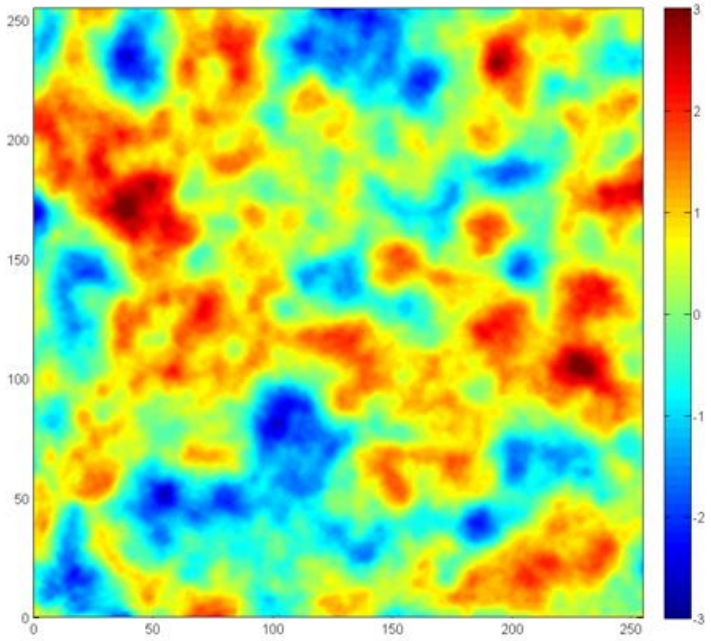


Figure 6: 2D (x-y) cross-section of a spatial SPG field.

Note that the speedup was for the spectral-space computations only, i.e. it did *not* include the cost of the discrete backward Fourier transform.

In summary, the 2D-in-space SPG took only 1 second on one CPU to perform the spectral-space model integration for as long as 100 hours of lead time. The respective cost of the backward Fourier transform performed every hour was about 4 seconds. The total cost was thus 5 seconds.

The same computations performed for the 3D-in-space grid with $300 \times 300 \times 64$ points took 60 seconds on one CPU for 100 hours of spectral-space model integration and 110 seconds for the hourly backward Fourier transform. The speedup of the spectral-space computations for the 3D scheme due to the two acceleration techniques was about 50 times.

7.5 Examples of the SPG fields

Figure 6 shows a "horizontal" x-y cross-section and Fig.7 a spatio-temporal x-t cross-section of a simulated pseudo-random field $\xi(t, x, y)$. Note that in each spatial direction, there were 300 grid points, whilst only 256 contiguous points are shown in the Figures. This is done in the SPG for practical purposes in order to avoid correlations between the opposite sides of the spatial domain, which would be spurious in real-world applications.

8 Application to the COSMO model

The SPG was embedded into the Fortran code of the limited-area meteorological non-hydrostatic model COSMO [34]. Within COSMO, the SPG code was parallelized using

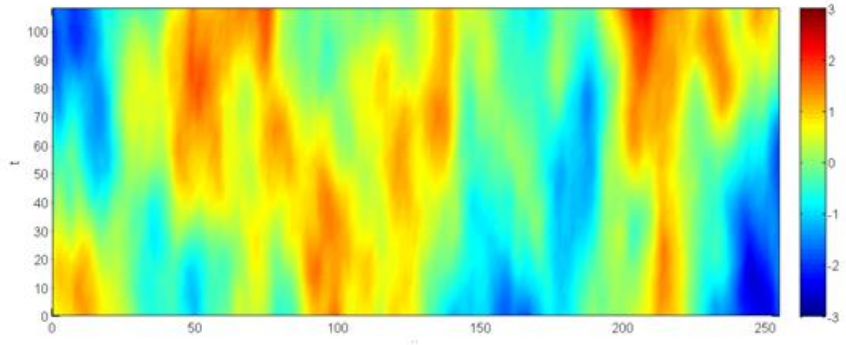


Figure 7: 2D (abscissa is x, ordinata is t) spatio-temporal cross-section of an SPG field.

MPI. The SPG was used to generate additive perturbations of the model's right-hand sides.

Figure 8 displays results of a numerical experiment, in which independent SPG perturbation fields for temperature and horizontal wind were simulated and added to the model fields every 15 minutes of lead time. The standard deviations of the SPG perturbations were specified as 0.005 K for temperature and 0.01 m/s for each of the two mutually orthogonal wind components. Besides, pressure perturbations were computed (and added to the model pressure 3D field) from the SPG temperature perturbation using the hydrostatic equation with the zero pressure perturbation at the model's top level.

The first generated by the SPG meridional wind perturbation field on the model level 25 (about 3 km above the ground) is displayed in Fig.8(top). The forecast (i.e. accumulated over time) meridional wind perturbation field after 3 hours of model integration is shown in Fig.8(bottom). Comparing the top and bottom panels of Fig.8 suggests that the perturbation field becomes more large-scale and, at the same time, less smooth over time. Specifically, the large-scale structure of the perturbation field becomes more large scale. This is to be expected because the time integration reduces (filters out) small-scale-in-time components of the spatio-temporal field and so, from the "proportionality of scales", filters out smaller scales also in space.

Besides, an opposite effect, namely appearance of a kind of fine structure can be seen in the forecast perturbation fields, see Fig.8(bottom). In particular, in the forecast perturbation field, there are many very localized features, which presumably develop due to a non-linear interaction with convection and effects related to steep orography. Finally, we note that in contrast to the "input" SPG model-error perturbation field, the "output" forecast perturbation field is clearly seen to be flow dependent (as desired in ensemble prediction and ensemble data assimilation schemes).

Figure 9 displays the growth of the meridional wind RMS forecast perturbation at the same model level 25 in response to the above SPG model-error perturbations. One can see that the magnitude of the forecast perturbation grows monotonically and "regularly" (as expected).

Finally, we note that at the time of writing, the numerical acceleration techniques described in section 7.4 were implemented only in the stand-alone version of the SPG. Without those accelerators, the cost of running the SPG within COSMO was about 0.8% of the total COSMO model wall-clock time per generated SPG field.

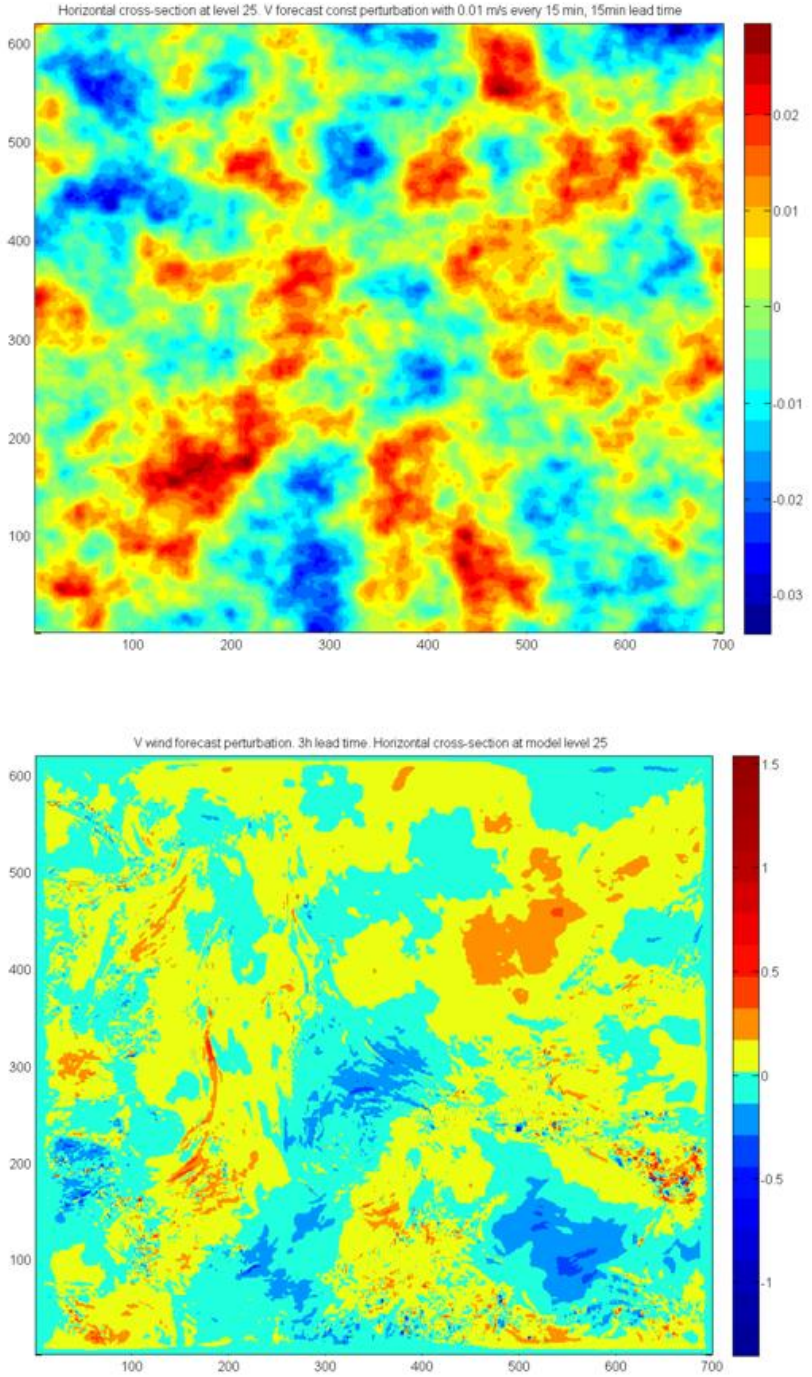


Figure 8: *The top panel*: The first SPG V-wind perturbation added to the COSMO field at the lead time 15 minutes. *The bottom panel*: the COSMO 3-h forecast V-wind perturbation field in response to the additive SPG perturbations of temperature, pressure, and both wind components added every 15 minutes of lead time.

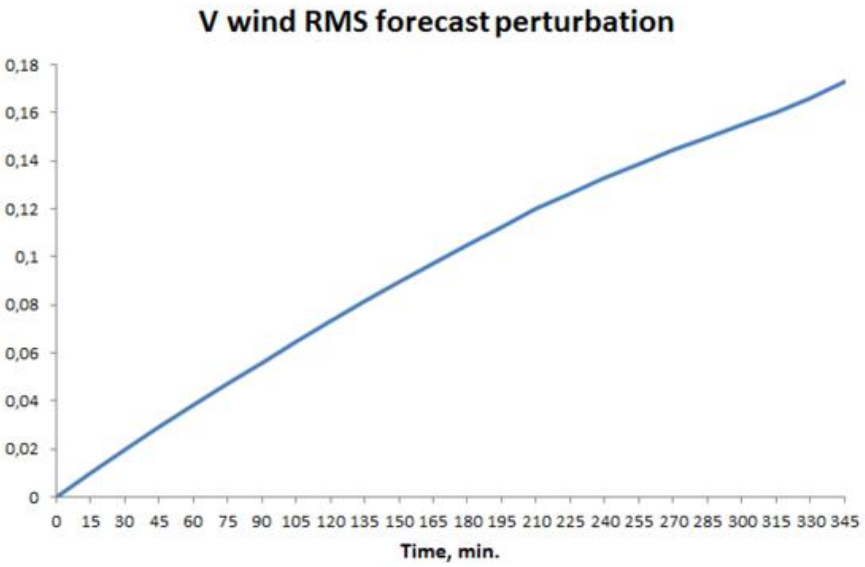


Figure 9: The COSMO forecast RMS V-wind perturbation in response to the SPG forcing.

9 Discussion

9.1 Physical-space or spectral-space SPG solver?

In this study, we have investigated both the spectral-space and the physical-space approximations of the SPG spatio-temporal model. We have found that both approaches can be used to build a practical SPG scheme. We have selected the spectral-space technique. Here, we briefly compare both approaches.

Advantages of the spectral-space technique are the following.

- Simplicity of realization. If the SPG model has constant coefficients, then the complicated SPG equation decouples into a series of simple OSDEs.
- Straightforward accommodation of non-local-in-physical-space spatial operators.

Advantages of the physical-space approach are:

- The relative ease of introduction of inhomogeneous and anisotropic capabilities to the SPG.
- The SPG solver can be implemented in domains with complex boundaries.
- Better suitability for an efficient implementation on massively parallel computers.

9.2 Extensions of the SPG

The proposed SPG technique can be extended in the future along the following lines.

- Development of a physical-space solver.

- Introduction of advection to the SPG model.
- Introduction of spatial inhomogeneity/anisotropy and non-stationarity.
- Introduction of non-Gaussianity. This can be done either by applying a nonlinear transform to the output SPG fields, or by introducing a non-Gaussian driving noise [as in 24, 25]. The former approach is simpler but the latter allows for much richer deviations from Gaussianity, including the multi-dimensional aspect.
- Going beyond additive and multiplicative perturbations for highly non-Gaussian variables like humidity and cloud fields.
- Simulation of several mutually correlated pseudo-random fields.
- Making the temporal order p a user defined variable. As noted above, the larger p the smoother the generated field.

10 Conclusions

10.1 Summary

- The proposed Stochastic Pattern Generator (SPG) produces pseudo-random spatio-temporal Gaussian fields on 2D and 3D spatial domains.
- The SPG model is defined on a standardized domain in space, specifically, on the unit 2D or 3D torus. Fields on a limited-area geophysical domain in question are obtained by mapping from the standardized domain.
- The SPG is based on a linear third-order in time stochastic model driven by the white in space and time Gaussian noise.
- The spatial operator of the stochastic model is built to ensure that solutions to the SPG model, i.e. the generated pseudo-random fields satisfy the "proportionality of scales" property: large-scale (small-scale) in space field components have large (small) temporal length scales.
- Besides the "proportionality of scales", the generated fields possess a number of other nice properties:
  - The spatio-temporal realizations are (almost surely) continuous.
  - With the appropriately scaled time coordinate, the spatio-temporal fields are isotropic in space-time.
  - The spatial and temporal correlation functions belong to the Matérn class.
  - The spatial and temporal correlations have the same shape.
- It is shown that the spatial operator of the SPG model can be effectively discretized both in physical space and spectral space.
- The basic SPG solver is spectral-space based.
- Two techniques to accelerate the spectral-space computations are proposed and implemented. The first technique selects the time step of the spectral-space numerical integration scheme to be dependent on the wavenumber, so that the discretization error is smaller for more energetic larger spatial scales and is allowed to be larger for

less energetic smaller scales. The second technique introduces a coarse grid in spectral space. The combined speedup for spectral-space computations from both techniques is as large as 50–80 times.

- The SPG is embedded in the COSMO model as a source of additive model-error perturbations. The numerical experiments show that the forecast perturbations in response to the SPG model-error perturbations behave as expected.
- For a peer reviewed publication on the SPG, see [35].

10.2 Applications

Potential applications of the SPG include ensemble prediction and ensemble data assimilation in meteorology, oceanography, hydrology, and other areas.

The SPG can be used to generate spatio-temporal perturbations of the model fields (in the additive or multiplicative or other mode), and of the boundary conditions.

Acknowledgements

The SPG has been developed as part of the Priority Project KENDA (Kilometer scale Ensemble Data Assimilation) of COSMO. We have used the discrete fast Fourier package `fft991` developed by C. Temperton at ECMWF in 1978. Christoph Schraff and Michael Baldauf kindly helped us to interpret the appearance of the small-scale noise in the COSMO forecast perturbation fields.

A Illustration of the "proportionality of scales" property

Figure 10 shows a realization of the spatio-temporal field with *non-separable* correlations that satisfy the "proportionality of scales" property (the top panel) and a realization of the field with *separable* spatio-temporal correlations (the bottom panel).

The non-separable spatio-temporal correlation function is defined as $B(x,t) = \exp(-r/L)$, where $r := \sqrt{x^2 + (Ut)^2}$, $U = 10$ m/s, $L = 200$ km, and the domain size in the x direction is 3000 km. The separable correlation function is $B(x,t) = \exp(-|x|/L) \cdot \exp(-|Ut|/L)$. So, both separable and non-separable fields have exactly the same spatial correlation functions and the same temporal correlation functions.

Note that both the separability and the exponential temporal correlation function is what the scale-independent first-order auto-regression used in [19, 9, 20, 21, 22] implies.

Comparing the two panels of Fig.10, one can see that the two fields are quite different. In the non-separable case, Fig.10(top), large spatial structures indeed tend to live longer than small structures, as it is expected from the "proportionality of scales" principle. In contrast, in the case with separable space-time correlations, Fig.10(bottom), the "longevity" of a spatial pattern is rather independent of its size (which is unphysical). Besides, in the non-separable case, a kind of spatio-temporal "organization" is evident, which is absent in the separable case. Finally, the field with non-separable correlations exhibits a sort of spatio-temporal isotropy, again, not visible in the separable case.

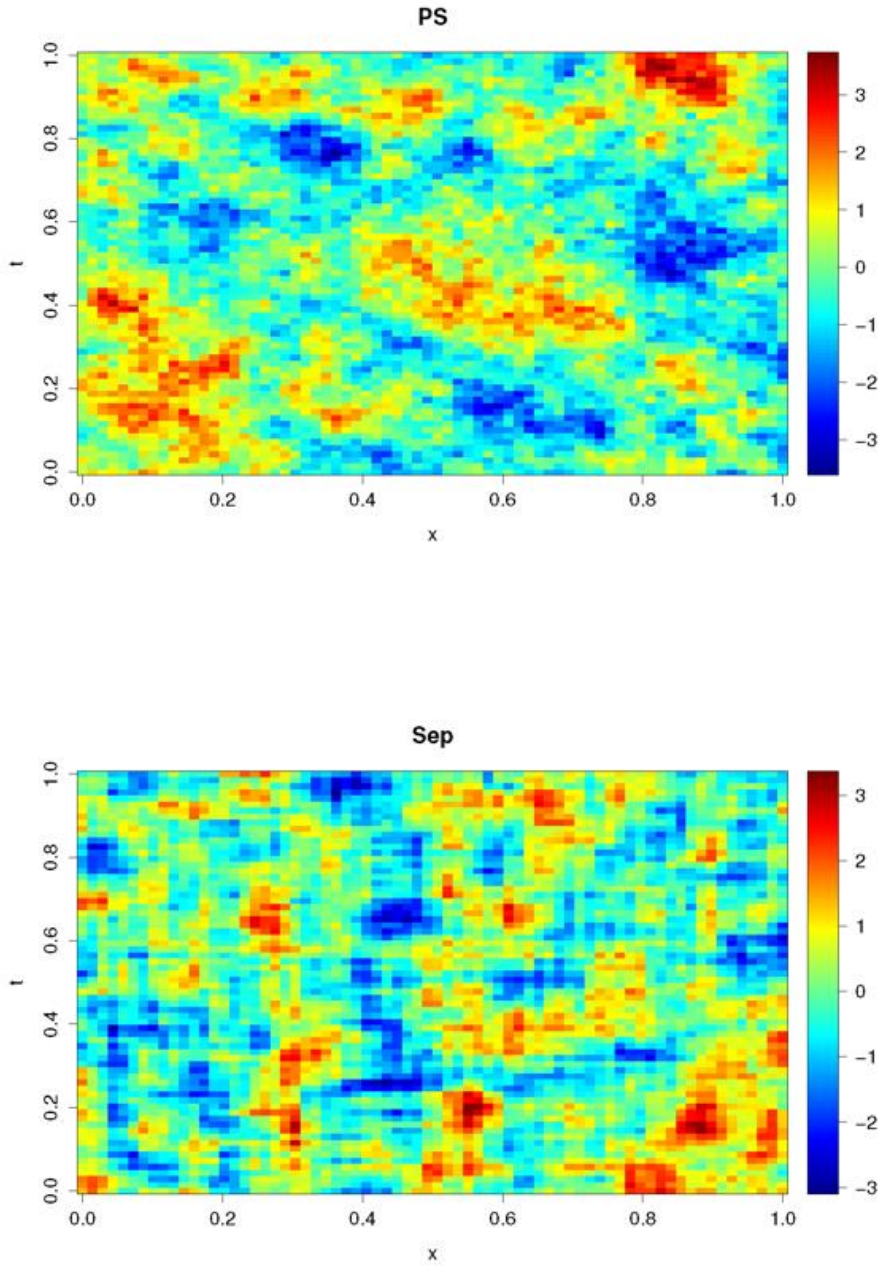


Figure 10: Simulated spatio-temporal fields. *Top*: With non-separable space-time correlations satisfying the "proportionality of scales" principle. *Bottom*: With separable space-time correlations.

B Spatio-temporal structure of the driving 4-D noise

Here, we recall the general definition of the white noise, define the spatial spectrum of the white noise on the d-dimensional unit torus, and find its spatial spectral decomposition in the spatio-temporal case. Then we introduce a colored in space and white in time noise, and find it spatial spectrum. Finally, we define the time discrete complex-valued white-noise process.

B.1 White noise

By definition, see e.g. [36, section 1.1.3] or [37, section 3.1.4], the *standard white noise* $\Omega(\mathbf{x})$ defined on a manifold $\mathbb{D}$ is a *generalized random field* that acts on a test function $\varphi(\mathbf{x})$ (where $x \in \mathbb{D}$) as follows:

$$(\Omega, \varphi) := \int \varphi(\mathbf{x})\, \Psi(\mathrm{d}\mathbf{x}), \tag{66}$$

where Ψ is the Gaussian orthogonal stochastic measure such that for any Borel set A, $\Psi(A)$ is a (complex, in general) Gaussian random variable with $\mathsf{E}\,\Psi(A) = 0$ and $\mathsf{E}\,|\Psi(A)|^2 = |A|$, where $|.|$ denotes the Lebesgue measure.

The equivalent definitions of the standard white noise are

$$\mathsf{E}\,|(\Omega, \varphi)|^2 := \int |\varphi(\mathbf{x})|^2\, \mathrm{d}\mathbf{x}, \tag{67}$$

and

$$\mathsf{E}\,(\Omega, \varphi) \cdot \overline{(\Omega, \psi)} := \int \varphi(\mathbf{x}) \overline{\psi(\mathbf{x})}\, \mathrm{d}\mathbf{x}, \tag{68}$$

where ψ is another test function. Thus, we have defined of the *standard* white noise. By the general Gaussian white noise, we mean a multiple of the *standard* white noise.

B.2 Spectrum of the white noise on $\mathbb{T}^d$

The formal Fourier transform of the spatial white noise $\Omega(\mathbf{s})$ (where $\mathbf{s} \in \mathbb{T}^3$),

$$\tilde{\Omega}_{\mathbf{k}} = \frac{1}{(2\pi)^d} \int_{\mathbb{T}^d} \Omega(\mathbf{s})\, \mathrm{e}^{-\mathrm{i}(\mathbf{k},\mathbf{s})}\, \mathrm{d}\mathbf{s}, \tag{69}$$

can be rigorously justified as the action of the white noise Ω on the test function

$$\chi(\mathbf{s}) := \frac{1}{(2\pi)^d}\, \mathrm{e}^{-\mathrm{i}(\mathbf{k},\mathbf{s})}. \tag{70}$$

Then, the spatial spectrum of $\Omega(\mathbf{s})$ is

$$b_{\mathbf{k}} := \mathsf{E}\,|\tilde{\Omega}_{\mathbf{k}}|^2 \equiv \mathsf{E}\,|(\Omega, \chi)|^2 = \int_{\mathbb{T}^d} |\chi(\mathbf{s})|^2\, \mathrm{d}\mathbf{s} = \frac{1}{(2\pi)^d}. \tag{71}$$

Here, the third equality is due to Eq.(67). We stress that it is the *modal* spectrum that is constant for the white noise (not the variance spectrum), see also remark at the end of section 5.3.

B.3 Space-integrated spatio-temporal white noise on $\mathbb{T}^d \times \mathbb{R}$

Let us consider the spatio-temporal white noise $\Omega = \Omega(t, \mathbf{s})$, where $t \in \mathbb{R}$ is time and $\mathbf{s} \in \mathbb{T}^d$ the spatial coordinate vector. Take a spatial test function $c(\mathbf{s})$ and define the temporal process $\Omega_1(t)$ formally as

$$\Omega_1(t) := \int_{\mathbb{T}^d} \Omega(t, \mathbf{s}) c(\mathbf{s}) \, \mathrm{d}\mathbf{s}, \tag{72}$$

so that it acts on a test function in the temporal domain, $\varphi(t)$, as

$$(\Omega_1, \varphi) := \int_{\mathbb{R}} \Omega_1(t) \varphi(t) \, \mathrm{d}t = \int_{\mathbb{R}} \int_{\mathbb{T}^d} \Omega(t, \mathbf{s}) c(\mathbf{s}) \varphi(t) \, \mathrm{d}\mathbf{s} \, \mathrm{d}t. \tag{73}$$

Here, we note that the latter double integral is nothing other than the result of action of the original white noise $\Omega(t, \mathbf{s})$ on the spatio-temporal test function $c(\mathbf{s}) \cdot \varphi(t)$. This enables us to mathematically rigorously *define* $\Omega_1(t)$ as the generalized random process that, with the fixed $c(\mathbf{s})$, acts on the test function $\varphi(t)$ as follows:

$$(\Omega_1(t), \varphi(t)) := (\Omega(t, \mathbf{s}),\, c(\mathbf{s})\varphi(t)). \tag{74}$$

Now, using the definition Eq.(67) of the white noise $\Omega(t, \mathbf{s})$, we have

$$\mathsf{E} \, |(\Omega(t, \mathbf{s}),\, c(\mathbf{s})\varphi(t))|^2 = \int_{\mathbb{T}^d} \int_{\mathbb{R}} |c(\mathbf{s})|^2 |\varphi(t)|^2 \, \mathrm{d}\mathbf{s} \, \mathrm{d}t = \int_{\mathbb{T}^d} |c(\mathbf{s})|^2 \, \mathrm{d}\mathbf{s} \int_{\mathbb{R}} |\varphi(t)|^2 \, \mathrm{d}t. \tag{75}$$

Since we have fixed $c(\mathbf{s})$, we observe that

$$\sigma^2 := \int |c(\mathbf{s})|^2 \, \mathrm{d}\mathbf{s} \tag{76}$$

is a constant such that

$$\mathsf{E} \, |(\Omega_1(t), \varphi(t))|^2 = \sigma^2 \int_{\mathbb{R}} |\varphi(t)|^2 \, \mathrm{d}t. \tag{77}$$

Comparing this equation with one of the definitions of the standard white noise, Eq.(67), we recognize $\Omega_1(t)$ as a general Gaussian white noise in time, i.e. the standard temporal white noise multiplied by σ. We call σ the *intensity* of the white noise.

B.4 Spatial spectrum of a spatio-temporal white noise

Now, we are in a position to derive the spatial spectrum of the standard spatio-temporal white noise $\Omega(t, \mathbf{s})$. In the formal Fourier decomposition

$$\Omega(t, \mathbf{s}) = \sum_{\mathbf{k}} \tilde{\Omega}_{\mathbf{k}}(t) \, \mathrm{e}^{\mathrm{i}(\mathbf{k}, \mathbf{s})}, \tag{78}$$

the elementary temporal processes $\tilde{\Omega}_{\mathbf{k}}(t)$ can be shown to be white noises in time. Indeed, again formally, we have

$$\tilde{\Omega}_{\mathbf{k}}(t) = \frac{1}{(2\pi)^d} \int_{\mathbb{T}^d} \Omega(t, \mathbf{s}) \, \mathrm{e}^{-\mathrm{i}(\mathbf{k}, \mathbf{s})} \, \mathrm{d}\mathbf{s}. \tag{79}$$

Here, we recognize an expression of the kind given by Eq.(72) with $c(\mathbf{s}) := \mathrm{e}^{-\mathrm{i}(\mathbf{k}, \mathbf{s})}/(2\pi)^{\mathrm{d}}$. Therefore, from Eq.(77), $\tilde{\Omega}_{\mathbf{k}}(t)$ is a temporal white noise with the intensity $\sigma^{\Omega}_{\mathbf{k}}$ squared equal to

$$(\sigma^{\Omega}_{\mathbf{k}})^2 = \int |c(\mathbf{s})|^2 \, \mathrm{d}\mathbf{s} = \frac{1}{(2\pi)^{2d}} \int_{\mathbb{T}^d} |\mathrm{e}^{-\mathrm{i}(\mathbf{k}, \mathbf{s})}|^2 \, \mathrm{d}\mathbf{s} = \frac{1}{(2\pi)^{\mathrm{d}}}. \tag{80}$$

In addition, using Eq.(68), it is easy to show that $\tilde{\Omega}_{\mathbf{k}}(t)$ and $\tilde{\Omega}_{\mathbf{k}'}(t)$ are mutually orthogonal for $\mathbf{k} \neq \mathbf{k}'$.

To summarize, $\tilde{\Omega}_{\mathbf{k}}(t)$ are mutually orthogonal white-in-time noises, all with equal intensities $\sigma_{\mathbf{k}}^{\Omega} = (2\pi)^{-d/2}$:

$$\tilde{\Omega}_{\mathbf{k}}(t) = \frac{1}{(2\pi)^{d/2}}\,\Omega_{\mathbf{k}}(t), \tag{81}$$

where $\Omega_{\mathbf{k}}(t)$ are the standard white noises.

B.5 Spectral decomposition of a white in time and colored in space noise

In order to introduce a white in time and colored in space noise, let us *convolve* the spatio-temporal white noise $\Omega(t, \mathbf{s})$ with a *smoothing kernel* in space $u(\mathbf{s})$, getting

$$\alpha(t, \mathbf{s}) := \int_{\mathbb{T}^d} u(\mathbf{s} - \mathbf{r})\,\Omega(t, \mathbf{r})\,\mathrm{d}\mathbf{r}. \tag{82}$$

In this equation, the stochastic integral is defined, for any t and $\mathbf{s}$, following Eq.(74) with $c(\mathbf{r}) := u(\mathbf{s} - \mathbf{r})$. Fourier transforming $u(\mathbf{s})$,

$$u(\mathbf{s}) = \sum_{\mathbf{k}} \tilde{u}_{\mathbf{k}}\,\mathrm{e}^{\mathrm{i}(\mathbf{k},\mathbf{s})}, \tag{83}$$

and, in space, $\alpha(t, \mathbf{s})$,

$$\alpha(t, \mathbf{s}) = \sum_{\mathbf{k}} \tilde{\alpha}_{\mathbf{k}}(t)\,\mathrm{e}^{\mathrm{i}(\mathbf{k},\mathbf{s})}, \tag{84}$$

we easily obtain that the elementary spectral processes $\tilde{\alpha}_{\mathbf{k}}(t)$ are independent white noises in time with the intensities squared

$$\sigma_{\mathbf{k}}^2 = (2\pi)^d |\tilde{u}_{\mathbf{k}}|^2, \tag{85}$$

so that the stochastic differential $\tilde{\alpha}_{\mathbf{k}}(t)\mathrm{d}t$ is

$$\tilde{\alpha}_{\mathbf{k}}(t)\,\mathrm{d}t = \sigma_{\mathbf{k}}\,\mathrm{d}W_{\mathbf{k}}(t). \tag{86}$$

Equivalently,

$$\tilde{\alpha}_{\mathbf{k}}(t) = \sigma_{\mathbf{k}}\,\Omega_{\mathbf{k}}(t). \tag{87}$$

B.6 Discretization of the spectral processes $\tilde{\alpha}_{\mathbf{k}}(t)$ in time

Being white noises, $\tilde{\alpha}_{\mathbf{k}}(t)$ have infinite variances. They become ordinary random processes if, e.g., we discretize them in time. With the time step Δt, we define the discretized process $\hat{\alpha}_{\mathbf{k}}(t_j)$ at the time instance t_j by replacing, in Eq.(86), $\mathrm{d}t$ with Δt and $\mathrm{d}W_{\mathbf{k}}$ with $\Delta W_{\mathbf{k}}$:

$$\hat{\alpha}_{\mathbf{k}}(t_j)\,\Delta t := \sigma_{\mathbf{k}}\,\Delta W_{\mathbf{k}}(t). \tag{88}$$

As $\mathsf{E}\,|\Delta W_{\mathbf{k}}(t)|^2 = \Delta t$, we obtain

$$\hat{\alpha}_{\mathbf{k}}(t_j) = \frac{\sigma_{\mathbf{k}}}{\sqrt{\Delta t}} \cdot \zeta_{\mathbf{k}j}, \tag{89}$$

where $\zeta_{\mathbf{k}j}$ are independent complex standard Gaussian random variables $CN(0, 1)$. The latter is defined as a complex random variable whose real and imaginary parts are mutually uncorrelated zero-mean random variables with variances equal to $1/2$. $CN(0, 1)$ is sometimes referred to as circularly symmetric complex Gaussian (normal) random variable [e.g. 33].

Equation (89) shows that the spatial spectrum of the time discrete driving noise is $\sigma_{\mathbf{k}}^2/\Delta t$.

C Physical-space approximation of the operator $\sqrt{1-\lambda^2\Delta}$

As we have discussed in section 5.5.1, the fractional power (square root) of the negated and shifted Laplacian operator, $\mathcal{L} := \sqrt{1-\lambda^2\Delta}$, is defined as the pseudo-differential operator with the symbol $\tilde{l}(\mathbf{k}) := \sqrt{1+\lambda^2\mathbf{k}^2}$. In the literature, one can find approaches to discretization of fractional powers of elliptic operators, e.g. finite elements were used in the spatial context in [38].

Here, we propose a simple technique to build a spatial discretization scheme that approximates the operator $\sqrt{1-\lambda^2\Delta}$ in the sense that the symbol of the approximating operator is close to $\sqrt{1+\lambda^2\mathbf{k}^2}$.

To this end, we do the following.

1. Perform the backward Fourier transform of the symbol $\tilde{l}(\mathbf{k})$, getting the function $l(\mathbf{s})$. As multiplication in Fourier space by $\tilde{l}(\mathbf{k})$ is equivalent to convolution in physical space with $l(\mathbf{s})$, we obtain that for any test function $\varphi(\mathbf{s})$,

$$(\mathcal{L}\varphi)(\mathbf{s}) = \int_{\mathbb{T}^3} l(\mathbf{s}-\mathbf{r})\,\varphi(\mathbf{r})\,\mathrm{d}\mathbf{r}. \tag{90}$$

   The crucial moment here is that the kernel function $l(\mathbf{s})$ appears to be oscillating while rapidly decreasing in modulus as $|\mathbf{s}|$ increases (see below). This enables its efficient approximation with a compact-support (truncated) function.

2. With the discretization on the grid with n points in each of the d dimensions on the torus $\mathbb{T}^d$, the kernel function $l(\mathbf{s})$ is represented by the set of its grid-point values $l(\mathbf{s_i})$, where $\mathbf{s} = (s_1, \ldots, s_d)$, $\mathbf{i} = (i_1, \ldots, i_d)$, and $\mathbf{s_i} = (s_1(i_1), \ldots, s_d(i_d))$. If $l(\mathbf{s})$ appears to be rapidly decreasing away from $\mathbf{s} = \mathbf{0}$, we truncate the $l(\mathbf{s_i})$ function by limiting its support near the origin, thus getting the function $l_{trunc}(\mathbf{s_i})$. E.g. in 3D, the support of $l_{trunc}(\mathbf{s_i})$ consists of the grid points $\mathbf{i} = (i_1, i_2, i_3)$ that simultaneously satisfy the following constraints: $|i_1| \le J$, $|i_2| \le J$, and $|i_3| \le J$, where J is the spatial order of the scheme. Below, we present results with $J = 1$ (3 grid points in the support of the truncated kernel function in each dimension) and $J = 3$ (7 grid points in the support in each dimension).

3. Fourier transform $l_{trunc}(\mathbf{s})$ back to the spectral space, getting the approximated symbol $\tilde{l}_{trunc}(\mathbf{k})$.

4. Compare $\tilde{l}(\mathbf{k})$ with $\tilde{l}_{trunc}(\mathbf{k})$ and conclude whether a parsimonious (that is, with a very small J) approximation is viable.

Now, we present the results. We found that for $d = 1$, $d = 2$, and $d = 3$, the goodness of fit was similar, so we examine the 3D case below.

We selected the grid of $n = 2 \cdot n_{max} = 256$ points in each of the three dimensions. We specified the spatial non-dimensional length scale λ to be much greater than the mesh size $h = 2\pi/n$ and much less than the domain's extents, 2π. Specifically, we chose $\lambda = 1/n_1$, where $n_1 := \sqrt{n_{max}}$. (The results were not much sensitive to changes in n_1 within the whole wavenumber range on the grid.)

Figure 11 displays the resulting kernel function $l(s)$ for positive s (note that $l(s)$ is an even function of the scalar distance s). One can see the remarkably fast decay of $|l(s)|$ with the growing s. Consequently, a stencil with just a few points in each dimension can be expected to work well.

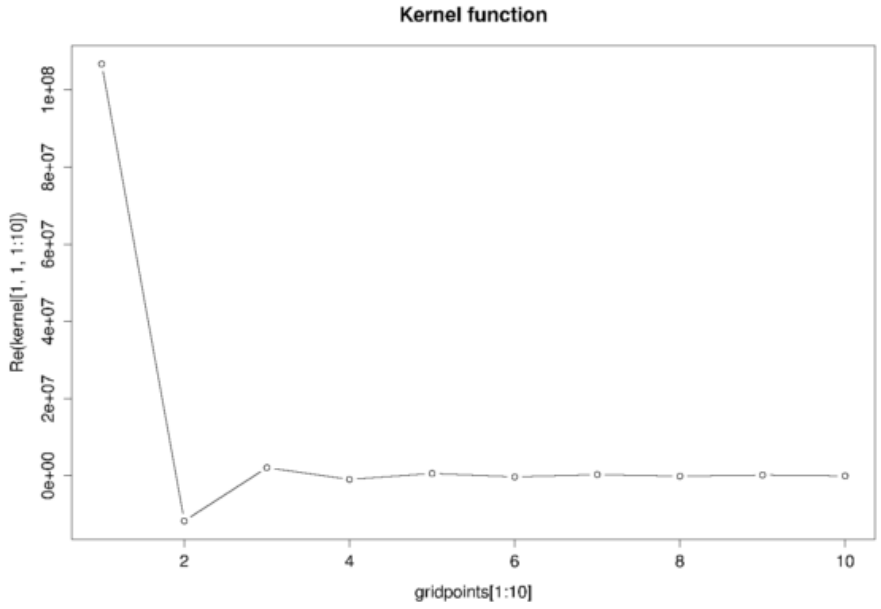


Figure 11: The kernel function

Figure 12 shows the exact and approximated symbols for the stencil that contains 3 grid points in each dimension (the left panel) and the stencil that contains 7 grid points in each dimension (the right panel). (The 5-point scheme worked not much better than the 3-point one and so its performance is not shown.)

From Fig.12, one can see that the 3-point scheme's performance is rather mediocre, whereas the 7-point scheme works very well (in terms of the reproduction of the operator's symbol).

Finally, we verified that the symbol $\tilde{l}_{trunc}(\mathbf{k})$ of the discrete operator for $J = 3, 5, 7$ was everywhere positive, which guarantees that the operator is positive definite and so the discretized SPG model should be stable.

To summarize, the operator $\sqrt{1-\lambda^2\Delta}$ can be approximated with parsimonious physical-space discretization schemes. For simulation of uncertainty in meteorology, where precise

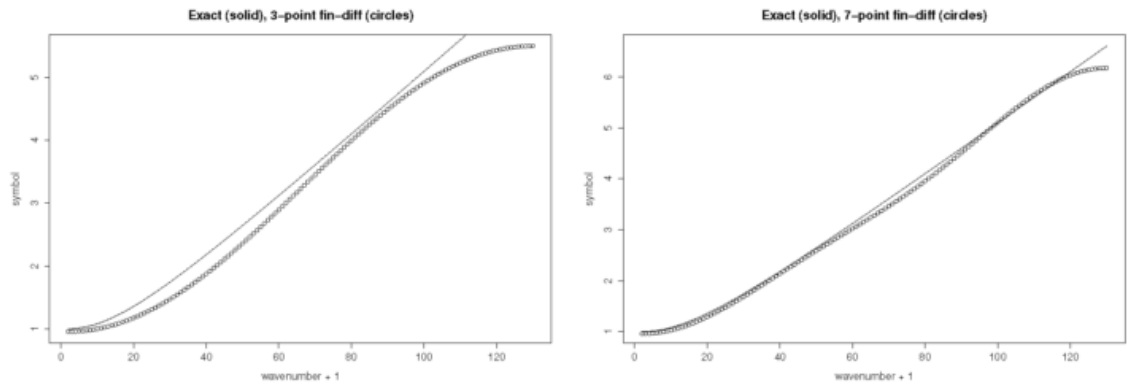


Figure 12: Goodness of fit of the symbol $\tilde{l}(\mathbf{k})$ (solid curve) by $\tilde{l}_{trunc}(\mathbf{k})$ (circles). Left: the 3-point stencil in each dimension. Right: the 7-point stencil

error statistics is not available, the simplest 3-point (in each direction) scheme seems most appropriate and computationally attractive. For more demanding applications, the 7-point scheme can be more appropriate.

D Stationary statistics of a higher-order OSDE

We examine the OSDE Eq.(38) in its generic form:

$$\boxed{\left(\frac{\mathrm{d}}{\mathrm{d}t}+a\right)^p \eta(t)=\sigma\Omega(t),} \tag{91}$$

where σ and a are the positive numbers, p is the positive integer, and $\Omega(t)$ is the standard white noise (see Appendix B).

The goal here is to find the variance and the correlation function of $\eta(t)$ in the stationary regime. The technique is to reduce the p-th order OSDE to a system of first-order OSDEs.

To simplify the exposition, we consider the third-order OSDE ($p=3$) and rewrite Eq.(91) as

$$\left(\frac{\mathrm{d}}{\mathrm{d}t}+a\right)\ \left\{\left(\frac{\mathrm{d}}{\mathrm{d}t}+a\right)\ \left[\left(\frac{\mathrm{d}}{\mathrm{d}t}+a\right)\eta(t)\right]\right\}=\sigma\Omega(t). \tag{92}$$

Here, by η_1 we denote the term in brackets,

$$\left(\frac{\mathrm{d}}{\mathrm{d}t}+a\right)\eta=:\eta_1 \tag{93}$$

and by η_2 the term in braces,

$$\left(\frac{\mathrm{d}}{\mathrm{d}t}+a\right)\eta_1=:\eta_2, \tag{94}$$

so that the original equation Eq.(91) can be rewritten as

$$\left(\frac{\mathrm{d}}{\mathrm{d}t}+a\right)\eta_2=\sigma\Omega. \tag{95}$$

In Eqs.(93)–(95), the last equation is the familiar first-order OSDE forced by the white noise, whereas the other equations are not forced by the white noise. Generalizing the above construction, Eqs.(92)–(95), to the arbitrary $p>0$, we form the following first-order vector-matrix OSDE (a system of first-order OSDEs):

$$\mathrm{d}\boldsymbol{\eta}+\mathbf{A}\boldsymbol{\eta}\mathrm{d}t=\boldsymbol{\Sigma}\boldsymbol{\Omega}\mathrm{d}t, \tag{96}$$

where $\boldsymbol{\eta}:=(\eta,\eta_1,\ldots,\eta_{p-2},\eta_{p-1})$, $\boldsymbol{\Omega}:=(0,0,\ldots,0,\Omega)$, and the design of the matrices $\mathbf{A}$ and $\boldsymbol{\Sigma}$ is obvious (not shown).

With Eq.(96) in hand, we derive a differential equation for the covariance matrix $\mathbf{P}:=\mathsf{E}\,\boldsymbol{\eta}\boldsymbol{\eta}^*$, where * denotes transpose complex conjugate [see e.g. 11, example 4.16]. First, we compute the increment of $\mathbf{P}$:

$$\Delta\mathbf{P}=\mathsf{E}\,(\boldsymbol{\eta}+\mathrm{d}\boldsymbol{\eta})(\boldsymbol{\eta}+\mathrm{d}\boldsymbol{\eta})^*-\mathsf{E}\,\boldsymbol{\eta}\boldsymbol{\eta}^*=\mathsf{E}\,\boldsymbol{\eta}\mathrm{d}\boldsymbol{\eta}^*+\mathsf{E}\,\mathrm{d}\boldsymbol{\eta}\boldsymbol{\eta}^*+\mathsf{E}\,\mathrm{d}\boldsymbol{\eta}\mathrm{d}\boldsymbol{\eta}^*. \tag{97}$$

Then, using Eq.(96) and the fact that $\mathsf{E}\,|\Omega\mathrm{d}t|^2=\mathsf{E}\,|\mathrm{d}W|^2=\mathrm{d}t$, we obtain the differential of $\mathbf{P}$ from Eq.(97):

$$\mathrm{d}\mathbf{P}=-\mathbf{A}\mathbf{P}\mathrm{d}t-\mathbf{P}\mathbf{A}^*\mathrm{d}t+\boldsymbol{\Sigma}\boldsymbol{\Sigma}^*\mathrm{d}t. \tag{98}$$

In the stationary regime $\mathrm{d}\mathbf{P}=0$, so the equation for the stationary covariance matrix is

$$\boxed{\mathbf{A}\mathbf{P}+\mathbf{P}\mathbf{A}^*=\boldsymbol{\Sigma}\boldsymbol{\Sigma}^*.} \tag{99}$$

Next, we look at the *first* diagonal entry of the resulting stationary covariance matrix $\mathbf{P}$, which represents the required $\mathsf{Var}\,\eta$ (because η is defined above to be the first entry of the

vector $\boldsymbol{\eta}$). Dropping tedious derivations, we present in Table 2 (second row) the formulas for the temporal orders $p = 1$, $p = 2$, $p = 3$, and for the general p.

Finally, we derive the temporal correlation function for the pth-order OSDE. To this end, we multiply Eq.(91) by $\eta(s)$ with $s < t$ and take expectation. Since a is non-stochastic, we may interchange the expectation and the differential operator $\left(\frac{\mathrm{d}}{\mathrm{d}t} + a\right)^p$, getting the pth-order ordinary differential equation for the temporal covariance function, whose solutions for different p are presented in row 3 of Table 2.

Table 2: **The variances $\mathsf{Var}\,\eta$ and correlation functions $C_\eta(t)$ of the stationary solution to Eq.(91) for different temporal orders p**

p	1	2	3	Arbitrary p
$\mathsf{Var}\,\eta$	$\frac{\sigma^2}{2a}$	$\frac{\sigma^2}{4a^3}$	$\frac{3\sigma^2}{16a^5}$	$\propto \frac{\sigma^2}{a^{2p-1}}$
$C_\eta(t)$	$\mathrm{e}^{-\mathrm{a\|t\|}}$	$(1 + a\|t\|)\,\mathrm{e}^{-\mathrm{a\|t\|}}$	$(1 + a\|t\| + \frac{a^2t^2}{3})\,\mathrm{e}^{-\mathrm{a\|t\|}}$	$\propto R_{p-1}(a\|t\|) \cdot \mathrm{e}^{-\mathrm{a\|t\|}}$

Here $R_{p-1}(x)$ is a polynomial of order $p - 1$.

E Smoothness of sample paths of the spatial Matérn random field for different ν

Here, we show how sample paths (realizations) of the Matérn random field with the smoothness parameter ν look. Specifically, in Fig.13, we present three plots with 1D cross-sections of randomly chosen realizations of the Matérn random field for the following three values of ν: 1/2, 3/2, and 5/2. The spatial length scale parameter λ is selected in each of the three cases in such a way that the spatial correlation function intersects the 0.7 level at approximately the same distance (we denote this distance by $L_{0.7}$): $L_{0.7} = 500$ km. Again, as in section 6.5 and Appendix A, we assume, for convenience, that the extent of the spatial domain in each coordinate direction is 3000 km (rather than 2π). For comparison, we also display a realization with $L_{0.7} = 1500$ km for $\nu = 1/2$ (the bottom panel of Fig.13).

One can see that, indeed, the larger ν, the smoother the realizations—in the sense that they have less small-scale "noise". By contrast, increasing the length scale λ (compare the top and bottom panels of Fig.13) makes the *large-scale* pattern smoother but does *not* remove the smallest scales. So, the *large-scale* behavior is determined by the length scale λ, whereas the degree of *small-scale* smoothness/roughness depends predominantly on the smoothness parameter ν.

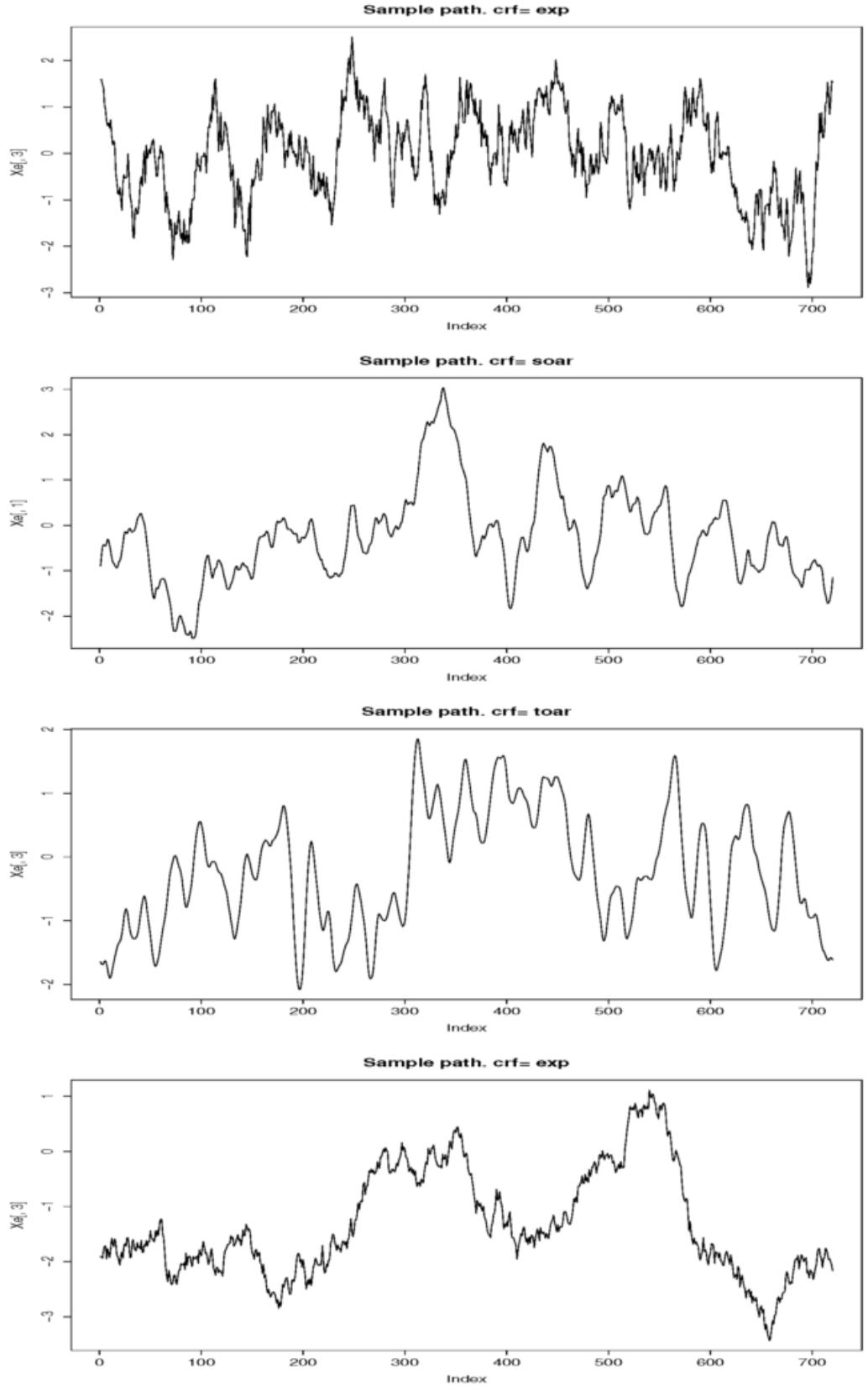


Figure 13: Sample paths for various ν and $L_{0.7}$. From the *top* to the *bottom*: $[\nu = \frac{1}{2}, L_{0.7} = 500]$, $[\nu = \frac{3}{2}, L_{0.7} = 500]$, $[\nu = \frac{5}{2}, L_{0.7} = 500]$, $[\nu = \frac{1}{2}, L_{0.7} = 1500]$

F Stationary statistics of a time discrete higher-order OSDE

Here, to simplify the exposition, we first examine the simplest first-order (i.e. with $p = 1$) OSDE and then give the results for the third-order OSDE used in the current version of the SPG.

F.1 First-order numerical scheme

Discretization of the Langevin Eq.(15) by an implicit scheme yields

$$\eta_i - \eta_{i-1} + a\eta_i \Delta t = \sigma \Delta W_i, \tag{100}$$

so that

$$\eta_i = \frac{\eta_{i-1} + \sigma \Delta W_i}{1 + a\Delta t}. \tag{101}$$

In the stationary regime, $\mathsf{Var}\,\eta_i = \mathsf{Var}\,\eta_{i-1}$, whence, bearing in mind that $\mathsf{Var}\,\Delta W_i = \Delta t$ and ΔW_i is independent on the values of η for all time moments up to and including the moment $i-1$, we apply the variance operator to both sides of Eq.(101) and obtain the stationary variance

$$V(\Delta t) := \lim_{i\to\infty} \mathsf{Var}\,\eta_i = \frac{\sigma^2}{2a + (g\Delta t)^2}. \tag{102}$$

Note that, as $\Delta t \to 0$, $V(\Delta t)$ tends to the continuous-time variance $\frac{\sigma^2}{2a}$, see Eq.(16).

F.2 Third-order numerical scheme

Consider the continuous-time OSDE, Eq.(91), with $p = 3$. The implicit scheme Eq.(62) we use to numerically solve it is reproduced here as

$$\eta_i = \frac{1}{\varkappa^3}\left[3\varkappa^2\eta_{i-1} - 3\varkappa\eta_{i-2} + \eta_{i-3} + \sigma(\Delta t)^2\,\Delta W_i\right], \tag{103}$$

where $\varkappa := 1 + a\Delta t$. Here, the goal is to find the stationary variance $V := \lim_{i\to\infty} \mathsf{Var}\,\eta_i$ along with lag-1 and lag-2 stationary covariances, $c_1 := \lim_{i\to\infty} \mathsf{E}\,\eta_i\eta_{i-1}$ and $c_2 := \lim_{i\to\infty} \mathsf{E}\,\eta_i\eta_{i-2}$, respectively. To reach this goal, we build three linear algebraic equations for the three unknowns, V, c_1, and c_2. The first equation is obtained by applying the variance operator to both sides of Eq.(103). The second and third equations are obtained by multiplying Eq.(103) by η_{i-1} and η_{i-2}, respectively, and applying the expectation operator to both sides of the resulting equations. Omitting the derivations, we write down the results:

$$V = \frac{\varkappa^4 + 4\varkappa^2 + 1}{(\varkappa^2 - 1)^5}\,(\Delta t)^5\sigma^2. \tag{104}$$

$$c_1 = \frac{3\varkappa(\varkappa^2 + 1)}{(\varkappa^2 - 1)^5}\,(\Delta t)^5\sigma^2, \qquad c_2 = \frac{6\varkappa^2}{(\varkappa^2 - 1)^5}\,(\Delta t)^5\sigma^2. \tag{105}$$

As in the first-order case, one can see that as $\Delta t \to 0$, V tends to the continuous-time variance $\frac{3}{16}\frac{\sigma^2}{a^5}$, see Table 2 in Appendix D.

References

[1] E.S. Epstein. Stochastic dynamic prediction. *Tellus*, 21(6):739–759, 1969.

[2] B.V. Tatarsky. The use of dynamic equations for a probabilistic forecasting of the pressure fields. *Izv. Akad. Nauk SSSR, FAO*, 5:293–297, 1969.

[3] E.J. Pitcher. Application of stochastic dynamic prediction to real data. *J. Atmos. Sci.*, 34(1):3–21, 1977.

[4] D. Orrell, L. Smith, J. Barkmeijer, and T.N. Palmer. Model error in weather forecasting. *Nonlin. Proc. Geophys.*, 8(6):357–371, 2001.

[5] J. Berner, U. Achatz, L. Batte, A. De La Camara, D. Crommelin, H. Christensen, M. Colangeli, S. Dolaptchiev, C.L. Franzke, P. Friederichs, et al. Stochastic parameterization: Towards a new view of weather and climate models. *arXiv preprint arXiv:1510.08682*, 2015.

[6] M. Tsyrulnikov and V. Gorin. Are atmospheric-model tendency errors perceivable from routine observations? *COSMO Newsletter No. 13*, pages 3–18, 2013.

[7] P.L. Houtekamer, H.L. Mitchell, and X. Deng. Model error representation in an operational ensemble Kalman filter. *Mon. Wea. Rev.*, 137(7):2126–2143, 2009.

[8] R. Buizza, M. Miller, and T.N. Palmer. Stochastic representation of model uncertainties in the ECMWF ensemble prediction system. *Q. J. R. Meterol. Soc.*, 125(560):2887–2908, 1999.

[9] J. Berner, G.J. Shutts, M. Leutbecher, and T.N. Palmer. A spectral stochastic kinetic energy backscatter scheme and its impact on flow-dependent predictability in the ECMWF ensemble prediction system. *J. Atmos. Sci.*, 66(3):603–626, 2009.

[10] L. Bengtsson, M. Steinheimer, P. Bechtold, and J.F. Geleyn. A stochastic parametrization for deep convection using cellular automata. *Q. J. R. Meterol. Soc.*, 139(675): 1533–1543, 2013.

[11] A.H. Jazwinski. *Stochastic processes and filtering theory*. Academic Press, 1970.

[12] L. Arnold. *Stochastic differential equations*. Wiley, 1974.

[13] M. Tsyrulnikov. Stochastic modelling of model errors: A simulation study. *Q. J. R. Meterol. Soc.*, 131(613):3345–3371, 2005.

[14] M. Tsyroulnikov. Proportionality of scales: An isotropy-like property of geophysical fields. *Q. J. R. Meterol. Soc.*, 127(578):2741–2760, 2001.

[15] N. Meunier and J. Zhao. Observations of photospheric dynamics and magnetic fields: from large-scale to small-scale flows. *Space Sci. Rev.*, 144(1-4):127–149, 2009.

[16] N. Cressie and H.C. Huang. Classes of nonseparable, spatio-temporal stationary covariance functions. *J. Amer. Statist. Assoc.*, 94(448):1330–1339, 1999.

[17] M.L. Stein. Space–time covariance functions. *J. Amer. Statist. Assoc.*, 100(469):310–321, 2005.

[18] T. Gneiting, M.G. Genton, and P. Guttorp. Geostatistical space-time models, stationarity, separability, and full symmetry. *Monographs Statist. Appl. Probab.*, 107:151, 2006.

[19] X. Li, M. Charron, L. Spacek, and G. Candille. A regional ensemble prediction system based on moist targeted singular vectors and stochastic parameter perturbations. *Mon. Wea. Rev.*, 136(2):443–462, 2008.

[20] N.E. Bowler, A. Arribas, S.E. Beare, K.R. Mylne, and G.J. Shutts. The local ETKF and SKEB: Upgrades to the MOGREPS short-range ensemble prediction system. *Q. J. R. Meterol. Soc.*, 135(640):767–776, 2009.

[21] T.N. Palmer, R. Buizza, F. Doblas-Reyes, T. Jung, M. Leutbecher, G.J. Shutts, M. Steinheimer, and A. Weisheimer. Stochastic parametrization and model uncertainty. *ECMWF Tech. Memo. n. 598, ECMWF, Shinfield Park, 42 pp.*, 2009.

[22] Bouttier F., Vié B., O. Nuissier, and L. Raynaud. Impact of stochastic physics in a convection-permitting ensemble. *Mon. Wea. Rev.*, 140(11):3706–3721, 2012.

[23] F. Lindgren, H. Rue, and J. Lindström. An explicit link between Gaussian fields and Gaussian Markov random fields: the stochastic partial differential equation approach. *J. Roy. Statist. Soc. B*, 73(4):423–498, 2011.

[24] S. Åberg and K. Podgórski. A class of non-Gaussian second order random fields. *Extremes*, 14(2):187–222, 2011.

[25] J. Wallin and D. Bolin. Geostatistical modelling using non-Gaussian Matérn fields. *Scand. J. Statist.*, 42(3):872–890, 2015.

[26] R.J. Adler. *The geometry of random fields.* Wiley, 1981.

[27] A.M. Yaglom. *Correlation theory of stationary and related random functions, Volume 1: Basic results.* Springer Verlag, 1987.

[28] M.A. Shubin. *Pseudodifferential operators and spectral theory.* Springer, 1987.

[29] M.L. Stein. *Interpolation of spatial data: some theory for kriging.* Springer, New York, 1999.

[30] P. Guttorp and T. Gneiting. Studies in the history of probability and statistics XLIX. On the Matern correlation family. *Biometrika*, 93(4):989–995, 2006.

[31] A.S. Monin and A.M. Yaglom. *Statistical fluid mechanics, Volume II: Mechanics of turbulence.* Courier Corp., 2013.

[32] J. Theiler, S. Eubank, A. Longtin, B. Galdrikian, and J.D. Farmer. Testing for nonlinearity in time series: the method of surrogate data. *Physica D*, 58(1-4):77–94, 1992.

[33] D. Tse and P. Viswanath. *Fundamentals of wireless communication.* Cambridge University Press, 2005.

[34] M. Baldauf, A. Seifert, J. Förstner, D. Majewski, M. Raschendorfer, and T. Reinhardt. Operational convective-scale numerical weather prediction with the COSMO model: description and sensitivities. *Mon. Wea. Rev.*, 139(12):3887–3905, 2011.

[35] M. Tsyrulnikov and D. Gayfulin. A limited-area spatio-temporal stochastic pattern generator for ensemble prediction and ensemble data assimilation. *Meteorol. Zeitschrift (under review)*, 2016.

[36] Y.A. Rozanov. *Markov random fields.* Springer, 1982.

[37] H.H. Kuo. White noise theory. *In "Handbook of stochastic analysis and applications" Kannan D. and Lakshmikantham V. (Eds.)*, pages 107–158, 2001.

[38] D. Simpson, F. Lindgren, and H. Rue. Think continuous: Markovian Gaussian models in spatial statistics. *Spatial Statist.*, 1:16–29, 2012.

List of COSMO Newsletters and Technical Reports

(available for download from the COSMO Website: www.cosmo-model.org)

COSMO Newsletters

No. 1: February 2001.

No. 2: February 2002.

No. 3: February 2003.

No. 4: February 2004.

No. 5: April 2005.

No. 6: July 2006.

No. 7: April 2008; Proceedings from the 8th COSMO General Meeting in Bucharest, 2006.

No. 8: September 2008; Proceedings from the 9th COSMO General Meeting in Athens, 2007.

No. 9: December 2008.

No. 10: March 2010.

No. 11: April 2011.

No. 12: April 2012.

No. 13: April 2013.

No. 14: April 2014.

No. 15: July 2015.

No. 16: July 2016.

COSMO Technical Reports

No. 1: Dmitrii Mironov and Matthias Raschendorfer (2001):
Evaluation of Empirical Parameters of the New LM Surface-Layer Parameterization Scheme. Results from Numerical Experiments Including the Soil Moisture Analysis.

No. 2: Reinhold Schrodin and Erdmann Heise (2001):
The Multi-Layer Version of the DWD Soil Model TERRA_LM.

No. 3: Günther Doms (2001):
A Scheme for Monotonic Numerical Diffusion in the LM.

No. 4: Hans-Joachim Herzog, Ursula Schubert, Gerd Vogel, Adelheid Fiedler and Roswitha Kirchner (2002):
LLM ¯ the High-Resolving Nonhydrostatic Simulation Model in the DWD-Project LITFASS.
Part I: Modelling Technique and Simulation Method.

No. 5: Jean-Marie Bettems (2002):
EUCOS Impact Study Using the Limited-Area Non-Hydrostatic NWP Model in Operational Use at MeteoSwiss.

No. 6: Heinz-Werner Bitzer and Jürgen Steppeler (2004):
Documentation of the Z-Coordinate Dynamical Core of LM.

No. 7: Hans-Joachim Herzog, Almut Gassmann (2005):
Lorenz- and Charney-Phillips vertical grid experimentation using a compressible nonhydrostatic toy-model relevant to the fast-mode part of the 'Lokal-Modell'.

No. 8: Chiara Marsigli, Andrea Montani, Tiziana Paccagnella, Davide Sacchetti, André Walser, Marco Arpagaus, Thomas Schumann (2005):
Evaluation of the Performance of the COSMO-LEPS System.

No. 9: Erdmann Heise, Bodo Ritter, Reinhold Schrodin (2006):
Operational Implementation of the Multilayer Soil Model.

No. 10: M.D. Tsyrulnikov (2007):
Is the particle filtering approach appropriate for meso-scale data assimilation ?

No. 11: Dmitrii V. Mironov (2008):
Parameterization of Lakes in Numerical Weather Prediction. Description of a Lake Model.

No. 12: Adriano Raspanti (2009):
COSMO Priority Project "VERification System Unified Survey" (VERSUS): Final Report.

No. 13: Chiara Marsigli (2009):
COSMO Priority Project "Short Range Ensemble Prediction System" (SREPS): Final Report.

No. 14: Michael Baldauf (2009):
COSMO Priority Project "Further Developments of the Runge-Kutta Time Integration Scheme" (RK): Final Report.

No. 15: Silke Dierer (2009):
COSMO Priority Project "Tackle deficiencies in quantitative precipitation forecast" (QPF): Final Report.

No. 16: Pierre Eckert (2009):
COSMO Priority Project "INTERP": Final Report.

No. 17: D. Leuenberger, M. Stoll and A. Roches (2010):
Description of some convective indices implemented in the COSMO model.

No. 18: Daniel Leuenberger (2010):
Statistical analysis of high-resolution COSMO Ensemble forecasts in view of Data Assimilation.

No. 19: A. Montani, D. Cesari, C. Marsigli, T. Paccagnella (2010):
Seven years of activity in the field of mesoscale ensemble forecasting by the COSMO–LEPS system: main achievements and open challenges.

No. 20: A. Roches, O. Fuhrer (2012):
Tracer module in the COSMO model.

No. 21: Michael Baldauf (2013):
A new fast-waves solver for the Runge-Kutta dynamical core.

No. 22: C. Marsigli, T. Diomede, A. Montani, T. Paccagnella, P. Louka, F. Gofa, A. Corigliano (2013):
The CONSENS Priority Project.

No. 23: M. Baldauf, O. Fuhrer, M. J. Kurowski, G. de Morsier, M. Müllner, Z. P. Piotrowski, B. Rosa, P. L. Vitagliano, D. Wójcik, M. Ziemiański (2013):
The COSMO Priority Project 'Conservative Dynamical Core' Final Report.

No. 24: A. K. Miltenberger, A. Roches, S. Pfahl, H. Wernli (2014):
Online Trajectory Module in COSMO: a short user guide.

No. 25: P. Khain, I. Carmona, A. Voudouri, E. Avgoustoglou, J.-M. Bettems, F. Grazzini (2015):
The Proof of the Parameters Calibration Method: CALMO Progress Report.

No. 26: D. Mironov, E. Machulskaya, B. Szintai, M. Raschendorfer, V. Perov, M. Chumakov, E. Avgoustoglou (2015):
The COSMO Priority Project 'UTCS' Final Report.

No. 27: J-M. Bettems (2015):
The COSMO Priority Project 'COLOBOC': Final Report.

No. 28: Ulrich Blahak (2016):
RADAR_MIE_LM and RADAR_MIELIB - Calculation of Radar Reflectivity from Model Output.

COSMO Technical Reports

Issues of the COSMO Technical Reports series are published by the *COnsortium for Small-scale MOdelling* at non-regular intervals. COSMO is a European group for numerical weather prediction with participating meteorological services from Germany (DWD, AWGeophys), Greece (HNMS), Italy (USAM, ARPA-SIMC, ARPA Piemonte), Switzerland (MeteoSwiss), Poland (IMGW), Romania (NMA) and Russia (RHM). The general goal is to develop, improve and maintain a non-hydrostatic limited area modelling system to be used for both operational and research applications by the members of COSMO. This system is initially based on the COSMO-Model (previously known as LM) of DWD with its corresponding data assimilation system.

The Technical Reports are intended

- for scientific contributions and a documentation of research activities,
- to present and discuss results obtained from the model system,
- to present and discuss verification results and interpretation methods,
- for a documentation of technical changes to the model system,
- to give an overview of new components of the model system.

The purpose of these reports is to communicate results, changes and progress related to the LM model system relatively fast within the COSMO consortium, and also to inform other NWP groups on our current research activities. In this way the discussion on a specific topic can be stimulated at an early stage. In order to publish a report very soon after the completion of the manuscript, we have decided to omit a thorough reviewing procedure and only a rough check is done by the editors and a third reviewer. We apologize for typographical and other errors or inconsistencies which may still be present.

At present, the Technical Reports are available for download from the COSMO web site (www.cosmo-model.org). If required, the member meteorological centres can produce hard-copies by their own for distribution within their service. All members of the consortium will be informed about new issues by email.

For any comments and questions, please contact the editor:

Massimo Milelli
Massimo.Milelli@arpa.piemonte.it

Consortium

for

Small-Scale Modelling

Technical Report No. 30

A Turbulence Kinetic Energy – Scalar Variance Turbulence Parameterization Scheme

April 2017

DOI: 10.5676/DWD_pub/nwv/cosmo-tr_30

Deutscher Wetterdienst
MeteoSwiss
Ufficio Generale Spazio Aereo e Meteorologia
ΕΘΝΙΚΗ ΜΕΤΕΩΡΟΛΟΓΙΚΗ ΥΠΗΡΕΣΙΑ
Instytucie Meteorogii i Gospodarki Wodnej
Administratia Nationala de Meteorologie
ROSHYDROMET
Agenzia Regionale per la Protezione Ambientale del Piemonte
Agenzia Regionale Prevenzione Ambiente Energia Emilia Romagna
Centro Italiano Ricerche Aerospaziali
Amt für GeoInformationswesen der Bundeswehr

www.cosmo-model.org

Editor: Massimo Milelli, ARPA Piemonte

A Turbulence Kinetic Energy – Scalar Variance Turbulence Parameterization Scheme

by

Dmitrii V. Mironov*[1] *and Ekaterina E. Machulskaya

German Weather Service,
Offenbach am Main,
Germany

[1]Corresponding author address: Deutscher Wetterdienst, FE14, Frankfurter Str. 135, D-63067 Offenbach am Main, Germany. Phone: +49-69-8062 2705, fax: +49-69-8062 3721. E-mail: dmitrii.mironov@dwd.de

1 Introduction 4

2 Quasi-Conservative Variables 7

3 Transport Equations for Second-Order Moments 7

4 Truncated Reynolds-Stress and Scalar-Flux Equations 10

5 Parameterization of Pressure Scrambling, Third-Order Transport and Dissipation Effects 11

5.1 Pressure Scrambling 11

5.2 Third-Order Transport 14

5.3 Dissipation 15

6 Time and Length Scales 15

7 Effect of Clouds on Mixing 17

8 Boundary-Layer Approximation 24

9 The (So-Called) Stability Functions 26

10 Interaction with the Underlying Surface 33

11 Equation for Scalar Skewness 35

12 Conclusions 38

13 Appendices 40

A Turbulence Kinetic Energy – Scalar Variance Turbulence Parameterization Scheme

Dmitrii V. Mironov[†] *and Ekaterina E. Machulskaya*

German Weather Service, Offenbach am Main, Germany

Abstract

A turbulence kinetic energy – scalar variance (TKESV) closure model (parameterization scheme) for moist atmosphere is developed. The scheme is formulated in terms of variables that are approximately conserved for phase changes in the absence of precipitation. These are the total water specific humidity and the liquid water potential temperature (or, if cloud ice is present, the ice-liquid water potential temperature). The scheme carries prognostic equations for the turbulence kinetic energy and for the variances and covariance of scalar quantities. The other second-moment equations, namely, the equations for the Reynolds stress and for the scalar fluxes, are reduced to the diagnostic algebraic expressions. In the present report, the set of governing equations of the TKESV scheme and parameterizations (closure assumptions) for the pressure-scrambling terms, the third-order transport (diffusion) terms, and the molecular destruction (dissipation) terms are discussed. Particular attention is paid to the pressure-scrambling terms in the Reynolds-stress and scalar-flux equations. The other issues that receive careful consideration are the effect of clouds on mixing (treated with the aid of statistical cloud schemes) and the interaction of the boundary layer with the underlying surface. Estimates of disposable parameters of the TKESV scheme are given.

[†]Corresponding author address: Deutscher Wetterdienst, FE14, Frankfurter Str. 135, D-63067 Offenbach am Main, Germany. Phone: +49-69-8062 2705, fax: +49-69-8062 3721. E-mail: dmitrii.mironov@dwd.de

1 Introduction

A turbulence parameterization scheme is an integral part of a physical parameterization package of any model of atmospheric circulation, including numerical weather prediction (NWP) and climate models. The importance of turbulence parameterization schemes will likely further increase as the resolution of the atmospheric models is refined. As the mesh size becomes small, quasi-organized flow structures, such as deep convective plumes that are chiefly responsible for non-local convective transport of momentum and scalars, are increasingly resolved. The focus of parameterizations of the sub-grid scale processes is then shifted towards motions at smaller scales and towards other issues, as e.g. the anisotropy of turbulence near the surface and in stably-stratified regions of the flow, and the interaction between boundary-layer turbulence and shallow clouds. Turbulence closure schemes based on truncated second-order moment equations are viable tools for describing these features.

There are many quite sophisticated and physically sound turbulence models (parameterization schemes) which proved to be very useful research tools. There is little chance, however, to use them in operational NWP and related applications for those schemes are computationally prohibitively expensive and are often specific to a particular mixing regime. A turbulence parameterization scheme should no doubt account for the essential physics of atmospheric turbulence. On the other hand, a usable scheme should be computationally efficient and should give a reasonably accurate solution for all mixing regimes (stably-stratified boundary layer, dry convective boundary layer, convective boundary layers capped by cumulus or stratus clouds, etc.) around the clock and at any point on the globe. Therefore, the key issue in developing turbulence parameterization schemes for NWP and related applications is to find the best compromise between physical realism and computational economy.

The so-called one-equation turbulence parameterizations schemes have been very popular in geophysical applications over several decades. Those schemes carry the turbulence kinetic energy (TKE) equation, including the time-rate-of-change (or substantial derivative if the TKE advection is included) and the third-order turbulent transport (diffusion) terms. All other second-moment equations, viz., the equations for the Reynolds stress, for the fluxes of scalar quantities (e.g. temperature and humidity), and for the scalar variances and scalar covariance, are reduced to diagnostic algebraic expressions. In spite of their numerous shortcomings (see a discussion in Mironov, 2009), one-equation TKE schemes (and even simpler algebraic schemes) have been and still are the draft horses of atmospheric turbulence modelling in NWP, climate studies, and related applications.

The present report describes a TKE – Scalar Variance (TKESV) turbulence parameterization scheme that is a natural step beyond one-equation TKE schemes. Apart from the TKE equation, the TKESV scheme carries prognostic transport equations for the scalar variances and covariance (see section 2 for the definition of quasi-conservative scalars utilized by the TKESV scheme). It is the authors' opinion that the level of complexity of the TKESV scheme is likely the minimum level of complexity that is required for NWP, climate modelling and related applications in terms of essential physics. A justification of this opinion is almost trivial. The key issue in modelling of any turbulent flow is an adequate description of the flow energy. In neutrally stratified flows, the kinetic energy of turbulence is a major concern. This explains why the one-equation schemes have been successfully used in modelling neutral flows. The situation is very different in flows where the buoyancy stratification is not neutral. In such flows, the turbulence potential energy (TPE) plays an important part along with the TKE. The TKE is spent to work against the gravity and is converted into the TPE in stably stratified flows. In convective flows, the TKE grows at the expense of the TPE. Since the atmospheric flows are virtually never hydrostatically neutral, and the TKE and the

TPE in stratified flows are equally important, it is difficult to adduce plausible arguments in favour of one form of energy over the other. Both energies possess equal rights and should be treated in a similar way. In the atmosphere, the TPE is characterized by the variances and covariance of the scalar quantities (see Appendix C). Hence, the scalar (co)variances should be treated as accurately as the TKE. An improved treatment of scalar (co)variances helps to improve the performance of atmospheric models in several respects. These are, for example, a consistent treatment of counter-gradient fluxes of scalars (which is not possible with the one-equation TKE schemes) and an improved representation of the fractional cloudiness. Furthermore, the TKESV scheme provides a framework for a consistent unified treatment of boundary-layer turbulence and shallow convection.

Examples of turbulence parameterization schemes that carry transport equations for both the TKE and the scalar variances are given in Kenjereš and Hanjalić (2002) (for the temperature-stratified atmosphere) and Nakanishi and Niino (2004) (for the moist atmosphere). Worthy of mention is a more complex scheme termed CLUBB (Cloud Layers Unified By Binormals), an assumed-PDF (probability distribution function) unified parameterization of turbulence and cloud processes in the Earth's atmosphere (numerous references and further information about CLUBB can be found at https://people.uwm.edu/vlarson/clubb/).

Interestingly enough, it was stated already by Mellor and Yamada in their popular 1974 paper (Mellor and Yamada, 1974) that the scheme (level 3 in their nomenclature) that carries transport equations for the TKE and for the potential-temperature variance is particularly attractive. The level 3 scheme outperforms an algebraic closure scheme, and little is gained if a more complex scheme that carries transport equations for all second-order moments involved is used. Thus the level 3 scheme represents an optimal choice. Mention should also be made of the analysis of the second-moment budgets in the cloud-topped boundary layers performed by Heinze et al. (2015) using large-eddy simulation (LES) data. It was found (among other things) that the third-order transport is of secondary importance in the Reynolds-stress and scalar-flux budgets but it plays a key role in maintaining the TKE and the scalar (co)variance budgets. These results support the design of the TKESV scheme.

In the present report, governing equations and closure assumptions (parameterizations) of the TKE–Scalar Variance scheme are formulated, and estimates of disposable parameters are given. In the remainder of this section, an outline of the report is given.

The TKESV scheme is formulated in terms of variables that are approximately conserved for phase changes in the absence of precipitation. These are the total water specific humidity and the liquid water potential temperature. If cloud ice is present, the ice-liquid water potential temperature is used. Quasi-conservative thermodynamic variables are introduced in section 2. Transport equations for the second-order moments of fluctuating velocity and scalar fields are given in section 3. The TKESV scheme carries "full" prognostic equations, i.e. the equations including the substantial derivative (that reduces to the time-rate-of-change in one-dimensional case, where the flow variables depend on the vertical coordinate only) and the third-order turbulent transport terms, for the TKE and for the variances and covariance of the scalar quantities. The equations for the Reynolds stress and for the scalar fluxes are reduced (truncated) to the diagnostic algebraic expressions by neglecting the substantial derivative and the third-order transport terms. The truncated Reynolds-stress and scalar-flux equations are presented in section 4.

The system of governing second-moment equations is not closed. There are four groups of terms that require parameterizations (closure assumptions). These are the pressure-scrambling terms in the Reynolds-stress and the scalar-flux equations, the third-order turbulent transport terms in the equations for the TKE and for the scalar variances and covariance, the dissipation rates of the TKE and of the scalar variances and covariance, and the buoy-

ancy terms (incorporating correlations of the velocity and scalars with the virtual potential temperature) in the Reynolds-stress, scalar-flux and TKE equations. Parameterizations of these terms are presented in sections 5 and 7. Particular attention is paid to the pressure-scrambling terms. Although parameterization of the pressure-scrambling effects is probably the most crucial issue in modelling atmospheric turbulence, this issue receives unduly little attention in the atmospheric modelling community. Formulations of the turbulence time and length scales are presented in section 6. An algebraic interpolation formula for the turbulence length scale that accounts for the limiting effect of stable density stratification is presented. A more advanced non-local length-scale formulation is also discussed. In section 7, we consider the effect of clouds on mixing intensity. The second-moment equations are coupled to a statistical cloud scheme, and parameterizations of the buoyancy terms in the Reynolds-stress, scalar-flux and TKE equations are developed with due regard for the presence of cloud condensate.

In section 8, the so-called boundary-layer approximation is invoked to obtain a one-dimensional version of the TKESV scheme. Note that in the majority of NWP models, including ICON and COSMO, one-dimensional schemes are used to parameterize turbulent mixing (unless these models are used in the LES mode). The so-called stability functions that appear in the algebraic formulations for the Reynolds stress and scalar fluxes (see e.g. Mellor and Yamada, 1974) are discussed in section 9 in much detail. The stability functions, resulting from the truncated Reynolds-stress and scalar-flux equations (where the third-order and the time-rate-of-change terms are neglected) with the linear parameterizations of the pressure-scrambling terms (linear in the second-order moments involved), are ill-behaved over a certain range of governing parameters (e.g. mean velocity shear and mean temperature gradient). Using rather plausible physical arguments, we develop regularized stability functions that are well-behaved in the entire range of governing parameters. The interaction of the boundary-layer flow with the underlying surface is discussed in section 10, where the focus is on the lower boundary conditions for the scalar variances and covariance.

The emphasis in sections 5 through 10 is on the baseline version of the TKESV scheme (TKESV-Bas). This somewhat simplified version of the scheme is based on the linear parameterizations of the pressure-scrambling terms, the simplest isotropic down-gradient parameterizations of the third-order transport terms, and the algebraic interpolation formula for the turbulence length scale. It utilizes an ad hoc correction to the Gaussian statistical cloud scheme to account for shallow cumuli (enhanced mixing due to clouds in spite of low fractional cloud cover). The lower boundary conditions for the scalar variances and covariance do not account for the heterogeneity of the underlying surface. It is the baseline version of the TKESV scheme in the boundary-layer approximation (i.e. the one-dimensional TKESV-Bas) that is intended for use within NWP models ICON and COSMO in the near future.

In the medium-term prospective, an extended version of the scheme (TKESV-Ext) can be used. TKESV-Ext incorporates advanced formulations of the pressure-scrambling terms and of the third-order transport terms, non-local formulation of the turbulence length scale, lower boundary conditions for the scalar (co)variances that are consistent with the tile approach to compute the surface fluxes over heterogeneous surfaces, and a statistical cloud scheme capable of describing cumulus regimes. These formulations are discussed in the respective sections under the heading ***Advanced Features***. The use of an advanced statistical cloud scheme, e.g. the scheme proposed by Naumann et al. (2013), requires knowledge of the triple correlations (skewness) of scalar quantities (more specifically, of linearized saturation deficit/excess). The scalar-skewness prognostic equation is developed in section 11.

Conclusions are given in section 12. The present report contains several Appendices. The aim

of the report is not only to present the governing equations and parameterization assumptions of the TKESV scheme, but also to elucidate their physical meaning and, importantly, their limitations. To this end, detailed derivations of at least some parameterizations should be presented (most notably, of the pressure-scrambling terms). Since the derivations are rather lengthy, they are given in Appendices. This allows to keep the main body of the text more concise.

2 Quasi-Conservative Variables

In order to account for the presence of cloud condensate, turbulence and shallow-convection models are formulated in terms of variables that are approximately conserved for phase changes in the absence of precipitation (Betts, 1973; Deardorff, 1976; Betts, 1986). One pair of moist quasi-conservative variables consists of the total water specific humidity q_t and the liquid water potential temperature θ_l defined as

$$q_t = q + q_l, \tag{1}$$

$$\theta_l = \theta - \frac{\theta}{T}\frac{L_v}{c_p} q_l. \tag{2}$$

Here, q is the water vapour specific humidity (the mass of water vapour per unit mass of moist air), q_l is the liquid water specific humidity (the mass of cloud water per unit mass of moist air), c_p is the specific heat of air at constant pressure, L_v is the heat of vapourization, θ is the potential temperature related to the absolute temperature T through $\theta = T(P_0/P)^{R_d/c_p}$, P and P_0 being the atmospheric pressure and its reference value, respectively, and R_d being the gas constant for dry air. No supersaturation is assumed, so that $q_l = q_t - q_s$ if $q_t > q_s$, where q_s is the saturation specific humidity, and $q_l = 0$ otherwise. Clearly, q_t and θ_l reduce to the dry variables q and θ, respectively, in unsaturated conditions. For the sake of simplicity the total water specific humidity and the liquid water potential temperature will also be referred to as simply humidity and temperature, respectively.

Advanced Features

The $q_t - \theta_l$ system outlined above can be extended to the case of three phases including cloud ice (Deardorff, 1976). To this end, the total water specific humidity is generalized to account for the presence of ice, and the ice-liquid water (i.e. total water) potential temperature is introduced:

$$q_t = q + q_l + q_i, \tag{3}$$

$$\theta_t = \theta - \frac{\theta}{T}\frac{L_v}{c_p} q_l - \frac{\theta}{T}\frac{L_i}{c_p} q_i, \tag{4}$$

where q_i is the solid water specific humidity (the mass of cloud ice per unit mass of moist air), and L_i is the heat of sublimation.

3 Transport Equations for Second-Order Moments

The basis for the development of second-order closure schemes is the set of transport equations for the second-order moments of fluctuating fields (e.g. Monin and Yaglom, 1971;

Mironov, 2009). For the moist atmosphere characterized by quasi-conservative variables θ_l and q_t, these are the equations for the Reynolds stress $\langle u_i' u_j' \rangle$, u_i being the velocity components[1], for the scalar fluxes $\langle u_i' \theta_l' \rangle$ and $\langle u_i' q_t' \rangle$, for the scalar variances $\langle \theta_l'^2 \rangle$ and $\langle q_t'^2 \rangle$, and for the scalar covariance $\langle \theta_l' q_t' \rangle$. The angle brackets denote mean quantities, and a prime denotes a turbulent fluctuation. Using the Boussinesq approximation and assuming that the Reynolds number is sufficiently high to neglect the molecular diffusion terms in the second-moment budget equations (a good approximation for the atmospheric flows), the equations read

$$\left(\frac{\partial}{\partial t} + \langle u_k \rangle \frac{\partial}{\partial x_k}\right) \langle u_i' u_j' \rangle =$$
$$- \left(\langle u_i' u_k' \rangle \frac{\partial \langle u_j \rangle}{\partial x_k} + \langle u_j' u_k' \rangle \frac{\partial \langle u_i \rangle}{\partial x_k} \right) - \left(\beta_i \langle u_j' \theta_v' \rangle + \beta_j \langle u_i' \theta_v' \rangle \right)$$
$$-2 \left(\epsilon_{imk} \Omega_m \langle u_k' u_j' \rangle + \epsilon_{jmk} \Omega_m \langle u_k' u_i' \rangle \right) + \left\langle p' \left(\frac{\partial u_i'}{\partial x_j} + \frac{\partial u_j'}{\partial x_i} \right) \right\rangle$$
$$- \frac{\partial}{\partial x_k} \left(\langle u_k' u_i' u_j' \rangle + \delta_{kj} \langle p' u_i' \rangle + \delta_{ki} \langle p' u_j' \rangle \right) - \epsilon_{ij}, \tag{5}$$

$$\left(\frac{\partial}{\partial t} + \langle u_k \rangle \frac{\partial}{\partial x_k}\right) \langle u_i' \theta_l' \rangle = - \langle u_k' \theta_l' \rangle \frac{\partial \langle u_i \rangle}{\partial x_k} - \langle u_i' u_k' \rangle \frac{\partial \langle \theta_l \rangle}{\partial x_k} - \beta_i \langle \theta_l' \theta_v' \rangle$$
$$-2 \epsilon_{imk} \Omega_m \langle u_k' \theta_l' \rangle - \left\langle \theta_l' \frac{\partial p'}{\partial x_i} \right\rangle - \frac{\partial}{\partial x_k} \langle u_k' u_i' \theta_l' \rangle - \epsilon_{\theta i}, \tag{6}$$

$$\left(\frac{\partial}{\partial t} + \langle u_k \rangle \frac{\partial}{\partial x_k}\right) \langle u_i' q_t' \rangle = - \langle u_k' q_t' \rangle \frac{\partial \langle u_i \rangle}{\partial x_k} - \langle u_i' u_k' \rangle \frac{\partial \langle q_t \rangle}{\partial x_k} - \beta_i \langle q_t' \theta_v' \rangle$$
$$-2 \epsilon_{imk} \Omega_m \langle u_k' q_t' \rangle - \left\langle q_t' \frac{\partial p'}{\partial x_i} \right\rangle - \frac{\partial}{\partial x_k} \langle u_k' u_i' q_t' \rangle - \epsilon_{qi}, \tag{7}$$

$$\frac{1}{2} \left(\frac{\partial}{\partial t} + \langle u_k \rangle \frac{\partial}{\partial x_k}\right) \langle \theta_l'^2 \rangle = - \langle u_k' \theta_l' \rangle \frac{\partial \langle \theta_l \rangle}{\partial x_k} - \frac{1}{2} \frac{\partial}{\partial x_k} \langle u_k' \theta_l'^2 \rangle - \epsilon_{\theta\theta}, \tag{8}$$

$$\frac{1}{2} \left(\frac{\partial}{\partial t} + \langle u_k \rangle \frac{\partial}{\partial x_k}\right) \langle q_t'^2 \rangle = - \langle u_k' q_t' \rangle \frac{\partial \langle q_t \rangle}{\partial x_k} - \frac{1}{2} \frac{\partial}{\partial x_k} \langle u_k' q_t'^2 \rangle - \epsilon_{qq}, \tag{9}$$

$$\left(\frac{\partial}{\partial t} + \langle u_k \rangle \frac{\partial}{\partial x_k}\right) \langle \theta_l' q_t' \rangle = - \langle u_k' q_t' \rangle \frac{\partial \langle \theta_l \rangle}{\partial x_k} - \langle u_k' \theta_l' \rangle \frac{\partial \langle q_t \rangle}{\partial x_k} - \frac{\partial}{\partial x_k} \langle u_k' \theta_l' q_t' \rangle - 2 \epsilon_{\theta q}. \tag{10}$$

Here, t is the time, x_i are the space coordinates, $\beta_i = g_i \alpha_T$ is the buoyancy parameter, g_i is the acceleration due to gravity, $\alpha_T = -\rho^{-1} \partial \rho / \partial T$ is the thermal expansion coefficient, ρ is the density, Ω_i is the angular velocity of the reference frame rotation, and p is the kinematic pressure (deviation of pressure from the hydrostatically balanced pressure divided by the reference density ρ_r). The Einstein summation convention for repeated indices is adopted. The last terms on the right-hand sides (r.h.s.) of Eqs. (5)–(10) are the molecular destruction (dissipation) rates of the Reynolds stress, of the scalar fluxes, and of the scalar variances and covariance. The quantity θ_v is the virtual potential temperature that is defined with due regard for the water loading effect (Lilly, 1968; Bannon, 2007),

$$\theta_v = \theta \left[1 + \left(\frac{R_v}{R_d} - 1 \right) q - q_l \right], \tag{11}$$

[1]The term "Reynolds stress" is used here in a somewhat loose way. Strictly speaking, the Reynolds stress tensor is $-\rho \langle u_i' u_j' \rangle$, where ρ is the fluid density. See e.g. Pope (2000).

where R_v is the gas constant for water vapour.

Setting $j = i$ in Eq. (5) yields the budget equation for the TKE, $e \equiv \frac{1}{2}\langle u_i'^2 \rangle$,

$$\frac{1}{2}\left(\frac{\partial}{\partial t} + \langle u_k \rangle \frac{\partial}{\partial x_k}\right)\langle u_i'^2 \rangle = -\langle u_i' u_k' \rangle \frac{\partial \langle u_i \rangle}{\partial x_k} - \beta_i \langle u_i' \theta_v' \rangle - \frac{\partial}{\partial x_k}\left(\frac{1}{2}\langle u_k' u_i'^2 \rangle + \langle u_k' p' \rangle\right) - \epsilon, \tag{12}$$

where the last term on the r.h.s. is the TKE dissipation rate, $\epsilon \equiv \frac{1}{2}\epsilon_{ii}$.

The pressure gradient-velocity covariance $\langle u_i' \partial p'/\partial x_j \rangle + \langle u_j' \partial p'/\partial x_i \rangle$ describes the combined effect of pressure transport and pressure scrambling in the Reynolds-stress equation. These are different physical processes that should be modelled in a different way. To this end, the pressure gradient-velocity covariance is decomposed to separate out the traceless part which does not alter the TKE but acts to redistribute the energy between the components, thus driving turbulence towards the isotropic state (hence the term "pressure scrambling"). The rest of the pressure gradient-velocity covariance describes the transport of the Reynolds stress in space by the fluctuating velocity and pressure fields. It should be mentioned that the decomposition of the pressure gradient-velocity covariance is not unique. Along with a somewhat more traditional decomposition into pressure-strain and pressure transport that is used in Eq. (5),

$$\left\langle u_i' \frac{\partial p'}{\partial x_j} \right\rangle + \left\langle u_j' \frac{\partial p'}{\partial x_i} \right\rangle = -\left\langle p' \left(\frac{\partial u_i'}{\partial x_j} + \frac{\partial u_j'}{\partial x_i}\right) \right\rangle + \left(\frac{\partial}{\partial x_j}\langle p' u_i' \rangle + \frac{\partial}{\partial x_i}\langle p' u_j' \rangle\right), \tag{13}$$

a decomposition into deviatoric and isotropic parts,

$$\left\langle u_i' \frac{\partial p'}{\partial x_j} \right\rangle + \left\langle u_j' \frac{\partial p'}{\partial x_i} \right\rangle = \left(\left\langle u_i' \frac{\partial p'}{\partial x_j} \right\rangle + \left\langle u_j' \frac{\partial p'}{\partial x_i} \right\rangle - \frac{2}{3}\delta_{ij}\frac{\partial}{\partial x_k}\langle u_k' p' \rangle\right) + \frac{2}{3}\delta_{ij}\frac{\partial}{\partial x_k}\langle u_k' p' \rangle, \tag{14}$$

has also been advocated (e.g. Speziale, 1985). The difference,

$$\frac{\partial}{\partial x_j}\langle p' u_i' \rangle + \frac{\partial}{\partial x_i}\langle p' u_j' \rangle - \frac{2}{3}\delta_{ij}\frac{\partial}{\partial x_k}\langle u_k' p' \rangle, \tag{15}$$

is both a transport term and a traceless term. Any fraction of this difference may be added to the pressure-strain and subtracted from the pressure transport, thus producing a new decomposition (Lumley, 1975).

The non-uniqueness of decomposition of the pressure gradient-velocity covariance does not matter much if a truncated equation for the Reynolds stress is used, where the third-order transport and pressure transport terms are neglected. No matter which approach is taken, the pressure-strain and the deviatoric part of the pressure gradient-velocity covariance are both traceless tensors that are modelled in the same way. Therefore, there is no general difference between the decompositions (13) and (14), or any other decomposition separating the traceless and the transport parts, as regards the pressure redistribution (the inter-component energy transfer)[2]. The two decompositions are essentially different as regards the pressure transport (Speziale, 1985). The pressure transport of the Reynolds stress is, however, neglected within the framework of the scheme considered here.

[2]Notice, however, that the way the traceless part of the pressure term is separated out does matter when data, e.g. large-eddy simulation or direct numerical simulation data, are used to evaluate disposable parameters in models (parameterizations) of the pressure redistribution terms.

Advanced Features

If cloud ice is considered, the virtual potential temperature is defined as

$$\theta_v = \theta \left[1 + \left(\frac{R_v}{R_d} - 1 \right) q - q_l - q_i \right]. \tag{16}$$

4 Truncated Reynolds-Stress and Scalar-Flux Equations

Within the framework of the TKESV scheme, the equations for the Reynolds stress and for the scalar fluxes are reduced (truncated) to the diagnostic algebraic expressions by neglecting the substantial derivatives, the third-order transport of $\langle u_i' u_j' \rangle$, $\langle u_i' \theta_l' \rangle$ and $\langle u_i' q_t' \rangle$, and the pressure transport of $\langle u_i' u_j' \rangle$. The resulting algebraic equations are conveniently recast in terms of the departure-from-isotropy tensor defined as

$$a_{ij} = \langle u_i' u_j' \rangle - \frac{2}{3} \delta_{ij} e. \tag{17}$$

Subtracting Eq. (12) times $\frac{2}{3}\delta_{ij}$ from Eq. (5) and neglecting the time-rate-of-change, advection by the mean flow, the third-order transport and the pressure transport, we obtain

$$\begin{aligned} &- \left[\frac{4}{3} e S_{ij} + \left(a_{ik} S_{jk} + a_{jk} S_{ik} - \frac{2}{3} \delta_{ij} a_{km} S_{km} \right) + \left(a_{ik} W_{jk} + a_{jk} W_{ik} \right) \right] \\ &- \left(\beta_i \langle u_j' \theta_v' \rangle + \beta_j \langle u_i' \theta_v' \rangle - \frac{2}{3} \delta_{ij} \beta_k \langle u_k' \theta_v' \rangle \right) - 2 \left(\epsilon_{imk} \Omega_m a_{kj} + \epsilon_{jmk} \Omega_m a_{ki} \right) \\ &- \Pi_{ij} - \epsilon_{ij}^d = 0, \end{aligned} \tag{18}$$

where $S_{ij} = \frac{1}{2} \left(\frac{\partial \langle u_i \rangle}{\partial x_j} + \frac{\partial \langle u_j \rangle}{\partial x_i} \right)$ and $W_{ij} = \frac{1}{2} \left(\frac{\partial \langle u_i \rangle}{\partial x_j} - \frac{\partial \langle u_j \rangle}{\partial x_i} \right)$ are the symmetric and the antisymmetric parts, respectively, of the mean-velocity gradient tensor, $\epsilon_{ij}^d = \epsilon_{ij} - \frac{2}{3}\delta_{ij}\epsilon$ is the deviatoric part of the Reynolds-stress dissipation tensor, and Π_{ij} is the traceless part of the pressure gradient-velocity covariance in the Reynolds-stress equation, see Eq. (13).

Neglecting the substantial derivative and the third-order transport terms in Eqs. (6) and (7), we obtain algebraic equations for the scalar fluxes $\langle u_i' \theta_l' \rangle$ and $\langle u_i' q_t' \rangle$. They read

$$\begin{aligned} &- \left(\frac{2}{3} e \delta_{ik} + a_{ik} \right) \frac{\partial \langle \theta_l \rangle}{\partial x_k} - \left(S_{ik} + W_{ik} \right) \langle u_k' \theta_l' \rangle - \beta_i \langle \theta_l' \theta_v' \rangle - 2 \epsilon_{imk} \Omega_m \langle u_k' \theta_l' \rangle \\ &- \Pi_{\theta i} - \epsilon_{\theta i} = 0, \end{aligned} \tag{19}$$

$$\begin{aligned} &- \left(\frac{2}{3} e \delta_{ik} + a_{ik} \right) \frac{\partial \langle q_t \rangle}{\partial x_k} - \left(S_{ik} + W_{ik} \right) \langle u_k' q_t' \rangle - \beta_i \langle q_t' \theta_v' \rangle - 2 \epsilon_{imk} \Omega_m \langle u_k' q_t' \rangle \\ &- \Pi_{qi} - \epsilon_{qi} = 0, \end{aligned} \tag{20}$$

where $\Pi_{\theta i}$ and Π_{qi} denote the pressure gradient-scalar covariances $\langle \theta_l' \partial p' / \partial x_i \rangle$ and $\langle q_t' \partial p' / \partial x_i \rangle$, respectively.

5 Parameterization of Pressure Scrambling, Third-Order Transport and Dissipation Effects

The second-moment equations (8), (9), (10), (12), (18), (19) and (20) are not closed. There are four groups of terms that should be parameterized. These are the pressure-scrambling terms, the third-order transport (diffusion) terms, the molecular destruction (dissipation) terms, and the buoyancy terms (incorporating correlations of the velocity and scalars with the virtual potential temperature). Parameterizations (closure assumptions) for the pressure-scrambling, third-order transport and dissipation terms are developed in sections 5.1, 5.2 and 5.3, respectively. The buoyancy terms are considered in section 7.

5.1 Pressure Scrambling

A common approach nowadays is to decompose the pressure-scrambling terms in the Reynolds-stress and scalar-flux equations into the contributions due to the non-linear turbulence interactions (that stem from the advection term in the equation of motion), mean velocity shear, buoyancy and the Coriolis effects, and to model (parameterize) these contributions separately (see e.g. Zeman, 1981; Mironov, 2001, 2009). Following this approach, we apply the return-to-isotropy parameterizations (Rotta, 1951; Monin, 1965) to the non-linear turbulence contributions to Π_{ij}, $\Pi_{\theta i}$ Π_{qi} (often referred to as slow parts of the pressure-scrambling terms) and utilize the simplest linear parameterizations of the mean velocity shear, buoyancy and Coriolis contributions (referred to as rapid parts of the pressure-scrambling terms). The following parameterizations of the pressure-scrambling terms are used in the TKESV-Bas scheme:

$$\begin{aligned}
\Pi_{ij} &= C_t^u \frac{a_{ij}}{\tau_{ru}} \\
&- C_{s1}^u S_{ij} e - C_{s2}^u \left(S_{ik} a_{kj} + S_{jk} a_{ki} - \frac{2}{3} \delta_{ij} S_{kl} a_{kl} \right) - C_{s3}^u \left(W_{ik} a_{kj} + W_{jk} a_{ki} \right) \\
&- C_b^u \left(\beta_i \left\langle u_j' \theta_v' \right\rangle + \beta_j \left\langle u_i' \theta_v' \right\rangle - \frac{2}{3} \delta_{ij} \beta_k \left\langle u_k' \theta_v' \right\rangle \right) \\
&- 2 C_c^u \left(\epsilon_{imk} \Omega_m a_{kj} + \epsilon_{jmk} \Omega_m a_{ki} \right), \qquad (21)
\end{aligned}$$

$$\Pi_{\theta i} = C_t^\theta \frac{\left\langle u_i' \theta_l' \right\rangle}{\tau_{r\theta}} - \left(C_{s1}^\theta S_{ij} + C_{s2}^\theta W_{ij} \right) \left\langle u_j' \theta_l' \right\rangle - C_b^\theta \beta_i \left\langle \theta_l' \theta_v' \right\rangle - 2 C_c^\theta \epsilon_{imj} \Omega_m \left\langle u_j' \theta_l' \right\rangle, \qquad (22)$$

$$\Pi_{qi} = C_t^q \frac{\left\langle u_i' q_t' \right\rangle}{\tau_{rq}} - \left(C_{s1}^q S_{ij} + C_{s2}^q W_{ij} \right) \left\langle u_j' q_t' \right\rangle - C_b^q \beta_i \left\langle q_t' \theta_v' \right\rangle - 2 C_c^q \epsilon_{imj} \Omega_m \left\langle u_j' q_t' \right\rangle, \qquad (23)$$

where $C_t^u = 1.8$, $C_{s1}^u = 4/5$, $C_{s2}^u = -6\alpha_5$, $C_{s3}^u = \frac{2}{3}(2 + 7\alpha_5)$, $C_b^u = 3/10$, $C_c^u = \frac{1}{3}(2 + 7\alpha_5)$, $C_t^\theta = C_t^q = 5.0$, $C_{s1}^\theta = C_{s1}^q = 3/5$, $C_{s2}^\theta = C_{s2}^q = 1$, $C_b^\theta = C_b^q = 1/3$ and $C_c^\theta = C_c^q = 1/2$ are dimensionless constants. An estimate of the yet undetermined disposable constant α_5 is obtained below. The return-to-isotropy time scales τ_{ru}, $\tau_{r\theta}$ and τ_{rq} in Eqs. (21)–(23) are taken to be proportional to the TKE dissipation time scale, $\tau_{ru} = \tau_{r\theta} = \tau_{rq} = \tau_\epsilon$, where $\tau_\epsilon = e/\epsilon$ and proportionality constants are set to one as they always occur in combination with the other constants. Parameterizations of the various time and length scales are discussed in section 6. A detailed derivation of Eqs. (21)–(23) is given in Appendix A. The properties of linear parameterizations of the pressure-scrambling terms, most notably their limitations, should be discussed in some detail.

It is readily seen that the linear parameterizations of the mean-velocity shear, buoyancy and Coriolis contributions to Π_{ij}, $\Pi_{\theta i}$ and Π_{qi} have the same form as the mean-velocity shear, buoyancy and Coriolis terms in the Reynolds-stress and scalar-flux equations (5)–(7) [or their truncated counterparts (18)–(20)]. Therefore, the effect of linear rapid parts of the pressure-scrambling terms, sometimes referred to as the implicit mean-velocity shear, buoyancy and Coriolis terms, is simply to partially offset the respective explicit terms already present in the Reynolds-stress and scalar-flux equations.

In the linear parameterizations of the pressure-scrambling terms, Eqs. (21)–(23), the numerical values of most dimensionless coefficients are fixed by mathematical constraints. In practice, however, those coefficients are often treated as disposable parameters whose values are adjusted to improve the overall performance of a turbulence model (parameterization scheme) in a particular flow regime. Although this approach may be considered legitimate in practical applications, caution must be exercised. Consider, for example, the coefficient C_b^θ in the buoyancy contribution to the pressure gradient-temperature covariance. As shown in Appendix A, the symmetry (A.11) and the normalization (A.13) constraints require that C_b^θ be equal to 1/3. This value corresponds to the isotropic limit and is consistent with the fact that the linear parameterizations of the pressure-scrambling terms are only valid for the flows where turbulence is not far from the isotropic state. The use of an empirical estimate of $C_b^\theta = 0.5$ advocated by a number of authors would improve the overall turbulence-scheme performance in the convective boundary layer driven by the surface buoyancy flux, but it would violate the isotropic constraint. One more important situation where the linear parameterizations fail is the so-called two-component limit (TCL). This is the limit that turbulence approaches when the velocity component in one direction vanishes. This occurs, for example, near the rigid boundary or in stably stratified layers, where the velocity component (both mean velocity and turbulent fluctuations) normal to the boundary or aligned with the vector of gravity, respectively, is suppressed. In order to satisfy the TCL constraint, C_b^θ should tend to one as the velocity component in one direction tends to zero (see Craft et al., 1996; Mironov, 2001, for details). Clearly, it is impossible to satisfy both the isotropic and the TCL constraints with one and the same value of C_b^θ. This shows a fundamental limitation of the linear parameterizations of the pressure-scrambling terms.

A consistent way out is to leave the coefficients of the linear terms intact, so that the isotropic limit is satisfied, and to include the non-linear terms, e.g. the terms non-linear in a_{ij} (e.g. Ristorcelli et al., 1995; Craft et al., 1996; Mironov, 2001). This would make the resulting turbulence model more flexible (capable of describing various flow regimes) and more suitable for strongly anisotropic flows. Non-linear parameterizations of the pressure-scrambling terms are inevitably complex, however. They are often inconvenient to use and are computationally expensive. It is therefore common in geophysical applications, including NWP, to put up with the shortcomings of linear parameterizations and apply Eqs. (21)–(23) without non-linear extensions. Another practically useful (albeit mathematically inconsistent) approach is to keep the functional form of Eqs. (21)–(23) but to replace some dimensionless constants with dimensionless functions of the flow governing parameters. Those functions should be constructed in such a way as to satisfy a number of limits. An approximation of $C_b^\theta(Ri)$, Ri being the gradient Richardson number, that satisfies that TCL constraint (a large positive Ri) and yields $C_b^\theta = 0.5$ at $Ri \leq 0$ (best-fit value for convective boundary layer) was proposed by Wyngaard (1975).

The TKESV-Bas scheme utilizes Eqs. (21)–(23) with the estimates of dimensionless constants given above. The estimates of the coefficients C_t^u, C_t^θ and C_t^q in the slow (return-to-isotropy) parts of the pressure-scrambling terms may require some fine tuning in order to improve the overall performance of the TKESV scheme. Most other dimensionless coefficients are fixed by mathematical constraints. We utilize their values given above, keeping in mind that these

values are actually suitable for nearly isotropic turbulence and may not be the best estimates for other flow regimes. The only remaining disposable coefficient α_5 should be determined by satisfying an additional constraint deemed important in terms of essential physics and/or practical significance. We determine α_5 so that the resulting equations of the TKESV scheme yield the classical logarithmic velocity profile in the vicinity of the underlying surface. The way this constraint is applied is described in Appendix A. The following expression for α_5 is obtained:

$$\alpha_5 = \frac{1}{22}\left[1-(1+11C_\alpha^*)^{1/2}\right], \qquad C_\alpha^* = 1+\frac{9C_t^u}{4}\left(\frac{4}{3}-C_{s1}^u\right)-\frac{9}{2}\left(\frac{C_t^u}{C_e}\right)^2, \tag{24}$$

where C_e is the dimensionless constant in the expression [third member of Eq. (A.30)] that relates the values of the TKE and of the friction velocity in the near-surface log-layer. Using $C_{s1}^u = 4/5$, $C_t^u = 1.8$ and $C_e = 3.33$, we obtain an estimate of $\alpha_5 = -0.164$. Optionally, the value of $\alpha_5 = -1/10$ can be used [see Eq. (26) and the subsequent text at the end of this section and Appendix B].

Advanced Features

Craft et al. (1996) proposed advanced parameterizations of the pressure-scrambling terms that satisfy both the isotropic limit and the strongly anisotropic two-component limit. Those parameterizations are rather complex and can hardly be used in NWP and related applications, at least in the short-term prospects. However, the TCL parameterizations of the buoyancy contributions $\Pi_{\theta i}^b$ and Π_{qi}^b to the pressure gradient-scalar covariances can be utilized within the framework of the TKESV scheme without making the scheme unduly complex and computationally expensive. Extending the formulation presented in Craft et al. (1996) to the case of moist air, we obtain

$$\Pi_{\theta i}^b = -\beta_j\left(\frac{1}{3}\delta_{ij}-a_{ij}\right)\langle\theta_l'\theta_v'\rangle, \qquad \Pi_{qi}^b = -\beta_j\left(\frac{1}{3}\delta_{ij}-a_{ij}\right)\langle q_t'\theta_v'\rangle. \tag{25}$$

In the isotropic limit, $a_{ij} = 0$ and the expressions (25) coincide with the third terms on the r.h.s. of Eqs. (22) and (23), respectively, where $C_b^\theta = C_b^q = 1/3$. In the two-component limit, the buoyancy contributions to the pressure-scrambling terms given by (25) cancel the buoyancy terms in the scalar-flux equations (19) and (20). The use of Eq. (25) helps to avoid spurious generation of scalar fluxes by the buoyancy forces in stably stratified regions of the flow, where the vertical velocity is suppressed and turbulence is driven towards the two-component state.

One point should be stressed in relation to Eq. (25). As discussed in section 7, the covariances $\langle\theta_l'\theta_v'\rangle$ and $\langle q_t'\theta_v'\rangle$ involving virtual potential temperature are parameterized in terms of linear combinations of $\langle\theta_l'^2\rangle$, $\langle q_t'^2\rangle$ and $\langle\theta_l'q_t'\rangle$. Since the TKESV scheme carries prognostic transport equations for the variances and covariance of scalar quantities, diagnostic equations (18)–(20) with due regard for the parameterizations (21)–(23), where the third terms on the r.h.s. of Eqs. (22) and (23) are replaced with the TCL formulations (25), remain linear in a_{ij} (and hence in $\langle u_i'u_j'\rangle$), $\langle u_i'\theta_l'\rangle$ and $\langle u_i'q_t'\rangle$. Then, the system of linear equations is readily solved, resulting in explicit diagnostic formulations for the Reynolds-stress and scalar-flux components (see section 9). This is not the case for one-equation TKE schemes, where diagnostic equations for the scalar variances and covariance are used [these are obtained from Eqs. (8)–(10) by neglecting the substantial derivative and the third-order transport terms]. Then, the use of Eq. (25) results in non-linear equations for a_{ij}, $\langle u_i'\theta_l'\rangle$, $\langle u_i'q_t'\rangle$, $\langle\theta_l'^2\rangle$, $\langle q_t'^2\rangle$ and $\langle\theta_l'q_t\rangle$.

As mentioned above, TKESV-Bas utilizes a constant value of dimensionless parameter α_5.

A more sophisticated approximation was proposed by Shih and Lumley (1985),

$$\alpha_5 = -\frac{1}{10}\left(1 + \frac{4}{5}F_l^{1/2}\right), \tag{26}$$

where $F_l = 1 - \frac{9}{8}(A_2 - A_3)$ is the so-called flatness parameter, and $A_2 = \hat{a}_{ij}\hat{a}_{ij}$ and $A_3 = \hat{a}_{ij}\hat{a}_{jk}\hat{a}_{ki}$ are the second and the third invariants, respectively, of the dimensionless departure-from-isotropy tensor $\hat{a}_{ij} = e^{-1}a_{ij}$. Although the use of Eq. (26) results in non-linear equations for a_{ij}, $\langle u_i'\theta_l'\rangle$ and $\langle u_i'q_t'\rangle$, the non-linearity can be treated in an approximate way, e.g. by evaluating F_l at the previous time step(s) during the integration of turbulence-moment equations in time. It should be mentioned that a constant value of $\alpha_5 = -1/10$ was adopted in a number of studies (e.g. Shih, 1996; Hanjalić, 1999). The value of $\alpha_5 = -1/10$ corresponds to $F_l = 0$, i.e. to the one-component or two-component limit of strongly anisotropic turbulence.

5.2 Third-Order Transport

The second group of terms that require closure assumptions includes turbulent transport (diffusion) terms. These terms enter the equations for the turbulence moments in the divergence form. They describe the transport of the quantity in question by the fluctuating velocity and the fluctuating pressure. Numerous formulations for the third-order turbulent transport have been proposed, ranging from the simplest down-gradient approximations to very complex formulations based on a sophisticated treatment of transport equations for the high-order turbulence moments. Simple isotropic down-gradient formulations have been very popular in various applications.

In the TKESV-Bas scheme, the simplest isotropic down-gradient parameterizations for the third-order transport terms in the TKE, scalar-variance and scalar-covariance equations are used. They read

$$\frac{1}{2}\left\langle u_i' u_k'^2\right\rangle + \left\langle u_i' p'\right\rangle = -C_e^d \tau_\epsilon e \frac{\partial e}{\partial x_i}, \tag{27}$$

$$\left\langle u_i'\theta_l'^2\right\rangle = -C_{\theta\theta}^d \tau_\epsilon e \frac{\partial\left\langle\theta_l'^2\right\rangle}{\partial x_i}, \qquad \left\langle u_i' q_t'^2\right\rangle = -C_{qq}^d \tau_\epsilon e \frac{\partial\left\langle q_t'^2\right\rangle}{\partial x_i},$$
$$\left\langle u_i'\theta_l q_t'\right\rangle = -C_{\theta q}^d \tau_\epsilon e \frac{\partial\left\langle\theta_l' q_t'\right\rangle}{\partial x_i}, \tag{28}$$

where C_e^d, $C_{\theta\theta}^d$, C_{qq}^d and $C_{\theta q}^d$ are dimensionless coefficients set equal to 0.1. Somewhat higher values of these coefficients may be used as needed. For example, an estimate of $C_{\theta\theta}^d = 0.3$ was advocated by Otić et al. (2005).

Advanced Features

The isotropic down-gradient diffusion formulations often perform poorly in strongly anisotropic flows, e.g. in the flows dominated by the effects of stratification and/or rotation. Generalized down-gradient diffusion approximations (Daly and Harlow, 1970) are somewhat more appropriate for such flows. The formulations for the diffusion terms in the TKE, scalar-variance and scalar-covariance equations read

$$\frac{1}{2}\left\langle u_i' u_k'^2\right\rangle + \left\langle u_i' p'\right\rangle = -C_e^{dg} \tau_\epsilon \left\langle u_i' u_k'\right\rangle \frac{\partial e}{\partial x_k}, \tag{29}$$

$$\langle u_i'\theta_l'^2\rangle = -C_{\theta\theta}^{dg}\tau_\epsilon \langle u_i'u_k'\rangle \frac{\partial \langle \theta_l'^2\rangle}{\partial x_k}, \qquad \langle u_i'q_t'^2\rangle = -C_{qq}^{dg}\tau_\epsilon \langle u_i'u_k'\rangle \frac{\partial \langle q_t'^2\rangle}{\partial x_k},$$
$$\langle u_i'\theta_l'q_t'\rangle = -C_{\theta q}^{dg}\tau_\epsilon \langle u_i'u_k'\rangle \frac{\partial \langle \theta_l'q_t'\rangle}{\partial x_k}, \tag{30}$$

where C_e^{dg}, $C_{\theta\theta}^{dg}$, C_{qq}^{dg} and $C_{\theta q}^{dg}$ are dimensionless coefficients set equal to 0.15. Higher values have also been proposed, e.g. $C_{\theta\theta}^{dg} = 0.22$ (Jones and Musogne, 1988; Hanjalić, 1999; Otić et al., 2005). Equations (29) and (30) reduce to Eqs. (27) and (28), respectively, if the Reynolds-stress anisotropy is neglected, i.e. a_{ij} is set to zero in the expression $\langle u_i'u_k'\rangle = a_{ik} + \frac{2}{3}\delta_{ik}e$.

5.3 Dissipation

Molecular destruction (dissipation) rates of the TKE and of the scalar variances and covariance can be determined from their own transport equations. The dissipation-rate equations are very complex, however. They contain a number of terms whose physical nature is poorly understood. In fact, all terms in the dissipation-rate equations that describe production, destruction and turbulent transport of the dissipation rates should be parameterized, and the validity of those parameterizations is uncertain. It has often been questioned whether prognostic transport equations for the dissipation rates are really necessary, or diagnostic expressions are sufficient, at least for flows in relatively simple geometries. The latter viewpoint is commonly held in geophysical applications.

In the TKESV scheme, the TKE dissipation rate is parameterized in terms of the TKE dissipation time scale τ_ϵ through the following algebraic expression:

$$\epsilon = \frac{e}{\tau_\epsilon}. \tag{31}$$

The dissipation rates of the scalar variances and the scalar covariance are parameterized as

$$\epsilon_{\theta\theta} = \frac{\langle \theta_l'^2\rangle}{2\tau_{\theta\theta}}, \qquad \epsilon_{qq} = \frac{\langle q_t'^2\rangle}{2\tau_{qq}}, \qquad \epsilon_{\theta q} = \frac{\langle \theta_l'q_t'\rangle}{2\tau_{\theta q}}, \tag{32}$$

where $\tau_{\theta\theta}$, τ_{qq} and $\tau_{\theta q}$ are the dissipation times scales of the scalar variances and the scalar covariance. These time scales are taken to be proportional to the TKE dissipation time scale (see the next section).

The deviatoric part ϵ_{ij}^d of the Reynolds-stress dissipation tensor is either neglected (on the assumption of local isotropy at small scales) or incorporated into a parameterization of the slow part Π_{ij}^t of the pressure redistribution term. Likewise, the temperature-flux and the humidity-flux dissipation rates, $\epsilon_{\theta i}$ and ϵ_{qi}, are incorporated into parameterizations of $\Pi_{\theta i}^t$ and Π_{qi}^t, respectively.

6 Time and Length Scales

The return-to-isotropy time scales in Eqs. (21)–(23) are taken to be proportional to the TKE dissipation time scale:

$$\tau_{ru} = \tau_{r\theta} = \tau_{rq} = \tau_\epsilon, \tag{33}$$

where proportionality constants between the various time scales are set to one as they always occur in combination with the other constants. Likewise, the dissipation time scales of the

scalar variances and the scalar covariance, Eq. (32), are taken to be proportional to the TKE dissipation time scale:

$$\tau_{\theta\theta} = \tau_{qq} = \tau_{\theta q} = R_\tau \tau_\epsilon, \tag{34}$$

where R_τ is the ratio of the scalar-variance/scalar-covariance dissipation time scale to the TKE dissipation time scale [e.g. $R_\tau = \tau_{\theta\theta}/\tau_\epsilon = \langle \theta_l'^2 \rangle \, \epsilon / (2e\epsilon_{\theta\theta})$ for the temperature variance]. The same value of R_τ is used for $\tau_{\theta\theta}$, τ_{qq} and $\tau_{\theta q}$. The estimates of R_τ given in the literature range from 0.3 to 1.0 (e.g. Dol et al., 1997). Following Kenjereš and Hanjalić (1995, 2000) and Hanjalić (2002), the value of $R_\tau = 0.5$ is utilized.

The TKE dissipation time scale is expressed in terms of the turbulence length scale l:

$$\tau_\epsilon = \frac{1}{C_\epsilon} \frac{l}{e^{1/2}}, \tag{35}$$

where $C_\epsilon = C_e^{-3/2}$, and C_e is a constant in the expression that relates the TKE and the friction velocity in the neutrally-stratified near-surface layer characterized by the logarithmic mean-velocity profile [see Eq. (A.30) in Appendix A]. We utilize an estimate of $C_e = 3.33$ (Umlauf and Burchard, 2003; Umlauf et al., 2003). The following interpolation formula is used in the TKESV-Bas scheme to compute the turbulence length scale:

$$\frac{1}{l} = \frac{1}{\kappa x_n} + \frac{1}{l_\infty} + \mathrm{H}\left(N^2\right) \frac{N}{C_{lb} e^{1/2}}, \tag{36}$$

where κ is the von Kármán constant, x_n is the distance normal to the surface, l_∞ is the length scale characteristic of the flow far away from the underlying surface, N is the buoyancy frequency, $\mathrm{H}(\zeta)$ is the Heaviside step function (equal to 1 if $\zeta \geq 0$, and to 0 if $\zeta < 0$), and C_{lb} is a dimensionless constant. If the last term on the r.h.s. is neglected, Eq. (36) reduces to the well-known Blackadar's formula (Blackadar, 1962) that yields the logarithmic velocity profile close to the underlying surface and prevents l from growing without bound far away from the surface. A conventional value of $\kappa = 0.4$ is utilized, and the l_∞ is set to a constant value of 200 m. The last term on the r.h.s. of Eq. (36) limits the length scale in stably stratified layers (where N^2 is positive) by the buoyancy length scale $l_b = C_{lb} N^{-1} e^{1/2}$ (e.g. Stull, 1973; Zeman and Tennekes, 1977; Brost and Wyngaard, 1978; Zilitinkevich and Mironov, 1992). An estimate of $C_{lb} = 1.0$ is used. The buoyancy frequency N is computed with due regard for the effect of cloud condensate on the static stability (see section 9).

Advanced Features

As an alternative to setting the time-scale ratio in Eq. (34) to a constant value, R_τ can be computed as a function of the scalar-flux correlation coefficient. The following expression was proposed by Craft et al. (1996):

$$R_\tau = \frac{2}{3\left(1 + A_{u\theta}\right)}, \qquad A_{u\theta} = \frac{\langle u_i' \theta' \rangle \, \langle u_i' \theta' \rangle}{e \, \langle \theta'^2 \rangle}, \tag{37}$$

where $A_{u\theta}$ is the heat-flux correlation coefficient. In the case of moist air, the time-scale ratio for the temperature variance, $R_\tau^{\theta\theta}$, and for the humidity variance, R_τ^{qq}, can be computed from Eq. (37) where θ is replaced with θ_l and q_t, respectively. The time scale ratio for the temperature-humidity covariance is then computed as $R_\tau^{\theta q} = \frac{1}{2}\left(R_\tau^{\theta\theta} + R_\tau^{qq}\right)$.

Following Bougeault and André (1986), Bougeault and Lacarrère (1989), Bechtold et al. (1992), Lappen and Randall (2001) and Golaz et al. (2002), an advanced non-local formulation for the turbulence length scale can be used instead of Eq. (36). The turbulence length scale is computed from the following relations:

$$e\left(x_i\right) = \int_{x_i}^{x_i + l_{up}} \beta_i \left[\theta_v^{par}\left(x_i, x_i'\right) - \theta_v^{env}\left(x_i'\right)\right] dx_i', \tag{38}$$

$$e\left(x_i\right) = \int_{x_i - l_{do}}^{x_i} \beta_i \left[\theta_v^{env}\left(x_i'\right) - \theta_v^{par}\left(x_i, x_i'\right)\right] dx_i', \tag{39}$$

$$\frac{1}{l} = \frac{1}{\kappa x_n} + \left(\frac{2}{l_{up} l_{do}}\right)^{1/2}. \tag{40}$$

The physical meaning of Eqs. (38)–(40) can be elucidates as follows. Consider a flat horizontal surface. The x_3-axis is aligned with the vector of gravity $(0, 0, -g_3)$ and is positive upward. The quantity l_{up} (l_{do}) is an estimate of the distance that an air parcel originating at the level x_3 travels upward (downward) until its energy $e\left(x_3\right)$ is spent working against gravity (l_{do} is limited by the distance to the surface). The virtual potential temperature $\theta_v^{par}\left(x_3, x_3'\right)$ of an ascending/descending air parcel is computed with due regard for the condensation/evaporation. As an air parcel is displaced from the level x_3 to the level x_3', the liquid water potential temperature $\theta_l^{par}\left(x_3'\right)$ and the total water specific humidity $q_t^{par}\left(x_3'\right)$ of the parcel are conserved, i.e. they remain equal to the values $\theta_l^{par}\left(x_3\right)$ and $q_t^{par}\left(x_3\right)$, respectively. However, the potential temperature θ^{par}, the specific humidity q^{par} and the liquid water specific humidity q_l^{par}, and hence the virtual potential temperature θ_v^{par}, are not conserved (because of phase changes) and are therefore re-computed at each level x_3' during the parcel ascend/descent. Note that the quantity $2^{-1/2}\left(l_{up} l_{do}\right)^{1/2}$, where l_{up} and l_{do} are computed from Eqs.(38) and (39), respectively, yields the buoyancy length scale $l_b = C_{lb} N^{-1} e^{1/2}$ with $C_{lb} = 1.0$ in stably stratified fluid characterized by a constant buoyancy frequency N. The first term on the r.h.s. of the interpolation formula (40) is required to recover the logarithmic velocity profile close to the underlying surface.

7 Effect of Clouds on Mixing

The thermodynamic structure of the atmosphere is heavily complicated by the presence of clouds. Clouds produce precipitation and interact with atmospheric radiation, strongly affecting the atmosphere energy budget. They also change the buoyancy of air parcels. As far as the parameterization of turbulence is concerned, the primary goal is to account for the effect of latent heat release/consumption on the buoyancy production/destruction of the Reynolds stress (including its trace, the TKE) and of the scalar fluxes. To this end, the buoyancy terms (the terms with β_i) in Eqs. (12), (18), (19) and (20) should be parameterized with due regard for the presence of cloud condensate. The problem essentially amounts to modelling the virtual potential temperature flux $\left\langle u_i' \theta_v' \right\rangle$ and the scalar-virtual potential temperature covariances $\left\langle \theta_l' \theta_v' \right\rangle$ and $\left\langle q_t' \theta_v' \right\rangle$ in terms of other moments that include fluctuations of u_i, θ_l and q_t.

Using the definition of the virtual potential temperature (11), the covariances incorporating θ_v' are represented as

$$\begin{aligned} \left\langle f' \theta_v' \right\rangle &= \left[1 + (R-1)\left\langle q_t \right\rangle - R\left\langle q_l \right\rangle\right] \left\langle f' \theta_l' \right\rangle + (R-1)\left\langle \theta \right\rangle \left\langle f' q_t' \right\rangle \\ &+ \left\{ \frac{\left\langle \theta \right\rangle}{\left\langle T \right\rangle} \frac{L_v}{c_p} \left[1 + (R-1)\left\langle q_t \right\rangle - R\left\langle q_l \right\rangle\right] - R\left\langle \theta \right\rangle \right\} \left\langle f' q_l' \right\rangle, \end{aligned} \tag{41}$$

where $R = R_v / R_d$, and a generic variable f stands for u_i, θ_l or q_t. In order to obtain Eq. (41), the third-order covariances and the pressure fluctuations are neglected. The latter assumption yields $\theta_l = \theta - \dfrac{\left\langle \theta \right\rangle}{\left\langle T \right\rangle} \dfrac{L_v}{c_p} q_l$. In the "dry" limit, where a given atmospheric-model

grid box is cloud free (but the water vapour may be present), Eq. (41) reduces to

$$\left\langle f'\theta'_v \right\rangle_d = \left[1 + (R-1)\left\langle q_t \right\rangle\right] \left\langle f'\theta'_l \right\rangle + (R-1)\left\langle \theta \right\rangle \left\langle f'q'_t \right\rangle, \tag{42}$$

where θ_l and q_t coincide with θ and q, respectively, as $q_l = 0$. In the "wet" limit, the entire atmospheric-model grid box is saturated, i.e. $q_l = q_t - q_s > 0$ at each point of the grid box. Then, $\langle f'\theta'_v \rangle$ can be expressed, to a good approximation, in terms of $\langle f'\theta'_l \rangle$ and $\langle f'q'_t \rangle$ as follows:

$$\begin{aligned} \left\langle f'\theta'_v \right\rangle_w &= \left[1 + (R-1)\left\langle q_t \right\rangle - R\left\langle q_l \right\rangle\right] \left\langle f'\theta'_l \right\rangle + (R-1)\left\langle \theta \right\rangle \left\langle f'q'_t \right\rangle \\ &+ \left[-\frac{\mathcal{A}\mathcal{P}}{\mathcal{Q}} \left\langle f'\theta'_l \right\rangle + \frac{\mathcal{A}}{\mathcal{Q}} \left\langle f'q'_t \right\rangle \right]. \end{aligned} \tag{43}$$

Here, $\mathcal{A} = \dfrac{\langle\theta\rangle}{\langle T\rangle}\dfrac{L_v}{c_p}\left[1 + (R-1)\langle q_t\rangle - R\langle q_l\rangle\right] - R\langle\theta\rangle$, $\mathcal{P} = \dfrac{\langle T\rangle}{\langle\theta\rangle}\langle q_{sl,T}\rangle$, $\mathcal{Q} = 1 + \dfrac{L_v}{c_p}\langle q_{sl,T}\rangle$, and $\langle q_{sl,T}\rangle \equiv \left.\dfrac{\partial q_s}{\partial T}\right|_{T=\langle T_l\rangle}$, T_l being the liquid water absolute temperature, is computed from the Clausius-Clapeyron equation, $\dfrac{\partial q_s}{\partial T} = \dfrac{L_v q_s}{R_v T^2}$. A first-order Taylor expansion of the saturation specific humidity $q_s(T)$ about $T = \langle T_l \rangle$ is used to express $\langle f'q'_l \rangle$ in terms of $\langle f'\theta'_l \rangle$ and $\langle f'q'_t \rangle$ [the last terms in brackets on the r.h.s. of Eq. (43)]. An expression is needed that is valid not only in the dry and wet limits, but also in the general case of fractional cloudiness. To this end, the following interpolation formula is used:

$$\begin{aligned} \left\langle f'\theta'_v \right\rangle &= \left[1 + (R-1)\left\langle q_t \right\rangle - R\left\langle q_l \right\rangle\right] \left\langle f'\theta'_l \right\rangle + (R-1)\left\langle \theta \right\rangle \left\langle f'q'_t \right\rangle \\ &+ \hat{\mathcal{R}} \left[-\frac{\mathcal{A}\mathcal{P}}{\mathcal{Q}} \left\langle f'\theta'_l \right\rangle + \frac{\mathcal{A}}{\mathcal{Q}} \left\langle f'q'_t \right\rangle \right]. \end{aligned} \tag{44}$$

where $\hat{\mathcal{R}}$ is the interpolation variable satisfying $0 \le \hat{\mathcal{R}} \le 1$. Equation (44) reduces to Eq. (42) and to Eq. (43) in the dry ($\hat{\mathcal{R}} = 0$) and wet ($\hat{\mathcal{R}} = 1$) limits, respectively.

The simplest way to determine $\hat{\mathcal{R}}$ is to set it equal to the fractional cloud cover $\hat{\mathcal{C}}$. This parameterization is used within the framework of one-equation TKE turbulence scheme of COSMO and ICON (see Raschendorfer, 1999, 2001; Baldauf et al., 2011). In order to compute the fractional cloud cover, a Gaussian statistical cloud scheme is used that is very similar to the scheme proposed by Sommeria and Deardorff (1977) (see also Mellor, 1977). Recall that statistical cloud schemes make use of probability distribution functions of the sub-grid scale (SGS) humidity and temperature (and possibly velocity) fluctuations. Once the PDF is specified, the fractional cloud cover is simply the integral over a saturated part of the PDF. The COSMO/ICON statistical cloud scheme is formulated in terms of s variable (Mellor, 1977) defined as $s = \mathcal{Q}^{-1}\left(\langle q_t\rangle - \langle q_{sl}\rangle + q'_t - \mathcal{P}\theta'_l\right)$, where $\langle q_{sl}\rangle = q_s(\langle T_l\rangle)$. The variable s accounts for the combined effect of humidity and temperature fluctuations (the latter ones change the local saturation vapour pressure). It is a measure of local oversaturation/undersaturation. A positive s is nothing but a local value of the liquid water specific humidity q_l computed with respect to the linearized saturation specific humidity curve[3]. Assuming that no supersaturation occurs, the fractional cloud cover is given by $\hat{\mathcal{C}} = \displaystyle\int_0^\infty G(s)ds$, where $G(s)$ is the PDF of s. The grid-box mean liquid water specific humidity is given by $\langle q_l \rangle = \displaystyle\int_0^\infty sG(s)ds$. Partial or full PDF moments of higher order can be computed in a similar manner. Following

[3]In fact, the quantity s has already been used above to express $\langle f'q'_l \rangle$ through $\langle f'q'_t \rangle$ and $\langle f'\theta'_l \rangle$ in Eq. (41), leading to Eq. (43)

Sommeria and Deardorff (1977) and Mellor (1977), a Gaussian PDF is utilized within the framework of the COSMO/ICON TKE turbulence scheme. The following relations hold:

$$\hat{\mathcal{C}} = \frac{1}{2}\left[1 + \mathrm{erf}\left(\frac{\langle s\rangle}{\sqrt{2}\sigma_s}\right)\right], \qquad \langle q_l\rangle = \hat{\mathcal{C}}\,\langle s\rangle + \frac{\sigma_s}{\sqrt{2\pi}}\exp\left(-\frac{\langle s\rangle^2}{2\sigma_s^2}\right), \tag{45}$$

where erf is the error function, $\langle s\rangle = \mathcal{Q}^{-1}\left(\langle q_t\rangle - \langle q_{sl}\rangle\right)$ is the mean value of s, and $\sigma_s \equiv \left\langle s'^2\right\rangle^{1/2} = \mathcal{Q}^{-1}\left(\left\langle q_t'^2\right\rangle + \mathcal{P}^2\left\langle \theta_l'^2\right\rangle - 2\mathcal{P}\left\langle q_t'\theta_l'\right\rangle\right)^{1/2}$ is its standard deviation. Note that σ_s depends on the variances of q_t and θ_l and on their covariance, providing an important link between the cloud cover and the dynamics of SGS motions. Within the framework of the one-equation TKE turbulence scheme, $\left\langle q_t'^2\right\rangle$, $\left\langle \theta_l'^2\right\rangle$ and $\left\langle q_t'\theta_l'\right\rangle$, and hence σ_s, are computed diagnostically through the down-gradient algebraic formulations. This is different from the TKESV scheme that carries prognostic equations for the scalar variances and covariance with due regard for the third-order transport. It is also worth noting that approximations of Eqs. (45) through piecewise polynomial (linear and quadratic) functions are used in COSMO/ICON to compute $\hat{\mathcal{C}}$ and $\langle q_l\rangle$ [see Eqs. (22) and (25) in Sommeria and Deardorff (1977) and Eqs. (47) below].

The use of $\hat{\mathcal{R}} = \hat{\mathcal{C}}$ in Eq. (44) along with the Gaussian formulations for $\hat{\mathcal{C}}$ and $\langle q_l\rangle$ may result in large errors in the determination of the buoyancy terms in the Reynolds-stress and scalar-flux equations. A prominent example is the convective boundary layer with shallow cumuli, where the PDFs of cloud-related variables are highly skewed. In the shallow cumulus regime, the atmospheric-model grid box is undersaturated in the mean and the fractional cloud cover is typically small (certainly, this holds if the horizontal model resolution is not too high and shallow cumulus clouds remain unresolved). However, these highly localized cumulus clouds account for much of the buoyancy terms in the Reynolds-stress, scalar-flux and TKE equations, and $\langle f'\theta_v'\rangle$ is closer to $\langle f'\theta_v'\rangle_w$ than to $\langle f'\theta_v'\rangle_d$. Then, $\hat{\mathcal{R}}$ in Eq. (44) is (considerably) larger than $\hat{\mathcal{C}}$ (see e.g. Lewellen and Lewellen, 2004).

In order to account for the skewed nature of convective motions associated with shallow cumuli, the following parameterization that interpolates between the Gaussian and the exponential formulations (Bougeault, 1981; Bechtold et al., 1995) is used within the framework of the TKESV-Bas scheme:

$$f = \begin{cases} f_{Gauss} & \text{at} \quad \tilde{s} \geq 0 \\ 0.5\left[(2+\tilde{s})\, f_{Gauss} - \tilde{s} f_{exp}\right] & \text{at} \quad -2 \leq \tilde{s} \leq 0 \\ f_{exp} & \text{at} \quad \tilde{s} \leq -2, \end{cases} \tag{46}$$

where $\tilde{s} = \langle s\rangle / \sigma_s$, and f stands either for the fractional cloud cover $\hat{\mathcal{C}}$ or for the grid-box mean liquid water specific humidity $\langle q_l\rangle$. The Gaussian formulations are given by

$$\begin{aligned} \hat{\mathcal{C}}_{Gauss} &= \begin{cases} 1 & \text{at} \quad \tilde{s} \geq 1.6 \\ 0.5\,(1+\tilde{s}/1.6) & \text{at} \quad -1.6 \leq \tilde{s} \leq 1.6 \\ 0 & \text{at} \quad \tilde{s} \leq -1.6, \end{cases} \\ \frac{\langle q_l\rangle_{Gauss}}{\sigma_s} &= \begin{cases} \tilde{s} & \text{at} \quad \tilde{s} \geq 1.6 \\ (\tilde{s}+1.6)^2/6.4 & \text{at} \quad -1.6 \leq \tilde{s} \leq 1.6 \\ 0 & \text{at} \quad \tilde{s} \leq -1.6. \end{cases} \end{aligned} \tag{47}$$

Equations (47) are the piecewise polynomial approximations of Eqs. (45). The exponential formulations are given by

$$\hat{\mathcal{C}}_{exp} = \exp\left(\tilde{s}-1\right), \qquad \langle q_l\rangle_{exp} = \sigma_s \exp\left(\tilde{s}-1\right). \tag{48}$$

At large negative $\tilde{s}$, the Gaussian relations (45) give a very small fractional cloud cover, and the approximations (47) give no clouds at all. A relatively thick exponential tail (as

compared to a Gaussian tail) is introduced to account, in an approximate way, for non-zero fractional cloud cover in the shallow cumulus regime. The buoyancy terms in the Reynolds-stress and scalar-flux equations are computed from Eq. (44), where the interpolation variable $\hat{\mathcal{R}}$ is given by

$$\frac{\hat{\mathcal{R}}}{\hat{\mathcal{C}}} = \begin{cases} 1 & \text{at} \quad \tilde{s} \geq 0 \\ 1 - 1.5\tilde{s} & \text{at} \quad -2 \leq \tilde{s} \leq 0 \\ 2 - \tilde{s} & \text{at} \quad \tilde{s} \leq -2. \end{cases} \tag{49}$$

Note that Eq. (49) may underestimate $\hat{\mathcal{R}}$ (perhaps quite considerably) at large negative $\tilde{s}$. Thus the above formulations with the exponential tail can only be considered as the first-order corrections to the Gaussian formulations. Note further that $\hat{\mathcal{C}}$, $\langle q_l \rangle$, and $\hat{\mathcal{R}}$ given by Eqs. (46)–(49) depend on the mean and the variance of s but do not explicitly depend on higher-order moments such as skewness. That is, the skewed nature of shallow cumulus clouds is accounted for implicitly in a rather ad hoc manner.

It should be recognized that the use of the interpolation formula (44) to determine the buoyancy terms in the Reynolds-stress and the scalar-flux equations can be avoided. If a cloud scheme employs a joint PDF for the scalars q_t and θ_l and for the vertical velocity u_3, all quantities $\langle f' q_l' \rangle$ including the liquid water specific humidity are determined in a straightforward way by means of integration over the saturated part of the PDF. In other words, the problem reduces to the determination of a number of partial moments using an assumed PDF. This approach is taken within the framework of CLUBB (Cloud Layers Unified By Binormals), an assumed-PDF unified parameterization of turbulence and cloud processes in the Earth's atmosphere (see references at https://people.uwm.edu/vlarson/papers/). Apart from its numerous advantages, the approach has shortcomings. For example, the cloud schemes based on a joint PDF require a large number of statistical moments of fluctuating scalar and velocity fields as an input. Furthermore, the joint-PDF schemes may place rather stringent requirements upon the input quality, i.e. a large number of irreducible moments of second, third and possibly higher order should be determined accurately. Comprehensive discussions of various issues related to the parameterization of clouds and cloud-turbulence interaction in atmospheric models are given in Tompkins (2003, 2005) and Machulskaya (2015). A cloud parameterization based on a joint scalar-velocity PDF may be incorporated into the TKESV scheme in the future. The TKESV-Bas scheme employs an interpolation formula (44) with $\hat{\mathcal{C}}$, $\langle q_l \rangle$, and $\hat{\mathcal{R}}$ determined through the approximations (46)–(49).

Advanced Features

Following Larson et al. (2001), Naumann et al. (2013) developed a statistical cloud scheme based on a double-Gaussian PDF of s,

$$\begin{aligned} G(s) &= aG_1(s) + (1-a)\,G_2(s) \\ &= \frac{a}{\sqrt{2\pi}\sigma_{s1}} \exp\left[-\frac{1}{2}\left(\frac{s-s_1}{\sigma_{s1}}\right)^2\right] + \frac{1-a}{\sqrt{2\pi}\sigma_{s2}} \exp\left[-\frac{1}{2}\left(\frac{s-s_2}{\sigma_{s2}}\right)^2\right]. \end{aligned} \tag{50}$$

Here, a and $1-a$ are the relative weights of the two Gaussian curves G_1 and G_2, respectively, and s_1 and s_2 and σ_{s1} and σ_{s2} are, respectively, their means and standard deviations. The PDF given by Eq. (50) is a five-parameter PDF. That is, five irreducible moments of s, e.g. five first moments, should be provided as input arguments to specify a, s_1, s_2, σ_{s1} and σ_{s2}. In order to reduce the number of input arguments, Naumann et al. (2013) used observational and numerical LES data to express σ_{s1} and σ_{s2} through the standard deviation σ_s and the skewness $S_s \equiv \langle s'^3 \rangle / \langle s'^2 \rangle^{3/2}$ of s. The following relations are proposed by Naumann et al.

(2013) (cf. Larson et al., 2001):

$$\begin{aligned}
\frac{\sigma_{s1}}{\sigma_s} &= \begin{cases} 1+\gamma_3\dfrac{S_s}{(\alpha+S_s^2)^{1/2}} & \text{at} \quad S_s \le 0 \\ 1+\gamma_1\dfrac{S_s}{\alpha^{1/2}} & \text{at} \quad S_s \ge 0, \end{cases} \\
\frac{\sigma_{s2}}{\sigma_s} &= \begin{cases} 1-\gamma_4\dfrac{S_s}{(\alpha+S_s^2)^{1/2}} & \text{at} \quad S_s \le 0 \\ 1-\gamma_2\dfrac{S_s}{(\alpha+S_s^2)^{1/2}} & \text{at} \quad S_s \ge 0, \end{cases}
\end{aligned} \tag{51}$$

where $\alpha = 2.0$, $\gamma_1 = 0.73$, $\gamma_2 = 0.46$, $\gamma_3 = 0.78$ and $\gamma_4 = 0.73$ are dimensionless constants (the notation used in Naumann et al., 2013, is retained).

With due regard for (51), only three irreducible moments of s should be provided, viz., $\langle s \rangle$, σ_s and S_s. The mean value of s is provided by the host atmospheric model. The variances and the covariance of the scalar quantities required to compute σ_s are determined within the framework of the TKESV scheme from the scalar (co)variance transport equations. The skewness of s is required to close the problem. The way to determine S_s is discussed in section 11. A cloud scheme based on Eqs. (50) and (51) represents a good compromise between physical realism and computational economy and is a viable choice for the extended version of the TKESV scheme. On the one hand, a double-Gaussian distribution (50) is very flexible and is capable of describing both symmetric and skewed PDFs, the latter one is required to describe the cumulus regime. On the other hand, the use of Eqs. (51) reduces the number of PDF input arguments to three (mean, variance, and skewness), making the cloud scheme reasonably inexpensive from the computational viewpoint.

Given the estimates of $\langle s \rangle$, σ_s and S_s, the weighting factor a is determined as a solution to the following equation:

$$\begin{aligned}
&S_s - \left\{ a\,(1-a) \left[1 - a \left(\frac{\sigma_{s1}}{\sigma_s} \right)^2 - (1-a) \left(\frac{\sigma_{s2}}{\sigma_s} \right)^2 \right] \right\}^{1/2} \\
&\times \left\{ 3 \left(\frac{\sigma_{s1}}{\sigma_s} \right)^2 - 3 \left(\frac{\sigma_{s2}}{\sigma_s} \right)^2 + \frac{1-2a}{a\,(1-a)} \left[1 - a \left(\frac{\sigma_{s1}}{\sigma_s} \right)^2 - (1-a) \left(\frac{\sigma_{s2}}{\sigma_s} \right)^2 \right] \right\} = 0,
\end{aligned} \tag{52}$$

where σ_{s1}/σ_s are σ_{s2}/σ_s are given by Eqs. (51). The mean values s_1 and s_2 are computed from

$$\begin{aligned}
\frac{s_1 - \langle s \rangle}{\sigma_s} &= \left(\frac{1-a}{a} \right)^{1/2} \left[1 - a \left(\frac{\sigma_{s1}}{\sigma_s} \right)^2 - (1-a) \left(\frac{\sigma_{s2}}{\sigma_s} \right)^2 \right]^{1/2}, \\
\frac{s_2 - \langle s \rangle}{\sigma_s} &= \left(\frac{a}{1-a} \right)^{1/2} \left[1 - a \left(\frac{\sigma_{s1}}{\sigma_s} \right)^2 - (1-a) \left(\frac{\sigma_{s2}}{\sigma_s} \right)^2 \right]^{1/2}.
\end{aligned} \tag{53}$$

Then, the fractional cloud cover and the grid-box mean liquid water specific humidity are computed from the following relations:

$$\begin{aligned}
\hat{\mathcal{C}} &= \frac{a}{2} \left[1 + \operatorname{erf} \left(\frac{s_1}{\sqrt{2}\sigma_{s1}} \right) \right] + \frac{1-a}{2} \left[1 + \operatorname{erf} \left(\frac{s_2}{\sqrt{2}\sigma_{s2}} \right) \right], \\
\langle q_l \rangle &= s_1 \frac{a}{2} \left[1 + \operatorname{erf} \left(\frac{s_1}{\sqrt{2}\sigma_{s1}} \right) \right] + s_2 \frac{1-a}{2} \left[1 + \operatorname{erf} \left(\frac{s_2}{\sqrt{2}\sigma_{s2}} \right) \right] \\
&+ \sigma_{s1} \frac{a}{\sqrt{2\pi}} \exp \left(-\frac{s_1^2}{2\sigma_{s1}^2} \right) + \sigma_{s2} \frac{1-a}{\sqrt{2\pi}} \exp \left(-\frac{s_2^2}{2\sigma_{s2}^2} \right).
\end{aligned} \tag{54}$$

The buoyancy terms in the Reynolds-stress and scalar-flux equations are computed from Eq. (44), where the interpolation variable $\hat{\mathcal{R}}$ is given by

$$\frac{\hat{\mathcal{R}}}{\hat{\mathcal{C}}} = \begin{cases} 1 & \text{at} \quad \tilde{s} \geq 0 \\ 1 + 1.5\tilde{s}^2 \exp\left(0.25 S_s\right) & \text{at} \quad \tilde{s} \leq 0. \end{cases} \tag{55}$$

It is significant that $\hat{\mathcal{R}}$ depends on the skewness of s in an explicit manner. This is different from Eq. (49), where $\hat{\mathcal{R}}$ explicitly depends on $\langle s \rangle$ and σ_s (via $\tilde{s} = \langle s \rangle / \sigma_s$) but there is no explicit dependence on S_s.

In order to obtain the weighting factor a, Eq. (52) with due regard for Eqs. (51) should be solved numerically at each atmospheric-model time step. Since the left-hand side (l.h.s.) of Eq. (52) is the seventh-order polynomial in a, in general no analytical solution $a\left(S_s\right)$ exists. In order to save computational resources, an approximate solution is used that interpolates between analytical asymptotic solutions valid at $S_s \to \pm\infty$ and $S_s \to \pm 0$. The asymptotic solutions are

$$\begin{aligned} a_{-\infty} &= 1 - \frac{C_{-\infty}}{S_s^2} && \text{at} \quad S_s \to -\infty \\ a_{-0} &= 1 + C_{-0} S_s && \text{at} \quad S_s \to -0 \\ a_{+0} &= C_{+0} S_s && \text{at} \quad S_s \to +0 \\ a_{+\infty} &= \frac{C_{+\infty}}{S_s^2} && \text{at} \quad S_s \to +\infty, \end{aligned} \tag{56}$$

where $C_{-\infty} = \gamma_3^3 \left(2 - \gamma_3\right)^3 \approx 0.862$, $C_{-0} = 8\alpha^{-3/2}\gamma_3^3 \approx 1.342$, $C_{+0} = 8\alpha^{-3/2}\gamma_2^3 \approx 0.275$, and $C_{+\infty} \approx 0.570$ are dimensionless constants. The value of $C_{+\infty}$ is a root of the cubic equation $\frac{4\gamma_1^6}{\alpha^3} C_{+\infty}^3 + \left[1 - \frac{3\gamma_1^2}{\alpha}\gamma_2^2 \left(2 - \gamma_2\right)^2\right] C_{+\infty} - \gamma_2^3 \left(2 - \gamma_2\right)^3 = 0$. Using (56), the weighting factor is computed from the following interpolation formulae:

$$\begin{aligned} \frac{1}{\left(1 - a\right)^n} &= \frac{1}{\left(1 - a_{-0}\right)^n} + \frac{1}{\left(1 - a_{-\infty}\right)^n} && \text{at} \quad S_s < 0 \\ a &= \frac{1}{2} && \text{at} \quad S_s = 0 \\ \frac{1}{a^m} &= \frac{1}{a_{+0}^m} + \frac{1}{a_{+\infty}^m} && \text{at} \quad S_s > 0, \end{aligned} \tag{57}$$

where the exponents n and m are tuning parameters estimated at 0.52 and 0.75, respectively.

As seen from Fig. 1, Eqs. (56) and (57) approximate the exact solution of Eqs. (51) and (52) very accurately at $S_s > 0$. A positive (and possibly large) skewness of s is characteristic of shallow cumulus regime that presents major difficulties in terms of modelling the effect of clouds on turbulent mixing. The agreement between the approximation and the exact solution is less favourable in the range of S_s from ca. -1 to ca. -4. This is not crucial, however. A negative S_s is characteristic of the stratus or stratocumulus clouds, but large negative values of S_s are rarely encountered. In the stratus (stratocumulus) regime, the atmospheric-model grid box is oversaturated in the mean ($\langle s \rangle > 0$), the fractional cloud cover is typically large, and the effect of clouds on mixing can be accounted for with the aid of relatively simple parameterization schemes. For example, assuming $\hat{\mathcal{R}} = \hat{\mathcal{C}}$, as in Eq. (55), does not lead to large uncertainties in the determination of the buoyancy terms in the Reynolds-stress and scalar-flux equations. Note that the error in a caused by the use of Eqs. (56) and (57) instead of the exact solution to Eqs. (51) and (52) does not exceed a few percent. This error is tolerable in the stratus regime.

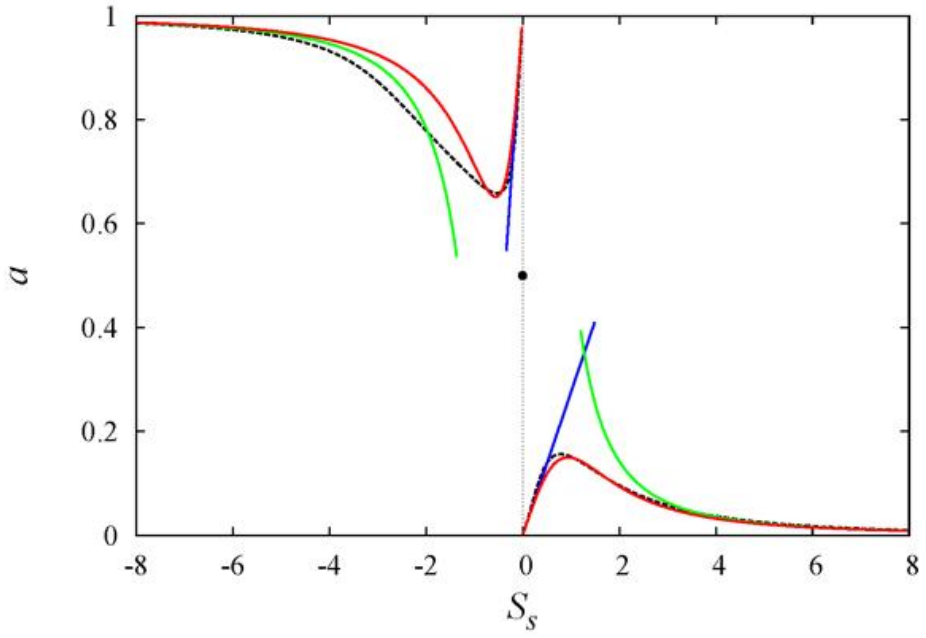


Figure 1: The weighting factor a as function of skewness S_s. Black dashed curves and black dot show numerical solution of Eqs. (51) and (52). Solid curves show the interpolation formulation given by Eqs. (56) and (57) – red, and the asymptotes a_{-0} and a_{+0} – blue, and $a_{-\infty}$ and $a_{+\infty}$ – green.

In order to account for the presence of cloud ice, a generalized total water specific humidity q_t and the ice-liquid (total) water potential temperature θ_t defined through Eqs. (3) and (4), respectively, should be utilized. The use of the $q_t - \theta_t$ system raises various tricky issues. A comprehensive discussion of those issues is beyond the scope of the present report. Here, a way to account for the cloud ice in a very approximate manner is briefly outlined.

Local saturation adjustment is performed in terms of the total cloud condensate $q_c = q_l + q_i$ computed as $q_c = q_t - q_s$ if $q_t > q_s$, and $q_c = 0$ if $q_t \leq q_s$. The saturation specific humidity is specified with respect to the water-ice mixed phase. The following parameterization of the mixed-phase q_s is used:

$$q_{sc} = (1 - F_i)\, q_{sl} + F_i q_{si}, \tag{58}$$

where $F_i = q_i / (q_l + q_i)$ is the cloud-ice fraction of the total cloud condensate, and q_{sl} and q_{si} are the saturation specific humidity for the vapour-liquid equilibrium and for the vapour-ice equilibrium, respectively. If cloud ice and cloud water are allowed to co-exist over a certain temperature range, a simple (e.g. polynomial) function of temperature can be used to determine F_i. A more attractive alternative is to employ a rate equation for F_i (see e.g. Deardorff, 1976):

$$\frac{dF_i}{dt} = -\mathrm{H}\,(T_{li} - T)\,\frac{(F_i - 1)}{\tau_{li}} - \mathrm{H}\,(T - T_{il})\,\frac{F_i}{\tau_{il}}, \tag{59}$$

where H is the Heaviside step function, τ_{li} and τ_{il} are the e-folding time scales of the liquid water to ice and ice to liquid water conversion, respectively, T_{li} is a threshold temperature, below which the conversion of liquid water to ice is assumed to occur, and T_{il} a threshold temperature, above which the cloud ice melting takes place (T_{il} may be set equal to the

fresh-water freezing point). In the quantities $\mathcal{A}$, $\mathcal{P}$ and $\mathcal{Q}$ that enter Eqs. (43) and (44), $\langle q_l \rangle$ should be replaced with $\langle q_c \rangle = \langle q_l \rangle + \langle q_i \rangle$, q_{sl} should be replaced with q_{sc}, and L_v should be replaced with the effective heat of vapourization-sublimation L_c. The latter quantity may be approximated through an interpolation formula similar to Eq. (58), that is $L_c = (1 - F_i)\, L_v + F_i L_i$.

A method to account for the effect of cloud ice described above is rather crude and can only be considered as a zero-order approximation. It should still be advantageous within a parameterization scheme of shallow clouds.

8 Boundary-Layer Approximation

A simplification typically made in geophysical applications, including NWP, is the so-called boundary-layer approximation. This approximation is fairly accurate for large-scale and meso-scale atmospheric models whose grid-box aspect ratio (the ratio of the horizontal grid size to the vertical grid size) is large. Within the framework of the boundary-layer approximation, all derivatives in the x_1 and x_2 horizontal directions in the second-moment equations are neglected and the grid-box mean vertical velocity $\langle u_3 \rangle$ is zero in the second-moment equations (but not in the equations for the mean fields). The equations become one-dimensional, i.e. the flow variables depend on the x_3 vertical coordinate only.

Equations (60)–(67) presented below are obtained using the baseline parameterizations of the third-order transport, dissipation and pressure-scrambling terms in the second-moment equations. The incorporation of more advanced formulations, given in the preceeding sections under the heading ***Advanced Features***, is fairly straightforward.

With due regard for the (baseline) parameterizations of the third-order transport and the dissipation terms given in sections 5.2, 5.3 and 6, the equations for the TKE and for the scalar variances and covariance in the boundary-layer approximation are

$$\begin{aligned} \frac{\partial e}{\partial t} = & - \left(\langle u_1' u_3' \rangle \frac{\partial \langle u_1 \rangle}{\partial x_3} + \langle u_2' u_3' \rangle \frac{\partial \langle u_2 \rangle}{\partial x_3} \right) - \beta_3 \langle u_3' \theta_v' \rangle \\ & + \frac{\partial}{\partial x_3} \left(C_e^d \tau_\epsilon e \frac{\partial e}{\partial x_3} \right) - \frac{e}{\tau_\epsilon}, \end{aligned} \tag{60}$$

$$\frac{1}{2} \frac{\partial \langle \theta_l'^2 \rangle}{\partial t} = - \langle u_3' \theta_l' \rangle \frac{\partial \langle \theta_l \rangle}{\partial x_3} + \frac{1}{2} \frac{\partial}{\partial x_3} \left(C_{\theta\theta}^d \tau_\epsilon e \frac{\partial \langle \theta_l'^2 \rangle}{\partial x_3} \right) - \frac{\langle \theta_l'^2 \rangle}{2 R_\tau \tau_\epsilon}, \tag{61}$$

$$\frac{1}{2} \frac{\partial \langle q_t'^2 \rangle}{\partial t} = - \langle u_3' q_t' \rangle \frac{\partial \langle q_t \rangle}{\partial x_3} + \frac{1}{2} \frac{\partial}{\partial x_3} \left(C_{qq}^d \tau_\epsilon e \frac{\partial \langle q_t'^2 \rangle}{\partial x_3} \right) - \frac{\langle q_t'^2 \rangle}{2 R_\tau \tau_\epsilon}, \tag{62}$$

$$\frac{\partial \langle \theta_l' q_t' \rangle}{\partial t} = - \langle u_3' q_t' \rangle \frac{\partial \langle \theta_l \rangle}{\partial x_3} - \langle u_3' \theta_l' \rangle \frac{\partial \langle q_t \rangle}{\partial x_3} + \frac{\partial}{\partial x_3} \left(C_{\theta q}^d \tau_\epsilon e \frac{\partial \langle \theta_l' q_t' \rangle}{\partial x_3} \right) - \frac{\langle \theta_l' q_t' \rangle}{R_\tau \tau_\epsilon}, \tag{63}$$

where the vertical x_3 axis is aligned with the vector of gravity so that the only non-zero component of the buoyancy parameter is β_3. The virtual potential temperature flux $\langle u_i' \theta_v' \rangle$ is expressed through the fluxes of liquid water potential temperature, $\langle u_i' \theta_l' \rangle$, and the total water specific humidity, $\langle u_i' q_t' \rangle$, using Eq. (44), and the interpolation variable $\hat{\mathcal{R}}$ is computed from Eqs. (46)–(49). The TKE dissipation time scale τ_ϵ is computed from

$$\tau_\epsilon = \frac{1}{C_\epsilon} \frac{l}{e^{1/2}}, \qquad \frac{1}{l} = \frac{1}{\kappa x_3} + \frac{1}{l_\infty} + \mathrm{H}\left(N^2\right) \frac{N}{C_{lb} e^{1/2}}. \tag{64}$$

In the atmospheric flows, the Coriolis terms in the Reynolds-stress and scalar-flux equations are typically small and can safely be neglected. With due regard for the (baseline) parameterizations of pressure-scrambling terms given in section 5.1 (the deviatoric part of the Reynolds-stress dissipation rate and the dissipation rates of temperature and humidity fluxes are incorporated into the slow parts of the respective pressure-scrambling terms), the algebraic equations for the departure-from-isotropy tensor (and hence for the Reynolds stress) and for the scalar fluxes in the boundary-layer approximation are

$$\begin{aligned}
&C_t^u a_{ij} + (1 - C_{s2}^u)\,\tau_\epsilon \left(a_{ik}S_{jk} + a_{jk}S_{ik} - \frac{2}{3}\delta_{ij}a_{km}S_{km} \right) \\
&+ (1 - C_{s3}^u)\,\tau_\epsilon \left(a_{ik}W_{jk} + a_{jk}W_{ik} \right) \\
&+ (1 - C_b^u)\,\tau_\epsilon \left(\delta_{i3}\beta_3 \left\langle u_j'\theta_v' \right\rangle + \delta_{j3}\beta_3 \left\langle u_i'\theta_v' \right\rangle - \frac{2}{3}\delta_{ij}\beta_3 \left\langle u_3'\theta_v' \right\rangle \right) \\
&= -\left(\frac{4}{3} - C_{s1}^u \right) \tau_\epsilon e S_{ij},
\end{aligned} \tag{65}$$

$$\begin{aligned}
&C_t^\theta \left\langle u_i'\theta_l' \right\rangle + a_{i3}\tau_\epsilon \frac{\partial \left\langle \theta_l \right\rangle}{\partial x_3} + \tau_\epsilon \left[\left(1 - C_{s1}^\theta \right) S_{ik} + \left(1 - C_{s2}^\theta \right) W_{ik} \right] \left\langle u_k'\theta_l' \right\rangle \\
&= -\frac{2}{3}\tau_\epsilon e \delta_{i3} \frac{\partial \left\langle \theta_l \right\rangle}{\partial x_3} - \left(1 - C_b^\theta \right) \tau_\epsilon \delta_{i3}\beta_3 \left\langle \theta_l'\theta_v' \right\rangle,
\end{aligned} \tag{66}$$

$$\begin{aligned}
&C_t^q \left\langle u_i'q_t' \right\rangle + a_{i3}\tau_\epsilon \frac{\partial \left\langle q_t \right\rangle}{\partial x_3} + \tau_\epsilon \left[(1 - C_{s1}^q) S_{ik} + (1 - C_{s2}^q) W_{ik} \right] \left\langle u_k'q_t' \right\rangle \\
&= -\frac{2}{3}\tau_\epsilon e \delta_{i3} \frac{\partial \left\langle q_t \right\rangle}{\partial x_3} - \left(1 - C_b^q \right) \tau_\epsilon \delta_{i3}\beta_3 \left\langle q_t'\theta_v' \right\rangle,
\end{aligned} \tag{67}$$

where the covariances $\langle u_i'\theta_v' \rangle$, $\langle \theta_l'\theta_v' \rangle$ and $\langle q_t'\theta_v' \rangle$ incorporating the virtual potential temperature are expressed through $\langle u_i'\theta_l' \rangle$ and $\langle u_i'q_t' \rangle$, $\langle \theta_l'^2 \rangle$ and $\langle \theta_l'q_t' \rangle$, and $\langle q_t'^2 \rangle$ and $\langle \theta_l'q_t' \rangle$, respectively, using Eq. (44). Within the framework of the boundary-layer approximation, $S_{13} = S_{31} = W_{13} = -W_{31} = \frac{1}{2}\partial \langle u_1 \rangle / \partial x_3$, $S_{23} = S_{32} = W_{23} = -W_{32} = \frac{1}{2}\partial \langle u_2 \rangle / \partial x_3$, and other components of S_{ij} and W_{ij} are zero. Estimates of disposable constants and parameters of TKESV-Bas are summarized in Appendix B.

Equations (65)–(67) constitute a system of 12 linear equations for a_{ij} (six independent components), $\langle u_i'\theta_l' \rangle$ (three independent components), and $\langle u_i'q_t' \rangle$ (three independent components). This system is readily solved, yielding explicit expressions for the Reynolds stress and scalar fluxes. Unfortunately, the solution to Eqs. (65)–(67) is non-realizable. That is, it yields physically meaningless values of a_{ij} (and hence of $\langle u_i'u_j' \rangle$), $\langle u_i'\theta_l' \rangle$ and $\langle u_i'q_t' \rangle$, such as infinite scalar fluxes or negative velocity variances, over a certain range of governing parameters (e.g. mean velocity shear and mean temperature gradient). A plausible way to circumvent these difficulties is considered in the next section.

9 The (So-Called) Stability Functions

The system of linear equations (65)–(67) yields explicit expressions for the Reynolds-stress and scalar-flux components. The expressions for $\langle u_3'u_1' \rangle$ and $\langle u_3'u_2' \rangle$ (components of the vertical flux of horizontal momentum) have the following down-gradient form:

$$\left\langle u_3'u_1' \right\rangle = -\mathcal{F}_{\mathrm{M}}\tau_\epsilon e \frac{\partial \left\langle u_1 \right\rangle}{\partial x_3}, \qquad \left\langle u_3'u_2' \right\rangle = -\mathcal{F}_{\mathrm{M}}\tau_\epsilon e \frac{\partial \left\langle u_2 \right\rangle}{\partial x_3}. \tag{68}$$

The expressions for the vertical scalar fluxes contain both the down-gradient terms and the non-gradient terms that describe the generation of scalar fluxes by buoyancy:

$$\left\langle u_3'\theta_l'\right\rangle = -\mathcal{F}_{\mathrm{H1}}\tau_\epsilon e\frac{\partial\left\langle\theta_l\right\rangle}{\partial x_3} - \mathcal{F}_{\mathrm{H2}}\tau_\epsilon\beta_3\left\langle\theta_l'\theta_v'\right\rangle, \tag{69}$$

$$\left\langle u_3'q_t'\right\rangle = -\mathcal{F}_{\mathrm{H1}}\tau_\epsilon e\frac{\partial\left\langle q_t\right\rangle}{\partial x_3} - \mathcal{F}_{\mathrm{H2}}\tau_\epsilon\beta_3\left\langle q_t'\theta_v'\right\rangle, \tag{70}$$

where the covariances $\langle\theta_l'\theta_v'\rangle$ and $\langle q_t'\theta_v'\rangle$ are expressed through $\langle\theta_l'^2\rangle$ and $\langle\theta_l'q_t'\rangle$ and $\langle q_t'^2\rangle$ and $\langle\theta_l'q_t'\rangle$, respectively, using Eq. (44). The quantities $\mathcal{F}_{\mathrm{M}}$, $\mathcal{F}_{\mathrm{H1}}$ and $\mathcal{F}_{\mathrm{H2}}$ are referred to as the "stability functions" (Mellor and Yamada, 1974). It should be emphasized at once that the stability functions are merely the notation introduced to represent the formulations of fluxes in a compact from. Basically, $\mathcal{F}_{\mathrm{M}}$, $\mathcal{F}_{\mathrm{H1}}$ and $\mathcal{F}_{\mathrm{H2}}$ reflect the parameterization assumptions invoked to arrive at the algebraic Reynolds-stress and scalar-flux equations, first of all, the parameterizations of the pressure-scrambling terms.

The functions $\mathcal{F}_{\mathrm{M}}$ and $\mathcal{F}_{\mathrm{H1}}$ that appear in the down-gradient terms in Eqs. (68)–(70) are functions of three dimensionless parameters. These are the squared dimensionless shear $(\tau_\epsilon S)^2$, the squared dimensionless buoyancy frequency $(\tau_\epsilon N)^2$, and the potential to kinetic energy ratio P/e. Here, S^2, N^2 and P are given by

$$S^2 = \left(\frac{\partial\left\langle u_1\right\rangle}{\partial x_3}\right)^2 + \left(\frac{\partial\left\langle u_2\right\rangle}{\partial x_3}\right)^2, \tag{71}$$

$$N^2 = -\beta_3\left(\mathcal{I}_\theta\frac{\partial\left\langle\theta_l\right\rangle}{\partial x_3} + \mathcal{I}_q\frac{\partial\left\langle q_t\right\rangle}{\partial x_3}\right), \tag{72}$$

$$P = \tau_\epsilon^2\beta_3^2\left[\mathcal{I}_\theta\left(\mathcal{I}_\theta\left\langle\theta_l'^2\right\rangle + \mathcal{I}_q\left\langle\theta_l'q_t'\right\rangle\right) + \mathcal{I}_q\left(\mathcal{I}_q\left\langle q_t'^2\right\rangle + \mathcal{I}_\theta\left\langle\theta_l'q_t'\right\rangle\right)\right], \tag{73}$$

$$\mathcal{I}_\theta = 1 + (R-1)\left\langle q_t\right\rangle - R\left\langle q_l\right\rangle - \hat{\mathcal{R}}\frac{\mathcal{A}\mathcal{P}}{\mathcal{Q}}, \qquad \mathcal{I}_q = (R-1)\left\langle\theta\right\rangle + \hat{\mathcal{R}}\frac{\mathcal{A}}{\mathcal{Q}}, \tag{74}$$

where $\mathcal{A}$, $\mathcal{P}$, $\mathcal{Q}$ and $\hat{\mathcal{R}}$ are defined in section 7. The quantity P characterizes potential energy of the turbulent flow and may be referred to as the turbulence potential energy[4]. Note that the buoyancy frequency and the TPE appear to depend on the interpolation variable $\hat{\mathcal{R}}$ and hence on the fractional cloud cover. As discussed in section 7, the covariances incorporating fluctuation of the virtual potential temperature cannot be computed exactly in the general case of fractional cloudiness. It is the use of the interpolation formula (44) to determine $\langle u_i'\theta_v'\rangle$, $\langle\theta_l'\theta_v'\rangle$ and $\langle q_t'\theta_v'\rangle$ that leads to the interpolation formulae (72) and (73) for N^2 and P, respectively. Instead of $(\tau_\epsilon S)^2$ and $(\tau_\epsilon N)^2$, $\mathcal{F}_{\mathrm{M}}$ and $\mathcal{F}_{\mathrm{H1}}$ can be presented in terms of $(\tau_\epsilon S)^2$ [or $(\tau_\epsilon N)^2$] and the gradient Richardson number $Ri = N^2/S^2$. The stability function $\mathcal{F}_{\mathrm{H2}}$ that appears in the non-gradient terms in Eqs. (69) and (70) depends on $(\tau_\epsilon S)^2$ and $(\tau_\epsilon N)^2$, or, alternatively, on $(\tau_\epsilon S)^2$ [or $(\tau_\epsilon N)^2$] and Ri, but does not depend on P/e.

The stability functions resulting from Eqs. (68)–(70) are ill-behaved over a certain range of governing parameters. Figure 2 shows $\mathcal{F}_{\mathrm{M}}$ and $\mathcal{F}_{\mathrm{H1}}$ as dependent on Ri and $(\tau_\epsilon S)^2$ at a fixed value of P/e. As seen from the figure, the stability functions have physically meaningless values, i.e. they tend to infinity or become negative over a part of their parameter

[4]Other definitions of TPE have also been used in the analyses of atmospheric turbulence, see Appendix C for a brief discussion.

space. The scalar-flux stability function $\mathcal{F}_{\mathrm{H2}}$ (not shown) is well-behaved and poses no complications. The expressions of $\mathcal{F}_{\mathrm{M}}$, $\mathcal{F}_{\mathrm{H1}}$ and $\mathcal{F}_{\mathrm{H2}}$ are rather lengthy and are not presented in this section. However, those expressions are drastically simplified in the case of shear-free (and rotation-free) flow, and the ill-behaviour of the stability functions can be easily demonstrated analytically. The analysis is presented in Appendix D.

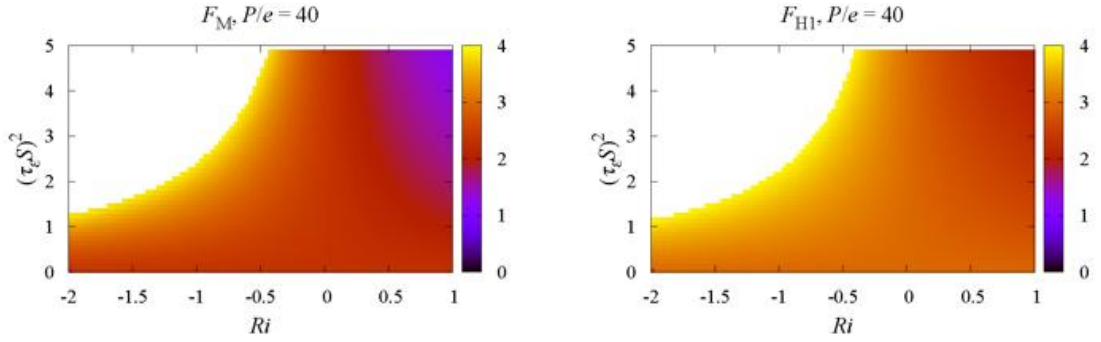


Figure 2: The momentum-flux $\mathcal{F}_{\mathrm{M}}$ (left panel) and the scalar-flux $\mathcal{F}_{\mathrm{H1}}$ (right panel) stability functions of the TKESV scheme as dependent on Ri and $(\tau_\epsilon S)^2$ at a fixed value of $P/e = 40$. The functions are computed with the estimates of dimensionless constants given in Table 1 (Appendix B), where the estimates of $C^u_{s2} = 3/5$ and $C^u_{s3} = 13/15$ are used. The values of $\mathcal{F}_{\mathrm{M}}$ and $\mathcal{F}_{\mathrm{H1}}$ are indicated by the colour scale. The white area is a part of the parameter space where the stability functions are ill-behaved.

In order to obtain the Reynolds-stress and scalar-flux formulations that remain in force over the entire parameter space, the stability functions should be modified (regularized) in one way or the other. A straightforward approach is to simply impose the upper and lower bounds on the stability functions themselves. Alternatively, realizability constraints may be imposed on the arguments, e.g. on $(\tau_\epsilon S)^2$ and $(\tau_\epsilon N)^2$, so that the stability functions cannot become infinite or negative (see e.g. Mellor and Yamada, 1982; Hassid and Galperin, 1994). These methods applied within the framework a one-equation TKE scheme may lead to either the model blow-up or to physically implausible solutions (Helfand and Labraga, 1988). One more method is to replace the ill-behaved stability functions with more simple functions that reveal no pathological behaviour. For example, the stability functions of the algebraic turbulence parameterization scheme, where all second-moment equations (including the TKE equation) are reduced to the diagnostic algebraic formulations, are well-behaved over their entire parameter space. The use of the algebraic-scheme stability functions within the one-equation TKE scheme yields regular solutions. However, the adjustment of the TKE towards the production-dissipation equilibrium state occurs on a too short time scale. In other words, turbulence responds too quickly to changes in the shear and buoyancy forcing. A more detailed discussion of the above (and some other) regularization methods is given in Helfand and Labraga (1988) (see also Hanjalić and Launder, 2011; Lazeroms et al., 2013, 2015, 2016).

An appealing way to tackle the problem was proposed by Helfand and Labraga (1988) (see also du Vachat, 1989; Helfand and Labraga, 1989). These authors analyzed the stability functions of the one-equation TKE scheme. Using rather plausible physical arguments, they developed regularized functions that reveal no pathological behaviour over their entire parameter space. In what follows, we extend the approach of Helfand and Labraga to the

TKESV scheme[5]. Following Helfand and Labraga (1988), we adhere to the Mellor and Yamada terminology (Mellor and Yamada, 1974, 1982; Yamada, 1977). The level 3 refers to the TKESV-like schemes that carry transport equations for the TKE and for the scalar variances and covariance, and the level 2 refers to the schemes, where all second-moment equations are reduced to the diagnostic algebraic formulations. One-equation TKE schemes are referred to as the level 2.5 schemes.

Within the framework of the level 2.5 scheme, the scalar-variance and scalar-covariance transport equations are truncated to the diagnostic expressions reflecting the steady-state balance between the mean-gradient production and the dissipation. The vertical scalar fluxes are given by the following down-gradient formulations:

$$\left\langle u_3' \theta_l' \right\rangle = -\mathcal{F}_{\mathrm{H}}^{2.5} \tau_\epsilon e \frac{\partial \left\langle \theta_l \right\rangle}{\partial x_3}, \qquad \left\langle u_3' q_t' \right\rangle = -\mathcal{F}_{\mathrm{H}}^{2.5} \tau_\epsilon e \frac{\partial \left\langle q_t \right\rangle}{\partial x_3}, \tag{75}$$

where $\mathcal{F}_{\mathrm{H}}^{2.5}$ is the level 2.5 scalar-flux stability function. The momentum-flux components $\langle u_3' u_1' \rangle$ and $\langle u_3' u_2' \rangle$ are given by Eqs. (68), where $\mathcal{F}_{\mathrm{M}}$ is replaced with the level 2.5 stability function $\mathcal{F}_{\mathrm{M}}^{2.5}$. The level 2.5 stability functions depend on $(\tau_\epsilon S)^2$ and $(\tau_\epsilon N)^2$, or, alternatively, on $(\tau_\epsilon S)^2$ [or $(\tau_\epsilon N)^2$] and Ri. The level 2.5 functions suffer from the same deficiencies as the level 3 functions, i.e. they are ill-behaved over a part of their parameter space.

Helfand and Labraga (1988) recast the functions $\mathcal{F}_{\mathrm{M}}^{2.5}\left(Ri, \tau_\epsilon^2 S^2\right)$ and $\mathcal{F}_{\mathrm{H}}^{2.5}\left(Ri, \tau_\epsilon^2 S^2\right)$ in terms of Ri and the ratio e/e_e of the actual TKE $e = e_{2.5}$ of the level 2.5 scheme (hence the subscript) to the equilibrium value of the TKE $e_e = e_2$ of the level 2 scheme. Within the framework of the level 2 scheme, all second-moment transport equations, including the TKE equation, are truncated to the diagnostic expressions by neglecting the time-rate-of-change, advection and third-order transport terms. That is, all second-order moments, including the TKE, are in the state of local production-destruction equilibrium. In order to change the variables $\left(Ri, \tau_\epsilon^2 S^2\right)$ to the variables $(Ri, e/e_e)$, the equality $\tau_\epsilon^2 S^2 = \left(\tau_\epsilon/\tau_{\epsilon e}\right)^2 \tau_{\epsilon e}^2 S^2 = \left(e_e/e\right) \tau_{\epsilon e}^2 S^2$ is used, where $\tau_{\epsilon e}$ is the equilibrium TKE dissipation time scale, i.e. τ_ϵ computed with e_e. The value of e_e, and hence of $\tau_{\epsilon e}^2 S^2$, for a given Ri is found by solving the equilibrium TKE equation of the level 2 scheme, which is a quadratic equation in e_e (in $\tau_{\epsilon e}^2 S^2$). Since the stability functions $\mathcal{F}_{\mathrm{M}}^2$ and $\mathcal{F}_{\mathrm{H}}^2$ are well-behaved over their entire parameter space (any value of Ri), a physically meaningful solution $e_e = e_2$ can always be found. Helfand and Labraga (1988) noticed that $\mathcal{F}_{\mathrm{M}}^{2.5}$ and $\mathcal{F}_{\mathrm{H}}^{2.5}$ become pathological in the case of growing turbulence, $e/e_e < 1$, where the TKE production (locally) dominates over the TKE dissipation. Figure 3 illustrates the pathological behaviour of the level 2.5 stability functions on the $Ri \times e/e_e$ plane. Note that $\mathcal{F}_{\mathrm{M}}^{2.5}$ and $\mathcal{F}_{\mathrm{H}}^{2.5}$ are computed with the estimates of dimensionless constants of TKESV-Bas (where $C_{s2}^u = 3/5$ and $C_{s3}^u = 13/15$), which are somewhat different from the estimates used by Helfand and Labraga (1988). As seen from the figure, $\mathcal{F}_{\mathrm{M}}^{2.5}$ and $\mathcal{F}_{\mathrm{H}}^{2.5}$ are well-behaved in the case of equilibrium or decaying turbulence, $e/e_e \geq 1$, but become pathological at $e/e_e < 1$.

The failure of the level 2.5 scheme is attributed to the closure assumptions used to develop the scheme, namely, (i) the neglect of the substantial derivative and the third order transport of the Reynolds stress, scalar fluxes and scalar variances and covariance, and (ii) the use of linear formulations of the pressure-scrambling terms in the Reynolds-stress and scalar-flux equations (see further discussion at the end of the present section). These closure assumptions are valid for the flows where turbulence is not far from the stationary, homogeneous, and isotropic state. Helfand and Labraga (1988) argue that it is precisely in the regime of growing TKE, where $e/e_e < 1$, that the turbulence becomes strongly anisotropic (also

[5]Helfand and Labraga (1988) considered dry atmosphere, where θ is the only thermodynamic variable that affects buoyancy. Our analysis deals with the moist atmosphere, using thermodynamic variables θ_l and q_t.

non-stationary and possibly non-homogeneous) and the above assumptions are too crude, leading to the ill-behaviour of the stability functions and to non-realizability of the turbulence closure scheme. In order to remedy the situation, Helfand and Labraga proposed to account, in an approximate way, for the effects of time-rate-of-change, advection and diffusion in those truncated second-moment equations in which these effects have been neglected. In other words, the idea is to restore to the second-moment equations some information that has been lost because of truncation. The following approximation was proposed:

$$\frac{d\mathcal{M}/dt + \mathcal{D}_\mathcal{M}}{\mathcal{G}_\mathcal{M}} = \frac{de/dt + \mathcal{D}_e}{\mathcal{G}_e}. \tag{76}$$

Here, $\mathcal{M}$ stands for the Reynolds stress, scalar fluxes, and (within the framework of the level 2.5 scheme) scalar variances and covariance, d/dt is the substantial derivative that coincides with $\partial/\partial t$ within the framework of the boundary-layer approximation, $\mathcal{D}$ is the diffusion rate of the respective second-order moment, and $\mathcal{G}$ is its production (generation) rate. The production rate $\mathcal{G}_\mathcal{M}$ includes the terms due to mean velocity shear and buoyancy (in the Reynolds-stress and scalar-flux equations), and due to mean scalar gradients (in the scalar-flux, scalar-variance and scalar-covariance equations). It should be mentioned that within the framework of the Helfand and Labraga approach the production rate is defined with due regard for the rapid parts of the pressure-scrambling terms. Equation (76) states that the ratio of the tendency of the second-order moment $\mathcal{M}$ due to d/dt and $\mathcal{D}$ to the production rate of $\mathcal{M}$ is the same as the respective ratio for the TKE.

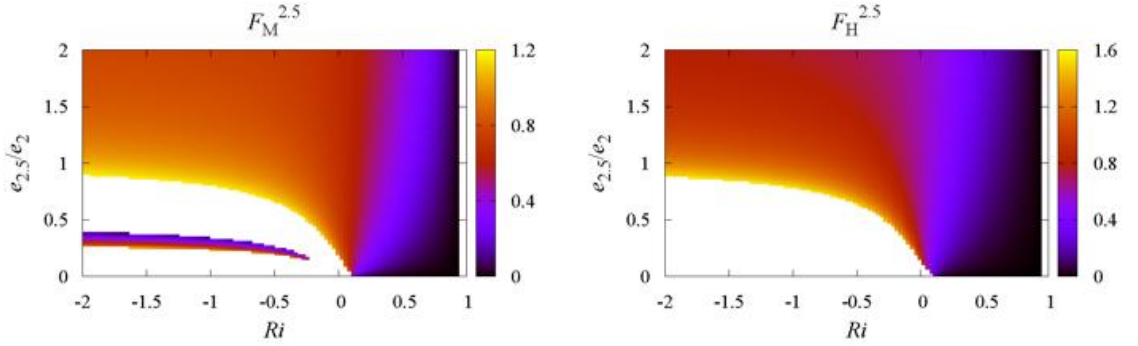


Figure 3: The stability functions of the level 2.5 scheme as dependent on Ri and $e/e_e = e_{2.5}/e_2$. The values of $\mathcal{F}_\mathrm{M}^{2.5}$ and $\mathcal{F}_\mathrm{H}^{2.5}$ are indicated by the colour scale. The white area is a part of the parameter space where the stability functions are ill-behaved.

Some comments on the validity of Eq. (76) are in order. Equation (76) is obviously exact in the regime of production-destruction equilibrium. In this regime, the production rate of any moment $\mathcal{M}$, including the TKE, is balanced by the destruction rate of $\mathcal{M}$ due to return-to-isotropy ($\mathcal{M}$ stands for the Reynolds stress or scalar flux) or viscous dissipation ($\mathcal{M}$ stands for the scalar variance, scalar covariance, or TKE). In the regime of production-destruction equilibrium, both the r.h.s. and the l.h.s. of Eq. (76) are zero. Equation (76) is also valid asymptotically if the production rate of the moment $\mathcal{M}$ strongly dominates over its destruction rate. A transport equation for $\mathcal{M}$ can be written in the following form:

$$\frac{d\mathcal{M}/dt + \mathcal{D}_\mathcal{M}}{\mathcal{G}_\mathcal{M}} = 1 - \frac{\epsilon_\mathcal{M}}{\mathcal{G}_\mathcal{M}}, \tag{77}$$

where $\epsilon_{\mathcal{M}}$ denotes the destruction rate of the moment $\mathcal{M}$. The r.h.s. of Eq. (77) approaches one as the ratio $\epsilon_{\mathcal{M}}/\mathcal{G}_{\mathcal{M}}$ tends to zero. If the ratio $\epsilon/\mathcal{G}_e$ for the TKE also tends to zero, both the r.h.s. and the l.h.s. of Eq. (76) approach one. In the real-world flows, this never holds exactly. However, $\epsilon_{\mathcal{M}}/\mathcal{G}_{\mathcal{M}} \ll 1$ may hold approximately following a rapid increase of forcing (by mean scalar gradient, mean velocity shear, or buoyancy), i.e. precisely in the regime of growing turbulence.

Using Eq. (76), the truncated, algebraic equations of the level 2.5 scheme can be modified to approximately account for (mimic) the effects of the time-rate-of-change and turbulent diffusion. To this end, approximations $d\mathcal{M}/dt + \mathcal{D}_{\mathcal{M}} = \alpha_e \mathcal{G}_{\mathcal{M}}$, where $\alpha_e = (de/dt + \mathcal{D}_e)/\mathcal{G}_e$ is known from the solution of the TKE equation, are added to the Reynolds-stress, scalar-flux and scalar-variance equations (recall that $d/dt = \partial/\partial t$ within the framework of the boundary-layer approximation). In substance, these modifications amount to multiplying the production terms in the algebraic equations by a factor $1 - \alpha_e$. The resulting system of the Reynolds-stress, scalar-flux and scalar-variance equations remains algebraic and linear. It is readily solved (see Helfand and Labraga, 1988, for details), giving the following expressions for the stability functions of the level 2.5 scheme:

$$\mathcal{F}_{\mathrm{M}}^{2.5} = \mathcal{F}_{\mathrm{Mr}}^{2.5} = \mathcal{F}_{\mathrm{M}}^{2} \left(\frac{e_{2.5}}{e_2} \right)^{1/2}, \qquad \mathcal{F}_{\mathrm{H}}^{2.5} = \mathcal{F}_{\mathrm{Hr}}^{2.5} = \mathcal{F}_{\mathrm{H}}^{2} \left(\frac{e_{2.5}}{e_2} \right)^{1/2}, \tag{78}$$

where the subscript "r" indicates the modified (regularized) stability functions. The regularized functions given by Eq. (78) are used in the case of growing turbulence, when the actual value of TKE $e_{2.5}$ of the level 2.5 scheme is less than the equilibrium TKE e_2 of the level 2 scheme. In the case of equilibrium or decaying turbulence, the original, non-modified stability functions of the level 2.5 scheme are used that are well-behaved at $e_{2.5}/e_2 \geq 1$ and pose no problem. Recall that the stability functions $\mathcal{F}_{\mathrm{M}}^2$ and $\mathcal{F}_{\mathrm{H}}^2$ of the level 2 algebraic scheme are well-behaved over their entire parameter space, and e_2 is found by solving the equilibrium TKE equation (a quadratic equation in e_2 that always has a physically meaningful solution). Figure 4 illustrates the regularized stability functions of the level 2.5 scheme that reveal no pathological behaviour.

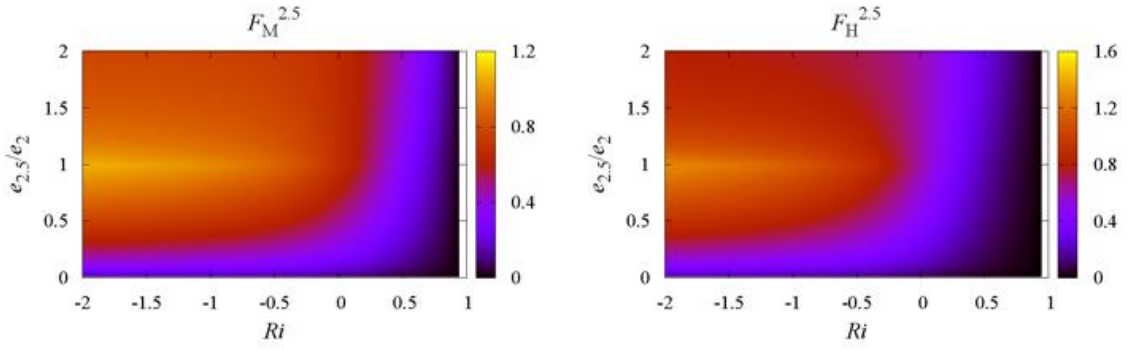


Figure 4: The regularized stability functions of the level 2.5 scheme as dependent on Ri and $e/e_e = e_{2.5}/e_2$. The values of $\mathcal{F}_{\mathrm{M}}^{2.5}$ and $\mathcal{F}_{\mathrm{H}}^{2.5}$ are indicated by the colour scale. In the case of growing turbulence, $e_{2.5}/e_2 < 1$, the stability functions are computed from Eq. (78).

The regularization method of Helfand and Labraga (1988) is now applied to the TKESV (level 3) scheme. Using Eq. (76), the Reynolds-stress and scalar-flux equations are modified, and the resulting system of algebraic equations for a_{ij}, $\langle u_i' \theta_l' \rangle$ and $\langle u_i' q_l' \rangle$ is solved (the

derivations are rather cumbersome and are omitted here). The following expressions of the stability functions $\mathcal{F}_{\mathrm{M}} = \mathcal{F}^3_{\mathrm{M}}$ and $\mathcal{F}_{\mathrm{H1}} = \mathcal{F}^3_{\mathrm{H1}}$ in Eqs. (68)–(70) are obtained (index "3" refers to the level 3, i.e. to the TKESV, scheme):

$$\mathcal{F}^3_{\mathrm{M}} = \mathcal{F}^3_{\mathrm{Mr}} = \mathcal{F}^{2.p}_{\mathrm{M}} \left(\frac{e_3}{e_{2.p}} \right)^{1/2}, \qquad \mathcal{F}^3_{\mathrm{H1}} = \mathcal{F}^3_{\mathrm{H1r}} = \mathcal{F}^{2.p}_{\mathrm{H1}} \left(\frac{e_3}{e_{2.p}} \right)^{1/2}, \tag{79}$$

where the subscript "r" indicates the regularized stability functions. In Eq. (79), the index "2.p" refers to the scheme that utilizes the equilibrium TKE equation but carries transport equations for the scalar variances and scalar covariance. That is, the TKE is determined diagnostically using the steady-state production-dissipation balance, whereas the scalar variances and covariance (and hence the TPE) are determined prognostically with due regard for the third-order turbulent transport[6]. The stability functions $\mathcal{F}^{2.p}_{\mathrm{M}}$ and $\mathcal{F}^{2.p}_{\mathrm{H1}}$ of the level 2.p scheme are well-behaved over their entire parameter space. The equilibrium TKE $e_e = e_{2.p}$ is found by solving the equilibrium TKE equation of the level 2.p scheme, which is a cubic equation in e_e. The regularized stability functions given by Eq. (79) are used in the case of growing turbulence, when $e_3/e_{2.p} < 1$. In the case of equilibrium or decaying turbulence, the original, non-modified stability functions of the level 3 (TKESV) scheme are used which are well-behaved at $e_3/e_{2.p} \geq 1$ and pose no problem.

Figure 5 shows the original, non-modified stability functions of the TKESV (level 3) scheme on the $Ri \times e_3/e_{2.p}$ plane at a fixed value of P/e_3. The stability functions are well-behaved in the case of equilibrium or decaying turbulence, $e_3/e_{2.p} \geq 1$, but become pathological in the case of growing turbulence, $e_3/e_{2.p} < 1$. Figure 6 shows the regularized stability functions of the TKESV (level 3) scheme. As seen from the figure, the stability functions reveal no pathological behaviour.

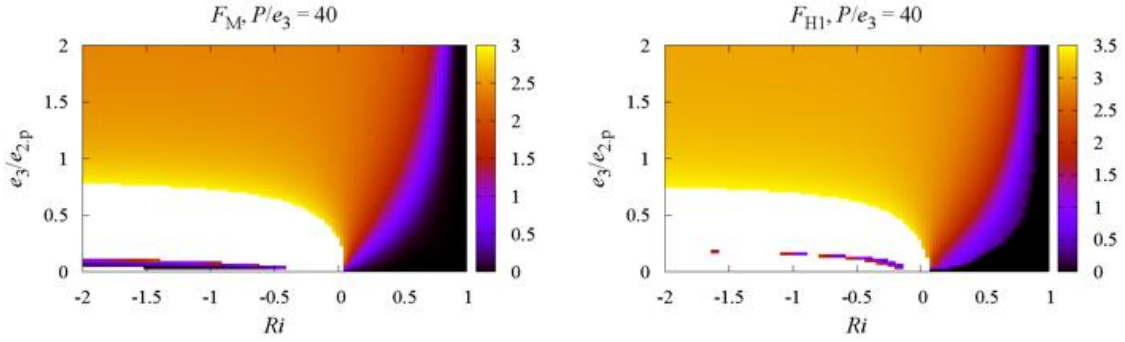


Figure 5: The original, non-regularized momentum-flux $\mathcal{F}_{\mathrm{M}} = \mathcal{F}^3_{\mathrm{M}}$ (left panel) and scalar-flux $\mathcal{F}_{\mathrm{H1}} = \mathcal{F}^3_{\mathrm{H1}}$ (right panel) stability functions of the TKESV (level 3) scheme as dependent on Ri and $e_3/e_{2.p}$ at a fixed value of $P/e_3 = 40$. The values of stability functions are indicated by the colour scale. The white area is a part of the parameter space where the stability functions are ill-behaved.

It is interesting to draw analogies between Eq. (78) and Eq. (79). As Eq. (78) shows, the regularized level 2.5 stability functions are expressed in terms of the level 2 stability

[6]The letter "p" in the label "2.p" is used to indicate potential energy. In a similar spirit, the level 2.5 scheme may be referred to as the "level 2.k" scheme, where "k" indicates kinetic energy, or, alternatively, the "level 2.e" scheme, where "e" is a conventional notation for the TKE.

functions. For the level 2.5 scheme, the level 2 scheme is the nearest lower-level realizable scheme whose stability functions are well-behaved over the entire parameter space. Likewise, for the level 3 scheme, the level 2.p scheme is the nearest lower-level realizable scheme. The level 2 and the level 2.p schemes differ significantly in the way they treat the scalar variances and covariance. However, both the level 2 and the level 2.p schemes utilize a steady-state equilibrium TKE equation, suggesting that it is the use of the TKE transport equation in combination with the algebraic formulations of the Reynolds stress and scalar fluxes that causes non-realizability of truncated turbulence closure schemes.

Note an important factor $(e_3/e_{2.p})^{1/2}$ in the expressions of the regularized level 3 stability functions, Eq. (79). It is this factor that takes care of a gradual transition of the TKE towards the production-dissipation equilibrium. Dropping the factor $(e_3/e_{2.p})^{1/2}$ in Eq. (79) would result in a too quick response of turbulence to changes in the forcing and in overestimation of momentum and scalar fluxes in the regime of growing TKE. The factor $(e_{2.5}/e_2)^{1/2}$ in Eq. (78) has a similar effect on the behaviour of the level 2.5 scheme.

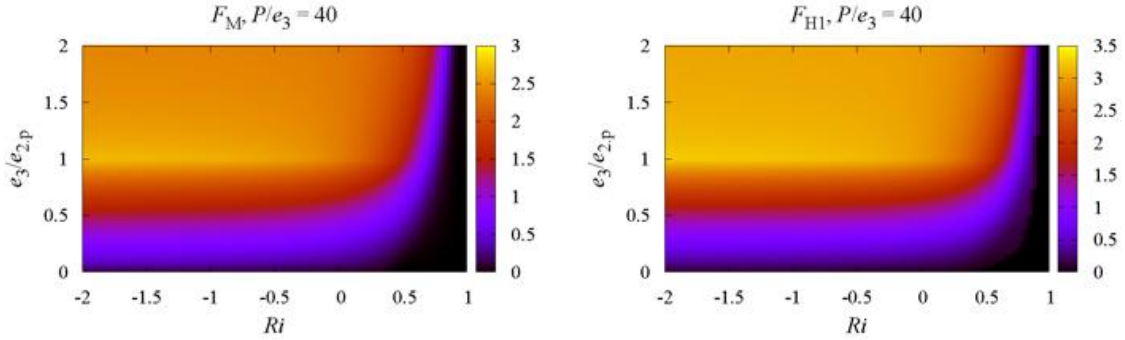


Figure 6: The regularized momentum-flux $\mathcal{F}_{\rm M} = \mathcal{F}^3_{{\rm M}r}$ (left panel) and scalar-flux $\mathcal{F}_{\rm H1} = \mathcal{F}^3_{{\rm H1}r}$ (right panel) stability functions of the TKESV (level 3) scheme as dependent on Ri and $e/e_e = e_3/e_{2.p}$ at a fixed value of $P/e_3 = 40$. The values of stability functions are indicated by the colour scale. In the case of growing turbulence, $e_3/e_{2.p} < 1$, the stability functions are computed from Eq. (79).

The idea of the regularization method of Helfand and Labraga (1988) is to restore to the second-moment equations some information that has been lost because of truncation. Equation (76) is used to approximately account for (mimic) the effects of the time-rate-of-change and turbulent diffusion in the Reynolds-stress and scalar-flux (and, in the case of level 2.5 scheme, in the scalar-variance and scalar-covariance) equations. An alternative interpretation can be suggested, however. As discussed above, the use Eq. (76) amounts to multiplying the production terms in the truncated equations by a factor $1-\alpha_e$, where $\alpha_e = (de/dt + \mathcal{D}_e)/\mathcal{G}_e$ depends on time t and vertical coordinate x_3. Consider, for example, the buoyancy production term in the liquid water potential temperature flux equation (66),

$$-\left(1 - C_b^\theta\right) \tau_\epsilon \beta_3 \left\langle \theta_l' \theta_v' \right\rangle , \tag{80}$$

where C_b^θ is a constant that stems from a linear model of the buoyancy contribution to the pressure-scrambling term in the temperature-flux equation. Recall that the use of linear parameterizations of the pressure-scrambling terms is identified as one reason for the failure

of truncated second-order schemes. If Eq. (76) is utilized, the buoyancy production term in the temperature-flux equation becomes

$$-\left[1-\alpha_e\left(t,x_3\right)\right]\left(1-C_b^\theta\right)\tau_\epsilon\beta_3\left\langle\theta_l'\theta_v'\right\rangle=-\left[1-C_{b*}^\theta\left(t,x_3\right)\right]\tau_\epsilon\beta_3\left\langle\theta_l'\theta_v'\right\rangle, \tag{81}$$

where $C_{b*}^\theta=C_b^\theta+\alpha_e\left(1-C_b^\theta\right)$ is no longer a constant, but a function of t and x_3. Note that $C_{b*}^\theta=C_b^\theta$ if $\alpha_e=0$, and the original, non-regularized formulation is recovered. If $\alpha_e=1$, then $C_{b*}^\theta=1$, which effectively satisfies the two-component limit constraint of strongly anisotropic turbulence. As discussed in section 5.1, it is not possible to satisfy the TCL constraint within the framework of a linear model of the pressure-scrambling terms if the value of C_b^θ is chosen so that to satisfy the isotropic limit. If Eq. (76) is utilized to modify the truncated temperature-flux equation, both the isotropic and the TCL constraints can be satisfied. Then, the Helfand and Labraga regularization procedure can be viewed as being conceptually similar to the use of non-linear parameterizations of the pressure-scrambling effects.

To conclude this section, we note that the regularized expressions have been obtained for all components of the Reynolds stress and scalar fluxes, not only for $\langle u_3'u_1'\rangle$, $\langle u_3'u_2'\rangle$, $\langle u_3'\theta_l'\rangle$, and $\langle u_3'q_t'\rangle$. Those regularized formulations are not presented here.

10 Interaction with the Underlying Surface

In order to describe the interaction of the boundary-layer turbulence with the underlying surface, the surface fluxes of momentum, heat and moisture should be specified and the boundary conditions for the TKE, scalar variances and scalar covariance should be imposed. The surface fluxes are assumed to be provided by the host atmospheric model (e.g. COSMO or ICON). A consideration of the surface flux calculation procedures is beyond the scope of the present report.

For the TKE, scalar-variance and scalar-covariance, the following boundary conditions at the underlying surface are used in the TKESV-Bas scheme:

$$-C_e^d\tau_\epsilon e\frac{\partial e}{\partial x_3}=0, \tag{82}$$

$$-C_{\theta\theta}^d\tau_\epsilon e\frac{\partial\left\langle\theta_l'^2\right\rangle}{\partial x_3}=0,\qquad -C_{qq}^d\tau_\epsilon e\frac{\partial\left\langle q_t'^2\right\rangle}{\partial x_3}=0,\qquad -C_{\theta q}^d\tau_\epsilon e\frac{\partial\left\langle\theta_l'q_t'\right\rangle}{\partial x_3}=0. \tag{83}$$

Equations (82) and (83) state that the fluxes of TKE, scalar variances and scalar covariance at the underlying surface are zero. That is, e, $\left\langle\theta_l'^2\right\rangle$, $\left\langle q_t'^2\right\rangle$ and $\left\langle\theta_l'q_t'\right\rangle$ are height-constant within the layer immediately adjacent to the underlying surface. This is consistent with the surface-layer similarity (cf. the log-layer relationships given in Appendix A). Notice, however, that the surface-layer relationships (the Monin-Obukhov similarity theory) are applicable to continuous turbulence over a homogeneous surface, and it is, strictly speaking, incorrect to apply the surface-layer similarity relationships over heterogeneous surfaces. Then, the boundary conditions (82) and (83) become inaccurate if a tile approach is used to compute the grid-box mean surface fluxes.

Advanced Features

In order to develop the surface boundary conditions for the scalar variances and covariance that are consistent with the tiled surface schemes, we make use of the following triple

decomposition:

$$f = \langle \overline{f} \rangle + \overline{f}'' + f^s, \tag{84}$$

where f is a generic variable. The angle brackets denote the quantity averaged horizontally over a grid box of a host model. An overbar denotes a mean over a tile, and a double prime denotes a fluctuation of a tile mean quantity about a grid-box mean quantity. The superscript "s" denotes a sub-tile fluctuation. By definition, $\left\langle \overline{f}'' \right\rangle = 0$. To simplify the discussion, we take $\overline{f^s} = 0$, although this assumption is not necessary (cf. Mironov and Sullivan, 2016).

Using Eq. (84), we obtain the following expression for the triple-correlation of the vertical velocity, u_3, and the two scalars, θ_l and q_t:

$$\begin{aligned} \langle u_3' \theta_l' q_t' \rangle &= \left\langle \overline{\left(\overline{u_3}'' + u_3^s\right)\left(\overline{\theta_l}'' + \theta_l^s\right)\left(\overline{q_t}'' + q_t^s\right)} \right\rangle \\ &= \left\langle \overline{u_3}''\overline{\theta_l}''\overline{q_t}'' \right\rangle + \left\langle \overline{u_3}''\overline{\theta_l^s q_t^s}'' \right\rangle + \left\langle \overline{\theta_l}''\overline{u_3^s q_t^s}'' \right\rangle + \left\langle \overline{q_t}''\overline{u_3^s \theta_l^s}'' \right\rangle + \langle \overline{u_3^s \theta_l^s q_t^s} \rangle . \end{aligned} \tag{85}$$

The first two terms on the r.h.s. of Eq. (85) are zero at the surface because of zero vertical velocity $\overline{u_3}$. The last term on the r.h.s. cannot be estimated unless a high-order closure model is applied to individual tiles. This is usually not the case. The third and the fourth terms on the r.h.s. of Eq. (85) are zero if the grid box of the host model is horizontally homogeneous. If the grid box is heterogeneous, the temperature $\overline{\theta_l}$ and humidity $\overline{q_t}$ differ between the tiles and so do the temperature and humidity fluxes, $\overline{u_3^s \theta_l^s}$ and $\overline{u_3^s q_t^s}$. Then, the third-order velocity-scalar covariance $\langle u_3' \theta_l' q_t' \rangle$, i.e. the flux of temperature-humidity covariance, is generally non-zero at the surface. The expressions for $\langle u_3' \theta_l'^2 \rangle$ and $\langle u_3' q_t'^2 \rangle$ are obtained from Eq. (85) by replacing q_t with θ_l and θ_l with q_t, respectively.

Notice a close analogy between the above analysis and the analysis of Mironov and Sullivan (2016). These authors used large-eddy simulation to explore the second-moment budgets in the stably stratified planetary boundary layer (PBL) over thermally homogeneous and thermally heterogeneous surfaces. Importantly, the LES-based second-moment budgets were estimated with due regard for the sub-grid scale contributions. Taking account of the SGS contributions revealed that the third-order velocity-scalar covariances are non-zero at the heterogeneous surfaces and are crucial for the maintenance of second-moment budgets in the heterogeneous PBL. That finding helped explain the enhanced vertical mixing in the stably-stratified PBL over thermally heterogeneous surfaces.

Based upon the above considerations, we propose the following surface boundary conditions for the scalar variances and scalar covariance that are consistent with the tiled surface schemes:

$$\begin{aligned} -C_{\theta\theta}^d \tau_\epsilon e \frac{\partial \langle \theta_l'^2 \rangle}{\partial x_3} = 2 \left\langle \overline{\theta_l}''\overline{u_3^s \theta_l^s}'' \right\rangle , \qquad -C_{qq}^d \tau_\epsilon e \frac{\partial \langle q_t'^2 \rangle}{\partial x_3} = 2 \left\langle \overline{q_t}''\overline{u_3^s q_t^s}'' \right\rangle , \\ -C_{\theta q}^d \tau_\epsilon e \frac{\partial \langle \theta_l' q_t' \rangle}{\partial x_3} = \left\langle \overline{\theta_l}''\overline{u_3^s q_t^s}'' \right\rangle + \left\langle \overline{q_t}''\overline{u_3^s \theta_l^s}'' \right\rangle . \end{aligned} \tag{86}$$

Note that the surface boundary condition (82) for the TKE remains in force, even though the tile approach may be used. This is readily shown by setting $\theta_l = u_i$ and $q_t = u_i$ in Eq. (85) (summation over repeated indices) and invoking the no-slip boundary condition for the flow velocity, $\overline{u_i} = 0$, at the underlying surface. Note that the term $\langle \overline{u_3^s u_i^s u_i^s} \rangle$ is not necessarily zero at the surface. It cannot be estimated, however, unless a high-order closure model is applied to individual tiles.

The surface boundary conditions given by Eqs. (86) provide an intimate coupling of the scalar variances and covariance with many other quantities characterizing the atmosphere and the soil. In order to illustrate this coupling, consider the moisture and heat balance equations at the underlying surface for individual tiles. The moisture balance equation reads

$$\overline{PP} + \rho\overline{u_3^s q_t^s} = \overline{G_q}, \tag{87}$$

where G_q is the ground moisture flux at the surface, and PP denotes the sum of all forms of precipitation, including (relatively slow) sedimentation of water droplets and ice crystals. Subtracting from Eq. (87) its horizontal mean, multiplying the result with $\overline{q_t}''$ and averaging horizontally, we obtain

$$\left\langle \overline{q_t}''\overline{u_3^s q_t^s}'' \right\rangle = \rho^{-1}\left[\left\langle \overline{q_t}''\overline{G_q}'' \right\rangle - \left\langle \overline{q_t}''\overline{PP}'' \right\rangle\right]. \tag{88}$$

The first term in brackets on the r.h.s. of Eq. (88) is generally non-zero since over heterogeneous surfaces both the total water content and the ground moisture flux vary between the tiles and are likely correlated. There is no good reason to assume that rain, snow, or hail falls differently onto some tiles than onto the others. However, if PP includes sedimentation of water droplets and ice crystals, then the difference between the tiles may be substantial and the covariance $\left\langle \overline{q_t}''\overline{PP}'' \right\rangle$ may appear to be different from zero. For example, if there is fog over some tiles but not over the other tiles, $\overline{PP}'' \neq 0$. Rain or snow falling through the fog layers may amplify the influence of fog via seeder-feeder effect.

Consideration of the heat balance of the underlying surface yields the following expression:

$$\left\langle \overline{\theta_l}''\overline{w^s\theta_l^s}'' \right\rangle =$$
$$(\rho c_p)^{-1}\left[\left\langle \overline{\theta_l}''\overline{G_\theta}'' \right\rangle - \left\langle \overline{\theta_l}''\overline{R_s}'' \right\rangle - \left\langle \overline{\theta_l}''\overline{R_l}'' \right\rangle - L_v\left(\left\langle \overline{\theta_l}''\overline{G_q}'' \right\rangle - \left\langle \overline{\theta_l}''\overline{PP}'' \right\rangle\right)\right]. \tag{89}$$

Here, G_θ is the ground heat flux at the surface, R_s is the solar radiation balance at the surface, and R_l is the net long-wave radiation at the surface. All terms on the r.h.s. of Eq. (89) are generally non-zero. The solar radiation balance varies between the tiles because of the difference in the tile albedo, and the long-wave radiation balance varies because of the difference in the tile temperature.

For the flux of temperature-humidity covariance, the following expression holds:

$$\left\langle \overline{\theta_l}''\overline{w^s q_t^s}'' \right\rangle + \left\langle \overline{q_t}''\overline{w^s\theta_l^s}'' \right\rangle = \rho^{-1}\left[\left\langle \overline{\theta_l}''\overline{G_q}'' \right\rangle - \left\langle \overline{\theta_l}''\overline{PP}'' \right\rangle\right]$$
$$(\rho c_p)^{-1}\left[\left\langle \overline{q_t}''\overline{G_\theta}'' \right\rangle - \left\langle \overline{q_t}''\overline{R_s}'' \right\rangle - \left\langle \overline{q_t}''\overline{R_l}'' \right\rangle - L_v\left(\left\langle \overline{q_t}''\overline{G_q}'' \right\rangle - \left\langle \overline{q_t}''\overline{PP}'' \right\rangle\right)\right], \tag{90}$$

where all terms on the r.h.s. of Eq. (90) are generally non-zero over heterogeneous surfaces. If ice is taken into account, a generalized formulation of q_t should be used, θ_l should be replaced with the total water potential temperature, and L_c should be replaced with an effective heat of vapourization-sublimation (see sections 2 and 7).

11 Equation for Scalar Skewness

In this section, a transport equation for the skewness (triple correlation) of the scalar variable s is developed. The s-skewness is required to utilize the double-Gaussian statistical cloud scheme proposed by Naumann et al. (2013) and is only used within the framework of the

extended version of the TKESV scheme. Thus this section discusses ***Advanced Features*** that are not used within the framework of TKESV-Bas.

Recall that the s variable defined as $s = \mathcal{Q}^{-1}\left(\langle q_t\rangle - \langle q_{sl}\rangle + q_t' - \mathcal{P}\theta_l'\right)$ accounts for the combined effect of humidity and temperature fluctuations, and is a measure of local oversaturation/undersaturation (see section 7 for details). A positive s is merely a local value of q_l computed with respect to the linearized saturation specific humidity curve. In order to determine the s skewness, $S_s \equiv \langle s'^3\rangle / \langle s'^2\rangle^{3/2}$, the variance of s, $\langle s'^2\rangle$, and its triple correlation, $\langle s'^3\rangle$, should be computed. The variance of s is given by

$$\langle s'^2\rangle = \mathcal{Q}^{-2}\left(\langle q_t'^2\rangle - 2\mathcal{P}\langle q_t'\theta_l'\rangle + \mathcal{P}^2\langle \theta_l'^2\rangle\right). \tag{91}$$

It can be computed in a straightforward way using the values of $\langle q_t'^2\rangle$, $\langle q_t'\theta_l'\rangle$ and $\langle \theta_l'^2\rangle$ determined within the framework of the TKESV scheme from the scalar (co)variance equations. The triple correlation of s is given by

$$\langle s'^3\rangle = \mathcal{Q}^{-3}\left(\langle q_t'^3\rangle - 3\mathcal{P}\langle q_t'^2\theta_l'\rangle + 3\mathcal{P}^2\langle q_t'\theta_l'^2\rangle - \mathcal{P}^3\langle \theta_l'^3\rangle\right). \tag{92}$$

As Eq. (92) suggests, the determination of $\langle s'^3\rangle$ requires knowledge of the four third-order scalar correlations. These correlations can be computed from their transport equations, where closure assumptions are required for a number of terms (third-order and fourth-order velocity-scalar correlations and molecular destruction terms). This would make the TKESV scheme unduly complex and computationally expensive. We therefore take a different, more simple approach. We combine the transport equations for $\langle q_t'^3\rangle$, $\langle q_t'^2\theta_l'\rangle$, $\langle q_t'\theta_l'^2\rangle$ and $\langle \theta_l'^3\rangle$ with due regard for Eq. (92) to formulate a single transport equation for $\langle s'^3\rangle$. To this end, we neglect the derivatives of $\mathcal{P}$ and $\mathcal{Q}$ with respect to time and space. Although an exact equation for the s-variable triple correlation can easily be derived, this is not required. The exact equation for $\langle s'^3\rangle$, including time and space derivatives of $\mathcal{P}$ and $\mathcal{Q}$, is cumbersome. Since $\mathcal{P}$ and $\mathcal{Q}$ depend on the grid-box mean quantities only, the uncertainties associated with neglect of the derivatives of $\mathcal{P}$ and $\mathcal{Q}$ are typically small unless the mean quantities change faster in space and time than higher-order moments (an unlikely situation). Note also that the skewness of s only serves to help determine the fractional cloud cover and its effect on the buoyancy production of the Reynolds stress and scalar fluxes. Then, $\langle s'^3\rangle$ is in a sense an auxiliary quantity, and it is legitimate to keep the $\langle s'^3\rangle$ equation reasonably simple at the expense of slightly reduced accuracy.

Combining transport equations for the four third-order moments on the r.h.s. of Eq. (92) and neglecting the derivatives of $\mathcal{P}$ and $\mathcal{Q}$ with respect to t and x_i, we obtain the following equation for the s-variable triple correlation:

$$\frac{1}{3}\left(\frac{\partial}{\partial t} + \langle u_i\rangle\frac{\partial}{\partial x_i}\right)\langle s'^3\rangle = -\langle u_i's'^2\rangle\frac{\partial\langle s\rangle}{\partial x_i} + \langle s'^2\rangle\frac{\partial\langle u_i's'\rangle}{\partial x_i} - \frac{1}{3}\frac{\partial\langle u_i's'^3\rangle}{\partial x_i} - \epsilon_{s3}, \tag{93}$$

where $\langle s\rangle = \mathcal{Q}^{-1}\left(\langle q_t\rangle - \langle q_{sl}\rangle\right)$. The terms on the r.h.s. of Eq. (93) represent production/destruction due to the mean scalar gradient and due to the scalar-flux divergence, fourth-order turbulent transport, and molecular destruction (dissipation), respectively. In order to close Eq. (93), parameterizations of the third-order, $\langle u_i's'^2\rangle$, and fourth-order, $\langle u_i's'^3\rangle$, velocity-scalar correlations and of the dissipation term, ϵ_{s3}, should be developed.

The dissipation rate of $\langle s'^3\rangle$ is parameterized through the following algebraic expression:

$$\epsilon_{s3} = \frac{\langle s'^3\rangle}{3R_{\tau s}\tau_\epsilon}, \tag{94}$$

where $R_{\tau s} = \tau_{s3}/\tau_\epsilon = \langle s'^3\rangle\,\epsilon/\left(3e\epsilon_{s3}\right)$ is the ratio of the $\langle s'^3\rangle$ dissipation time scale to the TKE dissipation time scale.

We adopt the following parameterization of the third-order velocity-scalar correlation:

$$\left\langle u_i' s'^2 \right\rangle = -C_{us2}^d \tau_\epsilon e \frac{\partial \left\langle s'^2 \right\rangle}{\partial x_i} + S_s \left\langle s'^2 \right\rangle^{1/2} \left\langle u_i' s' \right\rangle, \tag{95}$$

where C_{us2}^d is a dimensionless constant. In the case of nearly isotropic turbulence, the skewness S_s is small and Eq. (95) reduces to the down-gradient diffusion formulation. In the limiting case of strongly skewed PDF of s, the second term on the r.h.s of Eq. (95) becomes dominant. Then, Eq. (95) reduces to the form suggested by the top-hat representation of fluctuating quantities that is fundamental to the mass-flux approach widely used to parameterize cumulus convection in numerical models of the atmosphere. The simplest top-hat mass-flux model is formulated in terms of fractional areas of updraughts, a_u, and downdraughts, $a_d = 1 - a_u$. Alternatively, a PDF can be used which consists of only two Dirac delta functions, i.e. the probabilities of motions to be either updraughts or downdraughts are P_u and P_d, respectively, and $P_u + P_d = 1$. The second term on the r.h.s. of Eq. (95) is basically the mass-flux formulation recast in terms of the quantities used within the second-order closure framework (see Mironov, 2009, for a detailed discussion of the analogies between the mass-flux and the ensemble-mean second-order modelling frameworks). A skewness-dependent parameterization for the flux of potential-temperature variance [given by the second term on the r.h.s. of Eq. (95), where s is replaced with θ] was formulated in Mironov et al. (1999), Abdella and McFarlane (1999) and Abdella and Petersen (2000). An interpolation formula that incorporates both the down-gradient and the skewness-dependent terms was presented in Gryanik and Hartmann (2002). As different from previous studies, we apply these parameterization ideas to the scalar quantity s that accounts for the combined effect of temperature and humidity fluctuations.

The following parameterization of the fourth-order velocity-scalar correlation is adopted:

$$\left\langle u_i' s'^3 \right\rangle = 3 \left(1 + \frac{1}{3} S_s^2 \right) \left\langle s'^2 \right\rangle \left\langle u_i' s' \right\rangle - C_{us3}^d \tau_\epsilon e \frac{\partial \left\langle s'^3 \right\rangle}{\partial x_i}, \tag{96}$$

where C_{us3}^d is a dimensionless constant. The first term on the r.h.s. of Eq. (96) represents a generalization of the Millionshchikov hypothesis formulated in Gryanik and Hartmann (2002) and Gryanik et al. (2005) for convective boundary-layer turbulence. In the case of isotropic turbulence, S_s vanishes and the first term on the r.h.s. reduces to the classical Millionshchikov (1941) formulation. It states that the fourth-order moments can be considered as Gaussian, even though the third-order moments are nonzero. In the limiting case of very skewed turbulence, S_s is large and the first term on the r.h.s. of Eq. (96) takes on the form suggested by the top-hat mass-flux approach (cf. the formulation of $\left\langle u_i' s'^2 \right\rangle$). The expression $3 \left(1 + \frac{1}{3} S_s^2 \right) = 3 + S_s^2$ amounts to the simplest linear interpolation between the two limiting cases, where dimensionless coefficients 3 and 1 are chosen so that the limiting cases are satisfied exactly. The down-gradient diffusion term, the last term on the r.h.s. of Eq. (96), can be viewed as the smoothing operator that is added to the parameterization of the fourth-order turbulent transport term for numerical reasons. The use of the diffusion term can also be justified on physical grounds. To this end, one needs to consider the transport equation for the fourth-order term $\left\langle u_i' s'^3 \right\rangle$ and invoke a number of simplifying assumptions (e.g. use the Rotta-type closure for the pressure-scrambling terms and neglect turbulence anisotropy in the formulations of the mean-gradient terms).

Substituting Eqs. (94), (95) and (96) into Eq. (93) and using the boundary-layer approxi-

mation, we obtain the following equation for the s-variable triple correlation:

$$\frac{1}{3}\frac{\partial\left\langle s'^3\right\rangle}{\partial t} = -\left(S_s\left\langle s'^2\right\rangle^{1/2}\left\langle u_3's'\right\rangle - C^d_{us2}\tau_\epsilon e\frac{\partial\left\langle s'^2\right\rangle}{\partial x_3}\right)\frac{\partial\left\langle s\right\rangle}{\partial x_3} - \left\langle u_3's'\right\rangle\frac{\partial\left\langle s'^2\right\rangle}{\partial x_3}$$
$$+\frac{1}{3}\frac{\partial}{\partial x_3}\left(C^d_{us3}\tau_\epsilon e\frac{\partial\left\langle s'^3\right\rangle}{\partial x_3} - S_s^2\left\langle s'^2\right\rangle\left\langle u_3's'\right\rangle\right) - \frac{\left\langle s'^3\right\rangle}{3R_{\tau s}\tau_\epsilon}. \tag{97}$$

The following (tentative) estimates of disposable parameters are utilized: $C^d_{us2} = 0.1$, $C^d_{us3} = 0.1$, and $R_{\tau s} = 0.1$.

The surface boundary condition for $\left\langle s'^3\right\rangle$ should be specified that is applicable over both homogeneous and heterogeneous surfaces and is consistent with the tiled surface schemes. To this end, we make use of the triple decomposition (84) and express the fourth-order velocity-scalar covariance as follows:

$$\begin{aligned}\left\langle u_3's'^3\right\rangle &= \left\langle\overline{\left(\overline{u_3}'' + u_3^s\right)\left(\overline{s}'' + s^s\right)^3}\right\rangle \\ &= \left\langle\overline{u_3}''\overline{s}''^3\right\rangle + 3\left\langle\overline{u_3}''\overline{s}''\overline{s^{s2}}\right\rangle + \left\langle\overline{u_3}''\overline{s^{s3}}''\right\rangle \\ &+ 3\left\langle\overline{s}''^2\right\rangle\left\langle\overline{u_3^s s^s}\right\rangle + 3\left\langle\overline{s}''^2\overline{u_3^s s^s}''\right\rangle + 3\left\langle\overline{s}''\overline{u_3^s s^{s2}}''\right\rangle + \left\langle\overline{u_3^s s^{s3}}\right\rangle.\end{aligned} \tag{98}$$

The first three terms on the r.h.s. of Eq. (98) are zero at the surface because of zero vertical velocity $\overline{u_3}$. The last two terms on the r.h.s. cannot be estimated unless a high-order closure model is applied to individual tiles. The remaining two terms are generally non-zero over heterogeneous surfaces.

Using Eq. (98), we propose the following surface boundary condition for $\left\langle s'^3\right\rangle$:

$$3\left(1+\frac{1}{3}S_s^2\right)\left\langle s'^2\right\rangle\left\langle u_3's'\right\rangle - C^d_{us3}\tau_\epsilon e\frac{\partial\left\langle s'^3\right\rangle}{\partial x_3} = 3\left\langle\overline{s}''^2\right\rangle\left\langle\overline{u_3^s s^s}\right\rangle + 3\left\langle\overline{s}''^2\overline{u_3^s s^s}''\right\rangle. \tag{99}$$

Note that Eq. (99) represents the so-called Robin boundary condition, also referred to as the impedance boundary condition, or convective boundary condition. It is a weighted combination of Dirichlet and Neumann boundary conditions that relates the quantity in question ($\left\langle s'^3\right\rangle$ in our case) and its derivative normal to the domain boundary.

12 Conclusions

A turbulence kinetic energy – scalar variance (TKESV) turbulence parameterization scheme is developed. The scheme is formulated in terms of two scalars that are approximately conserved for phase changes in the absence of precipitation. These are the total water specific humidity and the liquid water potential temperature. The TKESV scheme carries prognostic transport equations (including the time-rate-of-change and the third-order turbulent transport terms) for the TKE, for the variances of scalar quantities, and for the scalar covariance. The other second-order moments, namely, the Reynolds stress and the scalar fluxes, are determined through the diagnostic algebraic expressions obtained by neglecting the time-rate-of-change and the triple correlations terms in the respective transport equations.

The focus of the present report is on the baseline version of the TKESV scheme (TKESV-Bas). TKESV-Bas is based on the linear (in the second-order moments involved) parameterizations of the pressure-scrambling terms in the Reynolds-stress and scalar-flux equations, the isotropic down-gradient parameterizations of the third-order transport terms in the TKE

and scalar (co)variance equations, and the algebraic interpolation formula for the turbulence length scale that incorporates a correction term due to stable density stratification. The various time scales, namely, the dissipation time scales in the TKE and the scalar (co)variance equations and the return-to-isotropy time scales in the Reynolds-stress and scalar-flux equations, are set proportional to each other and are expressed in terms of turbulence length scale and the TKE. The simplified boundary conditions for the scalar variances and covariance at the underlying surface are used that do not account for the surface heterogeneity within a grid box of a host atmospheric model. The effect of latent heat release/consumption on the buoyancy production/destruction of the Reynolds stress (including half of its trace, the TKE) and of the scalar fluxes is taken into account through the use of a statistical cloud scheme. The cloud scheme makes use of a combination of Gaussian and exponential PDFs of linearized saturation deficit/excess (s variable). The exponential PDF is used at strong grid-box mean undersaturation and is designed to account, in a rather approximate way, for the shallow cumulus regime. In that regime, mixing is known to be dominated by convective plumes although the fractional cloud cover is typically low. The so-called stability functions that appear in the algebraic formulations for the Reynolds stress and scalar fluxes are considered in much detail. The stability functions resulting from the truncated Reynolds-stress and scalar-flux equations (where the third-order and the time-rate-of-change terms are neglected) with the linear parameterizations of the pressure-scrambling terms are ill-behaved over a certain range of governing parameters (e.g. mean velocity shear and mean buoyancy gradient). Using plausible physical arguments, regularized stability functions are developed that are well-behaved over their entire parameter space and cause no pathological behaviour of the Reynolds stress and scalar fluxes.

It is the baseline version of the TKESV scheme in the boundary-layer approximation (i.e. the one-dimensional TKESV-Bas) that is intended for use in NWP models ICON and COSMO in the near future. In the medium-term prospective, an extended version of the scheme (TKESV-Ext) can be used. TKESV-Ext incorporates a number of advanced features discussed in the respective sections of the present report. These include improved formulations of the pressure-scrambling terms and of the third-order transport terms, non-local formulation of the turbulence length scale, lower boundary conditions for the scalar (co)variances that account for the surface heterogeneity and are consistent with the tile approach to compute surface fluxes, allowance for cloud ice through the use of the ice-liquid water potential temperature, and a statistical cloud scheme capable of describing cumulus regimes. The utilization of an advanced statistical cloud scheme, e.g. the scheme proposed by Naumann et al. (2013), requires knowledge of the scalar skewness. A prognostic transport equation for the skewness (triple correlation) of the s variable that accounts for the combined effect of humidity and temperature fluctuations is derived in section 11.

The TKESV-Bas scheme is implemented into the NWP models ICON and COSMO. Testing of TKESV-Bas is underway. Details of the implementation and results from numerical experiments will be reported in subsequent publications. Results of testing of an earlier version of the TKESV scheme through off-line single-column numerical experiments and through parallel experiments with the full-fledged COSMO model (including the entire data assimilation cycle) are reported in Machulskaya and Mironov (2013).

Acknowledgments.

The authors are grateful to Vittorio Canuto, Evgeni Fedorovich, Jean-Francois Geleyn, Vincent Larson, Ann Kristin Naumann, Matthias Raschendorfer, Bodo Ritter, Axel Seifert, and Peter Sullivan for useful discussions.

13 Appendices

Appendix A. Modelling Pressure-Scrambling Terms in the Reynolds-Stress and Scalar-Flux Equations

In this section, we demonstrate how models (parameterizations) of the pressure-scrambling terms in the Reynolds-stress and the scalar-flux equations are developed. By way of illustration, the formulation for the potential temperature θ is considered. Other scalar quantities, e.g. θ_l and q_t, are treated in the same way. We restrict our consideration to the parameterizations of Π_{ij} and $\Pi_{\theta i}$ which are linear in terms of the second-order moments of fluctuating fields. Some non-linear parameterizations of the pressure-scrambling terms are briefly discussed in section 5.1.

Decomposition

Taking the divergence of the transport equation for the fluctuating velocity, a Poisson equation for the fluctuating pressure is obtained. It reads

$$\frac{\partial^2 p'}{\partial x_k^2} = -\frac{\partial^2}{\partial x_k \partial x_l}\left(u_k' u_l' - \langle u_k' u_l' \rangle\right) - \beta_k \frac{\partial \theta'}{\partial x_k} - 2\epsilon_{kml}\Omega_m \frac{\partial u_l'}{\partial x_k} - 2\frac{\partial \langle u_k \rangle}{\partial x_l}\frac{\partial u_l'}{\partial x_k}. \tag{A.1}$$

The fluctuating pressure is decomposed into the contributions due to the non-linear turbulence interactions (denoted by the subscript t), buoyancy (subscript b), the Coriolis effects (subscript c), and mean-velocity shear (subscript s),

$$p' = p_t' + p_b' + p_c' + p_s', \tag{A.2}$$

which are found by solving the following set of Poisson equations:

$$\frac{\partial^2 p_t'}{\partial x_k^2} = -\frac{\partial^2}{\partial x_k \partial x_l}\left(u_k' u_l' - \langle u_k' u_l' \rangle\right), \qquad \frac{\partial^2 p_b'}{\partial x_k^2} = -\beta_k \frac{\partial \theta'}{\partial x_k},$$

$$\frac{\partial^2 p_c'}{\partial x_k^2} = -2\epsilon_{kml}\Omega_m \frac{\partial u_l'}{\partial x_k}, \qquad \frac{\partial^2 p_s'}{\partial x_k^2} = -2\frac{\partial \langle u_k \rangle}{\partial x_l}\frac{\partial u_l'}{\partial x_k}. \tag{A.3}$$

The (formal) solutions to Eqs. (A.3) read (Chou, 1945; Ristorcelli et al., 1995; Shih, 1996)

$$p_t = \frac{1}{4\pi}\int_{Vol}\left(\frac{\partial^2 u_k'' u_l''}{\partial x_k'' \partial x_l''} - \frac{\partial^2 \langle u_k u_l \rangle''}{\partial x_k'' \partial x_l''}\right)\frac{dVol}{|\mathbf{x}-\mathbf{x}''|}, \qquad p_b = \frac{1}{4\pi}\int_{Vol}\beta_k''\frac{\partial \theta''}{\partial x_k''}\frac{dVol}{|\mathbf{x}-\mathbf{x}''|},$$

$$p_c = \frac{1}{4\pi}\int_{Vol} 2\epsilon_{kml}\Omega_m \frac{\partial u_l''}{\partial x_k''}\frac{dVol}{|\mathbf{x}-\mathbf{x}''|}, \qquad p_s = \frac{1}{4\pi}\int_{Vol} 2\frac{\partial U_k''}{\partial x_l''}\frac{\partial u_l''}{\partial x_k''}\frac{dVol}{|\mathbf{x}-\mathbf{x}''|}, \tag{A.4}$$

where double-primed quantities are evaluated as functions of the integration variable. Small letters denote turbulent fluctuations, and capital letters denote mean quantities (this notation is used temporarily to avoid confusion between primed and double-primed quantities).

Using (A.2), the pressure-scrambling terms Π_{ij} and $\Pi_{\theta i}$ are decomposed into the contributions due to the non-linear turbulence interactions (superscript t), buoyancy (superscript b), the Coriolis effects (superscript c), and mean-velocity shear (superscript s),

$$\Pi_{ij} = \Pi_{ij}^t + \Pi_{ij}^b + \Pi_{ij}^c + \Pi_{ij}^s, \qquad \Pi_{\theta i} = \Pi_{\theta i}^t + \Pi_{\theta i}^b + \Pi_{\theta i}^c + \Pi_{\theta i}^s. \tag{A.5}$$

With due regard for Eqs. (A.4) these contributions are given by

$$\Pi_{ij}^{t} = -\left\langle p_t \left(\frac{\partial u_i}{\partial x_j} + \frac{\partial u_j}{\partial x_i} \right) \right\rangle = \frac{1}{4\pi} \int_{Vol} \left(\frac{\partial^3 \langle u_k'' u_l'' u_i \rangle}{\partial x_k'' \partial x_l'' \partial x_j''} + \frac{\partial^3 \langle u_k'' u_l'' u_j \rangle}{\partial x_k'' \partial x_l'' \partial x_i''} \right) \frac{dVol}{|\mathbf{x} - \mathbf{x}''|},$$

$$\Pi_{ij}^{b} = -\left\langle p_b \left(\frac{\partial u_i}{\partial x_j} + \frac{\partial u_j}{\partial x_i} \right) \right\rangle = \frac{1}{4\pi} \int_{Vol} \beta_k'' \left(\frac{\partial^2 \langle \theta'' u_i \rangle}{\partial x_k'' \partial x_j''} + \frac{\partial^2 \langle \theta'' u_j \rangle}{\partial x_k'' \partial x_i''} \right) \frac{dVol}{|\mathbf{x} - \mathbf{x}''|},$$

$$\Pi_{ij}^{c} = -\left\langle p_c \left(\frac{\partial u_i}{\partial x_j} + \frac{\partial u_j}{\partial x_i} \right) \right\rangle = \frac{1}{4\pi} \int_{Vol} 2\epsilon_{kml}\Omega_m \left(\frac{\partial^2 \langle u_l'' u_i \rangle}{\partial x_k'' \partial x_j''} + \frac{\partial^2 \langle u_l'' u_j \rangle}{\partial x_k'' \partial x_i''} \right) \frac{dVol}{|\mathbf{x} - \mathbf{x}''|},$$

$$\Pi_{ij}^{s} = -\left\langle p_s \left(\frac{\partial u_i}{\partial x_j} + \frac{\partial u_j}{\partial x_i} \right) \right\rangle = \frac{1}{4\pi} \int_{Vol} 2\frac{\partial U_k''}{\partial x_l''} \left(\frac{\partial^2 \langle u_l'' u_i \rangle}{\partial x_k'' \partial x_j''} + \frac{\partial^2 \langle u_l'' u_j \rangle}{\partial x_k'' \partial x_i''} \right) \frac{dVol}{|\mathbf{x} - \mathbf{x}''|}, \quad \text{(A.6)}$$

and

$$\Pi_{\theta i}^{t} = \left\langle \theta \frac{\partial p_t}{\partial x_i} \right\rangle = \frac{1}{4\pi} \int_{Vol} \frac{\partial^3 \langle u_k'' u_l'' \theta \rangle}{\partial x_k'' \partial x_l'' \partial x_i''} \frac{dVol}{|\mathbf{x} - \mathbf{x}''|},$$

$$\Pi_{\theta i}^{b} = \left\langle \theta \frac{\partial p_b}{\partial x_i} \right\rangle = \frac{1}{4\pi} \int_{Vol} \beta_k'' \frac{\partial^2 \langle \theta'' \theta \rangle}{\partial x_k'' \partial x_i''} \frac{dVol}{|\mathbf{x} - \mathbf{x}''|},$$

$$\Pi_{\theta i}^{c} = \left\langle \theta \frac{\partial p_c}{\partial x_i} \right\rangle = \frac{1}{4\pi} \int_{Vol} 2\epsilon_{kml}\Omega_m \frac{\partial^2 \langle u_l'' \theta \rangle}{\partial x_k'' \partial x_i''} \frac{dVol}{|\mathbf{x} - \mathbf{x}''|},$$

$$\Pi_{\theta i}^{s} = \left\langle \theta \frac{\partial p_s}{\partial x_i} \right\rangle = \frac{1}{4\pi} \int_{Vol} 2\frac{\partial U_k''}{\partial x_l''} \frac{\partial^2 \langle u_l'' \theta \rangle}{\partial x_k'' \partial x_i''} \frac{dVol}{|\mathbf{x} - \mathbf{x}''|}, \quad \text{(A.7)}$$

where quantities without double primes are evaluated at the point where Π_{ij} and $\Pi_{\theta i}$ are determined. The Π_{ij}^{t} and $\Pi_{\theta i}^{t}$ contributions are often referred to as slow parts and Π_{ij}^{b}, Π_{ij}^{c}, Π_{ij}^{s}, $\Pi_{\theta i}^{b}$, $\Pi_{\theta i}^{c}$ and $\Pi_{\theta i}^{s}$ as rapid parts, respectively, of the pressure-scrambling terms.

The integrals in Eqs. (A.6) and (A.7) are taken over the entire flow domain. In practice, however, the two-point correlations are assumed to diminish rapidly with distance from the point where the pressure terms are evaluated. Then, the volume of integration is reduced to a small region in the immediate vicinity of that point, and Π_{ij} and $\Pi_{\theta i}$ are modelled in terms of local quantities.

Slow Parts of Π_{ij} and $\Pi_{\theta i}$

We utilize the return-to-isotropy parameterizations (Rotta, 1951; Monin, 1965) for the slow (return-to-isotropy) contributions to the pressure-scrambling terms. They read

$$\Pi_{ij}^{t} = C_t^u \frac{\langle u_i u_j \rangle - \frac{2}{3}\delta_{ij} e}{\tau_{ru}} = C_t^u \frac{a_{ij}}{\tau_{ru}}, \qquad \Pi_{\theta i}^{t} = C_t^\theta \frac{\langle u_i \theta \rangle}{\tau_{r\theta}}, \quad \text{(A.8)}$$

where τ_{ru} and $\tau_{r\theta}$ are the relaxation return-to-isotropy time scales, and C_t^u and C_t^θ are dimensionless constants.

It is customary in geophysical and engineering applications to take the relaxation time scales τ_{ru} and $\tau_{r\theta}$ to be proportional to the TKE dissipation time scale $\tau_\epsilon = e/\epsilon$, that is $\tau_{ru} = \tau_{r\theta} = \tau_\epsilon$, where dimensionless proportionality constants are set to one as they always occur in combination with the other constants. Estimates of C_t^u and C_t^θ vary over a wide range. Values of C_t^u from 1 to 3 and of C_t^θ from 2 to 10 have been proposed (see e.g. Launder et al., 1975; Zeman and Tennekes, 1975; Zeman and Lumley, 1976; Dakos and Gibson, 1987; Speziale et al., 1991; Kenjereš and Hanjalić, 1995; Hanjalić et al., 1996; Craft et al., 1996; Dol et al., 1997; Hanjalić, 1999; Girimaji, 2000; Mironov, 2001; Hanjalić, 2002; Umlauf and Burchard, 2005). We adopt the estimates of $C_t^u = 1.8$ and $C_t^\theta = 5.0$, keeping in mind that some tuning may appear to be necessary. In particular, the estimate of $C_t^\theta = 3.0$ is found by a number of authors to be more appropriate for (mostly) buoyancy-driven flows.

Buoyancy Contributions to Π_{ij} and $\Pi_{\theta i}$

The formal expressions for the buoyancy, the Coriolis and the mean-velocity shear contributions (the so-called rapid contributions) to the pressure-scrambling terms are given by the second, the third and the fourth members of Eqs. (A.6) and (A.7), respectively. Assuming that the mean fields are approximately homogeneous over a distance of the order of the integral turbulence length scale, β_k can be taken outside the integrals (the same is true for $2\partial U_k/\partial x_l$ in the expressions for the mean-velocity shear contributions to the pressure-scrambling terms considered below). Then, the buoyancy contributions to the pressure-scrambling terms can be represented in the form (see e.g. Shih, 1996)

$$\Pi_{ij}^b = -\beta_k \left(X_{kij}^b + X_{kji}^b \right), \qquad \Pi_{\theta i}^b = -\beta_k Y_{ki}^b. \tag{A.9}$$

where, in view of the second members of Eqs. (A.6) and (A.7),

$$X_{kij}^b = -\frac{1}{4\pi} \int_{Vol} \frac{\partial^2 \langle \theta'' u_i \rangle}{\partial x_k'' \partial x_j''} \frac{dVol}{|\mathbf{x} - \mathbf{x}''|}, \qquad Y_{ki}^b = -\frac{1}{4\pi} \int_{Vol} \frac{\partial^2 \langle \theta'' \theta \rangle}{\partial x_k'' \partial x_i''} \frac{dVol}{|\mathbf{x} - \mathbf{x}''|}. \tag{A.10}$$

The tensors X_{kij} and Y_{ki} satisfy the following constraints:

$$\text{symmetry} \qquad X_{kij}^b = X_{jik}^b, \quad Y_{ki}^b = Y_{ik}^b, \tag{A.11}$$

$$\text{continuity} \qquad X_{kii}^b = 0, \tag{A.12}$$

$$\text{normalization} \qquad X_{kik}^b = \langle u_i \theta \rangle, \quad Y_{kk}^b = \langle \theta^2 \rangle. \tag{A.13}$$

Within the limits of linear approximations (in the second-order moments of fluctuating fields, i.e. in $\langle u_i u_j \rangle$, $\langle u_i \theta \rangle$ and $\langle \theta^2 \rangle$), the most general forms of X_{kij}^b and Y_{ki}^b that satisfy the symmetry constraints (A.11) are the following tensor polynomials:

$$X_{kij}^b = \alpha_1 \delta_{kj} \langle u_i \theta \rangle + \alpha_2 \left(\delta_{ki} \langle u_j \theta \rangle + \delta_{ji} \langle u_k \theta \rangle \right), \qquad Y_{ki}^b = \gamma_1 \delta_{ki} \langle \theta^2 \rangle. \tag{A.14}$$

Satisfying the continuity (A.12) and the normalization (A.13) constraints, we obtain $\alpha_1 = 2/5$, $\alpha_2 = -1/10$ and $\gamma_1 = 1/3$. With these estimates, Eqs. (A.9) and (A.14) yield the following formulations:

$$\Pi_{ij}^b = -\frac{3}{10} \left(\beta_i \langle u_j \theta \rangle + \beta_j \langle u_i \theta \rangle - \frac{2}{3} \delta_{ij} \beta_k \langle u_k \theta \rangle \right), \qquad \Pi_{\theta i}^b = -\frac{1}{3} \beta_i \langle \theta^2 \rangle. \tag{A.15}$$

Note that Eq. (A.15) contains no free parameters; the numerical values of all dimensionless coefficients in the expressions for Π_{ij}^b and $\Pi_{\theta i}^b$ are fixed by mathematical constraints.

Coriolis Contributions to Π_{ij} and $\Pi_{\theta i}$

Parameterizations of the Coriolis contributions to the pressure-scrambling terms are developed analogously to parameterizations of the buoyancy contributions. The Coriolis contributions are represented as

$$\Pi^c_{ij} = -2\epsilon_{kml}\Omega_m \left(X^c_{klij} + X^c_{klji}\right), \qquad \Pi^c_{\theta i} = -2\epsilon_{kml}\Omega_m Y^c_{kli}, \tag{A.16}$$

where

$$X^c_{klij} = -\frac{1}{4\pi}\int_{Vol} \frac{\partial^2 \langle u_l'' u_i\rangle}{\partial x_k'' \partial x_j''} \frac{dVol}{|\mathbf{x}-\mathbf{x}''|}, \qquad Y^c_{kli} = -\frac{1}{4\pi}\int_{Vol} \frac{\partial^2 \langle u_l'' \theta\rangle}{\partial x_k'' \partial x_i''} \frac{dVol}{|\mathbf{x}-\mathbf{x}''|}. \tag{A.17}$$

The tensor Y^c_{kli} is exactly the same tensor as X^b_{kij} that appears in the parameterization of Π^b_{ij}, see Eqs. (A.9)–(A.14). The tensor X^c_{klij} satisfies the following constraints:

$$\begin{aligned}
&\text{symmetry} && X^c_{klij} = X^c_{kilj}, \quad X^c_{klij} = X^c_{jlik}, && \text{(A.18)}\\
&\text{continuity} && X^c_{klii} = 0, && \text{(A.19)}\\
&\text{normalization} && X^c_{klik} = \langle u_l u_i\rangle . && \text{(A.20)}
\end{aligned}$$

Within the limits of a linear approximation, the most general form of X^c_{klij} that satisfies the symmetry constraints (A.18) is

$$\begin{aligned}
X^c_{klij} &= 2e\left[\alpha_1\delta_{li}\delta_{kj} + \alpha_2\left(\delta_{lk}\delta_{ji} + \delta_{lj}\delta_{ki}\right)\right]\\
&+ \alpha_3\delta_{li}a_{kj} + \alpha_4\delta_{kj}a_{li} + \alpha_5\left(\delta_{ij}a_{kl} + \delta_{lj}a_{ki} + \delta_{ki}a_{lj} + \delta_{lk}a_{ji}\right).
\end{aligned} \tag{A.21}$$

Satisfying the continuity (A.19) and the normalization (A.20) constraints, we obtain $\alpha_1 = 2/15$, $\alpha_2 = -1/30$, $\alpha_3 = -1/3 - 11\alpha_5/3$ and $\alpha_4 = 1/3 - 4\alpha_5/3$. Using Eqs. (A.16), (A.14) and (A.21) along with these estimates, we obtain

$$\Pi^c_{ij} = -\frac{2}{3}\left(2 + 7\alpha_5\right)\left(\epsilon_{imk}\Omega_m a_{kj} + \epsilon_{jmk}\Omega_m a_{ki}\right), \qquad \Pi^c_{\theta i} = -\epsilon_{imk}\Omega_m \langle u_k\theta\rangle , \tag{A.22}$$

with only one free coefficient α_5. An estimate of $\alpha_5 = -1/10$ was adopted in a number of studies (e.g Shih, 1996; Hanjalić, 1999).

Mean-Velocity Shear Contributions to Π_{ij} and $\Pi_{\theta i}$

The contributions to the pressure-scrambling terms due to the mean-velocity shear are parameterized in the same way as the contributions due to the Coriolis effects. The mean-velocity shear contributions are represented as

$$\Pi^s_{ij} = -2\frac{\partial U_k}{\partial x_l}\left(X^s_{klij} + X^s_{klji}\right), \qquad \Pi_{\theta i} = -2\frac{\partial U_k}{\partial x_l} Y^s_{kli}, \tag{A.23}$$

where

$$X^s_{klij} = -\frac{1}{4\pi}\int_{Vol} \frac{\partial^2 \langle u_l'' u_i\rangle}{\partial x_k'' \partial x_j''} \frac{dVol}{|\mathbf{x}-\mathbf{x}''|}, \qquad Y^s_{kli} = -\frac{1}{4\pi}\int_{Vol} \frac{\partial^2 \langle u_l'' \theta\rangle}{\partial x_k'' \partial x_i''} \frac{dVol}{|\mathbf{x}-\mathbf{x}''|}. \tag{A.24}$$

As is easy to see, the tensors X^s_{klij} and Y^s_{kli} are exactly the same tensors as X^c_{klij} and Y^c_{kli}, respectively, that appear in the parameterization of the Coriolis contributions to the

pressure-scrambling terms. Using the results of the previous sub-section, we obtain

$$\begin{aligned}
\Pi^s_{ij} = & - \frac{4}{5} S_{ij} e + 6\alpha_5 \left(S_{ik} a_{kj} + S_{jk} a_{ki} - \frac{2}{3} \delta_{ij} S_{kl} a_{kl} \right) \\
& - \frac{2}{3} \left(2 + 7\alpha_5 \right) \left(W_{ik} a_{kj} + W_{jk} a_{ki} \right), \\
\Pi^s_{\theta i} = & - \left(\frac{3}{5} S_{ik} + W_{ik} \right) \left\langle u'_k \theta' \right\rangle,
\end{aligned} \tag{A.25}$$

where S_{ij} and W_{ij} are the symmetric and the antisymmetric parts, respectively, of the mean-velocity gradient tensor.

Resulting Expressions for Π_{ij} and $\Pi_{\theta i}$

Combining Eqs. (A.8) with $\tau_{ru} = \tau_{r\theta} = \tau_\epsilon$, (A.15), (A.22) and (A.25) and returning to the notation with primes, we obtain the following parameterizations of the pressure-scrambling terms in the Reynolds-stress and the temperature-flux equations that are linear in the second-order moments of fluctuating fields:

$$\begin{aligned}
\Pi_{ij} = & \; C^u_t \frac{a_{ij}}{\tau_\epsilon} \\
& - C^u_{s1} S_{ij} e - C^u_{s2} \left(S_{ik} a_{kj} + S_{jk} a_{ki} - \frac{2}{3} \delta_{ij} S_{kl} a_{kl} \right) - C^u_{s3} \left(W_{ik} a_{kj} + W_{jk} a_{ki} \right) \\
& - C^u_b \left(\beta_i \left\langle u'_j \theta' \right\rangle + \beta_j \left\langle u'_i \theta' \right\rangle - \frac{2}{3} \delta_{ij} \beta_k \left\langle u'_k \theta' \right\rangle \right) \\
& - 2 C^u_c \left(\epsilon_{imk} \Omega_m a_{kj} + \epsilon_{jmk} \Omega_m a_{ki} \right),
\end{aligned} \tag{A.26}$$

$$\Pi_{\theta i} = C^\theta_t \frac{\left\langle u'_i \theta' \right\rangle}{\tau_\epsilon} - \left(C^\theta_{s1} S_{ij} + C^\theta_{s2} W_{ij} \right) \left\langle u'_j \theta' \right\rangle - C^\theta_b \beta_i \left\langle \theta'^2 \right\rangle - 2 C^\theta_c \epsilon_{imj} \Omega_m \left\langle u'_j \theta' \right\rangle, \tag{A.27}$$

where $C^u_t = 1.8$, $C^u_{s1} = 4/5$, $C^u_{s2} = -6\alpha_5$, $C^u_{s3} = \frac{2}{3}(2 + 7\alpha_5)$, $C^u_b = 3/10$, $C^u_c = \frac{1}{3}(2 + 7\alpha_5)$, $C^\theta_t = 5.0$, $C^\theta_{s1} = 3/5$, $C^\theta_{s2} = 1$, $C^\theta_b = 1/3$ and $C^\theta_c = 1/2$ are dimensionless coefficients. The only yet undetermined coefficient α_5 can be estimated by satisfying one or the other additional constraint. One way to determine α_5 is to require that the second-moment equations of the TKESV scheme subject to the surface-layer approximation yield the classical logarithmic velocity profile. Details are given in next sub-section.

Logarithmic Velocity Profile Constraints

Consider a fluid layer just above a flat rigid surface where (i) turbulence is stationary and horizontally homogeneous, and (ii) the effects of buoyancy, reference frame rotation, advection and third-order transport are negligible. It is further assumed that (iii) the surface layer is a small portion of the PBL, so that the directional wind shear is negligible, and turbulent fluxes can be considered approximately height-constant, equal to their surface values (in other words, changes of fluxes over the surface layer are small compared to their changes over the entire PBL). Under the assumptions (i)–(iii), the TKE equation (12) reduces to a balance between the shear production and the dissipation,

$$- \left\langle u'_i u'_k \right\rangle \frac{\partial \left\langle u_i \right\rangle}{\partial x_k} - \epsilon = 0, \tag{A.28}$$

and the Reynolds-stress equation (18) with due regard for the parameterization (21) of the pressure-scrambling term reduces to a balance between the shear production and pressure redistribution,

$$-C_t^u \frac{a_{ij}}{\tau_\epsilon} - \left(\frac{4}{3} - C_{s1}^u\right) e S_{ij} - \left(1 - C_{s2}^u\right)\left(a_{ik}S_{jk} + a_{jk}S_{ik} - \frac{2}{3}\delta_{ij}a_{kl}S_{kl}\right) - \left(1 - C_{s3}^u\right)\left(a_{ik}W_{jk} + a_{jk}W_{ik}\right) = 0, \tag{A.29}$$

where the deviatoric part ϵ_{ij}^d of the Reynolds-stress dissipation tensor is incorporated into the parameterization of the slow part Π_{ij}^t of the pressure redistribution term.

In the near-surface layer subject to the above assumptions (i)–(iii), the mean-velocity profile is logarithmic, and the following well-known relations hold true:

$$l = \kappa x_3, \quad -\left\langle u_1' u_3' \right\rangle = u_*^2, \quad e = C_e u_*^2, \quad \frac{\partial \left\langle u_1 \right\rangle}{\partial x_3} = \frac{u_*}{\kappa x_3}. \tag{A.30}$$

Here, κ is the von Kármán constant whose conventional value is 0.4, C_e is a dimensionless constants, and u_* is the surface friction velocity. The x_1 horizontal axis is taken to be aligned with the surface stress so that $\langle u_2' u_3' \rangle = 0$ and $\langle u_2 \rangle = 0$ (in the horizontally-homogeneous layer over a rigid surface, $\langle u_3 \rangle = 0$ by virtue of continuity).

It is straightforward to verify by substituting (A.30) into (A.28), where ϵ is expressed in terms of e and l through (31) and (35), that the logarithmic-layer TKE budget, Eq. (A.28), is satisfied if

$$C_\epsilon = C_e^{-3/2}. \tag{A.31}$$

Using the estimate of $C_e = 3.33$ (e.g. Umlauf and Burchard, 2003; Umlauf et al., 2003), we obtain $C_\epsilon = 0.165$.

With the x_1-axis aligned with $\langle u_1' u_3' \rangle$, the only non-zero components of S_{ij} and W_{ij} are $S_{13} = S_{31} = W_{13} = -W_{31}$. Then, Eq. (A.29) yields the following expressions for the Reynolds-stress components in the near-surface log-layer:

$$a_{12} = a_{23} = 0, \tag{A.32}$$

$$\left\{1 - \frac{4}{3}\left(\frac{1 - C_{s2}^u}{C_t^u}\right)^2 (\tau_\epsilon S_{13})^2 + 4\left(\frac{1 - C_{s3}^u}{C_t^u}\right)^2 (\tau_\epsilon W_{13})^2\right\} a_{13} + \frac{1}{C_t^u}\left(\frac{4}{3} - C_{s1}^u\right)\tau_\epsilon S_{13} e = 0, \tag{A.33}$$

$$\begin{aligned} a_{11} + \frac{\tau_\epsilon}{C_t^u}\left[\frac{2}{3}\left(1 - C_{s2}^u\right) S_{13} + 2\left(1 - C_{s3}^u\right) W_{13}\right] a_{13} &= 0, \\ a_{22} - \frac{\tau_\epsilon}{C_t^u}\left[\frac{4}{3}\left(1 - C_{s2}^u\right) S_{13}\right] a_{13} &= 0, \\ a_{33} + \frac{\tau_\epsilon}{C_t^u}\left[\frac{2}{3}\left(1 - C_{s2}^u\right) S_{13} - 2\left(1 - C_{s3}^u\right) W_{13}\right] a_{13} &= 0, \end{aligned} \tag{A.34}$$

Substituting Eqs. (17), (35), (A.30) and (A.31) along with the expressions $S_{13} = W_{13} = \frac{1}{2}\frac{\partial \langle u_1 \rangle}{\partial x_3}$, $C_{s2}^u = -6\alpha_5$ and $C_{s3}^u = \frac{2}{3}(2 + 7\alpha_5)$ into Eq. (A.33), we obtain the following quadratic equation for the disposable coefficient α_5:

$$44\alpha_5^2 - 4\alpha_5 - \left[1 + \frac{9C_t^u}{4}\left(\frac{4}{3} - C_{s1}^u\right) - \frac{9}{2}\left(\frac{C_t^u}{C_e}\right)^2\right] = 0. \tag{A.35}$$

The physically meaningful negative root of Eq. (A.35) is given by

$$\alpha_5 = \frac{1}{22}\left[1-(1+11C_\alpha^*)^{1/2}\right], \qquad C_\alpha^* = 1+\frac{9C_t^u}{4}\left(\frac{4}{3}-C_{s1}^u\right)-\frac{9}{2}\left(\frac{C_t^u}{C_e}\right)^2. \tag{A.36}$$

Using $C_{s1}^u = 4/5$, $C_t^u = 1.8$ and $C_e = 3.33$, we obtain $\alpha_5 = -0.164$.

With due regard for Eqs. (17), (35), (A.30), (A.31) and (A.33) and the expressions for $S_{13} = W_{13}$, C_{s2}^u and C_{s3}^u given above, Eqs. (A.34) yield the following estimates of the velocity variances in the near-surface log-layer:

$$\begin{aligned}
\langle u_1'^2\rangle &= \frac{2C_e}{3}\left(1-\frac{4\alpha_5}{C_t^u}\right)u_*^2,\\
\langle u_2'^2\rangle &= \frac{2C_e}{3}\left(1-\frac{1+6\alpha_5}{C_t^u}\right)u_*^2,\\
\langle u_3'^2\rangle &= \frac{2C_e}{3}\left(1+\frac{1+10\alpha_5}{C_t^u}\right)u_*^2.
\end{aligned} \tag{A.37}$$

It should be pointed out that with the above estimates of C_t^u, C_e and α_5 the velocity variances are always non-negative, i.e. the realizability requirements are satisfied.

Appendix B. Disposable Constants and Parameters of TKESV-Bas

Estimates of disposable constants and parameters of the baseline version of the TKESV scheme are summarized in Table 1. The values of $C^u_{s2} = 3/5$ and $C^u_{s3} = 13/15$ correspond to $\alpha_5 = -1/10$ [Eq. (26) with $F_l = 0$], i.e. to the one-component or two-component limit of anisotropic turbulence. These optional estimates are given in parentheses.

Table 1: Disposable Constants and Parameters of TKESV-Bas

Constant/ Parameter	Estimate	Equation for	Equation Nos.	Comments
C^d_e	0.1	e	(60)	
$C^d_{\theta\theta}$	0.1	$\langle \theta_l'^2 \rangle$	(61)	
C^d_{qq}	0.1	$\langle q_t'^2 \rangle$	(62)	
$C^d_{\theta q}$	0.1	$\langle \theta_l' q_t' \rangle$	(63)	
R_τ	0.5	$\langle \theta_l'^2 \rangle$, $\langle q_t'^2 \rangle$, $\langle \theta_l' q_t' \rangle$	(61)–(63)	
C_ϵ	0.165	τ_ϵ	(64)	$= C_e^{-3/2}$
κ	0.4	l	(64)	
C_{lb}	1.0	l	(64)	
l_∞	200 m	l	(64)	
C^u_t	1.8	$\langle u_i' u_j' \rangle$	(65)	
C^u_{s1}	4/5	$\langle u_i' u_j' \rangle$	(65)	
C^u_{s2}	0.986 (3/5)	$\langle u_i' u_j' \rangle$	(65)	$= -6\alpha_5$
C^u_{s3}	0.567 (13/15)	$\langle u_i' u_j' \rangle$	(65)	$= \frac{2}{3}(2 + 7\alpha_5)$
C^u_b	3/10	$\langle u_i' u_j' \rangle$	(65)	
C^θ_t	5.0	$\langle u_i' \theta_l' \rangle$	(66)	
C^θ_{s1}	3/5	$\langle u_i' \theta_l' \rangle$	(66)	
C^θ_{s2}	1	$\langle u_i' \theta_l' \rangle$	(66)	
C^θ_b	1/3	$\langle u_i' \theta_l' \rangle$	(66)	
C^q_t	5.0	$\langle u_i' q_t' \rangle$	(67)	
C^q_{s1}	3/5	$\langle u_i' q_t' \rangle$	(67)	
C^q_{s2}	1	$\langle u_i' q_t' \rangle$	(67)	
C^q_b	1/3	$\langle u_i' q_t' \rangle$	(67)	
C_e	3.33		(A.30)	Required to estimate C_ϵ through (A.31) and α_5 through (A.36)
α_5	-0.164 $(-1/10)$		(A.36), or (26)	Required to estimate C^u_{s2} and C^u_{s3}

Appendix C. Turbulence Potential Energy

The quantity P defined by Eqs. (73) and (74) naturally appears in the equations for the Reynolds stress and scalar fluxes. It is characteristic of the potential energy of turbulent flow and can therefore be referred to as the turbulence potential energy (TPE). By way of illustration, consider the temperature-stratified fluid where potential temperature θ is the only thermodynamic variable that affects buoyancy. Then, $q_l = 0$, $q_t = 0$, $\theta_l = \theta$, $\mathcal{I}_\theta = 1$, $N^2 = -\beta_3 \partial \langle\theta\rangle / \partial x_3$, and Eq. (73) is simplified to give

$$P = \tau_\epsilon^2 \beta_3^2 \left\langle \theta'^2 \right\rangle . \tag{C.1}$$

The definition of TPE is not unique, however. For example, the following definition of TPE has been used in the analyses of atmospheric turbulence (see e.g. Zilitinkevich et al., 2007; Mauritsen et al., 2007):

$$P_N = \frac{1}{2} N^{-2} \beta_3^2 \left\langle \theta'^2 \right\rangle . \tag{C.2}$$

A transport equation for P_N can be readily derived using the transport equation for buoyancy (potential temperature) variance. Assuming that N^2 varies slowly in space and time and using the boundary-layer approximation, we obtain

$$\frac{\partial P_N}{\partial t} = \beta_3 \left\langle u_3' \theta' \right\rangle - \frac{1}{2} \frac{\partial}{\partial x_3} \left(\frac{\beta_3^2}{N^2} \left\langle u_3' \theta'^2 \right\rangle \right) - \frac{\beta_3^2}{N^2} \epsilon_{\theta\theta}, \tag{C.3}$$

In the boundary-layer approximation, the transport equation for the TKE, $e \equiv \frac{1}{2} \left\langle u_i'^2 \right\rangle$, reads

$$\begin{aligned} \frac{\partial e}{\partial t} = & -\beta_3 \left\langle u_3' \theta' \right\rangle - \left(\left\langle u_1' u_3' \right\rangle \frac{\partial \langle u_1 \rangle}{\partial x_3} + \left\langle u_2' u_3' \right\rangle \frac{\partial \langle u_2 \rangle}{\partial x_3} \right) \\ & - \frac{\partial}{\partial x_3} \left(\frac{1}{2} \left\langle u_3' u_i'^2 \right\rangle + \left\langle u_3' p' \right\rangle \right) - \epsilon. \end{aligned} \tag{C.4}$$

The term $-\beta_3 \left\langle u_3' \theta' \right\rangle$ on the r.h.s. of Eq. (C.4) (the buoyancy flux) appears with the opposite sign on the r.h.s. of Eq. (C.3). It describes the conversion of the TPE into the TKE that occurs in unstable density (buoyancy) stratification, and vice versa where the stratification is stable. The use of TPE defined through Eq. (C.2) is advantageous as it makes the TPE transport equation particularly convenient and facilitates the analysis of turbulence energetics. For example, Eqs. (C.3) and (C.4) can be added, leading to the total (TPE+TKE) turbulence energy equation that has been used by some researchers in the analyses of stably-stratified turbulent flows (e.g. Zilitinkevich et al., 2007; Mauritsen et al., 2007; Zilitinkevich et al., 2009, 2013).

Note, however, that the TPE defined through Eq. (C.2) is a well-defined quantity (non-negative and finite) only if the flow is stably stratified ($N^2 > 0$). The quantity P_N bears a close analogy to the available potential energy defined as a part of the total potential energy of the stratified flow that can be converted into kinetic energy (see e.g. Vallis, 2006, for a comprehensive discussion). Where the buoyancy stratification is neutral ($N^2 = 0$) or unstable ($N^2 < 0$), P_N is infinite or negative and is not really convenient to use. For the Earth's atmosphere, where the buoyancy stratification is due to both temperature and humidity and the thermodynamics is strongly complicated by phase changes, a TPE transport equation as simple and elegant as Eq. (C.3) is difficult to derive. It is therefore advantageous to work with the variance and covariance equations for the scalar quantities that can be derived from the first principles in a fairly straightforward way. The quantity P defined by Eqs. (73)

and (74), or by Eq. (C.1) in the case of temperature-stratified flow, is merely a diagnostic quantity that naturally appears in the equations for the Reynolds stress and scalar fluxes. It has the physical meaning or turbulence potential energy but a separate transport equation for P is actually not needed.

Appendix D. Stability Functions in Shear-Free Flow

Consider a simple case of shear-free flow. With $S_{ij} = W_{ij} = 0$ (no mean velocity shear), the Reynolds-stress and scalar-flux equations (65)–(67) are considerably simplified (recall that the reference frame rotation is also neglected, $\Omega_i = 0$). The off-diagonal components of the Reynolds stress tensor are zero, $\langle u_1' u_2' \rangle = \langle u_1' u_3' \rangle = \langle u_2' u_3' \rangle = 0$, and so are the horizontal components of the scalar fluxes, $\langle u_1' \theta_l' \rangle = \langle u_2' \theta_l' \rangle = 0$ and $\langle u_1' q_t' \rangle = \langle u_2' q_t' \rangle = 0$. The diagonal components of the Reynolds stress tensor (i.e. the velocity variances) are given by

$$\left\langle u_1'^2 \right\rangle = \left\langle u_2'^2 \right\rangle = \frac{2}{3} e - \frac{2\left(1 - C_b^u\right)}{3 C_t^u} \tau_\epsilon \left(-\beta_3 \left\langle u_3' \theta_v' \right\rangle \right), \tag{C.1}$$

$$\left\langle u_3'^2 \right\rangle = \frac{2}{3} e + \frac{4\left(1 - C_b^u\right)}{3 C_t^u} \tau_\epsilon \left(-\beta_3 \left\langle u_3' \theta_v' \right\rangle \right), \tag{C.2}$$

and the vertical scalar fluxes are given by

$$\left\langle u_3' \theta_l' \right\rangle = -\mathcal{F}_{\mathrm{H1}} \tau_\epsilon e \frac{\partial \left\langle \theta_l \right\rangle}{\partial x_3} - \mathcal{F}_{\mathrm{H2}} \tau_\epsilon \beta_3 \left\langle \theta_l' \theta_v' \right\rangle, \tag{C.3}$$

$$\left\langle u_3' q_t' \right\rangle = -\mathcal{F}_{\mathrm{H1}} \tau_\epsilon e \frac{\partial \left\langle q_t \right\rangle}{\partial x_3} - \mathcal{F}_{\mathrm{H2}} \tau_\epsilon \beta_3 \left\langle q_t' \theta_v' \right\rangle, \tag{C.4}$$

$$\mathcal{F}_{\mathrm{H1}} = \left[1 + \frac{4\left(1 - C_b^u\right)}{3 C_t^u C_t^\theta} \tau_\epsilon^2 N^2 \right]^{-1} \left[\frac{2}{3 C_t^\theta} + \frac{4\left(1 - C_b^u\right)\left(1 - C_b^\theta\right)}{3 C_t^u \left(C_t^\theta\right)^2} \frac{P}{e} \right], \tag{C.5}$$

$$\mathcal{F}_{\mathrm{H2}} = \frac{1 - C_b^\theta}{C_t^\theta}, \tag{C.6}$$

where N^2 and P are given by Eqs. (72)–(74), and $C_t^q = C_t^\theta$ and $C_b^q = C_b^\theta$ are used to obtain Eq. (C.4). In the shear-free limit, $\mathcal{F}_{\mathrm{H2}}$ is merely a constant and $\mathcal{F}_{\mathrm{H1}}$ is a function of $\tau_\epsilon^2 N^2$ and P/e. There is no problem with the stability function $\mathcal{F}_{\mathrm{H1}}$ in the case of stable buoyancy stratification, where N^2 is positive (with the x_3-axis directed vertically upward, $\beta_3 < 0$). If the stratification is unstable, $N^2 < 0$ and the expression in the denominator (first set of square brackets) on the the r.h.s. of Eq. (C.5) may approach zero or become negative, leading to physically meaningless values of $\mathcal{F}_{\mathrm{H1}}$.

A similar problem with the stability functions is encountered within the framework of a one-equation closure scheme that carries prognostic transport equation for the TKE whereas all other second-moment equations, including the scalar-variance and scalar-covariance equations, are reduced to diagnostic algebraic expressions. By way of illustration, we further simplify the discussion and consider a temperature-stratified flow, where moisture effects are neglected and $\theta_l = \theta$. Within the framework of the one-equation TKE scheme, the following down-gradient formulation for the vertical potential-temperature flux holds:

$$\left\langle u_3' \theta' \right\rangle = -\mathcal{F}_{\mathrm{H}} \tau_\epsilon e \frac{\partial \left\langle \theta \right\rangle}{\partial x_3}, \tag{C.7}$$

$$\mathcal{F}_{\mathrm{H}} = \frac{2}{3 C_t^\theta} \left\{ 1 + \left[\frac{4\left(1 - C_b^u\right)}{3 C_t^u C_t^\theta} + 2 R_\tau \frac{1 - C_b^\theta}{C_t^\theta} \right] \tau_\epsilon^2 N^2 \right\}^{-1}. \tag{C.8}$$

As Eq. (C.8) suggests, $\mathcal{F}_{\mathrm{H}}$ may become infinite or negative in convective conditions, where $N^2 < 0$.

References

Abdella, K. and McFarlane, N. (1999). Reply. *J. Atmos. Sci.*, 56:3482–3483.

Abdella, K. and Petersen, A. C. (2000). Third-order moment closure through the mass-flux approach. *Boundary-Layer Meteorol.*, 95:303–318.

Baldauf, M., Seifert, A., Förstner, J., Majewski, D., Raschendorfer, M., and Reinhardt, T. (2011). Operational convective-scale numerical weather prediction with the COSMO model: description and sensitivities. *Mon. Weather Rev.*, 139:3887–3905.

Bannon, P. R. (2007). Virtualization. *J. Atmos. Sci.*, 64:1405–1409.

Bechtold, P., Cuijpers, J. W. M., Mascart, P., and Trouilhet, P. (1995). Modeling of trade wind cumuli with a low-order turbulence model: Toward a unified description of Cu and Sc clouds in meteorological models. *J. Atmos. Sci.*, 52:455–463.

Bechtold, P., Fravalo, C., and Pinty, J. P. (1992). Modeling of trade wind cumuli with a low-order turbulence model: Toward a unified description of Cu and Sc clouds in meteorological models. *J. Atmos. Sci.*, 49:1723–1744.

Betts, A. K. (1973). Non-precipitating cumulus convection and its parameterization. *Quart. J. Roy. Meteorol. Soc.*, 99:178–196.

Betts, A. K. (1986). A new convective adjustment scheme. Part I: Observational and theoretical basis. *Quart. J. Roy. Meteorol. Soc.*, 112:677–691.

Blackadar, A. K. (1962). The vertical distribution of wind and turbulent exchange in neutral atmosphere. *J. Geophys. Res.*, 67:3095–3102.

Bougeault, P. (1981). Modeling the trade-wind cumulus boundary layer. Part I: Testing the ensemble cloud relations against numerical data. *J. Atmos. Sci.*, 38:2414–2428.

Bougeault, P. and André, J.-C. (1986). On the stability of the third-order turbulence closure for the modeling of the stratocumulus-topped boundary layer. *J. Atmos. Sci.*, 43:15741581.

Bougeault, P. and Lacarrère, P. (1989). Parameterization of orography-induced turbulence in a mesobeta-scale model. *Mon. Weather Rev.*, 117:1872–1890.

Brost, R. A. and Wyngaard, J. C. (1978). A model study of the stably stratified planetary boundary layer. *J. Atmos. Sci.*, 35:1427–1440.

Chou, P.-Y. (1945). On velocity correlation and the solution of the equation of turbulent fluctuation. *Quart. Appl. Math.*, 3:38–54.

Craft, T. J., Ince, N. Z., and Launder, B. E. (1996). Recent developments in second-moment closure for buoyancy-affected flows. *Dynam. Atmos. Oceans*, 23:99–114.

Dakos, T. and Gibson, M. M. (1987). On modelling the pressure terms of the scalar flux equations. In et al., F. D., editor, *Turbulent Shear Flows 5*, pages 7–18, Berlin. Springer.

Daly, B. J. and Harlow, F. H. (1970). Transport equations in turbulence. *Phys. Fluids*, 13:2634–2649.

Deardorff, J. W. (1976). Usefulness of liquid-water potential temperature in a shallow-cloud model. *J. Appl. Meteorol.*, 15:98–102.

Dol, H. S., Hanjalić, K., and Kenjereš, S. (1997). A comparative assessment of the second-moment differential and algebraic models in turbulent natural convection. *Int. J. Heat and Fluid Flow*, 18:4–14.

du Vachat, R. J. (1989). Commenst on "Design of a nonsingular level 2.5 second-order closure model for the prediction of atmospheric turbulence". *J. Atmos. Sci.*, 46:1631–1632.

Girimaji, S. S. (2000). Pressure-strain correlation modelling of complex turbulent flows. *J. Fluid Mech.*, 422:91–123.

Golaz, J.-C., Larson, V. E., and Cotton, W. R. (2002). A PDF-based model for boundary layer clouds. Part I: Method and model description. *J. Atmos. Sci.*, 59:3540–3551.

Gryanik, V. M. and Hartmann, J. (2002). A turbulence closure for the convective boundary layer based on a two-scale mass-flux approach. *J. Atmos. Sci.*, 59:2729–2744.

Gryanik, V. M., Hartmann, J., Raasch, S., and Schröter, M. (2005). A refinement of the millionshchikov quasi-normality hypothesis for convective boundary layer turbulence. *J. Atmos. Sci.*, 62:2632–2638.

Hanjalić, K. (1999). Second-moment turbulence closures for CFD: Needs and prospects. *IJCFD*, 12:67–97.

Hanjalić, K. (2002). One-point closure models for buoyancy-driven turbulent flows. *Ann. Rev. Fluid Mech.*, 34:321–347.

Hanjalić, K., Kenjereš, S., and Durst, F. (1996). Natural convection in partitioned two-dimensional enclosures at high Rayleigh numbers. *Int. J. Heat Mass Tran.*, 39:1407–1427.

Hanjalić, K. and Launder, B. (2011). *Modelling Turbulence in Engineering and the Environment. Second-Moment Routes to Closure*. Cambridge University Press.

Hassid, S. and Galperin, B. (1994). Modeling rotating flows with neutral and unstable stratification. *J. Geophys. Res.*, 99:12,533–12,548.

Heinze, R., Mironov, D., and Raasch, S. (2015). Second-moment budgets in cloud-topped boundary layers: A large-eddy simulation study. *J. Adv. Model. Earth Syst.*, 7.

Helfand, H. M. and Labraga, J. C. (1988). Design of a nonsingular level 2.5 second-order closure model for the prediction of atmospheric turbulence. *J. Atmos. Sci.*, 45:113–132.

Helfand, H. M. and Labraga, J. C. (1989). Reply. *J. Atmos. Sci.*, 46:1633–1635.

Jones, W. P. and Musogne, P. (1988). Closure of Reynolds stress and scalar flux equation. *Phys. Fluids*, 31:3589–3604.

Kenjereš, S. and Hanjalić, K. (1995). Prediction of turbulent thermal convection in concentric and eccentric horizontal annuli. *Int. J. Heat Fluid Fl.*, 18:429–439.

Kenjereš, S. and Hanjalić, K. (2000). Convective rolls and heat transfer in finite-length Rayleigh-Bénard convection: A two-dimensional numerical study. *Phys. Rev. E.*, 62:7987–7998.

Kenjereš, S. and Hanjalić, K. (2002). Combined effects of terrain orography and thermal stratification on pollutant dispersion in a town valley: a T-RANS simulation. *J. Turbulence*, 3:1–25.

Lappen, C.-L. and Randall, D. A. (2001). Toward a unified parameterization of the boundary layer and moist convection. Part II: Lateral mass exchanges and subplume-scale fluxes. *J. Atmos. Sci.*, 58:2037–2051.

Larson, V. E., Wood, R., Field, P. R., Golaz, J.-C., Haar, T. H. V., and Cotton, W. R. (2001). Small-scale and mesoscale variability of scalars in cloudy boundary layers: One-dimensional probability density functions. *J. Atmos. Sci.*, 58:1978–1994.

Launder, B. E., Reece, G. J., and Rodi, W. (1975). Progress in the development of a Reynolds-stress turbulence closure. *J. Fluid Mech.*, 68:537–566.

Lazeroms, W. M. J., Brethouwer, G., Wallin, S., and Johansson, A. V. (2013). An explicit algebraic reynolds-stress and scalar-ux model for stably stratifid flows. *J. Fluid Mech.*, 723:91–125.

Lazeroms, W. M. J., Brethouwer, G., Wallin, S., and Johansson, A. V. (2015). Efficient treatment of the nonlinear features in algebraic reynolds-stress and heat-flux models for stratified and convective flows. *Int. J. Heat and Fluid Flow*, 53:15–28.

Lazeroms, W. M. J., Svensson, G., Bazile, E., Brethouwer, G., Wallin, S., and Johansson, A. V. (2016). Study of transitions in the atmospheric boundary layer using explicit algebraic turbulence models. *Boundary-Layer Meteorol.*, 161:19–47.

Lewellen, D. S. and Lewellen, W. S. (2004). Buoyancy flux modeling for cloudy boundary layers. *J. Atmos. Sci.*, 61:1147–1160.

Lilly, D. K. (1968). Models of cloud-topped mixed layers under a strong inversion. *Quart. J. Roy. Meteorol. Soc.*, 94:292–309.

Lumley, J. L. (1975). Pressure-strain correlation. *Phys. Fluids*, 18:750.

Machulskaya, E. (2015). Clouds and convection as subgrid-scale distributions. In Plant, R. S. and Yano, J.-I., editors, *Parameterization of Atmospheric Convection. Volume 2: Current Issues and New Theories*, chapter 25, pages 377–422. World Scientific, Imperial College Press.

Machulskaya, E. and Mironov, D. (2013). Implementation of TKE–Scalar Variance mixing scheme into COSMO. COSMO Newsletter 13. Available from http://www.cosmo-model.org.

Mauritsen, T., Svensson, G., Zilitinkevich, S. S., Esau, I., Enger, L., and Grisogono, B. (2007). A total turbulent energy closure model for neutrally and stably stratified atmospheric boundary layers. *J. Atmos. Sci.*, 64:4113–4126.

Mellor, G. L. (1977). The Gaussian cloud model relations. *J. Atmos. Sci.*, 34:356–358.

Mellor, G. L. and Yamada, T. (1974). A hierarchy of turbulence closure models for planetary boundary layers. *J. Atmos. Sci.*, 31:1791–1806.

Mellor, G. L. and Yamada, T. (1982). Development of a turbulence closure model for geophysical fluid problems. *Rev. Geophys.*, 20:851–875.

Millionshchikov, M. D. (1941). On the theory of homogeneous isotropic turbulence. *Doklady Acad. Nauk SSSR*, 32:611–614.

Mironov, D. V. (2001). Pressure–potential-temperature covariance in convection with rotation. *Quart. J. Roy. Meteorol. Soc.*, 127:89–110.

Mironov, D. V. (2009). Turbulence in the lower troposphere: second-order closure and mass-flux modelling frameworks. In Hillebrandt, W. and Kupka, F., editors, *Interdisciplinary Aspects of Turbulence*, volume 756 of *Lect. Notes Phys.*, pages 161–221. Springer-Verlag.

Mironov, D. V., Gryanik, V. M., Lykossov, V. N., and Zilitinkevich, S. S. (1999). Comments on "A New Second-Order Turbulence Closure Scheme for the Planetary Boundary Layer" by K. Abdella and N. McFarlane. *J. Atmos. Sci.*, 56:3478–3481.

Mironov, D. V. and Sullivan, P. P. (2016). Second-moment budgets and mixing intensity in the stably stratified atmospheric boundary layer over thermally heterogeneous surfaces. *J. Atmos. Sci.*, 73:449–464.

Monin, A. S. (1965). On the symmetry properties of turbulence in the near-surface layer of air. *Izv. Atmos. Oceanic Phys.*, 1:25–30.

Monin, A. S. and Yaglom, A. M. (1971). *Statistical Fluid Mechanics*, volume 1. MIT Press, Cambridge, Massachusetts.

Nakanishi, M. and Niino, H. (2004). An improved Mellor-Yamada level-3 model with condensation physics: its design and verification. *Boundary-Layer Meteorol.*, 112:1–31.

Naumann, A. K., Seifert, A., and Mellado, J. P. (2013). A refined statistical cloud closure using double-Gaussian probability density functions. *Geosci. Model Dev.*, 6:1641–1657.

Otić, I., Grötzbach, G., and Wörner, M. (2005). Analysis and modelling of the temperature variance equation in turbulent natural convection for low-Prandtl-number fluids. *J. Fluid Mech.*, 525:237–261.

Pope, S. B. (2000). *Turbulent Flows*. Cambridge University Press.

Raschendorfer, M. (1999). Special topic: The new turbulence parameterization of LM. Quarterly Report of the Operational NWP-Models of the Deutscher Wetterdienst, 19.

Raschendorfer, M. (2001). The new turbulence parameterization of LM. COSMO Newsletter 1. Available from http://www.cosmo-model.org.

Ristorcelli, J. R., Lumley, J. L., and Abid, R. (1995). A rapid-pressure covariance representation consistent with the taylor-proudman theorem materially frame indifferent in the two-dimensional limit. *J. Fluid Mech.*, 292:111–152.

Rotta, J. C. (1951). Statistische Theorie nichthomogener Turbulenz. 1. *Zs. Phys.*, 129:547–572.

Shih, T.-H. (1996). Constitutive relations and realizability of single-point turbulence closures. In M. Hallbäck, D. S. Henningson, A. V. Johansson, and P. H. Alfredsson, editor, *Turbulence and Transition Modelling*, pages 155–192. Kluwer Acad. Publ., Dordrecht, etc.

Shih, T.-H. and Lumley, J. L. (1985). Modeling of pressure correlation terms in Reynolds stress and scalar flux equations. Technical Report FDA-85-03, Sibley School of Mechanical and Aerospace Engineering, Cornell University.

Sommeria, G. and Deardorff, J. W. (1977). Subgrid-scale condensation in models of non-precipitating clouds. *J. Atmos. Sci.*, 34:344–355.

Speziale, C. G. (1985). Modeling the pressure gradient-velocity correlation of turbulence. *Phys. Fluids*, 28:69–71.

Speziale, C. G., Sarkar, S., and Gatski, T. B. (1991). Modeling the pressure-strain correlation of turbulence: an invariant dynamical system approach. *J. Fluid Mech.*, 227:245–272.

Stull, R. (1973). Inversion rise model based on penetrative convection. *J. Atmos. Sci.*, 30:1092–1099.

Tompkins, A. M. (2003). Impact of temperature and humidity variability on cloud cover assessed using aircraft data. *Quart. J. Roy. Meteorol. Soc.*, 129:2151–2170.

Tompkins, A. M. (2005). The parameterization of cloud cover. Technical memorandum, European Centre for Medium-Range Weather Forecasts, Reading, U.K.

Umlauf, L. and Burchard, H. (2003). A generic length-scale equation for geophysical turbulence models. *Journal of Marine Research*, 61:235–265.

Umlauf, L. and Burchard, H. (2005). Second-order turbulence closure models for geophysical boundary layers. A review of recent work. *Cont. Shelf Res.*, 25:795–827.

Umlauf, L., Burchard, H., and Hutter, K. (2003). Extending the $k - \omega$ turbulence model towards oceanic applications. *Ocean Modelling*, 5:195–218.

Vallis, G. K. (2006). *Atmospheric and Oceanic Fluid Dynamics. Fundamentals and Large-scale Circulation.* Cambridge University Press, Cambridge, etc.

Wyngaard, J. C. (1975). Modeling the planetary boundary layer – extension to the stable case. *Boundary-Layer Meteorol.*, 9:441–460.

Yamada, T. (1977). A numerical experiment on pollutant dispersion in a horizontally-homogeneous atmospheric boundary layer. *Atmos. Environ.*, 11:1015–1024.

Zeman, O. (1981). Progress in the modeling of planetary boundary layers. *Ann. Rev. Fluid Mech.*, 13:253–272.

Zeman, O. and Lumley, J. L. (1976). Modeling buoyancy driven mixed layers. *J. Atmos. Sci.*, 33:1974–1988.

Zeman, O. and Tennekes, H. (1975). A self-contained model for the pressure terms in the turbulent stress equations of the neutral atmospheric boundary layer. *J. Atmos. Sci.*, 32:1808–1813.

Zeman, O. and Tennekes, H. (1977). Parameterization of the turbulent energy budget at the top of the daytime atmospheric boundary layer. *J. Atmos. Sci.*, 34:111–123.

Zilitinkevich, S. S., Elperin, T., Kleeorin, N., iV. L'vov, and Rogachevskii, I. (2009). Energy- and flux-budget turbulence closure model for stably stratified flows. Part II: the role of internal gravity waves. *Boundary-Layer Meteorol.*, 133:139–164.

Zilitinkevich, S. S., Elperin, T., Kleeorin, N., and Rogachevskii, I. (2007). Energy- and flux-budget (EFB) turbulence closure model for stably stratified flows. Part I: steady-state, homogeneous regimes. *Boundary-Layer Meteorol.*, 125:167–191.

Zilitinkevich, S. S., Elperin, T., Kleeorin, N., Rogachevskii, I., and Esau, I. (2013). A hierarchy of energy- and flux-budget (EFB) turbulence closure models for stably-stratified geophysical flows. *Boundary-Layer Meteorol.*, 146:341–373.

Zilitinkevich, S. S. and Mironov, D. V. (1992). Theoretical model of thermocline in a fresh-water basin. *J. Phys. Oceanogr.*, 22:988–996.

List of COSMO Newsletters and Technical Reports

(available for download from the COSMO Website: www.cosmo-model.org)

COSMO Newsletters

No. 1: February 2001.

No. 2: February 2002.

No. 3: February 2003.

No. 4: February 2004.

No. 5: April 2005.

No. 6: July 2006.

No. 7: April 2008; Proceedings from the 8th COSMO General Meeting in Bucharest, 2006.

No. 8: September 2008; Proceedings from the 9th COSMO General Meeting in Athens, 2007.

No. 9: December 2008.

No. 10: March 2010.

No. 11: April 2011.

No. 12: April 2012.

No. 13: April 2013.

No. 14: April 2014.

No. 15: July 2015.

No. 16: July 2016.

COSMO Technical Reports

No. 1: Dmitrii Mironov and Matthias Raschendorfer (2001):
Evaluation of Empirical Parameters of the New LM Surface-Layer Parameterization Scheme. Results from Numerical Experiments Including the Soil Moisture Analysis.

No. 2: Reinhold Schrodin and Erdmann Heise (2001):
The Multi-Layer Version of the DWD Soil Model TERRA_LM.

No. 3: Günther Doms (2001):
A Scheme for Monotonic Numerical Diffusion in the LM.

No. 4: Hans-Joachim Herzog, Ursula Schubert, Gerd Vogel, Adelheid Fiedler and Roswitha Kirchner (2002):
LLM ¯ the High-Resolving Nonhydrostatic Simulation Model in the DWD-Project LITFASS.
Part I: Modelling Technique and Simulation Method.

No. 5: Jean-Marie Bettems (2002):
EUCOS Impact Study Using the Limited-Area Non-Hydrostatic NWP Model in Operational Use at MeteoSwiss.

No. 6: Heinz-Werner Bitzer and Jürgen Steppeler (2004):
Documentation of the Z-Coordinate Dynamical Core of LM.

No. 7: Hans-Joachim Herzog, Almut Gassmann (2005):
Lorenz- and Charney-Phillips vertical grid experimentation using a compressible nonhydrostatic toy-model relevant to the fast-mode part of the 'Lokal-Modell'.

No. 8: Chiara Marsigli, Andrea Montani, Tiziana Paccagnella, Davide Sacchetti, André Walser, Marco Arpagaus, Thomas Schumann (2005):
Evaluation of the Performance of the COSMO-LEPS System.

No. 9: Erdmann Heise, Bodo Ritter, Reinhold Schrodin (2006):
Operational Implementation of the Multilayer Soil Model.

No. 10: M.D. Tsyrulnikov (2007):
Is the particle filtering approach appropriate for meso-scale data assimilation ?

No. 11: Dmitrii V. Mironov (2008):
Parameterization of Lakes in Numerical Weather Prediction. Description of a Lake Model.

No. 12: Adriano Raspanti (2009):
COSMO Priority Project "VERification System Unified Survey" (VERSUS): Final Report.

No. 13: Chiara Marsigli (2009):
COSMO Priority Project "Short Range Ensemble Prediction System" (SREPS): Final Report.

No. 14: Michael Baldauf (2009):
COSMO Priority Project "Further Developments of the Runge-Kutta Time Integration Scheme" (RK): Final Report.

No. 15: Silke Dierer (2009):
COSMO Priority Project "Tackle deficiencies in quantitative precipitation forecast" (QPF): Final Report.

No. 16: Pierre Eckert (2009):
COSMO Priority Project "INTERP": Final Report.

No. 17: D. Leuenberger, M. Stoll and A. Roches (2010):
Description of some convective indices implemented in the COSMO model.

No. 18: Daniel Leuenberger (2010):
Statistical analysis of high-resolution COSMO Ensemble forecasts in view of Data Assimilation.

No. 19: A. Montani, D. Cesari, C. Marsigli, T. Paccagnella (2010):
Seven years of activity in the field of mesoscale ensemble forecasting by the COSMO–LEPS system: main achievements and open challenges.

No. 20: A. Roches, O. Fuhrer (2012):
Tracer module in the COSMO model.

No. 21: Michael Baldauf (2013):
A new fast-waves solver for the Runge-Kutta dynamical core.

No. 22: C. Marsigli, T. Diomede, A. Montani, T. Paccagnella, P. Louka, F. Gofa, A. Corigliano (2013):
The CONSENS Priority Project.

No. 23: M. Baldauf, O. Fuhrer, M. J. Kurowski, G. de Morsier, M. Müllner, Z. P. Piotrowski, B. Rosa, P. L. Vitagliano, D. Wójcik, M. Ziemiański (2013):
The COSMO Priority Project 'Conservative Dynamical Core' Final Report.

No. 24: A. K. Miltenberger, A. Roches, S. Pfahl, H. Wernli (2014):
Online Trajectory Module in COSMO: a short user guide.

No. 25: P. Khain, I. Carmona, A. Voudouri, E. Avgoustoglou, J.-M. Bettems, F. Grazzini (2015):
The Proof of the Parameters Calibration Method: CALMO Progress Report.

No. 26: D. Mironov, E. Machulskaya, B. Szintai, M. Raschendorfer, V. Perov, M. Chumakov, E. Avgoustoglou (2015):
The COSMO Priority Project 'UTCS' Final Report.

No. 27: J-M. Bettems (2015):
The COSMO Priority Project 'COLOBOC': Final Report.

No. 28: Ulrich Blahak (2016):
RADAR_MIE_LM and RADAR_MIELIB - Calculation of Radar Reflectivity from Model Output.

No. 29: M. Tsyrulnikov and D. Gayfulin (2016):
A Stochastic Pattern Generator for ensemble applications.

COSMO Technical Reports

Issues of the COSMO Technical Reports series are published by the *COnsortium for Small-scale MOdelling* at non-regular intervals. COSMO is a European group for numerical weather prediction with participating meteorological services from Germany (DWD, AWGeophys), Greece (HNMS), Italy (USAM, ARPA-SIMC, ARPA Piemonte), Switzerland (MeteoSwiss), Poland (IMGW), Romania (NMA) and Russia (RHM). The general goal is to develop, improve and maintain a non-hydrostatic limited area modelling system to be used for both operational and research applications by the members of COSMO. This system is initially based on the COSMO-Model (previously known as LM) of DWD with its corresponding data assimilation system.

The Technical Reports are intended

- for scientific contributions and a documentation of research activities,
- to present and discuss results obtained from the model system,
- to present and discuss verification results and interpretation methods,
- for a documentation of technical changes to the model system,
- to give an overview of new components of the model system.

The purpose of these reports is to communicate results, changes and progress related to the LM model system relatively fast within the COSMO consortium, and also to inform other NWP groups on our current research activities. In this way the discussion on a specific topic can be stimulated at an early stage. In order to publish a report very soon after the completion of the manuscript, we have decided to omit a thorough reviewing procedure and only a rough check is done by the editors and a third reviewer. We apologize for typographical and other errors or inconsistencies which may still be present.

At present, the Technical Reports are available for download from the COSMO web site (www.cosmo-model.org). If required, the member meteorological centres can produce hard-copies by their own for distribution within their service. All members of the consortium will be informed about new issues by email.

For any comments and questions, please contact the editor:

Massimo Milelli
Massimo.Milelli@arpa.piemonte.it

Consortium for Small-Scale Modelling

Technical Report No. 40

Analysis and Evaluation of TERRA_URB Scheme: PT AEVUS Final Report

December 2019

DOI: 10.5676/DWD_pub/nwv/cosmo-tr_40

Deutscher Wetterdienst
MeteoSwiss
Ufficio Generale Spazio Aereo e Meteorologia
ΕΘΝΙΚΗ ΜΕΤΕΩΡΟΛΟΓΙΚΗ ΥΠΗΡΕΣΙΑ
Instytucie Meteorogii i Gospodarki Wodnej
Administratia Nationala de Meteorologie
ROSHYDROMET
Agenzia Regionale Protezione Ambiente Piemonte
Agenzia Regionale Prevenzione Ambiente Energia Emilia Romagna
Centro Italiano Ricerche Aerospaziali
Amt für GeoInformationswesen der Bundeswehr
Israel Meteorological Service

www.cosmo-model.org

Editor: Massimo Milelli, ARPA Piemonte

Analysis and Evaluation of TERRA_URB Scheme:

PT AEVUS Final Report

Project participants:

***E. Bucchignani*[1], *P. Mercogliano*[1]‡, *V. Garbero*[2],**

***M. Milelli*[2], *M. Varentsov*[3], *I. Rozinkina*[3],**

***G. Rivin*[3], *D. Blinov*[3], *A. Kirsanov*[3],**

***H. Wouters*[4], *J.-P. Schulz*[5], *U. Schättler*[5]**

‡ Project Leader

[1] CIRA

[2] ArpaP

[3] Roshydromet

[4] UniGhent

[5] DWD

Contents

1 Introduction **3**

2 Tasks and achievements **4**

3 Activity performed at University of Ghent: perturbation experiments for Brussels during the 2003 heat wave (H. Wouters) **5**

4 Activity performed at DWD: Improved processes in the land surface model TERRA: Bare soil evaporation and skin temperature (J.-P. Schulz, G. Vogel) **7**

5 Activity performed ad CIRA: High resolution simulations for the representation of Urban Heat Islands over South Italy (E. Bucchignani, P. Mercogliano) **9**

5.1 Test case A: 8 - 10 August 2017 11

5.2 Test case B: 6 - 8 June 2019 15

6 Activities performed at RHM: high resolution simulations of the urban heat island of Moscow megacity (M. Varentsov, I. Rozinkina, G. Rivin, D. Blinov, A. Kirsanov) **17**

6.1 Test case A: 17 - 29 May 2014 20

6.2 Test case B: 1 - 15 January 2017 23

7 Activities performed at Arpa Piemonte (V. Garbero, M. Milelli) **25**

7.1 Test case A: July 2015 30

7.2 Test case B: October 2017 33

8 Conclusions **35**

9 Acknowledgements **36**

A Appendix **37**

Abstract

The main aim of PT AEVUS was the implementation and testing of the TERRA_URB scheme into the COSMO model. The PT was led by the Italian Aerospace Research Center (CIRA, Italy) and involved researchers from four institutions: ARPA Piemonte (Italy), Russian Hydrometeorological Center (RHM, Russia), German Meteorological Service (DWD, Germany) and the University of Ghent (Belgium). Several case studies have been selected in Europe, according to the availability of data from the different research teams involved in the task. Selected periods have been simulated, in order to test the capabilities of the COSMO model with TERRA_URB (TU) in reproducing the main features of specific dynamics such as the Urban Heat Islands (UHIs). The key conclusion of the work is that the version of COSMO model including TU, 5.05urb5, in general successfully simulates the key features of the UHIs. The outcomes of the PT have also stimulated the research groups to continue the activities in a new priority task (PT AEVUS 2) started in September 2019. The description of the PT with the Gantt chart and the related FTEs can be found on the COSMO web site: http://www.cosmo-model.org/content/tasks/pastTasks/pt_aevus.priv.pdf

1 Introduction

The modelling of urban environment has increased significantly in the last years; in fact, different parametrizations for the land use type have been developed. In COSMO model, cities are represented by natural land surfaces with an increased surface roughness length and a reduced vegetation cover (modification of soil and vegetation parameters of the TERRA model). However, in this representation, urban areas are still treated as water-permeable soil with aerodynamic, radiative and thermal parameters similar to the surrounding natural land. Therefore, this basic representation could not reliably capture the urban physics and associated urban-climatic effects including urban heat islands. For this reason, further developments of the parametrization of the urban land have been carried out. In the last years, three urban parametrizations have been incorporated in COSMO for the standard land-surface module TERRA-ML: a DCEP - multilayer urban canopy model, TEB - single layer urban canopy model, and TERRA_URB - bulk parametrization scheme with a prescribed anthropogenic heat flux. Anthropogenic heat emissions are included as an additional heat source to the first aboveground model layer. The urban canopy scheme DCEP coupled with COSMO-CLM has been evaluated extensively against data over Basel (Schubert and Grossman-Clarke, 2014), while TEB has been evaluated over Berlin (Trusilova et al. 2013). However, later study for Moscow revealed a problem in coupling between urban module and the atmospheric module in COSMO version with TEB scheme, which does not allow to adequately simulate the heat transfer from the urban surface to the lower atmosphere (Varentsov et al. 2017). TERRA_URB offers an intrinsic representation of the urban physics with modifications of the input data, soil module and land atmospheric interactions (the details can be found in Wouters et al. (2016)). TERRA_URB (in the following TU) includes the effects of buildings on the air flow without resolving the energy budgets of the buildings themselves, but using the externally calculated anthropogenic heat flux. This approach allows representing effects of multiple cities on the atmosphere without requiring additional data on the building structure. TU is computationally fast and is recommended for studies with spatial and temporal scales where the interactions between the urban canyon air and the atmosphere do not need to be resolved in detail. The latest version of TU implements the Semi-empirical Urban canopy parametrization (SURY). It translates urban-canopy parameters (containing 3D information) into bulk parameters. TU takes additional surface parameter input fields:

ISA (Impervious Surface Area, see Flanner, 2009) and AHF (Annual-mean anthropogenic Heat Flux, see Maucha et al.,2010), generated with EXTPAR via the WebPEP interface. By default, TU takes fixed values for the urban canopy parameters: variation of urban-canopy parameters is optional and could be don inside the model code. The aim of this PT is an evaluation and a deep verification of the performances of the code using a series of selected case studies, in particular in order to verify the capabilities in reproducing the urban dynamics and specific phenomena, e.g. Urban Heat Islands (UHIs) (Milelli, 2016), in order to decide if (and how) to improve the calibration of the namelist parameters, or the parametrization itself. Since the goal of the urban scheme is to catch small-scale features, only very-high resolution runs have been considered. This document is organized as follows: Section 2 contains a list and description of the subtasks in which the PT is organized. Sections 3 to 7 contain a description of the activities performed by the several research teams involved in the PT (UniGhent, DWD, CIRA, RHM, ArpaP) and the main conclusions are described in Section 8. A technical description of the TU implementation in COSMO model is included as Appendix to this report.

2 Tasks and achievements

A concise summary of the tasks and achievements during the project is presented in this section.

Task 0: installation and debugging of the beta COSMO version including TERRA_URB

The primary task of PT was installation and debugging of the different version of COSMO on the supercomputing facilities of the research centres involved in this PT. In total, 6 versions of the model were installed and tested, namely COSMO5.04g_urb1, COSMO5.05_urb1, COSMO5.05_urb2, COSMO5.05_urb3, COSMO5.05_urb4, COSMO5.05_urb5. These versions were consequently developed and updated during the PT. Initial releases contained a number of bugs (COSMO5.04g_urb1, COSMO5.05_urb1), which were found and fixed by PT participants during the debugging activities (details could be found in Appendix A). The revealed bugs were related with the implementation of TU itself, implementation of the skin-layer temperature scheme, input and output issues. All the problems and bugs, which were revealed during the PT AEVUS, were completely fixed in the recent release, COSMO5.05_urb5, which could be considered as a stable model version for further development.

Task 1: selection of case studies

The selection of certain periods for the each of study areas was based on the experience of each participating institution. In general, considered cases include the days with pronounced urban heat islands and extreme temperature events (warm weather in summer or cold weather in winter). More specifically, two regions have been considered in Italy: the urban areas of Turin and Naples, for which observations in urban and rural context are available. Simulations have been performed over periods selected in recent summer and winter seasons. Moscow (about 35 km diameter of urban landscapes, the biggest European city) with 50-80 km surrounding rural region has been chosen as test domain for Russia. Urban areas of Belgium, selecting summer and winter periods (from 2012 onwards) have been considered, performing an extensive evaluation using "standard" scores, with urban climate observations (in terms of air temperature at 2 m and UHI for Antwerp and Ghent, and boundary-layer temperatures and UHI observed from 100m high mast towers), boundary-layer profiles and satellite imagery.

Task 2: simulation setup and runs

Appropriate simulation setups have been selected for all the considered test cases. In particular, the reference configuration (ctrl) has been built in order to perform a comparison, ctrl (with TU scheme off) and ctrl-TU (with TU scheme on).

Task 3: calibration of TERRA_URB scheme

The TU scheme has two mandatory input fields, namely the Impervious Surface Area (ISA) and the annual-mean Anthropogenic Heat Flux (AHF), varying throughout the domain. The TU scheme also uses the Semi-Empirical Urban Canopy parametrization (SURY) (Wouters et al, 2016) in order to calculate the additional bulk parameters needed. These additional parameters are currently set to default values and hard-coded. Default values could not be suitable for the area under study, depending on the urban canopy properties. For this reason, it would be necessary to investigate the model sensitivity to these parameters, but for time constrains this task has been postponed to the follow-up of the PT.

Task 4: evaluation and verification of the case studies

The verification is the key point of the work. It has been used a dense network of weather stations, to determine the performance of the model in its various flavours, both at the surface and in the atmosphere.

Task 5: writing of the final report

A significant amount of documentation has been produced, and, in particular, the goal to make public the work performed within the COSMO PT, not only to the COSMO members but also to the wider scientific community, has been achieved.

3 Activity performed at University of Ghent: perturbation experiments for Brussels during the 2003 heat wave (H. Wouters)

A range of experiments has been performed to test the sensitivity of climate modelling to urban parametrization for Brussels during the heat wave of 2003 (1st August 2003 until 15th August 2003). The simulations have been performed on a 80x80 grid cell domain (0.025 degree resolution) centred over Brussels, and they are nested in Era-Interim (0.75 degree resolution) driven simulations over the EURO-CORDEX domain (0.11 degree resolution). Six perturbation experiments have been performed with different variants and parameters: the first one is a simulation with the default COSMO model 5.05 without urban parametrization (COSMO5.05 (no urb)). The second one is the initial implementation of TU2.3 (COSMO 5.05_urb_ini), which represents the buildings in the domain, but excluding the anthropogenic heat flux due to human activity.

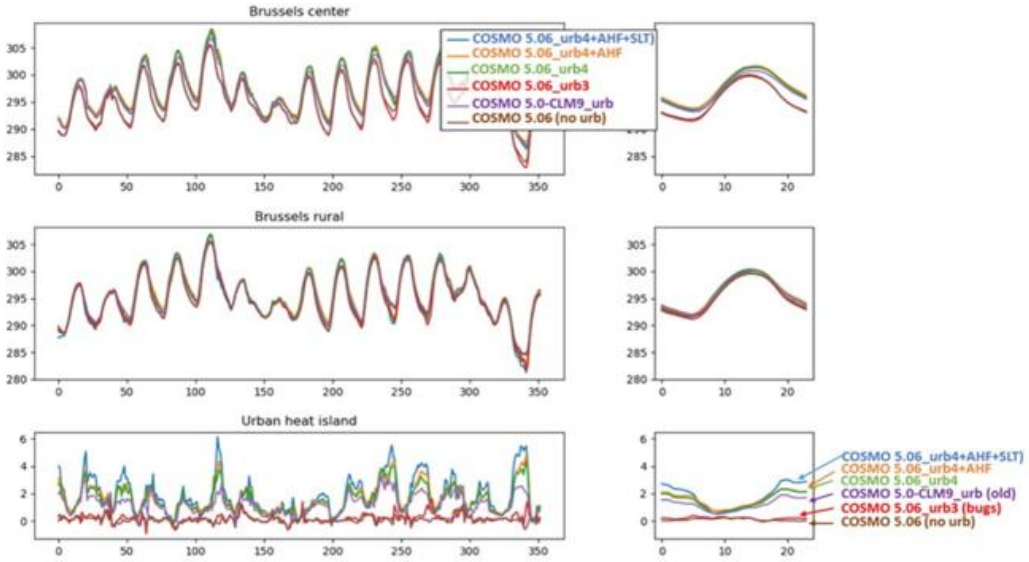


Figure 1: Model time series of T_2m for Brussels center, a rural location and the associated urban heat islands (urban-rural difference) during the heat wave of 2003 for the different perturbation experiments.

The third one refers to a simulation with the same version TU2.3, but implemented in a previous COSMO model (COSMO5.0_clm9_urb), which has been developed and used for climate applications. For description, evaluation and applications, see Wouters et al., 2015; Wouters et al., 2016; Wouters et al., 2017; Demuzere et al., 2017. A fourth simulation refers to a bug fix release of the implementation of TU2.3 into COSMO 5.05 (COSMO 5.05_urb4). The fifth simulation is analogous to the previous simulation, but including the anthropogenic heat flux. The last simulation is the same as the fifth simulation but activating the skin-layer resistance formulation that has been recently integrated into COSMO.

Time series and horizontal profiles of T_2m are shown in Figs. 1 and 2. They indicate that both the COSMO model version and the (urban) land-surface parametrization scheme substantially affect the urban heat wave model results, especially regarding the simulation of the UHI intensities. While the default COSMO model version did not show any UHI, the implementation of TU and additional bug fixes lead to a higher urban air temperature and hence a realistic simulation of the UHI intensity that is most pronounced during the evening and night time. While the formulation of the TU in the new COSMO model version (COSMO5.05_urb4) is similar to the implementation in the previous version (COSMO5.0_clm9_urb), urban heat island intensities now appear to be more pronounced. This suggests that not only the urban land-surface parametrization itself but also changes in the atmospheric model physics and the associated changes in the land-atmosphere feedbacks are determinant for urban climate modelling results. Moreover, the implementation of the skin-layer resistance formulation leading the higher decoupling of surface and air temperature and hence to lower temperature in the rural areas, also results in a more pronounced urban heat island intensity. Since the previous version was showing an overall underestimated UHI according to in situ measurements for Antwerp Belgium (Wouters et al., 2017), the higher UHI values suggest that the new implementation in COSMO5.05_urb4 may have a better model performance in representing urban climate than the previous one in COSMO5.0_clm9.

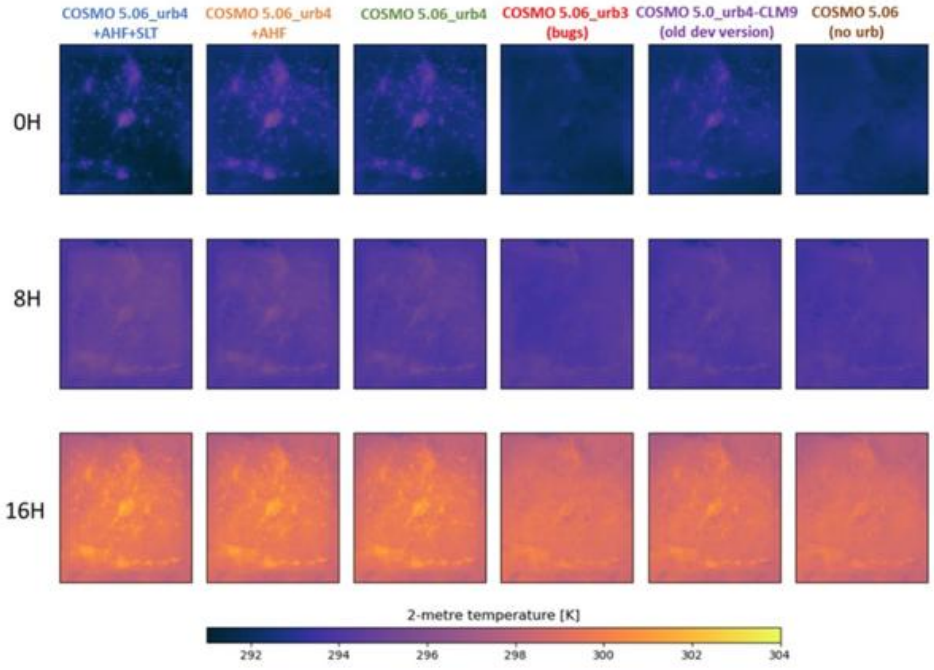


Figure 2: Horizontal profiles of modelled absolute 2-metre air temperature for Brussels at 0H 8H and 16H UTC averaged for the 2003 heat wave (1st August 2003 to 15th August 2003) for different perturbation experiments.

4 Activity performed at DWD: Improved processes in the land surface model TERRA: Bare soil evaporation and skin temperature (J.-P. Schulz, G. Vogel)

Land surface processes have a significant impact on near-surface atmospheric phenomena. They determine near surface sensible, latent heat fluxes, and the radiation budget, and thus influence atmosphere and land characteristics, such as temperature and humidity, the structure of the planetary boundary layer, and even cloud formation processes. All these processes are also very relevant for urban-atmospheric interactions. For example, the UHI is defined as a difference between urban and rural temperatures, so an adequate simulation of the UHI intensity, its dynamics and impacts on atmospheric processes in the model requires a realistic simulation of urban temperature and the rural temperate as well. The typical problem of COSMO model is an overestimation of nocturnal temperatures, which is also a problem for reproducing the observed UHI intensity (see Sec. 6 and Varentsov et al., 2017). It is therefore essential to simulate the land surface processes for rural areas in atmospheric models as realistically as possible.

Verifications have shown that the bare soil evaporation simulated by the land surface scheme TERRA of the COSMO model is systematically overestimated under wet conditions. Furthermore, it turned out that the amplitude of the diurnal cycle of the surface temperature is systematically underestimated. In contrast, the diurnal cycles of the temperatures in the soil are overestimated, instead. This means that the other components of the surface energy and water balances are biased as well, for instance, the surface turbulent heat fluxes as well as

the soil water content. Data from the Meteorological Observatory Lindenberg of the German Meteorological Service (DWD) were used to analyse this model behaviour. The erroneous formulation of bare soil evaporation was replaced by a scheme based on a resistance formulation, which efficiently reduces the simulated vapour flux (Schulz and Vogel 2016). In the standard model configuration of TERRA, there is no representation of the vegetation in the surface energy balance. This means, there is no energy budget including a temperature for the vegetation layer. Furthermore, the insulating effects by the vegetation at the sub-canopy level are missing as well. A scheme providing both of these missing model characteristics was implemented in TERRA, the so-called skin temperature formulation (Viterbo and Beljaars 1995, Schulz and Vogel 2017). As a result, the simulated diurnal amplitude of the surface temperature is increased and the one of the soil temperature is reduced.

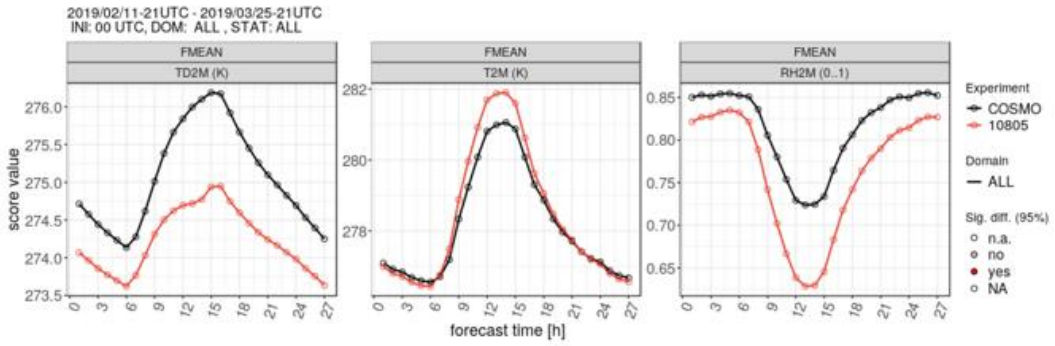


Figure 3: Diurnal cycles of the dew point temperature (TD2M), atmospheric temperature (T2M) and relative humidity (RH2M), all at 2-m above ground, averaged over the whole experimental period of 11 February to 25 March 2019. The COSMO operational reference version is depicted in black, the experiment in red.

A numerical experiment with the COSMO model was carried out that uses, beside the new formulations of bare soil evaporation and the skin temperature, a more realistic exponential root profile, a new interception reservoir for collecting dew on the leaves, and an improved formulation of the dependence of the soil thermal conductivity on soil moisture (Schulz et al. 2016). A comparison of this experiment with the operational COSMO model at DWD as reference is shown in Fig. 3. The experimental period is 11 February to 25 March 2019, i.e. six weeks. The figure shows the diurnal cycles of the dew point temperature, atmospheric temperature and relative humidity, all at 2-m above ground, averaged over the whole period. The experiment is substantially drier, as seen in the dew point temperature and relative humidity. This is mainly due to the new formulation of bare soil evaporation, which corrects for the systematically overestimated moisture fluxes of the reference model version. Furthermore, the simulated diurnal amplitude of the 2-m temperature is increased in the experiment. This is partly due to the decrease of the latent heat flux and its cooling effect, and partly due to the skin temperature formulation. The reference model version shows a substantial moist bias which is almost completely removed in the experiment (see Fig. 4). A pronounced cold bias during daytime in the reference model is considerably reduced in the experiment. The root mean square errors of the humidity and temperature fields are significantly reduced during the whole day.

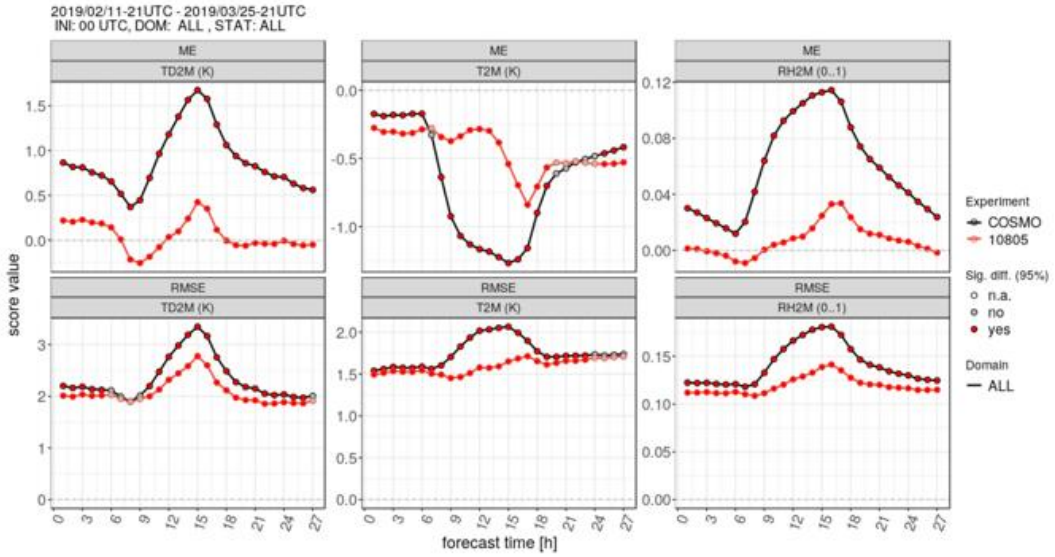


Figure 4: Same as Fig. 3, but for the mean error (ME) and the root mean square error (RMSE) of TD2M, T2M and RH2M.

5 Activity performed ad CIRA: High resolution simulations for the representation of Urban Heat Islands over South Italy (E. Bucchignani, P. Mercogliano)

Numerical simulations have been performed in order to test the capabilities of the COSMO-LM model with TU in reproducing the main climate features of urban areas, and in particular, of the UHIs in a selected area of southern Italy. Tests have been performed over a domain centred over Campania and Lazio region (Fig. 5), employing a spatial resolution of 0.009°(about 1 km), for two selected test cases: the first one (A) is 8-10 August 2017, since in these days the city of Naples experienced extreme temperature and uncomfortable conditions for the population. The second one (B) is 6-8 June 2019, since in these days a sudden increase of the daily maximum temperature was recorded, from about 27 °C to about 33 °C. Therefore, these periods represent a suitable benchmark to test the urban parametrization of COSMO-LM.

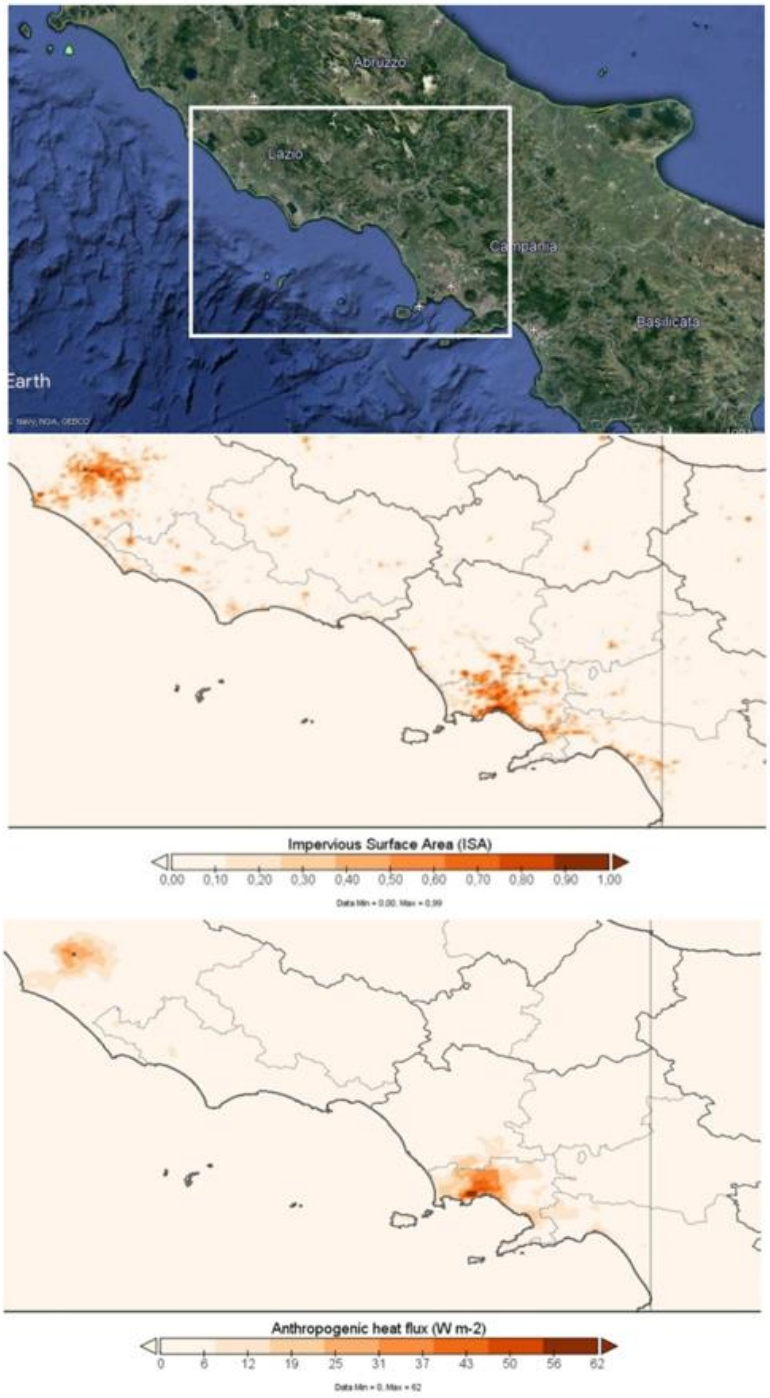


Figure 5: top: the computational domain; middle: impervious surface area; bottom: anthropogenic heat flux distributions.

Two different schemes of canopy parametrizations with respect to the surface energy balance have been considered: the "surface energy balance equation" solved at the ground surface (canopy energetically not represented, itype_canopy = 1) and the skin temperature formulation (itype_canopy = 2). In the second case, the value of implicitness of the vegetation-skin temperature parametrization (cimpl) must be specified. Previous sensitivity tests showed that this second option leads to a better representation of the urban/rural contrasts in surface-atmosphere exchanges, which was found to reduce the negative bias in the UHI in-

tensity. This option also allows investigating the effects of vegetation insulation on urban climate. For each day considered, the following simulations have been performed:

- **NOURB**: Setting OFF the TU scheme
- **URB**: Setting ON the TU scheme and itype_canopy =1
- **URB_itc2**: Setting ON the TU scheme and itype_canopy =2, cimpl =120
- **URB_itc22**: Setting ON the TU scheme and itype_canopy =2, cimpl = 600

Model evaluation has been performed in terms of 2m temperature (T_2m) and 2m relative humidity (Rel_hum) against the following observational data:

- hourly time series of T_2m and Rel_hum provided by the University of Naples, meteorological station located in Fuorigrotta quarter (urban area 14.19°E, 40.82°N).
- daily time series of T_2m and Rel_hum provided by SCIA ISPRA for the rural station of Grazzanise.

In the figures of the next section, observational values are identified as OBS.

5.1 Test case A: 8 - 10 August 2017

Fig. 6 shows the time series of T_2m over the period 8-10 Aug 2017 at the urban area of Naples (top) and the rural area of Grazzanise (bottom). For Grazzanise, only max and min daily observational values are available. The middle panel shows the spatial T_2m distribution for Aug 10th 2017 at 13.00 in a series of points close to Naples location (Naples is located in point 8). AHF is the Anthropogenic Heat Flux Distribution. In Naples, for this test case, it is evident (see also values shown in Tabs. 1-2-3) that URB simulation improves the representation of the mean daily T_2m values with respect to NOURB (improvements larger than 1 °C). Moreover, URB significantly increases the daily minimum values and this has a positive effect in the reduction of the bias. Benefits are achieved also for the daily maximum temperature, anyway a general underestimation with respect to observational data is still evident. The usage of "skin temperature scheme" does not provide any change, as it should not make a significant effect on the temperature in urban areas, because when TU is switched on, it uses a very high skin-layer conductivity for urban areas. Tab. 4 shows the spatial correlation values between simulated (all the simulations) and observed time series of T_2m, revealing that URB values are better correlated to observation than NOURB values. In Grazzanise as expected, URB simulation does not provide changes on the maximum temperature (Tab. 5), but an increase on the minimum one (Tab. 6). This has positive effects on reducing the bias in some days, but in other cases has a negative effect. The usage of itype_canopy=2, as expected in points where AHF is zero or very low, decreases the nocturnal temperatures in rural areas and increase the UHI intensity (urban-rural temperature difference). Setting cimpl = 600 does not provide relevant improvements. Fig. 7 shows the time series of relative humidity (Rel_hum) over the period 8-10 Aug 2017 at (a) the urban area of Naples and (c) the rural area of Grazzanise. For Grazzanise, only daily average observational values are available. Panel (b) shows the spatial Rel_hum distribution for Aug 10th 2017 at 13.00 in a series of points close to Naples location.

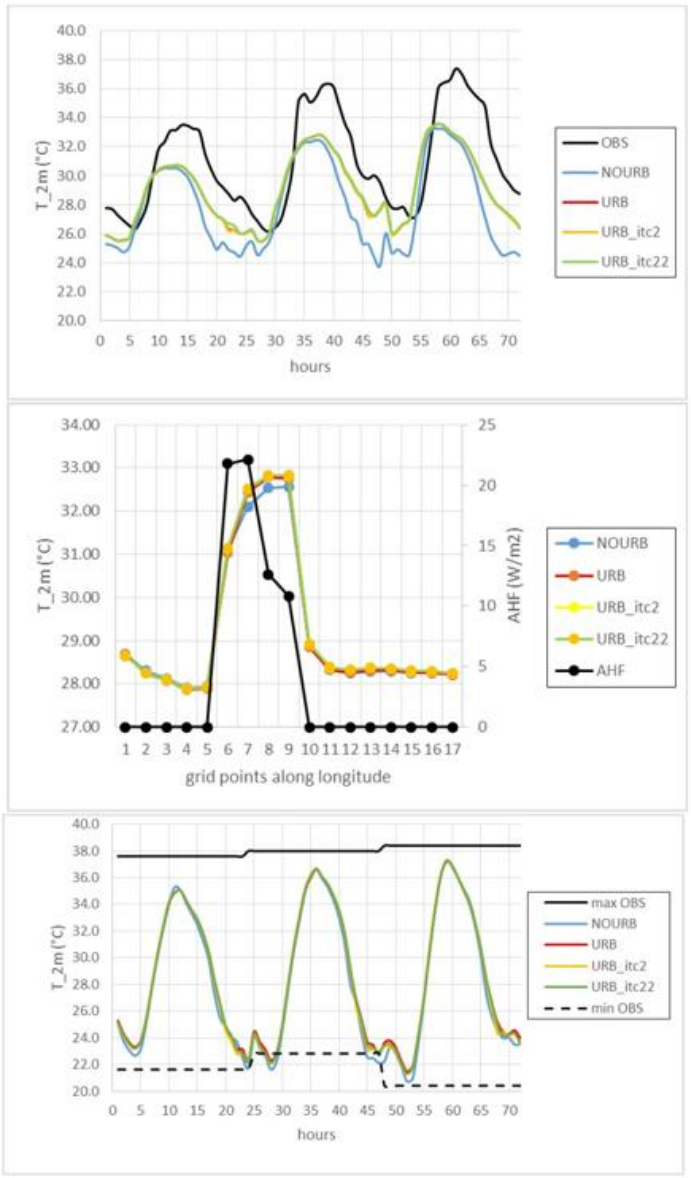


Figure 6: Time series of T_2m over the period 8-10 Aug 2017 at the urban area of Naples (top) and the rural area of Grazzanise (bottom); middle panel: spatial T_2m distribution for Aug 10th 2017 at 13.00 in a series of points close to Naples location (Naples is located in point 8). AHF is the Anthropogenic Heat Flux Distribution.

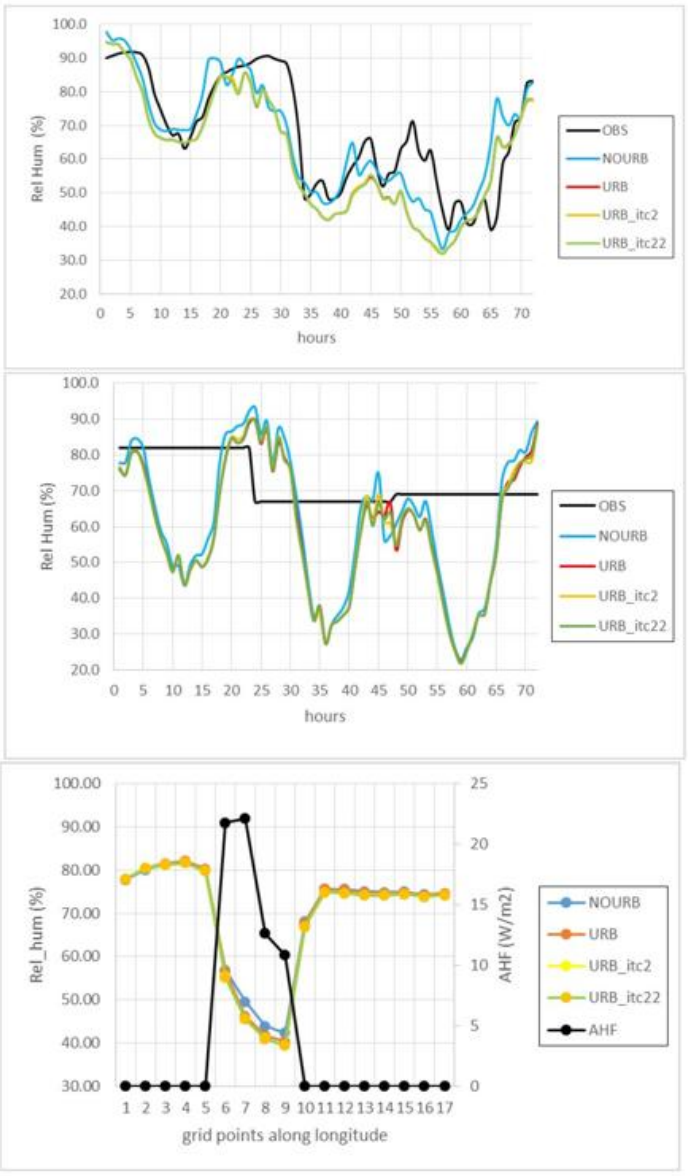


Figure 7: Time series of Rel_hum over the period 8-10 Aug 2017 at the urban area of Naples (top) and the rural area of Grazzanise (bottom). For Grazzanise, only daily average observational values are available; middle panel: spatial Rel_hum distribution for Aug 10th 2017 at 13.00 in a series of points close to Naples location

In Naples, URB simulation provides lower values of relative humidity with respect to NOURB (Tab. 7), leading to a general worsening of performances, with few exceptions. A slight improvement is recorded assuming itype_canopy =2: in fact Tab. 8 shows that in this case simulated values are better correlated to observations. A similar behaviour is recorded also in Grazzanise (Tab. 9), since in this rural area the usage of itype_canopy=2 provides slight better values with respect to itype_canopy = 1. In general, the configuration with itype_canopy=2 does not show consistent improvements with respect to other test cases where it has been tested. This is probably due to the short distance from the sea of the city of Naples. Further investigations need to be done to confirm this hypothesis.

	OBS	NOURB	URB	URB_itc2	URB_itc22
08 Aug 2017	33.5	30.5	30.7	30.7	30.7
09 Aug 2017	36.3	32.4	32.8	32.8	32.8
10 Aug 2017	37.4	33.2	33.6	33.6	33.6

Table 1: Daily maximum values of T_2m in Naples (urban) for the three days considered.

	OBS	NOURB	URB	URB_itc2	URB_itc22
08 Aug 2017	26.3	24.4	25.5	25.5	25.5
09 Aug 2017	26.1	23.7	25.5	25.5	25.5
10 Aug 2017	27.2	24.4	26.0	26.0	26.0

Table 2: Daily minimum values of T_2m in Naples (urban) for the three days considered.

	OBS	NOURB	URB	URB_itc2	URB_itc22
08 Aug 2017	29.9	27.2	28.0	28.0	28.1
09 Aug 2017	31.2	28.2	29.4	29.3	29.4
10 Aug 2017	31.8	28.2	29.8	29.7	29.8

Table 3: Daily mean values of T_2m in Naples (urban) for the three days considered.

	NOURB	URB	URB_itc2	URB_itc22
08 Aug 2017	0.74	0.84	0.84	0.85
09 Aug 2017	0.82	0.90	0.90	0.91
10 Aug 2017	0.76	0.76	0.76	0.77

Table 4: Spatial correlation between simulated and observed time series of T_2m in Naples (urban).

	OBS	NOURB	URB	URB_itc2	URB_itc22
08 Aug 2017	37.6	35.3	35.1	35.0	35.0
09 Aug 2017	38.0	36.6	36.6	36.7	36.6
10 Aug 2017	38.4	37.3	37.2	37.3	37.2

Table 5: Daily maximum values of T_2m in Grazzanise (rural) for the three days considered.

	OBS	NOURB	URB	URB_itc2	URB_itc22
08 Aug 2017	21.6	21.7	22.3	22.2	22.2
09 Aug 2017	22.8	21.6	22.2	22.0	22.1
10 Aug 2017	20.4	20.7	21.5	21.2	21.3

Table 6: Daily minimum values of T_2m in Grazzanise (rural) for the three days considered.

	OBS	NOURB	URB	URB_itc2	URB_itc22
08 Aug 2017	81.3	82.2	77.9	78.0	77.8
09 Aug 2017	66.5	61.0	56.4	56.4	56.4
10 Aug 2017	56.5	55.2	49.5	49.4	49.4

Table 7: Daily mean values of Rel_Hum in Naples (urban) for the three days considered.

	NOURB	URB	URB_itc2	URB_itc22
08 Aug 2017	0.89	0.85	0.89	0.89
09 Aug 2017	0.94	0.91	0.94	0.94
10 Aug 2017	0.34	0.33	0.33	0.34

Table 8: Spatial correlation between simulated and observed time series of Rel_Hum in Naples (urban).

	OBS	NOURB	URB	URB_itc2	URB_itc22
08 Aug 2017	82.0	70.2	67.0	67.2	67.0
09 Aug 2017	67.0	59.3	56.9	57.0	56.8
10 Aug 2017	69.0	56.5	53.8	53.8	53.7

Table 9: Daily mean values of Rel_Hum in Grazzanise (rural) for the three days considered.

5.2 Test case B: 6 - 8 June 2019

For this test case, only urban simulations assuming itype_canopy = 1 have been performed. Fig. 8 shows the time series of T_2m over the period 8-10 Aug 2017 at the urban area of Naples (top) and the rural area of Grazzanise (bottom). For Grazzanise, only max and min daily observational values are available. In the urban area of Naples, the maximum daily values increase of 0.6 °C (on 6th), 0.8 °C (on 7th) and 0.6 °C (on 8th), but anyway a general underestimation with respect to observational data is still evident. Improvements is confirmed by the higher values of correlation for URB simulation with observations (Tab. 10). In Grazzanise, URB simulation generally does not provide changes on the temperature values, apart from a few nocturnal values that are increased. The diurnal cycle amplitude is always underestimated with respect to observations. Fig. 9 shows the time series of Rel_hum over the period 8-10 Aug 2017 at (a) the urban area of Naples and (c) the rural area of Grazzanise. For Grazzanise, only daily average observational values are available. In Naples, URB simulation provides lower values of humidity, which are better correlated to observation than NOURB (Tab. 11). Also in the rural area of Grazzanise, URB provides a general increase of performances.

	NOURB	URB
06 Jun 2019	0.69	0.76
07 Jun 2019	0.72	0.83
08 Jun 2019	0.43	0.49

Table 10: Spatial correlation between simulated and observed time series of T_2m in Naples (urban).

	NOURB	URB
06 Jun 2019	0.38	0.58
07 Jun 2019	0.59	0.92
08 Jun 2019	0.28	0.55

Table 11: Spatial correlation between simulated and observed time series of Rel_hum in Naples (urban).

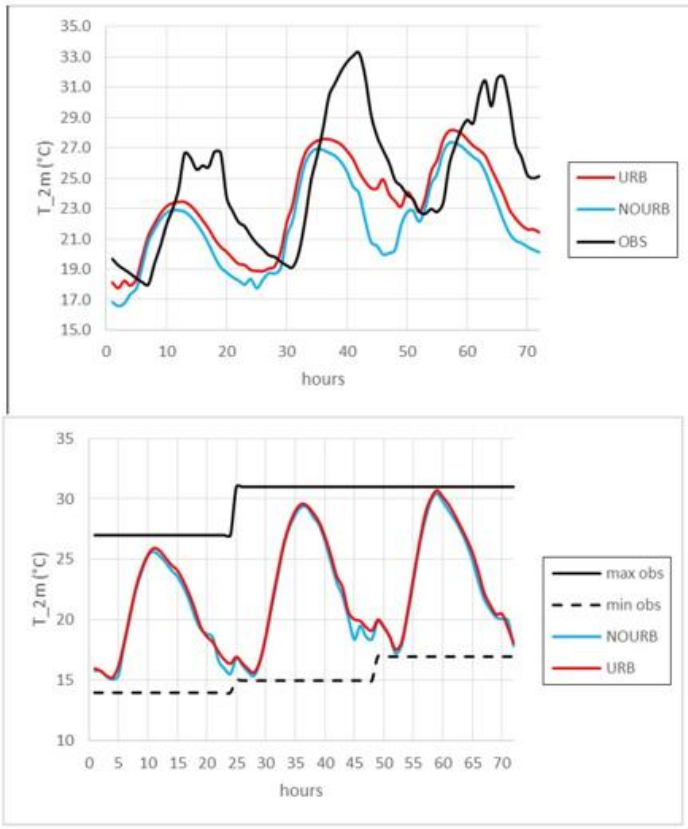


Figure 8: Time series of T_2m over the period 6-8 Jun 2019 at the urban area of Naples (top) and the rural area of Grazzanise (bottom).

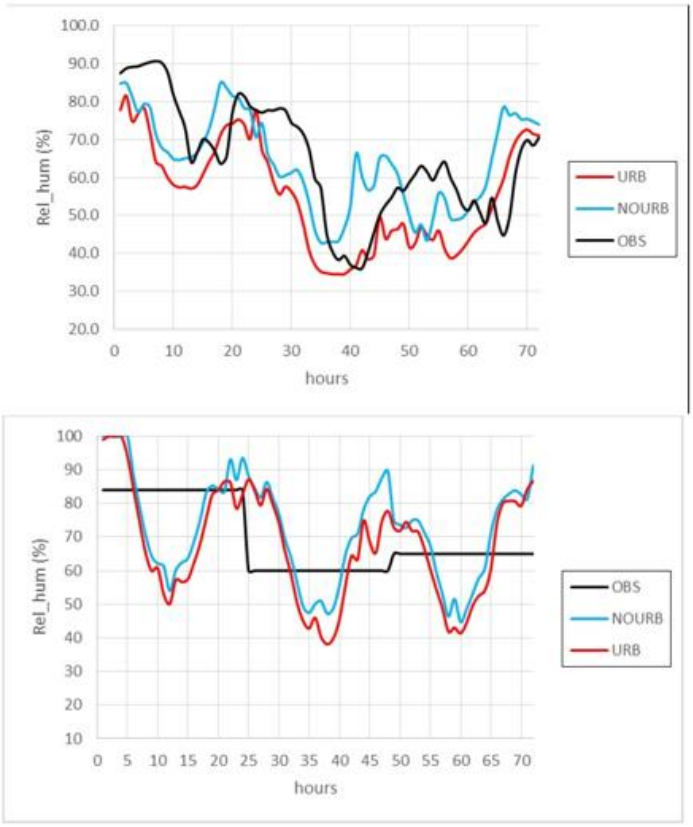


Figure 9: Time series of Rel_hum over the period 6-8 Jun 2019 at the urban area of Naples (top) and the rural area of Grazzanise (bottom).

6 Activities performed at RHM: high resolution simulations of the urban heat island of Moscow megacity (M. Varentsov, I. Rozinkina, G. Rivin, D. Blinov, A. Kirsanov)

The simulations for the selected cases were performed using the same modelling framework that was used in the previous modelling studies for Moscow (Varentsov et al., 2018; 2019). A chain of nested domains (D3-D1) was used, for a dynamic downscaling of the ERA-Interim reanalysis data for Moscow region for the periods of selected case-studies (about 15 days). The horizontal grid spacing for the domains D3, D2 and D1 was 12, 3 and 1 km respectively (Fig. 10). The TERRA_URB scheme was used only for the final D3 domain with 1-km grid step (180x180 grid cells). In contrast to tests for other cities, where default external parameters AHF and ISA from EXTPAR were used, for Moscow region these external fields were clarified based on OpenStreetMap data (Samsonov et al., 2015; Varentsov et al., 2017; Varentsov et al., 2017).

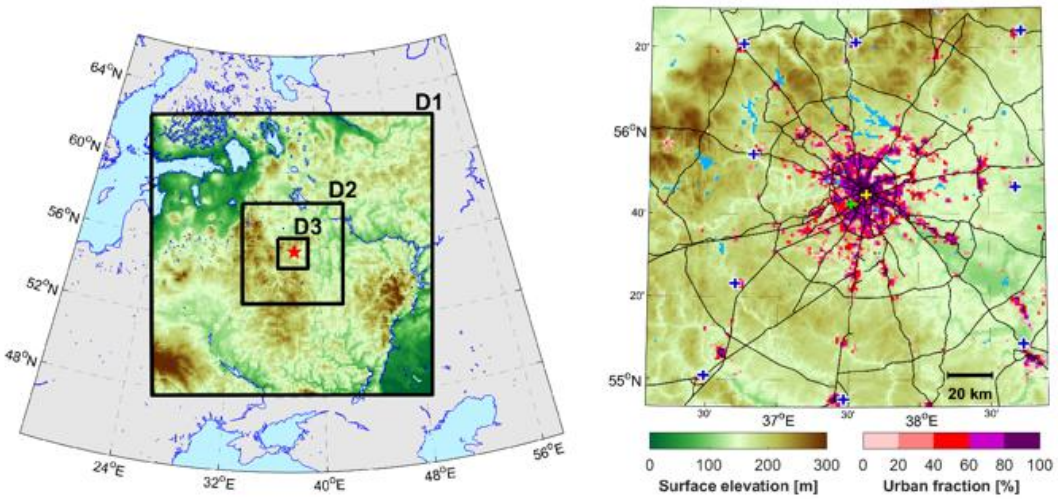


Figure 10: The configuration of the nested domains, used for simulations with the COSMO model, with surface elevation shown by the color scale, and water surfaces shown by the light-blue color (left). A detailed map of the finest D3 domain, used for the urban climate simulations with the COSMO-CLM model coupled to TERRA_URB, with urban fraction shown by an additional color scale (right). The location of the weather stations used for the estimation of the urban heat island (UHI) intensity is also shown (right). The yellow cross indicates Balchug station (considered as the city center), the green cross indicates MSU (Moscow State University) station, and blue crosses indicate the nine rural reference stations around Moscow. The black lines represent the primary road network (right).

For each considered case, three different simulations were performed. The older model version COSMO5.0_clm9_urb was used in the simulations called v5_REF and v5_MOD. In v5_REF simulations, the default values were used for the most of namelist settings; in the v5_MOD simulations, it was used the namelist settings that were carefully tuned in the previous modelling studies for Moscow in order to minimize the systematic model errors, including the well-known nocturnal warm bias. The most important differences between the tuned and default setup include the changes of the minimum coefficients of turbulent diffusion (tkhmin and tkmmin) and the scale of the subgrid thermal inhomogeneity (pat_len) according to (Cerenzia et al., 2014), the use of a new parametrization of bare soil evaporation (Schulz & Vogel, 2016) and a new skin-layer temperature scheme (Schulz & Vogel, 2017). The last set of simulations, v505_REF, was performed with a use of the new model version 5.05urb4. In general, the default namelist settings were used for v505_REF simulations, however, these settings are different from the default settings of the model version 5.0. It is important to highlight that all of new turbulence developments were switched on in simulations with 5.05 model version (loldtur = FALSE). The skin-layer temperature scheme was not used in the simulations with new model version. The key differences among namelist settings for v5_REF, v5_MOD and v505_REF simulations are given in Table 12.

The model verification was performed using the observational data from a dense network of the weather stations and air pollution control stations (more than 70 points in total within the D3 domain), as well as the data from the network of microwave temperature profilers MTP-5. MTP-5 profilers are remote sensing devises which provide temperature profile in the lowest 600 or 1000 m (depends on modification) with 50 m vertical resolution every 5 minutes. The MTP-5 data were provided by Lomonosov Moscow State University, A.M. Obukhov Institute of Atmospheric Physics of Russian Academy of Science (IAP RAS),

Parameter	v5_REF	v5_MOD	v5.05_REF
PHYCTL namelist			
itype_rootdp	1	2	2
itype_evsl	1	4	4
itype_heatcond	1	2	3
itype_canopy	1	2	1
calamrur (skin-layer conductivity)	-	30	-
loldtur	-	-	TRUE
TUNING namelist			
tkmmin & tkhmin	0.4	0.1 or 0.05	0.75
pat_len	500	100 or 50	100
DYNCTL namelist			
hd_corr_(t, u, p)	defaults	0.25 for all	defaults

Table 12: The key differences between namelist settings for v5_REF, v5_MOD and v5.05_REF simulations. Note that in v5_REF and v5_MOD the old turbulence was used as default.

Central Aerological Observatory (CAO) and Mosecomonitoring agency. The location of the observational sites in Moscow city and its closest surroundings is shown in Fig. 11.

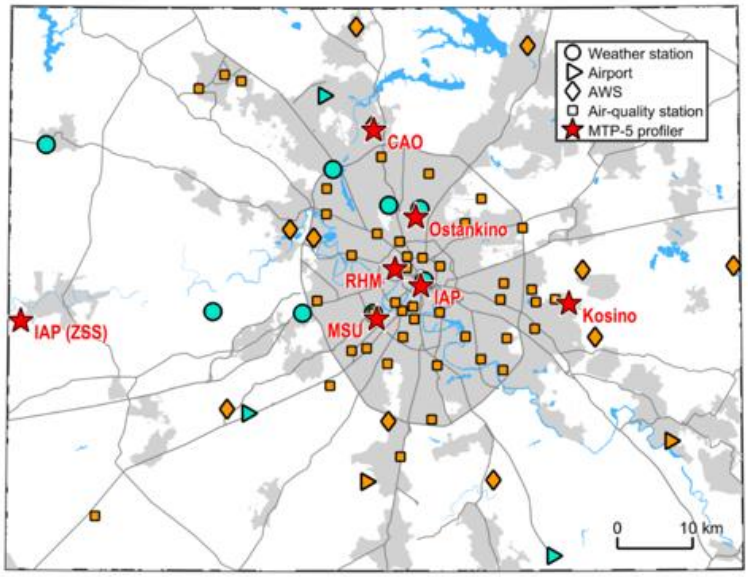


Figure 11: The location of the observational sites, used for the model verification for Moscow region. The orange colour indicates the relatively new observational sites; the cyan colour indicates the sites with long-term observational series.

The verification was focused mainly on the rural temperature and the UHI intensity (a difference between air temperature at the given urban site and mean rural temperature, averaged over 9 stations around Moscow, see Fig. 11). The UHI intensity was defined as a temperature anomaly with respect to the mean rural temperature, which was averaged over the 9 rural stations around Moscow. The greatest attention was paid to the UHI intensity in the city centre, where the Balchug weather station is located. Two case studies were considered for Moscow. The first case is from 17.05.2014 to 29.05.2014. It was a period in late spring (May) with warm, calm and clear weather which included several

days with intensive UHI. The second case study is from 01.01.2017 to 15.01.2017. It was a winter period which included a sub-period of the extremely cold weather from 6 to 10 of January, when temperature dropped below -35°Cin the countryside, and the intensive UHI was observed during more than one day under the conditions of strongly stable stratification of the atmosphere (Yushkov et al., 2019). The unique feature of winter period is that MTP-5 data were also available for city centre, for the IAP RAS site.

6.1 Test case A: 17 - 29 May 2014

For the first considered case in May 2014, the comparison between the modelling results and observations has clearly shown the significant difference between REF and MOD simulations with an older model version COSMO5.0_clm9_urb. The REF simulations strongly overestimate the nocturnal temperature at rural areas and underestimate the UHI intensity, while in the MOD simulations the nocturnal temperature and UHI intensity are much closer to the observations (Fig. 12).

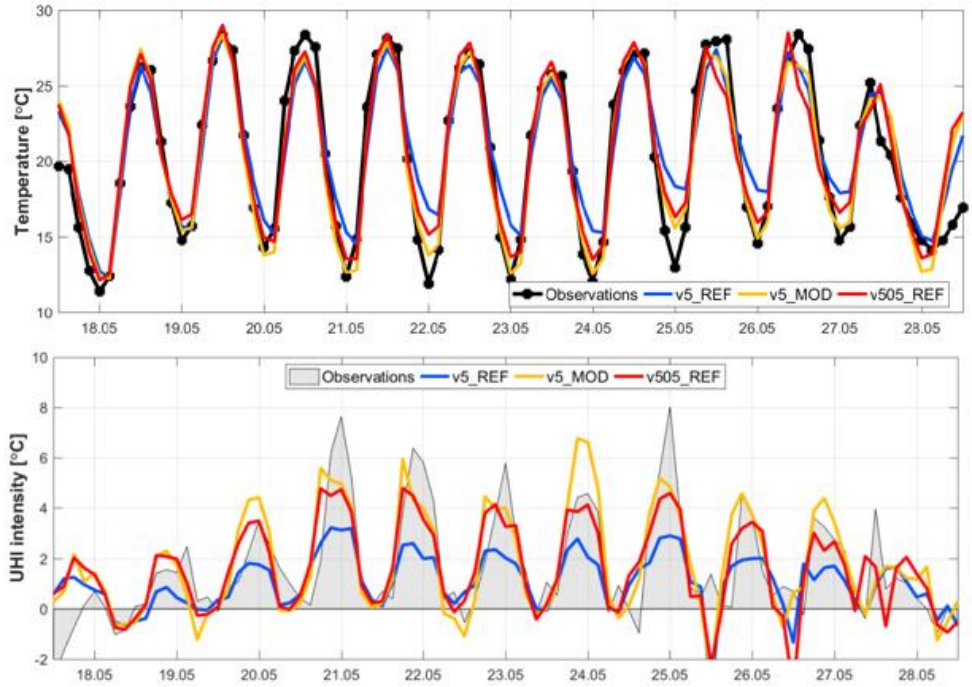


Figure 12: The variations of the mean rural air temperate and the UHI intensity for the city centre (temperature difference between the value for Balchug weather stations and the mean rural value) according to observations and modelling results for case (18-28 May 2014).

The new model version (v505_REF) simulates the rural temperate and UHI intensity almost as well as the old version with tuned settings (v5_MOD). A comparison between the simulated vertical temperature profiles and observations of MTP-5 profiler at a rural site (Zvenigorod, 50 km to the west from Moscow) and a suburb site (CAO, northern suburb of Moscow) has clearly shown that the differences between the different simulations in field of the near-surface temperature are densely linked with the differences in vertical temperature profiles. The v5_REF simulations strongly underestimate the strength of the nocturnal temperature ingestion, while v5_MOD and v505_DEF simulations reproduce it much closer to observations (Fig. 13). In general, v505_DEF simulations still slightly overestimate the

minimal nocturnal temperatures and slightly underestimate the maximum UHI intensity as well as the strength of nocturnal temperature invasion. However, the Skin Layer Temperature Scheme was not used in v505_DEF simulations, so we could expect that the use of Skin Layer Temperature Scheme in new model version will eliminate these biases. Figs. 14 and 15 show that v505_DEF simulation generally nicely captures the spatial structure of the nocturnal UHI of Moscow, as well as v5_MOD simulation.

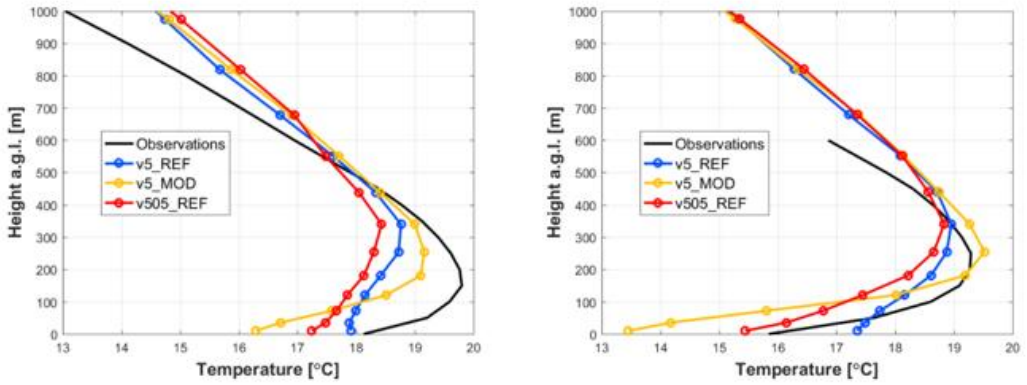


Figure 13: The observed and simulated nocturnal (00UTC) vertical temperature profiles, averaged over the period of 20-27 May 2014 for CAO suburb site (left) and Zvenigorod rural site(right).

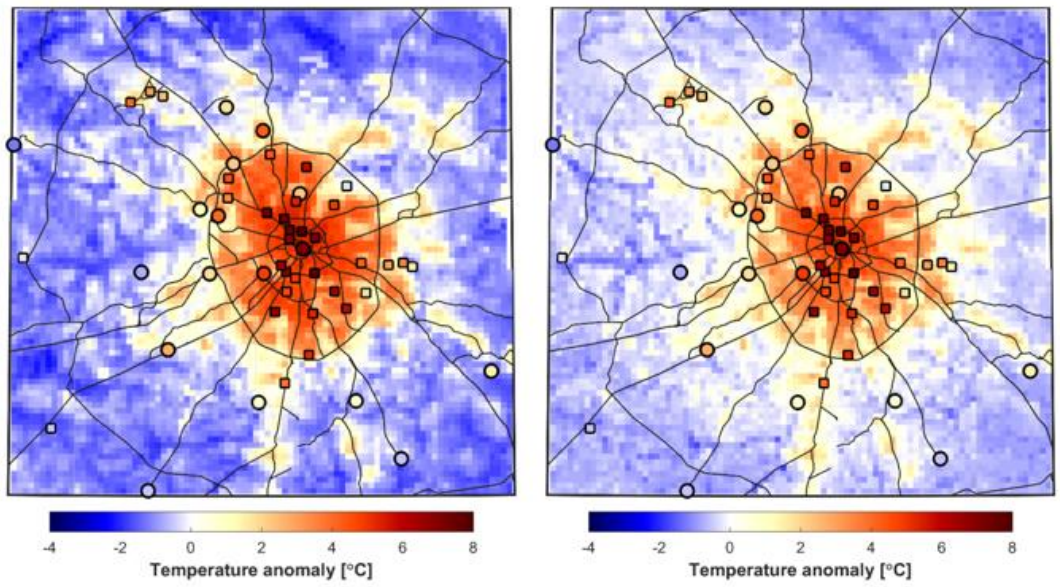


Figure 14: The spatial structure of the average nocturnal (00UTC) urban temperature anomaly in Moscow region according to observations (coloured squares and circles) and simulations v5_MOD (left) and v505_REF (right), shown as coloured background. The averaging is performed over 20-27 May 2014. The temperature anomaly is defined as a deviation from the mean rural value, averaged over 9 rural reference weather stations.

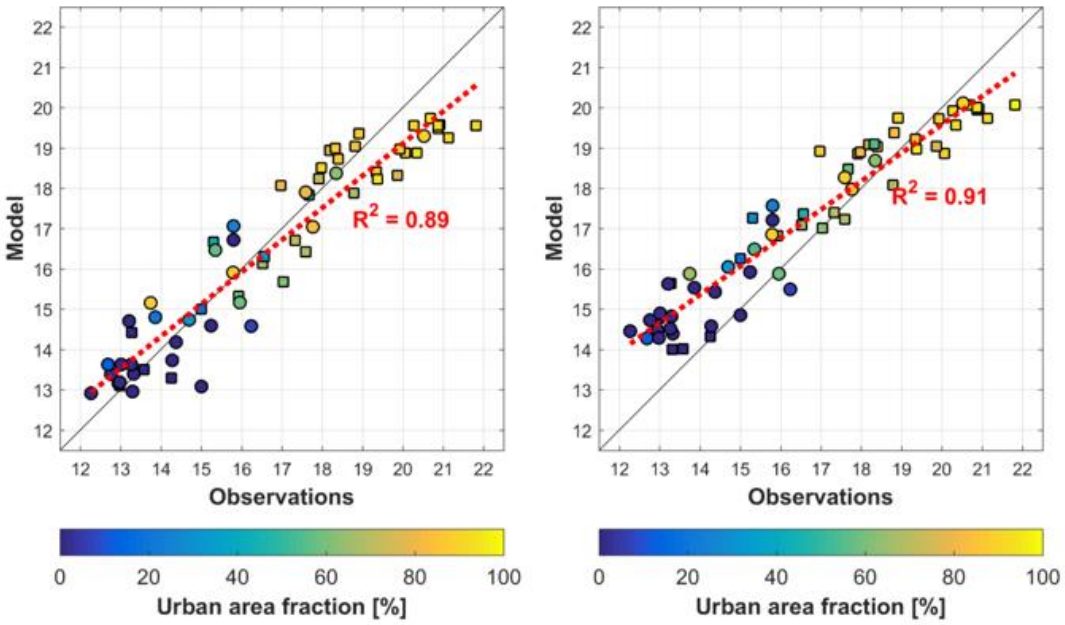


Figure 15: The dependence between the observed and modelled values of the mean nocturnal (00UTC) temperature for v5_MOD (left) and v505_REF (right) simulations. The averaging is performed over 20-27 May 2014. Each point corresponds to a different weather station (circles) or air-quality control stations (squares), the colour of the point represents the urban area fraction for corresponding model grid cell.

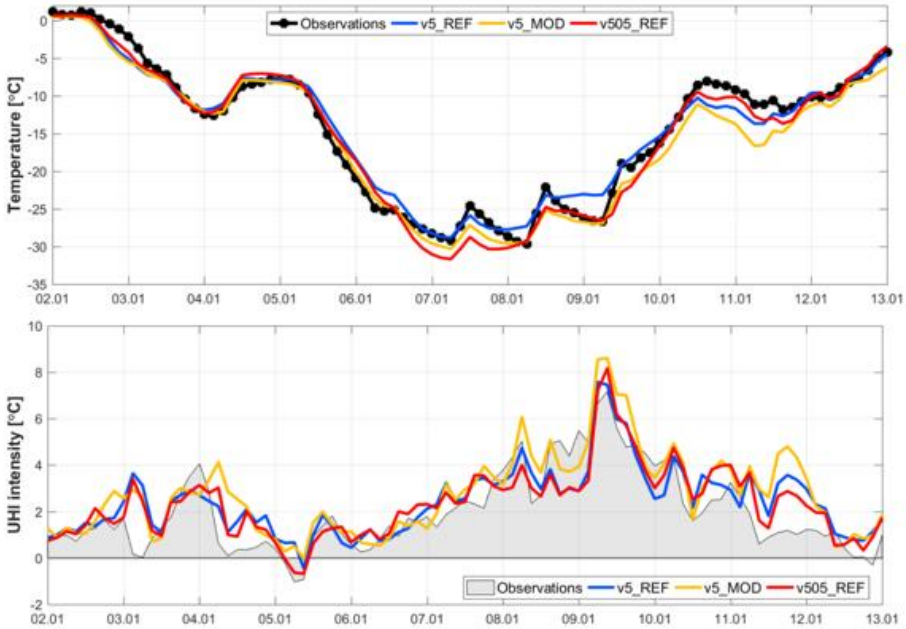


Figure 16: The variations of the mean rural air temperate and the UHI intensity for the city centre (temperature difference between the value for Balchug weather stations and the mean rural value) according to observations and modelling results for case (2-13 January 2017).

6.2 Test case B: 1 - 15 January 2017

For the winter case, all of the considered model runs generally nicely simulate the temporal dynamics of the mean rural air temperature and the UHI intensity for the city centre during this case (Fig. 16). The simulation with the newest model version, 5.05urb, has a cold bias for the peak of cooling at 7th of January, but shows the best correlation with observations, especially after the peak of cooling. Despite a very simple approach used for the AHF definition in TU, the simulations capture the dynamics of the UHI intensity quite nicely. The considered case allows verifying the model ability to simulate the spatial structure of the UHI in different conditions. At 8th of January the UHI was shifted to the southwest by prevailing north-eastern wind, and at the 9th January the UHI was collocated with the urban areas under calm weather conditions. The model generally successfully captures these features; however, the v505_REF simulation shows a lower agreement with observations than v5_MOD simulation (Fig. 17). The data from the network of MTP-5 profiles give a unique possibility to evaluate the vertical temperature profiles in the rural and urban sites during the period of frosty weather. All of the model runs successfully simulate the intensive temperature inversion in the lower atmosphere, which was observed during the last day of the frosty period and promoted the development of the UHI (Fig. 18). The model run with old model version without tuning, v5_REF underestimates the strength of inversion and overestimates the near-surface temperatures. The tuned model run with the old version (v5_MOD) captures the observed vertical temperature profile the best. The model run with the new version (v505_REF) also captures the near-surface temperatures and the inversion strength, but overestimates the height of inversion. All of the model runs successfully simulate the difference between rural and urban temperature profiles, including the UHI in the lowest 100 m above the ground, and a negative temperature anomaly over the city. Such anomaly corresponds to a so-called crossover-effect, which is known from the literature but is still poorly investigated (Khaikine et al., 2006; Lokoshchenko et al., 2016).

The key conclusion from the presented verification results is that the new version of COSMO model including TU, 5.05urb4, in general successfully simulates the key features of the UHI of Moscow megacity for the considered cases, including the spatio-temporal variations of the UHI intensity. The results obtained with the new version (v505_REF runs) are generally consistent with the results obtained with the old version COSMO5.0_clm9_urb (v5_REF and v5_MOD runs). Moreover, even without any special tuning, the simulations with the new model version (v505_REF runs) show almost as good verification results as the carefully tuned simulations with the old model version (v5_MOD runs). Such result indicates the improvements that come from a use of the new ICON-based model physics in the new model version. However, in some cases the new model version is still not perfect, which is shown based on the example of the extreme winter frosts in Moscow. Further improvements are expected from the tuning and calibration of the new model version, including the tuning for the namelist settings, the use of the skin-layer temperature scheme and the improvements of the external parameters for the TERRA_URB scheme.

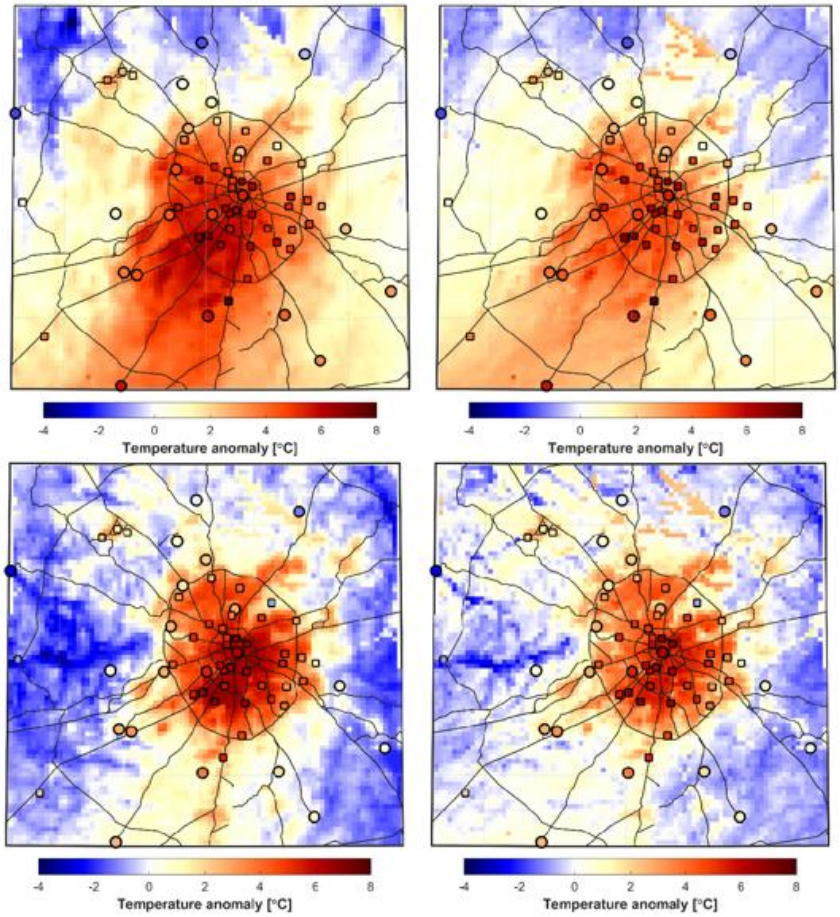


Figure 17: The spatial structure of the urban temperature anomaly in Moscow region according to observations (coloured squares and circles) and simulations v5_MOD (top left,bottom left) and v505_REF (top right, bottom right), shown as coloured background. The averaging is performed over the whole day of 8th of January 2017 (top panels) and 9th of January 2017 (bottom panels). The temperature anomaly is defined as a deviation from the mean rural value, averaged over 9 rural reference weather stations.

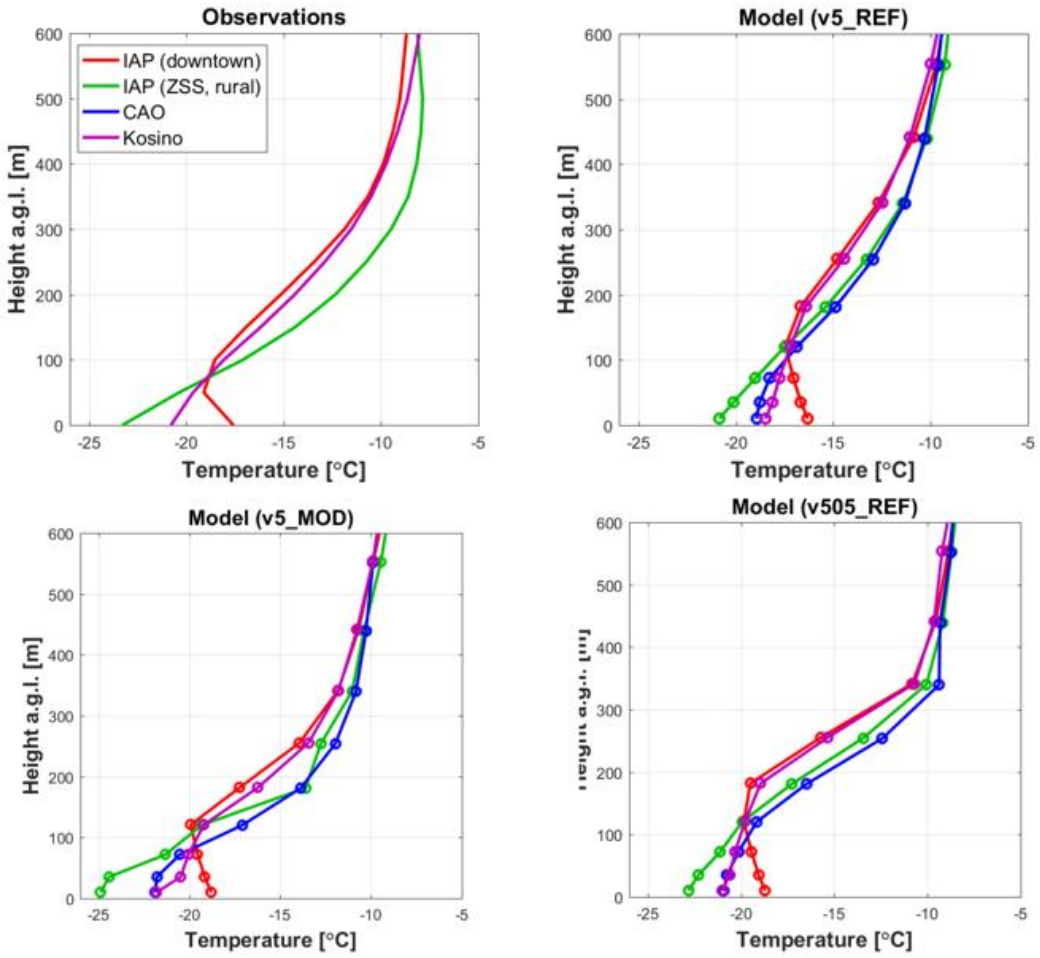


Figure 18: The vertical temperature profiles, averaged of 9th of January 2017, for four sites of Moscow region according to observations (top left) and different model runs (top right and bottom panels). The sites are: city centre (IAP site), rural area near Zvenigorod in 50 km to the west from Moscow (IAP ZSS site), Kosino site in the eastern suburb and CAO site in the northern suburb. The observations for CAO site are not available for the considered period.

7 Activities performed at Arpa Piemonte (V. Garbero, M. Milelli)

This study uses COSMO runs over a domain that includes the Piemonte region (Fig. 19) with a 1 km grid step (480x320 grid cells), driven by initial and boundary conditions provided by the ECMWF Operational Analysis at 9 km horizontal resolution every 6 hours. Simulations were conducted by activating or not the urban scheme TERRA_URB and by using different schemes to calculate the surface temperature, the canopy scheme or the skin conductivity scheme respectively. The urban scheme needs new external parameters (Fig. 21), ISA (impervious surface area) and AHF (anthropogenic heat flux), while the conductivity scheme requires the skin conductivity field (SKC, Fig. 22): all these parameters have been provided by EXTPAR.

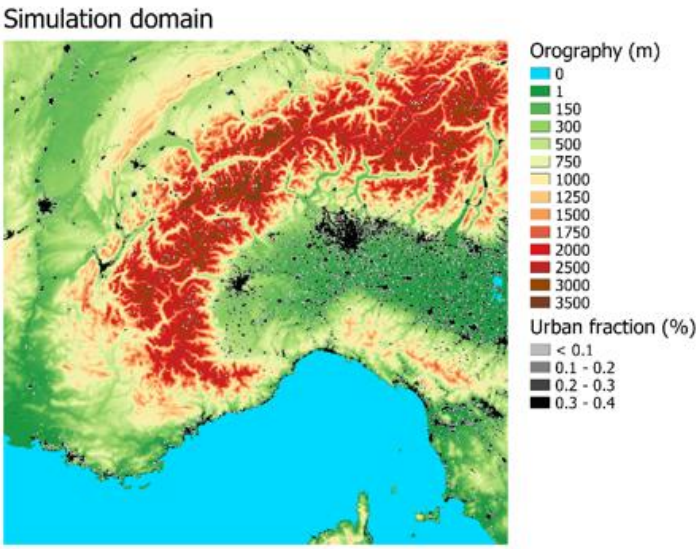


Figure 19: Domain of the simulations.

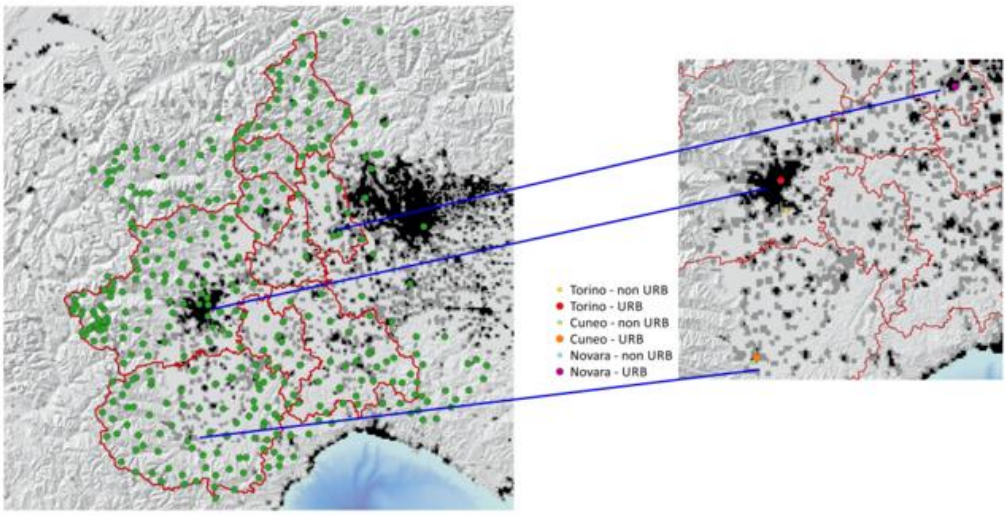


Figure 20: Ground network (left) with the rural/urban stations of the main cities, Torino, Cuneo and Novara (detail on the right).

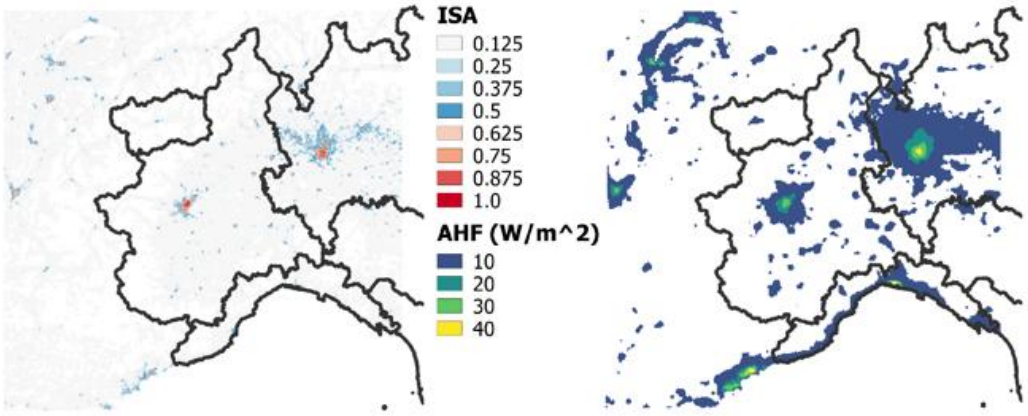


Figure 21: ISA (left) and AHF (right) fields.

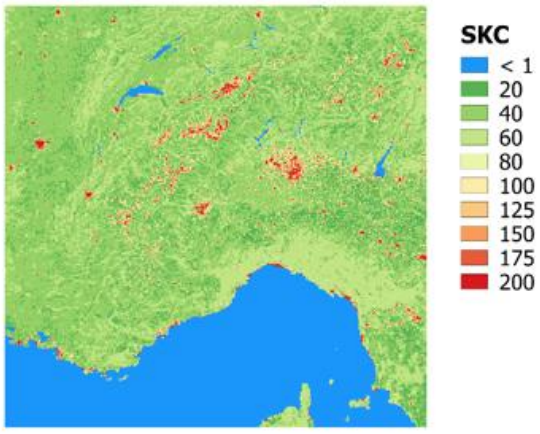


Figure 22: SKC field.

First of all a careful analysis of the UHI in the main cities has been conducted (see Fig. 20), starting from the study of Milelli (2016) and Milelli et al. (2017). In Figs. 24, 25 and 26 the UHI (difference between T2m_urban and T2m_rural) of Cuneo, Novara and Torino (respectively) has been compared. As expected, In Cuneo and Novara the effect is much less evident then in Torino, being smaller cities, nevertheless in Cuneo there is an indication of UHI influence. Therefore, for the selection of the case studies, we focused on the Torino area (Fig. 23), selecting stations 1 and 9 as reference for urban and rural area respectively. After looking at the UHI index defined as $T2m_urban - T2m_rural$ (see Fig. 27), two case studies

have been selected, one in July 2015 (case A) and the other one in October 2017 (case B). The general scheme of the runs is described in Tab. 13.



Figure 23: Location of the observation stations considered in the Torino area.

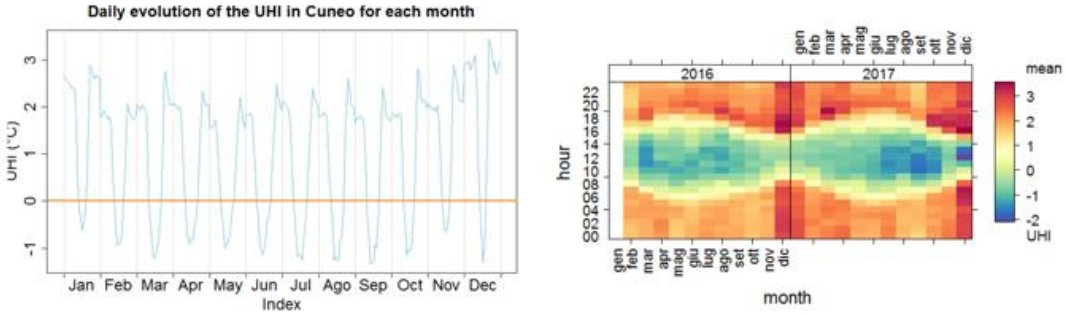


Figure 24: Mean daily UHI in Cuneo in 2016 and 2017 (left) and month by month (right).

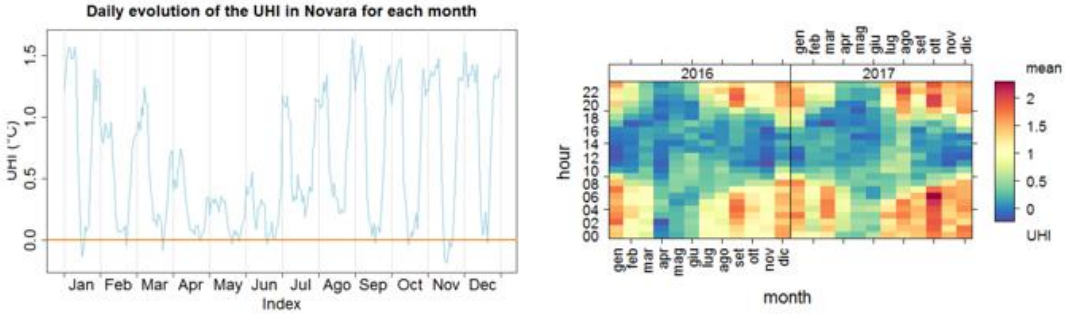


Figure 25: Mean daily UHI in Novara in 2016 and 2017 (left) and month by month (right).

		SKIN T	
		OFF	ON
TERRA_URB	OFF	CC1	CC2
	ON	UC1	UC2

Table 13: Scheme of the simulations.

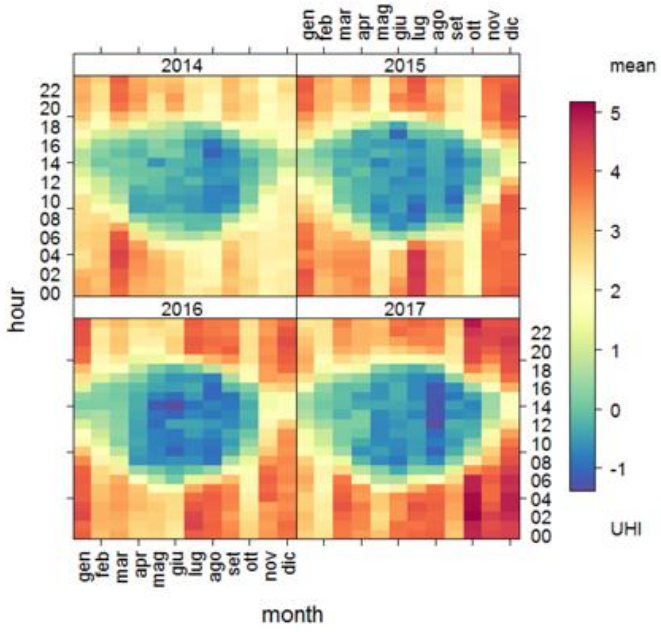


Figure 26: Mean daily cycle of UHI in Torino during 2014-2017 month by month.

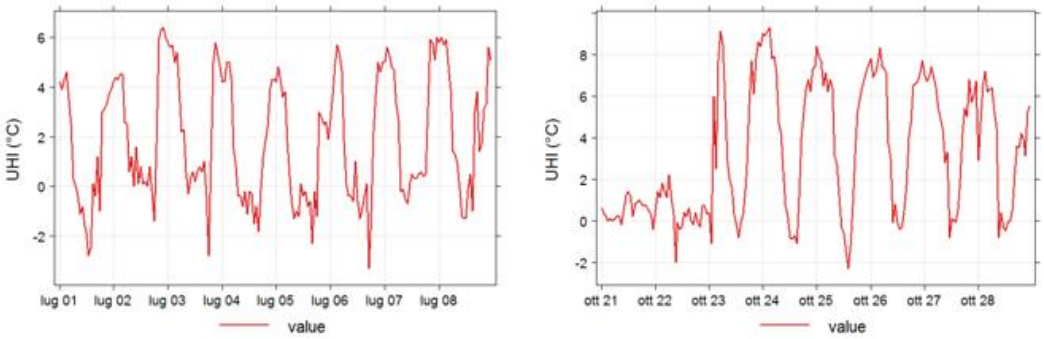


Figure 27: Detail of UHI in Torino in July 2015 (left) and October 2017 (right).

7.1 Test case A: July 2015

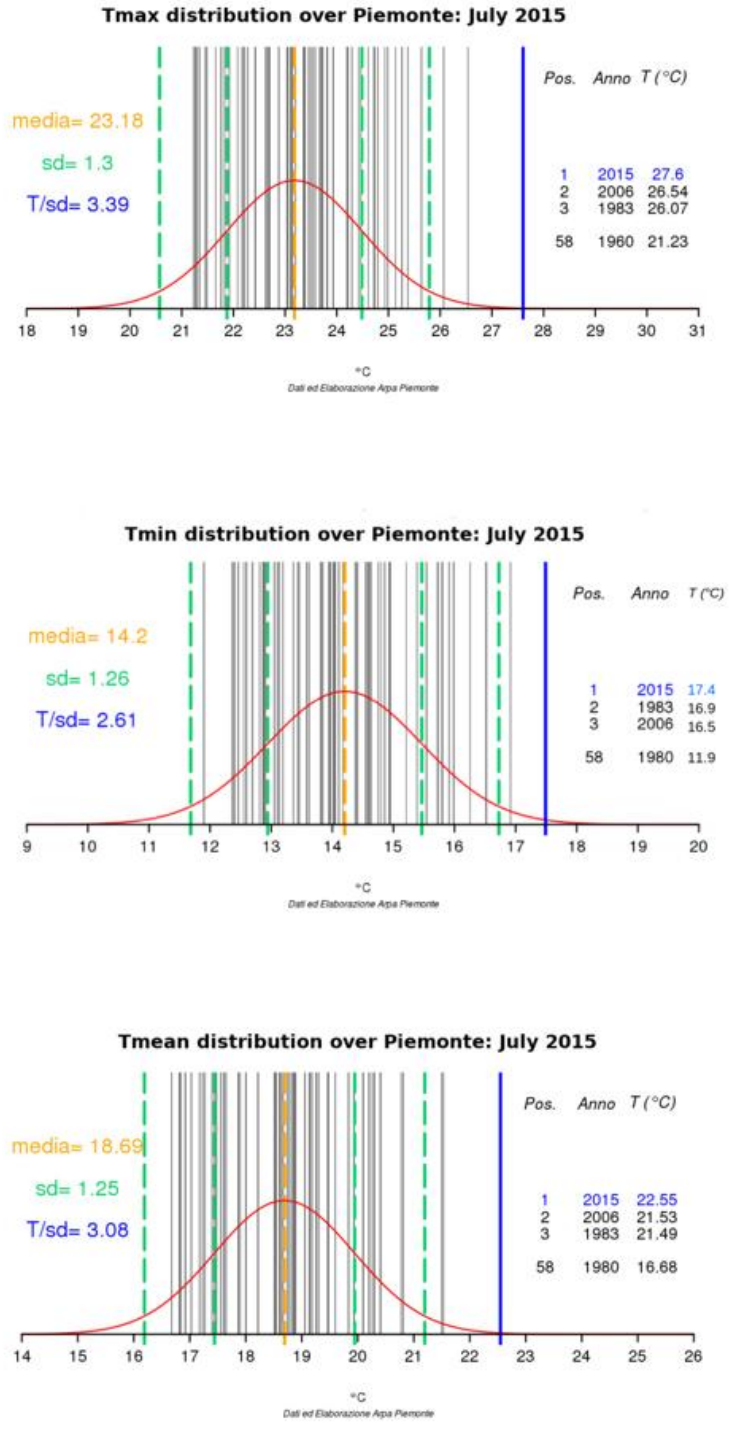


Figure 28: Distribution of T2m max (top), min (middle) and mean (bottom) in July 2015 over Piemonte.

During the first half of July 2015, an intense heat wave stroke Northern Italy with extreme temperature values and uncomfortable conditions for the population. In particular July 2015 has been the hottest July since 1958 (Fig. 28). It comes out that July 2015 is ranked first

in all the measurements. In Torino, the maximum temperature reached 38.5°C during that period and ground stations data pointed out the presence of a clear UHI effect. This is the reason why this area and this period represent a suitable benchmark to test the capabilities of COSMO, and in particular of the urban parametrisation. The simulation in hindcast mode focused on the first week (20150701 00UTC - 20150707 00UTC). In Fig. 29 is plotted the mean bias of UHI index averaged over the entire period of simulation, for the 4 runs. In general the introduction of TERRA_URB (UC1 and UC2) changes the sign and reduces the bias with respect to the respective runs without (CC1 and CC2), although in Cuneo and Novara there is a slight worsening. The effect is more pronounced using Torino Consolata which is in fact the referent urban station in Torino. The SKC scheme improves the UHI slightly (runs CC2 and UC2) with respect to CC1 and UC1.

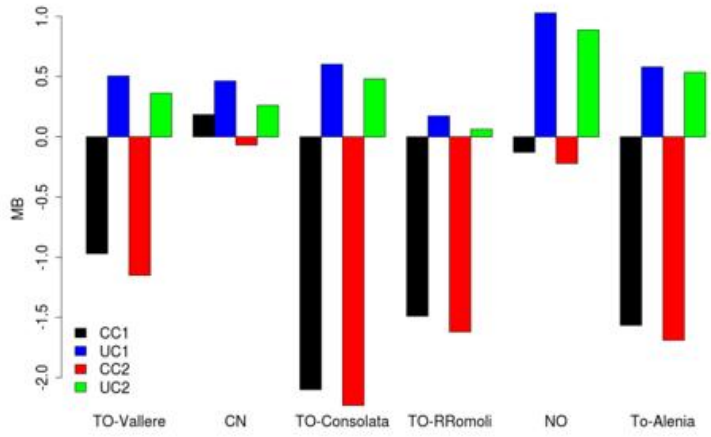


Figure 29: Mean Bias of UHI index over the entire period in a selection of stations. For Torino, different urban stations are used here.

Looking at the mean diurnal cycle, in Fig. 30 we plotted the MB and the RMSE using different samples of stations. In the top row the verification is performed with the whole network available (Fig. 20). The differences among the four runs are negligible, but this is a positive result because the impact of TERRA_URB should be limited to urban areas which are much less extended than rural ones. In the bottom row, the same plots have been made with urban stations only. There it is possible to appreciate the improvement of the new parametrisation, although there is a general heating as it can be better seen in the bias plot. Concerning the impact of SKC, a small difference (in positive direction) can be seen only during night time. Finally, having a look at Fig. 31, the time series of UHI index in Torino are plotted for the entire period. In each graph we compare only two pairs of runs, to better highlight the differences. In the first row it is evident the impact of TERRA_URB with a strong improvement during the night, catching the positive peaks of UHI. On the other hand, during day time the negative peaks of UHI are not seen by the model, with or without urban parametrisation. In the bottom row, SKC seems to have a neutral impact.

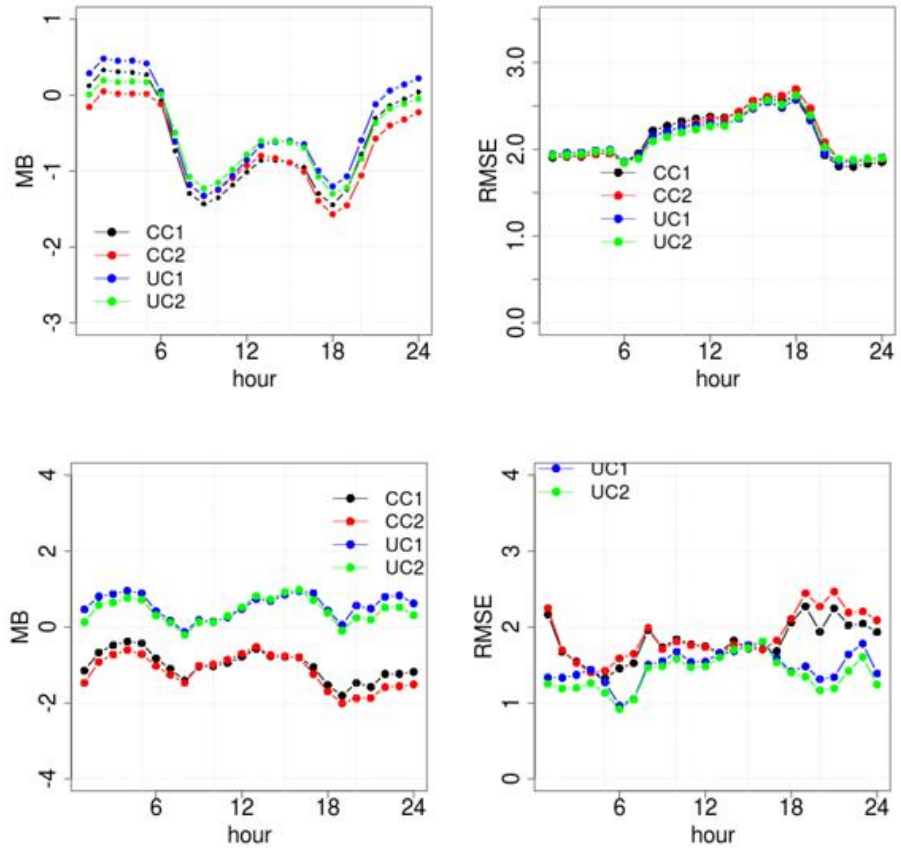


Figure 30: Mean Bias (left) and RMSE (right) using the four configurations in Table 13. All stations of Fig. 19 included (top row); only urban stations included (bottom row).

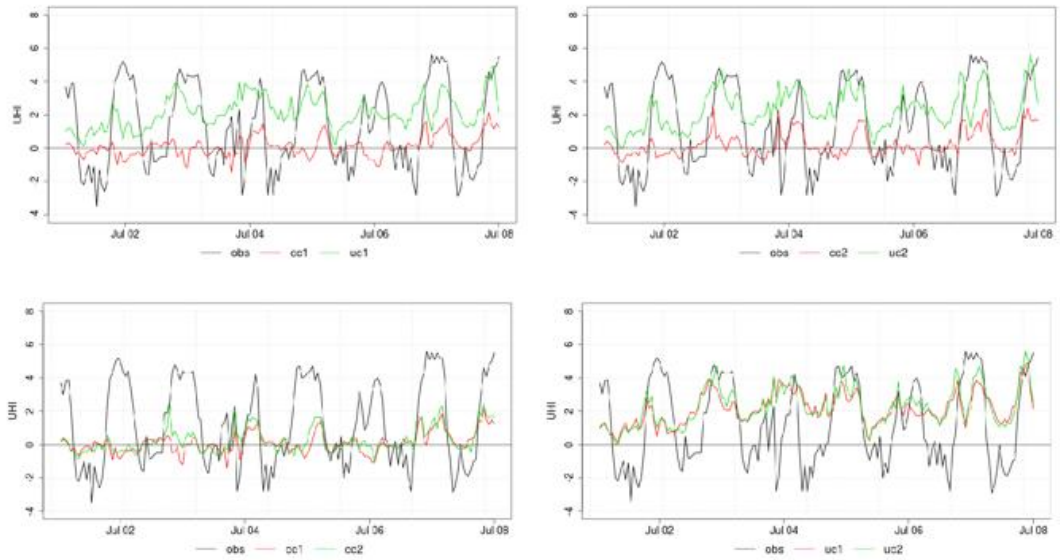


Figure 31: UHI index in Torino for the whole period of simulation. CC1 vs UC1 (top left), CC2 vs UC2 (top right), CC1 vs CC2 (bottom left), UC1 vs UC2 (bottom right).

7.2 Test case B: October 2017

A second test case has been selected, during a much more "normal" meteorological configuration (no heat wave), but standard autumn high pressure. It has to be pointed out that the UHI is more pronounced in this case, probably because the heating was already on. The simulation started on October 23 at 00UTC for 6 days, ending on October 29 at 00UTC, again in hindcast mode. In Fig. 32 the average bias shows a larger improvement with respect to the previous case, although in To-Vallere the T2m gets overestimated. Unfortunately there were problems with the Cuneo station which is not included. The improvement in urban areas is confirmed also from Fig. 33 (bottom row), but still with a general heating (the bias is shifted by 2 °C). In this test case, bias and rmse have higher values with respect to the previous test case. In Fig. 34 it is confirmed the positive impact during the night, but UC2 (bottom right panel) shows slightly better results than UC1 in the peaks. In other words, the amplitude of the cycle is larger with higher maxima and lower minima.

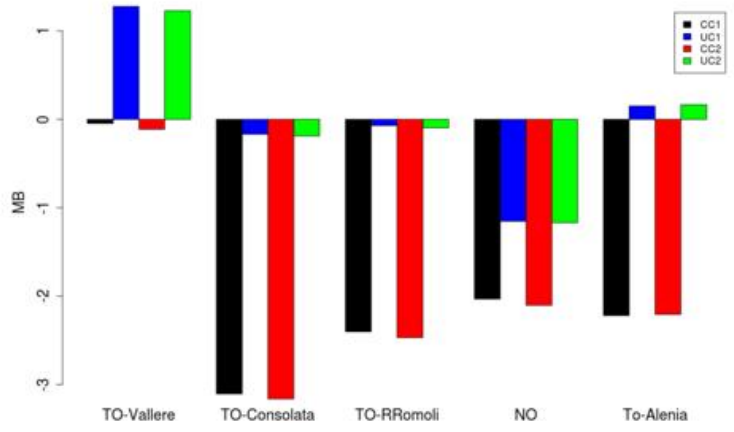


Figure 32: Mean Bias of UHI index over the entire period in a selection of stations. For Torino, different urban stations are used here.

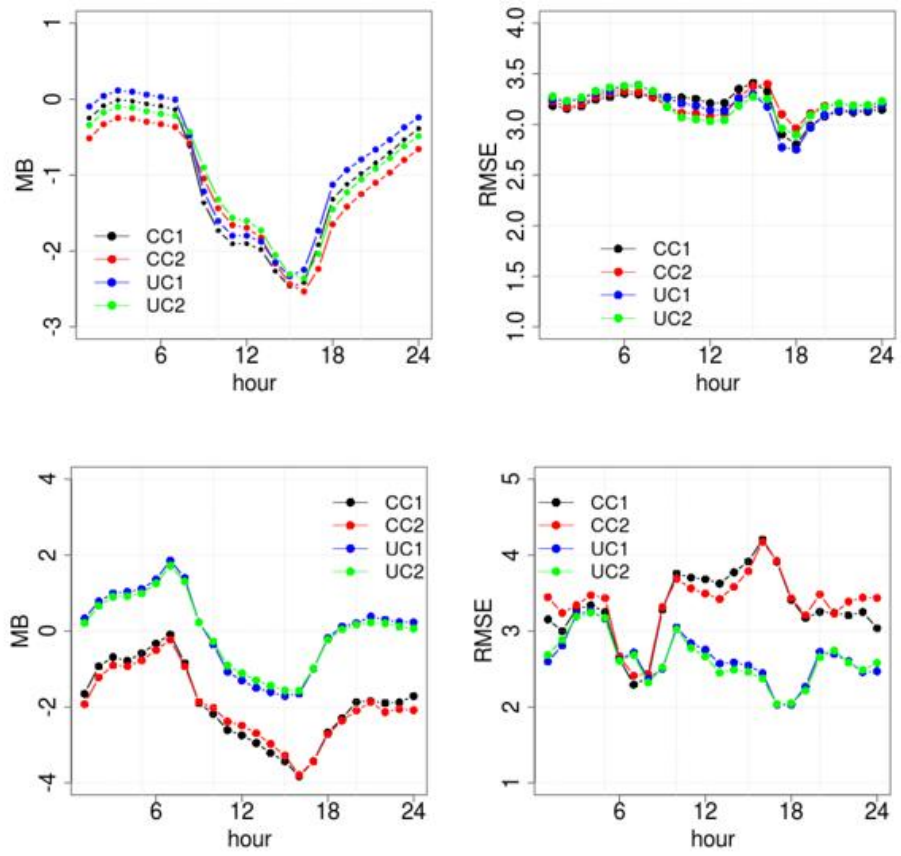


Figure 33: Mean Bias (left) and RMSE (right) using the four configurations in Table 13. All stations of Fig. 19 included (top row); only urban stations included (bottom row).

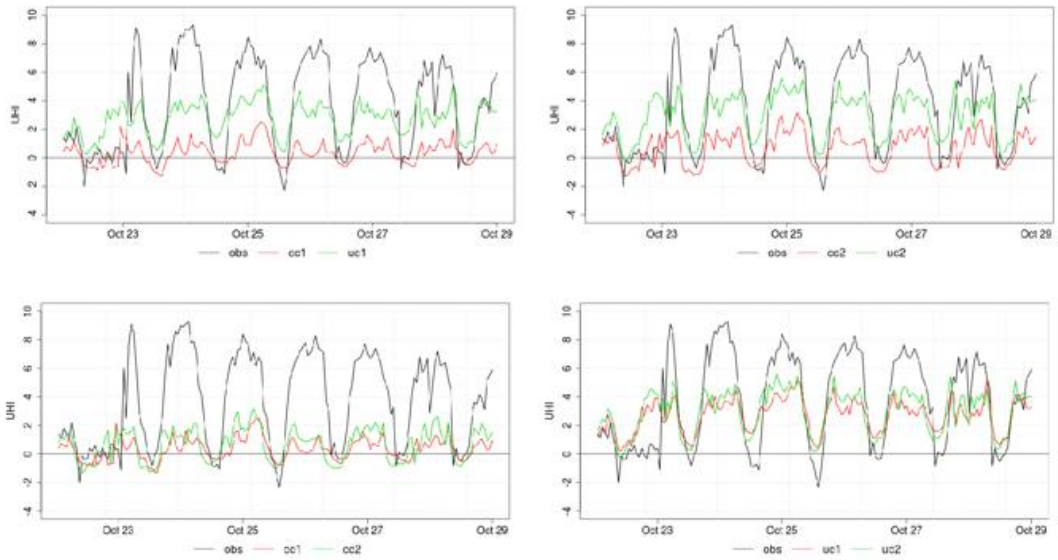


Figure 34: UHI index in Torino for the whole period of simulation. CC1 vs UC1 (top left), CC2 vs UC2 (top right), CC1 vs CC2 (bottom left), UC1 vs UC2 (bottom right).

8 Conclusions

In this report, the activities performed in the framework of PT AEVUS are presented. The main aim of this PT was an evaluation of the performance of a COSMO model version including the urban parametrization TERRA_URB (TU). It is a bulk parametrization scheme including prescribed Anthropogenic Heat Flux and Impervious Surface Area datasets which provides an intrinsic representation of the urban physics. For this purpose, modifications are applied to the model input data, the land surface scheme, and to the land-atmosphere interactions.

The activities were carried out by the modelling groups participating in the task, covering wide ranges of computational domains and periods. A support activity was carried out at DWD, in order to provide the so called skin temperature formulation as part of the land surface scheme TERRA. The skin temperature scheme provides an explicit representation of the vegetation canopy as a component of the surface energy balance. Therefore, it lead to a more efficient decoupling between the surface and the air temperature. In particular, the scheme allows for a more efficient night-time cooling, particularly in the rural areas, and therefore corrects for an important systematic model error of TERRA. As a result, the Urban Heat Island (UHI) intensity, i.e. the temperature difference between urban and rural areas, can be simulated more accurately. Experiments performed over the area of Brussels during the heat wave of 2003 revealed that TU allows an accurate representation of the UHI intensity, most pronounced during the evening and night-time. The numerical simulations over southern Italy on selected test cases have shown that the usage of TU produces a remarkable increase of temperature in urban areas, reducing the model bias. In rural areas, TU provides slight increases on both maximum and minimum temperature daily values, so that the diurnal cycle is always underestimated. Preliminary tests conducted using the skin temperature formulation have shown a reduction of the nocturnal temperatures in rural areas and an increase of the UHI intensity. A careful analysis and comparison with detailed near-surface and boundary layer observations has been conducted over the Moscow megacity area. Results reveal that the model with TU reasonably captures the spatial structure of the UHI by reducing the nocturnal temperature, including the spatio-temporal variations of the UHI intensity. The vertical structure of the UHI (only the lowest 100 m in the considered winter case) is well captured in comparison with the observed temperature profiles. Numerical simulations were conducted over the Piemonte region in order to test the capabilities of TU in simulating UHI in periods characterized by intense heat waves. It was found that the introduction of TU generally reduces the bias. Moreover, the usage of the skin temperature formulation improves the UHI representation slightly. Benefits provided by TU are particularly evident during the night, catching the positive peaks of UHI.

Overall, satisfactory results have been achieved in the framework of PT AEVUS. Further improvements are expected from a more accurate calibration and tuning of the last model version. In particular, an optimized namelist setting for an improved COSMO model performance will be specified, this includes the usage of the skin temperature scheme, and the external physiographic parameters will be improved. These activities will be carried out in the frame of the ongoing PT AEVUS2 (September 2019 - September 2020).

Summarizing, looking at the whole set of results, the authors believe that the TU scheme is suitable to be inserted into the main trunk of the COSMO model and to be distributed in the next official release.

9 Acknowledgements

The authors would like to thank all the scientists involved in the work. In particular Matthias Demuzere for the useful hints about the external datasets, Andreas Will for his suggestions, Pavel Khain for pointing out a few bugs and Jean-Marie Bettems for the support as Working Group Coordinator.

The authors are also thankful to Lomonosov Moscow State University, A.M. Obukhov Institute of Atmospheric Physics of Russian Academy of Science, Central Aerological Observatory and Mosecomonitoring agency and, personally, to Dr. Vladislav Yushkov, Dr. Irina Repina, Arseniy Artamonov and Evgeny Miller for providing the observation data used in the modelling study for Moscow. The simulations and data analysis for Moscow were partially supported by the Grant for the implementation of activities on the development of the system for monitoring and forecasting of, as well as warning against severe and adverse weather events in Moscow city (Resolution of the Government of Moscow No. 257-PP, April 3, 2018). RHM team is thankful to Prof. Dr. Alexander Kislov for scientific advising on the performed modelling studies for Moscow.

A Appendix

Implementing TERRA_URB in COSMO-Model Version 5.05

Ulrich Schättler

Deutscher Wetterdienst

Version 3.0, November 2019

The urban-canopy land-surface scheme TERRA_URB has been implemented in COSMO-Model Version 5.05. The TERRA_URB version used is 2.3, which is taken from the CCLM version COSMO-5.0-clm9. in the following we want to document this implementation into COSMO and try to highlight the technical differences to the implementation in COSMO-5.0-clm9.

Latest Actions in November 2019

This branch of the COSMO-Model is called COSMO-Model 5.05_urb5.
(`cosmo_191119_5.05_urb5.tar.bz2`).

NOTE:
The version `cosmo_191107_5.05_urb5.tar.bz2`, distributed early November 2019 was NOT CORRECT, due to a problem in the source code management.

Implemented a bug fix from Mikhail Varentsov in module `sfc_utilities.f90`, routine `diag_snowfrac_tg`, where usage of skin temperature `t_skin` has been forgotten in case of `itype_canopy = 2`.

Latest Actions in March 2019

This branch of the COSMO-Model is called COSMO-Model 5.05_urb4.
(`cosmo_190329_5.05_urb4.tar.bz2`).

Version 5.05_urb3 gives different results when running the model with `lterra_urb = .FALSE.` or running with `lterra_urb = .TRUE.`, and `ntiles = 0` and setting `FR_PAVED` and `AHF` to zero. In principle, these two runs should have the same results. This has been fixed by the following modifications:

- Treatment of `fr_snow` (fraction of snow): in the former TERRA_URB V5.0_clm19_urb2.3 the fraction of snow was computed at the beginning of TERRA. Now it is calculated in an extra routine, which is called after TERRA. This makes it necessary to introduce `fr_snow` as a tile variable to save the values of each tile for the next step. This was not done up to now, therefore using a value of the wrong tile in the next step.
- Treatment of `tl_freshsnow`: the values of the two tiles were not averaged up now, which gave wrong values for computing the surface albedo during a radiation step.
- The tile variables `tl_snow_melt`, `tl_runoff_s`, `tl_runoff_g` were not averaged to the 0-tile. This does not modify the results, as these are only diagnostic values. But now also the meteograph files `M_xxx` are identical.

Besides these real bugs, there were a few other modifications necessary ro really get bit reproducible results:

1. Setting of the natural tile `plcov`: all plants are considered to be in the natural tile, so `plcov` (urban tile) is 0.0 and the `plcov` (natural tile) has to be modified accordingly. But how it was done gave a different value even in grid points where `FR_PAVED=0.0` (no urban tile). Just for these cases I set `plcov` (natural tile) to the value read for `plcov` for the whole grid box (in module `sfc_tile_approach`, subroutine `tile_define_vegetation_canopy`, settings for `itl=1` (natural tile).
2. Averaging of the two tiles to the 0-tile in subroutine `tile_average_ground` (in module `sfc_tile_approach.f90`) is done with `temp**4` and then taking the 4th root of the result: `EXP (0.25_wp * LOG(temp))`. But this changes the result numerically. For now I do the averaging just as with the other variables.
3. `turb_transfer.f90`: calculation of variables `kbmo` and `dz_s0_h` for `lterra_urb=.TRUE.`: also these computations I modified in a way that they are bit reproducible in case there is only the natural tile.
4. `turb_interface.f90`: The transfer-scheme `turbtran` also uses the `ke`-values of the variables `tkvm`, `tkvh` and `tke`, but only the values for `ke1` are set in `turbtran`. The `ke`-values are only set in `turbdiff` (the atmospheric scheme). But `turbdiff` is not computed for all tiles, only for the averaged 0-tile. Therefore I do a copying of the 0-tile to the natural and the urban tile just for the `ke`-values.

Issues that have to be investigated / clarified:

- Re-think the formula of how `plcov` is modified to get the part of the urban tile (issue 1: above). What I did is only for urban tile=0, but what to do, if urban tile > 0 and natural tile > 0?
- Averaging of the temperatures with `**4`: this gives really big values (about 10E+9); is this really necessary? What is the advantage compared to the usual way? (issue 2: above)
- What to do with the `ke`-values of `tkvm`, `tkvh` and `tke` for the different tiles (issue 4: above)?

Additional technical changes and bug fixes:

- The rank of the external parameter `SKC` was erroneously set to 3, but has to be 2 (in `src_setup_vartab.f90`). Therefore the SKC could not be read and an error was reported by the model. This has been fixed now.
- Implemented additional debug output for a user-defined grid point in TERRA and the turbulence routines.

Latest Actions in October 2018

This branch of the COSMO-Model is called COSMO-Model 5.05_urb3.

- The skin temperature approach has been introduced by Jan-Peter Schulz

- The option `itype_canopy == 2` is fully working now

Latest Actions in September 2018

This branch of the COSMO-Model is called COSMO-Model 5.05_urb2.

- The files `ObjFiles` and `ObjDependencies` have been corrected. The definition of the new modules were missing (thanks to Mikhail).
- A bug fix in `turb_transfer.f90` has been implemented (similar to COSMO 5.05_1 from 31. July 2018).
- In the documentation some default values have been corrected (thanks to Pavel).

Latest Actions in April 2018

This branch of the COSMO-Model is called COSMO-Model 5.05_urb1.

- The former implementation of TERRA_URB in COSMO-Model 5.04g has been updated to the latest COSMO version 5.05.
- Output of tile variables has been implemented in GRIB1 and in restart files. A proper restart is now possible with this version.
- Modifications to the subroutine `tile_average_ground` to perform stable runs with different test cases (from module `sfc_tile_approach.f90`).
- Bug fix in `organize_physics.f90`: the variable `zqv_s` has to be set in all time steps, because this variable is used in the tracer module. This bug was the reason that there were no bit-identical results between version 5.04g and 5.04g_urb1 with setting `lterra_urb=.FALSE.`
- A few other technical modifications (described in DOCS/misc.global).

Latest "CAUTIONS" detected

- TERRA_URB cannot run with a coarse radiation grid. Something is going wrong in the radiation then. This has not been investigated further, because we want to remove this coarse radiation grid anyhow. For TERRA_URB you have to run with `nradcoarse=1`.

1. Using a Tile Approach in the COSMO-Model

1.1. Implementation of Tile Variables

The poor man's tile approach from TERRA_URB has been adopted in the COSMO-Model in a slightly different form. For every variable `var` an additional variable `tl_var` is declared in COSMO-5.0-clm9 with an extra dimension for the tiles. For example

surface roughness * g	`gz0 (ie,je)`	`tl_gz0 (ie,je,0:ntiles)`
fraction of plant cover	`plcov(ie,je)`	`tl_plcov(ie,je,0:ntiles)`

where `ntiles` is the number of tiles used. Before calling a routine which should use the tiles, the corresponding index from the tile-variable is copied to the usual variable and this is used in the routine. Afterwards, the result in the usual variable is copied to the corresponding tile index. Index 0 is used for aggregating the different values for the tiles.

In COSMO-Model 5.04g the new COSMO-ICON physics is written using argument lists for all subroutines. With this the copying of variables can be avoided easily by just writing a loop over all tiles around the call to subroutines. Therefore, in the implementation in COSMO-Model 5.04g we only use the tile-variable `tl_var(ie,je,0:ntiles)`. If no tiles are used, `ntiles` is 0 and the usual values are in `tl_var(:,:,0)`.

Implications to the rest of the COSMO-implementation:

- Throughout the COSMO-Model the use of tile-variables has to be adapted from `var(...)` to `tl_var(...,0)`, but not in the I/O.
- In the I/O we do not want to change the pointers in `src_setup_vartab.f90`. Some special implementation is needed for that. For more details see Section 3.

For the COSMO-ICON physics all variables are needed in a different data structure, which we call the blocked structure. One block consists of a part of the grid points of the two-dimensional domain and can be considered as a vector of grid columns. The name of the blocked variables is just the name of the variable with a suffix `_b`. For variables with a time dimension `tl_var(:,:,ntim=2)`, two variables in blocked format are allocated: `tl_var_b(:,:)` and `tl_var_new_b(:,:)`. Automatic copying of the `ijk`-structure to the block structure and back has been implemented for the tiles.

1.2. List of Variables with a Tile Dimension

The following table shows all variables from the COSMO-Model which are now implemented as tile variables (usual variable with dimensions, tile-variables now used in the COSMO-Model with dimensions, corresponding block variables with dimensions). The first line gives the dimensions of the variables in the program.

Two-dimensional variables:

(ie,je)	(ie,je,0:ntiles)	(nproma,0:ntiles)
gz0	tl_gz0	tl_gz0_b
plcov	tl_plcov	tl_plcov_b
lai	tl_lai	tl_lai_b
tai	tl_tai	tl_tai_b
sai	tl_sai	tl_sai_b
eai	tl_eai	tl_eai_b
tcm	tl_tcm	tl_tcm_b
tch	tl_tch	tl_tch_b
tfm	tl_tfm	tl_tfm_b
tfh	tl_tfh	tl_tfh_b
tfv	tl_tfv	tl_tfv_b
t_2m	tl_t_2m	tl_t_2m_b
qv_2m	tl_qv_2m	tl_qv_2m_b
td_2m	tl_td_2m	tl_td_2m_b
rh_2m	tl_rh_2m	tl_rh_2m_b
u_10m	tl_u_10m	tl_u_10m_b
v_10m	tl_v_10m	tl_v_10m_b
shfl_s	tl_shfl_s	tl_shfl_s_b
qvfl_s	tl_qvfl_s	tl_qvfl_s_b
lhfl_s	tl_lhfl_s	tl_lhfl_s_b
runoff_s	tl_runoff_s	tl_runoff_s_b
runoff_g	tl_runoff_g	tl_runoff_g_b
fr_snow	tl_fr_snow	tl_fr_snow_b
freshsnow	tl_freshsnow	tl_freshsnow_b
snow_melt	tl_snow_melt	tl_snow_melt_b

New two-dimensional variables for TERRA_URB:

(ie,je)	(ie,je,0:ntiles)	(nproma,0:ntiles)
frc	tl_frc	tl_frc_b
isa	tl_isa	tl_isa_b
isa_uc	tl_isa_uc	
sa_uc	tl_sa_uc	tl_sa_uc_b
w_imp	tl_w_imp	tl_w_imp_b
w_isa	tl_w_isa	tl_w_isa_b
kbmo	tl_kbmo	tl_kbmo_b

Two-dimensional variables with a time-dimension. Note that the time-dimension is always the last one!

(ie,je,ntim)	(ie,je,0:ntiles,ntim)	(nproma,0:ntiles,ntim)
t_snow	tl_t_snow	tl_t_snow_b
		tl_t_snow_new_b
t_s	tl_t_s	tl_t_s_b
		tl_t_s_new_b
t_sk	tl_t_sk	tl_t_sk_b
		tl_t_sk_new_b
t_g	tl_t_g	tl_t_g_b
		tl_t_g_new_b
qv_s	tl_qv_s	tl_qv_s_b
		tl_qv_s_new_b
w_i	tl_w_i	tl_w_i_b
		tl_w_i_new_b
w_p	tl_w_p	tl_w_p_b
		tl_w_p_new_b
w_s	tl_w_s	tl_w_s_b
		tl_w_s_new_b
w_snow	tl_w_snow	tl_w_snow_b
		tl_w_snow_new_b
h_snow	tl_h_snow	tl_h_snow_b
		tl_h_snow_new_b
rho_snow	tl_rho_snow	tl_rho_snow_b
		tl_rho_snow_new_b

And for the multi-layer snow model:

(ie,je,ntim)	(ie,je,0:ntiles,ntim)	(nproma,0:ntiles,ntim)
t_snow_mult	tl_t_snow_mult	tl_t_snow_mult_b
dzh_snow_mult	tl_dzh_snow_mult	tl_dzh_snow_mult_b
wliq_snow	tl_wliq_snow	tl_wliq_snow_b
w_snow_mult	tl_w_snow_mult	tl_w_snow_mult_b
rho_snow_mult	tl_rho_snow_mult	tl_rho_snow_mult_b

Three-dimensional variables:

(ie,je,ke1)	(ie,je,ke1,0:ntiles)	(nproma,ke1,0:ntiles)
tkvm	tl_tkvm	tl_tkvm_b
tkvh	tl_tkvh	tl_tkvh_b
edr	tl_edr	tl_edr_b

Three-dimensional variables with a time-dimension. Note that `kex` stands for a variable third dimension, because all these variables do have a different extent in the vertical. Again note that the time-dimension is the last one!

(ie,je,kex,ndim)	(ie,je,kex,0:ntiles,ndim)	(nproma,kex,0:ntiles,ndim)
tke	tl_tke	tl_tke_b
t_so	tl_t_so	tl_t_so_b
		tl_t_so_new_b
w_so	tl_w_so	tl_w_so_b
		tl_w_so_new_b
w_so_ice	tl_w_so_ice	tl_w_so_ice_b
		tl_w_so_ice_new_b

NOTE:

This is just a slightly different way of implementing the poor man's tile approach. It is not (and even not similar) to the tile approach used in ICON!

2. Additional Namelist Variables for TERRA_URB

Several new namelist variables have been implemented in COSMO-5.0-clm9, TERRA_URB 2.3 in the group `/PHYCTL/`. All but one have also been implemented in COSMO-Model 5.04g_urb1. The one not implemented is the logical variable `itype_tile`, which is redundant. The actions of `itype_tile` (0: no tiles, 1: tiles) can also be taken from the number of tiles being $= 0$ or > 0.

The implmented namelist variables are described shortly:

Name	Type	Definition / Purpose / Comments	Default
`ntiles`	`INT`	Number of total tiles. • If the COSMO-Model should run without tiles, the default `ntiles` $= 0$ has to be used. • If the COSMO-Model should run with tiles, `ntiles` has to be set explicitly (in contrast to COSMO-5.0-clm9, where the default of this variable was 2).	`0`
`lterra_urb`	`LOG`	To switch on/off the urban parametrization.	`.FALSE.`
`lurb_fab`	`LOG`	To switch on/off the urban fabric (in a bulk approach). It is only active, if also `lterra_urb` is set.	`.TRUE.`
`itype_ahf`	`INT`	Switch for anthropogenic heat flux. Options are: 0: no anthropogenic heat flux; 1: (default) anthropogenic heat according to *Flanner* (2009); latitudinal, annual, and diurnal-dependent anthropogenic heat flux based on an annual-mean input dataset.	`1`
`itype_kbmo_uf`	`INT`	$kB^{-1} = \ln(z_0/z_{0h})$ parametrization in the surface-layer transfer scheme for the urban fabric. Options are: 0: standard from the surface-layer transfer scheme 1: (default) external parametrization according to Brutsaert/Kanda 2: external from Zilitinkevich	`1`

Name	Type	Definition / Purpose / Comments	Default
itype_eisa	INT	Type of evaporation from impervious surfaces. Options are: 0: evaporation just like bare soil (of course, not recommended) 1: no evaporation (dry surface) 2: (default): density function of puddle depths (Wouters et al., 2015)	2
itype_canopy	INT	Type of canopy parametrization with respect to the surface energy balance. Options are: 1: Surface energy balance equation solved at the ground surface, canopy energetically not represented. 2: Skin temperature formulation by Schulz and Vogel (2017), based on Viterbo and Beljaars (1995). This is provided by the new COSMO/ICON code by Jan-Peter Schulz, which is recently adopted by TERRA URB. Model sensitivity tests show that this option leads to a better representation of the urban/rural contrasts in surface-atmosphere exchanges, hence largely improves urban climate modelling. This option also allows to investigate the vegetation insulation in urban areas on urban climate. Please note that this feature is still in experimental stage.	1
cimpl	REAL	value of implicitness of the vegetation-skin temperature parametrization.	120
calamrural	REAL	value of skin-layer conductivity for rural areas (in $Wm^{-2}K^{-1}$).	10
calamurb	REAL	value of skin-layer conductivity for rural areas (in $Wm^{-2}K^{-1}$).	1000

When activating `lterra_urb` the default of the above variables are used. Only the variable `ntiles` has to be set explicitly to 2!

3. Input and Output for the Tile Variables

The I/O implemented for the tile-variables in COSMO-5.0-clm9 is not practical with GRIB. A different method has now been implemented in COSMO-Model 5.05_urb1 for GRIB1 and for restart files (which uses GRIB1-like meta data).

A new namelist variable `lwrite_tiles` has been implemented in the namelist group `/GRIBOUT/`. If this variable is set to `.TRUE.`, all different tiles of a variable are written to output. To distinguish the different tiles, the additional element number is set to the number of the tile (in GRIB1 and in restart files). If writing a restart file, `lwrite_tiles` is set to `.TRUE.`, if `ntiles > 0`.

In order not to have to change the pointering in the module `src_setup_vartab.f90` we kept the *usual* arrays for the tile variables without the additional tile dimension, but put a "`z`" in front of the name, to make it different. In `src_input.f90` the fields are read into the fields

zvar and copied to the tile-variables tl_var afterwards.

In src_output.f90, all tile variables are added to the write_loop. If lwrite_tiles=.TRUE., a loop over all tiles is started to write all tile variables using the correct number of tile as additional element number. If lwrite_tiles=.FALSE., only tile 0 is written to output.

NOTE:

Implementation of all tile variables to NetCDF or GRIB2 is still ongoing.

4. Special Highlights of the Implementation in COSMO-Model 5.05_urb1

1. Implementation of the 2 new modules:

   - The module src_ahf has been named sfc_ahf. It contains one subroutine ahf. In COSMO-Model 5.04g_urb1 this routine is called in organize_physics.f90, after all parametrizations have been calculated and all data have been copied back to the ijk-data structure (because it is written for this data structure).
   - The module src_tile_approach.f90 has been named sfc_tile_approach.f90. It contains the subroutines
     - tile_define_urban_canopy:
     - tile_define_vegetation_canopy: These two routines are called in the module organize_data.f90 after reading the initial and the first two boundary data sets (not in src_input.f90 as in COSMO-5.0-clm9, because after the first boundary data set has been read, also the initial data can be modified again).
     - tile_filling: This new subroutine fills all tiles with the initial values and is also called in organize_data.f90, as the routines above.
     - tile_average_ground: This routine is written for the blocked data format now and is called just after TERRA.
     - tile_average_near_surface:
     - tile_average_near_surface_blocked: This routine is called after the call to the turbulence transfer scheme. It is now written with an argument list and is the blocked version of tile_average_near_surface.

2. The namelist variable tle has been renamed in ntiles (is a more "speaking name").

3. The external parameter data field for the total impervious surface-area index is called ISA in the version COSMO-5.0-clm9, but is now called FR_PAVED (similar to FR_LAND). This has already been implemented at DWD in the GRIB (shortNames) environment. The actual implementation in COSMO-Model 5.04g_urb1 accepts both names (but this is only a hack, because an extra GRIB 1 number is now used for ISA).

4. The new version of the turbulence scheme needs another external parameter SSO_STDH (from the SSO scheme). This parameter is not available in some test data set, therefore its usage has to be switched off, if necessary (modifications necessary in organize_physics and in organize_data.

5. In near_surface, a part "HSM" has been implemented, but only for itype_synd == 1, which is normally not used any more.
   This has not yet been implemented in COSMO-Model 5.04g_urb1.

6. In module `src_slow_tendencies_rk.f90`, a part has been implemented in subroutine `implicit_vert_diffusion_uvwt` for "additional security". In my opinion this is not necessary for COSMO-Model 5.05_urb1, because within TERRA and `tile_average_ground` all variables are only treated for landpoints.

7. Also in module `src_slow_tendencies_rk.f90`, the sensible heat flux is modified by substracting the field `ahf_now` when computing the vertical diffusion of the tendencies. With the new COSMO-ICON physics there is the possibility to compute this vertical diffusion after the physics. This is controlled with the namelist switch `itype_vdif`:

   -1: Vertical diffusion is computed in the dynamics (old behaviour)

   +1: Vertical diffusion is computed after the physics in the blocked data structure. Modification of the sensible heat flux with `ahf_now` is not yet implemented here (still have to think how to do it best).

5. Tests

A data set has been provided by Hendrik Wouters for 1st of July, 2012, for up to 15 hours in NetCDF data format. Tests have been performed with COSMO-5.0-clm9 and with COSMO-Model 5.04g_urb1. The following pictures show the 2m temperature computed by COSMO-5.0-clm9 (left) and by 5.04g_urb1 (right). This is just to show that the new version is running and not producing nonsense.

Runs have also been performed to test, whether the version COSMO-Model 5.04g_urb1 gives the same results as version COSMO-Model 5.04g without TERRA_URB. With the bug fix in `organize_physics.f90` (setting `zqv_s` in all time steps) this is now the case.

5.1 Problems with the Test Cases from Piemonte and Moscow

The version `cosmo_171113_5.04g_urb1` could not be used for test cases from Piemonte and Moscow. This model version crashes, no matter which configuration is used. These problems have been investigated:

5.2. Piemonte: Initial and Boundary Conditions derived from IFS Data

This data seems to be be problematic, because in the first few steps there are several grid points which have a negative value for the variable `QV_S`. This is also the case when using the former version COSMO-5.0-clm9, but this version does not crash, but silently ignores these values. Modifications in the computation of the 2m temperature now lead to crashes in such situations. This could be avoided using `itype_synd=1`.

We also prepared some ICON data for this test case, which did not show this behaviour regarding `QV_S`. But using the ICON data or the IFS data with `itype_synd=1` shows the same problems as the Moscow case.

5.3. Moscow: Initial Conditions without `SSO_STDH`

The new formulation of the turbulence scheme requires `SSO_STDH` as initial field, which was not present in the Moscow test data. To run this case two adaptations are necessary in the source code:

- `organize_data.f90`: Section 3.2, about line 1573: Comment the lines:

```
IF (itype_vdif > -2) THEN
  yvarini(nyvar_i + 1) = 'SSO_STDH  '
  nyvar_i = nyvar_i + 1
ENDIF
```

- `organize_physics.f90`: There are two calls to the subroutine `init_canopy`, in which you have to comment the lines with `d_pat` (line 1468 and 1702):

```
d_pat   = sso_stdh (:,j),     &
```

5.4. Analyzing the Problems

Depending on the configuration, the COSMO-Model shows a few different crashes:

- Crash in `turb_transfer` with negative values of `tl_qv_s` for tile 0.
- Crash in `gscp_graupel` with a negative value of `rho` or negative values of `tl_t_g`.

After some time of debugging, all crashes could be traced back to some calculations in the routine `tile_average_ground` in `sfc_tile_approach.f90`. This subroutine calculates the grid averages from the different tiles for all tile variables.

But for some variables not a grid averaged is used, but a new diagnosis is calculated. This is done for the sensible heat flux, the latent heat flux and the moisture flux. Also the variable `tl_qv_s` is computed again (and some variables necessary for that).

While these new computations seem to be ok for the old version COSMO-5.0-clm9, they seem to be problematic for the new version COSMO 5.05. Therefore we tested to use the fluxes as they are now computed in the physics from Version 5.05 and just aggregated `tl_qv_s` from the different tiles.

With this approach we could run the Piemonte and the Moscow cases without any problems using different configurations ("old" and "new" physics).

6. Major Changes between COSMO Versions 5.0 and 5.04g

6.1. Source Code

The following list gives the major changes in the COSMO-Model since version 5.0. Most of these changes had only a minor impact on the results. Only the bug fix in the dynamics for slope-dependent divergence damping coefficients showed clear differences in the results (with a better verification for our NWP tests).

The replacement of the turbulence and the soil and surface schemes by the ICON version has a major impact on the results, depending on the namelist configuration used (see Section A).

For a full list of changes for each version, please visit
`http://www.cosmo-model.org/content/model/releases/histories/default.htm`

Version 5.01:

- `src_slow_tendencies_rk.f90`: Use `t_g` instead of `t_s` for the flux computations.
- `pp_utilities.f90`: Optimization of the gamma-function.
- Removal of inconsistencies for the tracers
- Work in Dynamics:
  - targeted diffusion to avoid cold pools
  - reformulation of divergence damping coefficients in the new fast-waves solver
  - adaptation of the Runge-Kutta dynamical core to the SPPT (stochastic perturbation of physics tendencies)
- Modifications to lateral Davies relaxation

Version 5.02:

- Bug fix for computation of `kflat` (only when using GRIB2)
- Bug fix in use of MPI data types (only when using `ldatatypes=.TRUE.`

Version 5.03:

- Various bug fixes in the dynamics, TERRA and the radiation.

Version 5.04a:

- Bug fix in the dynamics for slope-dependent divergence damping coefficients

Version 5.04b:

- Introducing a new boundary condition module (only numerical changes)

Version 5.04a-g:

- Introducing ICON versions of parametrizations for turbulence, soil model, sea-ice scheme and FLake. But these schemes can be run in a configuration which reproduces the results from the corresponding COSMO schemes rather closely (see Section A).

6.2. Namelist Variables

The following namelist variables have been deleted or have changed their meaning (range, default value):

`/DYNCTL/`:

Name	Change	Comment
crltau	renamed	The new name now is crltau_inv and is just the inverse of crltau. Since the default is 1.0, this is not changed. Only if you used a different value, you have to adapt that now.
lexpl_lbc	deleted	No more explicit formulation of lateral boundary relaxation possible.
divdamp_slope	changed	This variable changed its default and the possible range (due to the bug fix). Before it was 10.0 < divdamp_slope <= 100.0 (with default 20.0). Now it is 0.1 < divdamp_slope <= 3.0 (with default 1.0).

/PHYCTL/:

In /PHYCTL/ the following namelist variables have been deleted, because now only the multi-layer version of TERRA is possible: lmulti_layer, nlgw, nlgw_ini, nlgw_bd

A few variables have been added for the COSMO-ICON physics: itype_vdif, ltkeshs, idiag_snowfrac, cwimax_ml

Please see the web site cited above for a description of these variables.

/TUNING/:

In /TUNING/ the following namelist variables have been deleted: wichfakt, securi

6.3. A Special Change for the Climate Mode

The treatment of statistically processed fields in the COSMO-Model is different for the NWP- or for the CLM-mode. This is especially true for fields that are accumulated, like the total precipitation TOT_PREC. In NWP-mode these fields are summed up from the beginning up to the end of the forecast, while in CLM-mode these fields are reset to 0.0 after every output step.

In COSMO-Model Version 5.04f we introduced special fields for cell tracking, which also have to be reset to 0.0 after every output. Therefore we had to change the handling of such fields and introduced additional namelist variables to control the way how and when statistically processed fields are reset.

We introduced 4 categories of statistically processed fields:

- Temperatures, e.g.: TMIN_2M, TMAX_2M
- Winds, e.g.: VMAX_10M, VABSMX_10M
- Summations, Averages, e.g.: TOT_PREC, ASHFL_S
- Cells, e.g.: LPI_MAX, TCOND_MAX

Resetting the variables for each category can now be controlled by the namelist variables

- ireset_temps
- ireset_winds

- `ireset_sums`
- `ireset_cells`

Possible values for these four variables are:

- `0`: no resetting at all (default for sums and averages)
- `1`: reset after given time interval (default for temps and winds)
- `2`: reset after every output (default for cells)

These defaults ensure the current behaviour of the COSMO-Model in NWP-mode.

In CLM Mode (`lbdclim=.TRUE.`), the namelist variable `ireset_sums = 2` has to be chosen to reset all summation variables after every output step!

7. Recommended Namelist Configurations for COSMO-Model 5.04g

At DWD we have problems when activating all new features in the COSMO-ICON physics, therefore it is difficult to recommend a special namelist configuration. We tested three different configurations:

- Old Settings: Turbulence and TERRA are run in a way to reproduce the results of the old COSMO-Versions as close as possible.
  These settings are now preferred at DWD.
- Conservative: The settings for the turbulence scheme activate the new parts of the code, while settings for TERRA still are for the old scheme. Alternatively, also some new features of TERRA can be activated (e.g. `itype_evsl=4`).
- Advanced: These settings come very close to the ICON settings, but COSMO results are not really satisfying. Please note that you need to run INT2LM also with special namelist settings:
  - `itype_aerosol = 2`
  - `itype_ndvi = 1`
  - `itype_rootdp = 4`
  - `lemiss = .TRUE.`
  - `lstomata = .TRUE.`

In addition to the namelist variables, that have to be set in a different way for the above configurations, there are also some hardcoded switches in the turbulence, that have to be different when reproducing the old COSMO-version of the turbulence. To be able to modify these switches at once, we implemented a new namelist switch `loldtur`. Per default `loldtur=.FALSE.` and the new way of running the turbulence is activated. To reproduce the old way, it has to be set to `.TRUE.` and all other namelist switches regarding turbulence have to be set for the "Old Settings".

The following table lists all namelist variables that have to be set for the three different configurations and specifies, which are related to turbulence, and which are not. Because

of ongoing problems with running the vertical diffusion after the physics, we only can recommend to use the former vertical diffusion in the dynamics. For this you have to set `itype_vdif=-1`:

Name	Old Settings	Conservative	Advanced
/TUNING/ (turbulence)			
tkhmin	0.4	0.75	0.75
tkmmin	0.4	0.75	0.75
rat_sea	20.0	7.5	7.5
patlen	500.0	750.0	750.0
turlen	150.0	500.0	500.0
a_hshr	0.2	2.0	2.0
c_soil	1.0	1.75	1.75
/PHYCTL/ (turbulence)			
loldtur	.TRUE.	.FALSE.	.FALSE.
itype_vdif	-1	-1	-1
ltkeshs	.FALSE.	.TRUE.	.TRUE.
itype_sher	1	0	0
imode_tran	1	0	0
imode_turb	1	1	1
icldm_tran	0	2	2
/PHYCTL/ (other)			
itype_aerosol	1	1	2
itype_root	1	1	2
itype_heatcond	1	3	3
itype_evsl	2	2	2
idiag_snowfrac	1	1	1
cwimax_ml	1.0E-6	0.0005	0.0005
lemiss	.FALSE.	.FALSE.	.TRUE.
lstomata	.FALSE.	.FALSE.	.TRUE.

References

Cerenzia I., Tampieri F., and Tesini M. S., 2014: Diagnosis of Turbulence Schema in Stable Atmospheric Conditions and Sensitivity Tests. COSMO Newsletter, 14

Demuzere, M., Harshan, S., Järvi, L., Roth, M., Grimmond, C.S., Masson, V., Oleson, K.W., Velasco, E., and Wouters, H., 2017: Impact of urban canopy models and external parameters on the modelled urban energy balance in a tropical city. *Q.J.R. Meteorol. Soc.*, **143**, 1581–1596, doi:10.1002/qj.302

Flanner, M. G., 2009: Integrating anthropogenic heat flux with global climate models, *Geophys. Res. Lett.*, **36**, L02801, 10.1029/2008GL036465

Khaikine, M.N., Kuznetsova, I.N., Kadygrov, E.N., and Miller, E.A., 2006: Investigation of temporal-spatial parameters of an urban heat island on the basis of passive microwave remote sensing. *Theoretical and Applied Climatology*, **84**, 161–169, doi:10.1007/s00704-005-0154-z

Lokoshchenko, M. A., Korneva, I. A., Kochin, A. V., Dubovetsky, A. Z., Novitsky, M. A., and Razin, P. Y., 2016: Vertical extension of the urban heat island above Moscow. *Doklady Earth Sciences*, **466**, **1**, 70–74, doi: 10.1134/S1028334X16010128

Maucha, G., Büttner, G., and Kosztra, B. 2010: European validation of GMES Data, Soil Sealing Enhancement, available at: http://www.eea.europa.eu/data-and-maps/figures/eea-fast-track-service-precursor

Milelli, M., 2016: Urban heat island effects over Torino. COSMO Newsletter, 16

Milelli, M., Bucchignani, E., Mercogliano, P., Garbero, V., 2017: Preliminary activity with COSMO-1 over Torino including TERRA_URB parameterisation. COSMO Newsletter, 17

Samsonov T. E., Konstantinov P. I., and Varentsov M. I., 2015: Object-oriented approach to urban canyon analysis and its applications in meteorological modeling. *Urban Climate*, **13**, 122–139, https://doi.org/10.1016/j.uclim.2015.07.007

Schubert, S., and Grossman-Clarke, S., 2014: Evaluation of the coupled COSMO-CLM/DCEP model with observations from BUBBLE. *Quarterly Journal of the Royal Meteorological Society*, **140**, **685**, 2465–2483, doi: 10.1002/qj.2311

Schulz, J.-P., Vogel, G., Becker, C., Kothe, S., Rummel, U., and Ahrens, B., 2016: Evaluation of the ground heat flux simulated by a multi-layer land surface scheme using high-quality observations at grass land and bare soil. *Meteor. Z.*, **25**, 607–620

Schulz, J.-P., and Vogel, G., 2016: An evaluation of the simulated bare soil evaporation of an atmospheric model. *Geophys. Res. Abstracts*, **18**, EGU2016-8559

Schulz, J.-P., and Vogel, G., 2017: An improved representation of the land surface temperature including the effects of vegetation in the COSMO model. *Geophys. Res. Abstracts*, **19**, EGU2017-7896

Trusilova, K., Fruh, B., Brienen, S., Walter, A., Masson, V., Pigeon, G., and Becker, P., 2013: Implementation of an Urban Parametrization Scheme into the Regional Climate Model COSMO-CLM. *J. Appl, Meteor. Climatol.*, **52**, 2296–2311

Viterbo, P., and Beljaars, C.M., 1995: An improved land surface parametrization scheme in the ECMWF model and its validation. *J. Climate*, **8**, 2716–2748

Varentsov M. I., Konstantinov P. I., and Samsonov T. E., 2017: Mesoscale modelling of the summer climate response of Moscow metropolitan area to urban expansion. *IOP Conf. Ser.:*

Earth Environ. Sci., **96**, 012009. https://doi.org/10.1088/1755-1315/96/1/012009

Varentsov M. I., Samsonov T. E., Kislov A. V., and Konstantinov P. I., 2017: Simulations of Moscow agglomeration heat island within framework of regional climate model COSMO-CLM [in Russian]. Moscow University Vestnik. Series 5. Geography, 6

Varentsov, M., Wouters, H., Platonov, V., and Konstantinov, P., 2018: Megacity-Induced Mesoclimatic Effects in the Lower Atmosphere: A Modelling Study for Multiple Summers over Moscow, Russia. *Atmosphere*, **9**, **50**, doi:10.3390/atmos9020050

Varentsov, M. I., Grishchenko, M. Y., and Wouters, H., 2019: Simultaneous assessment of the summer urban heat island in Moscow megacity based on in situ observations, thermal satellite images and mesoscale modeling. *Geography, Environment, Sustainability*, doi:10.24057/2071-9388-2019-10

Yushkov V. P., Kurbatova M. M., Varentsov M. I., Lezina E. A., Kurbatov G. A., Miller E. A., Repina I. A., Artamonov A. Y., and Kallistratova M. A., 2019, Modeling an Urban Heat Island during Extreme Frost in Moscow in January 2017. *Izvestiya, Atmospheric and Oceanic Physics*, **55**, 389–406, https://doi.org/10.1134/S0001433819050128

Wouters, H., Demuzere, M., Ridder, K.D., and Nicole, P.M., 2015: The impact of impervious water-storage parametrization on urban climate modelling. *Urban Clim.*, **11**, 24–50, https://doi.org/10.1016/j.uclim.2014.11.005.

Wouters, H., Demuzere, M., Blahak, U., Fortuniak, K., Maiheu, B., Camps, J., Tielemans, D., and van Lipzig, N., 2016: The efficient urban canopy dependency parametrization (SURY) v1.0 for atmospheric modelling: description and application with the COSMO-CLM model for a Belgian summer. *Geosci. Model Dev.*, **9**, 3027–3054, https://doi.org/10.5194/gmd-9-3027-2016

Wouters, H., De Ridder, K., Poelmans, L., Willems, P., Brouwers, J., Hosseinzadehtalaei, P., Tabari, H., Vanden Broucke, S., van Lipzig, N., and Demuzere, M., 2017: Heat stress increase under climate change twice as large in cities as in rural areas: a study for a densely populated midlatitude maritime region. *Geophys. Res. Lett.*, **44**, 8997–9007, doi:10.1002/2017GL074889

List of COSMO Newsletters and Technical Reports

(available for download from the COSMO Website: www.cosmo-model.org)

COSMO Newsletters

No. 1: February 2001.

No. 2: February 2002.

No. 3: February 2003.

No. 4: February 2004.

No. 5: April 2005.

No. 6: July 2006.

No. 7: April 2008; Proceedings from the 8th COSMO General Meeting in Bucharest, 2006.

No. 8: September 2008; Proceedings from the 9th COSMO General Meeting in Athens, 2007.

No. 9: December 2008.

No. 10: March 2010.

No. 11: April 2011.

No. 12: April 2012.

No. 13: April 2013.

No. 14: April 2014.

No. 15: July 2015.

No. 16: July 2016.

No. 17: July 2017.

No. 18: November 2018.

No. 19: October 2019.

COSMO Technical Reports

No. 1: Dmitrii Mironov and Matthias Raschendorfer (2001):
Evaluation of Empirical Parameters of the New LM Surface-Layer Parameterization Scheme. Results from Numerical Experiments Including the Soil Moisture Analysis.
DOI: 10.5676/DWD_pub/nwv/cosmo-tr_1

No. 2: Reinhold Schrodin and Erdmann Heise (2001):
The Multi-Layer Version of the DWD Soil Model TERRA_LM.
DOI: 10.5676/DWD_pub/nwv/cosmo-tr_2

No. 3: Günther Doms (2001):
A Scheme for Monotonic Numerical Diffusion in the LM.
DOI: 10.5676/DWD_pub/nwv/cosmo-tr_3

No. 4: Hans-Joachim Herzog, Ursula Schubert, Gerd Vogel, Adelheid Fiedler and Roswitha Kirchner (2002):
LLM ¯ the High-Resolving Nonhydrostatic Simulation Model in the DWD-Project LITFASS. Part I: Modelling Technique and Simulation Method.
DOI: 10.5676/DWD_pub/nwv/cosmo-tr_4

No. 5: Jean-Marie Bettems (2002):
EUCOS Impact Study Using the Limited-Area Non-Hydrostatic NWP Model in Operational Use at MeteoSwiss.
DOI: 10.5676/DWD_pub/nwv/cosmo-tr_5

No. 6: Heinz-Werner Bitzer and Jürgen Steppeler (2004):
Documentation of the Z-Coordinate Dynamical Core of LM.
DOI: 10.5676/DWD_pub/nwv/cosmo-tr_6

No. 7: Hans-Joachim Herzog, Almut Gassmann (2005):
Lorenz- and Charney-Phillips vertical grid experimentation using a compressible nonhydrostatic toy-model relevant to the fast-mode part of the 'Lokal-Modell'.
DOI: 10.5676/DWD_pub/nwv/cosmo-tr_7

No. 8: Chiara Marsigli, Andrea Montani, Tiziana Paccagnella, Davide Sacchetti, André Walser, Marco Arpagaus, Thomas Schumann (2005):
Evaluation of the Performance of the COSMO-LEPS System.
DOI: 10.5676/DWD_pub/nwv/cosmo-tr_8

No. 9: Erdmann Heise, Bodo Ritter, Reinhold Schrodin (2006):
Operational Implementation of the Multilayer Soil Model.
DOI: 10.5676/DWD_pub/nwv/cosmo-tr_9

No. 10: M.D. Tsyrulnikov (2007):
Is the particle filtering approach appropriate for meso-scale data assimilation ?
DOI: 10.5676/DWD_pub/nwv/cosmo-tr_10

No. 11: Dmitrii V. Mironov (2008):
Parameterization of Lakes in Numerical Weather Prediction. Description of a Lake Model.
DOI: 10.5676/DWD_pub/nwv/cosmo-tr_11

No. 12: Adriano Raspanti (2009):
COSMO Priority Project "VERification System Unified Survey" (VERSUS): Final Report.
DOI: 10.5676/DWD_pub/nwv/cosmo-tr_12

No. 13: Chiara Marsigli (2009):
COSMO Priority Project "Short Range Ensemble Prediction System" (SREPS): Final Report.
DOI: 10.5676/DWD_pub/nwv/cosmo-tr_13

No. 14: Michael Baldauf (2009):
COSMO Priority Project "Further Developments of the Runge-Kutta Time Integration Scheme" (RK): Final Report.
DOI: 10.5676/DWD_pub/nwv/cosmo-tr_14

No. 15: Silke Dierer (2009):
COSMO Priority Project "Tackle deficiencies in quantitative precipitation forecast" (QPF): Final Report.
DOI: 10.5676/DWD_pub/nwv/cosmo-tr_15

No. 16: Pierre Eckert (2009):
COSMO Priority Project "INTERP": Final Report.
DOI: 10.5676/DWD_pub/nwv/cosmo-tr_16

No. 17: D. Leuenberger, M. Stoll and A. Roches (2010):
Description of some convective indices implemented in the COSMO model.
DOI: 10.5676/DWD_pub/nwv/cosmo-tr_17

No. 18: Daniel Leuenberger (2010):
Statistical analysis of high-resolution COSMO Ensemble forecasts in view of Data Assimilation.
DOI: 10.5676/DWD_pub/nwv/cosmo-tr_18

No. 19: A. Montani, D. Cesari, C. Marsigli, T. Paccagnella (2010):
Seven years of activity in the field of mesoscale ensemble forecasting by the COSMO–LEPS system: main achievements and open challenges.
DOI: 10.5676/DWD_pub/nwv/cosmo-tr_19

No. 20: A. Roches, O. Fuhrer (2012):
Tracer module in the COSMO model.
DOI: 10.5676/DWD_pub/nwv/cosmo-tr_20

No. 21: Michael Baldauf (2013):
A new fast-waves solver for the Runge-Kutta dynamical core.
DOI: 10.5676/DWD_pub/nwv/cosmo-tr_21

No. 22: C. Marsigli, T. Diomede, A. Montani, T. Paccagnella, P. Louka, F. Gofa, A. Corigliano (2013):
The CONSENS Priority Project.
DOI: 10.5676/DWD_pub/nwv/cosmo-tr_22

No. 23: M. Baldauf, O. Fuhrer, M. J. Kurowski, G. de Morsier, M. Müllner, Z. P. Piotrowski, B. Rosa, P. L. Vitagliano, D. Wójcik, M. Ziemiański (2013):
The COSMO Priority Project 'Conservative Dynamical Core' Final Report.
DOI: 10.5676/DWD_pub/nwv/cosmo-tr_23

No. 24: A. K. Miltenberger, A. Roches, S. Pfahl, H. Wernli (2014):
Online Trajectory Module in COSMO: a short user guide.
DOI: 10.5676/DWD_pub/nwv/cosmo-tr_24

No. 25: P. Khain, I. Carmona, A. Voudouri, E. Avgoustoglou, J.-M. Bettems, F. Grazzini (2015):
The Proof of the Parameters Calibration Method: CALMO Progress Report.
DOI: 10.5676/DWD_pub/nwv/cosmo-tr_25

No. 26: D. Mironov, E. Machulskaya, B. Szintai, M. Raschendorfer, V. Perov, M. Chumakov, E. Avgoustoglou (2015):
The COSMO Priority Project 'UTCS' Final Report.
DOI: 10.5676/DWD_pub/nwv/cosmo-tr_26

No. 27: J-M. Bettems (2015):
The COSMO Priority Project 'COLOBOC': Final Report.
DOI: 10.5676/DWD_pub/nwv/cosmo-tr_27

No. 28: Ulrich Blahak (2016):
RADAR_MIE_LM and RADAR_MIELIB - Calculation of Radar Reflectivity from Model Output.
DOI: 10.5676/DWD_pub/nwv/cosmo-tr_28

No. 29: M. Tsyrulnikov and D. Gayfulin (2016):
A Stochastic Pattern Generator for ensemble applications.
DOI: 10.5676/DWD_pub/nwv/cosmo-tr_29

No. 30: D. Mironov and E. Machulskaya (2017):
A Turbulence Kinetic Energy – Scalar Variance Turbulence Parameterization Scheme.
DOI: 10.5676/DWD_pub/nwv/cosmo-tr_30

No. 31: P. Khain, I. Carmona, A. Voudouri, E. Avgoustoglou, J.-M. Bettems, F. Grazzini, P. Kaufmann (2017):
CALMO - Progress Report.
DOI: 10.5676/DWD_pub/nwv/cosmo-tr_31

No. 32: A. Voudouri, P. Khain, I. Carmona, E. Avgoustoglou, J.M. Bettems, F. Grazzini, O. Bellprat, P. Kaufmann and E. Bucchignani (2017):
Calibration of COSMO Model, Priority Project CALMO Final report.
DOI: 10.5676/DWD_pub/nwv/cosmo-tr_32

No. 33: N. Vela (2017):
VAST 2.0 - User Manual.
DOI: 10.5676/DWD_pub/nwv/cosmo-tr_33

No. 34: C. Marsigli, D. Alferov, M. Arpagaus, E. Astakhova, R. Bonanno, G. Duniec, C. Gebhardt, W. Interewicz, N. Loglisci, A. Mazur, V. Maurer, A. Montani, A. Walser (2018):
COsmo Towards Ensembles at the Km-scale IN Our countries (COTEKINO), Priority Project final report.
DOI: 10.5676/DWD_pub/nwv/cosmo-tr_34

No. 35: G. Rivin, I. Rozinkina, E. Astakhova, A. Montani, D. Alferov, M. Arpagaus, D. Blinov, A. Bundel, M. Chumakov, P. Eckert, A. Euripides, J. Förstner, J. Helmert, E. Kazakova, A. Kirsanov, V. Kopeikin, E. Kukanova, D. Majewski, C. Marsigli, G. de Morsier, A. Muravev, T. Paccagnella, U. Schättler, C. Schraff, M. Shatunova, A. Shcherbakov, P. Steiner, M. Zaichenko (2018):
The COSMO Priority Project CORSO Final Report.
DOI: 10.5676/DWD_pub/nwv/cosmo-tr_35

No. 36: A. Raspanti, A. Celozzi, A. Troisi, A. Vocino, R. Bove, F. Batignani (2018):
The COSMO Priority Project VERSUS2 Final Report.
DOI: 10.5676/DWD_pub/nwv/cosmo-tr_36

No. 37: A. Bundel, F. Gofa, D. Alferov, E. Astakhova, P. Baumann, D. Boucouvala, U. Damrath, P. Eckert, A. Kirsanov, X. Lapillonne, J. Linkowska, C. Marsigli, A. Montani, A. Muraviev, E. Oberto, M.S. Tesini, N. Vela, A. Wyszogrodzki, M. Zaichenko, A. Walser (2019):
The COSMO Priority Project INSPECT Final Report.
DOI: 10.5676/DWD_pub/nwv/cosmo-tr_37

No. 38: G. Rivin, I. Rozinkina, E. Astakhova, A. Montani, J-M. Bettems, D. Alferov, D. Blinov, P. Eckert, A. Euripides, J. Helmert, M.Shatunova (2019):
The COSMO Priority Project CORSO-A Final Report.
DOI: 10.5676/DWD_pub/nwv/cosmo-tr_38

No. 39: C. Marsigli, D. Alferov, E. Astakhova, G. Duniec, D. Gayfulin, C. Gebhardt, W. Interewicz, N. Loglisci, F. Marcucci, A. Mazur, A. Montani, M. Tsyrulnikov, A. Walser (2019):
Studying perturbations for the representation of modeling uncertainties in Ensemble development (SPRED Priority Project): Final Report.
DOI: 10.5676/DWD_pub/nwv/cosmo-tr_39

COSMO Technical Reports

Issues of the COSMO Technical Reports series are published by the *COnsortium for Small-scale MOdelling* at non-regular intervals. COSMO is a European group for numerical weather prediction with participating meteorological services from Germany (DWD, AWGeophys), Greece (HNMS), Italy (USAM, ARPA-SIMC, ARPA Piemonte), Switzerland (MeteoSwiss), Poland (IMGW), Romania (NMA) and Russia (RHM). The general goal is to develop, improve and maintain a non-hydrostatic limited area modelling system to be used for both operational and research applications by the members of COSMO. This system is initially based on the COSMO-Model (previously known as LM) of DWD with its corresponding data assimilation system.

The Technical Reports are intended

- for scientific contributions and a documentation of research activities,
- to present and discuss results obtained from the model system,
- to present and discuss verification results and interpretation methods,
- for a documentation of technical changes to the model system,
- to give an overview of new components of the model system.

The purpose of these reports is to communicate results, changes and progress related to the LM model system relatively fast within the COSMO consortium, and also to inform other NWP groups on our current research activities. In this way the discussion on a specific topic can be stimulated at an early stage. In order to publish a report very soon after the completion of the manuscript, we have decided to omit a thorough reviewing procedure and only a rough check is done by the editors and a third reviewer. We apologize for typographical and other errors or inconsistencies which may still be present.

At present, the Technical Reports are available for download from the COSMO web site (www.cosmo-model.org). If required, the member meteorological centres can produce hard-copies by their own for distribution within their service. All members of the consortium will be informed about new issues by email.

For any comments and questions, please contact the editor:

Massimo Milelli
Massimo.Milelli@arpa.piemonte.it

Consortium

for

Small-Scale Modelling

Technical Report No. 32

Calibration of COSMO Model,
Priority Project CALMO
Final report

September 2017

DOI: 10.5676/DWD_pub/nwv/cosmo-tr_32

Deutscher Wetterdienst
MeteoSwiss
Ufficio Generale Spazio Aereo e Meteorologia
ΕΘΝΙΚΗ ΜΕΤΕΩΡΟΛΟΓΙΚΗ ΥΠΗΡΕΣΙΑ
Instytucie Meteorogii i Gospodarki Wodnej
Administratia Nationala de Meteorologie
ROSHYDROMET
Agenzia Regionale Protezione Ambiente Piemonte
Agenzia Regionale Prevenzione Ambiente Energia Emilia Romagna
Centro Italiano Ricerche Aerospaziali
Amt für GeoInformationswesen der Bundeswehr
Israel Meteorological Service

www.cosmo-model.org

Editor: Massimo Milelli, ARPA Piemonte

Calibration of COSMO Model,

Priority Project CALMO

Final report.

Project participants:

A. Voudouri [*], ***P. Khain*** [1], ***I. Carmona*** [1], ***E. Avgoustoglou*** [2],

J.-M. Bettems [3], ***F. Grazzini*** [4], ***O. Bellprat*** [5]

with contributions from

P. Kaufmann [3] ***and E. Bucchignani*** [6]

[*] Project coordinator
Hellenic National Meteorological Service
El. Venizelou 14, Hellinikon GR16777, Greece

[1] Israel Meteorological Service

[2] Hellenic National Meteorological Service

[3] MeteoSwiss

[4] Agenzia Prevenzione Ambiente Energia Emilia Romagna

[5] Earth Science Department, Barcelona Supercomputing Center

[6] Centro Italiano Ricerche Aerospaziali

Contents

1 **Abstract** 3

2 **Methodology** 4

3 **Tasks and achievements** 6

4 **The Meta-model** *(P. Khain, I. Carmona)* 12

5 **Sensitivity experiments and fitting strategy** *(E. Avgoustoglou)* 14

6 **Verification of COSMO-2 calibration** *(with the contribution of P. Kaufmann)* 17

7 **A case study** *(E. Bucchignani, P. Mercogliano, M. Milelli)* 24

8 **Conclusions** 25

9 **Appendix: list of model parameters** 29

10 **Appendix: highlights of sensitivity experiments** 37

1 Abstract

Model parameter uncertainty is a major source of errors in regional climate and NWP model simulations (Stephens et al., 1990; Knutti et al., 2002). State-of-the-art NWP models are commonly tuned using expert knowledge without following a well-defined strategy (Duan et al., 2006; Skamarock, 2004; Bayler et al., 2000). This is also the case for the COSMO model where expert tuning is typically made once during the development of the model, for a certain target area, and for a certain model configuration, and is difficult if not impossible to replicate. It is questionable whether such a calibration is still optimal for different target regions (e.g. with a different climate) or for other model configurations (e.g. with a finer grid resolution). Furthermore, the lack of an objective process to re-calibrate the model is often a major roadblock for the implementation of new model features. A practicable objective multi-variate calibration method has been proposed by Neelin et al. (2010) and applied to COSMO model for regional climate simulations (RCM) by Bellprat et al. (2012a and 2012b, 2016). The objective method has shown to be at least as good as an expert tuning. Based on these results, a COSMO priority project (CALMO) has been proposed and accepted, at the COSMO GM 2012 in Lugano, aiming to implement this method for NWP applications. CALMO project officially started on January 2013 and was completed at the end of December 2016. This COSMO priority project was assigned to Working Group 3b. During these 4 years about 6.5 FTEs have been invested. The scientists involved in the project were from 4 different institutions (HNMS, IMS, MeteoSwiss and ARPA-SIMC). Although not all tasks were successful (see Sec. 4 for details), the developments done during this project resulted in a working and robust calibration framework for NWP applications, well documented, including the calibration code (see http://www.cosmo-model.org/content/tasks/priorityProjects/calmo/default.htm).

Furthermore, substantial knowledge transfer took place between ETHZ and MeteoSwiss on one side, and HNMS and IMS on the other side, which is also a very positive side effect of this project. CALMO project was implemented in three phases. In the first phase of the project the method has been tested using COSMO-7 for three parameters over two 20 days periods; in the second phase, COSMO-2 and six parameters have been calibrated over an entire year, and in the third phase calibration of COSMO-1 and five parameters over a one month period has been performed. CALMO project has shown that the method used by Bellprat for COSMO-CLM can be adapted to NWP applications. After the proper re-design, the meta-model (MM, hereafter) is able to reasonably reproduce full COSMO model simulations, for all cases considered (Khain et al., 2015, 2017). Furthermore, the optimum set of model parameters improves a COSI-type score[1], for all tested configurations, and the results of an independent verification seem to indicate that the operational verification scores are also improved (see Sec. 7 and Sec. 8). It should be noted that the history of the soil, which may substantially impact the effect of the calibration, was only switched on for the third phase of the project, and that the calibration of COSMO-1 was limited to one month, namely January 2013. This is a serious limitation, reducing the robustness of the current analysis. Furthermore, the issue of reducing the computational cost of the method has not been tackled. Therefore, considering the huge potential of this calibration method, a follow-up project called CALMO-MAX (CALilbration of MOdel Method Applied on eXtremes) has been accepted by the COSMO Steering Committee, and will take place from 06.2017 to 09.2019. A successful CALMO-MAX will provide a permanent affordable COSMO framework for objective model calibration. All details are available at http://www.cosmo-model.org/content/tasks/priorityProjects/calmoMax/default.htm.

[1]COSI score is a universal verification score used by the COSMO consortium

Much documentation about CALMO already exists and will not be duplicated in this document. More specifically two COSMO Technical Reports, No 25 and 31 (Khain et al. 2015, 2017) provide a very detailed description of many aspects of the project. All this documentation is accessible on the COSMO web. In Sec. 2 of this report, a short introduction to the calibration method is proposed and the appropriate modifications required for adapting the methodology from RCM to NWP are presented. The roadmap of the project and the progress achieved within each CALMO task are presented in Sec. 3. A short description of the MM is made in Sec. 4, while Sec. 5 is focused on sensitivity experiments and a new strategy for fitting the MM. Sec. 6 summarizes the verification of the COSMO-2 simulations computed with the optimal set of parameters and with the default parameters, using the standard verification system of MeteoSwiss. Sec. 7 presents a case study using the calibrated parameters. Conclusions are made in Sec. 8. A full commented list of unconfined model parameters is available in Appendix 9, and the results of sensitivity experiments for different model parameters and for different regions are presented in Appendix 10.

2 Methodology

The main goal of the CALMO project was the implementation of the calibration method proposed by Bellprat et al. (2012b) for regional climate modelling to NWP applications. For N unconfined model parameters, the calibration process aims at finding the values of these parameters which optimize a selected performance score (a scalar measure of the model quality depending on a set of model fields and the associated observations). The basic idea of the proposed approach is to fit a set of significant model fields in parameters space via N-dimensional quadratic polynomial (for each model field, for each region and each day, separately), the significant model fields being the ones contributing to the performance score. This is the so-called meta-model (MM). Once the MM has been fitted, using full COSMO model simulations, both the effect of the parameter setting and of the parameter space used (i.e. the maximal range of optimal values) can be determined without the use of the full model, and the optimization of the performance score becomes feasible. It is important to realize that the calibration of the model is computed for a specific score, i.e. for a specific class of model applications; one derives the values of the unconfined model parameters which provide the best results for these applications. However, to avoid over fitting the model, it is also necessary to choose a score representing enough aspects of the model. Furthermore, it is necessary to choose a score with enough associated observations of good quality. One major difference with the RCM calibration is the type of measure used to quantify the quality of the model (performance score). Whereas RCM uses monthly mean values computed over climate regions, NWP uses scores reflecting the daily cycle and the day to day variability of the weather parameters. Furthermore, the spatial resolution of a NWP model, and the spatial scales of interest, are typically finer than the ones of a RCM. This has of course consequences on the choice of the most significant model parameters to use in the calibration process. It is widely known that there are numerous unconfined parameters in the COSMO model related to sub-grid scale turbulence, surface layer parameterization, grid-scale clouds and precipitation, moist and shallow convection, radiation and the soil scheme. The selection of parameters to be calibrated is made with respect to their influence on the variables associated with daily forecasts such as daily minimum and maximum 2m temperature as well as 24h accumulated precipitation. Comprehensive experiments have been conducted to measure this sensitivity and to support the final choice of the most relevant parameters for the calibration process (see Appendix 2). Note that some expert knowledge is needed to preselect the set of unconfined parameters and to define a plausibility range of values for each of these parameters. The CALMO project has been carried out in three phases of increasing

complexity. For convenience, to be able to tackle the knowledge accumulated at MeteoSwiss, all model configurations have been based on MeteoSwiss production configuration. In the first phase of the project, the model was operated with horizontal resolution of 0.0625° (approximately 7km) for a domain extending mainly over Western Europe as shown in Fig. 1. The model vertical extension reached 23.5 km (30hPa) with 60 model levels in the atmosphere. The calibration was computed for two 20-days periods in 2008 (winter and summer), for 3 model parameters: asymptotic turbulence length scale, tur_len, minimal diffusion coefficients for heat, tkhmin, and scalar resistance for the latent and sensible heat fluxes in the laminar surface layer, rlam_heat. In the second phase of the project, the model was operated with horizontal resolution of 0.02o (approximately 2.2km) for a domain covering the Alpine Arc, in particular Switzerland and Northern Italy, as shown in Fig. 2. The same vertical structure was used as in the first project phase. The calibration was computed for the full year 2013, for 6 model parameters; with respect to the first phase of the project, the following three additional parameters have been considered: c_soil, the surface-area index of the evaporating fraction of grid points over land, v0snow, the factor in the terminal velocity for snow, and entr_sc, the mean entrainment rate of boundary layer humidity into the shallow convection clouds. In the third phase of the project, the model was operated with a horizontal resolution of 0.01° (approximately 1.1km) for the same domain as in phase 2 (Fig. 2), with 80 instead of 60 vertical levels. This is the only phase of the project where the soil memory was considered. The calibration was computed for January 2013, for 5 model parameters: besides tkhmin, tur_len, entr_sc, c_soil, also crsmin, the minimum value of stomatal resistance used by the BATS scheme for the plant transpiration has been considered. The theoretical minimum required number of full COSMO simulations to fit the meta-model is [2*N + 0.5*N*(N 1) + 1], where N is the number of unconfined model parameters to calibrate; this relation has been tested, and it has been found that more simulations are required to obtain a robust calibration. This has as consequence to increase the minimal amount of computing resources required for the calibration. The length of the model integrations used for the calibration is also an important parameter; this is emphasized by the fact that a seasonal dependency on the optimum parameter values has been found. Once the optimum values of the parameters have been determined, a final COSMO simulation using these optimum parameters is performed to assess any quality gain against the reference model configuration, as measured by a standard verification procedure.

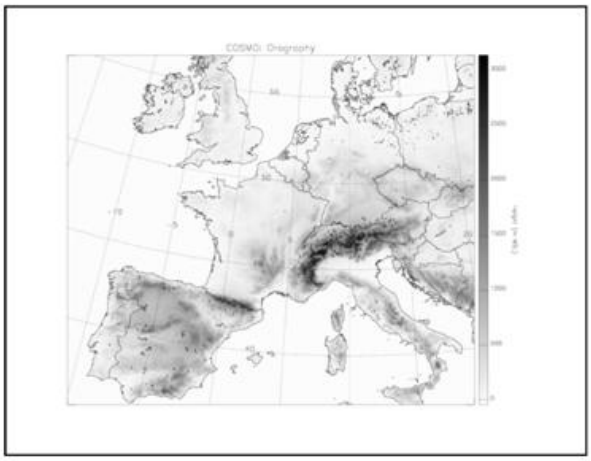


Figure 1: The simulation domain for the first phase of the project, with a 0.0625° grid size.

All necessary adaptations to transfer the calibration methodology from RCM to NWP have been performed in the framework of the CALMO project, which was defined with the following tasks:

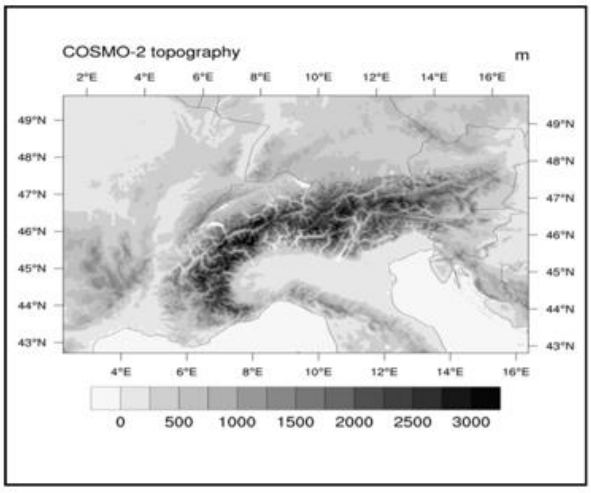


Figure 2: The simulation domain for the second and third phases of the project, with a grid size of 0.02°, respectively 0.01°.

- Preliminary work (e.g. acquire computing resources) (Task 1)
- Adaptation of the existing method for NWP applications (Task 2)
- Assessing the usefulness of the calibration method (Task 3)
- Define optimal methodology in terms of computing time and quality gain (Task 4)
- Documentation and dissemination of results (Task 5)

3 Tasks and achievements

A concise account of the tasks and achievements during the project is presented in this section.

Task 0: Administration and support

Due to the distributed nature of the project team (Greece, Switzerland, Israel and Italy), regular web conferences have been performed throughout the project to ensure the good information flow between all participants. The kick-off meeting took place in Zurich and three workshops have been successfully organized in Athens; additional workshops were also organized during the parallel sessions at the COSMO GM. The mailing list of the project (CALMO-ML, herein) has been widely used in order to support communication and information exchange between project participants (mailing list archive is available on-line). Although much effort has been invested to facilitate the communication within the project team, the rapid detection of critical problems and the timely solution of technical issues remained a real challenge due to the geographically distributed knowledge and team (as proven by the misunderstanding discussed in task 2.4). More in person meetings would certainly have been beneficial (but were difficult to realize due to the multiple tasks of the contributing scientists, including bench forecasting duties).

Task 1: Preliminary work

This task was divided into 4 subtasks, namely literature survey, knowledge transfer among contributing scientists, consolidation of CALMO methodology and technical infrastructure. The main deliverable of this task was the transfer of knowledge from RCM to NWP and

the working technical framework for performing the objective model calibration. Dr. Omar Bellprat / ETHZ, who contributed to the project in 2013, prepared an updated version of the calibration code, including minor changes to improve the MM estimation, and provided the appropriate documentation (see also sub-task 2.6). The entire project required significant computer resources for tasks 2 and 3. Computer resources were made available through a production project on the Piz Daint system hosted at the CSCS, using the GPU capable version of the COSMO model (the proposal is available at http://www.cosmo-model.org/content/tasks/priorityProjects/calmo/docs/CSCS_Proposal.pdf); more than one million node hours have been allocated to the CALMO project on this hybrid GPU system. In addition, a direct line has been established with the core model development team for the identification of key model parameters and for the variables to use in the performance score; discussions on this topic are available through the CALMO-ML.

Task 2: Adaptation of the method

Task 2 was divided into 8 subtasks, namely the documentation of the tuning parameters, the selection of a performance score, identification of key variables for NWP, setting up the experimental framework, collecting the appropriate data, modification of the meta model, computing and analyzing the results, and definition of a data thinning policy. The developments successfully performed in this task resulted in a working and robust calibration framework for NWP applications, well documented, including the calibration code. This task has also shown that a quadratic meta-model is able to reasonably reproduce full COSMO model simulations, for all cases considered.

2.1: Documentation of tuning parameters and choice of parameters subspace

A document listing most of the model tuning parameters, with a short documentation on their meaning, their default value, their allowed range, the associated model sensitivity, and other useful information (such as the code modules using the parameter) has been compiled and is available in Appendix 9 (note that this document is restricted to the physical parameterization schemes available in COSMO v.5.0). A selection of the parameters affecting turbulence, radiation, shallow convection, multilayer soil model, and diffusion parameterization schemes has been made and a set of sensitivity experiments have been performed by HNMS, discussed in Sec. 4 and, in more details, in Appendix 10. A shorter list of eight parameters to be considered for the optimization process at the time of the project was obtained: rlam_heat (the product of rlam_heat*rat_sea is kept constant), tkhmin (tkmmin= tkhmin, i.e. change tkmmin accordingly), tur_len, entr_sc, v0snow, crsmin, c_soil and kexpdec (f =2 in Decharme et al. 2006 formulation for hydraulic conductivity). Considering that one main goal of the calibration approach is to offer an alternative to the expert tuning, the list of tuning parameters should be kept up-to-date, and **this task should become a permanent task of COSMO**.

2.2: Selection of performance function(s)

A normalized RMSE, using both near surface daily minimum and maximum temperature and daily accumulated precipitation, suggested by IMS, described in Khain et al. (2015) and in Voudouri et al. (2017b), has been used as the performance score during the first stage of the project. It is known (Katz and Murthy, 1997) that several different measures have to be used for fully assessing the value of the forecast, in particular when considering precipitation. Therefore, more robust performance scores have been developed in the two last phases of the project: the normalized RMSE has been further improved and a COSI type score. All details are available in Khain et al (2017).

2.3: Identification of key-variables for NWP

The choice of key model variables used in the performance function is constrained by the accessibility of associated observations, with a good enough quality. Key variables used for daily weather forecasting, such as T2m daily minimum and maximum and daily accumulated precipitation, have been originally selected for the calibration. Besides their meteorological significance, observation based gridded analysis over Switzerland was also available for these variables. Additional variables have been introduced in the later phases of the project, such as the vertically integrated water vapor content, wind, temperature and humidity at significant levels, wind shear between significant levels, and stability indices, all evaluated at the location of upper air soundings stations. All details are available in Khain et al (2017).

2.4: Experimental set-up

The aim of this task was to define the exact configuration of the model simulations. The following aspects had to be considered: base model configuration (incl. grid resolution and set of physical parameterizations), domain size and location, set of external parameters, initial and boundary conditions (incl. soil initial conditions), type of simulation (e.g. hindcast, assimilation cycle and daily forecast), usage of additional analysis modules (e.g. soil moisture analysis, SST, snow pack), simulation length used for the calibration. The following paragraphs summarize the choices made in the three phases of the project.

CALMO first phase:

During the first phase of the project, the base model configuration is the COSMO-7 operational configuration operated at MeteoSwiss at the time. In particular, the model was operated on a horizontal grid with a grid size of 0.0625° (approximately 7km) for a domain extending mainly over Western Europe as shown in Fig. 1 above. Its vertical extension reached 23.5 km (30hPa) with 60 model levels in the atmosphere. The model was computed in forecast mode, with a daily 36-hour forecast starting from a fixed and prescribed analysis taken from the MeteoSwiss COSMO-7 operational archive. Lateral boundary conditions were also taken from the same MeteoSwiss operational archive. This means that the same sets of initial and lateral boundaries are used for all tests, including the reference simulation, independently from the set of unconfined model parameters values being tested. One consequence of this design is that the effect of a different set of model parameters values on the state of the soil are not propagated forward in time from one forecast to the next, or, in other words, the long-term memory of the soil is not active. According to WMO Annual Bulletin on the Climate, winter 2007/2008 was mild in Europe and, although summer 2008 has been warmer than usual, anomalies were confined in the normal range of variability of the thee recent years, without particularly strong and persistent departure from climatological averages (WMO, 2008). Therefore, 2008 was selected for the initial objective calibration approach as it was considered representative of a mean climatology over the area of interest. Two 20 days simulation periods, one during winter and one during summer, have been selected, namely 3-20.01.2008 (winter period) and 2-20.06.2008 (summer period). Although both periods are short, the forecast performance was evaluated over three different regions, yielding to a sample size which was considered adequate for this first phase of the project. The calibration of the model was restricted to the 12- to 36-hour lead time of the daily forecast, and to a limited domain covering Switzerland (verification domain), which is divided into three climatically unique areas, according to Frei (2013). The areas defined are: the area to the north of the Alpine crest, mostly coinciding with the Swiss Plateau; the area of Alpine crest, and the area to the south of the Alpine crest that mostly coincides with the Ticino region. Note that areas used by the meta-model should not be too small to avoid a noisy signal, which is not suited for a quadratic polynomial fit by the meta-model (this concerns in particular discontinuous fields like precipitation and CAPE). Finally, an additional simulation has been computed with the optimal set of unconfined parameters values, as provided by the meta-model, to

evaluate the impact of the calibration on the default model configuration.

CALMO second phase:

The base model configuration for the second phase is the COSMO-2 operational configuration operated at MeteoSwiss at the time of the project. The model was operated with a grid spacing of 0.02° (approximately 2.2km), for a domain covering the Alpine Arc, in particular Switzerland and Northern Italy, as shown in Fig. 2. Its vertical extension reached 23.5 km (30hPa) with 60 model levels in the atmosphere. As in the first phase of the project, the model was computed in forecast mode, with a daily 36-hour forecast starting from a fixed and prescribed analysis, meaning in particular that the long-term memory of the soil is again not active. In this phase of the project, the COSMO model was computed for a substantially longer period, considering the whole year of 2013 (from 01.01.2013 till 01.01.2014) instead of the 40 days period of the first phase of the project. The calibration was based on the 12- to 36-hour lead time of the daily forecast. In addition to Switzerland, Northern Italy was also added to the verification domain used for the calibration, and additional type of observations were considered. An additional experiment has also been computed with the optimal set of unconfined parameters values, to evaluate the impact of the calibration on the default model configuration.

CALMO third phase:

The base model configuration is the COSMO-1 operational configuration operated at MeteoSwiss at the time of the project (1.1 km grid mesh size, Alpine domain as in Fig. 2, 80 vertical levels). Unlike the two first phases of the project, the model was computed in hindcast mode (i.e. a free run without assimilation of observations) from 01.01.2013 till 01.02.2013, with prescribed lateral boundary conditions from the MeteoSwiss operational COSMO-7 archive. With this configuration, the impact of a new set of model parameters values on the state of the soil is propagated forward in time during the whole simulation period. The initial conditions of the soil model at the start of the hindcast run is derived from a three-year spin-up computed with a standalone soil model (so called TSA), for each set of unconfined model parameters which directly influences the soil parameterization. The advantages of computing a hindcast instead of a full assimilation cycle and a set of regular forecast, which would also keep the soil memory active, are the simplified configuration of the experiment and the reduced computational cost. Furthermore, studies have shown that, at least for a model domain of the size considered here, the differences between a hindcast and a full cycle are not significant, even after one year of simulation. In terms of computing resources, one day 1.1 km simulation costs approximately 10 times more than a similar one day 2.2 km simulation. The re-factored COSMO model version, capable of running on GPU-based hardware architectures, based on the version 5.0 of the COSMO model, was used in phases 2 and 3 of this project (Lapillonne and Fuhrer, 2013). Note also that the original plan was to use the same configurations for both the second and the third phase of the project (except for the resolution), both including the memory of the soil. However, misunderstanding between the PL and the WGC, which was realized too late, resulted in the configurations described here.

2.5: Collection of data

A gridded analysis of minimum and maximum daily 2-meter temperature, on a 2km grid, based only on observed 2m temperature at Swiss surface stations, is available over Switzerland (Frei, 2013). This analysis has been transformed to match the grid of the COSMO model, as described in the appendix A of Khain et al. 2015 (special care is needed due to the strong height dependency of the temperature field). A gridded product combining radar and rain gauges measurements has been used over Switzerland; 24-hours accumulated

precipitation have been derived from this product. All other observations, such as gridded T2m daily minimum and maximum over Northern Italy, gridded precipitation over Northern Italy, radio soundings, and gridded cloudy brightness temperature (MSG IR 10.8, and WV 6.2, not used) have been collected. The driving model used for the boundary conditions of all CALMO experiments is the operational COSMO-7 (7km resolution) computed at MeteoSwiss, and 3-hourly analysis available in the operational archive of MeteoSwiss have been used for that purpose. As already stated, an important issue that required careful consideration was the initialization of the soil, since multiple years are required for the deep soil to adapt itself to a change in the model climate (as induced e.g. by the choice of a different set of unconfined model parameters values). This is particularly crucial when considering unconfined parameter directly related to the parameterization of the soil. The approach adapted in this project was to compute a spin-up run with a much cheaper standalone soil, driven by prescribed atmospheric forcing, before starting each calibration experiment. Thus, TERRA standalone (TSA) has been consolidated to fulfill the requirements of the CALMO project. Systematic tests (sanity, performance) have been performed by IMS and soil initialization for CALMO experiments was computed. The consolidated TSA is now available through the COSMO web site (http://www.cosmo-model.org/content/support/software/default.htm).

2.6: Modifications on the meta-model

In the first phase, many adaptations of the original meta-model provided by Dr. Omar Bellprat have been performed to support the requirements for calibrating a NWP system instead of a RCM (e.g. the introduction of different statistical measures used as performance score, the manipulation of observational data sets). Significant work was then invested to improve the quadratic meta-model: defining a new set of regions, introducing an option not to average temperature extreme over regions, adding the support of atmospheric profiles, adjusting the RMSE-type performance score and introducing a new COSI performance score (Damrath, 2009), considering the conditions for a robust fit in parameter space, introducing a new method for logarithmic transformation of selected parameters, introducing a measure of model and observation uncertainties, developing an iterative method to obtain the optimal parameters via convergence in a n-dimensional parameter space of exceptional cardinality, and estimating the uncertainties on the optimal value of the model parameters. Sanity check of the meta-model has been performed, comparing the results of the meta-model with similar results of a full model run for a set of unconfined parameters not used in the calibration, both in the first and in the second phases of the project. All modifications and tests performed with the MM are discussed in details in Khain et al. 2017 and briefly described in Sec. 4 of this report. The MatLab code and the documentation is available at http://www.cosmo-model.org/content/support/software/default.htm#calmo.

2.7: Compute experiments and analyze results

This subtask was associated with the computation of at least [2*N + N *(N-1)/2 + 1] model simulations, each with a different set of model parameters values, each time over the selected time period, where N is the number of unconfined model parameters to calibrate. In the case of the COSMO-2 calibration, considering 6 model parameters, the minimum number of required simulations is 28. However, some additional simulations have been performed to better constrain the MM, and obtain a more robust set of optimum parameter values, resulting in a total of about 50 simulations, each simulation being computed over the entire year 2013. A control simulation has also been performed, using the optimum set of parameters, and the impact of the calibration on the model quality, compared with the configuration using the default parameters, is evaluated. The results of this verification are discussed in Sec. 6.

2.8 Data thinning policy and application

The standard amount of raw data produced by a one year COSMO-1 hindcast, i.e. for a single set of unconfined model parameters values, with hourly output, is of the order of 20 TB, whereas the allocated storage for the whole calibration project on Piz Daint was 70 TB. Consequently, an aggressive data thinning policy was required. Data thinning has been designed by HNMS and MeteoSwiss to provide all required data for standard verification on the full domain (SYNOP, upper air, radar composite), and to support the calibration based on minimum and maximum 2m temperature, radar composite, satellite brightness temperature and vertical profiles. Furthermore, a daily analysis was kept, in order to be able to restart a simulation from any day. Fieldextra was used for the data thinning. The data has been transferred from CSCS to ECMWF after the end of the project on Piz Daint. Although data thinning was applied, still a considerable amount of data is now being stored at the HNMS domain of ECMWF.

Task 3: Assessing the usefulness of the calibration method

The goal of this task was to show that the method is indeed able to improve the quality of the model. In addition, the sensitivity of the optimum with respect to the model resolution should have been investigated in this task, as well as the fair assessment of the impact of an improved resolution. The plan was to first calibrate the COSMO-2 configuration, and then a similar COSMO-1 configuration, both using a full year for the calibration. However, due to the many technical difficulties encountered during the project (see the Piz Daint allocation final report at
www.cosmo-model.org/content/tasks/priorityProjects/calmo/docs/CSCS_final_report.pdf), only the COSMO-2 calibration, without the memory of the soil, has been fully completed. Nevertheless, this task has shown that the optimum set of model parameters obtained with the calibration method improves a COSI-type score, for all tested configurations. More specifically, an improvement of the COSI-type score used by the MM of about 3-4% for the COSMO-2 configuration and of about 12% for the COSMO-1 configuration has been observed (all details are available in Khain et al. 2017). Interestingly, a strong seasonal dependency of the optimal parameters values has also been observed. Finally, the results of an independent verification indicate that the operational verification scores are also partly improved (see Sec. 6 for the COSMO-2 case).

3.1: Application of the method using COSMO-1

Calibration of COSMO-1 with five parameters has been performed (tkhmin, tur_len, entr_sc, c_soil, crsmin), but only for January 2013.

3.2: Analyse results

Analysis and discussion of the results have been made in Khain et al. 2015 and 2017, Voudouri et al. 2017c, and in the present report.

Task 4: Practicability of the method

An important objective of this project was to optimize the calibration procedure with respect to the required amount of computing resources, such that a model re-calibration can be computed on any reasonably powerful production system. As already mentioned under task 3, due to many technical problems met during the project, neither time nor human resources remained to tackle this issue. Instead of extending the project, it was decided to consolidate the goals already achieved, mainly a working and robust calibration framework for NWP applications, well documented, including the calibration code, and to design a follow-up project aiming at optimizing the method. The follow-up project, CALMO-MAX, has been accepted by the COSMO Steering Committee in spring 2017, and will take place from 06.2017 to 09.2019. The main goal of this new project is to provide a permanent afford-

able CALMO framework for objective model calibration. All details at http://www.cosmo-model.org/content/tasks/priorityProjects/calmoMax/default.htm.

Task 5: Documentation

A significant amount of documentation has been produced, and, in particular, the goal to make public the work performed within the COSMO Priority Project, not only to the COSMO members but also to the wider scientific community, has been achieved. A scientific paper focused on the preliminary results of this project has been published in Atmospheric Research (Voudouri et al., 2017b). Two papers (Voudouri et al., 2017a and Avgoustoglou et al., 2017) based on parts of the CALMO work have been presented at the 13th International Conference on Meteorology, Climatology and Atmospheric Physics (COMECAP 2016) which was held at Thessaloniki, in 19-21 September 2016; the contributions are included in the Conference Proceedings, published by Springer International Publisher AG as a book entitled: Perspectives on Atmospheric Sciences. Finally, a second manuscript summarizing the work using COSMO 2km has been submitted to Atmospheric Research. In addition, this final report and two COSMO technical reports are available. The documentation of the meta-model and a cookbook to facilitate its usage have also been prepared. All documentation is available on-line on the COSMO web site, at http://www.cosmo-model.org/content/tasks/priorityProjects/calmo/default.htm.

4 The Meta-model *(P. Khain, I. Carmona)*

The consolidation and extension of the MM is extensively discussed in Khain et al. 2015 and 2017, so only the basic ideas are described here. As in Neelin et al. (2010), the MM for a three model parameters combination, e.g. tur_len, tkhmin and rlam_heat, for a given day i and region r, states that the COSMO forecasted field $F_{i,r}$ (here Tmax, Tmin or Pr) may be approximated by a 3-dimensional polynomial of order 2:

$$F_{i,r} \cong F^d_{i,r} + c_{i,r} + \Sigma^3_{n=1} a^n_{i,r} x_n + \Sigma^3_{n=1} \Sigma^3_{m=1} B^{n,m}_{i,r} x_n x_m$$

where $x_{1,2,3}$ are the normalized parameters:

$$x_1 = \frac{rlam_heat - rlam_heat_d}{rlam_heat_{max} - rlam_heat_{min}}, x_2 = \frac{tkhmin - tkhmin_d}{tkhmin_{max} - tkhmin_{min}}, x_3 = \frac{tur_len - tur_len_d}{tur_len_{max} - tur_len_{min}}$$

The index d stands for the default unconfined parameter values. For default values of the 3 parameters, i.e. $(x_1 = 0, x_2 = 0, x_3 = 0)$, the approximated field should be close to $F^d_{i,r}$. The diagonal values of $B_{i,r}$ can be fitted along with the linear coefficients $a_{i,r}$ from the 2N end points of the $x_{1,2,3}$ ranges, along with the default case. Thus, an order-N first-fit procedure yields an estimate of the importance of quadratic non-linearity in addition to linear sensitivity. The off-diagonal $B_{i,r}$ coefficients can be evaluated from the corners of pairwise planes (or an equivalent number of suitably distributed points). Because the procedure is of order N2 it should in practice be done for a pruned subset of parameter directions. Thus, the minimum number of simulations to derive $c_{i,r}, a^{(n)}_{i,r}, B^{(n,m)}_{i,r}$ $(B^{(n,m)}_{i,r} = B^{(m,n)}_{i,r})$, with n,m=1,2,3, is equal to 2N + N(N-1)/2 + 1, which, for N=3, gives 10. Note that a different normalization of the unconfined model parameters than the linear transformation exemplified here with $x_{1,2,3}$ could be applied. In fact, it has been found that a logarithmic transformation provides a more robust fit when the default value of the concerned parameter is not centered in the parameter plausibility interval. It is important to realize that one polynomial is derived for each day i, for each region r, and for each meteorological field F, and that the MM is the collection of

all these polynomial functions. Once the MM has been fitted, the effect of any combination of the associated unconfined model parameters on the forecasted fields $F_{i,r}$ can be evaluated without the full NWP model. Once the MM is available, the calibration is based on the optimization of a performance score, function of the forecast fields $F_{i,r}$ and of the associated observations $O_{i,r}$. The RMSE-type performance score initially tested in CALMO first phase was adjusted, and a new **COSI performance score** was included based on the COSMO Index (COSI) developed by Ulrich Damrath (2009). The COSI score defined by user defined weights for the contributions of the various fields. In this project: $\omega_{Tmax} = 1, \omega_{Tmin} = 1, \omega_{Pr} = 1, \omega_{CAPE} = 0, \omega_{CIN} = 0$ (CAPE and CIN are usually noisy), $\omega_{TCWV} = 1$ (total column water vapor), $\omega_{WS1} = 0.33, \omega_{WS2} = 0.33, \omega_{WS3} = 0.33$ (wind shear between standard levels), $\omega_{T500} = 0.33, \omega_{T700} = 0.33, \omega_{T850} = 0.33, \omega_{RH500} = 0.33, \omega_{RH700} = 0.33, \omega_{RH850} = 0.33, \omega_{U500} = 0.2, \omega_{U700} = 0.2, \omega_{U850} = 0.2, \omega_{V500} = 0.2, \omega_{V700} = 0.2, \omega_{V850} = 0.2$ have been introduced. The adapted score for a combination of model parameters p is then defined by:

$$S_p = \frac{1}{12 \sum_{\Psi=1}^{18} \omega_\Psi} \left\{ \sum_{\Psi \neq 3} \omega_\Psi \sum_{mon=1}^{12} \left[1 - \frac{\sum_{\Psi regs} \sum_{\Psi days} (F_{\Psi,p,d,r,mon} - O_{\Psi,d,r,mon})^2}{\sum_{\Psi regs} \sum_{\Psi days} (O_{\Psi,d-1,r,mon} - O_{\Psi,d,r,mon})^2} \right] + \omega_3 \frac{\sum_{mon=1}^{12} \sum_{\Psi regs} \sum_{\Psi thr} ETS_{p,r,mon,thr}}{N_{\Psi days,mon} N_{\Psi regs,mon}} \right\}$$

where indices Ψ, r, mon, d refer to field, region, month and day of month mon, and where 1/3 < ETS < 1 (1 is the best) is the equitable threshold score for precipitation (region averaged precipitation with amounts thresholds thr of 0.1, 1, 3, 7.5, 10mm per 24h):

$$ETS_{p,r,mon,thresh} = \frac{H - \frac{(H+F)(H+M)}{N_{\Psi regs,mon}}}{H + M + F - \frac{(H+F)(H+M)}{N_{\Psi regs,mon}}}$$

where: H - Number of hits (i.e. both the model and the observations where above the given threshold); F - Number of false alarms; M - Number of misses. The result of the calibration procedure is the values of the parameters p which maximize (or minimize) the performance score S_p. To be able to solve this extreme problem on a standard computer in a reasonable amount of time, even for a large number of parameters p, an iterative method has been developed. In addition, the accuracy of the MM to represent COSMO results, has been examined both in the first phase for COSMO-7 and also in second phase for COSMO-2. In order to validate the quality of MM, an additional test simulation was performed for a parameter combination that was not used while fitting the MM. That allowed comparing the MM predictions for the specific parameters combination with the COSMO simulation results. These results are presented in Fig. 3 and Fig. 4 for COSMO-7 and COSMO-2 respectively. More specifically scatter plots for 24h accumulated precipitation (Pr) are presented for a 20-day interval during the calibration of COSMO-7 in Fig. 3. The y-axes show the MM estimation with respect to the reference (simulation with default parameters values), while the x-axes show the COSMO simulation results with respect to the reference. For Pr each point represents regions averages. The MM was constructed using the minimum number of simulations in Fig. 3a while in Fig. 3b the MM was constructed using additional "interaction" and "constrain" simulations. In both axes, the default simulation (REF) values were subtracted. The dots lying on the black straight lines show values for a region per day, which are accurately reproduced by the MM, the cloud of deviations from the line indicates MM error and the gray band shows the 95% percentile range of deviations. Reasonably high correlations R2 between COSMO forecasts and MM are observed. This is also the case in Fig. 4 for COSMO-2 where MM prediction of precipitation (Pr) for the tested parameter combination, vs COSMO-2 simulation results during the year 2013. The correlations given

in these figures represent a single parameter combination corresponding to one point in the 3- or 6-dimensional parameters space analyzed. However, it can be seen that regarding this tested parameter combination, the correlations R2 between the COSMO forecasts and the MM estimations are generally high. Consequently, the overall method seems to prove itself; one can use the MM to reproduce COSMO forecasts for various parameters combinations.

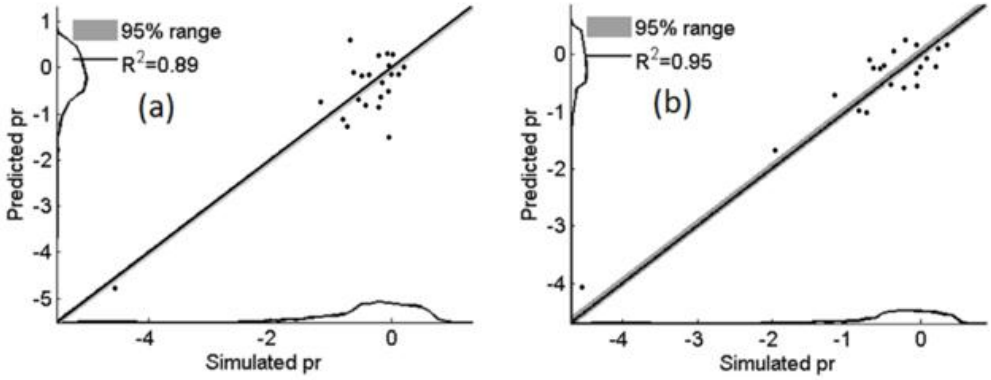


Figure 3: Estimating the MM quality for reproducing Pr field by comparing it with a test COSMO-7 simulation for the period 3-20.1.2008. (a) The MM was constructed using the minimum number of simulations; (b) the MM was constructed using additional "interaction" and "constrain" simulations. A slight improvement of the correlation is observed in this case. In both axes, the REF simulation values were subtracted.

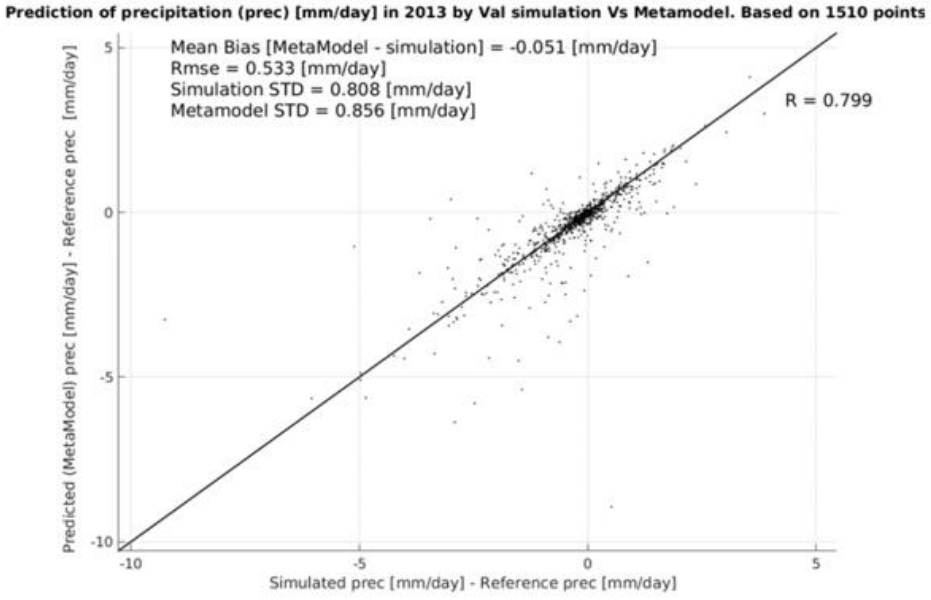


Figure 4: Pr Meta-Model prediction for the tested parameter combination, vs COSMO-2 simulation results during the year 2013. X axis presents the simulated Pr minus the reference simulation. Y axis presents the Meta-Model Pr minus the reference simulation.

5 Sensitivity experiments and fitting strategy *(E. Avgoustoglou)*

The goal of this effort was to gauge the sensitivity of COSMO model over a number of expected relatively high impact parameters. The list of parameters used for the sensitivity

experiments, extracted out of a wide list of free model parameters (shown in Appendix 9) and decided by CALMO project team over extensive communication and recommendations from COSMO experts. An extended set of parameters was tested over the wider Mediterranean area for a period of 62 dates from February, June, and December of 2013 with an emphasis over Switzerland. The sensitivity S with respect to a model variable P was estimated from the results of model runs for the two limits (min and max value) of the parameter selected, as well as for the default value, as follows:

$$S_{<P>}(\%) = \frac{< P >_{TEST} - < P >_{DEFAULT}}{< P >_{DEFAULT}} \bullet 100$$

$< P >$ stands for $< SNOWGSP >$ *or* $< TOTPREC >$ *or* $< CLCL >$ *or* $< CLCM >$ *or* $< CLCH >$ *or* $< CLCT >$

$$S_{\{\langle TOTPREC \rangle, \langle SNOWGSP \rangle, \langle CLCH \rangle, \langle CLCM \rangle, \langle CLCL \rangle\}} = \left|S_{\langle TOTPREC \rangle}\right| + \left|S_{\langle SNOWGSP \rangle}\right| + \left|S_{\langle CLCH \rangle}\right| + \left|S_{\langle CLCM \rangle}\right| + \left|S_{\langle CLCL \rangle}\right|$$

$$S_{\begin{bmatrix} TMIN\,2m \\ TMAX\,2m \end{bmatrix}} = \begin{bmatrix} < TMIN\,2m > \\ < TMAX\,2m > \end{bmatrix}_{TEST} - \begin{bmatrix} < TMIN\,2m > \\ < TMAX\,2m > \end{bmatrix}_{DEFAULT}$$

The results from the sensitivity experiments along with the highlights of this investigation are presented in Appendix 10 while an example is illustrated in Fig. 5. More details are available in Avgoustoglou et al., 2017. The impact for most of the parameters turned out to be important for all periods and domains. The weight of the parameter impact for the different domain, varies due to their climatological characteristics as expected. In principle, for almost all considered variables, at most 5 parameters show the greatest sensitivity and a choice among them should be expected to provide a sufficient kernel for the application of the MM. Towards the effort of model calibration and upon gauging the model sensitivity, when the number **n** of considered model parameters increases, the number of their pair combinations regarding their min and max values vastly increases $[O(2\mathbf{n})^2]$. **A methodology to help reduce the computing resources for fitting the meta-model is proposed here.** An efficient methodology to constrain the number of tests should be to indicate their impact according to some quantitative criteria and decide upon the resulting priority. The methodology is expected to be of practical value if two goals could be accomplished: (a) each test gets a priority number and (b) tests are performed according to it. If the number of tests becomes too expensive, the method should be flexible enough to be terminated at the priority that suits the available computational resources. The recommended truncation, however, needs to be supported by valid scientific arguments regarding the relative importance of the tests that will be included against those that will be omitted.

The specific steps followed in order to decide on the priority for model simulations needed to fit the MM is as follows: the first step is associated with the selection of the parameters to be used for calibration and decision on the model domain for which the MM will be used. The minimum number of simulations needed is [2N + N(N-1)/2 + 1] where N is the number of parameters selected including 1 simulation using default parameter value, 2 simulations using minimum and maximum value of each parameter and one simulation with an interaction terms between parameter pairs. **In order to decide on which interaction simulation per pair to use it is proposed to create a Priority Board Of Terms** (PBOT, see Fig. 6 below). It can easily be shown that the pair combinations for e.g. 7 parameters is 84. Consequently, the 84 empty white cells will be filled with priority numbers 1 to 84. Every empty white shell refers to a 2-parameters combination. The empty dark blue cells will not take any number due to single parameter assignment and due to double

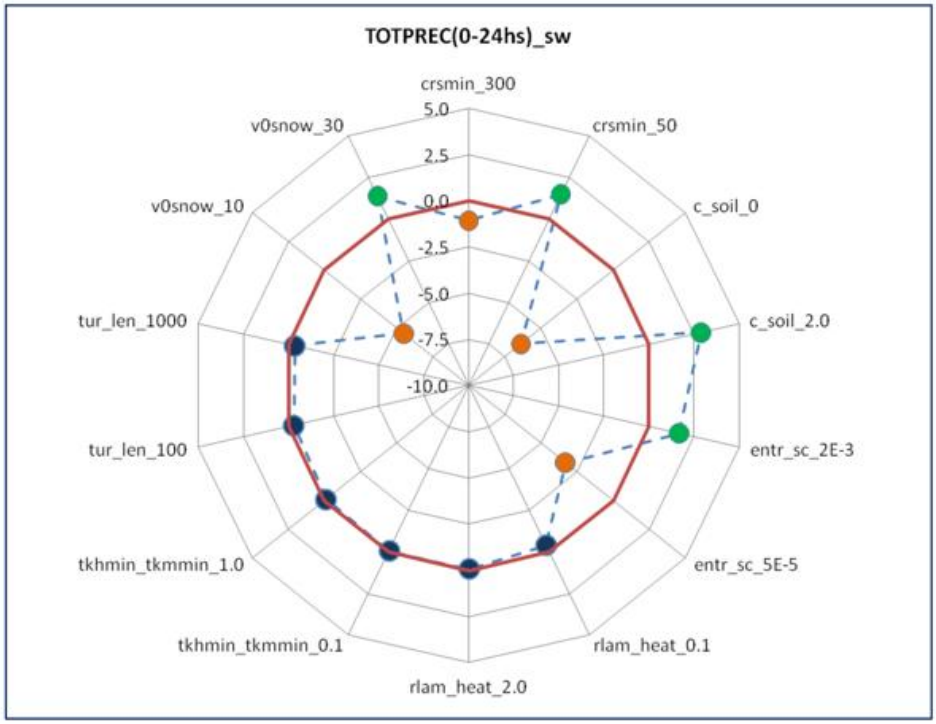


Figure 5: Spidertype graph for 24h accumulated precipitation.

counting in every test. Every number refers to the priority of the sensitivity run. For example, if the second empty white cell of the first line gets the number 5, the model runs with the combination will have priority 5, so 4 other parameter combinations have to be performed first. In addition, according to the importance of the model variables that will be used, a class is denoted in the PBOT (again, see Fig. 6 below). The subjective criteria on making this choice is discussed in detail in Avgoustoglou et al., 2017. The sensitivities (S) of the parameters used is defined and the sensitivity of the variable of the first priority class is presented in a **spider-type** graph, as shown for TOTPREC in Fig. 5. Once the spider type graph is created a set of priority numbers is given to fill the PBOT shown in Fig. 6. For example, the first set of priority numbers will be assigned to couple of parameters with opposite sensitivity, as shown by orange and green bullets on the spider graph, according to the radial distances between the orange and the green bullets. The second set of priority numbers will be assigned to PBOT according to the difference of the radial distances between couple of parameters with same sign sensitivity, etc. In more detail the methodology followed to perform the simulations needed to fit the MM can be found in:

http://www.cosmo-model.org/content/consortium/generalMeetings/general2015/parallel/WG3b_Euripides_Sept2015.pdf

and

http://www.cosmo-model.org/content/consortium/generalMeetings/general2016/wg3b/CALMO_Avgoustoglou.pdf

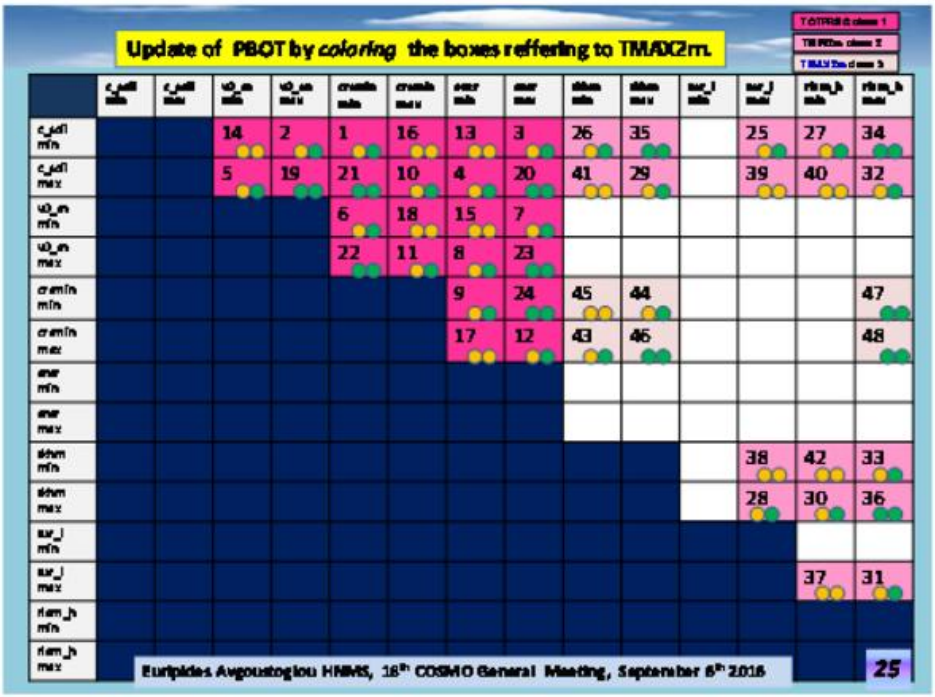


Figure 6: Final PBOT table indicating the hierarchy of interaction simulations to be performed for fitting the MM.

6 Verification of COSMO-2 calibration *(with the contribution of P. Kaufmann)*

By construction, the CALMO methodology provides a set of optimum values for unconfined model parameters, which optimizes a specified performance score (the COSI type score described in the previous section). In order to assess the robustness of this optimum, it is necessary to perform an independent verification of the simulation performed with the optimal set of parameters. A selection of verification plots produced with the standard MeteoSwiss verification system for the second phase of the CALMO project (COSMO-2 calibration) is presented in this section. Although limited in scope, this verification gives a first insight on the capacity of the CALMO methodology to provide a robust improvement of the quality of a specific model configuration. Simulations are performed over the entire year 2013, using default values (**DEF**) for 6 unconfined model parameters as well as using the optimum set of parameters (**BESTF2**) derived from the MM. The 6 parameters with their default and optimum values are summarized in Table 1. The optimum values are the ones obtained by using the COSI type performance score, with daily minimum and maximum of 2m temperature evaluated at grid points and not averaged (following the method 4 in Khain et al., 2017); a 3-4% improvement of the COSI type performance score has been obtained with BESTF2. The performance of the model for 2m temperature (T_2M), 2m dew point temperature (TD_2M), 10m wind speed (FF_10M), 12h accumulated precipitation (TOT_PREC12) and 1h accumulated precipitation (TOT_PREC1) is presented. All statistics are over the entire year 2013, the year which is also used for the calibration; all statistics are computed for Switzerland, using Swiss observing stations and the Swiss radar composite.

Diurnal cycle of mean model error in both cases DEF (blue line) and BESTF2 (red line) as well as mean model values and mean observation values (MOBS, black line) for **2m temperature** and **2m dew point temperature** are presented in Fig. 7 and Fig. 10. Improvement of 2m temperature mean error of about 0.2°C throughout the day is evident

Table 1: Calibration parameters and their values.

Parameter	Acronym	Default values	Optimum value (after method 4)
Factor for laminar resistance for heat	**rlam_heat**	1 (20 rat_sea)	1.273 (15.71092)
Minimal diffusion coefficient for heat	**tkhmin**	0.4	0.266
Maximal turbulent length scale (m)	**tur_len**	150	346.5
Entrainment rate for shallow convection	**entr_sc**	0.3e-3	0.1607e-3
Surface-area index of the evaporating fraction of grid points over land	**c_soil**	1	0.588
Factor for vertical velocity of snow	**v0snow**	20	12.3

in Fig. 7. This improvement is related to a warmer near surface temperature associated with BESTF2, which partly mitigates the cold bias observed with DEF over Switzerland. Considering the 2m dew point temperature, one observes a degradation of the mean error throughout the day associated with a drier surface layer, which increases the already dry bias observed with DEF. Left panel of Fig. 8 illustrates the mean 2m temperature model error for the optimum and the default cases, while mean observation and model values for all lead times during the entire year are shown in right panel. It is evident that model values obtained using the optimum set of parameters are closer to the observed ones. This is also supported by Fig. 9 where statistics for the whole 2013 are presented; incidentally, the overall minimum and maximum 2m temperature obtained with BESTF2 is closer to OBS than DEF (minimum observed is -30.9°C, with -28.9°C using BESTF2 and -28.8°C using DEF, while maximum observed is 37.1°C, with 37.9°C using BESTF2 and 38.1°C using DEF). For dew point 2m temperature, shown in Fig. 11 and Fig. 12, the observed mean value is equal to 2.13°C against 1.72°C using DEF and 1.47°C using BESTF2. It should be noted that the dew point temperature is not part of the performance score used to derive BESTF2.

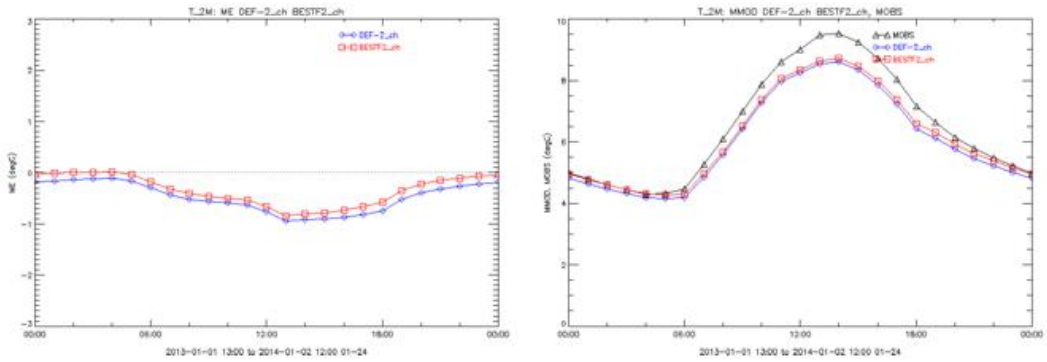


Figure 7: Verification of 2m temperature for 2013 over Switzerland. Diurnal cycle of mean model error (left panel) and mean model values compared to mean observations (right panel). An improvement of up to 0.2°C is observed.

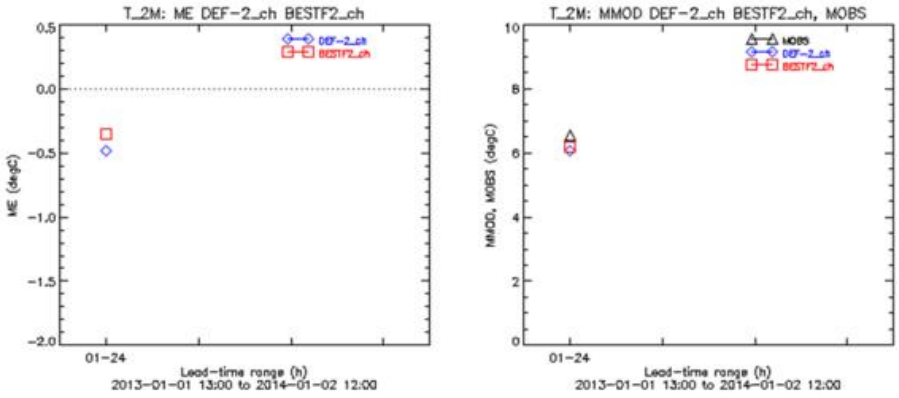


Figure 8: Verification of 2m temperature for 2013 over Switzerland. Mean model error (left panel) and mean model values compared to mean observations (right panel).

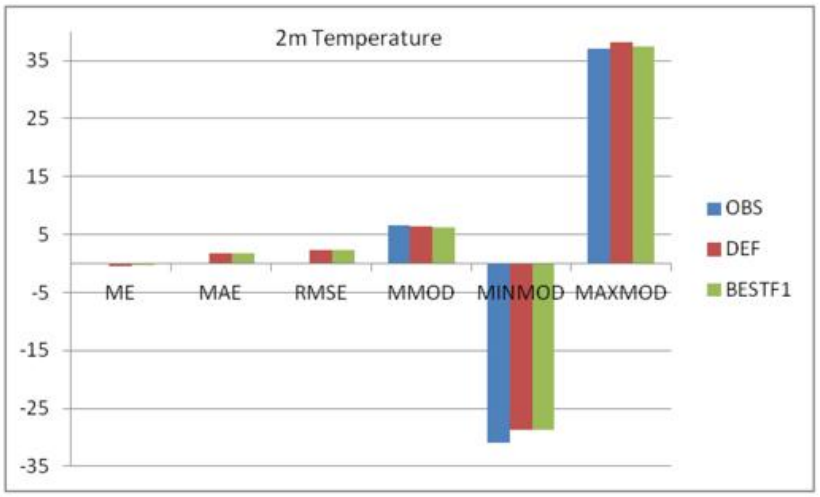


Figure 9: Statistics of 2m temperature for 2013 over Switzerland, showing observations (OBS) and model simulations using default parameter values (DEF) and optimum parameter values (BESTF2). The following quantities are shown: ME: mean error, MAE: mean absolute error, RMSE: root mean square, MMOD: mean value, MINMOD: minimal value, MAXMOD: maximal value.

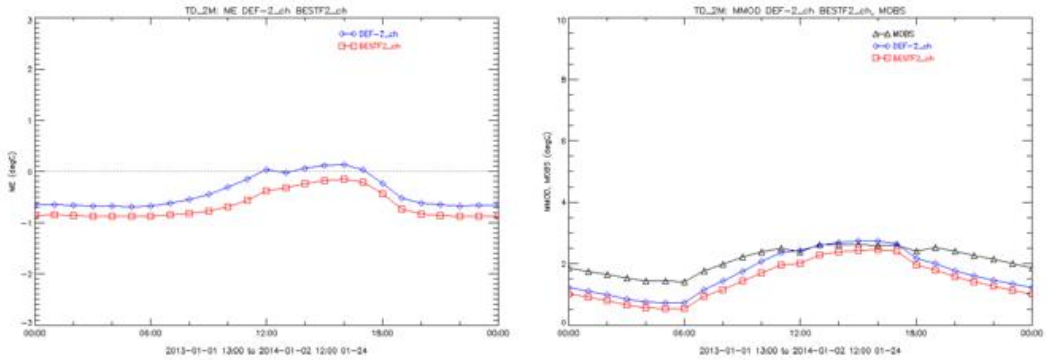


Figure 10: Verification of 2m dew point temperature for 2013 over Switzerland. Diurnal cycle of mean model error (left panel) and mean model values compared to mean observations (right panel).

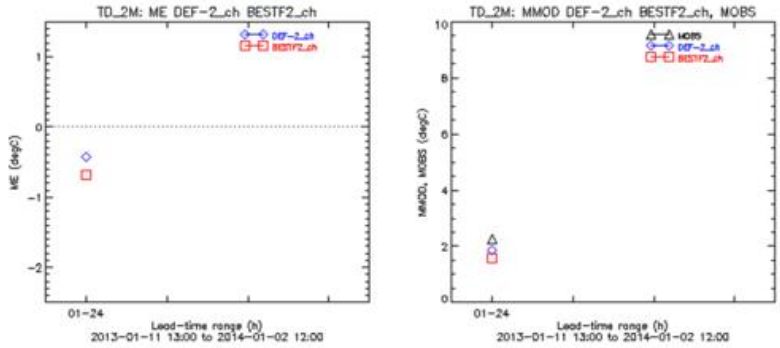


Figure 11: Verification of 2m dew point temperature for 2013 over Switzerland. Mean model error (left panel) and mean model values compared to mean observations (right panel) for dew point temperature.

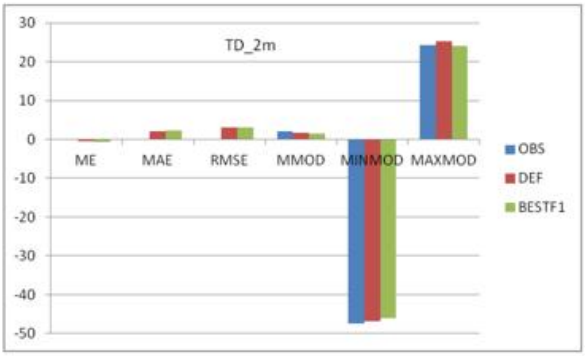


Figure 12: Statistics of 2m dew point temperature for 2013 over Switzerland, showing observations (OBS) and model simulations using default parameter values (DEF) and optimum parameter values (BESTF2). The following quantities are shown: ME: mean error, MAE: mean absolute error, RMSE: root mean square, MMOD: mean value, MINMOD: minimal value, MAXMOD: maximal value.

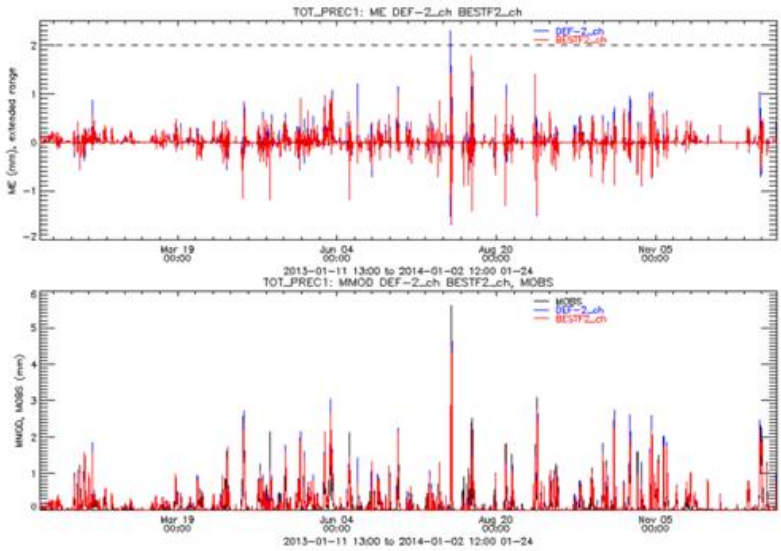


Figure 13: Time series of mean model error (upper panel) and mean model values compared to mean observations (lower panel) for hourly accumulated precipitation over Switzerland.

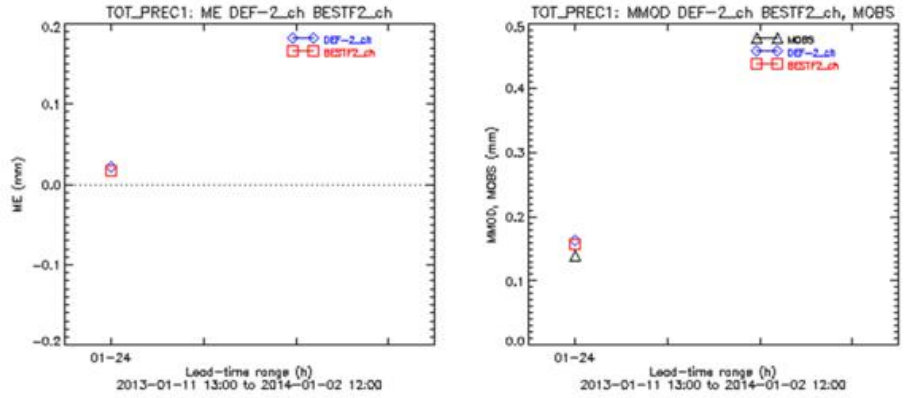


Figure 14: Mean model error (left panel) and mean model values compared to mean observations (right panel) for hourly accumulated precipitation over Switzerland.

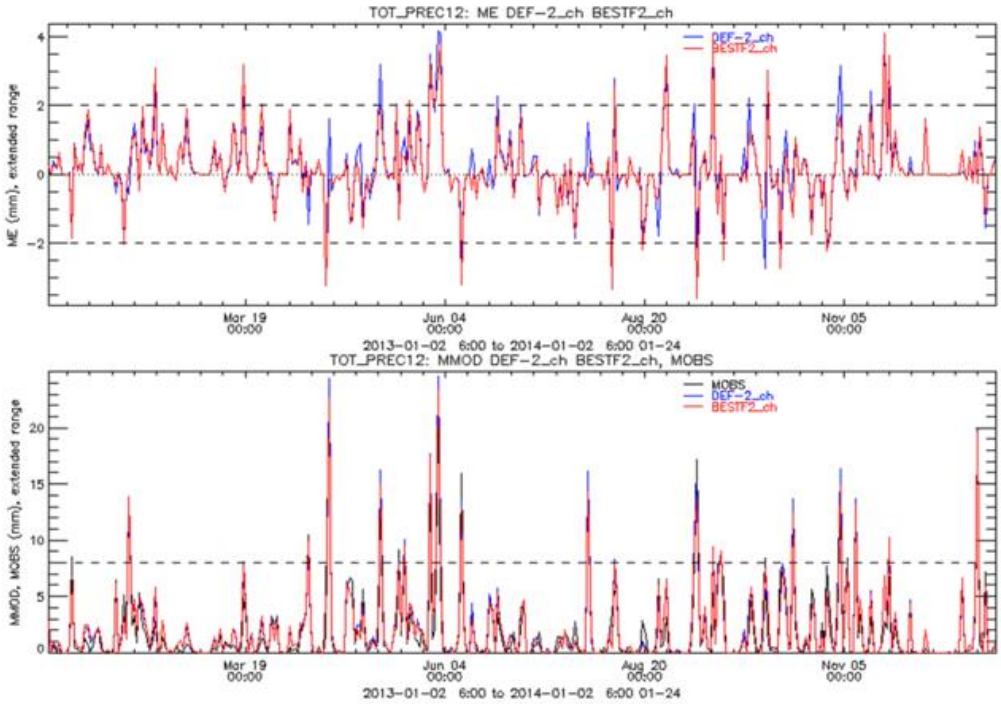


Figure 15: Time series of mean model error (upper panel) and mean model values compared to mean observations (lower panel) for 12-h accumulated precipitation over Switzerland.

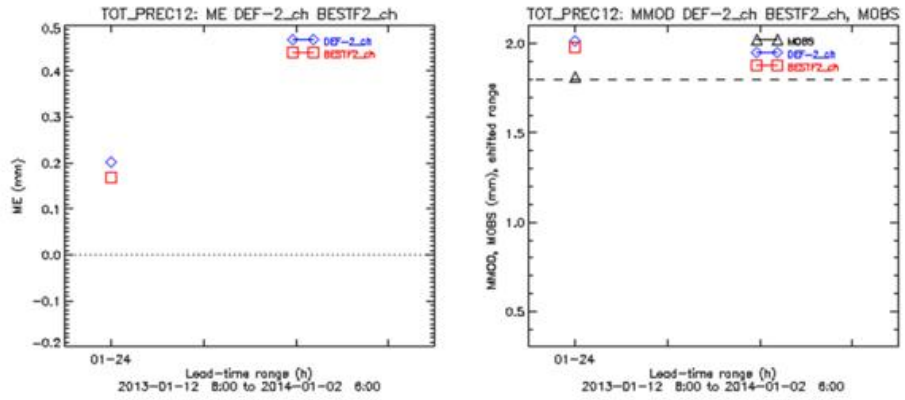


Figure 16: Mean model error (left panel) and mean model values compared to mean observations (right panel) for 12-h accumulated precipitation over Switzerland.

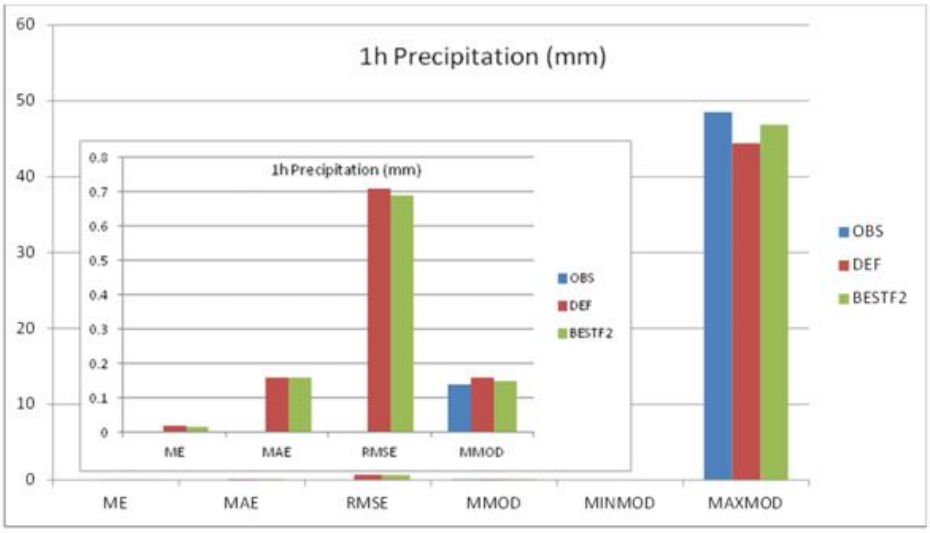


Figure 17: Statistics of hourly accumulated precipitation during entire 2013 over Switzerland, showing observations (OBS) and model simulations using default parameter values (DEF) and optimum parameter values (BESTF2). The following quantities are shown: ME: mean error, MAE: mean absolute error, RMSE: root mean square, MMOD: mean value, MINMOD: minimal value, MAXMOD: maximal value.

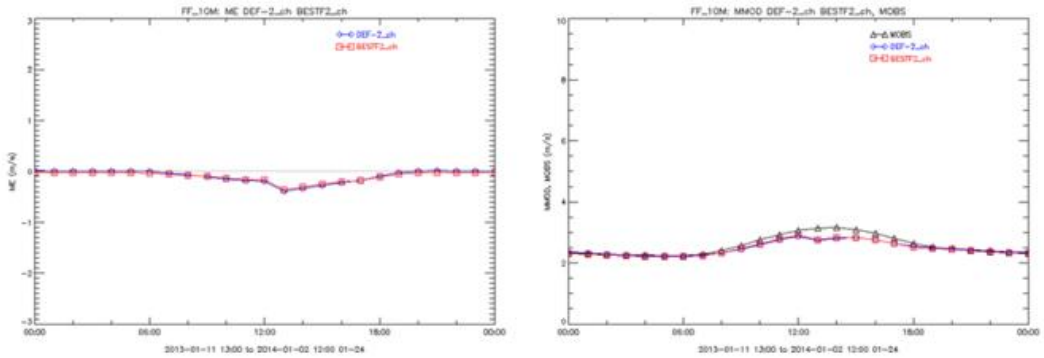


Figure 18: Verification of 10m wind speed for 2013 over Switzerland. Diurnal cycle of mean model error (left panel) and mean model values compared to mean observations (right panel).

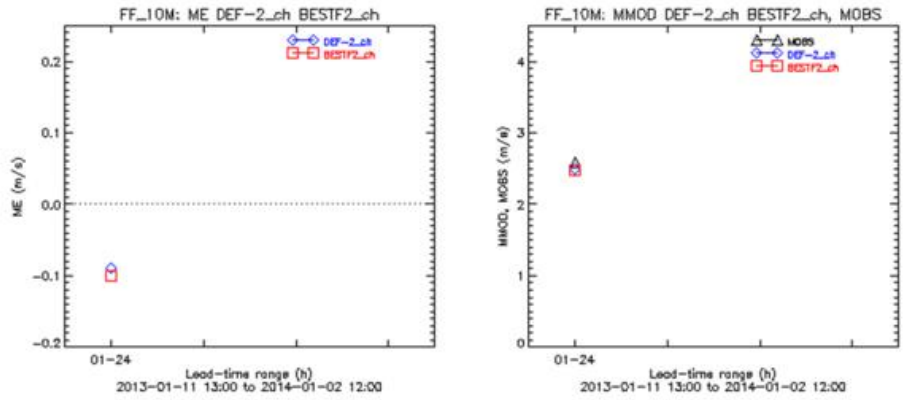


Figure 19: Verification of 10m wind speed for 2013 over Switzerland. Mean model error (left panel) and mean model values compared to mean observations (right panel).

Time series of mean model errors as well as mean model values, compared to mean observations for 12h and 1h accumulated precipitation are presented in Fig. 13 and Fig. 15 respectively. A slight improvement on mean error is visible for accumulated precipitation over the entire year, especially during the warm period of the year. Total scores for the diurnal cycle of the variable support this assertion, as shown in Fig. 14, Fig. 16 and Fig. 17: 1.79mm and 0.14mm mean observed values for 12h and 1h accumulated precipitation respectively, compared to 1.99mm and 0.16mm for the modeled values using default parameters and 1.96mm and 0.15mm using the optimum parameters.

Diurnal cycle of mean model error in both cases DEF (blue line) and BESTF2 (red line) as well as mean model values and mean observation values (MOBS, black line) for **10m wind speed** are presented in Fig. 18. Mean error total score and means for all lead times during the entire year for both model and observations is presented in Fig. 19. A very small degradation of the scores when using BESTF2 is observed (mean observed value 2.57 m/s, against 2.47 m/s using BESTF2 and 2.48 m/s using DEF).

7 A case study *(E. Bucchignani, P. Mercogliano, M. Milelli)*

The following case study illustrates the impact of using the CALMO calibrated values instead of the default parameters values. The interest of this study is that it uses the calibrated parameters with a different model configuration than the one used in the calibration, and for a different year. In the first half of July 2015, Piedmont region and Turin in particular experienced extreme temperature values and uncomfortable conditions for the population. In Turin, the maximum temperature since 1990 (38.5°C) has been recorded in July 2015. Ground stations data highlighted the presence of a UHI effect over Turin. This is the reason why this area and this period represent a suitable benchmark to test the capabilities of COSMO-CLM, and in particular of the urban parameterization. The computational domain considered is centered over Turin, discretized with 100 x 100 grid-points, employing a spatial resolution of 0.009° (about 1 km). The ECMWF IFS analysis at 0.075° have been used as forcing data. Three different simulations have been performed over the period 1 to 7 July 2015, respectively using the default set of control parameters **and two different sets of parameters derived from the COSMO-2 calibration performed in the CALMO project**[2], as listed in Table 2, in order to highlight the effects on the model results. Validation has been carried out against an observational dataset for daily values of temperature, provided by ARPA Piemonte. In the following, results related to Consolata station are shown, representative of an urban area. Table 3 shows the average observed T2m value, the average bias (model minus observation) over the simulated period and the maximum bias, obtained with the different configurations at Consolata. **Both calibrated configurations allow a significant reduction of the average bias. OPT2 allows also a reduction of the maximum bias.**

Table 2: Values of the control parameters for the three different configurations.

	Default	**OPT1**	**OPT2**
rlam_heat	1.0	0.74	1.24
tkhmin	0.4	0.176	0.233
tkmmin	0.4	0.4	0.233
tur_len	150	368.8	363.9
entr_sc	0.003	0.00014	0.000267
c_soil	1	0.663	0.492
v0snow	20	17.8	12.1
rat_sea	20	20	16.12903

Table 3: Values of observed T2m value (°C), average bias (model minus observation) over the simulated period and the maximum bias, obtained with the different configurations.

	OBS	**BIAS URB_DEF**	**BIAS URB_OPT1**	**BIAS URB_OPT2**
Average bias	29.4	0.68	0.36	0.43
Maximum bias	29.4	5.5	5.0	4.9

[2]This case study has been conducted before the definitive values of the calibrated parameters were available. This is the reason why two different sets are present, both differing from the final values listed in Khain 2017; the OPT2 set is the one which is the nearest to the final values obtained by CALMO.

8 Conclusions

The CALMO project was a considerable step towards complementing the usual expert tuning with an objective calibration methodology. Expert tuning is typically done once during the development of the model, for a certain target area, and for a certain model configuration, and is often difficult if not impossible to replicate. This is the hope placed in this new methodology to support on-demand calibration by any COSMO member, e.g. to define an optimal calibration over the target area of interest, to introduce a seasonal dependency on some unconfined model parameters values, or for a re-calibration after major model changes (e.g. higher horizontal or vertical resolution). Furthermore, the CALMO methodology could also be used for an unbiased assessment of different modules (e.g. parameterization schemes), and for optimal perturbation of parameters when run in ensemble mode. Starting with a rough model resolution of 7km and a short calibration period of 40 days, the method was extended to a finer 2.2km resolution. The simulation period was significantly increased from 40 days of 2008 to the entire year of 2013, to consistently incorporates the weather development on a seasonal basis. The verification area was enlarged to also consider Northern Italy. The daily minimum and maximum 2m temperature and the 24h accumulated precipitation was complemented with vertical wind, temperature, and humidity profiles and with total water column at soundings locations. The number of calibrated model parameters was increased from 3 to 6. The meta-model was adapted and extended. A new COSI performance score was included to act as a performance metric for NWP models. A new method for logarithmic transformation for selected parameters was developed along with an iterative method to obtain the optimal parameters via convergence in a 6-dimensional parameter space of exceptional cardinality. An estimation of error bars on the optimal parameters values has been introduced. Following these adaptations, the calibration of COSMO-2 was performed and the optimal parameters combination was obtained. Using the COSI performance score to quantify the quality of the simulation, which is a combination of root mean square score for continuous fields and equitable thread score for precipitation, a performance gain of 2-4% was observed. An independent verification of the optimal configuration shows a small reduction of the 2m temperature and precipitation biases, but also a small increase of the 2m dew point bias. This small impact is expected, given that the chosen model configuration is very similar to the model configuration used by the COSMO core development team, which has undergone exceptional expert tuning over a period of almost two decades; arguably this small impact confirms the validity of the calibration method. However, the main learning from the CALMO project is that the meta-model is able to reasonably reproduce the dependency of the model on the unconfined parameters. This is illustrated in Fig. 6, where the meta-model prediction is compared with the full model prediction for the daily accumulated precipitation at different locations. Thanks to these developments, **the calibration methodology can now be readily applied to a NWP system and the reliability of the calibration results can be trusted**. However, a full assessment of the impact of the soil memory is not available; this is an important issue, because it is expected that the impact of a new set of model parameters can be substantially stronger through the accumulation of heat and humidity in the soil over the full simulation period, as indeed observed in a preliminary experiment with a 1.1 km configuration of the COSMO model (a performance gain measured by the COSI score exceeding 10% has been observed following a one month calibration). Furthermore, in order for this method to be used by the COSMO community, **it is essential to reduce the computing cost of the calibration**. For these reasons, a follow-up project CALMO-MAX has been defined. Finally, it should be noted that the selection of unconfined model parameters used in the calibration process is a crucial but also user-dependent step. More specifically the calibration of the model towards better scores could be associated with the user specific needs for a detailed representation

of specific model variables and phenomena. Additional parameterization development and new model implementations is always needed but **calibration is always meaningful in order to complement the expert tuning!**

References

Avgoustoglou E., A. Voudouri, P. Khain, F. Grazzini and J.M. Bettems, 2017: Design and Evaluation of Sensitivity Tests of COSMO Model Over the Mediterranean Area. Perspectives on Atmospheric Sciences, Vol.1, Springer, pp 49-55

Bayler, Gail M.; Aune, R. M.; Raymond, W. H., 2000. NWP Cloud Initialization Using GOES Sounder Data and Improved Modeling of Nonprecipitating Clouds. Mon. Wea. Rev., 128, 3911-3921

Bellprat, O., S. Kotlarski, D. Lthi, and C. Schr. 2012a. Exploring perturbed physics ensembles in a regional climate model. Journal of Climate, 25, 4582-4599

Bellprat, O., S. Kotlarski, D. Lthi, and C. Schr. 2012b. Objective calibration of regional climate models. Journal of Geophysical Research, 117, D23115.

Bellprat, O., R. Elia, A. Frigon, S. Kotlarski, R. Laprise, D. Lthi, and C. Schr. 2016. Objective Calibration of Regional Climate Models: Application over Europe and North America. Journal of Climate. https://doi.org/10.1175/JCLI-D-15-0302.1

Damrath U., 2009, Presentation at 11th COSMO-GM Offenbach, Germany.
http://www.cosmo-model.org/content/consortium/generalMeetings/
general2009/wg5-versus2/ Ulrich_Damrath_Long_term_time_series_of_COSMO_EU.ppt

Decharme B., H. Douville, A. Boone, F. Habets and J. Noilhan, 2006. Impact of an Exponential Profile of Saturated Hydraulic Conductivity within the ISBA LSM: Simulations over the Rhne Basin. Journal of Hydrometeorology, Vol. 7, 61-80

Duan Q., J. Schaake, V. Andreassian, S. Franks, G. Goteti, H.V. Gupta, Y.M. Gusev, F. Habets, A. Hall, L. Hay, T. Hogue, M. Huang,G. Leavesley, X. Liang, O. Nasonova, J. Noilhan, L. Oudin,S. Sorooshian, T. Wagener, E.F. Wood. 2006. Model Parameter Estimation Experiment (MOPEX):An overview of science strategy and major results from the second and third workshops. Journal of Hydrology, 320, 317.

Frei, C. 2013: Interpolation of temperature in a mountainous region using nonlinear profiles and non-Euclidean distances. Int. J. Climatol. Published online: DOI:10.1002/joc.3786
Katz W. R. and A.H. Murthy, 1997. Economic value of weather and climate forecasts. Cambridge University Press, 222 pp.

Khain P., I. Carmona, A. Voudouri, E. Avgoustoglou, J-M. Bettems, F. Grazzini, 2015 The Proof of the Parameters Calibration Method: CALMO Progress Report, COSMO technical report, 25
www.cosmo-model.org/content/model/documentation/techReports/docs/techReport25.pdf

Khain P., I. Carmona, A. Voudouri, E. Avgoustoglou, J-M. Bettems, F. Grazzini, P. Kaufmann, 2017, CALMO - Progress Report, COSMO technical report, 31
www.cosmo-model.org/content/model/documentation/techReports/docs/techReport31.pdf

Knutti, R., T. F. Stocker, F. Joos, and G. K. Plattner, 2002: Constraints on radiative forcing and future climate change from observations and climate model ensembles. Nature 416(6882):719-23.

Lapillonne, X., and O. Fuhrer, 2013: Using compiler directives to port large scientific applications to GPUs: An example from atmospheric science. Parallel Processing Letters, in press.

Neelin, J. D., A. Bracco, H. Luo, J. C. McWilliams, and J. E. Meyerson. 2010. Consider-

ations for parameter optimization and sensitivity in climate models. Proc. of the National Academy of Sciences of the United States of America, 107, 21349-21354.

Skamarock, W.C., 2004. Evaluating Mesoscale NWP Models Using Kinetic Energy Spectra. Mon. Wea. Rev., 132, 3019-3032.

Stephens, Graeme L., Si-Chee Tsay, Paul W. Stackhouse, Piotr J. Flatau, 1990: The Relevance of the Microphysical and Radiative Properties of Cirrus Clouds to Climate and Climatic Feedback.J. Atmos. Sci., 47, 17421754.

Voudouri A., E. Avgoustoglou and P. Kaufmann, 2017a: Impacts of Observational Data Assimilation on Operational Forecasts. Perspectives on Atmospheric Sciences, Vol.1, Springer, pp 143-150

Voudouri A., Khain P., Carmona I., Bellprat O., Grazzini F., Avgoustoglou E. , Bettems J.M and Kaufmann P., 2017b: Objective calibration of numerical weather prediction models. Atm. Res. 190, pp 128-140

Voudouri A., Khain P., Carmona I., Avgoustoglou E., Kaufmann P, Grazzini F. and Bettems J.M 2017c: Optimization of high resolution COSMO model performance over Switzerland and Northern Italy (submitted)

9 Appendix: list of model parameters

The most interesting parameters for CALMO / COSMO-1 are highlighted:

in red: highest priority
in orange: medium priority
in yellow: lowest priority

Multilayer soil model

	name	description	value (min/max)	defined in	dependency on resolution, remarks
x	cdash	parameter for laminar conductance of heat and water vapour from leaves	0.05 $(m/s)^{1/2}$	data_soil	**not in use for COSMO-1 (aka itype_tran=2)**
x	cdmin	part of the tuning parameters for the maximum sustainable water flux in the soil	$2.5 \cdot 10^{-10} m^2/s$	data_soil	
x	cdsmin	minimum snow depth	0.01 m	data_soil	
x	cfinull	soil water suction at saturation	0.2 m	data_soil	
x	cf_snow	parameter for determination of fractional snow cover	0.015 m_{H2O}	data_soil	decrease cf_snow, if for smaller grid elements snow cover shall be increased, compare rhde for radiation
x	cf_w	parameter for determination of fractional water cover	0.001 m_{H2O}	data_soil	analogous to cf_snow
x	cik1	parameter for determination of maximum infiltration	0.02	data_soil	

	name	description	value (min/max)	defined in	dependency on resolution, remarks
x	ckrdi	scale for soil hydraulic conductivity	0.00001 m/s	data_soil	
x	cparcrit	scale for photosynthetically active radiation	100 W/m^2	data_soil	
x	crhosmax_ml	maximum density of snow	400 kg/m^3	data_soil	
x	crhosmin_ml	minimum density of snow	0.8	data_soil	
x	crhowm	fraction of saturated soil filled by water	50 kg/m^3	data_soil	
x	crsmax	maximum stomatal resistance	4000 s/m	data_soil	
x	crsmin	minimum stomatal resistance	150 s/m (50.0 – 300.0)	INPUT	
x	csatdef	scale for saturation deficit	4000 Pa	data_soil	
x	csvoro	parameter for influence of sub-grid scale orography on infiltration	1	data_soil	increase parameter for decreasing grid length to allow for more infiltration
x	ctau_i	time constant for drainage from interception store	1000 s	data_soil	modification in TERRA possible to avoid ctau_i $< 2\Delta$
x	ctend	maximum temperature for plant transpiration	313.15 K	data_soil	
x	cwimax_ml	parameter for determination of maximum interception store	0.000001 m	data_soil	
	kexpdec	hydraulic conductivity of soilr	2	src_soil_multlay.f90	

The soil model uses additional parameters which depend on the 8 soil types ice, rock, sand, sandy loam, loam, loamy clay, clay, and peat. Some additional values for sea water and for sea ice are given but not yet used in the model. All these parameters are defined in data_soil. Most of these parameters strongly effect the water and heat budgets at the soil surface. This in turn significantly effects the determination of the near surface values of temperature and humidity.

Turbulence (diffusion, vertical transport; atmosphere)

	name	description	value (min/max)	defined in	dependency on resolution, remarks
x	pat_len	length scale of subscale surface patterns over land	500 m (10.0 – 1000.0)		
x	c_diff	factor for turbulent diffusion of TKE	0.2 (0.01 – 10)		
x	a_stab	factor for stability correction of horizontal length scale	0		
x	a_heat	factor for turbulent heat transport	0.74		
x	a_mom	factor for turbulent momentum transport	0.92		
x	d_heat	Factor for turbulent heat dissipation	10.1 (12 – 15)		
x	d_mom	Factor for turbulent momentum dissipation	16.6 (12 – 15)		
x	tur_len	asymptotic maximal turbulent length scale	150 m (100 – 1000)		
x	tkesmot	time smoothing factor for TKE and diffusion coefficients	0.15		
x	tkmmin	Minimal diffusion coefficient for heat	$0.4m^2/s$(0.0 – 2.0)		
x	tkhmin	Minimal diffusion coefficient for momentum	$0.4m^2/s$(0.0 – 2.0)		

Turbulence (surface layer transfer)

	name	description	value (min/max)	defined in	dependency on resolution, remarks
x	rlam_mom	scaling factor of the laminar boundary layer for momentum	0.0		
x	rlam_heat	scaling factor of the laminar boundary layer for heat	1.0 (0.1 – 10.0)		
x	rat_lam	Ratio of laminar boundary thickness for q and h	1.0 (0.1 – 10.0)		
x	rat_can	Factor for canopy height	1.0 (0.0 – 10.0)		
x	rat_sea	ratio of laminar scaling factors for heat over sea and land	20 (1.0 – 100.0)		
x	c_lnd	surface area density of the roughness elements over land	2.0 (1.0 – 10.0)		
x	c_sea	surface area density of the waves over sea	1.5 (1.0 – 10.0)		
x	c_soil	surface area index of (evaporative) soil surfaces	1.0 (0.0 – 10.0)		
x	e_surf	Exponent to get the effective surface area	1.0 (0.1 – 10.0)		
x	z0m_dia	roughness length of a typical synoptic station	0.2 m (0.001 – 10.0)		

Grid scale precipitation

	name	description	value (min/max)	defined in	dependency on resolution, remarks
x	zaac	$zaac = \frac{3}{7}\frac{E_r}{\rho_w}(A_r B_r)^{2/9}$ $A_r = \rho_w \pi N_o^r$ $B_r = v_o^r \Gamma(4.5)/\Gamma(4)$ $E_r = 0.8$ $N_o^r = 8 \cdot 10^{-6} m^{-4}$ $v_o^r = 130 m^{1/2} s^{-1}$	1.72	hydor	parameter for the determination of the accretion rate
x	zaau	inverse of the time constant for autoconversion	$0.001 s^{-1}$	hydor	
x	zamc	parameter for the temperature dependent relation between mass and diameter of precipitation particles	$0.08 kg/m^2$	hydor	
x	zamelt	parameter for determination of melting of falling snow	$7.2 \cdot 10^{-6}$	hydor	
x	zamv	parameter for the temperature dependent relation between mass and diameter of precipitation particles	$0.02 kg/m^2$	hydor	
x	zanuc	inverse of the time constant for nucleation	$0.001 s^{-1}$	hydor	
x	zarim	$E_s \pi/4$ collection efficiency for snow particles	1.97	hydor	
x	zbdep	parameter β_{dep} (coef. for ice ventilation)	13	hydor	
x	zbev	parameter β_{ev} (coef. for drop ventilation)	8.05	hydor	
x	zbmelt	parameter β_{melt} (coef. for melting ice)	13	hydor	
x	zt1	parameter for the temperature dependent relation between mass and diameter of precipitation particles	253.15 K	hydor	
x	zt2	parameter for the temperature dependence of the distribution of water, ice, and mixed phase clouds	235.15 K	hydor	
x	v0snow	factor in the terminal velocity for snow	20 (10.0 – 30.0)		

	name	description	value (min/max)	defined in	dependency on resolution, remarks
x	rain_n0_fac	However, because on average, the parameterization of the frozen-phase growth processes in the current graupel scheme seems to be too inefficient to produce "enough" precipitation sized particles, we artificially reduce the evaporation of raindrops to get the "correct" rain amount at the surface, by tuning the N00 parameter with a factor rain_n0_factor ($\leqslant$ 1), N00_tuned = N00 $\cdot$ rain_n0_factor	1.0		
x	mu_rain		0		
x	qc0	cloud water threshold for autoconversion	0.0002 (0.0 – 0.01)		
x	qi0	cloud ice threshold for autoconversion	0.0 (0.0 – 0.01)		
	cloud_num	cloud droplet number concentration	5.0E8		
x	zxstar	separating mass between cloud and rain	separating mass between cloud and rain		

Radiation

	name	description	value (min/max)	defined in	dependency on resolution, remarks
x	csalb	solar albedo for dry soil	soil type dependent	data_soil	**Not in use for COSMO-1 (aka itype_albedo=3)**
x	csalb_snow	solar albedo for snow	0.7	data_soil	**Not in use for COSMO-1 (aka itype_albedo=3)**
x	csalb_p	solar albedo for plant covered soil	0.15	data_soil	**Not in use for COSMO-1 (aka itype_albedo=3)**
x	ctalb	thermal albedo for all soil types	0.004	data_soil	
x	ucl	determination of cloud cover in unsaturated conditions	1	constants	should be resolution dependent (ask Matthias how we can tune width of distribution!)
x	uc1	as ucl	0.8	constants	as ucl
x	uc2	as ucl	$sqrt(3)$	constants	as ucl
x	zclwfk	fraction of saturation humidity assumed for cloud liquid water content of convective clouds	0.01	organize_radiation	
x	zclwfs	as zclwfk, for non-convective sub-grid scale clouds	0.005	organize_radiation	**not used in code ?**
	IF (lzprog_qi) THEN zclws = 0.005_wp · zsex				
x	clc_diag	cloud cover at saturation in statistical cloud diagnostic	0.5 (0.2 – 0.8)		**not used by radiation, see turbulence**
x	q_crit	critical value for normalized oversaturation	1.6 (1.0 – 10.0)		**Not used by radiation, see turbulence (check why this is red!)**

Shallow convection

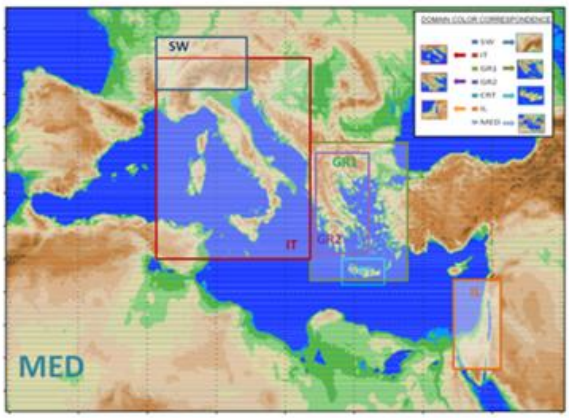
	name	description	value (min/max)	defined in	dependency on resolution, remarks
x	entr_sc	mean entrainment rate for shallow convection	3.0E-4 (5.0E-5 – 2.0E-3)		
x	thick_sc	limit for convective clouds to be "shallow" (in Pa)	2.5E4		

Sub-grid scale orographic drag

	name	description	value (min/max)	defined in	dependency on resolution, remarks
x	gkdrag	gravity wave drag constant	0.075		Not used in COSMO-1 (aka lsso=.false.)
x	gkwake	low level wake drag constant	0.5		Not used in COSMO-1 (aka lsso=.false.)

10 Appendix: highlights of sensitivity experiments

SELECTED DOMAINS



SENSITIVITY TESTS BLUEPRINT

13 parameters were considerd.

⊗

3 values/parameter including default.

⊗

The evaluation period consisted of 62 days from year 2013, i.e.: February 1-20, June 1-20, December 10-31.

‖

2418 runs based on COSMO.v5.0

- Horizontal grid size: 0.0625^0 (~7km).
- 649x393 grid points (wider mediterranean area), 60 levels.
- Integration time-step: 30 secs.
- Integration period: 48 hs.
- Boundary conditions : 6hr IFS Analysis.
- Computational Cost ~ 10^7 b.u. on Cray X C30 of ECMWF (gratis HNMS).

INVESTIGATED VARIABLES (AREA AVERAGES)

- **< TMAX2m >:** Maximum 2m temperature for 0-24 hr periods.
- **< TMIN2m >:** Minimum 2m temperature 0-24 hr periods.
- **< TOTPREC >:** 0-24 hr period accummulated precipitation (kg m^{-2}).
- **< SNOW_GSP >:** 0-24 hr periods accumulated grid-scale snow (kg m^{-2})
- **< CLCL >:** Low cloud cover (%) average of 3hr time steps 03-24 hs.
- **< CLCM >:** Medium cloud cover (%) average of 3hr time steps 03-24 hs.
- **< CLCH > :** High cloud cover (%) average of 3hr time steps 03-24 hs.
- **< CLCT > :** Total cloud cover (%) average of 3hr time steps 03-24 hs.

! The same investigation was performed for 24-48 hr periods with approximately the same performance.

GRAPH FEATURES

- The sensitivities of the considered variables are presented for every period as well as for the total number of days in succesive clustered column graphs: SW, IT, GR1, GR2, CRT, IL, MED.
- Domain color correspondance: SW IT GR1 GR2 CRT IL MED
- The idea behind the domain choices is to display the changes in sensitivities in reference to the relative location of the domains from the SouthEast (IL) to the NorthWest (SW) which is the focal domain of CALMO project at its present stage.
- On the horizonta axis, the sensitivities are presented for every pair of the parameter values under consideration.
- ● depicts the most sensitive parameters.
- ● depicts parameters with sensitivity of order 10% of ●.
- ● the sensitivity of **qi0** is displayed but not considered at this stage of the work.

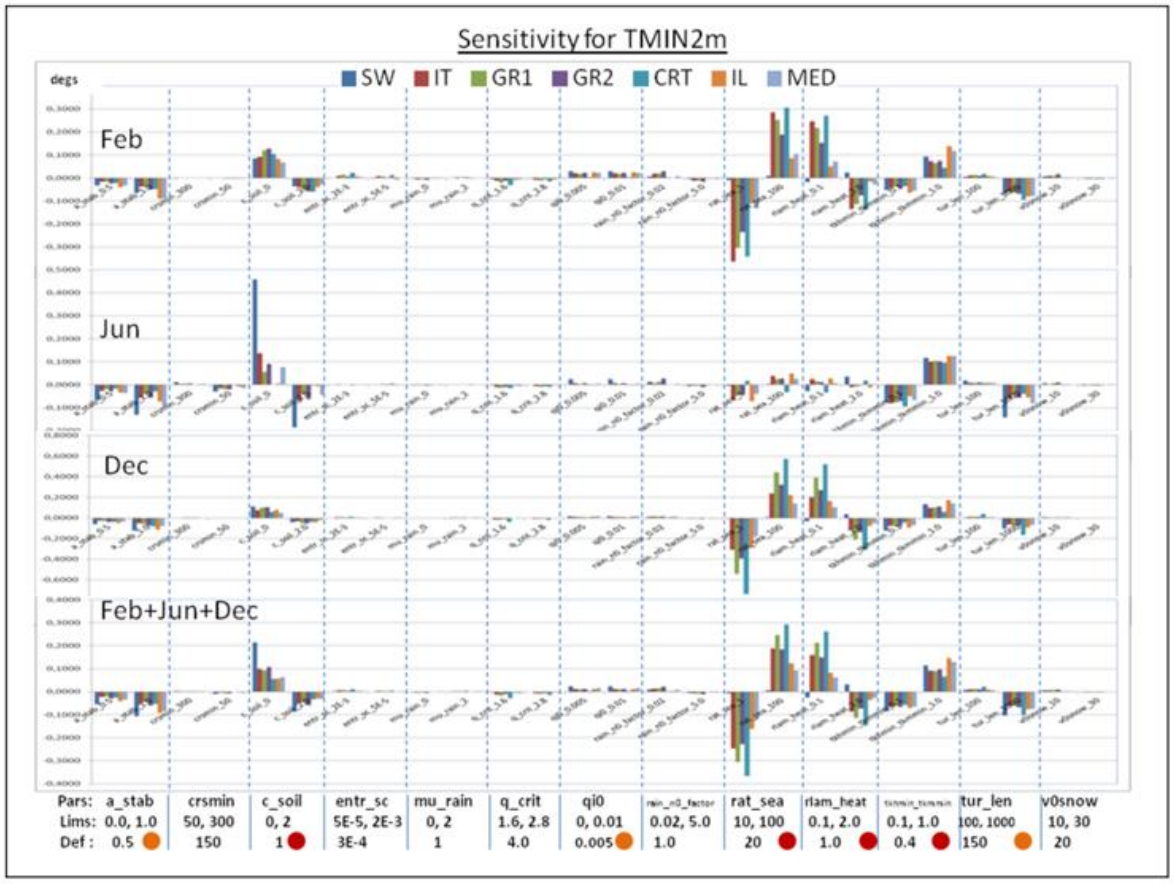
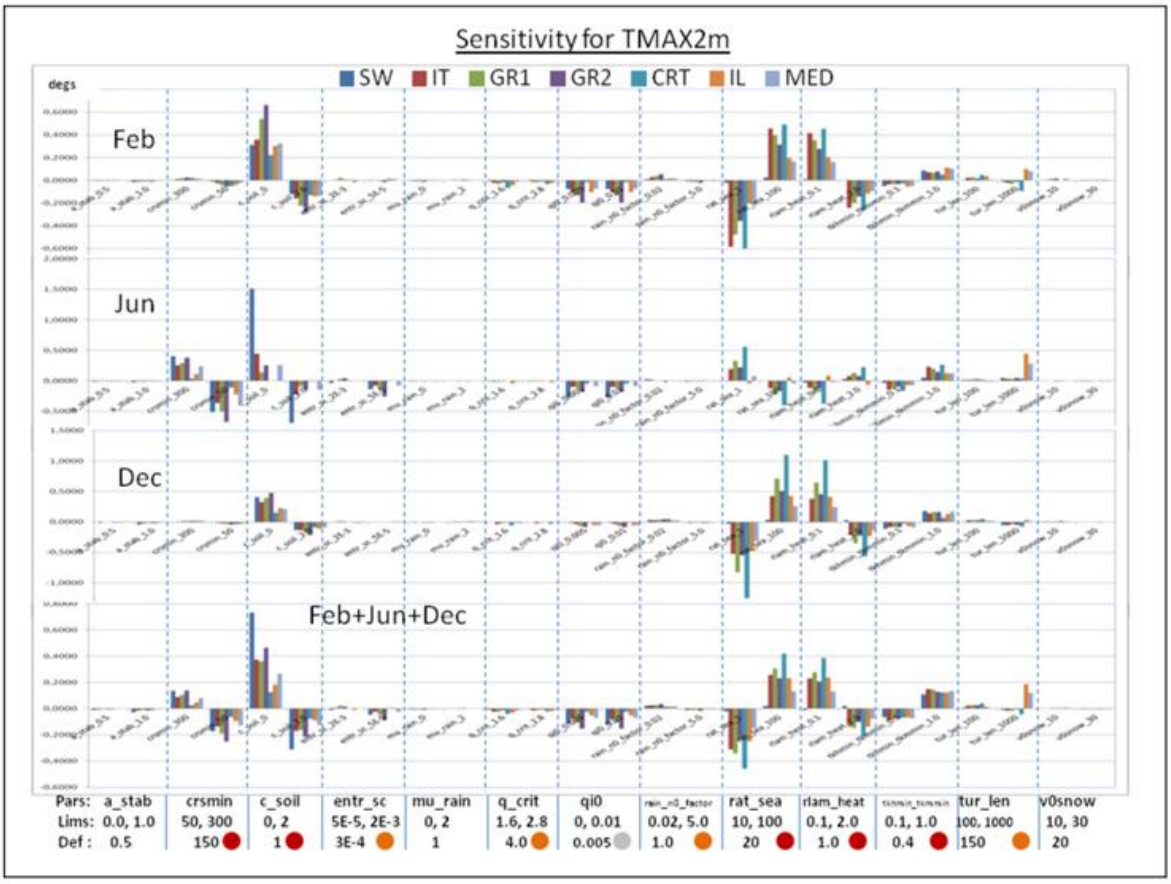
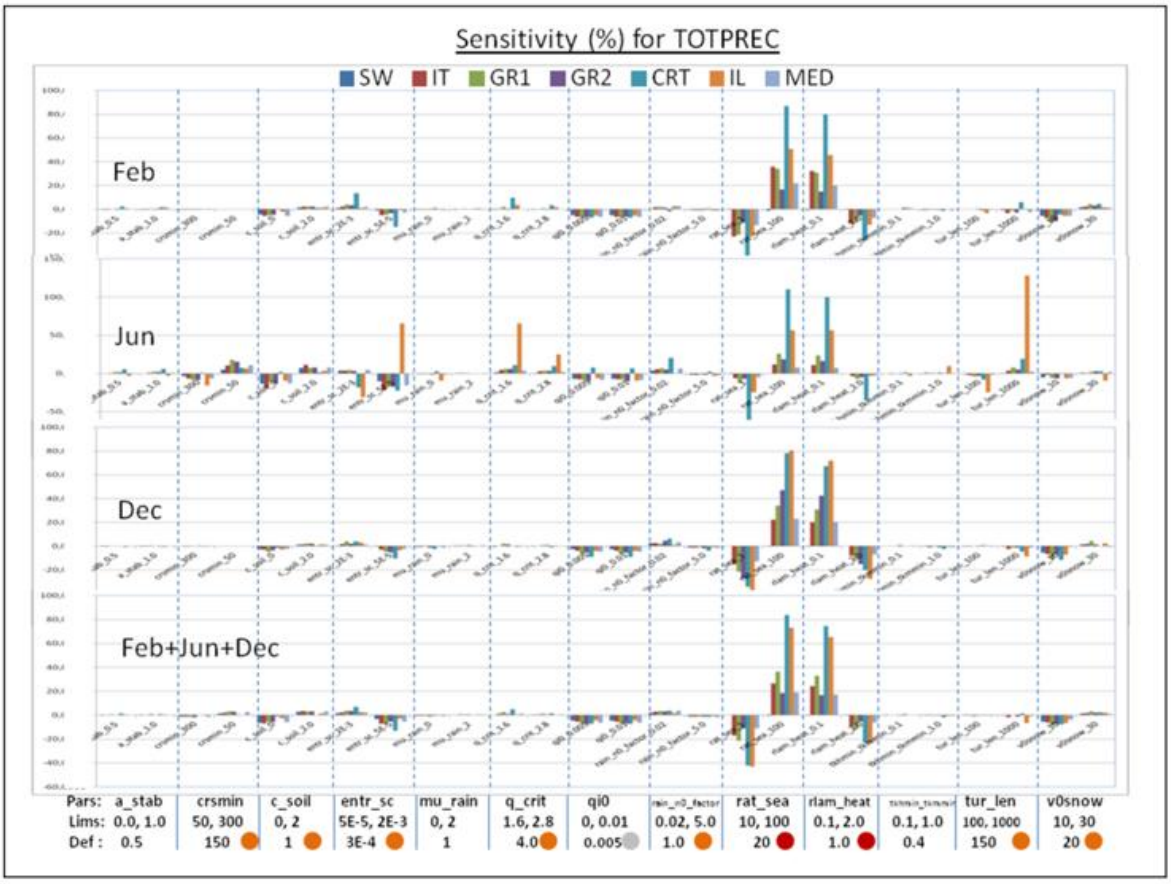
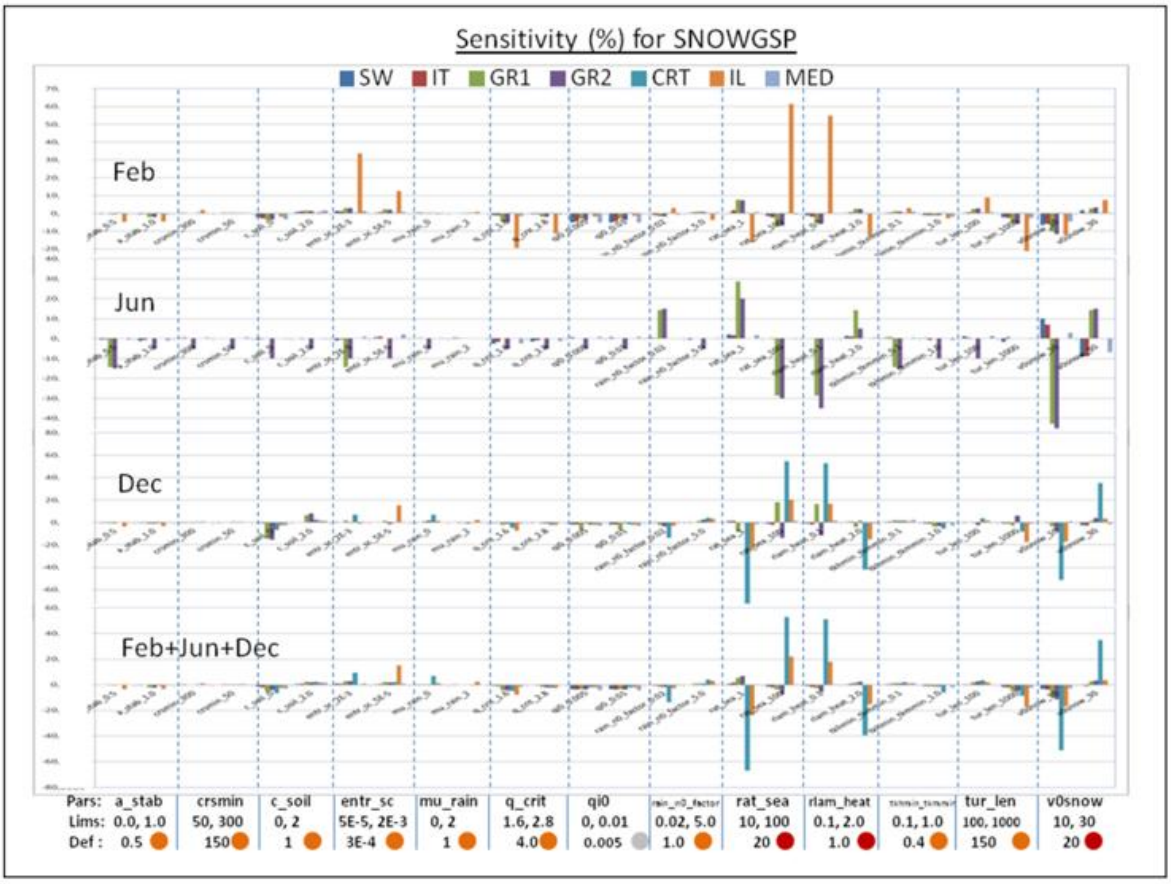
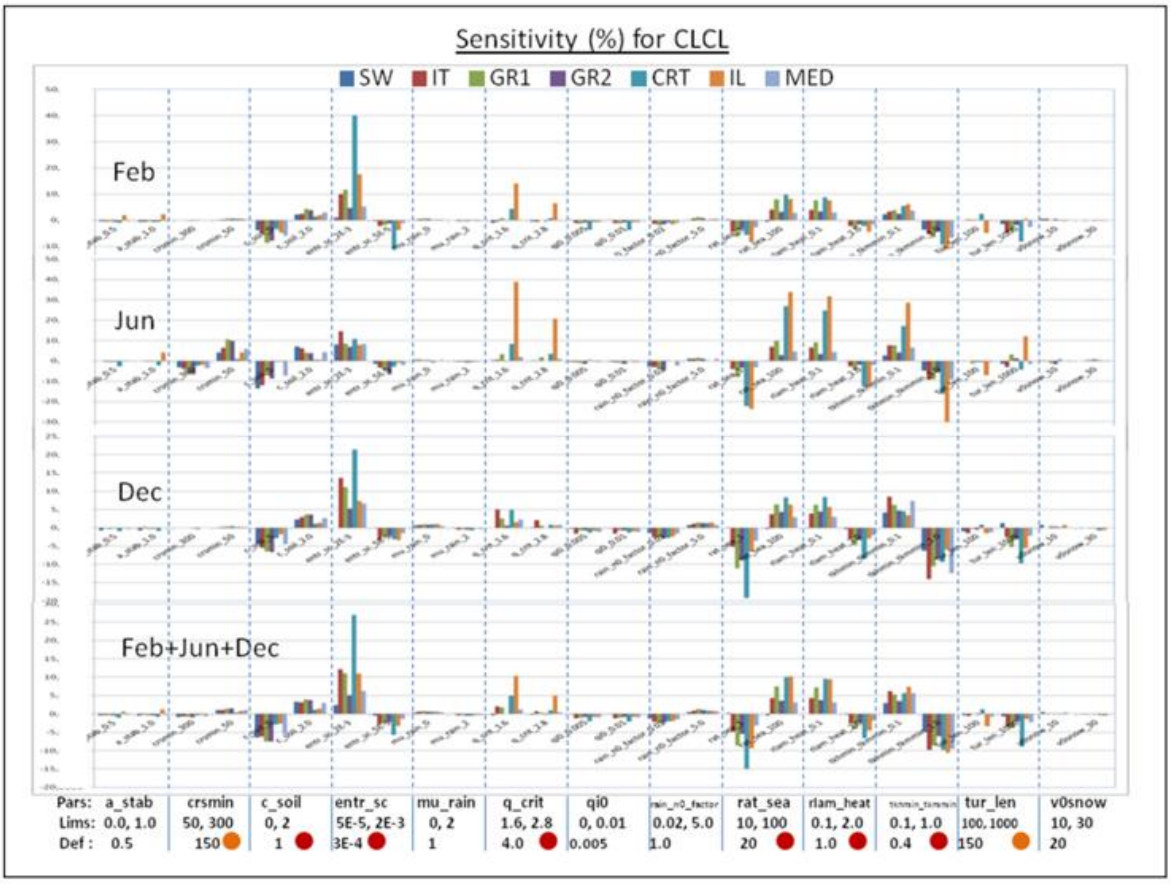


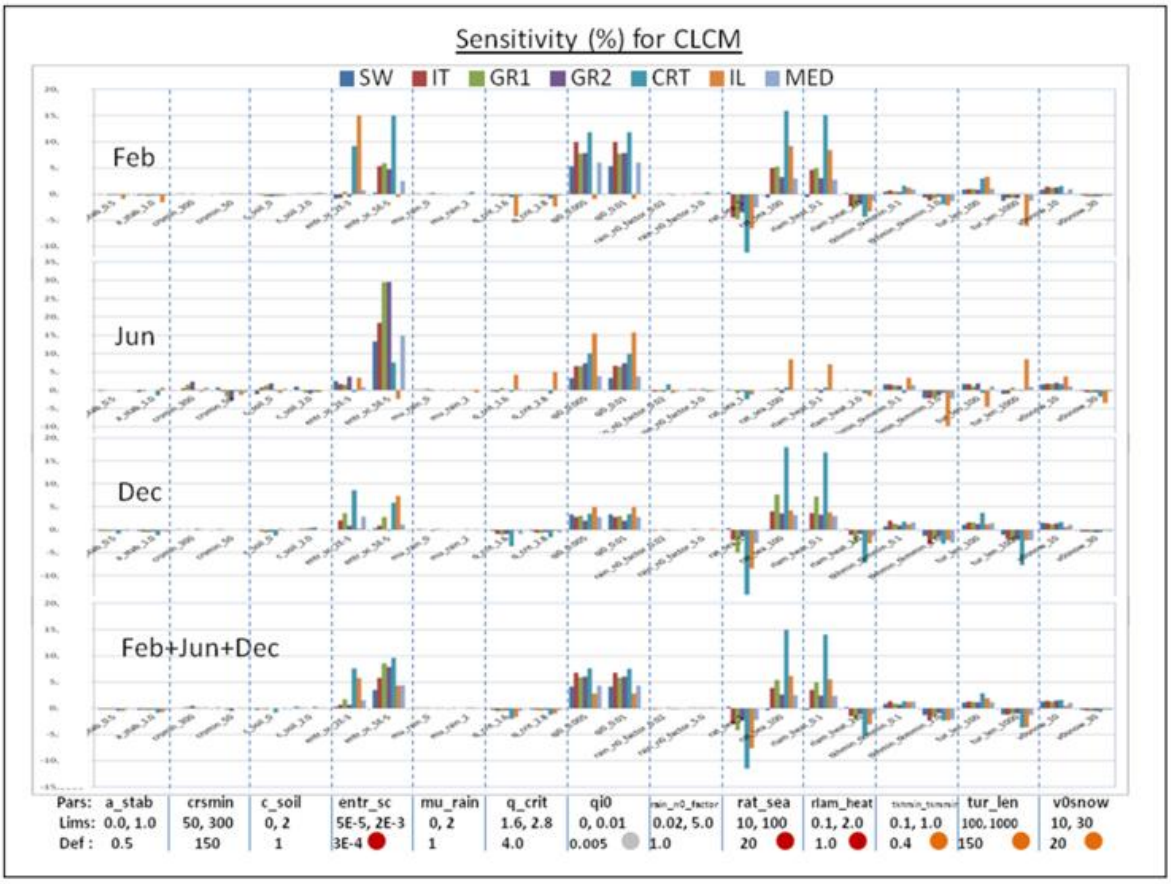
Figure 20: Description of parameter list. ∗c_lnd: Surface-area index of gridpoints over land (excluding leaf-area index). ∗∗The "gray" variable **qi0**, although its sensitivity will be shown, it is not accounted at this stage of our work due to caution regarding its use if different than its default value (communication with Axel Seifert).

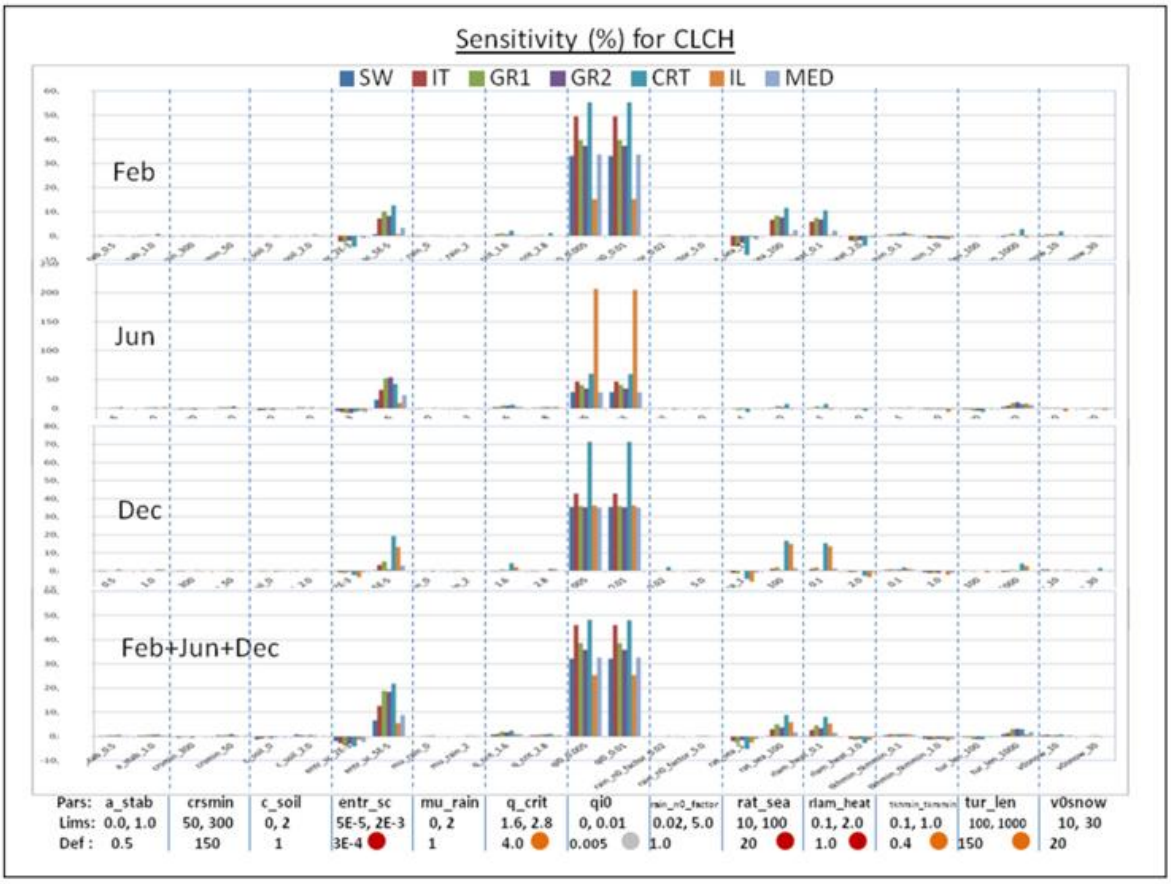

Sensitivity for TMAX2m
SW IT GR1 GR2 CRT IL MED
degs
Feb
Jun
Dec
Feb+Jun+Dec
Pars: a_stab crsmin c_soil entr_sc mu_rain q_crit qi0 rain_n0_factor rat_sea rlam_heat tur_len v0snow
Lims: 0.0, 1.0 50, 300 0, 2 5E-5, 2E-3 0, 2 1.6, 2.8 0, 0.01 0.02, 5.0 10, 100 0.1, 2.0 0.1, 1.0 100, 1000 10, 30
Def : 0.5 150 1 3E-4 1 4.0 0.005 1.0 20 1.0 0.4 150 20

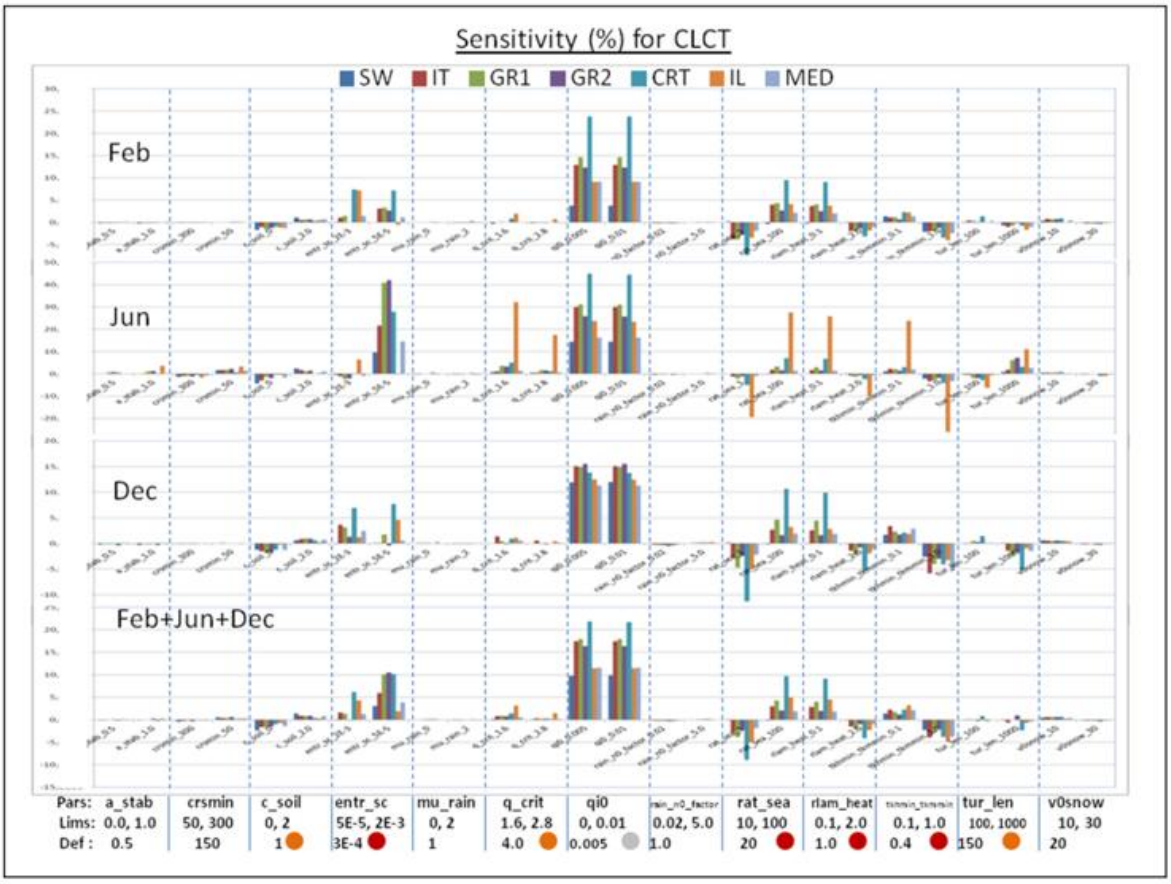

Sensitivity (%) for TOTPREC
SW IT GR1 GR2 CRT IL MED
Feb
Jun
Dec
Feb+Jun+Dec
Pars: a_stab crsmin c_soil entr_sc mu_rain q_crit qi0 rain_n0_factor rat_sea rlam_heat tkhmin_tkmmin tur_len v0snow
Lims: 0.0, 1.0 50, 300 0, 2 5E-5, 2E-3 0, 2 1.6, 2.8 0, 0.01 0.02, 5.0 10, 100 0.1, 2.0 0.1, 1.0 100, 1000 10, 30
Def : 0.5 150 1 3E-4 1 4.0 0.005 1.0 20 1.0 0.4 150 20

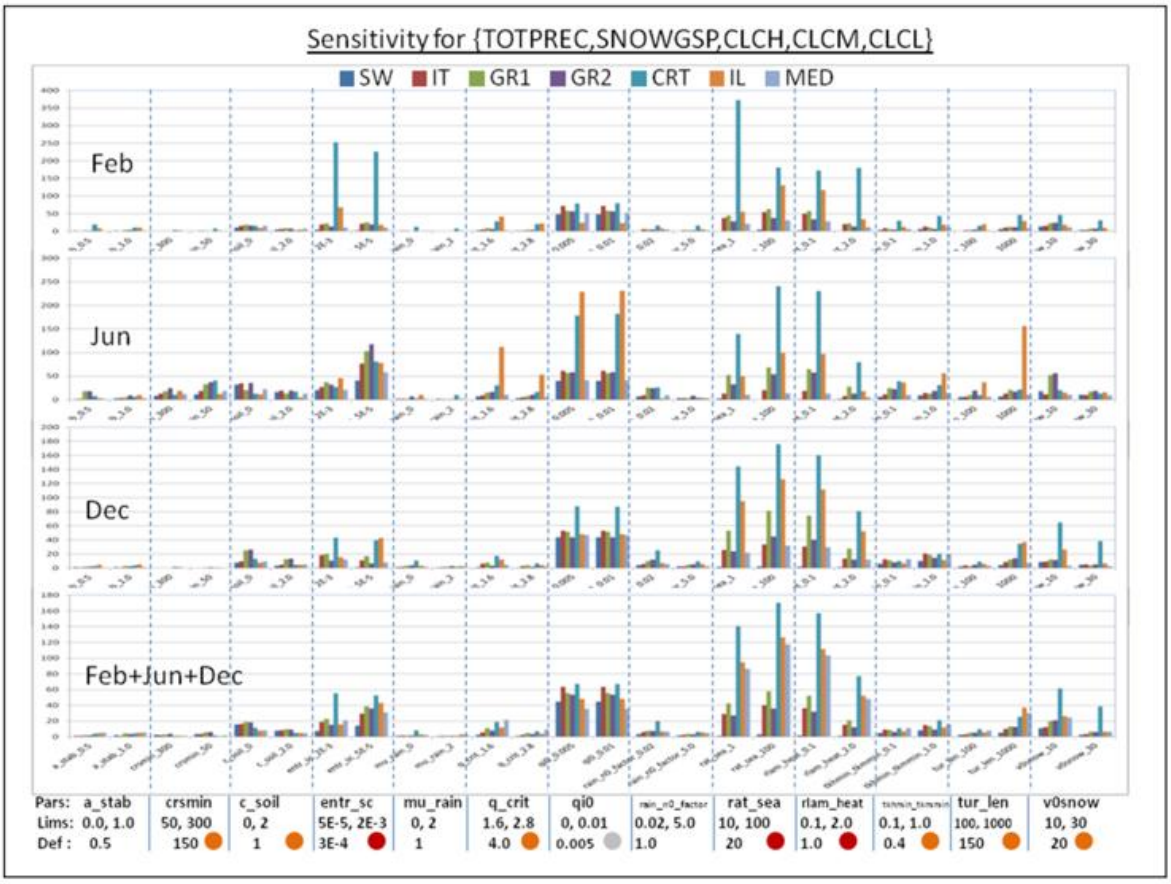

Sensitivity (%) for SNOWGSP
SW
IT
GR1
GR2
CRT
IL
MED
Feb
Jun
Dec
Feb+Jun+Dec
Pars: a_stab crsmin c_soil entr_sc mu_rain q_crit qi0 rain_n0_factor rat_sea rlam_heat tur_len v0snow
Lims: 0.0, 1.0 50, 300 0, 2 5E-5, 2E-3 0, 2 1.6, 2.8 0, 0.01 0.02, 5.0 10, 100 0.1, 2.0 0.1, 1.0 100, 1000 10, 30
Def : 0.5 150 1 3E-4 1 4.0 0.005 1.0 20 1.0 0.4 150 20


Sensitivity (%) for CLCL
SW
IT
GR1
GR2
CRT
IL
MED
Feb
Jun
Dec
Feb+Jun+Dec
Pars: a_stab crsmin c_soil entr_sc mu_rain q_crit qi0 rain_n0_factor rat_sea rlam_heat tur_len v0snow
Lims: 0.0, 1.0 50, 300 0, 2 5E-5, 2E-3 0, 2 1.6, 2.8 0, 0.01 0.02, 5.0 10, 100 0.1, 2.0 100, 1000 10, 30
Def : 0.5 150 1 3E-4 1 4.0 0.005 1.0 20 1.0 150 20


Sensitivity (%) for CLCM
SW
IT
GR1
GR2
CRT
IL
MED
Feb
Jun
Dec
Feb+Jun+Dec
Pars: a_stab crsmin c_soil entr_sc mu_rain q_crit qi0 rat_sea rlam_heat tur_len v0snow
Lims: 0.0, 1.0 50, 300 0, 2 5E-5, 2E-3 0, 2 1.6, 2.8 0, 0.01 0.02, 5.0 10, 100 0.1, 2.0 0.1, 1.0 100, 1000 10, 30
Def : 0.5 150 1 3E-4 1 4.0 0.005 1.0 20 1.0 0.4 150 20


Sensitivity (%) for CLCH
SW IT GR1 GR2 CRT IL MED
Feb
Jun
Dec
Feb+Jun+Dec
Pars: a_stab crsmin c_soil entr_sc mu_rain q_crit qi0 rat_sea rlam_heat tur_len v0snow
Lims: 0.0, 1.0 50, 300 0, 2 5E-5, 2E-3 0, 2 1.6, 2.8 0, 0.01 0.02, 5.0 10, 100 0.1, 2.0 0.1, 1.0 100, 1000 10, 30
Def : 0.5 150 1 3E-4 1 4.0 0.005 1.0 20 1.0 0.4 150 20


Sensitivity (%) for CLCT
SW
IT
GR1
GR2
CRT
IL
MED
Feb
Jun
Dec
Feb+Jun+Dec
Pars: a_stab crsmin c_soil entr_sc mu_rain q_crit qi0 rain_n0_factor rat_sea rlam_heat tkhmin_tkmmin tur_len v0snow
Lims: 0.0, 1.0 50, 300 0, 2 5E-5, 2E-3 0, 2 1.6, 2.8 0, 0.01 0.02, 5.0 10, 100 0.1, 2.0 0.1, 1.0 100, 1000 10, 30
Def : 0.5 150 1 3E-4 1 4.0 0.005 1.0 20 1.0 0.4 150 20


Sensitivity for {TOTPREC,SNOWGSP,CLCH,CLCM,CLCL}
SW IT GR1 GR2 CRT IL MED
Feb
Jun
Dec
Feb+Jun+Dec
Pars: a_stab crsmin c_soil entr_sc mu_rain q_crit qi0 rain_n0_factor rat_sea rlam_heat tur_len v0snow
Lims: 0.0, 1.0 50, 300 0, 2 5E-5, 2E-3 0, 2 1.6, 2.8 0, 0.01 0.02, 5.0 10, 100 0.1, 2.0 0.1, 1.0 100, 1000 10, 30
Def : 0.5 150 1 3E-4 1 4.0 0.005 1.0 20 1.0 0.4 150 20

List of COSMO Newsletters and Technical Reports

(available for download from the COSMO Website: www.cosmo-model.org)

COSMO Newsletters

No. 1: February 2001.

No. 2: February 2002.

No. 3: February 2003.

No. 4: February 2004.

No. 5: April 2005.

No. 6: July 2006.

No. 7: April 2008; Proceedings from the 8th COSMO General Meeting in Bucharest, 2006.

No. 8: September 2008; Proceedings from the 9th COSMO General Meeting in Athens, 2007.

No. 9: December 2008.

No. 10: March 2010.

No. 11: April 2011.

No. 12: April 2012.

No. 13: April 2013.

No. 14: April 2014.

No. 15: July 2015.

No. 16: July 2016.

No. 17: July 2017.

COSMO Technical Reports

No. 1: Dmitrii Mironov and Matthias Raschendorfer (2001):
Evaluation of Empirical Parameters of the New LM Surface-Layer Parameterization Scheme. Results from Numerical Experiments Including the Soil Moisture Analysis.

No. 2: Reinhold Schrodin and Erdmann Heise (2001):
The Multi-Layer Version of the DWD Soil Model TERRA_LM.

No. 3: Günther Doms (2001):
A Scheme for Monotonic Numerical Diffusion in the LM.

No. 4: Hans-Joachim Herzog, Ursula Schubert, Gerd Vogel, Adelheid Fiedler and Roswitha Kirchner (2002):
LLM ¯ the High-Resolving Nonhydrostatic Simulation Model in the DWD-Project LITFASS.
Part I: Modelling Technique and Simulation Method.

No. 5: Jean-Marie Bettems (2002):
EUCOS Impact Study Using the Limited-Area Non-Hydrostatic NWP Model in Operational Use at MeteoSwiss.

No. 6: Heinz-Werner Bitzer and Jürgen Steppeler (2004):
Documentation of the Z-Coordinate Dynamical Core of LM.

No. 7: Hans-Joachim Herzog, Almut Gassmann (2005):
Lorenz- and Charney-Phillips vertical grid experimentation using a compressible nonhydrostatic toy-model relevant to the fast-mode part of the 'Lokal-Modell'.

No. 8: Chiara Marsigli, Andrea Montani, Tiziana Paccagnella, Davide Sacchetti, André Walser, Marco Arpagaus, Thomas Schumann (2005):
Evaluation of the Performance of the COSMO-LEPS System.

No. 9: Erdmann Heise, Bodo Ritter, Reinhold Schrodin (2006):
Operational Implementation of the Multilayer Soil Model.

No. 10: M.D. Tsyrulnikov (2007):
Is the particle filtering approach appropriate for meso-scale data assimilation ?

No. 11: Dmitrii V. Mironov (2008):
Parameterization of Lakes in Numerical Weather Prediction. Description of a Lake Model.

No. 12: Adriano Raspanti (2009):
COSMO Priority Project "VERification System Unified Survey" (VERSUS): Final Report.

No. 13: Chiara Marsigli (2009):
COSMO Priority Project "Short Range Ensemble Prediction System" (SREPS): Final Report.

No. 14: Michael Baldauf (2009):
COSMO Priority Project "Further Developments of the Runge-Kutta Time Integration Scheme" (RK): Final Report.

No. 15: Silke Dierer (2009):
COSMO Priority Project "Tackle deficiencies in quantitative precipitation forecast" (QPF): Final Report.

No. 16: Pierre Eckert (2009):
COSMO Priority Project "INTERP": Final Report.

No. 17: D. Leuenberger, M. Stoll and A. Roches (2010):
Description of some convective indices implemented in the COSMO model.

No. 18: Daniel Leuenberger (2010):
Statistical analysis of high-resolution COSMO Ensemble forecasts in view of Data Assimilation.

No. 19: A. Montani, D. Cesari, C. Marsigli, T. Paccagnella (2010):
Seven years of activity in the field of mesoscale ensemble forecasting by the COSMO–LEPS system: main achievements and open challenges.

No. 20: A. Roches, O. Fuhrer (2012):
Tracer module in the COSMO model.

No. 21: Michael Baldauf (2013):
A new fast-waves solver for the Runge-Kutta dynamical core.

No. 22: C. Marsigli, T. Diomede, A. Montani, T. Paccagnella, P. Louka, F. Gofa, A. Corigliano (2013):
The CONSENS Priority Project.

No. 23: M. Baldauf, O. Fuhrer, M. J. Kurowski, G. de Morsier, M. Müllner, Z. P. Piotrowski, B. Rosa, P. L. Vitagliano, D. Wójcik, M. Ziemiański (2013):
The COSMO Priority Project 'Conservative Dynamical Core' Final Report.

No. 24: A. K. Miltenberger, A. Roches, S. Pfahl, H. Wernli (2014):
Online Trajectory Module in COSMO: a short user guide.

No. 25: P. Khain, I. Carmona, A. Voudouri, E. Avgoustoglou, J.-M. Bettems, F. Grazzini (2015):
The Proof of the Parameters Calibration Method: CALMO Progress Report.

No. 26: D. Mironov, E. Machulskaya, B. Szintai, M. Raschendorfer, V. Perov, M. Chumakov, E. Avgoustoglou (2015):
The COSMO Priority Project 'UTCS' Final Report.

No. 27: J-M. Bettems (2015):
The COSMO Priority Project 'COLOBOC': Final Report.

No. 28: Ulrich Blahak (2016):
RADAR_MIE_LM and RADAR_MIELIB - Calculation of Radar Reflectivity from Model Output.

No. 29: M. Tsyrulnikov and D. Gayfulin (2016):
A Stochastic Pattern Generator for ensemble applications.

No. 30: D. Mironov and E. Machulskaya (2017):
A Turbulence Kinetic Energy – Scalar Variance Turbulence Parameterization Scheme.

No. 31: P. Khain, I. Carmona, A. Voudouri, E. Avgoustoglou, J.-M. Bettems, F. Grazzini, P. Kaufmann (2017):
CALMO - Progress Report.

COSMO Technical Reports

Issues of the COSMO Technical Reports series are published by the *COnsortium for Small-scale MOdelling* at non-regular intervals. COSMO is a European group for numerical weather prediction with participating meteorological services from Germany (DWD, AWGeophys), Greece (HNMS), Italy (USAM, ARPA-SIMC, ARPA Piemonte), Switzerland (MeteoSwiss), Poland (IMGW), Romania (NMA) and Russia (RHM). The general goal is to develop, improve and maintain a non-hydrostatic limited area modelling system to be used for both operational and research applications by the members of COSMO. This system is initially based on the COSMO-Model (previously known as LM) of DWD with its corresponding data assimilation system.

The Technical Reports are intended

- for scientific contributions and a documentation of research activities,
- to present and discuss results obtained from the model system,
- to present and discuss verification results and interpretation methods,
- for a documentation of technical changes to the model system,
- to give an overview of new components of the model system.

The purpose of these reports is to communicate results, changes and progress related to the LM model system relatively fast within the COSMO consortium, and also to inform other NWP groups on our current research activities. In this way the discussion on a specific topic can be stimulated at an early stage. In order to publish a report very soon after the completion of the manuscript, we have decided to omit a thorough reviewing procedure and only a rough check is done by the editors and a third reviewer. We apologize for typographical and other errors or inconsistencies which may still be present.

At present, the Technical Reports are available for download from the COSMO web site (www.cosmo-model.org). If required, the member meteorological centres can produce hard-copies by their own for distribution within their service. All members of the consortium will be informed about new issues by email.

For any comments and questions, please contact the editor:

Massimo Milelli
Massimo.Milelli@arpa.piemonte.it

Consortium

for

Small-Scale Modelling

Technical Report No. 31

CALMO - Progress Report

May 2017

DOI: 10.5676/DWD_pub/nwv/cosmo-tr_31

Deutscher Wetterdienst
MeteoSwiss
Ufficio Generale Spazio Aereo e Meteorologia
ΕΘΝΙΚΗ ΜΕΤΕΩΡΟΛΟΓΙΚΗ ΥΠΗΡΕΣΙΑ
Instytucie Meteorogii i Gospodarki Wodnej
Administratia Nationala de Meteorologie
ROSHYDROMET
Agenzia Regionale Protezione Ambiente Piemonte
Agenzia Regionale Prevenzione Ambiente Energia Emilia Romagna
Centro Italiano Ricerche Aerospaziali
Amt für GeoInformationswesen der Bundeswehr
Israel Meteorological Service

www.cosmo-model.org

Editor: Massimo Milelli, ARPA Piemonte

CALMO - Progress Report

by

***P. Khain**[*], **I. Carmona**[*], **A. Voudouri**[**],*

***E. Avgoustoglou**[**], **J.-M. Bettems**[***],*

***F. Grazzini**[****], **P. Kaufmann**[***]*

[*] Israel Meteorological Service

[**] Hellenic National Meteorological Service

[***] MeteoSwiss

[****] Agenzia Prevenzione Ambiente Energia Emilia Romagna

Contents

1 Introduction - CALMO project **4**

2 Overview: different stages of the CALMO project **4**

3 Short overview of the tuned parameters **5**

4 Meta-Model **7**

4.1 Overview 7

4.2 Adaptations to the Meta-Model 8

4.2.1 Option not to average Tmax/Tmin over regions 8

4.2.2 Defining new regions for averaging the 24h accumulated precipitation (optional also for Tmax, Tmin) 9

4.2.3 Meta-Model predicts profiles characteristics 9

4.2.4 Logarithmic transformation for some of the parameters 10

5 Performance scores **10**

5.1 RMSE-type score 11

5.1.1 Observations variability is defined per month 11

5.1.2 Normalization weights 11

5.2 COSI-type score 11

6 Convergence to the optimal parameters combination **12**

6.1 Method 12

6.2 Uncertainty of the optimal parameters combination 13

7 TERRA stand-alone **13**

8 CALMO stage-2 **14**

8.1 Validation of CALMO stage-2 Meta-Model using arbitrary test simulation . . 14

8.2 Calibration results for entire year 2013 16

8.3 Calibration results - seasonal dependence 20

9 CALMO stage-3 **21**

9.1 Calibration results for January 2013 21

9.2 CALMO-2km vs CALMO-1km optimal parameters for January 2013 26

10 Summary **27**

A Appendix: Meta-Model code **30**

A.1 Algorithm 30

A.1.1 ReadData_and_MetaModel.m 30

A.1.2 PostProc.m 31

A.2 Structure 31

A.3 Subroutines 33

1 Introduction - CALMO project

The CALMO project is based on the objective calibration method which was developed and implemented in regional climate model by Omar Bellprat and Christoph Schär (ETH). The purpose of the CALMO project is to implement the calibration method of Bellprat et al. (2012) to NWP model COSMO. Briefly, the calibration method is the following:

- First, define the parameters for tuning and their allowed ranges. The selected parameters have to be the most significant for the verified fields. For example, for the maximum 2m-temperature we may need to focus on soil and radiation schemes parameters, while for precipitation, we may need to consider also microphysical parameters, etc.
- Define the forecast fields to be verified. It is important to select many meteorologically important fields in order to better reflect the weather conditions. Otherwise there is a danger that the calibration procedure will improve specific fields while degrading the overall skill of the forecast.
- Define the time periods and geographical regions for calibration. The time periods and the regions should be chosen to represent a meaningful forecast.
- Define the parameters (combinations) values for performing the COSMO simulations. The minimum required number of simulations to be performed is 2N + 0.5N(N - 1) + 1, where N is the number of calibrated parameters.
- Define the method to perform the COSMO simulations, i.e. initial and boundary conditions and the forecasts time ranges. For soil-related parameters, long term spin-up simulations of the COSMO soil scheme are needed for preparing proper initial conditions.
- After the simulations are performed, the Meta-Models are constructed, i.e. the forecasted fields are interpolated in parameters space via N-dimensional quadratic polynomial (for each field, for each region and each day, separately). These interpolation formulas (the Meta-Models) allow estimating the forecasted field value for arbitrary parameter values (for each region and each day) without performing real COSMO simulation.
- At the next stage, the parameters space is filled by a large number of parameters combinations. For each parameter combination, a forecast field time series is produced (using the Meta-Models), compared with the observations, and evaluated using a performance score.
- Finally, the parameters combination which obtained the best score is selected.
- In principle, it is reasonable to perform a real COSMO simulation with the selected parameters combination, and verify whether the forecasts are indeed better (than with the default parameters combination).

2 Overview: different stages of the CALMO project

The CALMO project included three stages. At CALMO-stage-1 we have performed a preliminary calibration of COSMO-7km. The detailed description of that stage is presented in

	Stage-1	Stage-2	Stage-3
Resolution	7km	2.2km	1.1km
Simulations domain	[17W-22E, 35N-57N]	[0E-17E,42N-50N]	[0E-17E, 42N-50N]
Calibration area	Switzerland	Switzerland and north Italy	Switzerland and north Italy
Calibrated atmospheric fields	T2m-max; T2m-min; 24h-precipitation	T2m-max; T2m-min; 24h-precipitation; sounding profiles diagnostics: CAPE; CIN; total column water vapor; vector wind shears between the levels 500-700mb/700-850mb/850-1000mb; temperature, relative humidity and wind components at 850, 700 and 500mb	T2m-max; T2m-min; 24h-precipitation; sounding profiles diagnostics: CAPE; CIN; total column water vapor; vector wind shears between the levels 500-700mb/700-850mb/850-1000mb; temperature, relative humidity and wind components at 850, 700 and 500mb
Simulations period	1-20/1/2008, 1-20/6/2008	1/1/2013-31/12/2013	1/1/2013-1/2/2013
Tuning parameters	rlam_heat, tkhmin, tur_len	rlam_heat, tkhmin, tur_len, entr_sc, c_soil, v0snow	tkhmin, tur_len, entr_sc, c_soil, crsmin

Table 1: Overview: different stages of the CALMO project

Khain et al. (2015). At CALMO-stages 2 and 3 we have performed several improvements of the calibration process. The main characteristics of the 3 stages are summarized in Table 1.

3 Short overview of the tuned parameters

In Table 2 we present the parameters which were tuned during the different stages of the CALMO project, and briefly describe their physical meaning.

	Used at stages:	Brief physical meaning:	Min	Default	Max
rlam_heat	1,2	rlam_heat $[no-units]$ is the parameter which linearly determines the heat resistance length of laminar layer; so that the higher is rlam_heat the higher is the resistance of laminar layer for heat transfer, and consequently, the lower is the heat transfer between the surface and the lower atmosphere	0.1	1	2
tkhmin	1,2,3	tkhmin $[m^2/s]$ and tkmmin $[m^2/s]$ determine the minimum limits for the turbulence coefficients. tkhmin presence is evident when the turbulent diffusion coefficients (then the mixing) are small, which occurs in stable conditions, mainly at night near the surface	0.1	0.4	1
tur_len	1,2,3	tur_len $[m]$ is l_∞ in Blackadar formula (Blackadar, 1962) for the turbulence length. The higher is tur_len, the higher are the turbulent coefficients (both vertical and horizontal) in the middle-upper atmospheric levels, and consequently the higher are the turbulent fluxes (mixing) for all the variables and tracers	100	150	1000
entr_sc	2,3	entr_sc $[m^{-1}]$ is the mean entrainment rate of boundary layer humidity into the shallow convection clouds. The higher is entr_sc, the more effective is the shallow convection vertical mixing	0.05e-3	0.3e-3	2e-3
c_soil	2,3	c_soil $[no-units]$ is the surface-area index of the evaporating fraction of gridpoints over land: c_soil $\in$ [0, c_lnd=2]. The higher is c_soil, the higher is the surface evaporation	0	1	2
v0snow	2	v0snow $[no-units]$ is the factor in the terminal velocity for snow	10	20	30
crsmin	3	crsmin $[s/m]$ is the minimum value of stomatal resistance used by the BATS approach for vegetation transpiration	50	150	200

Table 2: COSMO parameters tuned at different stages of the CALMO project

4 Meta-Model

4.1 Overview

The Meta-Model was widely discussed in Khain et al. (2015), so here we briefly present its basic idea. Following the theory of Meta-Model construction (see Bellprat et al., 2012 and Neelin et al., 2010), for any parameters combination (for example N=3 parameters combination of rlam_heat, tkhmin, tur_len), for a given day i and a region r, the COSMO field F (for example Tmax, Tmin, Pr, etc.) may be approximated by 3-dimensional polynomial of order 2:

$$F_{i,r} \approx F_{di,r} + c_{i,r} + \sum_{n=1}^{N} a_{i,r}^{(n)} x_n + \sum_{n,m=1(n\neq m)}^{N} B_{i,r}^{(n,m)} x_n x_m \qquad (1)$$

where

$$x_1 = \frac{rlam_heat - rlam_heat_d}{rlam_heat_{max} - rlam_heat_{min}}, x_2 = \frac{tkhmin - tkhmin_d}{tkhmin_{max} - tkhmin_{min}}, x_3 = \frac{tur_len - tur_len_d}{tur_len_{max} - tur_len_{min}}$$

The index d stands for default. For default values of the N=3 parameters, i.e. $[x_1 = 0, x_2 = 0, x_3 = 0]$, the approximated field should be close to $F_{di,r}$. The constants $c_{i,r}$, $a_{i,r}^{(n)}$, $B_{i,r}^{(n,m)}$ are obtained using several COSMO simulations, as described in the following. Each simulation (for given parameters values) yields a set of forecasted values $F_{i,r}$. When sufficient number of simulations is performed, one can interpolate the different known values of as function of $[x_1, x_2, x_3]$ using the 3D polynomial in eq. 1 above. The sufficient number is 2N + 0.5N(N - 1) + 1, so that for N=3 the sufficient number of simulations to be performed is 10. Next we discuss the ways to increase the quality and the representativeness of such fit. The following factors are important for the interpolation to be realistic (to be able to replace the COSMO simulations):

- The choice of parameters values (combinations) for COSMO simulations should be specific. In this work the design is chosen according to Bellprat et al. (2012) (see also Khain et al. (2015)). Moreover, one should use as many as possible additional constrain simulations (for additional parameters combinations).
- The simulated COSMO field $F_{i,r}$ should not be noisy as function of the parameters. In other words, the sensitivity of $F_{i,r}$ on the parameters should be higher than the noise level. However, various COSMO fields are noisy for various parameters. That issue was discussed and solved in Khain et al. (2015).
- The time periods i and the regions r should be chosen to represent a meaningful forecast of the field $F_{i,r}$. In that work we have chosen typical periods of 24 hours (maximum and minimum daily temperature, 24h accumulated precipitation, etc.) and climatically distinguishable regions. The choice of the regions will be discussed in sections 4.2.1 and 4.2.2 below.
- It is important to select many meteorological important fields F in order to better reflect the weather conditions. Otherwise there is a danger that the calibration procedure will improve specific fields while degrading the overall skill of the forecast. At CALMO-stages 2 and 3 we have included optimization of meteorological profiles characteristics. That will be discussed in section 4.2.3 below.

- The default values of the parameters should be located close to the center of their allowed ranges. Otherwise, in the empty parameter ranges, the parabolic fit may reach very high (or very low) unrealistic peaks. The problem is, that the default values of rlam_heat, tur_len and entr_sc are significantly shifted from the centers of their allowed ranges: for $[0.1, 1, 10]$, $[100, 500, 10000]$, and $[0.05e-3, 0.3e-3, 2e-3]$, for rlam_heat, tur_len and entr_sc, respectively. That problem will be discussed and solved in section 4.2.4 below.

4.2 Adaptations to the Meta-Model

From CALMO-stage-1 (see Khain et al. (2015)) to CALMO-stages 2 and 3 we have performed several adaptations to the Meta-Model codes.

4.2.1 Option not to average Tmax/Tmin over regions

For observations over Switzerland we use Frei (2014) gridded data after correction to the elevations of model grid points. Over Italy we use the observations interpolated to the model grid (without correction to the elevations of model grid points), while only the grid points in vicinity of the stations get a value. At CALMO-stage-1 we have divided Switzerland area into 3 regions, and averaged the maximum and minimum 2m temperatures (Tmax and Tmin, respectively) and 24h accumulated precipitation (Pr) over these regions, before comparing with observations. While for precipitation, this averaging reduces the noise, for Tmax and Tmin we lost a lot of information. Just for example, Tmax errors at two different grid points can yield no error on average (see Fig. 1).

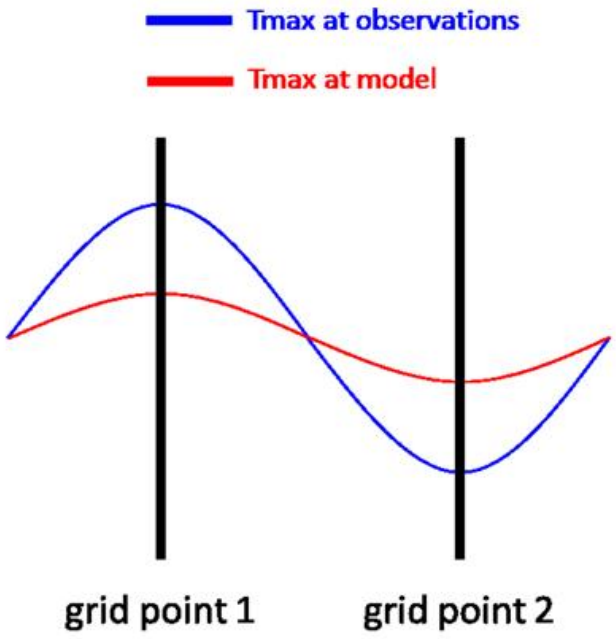


Figure 1: Schematic example for the reason not to average Tmax/Tmin over regions.

Moreover, at CALMO-stages 2 and 3 the Italian data are also analyzed. These data are not gridded (as Swiss ones), so that much less grid points are available for comparison of the model to the observations. In that case, region averaging would be based on much less points than over Switzerland. Therefore at CALMO-stages 2 and 3 we have added

the option (to the Meta-Model code) not to average Tmax and Tmin over regions, but to calculate the Meta-Model forecast for all the available grid-points in model and observations (about $N_{\Psi regs} \approx 10407$ for $\Psi = Tmax$ or $\Psi = Tmin$ for CALMO-stage-2, and similar number for CALMO-stage-3).

4.2.2 Defining new regions for averaging the 24h accumulated precipitation (optional also for Tmax, Tmin)

For observations over Switzerland we use the gridded MeteoSwiss radar composite (corrected by rain gauges) interpolated to the model grid. Over Italy we use the observations interpolated to the model grid, while only the grid points in vicinity of the stations get a value. In order to reduce the noise associated with precipitation fields, the precipitation model and observations values are averaged over $N_{Prregs,mon} = 6$ geographically unique regions, as presented in Fig. 2.

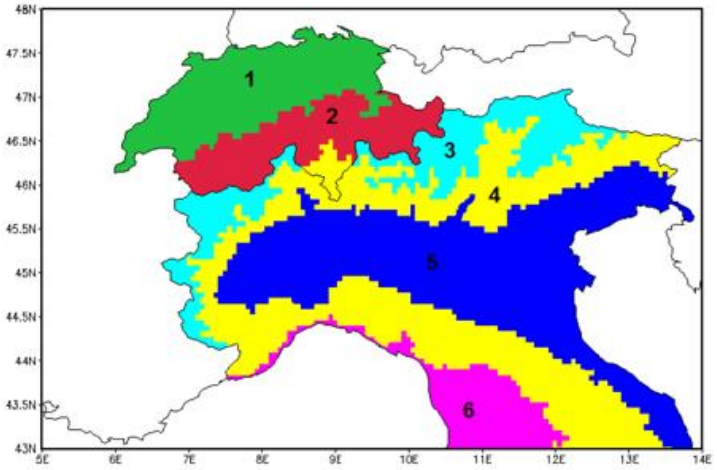


Figure 2: Geographically unique regions for precipitation averaging: 1-green: Swiss plateau (300m<h<1500m); 2-red: Swiss Alps (1500m<h); 3-cyan: Italian Alps (1500m<h); 4-yellow: Italian hills and Ticino (300m<h<1500m); 5-blue: Po Valley (h<300m); 6-magenta: Italian north-west coast (mainly h<300m).

4.2.3 Meta-Model predicts profiles characteristics

At CALMO-stage1 we have used the following fields: Ψ_1 - Daily maximum 2m temperature (Tmax); Ψ_2 - Daily minimum 2m temperature (Tmin); Ψ_3 - 24h accumulated precipitation (Pr). At CALMO-stages 2 and 3 we are using also the soundings data and the associated model profiles (at grid points near the soundings locations). The new verified fields are: Ψ_4 - Convective available potential energy (CAPE); Ψ_5 - Convective inhibition (CIN); Ψ_6 - Total column water vapor (TCWV); Ψ_7 - Vector wind shear between the levels of 500mb and 700mb (WS1); Ψ_8 - Vector wind shear between the levels of 700mb and 850mb (WS2); Ψ_9 - Vector wind shear between the levels of 850mb and 1000mb (WS3); $\Psi_{10,11,12}$ - Temperatures at 500mb (T500), 700mb (T700) and 850mb (T850) respectively; $\Psi_{13,14,15}$ - Relative humidity at 500mb (T500), 700mb (T700) and 850mb (T850) respectively; $\Psi_{16,17,18}$ - East-west wind component at 500mb (U500), 700mb (U700) and 850mb (U850) respectively; $\Psi_{19,20,21}$ - South-north wind component at 500mb (V500), 700mb (V700) and 850mb (V850) respectively. There are 11 available soundings at the CALMO-stages 2 and 3 domains, as presented in Fig. 3.

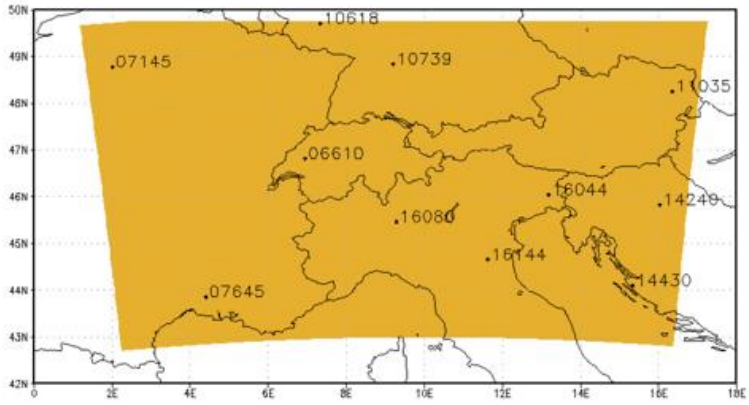


Figure 3: Available soundings inside CALMO-stages 2 and 3 domains.

Most of these soundings available twice per day, yielding about $N_{Prregs,mon} = 20{-}25$ (Ψ=any sounding field) profiles over the domain per day (depends on the sounding report quality).

4.2.4 Logarithmic transformation for some of the parameters

As discussed already in CALMO-stage 1 (Khain et al., 2015), the parabolic fit can accurately represent the dependency of the verified fields in parameters space only if the default values of the parameters are located close to the center of their allowed ranges. Otherwise, in the empty parameter ranges, the parabolic fit may reach very high (or very low) unrealistic peaks. The solution for that problem is transforming the problematic parameter/s to logarithm of the parameter/s. Such transformation brings the far away parameter values closer to the others, eliminating the empty parameter ranges, causing the parabolic fit to be more monotonic. In CALMO-stages 2 and 3, the problematic parameters are tur_len and entr_sc. Recently we have developed a method to objectively transform these parameters to logarithmic space:

$$x \rightarrow \hat{x} \equiv log(\alpha \frac{x - x_{min}}{x_{max} - x_{min}} + \beta).$$

The demand for the transformed default value to be exactly at the center between the minimum and maximum values, i.e. $\hat{x}_{max} - \hat{x}_d \stackrel{!}{=} \hat{x}_d - \hat{x}_{min}$ defines α and β. Applying the procedure yielded $\alpha = 72$, $\beta = 0.25$ for tur_len, and $\alpha = 9500$, $\beta = 210$ for entr_sc.

5 Performance scores

First, we have introduced user defined weights $\omega_{\Psi=1,...,21}$ (any positive numbers) for the contributions of various fields. For the results below, we have set: $\omega_{Tmax} = 1$, $\omega_{Tmin} = 1$, $\omega_{Pr} = 1$, $\omega_{CAPE} = 0$, $\omega_{CIN} = 0$, $\omega_{TCWV} = 1$, $\omega_{WS1} = 0.33$, $\omega_{WS2} = 0.33$, $\omega_{WS3} = 0.33$, $\omega_{T500} = 0.33$, $\omega_{T700} = 0.33$, $\omega_{T850} = 0.33$, $\omega_{RH500} = 0.33$, $\omega_{RH700} = 0.33$, $\omega_{RH850} = 0.33$, $\omega_{U500} = 0.2$, $\omega_{U700} = 0.2$, $\omega_{U850} = 0.2$, $\omega_{V500} = 0.2$, $\omega_{V700} = 0.2$, $\omega_{V850} = 0.2$. The fields CAPE and CIN (both observed and simulated) are generally noisy. Moreover, in the soundings data the number of reports (levels) is usually low, making the calculation of CAPE and CIN highly uncertain. Therefore at this work we set zero weights for these fields: $\omega_{CAPE} = 0$, $\omega_{CIN} = 0$. We have developed 2 optional performance scores for CALMO-stages 2 and 3, which are described below.

5.1 RMSE-type score

In contrast to CALMO-stage1, in stages 2 and 3 the number of regions (or grid-points) for comparing the model with observations very much depends on the forecasted field Ψ (and slightly depends on the month). Therefore the score for parameters combination p takes a more complicated form:

$$S_p = \left\{ \frac{1}{12 \sum_{\Psi=1}^{21} \omega_\Psi} \sum_{\Psi=1}^{21} \omega_\Psi \sum_{mon=1}^{12} \frac{1}{W_{\Psi,mon} N_{\Psi days,mon} N_{\Psi regs,mon}} \sum_{\Psi regs} \left[\frac{\sum_{\Psi days} (F_{\Psi,p,d,r,mon} - O_{\Psi,d,r,mon})^2}{\sigma^2_{\Psi,r,mon}} \right] \right\}^{1/2} \tag{2}$$

Where the fields Ψ_{1-21} where defined at Section 4.2.3 above.

5.1.1 Observations variability is defined per month

The quality of COSMO forecast strongly depends on the region and the season. For example, the forecast with Tmax error of 5K in the Alps at winter may be actually better than with error of 3K in the Swiss Plateau at summer. Therefore one needs to normalize the forecast errors by a value which reflects the forecast complexity for a given day and region. As at CALMO-stage 1, we normalize the forecast field Ψ errors by the observations standard deviation $\sigma_{\Psi,r,mon}$ at a given region (or grid-point) r over a period of a month $N_{\Psi days,mon} \approx 30$ (the period should not be too short in order to contain large enough sample, but not too long in order to represent the variability of a specific season):

$$\sigma_{\Psi,r,mon} = \sqrt{\frac{1}{N_{\Psi days,mon}} \sum_{\Psi days} (O_{\Psi,d,r,mon} - \overline{O}_{\Psi,d,r,mon})^2} \tag{3}$$

5.1.2 Normalization weights

Normalization weights are defined to set equal contributions for the various fields (N_p = 10000 - number of parameters combinations):

$$W_{\Psi,mon} = \frac{1}{N_p} \sum_{p=1}^{N_p} \frac{1}{N_{\Psi days,mon} N_{\Psi regs,mon}} \sum_{\Psi regs} \left[\frac{\sum_{\Psi days} (F_{\Psi,p,d,r,mon} - O_{\Psi,d,r,mon})^2}{\sigma^2_{\Psi,r,mon}} \right] \tag{4}$$

5.2 COSI-type score

The COSMO Index (COSI) was developed by Damrath (2009). We have adapted the score for CALMO use as following:

$$S_p = \frac{1}{12 \sum_{\Psi=1}^{18} \omega_\Psi} \left\{ \sum_{\Psi \neq 3} \omega_\Psi \sum_{mon=1}^{12} \left[1 - \frac{\sum_{\Psi regs} \sum_{\Psi days} (F_{\Psi,p,d,r,mon} - O_{\Psi,d,r,mon})^2}{\sum_{\Psi regs} \sum_{\Psi days} (O_{\Psi,d-1,r,mon} - O_{\Psi,d,r,mon})^2} \right] + \omega_3 \frac{\sum_{mon=1}^{12} \sum_{\Psi regs} \sum_{\Psi thr} ETS_{p,r,mon,thr}}{N_{\Psi days,mon} N_{\Psi regs,mon}} \right\} \tag{5}$$

where -1/3<ETS<1 (1 is the best) is the threshold dependent (we have chosen region averaged precipitation amounts thresholds of 0.1,1,3,7.5,10mm per 24h) precipitation score:

$$ETS_{p,r,mon,thresh} = \frac{H - \frac{(H+F)(H+M)}{N_{\Psi regs,mon}}}{H + M + F - \frac{(H+F)(H+M)}{N_{\Psi regs,mon}}} \tag{6}$$

where: H - Number of hits (i.e. both the model and the observations where above the given threshold); F - Number of false alarms; M - Number of misses.

6 Convergence to the optimal parameters combination

6.1 Method

After the Meta-Model is constructed we divide the parameters space into high number of points (parameters combinations), and calculate the score (see section 5) for each of the points in order to find the optimal one. In CALMO-stage 1, we have tuned 3 parameters, dividing the parameters space into 10000 points, i.e. roughly 21 bins for each of the parameters. In CALMO-stage 2, for example, the number of calibrated parameters is N=6, yielding huge number (about $21^6 \approx 10^8$) of points to be evaluated in order to find the optimal one. However, for computer time reasons it is not possible. Recently we have developed a method to overcome that problem and converge to the optimal parameters combination. At first iteration we sample 1000 points only and reveal the optimal regions in our N dimensional parameters space (according the uncertainty of the optimal 100 combinations). An example of the convergence after first iteration is presented in Fig. 4 below.

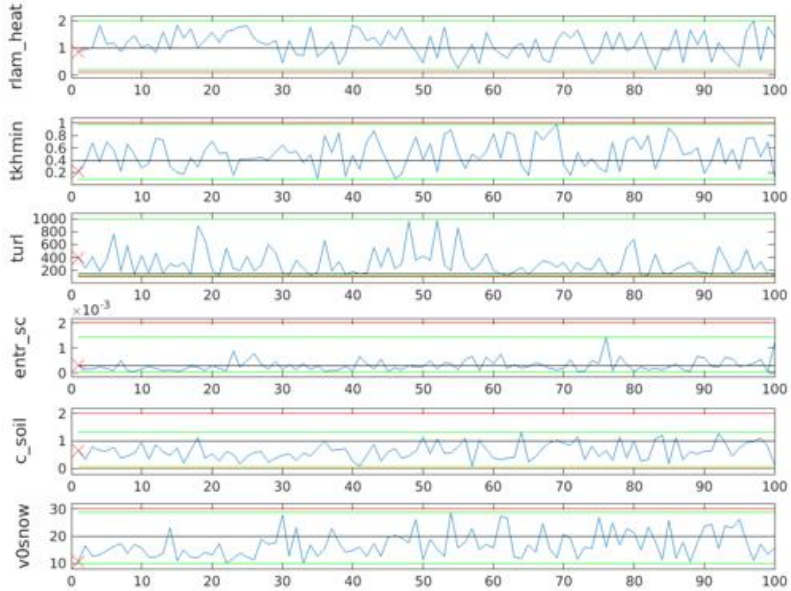


Figure 4: Example of convergence after first iteration. Each panel shows (in blue) the optimal 100 parameters values (in sorted order) among 1000 sampled combinations. The red lines represent the allowed ranges for each parameter, the green lines represent the uncertainty for each parameter after first iteration (following the optimal 100 values). Red crosses represent the best parameters combination after first iteration.

At second iteration we sample those regions (between the green lines in Fig. 4) by additional 1000 points, and reveal new, smaller, optimal regions (again according the uncertainty of the new optimal 100 combinations). We continue with these iterations until the solution converges to the optimal parameters combination. An example of the converged stage is presented in Fig. 5 below.

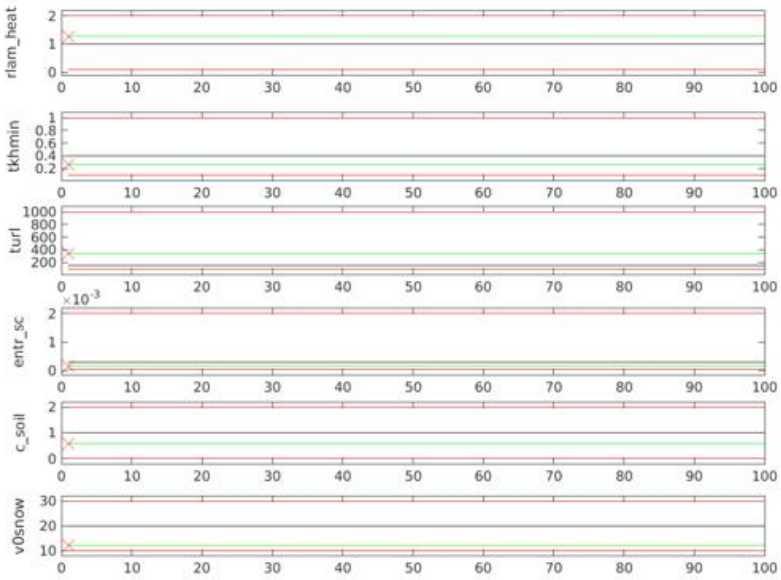


Figure 5: Example of convergence after last (35th) iteration.

6.2 Uncertainty of the optimal parameters combination

A question arises what is the uncertainty of the optimal parameters combination? In other words, what is the score sensitivity when slightly changing the parameters values with respect to the optimal parameters combination? To answer this question, we have followed the procedure described above, and determined the iteration at which the score reaches 90% of the optimal combination score. We define the parameters uncertainty (between the green lines in Fig. 4, for example) at that iteration as the uncertainty of the optimal parameters combination.

7 TERRA stand-alone

As part of CALMO-stages 2 and 3, among other parameters it was planned to tune also soil-scheme (TERRA) parameters (for example the hydraulic soil conductivity). In contrast to the regular COSMO parameters, the change in Terra parameters affects the COSMO forecasts with a significant delay (up to several years) via slow adaptation of the soil temperature and moisture profiles. Therefore, in order to tune TERRA parameters for specific year, one has to make the parameter changes several years earlier, and run the COSMO model in a cycle, slowly adapting the soil profiles to the parameter change. Moreover, errors in soil profiles caused by interpolation of soil fields from a coarse model disappear slowly, also on the scale of several years. Therefore, in order to obtain appropriate initial conditions in the soil (without interpolation errors), one again has to make the interpolation of soil fields several years earlier, and run the COSMO model in a cycle, slowly forgetting the interpolation errors. However, performing several years pre-run of the COSMO model (in a cycle mode)

is computationally expensive. Instead, it was decided to use the TERRA stand-alone (TSA) program driven by COSMO atmospheric analyses (from MeteoSwiss archive). The method was to initialize soil profiles from a coarse model interpolation, change the parameters of TSA (if needed), and run it for several years (prior to the tested year). Then, the obtained soil profiles were installed as initial soil conditions for the COSMO model runs (for the tested year). With we have run TSA for 3 years (2010-2012) with resolutions of 2.2 and 1.1 km, and prepared the soil initial conditions for the COSMO runs at 2013.

8 CALMO stage-2

8.1 Validation of CALMO stage-2 Meta-Model using arbitrary test simulation

In order to validate the Meta-Model quality, additional test simulation was performed for an arbitrary parameters combination [rlam_heat=1.24, tkmmin=0.233, tur_len=363.9, entr_sc=0.000267, c_soil=0.492 and v0snow=12.1], which was not used for building the Meta-Model. That allows comparing the Meta-Model prediction for this specific parameters combination with the real simulation results, over the entire 2013. Figs. 6-9 show scatter plots for maximum daily 2m-temperature (Tmax), minimum daily 2m-temperature (Tmin), 24h accumulated precipitation (Pr), and column integrated water vapor (TCWC), respectively. The y-axes show the Meta-Model estimation with respect to the reference (simulation with default parameters values), while the x-axes show the COSMO simulation results with respect to the reference. For Tmax and Tmin, each point represents grid-point comparison (according method IV as explained in section 8.2 below). For Pr each point represents regions averages. For TCWC each point represents a profile in one of the radiosondes locations.

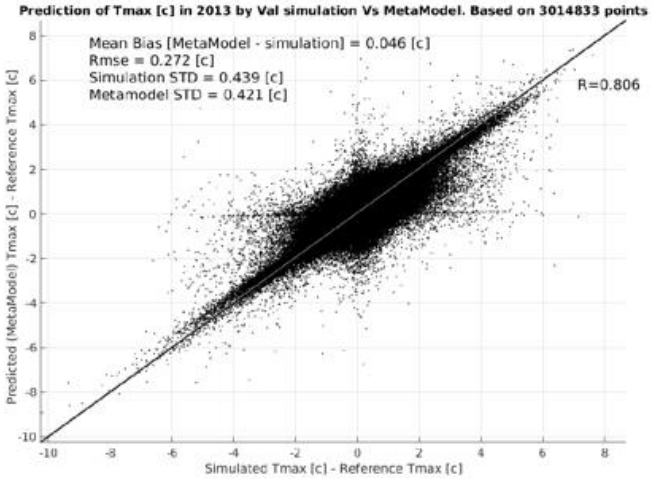


Figure 6: Tmax Meta-Model prediction for the tested parameter combination, vs COSMO simulation results during the year 2013. X axis presents the simulated Tmax minus the reference simulation. Y axis presents the Meta-Model Tmax minus the reference simulation.

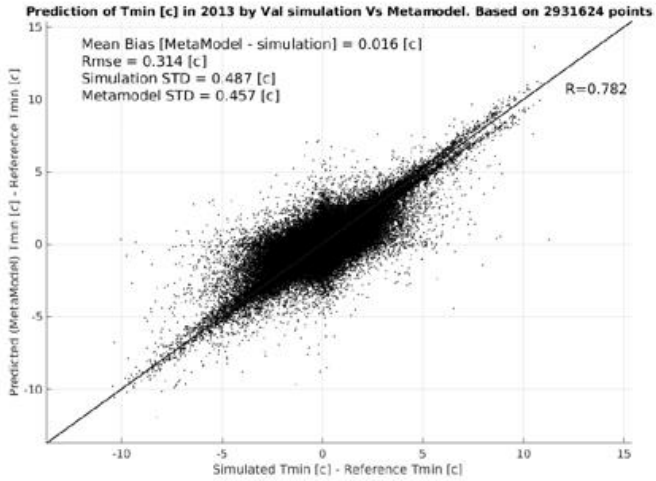


Figure 7: Tmin Meta-Model prediction for the tested parameter combination, vs COSMO simulation results during the year 2013. X axis presents the simulated Tmin minus the reference simulation. Y axis presents the Meta-Model Tmin minus the reference simulation.

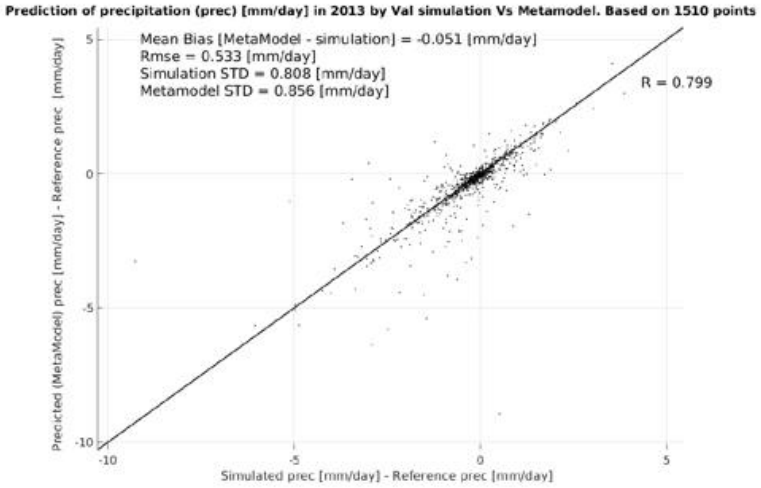


Figure 8: Pr Meta-Model prediction for the tested parameter combination, vs COSMO simulation results during the year 2013. X axis presents the simulated Pr minus the reference simulation. Y axis presents the Meta-Model Pr minus the reference simulation.

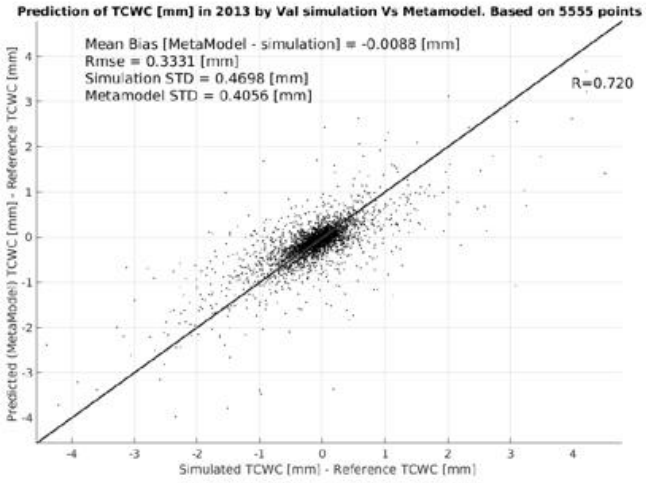


Figure 9: TCWC Meta-Model prediction for the tested parameter combination, vs COSMO simulation results during the year 2013. X axis presents the simulated TCWC minus the reference simulation. Y axis presents the Meta-Model TCWC minus the reference simulation.

Important to mention, that only one point (one parameters combination) in 6-dimensional parameters space was analyzed, so that correlations presented in Figs. 6-9 are not necessarily represent other possible parameters combinations. However, for the tested parameter combination, the correlations R between the COSMO forecasts and the Meta-Model estimations are generally high. Consequently, the overall method seems to prove itself: one can use the Meta-Model to reproduce COSMO forecasts for various parameters combinations.

8.2 Calibration results for entire year 2013

The calibration was performed using 4 different methods:

I Averaging Tmax and Tmin over regions (see Section 4.2.1 above), using RMSE-type score;

II Not averaging Tmax and Tmin over regions, using RMSE-type score;

III Averaging Tmax and Tmin over regions, using or the COSI score;

IV Not averaging Tmax and Tmin over regions, using the COSI score.

We have used the Meta-Model to calculate the overall score S_p (either RMSE-type (eq. 2) or COSI (eq. 5)) for any given parameters combination. Figs. 10-13 present the contours of S_p deviation, i.e. $S_p - \overline{S}_p$, for pairwise parameters combinations only, for the methods I,II,III,IV, respectively. Note that for RMSE-type score lower $S_p - \overline{S}_p$ means better parameters combination, while for COSI score, higher $S_p - \overline{S}_p$ is better. One can see that the optimal parameters regions are similar, regardless the method we used.

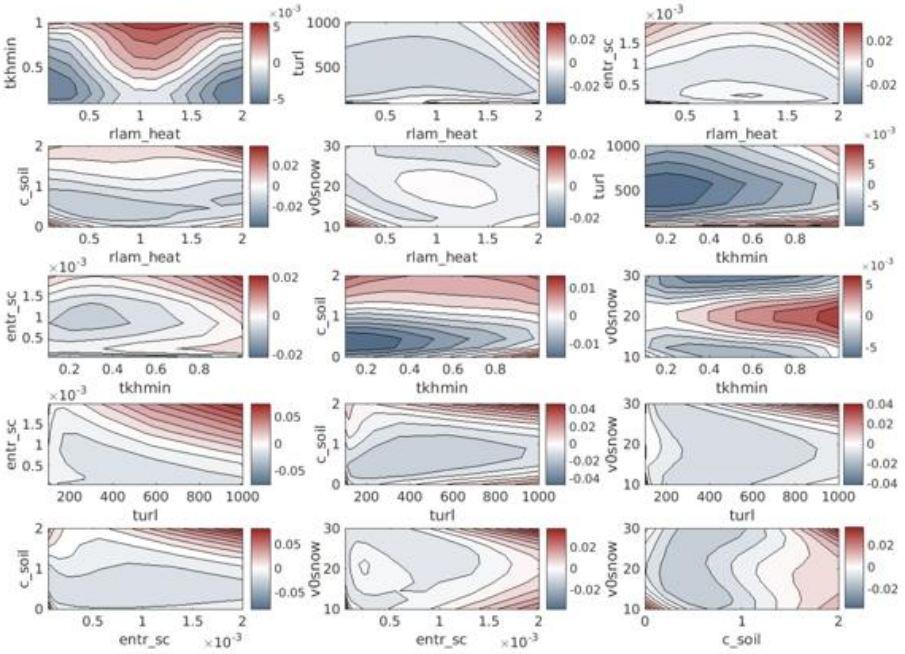


Figure 10: Method I - Contours of score deviation $S_p - \overline{S}_p$ (eq. 2), for pairwise parameters combinations. Lower $S_p - \overline{S}_p$ areas represent better parameters combinations.

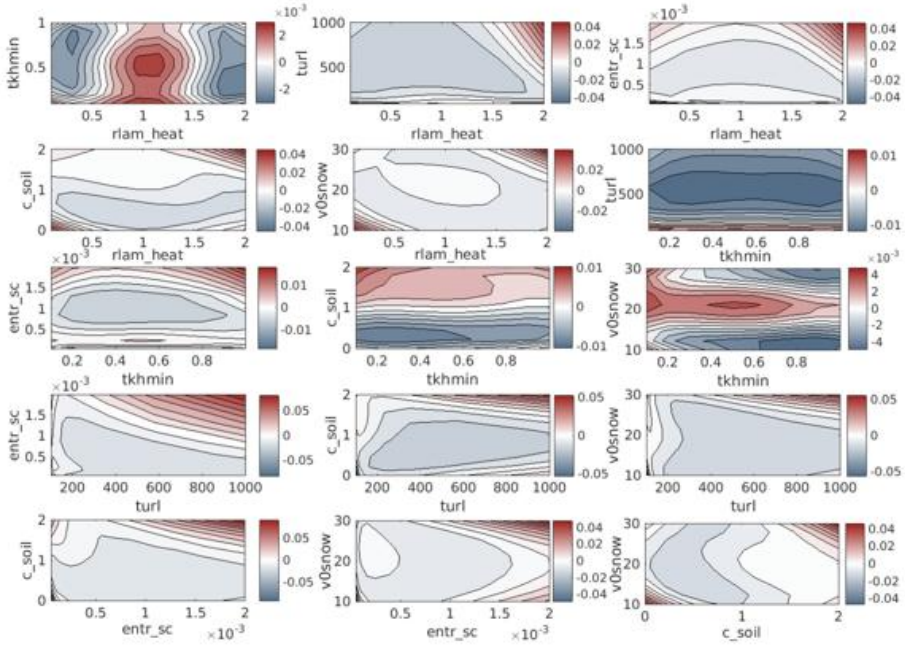


Figure 11: Method II - Contours of score deviation $S_p - \overline{S}_p$ (eq. 2), for pairwise parameters combinations. Lower $S_p - \overline{S}_p$ areas represent better parameters combinations.

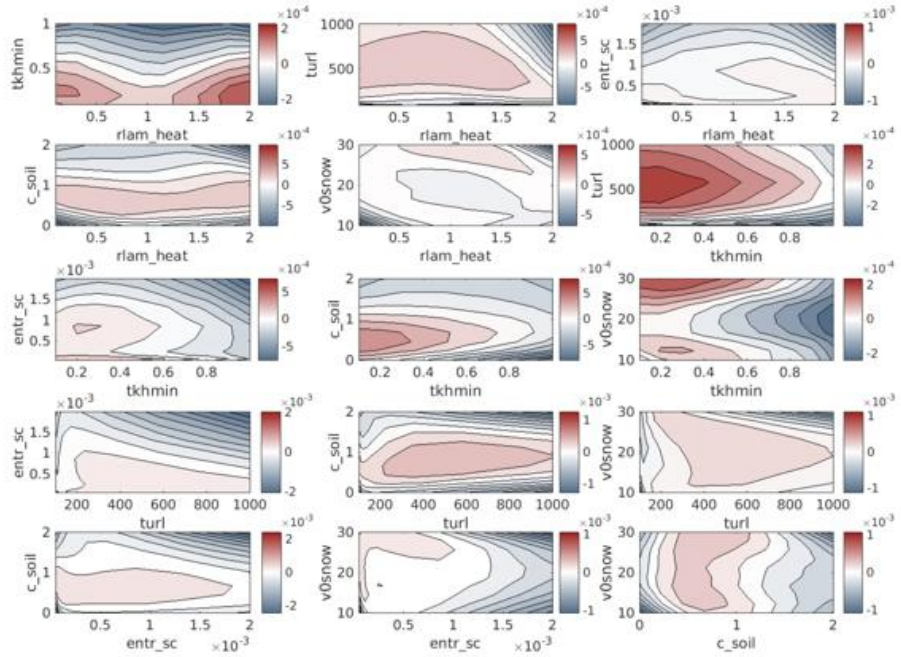


Figure 12: Method III - Contours of score deviation $S_p - \overline{S}_p$ (eq. 5), for pairwise parameters combinations. Lower $S_p - \overline{S}_p$ areas represent better parameters combinations.

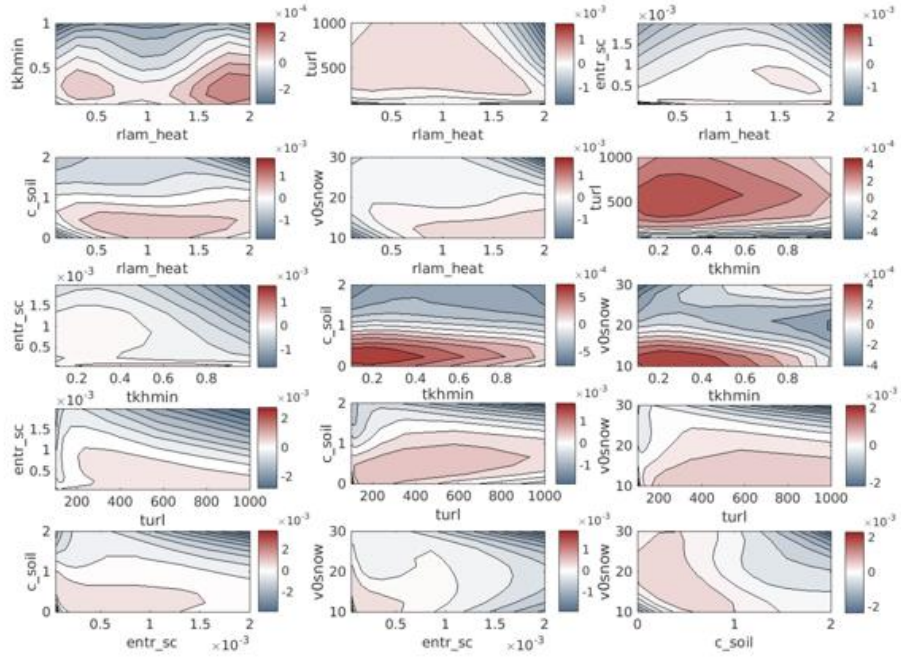


Figure 13: Method IV - Contours of score deviation $S_p - \overline{S}_p$ (eq. 5), for pairwise parameters combinations. Lower $S_p - \overline{S}_p$ areas represent better parameters combinations.

Figs. 14-15 present S_p scores distributions after first and last iterations, respectively (see Section 6 above), together with the score of the reference (REF) simulation, for methods I-IV.

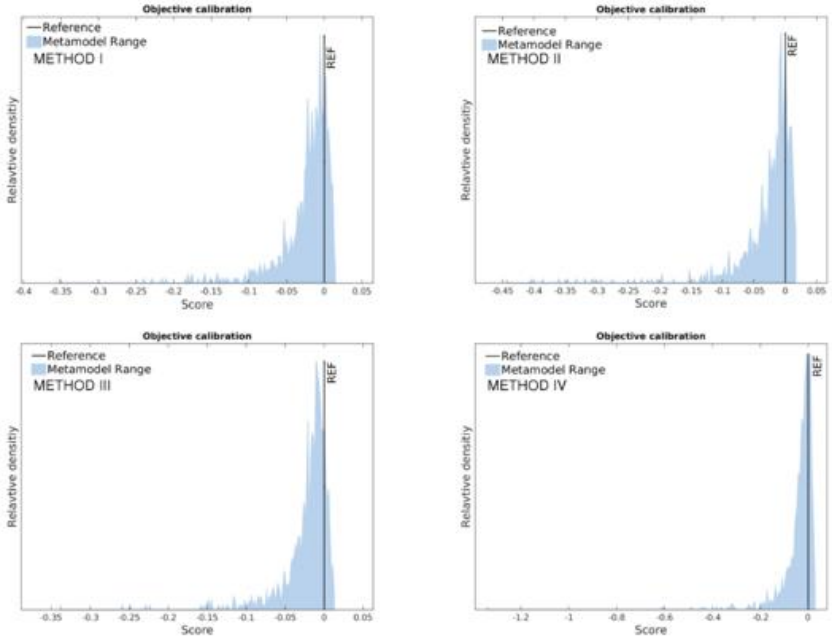


Figure 14: S_p scores distributions after **first** iteration, together with the score of the reference (REF) simulation, for methods I-IV. For convenience, the distributions are presented as function of $\widetilde{S}_p = 1 - S_p/S_{p,REF}$ for methods I, II and as function of $\widetilde{S}_p = S_p/S_{p,REF} - 1$ for methods III, IV. Therefore higher $\widetilde{S}_p > 0$ means better score with respect to the REF simulation.

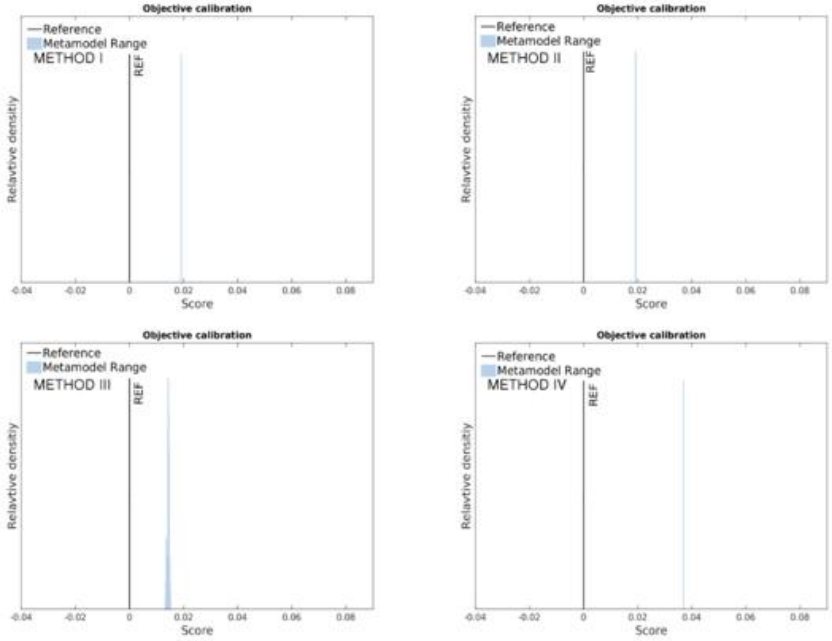


Figure 15: S_p scores distributions after **last** iteration, together with the score of the reference (REF) simulation, for methods I-IV. For convenience, the distributions are presented as function of $\widetilde{S}_p = 1 - S_p/S_{p,REF}$ for methods I, II and as function of $\widetilde{S}_p = S_p/S_{p,REF} - 1$ for methods III, IV. Therefore higher $\widetilde{S}_p > 0$ means better score with respect to the REF simulation.

Tables 3 and 4 present the optimal parameters combinations, as well as their uncertainties (see section 6.2) for the methods I-IV described above:

Method	rlam_heat	Tkhmin	tur_len
I	0.724 **0.835** 0.942 [-5.8% +5.6%]	0.179 **0.229** 0.282 [-5.6% +5.9%]	268.0 **309.3** 347.3 [-4.6% +4.2%]
II	0.836 **0.964** 1.077 [-6.7% +5.9%]	0.316 **0.372** 0.442 [-6.3% +7.8%]	390.2 **437.4** 503.9 [-5.2% +7.4%]
III*	**1.009**	**0.155**	**422.3**
IV	1.149 **1.273** 1.390 [-6.5% +6.2%]	0.205 **0.266** 0.351 [-6.8% +9.4%]	294.6 **346.5** 409.9 [-5.8% +7.0%]

Table 3: Optimal parameters combinations and their uncertainties for methods I-IV. *For method III there was no complete convergence to the optimal parameters combination, so the uncertainties are not presented.

Method	entr_sc (10^{-4})	c_soil	v0snow
I	0.643 **0.731** 0.866 [-4.5% +6.9%]	0.623 **0.681** 0.733 [-2.9% +2.6%]	18.7 **19.9** 21.2 [-6.0% +6.5%]
II	0.796 **0.798** 0.938 [-0.01% +0.7%]	0.679 **0.725** 0.760 [-2.3% 1.8%]	17.1 **18.5** 19.3 [-7.0% +4.0%]
III*	**0.832**	**0.735**	**18.8**
IV	1.261 **1.607** 2.104 [-1.8% +2.5%]	0.515 **0.588** 0.664 [-3.7% +3.8%]	11.6 **12.3** 13.3 [-3.5% +5.0%]

Table 4: Optimal parameters combinations and their uncertainties for methods I-IV. *For method III there was no complete convergence to the optimal parameters combination, so the uncertainties are not presented.

Assuming method IV as the most reasonable, the final optimal parameters combination with its uncertainty is:

- rlam_heat=1.273 instead of the default 1.0. Uncertainty: [1.149 1.390];
- tkhmin=0.266 instead of the default 0.4; Uncertainty: [0.205 0.351];
- tur_len=346.5 instead of the default 150; Uncertainty: [294.6 409.9];
- entr_sc=0.0001607 instead of the default 0.003; Uncertainty: [0.0001261 0.0002104];
- c_soil=0.588 instead of the default 1.0; Uncertainty: [0.515 0.664];
- v0snow=12.3 instead of the default 20; Uncertainty: [11.6 13.3].

8.3 Calibration results - seasonal dependence

In this section we analyzed the seasonal dependence of the optimal parameters combination during 2013. For that purpose we have performed parameters calibration for summer 2013 (Jul, Aug and Sep) and winter 2013 (Jan, Feb and Mar), separately. The results for the optimal parameters combinations, as well as their uncertainties are presented in Tables 5-6.

Cases	rlam_heat	Tkhmin	tur_len
Entire 2013	1.149 **1.273** 1.390 [-6.5% +6.2%]	0.205 **0.266** 0.351 [-6.8% +9.4%]	294.6 **346.5** 409.9 [-5.8% +7.0%]
Summer 2013	0.954 **1.071** 1.164 [-6.2% +4.9%]	0.186 **0.221** 0.270 [-3.9% +5.4%]	352.2 **357.5** 398.9 [-0.6% +4.6%]
Winter 2013	0.982 **1.112** 1.232 [-6.8% +6.3%]	0.791 **0.891** 0.929 [-11.1% +4.2%]	109.8 **117.2** 127.9 [-0.8% +1.2%]

Table 5: CALMO stage-2 optimal parameters combinations, as well as their uncertainties for method IV for the following cases: all months in 2013, summer 2013 (Jul, Aug and Sep) and winter 2013 (Jan, Feb and Mar).

Cases	entr_sc (10^{-4})	c_soil	v0snow
Entire 2013	1.261 **1.607** 2.104 [-1.8% +2.5%]	0.515 **0.588** 0.664 [-3.7% +3.8%]	11.6 **12.3** 13.3 [-3.5% +5.0%]
Summer 2013	4.439 **4.890** 5.495 [-2.3% +3.1%]	1.090 **1.150** 1.205 [-3.0% +2.8%]	20.2 **21.2** 22.3 [-5.5% +5.0%]
Winter 2013	1.387 **1.714** 2.076 [-1.7% +1.9%]	0.0 **0.041** 0.134 [-2.1% +4.7%]	29.2 **30.0** 30.0 [-4.0% +0.0%]

Table 6: CALMO stage-2 optimal parameters combinations, as well as their uncertainties for method IV for the following cases: all months in 2013, summer 2013 (Jul, Aug and Sep) and winter 2013 (Jan, Feb and Mar).

One can see significant differences at the optimal parameters combinations for summer and winter. This fact reflects different biases of atmospheric fields between the seasons (see for example the first CALMO progress report (Khain et al., 2015)). However, figuring out the atmospheric fields responsible for this behavior is beyond the scope of this report.

9 CALMO stage-3

9.1 Calibration results for January 2013

CALMO-stage-3 calibration was performed using method IV, i.e. not averaging Tmax and Tmin over regions, using the COSI score. As can be seen in Table 1, at that stage we have tuned 5 parameters: tkhmin, tur_len, entr_sc, c_soil, crsmin, for the period 1/1/2013 1/2/2013. As at CALMO-stage 2, we have used the Meta-Model to calculate the overall COSI score S_p (eq. 5) for any given parameters combination. Before presenting the results for the optimal 5-parameters combination, we first investigate the importance of each of the 5 parameters. This is done by performing the calibration several times, each time excluding one of the parameters. Figs. 16-20 present the contours of deviation, i.e. $S_p - \overline{S}_p$ (higher $S_p - \overline{S}_p$ is better), for pairwise parameters combinations only, in the following order:

- Case 1: Tuning parameters tkhmin, tur_len, entr_sc, c_soil (excluding crsmin) see Fig. 16;
- Case 2: Tuning parameters tkhmin, tur_len, entr_sc, crsmin (excluding c_soil) see Fig. 17;

- Case 3: Tuning parameters tkhmin, tur_len, c_soil, crsmin (excluding entr_sc) see Fig. 18;
- Case 4: Tuning parameters tkhmin, entr_sc, c_soil, crsmin (excluding tur_len) see Fig. 19;
- Case 5: Tuning parameters tur_len, entr_sc, c_soil, crsmin (excluding tkhmin) see Fig. 20.

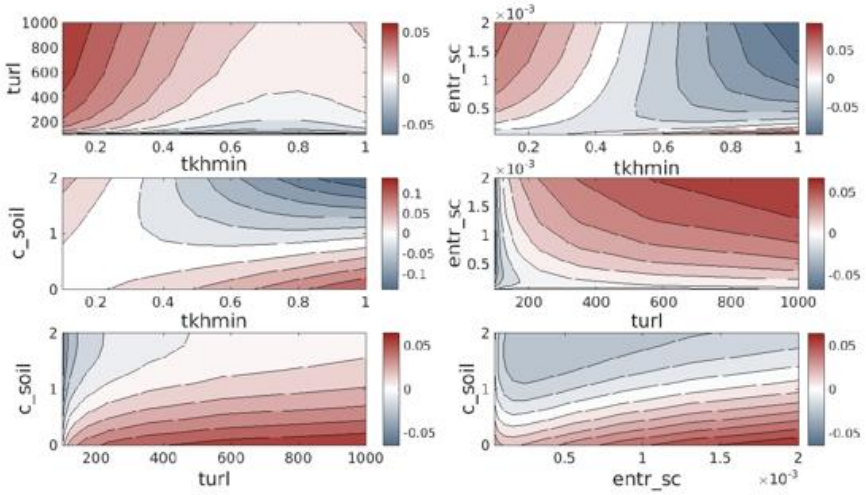


Figure 16: Contours of score deviation for method IV (eq. 5), for pairwise parameters combinations. Higher $S_p - \overline{S}_p$ areas represent better parameters combinations. The tuning is performed for parameters tkhmin, tur_len, entr_sc, c_soil (excluding crsmin) - case 1. Period: 1/1/2013-6/2/2013.

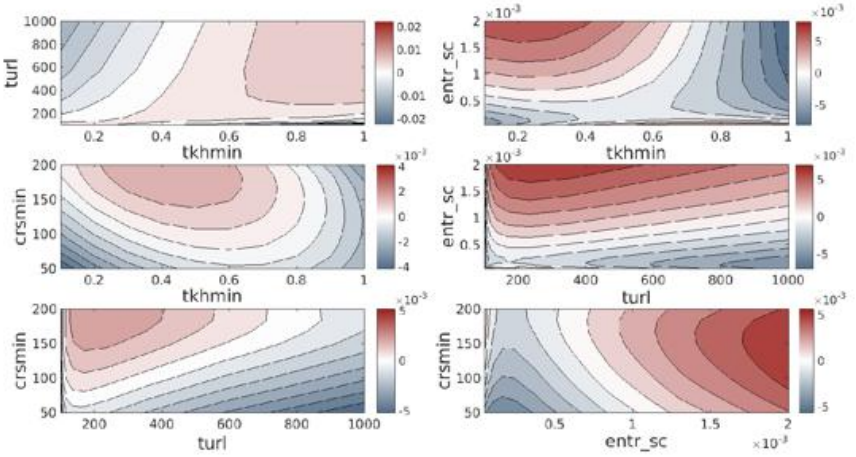


Figure 17: Contours of score deviation for method IV (eq. 5), for pairwise parameters combinations. Higher $S_p - \overline{S}_p$ areas represent better parameters combinations. The tuning is performed for parameters tkhmin, tur_len, entr_sc, crsmin (excluding c_soil) - case 2. Period: 1/1/2013-1/2/2013.

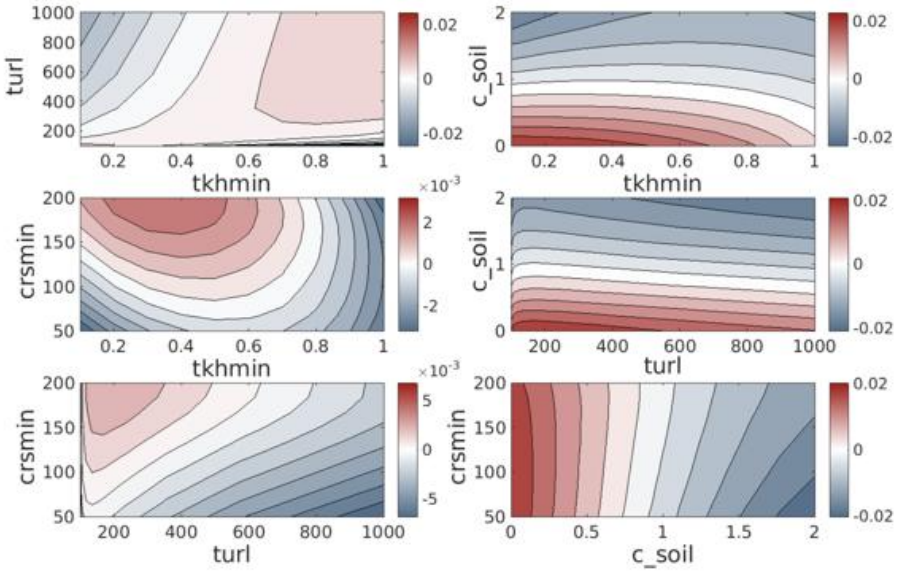


Figure 18: Contours of score deviation for method IV (eq. 5), for pairwise parameters combinations. Higher $S_p - \overline{S}_p$ areas represent better parameters combinations. The tuning is performed for parameters tkhmin, tur_len, c_soil , crsmin (excluding entr_sc) - case 3. Period: 1/1/2013-1/2/2013.

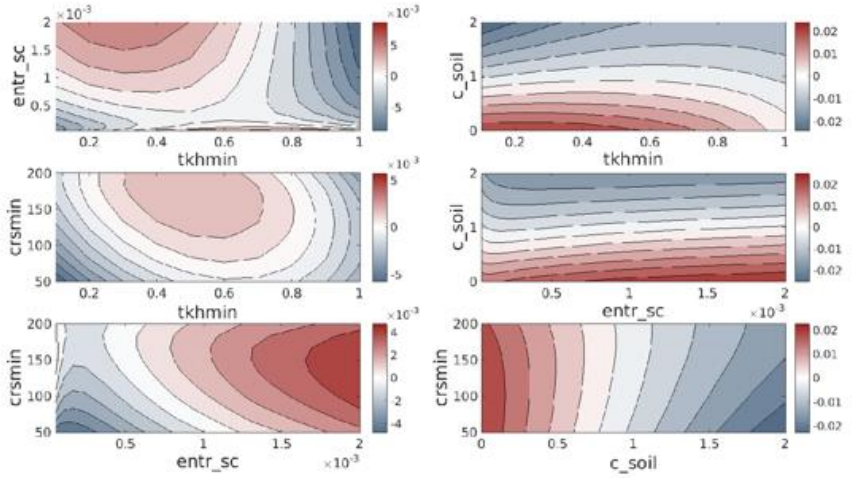


Figure 19: Contours of score deviation for method IV (eq. 5), for pairwise parameters combinations. Higher $S_p - \overline{S}_p$ areas represent better parameters combinations. The tuning is performed for parameters tkhmin, entr_sc, c_soil , crsmin (excluding tur_len) - case 4. Period: 1/1/2013-3/2/2013.

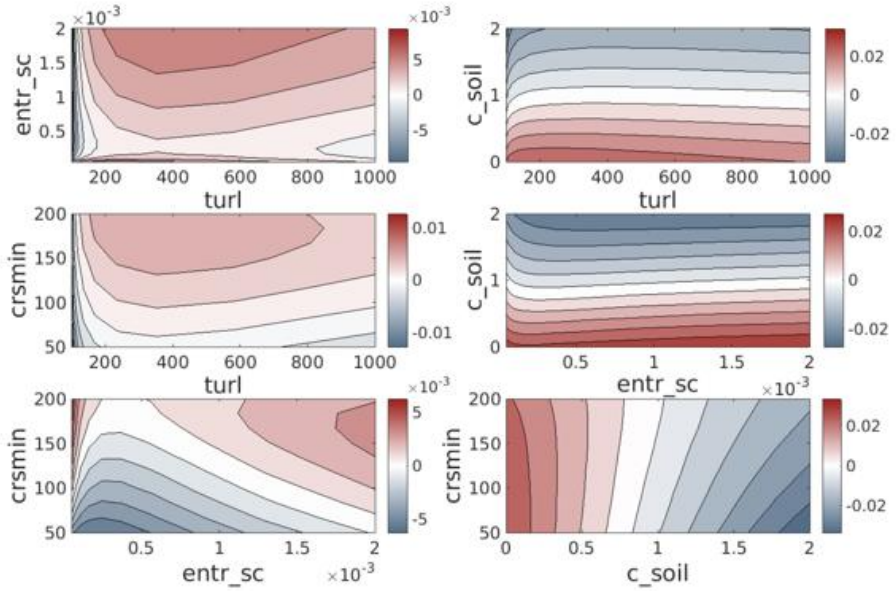


Figure 20: Contours of score deviation for method IV (eq. 5), for pairwise parameters combinations. Higher $S_p - \overline{S}_p$ areas represent better parameters combinations. The tuning is performed for parameters tur_len, entr_sc, c_soil , crsmin (excluding tkhmin) - case 5. Period: 1/1/2013-1/2/2013.

As can be seen from Figs. 16-20, the optimal and worst areas in parameters space differ between the 5 cases. This can be explained by an importance of parameters interactions (fourth term in eq. 1) with respect to the first order parameters variation (third term in eq. 1). However, the main reason for such behavior can be too small sample (for example, only 48% of the regions were rainy during the 32 days period). Following the analysis above, we have performed the calibration taking into account all the 5 parameters tkhmin, tur_len, entr_sc, c_soil, crsmin. Fig. 21 presents the contours of S_p deviation, i.e. $S_p - \overline{S}_p$ (higher $S_p - \overline{S}_p$ is better), for pairwise parameters combinations only.

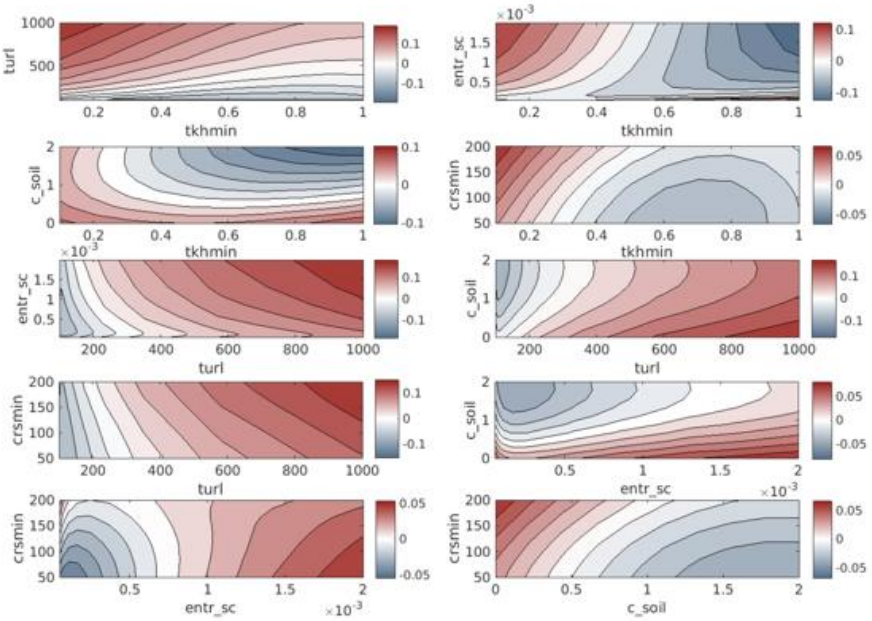


Figure 21: Contours of score deviation for method IV (eq. 5), for pairwise parameters combinations. Higher $S_p - \overline{S}_p$ areas represent better parameters combinations. The tuning is performed for all the 5 parameters tkhmin, tur_len, entr_sc, c_soil, crsmin. Period: 1/1/2013-1/2/2013.

Fig. 22 presents S_p scores distributions after first (left panel) and last (right panel) iterations, together with the score of the reference (REF) simulation.

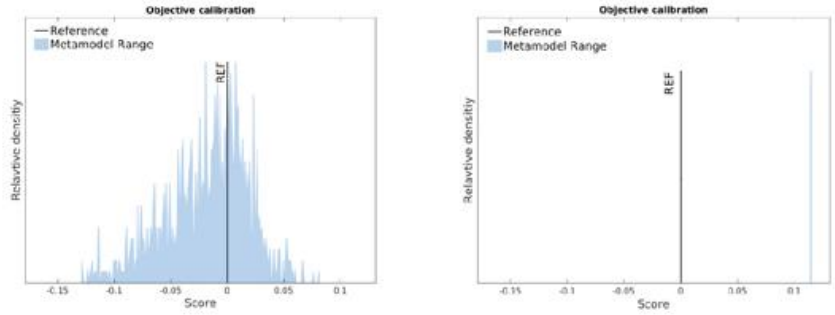


Figure 22: S_p scores distributions after **first** iteration (left) and **last** iteration (right), together with the scores of the reference (REF) simulation. For convenience, the distributions are presented as function of $\widetilde{S}_p = S_p/S_{p,REF} - 1$. Higher $\widetilde{S}_p > 0$ means better score with respect to the REF simulation.

Table 7 presents the optimal parameters combinations, as well as their uncertainties (see section 6.2), when calibrating 4 parameters (eliminating one parameter each time according cases 1-5 described above) and for the full calibration analysis, tuning all the 5 parameters:

Cases	tkhmin	tur_len	entr_sc (10^{-4})	c_soil	crsmin
1	0.986 **1.000** 1.000 [0.0% +1.6%]	100.0 **100.0** 101.0 [-0% +0.1%]	18.0 **20.0** 20.0 [1.0% +0.0%]	1.957 **2.000** 2.000 [2.0% +0.0%]	———
2	0.988 **1.000** 1.000 [-1.3% +0%]	100.0 **100.0** 100.2 [-0% +1.9%]	7.401 **8.985** 9.012 [-8.1% +0.1%]	———	150.1 **171.2** 171.6 [-8.4% +0.2%]
3*	**0.101**	**815.2**	———	**1.793**	**60.0**
4	0.100 **0.100** 0.111 [-0.0% +1.2%]	———	0.702 **0.704** 0.904 [-0.01% +1.0%]	1.978 **2.000** 2.000 [-1.1% +0%]	50.0 **50.0** 54.2 [-0.0% +1.7%]
5	———	100.0 **100.0** 100.3 [0.0% +0.03%]	4.284 **20.0** 20.0 [-8.1% +0.0%]	1.971 **2.000** 2.000 [-1.5% +0%]	50.0 **50.0** 54.3 [-0.0% +1.7%]
all 5 par.	0.983 **1.000** 1.000 [-1.9% +0.0%]	104.3 **109.3** 117.2 [-0.6% +0.9%]	18.0 **20.0** 20.0 [-10.3% +0.0%]	1.937 **2.000** 2.000 [-3.2% +0.0%]	186.3 **200.0** 200.0 [-5.5% +0.0%]

Table 7: Optimal parameters combinations and their uncertainties. *For case 3 there was no complete convergence to the optimal parameters combination, so the uncertainties are not presented

Taking into account the uncertainties using also cases 1-5, the final optimal parameters combination (with its uncertainty) is:

- tkhmin=**1** instead of the default 0.4; Uncertainty: [0.983 1];
- tur_len=**109.3** instead of the default 150; Uncertainty: [104.3 117.2];
- entr_sc=**0.002** instead of the default 0.003; Uncertainty: [0.0018 0.002];
- c_soil=**2** instead of the default 1.0; Uncertainty: [1.937 2];
- crsmin=**200** instead of the default 150; Uncertainty: [186.3 200].

One can see, that all the five parameters get their optimal values on the edges of their allowed ranges. As mentioned before, that can be explained by short calibration period i.e. too small sample (for example, only 48% of the regions were rainy during the 32 days period). In addition, more simulations have to be performed to validate the results. In CALMO-stage-3 only one interaction simulation was performed (in addition to the minimum required), while in CALMO-stage-2 13 additional interaction simulations were performed.

9.2 CALMO-2km vs CALMO-1km optimal parameters for January 2013

At this section we addressed the question does the optimal parameters combination changes with the model resolution, or more specifically, from CALMO-2km to CALMO-1km? As CALMO-1km results are available for January 2013 only, we have calibrated the parameters for CALMO-2km again but this time for January 2013. Tables 8 and 9 presents the CALMO-2km (Stage-2) and CALMO-1km (Stage-3) optimal parameters combinations, as well as their uncertainties for January 2013.

CALMO Stage	rlam_heat	Tkhmin	tur_len
Stage-2 Entire 2013	1.149 1.273 1.390 [-6.5% +6.2%]	0.205 0.266 0.351 [-6.8% +9.4%]	294.6 346.5 409.9 [-5.8% +7.0%]
Stage-2 Jan 2013	0.845 0.935 1.002 [-4.7% +3.5%]	0.191 0.220 0.262 [-3.2% +4.7%]	559.8 653.3 753.0 [-10.4% +11.1%]
Stage-3 Jan 2013	Default value*	0.983 1.000 1.000 [-1.9% +0.0%]	104.3 109.3 117.2 [-0.6% +0.9%]

Table 8: CALMO-2km (Stage-2) and CALMO-1km (Stage-3) optimal parameters combinations, as well as their uncertainties for method IV for January 2013 (in comparison with CALMO-2km for entire 2013 in the first row). *Note that in CALMO-1km the calibrated parameters are 'tkhmin', 'tur_len', 'entr_sc', 'c_soil' and 'crsmin'

CALMO Stage	entr_sc (10^{-4})	c_soil	v0snow
Stage-2 Entire 2013	1.261 1.607 2.104 [-1.8% +2.5%]	0.515 0.588 0.664 [-3.7% +3.8%]	11.6 12.3 13.3 [-3.5% +5.0%]
Stage-2 Jan 2013	2.346 2.764 3.242 [-2.1% +2.5%]	0.653 0.756 0.841 [-5.2% +4.3%]	11.2 11.8 12.3 [-3.0% +2.5%]
Stage-3 Jan 2013	18.0 20.0 20.0 [-10.3% +0.0%]	1.937 2.000 2.000 [-3.2% +0.0%]	Default value*

Table 9: CALMO-2km (Stage-2) and CALMO-1km (Stage-3) optimal parameters combinations, as well as their uncertainties for method IV for January 2013 (in comparison with CALMO-2km for entire 2013 in the first row). *Note that in CALMO-1km the calibrated parameters are ' tkhmin', 'tur_len', 'entr_sc', 'c_soil' and 'crsmin'

As can be seen from Tables 8 and 9, the optimal parameters for CALMO-2km and CALMO-1km are completely different. We see 4 possible reasons for that:

- The results are not statistically significant due to short calibration period (one month only).
- Different parameters combinations were analyzed in stages-2 and 3. In stage-2 we have tuned the combination of rlam_heat, tkhmin, tur_len, entr_sc, c_soil and v0snow while in stage-1 we have tuned the combination of tkhmin, tur_len, entr_sc, c_soil and crsmin. Parameters interactions might be significant, so that tuning part of parameters keeping others default is different from tuning them all together. Therefore we cannot state that the comparison performed in table 6 is a clean experiment.
- CALMO stage-2 and stage-1 simulations were performed in different ways. Stage-2 runs were initialized every 24 hours, while in stage-1 we have initialized the runs once at 1/1/2013 (using Terra-Standalone pre-runs), and performed single long runs keeping the soil memory. This soil memory may have a big influence on the model forecasts and the optimal parameters combinations.
- Physical reasons related to the change in resolution from 2.2km (stage-2) to 1.1km (stage-1) are probably significant, but at that stage we cannot state how much.

10 Summary

The CALMO project has several important achievements. In general, we have proved that the CALMO calibration method allows tuning parameters of NWP model. In order to adapt

the calibration method of Bellprat et al (2012) to NWP model, we have significantly improved the Meta-Model codes. The main developments are listed below:

- added the option not to average 2m-temperature over regions;
- added prediction of profiles characteristics;
- added quality control to the observed and simulated fields;
- added clever interpolation of observed 2m-temperature fields to the model grid;
- developed the RMSE-type and COSI scores;
- developed new method for logarithmic transformation for selected parameters;
- developed a method to converge to optimal parameters combination in huge N-dimensional parameters space;
- analyzed the uncertainty of the optimal parameters combination.

These new developments, mainly in the Meta-Model, performance score and the optimization algorithm (sections 4, 5, 6 above and Khain et al. (2015)) highly increased the reliability of the calibration results. As part of the CALMO project, we have calibrated the COSMO model in resolutions of 7km, 2.2km and 1.1km. For 2.2km and 1.1km resolutions we have used wide verification area, which included Switzerland and north of Italy. We have validated the model performance over many meteorological fields. Moreover, for 2.2km resolution, the calibration period was very long (entire 2013) and the number of the tuned parameters was high (six). These achievements yielded highly qualitative calibration analysis, making the calibration results especially reliable. Future study may have a lot of interesting and important directions. Using the Meta-Model, one can perform more specific calibrations:

- focusing on specific types of weather conditions (rain, extreme events, stable stratified nights, fogs, etc.);
- focusing on seasons (season-dependent parameters tuning);
- reducing the noise of the calibration method by matching specific parameters to related fields and weather situations, and performing the tuning for these matches only;
- analyzing the relative importance of constrain and interaction simulations for various parameters.

References

Bellprat, O., S. Kotlarski, D. Lüthi, and C. Schär, 2012: Objective calibration of regional climate models. *J. Geophys. Res.* **117**, D23.

Blackadar, A. K., 1962: The vertical distribution of wind and turbulent exchange in a neutral atmosphere. *J. Geophys. Res.*, **67**, 8, 30953102.

Khain P., Carmona I., Voudouri A., Avgoustoglou E., Bettems J.-M. and Grazzini F., 2015: The Proof of the Parameters Calibration Method: CALMO Progress Report. *COSMO Technical Report* **25**, 1-48. Available at:
www.cosmo-model.org/content/model/documentation/techReports/docs/techReport25.pdf

Neelin J. D., Bracco A., Luo H., McWilliams J. C. and Meyerson J. E., 2010: Considerations for parameter optimization and sensitivity in climate models. *Proc. of the National Academy of Sciences of the United States of America* **107**, 50, 21349-21354.

Frei C., 2014: Interpolation of temperature in a mountainous region using non-linear profiles and non-euclidean distances. *Int. J. Climatol.* **34**, 5, 1585-1605.

Damrath, U., 2009: Long-term trends of the quality of COSMO-EU forecasts. Presentation at the 11th COSMO General Meeting, Offenbach. Available at:
www.cosmo-model.org/content/consortium/generalMeetings/general2009/wg5-versus2.htm

A Appendix: Meta-Model code

A.1 Algorithm

In order to execute the program, one has to execute main.m. First it reads the user defined definitions from namelist.m. Then it divides the calibration period to several short (10 day) sub-periods (to save matlab memory) and executes ReadData_and_MetaModel.m for every period, to read observations and simulations data and build the meta-model regressions. After that stage is performed for all the sub-periods, it executes PostProc.m which performs the post-processing and saves the calibration results in .mat format files.

A.1.1 ReadData_and_MetaModel.m

First the observations data is read (via **read_calmo_obs.m**) into datamatrix.obsdata and datamatrix_so.obsdata structures, for near surface fields and sounding derived fields, respectively. The Swiss 2m-temperature (Tmax and Tmin) fields are interpolated to the model grid (via **build_temp_obs.m**) using several optional methods (including the one which takes into account the local observed 2m-temperature profile in the vicinity of the model grid point). Next, the 24-hours precipitation is interpolated to the model grid (via **build_rain_obs.m**). In addition, soundings data is read (via **read_sounding_obs.m**), followed by reading the Italian Tmax, Tmin and precipitation data (from netcdf files). After reading the observations, the simulations data is read (via **read_calmo_sim.m**), while the profiles data is read via **read_profiles_mod.m**. There are several types of simulations data: reference (default parameters combination) simulation is read into datamatrix.refdata structure for near surface fields (and datamatrix_so.refdata for profiles derived fields); min-max simulations (where one of the parameters gets its maximum or minimum value, while the others kept default) are read into datamatrix.moddata structure for near surface fields (and datamatrix_so.moddata for profiles derived fields); interaction simulations (where pair of parameters get their maximum or minimum value, while the others kept default) are read for near surface fields into datamatrix.moddata structure as well (and datamatrix_so.moddata for profiles derived fields); constrain simulations (where one of parameters gets some intermediate value, while the others kept default) are read into datamatrix.constrain structure for near surface fields (and datamatrix_so.constrain for profiles derived fields); validate simulation (where all the parameters get some intermediate value - needed for validating the meta-model at an arbitrary point in parameters space) is read into datamatrix.valdata structure for near surface fields (and datamatrix_so.valdata for profiles derived fields). After the observations and simulations data is read, there is an option (via avg_T parameter) to average part of the fields over regions (regions are defined in **regions_bmp.m**, similarly to definition of regions in Frei (2014) for Switzerland) so that the Meta-Model will be built to predict region-averaged fields, rather than the fields at every grid point. The averaging over regions is performed in **Frei_regions.m**. Next, we redefine data arrays to have the structure (fields,days,regions,simulations) (via **gpts_series.m**) and finally delete unrealistic sounding/profiles data (via **del_bad_sounding.m**). Next, the Meta-Models are created via **neelin_e.m** which uses **polyfitn.m** for performing the forecasts fits in N-dimensional parameters space. In case only precipitation is averaged over regions (avg_T=0), the Meta-Model structures metamodel_tmax, metamodel_tmin and metamodel_pr are created, while if temperature data is also averaged (avg_T=1), the Meta-Model structure metamodel_new includes all the data (for temperature and precipitation). In addition, the profiles Meta-Models are written into the structure metamodel_so (see definitions of the Meta-Model structures in the description of **neelin_e.m** function below). Finally, the Meta-Model structures are

saved in .mat format.

A.1.2 PostProc.m

First, the Meta-Model structures are loaded for all the periods. Then we calculate the weights for different fields via **weights_calc.m**, needed to equalize their contributions to the final score (see eq. 4). The weights calculation uses **neelin_p.m**. This function calculates pseudo-forecast using the Meta-Models, for an arbitrary parameters combination. Then a big structure "main_data" is created (and saved in .mat format), which includes all the model and observations structures, as well as the Meta-Model structures and the fields weights. Next, the function **planes.m** is called, which plot performance scores for pair-wise parameters cross sections. For that, it uses **neelin_p.m**, as well as the scores calculation **rmse_calc.m** and **cosi_calc.m**, for rmse-type and cosi-type scores, respectively. This is followed by the iterations loop, aimed to converge to the optimal parameters combination (see section 6). At each iteration, the function **lhopt.m** is called which uses **neelin_p.m** to calculate the scores distribution for a specific part of the parameters space (which is getting smaller from iteration to iteration). This distribution is plotted via **histplot.m**. In case the process converged to the optimal parameters combination, or the iterations number reached a predefined maximum ("iterations_num"), the loop is broken. Next, the "good enough" iteration is determined (parameter "iteration_goodenough") as the iteration at which the score reaches 90% of the optimal combination score. We define the parameters uncertainty (between the green lines at Fig. 4, for example) at that iteration as the uncertainty of the optimal parameters combination. Next **optparam.m** is called to plot the optimal parameters combination (before transforming parameters back from the log representation). In case some of the parameters were transformed to log space (see section 4.2.4), the optimal parameters combination and the uncertainties values are transformed back to the real parameters space via **log_turlen_entrsc.m**. Finally, the uncertainty ranges are saved in UB_reg.mat and LB_reg.mat, and the optimal parameters combination is saved in popt_reg.txt.

A.2 Structure

The Meta-Model code is written in Matlab and uses its Statistical Toolbox. It consists of 33 Matlab (.m) files, which are called in the following order:

1	main.m % main program to be called
2	ReadData_and_MetaModel.m % Read observations and simulations data, then fit the Meta-Models
3	namelist.m % read namelist
4	sims_def.m % choose parameters to be tuned
5	expval_inter_combs.m
6	**% stage A: Reading observations and simulations data:**
7	read_calmo_obs.m % Read observations data
8	build_temp_obs.m % Interpolate 2m-temperature observations grid to model grid
9	
10	build_rain_obs.m % Interpolate rain observations grid to model grid
11	var_meta_calmo.m % correct fields units
12	read_sounding_obs.m % Read sounding observations
13	get_press_levs.m
14	read_calmo_sim.m % Read simulations data
15	var_meta_calmo.m % correct fields units
16	read_profiles_mod.m % Read simulations data
17	get_press_levs.m
18	Frei_regions.m % Average part of the fields over predefined big regions
19	regions_bmp.m % Definition of regions over Switzerland and north Italy
20	gpts_series.m % Redefine data arrays to the following structure: (fields,days,regions,simulations)
21	del_bad_sounding.m % delete unrealistic sounding/profiles data
22	corr_so.m
23	**% stage B: create Meta-Models:**
24	neelin_e.m % create Meta-Models - forecasts fits in N-dimensional parameters space
25	allcomb.m
26	polyfitn.m % N-dimensional 2-nd order polynomial fit
27	**% stage C: Post-processing:**
28	PostProc.m % Post-processing: plot analysis results and calculate the optimal parameters combination
29	namelist.m % read namelist
30	sims_def.m % read parameters to be tuned
31	weights_calc.m % calculate weights for different fields, to equalize their contributions to the final score (assuming user defined weights are uniform)
32	neelin_p.m % calculate pseudo-forecast using the Meta-Models
33	ETS.m % calculate rain part of COSI score (in case weights are calculated for COSI score also)
34	planes.m % plot performance scores for pair-wise parameters cross sections
35	allcomb.m
36	divisor.m
37	neelin_p.m % calculate pseudo-forecast using the Meta-Models
38	rmse_calc.m % calculate RMSE-type score
39	cosi_calc.m % calculate COSI-type score
40	ETS.m % calculate rain part of COSI score
41	lhopt.m % calculate scores distribution as part of the iterative convergence algorithm
42	neelin_p.m % calculate pseudo-forecast using the Meta-Models
43	histplot.m % plot scores distribution as part of the iterative convergence algorithm
44	optparam.m % plot optimal parameters combination (before transforming parameters back from the log representation)
45	allcomb.m
46	log_turlen_entrsc.m % transforming tur_len and entr_sc parameters back from the log representation

A.3 Subroutines

The Meta-Model code includes the following subroutines:

```
function main()

% NAME
% main
% PURPOSE
% main program of the CALMO parameters tuning method
% NOTE
% Set main definitions at namelist.m file
% RUN
% from Bash: "matlab -nodesktop -nosplash -r main"
% from Matlab: F5 inside main.m
% INPUT
% -
% OUTPUT
% calibration results saved in .mat format
% AUTHORS
% Pavel Khain (pavelkh_il@yahoo.com)
% Itsik Carmona (carmonai@ims.gov.il)
% Originally: Omar Bellprat (omar.bellprat@gmail.com)

function ReadData_and_MetaModel(date_min,date_max)

% NAME
% ReadData_and_MetaModel
% PURPOSE
% Read observations and simulations data, then fit the Meta-Models
% INPUTS
% time period: from date_min 'dd-mmm-yyyy' to date_max 'dd-mmm-yyyy'
% OUTPUTS
% saved (in .mat format) observations and simulations fields as well as
% the Meta-Models coefficients

function [maindir simuldir obsdir extdir vars vars_2d avg_T vars_sound sims_opt ml score
w_user lhacc iterations_num best_percent date_min date_max]=namelist()

% NAME
% namelist
% PURPOSE
% Namelist of the calibration analysis
% INPUTS
% -
% OUTPUTS
% maindir - main directory
% simuldir - "maindir/simuldir": path to simulations files
% obsdir - "maindir/obsdir": path to observations files
% extdir - "maindir/extdir": path to "external data" files
% vars - calibrated fields groups. Can be any combinations of:
% 't2m_max','t2m_min','pr','sound'
```

```
% vars_2d - calibrated 2D fields. Can be any combinations of:
% 't2m_max','t2m_min','pr'
% avg_T - region average over Precipitation only (avg_T=0), or over
% Precipitation, Tmax and Tmin (avg_T=1)
% vars_sound - calibrated profiles fields:
% 'CAPE','CIN','TCWC','WSHEAR1','WSHEAR2','WSHEAR3','T850mb',
% 'T700mb','T500mb','RH850mb','RH700mb','RH500mb','U850mb',
% 'U700mb','U500mb','V850mb','V700mb','V500mb'
% sims_opt - Choose parameters to callibrate and the simulations to use. The
% possible values for sims_opt and their meaning appear in sims_def.m
% file
% ml - Minimum number of days (during given period) for valid soundings data. If
% less - current sounding fields are not analyzed
% score - 'rmse' or 'cosi' for RMSE-type and COSI-type scores, respectively
% w_user - array of user defined weights (for simlicity - from 0 to 1) for
% calibrated fields:
% tmax tmin pr cape cin ws1 ws2 ws3 T850mb T700mb T500mb RH850mb
% RH700mb R500mb U850mb U700mb U500mb V850 V700mb V500mb
% lhacc - Number of experiments to sample parameter space at each iteration
% iterations_num - Maximum number of iterations
% best_percent - "winners" percent of lhacc which is used to define the
% parameters space for the next iteration
% date_min - beginning of calibration period
% date_max - end of calibration period


function [paramn,paramnt,range,default,expval,valval,simval,sims_reg,sims_inter,
sims_con,valcon,param_log,date_min,date_max]=sims_def(sims_opt)

% NAME
% sims_def
% PURPOSE
% Choose parameters to tune and the simulations to use
% INPUTS
% sims_opt - defined by 5-digits number: sims_opt=ABCDE, where:
% A - number of parameters to calibrate (1,2,3,4,5,6,)
% B - serial number of combination for given A
% C - number of ADDITIONAL (to the minimum required) interaction
% parameter simulations (interaction terms)
% D - number of "constrain" 1D simulations (additional simulations
% where only one parameter is changed from default)
% E - number of parameters (among A) which are transformed to LOG
% space
% OUTPUTS
% paramn - Parameter names
% paramnt - Parameter names (for TEX interpreter)
% range - Parameters ranges (min and max)
% default - Parameters defaults
% sims_reg - Names of max-min simulations (where only 1 parameter is shifted to
% its max/min value)
% sims_inter - Names of interaction simulations (where 2 parameters are shifted
```

```
% to their max/min values)
% expval - Parameters values for max-min and interaction simulations
% simval - Name of "val" simulation (where all the parameters are shifted from
% their default values, in order to validate the Meta-Models)
% valval - Parameters values for "val" simulation
% sims_con - Name of "constrain" simulations (where each time one parameter is
% shifted from its default value, but not to its max/min values)
% valcon - Parameters values for "constrain" simulations
% param_log - Array of 0/1 numbers (having length of paramn), where ones stand
% for parameters which are transformed to log space
% date_min - The earliest allowed start date ('dd-mmm-yyyy') for chosen sims_opt
% date_max - The latest allowed end date ('dd-mmm-yyyy') for chosen sims_opt

function [VectorValues]=expval_inter_combs(temp_inter,range,default,paramn)

% NAME
% expval_inter_combs
% PURPOSE
% fill expval matrix for sims_def.m
% INPUTS
% temp_inter - one of the interaction simulations
% range - Parameters ranges (min and max)
% default - Parameters defaults
% paramn - Parameter names
% OUTPUTS
% expval matrix for sims_def.m

function [odata odata_s sound_exist]=read_calmo_obs(vars,date_lim,avg_type, size_vars_sound)

% NAME
% read_calmo_obs
% PURPOSE
% Read observations data from Switzerland and north Italy, as well as soundings
% data, for specified period
% INPUTS
% vars - calibrated fields groups. See namelist.m
% date_lim - Structure which includes the dates range of simulations to be read
% avg_type - Interpolation method of observations data to model grid. Can be:
% 'near_neighb','simple_mean','weight_mean','clever_mean'
% size_vars_sound - length(vars_sound) - number of soundings fields
% OUTPUTS
% odata - Data matrix with dimensions [Field,Day,1,Lon,Lat] (field can be
% Tmax,Tmin,Pr)
% odatas - Data matrix for profileswith dimensions [Field,Day,1,Hour,Sounding
% location]
% sound_exist - binary matrix [Day,Hour,Sounding location] with ones where the
% sounding data exist

function build_temp_obs(avg_type,maxminavg)

% NAME
```

```
% build_temp_obs
% PURPOSE
% This function interpolates the gridded temperature observations (by C. Frei) to the model
grid.
% METHOD
% When comparing smoothed topography model-grid 2m-temperature whith the
% observed 2m temperature, one shoud "correct" the observed
% 2m-temperature to correspond the model grid elevation. The correction may be
% performed using the neighboring grid points 2m-temperature profile,
% according the recommendation of C. Frei
% Steps:
% 1. Read any simulation file to obtain the model grid lat/lon
% (ex:aggregated_LTUR_2013011000.nc)
% 2. Read any simulation file to obtain the model grid altitude
% (ex:laf2013111600_filtered.nc)
% 3. Read any observations file to obtain the observations grid lat/lon (ex:
% TmaxD_ch01r.swisscors_201301010000_201302010000.nc)
% 4. Read gridded observations altitude ( ex: topo.swiss1_ch01r.swisscors.nc)
% 5. Interpolate the gridded observations to the model grid using one of the
% possible methods
% INPUTS
% avg_type - one of the interpolation methods:
% 'near_neighb','simple_mean','weight_mean','clever_mean'
% maxminavg - Which field to interpolate: 'Tmax','Tmin','Tavg'
% OUTPUTS
% saved (in .mat format) interpolated temperature observations

function build_rain_obs()

% NAME
% build_rain_obs
% PURPOSE
% This function interpolates the gridded rain observations to the model grid.
% METHOD
% 1. Read any simulation file to obtain the model grid lat/lon
% (ex:aggregated_LTUR_2013011000.nc)
% 2. Read gridded rain observations you need to interpolate (ex:
% CPCH_201301080000_01440_c2.nc)
% 3. Interpolate the gridded observations to the model grid using nearest
% neighbor
% INPUTS
% -
% OUTPUTS
% saved (in .mat format) interpolated precipitation observations
% AUTHOR
% Pavel Khain (pavelkh_il@yahoo.com)

function output=read_sounding_obs(year,month,day,height_step,windshear,windshearopt)

% NAME
% read_sounding_obs
```

```
% PURPOSE
% Read and interpolate soundings data, calculate sounding characteristics
% INPUTS
% year
% month
% day
% height_step - The interpolation height step in meters
% windshear - [v1u,v1d,v2u,v2d,v3u,v3d] - pressure levels for calculating wind shears:
% v1u - the upper pressure level for wshear1
% v1d - the bottom pressure level for wshear 1
% v2u - as mentioned above but for wshear 2
% v2d - as mentioned abobe but for wshear 2
% v3u - as mentioned above but for wshear 3
% v3d - as mentioned above but for wshear 3, whereas 1100 is the surface level or the lowest
level ("below surface")
% windshearopt - windshear calculation method: 'scalar' or 'vector'
% OUTPUTS
% output - Data matrix with dimensions [Field,Day,1,Hour,Sounding location]

function [mdata mdata_s]=read_calmo_sim(vars,sims,date_lim,sound_exist, size_vars_sound)

% NAME
% read_calmo_sim
% PURPOSE
% Read simulations data from, for specified period
% INPUTS
% vars - calibrated fields groups. See namelist.m
% sims - simulations names to be read. See namelist.m
% date_lim - Structure which includes the dates range of simulations to be read
% sound_exist - binary matrix [Day,Hour,Sounding location] with ones where the
%sounding data exist
% size_vars_sound - length(vars_sound) - number of soundings fields
% OUTPUTS
% mdata - Data matrix with dimensions [Field,Day,simulation,Lon,Lat] (field can
%be Tmax,Tmin,Pr)
% mdatas - Data matrix with dimensions [Field,Day,simulation,Hour,Sounding
% location]

function output = read_profiles_mod(simdir,year,month,day,simtype,height_step,
sound_exist,windshear,windshearopt)

% NAME
% read_profiles_mod
% PURPOSE
% Read and interpolate profiles data, calculate profiles characteristics
% INPUTS
% simdir - path to simulations files
% year
% month
% day
% simtype - simulation name
```

```
% height_step - The interpolation height step in meters
% sound_exist - binary matrix [Day,Hour,Sounding location] with ones where the
%sounding data exist
% windshear - [v1u,v1d,v2u,v2d,v3u,v3d] - pressure levels for calculating wind
% shears:
% v1u - the upper pressure level for wshear1
% v1d - the bottom pressure level for wshear 1
% v2u - as mentioned above but for wshear 2
% v2d - as mentioned abobe but for wshear 2
% v3u - as mentioned above but for wshear 3
% v3d - as mentioned above but for wshear 3, whereas 1100 is the surface
% level or the lowest level ("below surface")
% windshearopt - windshear calculation method: 'scalar' or 'vector'
% OUTPUTS
% output - Data matrix with dimensions [Field,Day,simulation,Hour,Sounding
% location]

function datamatrix_new = Frei_regions(datamatrix,lat,lon,vars, avg_T,unify_regions)

% NAME
% Frei_regions
% PURPOSE
% Average part of the surface fields over predefined big regions
% METHOD
% use image file (regions_italy_swiss_for_matlab.bmp) where each region has its
% color
% INPUTS
% datamatrix - Structure which includes observations and simulations data
% for surface fields ('t2m_max','t2m_min','pr'). Dimensions:
% [Field,Day,simulation,Lon,Lat]
% lat - latitudes of model domain
% lon - longitudes of model domain
% vars - calibrated fields groups. Can be any combinations of:
% 't2m_max','t2m_min','pr','sound'
% avg_T - region average over Precipitation only (avg_T=0), or over
% Precipitation, Tmax and Tmin (avg_T=1)
% unify_regions - array that defines which regions (out of 1-7) to unify (option
%to unify several regions into one bigger)
% OUTPUTS
% datamatrix_new - Structure which includes observations and simulations
% data for surface fields ('t2m_max','t2m_min','pr').
% Dimensions: [Field,Day,region,simulation]

function [area] = regions_bmp(lat,lon,img,unify_regions)

% NAME
% regions_bmp
% PURPOSE
% Definition of regions over Switzerland and north Italy
% METHOD
% Analyze image file (regions_italy_swiss_for_matlab.bmp) where each region has
```

```
% its color
% INPUTS
% lat - latitude
% lon - longitude
% img - image file (regions_italy_swiss_for_matlab.bmp) where each region has
% its color
% unify_regions - array that defines which regions (out of 1-7) to unify (option
% to unify several regions into one bigger)
% OUTPUTS
% area - region number to which lat lon belong

function datamatrix_t = gpts_series(datamatrix,vars,var)

% NAME
% gpts_series
% PURPOSE
% Redefine data arrays (which were not averaged over regions) to the following
% structure: (fields,days,regions,simulations)
% INPUTS
% datamatrix - Structure which includes observations and simulations data
% for surface fields ('t2m_max','t2m_min','pr'). Dimensions:
% [Field,Day,simulation,Lon,Lat]
% vars - calibrated fields groups. Can be any combinations of:
% 't2m_max','t2m_min','pr','sound'
% var - specific field group (one of vars)
% OUTPUTS
% datamatrix_new - Structure which includes observations and simulations
% data for surface fields ('t2m_max','t2m_min','pr').
% Dimensions: [Field,Day,region,simulation]

function datatemp=del_bad_sounding(datamatrix_so,ml,sims_reg,sims_inter, sims_con,simval,vars_sound)

% NAME
% del_bad_sounding
% PURPOSE
% delete unrealistic sounding/profiles data
% INPUTS
% datamatrix_so - Data matrix for profiles. Dimensions:
% [Field,Day,region,simulation]
% ml - Minimum number of days (during given period) for valid soundings data. If
% less - current sounding fields are not analyzed.
% sims_reg - Names of max-min simulations (where only 1 parameter is shifted to
% its max/min value)
% sims_inter - Names of interaction simulations (where 2 parameters are shifted
% to their max/min values)
% sims_con - Name of "constrain" simulations (where each time one parameter is
% shifted from its default value, but not to its max/min values)
% simval - Name of "val" simulation (where all the parameters are shifted from
% their default values, in order to validate the Meta-Models)
% vars_sound - calibrated profiles fields: 'CAPE','CIN','TCWC','WSHEAR1',
% 'WSHEAR2','WSHEAR3','T850mb','T700mb','T500mb','RH850mb',
```

```
% 'RH700mb','RH500mb','U850mb','U700mb','U500mb',
% 'V850mb','V700mb','V500mb'
% OUTPUTS
% datatemp - Data matrix for profiles. Dimensions: [Field,Day,region,simulation]

function metamodel=neelin_e(parameters, datamatrix_test,vars_2d)

% Quadratic regression metamodel as described in Neelin et al. (2010) PNAS and
% Bellprat (2012)
% NAME
% neelin_e
% PURPOSE
% Fit a mutlivariate quadratic quadratic regressions (metamodels)
% INPUTS
% From the structure parameters and datamatrix the following fields are
% processed
% parameters.experiments:
% Parameter values for each experiment with the dimension of [N,
% 2*N+N*(N-1)/2]
% The structure NEEDS to be as follows. Example for 2 parameters
% (p1,p2):
% [p1_l dp2 ] ! Low parameter value for p1 default dp2
% [p1_h dp2 ] ! High parameter value for p1 default dp2
% [dp1 p2_l] ! Low parameter value for p2 default dp1
% [dp1 p2_h] ! Hihg parameter value for p2 default dp1
% [p1_l p2_h] ! Experiments with interaction (no default)
% ! Additional experiments used to constrain interaction
% terms
% parameters.range:
% Range of values for each parameter to normalize the scale
% parameters.default:
% Default values of parameters to center the scale
% datamatrix_test.moddata:
% Modeldata corresponding to the dimensions of parameter.experiments
% datamatrix_test.refdata:
% Modeldata when using default parameter values to center the
% datamatrix fitted
% vars_2d - calibrated 2D fields. Can be any combinations of:
% 't2m_max','t2m_min','pr'
% OUTPUT
% structure metamodel.
% a: Metamodel parameter for linear terms [N,1]
% B: Metamodel parameter for quadratic and interaction terms
% [N,N]. Quadratic terms in the diagonal, interaction terms
% in the off-diagonal. Matrix symmetric, B(i,j)=B(j,i).
% c: Metamodel parameter for zero order (constant)

function PostProc(period)

% NAME
% PostProc
```

```
% PURPOSE
% plot analysis results and calculate the optimal parameters combination
% INPUTS
% time periods array (more precisely - initial dates of the periods):
% 'dd-mmm-yyyy','dd-mmm-yyyy',...
% OUTPUTS
% saved (in .mat format) analysis results

function [W_fin]=weights_calc(parameters,datamatrix_tmp,metamodel_tmp, w_user,score,fields)

% NAME
% weights_calc
% PURPOSE
% calculate weights for different fields, to equalize their contributions to the
% final score (assuming user defined weights are uniform).
% INPUTS
% parameters - structure parameters (see definitions in
% ReadData_and_MetaModel.m)
% datamatrix_tmp - structure datamatrix (see definitions in
% ReadData_and_MetaModel.m)
% metamodel_tmp - structure metamodel (see definitions in neelin_e.m)
% w_user - array of user defined weights (for simlicity - from 0 to 1) for
% calibrated fields:
% score - 'rmse' or 'cosi' for RMSE-type and COSI-type scores, respectively
% fields - field name (can be 't2m_max','t2m_min','pr',vars_sound)
% OUTPUT
% W_fin - weights array for different fields

function [dmatrix]=neelin_p(metamodel,parameters,datamatrix,pvector)

% NAME
% neelin_p
% PURPOSE
% Forecast using regression metamodel as described in Neelin et al. (2010) PNAS
% and Bellprat et al. (2012).
% METHOD
% Predict data using the metamodel for a parameter matrix
% INPUTS
% From the structure metamodel, parameters and datamatrix the following fields
% are
% processed (mind the same naming in the input)
% metamodel.a:
% Vector of linear terms of the metamodel [...,N,1] additional
% data dimensions possible (ex:a [Regions,Variables,Time,N,1])
% metamodel.B:
% Matrix of quadratic and interactions terms [...,N,N] additional
% data dimensions possible (ex:a [Regions,Variables,Time,N,N])
% metamodel.c: Metamodel parameter for zero order (constant)
% parameters.range:
% Range of values for each paramter to normalize the scale.
% parameters.default:
```

```
% Default values of parameters to center the scale
% datamatrix.reffdata:
% Modeldata of when using default parameter values to center the
% datamatrix
% pvector: Parameter values for one experiment with the
% dimension of [N,1] N=Number parameters
% OUTPUT
% dmatrix: Predicted data for parameter experiment

function ets = ETS (Obs,Model,thresrain)

% NAME
% ETS
% PURPOSE
% rain forecast. Answers the question: How well did the forecast "yes" events correspond
% to the observed "yes" events (accounting for hits that would be expected by chance)
% Range: -1/3 to 1; 0 indicates no skill. Perfect score: 1.
% NOTE
% be carefull with 0/0 when there is no rain both in nature and model (ex:
% "summer in Israel") !!!
% INPUTS
% parameters - structure parameters (see definitions in
% ReadData_and_MetaModel.m)
% datamatrix_tmp - structure datamatrix (see definitions in
% ReadData_and_MetaModel.m)
% metamodel_tmp - structure metamodel (see definitions in neelin_e.m)
% w_user - array of user defined weights (for simlicity - from 0 to 1) for
% calibrated fields:
% score - 'rmse' or 'cosi' for RMSE-type and COSI-type scores, respectively
% fields - field name (can be 't2m_max','t2m_min','pr',vars_sound)
% OUTPUT
% ets - rain forecast score

function planes(main_data,parameters,w_user,score,new_calc,predir,param_log)

% NAME
% planes
% PURPOSE
% Plot performance scores for pair-wise parameters cross sections
% INPUTS
% main_data - big structure, which includes the sub-structures:
% main_data.data - datamatrix structure
% main_data.metamodel metamodel structure
% main_data.field - field names
% main_data.W - weights array for different fields
% parameters structure:
% parameters.range:
% Range of values for each paramter to normalize the scale.
% parameters.default:
% Default values of parameters to center the scale
% datamatrix.reffdata:
```

```
% Modeldata of when using default parameter values to center the
% datamatrix
% w_user - array of user defined weights (for simlicity - from 0 to 1) for
% calibrated fields:
% tmax tmin pr cape cin ws1 ws2 ws3 T850mb T700mb T500mb RH850mb
% RH700mb R500mb U850mb U700mb U500mb V850 V700mb V500mb
% score - 'rmse' or 'cosi' for RMSE-type and COSI-type scores, respectively
% new_calc - 0 or 1: 0 by default, when main_data is devided into cells over
% periods. 1 - otherwise
% predir - path for saving output planes figures
% param_log - Array of 0/1 numbers (having length of paramn), where ones stand
% for parameters which are transformed to log space
% OUTPUT
% saved planes figures

function score=rmse_score(qfit,obsdata,W,w_user,new_calc)

% NAME
% rmse_score
% PURPOSE
% calculate RMSE-type score for Meta-Model predictions (regressions estimations)
% INPUTS
% qfit - metamodel predictions for given parameter combination
% obsdata - observations data
% W - weights for different fields, to equalize their contributions to the final
% score
% w_user - array of user defined weights (for simlicity - from 0 to 1) for
% calibrated fields
% new_calc - 0 or 1: 0 by default, when main_data is devided into cells over
% periods. 1 - otherwise
% OUTPUT
% score - RMSE-type score

function score=cosi_score(qfit,obsdata,W,w_user,new_calc)

% NAME
% cosi_score
% PURPOSE
% calculate COSI score for Meta-Model predictions (regressions
% estimations). Defined on the basis of the COSI score by Ulrich Damrath (DWD)
% INPUTS
% qfit - metamodel predictions for given parameter combination
% obsdata - observations data
% W - weights for different fields, to equalize their contributions to the final
% score
% w_user - array of user defined weights (for simlicity - from 0 to 1) for
% calibrated fields
% new_calc - 0 or 1: 0 by default, when main_data is devided into cells over
% periods. 1 - otherwise
% OUTPUT
% score - COSI score
```

```
function [Sopt,xstar,xopt,sc_stat,UB_next,LB_next]=lhopt(main_data,
parameters,w_user,score,new_calc,lhacc,tmp_str,iteration,
best_percent,UB_new,LB_new,param_log)

% NAME
% lhopt
% PURPOSE
% Optimise model parameters using a latin hypercube sampling. See Bellprat et al. (2012)
% METHOD
% Create a sample of parameters using a latin hypercube design
% and predict the model performance of the sample using the metamodel.
% INPUTS
% main_data - big structure, which includes the sub-structures:
% main_data.data - datamatrix structure
% main_data.metamodel metamodel structure
% main_data.field - field names
% main_data.W - weights array for different fields
% parameters structure:
% parameters.range:
% Range of values for each paramter to normalize the scale.
% parameters.default:
% Default values of parameters to center the scale
% w_user - array of user defined weights (for simlicity - from 0 to 1) for
% calibrated fields:
% tmax tmin pr cape cin ws1 ws2 ws3 T850mb T700mb T500mb RH850mb
% RH700mb R500mb U850mb U700mb U500mb V850 V700mb V500mb
% score - 'rmse' or 'cosi' for RMSE-type and COSI-type scores, respectively
% new_calc - 0 or 1: 0 by default, when main_data is devided into cells over
% periods. 1 - otherwise
% lhacc - Number of experiments to sample parameter space at each iteration
% tmp_str - path to the calibration results
% iteration - iteration number (of convergence process to the optimal parameters
% combination)
% best_percent - "winners" percent of lhacc which is used to define the
% parameters space for the next iteration
% UB_new - upper limit of parameters range at given iteration
% LB_new - lower limit of parameters range at given iteration
% param_log - Array of 0/1 numbers (having length of paramn), where ones stand
% for parameters which are transformed to log space
% OUTPUTS
% Sopt - Scores for all experiments at given iteration
% xstar - Latin hypercube parameter experiments at given iteration
% xopt - Parameter setting with highest score at given iteration
% sc_stat - score statistics at given iteration
% UB_next - upper limit of parameters range at NEXT iteration
% LB_next - lower limit of parameters range at NEXT iteration

function histplot(lhscore,score,best,predir,iteration)

% NAME
% histplot
```

```
% PURPOSE
% plot histogram of SCORES for meta-models predictions
% INPUTS
% lhscore - Scores for all experiments at given iteration
% score - 'rmse' or 'cosi' for RMSE-type and COSI-type scores, respectively
% best - 0 or 1: o by default, 1 if a special simulation exists and verified
% predir - path for saving output planes figures
% iteration - iteration number (of convergence process to the optimal parameters combination)
% OUTPUTS
% saved scores histogram for specific iteration

function optparam(parameters,lhscore,lhexp,popt,errm)

% NAME
% optparam
% PURPOSE
% Plot optimal parameters combination
% NOTE: not checked or adapted since early stage of the CALMO project !
% INPUTS
% parameters - parameters structure
% lhscore - Scores for all experiments (at last iteration)
% lhexp - Latin hypercube parameter experiments (at last iteration)
% popt - Parameter setting with highest score (at last iteration)
% errm - error of metamodel, set to 0.001 ???
% OUTPUTS
% Plot optimal parameters combination

function xnolog=log_turlen_entrsc(xlog,paramname)

% NAME
% log_turlen_entrsc
% PURPOSE
% convert the optimal parameters (tur_len and entr_sc) values from log-space
% back to the regular space
% INPUTS
% xlog - input vector of paramaeters values in log space
% paramname - parameter names
% OUTPUT
% xnolog - output vector of paramaeters values (tur_len and entr_sc) in regular
% space
```

List of COSMO Newsletters and Technical Reports

(available for download from the COSMO Website: www.cosmo-model.org)

COSMO Newsletters

No. 1: February 2001.

No. 2: February 2002.

No. 3: February 2003.

No. 4: February 2004.

No. 5: April 2005.

No. 6: July 2006.

No. 7: April 2008; Proceedings from the 8th COSMO General Meeting in Bucharest, 2006.

No. 8: September 2008; Proceedings from the 9th COSMO General Meeting in Athens, 2007.

No. 9: December 2008.

No. 10: March 2010.

No. 11: April 2011.

No. 12: April 2012.

No. 13: April 2013.

No. 14: April 2014.

No. 15: July 2015.

No. 16: July 2016.

COSMO Technical Reports

No. 1: Dmitrii Mironov and Matthias Raschendorfer (2001):
Evaluation of Empirical Parameters of the New LM Surface-Layer Parameterization Scheme. Results from Numerical Experiments Including the Soil Moisture Analysis.

No. 2: Reinhold Schrodin and Erdmann Heise (2001):
The Multi-Layer Version of the DWD Soil Model TERRA_LM.

No. 3: Günther Doms (2001):
A Scheme for Monotonic Numerical Diffusion in the LM.

No. 4: Hans-Joachim Herzog, Ursula Schubert, Gerd Vogel, Adelheid Fiedler and Roswitha Kirchner (2002):
LLM ¯ the High-Resolving Nonhydrostatic Simulation Model in the DWD-Project LITFASS.
Part I: Modelling Technique and Simulation Method.

No. 5: Jean-Marie Bettems (2002):
EUCOS Impact Study Using the Limited-Area Non-Hydrostatic NWP Model in Operational Use at MeteoSwiss.

No. 6: Heinz-Werner Bitzer and Jürgen Steppeler (2004):
Documentation of the Z-Coordinate Dynamical Core of LM.

No. 7: Hans-Joachim Herzog, Almut Gassmann (2005):
Lorenz- and Charney-Phillips vertical grid experimentation using a compressible nonhydrostatic toy-model relevant to the fast-mode part of the 'Lokal-Modell'.

No. 8: Chiara Marsigli, Andrea Montani, Tiziana Paccagnella, Davide Sacchetti, André Walser, Marco Arpagaus, Thomas Schumann (2005):
Evaluation of the Performance of the COSMO-LEPS System.

No. 9: Erdmann Heise, Bodo Ritter, Reinhold Schrodin (2006):
Operational Implementation of the Multilayer Soil Model.

No. 10: M.D. Tsyrulnikov (2007):
Is the particle filtering approach appropriate for meso-scale data assimilation ?

No. 11: Dmitrii V. Mironov (2008):
Parameterization of Lakes in Numerical Weather Prediction. Description of a Lake Model.

No. 12: Adriano Raspanti (2009):
COSMO Priority Project "VERification System Unified Survey" (VERSUS): Final Report.

No. 13: Chiara Marsigli (2009):
COSMO Priority Project "Short Range Ensemble Prediction System" (SREPS): Final Report.

No. 14: Michael Baldauf (2009):
COSMO Priority Project "Further Developments of the Runge-Kutta Time Integration Scheme" (RK): Final Report.

No. 15: Silke Dierer (2009):
COSMO Priority Project "Tackle deficiencies in quantitative precipitation forecast" (QPF): Final Report.

No. 16: Pierre Eckert (2009):
COSMO Priority Project "INTERP": Final Report.

No. 17: D. Leuenberger, M. Stoll and A. Roches (2010):
Description of some convective indices implemented in the COSMO model.

No. 18: Daniel Leuenberger (2010):
Statistical analysis of high-resolution COSMO Ensemble forecasts in view of Data Assimilation.

No. 19: A. Montani, D. Cesari, C. Marsigli, T. Paccagnella (2010):
Seven years of activity in the field of mesoscale ensemble forecasting by the COSMO–LEPS system: main achievements and open challenges.

No. 20: A. Roches, O. Fuhrer (2012):
Tracer module in the COSMO model.

No. 21: Michael Baldauf (2013):
A new fast-waves solver for the Runge-Kutta dynamical core.

No. 22: C. Marsigli, T. Diomede, A. Montani, T. Paccagnella, P. Louka, F. Gofa, A. Corigliano (2013):
The CONSENS Priority Project.

No. 23: M. Baldauf, O. Fuhrer, M. J. Kurowski, G. de Morsier, M. Müllner, Z. P. Piotrowski, B. Rosa, P. L. Vitagliano, D. Wójcik, M. Ziemiański (2013):
The COSMO Priority Project 'Conservative Dynamical Core' Final Report.

No. 24: A. K. Miltenberger, A. Roches, S. Pfahl, H. Wernli (2014):
Online Trajectory Module in COSMO: a short user guide.

No. 25: P. Khain, I. Carmona, A. Voudouri, E. Avgoustoglou, J.-M. Bettems, F. Grazzini (2015):
The Proof of the Parameters Calibration Method: CALMO Progress Report.

No. 26: D. Mironov, E. Machulskaya, B. Szintai, M. Raschendorfer, V. Perov, M. Chumakov, E. Avgoustoglou (2015):
The COSMO Priority Project 'UTCS' Final Report.

No. 27: J-M. Bettems (2015):
The COSMO Priority Project 'COLOBOC': Final Report.

No. 28: Ulrich Blahak (2016):
RADAR_MIE_LM and RADAR_MIELIB - Calculation of Radar Reflectivity from Model Output.

No. 29: M. Tsyrulnikov and D. Gayfulin (2016):
A Stochastic Pattern Generator for ensemble applications.

No. 30: D. Mironov and E. Machulskaya (2017):
A Turbulence Kinetic Energy – Scalar Variance Turbulence Parameterization Scheme.

COSMO Technical Reports

Issues of the COSMO Technical Reports series are published by the *COnsortium for Small-scale MOdelling* at non-regular intervals. COSMO is a European group for numerical weather prediction with participating meteorological services from Germany (DWD, AWGeophys), Greece (HNMS), Italy (USAM, ARPA-SIMC, ARPA Piemonte), Switzerland (MeteoSwiss), Poland (IMGW), Romania (NMA) and Russia (RHM). The general goal is to develop, improve and maintain a non-hydrostatic limited area modelling system to be used for both operational and research applications by the members of COSMO. This system is initially based on the COSMO-Model (previously known as LM) of DWD with its corresponding data assimilation system.

The Technical Reports are intended

- for scientific contributions and a documentation of research activities,
- to present and discuss results obtained from the model system,
- to present and discuss verification results and interpretation methods,
- for a documentation of technical changes to the model system,
- to give an overview of new components of the model system.

The purpose of these reports is to communicate results, changes and progress related to the LM model system relatively fast within the COSMO consortium, and also to inform other NWP groups on our current research activities. In this way the discussion on a specific topic can be stimulated at an early stage. In order to publish a report very soon after the completion of the manuscript, we have decided to omit a thorough reviewing procedure and only a rough check is done by the editors and a third reviewer. We apologize for typographical and other errors or inconsistencies which may still be present.

At present, the Technical Reports are available for download from the COSMO web site (www.cosmo-model.org). If required, the member meteorological centres can produce hard-copies by their own for distribution within their service. All members of the consortium will be informed about new issues by email.

For any comments and questions, please contact the editor:

Massimo Milelli
Massimo.Milelli@arpa.piemonte.it

Consortium for Small-Scale Modelling

Technical Report No. 14

COSMO Priority Project "Further Developments of the Runge-Kutta Time Integration Scheme (RK)": Final Report

October 2009

DOI: 10.5676/DWD_pub/nwv/cosmo-tr_14

Deutscher Wetterdienst

MeteoSwiss

Ufficio Generale Spazio Aereo e Meteorologia

ΕΘΝΙΚΗ ΜΕΤΕΩΡΟΛΟΓΙΚΗ ΥΠΗΡΕΣΙΑ

Instytucie Meteorogii i Gospodarki Wodnej

Administratia Nationala de Meteorologie

Agenzia Regionale per la Protezione Ambientale del Piemonte

Agenzia Regionale per la Protezione Ambientale dell' Emilia-Romagna: Servizio Idro-Meteo-Clima

Centro Italiano Ricerche Aerospaziali

Amt für GeoInformationswesen der Bundeswehr

www.cosmo-model.org

Editor: Massimo Milelli, ARPA Piemonte
Printed at Deutscher Wetterdienst, P.O. Box 100465, 63004 Offenbach am Main

COSMO Priority Project "Further Developments of the Runge-Kutta Time Integration Scheme (RK)": Final Report

Project participants:

M. Baldauf [‡]***, G. Ceci, J. Förstner, O. Fuhrer,***

A. Gassmann, H-J. Herzog, G. de Morsier, T. Reinhardt,

G. Rivin, L. Torrisi, P. L. Vitagliano, G. Zängl

[‡] Project Leader:
Michael Baldauf
Deutscher Wetterdienst
Offenbach
Germany

Contents

1 Summary **4**

2 Project report **5**

2.1 Task 1: Looking at pressure bias 5

2.1.1 Heat source term in p equation 7

2.1.2 New reference state 7

2.2 Task 2: Continue RK case studies 15

2.2.1 First difficulties and their solutions 15

2.2.2 General testing and some verification results 16

2.3 Task 3: A Tool for Testing Conservation Properties in the COSMO-Model . . 21

2.3.1 Introduction 21

2.3.2 'Shift-test' 22

2.3.3 Weisman-Klemp test case 22

2.4 Task 4: Advection of moisture quantities in conservation form 24

2.5 Task 5: Investigation of convergence 26

2.5.1 Hydrostatic linear mountain flow simulations 28

2.5.2 Hydrostatic non-linear mountain flow simulations 29

2.5.3 Non-hydrostatic linear mountain flow simulations 30

2.5.4 3D mountain flow tests 32

2.6 Task 6: Deep valleys + Task 7: Different filter options for orography 36

2.7 Task 8: Higher order discretization in the vertical 38

2.7.1 Addendum 39

2.8 Task 9: Physics coupling scheme 39

2.9 Task 10: Testing of alternative fast wave scheme 39

2.10 Task 13: Divergence damping in a true 3D-version 42

2.11 Task 14: Digital Filter Initialization (DFI) 42

2.12 Open points 44

2.13 Resources used 44

2.14 Lessons learned 44

3 Acknowledgements **44**

4 References **45**

1 Summary

The Priority Project Runge-Kutta started in October 2005 and ended after 3 years in September 2008. The starting point was an implementation of the Runge-Kutta (RK) method (Wicker and Skamarock 1998, Wicker and Skamarock 2002, Skamarock et al. 2005) into the COSMO-model at DWD beginning mid 2003 as the basic time integration scheme for use in high resolution applications. The aim was to replace the Klemp and Wilhelmson (1978) leapfrog-scheme later on. The Runge-Kutta method offers a substantial gain in accuracy at no additional costs. At the beginning of the Priority Project 10 tasks were defined (in a rather arbitrary order). During the project 4 additional tasks arose. These tasks can roughly be grouped into 3 classes:

- Repair detected model deficiencies:

  1 - Looking at pressure bias

  4 - Advection of moisture quantities in conservation form

  6 - Deep valleys

  7 - Different filter options for orography

  14 - DFI for RK

- New developments:

  8 - Higher order discretization in the vertical

  9 - Physics coupling scheme

  10 - Testing of alternative fast wave scheme

  13 - Divergence damping in a truly 3D-version

- Tool development:

  2 - Continue RK case studies

  3 - Conservation tool

  5 - Investigation of convergence

The two tasks

11 - Development of a more conservative dynamics

12 - Development of an efficient semi-implicit solver in combination with RK time integration scheme

were found to be too ambitious to be handled into this project. Indeed task 11 will evolve into an entirely new Priority Project ('Conservative Dynamical Core (CDC)').

Fortunately the tasks (1, 4, 6, 7, 14) which handle detected model deficiencies could be treated and came to a satisfactory end. This holds in particular for the rather tenacious problem of the pressure bias, task 1, which could be solved by a combination of several measures. The new moisture transport schemes are probably the main responsible for the improvements of the precipitation forecast, which were detected in the Priority Project 'Quantitative precipitation forecast' by comparing the old and new dynamical core (Leapfrog vs. RK). Also the tool development tasks (3, 5) could fulfil all the required deliverables.

The integration tool is now applied e.g. at the MPI Hamburg for budget inspections of moisture. A solver for analytic solutions for mountain flows is available, which was developed in particular for model validation. The tools for measuring the convergence rate are also available now. Task 2 had no concrete deliverables but accompanied the project by verifying the efforts of the projects by case studies and by identifying possible new problems of the dynamical core (e.g. the stability problem of thin layers near the ground). From the 'new development' tasks, task 9 is merely in an intermediate state. Task 8 (implicit vertical advection) could be brought to a satisfactory state some months after the official end of the project. At least, the necessary methodologies (needed efficient linear equation solver, model configuration items) are delivered and several studies were performed. Task 13 (3D-divergence) could not be treated at all. There was some time invested into task 10 to bring this version into a state for operational use. All in all it was found that some ideas contained there were promising, but a bigger effort is required to solve some more fundamental questions before it could be used.

2 Project report

2.1 Task 1: Looking at pressure bias

The pressure bias problem in RK core was pointed out in Torrisi (2005). Objective verification results using SYNOP observations showed a difference in mean sea-level pressure (MSLP) bias behaviour between 7 km Runge Kutta (RK) and LeapFrog (LF) runs (Fig. 1)

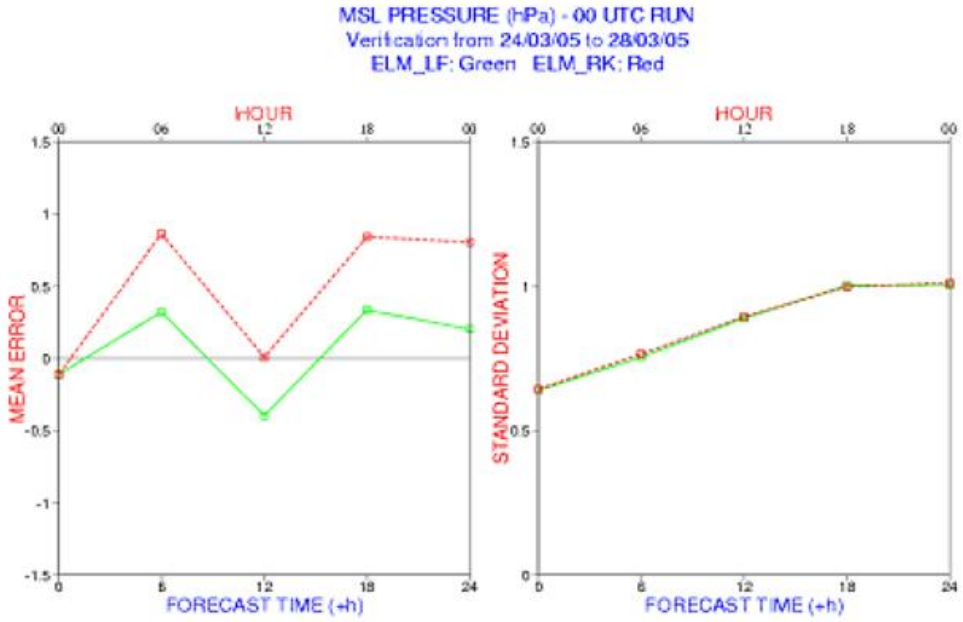


Figure 1: The pressure bias problem in the RK-dynamical core compared to the Leapfrog-scheme.

The pressure bias for RK runs, typically positive, tends to be larger (especially increasing

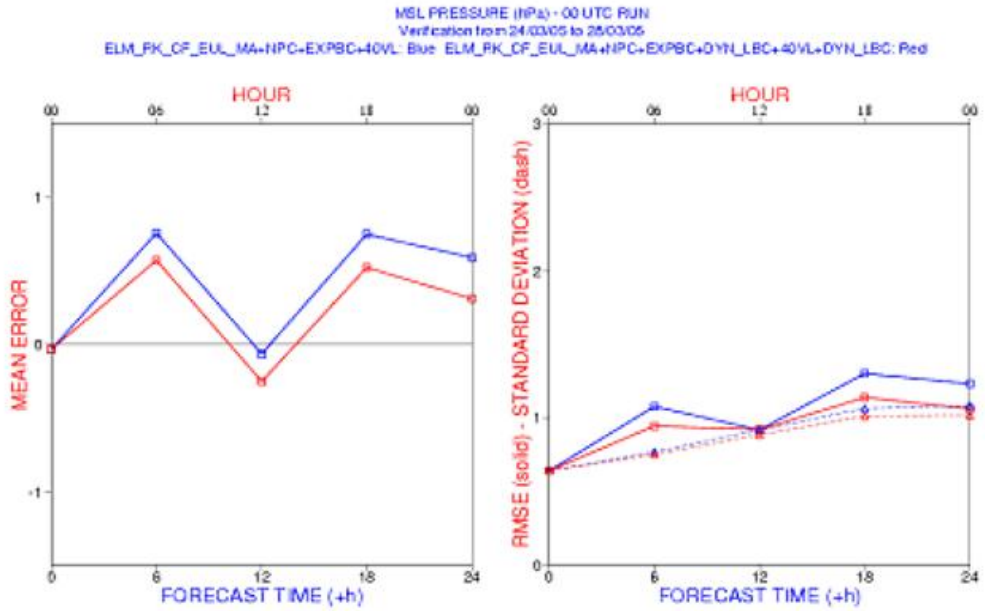


Figure 2: Positive effect of the dynamical bottom boundary condition on the PMSL.

with forecast time) leading to a worse RMSE. The implementation of the Gassmann formulation of the dynamical bottom boundary condition in the vertical pressure gradient term of the horizontal momentum equations brought an improvement in pressure bias behaviour for the RK dynamics (Fig. 2). Other work was done on RK core (change in metric term discretization, change in vertical average on half levels, etc), but no significant positive impact on the pressure bias was found. Objective verification results for the winter period 20 Jan - 04 Feb 2008 showed that 7 km RK/LF differences in pressure bias for COSMO-ME are almost negligible (Fig. 3). Generally, small RK/LF bias differences using 2.8/7 km grid spacing (depending on season, domain, location, etc) are still found (RK larger bias). RK/LF differences in MSLP bias are very big (especially at longer forecast times) using a 14 km grid spacing.

Other experiments showed that the pressure bias problem is not only present by changing the dynamical core (RK/LF), but it is evident also by using very large domain size and particularly clear using a 14 km grid spacing when compared to hydrostatic model runs (HRM). Objective verification results showed a difference in MSLP bias behaviour in 7 km RK (and LF) COSMO runs having domains of different sizes (the larger domain, the greater the bias difference - Fig. 4). Moreover, a large pressure bias difference was also found between 14 km COSMO and HRM runs on a Euro-Atlantic domain (Fig. 5). COSMO LF/RK runs have a larger bias increasing with forecast time. The pressure bias is a characteristics of COSMO model and is probably related to the model formulation. For this reason the effects on the pressure bias of two changes in the model formulation were addressed:

- Gassmann and Herzog (2006) reconsidered the derivation of prognostic temperature and pressure equations to remove some inconsistencies in the formulation of these equations;
- Zängl proposed a new reference atmosphere to overcome the problem of limitation in vertical extent of the model domain using the default reference atmosphere (model implementation in COSMO 4.5, September 2008).

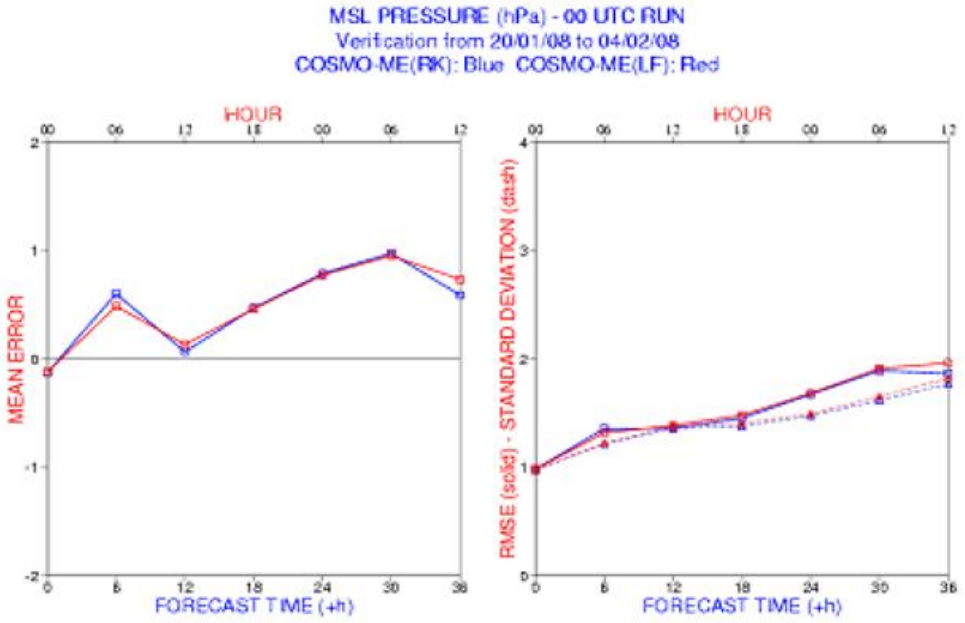


Figure 3: Comparison between RK and Leapfrog, 7 km resolution.

2.1.1 Heat source term in p equation

The pressure bias problem was also found in experiments using a coarser resolution (14 km) and enlarging the domain size (7 km). This could be an indication of some inconsistencies in the formulation of COSMO T/p budget equations. As suggested by Gassmann and Herzog (2006), a possible source of pressure bias could be neglecting the diabatic term in pressure equation. Preliminary real case experiments (winter period) without this approximation showed that the impact on the pressure bias is not general in 7 km runs (a slight deterioration around 12 UTC. Fig. 6), but it is apparent in 14 km runs (Fig. 7). Objective verification results (7 km) for a summer period were not so promising as those for the winter period (Fig. 8). No reduction of the amplitude of the pressure bias variation was found, but only a temporal shift in MSLP bias behaviour was present. More work would be needed. The pressure bias problem is typical for the COSMO model (not only of RK core !) and it seems to be mainly related to the model equation formulation. The use of a prognostic p-equation does not guarantee an exact mass conservation (accuracy depending on numerical algorithm), which is equivalent to introduce artificial sources or sinks in the continuity equation. Problems arise in applications such as data assimilation systems, where the pressure accuracy is important. A more conservative dynamical core is needed for the COSMO model.

2.1.2 New reference state

Introducing a reference state reduces the computational error in the calculation of pressure gradient terms in the equation of motion for not too large deviations of pressure from reference pressure.

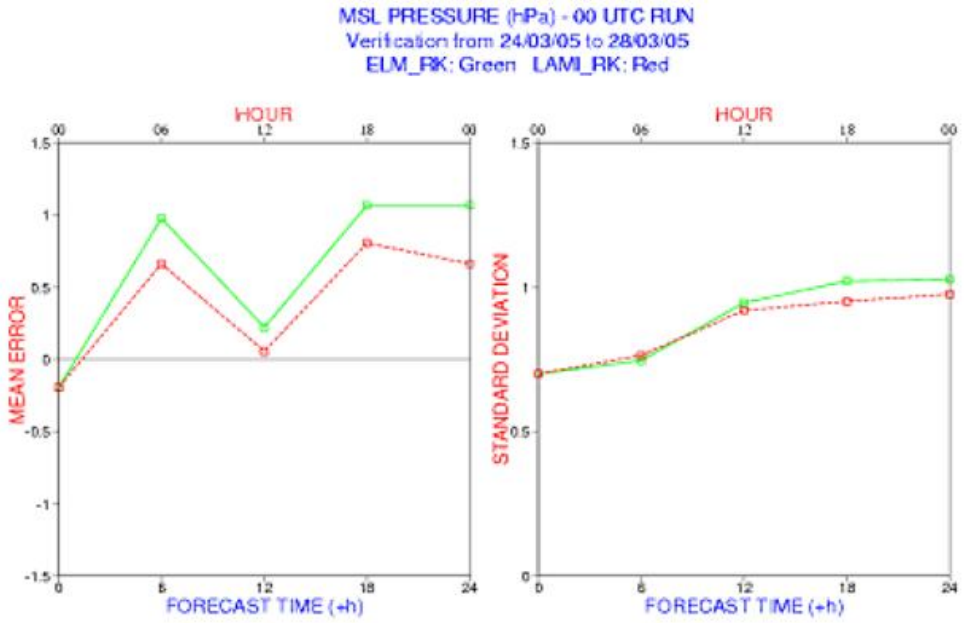


Figure 4: Influence of the domain size to the pressure bias.

At present, the reference atmosphere in the COSMO model is defined through the sea- level pressure, p_{00}, the sea-level temperature, T_{00}, and a generalized vertical temperature gradient

$$\frac{dT_0}{dlnp} = c_1. \tag{1}$$

Integration of the hydrostatic equation yields

$$T_0(z) = [T_{00}^2 - \frac{2gc_1}{R_d}(z - z_0)]^{1/2} \tag{2}$$

and

$$p_0(z) = p_{00}exp(\frac{T_0(z) - T_{00}}{c_1}) \tag{3}$$

From that follows

$$\frac{dT_0}{dz} = -\frac{gc_1}{R_d T_0} \tag{4}$$

which implies that the ordinary vertical temperature gradient becomes increasingly negative in the stratosphere. For the default values used in the COSMO model, p_{00} = 1000 hPa, T_{00} = 288.15 K and c_1 = 42 K, the reference temperature reaches 0 K at a height of 28923 m. This is clearly too restrictive for future plans to raise the model top to 10 hPa (about 30 km) or even higher. Another questionable property of the current reference atmosphere is

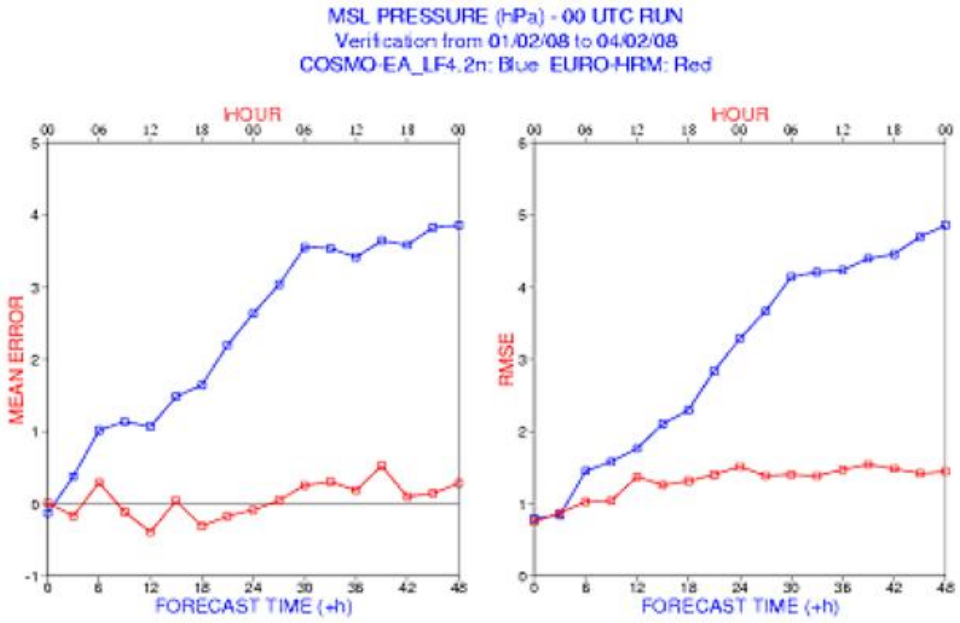


Figure 5: Comparison between COSMO-model and HRM for 14 km resolution.

that the base state pressure does not reach zero where the temperature does so. For the above-mentioned default values, $p_0 = 1.05$ hPa at the height where $T_0 = 0$ K.

To mitigate these problems, a new reference atmosphere has been implemented. Its temperature profile is defined through

$$T_0(z) = T_{00} + \Delta T exp(-z/H) \tag{5}$$

with reference values of $T_{00} = 213.15$ K, $\Delta T = 75$ K, and H = 10 km. For this temperature profile, the hydrostatic equation can be analytically integrated as well, yielding

$$p_0(z) = p_{00} exp[-\frac{gH}{R_d T_{00}} ln(\frac{exp(z/H)T_{00} + \Delta T}{T_{00} + \Delta T})] \tag{6}$$

and

$$T_0(p_0) = T_{00} + \frac{T_{00}\Delta T}{exp(-\frac{R_d T_{00}}{gH} ln\frac{p_0}{p_{00}})(T_{00} + \Delta T) - \Delta T} \tag{7}$$

With this definition, the temperature profile approaches an isothermal gradient in the stratosphere, which

- is closer to reality than an increasingly negative gradient and
- does not impose any limitation on the vertical extent of the model domain.

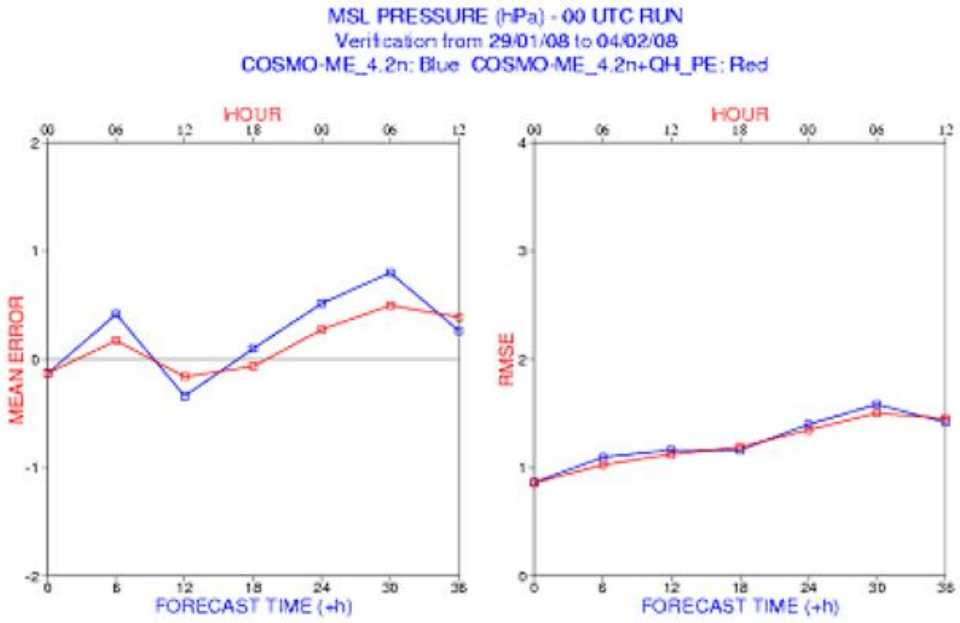


Figure 6: Influence of the diabatic terms in the pressure equations for 7 km resolution.

In the context of implementing the new reference atmosphere, an inconsistency in the computation of the reference pressure at the full model levels has been removed. Up to now, the reference pressure at full levels was set to the arithmetic mean of the reference pressure at the adjacent half levels, which is not consistent with the fact that the geometric height of the full levels is also assumed to be the arithmetic mean of the adjacent half levels. In the revised implementation, two possibilities for initializing the reference pressure are provided, both starting from an arithmetic averaging of height. One method directly uses the analytically integrated hydrostatic equation, the other one numerically integrates the hydrostatic equation from the bottom towards the model top. First experiments conducted with the new reference atmosphere and the corrected initialization of the reference pressure field indicate that both modifications could have a beneficial impact on the surface pressure forecast. Results are presented here for 72-hour forecasts on the COSMO-EU domain, starting on (i) 03 March 2008 (Fig. 9) and (ii) 30 May 2008 (Fig. 10). In all cases, initial data have been interpolated from the GME assimilation run, whereas lateral boundary conditions have been taken from the operational GME forecast. For reference, an experiment using the operational COSMO-EU setup (in particular the leapfrog core) is included. Moreover, an experiment using a non-approximated prognostic equation for perturbation pressure, as recently implemented by L. Torrisi, is shown. The surface pressure field has been validated against interpolated analyzes from GME assimilation runs every 12 hours.

The results reveal several interesting features:

- All experiments, except for the simulation with the non-approximated pressure equation in the March case, show a mostly negative slope in the pressure bias curves, with the bias turning from positive values at early forecast times into negative ones later on.

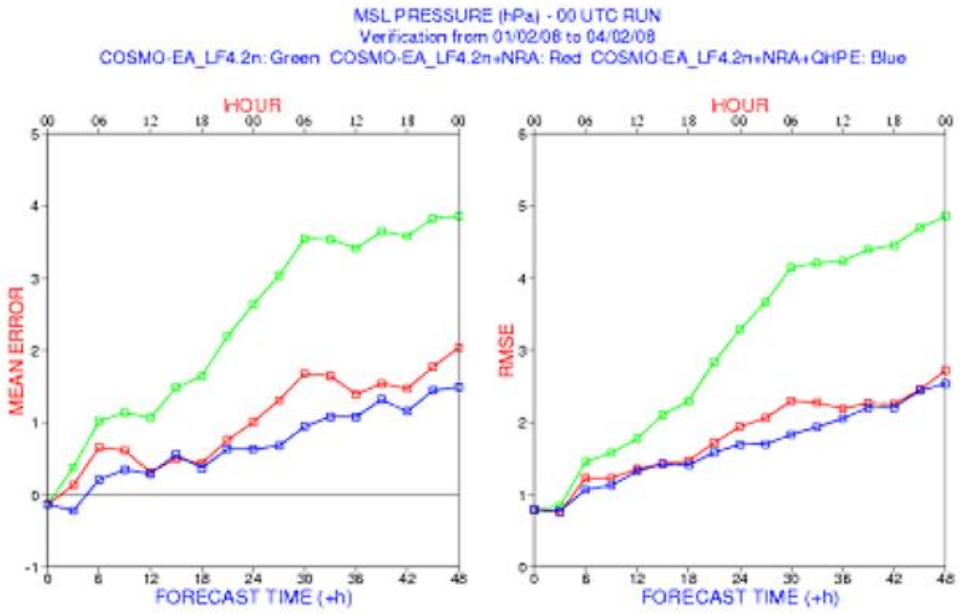


Figure 7: Influence of the diabatic terms in the pressure equations for 14 km resolution.

- Using the analytically integrated hydrostatic equation ("corr 2" in Fig. 9 and Fig. 10) induces a systematically more positive (or less negative) pressure bias than using the numerically integrated equation. This discrepancy is markedly larger for the old reference atmosphere than for the new one, particularly for the March case. Of all experiments using the Runge-Kutta core, the time-averaged bias is smallest when combining the new reference atmosphere with the analytically integrated hydrostatic equation.

- The rms error tends to be somewhat lower with the new reference atmosphere than with the old one. In the cases considered here, the Runge-Kutta core combined with the new reference atmosphere performs similarly well as the old Leapfrog core, whereas somewhat larger rms errors are obtained with the old reference atmosphere.

In summary, the most promising results have been obtained when combining the new reference atmosphere with initializing the reference pressure field from the analytically integrated hydrostatic equation. Thus, longer-term experiments should preferably be carried out with this setting. Objective verification results for only few runs using a 7 km grid spacing for the COSMO-ME showed a slight improvement around 06 UTC (Fig. 11). A dramatic improvement was found for 14 km runs (Fig. 12).

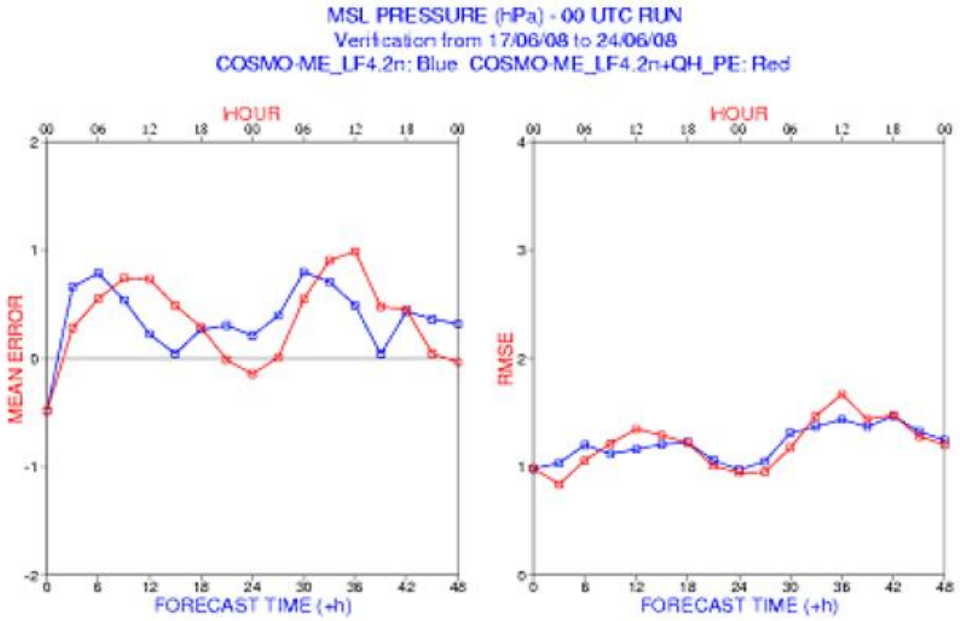


Figure 8: Influence of the diabatic terms in the pressure equations for 7 km resolution; summer period.

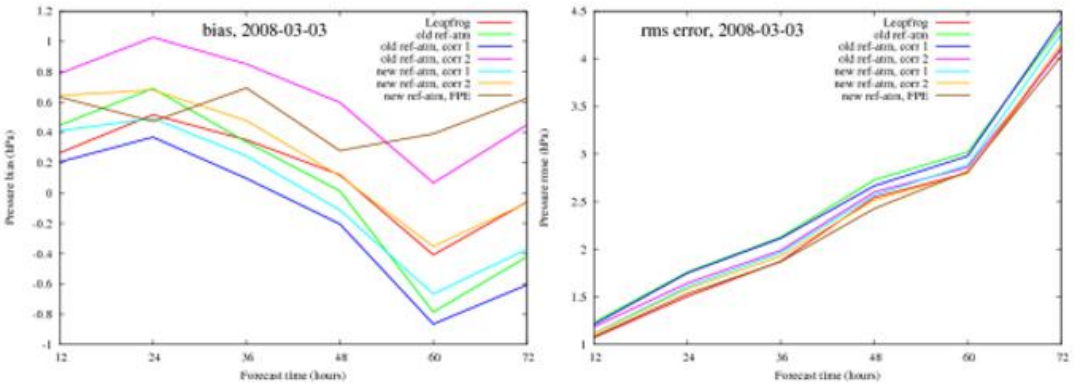


Figure 9: Bias and rms error of the surface pressure field for the experiments started at 00 UTC on 03 March 2008. The experiment denoted as "leapfrog" has been conducted with the operational COSMO-EU setup, all other experiments use the new Runge-Kutta core. The two methods available for calculating the base state pressure are denoted as "corr 1" for the discretized integration of the hydrostatic equation and as "corr 2" for the calculation based on the analytic formula. "FPE" stands for "full pressure equation", using the non-approximated prognostic equation for the perturbation pressure field.

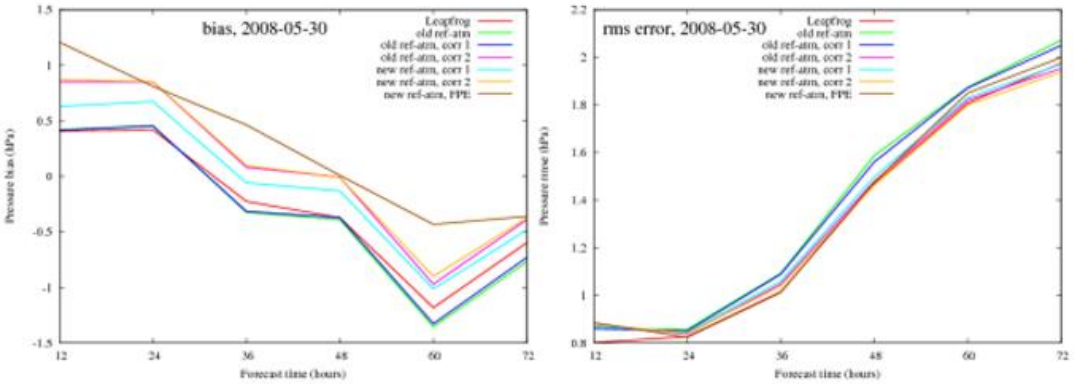


Figure 10: Same as Fig. 9, but for experiments initialized at 00 UTC on 30 May 2008.

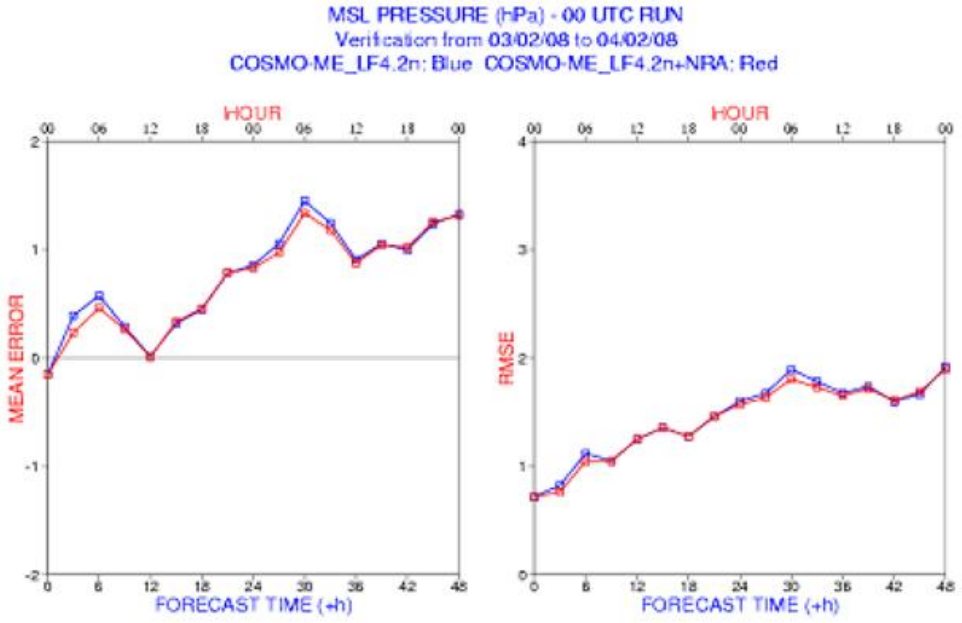


Figure 11: Slightly positive influence of the new reference atmosphere in 7 km runs.

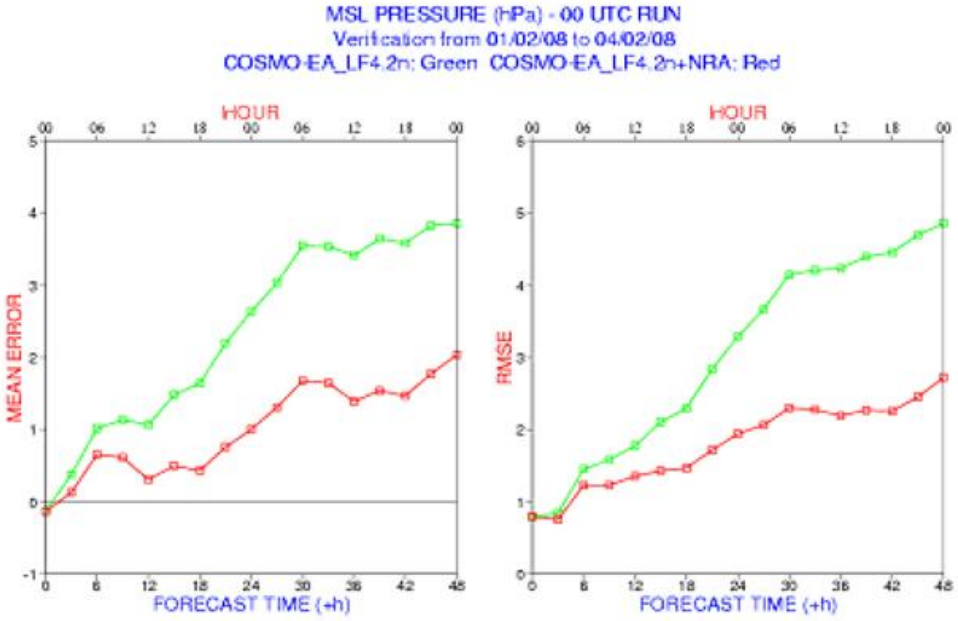


Figure 12: Bigger positive influence of the new reference atmosphere in 14 km runs.

2.2 Task 2: Continue RK case studies

The case studies done at MeteoSwiss were very closely linked with the set-up of the new model cascade which went operational on February 2008. This cascade consists of the new COSMO-7 model which is computed with a grid mesh of 6.6 km (0.06 degree resolution) and the imbedded COSMO-2 model covering the whole Alpine region which has a grid mesh of 2.2 km (0.02 degree resolution). The description of the different configuration of these 2 models can be found under:

http://www.cosmo – model.org/content/tasks/operational/default.htm

One feature is that they are both computed with the same 60 level distribution and use the Runge-Kutta dynamics. Originally it was planned to use a very fine vertical resolution (L60.1) of the planetary boundary layer, i.e. 29 levels below 2 km but operationally the level distribution of the driving model from ECMWF (IFS with 91 levels) was preferred (L60.2). This level distribution uses the bottom 43 levels directly from IFS and adapts the last levels so that the top of the model is at 23.6 km height. The bottom distribution has only 17 levels below 2 km and the level thicknesses are more or less constant (below 500 m) from the height of 5 km up to the tropopause. The problem with the very fine levels was finally solved by the work of Oliver Fuhrer with the stability analysis of the explicit vertical diffusion of TKE (see COSMO General meeting in Kracow, 2008).

2.2.1 First difficulties and their solutions

From a week's visit of Jochen Förstner (DWD) and Günther Zängl (at that time from München University) in March 2006 some interesting results were put together by the participants and are available in a separate Word report in German

ftp://ftp.cscs.ch/in/put/abc/morsier/Arbeitstreffen_Zusammenfassung.doc

Here are the main outputs:

- extra orographic smoothing, development of the lower bottom boundary conditions, and the p',T'-dynamics (see Task 6);
- the explicit lateral boundary condition helped to solve some of the unstable cases MeteoSwiss encountered but others needed extra horizontal diffusion at the lateral boundaries and just below the Rayleigh damping zone;
- use of the driving model orography at the boundaries with a smooth linear transition over 20 grid points to the high resolution orography in the inner domain (llbc_smooth in INT2LM);
- nice semi-idealized simulation of the thermal circulation in the Inn-valley.

During the whole project period many test cases were evaluated. Starting with 10 weather episodes from high precipitation MAP cases in 1999 to convective, storm and stratus cases and then to verification periods for COSMO 2.2 over the months of July to October 1995, 1997 and 1999 (COSMO-2 for WINDBANK). The encountered instabilities led to the following choices for the configuration of both COSMO 2.2 km and 6.6 km:

(see: *ftp://ftp.cscs.ch/in/put/abc/morsier/*200703*_gdm_RK_Langen.ppt*)

- the use of the SL advection of humidity variables instead of the Eulerian Bott 2nd order polynomials. These schemes are positive definite but the SL scheme uses multiplicative filling instead of clipping to achieve this property;
- the use of the standard 3rd order in time RK version instead of the more precise Total Variation Diminishing (TVD) variant which is also 3rd order in time but has less smoothing properties;
- the fixing of a bug in LM2LM in the shift of the boundary layer structure of the temperature (and horizontal winds). This helped to get the model started when downwards extrapolation into deep alpine valleys produced warm air bubbles.

2.2.2 General testing and some verification results

The choices made after the above first difficulties are still operational and the following list shows the systematic verification operated before the introduction of the 2 new models in February 2008:

(i) 6.6 km vs. 7 km

For the winter period a very slight improvement of the wind strength could be seen in the SYNOP verification over the whole domain. There were also some differences in the precipitation at the proximity of the boundaries and this also impacted on the cloud cover. But these effects were not significant.

(ii) Storm 18-20 Jan. 2007 (Kyrill)

This storm event was used to check the stability of the different numerical settings. Curiously the main differences were not seen in the wind speed but in the 2m temperature, on the total cloud cover and the precipitation. This is shown in Fig. 13.

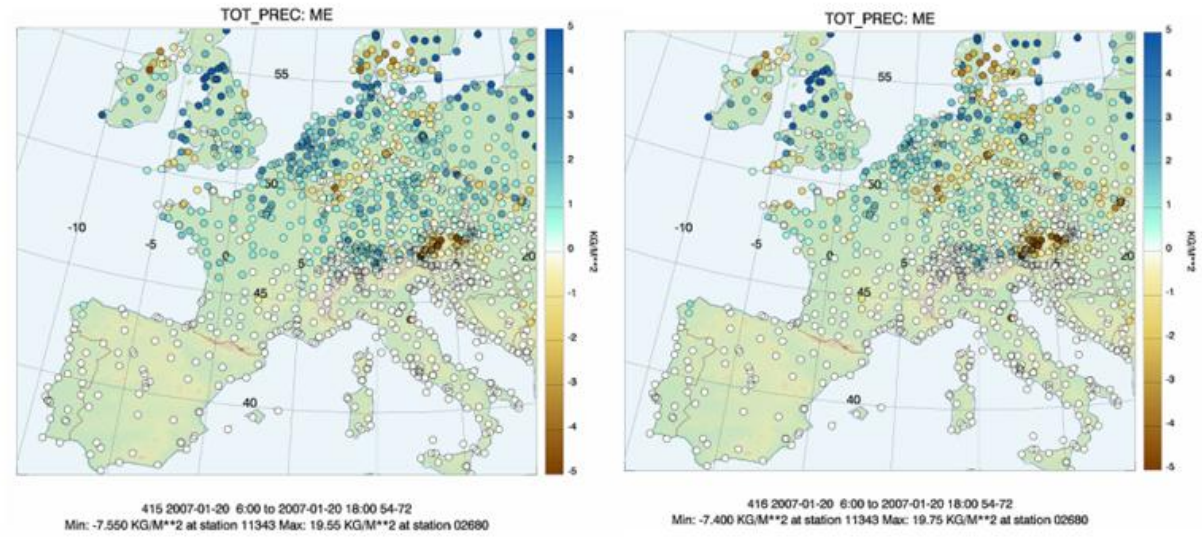


Figure 13: Kyrill precipitation in configuration COSMO 6.6L60.1 (left) and COSMO 6.6L60.2 (right).

(iii) 2.2 km, 7 km, 45 and 60 levels

These experiments were all conducted with their corresponding assimilation cycles to have the best initial and boundary conditions and to prevent differences to come from a common experiment setup. The results are illustrated with the upper-air verification in Fig. 14. There is a problem with the boundary layer of the fine 60 level version (L60.1 of version 424) and these results led to the choice of new vertical levels based on the IFS model (L60.2 of version 427) because the explicit vertical diffusion of the TKE with the very fine vertical model resolution was not stable (see Oliver Fuhrer's presentation at the General Meeting in Kracow in September 2008).

(iv) 2.2 km RK vs. 6.6 km RK vs. 7 km LF

(s3: JuneJulyAugust, s4: SeptOctNov, s1: DecJanFeb)

- S3: The differences in performance are generally small, but in a few cases, there are quite large differences. Notably the standard deviation of the surface pressure error is much decreased in COSMO-2 relatively to COSMO-7. This is probably a direct effect of the better representation of the topography in COSMO-2 and shows the limit of vertically interpolating surface pressure to the station height with a constant gradient. The smaller bias in the 2m-temperature shows that the gradient used in the vertical interpolation to the station high is not optimal. In contrast to surface pressure, using a constant gradient is not a problem, as the standard deviation confirms. Both of these effects show up in the Alpine domain because all stations are used for verification, regardless of the height difference between station and model surface. The precipitation deficit with strong precipitation in COSMO-7 is ameliorated in COSMO-2. The bias and the frequency bias of strong precipitation (> 10 mm/12h) are both much closer to their optimal value 0 and 1, respectively. For 4 different months the following Fig. 15 shows the much better performances of the Runge-Kutta scheme against the operational Leap-Frog for the same horizontal resolution of 7 km;
- S4: The pre-operational COSMO-6.6 with Runge-Kutta integration scheme generally performed about the same or slightly better than the operational COSMO-7 with Leap Frog in October 2007 and Runge-Kutta in November 2007. The exception is cloud coverage, where COSMO-6.6 has a clearly increased positive bias. Large differences are found in the precipitation, which is significantly reduced in COSMO-6.6. The positive bias in COSMO-7 is negative in COSMO-6.6 and slightly larger in absolute value. This is however mainly an effect of the few very much overestimated stations along the model boundary. The positive frequency bias for the smallest threshold (0.1 mm/12h) has decreased. For the largest threshold (10 mm/12h) however, the slight underestimation of the frequency of occurrence in COSMO-7 is amplified to a considerable underestimation in COSMO-6.6. Consequently, the probability of detection drops for this threshold by more than 5%.

(v) 6.6 km vs. 7 km RK

The pre-operational COSMO with 6.6 km resolution generally performs about the same or slightly better than the operational COSMO with 7 km grid spacing. The exception is dew point temperature, where COSMO-6.6 has an increased positive bias, but the standard deviation is still slightly smaller. A special case is the wind speed. It is notoriously underestimated at mountain tops by all COSMO versions due to the non-representativity of mountain tops for grid cell averages. The reduction in wind speed increases this negative bias, but it also decreases the positive bias at many stations in the Swiss Middleland, which is the more important aspect.

The previously found large differences in the precipitation between COSMO-7 and COSMO-6.6 have disappeared due to the fact that both versions now run with the Runge-Kutta integration scheme. Only for the large precipitation (> 10 mm/12h), COSMO-6.6 has a smaller frequency bias.

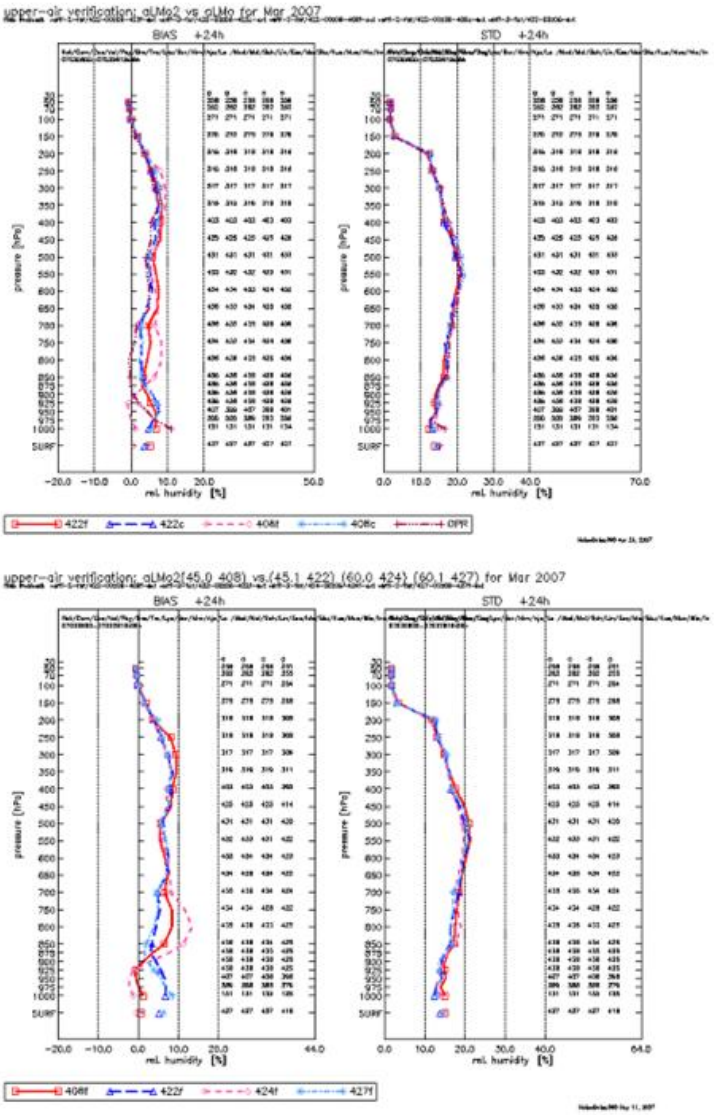


Figure 14: Upper-air (TEMP soundings) relative humidity verification (bias left and standard deviation right) of 24h forecasts in March 2007 for 5 different model versions: OPR: Leap Frog L45; 408: Runge-Kutta 7 km L45, 2 km L60.1; 422: Runge-Kutta L45; 424: Runge-Kutta L60.1; 427: Runge-Kutta L60.2. The letter "c" at the end of the experiment tags stands for coarse (7 km) and "f" for fine (2.2 km).

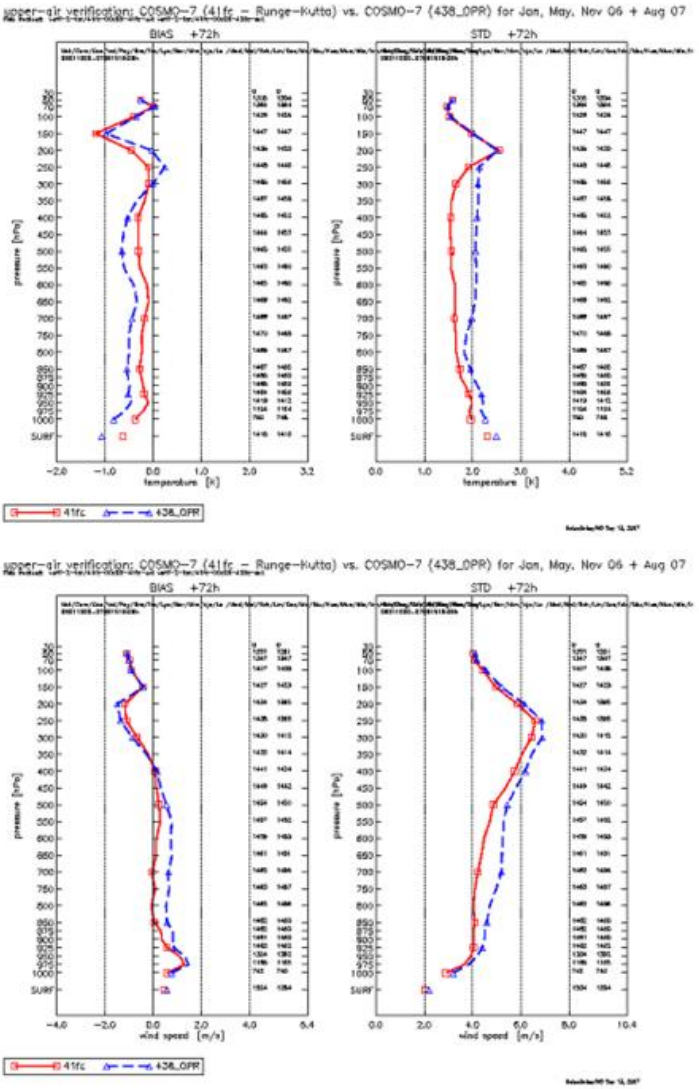


Figure 15: Upper-air (TEMP soundings) temperature (top) and wind speed (bottom) verification of 72h forecasts in Winter, Spring, Autumn 2006 and Summer 2007. The red curves are for the Runge-Kutta version and the blue curves are for Leap Frog.

2.3 Task 3: A Tool for Testing Conservation Properties in the COSMO-Model

2.3.1 Introduction

The fundamental equations of fluid mechanics, especially those used in Meteorology, can be formulated as conservation equations (or at least as balance equations) for mass, momentum and energy, as an example. Therefore a possible conservation of these variables (or others, like potential vorticity) should be obtained in a numerical model. Unfortunately this cannot be achieved in general but is guaranteed at most for a few variables in models which are formulated and also discretized in flux form. In all other cases it would be desirable to determine the strength of conservation violation. To this purpose, a tool was developed to determine budgets of arbitrary scalar variables for the COSMO-Model over an arbitrarily given cuboid volume inside of the model domain (see Fig. 16).

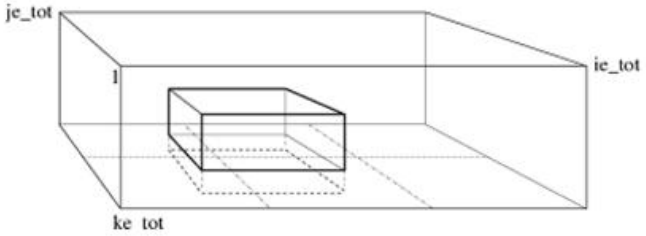


Figure 16: Integration area 'cuboid' lying in the model domain (in the transformed coordinate system). Here, a 3 * 2 domain decomposition is shown.

A general balance equation for a scalar ϕ (a generalized density) with an appropriate flux $\mathbf{f}_\phi$ reads in integral form (i.e. over a steady volume V):

$$\frac{d\Phi}{dt} + F_\Phi = Q_\Phi \tag{8}$$

total amount:

$$\Phi = \int_V \phi dv \tag{9}$$

total flux:

$$F_\Phi = \int_{\partial V} \mathbf{f}_\phi \cdot d\mathbf{A} \tag{10}$$

all sinks/sources:

$$Q_\Phi = \int_V q_\phi dv \tag{11}$$

In the case of ϕ being an integral conservative variable the right hand side of the first equation vanishes and the residuum $Res = d\Phi/dt + F_\phi$ describes the violation of conservation. Consequently, for the determination of these budgets, one has to be able to calculate volume integrals and surface integrals over fluxes in the model. The user of the 'conservation testing tool' first has to define the points in the model area which define the integration box volume (see Fig. 16). The coordinates of the corners of the cuboid imin_integ, imax_integ, jmin_integ, jmax_integ, kmin_integ, kmax_integ are read from the NAMELIST-parameter group DIACTL. In doing this the user is completely independent of any domain decomposition of the model parallelization. Secondly, one has to deliver a scalar field ϕ at the grid

position of the scalars (i, j, k) to calculate the volume integral over it. Thirdly, one has to deliver the vector field $\mathbf{f}_\phi$ whose components are defined at the grid positions of u, v, and w respectively to calculate the flux integral over the surface of the box. The details of the numerical implementation of these integrals and the subroutine calls to use the tool are described in Baldauf (2008b), section 2 and 5, respectively.

2.3.2 'Shift-test'

To test the abilities of the integration tool, a simple 'shift-test' is performed: an initial distribution is given and is simply shifted (or one could say: is transported by a perfect advection scheme) with a constant velocity through the model domain. On a discrete grid there occur some inaccuracies in the balance of this process which will lead to two artifacts. Firstly, a 'volume calculation artefact', which can arise for a transport with a non-integer Courant-number simply by a sampling error (this artefact is partly due to this artificial shift test, it cannot occur in a finite-volume schemes). Secondly, and more important, a 'flux calculation artefact' occurs due to errors in the estimation of the flux field $\mathbf{f}_\phi$ from the neighboring grid point values of ϕ. An unexpected result was that a simple upwind first order calculation is partly better than a second order centered difference or even higher order flux calculation (with or without higher order RK-time integration). However, recent studies by R. Petrik (MPI Hamburg) show that a Lax-Wendroff flux calculation seems to be the best choice. The addition of both artifacts can disturb the balance of conservation. In the tested example a relative error of the residuum of about 10^{-4} occurs. Nevertheless, the simple shift test did not show a significant programming error in the tool.

2.3.3 Weisman-Klemp test case

A first application of the integration tool was carried out with the idealized warm bubble test case (Weisman and Klemp, 1982). An ellipsoidal warm bubble serves as an initial disturbance with an increase of temperature of max $\Delta T = 2$ K. The atmosphere is in steady state at the beginning. The physics parameterizations are completely switched off, only the saturation adjustment (condensation and evaporation) is active. Therefore only water vapor q_v and cloud water q_c can occur. Further on there occur only advective fluxes $\mathbf{v}\rho_x$, but no turbulent or sedimentation fluxes. In Fig. 17 the balance of the moisture mass is shown. During the rising of the bubble (approximately the first 400 timesteps) moist air is sucked especially from the lower portions of the atmosphere. When the buoyancy is reduced, the bubble expands sidewards and blows out the moist air (timesteps 400-600). During this process the positive tendency of the mass change is not very well balanced by the negative tendency of the flux divergence (and vice versa); the residuum is rather big (Fig. 18). And therefore the relative error is about 0.7%. Therefore the question arises if this is a real error in the model or an artefact by the integration tool. Because the (conserving) Bott-advection scheme delivers very similar results, the problem seems not to be due to the Semi-Lagrange advection scheme, which was used here. The error in the total mass calculation of about 0.04% seems to be too small to explain this moisture mass change, too. Further effects of the 'flux integral artefact' could be excluded by an increase of the box volume by a factor of 2 in both x- and y-direction which does not change the residuum. This indicates, that the violation of the conservation is not induced by the inflow through the boundaries, but there seems to be a violation of conservation by the description of the physical process by the model.

A further experiment, where the the saturation adjustment was switched off showed a dras-

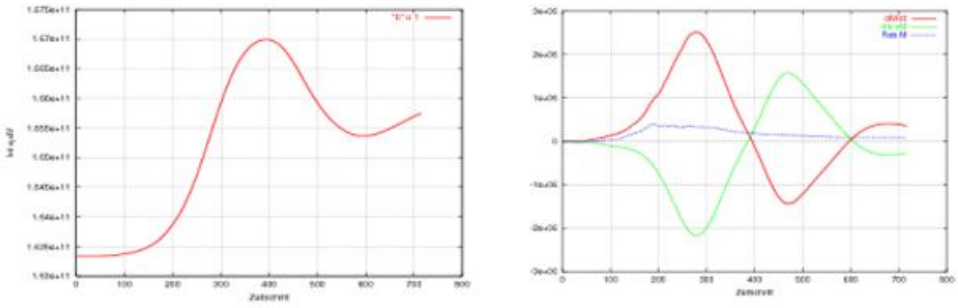


Figure 17: Weisman-Klemp-test case, density of moisture $\rho_x = \rho_v + \rho_c$, total mass of moisture (left); right: balance terms $\Delta\Phi/\Delta t$ (red), F_ϕ (green) and the residuum (blue).

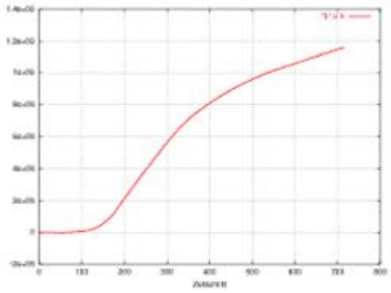


Figure 18: as Fig. 17 for the temporal integral of the residuum ΔM.

tically reduced residuum. This indicates, that the cause for the violation of conservation of moisture mass stems from the saturation adjustment. Indeed, the saturation adjustment in the COSMO-model conserves the specific mass (and specific energy) but not mass (and energy) themselves. This test serves as a first example to show in which way such a conservation testing tool can find hidden inconsistencies of the model. Although such a tool itself has some inherent, sometimes misleading properties as was discussed shortly for the 'shift-test', it can be used successfully at least in idealized simulations and can give valuable hints for the violation of conservation properties.

2.4 Task 4: Advection of moisture quantities in conservation form

This task is described in more detail and with further references in Förstner, Baldauf, and Seifert (2006). In the beginning of the development of COSMO-DE stable integration of the prognostic equations for the moisture quantities (q_x) was realized by doing two sequential Eulerian advection steps with half the time step of the dynamics to ensure Courant numbers less than one. Furthermore, to deal with the transport equations in advection form, after calculating the flux divergence the additional divergence term was subtracted, thereby destroying again the positive definiteness of the flux form advection scheme ("Flux Form - DIV"). Skamarock (2006) summarizes and presents ideas which combine several desirable properties of transport schemes used up to day. He concentrates on Eulerian schemes in flux-form and addresses splitting errors, mass conservation, Courant number restriction and positive definiteness. Following these ideas different schemes were implemented in the COSMO-DE in a Courant number independent (CRI) way. To switch to a "Conservation Form" of the equations, the specific moisture quantities are first multiplied with the air density. Then the resulting densities are transported and finally transformed back into the specific values. To do this a value for the air density, which was updated using the same advection scheme as for the moisture, is used. Since the advection is split into separate 1D steps for the different directions, a Strang-splitting approach is used to reduce the splitting error. To circumvent the Courant number restriction, the Courant number at each cell face is broken up into an integer and a remaining fractional part. While flux calculation is quite simple for the integer part only, the fractional part is dealt with a more sophisticated flux form transport scheme which is normally restricted to Courant numbers less than one. As a scheme with rather low numerical diffusion, a CRI version of Bott's (1989) positive definite advection was implemented into the COSMO-DE. The Bott scheme is realized in two variants with either second or fourth order polynomials for the calculation of the integrated (fractional) fluxes. When we compare the CPU time for a real case simulation, where advection is calculated for all six prognostic moisture variables q_v; q_c; q_i; q_r; q_s and q_g, while the fourth order version is slightly more expensive, the second order one is comparable to the semi-Lagrangian transport in this respect. All in all with the CRI version of the Bott scheme we get a high-order positive definite scheme at a reasonable computational cost. To verify the correct implementation and for comparison of the different schemes idealized advection tests were carried out with the COSMO-DE. As a first and also very common test, the solid body rotation of a tracer cone was simulated (Fig. 19). In the case shown, the angular velocity was rather high, leading to Courant numbers well above one. The schemes perform equally well, at least in two aspects: first the Courant number independence is fulfilled, since in each case we get a stable integration; second the circular shape of the cone is more or less retained, i.e. errors due to the directional splitting method used for the Bott scheme are negligible.

A tracer experiment where an almost uniform tracer distribution was transported in the flow field of a real case study clearly showed that it is not a good idea to use the "Flux Form - DIV" variant mentioned above and the "Conservation Form" of the equations is clearly to be preferred. Further details can be found in the newsletter article. The 2nd order Bott scheme is currently used for the advection of the moisture variables in the COSMO-DE. Additionally the Bott advection was tested in the COSMO-EU in a quasi operational setup. These tests were run over periods of several months. While most of the time these runs performed well and without serious deficiencies, a crash of the model could be traced back to the moisture advection. In this case the splitting error due to the splitting of the horizontal and vertical directions in combination with a very steep slope of the terrain led to this failure. Similar results were obtained at MeteoSwiss where the scheme failed in several cases due to the steep slopes in the Alpine region. It is possible to reduce the splitting error by a more complete

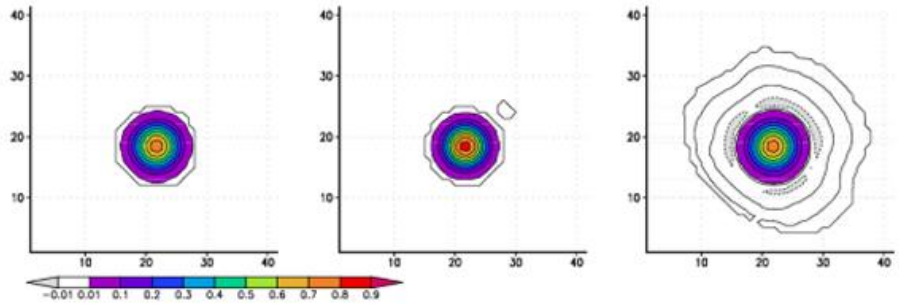


Figure 19: Solid body rotation of a tracer cone with an initial maximum of 1.0. Results after 80 time steps equivalent to one revolution. The Courant Number in the domain is close to a value of 3 near the lateral boundaries and approximately a value of 2.2 at the centre of the cone. Left: Bott (2nd order); Middle: Bott (4th order); Right: semi-Lagrange (tri-cubic).

but also more expensive (by a factor of 5/3 for the advection) form of the Strang splitting. In contrast, the semi-Lagrange advection is a multi-dimensional scheme, which needs no directional splitting and therefore proofed to be more robust in these situations. But it has the disadvantage to be a non-positive definite scheme, for which a simple clipping violates the conservation. This can be cured in a rough manner by a global acting multiplicative filling algorithm. In verifications done at CNMCA, the semi-Lagrangian scheme also gave slightly better scores for 7 km runs.

2.5 Task 5: Investigation of convergence

The aim of Task 5 is to study and analyze convergence properties of the Runge-Kutta dynamical core at high resolutions. Such properties can be inspected by considering different horizontal resolutions and a very good resolved vertical coordinate. Tests where done with:

- 2-dimensional linear mountain flows, both hydrostatic (Na/U $\gg 1$) and non-hydrostatic (Na/U ~ 1),
- 2-dimensional non-linear mountain flows (NH/U ~ 1),
- 3-dimensional mountain flows

For all mountain sizes 4 or 5 different horizontal resolutions were tested, in order to evaluate the spatial convergence of the scheme. For all cases the Brunt-Väisälä frequency N has been set equal to 0.01 Hz and the basic flow velocity U is 10 m/s. The mountain ridge has a Gaussian shape, $h(x) = Hexp[(-x^2/a^2)log2]$, where H is the mountain maximum height and a (the mountain width) is the horizontal distance from the mountain top where the height is H/2. The following results are all performed with the p'T'-dynamics. The Rayleigh damping layer starts at 11 km.

Several error measures (error norms) for the variables vertical velocity, kinetic energy, wave drag, U-momentum component were inspected:

- L0 = max $\mid F - F_{finestmesh} \mid$
- L1 = $1/N \sum \mid F - F_{finestmesh} \mid$
- L2 = $[1/N \sum (F - F_{finestmesh})^2]^{1/2}$

The reference solution in each case is a high resolution simulation on the finest mesh. The summation is performed over a subdomain containing the mountain.

The mountain wave drag will be computed by integrating the surface pressure in the x-direction.

$$D = \sum p'(x,0) dh/dx \Delta x \tag{12}$$

The vertical flow of the U- momentum component will be computed at each grid level by summing up all the cells in a grid level

$$D(z) = -\sum \rho_0(z) u'(x,z) w'(x,z) \Delta x \tag{13}$$

The values obtained will be compared, if possible, with the analytical solution (available in the linear hydrostatic case). To extract the effect of the improved horizontal discretization schemes, a very good resolved vertical coordinate Δz = 100 m was used which at least for the hydrostatic test cases should always lead to well converged solutions. There occurred some problems with the inflow and outflow boundaries, where the vertical velocity had positive values partially in the same order as the signal from the mountain (see Fig. 20, left). This error is too small to be noticeable in real-case applications; however, it becomes evident in idealized simulations with constant flow and a very low mountain (or no mountain at all). These artifacts could be reduced by initializing with the reference state, i.e. to set p'=0 and T'=0. An alternative solution for this problem was found by G. Zängl: the perturbations occur because the present initialization of the perturbation pressure field (executed in

src_artifdata for idealized simulations, otherwise in int2LM) is not exactly consistent with the discretized buoyancy term in the vertical momentum equation. To fix the problem, a new initialization procedure has been developed by solving the discretized vertical wind equation (for dw/dt = 0) for p'; ideally, this would ensure strict absence of buoyancy at the lateral model boundaries. The improvement by this measure can be seen in Fig. 20 (right).

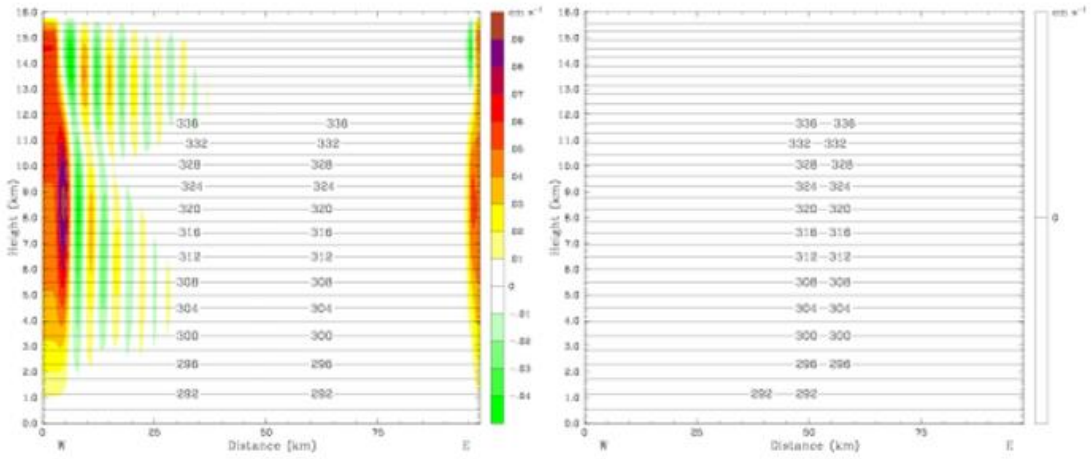


Figure 20: Comparison of the old p' initialization (left) which delivers error amplitudes of about w $\sim$ 1 mm/s and the new one (right) with error amplitudes of w $\sim 10^{-4}$ mm/s. Simulation with flat surface, u = 10m/s, and fixed relaxation b.c.'s, t = 12 h. Fields: Θ (contour interval 2 K), w (colors).

2.5.1 Hydrostatic linear mountain flow simulations

In case of a hydrostatic 2-dimensional mountain flow (mountain width a=10 km, mountain height H=10 m and U/Na=0.1), simulations have been performed with constant horizontal resolution Δx equal to 4000 m, 2000 m, 1000 m and 500 m, along either x- and y- directions ($\Delta x = \Delta y$). The extension in y-direction always covers 7 cells. The mountain ridge is located in the middle of the domain. As mentioned Δz=100 m with 195 vertical levels was set. The total simulation time is 60 h. For all the resolutions the same timestep dt=2.5 sec was used with a domain size of 500x19.5 km^2. The chosen horizontal resolutions are 4 km, 2 km, 1 km, 500 m (250 m). A comparison of L0, L1, L2 error norms for vertical velocity and kinetic energy for the two versions of the 3rd stage Runge-Kutta (TVD and 'standard') is shown in Fig. 21. The differences between the two schemes are quite small (note that for the TVD scheme the plot shows also the 250 m resolution), and only a small advantage of the 'standard' RK3 (Wicker and Skamarock, 2002) compared to the TVD-RK3 can be detected. The convergence is less than 2nd order for the resolutions simulated here, but the plots for the kinetic energy show that a nearly 2nd order convergence is approached for higher resolutions.

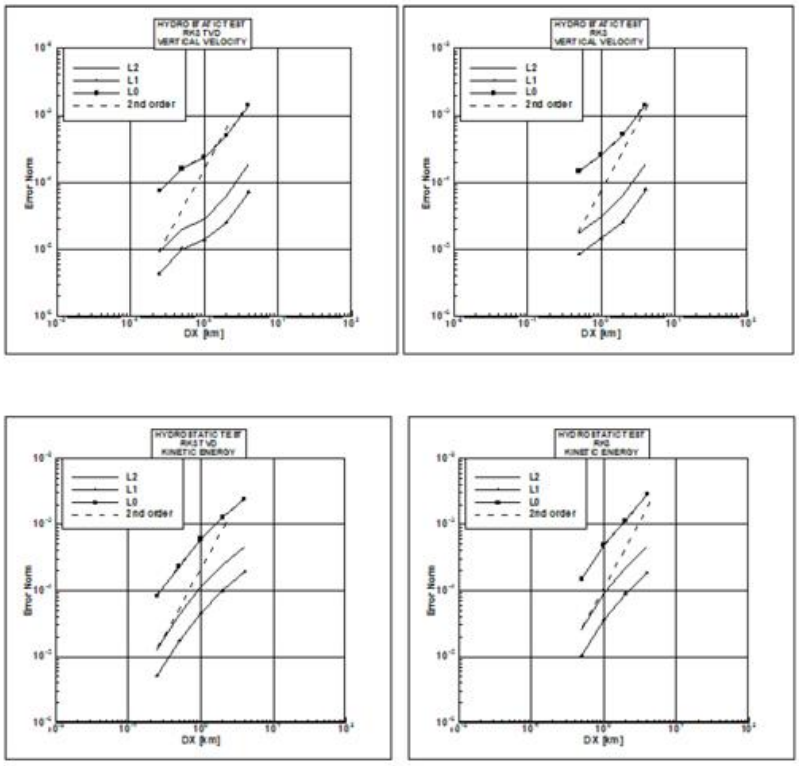


Figure 21: error norms L0, L1, L2 for vertical velocity and kinetic energy for the TVD Runge-Kutta and the standard Runge-Kutta scheme in the hydrostatic linear case. Dashed lines indicate 2nd order convergence.

2.5.2 Hydrostatic non-linear mountain flow simulations

Now the mountain has a height of H = 500 m with the same width than before (a=10 km). The simulation time had to be chosen a little bit longer to attain stationary results (Time = 100 h). Again the same time step dt = 2.5 sec has been chosen. The domain size was 500x19.5 km^2 and the horizontal resolution is 4 km, 2 km, 1 km, 500 m, (250 m). The height of the mountain was chosen in a manner that any non-stationary effect should occur. As the theory foresees, the wave breaking over a gaussian ridge takes place for NH/U>0.85 (which means H>850 m). Whereas the kinetic energy behaves completely similar for the two RK-schemes, the vertical velocity converges better in the TVD-variant.

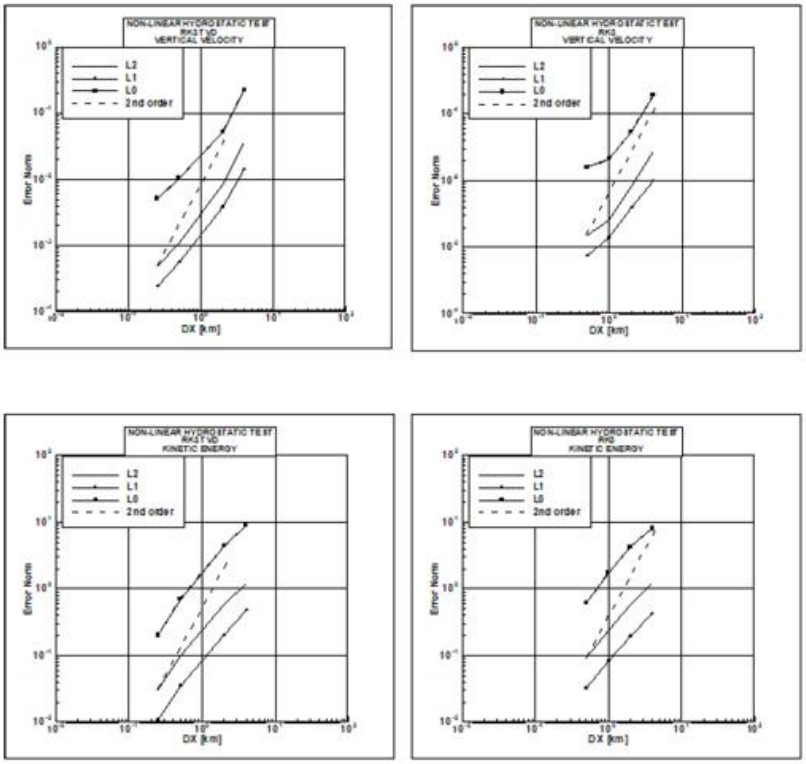


Figure 22: error norms L0, L1, L2 for vertical velocity and kinetic energy for the TVD Runge-Kutta and the standard Runge-Kutta scheme in the hydrostatic non-linear case. Dashed lines indicate 2nd order convergence.

2.5.3 Non-hydrostatic linear mountain flow simulations

In case of non-hydrostatic mountain flow (mountain width a=500 m, mountain height H=10 m which leads to U/Na=2.0), simulations with a constant horizontal resolution equal to 2000 m, 1000 m, 500 m, 250 m and 125 m ($\Delta x = \Delta y$) have been performed. Also in this case Δz has been set to 100 m and 195 vertical levels have been used. The total simulation time is 100 h, dt = 2.5 sec, and the domain size is 250x19.5 km^2; the horizontal resolutions are 1 km, 500 m, 250 m, 125 m. In this case no differences can be seen for the two RK-variants (Fig. 23 and Fig. 24).

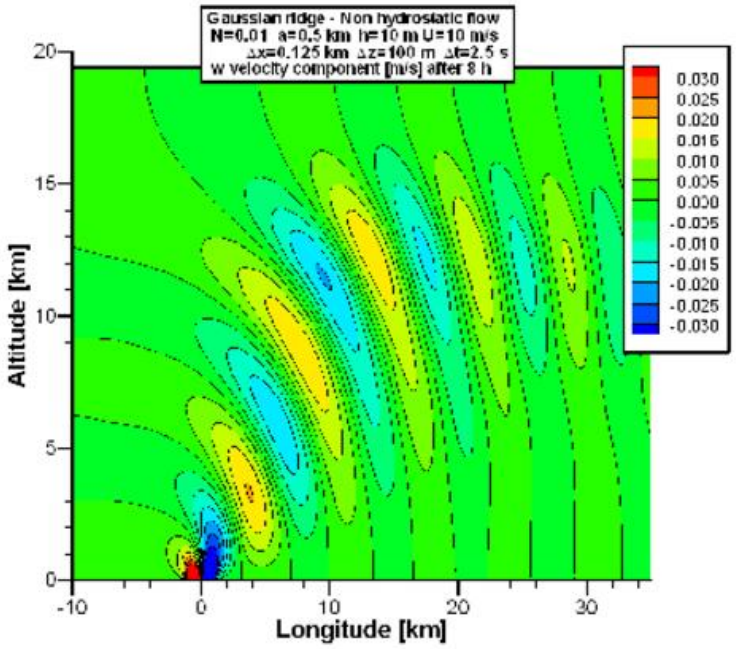


Figure 23: Non-hydrostatic flow example: vertical velocity.

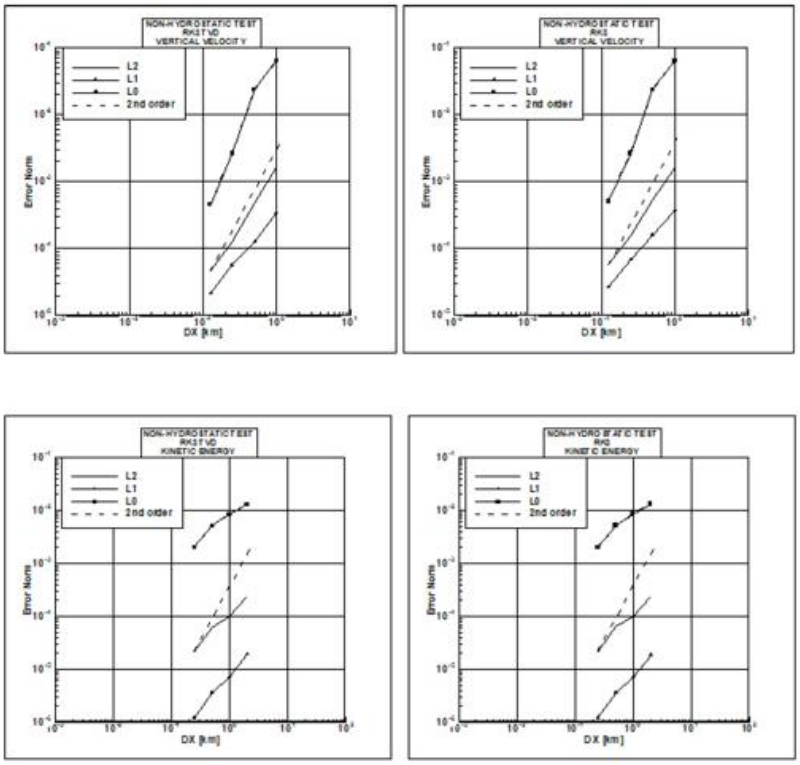


Figure 24: error norms L0, L1, L2 for vertical velocity and kinetic energy for the TVD Runge-Kutta and the standard Runge-Kutta scheme in the non-hydrostatic linear case. Dashed lines indicate 2nd order convergence.

2.5.4 3D mountain flow tests

In Gassmann (2002), chapter 5, the flow solutions obtained with different time integration schemes (Leap Frog and Runge Kutta) and resolutions for an Agnesi mountain were simulated and showed a rather different behaviour for different resolutions. The idea is to show that a similar behavior is only due to the different spatial scheme (i.e. 3rd order and 5th order upwind), and to the grid size.

In the present test case the mountain has again a gaussian shape, h=750 m, and a=10 km. It was not possible to get a steady solution for a 1500 m high mountain as in Gassmann (2002). The grid spacing ranges from 16 km to 4 km (smaller sizes up to 0.5 km were tested, but the solution does not change significantly) and the horizontal domains are 352 km x 352 km for the 16 km grid, 256 km x 256 km for the 8 km grid, 256 km x 128 km for the 4 km and smaller meshes (not shown here). Again 195 vertical levels with constant spacing of 100 m have been used. Reference dry atmosphere has been defined with constant Brunt-Väisälä frequency N=0.01 s^{-1}, ground Temperature 15 Celsius and ground pressure 10^5 Pa. Basic flow velocity U=10 m/s. Test runs were carried out for 20 hours, that is enough for disturbances traveling at 10 m/s to be advected away from the flow domain.

All the test cases have been computed with 3rd order Runge Kutta TVD time integration scheme (RK3), setting the iadv_order input parameter to 5 (that is indicated as UP5 in the pictures) and 3 (UP3 in the pictures).

In Fig. 25 something similar to Gassmann (2002), fig. 5.1 is shown, i.e. the vertical velocity component for different resolutions at the symmetry plane of the flow domain. The pictures cut away most of the Rayleigh damping layer, that starts from an altitude of 11 km and is 85 levels thick. In Fig. 26 the horizontal velocity component at the ground level is shown. The differences between the UP5 and UP3 schemes are visible. Note that in the coarsest resolution among the tests in Gassmann (2002) the grid size was about 3 times the mountain width (7 km / 2.6 km), that might explain the larger differences there.

The following conclusions from the convergence tests can be drawn:

- for 2D flows:
  - slightly less than 2nd order spatial convergence was reached. Obviously the convergence rate is dominated by the 'weakest' discretization, the fast waves scheme;
  - TVD and non-TVD 3 stages Runge Kutta show similar behaviour with slight advantages of the standard scheme in linear cases and slight advantages of TVD in non-linear cases;
  - the time step has minor effect (if any) on spatial convergence;
  - 2D flow tests are rather sensitive to a proper parameter setting for the upper and lateral boundary conditions (damping layers); fortunately these sensitivities are much less for 3D flows;
  - it was difficult to compare with analytical solutions (Baldauf, 2008c), due to boundary conditions (see below).
- for 3D flows:
  - the optimal damping parameter dt*nrdtau increases to $\sim$ 1000 s;
  - with poor resolutions different schemes can give different solutions. This is an indication that the resolutions are far from convergence. Here the higher order upwind schemes can improve the results (see Fig. 25 and Fig. 26);

– during this task, a program to calculate linear solutions for flow over mountains with very few approximations was developed. The theory behind it and implementation details are described in Baldauf (2008c). Fig. 27 shows the quite good similarity between this linear analytic solution and the COSMO-model simulation over a bell-shaped mountain with a high frequency modulation.

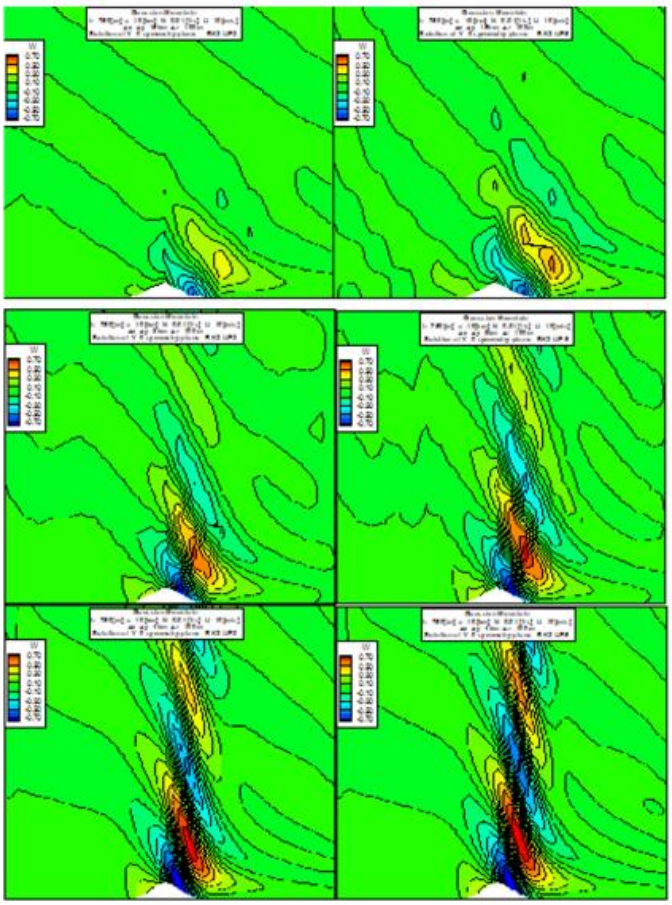


Figure 25: Velocity vertical component at the symmetry plane. On the left: solutions obtained with 3rd order upwind. On the right: solutions with 5th order upwind. From top to bottom horizontal grid spacing: 16 km, 8 km, 4 km. The horizontal size of the picture ranges from -96 km to 96 km, the vertical size from 0 to about 12.65 km.

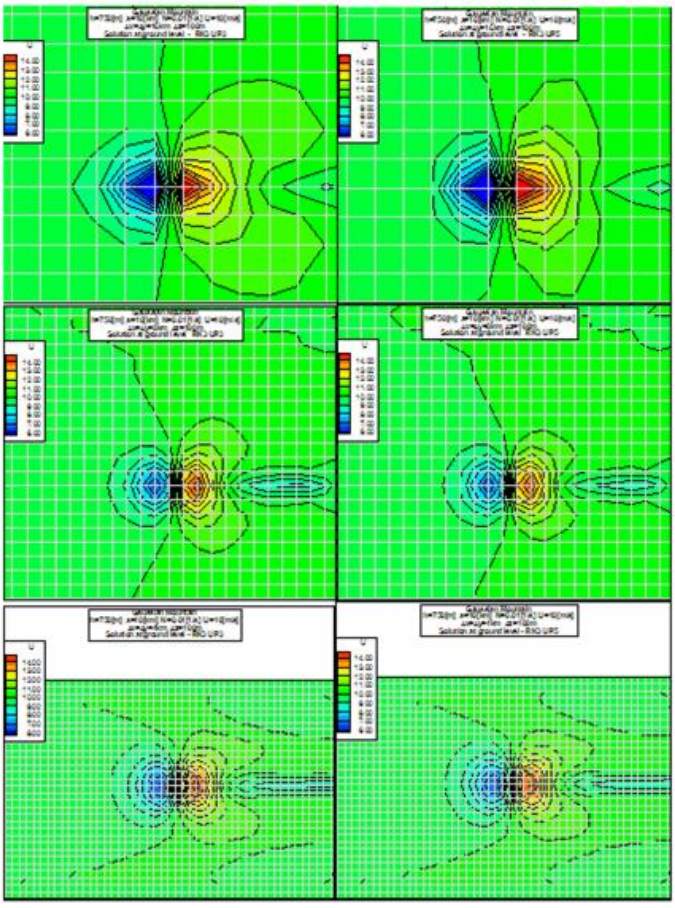


Figure 26: Velocity longitudinal component at the ground plane. On the left: solutions obtained with 3rd order upwind. On the right: solutions with 5th order upwind. From top to bottom horizontal grid spacing: 16 km, 8 km, 4 km. A gray circle (radius 10 km) indicates the mountain position.

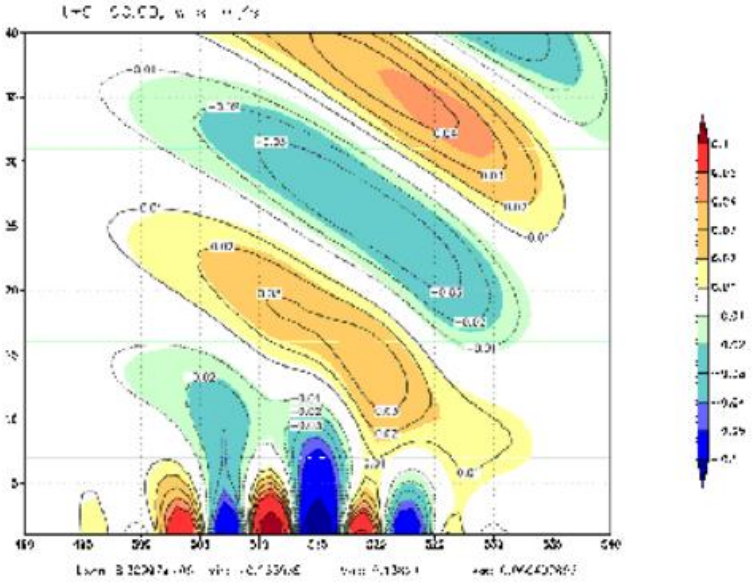


Figure 27: Comparison of the vertical velocity between COSMO-Simulation (colors) and the analytic solution (contours).

2.6 Task 6: Deep valleys + Task 7: Different filter options for orography

Task 7 is closely linked to task 6 since the filtering of orography is one measure to circumvent the problems in deep valleys. Namely the formation of unrealistic cold (or sometimes also hot) spots in the Alpine region. An example is given in Fig. 28 where on the left side a temperature plot of the Alpine region is given. In this case (3 Feb. 2005) the temperature in the first model layer reached an erroneous minimum of ≈200 K. The introduction of the "Dynamic Bottom Boundary Condition" (DYN_BBC) (Gassmann, 2004) was the key measure to circumvent the cold pool problem. This can be seen in the temperature difference plot in the right part of Fig. 28. The temperature in the run with the new bottom boundary condition is more than 70 K higher in the problematic region, i. e. no cold pool builds up. It can also be seen, that the changed BBC leads to significant changes only in the orographically structured regions. The basic equations for the DYN_BBC can be found below. For the layer right above the ground, the normal centered-difference approximation of the vertical pressure gradient term in the horizontal momentum equations ($\partial p^*/\partial\zeta$) is deteriorated. In the new formulation the momentum equations are set into the condition given in eq. 17.

$$\frac{\partial u}{\partial t} = -\frac{1}{\rho a cos\varphi}\left(\frac{\partial p^*}{\partial \lambda} + \frac{J_\lambda}{\sqrt{G}}\frac{\partial p^*}{\partial \zeta}\right) + f_u \tag{14}$$

$$\frac{\partial v}{\partial t} = -\frac{1}{\rho a}\left(\frac{\partial p^*}{\partial \varphi} + \frac{J_\varphi}{\sqrt{G}}\frac{\partial p^*}{\partial \zeta}\right) + f_v \tag{15}$$

$$\frac{\partial w}{\partial t} = \frac{1}{\rho\sqrt{G}}\frac{\partial p^*}{\partial \zeta} + g\frac{\rho_0}{\rho}\left(\frac{T - T_0}{T} - \frac{T_0 p^*}{T p_0}\right) + f_w \tag{16}$$

$$\frac{\partial \dot{\zeta}}{\partial t} = \frac{1}{\sqrt{G}}\left(\frac{1}{\rho a cos\varphi}\frac{\partial z}{\partial \lambda}\frac{\partial u}{\partial t} + \frac{1}{a}\frac{\partial z}{\partial \varphi}\frac{\partial v}{\partial t} - \frac{\partial w}{\partial t}\right) = 0 \tag{17}$$

In this way a dynamical expression for the vertical pressure gradient terms is found. The introduction of new filter options for the orography also helped to deal with the problems arising in deep valleys. A set of discrete local (i.e. applicable directly in the physical space) filters of different filter widths is used to filter the orography data. Their local nature makes it easy to combine the treatment with a local condition for the individual grid points. For the COSMO-DE first the orography is filtered globally to remove scales approximately smaller than 4Δ. In a second step a stronger filter (5Δ) is used for all points with a step of the orography still bigger than 625 m.

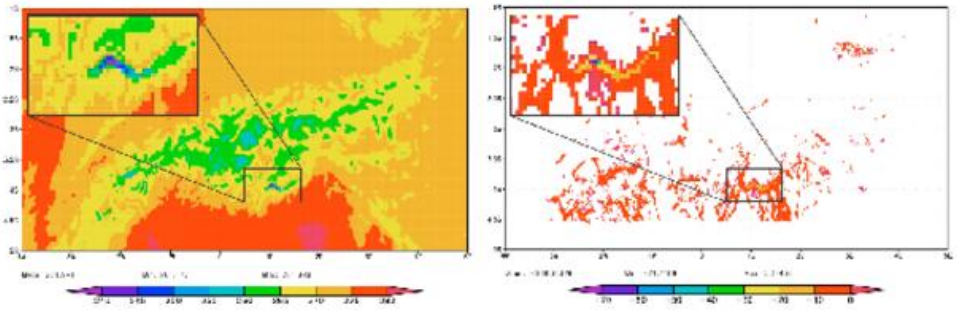


Figure 28: Left: Temperature in the lowest model layer in the Alpine region (init: 00 UTC, date: 2005020317) for a run using the old BBC. Right: Temperature difference of two runs using the old ("NO_DYN_BBC") and the new dynamic ("DYN_BBC") bottom boundary condition, i.e. "NO_DYN_BBC" - "DYN_BBC". Differences smaller 1 K are masked out.

2.7 Task 8: Higher order discretization in the vertical

For a model with increasing resolution, the vertical advection process gets increasing significance. This is the case in particular for convection resolving models with high vertical velocities and therefore a big amount of vertical transport. Due to the fact that the grid levels have a small distance in the lower part of the model, the vertical Courant numbers can reach values bigger than 1. This fact prevents the use of an explicit scheme. Indeed in the WRF model an explicit scheme is used also in the vertical. Tests with COSMO-DE (2.8 km horizontal resolution) show that a significant fraction of grid points in the model domain have vertical Courant numbers bigger than 1. To use an explicit scheme some sort of friction or simply a limitation of vertical velocities is needed. But this measure seems not adequate in a model which should not damp the resolved convection. The current model version contains an implicit scheme using centered differences 2nd order. It is absolutely stable but is not very accurate. Therefore an implicit scheme of 3rd order was implemented. It shows a better behaviour than the 2nd order scheme as can be seen in Fig. 29. But using this scheme in every Runge-Kutta step (as it is done with the 2nd order scheme) causes an increase in the overall computation time of about 30% and therefore is not ready for operational use. This amount can be hardly reduced by optimizing the scheme itself because each of the two steps, calculation of the coefficients of the 5 band diagonal equation system, and solving the linear equation system with a direct 5 band diagonal solver, takes approximately the same time.

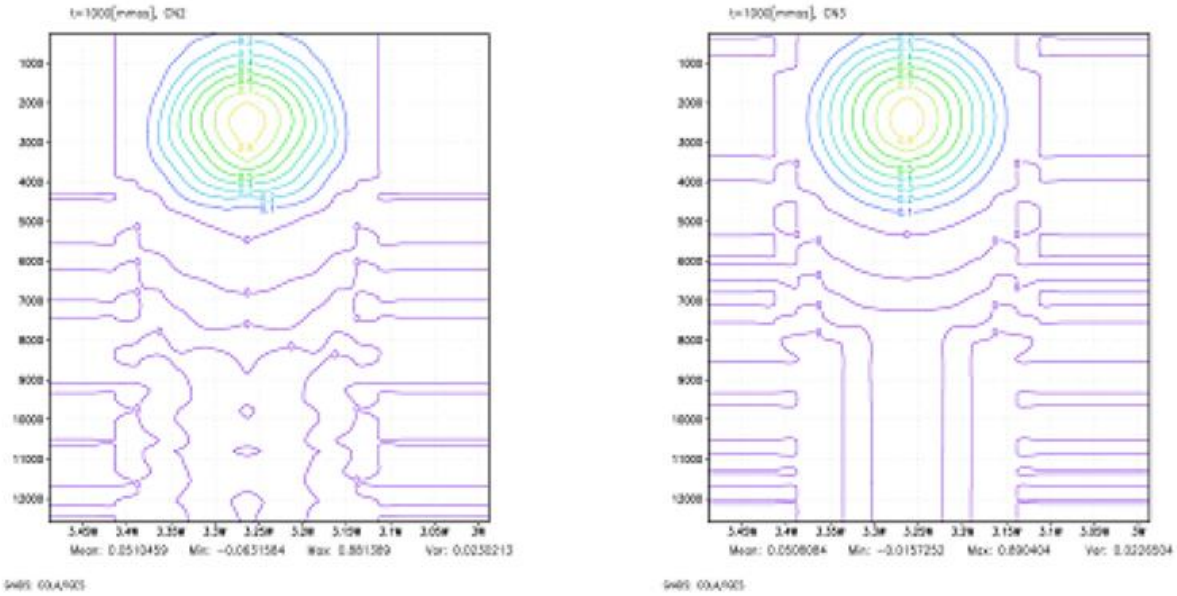


Figure 29: Implicit vertical advection; test with a constant velocity and starting with a cone distribution, 2nd order (left), 3rd order (right).

Not yet inspected is an alternative approach: the calculation of the vertical advection outside of the Runge-Kutta scheme. There are two reasons for that: first, the implicit advection needs no stabilization through the Runge-Kutta scheme, second, an implicit scheme is not very well suited for use in a Runge-Kutta substep. Questions of stability (in combination with the fast waves solver) and accuracy (splitting error) have to be inspected.

2.7.1 Addendum

Some months after finishing the Priority Project, the work on this task could be continued. The use of the implicit scheme outside of the RK-scheme leads to promising results. Pure 2D-advection tests show a strongly improved behaviour compared to the currently used scheme. The coupling with fast waves is stable and shows no significant splitting error as could be shown with linearized 2D shallow water equations. Beyond this, idealized and real test cases with the COSMO-model show a realistic behaviour of the new implicit scheme.

2.8 Task 9: Physics coupling scheme

A special procedure to couple microphysics and dynamics is described in the WRF documentation (Skamarock et al. 2005). A similar numerical treatment of latent heat is now implemented in the Runge-Kutta core of the COSMO-DE. In both models the microphysics parameterizations are calculated in one Eulerian time step after the Runge-Kutta integration of the dynamical core and the Marchuk-splitting method is used here to finally update the fields in a balanced way and complete the time step. The diabatic heating term in the prognostic equation for temperature includes the physical tendencies due to radiation, convection, turbulent mixing and latent heat conversion in the microphysics (e.g. the saturation adjustment). While the former tendencies are integrated within the acoustic steps, the last temperature tendency has not been part of this integration. The new variant uses the tendency due to latent heat conversion of the previous time step as an estimate which enters the integration of the fast waves in the same way than the other physical tendencies. After the Runge-Kutta update, this tendency estimate is subtracted again and the time step is completed as before. Tests with this new variant of coupling showed deficiencies especially in combination with the moist turbulence scheme. Especially vertical cross sections revealed 2Δz-structures of the TKE and cloud water fields. To circumvent these problems the temperature tendencies in the saturation adjustment step directly after the Runge-Kutta integration do not enter the summation of the latent heat tendencies. This could only be a preliminary solution. The reason for the mentioned problems should be studied further. Also other possibilities for the physics-dynamics coupling should be investigated.

2.9 Task 10: Testing of alternative fast wave scheme

In Gassmann (2005) a new split-explicit time integration scheme was proposed. This scheme is alternative to the Wicker-Skamarock type (1998, 2002) of splitting, which is closely related to the Runge-Kutta (RK) method. According to Gassmann this splitting method seems to have a stable and smaller splitting error compared to other existing split explicit schemes based on RK. The Gassmann scheme seems to be also more sensitive to the inconsistencies in the fast-waves terms than the RK version of Wicker and Skamarock. According to Gassmann along with this splitting method it is necessary to use the non-isotropic divergence damping and to include the vertical p*/T advection terms related to the vertical velocity w to have a consistent fast-mode solver. This implies the splitting up of vertical p*/T advection into two parts related to the two components of the contravariant vertical velocity ζ:

$$\dot{\zeta} = \dot{\xi} - \frac{1}{\sqrt{G}} w| \tag{18}$$

where

$$\dot{\xi} = \frac{1}{\sqrt{G}}(\frac{u}{acos\varphi}\frac{\partial z}{\partial \lambda} + \frac{v\partial z}{a\partial \varphi})| \tag{19}$$

the first one responsible for the actual vertical advection placed in the fast-waves solver and the second one accounting for a vertical advection component apparently present because of terrain-following coordinates involved in the slow-mode equations. A direct application of the free-slip condition is no longer possible in the p*/T slow vertical advection terms of the pressure and temperature equations. At the lower boundary the advective part of the model determines the w field:

$$w_{lowbound} = (\frac{u}{acos\varphi}\frac{\partial z}{\partial \lambda} + \frac{v\partial z}{a\partial \varphi})_{lowbound} \tag{20}$$

According to Gassmann (2006) the lower BC in this form is a slow term and it should be evaluated once per large time step and thus been held constant during the short time integration. Actually, in the slow part the full ξ=0 at the lower boundary is used (instead of ζ) in the vertical p*/T advection to avoid the evaluation of a vertical p*/T gradient which was not available in the numerical grid. A COSMO model version including the new time splitting scheme and fast-waves solver along with its documentation (Gassmann, 2006) was provided by Almut Gassmann (at that time Uni Bonn). All the tests performed with this version of code were not successful. The COSMO model crashed after a few hours of integration. Preliminary tests using the Gassmann splitting method implemented using the fast-waves solver of the RK core (without the vertical p*/T advection splitting and with the isotropic divergence damping) was successful (unofficial code) showing similar results to the default Wicker-Skamarock type RK scheme (MSLP scores are showed in Fig. 30). The above described formulation of the lower boundary condition used for the vertical p*/T advection splitting could probably be responsible for these crashes, but the issue how to formulate an appropriate lower boundary condition in this case has not been addressed.

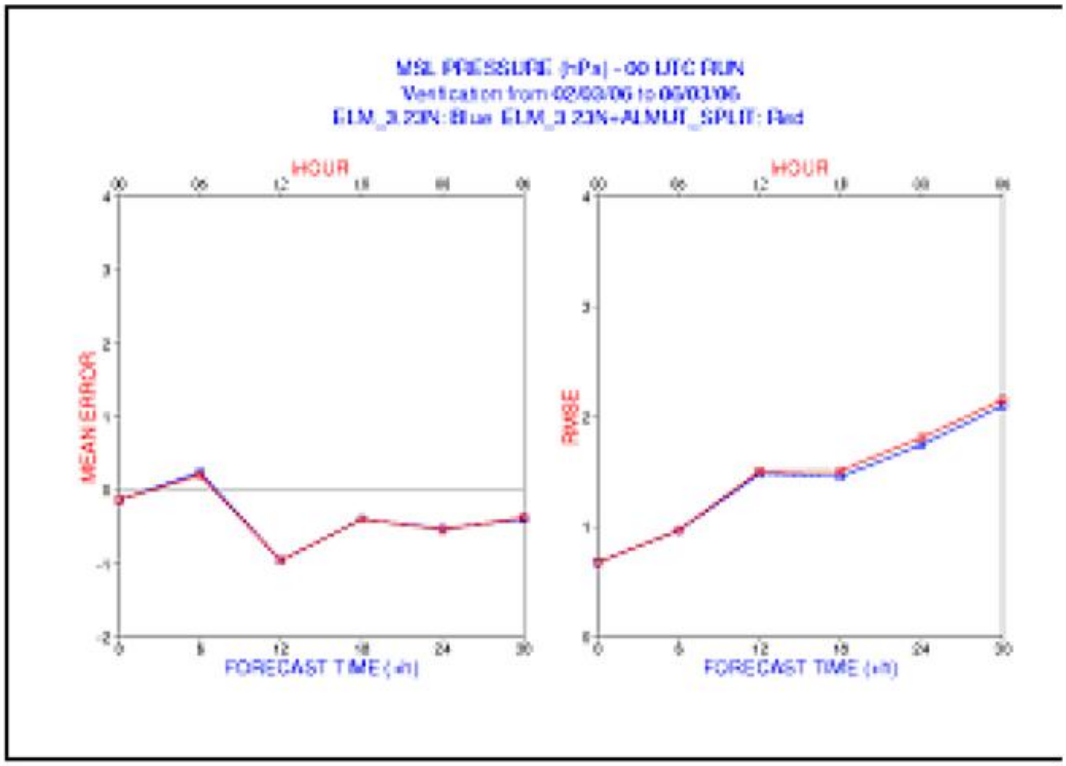


Figure 30: Comparison of pressure at MSL between the 'standard-RK' scheme and the 'Gassmann-RK'-scheme.

2.10 Task 13: Divergence damping in a true 3D-version

Cases occurred, where the up to now used 'quasi-2D' divergence filtering lead to unstable results. But a complete abandoning of the divergence filtering (as proposed by A. Gassmann for her dynamical core) also leads to several instabilities. This was also shown by stability analyzes of the RK-core by M. Baldauf. P. Prohl (DWD) could demonstrate that the Bryan-Fritsch-test case of a rising warm bubble is unstable with 'quasi-2D' divergence damping but becomes stable only with a full 3D (=isotropic) version (realized with a preliminary explicit formulation). For operational use an implicit version of 3D divergence damping is necessary. This task was defined relatively late and could not be treated during the project.

2.11 Task 14: Digital Filter Initialization (DFI)

DFI is an initialization scheme based on time filtering proposed by Lynch and McDonald (1990). The high frequencies are removed by applying a digital filter to a short time series of the prognostic model variables obtained by an integration from the initial data. The twice digital filter initialization (Lynch and Huang, 1994), implemented in COSMO model, consists of two model integrations subjected to a filter of span T: an adiabatic backward integration from 0 to -T and a diabatic forward integration from -T/2 to T/2 (see COSMO scientific documentation, part 1 for further details). The backward integration is realized by simply changing the time step Δt to $-\Delta t$. DFI did not work appropriately both in Leap-Frog (LF) and Runge-Kutta (RK) dynamical core. DFI using LF dynamics works correctly in COSMO model V3.23 with a 7 km grid spacing, after having fixed an error in the treatment of the boundary condition (dfi_initialization.f90). Some technical changes (mostly in the numerical functions of advection) were needed to run DFI using the RK core (dfi_initialization.f90, src_runge_kutta.f90, src_advection_rk.f90, fast_waves_rk.f90, numeric_utilities_rk.f90). All the odd order advection operators were changed to run in the backward model integration. The problem was that the odd order advection operators contain a dissipative term that needs a special treatment in the backward integration of the DFI. For example the 5th order horizontal advection operator is the sum of the 6th order advection operator and a dissipative term.

$$L_i^h(\phi)^{(5th)} = L_i^h(\phi)^{(6th)} + \frac{|u_i|}{60\Delta x}[-\phi_{i-3} + 6(\phi_{i-2} + \phi_{i+2}) - 15(\phi_{i-1} + \phi_{i+1}) + 20\phi_i - \phi_{i+3}] \quad (21)$$

The last term includes an absolute value of velocity and needs to be treated as the horizontal diffusion operator in the backward model run (sign of the diffusion coefficients reversed). The dissipative term of the odd order advection operators is multiplied to -1, when the integration time step is less than 0 (modifications in the next release of COSMO model). Additionally an optimization of the horizontal advection routines could be carried out by abandoning the concept of an operator acting on every grid point and using instead field operations, which can be much better optimized.

DFI using RK dynamics works well with a 7 km grid spacing after these changes. An example of the domain averaged surface pressure tendency and grid scale rain flux behaviours, as a function of the time step, are showed respectively in Fig. 31 and Fig. 32 for RK runs with (solid line) and without (dashed line) DFI. Some problems were found using RK core with a 2.8 km grid spacing. DFI worked only in some cases using the explicit version of the vertical advection.

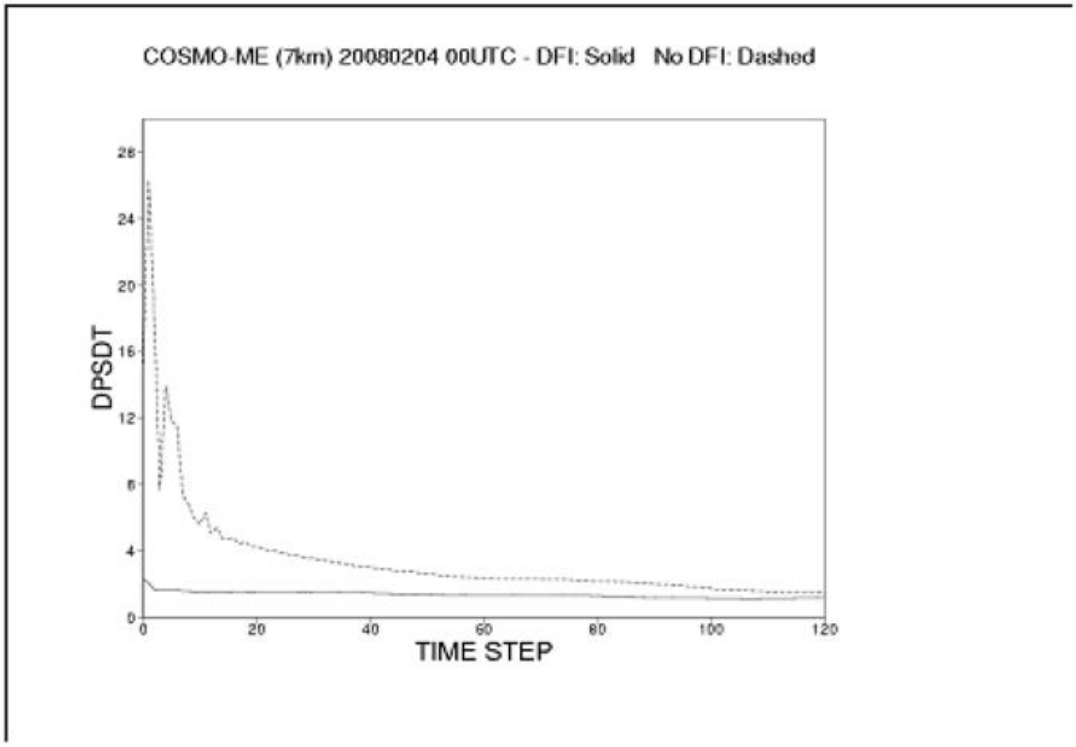


Figure 31: Domain averaged surface pressure tendency for a simulation with and without DFI.

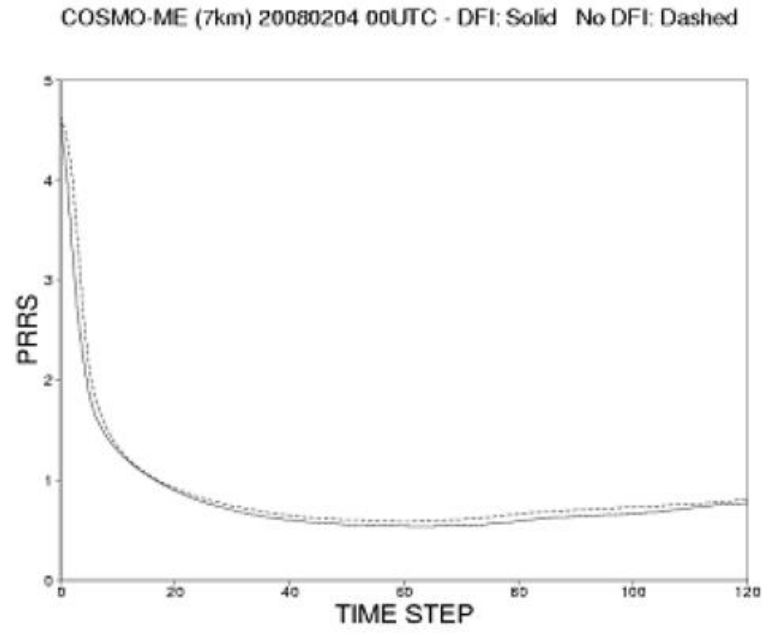


Figure 32: Grid scale rain flux for a simulation with and without DFI.

2.12 Open points

The Runge-Kutta scheme used here is adapted mainly from the WRF-model. The question that arises is if this basic scheme can be improved. A study about the stability of several combinations of Runge-Kutta schemes and horizontal advection schemes leads to only 3 useable combinations: namely RK3+upwind 3rd or 5th order and RK4 + centered difference 4th order (Baldauf, 2008a). This question was not yet inspected with the full COSMO model. Despite the fact that the pressure bias problem could be improved at least by the combination of several measures, the need of an at least mass conserving dynamical core is obvious. The problem of steep orography was solved by a slightly stronger filtering of the orography. Of course it would be more satisfying to solve this problem at the level of the discretization. Again, there is some hope to tackle this with a more conservative dynamical core (compare very interesting results with the EULAG model).

2.13 Resources used

0. Project leader	0.27
1. Looking at pressure bias	0.875
2. Continue RK case studies	0.623
3. Conservation	0.155
4. Advection of moisture quantities in conservation form	0.47
5. Investigation of convergence	0.775
6. Deep valleys	0.275
7. Different filter options for orography	0.05
8. Higher order discretization in the vertical	0.1
9. Physics coupling scheme	0.225
10. Testing of alternative fast wave scheme (Gassmann)	0.7
13. Divergence damping in a truly 3D-version	0
14. DFI corrections for RK	0.15
	sum= 4.668 FTE

2.14 Lessons learned

In this project people or rather small working groups from at least 4 different locations contributed to this project. Of course, it is not easy to communicate the relevant information among such different groups. During the project, the management instruments changed rather quickly (different forms of Excel-sheets, different web-based tools). During a project a more consistent reporting philosophy is certainly helpful. And, of course, only the most important reporting should be required.

3 Acknowledgements

List of contributing scientists during the whole project lifetime (in alphabetical order):

- Michael Baldauf (Deutscher Wetterdienst (DWD), Germany)
- Gabriella Ceci (Centro Italiano Ricerche Aerospaziali (CIRA), Italy)
- Jochen Förstner (Deutscher Wetterdienst (DWD), Germany)

- Oliver Fuhrer (MeteoSchweiz, Switzerland)
- Almut Gassmann (Max-Planck-Insitut, Hamburg, Germany)
- Hans-Joachim Herzog (Deutscher Wetterdienst (DWD), Germany)
- Guy de Morsier (MeteoSchweiz, Switzerland)
- Thorsten Reinhardt (Universität Köln, Germany)
- Gdaly Rivin (Federal Service for Hydrometeorology and Environmental Monitoring, Russia)
- Lucio Torrisi (Centro Nazionale di Meteorologia e Climatologia Aeronautica (CNMCA), Italy)
- Pier Luigi Vitagliano (Centro Italiano Ricerche Aerospaziali (CIRA), Italy)
- Günther Zängl (Deutscher Wetterdienst (DWD), Germany)

4 References

M. Baldauf (2008a): Stability analysis for linear discretization of the advection equation with Runge-Kutta time integration, J. Comput. Phys. 227, 6638-6659.

M. Baldauf (2008b): A Tool for Testing Conservation Properties in the COSMO-Model . COSMO-Newsletter No. 7.

M. Baldauf (2008c): A linear solution for flow over mountains and its comparison with the COSMO model, COSMO-Newsletter No. 9.

A. Bott (1989): A Positive Definite Advection Scheme obtained by Nonlinear Renormalization of the Advective Fluxes, Mon. Wea. Rev. 117/5, 1006-1015.

J. Förstner, M. Baldauf, A. Seifert (2006), Courant Number Independent Advection of the Moisture Quantities for the LMK, COSMO-Newsletter No. 6.

A. Gassmann (2002): Numerische Verfahren in der nichthydrostatischen Modellierung und ihr Einfluss auf die Güte der Niederschlagsvorhersage, PhD-Thesis, Berichte des Deutschen Wetterdienstes, Offenbach.

A. Gassmann (2004): Formulation of the LM's dynamical lower boundary condition, COSMO-Newsletter No. 4.

A. Gassmann, H.-J. Herzog (2006): Internal report, DWD, Offenbach.

J. B. Klemp, R. B. Wilhelmson (1978): The Simulation of Three-Dimensional Convective Storm Dynamics, J. Atmos. Sci. 35, 1070-1096.

P. Lynch, A. McDonald, 1990: A multi-level limited area slow equation model: application to initialization. Q. J. Roy. Met. Soc., 116, 595-609.

P. Lynch, X.-Y. Huang, 1994: Diabatic initialization using recursive filters. Tellus, 46A, 583-597.

W. C. Skamarock, J. B. Klemp, J. Dudhia, D. O. Gill, D. M. Barker, W. Wang, J. G. Powers (2005): A Description of the Advanced Research WRF Version 2, NCAR Technical Note, NCAR, Boulder, Colorado, USA.

W. C. Skamarock (2006): Positive-definite and Monotonic Limiters for Unrestricted-Time-Step Transport Schemes, Mon. Wea. Rev. 134, 2241-2250.

L. Torrisi (2005): Impact of Domain Size on LM Forecast, COSMO-Newsletter No. 5.

M. L. Weisman, J. B. Klemp, (1982): The dependence on numerically simulated convective storms on vertical wind shear and buoyancy. Mon. Wea. Rev., 110, 504-520.

L. J. Wicker, W. C. Skamarock (1998): A Time-Splitting Scheme for the Elastic Equations incorporating Second-Order Runge-Kutta Time Differencing, Mon. Wea. Rev. 126, 1992-1999.

L. J. Wicker, W. C. Skamarock (2002): Time Splitting Methods for Elastic Models using Forward Time Schemes, Mon. Wea. Rev. 130, 2088-2097.

List of COSMO Newsletters and Technical Reports

(available for download from the COSMO Website: www.cosmo-model.org)

COSMO Newsletters

No. 1: February 2001.

No. 2: February 2002.

No. 3: February 2003.

No. 4: February 2004.

No. 5: April 2005.

No. 6: July 2006.

No. 7: April 2008; Proceedings from the 8th COSMO General Meeting in Bucharest, 2006.

No. 8: September 2008; Proceedings from the 9th COSMO General Meeting in Athens, 2007.

No. 9: December 2008.

COSMO Technical Reports

No. 1: Dmitrii Mironov and Matthias Raschendorfer (2001):
Evaluation of Empirical Parameters of the New LM Surface-Layer Parameterization Scheme. Results from Numerical Experiments Including the Soil Moisture Analysis.

No. 2: Reinhold Schrodin and Erdmann Heise (2001):
The Multi-Layer Version of the DWD Soil Model TERRA_LM.

No. 3: Günther Doms (2001):
A Scheme for Monotonic Numerical Diffusion in the LM.

No. 4: Hans-Joachim Herzog, Ursula Schubert, Gerd Vogel, Adelheid Fiedler and Roswitha Kirchner (2002):
LLM ¯ the High-Resolving Nonhydrostatic Simulation Model in the DWD-Project LITFASS.
Part I: Modelling Technique and Simulation Method.

No. 5: Jean-Marie Bettems (2002):
EUCOS Impact Study Using the Limited-Area Non-Hydrostatic NWP Model in Operational Use at MeteoSwiss.

No. 6: Heinz-Werner Bitzer and Jürgen Steppeler (2004):
Documentation of the Z-Coordinate Dynamical Core of LM.

No. 7: Hans-Joachim Herzog, Almut Gassmann (2005):
Lorenz- and Charney-Phillips vertical grid experimentation using a compressible nonhydrostatic toy-model relevant to the fast-mode part of the 'Lokal-Modell'

No. 8: Chiara Marsigli, Andrea Montani, Tiziana Paccagnella, Davide Sacchetti, André Walser, Marco Arpagaus, Thomas Schumann (2005):
Evaluation of the Performance of the COSMO-LEPS System

No. 9: Erdmann Heise, Bodo Ritter, Reinhold Schrodin (2006):
Operational Implementation of the Multilayer Soil Model

No. 10: M.D. Tsyrulnikov (2007):
Is the particle filtering approach appropriate for meso-scale data assimilation ?

No. 11: Dmitrii V. Mironov (2008):
Parameterization of Lakes in Numerical Weather Prediction. Description of a Lake Model.

No. 12: Adriano Raspanti (2009):
COSMO Priority Project "VERification System Unified Survey" (VERSUS): Final Report

No. 13: Chiara Marsigli (2009):
COSMO Priority Project "Short Range Ensemble Prediction System" (SREPS): Final Report

No. 14: Michael Baldauf (2009):
COSMO Priority Project "Further Developments of the Runge-Kutta Time Integration Scheme" (RK): Final Report

COSMO Technical Reports

Issues of the COSMO Technical Reports series are published by the *COnsortium for Small-scale MOdelling* at non-regular intervals. COSMO is a European group for numerical weather prediction with participating meteorological services from Germany (DWD, AWGeophys), Greece (HNMS), Italy (USAM, ARPA-SIMC, ARPA Piemonte), Switzerland (MeteoSwiss), Poland (IMGW) and Romania (NMA). The general goal is to develop, improve and maintain a non-hydrostatic limited area modelling system to be used for both operational and research applications by the members of COSMO. This system is initially based on the COSMO-Model (previously known as LM) of DWD with its corresponding data assimilation system.

The Technical Reports are intended

- for scientific contributions and a documentation of research activities,
- to present and discuss results obtained from the model system,
- to present and discuss verification results and interpretation methods,
- for a documentation of technical changes to the model system,
- to give an overview of new components of the model system.

The purpose of these reports is to communicate results, changes and progress related to the LM model system relatively fast within the COSMO consortium, and also to inform other NWP groups on our current research activities. In this way the discussion on a specific topic can be stimulated at an early stage. In order to publish a report very soon after the completion of the manuscript, we have decided to omit a thorough reviewing procedure and only a rough check is done by the editors and a third reviewer. We apologize for typographical and other errors or inconsistencies which may still be present.

At present, the Technical Reports are available for download from the COSMO web site (www.cosmo-model.org). If required, the member meteorological centres can produce hard-copies by their own for distribution within their service. All members of the consortium will be informed about new issues by email.

For any comments and questions, please contact the editors:

Massimo Milelli
Massimo.Milelli@arpa.piemonte.it

Ulrich Schättler
Ulrich.Schaettler@dwd.de

Consortium

for

Small-Scale Modelling

Technical Report No. 16

COSMO Priority Project "INTERP": Final Report

December 2009

DOI: 10.5676/DWD_pub/nwv/cosmo-tr_16

Deutscher Wetterdienst

MeteoSwiss

Ufficio Generale Spazio Aereo e Meteorologia

ΕΘΝΙΚΗ ΜΕΤΕΩΡΟΛΟΓΙΚΗ ΥΠΗΡΕΣΙΑ

Instytucie Meteorogii i Gospodarki Wodnej

Administratia Nationala de Meteorologie

Agenzia Regionale per la Protezione Ambientale del Piemonte

Agenzia Regionale per la Protezione Ambientale dell' Emilia-Romagna: Servizio Idro-Meteo-Clima

Centro Italiano Ricerche Aerospaziali

Amt für GeoInformationswesen der Bundeswehr

www.cosmo-model.org

Editor: Massimo Milelli, ARPA Piemonte
Printed at Deutscher Wetterdienst, P.O. Box 100465, 63004 Offenbach am Main

COSMO Priority Project "INTERP": Final Report

Pierre Eckert

Pierre Eckert
MeteoSwiss
Geneva
Switzerland

Contents

1 Summary 4

2 General introduction 4

3 Fuzzy verification: theoretical aspects and application during the MAP D-PHASE DOP (T. Weusthoff, T. Bähler, F. Ament, MeteoSwiss) 6

3.1 Introduction . . . 6

3.2 Test bed . . . 8

3.2.1 Set-Up . . . 8

3.2.2 Perturbations and expected response . . . 8

3.2.3 Results of Sensitivity Studies . . . 9

3.2.4 Conclusions . . . 10

3.3 Application during the D-PHASE operations period (DOP) . . . 11

3.3.1 D-PHASE - Settings . . . 11

3.3.2 Results . . . 12

3.3.3 Conclusions and Outlook . . . 13

4 Verification of DWD-models against high resolution precipitation and SYNOP measurements (U. Damrath, DWD) 15

4.1 Introduction . . . 15

4.2 Methods . . . 15

4.3 Data . . . 15

4.4 Results . . . 16

4.5 Summary . . . 20

5 Post-processing of COSMO-7 and COSMO-2 Precipitation with the Neighborhood Method (P. Kaufmann, MeteoSwiss) 22

5.1 Introduction . . . 22

5.2 Optimizing the neighborhood . . . 22

5.2.1 Method . . . 22

5.2.2 Spatial radius of neighborhood . . . 22

5.2.3 Shape of the neighborhood . . . 22

5.2.4 Linearly fading weights . . . 23

5.2.5 Temporal radius . . . 25

5.3 Examples of products . . . 25

5.3.1 COSMO-7, threshold 25 mm / 6h 25
5.3.2 COSMO-2, threshold 25 mm / 6h 25
5.3.3 COSMO-7, threshold 50 mm / 24h 26
5.4 Conclusions and Outlook 26

6 Statistical properties of precipitation in boxes of various sizes (M. S. Tesini, C. Cacciamani, T. Paccagnella, ARPA-SIMC). 28

7 Open points 31

8 Contributing scientists 31

9 References 31

Project report

1 Summary

The project had the goal to explore various ways to verify very high resolution models taking into account the fact that this kind of model are not to be looked at one gridpoint, at least not for precipitation, on which the project finally focussed on. We explored methods which allow building statistics out of the distribution of values surrounding a gridpoint. These methods are commonly called fuzzy verification. Applying the various methods onto idealized precipitation patterns, upscaling and the fraction skill score were kept for their adequate properties. This is shown in Section 3. Verifications have then been carried out on different regions and seasons with the Swiss COSMO-2 (2.2 km) and the German COSMO-DE (2.8 km). It turns out that the useful scales of these models are situated between 30 and 50 km. This value can even be higher depending on the considered precipitation threshold. The verification scores of very high resolution models are however better than the corresponding high resolution models COSMO-7 and COSMO-EU which have a grid spacing of ≈ 7 km. Sections 3 and 4 show details on these facts. Optimal verification methods should lead to corresponding products. Upscaling is quite commonly used by building averages of precipitation around gridpoints or over hydrological catchments. A product linked to the fraction skill score is provided by the neighborhood method in which probabilities are built out of the distribution of precipitation included in a spatial and temporal neighborhood of an observation point. Optimization of the method and examples are shown in Section 5. It is also interesting to compare the distribution functions of both the observed and the modelled precipitation contained in boxes of 100 km x 100 km. Global models are clearly unable to reproduce the tails of the distributions while high resolution models behave better although not perfectly. This leaves possibilities to use higher moments of the distribution function like for instance some quantiles, or to calibrate the distribution as done with EPS. This work is exposed in Section 6.

2 General introduction

The project had the goal to investigate advanced postprocessing methods, including hydrological applications, but it soon appeared that the most challenging postprocessing was the one consisting of extracting pertinent information from the very variable fields provided by very high resolution models (1-3 km), in particular for precipitation. This report will thus target on the scale dependency of the precipitation verification. In very high resolution models (1-3 km), the precipitation fields show usually a lot of variability. Although not positioned at the right position at the right time, the structures are often more realistic than those given by high resolution models (5-10 km). Typical images are shown in Fig. 1.

Clearly, the forecasts that can be generated by these two forecasts will differ, the probability of exceeding some small threshold being smaller in the 2 km case. Even if one can argue that the 2 km forecast is more useful than the 7 km forecast, the classical verification scores will be smaller for the very high resolution model when looking at the grid scale (this is often referred to as the double penalty effect). Therefore, methods have been developed for extracting the information out of boxes of growing sizes. These so called fuzzy verification methods are described in various papers (non exhaustive list): Contiguous Rain Area (Ebert and McBride, 2000), Neighborhood method (Theis et al. 2005), Fraction skill score (Roberts 2005), Intensity scale technique (Casati et al. 2004, Mittermaier 2006). Other references can

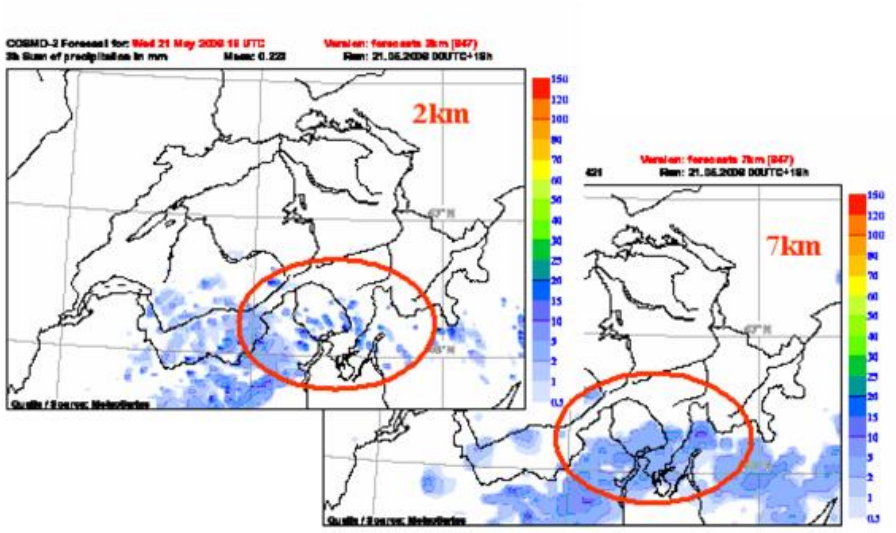


Figure 1: Example of precipitation field.

be found in Section 9. The generic behavior of such verifications has been sketched by N. Roberts (Fig. 2).

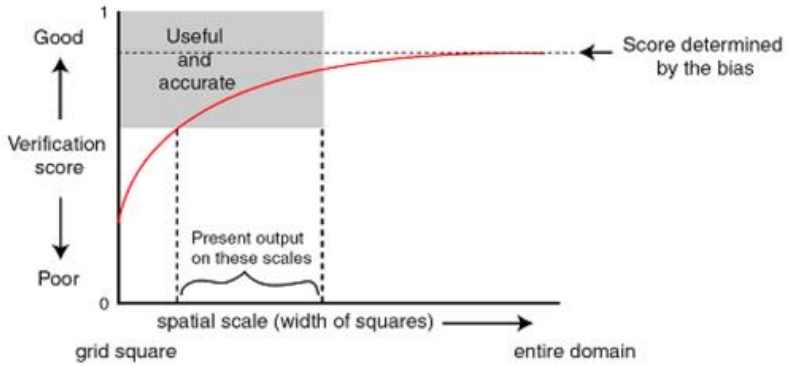


Figure 2: Generic behavior of verification.

The goal of the present project was to find out the highlighted "useful and accurate" scale. Of course, the other interesting question is to know if at this scale the very high resolution models show better scores than high resolution models. The scale dependency has been looked at from four different points of view which are reproduced in the following chapters:

- Fuzzy verification: theoretical aspects and application during the MAP D-PHASE DOP, by T. Bähler, F. Ament, T. Weusthoff
- Verification of DWD-models against high resolution precipitation and SYNOP measurements, by U. Damrath
- Post-processing of COSMO-7 and COSMO-2 Precipitation with the Neighborhood Method, by P. Kaufmann
- Statistical properties of precipitation in boxes of various sizes, by M. S. Tesini, C. Cacciamani, T. Paccagnella.

3 Fuzzy verification: theoretical aspects and application during the MAP D-PHASE DOP (T. Weusthoff, T. Bähler, F. Ament, MeteoSwiss)

3.1 Introduction

High resolution numerical weather forecast models are often punished when evaluated by traditional scores, which are based on a point wise comparison of observation and forecast. Although the structure of the observation may seem well forecasted by a high resolution model, a standard score may reveal a bad score due to e.g. spatial discrepancies. The coarser resolution model which cannot resolve the small-scale structure may in such a case get better scores although the subjective impression tells us different. However, so-called fuzzy verification methods try to avoid that problem by evaluating the forecast within a window around the region of interest. The forecast is hereby evaluated on increasing spatial scales by moving window domains of various sizes over the verification domain. The result is then presented as a function of spatial scale and threshold (see Fig. 3).

A variety of methods proposed by different authors can be allocated to "fuzzy verification", like those listed in Tab. 1. They are compiled by E.E. Ebert in form of a fuzzy verification toolbox - the IDL code can be downloaded from her webpage:
http://www.bom.gov.au/bmrc/wefor/staff/eee/beth_ebert.htm.

The different verification methods are in a first instance evaluated by means of idealized test cases. This way, three methods are identified to be well suited for the purpose of high resolution precipitation forecast. Those methods, namely the Fraction Skill Score, Upscaling and Intensity Scale, are then employed for the verification of precipitation forecasts of the Swiss COSMO models during the D-PHASE operations period.

Table 1: List of methods from the fuzzy verification toolbox (Ebert, 2008) which were evaluated by means of the test bed approach.

Acronym	**Method**	**Score**	**Decision model for useful forecast**
UP	Upscaling (Zepeda-Arce et al., 2000; Weygandt et al. 2004)	ETS	Resembles observation when averaged to coarser scales.
YN, MC	Anywhere in Window, 50% Coverage (Damrath, 2004)	ETS	Predicts event over minimum fraction of region.
FZ	Fuzzy logic (Damrath, 2004)	ETS	More correct than incorrect.
JP	Joint probability (Ebert, 2002)	ETS	More correct than incorrect.
ME	Multi-event contingency table (Atger, 2001)	HK	Predicts at least one event close to observed event.
IS	Intensity scale (Casati et al., 2004)	SS	Lower error than random arrangement of observations.
FB	Fractions skill score (Roberts and Lean, 2007)	FSS	Similar frequency of forecast and observed events.
PG	Pragmatic approach (Theis et al., 2005)	BS	Resembles forecast based on perfect knowledge of observations.
PP	Practically perfect hindcast (Brooks et al., 1998)	ETS ratio	Can distinguish events and non-events.
CS	Conditional square root of RPS (Germann and Zawadzki, 2004)	CSRR	High probability of matching observed value.
RM	Area-related RMSE (Rezacova et al., 2007)	RMSE	Similar intensity distribution as observed.

3.2 Test bed

3.2.1 Set-Up

The fuzzy verification package of E.E. Ebert contains a large number of methods and scores which are applicable for different purposes. In order to determine which of the available verification methods are suitable for verification of high resolution precipitation forecasts, the methods were tested in an idealized case study. A test bed was set up as follows (Fig. 3): a synthetically generated field that reflects a precipitation field containing simplified convective rain cells is modified by a perturbation generator which induces several known and assessable errors on that field. For each perturbation the resulting field was verified against the initial synthetic field by means of the fuzzy verification toolbox. In addition to that, the initial field was verified against itself, which represents a perfect forecast and should result in perfect scores. The observed response to the perturbations is then compared to the expected behavior. The sensitivity of the different methods and their cross-redundancy was determined. Working with a synthetic field - instead of radar data - provides the advantage of a simplified field with easier appreciation of the induced errors. However, the whole procedure was repeated with real radar data as will be presented in an upcoming publication. The results for the idealized cases are presented in the next section.

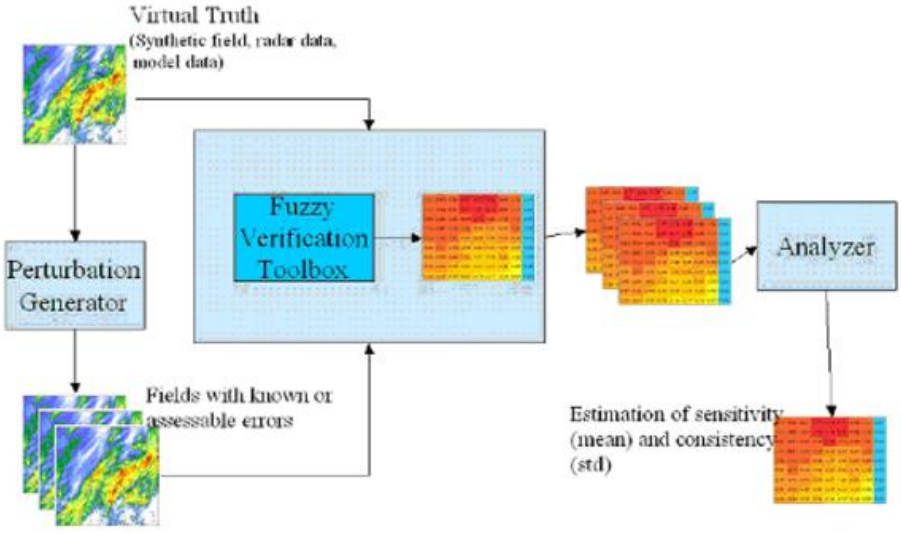


Figure 3: Test bed setup for the evaluation of fuzzy verification methods.

3.2.2 Perturbations and expected response

The synthetic field was perturbed by different perturbations for which a specific response was expected and additionally verified against itself ("perfect forecast"). Five types of perturbations are applied:

- XSHIFT - horizontal translation (10 gridpoints)
- BROWNIAN - no small scale

- LS_NOISE - wrong large scale forcing
- SMOOTH - high horizontal diffusion
- DRIZZLE - overestimation of low intensity precipitation

The appearance of the perturbations to the idealized precipitation fields is displayed in Fig. 4, while the expected response to each perturbation is shown in Fig. 5. Here, red boxes indicate scales where any sensitivity to the respective perturbation is expected, while blue boxes denote the scales for which no response is assumed.

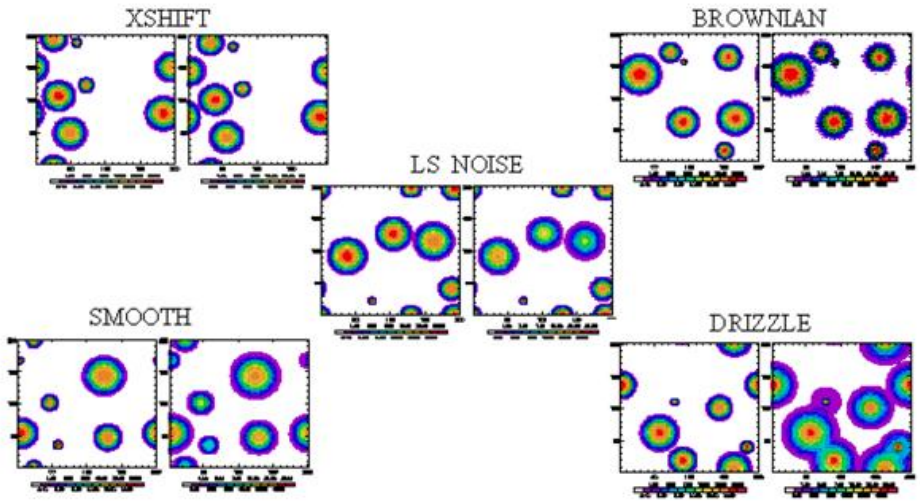


Figure 4: Perturbations on the synthetically precipitation field.

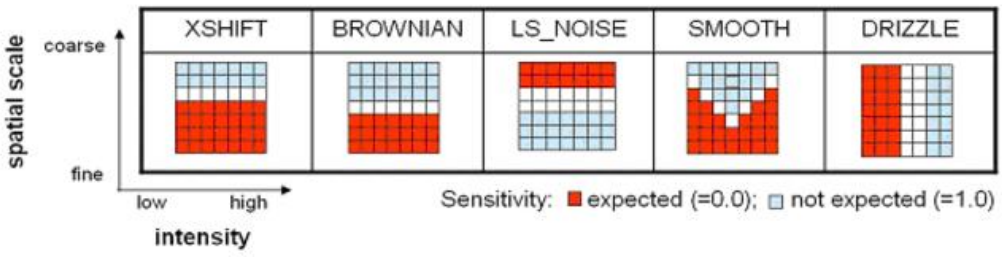


Figure 5: Expected response to the perturbations. Red boxes indicate that a response is expected on these scales why blue boxes indicate scales where no sensitivity to the perturbation is expected. When applying XSHIFT, for example, the verification results are expected to be sensitive for small scales and all thresholds.

3.2.3 Results of Sensitivity Studies

The sensitivity of the results is expressed by means of the difference between the expected behavior and the actual response to the perturbations. As measure for this difference, the contrast is calculated. It is defined as the mean value of the fuzzy boxes where no response was expected minus the mean value over all boxes where a response was expected:

contrast = mean(not_expected) - mean(expected)

The more the actual response equals the expected one, the higher the value of the contrast. The results of the idealized cases in terms of contrast are given in Fig. 6. Some methods were found to miss a perfect forecast, i.e. when the initial field was verified against itself, the scores did not give the perfect value, which is usually 1. Those "leaking scores" were not further considered (FZ, JP, ME, PG, CS). For the five perturbations, the scores revealed very different responses. Some are fairly good for all perturbations (e.g. UP and PP), while others are especially good for a special kind of perturbation but fail to detect others (e.g. YN and JP).

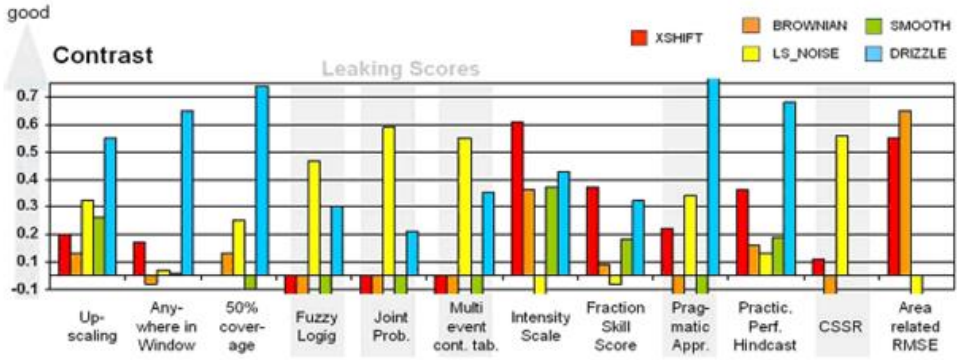


Figure 6: Results of the test bed experiment for the five perturbations on the idealized precipitation field.

Finally, the redundancy of the different methods was determined by calculating the correlation of the scores resulting from the test bed experiments. The scores for all window sizes and thresholds are therefore averaged over all perturbations and the correlation between the different scores is determined (Fig. 7). Three main groups of redundant methods have been identified this way: the first contains the methods UP, YN, MC, FB and PP, another group includes FZ, JP and a third one FB, PP. In addition it should be mentioned that the reliability is good for all scores - they show low standard deviations. Best performance in this respect was found for RM, which has, however, no intensity component and requires a lot of computational time. The Fraction Skill Score (FB) and Practically Perfect Hindcast (PP) generally show very good results. As both scores were found to be redundant, the more popular Fraction Skill Score was chosen as an appropriate method for the verification of quantitative precipitation of high resolution numerical models. To account for large scale error patterns, the Upscaling technique (UP) is added as a second method. Finally, Intensity Scale (IS) seems to be a promising technique, which is very fast and able to detect a specific scale of a spatial error.

3.2.4 Conclusions

Out of the huge set of methods which are available in the Fuzzy verification tool box, three methods and corresponding skill scores were identified to be suitable for a verification of high resolution quantitative precipitation forecast. The "Upscaling" method (UP) considers the mean value within each window to define an event (Zepeda-Arce et al. 2000; Weygandt et al. 2004), while for the "Fractions Skill Score" (FB) fractions of observed and forecast gridpoints exceeding a certain threshold are determined and a score is calculated based on these fractions (Roberts and Lean 2007). "Intensity Scale" (IS) uses a slightly different

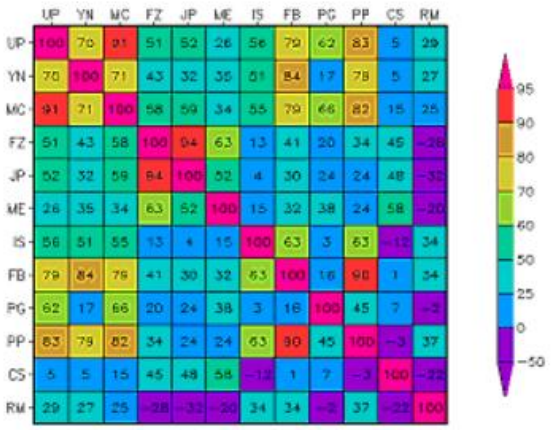


Figure 7: Correlation of the tested scores (see Tab. 1) derived from the averaged scores for each method.

approach: observation and forecast are transformed into binary images (rain larger then threshold or not) and a wavelet analysis is performed on the binary error image (Casati et al. 2004). For more information on the methods, the reader is referred to the given references.

3.3 Application during the D-PHASE operations period (DOP)

3.3.1 D-PHASE - Settings

The Forecast Demonstration Project (FDP) of the WWRP (World Weather Research Programme of WMO) D-PHASE (Demonstration of Probabilistic Hydrological and Atmospheric Simulation of flood Events in the Alpine region) was initiated to demonstrate the ability of forecasting heavy precipitation and related flooding events in the Alpine region. The D-PHASE operations period (DOP) covers the months from June to November 2007. During this time, several numerical and probabilistic models were run and alerts were issued based on those models. In this section, results of the verification of the quantitative precipitation forecast from two of those models, namely the Swiss COSMO models (COSMO-2 (2.2 km) and COSMO-7 (6.6 km)) are presented. The reference observation is the Swiss radar composite (NASS product). The verification is done on different spatial scales by varying the window sizes and for various thresholds defining an event. For the present analysis, window sizes of 1, 3, 5, 9 and 15 gridpoints were chosen for the coarser model and 1, 3, 9, 15, 27 and 45 for the high resolution model. The window sizes $whigh = 3*wcoarse$ of the high resolution model are comparable to window sizes $wcoarse$ of the coarse resolution model. The considered thresholds depend on the accumulation times that were evaluated. For 3 h accumulations, the following thresholds were chosen: 0.1, 0.2, 0.5, 1, 2, 5, 10, 20 mm/3h. For 24h accumulations, respective larger thresholds were chosen.

The scores are determined for 3h and 24h rain accumulations and are then aggregated on different time scales. Hereby, for the 3h accumulations always the latest model run is taken for both models beginning with a leadtime of 3h. This means that for COSMO-2 the leadtimes +3 to +6 are evaluated and for COSMO-7 (6.6 km) the leadtimes +3 to +15. It will be shown that the leadtime has no considerable influence on the difference in the skill of the two models. However, if all runs of the lower resolution model are available they should be

used for a "fair comparison". The 24h accumulations are only evaluated for the 00UTC runs of both models without any cutoff, i.e. for leadtimes +0 to +24.

3.3.2 Results

The results concerning the verification of quantitative precipitation forecasts during the D-PHASE Operations Period (DOP, June to November 2007) are presented for the two Swiss COSMO models. In Fig. 8, the scores calculated for 3h accumulations using the two methods UP and FB are given - the actual values for the score as well as the differences in the score's value of the two models for the respective scale. Generally, the skill increase with increasing window size and decreasing threshold for both methods and both models. For the Fraction Skill Score, which is displayed in the bottom row of the plot, useful scales are plotted in bold numbers. Those are the scales at which an acceptable level of skill is reached, which is given by $FSS_{uniform}$ lying halfway between random forecast skill and perfect forecast skill (Roberts and Lean 2007). The difference plot (COSMO-2 - COSMO-7) reveals that COSMO-2 has better skill on all scales. Especially small spatial scales (6.6 km to 50 km) and thresholds between 0.4 and 5 mm/3h can be pointed out here. According to the Fraction Skill Score, useful scales are especially those with low thresholds and large window sizes. The COSMO-2 precipitation forecast is hereby also useful on grid scale for very low precipitation thresholds, while COSMO-7 reaches a useful scale only for window sizes larger or equal 3 gridpoints.

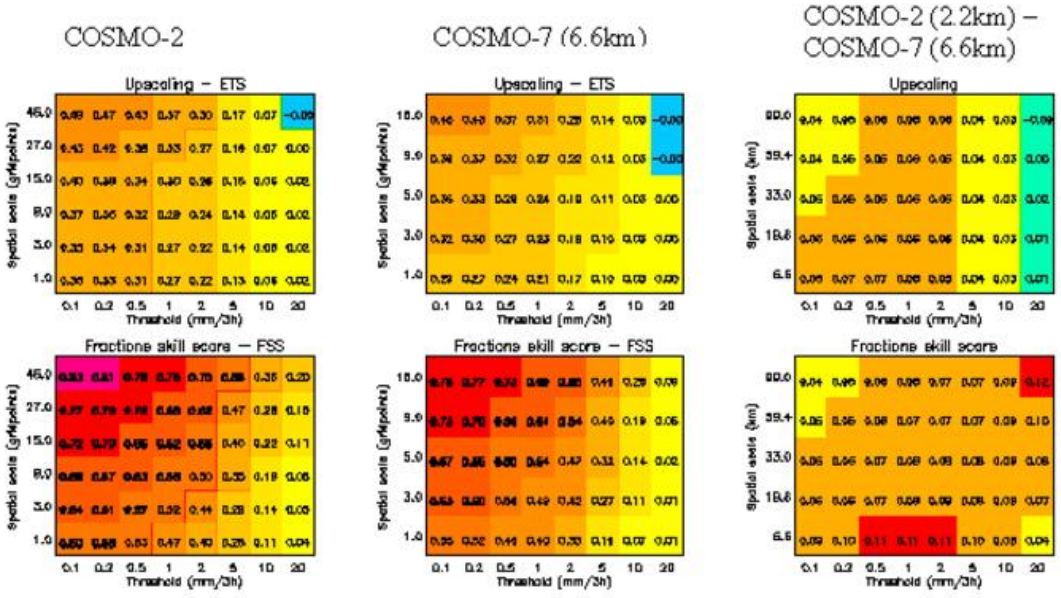


Figure 8: Verification results for the two methods UP (top row) and FB (bottom) and the period from June to November 2007 (3h accumulations). Displayed are the skill scores for the COSMO-2 (left), COSMO-7 (middle) and the differences between those two (right). For the latter, the spatial scale of the COSMO-7 in terms of gridpoints has to be multiplied by 3 to get the comparable spatial scale of COSMO-2.

The second example (Fig. 9) shows the results for 24h accumulations with only the 00UTC model runs used for verification. The skill is higher for both models on all scales and the useful scales are more numerous and almost identical for both models in terms of gridpoints. The difference plot looks slightly different from that for the 3h accumulations. The differences

in the skill of the two models are smaller and for a very small number of scales the coarser resolution model has slightly better skill. However, for the larger number of evaluated scales the skill of COSMO-2 is slightly better. This is especially true for the scales where the most pronounced differences were found for 3h accumulations.

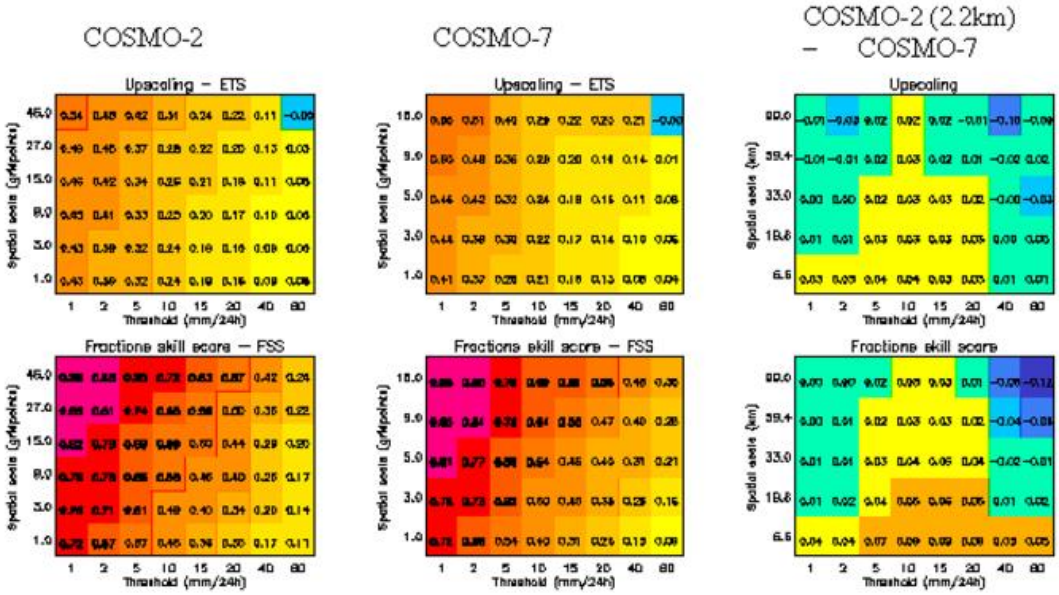


Figure 9: Verification results for the two methods UP (top row) and FB (bottom) and the period from June to November 2007 (24h accumulations). Displayed are the skill scores for the COSMO-2 (left), COSMO-7 (middle) and the differences between those two (right). For the latter, the spatial scale of the COSMO-7 in terms of gridpoints has to be multiplied by 3 to get the comparable spatial scale of COSMO-2.

In Fig. 10, the results of the verification by means of the "Intensity scale" method (IS) are shown. The advantage of this method is that each scale is evaluated separately, while for the other methods presented only the respective smaller scales are filtered. The results for the two models show no consistent behavior for the different scales. However, both accumulation times evaluated for each model reveal comparable skill. COSMO-2 has best skill for small windows (low thresholds) and for large window sizes. For a window size of 16 gridpoints, i.e. a spatial area of approx. 35 km x 35 km the score shows a relatively minimum. COSMO-7 behaves different: the skill is largest for high thresholds and large windows and a relative maximum in skill can be found for a spatial scale of 16 gridpoints, i.e. an area of approx. 105 km x 105 km. The test bed experiment revealed that the "Intensity scale" method is able to detect the specific scale of a spatial error. Imposing a perturbation in form of an horizontal shift, the response of the score was a minimum in skill for that specific scale. The results presented here are averaged over a period of 6 month. However, such a minimum in skill could be detected for the COSMO-2. To decide if this result is an artificial effect or originates from a shift in the precipitation forecast, more detailed investigations are needed.

3.3.3 Conclusions and Outlook

With fuzzy verification methods, forecasts are evaluated on different spatial scales and for varying thresholds. This procedure gives the chance to determine the scales on which a forecast model reveals the desired skill for a specific purpose. Furthermore, a better comparison

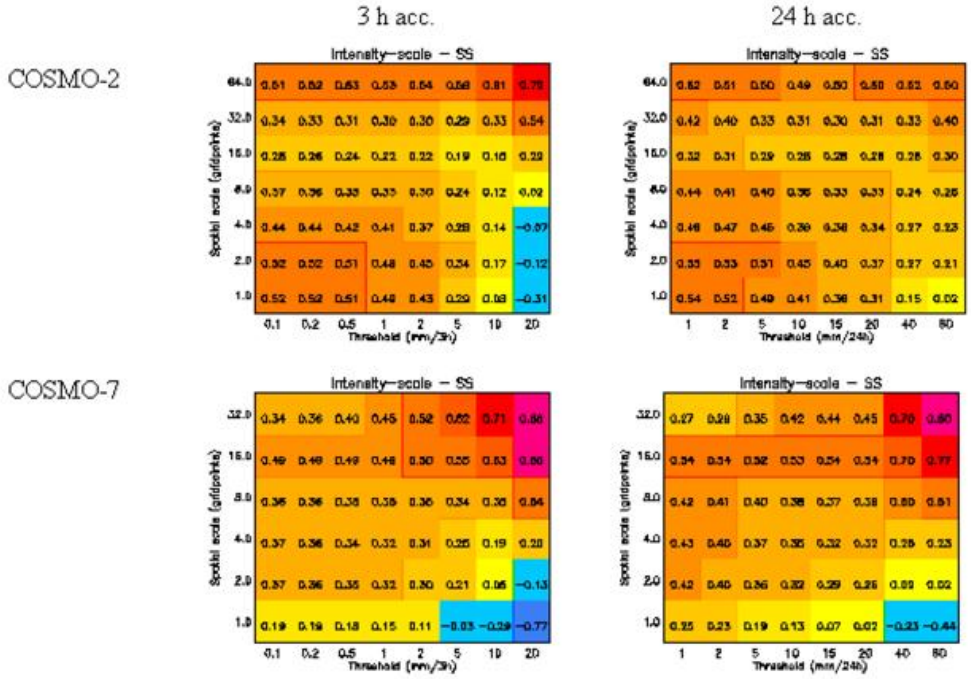


Figure 10: Verification results for the "Intensity scale" method (IS) for the period from June to November 2007 - 3h accumulations (left) and 24h accumulations (right). Displayed are the skill scores for the COSMO-2 (top) and COSMO-7 (bottom).

between models of different spatial resolution is possible. Three methods were chosen by means of a test bed experiment to be suitable for the purpose of precipitation verification and those methods were applied to the quantitative precipitation forecasts of the two Swiss COSMO models during the D-PHASE operations period. The three methods have different characteristics and thus give different results. The upscaling method dumps out high intensities by averaging over the respective window and spreads low intensities on the other hand. The resulting scores give an impression of the accuracy of the mean precipitation values. Fraction Skill Score in contrast considers the fraction of precipitation rates at grid-scale with values above a certain threshold and allows also a direct evaluation of high rain rates. However, due to the low sample of high rain rates, those scales are not classified as useful scales. The results of the two methods (UP and FB) reveal that the high resolution COSMO-2 (2.2 km) has better skill on all scales for 3h accumulations and on most scales for 24h accumulations. Useful scales, according to the Fraction Skill Score, are especially detected for low thresholds and large windows. The third method (IS) allows an evaluation for individual scales and reveals a more complex picture, which is harder to interpret. More detailed investigation is necessary to understand the results of this score. One of its main features is the ability to detect a horizontal shift of the forecast precipitation field. However, the three methods constitute an appropriate basis for the evaluation of quantitative precipitation forecasts of numerical models with different spatial resolutions. The results presented here are averaged over a rather long period of time (6 months). More information on the strength and problems of the individual models can be gained from conditional verification, e.g. stratified by weather types.

4 Verification of DWD-models against high resolution precipitation and SYNOP measurements (U. Damrath, DWD)

4.1 Introduction

Precipitation forecasts with high resolution models often show a high variability of forecasted patterns which have in some cases a characteristic size of only a few grid points. For those cases with observations with nearly the same characteristic size usually it cannot be expected that forecasted values and observed ones match correctly. Therefore, it is necessary to use verification methods that take into account that also right "signals" of forecasted events are judged beyond point by point verification which are further needful for weather elements with no high variability.

4.2 Methods

Traditional verification is carried out at DWD for nearly all weather elements which are observed near the ground and far from the ground. RMSE and BIAS are calculated for temperature, dew point depression, pressure wind (speed, direction and vector wind, no BIAS). Categorical scores are computed for cloud covers at different heights, gusts and precipitation in different classes. In order to check also the capability of the models to signal an event in a region of interest so called "fuzzy" techniques are used. These techniques are fully described by Ebert, 2008, Roberts and Lean 2008, and Casati, 2004. A lot of scores are defined within those frameworks and we have put our attention to the ETS from the upscaling method, the fractions skill score and a modification of the energy squared score. Using the energy squared score observed and forecasted fields are splitted in so called wavelets that contain the differences of values of a scale under consideration from the scale above. The modification relates to the original MSE Skill Score:

$$1 - \frac{2MSE(Y,X)}{En^2(X) + En^2(Y)} \tag{1}$$

to

$$1 - \frac{MSE(Y,X)}{En^2(X) + En^2(Y)} \tag{2}$$

MSE is the mean square difference between observed and predicted precipitation for a given wavelet, En^2 is the sum of the squared values for the given wavelet. The main difference between the wavelet method and the other methods is that with the wavelet method each scale can be separated but with the other methods an overview of all scales below the scale under consideration is given.

4.3 Data

For fuzzy verification forecasts of GME, COSMO-EU and COSMO-DE are compared on the same grid. That means that the forecasts of GME and COSMO-EU are transformed to the COSMO-DE grid. Observations are the values from the radar composite of DWD measurements which are also available on the grid of COSMO-DE. Traditional verification uses SYNOP observations and the forecasted value for the nearest grid point for COSMO-EU and an averaged value over 9 x 9 grid points for COSMO-DE in order to avoid scale dependent effects. Evaluations were made for all forecasts starting in an interval of 3 hours.

4.4 Results

Figs. 11 to 15 show exemplary the behavior of FSS, the ETS for August 2008 and these scores together with the modified energy squared score for January 2009. Also an example for traditional verification is presented (Figs. 16 and 17). These results are representative for most of the other months.

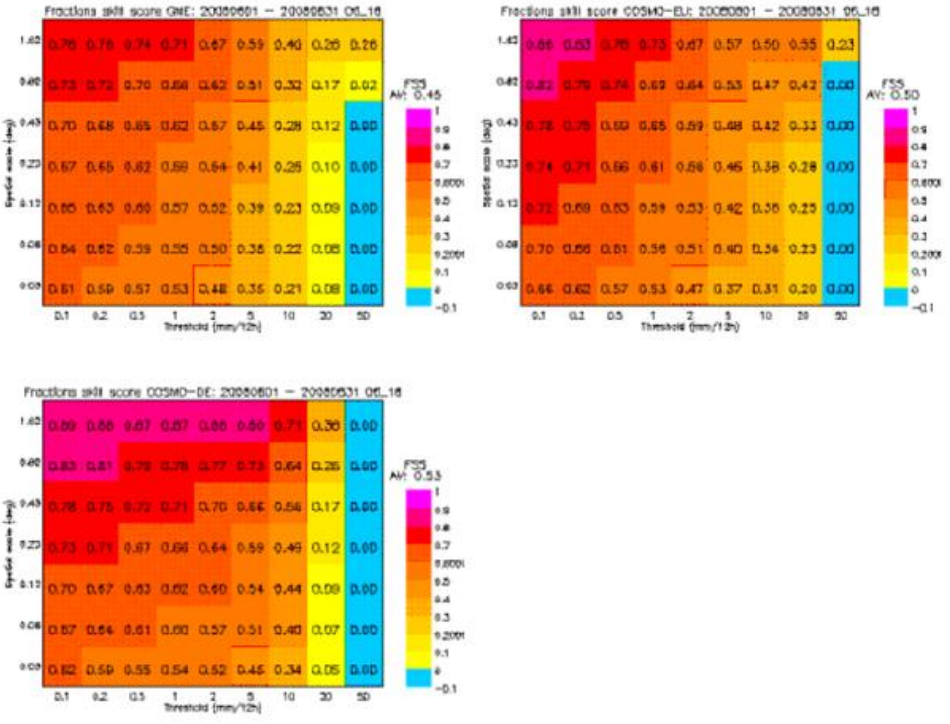


Figure 11: Fractions skill score for forecasts of GME, COSMO-EU and COSMO-DE for August 2008, forecast time 06-18 hours.

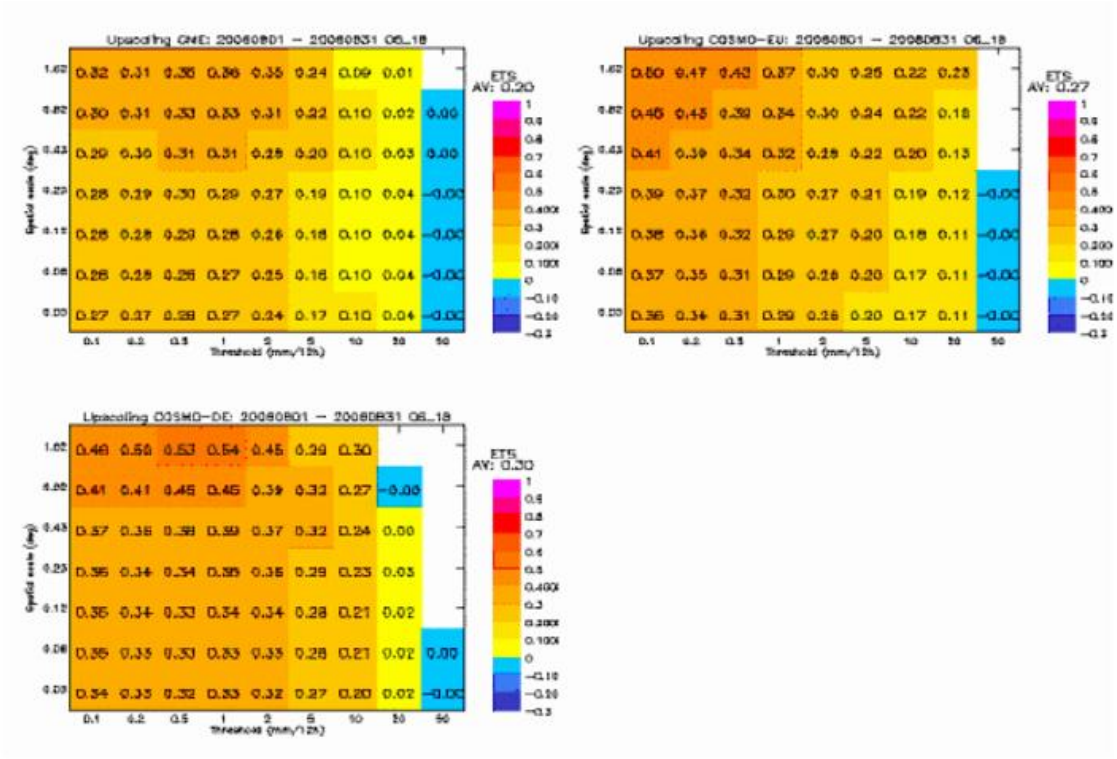


Figure 12: ETS from upscaling for forecasts of GME, COSMO-EU and COSMO-DE for August 2008, forecast time 06-18 hours.

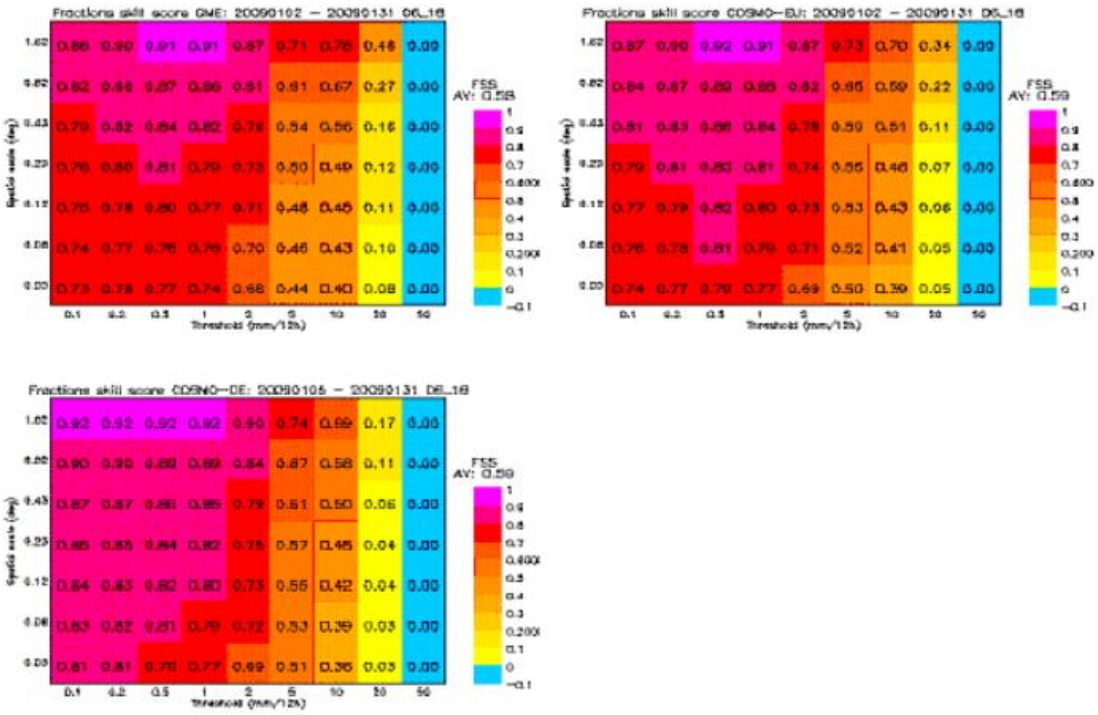


Figure 13: Fractions skill score for forecasts of GME, COSMO-EU and COSMO-DE for January 2009, forecast time 06-18 hours.

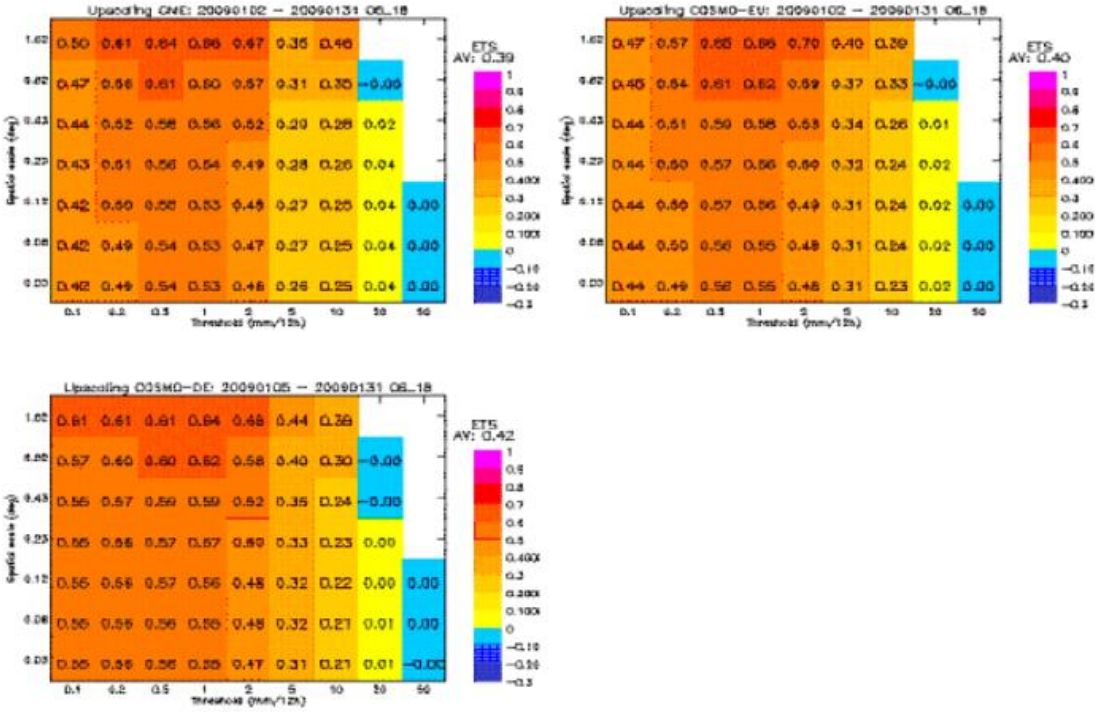


Figure 14: ETS from upscaling for forecasts of GME, COSMO-EU and COSMO-DE for January 2009, forecast time 06-18 hours.

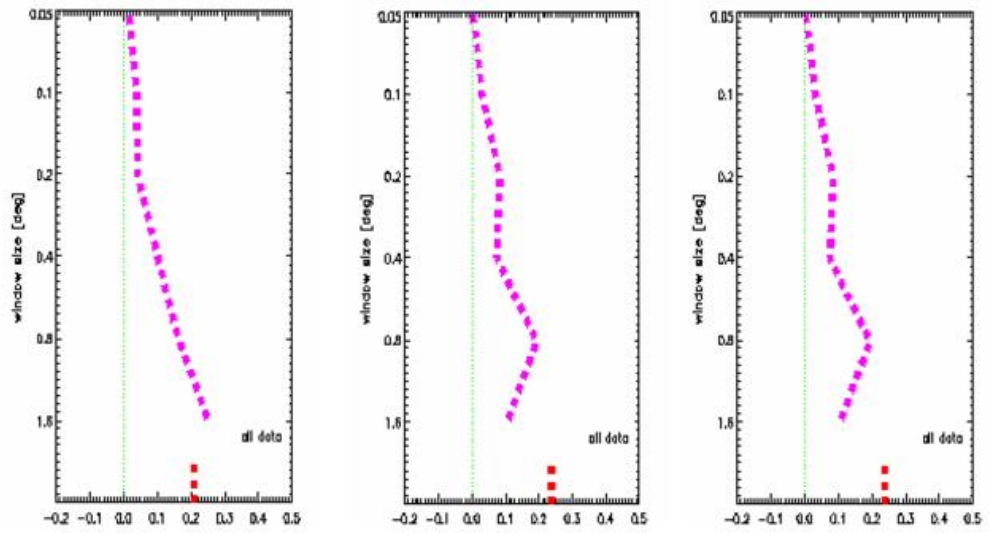


Figure 15: Modified energy squared score for forecasts of GME (left), COSMO-EU (center) and COSMO-DE (right) for January 2009, forecast time 06-18 hours; horizontal: skill score; vertical: window size; red mark: skill for all scale.

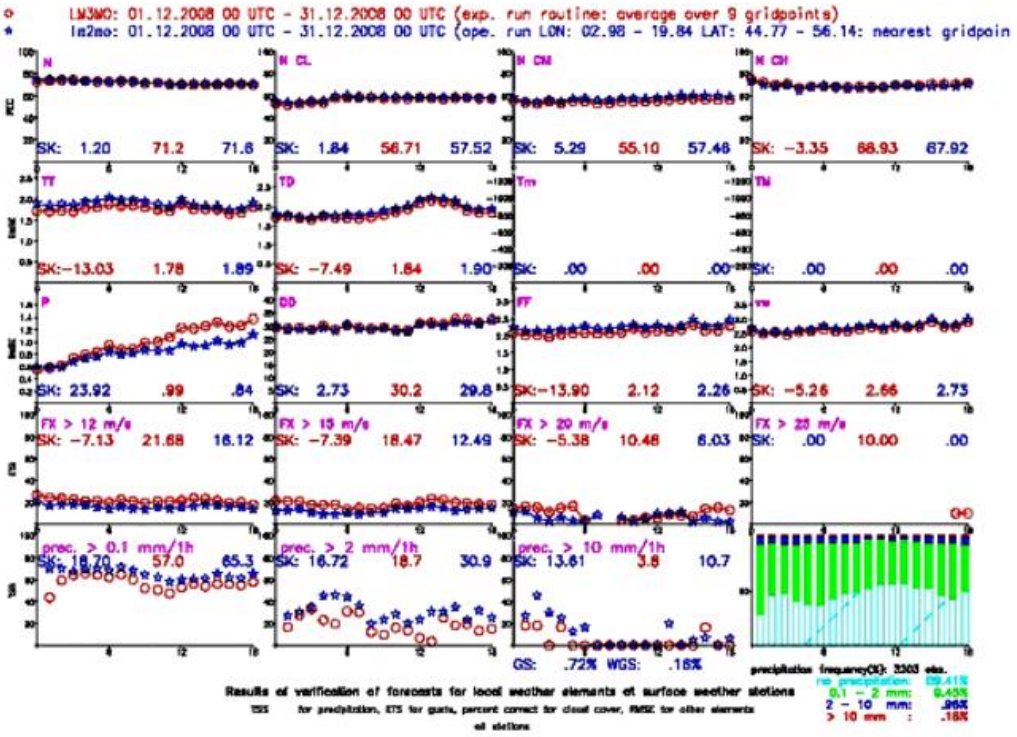


Figure 16: Example of traditional verification for surface weather elements for December 2008 (Start of forecasts 00UTC, scores measuring the quality of forecasts).

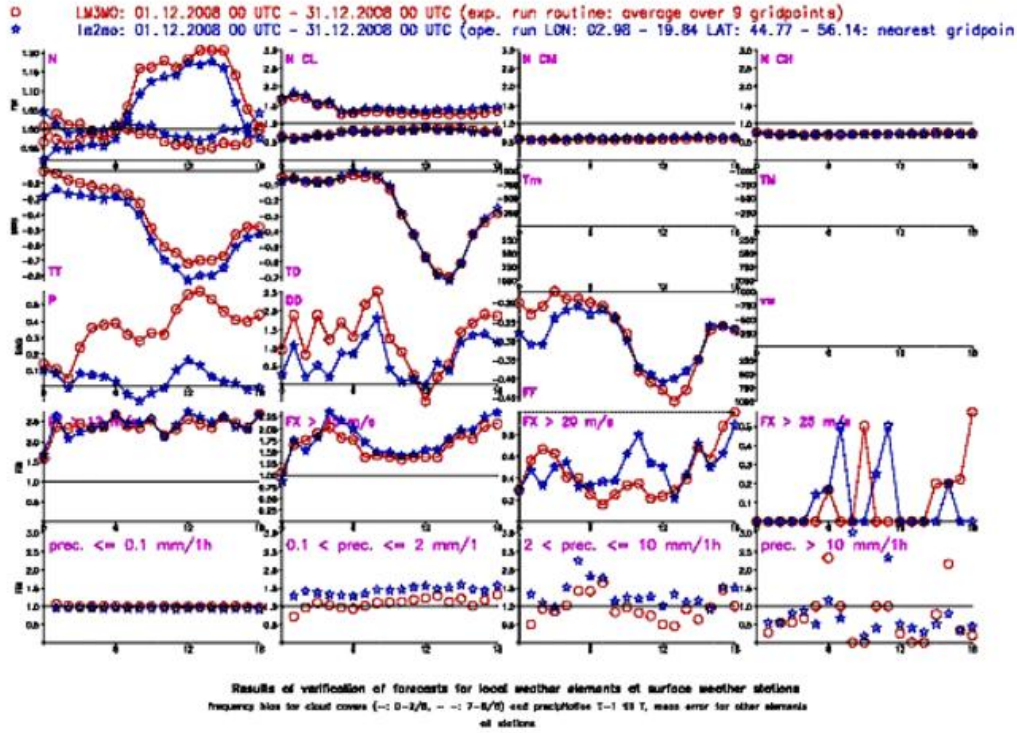


Figure 17: Example of traditional verification for surface weather elements for December 2008 (start of forecasts 00UTC, scores measuring the bias of forecasts).

This is a list of abbreviations which appear in Fig. 16:

- N: total cloud cover
- N CL: cloud cover of low clouds
- N CM: cloud cover of medium height clouds
- N CH: cloud cover of high clouds
- TT: 2m-temperature
- TD: 2m-dew point depression
- Tm: 2m-minimum temperature
- TM- 2m-maximum temperature
- P: pressure reduced to mean sea level
- DD: 10m-wind direction
- FF: 10m-wind speed
- vw: 10m-vector wind
- FX: gust over the given threshold
- Prec: precipitation for the given thresholds
- SK: skill of COSMO-EU agains COSMO-DE
- GS and WGS: global skill and weighted(different weights for each element) global skill over all elements
- red numbers: averages of the score for COSMO-DE
- blue numbers: averages of the score for COSMO-EU

4.5 Summary

Fuzzy verification methods show the following results which could be expected, but are assessed now:

- The quality of precipitation forecast is best for low precipitation values and large areas.
- For extreme precipitation values the dependency on the scale is as for low precipitation amounts. Higher quality occurs for larger areas. That means, indeed, that right "signals" often can be detected - especially by the models with finer resolution.
- Unfortunately, the number of those cases is relatively low and, therefore the statistical value of the scores is limited.
- The comparison between the models - and that follows from all the scores under consideration - indicate that the quality of forecasts increases in general with the degree of horizontal resolution.

- The question, whether the forecasts of a model has an economical benefit cannot be answered using these scores. It depends on the specific cost loss relationship. But if one can accept that a fractions skill score of above 0.5 or a ETS from upscaling is higher than 0.3 than one can find some areas in the graphics which indicate the horizontal scale and the amounts of precipitation that could be accepted as "good" forecasts.
- The example with the modified energy score shows that below a scale of 0.2° forecasts of GME have no skill. COSMO-models have a small skill below this range. For precipitation scales below 0.1 generally no skill can be expected.

Concerning the traditional verification it can be stated:

- Cloud covers are modeled with nearly the same quality for both models.
- COSMO-DE forecasts of temperature and dew point depression show small but systematic advantages against COSMO-EU.
- Although RMSE for pressure is for larger forecast times in COSMO-DE higher than in COSMO-EU (this is mainly related to the BIAS) wind forecasts of COSMO-DE are more trustable than those of COSMO-EU. This is also valid for gusts.
- QPF verification against SYNOP observations shows in general a frequency bias which is closer to 1 for COSMO-DE than for COSMO-EU. The small overestimation of COSMO-EU forecasts compared to COSMO-DE leads to a bit higher TSS for COSMO-EU. The evaluation of other scores that are not so strongly dependent on the frequency bias is under consideration.

5 Post-processing of COSMO-7 and COSMO-2 Precipitation with the Neighborhood Method (P. Kaufmann, MeteoSwiss)

5.1 Introduction

With increasing resolution, the numerical weather prediction models advance towards scales that are less and less deterministically predictable. This is especially true for precipitation with its high temporal and spatial variability. The time of onset and the location of a single convective cell for example cannot be predicted exactly due to the random nature of convection. This uncertainty in time and space needs to be accounted for when using high-resolution model output fields. The neighborhood method (Theis et al., 2005) accounts for the probability related to the spatial and temporal uncertainty on the scale of a few model grid cells. It solves the above-mentioned predictability problem by sampling a spatio-temporal neighborhood around each grid cell to derive a probabilistic forecast for that cell. Doing this, the neighborhood method provides a way to derive a probabilistic forecast from a deterministic model. In the present study, precipitation forecasts of the two Swiss models, the COSMO-7 with a grid spacing of 7 km (6.6 km after Feb. 2008), and the COSMO-2 with 2.2 km, are used as input.

5.2 Optimizing the neighborhood

5.2.1 Method

The neighborhood size has an important impact on the magnitude of the predicted probabilities. Theis (2005) found that she could not optimize the neighborhood size based on objective verification alone. With this unpromising perspective, I based the optimization for the Swiss COSMO models on case studies of precipitation cases. The optimization of the neighborhood uses a graphical comparison of the forecast probabilities with actual precipitation measurements of 2006 - 2008. An objective evaluation of the neighborhood determined in this way remains highly desirable and will be done this year (2009).

5.2.2 Spatial radius of neighborhood

Theis et al. (2005) tested three different sizes for the neighborhood: a small, a medium and a large neighborhood with a spatial radius of 3, 6 and 10 grid points, respectively. In this study, four sizes of 1, 3, 5, and 10 grid point radius are compared for COSMO-7 (Fig. 18). While the smallest radius retains most of the structural details, it also produces probabilities that are either very high or very low with much fewer points in between than are meaningful for a probabilistic forecast. The largest radius on the other hand only produces low probabilities, blurring the structural information very strongly. The ideal neighborhood radius is a trade-off between these extremes, lying for COSMO-7 somewhere in the range of 3 to 5 (Kaufmann, 2008) and for COSMO-2 between 8 to 15 grid points radius.

5.2.3 Shape of the neighborhood

Over homogeneous, flat terrain, a circular shape in space is the natural choice. In complex terrain or along surface property discontinuities however, it seems advantageous to account for the anisotropy. Theis et al. (2005) tested different anisotropic spatial shapes. The impact

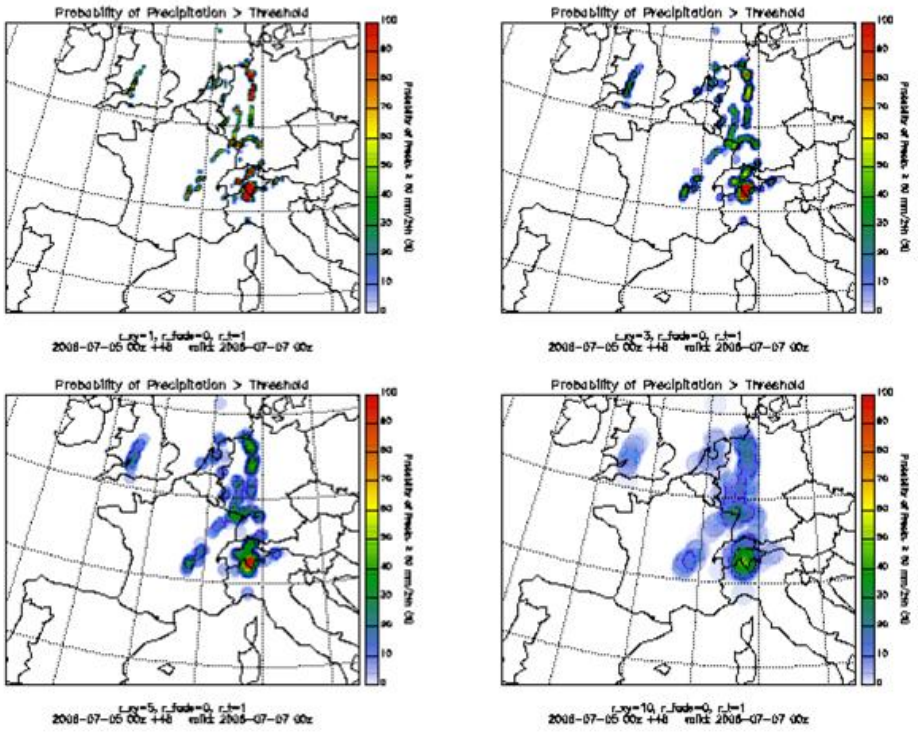


Figure 18: Probabilities of precipitation derived from COSMO-7 with a spatial neighborhood radius of 1, 3, 5, and 10 grid points, in this order.

proved to be quite small and at times even detrimental. Therefore, a circular neighborhood was chosen here, without further experimenting with the spatial shape.

The ellipsoidal shape of the neighborhood used by Theis et al. (2005) means that the spatial radius depends on the temporal distance to the central point. This implies a space-time dependency. It has at the same time the practical effect of smoothing the edges of the regions with high probabilities, because grid points near the central point contribute to the neighborhood at more time levels than those further away. If it is assumed that the time and space dimensions are independent, the spatial radius is constant in time, leading to a cylindrical neighborhood. This assumption is true if the ambient wind is nearly zero, and becomes increasingly inaccurate with increasing advection. The cylindrical neighborhood has the practical disadvantage of showing unreasonably sharp boundaries along the edges of precipitation. Smoothing of the edges has to be added to ameliorate this. A smoothing with linearly fading weights is introduced in the next section.

5.2.4 Linearly fading weights

The cylindrical neighborhood shape, in combination with localized strong precipitation peaks, leads to a dotted plot of probabilities, with a circular dot surrounding each major precipitation peak (Fig. 18). Such an unwanted feature could be smoothed out in an additional step, but it is more meaningful to do this as part of the neighborhood processing. This is achieved by adding an additional zone around the equally weighted neighborhood, with decreasing weights. For simplicity, the weights are chosen to decrease linearly. The meteorological reasoning behind such a zone is that given a convective rain forecast at the

central point, it is equally likely to appear within a certain radius, but the likelihood decreases beyond this radius and finally reaches zero at some larger distance. Fig. 19 shows the weight depending on the spatial distance of a grid cell to the neighborhood center for three neighborhood sizes.

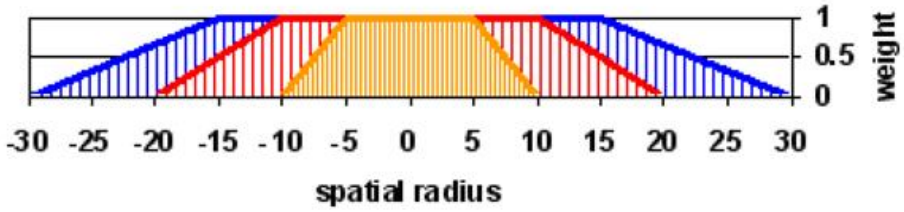


Figure 19: Weights of grid cells depending on the distance from the central cell, for tree different sizes of the neighborhood. Blue: Zone of equal weight and fading zone with 15 grid points radius each; red 10; orange: 5.

The result of adding such a fading zone is shown in Fig. 20. Here, the probability fields of the lower panels of Fig. 18 are repeated, but this time calculated with an additional linear fading zone of the same radius as the neighborhood itself. The areas are much smoother than in Fig. 18, and the peak values are somewhat decreased. This is because the total radius including the fading zone is now doubled.

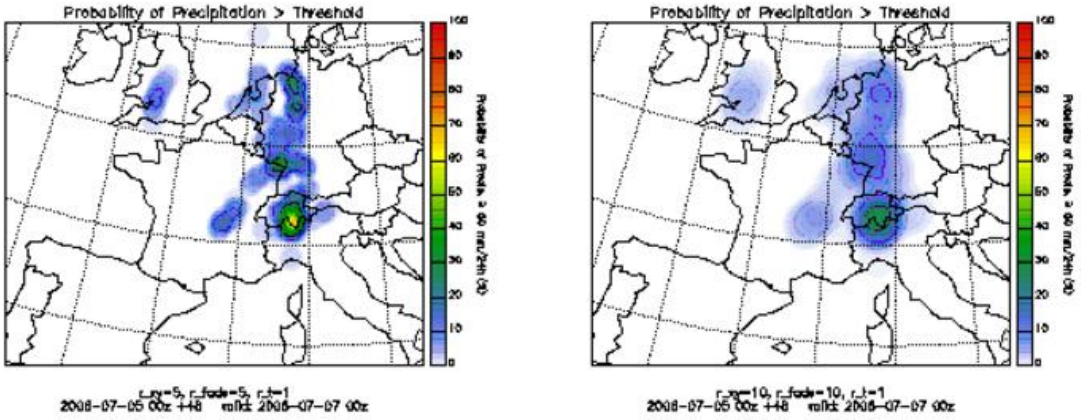


Figure 20: Same as lower two panels of Fig. 18 but with an additional fading zone of the same radius as the neighborhood, (left) 5 and (right) 10 grid points, added.

The cylindrical neighborhood shape with a fading zone is approximately equivalent with an ellipsoidal neighborhood with a larger temporal but smaller spatial radius (Fig. 21). With the same temporal radius, the linear fading provides smoother edges than the discrete weights of the ellipsoidal shape, while the values within the edges are retained. The smoother areas with non-zero probabilities are more realistic than the patchy areas of the ellipsoidal shapes.

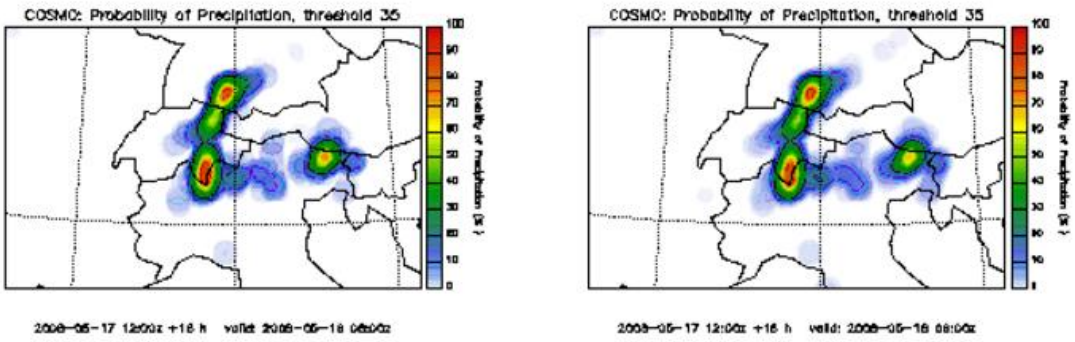


Figure 21: Approximately equivalent neighborhood shapes for COSMO-2. Left: ellipsoidal with 13 grid point radius, right: cylindrical with 8 grid point radius plus 8 grid point fading zone giving smoother transitions and edges. Shown is the 12h sum ending 18 May 2008 at 6:00 UTC.

5.2.5 Temporal radius

The temporal radius of the neighborhood represents the uncertainty in time of a rainfall prediction. For convective precipitation, it is known to span several hours. However, tests with temporal radius of 0, 1, 3, and 6 hours showed relatively little influence. The rainfall accumulation of 6 hours and even more so of 24 hours already has a smoothing effect on the time dimension, rendering the temporal extent of the neighborhood less critical. From the computational point of view, a smaller temporal radius is favorable because it is less costly.

5.3 Examples of products

5.3.1 COSMO-7, threshold 25 mm / 6h

Fig. 22 displays an example for a COSMO-7 product with a threshold of 25 mm per 6 hours. The situation shown occurred in August 2006, with a small region of strong precipitation over southern Switzerland. The probabilities for precipitation above the threshold level of 25 mm / 6h reach 50% in that region. Although probabilities and single precipitation events cannot be compared directly, large probabilities should coincide with rainfall above the threshold for a majority of cases. The probabilities generally decrease with increasing neighborhood size, thus a frequent occurrence of moderate probabilities with actual rainfall above the threshold as in Fig. 22 would indicate that the chosen neighborhood size is still slightly larger than optimal.

5.3.2 COSMO-2, threshold 25 mm / 6h

Fig. 23 shows on the left the product for COSMO-2 with a 25 mm per 6 hours threshold. On the right side, the actually occurred rainfall amount as measured at Swiss stations is shown. This is during the same episode already presented in Fig. 21, but 12 hours earlier.

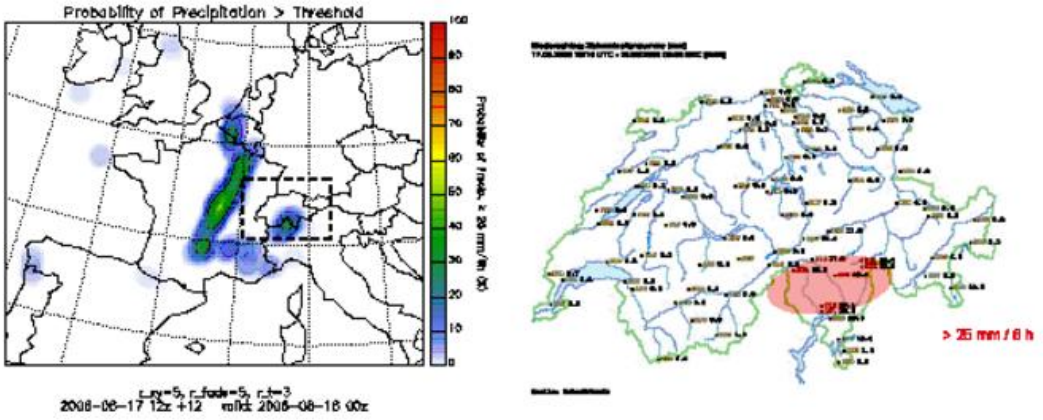


Figure 22: Probabilities predicted by the neighborhood method (left) and actual rainfall sum (right) for 2006-08-18 00:00 UTC.

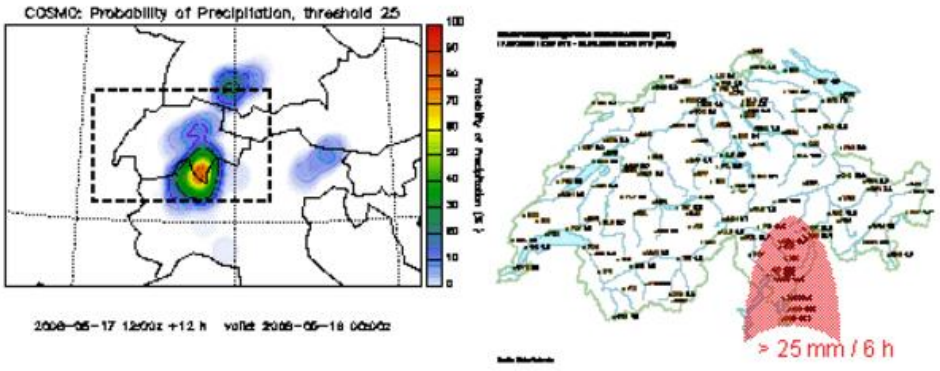


Figure 23: Probabilities predicted by the neighborhood method (left) and actual rainfall sum (right) in Switzerland (within dashed box in left figure) for 2008-05-18 06:00 UTC.

5.3.3 COSMO-7, threshold 50 mm / 24h

With a forecast range of just 24 hours, COSMO-2 cannot be used with the neighborhood method for 24h precipitation sums, unless the temporal radius is set to zero. The corresponding product for COSMO-7 (Fig. 24) shows a case with strong precipitation over northern Switzerland. The region of probabilities of 50% and more for precipitation above the threshold level of 50 mm / 24h nicely fits with the observed precipitation.

5.4 Conclusions and Outlook

The neighborhood method is used to derive a probabilistic forecast from a deterministic model. The probability is related to local-scale spatial and temporal model uncertainty. The resulting plots are compared to real cases and are optimized in this way. For COSMO-7, a spatial radius of 5 grid cells (33 km) with an additional zone of 5 grid cells with decreasing

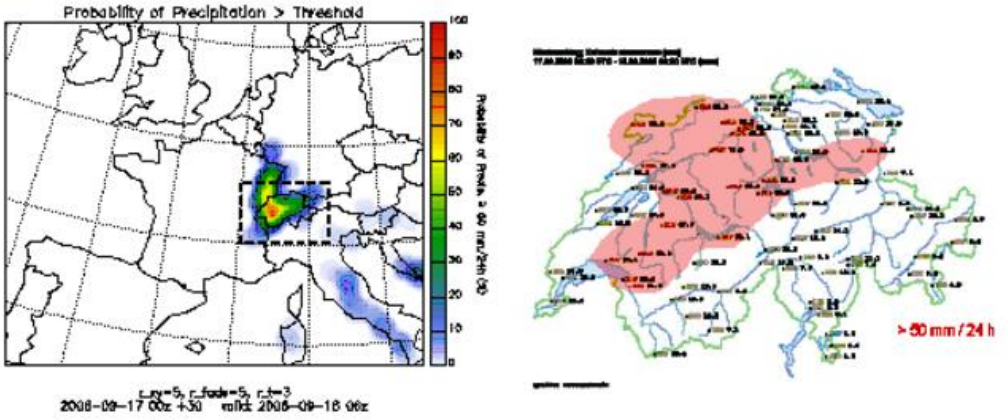


Figure 24: Probabilities predicted by the neighborhood method (left) and actual rainfall sum (right) for 2006-09-18 06:00 UTC.

weights and a temporal radius of 3 hours gives probabilities which are in accordance with the observed events and non-events. The radius of the zone with equal weight and of the zone with fading weights combine to an "effective" radius of approximately 7.5 grid cells (50 km). The temporal radius is currently chosen to be 3 hours for COSMO-7; however the extent of the neighborhood in time is of lesser importance. The respective values optimized in the same way for COSMO-2 are 10 grid cells (22 km) radius plus additional 10 grid cells for the fading zone, with a temporal radius of 1 hour. The two zones of the neighborhood add up to an "effective" radius of 15 grid cells (33 km). Compare this to the German Weather Service (DWD) which uses an ellipsoidal neighborhood with 13 grid point radius (36 km) for its 2.8 km resolution model. A throughout validation however, using objective verification, will have to follow to prove the quality of the probability forecast with the chosen neighborhood. Such a verification is planned for this year (2009). The neighborhood method is able to represent the local uncertainty concerning the prediction of the exact position and onset of precipitation. It does not account for the uncertainty related to synoptic forcing, which can be done using a model ensemble forecast. A combination of the ensemble and the neighborhood methods would combine both synoptic-scale and small-scale uncertainties.

6 Statistical properties of precipitation in boxes of various sizes (M. S. Tesini, C. Cacciamani, T. Paccagnella, ARPA-SIMC).

Model verification at ARPA-SIMC, in particular QPF, is operationally performed by using an upscaling method of both forecasted and observed fields over areas of selected size. The domain is divided in many squared areas and, for each area and for the chosen period of time, some indicators deduced by the distribution of the forecasted precipitation field (such as mean, maximum value, 90th percentile), are compared to those deduced by the distribution of the observed rainfall. Results concerning models performance depend on the considered distribution parameter; for example categorical verification scores for COSMO-I7 are better if the chosen indicator is the maximum value of precipitation in the area rather than those obtained selecting the mean value. Nevertheless all the distribution parameters are equally useful because they provide different information on the ability of the model in reproducing the precipitation field. Our interest is therefore addressed to the study of the distribution of the precipitation field, in order to analyze the capability of the models in reproducing precipitation statistical properties. Currently we focused on COSMO-I7 and ECMWF verification. The results suggest that verification methods based on the statistical description of model QPF and observations give more credit to high resolution model than the traditional standard verification, based on the comparison of model grid-point against observation (for example the choice of nearest grid point). We have applied a methodology based on the estimation of the distribution function of the observed/predicted precipitation field considering all points that fall in each area throughout the examined periods. Each area contains a lot of observation points as well as model grid-points: we assume that the occurrence of precipitation in each of these points is equiprobable. In order to consider well-founded this assumption, areas should be chosen carefully taking into account orographical and geographical features. The dimension of the selected areas is a critical point too. We followed a pragmatic approach for the choice of the dimension on the box: we should have enough forecast and observation points to perform significant statistics in each area. We chose squared areas of about 100 km x 100 km (see Fig. 25), containing about 200 COSMO-I7 grid-points or 16 IFS-ECMWF grid-points.

There are more than 1000 rain-gauges, belonging to regional/local administrations and provided by Italian Department of Civil Protection over the Italian territory, and the number of rain-gauges varies from 20 to 130 depending on the selected region. Tests on smaller area have been performed, but the results are very sensitive to the density of the observation points. We approached the problem mostly from a qualitatively point of view using a boxplot representation. A boxplot is a simple graphical summary of a dataset that can be useful to display differences between populations without making any assumptions of the underlying statistical distribution. It is possible to obtain information about the spread of the distribution and a roughly description of key measures that define it, such as the median, the quartiles, maximum and minimum values, and a range of values identified as "outliers". In this way we can, at least qualitatively, describe the type of precipitation: for instance the resulting distribution of a convective rainfall system possesses a long "tail" while the distribution of a widespread light rain event presents a distribution with a peak near a low amount of rainfall and little or no "tail". In this context, COSMO-I7 and IFS-ECMWF are used as representative of models with different horizontal resolution without focusing on their quality. In Fig. 26 the time-series of the daily forecasted/observed rainfall distribution are shown, obtained considering all the model grid-points and all the observed rain that fall daily (00-24UTC) within each area for ECMWF (blue), COSMO-I7 (red) and observations (green) during Autumn 2007. The number of stations in this area (131) is comparable with

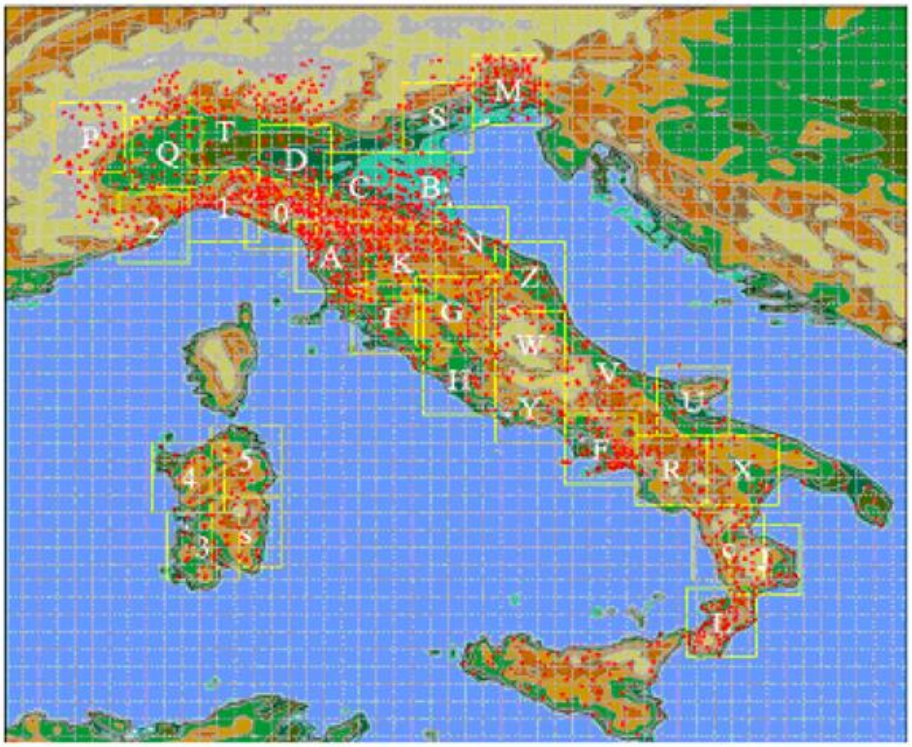


Figure 25: Box distribution.

COSMO-I7 grid-points (192), while ECMWF presents only 16 grid-points.

In general, we observe that COSMO-I7 is more realistic than ECMWF in reproducing the intra-box variability. However, COSMO-I7 presents both a large number of false alarms and high "spikes". On the other hand, ECMWF shows a greater number of missed alarms, especially if we chose high reference thresholds. According to most standard verification measures, COSMO-I7 forecast may have poor quality, but it might be very valuable to the forecaster since it provides additional information on the distribution and variability of the rain field over the considered region. The role of horizontal resolution is very important since it allows a more realistic simulation of the precipitation distribution, in particular for the "tails", that nevertheless represent the most interesting values of the rain field, especially for the emission of warning alerts to the Civil Protection. A better description of the distribution function of the observed precipitation field over each area represents a fundamental step in order to apply this methodology also to COSMO-I2, as the difference in the density of model grid-points and observations should represent a critical point. In fact, if we consider an area in which the number of model grid-points is significantly greater than the number of observations, such as the one shown in Fig. 27 where there are 34 stations, 212 COSMO-I7 grid-points and 16 ECMWF grid-points, we can see that "tail" of COSMO-I7 distribution is overestimated compared to the "tail" distribution of observations. Is it a sampling problem or does it depend on the behavior of the model in that area ? The question is still open.

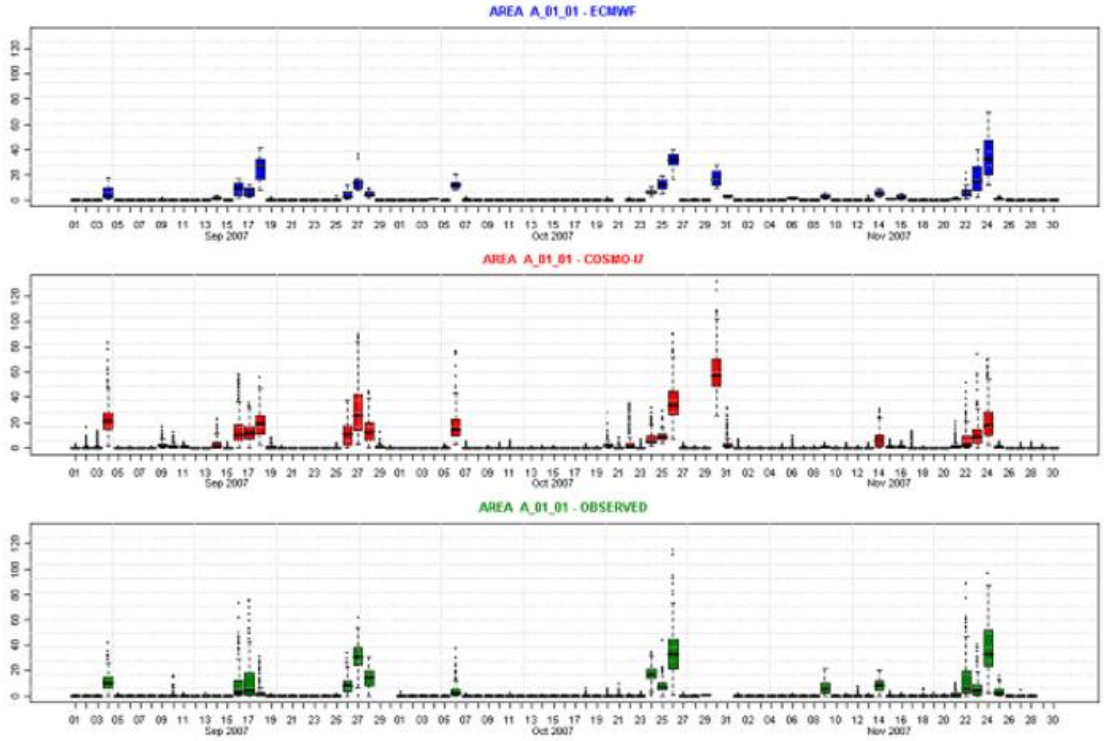


Figure 26: Time-series of the daily forecasted/observed rainfall.

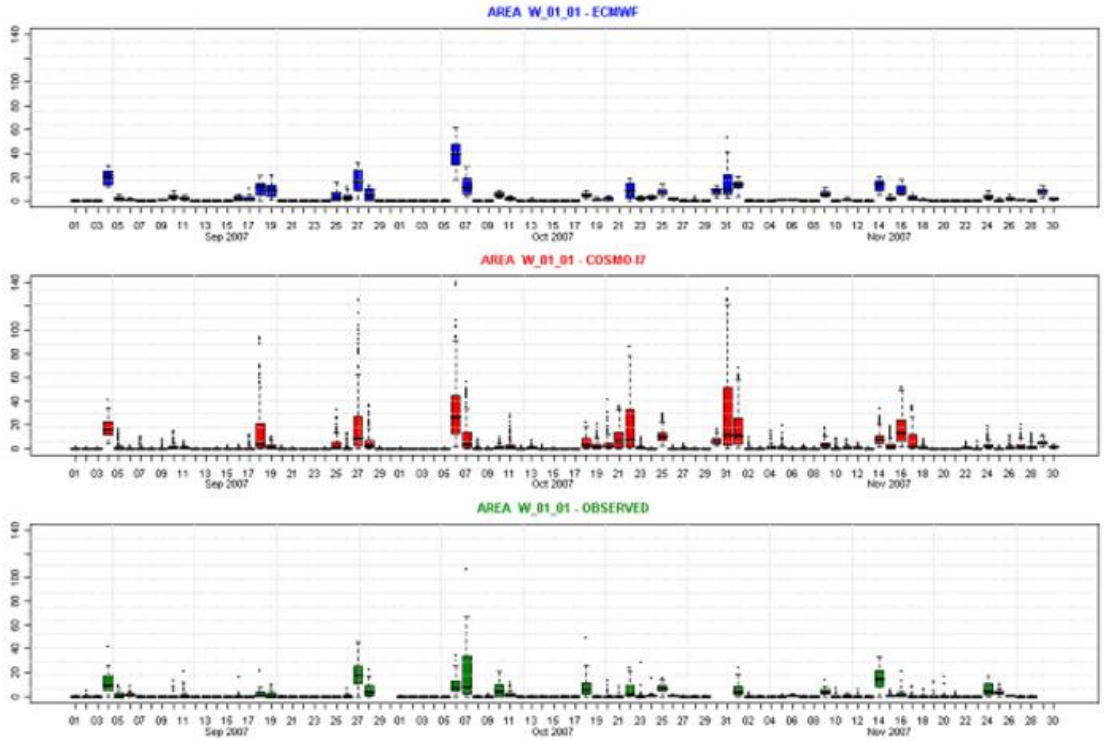


Figure 27: Example of area in which the number of model grid-points is significantly greater than the number of observations.

7 Open points

- The fact that precipitation patterns cannot be trusted at small scales is obviously dependent on the synoptic configuration. When a lot of uncertainty in the positioning is existent in purely convective situations, it is well possible that precipitation patterns are reproduced correctly in situations where orographic forcing is dominant (as long as the orography is correctly represented). Verification stratified by a weather type classification is thus recommended.
- By building statistics of precipitation values in a neighborhood of a gridpoint it is possible to build probabilistic precipitation forecasts. The same can be provided by Ensemble Prediction Systems (EPS), especially convection permitting EPS. Both methods should be compared by classical or fuzzy verification. Both systems can also be combined by applying the upscaling or the neighborhood method to the EPS.

8 Contributing scientists

The authors of the four articles are the contributing scientists.

9 References

Casati, B., Ross, G., Stephenson, D.B., 2004: A new intensity-scale approach for the verification of spatial precipitation forecasts. Meteorological Applications 11, 141-154.

Ebert, E.E., 2008: Fuzzy verification of high resolution gridded forecasts: A review and proposed framework. Meteorological Applications, 15, 51-64.

Kaufmann, P., 2008: Postprocessing of the aLMo [former name of COSMO-7] precipitation with the neighborhood method. COSMO Newsletter No. 7, DWD, Germany, 57-60. Available from http://www.cosmo-model.org.

Roberts, N.M., Lean, H.W., 2008: Scale-selective verification of rainfall accumulations from high-resolution forecasts of convective events. Monthly Weather Review 136, 78-97.

Theis, S., 2005: Deriving probabilistic short-range forecasts from a deterministic high- resolution model. Ph. D. thesis, University Bonn, Germany.

Theis, S., Hense, A., and Damrath, U., 2005: Probabilistic precipitation forecasts from a deterministic model: a pragmatic approach. Meteorol. Appl., 12, 257-268.

Weygandt, S.S., Loughe, A.F., Benjamin, S.G., Mahoney, J.L., 2004: Scale sensitivities in model precipitation skill scores during IHOP. 22nd Conference Severe Local Storms. American Meteorological Society, Hyannis, MA, 4-8 October 2004.

Zepeda-Arce, J., Foufoula-Georgiou, E., Droegemeier, K.K., 2000: Spacetime rainfall organization and its role in validating quantitative precipitation forecasts. Journal of Geophysical Research, 105(D8), 10, 129-10, 146.

List of COSMO Newsletters and Technical Reports

(available for download from the COSMO Website: www.cosmo-model.org)

COSMO Newsletters

No. 1: February 2001.

No. 2: February 2002.

No. 3: February 2003.

No. 4: February 2004.

No. 5: April 2005.

No. 6: July 2006.

No. 7: April 2008; Proceedings from the 8th COSMO General Meeting in Bucharest, 2006.

No. 8: September 2008; Proceedings from the 9th COSMO General Meeting in Athens, 2007.

No. 9: December 2008.

COSMO Technical Reports

No. 1: Dmitrii Mironov and Matthias Raschendorfer (2001):
Evaluation of Empirical Parameters of the New LM Surface-Layer Parameterization Scheme. Results from Numerical Experiments Including the Soil Moisture Analysis.

No. 2: Reinhold Schrodin and Erdmann Heise (2001):
The Multi-Layer Version of the DWD Soil Model TERRA_LM.

No. 3: Günther Doms (2001):
A Scheme for Monotonic Numerical Diffusion in the LM.

No. 4: Hans-Joachim Herzog, Ursula Schubert, Gerd Vogel, Adelheid Fiedler and Roswitha Kirchner (2002):
LLM ¯ the High-Resolving Nonhydrostatic Simulation Model in the DWD-Project LITFASS.
Part I: Modelling Technique and Simulation Method.

No. 5: Jean-Marie Bettems (2002):
EUCOS Impact Study Using the Limited-Area Non-Hydrostatic NWP Model in Operational Use at MeteoSwiss.

No. 6: Heinz-Werner Bitzer and Jürgen Steppeler (2004):
Documentation of the Z-Coordinate Dynamical Core of LM.

No. 7: Hans-Joachim Herzog, Almut Gassmann (2005):
Lorenz- and Charney-Phillips vertical grid experimentation using a compressible nonhydrostatic toy-model relevant to the fast-mode part of the 'Lokal-Modell'

No. 8: Chiara Marsigli, Andrea Montani, Tiziana Paccagnella, Davide Sacchetti, André Walser, Marco Arpagaus, Thomas Schumann (2005):
Evaluation of the Performance of the COSMO-LEPS System

No. 9: Erdmann Heise, Bodo Ritter, Reinhold Schrodin (2006):
Operational Implementation of the Multilayer Soil Model

No. 10: M.D. Tsyrulnikov (2007):
Is the particle filtering approach appropriate for meso-scale data assimilation ?

No. 11: Dmitrii V. Mironov (2008):
Parameterization of Lakes in Numerical Weather Prediction. Description of a Lake Model.

No. 12: Adriano Raspanti (2009):
COSMO Priority Project "VERification System Unified Survey" (VERSUS): Final Report

No. 13: Chiara Marsigli (2009):
COSMO Priority Project "Short Range Ensemble Prediction System" (SREPS): Final Report

No. 14: Michael Baldauf (2009):
COSMO Priority Project "Further Developments of the Runge-Kutta Time Integration Scheme" (RK): Final Report

No. 15: Silke Dierer (2009):
COSMO Priority Project "Tackle deficiencies in quantitative precipitation forecast" (QPF): Final Report

No. 16: Pierre Eckert (2009):
COSMO Priority Project "INTERP": Final Report

COSMO Technical Reports

Issues of the COSMO Technical Reports series are published by the *COnsortium for Small-scale MOdelling* at non-regular intervals. COSMO is a European group for numerical weather prediction with participating meteorological services from Germany (DWD, AWGeophys), Greece (HNMS), Italy (USAM, ARPA-SIMC, ARPA Piemonte), Switzerland (MeteoSwiss), Poland (IMGW) and Romania (NMA). The general goal is to develop, improve and maintain a non-hydrostatic limited area modelling system to be used for both operational and research applications by the members of COSMO. This system is initially based on the COSMO-Model (previously known as LM) of DWD with its corresponding data assimilation system.

The Technical Reports are intended

- for scientific contributions and a documentation of research activities,
- to present and discuss results obtained from the model system,
- to present and discuss verification results and interpretation methods,
- for a documentation of technical changes to the model system,
- to give an overview of new components of the model system.

The purpose of these reports is to communicate results, changes and progress related to the LM model system relatively fast within the COSMO consortium, and also to inform other NWP groups on our current research activities. In this way the discussion on a specific topic can be stimulated at an early stage. In order to publish a report very soon after the completion of the manuscript, we have decided to omit a thorough reviewing procedure and only a rough check is done by the editors and a third reviewer. We apologize for typographical and other errors or inconsistencies which may still be present.

At present, the Technical Reports are available for download from the COSMO web site (www.cosmo-model.org). If required, the member meteorological centres can produce hard-copies by their own for distribution within their service. All members of the consortium will be informed about new issues by email.

For any comments and questions, please contact the editors:

Massimo Milelli
Massimo.Milelli@arpa.piemonte.it

Ulrich Schättler
Ulrich.Schaettler@dwd.de

Consortium for Small-Scale Modelling

Technical Report No. 13

COSMO Priority Project "Short Range Ensemble Prediction System (SREPS)": Final Report

June 2009

DOI: 10.5676/DWD_pub/nwv/cosmo-tr_13

Deutscher Wetterdienst

MeteoSwiss

Ufficio Generale Spazio Aereo e Meteorologia

ΕΘΝΙΚΗ ΜΕΤΕΩΡΟΛΟΓΙΚΗ ΥΠΗΡΕΣΙΑ

Instytucie Meteorogii i Gospodarki Wodnej

Administratia Nationala de Meteorologie

Agenzia Regionale per la Protezione Ambientale del Piemonte

Agenzia Regionale per la Protezione Ambientale dell' Emilia-Romagna: Servizio Idro-Meteo-Clima

Centro Italiano Ricerche Aerospaziali

Amt für GeoInformationswesen der Bundeswehr

www.cosmo-model.org

Editor: Massimo Milelli, ARPA Piemonte
Printed at Deutscher Wetterdienst, P.O. Box 100465, 63004 Offenbach am Main

COSMO Priority Project "Short Range Ensemble Prediction System (SREPS)": Final Report

Chiara Marsigli
ARPA EMR - Servizio Idro-Meteo-Clima
Viale Silvani 2/3
40122 Bologna
Italia

Contents

Contents

1 Summary **3**

2 Project report **3**

2.1 Introduction 3

2.2 System description and implementation 4

2.2.1 The COSMO-SREPS system 4

2.2.2 Testing period and data 7

3 Results **8**

3.1 The spread-error relationship 8

3.2 How different perturbations contribute to the spread 12

3.3 How different perturbations contribute to the skill 15

3.4 Study on parameter perturbations 22

4 Open points **28**

5 Resources used **28**

6 Lessons learned **28**

7 Acknowledgements **29**

1 Summary

The project focused on building an ensemble system for the short-range using the COSMO model, called COSMO-SREPS. During the first phases of the project, the ensemble was designed and implemented, then it was tested over long periods, in order to derive a robust statistical assessment of its features. In particular the system was running during the whole DOP of the MAP D-PHASE project (June to November 2007). The analysis of its performances was carried out over two COSMO regions: an alpine area and Greece. The main findings are:

- A good correlation between spread and error is observed, but the system tends to be under-dispersive. The gap between the spread and the error has been observed for a number of meteorological variables, both surface and upper-air; the gap decreases moving from surface towards upper-air variables. This evaluation is influenced by the presence of a model Bias, especially evident for 2m temperature.
- It has been recognized the need of applying more model perturbations. An extensive testing of new and more diverse parameter perturbations has been carried out within the project, but it is needed to continue this testing in the following of the project, due to the great amount of time and resources required. Furthermore, it has been decided to add also perturbations in the lower boundary of the COSMO model, to represent better the model uncertainties.
- The different types of perturbation contribute differently to the spread and to the skill of the system. In particular, driving model perturbation is the main source of spread in the ensemble as well as the main source of ensemble skill. COSMO model perturbation (parameter perturbation) plays a minor role, but contributes to the ensemble spread as well, with an amount variable according to the considered meteorological variable.
- The quality of the different driving models and of the different parameter choices are generally equivalent, since none of the different components of the system is always over-performing the others. The only exceptions are: the use of GME-driven initial and boundary conditions improve the system performances in terms of 2m temperature in summer, probably due to the coherence between soil and atmospheric fields; the use of the Kain-Fritsch scheme for the parametrization of the deep convection improves the precipitation detection at the expense of a larger number of false alarms.
- The ensemble skill in the forecast of surface weather parameters is reasonable. An objective assessment of the system quality will be carried on in the framework of the D-PHASE project, where the system performances will be compared with those of other state-of-the-art ensemble systems.

2 Project report

2.1 Introduction

The SREPS Priority Project focused on the building up of a high-resolution ensemble system for the short-range. The project main tasks were to develop and implement such an ensemble, then to run it over extensive testing periods and to evaluate the system features and performances. The ensemble is called COSMO-SREPS (COSMO Short-Range Ensemble Prediction System) and it is based on 16 integrations of the limited-area non-hydrostatic

COSMO model at about 10 km of horizontal resolution, with 40 vertical levels. This system has been built to fulfil some needs that have recently arisen in the COSMO community:

- to have a short-range mesoscale ensemble to improve the support especially in situations of high impact weather
- to have a very short-range ensemble for data assimilation purposes
- to provide boundary conditions for the COSMO-DE-EPS convection-resolving ensemble, currently under development at DWD.

Therefore, the ensemble had to be designed to describe the uncertainty affecting the short-range predictions of surface weather parameters at a high spatial resolution. Aiming at this purpose, the strategy to generate the mesoscale ensemble members proposed by this project tried to take into account as many as possible sources of uncertainties which affect the scales of interest in the weather forecast at the short time range, in order to model many of the possible causes of the relevant forecast errors. Hence, perturbations have been applied both in the driving model and in the mesoscale model. The driving model error is described by means of a multi-analysis multi-boundary approach. Initial and boundary condition perturbations are applied by driving the 10-km COSMO runs with the four 25-km COSMO members of the Multi-Analysis Multi-Boundary SREPS system of INM. These four lower resolution COSMO runs, nested on four different global models (IFS, GME, GFS, UM) which use independent analyses, are provided by INM for this purpose. A representation of the smaller scale uncertainty is accomplished by applying limited-area model perturbations as well: the values of a number of parameters included in the sub-grid process parametrization schemes are randomly changed (within their range of variability) in the different ensemble members. The main issues which have been addressed in the system evaluation are:

- if the system shows a good spread/skill relationship, representative of the capability of the ensemble in describing the forecast error
- how the different perturbations contribute to the spread and to the skill of the system
- which is the ensemble skill in the forecast of surface weather parameters.

2.2 System description and implementation

2.2.1 The COSMO-SREPS system

COSMO-SREPS takes both initial and boundary conditions from 4 integrations of the COSMO-model, performed over the Euro-Atlantic area at 25 km of horizontal resolution, and differentiated from each other according to the global model used to drive the runs. The 4 integrations at 25 km are nested on the following global forecasting systems: ECMWF (IFS), DWD (GME), NCEP (NCEP) and UKMO (UM). Since these global systems are 4 different and independent state-of-the-art forecasting chains, a good deal of differentiation in the global models driving the limited-area runs is ensured. These integrations are performed by the Spanish weather Service (INM), which provides directly the fields generated by the 4 runs of the COSMO-model at 25 km. For each of the 4 sets of initial and boundary conditions, the COSMO-model integrations at 10 km of horizontal resolution are then performed over a domain covering Central and Southern Europe (Fig. 1). Each 25-km run drives 4

10-km integrations, which differentiates from one another for different choices of the parameters representative of sub-grid physical processes. Tab. 1 reports the parameters which were selected, together with their range of variability and the values selected for the experiments, as suggested by the COSMO scientists responsible for the development of parameterizations schemes. Tab. 2 shows the set-up of each ensemble member run in terms of both driving model and physics.

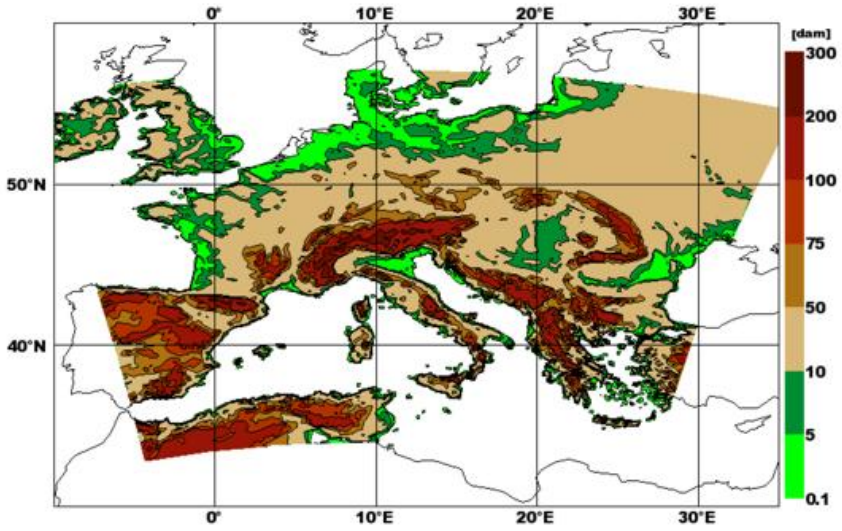


Figure 1: Integration domain of COSMO-SREPS (the model orography is shown).

Table 1: Perturbations applied to the model.

Perturbation name	Description	parameter range	default value	used value
SCHEMES				
Tiedtke	Scheme used for the parametrization of the deep convection		Tiedtke	Tiedtke
Kain-Fritsch	Scheme used for the parametrization of the deep convection		Tiedtke	Kain-Fritsch
PHYSICS				
pat_len	length scale of thermal surface patterns (influences mixing in the stable stratified atmosphere)	[0,10000] m	500	0, 10000
tur_len	maximal turbulent length scale (influences mainly stratospheric mixing)	[100,1000] m		1000

Table 2: Main features of the 16 runs which constitute the ensemble.

Member	Driving model of the LM-INM run	P1	P2	P3	P4
1	IFS	tiedtke=.T.	kainfri=.F.	tur_len=-1	pat_len=500
2	IFS	tiedtke=.F.	kainfri=.T.	tur_len=-1	pat_len=500
3	IFS	tiedtke=.T.	kainfri=.F.	tur_len=1000	pat_len=500
4	IFS	tiedtke=.T.	kainfri=.F.	tur_len=-1	pat_len=10000
5	GME	tiedtke=.T.	kainfri=.F.	tur_len=-1	pat_len=500
6	GME	tiedtke=.F.	kainfri=.T.	tur_len=-1	pat_len=500
7	GME	tiedtke=.T.	kainfri=.F.	tur_len=1000	pat_len=500
8	GME	tiedtke=.T.	kainfri=.F.	tur_len=-1	pat_len=10000
9	NCEP	tiedtke=.T.	kainfri=.F.	tur_len=-1	pat_len=500
10	NCEP	tiedtke=.F.	kainfri=.T.	tur_len=-1	pat_len=500
11	NCEP	tiedtke=.T.	kainfri=.F.	tur_len=1000	pat_len=500
12	NCEP	tiedtke=.T.	kainfri=.F.	tur_len=-1	pat_len=10000
13	UKMO	tiedtke=.T.	kainfri=.F.	tur_len=-1	pat_len=500
14	UKMO	tiedtke=.F.	kainfri=.T.	tur_len=-1	pat_len=500
15	UKMO	tiedtke=.T.	kainfri=.F.	tur_len=1000	pat_len=500
16	UKMO	tiedtke=.T.	kainfri=.F.	tur_len=-1	pat_len=10000

2.2.2 Testing period and data

The system was run over two main testing periods:

- 21 selected days of Autumn 2006, characterized by intense precipitation over either the Alpine area or Germany
- the MAP D-PHASE DOP (June to November 2007).

During Autumn 2006, 21 runs of the system were performed, on selected days characterized by intense precipitation over either the Alpine area or Germany. Fourteen runs were starting at 00 UTC, 7 runs at 12 UTC, on the basis of the availability of initial and boundary conditions. During the D-PHASE OP, 99 full runs of the COSMO-SREPS system were performed, covering not continuously the period, 50 in summer (JJA) and 49 in autumn (SON). Each full run (made up of 16 COSMO-model integrations at 10 km) started at 00UTC. The lack of continuity in the runs was mainly depending on the availability of initial and boundary conditions provided by INM. The analysis of the system was carried out over two COSMO regions:

- the Alpine area
- Greece

This is due to the availability of observations and to the COSMO scientists involved in the project. The climatology of two regions is very different, but both regions are quite complex from the geographical point of view (orography, proximity of the sea). In particular, it should be underlined that in Greece few and less intense precipitation events were observed during the D-PHASE period (this is why also the month of December has been included in the sample for Greece) and that summer 2007 was a remarkably warm one. Different data-sets have been used for the evaluation:

- high-res alpine: a dense network of stations covering northern-central Italy and Switzerland, providing precipitation data accumulated over 24h, from 06 to 06 UTC (about 1400 stations) (Fig. 2 left)
- high-res Italy: a dense network of stations covering northern-central Italy, providing precipitation data accumulated over 6h (about 900 stations) and 2m temperature data (about 600 stations)
- synop alpine: the SYNOP stations covering approximately the same area (43-48 ° N 6-14 ° E, 218 stations) (Fig. 2 right)
- synop Greece: the SYNOP stations covering Greece (about 90 stations) (Fig. 3)

Though the system performance was analyzed over both 2006 and 2007 testing periods, results are shown for the 2007 period only, due to the larger sample, which makes the analysis more statistically robust.

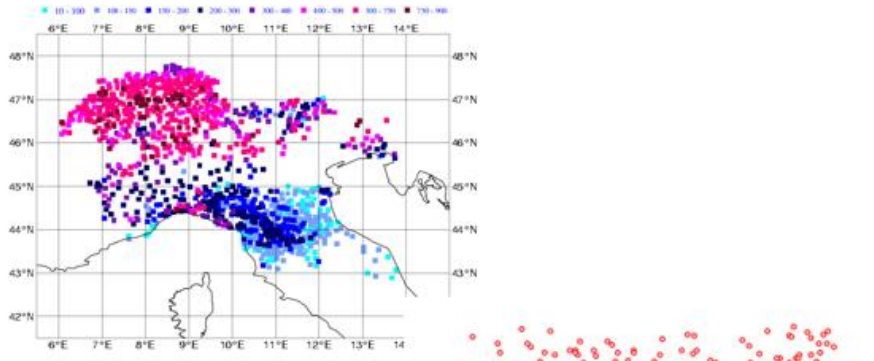


Figure 2: The high-res alpine dataset (left panel) and the synop alpine dataset (right panel). The high-res Italy dataset is made up by the Italian part only of the high-res alpine one.

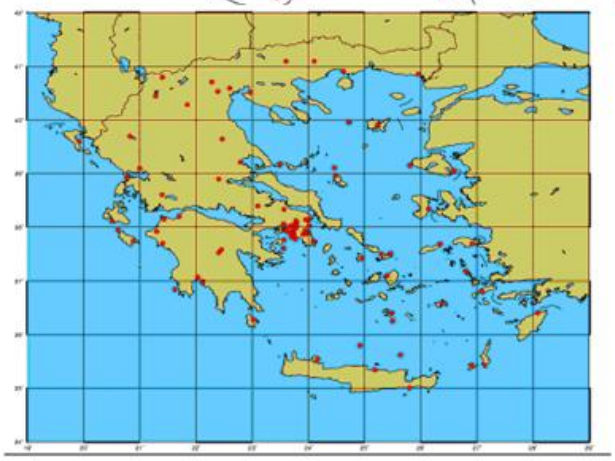


Figure 3: The synop Greece dataset.

3 Results

3.1 The spread-error relationship

The evaluation of the spread-error relationship was carried out on the Alpine area only, showing that the system still tends to be under-dispersive. The gap between the spread and the error has been observed for a number of meteorological variables, both surface and upper-air (2m temperature, mean-sea-level pressure, precipitation, temperature at 850 hPa, geopotential height at 500 hPa). Moving from surface towards upper-air variables, the gap decreases, but it is still detectable. In Fig. 4, the root-mean-square error of the ensemble mean and the root-mean-square spread of the ensemble (or ensemble standard deviation) are compared for the two seasons, in terms of 2m temperature. The error is computed by comparing forecasts interpolated on station points belonging to the synop alpine data-set with the corresponding observations, the spread is computed using these same interpolated forecast values, for homogeneity reasons.

The ensemble spread is bounded between 1 and 2 K in the summer season (Fig. 4, left panel), increasing with the forecast range and exhibiting a diurnal cycle, with values peaking at noon.

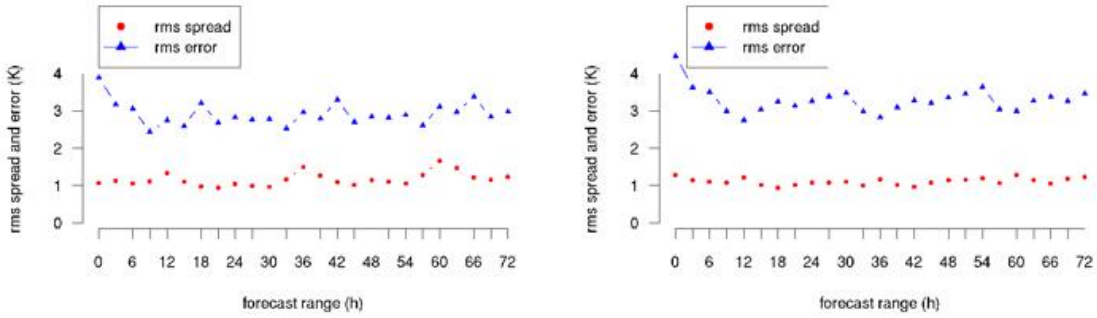


Figure 4: COSMO-SREPS spread (red) and error (blue) in terms of 2m temperature for summer (left) and autumn (right) 2007. Data are from the synop alpine dataset.

In autumn (right panel) the spread stays close to 1 K throughout the whole forecast range. In both seasons the ensemble mean error is quite larger than the spread, remaining below the 3 K value in summer, with peaks grater than 3 K at 18 UTC, while being generally above the 3 K value in autumn. The gap between the two measures is due to both the under-dispersion of the ensemble system and to the COSMO model systematic error, which should not be removed by ensemble techniques, but only by model improvement. In order to help in quantifying the contribution due to the model Bias, the same evaluation is repeated by using the COSMO-I7 analyses of 2m temperature instead of observed values in the computation of the ensemble mean error (Fig. 5). COSMO-I7 analyses are available at 00 and 12 UTC only.

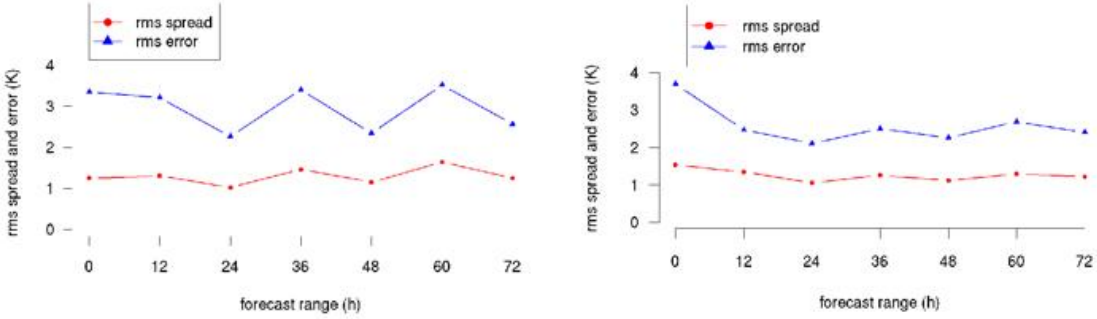


Figure 5: COSMO-SREPS spread (red) and error (blue) in terms of 2m temperature for summer (left) and autumn (right) 2007. Data are from the analysis of the COSMO model itself.

The root-mean-square spread values are the same, while the ensemble mean error is now reduced in both seasons. In summer the reduction is quite small, while is autumn the error is now bounded between 2 and 3 K, greatly improving the spread-error relationship. This indicates a dominance of the systematic error in autumn, which should be removed by model improvement and not addresses with ensemble techniques. A better representation of the spread/skill relationship of the ensemble is obtained by plotting the rms error as a function of the rms spread, after having divided the sample in classes of spread and computing for each class the average values of error and spread. This is shown in Fig. 6 for the 2m temperature

parameter, using data from the synop alpine data-set.

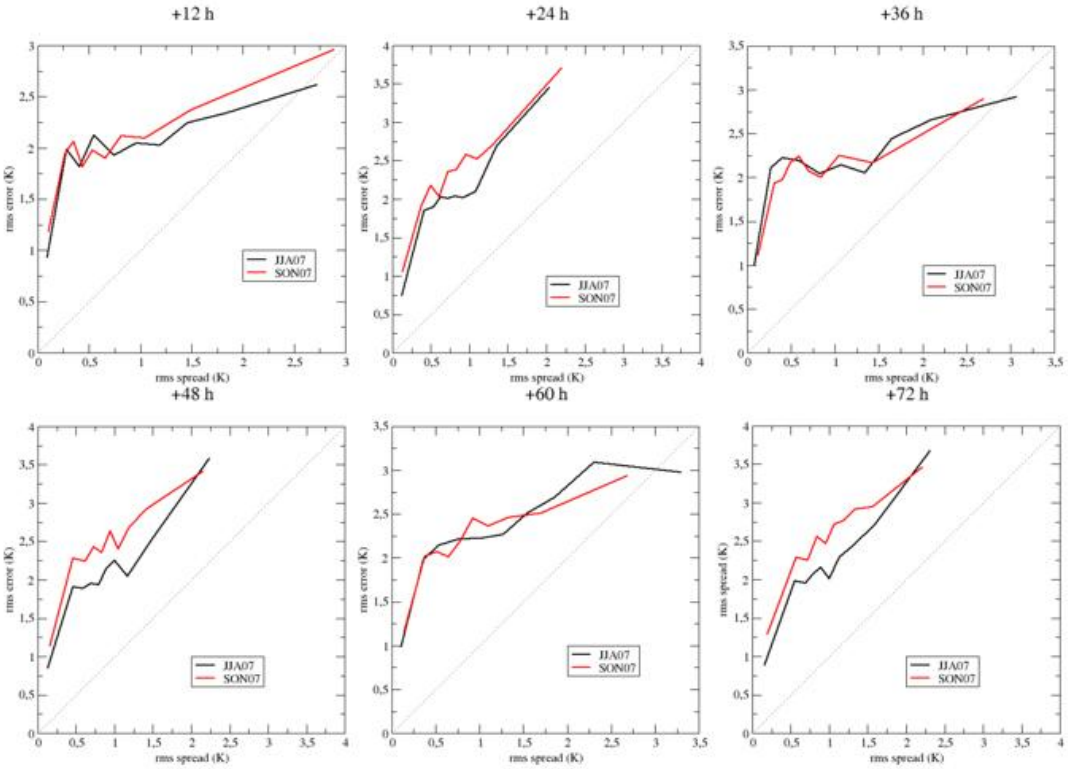


Figure 6: Spread/error relationship in terms of 2m temperature for summer (black line) and autumn (red line) 2007 for different forecast ranges (+12h, +24h, +36 h in the upper row, +48h, +60h, +72h in the lower row). Data are from the synop alpine dataset.

There is a clear correlation between error and spread, though at a given value of spread generally corresponds an higher value of error, even double. During the night (second, fourth and sixth panels, where data are from 00 UTC), the ensemble under-dispersion is less marked in the summer season. At 12 UTC (first, third and fifth panels) there two seasons exhibit a more similar behaviour, with a good relationship for high spread values. Moving from surface towards upper-air variables, the relationship exhibits only a little improvement. In Fig. 7, spread and error values in terms of temperature at 850 hPa are shown. The spread goes from 0.5 K at +12 h, increasing up to more than 1 K at the end of the period. The error grows similarly, being around the 2 K value. The spread/error relationship is shown in Fig. 8, indicating again the existence of a correlation but in presence of under-dispersion, though slightly less evident than for the surface variable.

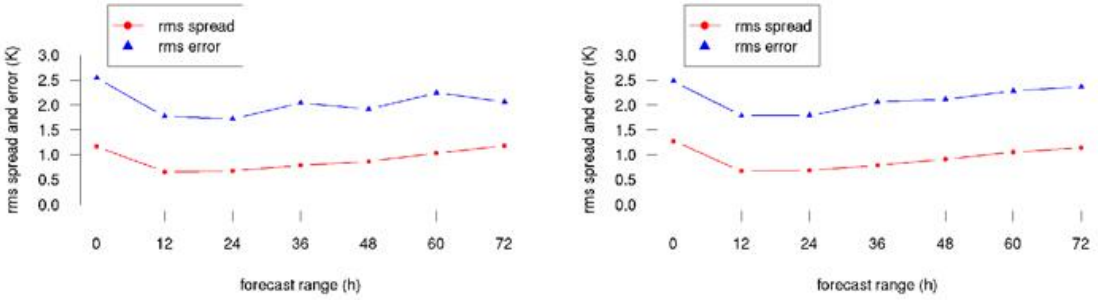


Figure 7: COSMO-SREPS spread (red) and error (blue) in terms of temperature at 850 hPa for summer (left) and autumn (right) 2007. Data are from the analysis of the COSMO model itself.

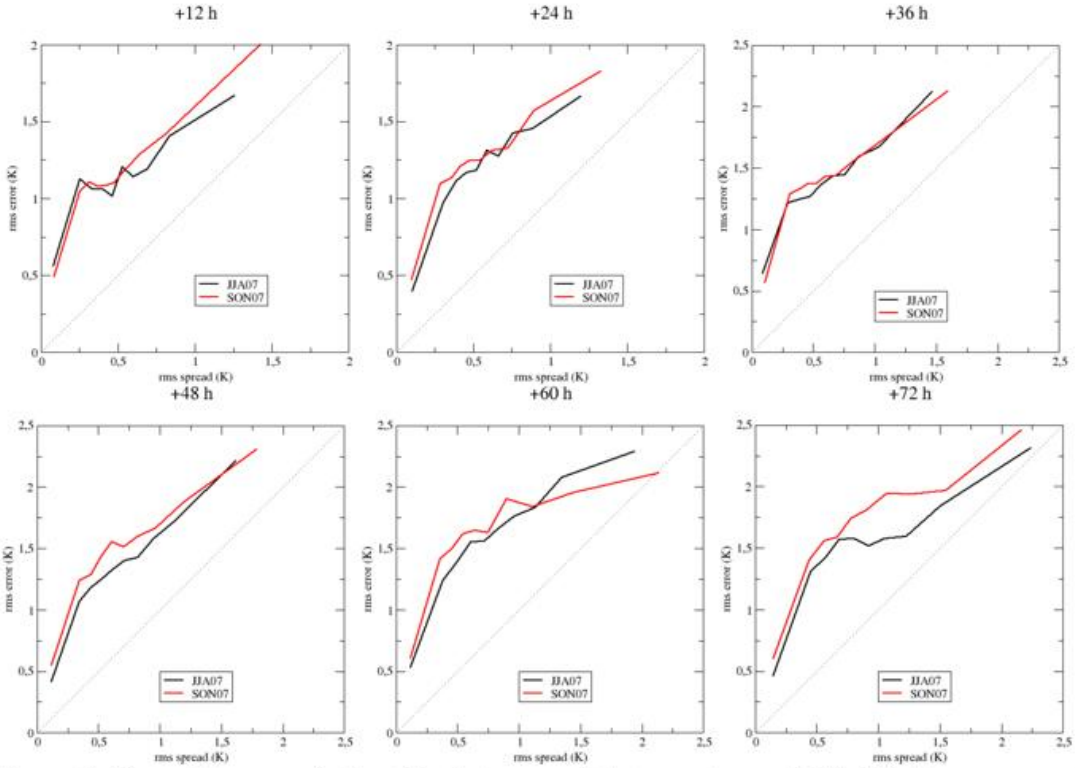


Figure 8: Spread/error relationship in terms of temperature at 850 hPa for summer (black line) and autumn (red line) 2007 for different forecast ranges (+12h, +24h, +36 h in the upper row, +48h, +60h, +72h in the lower row). Data are from the COSMO analyses.

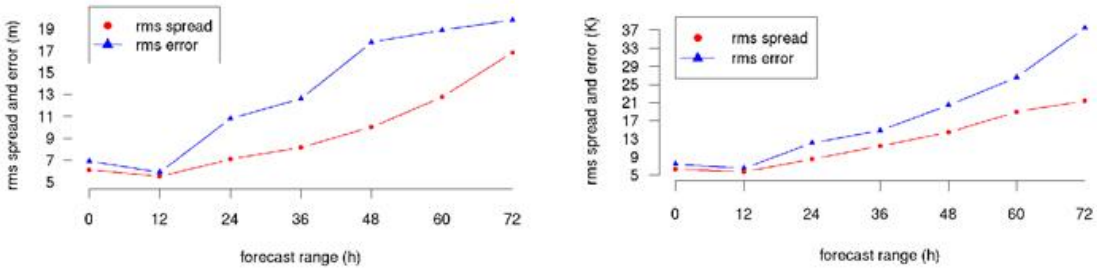


Figure 9: COSMO-SREPS spread (red) and error (blue) in terms of geopotential height at 500 hPa for summer (left) and autumn (right) 2007. Data are from the analysis of the COSMO model itself.

In Fig. 9, spread and error values in terms of geopotential at 500 hPa are shown. For this mid-tropospheric variable the ensemble spread is better able to describe the error, especially for the autumn season (right panel).

3.2 How different perturbations contribute to the spread

In order to quantify the contribution of each type of perturbation to the generation of spread in the ensemble, we have analyzed how the inner spread varies according to the two different methods used to group the ensemble elements. The 16 members can be subdivided into 4 groups of 4 elements each, in 2 different ways:

- considering groups of elements homogeneous in terms of initial and boundary conditions, but distinct for the model parameterizations;
- considering groups of elements homogeneous in terms of the model parameters, but distinct in terms of initial and boundary conditions.

The spread internal to the groups of the first type is due to parameter perturbations only (parameter spread), while the spread internal to the groups of the second type is due to driving-model perturbations only (driving-model spread). Each group is referred to after the common feature of their members, e.g. the group named *ecmwf* contains all the runs driven by the ECMWF global model, which have different parameter perturbations, while the group named *p1* contains all the runs with the same physics perturbation No. 1, with different initial and boundary conditions. For a complete characterizations of the 16 elements, see Tab. 2. In Fig. 10 the different spread components in terms of geopotential height at 500 hPa are shown.

The 4 upper lines represent the contribution to the spread due to different driving models only, while the 4 lower lines represent the contribution to the spread due to different physics parameters only. The driving-model spread is quite larger than the parameter one and increase rapidly with the forecast range. In terms of this mid-tropospheric variable, the perturbation of the parameters plays an almost negligible role, the parameter spread being about one order of magnitude lower than the driving-model one. In Fig. 11, the contributions to the spread are shown in terms of temperature at 850 hPa.

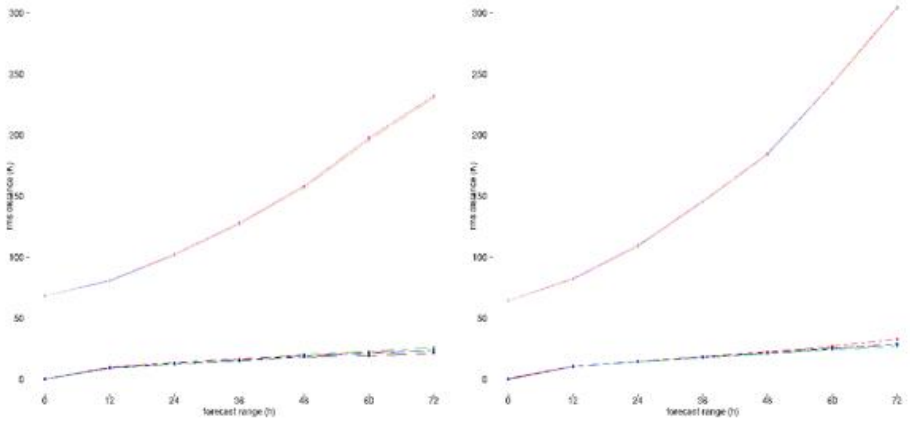


Figure 10: Spread (root-mean-square distance) of the ensemble members for the different forecast ranges, in terms of geopotential height at 500 hPa for the 50 summer runs (left panel) and for the 49 autumn runs (right panel). Each line represents the inner spread relative to a particular 4-member sub-ensemble. For each line, the legend denotes the feature which is common for a particular configuration of the 4-member sub-ensemble.

For this variable the driving-model spread is greater than the parameter one, but the two contributions are of the same order of magnitude. Parameter perturbations produce a spread of about 0.4-0.8 K, almost constant as forecast range increases, while driving-model perturbations produce a spread which ranges from 1 to 2 K, increasing with the forecast range.

Considering a surface variable, namely 2m temperature (Fig. 12), the spread components exhibit a different behaviour. In both season a larger contribution to the spread comes from the use of different initial and boundary conditions. In the summer season (left panel), the contribution is twice the one related to model physics perturbations, this holding throughout the entire forecast range. In the autumn season (right panel), instead, the contribution to the spread due to different initial and boundary conditions is only slightly larger than the one due to different physics configurations and the difference between the two tends to increase with increasing forecast range. It is worth mentioning that, locally on sub-areas or for single events, the main contribution can be provided for certain time ranges by the physical perturbations (not shown). It is also interesting to notice that the parameter spread (four lower lines in the panels) does not vary considerably depending upon the global model used to provide initial and boundary conditions to the COSMO-SREPS runs at which perturbations are then applied. As for the driving-model spread (four upper lines in the panels), this does not vary considerably depending upon the physics set-up adopted for the runs, with the exception of perturbation *p4* (grey line), which tends to give rise to lower spread.

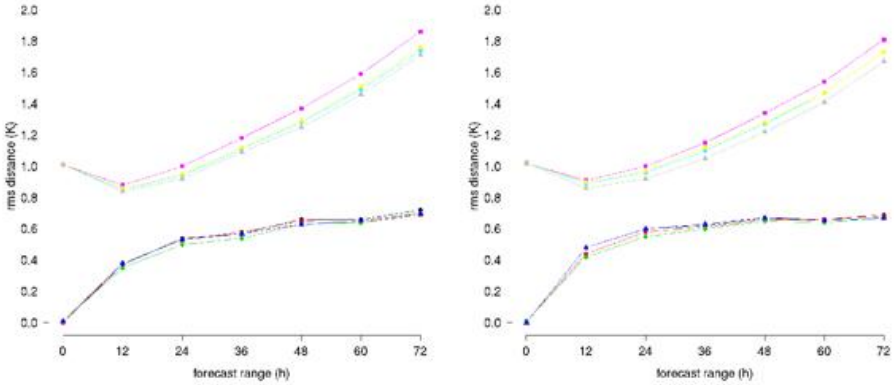


Figure 11: Same of Figure 10 but for temperature at 850 hPa.

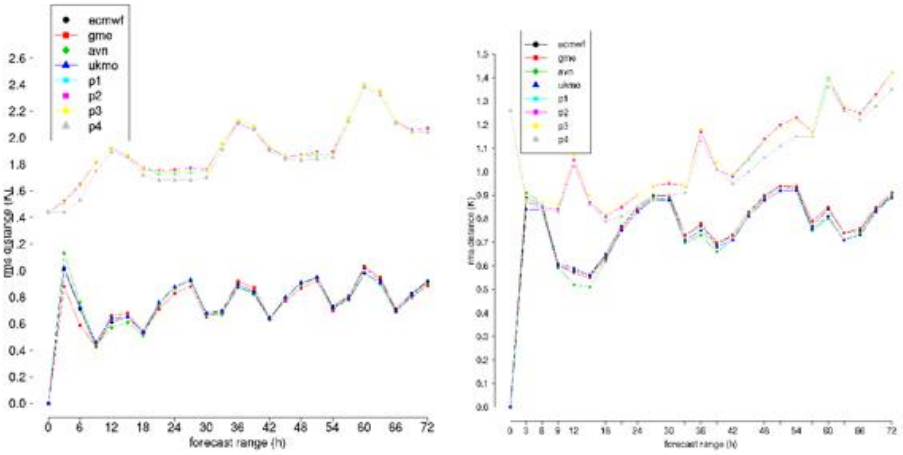


Figure 12: The same as in Figure 10 but in terms of 2-metre temperature. The sample is the high-res Italy dataset.

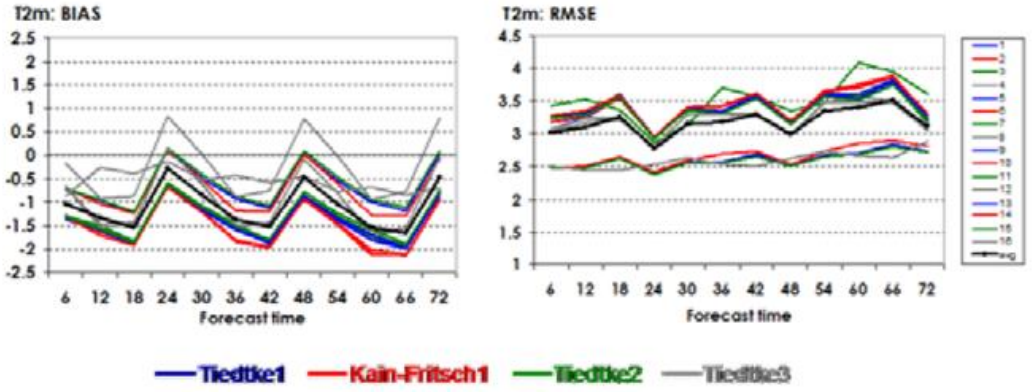


Figure 13: Bias and RMSE for temperature over Greece plotted with respect to effect of physical parameterisation. The thick black line represents the average of all the ensemble members.

A similar evaluation of the spread contribution in terms of 2m temperature was made over Greece (Fig. 13). Temperature Bias and RMSE of each ensemble member have been grouped with respect to the physical parametrization used for that member. It is indicated that that physics parameter perturbations were not producing a big impact in differentiating the scores obtained by the members.

3.3 How different perturbations contribute to the skill

In order to assess the contribution to the skill of the system provided by the different ensemble members, verification of the performances of the 16 runs has been also made, both in terms of temperature and precipitation. Results in terms of 2m temperature for summer 2007 are shown in Fig. 14 for northern and central Italy.

It is evident that the Bias of the GME-driven members is different from that of the other members, which are quite mixed up. In particular, GME-driven members are always warmer than the others. In terms of MAE, again the GME-driven members exhibit a peculiar behaviour, their error being the lowest. This indicates that the errors of the members of this group have lower absolute values, but probably most of them are of the "warmer type", hence sum up in the Bias with equal sign determining a Bias increase. Instead, the non-GME-driven members probably have some more "colder type" contributions to the Bias, though not enough to obtain a non-Biased forecast. Another interesting feature is the fact that members with physics perturbation *p4* (*pat_len*=10000) have the largest errors in the minimum temperatures (chain-dashed line with squares). The different behaviour of the GME-driven members is indeed present in both regions, as appears by considering the similar analysis carried out over Greece (Fig. 15). Nevertheless, conclusions about the Bias are different over the two areas: in Italy all the forecasts generally overestimate temperature, while in Greece all members underestimate temperature. This is an effect of the different climate conditions between the two regions. Looking at the error (mae or rmse) it seems that GME-driven members have better performance over both regions. It is worth pointing out that only the initial and boundary conditions provided to the GME-driven members are

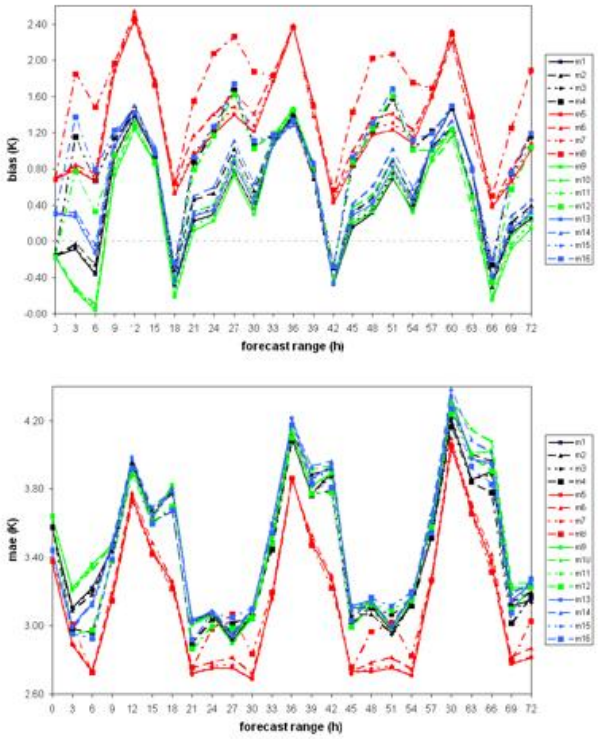


Figure 14: 2m temperature Bias (upper panel) and MAE (mean-absolute-error, lower panel) for the 16 COSMO-SREPS runs, computed over an alpine area (synop alpine dataset) for summer 2007.

characterized by a coherence between soil and atmosphere. In fact, in the 25-km COSMO runs performed by INM, the atmospheric fields are provided by the 4 different global models, while the soil fields are always provided by the GME run. Hence, the coherence between atmosphere and soil in the "father" runs can have a positive influence on the forecast of 2m temperature by the GME-driven members.

In order to identify the effect of the different months on temperature errors, both Bias and RMSE of the ensemble mean are calculated for each month (Fig. 16). It is clear that during summer months, especially June and July 2007, temperature is extremely underestimated. In fact, these two months were exceptionally warm with strong heat waves (the maximum temperature in Athens reached 46.2 °C in June). In autumn (here December is included as an autumn month), RMSE values remain close to 2 °C which is a statistically acceptable error value. It is worth underlining that the daily cycle of the error is inverse between summer and autumn months having its maxima during midday in the summer (also in September) and during night in autumn/winter. This is usual outcome for limited area models which is driven by soil parameterizations affecting the fluxes between soil and atmosphere. In Fig. 17, results in terms of 2m temperature for autumn 2007 are shown for northern and central Italy. During autumn, all the members exhibit a negative Bias, while in summer it was positive, but the error magnitude is almost the same (3-4 K). The 16 forecasts are quite mixed up, and the GME-driven members are included among the others. The performance of the IFS-driven members is slightly worse than the others, especially at the beginning of the forecast range. Members with physics perturbation *p4* are still characterized by a slightly different Bias, being generally warmer. Considering 24h precipitation forecast, the ensemble scores have been computed for each of the 4 groups of 4 elements which have been described at the

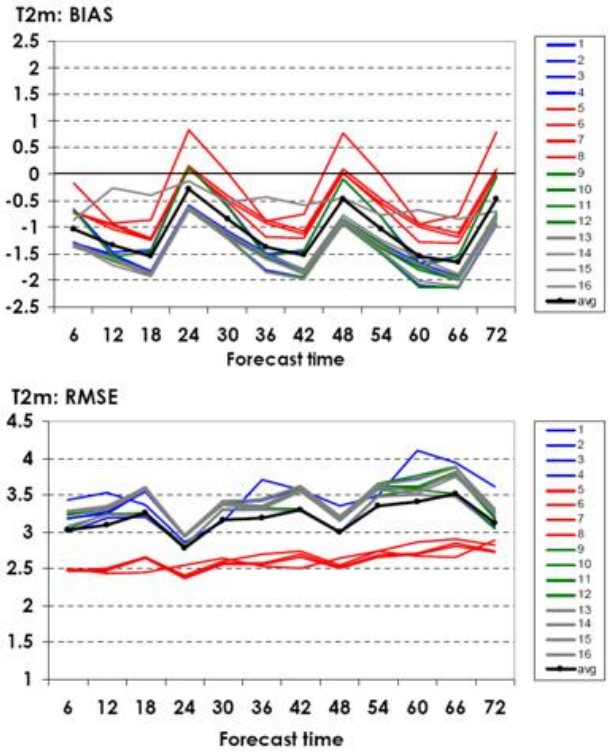


Figure 15: 2m temperature Bias (upper panel) and RMSE (lower panel) for the 16 COSMO-SREPS runs, computed over Greece for the whole period (June to December 2007).

beginning of section 3.2, in order to assess how the different forecast characteristics in terms of driving model and parameter contribute to the skill. The ROC area of the 4-member sub-ensembles are shown in Fig. 18 for the summer season and for the alpine area. The light blue line of each panel represents the ROC area of the full 16-member ensemble, which gives an indication of the COSMO-SREPS skill in forecasting precipitation for that period and in that particular area.

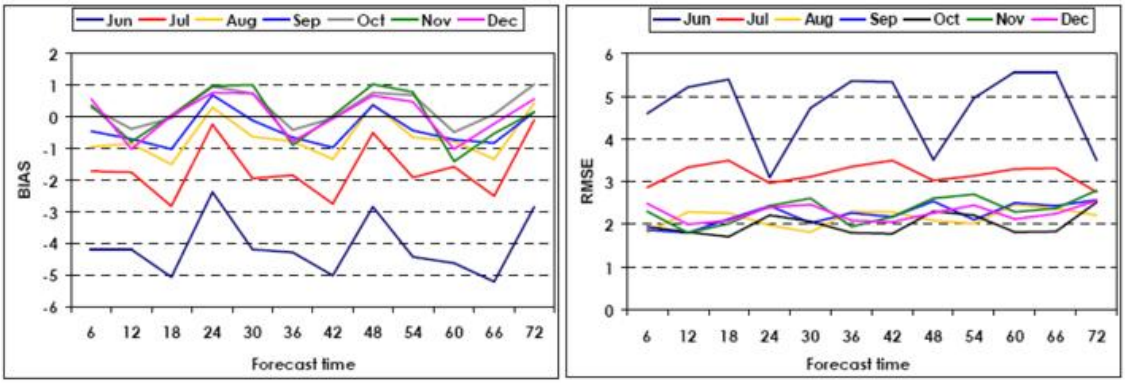


Figure 16: 2m temperature Bias (left panel) and RMSE (right panel) for the COSMO-SREPS ensemble mean, computed over Greece for the different months.

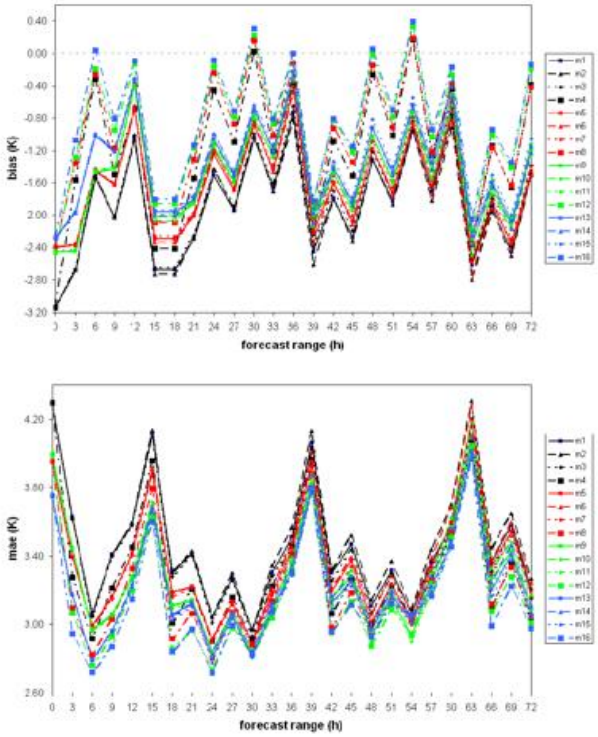


Figure 17: 2m temperature Bias (upper panel) and MAE (mean-absolute-error, lower panel) for the 16 COSMO-SREPS runs, computed over the alpine area (synop alpine dataset) for autumn 2007.

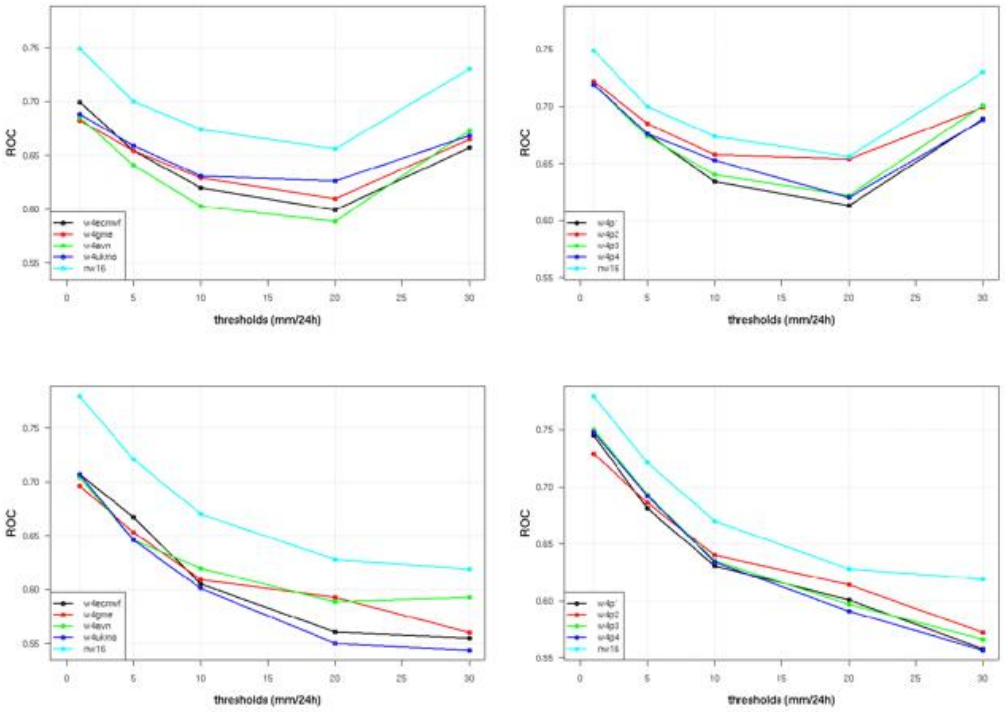


Figure 18: ROC area as a function of threshold for 24hr accumulated precipitation in the alpine area (high-res alpine data set) for the summer season. Left panels: full 16-member COSMO-SREPS (light blue line) vs. 4-member ensembles with identical 'mother run' (black: ECMWF, red: GME, green: GFS, blue: UKMO). Right panels: full 16-member COSMO-SREPS (light blue) vs. 4-member ensembles with identical physical perturbation (black: p1, red: p2, green: p3, blue p4). The upper panels are for the +30 h forecast range, while the lower panels are for the +54 h forecast range.

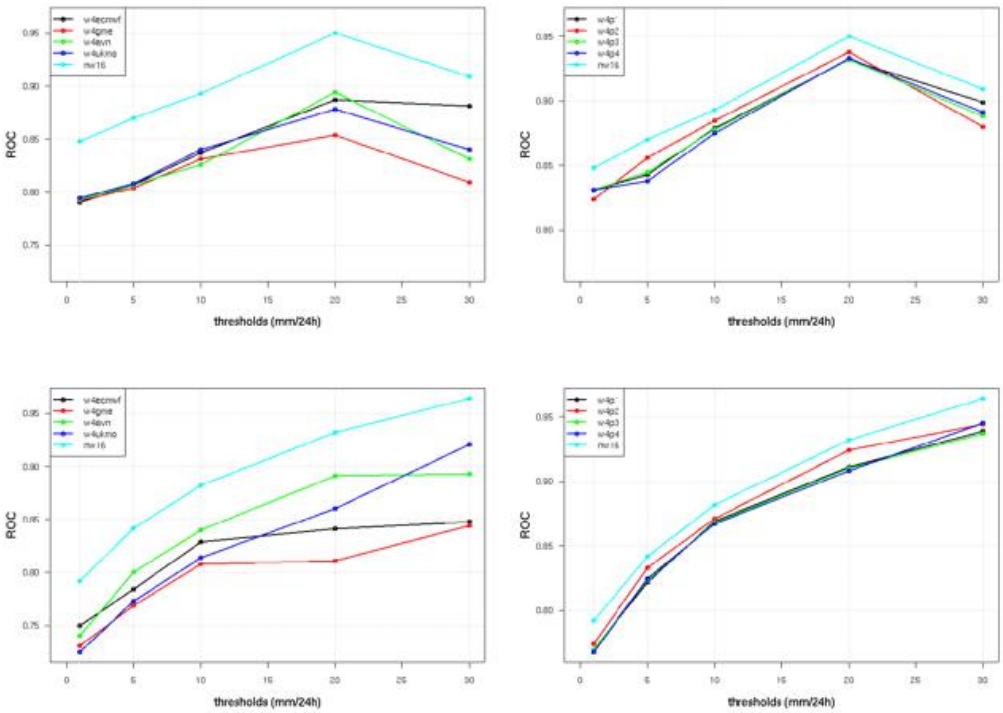


Figure 19: same of Fig. 18 but for the autumn season.

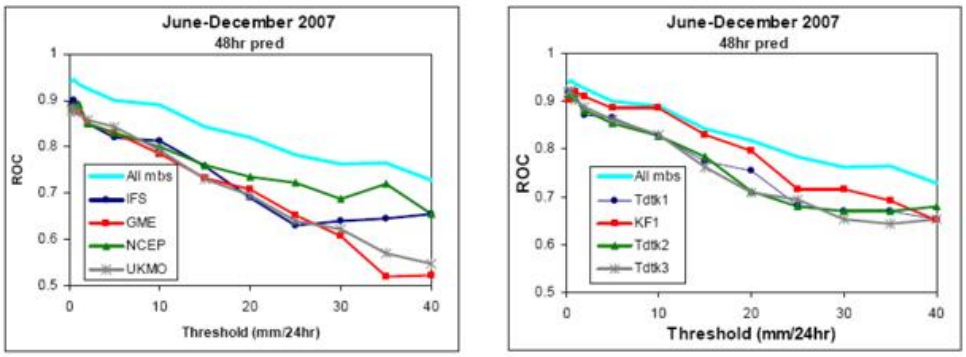


Figure 20: ROC area as a function of threshold for 24hr accumulated precipitation over Greece (synop Greece data set) for the whole period (June to December 2007). Left panel: full 16-member COSMO-SREPS (light blue line) vs. 4-member ensembles with identical 'mother run' (blue: ECMWF, red: GME, green: GFS, grey: UKMO). Right panel: full 16-member COSMO-SREPS (light blue) vs. 4-member ensembles with identical physical perturbation (blue: p1, red: p2, green: p3, grey p4). The forecast range is +48 h.

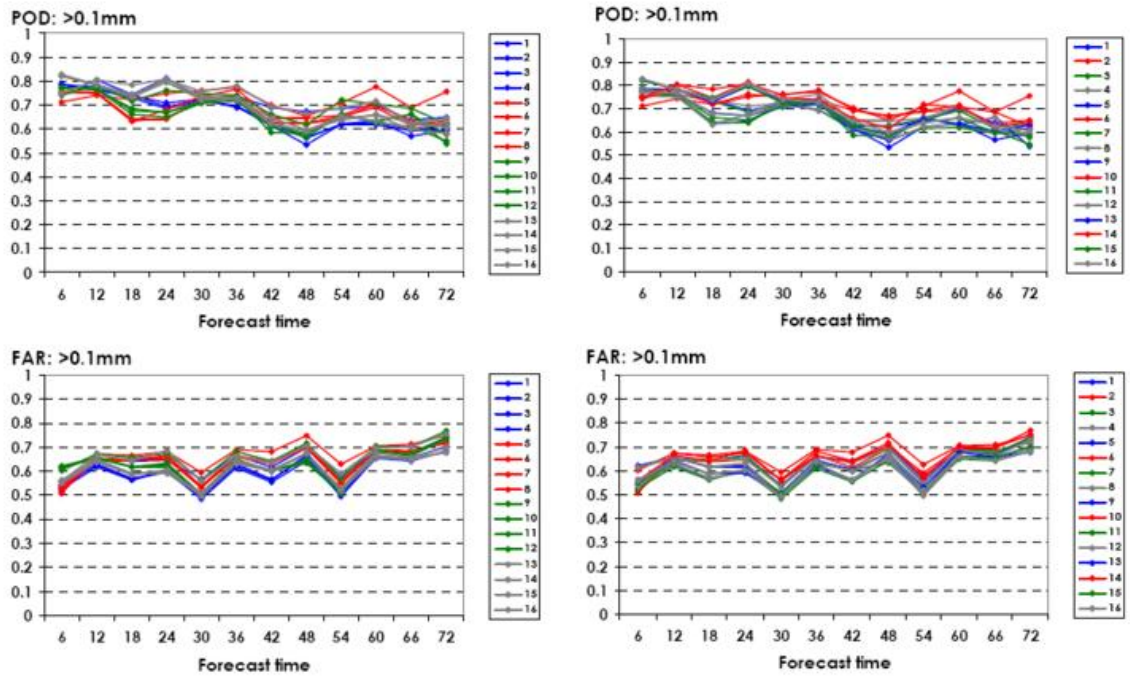


Figure 21: Probability of Detection (upper panels) and False Alarm Rate (lower panels) as a function of threshold for 6h accumulated precipitation over Greece (synop Greece data set) for the whole period (June to December 2007). In the left panels each line is coloured according to the driving-model of the member, while in the right panels each line is coloured according to the parameter set-up.

In the left panels, the other lines show the ROC area values of the 4-member ensembles made up by the 4 members nested on one particular global model. The 4 members are differentiated only in terms of the set-up of the physical parameterizations. Therefore, these represent the skill of ensembles, which are only model-perturbed, having the same initial and boundary conditions. Apart from the decrease in skill evident when passing from a 16-member to a 4-member ensemble, which is expected, it is worth pointing out that the different 4-member ensembles have different skill, which varies with the considered forecast range and also with threshold. In the right panels, the 4-member ensembles made up from identical physics perturbations are shown. Therefore, these represent the skill of ensembles, which are perturbed in the initial and boundary conditions only, but have the same model set-up. The comparison of each right panel with the corresponding left one suggests that perturbation of initial conditions generally yields more skillful performance than physical perturbation only. This is an indication of the fact that, the higher degree of diversity among members introduced by perturbing initial and boundary conditions determines a greater amount of skill with respect to the smaller-scale diversity introduced by the physics perturbations. As for the role of the different parameterizations, the 4-member ensemble where model perturbation *p2* (Kain-Fritsch convection scheme) is applied to each member (red line on the right panels) turns out to be more skillful that other 4-member ensembles. Results for the autumn season are shown in Fig. 19. It appears that scores for the autumn season are quite higher than those relative to the summer season, but the general features are the same. Again driving-model diversity gives rise to a more skillful forecast with respect to parameter diversity and the members of the Kain-Fritsch group tend to have more skill in terms of ROC area. The same evaluation has been performed also for Greece. Scores over Greece are shown in Fig. 20, for the whole period and at a +48h forecast range. It is

evident that larger skill resulted by varying the driving model only (lines in the right panel), compared to varying the physical parametrization only (lines in the left panel). The effect of the different initial conditions is not evident, while Kain-Fritsch parameterization provides the best score as the higher ROC area values suggest. From these results it is difficult to judge which driving-model leads to more skillful forecast, the results being dependent on the geographical area, on the season, on the forecast range and on the precipitation threshold. As for the different parameter choice, we should be careful in the evaluation of the Kain-Fritsch members. They have the best performance in terms of ROC area but the worst in terms of BSS (not shown). This is due to the fact that they always tend to produce slightly too much rain, as it is shown in Fig. 21, where Probability of Detection and False Alarm Rate for the 16 members over Greece is shown, in terms of 6-hour accumulated precipitation. Kain-Fritsch members have higher POD but also higher FAR. This result is confirmed over the alpine area (not shown).

3.4 Study on parameter perturbations

Beside the COSMO-SREPS suite, a parallel suite, called CSPERT, was implemented and run continuously at ECMWF (but not in real time) for the whole Autumn 2007 (September-October-November, 91 runs). Since the preliminary tests on COSMO-SREPS had identified a lack of spread due to an incomplete description of model uncertainty sources, this parallel suite was generated to choose more parameter perturbations for future implementation in COSMO-SREPS. This is necessary to increase the spread to values closer to the COSMO model error, especially for surface variables. The 16 perturbations involve also physical packages such as cloud and land schemes which had not been considered before (see Tab. 3). Initial and boundary conditions for the 16 runs were provided by the same run: the operational deterministic integration of ECMWF. The runs started daily at 00 UTC and the forecast range was 24 hours only, not 72 as in the COSMO-SREPS suite. This was done to save computer time, restricting the analysis to the shorter forecast range, where a good representation of the "error of the day" was needed also for data assimilation purposes.

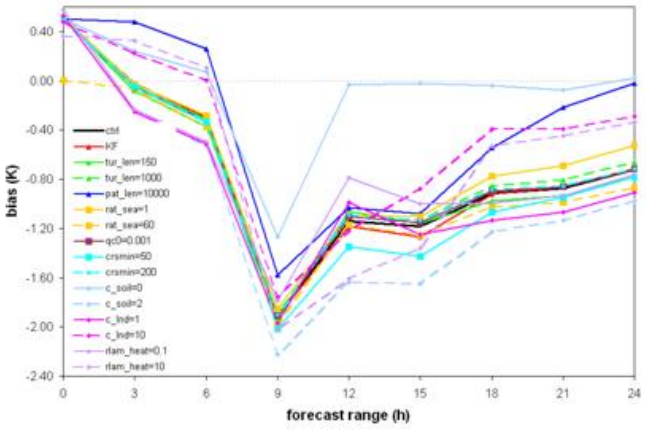


Figure 22: Mean Error (or BIAS) relative to the 16 CSPERT members in terms of 2m temperature, compared against observations over northern Italy for Autumn 2007.

In Fig. 22 and Fig. 23, an evaluation of the 16 runs is shown in terms of 2m temperature. The forecasts issued by the 16 members of the CSPERT suite were compared with non-GTS observations covering northern Italy (high-res Italy data-set, about 400 stations) for the

Table 3: Summary of the 16 perturbations applied in the CSPERT suite.

run nr.	**parameter name**	**parameter description**	**range**	**default**	**used**
1	**ctrl**				ope
2	**lconv**	convection scheme	T or KF	T	KF
3	**tur_len**	maximal turbulence length scale	[100,1000] m	500	150
4	**tur_len**	maximal turbulence length scale	[100,1000] m	500	1000
5	**pat_len**	length scale of thermal surface patterns	[0,10000] m	500	10000
6	**rat_sea**	ratio of laminar scaling factors for heat over sea	[1,100]	20	1
7	**rat_sea**	ratio of laminar scaling factors for heat over sea	[1,100]	20	60
8	**qc0**	cloud water threshold for autoconversion	[0,0.001]	0	0.001
9	**crsmin**	minimal stomatal resistance	[50,200] s/m	150	50
10	**crsmin**	minimal stomatal resistance	[50,200] s/m	150	200
11	**c_soil**	surface area index of the evaporating soil	[0,c_lnd]	1	0
12	**c_soil**	surface area index of the evaporating soil	[0,c_lnd]	1	2
13	**c_lnd**	surface area density of the roughness elements over land	[1,10]	2	1
14	**c_lnd**	surface area density of the roughness elements over land	[1,10]	2	10
15	**rlam_heat**	scaling factor of the laminar layer depth	[0.1,10]	1	0.1
16	**rlam_heat**	scaling factor of the laminar layer depth	[0.1,10]	1	10

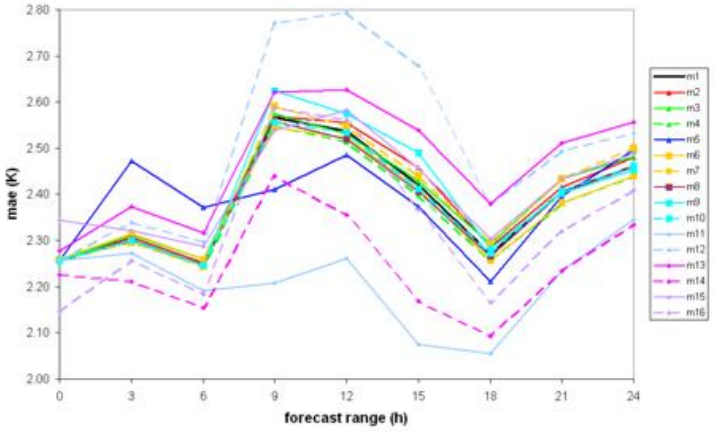


Figure 23: Mean Absolute Error (MAE) relative to the 16 CSPERT members in terms of 2m temperature, compared against observations over northern Italy for Autumn 2007.

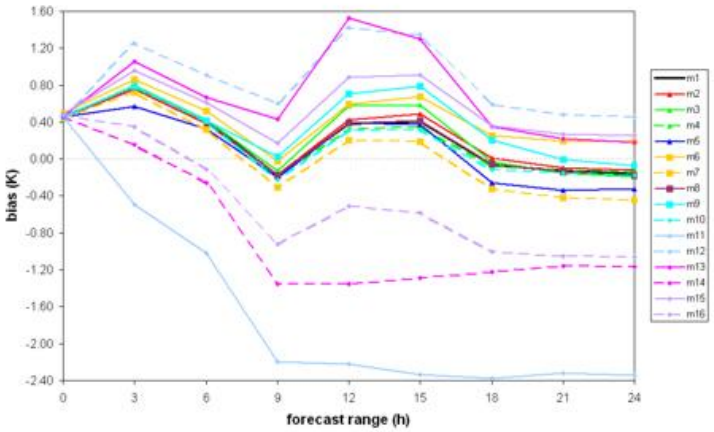


Figure 24: Mean Error (or BIAS) relative to the 16 CSPERT members in terms of 2m dew-point temperature, compared against observations over northern Italy for Autumn 2007.

whole Autumn 2007 period. This analysis shows that the perturbation of some parameters does not produce a detectable impact (at least in terms of 2m temperature), measured by the difference in score values between the run with that particular parameter set-up and the control run (thick black line). This is the case for the *qc0* and *tur_len* parameters. On the other hand, the perturbation of some parameters has a marked impact and could induce a significant increase of the ensemble spread. This is the case for the *c_soil*, *c_lnd* and *pat_len* parameters. It has to be underlined that if a particular parameter change produces a model integration which results to be statistically more or less skillful than the control run, this could be considered as a change to be implemented into all the runs to improve model performance and should not be used to produce ensemble perturbations. Of course we must be careful in this evaluation, the positive or negative impact should involve all the interesting meteorological variables and not just one. Furthermore, it is advisable to test the impact also on other seasons, characterized by different soil conditions and climatology. The good result obtained for 2m temperature by setting *c_soil*=0 should be regarded as suspicious, since this setting implies the suppression of any evaporation from

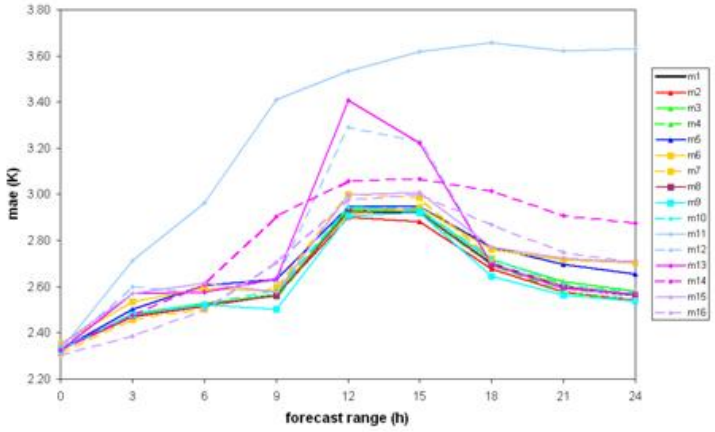


Figure 25: Mean Absolute Error (or MAE) relative to the 16 CSPERT members in terms of 2m dew-point temperature, compared against observations over northern Italy for Autumn 2007.

the bare soil. This is also evident by considering verification for other variables. Results of the evaluation in terms of 2m dew-point temperature are shown in Fig. 24 and Fig. 25. As it was expected, the run with *c_soil*=0 has the largest negative Bias and the largest error. The major impact is given by the runs with perturbation of the parameters *c_soil*, *c_lnd* and *rlam_heat*. Verification has been made also in terms of 6h precipitation forecasts (Fig. 26). The parameters producing the greater impact are *pat_len*, *c_soil*, *rlam_heat*, *rat_sea*. The major impact for the highest precipitation threshold is obtained by changing the scheme used for convection parametrization, namely using Kain-Fritsch instead of Tiedtke (perturbation *p2*, red line), as expected. As already underlined, the use of this scheme produces a positive Bias in precipitation, causing too many false alarms. The impact of the different set-up of the 16 runs on the selected meteorological variables is summarized in Tab. 4. The scores obtained by the 15 perturbed runs are evaluated against the score of the control run and a colour is assigned according to the performance:

- red: the perturbed run is worse than the control
- yellow: the perturbed run is slightly worse than the control
- light green: the perturbed run is slightly better than control
- dark green: the perturbed run is better than the control
- grey: the perturbed run is equivalent to the control
- white: no evaluation is possible, since the result changes with the forecast range

Looking at Tab. 4 it is evident that none of the runs performs continuously better than the control, so that its set-up can be used as the new control set-up. Some improvement is possible by choosing *rlam_heat*=10, *crsmin*=200 and *tur_len*=1000, but it is yet to be investigated what effect will be if these three values were implemented in the same run. Instead, the choice of *rlam_heat*=0.1, *c_lnd*=1, *c_soil*=2 and *tur_len*=150 has lead to a worsening of the performances. The fact that statistical behaviour of the various parameter set-ups "fluctuates" with respect to the control run (it is not always better nor worse) should

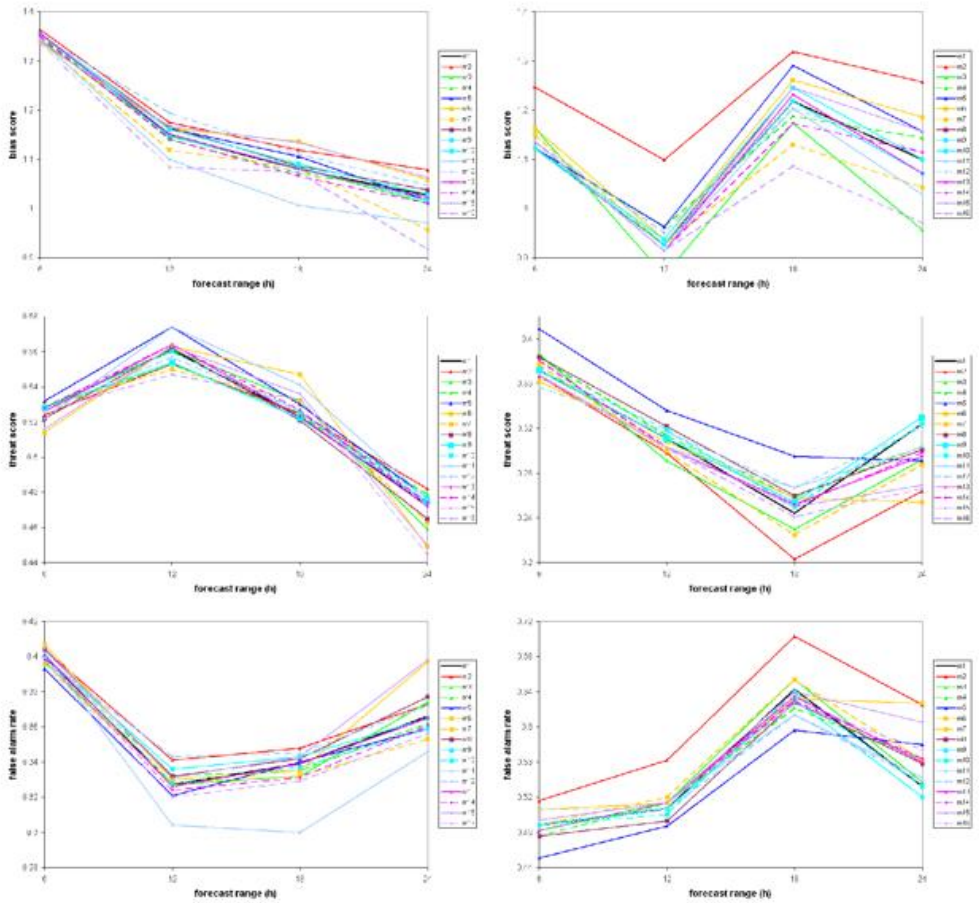


Figure 26: Bias Score (upper panels), Threat Score (middle panels) and False Alarm Rate (lower panels) relative to the 16 CSPERT members in terms of 2m 6h accumulated precipitation, for the 1mm/6h (left panels) and 10 mm/6h (right panels) thresholds.

be regarded as a positive outcome in this ensemble framework, since ensemble perturbations should be almost equivalent. The only set-ups which should be discarded are those which do not produce any (or a very small) impact (e.g. *tur_len* parameter). The analysis of these impacts is currently under study and will be completed during the CONSENS Priority Project. In particular, the CSPERT suite will be run for at least another season, probably summer, in order to assess the impact of the changes of the parameters in a quite different climatological situation. The outcome of the analysis will lead to the definition of a set of parameter perturbations to be applied in the future COSMO-SREPS suite.

Table 4: Summary of the performances of the 15 perturbed runs with respect to the control.

	t BIA	t MAE	td BIA	td MAE	tp1 BS	tp1 TS	tp1 FA	tp10 BS	tp10 TS	tp10 FA
KF										
tur_len=150										
tur_len=1000										
pat_len=10000										
rat_sea=1										
rat_sea=60										
qc=0.001										
crsmin=50										
crsmin=200										
c_soil=0										
c_soil=2										
c_lnd=1										
c_lnd=10										
rlam_heat=0.1										
rlam_heat=10										

4 Open points

- The system is under-dispersive (from the spread/skill relationship), hence there is a need to add more model perturbations
- It is difficult to assess in a statistically robust manner which parameters should be perturbed, since a large sample is needed. In fact, some values of the parameters can improve the forecast only for a certain season or for a certain meteorological variable. Furthermore, it is difficult to understand which choices of the parameter values can be made simultaneously in a run, unless some combinations are tried for a testing period
- Problems in running the system with continuity due to the difficulty of getting initial and boundary conditions every day
- The issue of perturbing the lower boundary was not addressed for reasons of lack of time and human resources
- The issue of perturbing the initial conditions at the mesoscale was not addressed for reasons of lack of time and human resources and it is abandoned for the moment

5 Resources used

- The computational resources needed to run the system are the Billing Units at ECMWF. These were provided by:
  - COSMO members (Germany, Italy (not for year 2008), Switzerland, Greece)
  - ECMWF through Special Projects: SPITLAEF and SPITFEAR

  The run of the system was computationally quite demanding, especially to carry on the testing of the new parameter perturbations.
- The verification task required quite an amount of resources in terms of FTEs, since it is a demanding task to obtain a statistically robust evaluation of the system performances. This had to be done for different seasons, different geographical regions and for a number of meteorological variables.

6 Lessons learned

Some Project tasks were not addressed due to lack of time and/or human resources: this was due mainly to a lack of experience in evaluating how much work was needed for a particular task, but also to the fact that, during the project, it was judged that it was more important to continue and further develop a certain line of research (not planned) instead of opening a new one. This is partly inherent in scientific research, since according to the results new questions can arise. Furthermore, since the work for the Priority Project is usually not the only one a scientist has to do, but it is done in addition to other operational and/or research work, new priorities can arise for her/him, which are not COSMO priorities but National or Regional Service ones. Finally, it happened that a task was temporally extended or shifted, for the same reasons already underlined, without undermining the project outcome. This should be considered in the project planning, allowing some flexibility in the time extension of the tasks.

7 Acknowledgements

List of contributing scientists

- Flora Gofa (HNMS)
- Petroula Louka (HNMS)
- Chiara Marsigli (ARPA-SIMC)
- Andrea Montani (ARPA-SIMC)
- Antonella Morgillo (ARPA-SIMC)
- Tiziana Paccagnella (ARPA-SIMC)

The cooperation with the Greek colleagues, which has been accounted for only as regards the verification task, was instead taking place also in the selection of the parameters to be perturbed and in the analysis of the impact of the new physics perturbations.

List of COSMO Newsletters and Technical Reports

(available for download from the COSMO Website: www.cosmo-model.org)

COSMO Newsletters

No. 1: February 2001.

No. 2: February 2002.

No. 3: February 2003.

No. 4: February 2004.

No. 5: April 2005.

No. 6: July 2006.

No. 7: April 2008; Proceedings from the 8th COSMO General Meeting in Bucharest, 2006.

No. 8: September 2008; Proceedings from the 9th COSMO General Meeting in Athens, 2007.

No. 9: December 2008.

COSMO Technical Reports

No. 1: Dmitrii Mironov and Matthias Raschendorfer (2001):
Evaluation of Empirical Parameters of the New LM Surface-Layer Parameterization Scheme. Results from Numerical Experiments Including the Soil Moisture Analysis.

No. 2: Reinhold Schrodin and Erdmann Heise (2001):
The Multi-Layer Version of the DWD Soil Model TERRA_LM.

No. 3: Günther Doms (2001):
A Scheme for Monotonic Numerical Diffusion in the LM.

No. 4: Hans-Joachim Herzog, Ursula Schubert, Gerd Vogel, Adelheid Fiedler and Roswitha Kirchner (2002):
LLM ¯ the High-Resolving Nonhydrostatic Simulation Model in the DWD-Project LITFASS.
Part I: Modelling Technique and Simulation Method.

No. 5: Jean-Marie Bettems (2002):
EUCOS Impact Study Using the Limited-Area Non-Hydrostatic NWP Model in Operational Use at MeteoSwiss.

No. 6: Heinz-Werner Bitzer and Jürgen Steppeler (2004):
Documentation of the Z-Coordinate Dynamical Core of LM.

No. 7: Hans-Joachim Herzog, Almut Gassmann (2005):
Lorenz- and Charney-Phillips vertical grid experimentation using a compressible nonhydrostatic toy-model relevant to the fast-mode part of the 'Lokal-Modell'

No. 8: Chiara Marsigli, Andrea Montani, Tiziana Paccagnella, Davide Sacchetti, André Walser, Marco Arpagaus, Thomas Schumann (2005):
Evaluation of the Performance of the COSMO-LEPS System

No. 9: Erdmann Heise, Bodo Ritter, Reinhold Schrodin (2006):
Operational Implementation of the Multilayer Soil Model

No. 10: M.D. Tsyrulnikov (2007):
Is the particle filtering approach appropriate for meso-scale data assimilation ?

No. 11: Dmitrii V. Mironov (2008):
Parameterization of Lakes in Numerical Weather Prediction. Description of a Lake Model.

No. 12: Adriano Raspanti (2009):
COSMO Priority Project "VERification System Unified Survey" (VERSUS): Final Report

No. 13: Chiara Marsigli (2009):
COSMO Priority Project "Short Range Ensemble Prediction System" (SREPS): Final Report

COSMO Technical Reports

Issues of the COSMO Technical Reports series are published by the *COnsortium for Small-scale MOdelling* at non-regular intervals. COSMO is a European group for numerical weather prediction with participating meteorological services from Germany (DWD, AWGeophys), Greece (HNMS), Italy (USAM, ARPA-SIMC, ARPA Piemonte), Switzerland (MeteoSwiss), Poland (IMGW) and Romania (NMA). The general goal is to develop, improve and maintain a non-hydrostatic limited area modelling system to be used for both operational and research applications by the members of COSMO. This system is initially based on the COSMO-Model (previously known as LM) of DWD with its corresponding data assimilation system.

The Technical Reports are intended

- for scientific contributions and a documentation of research activities,
- to present and discuss results obtained from the model system,
- to present and discuss verification results and interpretation methods,
- for a documentation of technical changes to the model system,
- to give an overview of new components of the model system.

The purpose of these reports is to communicate results, changes and progress related to the LM model system relatively fast within the COSMO consortium, and also to inform other NWP groups on our current research activities. In this way the discussion on a specific topic can be stimulated at an early stage. In order to publish a report very soon after the completion of the manuscript, we have decided to omit a thorough reviewing procedure and only a rough check is done by the editors and a third reviewer. We apologize for typographical and other errors or inconsistencies which may still be present.

At present, the Technical Reports are available for download from the COSMO web site (www.cosmo-model.org). If required, the member meteorological centres can produce hard-copies by their own for distribution within their service. All members of the consortium will be informed about new issues by email.

For any comments and questions, please contact the editors:

Massimo Milelli
Massimo.Milelli@arpa.piemonte.it

Ulrich Schättler
Ulrich.Schaettler@dwd.de

Consortium for Small-Scale Modelling

Technical Report No. 15

COSMO Priority Project "Tackle deficiencies in quantitative precipitation forecast (QPF)": Final Report

October 2009

DOI: 10.5676/DWD_pub/nwv/cosmo-tr_15

Deutscher Wetterdienst

MeteoSwiss

Ufficio Generale Spazio Aereo e Meteorologia

ΕΘΝΙΚΗ ΜΕΤΕΩΡΟΛΟΓΙΚΗ ΥΠΗΡΕΣΙΑ

Instytucie Meteorogii i Gospodarki Wodnej

Administratia Nationala de Meteorologie

Agenzia Regionale per la Protezione Ambientale del Piemonte

Agenzia Regionale per la Protezione Ambientale dell' Emilia-Romagna: Servizio Idro-Meteo-Clima

Centro Italiano Ricerche Aerospaziali

Amt für GeoInformationswesen der Bundeswehr

www.cosmo-model.org

Editor: Massimo Milelli, ARPA Piemonte
Printed at Deutscher Wetterdienst, P.O. Box 100465, 63004 Offenbach am Main

COSMO Priority Project "Tackle deficiencies in quantitative precipitation forecast (QPF)": Final Report

Project participants:

***S. Dierer*[1]‡, *M. Arpagaus*[1], *U. Damrath*[2], *A. Seifert*[2],**

***E. Avgoustoglou*[7], *T. Andreadis*[7], *M. Baldauf*[2], *R. Dumitrache*[9],**

***V. Fragkouli*[7], *F. Grazzini*[3], *W. Interewicz*[8], *P. Louka*[7]**

***P. Mercogliano*[6], *P. Mezzasalma*[3], *M. Milelli*[4], *D. Mironov*[2],**

***A. Morgillo*[3], *E. Oberto*[4], *A. Parodi*[5], *I. V. Pescaru*[9],**

***U. Pflüger*[2], *F. Schubiger*[1], *K. Starosta*[8], *M. S. Tesini*[3]**

‡ Project Leader

[1] MeteoSwiss

[2] DWD

[3] ArpaE

[4] ArpaP

[5] Uni. Genova

[6] CIRA

[7] HNMS

[8] IMGW

[9] NMA

Contents

1 Project report **3**

1.1 Introduction 3

1.2 Configuration and setup of the COSMO model 4

1.3 Selection and description of the test cases 6

1.4 Description of the sensitivity studies 9

1.5 Results of the sensitivity experiments 11

1.5.1 Change of the area averaged precipitation relative to the reference simulation 12

1.5.2 Change of the bias relative to the reference simulation 18

1.5.3 Cross experiments 21

1.6 Summary and conclusions 26

2 Workshops and meetings **28**

3 Presentation of QPF results **28**

4 Test cases description **29**

4.1 Germany 29

4.2 Switzerland 33

4.3 Emilia Romagna, Piemonte, Campania 39

4.4 Rome 45

4.5 Greece 49

4.6 Poland 52

4.7 Romania 58

5 Acknowledgements **62**

6 References **63**

1 Project report

1.1 Introduction

Quantitative precipitation forecasting (QPF) is an important reason to run a numerical weather prediction model - for forecasters and customers. Unfortunately, precipitation is also a very difficult parameter to quantitatively forecast. There are indications from verification and from forecasters in various COSMO countries, that the COSMO model - like other weather forecast models - has some serious deficiencies in quantitatively forecasting precipitation. This priority project aims at looking into the COSMO model deficiencies concerning QPF. The study is focused on the bias in area averaged accumulated precipitation rather than on local skill scores.

The QPF quality suffers from different sources of uncertainty such as inaccurate initial and boundary conditions, inaccuracies of numerical methods, and the incomplete description of physical processes. Especially, not all physical processes involved in the formation of precipitation are fully understood (Beard and Ochs, 1993), not to mention adequately represented in the model. Further limitations result from the fact, that some situations have a low predictability causing large errors in the precipitation forecast resulting from small errors in the initial conditions. This limited predictability especially occurs in situations which involve moist convection (Zhang et al., 2002; Walser et al., 2004; Hohenegger et al., 2006). The COSMO model, formerly known as Lokal Modell (LM, Steppeler et al., 2003), is a limited-area non-hydrostatic model that is developed within the consortium for small-scale modelling (COSMO). The model is designed for applications in the meso-β (20-200 km) and meso-γ (2-20 km) range and is used operationally at meteorological services in Germany, Greece, Italy, Poland, Romania, and Switzerland. A brief description of the model configuration and setup is given in Section 1.2. The objective verification of the operational forecasts as well as feedback by forecasters reveals deficiencies in the forecasts of precipitation. The kind of typical QPF error differs depending on the setup of the model for the operational forecasts in the different countries. The individual setups differ regarding size and location of the model domain, initial and boundary conditions as well as numerical methods or physical parameterizations. The aim of the present study is to investigate which parts of the modelling system have a significant impact on QPF. Investigations are focussing on numerical methods and physical parameterizations, while the effect of inaccurate initial and boundary conditions is disregarded in this study. Identifying the most important and/or weakest parts of the model will not necessarily lead to direct improvements, but can at least provide guidance for future research and development.

Investigations within the framework of this project are based on numerical sensitivity studies. Three to four test cases are selected for every implementation of the model representing typical forecast errors in the respective region. The test cases are selected such that the forecast error is unlikely to be caused by wrong synoptic conditions in the initial or boundary data. Altogether 25 test cases are selected that are representative for forecast errors in different geographical regions in Europe and for different meteorological situations (Section 1.3). For each of these test cases, 22 sensitivity studies regarding initial conditions, numerical methods and physical parameterizations (Section 1.4) are performed, and the effect and the importance of changes on the 24h area averaged precipitation is investigated (Section 1.5). The results and their implications are discussed in Section 1.6.

1.2 Configuration and setup of the COSMO model

The COSMO model is a non-hydrostatic limited-area atmospheric model developed within the Consortium for Small-scale Modelling (COSMO) for applications on the meso-β and meso-γ scale (Steppeler et al., 2003). The model is based on non-hydrostatic, fully compressible hydro-thermodynamical equations in advection form. The prognostic variables are horizontal and vertical wind components, pressure perturbation, temperature, specific humidity, cloud water and ice content, specific water content of rain and snow and turbulent kinetic energy. Generalized terrain-following height coordinates with rotated geographical coordinates are used.

The model equations are solved on an Arakawa C-grid with user-defined vertical grid staggering. They are spatially discretized with second-order finite differences. Time integration uses a second order leapfrog HE-VI (horizontally explicit, vertically implicit) time-split integration scheme including extensions proposed by Skamarock and Klemp (1992). A 4th order linear horizontal diffusion is calculated. 3-dimensional divergence damping and off-centering are applied in split time steps. Damping at the top of the model domain is done by Rayleigh damping in the upper layers. Data at the lateral boundaries are prescribed using a Davies-type one-way nesting.

Subgrid-scale turbulence is parameterized by a prognostic turbulent kinetic energy closure at level 2.5 including effects from subgrid-scale condensation and thermal circulations. The surface layer parametrization is based on turbulent kinetic energy and includes a laminar-turbulent roughness layer.

The formation of precipitation is described by a bulk microphysics parametrization including water vapor, cloud water and ice, rain and snow with a fully prognostic treatment of precipitation, i.e. three-dimensional transport of rain and snow is calculated. Condensation and evaporation are parameterized by saturation adjustment while depositional growth/sublimation of cloud ice is calculated using an explicit non-equilibrium growth equation. Subgrid-scale cloudiness used for radiation calculations is parameterized by an empirical function depending on relative humidity, ice content and height.

Moist convection is parameterized using a mass-flux scheme with an equilibrium closure based on moisture convergence following Tiedtke (1989). Radiation is calculated using a two-stream scheme for short- and longwave fluxes (eight spectral intervals) including a full cloud-radiation feedback. A multi-layer version of the soil model solving the heat conduction equation is applied. The simulations are performed using COSMO model version 3.19. Initial and boundary data are taken from GME forecasts (Majewski et al., 2002), no data assimilation is used. The horizontal grid size is 7 km and the number of vertical levels is varying between 40 and 45 for the different model implementations. The position of the model domain and its size also depends on the model implementation and is close to the operational setup of every involved meteorological service (Fig. 1).

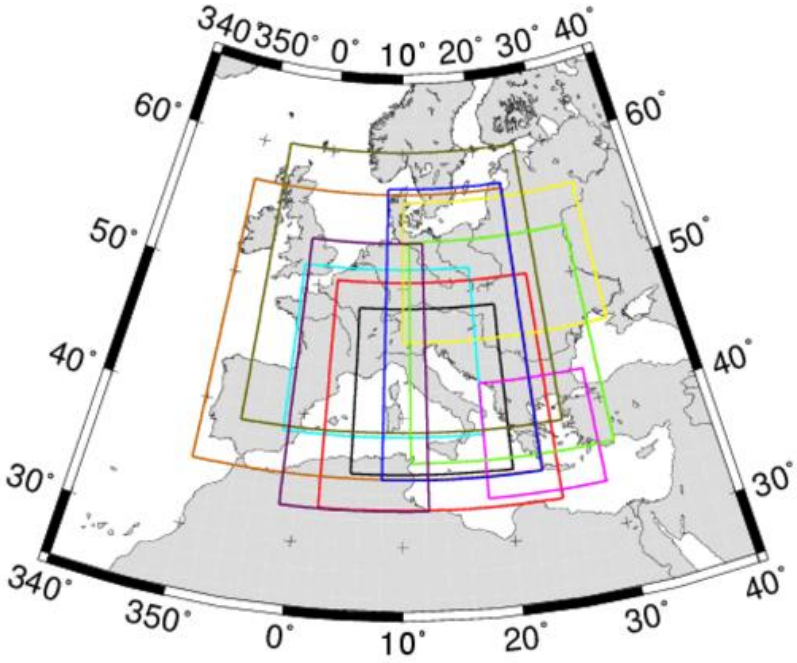


Figure 1: Position and size of the different model domains used for this study.

1.3 Selection and description of the test cases

The present study is focussing on the 24h precipitation sum of the first forecast day, that is, precipitation amounts between 6 and 30 hours lead time excluding the first 6 hours of the forecast (spin-up period). The first forecast day is chosen in order to ensure that initial and boundary conditions are close to reality and deficiencies of model forecasts are mainly due to numerical methods and physical parameterizations. The criterion for the test case selection is a poor forecast of the 24h precipitation sum on the first forecast day. The region of interest is specific for every involved meteorological service (Fig. 1).

The test cases are selected taking into account the typical QPF problems of the different regions of interest. No standard procedure for the selection is prescribed since operational verification procedures at the involved meteorological services are different. Based on operational QPF verification results and the experience of forecasters typical QPF errors are identified and single test cases are collected which reflect the most severe QPF errors and, hence, serve as a kind of prototype events for the observed QPF problems. In order to avoid wrong boundary forcing as a reason for bad QPF, the large-scale flow is checked to be reasonably well predicted. This selection resulted in a list of 53 test cases that were re-simulated with a COSMO reference version in order to exclude QPF errors due to out-dated model versions or inappropriate model settings. The reference version was COSMO model version 3.19, the newest version at that time, in the configuration described in Section 1.2. The boundary values for the reference simulations were taken from GME forecasts. If the QPF error disappeared or was completely changed in the re-forecast, the test case was excluded. The 25 test cases for which the original error was reproduced with the reference version remained on the list. Those test cases were characterized regarding the kind of QPF error (under-, overestimation), the kind of precipitation (mainly stratiform or convective) and the influence of fronts or orographic forcing. Three to four test cases per model implementation were selected by participants covering, if possible, different kinds of QPF errors. The test cases and their characteristics are summarized in Tab. 1.

The test cases fall into two main groups: underestimation of precipitation in convective weather situations (7 test cases) and overestimation of stratiform precipitation (9 test cases). There are 3 additional test cases with convective over- and 5 test cases with stratiform underestimation of precipitation and 1 test case that does not have a significant bias. The two dominant QPF errors correspond to specific geographical regions: 6 test cases of convective underestimation occur in regions where the weather is strongly affected by the vicinity to the Mediterranean Sea (Greece, Italy), and nine test cases of stratiform overestimation occur in countries in which the weather is less affected by the sea (Germany, Romania, Switzerland, and Poland). Thus, the geographical region and the kind of forecast error are closely related.

The QPF is evaluated based on the area averaged precipitation values calculated in evaluation regions that depend on the region of interest. The evaluation regions for the different test cases are defined in Section 4. The observed area averaged and maximum 24h precipitation values are compared with the simulated ones for all test cases (Fig. 2). Observed and simulated area averaged precipitation values are ranging from approximately 0.01 to 60 mm, differing strongly depending on the test case. Most of the test cases show significant differences between observed and simulated values except for the test cases 11 and 20, where the QPF error is not reflected by differences of area averaged or maximum precipitation values. Test case 11 is a situation with severe convective precipitation in the Piemonte region on the 17th of August 2006. The forecast error is underestimation of precipitation in the Toce catchment, while precipitation in the Ticino catchment is overestimated. The area averaged precipitation is calculated for a larger region and, thus, doesn't reflect the (large)

Table 1: Overview of selected test cases and their characteristics.

Case	Date	Meteorological service	Kind of error	Kind of precipitation	Fronts or orographic forcing
1	06.12.2004	Germany	overestimation	stratiform	warm sector
2	18.03.2005	Germany	overestimation	stratiform	cold front + orography
3	03.05.2005	Germany	overestimation	stratiform + convective	warm front
4	21.06.2005	Germany	underestimation	convective	cold front
5	02.02.2005	Switzerland	overestimation	stratiform	occluded front + orography
6	22.03.2005	Switzerland	overestimation	stratiform	warm front
7	12.07.2005	Switzerland	overestimation	convective	-
8	17.12.2005	Switzerland	overestimation	stratiform	orography
9	24.09.2004	Emilia Romagna	underestimation	convective	cold front + orography
10	10.04.2005	Emilia Romagna	overestimation	stratiform	occluded front + orography
11	17.08.2006	Piemonte	underestimation	convective	cold front + orography
12	09.09.2005	Campania	underestimation	convective	-
13	01.12.2005	Rome	underestimation	stratiform	cold front
14	03.12.2005	Rome	underestimation	stratiform	cold front + orography
15	17.12.2005	Rome	underestimation	stratiform + convective	cold front
16	15.09.2005	Greece	underestimation	convective	-
17	23.11.2005	Greece	underestimation	stratiform + convective	warm front
18	26.11.2005	Greece	underestimation	stratiform	orography
19	03.05.2005	Poland	underestimation	stratiform + convective	warm front
20	04.05.2005	Poland	average correct	stratiform	occluded front
21	10.06.2005	Poland	overestimation	stratiform + convective	-
22	09.08.2005	Poland	overestimation	stratiform	-
23	23.06.2005	Romania	overestimation	stratiform + convective	cold front
24	02.07.2005	Romania	overestimation	stratiform	cold front
25	12.07.2005	Romania	underestimation	stratiform	cold front

forecast error. A detailed description and discussion of this test case is given in Milelli et al. (2008). Test case 20 is a situation with stratiform precipitation on the 4th of August 2005. In the south-eastern part of Poland the forecast underestimates precipitation in a small region and north of this region the forecast overestimates precipitation. As a result, over- and underestimation are virtually canceling out and the area average is almost perfectly simulated. A discussion of both test cases is given in Section 4.

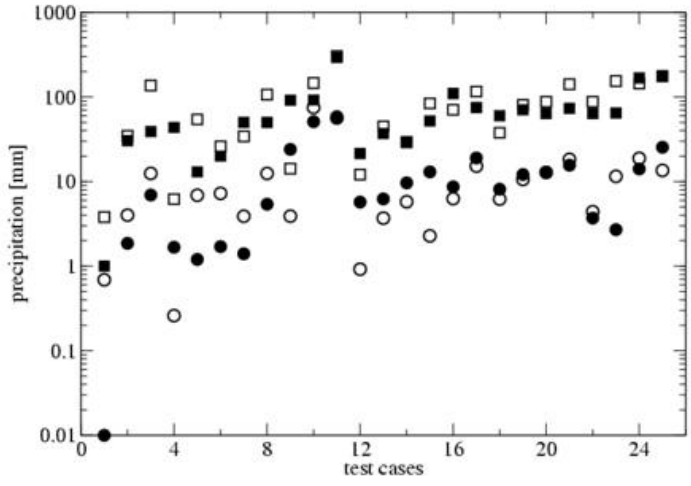


Figure 2: Observed (filled) and simulated (empty) area averaged (circles) and maximum 24h precipitation (squares).

Table 2: Overview of sensitivity studies regarding initial conditions.

No.	Sensitivity study	Expected	Kind of study
1	Reduction of soil moisture by 20%	Homogenous reduction of precipitation	idealized
2	Increase of soil moisture by 20%	Homogenous increase of precipitation	idealized
3	Reduction of initial humidity by 10%	Homogenous reduction of precipitation	idealized
4	Increase of initial humidity by 10%	Homogenous increase of precipitation	idealized

Table 3: Overview of sensitivity studies regarding numerics.

No.	Sensitivity study	Expected	Kind of study
5	Halved time step	Optimal case: nothing	idealized
6	Leapfrog, tri-cubic semi-Lagrange advection of QR and QS	Less diffusive advection of precipitation	option
7	Runge-Kutta, tri-cubic semi-Lagrange advection of QV, QC, QI QR and QS	Less diffusive, improved flow over terrain, improved advection of all moisture variables	option
8	Runge-Kutta, flux-form advection of QV, QC, QI, QR and QS	Less diffusive, improved flow over terrain, improve advection and mass conservation of all moisture variables	option
9	Runge-Kutta, flux form advection and T'-p' dynamics	Less diffusive, improved flow over terrain, improved advection and mass conservation and a better treatment of buoyancy terms	option
10	increased orography filtering	Slightly decreased orographic precipitation	idealized

1.4 Description of the sensitivity studies

Sensitivity experiments are divided into studies regarding initial conditions, numerical methods, and physical parameterizations. An overview of sensitivity experiments and expected changes is given in Tab. 2 to Tab. 4. The sensitivity experiments include idealized studies with changes that are not considered a possible configuration for operational applications (labeled 'idealized'), studies with optional schemes already included in the model ('option'), and studies with schemes that are currently under development and might be included soon ('development'). Sensitivity experiments regarding initial conditions, namely initial soil moisture and humidity are idealized studies. They are performed to have a reference in order to weight the effects of the other sensitivity experiments.

The sensitivity experiments regarding initial conditions are set up in an idealized way (Tab. 2). Soil moisture is increased (decreased) at all land grid points by 20%. The change is horizontally homogenous and is prescribed in all layers of the multi-layer soil model. The atmospheric water vapor mixing ratio is increased (decreased) by 10% in cloud free regions.

Table 4: Overview of sensitivity studies regarding physical parameterizations.

No.	Sensitivity study	Expected	Kind of study
Microphysics			
11	New warm rain scheme (Seifert and Beheng; 2001)	Reduced drizzle	option
12	Strong changes of ice microphysics and new warm rain scheme	Reduced drizzle and precipitation amount and increased transport of precipitation to mountain lee side	idealized
13	Moderate changes of ice microphysics and new warm rain scheme	Reduced drizzle and precipitation amount and increased transport of precipitation to mountain lee side	development
Convection			
14	Modified Tiedtke scheme	Weaker convection	development
15	Kain-Fritsch/Bechtold scheme	Modified convection	development
16	No parameterization of deep convection	Unrealistic up-scaling of convection, deteriorated forecast	idealized
Planetary boundary layer			
17/18	Decreased/increased scaling factor of height of laminar boundary layer for heat	Increased/decreased vertical exchange of heat and moisture	idealized
19/20	Decreased/increased stomata resistance	Increased/decreased vertical exchange of moisture	idealized
21/22	Decreased/increased laminar scaling factor for heat over sea	Increased/decreased vertical exchange of heat and moisture	idealized

Increased values might result in exceedance of the saturation value. In that test case the exceeding water vapor fraction is transformed to cloud water or cloud ice, respectively, but without considering latent heat release and, thus, a change in temperature.

Sensitivity experiments regarding numerical methods are changes of the time integration scheme in combination with different advection schemes (Tab. 3). For sensitivity experiments 7 to 9 the time integration scheme is changed from a leapfrog scheme to a two time-level 3rd order Runge-Kutta split-explicit scheme (Wicker and Skamarock, 1998). Advection of moisture variables in the reference simulation is calculated explicitly with a mix of various second-order spatial discretization, e.g., centered differences for moisture and cloud water, but upwind advection for cloud ice. Additional sensitivity studies are performed using a higher-order flux-form advection (Bott, 1989), a tri-cubic semi-Lagrange advection for water vapor and hydrometeors and a version using so-called T'-p'-dynamics, which is basically a reformulation of the dynamical core using perturbation temperature instead of total temperature. A sensitivity study with a halved time step is performed in order to confirm that the solution is insensitive against time step changes. The model orography is filtered in order to avoid numerically inaccurate solutions caused by mountain tops and valleys that are represented by only one grid point. The strength of filtering is increased in a sensitivity experiment in order to investigate its effect on orographically induced precipitation.

Sensitivity experiments regarding physical parameterizations are performed for microphysics, convection, and planetary boundary layer parameterizations. Microphysics studies include a sensitivity experiment using a one-moment variant of the warm rain scheme of Seifert and Beheng (2001) instead of the simpler Kessler-type formulation of autoconversion and accretion, and two studies with strong and moderate changes of ice microphysics (especially size, geometry of snow particles, and fall speed). Sensitivity experiments regarding convection include an idealized study without parametrization of deep convection, and a study using the mass flux Kain-Fritsch/Bechtold convection scheme (Bechtold et al., 2001) that is based on a CAPE closure instead of moisture convergence as used in the Tiedtke scheme. A further study is performed using the Tiedtke convection scheme with modifications regarding evaporation, turbulent entrainment and mixed-phase saturation adjustment. Three changes of the parameters of the planetary boundary layer parametrization change the vertical transport of heat and moisture. The vertical transport is decreased (increased) by a factor of 10 (50) in experiment 17 (18), by a factor of 3 (1.7) in experiment 19 (20), and by a factor of 20 (2) in experiment 21 (22). The change of stomata resistance affects the vertical exchange over land and is expected to be important for countries without strong influence by the sea (exp. 19/20). On the other hand, the change of the parameter affecting evaporation from the sea is expected to be important for countries with strong influence of the sea (exp. 21/22).

1.5 Results of the sensitivity experiments

The sensitivity experiments are performed and evaluated by the participating meteorological services. Model code and namelists are provided to everybody in order to ensure a consistent performance of sensitivity experiments. All sensitivity experiments (Tab. 2 to Tab. 4) are performed for all test cases (Tab. 1). However, some sensitivity experiments are missing for some test cases due to technical problems on different computational platforms.

A joint evaluation based on the area average of the 24h precipitation sum of lead times between +6 and +30 hours is performed. The area averaged precipitation value is calculated for the region of interest of every meteorological service. The evaluation regions are chosen sufficiently large in order to avoid changes by small-scale spatial shifts. The smallest evaluation region is about 100 km times 100 km. The evaluation regions are documented in

Section 4. The aim of the joint evaluation is an overview on the effect and its magnitude for different sensitivity experiments. Detailed investigations, e.g., of temporal development or small-scale spatial changes, are excluded from this joint evaluation. They are investigated by the participating groups individually. Due to the variety of details, these results are however not presented in this report.

1.5.1 Change of the area averaged precipitation relative to the reference simulation

We start with a joint evaluation based on the relative difference (Δrel) of the 24h area averaged precipitation of the sensitivity experiments (P_{exp}) with respect to the 24h area averaged precipitation of the reference simulation (P_{ref}):

$$\Delta rel = (P_{exp} - P_{ref})/P_{ref}. \tag{1}$$

The relative difference Δrel is very large for test cases 1, 4, and 12 because the area averaged value of the reference simulation P_{ref} is very small. Due to this dependency on the area averaged precipitation value of the reference simulation, relative differences are not comparable among different test cases. Thus, the relative difference allows comparing the effect of different sensitivity experiments, but not the test cases against each other.

An overview on the results for all sensitivity experiments and all test cases is given in Fig. 3, while Fig. 4 facilitates the comparison between different sensitivity experiments by condensing these results as follows: the sum for all test cases of the absolute values of the relative difference $\sum|\Delta rel|$ is shown as black bars whereas the sum of relative differences $\sum \Delta rel$ is given as grey bars. If a sensitivity experiment is causing an increase or decrease for most of the test cases, $\sum|\Delta rel|$ is about the same as $|\sum \Delta rel|$. On the other hand, the sum of absolute values is much higher than the sum of relative changes, if test cases with an increase and decrease of area averaged precipitation are canceling out.

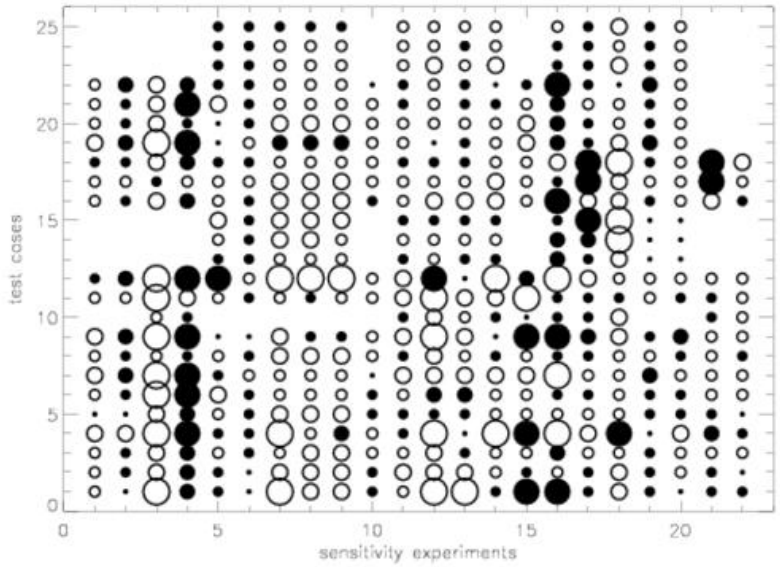


Figure 3: Difference of 24h area averaged precipitation in the sensitivity study and in the reference simulation relative to the 24h area averaged precipitation in the reference simulation Δrel [%]. Filled (empty) circles indicate an increase (decrease) of precipitation relative to the reference simulation. The big circles indicate a change bigger than 30%, medium ones between 10% and 30%, small ones between 0% and 10%, and tiny circles indicate cases with no change at all.

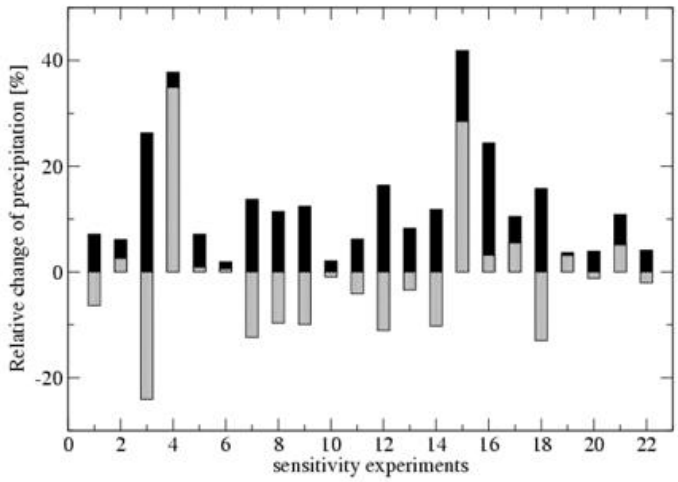


Figure 4: Relative difference of the 24h sum of area averaged precipitation in the sensitivity studies. The sum of the absolute values of the relative changes of area averaged values $\sum|\Delta rel|$ is given as black bars, whereas the sum of relative changes of area averaged precipitation $\sum \Delta rel$ is given as grey bars. The relation between grey and black bars indicates whether changes have predominantly one direction.

Initial conditions

Besides the Kain-Fritsch/Bechtold convection scheme (see below), the strongest changes in area averaged precipitation sums occur in the sensitivity experiments with changed initial humidity (exp. 3 and 4; cf. Fig. 4). The increase (decrease) of initial humidity by 10% causes an increase (decrease) of precipitation of more than 30% in about half of the test cases and between 10% and 30% for most of the other test cases (cf. Fig. 3). The change of initial humidity is predominantly acting as expected: an increase of initial humidity increases the average precipitation by 40% and a decreased initial humidity decreases it by 22%. Compared to the initial humidity changes, the average effect of the soil moisture changes by 20% results in a change in Δrel of less than 10% (exp. 1 and 2; cf. Fig. 3 and Fig. 4). The effect of initial soil moisture has a clear direction, and in those test cases where the change acts in the opposite direction, the effect is typically small. An explanation for the small effect of soil moisture changes might be that the first forecast day is evaluated. Soil moisture might act on a longer time scale and might be more important for longer forecast periods.

The strong impact of initial humidity is not surprising. Verifications of COSMO model results hint at an overestimation of atmospheric humidity. An example is the verification of the COSMO-EU model for the year 2007 using about 20 radio soundings in Europe. The comparison is carried out in the frame of the General Observation Period of the Priority Programme "Quantitative Precipitation Forecasts" of the German Research Foundation. Monthly bias and RMSE of mixing ratio are presented on the web page

http://gop.meteo.uni-koeln.de/gop/doku.php?id=data_quicklooks.

The monthly verification of the mixing ratio bias shows a great variety depending on radiosonde station and season. Examples for the radiosonde stations Lyon, Payerne, and Greifswald for January and July 2007 are shown in Fig. 5. The results show that the mixing ratio is overestimated above approximately 1000 m above ground in the model simulations during winter for these three radiosonde stations. The bias of initial humidity is generally relatively small, but increases significantly during the first 3 hours of simulation. In the summer months the overestimation of the mixing ratio in the model simulations is less pronounced. On the contrary, the mixing ratio bias at radiosonde stations in Italy and France show a tendency of underestimated humidity in the model simulations. Thus, over- and underestimation of simulated humidity might be an explanation for stratiform overestimation as well as convective underestimation. These results are only based on results of one model implementation, COSMO-EU, and for just one year, 2007. Still, the results motivate further investigations regarding the connection between simulated humidity and QPF deficiencies and possible reasons for over- or underestimated humidity in the COSMO model. The sensitivity studies confirm the expected great importance of simulated humidity for the precipitation forecast and, thus, it needs to be investigated if QPF deficiencies are partly based on wrong humidity.

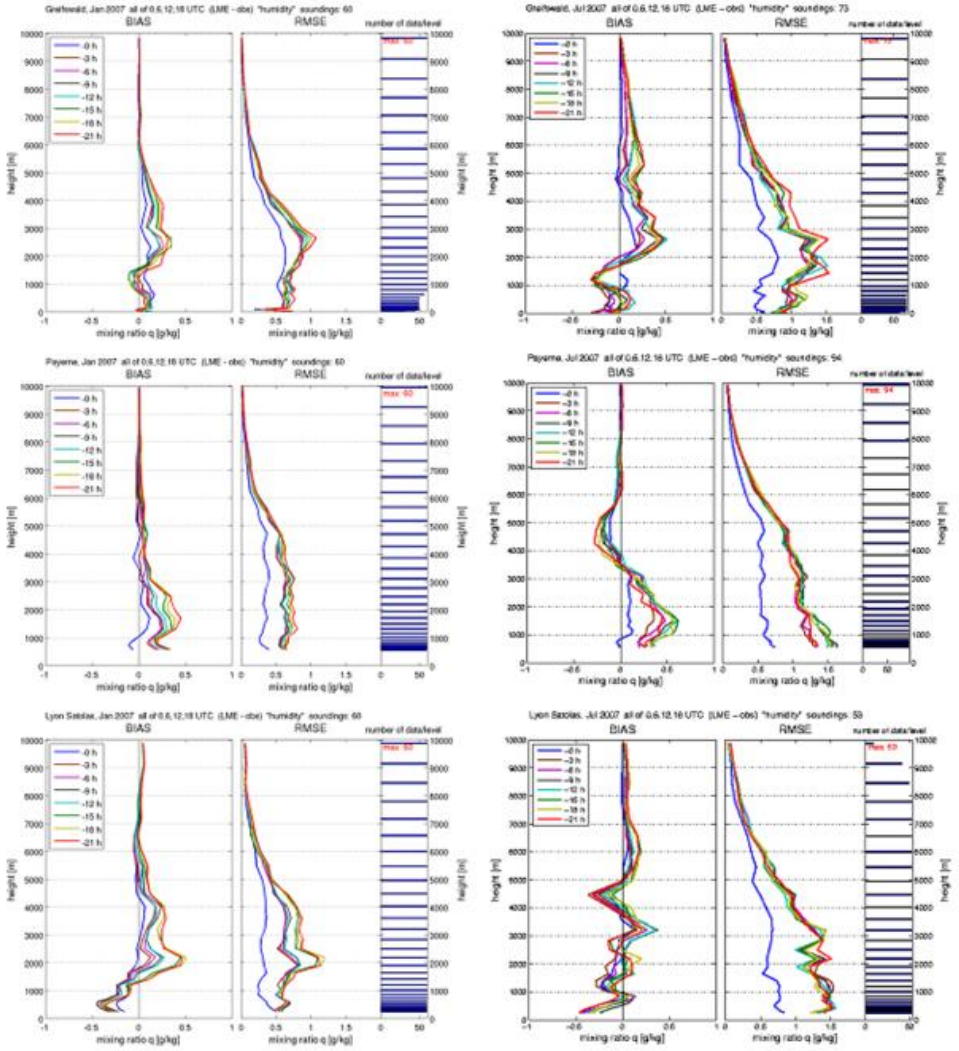


Figure 5: Monthly average Bias and Rmse for the observed and simulated vertical profile of mixing ratio at the radiosonde stations Greifswald (top), Payerne (middle), and Lyon (bottom) in January 2007 (left panels) and in July 2007 (right panels). The figures are taken from the GOP webpage: *http://gop.meteo.uni-koeln.de/gop/doku.php?id=data_quicklooks*.

Numerical methods

The strongest effect when changing numerical methods is the decrease of average precipitation when using the Runge-Kutta time integration scheme instead of Leapfrog (exp. 7 to 9; cf. Fig. 4). The Runge-Kutta scheme reduces the average precipitation amount by about 10%, for most of the test cases (cf. Fig. 4), stratiform as well as convective (cf. Fig. 3). The reason for this decrease has not yet been investigated. A possible explanation is that the centered differences, which are used in the reference simulation for advection of QV and QC, are not sufficiently accurate or lead to a significant mass error. Compared to this, the effect of the different variants of the Runge-Kutta scheme (exp. 7 to 9) is small. The effect is also small if the Leapfrog scheme is used with different advection schemes for mixing ratios of rain and snow (exp. 6; cf. Fig. 4), which leaves the improved advection of cloud and ice mixing ratios as the only possible explanation for the change in the average precipitation. Unfortunately, it was not possible to test this in a separate sensitivity experiment.

The impact of increased orography filtering and halved time step is negligible (exp. 5 and 10; cf. Fig. 4), i.e., changes remain below 10% for nearly all test cases. Only one test case with underestimated convective precipitation (test case 12) shows a significant relative increase of precipitation when changing the orography filtering, which is mainly due to the low area averaged precipitation value in the reference run. The absolute change from 0.92 mm in the reference run to 1.30 mm in the sensitivity experiment is small. Orography filtering and time step are part of the numerical methods and they should not have a significant impact on the results. Thus, insensitivity with respect to changes of orography filtering and time step is a positive result.

Physical parameterizations

The biggest change, besides the initial humidity changes, is caused by using a different convection scheme: Kain-Fritsch/Bechtold instead of Tiedtke (exp. 15). The sum of absolute values of relative changes of precipitation $\sum |\Delta rel|$ is about 40% resulting in an average increase of 30% (cf. Fig. 4). Changes are acting in both directions and there are many test cases with reduced average precipitation (cf. Fig. 3). Still, relative changes with increased average precipitation are bigger. This result is consistent with results from a comparison of the Kain-Fritsch/Bechtold and the Tiedtke scheme for Switzerland for summer 2006. The comparison showed that the Kain-Fritsch/Bechtold scheme tends to simulate higher area averaged precipitation values (Dierer and Schubiger, 2008). A test case with underestimated convective precipitation (case 4) is showing significantly better results with the Kain-Fritsch/Bechtold scheme which is triggering convection while the Tiedtke scheme misses the convective activity (Section 4).

Switching off convection causes average changes of 25% (exp. 16; cf. Fig. 4) with nearly neutral impact regarding increase or decrease of precipitation. There are some convective test cases where the lack of stabilization by the convection scheme causes an over-compensation by grid-scale precipitation (cases 9 and 16). In other convective test cases switching off the convection scheme reduces the average precipitation significantly or even inhibits precipitation (cases 4, 7, and 12). The effect for situations that are dominated by stratiform precipitation is typically small.

The sensitivity experiments with modified Tiedtke scheme tend to reduce the average precipitation by 11% (exp. 14; cf. Fig. 4) with the strongest impact on convective test cases. Regarding underestimation of convective precipitation, the other important QPF deficiency of the COSMO model besides stratiform overestimation, the modifications of the Tiedtke scheme seem not to improve QPF. The modified version of the Tiedtke scheme is further tested by DWD, e.g. exploring a revised formulation of evaporation of rain within the con-

vection scheme.

The strongest effect when changing microphysical schemes is caused by combining the changes of the warm rain scheme with the substantial changes in snow physics (exp 12): this sensitivity experiment causes an average change of 15% and an average reduction of precipitation of 11%. The snow microphysics changes of this sensitivity experiment are probably not realistic and lead to a significant overestimation of cloud cover in some test cases. The moderate changes in the microphysics scheme (exp. 13) cause differences of 7% with an average reduction of 4% (cf. Fig. 4). The number of test cases with increased and decreased average precipitation is approximately the same, but the effect of reducing average precipitation is bigger. There is no evidence that the change is acting differently on stratiform and convective precipitation.

The effect of changing the vertical exchange of heat and moisture is generally small (exp. 17 to 22; cf. Fig. 4), and most of the test cases are quite insensitive to changes of the vertical exchange (cf. Fig. 3). Only a strong decrease in the vertical exchange of moisture and temperature by a factor of 50 (exp 18) results in a significant average reduction of precipitation of 12% (cf. Fig. 4). The test cases that show a significant sensitivity towards change in the vertical exchange of heat and moisture are cases 15, 17, and 18. Two of these test cases are mainly convective (cases 15 and 17) and one is mainly stratiform (18), and all of them are influenced by the sea. Consistently, parameters changing evaporation from the sea (exp. 21 and 22) cause strong differences for these cases (no results available for case 15), while changes of stomata resistance hardly affect the results (exp. 19 and 20).

The ratio of grid-scale to parameterized convective precipitation varies by about 4% for the different sensitivity experiments and, thus, is hardly affected (not shown). The only exception is the sensitivity experiment with the modified Tiedtke scheme (exp. 14). For this sensitivity experiment, the ratio of grid-scale to total precipitation is on average increased by 10%, while the amount of total precipitation is decreased by about 11% (not shown). Thus, it seems that the modified Tiedtke scheme produces less convective precipitation without compensating the loss by grid-scale precipitation.

The maximum precipitation values are changing similar to the area averaged precipitation values, that is, the relative differences of maximum and area averaged precipitation values for the same sensitivity experiment and for the same test case are typically comparable (not shown). There are a few sensitivity experiments that show a different behaviour for maximum precipitation than for area averaged precipitation. Simulations with a tri-cubic semi-Lagrange advection scheme (exp. 6 and 7), the changes of the warm rain scheme (exp. 11 and 13), and the increase of vertical heat and moisture exchange over sea (exp. 21) cause changes of maximum precipitation that are significantly different from the difference in the area averaged values. The effects on maximum precipitation values in the sensitivity experiments with changed advection or warm rain scheme do not show a consistent picture: maximum values are decreased as well as increased for convective as well as for stratiform test cases (not shown). The major effect of the sensitivity experiments with changed vertical exchange is an increase of maximum values in one stratiform and two convective test cases (cases 7, 17, and 18; not shown).

The above results reflect the fact that the sensitivity experiments were originally designed to mainly investigate cases of stratiform precipitation overestimation. Just a few sensitivity experiments have the potential to increase the simulated precipitation for test cases with convective underestimation.

1.5.2 Change of the bias relative to the reference simulation

In this section, the evaluation of the sensitivity experiments is based on the absolute value of the ratio of the 24h area averaged precipitation bias of the sensitivity experiments and the 24h area averaged precipitation bias of the reference simulation:

$$|bias_{exp}/bias_{ref}| = (P_{exp} - P_{obs})/(P_{ref} - P_{obs}). \quad (2)$$

The evaluation of test case 20 is excluded from this evaluation, since the bias in the reference simulation is quasi-zero for this case. Test case 20 is discussed in Section 4.

The evaluation is focussing on some of the sensitivity experiments with significant relative difference Δrel, only: change of initial humidity (exp. 3 and 4), using Runge-Kutta (exp. 7 to 9), change of warm microphysical scheme and moderate snow physics changes (exp. 13), and using the modified Tiedtke (exp. 14) or Kain-Fritsch/Bechtold convection scheme (exp. 15). The idealized study of changed initial humidity is considered because of its strong impact on simulated precipitation and the hints that there are systematic errors of simulated humidity in the COSMO model. The other sensitivity studies considered are all realistic alternative options for running the model. The test cases are classified depending on their main characteristics: overestimation of stratiform and convective precipitation (Fig. 6, left) and underestimation of stratiform and convective precipitation (Fig. 6, right). The number of test cases in the different categories reflects the main QPF deficiencies found in the COSMO model. The two dominant errors are stratiform overestimation, which mainly occurs in countries not predominantly affected by the sea, and convective underestimation, mainly occurring in Mediterranean countries.

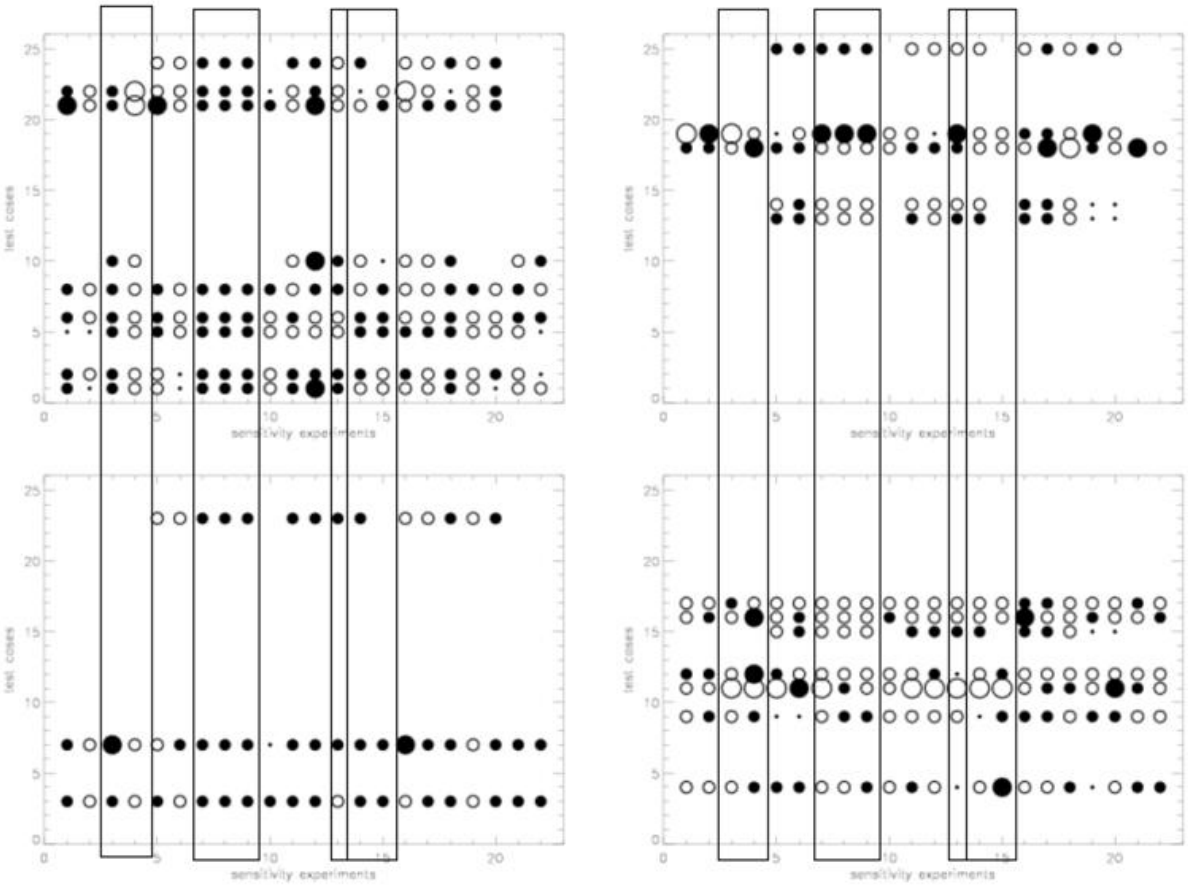


Figure 6: Ratio of the bias of the reference simulation and of the sensitivity study $|bias_{exp}/bias_{ref}|$ for cases with overestimation of stratiform (left, upper panel) and convective (left, lower panel) precipitation and with underestimation of stratiform (right, upper panel) and convective (right, lower panel) precipitation. Filled circles indicate a smaller bias, while empty circles indicate a higher bias than in the reference simulation. Big circles show a more than halved (doubled) bias and small circles an up to halved (doubled) bias. Points indicate no change. Case study 20 was excluded from this figure, because the bias was quasi-zero in the reference study.

Test cases with precipitation overestimation

The sensitivity experiments with decreased initial humidity and with Runge-Kutta time integration cause a decrease of area averaged precipitation for nearly all test cases (Section 1.5.1). For that reason, improved QPF for the test cases of overestimated precipitation can be expected. The decrease of initial humidity has a positive effect on all test cases with overestimation (Fig. 6, left), both for situations with stratiform as well as convective precipitation. On the other hand, an increase of initial humidity causes an even stronger overestimation. The Runge-Kutta time integration scheme, too, has a positive effect on all test cases with overestimated stratiform and convective precipitation. The sensitivity experiments with changes of warm rain scheme and moderate snow physics cause improvements but also worsening of QPF, the overall effect being slightly positive (Fig. 6). The effect of using the modified Tiedtke or the Kain-Fritsch/Bechtold scheme is small and mixed for the stratiform overestimation, but clearly positive for convective overestimation.

To summarize, reducing initial humidity and using Runge-Kutta time integration has a positive effect on overestimation of stratiform precipitation. These changes also have a positive effect on convective overestimation which are additionally reduced by using the modified Tiedtke scheme or the Kain-Fritsch/Bechtold convection scheme.

Test cases with precipitation underestimation

Increasing the initial humidity improves the QPF for most of the test cases. The results of the GOP (Section 1.5.1) show that there are stations in France and Italy where the COSMO-EU is underestimating the observed humidity. Since Italy is one of the countries with several test cases of underestimation, underestimated humidity in the atmosphere should be investigated as a possible reason affecting the underestimation of precipitation.

The Runge-Kutta time integration scheme tends to reduce the area averaged precipitation and, hence, gives overall worse results for the test cases with underestimated precipitation. Still, there are both convective and stratiform test cases with underestimated precipitation that are improved by using Runge-Kutta (4, 9, 19, and 25).

The change of warm rain scheme and moderate changes of the snow microphysics and the Kain-Fritsch/Bechtold scheme have a mixed impact, improving some (mainly stratiform cases for the former and mainly convective cases for the latter) and worsening other test cases. The modified Tiedtke scheme has a predominantly negative effect on QPF for test cases with precipitation underestimation.

Concerning convective underestimation, only, the sensitivity experiments don't reveal changes of numerical methods or physical parameterizations that have a clear positive impact on all these test cases. The sensitivity to the initial atmospheric humidity is however fairly large, and a good simulation of atmospheric humidity is mandatory for a decent QPF. Changing the convection scheme nevertheless has a significant impact on the results and, thus, further investigations regarding the convection scheme is the most promising step for these test cases. This is an ongoing task within COSMO: the IFS convection scheme has been implemented into the COSMO model and its performance is currently being tested.

The sensitivity experiments were also evaluated depending on the existence of fronts or orographic forcing of the precipitation, but no special characteristics were found. The characteristics of the sensitivity experiments described above remain valid independent of a frontal passage or orographic forcing.

Table 5: Overview of cross experiments.

No.	Sensitivity study
23	COSMO 4.0
24	COSMO 4.0 + 90% initial humidity + Runge-Kutta
25	COSMO 4.0 + Kain-Fritsch/Bechtold
26	COSMO 4.0 + 90% initial humidity + Runge-Kutta + Kain-Fritsch/Bechtold
27	COSMO 4.0 + modified Tiedtke scheme
28	COSMO 4.0 + 90% initial humidity + Runge-Kutta + modified Tiedtke scheme

1.5.3 Cross experiments

The cross experiments are set up to explore the positive effects of multiple changes. The focus is the overestimation of stratiform precipitation because several sensitivity experiments showed potential to improve this QPF deficiency. Changes of initial humidity, the Runge-Kutta time integration scheme, modified microphysics and modifications of the convection scheme had positive effects on test cases with overestimated stratiform precipitation. These changes are combined in the cross experiments that are described in Tab. 5. - Even if being highly idealized, the simulation with decreased humidity is included in the cross experiments due to indications that atmospheric humidity might be overestimated in the model and due to its great sensitivity to QPF.

The cross experiments are performed using version 4.0, the latest version of the COSMO model. This version is differing from the reference version (version 3.19) mainly by microphysics changes that are similar to the changes in the warm rain scheme and changes of snow physics in sensitivity experiment 13. The term 'reference version' will be used in the following for the reference simulation performed with COSMO 3.19. The modifications of the Tiedtke convection scheme for the cross experiments are, compared to the previous studies, expanded by an exchange of cloud water and cloud ice with grid-scale variables.

The comparison of simulated 24h area averaged precipitation values shows similar results with the reference version and with version 4.0 (Fig. 7). The simulations with version 4.0 reduce the average precipitation by 1 to 3 mm for most of the test cases. There are only two test cases (18 and 25) where the area averaged precipitation is significantly increased, and these are cases where (stratiform) precipitation is underestimated with the reference version. With the exception of the underestimated convective cases 9 and 11, this results in a neutral or slightly improved simulation of area averaged precipitation for all test cases. There are two test cases of stratiform overestimation that are clearly improved by using version 4.0 (cases 8 and 10). For test case 8 the overestimation is reduced by 2.5 mm, which is about 30%, and for test case 10 the overestimation is reduced by 11 mm, corresponding to 80% of the bias. Thus, COSMO version 4.0 has a significant positive impact on some test cases of overestimated stratiform precipitation and generally slightly improves the precipitation simulation.

The comparison of the results of the cross experiments to those of the reference version show a strong reduction of average precipitation for nearly all test cases and cross experiments (Fig. 8; compare with Fig. 3 for individual sensitivity experiments). Version 4.0 (exp. 23), as discussed before, has the tendency to reduce the area averaged precipitation, on average by 10 to 30%. The reduction of initial humidity and the use of the Runge-Kutta time integration scheme (exp. 24) reduce the area averaged precipitation by at least 10%, but for most of the test cases by over 30%. Comparing the effect of the cross experiment with reduced initial

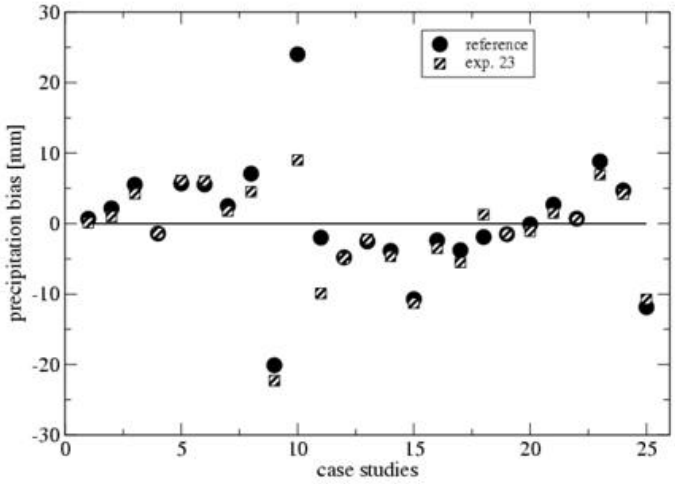


Figure 7: Bias of reference version (filled circles) and of the COSMO 4.0 version (striped squares).

humidity and Runge-Kutta scheme with their single effects leads to the conclusion that the effects of reduced initial humidity and Runge-Kutta time integration are adding up linearly without further non-linear amplification.

The test cases are again divided into cases with stratiform overestimation (Fig. 9) and cases with convective underestimation (Fig. 10) in order to study the effect of the cross experiments on different QPF deficiencies.

The results confirm that the cross experiments are reducing area averaged precipitation for most of the test cases and, thus, the bias of the test cases with overestimated stratiform precipitation is significantly improved for most of the cross experiments. 4 test cases have the best QPF results when using Kain-Fritsch/Bechtold, reduced initial humidity, and Runge-Kutta (exp. 26), 2 test cases when using only Kain-Fritsch/Bechtold (exp. 25) and 2 test cases when using the modified Tiedtke scheme, reduced initial humidity, and Runge-Kutta (exp. 28).

For test cases of underestimated convective precipitation the overall effect of the cross experiments is negative. Still, for two of the test cases (cases 4 and 16), the bias gets essentially zero if COSMO 4.0 is used together with the Kain-Fritsch/Bechtold scheme (exp. 25). For two other test cases (12 and 17), the bias is slightly improved using the Kain-Fritsch/Bechtold scheme. The increase of average precipitation in test case 12 is stronger than in the respective sensitivity experiment 15 that was performed with version 3.19 (Fig. 8 and Fig. 3) More generally, comparing the effect of using Kain-Fritsch/Bechtold in COSMO 3.19 and COSMO 4.0 seems to show that there is a tendency of a stronger impact of changing the convection scheme in version 4.0 (not shown). These results confirm that the convection parametrization is the most promising part of the model to concentrate on in order to improve the test cases with underestimated convective precipitation.

To summarize the effect of the cross experiments, 18 out of 25 test cases have been significantly improved by one of the cross experiments, including all 9 (3) test cases with overestimated stratiform (convective) precipitation. 5 test cases show the smallest bias if

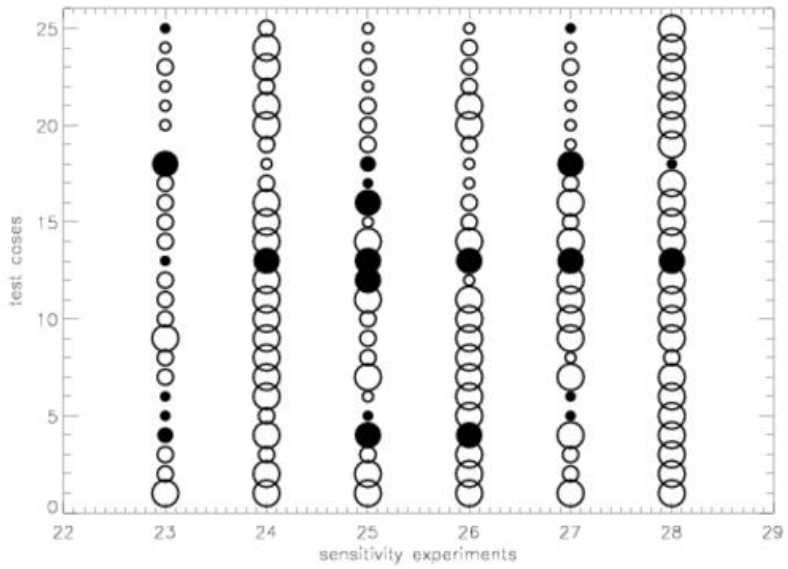


Figure 8: Difference of 24h area averaged precipitation in the cross experiments (23-28) and in the reference simulation relative to the 24h area averaged precipitation in the reference simulation Δrel [%]. Filled (empty) circles indicate an increase (decrease) of precipitation relative to the reference simulation. The big circles indicate an absolute change bigger than 30%, medium ones between 10% and 30% and small ones between 0% and 10%, tiny circles indicate cases with no change at all.

COSMO 4.0 is used with the Kain-Fritsch/Bechtold convection scheme. QPF of 3 test cases each is improved using reduced initial humidity, Runge-Kutta time integration, and Kain-Fritsch/Bechtold or modified Tiedtke scheme, respectively. 7 test cases are hardly affected or worse, 4 (3) of them being test cases of underestimated convective (stratiform) precipitation. The latter result is a consequence of the main focus of the cross experiments.

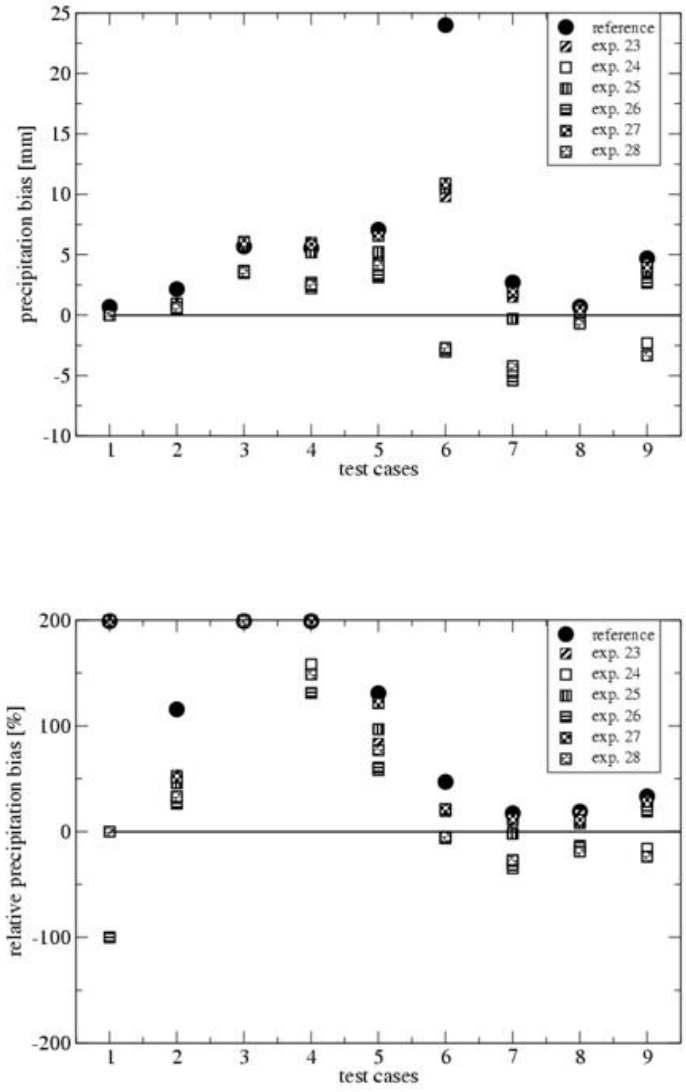


Figure 9: Absolute (upper panel) and relative (lower panel) precipitation bias ($(P_{exp} - P_{obs})$ and $(P_{exp} - P_{obs})/P_{obs}$, respectively) of the reference simulation (black circles) and the cross experiments compared to the observations for cases with overestimation of stratiform precipitation. The test cases are 1, 2, 5, 6, 8, 10, 21, 22, and 24.

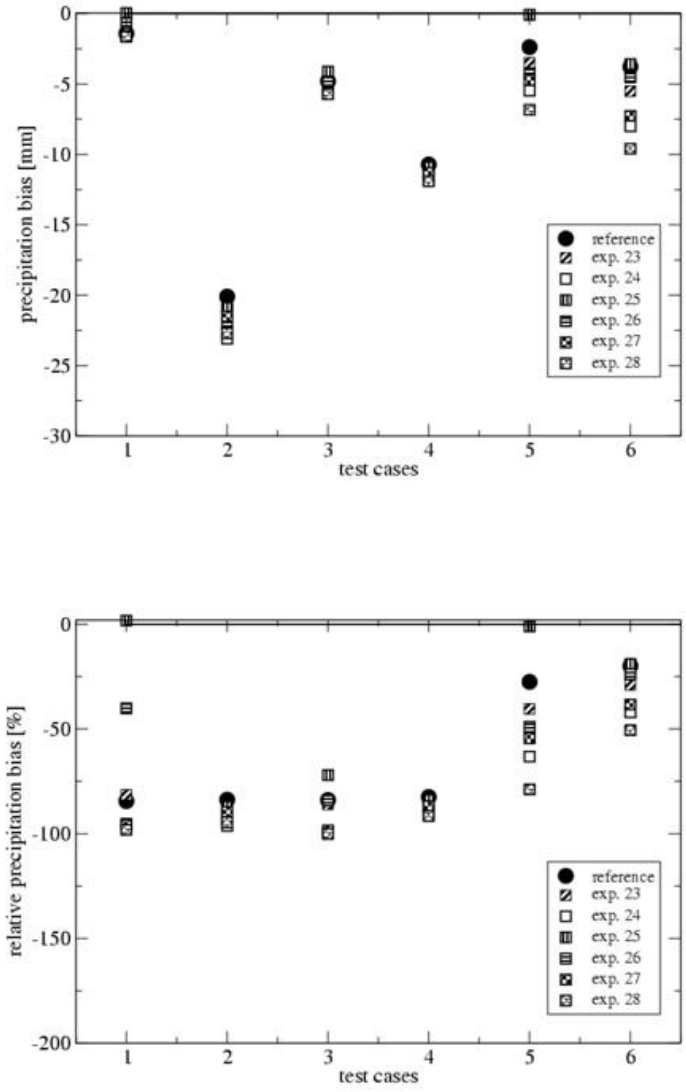


Figure 10: Absolute (upper panel) and relative (lower panel) precipitation bias ($(P_{exp} - P_{obs})$ and $(P_{exp} - P_{obs})/P_{obs}$, respectively) of the reference simulation (black circles) and the cross experiments compared to the observations for cases with underestimation of convective precipitation. The test cases are 4, 9, 12, 15, 16, and 17.

1.6 Summary and conclusions

Quantitative precipitation forecasting (QPF) is difficult ! Verification results and forecaster feedback suggest that the operational implementations of the COSMO model (7 to 14 km horizontal grid spacing), like many other numerical weather prediction models, have some problems in quantitatively forecasting precipitation. This was the motivation to launch the COSMO Priority Project 'Tackle deficiencies in quantitative precipitation forecasts'. The aim was to determine which parts of the modelling system have a significant impact on QPF quality and, thus, might have the potential to improve QPF. The focus of the project was on numerical methods and physical parameterizations, while the effects of inaccurate initial and boundary data were largely neglected.

In the first step of the project test cases were selected that reflect typical forecast errors for the different regions of interest of the participating meteorological services. To ensure that the observed COSMO model forecast deficiencies are not due to an old model version or a specific local model implementation, all test cases were re-run with a COSMO model reference version using a 7 km grid spacing. From the test cases, for which the COSMO model reference version reproduced the reported QPF problem, a list of 25 test cases was selected. The selected test cases thereby fall into two prominent groups of forecast errors: 9 test cases with stratiform overestimation, mainly in Germany, Switzerland, and Poland, and 7 test cases of convective underestimation, mainly in Italy and Greece. As a second step, a set of sensitivity studies concerning initial conditions, numerics, and model physics has been prepared. The list includes 22 sensitivity experiments as well as 6 cross-sensitivity runs that are simulated for all test cases. All in all, some 700 simulations had to be performed and analyzed. The evaluation of the sensitivity experiments is based on the 24h area averaged precipitation for selected evaluation regions with a minimum size of 100 km times 100 km. Hence, the focus is on large scale over- or underestimation of QPF. Problems of wrong small-scale localization or wrong temporal simulation are not looked at. The results of these sensitivity studies provide a broad overview of which parts of the modelling system are most relevant for QPF and suggest potential model variants that may lead to better quantitative precipitation forecasts.

The sensitivity experiments show that the strongest influence on QPF is caused by changes of the initial humidity and by using the Kain-Fritsch/Bechtold convection schemes. Both sensitivity experiments result in average relative differences of the area averaged precipitation values in the range of 30-40%. Using the Runge-Kutta time integration scheme instead of the Leapfrog scheme, applying a modified warm rain and snow physics scheme or a modified Tiedtke convection scheme all change the area averaged precipitation by roughly 10%. Finally, but only for the Roman and Greek test cases, which all have a strong influence from the sea, the heat and moisture exchange between surface and atmosphere is of great importance and can cause changes in the range of up to 25%.

The great importance of *atmospheric humidity* for the area averaged precipitation is not surprising. Still, these studies re-affirm this fact and the necessity to investigate the effect of humidity regarding QPF errors. There are indications from verification that there are indeed deficiencies in the humidity simulation. The comparison of radiosonde data and COSMO-EU profiles of mixing ratio performed in the frame of GOP shows that the model systematically overestimates atmospheric humidity, especially in the northern part of Europe. It also shows underestimation, especially in summer, in the southern part of Europe. These errors in the simulated atmospheric humidity field may strongly correspond to prevailing QPF errors of overestimated stratiform precipitation and underestimated convective precipitation. No detailed analysis of this interrelation has been performed that would allow to draw firm

conclusions, but the results of the sensitivity experiments provide motivation to have a closer look at the simulation of atmospheric humidity in order to prove or disprove its influence on QPF deficiencies.

The other important parameter influencing QPF, the *convection parametrization*, is also an expected one. The Kain-Fritsch/Bechtold scheme gives better results for 9 and worse results for 8 test cases. Test case 4, a case of underestimated convective precipitation, is significantly improved by using the Kain-Fritsch/Bechtold scheme. The scheme was tested in a quasi-operational test chain at MeteoSwiss in 2006 and showed promising results, especially regarding the diurnal cycle of precipitation. However, the test chain also revealed deficiencies. Further adaptations in order to avoid spin-up effects and overestimation of low precipitation amounts are required. Since no institute is currently developing this scheme or using it operationally, it was decided to implement and adapt the operational IFS convection scheme rather than continuing work on the very similar but unsupported Kain-Fritsch/Bechtold scheme. The other convection scheme used in the sensitivity experiments is the modified Tiedtke scheme which over all has a slightly negative impact on QPF. It improves the simulation of test cases with overestimated convective precipitation and has a neutral effect on overestimated stratiform precipitation, but it worsens test cases with underestimation of precipitation. This variant of the Tiedtke scheme is currently being revised and tested at DWD. Investigations regarding convection in the COSMO model are hence going on and it will be interesting to see how the new or further modified schemes perform in the COSMO model.

Using the *Runge-Kutta* time integration scheme instead of the Leapfrog scheme shows astonishing results: the area averaged precipitation values are significantly reduced,(by typically 10%) for most of the test cases. It is not yet fully understood why the scheme is predominantly reducing the precipitation amount, but it might be related to insufficient accuracy of the centered differences which are used in the reference simulation for advection of humidity and cloud water. Few test cases show an increase of area averaged precipitation with the Runge-Kutta scheme, and for those test cases it is a change in the right direction. Thus, the Runge-Kutta scheme has a positive effect on QPF for all cases with overprediction of precipitation as well as for some cases with underprediction of precipitation, and *is recommended for use.*

The *microphysics* changes similar to sensitivity experiment 13 are already included in COSMO version 4.0. They showed a positive impact on QPF for many test cases. The positive effect is confirmed by the comparison of COSMO version 4.0 to version 3.19 that shows a neutral or slightly positive impact on QPF for almost all the test cases when using the new model version.

The *cross experiments*, mainly targeted at the cases with overpredicted stratiform precipitation, confirm the main findings summarized above: Use of COSMO version 4.0 and the Runge-Kutta time integration scheme is encouraged, and more work on the simulation of atmospheric humidity as well as on further improvement of the convection schemes in needed to obtain better quantitative precipitation forecasts.

There are some limitations of this study which have to be kept in mind. To give just one example, all simulations were based on the same initial conditions, which can lead to an overestimation of the model sensitivity, since in a full NWP system that includes data assimilation, the initial conditions will always adjust to the new model physics or numerics. This effect of somewhat inconsistent initial conditions might, for example, contribute to the strong sensitivity of the accumulated precipitation which was found for the new microphysics in COSMO 4.0. Some of the reduction might be caused by the inconsistency of the old initial conditions, which are based on COSMO 3.19, and only the rest by the new microphysics in

COSMO 4.0. Still, the sensitivity studies shown here can provide some guidance and insight for improving or at least tuning the model to give better QPF results.

2 Workshops and meetings

- LM User Seminar, Langen, Germany, 8 March 2006
- COSMO General Meeting, Bucharest, Romania, 18 September 2006
- LM User Seminar, Langen, Germany, 8 March 2007
- Visit of Axel Seifert at MeteoSwiss, 24-25 April 2007
- COSMO General Meeting, Athens, Greece, 21 September 2007

3 Presentation of QPF results

- Silke Dierer et al.: LM User Seminar, Langen, Germany, 6-8 March 2007
- Federico Grazzini et al.: National Meeting of Geophysics, Ischia, Italy, 11-15 June 2007
- Massimo Milelli et al.: EMS, San Lorenzo de El Escorial, Spain, 1-5 October 2007
- Silke Dierer et al.: COSMO General Meeting, Athens, Greece, 19 September 2007
- Silke Dierer et al.: SRNWP Workshop, Bad Orb, Germany, 5-7 November 2007
- Antonella Morgillo et al.: SRNWP Workshop, Bad Orb, Germany, 5-7 November 2007

4 Test cases description

4.1 Germany

Simulation domain: 333 x 333 grid points, 7 km grid spacing, startlat = -9.75, startlon = -12.75, pollat = -40, pollon = -170

Evaluation domain: Germany

Responsible scientists: Uli Damrath (Task 1), Axel Seifert (Task 2)

Test case 06.12.2004

QPF problem: widespread overestimation of drizzle

Best sensitivity study: COSMO 4.0 with RK solves the problem. COSMO 4.0 with LF gives similar results. The main effect is due to the modification of the cloud microphysics in COSMO 4.0, especially the autoconversion rate.

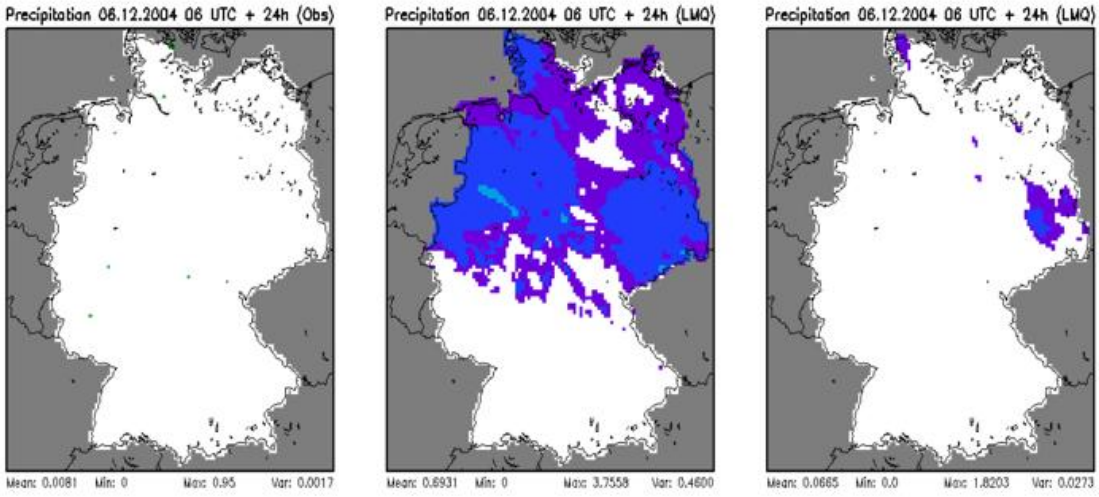


Figure 11: 24h precipitation sum from 06.12.2004, 06 UTC - 07.12.2004, 06 UTC from surface observations (left), the reference simulation (centre) and the sensitivity study with COSMO 4.0 and Runge-Kutta time integration (right).

Test case 18.03.2005

QPF problem: overestimation of stratiform precipitation

Best sensitivity study: no single sensitivity study was able to solve this case. The best improvement can be achieved by a combination of modifications which help to reduce the precipitation amounts in general, e.g. the cross-experiment A4 using COSMO 4.0 with Runge-Kutta core, KFB convection scheme and a reduction of the initial humidity.

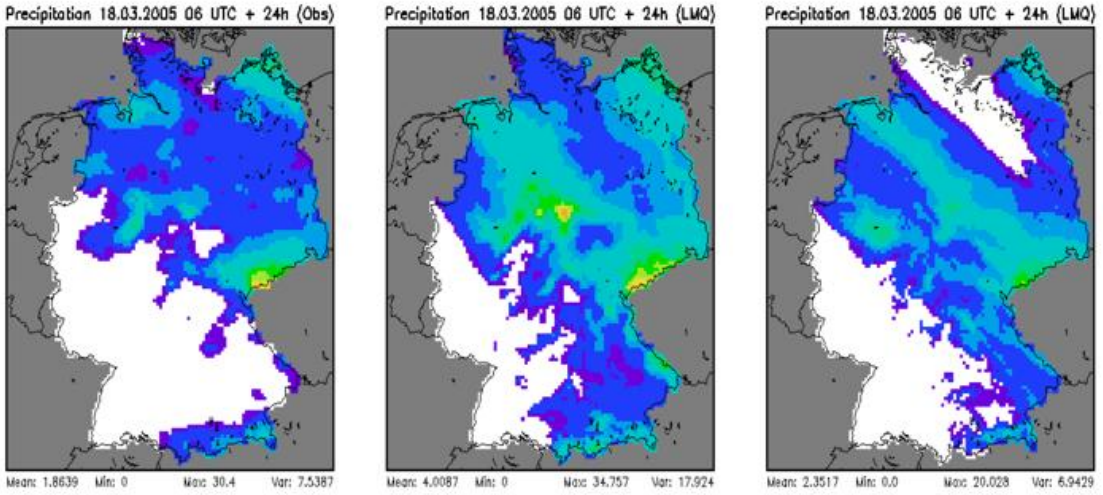


Figure 12: 24h precipitation sum from 18.03.2005, 06 UTC - 18.03.2005, 06 UTC from surface observations (left), the reference simulation (centre) and the sensitivity study with COSMO 4.0, Runge-Kutta time integration, KFB convection scheme and reduced initial humidity (right).

Test case 03.05.2005

QPF problem: overestimation of precipitation in a summertime event due to 'double-counting' of grid-scale and convective precipitation. Mean and maximum values are much too high. Probably caused by upscaling of convective motions to the grid-scale.

Best sensitivity study: COSMO 4.0 with Runge-Kutta and the modified Tiedtke convection scheme. The COSMO 4.0 with Runge-Kutta and KFB convection scheme does also a good job, but in this setup more of the overestimation of precipitation remains in the forecast. Detrainment of condensate from the convection scheme seems to help in this case.

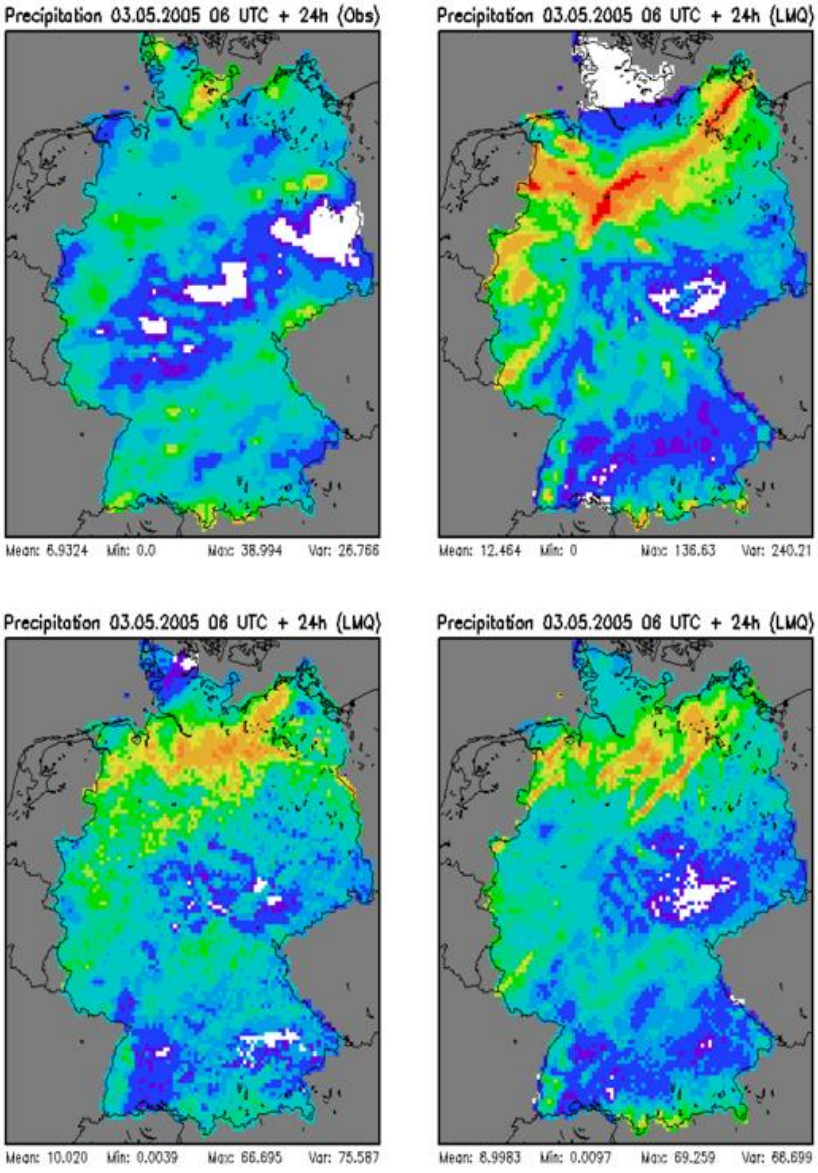


Figure 13: 24h precipitation sum from 03.05.2005, 06 UTC - 03.05.2005, 06 UTC from surface observations (upper left), the reference simulation (upper right), the sensitivity study with COSMO 4.0, Runge-Kutta time integration and KFB convection scheme (lower left) and an additional cross-sensitivity study COSMO 4.0 + Runge-Kutta + modified Tiedtke scheme.

Test case 21.06.2005

QPF problem: underestimation of the amount of precipitation in a convective event.

Best sensitivity study: the KFB scheme captures this event very well leading to a good forecast. This is a robust result independent from other choices, e.g. using RK vs LF or COSMO 3.19 vs 4.0.

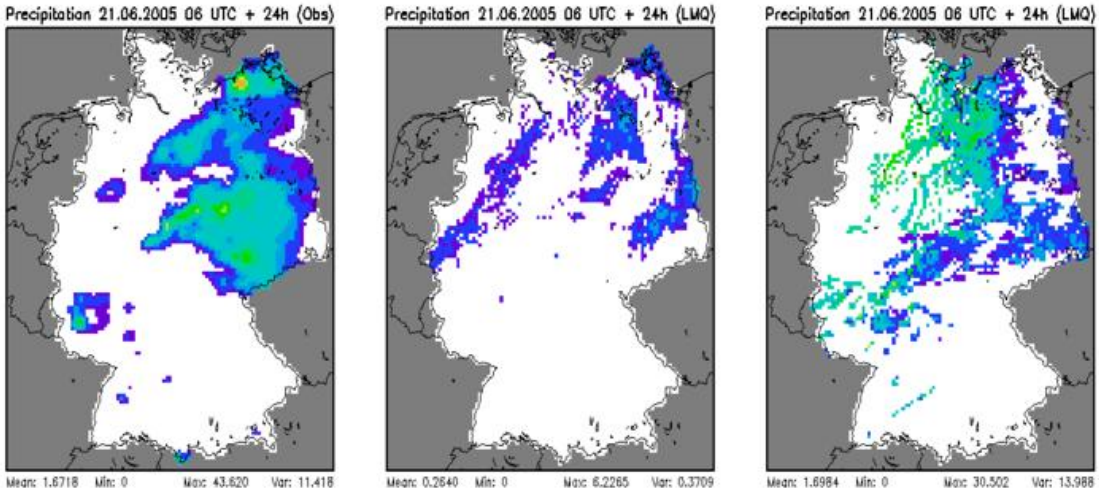


Figure 14: 24h precipitation sum from 21.06.2005, 06 UTC - 22.06.2005, 06 UTC from surface observations (left), the reference simulation (centre) and the sensitivity study with COSMO 3.19 and the KFB convection scheme (right).

4.2 Switzerland

Simulation domain: latitude 35.17/57.50; longitude -8.0/23.24

Evaluation domain: latitude 45.8/47.7; longitude 6.0/10.5

Responsible scientists: Silke Dierer and Francis Schubiger (Task 1), Silke Dierer (Task 2)

Test case 02.02.2005

QPF problem: northerly flow at 500 hPa, occluded front passing northeast of Switzerland. In the morning snow starting from north, locally rain. In the afternoon decaying snowfall. Overestimation of precipitation at the northern slopes of the Alps and in the mountains. Typical error pattern for situations with northerly flow.

Best sensitivity study: Runge-Kutta (independent of advection, in this case flux-form advection, exp. 8)

Best cross experiment: COSMO 4.0 with Kain-Fritsch/Bechtold, Runge-Kutta and reduced initial humidity (exp. 26)

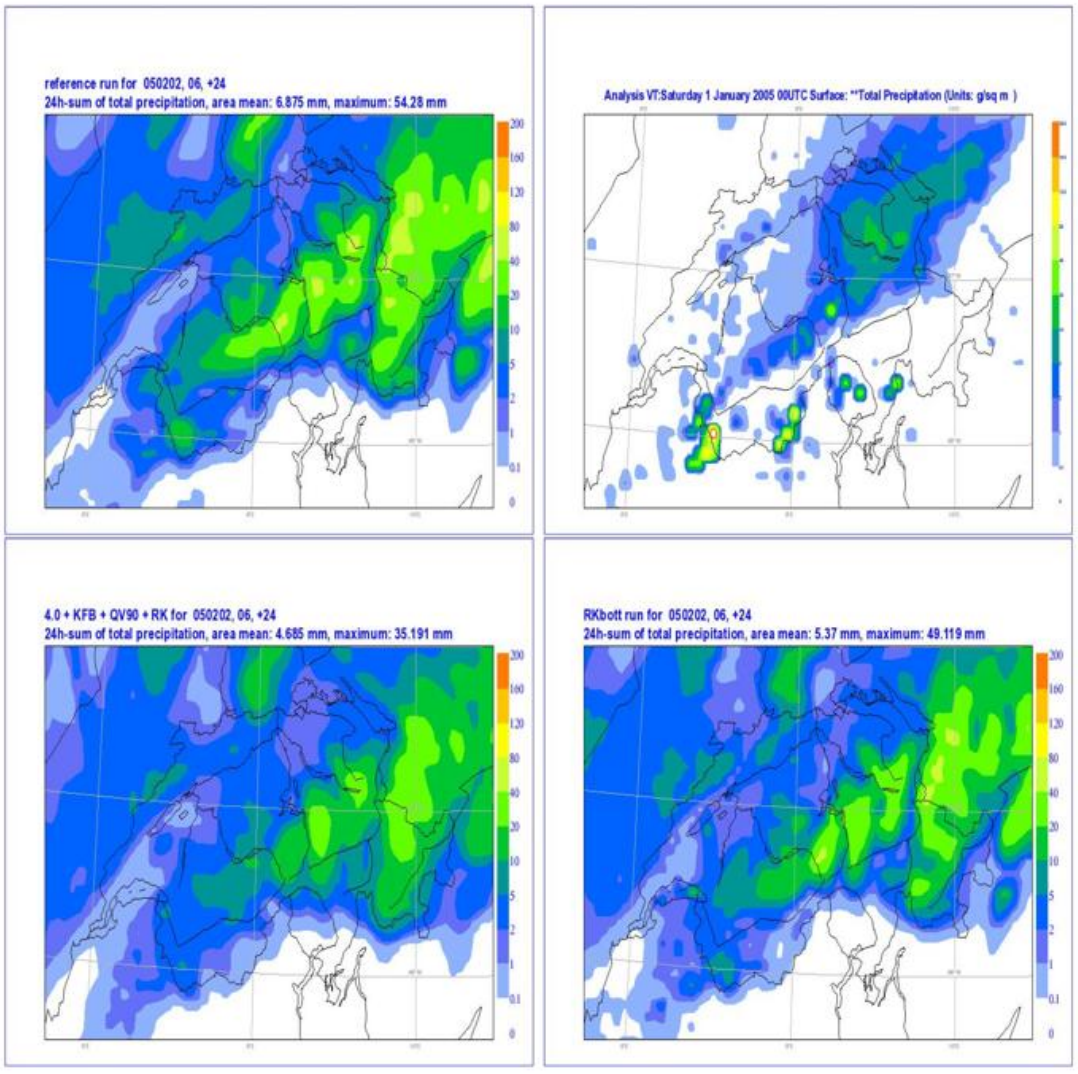


Figure 15: 24h precipitation sum from 02.02.2005, 06 UTC - 03.02.2005, 06 UTC from radar observations (upper panel, left), in the reference simulation (upper panel, right), in the sensitivity study with Runge-Kutta and flux-form advection (exp. 8, lower panel, left) and in the cross experiment with COSMO 4.0, Kain-Fritsch/Bechtold, Runge-Kutta and reduced initial humidity (exp. 26, lower panel, right).

Test case 22.03.2005

QPF problem: Switzerland is influenced by a high pressure system at 500 hPa with a weak south-westerly flow. A warm front is crossing Switzerland and, later, a cold front is crossing in the north. Overestimation of precipitation, mainly in the middle and eastern part of Switzerland.

Best sensitivity study: reduced initial humidity (exp. 3). Reducing the amount of precipitation to realistic values. Still, the location of precipitation remains wrong.

Best cross experiment: all studies with reduced initial humidity and Runge-Kutta very similar, lowest bias with reduced initial humidity, Runge-Kutta and Kain-Fritsch/Bechtold (exp. 26). Reducing the amount of precipitation to realistic values. Still, the location of precipitation remains wrong.

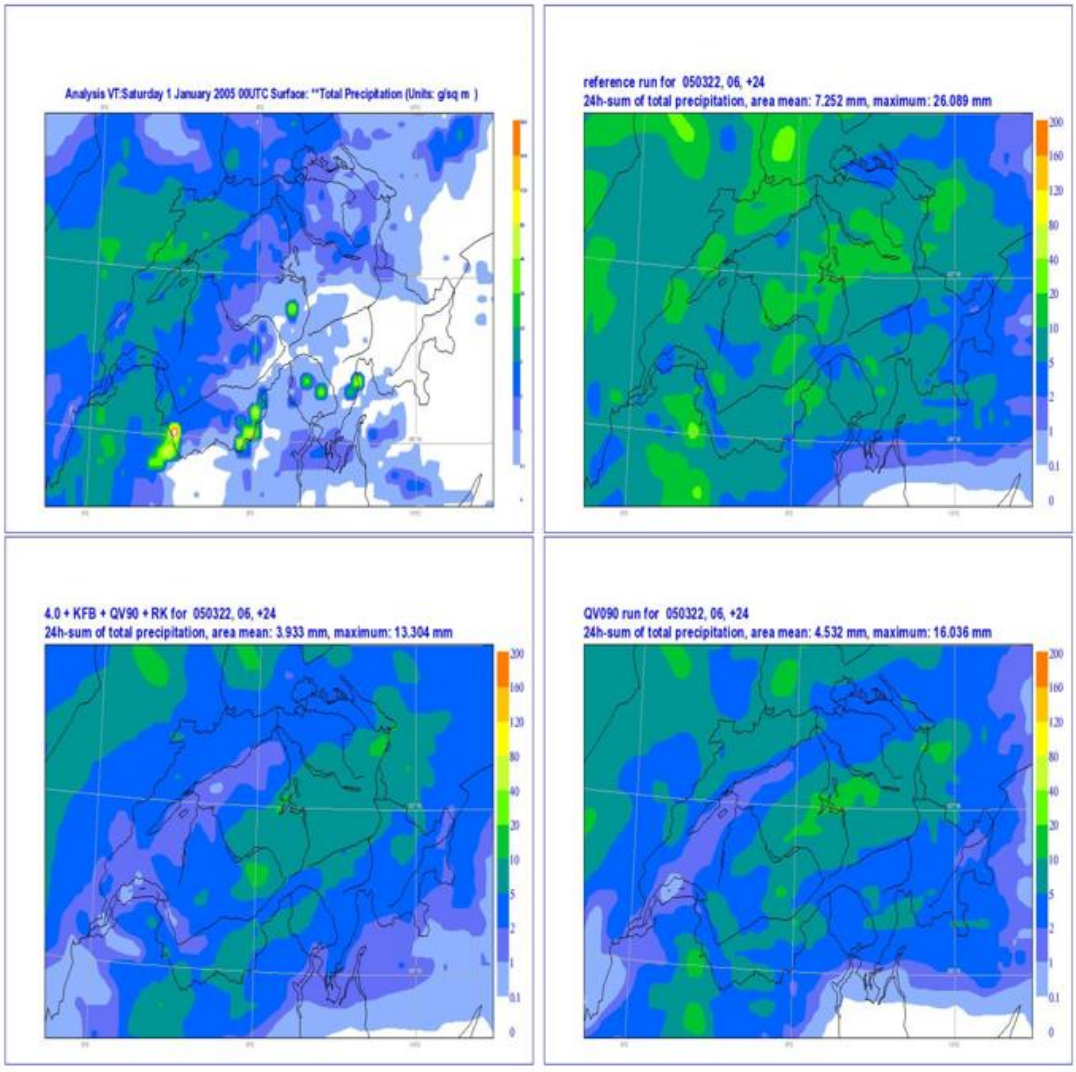


Figure 16: 24h precipitation sum from 22.03.2005, 06 UTC - 23.03.2005, 06 UTC from radar observations (upper panel, left), in the reference simulation (upper panel, right), in the sensitivity study with reduced initial humidity (exp. 3, lower panel, left) and in the cross experiment with COSMO 4.0, Kain-Fritsch/Bechtold, Runge-Kutta and reduced initial humidity (exp. 26, lower panel, right).

Test case 12.07.2005

QPF problem: low pressure system at 500 hPa over Croatia and influence of an Atlantic high pressure ridge towards Ireland: north-easterly flow at 500 hPa over the Alpine area. In the afternoon thunderstorms in Jura and Tessin. Those are hardly captured by the model. Wrong simulation of precipitation in the northern and eastern part of Switzerland.

Best sensitivity study: reduced initial humidity (exp. 3). Reducing and, thus, improving the amount of precipitation. Still, the location of precipitation remains wrong.

Best cross experiment: simulation with COSMO 4.0, reduced initial humidity, Runge-Kutta and Kain-Fritsch/Bechtold (exp. 26) improves the simulation of the precipitation north of Switzerland slightly improves the simulation of precipitation in the Tessin. Simulation of precipitation in the eastern part is reduced, but did not disappear.

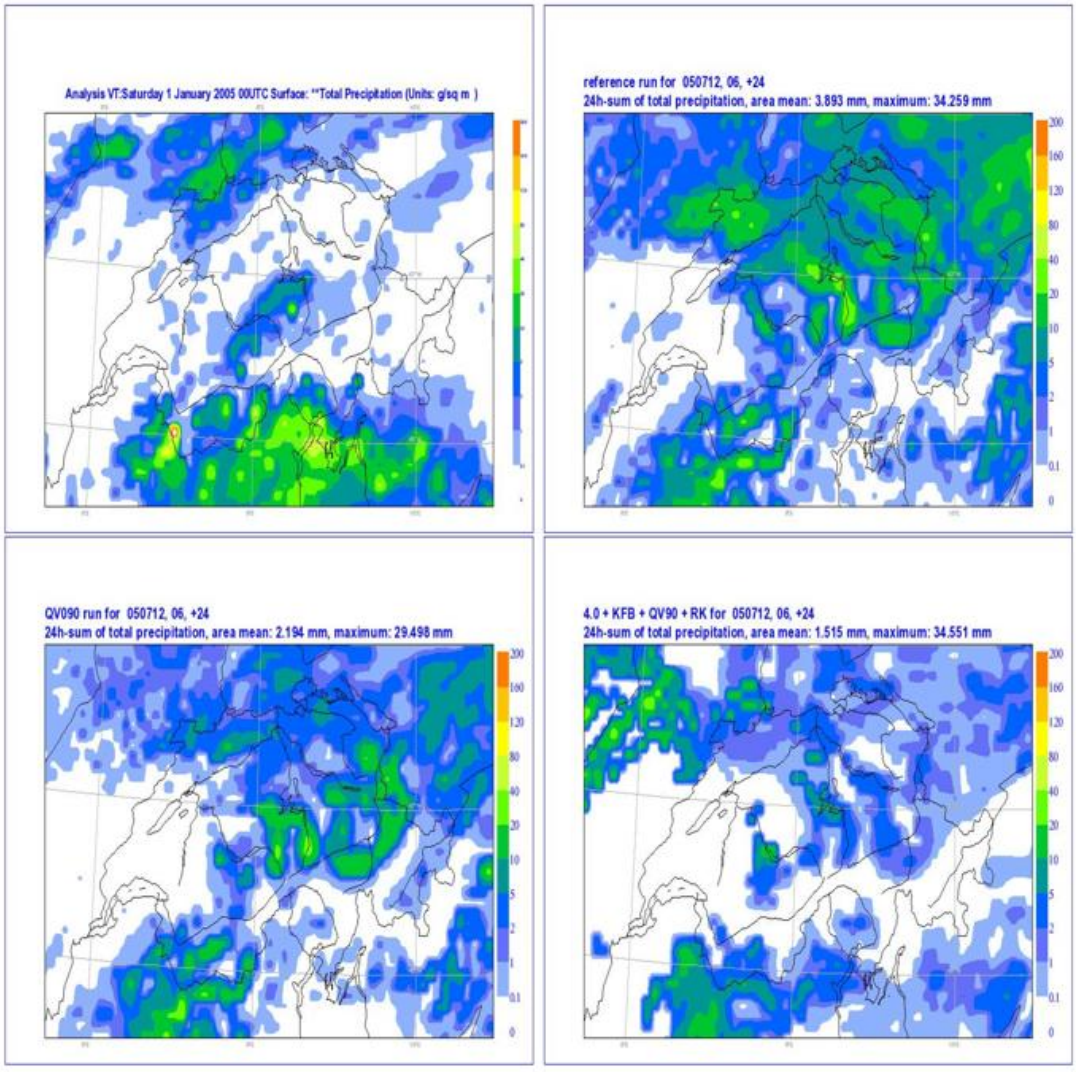


Figure 17: 24h precipitation sum from 12.07.2005, 06 UTC - 13.07.2005, 06 UTC from radar observations (upper panel, left), in the reference simulation (upper panel, right), in the sensitivity study with reduced initial humidity (exp. 3, lower panel, left) and in the cross experiment with COSMO 4.0, Kain-Fritsch/Bechtold, Runge-Kutta and reduced initial humidity (exp. 26, lower panel, right).

Test case 17.12.2005

QPF problem: northwesterly flow at 500 hPa, strong jet from Island to the Alps, very strong temperature gradient at 500 hPa over Switzerland. In the Alps and at the northern slopes constant snowfall, snow shower in the flat regions of Switzerland. Overestimation of precipitation in the middle and in the southern part of Switzerland. Typical error pattern for situations with northwesterly flow.

Best sensitivity study: Runge-Kutta (independent of advection, in this case flux-form advection, exp. 8). The average precipitation is reduced, but the region of precipitation remains too big.

Best cross experiment: COSMO 4.0 with reduced initial humidity, Runge-Kutta and Kain-Fritsch/Bechtold (exp. 26). Using COSMO 4.0 already gives a good reduction of the overestimation and using Runge-Kutta additionally increases this effect. While the amount of precipitation is in much better agreement now, there is still wrong simulation of precipitation in the Jura and in Graubünden.

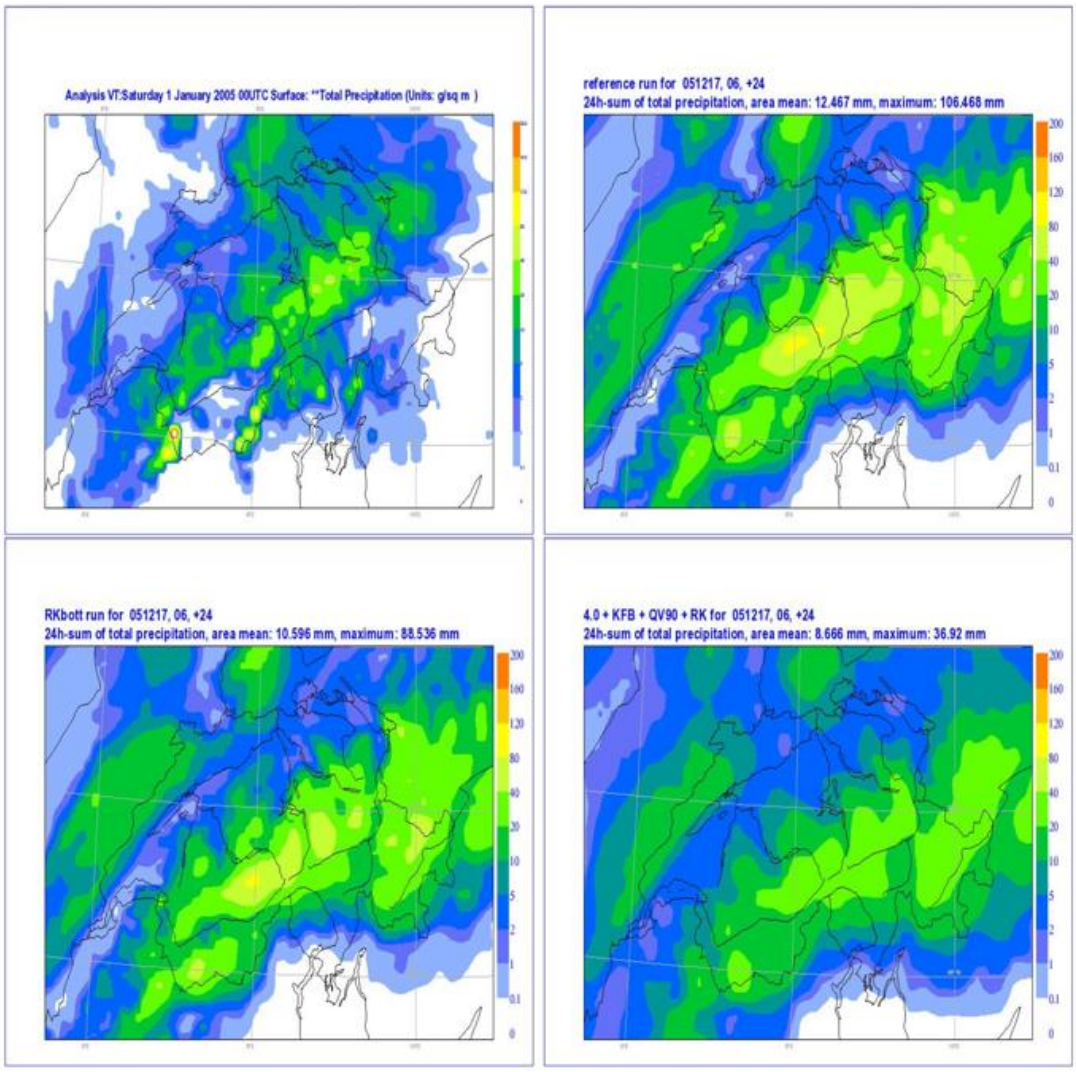


Figure 18: 24h precipitation sum from 17.12.2005, 06 UTC - 17.12.2005, 06 UTC from radar observations (upper panel, left), in the reference simulation (upper panel, right), in the sensitivity study with reduced initial humidity (exp. 3, lower panel, left) and in the cross experiment with COSMO 4.0, Kain-Fritsch/Bechtold, Runge-Kutta and reduced initial humidity (exp. 26, lower panel, right).

4.3 Emilia Romagna, Piemonte, Campania

Test case 24.09.2004

Simulation domain: latitude 32.81/50.51; longitude 2.16/24.76

Evaluation domain: latitude 43.75/45; longitude 10.5/12.2

Responsible scientists: Federico Grazzini (Task 1), Paola Mercogliano (Task 2)

QPF problem: deficiencies in the convection triggering caused by complex orography

Best sensitivity study: the best results for this test case (with stratiform and convective precipitation) has been found: increasing the initial humidity, switch off the convective parametrization; for the two runs in which has been Increased the vertical exchange of heat and moisture (on the soil and on the sea).

Best cross-experiment study: COSMO 4.0 with increased initial humidity, Runge-Kutta scheme for the numerics and Kain-Fritsch for the convection scheme (This particular experiment has not been reported in this paper but it has been considered only for this particular convective test case with strong underestimation).

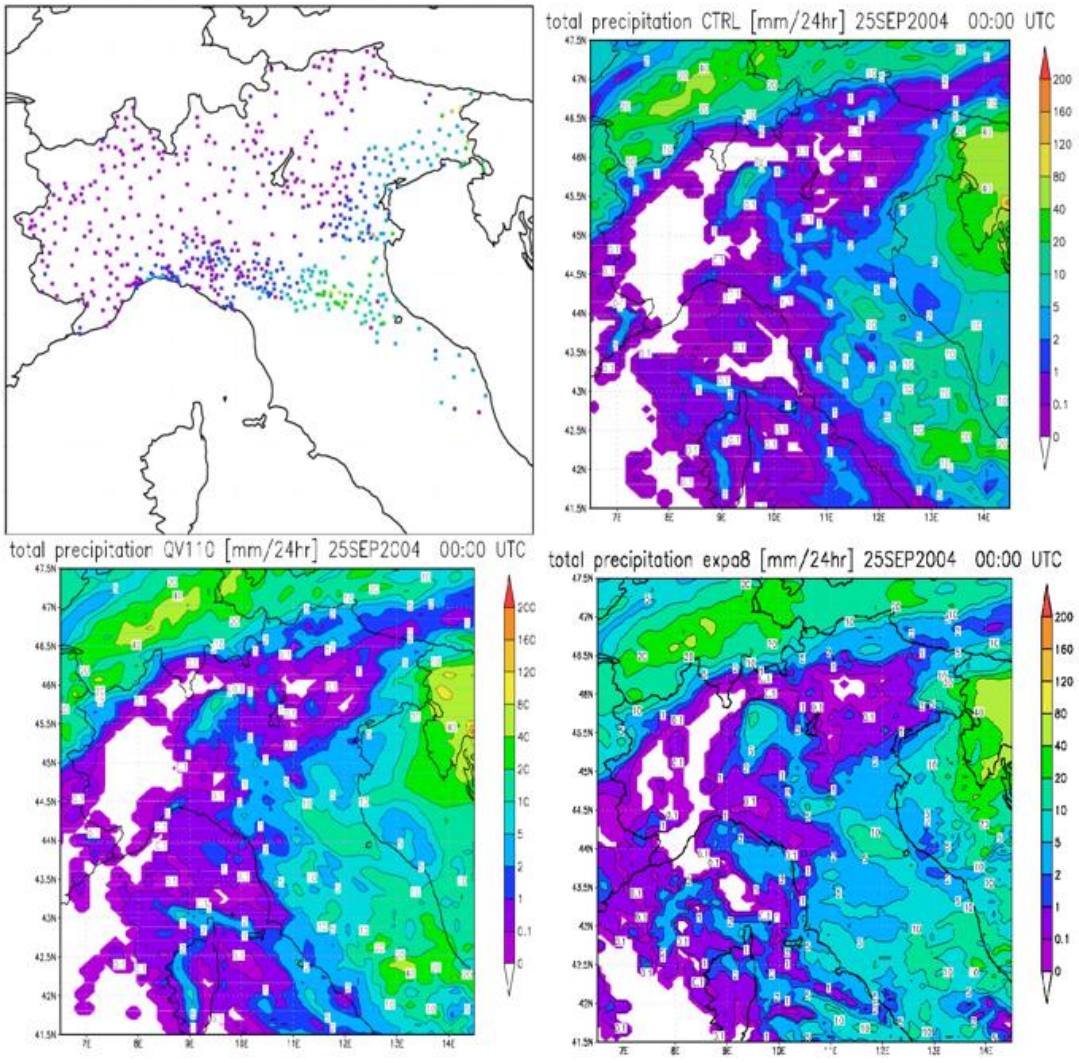


Figure 19: 24h precipitation sum from 24.09.2004, 00 UTC - 25.09.2004, 00 UTC from in situ observations of (upper panel, left), in the reference simulation (upper panel, right), in the sensitivity study with increased initial humidity (exp. 4, lower panel, left) and in the cross experiment with COSMO 4.0, Kain-Fritsch/Bechtold, Runge-Kutta and increased initial humidity (lower panel, right).

Test case 10.04.2005

Simulation domain: latitude 35.4/48.5; longitude 5/20.5

Evaluation domain: approximately 44.8N/43.8N, 10E/12.5E

Responsible scientists: Federico Grazzini (Task 1 and Task 2)

QPF problem: precipitation overestimation in a occluded front linked to a Mediterranean cyclone over Tirrenian Sea.

Best sensitivity study: the largest impact for our case of stratiform precipitation has been found with changes in the microphysics (Micro experiments) and with the introduction of version 4.0. In particular these versions contributed to reduce the overestimate of precipitation. A strong positive impact has been found in SEA40 and QV090.

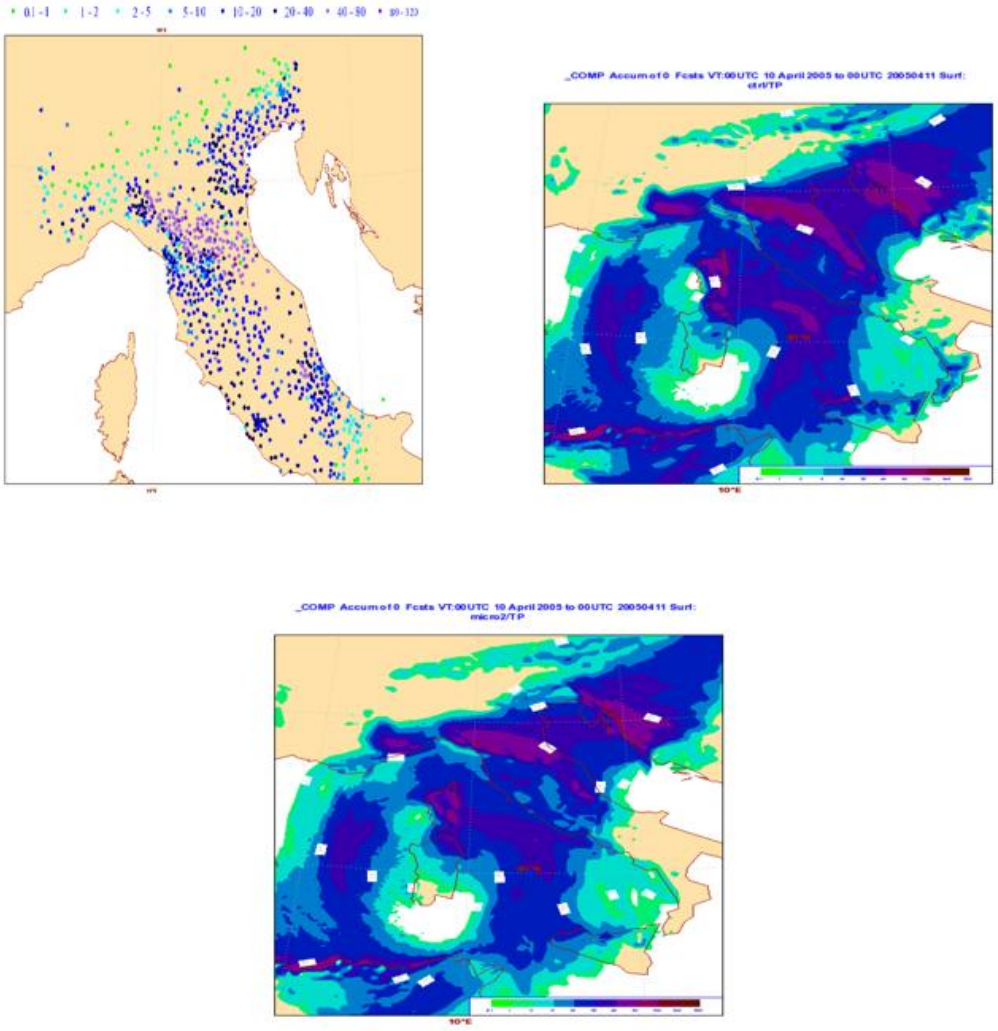


Figure 20: Observed precipitation (upper panel, left), in the reference run (upper panel, right), in the micro2 experiment (lower panel.

Test case 17.08.2006

Simulation domain: latitude 38.52N/51.48N; longitude 1.92W/17.98E

Evaluation domain: latitude 45.3N/46.6N; longitude 7.5E/9.3E

Responsible scientists: Elena Oberto (Task 1), Massimo Milelli (Task 2)

QPF problem: south-westerly flow at 500 hPa; cold frontal system with thunderstorms. Localized underestimation in the northern part of the region, both in the mean and in the maxima over the warning areas. Slight shift of the precipitation peak towards Tessin where the maximum value has been forecasted.

Best sensitivity study: actually it is difficult to find a simulation that gives better results than the ctrl. The stand-alone modifications (RK or QV or microphysics) do not improve the results.

Best cross experiment: a modification of Exp 24 (4.0 + QV090 + RK) in which humidity has been increased by 10% (fak=1.1) instead of being reduced by 10%. It has been called exp a7 (4.0 + QV110 + RK). Only in this case the relative error of the precipitation over the considered area is reduced (slightly) with respect to the other runs. Second place for the ctrl.

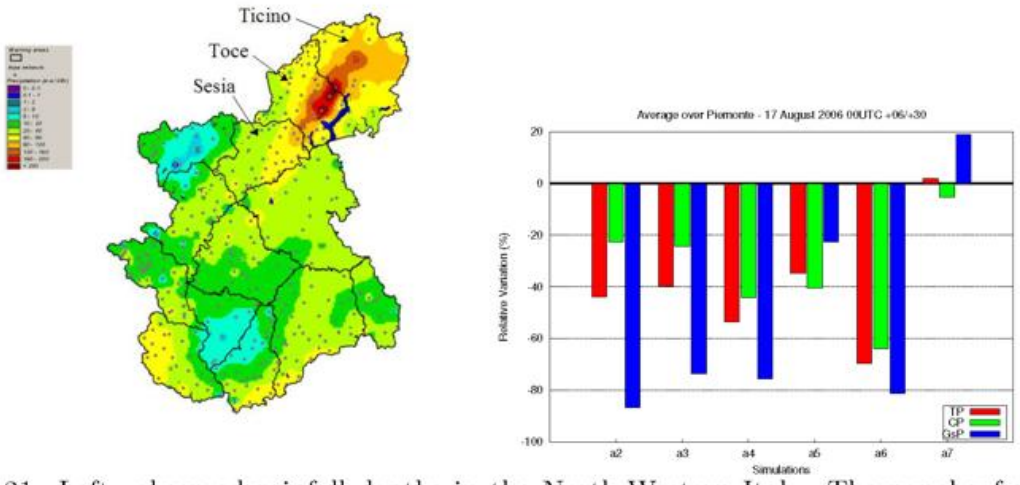


Figure 21: Left: observed rainfall depths in the North-Western Italy. The panel refers to the 24 h cumulated rainfall depth (06 UTC 17 August - 06 UTC 18 August). The rain gauges are plotted in grey and the warning areas in black. The affected areas, indicated with arrows, are Ticino (CH), Toce and, marginally, Sesia. Right: relative bias (%) of the different simulations with respect to the Ctrl run (a1) for different domains in the +6h/+30h time interval. Average performed over Piemonte region. Total Precipitation in red (TP), Convective Precipitation in green (CP) and Grid-scale Precipitation in blue (GsP). See Milelli et al. (2008) for more details.

Test case 09.09.2005

Simulation domain: latitude 32.81/50.51; longitude 2.16/24.76

Evaluation domain: latitude 40.5/41.5; longitude 13.8/15

Responsible scientists: Paola Mercogliano (Task 1 and Task 2)

QPF problem: deficiencies in the triggering of the afternoon convection along the coast line.

Best sensitivity study: the large impact on this convective case on the Italian coastal area has been obtained increasing the initial humidity, and changing the microphysics (in particular the experiment MICRO2).

Best cross-experiment study: COSMO 4.0 with increased initial humidity and using Runge-Kutta scheme fits well the average and the maximum value on the area (This particular experiment has not been reported in this paper but it has been considered only for this particular convective test case with strong underestimation).

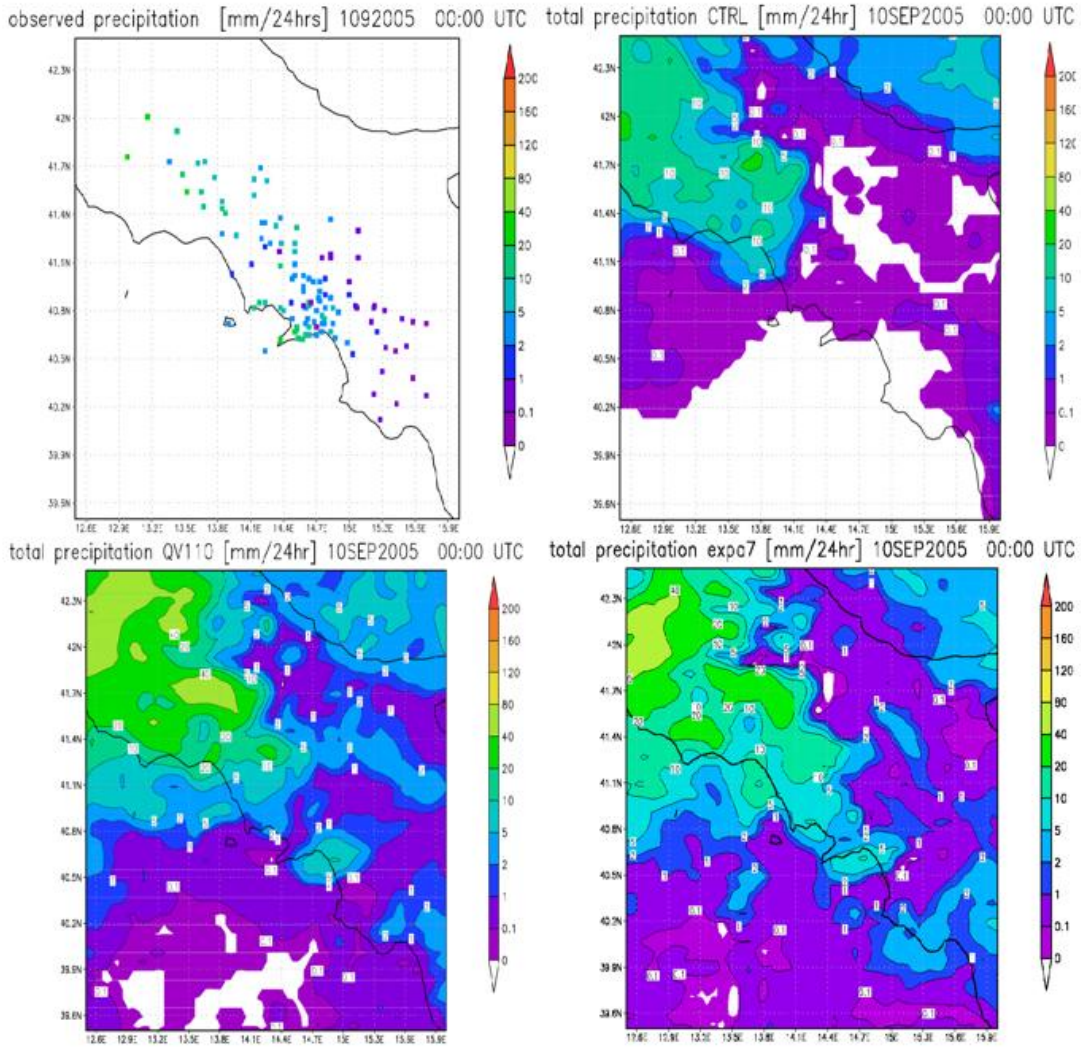


Figure 22: 24h precipitation sum from 09.09.2005, 00 UTC - 10.09.2005, 00 UTC from in situ observations of (upper panel, left), in the reference simulation (upper panel, right), in the sensitivity study with increased initial humidity (exp. 4, lower panel, left) and in the cross experiment with COSMO 4.0, Runge-Kutta and increased initial humidity (lower panel, right).

4.4 Rome

Simulation domain and evaluation domain: dlat=0.0625, dlon=0.0625, ielm_tot=321, jelm_tot=321, kelm_tot=40, pollat=40, pollon=-170.0, startlat_tot=-16.5, startlon_tot=-10.0

Responsible scientists: NN (Task 1), Rodica Dumitrache (Task 2)

Test case 01.12.2005

QPF problem:

- Sicily: 250 l/m^2 observation vs 25-50 l/m^2 model
- Ionian part of Calabria: 5 l/m^2 observation vs 25-50 l/m^2 model

Best sensitivity study: CTR, microphysics, numeric and surface simulations for Standard version tests

Best cross experiment: A1, A2, A6 for the LM 4.0 tests

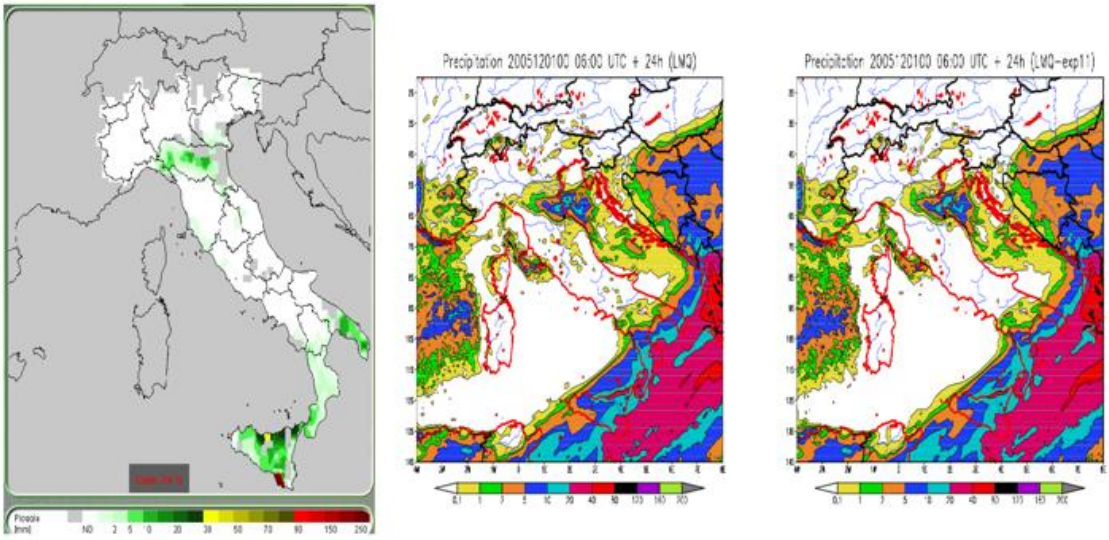


Figure 23: 24 h cumulated precipitation observation (left); 24h cumulated precipitation CTRL run (middle); 24h cumulated precipitation exp11 (right).

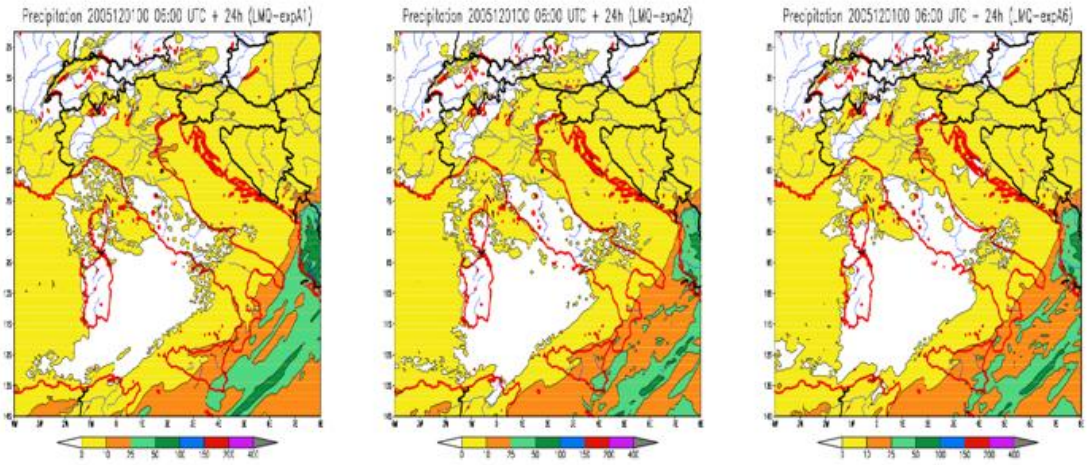


Figure 24: exp A1 (left); exp A2 (middle); exp A6 (right).

Test case 03.12.2005

QPF problem: east part of Liguria and north Toscana: 250 l/m^2 observation vs 0-10 l/m^2 model

Best sensitivity study: RLAM 50

Best cross experiment; CTRL 4.0

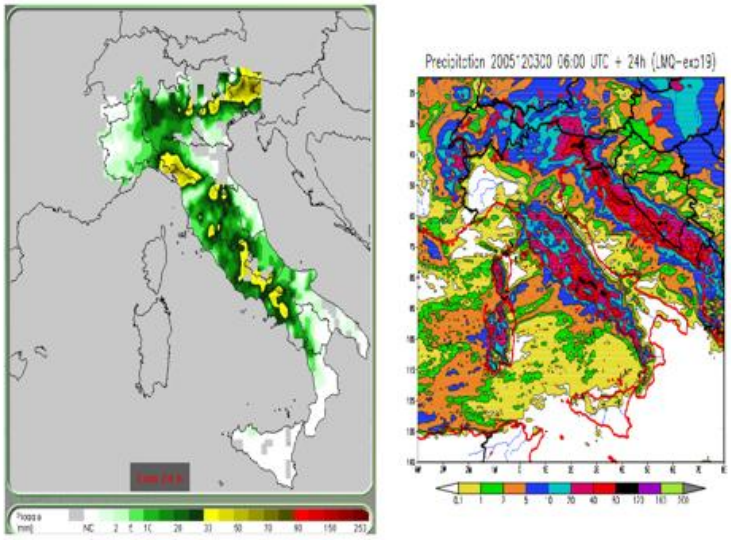


Figure 25: 24 h cumulated precipitation - observation (left); 24h cumulated precipitation exp 19 (right).

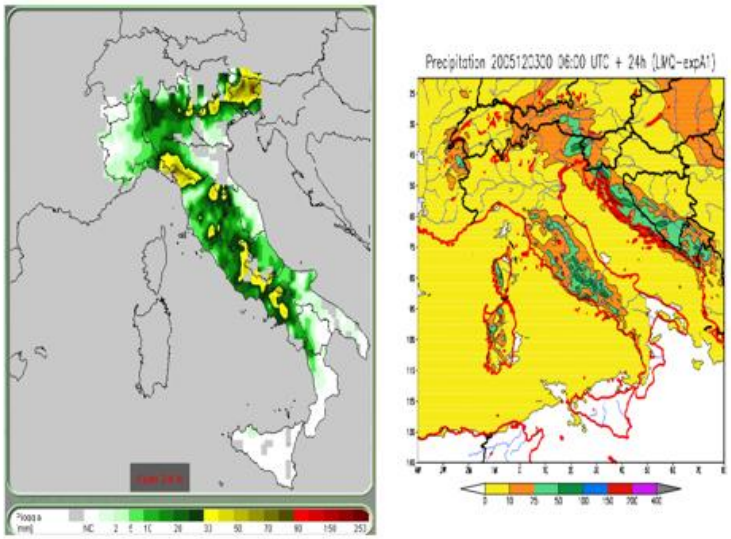


Figure 26: 24 h cumulated precipitation - observation (left); 24h cumulated precipitation exp A1 (right).

Test case 17.12.2005

QPF problem: Tyrrhenian part of Calabria: 10-50 l/m^2 observation vs 250-100 l/m^2 model

Best sensitivity study: numeric and surface simulations.

Best cross experiment: exp A3, A5.

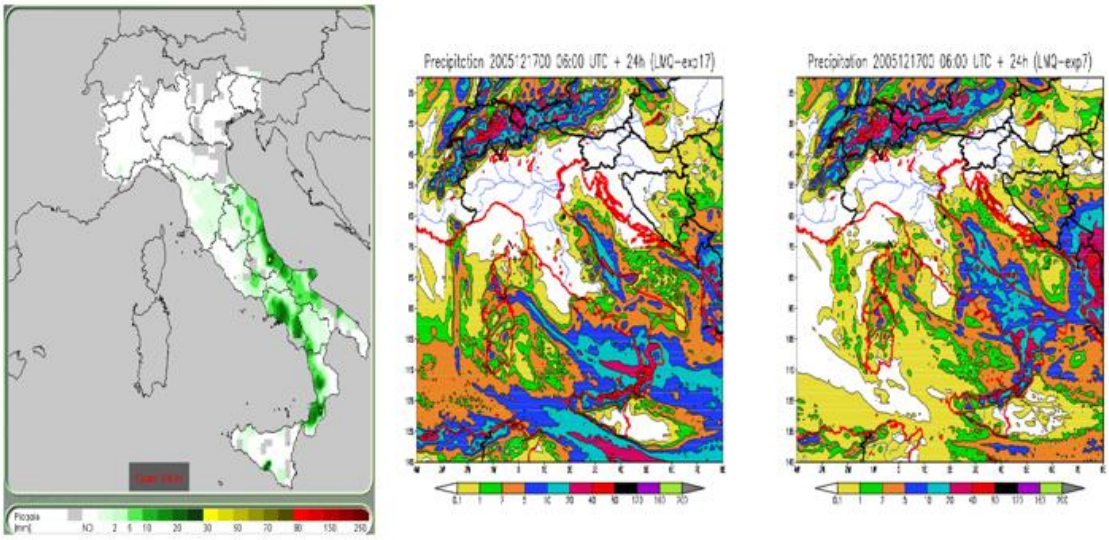


Figure 27: 24 h cumulated precipitation - observation (left); 24h cumulated precipitation exp 17(middle); 24h cumulated precipitation exp 7 (right).

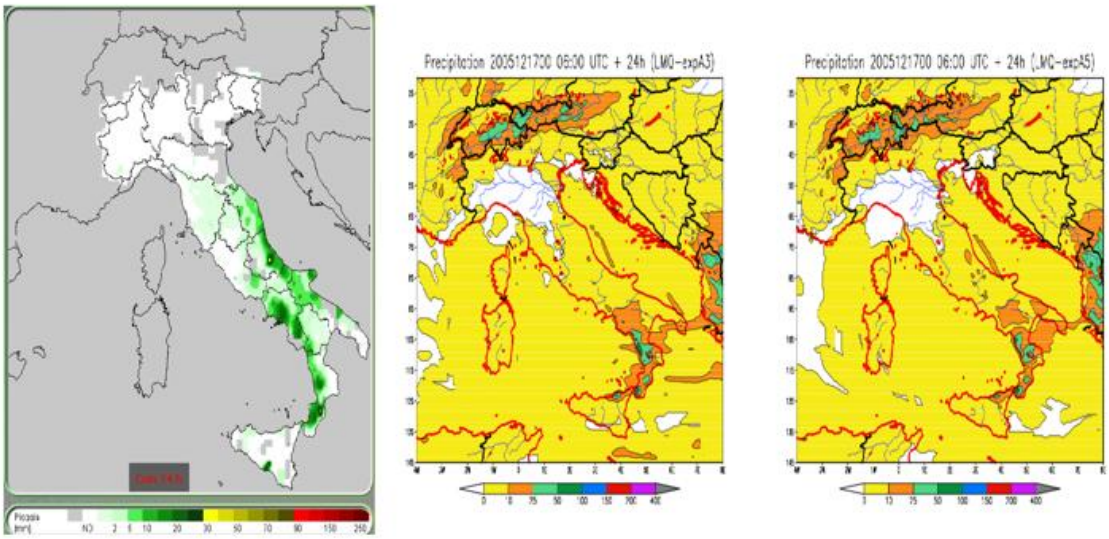


Figure 28: 24 h cumulated precipitations - observation (left); 24h cumulated precipitation exp A3 (middle); 24h cumulated precipitation exp A5 (right).

4.5 Greece

Simulation domain: latitude 33.5/42.5; longitude 18.0/29.0

Evaluation domain: latitude 34.5/41.5; longitude 19.0/28.5

Responsible scientists: P. Fragkouli (Task 1), E. Avgoustoglou (Task 2)

Test case 15.09.2005

QPF problem: trough over Southeast Europe, strong overestimation of precipitation over Crete.

Best sensitivity study: increase of atmospheric water vapor mixing ratio by 10% (exp.4). The average and the distribution of precipitation is improved, but the secondary precipitation centre over Central Aegean is missed.

Best experiment based on COSMO 4.0: in this case, the control run with COSMO 4.0 (exp. 23) showed rather significant preponderance over all cross experiments, however the overall precipitation simulation is poor.

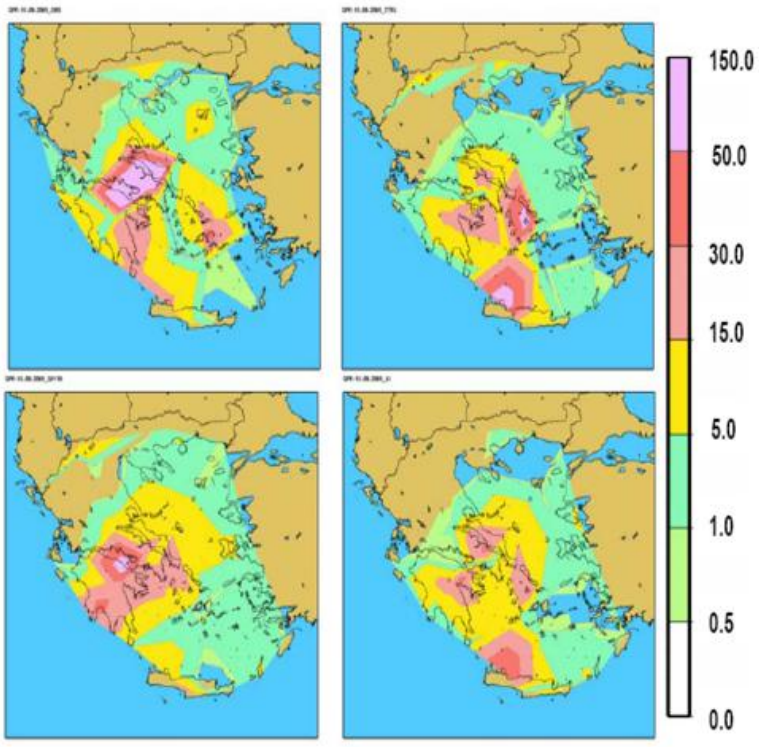


Figure 29: 24h precipitation sum in from 15.09.2005, 06 UTC - 16.09.2005, 06 UTC in the isohyet graphs based on synoptic observations from 63 meteorological stations (upper panel, left), in the reference simulation (upper panel right), in the sensitivity study with increase of water vapor mixing ratio (exp. 4, lower panel, left) and in the control experiment with COSMO 4.0 (exp. 23, lower panel, right).

Test case 23.11.2005

QPF problem: overestimation of precipitation in parts of Northern and Western Greece, eastwards moving fronts with extreme precipitation over Athens.

Best sensitivity study: increase of atmospheric water vapor mixing ratio by 10% (exp.4).The precipitation over the eastern and north-eastern parts of Greece is improved nevertheless underestimated over the central and western parts of the country.

Best cross experiment: COSMO 4.0 with Kain-Fritsch/Bechtold scheme (exp. 25).

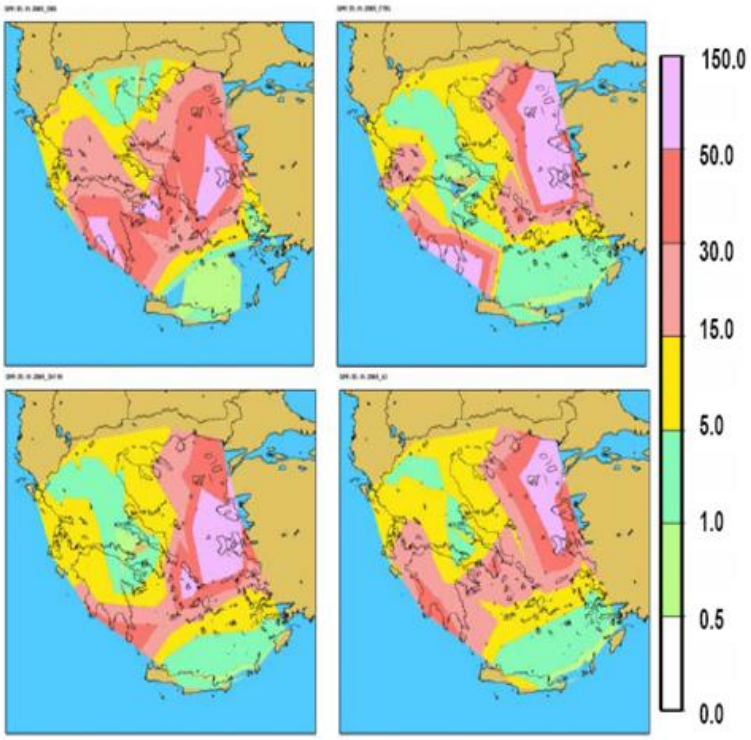


Figure 30: 24h precipitation sum in from 23.11.2005, 06 UTC - 24.11.2005, 06 UTC in the isohyet graphs based on synoptic observations from 60 meteorological stations (upper panel, left), in the reference simulation (upper panel right), in the sensitivity study with increase of water vapor mixing ratio (exp. 4, lower panel, left) and in the cross experiment with COSMO 4.0, Kain-Fritsch/Bechtold (exp. 25, lower panel, right).

Test case 26.11.2005

QPF problem: overestimation of extreme precipitation by a factor of 5 for the first forecast day.

Best sensitivity study: increase of atmospheric water vapor mixing ratio by 10% (exp.4). The average precipitation is improved but the simulation is wrong.

Best cross experiment: COSMO 4.0 with modified Tiedtke scheme (exp. 27).

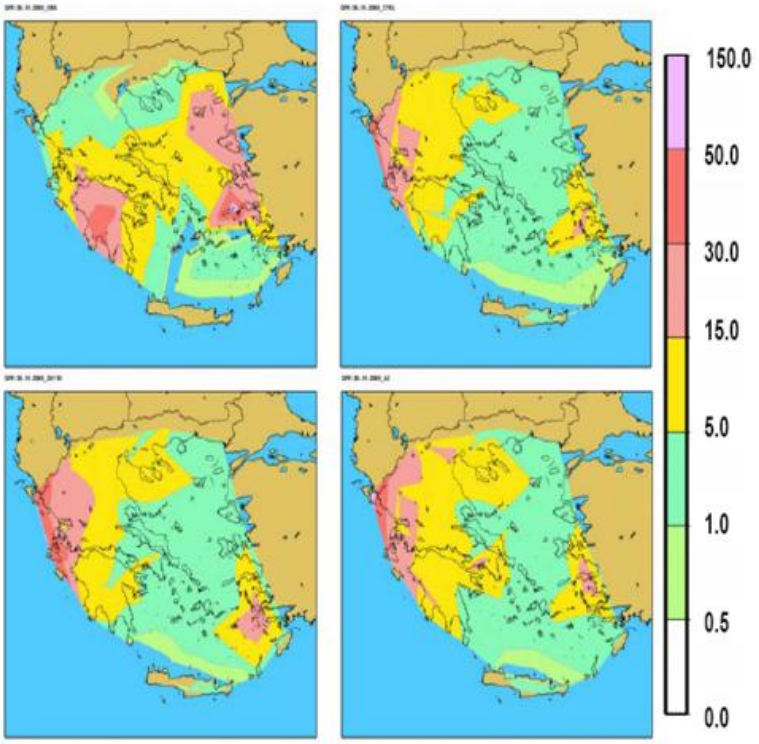


Figure 31: 24h precipitation sum in from 26.11.2005, 06 UTC - 27.11.2005, 06 UTC in the isohyet graphs based on synoptic observations from 59 meteorological stations (upper panel, left), in the reference simulation (upper panel right), in the sensitivity study with increase of water vapor mixing ratio (exp. 4, lower panel, left) and in the cross experiment with COSMO 4.0, modified Tiedtke (exp. 25, lower panel, right).

4.6 Poland

Simulation domain: latitude 45.9/56.5; longitude 10.0/32.8

Evaluation domain: latitude 49.0/54.3; longitude 12.8/26.1

Responsible scientists: Katarzyna Starosta (Task 1 and Task 2)

Test case 03.05.2005

QPF problem: a low with warm front is moving north of Poland from west to east. In the south-east of Poland a second low arises related with heavy precipitation in south-eastern part of the country. Underestimation of precipitation mainly in the south-eastern part of Poland is observed.

Best sensitivity study: the best result which reduces maximum precipitation and increases the average of precipitation to realistic values is observed in experiment 9 (Runge-Kutta, flux form and T'-p' dynamics).

Best cross experiment: these experiments do not increase average precipitation. Experiment with modified Tiedtke scheme reduces maximum precipitation (exp. 27), but the region without precipitation in south-east remains.

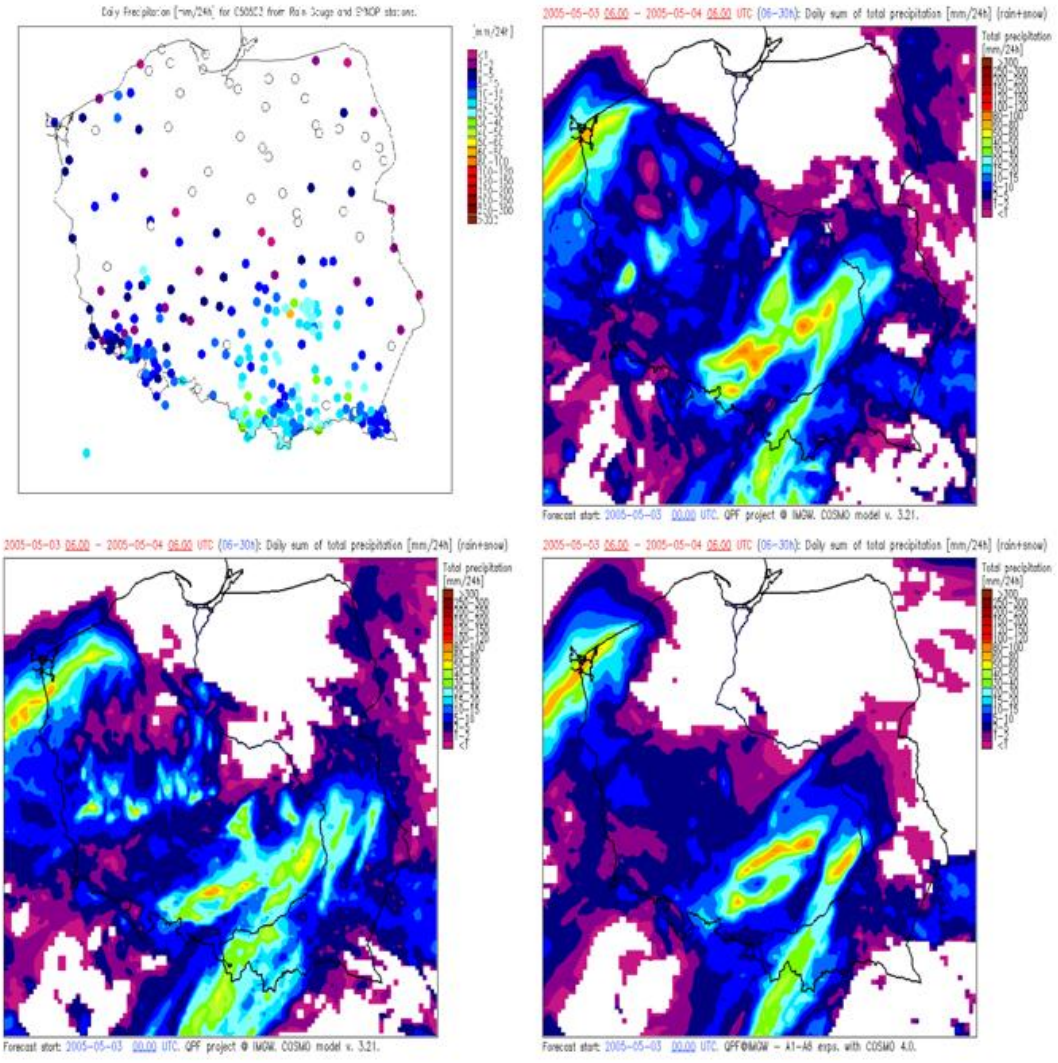


Figure 32: 24h precipitation sum from 03.05.2005, 06 UTC - 04.05.2005, 06 UTC from rain gauges observations (upper panel, left), in the reference simulation (upper panel, right), in the sensitivity study with Runge-Kutta and T'-p' dynamics (exp. 9, lower panel, left) and in the cross experiment with COSMO 4.0, modified Tiedtke scheme(exp. 27, lower panel, right).

Test case 04.05.2005

QPF problem: low over Ukraine moves from south to north provoking heavy precipitation in the south, centre and east of the Polish territory. In the south of the region there is underestimation of precipitation, but over central and eastern parts of territory there is an overestimation. The maximum of precipitation is overpredicted. Locally the difference of maximum precipitation is significant, but taking into account an average precipitation this difference disappears.

Best sensitivity study: the experiment with microphysics reduces the maximum of precipitation (exp. 11, exp. 13). Location of precipitation values still remains wrong.

Best cross experiment: reduction of initial humidity + Runge-Kutta (exp. 24) decreases in general the maximum of precipitation. Still, the location of precipitation values remains wrong.

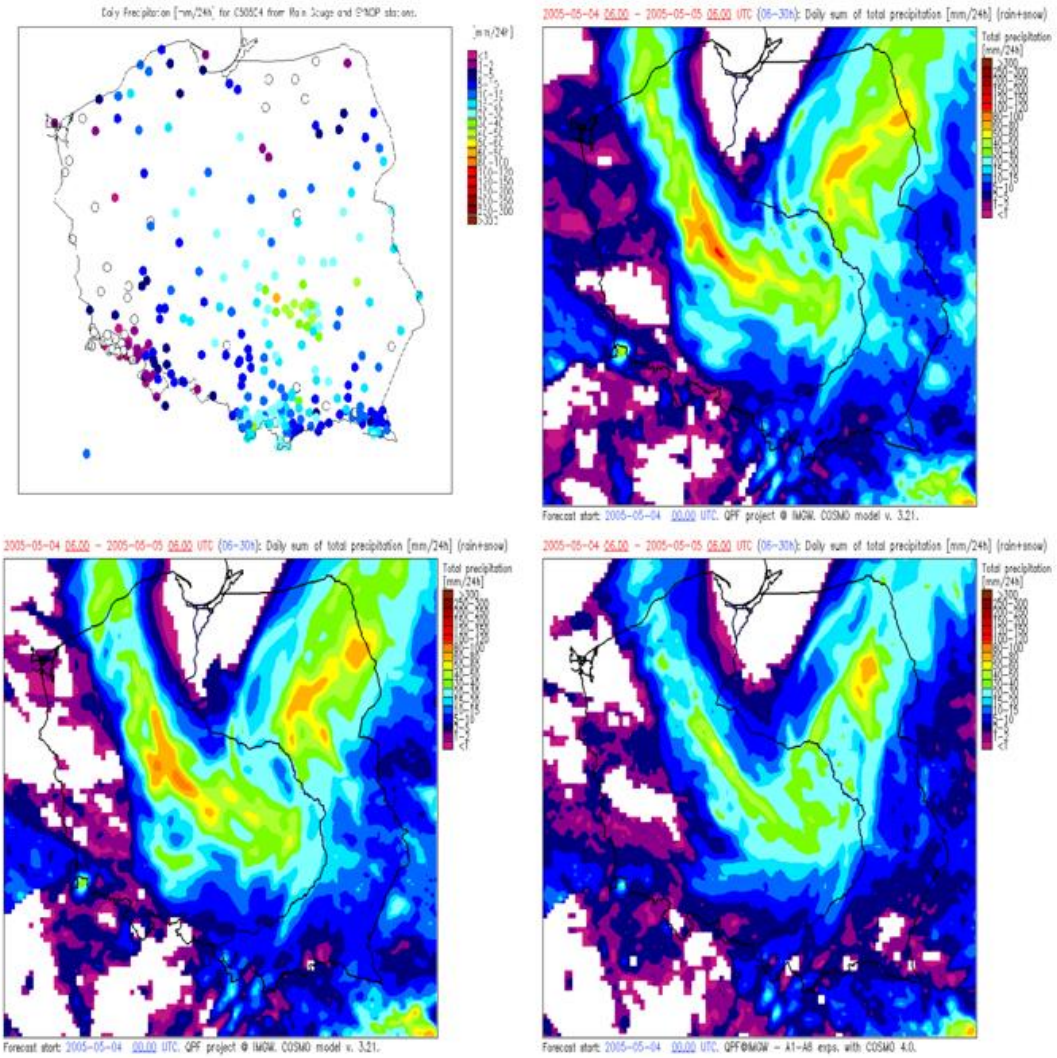


Figure 33: 24h precipitation sum from 04.05.2005, 06 UTC - 05.05.2005, 06 UTC from rain gauges observations (upper panel, left), in the reference simulation (upper panel, right), in the sensitivity study with new warm rain scheme (exp. 11, lower panel, left) and in the cross experiment with COSMO 4.0, Runge-Kutta and reduced initial humidity (exp. 24, lower panel, right).

Test case 10.06.2005

QPF problem: the heavy precipitation in the east is related to a low over Ukraine. The precipitation in western of Poland is connected with cold front. Overestimation is larger in maximum precipitation than in average precipitation. Over south-eastern parts of Poland there is a region where precipitation is not predicted. The region with maximum precipitation is located to the east and not to the south of the country.

Best sensitivity study: the experiments QV090 (exp. 3) and Mikro2 (exp. 12) reduce maximum precipitation but not ideally. Still, the location of precipitation in south-east remains wrong.

Best cross experiment: the experiment Kain-Fritsch/Bechtold (exp. 24) reduces average precipitation, and experiment 28 (reduced initial humidity + Runge-Kutta + modified Tiedtke scheme) reduces maximum value to realistic one, but decrease average value. Wrong location of maximum precipitation and the region with missing precipitation still exists.

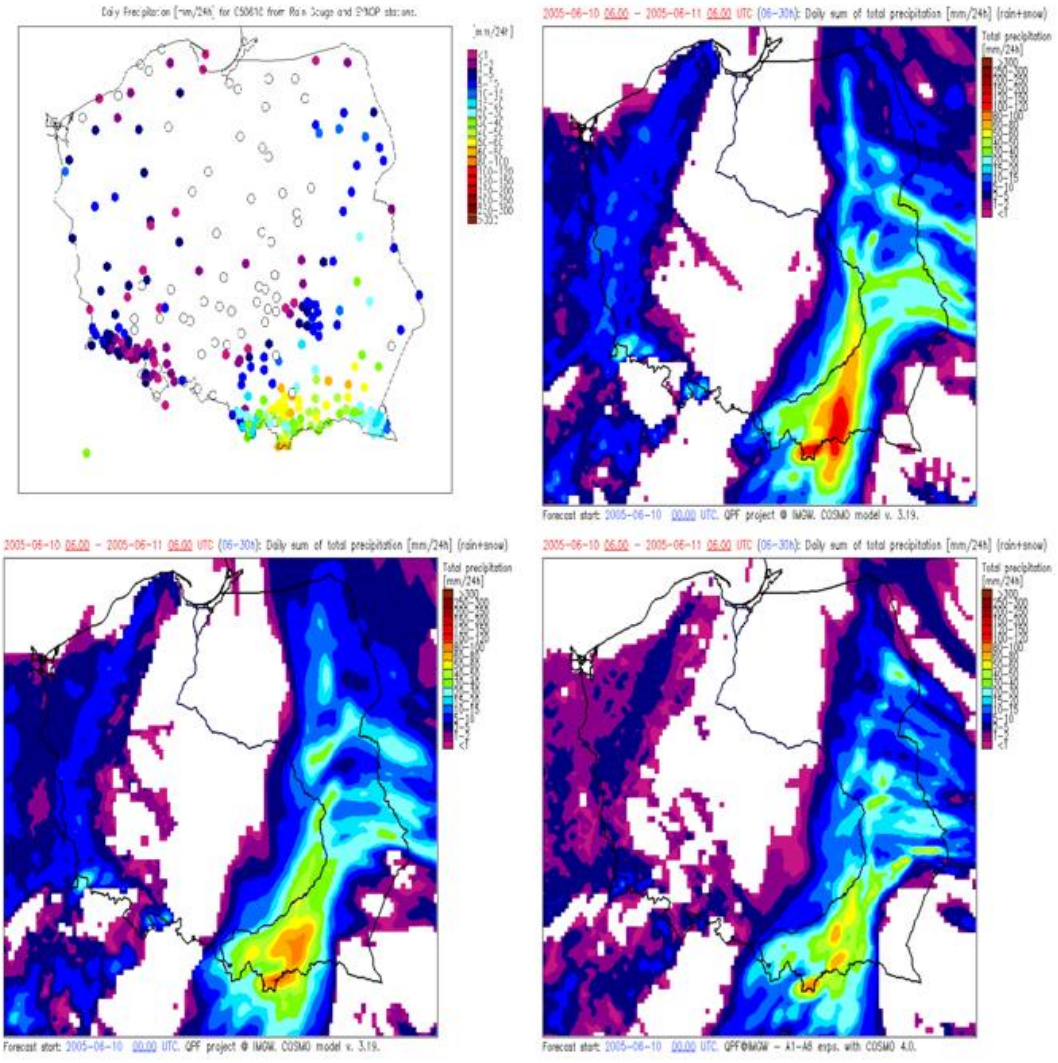


Figure 34: 24h precipitation sum from 10.06.2005, 06 UTC - 11.06.2005, 06 UTC from rain gauges observations (upper panel, left), in the reference simulation (upper panel, right), in the sensitivity study with changes of ice microphysics and new warm rain scheme (exp. 12, lower panel, left) and in the cross experiment with COSMO 4.0, modified Tiedtke scheme, Runge-Kutta and reduced initial humidity (exp. 28, lower panel, right).

Test case 09.08.2005

QPF problem: low moving from Belarus to Latvia. Overestimation recorded especially in north-east of Poland, while underestimation in south-east of Poland.

Best sensitivity study: the experiment with microphysics (exp. 11, 12) reduces the maximum value to realistic one.

Best cross experiment: the model version 4.0 improves the results.

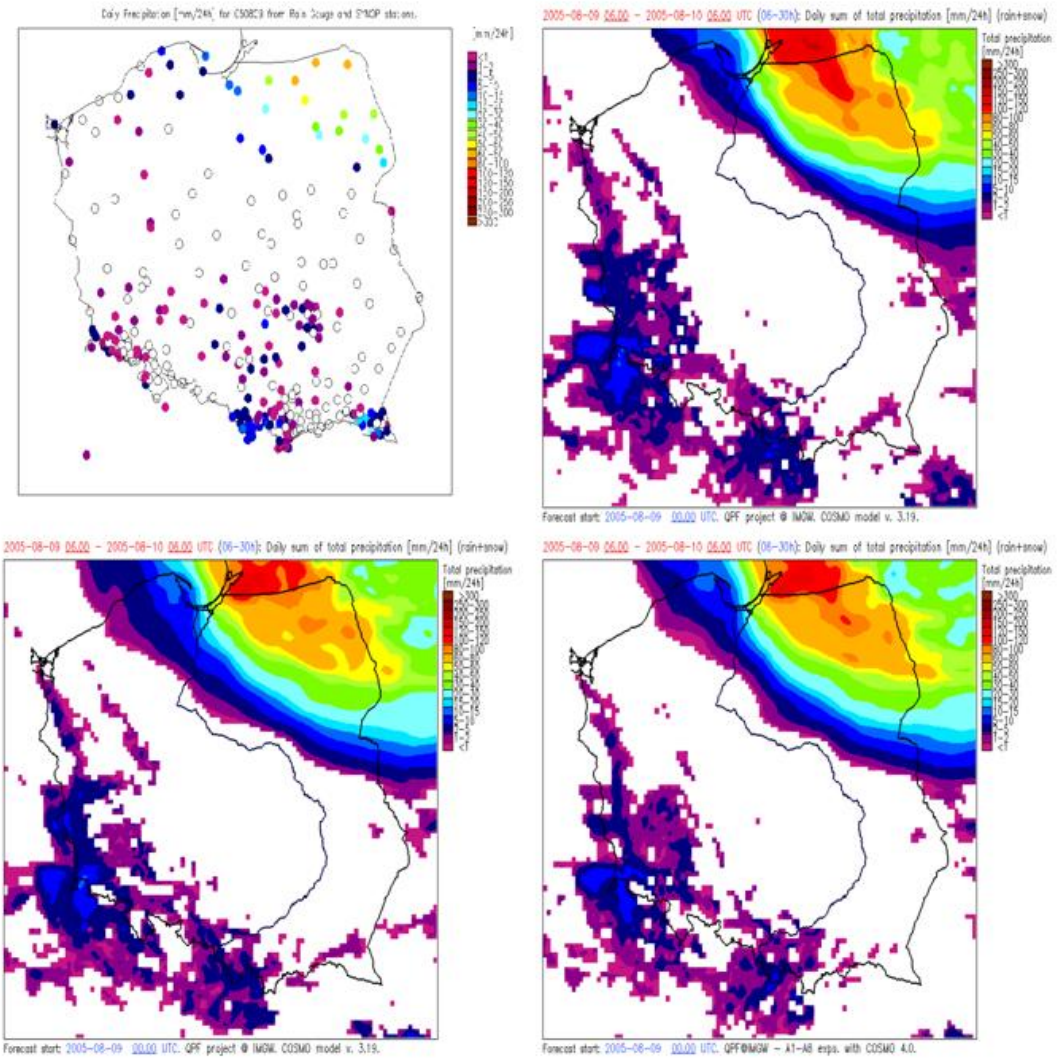


Figure 35: 24h precipitation sum from 09.08.2005, 06 UTC - 10.08.2005, 06 UTC from rain gauges observations (upper panel, left), in the reference simulation (upper panel, right), in the sensitivity study with changes of ice microphysics and new warm rain scheme (exp. 12, lower panel, left) and in the cross experiment with COSMO 4.0, (exp. 23, lower panel, right).

4.7 Romania

Simulation and evaluation domain: dlat=0.0625, dlon=0.0625, ielm_tot=301, jelm_tot=301, kelm_tot=40, pollat=40, pollon=-170.0, startlat_tot=-13.5, startlon_tot=0.625.

Responsible scientists: Rodica Dumitrache (Task 1 and Task 2).

QPF problem:

- E and central Moldova 50-100 l/m^2 observation vs 40-80 l/m^2 model;
- SE 25-50 l/m^2 observations vs 120-160 l/m^2 model overestimation;
- Littoral area 10-25 l/m^2 observations vs 40-80 l/m^2 model overestimation;
- NW - not observed – not simulated;
- SW not observed – 40-80 l/m^2 model overestimation;
- Center 25-50 l/m^2 observations vs 40-80 l/m^2 model.

Best sensitivity study: cloud microphysics, numeric and convective scheme simulations.

Best cross experiment: A2, A6.

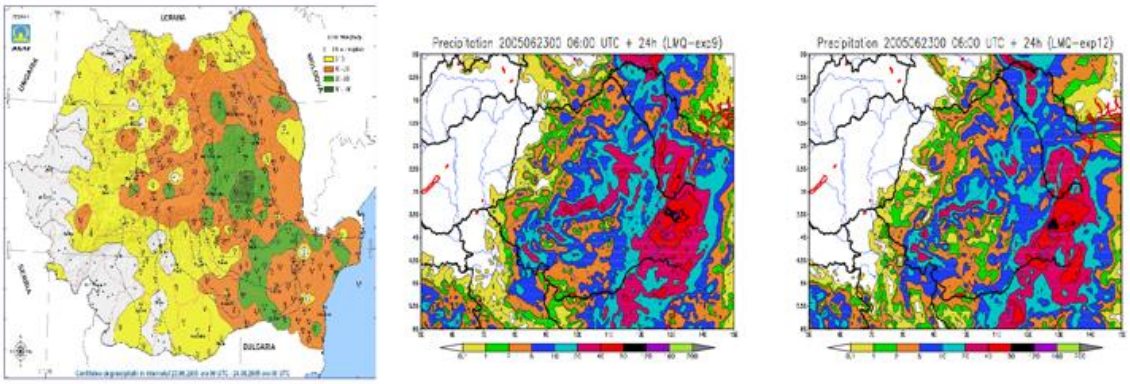


Figure 36: 24 hour cumulated precipitation - observation (left); 24h cumulated precipitation exp 9 (middle); 24h cumulated precipitation exp 12 (right).

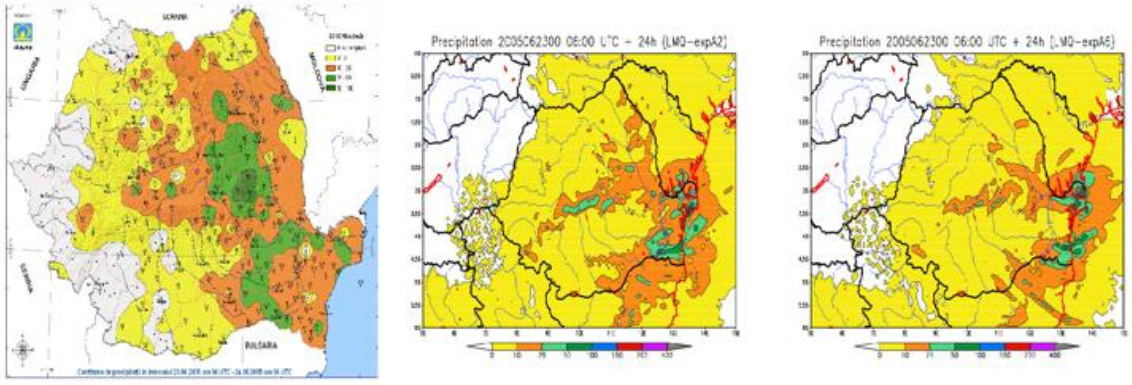


Figure 37: 24 hour cumulated precipitation - observation (left); 24h cumulated precipitation exp A2 (middle); 24h cumulated precipitation exp A6 (right).

Test case 02.07.2005

QPF problem:

- NE-E of the country (40 l/m^2 simulated vs no observed precipitation);
- West, SE and Carpathian region (120-160 l/m^2 simulated vs 25-50 l/m^2 observed);
- South of the country (20 l/m^2 simulated vs 66-110 l/m^2 observed).

Best sensitivity study: exp 18- RLAM 50.

Best cross experiment: exp A1, A6.

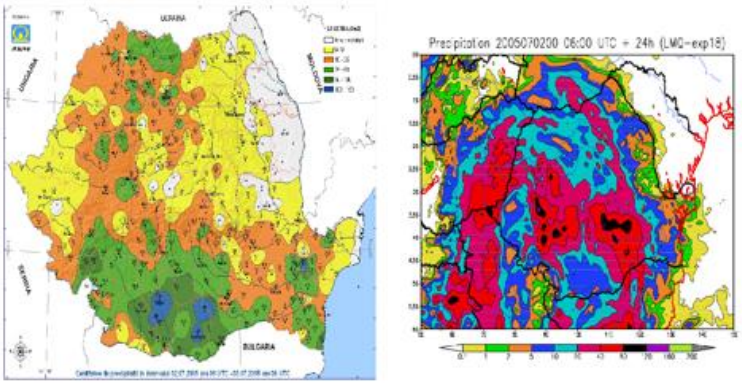


Figure 38: 24 hour cumulated precipitation - observation (left); 24h cumulated precipitation exp 18 (right).

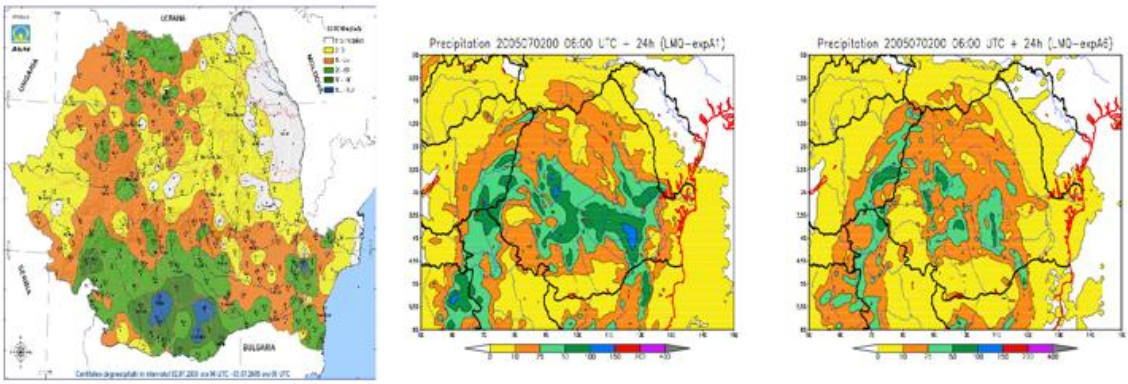


Figure 39: 24 hour cumulated precipitation - observation (left); 24h cumulated precipitation exp A1 (middle); 24h cumulated precipitation exp A6 (right).

Test case 12.07.2005

QPF problem:

- W 1-2 l/m^2 observations vs 20-40 l/m^2 model;
- SW 50-100 l/m^2 observations vs 2-5 l/m^2 model;
- SE 100-150 l/m^2 observations vs 10-20 l/m^2 model;
- Littoral area 1-2 l/m^2 observations vs 40-80 l/m^2 model.

Best sensitivity study: exp 17.

Best cross experiment; exp A1, A6.

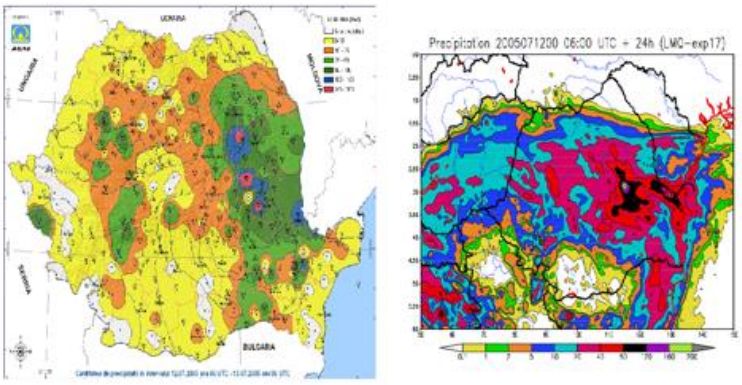


Figure 40: 24 hour cumulated precipitation - observation (left); 24h cumulated precipitation exp 17 (right).

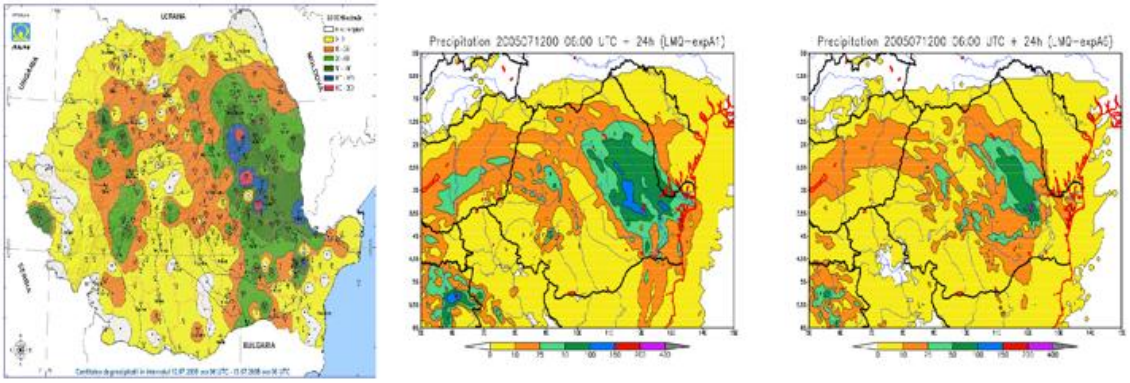


Figure 41: 24 hour cumulated precipitation - observation (left); 24h cumulated precipitation exp A1 (middle); 24h cumulated precipitation exp A6 (right).

5 Acknowledgements

List of contributing scientists during the whole project lifetime:

- S. Dierer (MeteoSchweiz, Switzerland)
- M. Arpagaus (MeteoSchweiz, Switzerland)
- U. Damrath (DWD, Germany)
- A. Seifert (DWD, Germany)
- E. Avgoustoglou (HNMS, Greece)
- T. Andreadis (HNMS, Greece)
- M. Baldauf (DWD, Germany)
- R. Dumitrache (NMA, Romania)
- V. Fragkouli (HNMS, Greece)
- F. Grazzini (ARPA-SIMC, Bologna, Italy)
- W. Interewicz (IMGW, Poland)
- P. Louka (HNMS, Greece)
- P. Mercogliano (CIRA, Italy)
- P. Mezzasalma (ARPA-SIMC, Bologna, Italy)
- M. Milelli (ARPA Piemonte, Torino, Italy)
- D. Mironov (DWD, Germany)
- A. Morgillo (ARPA-SIMC, Bologna, Italy)
- E. Oberto (ARPA Piemonte, Torino, Italy)
- A. Parodi (CIMA, Savona, Italy)
- I. V. Pescaru (NMA, Romania)
- U. Pflüger (DWD, Germany)
- F. Schubiger (MeteoSchweiz, Switzerland)
- K. Starosta (IMGW, Poland)
- M. S. Tesini (ARPA-SIMC, Bologna, Italy)

6 References

Beard, K. V. and H. T. Ochs III, 1993: Warm-Rain Initiation: An overview of microphysical mechanisms. J. Appl. Meteor., 32, 608-625.

Bechtold P., E. Bazile, F. Guichard, P. Mascart and E. Richard, 2001: A mass-flux convection scheme for regional and global models. Quart. J. Roy. Meteor. Soc., 127, 869-886.

Bott, A., 1989: A positive definite advection scheme obtained by nonlinear renormalization of the advective fluxes. Mon. Weather Rev., 117, 1006-1015.

Crewell, S., Mech, M., Reinhardt, T., Selbach, C., Betz, H.-D., Brocard, E., Dick, G., O' Connors, E., Fischer, J., Hanisch, T., Hauf, T., Huenerbein, A., Delobbe, L., Mathes, A., Peters, G., Wernli, H., Wiegner, M. and Wulfmeyer, V., 2008: General observation period 2007: Concept and first results. Meteorologische Zeitschrift, 17, 001-018.

Colle, B.A., C. F. Mass, and K. J. Westrick, 2000:MM5 precipitation verification over the Pacific Northwest during the 1997-1999 cool seasons. Wea. Forecasting, 15, 730-744.

Dierer S., and Schubiger F., 2008: Evaluation of the Kain-Fritsch/Bechtold Convection Scheme. COSMO Newsletter no. 7, 37-42.

Hohenegger, C., D. Lüthi, and C. Schär, 2006: Predictability mysteries in cloud-resolving models. Mon. Wea. Rev., 134, 2095-2107.

Jankov, I., Gallus, W.A., Segal, M. and Koch, S.E., 2007: Influence of initial conditions on the WRF-ARW model QPF response to physical parametrization changes. Wea. Forecasting, 22, 501-519.

Jenkner, J., Frei, C., Schwierz, C., 2008: Quantile-based short-range QPF evaluation over Switzerland. Meteorologische Zeitschrift, 17, pp. 827-848.

Majewski, D., D. Liermann, P. Prohl, B. Ritter, M. Buchhold, T. Hanisch, G. Paul, W. Wergen, and J. Baumgardner, 2002: The Operational Global Icosahedral-Hexagonal Gridpoint Model GME: Description and High-Resolution Tests. Mon. Wea. Rev., 130, 319-338.

Milelli, M., E. Oberto, and A. Parodi, 2008: Sensitivity experiments of a severe rainfall event in North-Western Italy: 17 August 2006. Adv. Sci. Res., Vol. 2, 133-138.

Seifert, A. and K.D. Beheng, 2001: A double-moment parametrization for simulating autoconversion, accretion and selfcollection. Atmos. Res., 59-60, 265-281.

Skamarock, W., and J. B. Klemp, 1992: The stability of time-splitting numerical methods for the hydrostatic and non-hydrostatic elastic systems. Mon. Wea. Rev., 120, 2109-2127.

Skamarock, W.C. and Weisman, M.L., 2009: The Impact of Positive-Definite Moisture Transport on NWP Precipitation Forecasts. Mon. Wea. Rev., 137, 488-494.

Stensrud, D.J., Bao, J.-W., Warner, T.T., 2000: Using Initial Condition and Model Physics Perturbations in Short-Range Ensemble Simulations of Mesoscale Convective Systems. Mon. Wea. Rev., 128, 2077-2107.

Steppeler, J., Hess, R., Doms, G., Schättler, U., and Bonaventura, L., 2003: Review of numerical methods for non-hydrostatic weather prediction models. Meteorology and Atmospheric Physics, 82, 287-301.

Tiedtke, M., 1989: A comprehensive mass flux scheme for cumulus parametrization in large scale models. Mon. Wea. Rev., 117, 1779-1800.

Walser, A., D. Lüthi and C. Schär, 2004: Predictability of Precipitation in a Cloud-Resolving Model. Mon. Wea. Rev., 132 (2), 560-577.

Wicker, L.J. and W.C. Skamarock, 1998: A Time-Splitting Scheme for the Elastic Equations Incorporating Second-Order Runge-Kutta Time Differencing. Mon. Wea. Rev., 126, 1992-1999.

Zängl, G., 2004, The sensitivity of simulated orographic precipitation to model components other than cloud microphysics. Quart. J. Roy. Met. Soc., 130, 1857-1875.

Zhang, F., C. Snyder, and R. Rotunno, 2002: Mesoscale Predictability of the "Surprise" Snowstorm of 24-25 January 2000. Mon. Wea. Rev., 130, 1617-1632.

List of COSMO Newsletters and Technical Reports

(available for download from the COSMO Website: www.cosmo-model.org)

COSMO Newsletters

No. 1: February 2001.

No. 2: February 2002.

No. 3: February 2003.

No. 4: February 2004.

No. 5: April 2005.

No. 6: July 2006.

No. 7: April 2008; Proceedings from the 8th COSMO General Meeting in Bucharest, 2006.

No. 8: September 2008; Proceedings from the 9th COSMO General Meeting in Athens, 2007.

No. 9: December 2008.

COSMO Technical Reports

No. 1: Dmitrii Mironov and Matthias Raschendorfer (2001):
Evaluation of Empirical Parameters of the New LM Surface-Layer Parameterization Scheme. Results from Numerical Experiments Including the Soil Moisture Analysis.

No. 2: Reinhold Schrodin and Erdmann Heise (2001):
The Multi-Layer Version of the DWD Soil Model TERRA_LM.

No. 3: Günther Doms (2001):
A Scheme for Monotonic Numerical Diffusion in the LM.

No. 4: Hans-Joachim Herzog, Ursula Schubert, Gerd Vogel, Adelheid Fiedler and Roswitha Kirchner (2002):
LLM ¯ the High-Resolving Nonhydrostatic Simulation Model in the DWD-Project LITFASS.
Part I: Modelling Technique and Simulation Method.

No. 5: Jean-Marie Bettems (2002):
EUCOS Impact Study Using the Limited-Area Non-Hydrostatic NWP Model in Operational Use at MeteoSwiss.

No. 6: Heinz-Werner Bitzer and Jürgen Steppeler (2004):
Documentation of the Z-Coordinate Dynamical Core of LM.

No. 7: Hans-Joachim Herzog, Almut Gassmann (2005):
Lorenz- and Charney-Phillips vertical grid experimentation using a compressible nonhydrostatic toy-model relevant to the fast-mode part of the 'Lokal-Modell'

No. 8: Chiara Marsigli, Andrea Montani, Tiziana Paccagnella, Davide Sacchetti, André Walser, Marco Arpagaus, Thomas Schumann (2005):
Evaluation of the Performance of the COSMO-LEPS System

No. 9: Erdmann Heise, Bodo Ritter, Reinhold Schrodin (2006):
Operational Implementation of the Multilayer Soil Model

No. 10: M.D. Tsyrulnikov (2007):
Is the particle filtering approach appropriate for meso-scale data assimilation ?

No. 11: Dmitrii V. Mironov (2008):
Parameterization of Lakes in Numerical Weather Prediction. Description of a Lake Model.

No. 12: Adriano Raspanti (2009):
COSMO Priority Project "VERification System Unified Survey" (VERSUS): Final Report

No. 13: Chiara Marsigli (2009):
COSMO Priority Project "Short Range Ensemble Prediction System" (SREPS): Final Report

No. 14: Michael Baldauf (2009):
COSMO Priority Project "Further Developments of the Runge-Kutta Time Integration Scheme" (RK): Final Report

No. 15: Silke Dierer (2009):
COSMO Priority Project "Tackle deficiencies in quantitative precipitation forecast" (QPF): Final Report

COSMO Technical Reports

Issues of the COSMO Technical Reports series are published by the *COnsortium for Small-scale MOdelling* at non-regular intervals. COSMO is a European group for numerical weather prediction with participating meteorological services from Germany (DWD, AWGeophys), Greece (HNMS), Italy (USAM, ARPA-SIMC, ARPA Piemonte), Switzerland (MeteoSwiss), Poland (IMGW) and Romania (NMA). The general goal is to develop, improve and maintain a non-hydrostatic limited area modelling system to be used for both operational and research applications by the members of COSMO. This system is initially based on the COSMO-Model (previously known as LM) of DWD with its corresponding data assimilation system.

The Technical Reports are intended

- for scientific contributions and a documentation of research activities,
- to present and discuss results obtained from the model system,
- to present and discuss verification results and interpretation methods,
- for a documentation of technical changes to the model system,
- to give an overview of new components of the model system.

The purpose of these reports is to communicate results, changes and progress related to the LM model system relatively fast within the COSMO consortium, and also to inform other NWP groups on our current research activities. In this way the discussion on a specific topic can be stimulated at an early stage. In order to publish a report very soon after the completion of the manuscript, we have decided to omit a thorough reviewing procedure and only a rough check is done by the editors and a third reviewer. We apologize for typographical and other errors or inconsistencies which may still be present.

At present, the Technical Reports are available for download from the COSMO web site (www.cosmo-model.org). If required, the member meteorological centres can produce hard-copies by their own for distribution within their service. All members of the consortium will be informed about new issues by email.

For any comments and questions, please contact the editors:

Massimo Milelli
Massimo.Milelli@arpa.piemonte.it

Ulrich Schättler
Ulrich.Schaettler@dwd.de

Consortium

for

Small-Scale Modelling

Technical Report No. 12

COSMO Priority Project
"VERification System Unified Survey
(VERSUS)": Final Report

June 2009

DOI: 10.5676/DWD_pub/nwv/cosmo-tr_12

Deutscher Wetterdienst

MeteoSwiss

Ufficio Generale Spazio Aereo e Meteorologia

ΕΘΝΙΚΗ ΜΕΤΕΩΡΟΛΟΓΙΚΗ ΥΠΗΡΕΣΙΑ

Instytucie Meteorogii i Gospodarki Wodnej

Administratia Nationala de Meteorologie

Agenzia Regionale per la Protezione Ambientale del Piemonte

Agenzia Regionale per la Protezione Ambientale dell' Emilia-Romagna: Servizio Idro-Meteo-Clima

Centro Italiano Ricerche Aerospaziali

Amt für GeoInformationswesen der Bundeswehr

www.cosmo-model.org

Editor: Massimo Milelli, ARPA Piemonte
Printed at Deutscher Wetterdienst, P.O. Box 100465, 63004 Offenbach am Main

COSMO Priority Project

"VERification System Unified Survey (VERSUS)":

Final Report

Adriano Raspanti

Adriano Raspanti
Ufficio Generale Spazio Aereo e Meteorologia
Viale dell'Universitá 4
00185 Roma
Italia

Contents

Contents

1 Summary **3**

2 Project report **3**

2.1 Open points 6

2.2 Resources used 7

2.3 Lessons learned 7

3 Acknowledgements **8**

1 Summary

The development of a complete Conditional Verification Tool has been the first priority and outcome of the VERSUS project. From a more general point of view the main purpose of VERSUS is the systematic evaluation of model performances in order to reveal, in a way different from the usual classical verification tools, model weaknesses. Once delivered and applied routinely, it should provide information to the all scientists and modelers, providing them hints which could be the causes of model deficiencies that can be seen in the operational verification. The typical approach to Conditional Verification consist of the selection of one or several forecast products and one or several mask variables or conditions, which would be used to define for example thresholds for the product verification (e.g. verification of T2M only for grid points with zero cloud cover in model and observations).

After the selection of the desired conditions, a classical verification tools is used to get statistical indexes. The more flexible way to perform a selection of forecasts and observations following a certain number of conditions, is to use an "ad hoc database", planned and designed for this purpose, where the mask or filter could be simple or complex SQL statements.

Through the development of VERSUS software we have achieved a unified tool able to perform operational standard verifications, operational conditional verifications along with experimental standard and conditional verifications, in batch and interactive mode.

The modularity of VERSUS easily allows updates and use of new verifications methods through the use and implementation of "R" language software package or even "ad hoc" algorithms (Fortran, C, PHP).

The verification software has been developed with an user friendly graphic interface, that makes easier the registration, modification and management of all the verification activities. The GUI is based on standard Web interface. This means also that the final architecture can be considered client-server kind.

2 Project report

The classical verification of forecast products is generally based on the evaluation of single elements (e.g. T2m, RR) over specific domains in space and time. The resulting numbers, tables and plots present measures of the overall performance of the model with regard to the product considered. Potential interdependencies between various products are a priori ignored (e.g. cloud cover & near surface temperature). The interpretation of classical verification results with regard to systematic deficiencies in the model simulation of specific processes is also far from trivial. Even though obvious failures of the model may be established, finding the reasons behind these failures is hampered by the integral properties of the classical approach, i.e. the averaging over spatial domains (and time) without consideration of specific details of the atmospheric and/or surface situation. However, a tool allowing a process or a situation dependent verification, e.g. the evaluation of the model forecast quality with regard to the diurnal cycle of near surface temperatures in the absence of clouds, would facilitate the task of finding the cause of model shortcomings and the model improvement. Formulating the verification of forecast products in conjunction with the existence of additional criteria, can be defined as Conditional Verification (CV).

The prime purpose of CV is the systematic evaluation of model performance in order to reveal typical shortcomings and the reasons behind them. Applied in a routine mode, it should also have the potential to provide information to the forecasters with regard to the

situation and product dependent model reliability (e.g. typical clear sky forecast errors for T2M in contrast to cloudy sky condition errors). Then the typical approach to CV could consist of the selection of one or several forecast products and one or several mask variables, which would be used to define thresholds for the product verification (e.g. verification of T2M for grid points with zero cloud cover in model and observations only). However, the masking requirements may occasionally be rather complex as in the cases where the forecast product depends strongly on the history of the evolution rather than the current state of a certain variable. For this reason, one could define at least four classes of masks:

- time-independent masks;
- time dependent masks concurrent to the product;
- time dependent masks with possible time-lag to the verified product;
- masks depending on an atmospheric situation classification.

The first class is certainly the simplest to handle, but it carries nevertheless a certain potential with regard to the purpose of the exercise. Apart from obvious masks like the application of a land-sea filter or the stratification of verification results with regard to orographic height, one could envisage masks like the model soil type, plant cover, roughness length etc. The application of such masks might well reveal that certain deficiencies are more pronounced within certain ranges of a particular mask than outside of that range and thereby lead to the detection of a more specific model deficiency.

The second class concerns more the direct interaction between various model products. Typical examples would be the verification of T2M in the presence or absence of snow, but also the verification of products like surface radiative fluxes classified by the cloud cover.

The third class allows in addition to take into account the history of the model (or observation) evolution. E.g. the near surface temperature, as an instantaneous model product, depends among others on the cloud cover which was present in the period before the verification time. In order to obtain a meaningful CV for such a product/mask combination, one would evaluate the verified variable with respect to the previous evolution and the current state of the mask variable.

Finally, the fourth class may need a sophisticated algorithm or even manual intervention in the stratification of all cases with regard to the mask criteria. For example, if we are interested in the performance of the model in stable wintertime conditions, it may not be sufficient to check for a temperature inversion near the earth's surface or relatively high pressure over the domain considered.

Masking conditions may be formulated in model or observation space or both, depending on the application. E.g. in order to obtain a detailed insight in the models ability to simulate the diurnal cycle of near surface temperatures in cloud-free conditions, neither simulated nor observed cloud cover must exceed the specified threshold value.

Generally, several masks may be applied at once, e.g. simultaneous application of cloud cover, soil moisture and plant cover thresholds. Obviously the size of the ensemble will depend on the number of criteria applied. Even though this could be detrimental for the evaluation of a few case studies, in an operational environment this problem would be alleviated by the large number of forecasts generated.

One drawback of CV may be the multitude of verification products arising, if various mask criteria are applied to a set of forecasts.

A generalized CV tool, which can handle all the potential applications mentioned above would require development resources which exceed those available. Consequently, in a first step a tool which is able to handle at least the more basic applications mentioned above, has been created. The name of this tool, as well as the COSMO priority project, is VERSUS (VERification System Unified Survey).

However, VERSUS has been developed in a flexible, user configurable way in order to allow future extensions towards a fully flexible tool. Nevertheless it can be already applied both to operational and experimental forecast products.

In order to give a general idea, in the following table a first attempt was made to define a small set of products to be verified in conjunction with corresponding criteria. This set should only be considered as a starting point. No attempt has been made to order the following table with regard to the expected benefit.

Verified variable	Mask variable(s)	Criteria	Remarks
T2m	CLC(t); local time	lower & upper thresholds in CLC; local time slots	cloud cover thresholds should be applied over the time period preceding the verification time and both to model and observations
T2m	Wsoil	lower & upper thresholds in soil moisture (relative to field capacity)	soil moisture is a multi-layer variable and it may be useful to compute an effective soil moisture as average over several layers
T2m	SHF/LHF	thresholds in Bowen ratio	Bowen ratio as an indirect measure of soil wetness needs to be considered as an average over time
CLC(L)	vertical stability index	stable versus unstable situations	differences in temperatures at various pressure levels may be used as a stability index; the distinction with regard to stability may be considered as an example for situation dependent masking, e.g. to focus on low level stratus or convective regimes
RR	vertical stability index	stable versus unstable situations	regime dependent precipitation verification
U10m	z0	low, medium, large z0	correlation between wind speed errors and roughness length may point to problems in external parameters
T2m	U10m	upper threshold in wind speed	exclude advection dominated situations in temperature verification
Td2m	Wsoil	lower & upper thresholds in soil moisture (relative to field capacity)	determine the error of dew point temperatures in the case of dry soils versus wet soils
T2m	Wsnow	no snow, broken snow, snow	the temperature error is likely to depend on snow cover, hence a broken snow deck might be an indicator for melting snow

The project started in an experimental version using the already developed Common Verification Suite (Fortran package). A number of other Fortran applications were developed to

implement some of the interdependencies of the table above. The results were encouraging because it was clear that applying a mask during the calculation of T2m standard verification, for example cloud/no-cloud, the model behaviour was really different and some clear indication arose from such a conditional verification.

On these basis it was decided to go further and to develop the VERSUS priority project and it was clear that the more flexible way to perform a selection of forecasts and observations following a certain number of conditions, is to design, build and use an "ad hoc database" where the mask or filter could be simple or complex SQL statements.

The project was planned on the development of ten tasks over a period of 3 years.

Of course not only conditional verifications, but also all the standards and common verification scores can be produced by VERSUS. For the comprehensive list of features of VERSUS package you can refer to the User Manual and Technical Manual, available in the installation package, on the VERSUS WEB GUI and soon on the COSMO website.

The following are only some of the most important features that can be found in VERSUS package:

- Verification (conditional or not) can be produced in batch or interactive mode;
- seasonal or monthly period can be produced in batch and interactive mode; any other time period can be produced in interactive way only;
- 3 different kind of users with different kind of privileges have been foreseen in VERSUS (see manuals for details);
- VERSUS can perform standard and conditional verification on continues and binary parameters for surface on-site observations;
- only standard verification is possible at the moment for upper-air observations;
- conditions can be imposed on both observation and forecasts spaces;
- VERSUS can be used not only for COSMO-models but also for, e.g., IFS and GME, provided the right information on the "model registration" module;
- VERSUS can calculate the usual standard statistical scores, both for continues and binary events. More scores can be introduced, through the GUI, using the "R" programming language;
- VERSUS can perform verification on different user-oriented stratifications, in time and/or space;
- all the scores, time series and daily cycles are produced in both text and graphical formats;
- graphic plots are highly configurable;
- all the possible activities are configurable through the web based GUI.

2.1 Open points

VERSUS has not been planned to cover all the existing verification methods, as well as all the possible products from a NWP. Moreover not all types of observation can be used at

present, with VERSUS software, for example observation from satellite and radar. In more detail, the open points in the VERSUS project are:

- development of probabilistic and ensemble forecasts verification;
- development of object-based and fuzzy verification methods applied to precipitation;
- new scores for extreme events (e.g. extreme dependency score);
- more in general, development of User-oriented verification;
- statistical features like Confidence intervals and Bootstrap method;
- use of non conventional obs (e.g. radar, satellite, raingauges) and gridded observations (precipitation analysis).

In order to face and solve these open points, an extension of VERSUS project has been proposed: VERSUS 2.

2.2 Resources used

The development of VERSUS needed the use of resources with special skill in database project, design and management. Of course expertise in verification methods has been used to fulfil and clarify the general requirements coming from documents, discussions, meetings and "wishes" inside the COSMO community.

Resources with skill in PHP programming and implementation of PHP graphic (JPGRAPH) modules have been used to create graphic package inside VERSUS. Resources with some skill in "R" programming language and in statistical packages have been employed too.

Finally, resources with skill in software and DB installation and customization on different LINUX platforms have been employed (e.g. testing phase).

2.3 Lessons learned

The project started at the end of 2005 with no clear technical specification or requirements but only with a joint document coming from WG3-WG5 workshop and some "wishes" from WG3. The lack of a Reference Document made the development of Conditional Verification (CV) package, and later VERSUS, more difficult and the direction and the solutions adopted inside the COSMO community were not clear even inside WG5 itself.

For this reason, the extension of VERSUS (the new project named VERSUS2) will have, as TASK0, the redaction of such a Reference Document (System Architecture Design and Overview), reviewed and accepted by all the members of the COSMO community. This task can be seen as the most important of the whole project. People involved in the actual development of requirements will have a clear reference document to follow, as well as a detailed description of what, why and how they have to implement. This TASK0 should avoid mistakes and delays due to misunderstandings or no full comprehension of the project itself.

The project leader has to "stress" and push people to communicate among them and with the PL himself. Communication is important for the exchange of suggestions, ideas, clarifications, for the release of deliverables and so on. Just to give an example: some parts

of VERSUS project were not really clear to everybody, almost until the end of the project itself, mainly due to poor communications.

3 Acknowledgements

This is the list of contributing scientists: Ulrich Damrath (DWD); Pirmin Kaufmann (MCH); Adriano Raspanti as PL (USAM); David Palella (USAM); Angela Celozzi (USAM); External Resources provided by USAM (ELSAG-DATAMAT); Flora Gofa (HNMS); Katarzyna Starosta (IMGW); Joanna Linkowksa (IMGW), Marek Lazanowicz (IMGW); Aurelia Lupascu (NMA); Rodica Dumitrache (NMA).

List of COSMO Newsletters and Technical Reports

(available for download from the COSMO Website: www.cosmo-model.org)

COSMO Newsletters

No. 1: February 2001.

No. 2: February 2002.

No. 3: February 2003.

No. 4: February 2004.

No. 5: April 2005.

No. 6: July 2006.

No. 7: April 2008; Proceedings from the 8th COSMO General Meeting in Bucharest, 2006.

No. 8: September 2008; Proceedings from the 9th COSMO General Meeting in Athens, 2007.

No. 9: December 2008.

COSMO Technical Reports

No. 1: Dmitrii Mironov and Matthias Raschendorfer (2001):
Evaluation of Empirical Parameters of the New LM Surface-Layer Parameterization Scheme. Results from Numerical Experiments Including the Soil Moisture Analysis.

No. 2: Reinhold Schrodin and Erdmann Heise (2001):
The Multi-Layer Version of the DWD Soil Model TERRA_LM.

No. 3: Günther Doms (2001):
A Scheme for Monotonic Numerical Diffusion in the LM.

No. 4: Hans-Joachim Herzog, Ursula Schubert, Gerd Vogel, Adelheid Fiedler and Roswitha Kirchner (2002):
LLM ¯ the High-Resolving Nonhydrostatic Simulation Model in the DWD-Project LITFASS.
Part I: Modelling Technique and Simulation Method.

No. 5: Jean-Marie Bettems (2002):
EUCOS Impact Study Using the Limited-Area Non-Hydrostatic NWP Model in Operational Use at MeteoSwiss.

No. 6: Heinz-Werner Bitzer and Jürgen Steppeler (2004):
Documentation of the Z-Coordinate Dynamical Core of LM.

No. 7: Hans-Joachim Herzog, Almut Gassmann (2005):
Lorenz- and Charney-Phillips vertical grid experimentation using a compressible nonhydrostatic toy-model relevant to the fast-mode part of the 'Lokal-Modell'

No. 8: Chiara Marsigli, Andrea Montani, Tiziana Paccagnella, Davide Sacchetti, André Walser, Marco Arpagaus, Thomas Schumann (2005):
Evaluation of the Performance of the COSMO-LEPS System

No. 9: Erdmann Heise, Bodo Ritter, Reinhold Schrodin (2006):
Operational Implementation of the Multilayer Soil Model

No. 10: M.D. Tsyrulnikov (2007):
Is the particle filtering approach appropriate for meso-scale data assimilation ?

No. 11: Dmitrii V. Mironov (2008):
Parameterization of Lakes in Numerical Weather Prediction. Description of a Lake Model.

No. 12: Adriano Raspanti (2009):
COSMO Priority Project "VERification System Unified Survey" (VERSUS): Final Report

COSMO Technical Reports

Issues of the COSMO Technical Reports series are published by the *COnsortium for Small-scale MOdelling* at non-regular intervals. COSMO is a European group for numerical weather prediction with participating meteorological services from Germany (DWD, AWGeophys), Greece (HNMS), Italy (USAM, ARPA-SIMC, ARPA Piemonte), Switzerland (MeteoSwiss), Poland (IMGW) and Romania (NMA). The general goal is to develop, improve and maintain a non-hydrostatic limited area modelling system to be used for both operational and research applications by the members of COSMO. This system is initially based on the COSMO-Model (previously known as LM) of DWD with its corresponding data assimilation system.

The Technical Reports are intended

- for scientific contributions and a documentation of research activities,
- to present and discuss results obtained from the model system,
- to present and discuss verification results and interpretation methods,
- for a documentation of technical changes to the model system,
- to give an overview of new components of the model system.

The purpose of these reports is to communicate results, changes and progress related to the LM model system relatively fast within the COSMO consortium, and also to inform other NWP groups on our current research activities. In this way the discussion on a specific topic can be stimulated at an early stage. In order to publish a report very soon after the completion of the manuscript, we have decided to omit a thorough reviewing procedure and only a rough check is done by the editors and a third reviewer. We apologize for typographical and other errors or inconsistencies which may still be present.

At present, the Technical Reports are available for download from the COSMO web site (www.cosmo-model.org). If required, the member meteorological centres can produce hard-copies by their own for distribution within their service. All members of the consortium will be informed about new issues by email.

For any comments and questions, please contact the editors:

Massimo Milelli
Massimo.Milelli@arpa.piemonte.it

Ulrich Schättler
Ulrich.Schaettler@dwd.de

Consortium for Small-Scale Modelling

Technical Report No. 34

COsmo Towards Ensembles at the Km-scale IN Our countries (COTEKINO), Priority Project final report

May 2018

DOI: 10.5676/DWD_pub/nwv/cosmo-tr_34

Deutscher Wetterdienst
MeteoSwiss
Ufficio Generale Spazio Aereo e Meteorologia
ΕΘΝΙΚΗ ΜΕΤΕΩΡΟΛΟΓΙΚΗ ΥΠΗΡΕΣΙΑ
Instytucie Meteorogii i Gospodarki Wodnej
Administratia Nationala de Meteorologie
ROSHYDROMET
Agenzia Regionale Protezione Ambiente Piemonte
Agenzia Regionale Prevenzione Ambiente Energia Emilia Romagna
Centro Italiano Ricerche Aerospaziali
Amt für GeoInformationswesen der Bundeswehr
Israel Meteorological Service

www.cosmo-model.org

Editor: Massimo Milelli, ARPA Piemonte

COsmo Towards Ensembles at the Km-scale IN Our countries (COTEKINO), Priority Project final report.

Project participants:

D. Alferov[1], ***M. Arpagaus***[2], ***E. Astakhova***[1], ***R. Bonanno***[3], ***G. Duniec***[4], ***R. Keane***[5], ***W. Interewicz***[4], ***R. Kohlhepp***[5], ***D. Leuenberger***[2], ***N. Loglisci***[3], ***E. Machulskaya***[5], ***C. Marsigli***[6‡], ***A. Mazur***[4], ***V. Maurer***[2], ***A. Montani***[6], ***G. Rivin***[1], ***I. Rozinkina***[1], ***L. Torrisi***[7], ***A. Walser***[2]

[1] Roshydromet

[2] MeteoSwiss

[3] ARPA Piemonte

[4] Instytucie Meteorogii i Gospodarki Wodnej

[5] Deutscher Wetterdienst

[6] Agenzia Prevenzione Ambiente Energia Emilia Romagna

[7] Ufficio Generale Spazio Aereo e Meteorologia

[‡] Project Coordinator

Contents

1 Introduction **3**

2 Initial Condition perturbations derived from KENDA **4**

3 Model perturbations **4**

3.1 Tests with the SPPT scheme 5

3.1.1 Tests at MCH 5

3.1.2 Tests at RHM 9

3.1.3 Tests at ARPA-SIMC 14

3.2 Test of the SKEB scheme in the 2.2 km ensemble at MCH 22

3.3 Information about improvements and a new strategy for model perturbations at DWD 23

4 Soil/surface perturbations **23**

4.1 IMGW 24

4.1.1 Preliminary sensitivity tests 24

4.1.2 Extensive test-cases and sensitivity tests 29

4.1.3 Test-bed and configuration for (quasi-)operational EPS, concept of time-lagged ICs/BCs 35

4.2 ARPA Piemonte 43

4.2.1 Sensitivity of COSMO model to different lower boundary initial conditions. 43

4.2.2 Implementing a soil perturbation technique in a high resolution ensemble system. 47

5 References **49**

Project leader

Chiara Marsigli (Arpa SIMC).

Contributing scientists

Dmitry Alferov (RHM), Marco Arpagaus (MCH), Elena Astakhova (RHM), Riccardo Bonanno (Arpa Piemonte), Grzegorz Duniec (IMGW), Richard Keane (DWD), Witold Interewicz (IMGW), Regina Kohlhepp (DWD), Daniel Leuenberger (MCH), Nicola Loglisci (Arpa Piemonte), Ekaterina Machulskaya (DWD), Chiara Marsigli (Arpa SIMC), Andrzeij Mazur (IMGW), Vera Maurer (MCH), Andrea Montani (Arpa SIMC), Gdaly Rivin (RHM), Inna Rozinkina (RHM), Lucio Torrisi (CNMCA), Andr Walser (MCH).

1 Introduction

In the recent years, more and more emphasis is being devoted to high-resolution rapid-update-cycle (RUC) NWP applications, since weather forecast is focusing more on high-impact weather (HIW) and small-scale intense phenomena (e.g. convection), also aiming at different applications (assistance to aviation, hydrology, civil protection). For this reason, NWP development is concentrating on high-resolution modelling, O(1km), and this is reflected in the COSMO strategy, which has lead to focusing the consortium development on high-resolution data assimilation, high-resolution modelling, high-resolution verification. Ensemble forecast was born to complement deterministic forecast, with products such as ensemble mean for medium-range predictions, ensemble spread to quantify the forecast uncertainty, meteograms for surface weather parameters, to present a spectrum of possible alternative scenarios. With the model resolution increase, the phenomena which are now described by NWP models are more and more stochastic in nature. For moist convection prediction, skill is manifested through the statistical properties of the forecasted convection instead of by deterministic modelling (Fritsch and Carbone 2004). Therefore, the weight given to ensemble forecast is now greater than it was some 10 years ago, since for the convection-permitting NWP models it is crucial to be able to forecast not only the "best scenario" but ideally the whole pdf or, more realistically, a good representation of it. The high-resolution of these systems prevents the possibility of running consortia ensembles, since it is prohibitive to cover a large domain with the required grid spacing. This is leading to the development of high-resolution ensembles on a national scale. Few years ago, DWD has started the development of a convection-permitting ensemble, COSMO-DE-EPS, which is operational over Germany at 2.8km horizontal resolution since May 2012 (Gebhardt et al., 2011). At the time of the COTEKINO PP, the system received initial condition perturbations from the 4 global scale operational analyses of DWD, ECMWF, NCEP and JMA. The four operational global runs of these institutions provides also boundary conditions to 4 COSMO runs at 7km horizontal resolution which drive in turn the COSMO-DE runs. Model physics perturbations are also applied, by changing the value of few parameters of the physics schemes. Then also Switzerland, Italy and Poland have started the development of convection-permitting ensembles in their countries. Furthermore, Russia has developed COSMO-RU2-EPS for assisting the Winter Olympics. Therefore, the need for a good strategy for convection-permitting ensemble has emerged at the Consortium level, requiring coordination among the activities taking place in the different countries, in order to share research and development work and to ensure good and timely exchange of in-

formation. This coordination has been organized through a Priority Project, COTEKINO (COsmo Towards Ensembles at the Km-scale IN Our countries). The COTEKINO Priority Project, which lasted for 2 years, was aimed at bringing to operations the COSMO ensemble forecasting systems for the convection-permitting scale. Several aspects of the design of convection-permitting ensembles have been taken into account, by organizing the Project in three Tasks: Initial Condition (Task 1, Section 2), Model perturbation (Task 2, Section 3) and Lower boundary perturbation (Task 3, Section 4). Boundary Conditions have not be considered in the Project. Anyway, a study about how to provide perturbed BCs to a convection-permitting ensemble has been carried out in Marsigli et al. (2014), showing that a direct nesting in a global ensemble of good quality may be a practicable solution, without the need of an intermediate step with a coarser resolution ensemble. The work carried out within the three Tasks is presented in the following Sections of this Report.

2 Initial Condition perturbations derived from KENDA

It is recognised that for the forecasting horizon of the convection-permitting ensembles, data assimilation plays a crucial role. What dominates ensemble spread in the first six hours are perturbed initial conditions (Peralta et al, 2012, Vié et al, 2011), which should include both a good estimate of the initial condition(s) and a good representation of its (their) uncertainties. Within the KENDA PP, a LETKF scheme for the km-scale has been developed, aiming at providing both deterministic analysis for driving high-resolution COSMO runs and a set of perturbed analyses to drive high-resolution ensembles. Though the KENDA development is included in the KENDA PP, how to set-up the system to provide ICs to a convection-permitting ensemble and how to derive ICs from KENDA was addressed in the COTEKINO PP. In particular, it was organised the communication about experiments and their results, the exchange of dedicated tools and the coordination with the KENDA PP itself. This activity has been carried out by Chiara Marsigli and Tiziana Paccagnella (ARPA-SIMC), Daniel Leuenberger and André Walser (MeteoSwiss), Richard Keane (DWD), from the COTEKINO PP side and by Christoph Schraff, Hendrik Reich and Roland Potthast (DWD) from the KENDA side. The coordination has been performed mainly thanks to meetings organized jointly with KENDA PP (COSMO GM 2014, CUS 2015). Results have been presented and discussed and further experiments have been agreed and planned. Tools for diagnostics have also been shared.

3 Model perturbations

The importance of model perturbations in ensemble forecasting has been recognised since some years. It is found that model perturbations usually play a smaller role with respect to initial conditions (at the beginning of the run) and boundary conditions (later) perturbations, but they may become crucial in specific weather situation (Marsigli et al, 2009; Gebhardt et al, 2011) and a poor representation of the model error may lead to severe underestimation of the ensemble spread (Vié et al., 2011). Several techniques have been developed to represent model error: perturbation of the physics schemes parameters (Marsigli, 2009; Gebhardt et al, 2011), random parameters (Bowler et al, 2008), SKEB (Shutts, 2005; Berner et al., 2009), SPPT (Buizza et al, 1999; Palmer et al, 2009), multi-physics, stochastic physics (Plant and Craig, 2008; Bengtsson et al., 2013). Interesting comparative studies have also been carried out (Berner et al, 2011; Hacker et al, 2011). While there are some results about the applicability of these techniques for the O(10km) scale, it is still not assessed how to use them for the O(1km) scale. From the COSMO-DE-EPS experience it is clear

that underdispersion severely affects the ensemble for surface variables, if only few physics parameters are perturbed. The SPPT scheme of ECMWF has been implemented in the COSMO code, to test its capability of representing model error in the LETKF ensemble. This code can be tested also for the ensemble forecasting set-ups, though it is argued that this approach may lead to serious unbalances in the model. Also, the scheme has been originally developed for the IFS model at coarser resolution and should be adapted for use at the O(1km) scale. On top of this, the SKEB scheme has been implemented in the COSMO model, opening the possibility of testing this approach for providing model perturbations to the convection-permitting ensembles. Finally, DWD has started the development of a new approach for model perturbation, aiming at simulating the model error as a continuous stochastic process with the same statistically properties as the empirically determined error of model tendencies.

3.1 Tests with the SPPT scheme

3.1.1 Tests at MCH

At MeteoSwiss, the SPPT scheme has been tested for the ensemble prediction system COSMO-E with 21 members for the Alpine area (see Fig. 1) and a mesh-size of 2.2 km and 60 model levels. The implementation of the SPPT in the COSMO code has been done by Lucio Torrisi and has been used in our first study to find an appropriate SPPT setup for the convection-resolving resolution as well as to understand the impact of the scheme on spread and error of temperature and humidity in COSMO-E. The main findings are:

- larger random numbers produce larger spread and faster spread growth
- larger correlation-lengths in space and time for the random numbers lead to substantially larger spread
- the spread increase due to SPPT decreases with increasing height above the surface

Details about this first study are given in Maurer et al. (2014).

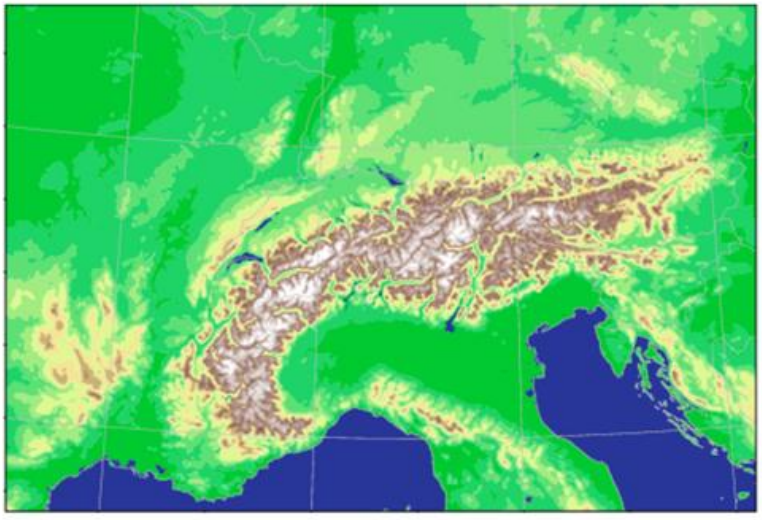


Figure 1: COSMO-E model domain for the experiments with orography.

In the course of the study, the SPPT implementation in COSMO has been reviewed and improved. In particular, perturbing the tendencies of the Coriolis force has been removed

as well as a few technical changes has been done to support single precision and to ensure the same results with different compilers. The revised SPPT code has been integrated into the official COSMO version 5.1. Further experiments for a summer period confirm these results and demonstrate that turning off the SPPT tapering below 850 hPa does not cause model stability problems and significantly increases the spread in the planetary boundary layer. Furthermore, deterministic forecasts for a summer and winter month in 2012 show no significant quality degradation with SPPT, even for rather strong stochastic perturbations of physical tendencies. Therefore, an aggressive SPPT parameter setting has been chosen for COSMO-E with:

- itype_vtaper_rn=2
- itype_qxpert_rn=1
- itype_qxlim_rn=0
- hinc_rn=6
- dlat_rn/dlon_rn=5.0
- stdv_rn=1.0
- range_rn=0.9
- lgauss_rn=.TRUE.
- lhorint_rn/ltimeint_rn =.TRUE.

This setup is used for further experiments to investigate the spread-error relationship in detail. To this end, 00 UTC COSMO-E forecasts are run for every second day from 26 July to 25 August 2012 for a summer period and from 3 December to 31 December 2012 for a winter period. Initial conditions including perturbations (if used) are taken from an early KENDA assimilation cycle in test mode which has been implemented at MeteoSwiss, while IFS-ENS control and members 1-20 are used to drive the COSMO-E forecasts at the lateral boundaries.The experiments are run with COSMO v5.0 including local modifications and with single precision (Rüdisühli et al., 2014). According to Jolliffe et al. (2011) the standard deviation of the ensemble mean error (STDE) needs to match the root mean ensemble variance (RMEV) for a reliable forecast.This is further discussed in Maurer et al. (2014). Fig. 2 shows RMEV (spread) and STDE (error) with respect to analysis for experiments without initial condition perturbations for temperature at the lowest model level,which is about 10m above surface. For summer, RMEV is clearly smaller than STDE in the first 4 days (i.e. roughly up to lead-time +96h) without SPPT and SPPT reduces the gap between RMEV and STDE to a large extend mainly by augmenting the daily cycle of RMEV. For the winter period, RMEV is clearly smaller than STDE in the first 3 days (i.e. roughly up to lead-time +72h) and the increase in RMEV due to the SPPT is much smaller. In the middle and upper troposphere the RMEV matches the STDE quite well except for the first day,also for the experiments with initial condition perturbations (not shown).

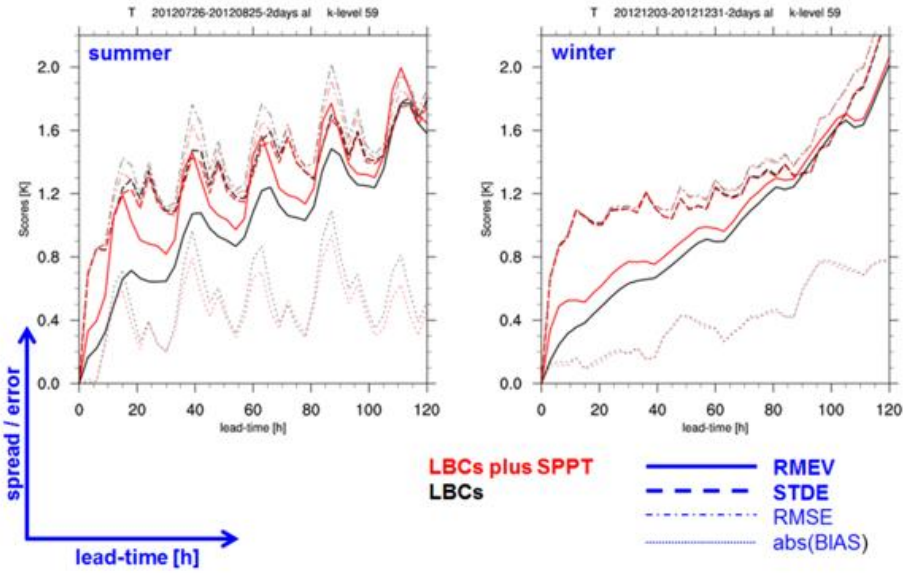


Figure 2: Root-mean ensemble variance (RMEV; bold solid), standard deviation of ensemble mean error against analysis (STDE; bold dashed), root mean square error of ensemble mean (RMSE; dashed-dotted) and the absolute value of the bias (dotted) for temperature as a function of forecast lead-time on the lowest model level at about 10m above surface averaged over the model domain for a summer (left) and winter (right) period without initial condition perturbations and with two different setups: boundary condition perturbations plus SPPT (red) and boundary condition perturbations only (black).

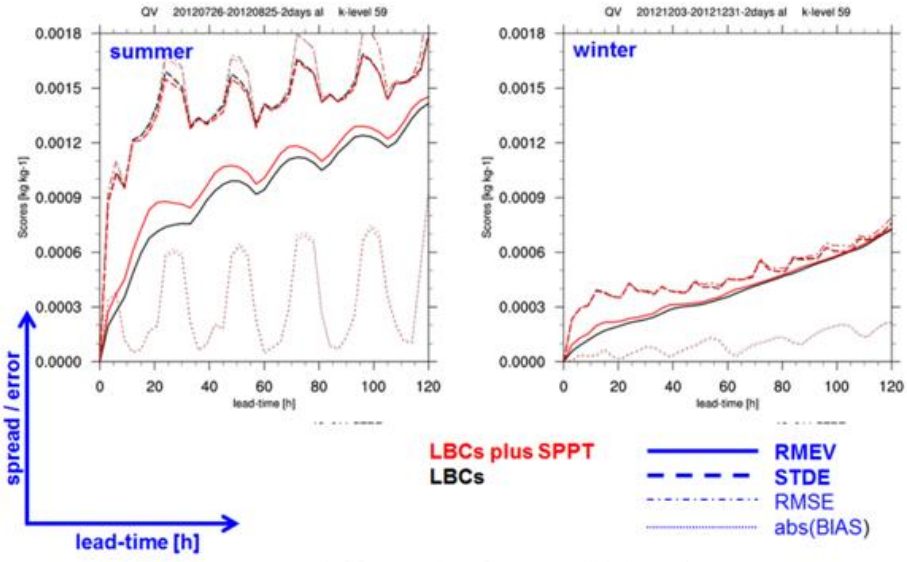


Figure 3: As Fig. 2 but for specific humidity.

Similar results are found for wind speed (not shown) but the underdispersiveness in winter with SPPT is clearly smaller than without. In contrast, the underspersiveness for specific humidity is much larger and SPPT does only slightly reduce the large gap between RMEV and STDE both in summer and winter (see Fig. 3). In the following, the vertical structure of the impact of SPPT is discussed for the summer period. Fig. 4 shows the RMEV, STDE, BIAS and RMSE differences for temperature between the summer experiments with and without SPPT for all model levels as a function of lead-time. The impact for temperature has an obvious daily cycle and is significant up to about level 42, i.e. up to about 2500m

above surface. Interestingly, SPPT does not only increase spread, it also decreases BIAS and STDE slightly (and thus RMSE as well). Similar results are found for wind speed and specific humidity in terms of RMEV, but the impact of SPPT clearly decreases with increasing lead-time (not shown).

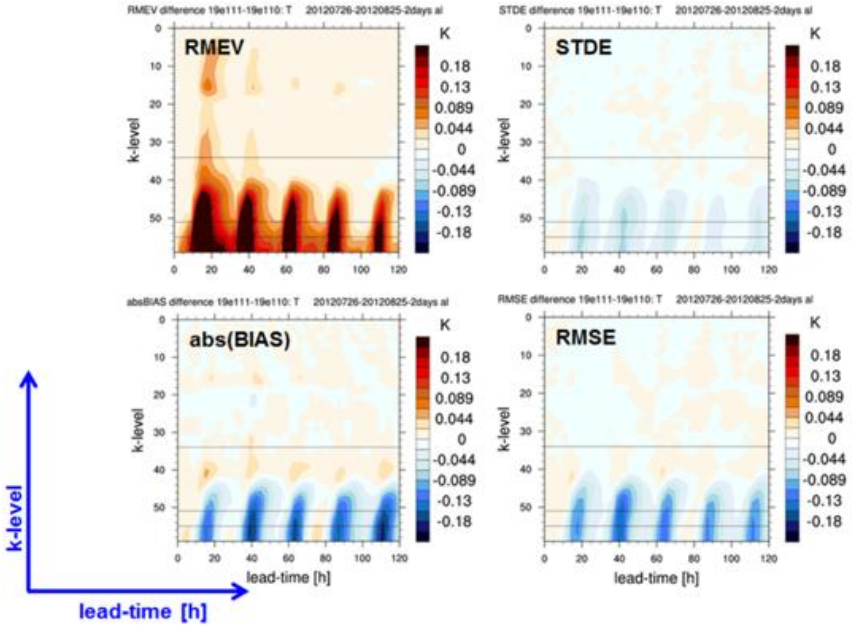


Figure 4: Difference between experiments with and without SPPT for RMEV (top left), STDE (top right), abs(BIAS) (bottom left), and RMSE (bottom right) for temperature on all model levels as a function of forecast lead-time for the summer period. The experiments use initial and lateral boundary condition perturbations.

In order to better understand the impact of SPPT, the tendency contributions from the different parametrizations are investigated. In the COSMO-E setup, the following parametrizations contribute to the sum of the temperature tendencies which is then perturbed by SPPT: turbulence, microphysics, shallow convection, and radiation. Fig. 5 shows the contribution of the different parametrizations on all model levels as a function of lead-time for a summer and winter day. It points out that for the summer day the tendencies from the turbulence scheme are at least an order of magnitude larger than the other ones. The tendencies show a daily cycle with values largest near-surface. This explains well the daily cycle of the SPPT impact on near-surface temperature in the summer period. For the winter day, the tendencies from the turbulence and radiation scheme are naturally smaller which explains the smaller impact of SPPT in winter. For the chosen day, they are of the same order of magnitude as the microphysics tendencies.

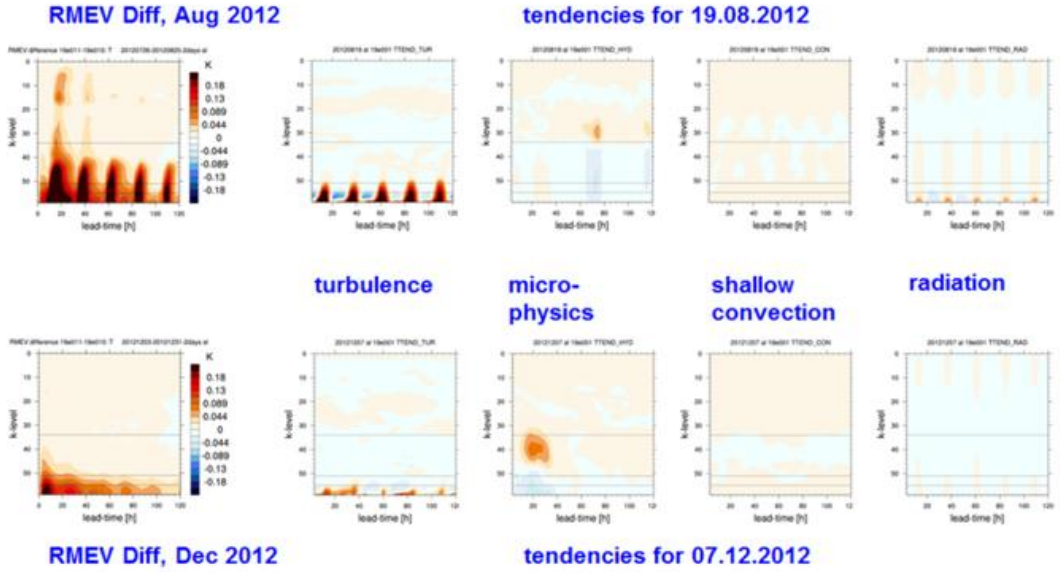


Figure 5: RMEV for temperature for the summer (top left) and winter (bottom left) period and temperature tendencies of the turbulence, microphysics, shallow convection and radiation scheme on all model levels as a function of lead-time for a summer (top) and winter (bottom) day. The sum of these temperature tendencies is perturbed by SPPT.

A further study has investigated the impact of an overlaid second smaller-scale spatial SPPT pattern and the impact of soil moisture perturbations. Both experiments show a positive impact for a summer case by further increasing the spread. However, they have only limited impact in winter when additional spread would be most helpful since then SPPT is less effective in representing model errors. In summary, the COSMO-E experiments show, primarily in summer, a significant improvement of RMEV, STDE, and BIAS due to SPPT in the lower troposphere for the entire forecast range, but they still lack spread in the first 3 days, in particular for humidity. In the middle and upper troposphere the experiments generally show a satisfactory spread-error relation, with the poorest results again for humidity which shows rather too little spread also at upper levels. The tendencies from the turbulence scheme generally show the largest physics tendencies and hence contribute strongest to the SPPT impact.

3.1.2 Tests at RHM

The goal of the RHM research was to assess the effect of stochastic perturbation of physical tendencies with different parameter settings in COSMO-Ru2-EPS (Montani et al., 2014). The ensemble consisted of 10 members, run with the COSMO model with a horizontal resolution of 2.2 km and 50 levels in vertical. The integration domain was the Sochi area. The initial and boundary conditions were provided by COSMO-S14-EPS (Montani et al., 2013). The period from 1 to 28 February 2014 was considered. The forecast length was 48h.The operational forecasts issued twice a day (00 and 12 UTC) during the Sochi Olympic Games 2014 were used as a reference experiment named noSPPT hereafter. The reference runs were carried out with COSMO model version 4.22. A set of experiments with COSMO-Ru2-EPS (the same EPS setting and period as in the reference experiment but model version 5.01) with different SPPT settings was held. The list of experiments and the corresponding SPPT settings are given in Table 1. In all experiments the distribution of random numbers was Gaussian (lgauss_rn=.true., default); a 5 deg x 5 deg coarse grid was used for random numbers (dlat_rn=dlon_rn=5); the random number field was changed every 6 hours (hinc_rn=6,

default); the tapering was prescribed by default near the surface and in the stratosphere (itypevtaperrn=1), and only one random number pattern with its correlation scales was applied (npattern_rn=1, default). The following SPPT parameters were varied:

- the standard deviation of the Gaussian distribution of random numbers stdv_rn;
- the upper limit imposed to the absolute value of random numbers range_rn;
- the parameters showing whether the random numbers are interpolated in space lhorint_rn and time ltimeint_rn;
- the parameter itype_qxpert_rn, showing which hydrometeor tendencies are perturbed;
- the parameter itype_qxlim_rn, determining the type of reduction/removal of the perturbation in case of negative or supersaturated values of specific water vapor content or negative other water-content related characteristics.

All SPPT runs completed successfully with no numerical instabilities. Both case study evaluation and probabilistic verification of monthly series of forecasts were carried out. The results of experiments SPPTtest and noSPPT were compared for the two cases: the tropospheric föhn event on February 7, 2014 and the heavy precipitation event on February 18, 2014. It was found that the SPPT effect on 2m T ensemble spread depends on orography (see Fig. 6). With SPPT the spread strongly increased over high mountains, moderately grew over low regions (including sea), and decreased over areas of medium heights. The strongest increase in the ensemble spread over high domains can be considered as a positive effect of SPPT introduction because the temperature forecasts above 1500 m were poor during the föhn (thus higher spread corresponded to less skilful forecast).

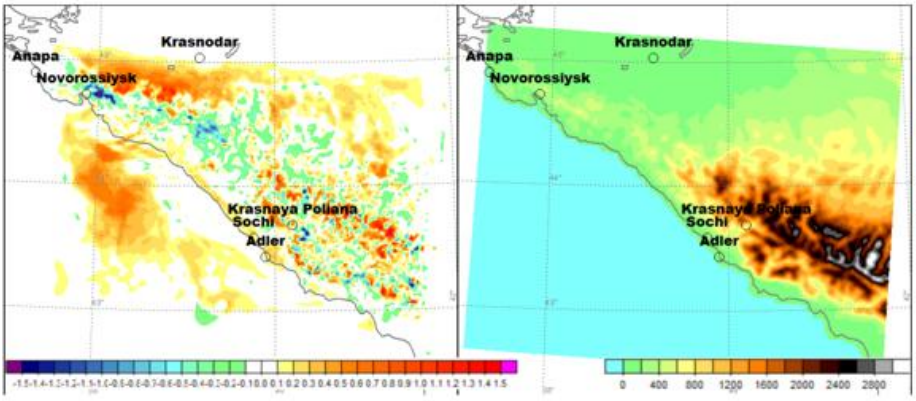


Figure 6: Left panel: difference of 2m temperature ensemble spread in experiments with and without SPPT (SPPTtest minus noSPPT). 30-h forecast starting at 00 UTC on February 6, 2014. Right panel: model orography.

For the case of heavy precipitation on February 18, 2014, the system with SPPT was more skilful in predicting the rain start. Also, it gave less false heavy rain areas and more correct peaks. However, the location of maximum precipitation was better predicted in the noSPPT experiment.

Perturbed parameters	**Experiment name and SPPT settings**						
	noSPPT	**SPPTtest**	**SPPTphys**	**SPPTintphys**	**SPPT_W**	**SPPT_W + phys**	**SPPT_W + intphys**
stdv_rn	N\A	0.4			1.0		
range_rn		0.8			0.9		
lhorint_rn		.FALSE. (no interpolation of perturbations)		.TRUE. (interpolated perturbations)	.FALSE. (no interpolation of perturbations)		.TRUE. (interpolated perturbations)
ltimeint_rn							
itype_qxpert_rn		0 (q_v only)	2 ($q_v, q_c, q_i, q_r, q_s, q_g$)				
itype_qxlim_rn		0 (no limitations imposed)	1 (do not perturb tt T- and tt q_v tendencies if new q_v are negative or supersaturated)		0 (no limitations imposed)	1 (do not perturb tt T- and tt q_v tendencies if new q_v are negative or supersaturated)	

Table 1: List of experiments with COSMO-Ru2-EPS and corresponding SPPT settings.

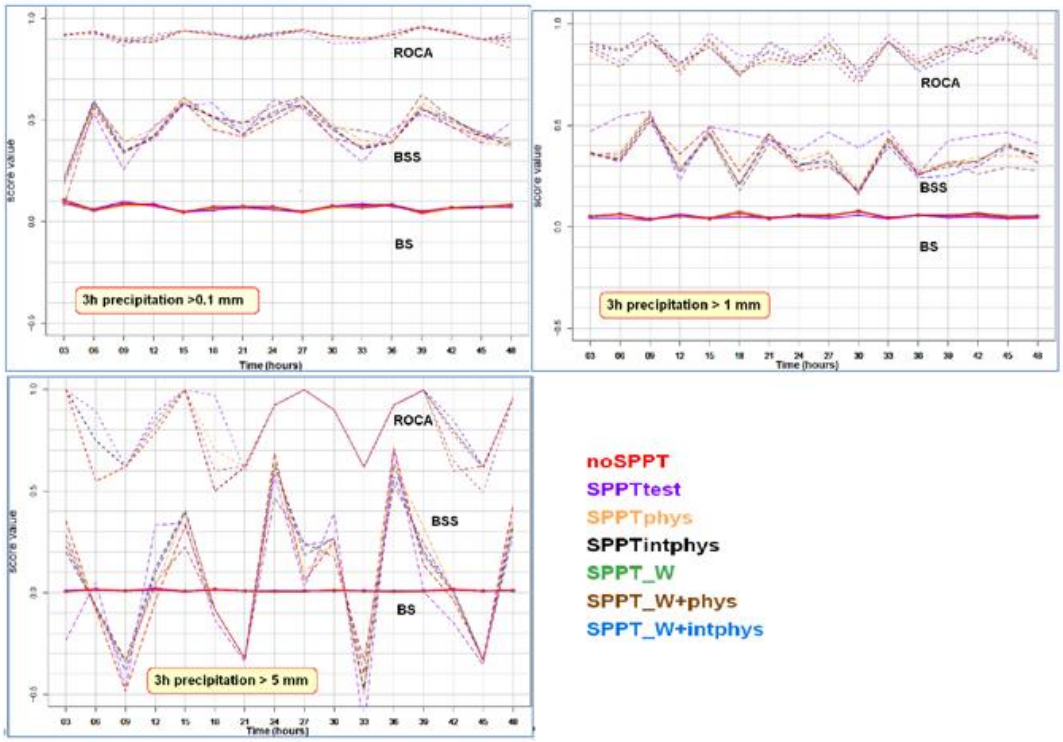


Figure 7: Verification of precipitation forecasts for various SPPT parameter settings.

The probabilistic verification was performed for the monthly (February 2014) series of COSMO-Ru2-EPS forecasts (56 in total, with no regard for the initial forecast time). The Brier score (BS), the Brier skill score (BSS) and the area under the ROC curve (ROCA) were computed for 3-hour total precipitation sum, 2-m air temperature, and 10-m wind speed. The verification was against observations at 31 meteorological stations in the Sochi region (http://frost2014.meteoinfo.ru). R-based utilities developed and kindly provided by A. Muravev were applied. Some positive effect of using SPPT was found for precipitation forecasts, especially for the event "3-h precipitation is greater than 1 mm". Though the application of different SPPT settings resulted in very close scores, SPPTtest was undoubtedly the best for the thresholds of 1 mm/3h and 5 mm/3h (Fig. 7). As for the 2-m temperature forecasts, SPPT did not improve their skill (Fig. 8). The experiment noSPPT was the best especially for high thresholds. SPPTtest, which demonstrated the best precipitation forecasts, was the worst in terms of 2-m temperature forecasts. Generally, the probabilistic scores for temperature differ more between the experiments than for precipitation. However, no sensitivity was found to interpolation of random numbers (parameters lhorint_rn, ltimeint_rn) and to the method applied to avoid problems with negative or supersaturated water vapor values (parameter itype_qxlim_rn). The verification results demonstrated the advantage of perturbing all hydrometeor tendencies and using wider distributions of random numbers.

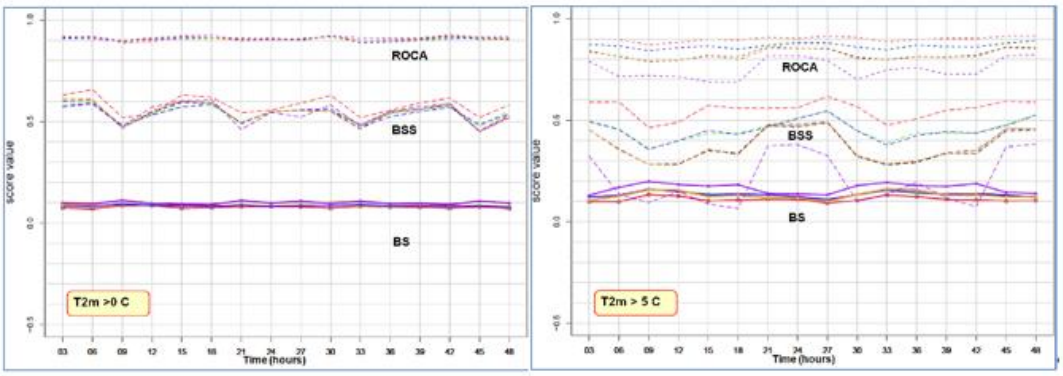


Figure 8: The same as Fig. 3 but for 2-m temperature.

The introduction of SPPT not only affected the probabilistic scores but also led to temperature biases that vary depending on the SPPT settings. Fig. 9 shows the monthly-averaged errors of the ensemble mean for different experiments at the Krasnaya Polyana station.

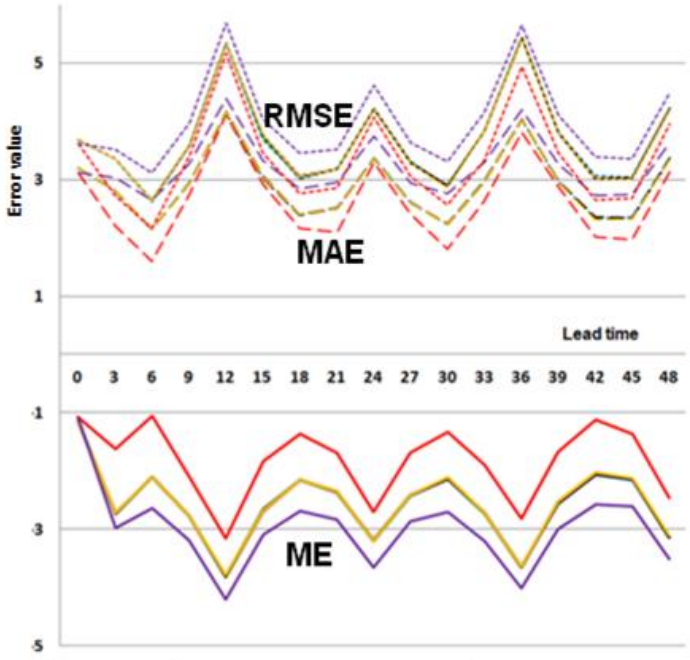


Figure 9: Mean error (ME, solid), mean absolute error (MAE, long-dashed), root-mean-square error (RMSE, dashed) for 2m T ensemble mean forecasts at Krasnaya Poliana station. Experiment as in Fig. 7.

The plot confirms the superiority of experiments with higher standard deviation of random number distribution and perturbation of all hydrometeor tendencies. High sensitivity of 2m T forecast skill to SPPT settings indicates that they could be improved as a result of SPPT tuning. Though SPPT seems to introduce biases to 2m T forecasts, it can improve the temperature distribution. The forecast histogram for experiment with SPPT in Fig. 10 looks more like the observation histogram than that for the experiment without SPPT.

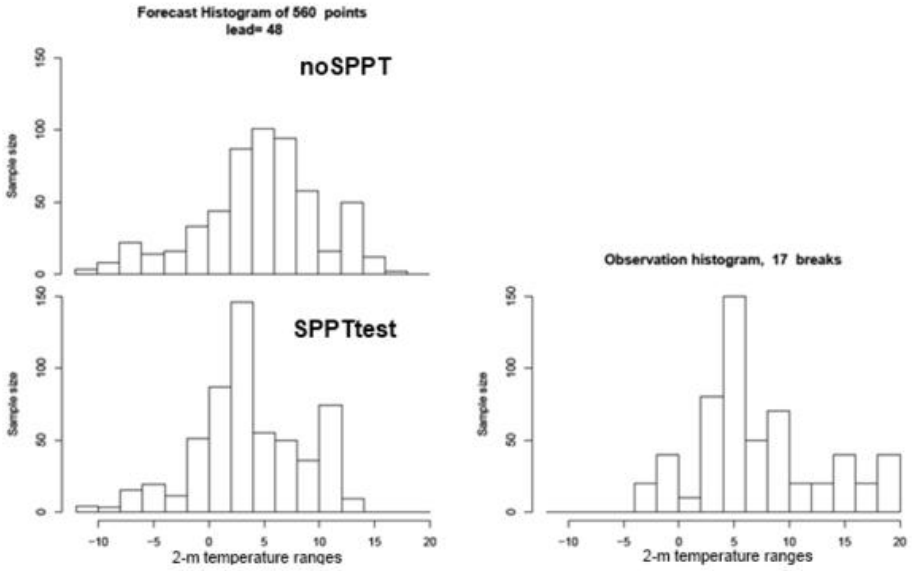


Figure 10: 2m T distribution histograms for noSPPT and SPPTtest 48-h forecasts and for observations at Krasnaya Polyana. February 1-28, 2014.

Wind speed forecast scores were rather poor both with and without SPPT. SPPT settings did not make significant difference.

Conclusions

Case studies in the Sochi mountainous area with COSMO-Ru2-EPS demonstrated that SPPT could be useful for precipitation forecasts, slightly improving the description of rain localization and start. The SPPT-related spread of 2m T ensemble forecasts correlates with the model orography. SPPT additional spread amplifies the coincidence between high-spread areas and the areas of less skilful forecast. The probabilistic verification of monthly series of COSMO-Ru2-EPS forecasts (56 in total) demonstrated a positive effect of using SPPT for precipitation forecasts, especially for the event "3-h precipitation is greater than 1 mm". Variations in the SPPT settings did not influence the results for precipitation much. SPPT worsens the 2m T forecasts, introducing temperature biases and deteriorating probabilistic scores. The verification showed rather large differences between the skills of experiments with various SPPT settings. At the same time, the eyeball analysis showed that the predicted temperature distribution became more realistic when physical tendencies were perturbed. Therefore, SPPT did not add value to temperature forecasts, but can sometimes improve the representation of distribution. It is possible to improve the 2m T forecast by varying the SPPT settings. For example, in most cases perturbations of all hydrometeor tendencies lead to better results than perturbations of specific water content tendency only. Also the increase of the range of standard deviation for the Gaussian distribution of random numbers and of the upper limit imposed to the absolute value of random numbers positively contributed to the results.

3.1.3 Tests at ARPA-SIMC

At ARPA-SIMC the SPPT scheme has been tested both in the COSMO-LEPS ensemble and in the COSMO-IT-EPS ensemble.

COSMO-LEPS

In the framework of the experimentation carried out in the PP, COSMO-LEPS was run for

Variables	2-m temperature, 10-m wind speed, 12-h cumulated precipitation
Period	22/11/2014 - 31/01/2015, starting at 12UTC
Verification period	35-55N, 0-20E (about 1000 synop reports/day)
Thresholds (for precipitation only)	1, 5, 10, 15, 25, 50 mm/12h
Method	Nearest grid point
Systems	OPER-CLEPS (v5.0) and SPPT-CLEPS (v5.1)

Table 2: Main features of the verification configuration.

about 70 days with SPPT switched on (SPPT-CLEPS) and its performance was compared to the operational set-up (OPER-CLEPS) for a number of surface variables. The verification network is provided by the synop reports which fall inside a domain covering Central and Southern Europe. On average, about 1000 observations are available for verification at each forecast range (Fig. 11).

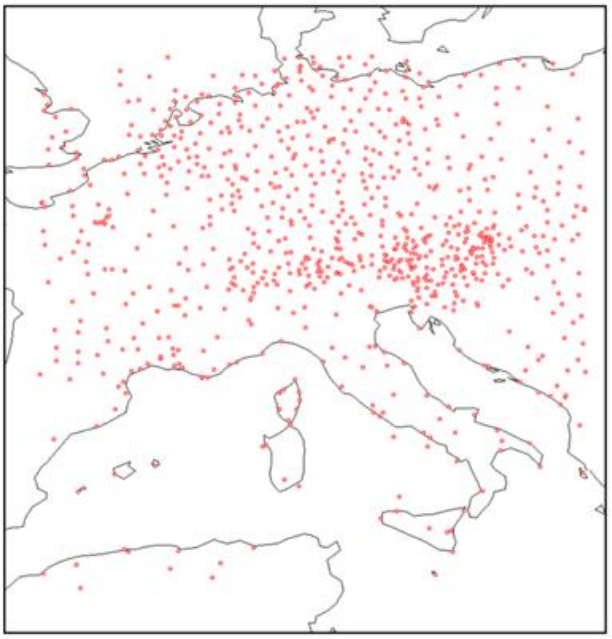


Figure 11: The verification domain used for inter-comparison between OPER-CLEPS and SPPT-CLEPS.

Table 2 summarises the main features of the experimentation.

As for the verification of temperature and wind-speed, the attention is focussed on the spread/skill relation of the two systems. As reported in Fig. 12, SPPT-CLEPS (blue lines) presents a larger spread than OPER-CLEPS for all forecast ranges. This is especially true for wind-speed and less evident for temperature. On the other hand, the impact on the forecast skill of the ensemble mean is negligible. In either cases, there is still a lack of spread in the short range, although the use of SPPT partly mitigates the underdispersion problem of COSMO-LEPS.

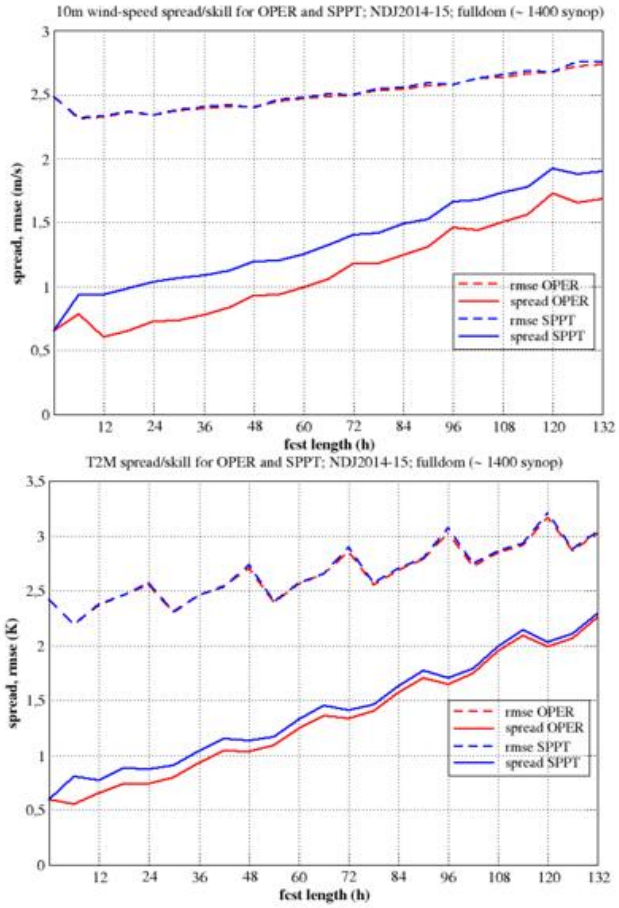


Figure 12: Spread/skill relation of OPER-CLEPS (red) and SPPT-CLEPS (blue) in terms of 2-m temperature (top panel) and 10-m wind speed (bottom panel) as a function of the forecast range. The rmse of the ensemble mean (spread) is reported as dashed (solid) line.

As for precipitation, the attention is focussed on the probabilistic prediction of 12-hour cumulated precipitation. In particular, the attention is focussed on the predictive skill of both systems for 2 types of events: 12-hour precipitation exceeding 1 mm and 10 mm. The left (right) panel of Figure 13 reports the values of the ROC area as a function of the forecast range for the 1mm (10 mm) threshold.

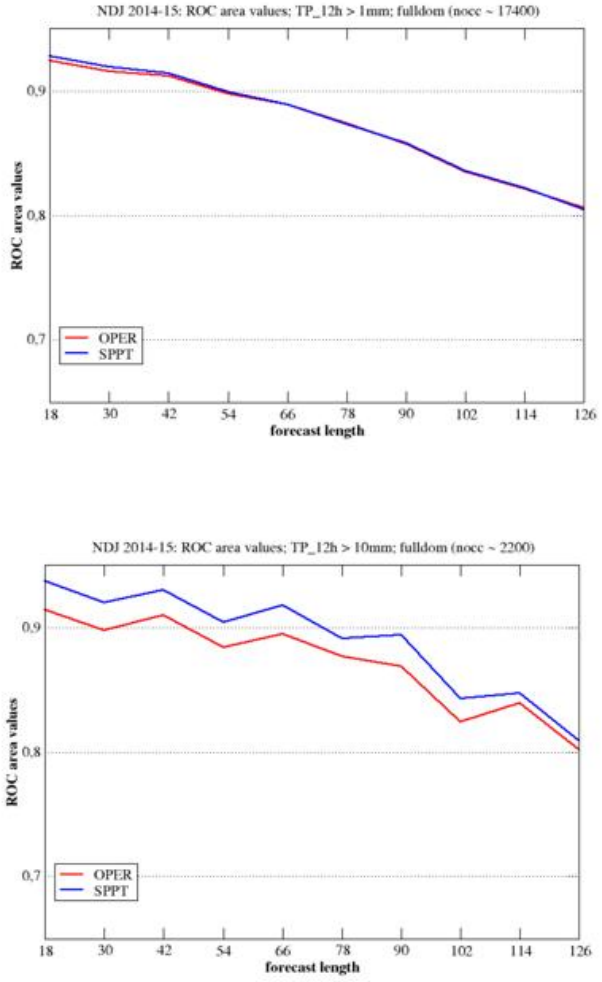


Figure 13: Roc area values for OPER-CLEPS (red) and SPPT-CLEPS (blue) as a function of the forecast range for the events: total precipitation over 12-hour exceeding 1 mm (top panel) and 10 mm (bottom panel).

It can be noticed that for the lower threshold, with about 17400 occurrences over the verifcation period of Table 2, the performance of OPER-CLEPS and SPPT-CLEPS is almost identical. On the other hand, for the higher threshold (about 2200 occurrences), some positive impact of using SPPT can be noticed. Therefore, on the basis of these encouraging results, it is planned to carry on the experimentation and assess the benefits of using SPPT also during summer months. In addition to that, it is also envisaged to study the possibility to run SPPT-CLEPS in single-precision mode, thus saving about 30% of computing resources and enabling the implementation of a larger-size COSMO-LEPS.

COSMO-IT-EPS

The COSMO-IT-EPS ensemble is an experimental convection-permitting ensemble running over Italy over selected cases/periods, aiming at the definition of an ensemble set-up to be operationally implemented as part of the Italian modelling chain. The COSMO model is run at 2.8 km of horizontal resolution, with 50 vertical levels, on an Italian domain. The ensemble has 16 members, which receive Initial and Boundary Conditions from the members of COSMO-LEPS. The aim of this work was to study the role of the physics perturbations focusing on severe rainfall events occurred in Italy. Three experimental ensemble set-ups

were run:

- no model perturbation (downscaling)
- perturbation of few physics parameters (PP)
- stochastic perturbation of physics tendencies (SPPT)

Two main rainfall events occurred in Italy in autumn 2014 were selected:

- Genova event, 9 October 2014
- Parma event, 13 October 2014

For the Genova event, the 6h accumulated precipitation estimated by radar during the 9th of October are shown in the first row of Fig. 14, while in the second row is shown the precipitation forecasted over the same time periods by the COSMO-I2 operational deterministic run.

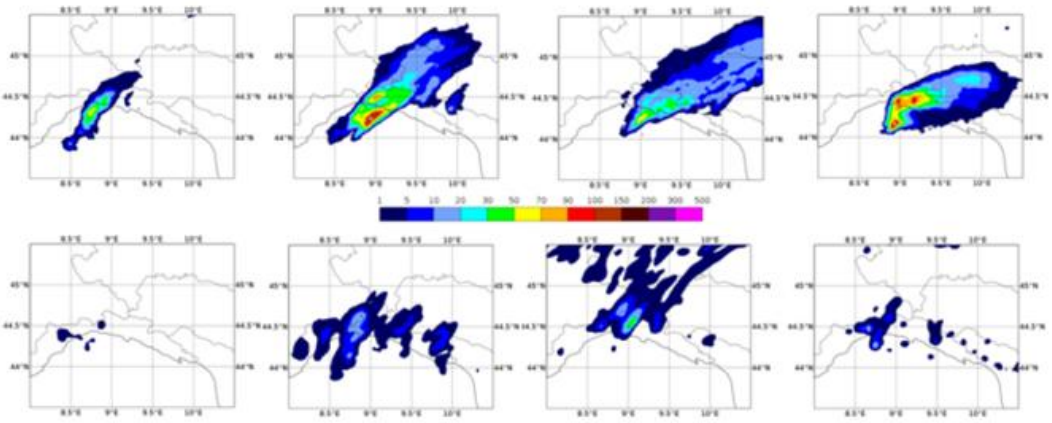


Figure 14: 6h accumulated precipitation during the 9th of October as estimated by radar (top row) and as forecasted by the COSMO-I2 operational deterministic run (bottom row).

For the Parma event, the precipitation accumulated over 24 hours, as measured by raingauges is shown in the left panel of Fig. 15, while in the right panel is shown the precipitation forecasted by the deterministic COSMO-2I model. The areas of maximum observed precipitation are highlighted in both plots by coloured ellipses.

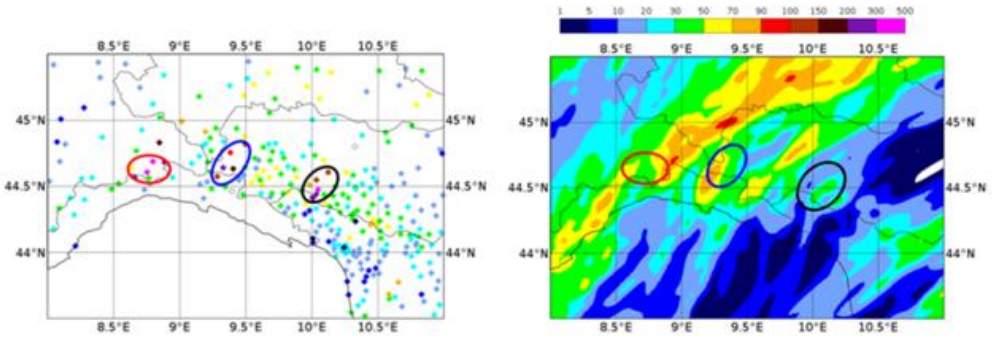


Figure 15: 24h accumulated precipitation during the 13th of October as measured by raingauges (left panel) and as forecasted by the COSMO-I2 operational deterministic run (right panel).

For the Genova event the behaviour of the 3 experimental suites is shown in the following figures, focussing on the 6h where the heaviest precipitation was observed, between 18 and 24 UTC of the 9th of October. In each figure, the precipitation forecasted by each ensemble member is shown, as well as the radar estimate in the uppermost right panel. In general, the ensemble members are able to forecast intense precipitation in the selected 6h period, but they tend to shift the structure toward the west (Fig. 16). The addition of parameter perturbations (PP, Fig. 17) permits to increase the diversity between the members and the introduction of the SPPT perturbation (Fig. 18) brings on top an enhancement of the precipitation forecasted by some members.

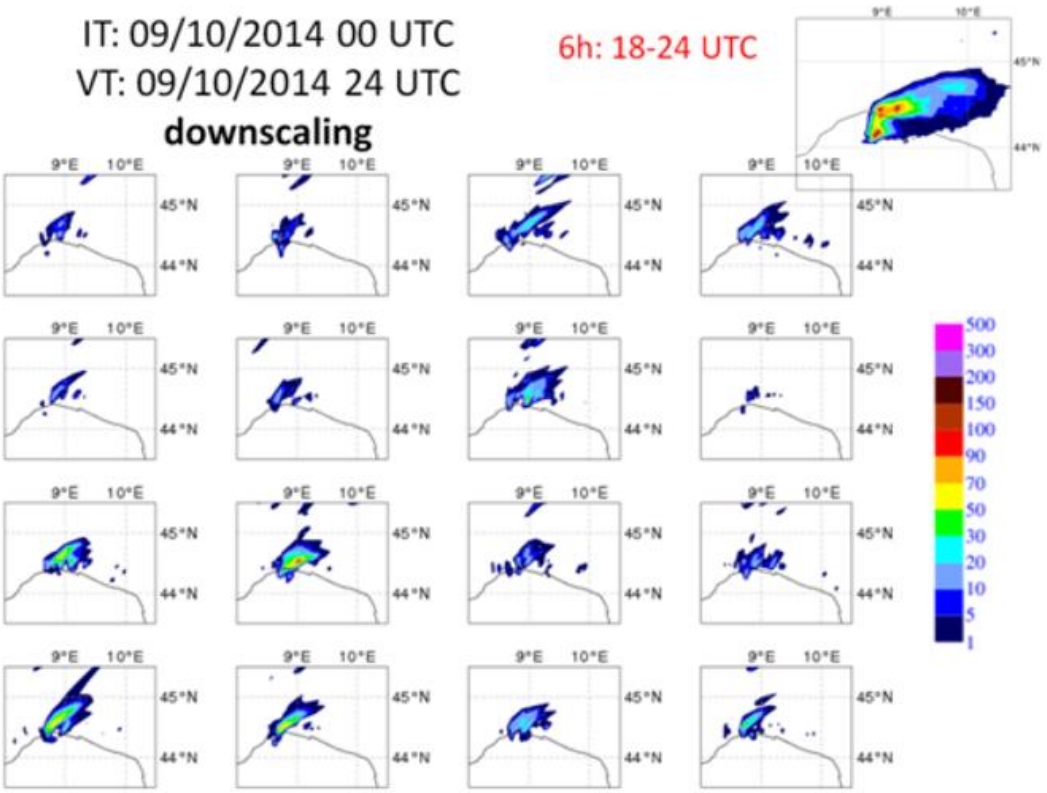


Figure 16: In the panels is shown the precipitation forecasted by each member of the downscaling ensemble accumulated over the 6 hours between 18 and 24 UTC of the 9th of October. The radar estimate for the same period is also shown in the uppermost right panel.

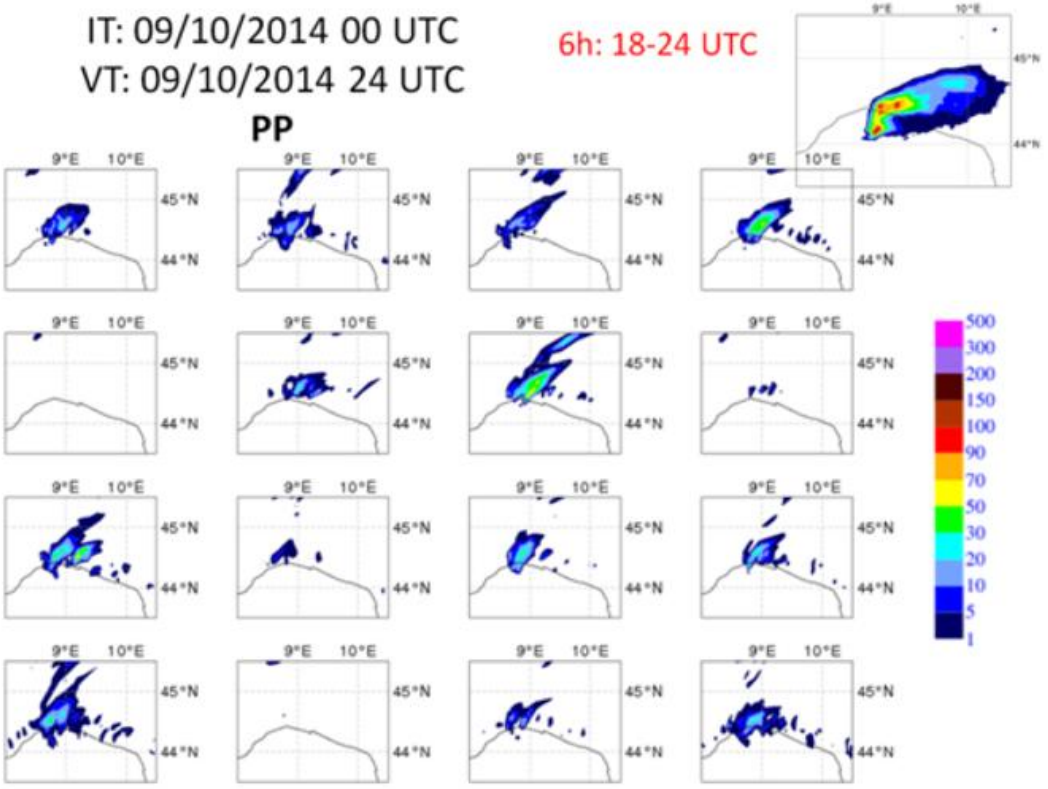


Figure 17: Same as Fig. 16 but for the PP ensemble.

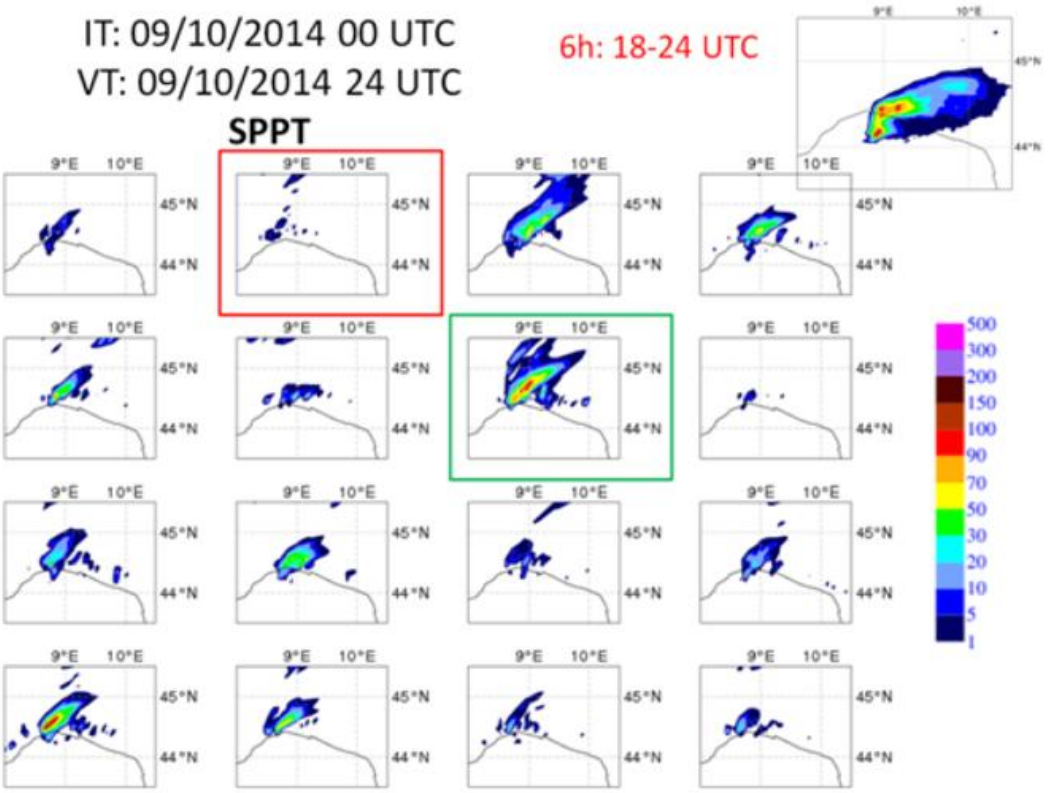


Figure 18: Same as Fig. 16 but for the SPPT ensemble.

The different role of the 2 perturbations in modifying the ensemble forecast for this case

is highlighted by considering the maps of ensemble mean and ensemble spread for the accumulated precipitation (Fig. 19). The PP ensemble (middle panel) forecasts an area of precipitation broader and more extended to the east than the downscaling ensemble (left panel), partly addressing the localisation error highlighted above, while the SPPT (right panel) mainly enhance the precipitation intensity, and adds spread particularly in the area where the precipitation peak was already forecasted by the downscaling ensemble.

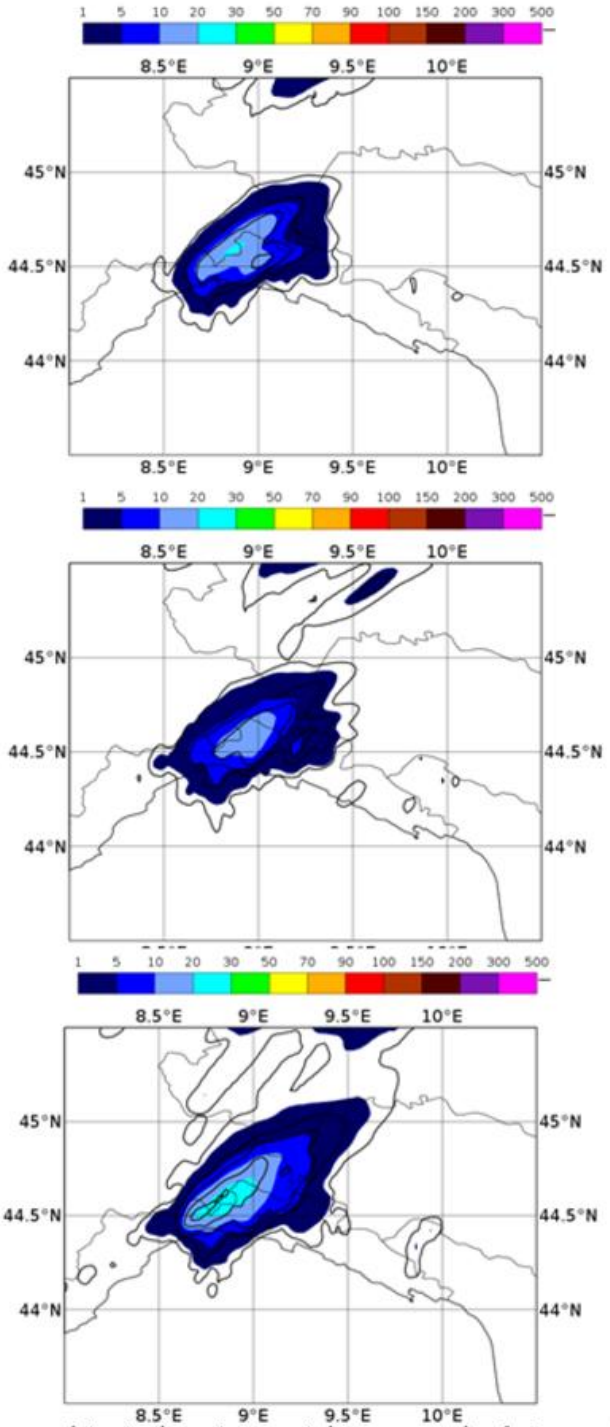


Figure 19: Ensemble mean (shaded) and spread (contouring) of the precipitation forecasted by the downscaling (left panel), PP (middle panel) and SPPT (right panel) ensemble, accumulated over the 6 hours between 18 and 24 UTC of the 9th of October.

Considering the Parma case, the precipitation forecasted over the 24h by 4 selected mem-

bers is shown in Fig. 20, for the downscaling ensemble (left column, labelled no physics perturbation in the Figure) and for the SPPT ensemble (right column). Also from this case is evident that SPPT tends to forecast more intense precipitation but does not address the issue of the localisation of the structures. Conclusions from these runs were drawn, by noticing that for the two cases the 2.8 km ensemble is able to provide scenarios different from the deterministic run, with few good members. The error in the localisation of the rainfall pattern is addressed by some model perturbations, but initial and boundary conditions seem to play a major role. Finally, SPPT-perturbed runs have a tendency towards more intense precipitation.

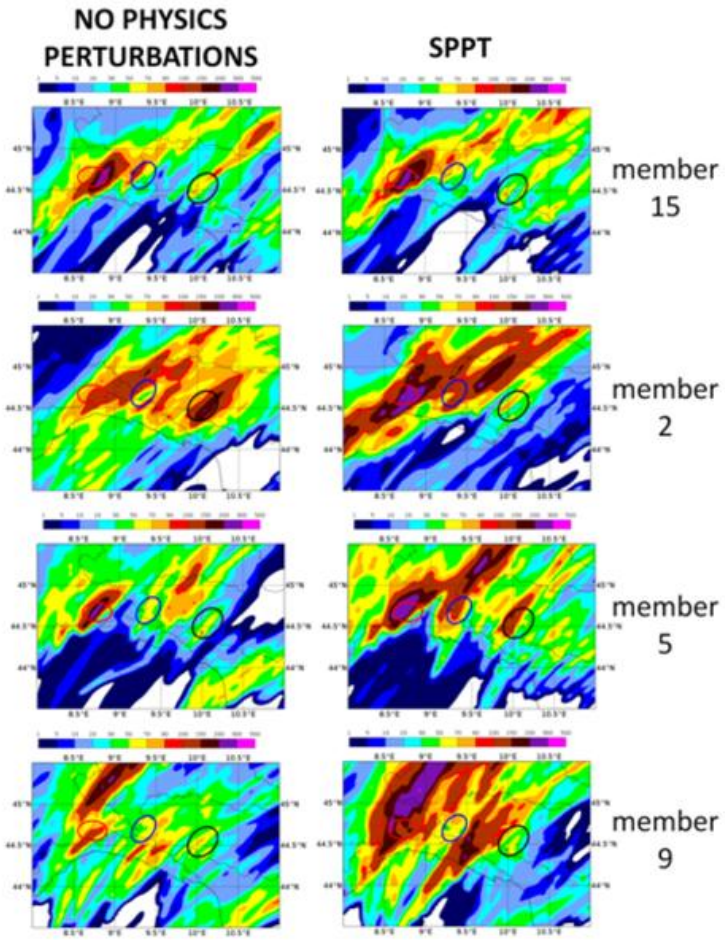


Figure 20: Precipitation forecasted by 4 members of the downscaling (left column) and SPPT (right column) ensembles, accumulated over 24 hours on the the 13th of October.

3.2 Test of the SKEB scheme in the 2.2 km ensemble at MCH

SKEB has not been further tested in COSMO, since the code is far from being ready for operational use due to performance issues. On the other hand, the generated perturbations are similar to those of the random pattern generator developed by RHM which has been implemented in COSMO with no performance problems. Hence, further work in this direction should preferably use this random pattern generator.

3.3 Information about improvements and a new strategy for model perturbations at DWD

At DWD, the research in model perturbations has been focussed on two aspects. On the one hand, the operationally used approach of fixed, non-stochastic perturbations of physics parameters has been extended and methodical modifications have been tested. On the other hand a prototype of a new model perturbation strategy with stochastic components has been developed and tested (model for the model error). The current set-up has been improved by including more parameters in the perturbation set up, i.e. the perturbation of minimum diffusion coefficients for heat and momentum has been added in the operational set-up in January 2014. Moreover, successful tests have been carried out for more perturbed parameters which have been selected with special focus on renewable energy applications. In general, adding more perturbed parameters led to a slight increase in ensemble spread with neutral or slightly positive impact on the root mean squared error of the ensemble mean. As a further methodical modification, which additionally helps to effectively perturb more parameters, a randomized selection of the perturbed values has been developed and first tests have been carried out. While there are still 2 -3 pre-defined different values for the parameters to be perturbed, there is a random approach how these perturbations are distributed within the 20 members. Under the condition that each parameter is perturbed in 50% of the members, a random selection of members which are actually perturbed is done for each parameter at each forecast start time. The selected perturbations stay fixed over the forecast range. Thus, the new method is not stochastic with respect to parameter values but used to distribute pre-defined values effectively among members and the EPS differs in this respect between forecast starts. Again, an increase of spread without degradation of skill (RMSE) has been observed. These refinements of the method became operational in November 2016. The research, which is intended to lead to a new perturbation strategy in upcoming years, is based on the assumption, that the temporal evolution of the model error itself can be described by an equation taking into account temporal and spatial coherence and a white noise stochastic component. The parameters of this model for the model error are estimated from past data and are considered to be weather-dependent. A prototype of this method has been implemented, tested and refined. Considerable resources will be denoted to further research on scientific and technical issues of this new strategy during the next years with the aim of operational implementation. Information on the advances concerning model perturbations has been provided to COSMO at the General Meetings and during the WG7 Meetings.

4 Soil/surface perturbations

The sensitivity of moist atmospheric processes to soil conditions has been demonstrated in numerous studies (Hacker 2010 and references therein). Although the physical representation of soil moisture in land surface schemes is known to have an influence on the quality of atmospheric predictions, the parametrization of the processes of soil moisture physics is not straightforward and the uncertainty in the parameters are little researched (Cloke et al, 2012). Some techniques have been proposed in the recent years: Cloke et al (2012) proposes a simple method, perturbation of 2 soil scheme parameters, in the ECMWF seasonal forecasting system; Sutton et al (2006) studied the impact of using two different soil moisture fields, estimated by 2 different LSM but with the same data and atmospheric forcing, showing that short-term precipitation is sensitive to the soil moisture, especially for a high-resolution run; a non-cycling surface breeding method has been proposed by Wang et al (2010), where short-range surface forecasts driven by perturbed atmospheric forcing are used for generating the

perturbation to surface ICs. A simple method is applied by Hacker (2010), who constructs perturbations of the soil moisture field that represent random, spatial correlated errors, to quantify the response to soil moisture perturbations. He recognises that this method is not suited for reproducing the characteristics of the actual soil moisture uncertainty, which varies locally with the properties of the soil, vegetation and background moisture itself (Hacker, 2010). In order to partly account for soil moisture uncertainty, in the COSMO PP CONSENS a methodology for soil moisture perturbation based on Sutton and Hamill (2004) was developed by HNMS (COSMO Technical Report No. 22). The method was never tested in ensemble mode but it could be revived and tested on the new ensembles under development. Other methods can be tested, among those available in literature, or proposed, according to the need of the COSMO countries and on the available resources. At DWD a simple method was developed to derive initial condition soil moisture perturbations from differences between COSMO-EU und COSMO-DE soil moisture. A long period test is now planned. Within the COTEKINO PP, work on soil/surface perturbation has been carried out at IMWG and at Arpa Piemonte. First a sensitivity study have been carried out, indicating a great sensitivity of COSMO run at 2.8 km to the soil conditions, in particular soil moisture and few TERRA parameters. Secondly, a scientific investigation of the possible strategies to be followed has been performed, including literature review and assessment of the more suitable methods. Then, techniques for lower boundary perturbation have been developed in the two Centres and have been implemented on selected cases. This work is described in detail in the following subsections.

4.1 IMGW

4.1.1 Preliminary sensitivity tests

The first part of this work focused on the test of different set-ups (configurations), in terms of parameters and methods. Shallow convection scheme was chosen as a basic (and invariant) setup to subsequent studies, because of the grid resolution used in the simulations (convection-permitting). As it was described in the previous work (Duniec and Mazur 2014), the other physical parametrizations and numerical schemes selected for the test were as follows (see also Schättler et al. 2016, for details):

- The various formulations of the advection:
  - Leapfrog: 3-timelevel HE-VI (Horizontally Explicit - Vertically Implicit) Integration. This scheme is used as default in Poland for the 7km resolution operational model, as well as for COSMO-EU at DWD
  - Runge - Kutta: 2-timelevel HE-VI Integration (irunge_kutta=1). This scheme is used in COSMO-DE
  - Runge - Kutta: 2-timelevel HE-VI Integration (irunge_kutta=2) - variant scheme with Total Variation Diminishing
- Vertical turbulent diffusion:
  - 1-D diagnostic closure (used in combination with leapfrog scheme only)
  - 1-D TKE-based diagnostic closure (used in COSMO-EU and in COSMO-DE)
- Type of parametrization for transpiration by vegetation:
  - Bucket version

– BATS version

All the above gives a total of 9 basic (reference) set-ups. Then soil-related parameters to be evaluated in the sensitivity test were chosen as follows:

- c_soil (with relation to c_lnd) - surface-area index of evaporating fraction from 0 to c_lnd (surface-area index of gridpoints over land, default 1.0),
- crsmin - minimum value of stomatal resistance (used in connection with BATS version only) from 50 to 200 (default 150.0),
- pat_len - length scale of subscale surface parameters over land from 0 to 10000 (default 500 m)

all the above are in the TUNING namelist. In addition:

- cz_bot_w_so - depth of bottom of last hydrological active soil layer, from 0.0 to last soil level depth (default 2.0 meters), in the PHYCTL namelist.

The general assumption for the preliminary assessment was to choose three to four values from a given parameter range, including minimum and maximum ones. Output fields selected for comparison were:

- Soil - soil temperature at 0 cm down (surface temp.).
- T2m - air temperature at 2m above ground level.
- Water - water + ice content of soil layers 1cm down the surface.
- U10m - zonal wind component, 10m above ground level.
- V10m - meridional wind component, 10m above ground level.

Statistical characteristics selected for the sensitivity analysis are here listed included the standard scores (BIAS, RMSE) as well as other measures here listed:

- the point-to-point difference field with centre of mass of field of differences is defined in Eq. 1 t_x being the value of the field at point r_x, average difference and RMS of difference (over entire domain)
- the maximum difference of values (MDV) defined in Eq. 2 where r and c are reference and changes, respectively
- the normalized difference of values NDV (Eq. 3) with $< T_x >$ defined in Eq. 4
- the R (Pearson) correlation coefficient (over entire domain) defined in Eq. 5

$$\overrightarrow{r_d} = \frac{\sum_{\overrightarrow{r_x}} t_x \cdot \overrightarrow{r_x}}{\sum_{\overrightarrow{r_x}} t_x} \tag{1}$$

$$MDV = max[|t_r(i,j) - t_c(i,j)|] \cdot sign[t_r(i,j) - t_c(i,j)] \tag{2}$$

$$NDV = \frac{\langle T_c \rangle - \langle T_r \rangle}{\langle T_r \rangle} \cdot 100\% \tag{3}$$

$$\langle T_x \rangle = \frac{\sum_{i=1}^{i_{max}} \sum_{i=j}^{j_{max}} t_x(i,j)}{i_{max} \cdot j_{max}} \tag{4}$$

$$R = \frac{\sum_{i=1}^{i_{max}} \sum_{j=1}^{j_{max}} (t_c(i,j) - \langle T_c \rangle) \cdot (t_r(i,j) - \langle T_r \rangle)}{\sqrt{\sum_{i=1}^{i_{max}} \sum_{i=j}^{j_{max}} (t_c(i,j) - \langle T_c \rangle)^2} \sqrt{\sum_{i=1}^{i_{max}} \sum_{j=1}^{j_{max}} (t_r(i,j) - \langle T_r \rangle)^2}} \tag{5}$$

As a case study basis eleven different synoptic situations were chosen (for Poland area); six of them were tested also in the framework of the COLOBOC Priority Project, and five new ones:

- 2009.02.01 (00 UTC) - low temperature, the ground was frozen solid
- 2009.02.22 (12 UTC) - sunny/fair day
- 2009.10.16 (00 UTC, 06 UTC) - ground covered with snow
- 2009.11.04 (12 UTC) - windy day with precipitation
- 2009.11.21 (06 UTC) - foggy day
- 2012.02.03 (00 UTC) - very cold day with air temperature below -20°C, ground frozen solid after two weeks of low air temperatures
- 2012.05.18 (00 UTC) - sunny/fair day, ground temperatures below 0°C
- 2012.07.01 (00 UTC) - sunny/fair/hot day
- 2012.12.14 (12 UTC) - again, very cold day with air temperature below -10°C
- 2012.12.16 (12 UTC) - right after previous, some warming in the air (higher temperature)

As a consequence of the results of these tests, the following conclusions were drawn (Duniec and Mazur, *ibidem*):

- No significant differences (sensitivities) with changes ofnumerical schemes (HE-VI, RK1 and/or RK2) were observed. Therefore, authors suggested to focus in the subsequent work on the COSMO operational configuration (i.e., 3-order standard Runge-Kutta scheme, 2-timelevel HE-VI integration)
- cz_bot_w_so has a noteworthy impact on values of water and ice content down to 1458 cm below ground level
- Parameter c_soil has a noteworthy impact on values of air temperature at 2m, dew point temperature and relative humidity at 2m, wind speed and direction at 10m and surface specific humidity
- For the other parameters no significant impact of the tested values against the reference ones was found.

Consequently, extended sensitivity tests were carried out with the following assumptions:

- CP-scale and model resolution forced the use of shallow convection scheme
- 3-order standard Runge-Kutta scheme was selected as a basic numerical scheme
- Different synoptic situations, i.e. the eleven cases listed above, were used to establish a relation between the stochastic variation of c_soil/cz_bot_w_so parameters and the skill of the ensemble members

The following figures (Figs. 21-28) show selected results from the sensitivity tests. Results are described in terms of the spatial distribution of the "spread" - i.e. standard deviation of the ensemble members vs. control (deterministic) run - for the selected parameter and presented as the "spread" (from left to right) of temperature (a), dew point (b), wind speed (c) and precipitation (d).

- c_soil sensitivity test results:

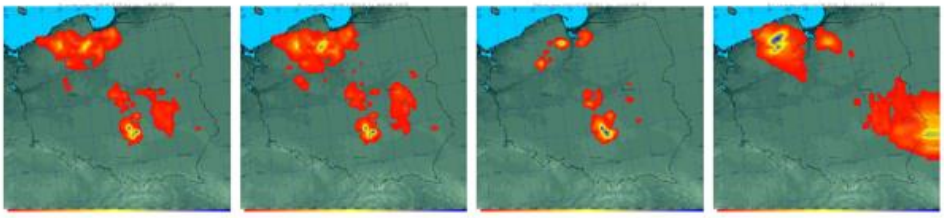


Figure 21: Winter case (December 14th, 2012). a, b, c, d from left to right respectively.

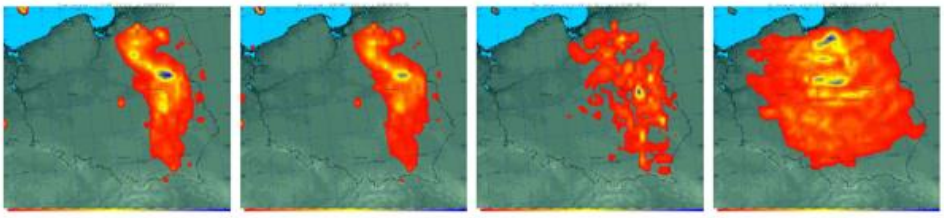


Figure 22: Spring case (February 22nd, 2009). a, b, c, d from left to right respectively.

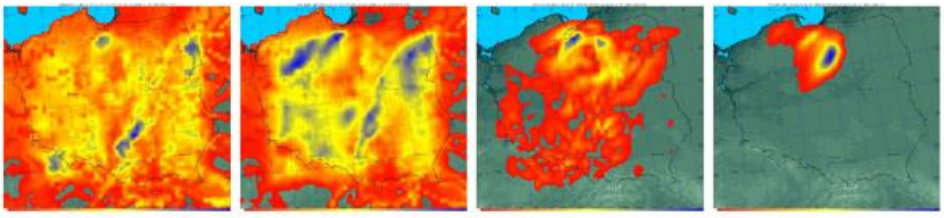


Figure 23: Summer case (July 1st, 2012). a, b, c, d from left to right respectively.

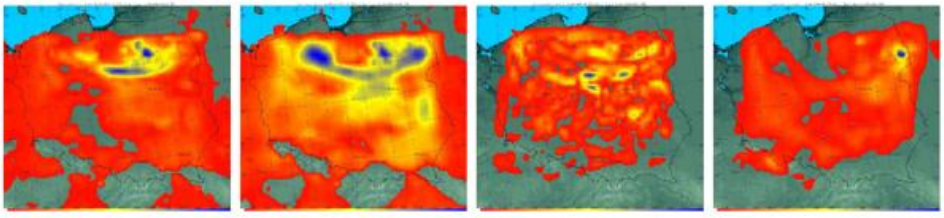


Figure 24: Autumn case (October 16th, 2009). a, b, c, d from left to right respectively.

- cz_bot_w_so sensitivity test results:

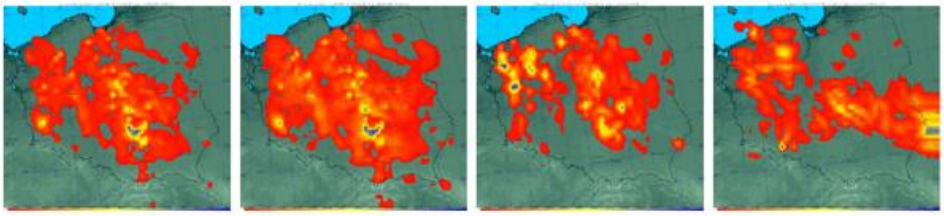


Figure 25: Winter case (December 14th, 2012). a, b, c, d from left to right respectively.

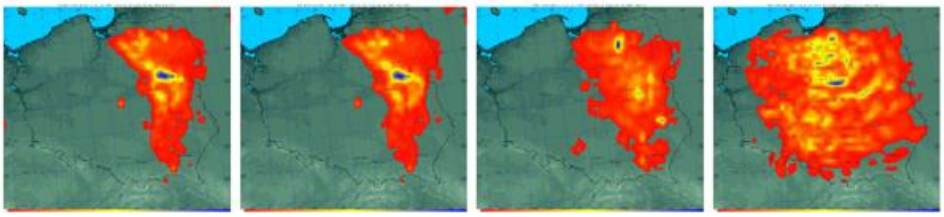


Figure 26: Spring case (February 22nd, 2009). a, b, c, d from left to right respectively.

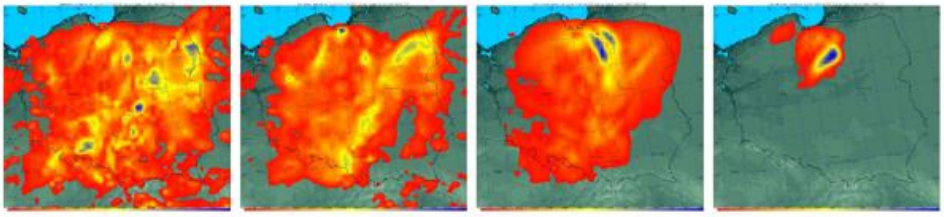


Figure 27: Summer case (July 1st, 2012). a, b, c, d from left to right respectively.

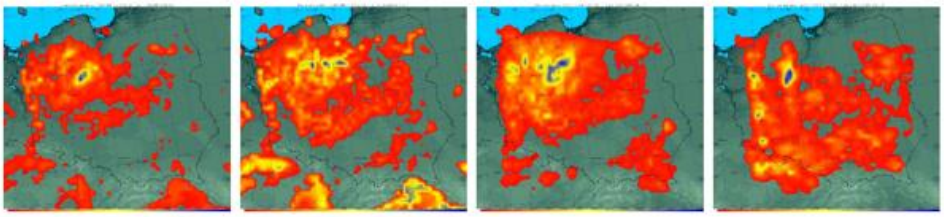


Figure 28: Autumn case (October 16th, 2009). a, b, c, d from left to right respectively.

It should be stressed that changes of cz_bot_w_so had a noteworthy impact on values of "deep soil" parameters, like water/ice and water content, temperature of soil layers down to 1458 cm (not shown). This influence varied from 10 to 25 percent of original (reference) value, and seemed to enlarge with increase of cz_bot_w_so. Impact on values of lower-atmosphere parameters like air temperature, dew point, precipitation amount or wind speed is regarded as negligible. Moreover, this parameter - which is of integer type, from 1 to 7 - seemed to be not very useful for the preparation of an ensemble. On the opposite, changes of c_soil seem to induce significant changes of values of air temperature, dew point temperature and relative humidity at 2m, wind speed/direction at 10m and surface specific humidity forecast against reference ones. Being a floating-point number it may be equal to any value in its range of variability (ie. from 0 to 2.0), so c_soil is (potentially) a much better candidate as a perturbation for an ensemble. Thus, all selected cases were studied in detail regarding changes of c_soil parameter (Mazur and Duniec, 2014a). The maximum "spread" (standard deviation of values against reference one) - is as big as 2°C(for temperature or dew point)

or 1.5 m/s (for wind-speed). Mean difference (over the entire domain) between maximum and minimum values was about 0.1°Cand 0.07 m/s, respectively. This order of changes pertained mostly to "warm" cases (late spring, summer, early fall), since the soil is at this time much more "subtle" to "stimuli" from a boundary layer. Thus, all the changes seemed to be much more visible during the warm season as above defined. Impact on values of soil parameters like water/ice and water content, or soil layers temperature is rather irrelevant. In the framework of the COTEKINO Priority Project it was planned to study the possibility to prepare a suitable ensemble in two different ways. The first one was a random setting of the value of c_soil globally and uniformly over the entire domain, which is easier to perform with no need for modification of the source code. The second approach proposed was a more "stochastic" one, consisting of a modification of the source code to perturb the values of c_soil from gridpoint to gridpoint over the domain in a random way. Subsequent activities were focused to build ensemble(s) in both ways and to compare results of these approaches. Having results of this approach as a first step (see Duniec and Mazur, 2014; Mazur and Duniec, 2014b), in the second phase further sensitivity tests were performed. This allowed for detailed selection of various configurations and for assessing methods of perturbation of important soil parameters.

4.1.2 Extensive test-cases and sensitivity tests

Effective ensemble members could be prepared using two methods:

- Set a unique random value of c_soil, globally on the whole domain. Easier to perform, by changing the namelists instead of modifying the model code
- An alternative approach - distribute the random values of the c_soil from point to point over the entire model domain by modifying the source code

The results are described in terms of spatial distribution of forecast "spread" - i.e. the standard deviation against mean value. As a case study basis, eleven events were chosen, covering four season and a diversity of synoptic situations. In Figs. 29 and 30 results of an application of the above mentioned point-to-point method for preparation of an ensemble, are presented.

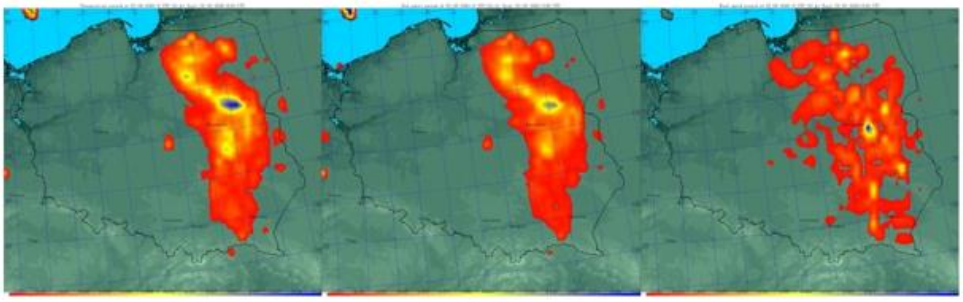


Figure 29: Spread of selected meteorological field from a c_soil based ensemble; winter case (February 22nd, 2009). Temperature (left), max spread value - 0.2°C, dew point temperature (middle), max spread value - 0.2°C, wind speed (right), max spread value - 0.1m/s.

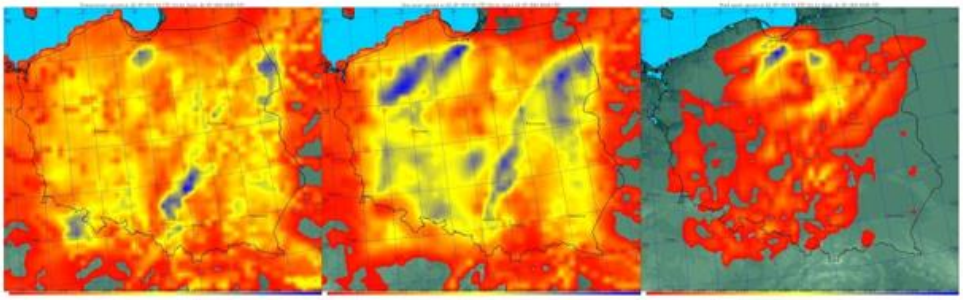


Figure 30: Spread of selected meteorological field over a c_soil based ensemble; summer case (July 1st, 2012). Temperature (left), max spread value - 0.7°C, dew point temperature (middle), max spread value - 0.9°C, wind speed (right), max spread value - 1.0m/s.

In Figs. 31-36 results of the comparison of ensemble forecasts with measurements at meteorological stations (seashore station Leba, midland station in Warsaw and Poznan, and the mountain station Zakopane) are shown for selected (winter and summer) cases.

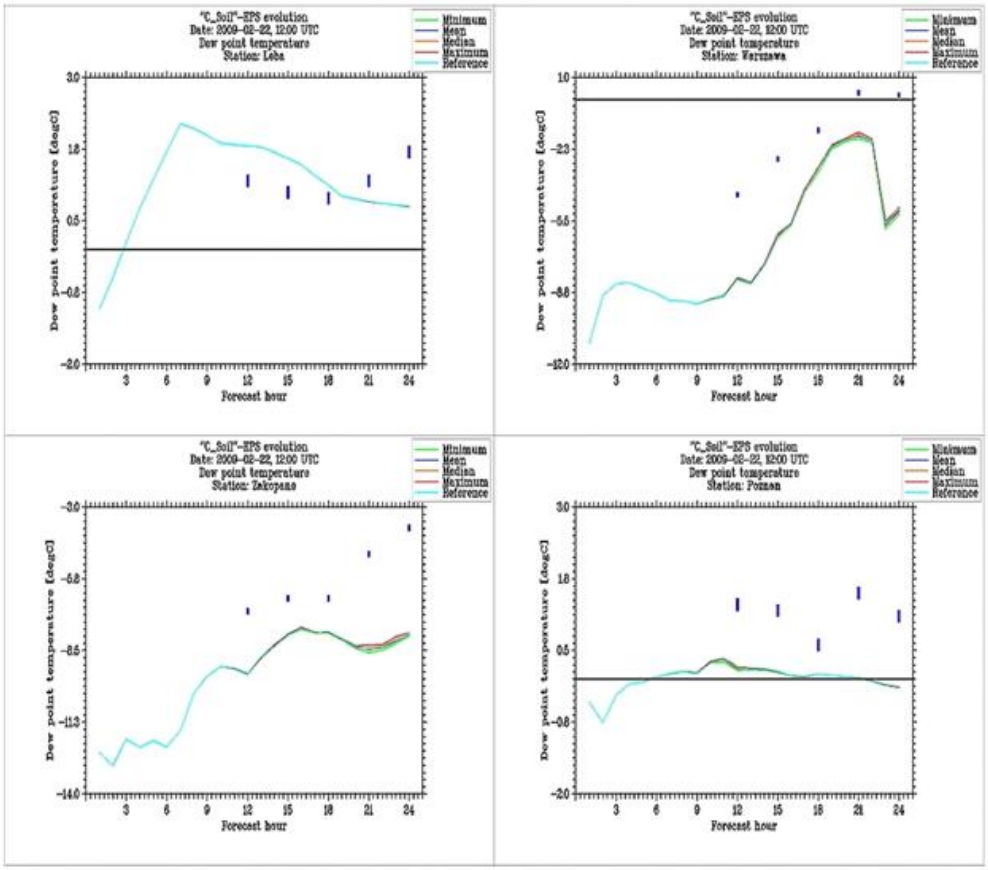


Figure 31: Ensemble forecast with c_soil, for the winter case, February 22nd, 2009. "Spaghetti-plots" against values measured at meteorological stations (vertical bars). Dew point temperature forecast at the following stations: upper left - Leba, upper right - Warsaw, lower left - Poznan , lower right - Zakopane.

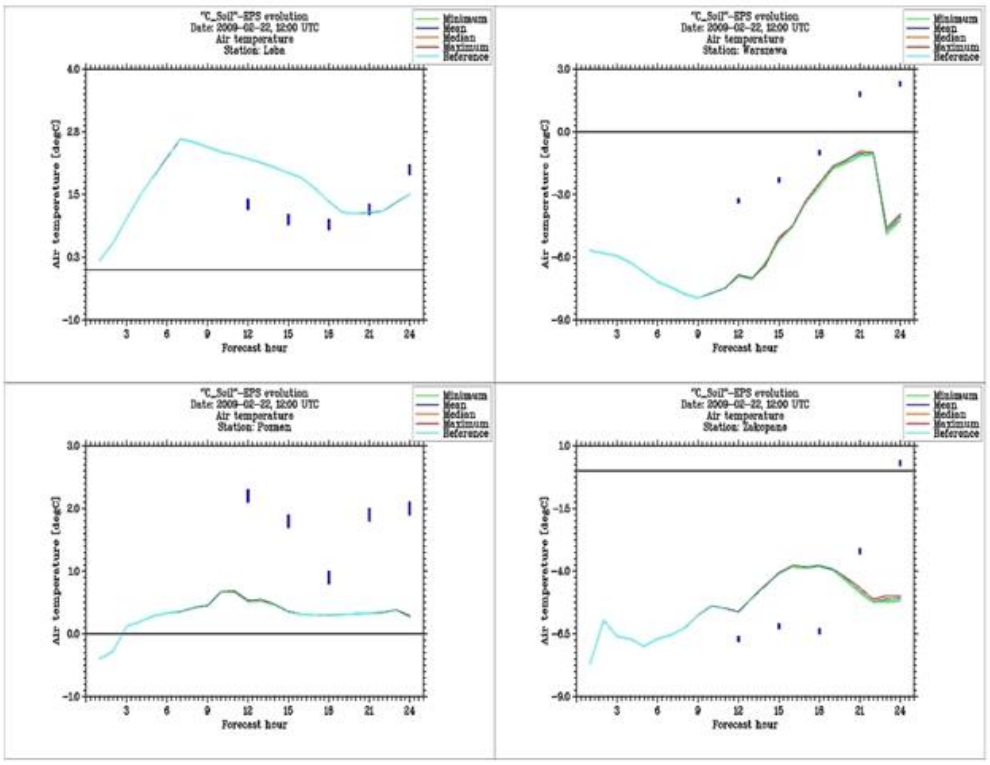


Figure 32: As above, but for air temperature forecast.

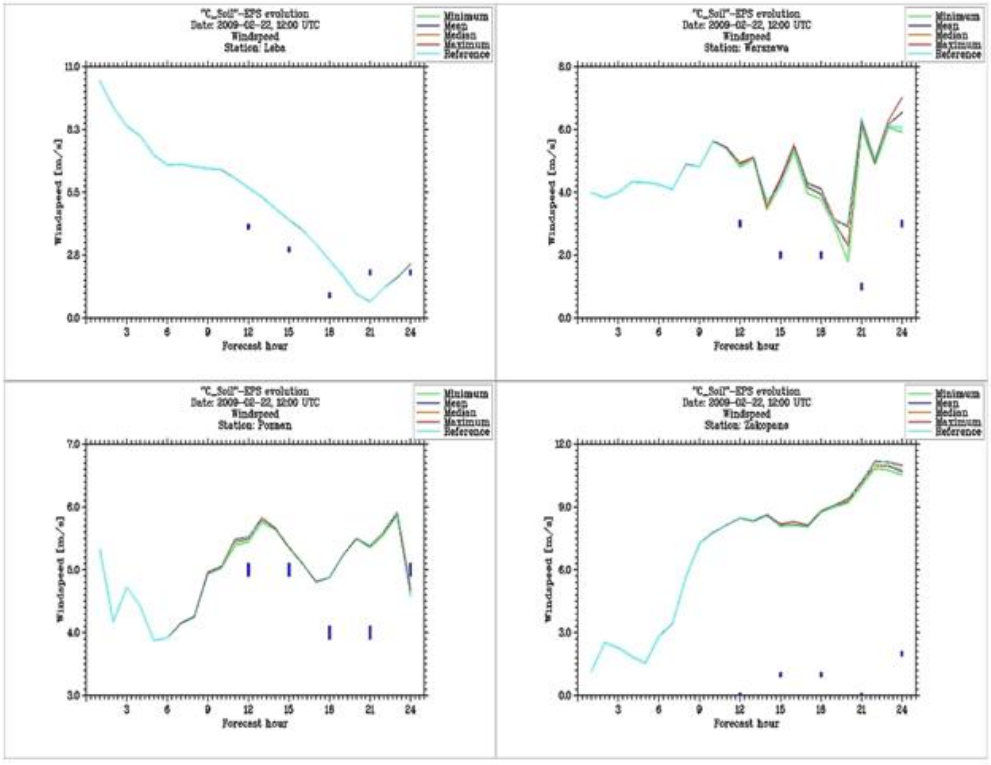


Figure 33: As above, but for wind speed forecast.

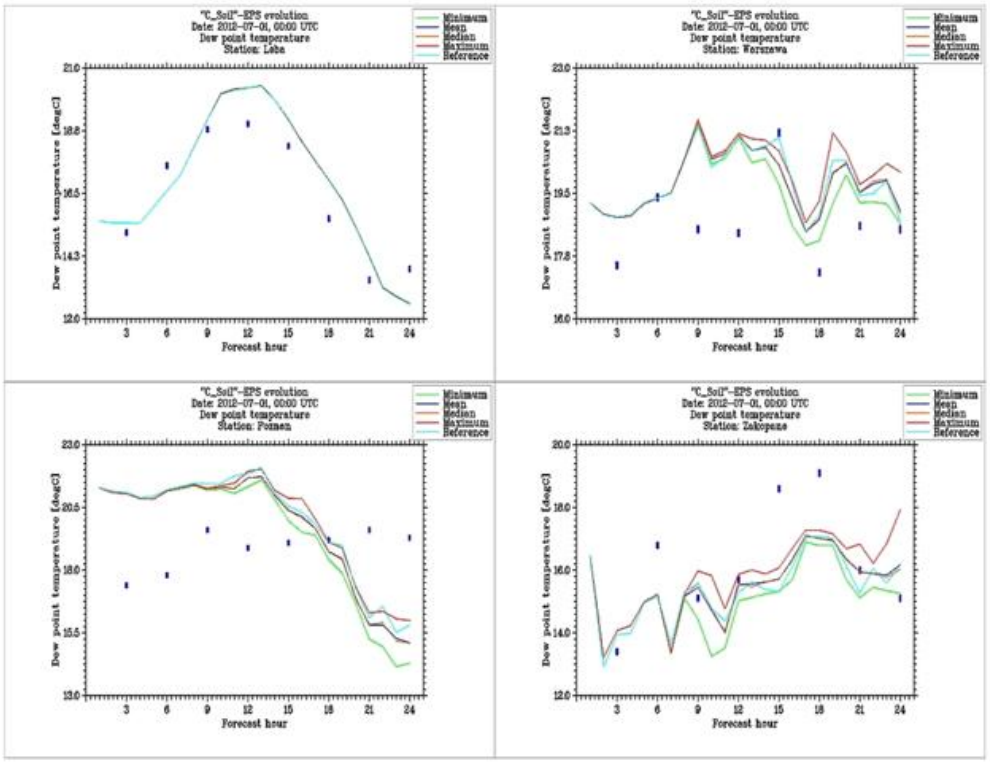


Figure 34: Ensemble forecast with c_soil, summer case, July 1st, 2012. "Spaghetti-plots" against values measured at meteorological stations. Dew point forecast at stations: upper left - Leba, upper right - Warsaw, lower left - Poznan, lower right - Zakopane.

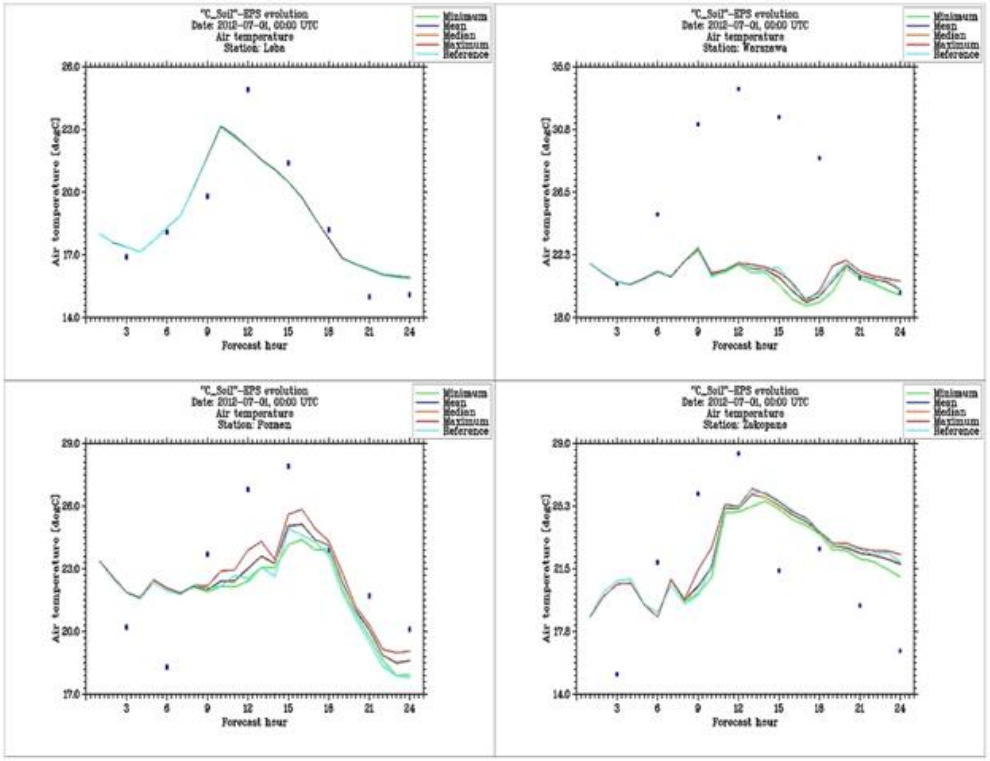


Figure 35: As above, but for air temperature forecast.

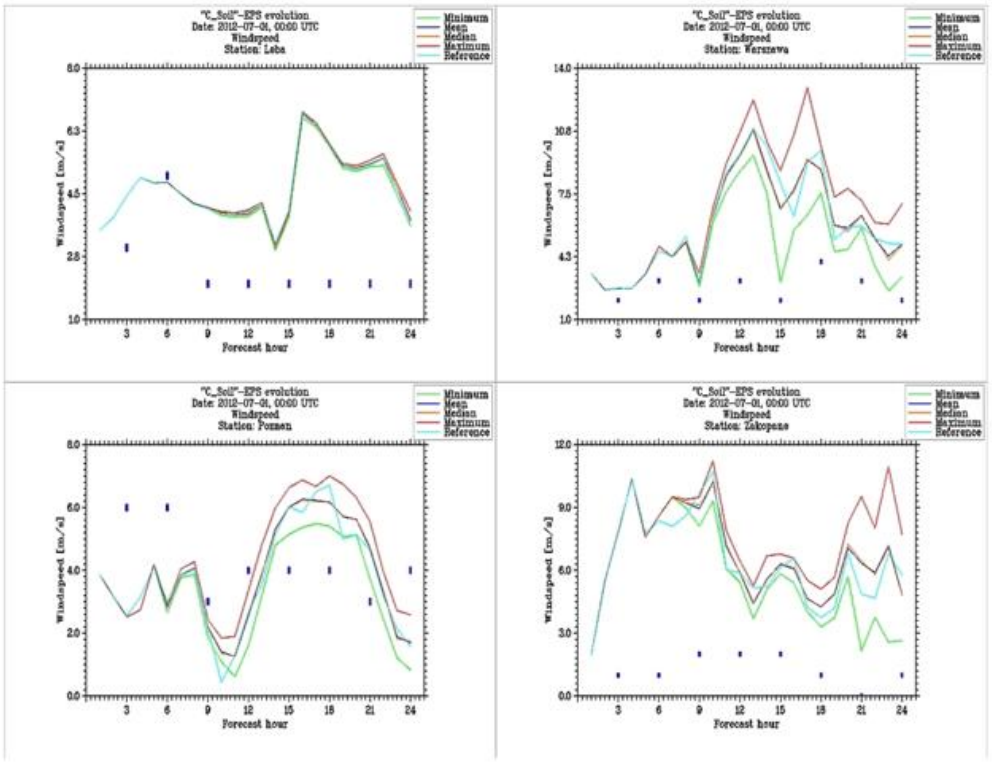


Figure 36: As above, but for wind speed forecast.

The next part of this study was to combine changes in the soil processes parametrization (Duniec and Mazur, 2014, developed by IMGW in the framework of WG3b activities) with the preparation of soil-based ensemble forecasts. After replacing the Dickinson equation with the temperature-dependent Darcy equation (see the above mentioned paper for detailed explanation), further improvements in forecasts can be seen. A quantitative effect of two different soil processes parametrization on a forecast quality was shown in Figs. 37-38. A comparison of these two forecasts was carried out by computation of a "distance" of a real value, measured at SYNOP stations, from an interval defined by the forecast spread, computed as the difference between minimum and maximum values over the ensemble. If the measured value was located inside the interval, this "distance" was identified as equal to zero. In the figures areas with "warm" colours (from yellow to red) represent an improvement of forecast (i.e., decrease of the "distance" of forecast spread from real values) caused by change of parametrization, whereas areas with "cold" colours (from blue to green) - represent a decrease of the forecast accuracy, both measured in [°C] in case of air temperature/dew point temperature, or [m/s] in case of wind speed. An overall improvement, defined by the sum of these "distances" calculated for all SYNOP stations and for every considered element, is presented in the Table 3.

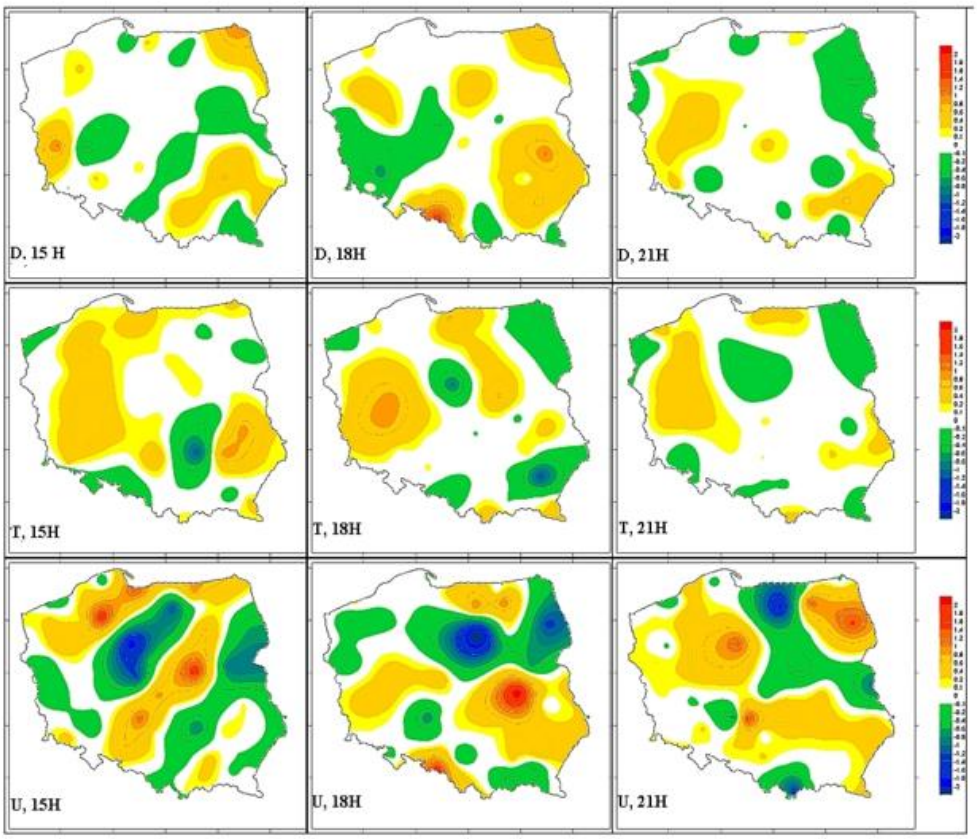


Figure 37: Comparison of "regular" c_soil-based ensemble forecast with the one combined with altered soil processes parametrization. Summer case, July 1st, 2012. Upper row - prediction of dew point temperature for 15th, 18th, and 21st hour of forecast, middle row - temperature forecast. lower row - wind speed forecast, similarly. Areas with "warm" colours represent improvement of forecast, areas with "cold" colours - worsening of forecast (see further explanation in text) due to change of soil processes parametrization. Scale units: °C in case of air temperature or of dew point temperature, or m/s in case of wind speed, all from -2.0 to 2.0.

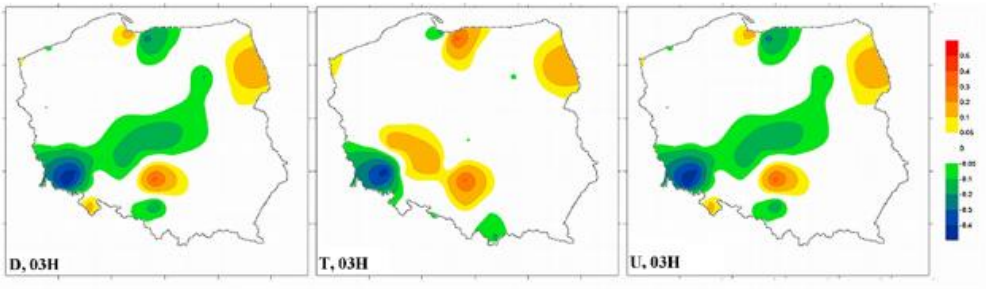


Figure 38: Comparison of "regular" c_soil-based ensemble forecast with the one combined with altered soil processes parametrization. Summer case, July 1st, 2012. Prediction of dew point temperature, air temperature and wind speed (from left to right) for 3rd hour of forecast. Areas with "warm" colours represent improvement of forecast, areas with "cold" colours - worsening of forecast due to change of soil processes parametrization. Scale units: °C in case of air temperature or of dew point temperature, or m/s in case of wind speed, all from -0.5 to 0.5.

It should also be stated, however, that this improvement can hardly be seen in the beginning of the forecast(s). It seems that the soil parametrization need some "spin-up" time to have a significant impact on the quality of an ensemble forecast of the atmospheric state.

hour of forecast	dew point (°C)	air temperature (°C)	wind speed (m/s)
3	-0.152	-0.071	-0.150
6	0.036	0.149	-0.201
9	-0.013	-0.181	0.143
12	-0.168	0.154	-0.115
15	1.714	4.205	2.016
18	4.701	2.460	1.720
21	1.103	1.969	2.751

Table 3: Indicator of overall improvement/worsening due to combination of ensemble preparations with changes of soil processes parametrization (for details see explanations in text).

In case of dew point and air temperature, significant improvement can be especially seen in the western, north-western and south-eastern part of Poland. In case of wind speed forecasts, the "area of improvement" was moving with forecast hour, in general, from west to east. This could be related to distribution of soil types (mainly areas with sand and loam) in Poland as adopted in the COSMO model (see Doms et al., 2011). Tests proved that small perturbations of selected parameter(s) were sufficient to induce significant changes in the forecast of the state of the atmosphere and to provide valid members in the ensemble. However, perturbations have had almost negligible impact in the areas with land fraction much less than one and during the cold season (perhaps due to the specific soil conditions, e.g. frozen ground). A detailed (seasonal/annual) performance analysis is needed for stochastic forecasts. Comparison of ensemble forecasts with observations at meteorological stations showed that, as in the case of deterministic forecasts, introduction of altered soil processes parametrization slightly improved the forecasts, mainly in the central/southern part of Poland, rather than closer to the sea or in mountain regions. All the results obtained from the tests allow to set-up an operationally running EPS at IMGW.

4.1.3 Test-bed and configuration for (quasi-)operational EPS, concept of time-lagged ICs/BCs

The first approach followed to establish an operational configuration has been carried out with BCs/ICs from COSMO-LEPS. Results were satisfactory from the point of view of the quality (i.e. skill) of the forecasts vs observations, however, time needed to prepare an operational forecast turned out to be unacceptably long, taking into account the downloading and pre-processing of BCs/ICs for the needs of EPS at IMGW. Thus, the idea of time-lagged initial and boundary conditions woke up. An explanation of the concept is presented below. At IMGW-NRI, the COSMO model runs in a deterministic mode using initial (IC) and boundary (BC) conditions from the ICON global model (previously from GME), as shown in Fig. 39. The non-hydrostatic ICON model runs at DWD using an icosahedral-hexagonal grid, with the highest spatial resolution over Europe equal to 13 km and a time span of at least 78 hours, four times per day. The ICON generates a set of IC/BCs for COSMO mesoscale model runs with a basic spatial resolution of 7 km and the domain covering the central part of Europe. This generates 78-hour forecasts. The COSMO model with 7 km horizontal resolution (COSMO-7 km) applies nudging-based data assimilation to correct global model forecasts, ingesting the most recent set of meteorological data acquired from the GTS/WMO network. Forecast results from the COSMO-7 km are further used as IC/BCs for a nested instance of a COSMO model with a higher resolution of 2.8 km and 36-hour forecasts. A set of the deterministic COSMO-2.8 km forecasts define the basis for the operational configuration

Model	Resolution min. (km)	Grid size (NxMxL)	Forecast length (h)
ICON (DWD, former: GME)	13	2949120 triangles	78
COSMO v5.01	7	415x460x40	36
COSMO v5.01	2.8	380x405x50	36

Table 4: Details of the configuration of deterministic models, status for year 2017.

of an ensemble forecasting system. More details of the configuration of deterministic models that run operationally at IMGW-NRI are presented in Table 4.

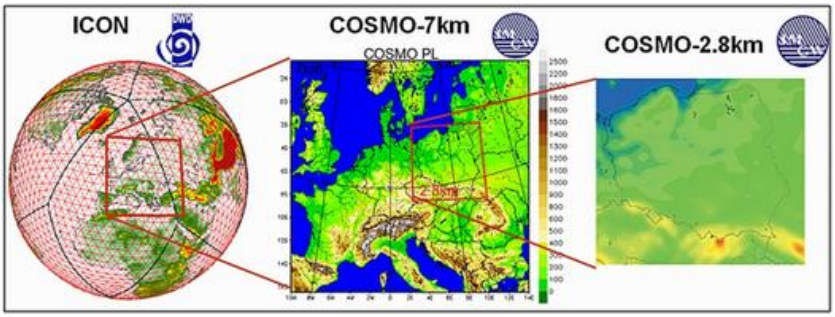


Figure 39: Operational configuration of deterministic COSMO-7 km model and 2.8 km resolution EPS runs at IMGW-NRI. From left to right - domain of ICON global model, domain of COSMO-7 km model running at IMGW-NRI, and a set of nested COSMO-2.8 km domains, forming a 20-members EPS.

In the recently developed EPS configuration, twenty ensemble members are run, based on the COSMO-2.8 km convection permitting (CP) forecasts. Every member of the ensemble applies perturbed lower boundary conditions, composed of a random noise of a specified amplitude added to perturbation of a parameter of the soil-model physical parametrization. The proper collection of adequate initial and boundary conditions (IC/BC) is a crucial issue. In the basic EPS configuration, the whole set of IC/BC was obtained from a single 78-hour deterministic run of the COSMO model with spatial resolution of 7 km. In order to increase the spread of the forecasts, we have further adopted the concept of time-lagged IC/BCs (see e.g. Lu et al., 2007; Chen et al., 2013), in which the set of deterministic CP forecasts is subdivided into groups starting at consecutive time windows: 00, 06, 12, and 18 UTC.

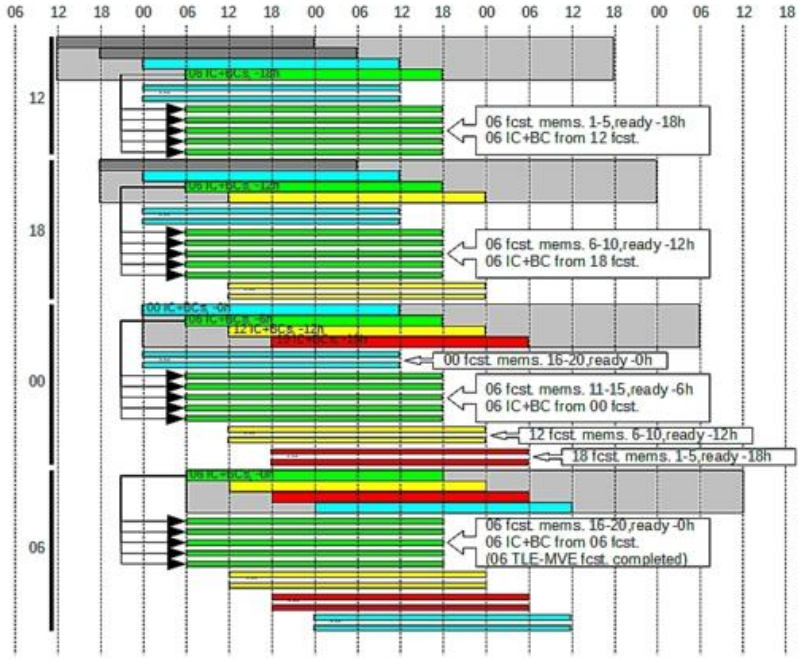


Figure 40: Operational setup of EPS based on Time-Lagged IC/BCs. X-axis - lead time (UTC), Y-axis - forecast individual initial time. The four different colours distinguish forecast nominal start time: blue - 00 UTC, green 06 UTC, yellow 12 UTC, and red 18 UTC.

In the final EPS configuration run operationally at IMGW-NRI, a set of twenty ensemble members is grouped into four bundles, each containing five elements as shown in Fig. 40. The uppermost group - members no. 01 to 05 - is finalized and ready for post-processing 18 hours before the nominal EPS start-up time in the current time window; the second group - members no. 06 to 10 - are gathered 12 hours before the current time window; the third group - members no. 11 to 15 - are prepared 6 hours before the current time window; and finally the lowermost group - members no. 16 to 20 - starts and is finalized in the current time window, completing the whole EPS forecast. The available forecast results (i.e., various meteorological fields) are ready for post-processing in order to provide selected statistics (ensemble mean, ensemble spread, probability of exceedance etc.) in graphical form, suitable for forecasting applications.

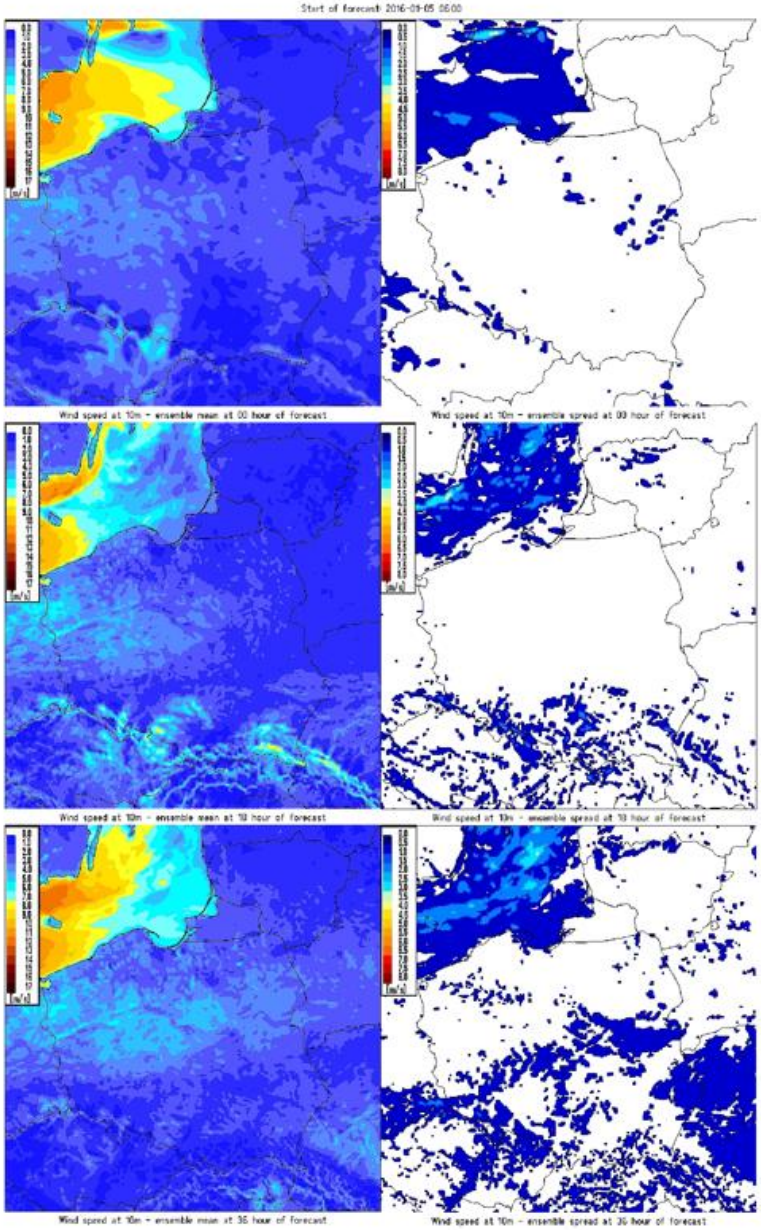


Figure 41: Ensemble mean (left) and ensemble spread (right) of wind speed at 10 m above ground level (m/s) at start (top), at 18th hour (middle) and at 36th hour (bottom) of forecast.

The EPS provides an estimate of the most probable and of alternative realisations of the event. The first two charts in Fig. 41 demonstrate examples of the ensemble mean and ensemble spread of selected meteorological fields (i.e., wind speed at 10 m above ground level). While ensemble spread has the general tendency for underestimation, it helps to objectively estimate the uncertainty of generated forecasts. The low values of the spread mean that forecasts converge toward a similar solution, leading to stronger anomalies. If the spread is large, the atmosphere is in a state where the small changes in the initial conditions may have a large effect on the forecast quality. In Fig. 42 an example of the probability of the exceedance of a selected threshold in the meteorological field is presented. This option is especially useful for calculating the probability of a predefined amount of precipitation (here: 1.5mm/3hours).

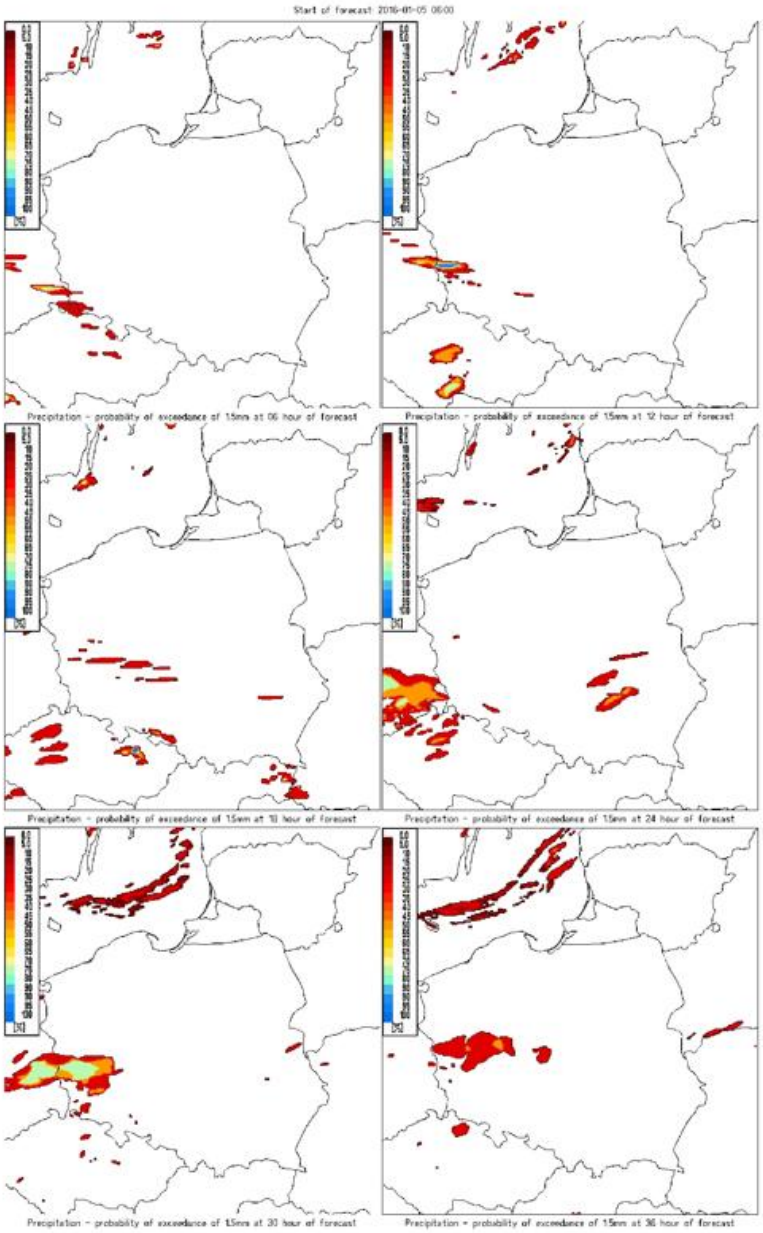


Figure 42: Probability (percentage) of exceedance of precipitation intensity of 1.5mm/3hours at 6th hour (top left), at 12th hour (top right), at 18th hour (mid. left), at 24th hour (mid. right), at 30th hour (bottom left) and at 36th hour (bottom right) of forecast.

In Fig. 43 an example of the so-called "spaghetti plots" is shown - the representation of a selected isopleth of a chosen meteorological field (here, the temperature at 2m above the ground) for every member in an ensemble. Since ensemble members generally diverge in time, these plots show many different model outputs. In the areas where the isopleth pattern is chaotic (i.e., resembling spaghetti) the confidence of the forecast is low. Spaghetti plots provide high confidence of a forecast in regions where members tend to coincide (i.e., contours follow a recognisable pattern through the sequence), and allows for identifying possible clustering of lines (e.g., bi-modal distributions). This particular chart shows an example of the amount of uncertainty in the forecast of air temperature. If there is a good agreement and the contours are close to one another (like in the presented case), then the confidence in the forecast can be high. The presented analysis (as the spread and other probabilistic statistics) derived from ensemble forecasts leads to an increase of confidence

in the forecast and may provide critical information that increases the awareness of a high impact event in advance.

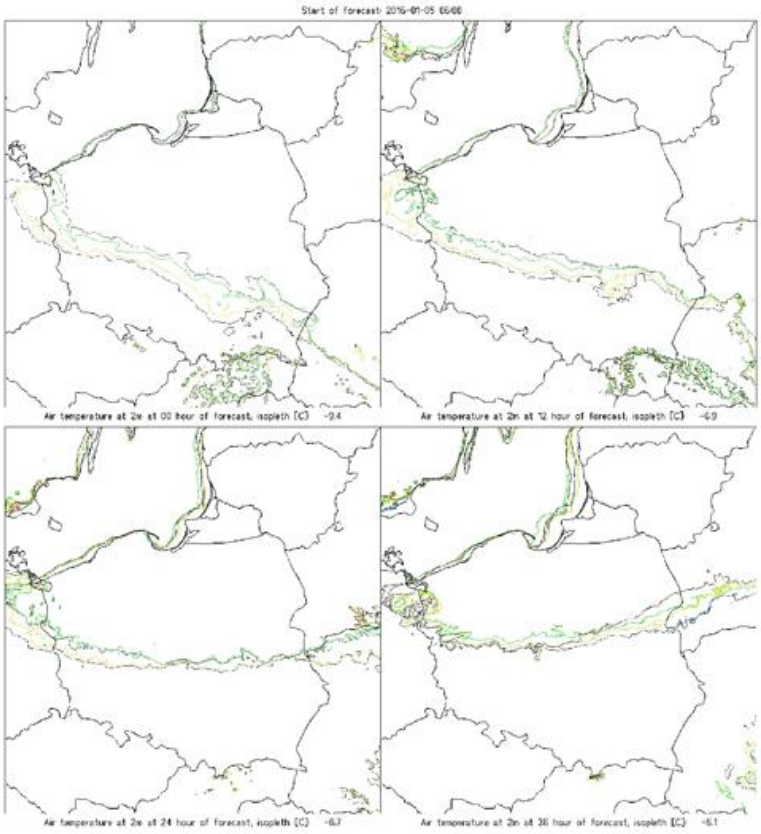


Figure 43: "Spaghetti plots" of air temperature (°C) at 2 m above ground level at the start (top left; isopleths -9.4°C), at the 12th hour (top right; -6.9°C), at the 18th hour (bottom left, -6.7°C) and at the 36th hour (bottom right; -6.1°C) of the forecast. Every coloured line represents the spatial distribution of isopleths for a single ensemble member.

The EPS results were compared with observations collected from 61 Polish SYNOP stations. In the following charts (Figs. 44-45) analysis of the model generated air temperature/dew point temperature forecast averaged for the whole day of 5-01-2016 are presented. In both cases, the EPS mean reproduces the main spatial features of the large-scale temperature distribution. The observed temperature is in a similar range (-20.7°C, -2.5°C) to the computed EPS mean (-20.8°C, -3.8°C).

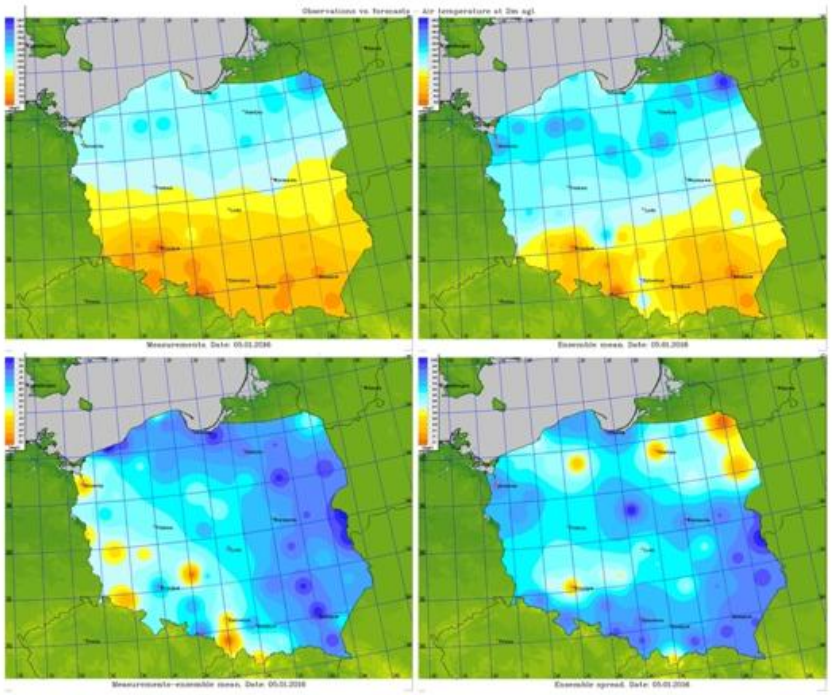


Figure 44: Comparison of the EPS derived temperature: ensemble mean (upper right), spread (lower right) with measurements (upper left), the absolute value of difference between measurement and ensemble mean (lower left).

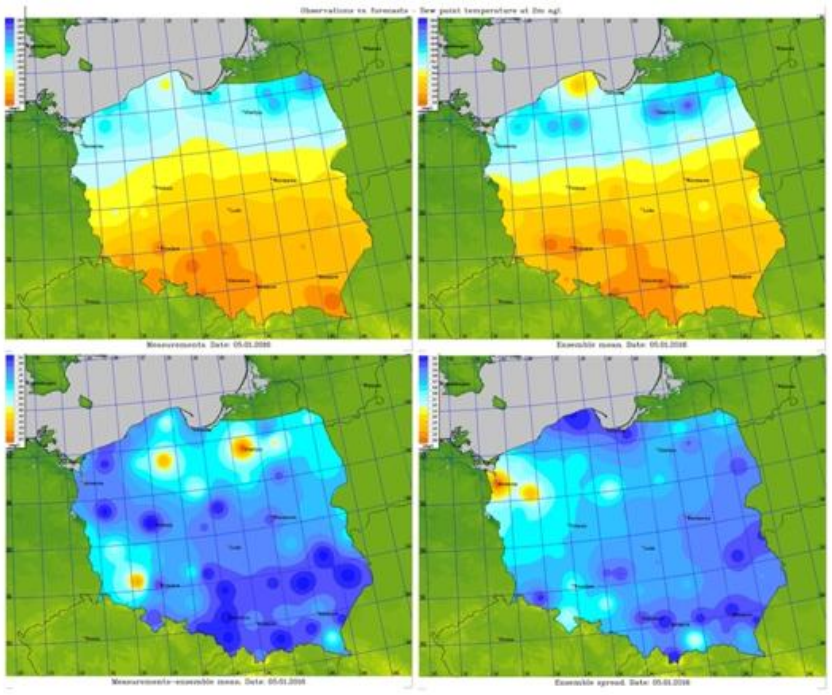


Figure 45: Same as Fig. 44 but for dew point temperature.

Similarly, the observed dew point temperature (Fig. 45) is in a similar range (-20.7°C, -2.0°C) than the EPS computed mean (-20.6°C, -1.6°C). In both cases, the model shows a bias when compared to observations with an absolute error of up to -6.1°Cfor temperature and -5.7°Cfor dew point temperature. For the temperature, larger error values (above 3°C) are well correlated with the air masses that came after the warm front crossing Poland during 5

January, 2016. Dew point temperature generally shows a small error - below 2°C- except in the north-eastern part of Poland, where we can observe a persistent lack of cloud coverage and in south-western areas, which may be correlated to a larger exceedance of precipitation intensity (see Fig. 42) that started in the afternoon hours of 5-01-2016 and developed further during the night and the morning hours of the following day. In summary, it should be stated, that our extensive tests conducted during the COTEKINO Priority Project proved that small perturbations of selected soil parameters were sufficient to induce significant changes in the forecast of the state of the atmosphere and to a provide valid members to the ensemble (Duniec and Mazur, 2014; Mazur and Duniec, 2014a). Changes of c_soil had a significant impact on values of air temperature, dew point temperature and relative humidity at 2m, wind speed/direction at 10m, and surface specific humidity (ibidem, see also Mazur and Duniec, 2015). The use of the concept of time-lagged initial and boundary conditions allowed us to obtain a valid ensemble and use it efficiently in an operational mode. Further work is intended to focus on "tuning" ensemble performance and to provide quantitative quality scores. For this purpose, a random number generator combined with perturbations of initial soil surface temperature and the dependence of the amplitude of perturbation on soil type will be implemented in the COSMO model. While the set of equally weighted time-lagged forecasts improves short-range forecasts, further progress may also be sought by adopting a regression approach to compute a set of weights for different time-lagged ensemble members. In this approach, the perturbation of the evaporating fraction in the soil has a significant impact on the forecast due to the increased stimulation of energy exchange between the surface and atmosphere. The maximum spread for the temperature is most likely of about 1.1°C, with increased value covering the entire northern and western parts of Poland. For the dew point temperature, we observe a higher spread of the amplitude up to 2.0°C, localized only in the north-western corner of the country. More advanced analysis of the EPS scores and of the correlation between EPS error and spread will be further provided in the context of specific applications. The examples of the probability of the occurrence of dry spells or of rainfall occurrence and distribution are both important in agriculture in assessing the influence of EPS forecasts on irrigation, crop growth or drought occurrence. For synoptic forecasters, the risk of the likelihood of a phenomena and its potential impact will have to be properly estimated to provide the objective basis for a decision to issue a warning. Overall, this phase of project task was focused on:

1. initiatory, quasi-operational implementation of EPS (BCs/ICs from a deterministic 7km runs of COSMO-PL)
2. Post-processing of results general charts/maps of mean/spread/max-min difference, spaghetti-charts of selected meteo elements
3. concept of time-lagged BCs/ICs - idea, technical aspects, details
4. time-lagged BCs/ICs - extended tests of the setup, case study results, quasi-operational implementation.

The work done in the framework of point 1 (and tests with ICs/BCs from COSMO-LEPS) has been presented at the COSMO User Seminars 2015. Further activities, related to points 2-3 have been presented at the COSMO General Meeting 2015, with particular emphasis on the comparison of the results of point 1 with those of points 3 and 4. A contribution has been also published in the COSMO Newsletters No. 14 and 15 as well as in the MHWM (Duniec and Mazur, 2014; Mazur and Duniec, 2015; Duniec et al., 2017).

4.2 ARPA Piemonte

The goal of this Task was to implement a soil perturbation technique in a high resolution ensemble system based on the Italian version of the limited area model COSMO at a resolution of 2.8 km taking into account soil surface uncertainties. To do this, we performed first a sensitivity test to assess the behaviour of the COSMO model to different lower boundary initial conditions. In fact, even if the sensitivity of the atmospheric moist processes to different soil condition initializations has been demonstrated in several studies, it cannot be generalized to a completely different modelling system. After that, we tried to find the best setting of a soil perturbation technique to be implemented in a high resolution ensemble system based on the Italian version of the limited area model COSMO at a resolution of 2.8 km taking into account soil surface uncertainties.

4.2.1 Sensitivity of COSMO model to different lower boundary initial conditions.

Different models with different spatial resolutions have been chosen to ensure a good variability among the soil moisture fields used to initialize COSMO model for the sensitivity test. A good variability in the ICs of soil moisture fields increases the chance to obtain a good spread among the ensemble members. The sensitivity test has been performed considering case studies taking into account summer and winter conditions, in order to evaluate the potential differences in sensitivity of the COSMO model in different seasons. For the model runs, COSMO model version 5.0 was used, with a horizontal resolution of 0.025 degrees (about 2.8 km), driven by ECMWF reanalysis at 0.125 degrees. The domain of integration is centered on Italy, with 45 vertical levels, 14 of which below 850 hPa. The variables that we opted to analyze for each case study to assess the changing spread due to different initializations were: 2 meters temperature and dew point, 10 meters wind speed (module), vertical velocity (w) at an altitude of about 1000 m, total precipitation, cloud cover, soil temperature and moisture. The spatial average of the spread for all the atmospheric and soil variables considered (Fig. 46), reveals a considerable spread increase for summer (red line), spring (orange line) and autumn (green line) cases, whereas in the winter one (blue line) the increase is less appreciable. Moreover, the diurnal cycle of some variables is evident (temperature, wind speed, and cloudiness), more pronounced in summer and spring conditions and almost absent in the winter stable case. The summer case, showing the highest values in spread and the most pronounced diurnal cycle, is also the one with the lowest initial mean spread. These results can be justified by the fact that during spring and summer seasons the fluxes, namely the exchanges of moisture and energy between soil and atmosphere, are stronger compared to autumn or winter conditions, especially during daytime. For this mechanism, variations in soil moisture may deeply affect the boundary layer and influence atmospheric processes leading to a considerable variability among COSMO runs.

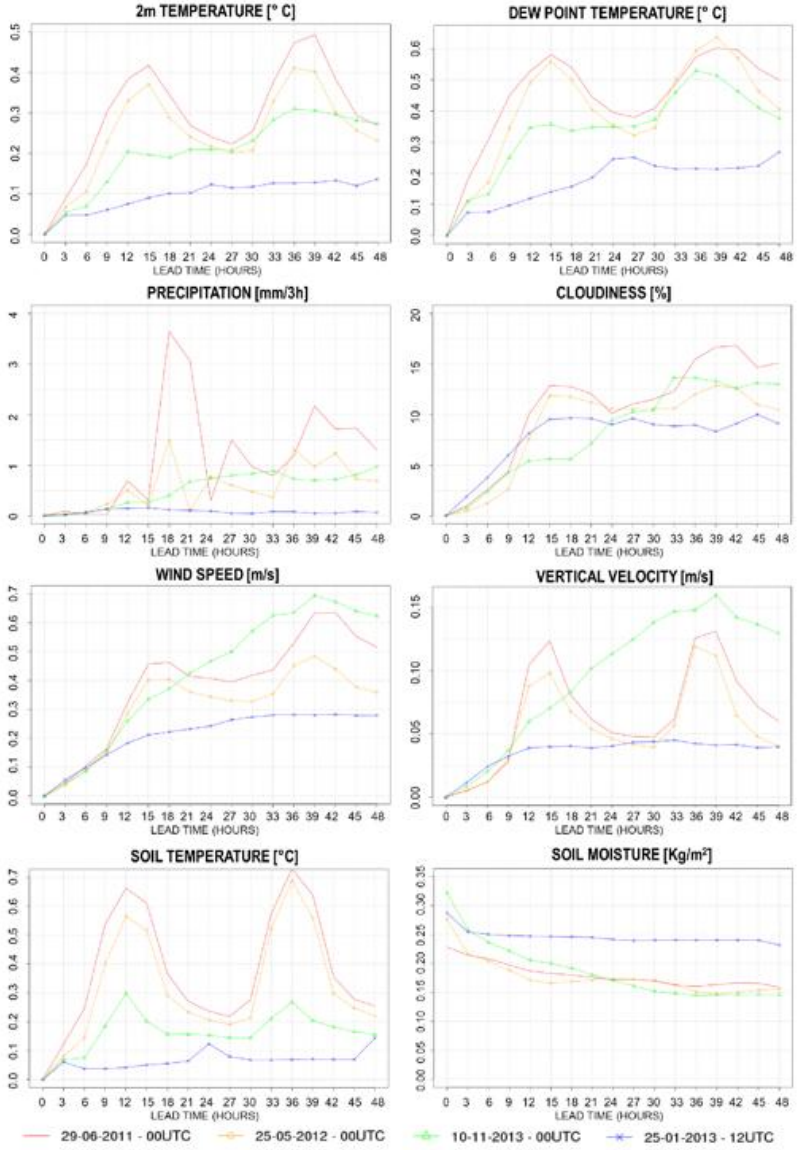


Figure 46: Spread of the variables indicated in panels averaged over the domain as a function of lead time.

This assumption is also confirmed by the behaviour of the soil moisture spread of the first soil layer (bottom right panel). For the winter stable case study, soil moisture spread remains nearly constant, because of the small fluxes leading to a limited exchange of moisture between soil and atmosphere. In other cases, where the fluxes are stronger, the initial spread in soil moisture tends to decrease, especially in the first day of the run. As regard the precipitation spread (left column, second row), the highest values are reached in summer case study with strong synoptic forcing, when events of heavy rainfall occurred. In general, for this variable and for all cases considered, a diurnal cycle is less evident or absent. In fact, for the two convective cases (spring and summer, respectively orange and red lines), thunderstorm events also occurred in the late evening and in the night time, where the cold front or an upper level trough interested some regions of the domain. Hence, in these convective cases, the highest spread generation occurs concurrently with convective phenomena. On the contrary, in the autumn case (green line), less convective precipitation leads to a more uniform spread increase. For the winter case (blue line), no spread appears because of stable synoptic

conditions. Moreover, the soil moisture spread remains nearly constant during the run, as already noticed. To explain this results we have to consider first that a strong inversion layer inhibits the moisture and heat transfer between soil and atmosphere and hence the variability from soil to the surface variable. Second, if the lower boundary layer is already close to the saturation, variations in the soil moisture content probably have a weak effect in the fog formation at the surface. These two points could explain why the influence of soil moisture perturbation in the surface variable is weak for winter case studies. As regard the wind speed and the vertical velocity (third row), the different behavior in spread between spring and summer case studies and the autumn one can be noticed. Considering the convective case studies analysed and as far as precipitation is concerned, we noticed that the areas of large spread are approximately also the regions where the convective phenomena took place (Fig. 47).

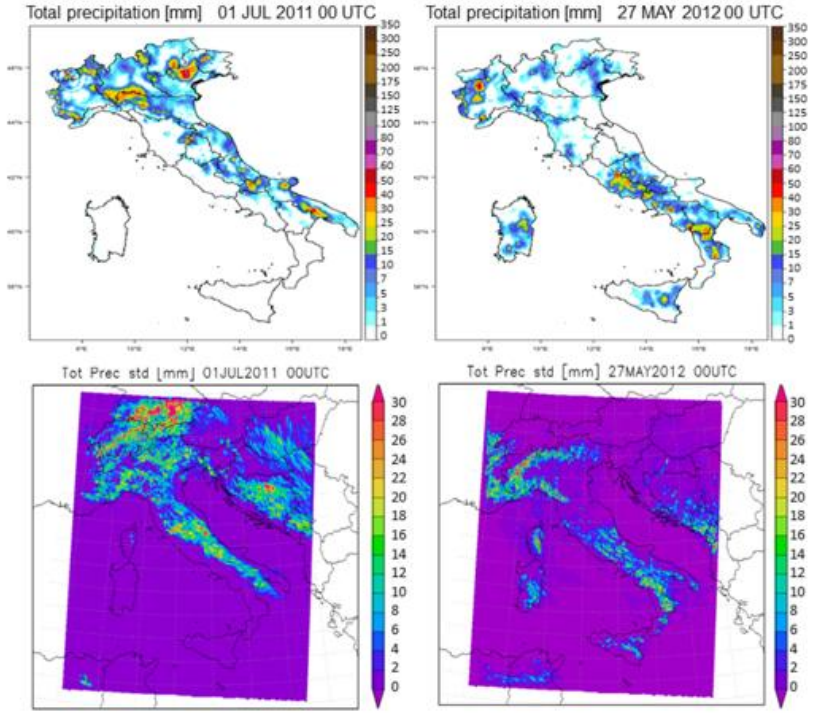


Figure 47: Total precipitation accumulated over 24 h (top row) and spread for this variable for the summer (left) and spring (right) cases.

This result indicates that the introduction of soil perturbation can add some skill to the ensemble system. Similar conclusion can be inferred considering the autumn case study, where the regions with the highest values of spread coincide with the regions of interesting weather (i.e. katabatic wind). In the winter case study, the spread increase is too weak and no noticeable signal can be detected. We investigated also if the different ICs of the soil have a contribution in the spread diffusion in the upper levels of the atmosphere. The spread of the main prognostic variables on longitudinal and latitudinal cross sections of the domain (Fig. 48), demonstrates that the soil moisture content change at the beginning of the simulations have a contribution in generating spread not only near the surface but even in the upper level of the atmosphere. In particular temperature spread is affected by the soil perturbation up to 850 hPa prognostic level, while the contribution to wind speed and water content spread propagates to higher levels affecting also the highest levels of the model integration. The speed of propagation of the spread in the upper atmosphere depends on the case study considered, because the phenomena involved in this study take place with

different time scales. The case studies associated with convective phenomena are the ones with the fastest spread propagation in the atmosphere. In the other cases, the propagation is slower and the spread diffuses less deeply in the upper levels of atmosphere.

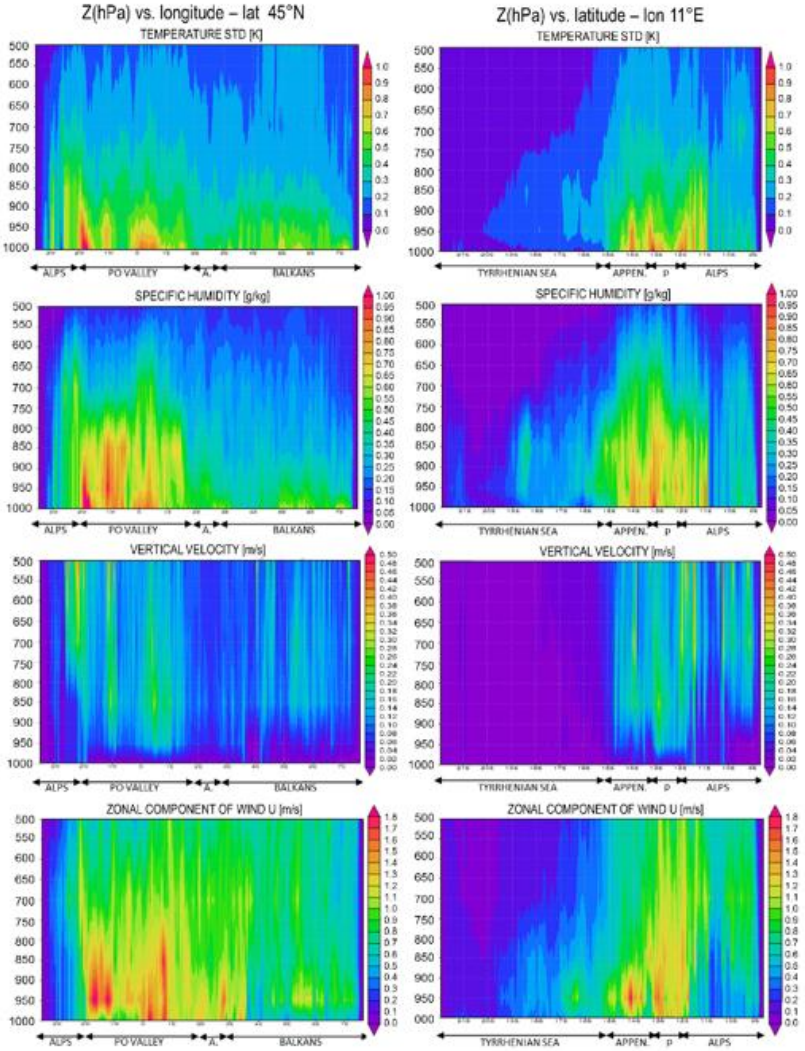


Figure 48: Spread of the main prognostic variables on longitudinal (left column) and latitudinal (right column) cross sections of the domain.

The results showed us that the model is very sensitive to soil moisture changes. This perturbation reflects in an increase of the spread of the main near-surface prognostic variables as well as upper in the atmosphere. The strength of the signal is higher in the case of convective case studies and weaker for the other cases. Moreover, in most of the analysed cases, it can be noticed that areas with large spread coincide with areas where "interesting" weather was observed, indicating that the soil moisture perturbation could potentially add some skill in the ensemble system. Considering the promising result of this study, we started the next phase of the priority project: test a perturbation technique in a full-fledged ensemble prediction system with ICs of soil and atmosphere as well as atmospheric BCs perturbed. Results of the sensitivity test are more extensively described in Bonanno and Loglisci (2014).

4.2.2 Implementing a soil perturbation technique in a high resolution ensemble system.

A first step to reach this goal was to choose between two available perturbation techniques. The first one (SHP hereafter, Spherical Harmonics Perturbation), proposed by Lavaysse et al. (2013), is based on perturbation of spectral coefficients in the expansion in spherical harmonics (in the horizontal) and Fourier harmonics (in the vertical). The second one (SPG hereafter, Stochastic Pattern Generator) is based on expansions in Fourier harmonics on a doubly periodic domain that contains the domain of interest (Tsyrulnikov and Gayfulin, 2016). This last SPG technique has been preferred because it gives a more irregular and noisy random field compared with the SHP technique. Moreover, SPG has the advantage of being less expensive from a computational point of view. Being SPG, with a specific setting, the selected technique to perturb soil field, we performed a sensitivity to initial soil moisture fields: the first coming from COSMO-EU (the operational run of DWD at the time of the experiments, with 7 km horizontal resolution over Europe), the second from the IFS model of ECMWF. This sensitivity test demonstrated that perturbing ECMWF initial soil moisture field gives a negative impact in terms of spread generation because of its highest values of soil moisture, close to saturation. To complete the sensitivity test, we tried to understand how sensitive the ensemble system is to the perturbation of other soil related external parameters such as LAI (Leaf Area Index), roughness length and vegetation cover. This last experiment revealed that the perturbations of external soil related parameters do not have a great impact on the generation of spread for 2-m temperature or soil moisture. The same results were obtained for other variables such as 2-m dew point, 10-m wind speed, precipitation, vertical velocity and soil temperature. Moreover, perturbing both the soil moisture and the external soil related parameters did not have a significant impact on the spread in the surface variables.

The selected perturbation method was, finally:

- SPG (Stochastic Pattern Generator), having the best numerical performances in terms of computational demands to compute the perturbed fields;
- Soil Moisture as the only field to be perturbed in the soil initial conditions, because perturbing other soil related external parameters and/or a combination of them do not produce enough spread compared to the one produced by soil moisture initial condition perturbation;
- Initial soil moisture field from the COSMOEU, because the use of ECMWF soil moisture analysis has a negative impact in terms of spread generation. Moreover, the use of COSMOEU soil moisture field guarantees, as an added value, that soil initial conditions come from the same modelling system.

The effects of an initial soil surface perturbation on surface prognostic variables have been analysed, but the soil initial perturbation have, indeed, an effect on the upper level atmosphere. In fact, latitude-height and longitude-height cross sections demonstrate how the soil moisture initial condition perturbation with SPG and the selected setting is able to propagate spread from the bottom layer to middle troposphere (Fig. 49).

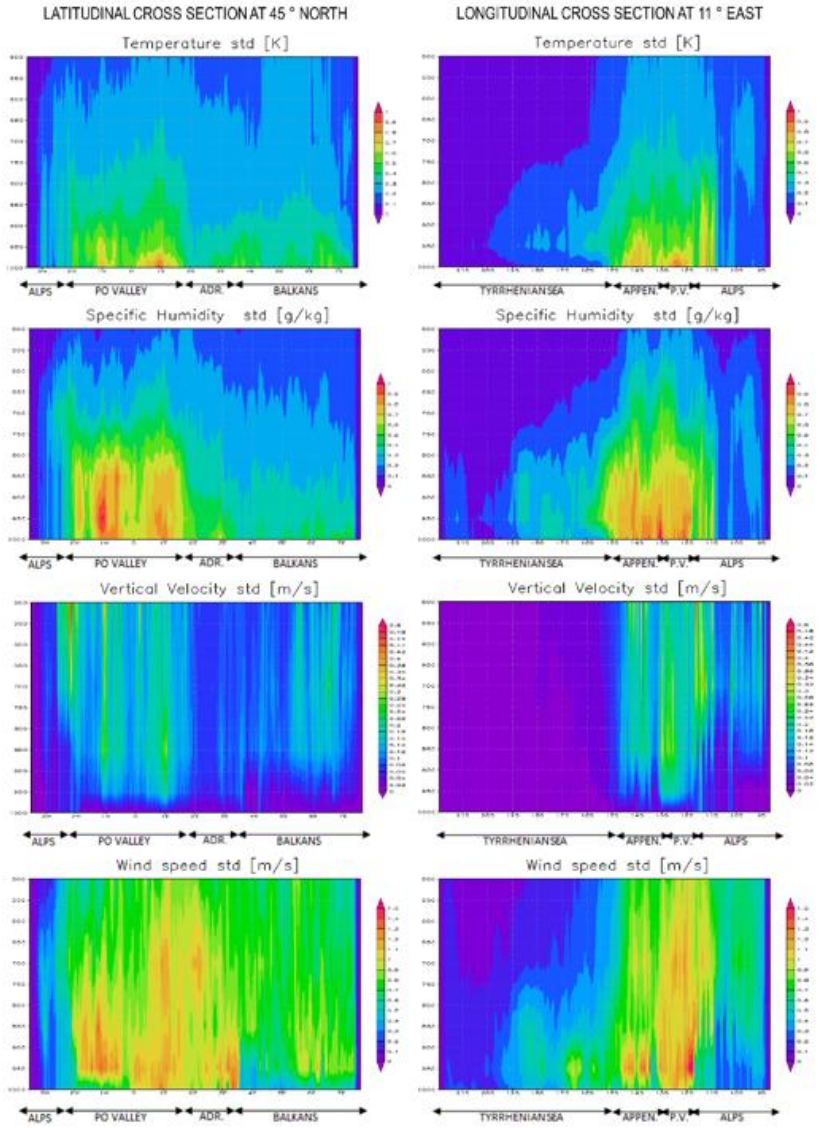


Figure 49: Spread of the main prognostic variables on longitudinal (left column) and latitudinal (right column) cross sections of the domain.

We finally compared the spread obtained with the selected soil perturbation technique with the one coming from an ensemble with perturbed atmospheric initial and boundary conditions, in this case COSMO-LEPS (Montani et al., 2011) (Fig. 50).

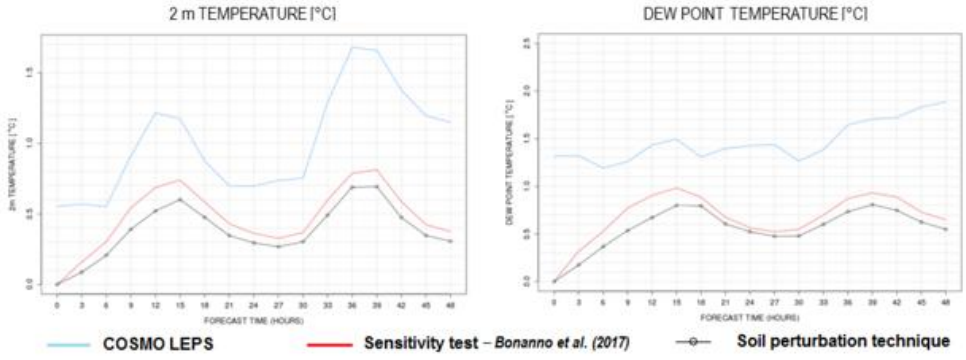


Figure 50: Spread of the variables indicated in panels averaged over the domain as a function of lead time, for the three systems COSMO-LEPS (blue line), a grouping of the runs performed in the sensitivity test (red line) and the ensemble generated by applying the soil perturbation technique based on SPG (black line).

Both systems produce comparable spreads as far as inland surface atmospheric variables are concerned. In fact, the main difference between the two EPSs is that COSMO-LEPS is able to produce spread also over the sea. Perturbing soil moisture initial condition has, naturally, a significant impact only for land areas. Over land the spread generated by the COSMO LEPS ensemble system is considerably higher than the one generated with the soil moisture perturbation. However, the latter is not negligible but gives a significant contribution, especially in the central hours of the day when the fluxes are higher. This fact led us to introduce the soil moisture perturbation into a full-fledged EPS expecting a positive contribution in term of spread generation. After this deep analysis, based on sensitivity of the model to soil uncertainties, we develop a perturbation technique able to generate randomly and numerically cheaply a perturbation of the soil moisture consistent with the model error of this important variable. This technique was successfully tested in a completely perturbed ensemble system based on the COSMO high resolution model, where perturbations act in the initial conditions of atmosphere and soil as well as in the boundary conditions of the atmosphere. Results have been published in COSMO Newsletter No. 15, Bonanno and Loglisci, 2015 and in a peer-reviewed paper (Bonanno and Loglisci, 2017).

5 References

Bengtsson L., Steinheimer M., Bechtold P. and Geleyn J.-F., 2013: A stochastic parametrization for deep convection using cellular automata. *Quarterly Journal of the Royal Meteorological Society*, **139**, 675, 1533–1543.

Berner J., Shutts G. J., Leutbecher M. and Palmer T. N., 2009: A spectral stochastic kinetic energy backscatter scheme and its impact on flow-dependent predictability in the ECMWF ensemble prediction system. *J. Atmos. Sci.*, **66**, 603–626.

Berner J., Ha S.-Y., Hacker J. P., Fournier A. and Snyder C., 2011: Model Uncertainty in a Mesoscale Ensemble Prediction System: Stochastic versus Multiphysics Representations. *Mon. Wea. Rev.*, **139**, 1972–1995.

Bonanno R. and Loglisci N., 2014: A sensitivity test to assess the impact of different soil moisture initializations on short range ensemble variability in COSMO model. COSMO Newsletter No. 14, available at
http://www.cosmo-model.org/content/model/documentation/newsLetters/default.htm.

Bonanno R. and Loglisci N., 2015: Setting up COSMO EPS perturbing lower boundary conditions: sensitivity and case studies. COSMO Newsletter No. 15, available at http://www.cosmo-model.org/content/model/documentation/newsLetters/default.htm.

Bonanno R. and Loglisci N., 2018: Introducing lower boundary conditions perturbations in a convection-permitting ensemble system: sensitivity to soil moisture perturbation. *Meteorol. Atmos. Phys.*, **130**, 1, 67–80.

Bowler N. E, Arribas A., Mylne K. R., Robertson K. B. and Beare S. E., 2008: The MOGREPS short-range ensemble prediction system. *Q. J. R. Meteorol. Soc.*, **134**, 703–722.

Buizza R., Miller M. and Palmer, T. N., 1999: Stochastic simulation of model uncertainties. *Q. J. R. Meteorol. Soc.*, **125**, 2887–2908.

Cloke H., Weisheimer A. and Pappenberger F., 2011: Representing uncertainty in land surface hydrology: fully coupled simulations with the ECMWF land surface scheme. Workshop on Model Uncertainty, 20-24 June 2011, ECMWF, Reading (UK).

Doms G. and Baldauf M., 2015: A Description of the Nonhydrostatic COSMO-Model, Part I: Dynamics and Numerics. www.cosmo-model.org.

Doms G., Förstner J., Heise E., Herzog H.-J., Mironov D., Raschendorfer M., Reinhardt T., Ritter B., Schrodin R., Schulz J.-P., Vogel G., 2011: A Description of the Nonhydrostatic Regional COSMO Model, Part II: Physical Parametrization. www.cosmo-model.org.

Duniec G. and Mazur A., 2014: COTEKINO Priority Project - Results of Sensitivity Tests, COSMO Newsletter No. 14, 106-113.

Duniec G., Interewicz W., Mazur A and Wyszogrodzki A., 2017: Operational Setup of the Soil-perturbed, Time-lagged Ensemble Prediction System at the Institute of Meteorology and Water Management - National Research Institute. *Meteorol. Hydrol. Water Manage.*, **5**, 2, 43–51.

Gebhardt C., Theis S., Paulat M., Ben Bouallegue Z., 2011: Uncertainties in COSMO-DE precipitation forecasts introduced by model perturbations and variation of lateral boundaries. *Atmospheric Research*, **100**, Issues 2-3, 168–177.

Hacker J. P., 2010: Spatial and temporal scales of boundary layer wind predictability in response to small-amplitude land surface uncertainty. *Journal of the Atmospheric Sciences*, **67**, 217–233.

Jolliffe I.P. and Stephenson D.B., 2011: Forecast Verification: A Practitioner's Guide in Atmospheric Science. Chapter 8 (Weigel, A.P.): Verification of Ensemble Forecast. Wiley.

Lavaysse C. M., Carrera S., Bélair N., Gagnon R., Frenette M., Charron M. and Yau M. K., 2013: Impact of surface parameter uncertainties within the Canadian Regional Ensemble Prediction System. *Mon. Wea. Rev.*, **141**, 1506–1526.

Marsigli C., 2009: COSMO-SREPS Priority Project "Short Range Ensemble Prediction System (SREPS): final report. COSMO Technical Report No 13.

Marsigli C., Montani A. and Paccagnella T., 2014: Provision of boundary conditions for a convection-permitting ensemble: comparison of two different approaches. Nonlin. *Processes Geophys.*, **21**, 393–403.

Maurer D., Walser A. and Arpagaus M., 2014: First COSMO-E Experiments with the Stochastically Perturbed Parametrization Tendencies (SPPT) Scheme, COSMO Newsletter No. 14, available at

http://www.cosmo-model.org/content/model/documentation/newsLetters/newsLetter14/.

Mazur A. and Duniec G., 2014a: Sensitivity test on the behaviour of different COSMO suites to different lower boundary initial conditions. Presented during COSMO User Seminar, 16-21.03.2014, Offenbach, Germany.

Mazur A. and Duniec G., 2014b: Soil state perturbations as an input for Ensemble Prediction System (EPS) forecast, Side, Antalya/Turkey, 14-16 October, 2014, Turkey.

Mazur A. and Duniec G., 2015: Ensemble Prediction System (EPS)-based forecast prepared from perturbations of soil conditions, COSMO Newsletter No. 15.

Montani A., Cesari D., Marsigli C. and Paccagnella T., 2011: Seven years of activity in the field of mesoscale ensemble forecasting by the COSMO-LEPS system: main achievements and open challenges. *Tellus A*, **63**, 605–624.

Montani A., Marsigli C. and Paccagnella T., 2013: Development of a COSMO-based limited-area ensemble system for the 2014 Winter Olympic Games. COSMO Newsletter, No. 13, 9399. Available online at
http://cosmo-model.org/content/model/documentation/newsLetters/newsLetter13/cnl13_12.pdf.

Montani A., Alferov D., Astakhova E., Marsigli C. and Paccagnella T., 2014: Ensemble forecasting for Sochi-2014 Olympics: the COSMO-based ensemble prediction systems. COSMO Newsletter, No. 14, 8894. Available online at
http://cosmo-model.org/content/model/documentation/newsLetters/newsLetter14/cnl14_10.pdf.

Palmer T. N., Buizza R., Doblas-Reyes F., Jung T., Leutbecher M., Shutts G. J., Steinheimer M. and Weisheimer A., 2009: Stochastic parametrization and model uncertainty. ECMWF Research Department Technical Memorandum n. 598, ECMWF, Shinfield Park, Reading RG2-9AX, UK, pp. 42.

Peralta C., Ben Bouallegue Z., Theis S., Gebhardt C. and Buchhold M., 2012: Accounting for initial condition uncertainties in COSMO-DE-EPS. *Journal of Geophysical Research: Atmospheres*, **117**, D7, 1–13.

Plant R. S. and Craig G. C., 2008: A Stochastic Parametrization for Deep Convection Based on Equilibrium Statistics. *Journal of the Atmospheric Sciences*, **65**, 87–105.

Rüdisühli S., Walser A., and Fuhrer O., 2014: COSMO in Single Precision, COSMO Newsletter No. 14, available at
http://www.cosmo-model.org/content/model/documentation/newsLetters/newsLetter14/.

Schättler U., Doms G. and Schraff C., 2016: A Description of the Nonhydrostatic COSMO-Model, Part VII: Users Guide, www.cosmo-model.org.

Shutts G., 2005: A kinetic energy backscatter algorithm for use in ensemble prediction systems. *Q. J. R. Meteorol. Soc.*, **131**, 3079–3102.

Sutton C.J. and Hamill T.M., 2004: Impacts of perturbed soil moisture conditions on short range ensemble variability. 84th AMS Annual Meeting, 20th Conference on Weather Analysis and Forecasting/16th Conference on Numerical Weather Prediction, 12-15 January 2004, Seattle, WA.

Sutton C., Hamill T. and Warner T., 2006: Will perturbing soil moisture improve warm-season ensemble forecasts? A proof of concept. *Mon. Weather Rev.*, **134**, 3174–3189.

Tsyrulnikov M. and D. Gayfulin D., 2016: A Stochastic Pattern Generator for ensemble applications. COSMO Technical Report No. 29, available at www.cosmo-model.org /con-

tent/model/documentation/techReports/default.htm.

Vié B., Nuissier O. and Ducroucq V., 2011: Cloud-resolving ensemble simulations of Mediterranean heavy precipitating events: uncertainty on initial conditions and lateral boundary conditions. *Monthly Weather Review*, **139**, 403–423.

Wang Y., Kann A., Bellus M., Pailleux J. and Wittmann C., 2010: A strategy for perturbing surface conditions in LAMEPS, *Atmos Sci Lett*, **11**, 108–113.

List of COSMO Newsletters and Technical Reports

(available for download from the COSMO Website: www.cosmo-model.org)

COSMO Newsletters

No. 1: February 2001.

No. 2: February 2002.

No. 3: February 2003.

No. 4: February 2004.

No. 5: April 2005.

No. 6: July 2006.

No. 7: April 2008; Proceedings from the 8th COSMO General Meeting in Bucharest, 2006.

No. 8: September 2008; Proceedings from the 9th COSMO General Meeting in Athens, 2007.

No. 9: December 2008.

No. 10: March 2010.

No. 11: April 2011.

No. 12: April 2012.

No. 13: April 2013.

No. 14: April 2014.

No. 15: July 2015.

No. 16: July 2016.

No. 17: July 2017.

COSMO Technical Reports

No. 1: Dmitrii Mironov and Matthias Raschendorfer (2001):
Evaluation of Empirical Parameters of the New LM Surface-Layer Parameterization Scheme. Results from Numerical Experiments Including the Soil Moisture Analysis.

No. 2: Reinhold Schrodin and Erdmann Heise (2001):
The Multi-Layer Version of the DWD Soil Model TERRA_LM.

No. 3: Günther Doms (2001):
A Scheme for Monotonic Numerical Diffusion in the LM.

No. 4: Hans-Joachim Herzog, Ursula Schubert, Gerd Vogel, Adelheid Fiedler and Roswitha Kirchner (2002):
LLM ¯ the High-Resolving Nonhydrostatic Simulation Model in the DWD-Project LITFASS.
Part I: Modelling Technique and Simulation Method.

No. 5: Jean-Marie Bettems (2002):
EUCOS Impact Study Using the Limited-Area Non-Hydrostatic NWP Model in Operational Use at MeteoSwiss.

No. 6: Heinz-Werner Bitzer and Jürgen Steppeler (2004):
Documentation of the Z-Coordinate Dynamical Core of LM.

No. 7: Hans-Joachim Herzog, Almut Gassmann (2005):
Lorenz- and Charney-Phillips vertical grid experimentation using a compressible nonhydrostatic toy-model relevant to the fast-mode part of the 'Lokal-Modell'.

No. 8: Chiara Marsigli, Andrea Montani, Tiziana Paccagnella, Davide Sacchetti, André Walser, Marco Arpagaus, Thomas Schumann (2005):
Evaluation of the Performance of the COSMO-LEPS System.

No. 9: Erdmann Heise, Bodo Ritter, Reinhold Schrodin (2006):
Operational Implementation of the Multilayer Soil Model.

No. 10: M.D. Tsyrulnikov (2007):
Is the particle filtering approach appropriate for meso-scale data assimilation ?

No. 11: Dmitrii V. Mironov (2008):
Parameterization of Lakes in Numerical Weather Prediction. Description of a Lake Model.

No. 12: Adriano Raspanti (2009):
COSMO Priority Project "VERification System Unified Survey" (VERSUS): Final Report.

No. 13: Chiara Marsigli (2009):
COSMO Priority Project "Short Range Ensemble Prediction System" (SREPS): Final Report.

No. 14: Michael Baldauf (2009):
COSMO Priority Project "Further Developments of the Runge-Kutta Time Integration Scheme" (RK): Final Report.

No. 15: Silke Dierer (2009):
COSMO Priority Project "Tackle deficiencies in quantitative precipitation forecast" (QPF): Final Report.

No. 16: Pierre Eckert (2009):
COSMO Priority Project "INTERP": Final Report.

No. 17: D. Leuenberger, M. Stoll and A. Roches (2010):
Description of some convective indices implemented in the COSMO model.

No. 18: Daniel Leuenberger (2010):
Statistical analysis of high-resolution COSMO Ensemble forecasts in view of Data Assimilation.

No. 19: A. Montani, D. Cesari, C. Marsigli, T. Paccagnella (2010):
Seven years of activity in the field of mesoscale ensemble forecasting by the COSMO–LEPS system: main achievements and open challenges.

No. 20: A. Roches, O. Fuhrer (2012):
Tracer module in the COSMO model.

No. 21: Michael Baldauf (2013):
A new fast-waves solver for the Runge-Kutta dynamical core.

No. 22: C. Marsigli, T. Diomede, A. Montani, T. Paccagnella, P. Louka, F. Gofa, A. Corigliano (2013):
The CONSENS Priority Project.

No. 23: M. Baldauf, O. Fuhrer, M. J. Kurowski, G. de Morsier, M. Müllner, Z. P. Piotrowski, B. Rosa, P. L. Vitagliano, D. Wójcik, M. Ziemiański (2013):
The COSMO Priority Project 'Conservative Dynamical Core' Final Report.

No. 24: A. K. Miltenberger, A. Roches, S. Pfahl, H. Wernli (2014):
Online Trajectory Module in COSMO: a short user guide.

No. 25: P. Khain, I. Carmona, A. Voudouri, E. Avgoustoglou, J.-M. Bettems, F. Grazzini (2015):
The Proof of the Parameters Calibration Method: CALMO Progress Report.

No. 26: D. Mironov, E. Machulskaya, B. Szintai, M. Raschendorfer, V. Perov, M. Chumakov, E. Avgoustoglou (2015):
The COSMO Priority Project 'UTCS' Final Report.

No. 27: J-M. Bettems (2015):
The COSMO Priority Project 'COLOBOC': Final Report.

No. 28: Ulrich Blahak (2016):
RADAR_MIE_LM and RADAR_MIELIB - Calculation of Radar Reflectivity from Model Output.

No. 29: M. Tsyrulnikov and D. Gayfulin (2016):
A Stochastic Pattern Generator for ensemble applications.

No. 30: D. Mironov and E. Machulskaya (2017):
A Turbulence Kinetic Energy – Scalar Variance Turbulence Parameterization Scheme.

No. 31: P. Khain, I. Carmona, A. Voudouri, E. Avgoustoglou, J.-M. Bettems, F. Grazzini, P. Kaufmann (2017):
CALMO - Progress Report.

No. 32: A. Voudouri, P. Khain, I. Carmona, E. Avgoustoglou, J.M. Bettems, F. Grazzini, O. Bellprat, P. Kaufmann and E. Bucchignani (2017):
Calibration of COSMO Model, Priority Project CALMO Final report

No. 33: N. Vela (2017):
VAST 2.0 - User Manual.

COSMO Technical Reports

Issues of the COSMO Technical Reports series are published by the *COnsortium for Small-scale MOdelling* at non-regular intervals. COSMO is a European group for numerical weather prediction with participating meteorological services from Germany (DWD, AWGeophys), Greece (HNMS), Italy (USAM, ARPA-SIMC, ARPA Piemonte), Switzerland (MeteoSwiss), Poland (IMGW), Romania (NMA) and Russia (RHM). The general goal is to develop, improve and maintain a non-hydrostatic limited area modelling system to be used for both operational and research applications by the members of COSMO. This system is initially based on the COSMO-Model (previously known as LM) of DWD with its corresponding data assimilation system.

The Technical Reports are intended

- for scientific contributions and a documentation of research activities,
- to present and discuss results obtained from the model system,
- to present and discuss verification results and interpretation methods,
- for a documentation of technical changes to the model system,
- to give an overview of new components of the model system.

The purpose of these reports is to communicate results, changes and progress related to the LM model system relatively fast within the COSMO consortium, and also to inform other NWP groups on our current research activities. In this way the discussion on a specific topic can be stimulated at an early stage. In order to publish a report very soon after the completion of the manuscript, we have decided to omit a thorough reviewing procedure and only a rough check is done by the editors and a third reviewer. We apologize for typographical and other errors or inconsistencies which may still be present.

At present, the Technical Reports are available for download from the COSMO web site (www.cosmo-model.org). If required, the member meteorological centres can produce hard-copies by their own for distribution within their service. All members of the consortium will be informed about new issues by email.

For any comments and questions, please contact the editor:

Massimo Milelli
Massimo.Milelli@arpa.piemonte.it

Consortium for Small-Scale Modelling

Technical Report No. 17

Description of some convective indices implemented in the COSMO model

April 2010

DOI: 10.5676/DWD_pub/nwv/cosmo-tr_17

Deutscher Wetterdienst

MeteoSwiss

Ufficio Generale Spazio Aereo e Meteorologia

ΕΘΝΙΚΗ ΜΕΤΕΩΡΟΛΟΓΙΚΗ ΥΠΗΡΕΣΙΑ

Instytucie Meteorogii i Gospodarki Wodnej

Administratia Nationala de Meteorologie

Agenzia Regionale per la Protezione Ambientale del Piemonte

Agenzia Regionale per la Protezione Ambientale dell' Emilia-Romagna: Servizio Idro Meteo

Centro Italiano Ricerche Aerospaziali

Amt für GeoInformationswesen der Bundeswehr

www.cosmo-model.org

Editor: Massimo Milelli, ARPA Piemonte
Printed at Deutscher Wetterdienst, P.O. Box 100465, 63004 Offenbach am Main

Description of some convective indices implemented in the COSMO model

D. Leuenberger, M. Stoll and A. Roches

MeteoSwiss
Krähbühlstrasse 58
8044 Zürich
Switzerland

Contents

1 Introduction **3**

2 Parcel theory **3**

3 Convective indices **3**

3.1 CAPE and CIN 3

3.1.1 CAPE and CIN based on the most unstable parcel 5

3.1.2 CAPE and CIN based on a mean layer parcel 7

3.1.3 CAPE_3KM on a mean layer parcel 7

3.2 Level of Free Convection 7

3.3 Lifting Condensation Level 8

3.4 Showalter Index (SI) 8

3.5 Surface Lifted Index (SLI) 8

3.6 $SWISS_{00}$ Index (SWISS00) 8

3.7 $SWISS_{12}$ Index (SWISS12) 9

3.8 Heat Index 9

3.9 Bulk Richardson number and height of the planetary boundary layer (PBL) . 10

3.9.1 Bulk Richardson Number 11

3.9.2 Height of the Planetary Boundary Layer 12

3.10 Supercell Detection Index 13

A Table of Constants **14**

B Grib parameters of indices **14**

1 Introduction

Convective indices describe characteristics of the thermodynamical state of the atmosphere with regard to convection and are widely used by forecasters to estimate the potential for convective precipitation. Some of the most popular indices include Convective Available Potential Energy (CAPE) and Convective INhibition (CIN). Most of these stability indices are related to the vertical structure of temperature, humidity and wind and can be calculated from radiosonde measurements or output of NWP models.

The following document describes the algorithms used in the COSMO model (Version 4.10) code to calculate a set of convective indices.

2 Parcel theory

A common way to assess the instability of the atmosphere is to apply the parcel method, which evaluates the buoyancy of an air parcel displaced a finite distance under a pseudo-adiabatic or reversible process. The advantages of using the parcel approach includes the ability to evaluate the stability of an unsaturated air mass to the displacement of the saturated parcel, the capability of measuring the total reservoir of potential energy for the convection of a parcel and the ability to assess *conditional instability*, which occurs, when a small displacement is stable but a sufficiently large one is not. The disadvantage of the parcel method is that it cannot account for the reaction of the environment to the parcel displacement. For a detailed description of the parcel theory we refer to [4].

3 Convective indices

3.1 CAPE and CIN

The potential energy PE estimates the available potential energy of the atmosphere. In the parcel theory framework it is calculated by integrating the buoyancy of a parcel lifted from a starting level z along the vertical parcel trajectory and ending at the equilibrium level z_{EL}. We define the potential energy PE of a parcel using the virtual temperature according to [3]

$$\mathrm{PE}(z) = g \cdot \int_z^{z_{\mathrm{EL}}} \frac{T_v^p - T_v^e}{T_v^e} dz \tag{1}$$

Here, g denotes gravitational acceleration, $T_v^{\{e,p\}}$ the virtual temperature $T_v = T(1 + \alpha q_v)$ of the environment and the parcel, respectively, q_v is the specific humidity and $\alpha = (R_v - R_d)/R_d \approx 0.608$. R_v and R_d denote the gas constants of water vapour and dry air, respectively. The ascent of the parcel is calculated dry adiabatically whenever the parcel is unsaturated (i.e. before reaching the condensation level) and pseudo-adiabatically when the parcel is saturated with respect to the environmental air. PE usually consists of a negative part accumulated below the level of free convection (LFC) z_{LFC}, commonly known as Convective INhibition (CIN)

$$\mathrm{CIN}(z) = -g \cdot \int_z^{z_{\mathrm{LFC}}} \frac{T_v^p - T_v^e}{T_v^e} dz \tag{2}$$

which is the energy that must be put into a parcel for its lifting until it gets positively buoyant and a positive part accumulated above the level of free convection, known as Convective

Available Potential Energy (CAPE)

$$\mathrm{CAPE}(z) = g \cdot \int_{z_{\mathrm{LFC}}}^{z_{\mathrm{EL}}} \frac{T_v^p - T_v^e}{T_v^e} dz \tag{3}$$

which is the energy released by the parcel once it is positively buoyant and rises without the addition of external energy. The relation PE(z) = CAPE(z) - CIN(z) holds.

Note that CAPE calculated with the parcel method is just an *upper bound* of the atmosphere's available potential energy due to the fact that the parcel cannot react with the environment (see [4]).

Since CAPE and CIN does not only depend on the thermodynamic structure of the sounding, but also on the parcel in question and on what thermodynamic process is applied in the parcel's displacement, there are many ways to calculate CAPE, which makes the comparison of different variants difficult. We adopted two CAPE and CIN methods which are widely used and robust in practice. They differ only by the definition of the starting parcel.

Implementation in COSMO and fieldextra The parcel ascent is performed using a parcel with given start temperature and humidity. It is then lifted dry adiabatically from model level to model level, preserving the potential temperature at the starting level

$$\theta = T\left(\frac{p_0}{p}\right)^{R_d/c_p} \tag{4}$$

until it reaches saturation at the lifted condensation level (LCL) z_{LCL}. Then it is further lifted pseudo-adiabatically, preserving the equivalent potential temperature at the lifting condensation level

$$\theta_e = T\left(\frac{p_0}{p}\right)^{R_d/c_p} \exp\left(\frac{L_v r_s}{c_p T}\right) \tag{5}$$

until it reaches the level of free convection z_{LFC} where $T^e = T^p$ and buoyancy gets positive. The parcel continues its ascent pseudo-adiabatically until it reaches the equilibrium level z_{EL}. $p_0 = 1000$ hPa, r_s is the saturation mixing ratio $r_s = R_d/R_v \cdot e_s/(p - e_s)$, e_s is the saturation water vapour pressure, c_p is the heat capacity at constant pressure of dry air and L_v is the latent heat of vapourization. All constants are defined as in the COSMO code and are listed in the Appendix for convenience. The main algorithm is as follows

- set start temperature, humidity and start level kstart for the ascent
- calculate potential temperature (θ) for start parcel
- loop over all levels
- if below LCL, perform dry ascent (θ const) to next level
- if at LCL, calculate equivalent potential temperature (θ_e)
- if above or at LCL, perform wet ascent (θ_e const) to next level
- calculate buoyancy $T_v^p - T_v^e$
- check for LFC (buoyancy changes from negative to positive)
- accumulate CAPE or CIN (dependent on sign of buoyancy)
- check for 500 hPa level and store $T_v^p - T_v^e$ (used for SI and SLI)
- end loop over all levels

Remarks

- The saturation water vapour pressure is approximated using Teten's formula (also used in the COSMO code)

$$e_s(T) = b_1 \exp\left(b_{2w}\frac{T - b_3}{T - b_{4w}}\right)$$

with b_1=610.78 Pa, b_{2w}=17.27, b_3=273.16 K and b_{4w}=35.86 K

- Since the temperature cannot be derived analytically from the equivalent potential temperature, it is calculated numerically using the Newton iteration method

$$\begin{aligned} T^{(k+1)} &= T^{(k)} - \frac{f(T^{(k)})}{f'(T^{(k)})} \\ f(T) &= T(\frac{p_0}{p})^{R_d/c_p}\exp(\frac{L_v r_s}{c_p T}) - \theta_e \end{aligned}$$

where k is the iteration index. There are usually less than 10 iterations needed for an accuracy of 0.003 K.

- Tests showed that very often a LFC is already found within the boundary layer even if significant capping inversions with a substantial amount of CIN are present above, implying that there are more than one LFC. Since CIN is defined as the part of PE below the LFC no CIN is present in these cases. To handle these situations in a meteorological meaningful way a check is done if the CIN within the capping inversion is larger than half (empirical value) the CAPE in the layer below. If this is the case, the LFC is set to the upper boundary of the CIN region (i.e. the second LFC) and CIN is defined as the CIN of the capping inversion.

- Since CIN is defined as the part of PE below the LFC, all contributions to CIN above the LFC are subtracted at the end of the ascent.

- In unstable situations (no LFC is present) or CAPE=0, CIN is set to "undefined value"

3.1.1 CAPE and CIN based on the most unstable parcel

The parcel with the largest CAPE value of all starting parcels within a certain layer above the earth's surface is chosen. By definition, the CAPE value of this parcel is an upper bound of all parcels starting within the given layer. This has the advantage that the CAPE value is independent of large vertical gradients of temperature and humidity often occurring in the surface layer. Therefore this variant of CAPE is a robust measure also during night when shallow surface-based inversions are present. CIN is calculated using the same starting parcel. For a graphical representation of an ascent using the most unstable parcel see Figure 1 (black line).

Implementation in COSMO and fieldextra To calculate the CAPE and CIN using the most unstable parcel (CAPE_MU and CIN_MU), an ascent is performed for each model level starting at the surface and ending at 300 hPa (adjustable parameter) above the surface. For each ascent the CAPE value is calculated and the parcel with the maximum value is taken as the starting parcel. CIN_MU is the CIN corresponding to this starting parcel. Since several ascents need to be performed for each grid point, these indices are computationally more expensive than the mean layer CAPE/CIN and the Showalter Index/Surface Lifted Index.

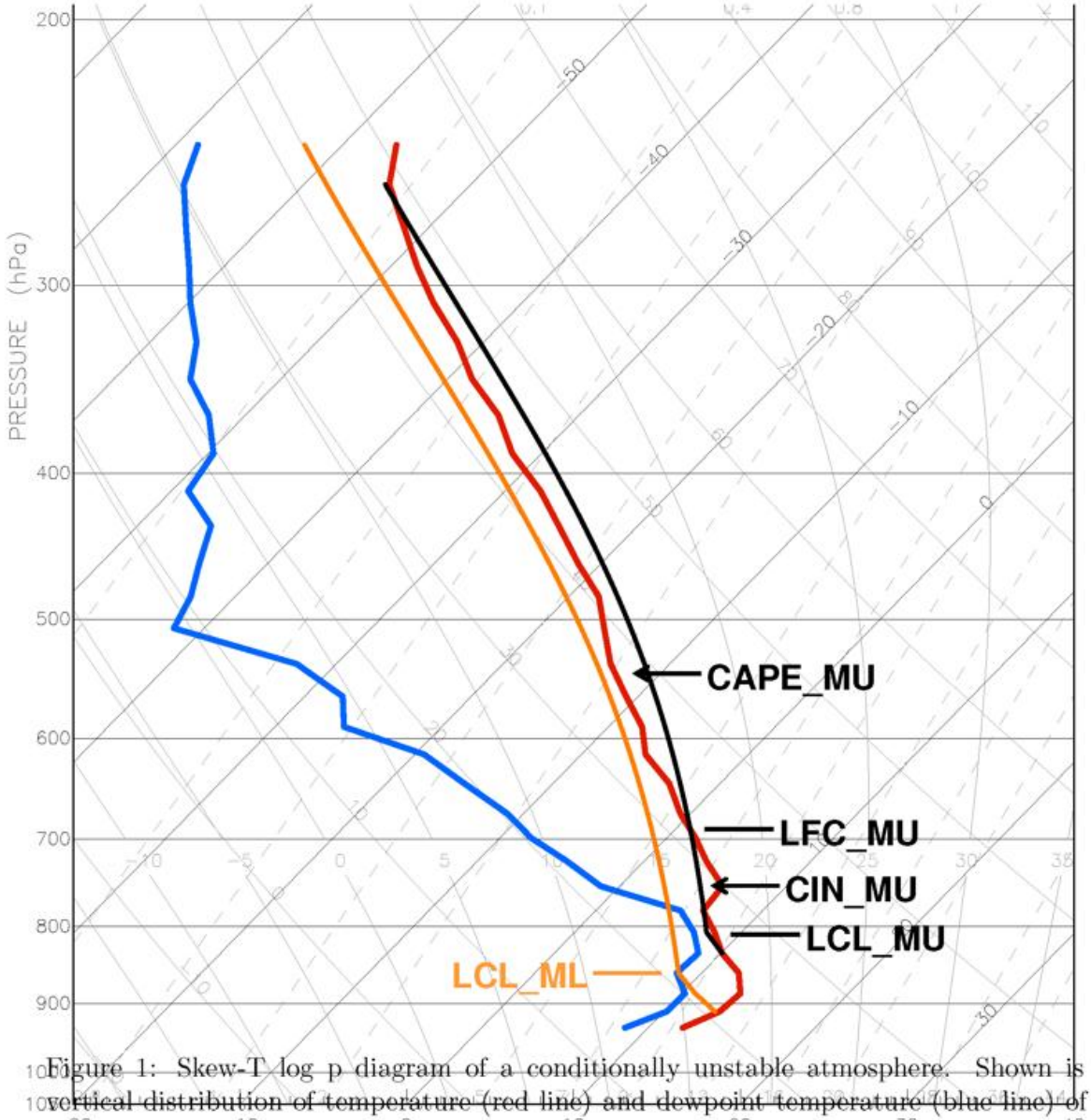


Figure 1: Skew-T log p diagram of a conditionally unstable atmosphere. Shown is the vertical distribution of temperature (red line) and dewpoint temperature (blue line) of the environment and two ascents using the parcel method starting from the most unstable parcel (black line) and a mean layer parcel (orange line). In the mean layer parcel ascent no level of free convection (LFC) is found, therefore CAPE_ML=0 and CIN_ML is undefined. In the most unstable parcel ascent a LFC (LFC_MU) is present, resulting in defined and non-negative CAPE_MU and CIN_MU. The lifting condensation levels are marked with LCL_MU and LCL_ML, respectively.

3.1.2 CAPE and CIN based on a mean layer parcel

In this case, the temperature and humidity of the starting parcel is calculated from that representative for a shallow surface layer (mean temperature and humidity of that layer). Like the CAPE/CIN using the most unstable parcel this results in a robust calculation without being too much dependent on the exact structure of the surface layer which may be not representative for the real atmosphere. CIN is calculated using the same string parcel. For a graphical representation of an ascent using the most unstable parcel see Figure 1 (orange line).

Implementation in COSMO and fieldextra To calculate the CAPE and CIN using a mean layer parcel (CAPE_ML and CIN_ML) a mean temperature and humidity from the lowest 50 hPa (adjustable parameter) above the surface are used for the "initialization" of the parcel. Only one ascent has to be performed per grid point.

3.1.3 CAPE_3KM on a mean layer parcel

CAPE_3KM is similar to the CAPE based on a mean layer parcel. The starting point for the parcel ascent is the same, whereas the ending point of the ascent is different. In case of CAPE based on a mean layer parcel, the ascent is performed until the equilibrium level z_{EL} is reached. For the CAPE_3KM the ascent is stopped at a height of 3 km above the ground. This particular CAPE is helpful for the forecasters. High values of CAPE_3KM tend to promote a stretching of the air columns and thus the development of tornadoes when high vorticity near the ground and high humidity occur simultaneously. Stretching is considered as significant when CAPE_3KM is greater than 150 J/kg (see [2]).

Implementation in COSMO and fieldextra The CAPE_3KM is computed exactly in the same way as the CAPE_ML excepting the fact that the ascent is stopped at 3 km above the ground.

3.2 Level of Free Convection

The Level of Free Convection LFC is the altitude at which the buoyancy is first positive, i.e. at which the lifted air parcel first becomes warmer than the surrounding air (see [4]). The PE of a lifted parcel is thus negative under the LFC (CIN) and we have to put some energy in the parcel in order to lift it. In opposite the PE of a lifted parcel is positive above the LFC (CAPE) and free convection occurs. The determination of the LFC is straightforward by computing the buoyancy at each level during the ascent and by searching the level at which the buoyancy sign changes.

Implementation in COSMO and fieldextra LFC is computed using a mean layer parcel (i.e. using mean values from the lowest 50 hPa above the surface as starting values for the parcel ascent).
The buoyancy is computed for each level:

$$Buo(k) = T_v^p(k) - T_v^e(k)$$

Then a sign change is searched: we test that $Buo(k) > 0$ and $Buo(k-1) < 0$. If it is the case k is the index corresponding to the LFC. The LFC is then computed as the height above the ground corresponding to this index k.

3.3 Lifting Condensation Level

Adiabatic expansion of moist air will always ultimately lead to saturation in the earth's atmosphere (see [4]). The LCL is the height at which a parcel, upon dry adiabatic lifting, will first achieve saturation (see [6]). It is often associated with the cloud base. At this point the parcel is just saturated with no cloud liquid water (see [12]). It is computed by comparing the current specific humidity with the specific humidity at saturation under the same conditions (pressure, temperature).

Implementation in COSMO and fieldextra We compute the LCL based on a mean layer parcel. We thus use a mean temperature and humidity from the lowest 50 hPa above the surface as starting values. Saturation humidity is computed for each level and the current specific humidity is compared to it. If the current specific humidity is greater or equal to the saturation value the LCL is found.

3.4 Showalter Index (SI)

The Showalter Index SI [9] is defined by the difference between the environmental temperature at 500 hPa and the 500 hPa temperature of an air parcel lifted dry adiabatically from 850 hPa to its condensation level and pseudo-adiabatically thereafter.

Implementation in COSMO and fieldextra For the calculation of the Showalter Index, an ascent is performed with a starting parcel at 850 hPa. SI is then equal to the temperature difference between the environment and the lifted parcel at 500 hPa. Only one ascent has to be performed per grid point. If the 850 hPa surface is below the topography, SI is set to "undefined value".

3.5 Surface Lifted Index (SLI)

The Surface Lifted Index SLI is defined by the difference between the environmental temperature at 500 hPa and the 500 hPa temperature of an air parcel lifted dry adiabatically from the surface to its condensation level and pseudo-adiabatically thereafter.

Implementation in COSMO and fieldextra For the calculation of the Surface Lifted Index, an ascent is performed with a starting parcel at the first model level. SLI is then equal to the temperature difference between the environment and the lifted parcel at 500 hPa. Only one ascent has to be performed per grid point.

3.6 $SWISS_{00}$ Index (SWISS00)

The $SWISS_{00}$ Index was especially designed for northern Switzerland during night conditions [5]. It is based on a combination of the Showalter Index, the wind shear between 3 and 6

km a.s.l. and the dewpoint depression on 600 hPa. This definition is similar to that of the SWEAT Index developed for the USA.

$$\mathrm{SWISS}_{00} = \mathrm{SI} + 0.4\mathrm{WSh}_{\text{3-6km}} + 0.1(T - T_d)_{\text{600hPa}}$$

where SI is the Showalter Index defined above and $\mathrm{WSh}_{\text{3-6km}}$ is the wind shear between 3 and 6 km.

Implementation in COSMO and fieldextra The SWISS_{00} Index is calculated as defined in section 3.6. The vertical wind shear is approximated by

$$\mathrm{WSh}_{\text{3-6km}} = \sqrt{u^2 + v^2}_{\text{6km}} - \sqrt{u^2 + v^2}_{\text{3km}}$$

3.7 SWISS_{12} Index (SWISS12)

The SWISS_{12} Index was especially designed for northern Switzerland during day conditions [5]. It is based on a combination of the Surface Lifted Index, the wind shear between ground and 3 km a.s.l. and the dewpoint depression on 650 hPa. This definition is similar to that of the SWEAT Index developed for the USA.

$$\mathrm{SWISS}_{12} = \mathrm{SLI} - 0.3\mathrm{WSh}_{\text{0-3km}} + 0.3(T - T_d)_{\text{650hPa}}$$

where SLI is the Surface Lifted Index defined above and $\mathrm{WSh}_{\text{0-3km}}$ is the wind shear between surface and 3 km.

Implementation in COSMO and fieldextra The SWISS_{12} Index is calculated as defined in section 3.7. The vertical wind shear is approximated by

$$\mathrm{WSh}_{\text{0-3km}} = \sqrt{u^2 + v^2}_{\text{3km}} - \sqrt{u^2 + v^2}_{\text{z(kdim)}}$$

z(kdim) is the height of the lowest model level.

3.8 Heat Index

The Heat Index (HI) is an index that combines air temperature and relative humidity in an attempt to determine the human-perceived equivalent temperature, how hot it feels, termed the felt air temperature. The human body normally cools itself by perspiration, or sweating, which evaporates and carries heat away from the body. However, when the relative humidity is high, the evaporation rate is reduced, so heat is removed from the body at a lower rate causing it to retain more heat than it would in dry air. Measurements have been taken based on subjective descriptions of how hot subjects feel for a given temperature and humidity, allowing an index to be made which create a correspondence between a temperature and humidity combination and a higher temperature in drier air.

The HI derives from a model comprising a collection of equations developed by Steadman [11]. It is the result of extensive bio-meteorological studies. The model is reduced by an iterative procedure to a relationship between temperature and relative humidity versus apparent temperature, Steadman developed a table based on this relationship.
The equation used commonly results from a multiple regression analysis performed on the data from Steadman's table [7] and is given by:

$$\begin{aligned} HI &= -42.379 + 2.0490T + 10.1433R - 0.2248TR - 6.8378 * 10^{-3}T^2 \\ &\quad - 5.4817 * 10^{-2}R^2 + 1.2287 * 10^{-3}T^2R + 8.5282 * 10^{-4}TR^2 - 1.99 * 10^{-6}T^2R^2 \end{aligned}$$

where T is the ambient dry bulb temperature (°F) and R is the relative humidity (%). This formula is only meaningful for temperatures above 80°F (corresponding to 26.7°C) and relative humidities above 40%.

The meaning of a Heat Index value can be summarized as follows:

Heat Index	Effects
<70°F	no effect for most of the people
71-79 °F	discomfort for half of the people
80-90°F	caution: fatigue is possible. Discomfort for all the people
91-105°F	extreme caution: sunstroke, heat cramps, heat exhaustion possible
106-130°F	danger: sunstroke, heat cramps, heat exhaustion likely
>130°F	extreme danger: heat strokes and sunstroke likely

Implementation in fieldextra The Heat Index is computed with the formula given in section 3.8 and for temperatures above 80°F (corresponds to 26.7°C) and relative humidities above 40%. For all other combinations of T and R the HI is flagged as undefined.

[7] does not mention at which height the temperature and the relative humidity should be considered. But this index attempts to determine the human-perceived equivalent temperature so the typical height is about 1.5-2 m. Thus, we choose to consider them at 2 meters height because of realism and simplicity. These outputs from the COSMO model are thus used:
- 2m temperature
- 2m relative humidity.

3.9 Bulk Richardson number and height of the planetary boundary layer (PBL)

The stability of the atmosphere plays a key role in the transport of air masses as well as in the transport of pollutants or humidity. The vertical transport is prevented in case of a stable stratified atmosphere whereas it is enhanced under unstable, or convective, conditions [12]. The dynamic stability is defined as the ability of an air mass to resist or recover from finite perturbations of a steady state. The perturbations are mechanically or thermally initiated [4].

The boundary layer is defined as the lowest part of the troposphere, whose behavior is directly influenced by the surface forcing with a response time of less than an hour [12]. This layer is turbulent, showing rapid fluctuations of the physical quantities, while the rest of the atmosphere (free atmosphere) is usually non turbulent or intermittently turbulent ([6]). Its thickness varies during the day cycle and during the year. It is generally thin at night and in the cool season and thicker during the day and in the warm season [12].

The characterization of the atmospheric stability and of the boundary layer height is crucial for a good comprehension of our atmosphere [8] and applications in air quality.

The following document describes the algorithms used in the COSMO model code to calculate the Bulk Richardson Number (BRN) and the height of the Planetary Boundary Layer (HPBL).

3.9.1 Bulk Richardson Number

The gradient Richardson Number is a dimensionless number relating the buoyant consumption term to the mechanical production term of the TKE budget equation [10].

$$Ri = \frac{(g/\theta_v)(\partial\theta_v/\partial z)}{(\partial u/\partial z)^2 + (\partial v/\partial z)^2} \tag{6}$$

Where θ_v is the virtual potential temperature in K, g is the acceleration due to gravity in m/s^2 , z is the height in m, u is the zonal wind in m/s and v is the meridional wind in m/s.

The Bulk Richardson Number BRN is an approximation of the gradient Richardson Number formed by approximating local gradients by finite difference across layers [12]. When approximating $\partial\theta_v/\partial z$ by $\Delta\theta_v/\Delta z$ and $\partial u/\partial z$ and $\partial v/\partial z$ by $\Delta u/\Delta z$ and $\Delta v/\Delta z$ respectively, we obtain the BRN:

$$BRN = \frac{g\Delta\theta_v\Delta z}{\theta_v[(\Delta u)^2 + (\Delta v)^2]} \tag{7}$$

We compute it between the ground and a height z:

$$BRN(z) = \frac{g(\theta_v(z) - \theta_{v_{ground}})(z - z_{ground})}{\theta_v(z)[(u(z) - u_{ground})^2 + (v - v_{ground})^2]} \tag{8}$$

Some authors [6] consider that $\theta_{v_{ground}} = \theta_v(z_{0,h})$ where $z_{0,h}$ is the energy roughness length [1]. In NWP models we consider however the surface values or the 2 meters values for the temperature related quantities and the 10 meters values for the winds.
According to [12], the bulk form of the Richardson Number, BRN, is used most frequently in meteorology because of the discrete nature of rawinsonde measurements and of numerical models.

[6] suggests this interpretation for the BRN:

BRN	Flow Type	Level of Turbulence due to Buoyancy	Level of Turbulence due to Shear
< 0, large	turbulent	large	small
< 0, small	turbulent	small	large
> 0, small	turbulent	none	large
> 0, large	laminar	none	small

Implementation in the COSMO model The BRN is computed according to equation (8). We consider no velocity at the ground, i.e. $u_{ground} = 0$ and $v_{ground} = 0$. The virtual

potential temperature at the denominator should be the mean virtual potential temperature for the whole layer. We thus have $\overline{\theta_v(z)} = [\sum_{k=1}^{n} \theta_v(k)]/(n+1)$, where n is the number of levels between the ground and the level k, instead of $\theta_v(z)$.
We thus obtain:

$$BRN(z) = \frac{g(\theta_v(z) - \theta_{v_{2m}})(z - z_{ground})}{\overline{\theta_v(z)}[u(z)^2 + v(z)^2]} \tag{9}$$

3.9.2 Height of the Planetary Boundary Layer

The height of the planetary boundary layer HPBL is a fundamental parameter characterizing the structure of the lowest troposphere [8]. It can be derived from profiles or parameterized. The second approach is used in NWP models. The parameterization is based on prognostic or diagnostic equations. The prognostic equations are more complicated and diagnostic methods are thus preferred.

The Bulk Richardson Number method is the standard way to derive HPBL from model outputs [8]. [10] considers it as a robust and fairly accurate method, which is particularly suited when the vertical resolution of the meteorological fields (temperature, winds) is limited.

This method consists in calculating the BRN and then in searching the height at which the BRN reaches a critical value, the critical Bulk Richardson Number. This level is the top of the boundary layer [10]. In the literature, one finds critical values between say 0.2 and 1. The method is however not very sensitive to this critical value. Values between 0.1 and 0.4 are generally admitted [10].
We have to notice that the diagnostic methods usually perform well under convective conditions, whereas their ability to predict the HPBL under stable conditions is poorer [8]. It can happen that the BRN profile never crosses the critical Bulk Richardson Number. In those cases it is thus impossible to find a HPBL with this method.

Implementation in the COSMO model There is no consensus in the literature about the critical Bulk Richardson Number. We decide to take into account the current stability conditions for the choice of the critical value. If the conditions are stable, we use a critical value $Ri_{B,cr}$ of 0.33 [14], whereas under convective conditions we use the value prescribed by [13] $Ri_{B,cr} = 0.22$.

The stability assessment is carried out in a simple way by computing the coefficient of the linear regression between the virtual potential temperature and the height in the 4 first model levels. If the coefficient is positive, the conditions are stable and if it is negative the conditions are known as convective. It is given by:

$$\beta = \frac{\sum_{i=1}^{4} z\theta_v - 1/4 \sum_{i=1}^{4} z \sum_{i=1}^{4} \theta_v}{\sum_{i=1}^{4} z^2 - 1/4 \sum_{i=1}^{4} z \sum_{i=1}^{4} z} \tag{10}$$

We then scan the levels starting at the bottom model level until a level satisfying this condition is reached: $BRN(z) > Ri_{B,cr}$. This level is the top of the PBL. If no such level is

found a missing value is returned.

We currently have not set some minimal and maximal threshold heights. It could be however useful when using this HPBL for certain applications (dispersion models for example).

3.10 Supercell Detection Index

The **Supercell Detection Index (SDI)** was devised by Wicker et al. [15] to help forecasters to detect the mesocyclone of a supercell from high resolution forecast models. At each horizontal grid point (i,j), the first Supercell Detection Index SDI_1 is defined as the product

$$\mathrm{SDI}_{1,ij} := \rho_{ij}\overline{\zeta_{ij}} \tag{11}$$

of the velocity-vorticity correlation

$$\rho_{ij} := \frac{< w'\zeta' >}{(< w'^2 >_{ij} < \zeta'^2 >_{ij})^{1/2}}$$

and the vertically averaged vorticity

$$\zeta_{ij} := (\nabla \times \mathbf{v})_{\mathbf{z}}.$$

Here, $< \ldots >$ denotes the average, taken over a sliding 3D slab of extensions 20 km * 20 km * [1.5 ... 5.5] km, and the overbar on ζ denotes a vertical average, taken in the height range [1.5 ... 5.5] km.
In contrast to other quantities that are used to predict tornados, like for instance the Storm Relative Environmental Helicity (SREH), or the near surface wind shear, the SDI_1 directly attempts at detecting the stream shape of a supercell in the model. That is the reason, why the SDI_1 can only be applied if the model resolution is sufficiently high. Hence it cannot be used for COSMO-7, since the resolution there is too low. The following threshold values of the SDI_1 for the detection of supercells are given in [15]:

$\lvert\mathrm{SDI}_1\rvert = 0.0003$ 1/s:	minimal threshold for supercells
$\lvert\mathrm{SDI}_1\rvert > 0.003$ 1/s:	significant signal for supercells

For regions of updraft, the product of correlation and vorticity is positive, and thus $\mathrm{SDI}_1 > 0$ holds true. For regions of downdraft $\mathrm{SDI}_1 < 0$.
Since the up- and downdrafts for supercells are coupled to each other, one is, however, rather interested in using the sign information to detect the sense of rotation of the supercells. Wicker et al. [15] thus define the second Supercell Detection Index SDI_2 at grid point (i,j) as

$$\mathrm{SDI}_{2,ij} := \begin{cases} \rho_{ij}|\overline{\zeta_{ij}}| & : \quad w > 0 \\ 0 & : \quad w \leq 0 \end{cases} \tag{12}$$

Thus it holds that $\mathrm{SDI}_2 > 0$ for regions of cyclonic updrafts, and $\mathrm{SDI}_2 < 0$ for regions of anticyclonic updrafts.
In practice, evaluation of the SDI_2 should be sufficient. The threshold values given for SDI_1 are of course also valid for SDI_2.

Implementation in the COSMO model Within COSMO, the Supercell Detection Indices SDI_1 and SDI_2 have been implemented by Axel Seifert (DWD) according to (11) and (12), respectively.

A Table of Constants

Name	Description	Value	Unit
g	Acceleration due to gravity	9.80665	m s^{-2}
R_d	Gas constant of dry air	287.05	$JK^{-1}kg^{-1}$
R_v	Gas constant of water vapour	461.51	$JK^{-1}kg^{-1}$
c_p	Specific heat of dry air at constant pressure	1005	$JK^{-1}kg^{-1}$
L_v	Latent heat of vapourization	$2.501 \cdot 10^6$	Jkg^{-1}

Table 1: Table of constants

B Grib parameters of indices

Name	Unit	GRIB Table	Grib Nr.	Level Type
CAPE_MU	1/s	201	143	1
CAPE_ML	J/kg	201	145	1
CIN_MU	J/kg	201	144	1
CIN_ML	J/kg	201	146	1
CAPE_3KM	J/kg	203	137	1
LCL_ML	m	203	135	1
LFC_ML	m	203	136	1
SWISS00	1	203	138	1
SWISS12	1	203	139	1
BRN	1	203	155	1
HPBL	m	203	156	1
HI	1	250	24	105
SDI_1	1/s	201	141	1
SDI_2	1/s	201	142	1

References

[1] Brutsaert W., 2005: Hydrology: An Introduction. *Cambridge University Press*, ISBN 13 978 0 521 82479 8

[2] Davies, J. M., 2002: On low-level thermodynamic parameters associated with tornadic and nontornadic supercells. *Preprints, 21st Conference on severe local storms, San Antonio, Amer. Meteor. Soc.*

[3] Doswell, C. A. and E. N. Rasmussen, 1994: The Effect of Neglicting the Virtual Temperature Correction on CAPE Calculations. *Wea. Forecasting*, **9**, 625-629.

[4] Emanuel, K. A., 1994: Atmoshperic Convection, Oxford University Press, pp. 580

[5] Huntrieser, H., H.H. Schiesser, W. Schmid and A. Waldvogel, 1997: Comparison of Traditional and Newly Developed Thunderstorm Indices for Switzerland. *Wea. Forecasting*, **12**, 108-125.

[6] Jacobson, M. Z., 1999: Fundamentals of atmospheric modeling, Cambridge University Press

[7] Rothfusz L.P., 1990: The Heat Index "Equation". *Technical Attachment of the Scientific Services Division, NWS Southern region Headquarters, Fort Worth, TX.*

[8] Seibert, P., Beyrich, F., Gryning, S. E., Joffre, S., Rasmussen, A., Tercier, P., 2000: Review and intercomparison of operational methods for the determination of the mixing height. *Atmospheric Environment*, **34**, 1001-1027.

[9] Showalter, A. K., 1953: A stability index for thunderstorm forecasting. *Bull. Amer. Meteor. Soc.*, **34**, 250-252

[10] Sørensen, J. H., Rasmussen, A., Svensmark, H., 1996: Forecast of Atmospheric Boundary-Layer Height Utilised for ETEX Real-Time Dispersion Modelling. *Phys. Chem. Earth*, **21**, No. 5-6, pp. 435-439

[11] Steadman R.G., 1979: The assessment of sutriness. Part I: A temperature-humidity index based on the human physiology and clothing science. *Journal of Applied Meteorology*, **18**, 861-873.

[12] Stull, R. B., 1988: An Introduction to Boundary Layer Meteorology, Kluwer Academic Publishers

[13] Vogelezang, D. H. P., and Holtslag, A. A. M., 1996: Evaluation and model impacts of alternative boundary-layer height formulations. *Boundary-Layer Meteorol.*, **81**, 245-269.

[14] Wetzel, P. J., 1982: Toward parameterization of the stable boundary layer. *J. Appl. Meteorol.*, **21**, 7-13.

[15] Wicker, L., Kain, J., Weiss, S., and Bright, D., 2005: A Brief Description of the Supercell Detection Index. *http://spc.noaa.gov/exper/Spring_2005/SDI-docs.pdf.*

List of COSMO Newsletters and Technical Reports

(available for download from the COSMO Website: www.cosmo-model.org)

COSMO Newsletters

No. 1: February 2001.

No. 2: February 2002.

No. 3: February 2003.

No. 4: February 2004.

No. 5: April 2005.

No. 6: July 2006.

No. 7: April 2008; Proceedings from the 8th COSMO General Meeting in Bucharest, 2006.

No. 8: September 2008; Proceedings from the 9th COSMO General Meeting in Athens, 2007.

No. 9: December 2008

No. 10: March 2010.

COSMO Technical Reports

No. 1: Dmitrii Mironov and Matthias Raschendorfer (2001):
Evaluation of Empirical Parameters of the New LM Surface-Layer Parameterization Scheme. Results from Numerical Experiments Including the Soil Moisture Analysis.

No. 2: Reinhold Schrodin and Erdmann Heise (2001):
The Multi-Layer Version of the DWD Soil Model TERRA_LM.

No. 3: Günther Doms (2001):
A Scheme for Monotonic Numerical Diffusion in the LM.

No. 4: Hans-Joachim Herzog, Ursula Schubert, Gerd Vogel, Adelheid Fiedler and Roswitha Kirchner (2002):
LLM ¯ the High-Resolving Nonhydrostatic Simulation Model in the DWD-Project LITFASS.
Part I: Modelling Technique and Simulation Method.

No. 5: Jean-Marie Bettems (2002):
EUCOS Impact Study Using the Limited-Area Non-Hydrostatic NWP Model in Operational Use at MeteoSwiss.

No. 6: Heinz-Werner Bitzer and Jürgen Steppeler (2004):
Documentation of the Z-Coordinate Dynamical Core of LM.

No. 7: Hans-Joachim Herzog, Almut Gassmann (2005):
Lorenz- and Charney-Phillips vertical grid experimentation using a compressible nonhydrostatic toy-model relevant to the fast-mode part of the 'Lokal-Modell'.

No. 8: Chiara Marsigli, Andrea Montani, Tiziana Paccagnella, Davide Sacchetti, André Walser, Marco Arpagaus, Thomas Schumann (2005):
Evaluation of the Performance of the COSMO-LEPS System.

No. 9: Erdmann Heise, Bodo Ritter, Reinhold Schrodin (2006):
Operational Implementation of the Multilayer Soil Model.

No. 10: M.D. Tsyrulnikov (2007):
Is the particle filtering approach appropriate for meso-scale data assimilation ?

No. 11: Dmitrii V. Mironov (2008):
Parameterization of Lakes in Numerical Weather Prediction. Description of a Lake Model.

No. 12: Adriano Raspanti (2009):
COSMO Priority Project "VERification System Unified Survey" (VERSUS): Final Report.

No. 13: Chiara Marsigli (2009):
COSMO Priority Project "Short Range Ensemble Prediction System" (SREPS): Final Report.

No. 14: Michael Baldauf (2009):
COSMO Priority Project "Further Developments of the Runge-Kutta Time Integration Scheme" (RK): Final Report.

No. 15: Silke Dierer (2009):
COSMO Priority Project "Tackle deficiencies in quantitative precipitation forecast" (QPF): Final Report.

No. 16: Pierre Eckert (2009):
COSMO Priority Project "INTERP": Final Report.

No. 17: D. Leuenberger, M. Stoll and A. Roches (2010):
Description of some convective indices implemented in the COSMO model.

COSMO Technical Reports

Issues of the COSMO Technical Reports series are published by the *COnsortium for Small-scale MOdelling* at non-regular intervals. COSMO is a European group for numerical weather prediction with participating meteorological services from Germany (DWD, AWGeophys), Greece (HNMS), Italy (USAM, ARPA-SIMC, ARPA Piemonte), Switzerland (MeteoSwiss), Poland (IMGW) and Romania (NMA). The general goal is to develop, improve and maintain a non-hydrostatic limited area modelling system to be used for both operational and research applications by the members of COSMO. This system is initially based on the COSMO-Model (previously known as LM) of DWD with its corresponding data assimilation system.

The Technical Reports are intended

- for scientific contributions and a documentation of research activities,
- to present and discuss results obtained from the model system,
- to present and discuss verification results and interpretation methods,
- for a documentation of technical changes to the model system,
- to give an overview of new components of the model system.

The purpose of these reports is to communicate results, changes and progress related to the LM model system relatively fast within the COSMO consortium, and also to inform other NWP groups on our current research activities. In this way the discussion on a specific topic can be stimulated at an early stage. In order to publish a report very soon after the completion of the manuscript, we have decided to omit a thorough reviewing procedure and only a rough check is done by the editors and a third reviewer. We apologize for typographical and other errors or inconsistencies which may still be present.

At present, the Technical Reports are available for download from the COSMO web site (www.cosmo-model.org). If required, the member meteorological centres can produce hard-copies by their own for distribution within their service. All members of the consortium will be informed about new issues by email.

For any comments and questions, please contact the editors:

Massimo Milelli
Massimo.Milelli@arpa.piemonte.it

Ulrich Schättler
Ulrich.Schaettler@dwd.de

Consortium

for

Small-Scale Modelling

Technical Report No. 6

Documentation of the Z-Coordinate Dynamical Core of LM

by

H.-W. Bitzer and J. Steppeler

April 2004

DOI: 10.5676/DWD_pub/nwv/cosmo-tr_6

Deutscher Wetterdienst

MeteoSwiss

Ufficio Generale per la Meteorologia

Hellenic National Meteorological Service

Amt für Wehrgeophysik

Il Servicio Meteorologico Regionale di ARPA

www.cosmo-model.org

Editors: G. Doms and U. Schättler, Deutscher Wetterdienst, P.O. Box 100465, 63004 Offenbach, Germany
Printed at Deutscher Wetterdienst, Offenbach am Main

A Description of the Z-Coordinate Dynamical Core of LM

Heinz-Werner Bitzer and Jürgen Steppeler

Deutscher Wetterdienst, Offenbach am Main, Germany

Table of Contents

1 Introduction **1**

2 Basic Numerical Concept **2**

2.1 Equations of Motion 2

2.2 Volume Elements and Grid Design 4

2.3 Computation of Sub-Surface Values of Meteorological Fields 7

2.4 Spatial Discretization 11

3 Time Integration and Numerical Solution **14**

3.1 Fast Tendencies 14

3.2 Method of Solution 17

3.3 Structure of the Tridiagonal Matrix 20

4 Numerical Smoothing **21**

4.1 Horizontal Diffusion 21

4.2 Vertical Diffusion 24

5 Results for Idealized Test Cases **26**

6 Summary **28**

References **30**

Appendix **31**

1 Introduction

Nonhydrostatic models using terrain-following coordinates, such as the Penn State-NCAR Mesoscale Model "MM5" (Dudhia, 1993) or the Lokal-Modell "LM" (Steppeler et al., 2002) are not well suited for predictions of flow near mountains in the environment of a stratified atmosphere. Numerical errors can be induced around steep slopes, due to numrical errors in connection with the terrain following coordinate transformation. The stratified atmosphere generates artificial forces, caused by numerical errors. These can produce artificial circulations which destroy clouds in the vicinity of mountains. For example, in the model LM, the condition that such numerical forces remain reasonably small is $\delta h < dz$, with δz being the layer thickness and δh the change of orography between one gridpoint and the next. This condition is violated in most operational models, even for larger scale operational hydrostatic applications. With fine meshes the model orography tends to be steeper than for coarser meshes. Therefore the circulations driven by numerical errors can be substantial (Sundqvist, 1976).

For models using the terrain following coordinate, such as MM5 or LM, a spatially homogeneous reference profile is introduced, in order to reduce this effect. If this reference profile is rather near to the real state of the atmosphere in the model, the error mentioned is absent, and nearly perfect simulations of gravitational waves can be done. This is the situation investigated in this paper. As in addition rather smooth grid representations of the mountain are used, the terrain following coordinate can be supposed to simulate these tests very well. For operational applications on large areas it will not be possible to choose a horizontally homogeneous atmospheric reference state in the way indicated. Therefore operational applications will always suffer from numerically generated artificial forces near mountains.

A method to reduce this error has been proposed by Mesinger (1988). This method reduces the coordinate deformation by having the model layers not following the mountains, but rather ending at mountains. The lower boundary is treated under the assumption that it is represented by a step function. While this coordinate has the expected advantages in low wind situations, it has disadvantages concerning the flow around smooth topography. In particular, Gallus and Klemp (2000) reported a failure to produce proper mountain induced gravitational waves. As opposed to this, the test case proposed by Gallus and Klemp (2000) is simulated properly using the terrain following coordinate. Another z-coordinate approach was proposed by Tripoli (private communication). It has been presented at the Third International Workshop on Non-Hydrostatic Modelling in Offenbach, 1999, and does not suffer from the problems mentioned above. A short report on the workshop is given by Saito (2001). The method by Tripoli is based on posing lower boundary values for the velocity components using assumptions on the vorticity. In the present paper a different method is used to obtain the approximation near the lower boundary. The free slip boundary condition is used and numerically evaluated using the finite volume approximation.

With simple equations a sufficient convergence condition is met when the domain boundary is a continuous spline. Such a condition is present in the z-coordinate atmospheric model described here, being based on the shaved element method, used in computational fluid dynamics and oceanography (Adcroft, 1997). A cartesian structured grid corresponding to the case without orography is assumed and the topography is assumed to be represented by a bilinear spline with nodes at the gridpoints with half values of the x-axis. There are three types of grid squares: those which are completely under the earth, those completely above the topography and those which are cut by the topography function. The first two classes of elements can be treated in an obvious way. The volumes which are cut by the orography are treated by the finite volume method.

Without further approximations this method may require very small time steps, since the elements cut from a volume may be rather small. One solution would be to use a semi-implicit discretization (Thomas et al., 2000). Here we use the time splitting method, as introduced by Klemp and Wilhelmson (1978b). This has been shown by Saito (1998) to have good operational efficiency with the model LM. The problem of a restrictive CFL criterion with small cut off elements is solved by using the thin wall aproximation, which is common in oceanography. An atmospheric use of this method was tested by Bonaventura (2000). The derivation of this method from the shaved element approach requires in addition to the vertical walls also the use of horizontal walls as opposed to Bonaventura (2000), who uses vertical walls only. Test integrations using this method in two space dimensions will be given in Section 3. The test problems proposed by Gallus and Klemp (2000) are simulated properly by the z-coordinate version of LM.

The present paper gives an extensive description of the z-coordinate, as implemented in the LM. THe tests involving an idealized bell shaped mountain are described. They perform well and the z-coordinate LM is now ready for further development towards operational implementation.

2 Basic Numerical Concept

2.1 Equations of Motion

The following numerical model simulates a 3d atmospheric flow in z-coordinates. Since the z-surfaces are horizontal, the governing equations are formulated in an orthogonal coordinate system on a sphere. The underlying mathematical structure consists of the full compressible Euler equations. The model takes gravity, coriolis force and metric terms into account, Reynolds stresses and viscosity are neglected. Physical processes like cloud physics, radiation and boundary layer physics are not included. The current version is suitable for idealized experiments in fluid flows and is the starting point to develop a weather forecast model in a z-coordinate system. The equations are the same as for the operational LM (Doms and Schaettler 2001) with the simplifications mentioned above. The equations read:

$$\frac{\partial u}{\partial t} = -\vec{v}\cdot\nabla u + \frac{uv}{a}\tan\varphi + fv - \frac{1}{\rho a\cos\varphi}\frac{\partial p}{\partial\lambda} \tag{1}$$

$$\frac{\partial v}{\partial t} = -\vec{v}\cdot\nabla v - \frac{u^2}{a}\tan\varphi - fu - \frac{1}{\rho a}\frac{\partial p}{\partial\varphi} \tag{2}$$

$$\frac{\partial w}{\partial t} = -\vec{v}\cdot\nabla w - \frac{1}{\rho}\frac{\partial p}{\partial z} - g \tag{3}$$

$$\frac{\partial p}{\partial t} = -\vec{v}\cdot\nabla p - \frac{c_p}{c_v}pD_3 \tag{4}$$

$$\frac{\partial T}{\partial t} = -\vec{v}\cdot\nabla T - \frac{1}{\rho c_v}pD_3 \tag{5}$$

The advection operator is definied by

$$\vec{v}\cdot\nabla = \frac{1}{a\cos\varphi}\left(u\frac{\partial}{\partial\lambda} + v\cos\varphi\frac{\partial}{\partial\varphi}\right) + w\frac{\partial}{\partial z} \tag{6}$$

and the threedimensional wind divergence by

$$D_3 = \frac{1}{a\cos\varphi}\left[\frac{\partial u}{\partial\lambda} + \frac{\partial}{\partial\varphi}(v\cos\varphi)\right] + \frac{\partial w}{\partial z} \tag{7}$$

The vertical acceleration due to the pressure gradient and gravity in (1.3) is expanded as

$$-\frac{1}{\rho}\frac{\partial p}{\partial z} - g = g\frac{\rho_0}{\rho}\left(\frac{T-T_0}{T} - \frac{T_0}{T}\frac{p'}{p_0}\right) - \frac{1}{\rho}\frac{\partial p'}{\partial z} \tag{8}$$

p' is the predicted pressure perturbation. p is the total pressure calculated as the sum of base-state pressure and predicted pressure perturbation:

$$p = p_0 + p' \tag{9}$$

The full set of model equations become

$$\frac{\partial u}{\partial t} = -\vec{v}\cdot\nabla u + \frac{uv}{a}\tan\varphi + fv - \frac{1}{\rho a\cos\varphi}\frac{\partial p'}{\partial\lambda} \tag{10}$$

$$\frac{\partial v}{\partial t} = -\vec{v}\cdot\nabla v - \frac{u^2}{a}\tan\varphi - fu - \frac{1}{\rho a}\frac{\partial p'}{\partial\varphi} \tag{11}$$

$$\frac{\partial w}{\partial t} = -\vec{v}\cdot\nabla w + g\frac{\rho_0}{\rho}\left[\frac{T-T_0}{T} - \frac{T_0}{T}\frac{p'}{p_0}\right] - \frac{1}{\rho}\frac{\partial p'}{\partial z} \tag{12}$$

$$\frac{\partial p'}{\partial t} = -\vec{v}\cdot\nabla p' + g\rho_0 w - \frac{c_p}{c_v}pD_3 \tag{13}$$

$$\frac{\partial T}{\partial t} = -\vec{v}\cdot\nabla T - \frac{1}{\rho c_v}pD_3 \tag{14}$$

The governing nonhydrostatic equations describe a compressible model atmosphere, thus meteorological unimportant sound waves are also part of the solution. According to the Courant Friedrich Levy criterion the fastest signal velocity, i.e. the sound velocity, determines the integration time step. In order to keep numerical efficiency, the mode-splitting time-integration method proposed be Klemp and Wilhelmson (1978) is applied. In practice the mode splitting time integration scheme in symbolic form can be written as:

$$\frac{\partial\psi}{\partial t} = s_\psi + f_\psi \tag{15}$$

Where ψ denotes a prognostic model variable, f_ψ the forcing terms due to the slow modes and s_ψ the source terms which are related to the acoustic and gravity wave mode (fast mode).

The full set of model equations can then be split:

a) slow tendencies

$$f_u = -\vec{v}\cdot\nabla u + \frac{uv}{a}\tan\varphi + fv \tag{16}$$

$$f_v = -\vec{v}\cdot\nabla v - \frac{u^2}{a}\tan\varphi - fu \tag{17}$$

$$f_w = -\vec{v}\cdot\nabla w \tag{18}$$

$$f_{p'} = -\vec{v}\cdot\nabla p' \tag{19}$$

$$f_T = -\vec{v}\cdot\nabla T \tag{20}$$

b) fast tendencies:

$$s_u = -\frac{1}{\rho a \cos\varphi}\frac{\partial p'}{\partial \lambda} \tag{21}$$

$$s_v = -\frac{1}{\rho a}\frac{\partial p'}{\partial \varphi} \tag{22}$$

$$s_w = -\frac{1}{\rho}\frac{\partial p'}{\partial z} + g\frac{\rho_0}{\rho}\left[\frac{T-T_0}{T} - \frac{T_0}{T}\frac{p'}{p_0}\right] \tag{23}$$

$$s_{p'} = g\rho_0 w - \frac{c_p}{c_v} pD_3 \tag{24}$$

$$s_T = -\frac{1}{\rho c_v} pD_3 \tag{25}$$

The f_ψ -terms denote the tendencies due to the slow modes. These terms are kept constant during the subcycle procedure. The equations for w' p' and T are coupled and solved implicitly.

Currently the model still runs with the originally introduced $\Delta\,(p_0)_k$ (thickness of layer k expressed by Δp_0) which is present in the entire programm code. So the vertical derivative is written as:

$$\frac{\partial}{\partial z} = -\frac{g\rho_0}{\Delta p_0}\frac{\partial}{\partial \zeta} \tag{26}$$

2.2 Volume Elements and Grid Design

The Arakawa C-Grid of the LM is used in the current model. Fig. 2.1 illustrates the staggering of the dependent model variables.

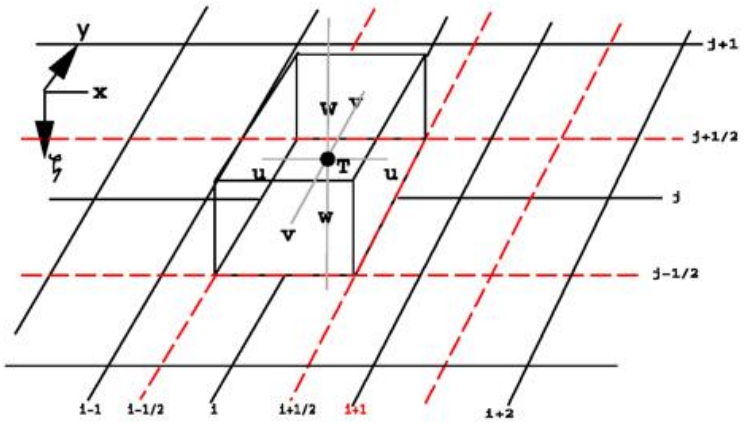


FIGURE 2.1: The three dimensional grid box.

Note, that the ζ -coordinate in the vertical is still used with $\Delta\zeta = 1$. Eq. (1.26) is applied to gain $\frac{\partial}{\partial z}(...)$.

The orography is definied at the corner points $(i + 1/2, j + 1/2)$ of a grid element (see Fig. 2.2).

Fig. 2.3 illustrates, how the surface of the orography intersects a column of volume elements.

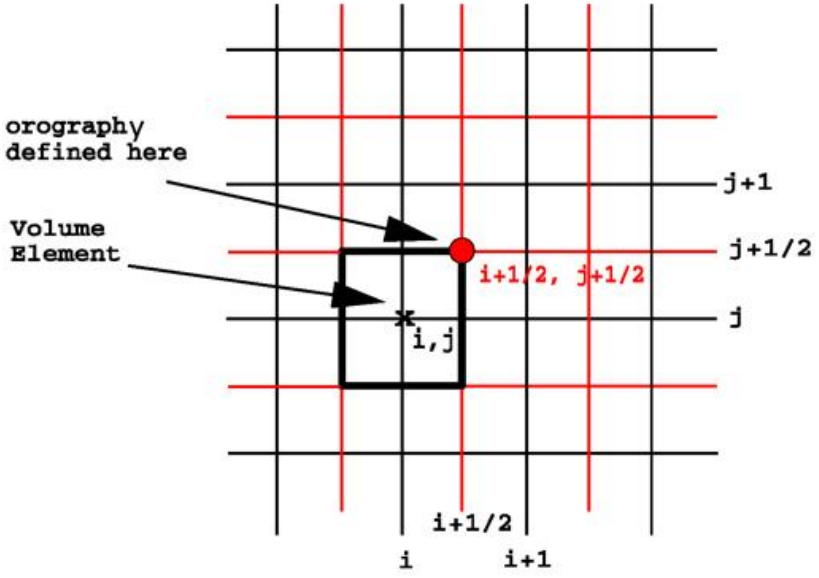


FIGURE 2.2: The horizontal grid and the definition of orography.

Fig. 2.4 illustrates for a bell shaped mountain, how the mountain's surface intersects the volume element. In the LM with terrain-following coordinates the horizontal pressure gradient is gained by applying the transformation formula which takes the vertical pressure difference along the sloped surface into account. Since the current model is formulated in z-coordinates, we have no metric term in the expression for (see Doms and Schättler, 2001) $\frac{\partial p}{\partial x}$ is not longer present. Instead a significant difference in the calculation of the spatial derivatives between the current model and the LM appears. As shown in Fig. 1.4 the volume element located at i, j, k is cut by the mountain's surface. In the advection term of equation (1.16),

$$-\vec{v} \cdot \nabla u = \underbrace{-u\frac{\partial u}{\partial x}}_{1} - v\frac{\partial u}{\partial y} - w\frac{\partial u}{\partial z} \tag{27}$$

the three terms have to be determined at position $i + 1/2, j, k$. For term 1 this is done in the following way, using the centered difference approximation

$$-u\frac{\partial u}{\partial x} = \overline{-\overline{u}^{x}\frac{\partial u}{\partial x}}^{x} = -\frac{1/2}{\Delta x}\left(u_{i,j,k}\Delta u_{i,j,k} + u_{i+1,j,k}\Delta u_{i+1,j,k}\right) \tag{28}$$

$$\text{with } u_{i,j,k} = \frac{1}{2}\left(u_{i-1/2,j,k} + u_{i+1/2,j,k}\right) \tag{29}$$

$$\Delta u_{i,j,k} = u_{i+1/2,j,k} - u_{i-1/2,j,k} \tag{30}$$

$$\Delta u_{i+1/j,k} = u_{i+11/2,j,k} - u_{i+1/2,j,k} \tag{31}$$

The velocity $u_{i-1/2,j,k}$ required in (1.29) and (1.30) which is denoted in Fig. 2.4 with u^*, is unknown, as it is underneath the mountain.

Fig. 2.5 gives a horizontal cross section through the grid. All values within the dashed area (see Fig. 2.5) lie underneath the mountain's surface. The solid line represents the

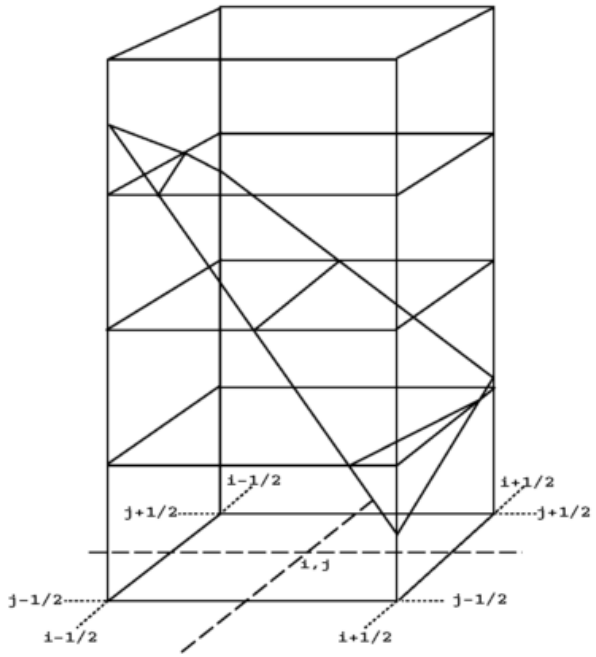


FIGURE 2.3: A column and the cells cut by a bilinear function representing the orography.

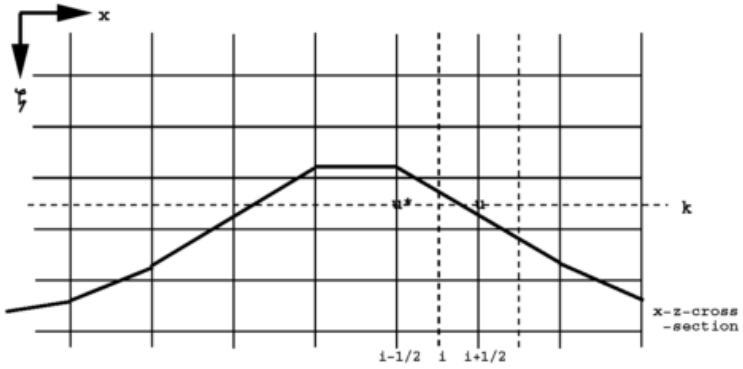


FIGURE 2.4: A vertical cross section through the grid and the boundary value u^* under the mountain.

intersection curve of the mountain's surface and a z-plane. Applying the formula

$$-v\frac{\partial u}{\partial y} = \overline{-\overline{v}^x \frac{\partial u}{\partial y}}^y = -\frac{1/2}{\Delta y}\left(v_{i+1/2,j+1/2,,k}\Delta u_{i+1/2,j+1/2,k} + v_{i+1/2,j-1/2,k}\Delta u_{i+1/2,j-1/2,k}\right) \quad (32)$$

with

$$v_{i+1/2,j-1/2,k} = \frac{1}{2}\left(\underline{v_{i,j-1/2,k}} + v_{i+1,j-1/2,k}\right) \quad (33)$$

and

$$\Delta u_{i+1/2,j-1/2,k} = u_{i+1/2,j,k} - \underline{u_{i+1/2,j-1,k}} \quad (34)$$

$v_{i,j-1/2,k}$ and $u_{i+1/2,j-1,k}$ are unknown quantities under the mountain. Our goal is, to determine a realistic value for $-u\frac{\partial u}{\partial x}$ and $-v\frac{\partial u}{\partial y}$ at point $i+1/2, j, k$. In order to do that the star values are computed.

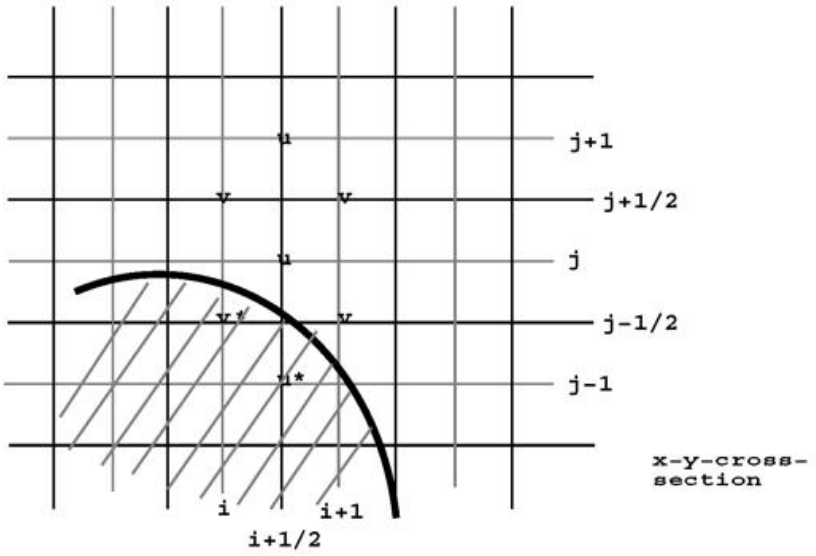


FIGURE 2.5: A horizontal cross section through the grid with boundary values in the horizontal

Please note, the star values are not computed in order to gain realistic values under the mountain. These quantities are artificial. The star values are just preliminary values, so called help values which are necessary to compute a realistic derivative at a point which lies very close at the boundary. In the horizontal plane (Fig. 2.5) the star quantities are those, which have at least one neighbour in the same plane positioned in the free atmosphere.

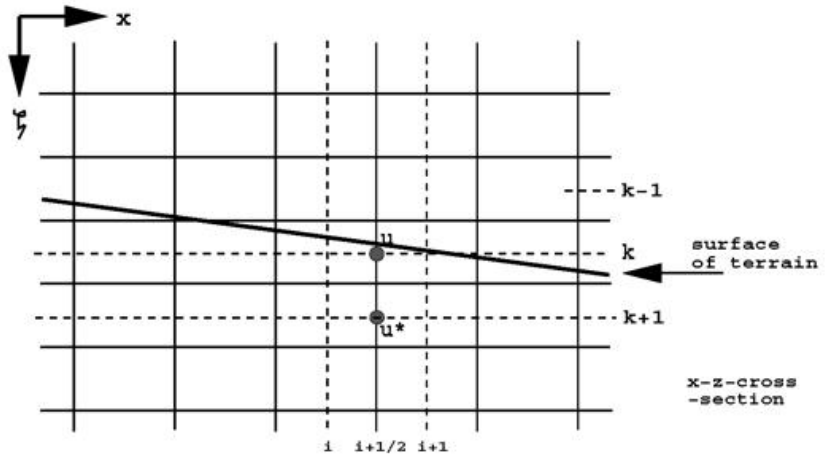


FIGURE 2.6: Boundary values u^* under flat terrain.

In many cases the surface of the terrain is flat (see Fig. 2.6). A star value under the surface is necessary for the correct evaluation of the vertical derivative. As illustrated in Fig. 2.6 u^* at $i+1/2, j, k+1$ is required for $\left.\frac{\partial u}{\partial \zeta}\right|_{i+1/2,j,k+1/2}$.

2.3 Computation of Sub-Surface Values of Meteorological Fields

The situation is represented in Fig. 2.7 where u^* as a help quantity has to be evaluated. In the current model a three point formula is applied.

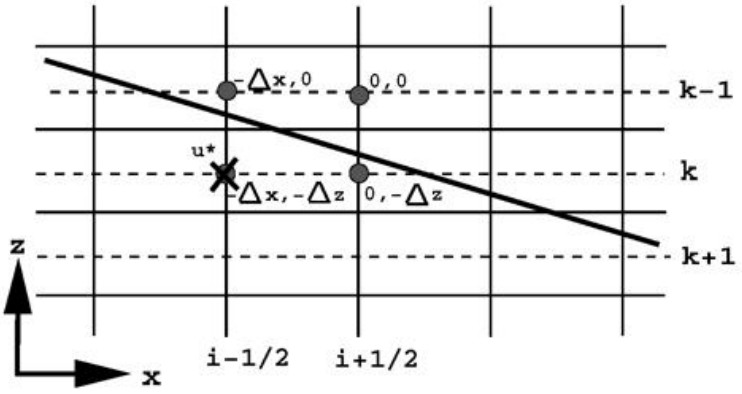


FIGURE 2.7: The interpolation of sub-surface boundary values $u^*$from surrounding values u.

Since the curvature of the spatial distribution of u is not taken into account the three points have to be chosen very close to the boundary. The method to yield u^* is based on the formula for a plane in a 3-dimensional space.

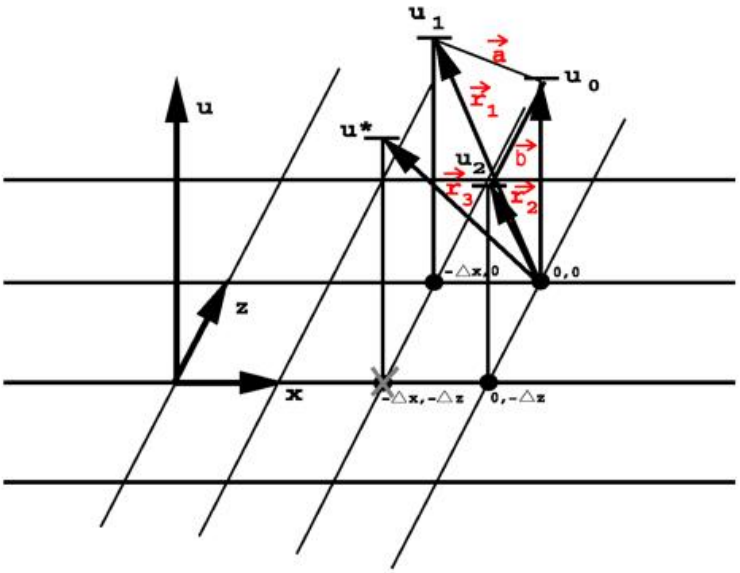


FIGURE 2.8: The plane used for the interpolation of u^*.

The plane is stretched by the vectors $\vec{a}$ and $\vec{b}$ in Fig. 2.8. The origin of the relative coordinate system is detoned with 0,0. The vectors $\vec{r_0}, \vec{r_1}, \vec{r_2}$ and $\vec{r_3}$ are the position vectors pointing to u_0, u_1, u_2 and u^*, they read:

$$\vec{r_0} = \begin{pmatrix} 0 \\ 0 \\ u_0 \end{pmatrix} ; \vec{r_1} = \begin{pmatrix} -\Delta x \\ 0 \\ u_1 \end{pmatrix} ; \vec{r_2} = \begin{pmatrix} 0 \\ -\Delta z \\ u_2 \end{pmatrix} ; \vec{r_3} = \begin{pmatrix} -\Delta x \\ -\Delta z \\ u_* \end{pmatrix} \tag{35}$$

The general formula of a plane in parameter representation is:

$$\vec{r} = \vec{r_0} + \lambda\vec{a} + \mu\vec{b} \tag{36}$$

where λ and μ are the parameters and $\vec{r}$ is a vector pointing to a point in the plane which

is stretched by $\vec{a}$ and $\vec{b}$. $\vec{a} = \vec{r_1} - \vec{r_0}$; $\vec{b} = \vec{r_2} - \vec{r_0}$ from (1.35) follows:

$$\vec{a} = \begin{pmatrix} -\Delta x \\ 0 \\ u_1 - u_0 \end{pmatrix} \quad ; \quad \vec{b} = \begin{pmatrix} 0 \\ -\Delta z \\ u_2 - u_0 \end{pmatrix} \tag{37}$$

The demand is: u^* is located within the plane. Thus, vector $\vec{r}$ in (1.36) can be replaced by $\vec{r_3}$:

$$\begin{pmatrix} -\Delta x \\ -\Delta z \\ u^* \end{pmatrix} = \begin{pmatrix} 0 \\ 0 \\ u_0 \end{pmatrix} + \lambda^* \begin{pmatrix} -\Delta x \\ 0 \\ u_1 - u_0 \end{pmatrix} + \mu^* \begin{pmatrix} 0 \\ -\Delta z \\ u_2 - u_0 \end{pmatrix} \tag{38}$$

The first two components of the vector equation (1.37) represent a linear system of equations for the unknowns λ^* and μ^*. The result is $\lambda^* = 1$, $\mu^* = 1$. For u^* we find the relation:

$$\begin{aligned} u^* &= u_0 + (u_1 - u_0) + (u_2 - u_0) \Rightarrow \\ u^* &= u_1 + u_2 - u_0 \end{aligned} \tag{39}$$

$$\begin{aligned} \text{substituting} \quad u^* &= u_{i-1/2,j,k} \\ u_1 &= u_{i-1/2,j,k-1} \\ u_2 &= u_{i+1/2,j,k} \\ u_0 &= u_{i+1/2,j,k-1} \qquad \text{yields} \end{aligned} \tag{40}$$

$$u_{i-1/2,j,k} = u_{i-1/2,j,k-1} + u_{i+1/2,j,k} - u_{i+1/2,j,k-1} \tag{41}$$

(1.41) is the answer for the preliminary value $u_{i-1/2,j,k}$ in case that the mountain is on the west side. For the other sides the formula looks very similar.

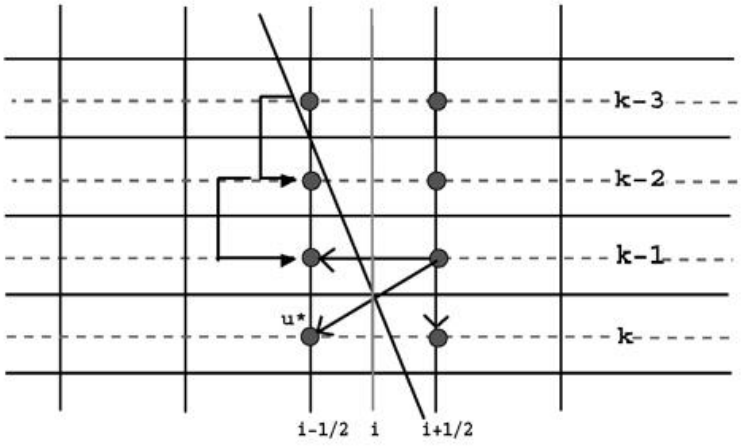


FIGURE 2.9: The interpolation in case of a steep mountain going from top to bottom.

Fig. 1.9 illustrates the situation in case of a steep slope. Applying (1.28) would fail for u^* if the calculation were started from below because $u_{i-1/2,j,k-1}$ is also unknown. Since the calculation procedure starts from upper levels downward, first $u_{i-1/2,j,k-1}$ is calculated because $u_{i-1/2,j,k-2}$ is available and finally u^* at k can be computed. In case of a flat terrain

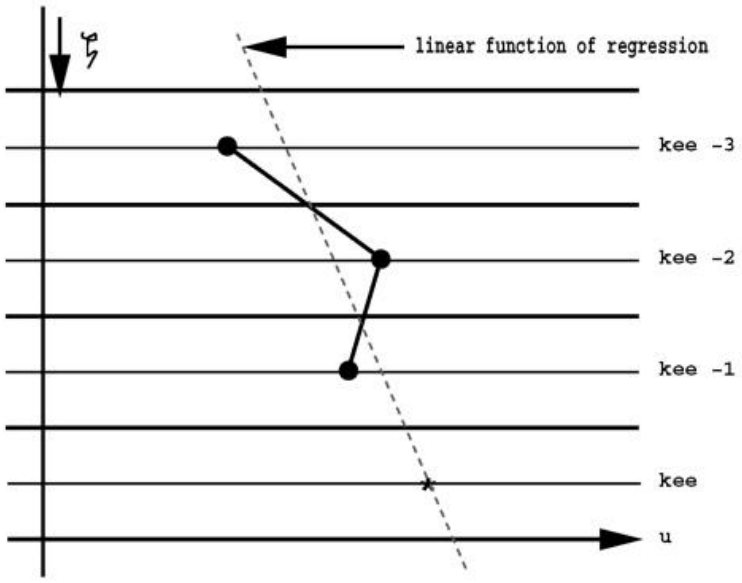


FIGURE 2.10: The linear regression used near the surface.

(Fig. 2.6) instead of the formula of a plane, a one dimensional linear function of regression is applied to compute u^*.

Let's assume that kee in Fig. 2.10 is the first level under the terrain with respect to the ζ-direction. Then $u_{i+1/2,j,kee-1}$, $u_{i+1/2,,j,kee}$ and $u_{i+1/2,j,kee-3}$ are taken to determine the linear function of regression:

$$
\begin{aligned}
u^*_{i+1/2,j,kee} &= um + 2us \qquad (42)\\
&\text{with}\\
um &= \frac{1}{3}\left(u_{i+1/2,j,kee-3} + u_{i+1/2,j,kee-2} + u_{i+1/2,j,kee-1}\right)\\
&\text{and}\\
us &= \frac{u_{i+1/2,j,kee-1} - u_{i+1/2,j,kee-3}}{2\Delta\zeta}\\
\text{because} \quad \Delta\zeta &= 1 \qquad \text{yields:}\\
us &= \frac{1}{2}\left(u_{i+1/2,j,kee-1} - u_{i+1/2,j,kee-3}\right)
\end{aligned}
$$

The preliminary star values of the other parameters are computed in the same way. Finally, all the necessary star values are processed and all the derivatives close to the boundary can be determined. The calculation procedure can be done in a subroutine which is called in the model before the slow tendencies are calculated. The advantage of this program structure is: no if statement is necessary while the slow tendencies are processed. At all the other gridpoints under the surface the field is filled with 0. For the calculation procedure they don't have any importance. In fact they must not have any importance. The program can be tested by writing strange numbers under the surface (except the star values). They should not have any impact on the solution of the flow field. Do loops in i-, j- and k-direction don't need to be interrupted at the boundaries. This is important in order to keep the integration sweeps in x-, y- and z-direction efficient.

2.4 Spatial Discretization

To present the difference form of equations (1.16)-(1.25) the following notations for horizontal and vertical averaging and differencing are defined.

$$\begin{aligned}
\overline{\psi}^{\lambda} &= \frac{1}{2}\left(\psi\left(\lambda+\frac{\Delta\lambda}{2}\right)+\psi\left(\lambda-\frac{\Delta\lambda}{2}\right)\right)\\
\overline{\psi}^{\varphi} &= \frac{1}{2}\left(\psi\left(\varphi+\frac{\Delta\varphi}{2}\right)+\psi\left(\varphi-\frac{\Delta\varphi}{2}\right)\right)\\
\overline{\psi}^{m\zeta} &= \frac{1}{2}\left(\psi_{k+1/2}+\psi_{k-1/2}\right)\\
\overline{\psi}^{h\zeta}_{k-1/2} &= \frac{\Delta\left(p_0\right)_{k-1}\psi_k+\Delta\left(p_0\right)_k\psi_{k-1}}{\Delta\left(p_0\right)_{k-1}+\Delta\left(p_0\right)_k}\\
\delta_{\lambda}\left(\psi\right) &= \psi\left(\lambda+\frac{\Delta\lambda}{2}\right)-\psi\left(\lambda-\frac{\Delta\lambda}{2}\right)\\
\delta_{\varphi}\left(\psi\right) &= \psi\left(\varphi+\frac{\Delta\varphi}{2}\right)-\psi\left(\varphi-\frac{\Delta\varphi}{2}\right)\\
\delta_{\varphi}\left(\psi\right) &= \psi\left(\zeta+\frac{1}{2}\right)-\psi\left(\zeta-\frac{1}{2}\right)
\end{aligned}$$

The vertical advection $-w\frac{\partial\psi}{\partial z}$ is still written with the contravariant vertical velocity $\dot{\zeta}$ (see LM operational version):

$$\begin{aligned}
-w\frac{\partial\psi}{\partial z} &= -\dot{\zeta}\frac{\partial\psi}{\partial\zeta} \qquad ; \qquad \dot{\zeta}_{k-1/2}=\frac{w^*_{k-1/2}}{\Delta\left(p_0\right)_{k-1/2}}=\frac{w_{k-1/2}}{\Delta z_{k-1/2}}\\
w^*_{k-1/2} &= -g\overline{(\rho_0)}^{h\zeta}_{k-1/2}w_{k-1/2} \qquad ; \qquad \Delta\left(p_0\right)_{k-1/2}=\frac{1}{2}\left(\Delta\left(p_0\right)_k+\Delta\left(p_0\right)_{k-1}\right)\\
\Delta z_{k-1/2} &= \frac{1}{2}\left(\Delta z_k+\Delta z_{k-1}\right)
\end{aligned} \tag{43}$$

With these notations the slow tendencies of (1.10) - (1.20) read:

$$\begin{aligned}
f_u &= -\frac{1}{a\overline{\cos\varphi}^{\varphi}\Delta\lambda}\overline{\overline{u}^{\lambda}\delta_{\lambda}\left(u\right)}^{\lambda}-\frac{1}{a\overline{\cos\varphi}^{\varphi}\Delta\varphi}\overline{\overline{v}^{\lambda}\cos\varphi\delta_{\varphi}\left(u\right)}^{\varphi}\\
&\quad \overline{-\dot{\zeta}^{\lambda}\delta_{\lambda}\left(u\right)}^{m\zeta}+\frac{u\overline{v}^{\lambda,\varphi}\overline{tan\varphi}^{\varphi}}{a}+\overline{f}^{\varphi}\overline{v}^{\lambda,\varphi}
\end{aligned} \tag{44}$$

$$\begin{aligned}
f_v &= -\frac{1}{a\cos^{\varphi}\Delta\lambda}\overline{\overline{u}^{\varphi}\delta_{\lambda}\left(v\right)}^{\lambda}-\frac{1}{a\cos\varphi\Delta\varphi}\overline{\overline{v}^{\varphi}\overline{\cos\varphi}^{\varphi}\delta_{\varphi}\left(v\right)}^{\varphi}\\
&\quad \overline{-\dot{\zeta}^{\varphi}\delta_{\zeta}\left(v\right)}^{m\zeta}-\frac{\left(\overline{u}^{\lambda,\varphi}\right)^2}{a}tan\varphi-\overline{f}^{\lambda}\overline{u}^{\lambda,\varphi}
\end{aligned} \tag{45}$$

$$f_w = -\frac{1}{a\overline{\cos^{\varphi}}^{\varphi}\Delta\lambda}\overline{\overline{u}^{h\zeta}\delta_{\lambda}\left(w\right)}^{\lambda}-\frac{1}{a\overline{\cos\varphi}^{\varphi}\Delta\varphi}\overline{\overline{v}^{h\zeta}\cos\varphi\delta_{\varphi}\left(w\right)}^{\varphi}-\overline{\dot{\zeta}^{m\zeta}\delta_{\zeta}\left(w\right)}^{m\zeta} \tag{46}$$

$$f'_p = -\frac{1}{a\overline{\cos^{\varphi}}^{\varphi}\Delta\lambda}\overline{u\delta_{\lambda}\left(p'\right)}^{\lambda}--\frac{1}{a\overline{\cos\varphi}^{\varphi}\Delta\varphi}\overline{v\cos\varphi\delta_{\varphi}\left(p'\right)}^{\varphi}-\overline{\dot{\zeta}\delta_{\zeta}\left(p'\right)}^{m\zeta} \tag{47}$$

$$f_T = -\frac{1}{a\overline{\cos^{\varphi}}^{\varphi}\Delta\lambda}\overline{u\delta_{\lambda}\left(T\right)}^{\lambda}-\frac{1}{a\overline{\cos\varphi}^{\varphi}\Delta\varphi}\overline{v\cos\varphi\delta_{\varphi}\left(T\right)}^{\varphi}-\overline{\dot{\zeta}\delta_{\varphi}\left(T\right)}^{m\zeta} \tag{48}$$

The slow tendencies are finally multiplied by the digital factors 0 or 1 depending on whether the location of the parameter is under the surface or in the free atmosphere respectively:

$$\begin{aligned} f_{u_{i,j,k}} &= f_{u_{i,j,k}} weightu_{i,j,k} \\ f_{v_{i,j,k}} &= f_{v_{i,j,k}} weightv_{i,j,k} \\ f_{w_{i,j,k}} &= f_{w_{i,j,k}} weight_{i,j,k} \\ f_{p'_{i,j,k}} &= f_{p'_{i,j,k}} weight_{i,j,k} \\ f_{T_{i,j,k}} &= f_{T_{i,j,k}} weight_{i,j,k} \end{aligned} \tag{49}$$

The tendencies of all the parameters under the surface are zero. This implies that those parameters keep their initial value and have to be set only once. The digital factors, here denoted with *weightu*, *weightv* and *weight* are processed in a special subroutine (*z_level.f90* of *src_artifdata.f90*) at the beginning of the program run. In the program code some coefficients can be separated from equations (1.44) - (1.48):

1. horizontal advection of u and v:

$$\begin{aligned} zfadsx(j) &= \frac{1/2}{a\cos\varphi_j \Delta\lambda} \\ zfadsy(j) &= \frac{1/2}{a\cos\varphi_j \Delta\varphi} \\ zfadvx(j) &= \frac{1/2}{a\cos\varphi_{j+1/2} \Delta\lambda} \\ zfpvoy(j) &= \frac{1/2}{a\cos\varphi_{j+1/2} \Delta\varphi} \end{aligned}$$

2. vertical advection of u:

$$\begin{aligned} zfkpx_{i+1/2,j,k+1/2} &= \frac{1}{2}\frac{w^*_{i,j,k+1/2} + w^*_{i+1,j,k+1/2}}{\Delta\left(p_0\right)_k + \Delta\left(p_0\right)_{k+1}} \\ zfkmx_{i+1/2,j,k-1/2} &= \frac{1}{2}\frac{w^*_{i,j,k-1/2} + w^*_{i+1,j,k-1/2}}{\Delta\left(p_0\right)_k + \Delta\left(p_0\right)_{k-1}} \end{aligned}$$

3. vertical advection of v:

$$\begin{aligned} zfkpx_{i,j+1/2,k+1/2} &= \frac{1}{2}\frac{w^*_{i,j,k+1/2} + w^*_{i,j+1,k+1/2}}{\Delta\left(p_0\right)_k + \Delta\left(p_0\right)_{k+1}} \\ zfkmx_{i,j+1/2,k-1/2} &= \frac{1}{2}\frac{w^*_{i,j,k-1/2} + w^*_{i,j+1,k-1/2}}{\Delta\left(p_0\right)_k + \Delta\left(p_0\right)_{k-1}} \end{aligned}$$

4. vertical advection of w:

$$\begin{aligned} zgcvx_{i,j,k} &= \frac{1}{4}\frac{w^*_{i,j,k-1/2} + w^*_{i,j,k+1/2}}{\Delta\left(p_0\right)_k} \\ zgavx_{i,j,k-1} &= \frac{1}{4}\frac{w^*_{i,j,k-11/2} + w^*_{i,j,k-1/2}}{\Delta\left(p_0\right)_{k-1}} \end{aligned}$$

In none of the previous equations a flux limiter does occur. The equations are not written in flux form.

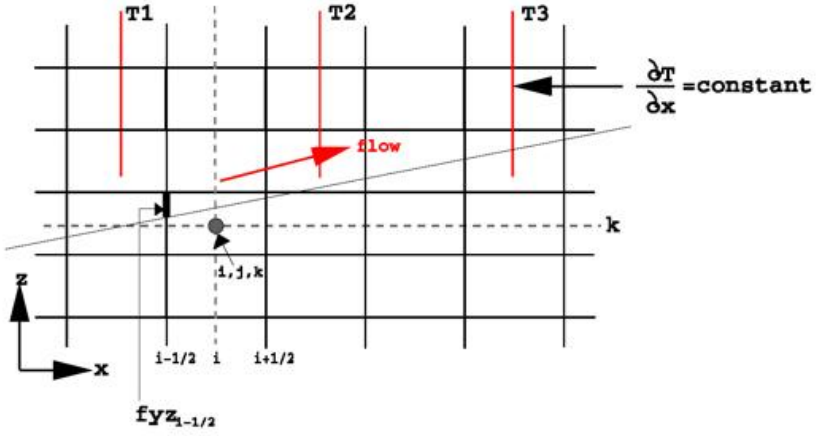


FIGURE 2.11a: Definition of the flux limiter in the grid.

Fig. 2.11a and Fig. 2.11b illustrate why the introduction of flux limiters in the advection terms would be faulty. The flux limiter $fyz_{i-1/2}$ is the fraction of the free interface of the volume $_{i,j,k}$ divided by the total area $\Delta y \Delta z$ of the interface. The so defined flux limiters take values between 0 and 1. If for example the temperature gradient $\frac{\partial T}{\partial x}$ is constant and the flow vector is parallel to the mountain's slope and constant with height, that means, a uniform flow uphill, then the advection $-u\frac{\partial T}{\partial x}$ is constant in the entire domain shown in Fig. 2.11a. Thus the volume element at $_{i,j,k}$ which is cut by mountains slope experiences the same temperature advection as all the other volume elements. For the mentioned volume element:

$$\frac{\partial T}{\partial t} = -\underline{fyz_{i-1/2}} u_{i-1/2} \left.\frac{\partial T}{\partial x}\right|_{i-1/2} \qquad \text{wrong!!} \tag{50}$$

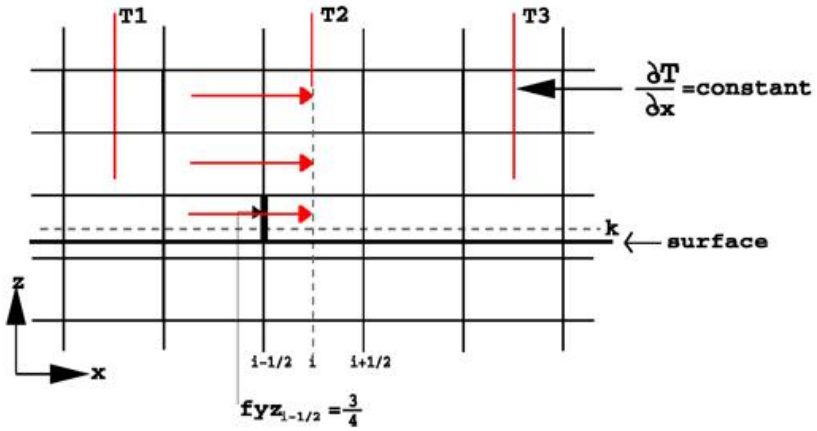


FIGURE 2.11b: Flux limiters for $\frac{\partial T}{\partial x}$ in the case of a horizontal terrain.

Fig. 2.11b illustrates the same situation in a simpler case. The current is uniform in x-direction and $\frac{\partial T}{\partial x} = const.$ The temperature gradient is assumed to be constant $\frac{\partial}{\partial z}\left(\frac{\partial T}{\partial x}\right) = 0$. The temperature tendency due to the advection $\frac{\partial T}{\partial t} = -u\frac{\partial T}{\partial x}$ is constant in the entire domain. If the surface would fill $\frac{1}{4}$ of the volume elements at level k, the free interfaces fyz of all the volume elements at that level would be $\frac{3}{4}$. If the carrier velocity u were premultiplied

by $fyz = \frac{3}{4}$ at level k, this would reduce the temperature tendency due to the advection of 25%, which would be wrong!

The explained treatment of the boundary values has to be done with much carefulness. The calculation of the corrrect derivatives close to the boundary are most important. The respond of the flow field is very sensitive with respect to the calculation of the boundary.

3 Time Integration and Numerical Solution

3.1 Fast Tendencies

According to the mode splitting time integration method proposed by Klemp and Wilhelmson (1978) the time step for stable explicit integration of the slow modes is subdivided into a number of small time steps. The tendencies represented in equations (1.21) - (1.25) are computed only once every big time step.

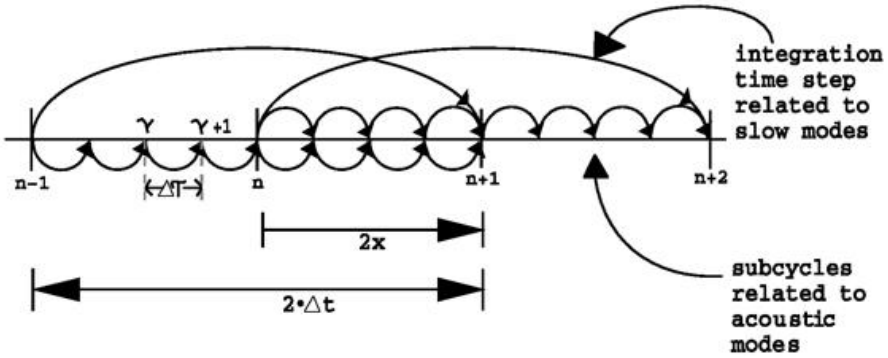


FIGURE 3.1: The Klemp Wilhelmson scheme.

Fig. 3.1 visualizes the mode splitting technique. The sound waves show up in the pressure gradient force, in the horizontal and vertical wind velocity and in the divergence term of the pressure tendency equation. High frequency oscillation is also caused by the buoyancy term. Additionally the vertical gravity wave propagation is also included in the reduced set of equations (1.21) - (1.25). As one can see from Fig. 3.1 the time step from n to $n+1$ is computet two times in the subcycle procedure. This will later be one of the reasons for approaches of a two time level integration scheme. The reduced set of equations which becomes subject to a split time integration using small time steps is revealed by rewriting the model equations (1.10) - (1.14) for the wind components, the pressure perturbation and the temperature in the following form:

$$\frac{\partial u}{\partial t} = \frac{1}{\rho a \cos^{\varphi}} \frac{\partial p'}{\partial \lambda} + f_u \tag{51}$$

$$\frac{\partial v}{\partial t} = \frac{1}{\rho a} \frac{\partial p'}{\partial \varphi} + fv \tag{52}$$

$$\frac{\partial w}{\partial t} = \frac{g}{\Delta p_0} \frac{\rho_0}{\rho} \frac{\partial p'}{\partial \zeta} + g \frac{\rho_0}{\rho} \left[\frac{T - T_0}{T} - \frac{T_0}{T} \frac{p'}{p_0} \right] + f_w \tag{53}$$

$$\frac{\partial p'}{\partial t} = g\rho_0 w - \frac{c_p}{c_v} p \left[D_h - \frac{g\rho_0}{\Delta p_0} \frac{\partial w}{\partial \zeta} \right] + f_{p'} \tag{54}$$

$$\frac{\partial T}{\partial t} = \frac{1}{\rho c_v} p \left[D_h - \frac{g\rho_0}{\Delta p_0} \frac{\partial w}{\partial \zeta} \right] + f_T \tag{55}$$

The threedimensional divergence D_3 in equation (1.7) is separated into a horizontal part D_h

$$D_h = \frac{1}{a\cos\varphi}\left[\frac{\partial u}{\partial\lambda} + \frac{\partial}{\partial\varphi}(v\cos\varphi)\right] \tag{56}$$

and a vertical part D_v

$$D_v = -\frac{g\rho_0}{\Delta p_0}\frac{\partial w}{\partial\zeta} \tag{57}$$

where the transformation (1.26) was applied in order to rewrite $\frac{\partial}{\partial z}$.

The set of equation (2.1) - (2.5) with acoustically active terms the big leapfrog time step $2\Delta t$ (see fig. 2.1) is subdivided into a number of small timesteps $\Delta\tau$. $2\Delta t$ must be an integer number times the small time step $\Delta\tau$. $\Delta\tau$ is determined by the fastest signal velocity, this means the sound speed:

$$\Delta\tau \leq \frac{\Delta s}{\sqrt{2}c_s} \qquad c_s = \text{ velocity of sound} \tag{58}$$

Δs is the horizontal spatial gridsize, $\Delta s = a\Delta\lambda = a\Delta\varphi$ with $\cos\varphi = 1$, supposed $\Delta\lambda = \Delta\varphi$. The vertical gridsize does not matter as long as the integration is carried out implicitely. For test cases the integration is sometimes carried out explicitely, then $\Delta\tau$ is limited by

$$\Delta\tau \leq \frac{\Delta z_{min}}{\sqrt{2}c_s} \tag{59}$$

where Δz_{min} is the minimum vertical grid spacing (usually this is the thickness of the lowest model layer).

Concerning the finite difference algorithms related to fast modes, second-order accurate differencing is used for spatial discretization of the reduced set of equations (2.1) - (2.5). The vertical velocity, the pressure pertubation and in the current model also $T - T_0$ are subject to time averaging with respect to the small time step $\Delta\tau$. Time averaging is realized in the same way as in the program code of the operationel LM

$$\overline{\psi}^{\tau} = \frac{1}{2}(1+\beta_{sw})\,\psi^{\nu+1} + \frac{1}{2}(1-\beta_{sw})\,\psi^{\nu}$$

see LM operational version (Doms and Schaettler, 1999). $\nu+1$ is the future time level related to the small steps $\Delta\tau$. The subcycle procedure is a 2 time level integration scheme. To simplify the notations we write

$$\beta^+ = \frac{1}{2}(1+\beta_{sw}) \qquad \text{and} \qquad \beta^- = \frac{1}{2}(1-\beta_{sw}) = 1-\beta^+$$

the model uses $\beta_{sw} = 0.4$ (i.e. $\beta^+ = 0.7$, $\beta^- = 0.3$). The time averaging is then realized with

$$\overline{\psi}^{\tau} = \beta^+\psi^{\nu+1} + \beta^-\psi^{\nu} \qquad \text{for} \qquad \psi = w, p', (T-T_0) \tag{60}$$

The finite difference equations derived from (2.1) - (2.6) are written in the following form, using definitions from Section 2.4.

$$u^{\nu+1} - u^{\nu} = -\frac{\Delta\tau}{\overline{\rho^n}^{\lambda} a\overline{\cos^{\varphi}}^{\varphi}\Delta\lambda}\delta_{\lambda}p'^{\nu} + f_u^n\Delta\tau \tag{61}$$

$$v^{\nu+1} - v^{\nu} = -\frac{\Delta\tau}{\overline{\rho^n}^{\varphi} a\Delta\varphi}\delta_{\varphi}p'^{\nu} + f_v^n\Delta\tau \tag{62}$$

$$\begin{aligned} w^{\nu+1} - w^{\nu} = {} & g\frac{\Delta\tau}{\Delta p_o}\frac{\overline{\rho_0}^{h\zeta}}{\overline{\rho^n}^{h\zeta}}\left[\beta^+\delta_{\zeta}\left(p'\right)^{\nu+1} + \beta^-\delta_{\zeta}\left(p'\right)^{\nu}\right] \\ & -g\Delta\tau\frac{\overline{\rho_0}^{h\zeta}}{\overline{\rho^n}^{h\zeta}}\left[\beta^+\overline{\frac{T_0}{T^n p_0}p'^{\nu+1}}^{h\zeta} + \beta^-\overline{\frac{T_0}{T^n p_0}p'^{\nu}}^{h\zeta}\right] \\ & -g\Delta\tau\frac{\overline{\rho_0}^{h\zeta}}{\overline{\rho^n}^{h\zeta}}\left[\beta^+\overline{\frac{T^{\nu+1}-T_0}{T^n}}^{h\zeta} + \beta^-\overline{\frac{T^{\nu}-T_0}{T^n}}^{h\zeta}\right] + f_w^n\Delta\tau \end{aligned} \tag{63}$$

$$\begin{aligned} p'^{\nu+1} - p'^{\nu} = {} & g\rho_0\Delta\tau\left[\beta^+\overline{w^{\nu+1}}^{m\zeta} + \beta^-\overline{w^{\nu}}^{m\zeta}\right] \\ & +g\frac{\rho_0\Delta\tau}{\Delta p_0}\frac{p^n c_p}{c_v}\left[\beta^+\delta_{\zeta}\left(fxyw^{\nu+1}\right) + \beta^-\delta_{\zeta}\left(fxyw^{\nu}\right)\right] \\ & -\Delta\tau\frac{p^n c_p}{c_v}D_h^{\nu+1} + f_{p'}^n\Delta\tau \end{aligned} \tag{64}$$

$$\begin{aligned} T^{\nu+1} - T^{\nu} = {} & g\frac{\rho_0\Delta\tau}{\Delta p_0}\frac{p^n}{\rho^n c_v}\left[\beta^+\delta_{\zeta}\left(fxyw^{\nu+1}\right) + \beta^-\delta_{\zeta}\left(fxyw^{\nu}\right)\right] \\ & -\Delta\tau\frac{p^n}{\rho^n c_v}D_h^{\nu+1} + f_T^n\Delta\tau \end{aligned} \tag{65}$$

The horizontal divergence D_h is computed at the centre of a grid box i, j, k even then when the volume contains only a little piece of air. The horizontal divergence reads:

$$D_h^{\nu+1} = \frac{1}{a\overline{\cos\varphi}^{\varphi}\Delta\lambda}\delta_{\lambda}\left(fyzu^{\nu+1}\right) + \frac{1}{a\overline{\cos\varphi}^{\varphi}\Delta\varphi}\delta_{\varphi}\left(\cos\varphi fxzv^{\nu+1}\right) \tag{66}$$

the vertical part D_v of equation (2.7) is:

$$D_v = \beta^+\delta_{\zeta}\left(fxyw^{\nu+1}\right) + \beta^-\delta_{\zeta}\left(fxyw^{\nu}\right) \tag{67}$$

The horizontal divergence D_h is first computed with the new velocities $u^{\nu+1}$ and $v^{\nu+1}$ at the new time level $\nu+1$. The equations (2.11), (2.12) and (2.16) remain in the explicit part of the integration procedure if the calculation is carried out implicitely. Most important now is the occurence of the so called flux limiters fxz, fyz and fxy. The last two letters denote the interfaces of a control volume, see Fig. 2.2. xz for example denotes an interface stretched in the xz-plane. All the flux limiters are non dimensional numbers between 0 and 1.

$fxy = \frac{s_{xy}}{\Delta x\Delta y}$ where s_{xy} is the real free interface expressed in m^2 and $\Delta x\Delta y$ is the total area of the interface. In case of fyz that reads: $fyz = \frac{s_{yz}}{\Delta y\Delta z}$. Only through these factors, in the divergence term the current feel the boundary. If the slope is small, $\frac{\Delta z}{\Delta x} < 1$ the factors are decreasing smoothly to zero as the flow is running in x-direction. Thus the current does not notice a step size topography but a smooth terrain as it should be. This is the most important difference of the shaved element method with respect to the Legoland topography. In equation (2.14) the flux limiters are affecting the pressure and the pressure again affects the vertical velocity. The term $g\rho_0 w$ is not premultiplied by the flux limiters. As we see, the

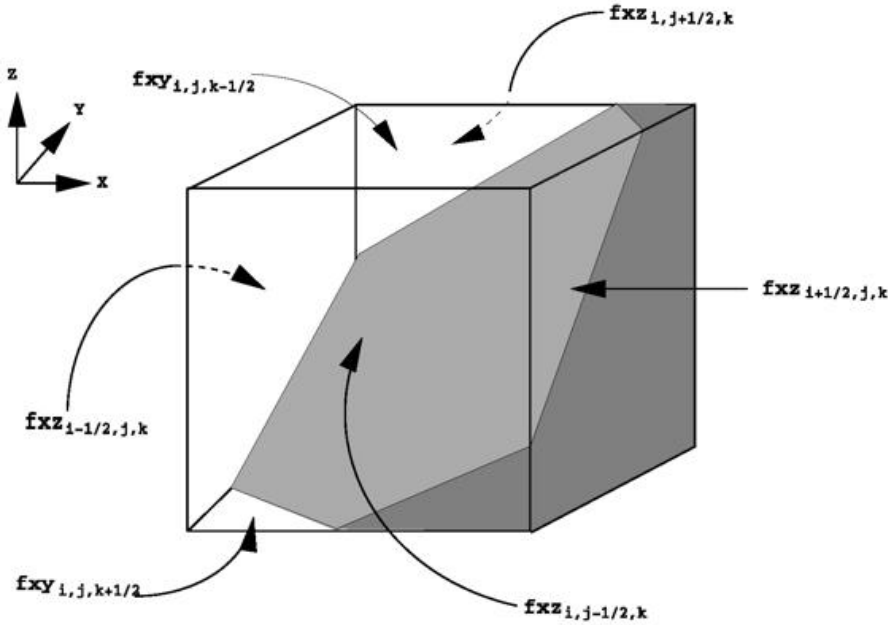


FIGURE 2.2: Flux limiters in three dimensions.

reference atmosphere is hiding here.

$$\begin{aligned} \frac{\partial p_0}{\partial z} &= -g\rho_0 \qquad \text{this implies} \\ g\rho_0 w &= -w\frac{\partial p_0}{\partial z} \end{aligned}$$

but $-w\frac{\partial p_0}{\partial z}$ is an advection term and above it was stated that the advection must be without a flux limiter.

3.2 Method of Solution

A vertically implicit integration scheme is applied for the solution of equation (2.1) - (2.5). Equations (2.3), (2,4) and (2.5) for the vertical velocity, the pressure perturbation and the temperature become coupled due to time averaging. In the current version the temperature deviation term

$$\frac{T^\nu - T_0}{T^n}$$

is drawn into the implicit calculation procedure. The temperature equation (2.15) in differencing form can be written as follows:

$$T_k^{\nu+1} = T_k^\nu + R_k \tag{68}$$

where R_k is the rest of the right hand side of equation. From (2.18) we gain:

$$T_k^{\nu+1} - (T_0)_k = T_k^\nu - (T_0)_k + R_k$$

respectively

$$\frac{T_k^{\nu+1} - (T_0)_k}{T_k^n} = \frac{T_k^\nu - (T_0)_k}{T_k^n} + \frac{R_k}{T_k^n} \tag{69}$$

In (2.19) we call $\frac{T_k^{\nu+1}-(T_0)_k}{T_k^n} = s_k^{\nu+1}$ and

$$\begin{aligned} \frac{T_k^\nu - (T_0)_k}{T^n} &= s_k^\nu \qquad \text{(2.19) then becomes} \\ s_k^{\nu+1} &= s_k^\nu + \frac{R_k}{T_k^n} \end{aligned} \tag{70}$$

with the substitutions (A.1) - (A.7), see appendix, the equation for the vertical velocity (2.13) can be written in the following way:

$$\begin{aligned} w_{k-1/2}^{\nu+1} - w_{k-1/2}^\nu &= g\Delta\tau 2y_{k-1/2}\left[\beta^+\left(p_k^{\nu+1} - p_{k-1}^{\nu+1}\right) + \beta^-\left(p_k^\nu - p_{k-1}^\nu\right)\right] \\ &\quad -g\Delta\tau\beta^+ 2y_{k-1/2}\left[(\Delta p_0)_{k-1}\frac{1}{2}x_k p_k^{\nu+1} + (\Delta p_0)_k\frac{1}{2}x_{k-1}p_{k-1}^{\nu+1}\right] \\ &\quad -g\Delta\tau\beta^- 2y_{k-1/2}\left[(\Delta p_0)_{k-1}\frac{1}{2}x_k p_k^{\nu} + (\Delta p_0)_k\frac{1}{2}x_{k-1}p_{k-1}^{\nu}\right] \\ &\quad +g\Delta\tau\beta^+ 2y_{k-1/2}\left[(\Delta p_0)_{k-1}\frac{1}{2}s_k^{\nu+1} + (\Delta p_0)_k\frac{1}{2}s_{k-1}^{\nu+1}\right] \\ &\quad +g\Delta\tau\beta^- 2y_{k-1/2}\left[(\Delta p_0)_{k-1}\frac{1}{2}s_k^{\nu} + (\Delta p_0)_k\frac{1}{2}s_{k-1}^{\nu}\right] \end{aligned} \tag{71}$$

After reorganizing the terms and applying (A.8) - (a.10), see appendix, the equation for the vertical velocity reads:

$$\begin{aligned} w_{k-1/2}^{\nu+1} &= w_{k-1/2}^\nu + C_{k-1/2}^w + \beta^+ C_{k-1/2}^{w1}\left[\alpha_{k-1/2}^B p_k^{\nu+1} - \alpha_{k-1/2}^T p_{k-1}^{\nu+1}\right. \\ &\quad \left. + \left((\Delta p_0)_{k-1}\frac{1}{2}s_k^{\nu+1} + (\Delta p_0)_k\frac{1}{2}s_{k-1}^{\nu+1}\right)\right] \end{aligned} \tag{72}$$

$$\begin{aligned} C_{k-1/2}^w &= (f_w^n)_{k-1/2}\,\Delta\tau + \beta^- C_{k-1/2}^{w1}\left[\alpha_{k-1/2}^B p_k^{\nu} - \alpha_{k-1/2}^T p_{k-1}^{\nu}\right. \\ &\quad \left. + \left((\Delta p_0)_{k-1}\frac{1}{2}s_k^{\nu} + (\Delta p_0)_k\frac{1}{2}s_{k-1}^{\nu}\right)\right] \end{aligned} \tag{73}$$

consequently the pressure tendency equation from (2.14) reads in differencing form:

$$\begin{aligned} p_k^{\nu+1} - p_k^\nu &= \left(f_p^n\right)_k\Delta\tau - \frac{p_k^n c_p}{c_v}\left(D_h^{\nu+1}\right)_k\Delta\tau + \beta^-\frac{1}{2}g\Delta\tau\,(\rho_0)_k \\ &\quad \left(w_{k+1/2}^\nu + w_{k-1/2}^\nu\right) + \beta^-\frac{g\,(\rho_0)_k}{(\Delta p_0)_k}\frac{p_k^n c_p}{c_v}\Delta\tau \\ &\quad \left(fxy_{k+1/2}w_{k+1/2}^\nu - fxy_{k-1/2}w_{k-1/2}^\nu\right) + \beta^+\frac{1}{2}g\Delta\tau \\ &\quad (\rho_0)_k\left(w_{k+1/2}^{\nu+1} + w_{k-1/2}^{\nu+1}\right) + \beta^+\frac{g\,(\rho_0)_k}{(\Delta p_0)_k}\frac{p_k^n c_p}{c_v}\Delta\tau \\ &\quad \left(fxy_{k+1/2}w_{k+1/2}^{\nu+1} - fxy_{k-1/2}w_{k-1/2}^{\nu+1}\right) \end{aligned} \tag{74}$$

Applying (A.11) and (A.12), (2.24) reads:

$$p_k^{\nu+1} = p_k^{\nu} + C_k^p + \beta^+ C_k^{p2}\left(w_{k+1/2}^{\nu} + w_{k-1/2}^{\nu}\right) + \beta^+ C_k^{p1} \left(fxy_{k+1/2} w_{k+1/2}^{\nu+1} - fxy_{k-1/2} w_{k-1/2}^{\nu+1}\right) \tag{75}$$

$$C_k^p = \left(f_p^n\right)_k \Delta\tau - \frac{p_k^n c_p}{c_v} \Delta\tau \left(D_h^{\nu+1}\right)_k + \beta^- C_k^{p2} \left(w_{k+1/2}^{\nu} + w_{k-1/2}^{\nu}\right) + \beta^- C_k^{p1} \left(fxy_{k+1/2} w_{k+1/2}^{\nu} - fxy_{k-1/2} w_{k-1/2}^{\nu}\right) \tag{76}$$

The temperature equation (2.15) completes the set of differencing equations:

$$T_k^{\nu+1} = T_k^{\nu} + \left(f_T^n\right)_k \Delta\tau - \frac{p_k^n}{\rho_k^n c_v} \Delta\tau \left(D_h^{\nu+1}\right)_k + \frac{g\left(\rho_0\right)_k \Delta\tau}{\left(\Delta\rho_0\right)_k} \frac{p_k^n}{\rho_k^n c_v} \left[\beta^+ \left(fxy_{k+1/2} w_{k+1/2}^{\nu+1} - fxy_{k-1/2} w_{k-1/2}^{\nu+1}\right) + \beta^- \left(fxy_{k+1/2} w_{k+1/2}^{\nu} - fxy_{k-1/2} w_{k-1/2}^{\nu+1}\right)\right] \tag{77}$$

As can be seen, the flux limiters show up in the vertical derivative of w, which is the vertical part of the divergence and they occur also in the horizontal part of the divergence $D_h^{\nu+1}$. For the vertically implicit solution procedure equations (2.22), (2.25) and (2.27) form a coupled system. Eliminating $p_k^{\nu+1}$ and $s_k^{\nu+1}$ at the future time step the w-equation (2.22) leaves $w^{\nu+1}$ as the only unknown. In order to eliminate $p_k^{\nu+1}$ and $p_{k-1}^{\nu+1}$ we use equation (2.25). The derivation of the additional term in (2.22)

$$\left(\left(\Delta p_o\right)_{k-1} \frac{1}{2} s_k^{\nu+1} + \left(\Delta p_0\right)_k \frac{1}{2} s_{k-1}^{\nu+1}\right) \tag{78}$$

which contains the vertical velocities at time step $\nu+1$ too is outlined in the appendix (A.13) - (A.16). Finally (A.15) with (A.16) are used in order to substitute the parenthesis (2.28) in the equation for the vertical velocity (2.22). After rearranging the terms this yields a linear tridiagonal equation system for $w^{\nu+1}$ which is written in the form:

$$a_{k-1/2} w_{k-11/2}^{\nu+1} + b_{k-1/2} w_{k-1/2}^{\nu+1} + c_{k-1/2} w_{k+1/2}^{\nu+1} = d_{k-1/2} \tag{79}$$

The matrix diagonals a, b and c and the inhomogeneous part d read:

$$a_{k-1/2} = -\beta^{+2} C_{k-1/2}^{w1} \left[\alpha_{k-1/2}^T \left(C_{k-1}^{p1} fxy_{k-11/2} - C_{k-1}^{p2}\right) - \left(\Delta p_0\right)_k C_{k-1}^{T1} fxy_{k-11/2}\right] \tag{80}$$

$$b_{k-1/2} = 1 + \beta^{+2} C_{k-1/2}^{w1} \left[\alpha_{k-1/2}^B \left(C_k^{p1} fxy_{k-1/2} - C_k^{p2}\right) + \alpha_{k-1/2}^T \left(C_{k-1}^{p1} fxy_{k-1/2} + C_{k-1}^{p2}\right) + \left(\Delta p_0\right)_{k-1} C_k^{T1} fxy_{k-1/2} - \left(\Delta p_0\right)_k C_{k-1}^{T1} fxy_{k-1/2}\right] \tag{81}$$

$$c_{k-1/2} = -\beta^{+2} C_{k-1/2}^{w1} \left[\alpha_{k-1/2}^B \left(C_k^{p1} fxy_{k+1/2} + C_k^{p2}\right) + \left(\Delta p_0\right)_{k-1} C_k^{T1} fxy_{k+1/2}\right] \tag{82}$$

$$d_{k-1/2} = w_{k-1/2}^{\nu} + C_{k-1/2}^w + \beta^+ C_{k-1/2}^{w1} \left[\alpha_{k-1/2}^B \left(p_k^{\nu} + C_k^p\right) - \alpha_{k-1/2}^T \left(p_{k-1}^{\nu} + C_{k-1}^p\right) + C_{k-1/2}^T\right] \tag{83}$$

The coefficients contain the flux limiters fxy and some additional terms with factors C^{T1} and C^T in the inhomogeneous part d which have their origin in the temperature equation. Actually, according to a suggestion of Janjic (19xx), the vertical advection of pressure pertubation $w\frac{\partial p'}{\partial z}$ should also be put into the implicit scheme - this wopuld further stabilize the integration. The matrix equation (2.29) can be solved for $w^{\nu+1}$ using a standard tridiagonal solver, provided that the vertical velocity at the upper and lower boundary is specified. At the top boundary the vertical velocity is set to zero. At the lower boundary we must allow the flow running parallel to the slope. Thus an appropriate value for w has to be taken at the lower boundary.

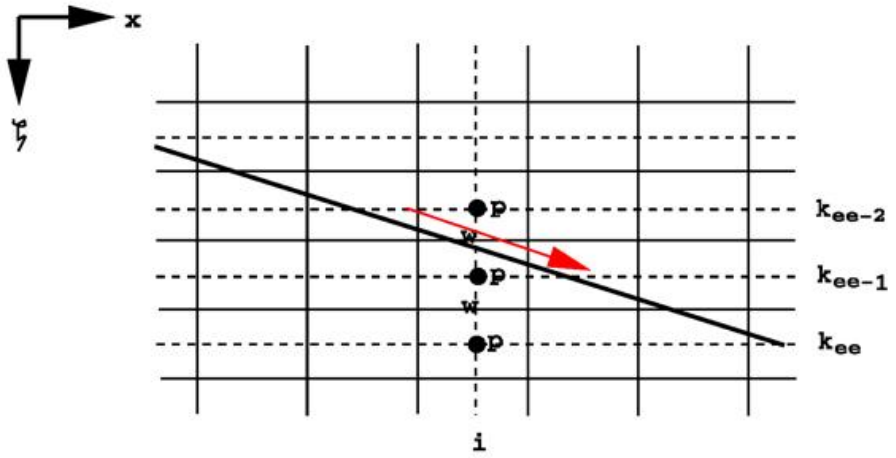


FIGURE 2.3: Boundary values of w under the surface

In Fig. 2.3 the volume element at $_{i,kee}$ lies completely under the surface. The prognostic equation (2.21) for the vertical velocity at $_{i,kee-11/2}$ requires the two pressure values $p_{i,kee-1}$ and $p_{i,kee-2}$ in order to calculate the pressure gradient at $_{i,kee-11/2}$. Since the pressure at $_{i,kee-1}$ is available this is no problem. The pressure at $_{i,kee-1}$ needs the vertical velocity at $_{i,kee-1/2}$. Normally this velocity would be not available but because it is a boundary value which is calculated according to equation (1.39) or (1.42) respectively. In the current model (1.39) or (1.42) is applied every small time step $\Delta\tau$. This is better rather than holding the boundary values constant during the entire subcycle procedure. The best value for the vertical velocity would yield if $w_{i,kee-1/2}$ were calculated dependent on the horizontal velocity with the demand that the total flow vector $\vec{v} = (u, v, w)$ at the surface is exactly tangential to the surface. Such a method is not implemented yet.

3.1 Structure of the Tridiagonal Matrix

In Section 1 the boundary values, necessary for the calculation of the derivatives close to the boundary were explained. The implicit scheme is related to the elimination of $w^{\nu+1}$ in a vertical column. The vertical do loop starts at k+1/2 and would normally end at $_{kee-1/2}$ because $w_{kee-1/2}$ is the lower boundary value. But kee is dependent on the orography, that means, kee is a function of i and j: kee = f(i,j) or in the current model: kee = kfin(i,j). The field kfin(i,j), contains the lowest k values at i,j this is the lowest level for w, the location of the lower boundary value. kfin(i,j) is calculated at the beginning of the program run in subroutine src_artifdata.f90 or z_level.f90 and is available in fast_waves.f90. The end of the do loop in vertical direction would be kee which is a function of i,j. Thus the k-loop had to be disposed to the interior of loop i and j; but this is not suitable. The tridiagonal equation system for $w^{\nu+1}$ runs as follows see Fig. 3.4.

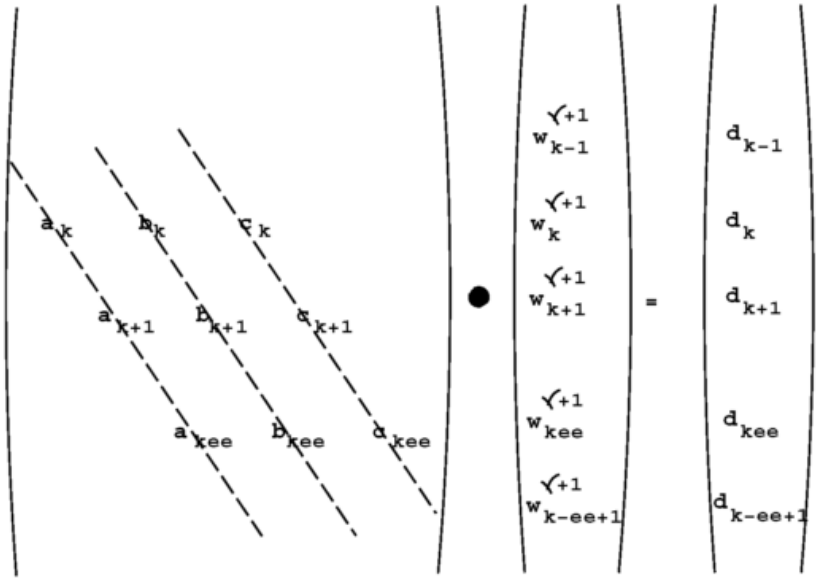


FIGURE 3.4: The matrix of the 1-d implicit scheme.

If we demand from the matrix system that the boundary value w_{kee} should be retrieved, then the coefficients and the inhomogeneous part read:

$$\begin{aligned} a_{kee} &= 0 \\ b_{kee} &= 1 \\ c_{kee} &= 0 \\ d_{kee} &= w^{\nu}_{kee} \end{aligned}$$

With these values w^{ν}_{kee} is reproduced in $w^{\nu+1}_{kee}$

For k > kee we set:

$$\begin{aligned} a_k &= 0 \\ b_k &= 1 \\ c_k &= 0 \\ d_k &= 0 \end{aligned}$$

which generates $w^{\nu+1}_k = 0$ for k > kee.

With this structure of tridiagonal system the do loops within the Gauss solver can be nested in the normal way: k-loop outside, j- and i-loop inside, and again this constellation is supposed to be numerically efficient.

4 Numerical Smoothing

4.1 Horizontal Diffusion

The program needs horizontal and vertical diffusion. At some boundaries some action is necessary in order to process the derivatives close to the boundaries. Here the second order

differencing scheme breaks down to order one. But there is another serious problem. Since the model only uses the complete spatial differences in the derivatives this implies very high errors for small volume elements in the calculation of the divergence term which acts on the pressure tendency equation (see Fig. 4.1). If the volume element is very small it kills the program run immedeately before one big time step is completed.

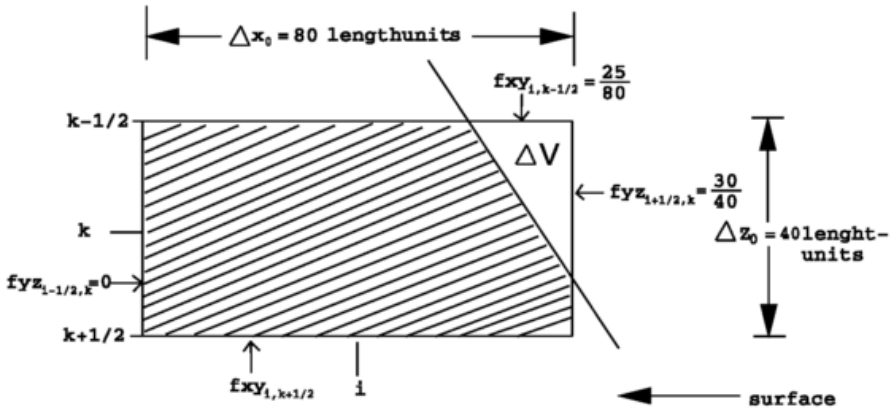


FIGURE 4.1: A small cut cell

Fig. 4.1 illustrates why this error occurs in the divergence term or in the pressure tendency equation which is used to represent the continuity equation. The correct volume Δv can be calculated as:

$$\Delta V = \frac{1}{2} fxy_{i,k-1/2} fxy_{j+1/2,k} \Delta x_0 \Delta z_0 \tag{84}$$

$$\begin{aligned} \frac{\Delta M}{\Delta t} = & -\rho(\Delta v) \left[\left(fyz_{i+1/2,k} u_{i+1/2,k} - fyz_{i-1/2,k} u_{i-1/2,k} \right) \Delta z_0 \right. \\ & \left. + \left(fxy_{i,k-1/2} w_{i,k-1/2} - fxy_{i,k+1/2} w_{i,k+1/2} \right) \Delta x_0 \right] \end{aligned} \tag{85}$$

Equation (3.1) represents the change of mass within the triangle ΔV. The continuity equation is retrieved by dividing (3.1) by ΔV :

$$\begin{aligned} \frac{\frac{\Delta M}{\Delta V}}{\Delta t} = & -\rho(\Delta v) \left[\left(fyz_{i+1/2,k} u_{i+1/2,k} - fyz_{i-1/2,k} u_{i-1/2,k} \right) \right. \\ & \frac{\boldsymbol{\Delta z_0}}{\frac{1}{2} fxy_{i,k-1/2} fyz_{i+1/2,k} \Delta x_0 \boldsymbol{\Delta z_0}} + \left(fxy_{i,k-1/2} w_{i,k-1/2} \right. \\ & \left. \left. - fxy_{i,k+1/2} w_{i,k+1/2} \right) \frac{\boldsymbol{\Delta x_0}}{\frac{1}{2} fxy_{i,k-1/2} fyz_{i+1/2,k} \boldsymbol{\Delta x_0} \Delta z_0} \right] \end{aligned} \tag{86}$$

divided by $\rho(\Delta v)$ yields:

$$\begin{aligned} \frac{1}{\rho} \frac{\Delta \rho}{\Delta t} = & -\left[\frac{1}{\Delta x_0} \left(fyz_{i+1/2,k} u_{i+1/2,k} - fyz_{i-1/2,k} u_{i-1/2,k} \right) \right. \\ & \frac{1}{\frac{1}{2} fxy_{i,k-1/2} fyz_{i+1/2,k}} + \frac{1}{\Delta z_0} \\ & \left(fxy_{i,k-1/2} w_{i,k-1/2} - fxy_{i,k+1/2} w_{i,k+1/2} \right) \\ & \left. \frac{1}{\frac{1}{2} fxy_{i,k-1/2} fyz_{i+1/2,k}} \right] \end{aligned} \tag{87}$$

From equation (3.4) it becomes obvious why the continuity equation or in the current model the pressure tendency equation cannot work for small volume elements. The current model uses the complete differences $\frac{1}{\Delta x_0}$ and $\frac{1}{\Delta z_0}$ but in reality the volume element is much smaller, the space differences Δx_0 and Δz_0 have to be premultiplied by $\left(\frac{1}{2} f x y_{i,k-1/2} f y z_{i+1/2,k}\right)$. This factor is missing in the current model. Unfortunately this factor can be of any smallness and in addition the factor would occure in the horizontal part of the divergence too. This is outside the implicit computation procedure which is directed only in the vertical. Thus the stability criterion would be dependent on the smallest volume element if the factor would be taken into account.

In order to overcome the problem we have to remove the very small volume elements. This is done in subroutine src_artifdata.f90 or in z_level.f90 respectively. Generally volume elements smaller than 1/60 or 1/120 of the total volume of an element are removed. In idealized experiments with a smooth Gaussian mountain the surface will be much rougher. The other volume elements greater than 1/60 or 1/120 are still not calculated correctly because of the mentioned missing factor in the divergence term. The current model is suffering from these deficiencies. The incorrect calculation of the derivatives in the divergence term results into wrong tendencies which appear as an overreaction and creates peaks of the parameters when stepped forward. Of course those peaks show up in the cut volume elements this means direct at the boundary. When we apply a diffusion in order to damp down the overreaction it should mainly act direct at the boundary. The horizontal diffusion is carried out sequentially, first in x- then in y-direction. The fourth order diffusion is drawn to the boundary in the following way:

```
work = 0
!
  do j = jstart-1 , jend+1
  do i = istart-1 , iend+1
    work(i,j) = weight(i+1,j)*(s(i+1,j)-s(i,j)) &
              - weight(i-1,j)*(s(i,j)-s(i-1,j))
  enddo
  enddo
!
  do j = jstart-1 , jend+1
  do i = istart-1 , iend+1
    dcoeff1 = dcoeff
    if((weight(i+1,j) < 0.5).and.(weight(i,j) > 0.5) dcoeff1 = alam
    if((weight(i-1,j) < 0.5).and.(weight(i,j) > 0.5) dcoeff1 = alam
    zsten = -dcoeff1*(weight(i+1,j)-(work(i+1,j)-work(i,j)) &
                     -weight(i-1,j)-(work(i,j)-work(i-1,j)))
!
    sten(i,j) = sten(i,j)+zsten
  enddo
  enddo
endif
```

In case if there is no boundary, the weight-factors are all 1. In this case the diffusion is working like in the operational LM with dcoeff1 = dcoeff which is the diffusion coefficient of the operational version. Now if the boundary is at the east side (see Fig. 4.2) the value at i+1 is beyond the boundary and weight (i+1,j) = 0. The program code above is acting in the following way:

$$\begin{aligned} work\,(i,j) &= -\Delta s_1 & \Delta s_1 &= s\,(i,j) - s\,(i-1,j) \\ work\,(i-1,j) &= \Delta s_1 - \Delta s_2 & \Delta s_2 &= s\,(i-1,j) - s\,(i-2,j) \end{aligned}$$

$$\begin{aligned} zsten &= -alam\,[-\,(work\,(i,j) - work\,(i-1,j))] \\ zsten &= alam\,[work\,(i,j) - work\,(i-1,j)] \\ zsten &= alam\,[\Delta s_2 - 2\Delta s_1] \end{aligned} \tag{88}$$

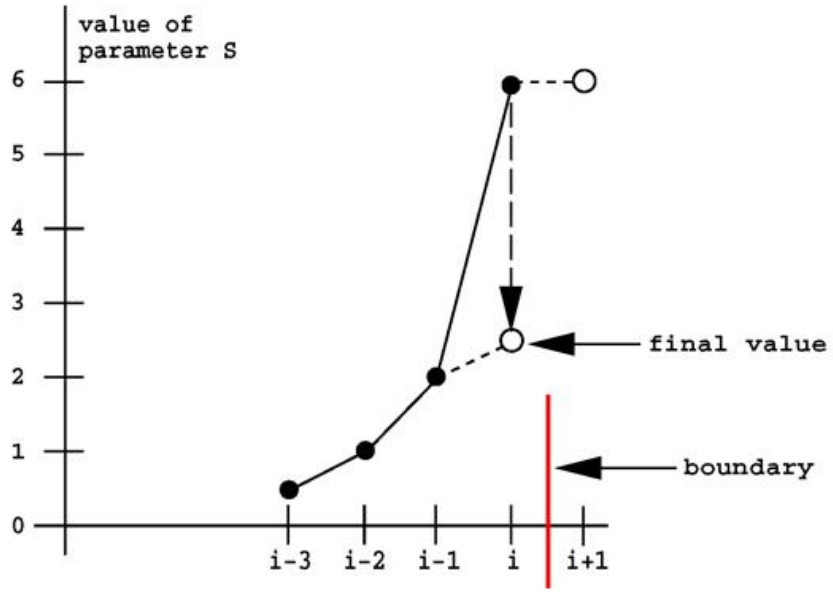


FIGURE 4.2: Action of horizontal diffusion

In the example of Fig. 4.2 $\Delta s_1 = 4$ and $\Delta s_2 = 1$ the tendency according to diffusion yields:

$$zsten = -7alam \tag{89}$$

zsten is negativ which implies, the fluctuating crazy boundary value s(i,j) = 6 is towed to lower values and calmed down. The final value, indicated in Fig. 4.2 with the short dashed line will be 2.5. Then $\Delta s_1 = \frac{1}{2}\Delta s_2$ and according to equation (3.5) zsten = 0. If a boundary is there the diffusion coefficient changes to

$$alam = \frac{1}{12dt2} \tag{90}$$

As illustrated in Fig. 4.2 the final value, caused by the diffusion, fits well into the general spatial distribution of the parameter s. But still the final value cannot represent the exact gradient of s if the gradient is unequal zero. Only if $\frac{\partial s}{\partial x} = 0$ then $\Delta s_2 = 0$ and from $\Delta s_1 = \frac{1}{2}\Delta s_2$ follows $\Delta s_1 = 0$; this implies, the final value s_i would be on the straight line defined by s_{i-2} and s_{i-1}. But it is very important to represent the correct vertical gradients of the velocity components and the temperature. The diffusion must not bend the profile off the gradient which has been established at gridpoints above the obstacle.

4.1 Vertical Diffusion

In order to sustain the established vertical gradient of the velocity and the temperature, the vertical diffusion in the current model effects on the difference function $s1(z) = s(z) - s_{lin}$.

The s(z) is the vertical profile of a parameter, for example u at gridpoint i,j (see Fig. 4.3). s_{lin} is the linear function of regression determined by the six last values above the surface. s_{lin} represents the vertical gradient of s(z) at the boundary properly. This is especially for the temperature gradient very important, otherwise the diffusion would generate artificial buoyancy which finally implies artificial motion at the obstacle.

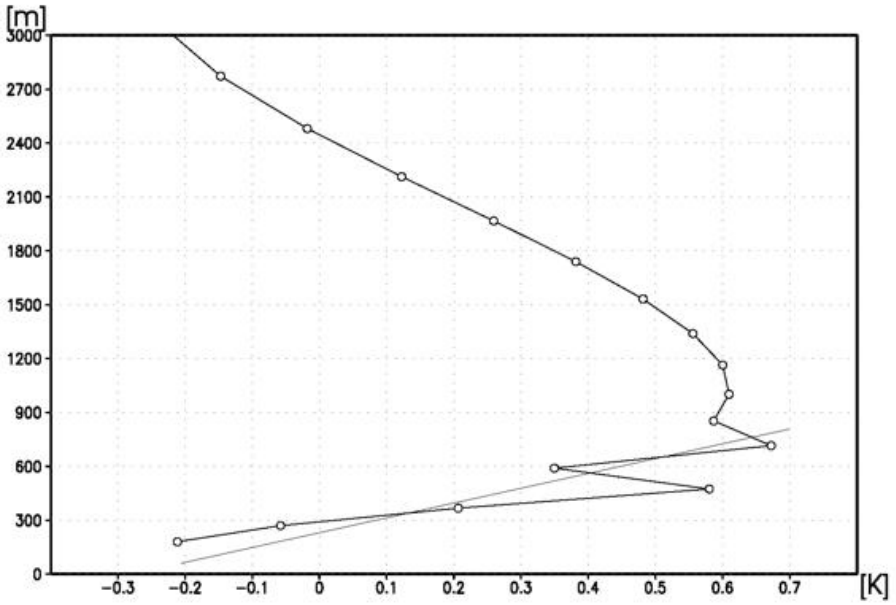


FIGURE 4.3: Vertical profile of the u-velocity with linear regression function.

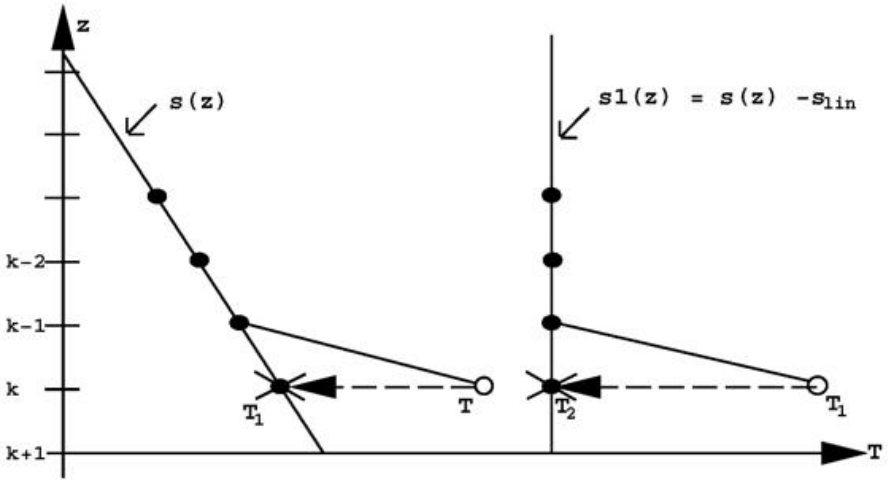


FIGURE 4.5: Action of diffussion for a temperature profile.

Fig. 4.4 shows a linear temperature profile s(z). The corresponding difference function s1(z) = s(z) - s_{lin} is represented on the right side of Fig. 3.4. Applying equation (3.5) for the vertical diffusion an s1(z) yields Δs_2 = s1(k-1) -s1(k-2) = 0 zsten in equation (3.5) is negativ and T_1 in Fig. 3.4 (right side) is nudged towards T_2. Since $\Delta s_2 = 0$ this demands $\Delta s_1 = 0$ if zsten should be 0. Δs_1 = s1(k)-s1(k-1)=0 this imlpies s1(k) = s1(k-1) in the equlibrium state when T_1 equals T_2. With this construction of the vertical diffusion the value T (Fig. 3.4, left side) is nudged towards T_1 which fits well into the vertical temperature distribution and in this way the vertical diffusion does not disturb an established vertical gradient. One particularity of the vertical diffusion has to be mentioned here: The diffusion coefficient is

decaying rapidly with height. Actually we need the diffusion right at the boundary rather than in the free flow domain. The existence of the vertical diffusion is absolutly necessary. One can drop horizontal diffusion rather than vertical diffusion at the boundary.

5 Results for Idealized Test Cases

The ability of the shaved element method can be tested on idealized experiments. The results presented below are carried out with a Gaussian mountain of $h_0 = 400$ m top height. The half width is set to $a = 10$ km. Since $\Delta x = 2$ km there are $5\Delta x$ to cover the half width. Thus the mountain is well resolved by sufficient gridpoints. The formula of the topography reads:

$$h(x,y) = \frac{h_0}{1 + \frac{x^2+y^2}{a^2}} \tag{91}$$

h_0	=	$400m$	top height of mountain
a	=	$10000m$	half width of mountain
u_0	=	10m/s	basic current.

The temperature lapse rate corresponds to an atmospheric stability $N = 0.01\ s^{-1}$. The Scorer number

$$s_c = \frac{N}{u_0} a \tag{92}$$

is in this case equal to 10, which means the horizontal scale of the mountain is much larger than the horizontal wave length of the buoyancy oscillation and the nonhydrostatic effect is small. Thus the results represents the almost hydrostatic case. For small amplitude mountains $\left(\frac{Nh_0}{u_0} << 1\right)$ the steady linear solution is known. The following solutions of the shaved element experiments are verified against the steady solution of the LM-operational version with terrain following coordinates. Of course the results have to be interpolated on the same z-levels which are used for the shaved element experiments, in order to yield a valid comparison. In all the experiments the uniform basic flow is from left to right with 10 m/s. All the experiments show the steady state solution.

Fig. 5.1 shows the u-velocity in a vertiacl cross section (x-z-plane). The plane cuts the mountain through it's centre. The numbers at the contour lines are given in m/s. The flow is decelerated upstream of the mountain and accelerated in the lee, which is realistic. There is no windshadow detectable. No artificial vorticity modification is necessary in order to gain this solution. In Fig. 5.2 the same solution is represented, but here processed with the LM operational version with the terrain following coordinate system. On the first glance glance one cannot detect any difference. If we look in detail we find an additional contour line in Fig. 5.2 at the right side of the plot in lower parts and in upper levels the 10.3 m/s contour line (right half of plot) is a little bit more extended than in the shaved element plot.

Fig. 5.3 and Fig. 5.4 illustrate the vertical velocity w of the shaved element method and the terrain following system respectively. Again the two plots are almost congruent. Small differencies are visible when we look at the - 0.35 m/s contour line in lower levels. The area of the minimum vertical velocity is a little bit larger in the shaved element experiment. One can see the same phnomena in upper levels with the - 0.15 m/s contour line.

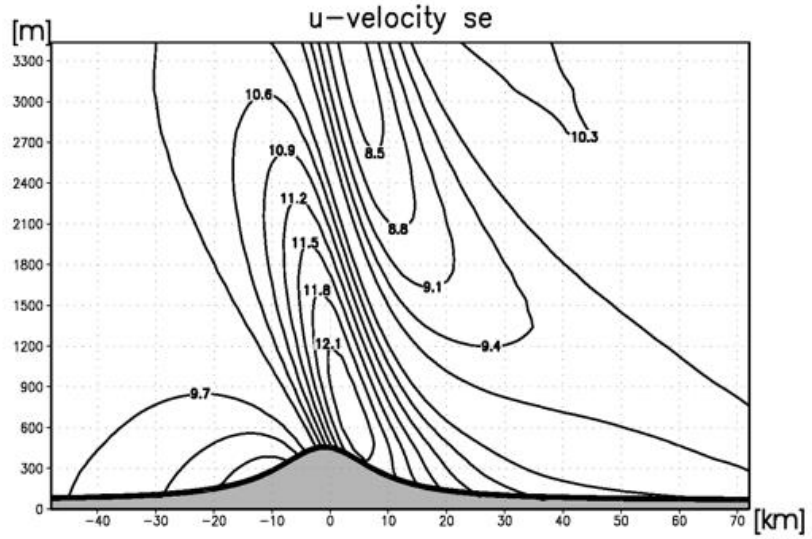


FIGURE 5.1: U-velocity in a vertical cross section computed by shaved elements.

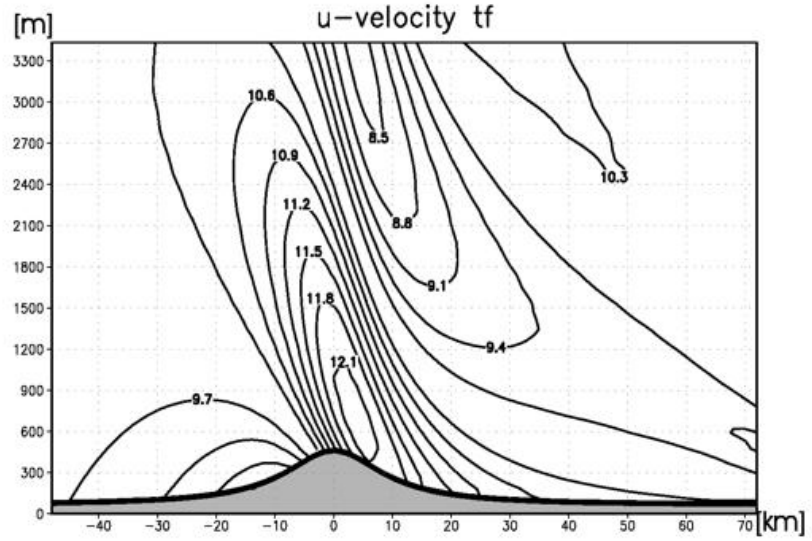


FIGURE 5.2: As in Fig. 5.1, but using the terrain following version of LM.

In Fig. 5.5 and 5.6 the vertical velocity is illustrated in a horizontal cross section at level z = 1164 m for both the shaved element experiments (Fig. 4.5) and the terrain following run (Fig. 5.6). There is no difference detectable.

Fig. 5.7 illustrates a vertical temperature profile which is the temperature deviation of the reference atmosphere (here shaved element experiment). The curvature of the profile in the lowest levels is remarkable. This means, the current model is able to simulate an inversion if the strongly bended profile is resolved with a few gridpoints. If the inversion is the represented just by one gridpoint, the vertical diffusion would act on it. From the mathematical point of view it would not make any sense to demand a resolution just by one gridpoint!

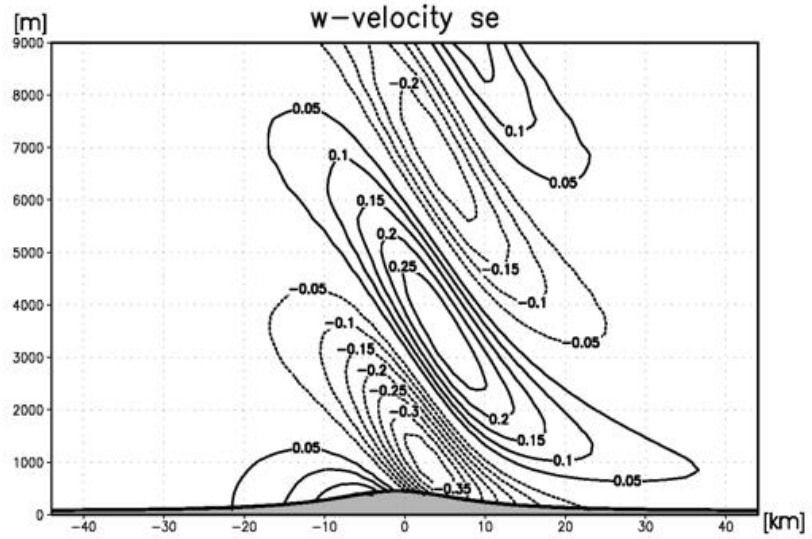


FIGURE 5.3: Vertical velocity in a vertical cross section computed by shaved elements.

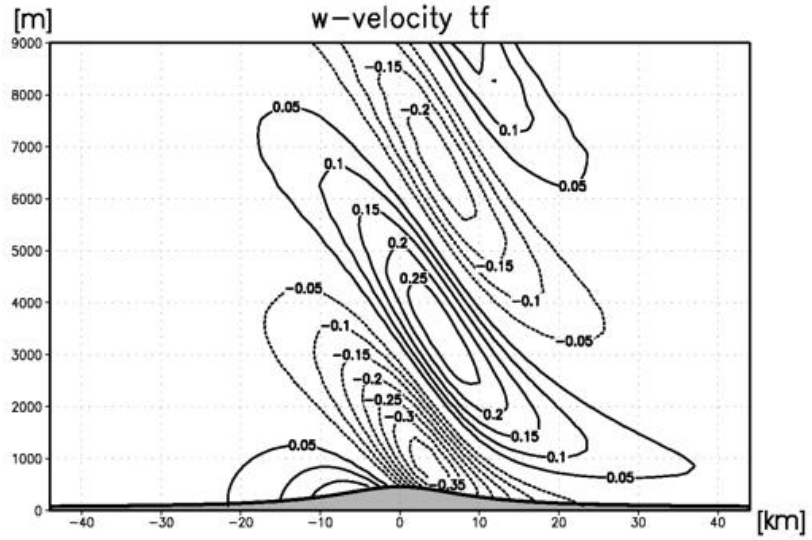


FIGURE 5.4: As in Fig. 5.3 but using the terrain following version of LM.

6 Summary

The new z-coordinate dynamical core of the LM has been described in detail. This version allows for a better orography representation by avoiding the forcing of the atmosphere by numerical errors in the presence of mountains. Problems concerning the prediction of precipitation which have been discussed in the literature in connection with similar approaches are solved by introducing a simplified version of the shaved element finite volume method using the thin wall approximation.

In this approach the mountains are represented by continuous linear splines. A regular grid is cut by this orographic function, which near the surface produces cut cells of different size and shape, which are treated by the finite volume method. For cells not cut by the orographic function the finite volume method produces the finite difference scheme of the operational

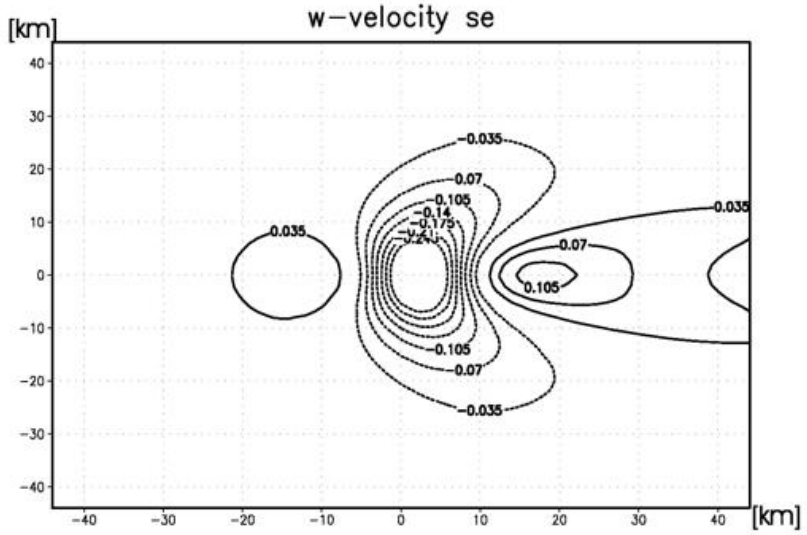


FIGURE 5.5: Vertical velocity in a horizontal cross section computed by shaved elements.

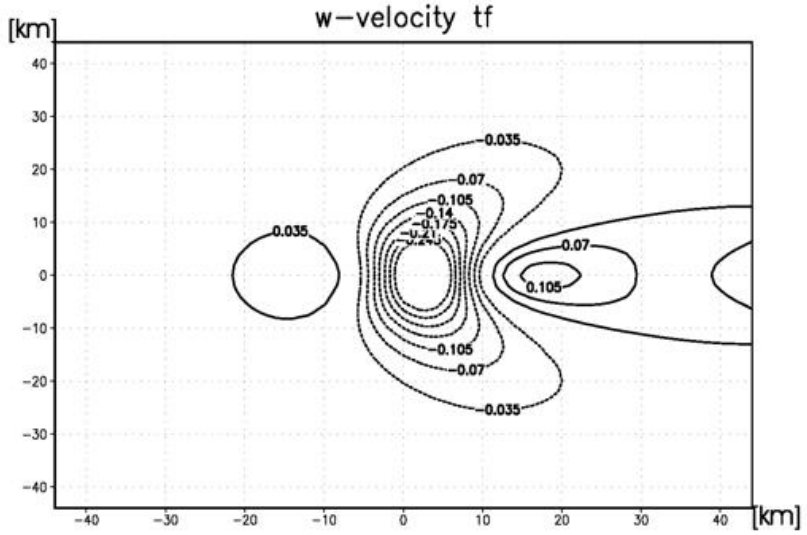


FIGURE 5.6: As in Fig. 5.5, but for the LM with terrain following coordinate.

LM, specialized for the case of flat terrain. The finite difference equations are based on centred difference approximation on the C-grid for those elements which are not cut by the topographic function. For the elements cut by the topographic function the finite difference equations are formulated using flux limiters in the horizontal and vertical directions. A small amount of numerical smoothing is required to stabilize the Leapfrog time-integration scheme.

A number of three-dimensional numerical tests have been performed with the new dynamical core. They showed that the method developed does not suffer from the problems reported in connection with the $\eta-$coordinate (Mesinger, 1988). Especially, the solutions for hydrostatic flow over a bell shaped-smooth mountain are rather similar to those obtained by a terrain following version of the model. Future work will focus on the inclusion of physical paramterizations to allow testing for real cases, aiming at an operational application of the z-coordinate version of the LM.

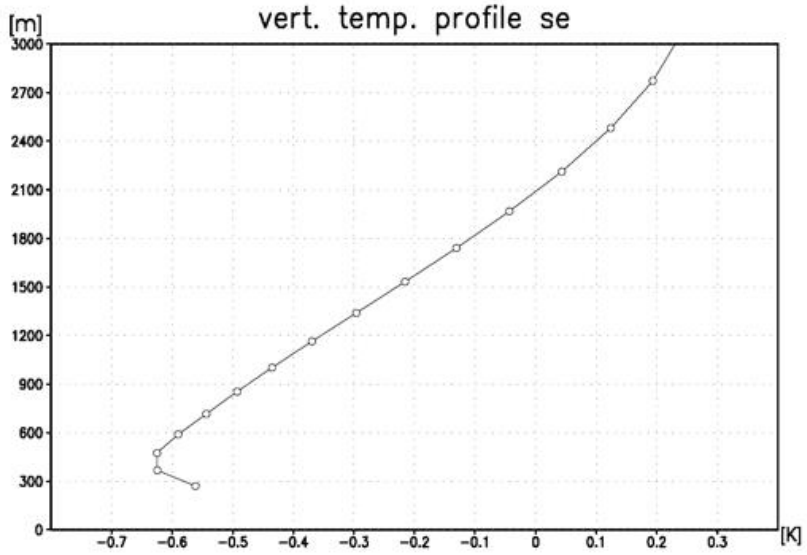


FIGURE 5.7: A vertical temperature profile simulated by shaved elements.

References

Doms, G. and U. Schättler, 1999: The Nonhydrostatic Limited Area Model LM. Part I: Scientific Documentation, DWD (available at www.cosmo-model.org).

Appendix

The following variable are used as substitutes / abbreviations for complex assembled expressions:

$$\frac{\overline{\rho_o}^{h\zeta}}{\overline{\rho^n}^{h\zeta}} = \frac{(\rho_0)_{k-1/2}}{(\rho^n)_{k-1/2}} = \frac{(\Delta p_0)_{k-1}(\rho_0)_k + (\Delta p_0)_k(\rho_0)_{k-1}}{(\Delta p_0)_{k-1}\rho_k^n + (\Delta p_0)_k \rho_{k-1}^n} \tag{93}$$

$$\begin{aligned}\frac{\overline{\rho_o}^{h\zeta}}{\overline{\rho^n}^{h\zeta}}\overline{A}^{h\zeta} &= \frac{(\rho_0)_{k-1/2}}{(\rho^n)_{k-1/2}} A_{k-1/2} = \frac{1}{(\Delta p_0)_{k-1} + (\Delta p_0)_k} \\ &\quad \frac{(\Delta p_0)_{k-1}(\rho_0)_k + (\Delta p_0)_k(\rho_0)_{k-1}}{(\Delta p_0)_{k-1}\rho_k^n + (\Delta p_0)_k \rho_{k-1}^n} \\ &\quad \left((\Delta p_0)_{k-1} A_k + (\Delta p_0)_k A_{k-1}\right)\end{aligned} \tag{94}$$

$$\frac{\overline{\rho_o}^{h\zeta}}{\overline{\rho^n}^{h\zeta}}\overline{A}^{h\zeta} = y_{k-1/2}\left((\Delta p_0)_{k-1} A_k + (\Delta p_0)_k A_{k-1}\right) \tag{95}$$

$$y_{k-1/2} = \frac{1}{(\Delta p_0)_{k-1} + (\Delta p_0)_k} \frac{(\Delta p_0)_{k-1}(\rho_0) + (\Delta p_0)_k(\rho_0)_{k-1}}{(\Delta p_0)_{k-1}\rho_k^n + (\Delta p_0)_k \rho_{k-1}^n} \tag{96}$$

$$\frac{1}{(\Delta p_0)_{k-1/2}} \frac{\overline{\rho_o}^{h\zeta}}{\overline{\rho^n}^{h\zeta}} = 2y_{k-1/2} \tag{97}$$

$$x_k = \left(\frac{T_0}{T^n p_0}\right)_k \tag{98}$$

$$s_k^\nu = \left(\frac{T^\nu - T_0}{T^n}\right)_k \tag{99}$$

$$C_{k-1/2}^{w1} = 2g\Delta\tau y_{k-1/2} \tag{100}$$

$$\alpha_{k-1/2}^B = 1 - (\Delta p_0)_{k-1}\frac{1}{2}x_k \tag{101}$$

$$\alpha_{k-1/2}^T = 1 + (\Delta p_0)_k \frac{1}{2}x_{k-1} \tag{102}$$

$$C_k^{p1} = \frac{g(\rho_0)_k \Delta\tau}{(\Delta p_0)_k}\frac{p_k^n c_p}{c_v} \tag{103}$$

$$C_k^{p2} = \frac{g}{2}(\rho_0)_k \Delta\tau \tag{104}$$

From the temperature equation (2.27) we gain:

$$\begin{aligned} T_k^{\nu+1} &= T_k^\nu + R_k \qquad\qquad T_k^{\nu+1} - T_{0_k} = T_k^\nu - T_{0_k} + R_k \\ R_k &= \text{rest of right hand side of equation} \\ \frac{T_k^{\nu+1} - T_{0_k}}{T_k^n} &= \frac{T_k^\nu - T_{0_k}}{T_k^n} + \frac{R_k}{T_k^n} \\ s_k^{\nu+1} &= s_k^\nu + \frac{R_k}{T_k^n} \end{aligned} \tag{105}$$

$$
\begin{aligned}
s_k^{\nu+1} &= s_k^{\nu} + \frac{(f_T^n)_k \Delta\tau}{T_k^n} - \left(\frac{p_k^n}{\rho_k^n c_v}\right)\left(D_h^{\nu+1}\right)_k \frac{\Delta\tau}{T_k^n} + \frac{g\,(\rho_0)_k}{(\Delta p_0)_k}\frac{\Delta\tau}{T_k^n} \\
&\quad \frac{p_k^n}{\rho_k^n c_v}\beta^- \left(fxy_{k+1/2} w_{k+1/2}^{\nu} - fxy_{k-1/2} w_{k-1/2}^{\nu}\right) + \frac{g\,(\rho_o)_k}{(\Delta p_0)_k} \\
&\quad \frac{\Delta\tau}{T_k^n}\frac{p_k^n}{\rho_k^n c_v}\beta^+ \left(fxy_{k+1/2} w_{k+1/2}^{\nu+1} - fxy_{k-1/2} w_{k-1/2}^{\nu+1}\right)
\end{aligned} \tag{106}
$$

$$
\begin{aligned}
\left((\Delta p_0)_{k-1}\frac{1}{2}s_k^{\nu+1} + (\Delta p_0)_k \frac{1}{2}s_{k-1}^{\nu+1}\right) &= C_{k-1/2}^T + \beta^+ (\Delta p_0)_{k-1} C_k^{T1} \\
&\quad \left(fxy_{k+1/2} w_{k+1/2}^{\nu+1} - fxy_{k-1/2} w_{k-1/2}^{\nu+1}\right) \\
&\quad +\beta^+ (\Delta p_0)_k C_{k-1}^{T1} \left(fxy_{k-1/2}\right. \\
&\quad \left. w_{k-1/2}^{\nu+1} - fxy_{k-11/2} w_{k-11/2}^{\nu+1}\right)
\end{aligned} \tag{107}
$$

$$
\begin{aligned}
C_{k-1/2}^T &= (\Delta p_0)_{k-1}\frac{1}{2}s_k^{\nu} + (\Delta p_0)_k \frac{1}{2}s_{k-1}^{\nu} + (\Delta p_0)_{k-1}\frac{(f_T^n)_k \Delta\tau}{2T_k^n} + (\Delta p_0)_k \\
&\quad \frac{(f_T^n)_{k-1}\Delta\tau}{2T_{k-1}^n} + (\Delta p_0)_{k-1}\frac{zcpr_k}{2T_k^n}\left[-zpnj_k\left(D_h^{\nu+1}\right)_k + \beta^-\right. \\
&\quad \left. zcp1_k\left(fxy_{k+1/2} w_{k+1/2}^{\nu} - fxy_{k-1/2} w_{k-1/2}^{\nu}\right)\right] + (\Delta p_0)_k \\
&\quad \frac{zcpr_{k-1}}{2T_{k-1}^n}\left[-zpnj_{k-1}\left(D_h^{\nu+1}\right)_k + \beta^- zcp1_{k-1}\right. \\
&\quad \left.\left(fxy_{k-1/2} w_{k-1/2}^{\nu} - fxy_{k-11/2} w_{k-11/2}^{\nu}\right)\right]
\end{aligned} \tag{108}
$$

with

$$
\begin{aligned}
zcpr_k &= \frac{1}{c_p \rho_k^n} \quad ; \quad zpnj_k = \frac{c_p}{c_v} p_k^n \Delta\tau \\
zcp1_k &= \frac{c_p}{c_v} p_k^n \Delta\tau\,(\rho_0)_k \frac{g}{(\Delta p_0)_k} \\
zcpr_k zcp1_k &= \frac{p_k^n \Delta\tau\,(\rho_0)_k\, g}{\rho_k^n c_v\,(\Delta p_0)_k} \quad \text{and} \quad c_k^{T1} = \frac{zcpr_k zcp1_k}{2T_k^n}
\end{aligned}
$$

List of COSMO Newsletters and Technical Reports

(available for download from the COSMO Website: www.cosmo-model.org)

COSMO Newsletters

Newsletter No.1, February 2001.

Newsletter No.2, February 2002.

COSMO Technical Reports

No. 1, Dmitrii Mironov and Matthias Raschendorfer (2001):
Evaluation of Empirical Parameters of the New LM Surface-Layer Parameterization Scheme. Results from Numerical Experiments Including the Soil Moisture Analysis.

No. 2, Reinhold Schrodin and Erdmann Heise (2001):
The Multi-Layer Version of the DWD Soil Model TERRA_LM.

No. 3, Günther Doms (2001):
A Scheme for Monotonic Numerical Diffusion in the LM.

No. 4, Hans-Joachim Herzog, Ursula Schubert, Gerd Vogel, Adelheid Fiedler and Roswitha Kirchner (2002):
LLM – the High-Resolving Nonhydrostatic Simulation Model in the DWD – Project LITFASS. Part I: Modelling Technique and Simulation Method.

No. 5, Jean-Marie Bettems (2002):
EUCOS Impact Study Using the Limited-Area Non-Hydrostatic NWP Model in Operational Use at MeteoSwiss.

No. 6, Heinz-Werner Bitzer and Jürgen Steppeler (2004):
Documentation of the Z-Coordinate Dynamical Core of LM.

COSMO Technical Reports

Issues of the COSMO Technical Reports series are published by the *Consortium for Small-Scale Modelling* at non-regular intervals. COSMO is a European group for numerical weather prediction with participating meteorological services from Germany (DWD, AWGeophys), Greece (HNMS), Italy (UGM, ARPA-SMR) and Switzerland (MeteoSwiss). The general goal is to develop, improve and maintain a non-hydrostatic limited area modelling system to be used for both operational and research applications by the members of COSMO. This system is initially based on the Lokal-Modell (LM) of DWD with its corresponding data assimilation system.

The Technical Reports are intended

- for scientific contributions and a documentation of research activities,
- to present and discuss results obtained from the model system,
- to present and discuss verification results and interpretation methods,
- for a documentation of technical changes to the model system,
- to give an overview of new components of the model system.

The purpose of these reports is to communicate results, changes and progress related to the LM model system relatively fast within the COSMO consortium, and also to inform other NWP groups on our current research activities. In this way the discussion on a specific topic can be stimulated at an early stage. In order to publish a report very soon after the completition of the manuscript, we have decided to omit a thorough reviewing procedure and only a rough check is done by the editors and a third reviewer. We apologize for typographical and other errors or inconsistencies which may still be present.

At present, the Technical Reports are available for download from the COSMO web site (www.cosmo-model.org). If required, the member meteorological centres can produce hard-copies by their own for distribution within their service. All members of the consortium will be informed about new issues by email.

For any comments and questions, please contact the editors:

Günther Doms
guenther.doms@dwd.de

Ulrich Schättler
ulrich.schaettler@dwd.de

Consortium

for

Small-Scale Modelling

Technical Report No. 5

EUCOS Impact Study Using the Limited-Area Non-Hydrostatic NWP Model in Operational Use at MeteoSwiss

by

J.-M. Bettems

March 2002

DOI: 10.5676/DWD_pub/nwv/cosmo-tr_5

Deutscher Wetterdienst

MeteoSwiss

Ufficio Generale per la Meteorologia

Hellenic National Meteorological Service

Amt für Wehrgeophysik

Il Servicio Meteorologico Regionale di ARPA

www.cosmo-model.org

Editors: G. Doms and U. Schättler, Deutscher Wetterdienst, P.O. Box 100465, 63004 Offenbach, Germany
Printed at Deutscher Wetterdienst, Offenbach am Main

EUCOS Impact Study Using the Limited-Area Non-Hydrostatic NWP Model in Operational Use at MeteoSwiss

Jean-Marie Bettems

jean-marie.bettems@meteoswiss.ch
Swiss Federal Office of Meteorology and Climatology (MeteoSwiss)
CH-8044 Zürich, Switzerland

Abstract

The EUCOS program aims to optimize the ground segment of the European observing system. A drastic reduction of the number of radiosondes has been proposed, compensated by a higher observing frequency of the remaining stations and additional AMDAR platforms. To assess the impact of such a scenario, sensitivity studies have been done with aLMo, the COSMO limited area NWP model in operational use at MeteoSwiss.

This non-hydrostatic model, in operational use at MeteoSwiss, is integrated on a 2700 km × 2300 km mesh covering occidental and central Europe, with a 7 km mesh size. A continuous assimilation cycle based on the nudging technique is used to assimilate all conventional observations. A 27 day test period has been defined (19.10.1999 - 14.11.1999) and daily 24 hour forecasts have been calculated to measure the impact of the proposed radiosonde network modification and to assess the effect of the additional AMDAR platforms on the model analysis and forecast quality.

A significant degradation of the model quality is associated with the reduction of the number of radiosonde stations at analysis time and in the very short range; the increased observation frequency does not compensate for the reduced horizontal resolution of the observing system. On the other side, the additional AMDAR platforms bring a clear local improvement of wind, temperature and humidity; however this improvement does not compensate the quality loss brought by the radiosonde network degradation. An improved horizontal coverage by AMDAR observations and additional information about local structures in the humidity field could be a necessary addition to the EUCOS scenario.

1 Context and Objectives

The main goal of the EUMETNET Composite Observing System program (EUCOS) is to define the optimum ground based observing system for the support of short range numerical weather prediction (NWP) over Europe. The current ground segment of the European observing system is quite dense over the continental area, but sparse over the ocean. A preliminary study [Pailleux et al., 1997] indicated that a significant reduction of the number of radiosondes over the data dense area and the addition of profiles over the Atlantic Ocean and the Mediterranean could optimize the NWP quality for the available financial resources. Based on this study two EUCOS network scenarios have been proposed: a first configuration using half the number of radiosonde stations over continental areas (about 40 remaining stations) but with higher sampling rate at these remaining stations (4 ascents a day) and

additional aircraft observations, and a second configuration which extends the first one by introducing new observations over sensitive areas of the Atlantic Ocean and Mediterranean.

In order to better evaluate the impact of these scenarios on NWP quality, it has been decided to perform observing system experiments (OSE) with both global and limited area NWP models. A special observing campaign took place from 20 September to 14 November 1999. 27 uniformly distributed radiosonde stations have been activated four times a day over the continent and 116 supplementary aircraft platforms providing wind and temperature were added. The set of all available observations collected during this period is the base for conducting EUCOS OSE[1].

A first impact study has been done with the ECMWF global model [Cardinali, 2000]: the observed impact on the short and medium range forecast was very small. It was also shown that during the two months of the EUCOS observing period the most sensitive areas where errors are fast growing were not located over Europe but over the North Pacific. However, this does not preclude an impact at smaller horizontal and shorter time scale (the ECMWF model used a T319 spectral truncation corresponding to a resolution of about 60km over Europe). Two countries committed to do OSE with their high resolution limited area models: the Danish Meteorological Institute with the HIRLAM model and its optimum interpolation analysis and MeteoSwiss with aLMo - its current operational model - and its associated continuous assimilation scheme. The results of the first study have been published [Amstrup, 2000], this report presents the results obtained with aLMo.

2 The NWP Model

In the frame of the Consortium for Small-scale Modelling (COSMO), the National Weather Services of Italy, Greece and Switzerland under the lead of the National Weather Service of Germany have developed a new non-hydrostatic meso-scale model called the Local Model. This model is based on the primitive hydro-thermodynamical equations describing non-hydrostatic flow in a moist atmosphere, without any scale approximations. The model equations are solved numerically using the finite difference method on a Arakawa C-grid with generalized terrain-following vertical coordinates. A thorough description of the Local Model itself can be found on the COSMO web site at www.cosmo-model.org or in the first COSMO newsletter [Doms, 2001].

The version of the Local Model running at MeteoSwiss is named aLMo (for *al*pine *mo*del). Two daily 48 h forecasts are calculated since the first of July 2000, and the model is used operationally since the first of April 2001. It is calculated on a 385 $\times$ mesh, with a 1/16 $^\circ$ mesh size (about 7 km), on a domain covering most of western Europe (see figure 2-1). In the vertical a 45 layers configuration is used; the vertical resolution in the lowest 2 km of the atmosphere is about 100 m (see figure 2-2). A filtered (smoothed) orography has been introduced in order to reduce the unrealistic forcing of 2 Δx waves produced by a mean orography. Lateral boundary conditions are assimilated by a 1-way nesting procedure according to Davies [Davies, 1976]. Rayleigh damping is applied in the 8 upper model layers, starting at 11 km, with a top boundary condition set by the driving model.

The model configuration defined for the OSE performed in this study is based on the operational configuration just described. The only differences are the driving model (the Global

[1]It has to be noted, that this EUCOS campaign coincided with the Special Observing Period of the Mesoscale Alpine Programme [Bougeault et al., 2001], whose data set offers a large potential for additional OSE's.



FIGURE 2-1. Domain and orography of aLMo (min: - 5 m, max: 3109 m).

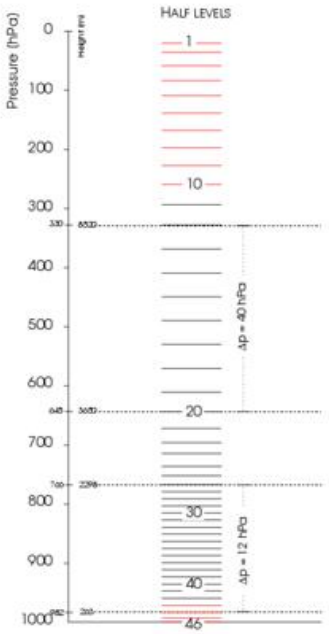


FIGURE 2-2. Vertical distribution of layers in aLMo.

Model of the German Weather Service is used for production, the ECMWF model for the OSE) and the initialization procedure (an interpolation of the driving model analysis is currently used in production, the nudging scheme is used for the OSE).

3 The Assimilation Scheme

Data assimilation with the Local Model is based on the nudging or Newtonian relaxation method. This technique has been implemented using relaxation of model dynamical fields towards direct observations [Schraff, 1997].

The observations being assimilated are horizontal wind, temperature, and relative humidity at all levels, and pressure at the lowest model level. Currently only conventional observing systems are used: surface observations (SYNOP, SHIP, DRIBU), aircraft observations (AIREP, AMDAR) and vertical soundings (TEMP, PILOT). The conditions defining the use of a specific observation are summarized in table 3-1.

TABLE 3-1. Conditions for assimilation of a specific observation.

	Surface Observation (SYNOP, SHIP, DRIBU)	**Vertical profile (TEMP, PILOT)**		**Aircraft (AIREP, AMDAR)**
		Standard level	Significant level	
Surface pressure	Height diff. [a] < 100m > −400m	Yes		No
Horizontal wind	Obs. height < 100m a.s.l.	Yes	Yes if > 100 hPa	Yes
Temperature	No	Yes	Yes if > 100 hPa	Yes
Relative humidity	Abs(height diff) < 160 m	Yes if > 300 hPa		No

[a] Difference between model orography and station height.

During aircraft ascent and descent phases, the aircraft observations are grouped together to form piecewise vertical profiles. All observations from the same aircraft are first collected and a base report is defined by selecting the report with the highest pressure. All observations within 15 minutes and 20 kilometers of the base report are then grouped in a multi-level report. This procedure is then repeated with the remaining reports. Finally each multi-level report is assimilated in a way similar to a TEMP profile (in particular a multi-level report is associated to a single location, neglecting any horizontal drift). As a result of this scheme, most aircraft observations are assimilated as part of multi-level reports below 700 hPa – with a vertical resolution of about 10 to 20 hPa – and as original single-level reports above 400 hPa.

The nudging weight (main coefficient of the nudging term in the model equations) is set to 6×10^{-4} s^{-1} which corresponds to an e-folding time of about half an hour. The temporal influence of a vertical profile extends from 3 h before the observation time to 1 h after, and the influence of surface and upper air single level observations extends from 1.5 h before the observation time to 0.5 h after. The typical half-width of the horizontal influence radius of an observation is between 120 km and 220 km, with smaller values near the ground and larger values aloft.

The conservation of the specific humidity is enforced when assimilating any temperature report. In order to better assimilate surface pressure information, a temperature and a partly geostrophic wind correction is associated with any surface pressure increment; hydrostatic upper-air pressure increments balancing the total analysis increments are also added. Because no soil model analysis is currently available at MeteoSwiss, the fields describing the soil state, including snow related quantities and sea surface temperature, are updated twice a day from the driving model analysis. A simple quality control is regularly performed by comparing the observation increments (difference between an observation and the corresponding model value) with predefined thresholds.

Since the first of March 2001, a continuous data assimilation cycle based on the configuration described above is in pre-operational mode at MeteoSwiss. Systematic subjective and objective verification, covering a 5 months period, has shown a consistent behaviour of this assimilation scheme and a clear positive impact on the forecasts.

The data assimilation scheme defined for the OSE performed in this study is based on the pre-operational scheme just described.

4 The Experimental Set-Up

Due to time constraints it was not possible to calculate EUCOS OSE for the whole EUCOS observing period. I chose the same four weeks as the one defined by the Danish Meteorological Institute, namely from 19 October 1999 00 UTC to 15 November 1999 00 UTC. This period includes 2 of the 3 case studies presented in the ECMWF report [Cardinali, 2000], and seven MAP heavy precipitation events (MAP is the Mesoscale Alpine Program, see the web site at www.map.ethz.ch or [Bougeault et al., 2001]); this last fact is of interest because we can anticipate a larger impact of the proposed EUCOS scenario on "wet" weather regimes due to the reduction of humidity observations.

Three observing systems called S1, S2 and S3 have been considered. S1 is the observing system which uses the same radiosonde and aircraft data as before the EUCOS campaign; S2 has 37 radiosonde stations less, but 13 more stations measuring every 6 hours; S3 has the same radiosonde configuration as S2, but is complemented by 121 more AMDAR plat-

TABLE 4-1. Typical number of observations assimilated by aLMo during a 24 h period (the active stations number differs from the blacklist derived value because only the stations inside aLMo domain are considered).

		TEMP	PILOT	AIRCRAFT	SYNOP	DRIBU
S1	active stations	55	12	135	1078	6
	active reports [a)]	202	24	4671	18542	146
S2	active stations	25	12	135	1078	6
	active reports	110	24	4671	18542	146
S3	active stations	25	12	216	1078	6
	active reports	110	24	21261	18542	146

a) all observations influencing the model flow during the considered 24−h period.

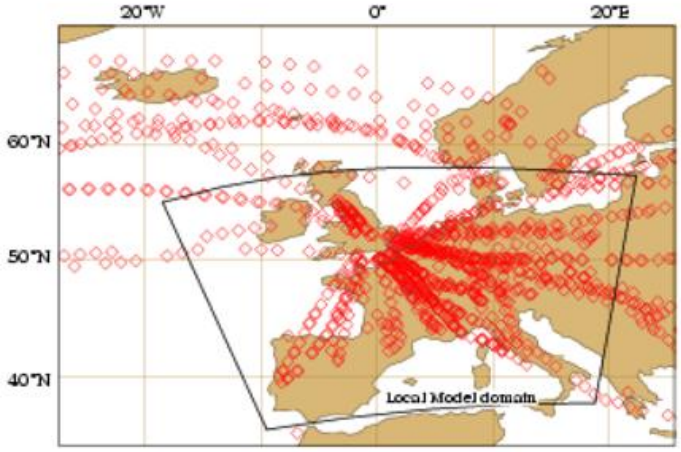


FIGURE 4-1. Typical daily coverage of activated AMDAR platforms in observing system S3 (red boxes).

forms. The blacklists used to define the different observing systems are available in the annex (supplementary soundings by stations which changed their operations during EUCOS observation campaign have not been included in S1, contrary to the ECMWF study). The typical number of bulletins assimilated by aLMo during a 24 h period for each of these observing systems is listed in table 4-1, and the typical daily coverage of AMDAR platforms in observing system S3 is displayed in figure 4-1.

A 27 days assimilation has been run with the Local Model for each of S1, S2 and S3. These three assimilation cycles have been started the 19 October 1999 at 00 UTC from the ECMWF operational 4-d variational analysis[2]. This same ECMWF analysis stream has been used to update the lateral boundary conditions every 6 hours, and to update the soil model once a day at 00 UTC (no soil model analysis is available at MeteoSwiss).

Daily 24 hour forecasts starting at 12 UTC have been run with aLMo for each of S1, S2 and S3. Initial conditions for these forecasts were obtained from the corresponding assimilation

[2]the MARS retrieval parameters are: stream *oper*, class *od*, type *4v*, expver *001*.

cycle, described in the previous section. Observations were still assimilated during the first forecast hour, in order to mirror the (pre-) operational configuration used at MeteoSwiss. Lateral boundary conditions were updated every 6 hours from the ECMWF operational deterministic forecast[3].

I would like to stress that all three experiments S1, S2 and S3 have been calculated with the same set of ECMWF lateral boundary conditions. Although EUCOS OSE dataset were available at ECMWF for both assimilation and forecast, it was not possible to use them: the liquid water field – required by aLMo – was missing in the ECMWF archive. However, in view of the weak impact observed in the ECMWF EUCOS OSE, this should not significantly alter the conclusions of this study.

5 Impact on Forecast Quality

The impact of the observing system modifications *on aLMo forecast quality* has been evaluated with two verification packages in operational use at MeteoSwiss: a package for the verification of the vertical structure of the atmosphere over the whole aLMo domain (section 5.1) and a package for the verification of near-surface weather parameters over Switzerland (section 5.2). One of the three cases presented in the ECMWF study [Cardinali, 2000] is also briefly presented (section 5.3).

5.1 Vertical Structure of the Atmosphere

A statistical verification of the vertical structure of the model atmosphere against radiosonde data for a set of 28 stations regularly distributed over the whole aLMo domain has been applied. The reference stations are Hemsby (03496), Crawley (03774), Camborne (03808), Long Kesh$^-$ (03920), Valentia (03953), Payerne$^+$ (06610), Brest$^-$ (07110), Trappes$^-$ (07145), Nancy$^-$ (07180), Lyon$^-$ (07481), Bordeaux$^+$ (07510), Nimes$^+$ (07645), Ajaccio$^-$ (07761), La Coruna (08001), Madrid$^-$ (08221), Mallorca$^+$ (08301), Schleswig (10035), Emden$^-$ (10200), Lindenberg^o (10393), Essen$^-$ (10410), Stuttgart$^-$ (10739), München$^-$ (10868), Wien (11035), Innsbruck^o (11120), Prag (11520), Udine (16044), Milano$^-$ (16080), San Pietro$^-$ (16144), Roma$^-$ (16245) and Cagliari (16560) (a "+" means increased observing frequency in S2, a "-" means not present in S2, a "o" means neither present in S1 nor in S2). A quality assessment in the frame of MAP [Häberli, 1998] has shown good observation scores for these stations. Bias and standard deviation for temperature, relative humidity (over water), wind direction and wind speed are calculated for the whole set of available forecasts and for different forecast times (+00 h, +06 h, +12 h, + 24h).

The main results of this verification can be summarized by the four statements presented below, and are illustrated by the statistical scores displayed in figures 5-1 to 5-5:

- Decreasing the spatial density of radiosondes and increasing the observing frequency of some (from S1 to S2) results in a significant increase of the standard deviation of both dynamical and thermodynamical fields *at analysis time* (+00 h). For instance, in the middle troposphere a 50% increase in variance of relative humidity is observed (fig. 5-2).

  This fact reflects a degradation of the mesoscale structures due to the modification of the observing system. This is consistent with one of the conclusion of an earlier observing system simulation experiment (OSSE), which showed that a high temporal

[3]the MARS retrieval parameters are: stream *oper*, class *od*, type *fc*, expver *001*.

resolution of wind profiler observations does not compensate for a poor horizontal resolution of the observing system [Bettems, 1999].

One can argue that the observed impact is maximized by the applied verification method, the scores being (partly) calculated at the exact locations where the observing network is modified. This is certainly true, but a relevant impact is also observed at locations where no observing system modification is applied, as shown in figures 5-6 and 5-7.

- Increasing the number of aircraft observations does not compensate for the quality loss observed by going from S1 to S2. In fact the global impact of a fourfold increase of AMDAR bulletins is only marginally positive on all verified parameters. This is not surprising for the humidity field - AMDAR do not contain humidity information - but such a weak impact on the wind field was not anticipated.

  However one should note the highly non-uniform distribution of AMDAR observations in the model domain (see figure 4-1) which could partly explain this fact. A look at figures 5-8 and 5-9 shows that AMDAR data have at least locally a remarkable impact, and are even able to improve the humidity field.

- All differences observed at analysis time have vanished *after 6 to 12 hours forecast.* This is again consistent with our experience, that for a limited area model similar to aLMo the impact of the initial conditions does not generally extend more than 12 to 18 hours into the forecast.

- A verification with a higher spatial granularity (Alpine region, the four quadrants west, north, east and south of the Alps) presents the same patterns.

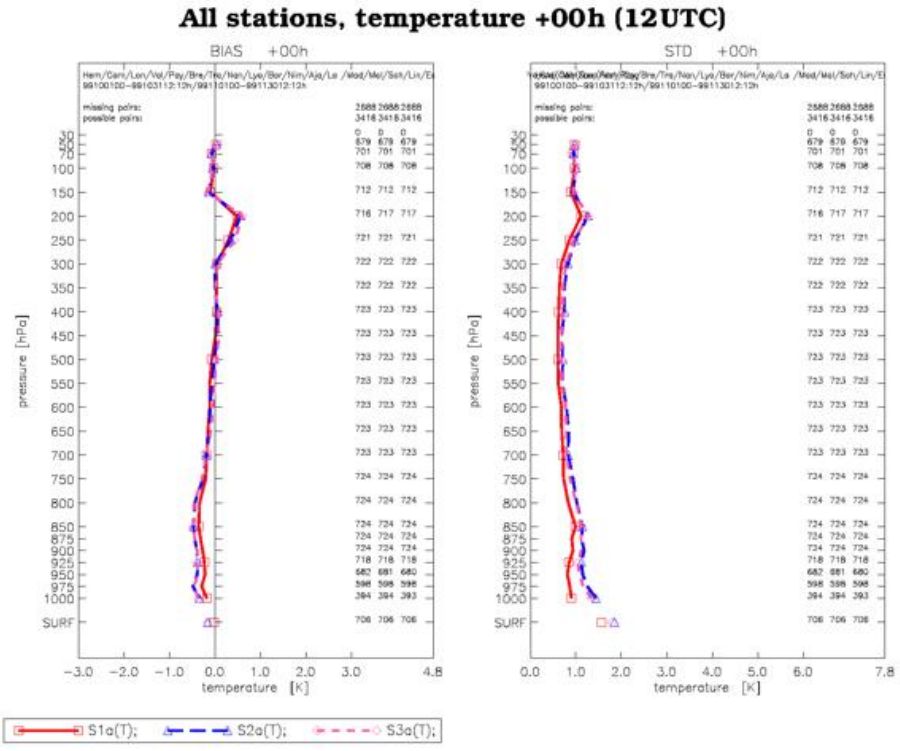


FIGURE 5-1. Bias (left panel) and standard deviation (right panel) of the temperature at initialization time calculated for the 27 forecasts against the 28 stations defined in section 5.1. Red curves are for observing system S1, blue curves for observing system S2 and magenta curves for observing system S3.

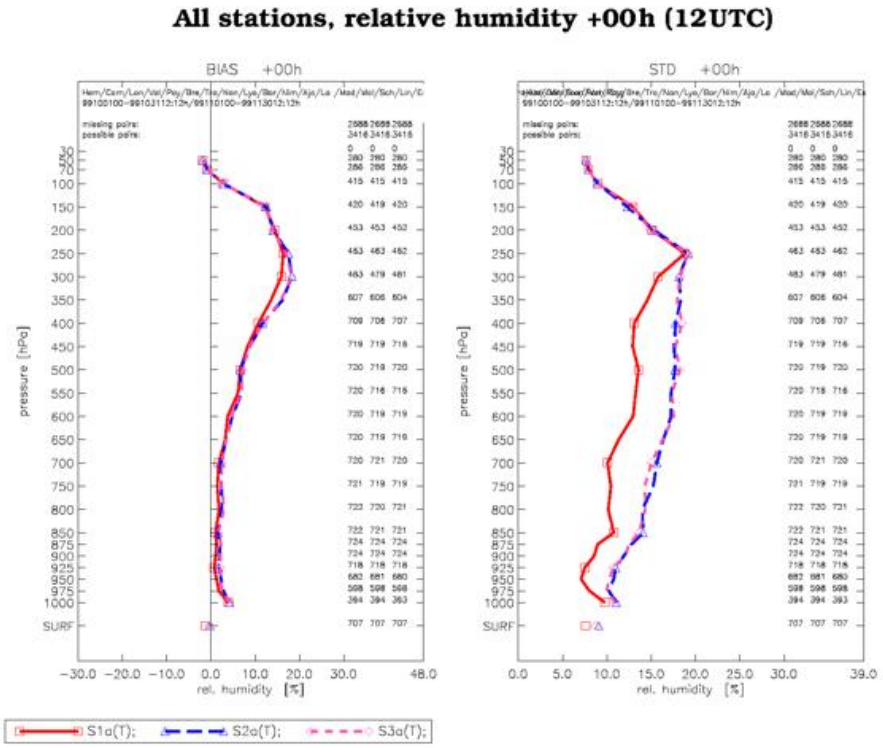


FIGURE 5-2. Bias (left panel) and standard deviation (right panel) of the relative humidity at initialization time calculated for the 27 forecasts against the 28 stations defined in section 5.1. Red curves are for observing system S1, blue curves for observing system S2 and magenta curves for observing system S3.

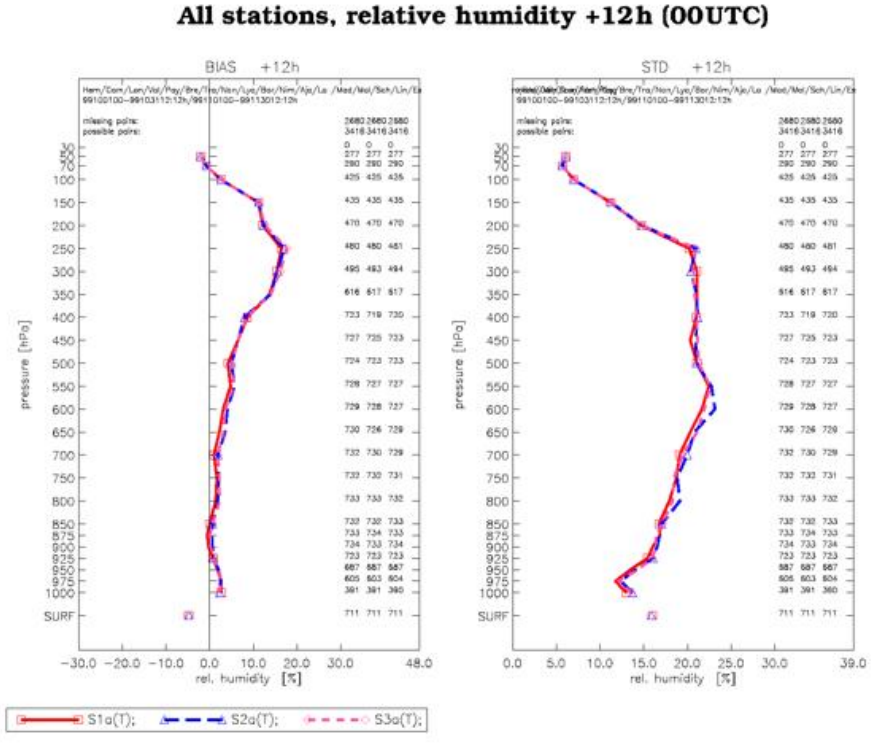


FIGURE 5-3. As in figure 5-2, after 12 hour forecast.

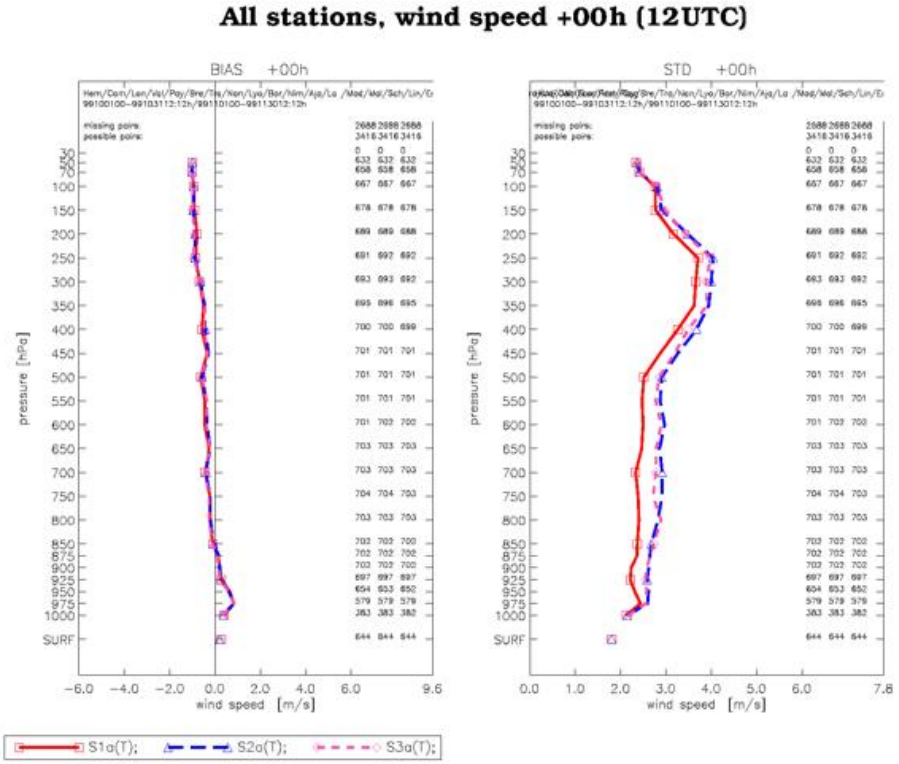


FIGURE 5-4. Bias (left panel) and standard deviation (right panel) of the wind speed at initialization time calculated for the 27 forecasts against the 28 stations defined in section 5.1. Red curves are for observing system S1, blue curves for observing system S2 and magenta curves for observing system S3.

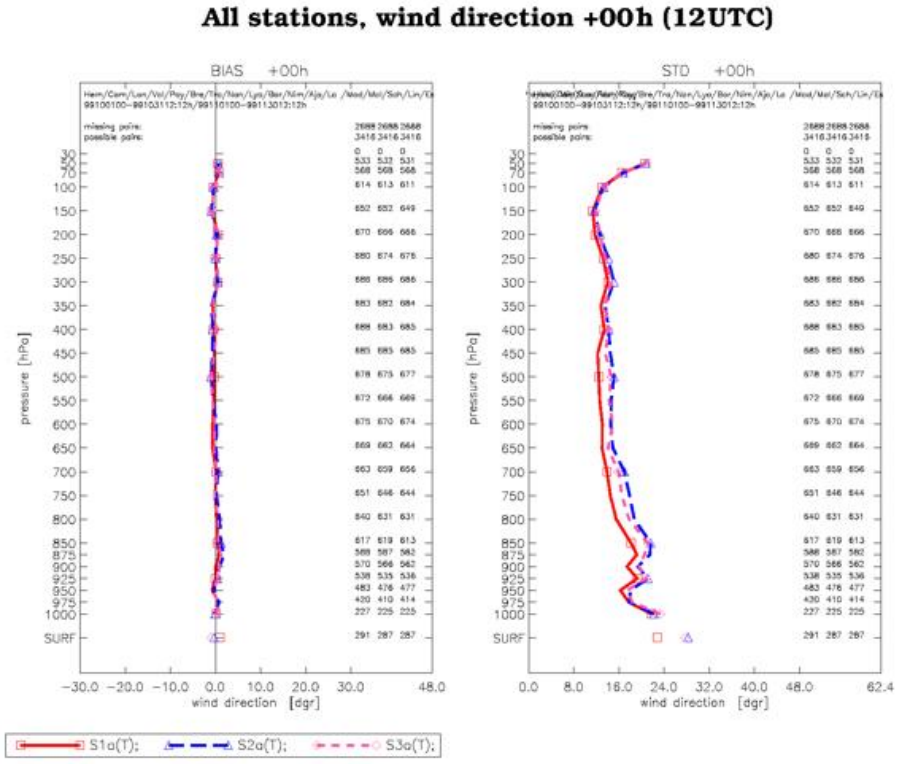


FIGURE 5-5. As in figure 5-4, for the wind direction.

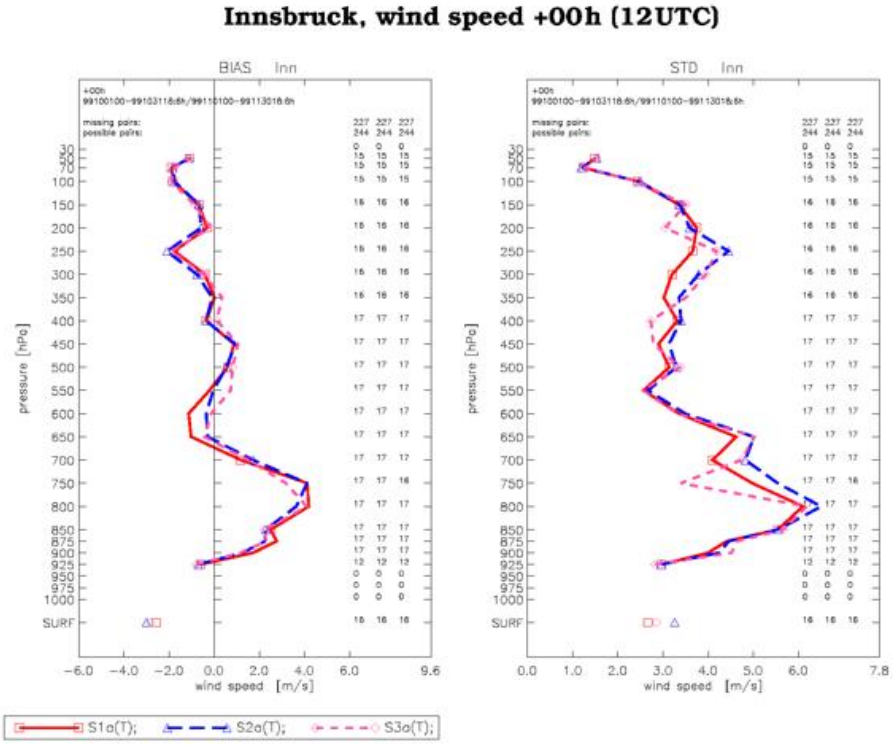


FIGURE 5-6. Bias (left panel) and standard deviation (right panel) of the wind speed at initialization time calculated for the 27 forecasts against the vertical sounding at Innsbruck. Red curves are for observing system S1, blue curves for observing system S2 and magenta curves for observing system S3. Innsbruck is a radiosonde station which is not used in our OSE.

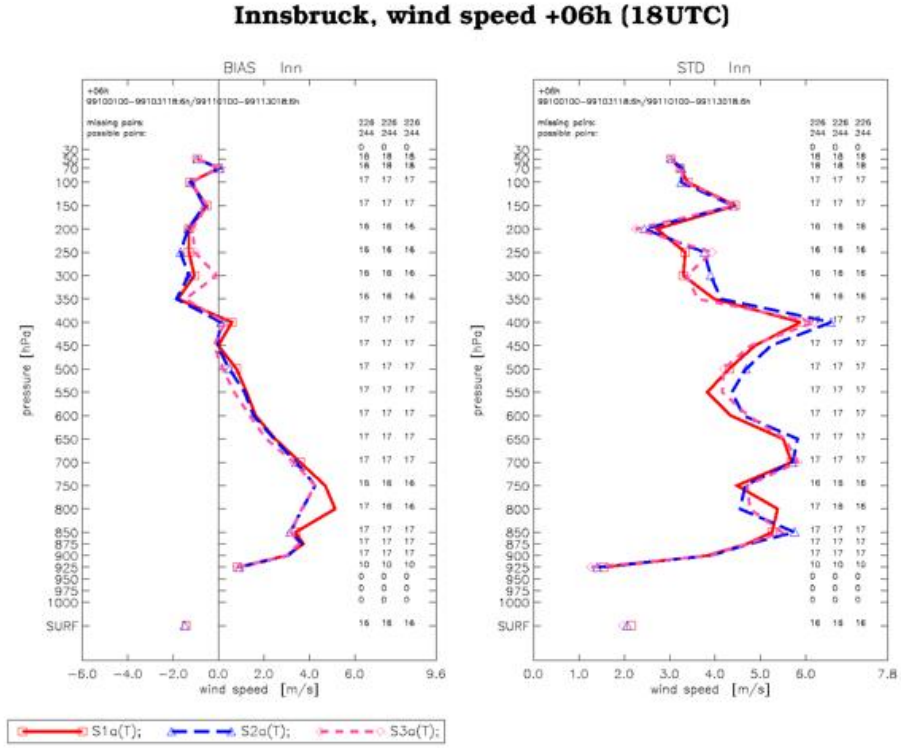


FIGURE 5-7. As in figure 5-6, after 6 hour forecast.

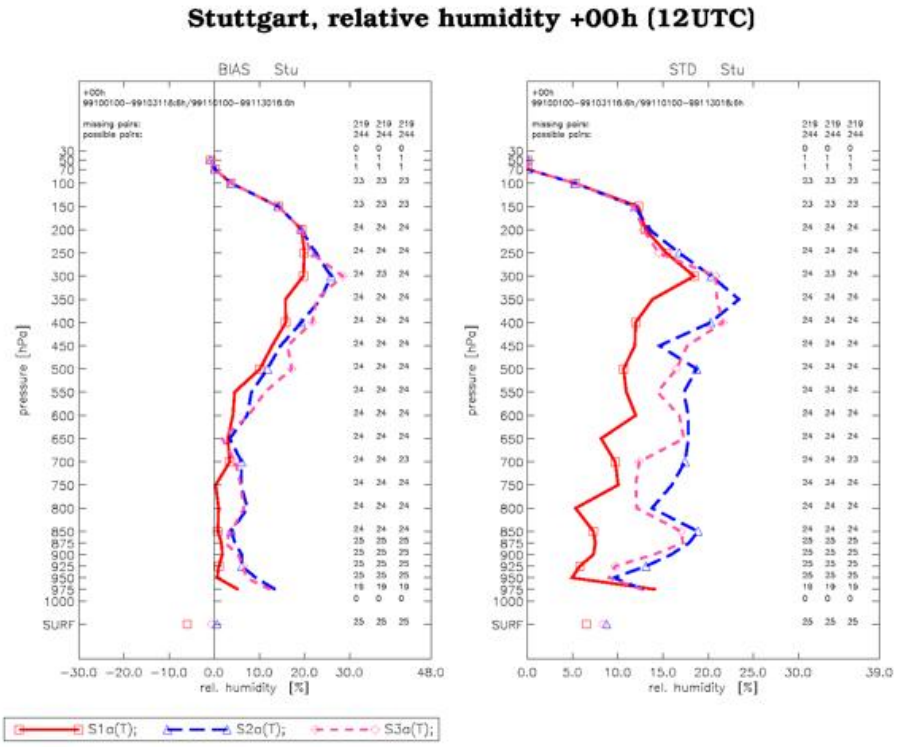


FIGURE 5-8. Bias (left panel) and standard deviation (right panel) of the relative humidity at initialization time calculated for the 27 forecasts against the vertical sounding at Stuttgart. Red curves are for observing system S1, blue curves for observing system S2 and magenta curves for observing system S3. Stuttgart is a radiosonde station which is blacklisted in S2 and S3, and is a location with many AMDARs data.

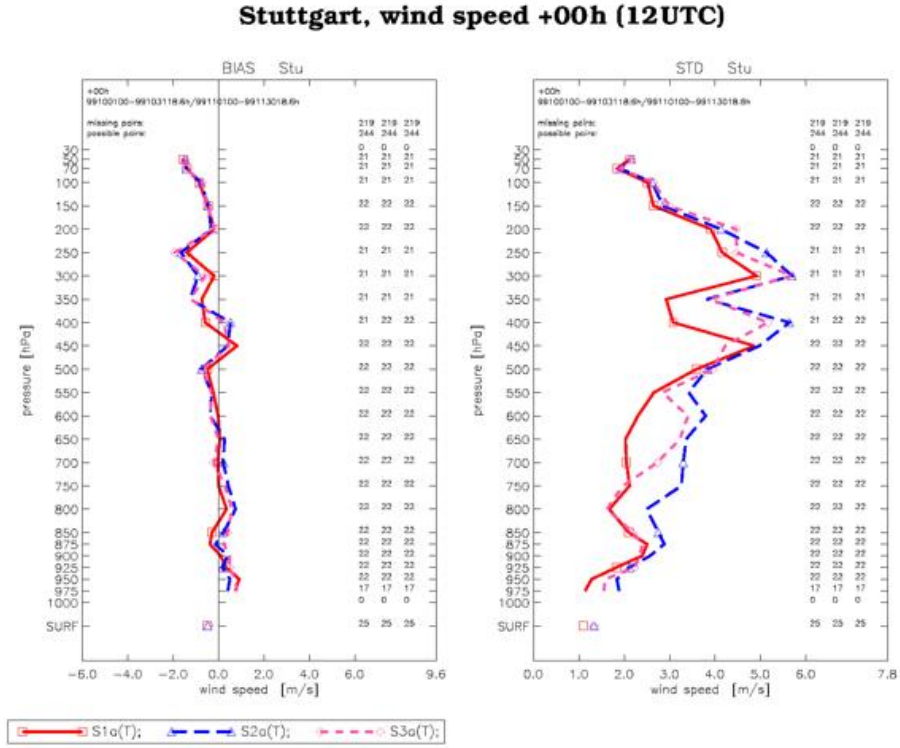


FIGURE 5-9. As in figure 5-8, for wind speed.

Another comment can be made about the figure 5-2: in all three experiments the humidity *bias* in the lower troposphere is about zero, meaning that the global water vapour budget is correct and very similar for all experiments (this is consistent with the fact that fluxes through lateral boundaries and soil model state are identical in S1, S2 and S3). What is clearly degraded by the reduction of the number of radiosonde stations is *the distribution* of humidity in the integration domain, resulting in the observed increase of standard deviation.

5.2 Near-Surface Weather Parameters over Switzerland

A statistical verification of 2-m temperature, 2-m dewpoint depression, 10-m wind, hourly sums of precipitation and cloud cover over *Switzerland* against data from the 72 stations of the Swiss automatic surface stations network (ANETZ) has been applied. Precipitation scores have also been calculated. To interpret these results it is important to realize that the observing system modifications associated with S2 resulted in a local increase of the number of radiosonde observations (Payerne station, on the Swiss Plateau, going from 2 to 4 daily soundings).

The results of this verification can be summarized by the three following statements and are illustrated by the statistical scores of figures 5-10 to 5-13:

- The sensitivity of the near-surface parameters to the modifications of the observing system is weaker than what has been observed in the verification of the vertical structure of the model atmosphere (e.g. compare the sensitivity of the wind speed standard deviation in fig. 5-4 and in fig. 5-10).
- Over Switzerland the modification of the radiosonde network results in a small degradation of the 10-m wind speed and direction (fig. 5-10) but induces a significant reduction in variance of precipitation, which even persists up to the end of the forecast (fig. 5-12.) The cloud cover bias is also slightly improved (fig. 5-11).

  The small degradation of the 10-m wind field associated with the increased sounding frequency probably reflects a weakness of our near-surface wind assimilation algorithm in presence of strong orographic forcing.

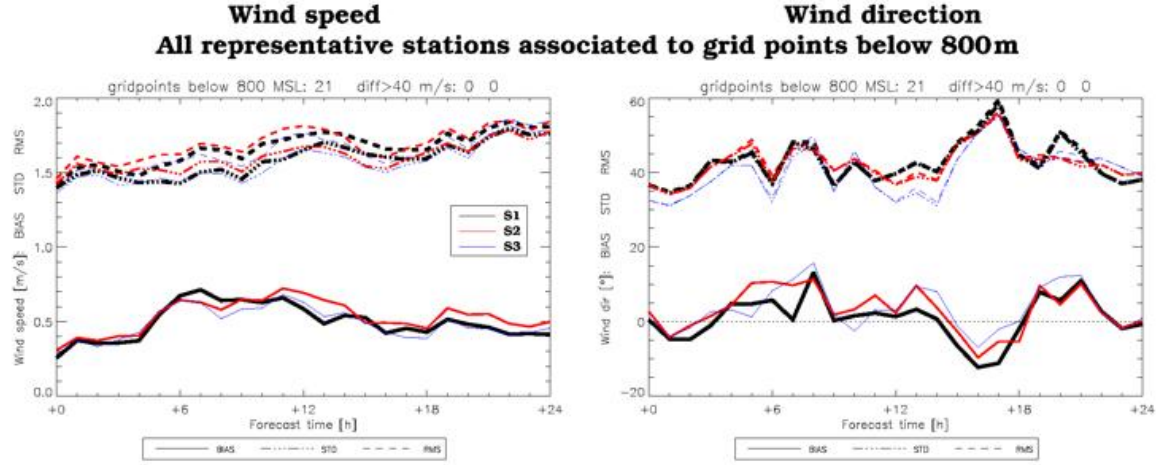


FIGURE 5-10. Hourly variation of some statistical scores for the 10-m wind speed (left panel) and for the 10-m wind direction (right panel), verified against the 21 representative ANETZ stations associated to a model grid point below 800 m. Black curves are for observing system S1, red curves for observing system S2 and blue curves for observing system S3. The plain lines represent the bias, the dotted lines represent the rms and the dash/dotted lines represent the standard deviation.

The observed improvement of cloudiness and precipitation reflects the better three-dimensional fields over Switzerland, due to the increased number of assimilated soundings. In contrast, this confirms the negative impact a reduction of the number of radiosonde observations can locally have on wet weather elements.

- One observes a small but clearly positive impact of AMDAR observations on the temperature standard deviation (compare in fig. 5-13 the impact on the 2-m temperature near an airport, at Kloten, and further away at Bern) and on the wind speed and direction (e.g. look at the wind speed standard deviation in fig. 5-10). This improvement is visible in the analysis *and* in the first 6 to 12 h forecast.

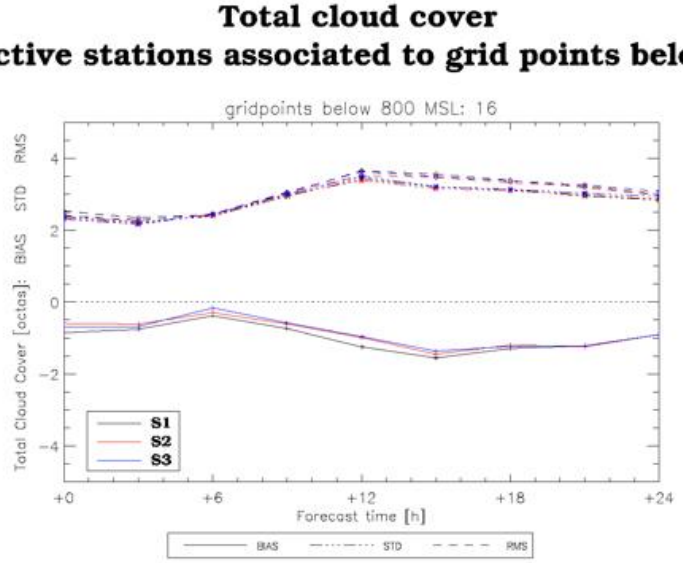


FIGURE 5-11. As figure 5-10, for the total cloud cover verified against the 16 active ANETZ stations associated to a model grid point below 800 m. All grid points within 30 km of an observation location are considered when calculating the scores.

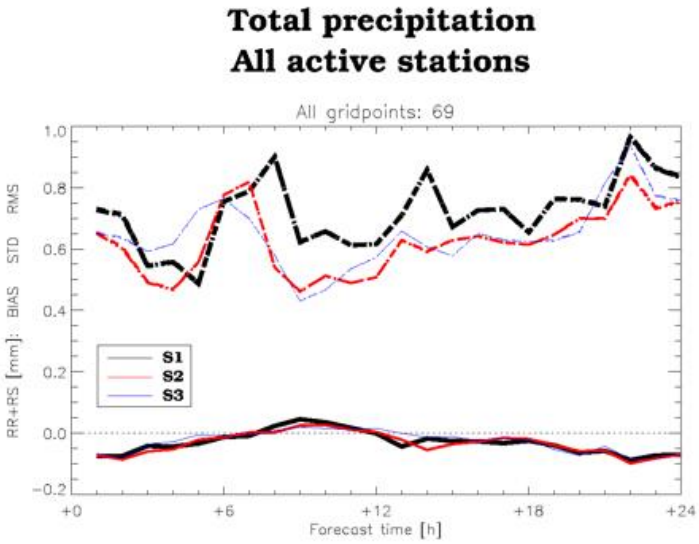


FIGURE 5-12. As figure 5-10, for the hourly total precipitation verified against all 69 active ANETZ stations. The plain lines represent the bias, the dash/dotted lines the standard deviation. A mean of 5 grid points around an observation is done before calculating the scores.

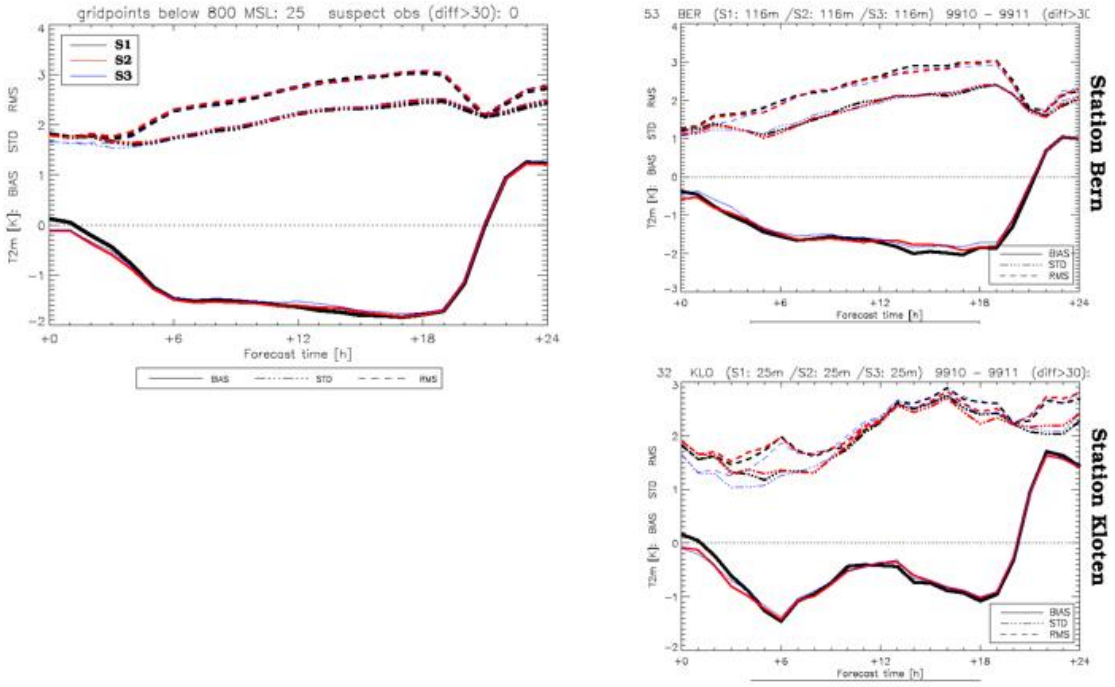


FIGURE 5-13. Upper left panel: hourly variation of bias (solid line) and standard deviation (dashed line) for the 2-m temperature, verified against the 25 active ANETZ stations associated to a model grid point below 800 m. Black curves are for observing system S1, red curves for observing system S2 and blue curves for observing system S3. Right panels: same as upper left panel but for a single ANETZ station. Both Bern and Kloten are on the Swiss Plateau, the latter one is also at an international airport location.

5.3 Case Study

A study of the forecast based on the 6th November 1999 12 UTC analysis has been done. This case is characterized by a blocking situation over the Western edge of the continent with a cut-off low over the South of Europe. Heavy precipitation – partly convective – has been observed in the Southern part of the Alps (Tessin, Lago Maggiore).

This case has been investigated at ECMWF [Cardinali, 2000] and it has been found that the synoptic situation was better described by forecast based on the observing system S1, the information from all the stations over the Atlantic border being very important for this particular meteorological situation.

No such synoptic scale differences are observed by looking at the high resolution short range forecast produced by aLMo; this is consistent with the fact that the synoptic structures are forced by the driving model, which is the same ECMWF operational deterministic forecast in all three experiments. However, smaller scale structures do exhibit significant differences, and a clear improvement of the location and the spread of the heavy precipitation region is brought by the additional AMDAR observations (see figure 5-14). The negative impact due to the suppression of Nancy and Stuttgart radiosondes – north of Switzerland – is also well visible.

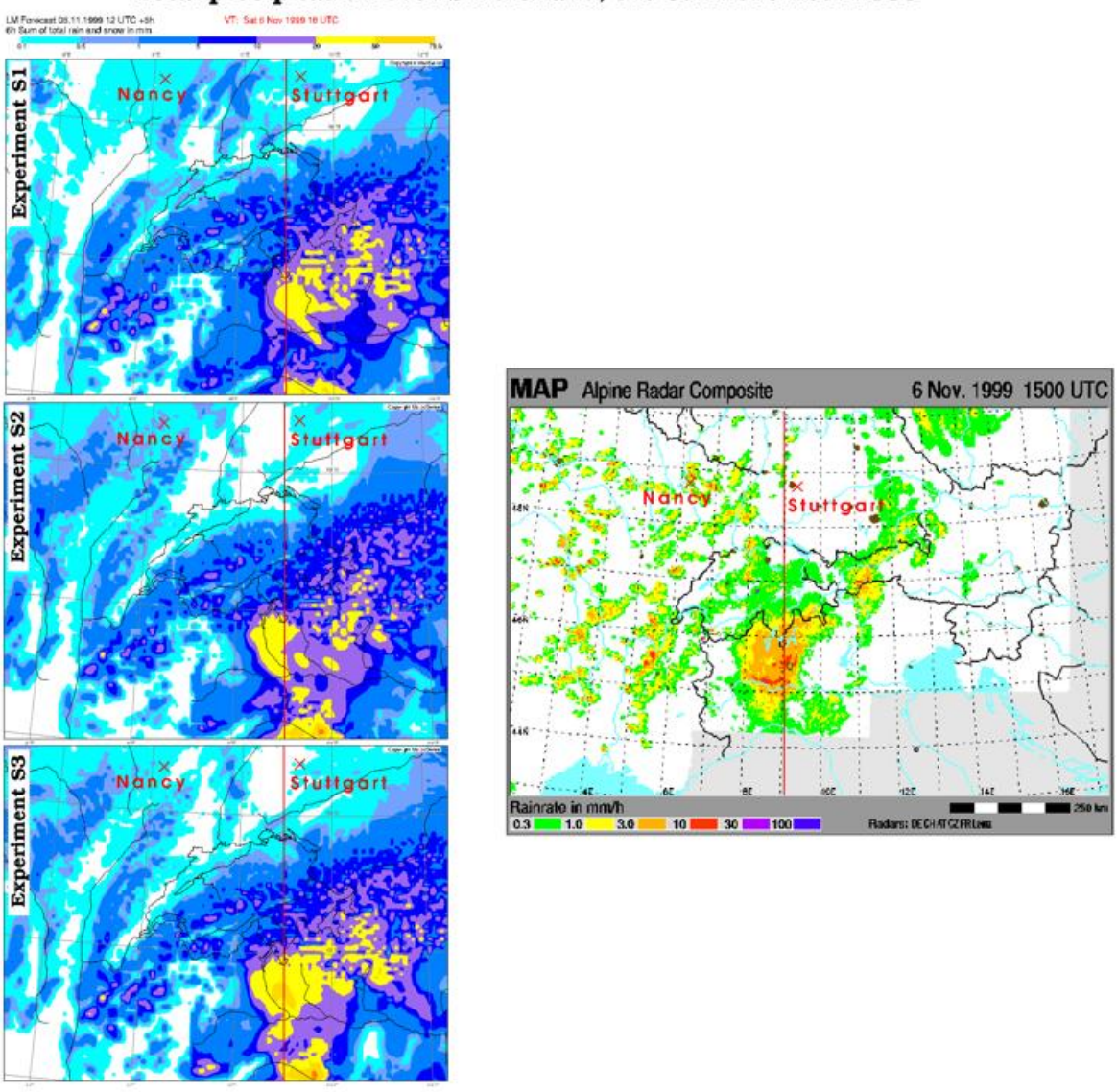


FIGURE 5-13. Sensitivity of a heavy precipitation event over Southern part of the Alps to the observing system. Left panels: 6 hours sum of total precipitation forecast over Switzerland, evaluated on the 6th November 1999 between 12 UTC (analysis time) and 18 UTC. Right panel: Total precipitation rate observed by the MAP Alpine Radar Composite on the 6th November 1999 at 15 UTC (data for the whole MAP period are available on-line at www.map.ethz.ch). Yellow areas in the left panels can be compared with light orange areas in the right panel, and correspond to about 20 to 50 mm precipitation in 6 hours.

6 Conclusion

The motivation of all EUCOS observing system experiments done at ECMWF [Cardinali, 2000], DMI [Amstrup, 2000] and MeteoSwiss was the evaluation of the impact of the proposed EUMETNET observing system modification on the quality of numerical weather forecast. It has been shown that a reduction of the number of active radiosonde stations had a very small but slightly negative impact on both the global ECMWF model and the DMI-HIRLAM-G limited area model, and the additional AMDAR data have been found to slightly degrade the quality of the forecast. The results obtained with aLMo differ substantially. To understand

this fact, one should keep in mind that the two other models have a coarser horizontal resolution (50 to 60 km instead of 7 km), and that the DMI-HIRLAM-G is integrated over a much larger domain than the EUCOS region and uses an intermittent data assimilation scheme. In the present study we have found:

- A *significant* degradation of the model quality at analysis time and in the very short range is associated with the reduction of the number of radiosonde stations. This degradation is mainly visible in the distribution of the 3-dimensional fields inside the model domain (meso-β structures).The quality of precipitation is also degraded.

  The increased observation frequency of the remaining stations does not compensate for the reduced horizontal resolution of the observing system, except in the surrounding of an upgraded station. This is consistent with previous OSSEs [Bettems, 1999].

- Measured over the *whole model domain* the impact of the additional AMDARs is positive but very small. However, a clear improvement of wind, temperature *and humidity* fields is *locally* observed, in regions well covered by AMDAR platforms. This improvement is significant, but does not compensate the quality loss brought by the radiosonde network degradation.

- Even in *regions well covered by radiosonde observations*, the AMDAR data bring a clear improvement of the forecast quality (e.g. see fig. 5-10).

These results suggest a degradation of the (mean) quality of high resolution short range numerical weather forecast associated with the introduction of one of the proposed EUCOS scenario, if no compensatory actions are taken. AMDAR observations have a clear potential, and an improved horizontal coverage (e.g. using regional flights) would certainly mitigate the expected quality loss. However additional information about local structures in the humidity field are needed.

Acknowledgements

This work would not have been possible without the great support of the Swiss Center for Scientific Computing (SCSC) which provided me with the necessary resources on their NEC SX5. I was able to calculate up to 9 days assimilation in 24 h, besides all the operational tasks of MeteoSwiss running on this machine, ... and all the jobs of the other users.

Many thanks also to Claudia Cardinali for providing me with the necessary blacklists for the OSE, and to Carsten Maasz for helping me with the MARS system at ECMWF.

My colleagues Marco Arpagaus and Francis Schubiger processed the OSE results with the verification packages to extract meaningful statistical scores, thanks for your effort!

Annex

This annex gives the blacklists defining the observing systems S1, S2 and S3. These lists have been provided by Mrs. Carla Cardinali from ECMWF and complemented by the information listed in table 1 of the document EUCOS-SPC-003 (radiosonde stations whose operating mode changed during EUCOS observing period).

Blacklist for TEMP, observing system S1:

All synoptic times (53 elements)

"11010", "11120", "07690", "11240", "06400", "06496", "06060", "07137", "07255", "07503", "10304", "10437", "10828", "10962", "06242", "03023", "03130", "03213", "03377", "03414", "03590", "03693", "03696", "03743", "11036", "11105", "11123", "07112", "07453", "07613", "07614", "07615", "07616", "07664", "10393", "11394", "10722", "06348", "01010", "06792", "03501", "03608", "03807", "03840", "16087", "16113", "16121", "06831", "06832", "06833", "06842", "06843", "06844"

00 UTC (3 elements)

"16754", "01152", "08579"

06 UTC (12 elements)

"11350", "07510", "07645", "10350", "16622", "16754", "01415", "08579", "08100", "08301", "06610", "08495"

12 UTC (2 elements)

"01152", "08579"

18 UTC (12 elements)

"11350", "07510", "07645", "10350", "16622", "16754", "01152", "01415", "08100", "08301", "06610", "08495"

Blacklist for TEMP, observing systems S2 and S3 (90 elements):

"06447", "06181", "02836", "07110", "07145", "07180", "07481", "07761", "10184", "10200", "10238", "10410", "10486", "10548", "10618", "10739", "10771", "10868", "16716", "16080", "16144", "16245", "16429", "01384", "01400", "08023", "08160", "08221", "08430", "02365", "03005", "03502", "03882", "03920", "11010", "11120", "07690", "11240", "06476", "06400", "06496", "06060", "07137", "07255", "07503", "10304", "10437", "10828", "10962", "06242", "03023", "03130", "03354", "03213", "03377", "03414", "03590", "03693", "03696", "03743", "11036", "11105", "11123", "07112", "07453", "07613", "07614", "07615", "07616", "07664", "10393", "11394", "10722", "06348", "01010", "02591", "06792", "03501", "03608", "03807", "03840", "16087", "16113", "16121", "06831", "06832", "06833", "06842", "06843", "06844"

Blacklist for AMDAR, observing systems S1 and S2 (121 elements):

"EU0088", "EU0123", "EU0143", "EU0175", "EU0201", "EU0204", "EU0221", "EU0245", "EU0249", "EU0254", "EU0263", "EU0274", "EU0285", "EU0291", "EU0300", "EU0312", "EU0332", "EU0341", "EU0347", "EU0354", "EU0357", "EU0363", "EU0372", "EU0385", "EU0393", "EU0405", "EU0482", "EU0574", "EU0720", "EU0807", "EU0934", "EU0947", "EU0961", "EU0985", "EU1002", "EU1222", "EU1495", "EU1593", "EU1673", "EU1688", "EU1692", "EU2378", "EU2399", "EU2547", "EU2578", "EU2590", "EU2618", "EU2630",

"EU2634", "EU2689", "EU2845", "EU2890", "EU2896", "EU2912", "EU2978", "EU2984", "EU3056", "EU3268", "EU3321", "EU3654", "EU3684", "EU3689", "EU3908", "EU4002", "EU4003", "EU4021", "EU4278", "EU4387", "EU4409", "EU4529", "EU4587", "EU4656", "EU4838", "EU5098", "EU5167", "EU5182", "EU5349", "EU5590", "EU5673", "EU6287", "EU6386", "EU6524", "EU6723", "EU6893", "EU6923", "EU7082", "EU7285", "EU7521", "EU7634", "EU7865", "EU7866", "EU8264", "EU8431", "EU8478", "EU8598", "EU8605", "EU8632", "EU8736", "EU8789", "EU8891", "EU8943", "EU9023", "EU9356", "EU9378", "EU9589", "EU9678", "EU9692", "EU9734", "EU9967", "EU0041", "EU0043", "EU0047", "EU0050", "EU0052", "EU0059", "EU0061", "EU0106", "EU0154", "EU0158", "EU0167", "EU0185"

Blacklist for PILOT, observing systems S1, S2 and S3 (20 elements):

"11036", "11105", "11123", "07112", "07453", "07613", "07614", "07615", "07616", "07664", "10393", "11394", "10722", "06348", "01010", "06792", "03501", "03608", "03807", "03840"

References

Amstrup, B., 2000: EUCOS observing system experiments with the DMI-HIRLAM Optimum Interpolation analysis and forecasting system. *Danish Meteorological Institute - Scientific Report*, 00-19.

Bettems, J.-M., 1999: The impact of hypothetical wind profiler networks on numerical weather prediction in the Alpine region. *Publications de l'Institut Suisse de Meteorologie*, 59.

Bougeault, P., P. Binder, A. Buzzi, R. Dirks, R. Houze, J. Kuettner, R. B. Smith, R. Steinacker, H. Volkert and all MAP Scientists, 2001: The MAP Special Observing Period. *Bull. Amer. Meteorol. Soc.*, 82, 433-462.

Cardinali, C., 2000: EUCOS Impact Study. *ECMWF Technical Memorandum*, 325.

Davies, H.C., 1976: A lateral boundary formulation for multilevel prediction models. *Quart. J. Roy. Meteor. Soc.*, 102, 405-418.

Doms, G. and U. Schättler, 2001: COSMO Newsletter, 1, 7-14.

Häberli, C., 1998: Quality assessment of upper air soundings in MAP. *The MAP Newsletter*, 9, 68-69.

Pailleux, J. et al., 1997: Impact of various observing systems on numerical weather prediction. *Proc. of the CGC/WMO workshop*, Geneva 7-9 April 1997, WMO/TD 868.

Schraff, C., 1997: Mesoscale Data Assimilation and Prediction of Low Stratus in the Alpine Region. *Meteorol. Atmos. Phys.*, 64, 21-50.

List of COSMO Newsletters and Technical Reports

(available for download from the COSMO Website: www.cosmo-model.org)

COSMO Newsletters

Newsletter No.1, February 2001.

Newsletter No.2, February 2002.

COSMO Technical Reports

No. 1, Dmitrii Mironov and Matthias Raschendorfer (2001): *Evaluation of Empirical Parameters of the New LM Surface-Layer Parameterization Scheme. Results from Numerical Experiments Including the Soil Moisture Analysis.*

No. 2, Reinhold Schrodin and Erdmann Heise (2001): *The Multi-Layer Version of the DWD Soil Model TERRA_LM.*

No. 3, Günther Doms (2001): *A Scheme for Monotonic Numerical Diffusion in the LM.*

No. 4, Hans-Joachim Herzog, Ursula Schubert, Gerd Vogel, Adelheid Fiedler and Roswitha Kirchner (2002): *LLM – the High-Resolving Nonhydrostatic Simulation Model in the DWD – Project LITFASS. Part I: Modelling Technique and Simulation Method.*

No. 5, Jean-Marie Bettems (2002): *EUCOS Impact Study Using the Limited-Area Non-Hydrostatic NWP Model in Operational Use at MeteoSwiss.*

COSMO Technical Reports

Issues of the COSMO Technical Reports series are published by the *Consortium for Small-Scale Modelling* at non-regular intervals. COSMO is a European group for numerical weather prediction with participating meteorological services from Germany (DWD, AWGeophys), Greece (HNMS), Italy (UGM, ARPA-SMR) and Switzerland (MeteoSwiss). The general goal is to develop, improve and maintain a non-hydrostatic limited area modelling system to be used for both operational and research applications by the members of COSMO. This system is initially based on the Lokal-Modell (LM) of DWD with its corresponding data assimilation system.

The Technical Reports are intended

- for scientific contributions and a documentation of research activities,
- to present and discuss results obtained from the model system,
- to present and discuss verification results and interpretation methods,
- for a documentation of technical changes to the model system,
- to give an overview of new components of the model system.

The purpose of these reports is to communicate results, changes and progress related to the LM model system relatively fast within the COSMO consortium, and also to inform other NWP groups on our current research activities. In this way the discussion on a specific topic can be stimulated at an early stage. In order to publish a report very soon after the completition of the manuscript, we have decided to omit a thorough reviewing procedure and only a rough check is done by the editors and a third reviewer. We apologize for typographical and other errors or inconsistencies which may still be present.

At present, the Technical Reports are available for download from the COSMO web site (www.cosmo-model.org). If required, the member meteorological centres can produce hard-copies by their own for distribution within their service. All members of the consortium will be informed about new issues by email.

For any comments and questions, please contact the editors:

Günther Doms
guenther.doms@dwd.de

Ulrich Schättler
ulrich.schaettler@dwd.de

Consortium

for

Small-Scale Modelling

Technical Report No. 1

Evaluation of Empirical Parameters of the New LM Surface-Layer Parameterization Scheme

Results from Numerical Experiments Including the Soil Moisture Analysis

by

Dmitrii Mironov and Matthias Raschendorfer

March 2001

Deutscher Wetterdienst

MeteoSwiss

Ufficio Generale per la Meteorologia

Hellenic National Meteorological Service

Amt für Wehrgeophysik

Il Servicio Meteorologico Regionale di ARPA

www.cosmo-model.org

Editors: G. Doms and U. Schättler, Deutscher Wetterdienst, P.O. Box 100465, 63004 Offenbach, Germany
Printed at Deutscher Wetterdienst, Offenbach am Main

COSMO Technical Reports

Issues of the COSMO Technical Reports series are published by the *Consortium for Small-Scale Modelling* at non-regular intervals. COSMO is a European group for numerical weather prediction with participating meteorological services from Germany (DWD, AWGeophys), Greece (HNMS), Italy (UGM, ARPA-SMR) and Switzerland (MeteoSwiss). The general goal is to develop, improve and maintain a non-hydrostatic limited area modelling system to be used for both operational and research applications by the members of COSMO. This system is initially based on the Lokal-Modell (LM) of DWD with its corresponding data assimilation system.

The Technical Reports are intended

- for scientific contributions and a documentation of research activities,
- to present and discuss results obtained from the model system,
- to present and discuss verification results and interpretation methods,
- for a documentation of technical changes to the model system,
- to give an overview of new components of the model system.

The purpose of these reports is to communicate results, changes and progress related to the LM model system relatively fast within the COSMO consortium, and also to inform other NWP groups on our current research activities. In this way the discussion on a specific topic can be stimulated at an early stage. In order to publish a report very soon after the completition of the manuscript, we have decided to omit a thorough reviewing procedure and only a rough check is done by the editors. We apologize for typographical and other errors or inconsistencies which may still be present.

The report series is also open for contributions from external users of the LM system at various universities and research institutes.

At present, the Technical Reports are available for download from the COSMO web site (www.cosmo-model.org). If required, the member meteorological centres can produce hard-copies by their own for distribution within their service. All members of the consortium will be informed about new issues by email.

For any comments and questions, please contact the authors of the present issue,

Dmitrii Mironov
dmitrii.mironov@dwd.de

Matthias Raschendorfer
matthias.raschendorfer@dwd.de

or the editors:

Günther Doms
guenther.doms@dwd.de

Ulrich Schättler
ulrich.schaettler@dwd.de

Evaluation of Empirical Parameters of the New LM Surface-Layer Parameterization Scheme

Results from Numerical Experiments Including the Soil Moisture Analysis

Dmitrii Mironov and Matthias Raschendorfer

Deutscher Wetterdienst, Abteilung Meteorologische Analyse und Modellierung,
Referat FE14, Frankfurter Str. 135, D-63067 Offenbach am Main, Germany
dmitrii.mironov@dwd.de, matthias.raschendorfer@dwd.de

1 Introduction

In this note, we outline some results from numerical experiments aimed at optimizing empirical parameters of the new LM surface-layer parameterization scheme (Raschendorfer 1999). This work is envisaged in frames of the COSMO Work Package 3.1. Both "component testing", where the fidelity of the individual model components are tested independently, and "system testing", where the overall performance of the model is tested (Wyngaard and Moeng 1993), have been performed. First, the new LM surface-layer parameterization scheme has been tested independently, using a single-column atmospheric model developed at DWD and observational data from the Lindenberg Meteorological Observatory (Beyrich 2000, Beyrich et al. 2000a, 2000b). By and large the new surface-layer parameterization scheme showed a rather promising performance. A number of shortcomings have been revealed, and the ways of improving the scheme have been suggested. Results from that study will be described in Mironov et al. (2001) in some detail. We will not further discuss them here.

Although results from component testing are extremely useful in understanding whether a parameterization in question appropriately accounts for the essential physical processes at work, they cannot be conclusive. As far as operational applications are concerned, they can only be suggestive. A parameterization scheme that performs well during independent component tests may not perform equally well in the full three-dimensional model environment due to shortcomings of the other model components which have previously been tuned to compensate each other's errors. Therefore, some tuning is usually required when an improved parameterization is implemented (although it should be avoided whenever possible, see Randall and Wielicki 1997, for discussion).

2 Background

Two types of tuning parameters are distinguished, *model parameters* and *external parameters*. Model parameters are usually independent of space and time but dependent on the model formulation. That is, they are constants in the context of a particular physical parameterization used, but more generally, are functions of other physical variables that are not accounted for. Classical examples of the model parameters are the von Kármán constant and the Charnock constant. External parameters describe the application-specific parts of the

model set-up, such as geometry of the model and characteristics of the model lower boundary. These may vary in space and some also in time. Examples of the external parameters are the aerodynamic roughness of the land surface (space dependent) and the leaf area index (space and time dependent).

The new LM surface-layer parameterization scheme (Raschendorfer 1999) is intimately connected with a new atmospheric turbulence mixing scheme, the latter being a version of the Mellor and Yamada (1974, 1982) level 2.5 closure using the turbulent kinetic energy as a prognostic variable. Both schemes are planned to be used for operational numerical weather prediction at DWD in spring 2001 (a detailed description of the new schemes will be published in a forthcoming issue of the COSMO technical report). The surface-layer scheme is formulated in such a way that dimensionless coefficients in the surface-layer Monin-Obukhov stability functions are expressed through the dimensionless coefficients of the Mellor-Yamada closure. As the Mellor-Yamada closure has been comprehensively tested in numerous applications (see Nurser 1996, for an overview), the estimates of its dimensionless coefficients are fairly reliable. This tends to reduce the number of LM model parameters to be tuned.

However, high complexity of the interaction of the atmosphere with the underlying surface requires the introduction of additional model parameters and external parameters into the LM surface-layer scheme. New model parameters have been introduced which directly affect the resistance of the air layer immediately adjacent to the underlying surface (laminar sub-layer, see Raschendorfer 1999, for details) to the transfer of momentum and of scalar quantities, respectively (in the LM code notation, these are RLAM_MOM and RLAM_HEAT). A new model parameter has been introduced (RAT_CAN in the LM code notation) that controls the "effective" height of the roughness (canopy) elements. It has a pronounced effect on the surface-layer resistance. This parameter would not be required if the above effective height is introduced as a space-dependent external parameter.

New external parameters have also been introduced in the surface-layer scheme to describe various types of the underlying surface in more detail (theses are the surface area indices of bare soil and of non-evaporating surface). Together with the leaf area index that is already present in the operational LM surface-layer scheme, these parameters have a major effect on evapotranspiration. More specifically, they govern the resistance to the transfer of water vapour from/to the upper soil layer and plants to/from the adjacent surface air layer. As these parameters have no influence on the resistance to the heat transfer, they can be used to change the Bowen ratio.

However, the evapotranspiration is also heavily dependent on the soil moisture. Within the LM data assimilation stream (based on the observational nudging analysis technique), the soil moisture field used to be a free-running prognostic model variable that was not corrected using observations. This was the situation until March 2000, when the soil moisture analysis (SMA) scheme was introduced (Hess 2001). With the SMA, the soil moisture can no longer be considered as a purely physical quantity. Rather it is a "fitting" quantity that is determined so that the predicted 2m temperatures at 12 UTC and 15 UTC give the best fit to the observations. The impact of the SMA is a maximum during warm sunny days. In cloud conditions with low radiation impact, the effect of the SMA is much lower. In these conditions, the influence of soil moisture on the 2m temperature is small. In a sense the soil moisture analysis is a "system testing procedure" that adjusts the time and space dependent model parameters, namely the soil moistures in the two soil layers, to improve the model performance for the 2m temperature. Notice that the resulting model soil moisture is not necessarily in agreement with the actual soil moisture. More likely the SMA adjusts the soil moisture so that to compensate for errors in the day-time 2m temperature introduced by

the other LM components. Clearly, an "ideal" model whose forecast is in perfect agreement with observations would not require any SMA-induced changes of the soil moisture. Thanks to the SMA, the abovementioned external parameters of the surface-layer scheme have now a minor effect on the forecast of the 2m temperature and of the 2m dew point. Any changes of the external parameters that affect evaporation would be compensated by changes in the soil moisture induced by the SMA.

The above is not true for the model parameters of the LM surface-layer scheme, first of all, for the parameters that affect the surface-layer resistance to the transfer of scalars (RAT_CAN and RLAM_HEAT). Setting these parameters incorrectly would not result in large errors in the day-time 2m temperature – the SMA would, to a great extent, make up for the deficiencies by appropriately changing the soil moisture. The shortcomings of the surface-layer scheme would, however, manifest themselves in the amplitude of the diurnal cycle of the weather elements, in the minimum temperatures at night and, most notably, in the 2m dew point. This was indeed the case in the previously performed parallel experiments, where the new LM surface-layer scheme was used but the new model parameters were not appropriately tuned (these are experiments No. 102, hereafter "exp_102", and No. 103, "exp_103"). Verification of results from those experiments, although showing a rather satisfactory overall performance of the new scheme, reveal a considerable negative bias of the 2m dew point. It therefore proved to be necessary to tune a number of parameters of the new LM surface-layer scheme with due regard for the SMA.

Although all empirical parameters of the surface-layer scheme are interrelated, as is the case for all turbulence models which are essentially non-linear, we have found that the 2m dew point is most sensitive to the model parameters that directly affect the surface-layer resistance to the transfer of scalar quantities (RAT_CAN and RLAM_HEAT). As explained above, setting these parameters correctly is hardly possible without the use of a full quasi-operational LM including the SMA. The 10m wind is most sensitive to the model parameter that directly affects the surface-layer resistance to the transfer of momentum (RLAM_MOM). As the results from "exp_102" and "exp_103" indicate, the 10m wind with the new surface-layer scheme has a slight positive bias that can be reduced by changing the value of the above parameter. Fortunately, a rough evaluation of this parameter could be made through the LM runs without the use of SMA that are much less expensive computationally.

Finally, a parameter referred to as "pattern length" (PAT_LEN in the LM code notation) helps improve predictions of the weather elements in a stably stratified boundary layer. This parameter controls the degree of enhancement of turbulence due to the sub-grid scale horizontal inhomogeneities of the surface temperature and thus affects turbulence transport. This is a feature of the new LM turbulence scheme which is not present in the operational LM. By tuning the pattern length, predictions of the minimum temperature and the nocturnal wind can be improved. Pattern length should be tuned together with the other model parameter (RLAM_MOM) that directly affects the surface-layer resistance to the transfer of momentum. A rough estimate of the pattern length could be obtained through the LM run without SMA.

Notice that pattern length is actually a location-dependent external parameter. It is related to the length scale of the inhomogeneities of the underlying surface which induce the surface temperature inhomogeneities. As this location dependence of pattern length cannot be rationally determined at present, a constant value is used in LM as if this parameter were a model parameter.

3 Experiments Performed

Since running the full LM suite in a quasi-operational mode over an extended period of time is computationally expensive, evaluating the model parameters by repeatedly performing long parallel experiments deemed unrealistic. Therefore, a series of particularly designed experiments has been performed. A few warm sunny days have been chosen, when the soil moisture changes due to SMA, and, therefore, also changes in evaporation and in the surface-layer specific humidity and dew point, are a maximum. The abovementioned empirical parameters of the surface-layer scheme are optimized by changing their values and repeating 24-hour long runs. The experiments are performed using the DWD Experimental Modelling System (Hanisch 1995).

Notice that the SMA cost function strongly depends on the background soil moisture fields. That is, the scheme accounts for the soil moisture during the past few days and, therefore, does not immediately respond to changes in the external forcing or in model physics. Then, the use of initial fields that are not in accord with the altered model parameters almost inevitably leads to an unsatisfactory prediction of the weather elements in question, first of all, the day-time 2m temperature. This would not have been the case if the SMA had enough time to overcome its "inertia" and set the soil moisture to match the altered model parameters. Therefore, a modified SMA binary (kindly prepared by Reinhold Hess) is used in our 24-hour experiments, where the effect of the background state is practically eliminated. In this way, the SMA is used to determine the initial soil moisture fields that fit the 12 UTC and 15 UTC observations of the 2m temperature. The LM forecast run is then performed for the same day, using these initial soil moisture fields. This is different from the operational SMA implementation, where the 12 UTC and 15 UTC observations of the 2m temperature from the last day are used to correct the soil moisture fields, and the twenty-four hour tendencies from the last-day routine forecast are then added to the above fields to get the initial fields for the next-day forecast run (see Hess 2001, for details).

A large number of 24-hour runs are performed over 2 April 2000, 20 June 2000 and 23 September 2000, to evaluate the abovementioned parameters of the surface-layer scheme. Other experiments have also been performed, but their results are of intermediate character and are not mentioned. Using the estimates of empirical parameters evaluated through the above experiments, further LM test runs are performed for several dates in January 2001. The first month of the new millennium is chosen for a rather cold weather kept over a considerable part of the LM domain for much of the month. As the effect of the soil moisture changes during cold winter periods are typically small, the SMA is not used. The initial fields are taken from the operational LM. The key experiments are listed in Table 1. The SMA Mode "NBSE" (no background state effect) indicates that a modified SMA binary is used, where the effect of the background state is practically eliminated. The SMA Mode "LM" indicates that the SMA is used in the same way as in operational LM.

In order to further test the performance of the surface-layer parameterization scheme in a quasi-operational mode, a parallel experiment, exp_3306, has been set up, where the SMA is used in the same way as in operational LM. This experiment is performed for the period from 24 September to 7 October 2000. This period partially covers the time span of the exp_102 parallel experiment that was performed with the new LM surface-layer scheme but the model parameters used in exp_102 were not tuned. In order to avoid a long spin-up period due to possible inconsistency of the background soil moisture fields and a modified LM physics, the initial fields for exp_3306 are taken from exp_3321, where the soil moisture is determined to match the modified model physics. A comprehensive verification of the exp_3306 results against observational data is carried out.

Table 1: Key experiments.

Experiment Number	Time Period	SMA Use	SMA Mode
exp_3268	2 Apr 2000	Yes	NBSE
exp_3329	20 Jun 2000	Yes	NBSE
exp_3321	23 Sep 2000	Yes	NBSE
exp_3306	24 Sep – 7 Oct 2000	Yes	LM
exp_23sep2000	23 Sep 2000	No	—
exp_14jan2001	14 Jan 2001	No	—
exp_16jan2001	16 Jan 2001	No	—

4 Results

A net result from the runs performed with the use of SMA in frames of the experiments exp_3268, exp_3229 and exp_3321 is that the values of the new LM parameters, namely (in LM code notation), of RAT_CAN=1.0, RLAM_HEAT=1.0, RLAM_MOM=0.1 and PAT_LEN=500 m, are plausible and are recommended for the operational use.

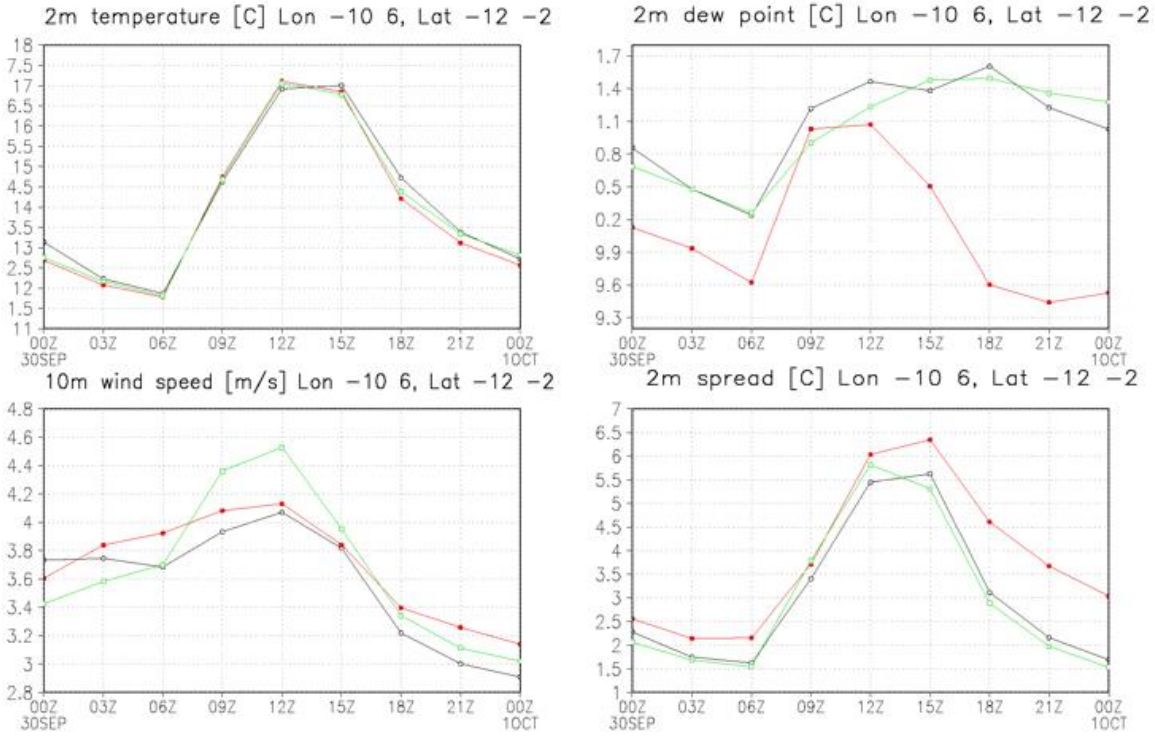


Figure 1: *The 2m temperature, 2m dew point, 10m wind speed and 2m spread from the LM analysis, black curves, from the LM operational forecast, red curves, and from a parallel experiment exp_3306, green curves. The time, UTC, and the date, 30 September 2000, are indicated at the x-axes.*

Figures 1 and 2 illustrate the performance of LM with the new physical package and the above estimates of empirical parameters versus the performance of the operational LM. The results are from a parallel experiment exp_3306. The 2m temperature, the 2m dew point,

the 10m wind speed and the 2m spread (2m temperature minus 2m dew point), predicted by the operational LM, out_LM, and by the new version of LM, exp_3306, are compared with the LM analysis, ana_LM. The curves show values of the weather elements averaged over a portion of the LM domain that is most densely covered with observations. Notice that the 2m temperature and the 2m dew point in the LM analysis come from the synoptic measurements. This is not the case for 10m wind that is a purely diagnostic quantity dependent on the interpolation procedure used in the surface-layer scheme. Therefore, the plots of 10m wind only indicate the difference between the various parameterizations.

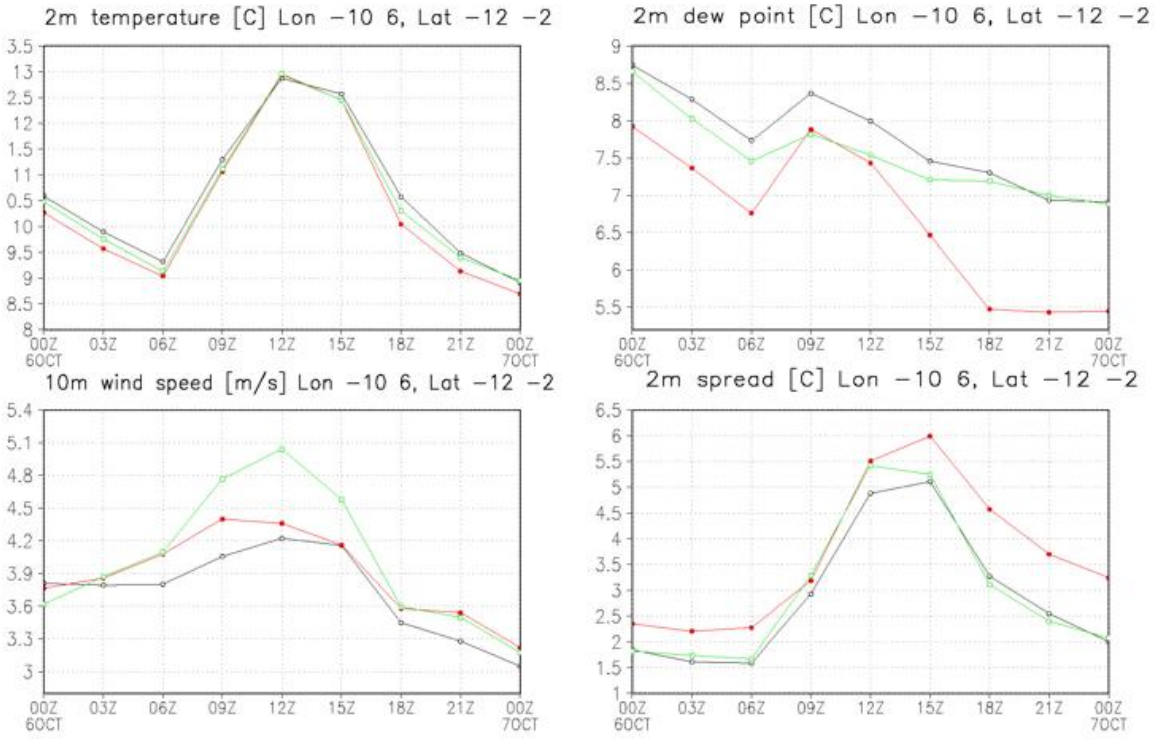


Figure 2: *The same as in Figure 1 for 6 October 2000.*

As seen from the figures, the new version of LM shows a better overall agreement with observations. A marked difference in the diurnal variation of the 2m dew point between the two versions of LM should be emphasised. In the operational LM, the diurnal course of the 2m dew point is a slightly modified re-scaled replica of the diurnal course of the 2m temperature. This is related to the diagnosis of the 2m dew point through the assumption of height-constant relative humidity in the surface layer. It leads to a strong underestimation of the dew point past 15h forecast time and, consequently, to an overestimation of the 2m spread. The latter quantity is of importance for the forecast of fogs. This overestimation is no longer the case with the new version of LM, where the diurnal course of the 2m dew point seems to be more physically realistic and compares better with observations.

Figure 3 compares the 2m temperature forecasts for 18 UTC on 16 January 2001. A test run is performed using the above values of the model parameters. The run is started at 00 UTC on 16 January 2001 with the initial fields from the operational LM. The SMA is not used. As seen from the figure, the 2m temperature is strongly underestimated by the operational LM over a considerable part of Central Europe and United Kingdom. A too rapid decrease of the temperature in the surface layer in the late afternoon hours is a long-standing problem of the LM. The deficiency is partially remedied in the new LM version. This counts in favour

of the new physical package.

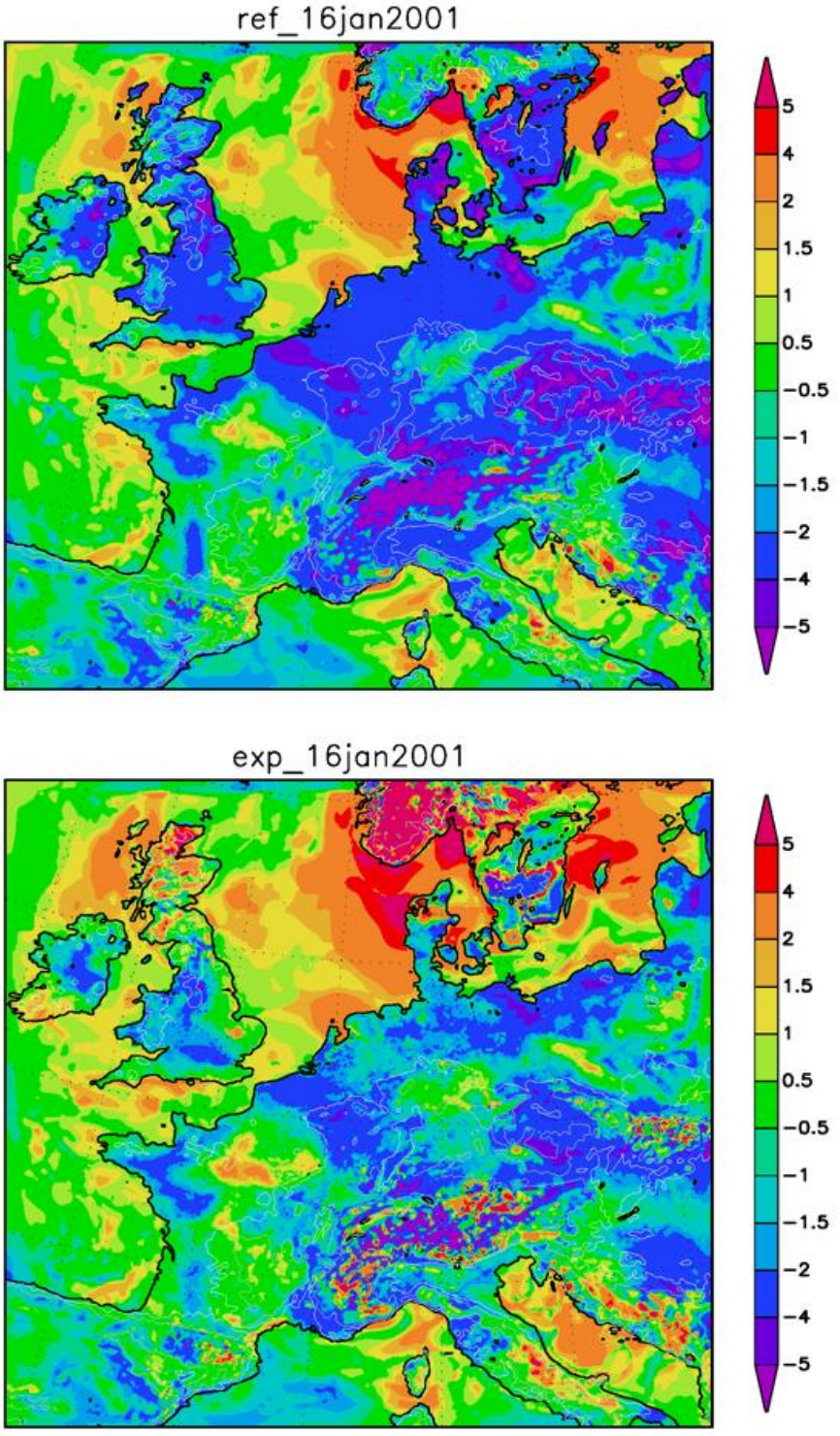


Figure 3: *Forecast error of the 2m temperature (° C), 18 UTC, 16 January 2001; the contour lines indicate the topographical heights of 200m (white) and 500m (grey); reference is the LM analysis. Upper panel: operational LM. Lower panel: test forecast with the tuned values of the model parameters as given in section 4.*

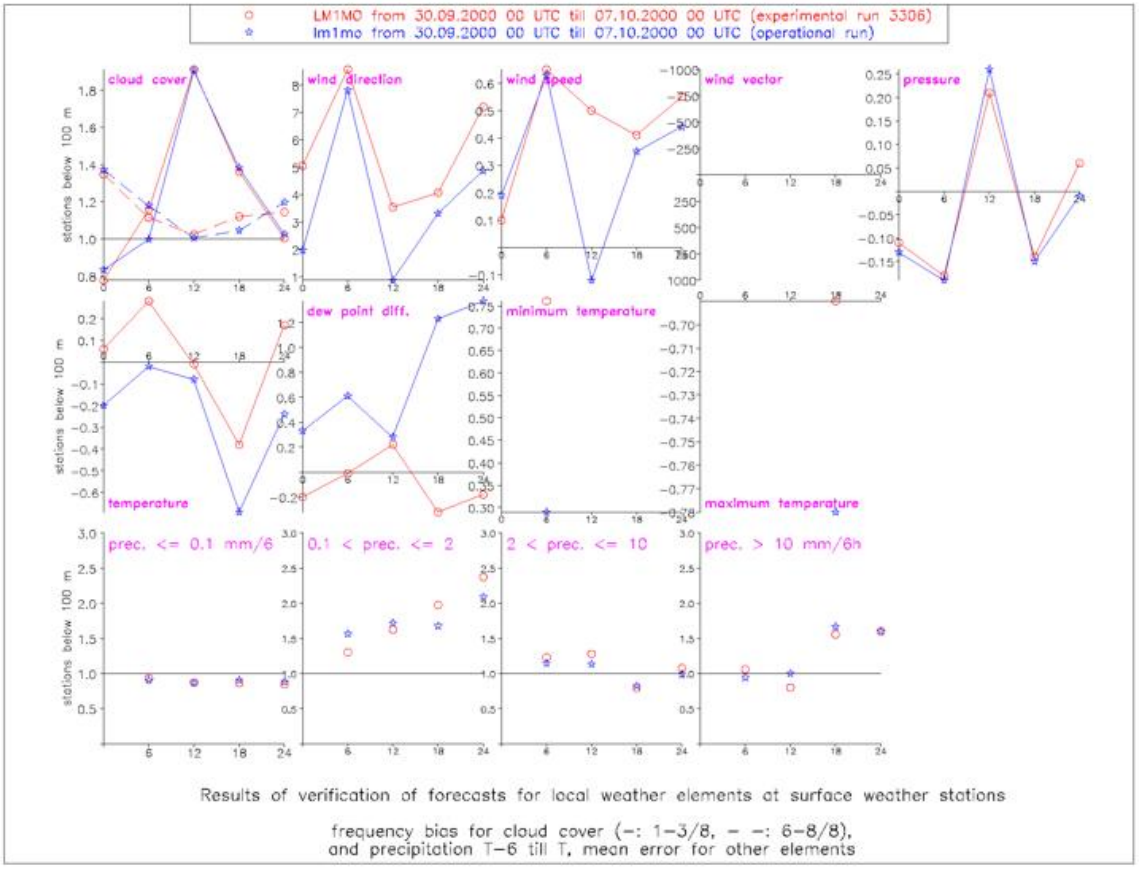


Figure 4: *Mean verification scores of all Synop Stations below 100 m for the period 30 September to 7 October 2000 (00 UTC) as a function of forecast time (00, 06, 12, 18 and 24 h). Red – experimental run exp_3306, blue – operational run.*
Mean error for all elements except for cloud cover and precipitation (frequency bias); numbers are mean values over all forecast times. Top (from left to right): cloud cover, wind direction, wind speed, wind vector and surface pressure. Middle (from left to right): temperature, dew point difference, minimum and maximum temperature. Bottom: frequency bias of 6 h precipitation amounts (prec) for the four indicated threshold intervals.

Figures 4 – 6 show results of verification of exp_3306 performed with the standard verification package of the DWD Department of Research and Development. For the weather stations whose height above the sea level does not exceed 100 m, the new version of LM reveals considerable lower mean error (Figure 4) of the 2m dew point and of the 2m temperature.

For these stations, the root-mean square error (Figure 5) is practically the same for the 2m temperature but is marginally smaller for the 2m dew point. The mean error is slightly higher for the 10m wind speed, however. The new LM version also shows a slight improvement in predicting the cloud cover, as seen in the upper left panel in Figure 5.

For all stations analysed (Figure 6) the major advantage of the new LM version is manifested in the mean error of the 2m dew point, particularly past 12h forecast time, and of the 2m temperature, particularly during the night time.

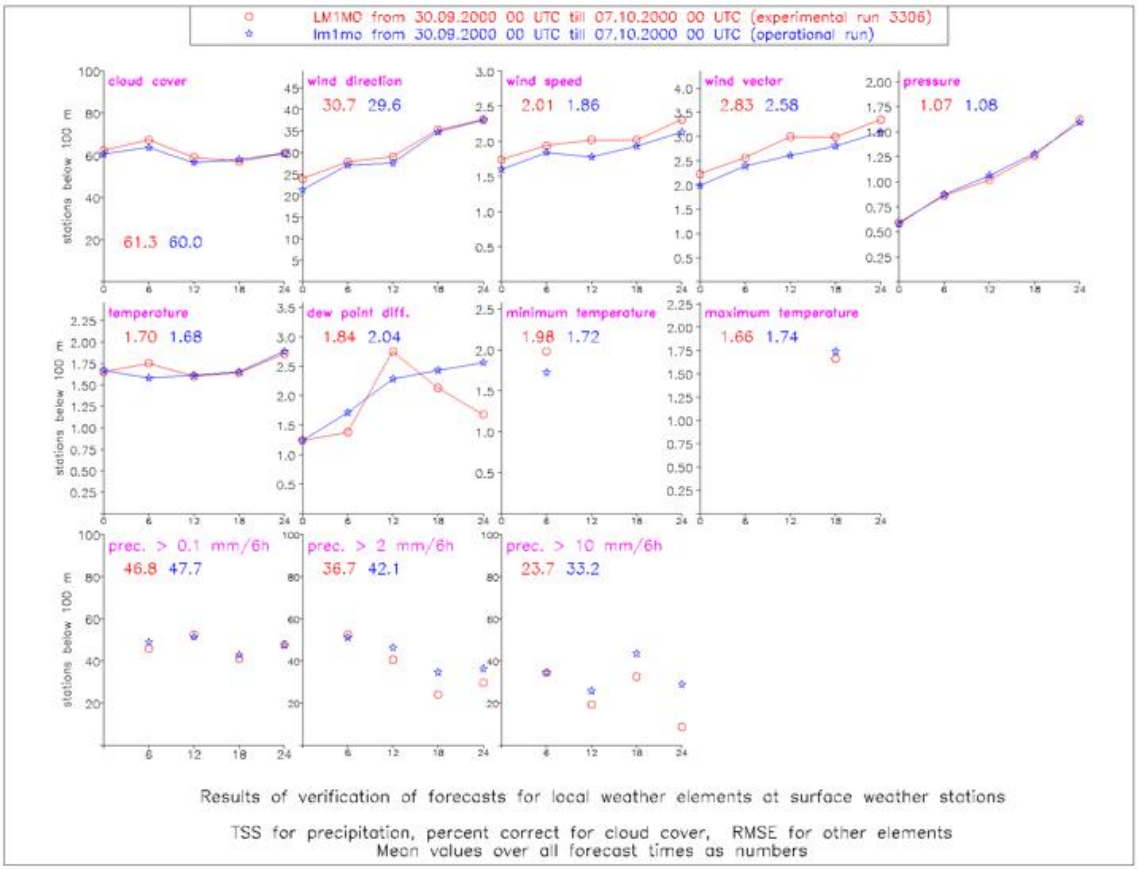


Figure 5: *As in Figure 4, but root-mean-square error for all elements exept for cloud cover (percent correct, upper panel left) and precipipitation (TSS, lower panel).*

5 Conclusions

A preliminary verification of results from the experiments described above lends considerable support to our estimates of parameters of the new LM surface-layer scheme. A negative bias of the 2m dew point is now largely reduced. The 10m wind is now reduced by about 0.4 $\mathrm{m \cdot s^{-1}}$ during the day and by about 0.1 $\mathrm{m \cdot s^{-1}}$ during the night as compared with exp_102. This reduction was suggested by verification (performed by Ulrich Damrath) of results from exp_102 against observations. As compared to the operational LM, the new parameterization scheme yields a number of improvements. Among them are a more realistic diurnal course of the 2m dew point as compared to the operational LM, and higher 2m temperatures during the evening and the night hours which are known to be underpredicted by the LM.

As a word of caution we note that in the experiments described above more emphasis has been placed on the performance of the surface-layer scheme over the land surface. The situation over the water surface motivates further investigation which may entail further modification of the surface-layer scheme.

Finally, the pattern length that is now kept constant independent of location should eventually be turned into a location-dependent two-dimensional field somewhat similar to what is now the aerodynamic roughness length of the land surface.

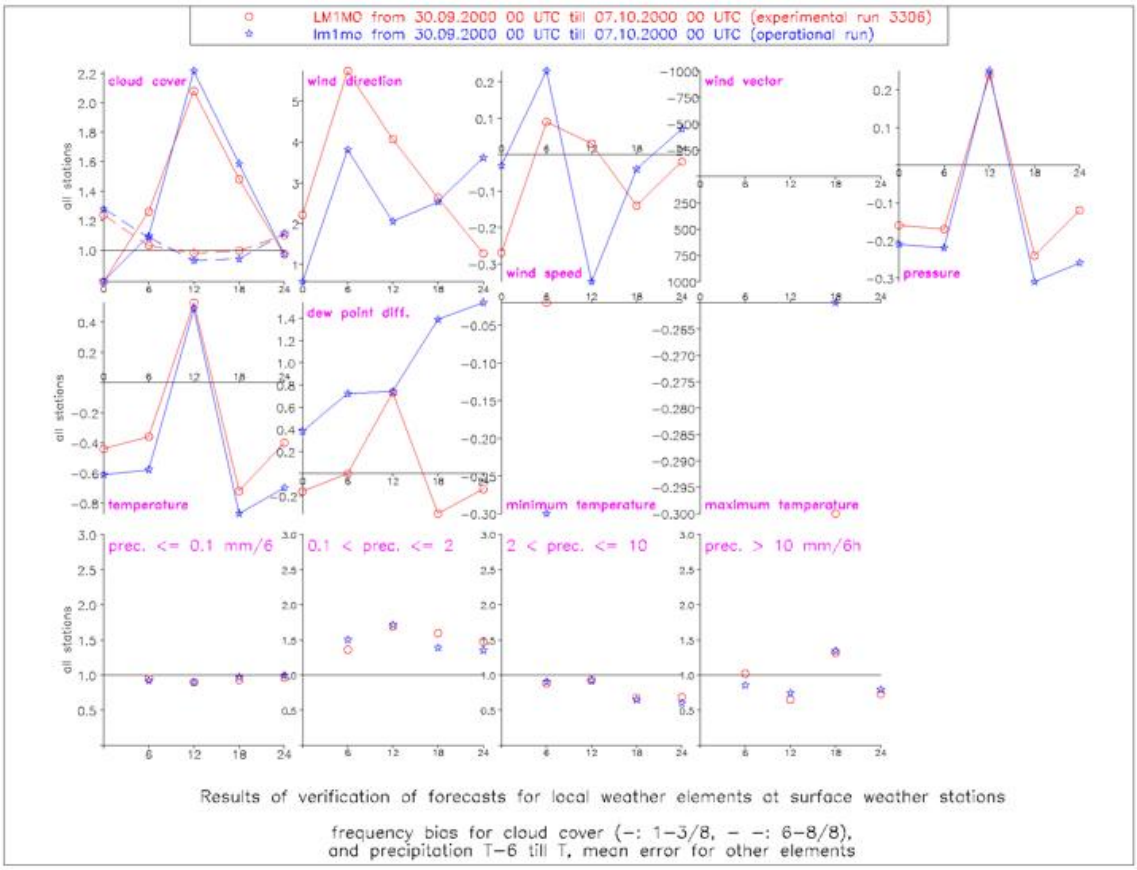


Figure 6: *As in Figure 4, but for all stations in the integration domain.*

Acknowledgements

We thank Erdmann Heise, Reinhold Hess, Günther Doms, Ulrich Damrath, Michael Buchhold and other colleagues at DWD for discussions and helpful suggestions. We are particularly grateful to Thomas Hanisch for innumerable suggestions concerning the use of the DWD Experimental Modelling System. Without his suggestions this work would have hardly ever been completed.

References

Beyrich, F., (Ed.), 2000: *LITFASS-98 Experiment. 25.51998 – 30.6.1998. Experiment Report.* Arbeitsergebnisse Nr. 62, Deutscher Wetterdienst, Geschäftsbereich Forschung und Entwicklung, Offenbach am Main, Germany, 78 pp.

Beyrich, F., H. de Bruin, and H. Schipper, 2000a: Experience from one-year continuous operation of a large aperture scintillometer over a heterogeneous land surface. Proc. 14th Symp. on *Boundary Layers and Turbulence*, 7 – 11 August 2000, Aspen-Snowmass, USA, P 1.12.

Beyrich, F., S. H. Richter, U. Weisensee, W. Kohsiek, F. Bosveld, H. Lohse, H. de Bruin, O. Hartogensis, J. Bange, and R. Vogt, 2000b: The LITFASS-98 Experiment: fluxes over

a heterogeneous land surface. Proc. 14th Symp. on *Boundary Layers and Turbulence*, 7 – 11 August 2000, Aspen-Snowmass, USA, P 1.3.

Hanisch, T., 1995: *Experimentiersystem des Deutschen Wetterdienstes.* DWD Internal Report, Deutscher Wetterdienst, Offenbach am Main, Germany.

Hess, R., 2001: Variational soil moisture analysis with first operational results. *COSMO Newsletter*, No. 1, Deutscher Wetterdienst, Offenbach am Main, Germany, 79–88.

Mellor, G. L., and T. Yamada, 1974: A hierarchy of turbulence closure models for planetary boundary layers. *J. Atmos. Sci.*, **13**, 1791-1806.

Mellor, G. L., and T. Yamada, 1982: Development of a turbulence closure model for geophysical fluid problems. *Rev. Geophys. Space Phys.*, **20**, 851-875.

Mironov, D., F. Beyrich, E. Heise, and M. Raschendorfer, 2001: The water surface roughness lengths for scalars: an observational study. In preparation. (Preliminary results are reported at the EGS XXVI General Assembly, Nice, France, 25 – 30 March 2001, Session OA14.03. Surface fluxes over land and ocean: Physics of sea-air, land-air and ice-air fluxes.)

Nurser, A. J. G., 1996: *A Review of Models and Observations of the Oceanic Mixed Layer.* Southampton Oceanographic Centre, Internal document No. 14, Southampton, U. K. 247 pp.

Randall, D. A., and B. A. Wielicki, 1997: Measurements, models, and hypotheses in the atmospheric sciences. *Bull. Amer. Met. Soc.*, **78**, 399-406.

Raschendorfer, M., 1999: Special topic: The new turbulence parameterization of LM. *Quarterly Report of the Operational NWP-Models of the Deutscher Wetterdienst*, No. 19, Deutscher Wetterdienst, Offenbach am Main, Germany, 3–12.

Wyngaard, J. C., and C.-H. Moeng, 1993: Large-eddy simulation in geophysical turbulence parameterization: an overview. *Large Eddy Simulation of Complex Engineering and Geophysical Flows*, B. Galperin and S. A. Orszag, Eds., Cambridge Univ. Press, 349–366.

Consortium

for

Small-Scale Modelling

Technical Report No. 8

Evaluation of the Performance of the COSMO-LEPS System

by

C. Marsigli, A. Montani, T. Paccagnella (ARPA-SIM)
D. Sacchetti (ARPAL)
A. Walser, M. Arpagaus (MeteoSwiss)
T. Schumann (DWD)

April 2005

DOI: 10.5676/DWD_pub/nwv/cosmo-tr_8

Deutscher Wetterdienst

MeteoSwiss

Ufficio Generale per la Meteorologia

Hellenic National Meteorological Service

Instytut Meteorologii i Gospodarki Wodnej

Il Servicio Meteorologico Regionale di ARPA

Amt für Wehrgeophysik

L'Agenzia Regionale per la Protenzione Ambientale del Piemonte

www.cosmo-model.org

Editors: G. Doms and U. Schättler, Deutscher Wetterdienst, P.O. Box 100465, 63004 Offenbach, Germany
Printed at Deutscher Wetterdienst, Offenbach am Main

Contents

1 Introduction **2**

2 Statistical analysis of the methodology **3**

3 Objective verification **5**

4 Parallel suite with model perturbations **14**

5 COSMO-LEPS Subjective verification – Contribution by ARPAL, Genova, Italy (Davide Sacchetti) **18**

5.1 Description of the methodology 18

5.1.1 Subjective evaluation of the precipitation field forecast by the 5 members 18

5.1.2 Subjective evaluation of the COSMO–LEPS probability maps 19

5.1.3 Individuation of the synoptic pattern 19

5.2 Results 21

6 Use of COSMO-LEPS at MeteoSwiss - Contribution by MeteoSwiss, Zürich, Switzerland (Andre' Walser and Marco Arpagaus) **25**

6.1 MeteoSwiss post-processing 25

6.2 Experience with COSMO-LEPS 26

6.3 Case study: Storm on 19 November 2004 28

6.4 Conclusions and outlook 29

7 Could the COSMO–LEPS system add value to operational forecasts of the DWD in the case of severe weather? - Contribution by the Central Forecast unit of the DWD in 2004 (Thomas Schumann) **30**

7.1 A case study - early winter over Germany (09 Nov, 2004) 32

7.2 Conclusions 34

8 Conclusions **36**

1 Introduction

The "experimental–operational" limited–area ensemble prediction system COSMO–LEPS has been running daily since November 2002 at the ECMWF computer system under the auspices of COSMO (Montani et al., 2003b). COSMO–LEPS aims at the development and pre–operational test of a "short to medium–range" (48–120 hours) probabilistic forecasting system using a LAM over a domain covering all countries involved in COSMO (Fig. 1).

A subjective evaluation of its performance is being carried out by the forecasters of the Meteorological Centres involved in the COSMO Consortium. Furthermore, the system is being objectively evaluated by ARPA–SIM using a set of probabilistic quality indices (Marsigli et al., 2005). In this report, a summary of the performance of COSMO–LEPS is presented, collecting also contributions coming from different COSMO partners.

In the first part, results obtained through an objective verification by ARPA–SIM are presented. In Section 2, an analysis of the methodology on which the system is based is shown, focusing on the results that led to a major modification of the system in June 2004. In Section 3, the quality of the system is assessed in an objective manner, making use of probabilistic indices. In Section 4, the operational suite has been compared with a parallel suite where a different scheme for the parameterization of the deep convection was used.

For a complete description of scores used in this report, the reader is referred to Wilks (1995), Stanski et al. (1989) and Talagrand et al. (1999) for the Brier Skill Score, Mason and Graham (1999) for the ROC Curves and the ROC area, to Richardson (2000) for the Cost-loss Analysis and to Buizza (1997) for the Percentage of Outliers.

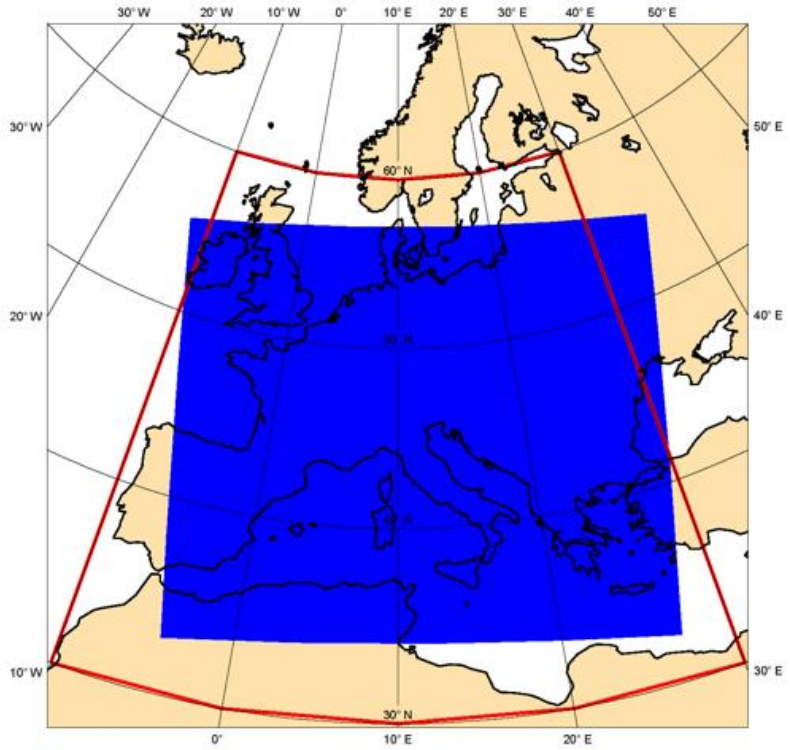


Figure 1: COSMO–LEPS operational domain (blue area) and clustering area (red frame).

In the second part, subjective evaluations of the system made by other COSMO partners are shown. In Section 5, the results from the subjective verification performed by the Regional

Agency for Prevention and Environment of the Liguria Region (ARPAL) are presented. In Section 6, the use of COSMO–LEPS by MeteoSwiss and the impressions got by the forecasters are described. In Section 7, the contribution by the forecasters of DWD is reported.

Finally, in Section 8 some conclusions are drawn.

2 Statistical analysis of the methodology

An analysis of the methodology on which COSMO–LEPS is based is presented in this section.

The idea of joining three consecutive EPS to form a super–ensemble is based on the need of enlarging the size of the ensemble on which the RM selection algorithm is applied. This permits to increase the ensemble spread and to have a wider part of the phase space spanned by the global ensemble members. Nevertheless, this is obtained by paying a price in terms of skill: the older is the EPS, the less skillful are their members. In order to quantify the relative effects of the increased spread and of the decreased skill, the Representative Members chosen with the current methodology are compared to those chosen using only one or two EPS. The three ensembles compared, are:

- the ensemble made up by the 5 RMs selected applying the Cluster Analysis and Representative Member Selection Algorithm on the three most recent EPS (referred to "3–EPS"), which is the original operational configuration
- the ensemble made up by the 5 RMs selected applying the Cluster Analysis and Representative Member Selection Algorithm on the two most recent EPS (referred to "2–EPS")
- the ensemble made up by the 5 RMs selected applying the Cluster Analysis and Representative Member Selection Algorithm on the most recent EPS (referred to "1–EPS")

This analysis is performed in terms of 24–hour precipitation. The forecast values at each grid point are compared with a proxy for the true precipitation occurred chosen as the +24 hours forecast by the ECMWF deterministic model. The extent to which this proxy is a good approximation for the truth is not important, because this is a comparison among different configurations of the same model. The period chosen for this test is September–November 2003 and the area is the clustering area (rectangle in Fig. 1).

Results show that the Brier Skill Score (the higher the better, see Wilks, 1995) is higher when the clustering is based on the most recent EPS only (Fig. 2, black line), while it is lower for the 3–EPS super–ensemble (blue line). The difference between the two is not so remarkable, but it remains at every forecast range. The 2–EPS super–ensemble (red line) has an intermediate skill, equal to the one of the 1–EPS ensemble at the first and last forecast ranges, its general performance being nearest to the one of the 1–EPS ensemble.

The percentage of outliers of the systems is also shown. This is the percentage of times the "truth" falls out of the range of the forecast values. The percentage of outliers (Fig. 3) of the 1–EPS ensemble (black line) is rather higher than the other two, for every forecast range, while there is almost no difference in terms of outliers between the 2–EPS (red line) and the 3–EPS (blue line) ensembles. These results seem to indicate that the use of just two EPS

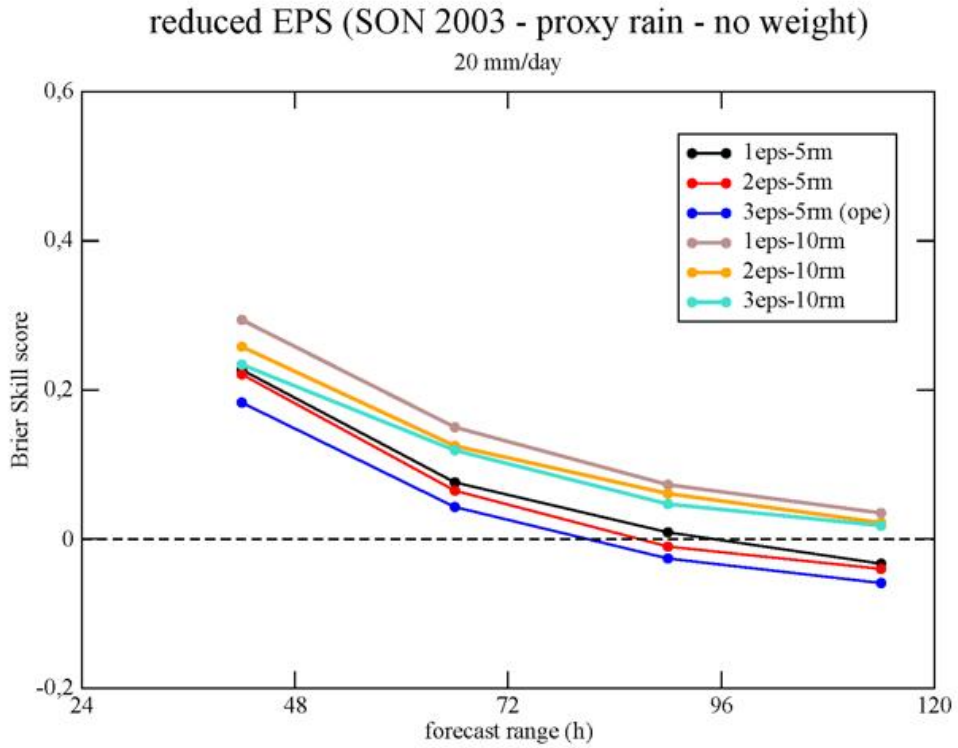


Figure 2: Brier Skill Score as a function of the forecast range for the event precipitation exceeding 20mm/24h relative to the RM EPS. The different configurations are: 5 clusters algorithm based on 1 EPS (black line), on 2 EPS (red line) and on 3 EPS (operational configuration, blue line); 10 clusters algorithm based on 1 EPS (gray line), on 2 EPS (orange line) and on 3 EPS (cyan line).

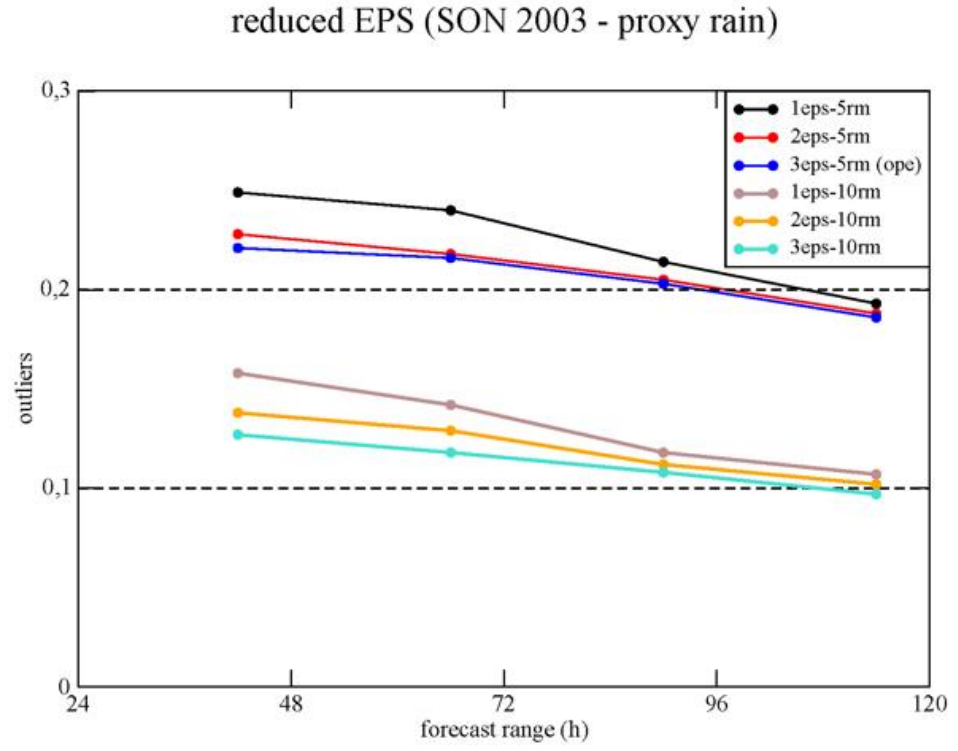


Figure 3: Percentage of outliers for the RM EPS, colours as in the previous figure.

in the super–ensemble can be a good compromise, permitting to decrease the percentage of outliers significantly but leading only to a small worsening of the skill.

In order to quantify the impact of the ensemble size on the performance of the system, the cluster analysis has been repeated by fixing the number of clusters to 10 and by selecting, then, 10 Representative Members. This has been done for each of the three ensemble configurations already considered, leading to the three configurations: 3–EPS–10RMs, 2–EPS–10RMs and 1–EPS–10RMs. The impact of the ensemble size proves to be quite remarkable, the difference between each 5–member ensemble and the correspondent 10–member ensemble being about 0.1 in terms of Brier Skill Score, for every configuration. This is shown in Fig. 2, where the blue line (3–EPS–5RMs) has to be compared with the cyan line (3–EPS–10RMs), the red line (2–EPS–5RMs) with the orange line (2–EPS–10RMs) and the black line (1–EPS–5RMs) with the brown line (1–EPS–10RMs). The impact of doubling the ensemble size is almost the same for every configuration and is predominant with respect to the impact of changing the number of EPS on which the Cluster Analysis is performed.

These results lead to two major modifications of the COSMO–LEPS methodology at the beginning of June 2004: the super–ensemble has been built by using only the 2 most recent EPS and the number of clusters has been fixed to 10, nesting Lokal Modell on each of the 10 RMs selected.

3 Objective verification

In order to quantify the added value brought about by the mesoscale probabilistic system, COSMO–LEPS is compared with the EPS. The comparison is made difficult by two main factors: the difference in the number of ensemble members (5 for COSMO–LEPS and 51 for the EPS) and the difference in terms of resolution (10 km for COSMO–LEPS and 80 km for the EPS). As the population of the ensembles is concerned, COSMO–LEPS is compared also with the small EPS ensemble made up by the 5 Representative Members. This permits to quantify the impact of the increased resolution alone. The problem of the very different resolutions of the two systems is tackled by upscaling both systems to a lower resolution: the grid point forecasts of both model are averaged over boxes of 1.5×1.5 degrees. The comparison is made in terms of 24–hour precipitation, against observed data from a very dense network of raingauges. Precipitation is cumulated from 06 to 06 UTC. In order to properly compare forecast values on grid points and observed values on station points, the observations within a box are averaged and the obtained value can be compared directly with the averaged forecast value. The comparison is carried out over a big area included in the COSMO–LEPS domain, covering Germany, Switzerland and Northern Italy. The very dense network of stations recording daily precipitation is shown in Fig. 4.

In order to avoid problems in the boxes at the boundaries of the domain covered by observations, an "observational mask" is used. This mask was built by assigning a value of 1 to a grid point only if its distance to at least one observation is less than 0.15 degrees; otherwise, it is assigned the value of 0. The mask relative to COSMO–LEPS and to the data–set used in this work is shown in Fig. 5. To compute the average or the maximum forecast value over a box, only grid points that are labelled 1 have been considered.

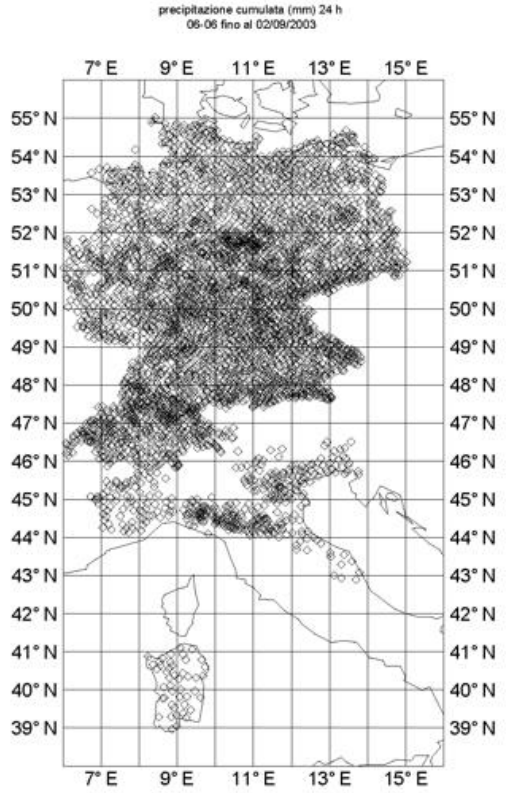


Figure 4: Network of station providing 24–hour precipitation (06 UTC to 06 UTC) for the COSMO verification.

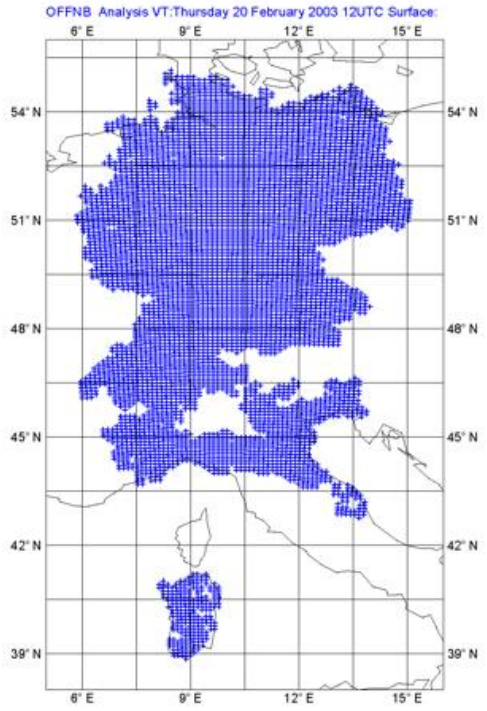


Figure 5: The "observational mask" used for COSMO–LEPS. Only grid points which are not too far from the area covered by the observations are considered.

The 3 ensemble systems compared are:

- the COSMO–LEPS system, made up of 5 members, 10 km of horizontal resolution, referred to as "cleps";
- the EPS mini–ensemble made up by the 5 Representative Members chosen from the super–ensemble, 80 km of horizontal resolution, referred to as "epsrm";
- the operational 51–member ECMWF EPS starting at the same initial time as COSMO–LEPS (the "youngest" EPS constituting the super–ensemble), 80 km of horizontal resolution, referred to as "eps51";

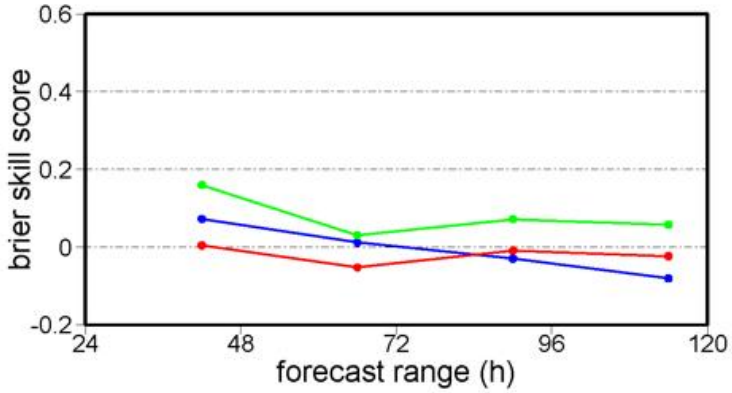


Figure 6: Brier Skill Score values for the precipitation threshold 20mm/24h. The blue line is relative to cleps, the red line is relative to epsrm, the green line is for eps51. Average observed and forecast values are compared.

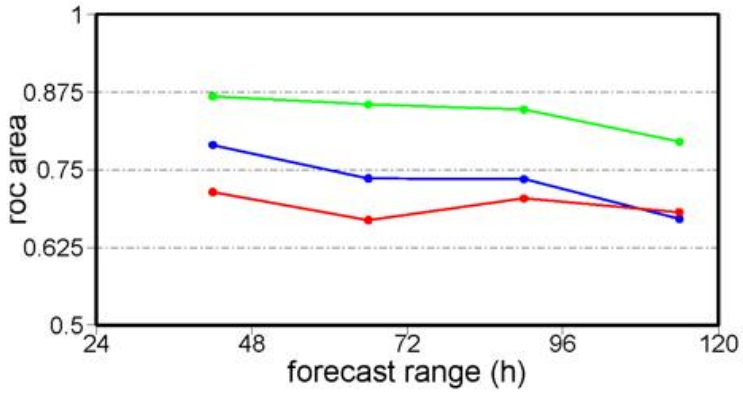


Figure 7: ROC area for the precipitation threshold 20mm/24h. The blue line is relative to cleps, the red line is relative to epsrm, the green line is for eps51. Average observed and forecast values are compared.

In Fig. 6 and Fig. 7 the Brier Skill Score and the ROC area are shown for the three systems (for both index, the higher the better). The average observed value of each box, obtained by computing the mean of all the observations falling in a box, is compared with the average forecast value relative to the same box, for each of the three forecasting systems. The event considered here is precipitation exceeding 20 mm / 24 h over 1.5 x 1.5 degree boxes. Since the observed and forecast values are averaged over an area of 1.5 x 1.5 degrees, this threshold is individuating an intense precipitation.

In terms of Brier Skill Score (Fig. 6) the three lines are rather close together. The BSS values of the full–size 51–member EPS (eps51, green line) are slightly higher than those of the other two systems, that is, its performance is slightly better. The difference between cleps and epsrm is slightly in favour of cleps for the first forecast ranges, while the reverse it is true at the +114 forecast range.

The differences in the performances of the three system are enlighted by the ROC area values (Fig. 7). The full–size 51–member EPS (eps51, green line) has the best scores at this threshold for every time range. The COSMO–LEPS system (cleps, blue line) has lower scores, but higher than those of the 5–RM EPS (epsrm, red line).

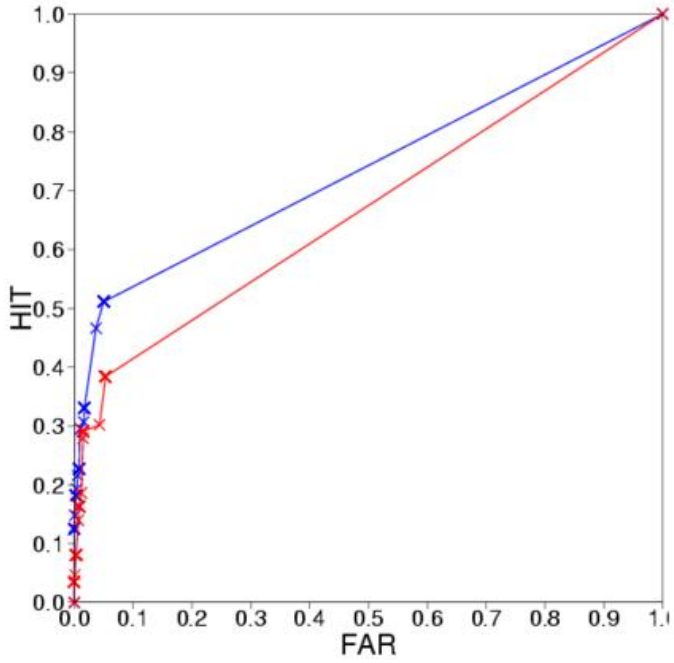


Figure 8: Average values: ROC Curves for the precipitation threshold 20mm/24h and for the +66h forecast range. The blue line is relative to cleps while the red line is relative to the epsrm.

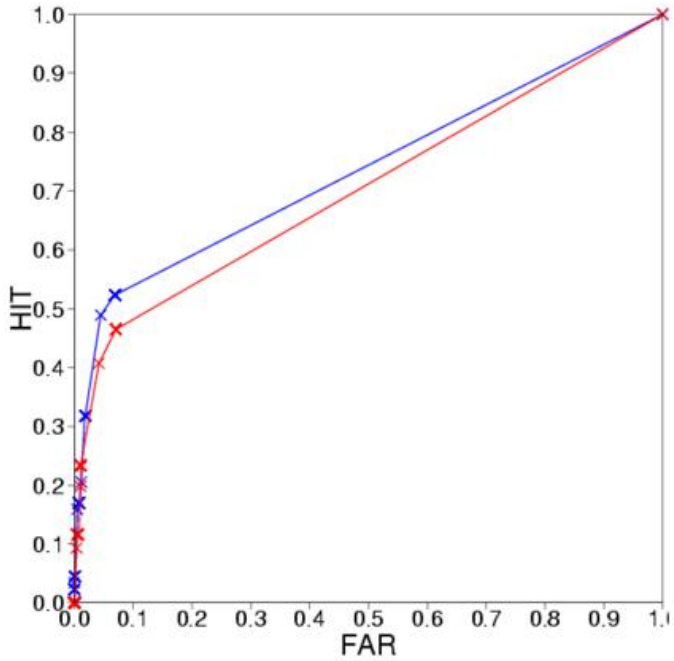


Figure 9: Average values: ROC Curves for the precipitation threshold 20mm/24h and for the +90h forecast range. The blue line is relative to cleps while the red line is relative to epsrm.

The ensemble size often plays a major role in the computation of the probabilistic indices, making a proper comparison between cleps and eps51 difficult. When the two systems with the same size are compared, "cleps" shows an improvement with respect to the "epsrm", especially in terms of ROC area. In order to better understand this result, the ROC Curves for these two systems are also reported.

The ROC Curves relative to COSMO–LEPS and to the 5–RM EPS are shown for the event "precipitation exceeding 20mm/24h", for the forecast ranges +66 hours (Fig. 8) and +90 hours (Fig. 9). The "cleps" curves (blue curves) are higher than the "epsrm" ones (red curves) for both forecast ranges. Considering the first cross from the top right in the diagram, it is evident that the two systems have comparable False Alarm Rates, but COSMO–LEPS obtains higher Hit Rate values. This cross is correspondent to the probabilistic issue "at least one ensemble member is forecasting the event", whose practical meaning can be understood referring to an alert situation. If a user has a damage from the considered event, he can avoid the related loss by taking a preventive action. In order to decide if the action has to be taken, he uses the probabilistic system, but he has to decide on which probability threshold to rely. The first cross of the diagram corresponds to the hit rate and false alarm rate a user can have, if he decides to take a protective action when at least one ensemble member forecasts the event, so he relies on a very low probability threshold. This situation is usually linked with cases in which the possible loss is very high (human lives) with respect to the cost of the preventive action.

Averaging the precipitation over boxes of this size permits to understand if the total amount of precipitation over a vast region is correctly forecast, without giving information on precipitation peaks, which are very important for hydro–geological purposes. A high–resolution system could play a major role in forecasting precipitation peaks, introducing information not available with a lower resolution model. For this reason, a comparison in terms of precipitation maxima has been performed: the maximum forecast value falling in a box is compared with the maximum observed value in the same box. The boxes are of the same size, 1.5×1.5 degrees. In this analysis, higher precipitation thresholds have been considered, due to the fact that the average precipitation over a large area and the maximum precipitation over the same area are two different quantities and can be considered to different "events" to be verified.

The BSS values relative to cleps for the 20 and 30 mm/24 thresholds (top and medium panels of Fig. 10, blue line) are well higher than both the epsrm and eps51 ones, indicating that COSMO–LEPS is more able to correctly forecast high precipitation values over a rather big area. Both eps51 and epsrm have almost no skill and no difference between the two is evident. At the highest threshold, all the three systems show almost no skill in terms of Brier Skill Score and it is not possible to find a difference between their performances.

In terms of ROC area (Fig. 11), cleps has the highest values for all the considered thresholds, exhibiting some skill even for the 50mm/24h thresholds. Then, the COSMO–LEPS system exhibits some skill in forecasting high precipitation peaks not reproduced by the lower resolution ensemble. According to this score measure, eps51 is more skillful than epsrm, showing the positive impact of the ensemble population on this index.

The difference of the behaviour of the scores in the evaluation of the three ensemble systems is due to the characteristics of these scores. In particular, the Brier Skill Score is more sensitive to the probability with which a forecast is issued: an event correctly forecast with low probability has a positive impact on the ROC area and a negative one on the Brier Skill Score. For this reason, it is better to look at a number of indices when evaluating the performances of a forecasting system.

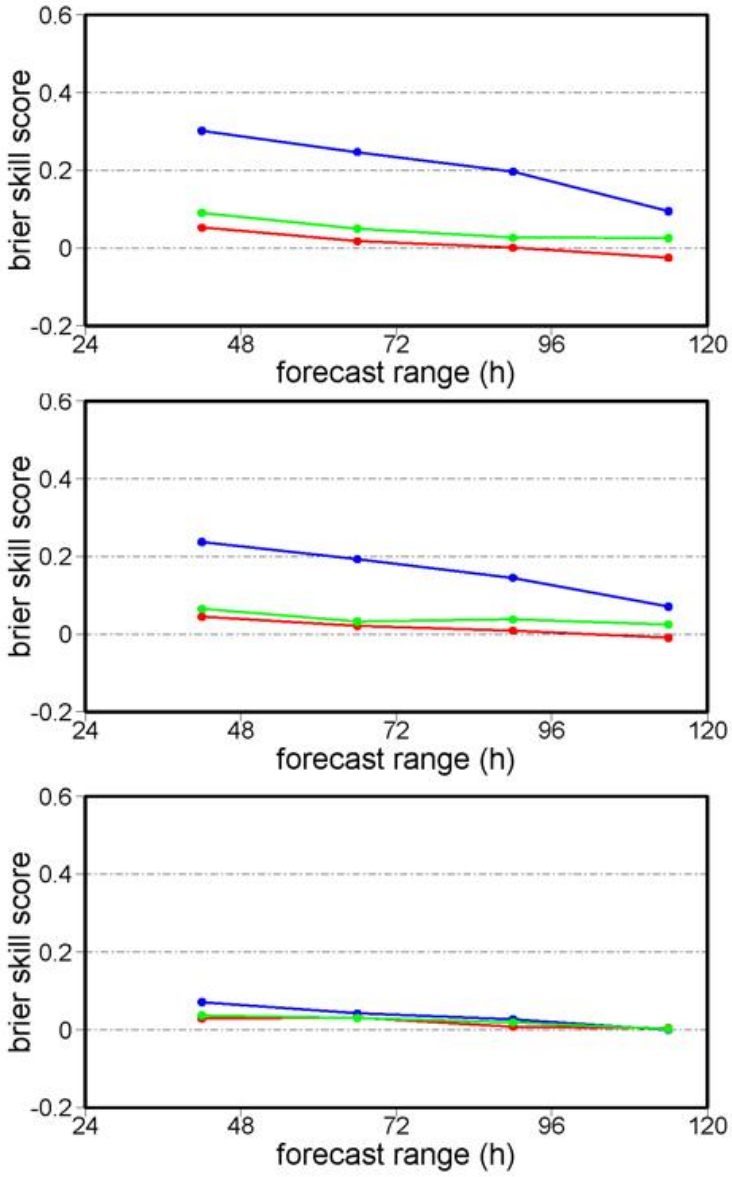


Figure 10: Brier Skill Score values for the precipitation threshold 20mm/24h (top panel), 30mm/24h (medium panel) and 50mm/24h (bottom panel). The blue line is relative to cleps, the red line is relative to epsrm, the green line is for eps51. Maximum observed and forecast values are compared.

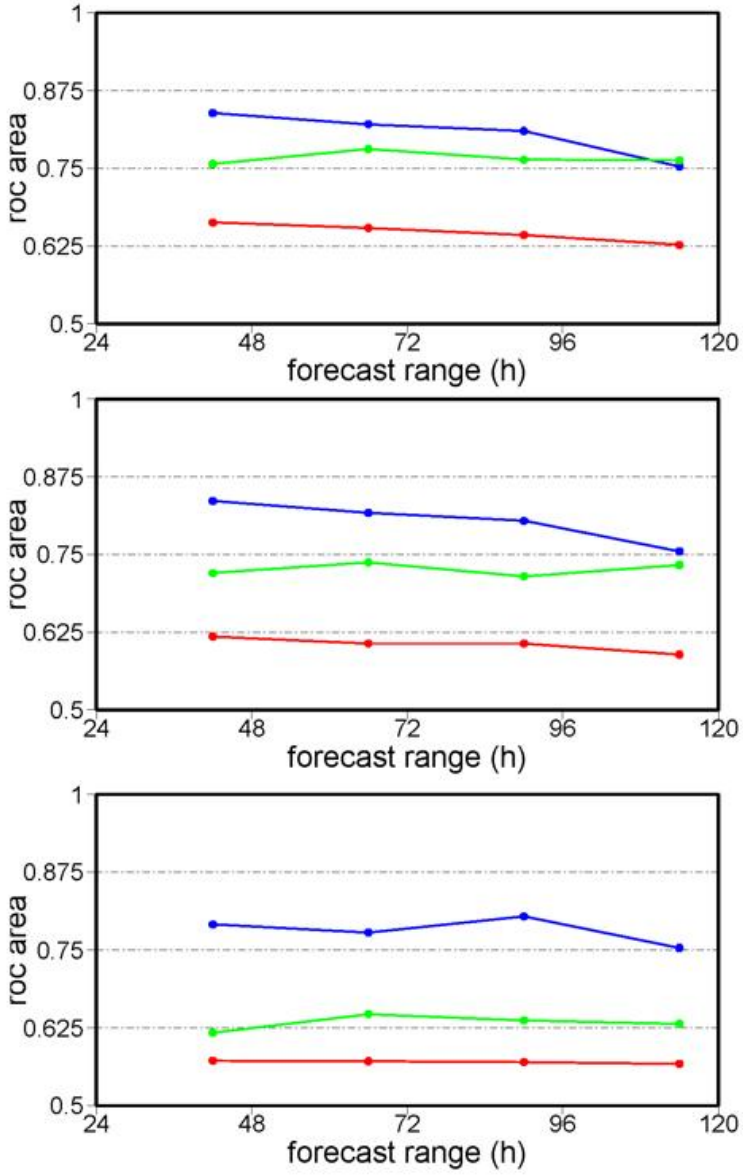


Figure 11: ROC area for the precipitation threshold 20mm/24h (top panel), 30mm/24h (medium panel) and 50mm/24h (bottom panel). The blue line is relative to cleps, the red line is relative to epsrm, the green line is relative to eps51. Maximum observed and forecast values are compared.

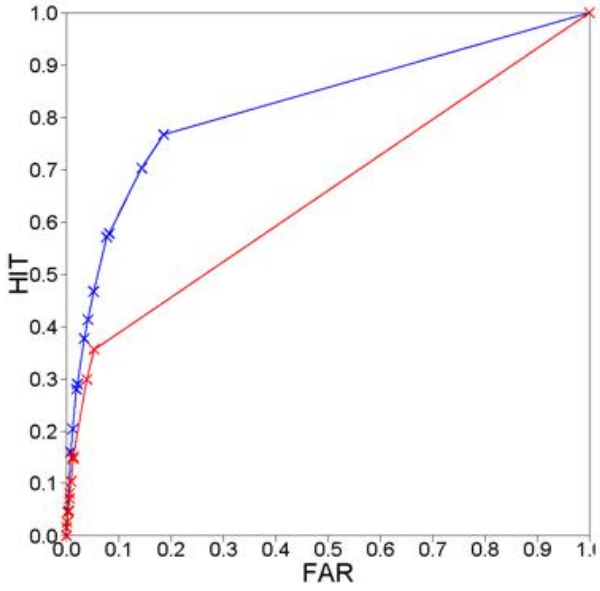


Figure 12: Maximum values: ROC Curves for the precipitation threshold 20mm/24h and for the +66h forecast range. The blue line is relative to cleps while the red line is relative to the epsrm.

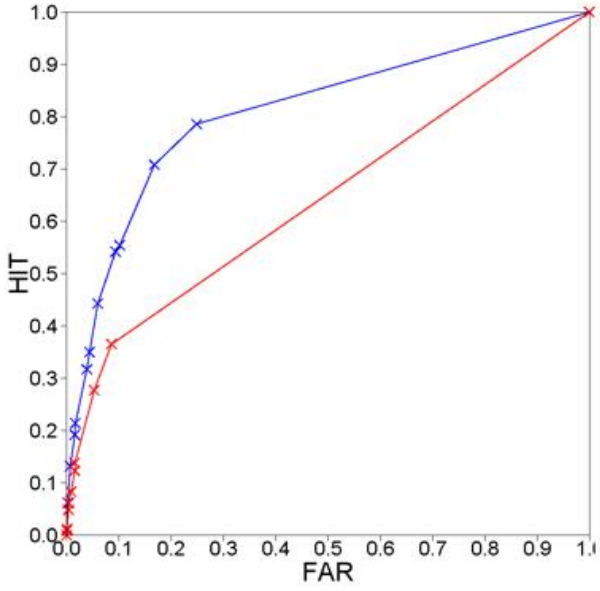


Figure 13: Maximum values: ROC Curves for the precipitation threshold 20mm/24h and for the +90h forecast range. The blue line is relative to cleps while the red line is relative to epsrm.

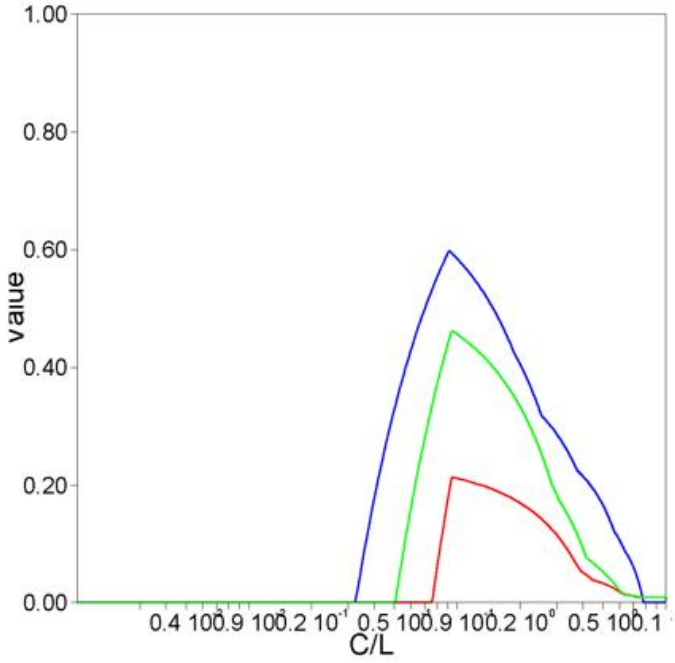


Figure 14: Envelope of the cost-loss curves for the precipitation threshold 30mm/24h (maximum values) for the +66h forecast range. The blue line is relative to cleps, the green line is relative to eps51 and the red line is relative to epsrm.

A general decrease of the cleps scores with increasing forecast range is evident for both BSS and ROC area, the score of cleps reaching that of eps51 at the +114 h forecast range for almost all the thresholds.

The ROC Curves relative to COSMO–LEPS and to the 5–RM EPS are shown for the event "maximum precipitation exceeding 20mm/24h", for the forecast ranges +66 hours (Fig. 12) and +90 hours (Fig. 13). The "cleps" curves (blue curves) are well above the "epsrm" ones (red curves) for both forecast ranges. Considering the first cross from the top right in the diagrams (correspondent to the probabilistic issue "at least one ensemble member is forecasting the event"), the relationship between Hit Rate and False Alarm Rate of the two systems can be easily understood. At the +66 h (+90 h) forecast range, COSMO–LEPS produces more false alarms, FAR being around 0.2 (0.25) for cleps and 0.05 (0.1) for epsrm, but it has a more than double Hit Rate, HIT being around 0.75 (0.8) for cleps and 0.35 (0.35) for epsrm.

Finally, the cost-loss curves relative to the event "maximum precipitation over the box exceeding 30 and 50 mm/24h" are shown for the +66 hour forecast range (figures 14 and 15, respectively. This curves quantify the "value" of the forecast systems (expressed as a percentage, 100% is the value of a perfect forecast system) as a function of the ratio between cost (C) and loss (L). This ratio depends on the user, who incur a loss (L) if a dangerous meteorological event occurs and who can prevent this event by taking an action which cost is C. Each user has to find the position corresponding to his/her own "C/L" on the x–axis of this graph, then he/she can find the value he/she could obtain by using the forecasting system in order to decide when to take a preventive action.

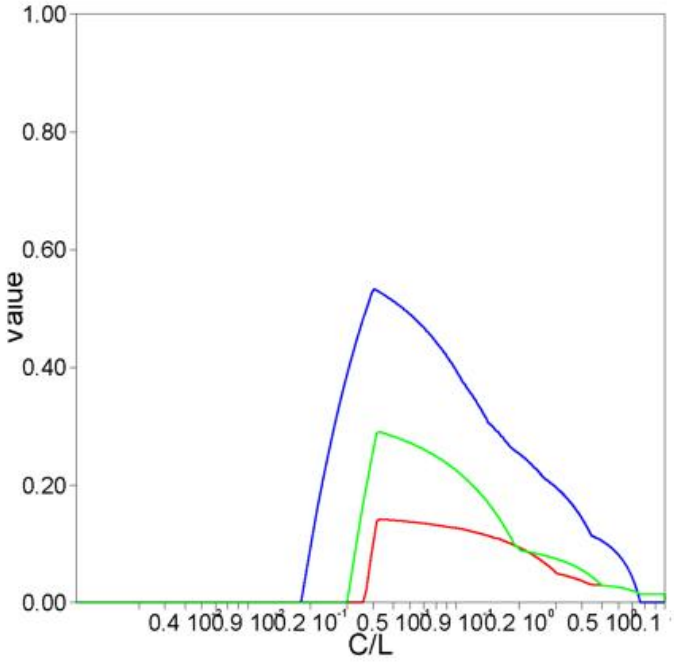


Figure 15: Envelope of the cost-loss curves for the precipitation threshold 50mm/24h (maximum values) for the +66h forecast range. The blue line is relative to cleps, the green line is relative to eps51 and the red line is relative to epsrm.

4 Parallel suite with model perturbations

The COSMO–LEPS members are differentiated only by their initial and boundary conditions, which come from different members of the ECWMF EPS. More spread can be easily added to the mesoscale ensemble by nesting in each of the selected EPS Representative Member more than one limited–area model or, more simply, the same model in different configurations. This is a simple way of adding model perturbations in the ensemble formulation. This was attempted for the COSMO–LEPS system by integrating a pair of LM runs for each set of initial and boundary conditions, the twin runs being different only in the scheme used for the parameterization of the convection. This lead to a 10 member limited–area ensemble. At the same time, two 5–member suite have become available, differentiated only by the configuration of the limited–area model. Then, starting from September 2003 to May 2004, a second suite, parallel to the standard one was running. In the standard suite the Tiedtke scheme was used for the parameterization of the convection, while in the parallel suite the Kain–Fritsch scheme was used. The two systems are referred to as "Tiedtke suite" and"Kain–Fritsch suite".

The 10–member COSMO–LEPS, obtained by simply joining the two suites, is then a system in which perturbations in the model are added to the usual perturbations in the initial and boundary conditions. This system is referred to as "combined suite".

A comparison of the three suites is made in terms of 24–hour precipitation using observed data from a network of raingauges covering Northern Italy (about 600 stations). The comparison is made over boxes of 0.5×0.5 degrees that covers this area. The average (maximum) of the forecast values falling in each box are compared with the average (maximum) of the observed values falling in the same box. The values are computed by considering, for each

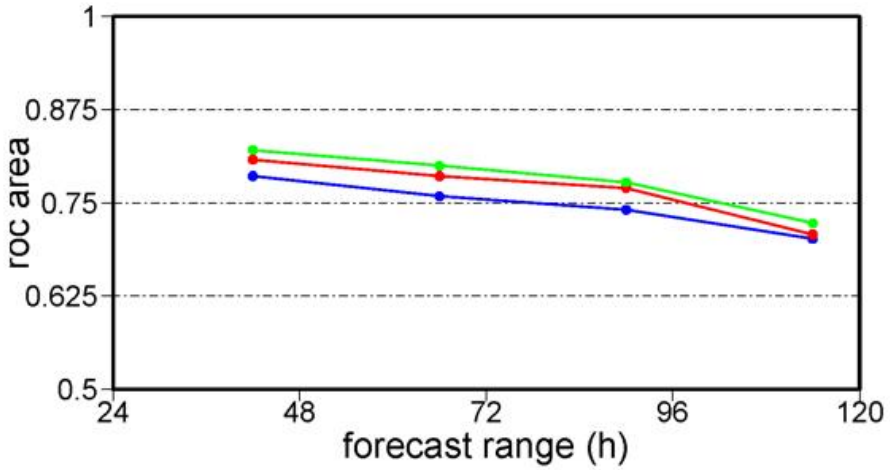


Figure 16: ROC area values as a function of the forecast range for averaged precipitation over 0.5×0.5 degrees boxes exceeding 20mm/24h. The blue line is relative to the Tiedtke suite (operational), the red line is relative to the Kain–Fritsch suite and the green line is for the 10–member combined suite.

box, only the model grid points that lies within a small distance from at least one observation point, following the "observational mask" technique described in the previous section.

In Fig. 16 the ROC area values computed in terms of average values over 0.5×0.5 degrees boxes are shown. The precipitation threshold is 20mm/24h. In terms of ROC area, the Kain–Fritsch suite (red line) improves with respect to the Tiedtke suite (blue line). The score of the combined suite (green line) is a little higher than both 5–member suites, but it is very similar to the one of the Kain–Fritsch suite. This seems to suggest that adding this kind of model perturbations without changing also initial and boundary conditions is not very useful, the spread added by using two different convection scheme being much lower than the other. In order to better understand the difference between the two schemes on the skill in forecasting precipitation, the ROC diagram at the +90h forecast range is reported in Fig. 17.

Looking at the first crosses from the top right corner (low probability classes), the Hit Rate of the Kain–Fritsch suite is rather higher than that of the Tiedtke suite, while only a small increase in terms of False Alarm Rate is shown.

When verification is repeated in terms of maximum values over the same boxes, different results are obtained. Considering maximum values over boxes, a higher precipitation threshold (50mm/24h) is chosen for this analysis. As shown in Fig. 18, higher ROC area values are relative to the Tiedtke suite (blue line), but the difference between the two is narrowing for increasing forecast range. The combined suite line (green) is still the highest, but only by a very little amount.

Considering the ROC Curves at the +90h forecast range (Fig. 19), it appears that the small difference between the two suites is due to a little increase in terms of Hit Rate for the Tiedtke suite, while the False Alarm Rate are almost identical.

Actually, it does not seem possible to establish from these results which convection scheme lead to the best performance of the mesoscale ensemble. Furthermore, it is evident that using this kind of model perturbation in order to increase the ensemble spread does not lead to the expected results, the performance of the 10–member ensemble being almost identical

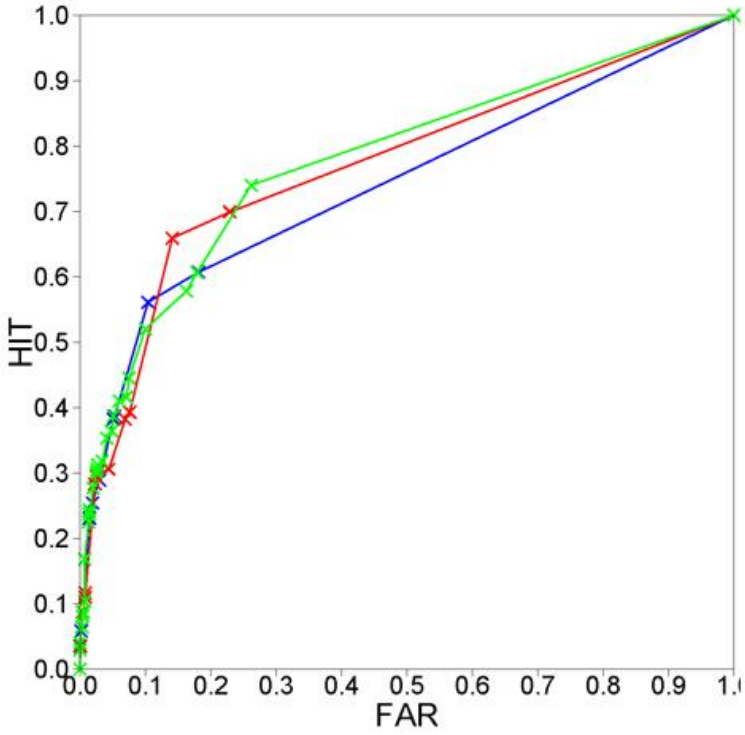


Figure 17: ROC Curves for the precipitation threshold 20mm/24h (average values) and for the +90h forecast range. The blue line is relative to the Tiedtke suite (operational), the red line is relative to the Kain–Fritsch suite and the green line is for the 10–member combined suite.

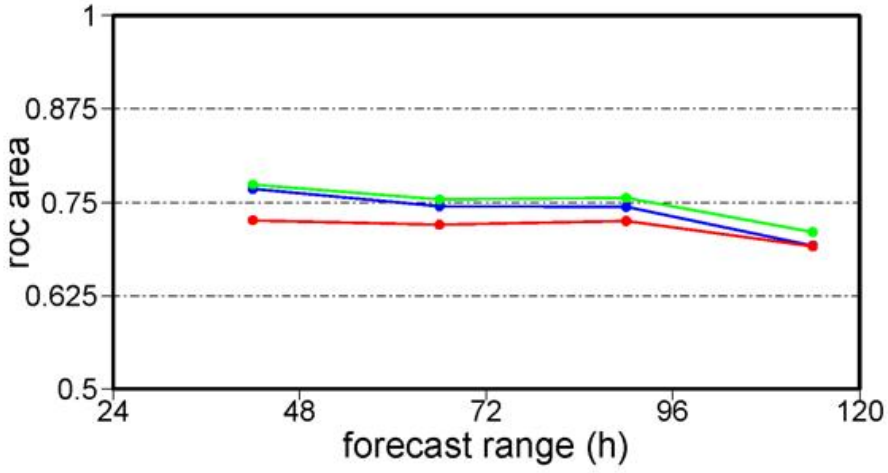


Figure 18: ROC area values as a function of the forecast range for maximum precipitation over 0.5 x 0.5 degrees boxes exceeding 50mm/24h. The blue line is relative to the Tiedtke suite (operational), the red line is relative to the Kain–Fritsch suite and the green line is for the 10–member combined suite.

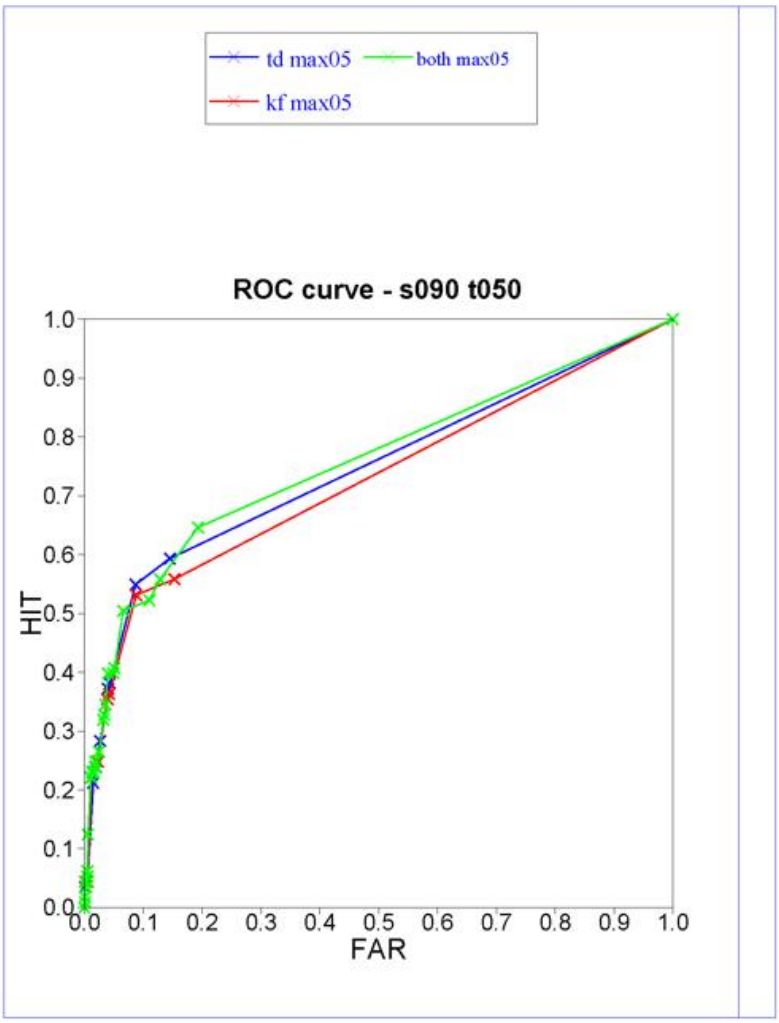


Figure 19: ROC Curves for the precipitation threshold 50mm/24h and for the +90h forecast range. The blue line is relative to the Tiedtke suite (operational), the red line is relative to the Kain–Fritsch suite and the green line is for the combined suite.

to those of both 5–member ensembles. Due to this result, we decided to move to a 10–member COSMO–LEPS by selecting 10 Representative Members out of the EPS, to benefit from the spread introduced by the different initial and boundary conditions. Nevertheless, trying to benefit also from the little spread added by this kind of model perturbations, we decided to perform the 10 LM runs by using both the Tiedtke and Kain–Fritsch schemes for the parameterization of the convection. Then, from June 2004, also this modification was introduced in the COSMO–LEPS suite and the convection parameterization scheme used by each single run is selected randomly.

5 COSMO-LEPS Subjective verification – Contribution by ARPAL, Genova, Italy (Davide Sacchetti)

This analysis aims at evaluating from a quantitative point of view the subjective judgements by the forecasters on the usefulness of COSMO–LEPS as a tool for operational weather forecast. The followed methodology is described in section 5.1 while the results are presented in section 5.2.

5.1 Description of the methodology

The questions we have tried to answer are:

- do the members provide weather scenarios actually different from the forecaster's point of view?
- do the members provide useful informations on both the amount and the localization of the precipitation?
- is the most weighted member the more skillful?
- what kind of information can be obtained by the forecasters from the probability maps for the exceeding of a threshold?
- does the system performance depend on the synoptic situation?

In order to answer these questions, the forecasters have been asked to judge the COSMO–LEPS products following a scheme developed for this purpose.

5.1.1 Subjective evaluation of the precipitation field forecast by the 5 members

A qualitative analysis of the skill of the forecast provided by the 5 COSMO–LEPS members is performed through three steps:

- identification of the member(s) which better forecasts the localization of the precipitation maxima over the considered area
- identification of the member(s) which better forecasts the amount of maxima of precipitation over the considered area
- How many members are significantly different?

In Fig. 20 the mask used by the forecaster for the evaluation of the 5 different scenarios provided by COSMO-LEPS is shown.

It is also possible to signal that no one of the members is representative of the observed scenario.

At this stage the forecaster does not know the weights which are assigned to each member; the comparison between his/her choice and the "a priori" probabilities are carried out afterwards.

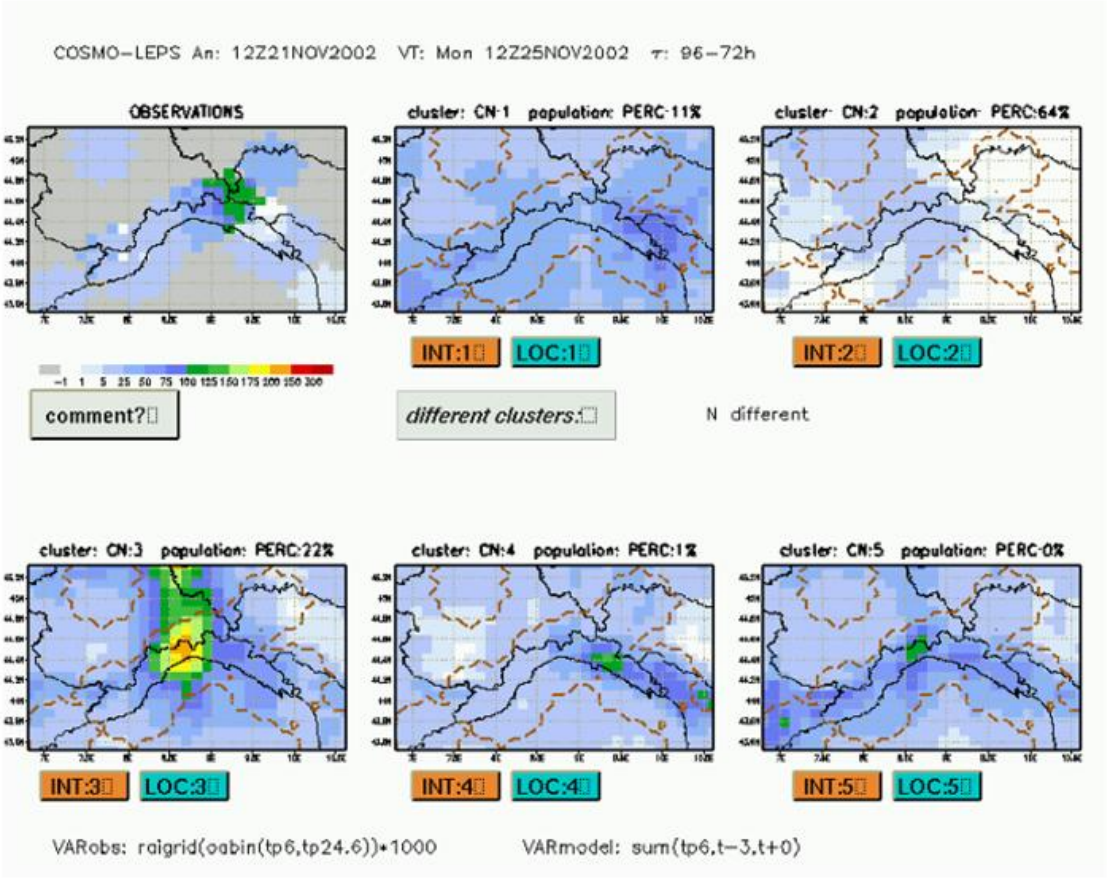


Figure 20: Mask used by the forecasters of the ARPAL Hydro–meteorological Service for the subjective evaluation of the forecast provided by the 5 COSMO–LEPS members.

5.1.2 Subjective evaluation of the COSMO–LEPS probability maps

A qualitative analysis of the skill of the forecast provided by the COSMO–LEPS probability forecast is performed. For each precipitation threshold (20, 50, 100 mm/24h), the probability map is compared with a map of observed precipitation cut at the corresponding threshold (only values exceeding the threshold). The forecaster assigns a score (agreement: poor, reasonable, good) to the probability fields on the basis of their usefulness. This is evaluated only in terms of the "alarm level" suggested by the probability maps, that is on the forecast precipitation amount, giving only small importance to the correct localization of the phenomena. In this phase what is more important is the capability of providing a signal of an intense event.

In Fig. 21 the mask used by the forecaster for the evaluation of the COSMO–LEPS probability maps is shown.

5.1.3 Individuation of the synoptic pattern

Finally, the performance of COSMO–LEPS is related to the synoptic situation associated with the considered event. The forecasters have to answer to the following question: to which synoptic pattern is it possible to associate the considered event? They can choose between four possibilities, which are listed in Table 5.1.3.

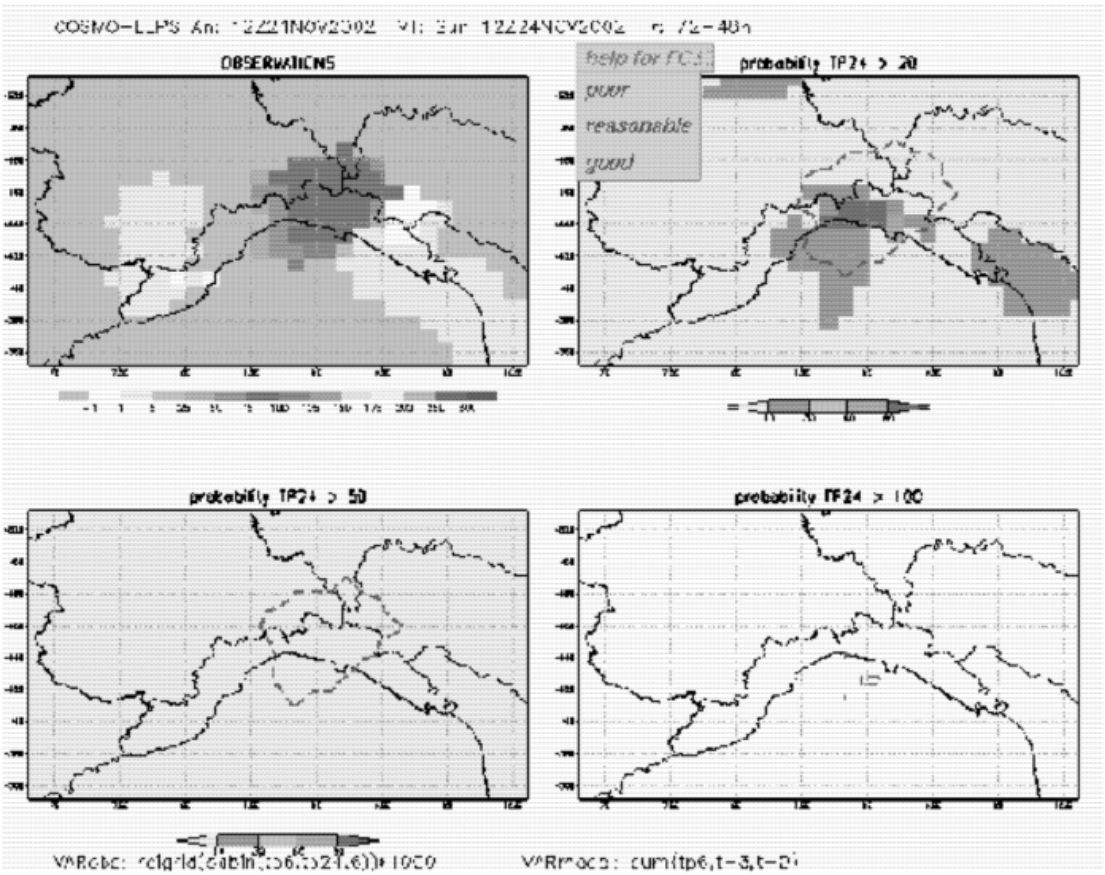


Figure 21: Mask used by the forecasters of the ARPAL Hydro–meteorological Service for the subjective evaluation of the forecast provided by the COSMO–LEPS probability maps.

Table 1: Medium range weather types

Name	Description	Main characteristics of the weather
straight flow	rapid, straight, perturbed	rainy, often windy
undulating flow	alternating ridge and trough, unsettled weather	a rainy period is followed by a sunny one; there is at least one rainy period
warm blocked	anticyclonic conditions	dry weather, sunny in summer, sometimes foggy or dull weather in winter
cold blocked	low-pressure conditions	cool or cold weather, often rainy

5.2 Results

In Fig. 22 the usefulness for the forecasters of the COSMO–LEPS scenarios in terms of precipitation intensity is assessed for different forecast ranges. In the left panel the analysis is relative to the evaluation directly made by the forecasters, ignoring the weight given to each member according to the cluster population, while in the right panel weights have been associated to the COSMO–LEPS members.

A positive impact of the weighting procedure is evident, for all the precipitation intensities and for all the forecast ranges.

The same analysis has been repeated in terms of localization of the precipitation (Fig. 23).

The positive impact of the weighting procedure on the localization is well evident, especially for moderate and intense precipitation.

How the usefulness of the forecasts differentiate with the synoptic situation is shown in Fig. 24.

The "warm blocked" situation seems to be the more predictable, while the "straight" flow is the less predictable. The performances both in terms of intensity and localization improve when the ensemble members are weighted according to the cluster population.

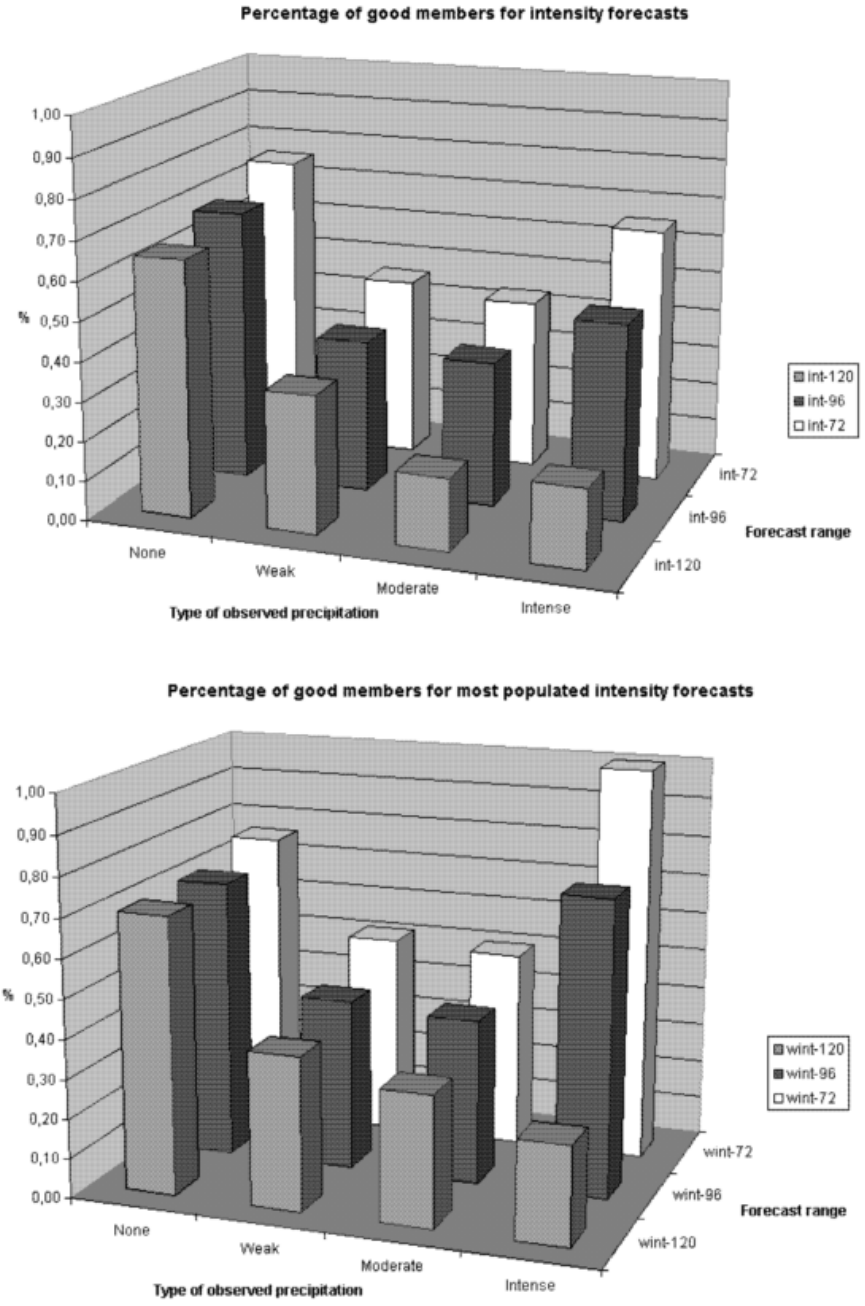


Figure 22: Percentage of "good" members in terms of intensity for four classes of intensity and for the different forecast ranges (+72h, +96h, +120h). The percentage is computed by not weighting (top panel) and by weighting (bottom panel) the ensemble members.

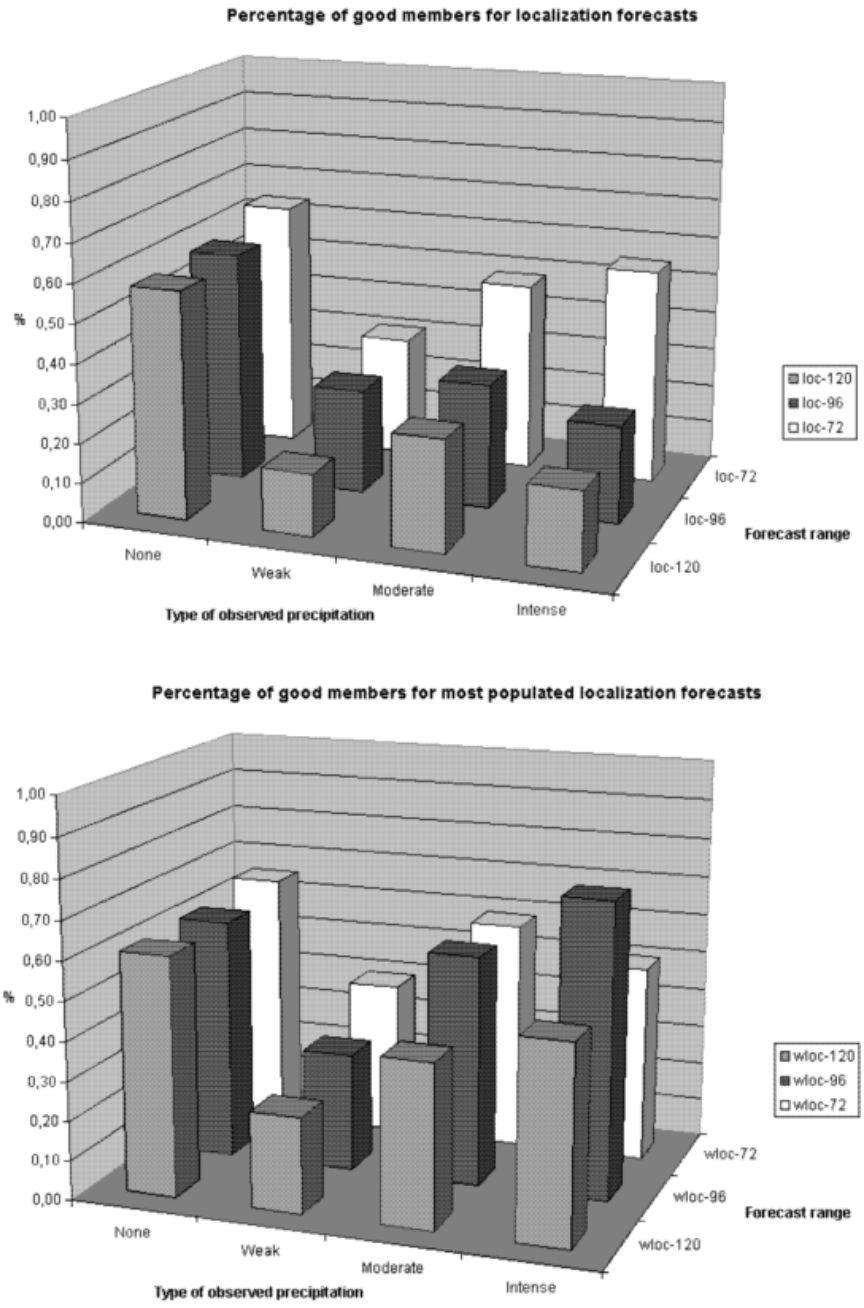


Figure 23: Percentage of "good" members in terms of localization for four classes of intensity for the different forecast ranges (+72h, +96h, +120h). The percentage is computed by not weighting (top panel) and by weighting (bottom panel) the ensemble members.

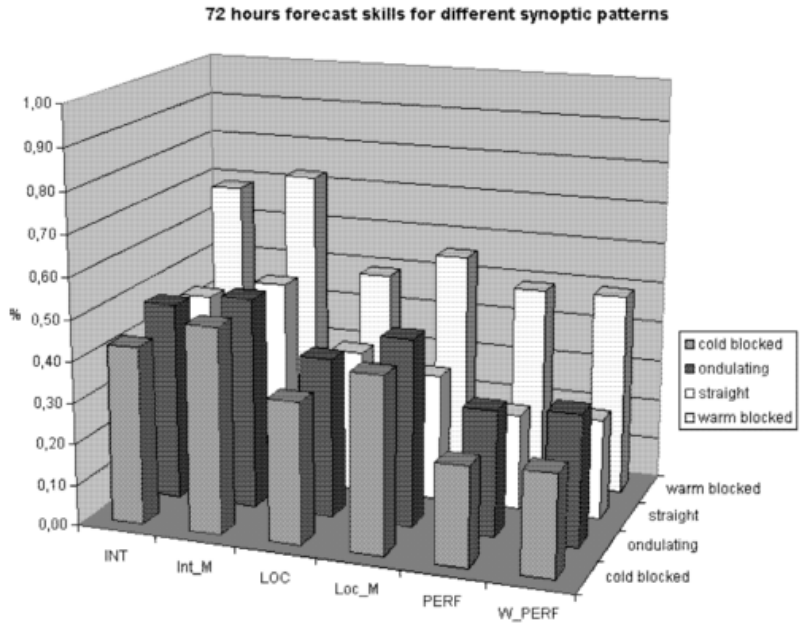


Figure 24: Percentage of "good" members in terms of intensity (int) and localization (loc) for the four types of synoptic situation for the +72h forecast range. A label M is added to int and loc if the percentage is computed by weighting the ensemble members.

6 Use of COSMO-LEPS at MeteoSwiss - Contribution by MeteoSwiss, Zürich, Switzerland (Andre' Walser and Marco Arpagaus)

The quasi-operational COSMO-LEPS has made probabilistic short to early-medium range forecasts available at MeteoSwiss. It motivated scientists and forecasters from the weather department to look closer into the topic of probabilistic weather forecasting and provides an excellent basis for research in this field. Since the optimal use of probabilistic forecasts needs a knowledge transfer from scientists to forecasters, the introduction of COSMO-LEPS had both technical and educational aspects.

This chapter is structured as follows: The MeteoSwiss post-processing of COSMO-LEPS is described in section 6.1. Section 6.2 discusses the experience with COSMO-LEPS from the perspective of the forecasters, while section 6.3 presents the use of COSMO-LEPS forecasts exemplified for a storm event. Finally, conclusions and an outlook are provided in section 6.4.

6.1 MeteoSwiss post-processing

The setup of the MeteoSwiss post-processing of COSMO-LEPS output has been strongly supported by our colleagues of ARPA-SIM and is summarised in Fig. 6.1. This post-processing starts as soon as the COSMO-LEPS forecasts are available at ECMWF and consists of

(i) a transfer of COSMO-LEPS probabilistic model output (PMO) and direct model output (DMO) of all ensemble members to the MeteoSwiss post-processing server at the CSCS[1],

(ii) using the DMO to calculate customer-specific PMO, and

(iii) a visualisation of the PMO in the form of probability maps and meteograms, the latter of which is described in the following paragraph.

These COSMO-LEPS products are presented on the intranet of MeteoSwiss and some selected products are printed out automatically and pinned to the weather board in the meteorological operations room.

A very popular output of the post-processing is the mentioned meteogram. It is currently produced for about 30 grid points within the model domain and summarises the 5-day COSMO-LEPS forecast in terms of cloud cover, precipitation, wind gusts and temperature. Figure 6.1 shows the meteogram for the grid point closest to Zürich from the forecast started on 25 August 2004 1200 UTC. For each variable the median of the 10 COSMO-LEPS members is displayed as red line. The middle two quartiles (25% to 75% probability of occurrence) are indicated by the grey shaded area, and the minimum and maximum values, respectively, by the dashed lines. Median and quartiles are calculated by weighting the members according to the cluster population and with a linear interpolation between the discrete cumulative probabilities for every three hours (corresponding to the current output frequency of the COSMO-LEPS members). Additionally, the meteogram shows the deterministic forecast

[1]Swiss National Supercomputing Centre, Manno.

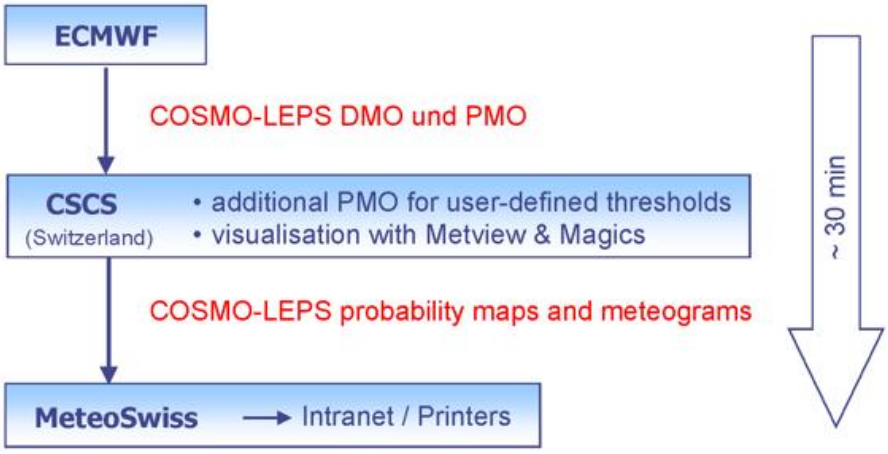


Figure 25: Flow chart of the MeteoSwiss post-processing of COSMO-LEPS output.

of the operational high-resolution model at MeteoSwiss (aLMo) as blue lines. Since the aLMo forecast initialized 12 hours later than COSMO-LEPS is available shortly after the COSMO-LEPS forecast, this newer 72-h forecast is displayed in the meteogram.

The width of the grey shaded area together with the spread between the minimum and maximum values give a measure of the uncertainty of the most likely scenarios given by the aLMo and the COSMO-LEPS median. It is expected that aLMo is the better estimate than the median for short lead-times, however, without yet knowing how long "short" in this context is. Temperature and wind gust forecast show the typical case with increasing spread with increasing forecast time. Clearly, the prediction of cloud cover is associated with the highest uncertainty, this being often associated with a similar uncertainty in the forecast for precipitation.

6.2 Experience with COSMO-LEPS

The change from predicting precipitation amounts to predicting probabilities of occurrence for a certain threshold is a radical paradigm shift which clearly demands some training for forecasters not familiar with probabilistic forecasts. This was essential for the introduction of COSMO-LEPS forecasts at MeteoSwiss. Meanwhile, about half of the forecasters already use COSMO-LEPS together with other products to prepare their weather bulletins for the next few days.

The overall feedback on COSMO-LEPS from the forecasters is clearly positive. They mainly use probability maps of 24-h accumulated precipitation and maximal daily wind gusts for forecast days 2 to 4 (for an example of a probability map, cf. Fig. 28). COSMO-LEPS products for other variables are not yet considered frequently. In addition, some forecasters also look at a small set of meteograms. Forecasters describe the use of COSMO-LEPS for the current bulletin as "considering an additional opinion besides the other models", which are mainly aLMo and deterministic ECMWF. E.g., for forecasting precipitation amounts, a high probability for a threshold below the predicted value and a low probability above would be considered a confirmation of the predicted deterministic estimates.

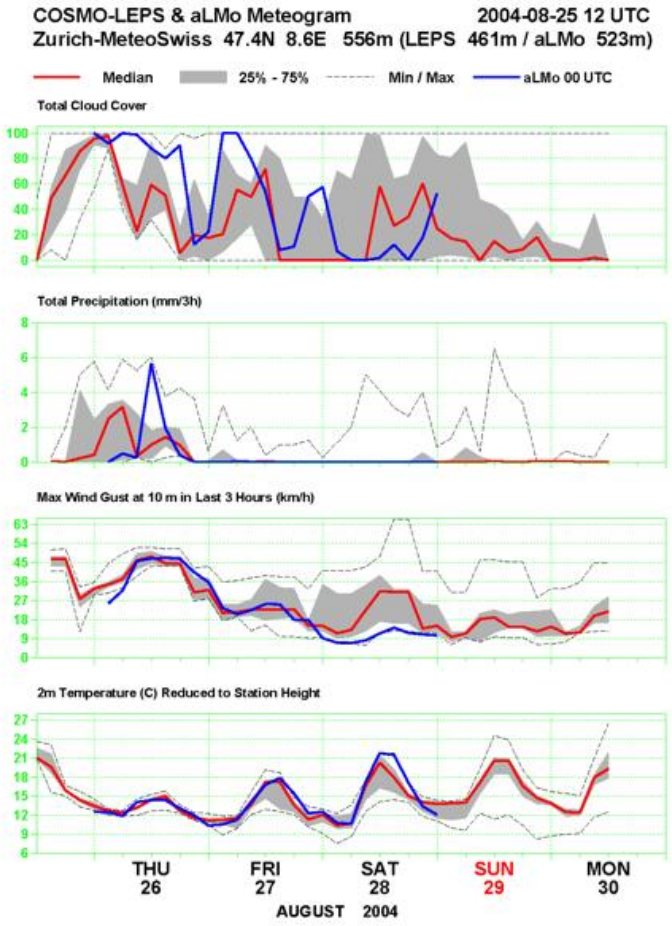


Figure 26: Meteogram as derived from the COSMO-LEPS and aLMo output in terms of cloud cover, precipitation, max. wind gusts, and temperature (see text). Example for Zürich from the forecast starting on 25 August 2004 1200 UTC.

COSMO-LEPS forecasts are studied more thoroughly when they show considerable probabilities for a threshold which represents a warning level or if forecasters have other indications for an extreme precipitation or storm event. Since such extreme events often have low predictability even in the short-range, COSMO-LEPS PMO is also considered for this forecast-range (for which COSMO-LEPS is not designed) due to the lack of an alternative. There is no verification done yet concerning the performance of warnings from forecasters compared to COSMO-LEPS itself in terms of hit rate and false alarm rate. Such a verification for Switzerland would be of strongest interest for the forecasters and would possibly help to extend the use of COSMO-LEPS (personal communication from a forecaster). In discussions with forecasters the following concerns about COSMO-LEPS turn up frequently:

- There is little confidence that COSMO-LEPS is able to predict reliably the probability for convective precipitation events in summer.
- Due to the rather coarse horizontal resolution, it is not expected that COSMO-LEPS is able to give warnings for extreme events related to small-scale orography such as Föhn.
- For short lead-times, the use of the super-ensemble could smooth the predicted probability distribution, reducing the probability for an extreme event and hence the hit rate.

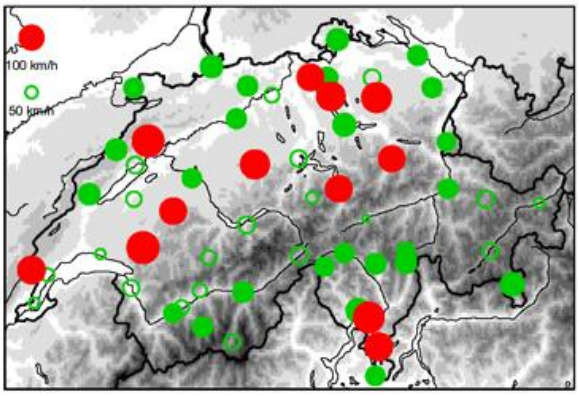


Figure 27: Observed maximal wind gusts on 19 November 2004 as size of centered circles (scale is indicated in the panel) for 59 stations below 2000 m a.s.l. of the Swiss automatic observation network. Green and red filled circles indicate wind gusts above 70 km/h and 100 km/h, respectively. The grey shaded background represents the topography.

Overall, the use of PMO has clearly increased due to the availability of COSMO-LEPS products which are acknowledged by the forecasters. However, the entire potential of COSMO-LEPS is not yet exploited since forecasters are not instructed to complement the weather bulletins with a level of confidence, e.g. with a probability of occurrence for the predicted event. This would mean an even more profound paradigm shift, which clearly needs more confidence in the ability of COSMO-LEPS (or other high-resolution probabilistic weather forecasting system) to predict the probability distributions reliabe for the most important parameters such as temperature, horizontal wind, precipitation, and cloud cover.

6.3 Case study: Storm on 19 November 2004

In this section, the COSMO-LEPS forecasts and their use are discussed on the basis of a case study. In the early morning of 19 November 2004 a cold front crossed Switzerland in a strong westerly flow producing maximal wind gusts of 60-90 km/h on the Swiss Plateau and slightly above 100 km/h in somewhat elevated places, in Alpine valleys, and in the Lago Maggiore Area to the south of the Alps. Figure 6.3 shows the observed maximal wind gusts for 59 stations located below 2000 m a.s.l. of the Swiss automatic network with green and red filled circles indicating maximal gusts above 70 km/h and 100 km/h, respectively, where the latter value corresponds to the warning threshold for the regional authorities.

On 17 November the forecasters on duty decided to issue a pre-warning for wind gusts between 80-100 km/h on the Swiss Plateau during the night from 18 November to 19 November. They based the warning on (i) the mean 850 hPa flow of the deterministic ECMWF forecast, (ii) the predicted aLMo wind gusts, and (iii) the COSMO-LEPS probability maps for maximal 10 m wind gusts. On the following day, this warning was confirmed and a new warning for the Ticino was issued for wind gusts of 75-100 km/h embedded in a strong north Föhn.

While ECMWF and aLMo suggested wind gusts somewhat above and slightly below 100 km/h, respectively, COSMO-LEPS indicated in the four consecutive forecasts started on 15, 16, 17, and 18 November 1200 UTC high probabilities for wind gusts below 100 km/h, but negligible probabilities for wind gusts above this value, shown in Fig. 28. Only the forecast started on 18 November (Fig. 28d) predicted considerable probabilities for maximal wind gusts above 100 km/h for the eastern part of the Swiss Plateau.

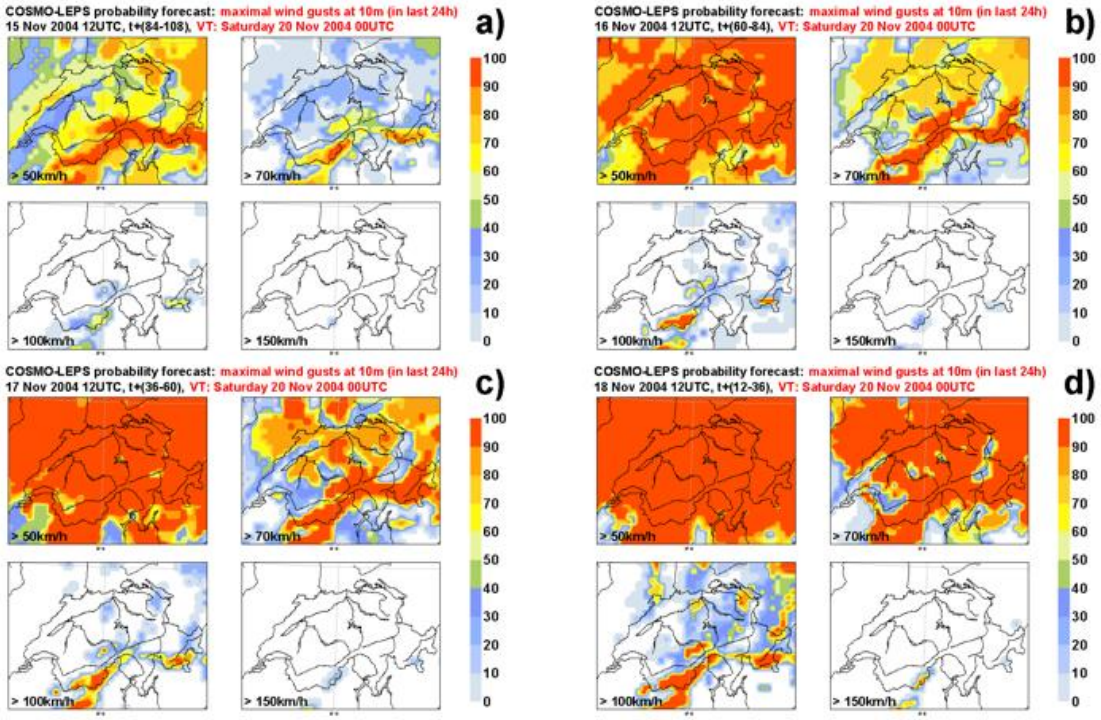


Figure 28: Probability forecast for maximal wind gusts above 50, 70, 100, and 150 km/h, respectively, from four consecutive COSMO-LEPS forecasts for 19 Nov 2004 initialised at (a) 15 Nov, (b) 16 Nov, (c) 17 Nov, and (d) 18 Nov 1200 UTC.

Overall, COSMO-LEPS supported the forecasters well in this case by suggesting a high probability for maximal wind gusts at the observed level on the Swiss Plateau without suggesting a more extreme event. However, COSMO-LEPS missed the wind gusts above 100 km/h at the elevated places in western Switzerland and - as expected - in the Alpine valleys including the strong north Föhn in the Ticino. Considering the four consecutive forecasts, the steady increase in the probabilities for maximal wind gusts below the observations with decreasing lead-time is remarkable, whereas a corresponding decrease of probabilities for maximal wind gusts above the observations cannot be seen. A sharpening of the predicted probability density function with decreasing lead-time as can be partly observed for this case is a key characteristic of a well-designed EPS.

6.4 Conclusions and outlook

The developed probabilistic COSMO-LEPS products try to visualize the complex information of COSMO-LEPS forecast in a concise way. They complement the deterministic forecast products of aLMo and are appreciated both from forecasters and scientists as subjectively skillful information.

We are convinced that high-resolution EPSs such as COSMO-LEPS have a great potential for further improvements in terms of forecast skill. It is planned to continue our research activities in this field in close collaboration with the ARPA-SIM focusing on potential high-impact weather. A key goal is the comparison to different available and newly developed forecasting approaches such as ECMWF extreme forecasts index and neural networks. In addition, a model-based climatology will be assembled to assess the return periods of high-impact weather events as a function of forecast lead-time and compared to observations.

Moreover, this model climatology will allow to identify model biases related to intrinsic model deficiencies.

The interest in high-resolution EPSs will undoubtfully further increase and it is worth to mention here, that the executive board of MeteoSwiss recently declared probabilistic forecasting as a strategic goal.

7 Could the COSMO–LEPS system add value to operational forecasts of the DWD in the case of severe weather? - Contribution by the Central Forecast unit of the DWD in 2004 (Thomas Schumann)

Since 31 January 2003 products of the COSMO–LEPS system are available in the DWD intranet for use in operational forecasts. COSMO–LEPS as a limited area ensemble prediction system is running once a day, driven (since 01 June, 2004) from 10 selected EPS members of 2 consecutive (12-hr lagged) runs of the ECMWF global model. The forecast range is beginning at H+48 in the short range and ending at H+120 in the early medium range from the last of the both ECMWF runs. The main objective of the COSMO–LEPS system is to identify severe weather patterns within a certain time range over a limited area by using probabilistic methods. To reach this, LM-based probabilistic products will be calculated, disseminated and presented to the forecaster in a user-friendly design by using the DWDs intranet or the meteorological application system via workstations. Beginning in March 2003 the COSMO–LEPS system at the DWD will be used pre-operational as well during the medium range as for short range forecasts. COSMO–LEPS is an additional source of information, forecast plots will be checked whether possible severe events could be identified by relevant signals in the probability maps or not. This is dependent of course from the synoptic situation. Products such as a direct model output from COSMO–LEPS were not generated. In the Central Forecast unit a subjective, very comprehensive verification of the COSMO–LEPS probabilistic forecasts has been carried out. The verification has been done by comparing observations against the forecasts verifying at the time of the observation by continuous tables for each weather parameter including a short description of the event. This task is still a part of the operational medium range forecast shift carried out by the duty forecaster of this shift and will be continued. Another verification method used in the Central Forecast Unit is the preparation of case studies. If a severe event occurred the observed values of a certain weather parameter will be compared with the probability forecasts of COSMO–LEPS at certain thresholds verifying at the time of the occurrence of severe weather. Forecasts of other models or centers will be included. The objective of the verification of the COSMO–LEPS system is:

- Is COSMO–LEPS able to add value to the prediction of severe weather events?
- Could COSMO–LEPS outperform other models?
- What are typical weak points and what are the strength of COSMO–LEPS?
- Are there any changes in the COSMO–LEPS system required (design, thresholds, weather parameters, forecast range)?

To answer these questions we have to go more into detail how COSMO–LEPS performs related to weather parameters provided from the system. An overview has been prepared as a result of the continuous verification, forecasters experience and several case studies. This is provided by Table 2.

Parameter	General remarks Predictability by COSMO–LEPS	Further comments / recommendations
Temperature Minimum of the day	Very poor, mostly no signals	Useful in a few cases only without near surface inversion. Outperformed by the KALMAN / MOS output from LM or ECMWF deterministic model.
Temperature Maximum of the day	Sometimes useful	Realistic regional assignment, even heat islands (large cities) visible. Poor results in the case of extreme heat waves (underestimation of temperature maximum). Outperformed by the KALMAN / MOS output from LM or ECMWF deterministic model.
Maximum wind gusts of the day	Major synoptic scale storms: Good forecasts. Convective gusts: No correct signals	Realistic regional assignment, orographic effects well represented. COSMO–LEPS adds value to forecasts. Prediction of gusts caused by convection events not possible. If signals presented they are wrong located, orographic effects overestimated. Thresholds should be changed, levels 30 and 35 m/s more important for severe weather prediction than 10 and 15 m/s
Snow fresh fallen during the last day	Sometimes useful	Synoptic-scale events: Realistic regional assignment, orographic effects well represented. COSMO–LEPS adds value to forecasts. Poor results in the case of minor severe / small scale events
Total precipitation accumulated over 24 hours	Often useful	large-scale events: Realistic regional assignment, orographic effects well represented. COSMO–LEPS could add value to forecasts. Poor results in the case of minor severe / small scale, convective or convective-mixed events
Convective precipitation Thunderstorm (CAPE)	Very poor, mostly no signals. CAPE: more cases needed	Prediction of heavy precipitations caused by convective or convective-mixed events not possible. If signals presented they are wrong located, orographic effects overestimated

Table 2: Overview on Forecasters experience

To summarize this and to answer the questions above, it has to be concluded that COSMO–LEPS did not always met the forecasters requirements and expectations. Valuable predictions of severe events provided only if the event is non-convective and at least a synoptic-scale one. In this situations COSMO–LEPS will be able to add value to the prediction of severe events by providing probabilities exceeding certain thresholds. Then other models mostly are performing very well, too. COSMO–LEPS could outperform other models in areas with clear orographic structure only. This is the strength of COSMO–LEPS and why it has been designed: Provide the forecaster a hint what could happen in these areas in the case of severe weather. COSMO–LEPS has been adjusted to deal with the orography of the Alps and the surrounding mountains of the Mediterranean Sea and not with the highlands over Central Germany. Another point is that COSMO–LEPS is reflecting the weaknesses of the driving ECMWFs EPS and the nested LM. This has been characterized by the problems of

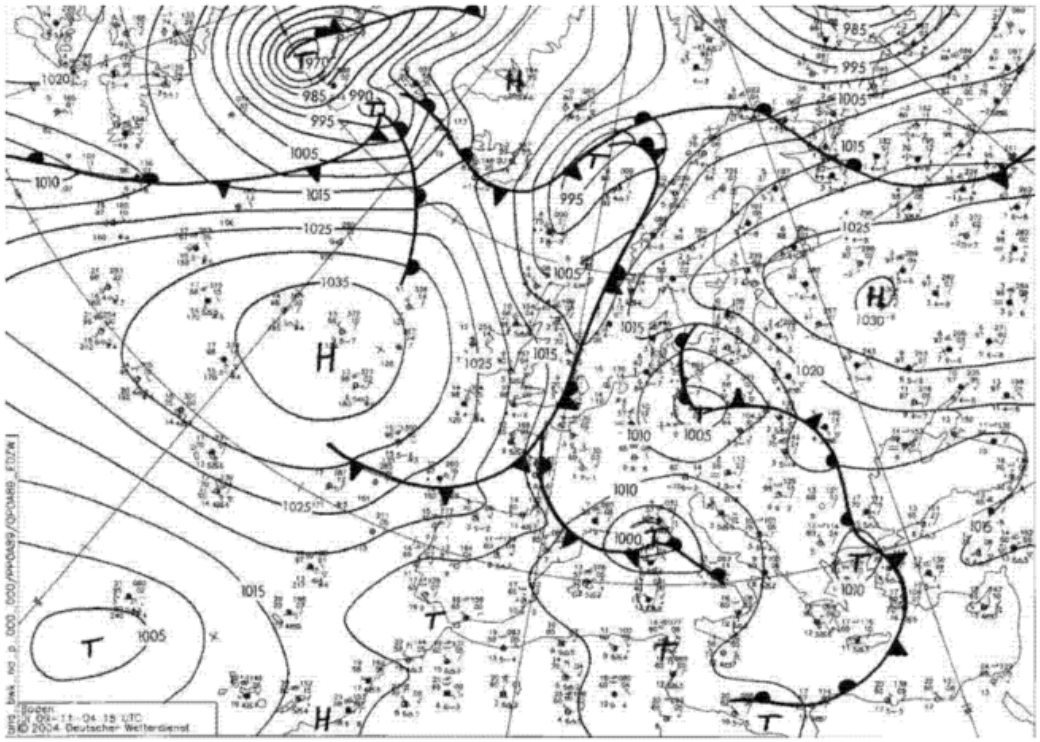


Figure 29: MSLP Analysis, 09 Nov 2004, 18 UTC.

COSMO–LEPS predicting convective gusts and precipitation and due to the poor vertical resolution in the lower troposphere in the forecast of the daily temperature minimum as well as for the temperature maximum in the case of extreme heat waves. Further verification is required to detect changes in the model behavior caused by the variation of the configuration since 06/2004.

7.1 A case study - early winter over Germany (09 Nov, 2004)

The synoptic situation was characterized by a huge cut off-low with embedded centers over the west part of Germany and the southern Adriatic Sea. Crossing the eastern part of the Alps the second center has been induced a cyclogenesis. The resulting low passed the Czech Republic and has been moved over Northeastern Germany (see Fig. 29, SLP Analysis 09 Nov 2004, 18 UTC.). The low caused the first winter outbreak over Germany in 2004/2005. Widespread areas have been covered by fresh fallen snow (Fig. 30, snow cover over Germany in centimeter, 10 Nov 2004, 06 UTC). The early winter outbreak lead to chaotic situations in the traffic including disruptions of streets by broken trees because of wet snow (Fig. 31, impressions from the winter outbreak over central parts of Germany).

How has COSMO–LEPS predicted this winter outbreak? That will be demonstrated by Fig. 32. On the left the probability of exceeding 10 centimeter fresh fallen snow is shown, the right shows the 20 centimeter-threshold. The first row are the 120-hr forecasts verifying on 10 November, 12 UTC. Already during the early medium range COSMO–LEPS has been shown relevant signals. In the highlands over the central part of Germany 10 centimeter fresh fallen snow is likely and up to 20 centimeter is possible. Over the southwestern part of Germany not more than 10 centimeter snow has to be expected. In this situation COSMO–LEPS has provided an "early warning". Therefore it was possible to describe this scenario

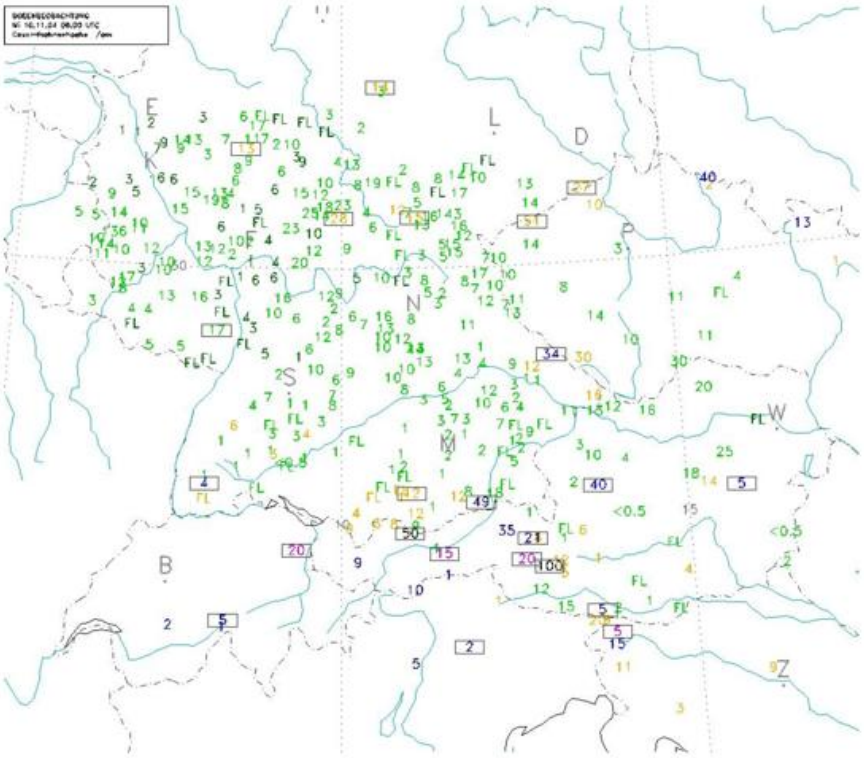


Figure 30: Fresh fallen snow, 10 Nov 2004, 06 UTC



Figure 31: Impressions from the winter outbreak over central parts of Germany 10 Nov, 2004

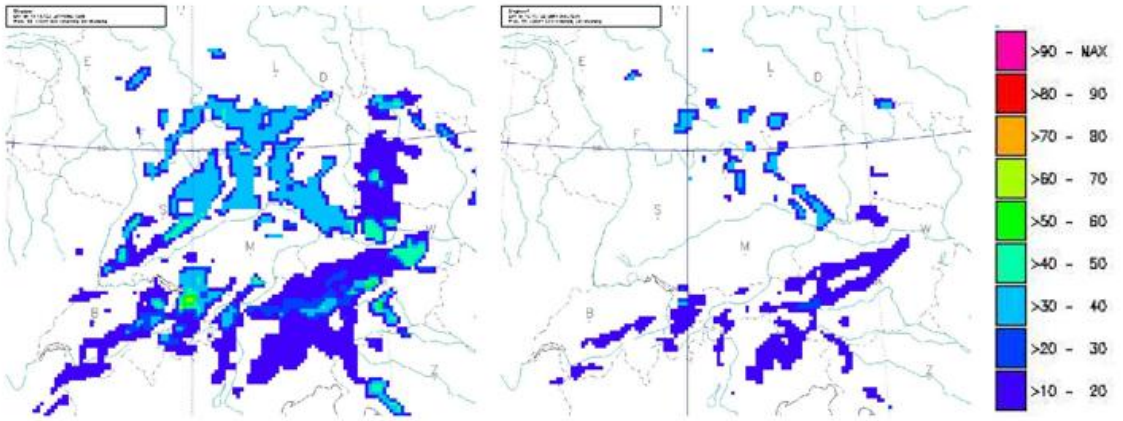


Figure 32: 120 hr-forecast, verifying at the 10 Nov 2004, 12 UTC. Left: Threshold 10 centimeter, right: 20 centimeter fresh fallen snow.

early in the weather reports, from a forecasters point of view this early winter outbreak was not a surprise.

The signal has been developed by the forecasts of the following days (see Fig. 33). The closer the event comes, the more the pattern has been shifted into northwesterly direction. Comparing against observations this was correct. The maximum of snow has been predicted already during the medium range. The orographic representation of the probabilities shown here even allows predictions that in the Upper Rhine valley, the lower-evaluated part of the Rhein-Main-area and the Wetterau snow will be unlikely or the snow depth will not exceed a few centimeter as it has been observed close to the Danube river or in the Hunsrück highlands.

This case study demonstrates a successful forecast of COSMO–LEPS how the system is working and how it could be used to improve the forecasters guidance. During the majority of the severe weather cases the signals provided by COSMO–LEPS were less developed and consequently the forecasts less helpful.

7.2 Conclusions

The COSMO–LEPS system did not always meet forecasters expectations. The guidance provided by COSMO–LEPS to predict the temperature minimum of the day and convective events (related gusts and heavy precipitation) is poor and useful in a few cases only. COSMO–LEPS will add value to the prediction of large scale precipitation and wind gusts if the causing event is a synoptic or larger scale one. The regional assignment is mostly realistic, orographic effects are well represented, weak, but realistic and useful signals often have been shown already during the medium range. The majority of severe weather warnings will be caused by smaller scale events related often with heavy convection. The prediction of such events needs to be improved as well by COSMO–LEPS as by the driving ECMWFs EPS and the nested LM. A small number of cases does not allow final conclusions, further verification (continuous or case-sensitive) is required. A problem is the re-calculation of the COSMO–LEPS forecasts for "historical" weather events again. This might be too expensive. An archiving of the set of derived probability forecasts in the MARS archive of the ECMWF would be helpful.

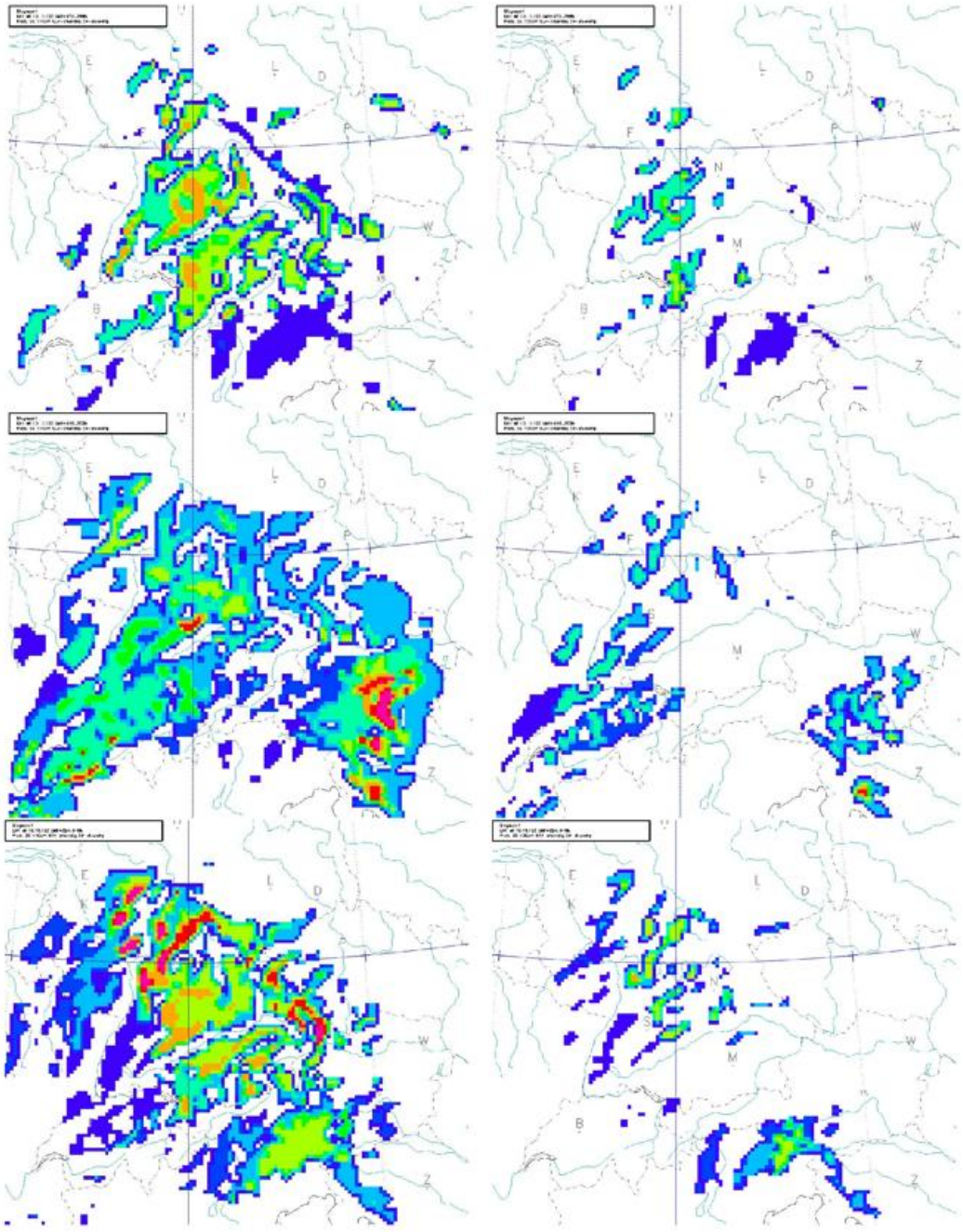


Figure 33: 96 hr-forecast (top), 72 hr-forecast (center) and 48 hr-forecast (bottom) verifying at the 10 Nov 2004, 12 UTC. Left: Threshold 10 centimeter, right: 20 centimeter fresh fallen snow. Color scheme is the same as in Fig. 32.

8 Conclusions

The high–resolution system COSMO–LEPS has been designed as a tool for the prediction of heavy precipitation in a probabilistic perspective. On a case study basis (Montani et al., 2003b and Marsigli et al., 2004), the system has proved to be successful in the prediction of intense rainfall events. An objective probabilistic verification is being carried out at ARPA–SIM so as to assess both the abilities and shortcomings of the system, to address future developments of the system and to provide guidelines to the users. Furthermore, the other COSMO partners have submitted the systems to a careful subjective evaluation, trying to assess the usefulness in a quasi–operational framework.

With regard to the objective verification, in this report the COSMO–LEPS performances in forecasting precipitation has been presented. The period considered is September–November 2003 and forecast precipitation cumulated over 24 hours is compared with observed data.

In order to quantify the added value provided by the mesoscale probabilistic system, COSMO–LEPS has been compared with the ECMWF EPS. To make an appropriate comparison of the two systems, the differences in the number of ensemble members (5 for COSMO–LEPS and 51 for the EPS) and in the horizontal resolution (10 km for COSMO–LEPS and 80 km for the EPS) have been considered. As far as the population of the ensembles is concerned, the reduced EPS made up of the 5 Representative Members has also been analysed, allowing to quantify the impact of the increased resolution alone. On the other hand, the problem of the very different resolutions of the two systems is tackled by upscaling both systems to a lower resolution: the grid point forecasts of both model are aggregated over boxes of 1.5×1.5 degrees. The observations are also aggregated over the same boxes.

A comparison in terms of average precipitation values over 1.5×1.5 degree boxes shows that EPS performs better. Nevertheless, COSMO–LEPS outperforms the reduced EPS composed of the 5 Representative Members in terms of ROC area, in particular showing a higher Hit Rate. When the comparison is carried out in terms of maximum values over boxes of the same size, COSMO–LEPS scores are the highest, in terms of both Brier Skill Score and ROC area. This is due to the capability of the mesoscale system to forecast high precipitation values. The analysis of the ROC Curves shows that this improvement is not associated to a dramatic increase of the false alarms.

Considering average precipitation over a quite large area, EPS is performing better than the mesoscale system. Nevertheless, it is worth noting that meteo–hydrological applications often requires information on a more local scale. The skill of the COSMO–LEPS system in forecasting the occurrence of precipitation maxima is a clear indication of the usefulness of the system in forecasting intense and localized events.

Finally, COSMO–LEPS scores are worsening at the 5 day forecast range, leading to a reduction of the improvement with respect to the global systems. This could be linked to the increase of the limited–area model error, which, at this time range, becomes large enough to overwhelm the improvement produced by LM in terms of predictability of mesoscale structures.

A comparison of the COSMO–LEPS scores with and without the application of the weighted procedure has not been presented in this report. Results (not shown) indicate that no benefit is added by weighting the COSMO–LEPS members according to the cluster population. These results were obtained in terms of precipitation, verified against observations. Nevertheless, a positive impact is evident in the subjective verification performed by ARPAL, where it is shown that weighting the members improves the COSMO–LEPS performances,

both in terms of intensity and localization of the precipitation, especially for moderate and intense precipitation.

An analysis of the COSMO–LEPS methodology, leading to the choice of the Representative Members, has been also shown, addressing the topics of the super–ensemble size (1 EPS, 2 EPS, 3 EPS) and of the number of Representative Members (5 or 10). The analysis has been performed by verifying the precipitation forecast by the reduced EPS made up by the RMs without running the nested LAM. The forecast are compared with ECMWF proxy rain over the same season (Autumn 2003).

We showed that the use of just two EPS in the super–ensemble seems to be a suitable compromise between the need to decrease the percentage of outliers and the need to maintain a high skill. Furthermore, doubling the number of Representative Members (from 5 to 10) produces the greatest improvement of the skill.

These results led to a modification of the COSMO–LEPS methodology at the beginning of June 2004: the super–ensemble has been built by using only the 2 most recent EPS and the number of clusters has been fixed to 10, nesting Lokal Modell on each of the selected 10 RMs. The 10 Lokal Modell runs are performed by using both the Tiedtke and Kain–Fritsch schemes for the parameterization of the convection. The scheme used within each single run is randomly selected. This choice was adopted since we did not see any significant difference when using either the Tiedtke scheme or the Kain–Fritsch scheme.

The new configuration of COSMO–LEPS system is being currently verified and the impact of the modifications on the system performance is addressed. The verification methodology is still under development, focusing on the proper way of performing a probabilistic verification of an high–resolution forecast system.

References

Buizza R., Potential forecast skill of ensemble prediction and spread and skill distributions of the ECMWF ensemble prediction system, *Monthly Weather Review*, *125*, 99–119, 1997.

Marsigli, C., Montani, A., Nerozzi, F., Paccagnella, T., Tibaldi, S., Molteni, F., Buizza, R., A strategy for High–Resolution Ensemble Prediction. Part II: Limited–area experiments in four Alpine flood events, *Quart. J. Roy. Meteor. Soc.*, *127*, 2095–2115, 2001.

Marsigli, C., Montani, A., Nerozzi, F., Paccagnella, T., Probabilistic high–resolution forecast of heavy precipitation over Central Europe, *Natural Hazards and Earth System Sciences*, *4*, 315–322, 2004.

Marsigli, C., Boccanera F., Montani, A., Paccagnella, T., The COSMO–LEPS mesoscale ensemble system: validation of the methodology and verification, *Nonlinear Processes in Geophysics*, in print, 2005.

Mason, S. J. and Graham, N. E., Conditional probabilities, relative operating characteristics and relative operating levels, *Weather and Forecasting*, *14*, 713–725, 1999.

Molteni, F., Buizza, R., Palmer, T.N., Petroliagis, T., The ECMWF Ensemble Prediction System: Methodology and validation, *Quart. J. Roy. Meteor. Soc.*, *122*, 73–119, 1996.

Molteni, F., Buizza, R., Marsigli, C., Montani, A., Nerozzi, F. and Paccagnella, T., A strategy for High–Resolution Ensemble Prediction. Part I: Definition of Representative

Members and Global Model Experiments, *Quart. J. Roy. Meteor. Soc.*, *127*, 2069–2094, 2001.

Montani, A., Marsigli, C., Nerozzi, F., Paccagnella, T. and Buizza, R., Performance of ARPA–SMR Limited–area Ensemble Prediction System: two flood cases. *Nonlinear Processes in Geophysics*, *8*, 387–399, 2001.

Montani, A., Marsigli, C., Nerozzi, F., Paccagnella, T., Tibaldi, S. and Buizza R., The Soverato flood in Southern Italy: performance of global and limited–area ensmeble forecasts, *Nonlinear Processes in Geophysics*, *10*, 261–274, 2003a.

Montani, A., Capaldo, M., Cesari, D., Marsigli, C., Modigliani, U., Nerozzi, F., Paccagnella, T., Patruno, P. and Tibaldi, S., Operational limited–area ensmeble forecasts based on the Lokal Modell, *ECMWF Newsletter Summer 2003*, *98*, 2–7, 2003b.

Richardson, D. S., Skill and relative economic value of the ECWMF ensemble prediction system, *Quart. J. Roy. Meteor. Soc.*, *126*, 649–667, 2000.

Stanski, H. R., Wilson, L. J. and Burrows, W. R., Survey of common verification methods in meteorology, *WMO World Weather Watch Tech. Rep.*, 8, pp. 144, 1989

Talagrand, O., Vautard, R. and Strauss, B, 1999, Evaluation of probabilistic prediction systems, *Proceedings of the ECMWF workshop on predictability*, 20–22 October 1997, Reading, UK, pp. 372, 1999.

Wilks, D. S., Statistical methods in the atmospheric sciences, Academic Press, New York, 467 pp., 1995.

List of COSMO Newsletters and Technical Reports

(available for download from the COSMO Website: www.cosmo-model.org)

COSMO Newsletters

No. 1: February 2001.

No. 2: February 2002.

No. 3: February 2003.

No. 4: February 2004.

No. 5: April 2005.

COSMO Technical Reports

No. 1: Dmitrii Mironov and Matthias Raschendorfer (2001):
Evaluation of Empirical Parameters of the New LM Surface-Layer Parameterization Scheme. Results from Numerical Experiments Including the Soil Moisture Analysis.

No. 2: Reinhold Schrodin and Erdmann Heise (2001):
The Multi-Layer Version of the DWD Soil Model TERRA_LM.

No. 3: Günther Doms (2001):
A Scheme for Monotonic Numerical Diffusion in the LM.

No. 4: Hans-Joachim Herzog, Ursula Schubert, Gerd Vogel, Adelheid Fiedler and Roswitha Kirchner (2002):
LLM ¯ the High-Resolving Nonhydrostatic Simulation Model in the DWD-Project LITFASS.
Part I: Modelling Technique and Simulation Method.

No. 5: Jean-Marie Bettems (2002):
EUCOS Impact Study Using the Limited-Area Non-Hydrostatic NWP Model in Operational Use at MeteoSwiss.

No. 6: Heinz-Werner Bitzer and Jürgen Steppeler (2004):
Documentation of the Z-Coordinate Dynamical Core of LM.

No. 7: Hans-Joachim Herzog, Almut Gassmann (2005):
Lorenz- and Charney-Phillips vertical grid experimentation using a compressible nonhydrostatic toy-model relevant to the fast-mode part of the 'Lokal-Modell'

No. 8: Chiara Marsigli, Andrea Montani, Tiziana Paccagnella, Davide Sacchetti, André Walser, Marco Arpagaus, Thomas Schumann (2005):
Evaluation of the Performance of the COSMO-LEPS System

COSMO Technical Reports

Issues of the COSMO Technical Reports series are published by the *Consortium for Small-Scale Modelling* at non-regular intervals. COSMO is a European group for numerical weather prediction with participating meteorological services from Germany (DWD, AWGeophys), Greece (HNMS), Italy (UGM, ARPA-SMR) and Switzerland (MeteoSwiss). The general goal is to develop, improve and maintain a non-hydrostatic limited area modelling system to be used for both operational and research applications by the members of COSMO. This system is initially based on the Lokal-Modell (LM) of DWD with its corresponding data assimilation system.

The Technical Reports are intended

- for scientific contributions and a documentation of research activities,
- to present and discuss results obtained from the model system,
- to present and discuss verification results and interpretation methods,
- for a documentation of technical changes to the model system,
- to give an overview of new components of the model system.

The purpose of these reports is to communicate results, changes and progress related to the LM model system relatively fast within the COSMO consortium, and also to inform other NWP groups on our current research activities. In this way the discussion on a specific topic can be stimulated at an early stage. In order to publish a report very soon after the completition of the manuscript, we have decided to omit a thorough reviewing procedure and only a rough check is done by the editors and a third reviewer. We apologize for typographical and other errors or inconsistencies which may still be present.

At present, the Technical Reports are available for download from the COSMO web site (www.cosmo-model.org). If required, the member meteorological centres can produce hard-copies by their own for distribution within their service. All members of the consortium will be informed about new issues by email.

For any comments and questions, please contact the editors:

Ulrich Schättler
ulrich.schaettler@dwd.de

Andrea Montani
amontani@smr.arpa.emr.it

Consortium for Small-Scale Modelling

Technical Report No. 10

Is the Particle Filtering Approach appropriate for Meso-Scale Data Assimilation ?

December 2007

DOI: 10.5676/DWD_pub/nwv/cosmo-tr_10

Deutscher Wetterdienst

MeteoSwiss

Ufficio Generale Spazio Aereo e Meteorologia

ΕΘΝΙΚΗ ΜΕΤΕΩΡΟΛΟΓΙΚΗ ΥΠΗΡΕΣΙΑ

Instytucie Meteorogii i Gospodarki Wodnej

Administratia Nationala de Meteorologie

Agenzia Regionale per la Protezione Ambientale del Piemonte

Agenzia Regionale per la Protezione Ambientale dell' Emilia-Romagna: Servizio Idro Meteo

Centro Italiano Ricerche Aerospaziali

Amt für GeoInformationswesen der Bundeswehr

www.cosmo-model.org

Editor: Massimo Milelli, ARPA Piemonte
Printed at Deutscher Wetterdienst, P.O. Box 100465, 63004 Offenbach am Main

Is the Particle Filtering Approach appropriate for Meso-Scale Data Assimilation ?

Mikhail D. Tsyrulnikov

Mikhail D. Tsyrulnikov
Hydrometeorological Centre of Russia
11-13 B. Predtechensky Lane
123242 Moscow
Russia

Contents

1 Introduction **3**

2 Nonlinear filtering **3**

2.1 Statement of the problem and notation 3

2.2 Sequential non-linear filtering 4

3 Monte-Carlo filters **5**

4 The bootstrap (SIR) filter **5**

5 Inherent advantages and disadvantages of the SIR filter **7**

5.1 Advantages 7

5.2 Disadvantages 7

6 Extensions to the SIR filter **7**

7 Non-meteorological and non-oceanographic applications of particle filtering **9**

8 Applications of particle filtering in meteorology and oceanography **10**

8.1 A meteorological review 10

8.2 Work of P. J. Van Leeuwen 11

9 Summary of the disadvantages of a hypothetical particle-filtering based meso-scale data assimilation scheme **12**

10 Conclusions **14**

11 Acknowledgements **14**

12 References **14**

1 Introduction

This review aims to discuss the suitability of *particle filtering* as a method of choice for the future COSMO meso-scale data assimilation system.

2 Nonlinear filtering

In this introductory section some basic facts on nonlinear filtering are given in order to facilitate the subsequent discussion of the particle filtering technique.

2.1 Statement of the problem and notation

Let us be interested in the system (atmospheric, oceanic...) state, X, at the time instant t_k, X_k. The information we have on X_k is twofold:

1. We have the deterministic model,

$$X_k^f = \mathcal{M}_{k-1}(X_{k-1}^a), \tag{1}$$

   where the superscript "a" means "analysis" (forecast initial conditions) and "f" forecast.

2. We have observations Y_s, $s = k, k-1, k-2, ...$, which are related to the state in the known way:

$$Y_s = H_s(X_s) + \eta_s, \tag{2}$$

   where η_s is the observation error, which includes both the measurement error and the error in the observation operator H_s (representativeness error).

We assume that the deterministic model, Eq. (1), *approximates* the true system evolution, so that if we substitute, into Eq. (1), the *true system* states (not the *model* states), a discrepancy arises, which is called "model error", ξ:

$$X_k = \mathcal{M}_{k-1}(X_{k-1}) - \xi_{k-1}. \tag{3}$$

We stress that this equation is a stochastic dynamic model for the *true* system state.

In order to properly assimilate the information contained both in the observations and the model, we assume the error sources, η_s and ξ_s ($s = k, k-1, k-2, ...$), to be independent of X and governed by the respective stochastic models, so that their probability distributions are known, $p(\eta_s)$ and $p(\xi_s)$, respectively. For the assimilation to be *sequential*, we require that both η_s and ξ_s are *white* sequences. For simplicity, we also assume that observation errors and model errors are (probabilistically) independent.

2.2 Sequential non-linear filtering

In data assimilation, our goal is the conditional distribution of the state, given all current and past observations (called posterior distribution):

$$p(X_k|Y_{:k}), \tag{4}$$

where " $:k$" means "up to k" (at the time moments $t_k, t_{k-1}, t_{k-2}, ...$).

To develop an assimilation technique, we break up the observations into the present and past batches: $Y_{:k} = (Y_{:k-1}, Y_k)$. Then, we transform Eq. (4) using the Bayes theorem:

$$p(X_k|Y_{:k}) = p(X_k|Y_{:k-1}, Y_k) \propto p(X_k|Y_{:k-1}) \cdot p(Y_k|X_k, Y_{:k-1}). \tag{5}$$

Here, $p(X_k|Y_{:k-1})$ is the *predictive* (prior) distribution (density) and

$$p(Y_k|X_k, Y_{:k-1}) = p(Y_k|X_k) \tag{6}$$

is the likelihood; the equality in Eq. (6) follows from the assumption that the observation error sequence is white.

Thus,

$$p(X_k|Y_{:k}) \propto p(X_k|Y_{:k-1}) \cdot p(Y_k|X_k). \tag{7}$$

The likelihood is assumed to be known (from the observation operator and the observation error probability distribution), so all it remains to be found is the predictive probability density. From Eq. (3), we have:

$$p(X_k|Y_{:k-1}) = p[\mathcal{M}_{k-1}(X_{k-1}) - \xi_{k-1} = X_k|Y_{:k-1}].$$

Here, both X_{k-1} and ξ_{k-1} are random and unknown, so we use the "complete probability rule": $p(X) = \mathbf{E}p(X|\vartheta)$, with ϑ being some random variable (vector):

$$p(X_k|Y_{:k-1}) = \mathbf{E}_{X_{k-1}} p[\xi_{k-1} = \mathcal{M}_{k-1}(X_{k-1}) - X_k|X_{k-1}, Y_{:k-1}] \tag{8}$$

(here the conditional expectation is taken over X_{k-1}). Using the *previous* posterior density, $p(X_{k-1}|Y_{:k-1})$, we obtain from Eq. (8):

$$p(X_k|Y_{:k-1}) = \int p(X_{k-1}|Y_{:k-1}) \cdot p[\xi_{k-1} = \mathcal{M}_{k-1}(X_{k-1}) - X_k] \mathrm{d}X_{k-1}. \tag{9}$$

The fact that the second p.d.f. in the r.h.s. of this equation is unconditional, follows from the assumptions indicated above in the last paragraph of the previous subsection.

Using the explicit transition probability density, $p(X_k|X_{k-1})$, we can rewrite Eq. (9) as

$$p(X_k|Y_{:k-1}) = \int p(X_{k-1}|Y_{:k-1}) \cdot p(X_k|X_{k-1}) \mathrm{d}X_{k-1}. \tag{10}$$

Thus, Eqs. (7) and (9) provide the desired sequential non-linear assimilation algorithm: having the posterior density at time t_{k-1}, $p(X_{k-1}|Y_{:k-1})$, we compute (in theory) the prior density at time t_k (using Eq. (9)) and then update it using current observations, Eq. (7). At the very beginning of the assimilation process, we specify some initial distribution $p_0(X)$.

3 Monte-Carlo filters

For high-dimensional systems like the atmosphere, the above non-linear sequential assimilation technique in its pure and non-approximated form is absolutely unsuitable, mainly, due to the complexity of the integral in Eq. (9) or (10). The analysis (measurement update) step, Eq. (7), may become feasible for high-dimensional systems if the observation operator is only weakly non-linear and the observation-error distribution is multivariate Gaussian (3D-Var). But the forecast step (time update) in its exact form is prohibitively expensive even for linearized (tangent-linear) dynamics and Gaussian model errors, when the Kalman filter is applicable. Simplified Kalman filters have not yet proven to be successful, so we resort to Monte-Carlo methods.

One of such methods, known as the Ensemble Kalman Filter (EnKF), relies on the Gaussian approximation of the predictive distribution (Evensen, 1994 and Houtekamer and Mitchell, 2005). But this approximation may become too restrictive if we attempt to treat highly non-linear atmospheric processes that involve moisture, clouds, precipitation etc. at fine spatial resolution. This leads us to turn our attention to fully non-linear assimilation methods known as "particle filters". The basic particle filter is called the bootstrap or SIR filter. The term SIR means "sequential importance resampling" or "sampling importance resampling".

4 The bootstrap (SIR) filter

The simplest particle filter proposed by Rubin (1987) relies on the *discrete* (point-support) approximation to the probability distributions in question (just like the statistical technique known as bootstrap (Efron and Tibshirani, 1993)). Namely, we proceed as follows

1. At the discrete time moment t_{k-1}, approximate the posterior distribution, $p(X_{k-1}|Y_{:k-1})$, by the *discrete* distribution, so that the whole probability mass is concentrated in N points (particles), $\{X^-_{k-1}(j)\}_{j=1}^N$ (the sign "$-$" means "before sampling from the posterior distribution"):

$$\hat{p}(X_{k-1}|Y_{:k-1}) = \sum_{j=1}^{N} w_{k-1}(j) \cdot \delta[X_k - X^-_{k-1}(j)], \tag{11}$$

   where the hat denotes an estimate and $w_{k-1}(j)$ are the weights.

2. Resampling: draw N samples from this discrete distribution: $\{X^+_{k-1}(j)\}_{j=1}^N$ (the sign "$+$" means "after sampling from the posterior distribution"). Now, all $\{X^+_{k-1}(j)\}$ are independent and identically distributed samples from the approximate posterior density Eq. (11).

3. Feed the time evolution model, Eq. (3), with $X_{k-1} = X^+_{k-1}(j)$, $j = 1, 2, ..., N$, and obtain (as it can be easily seen) a set of N samples from the approximate predictive (prior) distribution:

$$X^-_k(j) = \mathcal{M}_{k-1}[X^+_{k-1}(j)] - \xi_{k-1}(j), \tag{12}$$

   where $\xi_{k-1}(j)$ is the j-th pseudo-random realization of the model error on the (t_{k-1}, t_k) time interval.

4. Regard this sample from the approximate prior distribution as the discrete distribution with equal weights:

$$\hat{p}(X_k|Y_{:k-1}) = \frac{1}{N}\sum_{j=1}^{N}\delta[X_k - X_k^-(j)]. \tag{13}$$

This is a virtual step, nothing is computed here. Actually, we can drop the assumption that the *prior* distribution is approximated by the discrete one, instead, we can derive the SIR equations by considering the analysis step as an importance sampler from the posterior (at time t_k) distribution (Pitt and Shephard, 1999), but we will not elaborate on this.

5. Accomplish the analysis step, Eq. (7), with the point-mass prior distribution, Eq. (13):

$$\hat{p}(X_k|Y_{:k}) \propto \frac{1}{N}\sum p(Y_k|X_k^-(j)) \cdot \delta[X_k - X_k^-(j)].$$

Denoting $p(Y_k|X_k^-(j)) =: w'_k(j)$ and normalizing $w'_k(j)$ (in order to obtain a proper discrete distribution),

$$w_k(j) = \frac{w'_k(j)}{\sum_{i=1}^{N} w'_k(i)}, \tag{14}$$

we get the point-mass approximation to the posterior distribution:

$$\hat{p}(X_k|Y_{:k}) = \sum_{j=1}^{N} w_k(j) \cdot \delta[X_k - X_k^-(j)]. \tag{15}$$

6. Now, we go to step 1 above and the process repeats.

Note that in the resampling step, if, for some j, the respective weight $w_k(j)$ is large, then, likely, this particle will be sampled several times, $N_j > 1$, but if $w_k(j)$ is small, then, likely, $N_j = 0$. So, the least likely (as identified by the likelihoods) particles are killed, whereas the most likely particles multiply ("survival of the fittest").

Finally, we discuss how the ordinary deterministic analysis can be obtained with the particle filtering assimilation scheme. As it can be easily seen from Eq. (15), the mean of the posterior distribution is

$$\hat{X}_k = \int X_k \cdot \hat{p}(X_k|Y_{:k})\mathrm{d}X_k = \sum w_k(j) \cdot X_k^-(j). \tag{16}$$

This mean provides the best estimate, in the mean-square sense, of the current state of the system, given all present and past observations. So, $\hat{X}_k$ can be used as the "analysis".

Eq. (16) implies that the analysis is just a linear combination of an inevitably small number of particles. This has very serious consequences for the applicability of a particle filtering data assimilation scheme for such a highly variable system as the atmosphere (see the discussion below).

5 Inherent advantages and disadvantages of the SIR filter

5.1 Advantages

The advantages of particle filtering include its great simplicity, substantial modularity, generality (no linearity, no Gaussianity needed). These are discussed in the referenced literature, so it is not necessary to dwell on this in the critical review here.

5.2 Disadvantages

In the literature, two main drawbacks of the SIR filter were indicated.

First, an "impoverishment" of the particle swarm is often observed. This effect arises if the predictive density appears to be substantially dissimilar to the likelihood. If this happens, most of the "forecast" particles are rejected, leaving only a small number of heavily weighted "survivors". As a consequence, the diversity of the swarm of particles becomes too weak, the point-mass approximation too poor, the filter ceases to follow the truth (degeneracy of the filter). The above dissimilarity of the predictive density and the likelihood may be a result of either very small model error or very small observational error.

Second, if the posterior distribution has heavy tails (outliers happen), then a very large ensemble size is needed in order to represent these distant areas in phase space. This is because their probability mass, p_{out}, is so small that, in order to obtain a single "representer" of these areas (provided we consider these outliers meteorologically important, say, indicating possible severe weather events), the ensemble size should satisfy the inequality $N \cdot p_{out} > 1$, so $N_{min} = p_{out}^{-1}$, which can be large. It becomes even larger if we wish to have several "representers" in these remote areas in phase space. If, moreover, a *difference* between various outlying areas is of interest to us (which is certainly the case for meso-scale modelling and filtering), p_{out} is divided into several even smaller probabilities, thus making N_{min} further larger.

6 Extensions to the SIR filter

A number of improvements and extensions to the basic bootstrap (SIR) filter have been proposed in order to mitigate the above problems of the basic scheme.

To overcome the "impoverishment" problem Gordon et al. (1993) proposed the technique called jittering. With this technique, one adds small random noise to the posterior sample, thus making coincident particles differ from each other. This introduces the desired diversity in the set ("swarm") of particles.

Another technique (Rubin, 1987), called "particle boosting" consists in multiplying, at the prediction step, the number of particle candidates $N_+ = mN$, where m is an integer. Then, one randomly takes N particles from the set of mN candidates. This also increases the diversity, as desired. But this technique greatly increases the computational cost if the forecast step is expensive (as is the case in the atmospheric data assimilation problem).

Musso et al. (2001) proposed "regularized particle filters", in which the point-mass approximation is replaced by the kernel density approximation, see also the "smooth bootstrap" technique (Stavropoulos and Titterington, 2001). Again, the forecast particles become more

different as a result of kernel smoothing, which can prevent the particles' swarm from "impoverishment" and even degeneracy.

Xiong et al. (2006), similarly, proposed to use a posterior Gaussian resampling technique in order to introduce variability in the ensemble sample (see below).

Liu et al. (2001) discuss reweighting as a means to control the balance between "diversity" and "focus" in the posterior swarm of particles. As a generic choice, they recommend to use

$$\pi_k(j) = \sqrt{w_k(j)} \tag{17}$$

as the probabilities of the particles $X_k(j)$. But then, in the prior discrete distribution, Eq. (13), $1/N$ should be replaced by $(1/N) \cdot w_k(j)/\pi_k(j)$. Using the square root in the definition of the probabilities $\pi_k(j)$, allows us to tolerate, to some extent, low-weight particles (outliers), which enhances diversity. Other than the square root choices are also possible.

So, even if the weights happen to differ considerably one from another, we may sample from a more uniform discrete distribution. This means that for a heavily weighted particle, we may not launch too many forecasts from the same (or similar) initial conditions (which looks as a wasting of computer time, even though model-error perturbations can make these forecasts slightly diverge). Instead, we may just remember that this particle has high weight and use this knowledge in the subsequent analysis. Similarly, we may let "light" particles "live", thus preventing the particles' swarm from collapsing.

Pitt and Shephard (1999) proposed to use a more complex sampling scheme, in which the so-called proposal distribution (importance distribution) for importance sampling from the posterior distribution becomes *dependent on current observations* (in the basic SIR formulation, the proposal distribution is the approximate prior distribution). Introducing current observations into the proposal density can, obviously, decrease the above dissimilarity between $p(X_k|Y_{:k-1})$ and $p(Y_k|X_k)$, thus alleviating the "impoverishment" problem. As they report, using the proposal distribution dependent on current observations significantly increases the efficiency of the sampling scheme (less very-low-probability particles). But their "auxiliary filter" requires multiple *evaluations* of the proposal density and the time transition density, which would be very time consuming in the atmospheric data assimilation context.

A simpler technique to use current observations with the aim to appropriately change the importance sampling distribution is "prior editing" proposed by Gordon et al. (1993). With this technique, one enhances the ensemble size at the prediction step and removes the particles with small likelihoods at the current time step. But, similarly to "particle boosting" (see above), this technique is computationally inefficient in our case in view of the high cost of the forecast.

Another technique to skip hopelessly bad (not supported by observations) particles was developed by Van Leeuwen (2003), see below.

Djuric (2001) proposed to combine the well-known from the seventies (Anderson and Moore, 1979) Gaussian sum filter with the SIR methodology. Such a combination can cope with the outliers problem and the "impoverishment" problem of the SIR technique.

More on different flavors of particle filtering can be found in Farnhead (1998).

The above brief review of the techniques developed to improve the basic SIR formulation demonstrates that there are a number of ways to make the SIR filter more efficient. However, Stavropoulos and Titterington (2001) note that *"in general the more sophisticated methods did not lead to noticeable improvement over the simpler versions of particle filtering"*.

7 Non-meteorological and non-oceanographic applications of particle filtering

In the last 15 years, a substantial literature arose devoted to applications of particle filtering. The main areas of applications include target tracking, navigation, positioning, computer vision, signal processing, financial time series modelling, bio-medical applications etc. The common point of all these papers is the low dimensionality of the dynamical systems under investigation. A few examples follow.

Marss (2001) reported on a successful implementation of a particle filter for a 3-D system. Koller and Lerner (2001) worked on a system with 33,000 discrete states. If we assume that in Euclidean space, about 30 points are enough to represent the function's behavior along each axis, we find that 33,000 points roughly correspond to the 3-D case. McGinnity and Irwin (2001) worked with systems whose dimensionality ranged from 1 to 4. It was not possible to find any high-dimensional (more than 10-D) particle filter applications in the statistical literature among tens of available papers.

For such low-dimensional systems, it is of interest for us to look at the ensemble sizes in use. About 40 papers have been checked and those with practical or near-practical applications have been selected. Then, the ensemble sizes reported by the authors has been indicated. The resulting distribution follows.

50

100

200, 200, 200

400

500, 500, 500

1000, 1000, 1000, 1000, 1000

3000

4000, 4000

5000, 5000, 5000

8000

9000

10000, 10000

50000, 50000

100000

50KF

The median of this distribution is about 3000, which is not encouraging for us. The $N = 50$ case corresponds to a simple 2-D mobile robot localization problem. 50KF means 50 Kalman filters in a mixture Kalman filtering scheme.

A personal interpretation of these results is that the particle filtering technique works if we can really *approximate* (in the weak sense) the true distribution by a point-mass distribution. In our effectively high-dimensional case this is certainly not possible.

8 Applications of particle filtering in meteorology and oceanography

8.1 A meteorological review

In the meteorological literature, the use of particle filters was proposed by Anderson and Anderson (1999), Pham (2001), Kim et al. (2003), Xiong at al. (2006), Eyink and Kim (2006), and Nakano et al. (2007).

Anderson and Anderson (1999) used a kernel smoothing (of the prior density) in a Gaussian sum filter without resampling. They used the three-variable Lorenz model and the ensemble size $N = 40$. They also showed that for a 3000-D global barotropic model in an idealized setting, their kernel filter with $N = 40$ was capable of doing the assimilation job. However, it is difficult to judge the relative merit of their filter as compared with other, more traditional approaches. Anderson and Anderson (1999) argue that a small ensemble size may be sufficient if the system "lives" on a low-dimensional attractor. But on the meso-scale, we hardly can assume that the attractor (if it exists) is low-dimensional — in view of the highly variable and diverse atmospheric behaviour on the meso scale. Besides, at every assimilation time step, observations will inevitably push the system off the attractor.

Pham (2001) proposed to use, in the meteorological and oceanographic context, a SIR filter with kernel smoothing of the posterior density. He applied the filter for the three-variable (just three degrees of freedom) Lorenz system and found that for good performance, 50 particles were needed. This is not a promising result for us because the dimensionality of our phase space is about one million.

Kim et al. (2003) used the SIS (sequential importance sampling) and SIR filters for a one-dimensional non-linear stochastic differential equation. They checked the ensemble sizes of 100 and 10^4 and found that 10^4 particles were needed for SIS and 100 for SIR. Again, this is not a good result for us, in view of the extremely low dimensionality of their phase space, $n = 1$. They also proposed a parametric particle filter, in which the prior density is approximated by a density from the exponential family. In their experiments, they found that this filter performed better than SIR (nothing is said about SIS). The parametrization idea seems fruitful, but in the implementation of their analysis step, only two free parameters of the parametric density were updated, which is not acceptable for us, since we wish to control, in the analysis, many meso-scale features across the domain of interest.

Xiong et al. (2006) proposed to use a posterior Gaussian resampling technique in order to fight "impoverishment" of the ensemble sample. This method is not useful for us because it is the non-Gaussianity that has drawn our attention to particle filtering. Besides, in other respects (especially in the analysis scheme), the technique of Xiong et al. (2006) does not differ from the basic SIR formulation. For the three-variable Lorenz system, the ensemble size in their numerical experiments ranged from 100 to 1000. Again, this is not encouraging for us, because we have to build a hyper-dimensional meso-scale data assimilation system.

Eyink and Kim (2006) proposed several methods based on the maximum entropy principle. The methods were checked on low-dimensional systems, but the authors claimed that they were preparing a paper in which they would report on a successful application of these methods for high-dimensional oceanic thermohaline circulation assimilation.

A device to fight the "impoverishment" problem was proposed by Nakano et al. (2007). Their suggestion is not to kill low-weight particles (thus, reducing the desirable diversity) but to use them in a particle merging scheme. The merging is a linear combination (with

the weights independent of the physical-space coordinates) selected to preserve the first two moments of the multivariate posterior distribution. They tested their merging technique in experiments with the three-variable Lorenz model and the 40-variable Lorenz-96 model. While the merging technique itself does not seem to lead to vital improvements in the meso-scale data assimilation context, their results are interesting for us in the ensemble sizes they used. Namely, for the 40-D case, even as many as 260,000 members were not enough for the performance of their filter to converge (to stop improving). This result, again, indicates that in our 10^{-6}-D case, the ensemble size necessary for a particle filter to properly work will be enormous, thus prohibiting the use of the particle filtering idea for atmospheric data assimilation.

8.2 Work of P. J. Van Leeuwen

In the oceanographic context, Van Leeuwen (2003) tested three formulations of particle filters: first he used the standard SIR (with a slight modification of sampling from the discrete probability distribution), second he proposed the local SIR (LSIR) and third, the guided SIR (GSIR).

He noticed that the SIR analysis is essentially global, so that on one domain's sub-area, one subset of particles appears to be consistent with the observations, whereas in other sub-areas, quite different particles can be supported by observations. In order to let the observations influence not just the global weights but local neighborhoods, he proposed to make the weights spatially variable by performing the SIR analysis step many times for every grid point with local data selection, like in optimum interpolation (OI). This can introduce the necessary locality of the observational usage, but the great problem arises: what should be the posterior particles if at different grid points different particles were selected. Van Leeuwen (2003) used a simple gluing of the particles, which was not successful in his experiments and does not seem to be a suitable approach in meso-scale assimilation for the two following reasons.

1. From a theoretical point of view, this device violates the particle representation, so that we, seemingly, cannot justify how to *change* ("break") the particles at the analysis step. How can we find the posterior distribution if the prior particles are completely destroyed by "gluing" ? If "gluing" is an approximation, a question arises: is there a *proof* that the error of this approximation tends, in some sense, to zero as the ensemble size tends to infinity ? Without mathematically-based answers to these questions, the technique becomes largely *ad hoc*, which should be considered as a serious drawback.

2. From a practical point of view, "gluing", or equivalently, building the new posterior particles of patches from different ensemble members (presumably, as many patches as many different meso-scale features are present across the analysis domain) violates the dynamical and physical balances in the new particles. This will certainly lead to generation of spurious gravity waves (as noted by the author of the technique) and also to spurious fluxes of heat, water, and momentum, giving rise to the well-known "spin-up" phenomenon, which is highly undesirable in the data assimilation context because a *short-* or *very-short-range* forecast is used at the analysis step as a source of a priori information. In addition, like in OI, local data selection will lead to small-scale noise, which can mask important meteorological details on the meso scale.

So, in the present form, the LSIR technique seems to be not suitable for meso-scale data assimilation.

The GSIR technique of Van Leeuwen (2003) aims to reduce the ensemble size by removing "bad" particles at the very early stages of the forecast. This is possible because we can start the ensemble forecast step *after* we receive current observations (although, at the price of some time delay in issuing the analysis, which may be not desirable in the operation context). For meso-scale data assimilation, the GSIR idea can be useful, among others, but GSIR remains a *global* technique (the weights do not vary across the domain), which prohibits its direct use. The reason for this, as explained below, is that in the global ensemble, the number of global particles should be comparable with the number of effective degrees of freedom we wish to control in the analysis. In the meso-scale, the latter can be very large as compared with the affordable ensemble size.

As for the numerical experiments of Van Leeuwen (2003), it is worth noting that his assimilation/forecast results were not compared with observations. There was also no comparison with other assimilation methods. Besides, in his experiments the assimilated fields look smoother than atmospheric meso-scale patterns.

Concerning the applicability of the results obtained for *oceanic* data assimilation to atmospheric problems, it should be mentioned that the atmosphere is much better observed than the ocean. This implies that oceanic forecasts are relatively much worse than the atmospheric ones. As a result of this, oceanic data assimilation works in a rather different "regime" than the atmospheric one, which reduces the applicability of oceanic results to atmospheric data assimilation, in particular, on the meso-scale.

9 Summary of the disadvantages of a hypothetical particle-filtering based meso-scale data assimilation scheme

The main problem: critically insufficient ensemble size to resolve meso-scale details of meteorological fields and to allow efficient observational usage.

1. Mathematically, we cannot even imagine to approximate a million-dimensional density by a handful of phase-space points (particles). This is completely "unmathematical". Even if we take into account that not all of these numerous degrees of freedom are equally important and the effective number of degrees of freedom, n_{eff} is substantially less, n_{eff} remains, as it follows from physical arguments for meso-scale modelling, orders of magnitude larger than any practically imaginable ensemble size.

2. Meteorologically, an inevitably small ensemble size does not allow us to *resolve* small-scale meso-scale details, as discussed below in this section.

3. Practically, a particle filtering based analysis scheme would imply **critically inefficient use of observations** (as compared to OI and Var).

   In a particle-filter atmospheric data assimilation scheme, tens of thousands, and very soon, millions of observations can influence the analysis only through a few (30-50) free parameters, the particle weights (a "bottleneck"). So, information contained in a huge number of observations, before correcting the forecast fields, should be "summarized" in an extremely small number of particle weights. Obviously, such a tremendous "compression" of observational data is impossible without an immense loss of information. But if we waste valuable observational information, we cannot hope to design an efficient assimilation system.

   In other words, in the SIR filter, local corrections due to local observation-minus-forecast differences are virtually impossible because only the *combined* effect of *all*

observations does influence the analysis (through the particle weights), see Eq. (16).

The most severe consequence of the small ensemble size is that the number of degrees of freedom of the meso-scale field we wish to resolve appears to be orders of magnitude larger than the number of adjustable parameters (the particle weights) at the analysis step. Indeed, if we intend, in the analysis, to resolve meteorological details of the size of kilometers, then we have to design an analysis scheme capable of controlling the analysis fields with this granularity. In other words, if in the analysis we admit a feature (say, a cloud system) of the size of 10 km, and observations indicate that we have to correct the forecast in this 10-km area, then the analysis technique should allow this. And this job has to be done simultaneously, in other 10-km "boxes", independently of each other. In a 1000 by 1000 km domain there are 10,000 horizontal "boxes". In the vertical, similarly, if we aim at details, say, 500-m deep, then 10 to 20 vertical "boxes" have to be resolved. Thus, in total, we obtain $10,000 \cdot 20 = 200,000$ 3-D "boxes" or degrees of freedom. But, in the SIR analysis, we have only N (recall, N is the ensemble size) free parameters, with N being about 30–50. Obviously, it is absolutely impossible to control 200,000 degrees of freedom with such a tiny number of adjustable parameters.

Otherwise stated, the SIR analysis equation, Eq. (16), can be viewed as an expansion of the analysis field in the basis functions $X_k^-(j)$, the particles' fields (a kind of *spectral* technique). But the number of the basis functions, N, is so incredibly small as compared to the number of meso-scale details to be resolved, that we have to conclude that the SIR filter is inappropriate with a reasonable (for us) ensemble size. With $N = 50$, only about 50 details over the whole 3-D analysis domain can be resolved, which is far too small for a state-of-the-art and a prospective meso-scale data assimilation system.

The LSIR Ansatz of Van Leeuwen (2003) could be a remedy but it seems to lack mathematical and meteorological justification (see above).

In addition to the above small-ensemble-size issues, the following practical points are worth noting.

1. In 3D and 4D-Var analysis schemes, the very important role of the prior (background) probability distribution (covariances) is well established. To obtain a good analysis, very sophisticated background-error covariance models have been proposed. In particular, control of multivariate covariances, non-separability (vertical by horizontal) of 3-D correlations and other aspects are shown to be of great importance for a successful background-error covariance model. With a particle filter, we do not care about these issues at all, completely relying on the (small) swarm of particles. But particles are selected, to a large extent, at random, so the implied probability distribution is also random (significantly contaminated by sampling noise). Is it good to use this random prior distribution as if it were the true one?

2. As noted by Anderson and Anderson (1999), the SIR filter may fail if the forecast model is *biased*. In this case, all particles can be biased, so that the observations will be not capable of removing this bias at all (because the observation has only "the right" to select from prior particles, which are all biased).

3. The SIR analysis algorithm is so incredibly simple that we may question: why the substantial *simplification* of the analysis technique (from the complicated 3D-Var to the extremely simple SIR) will lead to an improvement? Common practice shows that the converse is almost always the case.

10 Conclusions

The SIR filter is *not* recommended for meso-scale data assimilation because it would imply, for an affordable ensemble size, first, critically inefficient observational usage and second, lack of high-resolution meso-scale fields' analysis corrections.

The LSIR filter is also *not* recommended for meso-scale data assimilation in its present form because of lack of its mathematical and meteorological justification.

11 Acknowledgements

This study has been supported by the Russian Foundation for Basic Research under grant 06-05-08076. I also appreciated valuable discussions with D.B. Kiktev.

12 References

Anderson, J.L., and S.L. Anderson, 1999: A Monte Carlo implementation of the nonlinear filtering problem to produce ensemble assimilations and forecasts, Mon. Wea. Rev., 127, 2741-2758.

Andersson, P., and J.B. Moore, 1979: Optimal Filtering, Prentice-Hall, New Jersey.

Djuric, P.M., 2001: Sequential estimation of signals under model, in "Sequential Monte Carlo Methods in Practice", Eds. A. Doucet, N. Freitas, and N. Gordon.", Springer, 381-400.

Efron, B., and R.J. Tibshirani, 1993: An Introduction to the Bootstrap, Chapman and Hall, London.

Evensen, G., 1994: Sequential data assimilation with a nonlinear quasi-geostrophic model using Monte-Carlo methods to forecast error statistics, J. Geophys. Res., 99 (C5), 10143-10162.

Eyink, G.L., and S. Kim., 2006: A maximum entropy method for particle filtering, J. Statist. Phys., 123 (5), 1071-1128.

Farnhead, P., 1998: Sequential Monte Carlo Methods in filter theory, Ph.D. Thesis, Oxford Univ., http://www.maths.lancs.ac.uk/ fearnhea/publications/.

Gordon, N.J., D.J. Salmond, and A.F.M. Smith, 1993: Novel approach to nonlinear/non-Gaussian Bayesian state estimation, IEEE Proceedings-F, 140(2), 107-113.

Houtekamer, P.L., and H.L. Mitchell, 2005: Ensemble Kalman filtering, Quart. J. Roy. Meteorol. Soc., 131, 3269-3289.

Kim., S., G.L. Eyink, J.M. Restrepo, F.J. Alexander, and G. Johnson, 2003: Ensemble filtering for nonlinear dynamics, Mon. Wea. Rev., 131, 2586-2594.

Koller, D., and U. Lerner, 2001: Sampling in factored dynamic system, in "Sequential Monte Carlo Methods in Practice", Eds. A. Doucet, N. Freitas, and N. Gordon.", Springer, 445-464.

Liu, J.S., R. Chen, and T. Logvinenko, 2001: A theoretical framework for sequential importance sampling with resampling, in "Sequential Monte Carlo Methods in Practice", Eds. A. Doucet, N. Freitas, and N. Gordon.", Springer, 225-246.

Marrs, A.D., 2001: In-Situ ellipsometry solution using sequential Monte Carlo, in "Sequential Monte Carlo Methods in Practice", Eds. A. Doucet, N. Freitas, and N. Gordon.", Springer, 465-478.

McGinnity, S., and G.W. Irwin, 2001: Manoeuvring target tracking using a multiple-model bootstrap filter, in "Sequential Monte Carlo Methods in Practice", Eds. A. Doucet, N. Freitas, and N. Gordon.", Springer, 479-498.

Musso, C., N. Oudjane, and F. Le Gland, 2001: Improving regularized particle filters, in "Sequential Monte Carlo Methods in Practice", Eds. A. Doucet, N. Freitas, and N. Gordon.", Springer, 247-272.

Nakano, S., G. Ueno, and T. Higuchi, 2007: Merging particle filter for sequential data assimilation, Nonlin. Proc. Geophys., 14, 395-408.

Pham, D.T., 2001: Stochastic methods for sequential data assimilation in strongly nonlinear systems, Mon. Wea. Rev., 129, 1194-1207.

Pitt, M.K., and N. Shephard, 1999: Filtering via simulation: Auxiliary particle filters, J. Amer. Statist. Assoc., 94(446), 590-599.

Rubin, D.B., 1987: Comment on 'The calculation of posterior distributions by data augmentation', J. Amer. Statist. Ass., 82, 543-546.

Stavropoulos, P., and D.M. Titterington, 2001: Improved particle filters and smoothing, in "Sequential Monte Carlo Methods in Practice", Eds. A. Doucet, N. Freitas, and N. Gordon.", Springer, 295-318.

Van Leeuwen, P.J., 2003: Nonlinear ensemble data assimilation for the Ocean, ECMWF Seminar "Recent developments in data assimilation for atmosphere and ocean".

Xiong, X., I.M. Navon, and B. Uzunoglu, 2006: A note on the particle filter with posterior Gaussian resampling, Tellus, 58A, 456-460.

List of COSMO Newsletters and Technical Reports

(available for download from the COSMO Website: www.cosmo-model.org)

COSMO Newsletters

No. 1: February 2001.

No. 2: February 2002.

No. 3: February 2003.

No. 4: February 2004.

No. 5: April 2005.

No. 6: July 2006; Proceedings from the COSMO General Meeting 2005.

No. 7: July 2007; Proceedings from the COSMO General Meeting 2006.

COSMO Technical Reports

No. 1: Dmitrii Mironov and Matthias Raschendorfer (2001):
Evaluation of Empirical Parameters of the New LM Surface-Layer Parameterization Scheme. Results from Numerical Experiments Including the Soil Moisture Analysis.

No. 2: Reinhold Schrodin and Erdmann Heise (2001):
The Multi-Layer Version of the DWD Soil Model TERRA_LM.

No. 3: Günther Doms (2001):
A Scheme for Monotonic Numerical Diffusion in the LM.

No. 4: Hans-Joachim Herzog, Ursula Schubert, Gerd Vogel, Adelheid Fiedler and Roswitha Kirchner (2002):
LLM ¯ the High-Resolving Nonhydrostatic Simulation Model in the DWD-Project LITFASS.
Part I: Modelling Technique and Simulation Method.

No. 5: Jean-Marie Bettems (2002):
EUCOS Impact Study Using the Limited-Area Non-Hydrostatic NWP Model in Operational Use at MeteoSwiss.

No. 6: Heinz-Werner Bitzer and Jürgen Steppeler (2004):
Documentation of the Z-Coordinate Dynamical Core of LM.

No. 7: Hans-Joachim Herzog, Almut Gassmann (2005):
Lorenz- and Charney-Phillips vertical grid experimentation using a compressible nonhydrostatic toy-model relevant to the fast-mode part of the 'Lokal-Modell'

No. 8: Chiara Marsigli, Andrea Montani, Tiziana Paccagnella, Davide Sacchetti, André Walser, Marco Arpagaus, Thomas Schumann (2005):
Evaluation of the Performance of the COSMO-LEPS System

No. 9: Erdmann Heise, Bodo Ritter, Reinhold Schrodin (2006):
Operational Implementation of the Multilayer Soil Model

No. 10: M.D. Tsyrulnikov (2007):
Is the particle filtering approach appropriate for meso-scale data assimilation ?

COSMO Technical Reports

Issues of the COSMO Technical Reports series are published by the *COnsortium for Small-scale MOdelling* at non-regular intervals. COSMO is a European group for numerical weather prediction with participating meteorological services from Germany (DWD, AWGeophys), Greece (HNMS), Italy (USAM, ARPA-SIM, ARPA Piemonte), Switzerland (MeteoSwiss), Poland (IMGW) and Romania (NMA). The general goal is to develop, improve and maintain a non-hydrostatic limited area modelling system to be used for both operational and research applications by the members of COSMO. This system is initially based on the COSMO-Model (previously known as LM) of DWD with its corresponding data assimilation system.

The Technical Reports are intended

- for scientific contributions and a documentation of research activities,
- to present and discuss results obtained from the model system,
- to present and discuss verification results and interpretation methods,
- for a documentation of technical changes to the model system,
- to give an overview of new components of the model system.

The purpose of these reports is to communicate results, changes and progress related to the LM model system relatively fast within the COSMO consortium, and also to inform other NWP groups on our current research activities. In this way the discussion on a specific topic can be stimulated at an early stage. In order to publish a report very soon after the completion of the manuscript, we have decided to omit a thorough reviewing procedure and only a rough check is done by the editors and a third reviewer. We apologize for typographical and other errors or inconsistencies which may still be present.

At present, the Technical Reports are available for download from the COSMO web site (www.cosmo-model.org). If required, the member meteorological centres can produce hard-copies by their own for distribution within their service. All members of the consortium will be informed about new issues by email.

For any comments and questions, please contact the editors:

Massimo Milelli
Massimo.Milelli@arpa.piemonte.it

Ulrich Schättler
Ulrich.Schaettler@dwd.de

Consortium

for

Small-Scale Modelling

Technical Report No. 4

LLM - the High-Resolving Nonhydrostatic Simulation Model in the DWD Project LITFASS Part I: Modelling Technique and Simulation Method

by

H.-J. Herzog, U. Schubert, G. Vogel, A. Fiedler

March 2002

DOI: 10.5676/DWD_pub/nwv/cosmo-tr_4

Deutscher Wetterdienst

MeteoSwiss

Ufficio Generale per la Meteorologia

Hellenic National Meteorological Service

Amt für Wehrgeophysik

Il Servicio Meteorologico Regionale di ARPA

www.cosmo-model.org

Editors: G. Doms and U. Schättler, Deutscher Wetterdienst, P.O. Box 100465, 63004 Offenbach, Germany
Printed at Deutscher Wetterdienst, Offenbach am Main

LLM – the High-Resolving Nonhydrostatic Simulation Model in the DWD – Project LITFASS.

Part I

Modelling Technique and Simulation Method.

Hans-Joachim Herzog, Ursula Schubert, Gerd Vogel, Adelheid Fiedler and Roswitha Kirchner

Deutscher Wetterdienst, Meteorologisches Observatorium Potsdam

Table of Contents

1 Introduction **1**

2 Model Description **4**
- 2.1 The Model Equations . . . 4
- 2.2 Numerical Aspects . . . 6
- 2.3 Lateral and Upper Boundary Techniques . . . 8
- 2.4 Lower Boundary Condition and Forcing . . . 15
- 2.5 Model Physics Different to LM . . . 16
- 2.6 Specification of the Horizontal Integration Area . . . 16

3 Parameterization of Subgrid-Scale Turbulence **19**
- 3.1 The SGS-TKE Model . . . 19
- 3.2 Numerical Treatment . . . 23

4 External Forcing at the Lateral and Upper Boundary **30**
- 4.1 Method . . . 30
- 4.2 Technical Approach . . . 33

5 Physical Forcing at the Lower Boundary **35**
- 5.1 External Parameters . . . 35
- 5.2 Radiative Forcing . . . 46
- 5.3 Precipitation Forcing . . . 57
- 5.4 Soil Moisture Modelling . . . 59

References **63**

An Epilogue to Part I **66**

1 Introduction

At the Deutscher Wetterdienst (DWD) an internal project named LITFASS (Lindenberg Inhomogeneous Terrain - Fluxes between Atmosphere and Surface - a long-term Study) was founded (Müller et al. 1995) and is running up to summer 2001. The aim of that project is to determine by measurement and model simulation area-averaged turbulent fluxes of momentum, heat and moisture representative for an inhomogeneous landscape typical of Central Europe and far enough to the south-east of Berlin.

The project takes advantage of the given infra-structure of the Research Division at DWD, where model research capacity is brought together with considerable and very complex measurement capacity at and over a defined area around the Meteorological Observatory Lindenberg (MOL). LITFASS consists of two main components, a measurement/observation component, (cf. Beyrich 2000) and a numerical simulation component, which serves in a judicious and mutual way to finally help improving the parameterization of subgrid-scale fluxes at and near to the underlying surface for the operational NWP-models. For these models at DWD, and for those elsewhere, one is confronted with the notoric problem that parameterization of subgrid-scale turbulent fluxes is far from being completely solved, and so, for instance, the prediction of 2m-parameters often fails to be satisfactory.

At the end of the project time, after a great, joint achievement and with a noticeable research investment the conclusion may be drawn that due to LITFASS a complex long-term validation system could be established from which the above mentioned task can be tackled with a permanently available measurement system and an appropriate and reliable numerical simulation model. The concern of this paper is to present the numerical simulation component of LITFASS. It represents the 'heart' of the project. From utmost importance is that that model is tightly related to the high-resolution part of the new operational NWP-system, namely to the non-hydrostatic 'Lokal-Modell' (LM), which in the present mode is running with a 7 km horizontal gridpoint distance and 35 vertical layers (cf. Doms and Schättler 1999). Since the model presented here is derived from the LM, it will be designated as LITFASS-Lokal-Modell or LES-Lokal-Modell. The generic abbreviation is LLM. The strict relation to the LM is deliberately organized so as to have a high degree of consistency by using a unified program code, having similar dynamics, numerics and therefore a close reference to the LM-validation from the point of view of the LLM over the defined Lindenberg-observational and LLM-simulation area.

The latter aspect is of particular importance, because the LLM is the simulation tool to determine explicitly the relevant turbulence structures in the integration area as 'true' area-averaged fluxes which are then allowed to compare with the corresponding subgrid-scale fluxes of the LM. This is in the narrow sense the main task of the LLM. It is integrated with a very high horizontal and vertical grid resolution. The integration area covers the planetary boundary layer in the vertical. Its horizontal size corresponds to an area of 14×14 km^2 (or even larger: 20×20 km^2) in which the MOL is placed. A detailed physiographic description of the underlying surface is taken into account. In contrast to common LES models (e.g. Mason 1994, Mason and Brown 1999, Chlond 1999, Stevens 2000, Kanak et.al. 2000) which are sophisticated instruments to investigate the energy-relevant turbulence structures under clearly defined and controlled conditions (horizontally homogeneous vertical profile of wind, temperature, water content plus small randomized perturbations defining an initial state, homogeneous properties of the underlying surface with prescribed time-independent surface fluxes, or regular or stylized pattern of surface inhomogeneities, double-periodic lateral continuation of the integration domain etc.), the LLM is designed as a 'real-world'-LES model operating under general meteorological conditions.

Demonstrating the unity with the measurement component of LITFASS, the LLM integration mode is characterized by a time-dependent external forcing at the lateral and upper boundary derived from available time sequences of measured vertical profiles, and also by the physical forcing at the surface deduced from temporally variable ground-based measurements of radiation (supported by satellite data) and precipitation, and by observations describing updated surface parameters (vegetation parameters). All the LLM simulations are mainly related to two intensive measurement campaigns in the Lindenberg field. The first one is the 'LITFASS-98 Experiment' (25 May - 30 June 1998) (cf. Beyrich 2000), and the second one is an experiment named 'LINEX-2000' which took place during August/September 2000.

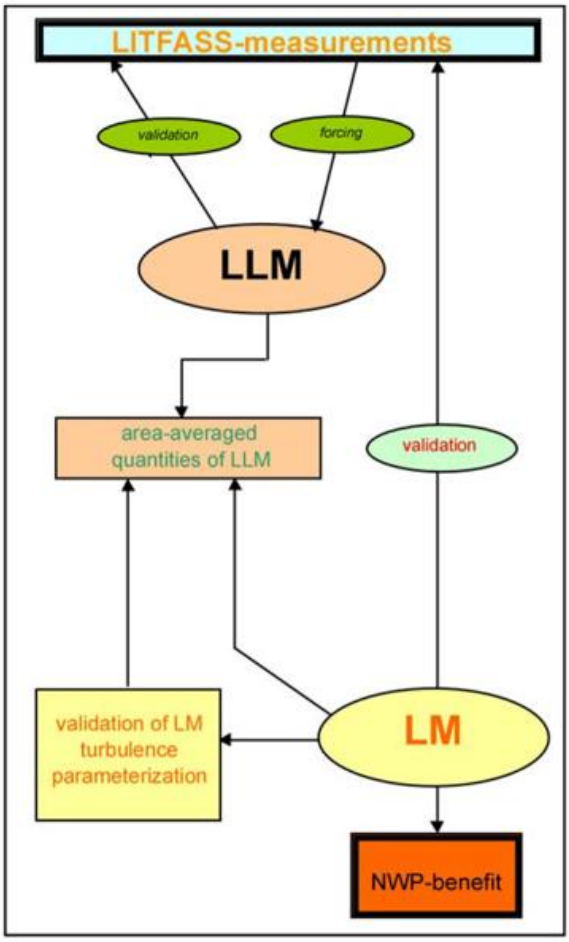


Figure 1.1: The meaning of the DWD project LITFASS from the point of view of bridging observation and simulation by use of the LLM as a tool to validate and help improving NWP models like the LM.

The entire paper is organized as follows. In Chapter 2 the model design is described. It concerns the model equations, the numerics with the vertical and horizontal grid spacing, the specific lateral, upper and lower boundary treatment, a description and explanation of the physics relevant to the LLM integration mode and, finally, the definition and position of the LLM simulation area. Chapter 3 contains a detailed discussion of the LLM-specific incorporation of the three-dimensional subgrid-scale turbulent fluxes concerning both numerical aspects and their parameterization using a prognostic scheme for the turbulent kinetic energy (TKE).

The Chapters 4 and 5 are of particular meaning with respect to the 'real-world' properties of the LLM. Chapter 4 describes how the LLM is externally driven in a lateral and upper boundary zone due to time-sequences of meteorological vertical profiles derived from different measurement sites and vertical sounding systems. In addition to this, the physical forcing of the LLM from the heterogeneous underlying surface is thoroughly discussed in Chapter 5. Here, an important aspect of the LLM integration mode is pointed out. It concerns the careful documentation of the external parameters related to the coupled soil model, and a broader description of methods is given, how to deduce the in homogeneous distribution of surface radiation components and precipitation. The actual time variation of the soil moisture distribution is also taken into account.

In Chapter 6 the model validation is carried out in detail. It reflects the primary claim to have obtained by LITFASS a reliable LLM as a simulation tool on the base of measurements. The following Chapter 7 involves a theoretical consideration. It will be shown in the context of the model equations how area-averaged subgrid- plus grid-scale fluxes are to be formulated in the LLM for referring them to the subgrid-scale fluxes of the LM. As a conclusion, the quantitative comparison of model results from LLM versus LM is particularly demonstrated in Chapter 8. Beyond the given presentation, in an additional Chapter 9 the efforts of programming and program organization on the high-capacity computers at DWD (Cray T3E) and the ECMWF (Fujitsu/VPP 700/116) are dealt with, which have guaranteed the feasibility of the computationally extensive task of LLM simulations. Summing up all partial results, a rather complex and upgraded validation system has been achieved, which makes up the main result of the present state of LLM development. This is shown in Fig. 1.1. It must be understood as a platform ready to start from for systematic and continuous work of NWP activities in the field of parameterization.

The present issue does not contain the entire content listed above, but rather Chapters 1 - 5. These Chapters together built a logical unit. They describe with a fairly completeness the LLM-design including all specific and technical aspects. While writing and preparing the full text we made an incidental decision to publish immediately that part just completed as Part I, before Part II with the following Chapters 6 - 9 will be issued next.

Remark
This paper here submitted to the COSMO community is an improved und updated version of an equally entitled contribution in *Deutscher Wetterdienst, Forschung und Entwicklung, Arbeitsergebnisse Nr.67, Offenbach, Juli 2001.*

2 Model Description

The LLM (LITFASS/LES-Lokal-Modell) is derived from the LM (Lokal-Modell) after having made a deliberate decision in this way. The most important reason for this is obvious, because the LM is the high-resolution model component of the new operational NWP-system at the DWD, and the LITFASS-project was from the very beginning thought to become directly useful to the NWP. As the LM is a nonhydrostatic, compressible model, it is from the point of view of these general properties immediately suitable to be used also as a very high-resolving model within the context of LITFASS. Therefore, the basic equations are, apart from minor modifications, for the LLM identical with the LM equation set. This makes the following model description short enough, where we, however, need the full reference to Doms and Schättler (1999).

2.1 The Model Equations

As discussed above, the LLM equations are borrowed from the LM. We write them here in the following form:

$$\begin{aligned}\frac{\partial u}{\partial t} &= -\frac{1}{\rho}\left(\frac{\partial p'}{\partial x}-\frac{1}{\sqrt{\gamma}}\frac{\partial p_0}{\partial x}\frac{\partial p'}{\partial \zeta}\right)-\left(\frac{\partial K}{\partial x}-vV\right)-\dot{\zeta}\frac{\partial u}{\partial \zeta}-\frac{1}{\rho}\left(\nabla\cdot\underline{\underline{F}}\right)\cdot\underline{e}_1 \\ &\quad + M_u^{LB}+M_u^{UB}+D_u \qquad (1)\end{aligned}$$

$$\begin{aligned}\frac{\partial v}{\partial t} &= -\frac{1}{\rho}\left(\frac{\partial p'}{\partial y}-\frac{1}{\sqrt{\gamma}}\frac{\partial p_0}{\partial y}\frac{\partial p'}{\partial \zeta}\right)-\left(\frac{\partial K}{\partial y}+uV\right)-\dot{\zeta}\frac{\partial v}{\partial \zeta}-\frac{1}{\rho}\left(\nabla\cdot\underline{\underline{F}}\right)\cdot\underline{e}_2 \\ &\quad + M_v^{LB}+M_v^{UB}+D_v \qquad (2)\end{aligned}$$

$$\begin{aligned}\frac{\partial w}{\partial t} &= \frac{g}{\sqrt{\gamma}}\frac{\rho_0}{\rho}\frac{\partial p'}{\partial \zeta}+g\frac{\rho_0}{\rho}\left\{\frac{(T-T_0)}{T}-\frac{T_0 p'}{T p_0}+\left(\frac{R_v}{R_d}-1\right)q^v-q^l\right\} \\ &\quad -\left(u\frac{\partial w}{\partial x}+v\frac{\partial w}{\partial y}\right)-\dot{\zeta}\frac{\partial w}{\partial \zeta}-\frac{1}{\rho}\left(\nabla\cdot\underline{\underline{F}}\right)\cdot\underline{e}_3+M_w^{UB}+D_w \qquad (3)\end{aligned}$$

$$\begin{aligned}\frac{\partial p'}{\partial t} &= g\rho_0 w-\frac{c_{pd}}{c_{vd}}p\left(D_H-\frac{g\rho_0}{\sqrt{\gamma}}\frac{\partial w}{\partial \zeta}\right)-\left(u\frac{\partial p'}{\partial x}+v\frac{\partial p'}{\partial y}\right)-\dot{\zeta}\frac{\partial p'}{\partial \zeta} \\ &\quad +M_{p'}^{LB}+M_{p'}^{UB} \qquad (4)\end{aligned}$$

$$\begin{aligned}\frac{\partial T}{\partial t} &= -\frac{p}{\rho c_{vd}}\left(D_H-\frac{g\rho_0}{\sqrt{\gamma}}\frac{\partial w}{\partial \zeta}\right)-\left(u\frac{\partial T}{\partial x}+v\frac{\partial T}{\partial y}\right)-\dot{\zeta}\frac{\partial T}{\partial \zeta} \\ &\quad +Q_T-\frac{1}{\rho c_{pd}}\nabla\cdot\underline{H}+M_T^{LB}+M_T^{UB}+D_T \qquad (5)\end{aligned}$$

$$\begin{aligned}\frac{\partial q^k}{\partial t} &= -\left(u\frac{\partial q^k}{\partial x}+v\frac{\partial q^k}{\partial y}\right)-\dot{\zeta}\frac{\partial q^k}{\partial \zeta} \\ &\quad +Q_k-\frac{1}{\rho}\nabla\cdot\underline{F}_{q^k}+M_{q^k}^{LB}+M_{q^k}^{UB}+D_{q^k} \qquad (6)\end{aligned}$$

with $k = v, l$ (denoting water vapour or cloud liquid water, respectively) and with the definitions

$$p = \rho R_d \left\{ 1 + (R_v/R_d - 1)q^v - q^l - q^f \right\} T \tag{7}$$

$$\dot{\zeta} = -\frac{1}{\sqrt{\gamma}} \left(u\frac{\partial p_0}{\partial x} + v\frac{\partial p_0}{\partial y} + g\rho_0 w \right) \tag{8}$$

$$D_H = \left(\frac{\partial u}{\partial x} - \frac{1}{\sqrt{\gamma}} \frac{\partial p_0}{\partial x} \frac{\partial u}{\partial \zeta} \right) + \left(\frac{\partial v}{\partial y} - \frac{1}{\sqrt{\gamma}} \frac{\partial p_0}{\partial y} \frac{\partial v}{\partial \zeta} \right) \tag{9}$$

$$K = \frac{1}{2}\left(u^2 + v^2\right), \quad V = \frac{\partial v}{\partial x} - \frac{\partial u}{\partial y} + f \tag{10}$$

The formulation makes reference to a defined basic state, which is hydrostatic, dry and at rest. For the temperature and the pressure follows $p = p_0(z) + p'$, $T = T_0 + T'$, and the density of the basic state is $\rho_0 = p_0/(R_d T_0)$. Because the LLM integration domain has a rather limited horizontal extension (see below in 2.6), the horizontal partial derivatives are here symbolized in local cartesian coordinates ($\partial x := a\cos\varphi\partial\lambda$, $\partial y = a\partial\varphi$) instead of spherical ones. Spherical metric terms are therefore dropped, and the variation of the Coriolis parameter is neglected. Furthermore, the equations are formulated with a terrain-following vertical coordinate ζ in such a way, that the momentum equations are related to the physical wind components u, v, w. $\dot{\zeta}$ denotes a contravariant vertical velocity which by use of (8) is related to u, v, w.

The factor $\sqrt{\gamma}$ is defined by $\sqrt{\gamma} = \partial p_0/\partial\zeta$, where $\sqrt{\gamma}/(g\rho_0)$ is the Jacobian of the transformation from the z- to the ζ-coordinate. The horizontal wind divergence D_H, the kinetic energy of the horizontal wind K, and the absolute vorticity V are defined by (9) and (10). The equation of state for a mixture of dry air, water vapour and liquid water is given by (7), q^v and q^l denote the specific contents of water vapour and liquid water, respectively. Thus, (6) consists of two equations for both these moisture variables. The ice phase is not taken into account in the LLM. In contrast to the LM, we consider here the turbulent fluxes of momentum, heat and moisture in all three space directions. Therefore, F denotes in (1), (2), (3) the turbulent momentum flux tensor with its 6 components, and H, F_{q^v} and F_{q^l} the three-dimensional turbulent vector fluxes of heat, water vapour and liquid water. In addition, in the prognostic equations (1), (2), (3), (5), (6) a non-physical computational mixing is implied, where a linear fourth-order horizontal diffusion symbolized by the terms D_ψ ($\psi = u, v, w, T, q^v, q^l$) is applied.

The source terms Q_T and Q_{q^k} need also to be explained. Q_T represents the rate of diabatic heating/cooling due to phase changes of water. The atmospheric effect of radiation is deliberately neglected. This will be discussed from the point of view of the external model forcing in Sections 2.5 and Chapters 4 and 5. The terms Q_{q^v} and Q_{q^l} contain the cloud microphysical source and sink terms and the precipitation flux.

In order to complete the formal model description, the terms M_ψ^{LB} and M_ψ^{UB} must be mentioned. They have no physical background. They represent relaxation terms, acting in a *lateral boundary* zone (=superscript LB) and *upper boundary* model layer (=superscript UB), in order to bring the LLM solution within those boundary zones outward to an externally driving state deduced from measured vertical profiles. This aspect is discussed in Section 2.3 and in Chapter 4. For the rest of symbols in the equations above the meteorological standard notion is valid: R_d and R_v are the special gas constant for dry air and water vapour, respectively, g is the gravity constant, and c_{pd} (c_{vd}) denotes the specific heat capacity at constant pressure (volume).

2.2 Numerical Aspects

As argued above in the description of the continuous LLM equations, we can be brief in discussing the numerics of the LLM as far as taken directly from the LM numerical scheme. This concerns horizontal, vertical and time differences. The horizontal gridpoint position of variables is ordered in a C-grid scheme after the well-known Arakawa nomenclature: At a central point of each gridbox almost all scalar variables inclusively w are placed, while horizontal wind components are positioned halfway from that point as normal components with respect to the box sides (u to 'right' and 'left'; v 'above' and 'below'). The vertical grid is a so called Lorenz-grid. Here, most of variables are placed in the middle of each layer, which is at the so called main levels, while the vertical velocity and also the turbulent vertical flux terms are placed at half levels, which are the interfaces between those layers. The fundamentals of the vertical layer structure can easily be characterized from a strict quotation of Doms and Schättler (1999, cf. Subsection 2.5.3 in the LM-Scientific Documentation).

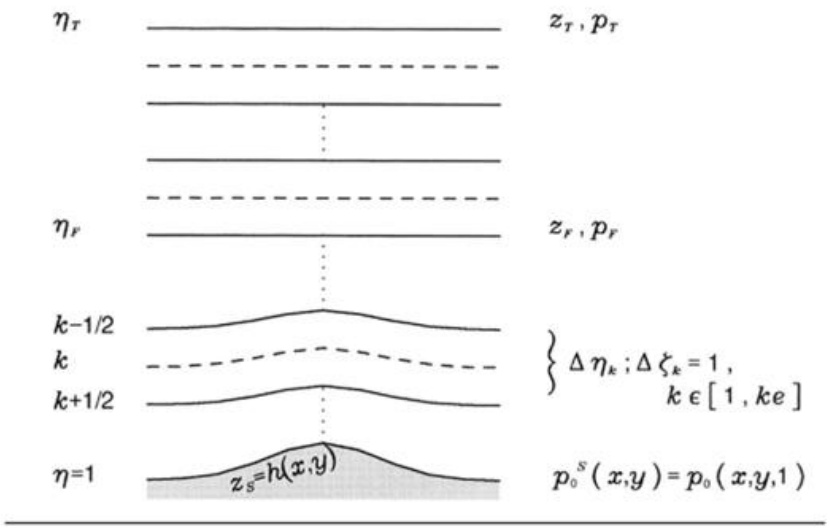


Figure 2.1: Vertical differencing scheme based on the terrain-following hybrid vertical coordinate η with some mapping $\eta = m(\zeta)$ onto the generalized coordinate ζ with the convenient property $\Delta\zeta_k = 1$. The LLM values are $z_T = 3000$ m, $p_T = 693.9075$ hPa, $\eta_T = p_T/p_{SL}$, $p_{SL} = 1000$ hPa, $z_F = 1000$ m, $p_F = 887.27$ hPA and $\eta_F = p_F/p_{SL}$. z_s is the orographic height which is also given by a standard surface pressure distribution $p_0^s(x, y)$ on $\eta = 1$.

An important aspect of the terrain-following vertical coordinate used in the LLM is specified as a pressure-based hybrid coordinate that involves a defined height of $z_F = 1000$ m separating the entire vertical domain into a terrain-following part below and a pure z-coordinate above it (Fig. 2.1). Thus, the lower model boundary is a coordinate surface formed by the highly resolved orography plus a seasonally varying field of the displacement height. The upper boundary is assumed at 3000 m height. This vertical depth of the LLM is divided into 39 layers, where the layers nearest to the lower boundary are very thin. The thickness is spreaded from 4 m to 25 m in the first two-hundred meters with 15 layers. Above, the layer thickness increases gradually up to 100 m at 425 m height where it remains so up to about 1000 m. From there the resolution becomes still coarser with a thickness of 150 m up to model top height (Tab. 2.1).

With a horizontal mesh width of $\Delta \simeq 100$ m the aspect ratio $\alpha = \Delta z/\Delta$ varies between $1/25 \leq \alpha \leq 3/2$. The vertical depth of 3000 m has been fixed after test integrations of a 52-layer model version with a model top height chosen for sake of caution at 5000 m for

k	$z(m)$	$p_0(z)$ (Pa)
1	3000.0	69390.8
2	2850.0	70704.6
3	2700.0	72039.5
4	2550.0	73395.5
5	2400.0	74773.5
6	2250.0	76173.1
7	2100.0	77594.8
8	1950.0	79039.1
9	1800.0	80506.1
10	1650.0	81006.1
11	1500.0	83509.5
12	1350.0	85046.7
13	1200.0	86607.8
14	1050.0	88193.2
15	925.0	89533.2
16	825.0	90617.7
17	725.0	91713.3
18	625.0	92820.2
19	525.0	93939.5
20	425.0	95068.2

k	$z(m)$	$p_0(z)$ (Pa)
21	350.0	95923.1
22	300.0	96496.7
23	266.0	96888.4
24	233.0	97269.9
25	200.0	97652.6
26	175.0	97943.5
27	150.0	98235.0
28	125.0	98527.3
29	105.0	98761.7
30	90.0	98937.8
31	77.5	99084.7
32	65.0	99231.9
33	52.5	99379.2
34	42.5	99497.2
35	32.5	99615.3
36	22.5	99733.5
37	15.0	99822.3
38	9.0	99893.3
39	4.0	99525.8
40	0.0	100000.0

Table 2.1: Vertical structure of layers. The index $k \in [1, 40]$ counts the half-levels with associated heights and basic-state pressure values.

a convective case. The outcome has indicated that a 3000 m upper boundary height is sufficient.

The time differencing scheme used for the LLM integration is completely taken from the LM-code as the dominant scheme amongst three options. In brief, we selected the mode-splitting time integration method originally proposed by Klemp and Wilhelmson (1978), refined by Skamarock and Klemp (1992) and completed by further implicit manipulations. In this line the model equations are split up into a slowly varying part and a fast one. The former consists of horizontal advection, vertical advection, turbulent diffusion in all three space directions, horizontal computational mixing and source/sink terms. The water balance equations for vapour and liquid water and the turbulent kinetic energy equation are exclusively slow equations, while the momentum equations for the wind components u, v, w, the temperature equation and the prognostic perturbation pressure equation have also a fast part.

In the slow equations/equation parts different terms are treated differently as follows. The horizontal advection is integrated by use of the leap-frog scheme. The vertical advection and the vertical turbulent flux terms are approximated by an implicit Crank-Nicholson scheme, and the horizontal turbulent flux terms, the computational mixing (fourth-order diffusion), and the source/sink-terms as well, are formulated by a simple forward scheme. The corresponding time step (large time step) is chosen $\Delta t = 2$ s with respect to the horizontal gridpoint distance $\Delta = 96.5$ m. The entire time marching per Δt consists in extrapolating the fast equation part with a small timestep $\Delta\tau$ several times over each time span $2\Delta t$ keeping the before determined slow tendencies fixed over this intervall. The fast-mode part involves, apart from the slow tendencies of momentum, temperature and perturbation pressure, all terms representing inertial-gravity waves and sound-waves. Those terms describing

vertically propagating waves are treated implicitly in order to prevent any dependence on high vertical grid resolution. Thus, the choice of the small time increment $\Delta\tau$ is governed by the linear stability condition $\Delta\tau \leq \Delta/(\sqrt{2}\,c_s)$ with an estimate for the sound speed $c_s = (R_d(c_{pd}/c_{vd}) \times 303K)^{1/2}$. With respect to the relation $\Delta\tau = 2\Delta t$ follows $N = 22$ as the number of small timesteps over twice the large step giving $\Delta\tau = 0.182$ s.

Each time step Δt ends with the application of a Robert-Asselin time filter followed by the upper and lateral boundary relaxation technique in order to match the inner LLM solution with an external forcing. The latter aspect is of special interest for the LLM integration mode and will therefore be discussed separately in the next Section.

Lest we ignore possibly a time integration scheme being less time consuming than the mode splitting scheme, it was mandatory for us to test further options available for the LM. Thomas et al. (1998 a, b) had developed a three-dimensional semi-implicit time integration method suitable for a non-hydrostatic compressible model which they also introduced in the LM program code. Their method rests on a GMRES (General Minimal Residual Krylov Iterative Solver) algorithm and seemed to promise computational advantages. Therefore, rather time-expensive tests of that scheme applied to the LLM have been carried out (Herzog and Fiedler 1999). The computational efficiency of the fully 3D semi-implicit (SI) time-scheme versus the above described split-explicit (SE) scheme has been investigated by comparable real data runs for the 14.06.97 day. Unfortunately, the outcome of these runs was negative. Compared to the SE reference run with the 'slow mode'-time step of $\Delta t = 2$ s the SI runs led to an unexpected computational overhead. The slow convergence rate of the elliptic solver could not be influenced by an enlarged Krylow space dimension and an aspect ratio $\Delta z/\Delta$ chosen always smaller than unity. The conclusion had to be drawn that the SI-scheme cannot compete with the SE-scheme in case of the LLM which simulates the planetary boundary layer with its inherent three-dimensional micro-scale structures. For a comparably larger-scale LM computational problems discussed seem different (Saito et al. 1998).

2.3 Lateral and Upper Boundary Techniques

Integrating a very high-resolving model over a rather limited area like the LLM, one is confronted with an extremly underestimated problem in view of external atmospheric information needed to drive the model via its lateral boundaries and the upper boundary as well. We assume the relatively low-resolved boundary data provided from measurements (cf. Chapter 4) to be in general variable in time. For that reason it is important to have some desirable control of such boundary forcing. Particularly, the effect of local physical forcing in the near-surface Planetary Boundary Layer domain of the LLM should be maintained as far as possible. Trying to find a solution, a pragmatic, engineering strategy is reasonable to be pursued. Unfortunately, there is no standard method that has been demonstrated to be satisfactory for the wide-spread spectrum of atmospheric motions, and so for the LLM problem neither.

In view of this, rather extended numerical experiments have been made both as transparent simplified tests and as complex real-data model runs, in order to come to a decision for an acceptable compromise. Basically, two types of lateral boundary methods have been tested. The first type is the *radiation condition* in its approximate form (Orlanski 1976). The principal difficulty to incorporate a radiation condition into a realistic model is that the speed normal to the boundary is generally unknown. The approach (Miller and Thorpe 1981) locally diagnoses the normal speed component, whereas in Klemp and Wilhelmson (1978) it is specified to be a representative phase speed of internal gravity waves. In each case

tested, the approach remains approximative and is linear. The boundary condition becomes, however, necessarily nonlinear which means that this type of method works successful only when the solution is dominated by a single wave. In all other cases we are mainly interested in, the solution is severely polluted with errors. By the way, there is also no convincing theoretical support for the radiative idea, since the original variables are not characteristic. The outcome of numerous test integrations gave us a sufficient reason to discard this type of lateral boundary technique from further consideration.

The second type uses a certain *adjustment or 'sponge' effect* in a zone next to the lateral boundary (Davies 1976, Perkey and Kreitzberg 1976, Chen 1973, Miyakoda and Rosati 1977 etc.). Our interest is to apply a method of that type which was introduced in a particularly easy and therefore practicable form by Kallberg and Gibson (1977) starting from Davies' original approach. The so called 'Davies-Kallberg'-technique is a preferable method which is always available because of its ease to be used in general situations, where the boundary data are time-dependent. The property of easy use is also a very important aspect in view of parallel programming. Nevertheless, one must not ignore the inevitable shortcomings of the Davies-Kallberg boundary relaxation or blending method from which dynamical imbalances in the relevant boundary adjustment zone may be produced.

Before we start describing a version of the Davies-Kallberg technique applied to the LLM regime, some remarks concerning a hybrid method are given. The latter one has also been tested because there were arguments in literature (Arakawa 1984) for a pragmatic solution, in which a scheme that is nonreflective – at least for idealized cases – is combined with some adjustments near the boundary. An attempt was therefore made to adapt such a method to the compressible, non-hydrostatic LLM with its specific time-splitting technique. The working hypothesis was to introduce also a mode splitting for the radiative scheme. In doing so, the acoustic-gravity equation part is treated with open boundaries at each short timestep. For the advection part, however, a mixed scheme is applied: At the outflow boundary points a radiative scheme is used again, but now for the advective wind speed, while at outflow points a modified Davies-scheme operates.

In short, this rather sophisticated scheme works well in case of simplified flow situations, where outflow points and inflow points can easily be separated (e. g. the most simple case of a diagonal basic current). In more general cases problems emerge at boundary points, where the relaxation scheme and the radiative scheme influence and conflict with each other in an uncontrolled way. Therefore, this method was also discarded, which has finally led to our choice of a 'pure' Davies-Kallberg technique. That method is applied in the LLM in a modified form.

The prototype for each prognostic LLM equation may be written

$$\frac{\psi_j^{(\tau+1)} - \psi_j^{(\tau-1)}}{2\Delta t} = RHS_j^{(\tau-1,\tau,\tau+1)} - \mu_j \left(\psi_j - \psi_j^B\right)^{(\tau+1)} . \tag{11}$$

In a more symbolized form the tendency is approximated by a centered time difference with $2\Delta t$. In $RHS_j^{(\tau-1,\tau,\tau+1)}$ all terms of each equation are absorbed, and the second term on the r. h. s. represents the lateral boundary relaxation term of interest. Towards the boundary the inner LLM solution is forced to become equal to the external solution represented by the boundary data ψ_j^B. The index j numbers the gridpoints of a grid row inwards and normal to the boundary point $j = 0$.

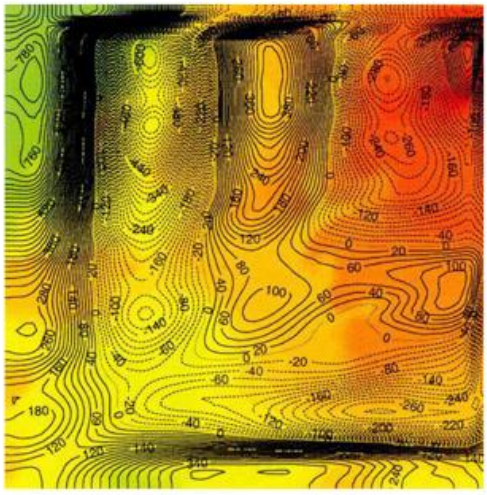
In line with the philosophy of that relaxation term, abbreviated by M_ψ^{LB} in the model equations, the relaxation coefficient μ_j is a prescribed function of distance of an inner gridpoint

j to the boundary point. At the boundary the coefficient becomes infinity and it approaches to zero in the inner region defining so the prescribed width of the lateral boundary relaxation zone. The time levels $\tau - 1$, τ, $\tau + 1$ in (11) indicate in a common way of notation the different time difference approximations (leap-frog centered, forward and implicit treatment of involved terms) in the prototype equation. As known from many descriptions of Kallberg's approach, the equation type (11) can be brought into an astonishing simple linear form

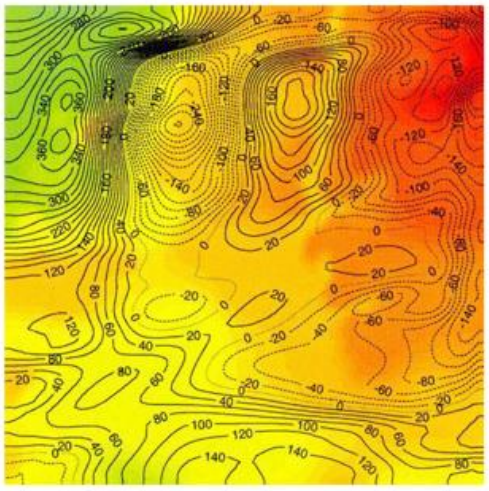
$$\psi_j \;=\; (1 - \alpha_j)\, \psi_j^{LLM} + \alpha_j \psi_j^B \;, \tag{12}$$

where the internal LLM data ψ_j^{LLM} – not influenced by the relaxation term M_ψ^{LB} – are linearly combined with the external driving boundary data ψ_j^B to produce per timestep the boundary data adjustment of the inner solution in terms of ψ_j. Far from being ideal the simple procedure is thought to avoid most of dangerous reflections and contaminations originating from overestimated and generally unfitted boundary data. The blending weights α_j are related to the relaxation coefficients μ_j by

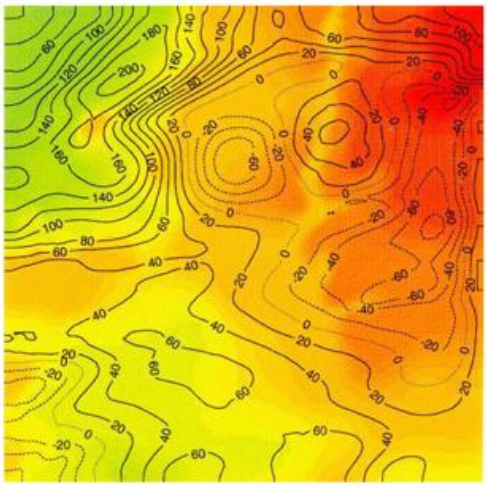
$$\alpha_j \;=\; \frac{2\Delta t \mu_j}{1 + 2\Delta t \mu_j} \;. \tag{13}$$



a=0.5, max = 884mm/s, min = -675mm/s



a=0.25, max = 388mm/s, min = -302mm/s



a=0.125, max = 206 mm/s, min = -86 mm/s

Figure 2.2: Horizontal section of vertical velocity w at altitude z = 1500 m after an one-hour integration over a LLM subdomain of 81 × 81 gridpoints assuming a basic flow over the real orography with U = 10 m/s. The w-field is shown for three values of the Kallberg-parameter a. Top left: a = 0.5, top right: a = 0.25, bottom left: a = 0.125.

For the α_j-weights follows $0 \leq \alpha_j \leq 1$ with $\alpha_{j=0} = 1$. Formula (13) is, however, unpractical to be used. Since Kallberg (1977) it is common practice to apply an ad hoc formula

$$\alpha_j = 1 - \tanh(aj); \quad j = 0, 1, 2, ..., \tag{14}$$

which describes a damping curve like (13). The parameter a determines the essential decrease of that curve because of $(\partial\alpha/\partial j)_{j=0} = -a$. In many limited area models (e.g. EM, DM, LM) the value $a = 0.5$ has shown to be sufficient. To find out an appropriate steepness of the α_j-curve for the LLM with its significantly higher grid resolution, some numerical experimentation was carried out starting from the default value $a = 0.5$. The result is shown in Fig. 2.2. It suggests an α_j-curve with a sufficiently weaker slope. Thus, $a = 0.125$ is chosen further on instead of 0.25 or 0.5. Fig. 2.3 demonstrates the weight curves (14) for those three slope values.

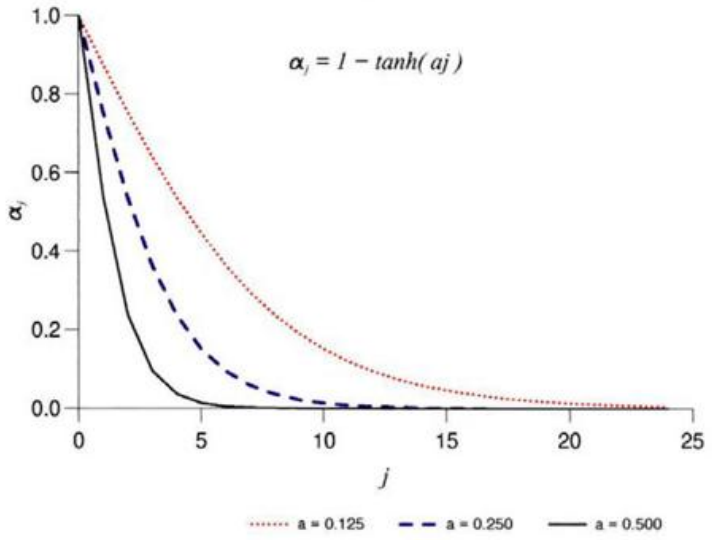


Figure 2.3: Boundary weight curve (Equation (14), see text) as a function of distance of an inner gridpoint j to the boundary point $j = 0$ for three different slope parameters a = 0.5, 0.25, 0.125.

In order to obtain more insight from the result shown in Fig. 2.2, it is illuminating to take into account also the first and second derivative of relation (12):

$$\frac{\partial\psi}{\partial x} = (1-\alpha)\frac{\partial\psi^{LLM}}{\partial x} + \alpha\frac{\partial\psi^{B}}{\partial x} - \frac{\partial\alpha}{\partial x}(\psi^{LLM} - \psi^{B}), \tag{15}$$

$$\frac{\partial^2\psi}{\partial x^2} = (1-\alpha)\frac{\partial^2\psi^{LLM}}{\partial x^2} + \alpha\frac{\partial^2\psi^{B}}{\partial x^2} - 2\frac{\partial\alpha}{\partial x}\left(\frac{\partial\psi^{LLM}}{\partial x} - \frac{\partial\psi^{B}}{\partial x}\right) - \frac{\partial^2\alpha}{\partial x^2}(\psi^{LLM} - \psi^{B}). \tag{16}$$

x is a continuous coordinate measured in grid distance units. While the blending formula (12) is actually applied per timestep for prognostic variables ψ $(= u, v, T, p)$, one obtains, in effect, due to (15) and (16), no similar blending of $\partial\psi/\partial x$ (which, for instance, is related to the horizontal wind divergence and vorticity) and $\partial^2\psi/\partial x^2$ (related to the horizontal gradient of vertical motion, respectively). It can be seen that the dissimilarity is fundamentally marked by the always existing difference between inner solution (ψ^{LLM}, $\partial\psi^{LLM}/\partial x$) and the external one ($\psi^{B}$, $\partial\psi^{B}/\partial x$). (15) and (16) tell us furthermore that the significant

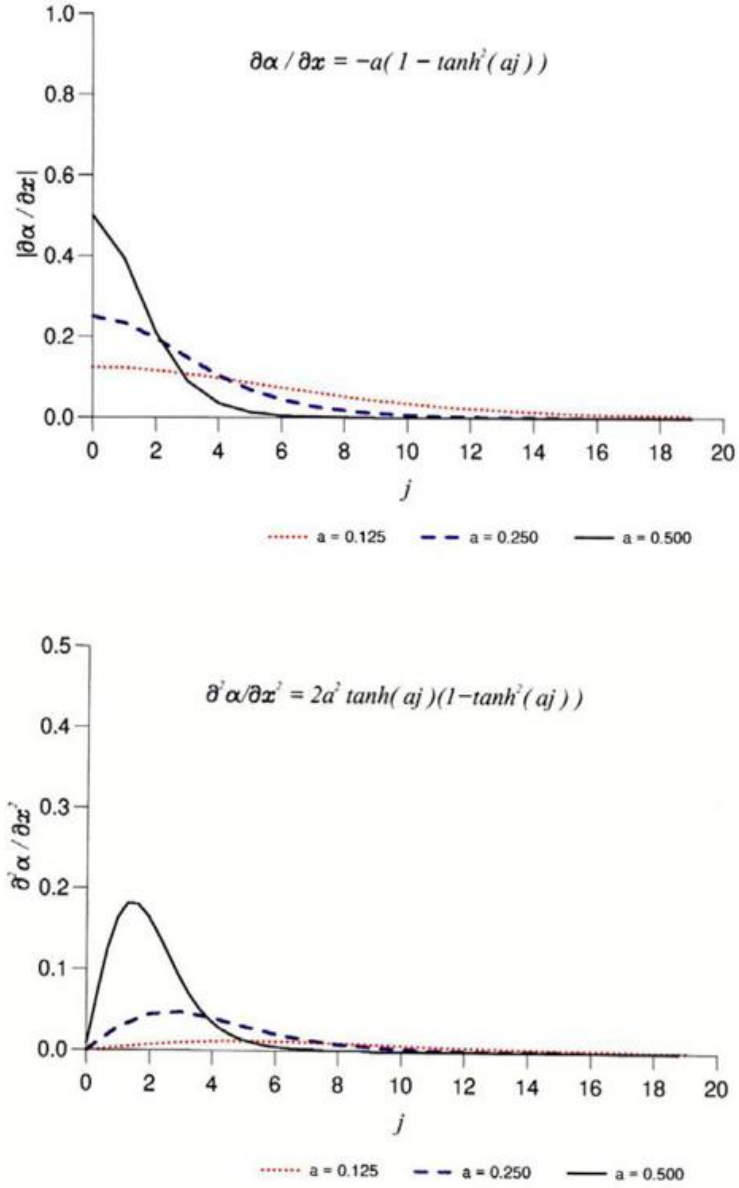


Figure 2.4: The first (top) and second (bottom) derivatives of the Kallberg boundary weight function α (x is measured in grid distance units) for $a = 0.5, 0.25, 0.125$.

difference is multiplied by $\partial\alpha/\partial x$ and $\partial^2\alpha/\partial x^2$. By an appropriate choice of the weights α we are, however, able to keep the unwanted effect due to those terms rather small. This depends obviously on the choice of the parameter a. Fig. 2.4 shows in addition to Fig. 2.3 the functions

$$\frac{\partial\alpha}{\partial x} = -a(1 - \tanh\{ax\}), \quad \frac{\partial^2\alpha}{\partial x^2} = 2a^2 \tanh\{ax\}(1 - \tanh^2\{ax\}) . \tag{17}$$

The conclusion from Fig. 2.3 together with Fig. 2.4 is that $a = 0.125$ is the best value to be used in case of the LLM. The strong gradient of w in a short distance from the boundary, as shown in Fig. 2.2 for $a = 0.5$, may be explained by use of the continuity equation summing up the gradient of the horizontal wind divergence from the earth surface to the height z.

In this way the vertically accumulated effect of the $\partial\alpha/\partial x$ and $\partial^2\alpha/\partial x^2$-terms in (16) is involved. It is not demonstrated here from the background experiment of Fig. 2.2 that the near-boundary gradient of vertical motion shown for $a = 0.5$ is actually not observed on the lowest model levels but will be formed and amplified with increasing height. All our experimentation with numerous real data cases so far have indicated that with $a = 0.125$ the unwanted gradients discussed do vanish.

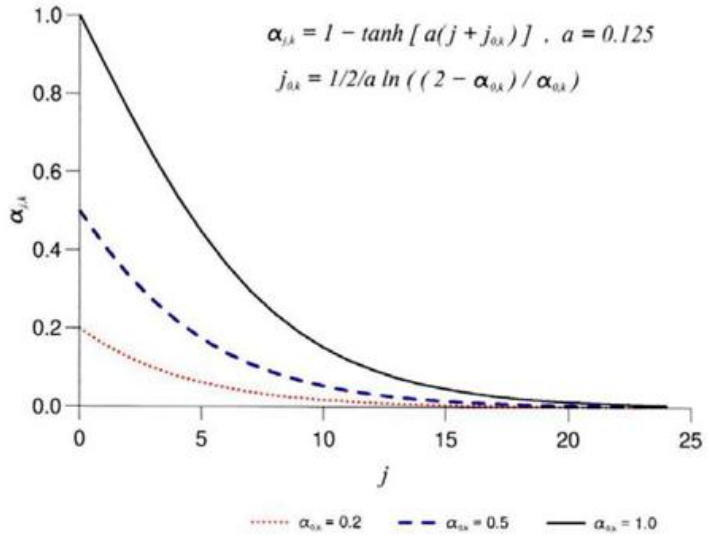


Figure 2.5: Plot of vertically varying weight function $\alpha_{j,k}$ showing how in the LLM the external boundary data influence is reduced downwards by using a phase parameter $\alpha_{0,k}$ in the intervall $0.2 \leq \alpha_{0.k} \leq 1$ (see text).

In order to complete the description of the LLM-specific lateral boundary technique another engineering component is added to the original Kallberg approach. The motivation follows from the decision to use the weight curve parameter $a = 0.125$. Though necessary, some nuisance might come from the relatively far inward reaching influence of boundary data information connected with a low-steepness curve. To alleviate possible problems from this, the following vertically varying weight functions differing from (14) are introduced:

$$\alpha_{j,k} = 1 - \tanh\left[a(j + j_{0,k})\right] , \tag{18}$$

with a phase parameter

$$j_{0,k} = \frac{1}{2a} \ln\left(\frac{2 - \alpha_{0,k}}{\alpha_{0,k}}\right) .$$

k is the vertical model level index, and a is always equal to 0.125 (Fig. 2.5). The new parameters $\alpha_{0,k}$ are user-prescribed values, which for the lowest LLM levels $14 \leq k \leq 39$ (cf. Tab.2.1) are linearly distributed in the range $0.2 \leq \alpha_{0,k} \leq 1$ by $\alpha_{0,k} = 1 - 0.8(k-14)/39-14)$. This empirical operation, entirely determined from experimentation, makes sure that the influence of the always not exactly adapted boundary data is in the planetary boundary layer towards the earth surface gradually diminished, where, however, the near-surface turbulent fluxes produced in the LLM are allowed to remain dominating. Instead of (12) a similar blending formula, now also depending on k, must be applied, which evaluates the above described weights (18) instead of (14),

$$\psi_{j,k} = (1 - \alpha_{j,k})\, \psi^{LLM}_{j,k} + \alpha_{j,k} \psi^{B}_{j,k} . \tag{19}$$

It follows from this philosophy that in any case of $\alpha_{0,k} < 1$ also internal LLM information is needed at the boundary points which from the numerical integration is not directly available. Therefore, a simple linear extrapolation as computational boundary condition is additionally applied.

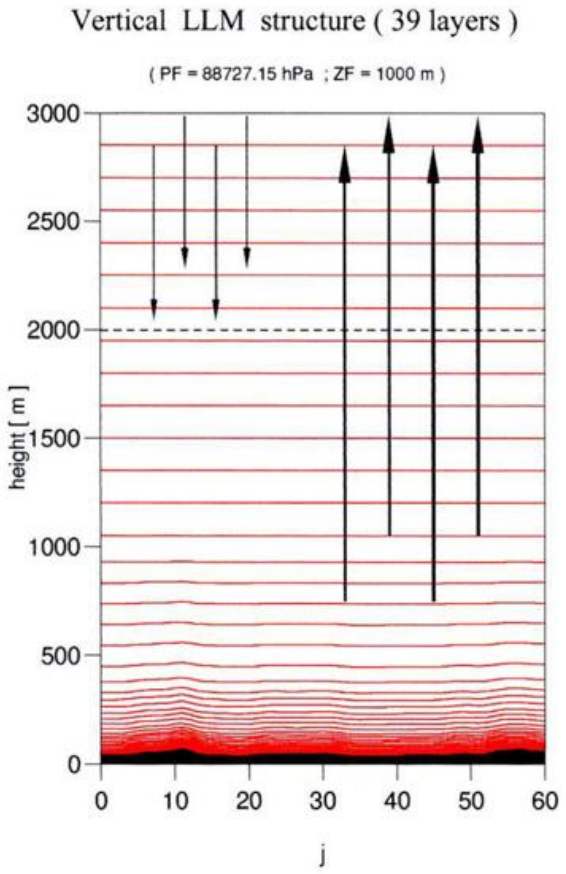


Figure 2.6: Position of the Rayleigh damping layer connected with vertical layering of the LLM.

In the following the *upper boundary technique* will be explained. It is directly adopted from the LM-scheme. The method is similar to the lateral boundary technique, which is a Rayleigh-damping mechanism. In the model equations (1) - (6) this is symbolized by the terms M_ψ^{UB}. Here, the vertical motion w is included. The original motivation for that sort of upper boundary relaxation is to allow an upper lid condition $w = 0$ at the top of the model, from which artificial gravity wave reflection can take place. The Rayleigh damping method prevents that by absorption of energy of those waves penetrating upward through an upper absorption zone before arriving the top elevation. In case of the LLM, the purpose of that method is, however, twofold. In addition, the technique is thought to be an adaptation method as at the lateral boundary in order to match the inner solution also in an upper boundary zone with an outer solution which serves as a driver from measured data in the free atmosphere (cf. Chapter 4). Similar to equation (11) the mechanism rests here on a prognostic equation like that

$$\frac{\psi_k^{(\tau+1)} - \psi_k^{(\tau-1)}}{2\Delta t} = \cdots - \nu_k^{rd} \left(\psi_k - \psi_k^B\right)^{(\tau+1)} . \tag{20}$$

In (20) only a relaxation term M_ψ^{UB} is of interest. The vertical model level index k emphasizes its operation in vertical direction. ν_k^{rd} is a relaxation coefficient corresponding to a reciprocal relaxation time. After Ikawa and Saito (1991) it is assumed to have the form

$$\nu_k^{rd} = \frac{1}{2N_{rd}\Delta t}\left[1 - \cos\left(\pi\frac{z_k - z_{rd}}{z_T - z_{rd}}\right)\right] . \tag{21}$$

The parameters in formula (21) are specified as follows: $\Delta t = 2$ s, $N_{rd} = 10$, $z_T = 3000$ m and $z_{rd} = 2000$ m. They define a Rayleigh damping layer being 1000 meters thick and resolved by the 7 uppermost layers, $k \in [1, 7]$ (Fig. 2.6). From the cosine-profile function follows an increasing absorption effect towards the model top. There, the damping effect reaches its maximum. The parameter $N_{rd} = 10$ means, that the perturbation $(\psi - \psi^B)$ will be reduced to its e^{-1}-th part at the top height $z_T = 3000$ m after 10 large LLM timesteps. For levels below 2000 meters the method is ineffective. The practical execution of the Rayleigh damping is similar to the lateral boundary technique, where a blending like (11) or (19) is applied. The associated weight function is here $\alpha_k = 2\Delta t\nu_k^{rd}/(1 + 2\Delta t\nu_k^{rd})$.

A radiative scheme instead of the presently applied method is still under development. The hydrostatic radiation condition after Klemp and Durran (1983) and Bougeault (1983) successfully introduced in the former DM/HRM (Herzog 1995, Binder and Herzog 1995), seems not directly suited in the non-hydrostatic and compressible world of LM/LLM.

2.4 Lower Boundary Condition and Forcings

For the sake of completeness, the lower boundary condition/treatment must be added here after having described the LLM-specific lateral and upper boundary technique in the previous Section. Because the lower bounding surface is the earth surface (without deeper thinking how it is defined from the point of view of modelling), it is assumed rigid. Frictional forces are important at that surface. Therefore, the classical adherence condition or non-slip condition holds there. Consequently, the horizontal wind components u and v vanish at the surface. Since the contravariant vertical motion $\dot{\zeta}$ in the LM/LLM-equations always vanishes then, it follows from equation (8) a vanishing physical vertical velocity, that is $w = 0$.

The boundary layer processes are of vital interest in LLM modelling. Thus, the turbulent fluxes of momentum, heat and moisture at the surface must be available as exact as possible. For their determination the surface temperature and moisture must be known. These parameters again are determined from an LLM-coupled prognostic soil model 'terra'. That model is also incorporated in the present operational LM version and was already operating in the former DWD-models EM and DM/HRM (Jacobsen and Heise 1982). Intensive work is underway to insert for the thermal part, still being an 'extended force-restore' method, a higher resolved heat conduction equation.

All the external parameters needed have been derived in case of the LLM problem from a detailed physiographic description of the landscape around Lindenberg. Furthermore, horizontally distributed, time-varying fields of precipitation and short-wave plus long-wave radiation balance at the earth surface determined from measurements constitute the physical forcing of LLM from the underlying surface. This aspect is of greatest importance for reasonable and successful LLM simulations. Therefore, the LLM forcing from the earth surface is the matter of thorough discussion in Chapter 5.

2.5 Model Physics Different to LM

In view of the fact that near-surface turbulent fluxes are very sensitive to forcing from the underlying surface, that process must be kept as close as possible to reality. This will be achieved by using real surface precipitation and radiation balance fields for that forcing as mentioned above in Section 2.4. The consequence is, however, to make an operation in both the cloud-precipitation scheme and the radiation parameterization scheme as they are originally available from the LM.

In contrast to well-defined LES studies taking into account cloud-radiation interaction and a precipitation scheme, the LLM real-case simulations cannot operate with that philosophy. Although forming of clouds and precipitation is in the LLM allowed, the precipitation flux reaching the earth is ignored and replaced by a real-data precipitation field. Furthermore, the radiation scheme available from the LM is even completely discarded. The radiative long- and short-wave balance field at the surface is exclusively deduced from measurements and supported by satellite information (cf. Chapter 5). The input-frequency of the radiation balance and of the surface precipitation field amounts to 10 minutes. In this way the ground surface and therefore the soil model 'terra' perceives radiation and precipitation as would be obtained from properly simulated atmospheric conditions like cloudiness and radiation in and over the LLM integration domain.

A weak point of this strategy might be the omission of any radiation scheme in the atmospheric part of the LLM. This is just taken into the bargain in order to avoid an erroneous radiative heating/cooling from insufficient simulations of all conditions influencing the radiation processes. To keep on the right way, it is tacitly assumed that the long-wave radiative effect on the temperature field is implied in the measured vertical profiles from which the LLM is driven from outside with an 1 hour-updating frequency. Summing up that, the reduction in the precipitation and radiation parameterization in case of LLM studies is believed to be compensated by sets of real forcing data where these processes are implicitly contained.

In the LLM also the soil model 'terra' (already commented in Section 2.4) is incorporated, which is directly taken from the LM system. For a detailed description we refer to the LM Scientific Documentation (Doms and Schättler 1999, Chapter 10). Its use in the LLM and minor adjustments are detailed in Chapter 5, where the forcing of LLM will be discussed thoroughly.

The most important sub-grid parameterization in the LLM is undoubtedly an adequate turbulence scheme. Because this physical component has been developed as a primary task of the LLM-development, it deserves to be documented in the present report in the following Chapter 3.

2.6 Specification of the Horizontal Integration Area

This Section deals with a technical issue concerning the exact size and placement of the horizontal grid net . Its fixation must be explained from a historical situation when the 'Deutschland-Modell' (DM) was in operational use. At the beginning of the LITFASS-project there was a common agreement to think of an integration area for the LLM having exactly the size of a DM-gridbox. The gridbox selected encloses the location of the Lindenberg Observatory and contains almost all measurement places in it (Beyrich 2000). The size of that gridbox (so called 'Lindenberg gridbox') is defined by a mesh width of the DM which is $(\Delta\lambda')_{DM} = (\Delta\varphi')_{DM} = 0.125^\circ$ defining an area of about 14×14 km^2. The primes refer

to a rotated latitude-longitude coordinate system (λ', φ') with its rotated north pole at a location $\lambda = 170.0^\circ W$, $\varphi = 32.5^\circ N$ given in geographical coordinates.The same rotated system is valid for the LM (cf. Doms et al. 1999, Chapter 4; Schättler and Doms 1998, p. 27), and so for the LLM. The DM-gridpoint is positioned exactly in the centre of the Lindenberg gridbox. It coincides with an LM-gridpoint and an LLM-gridpoint as well. In terms of a C-grid valid for DM, LM and LLM this gridpoint is a so called 'mass'-point, where almost all model variables and parameters but the horizontal wind components are placed. (We tacitly make the agreement that all gridpoints considered are the mass-points of a C-grid where the places of u and v are automatically related to.)

The coordinates of the central gridpoint are given by $\lambda' = 2.5^\circ$ and $\varphi' = -5.25^\circ$, corresponding to $\lambda = 14.0617^\circ W$ and $\varphi = 52.1752^\circ N$. For the transformation $(\lambda', \varphi') \leftrightarrow (\lambda, \varphi)$ we refer to Schrodin (1995). The size of the standard LLM integration area is shown in Fig. 2.7 a,b. It is a square having 145×145 gridpoints. Therefore, the LLM mesh width can be found from $(\Delta\varphi)_{DM}/144 = (\Delta\varphi)_{LLM} = (\Delta\varphi)_{LLM} \simeq 96.53$ m (assuming $a = 6371229$ m for the earth radius and 111.19892 km for a 1°-distance on a great circle). With a gridpoint indexing $i \in [1, 145]$ in west-east direction and $j \in [1, 145]$ in south-north direction, the central point is determined by $(i, j) = (73, 73)$. In the following the coordinates of the four corner points are noted.

LLM domain corners	λ' (°)	ϕ' (°)	λ ($^\circ E$)	ϕ ($^\circ N$)
lower left $(i = 1, j = 1)$	2.4375	- 5.3125	13.9544	52.1165
upper left $(i = 1, j = 145)$	2.4375	- 5.1875	13.9663	52.2413
lower right $(i = 145, j = 1)$	2.5625	- 5.3125	14.1567	52.1091
upper right $(i = 145, j = 145)$	2.5625	- 5.1875	14.1692	52.2339

Besides this standard area another option of integration area has been agreed with the people of the measurement branch, which is the so called 'extended Lindenberg' - area having all local measurement points enclosed and more possibilities of testing the LLM. Compared to the standard area it is extended about 2km to south and north and 4km to north and west. The total is about 20×20 km^2 covered by 199×199 gridpoints. It corresponds to the entire area shown in Fig. 2.7. In order to note at least the relative placement of that 'extended area', the corner points of the 'standard area' are to be noted in terms of the 'extended area' indices $i_{ext} \in [1, 199]$ and $j_{ext} \in [1, 199]$:

$$\begin{aligned} (1,1) &= (37,19)_{ext} \\ (1,145) &= (37,163)_{ext} \\ (145,1) &= (181,19)_{ext} \\ (145,145) &= (181,163)_{ext} \end{aligned}$$

Finally, the location of the corner points of the central LM-gridbox ($\simeq 7 \times 7$ km^2) is given in terms of the 'standard area' gridpoint indices $i \in [1, 145]$ and $j \in [1, 145]$: (37,37), (37,109), (109,37) and (109,109).

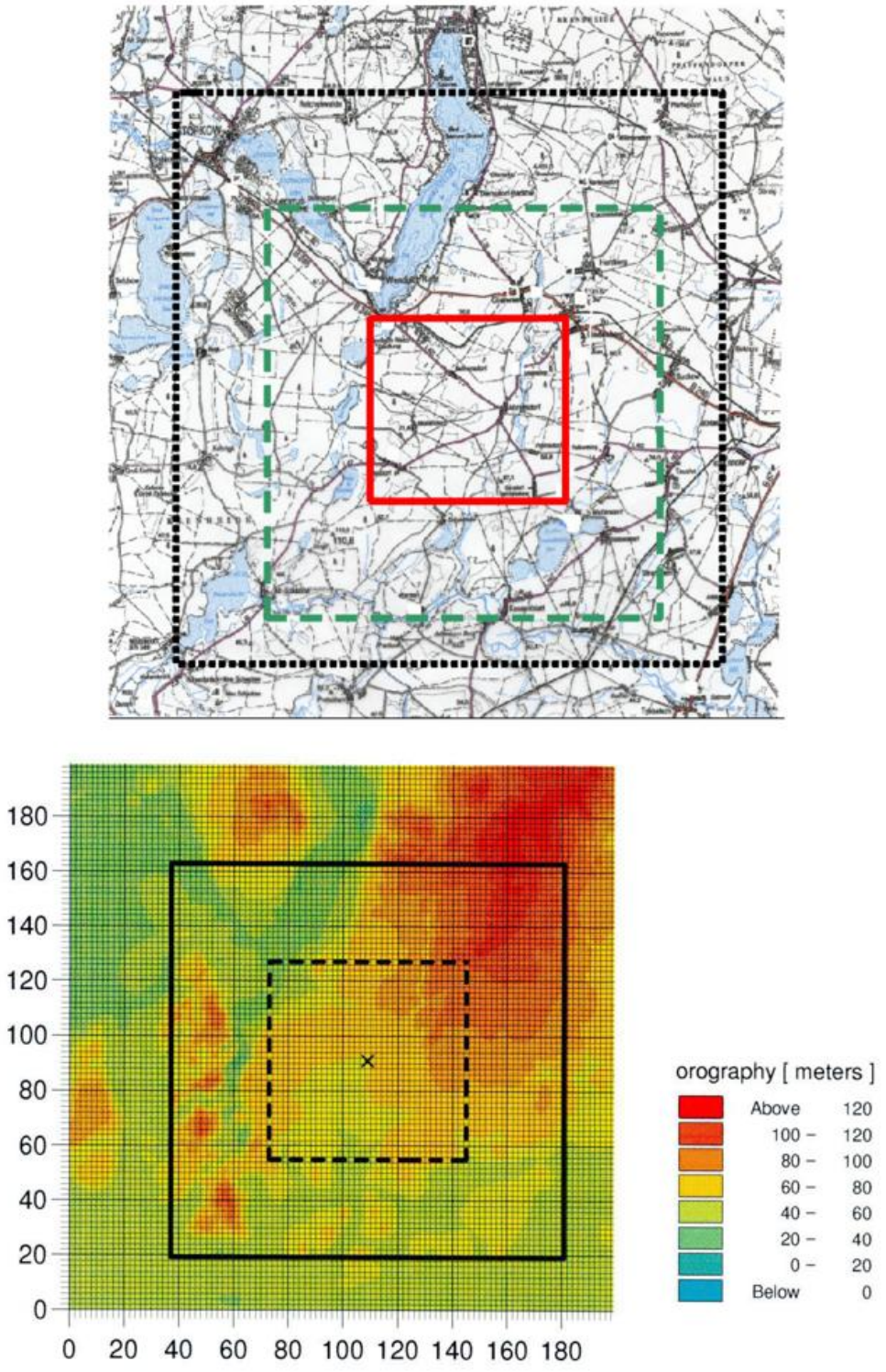


Figure 2.7: Position of the LLM integration area laid over a map of Lindenberg (top) and over a grid net with twice the mesh width and underlaying orography.

Top: Black broken line – boundary of the extended area ($\sim 20 \times 20$ km^2, 199×199 gridpoints). Green dashed line – boundary of standard area ($\sim 14 \times 14$ km^2, 145×145 gridpoints). Red full line – boundary of centered LM grid box ($\sim 7 \times 7$ km^2).

Bottom: Whole area corresponding to the extended area, with standard area (black line) and LM grid box (dashed line) in it. The cross point marks the central LM gridpoint.

3 Parameterization of Subgrid-Scale Turbulence

The parameterization of subgrid-scale (actually subfilter) turbulent processes, also called a subgrid-scale (SGS) model, is of particular meaning for the LES-like LLM. Because such an SGS model was not available from the LM system, we had to do an extra development. For this, a completely three-dimensional flux scheme was necessary to implement instead of only vertical turbulent flux terms as included in the given LM scheme. This part of work was with considerable effort an extension of the original LM code. In a further step, the SGS model itself, which must be written as function of the resolved scales (unaffected by a filter application), seems to be easier for the LLM compared to LM. Namely, in the latter the parameterization embraces more complex processes than in case of the LLM. The SGS model we decided to use is a prognostic turbulent kinetic energy (TKE) scheme taking into account the three space directions. This is documented in the following. In a first step, the SGS model is described, while in the following step the numerical incorporation is exactly demonstrated for the first time.

3.1 The SGS - TKE Model

We start from the LLM equation set (1)-(3), (5), (6) (see Section 2.1), which is rewritten here, emphasizing the turbulent flux terms:

$$\begin{aligned}
\frac{\partial u}{\partial t} &= \ldots - \frac{1}{\rho}\left(\nabla \cdot \underline{\underline{F}}\right) \cdot \underline{e}_1 \\
\frac{\partial v}{\partial t} &= \ldots - \frac{1}{\rho}\left(\nabla \cdot \underline{\underline{F}}\right) \cdot \underline{e}_2 \\
\frac{\partial w}{\partial t} &= \ldots - \frac{1}{\rho}\left(\nabla \cdot \underline{\underline{F}}\right) \cdot \underline{e}_3 \\
\frac{\partial T}{\partial t} &= \ldots - \frac{1}{\rho c_{pd}} \nabla \cdot \underline{H} \\
\frac{\partial q^k}{\partial t} &= \ldots - \frac{1}{\rho} \nabla \cdot \underline{F}_{q^k}
\end{aligned}$$

For the following the three-dimensionality of those terms is completely retained. $\underline{\underline{F}}$ denotes the turbulent momentum flux tensor with its 6 independent components τ_{ij} $(i, j = 1,2,3)$, and $\underline{H}$ and $\underline{F}_{q^k}$ are the vector fluxes of heat and water components. From these fragments of equations we change, as often usual, to the more convenient tensor notation:

$$\frac{\partial u_i}{\partial t} = \cdots - \frac{1}{\rho} \frac{\partial \tau_{ij}}{\partial x_j}\,, \tag{22}$$

$$\frac{\partial X^n}{\partial t} = \cdots - \frac{1}{\rho} \frac{\partial Y_j^n}{\partial x_j}\,, \tag{23}$$

where there is $(u_i) = (u, v, w)$, $(\tau_{ij}) = \underline{\underline{F}}$, $(X^1, X^2) = (T, q^k)$, $(Y_j^1) = \underline{H}$ and $(Y_j^1) = \underline{F}_{q^k}$ for $i = 1,\ 2,\ 3$ and $j = 1,\ 2,\ 3$. The fluxes are specified by use of a first-order closure assumption. It means that the fluxes are set proportional to the local gradient multiplied by a local turbulence coefficient:

$$\tau_{ij} = -\rho K_m \left(\frac{\partial u_i}{\partial x_j} + \frac{\partial u_j}{\partial x_i} \right)\,, \tag{24}$$

$$Y_j^1 = -c_p \pi \rho K_h \frac{\partial \Theta_v}{\partial x_j}, \qquad Y_j^2 = -\rho K_h \frac{\partial q^k}{\partial x_j}. \tag{25}$$

For this specification we refer, for instance, to Mason (1994), and Mason and Brown (1999). There, a distinction is drawn between a turbulence coefficient for momentum, K_m, and heat, K_h, respectively. Here, ρ is density, Θ_v denotes virtual potential temperature and π is the Exner function. The SGS-TKE model is determined by specifying the turbulence coefficients after Prandtl and Kolmogorov:

$$K_m = \phi_m \Lambda \sqrt{\overline{e}}, \qquad K_h = \phi_h \Lambda \sqrt{\overline{e}}. \tag{26}$$

Apart from having still undetermined factors ϕ_m, ϕ_h, that $K_{m,h}$-specification needs the knowledge of turbulent kinetic energy, $\overline{e}$, and some assumption, how to set the turbulence length scale Λ. In order to come to a closure of the system, we need a relation/equation, which allows the calculation of TKE from the resolved/filtered fluid regime. For that purpose we invoke the prognostic TKE-equation which may be written

$$\frac{\partial \overline{e}}{\partial t} + u_j \frac{\partial \overline{e}}{\partial x_j} = \delta_{i3} \frac{g}{\overline{\Theta}_v} (\overline{u_i' \Theta_v'}) - \overline{u_i' u_j'} \frac{\partial \overline{u_i}}{\partial x_j} - \frac{\partial (\overline{u_j' e})}{\partial x_j} - \frac{1}{\rho} \frac{\partial (\overline{u_i' p'})}{\partial x_i} - \varepsilon. \tag{27}$$

Here, the TKE is defined by

$$\overline{e} = \frac{1}{2} (\overline{u_i' u_i'}) \tag{28}$$

and $e = u_i' u_i'/2$. We quote Stull (1988, p. 152) for the derivation of that TKE-equation (27). The physical meaning of all terms, and so the definition of variables in it, can also be found in Stull's bible of turbulence quoted. It is important to note here that the derivation of (27) implies the Boussinesq-approximation, the hypothesis of Reynolds averaging and the assumption of incompressibility and shallow convection. This is not strictly in agreement with the more general LM/LLM-equations and, we may think that it does not need so. Here, we remind of experiences that errors in the parameterization of SGS processes in case of an LLM-like resolution do not influence the resolved scales in a significant manner. In view of determining K_m and K_h according to (26a,b), one needs in a further step suitable parameterizations in (27). Here, the 'flux-gradient' specification, like (24) and (25), is also used,

$$\overline{u_i' u_j'} = -K_m \left(\frac{\partial u_j}{\partial x_i} + \frac{\partial u_i}{\partial x_j} \right) \tag{29}$$

$$\overline{u_i' \Theta_v'} = -K_h \frac{\partial \Theta_v}{\partial x_i} \tag{30}$$

in order to make the buoyant production term and the shear production term applicable. The term describing the turbulent transport of TKE and the pressure correlation term are collected,

$$\frac{\partial (\overline{u_j' e})}{\partial x_j} + \frac{1}{\rho} \frac{\partial (\overline{u_j' p'})}{\partial x_j} \simeq \frac{\partial}{\partial x_j} \left(\overline{u_j' e + \frac{u_j' p'}{\rho}} \right), \tag{31}$$

in order to parameterize the resulting flux also in accordance with a gradient specification:

$$\overline{u_j' \left(e + \frac{p'}{\rho} \right)} = -2 K_m \frac{\partial \overline{e}}{\partial x_j}. \tag{32}$$

For the latter we refer to Stevens et al. (1999). Finally, as usual the dissipation term is set equal to

$$\varepsilon \;=\; c_\varepsilon \frac{(\overline{e})^{3/2}}{\Lambda}\,. \tag{33}$$

The length scale Λ will be defined later. The value of c_ε is assumed different in literature. Here, we adopt $c_\varepsilon = 0.93$ (Stevens et al. 1999). In that way the following TKE-equation is found to be useful for our purpose:

$$\frac{\partial \overline{e}}{\partial t} + u_j \frac{\partial \overline{e}}{\partial x_j} \;=\; -K_h N^2 + K_m S^2 + 2\frac{\partial}{\partial x_j}\left(K_m \frac{\partial \overline{e}}{\partial x_j}\right) - c_\varepsilon \frac{(\overline{e})^{3/2}}{\Lambda}\,. \tag{34}$$

(The tacit change of denotation for the resolved/filtered variables must be noted, that is $\overline{u}_j = u_j$, $\overline{\Theta}_v = \Theta_v$, etc.) There we have introduced the Brunt-Väisälä frequency squared

$$N^2 \;=\; \frac{g}{\Theta_v}\frac{\partial \Theta_v}{\partial z}\,, \tag{35}$$

and the definition

$$S^2 \;=\; 2S_{ij}S_{ij} \;=\; \left(\frac{\partial u_i}{\partial x_j} + \frac{\partial u_j}{\partial x_i}\right)\frac{\partial u_i}{\partial x_j} \;=\; \frac{1}{2}\left(\frac{\partial u_i}{\partial x_j} + \frac{\partial u_j}{\partial x_i}\right)^2\,, \tag{36}$$

where S_{ij} is the strain tensor and S^2 the deformation squared.

By solving the TKE from the prognostic equation (34), we would be able to determine K_m, K_h according to (26a,b), provided the coefficients ϕ_m and ϕ_h are known. Therefore, we think about these factors how to determine them as some reasonable functions of stability and having then a stability-dependent Prandtl-number

$$Pr \;=\; \frac{K_m}{K_h} \;=\; \frac{\phi_m}{\phi_h}\,. \tag{37}$$

In order to come to a reasonable solution, we start as an interlude from another more simple SGS-model, that is the extension of the Smagorinsky (1963) model presented by Brown et al. (1994) (cf. also Mason and Brown 1999). We call it, in brief, a Smagorinsky-SGS-model. It is characterized by the following K_m-, K_h-specification:

$$K_m \;=\; \lambda^2 S F_m(Ri)\,, \quad K_h \;=\; \lambda^2 S F_h(Ri)\,. \tag{38}$$

The stability dependence is imposed through the functions F_m and F_h. These functions are based on observations which are loosely the 'Kansas data'. S is defined in (36), and λ is the length scale in the Smagorinsky model. That length scale may be rewritten

$$\lambda \;=\; c_s \Lambda \tag{39}$$

defining the constant c_s. We assume here $c_s = 0.25$. Λ is a length scale closely related to the grid spacing as a measure of the numerical resolution envisaged and may be identical with the length scale Λ in the Prandtl-Kolmogorov specification (26). Following Brown et al. (1994) the stability functions F_m and F_h are specified as separate functions for statically unstable conditions and statically stable conditions, and it is ensured that these functions match in value (not in gradient) at $Ri = 0$. Anticipating our three-dimensional TKE-model, the local Richardson number may be defined as

$$Ri \;=\; \frac{N^2}{S^2} \tag{40}$$

with reference to (35) and (36).

For the unstable case, $Ri < 0$, one assumes

$$F_m = (1 - 16Ri)^{1/2}\,, \quad F_h = (1 - 40Ri)^{1/2} Pr_N^{-1}\,, \tag{41}$$

while in case of stability, $0 \leq Ri \leq Ri_c$,

$$F_m = (1 - Ri/Ri_c)^4\,, \quad F_h = (1 - Ri/Ri_c)^4(1 - 1.2Ri) Pr_N^{-1} \tag{42}$$

is used. The critical value of Ri is taken $Ri_c = 0.25$. The value $Pr_N^{-1} = 0.7$ which is the Prandtl number in neutral condition is chosen consistent with the Kansas data and LES experiments. In order to specify the length scale Λ we deviate from Brown et al. (1994) and introduce

$$\Lambda = (\Delta x \Delta y \Delta z)^{1/3} f(a_1, a_2)\,. \tag{43}$$

The function $f(a_1, a_2)$ serves as a corrective factor in case of an anisotropic grid and has been proposed by Scotti et al. (1993, 1997). If $\Delta_1, \Delta_2, \Delta_3$ are the dimensions of a grid box, where we can always assume $\Delta_1 \leq \Delta_2 \leq \Delta_3$, the two aspect ratios of the given grid are defined as

$$a_1 = \frac{\Delta_1}{\Delta_3}\,, \quad a_2 = \frac{\Delta_2}{\Delta_3}\,. \tag{44}$$

For the present LLM grid configuration (cf. Section 2.2) the relevant aspect ratio $\Delta z/\Delta$ (with $\Delta x = \Delta y = \Delta$ and $(\Delta x \Delta y \Delta z)^{1/3} = \Delta^{2/3}\Delta z^{1/3}$) ranges from 1/25 to 3/2. Thus, we meet with a 'pancake-like' grid ($\Delta z/\Delta \leq 1$) and a 'pencil-like' grid ($\Delta z/\Delta > 1$). Scotti et al. (1993) have shown on the base of theoretical arguments for isotropic turbulence that there exists an estimate for the grid anisotropy function as follows

$$f(a_1, a_2) \simeq \cosh\left[\frac{4}{27}(\ln^2 a_1 - \ln a_1 \ln a_2 + \ln^2 a_2)\right]^{1/2}\,. \tag{45}$$

In case of $\Delta z/\Delta \leq 1$ ($\Delta_1 = \Delta z, \Delta_2 = \Delta_3 = \Delta$):

$$\begin{aligned} a_1 &= \Delta z/\Delta \leq 1 \quad a_2 = 1 \\ f(a_1, a_2) &= f(\Delta z/\Delta) = \cosh(0.3849 \ln[\Delta z/\Delta])\,. \end{aligned} \tag{46}$$

In case of $\Delta z/\Delta > 1$ ($\Delta_1 = \Delta_2 = \Delta, \Delta_3 = \Delta z$):

$$\begin{aligned} a_1 &= \Delta/\Delta z = a_2 \\ f(a_1, a_2) &= f(\Delta/\Delta z) = \cosh(0.3849 \ln[\Delta/\Delta z])\,. \end{aligned} \tag{47}$$

In case of grid isotropy we have $f = 1$, of course. By now, our Smagorinsky SGS model is sufficiently described. In passing, it was the first SGS model we had incorporated in the LLM scheme. Here it serves as a special case of the general TKE model, in order to deduce the specifications of ϕ_m and ϕ_h in (26) from that. In this line, we recall the Smagorinsky model to be the equilibrium limit of the prognostic TKE equation (34). It can actually be shown the equivalence of the K_m-, K_h-specifications (38) and (26), provided that the equilibrium TKE equation

$$K_m S^2 - K_h N^2 - c_\varepsilon \frac{(\overline{e})^{3/2}}{\Lambda} = 0 \tag{48}$$

is valid. From that special case the equality

$$K_m = \phi_m \Lambda \sqrt{\overline{e}} = c_s^2 \Lambda^2 S F_m(Ri)\,, \quad K_h = \phi_h \Lambda \sqrt{\overline{e}} = c_s^2 \Lambda^2 S F_h(Ri)\,, \tag{49}$$

is used to find the TKE

$$\overline{e} = \phi_m c_\varepsilon^{-1} \Lambda^2 S^2 \left(1 - Pr^{-1} Ri\right)\,, \tag{50}$$

which is, therefore associated to the Smagorinsky model. The Prandtl-number is

$$Pr = \frac{\phi_m}{\phi_h} = \frac{F_m}{F_h}\,. \tag{51}$$

With $-\infty \leq Ri \leq Ri_c = 0.25$ and $Pr = Pr_N = 0.7$ for $Ri = 0$ it follows the stability dependence of Pr in a range

$$0.4427 \leq Pr \leq 1 \tag{52}$$

in accordance with the Kansas data-fitted stability functions F_m and F_h. By inserting (50) in (49), an expression for ϕ_m is then easily found:

$$\phi_m = c_s^{4/3} c_\varepsilon^{1/3} F_m^{2/3}(Ri) \left(1 - Pr^{-1} Ri\right)^{-1/3}\,. \tag{53}$$

That result is now used to be valid in specifying ϕ_m in (26) for the general problem to solve the prognostic TKE equation (34). ϕ_h follows by use of (51) from the known functions F_m and F_h. The grid scale length is found to be

$$\Lambda = \Delta^{2/3} \Delta z^{1/3} \begin{cases} \cosh[0.3849 \ln(\Delta z/\Delta)]\,, & \Delta z/\Delta \leq 1\,, \\ \cosh[0.3849 \ln(\Delta/\Delta z)]\,, & \Delta/\Delta z < 1\,. \end{cases} \tag{54}$$

3.2 Numerical Treatment

We focus our attention first on the incorporation of the three-dimensional 'divergence of turbulent flux'-terms in the given numerical LM-scheme. For this reason, we write down the discretized form of those terms as parts of the momentum, heat and moisture transport equations. For the momentum equations we have

$$\left(\frac{\partial u}{\partial t}\right)^{(n)} = \cdots - \frac{1}{\overline{\rho^{(n)}}^{\lambda} a \cos\varphi} \left(\delta_\lambda \tau_{11} + \cos\varphi \delta_\varphi \tau_{12}\right)^{(n,n-1)} + \frac{g}{\overline{\sqrt{\gamma}}^{\lambda}} \overline{\left(\frac{\rho_0}{\rho^{(n)}}\right)}^{\lambda} \left(\delta_\zeta \tau_{13}\right)^{(n-1,n,n+1)} \tag{55}$$

$$\left(\frac{\partial v}{\partial t}\right)^{(n)} = \cdots - \frac{1}{\overline{\rho^{(n)}}^{\varphi} a \cos\varphi} \left(\delta_\lambda \tau_{12} + \cos\varphi \delta_\varphi \tau_{22}\right)^{(n,n-1)} + \frac{g}{\overline{\sqrt{\gamma}}^{\varphi}} \overline{\left(\frac{\rho_0}{\rho^{(n)}}\right)}^{\varphi} \left(\delta_\zeta \tau_{23}\right)^{(n-1,n,n+1)} \tag{56}$$

$$\left(\frac{\partial w}{\partial t}\right)^{(n)} = \cdots - \frac{1}{\overline{\rho^{(n)}}^{\zeta} a \cos\varphi} \left(\delta_\lambda \tau_{13} + \cos\varphi \delta_\varphi \tau_{23}\right)^{(n,n-1)} + \frac{g}{\overline{\sqrt{\gamma}}^{\zeta}} \overline{\left(\frac{\rho_0}{\rho^{(n)}}\right)}^{\zeta} \left(\delta_\zeta \tau_{33}\right)^{(n-1,n,n+1)} \tag{57}$$

Here, the slow tendencies are approximated as

$$\left(\frac{\partial\psi}{\partial t}\right)^{(n)} = \frac{\psi^{(n+1)} - \psi^{(n-1)}}{2\Delta t}\,, \quad \psi = (u, v, w, T, q^k)\,. \tag{58}$$

Δt is the 'large' timestep. For the 6 turbulent stress components we assume

$$\tau_{11} = -\frac{\left(\rho\overline{K}_m^{\varphi}\right)^{(n)}}{a\cos\varphi} 2\delta_\lambda u^{(n-1)} \tag{59}$$

$$\tau_{12} = -\frac{\left(\overline{\rho K}_m^{\lambda,\varphi}\right)^{(n)}}{a\cos\varphi}\left(\delta_\lambda v^{(n-1)} + \cos\varphi\delta_\varphi u\right)^{(n-1)} \tag{60}$$

$$\tau_{13} = -\frac{\left(\overline{\rho K}_m^{\lambda}\right)^{(n)}}{a\cos\varphi}\delta_\lambda w^{(n-1)} + g\overline{\left(\overline{\left[\frac{\rho_0\rho^{(n)}}{\sqrt{\gamma}}\right]}^{\zeta} K_m^{(n)}\right)}^{\lambda}\left(\beta_d^+\delta_\zeta u^{(n+1)} + \beta_d^-\delta_\zeta u^{(n-1)}\right) \tag{61}$$

$$\tau_{23} = -\frac{\left(\rho\overline{K}_m^{\varphi}\right)^{(n)}}{a}\delta_\varphi w^{(n-1)} + g\overline{\left(\overline{\left[\frac{\rho_0\rho^{(n)}}{\sqrt{\gamma}}\right]}^{\zeta} K_m^{(n)}\right)}^{\varphi}\left(\beta_d^+\delta_\zeta v^{(n+1)} + \beta_d^-\delta_\zeta v^{(n-1)}\right) \tag{62}$$

$$\tau_{22} = -\frac{\left(\rho\overline{K}_m^{\zeta}\right)^{(n)}}{a} 2\delta_\varphi v^{(n-1)} \tag{63}$$

$$\tau_{33} = g\overline{\left(\overline{\left[\frac{\rho_0\rho^{(n)}}{\sqrt{\gamma}}\right]}^{\zeta} K_m^{(n)}\right)}^{\zeta} 2\left(\overline{\beta_d^+}^{\zeta}\delta_\zeta w^{(n+1)} + \overline{\beta_d^-}^{\zeta}\delta_\zeta w^{(n-1)}\right) \tag{64}$$

We have strictly adopted here and in the following formulae all the rules and definitions of differencing and averaging operators applied in the LM numerics as documented in the work of Doms and Schättler (1999). In a similar way the turbulent fluxes of sensible heat and moisture are considered in the following approximations.

$$\left(\frac{\partial T}{\partial t}\right)^{(n)} = \cdots - \frac{1}{\rho^{(n)} a\cos\varphi}\left(\delta_\lambda h_1 + \cos\varphi\delta_\varphi h_2\right)^{(n,n-1)} + \frac{g}{\sqrt{\gamma}}\left(\frac{\rho_0}{\rho^{(n)}}\right)\left(\delta_\zeta h_3\right)^{(n-1,n,n+1)} \tag{65}$$

$$h_1 = -\frac{\left(\overline{\pi\rho K}_h^{\lambda}\right)^{(n)}}{a\cos\varphi}\delta_\lambda\left(T/\pi\right)^{(n-1)} \tag{66}$$

$$h_2 = -\frac{\left(\overline{\pi\rho K}_h^{\varphi}\right)^{(n)}}{a}\delta_\varphi\left(T/\pi\right)^{(n-1)} \tag{67}$$

$$h_3 = g\left(\overline{\left[\frac{\pi\rho_0\rho^{(n)}}{\sqrt{\gamma}}\right]}^{\zeta} K_h^{(n)}\right)\left(\beta_d^+\delta_\zeta(T/\pi)^{(n+1)} + \beta_d^-\delta_\zeta(T/\pi)^{(n-1)}\right) \tag{68}$$

$$\left(\frac{\partial q^k}{\partial t}\right)^{(n)} = \cdots - \frac{1}{\rho^{(n)} a\cos\varphi}\left(\delta_\lambda F_1^k + \cos\varphi\delta_\varphi F_2^k\right)^{(n,n-1)} + \frac{g}{\sqrt{\gamma}}\left(\frac{\rho_0}{\rho^{(n)}}\right)\left(\delta_\zeta F_3^k\right)^{(n-1,n,n+1)} \tag{69}$$

$$F_1^k = -\frac{\left(\overline{\rho K}_h^{\lambda}\right)^{(n)}}{a\cos\varphi}\delta_\lambda(q^k)^{(n-1)} \tag{70}$$

$$F_2^k = -\frac{\left(\overline{\rho K}_h^{\varphi}\right)^{(n)}}{a}\delta_\varphi(q^k)^{(n-1)} \tag{71}$$

$$F_3^k = g\left(\overline{\left[\frac{\rho_0\rho^{(n)}}{\sqrt{\gamma}}\right]}^{\zeta} K_h^{(n)}\right)\left(\beta_d^+\delta_\zeta(q^k)^{(n+1)} + \beta_d^-\delta_\zeta(q^k)^{(n-1)}\right) \tag{72}$$

In these terms of interest, metrical simplifications are implied, that is, metrical terms both related to spherical coordinates and the generalized, terrain-following vertical coordinate are dropped. As can be seen, all horizontal turbulent diffusion terms are treated by forward-in-time differences, and so those terms of vertical momentum fluxes arising from the consideration of horizontal inhomogeneities. The rest of vertical diffusion terms is treated partially implicit by a Crank-Nicholson scheme. This leads together with the vertical advection terms to a tridiagonal vertical structure equation to be solved by a Gaussian elimination procedure as provided from the LM code. In case of the LLM the given method has also been applied due to the τ_{33}-term in the w-equation (57).

On this level the numerical treatment considered is independent of any specified SGS model. With the preparations shown the numerics of the SGS-TKE model must now be put forward. Therefore, we start from the TKE equation (34), which is here rewritten in spherical coordinates neglecting metrical terms and by use of the LM-specific vertical coordinate. We have instead of (34)

$$\begin{aligned}\frac{\partial\overline{e}}{\partial t} = & -\frac{1}{a\cos\varphi}\left(u\frac{\partial\overline{e}}{\partial\lambda} + v\cos\varphi\frac{\partial\overline{e}}{\partial\varphi}\right) - \dot{\zeta}\frac{\partial\overline{e}}{\partial\zeta} - K_h N^2 + K_m S^2 - c_\varepsilon\frac{(\overline{e})^{3/2}}{\Lambda} \\ & + \frac{1}{a\cos\varphi}\frac{\partial}{\partial\lambda}\left(2K_m\frac{\partial\overline{e}}{a\cos\varphi\partial\lambda}\right) + \frac{1}{a}\frac{\partial}{\partial\varphi}\left(2K_m\frac{\partial\overline{e}}{a\partial\varphi}\right) \\ & + \frac{g\rho_0}{\sqrt{\gamma}}\frac{\partial}{\partial\zeta}\left(\frac{g\rho_0}{\sqrt{\gamma}}2K_m\frac{\partial\overline{e}}{\partial\zeta}\right),\end{aligned} \tag{73}$$

where

$$N^2 = \frac{g}{\Theta_v}\frac{\partial\Theta_v}{\partial z}, \tag{74}$$

and

$$\begin{aligned}S^2 = & 2\left[\left(\frac{\partial u}{a\cos\varphi\partial\lambda}\right)^2 + \left(\frac{\partial v}{a\partial\varphi}\right)^2 + \left(\frac{g\rho_0}{\sqrt{\gamma}}\frac{\partial w}{\partial\zeta}\right)^2\right] \\ & + \left(\frac{\partial u}{a\partial\varphi} + \frac{\partial v}{a\cos\varphi\partial\lambda}\right)^2 + \left(\frac{\partial w}{a\cos\varphi\partial\lambda} - \frac{g\rho_0}{\sqrt{\gamma}}\frac{\partial u}{\partial\zeta}\right)^2 \\ & + \left(\frac{\partial w}{a\partial\varphi} - \frac{g\rho_0}{\sqrt{\gamma}}\frac{\partial v}{\partial\zeta}\right)^2.\end{aligned} \tag{75}$$

Next, the differencing in space and time must be carried out. This has to be made also by strict adaptation to the LM numerics. In detail, the C-grid in the horizontal and the Lorenz-grid in the vertical is mandatory to be used inclusively the appropriate differencing and averaging. Concerning the time difference scheme a 'mixed' scheme is applied: horizontal advection is approximated by a leap-frog scheme, for vertical advection plus vertical diffusion

a partially implicit Crank-Nicholson scheme is applied, and horizontal diffusion as well as source/sink-terms like shear production, buoyant production/consumption, dissipation are treated by a time-forward scheme. In effect, by use of a Gaussian elimination algorithm a tridiagonal form for solving the slow-mode regime of the LLM will be found. The resulting $\overline{e}^{(n+1)}$ is then available to specify K_m and K_h. Here we skip the rather lengthy derivation of that tridiagonal form from the discretized TKE-equation. It may suffice to write down the relevant result. In order to support the following notation of differencing, averaging and the definition of the placement of variables on different gridpoints we refer to Figure 3.1 and Figure 3.2.

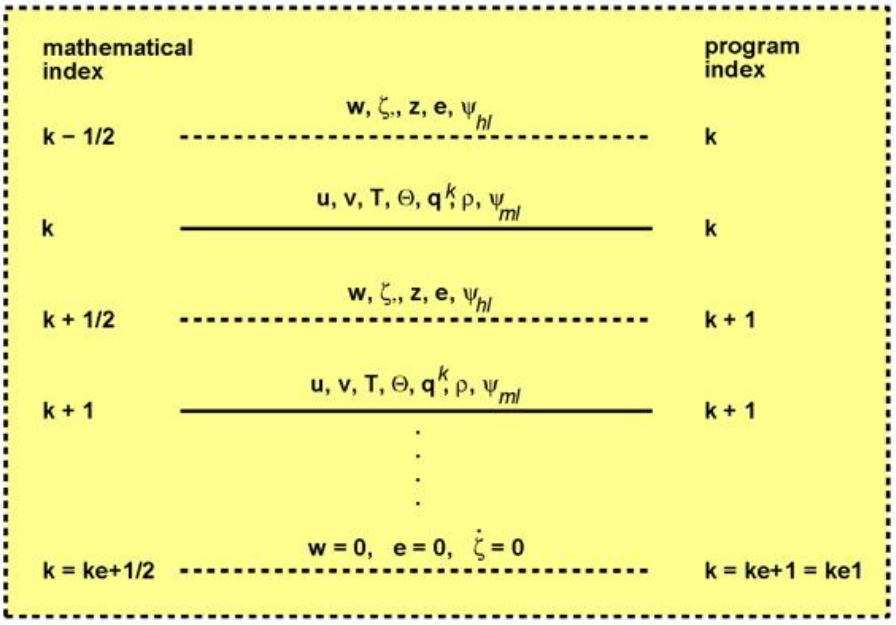


Figure 3.1: Vertical grid scheme (Lorenz-grid) with placement of variables at half-levels (dashed lines) and main levels (black lines). Further half-level variables (ψ_{hl}) and main-level variables (ψ_{ml}) are:
$\psi_{hl} = (\tau_{13}, \tau_{23}, h_3, F_3, K_m, K_h, S, N^2, Ri, \beta_v^{+,-}, \beta_d^{+,-})$,
$\psi_{ml} = (\tau_{11}, \tau_{12}, \tau_{22}, \tau_{33}, h_1, h_2, F_1, F_2, \sqrt{\gamma}, p_0, \rho_0)$.

The tridiagonal structural equation for determining $\overline{e}^{(n+1)}$, which is TKE at vertical half-level k (in accordance with program code indexing) and time level $n+1$, may be written

$$\begin{aligned} B_2\overline{e}_2^{(n+1)} + C_2\overline{e}_3^{(n+1)} &= D_2^{(n,n-1)} \\ A_k\overline{e}_{k-1}^{(n+1)} + B_k\overline{e}_k^{(n+1)} + C_k\overline{e}_{k+1}^{(n+1)} &= D_k^{(n,n-1)} \quad (k \in [3, ke-1]) \\ A_{ke}\overline{e}_{ke-1}^{(n+1)} + B_{ke}\overline{e}_{ke}^{(n+1)} &= D_{ke}^{(n,n-1)} \end{aligned} \tag{76}$$

The functions $D_k^{(n,n-1)}$ for $k \in [2, ke]$ in (76) are known. They contain only variables at the present and previous time level. The same is valid for the coefficients A_k, B_k, C_k. By use of the Gaussian elimination procedure the $\overline{e}_k^{(n+1)}$ follow by assuming the boundary condition $\overline{e}_1 = \overline{e}_{ke1} = 0$. For the coefficients A_k, B_k, C_k and D_k we find:

$$
\begin{aligned}
A_k &= \beta_v^+ A_k^v + \overline{\beta_d^+}^{\,\zeta} A_k^d \\
A_k^v &= -\frac{(\sqrt{\gamma})_k \overline{(W^c)}^{\zeta}_{k-1}}{\overline{(\sqrt{\gamma})}^{\zeta}_k \left((\sqrt{\gamma})_k + (\sqrt{\gamma})_{k-1}\right)}, \quad A_k^d = -\frac{2g^2 \overline{(\rho_o)}^{\zeta}_k}{\overline{(\sqrt{\gamma})}^{\zeta}_k} \overline{\left(\frac{\overline{(\rho_o)}^{\zeta}}{\overline{(\sqrt{\gamma})}^{\zeta}} K_m^{(n)} \right)}^{\zeta}_{k-1} \\
B_k &= \frac{1}{2\Delta t} - A_k - C_k \\
C_k &= \beta_v^+ C_k^v + \overline{\beta_d^+}^{\,\zeta} C_k^d \qquad (77) \\
C_k^v &= \frac{(\sqrt{\gamma})_{k-1} \overline{(W^c)}^{\zeta}_k}{\overline{(\sqrt{\gamma})}^{\zeta}_k \left((\sqrt{\gamma})_k + (\sqrt{\gamma})_{k-1}\right)}, \quad C_k^d = -\frac{2g^2 \overline{(\rho_o)}^{\zeta}_k}{\overline{(\sqrt{\gamma})}^{\zeta}_k} \overline{\left(\frac{\overline{(\rho_o)}^{\zeta}}{\overline{(\sqrt{\gamma})}^{\zeta}} K_m^{(n)} \right)}^{\zeta}_{k} \\
D_k &= \frac{1}{2\Delta t} \overline{e}_k^{(n-1)} + \Sigma_k^{(n,n-1)} + (\beta_v^- A_k^v + \overline{\beta_d^-}^{\,\zeta} A_k^d)(\overline{e}_k^{(n-1)} - \overline{e}_{k-1}^{(n-1)}) \\
&\quad - (\beta_v^- C_k^v + \overline{\beta_d^-}^{\,\zeta} C_k^d)(\overline{e}_{k+1}^{(n-1)} - \overline{e}_k^{(n-1)})
\end{aligned}
$$

with the further definition

$$
W_k^c = \overline{(\sqrt{\gamma})}^{\zeta}_k \dot{\zeta}_k \,. \qquad (78)
$$

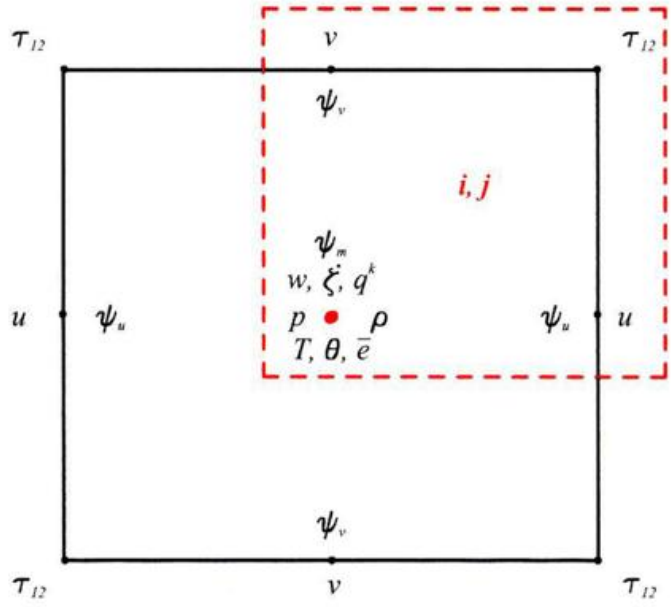


Figure 3.2: Position of variables in the horizontal grid (C-grid). Dashed-line square embraces a cluster of variables having the same horizontal program index pair i, j. Further variables at mass point (ψ_m), u-point (ψ_u) and v-point (ψ_v) are:
$\psi_m = (\tau_{11}, \tau_{22}, \tau_{33}, h_3, F_3, K_m, K_h, S, N^2, Ri, \sqrt{\gamma}, p_0, \rho_0)$,
$\psi_u = (\tau_{13}, h_1, F_1)$, $\psi_v = (\tau_{23}, h_2, F_2)$.

The auxiliary variable $\Sigma_k^{(n,n-1)}$, emerging in the expression for D_k, implies horizontal advection and turbulent horizontal diffusion of TKE as well as source/sink-terms as follows:

$$\begin{aligned}
\Sigma_k^{(n,n-1)} &= -\frac{1}{\overline{\sqrt{\gamma}}^{\zeta} a\cos\varphi}\left[\left(\overline{\overline{\sqrt{\gamma}}^{\zeta} u}^{\zeta}\,\delta_\lambda \overline{e}\right)^{\lambda} + \left(\overline{\overline{\sqrt{\gamma}}^{\zeta} v}^{\zeta}\cos\varphi\,\delta_\varphi \overline{e}\right)^{\varphi}\right] \\
&\quad + \frac{1}{a\cos\varphi}\delta_\lambda\left(2(\overline{K_m}^{\lambda})^{(n)}\frac{\delta_\lambda(\overline{e})^{(n-1)}}{a\cos\varphi}\right) + \frac{1}{a}\delta_\varphi\left(2(\overline{K_m}^{\varphi})^{(n)}\frac{\delta_\varphi(\overline{e})^{(n-1)}}{a}\right) \\
&\quad - K_h^{(n)}(N^2)^{(n-1)} + K_m^{(n)}(S^2)^{(n-1)} - c_\varepsilon\frac{((\overline{e})^{3/2})^{(n-1)}}{\Lambda}\,.
\end{aligned} \tag{79}$$

To complete the description of the tridiagonal form, we need finally the difference approximation of S^2 and Ri. For the deformation squared we have

$$\begin{aligned}
S^2 &= 2\left[\left(\frac{\overline{\delta_\lambda u}^{\zeta}}{a\cos\varphi}\right)^2 + \left(\frac{\overline{\delta_\varphi v}^{\zeta}}{a}\right)^2 + \left(\frac{g\overline{\rho_0}^{\zeta}}{\overline{\sqrt{\gamma}}^{\zeta}}\delta_{2\zeta} w\right)^2\right] \\
&\quad + \left(\frac{\delta_\varphi \overline{\overline{u}^{\lambda,\varphi}}^{\zeta}}{a} + \frac{\partial\overline{\overline{v}^{\lambda,\varphi}}^{\zeta}}{a\cos\varphi}\right)^2 + \left(\frac{\delta_\lambda \overline{w}^{\lambda}}{a\cos\varphi} - \frac{g\overline{\rho_0}^{\zeta}}{\overline{\sqrt{\gamma}}^{\zeta}}\delta_\zeta \overline{u}^{\lambda}\right)^2 \\
&\quad + \left(\frac{\delta_\varphi \overline{w}^{\varphi}}{a} - \frac{g\overline{\rho_0}^{\zeta}}{\overline{\sqrt{\gamma}}^{\zeta}}\delta_\varphi \overline{v}^{\varphi}\right)^2
\end{aligned} \tag{80}$$

and the local Richardson number is written

$$Ri = 2g\frac{(\Theta_{v,k} - \Theta_{v,k-1})\left(\sqrt{\gamma}_{k-1} + \sqrt{\gamma}_k\right)}{(z_{k+1} - z_{k-1})\left(\sqrt{\gamma}_{k-1}\Theta_{v,k} + \sqrt{\gamma}_k\Theta_{v,k-1}\right) S^2} \tag{81}$$

provided $S^2 > S^2_{min} > 0$. The equilibrium case (50) is used to determine an initial value of $\overline{e}_k$. A final remark is made concerning the incorporation of the turbulent surface fluxes. They are determined just as in the LM (cf. Doms and Schättler 1999, Chapter 6). A stability and roughness-length dependent formulation is used, which is based on modified Businger relations. As known, the approach makes use of a drag-law relation

$$F^{\psi}_{sfc} = -\rho\, C^d_{\psi}\,|\vec{v}_h|\,(\psi - \psi_{sfc}) \tag{82}$$

specified for $\psi = (u, v, T, q^k)$. The surface flux F^{ψ}_{sfc} follows then according to (82), provided the drag coefficient is given by a parameterization

$$C^d_{\psi} = \frac{\chi^2}{[\ln(h/z_0)]^2}\, f_\psi(Ri_B, h/z_0) \tag{83}$$

dependent on the bulk Richardson number

$$Ri_B = g\frac{(\Theta - \Theta_{sfc})\,(h - z_0)}{\Theta_{sfc}(u^2 + v^2)} \tag{84}$$

as a measure of stability. With given surface values ψ_{sfc}, Θ_{sfc}, provided from the soil model 'terra', the surface flux will be determined using atmospheric values ψ, Θ and $|\vec{v}_h|$ at the

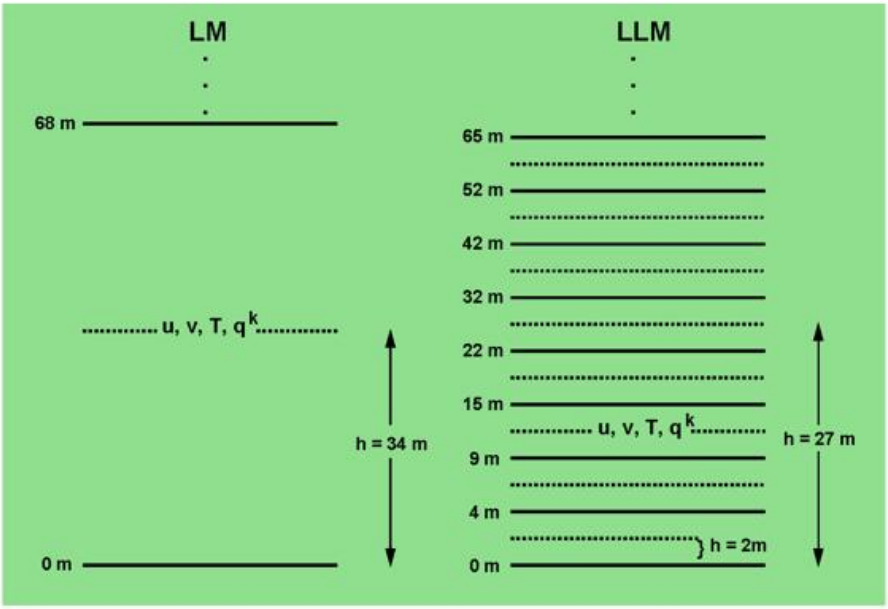


Figure 3.3: Different vertical resolution of the Prandtl-layer in LM (left) and in LLM (right). Further explanation see text.

model altitude h within the Prandtl-layer. In case of the LM this altitude is assumed to be placed at the lowest main-level being $h = 34$ m (Fig 3.3, left). By direct use of that LM-algorithm in case of the LLM the height h would also be positioned at the lowest model main-level, which is only about 2 meters above ground. In order to avoid a value of h too near to the roughness-length z_0, it has been set sufficiently higher than z_0 (Fig 3.3, right). Consequently, some more involved manipulations in the given LM-numerics not mentioned in detail were necessary to be done for that kind of LLM adaptation.

4 External Forcing at the Lateral and Upper Boundary

Since the LLM is thought to be a 'real-world' - LES model with its declared bridge-function in the scope of an observation-simulation conception, it must externally be driven somehow by real-world time-dependent states of the boundary layer atmosphere and the underlying surface. The initial state must also be a realistic one to start the LLM simulation from. While the physical forcing from the underlying surface will be treated in the following Chapter 5, we are dealing here with the atmospheric part of forcing the LLM.

4.1 Method

Before we describe some technical details, how lateral and upper boundary data, and initial data as well, are organized by use of time sequences of measured vertical profiles available, some general remarks about the strategy of an external LLM-driving are necessary. In contrast to 'pure' LES studies the LLM simulations have been planned to cover a wide range of real meteorological weather situations. This needs a more general approach not limited to special cases. This statement does not deny the general virtue of large eddy simulations which by fortunate circumstances can investigate general problems from simplified modelling, e.g. by ignoring the lateral limitation of the integration area. In our case a limited area integration mode must be accepted, and the technique to handle that problem had to be borrowed from the field of NWP. The method of interest has been described in Section 2.3. As explained there, the boundary technique is chosen in such a way that it anticipates the specific problem of application. From the point of view of information content of measured data we meet with a very underestimated problem for providing the LLM with initial and boundary data. In Fig. 4.1 the following argumentation is to be supported. In that manner we are forced to assume only one measured vertical profile for each relevant LLM variable like horizontal wind, temperature and moisture.

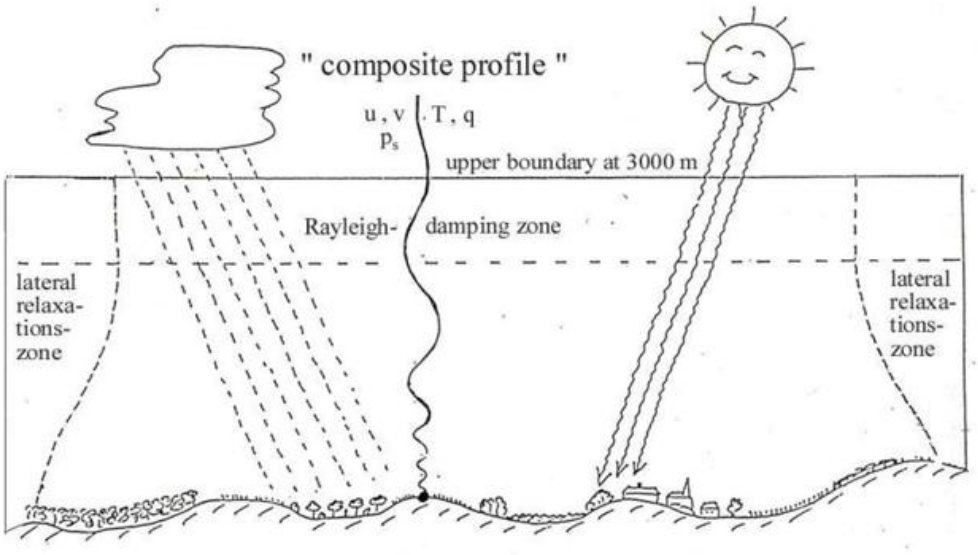


Figure 4.1: A sketch showing how the LLM is externally driven by taking into account a detailed physiographic description of the underlying surface plus surface measurements of precipitation and radiation and by use of a driving composite profile which operates through a vertical and lateral transmission zone.

We call it a 'composite profile' (CP), because it is deduced from vertical profiles of different sounding systems available at and around the MOL (Görsdorf et al. 2000), and it may be available at a time frequency of say, one hour. This CP is assumed to be associated to a distinct location laying in the interior of the LLM integration area. Further, the CP gives the only base of temporally and vertically distributed information for constructing the three-dimensional initial and boundary data due to a quasi-horizontal distribution of that given vertical profiles. How this is carried out will be shown in the next section.

Here some arguments to support this approach will be given. By horizontally distributing the CP we make use of the 'hypothesis of fast local adaptation', provided that the physical forcing from the underlying surface works well (cf. Sections 2.4, 2.5, Chapter 5 and Fig. 4.1). Therefore, the near-surface information of a CP is unsuitable at other places than the original location which is assumed to be assimilated by the LLM very fast and in case of boundary data in a rather short distance from the boundary. The mechanism of dominating near-surface turbulent fluxes, essentially coined by carefully treated lower boundary properties, makes thus the CP-data model-friendly and brings them automatically into a 'ready-to-eat' form. From the point of view of the lateral boundary technique this kind of near-surface adaptation is deliberately supported by reduced boundary weights. Towards higher levels of the LLM the CP information approaches to larger scales and even to scales governing the free atmosphere up to 3 kilometers. Because the essential integration mode of the LLM is given by a non-stationary boundary data forcing, the time-dependent boundary data rely on time series of CPs with an up-dating frequency of 1 hour with a linear time interpolation onto every 2-second timestep.

It is important to note that by use of that CP sequence the LLM perceives relevant large-scale information in an implicit way. That is, changes of the temperature profile imply realistic effects of large scale warm/cold air advection, changes of stability indicating large-

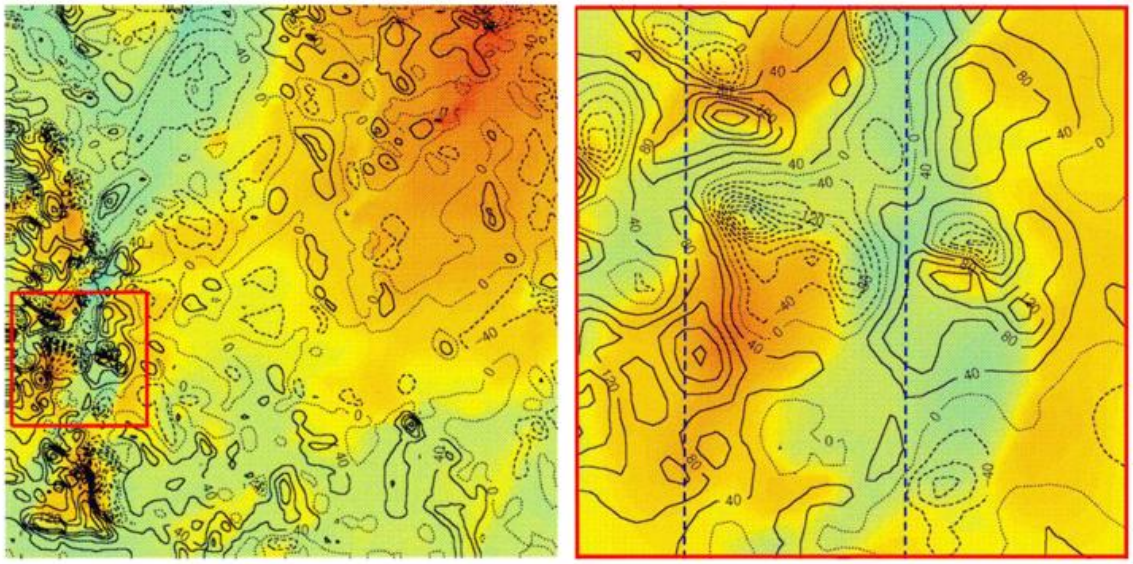


Figure 4.2a: Results from a 24-h integration after 12 hours, on 14 June 1997 at noon, for vertical motion w. Left: in a horizontal section over the whole 145 × 145 gridpoint area at a model level about 100 m above ground. Right: enlargement for the red-marked 3.5 × 3.5 km^2 sub-area, where the vertical velocity varies in an interval -310 mm/s $\leq w \leq$ 277 mm/s. Cross sections along the two dashed lines are shown in Fig. 4.2b.

scale divergence and so subsidence, and also effects of radiative warming/cooling. From each profile an estimate of the geostrophic wind and so the large-scale pressure gradient is derived for determining the pressure field of the initial and boundary data.

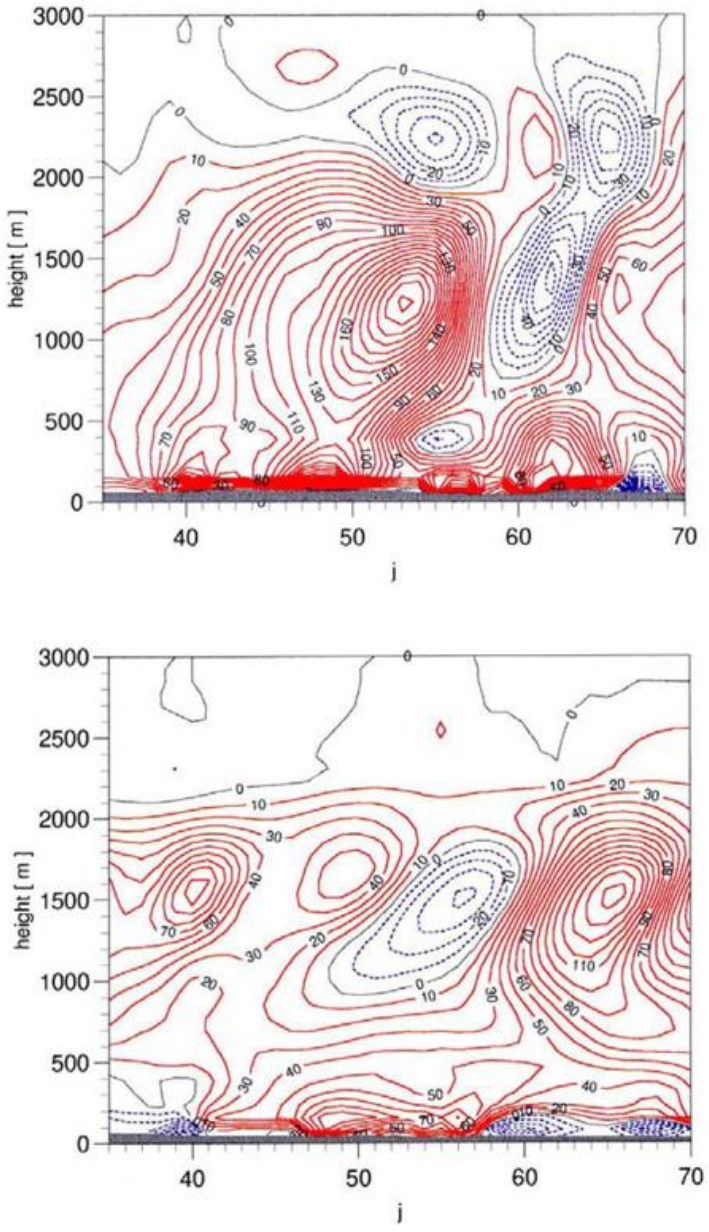


Figure 4.2b: South-north vertical cross sections of vertical velocity (isolines in mm/s, negative values dashed) along the two dashed lines in Fig 4.a. Top: Cross section referring to the left dashed line in Fig. 4.2a. Bottom: Cross section referring to the right dashed line in Fig.4.2a.

Concerning the ability of local adaptation even in the very proximity of the lateral boundary, an example is shown in Figs. 4.2a and 4.2b, where the fine-scale structures are obviously established against the external influence of the boundary data derived from CP's. The example of a 24-hour simulation has been carried out on 14 June 1997. The vertical motion is shown in a horizontal section covering the whole area of 145 × 145 gridpoints, after a 12-

hour integration time, at noon (Fig. 4.2a, left). By zooming over an indicated 3.5×3.5 km^2 sub-area (Fig. 4.2a, right) and by further inspection from two selected south-north-vertical cross sections coherent w-structures related to local orographic structures are observed (Fig. 4.2b). With that case a rather involved synoptic situation has been chosen by chance. The basic current at noon was directed from WSW.

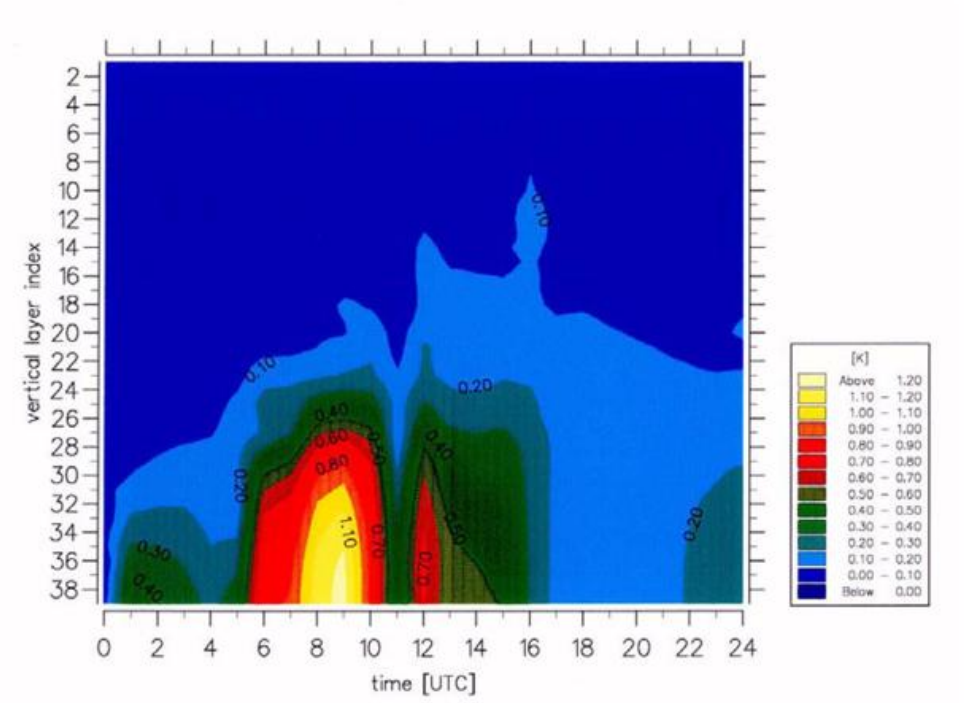


Figure 4.3: The standard deviation of temperature as a function of height and time for the LITFASS day 1 June 1998.

For another 'non-textbook case' (1 June 1998, arbitrarily selected from the LITFASS '98 period) the standard deviation of temperature deduced from the standard LLM integration domain with its variation in time and along the vertical is shown in Fig. 4.3. It demonstrates here in a more qualitative manner the local forcing by the inhomogeneities of the underlying surface: Though the standard deviation is not too large for such a case in June, it shows a rather changable variation over the day with convective intervals in the morning and significant rainfall in the late afternoon and evening.

4.2 Technical Approach

Assuming given vertical profiles of horizontal wind, temperature and moisture as a Composite Profile (CP) constructed from different measurement systems at MOL (Görsdorf et al. 2000, Beyrich 2000) and from the Falkenberg measurement site ('Gemeinsames Messfeld' = GM), the specific task is to determine the initial field and the boundary data fields from that information by use of a reasonable extrapolation approach with the above mentioned philosophy behind. As a matter of fact, those profiles are from technical reasons hourly available, which defines the updating frequency of boundary data for the LLM. By an agreement the CP provides u^M, v^M, T^M and the specific humidity q^M at all LLM-main levels along a vertical gridpoint column (the superscript M denotes a measured value). The surface pressure p_s^M is also assumed to be known.

The location of this vertical profile is given at the horizontal gridpoint i=118, j=67 with respect to the LLM standard grid net (cf. Section 2.6). As a first step, the variables u^M, v^M, T^M are horizontally distributed on (terrain-following) model levels. Due to a lack of more information this procedure has to be tolerated having in mind that the orography in the LLM area is formed by a gently undulating earth surface with surface heights in between about 40 and 120 meters above sea level. Above 1000 meters the model levels are genuinely horizontal (cf. Section 2.2). In mountainous regions this method seems insufficient. Here, the surface pressure field p_s is calculated on the base of p_s^M using T_{ke}^v and the given orographic height values z_s:

$$p_s = p_s^M \exp\left[-\frac{g(z_s - z_s^M)}{RT_{ke}^v}\right] . \tag{86}$$

T_{ke}^v is the virtual temperature at the lowest main level ($ke = 39$). In a further step the large-scale pressure gradient is determined from averaging the five uppermost wind values of the CP which are assumed to be representative for the free atmosphere. From this gradient assuming barotropy a pressure correction is added to the ps-field. In the following step the perturbation pressure field $p'_{ke} = p - p_0(z)$ is calculated for each vertical gridpoint column using p_s and a first guess value of virtual temperature T_{ke}^v. For the present we obtain

$$p'_{ke} = p_s \exp\left[-\frac{g(z_{ke} - z_s)}{RT_{ke}^v}\right] - p_{0,ke} . \tag{87}$$

Next, the p'_{ke} for $k < ke$ can be determined upwards by a recurrent formula following from the hydrostatic equation, which is here the LM-consistent differencing analogue of a balance equation with the first three terms on the r.h.s. of equation (3) (these are vertical pressure gradient -, buoyant- and water loading term). A more detailed description of that hydrostatic approach with an iterative improvement of T^v is given in Doms and Schättler (1999).

Normally, the given CP information consists of a synthesis of measured data from radiosonde, wind profiler, RASS, microwave profiler and 100m-mast. In a program module src_obsdata.f90 that CP estimate is used to construct both the initial field and the hourly boundary data fields as described above. As an important generalization the latest completion in this program module is the possibility to use a pseudo-CP having data exclusively from an LM-profile over the central gridpoint (i,j) = (73,73). In parallel to genuine CP-driven runs some selected 24h-runs with LM-profile forcing from the LITFASS '98 episode have been successfully carried out (cf. Chapter 6). The option of an LM-profile forcing is seen to be a necessary step for integrating the LLM off from Lindenberg over a transportable area imbedded in the LM integration domain. Moreover, that kind of forcing is of interest for a broader LM validation by use of the LLM as the declared validation tool.

In view of the following Chapter 5, where the physical forcing from the surface is dealt with, we add some further functions of the mentioned module src_obsdata.f90 providing the LLM with inhomogeneous fields of soil parameters. These are: land/water fraction per gridbox and soil typ as time-fixed values; all other parameters are in principle temporally variabel due to the annual vegetation cycle: orographic plus displacement height, roughness length, root depth, leaf-area index, degree of plant covering. Finally, two-dimensional fields of the water content of the upper (0-10cm) and medium (10-100cm) soil layer of the soil model 'terra', following from a homogeneous distribution of measured values or a longer series of precursory LLM runs with the desired effect of an inhomogeneous soil moisture spin-up, are read for starting the actual run. All these values have to be distributed among all computing processors.

5 Physical Forcing at the Lower Boundary

As already outlined, the most important forcing of the LLM is caused from the underlying surface with its natural inhomogeneities. In contrast to the lateral and upper boundary, the lower one is a physical interface, where the exchange of energy and water between atmosphere and soil takes place. These processes are characterized by the presence of turbulent near-surface fluxes of momentum, heat and moisture. In a complex way these fluxes depend strongly on physical conditions as e.g. local soil properties, soil moisture, radiation received at the surface, specific land use and realistic orography. In order to have a local forcing from below as exact as possible in the sense of 'real-world' - simulations with the LLM, the careful treatment of the mentioned physical properties is found to be a main task of the LLM development.

In that way, the detailed physiographic description of the underlying surface consists in deriving external parameters which are the key parameters of the coupled soil model to describe the dominating processes of soil, surface and vegetation with them. These parameters will be described in Section 5.1. To determine the relevant energetic processes at the bounding surface, it is important to know the short- and long-wave radiation balance there as well as the precipitation flux reaching the earth surface. These fields are derived from all the surface radiation and precipitation measurements available over the Lindenberg area. This is shown in detail in the following Sections 5.2 and 5.3. Since realistic LLM simulations are strongly dependent on a proper soil moisture distribution in connection with the given soil model, but soil moisture measurements are extremely sparse, an empirical adaptation method by using the LLM system itself is carried out and described in Section 5.4.

5.1 External Parameters

The kind and number of external parameters depend on the soil model in the LLM. Apart from minor changes, the soil model, which is the program module 'terra', is identically taken from the LM. In order to determine the appropriate external parameters over the high-resolving LLM grid, a comprehensive physiographic data set has been made available. It consists of orography data, of actualized airborne land use information (Zimmermann 1994a, b) and of soil property data (Hierold et al., 1997). All these data were provided in a vectorized form and had been transformed to LLM gridpoint data by Rosenow (1998).

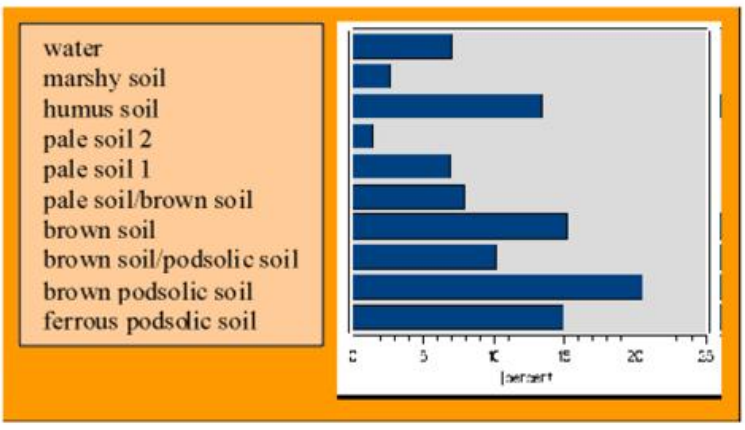


Figure 5.1: Soil type cover in percent of the total LLM area.

In the following a short description is given how the external parameters of interest are deduced from these data. According to a given soil map having 27 different soil types in the LLM simulation area, these types had to be reduced and fitted to only 9 types distinguished in the soil model. Fig 5.1 shows a histogram with the coverage of relevant soil types in percent of the total area of 199 × 199 gridpoints (see Section 2.6). The most frequent soils are brown-podsolic soil (20.5%), brown soil (15.2%) and ferrous podsolic soil (14.9%), while the coverage of water amounts to 7%.

In Fig. 5.2 the areal distribution of soil types is shown indicating the predominance of brown soils in the eastern part, whereas ferrous podsolic soils are found in the west. At some locations in the southern part and also in the proximity of lakes marshy soils sometimes prevail.

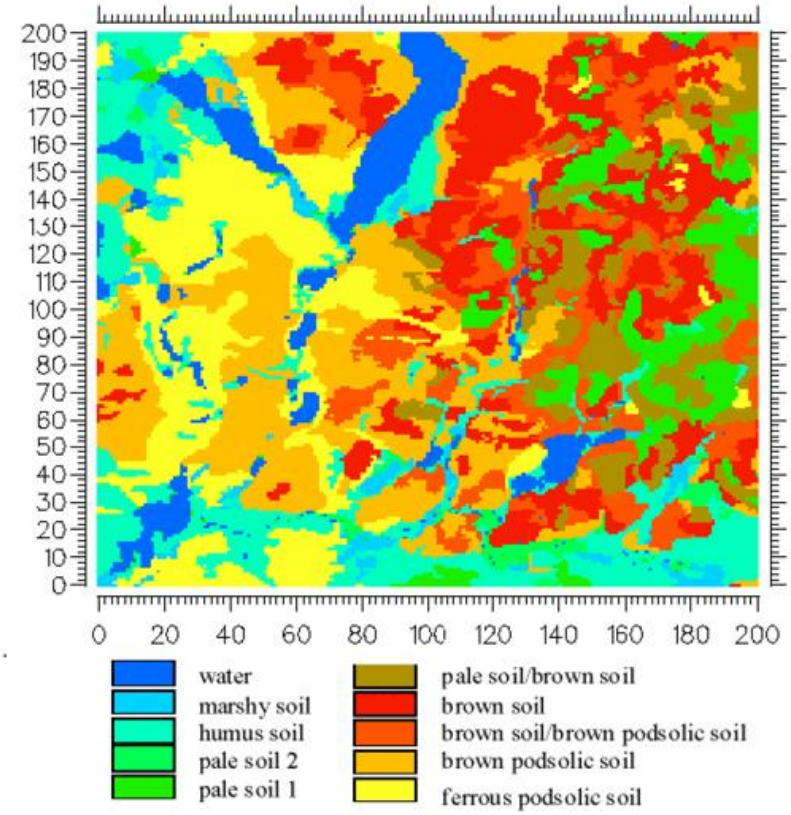


Figure 5.2: Distribution of soil types over the LLM area.

In the following Fig 5.3 topographic information is compiled showing e.g. the placement of important settlements, roads and lakes, and indicating specific locations associated to horizontal gridpoint indices. To add still more information, Tab. 5.1 provides a list of local soil parameters as valid in 'terra'. These parameters are additionally put in relation to processes like water storage, vertical water transfer within the soil, transpiration of plants and radiation near the surface. In order to demonstrate the horizontal heterogeneity of soil parameters, in Figs. 5.4 and 5.5 are shown the patterns of field capacity (a measure of maximal ability to store water in a soil layer) and soil heat capacity, respectively. Comparing both fields, it can be seen that podsolic soils in the west are able to store somewhat more of water and have a larger thermal inertia than brown soils in the eastern part. In contrast, marshy soils indicate a relatively high field capacity, but a relatively low soil heat capacity.

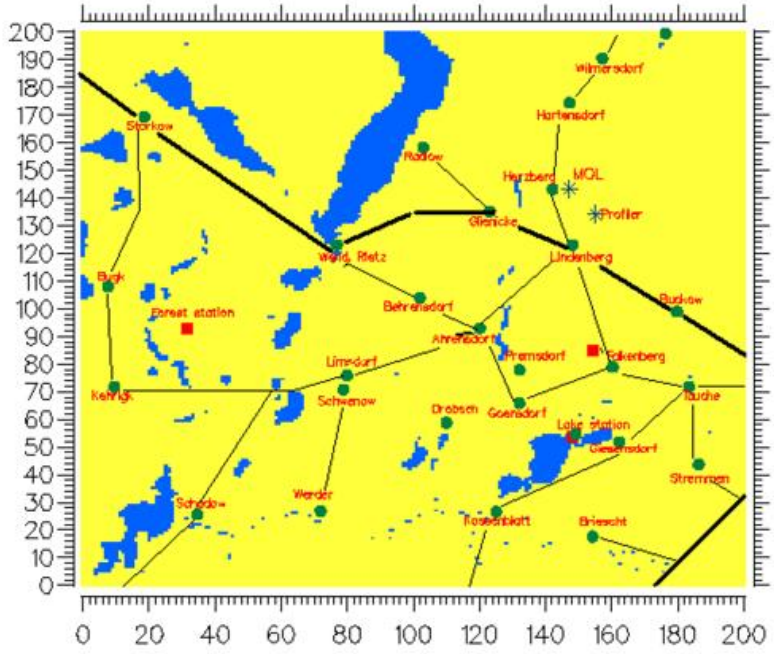


Figure 5.3: Map of local topographic information.

soil parameter	interval	dimension	main impact on
field capacity	0.11 - 0.75	fraction of volume	maximal soil water storage
pore volume	0.36 - 0.90	fraction of volume	infiltration and soil water storage
minimal infiltration rate	0.0002 - 0.0032	kg/(s*m²)	water influx into soil and surface runoff
plant wilting point	0.05 - 0.26	fraction of volume	transpiration
air dryness point	0.012 - 0.098	fraction of volume	transpiration
parameter to determine the hydraulical diffusivity *cdw0* *)	106 - 18400	10^{-9}m²/s	vertical soil water transfer
hydraulical conductivity *ckw0* *)	58 - 47900	10^{-9}m²/s	vertical soil water transfer
soil heat capacity *crhoc* *)	0.58+6 - 1.35+6	J/(K*m³)	thermal inertia of soil
albedo	0.10 - 0.35	fraction of 1	solar energy balance at surface
emissivity	0.90 - 0.98	fraction of 1	emission of IR-radiation from the ground

*) detailed description cf. LM-documentation (Doms and Schättler, 1999)

Table 5.1: Local soil parameters used in LLM.

Another sort of external parameters concerning the simulation of effects related to the coupled surface-vegetation system must be derived from the given land use data. The original data set comprises 35 biotopes resolving details smaller than the LLM grid mesh distance of about 100m. In view of the limited vegetation parameterization model the number of biotopes had to be reduced to 13 main types with water included. The resulting parameters distinguish between vegetation with constant height and a monthly varying leaf area index (e.g. forest, grass- and greenland as well as fen) and those having even daily variations (agricultural plants).

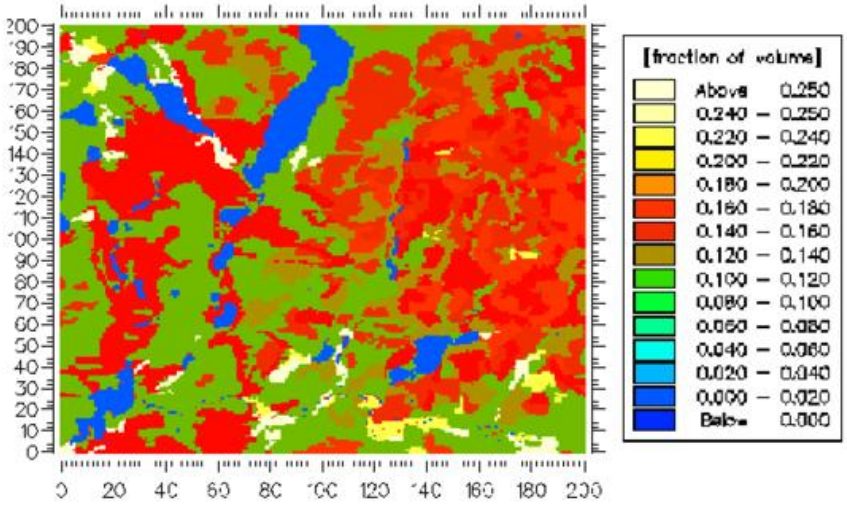


Figure 5.4: Field capacity distribution of the relevant soil types.

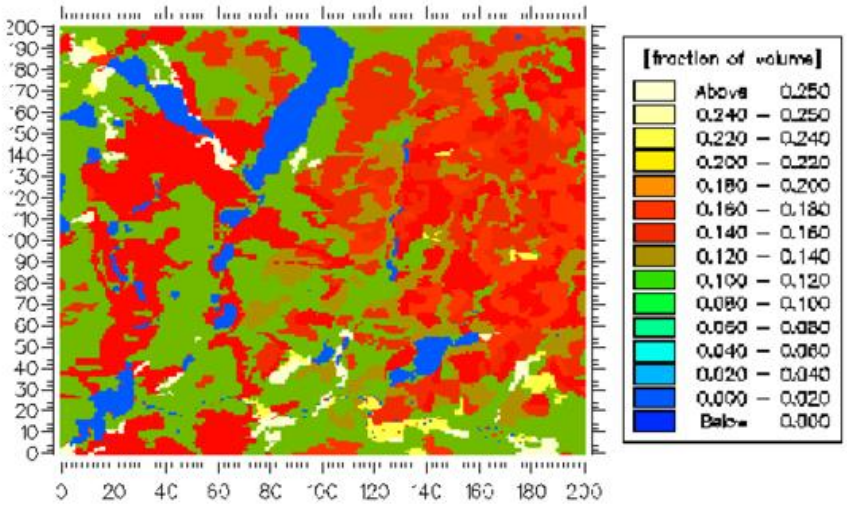


Figure 5.5: Distriubution of soil heat capacity.

As can be seen in Tab. 5.2 the predominant land use pattern is significantly influenced by human activity. The result is a high amount of coniferous forest (40.5%) and farmland (27.5%), while forest of deciduous trees has a portion of 8%. Greenland (here defined as fallow land, covered by several uncultured plants differing from forest) covers 14.5% of the total area.

Forests and fields are unequally distributed over the whole integration domain. According to the land use map shown in Fig. 5.6, forest prevails in the south-west while farmland dominates in the north-eastern part of the region. The most important agricultural plants are triticale, maize and rape. The variety seen in the actual land use map of June 1998 is largely determined from the different sorts of agricultural plants growing in that season. This concerns our simulation period for the LITFASS-98 experiment. In order to adapt the associated parameter distribution to the LINEX-2000 experiment (August-September 2000), the agricultural areas are assumed to be covered by grass after the harvest. That amounts to be an area portion of 28.6% for grassland compared to only 1.1% during June 1998.

Type of land use	coverage during LITFASS-98 [percent]	coverage during LINEX-2000 [percent]
water (lake, river)	7.0	7.0
coniferious forest	40.5	40.5
deciduous forest and settlements	8.0	8.0
triticale	17.2	-
maize	4.4	-
rape	2.8	-
barlay	1.6	-
lucern	0.5	-
sunflowers	0.5	-
wheat	0.5	-
greenland	14.9	14.9
grassland	1.1	28.6
marshland	0.9	0.9

Table 5.2: Land use cover in percent for the campaigns LITFASS-98 and LINEX-2000.

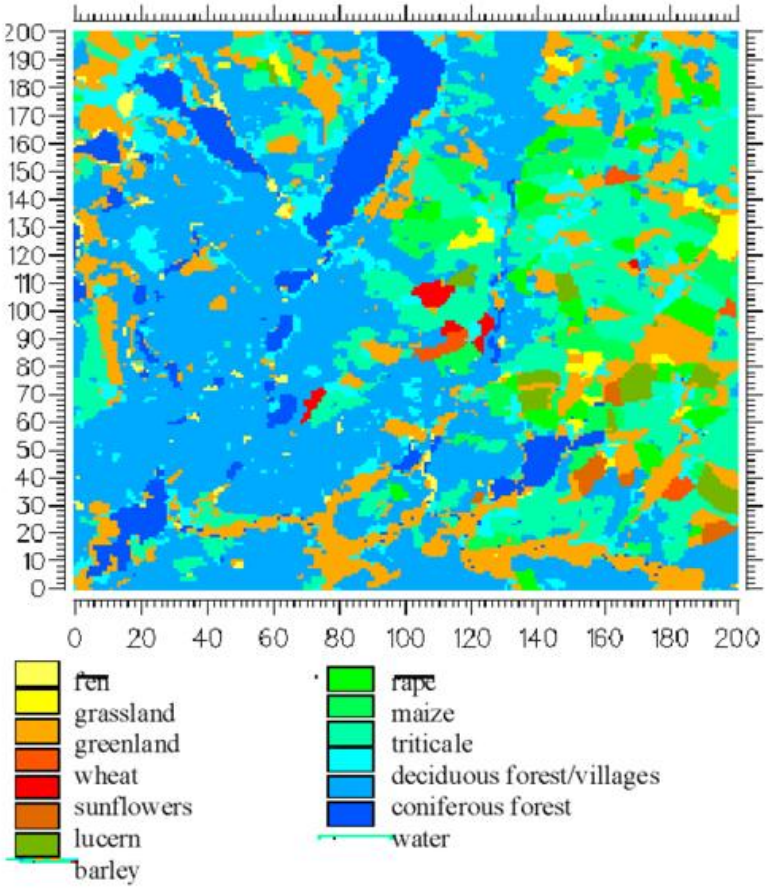


Figure 5.6: Land use cover (see text).

The external parameter set required for the LLM simulations is eventually listed in Tab. 5.3. In addition, the relevant land-surface processes playing a major role in driving the LLM from below are noted in that table.

Among all parameter maps, the landpoint mask can be obtained immediately from the map of soil types indicating where areas of water are located. Considering the fine grid resolution, it suffices to entirely assume a grid point to be either water or land. Concerning the specification of the root depth parameter, it is necessary to accept facts given by the present soil model. With respect to the hydrological part this model is assumed to have two active vertical layers, from 0 - 10 cm and 10 cm - 1 m depth. Therefore, in case of forest and greenland a constant root depth of 0.5 m has been chosen, while the root depth of farm- and grassland as well as fen is taken 0.05 m.

Some more effort is needed to determine the other external parameters mentioned in Tab. 5.3, since they depend explicitly on the type of vegetation. For the sake of convenience they have been estimated separately for vegetation and bare soil, before the final fields are determined by averaging both components with weights of the given degree of plant covering. This approach seems to be valid for the surface roughness length and the displacement height.

external parameter	interval	dimension	main impact on
landpoint mask	0 or 1		distribution of land and water gridpoints
roughness length	0.0002 - 1.52	m	vertical wind profile
displacement length	0 - 12	m	vertical wind profile
leaf area index	0 - 8	m^2/m^2	transpiration of plants
fractional plant cover	0 - 0.99	fraction	vegetation and bare soil components of the external parameters
root depth	0.05 or 0.50	m	transpiration of plants
albedo	0.10 - 0.35	fraction	solar energy balance at surface
emissivity	0.90 - 0.98	fraction	emission of IR-radiation from the ground

Table 5.3: Local external parameters used in the soil/vegetation module of LLM.

land use type	vegetation height [m]	LAI-variation in the annual course
coniferious forest	~15	8.0
deciduous forest	10	0.1 - 8.0
grassland	0.15	0.2 - 1.4
greenland	4	0.1 - 4.0
marshland	1	0.1 - 4.0

Table 5.4: Vegetation heights and LAI-values for some land use types.

In case of vegetation these values depend on the actual height of plants and the leaf area index. For some sorts of vegetation it is sufficient to use fixed plant heights, which are given in Tab. 5.4. Based on observational data from Lindenberg area a forest of coniferous trees is, on average, assumed to have a height of 15 m with a random variation superimposed within an intervall of ± 5 m. Only in case of agricultural plants the vegetation height is assumed time-variable.

For agricultural plants the time-variation of the plant height h_v and the LAI is considered over the vegetation period until the harvest using simple formulae proposed by Vogelgesang (1993) and Jürrens, respectively. For both parameters $\psi = (h_v, LAI)$ a linear time-interpolation formula is applied, where n counts the Julian days during the annual course:

$$\psi = \begin{cases} \psi_s & , n \leq n_s \\ \psi_s + \frac{\psi_z - \psi_s}{n_z - n_s}(n - n_s) & , n_z < n \leq n_s \\ \psi_s + \frac{\psi_{max} - \psi_z}{n_{max} - n_z}(n - n_z) & , n_{max} < n \leq n_e \\ \psi_s & , n_e < n \end{cases} \tag{88}$$

$\psi_s, \psi_z, \psi_{max}$ denote the values of parameters at selected Julian days n_s, n_z and n_{max}, where n_s is a Julian day at the very beginning after the seed-time, n_z marks a day characterizing a particular change of the plant property in order to ameliorate the linear approach due to a nonlinear growth in reality, and n_{max} denotes a day when the plant has obtained its maximal height, n_e is the day of the harvest.

Thus, both key parameters indicate the progress of plant growth and the degree of maturity (cf. Tab's. 5.5 and 5.6). In Fig. 5.7 the time-variation of the plant height as used in the LLM is shown in comparison to some measured heights (triangles), where these measurements are used to derive the parameters in (88). In view of these curves the model-relevant time of the LITFASS-98 experiment (1-20 June 1998) can be characterized by the end of a rapid growth, with exception of maize. Most of plants have obtained their maturity stage. In the following Fig. 5.8 a time-averaged field of LAI over the same LITFASS-98 period is depicted illustrating the typical physiographic structure of the Lindenberg simulation area. High LAI-values of about 8 are found in the south-west, while values of about 2 - 4 can be found in the eastern part of the area. The minimum value is found to be not below 0.7.

kind of vegetation	phenological dates							n_s	n_z	n_{max}
	EMG	STE	EE	TE	CC	FL	HV			
wheat	100	139	154	-	-	-	240	EMG	STE-10	EE-5
barley	60	103	142	-	-	-	240	EMG	STE-10	EE+15
triticale	90	101	140	-	-	-	240	EMG	STE	EE+10
maize	140	-	-	199	-	-	240	EMG	TE-40	TE
sunflowers	100	-	-	-	140	161	240	EMG	CC	FL
lucern	60	-	-	-	140	161	240	EMG	CC	FL
rape	100	-	-	-	135	161	240	EMG	CC	FL

Table 5.5: Dates (in Julian days) of phenological events and characteristic plant heights after Löpmeier (1983), Jürrens (1996) and own studies (see text). EMG: emergence; STE: stem elongation; EE: ear emergence, heading; TE: tessel emergence, heading; CC: canopy closed, crop cover complete; FL flowering; HR: harvest.

kind of vegetation	LAI_s [m^2m^{-2}]	LAI_z [m^2m^{-2}]	LAI_{max} [m^2m^{-2}]	h_s [m]	h_z [m]	h_{max} [m]
wheat	0.0	0.4	3.9	0.10	0.60	0.80
barlay	0.3	0.6	3.7	0.12	0.60	0.80
triticale	0.3	0.8	3.1	0.12	-	1.10
maize	0.0	0.3	4.2	0.10	-	1.80
sunflowers	0.3	3.0	4.0	0.10	1.70	1.90
lucern	0.3	3.0	4.0	0.10	1.20	1.40
rape	0.3	3.0	4.0	0.10	1.60	1.65

Table 5.6: LAI-values and typical vegetation heights.

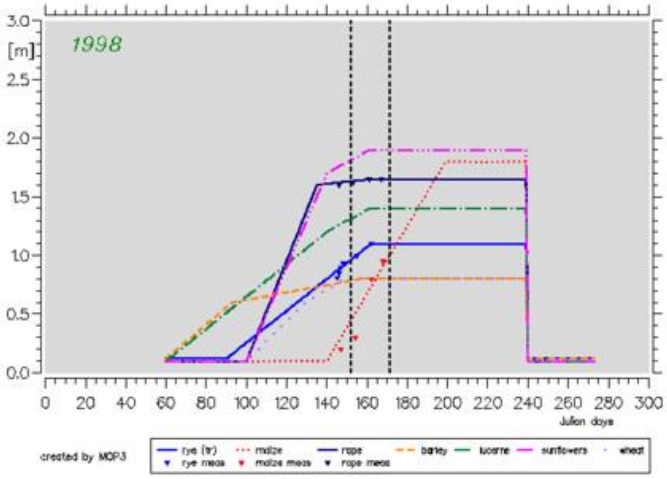


Figure 5.7: Time-variation of the plant height (see text).

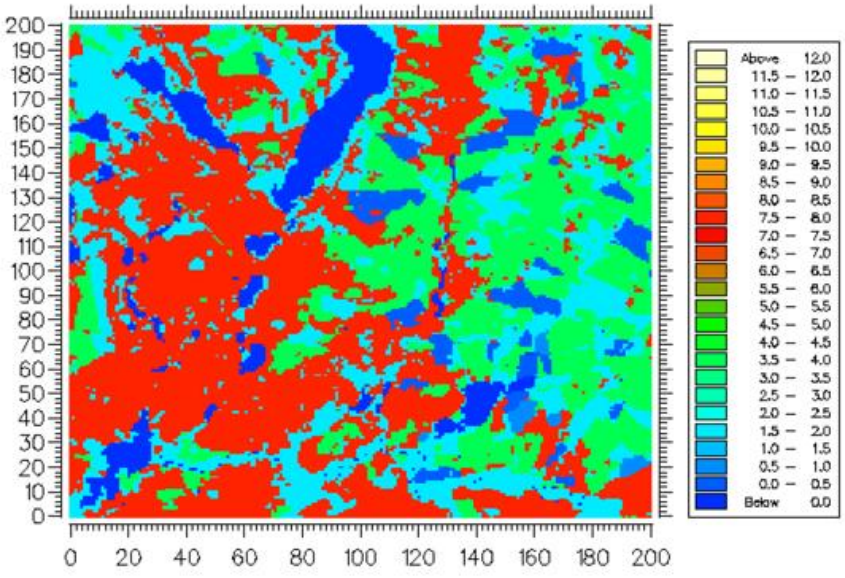


Figure 5.8: Time-averaged field of LAI over the LITFASS-98 simulation period.

In a following step it is necessary to determine the roughness length z_{0v} [m] and the displacement height d_v [m] over vegetation in dependence of the plant height h_v and LAI. In case of a forest with conifers and/or deciduous trees we use formulae by Brücher (1997):

$$z_{0v} = 0.1 h_v \,, \quad d_v = 0.67 h_v \,. \tag{89}$$

Having green- or grassland, fen or agricultural plants, an approach of Bailey and Davies (1980) is taken instead, where the LAI is also involved:

$$z_{0v} = 0.0275 + 0.281 h_v - 0.028 LAI \,, \quad d_v = 0.245 h_v + 0.091 LAI \,. \tag{90}$$

The only exception is made for z_{0v} in case of maize, where the LAI is not taken into account (Uchijima 1976):

$$z_{0v} = 0.062 h_v^{1.08} \tag{91}$$

We use the fractional plant cover expressed as a function of the LAI (Vogelgesang 1993),

$$f_p = 1.0 - \exp\left(-0.4\, LAI\right) . \tag{92}$$

Gridpoint values of the roughness length and of the displacement height over a gridbox area are weighted averages from the partial areas with vegetation and bare soil:

$$\begin{aligned} z_0 &= (1.0 - f_p)\, z_{0,surf} + f_p\, z_{0,v} \,, \\ d &= (1.0 - f_p)\, d_{surf} + f_p\, d_v \,. \end{aligned} \tag{93}$$

In the case of bare soil we assume $z_{0,surf} = 0.01$ m and $d_{surf} = 0$ m. For a water surface, $z_{0,surf} = 0.0002$ m is taken. Any dependence on the wind speed is ignored. By z_0 a roughness length $z_{0,M}$ is actually meant, which is defined for momentum fluxes. For latent and sensible heat fluxes we assume a similar length defined as

$$z_{0,H} = 0.1\, z_{0,M} \tag{94}$$

which is taken from Jürrens (1996). The surface heterogeneity is demonstrated for the LITFASS-98 period in terms of time-averaged fractional plant cover f_p and roughness length

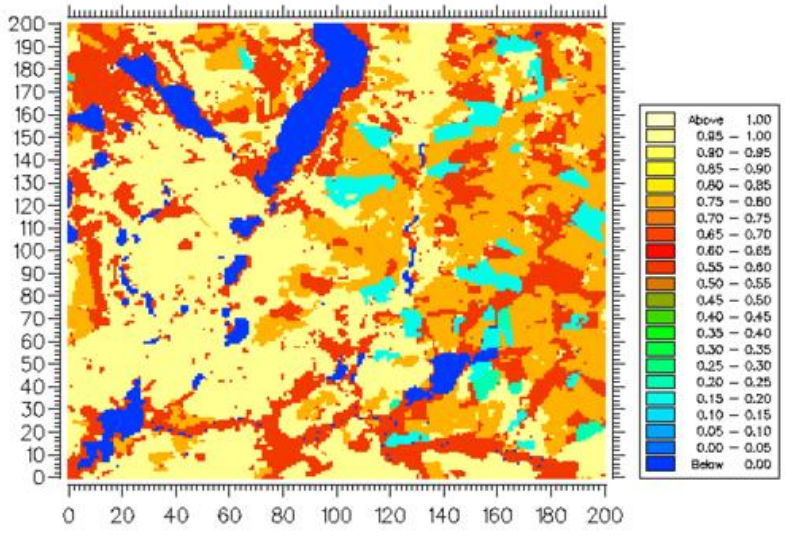


Figure 5.9: Time-averaged field of plant cover (%) over the LITFASS-98 simulation period.

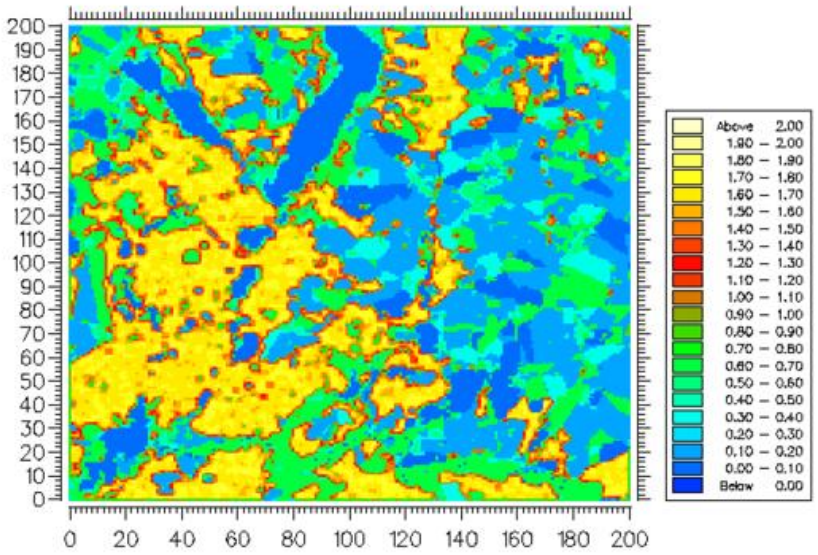


Figure 5.10: Time-averaged field of surface roughness over the LITFASS-98 simulation period.

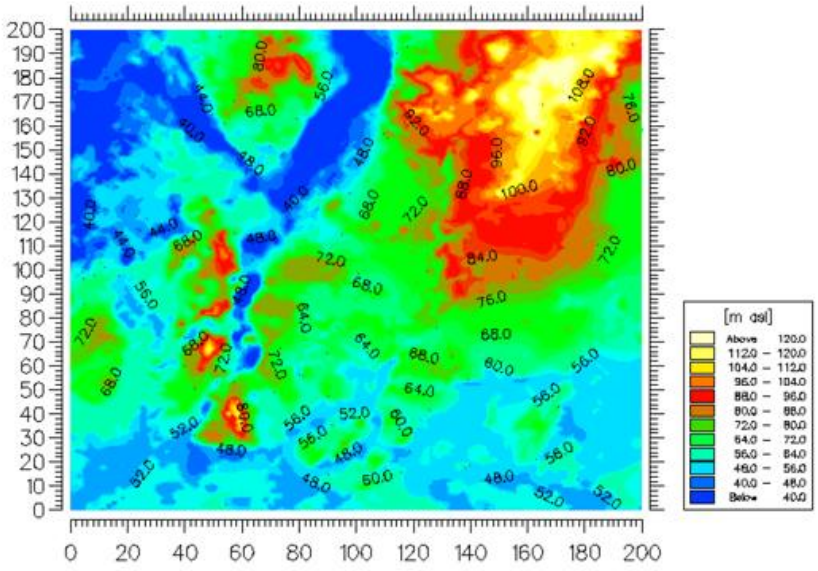


Figure 5.11: Orography plus time-averaged field of displacement height over the LITFASS-98 simulation period.

$z_{0,M}$ in Fig's. 5.9 and 5.10. For the sake of practical convenience the actual field of the displacement height is always added to the time-fixed orography (cf. Fig 2.7b) to have actually a time-variable orography field. That field averaged over the relevant period of LITFASS-98 is shown in Fig. 5.11.

A further group of external parameters immediately relevant to the radiative processes at the surface is related to the reflection of incoming solar radiation and to emission of infrared radiation from the ground. These parameters are albedo and emissivity. They were provided separately for vegetation and bare soil. The influence of precipitation on those parameters will be considered in the following Section 5.2 where the radiation balance components will

be deduced from measurements. Here, the values of albedo for vegetation are differently updated (daily or monthly) in dependence of the average growth rate of each plant type. The corresponding data source has been extracted from a VDI Guideline (1994). Finally, we show as examples the distribution of the 'dry' albedo over the total LLM-integration area in Fig. 5.12 and the 'dry' emissivity of vegetation (Fig. 5.13) indicating the specific heterogeneity from this point of view. These values are also averaged in time over the LITFASS-98 period.

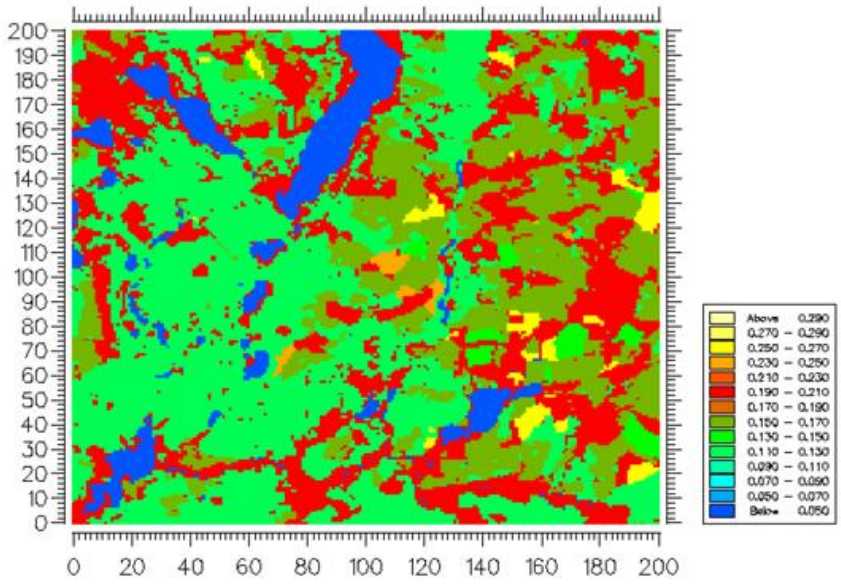


Figure 5.12: Time-averaged field of albedo (vegetation) over the LITFASS-98 simulation period.

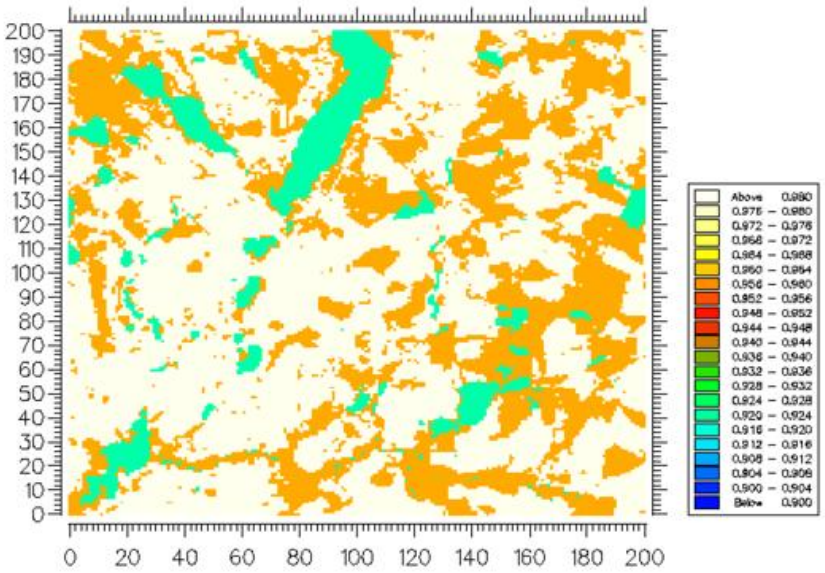


Figure 5.13: Time-averaged field of emissivity (vegetation) over the LITFASS-98 simulation period.

5.2 Radiative Forcing

The task we describe here consists in determining the radiation components of the energy balance at the surface by use of all radiation measurements available in and around the LLM integration area. Satellite information is also taken into account. All these different data sources relevant for our purpose to derive the radiative forcing are compiled in Tab. 5.7. The ground-based radiation measurements are of greatest importance. They are recorded, first of all, at the BSRN-station near the MOL, serving as the reference station, at the radiation measurement site Falkenberg, and at other Energy Balance Stations (EBS) (Lake Kossenblatt, in a pine forest near Storkow, and two special measurement places, in a barley and a triticale field). The latter were only available over the LITFASS-98 period.

Beyond this measurement campaign, further Global Radiation measurement stations have been added since summer 2000 to have meanwhile 8 of them. In Fig. 5.14 the net of radiation measurement points from these different sites is shown, where the mean local METEOSAT pixel positions relevant to our approach are also depicted. As one can see, the area of interest

Data sources available for the radiative forcing of the LLM

■ Satellite-based radiation data	{derived by PODLASLY und BERGER et al. (1999)}
Global Radiation	based on NOAA-measurements (25.05.-30.09.1998) area resolution 1 x 1 km, Northeastern Germany once or twice per day
Temperature planetary albedo	based on METEOSAT data (25.05. - 30.09.1998) area-resolution 7 x 7 km², Northeastern Germany (half-)hourly
■ Ground-based radiation measurements	
Global Radiation Reflected Solar Radiation Diffuse Solar Radiation Direct-beam Solar Radiation	BSRN-station
Global Radiation at horizontal surface Reflected Solar Radiation Thermal Radiation of the atmosphere Emitted thermal radiation from ground	Measurement site Falkenberg
Global Radiation Thermal Radiation of the atmosphere Radiation balance	Forest site Storkow Lake site Kossenblatt measurements at special sites (barley, triticale) [Global radiation network since 2000 (8 sites)]
■ Meteorological data	
precipitation temperature (2m) water vapour pressure (2m)	LITFASS-network (21 sites) Energy balance stations and special sites

Table 5.7: Data base available for radiative forcing.

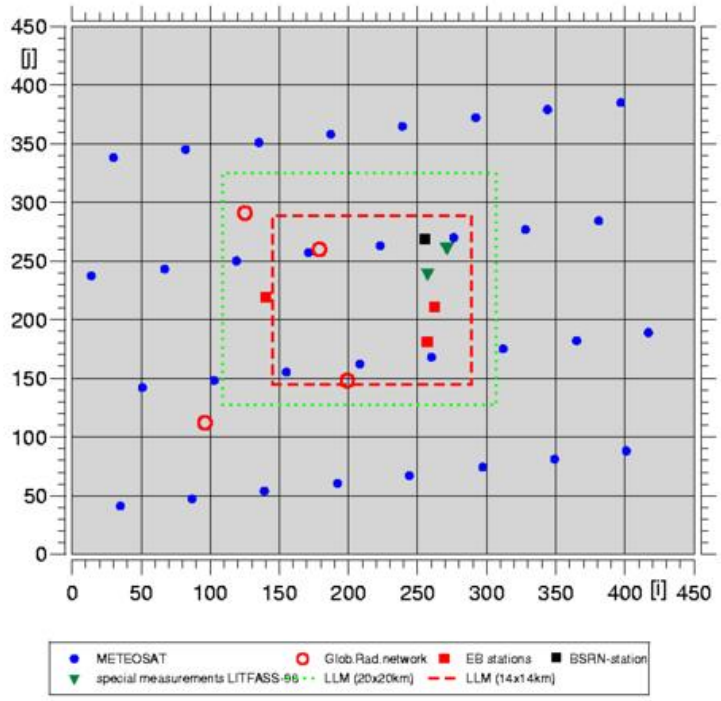


Figure 5.14: Placement of measurement sites recording radiation data.

is chosen considerably larger than the local LLM integration area to be able in any case to apply an interpolation method. In the background NOAA-data are also exploited in order to support the METEOSAT information with its coarser horizontal and spectral resolution. Normal meteorological information, like precipitation, 2m-temperature and water vapour pressure is also involved (Tab. 5.7). These data are provided from a special LITFASS precipitation network with 21 measurement points (see Section 5.3). For further explanation of the instrumental design concerning the radiation measurements during the LITFASS-98 main experimental phase we refer to Beyrich (2000).

For our purpose the satellite data have been made available by Podlasly and Berger (1999). They provided us with a comprehensive data set of METEOSAT and NOAA measurements over the period 25 May - 30 September 1998 with our LITFASS simulation time interval embedded. The METEOSAT data consist of temperature and planetary albedo, while the Global Radiation was derived directly from the NOAA satellite. In the latter case the radiation data have a high resolution of about 1×1 km^2 which would be appropriate for LLM. Unfortunately, these data are available only once ore twice a day over the area of interest. In contrast, the METEOSAT information can be obtained in a relatively high time-resolution, that is every 30 minutes, but due to its poor spectral resolution the Global Radiation data cannot be similarly derived (cf. Podlasly and Berger 1999).

This dilemma of different shortcomings of the two available satellite data sources can be reduced by a method to combine both. In effect, our approach rests on deducing a Global Radiation field from these satellite data by combining the available information with the ground-based measurements of Global Radiation as the key radiation component relevant to the LLM forcing. For the LITFASS-98 period the method cannot do without satellite information due to the small number of ground-based radiation stations inside the LLM

integration area. The following approach may be characterized as some calibration of the available METEOSAT information of temperature and planetary albedo by the Global Radiation field, derived from NOAA data at METEOSAT pixels.

The area of satellite data shown in Fig. 5.15, which covers Northeast Germany with the LLM-area as a tiny sub-area in the eastern part in it. In this figure the 18 June 1998 at 12.30 UTC is chosen, when the NOAA data coincide almost exactly in time with the METEOSAT information. At first glance, the Global Radiation from NOAA data (Fig.5.15a) seems to be not highly correlated neither to the temperature (Fig. 5.15b) nor to the albedo (Fig. 5.15c). Here, qualitative arguments might be helpful to put forward the matter. In this line, we generally expect a significant relation between cloudiness on the one hand and temperature and albedo on the other hand. In case of compact clouds the satellite measures deeper temperatures together with a higher albedo, which must be correlated with a correspondingly reduced Global Radiation at the ground. Inversely, one expects in cloudless areas with relatively high values of temperature and smaller values of albedo increased values of Global Radiation at the ground.

This leads us to the definition of an Insolation parameter s, which is an appropriate combination of albedo *and* temperature, as available from METEOSAT data, in such a way that

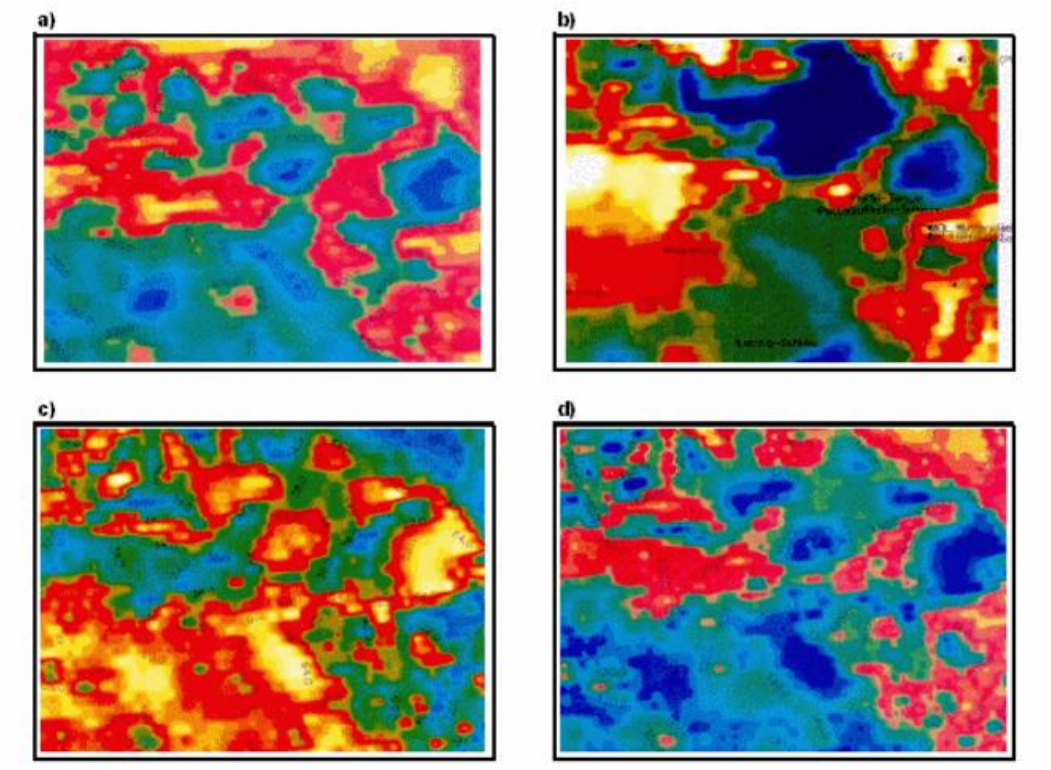


Figure 5.15:
a) Field of Global Radiation derived from NOAA data and adapted to the coarser METEOSAT resolution.
b) Temperature field based on METEOSAT data.
c) Field of Planetary albedo based on METEOSAT data.
d) Field of Insolation parameter.
All fields refer to north-east Germany (18 June 1998, 12:30 UTC).

it has a significantly high correlation to the known Global Radiation fields directly gained from the NOAA satellite. A comparison of the s-field in Fig. 5.15d with the NOAA Global Radiation field in Fig. 5.15a demonstrates such a desired correlation. By use of all available NOAA- and METEOSAT data taken out of the entire data set the Insolation parameter has been found as a result of statistics:

$$s = a_s T\,(1.0 - 0.01\alpha_p) + b_s\,. \tag{95}$$

α_p is the planetary albedo [%] and T [K] the temperature from METEOSAT, the constants are found to be $a_s = 0.0053K^{-1}$ and $b_s = 0.0227$. After deriving relation (95) from NOAA Global Radiation data, it can now be used to determine from the METEOSAT information (from T and α_p) the Insolation parameter field s every 30 minutes.

In the next step a local fitting of the s-field to the Global Radiation measurements at the ground is performed such that the s-field is slightly shifted in the horizontal until a measure of distance to the Global Radiation values at the given 5 measurement points becomes minimal. In Fig. 5.16 the s-field is shown for the same selected time as in Fig. 5.15 after the operations just described. Although this field has a relatively coarse structure due to the METEOSAT-pixel resolution and a 30 minutes-resolution in time, compared to the LLM-scale resolution, the s-field serves as a necessary background information towards a horizontally inhomogeneous and time-variable Global Radiation field at the surface. Thus, at measurement points associated Global Radiation (G-) and s-values are used to deduce a linear s, G-relation. In such a way we obtain all s-values available as G-values which are finally exploited as additional information to the genuine surface measurements in a horizontal interpolation onto the LLM-gridpoints.

Since the ground-based measured values are delivered every 10 minutes, a further time-interpolation from 30 down to 10 minutes is carried out to obtain finally a surface Global Radiation field G over the 20×20 km^2 LLM integration domain with 199×199 gridpoints and a 10-minute input frequency. As can be seen from Fig. 5.17, the method described above is able to provide the LLM with a horizontally inhomogeneous G-field, where real

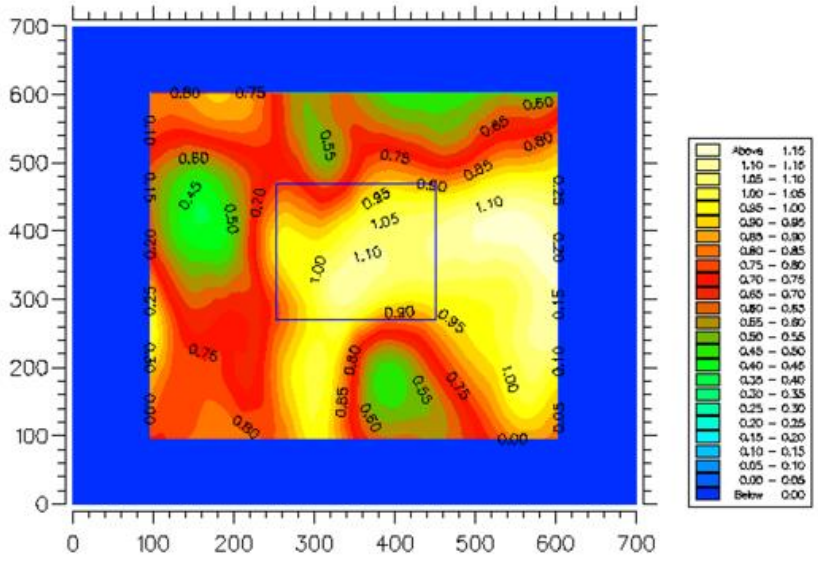


Figure 5.16: Distribution of Insolation parameter for 18 June 1998, 12:30 UTC. The LLM area is embedded in the centre.

cloudiness is involved. This approach has been used for all LLM integrations over our LITFASS-98 simulation period (1 June-20 June 1998). As mentioned above, the number of Global Radiation recording stations was only extended after this period, in summer 2000. In order to demonstrate the additional gain of information from this further technical effort, Fig. 5.18 shows the sequence of G in 10minute-time intervals over the LLM-area with rapid time-changes of that radiation pattern accompanied with rather sharp gradients.

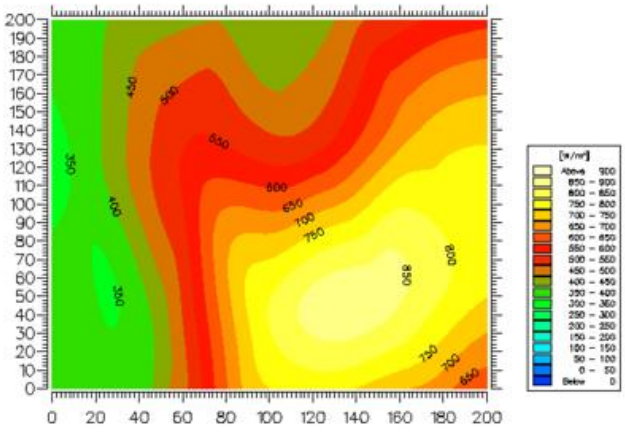


Figure 5.17: Global Radiation field in the LLM area for 18 June 1998, 12:30 UTC (see text).

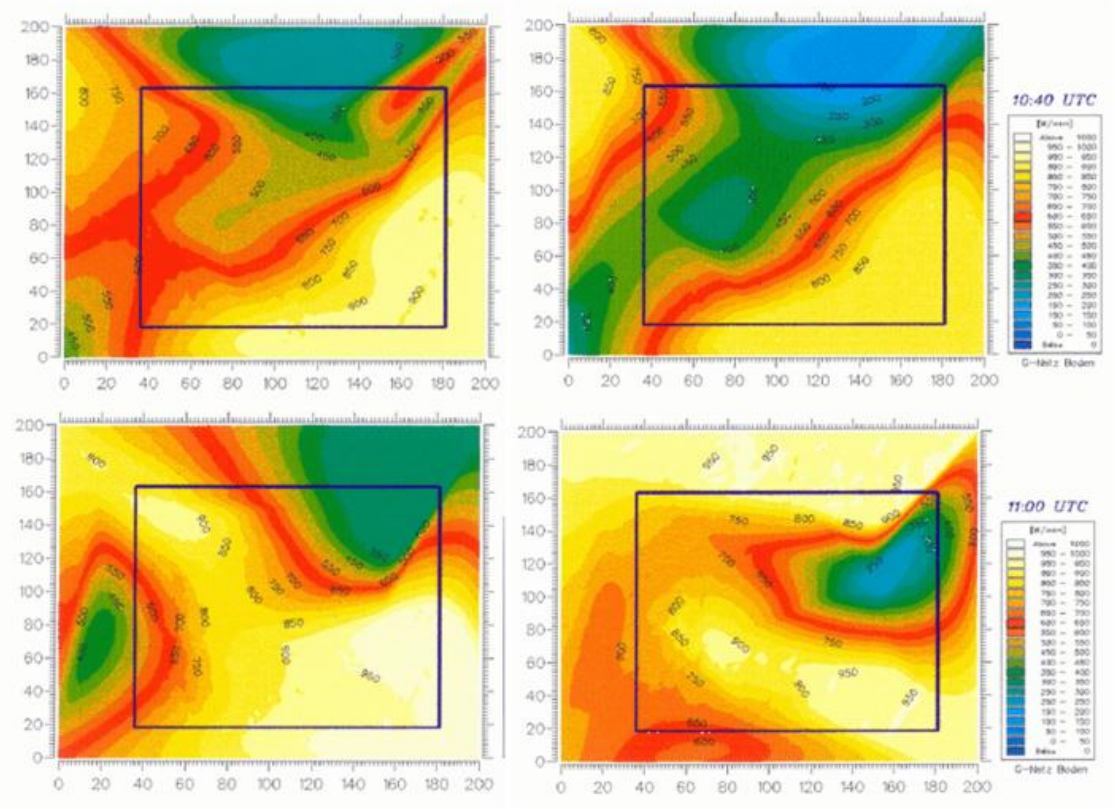


Figure 5.18: Time sequence of Global Radiation fields deduced every 10 minutes from an extended surface network on 21 June 2000. Top left: 10:30 UTC; top right: 10:40 UTC; bottom left: 10:50 UTC; bottom right: 11:00 UTC.

The Global Radiation G found in this way is, however, not the final result. To make the incoming solar radiation flux still more realistic, the inclination of the natural surface has to be taken into account. The corresponding correction necessary is, however, effective only to the Direct-beam Solar Radiation I. For that purpose we need an approach to split up G into its components I plus Diffuse Solar Radiation D, that is $G = I + D$. Assuming that this splitting has been carried out, the correction of I due to the orographic inclination can be performed. All details of that operation including the derivation of the inclination angle from the given orography up to the determination of the modified solar height (depending on the varying sun position over the day and the season) will be dropped here. This method is standard.

The splitting procedure needs, however, further explanation, and for that purpose we introduce a Global Radiation Reduction factor R_s, which may be defined with reference to Davies et al. (1975) as

$$G = G_0 R_s \,. \tag{96}$$

This relation separates the Global Radiation at the ground, G, into a Global Radiation component of the cloudless case G_0 multiplied by a Reduction factor R_s. The latter describes the reducing influence of clouds in the solar spectrum. After Davies et al. (1975) the parameterization of G_0 and R_s may be given as follows.

$$G_0 = a_R + \frac{b_R}{2}\left(\frac{r_0}{r}\right)^2 S \sin\gamma \left[\psi_{wa}(\psi_{ws}\psi_{rs}\psi_0 + \sqrt{\psi_0})\right] , \tag{97}$$

$$R_s = \left[1 - \left(1 - \frac{a}{G_0 m_a}\exp(-b m_a)\right) n\right] (1 - \alpha_c \alpha_g n) , \tag{98}$$

with the following explanations and definitions of parameters in the G_0-relation (97): $(r/r_0)^2$, γ, S are measures of astronomical excentricity, solar height at given location and time, and solar constant, respectively. ψ_{wa}, ψ_{ws}, ψ_{rs}, ψ_0 are transmission coefficients due to water vapour absorption, water vapour scattering, Rayleigh-scattering and scattering from dust. The regression coefficients a_R and b_R are introduced to fit this relation to the local conditions of Lindenberg.

The R_s-relation (98) depends on parameters describing different cloud properties, a and b are coefficients specifying the cloud type, a_c is the cloud albedo seen from below, n describes the cloud coverage ($0 \le n \le 1$), m_a defines the optical mass of the atmosphere and α_g is the albedo of the ground. The reliability of relation (96) together with the parameterizations of G_0 and R_s has been proved by use of NOAA-radiation fields. For the problem discussed here and in the following we confine the parameterization to G_0. The determination of the Reduction factor R_s follows from (96) by use of ground measurements of G (actually determined from ground measurements and METEOSAT/NOAA-satellite data as described above). Such an R_s-field is shown in Fig. 5.23a.

After having found R_s, it is possible now to separate D and/or I from the preliminary G. Therefore, we assume that the ratio D/G is a function of R_s:

$$\frac{D}{G} = \frac{D}{D+I} = f(R_s) \,. \tag{99}$$

For the cloudless case, with $R_s = 1$, we expect the ratio to have a minimum, $f(1) = D/G_0$. If the sky becomes overcast ($I \to 0$), R_s approaches to a minimum and the ratio to unity. Fortunately, the Diffuse Solar Radiation D is directly recorded at the BSRN-station at MOL and each 10 minutes available. Taking advantage of these data, the function $f(R_s)$ can be determined. In Fig. 5.19 the ratio D/G is plotted against R_s from measurements and by

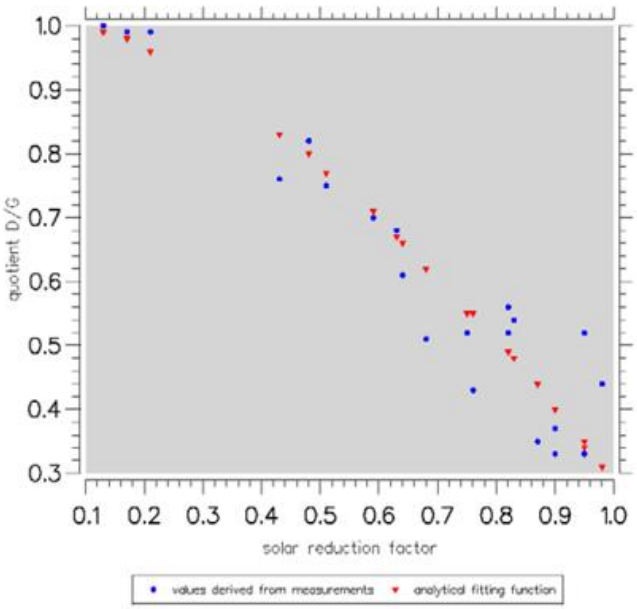


Figure 5.19: Quotient D/G as empirical function of solar Reduction factor (see text).

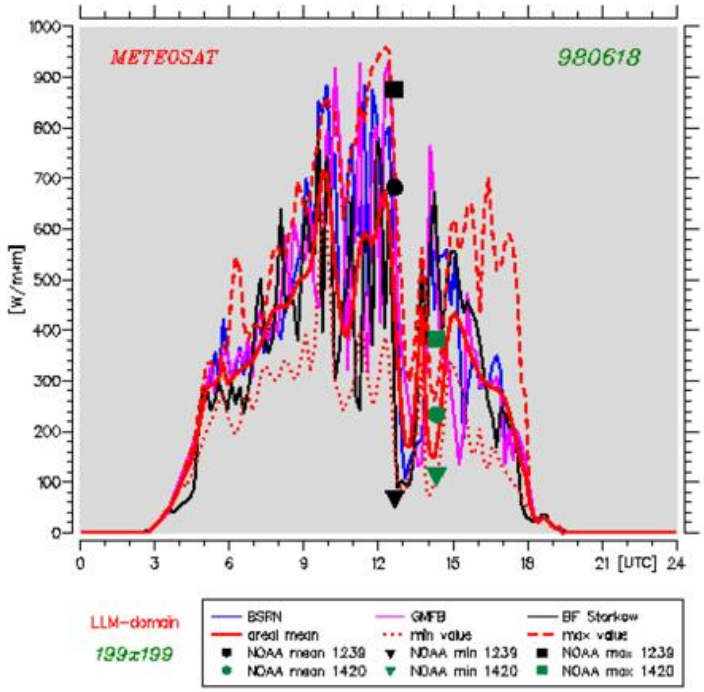


Figure 5.20: Diurnal variation of measured and derived Global Radiation over the LLM area (18 June 1998). Time variations of deduced area-average, -maximum and -minimum against selected NOAA- and surface measurements of Global Radiation at BSRN-station, forest station (BF Storkow) and Falkenberg site (GMFB).

using an analytical curve fitted to these data. The latter is assumed to be the appropriate tool to separate D and/or I from the given G which makes it immediately possible to modify I in the above sense and use that result together with the unchanged D to obtain the final composite of G.

Before we continue to derive further radiation balance components for the radiative forcing of the LLM the time-variation of G is shown in Fig. 5.20 for the same selected day (18 June 1998) from the LITFASS-98 period as in previous figures. This day was a particular occasion for LLM-simulations because of a helicopter flight with a sonde. By chance, this day was characterized by prevailing convective weather. The time-variations of G show in general rapidly passing small-scale cloud patterns accompanied by sharp peaks and gaps in the morning. At noon, a compact cloud field covers the entire LLM-area, from which a maximum of about 900 Wm^2 has been reduced down to 100 Wm^2. As seen in the figure, the various plots of G refer to three different recording stations and show in parallel the time-variations of the area-average, -maximum and -minimum which demonstrates the considerable spread of G-variations over the LLM-domain and so the radiative inhomogeneity at the surface.

In order to complete the Solar Radiation balance SB, we have to determine the Reflected Solar Radiation G_r, too, and to subtract it from the Global Radiation G:

$$SB = G - G_r\,. \tag{100}$$

Since D and I have already been derived in connection with the determination of G, we are now immediately able to carry out the necessary separation of G_r into the diffuse and the direct-beam component:

$$G_r = \alpha_d D + \alpha_{par} I\,. \tag{101}$$

Therefore, in accordance with (101), the determination of G_r can be reduced to the determination of the diffuse albedo α_d and the albedo of a parallel radiation beam α_{par}. Concerning the diffusive albedo α_d, we refer to comments at the end of Section 5.1 about the availability of external parameters like dry, diffuse albedo and emissivity, which are already prepared to be used separately for bare soil and vegetation. In case of precipitation both albedo components are modified provided the actual amount of rainfall exceeds 0.5mm over a 10minutes-interval. Then the surface is assumed to be wet. In this case the albedo of vegetation is reduced by 10 percent and the albedo of wet bare soil is treated in accordance to the VDI Guideline (1994). The diffuse albedo follows then by use of a weighted average of both components with the

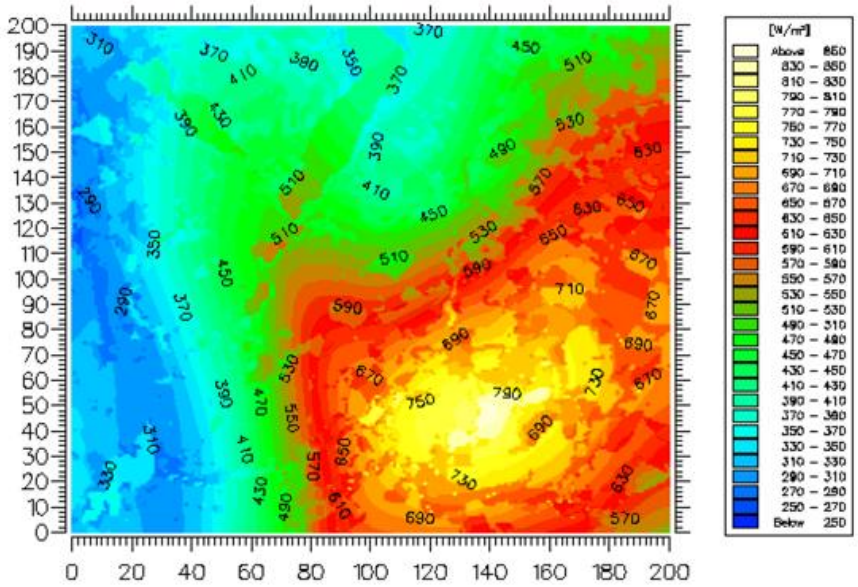


Figure 5.21: Example of Solar Radiation balance field over the LLM area (18 June 1998, 12:30 UTC).

fractional plant cover. This is similar to the treatment of the roughness length in (93). In the following step, the albedo of a parallel radiation beam is calculated as a function of α_d and solar height γ (Ritter, cf. Doms and Schättler 1999):

$$\alpha_{par} = \frac{1 + \frac{\gamma}{2(\alpha_d - 1)}}{\left(1 + \frac{\gamma}{\alpha_d - 1}\right)^2} . \tag{102}$$

Using α_d and α_{par}, the reflected component G_r can be found from (101), which leads to the Solar Radiation balance (100). An example of an SB-field is shown in Fig. 5.21.

In a final step we still have to determine the Thermal Radiation of the atmosphere A and the Thermal Radiation E emitted from the ground. In case of A we need a method which also operates on the basis of available Global Radiation data G. In a similar way an Amplification Factor M_{IR} is introduced in order to determine A by use of a reference value

$$A_0 = (\alpha_{IR} - \beta_{IR} \exp\{-\gamma_{IR} e_{2m}\})\ \sigma T_{2m}^4 , \tag{103}$$

valid for cloud-free conditions (Rietschel 1994), that is, by

$$A = M_{IR} A_0 . \tag{104}$$

Here, the general problem is shifted to the determination of M_{IR}, while A_0 can easily be approximated by use of temperature T_{2m} and water vapoure pressure e_{2m} at 2 meters above the ground as meteorological input-parameters taken from measurements. During simulation runs these data are directly provided from the LLM in order to determine the A_0-values in a consistent manner to the model. α_{IR}, β_{IR} and γ_{IR} are empirical constants with reference to Rietschel (1994), and σ is the Stefan-Boltzmann constant. The true problem is to estimate

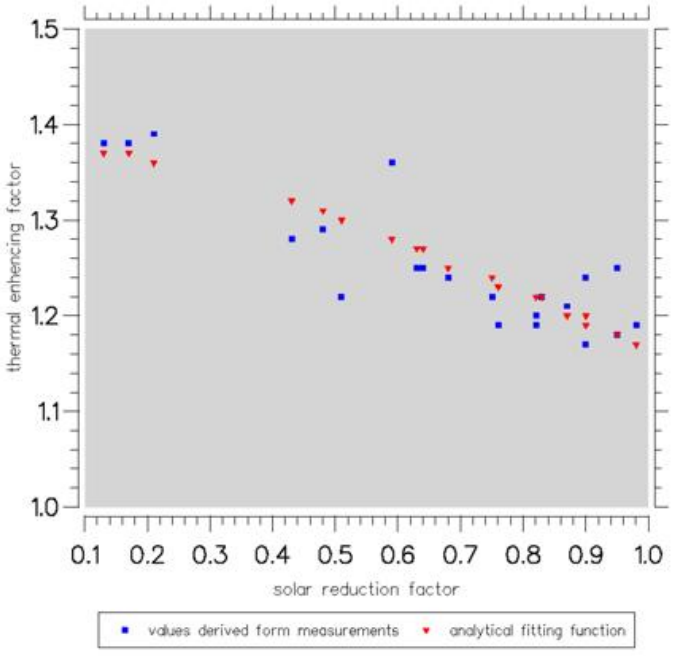


Figure 5.22: Empirical relationship between thermal Amplification factor and solar Reduction factor for a given time interval on 18 June 1998, 9 - 12 UTC (see text).

the factor $M_{IR} \geq 1$. In order to have an approach consistent with our treatment of the Solar Radiation component, it is reasonable to find out an empirical relation between R_s and M_{IR}, which is expected to have in a crude manner a reciprocal proportionality. This means, the enhancement of Thermal Radiation from the atmosphere compared to the cloud free case must directly be related to a reduced Global Radiation, which is expressed by a decreasing Reduction factor R_s. In our approach, this relation has been determined every 10 minutes and is shown for a selected time interval in Fig. 5.22. On the basis of this operation M_{IR} is given and the estimation of A follows using (104). Fig 5.23a,b demonstrates the consistent relation between R_s and M_{IR}.

In the following the Thermal Radiation emitted from the ground,

$$E = \varepsilon \sigma T_{sfc}^4 \tag{105}$$

must be estimated, Here, the problem confines to the use of the infrared emissivity ε, which has already been provided as an external parameter field. Similar to the diffuse albedo, these values have been provided separately for vegetation and bare soil and possibly modified owing to precipitation.

We close the Section with a marginal remark concerning the Photosynthetically active Radiation P, which is needed in the vegetation parameterization part after Dickinson of the soil model 'terra'. P is approximated by the very simple relation $P = 0.5G$. A view on Fig. 5.24 may finally serve us as a summary of the present section. This figure is self-explaining. To organize the important forcing due to radiation processes from below, four groups of input data are of interest. These are ground-based radiation measurements, preprocessed satellite data from NOAA- and METEOSAT-instruments, meteorological near-surface data and basic data as orography, land use and soil type maps to derive relevant external parameters from them. All these data are stored in order to make a synthesis having finally the ground-based fields relevant for the radiative forcing (Solar Radiation balance, infrared Amplification factor, precipitation (cf. Section 5.3), infrared emissivity, Photosynthetically active Radiation) and the external parameters (cf. Section 5.1) which are orography plus displacement height, roughness length, LAI, fractional plant cover, root depth and landpoint mask.

These data are always ready for LLM-access. In case of radiation data their input to the LLM takes place every 10 minutes of integration time. All computer runs are carried out at

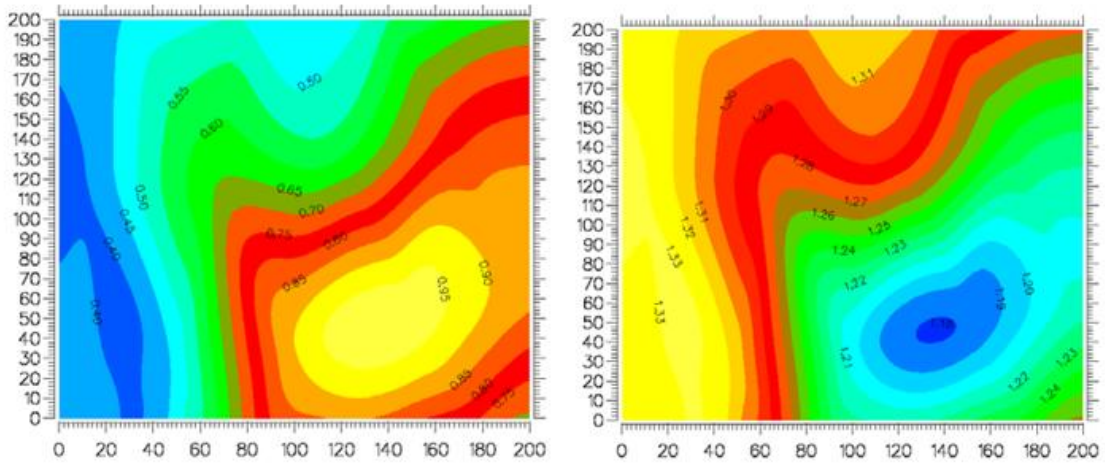


Figure 5.23: Consistent distributions of solar Reduction factor (left) and thermal Amplification factor (right) over the LLM area.

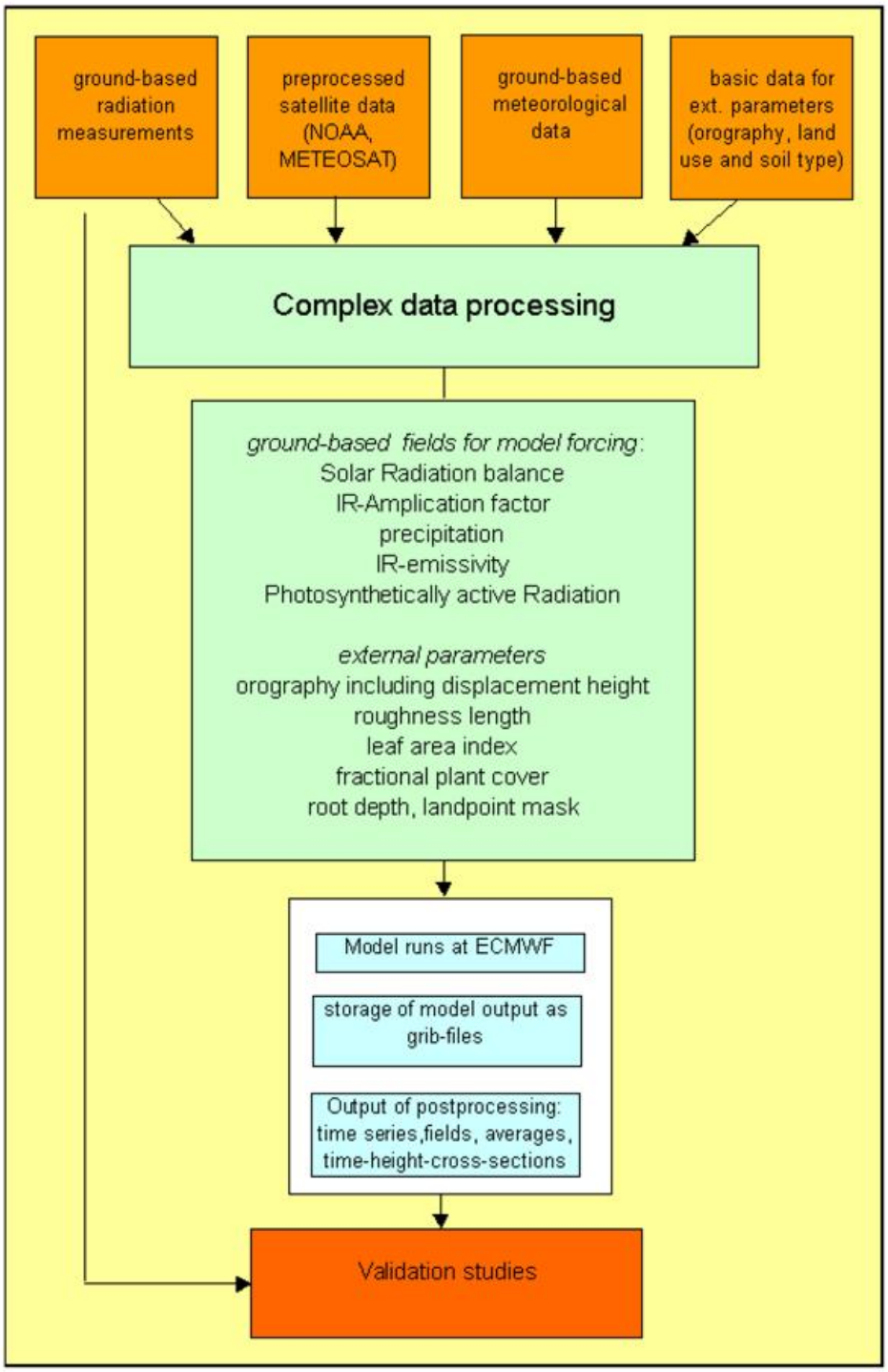


Figure 5.24: Summarizing scheme of data processing for physical forcing at lower boundary.

ECMWF on the VPP700 machine where all LLM output-arrays are also stored as Grib-files, and so the postprocessing is organized to be performed there, before results as time-series, selected fields, averages and specified sections of fields are transferred to Potsdam. There, the validation of the LLM products is executed by direct use of measurements, which are e.g. ground-based Radiation balance records. Ultimately, this kind of validation is part of a more general validation system as shown in Fig. 1.1.

5.3 Precipitation Forcing

We have already explained in Section 2.5 that in view of real-case simulations with the LLM its precipitation parameterization is ignored and the precipitation flux reaching the earth surface is inserted by a real-data field. This philosophy is similar to what has been carried out in the previous Section concerning the radiative forcing. In the following we describe the way how the horizontal distribution of precipitation at the surface is analyzed from given measurements. For that purpose a special network of Hellmann gauges commonly in use and automatically recording pluviometers has been established. RADAR data are not available.

In Fig. 5.25 the placement of 19 Hellmann gauges and 12 pluviometers is depicted. As can be seen, most of the pluviometers are placed within the extended LLM-area (199 × 199 gridpoints), while the gauges are distributed also far outside. At 7 places gauges and pluviometers have the same location. For these stations the pluviometer measurements are only used. Both instruments differ from each other by summing up the rainwater over quite different time intervals. In the gauges the rain water is gathered to obtain sums over 24 hours, normally observed at 5, 6 or 7 UTC in the morning, while the pluviometer records yield very high-resolved sums over every 10 minutes. By a simple operation the pluviometer values will be used as reference measurements to derive pseudo-values from the 24hour-Hellmann-data with the same high time-resolution. Then all measurements are put together for a following analysis.

The production of such pseudo-values may be demonstrated by Fig. 5.26. In Fig. 5.26a a pluviometer record is shown over 1 June 1998 at the village Limsdorf, placed in the LLM-area. Already in the morning a maximum of 5.6 mm/10min occurred during a heavy shower, and further showers with diminishing intensity took place during the second half of this day.

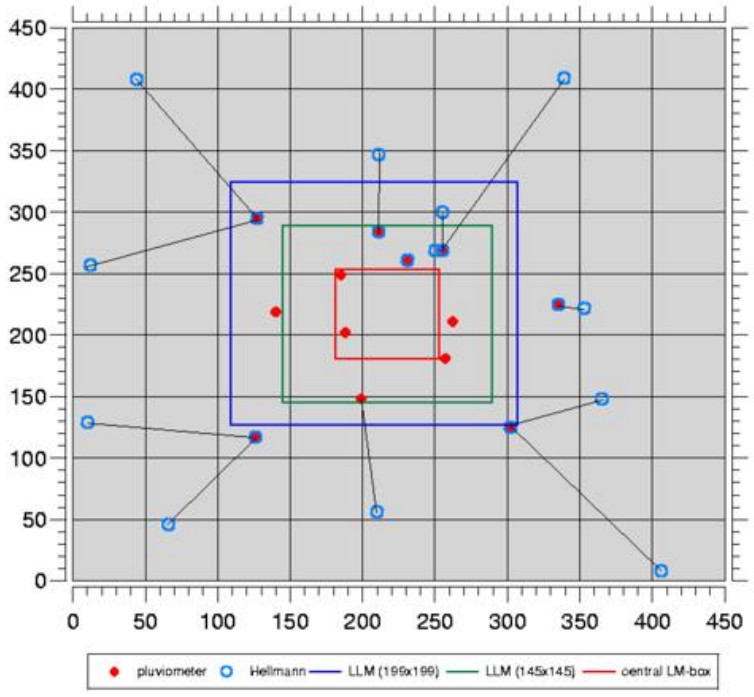


Figure 5.25: Placement of pluviometers and Hellmann gauges within and around the LITFASS area.

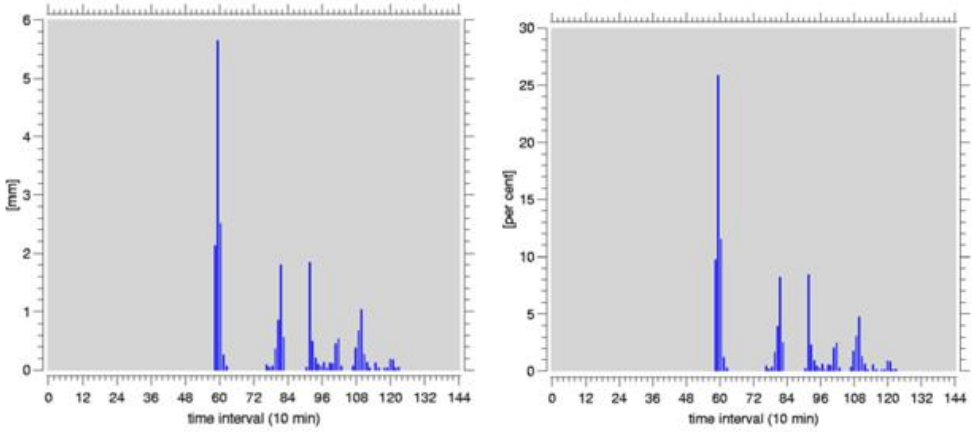


Figure 5.26: Time series of precipitation sums on 1 June 1998 at Limsdorf.
Left: Precipitation sums (mm/10min) in the diurnal course (144 time intervals of 10 minutes).
Right: Percentage distribution of 10-minute precipitation sums referred to daily sum (144 time intervals of 10 minutes).

The total sum amounts to 21.8 mm/day. With reference to this sum the time-series shown can easily be transformed into a corresponding time-variable percentage-distribution (Fig. 5.26b). Such a percentage-distribution found from each given pluviometer is then assumed to be valid for the nearest Hellmann-stations. (This is symbolized by connecting lines in Fig. 5.25). From this approximation the pseudo-values with a 10minute-resolution can be determined from the 24 hour-sum of the respective gauge. The irregular horizontal distribution of precipitation obtained every 10 minutes as explained above is the data basis for the following interpolation onto the LLM-gridpoints. This interpolation rests on a triangulation standard method.

The outcome of such treatment is shown in Fig. 5.27 for the same convection situation of the 1 June 1998 at 9:50 UTC, with a maximum near Limsdorf (cf. the peak at this time in

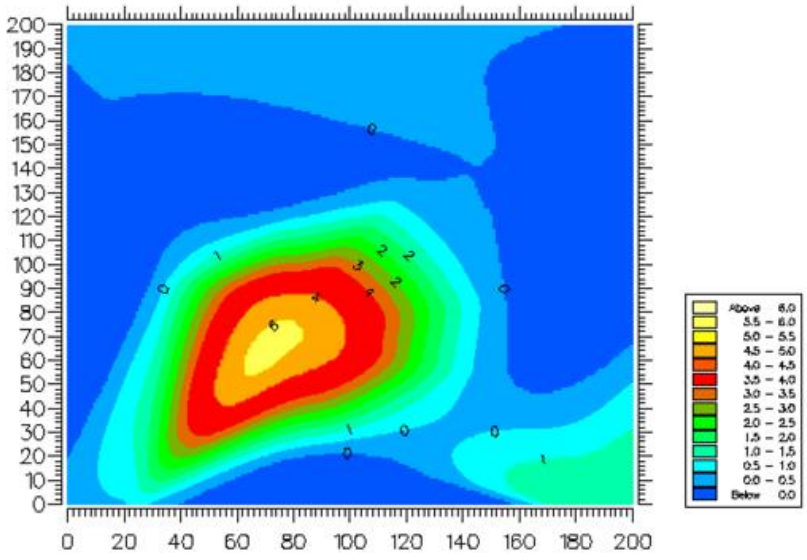


Figure 5.27: Deduced precipitation field over the LLM area on 1 June 1998, 9:50 UTC.

Fig. 5.26a). In this way precipitation forcing fields are made ready for the LLM-access every 10 minutes similar to that of radiation data. In case of large-scale precipitation our method presented seems to be sufficient. In case of convective rain events, however, further research supported from RADAR data is desirable in order to find out more adequate fine-scale field structures.

5.4 Soil-Moisture Modelling

Soil-moisture modelling is a specific problem of great importance for real-world simulations with the LLM. Obviously, that topic is seen to be closely related to the precipitation analysis we have treated in Section 5.3. The soil-moisture is a very complex factor caused by water influx due to precipitation. It interacts permanently with a diversity of processes like interception, surface runoff, infiltration, evapotranspiration, vertical water transport within the soil and runoff into the ground water. These processes again depend strongly on the soil properties, and they have very different characteristic time-scales. The longest of them make up the memory of the soil which is important to consider for the soil moisture initialization. This problem is of particular interest and must be solved in a pragmatic way.

While the LLM integration mode is generally characterized by a time-dependent external forcing founded on measurements – these are composite profiles (Chapter 4), external parameters (Section 5.1), surface radiation (Section 5.2) and precipitation (Section 5.3) – soil moisture measurements are only available at one measurement point at the Falkenberg site. As will be pointed out, this single measurement is absolutely insufficient to support an initialization approach needed and seems also to be unsuitable for the validation of simulation. It follows that LLM-simulations themselves are thought to be used as a possible soil moisture initialization procedure. These LLM-integrations are pre-runs started sufficiently long before the beginning of the actual run in order to produce a soil moisture spin-up towards a realistic initial field. The initial soil-moisture state of such a spin-up LLM-run is assumed to be a reasonable approximation, and this run will be controlled from the real time-dependent radiative and precipitation forcing as discussed above. We have to be aware, however, that

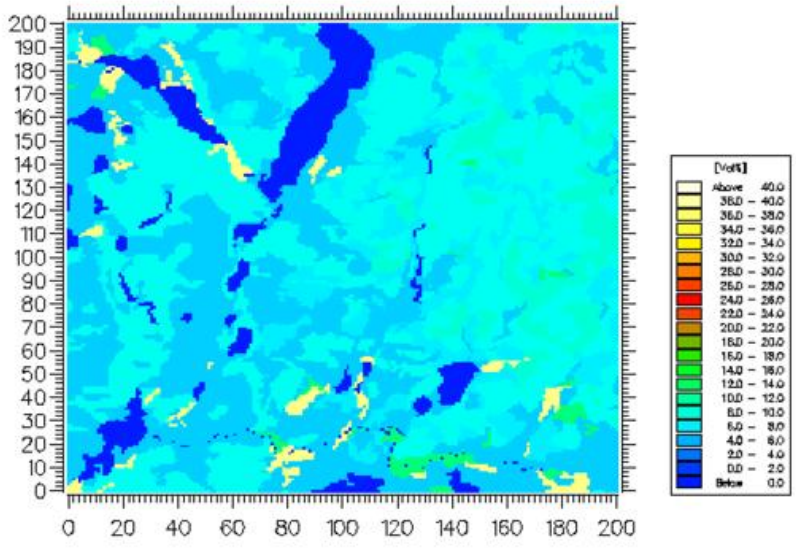


Figure 5.28: Initial field of soil moisture referred to the upper soil-model layer (1 June 1998, 00 UTC).

the approach is dependent on the potential of the coupled soil-model (Jacobsen and Heise 1982, Doms and Schättler 1999).

Because all LLM-simulations we have made were strictly connected with the measurement equipment installed for the project LITFASS-98 and further on for LINEX 2000, corresponding pre-runs were dictated from these facts and from the availability of real data before these campaigns. In case of LITFASS-98 it would have been desirable to have the basic data for the radiative forcing and of precipitation already since April 1998, in order to start the spin-up simulations in time with respect to a very dry May. Unfortunately, satellite data have not been available in that time, and the rain gauge network was still in preparation. While in case of LINEX 2000 the spin-up runs were possible already since 10 August 2000, our LITFASS-98 simulation had to be performed without such a desirable soil-moisture spin-up before.

For LINEX 2000 the spin-up start at 10 August was accepted due to heavy rain during August which makes the soil-memory from the months before possibly lost. In case of LITFASS-98 with its simulation time from 1 June to 20 June 1998 we are going to point out the soil moisture course from LLM-integrations over that time at a selected gridpoint which coincide with the only measurement point, and the model had to start with an approximate soil-moisture field without a necessary pre-run. That approximation is as follows. By use of the only measured value the percentage of the field capacity at the measurement point is known as an additional useful information. Since the horizontally inhomogeneous distribution of the field capacity over the LLM-domain is also known from the associated soil-type map, the assumption of the same percentage at each gridpoint leads immediately to an inhomogeneous soil-moisture field. This is assumed to be valid for both active model layers. In Fig. 5.28 the result is shown for the 1 June 1998. It is valid for the upper layer of the soil-model 'terra' having a thickness of 0.1m. (The present soil-model version has two active layers. The second layer, below, reaches from 0.1 m to 1 m depth.)

In the Fig. 5.29 the time variation of the soil-moisture at the gridpoint Falkenberg is shown as the result of an extensive LLM-simulation over all 20 days of the LITFASS-98 simulation period against the measurements there. For that experiment the LLM has externally

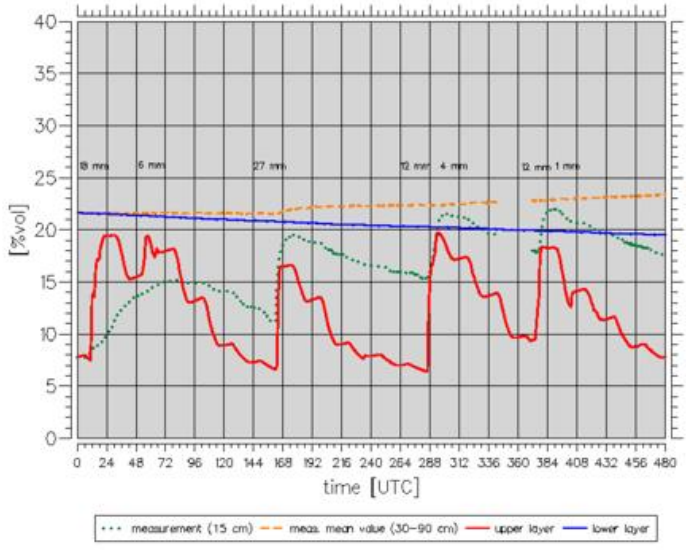


Figure 5.29: Time series of measured and LLM-simulated soil moisture over the LITFASS-98 simulation period from 1 June - 20 June 1998.

been driven at the lateral and upper boundaries only by radiosonde information, because composite profiles have been available only at 9 days of the whole simulation period (9-14, 18-20 June 1998). In parallel to the measured and simulated soil-moisture curves the 24 hour-rain-sums at 7 days with precipitation can also be seen in Fig. 5.29.

Prior to an interpretation of the LLM-results against measurements some comments about the measurements must be given. It is important to note that the uppermost measurement point is in a depth of 0.15 m, while further three points are placed at depths of 0.3, 0.6 and 0.9 m. In order to have initial values from these points for the given soil-model, the value at 0.15 m depth is used to be valid in the uppermost active model layer with its thickness of 0.1 m, while a vertical mean taken from the three lowest points is assumed to be valid in the second active soil-model layer.

Fig. 5.29 demonstrated that these values seem to be unsuitable for the model validation. At least, it can be seen that for the uppermost layer the curve derived from measurements differs significantly from the LLM-simulation. The reason is that the upper measurement point with its depth of 0.15 m is not appropriate to be used in the upper soil-model layer having a depth of 0.1 m. But it is unavoidable to do so. As one can see this kind of initialization error seems incidentally diminished due to considerable precipitation on 1 June 1998. The model simulation shows a more believable result in the upper layer compared to the measured values (which are provided every 10 minutes). Already in the afternoon of that first day a strong shower led to a considerable increase of the soil moisture in the upper layer from 8 %vol. to about 20 %vol. As a consequence, the second integration day started from a much higher soil moisture value while the measured one remained much smaller from a rather slow growth rate. On the second day no precipitation occurred. This led to a decrease of soil-moisture. Measurements, however, indicated a further slow increase. The moisture was obviously transported downwards with some delay. After a further moisture increase from precipitation on 3 June the upper model layer dried out over the next days down to 7 % vol. The degree of drying out seems to be caused by a small plant cover of 0.27 due to assumed grassland. That decrease is, however, not continuous and shows a diurnal course.

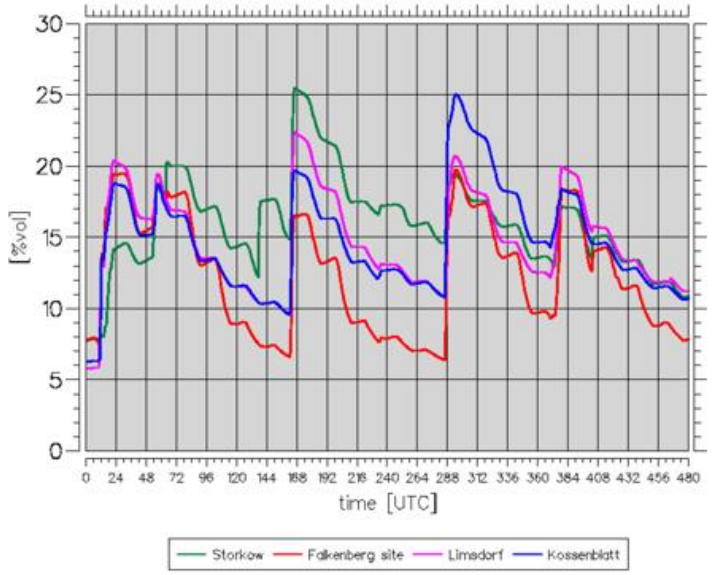


Figure 5.30: Time series of LLM-simulated soil moisture at different locations within the LLM area from 1 June - 20 June 1998.

Here, we drop a further quantitative discussion in this way.

In general, it should be noticed that the soil moisture of the uppermost layer in the model indicates a very sensitive response to precipitation, and it tends to be either significantly higher or smaller than the measured values. From that point of view we have made the decision to initialize each 24-hour run with a simulated moisture value, while the virtue of the measurement is not obvious as long as it is recorded actually 5 cm deeper than the 10-cm thickness of the uppermost soil-model layer. In case of the second active layer a comparison between measured and simulated values cannot be qualified although they show a slightly contrary trend.

Coming to an end, in Fig. 5.30 we show to what extent the soil-moisture can vary over the LLM-integration area as the result of simulations over the above mentioned 20-day LITFASS-98 period as in the previous Fig 5.29. In Fig. 5.30 the same time-variation of the soil-moisture from the uppermost layer at the Falkenberg measurement site is shown and further curves from three selected locations (Fig. 5.31) are added to demonstrate the possible inhomogeneity following from LLM-integrations. The added places are the stations Storkow, Limsdorf and Kossenblatt, where on average over the LITFASS-98 simulation period relative maxima of precipitation occurred.

The corresponding curves in Fig. 5.30 are a sample from the inhomogeneous soil-moisture distribution demonstrating one aspect of a great manifold of results from the rather extensive simulations with the LLM. The simulated soil-moisture variations in time and location indicate the result of a complex interplay between the processes in the soil, in the near-surface atmospheric region and at the interface between both subsystems. Here, these special results were shown first of all to complete the description and documentation of the present state of the LLM implying a great variety of aspects, theories and pragmatic concepts in strict relation to the observational potential and the richness of an elaborated data-pool due to the LITFASS project.

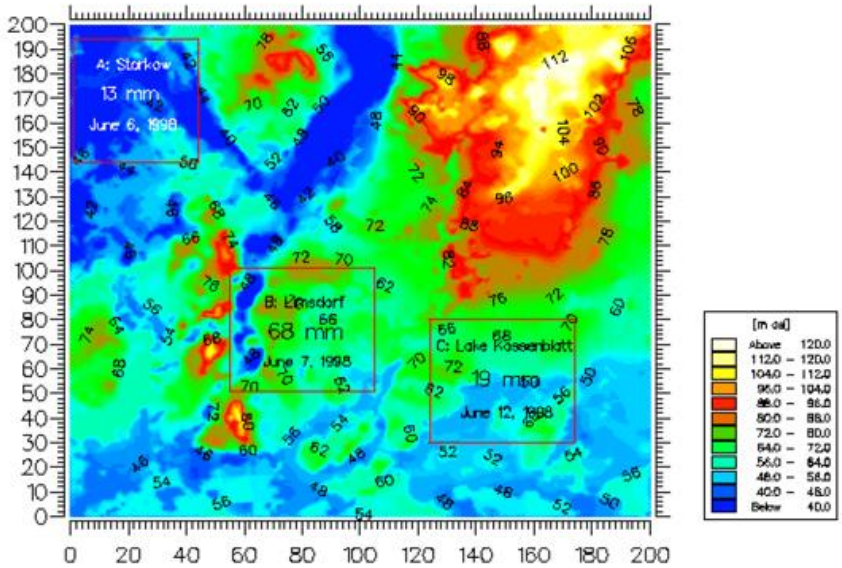


Figure 5.31: Locations with measured maximum precipitation sums over the LITFASS-98 simulation period.

References

Arakawa, A., 1984: Boundary conditions in limited-area models. *Short- and Medium Range Weather Prediction Research Publ. Series*, No. 13, 403-433.

Bailey, W. C., and J. A. Davies, 1980: Bulk stomatal resistance control on evaporation. Agricultural Canada Research Station, Beaverlodge, Alberta Department of Geography, Mc. Master University Hamilton, Ontario.

Beyrich, F. (ed.), 2000: LITFASS-98 Experiment 25.05.1998-30.06.1998. *Experiment Report, Deutscher Wetterdienst, Forschung und Entwicklung, Arbeitsergebnisse Nr. 62*, 78 p.

Binder, P., and H.-J. Herzog, 1995: A radiative upper boundary condition in for a 3-dimensional meso-γ-scale NWP model. *Res. Activities in Atmosph. and Ocean, Modelling Rep. No. 21*, WMO/TD-No. 665.

Bougeault, Ph., 1983: A non-reflective upper boundary condition for limited-height hydrostatic models. *Mon. Wea. Rev.*, 111, 420-429.

Brown, A. R., S. H. Derbyshire, and P. J. Mason, 1994: Large-eddy simulation of stable atmosheric boundary layers with a revised stochastic subgrid model. *Q. J. R. Meteorol. Soc.*, 120, 1485-1512.

Brücher, W., 1997: Numerische Studien zum Mehrfachnesting mit einem nicht-hydrostatischen Modell. *Mitteilungen aus dem Institut für Geophysik und Meteorologie der Universit zu Köln.* Heft 119.

Chen, J. H., 1973: Numerical boundary conditions and computational modes. *J. of Comput. Physics*, 13, 522-535.

Chlond, A., 1999: Grobstruktursimulation- eine Methode zur Berechnung turbulenter atmosphärischer Strömungen. *Max-Planck-Institut für Meteorologie, Examensarbeit Nr. 66*, Hamburg, Juli 1999, 181 S.

Davies, H. C., 1976: A lateral boundary formulation for multi-level prediction models. *Quart. J. R. Met. Soc.*, 102, 405-418.

Davies, A., W. Schertzer, and M. Nunez, 1975: Estimating global solar radiation. *Boundary-Layer Meteorology*, 9, 33-52.

Doms, G., and U. Schättler, 1999: The Nonhydrostatic Limited-Area Model LM (Lokal Modell) of DWD. Part I: Scientific Documentation, Prelim. Vers. LM_F90, Jan. 1999, 169 p., Deutscher Wetterdienst, Geschäftsbereich Forschung und Entwicklung, Postbox 100465, D-63004, Offenbach, Germany; available at *www.cosmo-model.org.*

Görsdorf, U., F. Beyrich, H. Dier, U. Leiterer, J. Güldner, and H.-J. Herzog, 2000: Composite vertical profiles of wind, temperature and humidity for use in numerical modelling. *Extended Abtracts of 5th Int. Symposium on Tropospheric Profiling: Needs and Technology*, pp.65-68, Adelaide, Australia.

Herzog, H.-J., 1995: Testing a radiative upper boundary condition in a nonlinear model with hybrid vertical coordinate. *Meteorol. and Atmosph. Phys.*, 55, 185-204.

Herzog, H.-J., and A. Fiedler, 1999: Bericht über 3D semi-implizite Testläufe mit einer LES-Version des Lokalmodells. Internal Working Report, August 1999.

Hierold, W., U. Schumacher, R. Ziethen and D. Becker, 1977: Bodenübersichtskarte für das LITFASS-Gitterelement Lindenberg des DWD. Zentrum für Agrarlandschafts- und Landnutzungsforschung e.V., Forschungsstation Eberswalde.

Ikawa, M., and K. Saito, 1991: Description of a nonhydrostatic model developed at the forecast research department of the MRI. *Techn. Reports of the Met. Res. Institute*, No. 28, Dec. 1991, 238 p.

Jacobsen, I., and E. Heise, 1982: A new economic method for the computation of the surface temperature in numerical models. *Contrib. Atm. Phys.*, 55, 128-141.

Jürrens, R., 1996: Parameterisierung der Gebietsverdunstung zur Verwendung in meso- und makroskaligen meteorologischen Simulationsmodellen. *Berichte des Instituts für Meteorologie und Klimatologie der Universität Hannover*, Band 53.

Kallberg, P. W., and J. K. Gibson, 1977: Lateral boundary conditions for a limited area version of the EMWF-model. *The GARP Programme on Numerical Experimentation, Report No. 44*, 103-105.

Kanak, K. M., D. K. Lilly, and J. T. Snow, 2000: The formation of vertical vortices in the convective boundary layer. *Q. J. R. Meteorol. Soc.*, 126, 2789-2810.

Klemp, J. B., and R. D. Durran, 1983: An upper boundary condition permitting internal gravity wave radiation in numerical mesoscale models. *Mon. Wea. Rev.*, 111, 430-444.

Klemp, J. B., and R. B. Wilhelmson, 1978: The simulation of three-dimensional convective storm dynamics. *J. Atm. Sci.*, 35, 1070-1096.

Löpmeier, F. J., 1983: Agrarmeteorologisches Modell zur Berechnung der aktuellen Verdunstung (AMBAV). *Beiträge zur Agrarmeteorologie*, Nr. 7, Deutscher Wetterdienst, Zentrale agrarmeteorologische Forschungsstelle Braunschweig.

Mason, P. J., 1994: Large-eddy simulation: A critical review of the technique. *Q. J. R. Meteorol. Soc.*, 120, 1-26.

Mason, P. J., and A. R. Brown, 1999: On Subgrid Models and Filter Operations in Large Eddy Simulations. *J. Atm. Sci.*, 56, 2101-2114.

Miller, M. J., and A. J. Thorpe, 1981: Radiation conditions for the lateral boundaries of limited-area numerical models. *Quart. J. R. Met. Soc.*, 107, 615-628.

Miyakoda, K., and A. Rosati, 1977: One-way nested grid models: The interface conditions and the numerical accuracy. *Mon. Wea. Rev.*, 105, 1072-1107.

Müller, E. et al., 1995: LITFASS - a nucleus for a BALTEX field experiment. *Deutscher Wetterdienst, Forschung und Entwicklung, Arbeitsergebnisse Nr. 33*, 17 p.

Orlanski, J., 1976: A simple boundary condition for unbounded hyperbolic flows. *J. of Comput. Physics*, 21, 251-269.

Perkey, D. J., and C. W. Kreitzberg, 1976: A time dependent lateral boundary scheme for limited area primitive equation models. *Mon. Wea. Rev.*, 104, 744-755.

Podlasly, Ch., and F. Berger, 1999: Bereitstellung von Strahlungsgrössen aus NOAA- und METEOSAT-Messungen für den Strahlungsantrieb des LLM. Abschlussbericht zum DWD-Projekt MOP/63/98. Technische UniversitätDresden, Institut für Hydrologie und Meteorologie, Lehrstuhl für Meteorologie.

Rietschel, 1994: Raumklimatechnik, Band 1 Grundlagen. Hrsg.: Esdorn, H., Springer-Verlag, Berlin Heidelberg New York.

Rosenow, W., 1998: Personal communication.

Saito, K., G. Doms, U. Schättler, and J. Steppeler, 1998: 3-D Mountain Waves by the Lokal-Modell of DWD and the MRI Mesoscale Nonhydrostatic Model. *Papers in Meteorol. and Geophys.* 49, 1, 7-19.

Scotti, A., C. Meneveau, and D. K. Lilly, 1993: Generalized Smagorinsky model for anisotropic grids. *Phys. Fluids*, A5 (9), 2306-2308.

Scotti, A., C. Meneveau, and M. Fatica, 1997: Dynamic Smagorinsky model on anisotropic grids. *Phys. Fluids*, 9 (6), 1856-1858.

Skamarock, W. C., and J. B. Klemp, 1992: The stability of time-split numerical methods for the hydrostatic and the nonhydrostatic elastic equations. *Mon. Wea. Rev.*, 120, 2109-2127.

Smagorinsky, J., 1963: General circulation experiments with the primitive equations: 1. The basic experiment. *Mon. Wea. Rev.*, 91, 99-164.

Stevens, D. E. et al., 2000: Small-Scale Processes and Entrainment in a Stratocumulus Marine Boundary Layer. *J. Atm. Sci.*, 57, 567-581.

Stull, R. B., 1988: An introduction to boundary layer Meteorology. Kluwer Academic Publishers, Dordrecht/Boston/London, 666 p.

Thomas, S., and C. Girard, 1998 a: Semi-implicit scheme for the DWD LM model. Internal Working Report, August 1998, 27 p.

Thomas, S., C. Girard, and R. Benoit, 1998 b: A new adiabatic Kernel for the MC2 model. *Atmosphere-Ocean*, 36(3), 241-270.

Uchijima, Z., 1976: Maize and rice. In: J.L. Monteith, Ed.: Vegetation and the atmosphere, Volume 2, Academic Press London.

VDI Guideline 1994: Wechselwirkungen zwischen Atmosphäre und Oberflächen. Berechnung der kurz- und langwelligen Strahlung. *Verein Deutscher Ingenieure VDI 3789 Blatt 2*, Oktober 1994.

Vogelgesang, R., 1993: Agrarmeteorologisches Modell zur Berechnung von aktueller Verdunstung und Bodenfeuchte. *Deutscher Wetterdienst, Abteilung Agrarmeteorologie, FE-Vorhaben AM 1 -Nr. 85/01.*

Zimmermann, F., 1994 a: Biotopkartierung Brandenburg - Kartierungsanleitung. Landesumweltamt Brandenburg, Potsdam.

Zimmermann, F., 1994 b: Biotopkartierung Brandenburg - Erfassungsstand und Umsetzung. *Naturschutz und Landschaftspflege*, Heft 2, Potsdam.

An Epilogue to Part I

Although in the Introduction announced that the entire LLM-report will contain nine Chapters, the presented Part I with its first five Chapters may be already reason enough to us for some comments and acknowledgements. First of all, the authors dedicate their paper to Dr. E. Müller. He gave the decisive impetus to the LITFASS-project, and it was particularly his basic idea to determine near-surface turbulent fluxes over a realistic inhomogeneous area like Lindenberg by use of a high-resolving nonhydrostatic simulation model. It was a great challenge for us to start working in this field and to bring that task till to the present state. We will not deny our feeling to have worked not only hard over a longer time but to have also always been conscious of taking part in a DWD-pilot project of sustainable meaning, where all the investment over that project time is now available to connect observatory capacity immediately with the urgent needs of NWP - and to have contributed so far with our efforts in this line. We appreciate very much E. Müller's productive impatience, criticism and his permanent interest over most of the project time until his retirement.

Furthermore, all the countless working meetings and discussions in various circles of colleagues from the NWP modelling groups of the Research/Development field and the Observatory Lindenberg have been indispensible. In that way a close cooperation with Dr. E. Heise, the leader of the NWP-parameterization group, must be emphasized, who himself was involved in the LITFASS-project from the very beginning. In the first years of the project Prof. Th. Foken has been the leader and coordinator. After that, Dr. F. Beyrich's intensive conduction of LITFASS brought us great benefit due to his indivisible sense of responsibility both for the measurement - and the simulation component. Concerning important details, we are thankful to Prof's H. Fortak, G. Groß and to Dr. A. Dörnbrack for several hints, advices and their general interest to our topic. Almost all extensive LLM-integrations has been carried out at the ECMWF. The care for the great many of series of LLM-runs was excellent. We are very grateful to the people in the Computing Centre there, who were involved with our jobs. In particular, N. Kreitz from the User Support has actually supported us very intensively.

Concerning ourselves, the first author was told to be responsible for the whole LLM-subproject of LITFASS, while he is also responsible for the subjects of Chapters 1-4 and 7 in Part II. Dr. G. Vogel is responsible for the content of Chapter 5 and in Part II for Chapters 6 and 8. Mrs. Dr. U. Schubert's contributions are overlapping. She has solved all problems of programming and program organization concerning the specific LLM-problem of external real-data updating at low, lateral and upper boundaries, and moreover, she has organized and managed all computing runs at ECMWF, the postprocessing there included. She wrote Chapter 9 about the LLM-computing problems. Mrs. A. Fiedler is responsible for all programs in parallel code contained in Chapters 2-4 (lateral boundary technique, inclusion of 3D-turbulent flux termes, TKE-SGS model) and for preparing all Figures in these Chapters. Mrs. R. Kirchner's contributions and untiring efforts concern the widespread delivery and preparation of model- and measurement data necessary for the LLM and for different purposes of validation. Finally, the authors are very grateful to Mrs. E. Sulz for her reliable assistance in the wide field of postprocessing and to Mrs. Ch. Baudach, who wrote the text in that final form.

List of COSMO Newsletters and Technical Reports

(available for download from the COSMO Website: www.cosmo-model.org)

COSMO Newsletters

Newsletter No.1, February 2001.

Newsletter No.2, February 2002.

COSMO Technical Reports

No. 1, Dmitrii Mironov and Matthias Raschendorfer (2001): *Evaluation of Empirical Parameters of the New LM Surface-Layer Parameterization Scheme. Results from Numerical Experiments Including the Soil Moisture Analysis.*

No. 2, Reinhold Schrodin and Erdmann Heise (2001): *The Multi-Layer Version of the DWD Soil Model TERRA_LM.*

No. 3, Günther Doms (2001): *A Scheme for Monotonic Numerical Diffusion in the LM.*

No. 4, Hans-Joachim Herzog, Ursula Schubert, Gerd Vogel, Adelheid Fiedler and Roswitha Kirchner (2002): *LLM – the High-Resolving Nonhydrostatic Simulation Model in the DWD – Project LITFASS. Part I: Modelling Technique and Simulation Method.*

COSMO Technical Reports

Issues of the COSMO Technical Reports series are published by the *Consortium for Small-Scale Modelling* at non-regular intervals. COSMO is a European group for numerical weather prediction with participating meteorological services from Germany (DWD, AWGeophys), Greece (HNMS), Italy (UGM, ARPA-SMR) and Switzerland (MeteoSwiss). The general goal is to develop, improve and maintain a non-hydrostatic limited area modelling system to be used for both operational and research applications by the members of COSMO. This system is initially based on the Lokal-Modell (LM) of DWD with its corresponding data assimilation system.

The Technical Reports are intended

- for scientific contributions and a documentation of research activities,
- to present and discuss results obtained from the model system,
- to present and discuss verification results and interpretation methods,
- for a documentation of technical changes to the model system,
- to give an overview of new components of the model system.

The purpose of these reports is to communicate results, changes and progress related to the LM model system relatively fast within the COSMO consortium, and also to inform other NWP groups on our current research activities. In this way the discussion on a specific topic can be stimulated at an early stage. In order to publish a report very soon after the completition of the manuscript, we have decided to omit a thorough reviewing procedure and only a rough check is done by the editors and a third reviewer. We apologize for typographical and other errors or inconsistencies which may still be present.

At present, the Technical Reports are available for download from the COSMO web site (www.cosmo-model.org). If required, the member meteorological centres can produce hard-copies by their own for distribution within their service. All members of the consortium will be informed about new issues by email.

For any comments and questions, please contact the editors:

Günther Doms
guenther.doms@dwd.de

Ulrich Schättler
ulrich.schaettler@dwd.de

Consortium

for

Small–Scale Modelling

Technical Report No. 7

Lorenz- and Charney-Phillips vertical grid experimentation using a compressible nonhydrostatic toy-model relevant to the fast-mode part of the 'Lokal - Modell'

by

H.-J. Herzog and A. Gassmann

Res severa verum gaudium !

February 2005

DOI: 10.5676/DWD_pub/nwv/cosmo-tr_7

Deutscher Wetterdienst

MeteoSwiss

Ufficio Generale per la Meteorologia

Hellenic National Meteorological Service

Instytut Meteorologii i Gospodarki Wodnej

Il Servicio Meteorologico Regionale di ARPA

Amt für Wehrgeophysik

L'Agenzia Regionale per la Protenzione Ambientale del Piemonte

www.cosmo-model.org

Editors: G. Doms and U. Schättler, Deutscher Wetterdienst, P.O. Box 100465, 63004 Offenbach, Germany
Printed at Deutscher Wetterdienst, Offenbach am Main

Contents

1 Introduction **3**

2 A duplicate of Arakawa and Konor's simulation **5**

3 An LM fast-wave toy-model **7**
3.1 Model equation set 7
3.2 Time differencing scheme 9
3.3 Vertical discretisation with an L-grid 10
3.4 Numerical integration algorithm with an L-grid 12
3.5 Simulations with L-grid model version 15
3.6 Vertical grid-staggering with a CP-grid 17
3.7 Simulation with the CP-grid model version 18

4 Application of a radiative upper boundary condition **22**
4.1 Derivation of the Klemp-Durran-Bougeault type of a radiative upper boundary condition 22
4.2 Implementation of the KDB - RUBC 24
4.3 Results with KDB-RUBC 29

5 Simulations with LM - layering **32**

6 Conclusion **34**

7 References **35**

1 Introduction

It is well known that in numerical atmospheric simulation models for vertical discretisation a so-called Lorenz (L-)-grid or a Charney-Phillips (CP-)-grid is normally applied in order to define the staggered placement of model variables at grid points along the vertical. In case of an L-grid the variables of temperature, pressure and horizontal momentum are placed at 'main-levels', each of them centred within a finite model layer, while the vertical velocity is assumed to be positioned at 'half-levels', which are the interface levels between adjacent model layers. The difference of the CP-grid to the L-grid consists in having placed temperature together with vertical velocity at half-levels. For instance, the Lokal-Modell of the DWD uses an L-grid, while the Unified Model of the United Kingdom Met Office is based on a CP-grid. A representative discussion of pros and cons concerning both types of vertical grid staggering can be found in a thorough paper by Arakawa (2000). There, Arakawa gives statements and draws conclusions from his own work and so from many other authors that the CP-grid seems preferable compared to the L-grid also widespread in use. In order to characterise an obvious shortcoming of the L-grid we quote from Arakawa's article (2000, p.721-780) the following statement: 'The problem with the L-grid is due to the existence of an extra degree of freedom in the vertical distribution of θ that cannot be controlled by any baroclinic (or internal) modes... This extra degree of freedom introduces a vertical "computational mode" in the solution, characterised by a zigzag vertical structure of θ, which has no counterpart in the solutions of the continuous equation... It is important to note, that this problem with the L Grid is a property of the grid rather than of a particular scheme. An increase in order of accuracy does not reduce the error due to this mode because a computational mode cannot become "accurate" since there is no corresponding true solution with which to compare it.'
This statement is a more general motivation, but due to the fact that the Lokal-Modell (=LM) as a model of particular interest uses an L-grid, our concern and starting point comes immediately from a paper by Arakawa and Konor (1996). In this article the main point we are interested in is the author's comparing numerical simulations with the L-grid and the CP-grid. For this, they use two linearised versions of a primitive equation model for meridionally uniform perturbations, one for the grid type L and the other for the CP-grid. In order to show the existence of a computational mode produced by the L-grid and to demonstrate that this artificial effect is avoided in case of a CP-grid, a local initial potential temperature perturbation as one specific set of integration is imposed on a resting isothermal ($T_0 = 250K$) basic state on a zonally cyclic f-plane. The model uses simple centered vertical differences on a p-coordinate and 40 equally spaced layers below 100 Pa. For a detailed description of the model equations and the experimental set-up we refer to Arakawa and Konor (1996). The unbalanced initial perturbation in θ' is set equal to 0.5 K at levels with vertical index k=39/39.5 (k-index is counted downward), and with opposite sign at the adjacent level designed by k=38/38.5 for the L-grid/CP-grid, and $\theta' = 0$ everywhere else.
As an introduction for our own numerical experimentation we deliberately describe and show the experimental set-up and important results from Arakawa and Konor, concerning the isolated effect of a computational mode due to the L-grid. In Figure 1 an important result from the author's original paper is therefore shown again (original Figure 3 from Monthly Weather Review 124, at page 521): The original legend is sufficiently self-explaining. It shows in a time-height plot the evolution over 48 hours integration time of an initially specified spectral perturbation amplitude for two horizontal wave components with a wavelength of 100 km and 250 km, respectively. From another quotation in the relevant paper that simulation result may be characterised as follows. In case of the L-grid simulation '... The flow is dominated by stationary components... The vertically propagating oscillatory component is weak, having significant amplitudes only during early hours.' A pure artificial vertical zigzag structure is obvious. For the CP-grid, however, '... The simulation shows vertical propagation and almost complete dispersion of initial perturbations...' and a stationary computational mode does not occur.

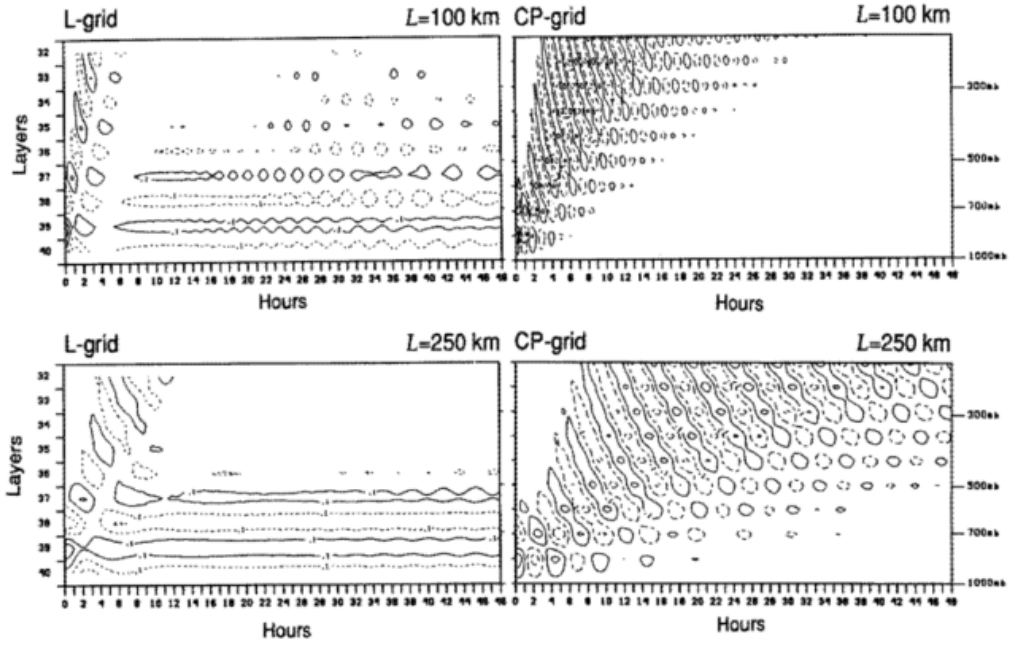


FIG. 3. Time evolution of the potential temperature perturbation θ' (K) in the lower portion of the vertical domain obtained from the models based on the Lorenz (left panels) and Charney–Phillips (right panels) grids for horizontal wavelengths L = 100 km (upper panels) and L = 250 km (lower panels). Simulations are started from unbalanced θ' at two adjacent levels with opposite signs. Solid and dashed lines correspond to positive and negative values, respectively. The contour interval is 0.2 K starting from ±0.1 K.

Figure 1: Original figure taken from Arakawa, A., and C.S. Konor, 1996 (see References)

In a first step of our following numerical simulations we are going to copy as exact as possible both the hydrostatic simulation model and the numerical set-up from Arakawa and Konor's paper, who provide the reader with a fairly good description of their approach. On this ground we were then easily able to copy the results from and could have obtained in such a way a comfortable method, and also an appropriate calibration tool, for our concern with a nonhydrostatic model having important characteristics of the fast-mode part of the LM. With the adopted thickness and number of model layers we were able to demonstrate for the LM-like compressible nonhydrostatic model with L-grid versus CP-grid simulation results similar to Arakawa and Konor's in case of hydrostatic gravity waves, where a computational mode is revealed in case of the L-grid type model, while it is avoided by using a CP-type model. To obtain this sort of simulations in a fairly neat form, we felt it necessary to introduce, in addition, a non-reflective upper boundary condition. Instead of a Rayleigh relaxation-type we have applied an radiative upper boundary condition (=RUBC) as suggested from Klemp and Durran (1983) and Bougeault (1983). Within the scope of this LM-toy model with essential components of the fast mode part of the real LM the possible occurrence of a computational mode due to the L-grid and the application of a CP-grid instead in order to avoid this numerical nuisance will be demonstrated. At this stage of work it seems however too early for a generalisation of that simulation results to draw already the conclusion that the vertical grid staggering in the LM should be changed from the L- to the CP-grid immediately. Neverthless, the results demonstrated in this contribution give serious hints that the LM is suspected to have possible unwanted numerical shortcomings related to the applied L-grid which are worth studying further in a more specific and systematic manner. The importance of this should be underlined by still another quotation from the key paper of Arakawa and Konor: 'The problem of the existence of the computational mode can be serious, especially in the models that include moist processes, since the computational mode can spuriously interact with the physical mode through inherently nonlinear condensation and associated processes. An example of the latter is the effect of cloud layers generated by the zigzag vertical structure of the potential temperature on the radiation field.'

2 A duplicate of Arakawa and Konor's simulation

As explained above we are interested in an almost exact repetition of numerical simulations from Arakawa and Konor (1996). Their results have been depicted in our Figure 1 (taken from the original paper). With strict quotation from that paper all the background may be assumed to be known, that is, how this simulation experiment has been conducted and the model and the numerics were

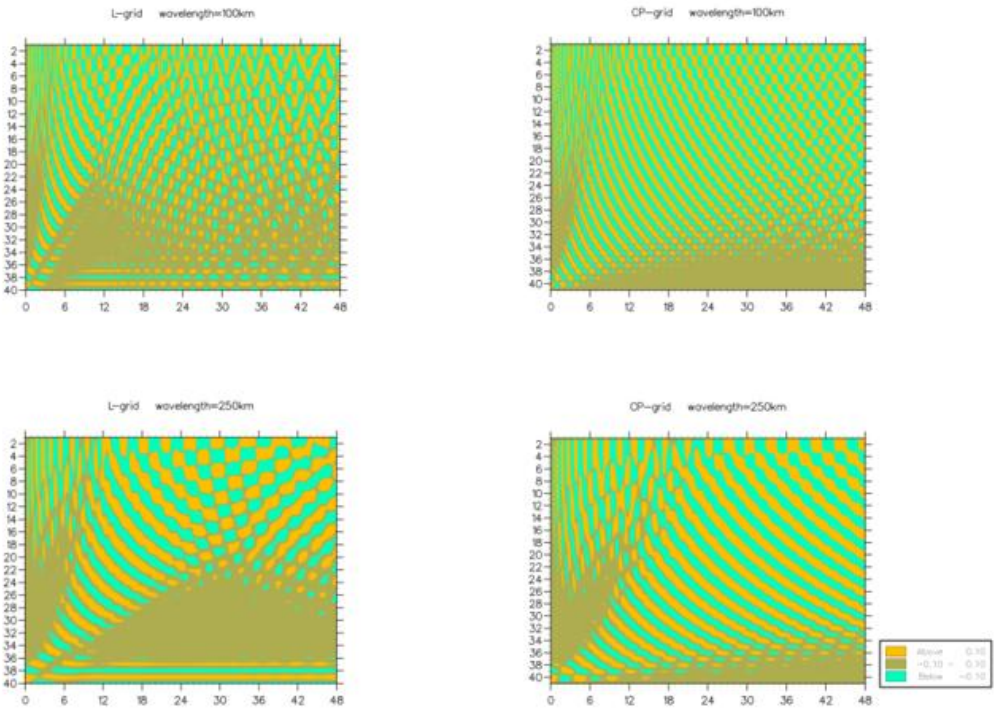


Figure 2: Almost the same result as in Figure 1, but over the entire integration domain, for L-grid (left panels) and CP-grid (right panels) and for horizontal wavelengths 100km (upper panels) and 250km (lower panels). For more details see text.

designed. Moreover, the comments describing the special experiment were already noted in the Introduction and need not be repeated here. In order to almost copy the result of interest shown in Figure 1, we decided to apply the leap-frog scheme as an sufficient numerical time-integration method, and for sake of caution, an Asselin time filter is added at every time step. In case of the model version with L=250km, the time step is chosen $\Delta t = 90s$, for L=100km we used $\Delta t = 30s$. In this way we are now in a position to be able to show the almost identical outcome, but here over the entire integration area, from the lower boundary (at 100000 Pa) up to the upper boundary (at 100 Pa) over 40 equally spaced layers, where the time evolution of the potential temperature perturbation in the lowest 9 layers of Figure 1 is recovered fairly good in Figure 2. In addition to a qualitative discussion of Figure 1 , and so of Figure 2, we make out that the gravity wave perturbations, here expressed in terms of potential temperature and caused by the defined initial state, propagate upward over a wider range of signal velocities different in dependence of an L-grid or a CP-grid, and that in any case these propagating perturbations are reflected at the upper boundary due to an lid condition imposed there. The reflected wave component as an obvious artificial phenomenon can then 'contaminate' in case of the L-grid even the computational mode of our concern. For the smaller spectral component with L=100km the degree of reflection seems more obvious than for L=250km, and for the experimental set with an CP-grid the strength of reflection seems apparently reduced compared to the model version with L-grid.

In the following we are interested in eliminating the reflected wave mode, which may be done by use of a radiative upper boundary condition (RUBC) instead of the lid condition. For the Arakawa-Konor model (AKM), which is linear and a hydrostatic one, the Klemp-Durran-Bougeault typ of an RUBC (=KDB-RUBC) is expected to be sufficient as an appropriate tool. Since the model variables in the AKM are spectral amplitudes of a horizontal wave component depending on pressure and time, the application of the KDB-RUBC is ideal. As known, this BC is local in time but global over the upper boundary level. In general, this needs the Fourier transforms of vertical motion and a mass variable at the upper boundary. Here, the RUBC is easily formulated in terms of the defined model variables without an additional transform. The reader may be convinced about this from a necessary reference to the original paper of Arakawa and Konor (1996). After a thorough and classical analysis we can derive the appropriate RUBC for the given AKM. It reads

$$\hat{\omega}_{top} = -\frac{k\ p_{top}}{c_0}\hat{\phi}_{top} \tag{1}$$

instead of the lid condition $\hat{\omega}_{top} = 0$. For the perturbation geopotential and vertical velocity variables of the given model we have

$$\phi^{'}(x,p,t) = \hat{\phi}(p,t)\ sin\, kx \quad , \quad \omega^{'}(x,p,t) = \hat{\omega}(p,t)\ sin\, kx \tag{2}$$

with horizontal wavenumber $k = 2\pi/L$, $p_{top} = 100\,Pa$, and the parameter $c_0 = +\sqrt{\kappa R T_0}, \kappa = c_p/c_v$. Here we make use of the normal meteorological notation also valid for the AKM . This form of a KDB-RUBC has been applied in the AKM for both its L-grid and its CP-grid version. It is important to note that in accordance with (1) the geopotential needed at the upper boundary (the uppermost half-level) must be extrapolated by use of an uncentered difference form of the hydrostatic equation different for L-grid and CP-grid due to different positions of the potential temperature on these grids. In that way we have repeated the AKM simulations, and the corresponding results are shown in Figure 3 [1] for the case with L =100km.

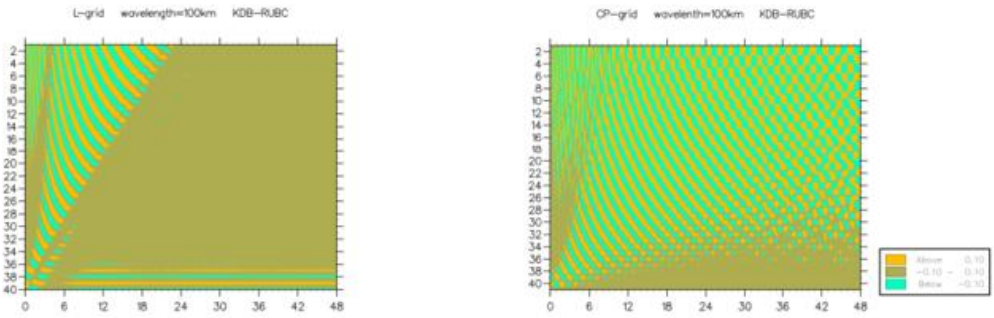


Figure 3: Repetition of Arakawa and Konor's (1996) simulation for L-grid and CP- grid with L =100km, but a radiative upper boundary condition taken into account (compare with upper panel of Figure 2).

A comparison with Figure 2 demonstrates that the reflection from the upper boundary could be removed as desired. Similar results not shown here were found for the wavelength L= 250km. In contrast to the CP-grid, we observe for the L-grid simulation a significant limitation of the gravity wave dispersion process accompanied by the stationary zigzag phenomenon of a computational mode.

[1] It needs a technical remark concerning Figures 2 and 3 and so on all Figures of this type. The contour colours are meant as follows: *brown* covers an interval from $\pm\,0.1\ K$, *yellow* covers values $>\ 0.1\ K$, and *green* is valid for $<\ -0.1\ K$

3 An LM fast-wave toy-model

With the information from Arakawa and Konor's simulation example, we turn now to the compressible nonhydrostatic equations in a linearised form, having in mind the relation to the fast-mode part of the LM. For this we refer to a thorough description of the LM dynamics and numerics documented by Doms and Schättler (2002). On this ground we are going to derive an appropriate simulation model with properties as much as possible of Arakawa and Konor's model set-up.

3.1 Model equation set

Starting point is the following equation set

$$\frac{\partial u'}{\partial t} = -\frac{1}{\bar{\rho}}\left(\frac{\partial p'}{\partial x} - \frac{1}{\sqrt{\gamma}}\frac{\partial \bar{p}}{\partial x}\frac{\partial p'}{\partial \zeta}\right) + f_0 v' \tag{3}$$

$$\frac{\partial v'}{\partial t} = \quad -f_0 v' \tag{4}$$

$$\frac{\partial w'}{\partial t} = \frac{g}{\sqrt{\gamma}}\frac{\partial p'}{\partial \zeta} - g\left(\frac{p'}{\bar{p}} - \frac{T'}{\bar{T}}\right) \tag{5}$$

$$\frac{\partial p'}{\partial t} = g\bar{\rho}w' - \kappa\bar{p}\left(\frac{\partial u'}{\partial x} - \frac{1}{\sqrt{\gamma}}\frac{\partial \bar{p}}{\partial x}\frac{\partial u'}{\partial \zeta} - \frac{g\bar{\rho}}{\sqrt{\gamma}}\frac{\partial w'}{\partial \zeta}\right) \tag{6}$$

$$\frac{\partial T'}{\partial t} = \frac{g\bar{\rho}}{\sqrt{\gamma}}\frac{d\bar{T}}{d\zeta}w' - \frac{\kappa}{c_p}\frac{\bar{p}}{\bar{\rho}}\left(\frac{\partial u'}{\partial x} - \frac{1}{\sqrt{\gamma}}\frac{\partial \bar{p}}{\partial x}\frac{\partial u'}{\partial \zeta} - \frac{g\bar{\rho}}{\sqrt{\gamma}}\frac{\partial w'}{\partial \zeta}\right) \tag{7}$$

These equations follow approximately from the fast-mode equation part of the LM by consequent linearisation. The perturbation variables (primed entities) are assumed to be meridionally uniform. Spherical metric terms have been dropped for the sake of simplicity. The variables $\bar{p}$, $\bar{\rho}$, $\bar{T}$ constitute a hydrostatic basic state. The vertical coordinate ζ is meant just as in the LM. In relation to the usual z-coordinate the following operator is valid

$$\frac{\partial}{\partial z} = -\frac{g\bar{\rho}}{\sqrt{\gamma}}\frac{\partial}{\partial \zeta} \tag{8}$$

Here, the reciprocal pre-factor $\left(\sqrt{\gamma}\right) / \left(g\bar{\rho}\right)$ is defined as the Jacobian of the transformation from the z- to the ζ - coordinate. The equation set (3) - (7) deviates slightly from the present formulation in the fast-wave part of the LM. In order to take into account inertia-gravity waves, that is without separation of the rotational effect, the Coriolis terms are included here. Further, we emphasize the presence of the first term on the right-hand side of equation (7), which is significant in case of a non-isothermal basic state as it is for the LM. There, a polytropic state is stipulated. Neglecting the term in that case leads however to an inconsistency concerning the gravity wave energetics and an overestimation of the gravity wave frequencies. To evade this problem a-priori, a prognostic equation for θ' should be used rather than for T'. We do so , although from the discussed point of view unnecessary, because we prefer an isothermal basic state which makes that term vanishing.

With this choice we are deliberately in accordance with the basic state of the AKM. Without any loss of physical background the vertical z- coordinate is simply taken, and a horizontally plane terrain may be sufficient for our considerations to be assumed. Thus, we change with these assumptions from (3) - (7) to a physically identical set

$$\frac{\partial u^{'}}{\partial t} = -\frac{1}{\bar{\rho}}\frac{\partial p^{'}}{\partial x} + f_0 v \tag{9}$$

$$\frac{\partial v^{'}}{\partial t} = -f_0 u^{'} \tag{10}$$

$$\frac{\partial w^{'}}{\partial t} = -\frac{1}{\bar{\rho}}\frac{\partial p^{'}}{\partial z} - \frac{g}{\bar{\rho}\, c_s^2}\, p^{'} + \frac{g}{\bar{\theta}}\theta^{'} \tag{11}$$

$$\frac{\partial p^{'}}{\partial t} = g\bar{\rho} w^{'} - c_s^2 \bar{\rho}\left(\frac{\partial u^{'}}{\partial x} + \frac{\partial w^{'}}{\partial z}\right) \tag{12}$$

$$\frac{\partial \theta^{'}}{\partial t} = -\frac{N^2}{g}\bar{\theta}\; w^{'} \tag{13}$$

For the isothermal basic state we have

$$N^2 = \frac{g}{\bar{\theta}}\frac{d\bar{\theta}}{d\, z} = \frac{g^2}{c_p\, T_0}\;\;,\;\; \bar{\theta} = T_0\; exp\left(\frac{N^2}{g} z\right)\;\;,\;\; \bar{\rho} = \frac{p_s}{R\, T_0}\; exp\left(-\frac{g}{c_p T_0} z\right) \tag{14}$$

with the familiar constants $c_s^2 = \kappa \bar{p}/\bar{\rho} = \kappa\; RT_0\;\;,\;\; \kappa = c_p/c_v\;\;,\;\; T_0 = 250K$, and $p_s = 100000\, Pa$ at the lower boundary. In order to perform similar numerical experiments as Arakawa and Konor (1996) demonstrated, we assume also that the perturbations are horizontally standing waves in the forms:

$$\begin{gathered} u^{'}(x,z,t) = \hat{u}(z,t)\, cos\, kx\;\;,\;\; v^{'}(x,z,t) = \hat{v}(z,t)\, cos\, kx \\ w^{'}(x,z,t) = \hat{w}(z,t)\, sin\, kx\;\;,\;\; p^{'}(x,z,t) = \hat{p}(z,t)\, sin\, kx\;\;,\;\; \theta^{'}(x,z,t) = \hat{\theta}(z,t)\, sin\, kx \end{gathered} \tag{15}$$

$k = 2\pi/L$ is the zonal wavenumber with the wavelength L. Inserting the wave-components (15) into the above equation set, we obtain a simple prognostic equation system for the perturbation amplitudes of their horizontal wave-components with wavelength L:

$$\frac{\partial \hat{u}}{\partial t} = -\frac{k}{\bar{\rho}}\hat{p} + f_0 \hat{v} \tag{16}$$

$$\frac{\partial \hat{v}}{\partial t} = -f_0 \hat{u} \tag{17}$$

$$\frac{\partial \hat{w}}{\partial t} = -\frac{1}{\bar{\rho}}\frac{\partial \hat{p}}{\partial z} - \frac{g}{\hat{\rho} c_s^2}\hat{p} + \frac{g}{\bar{\theta}}\hat{\theta} \tag{18}$$

$$\frac{\partial \hat{p}}{\partial t} = g\bar{\rho}\hat{w} - c_s^2\bar{\rho}\left(\frac{\partial \hat{w}}{\partial z} - k\,\hat{u}\right) \tag{19}$$

$$\frac{\partial \hat{\theta}}{\partial t} = -\frac{N^2\bar{\theta}}{g}\hat{w} \tag{20}$$

The associated local total energy budget equation reads

$$\frac{\partial}{\partial t}\left[\frac{1}{2}\bar{\rho}\left(\hat{u}^2+\hat{v}^2+\hat{w}^2\right) + \frac{1}{2c_s^2\bar{\rho}}\hat{\rho}^2 + \frac{g^2\bar{\rho}}{2N^2}\left(\frac{\hat{\theta}}{\bar{\theta}}\right)^2\right] = -\frac{\partial\left(\hat{p}\;\hat{w}\right)}{\partial z} \tag{21}$$

and, for some reasoning further below, we note here the normal mode frequencies for the internal gravity waves solution (ω_g) and the acoustic wave solution (ω_a) of the equation set (16) - (20) with the rotational effect ignored $(f_0 = 0)$, following an usual analysis:

$$\omega_a^2 \approx c_s^2\left(k^2+n^2+\frac{1}{4H^2}\right) \tag{22}$$

$$\omega_g^2 \approx \frac{k^2N^2}{k^2+n^2+\frac{1}{4H^2}} \tag{23}$$

n denotes a vertical wavenumber, and H , $\left(H^{-1} = g/c_s^2 + N^2/g\right)$, a constant vertical scale height.

3.2 Time differencing scheme

For our linear system (16) - (20) we are going to adopt the time integration scheme as close as possible from the fast mode part of the LM. To compare that with the LM we refer to the thorough LM-documentation by Doms and Schättler (2002) and there with further quotations of Skamarock and Klemp (1992), Ikawa (1988), and Dudhia (1993). With that application we have here

$$\frac{\hat{u}^{(\tau+1)} - \hat{u}^{(\tau)}}{\Delta t} = -\frac{k}{\bar{\rho}}\hat{p}^{(\tau)} + f_0\hat{v}^{(\tau+1)} \tag{24}$$

$$\frac{\hat{v}^{(\tau+1)} - \hat{v}^{(\tau)}}{\Delta t} = -f_0\hat{u}^{(\tau+1)} \tag{25}$$

$$\begin{aligned}\frac{\hat{w}^{(\tau+1)} - \hat{w}^{(\tau)}}{\Delta t} = &-\frac{1}{\bar{\rho}}\left(\beta^+\frac{\partial \hat{p}^{(\tau+1)}}{\partial z} + \beta^-\frac{\partial \hat{p}^{(\tau)}}{\partial z}\right)\\ &-\frac{g}{\bar{\rho}c_s^2}\left(\beta^+\hat{p}^{(\tau+1)} + \beta^-\hat{p}^{(\tau)}\right) + \frac{g}{\bar{\theta}}\hat{\theta}^{(\tau)}\end{aligned} \tag{26}$$

$$\begin{aligned}\frac{\hat{p}^{(\tau+1)} - \hat{p}^{(\tau)}}{\Delta t} = &\;g\bar{\rho}\left(\beta^+\hat{w}^{(\tau+1)} + \beta^-\hat{w}^{(\tau)}\right)\\ &-c_s^2\bar{\rho}\left(\beta_+\frac{\partial \hat{w}^{(\tau+1)}}{\partial z} + \beta^-\frac{\partial \hat{w}^{(\tau)}}{\partial z}\right) + c_s^2\bar{\rho}\,k\,\hat{u}^{(\tau+1)}\end{aligned} \tag{27}$$

$$\frac{\hat{\theta}^{(\tau+1)} - \hat{\theta}^{(\tau)}}{\Delta t} = -\frac{N^2\bar{\theta}}{g}\left(\beta^+\hat{w}^{(\tau+1)} + \beta^-\hat{w}^{(\tau)}\right) \tag{28}$$

As one can see, the terms for vertically propagating waves are treated implicitly. For the weights of averaging these terms we have

$$\beta^+ = \frac{1}{2}(1+\varepsilon) \quad , \quad \beta^- = \frac{1}{2}(1-\varepsilon) \tag{29}$$

with the LM default-value $\varepsilon = 0.4$, determining the strength of implicity of the scheme. Since the scheme in this form behaves neutral for acoustic waves, a so-called divergence damping is added in the horizontal momentum equations as a remedy, which in our case means that in equation (24) the pressure in the gradient term is replaced such

$$\hat{p}^{(\tau)} := \hat{p}^{(\tau)} + \alpha_d\,\Delta t\,\bar{\rho}c_s^2\left(k\,\hat{u}^{(\tau)} - \frac{\partial\hat{w}^{(\tau)}}{\partial z}\right) \tag{30}$$

$\alpha_d = 0.1$ is the default-value used in the LM. We drop here critical remarks concerning this measure. The inclusion of the rotation terms in the momentum equations deviates from the LM fast-mode part, but is a concession to the AKM with which we want to compare our solutions. For the sake of stability these terms are formulated implicitly.

3.3 Vertical discretisation with an L-grid

In addition to the semi-discrete equations (24)- (28) with an LM-specific time differencing scheme, we want to exactly apply the vertical layering from the AKM with either an L-grid or a CP-grid. We introduce the L-grid first. In this way the scheme is shown in Figure 4

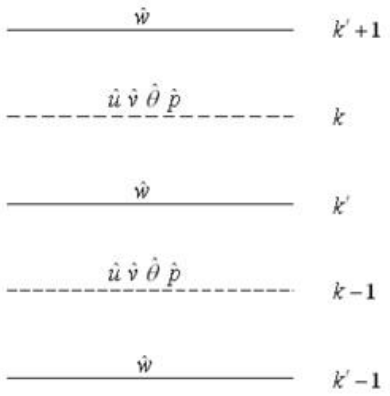


Figure 4: Vertical staggering of variables of LM fast-wave toy-model with equally spaced layers in accordance with AKM (see text)

As can be seen, the variables $\hat{u}, \hat{v}, \hat{\theta}, \hat{p}$ (and also $\bar{\rho}, \bar{\theta}$, not shown in Figure 4) are positioned at main-levels indicated with indices $k \in [1, ke]$, while the perturbation amplitude of vertical velocity, $\hat{w}$, is defined at so-called half-levels with index numbering $k' \in [1, ke1]$. Coinciding with the numerical set-up in the AKM, we assume 40 model layers, which means $ke = 40$ and $ke1 = ke + 1$. In accordance with a vertical z-coordinate the index k is counted upward here, which is in contrast to

the LM with its terrain-following coordinate. The thickness of model-layers is constant. It is given by

$$\Delta z = \frac{1}{40}\frac{RT_0}{g} ln(1000) \qquad . \tag{31}$$

With that scheme we introduce simple centred differences in the vertical in the equation system (24) - (28), which leads straightforward to the following difference equation system:

$$\hat{u}_k^{(\tau+1)} = \hat{u}_k^{(\tau)} - \Delta t \frac{k}{\bar{\rho}} \hat{p}_k^{(\tau)} + f_0 \, \Delta t \, \hat{v}_k^{(\tau+1)} \tag{32}$$

$$\hat{v}_k^{(\tau+1)} = \hat{v}_k^{(\tau)} - \Delta t \, f_0 \, \hat{u}_k^{(\tau+1)} \tag{33}$$

for $k \in [1, ke]$.

$$\begin{aligned} \hat{w}_{k'}^{(\tau+1)} = \hat{w}_{k'}^{(\tau)} &- \frac{2}{\bar{\rho}_{k-1} + \bar{\rho}_k} \left(\frac{\Delta t}{\Delta z}\right) \beta^+ \left(\hat{p}_k^{(\tau+1)} - \hat{p}_{k-1}^{(\tau+1)}\right) \\ &- \frac{2}{\bar{\rho}_{k-1} + \bar{\rho}_k} \left(\frac{g \Delta t}{2c_s^2}\right) \beta^+ \left(\hat{p}_k^{(\tau+1)} + \hat{p}_{k-1}^{(\tau+1)}\right) + C_{k'}^w \end{aligned} \tag{34}$$

with

$$\begin{aligned} C_{k'}^w = &- \frac{2}{\bar{\rho}_{k-1} + \bar{\rho}_k} \left(\frac{\Delta t}{\Delta z}\right) \beta^- \left(\hat{p}_k^{(\tau)} - \hat{p}_{k-1}^{(\tau)}\right) \\ &- \frac{2}{\bar{\rho}_{k-1} + \bar{\rho}_k} \left(\frac{g \Delta t}{2c_s^2}\right) \beta^- \left(\hat{p}_k^{(\tau)} + \hat{p}_{k-1}^{(\tau)}\right) + \frac{g \Delta t}{2} \left(\left(\frac{\hat{\theta}^\tau}{\bar{\theta}}\right)_k + \left(\frac{\hat{\theta}^\tau}{\bar{\theta}}\right)_{k-1}\right) \end{aligned} \tag{35}$$

$$\begin{aligned} \hat{p}_k^{(\tau+1)} = \hat{p}_k^{(\tau)} &- \left(\frac{c_s^2 \Delta t}{\Delta z}\right) \bar{\rho}_k \; \beta^+ \left(\hat{w}_{k'+1}^{(\tau+1)} - \hat{w}_{k'}^{(\tau+1)}\right) \\ &+ \left(\frac{g \Delta t}{2}\right) \bar{\rho}_k \; \beta^+ \left(\hat{w}_{k'+1}^{(\tau+1)} + \hat{w}_{k'}^{(\tau+1)}\right) + C_k^p \end{aligned} \tag{36}$$

with

$$\begin{aligned} C_k^p = &- \left(\frac{c_s^2 \Delta t}{\Delta z}\right) \bar{\rho}_k \; \beta^- \left(\hat{w}_{k'+1}^{(\tau)} - \hat{w}_{k'}^{(\tau)}\right) \\ &+ \left(\frac{g \Delta t}{2}\right) \bar{\rho}_k \; \beta^- \left(\hat{w}_{k'+1}^{(\tau)} + \hat{w}_{k'}^{(\tau)}\right) + \Delta t \, c_s^2 \, k \, \bar{\rho}_k \, \hat{u}_k^{(\tau+1)} \end{aligned} \tag{37}$$

for $k \in [1, ke]$.

$$\hat{\theta}_k^{(\tau+1)} = \hat{\theta}_k^{(\tau)} - \left(\frac{N^2 \bar{\theta}}{g}\right)_k \Delta t \left[\beta^+ \left(\frac{\hat{w}_{k'}^{(\tau+1)} + \hat{w}_{k'+1}^{(\tau+1)}}{2}\right) + \beta^- \left(\frac{\hat{w}_{k'}^{(\tau)} + \hat{w}_{k'+1}}{2}\right)\right] \tag{38}$$

for $k \in [1, ke]$.

For the application of these difference equations boundary conditions for $\hat{w}$ have to be taken into account

$$\begin{aligned} &\text{at the lower boundary:} \quad \hat{w}_1 = 0 \quad \text{and} \\ &\text{at the upper boundary:} \quad \hat{w}_{ke1} = 0 \quad \text{(lid-condition).} \end{aligned} \tag{39}$$

(It should be mentioned, that our notation is not quite consistent, since the symbol k is used to indicate both the horizontal wavenumber and a vertical gridpoint index as subscript. The physical background may, however, prevent any confusion!)

3.4 Numerical integration algorithm with an L-grid

Here, we rewrite the difference equations (32)-(39) with its implicit formulation of time differences to come to an explicit time integration process. This will be done just as demonstrated in Doms and Schättler (2002) for the LM. For the *horizontal momentum equations* (32) and (33) it follows easily

$$\hat{u}_k^{(\tau+1)} = \left(1 + \Delta t^2 \, f_0^2\right)^{-1} \left(\hat{u}_k^{(\tau)} + \Delta t \, f_0 \, \hat{v}_k^{(\tau)} - \Delta t \, \frac{k}{\bar{\rho}_k} \, \hat{p}_k^{(\tau)} \right) \tag{40}$$

$$\hat{v}_k^{(\tau+1)} = \hat{v}_k^{(\tau)} - \Delta t \, f_0 \, \hat{u}_k^{(\tau+1)} \tag{41}$$

with an additional *divergence damping* approach, where the pressure perturbation in (40) is altered:

$$\hat{p}_k^{(\tau)} := \hat{p}_k^{(\tau)} + \alpha_d \, \Delta t \, \bar{\rho}_k \, c_s^2 \left(k \, \hat{u}_k^{(\tau)} - \frac{\hat{w}_{k'+1}^{(\tau)} - \hat{w}_{k'}^{(\tau)}}{\Delta z} \right) \quad . \tag{42}$$

Due to the implicit treatment of the Coriolis terms the prognostic time-step of $\hat{u}$ is carried out first before the $\hat{v}$ - prognosis can follow.

An explicit procedure for the *vertical velocity* component must be derived next. For that purpose the pressure perturbation amplitude at the prognostic time-level $\tau + 1$, $\hat{p}_k^{(\tau+1)}$, in equation (34) is eliminated using equation (36). In the well-known manner a tri-diagonal vertical structural equation for $\hat{w}_{k'}^{(\tau+1)}$ is explicitly obtained:

$$\begin{aligned} B_2 \; \hat{w}_2^{(\tau+1)} + C_2 \; \hat{w}_3^{(\tau+1)} &= D_2^{(\tau)} \\ A_{k'} \; \hat{w}_{k'-1}^{(\tau+1)} + B_{k'} \; \hat{w}_{k'}^{(\tau+1)} + C_{k'} \; \hat{w}_{k'+1}^{(\tau+1)} &= D_{k'}^{(\tau)} \quad ; \quad k' \in \left[3, ke' - 1\right] \\ A_{ke'} \; \hat{w}_{ke'-1}^{(\tau+1)} + B_{ke'} \; \hat{w}_{ke'}^{(\tau+1)} &= D_{ke'}^{(\tau)} \end{aligned} \tag{43}$$

The right-hand side terms $D_{k'}^{(\tau)}$, at time-level τ, are known, and the time-independent coefficients $A_{k'}$,$B_{k'}$,$C_{k'}$ either. Thus, the time-extrapolated values of $\hat{w}_{k'}^{(\tau+1)}$, for $k' \in \left[2, ke'\right]$, can be determined from a Gaussian elimination process with an adherence condition at the lower boundary, $\hat{w}_1 = 0$, and a lid-condition at the upper boundary, $\hat{w}_{ke1} = 0$. The coefficients $A_{k'}$,$B_{k'}$,$C_{k'}$ and the function $D_{k'}^{(\tau)}$ in (43) read

$$A_{k'} = \left(\beta^+\right)^2 \frac{\bar{\rho}_{k-1}}{\left(\bar{\rho}_{k-1} + \bar{\rho}_k\right)/2} \left[\left(\frac{c_s\,\Delta t}{\Delta z}\right)^2 - \left(\frac{g\,\Delta t}{2c_s}\right)^2\right] = \left(\frac{\bar{\rho}_{k-1}}{\bar{\rho}_k}\right) C_{k'} \qquad \text{for } k' \in \left[3, ke'\right] \tag{44}$$

$$C_{k'} = \left(\beta^+\right)^2 \frac{\bar{\rho}_k}{\left(\bar{\rho}_{k-1} + \bar{\rho}_k\right)/2} \left[\left(\frac{c_s\,\Delta t}{\Delta z}\right)^2 - \left(\frac{g\,\Delta t}{2c_s}\right)^2\right] = \left(\frac{\bar{\rho}_k}{\bar{\rho}_{k-1}}\right) A_{k'} \qquad \text{for } k' \in \left[2, ke' - 1\right] \tag{45}$$

$$B_{k'} = 1 + 2\left(\beta^+\right)^2 \left[\left(\frac{c_s\,\Delta t}{\Delta z}\right)^2 + \left(\frac{g\,\Delta t}{2c_s}\right)^2\right] + 2\left(\beta^+\right)^2 \left(\frac{\bar{\rho}_k - \bar{\rho}_{k-1}}{\bar{\rho}_k + \bar{\rho}_{k-1}}\right) \left(\frac{g\,(\Delta t)^2}{\Delta z}\right) \qquad \text{for } k' \in \left[2, ke'\right] \tag{46}$$

$$\begin{aligned} D_{k'} = \hat{w}_{k'}^{(\tau)} &- \frac{2\beta^+}{\left(\bar{\rho}_{k-1} + \bar{\rho}_k\right)} \left(\frac{\Delta t}{\Delta z}\right) \left[\left(\hat{p}_k^{(\tau)} - \hat{p}_{k-1}^{(\tau)}\right) + \left(C_k^p - C_{k-1}^p\right)\right] \\ &- \frac{2\beta^+}{\left(\bar{\rho}_{k-1} + \bar{\rho}_k\right)} \left(\frac{g\,\Delta t}{2c_s^2}\right) \left[\left(\hat{p}_k^{(\tau)} + \hat{p}_{k-1}^{(\tau)}\right) + \left(C_k^p + C_{k-1}^p\right)\right] + C_{k'}^w \end{aligned} \qquad \text{for } k' \in \left[2, ke'\right] \tag{47}$$

with the auxiliary variables:

$$C_k^p = -\beta^-\, c_s^2 \left(\frac{\Delta t}{\Delta z}\right) \bar{\rho}_k \left(\hat{w}_{k'+1}^{(\tau)} - \hat{w}_{k'}^{(\tau)}\right) + \beta^- \left(\frac{g\,\Delta t}{2}\right) \bar{\rho}_k \left(\hat{w}_{k'+1}^{(\tau)} + \hat{w}_{k'}^{(\tau)}\right) + \Delta t\, c_s^2\, k\, \bar{\rho}_k\, \hat{u}_k^{(\tau+1)} \qquad \text{for } k \in [1, ke] \tag{48}$$

$$\begin{aligned} C_{k'}^w = &- \frac{2\beta^-}{\left(\bar{\rho}_{k-1} + \bar{\rho}_k\right)} \left(\frac{\Delta t}{\Delta z}\right) \left(\hat{p}_k^{(\tau)} - \hat{p}_{k-1}^{(\tau)}\right) - \frac{2\beta^-}{\left(\bar{\rho}_{k-1} + \bar{\rho}_k\right)} \left(\frac{g\,\Delta t}{2c_s^2}\right) \left(\hat{p}_k^{(\tau)} + \hat{p}_{k-1}^{(\tau)}\right) \\ &+ \left(\frac{g\,\Delta t}{2}\right) \left[\left(\frac{\hat{\theta}_k^{(\tau)}}{\bar{\theta}_k^{(\tau)}}\right) + \left(\frac{\hat{\theta}_{k-1}}{\bar{\theta}_{k-1}}\right)\right] \end{aligned} \qquad \text{for } k' \in \left[2, ke'\right] \tag{49}$$

The Gaussian elimination procedure is then applied to (43)- (49) in a common way. By a 'top-down sweeping' the following auxiliary entities are determined first:

$$E_{ke'} := -\frac{A_{ke'}}{B_{ke'}} \qquad , \qquad F_{ke'} := \frac{D_{ke'}}{B_{ke'}} \tag{50}$$

and then for $k' \in \left[ke' - 1, 2\right]$:

$$\begin{aligned} E_{k'} &:= -\frac{A_{k'}}{B_{k'} + C_{k'} E_{k'+1}} \qquad , \qquad F_{k'} := \frac{D_{k'} - C_{k'} F_{k'+1}}{B_{k'} + C_{k'} E_{k'+1}} \\ E_1 &:= 0 \qquad , \qquad F_1 := \frac{D_2 - C_2 F_3}{B_2 + C_2 E_3} = \hat{w}_2^{(\tau+1)} \end{aligned} \tag{51}$$

From all following 'down-top sweeping' the vertical motion perturbation is easily calculated:

$$\hat{w}_{k'}^{(\tau+1)} = E_{k'} \hat{w}_{k'-1}^{(\tau+1)} + F_{k'} \qquad k' \in \left[3, ke'\right] \tag{52}$$

Once the prognostic *vertical motion perturbation* is calculated, the *pressure perturbation* and the *potential temperature perturbation* at that time-level can immediately be found from the equations ((36), (37)) and (38).

To complete the numerical integration algorithm, we list the constants how they are chosen in this model:

$f_0 = 10^{-4}\, s^{-1}$ - Coriolis parameter

$k \ = 2\pi / L$ - wavenumber associated with wavelength $L = 100, 250km$

$R \ = 287 m^2\, s^2\, K^{-1}$ - gas constant

$g \ = 9.80665 m\, s^{-2}$ - gravity constant

$c_p = 1005 J\, K^{-1}\, kg^{-1}$,

$c_v = 718 J\, K^{-1}\, kg^{-1}$ - specific heat at constant pressure and constant volume, respectively

$\varepsilon \ = 0.4$ - implicity parameter (see Subsection 3.2, (29))

$\alpha_d = 0.1, ...0.3$ - divergence damping parameter (see 3.2, (30))

$T_0 = 250K$ - assumption of an isothermal model atmosphere

$p_s = 100000Pa$ - pressure at lower boundary

$c_s^2 = \kappa\, RT_0\,, \ \ \kappa = c_p / c_v$ - constant sound wave speed squared

$\Delta t = 1s, ...10s$ - time-step

$\Delta z = (1/40)\, RT_0\, 1n\,(1000)\,/g$ - constant model layer thickness of the 40-layer model

together with formulae to calculate basic state parameters in the difference equations above

$$\bar{\rho}_k = \frac{p_s}{RT_0} \exp\left(-\frac{g}{RT_0}\, z_k\right) \;,\; \bar{\theta}_k = T_0 \exp\left(\frac{g}{c_p\, T_0}\, z_k\right)$$

$$\left(\frac{N^2\bar{\theta}}{g}\right)_k = \left(\frac{d\bar{\theta}}{d\, z}\right)_k = \frac{g}{c_p} \exp\left(\frac{g}{c_p\, T_0} z_k\right) \qquad \text{for } k \in [1, ke] \;.$$

3.5 Simulations with L-grid model version

Based on the model algorithm for a vertical L-grid, described in the previous Subsection 3.4, we carry out simulations similar to Arakawa and Konor's (1996) with their model (AKM). It serves us to calibrate our LM toy-model. Therefore, our concern is mainly to simulate hydrostatic gravity waves, which is guaranteed with the choice of relatively large horizontal wavelengths of $L = 100, 250km$ compared to the initially produced vertical wavelength. On a state of rest a local zig-zag initial perturbation in θ' is imposed to $\pm 0.5K$ at the vertical gridpoints indexed with $k = 2/3$, and $\theta' = 0$ everywhere else. From this manipulation sound- and gravity waves are generated, and their propagation can then be simulated in terms of a dispersion process. Besides linearisation, our approach differs from the leap-frog / split-explicit time-scheme of the LM in such a way, that we run the fast-mode model part in a stand-alone form not linked within a splitting scheme with the slow-mode model part. In a first set of simulations we assume a horizontal wavelength of $L = 250km$

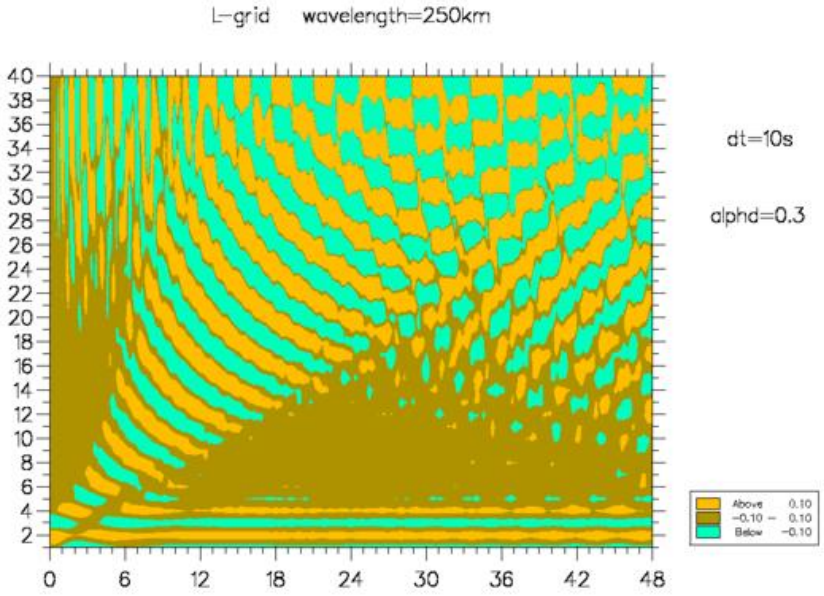


Figure 5: Linear LM fast-mode simulation with L-grid for a horizontal wave length of 250km. Time evolution of the potential temperature perturbation amplitude over 48 hours integration time with time-step $\Delta t = 10s$ and a divergence damping parameter of $\alpha_d = 0.3$ (Further explanation see text, contour interval similar to previous figures).

On an empirical ground the time-step is chosen $\Delta t = 10s$ and the divergence damping parameter has been set $\alpha_d = 0.3$ in order to damp out acoustic waves. Over 48 hours integration time the simulation shows, how a gravity wave dispersion process takes place from the assumed initial potential temperature perturbation in case of the L-grid staggering of variables and influenced by an upper lid-condition. Obviously, wave perturbations propagate only partially upward, where they are reflected at the upper boundary to reach lower parts of the integration domain again, while another wave mode remains to be stationary as a pure computational mode (Fig. 5).

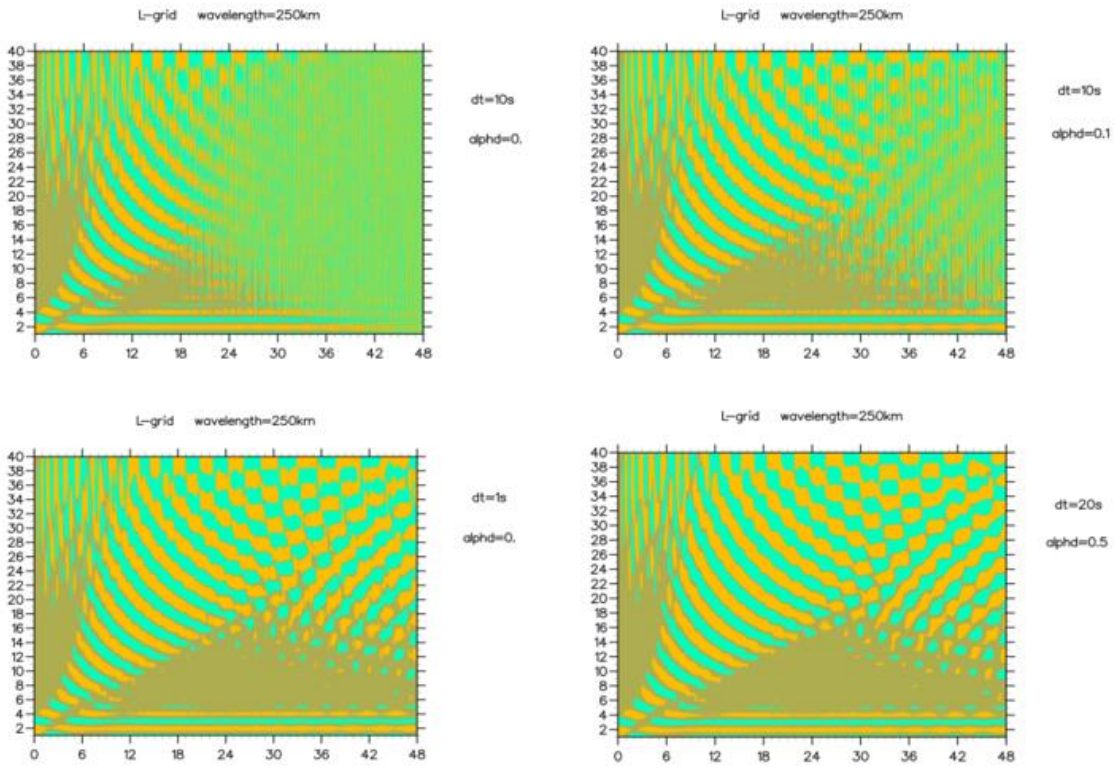


Figure 6: Further simulations with L-grid for a 250km horizontal wavelength over 48 hours integration time in dependence of varying time-step $\Delta t = 1, 10, 20s$ and divergence damping parameter of $\alpha_d = 0., 0.1, 0.5$, and compared to the simulation with $\Delta t = 10s$ and $\alpha_d = 0.3$ in Fig. 5.

From an empirical point of view the Figures 5 and 6 show that the simulation with $\Delta t = 10s$ brings about an optimal result, if the divergence damping term is switched on with $\alpha_d = 0.3$ while the choice of $\alpha_d = 0.1$ (LM-default value, see upper right panel of Figure 6) leads to an unsatisfactory solution, which tends to make the matter still worse, if $\alpha_d = 0$ (upper left panel of Figure 6) is taken. We interpret this outcome as an accuracy problem due to the choice of a time-step as large as $\Delta t = 10s$. Related truncation errors seem to become the cause of artificial, horizontally propagating acoustic waves, which however can be damped, if the divergence damping mechanism is taken into account. Due to this, the choice of $\alpha_d = 0.3$ is shown to be sufficient, while $\alpha_d = 0.1$ is still too small to be effective. In the lower right panel of Figure 6 it is shown that even with a time-step of $\Delta t = 20s$, which is connected with a still more reduced time-difference accuracy, the simulation becomes successful, provided the divergence damping effect is sufficiently increased (e.g. $\alpha_d = 0.5$). If in contrast to this the time-difference accuracy is improved by using a sufficiently small time-step of $\Delta t = 1s$ there seems to be no reason to apply any divergence damping, since no spurious acoustic waves occur (lower left panel in Figure 6). Here we speculate about the nature of this kind of time-difference accuracy. From a physical point of view, an inherent hydrostatic adjustment process seems to take place, where the horizontally propagating acoustic modes play the role of a catalyst. If the timestep is small enough, the simulation is accurate to model the adaptation well enough in analogy to the well-known geostrophic adjustment, which must be simulated properly to avoid noisy gravity waves. This means here that larger timesteps appear to produce spurious acoustic waves which are then necessery to be damped out using some remedy in terms of an stronger divergence damping parameter. The same qualitative result can also be shown from simulations with a horizontal wavelength of $L = 100km$ for the assumed initial potential temperature perturbation (Figure 7). With $\Delta t = 1s$ and $\alpha_d = 0.3$ one obtains an optimal result, while with the same time-step, but ignored

divergence damping, the solution tends to become noisy. If then the time-step is further increased up to $\Delta t = 5s$ the emergence of spurious horizontally propagating acoustic waves is obvious, and the gravity wave solution is almost destroyed. The choice of an increased divergence damping parameter, $\alpha_d = 0.5$, makes, however, this larger time-step applicable and leads to a solution comparable with that from $\Delta t = 1s$ and $\alpha_d = 0.3$. With the specific time-differencing scheme suitable, and applied here to the compressible nonhydrostatic equations, we were able to recover the hydrostatic gravity wave solutions for a 100km- and 250km horizontal wavelength as found from the hydrostatic AKM concerning the L-grid. This has been demonstrated by comparing the appropriate solutions of Figure 2 with those of Figures 5 , 6 and 7 . Of particular interest is here, too, that the L-grid causes an unwanted stationary zigzag-computational mode which we know to be avoided in the AKM when introducing the CP-grid staggering instead. This change to the CP-grid must be managed in the following for our toy-model.

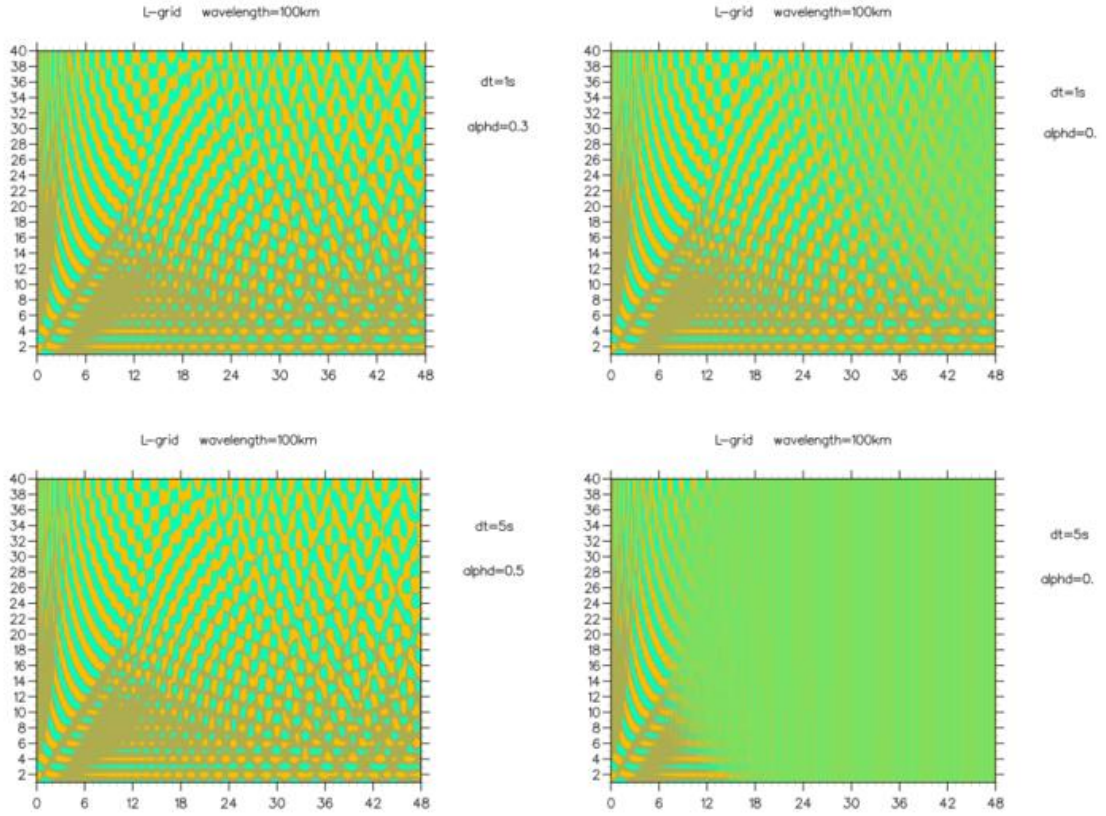


Figure 7: Simulations with L-grid for a 100km horizontal wavelength over 48 hours integration time for time steps $\Delta t = 1s$ and $5s$ in dependence of divergence damping parameter of $\alpha_d = 0., 0.3, 0.5$.

3.6 Vertical grid-staggering with a CP-grid

We refer strictly to our description of the L-grid algorithm in Subsections 3.3 and 3.4 . In order to define here the vertical differencing for a CP-grid option of the LM fast-wave toy-model, we need only list the differences to the L-grid formulation. In contrast to the L-grid scheme (see Figure 4) the CP-grid staggering scheme is shown in Figure 8.

In this case the variables $\hat{u}$, $\hat{v}$, $\hat{p}$ are placed at main-levels indicated with indices $k \in [1, k]$, while $\hat{w}$ and $\hat{\theta}$ are defined at half-levels indexed with $k' \in [1, ke1]$. For the basic state we assume again $\bar{\rho}$ to be positioned at main-levels, but $\bar{\theta}$ now at half-levels together with its perturbation value $\hat{\theta}$. To make the

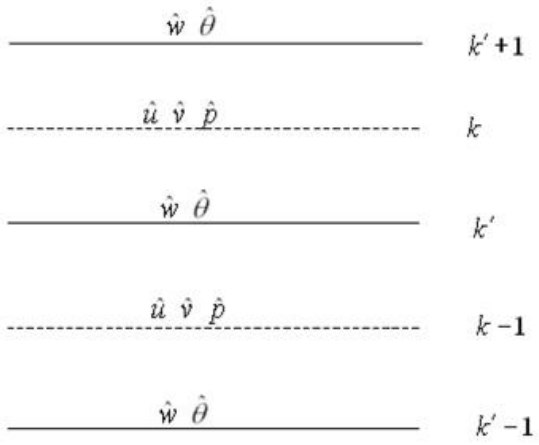


Figure 8: Scheme of vertical staggering according to CP-grid

matter simple enough, we comment here only the changes from the numerical integration algorithm written down in the Subsection 3.4 for the L-grid. The horizontal momentum equations (40), (41) with the divergence damping (42) included remain as they stand there. The Gaussian elimination procedure to compute the vertical velocity from a tri-diagonal vertical structural equation system (43) remains also formally untouched . Only the term $C^w_{k'}$ involved, obtains a more simple form compared to (49). Due to a more natural formulation of the buoyancy term with a CP-grid, its vertical averaging is avoided. Instead of (35) we have

$$C^w_{k'} = \ldots \quad g\Delta t \left(\frac{\hat{\theta}^{(\tau)}}{\bar{\theta}} \right)_{k'} \qquad \text{for} \quad k' \in \left[2, ke' \right] \tag{53}$$

The first two terms on the right-hand side of equation (35)/(49) are identically introduced in (53) written in symbolic form by dots. The pressure perturbation equation ((36), (37)) is used without any change, while a minimal modification is made for the potential temperature perturbation equation (38):

$$\hat{\theta}^{(\tau+1)}_{k'} = \hat{\theta}^{(\tau)}_{k'} - \left(\frac{N^2 \bar{\theta}}{g} \right)_{k'} \Delta t \left(\beta^+ \hat{w}^{(\tau+1)}_{k'} + \beta^- \hat{w}^{(\tau)}_{k'} \right) \qquad \text{for} \quad k' \in [1, ke1] \tag{54}$$

The boundary conditions (39) are assumed here, too, and the list of constants used in the L-grid version is also valid. With this specifications we are going to carry out similar simulations with the CP-grid model version to show the impact of the CP-grid against the L-grid as already demonstrated with the hydrostatic AKM in Section 2.

3.7 Simulation with the CP-grid model version

Here we carry out simulations on the basis of the CP-grid model version described in Subsection 3.6 . With reference to 3.5, the numerical set-up is chosen to compare the results with the previous L-grid simulations. For horizontal wavelengths $L = 100, 250km$ with time-step $\Delta t = 1s$ and $10s$, respectively, and $\alpha_d = 0.3$ in each case, the CP-grid results are shown in Figure 9, compared with the corresponding L-grid simulations over 48 hours integration time. This result can be compared with that in Figure 2, where analogous runs have been shown with the hydrostatic AKM. The similarity of results between Figure 2 and Figure 9 was expected to be found in this way, because in both situations

hydrostatic gravity waves were simulated due to the same, relatively long horizontal wavelengths of the assumed initial perturbation. Therefore, the discussion of the results depicted in Figure 9 is qualitatively the same as that about Arakawa and Konor's simulation shown in Figure 2, and need not be repeated here. So we can refer to our discussion in Section 2. On the whole, we can state that a computational mode in the L-grid nonhydrostatic model version is possible to occur - here deliberately provoked by a special initial perturbation - and due to the introduction of a CP-grid instead this unphysical nuisance is removed, and, moreover, we observe that the CP-grid seems to support the gravity wave dispersion process much better.

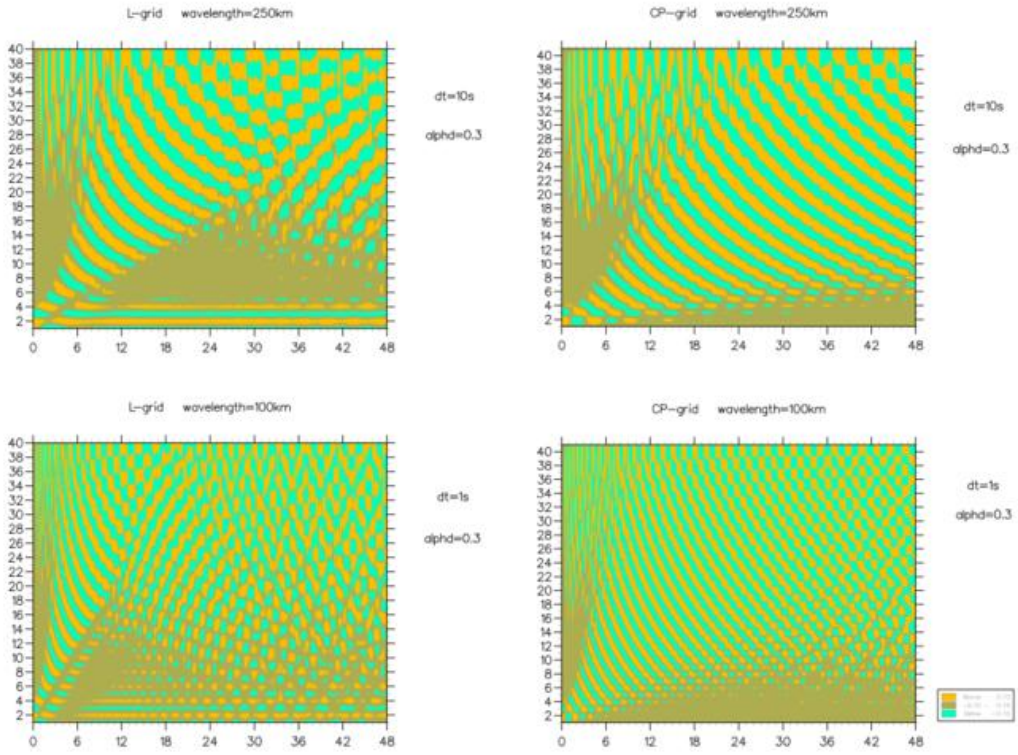


Figure 9: Comparison of L-grid simulations with corresponding CP-grid runs for horizontal wave components with $L = 100, 250km$ wave length over 48hours integration time.

In order to demonstrate further aspects of the possible occurrence of a computational mode in the L-grid, Arakawa and Konor (1996) carried out still a second set of simulations with their AKM not mentioned up to now in this paper. We will add this in brief from the point of view of the LM toy-model. In this set, the initial conditions are modified in a way that $\theta^{'} = 0$ is assumed everywhere without any local perturbation imposed. Instead, a Newtonian-type diabatic heating term is added in the prognostic equation for $\hat{\theta}$, (20), on its right-hand side, using a time-independent equilibrium value amplitude $\hat{\theta}^*$. The modified potential temperature equation reads then

$$\frac{\partial \hat{\theta}}{\partial t} = -\frac{N^2 \bar{\theta}}{g}\,\hat{w} - \lambda\left(\hat{\theta} - \hat{\theta}^*\right) \tag{55}$$

with $\hat{\theta}^* = 10K$ for the equilibrium value, and $\lambda = 1/86400\,s^{-1}$ for the relaxation constant. This term is applied at only one single model level, at $k = 4$ and $k^{'} = 4$, respectively. These parameters are identical with those in Arakawa and Konor's paper. In Figure 10 we show the corresponding results from this set of simulations.

The simulation with the horizontal wavelength of 250 km is not shown here. It brings qualitatively

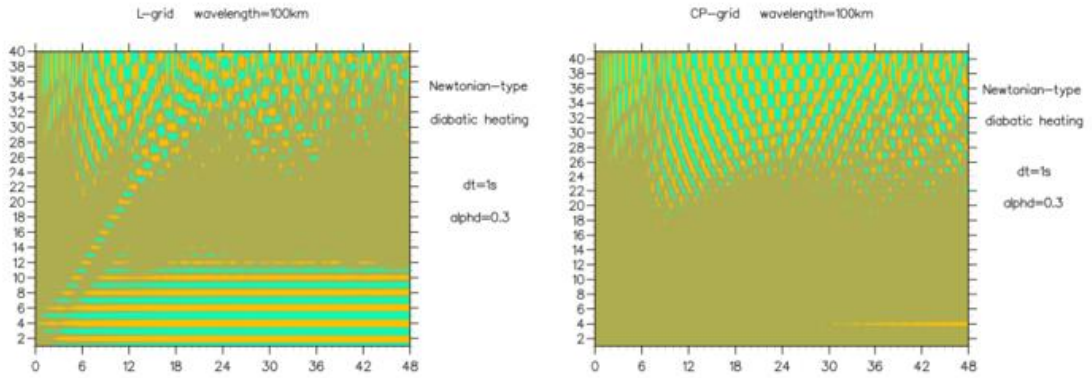


Figure 10: Simulation with Newtonian-type heat forcing at a single model level for horizontal wavelength of 100km and L-grid against CP-grid.

an analogous result as shown for the 100km-wave component. Since for both these large wavelengths the nonhydrostatic model simulates wave solutions comparable with the hydrostatic approximation, the results can be compared directly with the corresponding AKM-simulations (see Figure 4 in Arakawa and Konor 1996). Thus, the same qualitative discussion of the result in Figure 10 is valid and, with reference to Arakawa and Konor (1996), needs not be repeated here. In particular, we see the generation of a spurious zigzag distribution of the potential temperature perturbation due to the L-grid, which does not occur when using the CP-grid instead. We add still another experiment, where the effect of a subgrid-scale convective forcing is simulated with the given toy-model. For that purpose the continuity equation is thought to be extended to take into account an additional term describing the divergence of a subgrid mass flux. In terms of equation (19), which is the continuity equation for the given system, we add an expression of the vertical divergence of a vertical mass flux like this:

$$\frac{\partial \hat{p}}{\partial t} = g\bar{\rho}\,\hat{w} - c_s^2\,\bar{\rho}\left(\frac{\partial \hat{w}}{\partial z} - k\hat{u}\right) - c_s^2\,\frac{\partial \hat{F}_z}{\partial z} \tag{56}$$

With background values $w' \sim 5m\,s^-1$, $\rho' \sim 10^{-3}kg\,m^{-3}$, $\Delta z \sim 10^3 m$ we make use of an estimate

$$\left|c_s^2\,\partial\,\hat{F}_z/\partial z\right| \sim 0.5kg\,m^{-1}\,s^3 \qquad .$$

The positive value is imposed at an altitude corresponding to level $k = 3$, while its negative value holds at $k = 8$. Otherwise this term is set equal zero. Thus, a step-like vertical distribution of an constant mass flux directed upward in between an interval $3 \leq k \leq 8$ is imposed, while it is zero below and above. In the simulation with this kind of forcing the term of concern is assumed to be constant in time. In this experimental set-up no initial local perturbation is otherwise imposed.

Due to this specification of a vertical massflux distribution the following result is expected: massflux divergence (convergence) is accompanied with flow convergence (divergence) at $k = 3$ ($k = 8$). Thus, we observe at $k = 8$ downward motion of air with higher θ from above, which leads to local heating there, while upward motion right next at $k = 9$ carries air with lower θ from below bringing local cooling. The same takes place at $k = 3$, and $k = 4$, respectively, but in reverse order and somewhat weaker. As demonstrated in Figure 11, the typical difference of simulation results between L-grid and CP-grid is observed. The L-grid produces a stationary computational zig-zag structure, while the physical solution expected cannot be reproduced. The CP-grid, however, avoids this non-physical phenomenon and seems even necessary to properly simulate the adopted process.

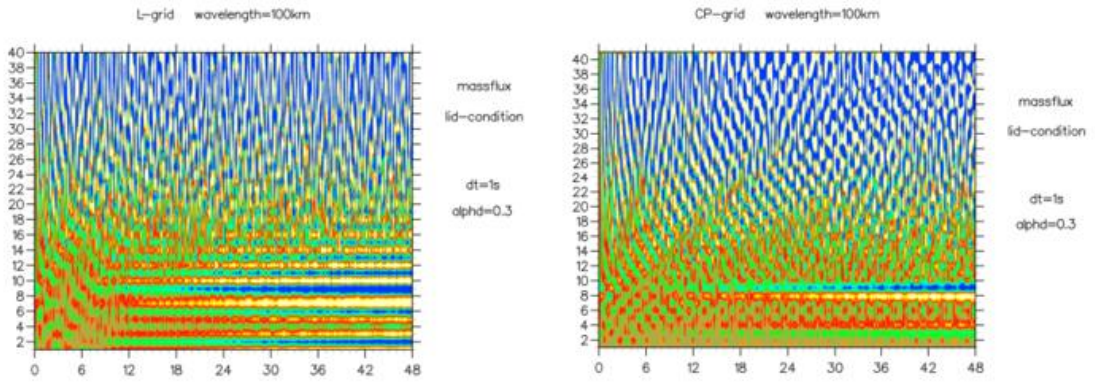


Figure 11: Time evolution of the potential temperature perturbation with imposed subgrid-scale massflux (see text) for horizontal wavelength of 100km with L-grid versus CP-grid. (contour colour interval here 0.01K in between (-0.1; + 0.1).

In all Figures above the simulation results have been shown over the entire integration domain. There we have always tacitly accepted that the internal gravity wave pattern propagating upward arrive eventually at the upper model boundary, where they are reflected owing to the assumed lid-condition $\hat{w}_{top} = 0$ with a following contamination of the physical solution. These results suggest urgently the implementation of an absorbing upper boundary condition instead of the reflective lid-condition here still applied. This will be our concern in the next section.

4 Application of a radiative upper boundary condition

In all our results shown by now it can be observed that reflecting wave components occur which propagate downward as an unnatural phenomenon to contaminate then internal solutions, and, moreover, veil and distort even unphysical modes like zigzag patterns owing to an L-grid which might then not always be detected easily from. With this motivation, but also from much more general reasons, it is strongly indicated to improve any model of concern in order to get rid of an upper lid-condition and introduce an absorbing or non-reflecting upper condition instead. Here, we are interested in applying a radiative boundary condition for our compressible nonhydrostatic toy-model as a desirable improvement in the above sense. Moreover, we have in mind to start finding out in principle a way to extend this application to the real LM. In the following Section, however, we deal with that problem in the narrow sense. It needs no explanation, why we are here particularly interested in applying a radiative boundary condition, since our toy-model is a simple horizontally spectral model. Thus, we operate always in the Fourier space with a monochromatic wave component which allows the direct application of a radiative boundary condition, while normally a Fourier transform is necessary to apply.

4.1 Derivation of the Klemp-Durran-Bougeault type of a radiative upper boundary condition

The following analysis starts from the toy-model equations (16) - (20) with all their explanations given in Section 3. The only modification is thought to be done in the prognostic $\hat{w}$ - equation, where a hydrostatic switch μ is added to be multiplied with the vertical acceleration term in (18). Setting $\mu = 1$ gives the full nonhydrostatic system while $\mu = 0$ reduces the system to the hydrostatic model equations. With this notation we carry out the elimination of the horizontal momentum components and the potential temperature perturbation amplitude to obtain two relationships for pressure and vertical momentum:

$$\left[\frac{1}{c_s^2}\left(\frac{\partial^2}{\partial t^2}+f_0^2\right)+k^2\right]\frac{\partial \hat{p}}{\partial t}=-\left(\frac{\partial^2}{\partial t^2}+f_0^2\right)\left(\frac{\partial}{\partial z}+\frac{N^2}{g}\right)(\bar{\rho}\hat{w}) \tag{57}$$

$$\left(\frac{\partial}{\partial z}+\frac{g}{c_s^2}\right)\frac{\partial \hat{p}}{\partial t}=-\left(\mu\frac{\partial^2}{\partial t^2}+N^2\right)(\bar{\rho}\hat{w}) \tag{58}$$

The z- and t- dependencies may now be separated

$$\begin{pmatrix}\hat{p}\\ \bar{\rho}\hat{w}\end{pmatrix}=\mathrm{Re}\begin{pmatrix}P(z)\\ W(z)\end{pmatrix}\exp(-i\omega t) \tag{59}$$

allowing the following to be written:

$$\left[\frac{\partial^2}{\partial z^2}+\left(\frac{g}{c_s^2}+\frac{N^2}{g}\right)\frac{\partial}{\partial z}+\frac{N^2}{c_s^2}\right]\begin{pmatrix}P\\ W\end{pmatrix}+\left(\frac{N^2-\mu^2\omega}{\omega^2-f_0^2}\right)\left(k^2-\frac{\omega^2-f_0^2}{c_s^2}\right)\begin{pmatrix}P\\ W\end{pmatrix}=0 \tag{60}$$

Normalising equation (60), the change of variables is made

$$\begin{pmatrix}P(z)\\ W(z)\end{pmatrix}=\begin{pmatrix}\tilde{P}(z)\\ \tilde{W}(z)\end{pmatrix}\exp\left(-\frac{z}{2H}\right) \tag{61}$$

using the definition of a reciprocal vertical scale height

$$\frac{1}{H} = -\frac{1}{\bar{\rho}}\frac{d\bar{\rho}}{dz} = \frac{N^2}{g} + \frac{g}{c_s^2} \qquad , \tag{62}$$

finally leaves the well-known wave equation

$$\frac{d^2}{dz^2}\begin{pmatrix}\tilde{P}\\ \tilde{W}\end{pmatrix} + n^2\begin{pmatrix}\tilde{P}\\ \tilde{W}\end{pmatrix} = 0 \tag{63}$$

with the vertical wavenumber squared

$$n^2 = \frac{\left(N^2 - \mu^2\omega^2\right)k^2}{\omega^2 - f_0^2} + \frac{\mu^2\omega^2}{c_s^2} - \frac{1}{4H^2} \tag{64}$$

The general solution of (63) reads

$$\tilde{W}(z) = a\,\exp(i\,n\,z) + b\,\exp(-i\,n\,z) \tag{65}$$

and similar for $\tilde{P}(z)$. The relationship (64) constitutes a rather general dispersion equation to determine the frequency ω for acoustic and inertia-gravity modes. A fairly detailed discussion for $\mu = 1$ can be found in Gossard and Hooke (1975, p. 112). In a next step we are interested in considering the vertical energy flux averaged over a periodic time length $2\pi/\omega$. For the present we find

$$\begin{aligned}\overline{\hat{p}\hat{w}} = \overline{\mathrm{Re}\left(P\exp(-i\omega t)\right)\mathrm{Re}\left(\frac{W}{\bar{\rho}}\exp(-i\omega t)\right)} &= \frac{1}{4\bar{\rho}}\left(P\overset{*}{W} + \overset{*}{P}W\right)\\ &= \frac{1}{2\bar{\rho}(0)}\mathrm{Re}\left(\overset{*}{\tilde{W}}\tilde{P}\right)\end{aligned} \tag{66}$$

The upper stars in (66) denote complex-conjugate entities. This general expression needs to be more specified in view of introducing now the Klemp-Durran-Bougeault radiative boundary condition (= KDB-RUBC) with its rather restricting assumptions. We are motivated to do so, since it is common that a radiative boundary condition following from the general case is impracticable to be applied due to its global properties in space and time. In contrast, the KDB-RUBC seems here particularly attractive, because it is local in time, and the global character in space is not an obstacle at all due to the specific definition of model variables. The list of assumptions to arrive at the KDB-RUBC is:

- hydrostatic approximation $(\mu = 0)$
- anelastic condition $\left(c_s^2 \to \infty\right)$
- isothermal basic state
- no rotation $(f_0 = 0)$ (67)
- Boussinesq - approximation $\left(\frac{\partial}{\partial z} \gg \frac{1}{H}, n^2 \gg \frac{1}{H^2}\right)$

With this limitations the dispersion equation reduces to

$$\omega n = \pm N\, k \tag{68}$$

and from (57) follows with (59) and (61) the relation

$$\tilde{P} = i\frac{\omega}{k^2}\frac{d\tilde{W}}{dz} \qquad . \tag{69}$$

Inserting (69) in (66) leads, together with (65), to

$$\overline{\hat{p}\hat{w}} = -\frac{\omega n}{2\bar{\rho}_0 k^2}\left(|a|^2 - |b|^2\right) \tag{70}$$

At this point we have to specify the energy flux (70) at the upper boundary. In accordance with a condition of outgoing wave energy there, it is inferred from the energy budget equation (21) by integration from the bottom to the upper boundary that

$$\overline{(\hat{p}\hat{w})}_{top} > 0 \tag{71}$$

must hold. With always $n > 0$ (cf. with (65)) we start assuming $\omega n = Nk > 0$. In accordance with the desirable condition (71) it follows from (70) at the upper boundary $a = 0$. In this case we infer from (65) $d\tilde{W}/dz = -in\tilde{W}$, and via (69) we arrive at

$$\tilde{P}_{top} = \frac{N_{top}}{k}\tilde{W}_{top} \qquad . \tag{72}$$

If, however, $\omega n = -N\,k < 0$, we find with $b = 0$ from (65), (69), (70) the same result as (72). Provided that $z_{top} < \infty$, we finally obtain by use of (61) and then ((57), (58)) the KDB-RUBC in the form

$$\hat{p}_{top} = \frac{(\bar{\rho}N)_{top}}{k}\hat{w}_{top} \qquad . \tag{73}$$

In our case $k > 0$ is always valid. A direct application of (73) would be possible in our toy-model, provided the limiting assumptions behind this RUBC can be neglected compared to its desirable advantages. Apart from the original references (Klemp and Durran 1983, Bougeault 1983) we refer particularly to Durran (1999) who gave in his monography an excellent overview about this subject. Moreover, Durran has suggested an interesting computational method, how to incorporate the KDB-RUBC in a nonhydrostatic linear model algorithm. In the following we want to take up with his idea in order to apply it for the present model scheme.

4.2 Implementation of the KDB - RUBC

Before we put forward the matter, it seems worth thinking about, if there is really a good reason to deal with the KDB-RUBC in connection with a compressible nonhydrostatic model because of rather limited assumptions implied in this boundary condition. We are motivated to do so because of a reasoning as follows. The time differencing scheme used and described in Section 3.2, which

is essentially the time scheme in the fast-wave part of the LM, treats those terms responsible for vertically propagating acoustic waves implicitly in order to damp them significantly. Moreover, the divergence damping modifying the horizontal pressure gradient term serves to damp acoustic waves, so that, on the whole, acoustic modes seem to be significantly removed, while gravity modes, as the essential physical content of this equation part, remain untouched due to these numerical techniques. Having almost only gravity modes involved in this scheme we want to make, in addition, sure the applicability of the KDB-RUBC by treating approximately hydrostatic gravity waves (which makes then the solution comparable with the simulations from Arakawa and Konor who used a hydrostatic system). In this line we carry out a special simulation with our toy-model stipulating now $k = 0$ for an infinite horizontal wavelength and the case of no rotation, $f_0 = 0$. The model is initialised again with the above defined zigzag-perturbation for $\hat{\theta}$ with $\pm 0.5K$ at vertical gridpoints indexed with k=2 and k=3, respectively. In contrast to the complete equation system (16) - (20) the reduced one leads instead of the dispersion relations (22) and (23) here to a stationary gravity solution $\omega_g^2 = 0$ and to acoustic wave modes propagating vertically only, $\omega_a^2 \approx c_s^2\, n^2$. This simulation is shown in Figure 12. It supports the possible application of the KDB-RUBC.

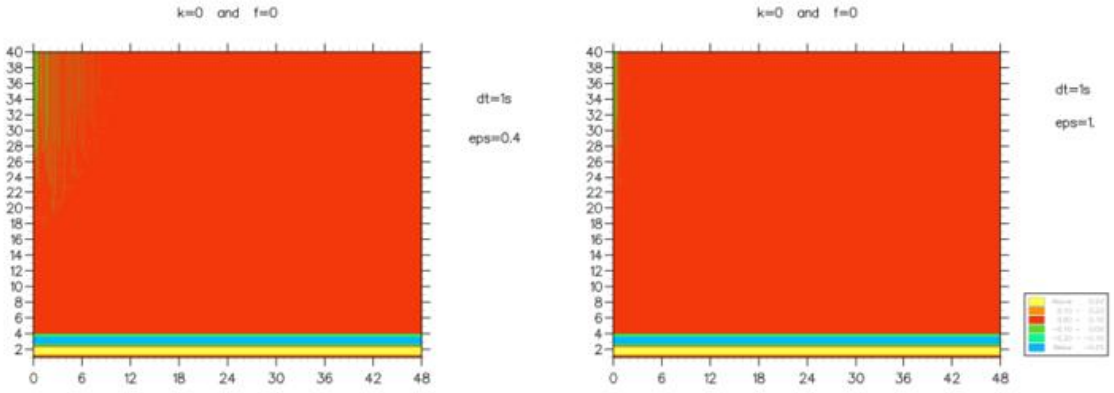


Figure 12: No rotation case simulation over 48 hours integration time with zero horizontal wavenumber. Lower stripe demonstrates a stationary gravity mode with no dispersion at all in both panels. Vertically propagating acoustic waves are treated implicitly, in the left panel with $\varepsilon = 0.4$, and in the right panel fully implicit with $\varepsilon = 1$. (plot valid both for L- and CP-grid).

Figure 12 demonstrates that the propagation of gravity modes have been suppressed. The local initial potential temperature perturbation can therefore not trigger a dispersion process compared to the more general toy-model simulations discussed above. Instead, the initial zig-zag perturbation remains so during the integration owing to a stationary mode, $\omega_g^2 = 0$. Due to the existence of a vertically propagating acoustic mode we can, however, test how the implicit time-scheme does work to damp off this mode in dependence of the implicity parameter ε. In an isolated manner we can observe that with the LM default-value $\varepsilon = 0.4$, that is with the implicity weights $\beta^+ = 0.7$ and $\beta^- = 0.3$, the acoustic mode, also caused by the special initial perturbation, is significantly reduced and eventually totally removed. In case of a fully implicit treatment ($\varepsilon = 1$, that corresponds to $\beta^+ = 1$ and $\beta^- = 0$) the effect of filtering out the acoustic mode is still more obvious. Since the implicit technique seems sufficient to remove vertically propagating acoustic waves, we conclude that the introduction of the KDB-RUBC, exclusively effective for (hydrostatic) gravity modes, may be possible to be used also in a nonhydrostatic compressible model frame provided that acoustic modes are sufficiently removed by appropriate numerical methods. From this thinking we are motivated to apply the KDB-RUBC in the given model. We start from the model equations with the given time- and vertical differencing scheme, described above in Subsection 3.2, 3.3 and 3.4 (equations (24) - (30), (31) - (39), and more directly, equations (40) - (51)). To demonstrate the method, we use the

vertical L-grid version first. The adaptation to the CP-grid is then easy to be done. Fortunately, a *first method* how to accomplish our approach, has been proposed by Durran (1999, p.429-430), which seems encouraging to be adopted for our purpose.

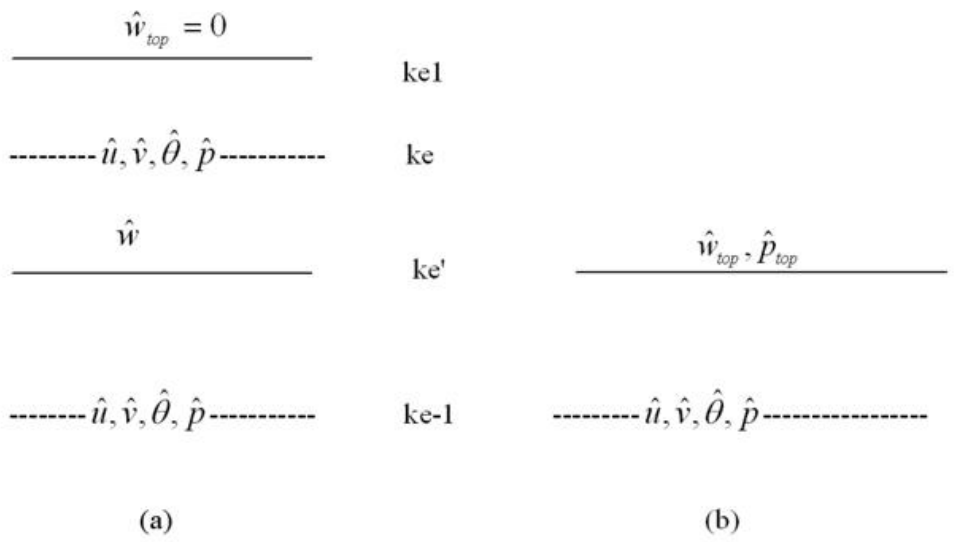


Figure 13: Change of uppermost gridpoint placement from case with (a) upper lid-condition to case (b) for introducing an RUBC according to Durran's (1999) approach.

According to Durran (1999), we change the numerical integration algorithm shown in Subsections 3.3 and 3.4 as follows. As indicated in Figure 13, we reduce the number of vertical computational gridpoints from ke to $ke-1$. Thus, the horizontal momentum equations ((40), (41)), with (42) involved, the pressure perturbation equation (27) and the potential temperature equation (28) are applied at vertical gridpoints $k \in [1, ke-1]$. With these difference equations for $k = ke-1$ there is, in particular, an access to $\hat{w}_{ke'}^{(\tau,\tau+1)} = \hat{w}_{top}^{(\tau,\tau+1)}$ which appears to be now the non-zero upper boundary value. Durran's approach consists then in changing in the tri-diagonal structural equation set for $\hat{w}_{k'}^{(\tau+1)}$, (43), the latter equation for $k = ke'$. This will be elaborated next. We start from the prognostic $\hat{w}_{k'}^{(\tau+1)}$ - equation (34) which must be reformulated for $k = ke'$ in such a way that an access to $\hat{p}_{ke}^{(\tau,\tau+1)}$ is avoided. This is made by using forward differences for the corresponding terms in (34) together with (35), where we define a new pressure value at the half-indexed gridpoint $k' = ke'$, $\hat{p}_{ke'}^{(\tau,\tau+1)} = \hat{p}_{top}^{(\tau)}$. This becomes necessary due to the proportionality of spectral perturbation pressure and vertical motion in the KDB-RUBC (73). So we have

$$\begin{aligned}\hat{w}_{top}^{(\tau+1)} = \hat{w}_{top}^{(\tau)} &- \frac{4}{\bar{\rho}_{ke-1} + \bar{\rho}_{ke}} \left(\frac{\Delta t}{\Delta z}\right) \beta^{+} \left(\hat{p}_{top}^{(\tau+1)} - \hat{p}_{ke-1}^{(\tau+1)}\right) \\ &- \frac{2}{\bar{\rho}_{ke-1} + \bar{\rho}_{ke}} \left(\frac{g\Delta t}{c_s^2}\right) \beta^{+} \hat{p}_{top}^{(\tau+1)} + C_{top}^{w}\end{aligned} \tag{74}$$

with a similar change in C_{top}^{w}:

$$\begin{aligned}C_{top}^{w} = -\frac{4\beta^{-}}{\bar{\rho}_{ke-1} + \bar{\rho}_{ke}} \left(\frac{\Delta t}{\Delta z}\right) \left(\hat{p}_{top}^{(\tau)} - \hat{p}_{ke-1}^{(\tau)}\right) - \frac{2\beta^{-}}{\bar{\rho}_{ke-1} + \bar{\rho}_{ke}} \left(\frac{g\Delta t}{c_s^2}\right) \hat{p}_{top}^{(\tau)} \\ + \frac{g\Delta t}{2} \left(\frac{\hat{\theta}_{ke-1}}{\bar{\theta}_{ke}} + \frac{\hat{\theta}_{ke-1}}{\bar{\theta}_{ke-1}}\right)\end{aligned} \tag{75}$$

and some reasonable approximation for the latter term in (75). In the next step, equation (36) for $k = ke - 1$ is used to eliminate $\hat{p}_{ke-1}^{(\tau+1)}$ from equation (74) which leads in contrast to the general procedure of Subsection 3.4 to a more specific relationship

$$A_{top}\hat{w}_{ke'-1}^{(\tau+1)} + B_{top}\hat{w}_{top}^{(\tau+1)} = D_{top}^{(\tau)} - \tilde{\alpha}_{top}\hat{p}_{top}^{(\tau+1)} \tag{76}$$

with coefficients A_{top}, B_{top}, differing from the former $A_{ke'}$, $B_{ke'}$ in (43), and with an additional coefficient $\tilde{\alpha}_{top}$:

$$A_{top} = -\left(\beta^{+}\right)^{2} \frac{\bar{\rho}_{ke-1}}{\left(\bar{\rho}_{ke-1} + \bar{\rho}_{ke}\right)/2} \left[2\left(\frac{c_s \Delta t}{\Delta z}\right)^{2} + g\frac{(\Delta t)^{2}}{\Delta z}\right] \tag{77}$$

$$B_{top} = 1 + \left(\beta^{+}\right)^{2} \frac{\bar{\rho}_{ke-1}}{\left(\bar{\rho}_{ke-1} + \bar{\rho}_{ke}/2\right)} \left[2\left(\frac{c_s \Delta t}{\Delta z}\right)^{2} - g\frac{(\Delta t)^{2}}{\Delta z}\right] \tag{78}$$

$$\tilde{\alpha}_{top} = \frac{4\beta^{+}}{\left(\bar{\rho}_{ke-1} + \bar{\rho}_{ke}\right)} \left[\left(\frac{\Delta t}{\Delta z}\right) + \left(\frac{g\Delta t}{2c_s^{2}}\right)\right] \tag{79}$$

The right hand side term $D_{top}^{(\tau)}$ reads

$$D_{top}^{(\tau)} = \hat{w}_{top}^{(\tau)} + 4\beta^{+}\frac{(\Delta t/\Delta z)}{\left(\bar{\rho}_{ke-1} + \bar{\rho}_{ke}\right)} \left(\hat{p}_{ke-1}^{(\tau)} + C_{ke-1}^{p}\right) + C_{top}^{w} \tag{80}$$

Here we arrive at a point, where the KDB-RUBC (73) needs to be introduced explicitly. We use it in the form

$$\hat{p}_{top}^{(\tau+1,\tau)} = \left(\frac{N\bar{\rho}}{k}\right)_{top} \hat{w}_{top}^{(\tau+1,\tau)} \qquad \Rightarrow \qquad b_{top}\ \hat{w}_{top}^{(\tau+1,\tau)} \tag{81}$$

with the definition

$$b_{top} := \left(\frac{N\bar{\rho}}{k}\right)_{top} = \frac{g\sqrt{\kappa - 1}}{2c_s k}\left(\bar{\rho}_{ke-1} + \bar{\rho}_{ke}\right) \quad , \quad \kappa = c_p/c_v \tag{82}$$

for the assumed isothermal basic state. The KDB-RUBC ((81) , (82)) is then inserted in (76) to eliminate $\hat{p}_{top}^{(\tau+1)}$. In contrast to the Gaussian elimination procedure in Subsection 3.4, the 'top down sweeping' for the auxiliary entities $E_{k'}$, $F_{k'}$ begins here instead of (50) with

$$E := -\frac{A_{top}}{B_{top} + \tilde{\alpha}_{top}b_{top}} \qquad and \qquad F_{ke'} := -\frac{D_{top}}{B_{top} + \tilde{\alpha}_{top}b_{top}} \tag{83}$$

while the other entities for $k' \in \left[ke' - 1, 2\right]$ remain unchanged as in (51). It should be noticed that $\hat{p}_{top}^{(\tau)}$ in C_{top}^{w} is eliminated by using ((81) , (82)) either. The following 'down-top sweeping' to calculate the vertical motion $\hat{w}_{k'}^{(\tau+1)}$ for $k' \in \left[3, ke'\right]$ is then accomplished according to (52). The prognostic step for the pressure perturbation and also for the potential temperature follows as usual to complete one time-step cycle.

Apart from this Durran-method we suggest still a *second method*. This approach attempts to avoid the introduction of the KDB-RUBC into the vertically implicit time-scheme, but it applies this boundary condition in an explicit way rather. We demonstrate this as follows. For that purpose we need not modify the uppermost gridpoint placement as necessary in the previous method and shown in Figure 13a, b. The gridpoint arrangement demonstrated in Figure 13a is maintained, and the only modification is to assume $\hat{w} \neq 0$ at the upper boundary (at $k^{'} = ke1$) owing to the RUBC:

$$\hat{w}_{top}^{(\tau+1,\tau)} = \frac{kc_s}{g\bar{\rho}_{top}\sqrt{\kappa-1}}\hat{p}_{top}^{(\tau+1,\tau)} \tag{84}$$

which is a rearranged form of the KDB-RUBC ((81) , (82)). Provided this vertical motion value is prescribed at the upper boundary, the prognostic step for pressure with (36) and for potential temperature (38) is possible for $k = ke$ with easy access to this boundary value. In order to execute the prognostic step for the vertical motion before by solving its tri-diagonal vertical structural equation set, the corresponding equation for $k^{'} = ke^{'}$ is slightly modified compared to the form in (43). Taking into account the significant boundary value, its contribution is added to the $ke^{'}$ - equation as follows

$$A_{ke'}\hat{w}_{ke'-1}^{(\tau+1)} + B_{ke'}\hat{w}_{ke'}^{(\tau+1)} = D_{ke'}^{(\tau)} - C_{ke'}\hat{w}_{top}^{(\tau)} \tag{85}$$

Here, the closure approximation is made to put the boundary value term on the right-hand side, where it is applied at the discrete time level τ instead of $\tau + 1$. From a practical point of view this small retardation is found to be irrelevant. In order to determine $\hat{w}_{top}$ from the KDB-RUBC (84), we need, however, the perturbation pressure $\hat{p}_{top}$ which is not directly available from the general time-stepping procedure. Thus, an extrapolation technique is invoked. The practical experimentation has shown that the application of some formal mathematical extrapolation is unsuitable. A successful method consists in using an adequate hydrostatic extrapolation. For that purpose it has shown to be necessary to use the consistent hydrostatic part of the prognostic $\hat{w}$ - equation with the given time-scheme included. In the present case we have to use the hydrostatic part of (26) which is here applied with L-grid and forward vertical differences:

$$\beta^{+}\frac{\hat{p}_{top}^{(\tau+1)} - \hat{p}_{ke}^{(\tau+1)}}{\Delta z/2} + \beta^{-}\frac{\hat{p}_{top}^{(\tau)} - \hat{p}_{ke}^{(\tau)}}{\Delta z/2} = -\frac{g}{c_s^2}\left(\beta^{+}\hat{p}_{ke}^{(\tau+1)} + \beta^{-}\hat{p}_{ke}^{(\tau)}\right) + \frac{g\bar{\rho}_{ke}}{\bar{\theta}_{ke}}\hat{\theta}_{ke}^{(\tau)} \tag{86}$$

This relation makes it possible to determine $\hat{p}_{top}^{(\tau)}$ as the input value in the KDB-RUBC (84) to determine $\hat{w}_{top}^{(\tau)}$, provided the prognostic step for the perturbation pressure with equation ((36), (37)) is made before.

This is our *second method* which is an explicit approach compared to the *first method* suggested from Durran (1999). The following application of both methods to our nonhydrostatic toy-model will be shown to be practically equivalent, though the Durran-approach demonstrates a perfect incorporation and adaptation to the given vertically implicit time-scheme, while our *second method* brings about some slight inaccuracies concerning the precise time-level assignment for $\hat{w}_{top}$ within the given time-scheme. Nevertheless, the latter approach promises to be a more simple method without troublesome preparatory changes in a given model and with more convenient properties for using different time-schemes. For numerical experimentation it becomes much more easy in the programming code to switch on/off the RUBC.

4.3 Results with KDB-RUBC

Here, we carry out toy-model simulations with KDB-RUBC instead of an upper lid-condition. We are going to apply both methods as explained in the previous Subsection, but the results shown in the following do not differ from each other at all. All the results up to now demonstrated with upper lid-condition have been repeated with KDB-RUBC involved and will be shown in the next Figures against the corresponding model version with upper lid. Figure 14 gives a comparison of lid-condition against RUBC for L- and CP-grid and in each panel for a horizontal wave component with 250km-wavelength.

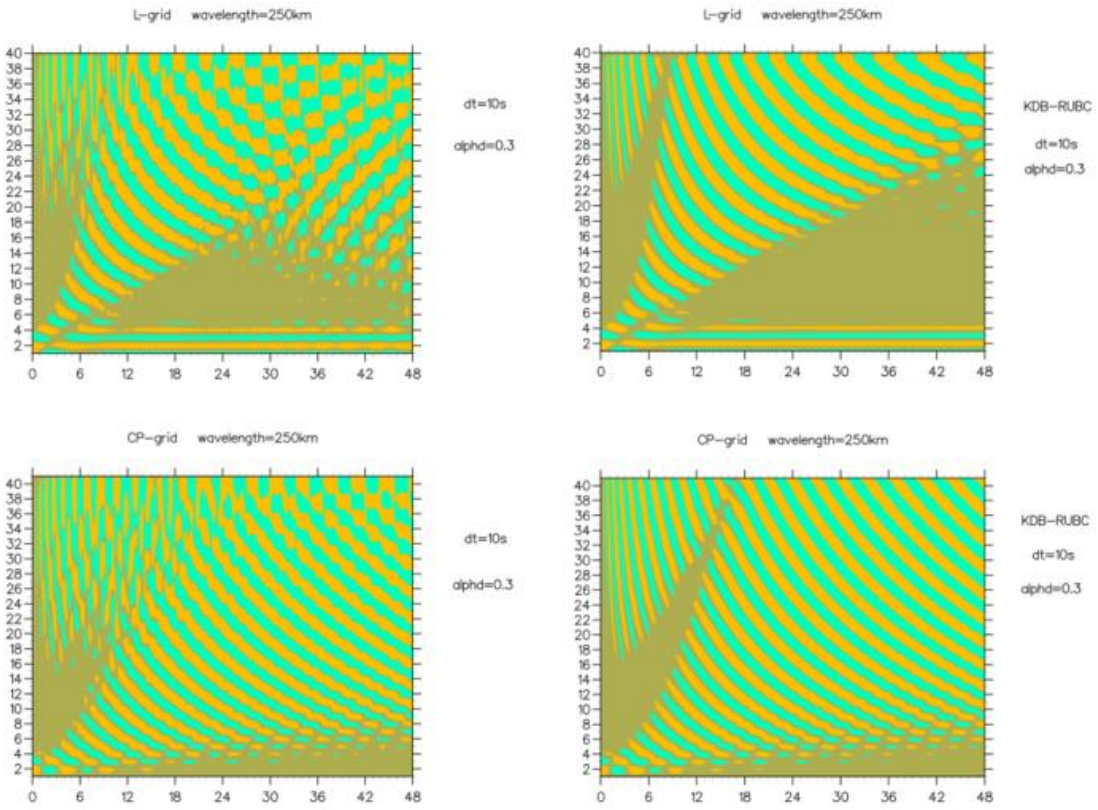


Figure 14: Simulations over 48 hours with 250km horizontal wavelength and both L- and CP-grid. Panels on the left row show the integrations with upper lid-condition, and the panels on the right row demonstrate the solution with KDB-RUBC involved.

The same type of simulation results follow immediately in Figure 15 for the potential temperature perturbation amplitude of a 100km horizontal wavelength.

In both figures (Figures 14, 15) the effect of the KDB-RUBC is clearly demonstrated. The reflective mode is essentially removed against the case with upper-lid condition. Thus, the advantages of the CP-grid on the one side and the disadvantages of the L-grid on the other side are much better revealed if a radiative upper boundary is assumed. In this case it is demonstrated best, how a dispersion process, here initiated by some special local imbalance of the hydrostatic basic state can be properly simulated. In spite of very specific and isolated simulations, deliberately adopted from Arakawa and Konor (1996) for methodical reasons, we still draw a more general conclusion that the L-grid can produce obvious shortcomings concerning the simulation of a possible dispersion process on the background of a given spectrum of internal gravity modes. Only in case of a CP-grid this dispersion process can be supported by a wide range of internal modes and is therefore simulated quite well, while using an L-grid, significant distortions of that process occur. In the latter case the associ-

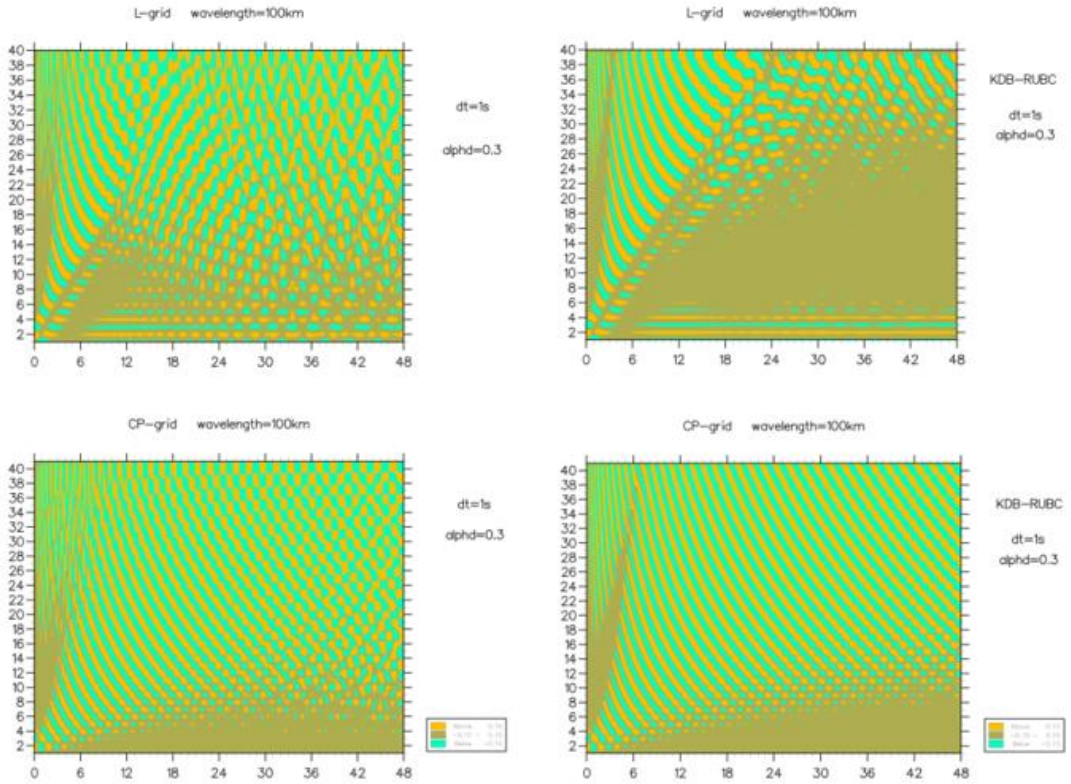


Figure 15: The same as in Figure 14 , but for 100km horizontal wavelength instead of 250km. Further explanation see text.

ated spectrum of internal modes is distorted, becomes shrunk, and brings about even an unphysical stationary mode.

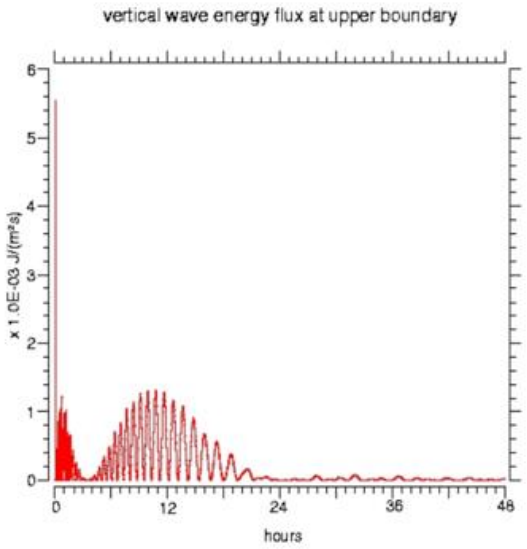


Figure 16: Vertical flux of wave energy over 48hour simulation with L-grid and 100km horizontal wavelength indicating how effective the KDB-RUBC operates

In Figure 16 we show the effectiveness of the KDB-RUBC for the L-grid simulation associated to the upper right panel of Figure 15. There can be seen the quantitative evaluation of the vertical flux of mechanical wave energy at the upper boundary in terms of $(\hat{p}\hat{w})_{top}$. This expression has to have a

positive sign in case of outgoing radiation, and Figure 16 demonstrates this positiveness over the 48 hour simulation time. The fastest vertically propagating signals associated to highest frequencies of the energy flux arrive at the upper boundary first, while after some gap the bulk of energy impinges on the model top at around 12 hour integration time having then the broadest amount of outgoing energy with slower frequencies. After that time increasingly less wave energy propagates upward, because most of it remains trapped as a stationary computational mode due to the L-grid properties, and, thus, the amount of outgoing energy dyes off over the following time.

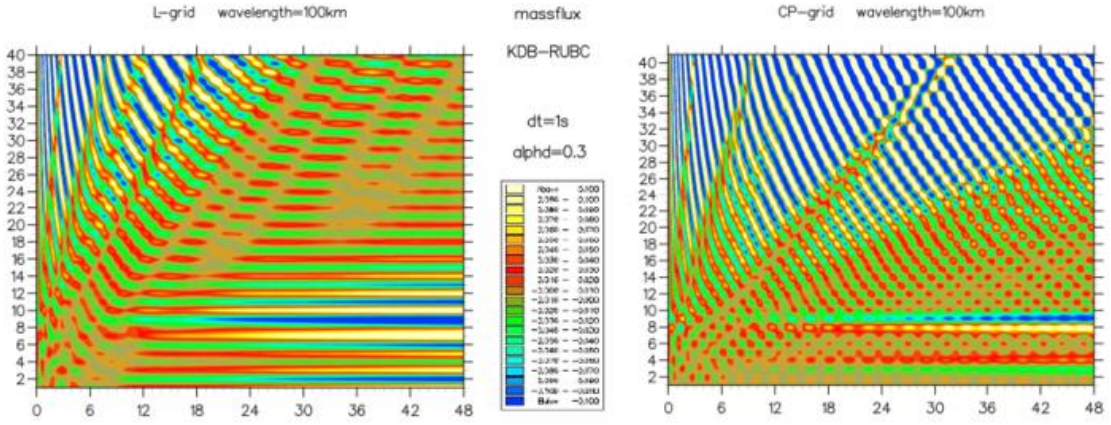


Figure 17: Time evolution of the potential temperature perturbation with imposed subgrid-scale massflux with L-grid versus CP-grid and with KDB-RUBC (compare with Fig.11).

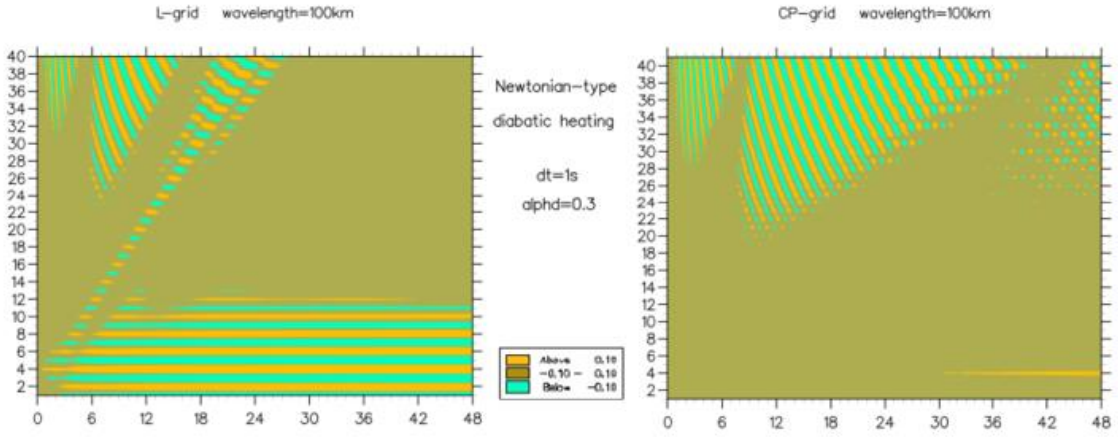


Figure 18: Simulation with Newtonian-type heat forcing at a single model level for horizontal wavelength of 100km and L-grid versus CP-grid, here with KDB-RUBC taken into account (compare with Fig.10).

Finally, we demonstrate the KDB-RUBC influence also from simulations already discussed in Subsection 3.7 for L-grid versus CP-grid, but executed there with upper lid-condition, where a simplified convective massflux and an Newtonian-heating case has been shown. A direct comparison without and with KDB-RUBC can be seen from Figure 10 versus Figure 18 in case of the Newtonian-heating simulation, and Figure 11 versus Figure 17 concerns the vertical massflux situation. The finding is also here that due to the impact of the KDB-RUBC the advantages of the CP-grid choice is much more distinct against the more distinct shortcomings of comparable L-grid simulations.

5 Simulations with LM - layering

All our previous simulations have used a vertical layering as proposed from Arakawa and Konor (1996). Instead of their choice of 40 geometrically equidistant vertical layers, we want to adopt now the vertically non-equidistant distribution of layers as valid in the LM. According to this a new experimental set-up with 35 layers is chosen from the COSMO LM-documentation by Doms and Schättler (2002, A description of the Nonhydrostatic Regional Model LM, Part I: Dynamics and Numerics, LM_F90 2.18, Nov.2002, at pages 57, 58 in Tables 4.1 and 4.2). In accordance with this the new vertically dicretised structure is formed by 35 main-levels and 36 half-levels, respectively. Since we remain here with a vertical z_k - coordinate as in the constant-layer model version above, the vertical z_k - distribution is adopted from the tables referred. For the present the basic state is assumed to be isothermal and not yet polytropic as normally used in the LM. On this basis the given LM fast-mode toy-model has been reformulated and extended to have then the LM - vertical layering. This has been made both for the vertical L-grid and the CP-grid staggering and in each case with KDB-RUBC omitted or involved. The documentation of all these modifications is rather lengthy and will therefore be dropped here.

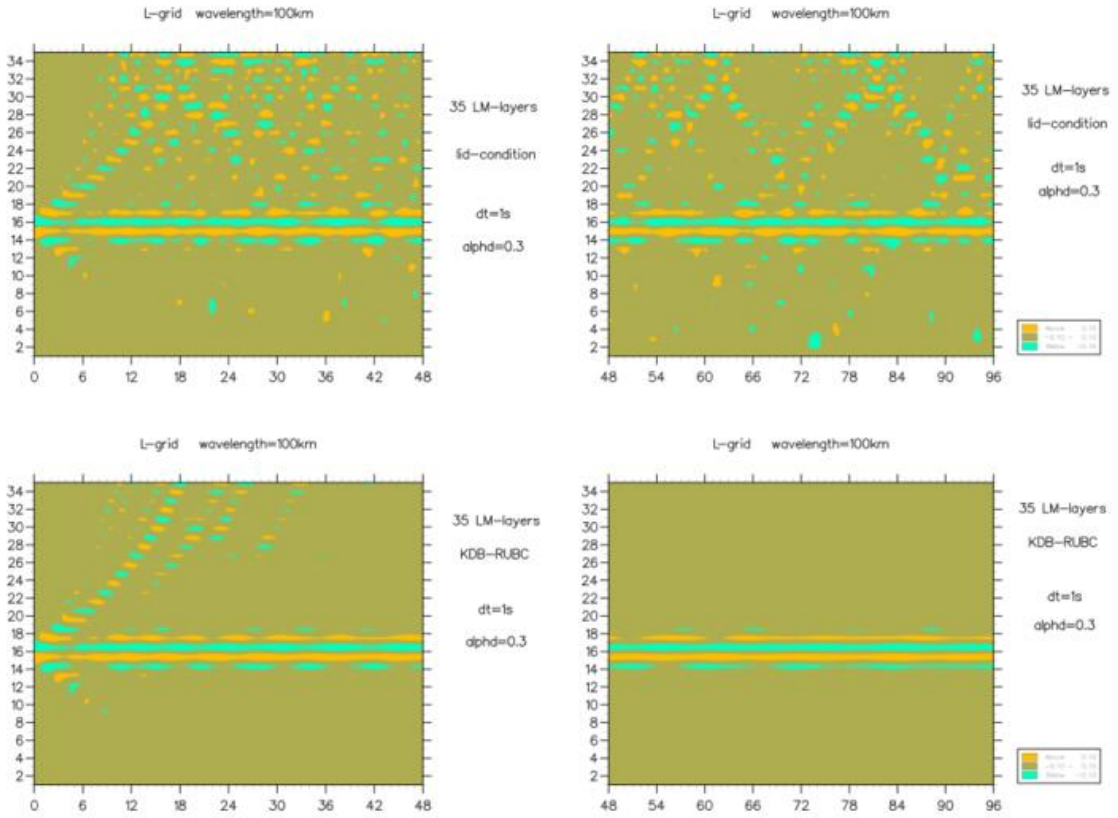


Figure 19: Time-height plot of potential temperature perturbation over 96-hour simulation time for L-grid with non-equidistant LM-layering , starting from an initial zig-zag perturbation. Upper row of panels: upper lid-condition. Lower row of panels: use of KDB-RUB. Each right panel is the continuation in time of the corresponding left one.

A simulation up to 96 hour integration time is shown in this context in Figure 19, where the typical L-grid deficiency can also be demonstrated and is more obvious with KDB-RUBC involved. The latter measure avoids a reflective mode downward from the upper boundary, so that almost all wave energy from the initial zig-zag perturbation with $\pm 0.5K$ prescribed only at vertical gridpoints $k = 15/16$ remains concentrated in an unphysical computational mode all over the integration time. It is interesting to note that the dispersion process triggered by the initial perturbation assumed here brings

about quite a different behaviour compared to all previous simulations with an equidistant layering adopted from Arakawa and Konor (1996). We postpone a deeper discussion of this numerical aspect beyond this report. Nevertheless, an anyhow triggered dispersion process with internal gravity modes involved depends for a given source strength on the thickness of layers and the way how the thickness of layers is varied through the depth of the model atmosphere (Gassmann 2003). In contrast to the L-grid simulation we show the comparable CP-grid case in the following Figure 20.

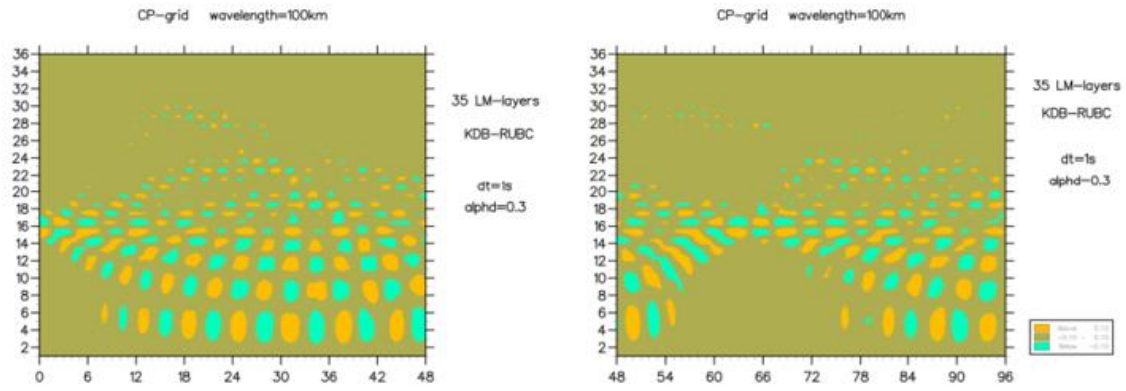


Figure 20: Comparable to Fig 19 the simulation with CP-grid property and KDB-RUBC involved.

We show here the simulation with KDB-RUBC only, since the related case with upper lid-condition has found to be not significantly different when using the CP-grid and having an initial zig-zag triggering at levels as assumed here. Compared to the result in Figure 19 it is demonstrated that the stationary computational mode is removed as expected, but the propagation of gravity modes behaves clearly different. Almost all wave energy seems trapped in the lower part of the model atmosphere where even reflections at the lower boundary can be observed. Although worth discussing these aspects we skip that here and restrict ourselves to the demonstration of L-grid shortcomings versus CP-grid advantages also in case of a vertical distribution of layer thickness used in the LM.

6 Conclusion

Starting point of our contribution was a paper by Arakawa and Konor (1996), in which these authors have carried out numerical simulations demonstrating important differences between the vertical grid type L and CP. They have shown that the L-grid version of their linear primitive model produces a computational mode without any physical meaning, while a model version with the CP-grid instead avoids this shortcoming. A thorough discussion including also quotations from many other authors are found in Arakawa (2000). We were particularly interested in the approach of Arakawa and Konor, because they have used a linearised hydrostatic model version as a simple and serious research tool, which is easy to copy for own investigations. After methodical studies with this model and with the identical experimental set-up we have then changed the model type to a compressible nonhydrostatic equation set in view of the linear fast-mode part of the LM. In order to be able to compare the solutions from this system with Arakawa and Konor's (1996) as close as possible, the design of vertical differencing (40 equally spaced layers), the choice of a basic state (isothermal and at rest) and the specific initialisation exactly remains as suggested by Arakawa and Konor. The model equations are written in spectral form for a horizontal wave component with vertically dependent perturbation amplitudes. The time-evolution of them can thus be investigated so as they are affected by the presence of gravity and sound wave modes. The given model design separates the combined effect of vertical differencing (layering, staggering) and LM - fast wave time-scheme with divergence damping involved in an isolated manner. First of all we apply this model tool in order to study computational influences on the dispersion process triggered by initially defined perturbations when using either the L-grid or the CP-grid. Within the scope of this investigation with a compressible nonhydrostatic model type very similar to the linearised LM fast mode equation part, we were also able to show that the CP-grid model version is clearly superior to an application of the L-grid in that model. Thus, there is a strong suspicion that the disadvantages of the L-grid demonstrated are expected to be possible also with the LM.

An important by-product of our simulations with L-grid versus CP-grid is that we have succeeded in incorporating the KDB-RUBC in the given scheme. The results without it suffer from strong reflections of gravity wave energy as a nuisance at and from the upper model-lid downward. Our investigation has shown that the application of the KDB-RUBC is possible and also successful in case of the nonhydrostatic compressible LM-like fast-mode model. Two methods how to incorporate the KDB-RUBC in this model has been tested. The first one is adopted from Durran (1999), and a second one is an explicit method. Both methods are equally successful showing almost identical results. In view of the present studies the impact of simulations with the KDB-RUBC included show that the advantage of a CP-grid is found to be much more distinct against the more distinct disadvantages with the L-grid.

Finally, we emphasise the meaning of our simple simulation model, that it is closely related to the linearised LM – fast mode equation part. In the sense of *res severa verum gaudium* it is a nice toy-model to study with it different options of time difference approximations in order to come then to an optimal time scheme for the LM as a whole. Furthermore, it is also possible to make studies concerning the proper way of layering through the vertical which seems also far from optimal.

Acknowledgement: The authors appreciate Peter Meyring's important help to convert the original text into the desirable LaTeX-form.

7 References

Arakawa, A. 2000: Future Development of General Circulation Models, in: General Circulation Model Development. Past, Present, and Future. Ed. By. Randall, International

Arakawa, A., and C.S. Konor, 1996: Vertical Differencing of the Primitive Equations Based on the Charney-Phillips Grid in Hybrid $\sigma - p$ Vertical Coordinates. Monthly Wea. Rev., 124, 511-528.

Bougeault, Ph., 1983: A nonreflective upper boundary condition for limited-height hydrostatic models. Monthly Wea. Rev., 111, 420-429.

Doms,G., and U. Schättler, 2002: A Description of the Nonhydrostatic Regional Model LM. Part I: Dynamics and Numerics. COSMO-Document, Nov. 2002, 134 pp.

Dudhia, J., 1993: A nonhydrostatic version of the Penn.State/ NCAR mesoscale model: Validation tests and simulation of an Atlantic cyclone and cold front. Monthly Wea. Rev., 121, 1493-1513.

Durran, D.R., 1999: Numerical methods for Wave Equations in Geophysical Fluid Dynamics. Springer-Verlag New York Berlin Heidelberg, 465 pp.

Gassmann, A., 2003: Formulation of the LM's Dynamical Lower Boundary Condition. COSMO Newsletter No.4, 155-158.

Gossard, E.E., and W.H. Hook, 1975: Waves in the Atmosphere. Elsevier Scientific Publishing Company Amsterdam-Oxford-New York, 456 pp

Ikawa, M., 1988: Comparison of some schemes for nonhydrostatic models with orography. J.Meteor.Soc.Jap., 66, 735-776.

Klemp, J.B., and D.R. Durran, 1983: An upper boundary condition permitting internal gravity wave Radiation in numerical mesoscale models. Monthly Wea. Rev., 111, 430-444.

Skamarock, W.C., and J.B. Klemp, 1992: The stability of time-split numerical methods for the hydrostatic and the nonhydrostatic elastic equations. Monthly Wea. Rev., 120, 2109-2127.

Author's adress:

Hans-Joachim Herzog,
DWD FE14, Potsdam
eMail: hans-joachim.herzog@dwd.de

Almut Gassmann,
Meteorological Institute, University Bonn
eMail: almut.gassmann@uni-bonn.de

List of COSMO Newsletters and Technical Reports

(available for download from the COSMO Website: www.cosmo-model.org)

COSMO Newsletters

Newsletter No.1, February 2001.

Newsletter No.2, February 2002.

Newsletter No.3, February 2003.

Newsletter No.4, February 2004.

COSMO Technical Reports

No. 1, Dmitrii Mironov and Matthias Raschendorfer (2001):
Evaluation of Empirical Parameters of the New LM Surface-Layer Parameterization Scheme. Results from Numerical Experiments Including the Soil Moisture Analysis.

No. 2, Reinhold Schrodin and Erdmann Heise (2001):
The Multi-Layer Version of the DWD Soil Model TERRA_LM.

No. 3, Günther Doms (2001):
A Scheme for Monotonic Numerical Diffusion in the LM.

No. 4, Hans-Joachim Herzog, Ursula Schubert, Gerd Vogel, Adelheid Fiedler and Roswitha Kirchner (2002):
LLM — the High-Resolving Nonhydrostatic Simulation Model in the DWD — Project LITFASS. Part I: Modelling Technique and Simulation Method.

No. 5, Jean-Marie Bettems (2002):
EUCOS Impact Study Using the Limited-Area Non-Hydrostatic NWP Model in Operational Use at MeteoSwiss.

No. 6, Heinz-Werner Bitzer and Jürgen Steppeler (2002):
Documentation of the Z-Coordinate Dynamical Core of LM.

No.7, Hans-Joachim Herzog, Almut Gassmann (2005):
Lorenz- and Charney-Phillips vertical grid experimentation using a compressible nonhydrostatic toy-model relevant to the fast-mode part of the 'Lokal-Modell'

COSMO Technical Reports

Issues of the COSMO Technical Reports series are published by the *Consortium for Small-Scale Modelling* at non-regular intervals. COSMO is a European group for numerical weather prediction with participating meteorological services from Germany (DWD, AWGeophys), Greece (HNMS), Italy (UGM, ARPA-SMR) and Switzerland (MeteoSwiss). The general goal is to develop, improve and maintain a non-hydrostatic limited area modelling system to be used for both operational and research applications by the members of COSMO. This system is initially based on the Lokal-Modell (LM) of DWD with its corresponding data assimilation system.

The Technical Reports are intended

- for scientific contributions and a documentation of research activities,
- to present and discuss results obtained from the model system,
- to present and discuss verification results and interpretation methods,
- for a documentation of technical changes to the model system,
- to give an overview of new components of the model system.

The purpose of these reports is to communicate results, changes and progress related to the LM model system relatively fast within the COSMO consortium, and also to inform other NWP groups on our current research activities. In this way the discussion on a specific topic can be stimulated at an early stage. In order to publish a report very soon after the completition of the manuscript, we have decided to omit a thorough reviewing procedure and only a rough check is done by the editors and a third reviewer. We apologize for typographical and other errors or inconsistencies which may still be present.

At present, the Technical Reports are available for download from the COSMO web site (www.cosmo-model.org). If required, the member meteorological centres can produce hardcopies by their own for distribution within their service. All members of the consortium will be informed about new issues by email.

For any comments and questions, please contact the editors:

Ulrich Schättler
ulrich.schaettler@dwd.de

Andrea Montani
amontani@smr.arpa.emr.it

Consortium for Small-Scale Modelling

Technical Report No. 24

Online Trajectory Module in COSMO: A short user guide

September 2014

Version 1.0

DOI: 10.5676/DWD_pub/nwv/cosmo-tr_24

Deutscher Wetterdienst
MeteoSwiss
Ufficio Generale Spazio Aereo e Meteorologia
ΕΘΝΙΚΗ ΜΕΤΕΩΡΟΛΟΓΙΚΗ ΥΠΗΡΕΣΙΑ
Instytucie Meteorogii i Gospodarki Wodnej
Administratia Nationala de Meteorologie
ROSHYDROMET
Agenzia Regionale per la Protezione Ambientale del Piemonte
Agenzia Regionale per la Protezione Ambientale dell'Emilia-Romagna
Centro Italiano Ricerche Aerospaziali
Amt für GeoInformationswesen der Bundeswehr



www.cosmo-model.org

Editor: Massimo Milelli, ARPA Piemonte

Online Trajectory Module in COSMO: A short user guide

by

***A. K. Miltenberger**[*], **A. Roches**[**], **S. Pfahl**[*], **H. Wernli**[*]*

[*]Institute for Atmospheric and Climate Science, ETHZ
Universitätstrasse 16
8092 Zürich
Switzerland
[**]C2SM
Universitätstrasse 16
8092 Zürich
Switzerland

Revision	Modifications	Date	Author
1.0	Initial Release	September 2014	Annette K. Miltenberger (ETHZ) Anne Roches (C2SM) Tobias Selz (LMU)

1 Introduction **4**

2 Scientific rational **4**

3 Implementation overview **5**

4 Namelist settings **5**

5 Start file **6**

6 Output **7**

7 Implementation details **9**

7.1 Workflow overview 9

7.2 Maximal values for array allocation 10

7.3 Restrictions of use 11

7.4 Traced variables 11

7.5 Communication strategy 12

7.6 Trajectory positions 12

Abstract

An online trajectory module is implemented in COSMO 5.1 and higher versions. The module is a diagnostic tool that enables to compute trajectories (i.e., to follow air parcels) and to trace any prognostic variable as well as diagnostic variables along the trajectories. The trajectory position is updated at each model time step based on the model wind fields, which allows to calculate trajectories very accurately for high spatial resolutions.

1 Introduction

The Lagrangian description of atmospheric motion is a valuable approach to study numerous phenomena ranging from large spatial scales, as extratropical cyclones (e.g., Wernli and Davies, 1997), to small scales, as the entrainment in stratocumulus clouds (e.g., Stevens et al., 1996). It is also very common to investigate the dispersion of atmospheric pollutants (e.g., Weil et al., 2012).

While many trajectory models for offline computation are currently available, they rely on the output of numerical weather prediction models. To capture the spatial and temporal variability of the wind field, that can be represented in the Eulerian model at high spatial resolution, model output would be required at a minute-scale temporal resolution (about 5 min for 2.2 km grid spacing) for the trajectory calculation. The temporal resolution of the wind field data has been shown to significantly influence the trajectory path (e.g., Rössler et al. 1992). It thus appears very attractive for a NWP model to incorporate a module for online trajectory computation, which allows to use the wind field at every model timestep and hence allows a very accurate calculation of trajectories also for high resolution applications.

This technical report describes shortly the implementation of the online trajectory module in the official COSMO code and presents the technical aspects that are relevant for the user of the module. It is based on the user guide published as supplement material of Miltenberger et al. (2013). Discrepancies that can be observed between both documents reflect the changes made to the code between the first version and the version that is currently implemented in the official COSMO version 5.1 and higher.

For a detailed documentation, the reader should refer to Miltenberger et al. (2013), where the scientific rational, the workflow and an example of scientific application are provided. The module has been tested on several platforms and applied in multiple research projects, demonstrating its versatility and scientific soundness.

2 Scientific rational

The scientific reasoning for implementing an online trajectory module into an atmospheric model is thoroughly described in Miltenberger et al. (2013). This paper is freely accessible at *http://www.geosci-model-dev.net/6/1989/2013/gmd-6-1989-2013.pdf*.

This comprehensive scientific documentation provides also insights in the workflow and the trajectory integration scheme. It discusses error sources for the trajectory calculation and

their relative importance and assesses the overall performance of the model. In addition a case study of an alpine foehn event is presented, demonstrating the scientific soundness of the method and the advantage of the online trajectory computation over offline trajectory computation using standard COSMO model output.

3 Implementation overview

The online trajectory module consists of two different source files, namely `data_traj.f90` and `src_traj.f90`. While the first file contains the definition of datatypes and the declaration of some variables used across the whole module (in particular some maximal values for the dimensioning of module arrays), the allocation of the module variables, the forward integration of the trajectories, the communication between the processors and the I/O subroutines are available in the second file. The interfaces to the rest of the COSMO code are slim: four calls to the organizing routine of the module in `lmorg.f90` and one call in `organize_data` as well as a global switch to activate/deactivate the module.

The module is controlled by a namelist and requires a text file containing the start positions of the trajectories (startfile).

In the following sections the technical details related to the use of the module and its implementation are described. Section 4 provides an overview of all relevant namelist swiches and section 5 explains how the start information of the trajectories should be specified. Reading these two sections should be enough to setup a trajectory computation. In section 6, more information about the output files produced by the trajectory module is provided while section 7 details the current implementation and should ease code comprehension and further extension.

4 Namelist settings

The online trajectory module can be switched on and off by an additional namelist parameter in the namelist group `RUNCTL` named `ltraj`, which is set to `FALSE` by default. The user-defined parameters for the trajectory calculation can be specified in a separate namelist named `INPUT_TRAJ` in a namelist group called `TRAJCTL`. These parameters are described below.

- `istart_mode_traj` : Specification mode of the trajectory start times:
  - `istart_mode_traj= 1` : A comma separated list of start times has to be given through the namelist parameter `hstart_traj` or `nstart_traj`. The list contains the start times in hours after model start (`hstart_traj`) or in model time steps (`nstart_traj`). Trajectories are always started at the same spatial locations for each specified start time. `nstart_traj` has priority over `hstart_traj` if both are specified.
  - `istart_mode_traj = 2` : Trajectories are started repeatedly at fixed time intervals from the same spatial locations. The first start time (in hours after the model start), the last start time (in hours after the model start) and the time interval (in hours) are specified through the namelist parameter `hcomb_start_traj` (a comma separated list of the three elements). The same triplet can be expressed in model time steps through the namelist parameter `ncomb_start_traj`. `ncomb_start_traj` has priority over `hcomb_start_traj` if both are specified.

  - `istart_mode_traj = 3` : Trajectories are started repeatedly at the times and locations provided in the startfile. The start times should be provided in hours and the entries in the startfile should be sorted according to starting time. Except for `nstop_traj` resp. `hstop_traj` all other namelist parameters pertaining to the start times (`hcomb_start_traj`, `ncomb_start_traj`, `hstart_traj`, `nstart_traj`) have no effect.
- `startfile_traj` : Path of the start file. The path can be a relative path and is limited to 100 characters. A description of the start file is provided in section 5.
- `hstop_traj` or `nstop_traj`: Time at which the trajectory calculation stops in hours after model start or in model time steps, respectively. It only has to be specified if the trajectory calculation should stop before the model integration. It has to be a multiple of the model time step. `nstop_traj` has priority over `hstop_traj` if both are specified.
- `ydir_traj` : Directory to which the trajectory output will be written. The directory specification is limited to 100 characters.
- `hinc_out_traj` or `ninc_out_traj`: Output frequency of the trajectory positions (and traced variables) in hours or in number of model time steps respectively. `hinc_out_traj` has to be a multiple of the model time step and `ninc_out_traj` has to be a whole number. If both parameters are specified, `ninc_out_traj` has priority over `hinc_out_traj`.
- `tracevar_traj` : Names of the variables which should be traced along the trajectories. The naming should be consistent with the table in the COSMO source file `src_setup_vartab.f90`, which is also used for the COSMO model output.

An example of the namelist `TRAJCTL` is given in Listing 1.

Listing 1: Namelist example

```
cat > INPUT_TRAJ << end_input_traj
 &TRAJCTL
  nstop_traj= 4320,
  hstop_traj = 24.0,
  istart_mode_traj = 1,
    hstart_traj = 3.0,6.0,12.0,
    nstart_traj = 540,1080,2160,
    !hcomb_start_traj=
    !ncomb_start_traj=
  startfile_traj = './startfile_case_n.txt',
  ydir_traj = './output_traj',
  !hinc_out_traj = 0.0333,
  ninc_out_traj = 6,
  tracevar_traj = 'T','P','QV','QC','QR','RELHUM',
/
end_input_traj
```

5 Start file

A start file containing the start positions (and times) of the trajectories has to be provided. It is specified by the user via the namelist parameter `startfile_traj` (see section 4). It contains the rotated longitudes, the rotated latitudes and the height and optionally the times at which the trajectories are started.

It is a textfile and it must comply with strict formatting rules.

The first 3 lines are header lines:

- First line: It contains the reference date, i.e., the date at which the COSMO simulation starts. This line is not considered by the program.
- Second line: Description of the file data columns. It should either be `"time lon lat z"` or `"lon lat z"` (without quotes). Only the first four non blank characters of this line will be analyzed by the program and in case the first four characters match the keyword `time`, the program will read the first data column as being the start times and expect the second column to be the rotated longitudes. If the first four characters do not match the keyword `time`, the first data column is assumed to contain the rotated longitudes.
- Third line: It is not relevant for the program. It traditionally contains only `"-------"` symbols.

The following lines in the file are content lines. In case the keyword `time` is present on the second line, the program reads the first column as the start times, the second as the rotated longitudes, the third as the rotated latitudes and the fourth as the height. If the keyword `time` is not present on the second line, the first column is read as the rotated longitudes, the second as the rotated latitudes and the third as the height. Column delimiters are blank spaces. The longitudes have to range between `-180.0` and `180.0` degrees and the latitudes can be comprised between `-90.0` and `90.0` degrees. They are expressed in the same referential than COSMO (i.e., same rotated pole coordinates). The height has to be given in meters AMSL. If time data is provided, it must be in hours after model start. The entries in the startfile should be sorted according to starting time.

The start file is read in an endless loop and all lines (except the 3 header lines) are considered as data.

Make sure that your start file fulfills the format requirements explained above!

A startfile should look similar to the example provided in Listing 2.

Listing 2: Start file example

```
Reference Date 19870725_0000
time lon lat z
----------------
 10.00    -8.000   -2.500 9000.000
 10.00    -8.000   -2.500 9100.000
 10.00    -8.000   -2.500 9200.000
```

6 Output

For all trajectories, their position as well as the value of the traced variables are written to file at the output frequency specified by the user via the namelist parameter `hinc_out_traj` or `ninc_out_traj` (see section 4) in the output directory specified by the user (`ydir_traj`, see section 4). Only NetCDF format is supported.
The output is split in the following way: The trajectories that start together at a given start time are considered as a group. If the group is too large to be contained in one single file,

the trajectories are further split over several files, according to their position in the start file. A limit of 2 GB is set as maximal file size in order to ease postprocessing. At all output time steps comprised between the start of the trajectory group and the end of the trajectory simulation (see namelist parameter `hstop_traj` or `nstop_traj` in section 4), the positions and traced variable values for the group of trajectories are written to one (or several) files. The files can thus have different lengths (for different start times).

One or several files `traj_tXXXXXX_pYYY.nc` are thus produced, where `XXXXXX` is the start time of the trajectory group expressed in minutes after the model start and `YYY` is the number of the file in the file set containing the trajectories starting at `XXXXXX` after the model start.

The output files follow the CF conventions. Some global attributes (reference date, duration of the simulation for the group of trajectories, coordinates of the rotated pole and output frequency) are written to each file. A variable `time` indicates the time elapsed since the model start in seconds. For each instance of `time` (first dimension) and for each trajectory identified by its ID (`id` as second dimension), the longitude, latitude and height (variables `longitude`, `latitude` and `z`) are written as well as the value of the traced variables. For each of these variables, the short name, the long name and the units are provided as attributes.

The header of an output file (here for 13507 trajectories starting after 120 minutes) thus looks like the example provided in Listing 3.

Listing 3: Output file example

```
netcdf traj_t000120_p001 {
dimensions:
        id = 13507 ;
        time = 541 ;
variables:
        float time(time) ;
                time:standard_name = "time" ;
                time:long_name = "time" ;
                time:units = "seconds" ;
        float longitude(time, id) ;
                longitude:standard_name = "grid_longitude" ;
                longitude:long_name = "rotated longitudes" ;
                longitude:units = "degrees" ;
        float latitude(time, id) ;
                latitude:standard_name = "grid_latitude" ;
                latitude:long_name = "rotated latitudes" ;
                latitude:units = "degrees" ;
        float z(time, id) ;
                z:standard_name = "height" ;
                z:long_name = "height above mean sea level" ;
                z:units = "m AMSL" ;
        float T(time, id) ;
                T:standard_name = "air_temperature" ;
                T:long_name = "temperature" ;
                T:units = "K" ;
        float P(time, id) ;
                P:standard_name = "air_pressure" ;
                P:long_name = "pressure" ;
                P:units = "Pa" ;
```

```
        float U(time, id) ;
                U:standard_name = "grid_eastward_wind" ;
                U:long_name = "U-component of wind" ;
                U:units = "m s-1" ;
        float QV(time, id) ;
                QV:standard_name = "specific_humidity" ;
                QV:long_name = "specific humidity" ;
                QV:units = "kg kg-1" ;
        float QI(time, id) ;
                QI:standard_name = "mass_fraction_of_cloud_ice_in_air
                    " ;
                QI:long_name = "specific cloud ice content" ;
                QI:units = "kg kg-1" ;
        float RELHUM(time, id) ;
                RELHUM:standard_name = "relative_humidity" ;
                RELHUM:long_name = "relative humidity" ;
                RELHUM:units = "%" ;

// global attributes:
                :ref_year = 2011 ;
                :ref_month = 11 ;
                :ref_day = 20 ;
                :ref_hour = 12 ;
                :ref_min = 0 ;
                :ref_sec = 0 ;
                :duration_in_sec = 10800. ;
                :pollon = -171.5 ;
                :pollat = 47.5 ;
                :output_timestep_in_sec = 20. ;
}
```

7 Implementation details

7.1 Workflow overview

An organizing routine `organize_traj` is called four times from `lmorg.f90`:

1. Once at the beginning of the initialization phase with the action `'input'`. The namelist `INPUT_TRAJ` is read as well as the start file. Necessary checks are performed in order to ensure that the specifications made by the user are meaningful. The user can proof the settings by inspecting the `YUSPECIF` file.

2. Once later on during the initialization phase with the action `'init'`. Arrays required for the whole trajectory simulation are allocated. A data structure is filled for all traced variables (see section 7.4). The rank of the eight surrounding processing elements for each processing element is defined in a parallel case. The position of the trajectories are initialized using the information read from the start file. Also, a status flag indicating if the trajectory has to be computed (`alive`), has left the domain (`dead`) or is not yet started (`embryonic`) is initialized using the start times read from or derived from the namelist settings (see section 4). In case the simulation is started from a restart file, the start positions are read directly from the restart file instead of the start file. The number of required output files is computed and the split of the trajectories among these files is determined. All NetCDF files are created and the global attributes are

written to the files. The variables are defined and their attributes written. In case the simulation is started from a restart file, this information is read from already existing output files. The NetCDF files will be kept open for the whole trajectory simulation.

3. Once at the end of each time step, where the other diagnostics are computed, with the action `'compute'`. For each compute time step of the trajectories (i.e., for each time step comprised between the start of the first trajectory and the end of the trajectory computation, both specified by the user via namelist parameters), it is checked for each trajectory, if it should be computed or not on each processor. In case it has to be computed, the forward integration is performed (see Miltenberger et al., 2013 for more details) and in case the trajectory leaves the processor domain after its integration, it is added to a buffer for communicating the new position to the relevant neighbor processor. After this has been done for all trajectories, the communication of all trajectories that have to be passed to a neighbor processor is performed. Finally output is performed, if the time step corresponds to an output time step.

4. Once at the end of the simulation with the action `'finalize'`. All NetCDF files are closed and the memory used for the trajectory simulation is freed.

In addition an organizing routine `organize_traj_restart('restart')` is called from `organize_data('results')` at the end of the time step in order to write out the trajectories to an extra restart file if needed.

7.2 Maximal values for array allocation

Some restrictions have to be set regarding the maximal size of arrays used in the module. All the maximal values are defined as parameters in the module `data_traj.f90`.
In case these maximal values have to be increased, one can simply change the values of the parameters listed below in `data_traj.f90` and test, if the model still works on the platform used.

The parameters are:

- `nmax_traj_starttime=100`: Maximal number of trajectory start times. It means that up to 100 values can be provided by the user through the namelist parameters `hstarts_traj` or `nstarts_traj` or that the namelist triplet `hcomb_start_traj` or `ncomb_start_traj` does not lead to more than 100 values. This parameter should be increased with caution!

- `nmax_traj_startpt=50000`: Maximal number of trajectories that can start at a given start time (from different locations). It thus means that a maximum of `100*50000=5 mio.` trajectories is imposed. Please note that so far, the module has been tested only with up to about 2 mio. of trajectories. If increasing this parameter or the previous one, intensive testing should be done.

- `nmax_traced_var=30`: Maximal number of variables that can be traced along the trajectories. This parameter could be increased, if more variables should be traced, but testing is recommended.

- `nmax_out_per_start_t=100`: Maximal number of output files per start time. It corresponds to the part `YYY` in the output filename `traj_tXXXXXX_pYYY.nc`. Please note that this could not be increased to more than 999 without modifying the naming scheme

of the output files. At the moment, we cannot produce more than `100*100=10'000` output files (`nmax_traj_starttime` times `nmax_out_per_start_t`).

- `nmax_nc_size=2*2^30`: Maximal size of an output file. The file size is currently limited to 2 GB in order to ease post-processing. If increasing this value, some post-processing facilities might fail.
- `header_nc_size=2*2^20`: Reserved space for the header in an output file (2 MB). If more information is added to the header in the future, it might be necessary to increase this number.

7.3 Restrictions of use

The periodic boundary conditions are not yet implemented for the trajectories. The trajectory module can be used in combination with periodic boundary conditions (`lperi_x` and `lperi_y`) and the trajectories will be computed using periodic winds but the trajectories themselves are not cycled.

Other configurations are supported.

7.4 Traced variables

A new data type `trajtrace_type` is defined in `data_traj.f90` to hold the needed information to handle properly the traced variables. Most of the information is inherited from the `var` structure available in `src_setup_vartab.f90`. It contains the following elements:

- `name`: name of the traced variable
- `levtyp`: level type (GRIB related)
- `ntri`: time range indicator (GRIB related)
- `rank`: rank
- `p4`: pointer to a 4-dimensional field
- `p3`: pointer to a 3-dimensional field
- `idef_stat`: status indicating if the variable has been computed already or if it should be derived from other model variables
- `istag`: staggering flag (`0`: no staggering; `1`: zonal staggering; `2`: meridional staggering; `3`: vertical staggering)
- `units`: units (NetCDF related)
- `sdname`: standard name (NetCDF related)
- `lgname`: long name (NetCDF related)

Only COSMO model variables can be traced. The name of the traced variables must match exactly the name of the corresponding variable in the `var` structure (in `src_setup_vartab.f90`). Only 4-dimensional and 3-dimensional variables in space can be traced. The traced variables

must be instantaneous values (i.e., have a time range indicator of 0), since it is not clear what should be traced in case of accumulated values or statistical quantities (mean, min, max). The variables can be on the half-levels or on the full-levels. They can be staggered in zonal direction (`U`) or in meridional direction (`V`). All variables that are valid at each time step in the model (`idef_stat=1` in `src_setup_vartab.f90`), i.e., all prognostic variables and several diagnostics, can be traced. The other model variables (`idef_stat=0` in `src_setup_vartab.f90`) must be derived before being written to the COSMO output. Only a subset of these variables has been implemented for tracing so far:

- `P`: total pressure
- `RELHUM`: relative humidity
- `POT_VORTIC`: potential vorticity

Other variables could easily be implemented by making use of the subroutines used in `src_output.f90` (e.g., `curl`).

At each output step the traced variables are interpolated to the trajectory position using a linear interpolation. The computed values for the traced variables as well as the trajectory ID and position (longitude, latitude and height) are gathered on processor 0, which writes the data to file.

7.5 Communication strategy

For each trajectory that leaves a processor, its ID as well as the three components of its position (longitude, latitude and height) are packed in a buffer dimensioned with the 8 neighbors and with the number of trajectories times the four needed pieces of information (ID, longitude, latitude and time). After having looped over all trajectories, actual communication is performed. For this, a "pairwise" non-blocking (`MPI_ISEND` and `MPI_IRECV`) communication strategy has been chosen. Two slices of the buffer for opposite neighbor processors (e.g., northern and southern neighbor) are communicated at a time. This is faster than communicating in each direction one after the other and requires less memory than a communication in all directions at a time. This solution is thus a compromise between performance in terms of communication speed and memory consumption. This could easily be changed if desired. The `MPI_IRECV` are pre-posted in order to improve performance.

7.6 Trajectory positions

The trajectory positions in the index space must be determined several times during a trajectory computation time step: To determine the winds at the trajectory position in order to update its position, to interpolate the orography at the trajectory position (in order to check if the trajectory has reached the ground), and finally to interpolate the traced variables to the trajectory location in case output must be performed. This computation is sensitive to the reference system and rounding errors thus occur when changing the domain decomposition. They are very small (typically differences of $O(10^{-9})$ for the longitudes and latitudes, $O(10^{-6})$ for height, $O(10^{-7})$ for traced temperature, $O(10^{-8})$ for traced wind or pressure, $O(10^{-10})$ for the traced humidity variables are observed) and do not affect the physical interpretation of the trajectories.

The required horizontal interpolation combined with the formulation of the lower boundary condition in the model (wind extrapolation) leads to trajectories that intersect the terrain, which is physically impossible. Any trajectory that reaches the ground is then lost for the rest of the simulation. In order to avoid unreasonable loss of trajectories, a trajectory that reaches the ground is reset to 10 meters above ground during the Euler forward integration (see Miltenberger et al., 2013 for more details). A hardcoded switch `ljump` controls this feature and could easily be set to `FALSE`, in order to let the trajectories leave the domain at the ground during the forward integration. Similarly, the value of the hardcoded parameter `hjump` that defines the height, at which the trajectories are reset (currently 10 meters above ground) can easily be modified.

References

Miltenberger A.K., Pfahl S., Wernli H., 2013: An online trajectory module (version 1.0) for the nonhydrostatic numerical weather prediction model COSMO. *Geosci. Model Dev.* **6**, 1989-2004, doi:10.5194/gmd-6-1989-2013.

Röessler, C. E., Paccagnella, T., Tibaldi, S., 1992: A three-dimensional atmospheric trajectory model: Application to a case study of Alpine lee cyclogenesis. *Meteorol. Atmos. Phys* **50**, 211-229.

Stevens B., Feingold G., Cotton W. R., Walko R. L., 1996: Elements of the microphysical structure of numerically simulated nonprecipitating stratocumulus. *J. Atmos. Sci.* **53**, 980-1006, doi:10.1175/1520-0469(1996)053<0980:EOTMSO>2.0.CO;2.

Weil J., Sullivan P.P., Patton E., Moeng C.-H., 2012: Statistical variability of dispersion in the convective boundary layer: Ensembles of simulations and observations. *Bound.-Lay. Meteorol.* **145**, 185-210, doi:10.1007/s10546-012-9704-y.

Wernli H., Davies H.C., 1997: A lagrangian-based analysis of extratropical cyclones. I: The method and some applications. *Q.J.R. Meteorol. Soc.* **123**, 467-489, doi:10.1002/qj.49712353811.

List of COSMO Newsletters and Technical Reports

(available for download from the COSMO Website: www.cosmo-model.org)

COSMO Newsletters

No. 1: February 2001.

No. 2: February 2002.

No. 3: February 2003.

No. 4: February 2004.

No. 5: April 2005.

No. 6: July 2006.

No. 7: April 2008; Proceedings from the 8th COSMO General Meeting in Bucharest, 2006.

No. 8: September 2008; Proceedings from the 9th COSMO General Meeting in Athens, 2007.

No. 9: December 2008.

No. 10: March 2010.

No. 11: April 2011.

No. 12: April 2012.

No. 13: April 2013.

No. 14: April 2014.

COSMO Technical Reports

No. 1: Dmitrii Mironov and Matthias Raschendorfer (2001):
Evaluation of Empirical Parameters of the New LM Surface-Layer Parameterization Scheme. Results from Numerical Experiments Including the Soil Moisture Analysis.

No. 2: Reinhold Schrodin and Erdmann Heise (2001):
The Multi-Layer Version of the DWD Soil Model TERRA_LM.

No. 3: Günther Doms (2001):
A Scheme for Monotonic Numerical Diffusion in the LM.

No. 4: Hans-Joachim Herzog, Ursula Schubert, Gerd Vogel, Adelheid Fiedler and Roswitha Kirchner (2002):
LLM ¯ the High-Resolving Nonhydrostatic Simulation Model in the DWD-Project LITFASS.
Part I: Modelling Technique and Simulation Method.

No. 5: Jean-Marie Bettems (2002):
EUCOS Impact Study Using the Limited-Area Non-Hydrostatic NWP Model in Operational Use at MeteoSwiss.

No. 6: Heinz-Werner Bitzer and Jürgen Steppeler (2004):
Documentation of the Z-Coordinate Dynamical Core of LM.

No. 7: Hans-Joachim Herzog, Almut Gassmann (2005):
Lorenz- and Charney-Phillips vertical grid experimentation using a compressible nonhydrostatic toy-model relevant to the fast-mode part of the 'Lokal-Modell'.

No. 8: Chiara Marsigli, Andrea Montani, Tiziana Paccagnella, Davide Sacchetti, André Walser, Marco Arpagaus, Thomas Schumann (2005):
Evaluation of the Performance of the COSMO-LEPS System.

No. 9: Erdmann Heise, Bodo Ritter, Reinhold Schrodin (2006):
Operational Implementation of the Multilayer Soil Model.

No. 10: M.D. Tsyrulnikov (2007):
Is the particle filtering approach appropriate for meso-scale data assimilation ?

No. 11: Dmitrii V. Mironov (2008):
Parameterization of Lakes in Numerical Weather Prediction. Description of a Lake Model.

No. 12: Adriano Raspanti (2009):
COSMO Priority Project "VERification System Unified Survey" (VERSUS): Final Report.

No. 13: Chiara Marsigli (2009):
COSMO Priority Project "Short Range Ensemble Prediction System" (SREPS): Final Report.

No. 14: Michael Baldauf (2009):
COSMO Priority Project "Further Developments of the Runge-Kutta Time Integration Scheme" (RK): Final Report.

No. 15: Silke Dierer (2009):
COSMO Priority Project "Tackle deficiencies in quantitative precipitation forecast" (QPF): Final Report.

No. 16: Pierre Eckert (2009):
COSMO Priority Project "INTERP": Final Report.

No. 17: D. Leuenberger, M. Stoll and A. Roches (2010):
Description of some convective indices implemented in the COSMO model.

No. 18: Daniel Leuenberger (2010):
Statistical analysis of high-resolution COSMO Ensemble forecasts in view of Data Assimilation.

No. 19: A. Montani, D. Cesari, C. Marsigli, T. Paccagnella (2010):
Seven years of activity in the field of mesoscale ensemble forecasting by the COSMO–LEPS system: main achievements and open challenges.

No. 20: A. Roches, O. Fuhrer (2012):
Tracer module in the COSMO model.

No. 21: Michael Baldauf (2013):
A new fast-waves solver for the Runge-Kutta dynamical core.

No. 22: C. Marsigli, T. Diomede, A. Montani, T. Paccagnella, P. Louka, F. Gofa, A. Corigliano (2013):
The CONSENS Priority Project.

No. 23: M. Baldauf, O. Fuhrer, M. J. Kurowski, G. de Morsier, M. Müllner, Z. P. Piotrowski, B. Rosa, P. L. Vitagliano, D. Wójcik, M. Ziemiański (2013):
The COSMO Priority Project 'Conservative Dynamical Core' Final Report.

COSMO Technical Reports

Issues of the COSMO Technical Reports series are published by the *COnsortium for Small-scale MOdelling* at non-regular intervals. COSMO is a European group for numerical weather prediction with participating meteorological services from Germany (DWD, AWGeophys), Greece (HNMS), Italy (USAM, ARPA-SIMC, ARPA Piemonte), Switzerland (MeteoSwiss), Poland (IMGW) and Romania (NMA). The general goal is to develop, improve and maintain a non-hydrostatic limited area modelling system to be used for both operational and research applications by the members of COSMO. This system is initially based on the COSMO-Model (previously known as LM) of DWD with its corresponding data assimilation system.

The Technical Reports are intended

- for scientific contributions and a documentation of research activities,
- to present and discuss results obtained from the model system,
- to present and discuss verification results and interpretation methods,
- for a documentation of technical changes to the model system,
- to give an overview of new components of the model system.

The purpose of these reports is to communicate results, changes and progress related to the LM model system relatively fast within the COSMO consortium, and also to inform other NWP groups on our current research activities. In this way the discussion on a specific topic can be stimulated at an early stage. In order to publish a report very soon after the completion of the manuscript, we have decided to omit a thorough reviewing procedure and only a rough check is done by the editors and a third reviewer. We apologize for typographical and other errors or inconsistencies which may still be present.

At present, the Technical Reports are available for download from the COSMO web site (www.cosmo-model.org). If required, the member meteorological centres can produce hard-copies by their own for distribution within their service. All members of the consortium will be informed about new issues by email.

For any comments and questions, please contact the editors:

Massimo Milelli
Massimo.Milelli@arpa.piemonte.it

Consortium for Small-Scale Modelling

Technical Report No. 9

Operational Implementation of the Multilayer Soil Model

July 2006

DOI: 10.5676/DWD_pub/nwv/cosmo-tr_9

Deutscher Wetterdienst

MeteoSwiss

Ufficio Generale Spazio Aereo e Meteorologia

ΕΘΝΙΚΗ ΜΕΤΕΩΡΟΛΟΓΙΚΗ ΥΠΗΡΕΣΙΑ

Instytucie Meteorogii i Gospodarki Wodnej

Administratia Nationala de Meteorologie

Agenzia Regionale per la Protezione Ambientale del Piemonte

Agenzia Regionale per la Protezione Ambientale dell' Emilia-Romagna: Servizio Idro Meteo

Centro Italiano Ricerche Aerospaziali

Amt für GeoInformationswesen der Bundeswehr

www.cosmo-model.org

Editor: Massimo Milelli, ARPA Piemonte
Printed at Deutscher Wetterdienst, P.O. Box 100465, 63004 Offenbach am Main

Operational Implementation of the Multilayer Soil Model

E. Heise, B. Ritter, R. Schrodin

DWD
Offenbach
Germany

Contents

1 Introduction, configuration of the multi-layer soil model 3

2 Operational use of the multi-layer soil model in the global model (GME) of DWD 5

2.1 Instability problems in connection with the interception store 5

2.2 Negative near surface temperature bias in the presence of snow, implementation of a prognostic treatment of snow density 5

2.3 High-frequency small-amplitude waves in the surface temperature 6

2.4 Unfavourable interaction with the snow analysis 6

2.5 Limitation of transfer coefficients to alleviate stability problems in the multi-layer soil model 7

2.5.1 Turbulent transfer coefficient limitation at the surface 7

2.5.2 Final remarks 10

3 Pre-operational and operational use in LME 10

4 Verification of soil temperature prediction over Germany 10

5 Long-term diagnostics for LME and GME 11

5.1 Soil temperature 11

5.2 Soil water content 14

6 Changes after the operational implementation 16

6.1 Dependence of snow albedo on time and on forest cover 16

6.2 Increase of infiltration at the expense of surface runoff 17

7 Suggested future work 17

8 Summary 18

9 Acknowledgement 18

10 References 18

1 Introduction, configuration of the multi-layer soil model

During the last years a new multi-layer version of the GME/LM soil model was developed (Schrodin and Heise, 2002; Heise et al., 2003) to replace the former operational 2-layer version. It became operational in GME on September 27, 2004, and in LM with the new extended model area LME on September 28, 2005. The aim of this report is to describe the present state of experience gained with the new soil model during the first years of (pre)operational use.
The main reason for increasing the number of layers was the need to take into account for freezing/melting processes in the soil, which in the 2-layer model are neglected. Because of the comparably thick uppermost layer in that version, freezing/melting effects would cause near surface temperatures to stick close to 0^oC for much too long periods in situations where in reality temperatures change around the freezing point with considerable amplitudes. But the omission of freezing/melting results in too large amplitudes of the near surface temperature in these situations. Therefore, a new version of the soil model was developed. It's main characteristic is a very high resolution in the uppermost layers of the soil. In order to avoid problems with prescribing the lower boundary condition for the thermal part, it was decided to extend the soil model to a depth, in which the annual variation of temperature is negligible. The solution

$$\delta = \Delta T_s e^{z/D} e^{i(\omega t + z/D)} \tag{1}$$

of the heat conduction equation (where δ is the temperature difference to a constant deep soil temperature, ΔT_s is the amplitude of a periodic variation of the soil surface temperature with frequency ω, D is the e-folding depth for the temperature wave, and z is the vertical coordinate, negative downward), shows the amplitude reduction of the surface temperature wave with increasing depth in the soil. For typical values of the e-folding depth of an annual temperature wave in the soil ($D \approx 2m$) an amplitude reduction to roughly 3 % of the surface value is achieved in a depth of 7 m. This led to the layer structure as given in Figure 1. In correspondence with the solution of the heat conduction equation, the layer thickness increases exponentially with depth. An additional layer with a temperature being constant in time is added below 7.29 m. Here the annual mean atmospheric near-surface temperature is prescribed as a boundary condition.

In contrast to the former two-layer version, identical layer structures are used in the thermal and the hydrologic parts, respectively. However, in contrast to the thermal part no straightforward solution for the lower boundary condition is available for the hydrologic part. Therefore, we tentatively follow a suggestion expressed in the context of the EU-project ELDAS (http://www.knmi.nl/samenw/eldas/) and prescribe a flux-boundary-condition in a depth of 2.43 m. In this depth we only consider the gravitational drainage of water and neglect any water transport due to vertical soil water gradients. In ELDAS a detailed verification has been performed of multi-annual quasi two-dimensional simulations using the multi-layer soil model. Here data from the Rhône-AGGregation Experiment (Boone et al., 2001) have been used partly as forcing data and partly as verification data. The verification concentrated on the annual courses of the snow budget and of the runoff production. The results led to some reformulation of aspects of the soil model.
The soil model is still strictly one-dimensional, i. e., all horizontal transports of water and energy in the soil are neglected. The effect of freezing/melting of soil water/ice is taken into account. The formulation accounts for the capability of the soil to retain a certain amount of liquid water at temperatures well below the freezing point. A single layer snow module complements the soil model.
For details of the soil model formulation the reader should refer to the extended documentation of the soil model (Doms et al., 2005).

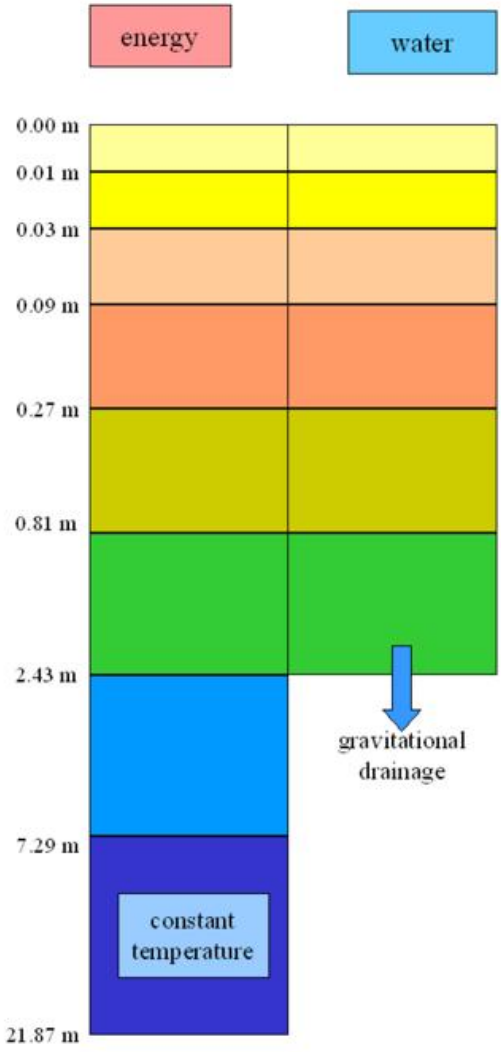


Figure 1:
Structure of the soil model

2 Operational use of the multi-layer soil model in the global model (GME) of DWD

Since September 2004 the multi-layer soil model is in operational use in the global model GME of the German Weather Service. A more than one year pre-operational run with GME preceded the operational introduction. During the operational use in GME some previously undetected problems were discovered, and a flux limiter was introduced.

2.1 Instability problems in connection with the interception store

In some cases an unfavourable interaction between the thin uppermost layer of the soil and the interception store was observed. As the interception store is not as important in the multi-layer model as in the former two layer model which used a thickness of the first layer of 0.1 m, the interception store was deactivated by setting it's maximum value to 10^{-6} m. The code related to the interception store was retained in order to allow for a later reuse of the interception store formulation.

2.2 Negative near surface temperature bias in the presence of snow, implementation of a prognostic treatment of snow density

In March 2005 excessive low temperatures were simulated over an old snow pack in southern Germany. The problem was traced back to the prescribed low density of the snow, which did not depend on external influences. The low value of snow density results in a) low heat conduction through the snow, and in b) a comparably thick snow layer for a given value of snow water equivalent. Both effects result in a very effective isolation between the soil surface and the top of the snow layer, leading to a de facto decoupling between soil and atmosphere. In order to overcome this problem, a time-dependent formulation of snow density was tested and implemented in GME. This formulation combines an ageing function, which simulates the various processes involved in the complex metamorphosis of an existing snow pack in a very crude way, with a reduction of the mean snow density in situations of fresh snow fall. The new value $\rho_{snow,new}$ of snow density at the end of time-step Δt is given by

$$\rho_{snow,new} = \left\{ \rho_{snow,age} W_{snow,old} + \rho_{snow,fresh} RR_{snow} \frac{\Delta t}{\rho_w} \right\} / W_{norm} \tag{2}$$

Here $W_{snow,old}$ is the snow water equivalent at the beginning of time-step Δt, ρ_w is the density of water. The ageing is accounted for by

$$\rho_{snow,age} = \rho_{snow,max} + (\rho_{snow,old} - \rho_{snow,max}) e^{-C_{age} \Delta t / \tau_\rho}, \tag{3}$$

where $\rho_{snow,old}$ is the snow density at the beginning of time-step Δt, and

$$C_{age} = 0.2 + (0.4 - 0.2) \cdot \frac{T_{snow} - T_{min}}{T_0 - T_{min}} \tag{4}$$

T_0 is the freezing point and we use $T_{min} = 258.15$ K. The time constant is set to $\tau_\rho = 1d$. The density of fresh falling snow is parameterized by

$$\rho_{snow,fresh} = \rho_{s,f,min} + (\rho_{s,f,max} - \rho_{s,f,min}) \cdot \frac{T_{low} - T_{min}}{T_0 - T_{min}}, \tag{5}$$

where $\rho_{s,f,min} = 50\ kg/m^3$, $\rho_{s,f,max} = 150\ kg/m^3$, and T_{low} is the temperature in the lowest atmospheric level. Finally, RR_{snow} is the rate of snowfall, and $W_{norm} = W_{snow,old} + RR_{snow}\frac{\Delta t}{\rho_w}$. The whole range of snow densities is restricted to $\rho_{snow,min} = 50\ kg/m^3$ and $\rho_{snow,max} = 400\ kg/m^3$.

In connection with the implementation of a time dependent snow density the determination of the snow heat conductivity was changed to

$$\lambda_{snow} = \lambda_{ice} \left\{ \frac{\rho_{snow}}{\rho_{ice}} \right\}^{1.88}, \tag{6}$$

where $\lambda_{ice} = 2.22\ W/(mK)$ is the heat conductivity of ice.

These changes became operational in GME on December 7, 2005.

2.3 High-frequency small-amplitude waves in the surface temperature

There is a tendency of the multi-layer soil model to produce $2\Delta t$-waves of small amplitude in the soil surface temperature. Normally these waves are not harmful to the rest of the (atmospheric) model. But in one case the effect became a problem because of an unfavourable coupling with atmospheric temperatures at grid-points with very large values of the roughness length. The small wave in the surface temperature combined with a more or less constant atmospheric temperature resulted in an alternation between stable and unstable stratification. Because of the large roughness length this led to a large-amplitude $2\Delta t$-wave in the transfer coefficient which resulted in a large-amplitude $2\Delta t$-wave in the diagnosed gusts. The runs with the LME seem not to be prone to this problem as LME uses a different formulation of the surface layer processes. In GME since August 24, 2005, the roughness length is restricted to 50 % of the height of the lowest atmospheric main level in order to overcome this problem.

2.4 Unfavourable interaction with the snow analysis

During the test-phase of the multi-layer soil model in combination with the assimilation cycle of GME it happened that snow cover was analysed in grid-elements with a soil surface temperature above the freezing point. As the analysed snow has the priority over the first guess of the model (zero snow cover in these grid-elements), an adjustment of soil temperatures is necessary. This was done by reducing the soil surface temperature to $0^o C$. In order to avoid too strong vertical gradients of the soil temperature across the first layer, a correction was applied to all soil layers with the temperature increment at the surface being linearly reduced to zero in the depth of the main level of the climate layer. In some parts of the Himalayas this led to soil temperatures of $0\,K$ during summer. The reason was a perpetual insertion of a few mm of snow in each analysis step. During the forecast this snow melted very fast, and soil surface temperatures increased considerably. But the next snow cover analysis again produced snow, and the correction had to be applied again. In the upper soil layers the energy gain due to solar radiation compensated the artificial temperature reduction in the analysis step and prevented temperatures from decreasing too much. But in the lower soil layers there was no effect counteracting the continual reduction of temperature. Therefore, the correction had to be modified. Now it is applied only in those uppermost layers, which exhibit temperatures above the freezing point. This version is applied since the start of the operational use of the multi-layer soil model in GME.

2.5 Limitation of transfer coefficients to alleviate stability problems in the multi-layer soil model

The continuous evolution of atmospheric and soil state variables which occur in the real world is not always guaranteed in the context of an NWP model. Abrupt changes may be caused in data assimilation steps but also within the actual forecast, where abrupt changes in the forcing terms (e.g. solar radiative surface flux) may be introduced as a consequence of a numerical method (e.g. rather infrequent calls of the radiative transfer scheme). If the inertia of model and soil layers is sufficiently large compared to the magnitude of the disturbances, a new balanced state can be achieved within a limited number of forecast time steps. If, in contrast, the disturbance is large compared to the model inertia, overshooting reactions may occur, which can subsequently lead to numerical instability.

The current multi-layer soil model, which features a top layer thickness of 1 cm, is prone to such over-reactions, following significant instantaneous changes in variables like snow water content or near surface wind in the analysis step or abrupt changes in the solar forcing caused by large variations in cloud cover between radiation time steps.

2.5.1 Turbulent transfer coefficient limitation at the surface

The overshooting reaction can be alleviated in many situations through the introduction of a situation-dependent upper limit for the turbulent fluxes exchanged between atmosphere and soil. For this purpose the flux will, if possible, be constrained such that the temporal tendency of the uppermost soil layer, i.e. the one with the smallest thermal inertia, does not exceed a prescribed limit in a single model time step.

The temperature tendency for each soil layer follows from:

$$\rho_{soil} c_{soil} \frac{\partial T_{soil}}{\partial t} = -\frac{\partial G}{\partial z} \tag{7}$$

with a typical value of the soil heat capacity of

$$\rho_{soil} c_{soil} = 1.4 \cdot 10^6 \frac{J}{m^3 K} \tag{8}$$

In (7) T_{soil} represents the soil temperature, z the soil depth and G the soil heat flux, which at the upper boundary is replaced by the surface fluxes of radiation, sensible and latent heat flux. For simplicity we will ignore the contributions by internal sources and sinks like melting and freezing of soil water.

Postulating an upper limit for the temporal temperature increment $\Delta T_{soil,max}$, we may derive a threshold for the heat flux at the earths surface. In discretized form we obtain:

$$\left| \frac{G(0) - G(1)}{z(0) - z(1)} \right| \leq \rho_{soil} c_{soil} \frac{\Delta T_{soil,max}}{\Delta t} \tag{9}$$

where the depths z refer to the half levels of the soil model grid and may be replaced by the thickness of the first soil layer, which we will denote byΔz_{soil}.

The presence of snow on the ground may be incorporated in (9) through the addition of a component representing a potential heating and melting of the snow layer. Based on (9) we then obtain:

$$\begin{aligned} &|G(0) - G(1)| \leq \\ &\left(\rho_{soil} c_{soil} \Delta T_{soil,max} \Delta z_{soil} + \rho_{H_2O} W_{snow} (c_{snow} \Delta T^0_{soil,max} + L_{melt})\right) / \Delta t \end{aligned} \tag{10}$$

The superscript "0" in the snow heating term reflects the fact that snow temperatures must not exceed the melting temperature. In this approach the latent heat of fusion should of course only be considered for events when the overall energy budget of the surface layer indicates a heating and the energy required for snow melting would therefore contribute to the thermal inertia of the uppermost soil layer and moderate the layer temperature tendency. A snow layer of 10 cm would typically have a heat capacity which is larger than the corresponding value of the uppermost soil layer and the energy required to melt such an amount of snow is even larger, provided the temperature increments are not excessively large. However, for simplicity, we will omit the snow contribution in the following. These effects may simply be added in the final form of the derived equations.

The flux at the upper boundary G(0) can be decomposed in the individual contributions from sensible heat flux J_s, latent heat flux J_q, net solar F_s and net thermal radiative flux F_t. Using this decomposition, we obtain:

$$\begin{aligned} &|J_s + J_q + F_s + F_t - G(1)| \leq \\ &\quad \left(\rho_{soil} c_{soil} \Delta T_{soil,max} \Delta z_{soil} + \rho_{H_2O} W_{snow} (c_{snow} \Delta T^0_{soil,max} + L_{melt})\right) / \Delta t \end{aligned} \tag{11}$$

This equation poses an upper limit on the total flux divergence for the uppermost soil layer. Since radiative fluxes are computed independently and the soil heat flux at the lower boundary of the layer is generally small compared to the other contributions, we will try to comply with the imposed limitation through an adjustment of the sensible (and latent) heat flux. As the sensible heat flux is computed from the relation:

$$J_s = C_D |\vec{u}| \rho_a c_a \Delta T_{as} \tag{12}$$

where ΔT_{as} represents the temperature difference between atmosphere and the earths surface, $|\vec{u}|$ the near surface wind speed and C_D the dimensionless transfer coefficient for heat. The atmospheric heat capacity has a typical value of $\rho_a c_a \approx 1000 J/(m^3 K)$.

A similar equation holds for the latent heat flux, i.e.

$$J_q = C_D |\vec{u}| \rho_a L_v \Delta q_{as} \tag{13}$$

with latent heat of condensation and moisture difference between surface and atmosphere as relevant properties.

Substitution of the turbulent flux equations (12) and (13) into (11), gives:

$$\begin{aligned} &|C_D |\vec{u}| \rho_a (c_a \Delta T_{as} + L_v \Delta q_{as}) + F_s + F_t - G(1)| \leq \\ &\quad \left(\rho_{soil} c_{soil} \Delta T_{soil,max} \Delta z_{soil} + \rho_{H_2O} W_{snow} (c_{snow} \Delta T^0_{soil,max} + L_{melt})\right) / \Delta t \end{aligned} \tag{14}$$

As all other properties are either fixed or can not be changed without major complications, we will attempt to comply with the soil temperature tendency limitation through a constraint to the surface-atmosphere transfer coefficient. In order to isolate the transfer coefficient in (14), we must now introduce a distinction between heating and cooling situations for the topmost soil layer.

Let us first consider a heating of the soil, i.e. the sum of all contributions on the left hand side of (14) is positive even before taking the absolute value. In this case, we may rewrite (14) as:

$$\begin{aligned} C_D |\vec{u}| \rho_a (c_a \Delta T_{as} + L_v \Delta q_{as}) \leq \\ \left(\rho_{soil} c_{soil} \Delta T_{soil,max} \Delta z_{soil} + \rho_{H_2O} W_{snow} (c_{snow} \Delta T^0_{soil,max} + L_{melt})\right) / \Delta t \\ - F_s - F_t + G(1) \end{aligned} \tag{15}$$

Despite the supposition of an overall heating, the energy transfer by turbulent fluxes may in certain situations be directed from the soil to the atmosphere. In such situations a reduction of the turbulent transfer coefficients would be counterproductive to our intention of limiting the heating of the first soil layer. In these cases we will therefore retain the original unlimited transfer coefficient. If turbulent fluxes would provide a positive contribution to the energy budget of the soil and thereby enhance the overall heating in situations when atmosphere and soil are not in balance (e.g. after the data assimilation step) a limitation of the transfer coefficient can alleviate the problem. In this situation, we may solve (15) for C_D to obtain the following constraint for the transfer coefficient:

$$\begin{aligned} C_D \leq \{ \left(\rho_{soil} c_{soil} \Delta T_{soil,max} \Delta z_{soil} + \rho_{H_2O} W_{snow} (c_{snow} \Delta T^0_{soil,max} + L_{melt}) \right) / \Delta t \\ - F_s - F_t + G(1) \} \; / \; \{ |\vec{u}| \rho_a (c_a \Delta T_{as} + L_v \Delta q_{as}) \} \end{aligned} \tag{16}$$

The physical meaning of (16) is obvious. Compared to the threshold soil temperature tendency the remaining possible contributions by turbulent fluxes to the heating of the first soil layer is diminished by the potential contributions of radiative fluxes at the surface and the internal heat flux between soil layer 1 and 2. In the presence of snow a (substantial) part of the energy gain may be used for the heating and/or melting of the snow layer, thereby allowing an overall larger total energy input.

Let us now consider a cooling of the soil, i.e. the sum of all contributions on the left hand side of (14) is negative before taking the absolute value. In this case, we may rewrite the equation:

$$\begin{aligned} C_D |\vec{u}| \rho_a (c_a \Delta T_{as} + L_v \Delta q_{as}) + F_s + F_t - G(1) \geq \\ -(\rho_{soil} c_{soil} \Delta T_{soil,max} \Delta z_{soil} + \rho_{H_2O} W_{snow} c_{snow} \Delta T^0_{soil,max}) / \Delta t \end{aligned} \tag{17}$$

leading to:

$$\begin{aligned} C_D |\vec{u}| \rho_a (c_a \Delta T_{as} + L_v \Delta q_{as}) \geq \\ -(\rho_{soil} c_{soil} \Delta T_{soil,max} \Delta z_{soil} + \rho_{H_2O} W_{snow} c_{snow} \Delta T^0_{soil,max}) / \Delta t - F_s - F_t + G(1) \end{aligned} \tag{18}$$

Note that the snow melting term has vanished since no melting will take place, if the overall forcing is negative. A limitation of the transfer coefficient in this situation can only alleviate the temperature tendency problem of the first soil layer, if the turbulent fluxes at the surface would contribute to an energy loss. Solving for the transfer coefficient, we obtain:

$$\begin{aligned} C_D \leq \{ (-\rho_{soil} c_{soil} \Delta T_{soil,max} \Delta z_{soil} + \rho_{H_2O} W_{snow} c_{snow} \Delta T^0_{soil,max}) / \Delta t \\ - F_s - F_t + G(1) \} \; / \; \{ |\vec{u}| \rho_a (c_a \Delta T_{as} + L_v \Delta q_{as}) \} \end{aligned} \tag{19}$$

Note the reversal from $\geq$ to $\leq$ when going from (18) to (19) due to the division by a negative quantity. In the absence of other contributions (e.g. from radiative fluxes) the energy loss through turbulent fluxes from the earths surface to the atmosphere is simply constrained to keep the cooling of the first soil layer below the specified threshold value. Positive contributions to the energy balance of the soil layer (e.g. by solar radiation or an upward heat flux within the soil) imply a larger potential for an energy loss through turbulence without violation of the imposed threshold.

2.5.2 Final remarks

The above derivation of a threshold equation for the transfer coefficient does not consider that the heat conduction equation is solved implicitly in the soil scheme. However, the upper limit for the temperature increment within one time step has to be chosen rather arbitrarily anyway. And the whole mechanism is only intended for a "soft" relaxation towards a more balanced atmospheric and soil structure in hopefully rare cases of "unphysical" changes of individual state variables or forcing components. In situations were a limitation of the transfer coefficient were counterproductive, the temporal tendency of the uppermost soil layer remains unchanged. If such a situation would lead to an unstable behaviour of the soil scheme, one would either have to reduce the model time step or extend the flux limitation approach to other forcing terms like the surface radiative fluxes.

3 Pre-operational and operational use in LME

In January 2005 the pre-operational test-suite of LME was initiated using the multi-layer soil model. Because at this time GME had been running pre-operationally and operationally for more than one year, temperatures and water content values in the LME-soil could be initialised by interpolation of the respective GME-fields. Therefore, the initial values could be regarded as being fairly adjusted to the model climate. No long spin-up period had to be anticipated. The soil moisture assimilation scheme was transferred from LM to LME with some adjustment because of the different layer structure. On September 28, 2005, LME replaced LM as the operational limited area model. Since the start in January no serious problem was noted in the LME soil model.
Most of the changes made during the first year of operational GME-runs with the new soil model were implemented step by step also in LME. The large negative bias of near surface temperatures observed for the GME in March 2005 was reduced in the LME by a provisional - and in fact not correct - method to convert snow heights to snow water equivalent in the LME-analysis. Purely by chance this method considerably reduced the problem. On January 05, 2006, the time-dependent treatment of snow density became operational in LME.
LME seems not to be prone to the problem with the small amplitude waves in surface temperatures as it uses a different formulation of the surface layer processes. Although no problems in the interaction with the snow analysis were noted, the respective method of GME was copied into LME.

4 Verification of soil temperature prediction over Germany

A soil model with a large active depth used operationally obviously needs to be validated in detail. However, observations of the prognostic soil variables at different depths are not available over the whole LME domain. Fortunately, all synoptic stations over Germany regularly report soil temperatures in different depths (2 cm, 5 cm, 10 cm, 20 cm, 50 cm, and 100 cm). This allows a direct comparison of observed/simulated temperatures in depths of 5/6 cm, 20/18 cm, and 50/54 cm. Figures 2 through 7 show observed and simulated temperatures in these three pairs of depths. As to be anticipated in early autumn, temperatures increase with increasing depth both in the observations and in the model.
Unfortunately it is difficult to obtain realistic area mean values. In the case of the observations they can only be estimated by taking the arithmetic average of the values reported. The respective values of the model simulations, computed by the plot-software, are biased by the

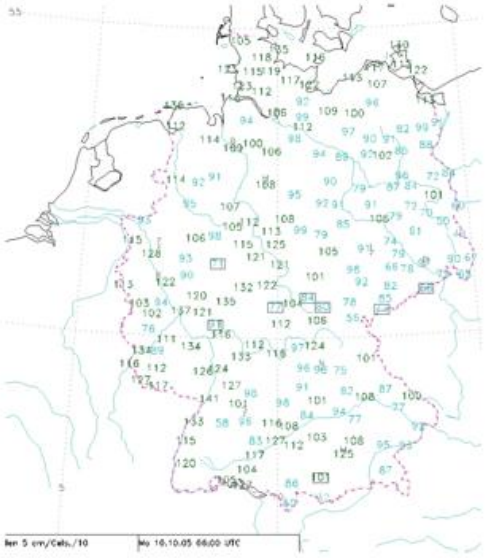


Figure 2:
Distribution of observed soil temperature $[0.1^0C]$ at 5 cm depth, 10 October 2005, 06 UTC.

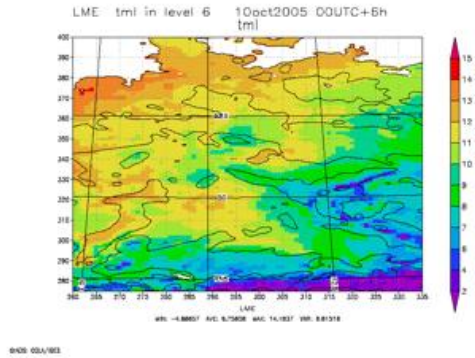


Figure 3:
Distribution of predicted soil temperature $[^0C]$ at 6 cm depth, 10 October 2005, 06 UTC.

inclusion of some part of the Alps with very low temperatures. Only very few observations are representative of higher regions, whereas the model simulations show comparably large areas with rather low temperatures because of comparably high values of the orography. Taking these effects into account, the area mean values seem to be in fairly good agreement between observation and simulation, but there seems to be some small warm bias in the model. The Upper Rhine Valley is correctly simulated as the warmest region in Germany. Although the eastern parts of northern Germany are simulated colder than the western parts, the difference is not as pronounced as in the observations. In contrast to this, some temperatures at the mountain peaks of the Thuringian Forest and of the Ore Mountains are colder in the simulations than in the observations.

5 Long-term diagnostics for LME and GME

The long-term behaviour of a soil model like the present has to be diagnosed carefully. Slow drifts might occur, especially for soil water content. A potential risk of a systematic drift in the soil temperatures is alleviated through the existence of the climate layer as a lower boundary condition. However, any systematic drift of temperatures or water content in the soil would have an impact on near surface temperatures. It is therefore mandatory to monitor the long term evolution of the soil variables in the model. For this purpose some statistical properties of the soil variables are checked on a regular basis. This monitoring is applied for layers below 0.09 m only. The rather thin three uppermost layers are excluded, as they immediately react to the atmospheric forcing. They are not characteristic of the long-term behaviour of the soil model.

5.1 Soil temperature

For the whole LME-area Table 1 shows the minimum (Min), the area averaged (Ave), and the maximum (Max) values of temperature for all soil model levels included in the diagnostic

Table 1: Minimum value (Min), area-mean (Ave), and maximum value (Max) of LME soil temperatures (^0C) in different levels of the soil model, 15 Feb 2005 - 01 Feb 2006

depth	**0.18 m**			**0.54 m**			**1.62 m**			**4.86 m**		
	Min	**Ave**	**Max**	**Min**	**Ave**	**Max**	**Min**	**Ave**	**Max**	**Min**	**Ave**	**Max**
2005												
15 Feb	-15.55	0.81	19.12	-13.25	2.30	18.46	-10.25	5.16	22.57	-11.46	9.06	29.31
15 Mar	-13.35	2.75	23.08	-12.69	3.25	24.05	-10.48	5.09	23.78	-11.46	9.05	29.15
15 Apr	-11.26	7.93	28.45	-11.51	6.94	29.75	-10.68	6.26	25.96	-11.46	9.05	29.15
15 May	-7.65	12.35	33.89	-8.27	10.94	33.54	-8.57	7.18	27.60	-14.87	8.08	24.72
15 Jun	-6.06	16.08	37.77	-6.34	14.94	36.87	-7.11	10.07	32.60	-14.87	8.09	24.80
15 Jul	-5.01	19.69	40.52	-5.27	18.03	40.79	-6.39	12.25	35.82	-14.87	8.14	26.68
15 Aug	-4.83	19.07	38.43	-3.73	18.55	40.94	-5.26	13.91	37.85	-14.88	8.29	28.61
01 Sep	-4.45	17.45	38.11	-4.50	17.64	39.47	-5.24	14.10	37.59	-14.87	8.33	29.67
11 Sep	-4.64	16.45	37.26	-4.89	16.06	38.11	-4.99	14.06	36.81	-14.87	8.33	30.11
21 Sep	-5.98	13.97	35.46	-5.06	15.25	37.12	-5.06	13.87	36.11	-14.87	8.33	30.11
01 Oct	-6.79	13.68	31.33	-6.46	14.65	33.75	-5.62	13.50	34.91	-14.87	8.33	30.11
11 Oct	-11.68	11.98	32.16	-6.72	13.28	34.16	-6.00	13.04	33.70	-14.87	8.33	30.11
21 Oct	-12.36	8.79	30.75	-8.31	11.14	31.61	-6.35	12.44	32.76	-14.87	8.33	30.11
01 Nov	-12.42	7.66	26.98	-10.37	9.75	28.64	-6.87	11.64	31.31	-14.87	8.33	30.11
11 Nov	-15.92	6.59	22.32	-10.86	8.63	26.37	-7.22	10.86	29.99	-14.87	8.33	30.10
21 Nov	-17.71	4.57	22.74	-13.36	6.78	24.04	-7.57	9.99	27.94	-14.87	8.33	29.99
01 Dec	-14.07	4.14	23.90	-13.03	5.68	25.50	-8.82	9.01	26.58	-14.87	8.33	29.36
11 Dec	-14.10	2.86	23.27	-12.00	5.12	25.31	-9.40	8.24	26.11	-14.87	8.33	28.73
21 Dec	-13.35	1,95	19.87	-11.77	3.95	22.56	-9.46	7.48	25.47	-14.87	8.32	28.11
2006												
01 Jan	-13.38	2.05	19.76	-13.11	3.37	20.78	-10.13	6.71	24.25	-14.87	8.31	27.42
11 Jan	-13.57	0.88	17.65	-11.61	2.84	21.19	-10.23	6.13	23.72	-14.87	8.27	26.99
21 Jan	-21.32	-0.93	17.75	-12.80	2.05	18.82	-9.86	5.57	22.95	-14.87	8.24	26.47
01 Feb	-14.79	-0.17	17.63	-10.96	1.45	19.61	-9.53	5.05	22.67	-14.87	8.21	26.04
11 Feb	-14.86	0.05	17.96	-10.91	1.47	19.76	-9.40	4.75	22.07	-14.87	8.19	26.03
21 Feb	-11.26	1.45	19.49	-10.29	2.22	20.34	-9.39	4.62	21.86	-14.87	8.18	26.03
01 Mar	-10.77	1.63	24.65	-10.23	2.57	23.60	-9.40	4.57	21.98	-14.87	8.14	26.03

Table 2: Area-mean (Ave) and maximum (Max) values of LME soil water content (vol %) in different layers of the soil model, 15 Feb 2005 - 11 Apr 2006, whole model area

depth	**0.09-0.27 m**		**0.27-0.81 m**		**0.81-2.43 m**	
	Ave	**Max**	**Ave**	**Max**	**Ave**	**Max**
2005						
15 Feb	26.87	82.13	22.42	80.02	24.39	68.62
15 Mar	27.27	84.18	22.84	76.72	24.34	69.67
15 Apr	24.15	85.46	23.39	77.02	24.27	70.60
15 May	22.32	82.59	22.88	85.40	24.50	72.49
15 Jun	21.84	82.86	22.17	80.45	24.63	74.01
15 Jul	20.23	85.46	20.29	80.66	24.65	74.69
15 Aug	21.27	85.91	19.30	80.50	24.57	75.54
01 Sep	19.68	82.93	18.20	78.61	24.52	75.71
11 Sep	19.66	82.17	18.04	78.30	24.47	75.69
21 Sep	21.18	81.99	18.85	78.57	24.43	75.64
01 Oct	20.00	81.97	18.46	78.72	24.40	75.61
11 Oct	19.46	81.91	18.16	85.05	24.37	75.66
21 Oct	21.45	82.02	18.61	79.07	24.34	75.76
01 Nov	22.15	82.11	18.77	79.31	24.31	75.99
11 Nov	21.77	82.25	18.50	80.05	24.31	76.31
21 Nov	23.18	82.22	18.76	80.53	24.30	76.68
01 Dec	24.20	82.60	19.52	79.53	24.30	76.95
11 Dec	24.02	82.61	19.94	78.97	24.36	77.11
21 Dec	23.54	85.61	19.89	79.51	24.42	77.26
2006						
01 Jan	23.65	86.24	19.79	79.45	24.45	77.47
11 Jan	23.39	85.83	19.88	78.54	24.48	77.56
21 Jan	23.80	85.47	19.97	78.75	24.49	77.56
01 Feb	24.24	86.12	20.33	79.09	24.49	77.60
11 Feb	24.33	86.21	20.93	78.64	24.49	77.67
21 Feb	24.85	85.84	21.35	79.08	24.50	77.75
01 Mar	25.09	85.52	21.74	78.75	24.54	77.83
11 Mar	25.04	85.51	21.83	79.07	24.58	77.81
21 Mar	24.46	85.37	21.89	79.01	24.65	77.70
01 Apr	24.22	85.29	21.72	79.11	24.73	77.83
11 Apr	24.51	85.34	22.31	79.82	24.79	77.65

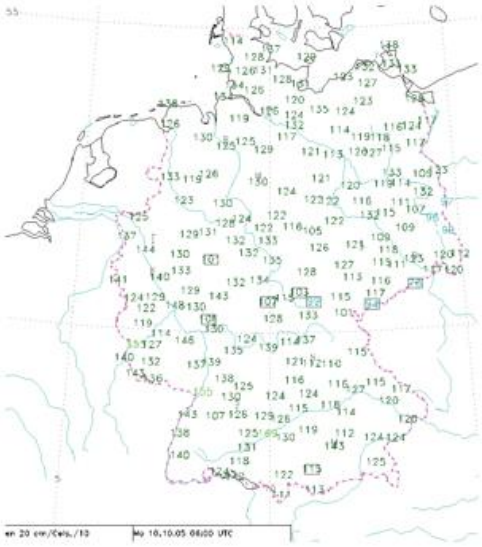


Figure 4:
Distribution of observed soil temperature $[0.1^0C]$ at 20 cm depth, 10 October 2005, 06 UTC.

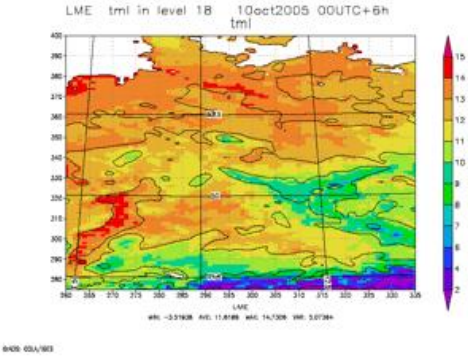


Figure 5:
Distribution of predicted soil temperature $[^0C]$ at 18 cm depth, 10 October 2005, 06 UTC.

evaluation since the start of the pre-operational LME runs in 2005. The respective values for the climatological boundary condition are: Min -11.74 ^0C, Ave 9.21 ^0C and Max 29.62 ^0C, being constant in time. The downward propagation of the annual temperature wave is clearly visible. The phase is in accord with the analytical solution of the heat conduction equation. Also, the decrease of temperature variations with increasing depth shows up in the results. In general the results appear to be realistic. There seems to be a slight discontinuity from April to May. The reason for this is a new start of LME on May 09. This was required by a new data-set of external parameters. After one year of simulation the temperatures are rather close to the initial values on 15 February, 2005. There is only a small decrease in average temperatures by less than 1 K, whereas the minimum values are slightly warmer. No uniform change is present in the maximum values. In general these results confirm the long-term stability of the soil model with respect to temperature.

5.2 Soil water content

Results for the behaviour of soil water content in LME are shown in Table 2. In the layer 0.09-0.27 m the maximum occurs in March after the snow melting in most of the model-area is finished. This high water content slowly penetrates to deeper layers. The maximum occurs in April in the layer 0.27-0.81 m and as late as August in the layer 0.81-2.43 m. Also the drying in summer is obvious, the minimum is simulated in October and November. For the whole LME-area the minimum value of soil water content is always zero because of the presence of grid-points with soil type ice or rock. For these soil types hydrological processes are not simulated and a water content of zero is prescribed. Therefore minimum values are not shown in this table. In the layers from 0.27 to 2.43 m a small decrease in average soil water content is observed. This could be a result of unsuitable initial conditions. But other data confirm a tendency of the soil model to decrease soil water content at least in part of the model area. The statistics are also available for some small regions, namely Iceland, Lapland, the Alps, and Asia Minor. Whereas for Iceland an increase in soil moisture is simulated, for the Alps a loss of 25% of the initial value is simulated for the layers from 0.27

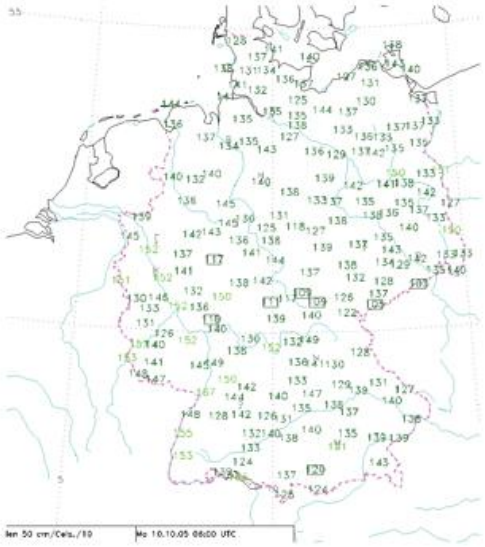


Figure 6:
Distribution of observed soil temperature $[0.1^0C]$ at 50 cm depth, 10 October 2005, 06 UTC.

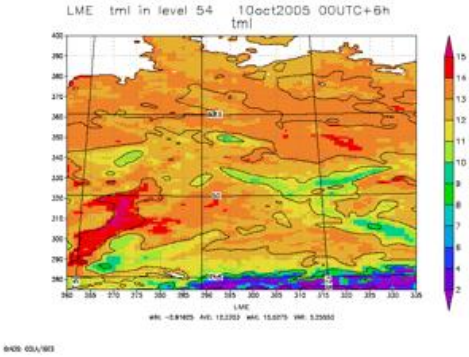


Figure 7:
Distribution of predicted soil temperature $[^0C]$ at 54 cm depth, 10 October 2005, 06 UTC.

to 2.43 m. A small decline in soil water content is also simulated for Lapland and for Asia Minor.

At the German Weather Service soil water content is measured on a regular basis in the area of the observatory Lindenberg (federal state of Brandenburg). For the year 2005 the results of the pre-operational and operational LME-runs are compared to direct measurements and to simulations performed with the model system AMBAV of the department for agricultural meteorology. AMBAV includes the very high resolution model AMBETI (Braden, 1995), which in AMBAV is driven by observations. The results of AMBAV-simulations can be used as surrogates for soil moisture measurements. Figure 8 shows a comparison of LME-forecast (6 to 30 hour forecasts for each day are combined to one quasi-annual result), direct measurements and AMBAV-results for the layer 9 to 27 cm. Taking into account for the limited comparability of direct soil water content measurements and model simulations for a rather large area (7 x 7 km^2), the results agree fairly well until the end of the second quarter of the year. But in July and August there is excessive drying in the LME-results. This effect is only partly compensated in September. In December the moisture values are much lower (roughly 50 %) than in January.

It must be noted that at DWD the operational LME is run including a soil moisture assimilation scheme (SMA). The SMA reacts on errors in the predicted 2m-temperatures, changing soil water content in order to minimize the error. The SMA partly counteracts changes of soil water content due to forcing by precipitation, evapotranspiration and runoff. During the pre-operational phase in 2005, the SMA-increments of soil water content in LME were compared with the respective changes in the operational LM (at the time with the old two-layer soil model). The average values for the LM-area turned out to be very similar in both models. This indicates that on average the multi-layer model and the old two layer model react in a nearly identical manner on the forcing of soil water content.

In Table 3 the soil water content values for GME are presented. Only the values determined for the LME-area are shown, in order to allow a comparison with the values for LME in Table 2. Obviously there is a much stronger decrease in soil water content in GME compared to LME in the upper layers during summer. This is consistent with the effect of the SMA, which in summer on average moistens the soil. But at the end of the one year period shown

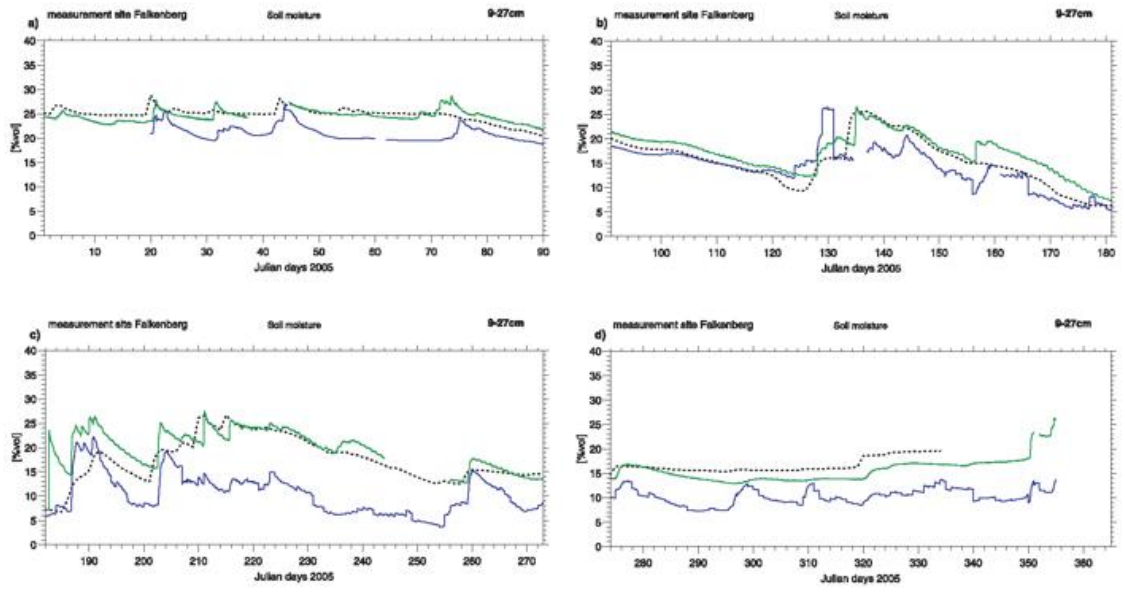


Figure 8:
Soil moisture (Vol %) in the layer 9 - 27 cm for the year 2005. Green: direct measurements, dotted: AMBAV-simulations, blue: LME-forecasts. a) January -March, b) April - June, c) July - September, d) October - December. See text for details.

in Table 3 the vaues are quite similar to the values in April 2005.

6 Changes after the operational implementation

The operational results of GME and LME with the multi-layer soil model revealed some problems. This resulted in changes of the soil model, which are described in this section.

6.1 Dependence of snow albedo on time and on forest cover

The first operational version of the multi-layer soil model used a constant snow albedo for solar radiation of 70%. Forest cover was not used to decrease the mean solar albedo in the case of existing snow decks. GME-results - especially in North America - revealed a strong negative temperature bias in spring. This could well be the effect of too high albedo values of old snow decks and snow cover in forested areas. This led to a reformulation of snow albedo. A snow-age indicator f_{snow} is introduced, being 1 for 'fresh' snow and 0 for 'old' snow. The albedo of snow is determined by

$$\alpha_{snow} = \alpha_{snow,max} \cdot f_{snow} + \alpha_{snow,min} \cdot (1 - f_{snow}), \tag{20}$$

where $\alpha_{snow,max} = 0.7$ and $\alpha_{snow,min} = 0.4$. The snow-age indicator is updated every time-step. One effect is a slow ageing term $\Delta t/\tau_\alpha$ with the time-step Δt of the model and a time constant $\tau_\alpha = 28d$. The second effect is a regeneration by falling snow: RR_{snow}/RR_{norm}, where RR_{snow} is the predicted rate of snowfall, and $RR_{norm} = 5mm/d$. Then the change of f_{snow} in one time-step Δt is given by

$$\Delta f_{snow} = f_{snow}\,[RR_{snow}/RR_{norm} - \Delta t/\tau_\alpha] \tag{21}$$

Table 3: Area-mean (Ave) and maximum (Max) values of GME soil water content (vol %) in different layers of the soil model, 15 Apr 2005 - 15 Apr 2006, values are average and maximum for the LME-area

depth	**0.09-0.27 m**		**0.27-0.81 m**		**0.81-2.43 m**	
	Ave	**Max**	**Ave**	**Max**	**Ave**	**Max**
2005						
15 Apr	24.49	80.11	23.91	78.35	25.19	72.03
15 May	22.74	76.67	22.59	75.97	25.27	73.15
15 Jun	19.89	75.77	18.46	73.30	25.08	73.63
15 Jul	17.10	72.11	15.14	69.09	24.68	73.60
15 Aug	19.40	74.24	13.90	66.16	24.21	73.12
15 Sep	18.39	77.00	13.73	68.75	23.96	72.65
15 Oct	17.88	79.87	14.72	79.59	23.86	72.59
15 Nov	22.28	81.20	16.92	79.15	23.82	73.55
15 Dec	24.97	81.08	20.25	79.53	23.98	75.16
2006						
15 Jan	25.88	80.79	21.60	79.38	24.19	76.90
15 Feb	26.78	80.90	22.38	79.93	24.28	78.30
15 Mar	26.75	81.97	23.26	78.66	24.51	79.15
15 Apr	25.33	79.50	23.18	79.07	24.72	79.63

The snow-age indicator is initialised with 1.
Having determined the albedo of snow by (20), the value is reduced depending on forest cover. Although separate values are available for evergreen and for deciduous forests, respectively, at present we only use the total fractional forest cover σ_{forest} to compute the final snow albedo α_{sf} by

$$\alpha_{sf} = \alpha_{snow} \cdot (1 - \sigma_{forest}) + \alpha_{forest} \cdot \sigma_{forest}, \tag{22}$$

with $\alpha_{forest} = 0.2$.

6.2 Increase of infiltration at the expense of surface runoff

The indications given in the chapter on the long-term diagnostics for LME and GME on a possible drying of the soil led to some investigation of likely reasons for this behaviour. It turned out that the extremely low value of 10^{-6} m prescribed as the maximum value of the water content in the interception store had an unwanted effect on infiltration. As nearly no rain could be stored in the interception store, being available for later infiltration, nearly all rain was converted to runoff (see the paragraph on 'Interception store, Infiltration of Rain and Runoff from Interception Store' in the extended LM-documentation (Doms et al., 2005)). The parameter α tended to be 1, therefore in $I_{rain} = (1 - \alpha)P_r$ no rain is converted to infiltration. This situation was improved by artificially prescribing $\alpha = 0$. In GME a remarkable effect occurred, especially in the areas of high convective precipitation in the tropics. In LME only a very small effect could be noted, because the soil moisture assimilation masked most of the possible impact.

7 Suggested future work

There are especially three areas for future model improvement:

- The drying of the soil deserves further attention. A flux equal to zero at the lower

boundary of the hydrologically active layers should be tested. This could especially be advantageous in areas with long periods of snow cover. As long as the deeper soil layers are not completely frozen, the gravitational flux will reduce the water content. This might be the reason for extremely low soil moisture values in the Alps.

- A tile approach, which distinguishes between - at least - snow-covered and snow-free parts of a grid element will be helpful for temperature prediction in the case of melting snow. Presently the soil surface temperature sticks to 0^oC as long as some part of the grid element is snow-covered. This leads to much too cold 2m-temperatures in situations with melting snow. In reality the soil surface temperature in the snow-free areas of the grid element can be considerably warmer than 0^oC.

- With a much larger effort the implementation of a multi-layer snow module should be considered. Such a model can deal with the layered structure of old snow decks and with the downward transport of water (rain or melted snow) through the snow. Also, the problem of snow density can be dealt with in a much more consistent manner.

8 Summary

A multi-layer soil model was implemented and tested in GME and LME. As a main new feature the model includes the effect of freezing/melting of soil water/ ice. Thorough testing in the global model GME preceded the pre-operational (since January 2005) and operational (since September 28, 2005) use in LME. The soil moisture assimilation scheme of LM was adjusted to the new layer structure and used in the pre-operational LME-runs since May 2005. A lot of minor and also some major bugs in the model were detected and corrected through the (pre)operational runs. Additionally, some improvements have been introduced in the code in the years 2005 and 2006. The long-term behaviour of soil water content still deserves special attention.

9 Acknowledgement

A lot of technical problems in the interplay of analysis, interpolation from GME to LME and operational LME-runs had to be solved with the help of M. Buchhold, Th. Hanisch and U. Schättler. M. Arpagaus and his colleagues at Meteoswiss used the multi-layer soil model in parallel runs and provided a lot of input for the improvement of the model. P. Meyring performed the diagnostic evaluation of the model results and assisted in solving problems with different graphic formats.

10 References

Boone, A., F. Habets, and J. Noilhan, 2001: The Rhône-AGGregation Experiment, GEWEX News, WCRP, 11(3), 3-5.

Braden, H., 1995: The model AMBETI. A detailed description of a soil-plant-atmosphere model. Berichte des Deutschen Wetterdienstes, Nr. 195, 117 pp.

Doms, G., J. Förstner, E. Heise, H.-J. Herzog, M. Raschendorfer, R. Schrodin, Th. Reinhardt, and G. Vogel, 2005: A description of the Nonhydrostatic Regional Model LM, Part II: Physical parameterization. See: www.cosmo-model.org

Heise, E., M. Lange, B. Ritter, and R. Schrodin, 2003: Improvement and Validation of the Multi-Layer Soil Model. COSMO Newsletter No. 3, February 2003, 198-203.

Schrodin, E., and E. Heise, 2002: A New Multi-Layer Soil Model. COSMO Newsletter No. 2, February 2002,149-151

List of COSMO Newsletters and Technical Reports

(available for download from the COSMO Website: www.cosmo-model.org)

COSMO Newsletters

No. 1: February 2001.

No. 2: February 2002.

No. 3: February 2003.

No. 4: February 2004.

No. 5: April 2005.

No. 6: July 2006; Proceedings from the COSMO General Meeting 2005.

COSMO Technical Reports

No. 1: Dmitrii Mironov and Matthias Raschendorfer (2001):
Evaluation of Empirical Parameters of the New LM Surface-Layer Parameterization Scheme. Results from Numerical Experiments Including the Soil Moisture Analysis.

No. 2: Reinhold Schrodin and Erdmann Heise (2001):
The Multi-Layer Version of the DWD Soil Model TERRA_LM.

No. 3: Günther Doms (2001):
A Scheme for Monotonic Numerical Diffusion in the LM.

No. 4: Hans-Joachim Herzog, Ursula Schubert, Gerd Vogel, Adelheid Fiedler and Roswitha Kirchner (2002):
LLM ¯ the High-Resolving Nonhydrostatic Simulation Model in the DWD-Project LITFASS.
Part I: Modelling Technique and Simulation Method.

No. 5: Jean-Marie Bettems (2002):
EUCOS Impact Study Using the Limited-Area Non-Hydrostatic NWP Model in Operational Use at MeteoSwiss.

No. 6: Heinz-Werner Bitzer and Jürgen Steppeler (2004):
Documentation of the Z-Coordinate Dynamical Core of LM.

No. 7: Hans-Joachim Herzog, Almut Gassmann (2005):
Lorenz- and Charney-Phillips vertical grid experimentation using a compressible nonhydrostatic toy-model relevant to the fast-mode part of the 'Lokal-Modell'

No. 8: Chiara Marsigli, Andrea Montani, Tiziana Paccagnella, Davide Sacchetti, André Walser, Marco Arpagaus, Thomas Schumann (2005):
Evaluation of the Performance of the COSMO-LEPS System

No. 9: Erdmann Heise, Bodo Ritter, Reinhold Schrodin (2006):
Operational Implementation of the Multilayer Soil Model

COSMO Technical Reports

Issues of the COSMO Technical Reports series are published by the *Consortium for Small-Scale Modelling* at non-regular intervals. COSMO is a European group for numerical weather prediction with participating meteorological services from Germany (DWD, AWGeophys), Greece (HNMS), Italy (UGM, ARPA-SMR, ARPA Piemonte) and Switzerland (MeteoSwiss). The general goal is to develop, improve and maintain a non-hydrostatic limited area modelling system to be used for both operational and research applications by the members of COSMO. This system is initially based on the Lokal-Modell (LM) of DWD with its corresponding data assimilation system.

The Technical Reports are intended

- for scientific contributions and a documentation of research activities,
- to present and discuss results obtained from the model system,
- to present and discuss verification results and interpretation methods,
- for a documentation of technical changes to the model system,
- to give an overview of new components of the model system.

The purpose of these reports is to communicate results, changes and progress related to the LM model system relatively fast within the COSMO consortium, and also to inform other NWP groups on our current research activities. In this way the discussion on a specific topic can be stimulated at an early stage. In order to publish a report very soon after the completition of the manuscript, we have decided to omit a thorough reviewing procedure and only a rough check is done by the editors and a third reviewer. We apologize for typographical and other errors or inconsistencies which may still be present.

At present, the Technical Reports are available for download from the COSMO web site (www.cosmo-model.org). If required, the member meteorological centres can produce hard-copies by their own for distribution within their service. All members of the consortium will be informed about new issues by email.

For any comments and questions, please contact the editors:

Massimo Milelli
Massimo.Milelli@arpa.piemonte.it

Ulrich Schättler
Ulrich.Schaettler@dwd.de

Consortium

for

Small-Scale Modelling

Technical Report No. 11

Parameterization of Lakes in Numerical Weather Prediction. Description of a Lake Model

August 2008

DOI: 10.5676/DWD_pub/nwv/cosmo-tr_11

Deutscher Wetterdienst

MeteoSwiss

Ufficio Generale Spacio Aero e Meteorologia

ΕΘΝΙΚΗ ΜΕΤΕΩΡΟΛΟΓΙΚΗ ΥΠΗΡΕΣΙΑ

Instytucie Meteorogii i Gospodarki Wodnej

Administratia Nationala de Meteorologie

Agenzia Regionale per la Protezione Ambientale dell Piemonte

Agenzia Regionale per la Protezione Ambientale dell Emilia-Romagna: Servizio Idro Meteo

Centro Italiano Ricerche Aerospaziali

Amt für GeoInformationswesen der Bundeswehr

www.cosmo-model.org

Editor: Massimo Milelli, ARPA Piemonte
Printed at Deutscher Wetterdienst, P.O. Box 100465, 63004 Offenbach am Main

Parameterization of Lakes in Numerical Weather Prediction. Description of a Lake Model

Dmitrii V. Mironov[†]

German Weather Service, Offenbach am Main, Germany

Abstract

A lake model intended for use as a lake parameterization module in numerical weather prediction (also in climate modelling and other environmental applications) is developed. The model is capable of predicting the vertical temperature structure and mixing conditions in lakes of various depth on the time scales from a few hours to many years. It is based on a two-layer parametric representation of the evolving temperature profile and on the integral budget of energy for the layers in question. The structure of the stratified layer between the upper mixed layer and the basin bottom, the lake thermocline, is described using the concept of self-similarity (assumed shape) of the temperature-depth curve. The same concept is used to describe the temperature structure of the thermally active upper layer of bottom sediments and of the ice and snow cover. An entrainment equation is used to compute the depth of a convectively-mixed layer. A relaxation-type equation is used to compute the wind-mixed layer depth in stable and neutral stratification, where a multi-limit formulation for the equilibrium mixed-layer depth accounts for the effects of the earth's rotation, of the surface buoyancy flux, and of the static stability in the thermocline. Both mixing regimes are treated with due regard for the volumetric character of solar radiation heating. Simple thermodynamic arguments are invoked to develop the evolution equations for the ice and snow depths. In this way, the problem of solving partial differential equations (in depth and time) for the temperature and turbulence quantities is reduced to solving ordinary differential equations for the time-dependent parameters that specify the evolving temperature profile. The result is a computationally efficient bulk model that incorporates much of the essential physics.

Empirical constants and parameters of the proposed model are estimated, using independent empirical and numerical data. Importantly, they should not be re-evaluated when the model is applied to a particular lake. The only lake-specific parameters are the lake depth, the optical characteristics of lake water, the temperature at the bottom of the thermally active layer of bottom sediments, and the depth of this layer. These external parameters are not part of the model physics, however. In this way, the model does not require re-tuning, a procedure that may improve an agreement with a limited amount of data but should generally be avoided as it greatly reduces the predictive capacity of a physical model.

The present report contains a brief overview of previous studies and a description of the lake model. Results from single-column numerical experiments with the proposed model, termed FLake, details of the implementation of FLake into the limited-area numerical weather prediction model COSMO, and results from numerical experiments with the coupled COSMO-FLake system are described elsewhere.

[†]Corresponding author address: Deutscher Wetterdienst, Forschung und Entwicklung, FE14, Frankfurter Str. 135, D-63067 Offenbach am Main, Germany. Phone: +49-69-8062 2705, fax: +49-69-8062 3721, e-mail: dmitrii.mironov@dwd.de.

Contents

1 Introduction **1**

2 Background **3**

2.1 The Concept of Self-Similarity of the Temperature Profile 3

2.2 Empirical Evidence 4

2.3 Theoretical Explanation 5

2.4 Bottom Sediments 8

2.5 Ice and Snow Cover 11

2.6 Applications 11

3 Model Description **12**

3.1 Equation of State 12

3.2 The Water Temperature 15

3.2.1 Parameterization of the Temperature Profile and the Heat Budget . . 15

3.2.2 The Mixed-Layer Depth 16

3.3 The Water - Bottom Sediment Interaction 19

3.3.1 Parameterization of the Temperature Profile and the Heat Budget . . 19

3.3.2 Heat Flux through the Bottom 20

3.4 Ice and Snow Cover 20

3.4.1 Parameterization of the Temperature Profile and the Heat Budget . . 20

3.4.2 Snow and Ice Thickness 21

3.4.3 The Temperature Profile beneath the Ice 22

3.5 Empirical Relations and Model Constants 23

3.5.1 The Shape Functions 23

3.5.2 Constants in the Equations for the Mixed-Layer Depth 28

3.5.3 Thermodynamic Parameters 28

4 Conclusions **29**

5 Appendices **31**

1 Introduction

Lakes significantly affect the structure of the atmospheric boundary layer and therefore the surface fluxes of heat, water vapour and momentum. This effect has not been systematically studied so far and is poorly understood. In most numerical weather prediction (NWP) models, the effect of lakes is either entirely ignored or is parameterized very crudely. At present, a large number of small-to-medium size lakes are indistinguishable sub-grid scale features. These lakes will become resolved scale features as the horizontal resolution is increased. Then, a physically sound model (parameterization scheme) is required to predict the lake surface temperature and the effect of lakes on the structure and transport properties of the atmospheric boundary layer[1]. Apart from being physically sound, a lake model must meet stringent requirements of computational economy.

There are several aspects of the problem. For one thing, the interaction of the atmosphere with the underlying surface is strongly dependent on the surface temperature and its time-rate-of-change. It is common for NWP models to assume that the water surface temperature can be kept "frozen" over the forecast period. That is, once the NWP model has been initialised, the surface temperature of the grid points of the type "water" is kept constant in time. The assumption is to some extent justified for seas and deep lakes. It is doubtful for small-to-medium size relatively shallow lakes, where short-term variations of the surface temperature (with a period of several hours to one day) reach several degrees. A large number of such lakes become resolved scale features as the horizontal resolution is increased. The use of a horizontal grid size of about three kilometres or even less will soon become a common practice in short-range weather forecast. In NWP models with coarser resolution, many small-to-medium size lakes remain sub-grid scale features. However, the presence of these lakes cannot be ignored due to their aggregate effect on the grid-scale surface fluxes. This also holds for climate models concerned with the time scales ranging from many days to many years.

Initialisation of the water-type grid points of an NWP model often presents considerable difficulties. In case the observational data for several water points are not available, these points are initialised by means of interpolation (often quite sophisticated) between the nearest water-type points for which the surface temperature is known (from satellite data or from in situ measurements). Such procedure is not too harmful for sea points. Large horizontal gradients of the sea surface temperature (SST) are comparatively rare, so that the interpolated SST is expected to be a reasonably good approximation of the actual SST. In contrast to open sea, lakes are enclosed water bodies of a comparatively small horizontal extent. The lake surface temperature is a result of a complex interplay of physical processes in the lake in question. It has little or nothing to do with the surface temperature obtained by means of interpolation between the alien water bodies.

Another important aspect of the problem is that lakes strongly modify the structure and the transport properties of the atmospheric boundary layer. A major outstanding question is the parameterization of the roughness of the water surface with respect to wind and to scalar quantities, such as potential temperature and specific humidity. A detailed consideration of this aspect of the problem is beyond the scope of the present report.

An interest in the problem of lakes has led to the development of several lake models (parameterization schemes) for use in NWP and climate studies. Three-dimensional lake models

[1]The terms "model" and "parameterization scheme" may be used interchangeably in this context. The term "parameterization scheme" is more often used in the NWP and climate modelling community to discriminate a component (module) of a complex modelling system from its host that is referred to as an NWP (climate) model.

account for both vertical and horizontal transport of momentum and heat and provide detailed information about the lake temperature structure. However, a very high computational cost limits their utility to only a few large lakes, such as Lake Victoria (Song et al. 2004), Laurentian Great Lakes (León et al. 2005), Great Slave Lake (León et al. 2007, Long et al. 2007) and Great Bear Lake (Long et al. 2007), and to research applications. The use of three-dimensional lake models (or ocean models customised for lakes) as lake parameterization schemes in NWP and other operational applications will most likely be impossible for some years to come. One-dimensional lake models range from the simplest one-layer slab models to rather sophisticated turbulence closure models based on the transport equations for the second-order turbulence moments. One-layer models characterise the entire water column by a single value of temperature, assuming a complete mixing down to the lake bottom (Ljungemyr et al. 1996), or to the bottom of a mixed layer of a fixed depth which may vary spatially (Goyette et al. 2000). Although this assumption results in a bulk model that is computationally very efficient, it is an oversimplification from the physical point of view. As most lakes are stratified over a considerable part of the year, neglecting the lake thermocline results in large errors in the surface temperature. Second-order turbulence closure models, e.g. models that carry transport equations for the turbulence kinetic energy (TKE) and its dissipation rate (Omstedt and Nyberg 1996, Omstedt 1999, Blenckner et al. 2002, Stepanenko 2005, Stepanenko et al. 2006) or for the TKE only (Tsuang et al. 2001)[2], may describe the lake thermocline with reasonable accuracy. These models are computationally rather expensive, however. Their use to treat a large number of lakes can hardly be afforded in operational applications. Hostetler (see Hostetler and Bartlein 1990, Hostetler 1991, Hostetler et al. 1993, Barrette and Laprise 2005) developed a lake model that uses an algebraic stability-dependent formulation for the turbulent heat conductivity and a convective adjustment procedure. As a lake parameterization scheme, that lake model was coupled to a number of atmospheric models. It enjoyed wide popularity in climate studies (Hostetler and Benson 1990, Hostetler 1991, Hostetler and Giorgi 1992, Bates et al. 1993, 1995, Hostetler et al. 1993, 1994, Bonan 1995, Small et al. 1999). MacKay (2005) developed a hybrid model, where the solution of the non-steady heat transfer equation on a numerical grid is combined with the bulk treatment of the upper mixed layer following Imberger (1985) and Spigel et al. (1986).

In the present report, a lake model capable of predicting the vertical temperature structure in lakes of various depth on the time scales from a few hours to many years is described. The model is based on a two-layer parameterization of the evolving temperature profile and on the integral energy budget for the layers in question. The structure of the stratified layer between the upper mixed layer and the basin bottom, the lake thermocline, is described using the concept of self-similarity (assumed shape) of the temperature-depth curve. The same concept is used to describe the temperature structure of the thermally active upper layer of bottom sediments and of the ice and snow cover. In this way, the problem of solving partial differential equations (in depth and time) for the temperature and turbulence quantities is reduced to solving ordinary differential equations for the time-dependent parameters that specify the temperature profile. This approach, that is based on what could be called "verifiable empiricism", offers a very good compromise between physical realism and computational economy. In Section 2, the concept of self-similarity of the temperature profile is outlined and a brief overview of previous studies along this line is given. A lake model is presented in Section 3. Conclusions are presented in Section 4.

[2]The model of Tsuang et al. (2001) is not strictly one dimensional as it incorporates a simplified scheme to account for horizontal advection of momentum, heat and turbulence kinetic energy.

2 Background

2.1 The Concept of Self-Similarity of the Temperature Profile

The concept of self-similarity of the temperature profile $\theta(z,t)$ in the thermocline was put forward by Kitaigorodskii and Miropolsky (1970) to describe the vertical temperature structure of the oceanic seasonal thermocline. The essence of the concept is that the dimensionless temperature profile in the thermocline can be fairly accurately parameterized through a "universal" function of dimensionless depth, that is

$$\frac{\theta_s(t) - \theta(z,t)}{\Delta\theta(t)} = \Phi_\theta(\zeta) \quad \text{at} \quad h(t) \le z \le h(t) + \Delta h(t). \tag{1}$$

Here, t is time, z is depth, $\theta_s(t)$ is the temperature of the upper mixed layer of depth $h(t)$, $\Delta\theta(t) = \theta_s(t) - \theta_b(t)$ is the temperature difference across the thermocline of depth $\Delta h(t)$, $\theta_b(t)$ is the temperature at the bottom of the thermocline, and $\Phi_\theta \equiv [\theta_s(t) - \theta(z,t)]\,/\Delta\theta(t)$ is a dimensionless "universal" function of dimensionless depth $\zeta \equiv [z - h(t)]\,/\Delta h(t)$ that satisfies the boundary conditions $\Phi_\theta(0) = 0$ and $\Phi_\theta(1) = 1$. In what follows, the arguments of functions dependent on time and depth are not indicated, unless it is indispensable. The temperature profile given by Eq. (1) is illustrated in Fig. 1.

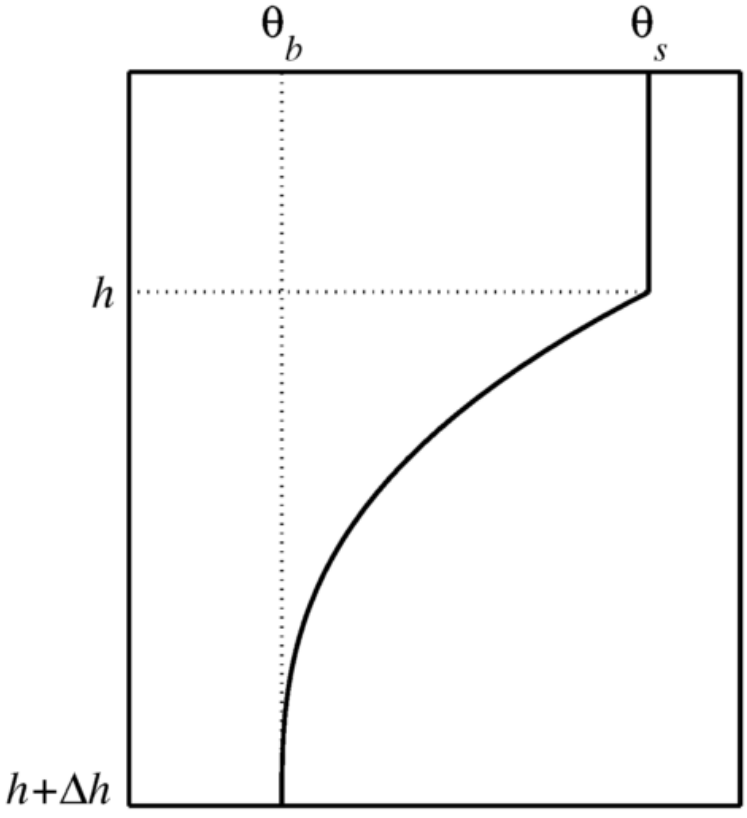


Figure 1: Schematic representation of the temperature profile in the upper mixed layer and in the thermocline. See text for notation.

The idea of self-similarity of the temperature profile in the thermocline can be traced back to the famous work of Munk and Anderson (1948). Although these authors did not present Eq. (1) in its explicit form, the following quotation is a qualitative statement of the idea (Munk and Anderson 1948, p. 276):

> ...the upper layers are stirred until an almost homogeneous layer is formed, bounded beneath by a region of marked temperature gradient, the thermocline. ...If the wind increases in intensity the thermocline moves downward, but the characteristic *shape* of the temperature-depth curve remains essentially unchanged. (Original authors' italic.)

In this connection, the work of Ertel (1954) should be mentioned. Ertel considered the formation and deepening of the thermocline in a fresh-water lake during the summer heating period, using an analytical solution to the linear heat transfer equation. He defined the thermocline ("thermische Sprungschicht" – the temperature jump layer, as termed in op. cit.) as a layer where the vertical temperature gradient exceeds 1 $\mathrm{K{\cdot}m^{-1}}$. Ertel did not present his results in the form given by Eq. (1). He found, however, that the ratio of the depth from the upper boundary of the thermocline to the bend point of the temperature profile to the depth from the bend point to the bottom of the thermocline is constant. In other words, the *shape* of the temperature-depth curve in the thermocline is independent of time.

The concept of self-similarity of the temperature profile in the thermocline can be considered as a natural extension of the concept of the temperature uniform mixed layer that has been successfully used in geophysical fluid dynamics over several decades. Indeed, using the mixed-layer temperature θ_s and its depth h as appropriate scales, the mixed-layer concept can be expressed as $\theta(z,t)/\theta_s(t) = \vartheta[z/h(t)]$, where a dimensionless function ϑ is simply a constant equal to one. The use of $\Delta\theta$ and Δh as appropriate scales of temperature and depth, respectively, in the thermocline leads to Eq. (1), where Φ_θ is not merely a constant but a more sophisticated function of ζ. It should be emphasised that neither the mixed-layer concept nor the concept of self-similarity of the thermocline is well justified theoretically. Both concepts heavily rely on empirical evidence and should therefore be considered phenomenological. However, this phenomenological approach appears to describe the observed temperature structure to a degree of approximation that is sufficient for many applications.

2.2 Empirical Evidence

In order to obtain an analytical approximation of the dimensionless function $\Phi_\theta(\zeta)$ in Eq. (1), Kitaigorodskii and Miropolsky (1970) took a geometrical approach similar to what is often referred to as the Pohlhausen method in the boundary-layer theory. They expressed Φ_θ as a fourth-order polynomial in ζ and invoked five boundary conditions to specify the polynomial coefficients. Apart from the conditions $\Phi_\theta(0) = 0$ and $\Phi_\theta(1) = 1$ that simply follow from the definition of Φ_θ and ζ, they assumed neutral temperature stratification at the bottom of the thermocline, $\Phi'_\theta(1) = 0$, and a smooth matching to the temperature profile in the underlying layer, $\Phi''_\theta(1) = 0$. Furthermore, they assumed that the temperature-depth curve has a maximum curvature at the upper boundary of the thermocline, $\Phi'''_\theta(0) = 0$. The resulting expression,

$$\Phi_\theta = \frac{8}{3}\zeta - 2\zeta^2 + \frac{1}{3}\zeta^4, \tag{2}$$

was tested against monthly-mean temperature profiles recorded at the ocean weather ships "Papa" (Kitaigorodskii and Miropolsky 1970) and "Tango" (Kitaigorodskii 1970).

One more polynomial approximation of $\Phi_\theta(\zeta)$ was proposed by Arsenyev and Felzenbaum (1977). These authors also took a geometrical approach (the Pohlhausen method) but, unlike Kitaigorodskii and Miropolsky (1970), did not make use of the condition $\Phi'''_\theta(0) = 0$. The

resulting third-order polynomial,

$$\Phi_\theta = 1 - (1-\zeta)^3, \tag{3}$$

has subsequently enjoyed wide popularity.

The concept of self-similarity of the temperature profile in the thermocline received support through laboratory studies (Linden 1975, Voropaev 1977, Wyatt 1978). Linden (1975) modified the Kitaigorodskii and Miropolsky (1970) expression (2) in order to account for the stable density stratification in a quiescent layer below the thermocline. He proposed the expression (in op. cit., it is given in terms of density)

$$\Phi_\theta = \zeta + (1-\Gamma)\left(\frac{5}{3}\zeta - 2\zeta^2 + \frac{1}{3}\zeta^4\right), \tag{4}$$

where $\Gamma = -(\Delta\theta/\Delta h)^{-1}(\partial\theta/\partial z)|_{h+\Delta h}$ is the temperature gradient just below the thermocline relative to the mean temperature gradient within the thermocline [by virtue of a smooth matching of the temperature profile in the thermocline and in the layer below, $\Gamma = \Phi'_\theta(1)$]. Equation (4) revealed a good agreement with data from measurements in a laboratory tank, where turbulence was generated by an oscillating grid.

Empirical data taken in natural conditions (Miropolsky et al. 1970, Nesterov and Kalatsky 1975, Kharkov 1977, Reshetova and Chalikov 1977, Efimov and Tsarenko 1980, Filyushkin and Miropolsky 1981, Mälkki and Tamsalu 1985, Tamsalu and Myrberg 1998) also lent support to the concept of self-similarity of the thermocline. However, the scatter of data around the temperature-depth curves proved to be quite large. Reshetova and Chalikov (1977) attempted to extend the self-similarity concept to parameterize the vertical profile of salinity in the ocean.

Filyushkin and Miropolsky (1981) noticed that the shape of the temperature-depth curve depends on the mixed-layer state. They proposed to differentiate between the two cases: the mixed-layer deepening, $dh/dt > 0$, and its stationary state or retreat, $dh/dt \leq 0$. Mälkki and Tamsalu (1985) developed the following empirical approximations for these two cases:

$$\Phi_\theta = \begin{cases} 1-(1-\zeta)^3 & \text{if} \quad dh/dt > 0 \\ 1-4(1-\zeta)^3+3(1-\zeta)^4 & \text{if} \quad dh/dt \leq 0. \end{cases} \tag{5}$$

These expressions were tested against data from measurements in the Baltic Sea (Mälkki and Tamsalu 1985, Tamsalu and Myrberg 1998). The first line of Eq. (5) that corresponds to the mixed-layer deepening coincides with Eq. (3) developed from simple geometrical arguments by Arsenyev and Felzenbaum (1977). In case of the mixed-layer stationary state or retreat, the form of the temperature-depth curve is essentially different. The temperature profiles in the thermocline and in the mixed layer match smoothly, and the vertical temperature gradient is a maximum within the thermocline, not at its upper boundary. Data taken in Lake Ladoga, Russia, and Lake Sevan, Armenia, corroborated the occurrence of two types of self-similar temperature profiles in the thermocline (Zilitinkevich 1991).

2.3 Theoretical Explanation

A plausible theoretical explanation for the observed self-similarity of the temperature profile in the thermocline was offered in case of the mixed-layer deepening (Barenblatt 1978, Turner 1978, Shapiro 1980, Zilitinkevich et al. 1988, Zilitinkevich and Mironov 1989, Mironov 1990, Zilitinkevich and Mironov 1992). These authors analysed the heat transfer equation

$$\frac{\partial\theta}{\partial t} = \frac{\partial}{\partial z}K_H\frac{\partial\theta}{\partial z}, \tag{6}$$

where K_H is the temperature conductivity (the heat conductivity divided by the density ρ and specific heat c of the medium in question). Introducing a vertical co-ordinate moving with the mixed layer-thermocline interface, $z' = z - h(t)$, they considered a travelling wave-type solution to Eq. (6). Assuming constant temperatures at the upper and lower boundaries of the thermocline, $\partial\theta_s/\partial t = \partial\theta_b/\partial t = 0$, Eq. (6) becomes

$$-\dot{h}\frac{d\theta}{dz'} = \frac{d}{dz'}K_H\frac{d\theta}{dz'}, \tag{7}$$

where $\dot{h} \equiv dh/dt > 0$ is the rate of the mixed-layer deepening.

Barenblatt (1978) took K_H to be constant and considered a solution to Eq. (7) in a half-space $z' > 0$. Using boundary conditions $\theta = \theta_s$ at $z' = 0$ and $\theta = \theta_b$ at $z' = \infty$, he obtained the solution

$$\Phi_\theta = 1 - \exp(-\dot{h}z'/K_H). \tag{8}$$

Since the thermocline has an infinite thickness, the above solution cannot be recast in terms of $\Phi_\theta(\zeta)$. However, Eq. (8) appears to be a fairly close approximation to the empirical polynomials proposed by Kitaigorodskii and Miropolsky (1970) and Arsenyev and Felzenbaum (1977) at certain values of $\dot{h}/K_H$.

Turner (1978) examined both the simplest case of $K_H = const$ and a more sophisticated case, where K_H is proportional to the vertical temperature gradient,

$$K_H = -\frac{\dot{h}l^2}{\Delta\theta}\frac{\partial\theta}{\partial z}, \tag{9}$$

l being a characteristic eddy length scale. Assuming $K_H \propto -\partial\theta/\partial z$, he added the factor $\dot{h}l^2/\Delta\theta$ to the r.h.s. of Eq. (9) "to be consistent dimensionally". In support of Eq. (9), Turner considered generation of turbulence by breaking internal gravity waves. He wrote (Turner 1978, p. 6): "It seems likely that the energy required to produce this addition mixing below the surface layer will be supplied by internal waves propagating into the gradient region, and then breaking. ... Clearly, the wave breaking and the density distribution must be intimately linked: for a given energy level breaking will occur preferentially in regions where the density gradient is high." Numerical experiments with a mixed-layer model (Kamenkovich and Kharkov 1975, Gill and Trefethen, unpublished manuscript referred to by Turner 1978) lend some support to this idea. They show an improved fit to ocean data if the effective temperature conductivity in the thermocline is taken proportional to the vertical temperature (density) gradient. Taking $l = const$ and using boundary conditions $\theta = \theta_s$ at $z = h$ and $\theta = \theta_b$ at $z = h + \Delta h$, and an additional condition $\partial\theta/\partial z = 0$ at $z = h + \Delta h$ that serves to determine l, the solution to Eqs. (7) and (9) is

$$\Phi_\theta = 1 - (1 - \zeta)^2, \qquad l = \frac{1}{2}\Delta h. \tag{10}$$

Obviously, it is difficult to give preference to the above expression for $\Phi_\theta(\zeta)$ over the expressions developed by Kitaigorodskii and Miropolsky (1970) and Arsenyev and Felzenbaum (1977), or vice versa, on purely empirical ground by virtue of a large scatter of empirical data.

Zilitinkevich et al. (1988) pointed out that Eq. (9) is not consistent with the proposed wave breaking mechanism of mixing in the thermocline, although the mechanism per se is physically credible. The point is that Eq. (9) does not contain the buoyancy parameter $\beta = g\alpha_T$, where g is the acceleration due to gravity and α_T is the thermal expansion coefficient, which must obviously be taken into account. Indeed, there would be no internal

gravity waves and no wave breaking mechanism of mixing were it not for the density changes associated with the temperature changes and not for the gravity that cause the buoyancy effects in a temperature-stratified fluid. Using β, $\partial\theta/\partial z$ and l as the governing parameters, Zilitinkevich et al. (1988) invoked dimensional arguments to obtain the following expression for the effective temperature conductivity in the thermocline:

$$K_H = l^2 N, \tag{11}$$

where $N = (-\beta\partial\theta/\partial z)^{1/2}$ is the buoyancy frequency (the constant of proportionality is incorporated into l). It is easy to verify that Eqs. (7) and (11) subject to the same boundary conditions as used by Turner (1978) have the following solution:

$$\Phi_\theta = 1 - (1-\zeta)^3, \qquad l = 3^{-3/4}(\beta\Delta\theta)^{-1/4}\Delta h^{3/4}\dot{h}^{1/2}. \tag{12}$$

The above expression for the temperature profile shape function $\Phi_\theta(\zeta)$ appears to coincide with the third-order polynomial (3) developed earlier from simple geometrical arguments by Arsenyev and Felzenbaum (1977) and on the basis of empirical data by Mälkki and Tamsalu (1985).

In the models of Turner (1978) and Zilitinkevich et al. (1988), the eddy length scale l was treated as a bulk quantity characteristic of the thermocline as a whole. Zilitinkevich and Mironov (1992, see also Zilitinkevich and Mironov 1989, and Mironov 1990) proposed to treat l as a depth-dependent quantity. To this end, they employed the transport equation for the turbulence kinetic energy in its stationary form,

$$\frac{\partial e}{\partial t} = -\frac{\partial F}{\partial z} - \beta\mathcal{Q} - \epsilon = 0, \tag{13}$$

where e is the TKE per unit mass, F is the vertical TKE flux (the sum of the third-order velocity correlations and the pressure-velocity correlation), $\mathcal{Q}$ is the vertical turbulent temperature flux, and ϵ is the TKE dissipation rate. The temperature flux is also referred to as the kinematic heat flux, that is the heat flux divided by the density ρ and specific heat c. A calligraphic letter is used to avoid confusion with the heat flux $Q = \rho c\mathcal{Q}$. The following expression that is known to hold in strongly stable layers (see e.g. Zeman and Tennekes 1977, Brost and Wyngaard 1978, Otte and Wyngaard 2001) was used to relate the length scale to the TKE:

$$l = \frac{e^{1/2}}{N}. \tag{14}$$

The problem was closed through the use of a down-gradient approximation for the fluxes,

$$\mathcal{Q} = -K_H\frac{\partial\theta}{\partial z}, \qquad F = -K_E\frac{\partial e}{\partial z}, \tag{15}$$

and the Kolmogorov-Heisenberg hypothesis for the eddy exchange coefficients and the TKE dissipation rate,

$$\frac{K_H}{C_H} = \frac{K_E}{C_E} = le^{1/2}, \qquad \epsilon = C_\epsilon\frac{e^{3/2}}{l}, \tag{16}$$

where C_H, C_E and C_ϵ are dimensionless constants.

Considering the problem in a half-space $z' > 0$, the travelling wave-type solution to Eqs. (7), (13), (14), (15) and (16) subject to boundary conditions $\theta = \theta_s$, $e = e_h$ at $z' = 0$ and $\theta = \theta_b$, $e = 0$ at $z' = \infty$ is

$$\Phi_\theta = 1 - \exp(E_* - E_*/\eta), \qquad 6^{1/2}\exp(-E_*)\int_\eta^1 \eta'^2\exp(E_*/\eta')d\eta' = \xi. \tag{17}$$

Here, $\eta^2 = e_h^{-1} e$ and $\xi = C_e^{-1/2} e_h^{-1/2} N_h z'$ are the dimensionless TKE and the dimensionless vertical co-ordinate, respectively, $E_* = C_H^{-1}(6C_e)^{1/2} e_h^{-1/2} \dot{h}$ is the dimensionless rate of the mixed-layer deepening, e_h and N_h are the TKE and the buoyancy frequency, respectively, at the mixed layer-thermocline interface $z = h$, and $C_e = C_E(C_H + C_\epsilon)^{-1}$ is a dimensionless constant. The solution (17) describes a family of the temperature-depth curves where the shape of the curve depends upon E_*. At $E_* \geq 2$, the vertical temperature gradient is a maximum at the mixed layer-thermocline interface, $z = h$, whereas at $E_* < 2$, the temperature gradient is a maximum at $z > h$. The temperature profile given by Eq. (17) is quite similar to the third-order polynomial (3) at certain values of E_*.

An extension of the $K_H = const$ solution to Eq. (7) was developed by Shapiro (1980). He assumed that the mixed-layer temperature θ_s and the rate of the mixed-layer deepening $\dot{h}$ do not remain constant, as in the case considered by Barenblatt (1978) and Turner (1978), but experience small-amplitude fluctuations. Then, an additional term appears on the r.h.s. of Eq. (7), namely $\left\langle \dot{h}'' \partial \theta_s'' / \partial z \right\rangle$, where the angle brackets denote an ensemble mean and a double prime denotes a fluctuation therefrom. An analysis of the resulting solution showed an increase of the temperature gradient just below the mixed layer-thermocline interface and an overall cooling of the thermocline as compared to the case of constant θ_s and $\dot{h}$ when the fluctuations of θ_s and of $\dot{h}$ are coherent.

The analytical travelling wave-type solutions considered above are conditioned by a constant rate of the mixed-layer deepening and constant temperatures at the upper and lower boundaries of the thermocline (the mean values of $\dot{h}$, θ_s and θ_b are constant although these quantities may experience high-frequency small-amplitude fluctuations, cf. Shapiro 1980). If these quantities are not constant but vary slowly with time, the analytical solutions are not exact but approximate. If these quantities undergo fast changes, a travelling wave-type solution to the heat transfer equation can no longer serve as a theoretical explanation for the observed self-similarity of the temperature profile in the thermocline. It should be pointed out that all the above theoretical models apply to the case of the mixed-layer deepening. No theoretical explanation for the self-similarity of the temperature profile in case of the mixed-layer stationary state or retreat has been offered so far. The self-similarity at $dh/dt \leq 0$ is based on the empirical evidence only and should therefore be considered purely phenomenological.

2.4 Bottom Sediments

A distinctive feature of shallow lakes is a strong thermal interaction between the water body and the bottom sediments. A sizable portion of the heat received from the atmosphere during spring and summer can be accumulated in the thermally active upper layer of bottom sediments. This heat is then returned back to the water column during autumn and winter, leading to a hysteresis-like behaviour of the seasonal temperature cycle of the water column-bottom sediment system. A straightforward approach to describe the evolution of the temperature structure of bottom sediments is to use the equation of heat transfer with a priori knowledge of the thermal diffusivity of sediments (see e.g. Gu and Stefan 1990, Fang and Stefan 1996, 1998, and references therein). The major shortcoming of this approach is that the thermal diffusivity is strongly dependent on the composition of the sediments and on the amount of organic matter they contain and is, therefore, rarely well known.

Golosov and Kreiman (1992) proposed an alternative way of describing the vertical temperature structure of bottom sediments. Their approach is based on a two-layer self-similar parametric representation of the evolving temperature profile in the sediments that is concep-

tually similar to a parametric representation of the temperature profile in the thermocline. Observations suggest (a summary of observational studies is given in Ryanzhin 1997) that the temperature profile in the bottom sediments has the form of a travelling thermal wave. Typical temperature profiles in the lake bottom sediments are illustrated in Fig. 2. The wave starts at the water-sediment interface $z = D$ and propagates downward as the lake water and the bottom sediments are heated during spring and summer. When heating ceases and cooling sets in, a new wave starts at $z = D$. It propagates downward as the lake water and the sediments are cooled during autumn and winter, thus closing the annual cycle. The layer $D \le z \le L$, where seasonal temperature changes take place, is the thermally active layer of bottom sediments. Importantly, a characteristic *shape* of the temperature-depth curve remains approximately the same. Motivated by this empirical evidence, a two-layer parametric representation of the temperature profile in the bottom sediments was proposed by Golosov and Kreiman (1992) and further developed by Golosov et al. (1998). The expression of Golosov et al. (1998) reads

$$\theta(z,t) = \begin{cases} \theta_b(t) - [\theta_b(t) - \theta_H(t)]\,\Phi_{B1}(\zeta_{B1}) & \text{at} \quad D \le z \le H(t) \\ \theta_H(t) - [\theta_H(t) - \theta_L]\,\Phi_{B2}(\zeta_{B2}) & \text{at} \quad H(t) \le z \le L. \end{cases} \tag{18}$$

Here, θ_L is the (constant) temperature at the outer edge $z = L$ of the thermally active layer of the sediments, θ_H is the temperature at the depth H where the vertical temperature gradient is zero, and $\Phi_{B1} \equiv (\theta_b - \theta)/(\theta_b - \theta_H)$ and $\Phi_{B2} \equiv (\theta_H - \theta)/(\theta_H - \theta_L)$ are dimensionless functions of dimensionless depths $\zeta_{B1} \equiv (z - D)/(H - D)$ and $\zeta_{B2} \equiv (z - H)/(L - H)$, respectively. Using empirical polynomial approximations of $\Phi_{B1}(\zeta_{B1})$ and $\Phi_{B2}(\zeta_{B2})$, Golosov et al. (1998) developed a simple procedure for calculating the heat flux through the water-sediment interface. Simulations of the seasonal cycle of temperature in the bottom sediments of several lakes using that procedure showed a satisfactory agreement with observations (Golosov et al. 1998, Kondratiev et al. 1998). In the present study, the approach of Golosov and Kreiman (1992) and Golosov et al. (1998) is used to develop a simple parameterization for calculating the heat flux through the water-bottom sediment interface. It is presented in Section 3.3.

A plausible theoretical explanation for the observed self-similarity of the temperature profile in bottom sediments was offered by Mironov et al. (2003). Assuming a travelling wave-type behaviour of the temperature profile, these authors considered the temperature distribution in the layer from the water-bottom sediment interface $z = D$ to the depth $z = H$ penetrated by the wave. They showed that in the simplest case of constant temperature diffusivity K_H the heat transfer equation (6) subject to the boundary conditions $\Phi_{B1}(0) = 0$ and $\Phi_{B1}(1) = 1$ has an analytical solution in the form

$$\Phi_{B1} = \frac{\Pi_D}{\Pi_D - \Pi_H}\left(1 + \frac{\exp\left(-E\zeta_{B1}^2/4\right)}{\zeta_{B1}^{1/2}} \times \right.$$

$$\left. \left\{ P\left[\frac{W_{p,1/4}(E/2)}{M_{p,1/4}(E/2)} M_{p,1/4}(E\zeta_{B1}^2/2) - W_{p,1/4}(E\zeta_{B1}^2/2)\right] - \frac{\Pi_H}{\Pi_D}\exp(E/4) \right\} \right). \tag{19}$$

Here, $E = K_H^{-1}(H - D)dH/dt$ is the dimensionless rate of propagation of the thermal wave, $\Pi_D = K_H^{-1}(\theta_b - \theta_H)^{-1}(H - D)^2 d\theta_b/dt$ and $\Pi_H = K_H^{-1}(\theta_b - \theta_H)^{-1}(H - D)^2 d\theta_H/dt$ are the dimensionless time rates of change of the temperature at the water-sediment interface $z = D$ and of the temperature at the depth $z = H$ penetrated by the wave, respectively, M and W are the Whittaker functions (Abramowitz and Stegun 1964, Chapter 13), $p = -\left[2(\Pi_D - \Pi_H) + E\right]/4E$, $P = 2^{1/4}\pi^{-1/2}E^{-1/4}\Gamma\left[(2E + \Pi_D - \Pi_H)/2E\right]$, and Γ is the Gamma function.

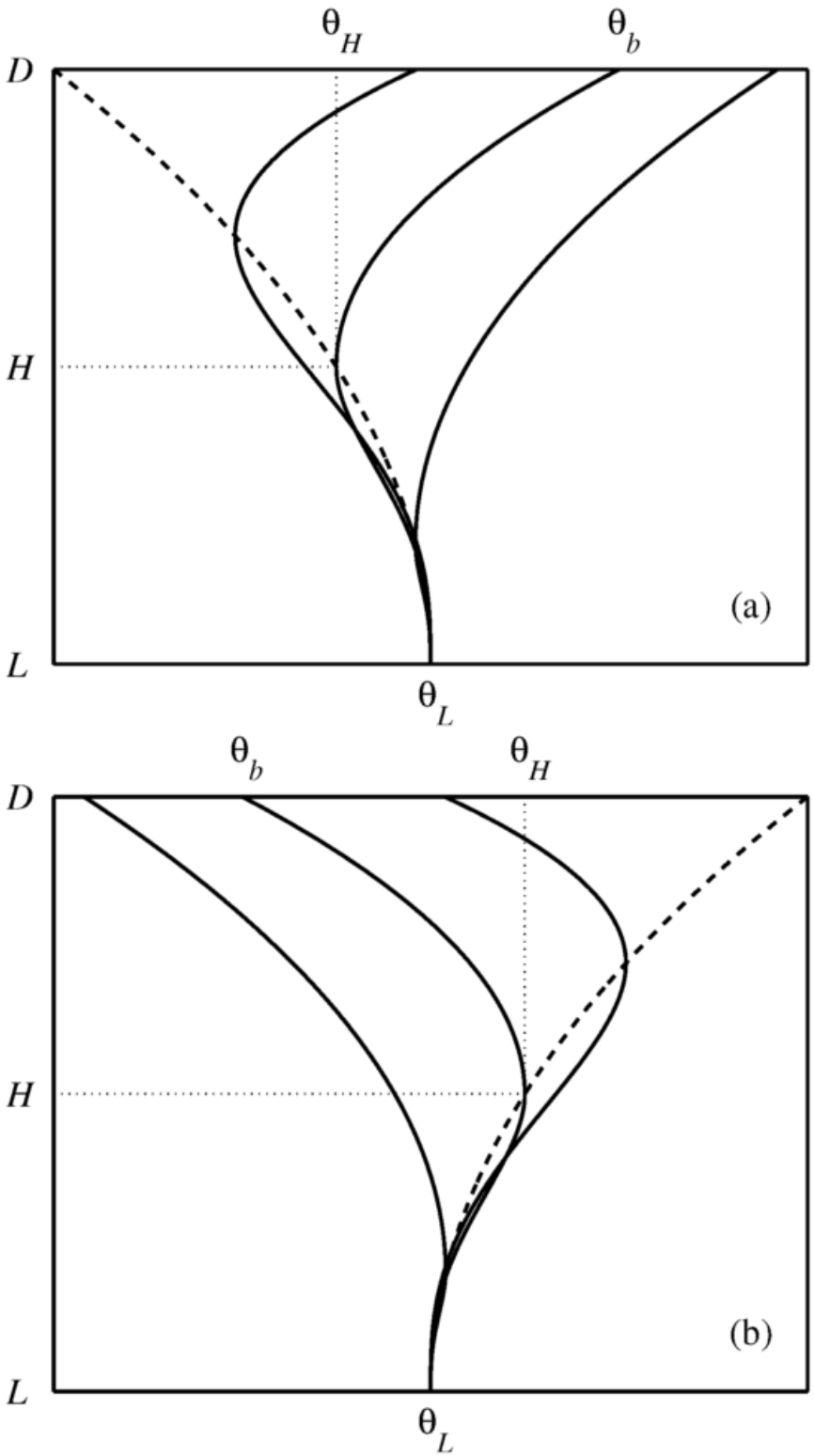


Figure 2: Schematic representation of the temperature profile in bottom sediments during periods of (a) heating and (b) cooling. Dashed curves show the initial temperature profiles, i.e. the profiles developed towards the end of the previous period of cooling (heating). See text for details.

The solution (19) is conditioned by a constant dimensionless propagation rate of the thermal wave and constant time rates of change of the temperature at the water-sediment interface and of the temperature at the depth penetrated by the wave. In case E, Π_D and Π_H are not constant but vary slowly with time, Eq. (19) is not exact but approximate. If these quantities undergo fast changes, the analytical solution (19) can no longer serve as a theoretical explanation for the observed self-similarity of the temperature profile in bottom sediments. Equation (19) appears to compare favourably with data from measurements in a number of lakes, with data from laboratory experiments and with a phenomenological polynomial approximation of the temperature profile in bottom sediments developed by Golosov et al. (1998) on the basis of empirical data.

2.5 Ice and Snow Cover

Many lakes are frozen over a considerable part of the year so that the atmosphere does not directly communicate with the lake water. The atmosphere-lake interaction occurs through the air-ice or, if snow is present, through the air-snow interface. An ice-snow model is therefore required to predict the surface temperature. Use of sophisticated ice models with rheology is a standard practice in climate modelling where the integration is performed over many decades. For NWP and related applications, a sophisticated dynamic-thermodynamic ice model is not required (and most often cannot be afforded because of its high computation cost). A simplified thermodynamic model is usually sufficient. Such model is developed in Section 3.4. As regards the thermodynamics of ice and snow, the model is broadly similar to most other models developed to date (summaries are given by e.g. Leppäranta 1993, and Launiainen and Cheng 1998). A distinguishing feature of the present model is the treatment of the heat transfer through the ice and snow. Most currently used ice and snow models carry the heat transfer equation that is solved on a finite-difference grid where the number of grid points and the grid spacing differ with the application. Here the integral, or bulk, approach is used. It is based on a parametric representation of the temperature profile within ice and snow and on the integral heat budgets of the ice and snow layers.

2.6 Applications

A number of computationally efficient models based on the self-similar representation of the temperature profile have been developed and successfully applied to simulate the evolution of the mixed layer and seasonal thermocline in the ocean (Kitaigorodskii and Miropolsky 1970, Miropolsky 1970, Kitaigorodskii 1970, Kamenkovich and Kharkov 1975, Arsenyev and Felzenbaum 1977, Kharkov 1977, Filyushkin and Miropolsky 1981). Filyushkin and Miropolsky (1981) assumed that both the temperature profile and the profile of the vertical heat flux in the thermocline can be represented in a self-similar form. We return to this issue in Section 3.2.1. The self-similarity concept has also been applied to model the atmospheric convectively mixed layer capped by the temperature inversion (Deardorff 1979, Fedorovich and Mironov 1995, Mironov 1999, Pénelon et al. 2001).

Models of the seasonal cycle of temperature and mixing in medium-depth fresh-water lakes, based on the self-similar representation of the evolving temperature profile, have been developed and successfully applied by Zilitinkevich and Rumyantsev (1990), Zilitinkevich (1991), Mironov et al. (1991), Zilitinkevich et al. (1992), Mironov (1992), Golosov et al. (1998), and Kondratiev et al. (1998). An attempt has been made to apply the above self-similarity concept to shallow lakes and to consider short-term (diurnal) variations of temperature and mixing conditions (Kirillin 2001a, 2001b). As different from the ocean and the atmo-

sphere, where the thermocline (capping inversion) is underlain (overlain) by a deep stably or neutrally stratified quiescent layer, the above lake models assume a two-layer temperature structure, where the thermocline extends from the bottom of the mixed layer down to the basin bottom. This assumption is fair for most lakes, except for very deep lakes such as Lake Baikal.

3 Model Description

In this section, a lake model based on a self-similar parametric representation (assumed shape) of the evolving temperature profile in the water column, in the bottom sediments, and in the ice and snow is developed. The same basic concept is used to describe the temperature structure of the four media in question (snow, ice, water, and bottom sediment). The lake model proposed by Mironov et al. (1991) is taken as a starting point. It is modified and further developed to account for specific features of shallow lakes and to consider both seasonal and diurnal variations of temperature and mixing conditions. The lake water is treated as a Boussinesq fluid, i.e. the water density is taken to be constant equal to the reference density except when it enters the buoyancy term in the TKE equation and the expression for the buoyancy frequency. The other thermodynamic parameters are considered constant except for the snow density and the snow heat conductivity (see Section 3.5.3 and Appendix B).

The model presented in what follows is a bulk model. It incorporates the heat budget equations for the layers in question. An entrainment equation for the depth of a convectively-mixed layer and a relaxation-type equation for the depth of a wind-mixed layer in stable and neutral stratification are developed on the basis of the TKE equation integrated over the mixed layer. Simple thermodynamic arguments are invoked to develop the evolution equations for the ice and snow depths. The resulting system of ordinary differential equations for the time-dependent prognostic quantities that characterise the evolving temperature profile, see Figs. 3 and 4, is closed with algebraic (or transcendental) equations for diagnostic quantities, such as the heat flux through the lake bottom and the equilibrium mixed-layer depth in stable or neutral stratification. Finally, we end up with a lake model that is computationally very efficient but still incorporates much of the essential physics.

3.1 Equation of State

We utilise the quadratic equation of state of the fresh water,

$$\rho_w = \rho_r \left[1 - \frac{1}{2} a_T \left(\theta - \theta_r \right)^2 \right], \tag{20}$$

where ρ_w is the water density, $\rho_r = 999.98 \approx 1.0 \cdot 10^3$ kg·m^{-3} is the maximum density of the fresh water at the temperature $\theta_r = 277.13$ K, and $a_T = 1.6509 \cdot 10^{-5}$ K^{-2} is an empirical coefficient (Farmer and Carmack 1981). Equation (20) is the simplest equation of state that accounts for the fact that the temperature of maximum density of the fresh water exceeds its freezing point $\theta_f = 273.15$ K. According to Eq. (20), the thermal expansion coefficient α_T and the buoyancy parameter β depend on the water temperature,

$$\beta(\theta) = g\alpha_T(\theta) = g a_T(\theta - \theta_r), \tag{21}$$

where $g = 9.81$ m·s^{-2} is the acceleration due to gravity.

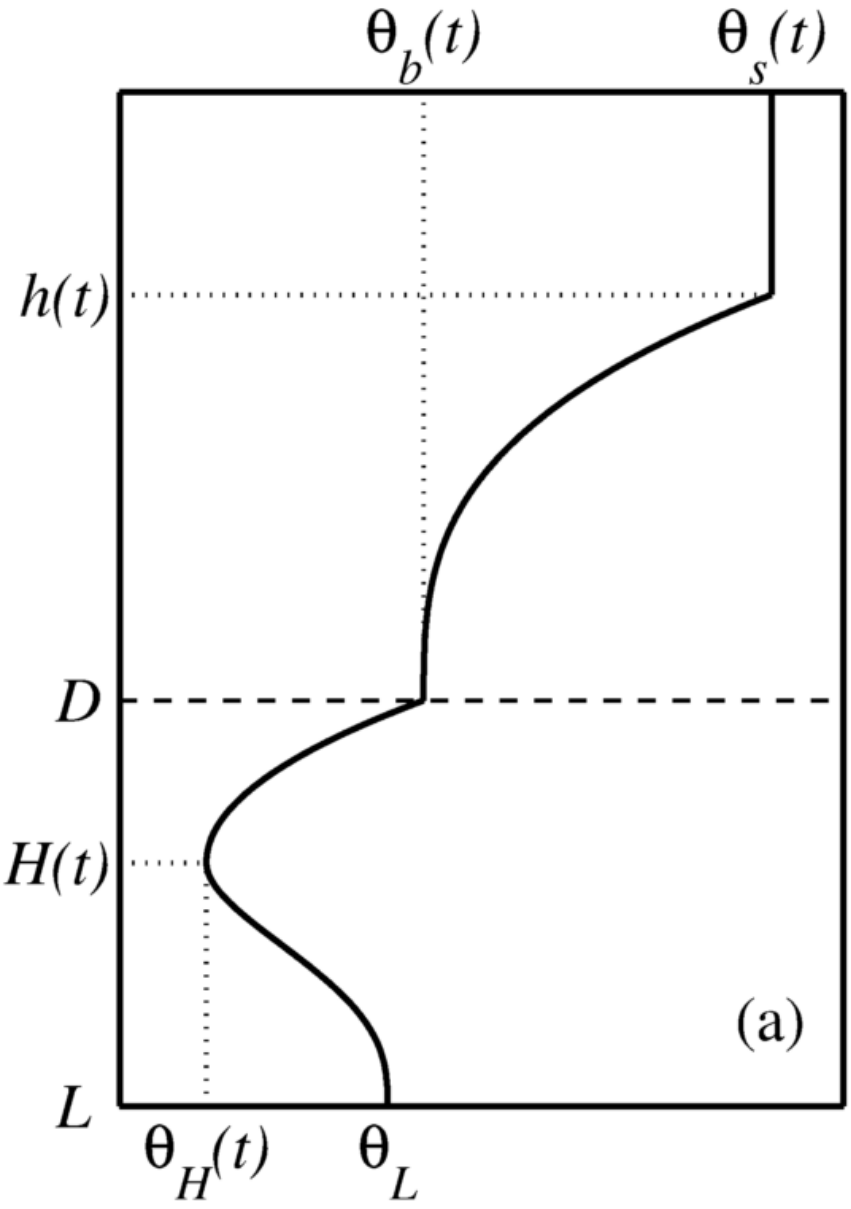


Figure 3: Schematic representation of the temperature profile in the mixed layer, in the thermocline, and in the thermally active layer of bottom sediments. The evolving temperature profile is specified by several time-dependent quantities. These are the mixed-layer temperature $\theta_s(t)$ and its depth $h(t)$, the temperature $\theta_b(t)$ at the water-bottom sediment interface, the shape factor $C_\theta(t)$ with respect to the temperature profile in the thermocline, the temperature $\theta_H(t)$ at the lower boundary of the upper layer of bottom sediments penetrated by the thermal wave, and the depth $H(t)$ of that layer. The temperature θ_L at the outer edge $z = L$ of the thermally active layer of bottom sediments is constant.

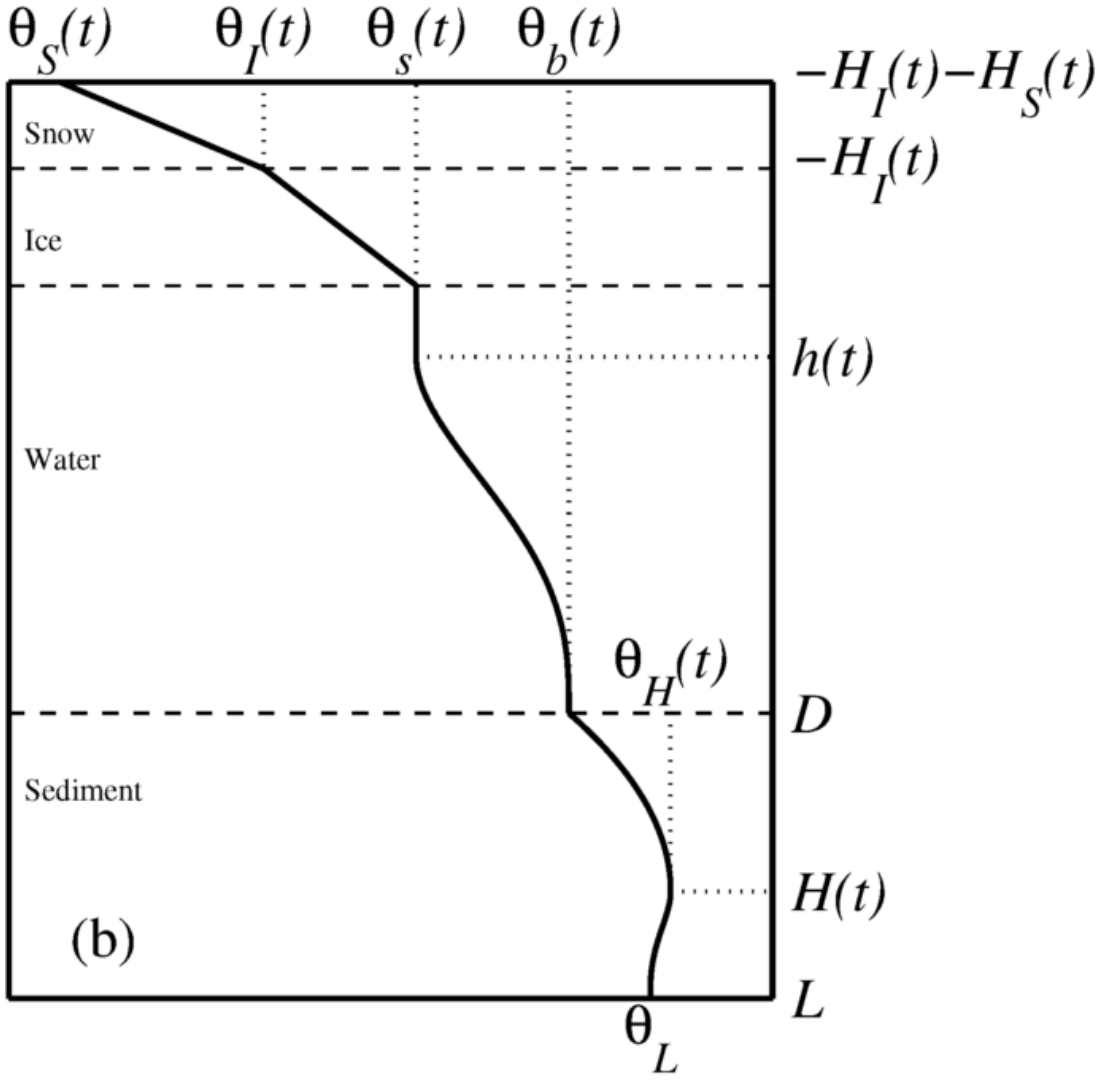


Figure 4: Apart from $\theta_s(t)$, $h(t)$, $\theta_b(t)$, $C_\theta(t)$, $\theta_H(t)$, and $H(t)$ (see Fig. 3), four additional quantities are computed in case the lake is covered by ice and snow. These are the temperature $\theta_S(t)$ at the air-snow interface, the temperature $\theta_I(t)$ at the snow-ice interface, the snow depth $H_S(t)$, and the ice depth $H_I(t)$.

3.2 The Water Temperature

3.2.1 Parameterization of the Temperature Profile and the Heat Budget

We adopt the following two-layer parameterization of the vertical temperature profile:

$$\theta = \begin{cases} \theta_s & \text{at} \quad 0 \le z \le h \\ \theta_s - (\theta_s - \theta_b)\Phi_\theta(\zeta) & \text{at} \quad h \le z \le D, \end{cases} \tag{22}$$

where $\Phi_\theta \equiv (\theta_s - \theta) / (\theta_s - \theta_b)$ is a dimensionless function of dimensionless depth $\zeta \equiv (z - h) / (D - h)$. The thermocline extends from the mixed-layer outer edge $z = h$ to the basin bottom $z = D$.

According to Eq. (22), h, D, θ_s, θ_b, and the mean temperature of the water column, $\overline{\theta} \equiv D^{-1} \int_0^D \theta dz$, are related through

$$\overline{\theta} = \theta_s - C_\theta(1 - h/D)(\theta_s - \theta_b), \tag{23}$$

where

$$C_\theta = \int_0^1 \Phi_\theta(\zeta) d\zeta \tag{24}$$

is the shape factor.

The parameterization of the temperature profile (22) should satisfy the heat transfer equation

$$\frac{\partial}{\partial t}(\rho c \theta) = -\frac{\partial}{\partial z}(Q + I), \tag{25}$$

where Q is the vertical turbulent heat flux, and I is the heat flux due to solar radiation.

Integrating Eq. (25) over z from 0 to D yields the equation of the total heat budget,

$$D\frac{d\overline{\theta}}{dt} = \frac{1}{\rho_w c_w}\left[Q_s + I_s - Q_b - I(D)\right], \tag{26}$$

where c_w is the specific heat of water, Q_s and I_s are the values of Q and I, respectively, at the lake surface, and Q_b is the heat flux through the lake bottom. The radiation heat flux I_s that penetrates into the water is the surface value of the incident solar radiation flux from the atmosphere multiplied by $1 - \alpha_w$, α_w being the albedo of the water surface with respect to solar radiation. The surface flux Q_s is a sum of the sensible and latent heat fluxes and the net heat flux due to long-wave radiation at the air-water interface.

Integrating Eq. (25) over z from 0 to h yields the equation of the heat budget in the mixed layer,

$$h\frac{d\theta_s}{dt} = \frac{1}{\rho_w c_w}\left[Q_s + I_s - Q_h - I(h)\right], \tag{27}$$

where Q_h is the heat flux at the bottom of the mixed layer.

Given the surface fluxes Q_s and I_s (these are delivered by the driving atmospheric model or are known from observations), and the decay law for the flux of solar radiation (Section 3.5.3), Eqs. (23), (26) and (27) contain seven unknowns, namely, h, $\overline{\theta}$, θ_s, θ_b, Q_h, Q_b and C_θ. The mixed layer depth, the bottom heat flux and the shape factor are considered in Section 3.2.2, Section 3.3 and Section 3.5.1, respectively. One more relation is required. Following Filyushkin and Miropolsky (1981, see also Tamsalu et al. 1997, and Tamsalu and Myrberg

1998), we assume that in case of the mixed layer deepening, $dh/dt > 0$, the profile of the vertical turbulent heat flux in the thermocline can be represented in a self-similar form. That is

$$Q = Q_h - (Q_h - Q_b)\Phi_Q(\zeta) \qquad \text{at} \;\; h \le z \le D, \tag{28}$$

where the shape function Φ_Q satisfies the boundary conditions $\Phi_Q(0) = 0$ and $\Phi_Q(1) = 1$. Equation (28) is suggested by the travelling wave-type solution to the heat transfer equation. If the mixed layer and the thermocline develop on the background of a deep stably or neutrally stratified quiescent layer (this situation is encountered in the ocean and in the atmosphere), the travelling wave-type solution shows that both the temperature profile and the profile of the turbulent heat flux are described by the same shape function, i.e. $\Phi_\theta(\zeta) = \Phi_Q(\zeta)$. In lakes, the thermocline usually extends from the bottom of the mixed layer down to the basin bottom. In this case, the travelling wave-type solution to the heat transfer equation also suggests self-similar profiles of the temperature and of the heat flux, however the relation between the shape functions $\Phi_\theta(\zeta)$ and $\Phi_Q(\zeta)$ is different. The issue is considered in Appendix A.

Integrating Eq. (25) with due regard for Eqs. (22) and (28) over z' from h to $z > h$, then integrating the resulting expression over z from h to D, we obtain

$$\frac{1}{2}(D-h)^2\frac{d\theta_s}{dt} - \frac{d}{dt}\left[C_{\theta\theta}(D-h)^2(\theta_s - \theta_b)\right] =$$

$$\frac{1}{\rho_w c_w}\left[C_Q(D-h)(Q_h - Q_b) + (D-h)I(h) - \int_h^D I(z)dz\right], \tag{29}$$

where

$$C_Q = \int_0^1 \Phi_Q(\zeta)d\zeta \tag{30}$$

is the shape factor with respect to the heat flux, and

$$C_{\theta\theta} = \int_0^1 d\zeta \int_0^{\zeta'} \Phi_\theta(\zeta')d\zeta' \tag{31}$$

is the dimensionless parameter. The analysis in Appendix A suggests that $C_Q = 2C_{\theta\theta}/C_\theta$.

In case of the mixed-layer stationary state or retreat, $dh/dt \le 0$, Eq. (28) is not justified. Then, the bottom temperature is assumed to be "frozen",

$$\frac{d\theta_b}{dt} = 0. \tag{32}$$

If $h = D$, then $\theta_b = \theta_s = \overline{\theta}$ and the mean temperature is computed from Eq. (26).

3.2.2 The Mixed-Layer Depth

Convection

Convective deepening of the mixed layer is described by the entrainment equation. This equation is conveniently formulated in terms of the dependence of the so-called entrainment ratio A on one or the other stratification parameter. The entrainment ratio is a measure of the entrainment efficiency. It is commonly defined as a negative of the ratio of the heat flux due to entrainment at the bottom of the mixed layer, Q_h, to an appropriate heat flux scale,

Q_*. In case of convection driven by the surface flux, where the forcing is confined to the boundary, the surface heat flux Q_s serves as an appropriate flux scale. This leads to the now classical Deardorff (1970a, 1970b) convective scaling, where h and $|h\beta Q_s/(\rho_w c_w)|^{1/3}$ serve as the scales of length and velocity, respectively.

The Deardorff scaling is unsuitable for convective flows affected by the solar radiation heating that is not confined to the boundary but is distributed over the water column. If the mixed-layer temperature exceeds the temperature of maximum density, convective motions are driven by surface cooling, whereas radiation heating tends to stabilise the water column, arresting the mixed layer deepening (Soloviev 1979, Mironov and Karlin 1989). Such regime of convection is encountered in the oceanic upper layer (e.g. Kraus and Rooth 1961, Soloviev and Vershinskii 1982, Price et al. 1986) and in fresh-water lakes (e.g. Imberger 1985). If the mixed-layer temperature is below that of maximum density, volumetric radiation heating leads to de-stabilisation of the water column and thereby drives convective motions. Such regime of convection is encountered in fresh-water lakes in spring. Convective mixing often occurs under the ice, when the snow cover overlying the ice vanishes and solar radiation penetrates down through the ice (e.g. Farmer 1975, Mironov and Terzhevik 2000, Mironov et al. 2002, Jonas et al. 2003).

In order to account for the vertically distributed character of the radiation heating, we make use of a generalised convective heat flux scale

$$Q_* = Q_s + I_s + I(h) - 2h^{-1}\int_0^h I(z)dz, \tag{33}$$

and define the convective velocity scale and the entrainment ratio as

$$w_* = \left[-h\beta(\theta_s)Q_*/(\rho_w c_w)\right]^{1/3}, \qquad A = -Q_h/Q_*, \tag{34}$$

respectively. In order to specify A, we employ the entrainment equation in the form

$$A + \frac{C_{c2}}{w_*}\frac{dh}{dt} = C_{c1}, \tag{35}$$

where C_{c1} and C_{c2} are dimensionless constants (the estimates of these and other empirical constants of the model are discussed in Section 3.5.2 and summarised in Appendix B). The second term on the l.h.s. of Eq. (35) is the spin-up correction term introduced by Zilitinkevich (1975). This term prevents an unduly fast growth of h when the mixed layer is shallow. If the spin-up term is small, Eq. (35) reduces to a simple relation $A = C_{c1}$ that proved to be a sufficiently accurate approximation for a large variety of geophysical and laboratory convective flows (Zilitinkevich 1991).

Equations (33), (34) and (35) should be used to compute the mixed-layer depth when the buoyancy flux $B_* = \beta(\theta_s)Q_*/(\rho_w c_w)$ is negative. The quantity $-hB_* \equiv w_*^3$ is a measure of the generation rate of the turbulence kinetic energy in a layer of depth h by the buoyancy forces (see a discussion in Mironov et al. 2002). A negative B_* indicates that the TKE is generated through convective instability. Otherwise, the TKE is lost to work against the gravity. This occurs when the density stratification is stable. A different formulation for the mixed-layer depth is then required.

Stable and Neutral Stratification

Mironov et al. (1991) used a diagnostic equation to determine the wind-mixed layer depth in stable and neutral stratification. That is, h was assumed to adjust to external forcing on a time scale that does not exceed the model time step. This assumption is fair if seasonal

changes of temperature and mixing conditions are considered and the model time step is typically one day. The assumption is likely to be too crude to consider diurnal variations. To this end, we utilise a relaxation-type rate equation for the depth of a stably or neutrally stratified wind-mixed layer. It reads

$$\frac{dh}{dt} = \frac{h_e - h}{t_{rh}}. \tag{36}$$

Here, h_e is the equilibrium mixed-layer depth, and t_{rh} is the relaxation time scale given by

$$t_{rh} = \frac{h_e}{C_{rh} u_*}, \tag{37}$$

where $u_* = |\tau_s/\rho_w c_w|^{1/2}$ is the surface friction velocity, τ_s being the surface stress, and C_{rh} is a dimensionless constant. A rate equation (36) with the relaxation time scale proportional to the reciprocal of the Coriolis parameter [that is a particular case of Eq. (37) with h_e specified through Eq. (38)] was favourably tested by Zilitinkevich et al. (2002) and Zilitinkevich and Baklanov (2002) against data from atmospheric measurements and was recommended for practical use.

In order to specify h_e, we make use of a multi-limit formulation for the equilibrium depth of a stably or neutrally stratified boundary layer proposed by Zilitinkevich and Mironov (1996). Based on the analysis of the TKE budget, these authors proposed a generalised equation for the equilibrium boundary-layer depth that accounts for the combined effects of rotation, surface buoyancy flux and static stability at the boundary-layer outer edge [Eq. (30) in op. cit.]. That equation reduces to the equations proposed earlier by Rossby and Montgomery (1935), Kitaigorodskii (1960) and Kitaigorodskii and Joffre (1988) in the limiting cases of a truly neutral rotating boundary layer, the surface-flux-dominated boundary layer, and the imposed-stability-dominated boundary layer, respectively. It also incorporates the Zilitinkevich (1972) and the Pollard, Rhines and Thompson (1973) equations that describe the intermediate regimes, where the effects of rotations and stratification essentially interfere and are roughly equally important. We adopt a simplified version of the Zilitinkevich and Mironov (1996) equation [Eq. (26) in op. cit.] that does not incorporate the Zilitinkevich (1972) and the Pollard et al. (1973) scales. It reads

$$\left(\frac{f h_e}{C_n u_*}\right)^2 + \frac{h_e}{C_s L} + \frac{N h_e}{C_i u_*} = 1, \tag{38}$$

where $f = 2\Omega \sin\phi$ is the Coriolis parameter, $\Omega = 7.29 \cdot 10^{-5}$ s^{-1} is the angular velocity of the earth's rotation, ϕ is the geographical latitude, L is the Obukhov length, N is the buoyancy frequency below the mixed layer, and C_n, C_s and C_i are dimensionless constants. A generalised formulation for the Obukhov length is used, $L = u_*^3/(\beta Q_*/\rho_w c_w)$, that accounts for the vertically distributed character of the solar radiation heating (note that the von Kármán constant is not included into the definition of L). A mean-square buoyancy frequency in the thermocline, $\overline{N} = \left[(D-h)^{-1} \int_h^D N^2 dz\right]^{1/2}$, is used as an estimate of N in Eq. (38).

One further comment is in order. Zilitinkevich et al. (2002, 2007) reconsidered the problem of the equilibrium stable boundary-layer depth. They concluded that the Zilitinkevich (1972) scale, $|u_* L/f|^{1/2}$, and the Pollard et al. (1973) scale, $u_*/|Nf|^{1/2}$, are the appropriate depth scales for the boundary layers dominated by the surface buoyancy flux and by the static stability at the boundary-layer outer edge, respectively. In other words, h_e depends on the Coriolis parameter no matter how strong the static stability. This is different from Eq. (38) where the limiting scales are L and u_*/N, respectively. The problem was further examined by Mironov and Fedorovich (2008). They showed that the above scales are particular cases of

more general power-law formulations, namely, $h/L \propto (|f|L/u_*)^{-p}$ and $hN/u_* \propto (|f|/N)^{-q}$ for the boundary layers dominated by the surface buoyancy flux and by the static stability at the boundary-layer outer edge, respectively. The Zilitinkevich (1972) and Pollard et al. (1973) scales are recovered with $p = 1/2$ and $q = 1/2$, whereas the Kitaigorodskii (1960) and Kitaigorodskii and Joffre (1988) are recovered with $p = 0$ and $q = 0$. Scaling arguments are not sufficient to fix the exponents p and q. They should be evaluated on the basis of experimental data. Available data from observations and from large-eddy simulations are uncertain. They do not make it possible to evaluate p and q to sufficient accuracy and to conclusively decide between the alternative formulations for the boundary-layer depth. Leaving the evaluation of p and q for future studies, we utilise Eq. (38). This simple interpolation formula is consistent with the complexity of the present lake model and is expected to be a sufficiently accurate approximation for most practical purposes.

One more limitation on the equilibrium mixed-layer depth should be taken into account. Consider the situation where the mixed-layer temperature exceeds the temperature of maximum density, the surface flux Q_s is negative, whereas the heat flux scale Q_* given by Eq. (33) is positive (this can take place if $-Q_s/I_s < 1$). A positive Q_* indicates the the mixed layer of depth h is statically stable. A negative Q_s, however, indicates that convective instability should take place, leading to the development of a convectively mixed layer whose deepening is arrested by the solar radiation heating. The equilibrium depth h_c of such mixed layer is given by (see e.g. Mironov and Karlin 1989)

$$Q_*(h_c) = Q_s + I_s + I(h_c) - 2h_c^{-1} \int_0^{h_c} I(z)dz = 0. \tag{39}$$

This regime of convection is encountered on calm sunny days. If the wind suddenly ceases, Eq. (38) predicts a very shallow stably-stratified equilibrium mixed layer to which the mixed layer of depth $h > h_e$ should relax. In fact, however, the mixed layer would relax towards a convectively mixed layer whose equilibrium depth is given by Eq. (39). In order to account for this constraint, we require that $h_e \geq h_c$ if $Q_*(h) > 0$ and $\theta_s > \theta_r$.

3.3 The Water - Bottom Sediment Interaction

3.3.1 Parameterization of the Temperature Profile and the Heat Budget

We adopt a two-layer parametric representation, Eq. (18), of the evolving temperature profile in the thermally active layer of bottom sediments proposed by Golosov et al. (1998). The parameterization (18) should satisfy the heat transfer equation (25), where the heat flux Q is due to molecular heat conduction and the bottom sediments are opaque to radiation. Integrating Eq. (25) over z from $z = D$ to $z = H$ with due regard for Eq. (18), we obtain

$$\frac{d}{dt}\left[(H-D)\theta_b - C_{B1}(H-D)(\theta_b - \theta_H)\right] - \theta_H \frac{dH}{dt} = \frac{1}{\rho_w c_w}\left[Q_b + I(D)\right], \tag{40}$$

where the heat flux at $z = H$ is zero by virtue of the zero temperature gradient there.

Integrating Eq. (25) over z from $z = H$ to $z = L$, we obtain

$$\frac{d}{dt}\left[(L-H)\theta_H - C_{B2}(L-H)(\theta_H - \theta_L)\right] + \theta_H \frac{dH}{dt} = 0, \tag{41}$$

where the heat flux at $z = L$ (the geothermal heat flux) is neglected.

The shape factors C_{B1} and C_{B2} are given by

$$C_{B1} = \int_0^1 \Phi_{B1}(\zeta_{B1})d\zeta_{B1}, \qquad C_{B2} = \int_0^1 \Phi_{B2}(\zeta_{B2})d\zeta_{B2}. \tag{42}$$

3.3.2 Heat Flux through the Bottom

The bottom heat flux Q_b is due to molecular heat conduction through the uppermost layer of bottom sediments. It can be estimated as the product of the negative of the temperature gradient at $z = D + 0$ and the molecular heat conductivity. The uppermost layer of bottom sediments is saturated with water. Its water content typically exceeds 90% and its physical properties, including the heat conductivity, are very close to the properties of the lake water. Then, the heat flux through the lake bottom is given by

$$Q_b = -\kappa_w \frac{\theta_H - \theta_b}{H - D} \Phi'_{B1}(0), \tag{43}$$

where κ_w is the molecular heat conductivity of water. This relation closes the problem.

It should be stressed that Eqs. (40), (41) and (43) do not contain the molecular heat conductivity of bottom sediments, a quantity that is rarely known to a satisfactory degree of precision. It is through the use of the integral (bulk) approach, based on the parameterization (18) of the temperature profile, that the molecular heat conductivity of bottom sediments is no longer needed.

3.4 Ice and Snow Cover

In this section, a two-layer thermodynamic (no rheology) model of the ice and snow cover is described. It is based on a self-similar parametric representation of the temperature profile within ice and snow and on the integral heat budgets of the ice and snow layers. The approach is, therefore, conceptually similar to the approach used above to describe the temperature structure of the mixed layer, of the lake thermocline, and of the thermally active layer of bottom sediments. Notice that the assumption about the shape of the temperature profile within the ice, the simplest of which is the linear profile, is either explicit or implicit in a number of ice models developed to date. A model of ice growth based on a linear temperature distribution was proposed by Stefan as early as 1891.

3.4.1 Parameterization of the Temperature Profile and the Heat Budget

We adopt the following parametric representation of the evolving temperature profile within ice and snow:

$$\theta(z,t) = \begin{cases} \theta_f - [\theta_f - \theta_I(t)]\Phi_I(\zeta_I) & \text{at} \quad -H_I(t) \le z \le 0 \\ \theta_I(t) - [\theta_I(t) - \theta_S(t)]\Phi_S(\zeta_S) & \text{at} \quad -[H_I(t) + H_S(t)] \le z \le -H_I(t). \end{cases} \tag{44}$$

Here, z is the vertical co-ordinate (positive downward) with the origin at the ice-water interface, H_I is the ice thickness, H_S is the thickness of snow overlaying the ice, θ_f is the fresh-water freezing point, θ_I is the temperature at the snow-ice interface, and θ_S is the temperature at the air-snow interface. Notice that the freezing point of salt water is a decreasing function of salinity. A model that accounts for this dependence and is applicable to the ice over salt lakes or seas is presented by Mironov and Ritter (2004). Dimensionless universal functions $\Phi_I \equiv (\theta_f - \theta)/(\theta_f - \theta_I)$ and $\Phi_S \equiv (\theta_I - \theta)/(\theta_I - \theta_S)$ of dimensionless depths $\zeta_I \equiv -z/H_I$ and $\zeta_S \equiv -(z + H_I)/H_S$, respectively, satisfy the boundary conditions $\Phi_I(0) = 0$, $\Phi_I(1) = 1$, $\Phi_S(0) = 0$, and $\Phi_S(1) = 1$.

According to Eq. (44), the heat fluxes through the ice, Q_I, and through the snow, Q_S, due to molecular heat conduction are given by

$$Q_I = -\kappa_i \frac{\theta_f - \theta_I}{H_I} \frac{d\Phi_I}{d\zeta_I}, \qquad Q_S = -\kappa_s \frac{\theta_I - \theta_S}{H_S} \frac{d\Phi_S}{d\zeta_S}, \tag{45}$$

where κ_i and κ_s are the heat conductivities of ice and snow, respectively.

The parameterization of the temperature profile (44) should satisfy the heat transfer equation (25). Integrating Eq. (25) over z from the air-snow interface $z = -(H_I + H_S)$ to just above the ice-water interface $z = -0$ with due regard for the parameterization (44), we obtain the equation of the heat budget of the snow-ice cover,

$$\frac{d}{dt}\{\rho_i c_i H_I [\theta_f - C_I(\theta_f - \theta_I)] + \rho_s c_s H_S [\theta_I - C_S(\theta_I - \theta_S)]\} - \rho_s c_s \theta_S \frac{d}{dt}(H_I + H_S) =$$

$$Q_s + I_s - I(0) + \kappa_i \frac{\theta_f - \theta_I}{H_I} \Phi_I'(0). \tag{46}$$

Here, ρ_i and ρ_s are the densities of ice and of snow, respectively, c_i and c_s are specific heats of these media, and Q_s and I_s are the values of Q and I, respectively, at the air-snow or, if snow is absent, at the air-ice interface. The radiation heat flux I_s that penetrates into the interior of snow-ice cover is the surface value of the incident solar radiation flux from the atmosphere multiplied by $1 - \alpha_i$, α_i being the albedo of the ice or snow surface with respect to solar radiation. The dimensionless parameters C_I and C_S, the shape factors, are given by

$$C_I = \int_0^1 \Phi_I(\zeta_I) d\zeta_I, \qquad C_S = \int_0^1 \Phi_S(\zeta_S) d\zeta_S. \tag{47}$$

The heat flux at the snow-ice interface is assumed to be continuous, that is

$$-\kappa_i \frac{\theta_f - \theta_I}{H_I} \Phi_I'(1) = -\kappa_s \frac{\theta_I - \theta_S}{H_S} \Phi_S'(0). \tag{48}$$

Equations (46) and (48) serve to determine temperatures at the air-snow and at the snow-ice interfaces, when these temperatures are below the freezing point, i.e. when no melting at the snow surface (ice surface, when snow is absent) takes place. During the snow (ice) melting from above, the temperatures θ_S and θ_I remain equal to the freezing point θ_f, and the heat fluxes Q_S and Q_I are zero.

3.4.2 Snow and Ice Thickness

The equations governing the evolution of the snow thickness and of the ice thickness are derived from the heat transfer equation (25) that incorporates an additional term on its right-hand side, namely, the term $f_M(z) L_f dM/dt$ that describes the rate of heat release/consumption due to accretion/melting of snow and ice. Here, M is the mass of snow or ice per unit area, L_f is the latent heat of fusion, and $f_M(z)$ is a function that satisfies the normalization conditions $\int_{H_I}^{H_I+H_S} f_M(z) dz = 1$ and $\int_0^{H_I} f_M(z) dz = 1$ for snow and ice, respectively.

The accumulation of snow is not computed within the ice-snow model. The rate of snow accumulation is assumed to be a known time-dependent quantity that is provided by the atmospheric model or is known from observations. Then, the evolution of the snow thickness during the snow accumulation and no melting is computed from

$$\frac{d\rho_s H_S}{dt} = \left(\frac{dM_S}{dt}\right)_a, \tag{49}$$

where $M_S = \rho_s H_S$ is the snow mass per unit area, and $(dM_S/dt)_a$ is the (given) rate of snow accumulation.

When the temperature θ_I at the upper surface of the ice is below the freezing point θ_f, the heat conduction through the ice causes the ice growth. This growth is accompanied by a release of heat at the lower surface of the ice that occurs at a rate $L_f dM_I/dt$, where $M_I = \rho_i H_I$ is the ice mass per unit area. The normalization function f_M is equal to zero throughout the snow-ice cover except at the ice-water interface where $f_M = \delta(0)$, $\delta(z)$ being the Dirac delta function. Integrating Eq. (25) from $z = -0$ to $z = +0$ with due regard for this heat release yields the equation for the ice thickness. It reads

$$L_f \frac{d\rho_i H_I}{dt} = Q_w + \kappa_i \frac{\theta_f - \theta_I}{H_I} \Phi'_I(0), \tag{50}$$

where Q_w is the heat flux in the near-surface water layer just beneath the ice. If the r.h.s. of Eq. (50) is negative, i.e. the negative of the heat flux in the water, Q_w, exceeds the negative of the heat flux in the ice, $Q_I|_{z=0}$, ice ablation takes place.

As the atmosphere heats the snow surface, the surface temperature eventually reaches the freezing point and the snow and ice melting sets in. This process is accompanied by a consumption of heat at rates $L_f d\rho_s H_S/dt$ and $L_f d\rho_i H_I/dt$ for snow and ice, respectively. Notice that the exact form of the normalization function f_M is not required by virtue of the normalization conditions considered above. Integrating Eq. (25) from $z = -(H_I + H_S) - 0$ to $z = -H_I$ with due regard for the heat loss due to snow melting and adding the (given) rate of snow accumulation yields the equation for the snow thickness,

$$L_f \frac{d\rho_s H_S}{dt} = -(Q_s + I_s) + I(-H_I) + L_f \left(\frac{dM_S}{dt}\right)_a + c_s \theta_f H_S \frac{d\rho_s}{dt}, \tag{51}$$

where the last term on the r.h.s. originates from the dependence of the snow density on the snow depth (see Section 3.5.3).

Integrating Eq. (25) from $z = -H_I$ to $z = +0$ with due regard for the heat loss due to ice melting yields the equation for the ice thickness,

$$L_f \frac{d\rho_i H_I}{dt} = Q_w + I(0) - I(-H_I), \tag{52}$$

If the ice melts out earlier than snow, the snow depth is instantaneously set to zero.

3.4.3 The Temperature Profile beneath the Ice

The simplest assumption is to keep the temperature profile unchanged over the entire period of ice cover. This assumption is fair for deep lakes, where the heat flux through the bottom is negligibly small. In shallow lakes, this assumption may lead to an underestimation of the mean temperature. The heat accumulated in the thermally active upper layer of bottom sediments during spring and summer is returned back to the water column during winter, leading to an increase of the water temperature under the ice. The water temperature under the ice can also increase due to heating by solar radiation penetrating down through the ice. The thermodynamic regimes encountered in ice-covered lakes are many and varied. Their detailed description requires a set of sophisticated parameterizations. The use of such parameterizations in the framework of the present lake model is, however, hardly justified. The point is that it is the snow (ice) surface temperature that communicates information to the atmosphere, the water temperature is not directly felt by the atmospheric surface layer. It is, therefore, not vital that the temperature regimes in ice-covered lakes be described in great detail. Only their most salient features should be accounted for, first of all, the heat budget of the water column.

When the lake is ice-covered, the temperature at the ice-water interface is fixed at the freezing $\theta_s = \theta_f$. In case the bottom temperature is less than the temperature of maximum density, $\theta_b < \theta_r$, the mixed-layer depth and the shape factor are kept unchanged, $dh/dt = 0$ and $dC_\theta/dt = 0$, the mean temperature $\overline{\theta}$ is computed from Eq. (26) and the bottom temperature θ_b is computed from Eq. (23). If the entire water column appears to be mixed at the moment of freezing, i.e. $h = D$ and $\theta_s = \overline{\theta} = \theta_b$, the mixed layer depth is reset to zero, $h = 0$, and the shape factor is set to its minimum value, $C_\theta = 0.5$ (see Section 3.5.1).

The heat flux from water to ice is estimated from

$$Q_w = -\kappa_w \frac{\theta_b - \theta_s}{D}, \tag{53}$$

if $h = 0$, and $Q_w = 0$ otherwise. Notice that the estimate of Q_w given by Eq. (53) and the shape factor $C_\theta = 0.5$ correspond to a linear temperature profile over the entire water column. A linear profile is encountered in ice-covered shallow lakes when $\theta_b < \theta_r$ and the heat flux is from the bottom sediments to the lake water.

As the bottom temperature reaches the temperature of maximum density, convection due to bottom heating sets in. To describe this regime of convection in detail, a convectively mixed layer whose temperature is close to θ_r, and a thin layer adjacent to the bottom, where the temperature decreases sharply from $\theta_b > \theta_r$ to θ_r, should be thoroughly considered. We neglect these peculiarities of convection due to bottom heating and adopt a simpler model where the bottom temperature is fixed at the temperature of maximum density, $\theta_b = \theta_r$. The mean temperature $\overline{\theta}$ is computed from Eq. (26). If $h > 0$, the shape factor C_θ is kept unchanged, and the mixed-layer depth is computed from Eq. (23). As the mixed-layer depth approaches zero, Eq. (23) is used to compute the shape factor C_θ that in this regime would increase towards its maximum value C_θ^{max}. The heat flux from water to ice is estimated from

$$Q_w = -\kappa_w \frac{\theta_b - \theta_s}{D} \max\left[1, \Phi'_\theta(0)\right], \tag{54}$$

if $h = 0$, and $Q_w = 0$ otherwise.

One more regime of convection is often encountered in ice-covered lakes. In late spring, the snow overlying the ice vanishes and solar radiation penetrates down through the ice. As the mixed-layer temperature is below that of maximum density, the volumetric radiation heating leads to de-stabilisation of the water column and thereby drives convective motions. Such regime of convection was analysed by Farmer (1975), Mironov and Terzhevik (2000), Mironov et al. (2002), and Jonas et al. (2003), among others. A parameterization of convection due to solar heating (e.g. a parameterization based on a bulk model developed by Mironov et al. 2002) can, in principle, be incorporated into the present model. We do not do so, however, considering that the major effect of convection beneath the ice is to redistribute heat in the vertical and that it takes place over a very limited period of time.

3.5 Empirical Relations and Model Constants

3.5.1 The Shape Functions

In the lake model proposed by Mironov et al. (1991), a polynomial approximation of the shape function with respect to the temperature profile in the thermocline was used. The temperature-depth curve was assumed to be bounded by the two limiting curves given by Eq. (5). The shape function $\Phi_\theta(\zeta)$ evolves towards the first line of Eq. (5) during the mixed-layer deepening, and towards the second line of Eq. (5) during the mixed-layer stationary

state or retreat. The corresponding limiting values of the shape factor C_θ are 0.75 and 0.6, respectively. The adjustment of the temperature-depth curve occurs on a certain relaxation time scale that was estimated on the basis of the similarity theory for stably stratified turbulent flows (see Mironov et al. 1991 for details).

Recall that the approximations (5) are based on the observational data taken in the Baltic Sea. Theoretical analysis of Zilitinkevich et al. (1988) also holds for the ocean or sea, where the thermocline is underlain by a deep quiescent layer. Shallow and medium-depth lakes usually have a two-layer temperature structure, where the thermocline extends from the bottom of the mixed layer down to the basin bottom. Empirical data indicate a greater variety of shapes of the temperature-depth curve in lakes than in the ocean or sea (Kirillin 2001a, 2001b). During the mixed-layer deepening, the dimensionless temperature gradient just below the mixed layer-thermocline interface and the shape factor often exceed their limiting values of $\Phi'_\theta(0) = 3$ and $C_\theta = 0.75$, respectively, suggested by the first line of Eq. (5). These findings are corroborated by the theoretical analysis in Appendix A. Based upon these empirical and theoretical findings, we allow a wider range of variation in Φ_θ.

We adopt the following polynomial approximation of the shape function $\Phi_\theta(\zeta)$ with respect to the temperature profile in the thermocline:

$$\Phi_\theta = \left(\frac{40}{3}C_\theta - \frac{20}{3}\right)\zeta + (18 - 30C_\theta)\,\zeta^2 + (20C_\theta - 12)\,\zeta^3 + \left(\frac{5}{3} - \frac{10}{3}C_\theta\right)\zeta^4. \tag{55}$$

The shape factor C_θ is computed from

$$\frac{dC_\theta}{dt} = \mathrm{sign}(dh/dt)\frac{C_\theta^{max} - C_\theta^{min}}{t_{rc}}, \qquad C_\theta^{min} \le C_\theta \le C_\theta^{max}, \tag{56}$$

where t_{rc} is the relaxation time scale, and sign is the signum function, $\mathrm{sign}(x)=-1$ if $x \le 0$ and $\mathrm{sign}(x)=1$ if $x > 0$. The minimum and maximum values of the shape factor are set to $C_\theta^{min} = 0.5$ and $C_\theta^{max} = 0.8$. The shape function $\Phi_\theta(\zeta)$ given by Eq. (55) is illustrated in Fig. 5. As seen from the figure, the dimensionless temperature profiles lie in the area bounded by the lower and the upper solid curves. During the mixed-layer deepening, $dh/dt > 0$, the temperature profile evolves towards the limiting curve, characterised by a maximum value of the shape factor, $C_\theta^{max} = 0.8$, and the maximum value of the dimensionless temperature gradient at the upper boundary of the thermocline, $\Phi'_\theta(0) = 4$. During the mixed-layer stationary state or retreat, $dh/dt \le 0$, the temperature profile evolves towards the other limiting curve, characterised by a minimum value of the shape factor, $C_\theta^{min} = 0.5$, and the zero temperature gradient at the upper boundary of the thermocline, $\Phi'_\theta(0) = 0$. Notice that $C_\theta^{min} = 0.5$ is consistent with a linear temperature profile that is assumed to occur under the ice when the bottom temperature is less than the temperature of maximum density (see Section 3.4.3).

According to Eq. (55), the dimensionless parameter $C_{\theta\theta}$ defined through Eq. (31) is given by

$$C_{\theta\theta} = \frac{11}{18}C_\theta - \frac{7}{45}. \tag{57}$$

The relaxation time t_{rc} is estimated from the following scaling arguments. The time t_{rc} is basically the time of the evolution of the temperature profile in the thermocline from one limiting curve to the other, following the change of sign in dh/dt. Then, a reasonable scale for t_{rc} is the thermal diffusion time through the thermocline, that is a square of the thermocline thickness, $(D-h)^2$, over a characteristic eddy temperature conductivity, K_{H*}. With due regard for the stable stratification in the thermocline, K_{H*} is estimated from Eqs. (14) and (16). Using a mean-square buoyancy frequency in the thermocline, $\overline{N} =$

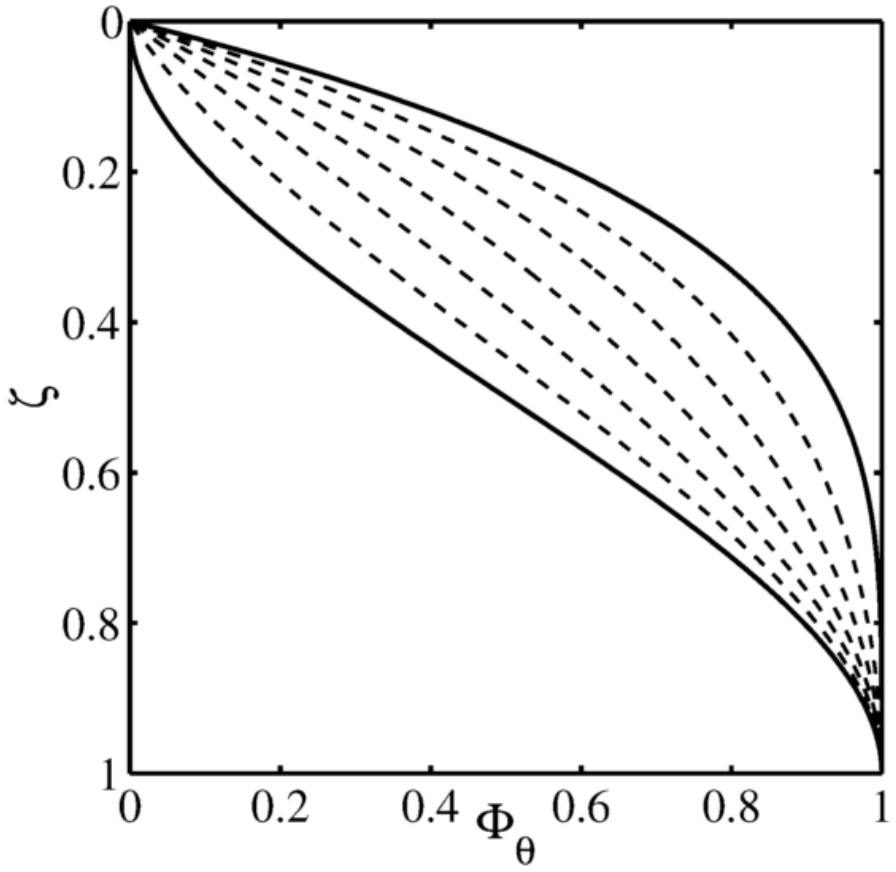


Figure 5: The fourth-order polynomial approximation of the shape function $\Phi_\theta(\zeta)$ with respect to the temperature profile in the thermocline. The curves are computed from Eq. (55) with seven different values of the shape factor C_θ ranging from $C_\theta = C_\theta^{min} = 0.5$, lower solid curve, to $C_\theta = C_\theta^{max} = 0.8$, upper solid curve, $\Delta C_\theta = 0.05$ apart.

$\left[(D-h)^{-1}\int_h^D N^2 dz\right]^{1/2}$, as an estimate of N and assuming that the TKE in the thermocline scales either on the convective velocity w_*, Eq. (34), or on the surface friction velocity u_*, we propose

$$t_{rc} = \frac{(D-h)^2\overline{N}}{C_{rc}u_T^2}, \qquad u_T = \max(w_*, u_*), \tag{58}$$

where C_{rc} is a dimensionless constant estimated at 0.003 (this value may be altered as new information becomes available).

We adopt the following polynomial approximations of the shape functions $\Phi_{B1}(\zeta_{B1})$ and $\Phi_{B2}(\zeta_{B2})$ with respect to the temperature profile in bottom sediments (cf. Golosov et al. 1998):

$$\Phi_{B1} = 2\zeta_{B1} - \zeta_{B1}^2, \qquad \Phi_{B2} = 6\zeta_{B2}^2 - 8\zeta_{B2}^3 + 3\zeta_{B2}^4. \tag{59}$$

which are the simplest polynomials that satisfy a minimum set of constraints. The conditions $\Phi_{B1}(0) = \Phi_{B2}(0) = 0$ and $\Phi_{B1}(1) = \Phi_{B2}(1) = 1$ follow from the definition of ζ_{B1}, ζ_{B2}, Φ_{B1}, and Φ_{B2}. The conditions $\Phi'_{B1}(1) = \Phi'_{B2}(0) = \Phi'_{B2}(1) = 0$ provide a zero temperature

gradient at the depths $z = H$ and $z = L$, and the condition $\Phi''_{B2}(1) = 0$ follows from the requirement that the temperature θ_L at the outer edge $z = L$ of the thermally active layer of the sediments is constant in time. The shape functions given by Eq. (59) are illustrated in Fig. 6. The shape factors that correspond to Eq. (59) are $C_{B1} = 2/3$ and $C_{B2} = 3/5$.

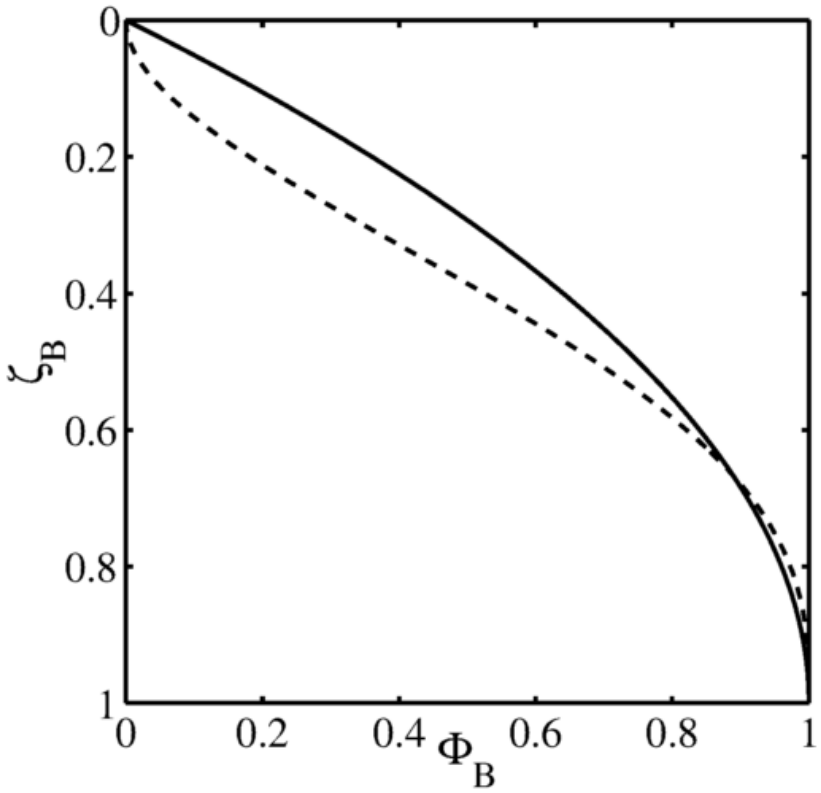


Figure 6: The polynomial approximations of the shape functions $\Phi_{B1}(\zeta_{B1})$, solid curve, and $\Phi_{B2}(\zeta_{B2})$, dashed curve, with respect to the temperature profile in bottom sediments. The curves are computed from Eq. (59).

As a zero-order approximation, the simplest linear temperature profile within snow and ice can be assumed, $\Phi_S(\zeta_S) = \zeta_S$ and $\Phi_I(\zeta_I) = \zeta_I$. This gives $C_S = C_I = 1/2$. Although a linear profile is a good approximation for thin ice, it is likely to result in a too thick ice in cold regions, where the ice growth takes place over a long period, and in a too high thermal inertia of thick ice. A slightly more sophisticated approximation was developed by Mironov and Ritter (2004) who assumed that the ice thickness is limited by a certain maximum value H_I^{max} and that the rate of ice growth approaches zero as H_I approaches H_I^{max} (the snow layer over the ice was not considered). They proposed

$$\Phi_I = \left[1 - \frac{H_I}{H_I^{max}}\right]\zeta_I + \left[(2 - \Phi_{*I})\frac{H_I}{H_I^{max}}\right]\zeta_I^2 + \left[(\Phi_{*I} - 1)\frac{H_I}{H_I^{max}}\right]\zeta_I^3, \tag{60}$$

where Φ_{*I} is a dimensionless constant. The shape factor that corresponds to Eq. (60) is

$$C_I = \frac{1}{2} - \frac{1}{12}(1 + \Phi_{*I})\frac{H_I}{H_I^{max}}. \tag{61}$$

The physical meaning of the above expressions can be elucidated as follows. The relation $\Phi'_I(0) = 1 - H_I/H_I^{max}$ that follows from Eq. (60) ensures that the ice growth is quenched

as the ice thickness approaches its maximum value. Equation (61) suggests that the shape factor C_I decreases with increasing ice thickness. A smaller C_I means a smaller relative thermal inertia of the ice layer of thickness H_I [the absolute thermal inertia is measured by the term $C_I H_I$ that enters the l.h.s. of Eq. (46)]. This is plausible as it is mostly the upper part of thick ice, not the entire ice layer, that effectively responds to external forcing. For use in the global numerical weather prediction model GME of the German Weather Service, Mironov and Ritter (2004) proposed an estimate of $H_I^{max} = 3$ m. This value is typical of the central Arctic in winter. The allowable values of Φ_{*I} lie in the range between -1 and 5. $\Phi_{*I} > 5$ yields an unphysical negative value of C_I as the ice thickness approaches H_I^{max}. $\Phi_{*I} < -1$ gives C_I that increases with increasing H_I. There is no formal proof that this may not occur, but it is very unlikely. A reasonable estimate is $\Phi_{*I} = 2$. With this estimate C_I is halved as H_I increases from 0 to H_I^{max}. Notice that the linear temperature profile is recovered as $H_I/H_I^{max} \ll 1$, i.e. when the ice is thin. The polynomial (60) is illustrated in Fig. 7.

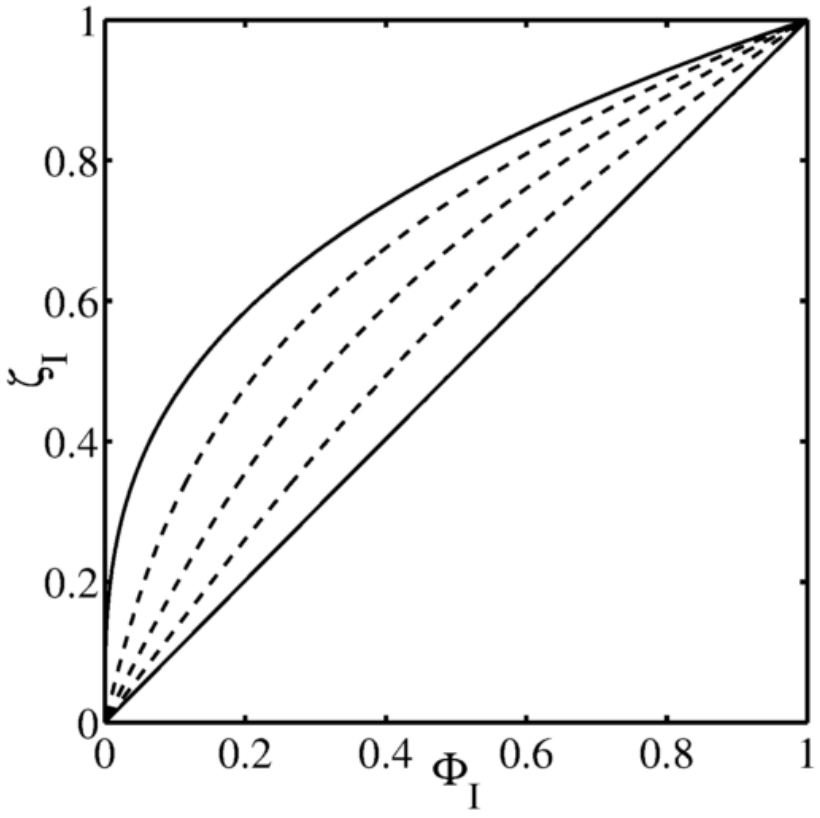


Figure 7: The approximation of the temperature profile shape function $\Phi_I(\zeta_I)$ given by Eq. (60). The curves are computed with $\Phi_{*I} = 2$ and (from right to left) $H_I/H_I^{max} = 0.01$, $H_I/H_I^{max} = 0.25$, $H_I/H_I^{max} = 0.5$, $H_I/H_I^{max} = 0.75$ and $H_I/H_I^{max} = 1.0$.

One further comment is in order regarding the shape functions Φ_θ, Φ_{B1}, Φ_{B2}, Φ_S and Φ_I. These functions have been determined using a geometrical approach (the Pohlhausen method). The essence of the approach is to use a polynomial approximation of the function in question and to invoke a minimum set of physical constraints to determine the polynomial coefficients. In spite of the utter simplicity of this approach, it often yields very accurate results. Prominent examples are the boundary-layer similarity models developed by Long

(1974) and Zilitinkevich (1989a, 1989b).

It should be stressed that, although the shape functions are useful in that they provide a continuous temperature profile trough the snow, ice, water and bottom sediments, their exact shapes are not required in the present model. It is not $\Phi_\theta(\zeta)$, $\Phi_{B1}(\zeta_{B1})$, $\Phi_{B2}(\zeta_{B2})$, $\Phi_S(\zeta_S)$ and $\Phi_I(\zeta_I)$ per se, but the shape factors C_θ, C_{B1}, C_{B2}, C_S and C_I, and the dimensionless gradients $\Phi'_\theta(0)$, $\Phi'_{B1}(0)$, $\Phi'_S(0)$, $\Phi'_I(0)$ and $\Phi'_I(1)$, that enter the model equations. The estimates of these parameters are summarised in Table 1 (Appendix B).

3.5.2 Constants in the Equations for the Mixed-Layer Depth

The estimates of $C_{c1} = 0.2$ and $C_{c2} = 0.8$ in Eq. (35) were recommended by Zilitinkevich (1991). They were obtained using laboratory, atmospheric and oceanic data. Apart from being commonly used in mixed-layer models of penetrative convection driven by the surface buoyancy flux, these values were successfully used by Mironov and Karlin (1989) to simulate day-time convection in the upper ocean that is driven by surface cooling but inhibited by radiation heating, and by Mironov and Terzhevik (2000) and Mironov et al. (2002) to simulate spring convection in ice-covered lakes where convective motions are driven by volumetric radiation heating of the water at temperature below the temperature of maximum density (Mironov et al. 2002 used $C_{c2} = 1.0$). A slightly modified estimate of $C_{c1} = 0.17$ was obtained by Fedorovich et al. (2004) from large-eddy simulation data. We adopt the estimates of $C_{c1} = 0.17$ and $C_{c2} = 1.0$ for use in the equation of convective entrainment.

For use in Eq. (38) for the equilibrium mixed-layer depth in stable or neutral stratification, we adopt the estimates of $C_n = 0.5$, $C_s = 10$ and $C_i = 20$ obtained by Zilitinkevich and Mironov (1996). The estimates of C_s and C_i are based on a limited amount of data and may need to be slightly altered as new (and better) data become available. The estimate of C_n was corroborated by the results from further studies (Zilitinkevich and Esau 2002, 2003) and is reliable.

The estimates of the dimensionless constant C_{rh} in the relaxation-type rate equation for the depth of a stably or neutrally stratified wind-mixed layer, Eqs. (36) and (37), are not abundant. Kim (1976) and Deardorff (1983) recommended that the value of $C_{rh} = 0.28$ be used to describe entrainment into a homogeneous fluid. The same value was used by Zeman (1979), and a slightly lower value of $C_{rh} = 0.26$ by Zilitinkevich et al. (1979). The rate equations given by Khakimov (1976) and Zilitinkevich et al. (2002) use the reciprocal of the Coriolis parameter as the relaxation time scale. Their rate equations suggest the values of $C_{rh} = 0.45$ and $C_{rh} = 0.5$, respectively. A similar form of the rate equation was proposed earlier by Deardorff (1971) who used a much lower value of $C_{rh} = 0.025$. We adopt an estimate of $C_{rh} = 0.03$ suggested by the sensitivity experiments with the present lake model (keeping in mind that this value may need to be altered).

The estimates of dimensionless constants in the equations for the mixed-layer depth are summarised in Table 1 (Appendix B).

3.5.3 Thermodynamic Parameters

The exponential approximation of the decay law for the flux of solar radiation is commonly used in applications. It reads

$$I(t,z) = I_s(t) \sum_{k=1}^{n} a_k \exp[-\gamma_k(z + H_S + H_I)], \tag{62}$$

where I_s is the surface value of the solar radiation heat flux multiplied by $1-\alpha$, α being the albedo of the water, ice or snow surface with respect to solar radiation, n is the number of wavelength bands, a_k are fractions of the total radiation flux for different wavelength bands, and $\gamma_k(z)$ are attenuation coefficients for different bands. The attenuation coefficients are piece-wise constant functions of height, i.e. they have different values for water, ice and snow but remain depth-constant within these media. The optical characteristics of water are lake-specific and should be estimated in every particular case. Rough estimates of a_k and γ_k for ice and snow are given by Launiainen and Cheng (1998).

The lake model includes a number of thermodynamic parameters. They are summarised in Table 2 (Appendix B). These thermodynamic parameters can be considered constant except for the snow density and the snow heat conductivity that depend, among other things, on the snow thickness and the snow age. As a first approximation, the following empirical formulations (Heise et al. 2003) can be used that relate ρ_s and κ_s to the snow thickness:

$$\rho_s = \min\left\{\rho_s^{max}, |1 - H_S\Gamma_{\rho_s}/\rho_w|^{-1}\,\rho_s^{min}\right\}, \tag{63}$$

where $\rho_s^{min} = 100$ kg·m^{-3} and $\rho_s^{max} = 400$ kg·m^{-3} are minimum and maximum values, respectively, of the snow density, and $\Gamma_{\rho_s} = 200$ kg·m^{-4} is an empirical parameter, and

$$\kappa_s = \min\left\{\kappa_s^{max}, \kappa_s^{min} + H_S\Gamma_{\kappa_s}\rho_s/\rho_w\right\}, \tag{64}$$

where $\kappa_s^{min} = 0.2$ J·m^{-1}·s^{-1}·K^{-1} and $\kappa_s^{max} = 1.5$ J·m^{-1}·s^{-1}·K^{-1} are minimum and maximum values, respectively, of the snow heat conductivity, and $\Gamma_{\kappa_s} = 1.3$ J·m^{-2}·s^{-1}·K^{-1} is an empirical parameter.

4 Conclusions

A lake model suitable to predict the vertical temperature structure in lakes of various depths on time scales from a few hours to many years is developed. The model, termed FLake, is based on a two-layer parametric representation of the evolving temperature profile and on the integral budget of energy for the layers in question. The structure of the stratified layer between the upper mixed layer and the basin bottom, the lake thermocline, is described using the concept of self-similarity (assumed shape) of the temperature-depth curve. The same concept is used to describe the temperature structure of the thermally active upper layer of bottom sediments and of the ice and snow cover. An entrainment equation is used to compute the depth of a convectively-mixed layer. A relaxation-type equation is used to compute the wind-mixed layer depth in stable and neutral stratification, where a multi-limit formulation for the equilibrium mixed-layer depth accounts for the effects of the earth's rotation, of the surface buoyancy flux, and of the static stability in the thermocline. Both mixing regimes are treated with due regard for the volumetric character of solar radiation heating. Simple thermodynamic arguments are invoked to develop the evolution equations for the ice and snow depths. Using the integral (bulk) approach, the problem of solving partial differential equations (in depth and time) for the temperature and turbulence quantities is reduced to solving ordinary differential equations for the time-dependent parameters that specify the evolving temperature profile. The result is a computationally efficient lake model that incorporates much of the essential physics.

It must be emphasised that the empirical constants and parameters of FLake are not application-specific. That is, once they have been estimated using independent empirical and numerical data, they should not be re-evaluated when the model is applied to a particular lake. There are, of course, lake-specific external parameters, such as depth to the

bottom and optical characteristics of water, but these are not part of the model physics. In this way FLake does not require "re-tuning", a procedure that may improve an agreement with a limited amount of data and is sometimes justified. This procedure should, however, be considered as a bad practice and must be avoided whenever possible as it greatly reduces the predictive capacity of a physical model (Randall and Wielicki 1997).

Apart from the depth to the bottom and the optical characteristics of lake water, the only lake-specific parameters are the depth L of the thermally active layer of bottom sediments and the temperature θ_L at that depth. These parameters should be estimated only once for each lake, using observational data or empirical recipes (e.g. Fang and Stefan 1998). In a similar way, the temperature at the bottom of the thermally active soil layer and the depth of that layer are estimated once and then used in an NWP model as two-dimensional external-parameter arrays.

The proposed lake model is intended for use, first of all, in NWP and climate models as a module (parameterization scheme) to predict the lake surface temperature. Apart from NWP and climate modelling, practical applications where simple bulk models are favoured over more accurate but more sophisticated models (e.g. second-order turbulence closures) include modelling aquatic ecosystems. For ecosystem modelling, a sophisticated physical module is most often not required because of insufficient knowledge of chemistry and biology.

Acknowledgements

The author is grateful to Erdmann Heise, Sergej Golosov, Georgiy Kirillin, Ekaterina Kourzeneva, Bodo Ritter, Natalia Schneider and Arkady Terzhevik for useful discussions. The work was partially supported by the EU Commissions through the projects INTAS-01-2132 and INTAS-05-1000007-431.

5 Appendices

Appendix A. Temperature Profile in the Lake Thermocline – A Self-Similar Travelling Wave-Type Solution

In Section 2.3, a travelling wave-type self-similar solution to the heat transfer equation obtained by Zilitinkevich et al. (1988) is discussed. These authors analysed the heat transfer equation in the form

$$\partial\theta/\partial t = -\partial\mathcal{Q}/\partial z, \tag{A.1}$$

where $\mathcal{Q}$ is the vertical turbulent temperature flux, subject to the boundary conditions

$$\theta = \theta_s \quad \text{at} \quad z = h, \qquad \theta = \theta_b \quad \text{at} \quad z = h + \Delta h. \tag{A.2}$$

They assumed that the temperatures at the upper and lower boundaries of the thermocline are constant, $\theta_s = const$ and $\theta_b = const$, the mixed layer deepens at a constant rate, $dh/dt \equiv \dot{h} = const > 0$, whereas the thickness of the thermocline does not change with time, $d\Delta h/dt = 0$. Then, the heat transfer equation (A.1) takes the form

$$\dot{h}d\theta/d\zeta = d\mathcal{Q}/d\zeta, \tag{A.3}$$

where $\zeta = (z-h)/\Delta h$ is the dimensionless depth. In order to close the problem, Zilitinkevich et al. (1988) used the down-gradient formulation for the temperature flux, $\mathcal{Q} = -K_H\partial\theta/\partial z$, and the expression $K_H = l^2N$ for the effective temperature conductivity in the thermocline, where l is the eddy length scale. Taking $l = const$, they invoked an additional condition $\partial\theta/\partial z = 0$ at $z = h + \Delta h$ to determine l. The solution to the problem reads

$$\Phi_\theta = 1 - (1-\zeta)^3, \qquad l = 3^{-3/4}(\beta\Delta\theta)^{-1/4}\Delta h^{3/4}\dot{h}^{1/2}. \tag{A.4}$$

The temperature profile shape function Φ_θ is given by the third-order polynomial in ζ. This polynomial was developed earlier by Arsenyev and Felzenbaum (1977) on the basis of simple geometrical arguments and by Mälkki and Tamsalu (1985) on the basis of data from measurements in the Baltic Sea.

The Zilitinkevich et al. (1988) solution (A.4) is conditioned by the assumption $d\Delta h/dt = 0$. This situation is illustrated in Fig. 8(a). It is characteristic of the ocean or sea, where the mixed layer grows into a neutrally stratified deep quiescent layer, whereas the thickness of the thermocline remains approximately unchanged. In lakes, the thermocline is usually pressed against the basin bottom so that an increase of the mixed-layer thickness is accompanied by a decrease of the thickness of the thermocline, $dh/dt = -d\Delta h/dt$. This situation is illustrated in Fig. 8(b). With $dh/dt = -d\Delta h/dt = const > 0$, the heat transfer equation (A.1) takes the form

$$\dot{h}(1-\zeta)d\theta/d\zeta = d\mathcal{Q}/d\zeta. \tag{A.5}$$

It is easy to verify that Eq. (A.5) subject to the same boundary conditions and closure relations as used by Zilitinkevich et al. (1988) possesses a solution in the form

$$\Phi_\theta = 1 - (1-\zeta)^5, \qquad l = 180^{-1/4}(\beta\Delta\theta)^{-1/4}\Delta h^{3/4}\dot{h}^{1/2}. \tag{A.6}$$

Equations (A.4) and (A.6) reveal a number of differences between the lake thermocline that is pressed against the bottom and the ocean thermocline that is underlain by a deep neutrally

stratified quiescent layer. The eddy length scale l characteristic of the lake thermocline is $(20/3)^{1/4}$ times smaller than l characteristic of the ocean thermocline. The temperature profile in the lake thermocline is characterised by a sharper temperature gradient near the thermocline top. The dimensionless temperature gradients at the top of the thermocline, $-(\Delta\theta/\Delta h)^{-1}(\partial\theta/\partial z)|_{z=h} \equiv \Phi'_\theta(0)$, $\Delta\theta = \theta_s - \theta_b$ being the temperature difference across the thermocline, are $\Phi'_\theta(0) = 5$ for the lake and $\Phi'_\theta(0) = 3$ for the ocean. The temperature profile shape factor is $C_\theta = 5/6$ for the lake and $C_\theta = 3/4$ for the ocean.

As Eq. (A.3) suggests, the self-similar oceanic thermocline is characterised by the shape function $\Phi_\theta \equiv (\theta_s - \theta)/(\theta_s - \theta_b)$ with respect to the temperature that coincides with the shape function $\Phi_Q \equiv (\mathcal{Q}_h - \mathcal{Q})/(\mathcal{Q}_h - \mathcal{Q}_b)$ with respect to the temperature (heat) flux. For the lake thermocline, the relation between Φ_θ and Φ_Q is more sophisticated. Equation (A.5) yields

$$\Phi_Q(\zeta) = C_\theta^{-1}\left[(1-\zeta)\Phi_\theta(\zeta) + \int_0^\zeta \Phi_\theta(\zeta')d\zeta'\right]. \tag{A.7}$$

The above relation suggests that the dimensionless shape-function parameters C_Q, $C_{\theta\theta}$ and C_θ defined by Eqs. (30), (31) and (24), respectively, are related through $C_Q = 2C_{\theta\theta}/C_\theta$.

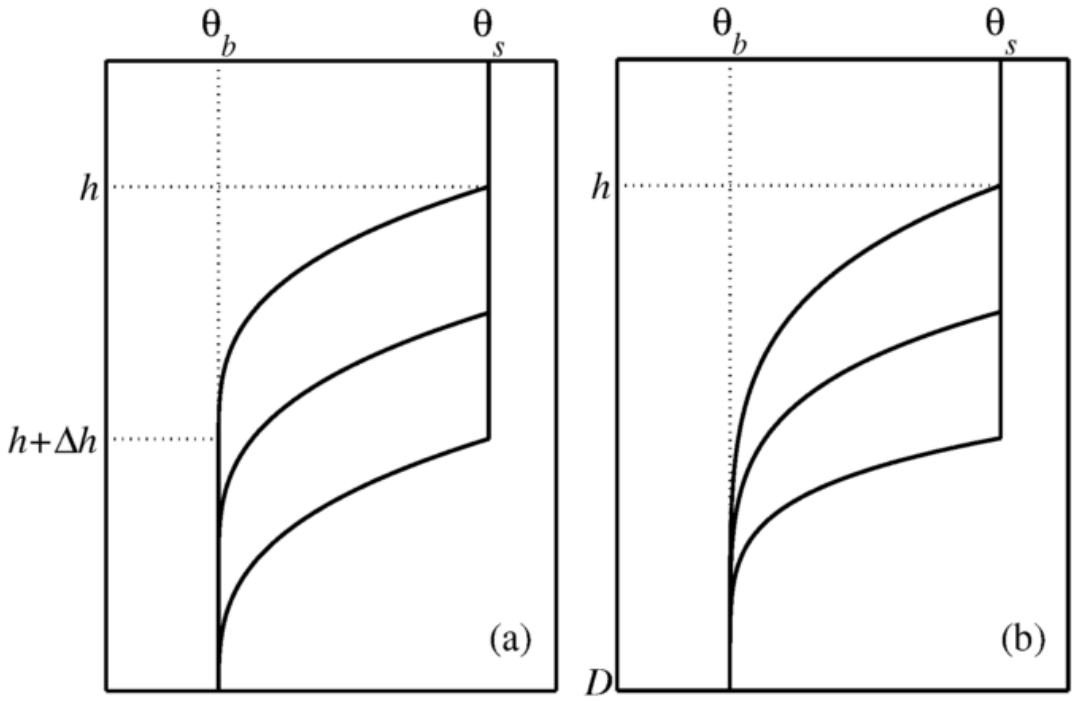


Figure 8: Self-similar temperature profile during the mixed-layer deepening. (a) In a neutrally stratified deep ocean, the mixed-layer depth increases, $dh/dt > 0$, whereas the depth of the thermocline remains constant, $d\Delta h/dt = 0$. (b) In lakes, the thermocline is pressed against the bottom, $\Delta h = D - h$, so that $dh/dt = -d\Delta h/dt$.

Appendix B. A Summary of Model Parameters

Table 1: Empirical Constants and Parameters

Constant/ Parameter	Recommended Value/ Computed from	Comments
C_{c1}	0.17	
C_{c2}	1.0	
C_n	0.5	
C_s	10	
C_i	20	
C_{rh}	0.03	
C_{rc}	0.003	
C_θ	Eq. (56)	
C_θ^{min}	0.5	
C_θ^{max}	0.8	
$C_{\theta\theta}$	Eq. (57)	
C_Q	$2C_{\theta\theta}/C_\theta$	
C_{B1}	2/3	
C_{B2}	3/5	
C_I	1/2	Optionally Eq. (61)
C_S	1/2	
$\Phi'_\theta(0)$	Eqs. (55) and (56)	
$\Phi'_{B1}(0)$	2	
$\Phi'_I(0)$	1	Optionally Eq. (60)
$\Phi'_I(1)$	1	Optionally Eq. (60)
$\Phi'_S(0)$	1	
Φ_{*I}	2	
H_I^{max}	3 m	

Table 2: Thermodynamic Parameters

Notation	Parameter	Dimensions	Estimate/ Computed from
g	Acceleration due to gravity	$\mathrm{m{\cdot}s^{-2}}$	9.81
θ_r	Temperature of maximum density of fresh water	K	277.13
θ_f	Fresh water freezing point	K	273.15
a_T	Coefficient in the fresh-water equation of state	$\mathrm{K^{-2}}$	$1.6509 \cdot 10^{-5}$
ρ_w	Density of fresh water	$\mathrm{kg{\cdot}m^{-3}}$	Eq. (20)
ρ_r	Maximum density of fresh water	$\mathrm{kg{\cdot}m^{-3}}$	$1.0 \cdot 10^3$
ρ_i	Density of ice	$\mathrm{kg{\cdot}m^{-3}}$	$9.1 \cdot 10^2$
ρ_s	Density of snow	$\mathrm{kg{\cdot}m^{-3}}$	Eq. (63)
L_f	Latent heat of fusion	$\mathrm{J{\cdot}kg^{-1}}$	$3.3 \cdot 10^5$
c_w	Specific heat of water	$\mathrm{J{\cdot}kg^{-1}{\cdot}K^{-1}}$	$4.2 \cdot 10^3$
c_i	Specific heat of ice	$\mathrm{J{\cdot}kg^{-1}{\cdot}K^{-1}}$	$2.1 \cdot 10^3$
c_s	Specific heat of snow	$\mathrm{J{\cdot}kg^{-1}{\cdot}K^{-1}}$	$2.1 \cdot 10^3$
κ_w	Molecular heat conductivity of water	$\mathrm{J{\cdot}m^{-1}{\cdot}s^{-1}{\cdot}K^{-1}}$	$5.46 \cdot 10^{-1}$
κ_i	Molecular heat conductivity of ice	$\mathrm{J{\cdot}m^{-1}{\cdot}s^{-1}{\cdot}K^{-1}}$	2.29
κ_s	Molecular heat conductivity of snow	$\mathrm{J{\cdot}m^{-1}{\cdot}s^{-1}{\cdot}K^{-1}}$	Eq. (64)

References

Abramowitz, M., and I. A. Stegun, 1964: *Handbook of Mathematical Functions.* National Bureau of Standards, Applied Mathematics Series 55.

Arsenyev, S. A., and A. I. Felzenbaum, 1977: Integral model of the active ocean layer. *Izv. Akad. Nauk SSSR. Fizika Atmosfery i Okeana*, **13**, 1034–1043.

Barenblatt, G. I., 1978: On the self-similar distribution of temperature and salinity in the upper thermocline. *Izv. Akad. Nauk SSSR. Fizika Atmosfery i Okeana*, **14**, 1160–1166.

Barrette, N., and R. Laprise, 2005: A one-dimensional model for simulating the vertical transport of dissolved CO_2 and CH_4 in hydroelectric reservoirs. *Greenhouse Gas Emissions: Fluxes, and Processes, Hydroelectric Reservoirs and Natural Environments*, A. Tremblay, L. Varfalvy, C. Roehm, and M. Garneau, Eds., Environmental Science Series, Springer, Berlin–Heidelberg–New York, 575–595.

Bates, G. T, F. Giorgi, and S. W. Hostetler, 1993: Towards the simulation of the effects of the Great Lakes on regional climate. *Mon. Weather Rev.*, **121**, 1373–1387.

Bates, G. T, S. W. Hostetler, and F. Giorgi, 1995: Two-year simulation of the Great Lakes region with a coupled modeling system. *Mon. Weather Rev.*, **123**, 1505–1522.

Blenckner, T., A. Omstedt, and M. Rummukainen, 2002: A Swedish case study of contemporary and possible future consequences of climate change on lake function. *Aquat. Sci.*, **64**, 171–184.

Bonan, G. B., 1995: Sensitivity of a GCM simulation to inclusion of inland water surfaces. *J. Climate*, **8**, 2691–2704.

Brost, R. A., and J. C. Wyngaard, 1978: A model study of the stably stratified planetary boundary layer. *J. Atmos. Sci.*, **35**, 1427–1440.

Deardorff, J. W., 1970a: Preliminary results from numerical integrations of the unstable planetary boundary layer. *J. Atmos. Sci.*, **27**, 1209–1211.

Deardorff, J. W., 1970b: Convective velocity and temperature scales for the unstable planetary boundary layer and for Rayleigh convection. *J. Atmos. Sci.*, **27**, 1211–1213.

Deardorff, J. W., 1971: Rate of growth of the nocturnal boundary layer. Paper presented at Symposium on Air Pollution, Turbulence and Diffusion, Las Cruces, N. M., NCAR ms. No. 71-246.

Deardorff, J. W., 1979: Prediction of convective mixed-layer entrainment for realistic capping inversion structure. *J. Atmos. Sci.*, **36**, 424–436.

Deardorff, J. W., 1983: A multi-limit mixed-layer entrainment formulation. *J. Phys. Oceanogr.*, **13**, 988–1002.

Efimov, S. S., and V. M. Tsarenko, 1980: On a self-similarity of the temperature distribution in the upper thermocline. *Izv. Akad. Nauk SSSR. Fizika Atmosfery i Okeana*, **16**, 620–627.

Ertel, H., 1954: Theorie der thermischen Sprungschiht in Seen. *Acta Hydrophys.*, Bd. 2, 151–171.

Fang, X., and H. G. Stefan, 1996: Dynamics of heat exchange between sediment and water in a lake. *Water Resour. Res.*, **32**, 1719–1727.

Fang, X., and H. G. Stefan, 1998: Temperature variability in lake sediments. *Water Resour. Res.*, **34**, 717–729.

Farmer, D. M., 1975: Penetrative convection in the absence of mean shear. *Quart. J. Roy. Meteorol. Soc.*, **101**, 869–891.

Farmer, D. M., and E. Carmack, 1981: Wind mixing and restratification in a lake near the temperature of maximum density. *J. Phys. Oceanogr.*, **11**, 1516–1533.

Fedorovich, E., R. Conzemius, and D. Mironov, 2004: Convective entrainment into a shear-free, linearly stratified atmosphere: bulk models reevaluated through large eddy simulations. *J. Atmos. Sci.*, **61**, 281–295.

Fedorovich, E. E., and D. V. Mironov, 1995: A model for shear-free convective boundary layer with parameterized capping inversion structure. *J. Atmos. Sci.*, **52**, 83–95.

Filyushkin, B. N., and Yu. Z. Miropolsky, 1981: Seasonal variability of the upper thermocline and self-similarity of temperature profiles. *Okeanologia*, **21**, 416–424.

Golosov, S. D., and K. D. Kreiman, 1992: Heat exchange and thermal structure within "water-sediments" system. *Water Resources (Vodnye Resursy)*, **6**, 92–97.

Golosov, S., I. Zverev, and A. Terzhevik, 1998: *Modelling Thermal Structure and Heat Interaction between a Water Column and Bottom Sediments.* Report No. 3220 [LUTVDG/(TVVR-3220) 1-41(1998)], Dept. of Water Resources Engineering, Inst. of Technology, Univ. of Lund, Lund, Sweden, 41 p.

Goyette, S., N. A. McFarlane, and G. M. Flato, 2000: Application of the Canadian regional climate model to the Laurentian Great Lakes region: implementation of a lake model. *Atmosphere-Ocean*, **38**, 481–503.

Gu, R., and H. G. Stefan, 1990: Year-round temperature simulation of cold climate lakes. *Cold Reg. Sci. Technol.*, **18**, 147–160.

Heise, E., M. Lange, B. Ritter, and R. Schrodin, 2003: Improvement and validation of the multi-layer soil model. *COSMO Newsletter*, No. 3, Consortium for Small-Scale Modelling, Deutscher Wetterdienst, Offenbach am Main, Germany, 198-203.

Hostetler, S. W., 1991: Simulation of lake ice and its effect on the late-Pleistocene evaporation rate of Lake Lahontan. *Clim. Dynam.*, **6**, 43–48.

Hostetler, S. W., and P. J. Bartlein, 1990: Simulation of lake evaporation with application to modeling lake level variations of Harney-Malheur Lake, Oregon. *Water Resour. Res.*, **26**, 2603–2612.

Hostetler, S. W., G. T. Bates, and F. Giorgi, 1993: Interactive coupling of a lake thermal model with a regional climate model. *J. Geophys. Res.*, **98**, 5045–5057.

Hostetler, S. W., and L. V. Benson, 1990: Paleoclimatic implications of the high stand of Lake Lahontan derived from models of evaporation and lake level. *Clim. Dynam.*, **4**, 207–217.

Hostetler, S. W., and F. Giorgi, 1992: Use of a regional atmospheric model to simulate lake-atmosphere feedbacks associated with Pleistocene Lakes Lahontan and Bonneville. *Clim. Dynam.*, **7**, 39–44.

Hostetler, S. W., F. Giorgi, G. T. Bates, and P. J. Bartlein, 1994: Lake-atmosphere feedbacks associated with paleolakes Bonneville and Lahontan. *Science*, **263**, 665–668.

Imberger, J., 1985: The diurnal mixed layer. *Limnol. Oceanogr.*, **30**, 737–770.

Jonas, T., A. Y. Terzhevik, D. V. Mironov, and A. Wüest, 2003: Investigation of radiatively-driven convection in an ice covered lake using temperature microstructure technique. *J. Geophys. Res.*, **108**, 14-1–14-18.

Kamenkovich, V. M., and B. V. Kharkov, 1975: On the seasonal variation of the thermal structure of the upper layer in the ocean. *Okeanologia*, **15**, 978–987.

Khakimov, I. R., 1976: The wind profile in the neutrally stratified atmospheric boundary layer. *Izv. Akad. Nauk SSSR. Fizika Atmosfery i Okeana*, **12**, 628–630.

Kharkov, B. V., 1977: On the structure of the upper ocean layer. *Okeanologia*, **17**, 37–43.

Kim, J.-W., 1976: A generalized bulk model of the oceanic mixed layer. *J. Phys. Oceanogr.*, **6**, 686–695.

Kirillin, G., 2001a: On self-similarity of thermocline in shallow lakes. *Proc. 6th Workshop on Physical Processes in Natural Waters*, X. Casamitjana, Ed., University of Girona, Girona, Spain, 221–225.

Kirillin, G., 2001b: On a self-similarity of the pycnocline. *Proc. 2001 International Symposium on Environmental Hydraulics*, Arizona State University, Tempe, Arizona, USA.

Kitaigorodskii, S. A., 1960: On the computation of the thickness of the wind-mixing layer in the ocean. *Izv. AN SSSR. Ser. geofiz.*, No. 3, 425–431.

Kitaigorodskii, S. A., 1970: *The Physics of Air-Sea Interaction.* Gidrometeoizdat, Leningrad, 284 p. (In Russian. English translation: Israel Progr. Scient. Translation, Jerusalem, 1973, 236 p.)

Kitaigorodskii, S. A., and S. M. Joffre, 1988: In search of simple scaling for the heights of the stratified atmospheric boundary layer. *Tellus*, **40A**, 419–433.

Kitaigorodskii, S. A., and Yu. Z. Miropolsky, 1970: On the theory of the open ocean active layer. *Izv. Akad. Nauk SSSR. Fizika Atmosfery i Okeana*, **6**, 178–188.

Kondratiev, S. A., S. D. Golosov, K. D. Kreiman, and N. V. Ignatieva, 1998: Modelling hydrological processes and mass transfer in a watershed-lake system. *Water Resources (Vodnye Resursy)*, **25**, 571–580.

Kraus, E. B., and C. Rooth, 1961: Temperature and steady state vertical heat flux in the ocean surface layer. *Tellus*, **13**, 231–238.

Launiainen, J., and B. Cheng, 1998: Modelling of ice thermodynamics in natural water bodies. *Cold. Reg. Sci. Technol.*, **27**, 153–178.

León, L. F., D. Lam, W. Schertzer, and D. Swayne, 2005: Lake and climate models linkage: a 3-D hydrodynamic contribution. *Advances in Geosciences*, **4**, 57–62.

León, L. F., D. C. L. Lam, W. M. Schertzer, D. A. Swayne, and J. Imberger, 2007: Towards coupling a 3D hydrodynamic lake model with the Canadian Regional Climate Model: Simulation on Great Slave Lake. *Environ. Modell. Softw.*, **22**, 787–796.

Leppäranta, M., 1993: A review of analytical models of sea-ice growth. *Atmosphere-Ocean*, **31**, 123–138.

Linden, P. F., 1975: The deepening of a mixed layer in a stratified fluid. *J. Fluid Mech.*, **71**, 385–405.

Ljungemyr, P., N. Gustafsson, and A. Omstedt, 1996: Parameterization of lake thermodynamics in a high-resolution weather forecasting model. *Tellus*, **48A**, 608–621.

Long, R. R., 1974: Mean stress and velocities in the neutral, barotropic planetary boundary layer. *Boundary-Layer Meteorol.*, **7**, 475–487.

Long, Z., W. Perrie, J. Gyakum, D. Caya, and R. Laprise, 2007: Northern lake impacts on local seasonal climate. *J. Hydrometeorology*, **8**, 881–896.

MacKay, M. D., 2005: Regional climate impacts of small lakes: a sub-gridscale lake model for CLASS. *Proc. 15th International Northern Research Basins Symposium and Workshop*, A. Semadeni-Davies, L. Bengtsson, and G. Westerström, Eds., Dept. of Water Resources Engineering, Lund University, Lund, Sweden, and Environmental Engineering Dept., Luleå University of Technology, Luleå, Sweden, 121–130.

Mälkki, P., and R. E. Tamsalu, 1985: Physical Features of the Baltic Sea. *Finnish Marine Research*, No. 252, Helsinki, 110 p.

Mironov, D. V., 1990: On the calculation of the temperature profile in a fresh-water thermocline. *Izv. Akad. Nauk SSSR. Fizika Atmosfery i Okeana*, **26**, 880–883.

Mironov, D. V., 1992: A one-dimensional parameterised model for the evolution of the temperature profile and mixing conditions in a lake. *Lake Ladoga – Criteria of the Ecosystem State*, N. A. Petrova and A. Yu. Terzhevik, Eds., "Nauka" Publishing House, St. Petersburg, 36–41.

Mironov, D. V., 1999: *The SUBMESO Meteorological Preprocessor. Physical Parameterisations and Implementation.* Technical Note, Laboratoire de Mécanique des Fluides UMR CNRS 6598, Ecole Centrale de Nantes, Nantes, France. 25 p.

Mironov, D. V., and E. Fedorovich, 2008: Effect of the Earth's rotation on the equilibrium depth of a stably stratified barotropic planetary boundary layer. 18th Symposium on Boundary Layers and Turbulence 9-13 June 2008, Stockholm, Sweden, manuscript 16B.1.

Mironov, D. V., S. D. Golosov, S. S. Zilitinkevich, K. D. Kreiman, and A. Yu. Terzhevik, 1991: Seasonal changes of temperature and mixing conditions in a lake. *Modelling Air-Lake Interaction. Physical Background*, S. S. Zilitinkevich, Ed., Springer-Verlag, Berlin, etc., 74–90.

Mironov, D. V., S. D. Golosov, and I. S. Zverev, 2003: Temperature profile in lake bottom sediments: an analytical self-similar solution. *Proc. 7th Workshop on Physical Processes in Natural Waters*, A. Yu. Terzhevik, Ed., Northern Water Problems Institute, Russian Academy of Sciences, Petrozavodsk, Karelia, Russia, 90–97.

Mironov, D. V., and L. N. Karlin, 1989: Penetrative convection due to surface cooling with vertically distributed heating. *Dokl. Akad. Nauk SSSR.*, **309**, 1336–1340.

Mironov, D., and B. Ritter, 2004: A New Sea Ice Model for GME. Technical Note, Deutscher Wetterdienst, Offenbach am Main, Germany, 12 p.

Mironov, D. V., and A. Yu. Terzhevik, 2000: Spring convection in ice-covered fresh-water lakes. *Izv. Akad. Nauk SSSR. Fizika Atmosfery i Okeana*, **36**, 627–634.

Mironov, D., A. Terzhevik, G. Kirillin, T. Jonas, J. Malm, and D. Farmer, 2002: Radiatively driven convection in ice-covered lakes: Observations, scaling, and a mixed layer model. *J. Geophys. Res.*, **107**, 7-1–7-16.

Miropolsky, Yu. Z., 1970: Non-stationary model of the wind-convection mixing layer in the ocean. *Okeanologia*, **6**, 1284–1294.

Miropolsky, Yu. Z., B. N. Filyushkin, and P. P. Chernyshkov, 1970: On the parametric description of temperature profiles in the active ocean layer. *Okeanologia*, **10**, 1101–1107.

Munk, W. H., and E. R. Anderson, 1948: Notes on a theory of the thermocline. *J. Marine Res.*, **7**, 276–295.

Nesterov, E. S., and V. I. Kalatsky, 1975: Parameterisation of the vertical temperature profile in the active layer in North Atlantic. *Trudy Gidrometzentra SSSR (Proc. Hydrometeorological Centre of the USSR)*, No. 161, 35–39.

Omstedt, A., 1999: Forecasting ice on lakes, estuaries and shelf seas. *Ice Physics and the Natural Environment*, Edited by J. S. Wettlaufer, J. G. Dash, and N. Untersteiner, Eds., NATO ASI Series, Vol. I 56, Springer, Berlin–Heidelberg, 185–207.

Omstedt, A., and L. Nyberg, 1996: Response of Baltic Sea ice to seasonal, interannual forcing and to climate change. *Tellus*, **4BA**, 644–662.

Otte, M. J., and J. C. Wyngaard, 2001: Stably stratified interfacial-layer turbulence from large-eddy simulation. *J. Atmos. Sci.*, **58**, 3424–3442.

Pénelon, T., I. Calmet, and D. V. Mironov, 2001: Micrometeorological simulation over a complex terrain with SUBMESO: a model study using a novel pre-processor. *Int. J. Envir. and Pollution*, **16**, 583–602.

Pollard, R. T., P. B. Rhines, and R. O. R. Y. Thompson, 1973: The deepening of the wind-mixed layer. *Geophys. Fluid Dyn.*, **3**, 381–404.

Price, J. F., R. A. Weller, and R. Pinkel, 1986: Diurnal cycling: observations and models of the upper ocean response to diurnal heating. *J. Geophys. Res.*, **91**, 8411–8427.

Randall, D. A., and B. A. Wielicki, 1997: Measurements, models, and hypotheses in the atmospheric sciences. *Bull. Amer. Met. Soc.*, **78**, 399–406.

Reshetova, O. V., and D. V. Chalikov, 1977: On the universal structure of the active layer in the ocean. *Okeanologia*, **17**, 774–777.

Rossby, C. G., and R. B. Montgomery, 1935: The layer of frictional influence in wind and ocean currents. *Pap. Phys. Oceanogr. Meteorol.*, **3**, 1–101. (M.I.T. and Woods Hole Oceanogr. Inst.)

Ryanzhin, S. V., 1997: *Thermophysical Properties of Lake Sediments and Water-Sediments Heat Interaction.* Report No. 3214, Dept. of Water Resources Engineering, Inst. of Technology, Univ. of Lund, Lund, Sweden, 95 p.

Shapiro, G. I., 1980: Effect of fluctuations in the turbulent entrainment layer on the heat and mass transfer in the upper thermocline. *Izv. Akad. Nauk SSSR. Fizika Atmosfery i Okeana*, **16**, 433–436.

Small, E. E., L. C. Sloan, S. Hostetler, and F. Giorgi, 1999: Simulating the water balance of the Aral Sea with a coupled regional climate-lake model. *J. Geophys. Res.*, **104**, 6583–6602.

Soloviev, A. V., 1979: Fine thermal structure of the ocean surface layer in the POLYMODE-77 region. *Izv. Akad. Nauk SSSR. Fizika Atmosfery i Okeana*, **15**, 750–757.

Soloviev, A. V., and N. V. Vershinskii, 1982: The vertical structure of the thin surface layer of the ocean under conditions of low wind speed. *Deep-Sea Res.*, **29**, 1437–1449.

Song, Y., F. H. M. Semazzi, L. Xie, and L. J. Ogallo, 2004: A coupled regional climate model for the Lake Victoria basin of East Africa. *Int. J. Climatol.*, **24**, 57–75.

Spigel, R. H., J. Imberger, and K. N. Rayner, 1986: Modeling the diurnal mixed layer. *Limnol. Oceanogr.*, **31**, 533–556.

Stefan, J., 1891: Ueber die Theorie der Eisbildung, insbesondere über die Eisbildung im Polarmeere. *Ann. Phys.*, **42**, 269–286.

Stepanenko, V. M., 2005: Numerical modeling of thermal regime of shallow lakes. *Computational Technologies*, **10**, 100–106.

Stepanenko, V. M., P. M. Miranda, and V. N. Lykosov, 2006: Numerical modeling of mesoscale interaction between atmosphere and hydrologically heterogeneous land. *Computational Technologies*, **11**, 118–127.

Tamsalu, R., and K. Myrberg, 1998: A theoretical and experimental study of the self-similarity concept. *MERI, Report Series of the Finnish Institute of Marine Research*, No. 37, 3–13.

Tamsalu, R., P. Mälkki, and K. Myrberg, 1997: Self-similarity concept in marine system modelling. *Geophysica*, **33**, 51–68.

Tsuang, B.-J., C.-Y. Tu, and K. Arpe, 2001: *Lake Parameterization for Climate Models.* Report No. 316 (ISSN 0937-1060), Max-Planck-Institut für Meteorologie, Hamburg, Germany, 72 p.

Turner, J. S., 1978: The temperature profile below the surface mixed layer. *Ocean Modeling*, No. 11, 6–8.

Voropaev, S. I., 1977: Laboratory modelling of the mixing process in a stratified fluid. *Proc. 1st Soviet Oceanography Congress*, Moscow, 20–25 June 1977, No. 1, *Oceanic Physics, Marine Technology*, p. 81.

Wyatt, L. R., 1978: Mixed layer development in an annular tank. *Ocean Modeling*, No. 17, 6–8.

Zeman, O., 1979: Parameterization of the dynamics of stable boundary layers and nocturnal jets. *J. Atmos. Sci.*, **36**, 792–804.

Zeman, O., and H. Tennekes, 1977: Parameterization of the turbulent energy budget at the top of the daytime atmospheric boundary layer. *J. Atmos. Sci.*, **34**, 111–123.

Zilitinkevich, S. S., 1972: On the determination of the height of the Ekman boundary layer. *Boundary-Layer Meteorol.*, **3**, 141–145.

Zilitinkevich, S. S., 1975: Comments on "A Model for the Dynamics of the Inversion Above a Convective Boundary Layer". *J. Atmos. Sci.*, **32**, 991–992.

Zilitinkevich, S. S., 1989a: Velocity profiles, resistance law and dissipation rate of mean flow kinetic energy in a neutrally and stably stratified planetary boundary layer. *Boundary-Layer Meteorol.*, **46**, 367–387.

Zilitinkevich, S. S., 1989b: Temperature profile and heat transfer law in neutrally and stably stratified planetary boundary layer. *Boundary-Layer Meteorol.*, **46**, 367–387.

Zilitinkevich, S. S., 1991: *Turbulent Penetrative Convection.* Avebury Technical, Aldershot, 179 p.

Zilitinkevich, S., and A. Baklanov, 2002: Calculation of the height of the stable boundary layer in practical applications. *Boundary-Layer Meteorol.*, **105**, 389–409.

Zilitinkevich, S., A. Baklanov, J. Rost, A.-S. Smedman, V. Lykosov, and P. Calanca, 2002: Diagnostic and prognostic equations for the depth of the stably stratified Ekman boundary layer. *Quart. J. Roy. Meteorol. Soc.*, **128**, 25–46.

Zilitinkevich, S. S., D. V. Chalikov, and Yu. D. Resnyansky, 1979: Modelling the oceanic upper layer. *Oceanologica Acta*, **2**, 219–240.

Zilitinkevich, S., and I. Esau, 2002: On the integral measures of the neutral barotropic planetary boundary layer. *Boundary-Layer Meteorol.*, **104**, 371–379.

Zilitinkevich, S., and I. Esau, 2003: The effect of baroclinicity on the depth of neutral and stable planetary boundary layers. *Quart. J. Roy. Meteorol. Soc.*, **129**, 3339–3356.

Zilitinkevich, S., I. Esau, and A. Baklanov, 2007: Further comments on the equilibrium height of neutral and stable planetary boundary layers. *Quart. J. Roy. Meteorol. Soc.*, **133**, 265–271.

Zilitinkevich, S. S., E. E. Fedorovich, and D. V. Mironov, 1992: Turbulent heat transfer in stratified geophysical flows. *Recent Advances in Heat Transfer*, B. Sundén and A. Žukauskas, Eds., Elsevier Science Publisher B. V., Amsterdam, etc., 1123–1139.

Zilitinkevich, S. S., K. D. Kreiman, and A. I. Felzenbaum, 1988: Turbulence, heat exchange and self-similarity of the temperature profile in a thermocline. *Dokl. Akad. Nauk SSSR.*, **300**, 1226–1230.

Zilitinkevich, S. S., and D. V. Mironov, 1989: A theoretical model of thermocline evolution in a fresh-water basin. *Izv. Akad. Nauk SSSR. Fizika Atmosfery i Okeana*, **25**, 969–978.

Zilitinkevich, S. S., and D. V. Mironov, 1992: Theoretical model of the thermocline in a freshwater basin. *J. Phys. Oceanogr.*, **22**, 988–996.

Zilitinkevich, S. S., and D. V. Mironov, 1996: A multi-limit formulation for the equilibrium depth of a stably stratified boundary layer. *Boundary-Layer Meteorol.*, **81**, 325–351.

Zilitinkevich, S. S., and V. A. Rumyantsev, 1990: A parameterized model of the seasonal temperature changes in lakes. *Environ. Softw.*, **5**, 12–25.

List of COSMO Newsletters and Technical Reports

(available for download from the COSMO Website: www.cosmo-model.org)

COSMO Newsletters

No. 1: February 2001.

No. 2: February 2002.

No. 3: February 2003.

No. 4: February 2004.

No. 5: April 2005.

No. 6: July 2006; Proceedings from the COSMO General Meeting 2005.

No. 7: July 2007; Proceedings from the COSMO General Meeting 2006.

No. 8: August 2007; Proceedings from the COSMO General Meeting 2007.

COSMO Technical Reports

No. 1: Dmitrii Mironov and Matthias Raschendorfer (2001):
Evaluation of Empirical Parameters of the New LM Surface-Layer Parameterization Scheme. Results from Numerical Experiments Including the Soil Moisture Analysis.

No. 2: Reinhold Schrodin and Erdmann Heise (2001):
The Multi-Layer Version of the DWD Soil Model TERRA_LM.

No. 3: Günther Doms (2001):
A Scheme for Monotonic Numerical Diffusion in the LM.

No. 4: Hans-Joachim Herzog, Ursula Schubert, Gerd Vogel, Adelheid Fiedler and Roswitha Kirchner (2002):
LLM ¯ the High-Resolving Nonhydrostatic Simulation Model in the DWD-Project LITFASS.
Part I: Modelling Technique and Simulation Method.

No. 5: Jean-Marie Bettems (2002):
EUCOS Impact Study Using the Limited-Area Non-Hydrostatic NWP Model in Operational Use at MeteoSwiss.

No. 6: Heinz-Werner Bitzer and Jürgen Steppeler (2004):
Documentation of the Z-Coordinate Dynamical Core of LM.

No. 7: Hans-Joachim Herzog, Almut Gassmann (2005):
Lorenz- and Charney-Phillips vertical grid experimentation using a compressible nonhydrostatic toy-model relevant to the fast-mode part of the 'Lokal-Modell'.

No. 8: Chiara Marsigli, Andrea Montani, Tiziana Paccagnella, Davide Sacchetti, André Walser, Marco Arpagaus, Thomas Schumann (2005):
Evaluation of the Performance of the COSMO-LEPS System.

No. 9: Erdmann Heise, Bodo Ritter, Reinhold Schrodin (2006):
Operational Implementation of the Multilayer Soil Model.

No. 10: Mikhail D. Tsyrulnikov (2007):
Is the particle filtering approach appropriate for meso-scale data assimilation?

No. 11: Dmitrii V. Mironov (2008):
Parameterization of Lakes in Numerical Weather Prediction. Description of a Lake Model.

COSMO Technical Reports

Issues of the COSMO Technical Reports series are published by the *COnsortium for Small-scale MOdelling* at non-regular intervals. COSMO is a European group for numerical weather prediction with participating meteorological services from Germany (DWD, AWGeophys), Greece (HNMS), Italy (USAM, ARPA-SIM, ARPA Piemonte), Switzerland (MeteoSwiss), Poland (IMGW), Romania (NMA), and Russia (ROSHYDROMET). The general goal is to develop, improve and maintain a non-hydrostatic limited area modelling system to be used for both operational and research applications by the members of COSMO. This system is initially based on the COSMO-Model (previously known as LM) of DWD with its corresponding data assimilation system.

The Technical Reports are intended

- for scientific contributions and a documentation of research activities,
- to present and discuss results obtained from the model system,
- to present and discuss verification results and interpretation methods,
- for a documentation of technical changes to the model system,
- to give an overview of new components of the model system.

The purpose of these reports is to communicate results, changes and progress related to the COSMO-Model relatively fast within the COSMO consortium, and also to inform other NWP groups on our current research activities. In this way the discussion on a specific topic can be stimulated at an early stage. In order to publish a report very soon after the completion of the manuscript, we have decided to omit a thorough reviewing procedure and only a rough check is done by the editors and a third reviewer. We apologize for typographical and other errors or inconsistencies which may still be present.

At present, the Technical Reports are available for download from the COSMO web site (www.cosmo-model.org). If required, the member meteorological centres can produce hard-copies by their own for distribution within their service. All members of the consortium will be informed about new issues by email.

For any comments and questions, please contact the editors:

Massimo Milelli
Massimo.Milelli@arpa.piemonte.it

Ulrich Schättler
Ulrich.Schaettler@dwd.de

Consortium for Small-Scale Modelling

Technical Report No. 41

Performance On Massively Parallel Architectures (POMPA): Final report

February 2020

DOI: 10.5676/DWD_pub/nwv/cosmo-tr_41

Deutscher Wetterdienst
MeteoSwiss
Ufficio Generale Spazio Aereo e Meteorologia
ΕΘΝΙΚΗ ΜΕΤΕΩΡΟΛΟΓΙΚΗ ΥΠΗΡΕΣΙΑ
Instytucie Meteorogii i Gospodarki Wodnej
Administratia Nationala de Meteorologie
ROSHYDROMET
Agenzia Regionale Protezione Ambiente Piemonte
Agenzia Regionale Prevenzione Ambiente Energia Emilia Romagna
Centro Italiano Ricerche Aerospaziali
Amt für GeoInformationswesen der Bundeswehr
Israel Meteorological Service

www.cosmo-model.org

Editor: Massimo Milelli, ARPA Piemonte

Performance On Massively Parallel Architectures

(POMPA): Final report

Project leaders:

X. Lapillonne[1], ***O. Fuhrer***[1‡]

[1] MeteoSwiss

[‡] from 2010 to 2015

Contents

1 Introduction 3

2 Main achievements 4

3 Applications of the GPU and single precision capability 7

4 Lessons learned and outlook 7

Executive summary

Efficient use of high-performance computing (HPC) systems is key to enable higher resolution, larger computational domains, more complex physical parametrizations, or more ensemble members. Due to the end of Moore's Law, HPC systems achieve higher performance via a massive increase in processor cores accompanied by a stagnant or decreasing clock frequency and by employing specialized hardware such as GPUs. The main outcomes of this project are a GPU-capable version of the COSMO model and the possibility to run the model in single precision. Both developments have been merged into the official release of the model and are already in use by several members of the COSMO community. The port to GPU was achieved by using a domain-specific language (DSL) for the dynamics and OpenACC compiler directives for the other components of the model. The resulting code is about a factor 3-4x faster on current state-of-the-art GPUs as compare to traditional multi-core CPUs.

1 Introduction

Numerical weather prediction can greatly benefit from progress in computational technology by increasing resolution, model complexity or the number of ensemble members in probabilistic prediction system. In the recent years, performance increase in hardware stems from massive increase in the number of processing units (cores) and specialized hardware such as Graphics Processing Units (GPUs). In order to benefit from current hardware, scientific models need to be adapted. The aim of the POMPA project was to prepare the COSMO model for these hardware architectures and render it performance portable across architectures. The project leveraged efforts from the High Performance and High Productivity Computing (HP2C) initiative and the Platform for Advanced Scientific Computing (PASC) in Switzerland which addressed these challenges.

The following actions were planned in the project:

- Holistic performance analysis and documentation (Task 1)
- Improve generic scalability of the current model implementation:
  - Redesign memory layout and data structures for better cache awareness and easier load-balancing (Task 2)
  - Optimization of current parallelization and introduction of a hybrid parallelization employing MPI and OpenMP (Task 3)
  - Improve performance of I/O (Task 4)
  - Develop a switchable singe/double precision model version (Task 8)
- Explore emerging technologies:
  - Design a new implementation of the dynamical core optimized for multi-core processors and GPUs (Task 5)
  - Re-engineering the implementation of the physical parametrizations (Task 6)
  - Develop a GPU-capable version of COSMO (Task 7)

This report provides only a general overview of the main outcomes of the POMPA project, while further details can be found in several papers and reports published during this project

which are referenced thereafter in particular. In Sec. 2 we discuss main achievements of the projects associated with the different tasks. In Sec. 3 we present the lessons learned during this work and finally some overview and recommendation for future work are discussed.

2 Main achievements

The performance analysis of the model (Task 1) shows that for a typical application most of the computational time (60%) is spend in the dynamical core, which only represents a relatively small fraction of the code (20%), see Fig. 1. Most of the optimizations therefore focused on this part and a re-write using a Domain Specific Language (DSL) was considered.

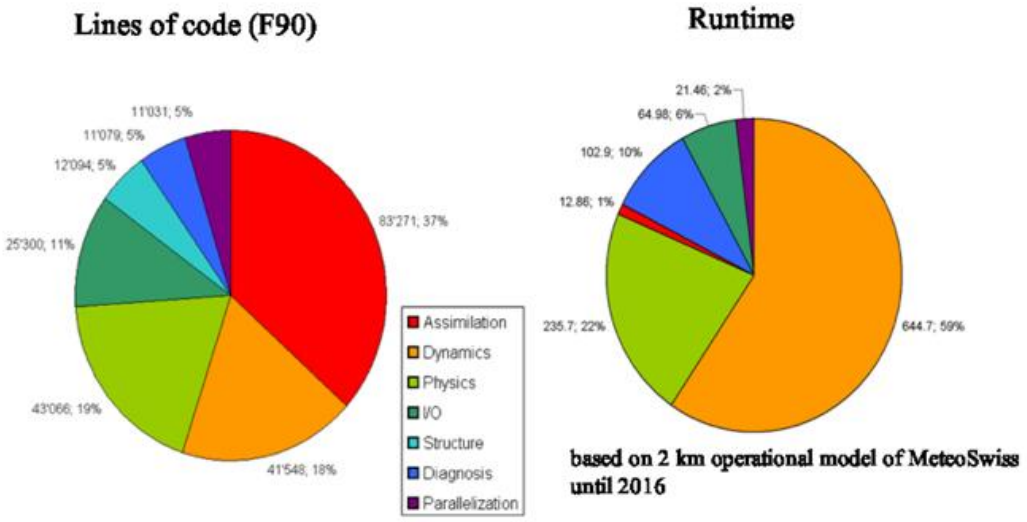


Figure 1: COSMO components timing.

The DSL approach allows a separation of concerns between the user code and the hardware specific optimizations which are implemented in a so-called back-end. A given user code is in principle portable to and efficient on all architectures supported by the library that implements the DSL. The COSMO dynamical core was re-written using the STELLA Library which was developed as part of the project and for which an x86 CPU and a GPU back-end have been implemented. A detailed description of the STELLA library can be found in [Gysi 2015]. The CPU back-end employs OpenMP for threading (Task 3 and 5) while the GPU back-end relies on the CUDA language (Task 5). The specific data storage layout is hidden from the STELLA user allowing to change the underlying data structures for optimal performance on a given target hardware architecture (Task 2). Furthermore the library relies heavily on cache optimizations (Task 2).

For an application such as COSMO which has low compute intensity, i.e. low number of floating-point operations as compared to memory accesses, having only the dynamical core running on GPU is not a performant solution for running on an hybrid GPU system. This would indeed require costly synchronization between the host CPU and the GPU at every time steps which would counteract all performance gains obtained by using GPUs. It was therefore decided to adopt a so-called full GPU port strategy which means that every component of the model reading or writing three dimensional fields needs to run on the GPU see Fig. 2. The dynamics and communication are ported to GPU using the DSL while a

compiler-based directive approach OpenACC (Task 7) is considered [Lapillonne 2014]. A detailed description of the COSMO GPU port can be found in [Fuhrer 2014].

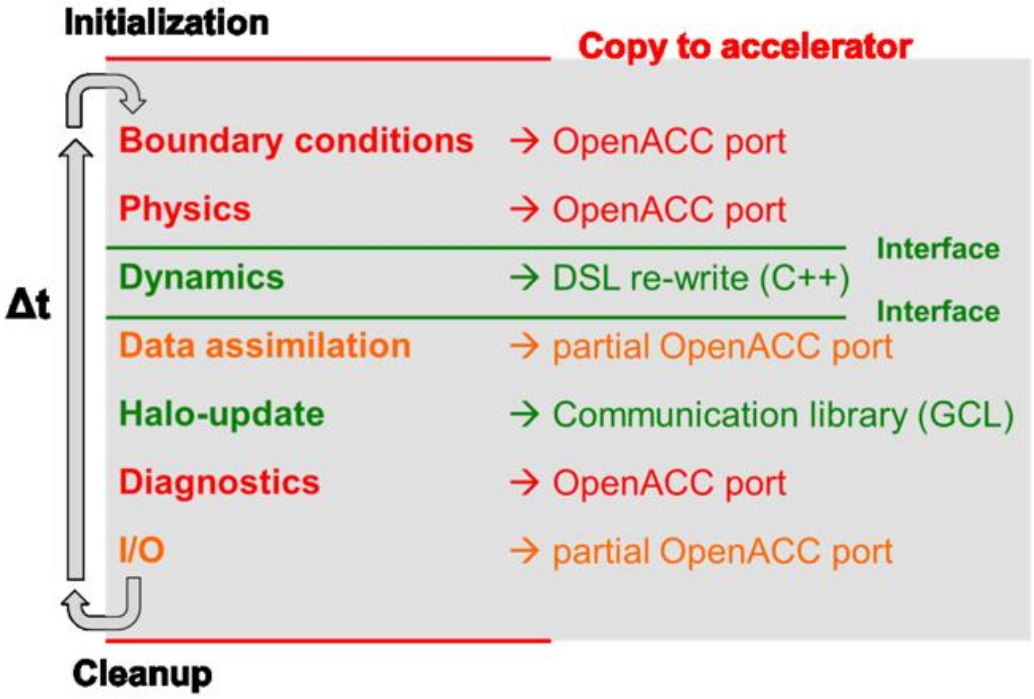


Figure 2: COSMO time loop. Full GPU port strategy.

The GPU capability of COSMO are available from COSMO version 5.6 on for the COSMO community. When comparing the runtime of COSMO on CPU and GPUs of similar generation the code runs typically 3 to 5 time faster on GPU (Fig. 3).

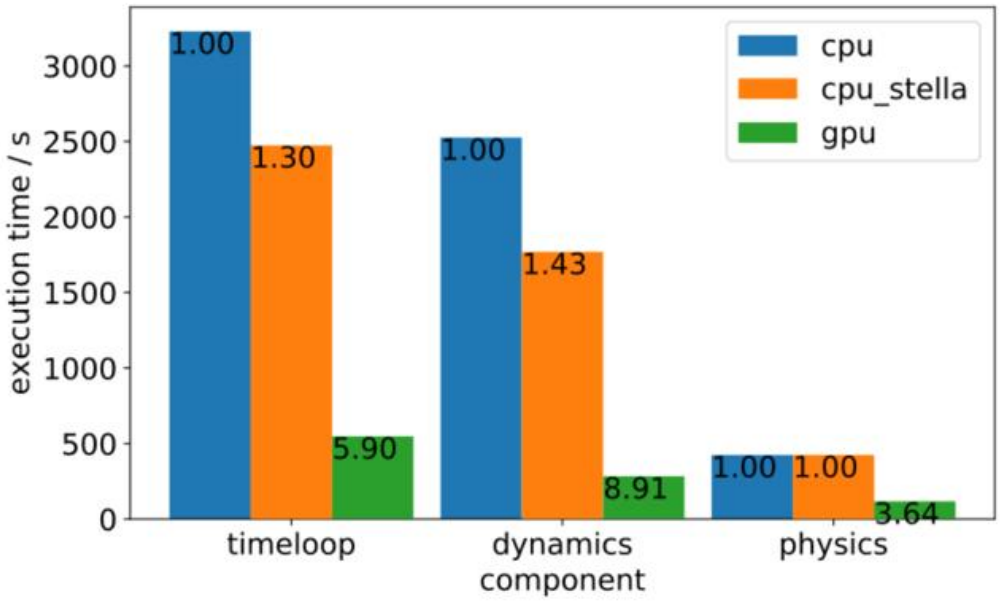


Figure 3: Performance comparison of a COSMO-1 6h benchmark on Piz Daint supercomputer. The CPU benchmark is run on 32 Intel Haswell (12 cores - Xeon E5-2690 v3) CPUs while the GPU is run using 32 P100 Nvidia cards. The speedup as compared to the reference Fortran code (i.e. without the DSL dynamics) is given inside the bars. The code used is COSMO 5.6 release-candidate.

In parallel to the GPU port, the physical parametrizations have been restructured to be shared with the ICON model using a block format (Task 6). This can in principle improve performance on CPU since it could increase cache reuse between the different parametrizations. This gain is however counterbalanced by the fact that one needs to copy the input and output data from the original ijk COSMO data structure to the block format. This change has a neutral effect on performance, but allows to share physics between the ICON and COSMO model.

The COSMO code was furthermore adapted to run using single precision floating point number (Task 8), in addition to double precision. A detailed description of the required adaptation can be found in [Rudisuhli 2014]. This provides an additional performance improvement ranging from a speed up factor of 1.2x to 1.3x depending on the architecture.

Finally, although the C++ dynamical core is making use of OpenMP parallelization on CPU, the rest of the code also had to be ported to OpenMP (Task 3). As compared to a flat MPI parallelization, introducing threading using OpenMP in the Fortran part did not lead to significant performance improvements. Unless more aggressive optimizations such as blocking would be introduced in the Fortran code (which would significantly reduce the maintainability and readability of the code), it was to be expected that a memory bandwidth bound code would not yield significant performance improvements. As a consequence, the changes introduced for hybrid MPI+OpenMP parallelism were not prioritized high enough to be introduced into the official version of the COSMO code.

3 Applications of the GPU and single precision capability

The COSMO model is run operationally at MeteoSwiss on GPU-based hardware and in single precision since 2016. The high performance computing system employs a fat-node design with multiple GPUs per CPU socket. From the operational point of view the use of a GPU system did not bring new issues, and the system is running stably as compared to the previous CPU only operational system. Currently, the system is being upgraded by a system with a similar fat node design but latest-generation hardware. The COSMO-LEPS ensemble forecast run at ECMWF is running in single precision, the performance gain associated with switching from single precision to double precision has enabled to run more ensemble members. Several groups at ETH Zurich are running the COSMO model on GPUs for climate applications on the Piz Daint supercomputer. This allowed researchers to run high-resolution (2-km) simulations on continental scale domain [Leutwyler 2016]

4 Lessons learned and outlook

With the advent of GPU-accelerated systems, the days where vendors would port applications to a specific hardware architecture within the framework of a procurement benchmark are over and the load of maintaining a code base that is ready to run on different hardware architectures has been shifted to the code maintainers and developers. Since hardware architectures are evolving rapidly and the lifetime of a supercomputer typically is between 3-6 years, this requires a tight collaboration with institutions and individuals who have an in-depth understanding of and outlook on developments in the HPC hardware sector.

As a side effect of this project the development infrastructure of COSMO has been greatly improved. The GPU as well as single/double precision capability of the model have increased the maintenance complexity, such that manual testing is not an option anymore. The Jenkins continuous integration platform is now being used to automatically test the main source code as well as development branches on all supported hardware architectures and floating point precision using the COSMO technical testsuite. The code is now hosted on the development infrastructure github which provides a modern interface for software development and in particular allows for online code reviews. Without these tools, the project could not have been such a success, and this type of infrastructure and workflow should be used in the future in the COMO community.

For the port to GPUs different technologies have been used. The OpenACC compiler directives have proven to be very efficient for incrementally porting large existing code bases. It also has the advantage of being moderately intrusive, as compared to a full re-write, and is well accepted by the developer community. On the other hand, adding directives to an existing legacy code make the code much harder to maintain. Indeed, several targets need now to be supported but the Fortran code does not provide component or unit testing functionality such that bugs introduced with changes or associated to a new compiler version require considerable amount of time to be identified. Further, the OpenACC programming model has proven not to be very robust, with the few compilers that support it introducing regressions when new versions come out. Cray has decided to drop support for OpenACC in the future and thus currently the only compiler supporting OpenACC is the PGI compiler owned by NVIDIA. An alternative implementation of OpenACC exists in GCC, but is not in a state that can be used for production. For some components, optimizations for GPU have adverse effects on CPU performance such that either the CPU performance has been given priority, or separate code for GPU has been introduced using ifdef pre-processor macro.

For the most critical component ported with OpenACC a source-to-source translation tool CLAW [Clement 2018], doing automatic code transformation, has been also used.

The STELLA DSL approach has proven successful to achieve performance portability. However, the project has shown that acceptance of this new technology by the end user (dycore developer) is very limited. In fact, there are currently two versions of the COSMO dynamical core in the official code, namely the Fortran and the DSL version. One possible reason for this is that the resulting C++ code is rather complex to handle for someone used to pure Fortran code. In addition, because of time constraints on both the DSL developer and end dycore user the exchange while developing the library was very limited, such that the final product did not meet the expectation of the end user. For a future project we recommend more focus and the usability of such a DSL approach as well as a better integration between the DSL developers and the end-users.

References

Clement, V., Ferrachat, S., Fuhrer, O., Lapillonne, X., Osuna, C. E., Pincus, R., ... & Sawyer, W. (2018, July). The CLAW DSL: Abstractions for Performance Portable Weather and Climate Models. In Proceedings of the Platform for Advanced Scientific Computing Conference (p. 2). ACM

Fuhrer, O., Osuna, C., Lapillonne, X., Gysi, T., Cumming, B., Bianco, M., Arteaga, A. and Schulthess, T.C., 2014. Towards a performance portable, architecture agnostic implementation strategy for weather and climate models. Supercomputing frontiers and innovations, 1(1), pp.45-62

Gysi, T., Osuna, C., Fuhrer, O., Bianco, M. and Schulthess, T.C., 2015, November. STELLA: a domain-specific tool for structured grid methods in weather and climate models. In Proceedings of the International Conference for High Performance Computing, Networking, Storage and Analysis (p. 41). ACM

Lapillonne, X., Fuhrer, O. (2014). Using compiler directives to port large scientific applications to GPUs: An example from atmospheric science. Parallel Processing Letters, 24(01), 1450003

Leutwyler, D., Fuhrer, O., Lapillonne, X., Lüthi, D., Schär, C. (2016). Towards European-scale convection-resolving climate simulations with GPUs: a study with COSMO 4.19. Geoscientific Model Development, 9(9), 3393-3412

Rudisuhli, S., Walser, A., Fuhrer, O. 2014, COSMO in Single Precision, COSMO Newsletter no. 14, p.18, www.cosmo-model.org

List of COSMO Newsletters and Technical Reports

(available for download from the COSMO Website: www.cosmo-model.org)

COSMO Newsletters

No. 1: February 2001.

No. 2: February 2002.

No. 3: February 2003.

No. 4: February 2004.

No. 5: April 2005.

No. 6: July 2006.

No. 7: April 2008; Proceedings from the 8th COSMO General Meeting in Bucharest, 2006.

No. 8: September 2008; Proceedings from the 9th COSMO General Meeting in Athens, 2007.

No. 9: December 2008.

No. 10: March 2010.

No. 11: April 2011.

No. 12: April 2012.

No. 13: April 2013.

No. 14: April 2014.

No. 15: July 2015.

No. 16: July 2016.

No. 17: July 2017.

No. 18: November 2018.

No. 19: October 2019.

COSMO Technical Reports

No. 1: Dmitrii Mironov and Matthias Raschendorfer (2001):
Evaluation of Empirical Parameters of the New LM Surface-Layer Parameterization Scheme. Results from Numerical Experiments Including the Soil Moisture Analysis.
DOI: 10.5676/DWD_pub/nwv/cosmo-tr_1

No. 2: Reinhold Schrodin and Erdmann Heise (2001):
The Multi-Layer Version of the DWD Soil Model TERRA_LM.
DOI: 10.5676/DWD_pub/nwv/cosmo-tr_2

No. 3: Günther Doms (2001):
A Scheme for Monotonic Numerical Diffusion in the LM.
DOI: 10.5676/DWD_pub/nwv/cosmo-tr_3

No. 4: Hans-Joachim Herzog, Ursula Schubert, Gerd Vogel, Adelheid Fiedler and Roswitha Kirchner (2002):
LLM ¯ the High-Resolving Nonhydrostatic Simulation Model in the DWD-Project LITFASS. Part I: Modelling Technique and Simulation Method.
DOI: 10.5676/DWD_pub/nwv/cosmo-tr_4

No. 5: Jean-Marie Bettems (2002):
EUCOS Impact Study Using the Limited-Area Non-Hydrostatic NWP Model in Operational Use at MeteoSwiss.
DOI: 10.5676/DWD_pub/nwv/cosmo-tr_5

No. 6: Heinz-Werner Bitzer and Jürgen Steppeler (2004):
Documentation of the Z-Coordinate Dynamical Core of LM.
DOI: 10.5676/DWD_pub/nwv/cosmo-tr_6

No. 7: Hans-Joachim Herzog, Almut Gassmann (2005):
Lorenz- and Charney-Phillips vertical grid experimentation using a compressible nonhydrostatic toy-model relevant to the fast-mode part of the 'Lokal-Modell'.
DOI: 10.5676/DWD_pub/nwv/cosmo-tr_7

No. 8: Chiara Marsigli, Andrea Montani, Tiziana Paccagnella, Davide Sacchetti, André Walser, Marco Arpagaus, Thomas Schumann (2005):
Evaluation of the Performance of the COSMO-LEPS System.
DOI: 10.5676/DWD_pub/nwv/cosmo-tr_8

No. 9: Erdmann Heise, Bodo Ritter, Reinhold Schrodin (2006):
Operational Implementation of the Multilayer Soil Model.
DOI: 10.5676/DWD_pub/nwv/cosmo-tr_9

No. 10: M.D. Tsyrulnikov (2007):
Is the particle filtering approach appropriate for meso-scale data assimilation ?
DOI: 10.5676/DWD_pub/nwv/cosmo-tr_10

No. 11: Dmitrii V. Mironov (2008):
Parameterization of Lakes in Numerical Weather Prediction. Description of a Lake Model.
DOI: 10.5676/DWD_pub/nwv/cosmo-tr_11

No. 12: Adriano Raspanti (2009):
COSMO Priority Project "VERification System Unified Survey" (VERSUS): Final Report.
DOI: 10.5676/DWD_pub/nwv/cosmo-tr_12

No. 13: Chiara Marsigli (2009):
COSMO Priority Project "Short Range Ensemble Prediction System" (SREPS): Final Report.
DOI: 10.5676/DWD_pub/nwv/cosmo-tr_13

No. 14: Michael Baldauf (2009):
COSMO Priority Project "Further Developments of the Runge-Kutta Time Integration Scheme" (RK): Final Report.
DOI: 10.5676/DWD_pub/nwv/cosmo-tr_14

No. 15: Silke Dierer (2009):
COSMO Priority Project "Tackle deficiencies in quantitative precipitation forecast" (QPF): Final Report.
DOI: 10.5676/DWD_pub/nwv/cosmo-tr_15

No. 16: Pierre Eckert (2009):
COSMO Priority Project "INTERP": Final Report.
DOI: 10.5676/DWD_pub/nwv/cosmo-tr_16

No. 17: D. Leuenberger, M. Stoll and A. Roches (2010):
Description of some convective indices implemented in the COSMO model.
DOI: 10.5676/DWD_pub/nwv/cosmo-tr_17

No. 18: Daniel Leuenberger (2010):
Statistical analysis of high-resolution COSMO Ensemble forecasts in view of Data Assimilation.
DOI: 10.5676/DWD_pub/nwv/cosmo-tr_18

No. 19: A. Montani, D. Cesari, C. Marsigli, T. Paccagnella (2010):
Seven years of activity in the field of mesoscale ensemble forecasting by the COSMO–LEPS system: main achievements and open challenges.
DOI: 10.5676/DWD_pub/nwv/cosmo-tr_19

No. 20: A. Roches, O. Fuhrer (2012):
Tracer module in the COSMO model.
DOI: 10.5676/DWD_pub/nwv/cosmo-tr_20

No. 21: Michael Baldauf (2013):
A new fast-waves solver for the Runge-Kutta dynamical core.
DOI: 10.5676/DWD_pub/nwv/cosmo-tr_21

No. 22: C. Marsigli, T. Diomede, A. Montani, T. Paccagnella, P. Louka, F. Gofa, A. Corigliano (2013):
The CONSENS Priority Project.
DOI: 10.5676/DWD_pub/nwv/cosmo-tr_22

No. 23: M. Baldauf, O. Fuhrer, M. J. Kurowski, G. de Morsier, M. Müllner, Z. P. Piotrowski, B. Rosa, P. L. Vitagliano, D. Wójcik, M. Ziemiański (2013):
The COSMO Priority Project 'Conservative Dynamical Core' Final Report.
DOI: 10.5676/DWD_pub/nwv/cosmo-tr_23

No. 24: A. K. Miltenberger, A. Roches, S. Pfahl, H. Wernli (2014):
Online Trajectory Module in COSMO: a short user guide.
DOI: 10.5676/DWD_pub/nwv/cosmo-tr_24

No. 25: P. Khain, I. Carmona, A. Voudouri, E. Avgoustoglou, J.-M. Bettems, F. Grazzini (2015):
The Proof of the Parameters Calibration Method: CALMO Progress Report.
DOI: 10.5676/DWD_pub/nwv/cosmo-tr_25

No. 26: D. Mironov, E. Machulskaya, B. Szintai, M. Raschendorfer, V. Perov, M. Chumakov, E. Avgoustoglou (2015):
The COSMO Priority Project 'UTCS' Final Report.
DOI: 10.5676/DWD_pub/nwv/cosmo-tr_26

No. 27: J-M. Bettems (2015):
The COSMO Priority Project 'COLOBOC': Final Report.
DOI: 10.5676/DWD_pub/nwv/cosmo-tr_27

No. 28: Ulrich Blahak (2016):
RADAR_MIE_LM and RADAR_MIELIB - Calculation of Radar Reflectivity from Model Output.
DOI: 10.5676/DWD_pub/nwv/cosmo-tr_28

No. 29: M. Tsyrulnikov and D. Gayfulin (2016):
A Stochastic Pattern Generator for ensemble applications.
DOI: 10.5676/DWD_pub/nwv/cosmo-tr_29

No. 30: D. Mironov and E. Machulskaya (2017):
A Turbulence Kinetic Energy – Scalar Variance Turbulence Parameterization Scheme.
DOI: 10.5676/DWD_pub/nwv/cosmo-tr_30

No. 31: P. Khain, I. Carmona, A. Voudouri, E. Avgoustoglou, J.-M. Bettems, F. Grazzini, P. Kaufmann (2017):
CALMO - Progress Report.
DOI: 10.5676/DWD_pub/nwv/cosmo-tr_31

No. 32: A. Voudouri, P. Khain, I. Carmona, E. Avgoustoglou, J.M. Bettems, F. Grazzini, O. Bellprat, P. Kaufmann and E. Bucchignani (2017):
Calibration of COSMO Model, Priority Project CALMO Final report.
DOI: 10.5676/DWD_pub/nwv/cosmo-tr_32

No. 33: N. Vela (2017):
VAST 2.0 - User Manual.
DOI: 10.5676/DWD_pub/nwv/cosmo-tr_33

No. 34: C. Marsigli, D. Alferov, M. Arpagaus, E. Astakhova, R. Bonanno, G. Duniec, C. Gebhardt, W. Interewicz, N. Loglisci, A. Mazur, V. Maurer, A. Montani, A. Walser (2018):
COsmo Towards Ensembles at the Km-scale IN Our countries" (COTEKINO), Priority Project final report.
DOI: 10.5676/DWD_pub/nwv/cosmo-tr_34

No. 35: G. Rivin, I. Rozinkina, E. Astakhova, A. Montani, D. Alferov, M. Arpagaus, D. Blinov, A. Bundel, M. Chumakov, P. Eckert, A. Euripides, J. Förstner, J. Helmert, E. Kazakova, A. Kirsanov, V. Kopeikin, E. Kukanova, D. Majewski, C. Marsigli, G. de Morsier, A. Muravev, T. Paccagnella, U. Schättler, C. Schraff, M. Shatunova, A. Shcherbakov, P. Steiner, M. Zaichenko (2018):
The COSMO Priority Project CORSO Final Report.
DOI: 10.5676/DWD_pub/nwv/cosmo-tr_35

No. 36: A. Raspanti, A. Celozzi, A. Troisi, A. Vocino, R. Bove, F. Batignani (2018):
The COSMO Priority Project VERSUS2 Final Report.
DOI: 10.5676/DWD_pub/nwv/cosmo-tr_36

No. 37: A. Bundel, F. Gofa, D. Alferov, E. Astakhova, P. Baumann, D. Boucouvala, U. Damrath, P. Eckert, A. Kirsanov, X. Lapillonne, J. Linkowska, C. Marsigli, A. Montani, A. Muraviev, E. Oberto, M.S. Tesini, N. Vela, A. Wyszogrodzki, M. Zaichenko, A. Walser (2019):
The COSMO Priority Project INSPECT Final Report.
DOI: 10.5676/DWD_pub/nwv/cosmo-tr_37

No. 38: G. Rivin, I. Rozinkina, E. Astakhova, A. Montani, J-M. Bettems, D. Alferov, D. Blinov, P. Eckert, A. Euripides, J. Helmert, M.Shatunova (2019):
The COSMO Priority Project CORSO-A Final Report.
DOI: 10.5676/DWD_pub/nwv/cosmo-tr_38

No. 39: C. Marsigli, D. Alferov, E. Astakhova, G. Duniec, D. Gayfulin, C. Gebhardt, W. Interewicz, N. Loglisci, F. Marcucci, A. Mazur, A. Montani, M. Tsyrulnikov, A. Walser (2019):
Studying perturbations for the representation of modeling uncertainties in Ensemble development (SPRED Priority Project): Final Report.
DOI: 10.5676/DWD_pub/nwv/cosmo-tr_39

No. 40: E. Bucchignani, P. Mercogliano, V. Garbero, M. Milelli, M. Varentsov, I. Rozinkina, G. Rivin, D. Blinov, A. Kirsanov, H. Wouters, J.-P. Schulz, U. Schättler (2019):
Analysis and Evaluation of TERRA_URB Scheme: PT AEVUS Final Report.
DOI: 10.5676/DWD_pub/nwv/cosmo-tr_40

COSMO Technical Reports

Issues of the COSMO Technical Reports series are published by the *COnsortium for Small-scale MOdelling* at non-regular intervals. COSMO is a European group for numerical weather prediction with participating meteorological services from Germany (DWD, AWGeophys), Greece (HNMS), Italy (USAM, ARPA-SIMC, ARPA Piemonte), Switzerland (MeteoSwiss), Poland (IMGW), Romania (NMA) and Russia (RHM). The general goal is to develop, improve and maintain a non-hydrostatic limited area modelling system to be used for both operational and research applications by the members of COSMO. This system is initially based on the COSMO-Model (previously known as LM) of DWD with its corresponding data assimilation system.

The Technical Reports are intended

- for scientific contributions and a documentation of research activities,
- to present and discuss results obtained from the model system,
- to present and discuss verification results and interpretation methods,
- for a documentation of technical changes to the model system,
- to give an overview of new components of the model system.

The purpose of these reports is to communicate results, changes and progress related to the LM model system relatively fast within the COSMO consortium, and also to inform other NWP groups on our current research activities. In this way the discussion on a specific topic can be stimulated at an early stage. In order to publish a report very soon after the completion of the manuscript, we have decided to omit a thorough reviewing procedure and only a rough check is done by the editors and a third reviewer. We apologize for typographical and other errors or inconsistencies which may still be present.

At present, the Technical Reports are available for download from the COSMO web site (www.cosmo-model.org). If required, the member meteorological centres can produce hard-copies by their own for distribution within their service. All members of the consortium will be informed about new issues by email.

For any comments and questions, please contact the editor:

Massimo Milelli
Massimo.Milelli@arpa.piemonte.it

Consortium

for

Small-Scale Modelling

Technical Report No. 28

RADAR_MIE_LM and RADAR_MIELIB
Calculation of Radar Reflectivity from Model Output

January 2016

DOI: 10.5676/DWD_pub/nwv/cosmo-tr_28

Deutscher Wetterdienst
MeteoSwiss
Aeronautica Militare - Reparto per la Meteorologia
ΕΘΝΙΚΗ ΜΕΤΕΩΡΟΛΟΓΙΚΗ ΥΠΗΡΕΣΙΑ
Instytucie Meteorogii i Gospodarki Wodnej
Administratia Nationala de Meteorologie
ROSHYDROMET
Agenzia Regionale per la Protezione Ambientale del Piemonte
Agenzia Regionale per la Protezione Ambientale dell'Emilia-Romagna
Centro Italiano Ricerche Aerospaziali
Amt für GeoInformationswesen der Bundeswehr



www.cosmo-model.org

Editor: Massimo Milelli, ARPA Piemonte

RADAR_MIE_LM and RADAR_MIELIB

Calculation of Radar Reflectivity from Model Output

Ulrich Blahak*

* Ulrich Blahak
Deutscher Wetterdienst
Frankfurter Str. 135
63067 Offenbach am Main
Germany

Contents

Contents 2

1 Preface 5

2 Introduction 6

3 Factors contributing to the radar "bright band" 7

4 Theoretical basis 7
4.1 Equivalent radar reflectivity factor . . . 7
4.2 Extinction . . . 8
4.3 Backscattering and extinction by spheres . . . 8
4.4 Backscattering and extinction by two-layered spheres . . . 10
4.5 Refractive index of hydrometeors . . . 10
4.5.1 Water . . . 12
4.5.2 Ice . . . 13
4.5.3 Mixtures of ice, air and water . . . 14
4.5.4 Mixtures of ice, air and water — Wieners formula . . . 14
4.5.5 Mixtures of ice, air and water — Maxwell-Garnetts formula . . . 16
4.5.6 Mixtures of ice, air and water — Bruggemann formula . . . 17

5 Routines in `radar_mielib` 18
5.1 Refractive index of pure ice and water . . . 18
5.1.1 `FUNCTION m_complex_water_ray` . . . 18
5.1.2 `FUNCTION m_complex_water_liebe` . . . 19
5.1.3 `FUNCTION m_complex_ice_ray` . . . 20
5.1.4 `FUNCTION m_complex_ice_warren` . . . 21
5.1.5 `FUNCTION m_complex_ice_maetzler` . . . 22
5.2 Refractive index of mixture materials . . . 23
5.2.1 `FUNCTION m_complex_oguchi` . . . 23
5.2.2 `FUNCTION m_complex_maxwellgarnett` . . . 24
5.2.3 `FUNCTION m_complex_bruggemann` . . . 25
5.2.4 `FUNCTION get_m_mix` . . . 26
5.2.5 `FUNCTION get_m_mix_nested` . . . 28
5.3 Backscattering cross section for single precipitation particles . . . 31
5.3.1 `SUBROUTINE MIE_DRY_GRAUPEL` . . . 31
5.3.2 `SUBROUTINE RAYLEIGH_DRY_GRAUPEL` . . . 33
5.3.3 `SUBROUTINE MIE_DRYHAIL` . . . 35
5.3.4 `SUBROUTINE MIE_DRYSNOW` . . . 36
5.3.5 `SUBROUTINE MIE_DRYSNOW_TWOSPH` . . . 38
5.3.6 `SUBROUTINE MIE_WATERSPH_WETHAIL` . . . 40
5.3.7 `SUBROUTINE MIE_SPONGY_WETHAIL` . . . 41
5.3.8 `SUBROUTINE MIE_WATERSPH_WETGR` . . . 43
5.3.9 `SUBROUTINE MIE_SOAK_TWOSPH_WETGR` . . . 45
5.3.10 `SUBROUTINE MIE_MEAN_WETGR` . . . 47
5.3.11 `SUBROUTINE MIE_SOAK_WETGR` . . . 48
5.3.12 `SUBROUTINE RAYLEIGH_SOAK_WETGR` . . . 50
5.3.13 `SUBROUTINE MIE_WETSNOW_TWOSPH` . . . 51

6 `radar_mie_lm`: Interface functions for the LM 54

6.1 An approximation for the degree of melting applicable for bulk microphysical schemes . . . 54

6.2 An efficient Rayleigh-Approximation for melting hydrometeors with Oguchis refractive index formulation . . . 59

6.3 Controlling reflectivity calculations in LM — relevant namelist parameters and their setting . . . 60

6.4 Tables of namelist parameter settings for the EMA choice . . . 64

6.5 Additions to LM-runscripts to enable reflectivity calculations . . . 67

7 Backscattering cross sections of dry ice particles 68

7.1 One-layered sphere . . . 68

7.2 Two-layered sphere . . . 71

8 Backscattering cross sections for melting ice particles relative to the mass-equivalent water drop 73

8.1 Rayleigh: soaked wet graupel, LM-scheme . . . 74

8.2 Rayleigh: soaked wet graupel, Seifert/Beheng-scheme . . . 77

8.3 Rayleigh: soaked wet snow, LM-scheme . . . 80

8.4 Rayleigh: soaked wet snow, Seifert/Beheng-scheme . . . 82

8.5 Mie: soaked twosphere wet graupel, LM-scheme . . . 84

8.6 Mie: soaked twosphere wet graupel, Seifert/Beheng-scheme . . . 86

8.7 Mie: soaked twosphere wet snow, LM-scheme . . . 88

8.8 Mie: soaked twosphere wet snow, Seifert/Beheng-scheme . . . 90

8.9 Mie: soaked wet graupel, LM-scheme . . . 92

8.10 Mie: soaked wet graupel, Seifert/Beheng-scheme . . . 95

8.11 Mie: soaked wet snow, LM-scheme . . . 98

8.12 Mie: soaked wet snow, Seifert/Beheng-scheme . . . 100

8.13 Mie: watersphere wet graupel, LM-scheme . . . 102

8.14 Mie: watersphere wet graupel, Seifert/Beheng-scheme . . . 103

8.15 Mie: watersphere wet snow, LM-scheme . . . 104

8.16 Mie: watersphere wet snow, Seifert/Beheng-scheme . . . 105

8.17 Mie: spongy wet hail, Seifert/Beheng-scheme . . . 106

8.18 Mie: watersphere wet hail, Seifert/Beheng-scheme . . . 107

8.19 Mie: twosphere soaked wet snow, LM-scheme . . . 108

8.20 Mie: twosphere soaked wet snow, Seifert/Beheng-scheme . . . 138

9 Index of the Figures of Section 8 **168**

9.1 Rayleigh: soaked wet graupel, LM-scheme 168
9.2 Rayleigh: soaked wet graupel, Seifert/Beheng-scheme 168
9.3 Rayleigh: soaked wet snow, LM-scheme 168
9.4 Rayleigh: soaked wet snow, Seifert/Beheng-scheme 168
9.5 Mie: soaked twosphere wet graupel, LM-scheme 168
9.6 Mie: soaked twosphere wet graupel, Seifert/Beheng-scheme 169
9.7 Mie: soaked twosphere wet snow, LM-scheme 169
9.8 Mie: soaked twosphere wet snow, Seifert/Beheng-scheme 169
9.9 Mie: soaked wet graupel, LM-scheme 169
9.10 Mie: soaked wet graupel, Seifert/Beheng-scheme 169
9.11 Mie: soaked wet snow, LM-scheme 169
9.12 Mie: soaked wet snow, Seifert/Beheng-scheme 170
9.13 Mie: watersphere wet graupel, LM-scheme 170
9.14 Mie: watersphere wet graupel, Seifert/Beheng-scheme 170
9.15 Mie: watersphere wet snow, LM-scheme 170
9.16 Mie: watersphere wet snow, Seifert/Beheng-scheme 170
9.17 Mie: spongy wet hail, Seifert/Beheng-scheme 170
9.18 Mie: watersphere wet hail, Seifert/Beheng-scheme 171
9.19 Mie: twosphere soaked wet snow, LM-scheme 171
9.20 Mie: twosphere soaked wet snow, Seifert/Beheng-scheme 173

References **176**

1 Preface

This Technical Report describes a new implementation of the computation of radar reflectivity values on the native model grid points, which will soon become available in the COSMO-Model together with the new Efficient Modular VOlume scanning RADar forward Operator (EMVORADO).

While the abovementioned computation of grid point reflectivities is one of several processing steps within the EMVORADO, it can also be used on its own, without the "full" EMVORADO-simulation of polar volumetric radar data. In that sense, it is a replacement for the presently very simple Rayleigh-type 'DBZ' computation available in the COSMO module `pp_utilities.f90`, which is currently used for output diagnosis in the COSMO `GRIBOUT`-namelist(s). Well, "replacement" is not entirely correct, because the present method will still be available as one of several options. The new options are the more accurate (and more expensive) Mie-scattering, but also two new variants of Rayleigh-type approximations of different complexity and cost, which differ from the current simple one mainly by a better treatment of partially melted particles (the famous radar "bright band").

The present report is restricted to this "stand-alone" aspect. It covers the theoretical aspects of the unattenuated equivalent radar reflectivity factor (loosely called "reflectivity"), including the refractive index of hydrometeors, which is the basic material parameter, which determines the interaction with electromagnetic radiation. The latter possesses various possible and uncertain definitions for the ice-water-air-mixture of partially melted particles. Moreover, details of the implementation of these aspects into the new libraries `radar_mielib_vec.f90` and `radar_mie_lm_vec.f90` are described, before the report concludes with an exhaustive sensitivity study on the various (and uncertain!) choosable options for the backscattering cross section of partially melted particles.

Although developed in the framework of the COSMO-model, the new libraries can in principle be coupled to any other NWP model.

I have written most contents of this report alongside the code development during my Post-Doc time at the Institute of Meteorology and Climate Research, Tropospheric Branch (IMK-TRO), Karlsruhe Institute of Technology (KIT) in Germany. This work started in early 2005, when I first came into contact with numerical modeling and the COSMO-model, and was largely finished by 2010 when I started at Deutscher Wetterdienst. In 2005, the model still had its traditional name "Lokalmodell" LM, and I preserved this acronym at many places in the code in order to not forget the roots.

Later, together with Yuefei Zeng and Dorit Jerger (PhD-projects with financial support through DWD's Extramural Reserach Programme) as well as our mentor Klaus-Dieter Beheng from IMK-TRO, we built the full EMVORADO-framework on top. But this is a different story.

Ulrich Blahak

2 Introduction

The program package `radar_mielib` provides Fortran-90 routines for the calculation of gridbox values of the equivalent radar reflectivity factor from model output based on Mie-scattering functions as well as Rayleigh approximation. Water drops and a variety of different kinds of dry and melting ice particles are considered (graupel, snow, cloud ice, hail).

Whereas `radar_mielib` contains quite general subroutines, the library `radar_mie_lm` provides the necessary interface routines to use them with the Lokalmodell (LM) of the German Weather Service (DWD) together with the two-moment bulk microphysical scheme of Seifert and Beheng (2006) or the standard one-moment bulk microphysical schemes.

Note that in calculating gridbox values, propagation effects (extinction) and the spatial averaging properties (beam function) of radar systems are not considered. The neglect of attenuation confines the applicability of the calculated reflectivity values to quantitative comparisons at radar wavelengths with negligible attenuation only, e.g., S-band, or to situations or research questions where attenuation is not of primary importance. At shorter wavelengths (C-band, X-band) those effects have to be kept in mind when comparing with real radar data. The shorter the wavelength the stronger is attenuation. However, calculation of the extinction cross section is contained in the basic scattering routines in `radar_mielib`, but is not used further by routines in `radar_mielib` and `radar_mie_lm` which build upon them. Only a full radar forward operator, considering true ray paths from the antenna through the atmosphere, could make use of this information.

Special emphasis is given to the description of melting ice particles. It is well known, however, that this is a highly underdetermined problem, since, on one hand, the particles shapes are different from spherical and, on the other hand, the effective refractive index of the particle material (mixture of ice, water, and air) is very sensitive to the type and topology of mixture and the particles bulk density. Moreover, there is no absolutely precise theoretical description of the effective refractive index of such complex mixtures like in snow- and graupel particles — consequently, a large number of formulas for different applications are on the market.

In `radar_mielib`, the problem is tackled by providing routines for 3 different mixing formulas for the refractive index (Maxwell-Garnett, Wiener, Bruggemann), whereas only spherical shapes are considered. In case of Mie-scattering, also a concentric two-layer-sphere particle model is implemented, which can be used for, e.g., snowflakes and melting hail- and graupel particles. Moreover, different melting topologies are considered, e.g., accumulation of meltwater on the outside or fully soaked particles, melting taking place only on the outside or partly within the ice structure. Combining the tools leaves one with an infinite number of possibilities to describe a melting particle. Especially the Maxwell-Garnett mixing rule allows 15 different refractive index values for a single set of ice-water-air volume fractions. From this it can clearly be seen that there is a large natural variability, which has to be considered when comparing calculated with measured radar reflectivities. Sensitivity studies with the help of the tools from `radar_mielib` at least provide a lower bound for this high variability.

In the following sections, the tools of `radar_mielib` are described in detail. To facilitate their proper use, calculated backscatter coefficients for different types of melting particles (snow, graupel and hail) as a function of the degree of melting and particle mass are presented, considering about 800 different combinations of particle types and mixing rules. The different particle types are taken from the cloud microphysical schemes of the COSMO-model (formerly "Lokalmodell" (LM) of the German Weather Service (DWD) — the standard 1-moment scheme as well as the 2-moment scheme of Seifert and Beheng (2006).

3 Factors contributing to the radar "bright band"

There are different (and sometimes competing) factors contributing to the observed radar bright band:

- Backscattering of single melting particles is enhanced in the presence of meltwater.
- Thinning of the number densitiy (number of particles per volume of air) by increasing fall speed with increasing degree of melting reduces backscattering.
- Upper part of the melting layer: particle breakup is dominant.
  Lower part: particle coalescence is dominant.

It should be emphasized that the backscattering enhancement of single melting particles treatable by the routines in `radar_mielib` is only one of several processes contributing to the observed radar bright band. Therefore, the results presented later in Section 8 about backscattering cross sections of single particles as function of the degree of melting attribute only to this part of the reflectivity maximum.

4 Theoretical basis

In this section formulas are collected to calculate the unattenuated equivalent radar reflectivity factor Z_e from model output which are implemented in `radar_mielib`. To simulate a real radar measurement, also attenuation, beam propagation and the beam smoothing function would have to be included, which is omitted here.

4.1 Equivalent radar reflectivity factor

Consider the assumption of incoherent single scattering beeing the dominant effect in radar backscattering. Then, the equivalent radar reflectivity factor is commonly defined as

$$Z_e \;=\; \frac{\lambda_0^4}{\pi^5\;|K_{w,0}|^2}\;\int\limits_0^\infty \sigma_b(D)\,N(D)\,dD \quad , \tag{1}$$

where λ_0 is the radar wavelength, $N(D)$ the particle size distribution as a function of the (spherical) particle diameter D, and σ_b denotes the backscattering cross section of a particle having diameter D. $|K_{w,0}|$ is a reference value of the dielectric factor used in the radar software, usually taken as 0.93 (water, $T = 0°$C, $lambda_0 \approx 5 - 10$ cm). $N(D)$ depends also on time and location, but the explicit dependence is omitted for brevity.

Z_e would be output by a radar in case of a homogeneous spatial hydrometeor distribution across the range cell and no attenuation on the path to the cell. Written in the above notation, it is implicitly assumed that there is a unique relation between size (D) and $\sigma_b(D)$ as it is the case for water drops to a good degree of approximation. Taking into account also ice particles complicates the description, since then, this uniqueness breaks down and we have to extend the dependencies of N and σ to particle shape and particle effective refractive index ($\sigma_b(\text{shape}, D, \lambda_0, m)$).

As a compromise, one might define different types of ice hydrometeors (e.g., graupel, snow, hail) in a way that for these subtypes, a unique relation of σ and D exists. Then, Z_e is the sum of the contribution of each hydrometeor type. In fact, current microphysical descriptions in numerical weather prediction models classify ice hydrometeors in different types in a way to also let σ only depend on D.

As an example, the procedure to calculate Z_e from the output of a two-moment bulk microphysical scheme is as follows:

- $f(D)$: assume certain master function for $N(D)$, e.g., a four-parametric generalized gamma distribution. 2 free parameters are then deduced from the model predicted two moments (e.g., hydrometeor number- and mass density), and the other two parameters have to be fixed.
- Hydrometeors are a mixture of ice, air and water.
  - Choose appropriate formula to calculate m as a function of T, λ, material, density and the degree of melting f_{melt}. For this, several state-of-the-art effective medium approximations could be used, but this is always a delicate choice. A huge uncertainty and variability has to be expected there.
  - If the microphysics scheme does not predict f_{melt}, it has to be estimated from whatever information is available (temperature, particle size, etc.). This is a particularly difficult thing especially if there is no information about the particles history. Temperature and ventilation factors along backwards trajectories would be desireable for this task but are very costly to determine.
- σ_b: apply Mie-scattering (one- or twolayered sphere) or Rayleigh-Approximation to calculate σ_b.
- $Z_e = \sum$ (all hydrometeor categories)

For the LM, these tasks are accomplished by interface subroutines in the library `radar_mie_lm`, building on the more general tools provided by `radar_mielib`.

4.2 Extinction

For completeness, the formula for the twoway attenuation coefficient k_2 is given here:

$$k_2 \;=\; \frac{20}{\ln 10} \int_0^\infty \sigma_{ext}(D)\, N(D)\, dD \quad . \tag{2}$$

σ_{ext} is the extinction cross section, depending on D as well as λ_0. Applying Lambert-Beer's extinction law, integration of k_2 along the radar beam yields the attenuation factor. Again, there are issues about beam smoothing and propagation path which render an accurate calculation from model data very difficult and costly (apart from considering different hydrometeor types).

The calculation of σ_{ext} is implemented in all basic scattering subroutines but is not used further up to now (2008). This could however be extended by users who whish to develop, e.g., a complete radar simulator including propagation effects.

4.3 Backscattering and extinction by spheres

Consider a plane parallel electromagnetic wave incident on a spherical object with refractive index m (complex) different to that of the surrounding medium, m_0 (real, no extinction). The Mie-solution of maxwells equations at a large distance from the scatterer leads to the formula for σ_b,

$$\sigma_b \;=\; \frac{4\,\pi}{k^2} \left| \sum_{n=1}^{\infty} (-1)^n \left(n + \frac{1}{2}\right) (a_n \,-\, b_n) \right|^2 \quad . \tag{3}$$

a_n und b_n are the socalled Mie scattering coefficients of order n which depend only on the Mie-parameter $\alpha = \pi\lambda_0 m_0/D$ and the relative refractive index m/m_0 of the particle

material. They in turn involve spherical bessel functions of the arguments α and $\alpha m/m_0$ and are omitted here.

As an alternative, a_n and b_n can be efficiently calculated by recurrence formulas derived by, e.g., Deirmendjian (1969) or Bohren and Huffman (1983). These formulas themselves build on recurrence relations for the involved spherical bessel functions. The subroutine `SPHERE_SCATTER_BH()` of `radar_mielib` makes use of these relations.

A further simplification is the so called **Rayleigh-approximation** for particles having D small compared to λ_0. Series expansions of a_n and b_n in equation (3) and retention of only the leading term yield the approximation

$$\sigma_b \;=\; \frac{\pi^5}{\lambda_0^4}\left|\frac{m^2-1}{m^2+2}\right|^2 D^6 \;=\; \frac{\pi^5}{\lambda_0^4}\,|K|^2\;D^6 \qquad \text{with}\;\; \frac{m^2-1}{m^2+2} \;=\; K \tag{4}$$

where m_0 is set to 1 (air), so m/m_0 reduces to just m. K is called the dielectric factor. The Validity of the approximation depends on the Mie parameter and m/m_0. Generally, larger m/m_0 yield a more restrictive size criterion. For water spheres a comparison of exact formula and approximation yields $D < \lambda_0/20$, for ice spheres $D < \lambda_0/5$. Bohren and Huffman (1983) formulate the condition as $|m/m_0|\,\pi D_k/\lambda_0 \ll 1$.

When the particles are very small compared with the wavelength, the Rayleigh-approximation is also valid for nonspherical particles. The smaller the particle the less important is its shape. D has then to be taken as the diameter of the volume equivalent sphere.

In case of $m = \text{const.}$ (e.g., for water drops or dry ice spheres) and application of the Rayleigh approximation for σ_b, Z_e is simply given by the 6. moment of the size distribution $N(D)$,

$$Z_e \;=\; \frac{|K_w|^2}{|K_{w,0}|^2}\int\limits_0^\infty D^6\,N(D)\,dD \quad , \tag{5}$$

where water drops have been assumed in the formula without loss of generality. Z_e is equivalent to the 6. Moment of the size distribution of (hypothetically) measured water drops, which explaines the name "equivalent reflectivity factor". In cases of $N(D)$ beeing a certain type of function (e.g., a generalized gamma distribution), the integral in (5) can be solved analytically, involving gamma functions.

The extinction coefficient σ_{ext} for spherical particles is given by

$$\sigma_{ext} \;=\; \frac{4\,\pi}{k^2}\,\Re\left\{\sum_{n=1}^{\infty}\left(n+\frac{1}{2}\right)\,(a_n\,+\,b_n)\right\} \quad . \tag{6}$$

A similar approximation as in equation (4) yields

$$\sigma_{ext} \;=\; \frac{\pi^2}{\lambda_0}\Im\{-K\}\;D^3 \;+\; \frac{2}{3}\,\frac{\pi^5}{\lambda_0^4}\,|K|^2\;D^6 \quad , \tag{7}$$

with K having the same meaning as in equation (4). Two terms have been retained here since they might be of same order in certain situations. The first term describes the losses by absorption, second term the losses by scattering in all directions.

In case of a small water drop σ_{ext} is dominated by the absorption term (example with subscript $_w$ for water: $\lambda_0 = 1$ cm, $m_w = 4.97 - 2.79i$ (10°C) after Ray (1972), $|K_w|^2 = 0.91$, $\Im\{-K\} = 0.07$, $D = 0.1$ mm $\Rightarrow$ absorption term $= 7 \cdot 10^{-11}$ m^2, scattering term $= 3 \cdot 10^{-14}$ m^2, geometrical cross section $= 8 \cdot 10^{-9}$ m^2. In case of small ice particles both

Can't show picture #1 because `tr28_ub2-pics.pdf` not found. Create it from `tr28_ub2.dvi` using `dvips` and `ps2pdf`!

Figure 1: Convention for the refractive indices m_0, m_1, m_2 and for the radii r_1, r_2 in the calculation of the scattering functions for a two-layered sphere.

terms are important, since $\Im\{-K_i\} \ll |K_i|^2$ (subscript $_i$ for ice). Ice absorbs microwave radiation much less than water.

For water droplets in the microwave region, the approximation (7) is only valid for $D < \lambda_0/100$, whereas for ice spheres $D < \lambda_0/2$, which is by far less restrictive. The same rule of thumb as in the case of backscattering applies here as well: the larger $|m/m_0|$, the more restrictive is the size criterion on D. As soon as the particles contain water in any volume fraction, one should not calculate σ_{ext} by the above approximation, but with the exact formula (6).

4.4 Backscattering and extinction by two-layered spheres

Today, exact solutions to the scattering problem of N-layered spheres are available which reduce to the classical Mie-formula for a simple sphere. Since some hydrometeors like melting hail (ice core, spongy ice/water-shell) can be well approximated by a two-layered sphere, formulas for backscattering- and extinction cross sections for this configuration are included into `radar_mielib` as well.

As in the case of simple spheres, important parameters are the two Mie-parameters

$$\alpha_1 = \frac{2\,\pi\,r_1\,m_0}{\lambda_0} \quad ; \qquad \alpha_2 = \frac{2\,\pi\,r_2\,m_0}{\lambda_0} \quad . \tag{8}$$

defined by the shell and core radii r_1 and r_2, resp., as well as the corresponding relative refractive indices m_1 and m_2 (see Figure 1).

Depending on these parameters, the scattering coefficients a_n and b_n can be calculated analytically and then plugged into equation (3) and (6). To this end, formulas for a_n and b_n given by, e.g., Kerker (1969) are implemented into `radar_mielib` (subroutine `COATEDSPHERE_SCATTER()`) or, as a second alternative, an efficient subroutine making advantage of the recurrence relations for the spherical Bessel and Hankel functions given in the appendix of Bohren and Huffman (1983) is provided (subroutine `COATEDSPHERE_SCATTER_BH()`). The rather long and cumbersome formulas for a_n and b_n are omitted here. We refer the reader to the cited literature.

Note that numerical instabilities in calculating Bessel-functions by utilizing efficient recurrence relations (as is done here) are known to be problematic in case of large arguments to the Bessel functions. In the `radar_mielib`-subroutine `COATEDSPHERE_SCATTER()`, backward recurrence for the Bessel- and Hankel functions (programs taken from Zhang and Jin, 1996) are utilized, which is more stable than the forward recurrence implemented into subroutine `COATEDSPHERE_SCATTER_BH()`. However, `COATEDSPHERE_SCATTER()` is slower than `COATEDSPHERE_SCATTER_BH()`. Application of these routines to hydrometeor scattering in the microwave region should not be problematic, so both routines can be used.

4.5 Refractive index of hydrometeors

Up to this point, general formulas for the computation of the backscatter- and extinction cross section of spherical particles were given. An important parameter herein is the complex refractive index of the particle material $m = m' + im''$ (m_1, m_2 for the two-layered

sphere), which will be presented in the next sections. m is connnected to the relative dielectric constant $\epsilon = \epsilon' + i\epsilon''$ by the relation $\epsilon = m^2$. Note that in this paper the convection with negative imaginary part of m and ϵ is used which corresponds to a timefactor $\exp(i\omega t)$ in the description of electromagnetic waves. Under the assumption $\epsilon'' < 0$, $m'' < 0$ the following conversion formulas apply:

$$\epsilon' = m'^2 - m''^2 \tag{9}$$

$$\epsilon'' = 2\, m'\, m'' \tag{10}$$

$$m' = \sqrt{\frac{\sqrt{\epsilon'^2 + \epsilon''^2} + \epsilon'}{2}} \tag{11}$$

$$m'' = -\sqrt{\frac{\sqrt{\epsilon'^2 + \epsilon''^2} - \epsilon'}{2}} \quad . \tag{12}$$

The last two equations define the principal arm of the complex root function, as it is implemented also in most programming languages.

Hydrometeors consist of air, ice and/or water, so values of m for these materials are needed. For air, $m = 1$ is a very good approximation. For ice and water, m basically depends on wavelength and temperature. With these values, pure water and ice particles can be treated. These are given in subsubsection 4.5.1 and 4.5.2.

Things get by far more complicated in the case of dry snow particles (mixture of ice and air) or melting snow particles (mixture of ice, air and water). Here the task is to find an effective value m_{eff}, which leads to the same scattering functions when applied in the Mie-formulae that are observed for the mixture particle, whose scattering pattern highly depends on the topology of the mixture. This is a very difficult task, and consequently, there are a lot of mixing formulas on the market applicable to certain special situations. A general solution to the problem seems to be not existent. Moreover, mixing rules applicable for backscattering might not be applicable for extinction and vice versa (e.g., for granular mixtures with spatially inhomogeneous material distribution), since it is sometimes not possible to describe the directional scattering by a single value of m_{eff}.

In subsubsection 4.5.4 to subsubsection 4.5.6, some mixing formulas are presented which are currently used by the radar meteorological community for the mixture topologies encountered in dry and melting hydrometeors.

Can't show picture #2 because `tr28_ub2-pics.pdf` not found. Create it from `tr28_ub2.dvi` using `dvips` and `ps2pdf`!

Figure 2: Complex refractive index of water after Ray (1972) as a function of wavelength λ_0 in m and temperature in °C (only his equations (5) and (6) are used). **Red:** real part, **blue:** negative imaginary part. Several curves are shown at constant temperatures of -10°C to 30°C in steps of 10°C.

Can't show picture #3 because `tr28_ub2-pics.pdf` not found. Create it from `tr28_ub2.dvi` using `dvips` and `ps2pdf`!

Figure 3: Complex refractive index of water after Liebe et al. (1991) as a function of wavelength λ_0 in m and temperature in °C. **Red:** real part, **blue:** negative imaginary part. Several curves are shown at constant temperatures of -10°C to 30°C in steps of 10°C.

4.5.1 Water

Two models (formulas) for the complex index of refraction of water, m_w, are implemented into `radar_mielib` as functions. They give m_w as a function of wavelength λ_0 and temperature T. The first is the model of Ray (1972), which is applicable to the temperature range from -10°C to 30°C and to the wavelength range of about 1 mm to 1 m. Figure 2 depicts the real and imaginary parts of m_w for this model as a function of λ_0 and T. One clearly sees the anomaleous dispersion signal connected to a classical Debye relaxation mode in the microwave region. With higher frequency (shorter wavelength) the real part drops down reflecting an increase in propagation phase speed, whereas in the same frequency range, the imaginary part has a distinct maximum, reflecting strong absorption. The complete formulas of Ray (1972) also contain several rotational and absorption bands in the infrared region, parameterized as gaussian peaks, but this is omitted in the `radar_mielib` function. Only the formulas (5) and (6) of Ray (1972) are used, which limits the applicability to the microwave region.

Another model is given by Liebe et al. (1991) with a slightly different application range, namely 300 μm $< \lambda_0 <$ 0.3 m and -3°C $< T <$ 30°C. Figure 3 shows the real and imaginary parts of m_w for this model. The prominent Debye relaxation mode is also present here, as it should.

A comparison of both models can be found in Figure 4 for a temperature of 25°C, together with a model based on measurements of Segelstein (1981). The latter is only available for the temperature of 25°C. Nearly no differences between these descriptions are visible the wavelength range 5 mm to 20 cm, so all descriptions equally can be used in the microwave region, all giving similar results. Looking at other temperatures, nearly no differences between Rays and Liebes model can be found for the wavelength range 1 cm to 10 cm. At larger wavelength, the imaginary part is larger for Rays model, whereas at shorter wavelengths, the opposite is found. Liebes model should be used for $\lambda_0 <$ 1 cm, whereas both models are applicable from 1 cm to 10 cm, and Rays model is better from 10 cm to 1 m.

Can't show picture #4 because `tr28_ub2-pics.pdf` not found. Create it from `tr28_ub2.dvi` using `dvips` and `ps2pdf`!

Figure 4: Comparison of the complex refractive index of water as function of wavelength in m at a temperature of 25°C for 3 different formulations. **Black:** Ray (1972), **blue:** Segelstein (1981), **red:** Liebe et al. (1991). **Solid lines:** real part, **Dashed lines:** imaginary part.

Can't show picture #5 because `tr28_ub2-pics.pdf` not found. Create it from `tr28_ub2.dvi` using `dvips` and `ps2pdf`!

Figure 5: Complex refractive index of ice after Ray (1972) as a function of wavelength λ_0 in m and temperature in °C. **Red, right ordinate:** real part. **Blue, left ordinate (logarithmic scale):** negative imaginary part. Several curves are shown at constant temperatures of -20°C, -10°C and 0°C.

Can't show picture #6 because `tr28_ub2-pics.pdf` not found. Create it from `tr28_ub2.dvi` using `dvips` and `ps2pdf`!

Figure 6: Complex refractive index of ice after Warren (1984) as a function of wavelength λ_0 in m and temperature in °C. **Red, right ordinate:** real part. **Blue, left ordinate (logarithmic scale):** negative imaginary part. Several curves are shown at constant temperatures from -60°C to 0°C in steps of 10°C.

Can't show picture #7 because `tr28_ub2-pics.pdf` not found. Create it from `tr28_ub2.dvi` using `dvips` and `ps2pdf`!

Figure 7: Complex refractive index of ice after Mätzler (1998) as a function of wavelength λ_0 in m and temperature in °C. **Red, right ordinate:** real part. **Blue, left ordinate (logarithmic scale):** negative imaginary part. Several curves are shown at constant temperatures from -60°C to 0°C in steps of 10°C.

4.5.2 Ice

For the complex refractive index of ice, m_i, three models are available in `radar_mielib`. The first is again a model of Ray (1972), from the same paper as previously the model for water. The corresponding real and imaginary parts of m_i are depicted in Figure 5 as functions of λ_o and T. The range of validity is given by the author to be 0.001 m $< \lambda_0 <$ 10^7 m and -20°C $< T <$ 0°C. Ray (1972) deduced it from then available measurements from the literature, but not fulfilling the Kramers-Kronig-relations (see, e.g., Bohren and Huffman, 1983), as criticized, e.g., by Warren (1984). The use of this model is therefore not recommended.

As a second and better model, the descrete m_i-tables given by Warren (1984) are implemented, as shown in Figure 6. The author critically and carefully reviewed the existing measurements in literature, combined with own measurements to deduce his lookup tables. Here the Kramers-Kronig-relations are fulfilled. Values of m_i at intermediate values of λ_0 and T are linearily interpolated. In the original paper, the range of validity is given as 45 nm $< \lambda_0 <$ 8.6 m and -60°C $< T <$ 0°C.

Third, the formula of Mätzler (1998) is available (see Figure 7). The author gives the range of validity as 0.1 mm $< \lambda_0 <$ 30 m and -250°C $< T <$ 0°C.

Can't show picture #8 because `tr28_ub2-pics.pdf` not found. Create it from `tr28_ub2.dvi` using `dvips` and `ps2pdf`!

Can't show picture #9 because `tr28_ub2-pics.pdf` not found. Create it from `tr28_ub2.dvi` using `dvips` and `ps2pdf`!

Figure 8: Comparison of the complex refractive index of ice as function of wavelength in m at temperatures of -2°C (solid lines) and -20°C (dashed lines) for 3 different formulations. **Upper panel:** real part. **Lower panel:** imaginary part. **Black:** Ray (1972), **blue:** Warren (1984), **red:** Mätzler (1998).

While very similar for the real part of m_i, it can be seen from Figure 8 that especially the model of Ray (1972) predicts a totally different behaviour of the imaginary part of m_i with wavelength than the other two models. Here, the models of Warren (1984) and Mätzler (1998) are in qualitative agreement, but Mätzler (1998) gives lower values of the imaginary part up to a factor of 8 compared to Warren (1984). The author of this document feels not to be in a position to recommend using one or the other, but using the model of Ray (1972) is not recommended because of the abovementioned reasons.

4.5.3 Mixtures of ice, air and water

In literature, many different formulations of the refractive index of a mixture material are presented termed "Effective Medium Approximations" (EMA). Mostly they have their origin in the field of physical chemistry. It is a very old concept dating back to the late 19th century but nevertheless still an actual topic in research. In the meteorological community dealing with radar measurements, mostly three formulations are used which are also part of `radar_mielib`. These will be introduced in the following subsections.

The general problem is to find an effective value for the refractive index m_{eff} of a mixture material leading to the same scattering pattern when replacing the actual mixture particle by a homogeneous particle and measuring/ calculating the scattering functions by some theory using m_{eff}. Many theoretical and experimental attempts can be found in literature, but we cannot go into detail here. A starting point for further study could be the book of Bohren and Huffman (1983) or the article of shortciteNstroud1978.

It is immediately clear that such a technique inevitably gets complicated or leads to errors when applying it to particles which are not truly homogeneously mixed (mixture may have a macroscale topography) and/or when at least one of the mixture components is a strong dielectric like water. Some EMAs may be valid only for extinction or scattering in a certain direction depending on the method of their derivation.

4.5.4 Mixtures of ice, air and water — Wieners formula

Otto Wiener (1912) presented a quite general theory for a homogeneous mixture of inclusions (grains, fibres, layers, etc.) of N materials which are embedded in a homogeneous background medium with dielectric constant ϵ_0. In case of spherical inclusions, he states

$$\frac{\epsilon_{eff} - \epsilon_0}{\epsilon_{eff} + f\,\epsilon_0} \;=\; \sum_{j=1}^{N} p_j \, \frac{\epsilon_j - \epsilon_0}{\epsilon_j + f\,\epsilon_0} \quad . \tag{13}$$

p_j denotes the relative volume fraction of the species j on the overall particle volume,

$$p_j \;=\; \frac{V_j}{V_m}, \quad \text{where} \;\; V_m \;= \text{Volume of mixture particle} \tag{14}$$

and ϵ_j is its dielectric constant. **Note that in fact N+1 materials are contained in the mixture!** The parameter f in general depends on the shape, orientation, mutual distance and alignment within the mixture body. Let us denote the partial volume fraction of the background medium with p_0 and the partial volume by V_0, then it is

$$p_0 + \sum_{j=1}^{N} p_j \;=\; 1 \qquad \text{and} \qquad V_0 + \sum_{j=1}^{N} V_j \;=\; V_m \tag{15}$$

A good review of the original paper by Wiener is given by Lichtenecker (1926).

Formula (13) was derived under the assumption of a mixture of equally shaped and equally sized inclusions of N species into the background medium. In order to be applicable, one has to specify a value for the parameter f. Wiener (1912) showed that this can be accomplished under the following constraints:

- All inclusions have to be sufficiently separated so that the electromagnetic field inbetween can be regarded as homogeneous. This implies $p_0 > 0$ (in fact $p_0 \gg p_1, p_2$) so that the condition of large grain separation distances can be fullfilled.
- ϵ_0 has to be either the largest or the smallest value of all ϵ_x involved and it has to be significantly different to the adjacent ϵ_x.
- Isotropic distribution of the grains within the matrix medium.

Under these circumstances the parameter f depends largely only on the shape of the inclusions and attains the value 2 for spherical inclusions (Wiener then denotes f by "Formzahl" — shape number). A more detailed discussion of these constraints can be found in the original literature. However, since the classical derivations were done for real ϵ_x, it remains somehow unclear how to formulate these constraints for complex ϵ_x.

Often a seemingly similar formula is used by the radarmeteorological community in a way to set $\epsilon_0 = 1$ (vacuum, air) (see e.g., the review article by Oguchi (1983)) and at the same time assuming that there is no contribution of the background medium to the particles volume ($p_0 = 0$). The formula then reduces to an older formula (Lorenz-Lorentz, Clausius, Mosotti et others, see, e.g., Wiener, 1912 or Lichtenecker, 1926),

$$\frac{\epsilon_{eff} - 1}{\epsilon_{eff} + u} = \sum_{j=1}^{N} p_j \frac{\epsilon_j - 1}{\epsilon_j + u} \tag{16}$$

$$\sum_{j=1}^{N} p_j = 1 \quad .$$

In the following, formula (16) is referred to as Oguchis[1] formula. Oguchi (1983) designates the parameter u as shape parameter, similar to f in equation (13), and states that in case of spherical inclusions u attains the value 2.

The problem with this formula is that in neglecting the partial volume of the background medium, the assumption of mutual "large enough" distances between the inclusions is violated and the formula seems not to be applicable in general. Debye (1929) therefore restricts the formula to weak dielectrics and to the case of molecular mixtures which he regards as suspended spheres (single atoms) in vacuum (same argumentation in Bohren and Huffman (1983)). It is clearly not applicable to a melting ice particle with low air contribution since water is a strong dielectric. This was also found experimentally by Joss and Aufdermaur (1965).

However, when the background medium within the particle is air ($\epsilon_0 = 1$) with a considerable volume fraction and the particle is a mixture of ice and air (dry snow flake, graupel), the formula might be applicable since ice is a weak dielectric. The mixing term containing the air volume in (16) then vanishes and a "classical" formula used by radar meteorologists for many years (e.g., Battan, 1973) is recovered (also by appropiately using formula (13), which corroborates the validity of (16) for this special case).

[1]Oguchi (1983) wrongly attributes equation (16) to Otto Wiener, whereas the latter showed in his 1912 paper, why and under what circumstances this formula is not applicable. Wiener derived equation (13) instead, among formulas for other mixing topologies.

4.5.5 Mixtures of ice, air and water — Maxwell-Garnetts formula

Maxwell-Garnetts formula (Maxwell Garnett, 1904) is a special case of a more general formulation, see Stroud (1975), in the limiting case of small spherical inclusions of random size suspended in a background medium ("matrix"), similar as is the Wiener-formula, except for the random size. (In fact, it will be shown later in this section to be exactly equal to Wieners formula in case of spherical inclusions.)

Bohren and Huffman (1983) derive the following formulation similar to the original paper of Maxwell Garnett (1904)

$$\epsilon_{eff} = \frac{p_1 \epsilon_1 + \sum_{j=2}^{N} p_j \beta_j \epsilon_j}{p_1 - \sum_{j=2}^{N} p_j \beta_j} \tag{17}$$

$$\beta_j = \frac{3\epsilon_1}{\epsilon_j + 2\epsilon_1} \quad , \tag{18}$$

where p_j denotes again the relative volume fraction of the species j on the overall particle volume,

$$p_j = \frac{V_j}{V_m}, \quad \text{where } V_m = \text{Volume of mixture particle} \tag{19}$$

and ϵ_j is its dielectric constant. It is

$$\sum_{j=1}^{N} p_j = 1 \quad .$$

in this case. Here, index 1 corresponds to the matrix medium and indices larger than 1 denote inclusion materials.

Bohren and Battan (1982) extended this model to spheroidal inclusions, which have random size, which are randomly oriented within the matrix medium and which have random principal axes ratios (shapes). For this, only the coefficients β_j have to be replaced by

$$\beta_j = \frac{2\epsilon_1}{\epsilon_j - \epsilon_1} \left(\frac{\epsilon_j}{\epsilon_j - \epsilon_1} \ln\left(\frac{\epsilon_j}{\epsilon_1}\right) - 1 \right) \quad . \tag{20}$$

The complex logarithm denotes the principal arm. Note that this formulation is not invariant to a change in the matrix-species, but it is invariant to interchange the inclusions.

In case of a three-component mixture (as is the case with melting snow and graupel particles), formula (17) leads to numerous possibilities to specify matrix and inclusions. There are 3 possibilities to specify one material as matrix and the other two as inclusions. 12 additional possibilities arise by a two-fold application of a two-component mixture: one material is regarded as the matrix (3 possibilities), whereas the inclusion itself is regarded as a two-component mixture with 2 possibilities to specify matrix and inclusion. This leads to 6 possibilities. Changing further the roles of matrix and inclusion for the hosting material and the two-component sub-mixture, another 6 possibilities arise. Every possibility leads to different results. The degree of freedom (and the uncertainty about what to do) is therefore very large. In addition spherical and spheroidal inclusions can be discriminated, further doubling the number of possible choices.

An interesting comparison to the Wiener-formula can be made in rewriting equation (17) for spherical inclusions (β_j with equation (4.5.5)). After some manipulation,

$$\frac{\epsilon_{eff} - \epsilon_1}{\epsilon_{eff} + 2\epsilon_1} = \sum_{j=2}^{N} p_j \frac{\epsilon_j - \epsilon_1}{\epsilon_j + 2\epsilon_1} \quad . \tag{21}$$

Changing the index convention to Wieners formula ($1 \to 0$, $N \to N-1$) leads to the formula

$$\frac{\epsilon_{eff} - \epsilon_0}{\epsilon_{eff} + 2\epsilon_0} = \sum_{j=1}^{N} p_j \frac{\epsilon_j - \epsilon_0}{\epsilon_j + 2\epsilon_0} \quad . \tag{22}$$

Now the species 1 to N are the inclusions and the species 0 is the matrix. Comparing to equation (13) with $f = 2$ (spherical inclusions), both formulas turn out to be exactly equal. Therefore, the same constraints concerning the applicability as for the Wiener-formula also apply to Maxwell-Garnetts fromula. In particular, in the case of $p_1 \to 0$, the matrix material vanishes and the Maxwell-Garnett formula might no longer be applicable. In this case, another formula might be better suited, which will be described in subsubsection 4.5.6. On the other hand, Wieners formula with $f = 2$ does not require the spherical inclusions to be all of equal size.
In recent studies, mainly the Maxwell-Garnett formulation with the assumption of randomly oriented and randomly shaped small spheroidal inclusions is preferred in the literature, but with different assumptions about matrix and inclusions.

4.5.6 Mixtures of ice, air and water — Bruggemann formula

Another limiting case of the more general formulation of Stroud (1975) is the formula given by Bruggemann (1935),

$$\sum_{j=1}^{N} p_j \frac{\epsilon_j - \epsilon_{eff}}{\epsilon_j + 2\epsilon_{eff}} = 0 \tag{23}$$

$$p_j = \frac{V_j}{V_m}, \quad \text{where } V_m = \text{Volume of mixture particle}$$

$$\sum_{j=1}^{N} p_j = 1 \quad .$$

It is applicable for a homogeneous mixture of subscale macroscopic granules of different materials (index j) in "dense packing" configuration without giving a special meaning to one of the component materials (Chýlek and Srivastava, 1983). In that sense, the mixing topology assumed for this formula might be regarded as the limiting case of vanishing matrix material (cf. end of subsubsection 4.5.5). It is based on an approximation of the Mie forward scattering function $S_1(0) = S_2(0)$ for the single granules in that only the leading term with coefficient a_1 in equation (3) is retained. The single granules therefore have to be very small compared to the wavelength. Formula (23) is invariant to interchanging the species, as is Oguchis formula (16).
The implicit equation (23) leads to the problem of finding the roots of a complex polynomial of order N in ϵ_{eff}. After the fundamental theorem of algebra there are exactly N complex roots. For $N \leq 3$ there exist analytical solutions ($N = 3$: Cardani's formula, e.g.), and for $N > 3$, these can be found, e.g., iteratively by Laguerre's method (Press et al., 2001).
However, only one of these roots has physical meaning and can be assigned to $m_{eff} = \sqrt{\epsilon_{eff}}$. Usually, the constraints of a negative imaginary part of ϵ_{eff} (by convention in `radar_mielib`) together with the real part of ϵ_{eff} beeing inbetween the range of real parts of the ϵ_j, the physical meaningful root ϵ_{eff} can be identified, at least for a three-component mixture of ice, air and water, as is needed for our purpose.

5 Routines in `radar_mielib`

To calculate Z_e by integration of equation (1) (Page 7), information about the particle size distribution and about the backscattering cross section σ_b as function of particle type, size and degree of melting is needed, which in turn requires information about the effective particle refractive index m_{eff}. The theoretical basics for σ_b (one- and two-layered Mie scattering, Rayleigh approximation) and m_{eff} were briefly discussed in earlier sections, and, in particular, different EMA approximations for m_{eff} were summarized. Up to now and in the remainder of this document, the particle size distributions itself are not treated in detail, since their proper treatment depends strongly on the application: for a bin microphysical scheme resolving explicitely the size distributions of different hydrometeor types, no assumptions have to be drawn about it, whereas for a bulk microphysical scheme, usually a parametric function prototype ("master function" approach) is chosen whose free parameters are diagnosed from model variables. Therefore, the main focus of this document is on the properties of single particles, whereas the integration over the entire size distribution is left for the user.

Before we turn to more detailed investigations of the differences caused by applying different combinations of EMA formulations and melting models for single particles (one-layered or two-layered spheres, different mixing material assumptions) in subsequent sections, a complete list of subroutines and functions from `radar_mielib` will be given in the following subsections providing tools for calculation of σ_b and m_{eff} of single particles.

Later in Section 6, the library `radar_mie_lm` is exemplified to show how these tools can be combined for reflectivity calculations in a mesoscale NWP-model. `radar_mie_lm` provides interface reflectivity calculation subroutines for the LM.

5.1 Refractive index of pure ice and water

5.1.1 `FUNCTION m_complex_water_ray (lambda, T)`

```
INTEGER, PARAMETER    :: kinddp = KIND(1.0d0)
COMPLEX(kind=kinddp)  :: m_complex_water_ray
DOUBLE PRECISION      :: T, lambda
```

Description:

Refractive index of water after Ray (1972), see subsubsection 4.5.1 on Page 12.
Valid for -10°C $< T <$ 30°C, 0.001 m $< \lambda_0 <$ 1 m.

Input parameters:

`kinddp`	kind parameter for double precision
`lambda`	radar wavelength in m
`T`	temperature in °C

Example:

```
mwater = m_complex_water_ray(0.055, 10.0)
```

5.1.2 FUNCTION m_complex_water_liebe (lambda, T)

```
INTEGER, PARAMETER    :: kinddp = KIND(1.0d0)
COMPLEX(kind=kinddp)  :: m_complex_water_liebe
DOUBLE PRECISION      :: T, lambda
```

Description:

Refractive index of water after Liebe et al. (1991), see subsubsection 4.5.1 on Page 12.
Valid for -3°C $< T <$ 30°C, 0.0003 m $< \lambda_0 <$ 0.3 m.

Input parameters:

`kinddp`	kind parameter for double precision
`lambda`	radar wavelength in m
`T`	temperature in °C

Example:

```
mwater = m_complex_water_liebe(0.055, 10.0)
```

5.1.3 FUNCTION m_complex_ice_ray (lambda, T)

```
INTEGER, PARAMETER    :: kinddp = KIND(1.0d0)
COMPLEX(kind=kinddp) :: m_complex_ice_ray
DOUBLE PRECISION      :: T, lambda
```

Description:

Refractive index of ice after Ray (1972), see subsubsection 4.5.2 on Page 13.
Valid for -20°C $< T <$ 0°C, 0.001 m $< \lambda_0 <$ 10^7m.

Input parameters:

`kinddp`	kind parameter for double precision
`lambda`	radar wavelength in m
`T`	temperature in °C

Example:

```
mice = m_complex_ice_ray(0.055, -10.0)
```

5.1.4 FUNCTION m_complex_ice_warren (lambda, T)

```
INTEGER, PARAMETER   :: kinddp = KIND(1.0d0)
COMPLEX(kind=kinddp) :: m_complex_ice_warren
DOUBLE PRECISION     :: T, lambda
```

Description:

Refractive index of ice after Warren (1984), see subsubsection 4.5.2 on Page 13.
Valid for -60°C $< T <$ 0°C, $45 \cdot 10^{-9}$ m $< \lambda_0 <$ 8.6 m.

Input parameters:

`kinddp`	kind parameter for double precision
`lambda`	radar wavelength in m
`T`	temperature in °C

Example:

```
mice = m_complex_ice_warren(0.055, -10.0)
```

5.1.5 FUNCTION m_complex_ice_maetzler (lambda, T)

```
INTEGER, PARAMETER    :: kinddp = KIND(1.0d0)
COMPLEX(kind=kinddp) :: m_complex_ice_maetzler
DOUBLE PRECISION      :: T, lambda
```

Description:

Refractive index of ice after Mätzler (1998), see subsubsection 4.5.2 on Page 13.
Valid for -250°C $< T <$ 0°C, 0.0001 m $< \lambda_0 <$ 30 m.

Input parameters:

`kinddp`	kind parameter for double precision
`lambda`	radar wavelength in m
`T`	temperature in °C

Example:

```
mice = m_complex_ice_maetzler(0.055, -10.0)
```

5.2 Refractive index of mixture materials

5.2.1 FUNCTION m_complex_oguchi (vol1, vol2, vol3, m1, m2, m3, fehler)

```
INTEGER, PARAMETER    :: kinddp = KIND(1.0d0)
COMPLEX(kind=kinddp) :: m_complex_oguchi
COMPLEX(kind=kinddp) :: m1, m2, m3
DOUBLE PRECISION      :: vol1, vol2, vol3
INTEGER, INTENT(out) :: fehler
```

Description:

Refractive index m_{eff} of a three-component mixture material after Oguchi (1983), see equation (16) in subsubsection 4.5.4 on Page 15.

Input parameters:

`kinddp`	kind parameter for double precision
`m1, m2, m3`	complex index of refraction for the three mixture components 1, 2 and 3
`vol1, vol2, vol3`	corresponding volume fractions (conform with p_1, p_2, p_3 from equation (16), $\sum p_j \stackrel{!}{=} 1$)

Output parameters:

`m_complex_oguchi`	complex refractive index m_{eff} of the mixture material, function result
`fehler`	error status (side effect): 0 = no error, 1 = error encountered

Example:

```
mmix = m_complex_oguchi(0.5, 0.3, 0.2, mwater, mice, mair, errorflag)
```

5.2.2 FUNCTION m_complex_maxwellgarnett (vol1, vol2, vol3, m1, m2, m3, inclusionstring, fehler)

```
INTEGER, PARAMETER   :: kinddp = KIND(1.0d0)
COMPLEX(kind=kinddp) :: m_complex_maxwellgarnett
COMPLEX(kind=kinddp) :: m1, m2, m3
DOUBLE PRECISION     :: vol1, vol2, vol3
CHARACTER(len=*)     :: inclusionstring
INTEGER, INTENT(out) :: fehler
```

Description:

Refractive index of a three-component mixture material after Maxwell Garnett (1904), see subsubsection 4.5.5 on Page 16. Both formulas for spherical (equation (18)) and spheroidal (equation (20)) inclusions are implemented and can be chosen via a keyword parameter. The choice which material is the matrix and which are the inclusions is done via the order number of the material: No. 1 denotes the matrix, No. 2 and 3 represent the inclusions (see below).

Input parameters:

`kinddp`	kind parameter for double precision
`m1, m2, m3`	complex index of refraction for the three mixture components 1, 2 and 3. Index 1 denotes the matrix material and 2 and 3 represent the inclusions
`vol1, vol2, vol3`	corresponding volume fractions (conform with p_1, p_2, p_3 from equation (17), $\sum p_j \stackrel{!}{=} 1$)
`inclusionstring`	A string constant to choose if spherical or spheroidal inclusions should be assumed: `'spherical'` — spherical inclusions `'spheroidal'` — spheroidal inclusions

Output parameters:

`m_complex_maxwellgarnett`	complex refractive index m_{eff} of the mixture material, function result
`fehler`	error status (side effect): 0 = no error, 1 = error encountered

Example:

```
mmix = m_complex_maxwellgarnett(0.5, 0.3, 0.2, mwater, mice, mair, 'spheroidal', errorflag
```

5.2.3 FUNCTION m_complex_bruggemann (volair, volice, volwater, mair, mice, mwater, fehler)

```
INTEGER, PARAMETER   :: kinddp = KIND(1.0d0)
COMPLEX(kind=kinddp) :: m_complex_bruggemann
COMPLEX(kind=kinddp) :: mair, mice, mwater
DOUBLE PRECISION     :: volair, volice, volwater
INTEGER, INTENT(out) :: fehler
```

Description:

Refractive index of a three-component mixture of air, ice and water after Bruggemann (1935), see equation (23) in subsubsection 4.5.6 on Page 17.

Note: This routine is especially designed for mixtures of air, ice and water!

Input parameters:

`kinddp`	kind parameter for double precision
`mair, mice, mwater`	complex index of refraction for air, ice and water
`volair, volice, volwater`	corresponding volume fractions (conform with p_1, p_2, p_3 from equation (23), $\sum p_j \stackrel{!}{=} 1$)

Output parameters:

`m_complex_bruggemann`	complex refractive index m_{eff} of the mixture material, function result
`fehler`	error status (side effect): 0 = no error, 1 = error encountered

Example:

```
mmix = m_complex_bruggemann(0.5, 0.3, 0.2, mwater, mice, mair, errorflag)
```

5.2.4 FUNCTION get_m_mix (m_a, m_i, m_w, volair, volice, volwater, mixingrulestring, matrixstring, inclusionstring, fehler)

```
INTEGER, PARAMETER                :: kinddp = KIND(1.0d0)
COMPLEX(kind=kinddp)              :: get_m_mix
COMPLEX(kind=kinddp), INTENT(in)  :: m_a, m_i, m_w
DOUBLE PRECISION, INTENT(in)      :: volair, volice, volwater
CHARACTER(len=*), INTENT(in)      :: mixingrulestring
CHARACTER(len=*), INTENT(in)      :: matrixstring
CHARACTER(len=*), INTENT(in)      :: inclusionstring
INTEGER, INTENT(out)              :: fehler
```

Description:

Interface routine to the basic functions `m_complex_oguchi()`, `m_complex_maxwellgarnett()` and `m_complex_bruggemann()` for a three-component mixture. Three keyword parameter strings determine, which mixingrule and, if necessary, which matrix material should be chosen. **Note: This routine is especially designed for mixtures of air, ice and water!**

Input parameters:

`kinddp`	kind parameter for double precision
`m_a, m_i, m_w`	complex index of refraction for air, ice and water, resp.
`volair, volice, volwater`	corresponding volume fractions (conform with p_1, p_2, p_3 from equation (23), $\sum p_j \stackrel{!}{=} 1$)

`mixingrulestring`	A string constant to choose the mixing rule:
	`'oguchi'` — `m_complex_oguchi()`, spherical inclusions
	`'maxwellgarnett'` — `m_complex_maxwellgarnett()`
	`'bruggemann'` — `m_complex_bruggemann()`

`matrixstring`	In case of `mixingrulestring = 'maxwellgarnett'`, choice of the matrix material: `'air'` — air `'ice'` — ice `'water'` — water
`inclusionstring`	A string constant to choose if spherical or spheroidal inclusions should be assumed: `'spherical'` — spherical inclusions `'spheroidal'` — spheroidal inclusions

Output parameters:

`get_m_mix`	complex refractive index m_{eff} of the mixture material, function result
`fehler`	error status (side effect): 0 = no error, 1 = error encountered

Example:

```
mmix = get_m_mix(mair, mice, mwater, 0.2, 0.3, 0.5, 'maxwellgarnett', &
                 'ice', 'spheroidal', errorflag)
```

5.2.5 FUNCTION get_m_mix_nested (m_a, m_i, m_w, volair, volice, volwater, mixingrulestring, hoststring, matrixstring, inclusionstring, hostmatrixstring, hostinclusionstring, kumfehler)

```
INTEGER, PARAMETER                :: kinddp = KIND(1.0d0)
COMPLEX(kind=kinddp)              :: get_m_mix_nested
COMPLEX(kind=kinddp), INTENT(in)  :: m_a, m_i, m_w
DOUBLE PRECISION, INTENT(in)      :: volair, volice, volwater
CHARACTER(len=*), INTENT(in)      :: mixingrulestring
CHARACTER(len=*), INTENT(in)      :: hoststring
CHARACTER(len=*), INTENT(in)      :: matrixstring
CHARACTER(len=*), INTENT(in)      :: inclusionstring
CHARACTER(len=*), INTENT(in)      :: hostmatrixstring
CHARACTER(len=*), INTENT(in)      :: hostinclusionstring
INTEGER, INTENT(out)              :: kumfehler
```

Description:

Interface routine to the basic functions `m_complex_oguchi()`, `m_complex_maxwellgarnett()` and `m_complex_bruggemann()` for a three-component mixture. The difference to `get_m_mix()` (subsubsection 5.2.4) is that, once a particular mixing rule is chosen, additionally a twofold mixing of two two-component mixtures is possible. This offers for the Maxwell-Garnett rule 30 different choices in total. If this twofold mixing is specified, first m_{eff} of a mixture of two of the three components is calculated ("inner" mixing material), and later, this effective medium is mixed with the remaining third compontent ("outer" mixture). **Note that the twofold application of two two-component mixtures with different mixing rules is not implemented so far.** In case of Bruggemann- and Oguchi-rule, it does not make any difference if choosing the three-component or twofold two-component mixing.

Six keyword parameter strings determine, which mixingrule and (if necessary) if twofold two-component or three-component mixture with which matrix material(s) should be chosen (see below for details). **Note: This routine is especially designed for mixtures of air, ice and water!**

Input parameters:

`kinddp`	kind parameter for double precision
`m_a, m_i, m_w`	complex index of refraction for air, ice and water, resp.
`volair, volice, volwater`	corresponding volume fractions (conform with p_1, p_2, p_3 from equation (23), $\sum p_j \stackrel{!}{=} 1$)

`mixingrulestring`	A string constant to choose the mixing rule:
	`'oguchi'` — `m_complex_oguchi()`, spherical inclusions
	`'maxwellgarnett'` — `m_complex_maxwellgarnett()`
	`'bruggemann'` — `m_complex_bruggemann()`

`hoststring`	Determines which material should be the hosting ("outer") material in a twofold two-component mixture or if a three-component mixture should be chosen: `'none'` — onefold three-component mixture `'air'` — air `'ice'` — ice `'water'` — water

`matrixstring`
: In case of twofold two-component mixture (`hoststring` $\neq$ `'none'`) and Maxwell-Garnett mixing rule, choice of the matrix material of the "inner" mixture:
`'air'` — air
`'ice'` — ice
`'water'` — water
(not equal to `hoststring`!)

  In case of three-component mixture (`hoststring = 'none'`), the usual choice of the matrix material:
`'air'` — air
`'ice'` — ice
`'water'` — water

`inclusionstring`
: A string constant to choose if spherical or spheroidal inclusions should be assumed (in case of twofold two-component mixture, for the "inner" mixture):
`'spherical'` — spherical inclusions
`'spheroidal'` — spheroidal inclusions

`hostmatrixstring`
: In case of `mixingrulestring = 'maxwellgarnett'` and twofold two-component mixture, choice of the matrix material of the "outer" mixture (no meaning in case of `hoststring = 'none'`):
`'air'` — air
`'ice'` — ice
`'water'` — water
`'airice'` — air/ice-mixture
`'airwater'` — air/water-mixture
`'icewater'` — ice/water-mixture

`hostinclusionstring`
: In case of twofold two-component mixture, for the "outer" mixture, a string constant to choose if spherical or spheroidal inclusions should be assumed:
`'spherical'` — spherical inclusions
`'spheroidal'` — spheroidal inclusions

Note that not all combinations of these six keyword parameter strings does make sense. Nonsense combinations will lead to an error ($m_{eff} = -999.99$), a corresponding error message and `kumfehler` $\neq$ `0`.

Output parameters:

`get_m_mix`
: complex refractive index m_{eff} of the mixture material, function result

`kumfehler`
: error status (side effect): 0 = no error, 1 = error encountered

Example:

```
mmix = get_m_mix_nested(mair, mice, mwater, 0.2, 0.3, 0.5, &
             'maxwellgarnett', 'air', 'water', 'spherical', &
             'icewater', 'spheroidal', errorflag)
```

5.3 Backscattering cross section for single precipitation particles

5.3.1 SUBROUTINE MIE_DRY_GRAUPEL (x_g,a_geo,b_geo,m_i,lambda,C_back, mixingrulestring, matrixstring, inclusionstring)

```
INTEGER, PARAMETER                :: kinddp = KIND(1.0d0)
DOUBLE PRECISION, INTENT(in)      :: x_g, lambda, a_geo, b_geo
COMPLEX(kind=kinddp), INTENT(in) :: m_i
CHARACTER(len=*), INTENT(in)      :: mixingrulestring
CHARACTER(len=*), INTENT(in)      :: matrixstring
CHARACTER(len=*), INTENT(in)      :: inclusionstring
DOUBLE PRECISION, INTENT(out)     :: C_back
```

Description:

Backscattering cross section σ_b (Mie-scattering) of a dry graupel/snow/hail particle, assumed as a **sphere of homogeneous ice-air mixture material**. The particle bulk density is derived from the inverse mass-size-relation (40) with coefficients a_{geo} and b_{geo} assuming spherical shape. `mixingrulestring`, `matrixstring` and `inclusionstring` determine the effective medium approximation used to calculate the effective refractive index of the particles, which is done by function `get_m_mix` (Subsection 5.2).

For relatively small particles, the Rayleigh approximation can be applied instead by using subroutine `RAYLEIGH_DRY_GRAUPEL()` (subsubsection 5.3.2).

Input parameters:

`kinddp`	kind parameter for double precision
`x_g`	Mass of particle in kg (without air fraction)
`a_geo`	Coefficient a_{geo} of the inverse mass-size-relation (40)
`b_geo`	Coefficient b_{geo} of the inverse mass-size-relation (40)
`m_i`	Complex refractive index of ice
`lambda`	Radar wavelength in m

`mixingrulestring`	A string constant to choose the mixing rule:
	`'oguchi'` — `m_complex_oguchi()`, spherical inclusions
	`'maxwellgarnett'` — `m_complex_maxwellgarnett()`
	`'bruggemann'` — `m_complex_bruggemann()`

`matrixstring`	In case of `mixingrulestring = 'maxwellgarnett'`, choice of the matrix material: `'air'` — air `'ice'` — ice `'water'` — water (does not make sense here)
`inclusionstring`	A string constant to choose if spherical or spheroidal inclusions should be assumed: `'spherical'` — spherical inclusions `'spheroidal'` — spheroidal inclusions

Output parameters:

`C_back`	Backscattering cross section σ_b in m^2

Example:

```
CALL MIE_DRY_GRAUPEL(2.3e-3, a_geo, b_geo, m_i, 0.055, C_back, &
     'maxwellgarnett', 'ice', 'spheroidal')
```

5.3.2 SUBROUTINE RAYLEIGH_DRY_GRAUPEL (x_g,a_geo,b_geo,m_i,lambda,C_back, mixingrulestring, matrixstring, inclusionstring)

```
INTEGER, PARAMETER                :: kinddp = KIND(1.0d0)
DOUBLE PRECISION, INTENT(in)      :: x_g, lambda, a_geo, b_geo
COMPLEX(kind=kinddp), INTENT(in) :: m_i
CHARACTER(len=*), INTENT(in)      :: mixingrulestring
CHARACTER(len=*), INTENT(in)      :: matrixstring
CHARACTER(len=*), INTENT(in)      :: inclusionstring
DOUBLE PRECISION, INTENT(out)     :: C_back
```

Description:

Backscattering cross section σ_b (Rayleigh approximation) of a dry graupel/snow/hail particle, assumed as a **sphere of homogeneous ice-air mixture material**. The particle bulk density is derived from the inverse mass-size-relation (40) with coefficients a_{geo} and b_{geo} assuming spherical shape. `mixingrulestring`, `matrixstring` and `inclusionstring` determine the effective medium approximation used to calculate the effective refractive index of the particles, which is done by function `get_m_mix` (Subsection 5.2).

Input parameters:

`kinddp`	kind parameter for double precision
`x_g`	Mass of particle in kg (without air fraction)
`a_geo`	Coefficient a_{geo} of the inverse mass-size-relation (40)
`b_geo`	Coefficient b_{geo} of the inverse mass-size-relation (40)
`m_i`	Complex refractive index of ice
`lambda`	Radar wavelength in m

`mixingrulestring`	A string constant to choose the mixing rule:
	`'oguchi'` — `m_complex_oguchi()`, spherical inclusions
	`'maxwellgarnett'` — `m_complex_maxwellgarnett()`
	`'bruggemann'` — `m_complex_bruggemann()`

`matrixstring`	In case of `mixingrulestring = 'maxwellgarnett'`, choice of the matrix material: `'air'` — air `'ice'` — ice `'water'` — water (does not make sense here)
`inclusionstring`	A string constant to choose if spherical or spheroidal inclusions should be assumed: `'spherical'` — spherical inclusions `'spheroidal'` — spheroidal inclusions

Output parameters:

`C_back`	Backscattering cross section σ_b in m^2

Example:

```
CALL RAYLEIGH_DRY_GRAUPEL(2.3e-3, a_geo, b_geo, m_i, 0.055, C_back, &
     'maxwellgarnett', 'ice', 'spheroidal')
```

5.3.3 SUBROUTINE MIE_DRYHAIL (x_h,a_geo,b_geo,m_i,lambda,C_back)

```
INTEGER, PARAMETER                :: kinddp = KIND(1.0d0)
DOUBLE PRECISION, INTENT(in)      :: x_h, lambda, a_geo, b_geo
COMPLEX(kind=kinddp), INTENT(in) :: m_i
DOUBLE PRECISION, INTENT(out)     :: C_back
```

Description:

Backscattering cross section σ_b (Mie-scattering) of a dry hail particle, assumed as a **homogeneous ice sphere**. It is an approximation to `MIE_DRY_GRAUPEL()` (subsubsection 5.3.1) in the sense that although the particle bulk density is permitted to deviate from pure ice, but solid ice is assumed for the particles refractive index (m_i). The purpose of this is to save computation time in case of high density ice particles. Therefore, this routine is only applicable to particle types whose coefficients a_{geo} and b_{geo} of the inverse mass-size-relation (40) represent nearly solid ice particles.

For smaller particles, the Rayleigh approximation can be applied by subroutine `RAYLEIGH_DRY_GRAUPEL` instead (subsubsection 5.3.2).

Input parameters:

`kinddp`	kind parameter for double precision
`x_h`	Mass of hail particle in kg
`a_geo`	Coefficient a_{geo} of the inverse mass-size-relation (40)
`b_geo`	Coefficient b_{geo} of the inverse mass-size-relation (40)
`m_i`	Complex refractive index of ice
`lambda`	Radar wavelength in m

Output parameters:

`C_back`	Backscattering cross section σ_b in m^2

Example:

```
CALL MIE_DRYHAIL(2.3e-3, a_geo, b_geo, m_i, 0.055, C_back)
```

5.3.4 SUBROUTINE MIE_DRYSNOW (x_s,a_geo,b_geo,m_i,lambda,C_back, mixingrulestring, matrixstring, inclusionstring)

```
INTEGER, PARAMETER                :: kinddp = KIND(1.0d0)
DOUBLE PRECISION, INTENT(in)      :: x_s, lambda, a_geo, b_geo
COMPLEX(kind=kinddp), INTENT(in) :: m_i
CHARACTER(len=*), INTENT(in)      :: mixingrulestring
CHARACTER(len=*), INTENT(in)      :: matrixstring
CHARACTER(len=*), INTENT(in)      :: inclusionstring
DOUBLE PRECISION, INTENT(out)     :: C_back
```

Description:

Backscattering cross section σ_b (Mie-scattering) of a dry graupel/snow/hail particle, assumed as a **sphere of homogeneous ice-air mixture material**. The particle bulk density is derived from the inverse mass-size-relation (40) with coefficients a_{geo} and b_{geo} assuming spherical shape. `mixingrulestring`, `matrixstring` and `inclusionstring` determine the effective medium approximation used to calculate the effective refractive index of the particles, which is done by function `get_m_mix` (Subsection 5.2).

For smaller particles, the Rayleigh approximation can be applied by using subroutine `RAYLEIGH_DRY_GRAUPEL` instead (subsubsection 5.3.2).

The only difference to subroutine `MIE_DRY_GRAUPEL` (subsubsection 5.3.1) is that a equivalent spherical diameter threshold of 10^{-12} m is used instead of 10^{-6} m below which C_back is set to 0 to save computation time.

Input parameters:

`kinddp`	kind parameter for double precision
`x_s`	Mass of particle in kg (without air fraction)
`a_geo`	Coefficient a_{geo} of the inverse mass-size-relation (40)
`b_geo`	Coefficient b_{geo} of the inverse mass-size-relation (40)
`m_i`	Complex refractive index of ice
`lambda`	Radar wavelength in m

`mixingrulestring`	A string constant to choose the mixing rule:
	`'oguchi'` — `m_complex_oguchi()`, spherical inclusions
	`'maxwellgarnett'` — `m_complex_maxwellgarnett()`
	`'bruggemann'` — `m_complex_bruggemann()`

`matrixstring`	In case of `mixingrulestring = 'maxwellgarnett'`, choice of the matrix material: `'air'` — air `'ice'` — ice `'water'` — water (does not make sense here)
`inclusionstring`	A string constant to choose if spherical or spheroidal inclusions should be assumed: `'spherical'` — spherical inclusions `'spheroidal'` — spheroidal inclusions

Output parameters:

`C_back`	Backscattering cross section σ_b in m^2

Example:

```
CALL MIE_DRYSNOW(3.4e-5, a_geo, b_geo, m_i, 0.055, C_back, &
     'maxwellgarnett', 'ice', 'spheroidal')
```

5.3.5 SUBROUTINE MIE_DRYSNOW_TWOSPH (x_s,a_geo,b_geo,m_i,radienverh,lambda,C_back, mixingrulestring_shell, matrixstring_shell, inclusionstring_shell, mixingrulestring_core, matrixstring_core, inclusionstring_core)

```
INTEGER, PARAMETER                :: kinddp = KIND(1.0d0)
DOUBLE PRECISION, INTENT(in)      :: x_s, lambda, a_geo, b_geo
DOUBLE PRECISION, INTENT(in)      :: radienverh
COMPLEX(kind=kinddp), INTENT(in) :: m_i
CHARACTER(len=*), INTENT(in)      :: mixingrulestring_shell
CHARACTER(len=*), INTENT(in)      :: matrixstring_shell
CHARACTER(len=*), INTENT(in)      :: inclusionstring_shell
CHARACTER(len=*), INTENT(in)      :: mixingrulestring_core
CHARACTER(len=*), INTENT(in)      :: matrixstring_core
CHARACTER(len=*), INTENT(in)      :: inclusionstring_core
DOUBLE PRECISION, INTENT(out)     :: C_back
```

Description:

Backscattering cross section σ_b (Mie-scattering) of a dry snowflake, assumed as a **two-layered sphere of homogeneous ice-air mixture material in each layer, the core having higher bulk density than the shell (see Subsection 7.2).** The overall particle bulk density is derived from the inverse mass-size-relation (40) with coefficients a_{geo} and b_{geo} assuming spherical shape. Note that b_{geo} has to represent a decreasing bulk density with size.

To model a snowflake by a two-layered sphere with a denser core and a less dense shell, additional information is necessary to assign the different bulk densities to core and shell, preserving overall particle mass. To this end, as additional parameter, the ratio of the inner to the outer sphere radius, `radienverh`, has to be specified with a value between 0 and 1. With this parameter, the procedure discribed later in Subsection 7.2 on Page 71 is applied to assign different bulk densities to core and shell.

Further, the input parameters `mixingrulestring_shell`/ `mixingrulestring_core`, `matrixstring_shell`/ `matrixstring_core` and `inclusionstring_shell`/ `inclusionstring_core` determine the effective medium approximation used to calculate the effective refractive index of the particles shell/ core, which is done by function `get_m_mix` (Subsection 5.2).

This routine uses the formulae of Bohren and Huffman (1983) for the backscattering cross section of a two-layered sphere (subroutine `COATEDSPHERE_SCATTER_BH()`), see Subsection 4.4.

Input parameters:

`kinddp`	kind parameter for double precision
`x_s`	Mass of particle in kg (without air fraction)
`a_geo`	Coefficient a_{geo} of the inverse mass-size-relation (40)
`b_geo`	Coefficient b_{geo} of the inverse mass-size-relation (40)
`radienverh`	Ratio of the inner to the outer sphere radius
`m_i`	Complex refractive index of ice
`lambda`	Radar wavelength in m

`mixingrulestring_shell/` `mixingrulestring_core`	String constants to choose the mixing rule:
	`'oguchi'` — `m_complex_oguchi()`, spherical inclusions
	`'maxwellgarnett'` — `m_complex_maxwellgarnett()`
	`'bruggemann'` — `m_complex_bruggemann()`

`matrixstring_shell/` `matrixstring_core`	In case of `mixingrulestring = 'maxwellgarnett'`, choice of the matrix material: `'air'` — air `'ice'` — ice `'water'` — water (does not make sense here)
`inclusionstring_shell/` `inclusionstring_core`	String constants to choose if spherical or spheroidal inclusions should be assumed: `'spherical'` — spherical inclusions `'spheroidal'` — spheroidal inclusions

Output parameters:

`C_back`	Backscattering cross section σ_b in m^2

Example:

```
CALL MIE_DRYSNOW_TWOSPH(3.4e-5, a_geo, b_geo, m_i, 0.055, C_back, &
     'maxwellgarnett', 'air', 'spheroidal', &
     'maxwellgarnett', 'ice', 'spheroidal')
```

5.3.6 SUBROUTINE MIE_WATERSPH_WETHAIL (x_h,fmelt,m_i,m_w,lambda,C_back)

```
INTEGER, PARAMETER                :: kinddp = KIND(1.0d0)
DOUBLE PRECISION, INTENT(in)      :: x_h, fmelt, lambda
DOUBLE PRECISION, INTENT(out)     :: C_back
COMPLEX(kind=kinddp), INTENT(in) :: m_i, m_w
```

Description:

Backscattering cross section σ_b of a melting hail particle, assumed as a **solid spherical ice core with spherical water coating**, calculated by the two-sphere Mie-formulae. Here, the formulae of Kerker (1969) are applied (subroutine `COATEDSPHERE_SCATTER()`), see Subsection 4.4.

To speed up computation (but with some loss of stability), the **subroutine** `MIE_WATERSPH_WETHAIL_BH()` can be used instead with exactly the same input- and output parameters. This routine utilizes the formulae of Bohren and Huffman (1983) (subroutine `COATEDSPHERE_SCATTER_BH()`) instead of Kerker (1969), see Subsection 4.4.

Input parameters:

`kinddp`	kind parameter for double precision
`x_h`	Mass of hail particle in kg
`fmelt`	degree of melting, $f_{melt} = x_w/x_h$ (x_w = mass of water contained in the particle)
`m_i`	Complex refractive index of ice
`m_w`	Complex refractive index of water
`lambda`	Radar wavelength in m

Output parameters:

`C_back`	Backscattering cross section σ_b in m^2

Example:

```
CALL MIE_WATERSPH_WETHAIL(2.3e-3, 0.7, m_i, m_w, 0.055, C_back)
```

Example sensitivity studies:

The dependence of σ_b on the degree of melting and on particle size for a specific temperature of $T = 5°C$ is studied in detail in Subsection 8.18 on Page 107.

5.3.7 SUBROUTINE MIE_SPONGY_WETHAIL (x_h,fmelt,f_water,m_i,m_w,lambda,C_back, mixingrulestring, matrixstring, inclusionstring)

```
INTEGER, PARAMETER                :: kinddp = KIND(1.0d0)
DOUBLE PRECISION, INTENT(in)      :: x_h, fmelt, f_water, lambda
COMPLEX(kind=kinddp), INTENT(in) :: m_i, m_w
CHARACTER(len=*), INTENT(in)      :: mixingrulestring
CHARACTER(len=*), INTENT(in)      :: matrixstring
CHARACTER(len=*), INTENT(in)      :: inclusionstring
DOUBLE PRECISION, INTENT(out)     :: C_back
```

Description:

Backscattering cross section σ_b of a melting hail particle, assumed as a **solid spherical ice core with a spherical coating of a "spongy" ice-water mixture**, calculated by the two-sphere Mie-formulae. Here, the formulae of Kerker (1969) are applied (subroutine `COATEDSPHERE_SCATTER()`), see Subsection 4.4. The mass fraction of water (`f_water`) in the outer spongy shell has to be preset and is held fixed throughout the melting process, as long as the inner ice core is not completely melted. After the inner core has completely vanished, `f_water` is increased automatically to represent now the melted fraction of the remaining homogeneous spherical particle.

It seems reasonable to assume larger values of `f_water` during later melting stages (larger `fmelt`) than for earlier melting stages (small `fmelt`).

To speed up computation (but with some loss of stability), the **subroutine** `MIE_SPONGY_WETHAIL_BH()` can be used instead with exactly the same input- and output parameters. This routine utilizes the formulae of Bohren and Huffman (1983) (subroutine `COATEDSPHERE_SCATTER_BH()`) instead of Kerker (1969), see Subsection 4.4.

Input parameters:

`kinddp`	kind parameter for double precision
`x_h`	Mass of hail particle in kg
`fmelt`	Degree of melting, $f_{melt} = x_w/x_h$ (x_w = mass of water contained in the particle)
`f_water`	Mass fraction of water in the outer spongy shell ($x_{water}/(x_{ice} + x_{water})$)
`m_i`	Complex refractive index of ice
`m_w`	Complex refractive index of water
`lambda`	Radar wavelength in m

`mixingrulestring`	A string constant to choose the mixing rule for the ice-water shell:
	`'oguchi'` — `m_complex_oguchi()`, spherical inclusions
	`'maxwellgarnett'` — `m_complex_maxwellgarnett()`
	`'bruggemann'` — `m_complex_bruggemann()`

`matrixstring`	In case of `mixingrulestring = 'maxwellgarnett'`, choice of the matrix material for the ice-water shell: `'air'` — air (does not make sense here) `'ice'` — ice `'water'` — water
`inclusionstring`	A string constant to choose if spherical or spheroidal inclusions should be assumed for the ice-water shell: `'spherical'` — spherical inclusions `'spheroidal'` — spheroidal inclusions

Output parameters:

`C_back`	Backscattering cross section σ_b in m^2

Example:

```
CALL MIE_SPONGY_WETHAIL(2.3e-3, 0.7, 0.5, m_i, m_w, 0.055, C_back)
```

Example sensitivity studies:

The dependence of σ_b on the degree of melting and on particle size for a specific temperature of $T = 5°\mathrm{C}$ is studied in detail in Subsection 8.17 on Page 106.

5.3.8 SUBROUTINE MIE_WATERSPH_WETGR (x_g,a_geo,b_geo,fmelt,m_w,m_i,lambda,C_back, mixingrulestring, matrixstring, inclusionstring)

```
INTEGER, PARAMETER                :: kinddp = KIND(1.0d0)
DOUBLE PRECISION, INTENT(in)      :: x_g, lambda, a_geo, b_geo, fmelt
COMPLEX(kind=kinddp), INTENT(in) :: m_w, m_i
CHARACTER(len=*), INTENT(in)      :: mixingrulestring
CHARACTER(len=*), INTENT(in)      :: matrixstring
CHARACTER(len=*), INTENT(in)      :: inclusionstring
DOUBLE PRECISION, INTENT(out)     :: C_back
```

Description:

Backscattering cross section σ_b (Mie-scattering, two-layered sphere) of a melting graupel particle, assumed as a **two-layered sphere composed of a homogeneous ice-air mixture core and a spherical water shell**. The bulk density (ice mass per particle volume) of the original unmelted particle is derived from the inverse mass-size-relation (40) with coefficients a_{geo} and b_{geo} assuming spherical shape. `fmelt` denotes the melted mass fraction or the degree of melting, f_{melt}, resp. It is assumed that the particle melts entirely at the outside of the ice-air core and that the meltwater is accumulated in a spherical shell. `mixingrulestring`, `matrixstring` and `inclusionstring` determine the effective medium approximation used to calculate the effective refractive index of the particle ice-air core, which is done by function `get_m_mix` (Subsection 5.2). Such a melting model should be applicable to relatively high-density graupel and/ or at later melting stages (`fmelt` > approx. 0.5).

For the calculation of the two-sphere backscattering cross section, the formulae of Kerker (1969) are applied (subroutine `COATEDSPHERE_SCATTER()`), see Subsection 4.4.

To speed up computation (but with some loss of stability), the **subroutine** `MIE_WATERSPH_WETGR_BH()` can be used instead with exactly the same input- and output parameters. This routine utilizes the formulae of Bohren and Huffman (1983) (subroutine `COATEDSPHERE_SCATTER_BH()`) instead of Kerker (1969), see Subsection 4.4.

Input parameters:

`kinddp`	kind parameter for double precision
`x_g`	Mass of particle in kg (without air fraction)
`a_geo`	Coefficient a_{geo} of the inverse mass-size-relation (40)
`b_geo`	Coefficient b_{geo} of the inverse mass-size-relation (40)
`fmelt`	Degree of melting, $f_{melt} = x_w/x_g$ (x_w = mass of water contained in the particle)
`m_w`	Complex refractive index of water
`m_i`	Complex refractive index of ice
`lambda`	Radar wavelength in m

`mixingrulestring`	A string constant to choose the mixing rule for the ice-air core:
	`'oguchi'` — `m_complex_oguchi()`, spherical inclusions
	`'maxwellgarnett'` — `m_complex_maxwellgarnett()`
	`'bruggemann'` — `m_complex_bruggemann()`

`matrixstring`	In case of `mixingrulestring = 'maxwellgarnett'`, choice of the matrix material for the ice-air core: `'air'` — air `'ice'` — ice `'water'` — water (does not make sense here)
`inclusionstring`	A string constant to choose if spherical or spheroidal inclusions should be assumed for the ice-air core: `'spherical'` — spherical inclusions `'spheroidal'` — spheroidal inclusions

Output parameters:

`C_back`	Backscattering cross section σ_b in m^2

Example:

```
CALL MIE_WATERSPH_WETGR(2.3e-3, a_geo, b_geo, &
          0.45, m_w, m_i, 0.055, C_back, &
          'maxwellgarnett', 'ice', 'spheroidal')
```

Example sensitivity studies:

The dependence of σ_b on the degree of melting and on particle size for a specific temperature of $T = 5°C$ is studied in detail in subsequent sections for the 4 different inverse mass-size-relations given in Subsection 7.1. These are:

- for inverse mass-size-relation (36) in Subsection 8.9 on Page 92,
- for inverse mass-size-relation (37) in Subsection 8.10 on Page 95,
- for inverse mass-size-relation (38) in Subsection 8.11 on Page 98,
- for inverse mass-size-relation (39) in Subsection 8.12 on Page 100.

5.3.9 SUBROUTINE MIE_SOAK_TWOSPH_WETGR (x_g,a_geo,b_geo,fmelt,m_w,m_i,lambda,C_back, mixingrulestring_iceair, matrixstring_iceair, inclusionstring_iceair, mixingrulestring_icewater, matrixstring_icewater, inclusionstring_icewater)

```
INTEGER, PARAMETER                :: kinddp = KIND(1.0d0)
DOUBLE PRECISION, INTENT(in)      :: x_g, lambda, a_geo, b_geo, fmelt
COMPLEX(kind=kinddp), INTENT(in) :: m_w, m_i
CHARACTER(len=*), INTENT(in)      :: mixingrulestring
CHARACTER(len=*), INTENT(in)      :: matrixstring
CHARACTER(len=*), INTENT(in)      :: inclusionstring
DOUBLE PRECISION, INTENT(out)     :: C_back
```

Description:

Backscattering cross section σ_b (Mie-scattering, two-layered sphere) of a melting graupel/snow particle, assumed as a **two-layered sphere composed of a homogeneous ice-air mixture core and a spherical ice-water mixture shell**. The bulk density (ice mass per particle volume) of the original unmelted particle is derived from the inverse mass-size-relation (40) with coefficients a_{geo} and b_{geo} assuming spherical shape. `fmelt` denotes the melted mass fraction or the degree of melting, f_{melt}, resp. It is assumed that the particle melts entirely on its outside and that the meltwater is soaked into the particle, displacing the air inclusions entirely from the outside. In this way, a spherical ice-water mixture shell forms around the ice-air core, growing to the inside with growing melt fraction, up to the melt fraction where the particle is completely soaked and the core has vanished. For a larger melt fraction, the particle is assumed as a sphere of homogeneous ice-water mixture.

Such a melting model should be applicable to graupel with intermediate density at all melting stages or to high-density graupel during an early melting stage (`fmelt` < approx. 0.5).

`mixingrulestring_iceair`/ `mixingrulestring_icewater`, `matrixstring_iceair`/ `matrixstring_icewater` and `inclusionstring_iceair`/ `inclusionstring_icewater` determine the effective medium approximation used to calculate the effective refractive index of the particle ice-air core/ ice-water shell. Both calculations are performed using the function `get_m_mix` (Subsection 5.2).

For the calculation of the two-sphere backscattering cross section, the formulae of Kerker (1969) are applied (subroutine `COATEDSPHERE_SCATTER()`), see Subsection 4.4.

To speed up computation (but with some loss of stability), the **subroutine** `MIE_SOAK_TWOSPH_WETGR_BH()` can be used instead with exactly the same input- and output parameters. This routine utilizes the formulae of Bohren and Huffman (1983) (subroutine `COATEDSPHERE_SCATTER_BH()`) instead of Kerker (1969), see Subsection 4.4.

Input parameters:

`kinddp`	kind parameter for double precision
`x_g`	Mass of particle in kg (without air fraction)
`a_geo`	Coefficient a_{geo} of the inverse mass-size-relation (40)
`b_geo`	Coefficient b_{geo} of the inverse mass-size-relation (40)

`fmelt`	Degree of melting, $f_{melt} = x_w/x_g$ (x_w = mass of water contained in the particle)
`m_w`	Complex refractive index of water
`m_i`	Complex refractive index of ice
`lambda`	Radar wavelength in m

`mixingrulestring_iceair`/ `mixingrulestring_icewater`	String constants to choose the mixing rule for the ice-air core/ ice-water shell:
	`'oguchi'` — `m_complex_oguchi()`, spherical inclusions
	`'maxwellgarnett'` — `m_complex_maxwellgarnett()`
	`'bruggemann'` — `m_complex_bruggemann()`

`matrixstring_iceair`/ `matrixstring_icewater`	In case of `mixingrulestring = 'maxwellgarnett'`, choice of the matrix material for the ice-air core/ ice-water shell: `'air'` — air (not for `matrixstring_icewater`) `'ice'` — ice `'water'` — water (not for `matrixstring_iceair`)
`inclusionstring_iceair`/ `inclusionstring_icewater`	String constants to choose if spherical or spheroidal inclusions should be assumed for the ice-air core/ ice-water shell: `'spherical'` — spherical inclusions `'spheroidal'` — spheroidal inclusions

Output parameters:

`C_back`	Backscattering cross section σ_b in m^2

Example:

```
CALL MIE_SOAK_TWOSPH_WETGR(2.3e-3, a_geo, b_geo, &
          0.45, m_w, m_i, 0.055, C_back, &
          'maxwellgarnett', 'ice', 'spheroidal', &
          'maxwellgarnett', 'water', 'spheroidal')
```

Example sensitivity studies:

The dependence of σ_b on the degree of melting and on particle size for a specific temperature of $T = 5°C$ is studied in detail in subsequent sections for the 4 different inverse mass-size-relations given in Subsection 7.1. These are:

- for inverse mass-size-relation (36) in Subsection 8.5 on Page 84,
- for inverse mass-size-relation (37) in Subsection 8.6 on Page 86,
- for inverse mass-size-relation (38) in Subsection 8.7 on Page 88,
- for inverse mass-size-relation (39) in Subsection 8.8 on Page 90.

5.3.10 SUBROUTINE MIE_MEAN_WETGR (x_g,a_geo,b_geo,fmelt,m_w,m_i,lambda,C_back, mixingrulestring_iceair, matrixstring_iceair, inclusionstring_iceair, mixingrulestring_icewater, matrixstring_icewater, inclusionstring_icewater)

```
INTEGER, PARAMETER                :: kinddp = KIND(1.0d0)
DOUBLE PRECISION, INTENT(in)      :: x_g, lambda, a_geo, b_geo, fmelt
COMPLEX(kind=kinddp), INTENT(in) :: m_w, m_i
CHARACTER(len=*), INTENT(in)      :: mixingrulestring_iceair
CHARACTER(len=*), INTENT(in)      :: matrixstring_iceair
CHARACTER(len=*), INTENT(in)      :: inclusionstring_iceair
CHARACTER(len=*), INTENT(in)      :: mixingrulestring_icewater
CHARACTER(len=*), INTENT(in)      :: matrixstring_icewater
CHARACTER(len=*), INTENT(in)      :: inclusionstring_icewater
DOUBLE PRECISION, INTENT(out)     :: C_back
```

Description:

Backscattering cross section σ_b of a melting graupel particle (Mie-scattering, two-layered sphere model), assumed as melt fraction weighted mean of the backscattering coefficients calculated with the subroutines `MIE_WATERSPH_WETGR()` (subsubsection 5.3.8) and `MIE_SOAK_TWOSPH_WETGR()` (subsubsection 5.3.9):

$$C_{back} \;=\; f_{melt}\, C_{watersphere} \;+\; (1.0 \;-\; f_{melt})\, C_{soak_twosphere} \quad .$$

In this way, the melting particle is assumed to soak the meltwater during the early stage of melting and to accumulate more and more meltwater on the outside at later melting stages.

`mixingrulestring_iceair`, `matrixstring_iceair` and `inclusionstring_iceair` determine the choice of the effective medium approximation for the two-component ice-air core in subroutine `MIE_WATERSPH_WETGR()` as well as in subroutine `MIE_SOAK_TWOSPH_WETGR()`. `mixingrulestring_icewater`, `matrixstring_icewater` and `inclusionstring_icewater` do the same for the ice-water shell in `MIE_SOAK_TWOSPH_WETGR()`.

Input- and output parameters are virtually the same as in subsubsection 5.3.9 on Page 45!

Example:

```
CALL MIE_MEAN_WETGR(2.3e-3, a_geo, b_geo, &
          0.45, m_w, m_i, 0.055, C_back, &
          'maxwellgarnett', 'ice', 'spheroidal', &
          'maxwellgarnett', 'water', 'spheroidal')
```

Example sensitivity studies:

Not shown in the present document.

5.3.11 SUBROUTINE MIE_SOAK_WETGR (x_g,a_geo,b_geo,fmelt,meltratio_outside,m_w,m_i,lambda,C_back, mixingrulestring, matrixstring, inclusionstring, hoststring, hostmatrixstring, hostinclusionstring)

```
INTEGER, PARAMETER                :: kinddp = KIND(1.0d0)
DOUBLE PRECISION, INTENT(in)      :: x_g, lambda, a_geo, b_geo, fmelt
DOUBLE PRECISION, INTENT(in)      :: meltratio_outside
COMPLEX(kind=kinddp), INTENT(in) :: m_w, m_i
CHARACTER(len=*), INTENT(in)      :: mixingrulestring
CHARACTER(len=*), INTENT(in)      :: matrixstring
CHARACTER(len=*), INTENT(in)      :: inclusionstring
CHARACTER(len=*), INTENT(in)      :: hoststring
CHARACTER(len=*), INTENT(in)      :: hostmatrixstring
CHARACTER(len=*), INTENT(in)      :: hostinclusionstring
DOUBLE PRECISION, INTENT(out)     :: C_back
```

Description:

Backscatter cross section σ_b (Mie-scattering) of a melting graupel/snow particle, assumed as a **sphere composed of a homogeneous ice-water-air mixture material**. The bulk density (ice mass per particle volume) of the original unmelted particle is derived from the inverse mass-size-relation (40) with coefficients a_{geo} and b_{geo} assuming spherical shape. `fmelt` denotes the melted mass fraction or the degree of melting, f_{melt}, resp.

It is assumed that the particle melts partly on the outside and on the inside, within the ice structure, and that the meltwater is completely soaked and distributed homogeneously within the particle, displacing the air inclusions. The fraction of meltwater coming from the outside has to be preselected as input parameter `meltratio_outside` (between 0 and 1), which is the ratio when melting starts ($f_{melt} = 0$). Choosing `meltratio_outside` < 1 leads to larger particles compared to `meltratio_outside` $= 1$.

If f_{melt} is large enough (depending on bulk density and the actual `meltratio_outside`, see below), the meltwater completely fills the ice structure. Now the ice core melts homogeneously and the particle is assumed to be a homogeneous mixture of ice and water.

However, if `meltratio_outside` is sufficiently small, it could happen that the entire ice skeleton would be melted before all the air inclusions are filled with meltwater. Such particle would be unstable and splash into pieces sooner or later. To avoid this unrealistic asymptotic behaviour, the actual value of `meltratio_outside` increases linearily with growing f_{melt} from its value at $f_{melt} = 0$ (input parameter) to a value of 1 for $f_{melt} = 1$. In this way, the particle in any case converges to a water drop for $f_{melt} \to 1$.

Once the volume fractions of ice, water and air are derived based on the above assumptions, the effective refractive index of the particle is calculated by the function `get_m_mix_nested`, subsubsection 5.2.5. By proper choice of the input parameters `mixingrulestring`, `matrixstring`, `inclusionstring`, `hoststring`, `hostmatrixstring` and `hostinclusionstring`, the application of many different EMAs is possible, see subsubsection 5.2.5 on Page 28. Mie scattering is finally applied to calculate the backscattering cross section.

For small particles, the Rayleigh approximation can be applied instead to speed up the computation, by using subroutine `RAYLEIGH_SOAK_WETGR()` instead (subsubsection 5.3.12).

Input parameters:

`kinddp`	kind parameter for double precision
`x_g`	Mass of particle in kg (without air fraction)
`a_geo`	Coefficient a_{geo} of the inverse mass-size-relation (40)
`b_geo`	Coefficient b_{geo} of the inverse mass-size-relation (40)
`fmelt`	Degree of melting, $f_{melt} = x_w/x_g$ (x_w = mass of water contained in the particle)
`meltratio_outside`	Subpart ratio of the meltwater mass x_w which melts on the outside of the particle when melting starts ($f_{melt} = 0$). Value between 0 and 1. The complementary subpart of x_w is assumed to melt within the ice structure. The actual value depends on f_{melt} and increases linearily to 1 for $f_{melt} = 1$.
`m_w`	Complex refractive index of water
`m_i`	Complex refractive index of ice
`lambda`	Radar wavelength in m
`mixingrulestring`, `matrixstring`, `inclusionstring`, `hoststring`, `hostmatrixstring`, `hostinclusionstring`	see subroutine `get_m_mix_nested()`, subsubsection 5.2.5.

Output parameters:

`C_back`	Backscattering cross section σ_b in m^2

Example:

```
CALL MIE_SOAK_WETGR(2.3e-3, a_geo, b_geo, &
          0.45, 0.7, m_w, m_i, 0.055, C_back, &
          'maxwellgarnett', 'water', 'spheroidal', &
          'air', 'icewater', 'spheroidal')
```

Example sensitivity studies:

The dependence of σ_b on the degree of melting and on particle size for a specific temperature of $T = 5°C$ is studied in detail in subsequent sections for the 4 different inverse mass-size-relations given in Subsection 7.1. These are:

- for inverse mass-size-relation (36) in Subsection 8.13 on Page 102,
- for inverse mass-size-relation (37) in Subsection 8.14 on Page 103,
- for inverse mass-size-relation (38) in Subsection 8.15 on Page 104,
- for inverse mass-size-relation (39) in Subsection 8.16 on Page 105.

5.3.12 SUBROUTINE RAYLEIGH_SOAK_WETGR (x_g,a_geo,b_geo,fmelt,meltratio_outside,m_w,m_i,lambda,C_back, mixingrulestring, matrixstring, inclusionstring, hoststring, hostmatrixstring, hostinclusionstring)

```
INTEGER, PARAMETER                :: kinddp = KIND(1.0d0)
DOUBLE PRECISION, INTENT(in)      :: x_g, lambda, a_geo, b_geo, fmelt
DOUBLE PRECISION, INTENT(in)      :: meltratio_outside
COMPLEX(kind=kinddp), INTENT(in) :: m_w, m_i
CHARACTER(len=*), INTENT(in)      :: mixingrulestring
CHARACTER(len=*), INTENT(in)      :: matrixstring
CHARACTER(len=*), INTENT(in)      :: inclusionstring
CHARACTER(len=*), INTENT(in)      :: hoststring
CHARACTER(len=*), INTENT(in)      :: hostmatrixstring
CHARACTER(len=*), INTENT(in)      :: hostinclusionstring
DOUBLE PRECISION, INTENT(out)     :: C_back
```

Description:

Backscatter cross section σ_b according to Rayleigh approximation of a melting graupel/snow particle, assumed as a **sphere composed of a homogeneous ice-water-air mixture material**. This subroutine uses the same principles to determine the effective refractive index of the melting particle as `MIE_SOAK_WETGR()` except that the backscattering cross section is calculated applying Rayleigh approximation instead of Mie-scattering. See subroutine `MIE_SOAK_WETGR()` in subsubsection 5.3.11 for further details.

Input- and output parameters the same as in subsubsection 5.3.11 on Page 48!

Example:

```
CALL MIE_SOAK_WETGR(2.3e-3, a_geo, b_geo, &
          0.45, 0.7, m_w, m_i, 0.055, C_back, &
          'maxwellgarnett', 'water', 'spheroidal', &
          'air', 'icewater', 'spheroidal')
```

Example sensitivity studies:

The dependence of σ_b on the degree of melting and on particle size for a specific temperature of $T = 5°C$ is studied in detail in subsequent sections for the 4 different inverse mass-size-relations given in Subsection 7.1. These are:

- for inverse mass-size-relation (36) in Subsection 8.1 on Page 74,
- for inverse mass-size-relation (37) in Subsection 8.2 on Page 77,
- for inverse mass-size-relation (38) in Subsection 8.3 on Page 80,
- for inverse mass-size-relation (39) in Subsection 8.4 on Page 82.

5.3.13 SUBROUTINE MIE_WETSNOW_TWOSPH (x_s,a_geo,b_geo,fmelt,meltingratio_outside,m_w,m_i,lambda,radienverh,C_back, mixingrulestring_shell, matrixstring_shell, inclusionstring_shell, mixingrulestring_core, matrixstring_core, inclusionstring_core, hoststring_shell, hostmatrixstring_shell, hostinclusionstring_shell, hoststring_core, hostmatrixstring_core, hostinclusionstring_core)

```
INTEGER, PARAMETER                :: kinddp = KIND(1.0d0)
DOUBLE PRECISION, INTENT(in)      :: x_g, lambda, a_geo, b_geo, fmelt
DOUBLE PRECISION, INTENT(in)      :: meltingratio_outside
DOUBLE PRECISION, INTENT(in)      :: radienverh
COMPLEX(kind=kinddp), INTENT(in) :: m_w, m_i
CHARACTER(len=*), INTENT(in)      :: mixingrulestring_shell
CHARACTER(len=*), INTENT(in)      :: matrixstring_shell
CHARACTER(len=*), INTENT(in)      :: inclusionstring_shell
CHARACTER(len=*), INTENT(in)      :: hoststring_shell
CHARACTER(len=*), INTENT(in)      :: hostmatrixstring_shell
CHARACTER(len=*), INTENT(in)      :: hostinclusionstring_shell
CHARACTER(len=*), INTENT(in)      :: mixingrulestring_core
CHARACTER(len=*), INTENT(in)      :: matrixstring_core
CHARACTER(len=*), INTENT(in)      :: inclusionstring_core
CHARACTER(len=*), INTENT(in)      :: hoststring_core
CHARACTER(len=*), INTENT(in)      :: hostmatrixstring_core
CHARACTER(len=*), INTENT(in)      :: hostinclusionstring_core
DOUBLE PRECISION, INTENT(out)     :: C_back
```

Description:

Backscatter cross section σ_b (Mie-scattering, two-layered sphere) of a melting soaked graupel/snow particle, assumed as a **spherical core of a homogeneous ice-water-air mixture material and a shell of a similar ice-water-air mixture material but with lower bulk density**.

This subroutine uses the same principles to determine the effective refractive index of the melting particle as `MIE_SOAK_WETGR()`, applied to core and shell. A further input parameter is the ratio between the outer and inner sphere radii, `radienverh`. The initial masses of the unmelted core and shell are derived from the inverse mass-size-relation (40) with coefficients a_{geo} and b_{geo} assuming spherical shape, in a similar way as in subroutine `MIE_DRYSNOW_TWOSPH()`, subsubsection 5.3.5. See subroutine `MIE_SOAK_WETGR()` in subsubsection 5.3.11 for further details. Note that the input parameter `meltratio_outside` from `MIE_SOAK_WETGR()` is termed `meltingratio_outside` here.

To calculate the backscattering coefficient of the two-layered spherical particle, the formulae of Bohren and Huffman (1983) are applied (subroutine `COATEDSPHERE_SCATTER_BH()`), see Subsection 4.4.

Input parameters:

`kinddp`	kind parameter for double precision
`x_s`	Mass of particle in kg (without air fraction)
`a_geo`	Coefficient a_{geo} of the inverse mass-size-relation (40)

`b_geo`	Coefficient b_{geo} of the inverse mass-size-relation (40)
`fmelt`	Degree of melting, $f_{melt} = x_w/x_s$ (x_w = mass of water contained in the particle). Same value for core and shell.
`meltingratio_outside`	Subpart ratio of the meltwater mass x_w which melts on the outside of the particle when melting starts ($f_{melt} = 0$). Value between 0 and 1. The complementary subpart of x_w is assumed to melt within the ice structure. The actual value depends on f_{melt} and increases linearily to 1 for $f_{melt} = 1$. Same value for core and shell.
`radienverh`	Ratio of the inner to the outer sphere radius
`m_w`	Complex refractive index of water
`m_i`	Complex refractive index of ice
`lambda`	Radar wavelength in m
`mixingrulestring_shell`, `matrixstring_shell`, `inclusionstring_shell`, `hoststring_shell`, `hostmatrixstring_shell`, `hostinclusionstring_shell`	Parameters determining the effective refractive index of the shell ice-water-air mixture material, see subroutine `get_m_mix_nested()`, subsubsection 5.2.5.
`mixingrulestring_core`, `matrixstring_core`, `inclusionstring_core`, `hoststring_core`, `hostmatrixstring_core`, `hostinclusionstring_core`	Parameters determining the effective refractive index of the core ice-water-air mixture material, see subroutine `get_m_mix_nested()`, subsubsection 5.2.5.

Output parameters:

`C_back`	Backscattering cross section σ_b in m^2

Example:

```
CALL MIE_WETSNOW_TWOSPH(2.3e-3, a_geo, b_geo, &
          0.45, 0.7, m_w, m_i, 0.055, 0.5, C_back, &
          'maxwellgarnett', 'water', 'spheroidal', &
          'maxwellgarnett', 'ice', 'spheroidal', &
          'air', 'icewater', 'spheroidal', &
          'water', 'water', 'spheroidal')
```

Example sensitivity studies:

The dependence of σ_b on the degree of melting and on particle size for a specific temperature of $T = 5°C$ is studied in detail in subsequent sections for the 2 different inverse mass-size-relations for snow given in Subsection 7.1. These are:

- for inverse mass-size-relation (38) in Subsection 8.19 on Page 108,
- for inverse mass-size-relation (39) in Subsection 8.20 on Page 138.

6 radar_mie_lm: Interface functions for the LM

As previously mentioned, the library radar_mie_lm provides interface routines for the LM to calculate Z_e as a sum of Integrals of the form equation (1) (Page 7) over the different hydrometeor types which are implemented into the LM microphysical schemes (cloud droplets, rain, cloud ice, snow, graupel and, depending on the scheme, hail). These interface functions call the subroutines for the basic particle properties m_{eff} and σ_b, which are provided by radar_mielib and were previously described in Section 5. For the particle size distributions, generalized gamma distributions are assumed for all hydrometeor types, which is consistent with the assumption in the bulk microphysical schemes of the LM. The parameters of these size distributions are derived from model variables (mass density, and in case of two-moment scheme, number density) consistent to the assumptions drawn for the applied microphysical scheme. Note that the exponential and gamma size distribution are a special case of the generatilzed gamma distribution.

For Mie-scattering as well as for Rayleigh approximation with general EMA approximation, the integration of Z_e is done over a finite size interval $[D_{min}; D_{max}]$ beeing prescribed in a reasonable way within the interface routines and beeing generally different for each hydrometeor category. There are also two much more efficient approaches implemented in radar_mielib utilizing Rayleigh approximation together with Oguchis EMA approximation, which enables analytical solutions of the reflectivity integral (see Subsection 6.2).

The degree of melting f_{melt} (melted mass fraction) of the single particles is estimated as a function of size and ambient temperature by a parameterization which will be presented in Subsection 6.1. Two important parameters of this parameterization, T_{min} and $f_{meltbegin}$ (see Subsection 6.1), are also specified in the interface routines in a reasonable way, but can certainly be changed by the user. Note that the estimated degree of melting can only be regarded as a very simplified and uncertain approximation since important information is not available for a more thorough description, e.g., the temperature and riming rate along the particle backward trajectories (the "melting history"). See Subsection 6.1 for a more detailed description.

The user can choose by appropriate settings of certain namelist parameters (described in Subsection 6.3), if full Mie-scattering or Rayleigh approximation with one of 3 different levels of simplification for m_{eff} of snow, graupel and hail is applied (see also Subsection 6.5 for an example of the relevant namelist parameters added to namelist GRIBOUT). These different levels of simplification can lead to largely different results for Z_e in case of melting hydrometeors, whereas in case of dry ice particles no significant differences are observed. The physical reason for this behaviour is that ice is only a weak dielectric whereas water is a strong dielectric (permanently polar molecules) so that the choice of a certain EMA-formulation becomes important primarily in the presence of water within a mixture particle.

6.1 An approximation for the degree of melting applicable for bulk microphysical schemes

This section describes a simple parameterization of the degree of melting f_{melt} (melted mass fraction) of hydrometeors, which can be used with bulk microphysical models which in turn do not explicitly predict the degree of melting. First of all, let us recall the definition of f_{melt},

$$f_{melt} = \frac{x_w}{x_{i,0}} \quad , \tag{24}$$

where x_w is the mass of meltwater and $x_{i,0}$ is the unmelted mass of the particle, only counting the ice fraction, not the enclosed air. Values for f_{melt} are in the range of $[0, 1]$. 0 means unmelted and 1 means fully melted.

Generally, f_{melt} depends on the time a certain particle has spent in a certain environment (T, riming rate, rate of turbulent heat transfer towards the particle, determined by, e.g., Reynolds number and particle surface roughness, etc.). This means that for an accurate calculation, the exact trajectory of each single particle has to be known together with a detailed solution of the equation of heat exchange of particles with the environment, considering also the feedback on the environmental temperature. In a numerical weather prediction model, this can hardly be done.

Therefore, to construct a parameterization f_{melt}, some assumptions have to be made to simplify the problem. We draw the following assumptions:

- In the environment, T decreases with height and no intense vertical motions are present, so that particles found at a specific time and place originate from regions above, not below.
- Every hydrometeor category can be assigned its own parameterization of f_{melt}, following the same master function (see below), but with different parameters.
- Within each hydrometeor class, the rate of heat exchange with the environment is a function of particle size only.
- It follows from the previous assumptions, that the particles all begin to melt at a certain temperature level T_{min}, e.g., 0°C or slightly below,
- that f_{melt} only depends on the environmental temperature T and particle diameter D,
- in particular that at a given temperature, f_{melt} is larger for smaller particles — we assume a simple dependence $f_{melt} \sim D^{-a}$ with $a > 0$.
- It is further assumed that below the height of a certain temperature level T_{max}, all particles are fully melted.

From these assumptions it follows that for a given environmental temperature there is a certain particle size D_{fm} at which the particles are just melted. Larger particles obey $f_{melt} < 1$. D_{fm} has to be 0 for $T = T_{min}$ and $D_{fm} \Rightarrow \infty$ for $T \Rightarrow T_{max}$. A simple *ansatz* for D_{fm} fulfilling these constraints is, for example, an inverse exponential formula with respect to temperature,

$$D_{fm}^a \;=\; D_{ref}^a \;\ln\left(\frac{T_{max} \;-\; T_{min}}{T_{max} \;-\; T}\right) \quad , \tag{25}$$

with $T_{min} \leq T < T_{max}$. The exponent a has been introduced here for later convenience. D_{ref} is a scaling parameter and has to be specified properly. D_{ref} represents the value of D_{fm} at a temperature $T = T_{1/e}$, where

$$T_{1/e} \;=\; T_{max} - \frac{1}{e}\,(T_{max} \;-\; T_{min}) \quad , \tag{26}$$

the e-folding value of T within the interval $[T_{min}, T_{max}]$.

Now, requiring that $f_{melt}(D_{fm}) = 1$ and $f_{melt} \sim D^{-a}$ immediately leads to

$$f_{melt} \;=\; \left(\frac{D_{fm}}{D}\right)^a \;=\; \left(\frac{D_{ref}}{D}\right)^a \ln\left(\frac{T_{max} \;-\; T_{min}}{T_{max} \;-\; T}\right) \;=\; \mathrm{fct}(D,T) \tag{27}$$

again for $T_{min} \leq T < T_{max}$. This function has to be limited to the codomain $f_{melt} \in [0,1]$ and extended to arbitrary temperatures by the constraints $f_{melt}(D_{fm}) = 0$ for $T < T_{min}$ and $f_{melt}(D_{fm}) = 0$ for $T < T_{max}$, which finally leads to the formulation

$$f^*_{melt} = \begin{cases} 0 & , \; T < T_{min} \\ \left(\frac{D_{ref}}{D}\right)^a \ln\left(\frac{T_{max} - T_{min}}{T_{max} - T}\right) & , \; T_{min} \leq T < T_{max} \\ 1 & , T \geq T_{max} \end{cases}$$

$$f_{melt} = \min[\, \max[\, f^*_{melt}\,, 0\,]\,, 1\,] \quad . \tag{28}$$

This formulation is intended to describe f_{melt} in a temperature regime in which the sensible heat flux from the environment to the particle is an important mechanism in enhancing the temperature of the particle. The parameter T_{min} denotes the temperature where this melting process starts. In that regime, the abovementioned assumptions leading to formula (27) may be more or less reasonable.

However, it may be desireable to also include the effects of melting at lower temperatures $T < T_{min}$ caused by high riming rates and too small a transfer of latent heat of freezing away from the particle, as it is sometimes observed for, e.g., high density graupel particles. This effect may be active for large particles in the temperature range of $-10 < T < 0°\mathrm{C}$. To this end, a simple extension to formula (27) is proposed, based on the (maybe contradictory) assumption that the effect on f_{melt} does not depend on particle size. Without a more sound theoretical basis, we would not dare to go any further than a linear dependence on size or a stepfunction, and we limit ourselves to the even simpler constance assumption above. Concerning the temperature dependence at fixed size, a linear *ansatz* is used.

Introducing the two new parameters T_{mb} and f_{tmin} (T_{mb} = Temperature, at which riming induced melting starts, f_{tmin} = degree of melting reached at T_{min}), the following extended formula

$$f^*_{melt} = \begin{cases} 0 & , \; T < T_{mb} \\ \frac{f_{tmin}}{T_{min} - T_{mb}}\,(T - T_{mb}) & , \; T_{mb} \leq T < T_{min} \\ (1 - f_{tmin})\left(\frac{D_{ref}}{D}\right)^a \ln\left(\frac{T_{max} - T_{min}}{T_{max} - T}\right) + f_{tmin} & , \; T_{min} \leq T < T_{max} \\ 1 & , T \geq T_{max} \end{cases}$$

$$f_{melt} = \min[\, \max[\, f^*_{melt}\,, 0\,]\,, 1\,] \tag{29}$$

is implemented into `radar_mie_lm`.

Formula (29) is used if $T_{mb} < T_{min}$ whereas the extension is switched off choosing $T_{mb} \geq T_{min}$, which leads to application of formula (28).

Figure 9 shows f_{melt} as function of T and D after formula (29) for an exemplaric parameter set of T_{mb}, T_{min}, T_{max}, f_{tmin} and D_{ref}, suitable for high density graupel or hail particles. It can be seen that a distinct transition between the riming- and environmental temperature-induced melting processes can be modeled by appropriate parameter settings of the parameterization (29).

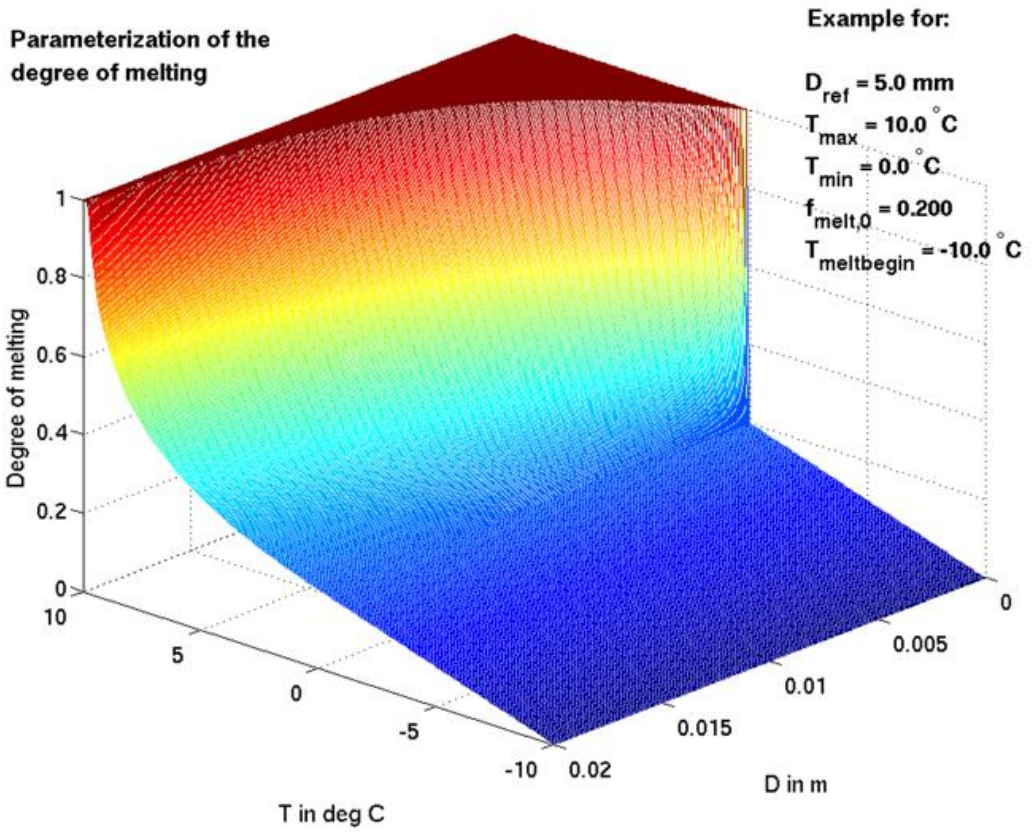


Figure 9: Parameterization function for the degree of melting f_{melt} as function of temperature in °C and particle diameter in mm for an exemplaric parameter set of formula (29), applicable to graupel or hail particles, see annotations. The exponent parameter a is 1.0.

The implementation into `radar_mie_lm` is as follows: for graupel- and hail particles, the parameters T_{mb} and f_{tmin} are set equal to the values annotated in Figure 9 by default. T_{min} is set to 0°C for all species. D_{ref} is chosen as min[6 mm, $\overline{D}(\overline{x})$], with $\overline{D}(\overline{x})$ beeing the mean mass spherical equivalent diameter of the particle spectrum. For snow- and cloud ice particles, the riming-induced melting is switched off by choosing $T_{mb} > T_{min}$ by default, and D_{ref} is the same as for graupel and hail. Based on explicit simulations of melting particles carried out with a spectral bin microphysical model (Hebrew University Cloud Model HUCM), the exponent a is chosen as 0.5 for snow and cloud ice, 0.6 for graupel and 0.8 for hail particles.

To give the user some more control over the riming-induced melting degree parameterization at $T < 0$°C, the parameters T_{mb} and f_{tmin} are available as namelist parameters for the snow-, graupel- and hail categories.

So far the parameter T_{max} remains to be discussed. This parameter denotes the temperature above which even the largest particles are assumed to be fully melted. From physical arguments it would seem reasonable to specify a fixed value (e.g., 10°C). However, there might be situations, e.g., strong convective downdrafts, in which the particles may "survive" longer. To account for this, a dynamic approach is chosen to make use of the information about the melting process and T_{max} which is provided by the melting parameterization of the cloud microphysical scheme itself: If there are particles of the specific type are present at locations with T exceeding the above fixed value, T_{max} is dynamically adjusted to the temperature of the lowest model height level where these melting hydrometeors are present. The fixed minimum value is presently chosen as 5°C for snow and cloud ice, 10°C for graupel and 20°C for hail. This is done every timestep at every horizontal gridpoint. This "precipitation-column"-approach should be reasonable in case of coarse numerical horizontal grid resolution and/or low windspeed. To prevent problems in case of high grid resolution and high windspeed, T_{max} is further set to its maximum value within a "search area" of 10 x 10 km^2 centered around each gridpoint, providing a certain degree of smoothing.

The following subroutines in `radar_mie_lm` are connected to the f_{melt}-parameterization:

- `degree_of_melting_fun()`:

  master function (29), input parameters are D, T_{mb}, T_{min}, T_{max}, f_{tmin} and D_{ref}. Output parameter is f_{melt}.

- `initialize_tmax()`:

  Determination of T_{max}, separately for every hydrometeor category.

- Subroutines which itself call `degree_of_melting_fun()` with suitable input parameter sets for each hydrometeor type:

  - `degree_of_melting_ice()`, `degree_of_melting_ice_sb()`
  - `degree_of_melting_snow()`, `degree_of_snow_hail_sb()`
  - `degree_of_melting_graupel()`, `degree_of_graupel_hail_sb()`
  - `degree_of_melting_hail()`, `degree_of_melting_hail_sb()`

The results of the reflectivity calculations using the presented parameterization for f_{melt} look qualitatively promising for stratiform precipitation (radar "bright band"), but there will almost certainly be problems in case of deep convective events. It has to be mentioned, too, that up to now no attempt to verify or calibrate the formula (29) and its parameters has been undertaken aside the abovementioned tests using the HUCM bin microphysical model. Therefore, the above parameterization remains speculative to some degree. However, since almost no suitable measurements of the degree of melting in clouds are existing, the verification/calibration would have to rely on further simulations with HUCM or on a suitable detailed Lagrangian melting model. But even such a Lagrangian model would require

certain assumptions on the vertical and horizontal structure of precipitation and horizontal and vertical windspeed and therefore it is unclear whether the results of such a verification/calibration approach would be applicable in general.

6.2 An efficient Rayleigh-Approximation for melting hydrometeors with Oguchis refractive index formulation

There is a nice closed analytical solution for Z_e in Rayleigh approximation if a generalized gamma distribution is assumed for the particle mass distribution and Oguchis EMA formula for m_{eff} with shape factor $u = 2$ (equation (16) on Page 15) is applied. A further precondition is that the same degree of melting is assumed for all particles, regardless of their size. However, this EMA approximation is not valid in case of a mixture of strong and/or strongly differing dielectric materials, as is the case with melting hydrometeors.

Nevertheless, this approach is implemented into `radar_mie_lm` because of its computational efficiency. It has to be remembered that it can be safely applied for rain and for dry ice particles but may lead to much too small reflectivity values for melting hydrometeors.

Now, recalling that the dielectric factor K in the Rayleigh approximation equals $(\epsilon-1)/(\epsilon+2)$, Oguchis formula (16) with $u = 2$ for the effective refractive index of an ice-water-air mixture reads

$$\begin{aligned} \frac{\epsilon_{eff}-1}{\epsilon_{eff}+2} &= \frac{\epsilon_i-1}{\epsilon_i+2}\,p_i + \frac{\epsilon_w-1}{\epsilon_w+2}\,p_w + \frac{\epsilon_a-1}{\epsilon_a+2}\,p_a \\ K_{eff} &= K_i\,p_i + K_w\,p_w + K_a\,p_a \quad , \end{aligned} \tag{30}$$

where indices i, w, a and s denote ice, air, water and the mixture particle, and p_i, p_w, p_a are the respective volume fractions. Since

$$p_x = \frac{V_x}{V} = \frac{m_x}{\rho_x V} \qquad x \in i,w,a \quad , \tag{31}$$

where V_X is partial volume of material x, V is total particle volume, m_x is partial mass of material x and ρ_x is the material's density, equation (30) can be rewritten to

$$K_{eff} = \frac{1}{V}\left(K_i\,\frac{m_i}{\rho_i} + K_w\,\frac{m_w}{\rho_w} + K_a\,\frac{m_a}{\rho_a}\right) \quad . \tag{32}$$

To a very good approximation, $K_a = 0$, and using the definition of partial densities $\rho_{p,s} = m_i/V$ and $\rho_{p,w} = m_w/V$,

$$K_{eff} = K_i\,\frac{\rho_{p,s}}{\rho_i} + K_w\,\frac{\rho_{p,w}}{\rho_w} \quad . \tag{33}$$

K_x are complex numbers, $K_x = K_{x,r} + i\,K_{x,i}$, so the square of the modulus of K_{eff} is

$$|K_{eff}|^2 = |K_i|^2\left(\frac{\rho_{p,s}}{\rho_i}\right)^2 + |K_w|^2\left(\frac{\rho_{p,w}}{\rho_w}\right)^2 + 2\,\frac{\rho_{p,s}\rho_{p,w}}{\rho_i\rho_w}\left(K_{i,r}K_{w,r} + K_{i,i}K_{w,i}\right) \quad . \tag{34}$$

Defining $x = m_i + m_w$ as mass of a melting particle without its air contribution and f_{melt} as its degree of melting, so that $m_i = (1 - f_{melt})x$ and $m_w = f_{melt}x$, the Rayleigh reflectivity (equation (5)) for a population of melting particles is

$$
\begin{aligned}
Z_e &= \frac{1}{|K_{w,0}|^2} \int_0^\infty |K_{eff}|^2 \, D^6 \, N(D) \, dD \\
&= \frac{1}{|K_{w,0}|^2} \int_0^\infty |K_{eff}|^2 \, D(x)^6 \, N(x) \, dx \\
&= \frac{1}{|K_{w,0}|^2} \left[\frac{|K_i|^2}{\rho_i^2} \int_0^\infty \left(\frac{6V}{\pi}\right)^2 \frac{m_i^2}{V^2} \, N(x) \, dx + \right. \\
&\quad \left. \frac{|K_w|^2}{\rho_w^2} \int_0^\infty \left(\frac{6V}{\pi}\right)^2 \frac{m_w^2}{V^2} \, N(x) \, dx + 2 \, \frac{K_{i,r}K_{w,r} + K_{i,i}K_{w,i}}{\rho_i \rho_w} \int_0^\infty \left(\frac{6V}{\pi}\right)^2 \frac{m_i m_w}{V^2} \, N(x) \, dx \right] \\
&= \frac{6^2}{\pi^2 \, |K_{w,0}|^2} \left[\frac{|K_i|^2}{\rho_i^2} \int_0^\infty (1 - f_{melt})^2 \, x^2 \, N(x) \, dx + \right. \\
&\quad \left. \frac{|K_w|^2}{\rho_w^2} \int_0^\infty f_{melt}^2 \, x^2 \, N(x) \, dx + 2 \, \frac{K_{i,r}K_{w,r} + K_{i,i}K_{w,i}}{\rho_i \rho_w} \int_0^\infty f_{melt} \, (1 - f_{melt}) \, x^2 \, N(x) \, dx \right] \\
&= \frac{6^2}{\pi^2 \, |K_{w,0}|^2} \left[\frac{|K_i|^2}{\rho_i^2} \, (1 - f_{melt})^2 + \frac{|K_w|^2}{\rho_w^2} \, f_{melt}^2 + 2 \, \frac{K_{i,r}K_{w,r} + K_{i,i}K_{w,i}}{\rho_i \rho_w} \, f_{melt} \, (1 - f_{melt}) \right] M_2 \quad ,
\end{aligned}
\tag{35}
$$

where M_2 denotes the second moment of the particle mass distribution function. The last equality in equation (35) is only valid if all particles obey the same degree of melting, independent of their size. equation (35) is especially attractive since it only envolves the calculation of the second moment with respect to mass, which in most cases is far more efficient since, for certain types of distribution functions $N(x)$ (e.g., generalized gamma distribution), M_2 can be written in closed analytical form.

Note, however, that a systematical underestimation of Z_e might possibly occur, since it is assumed here (as in all other routines of `radar_mie_lm`) that the mass of meltwater is contained in the particle mass x and the second moment M_2, which contrasts the treatment of melting in most microphysical schemes, where the meltwater is (partially or completely) shedded to rainwater.

6.3 Controlling reflectivity calculations in LM — relevant namelist parameters and their setting

To enable output of radar reflectivity in LM, the user simply has to specify the output variable `'dBZ'` within the list of output variables in the `GRIBOUT`-namelist. `'dBZ'` is implemented for model level output as well as for pressure-level- or height-level interpolation. In case of interpolated output, the reflectivity is calculated first on model levels and subsequently interpolated to output pressure/height levels. In standard LM, the interpolation is done by cubic tension splines. However, reflectivity is a positive definite quantity and can vary over several orders of magnitude between adjacent grid points. In this case, cubic splines can lead to serious undershoots producing negative values. We therefore changed the interpolation in

our LM version to simple linear interpolation, but unfortunately this is not available in the operational LM version.

Once reflectivity output is chosen, the basic namelist parameter to control the kind of reflectivity calculation is

- `dbz%itype_refl`, namelist `GRIBOUT` (`INTEGER`: 1, 2, 3, or 4).

The radarwavelength can be specified by

- `dbz%lambda_radar`, namelist `GRIBOUT` (`REAL`).

To choose the parameters of the parameterization for the degree of melting in Subsection 6.1, which influence the riming-induced melting for $T < 0°C$ (namelist `GRIBOUT`, `REAL`):

- `dbz%Tmeltbegin_s` (T_{mb} for snow)
- `dbz%meltdegTmin_s` (f_{tmin} for snow)
- `dbz%Tmeltbegin_g` (T_{mb} for graupel)
- `dbz%meltdegTmin_g` (f_{tmin} for graupel)
- `dbz%Tmeltbegin_h` (T_{mb} for hail; only for `itype_gscp` $\geq$ 2000)
- `dbz%meltdegTmin_h` (f_{tmin} for hail; only for `itype_gscp` $\geq$ 2000)

To further choose different EMA approximations of m_{eff} for different hydrometeor types, the following namelist parameters apply (namelist `GRIBOUT`, `CHARACTER(len=12)`):

- `dbz%ctype_drysnow_mie`
- `dbz%ctype_wetsnow_mie`
- `dbz%ctype_drygraupel_mie`
- `dbz%ctype_wetgraupel_mie`
- `dbz%ctype_dryhail_mie` (only for `itype_gscp` $\geq$ 2000)
- `dbz%ctype_wethail_mie` (only for `itype_gscp` $\geq$ 2000)
- `dbz%ctype_drysnow_ray`
- `dbz%ctype_wetsnow_ray`
- `dbz%ctype_drygraupel_ray`
- `dbz%ctype_wetgraupel_ray`
- `dbz%ctype_dryhail_ray` (only for `itype_gscp` $\geq$ 2000)
- `dbz%ctype_wethail_ray` (only for `itype_gscp` $\geq$ 2000)

Their setting depends in turn on `dbz%itype_refl`. The listing below and the subsequently linked tables show the different possible combinations of these parameters and the corresponding `radar_mielib` functions which are used to calculate radar reflecitvity.

Further, in case of graupel particles and application of Mie-scattering (`dbz%itype_refl=1`), the namelist parameter `dbz%igraupel_type` (=1, 2, or 3) provides three possibilities for the melting model of graupel, see the listing below.

In case of melting hydrometeors, the degree of melting is derived from the parameterization described in Subsection 6.1 before calculating reflectivity according to the following listing.

The followin listing shows combinations of the namelist parameter `dbz%itype_refl` with the other namelist parameters mentioned previously in this section. The links in the right column lead to the description of the corresponding `radar_mielib` subroutine and to subsequent tables which describe in detail the possible settings of the corresponding namelist parameter for the EMA approximation:

- `dbz%itype_refl` = **1:**

  Mie scattering, general EMA approximation

  - **Cloud drops:**
    Rayleigh approximation, analytical solution of (5)
  - **Cloud ice:**
    dry / melting: Rayleigh approximation (35) with EMA after Oguchi
  - **Rain:**
    Mie scattering, numerical solution using (3): `SPHERE_SCATTER_BH()`
  - **Snow:**
    dry ($T \leq 0°C$):
    `MIE_DRYSNOW_TWOSPH()` — `dbz%ctype_drysnow`: 6-character code, composed of two 3-character codes after Table 38 for core and shell, resp.

    melting ($T > 0°C$):
    `MIE_WETSNOW_TWOSPH()` — `dbz%ctype_wetsnow`: 12-character code, composed of two 6-character codes after Table 40 for core and shell, resp.
    `meltingratio_outside` = 0.7
    `radienverh` = 0.5

  - **Graupel:**
    dry ($T \leq$ -10°C):
    `MIE_DRY_GRAUPEL()` — `dbz%ctype_drygraupel`

    melting ($T >$ -10°C):
    depends on namelist parameter `dbz%igraupel_type`:
    - `dbz%igraupel_type` = 1:
      `MIE_SOAK_WETGR()` — `dbz%ctype_wetgraupel`
      `meltratio_outside` = 0.7
    - `dbz%igraupel_type` = 2:
      `MIE_SOAK_TWOSPH_WETGR()` — `dbz%ctype_wetgraupel`
    - `dbz%igraupel_type` = 3:
      `MIE_WATERSPH_WETGR()` — `dbz%ctype_wetgraupel`

  - **Hail:**
    dry ($T > 0°C$): `MIE_DRY_GRAUPEL()` — `dbz%ctype_dryhail`
    melting ($T \leq 0°C$): `MIE_SPONGY_WETHAIL()` — `dbz%ctype_wethail_ray`
    `fwater` = 0.5

- `dbz%itype_refl` = **2:**

  Rayleigh approximation with general EMA approximation

  - **Cloud drops:**
    Rayleigh approximation, analytical solution of (5)

- **Cloud ice:**
  dry / melting:Rayleigh approximation with EMA after Oguchi
- **Rain:**
  Rayleigh approximation, analytical solution of (5)

- **Snow:**
  dry ($T > 0°C$):
  `RAYLEIGH_DRY_GRAUPEL()` — `dbz%ctype_drysnow_ray`

  melting ($T \leq 0°C$):
  `RAYLEIGH_SOAK_WETGR()` — `dbz%ctype_wetsnow_ray`

- **Graupel:**
  dry ($T \leq$ -10°C):
  `RAYLEIGH_DRY_GRAUPEL()` — `dbz%ctype_drygraupel_ray`

  melting ($T >$ -10°C):
  `RAYLEIGH_SOAK_WETGR()` — `dbz%ctype_wetgraupel_ray`

- **Hail:**
  dry ($T \leq 0°C$):
  `RAYLEIGH_DRY_GRAUPEL()` — `dbz%ctype_dryhail_ray`

  melting ($T > 0°C$):
  `RAYLEIGH_SOAK_WETGR()` — `dbz%ctype_wethail_ray`

- `dbz%itype_refl` = **3:**

  Rayleigh approximation with EMA after Oguchi for cloud ice, snow, graupel and hail (analytical formula from Subsection 6.2), Rayleigh approximation (5) for cloud droplets and rain drops.

- `dbz%itype_refl` = **4:**

  Very simple and efficient Rayleigh approximation from `pp_utilities.f90` for all particles, crude description of melting particles

6.4 Tables of namelist parameter settings for the EMA choice

Table 38: 3-character Coding of the namelist-parameters `dbz%ctype_XXX` for two-component ice-air mixture materials and different EMA approximations, controlling the keywords of function `get_m_mix()`. Question marks denote wildcards for arbitrary characters.

mixingrulestring (1. character)	matrixstring (2. character)	inclusionstring (3. character)	ctype-Code
'bruggemann' -- 'b'	N/A	N/A	'b??'
'oguchi' -- 'o'	N/A	N/A	'o??'
'maxwellgarnett' -- 'm'	'ice' -- 'i'	'spherical' -- 'k'	'mik'
		'spheroidal' --'s'	'mis'
	'air' -- 'a'	'spherical' -- 'k'	'mak'
		'spheroidal' --'s'	'mas'

Table 39: Similar to Table 38: 3-character Coding of the namelist-parameters `dbz%ctype_XXX` for two-component ice-water mixture materials and different EMA approximations, controlling the keywords of function `get_m_mix()`. Question marks denote wildcards for arbitrary characters.

mixingrulestring (1. character)	matrixstring (2. character)	inclusionstring (3. character)	ctype-Code
'bruggemann' -- 'b'	N/A	N/A	'b??'
'oguchi' -- 'o'	N/A	N/A	'o??'
'maxwellgarnett' -- 'm'	'ice' -- 'i'	'spherical' -- 'k'	'mik'
		'spheroidal' --'s'	'mis'
	'water' -- 'w'	'spherical' -- 'k'	'mwk'
		'spheroidal' --'s'	'mws'

Table 40: 6-character Coding of the namelist-parameters **dbz%ctype_XXX** for three-component ice-water-air mixture materials and different EMA approximations, controlling the keywords of function **get_m_mix_nested()**. Question marks denote wildcards for arbitrary characters. Note that **inclusionstring** and **hostinclusionstring** are only displayed as representing spheroidal inclusions (i.e., character **'s'**), but both can also specify spherical inclusions by a character **'k'** instead, leading to 4 times more possibilities as laid out in the table below.

mixingrulestring (1. character)	hoststring (2. character)	matrixstring (3. character)	inclusionstring (4. character)	hostmatrixstring (5. character)	hostinclusionstring (6. character)	ctype-Code
'bruggemann' -- 'b'	N/A	N/A	N/A	N/A	N/A	'b?????'
'oguchi' -- 'o'	N/A	N/A	N/A	N/A	N/A	'o?????'
'maxwellgarnett' -- 'm'	'none' -- 'n'	'ice' -- 'i'	'spherical' -- 'k'	N/A	N/A	'mnik??'
			'spheroidal' -- 's'	N/A	N/A	'mnis??'
		'water' -- 'w'	'spherical' -- 'k'	N/A	N/A	'mnwk??'
			'spheroidal' -- 's'	N/A	N/A	'mnws??'
		'air' -- 'a'	'spherical' -- 'k'	N/A	N/A	'mnak??'
			'spheroidal' -- 's'	N/A	N/A	'mnas??'
	'ice' -- 'i'	'air' -- 'a'	'spheroidal' -- 's'	'ice' -- 'i'	'spheroidal' -- 's'	'miasis'
			'spheroidal' -- 's'	'airwater' -- 'r'	'spheroidal' -- 's'	'miasrs'
		'water' -- 'w'	'spheroidal' -- 's'	'ice' -- 'i'	'spheroidal' -- 's'	'miwsis'
			'spheroidal' -- 's'	'airwater' -- 'r'	'spheroidal' -- 's'	'miwsrs'
	'water' -- 'w'	'ice' -- 'i'	'spheroidal' -- 's'	'water' -- 'w'	'spheroidal' -- 's'	'mwisws'
			'spheroidal' -- 's'	'airice' -- 's'	'spheroidal' -- 's'	'mwisss'
		'air' -- 'a'	'spheroidal' -- 's'	'water' -- 'w'	'spheroidal' -- 's'	'mwasws'
			'spheroidal' -- 's'	'airice' -- 's'	'spheroidal' -- 's'	'mwasss'
	'air' -- 'a'	'ice' -- 'i'	'spheroidal' -- 's'	'air' -- 'a'	'spheroidal' -- 's'	'maisas'
			'spheroidal' -- 's'	'icewater' -- 'm'	'spheroidal' -- 's'	'maisms'
		'water' -- 'w'	'spheroidal' -- 's'	'air' -- 'a'	'spheroidal' -- 's'	'mawsas'
			'spheroidal' -- 's'	'icewater' -- 'm'	'spheroidal' -- 's'	'mawsms'

Table 41: 6-character coding of the namelist-parameters `dbz%ctype_XXX` for a two-layered particle, composed of a two-component ice-air mixture core and a two-component ice-water shell, and for different EMA approximations, controlling the keywords of function `get_m_mix()`. Question marks denote wildcards for arbitrary characters. The code is a combination of two 3-character codes similar to Table 38 and Table 39. There are 36 possibilities altogether, namely all combinations of 3-character codes from part 1 (core material) and part 2 (shell material) of the table.

Part 1: 1.-3. character, ice-air mixture of particle core

mixingrulestring (1. character)	matrixstring (2. character)	inclusionstring (3. character)	ctype-Code (1:3)
'bruggemann'	N/A	N/A	'b??'
'oguchi'	N/A	N/A	'o??'
'maxwellgarnett'	'ice'	'spherical'	'mik'
		'spheroidal'	'mis'
	'air'	'spherical'	'mak'
		'spheroidal'	'mas'

Part 2: 4.-6. character, ice-water mixture of particle shell

mixingrulestring (4. character)	matrixstring (5. character)	inclusionstring (6. character)	ctype-Code (4:6)
'bruggemann'	N/A	N/A	'b??'
'oguchi'	N/A	N/A	'o??'
'maxwellgarnett'	'ice'	'spherical'	'mik'
		'spheroidal'	'mis'
	'water'	'spherical'	'mwk'
		'spheroidal'	'mws'

6.5 Additions to LM-runscripts to enable reflectivity calculations

An example for the necessary additions to the namelist GRIBOUT to enable reflectivity calculation and output at each output timestep:

```
yvarml = ... , 'DBZ       ', ...
yvarzl = ... , 'DBZ       ', ...
yvarpl = ... , 'DBZ       ', ...

dbz%itype_refl = 1,

  dbz%lambda_radar = 0.055,

  dbz%Tmeltbegin_s  = 273.16,
  dbz%meltdegTmin_s = 0.0,
  dbz%Tmeltbegin_g  = 263.16,
  dbz%meltdegTmin_g = 0.2,
  dbz%Tmeltbegin_h  = 263.16,
  dbz%meltdegTmin_h = 0.2,

  ! Settings for itype_refl=1
  ! (effektive refractive index for Mie-scattering):

    dbz%ctype_drysnow_mie=    'masmas      ',
    dbz%ctype_wetsnow_mie=    'mawsasmawsas',
    dbz%ctype_drygraupel_mie= 'mis         ',

    ! Type of melting model for the Mie-calculations for
    ! partially melted graupel (1=soak, 2=twosphere, 3=watersphere):
    ! ( + corresponding ctype_wetgraupel_mie -- change accordingly!)

    dbz%igraupel_type=1,
    dbz%ctype_wetgraupel_mie= 'mawsms      ',

    ! Effective only for itype_gscp >= 2000:

    dbz%ctype_dryhail_mie=    'mis         ',
    dbz%ctype_wethail_mie=    'mws         ',

  ! Settings for itype_refl=2
  ! (effektive refractive index for Rayleigh-scattering):

    dbz%ctype_drysnow_ray=    'mas         ',
    dbz%ctype_wetsnow_ray=    'mawsas      ',
    dbz%ctype_drygraupel_ray= 'mis         ',
    dbz%ctype_wetgraupel_ray= 'mawsms      ',

    ! Nur bei itype_gscp >= 2000 wirksam:

    dbz%ctype_dryhail_ray=    'mis         ',
    dbz%ctype_wethail_ray=    'mawsms      ',
```

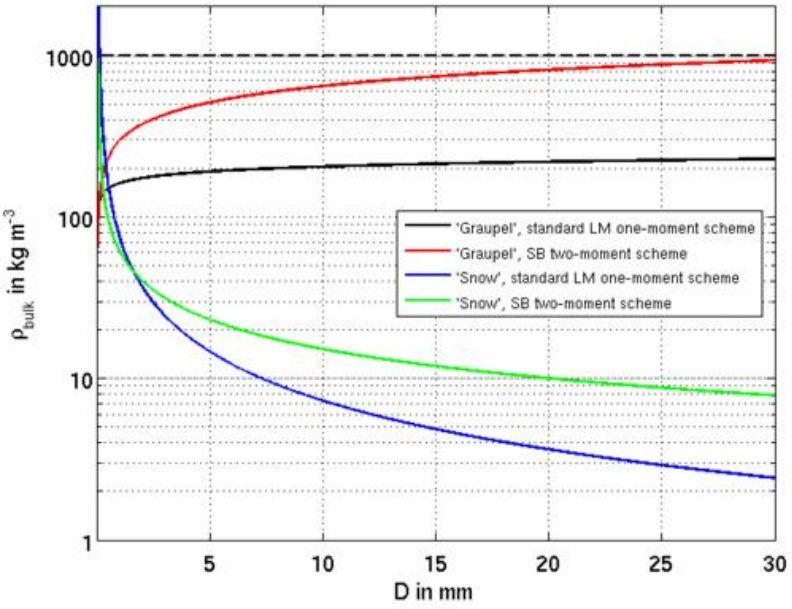


Figure 10: Bulk density of snow/graupel particles in $\mathrm{kg\,m^{-3}}$ as funktion of sphere equivalent diameter in mm, deduced from the 4 different inverse mass-size-relations presented in equations (36), (37), (38) and (39).

7 Backscattering cross sections of dry ice particles

We now turn to a more detailed investigation on the backscattering properties of single precipitation particles. In this section, the focus is on results for dry ice particles. In later sections, similar investigations will also be presented for melting ice particles.

For dry ice particles, basically two different particle models are available in `radar_mielib` if Mie-scattering is assumed. These are the one-layered ordinary sphere (suitable, e.g., for graupel and hail particles) and the two-layered sphere (e.g., for snow flakes). With Rayleigh scattering, only one-layered spheres are accounted for, since the Rayleigh approximation is an approximation to the Mie scattering functions for ordinary spheres.

In the following, the two different particle models are briefly described, together with a short examination of the differences in Z_e which they produce for the **C-Band radar wavelength $\lambda_0 = 5.5$ cm.**

7.1 One-layered sphere

In this section, the differences in Z_e caused by the application of different EMAs in case of different particle bulk densities is examined at $\boldsymbol{\lambda_0 = 5.5}$ **cm (C-Band)** to provide a qualitative guideline what to expect from what combination of these settings. The focus here is on dry ice particles which are assumed to be one-layered spheres of a homogeneous two-compontent mixture of ice and air. This particle model should be applicable to graupel and hail particles and in case of Rayleigh approximation, it has to be applied to all kinds of ice particles.

To this end, backscatter cross sections of graupel particles were calculated as a function of particle diameter by the `radar_mielib` subroutine `MIE_DRY_GRAUPEL()` (subsubsection 5.3.1) or, in case of Rayleigh approximation, by subroutine `RAYLEIGH_DRY_GRAUPEL()` (subsubsection 5.3.2). This was done for two different temperatures (T = -10°C, T = -20°C) and for

the mixing rules presented in subsubsection 4.5.4, applied to a two-component mixture. To show the dependence on particle bulk density (important to deduce the volume fractions of ice and air for the EMAs), this parameter is derived alternatively from the four inverse mass-size-relations

$$\frac{D}{D_0} = 0.19091 \left(\frac{x}{x_0}\right)^{0.32258} \quad \text{("Graupel", standard LM one-moment scheme)} \tag{36}$$

$$\frac{D}{D_0} = 0.11 \left(\frac{x}{x_0}\right)^{0.3} \quad \text{("Graupel", SB two-moment scheme)} \tag{37}$$

$$\frac{D}{D_0} = 5.12989 \left(\frac{x}{x_0}\right)^{0.5} \quad \text{("Snow", standard LM one-moment scheme)} \tag{38}$$

$$\frac{D}{D_0} = 1.33398 \left(\frac{x}{x_0}\right)^{0.41667} \quad \text{("Snow", SB two-moment scheme)} \quad , \tag{39}$$

assuming equivalent spherical particles. x is the particle mass (without the mass of the enclosed air), D its diameter and x_0 and D_0 are constant scaling parameters of 1 kg and 1 m, resp. The general form of the inverse mass-size-relation used throughout this document is

$$\frac{D}{D_0} = a_{geo} \left(\frac{x}{x_0}\right)^{b_{geo}} \quad , \tag{40}$$

with a_{geo} and b_{geo} beeing dimensionless constants.

equation (36) and (38) are taken from the operational one-moment bulk microphysical scheme of the LM, and equation (37) and (39) from the two-moment bulk microphysical scheme of Seifert and Beheng (2006). Figure 10 presents the resulting particle bulk densities as function of size and shows that, with these 4 different relations, nearly the whole range of possible bulk densities occuring in nature is covered.

For the refractive index of ice, the model of Mätzler (1998) (cf. Figure 6 on Page 13) is used in the following.

The results (Figure 11) show that there is no substantial difference at the two assumed temperatures. In addition, all applied mixing rules lead to nearly the same backscattering cross section for a given particle (the variation range of σ_b for different EMAs is less than 3 dB — a factor of two — which is not much). Considerable differences occur for larger particles when Rayleigh scattering is assumed instead of Mie scattering. Most important, the backscattering cross section shows a strong increase with particle bulk density, as shown by the four different used mass-size-relations.

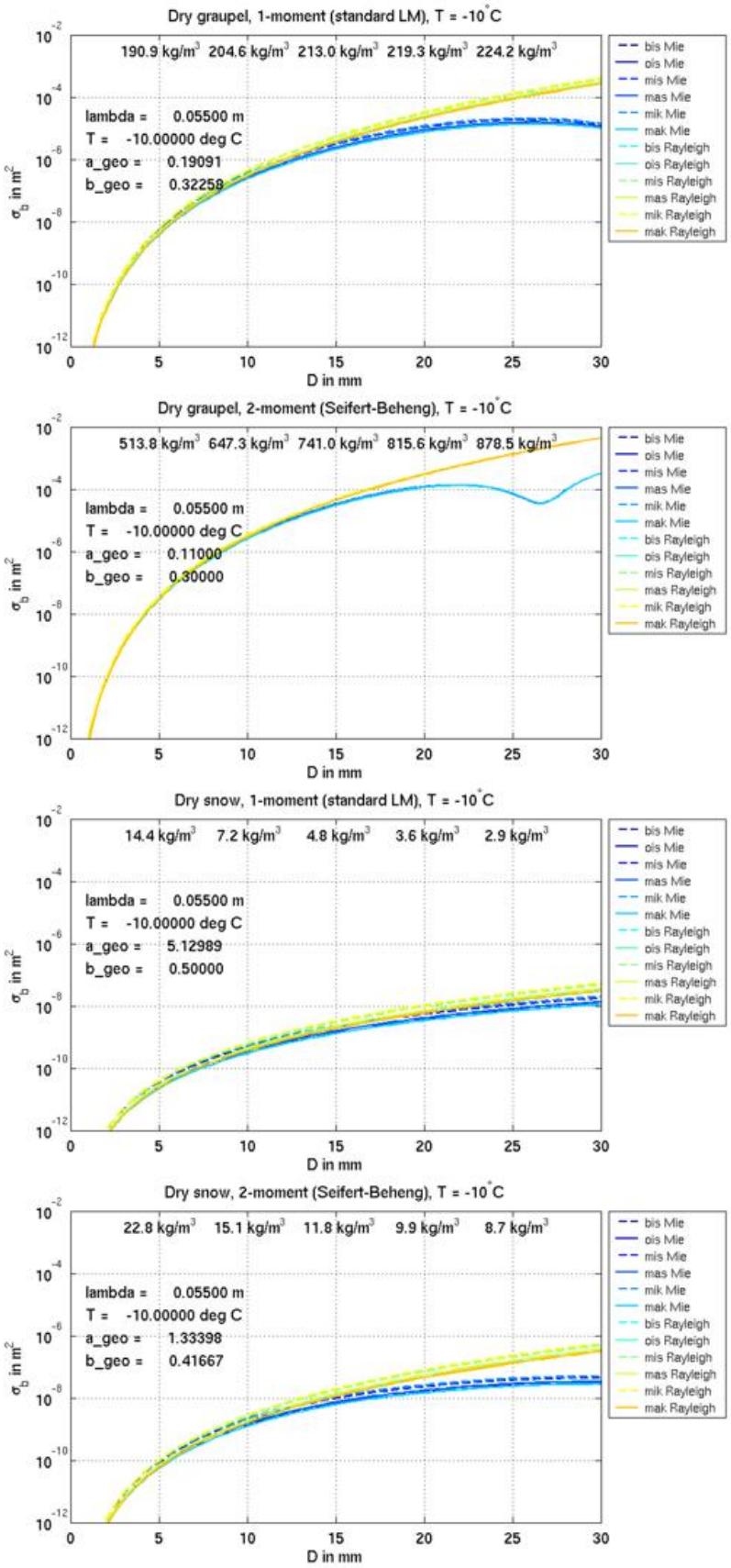


Figure 11: Backscattering cross section σ_b in m^2 as a function of particle diameter, EMA (see legend and explanation in Table 38 in combination with section 5.2.4) for T = -10°C. **Panels from top to bottom:** Graupel with mass-size-relation (36) from the LM standard microphysics scheme, graupel from Seifert and Beheng two-moment scheme (equation (37)), snow from the LM standard scheme (equation (38)), snow from the two-moment scheme (equation (39)).

7.2 Two-layered sphere

Backscattering cross sections for a two-layered sphere (cf. Figure 1 on Page 10) were calculated by using the `radar_mielib` subroutine `MIE_DRYSNOW_TWOSPH()` (subsubsection 5.3.5). Here, an additional important parameter is the ratio between the inner sphere and outer sphere radii. This ratio has to be preset and is a fixed input parameter for subroutine `MIE_DRYSNOW_TWOSPH()`. Without loss of generality, a value of 0.5 is used throughout `radar_mie_lm`, but this can be changed by the user. As mentioned before, this model is applicable to snow particles, as shown by, e.g., Fabry and Szyrmer (1999).

A similar comparison as presented in the last Subsection 7.1 is repeated here for snow particles of two different mass-size-relations as a function of particle diameter, temperature and mixing rule. The inverse mass-size-relations were given earlier in equation (38) and (39) in Subsection 7.1.

For the refractive index of ice, again the model of Mätzler (1998) (cf. Figure 6 on Page 13) is used in the following.

A comment is necessary on the derivation of the particle bulk densities in the inner and outer spherical shells. Note that for snow flakes, it is observed that the bulk density usually decreases with size, reflected by the mass-size-relations found in literature. To explain this behaviour, Fabry and Szyrmer (1999) present an interesting *Gedankenexperiment*: Snow flakes preferably form by aggregation of smaller ice and snow particles. Thats why they are called "aggregates" in technical terms. Consider now without loss of generality a population of equally sized snow flakes having equal bulk density. Through collision and sticking, larger flakes are formed. In the extreme case of flakes aggregating around a single "embryonal flake" in dense sphere packing, the resulting flake would be double in diameter with a nearly equal but slightly lower bulk density. In reality, this dense packing will almost never be fully realised and there will always be some voids causing the overall bulk density to be even lower. Generalization to an initial population of differently sized snow flakes, the outcome will always be a decreasing mean bulk density with snow flake diameter.

To model this, the bulk densities of the inner and outer shell of the two-layered spherical particles are calculated in the following way: Given a fixed mass-size-relation representing a decreasing bulk density with diameter, a certain snowflake diameter and an assumed ratio of inner to outer shell diameter (e.g., 0.5), at first the inner core is assigned the density found by applying the inner sphere diameter within the mass-size-relation. Then, given the total mass by applying the outer sphere diameter within the mass-size-relation, the mass of the outer spherical shell is just the difference of total mass minus mass of inner sphere. From this and the preset and fixed ratio of inner to outer sphere radius, the bulk density of the outer shell can be calculated.

From the bulk densities of core and shell, the corresponding volume fractions of ice and air are calculated further. To get m_{eff} of core and shell, the volume fractions are plugged into the different formulas for the EMA approximations presented earlier in this document. Table 38 gives the 6 possible different settings for an ice-air mixture material (cf. subsubsection 5.2.4). With this, backscattering coefficients are calculated as function of size and all implemented combinations of EMA approximations for core and shell ($6 \times 6 = 36$) . This was done for both inverse mass-size relations mentioned earlier in this section. In all cases, the temperature was set to -10°C.

Figure 12 shows the results for both mass-size relations in a simplified way (upper panel: relation (38), lower panel: relation (39)). In each figure, the blue "strip" marks the envelope (variation range) of σ_b as function of size and EMA for the two-layered Mie calculation. For

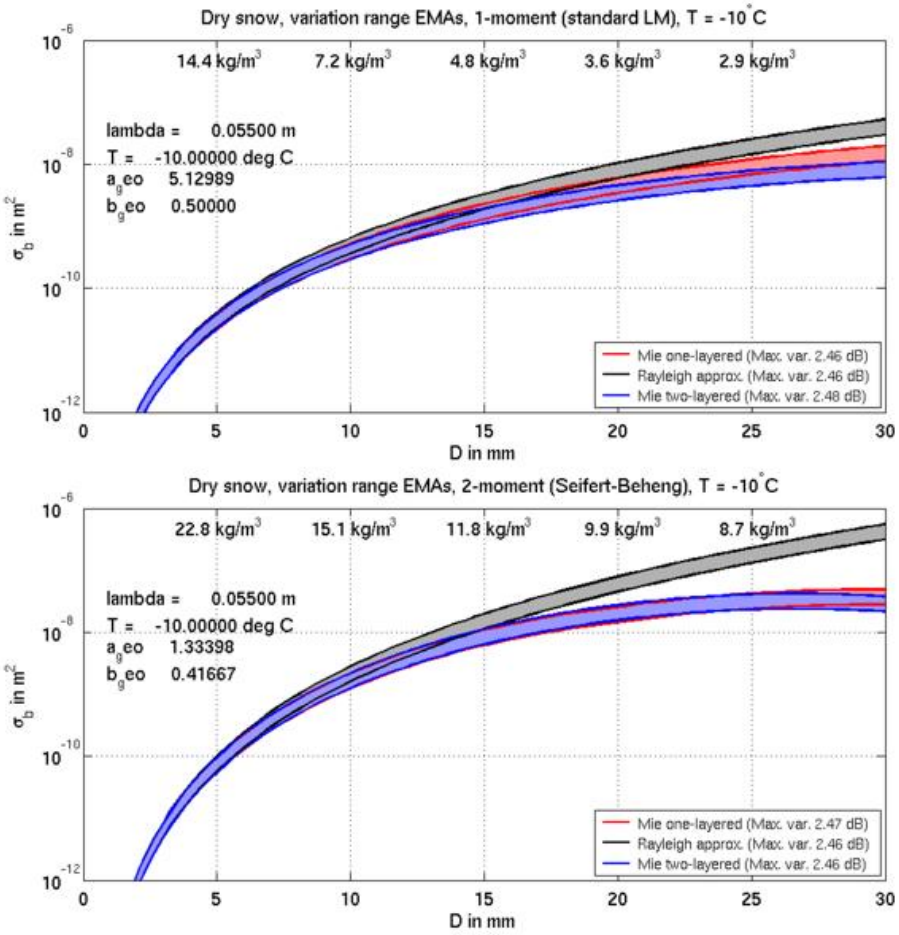


Figure 12: Variation range of Backscattering cross section σ_b for snow in m^2 as a function of particle diameter considering all possible combinations of the implemented EMAs for a two-layered sphere at T = -10°C. See text for explanation. **Upper panel:** Snow with mass-size-relation (38) from the LM standard microphysics scheme, **lower panel:** snow from Seifert and Beheng two-moment scheme (equation (39)).

comparison, the red "strip" gives the corresponding results considering Mie scattering by simple spheres only (6 different EMA approximations), and further applying Rayleigh approximation leads to the grey "strip". It is found that imposing different EMA-approximations leads to only moderate variations of σ_b for a given size. This can be explained by the fact that ice is weak dielectric only and nearly every different choice of an EMA approximation leads to the nearly the same m_{eff}. Moreover, in case of $\lambda_0 = 5.5$ cm as considered here, for particles with $D < 15$ mm it does not make a large difference if choosing a two-sphere particle model or simple spheres, or if choosing an even simpler Rayleigh approximation. For larger particles, the two-sphere model produces slightly smaller backscattering cross sections than the simple sphere model (larger difference for less dense particles) and the Rayleigh approximation becomes unrealistic.

As a result, considering the large numerical effort, application of Mie scattering for dry snowflakes makes sense in case for large snowflakes whereas a further complication by using the two-layered sphere model seems to be unnecessary in this case.

However, it will be shown in the next section that in case of melting snowflakes, the two-layered sphere model leeds to significantly different results compared to simple spheres.

8 Backscattering cross sections for melting ice particles relative to the mass-equivalent water drop

For melting ice particles, the presence of water (a strong dielectric) within the ice structure of melting particles poses a particular problem when it comes to the proper choice of an effective medium approximation. In fact, is there a proper choice at all? The answer to this question stronly depends on the mixture topology of the ice-water-air mixture. Whereas for nearly solid hail it seems quite easy, the structure of melting intermediate- or low-density graupel or snowflakes is more difficult to treat.

Therefore, `radar_mielib` and `radar_mie_lm` provide no definite answer (the one and only solution) but permit the user to choose between many different possibilities to get a feeling for the range of uncertainty of the resulting reflectivity value. However, there are theoretical and experimental results presented in literature providing guidelines which EMA formulation and particle model should work better for certain hydrometeor types. Some basic discussion was presented earlier in the sections describing different EMA approximations For more detailed informations, the reader is kindly referred to the corresponding literature. A starting point could be, e.g., the book of Bohren and Huffman (1983) and a number of subsequent articles by C. Bohren and coauthors. The literature is so numerous that we omit further citing here.

For LM users, the "hints" and guidelines from literature are reflected by reasonable default parameter values for the corresponding subroutines in `radar_mie_lm`, which can, of course, be changed. And to provide some guideline about what happens to Z_e if the default parameter settings are changed, the following sections provide a detailed sensitivity investigation of the backscattering cross sections of melting hydrometeors considering all possible parameter settings for the most basic particle models implemented into `radar_mielib`.

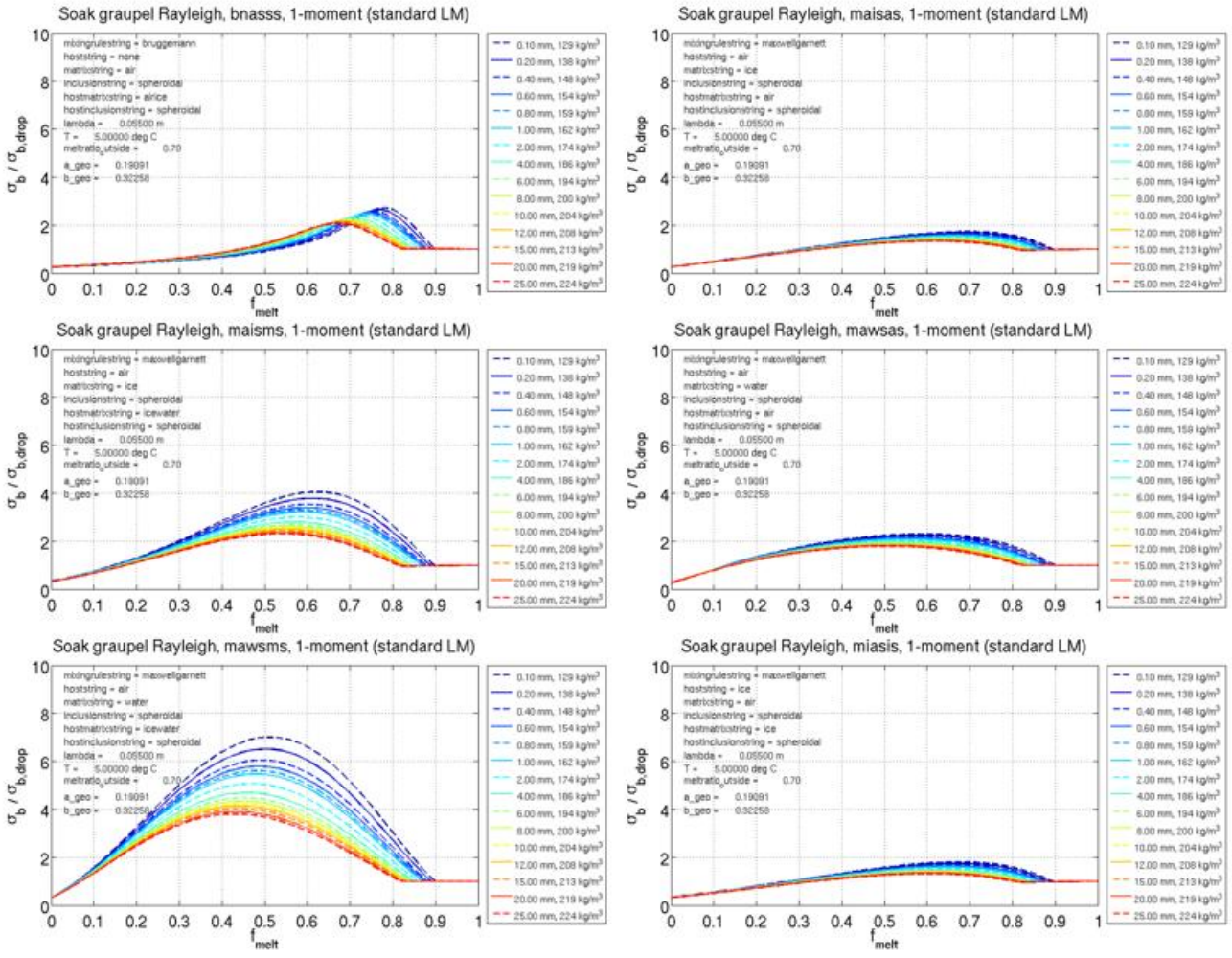
To this end, the same 4 different inverse mass-size relations as in Subsection 7.1 are applied to deduce the mass of the initally unmelted particle which is varied from small to large values. Subsequent variation of the degree of melting f_{melt} and the particle model together with the EMA approximation leads to a very large compilation of results which is presented in the following subsections.

The results apply to a **C-Band radar wavelength of $\lambda_0 = 5.5$ cm and to a temperature of 5°C.**

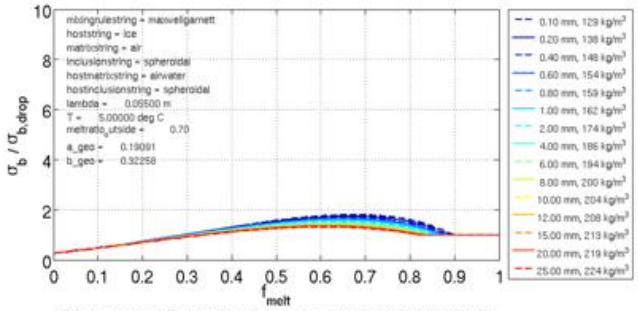
8.1 Rayleigh: soaked wet graupel, LM-scheme

Results are shown for calculations of the backscattering cross section σ_b with subroutine `RAYLEIGH_SOAK_WETGRAUPEL()` (Rayleigh approximation), see subsubsection 5.3.12 on Page 50. The following figures show the ratio of σ_b to the backscattering cross section $\sigma_{b,drop}$ of the resulting water drop, if the particle would be completely melted, as function of f_{melt} and the unmelted particle diameter for different EMA-formulations of the particles effective refractive index m_{eff}. The particle bulk density as function of size is determined by equation (36) on Page 69. A depiciton of the resulting bulk density as function of particle size can be found in Figure 10 (black solid line).

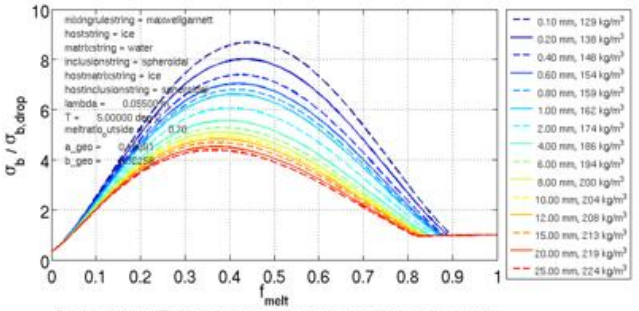
Every figure represents one particular EMA-formulation for m_{eff}, which is obtained by using function `get_m_mix_nested()` (subsubsection 5.2.5 on Page 28). The input parameter set for `get_m_mix_nested()` can be found in the text annotation within each graph. For users of the LM, the corresponding setting of the namelist-parameter `ctype_wetgraupel_ray` can be found as 6-character code in the figures title. For explanation of this code, see Table 40. The results of this section apply to the LM for graupel and snow particles in case of application of the standard one-moment bulk microphysical scheme (namelist-parameter `itype_gscp` $<$ 100) together with `itype_refl` $= 2$.



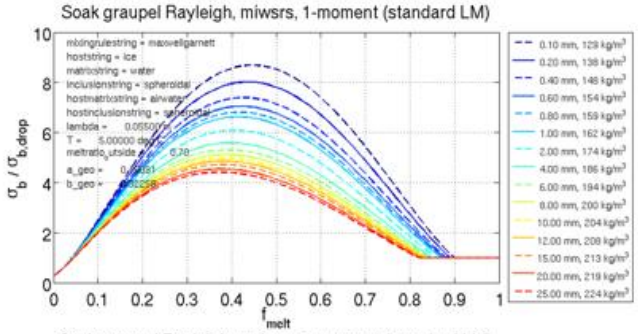
Soak graupel Rayleigh, miasrs, 1-moment (standard LM)



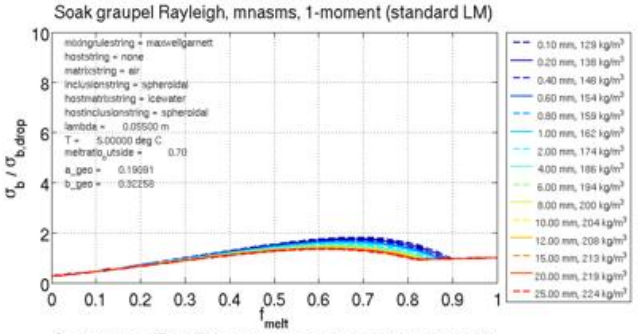
Soak graupel Rayleigh, miwsis, 1-moment (standard LM)



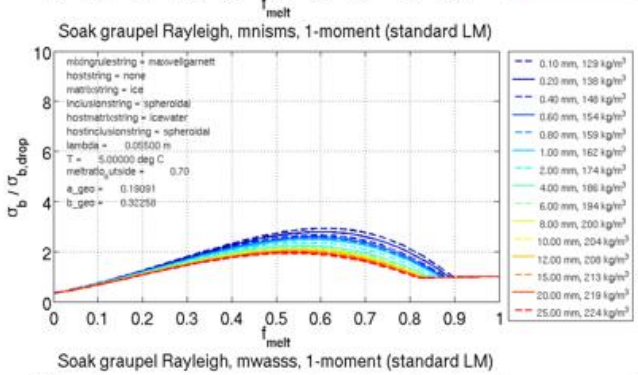
Soak graupel Rayleigh, miwsrs, 1-moment (standard LM)



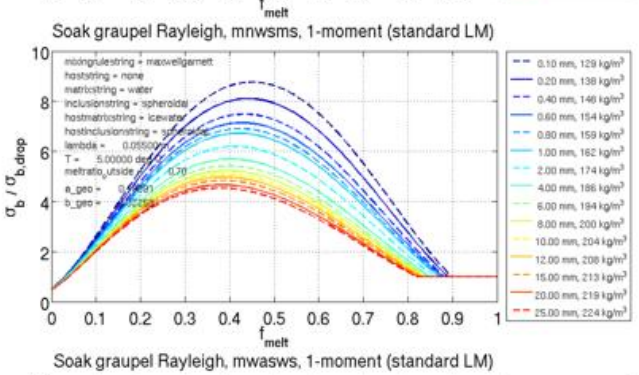
Soak graupel Rayleigh, mnasms, 1-moment (standard LM)



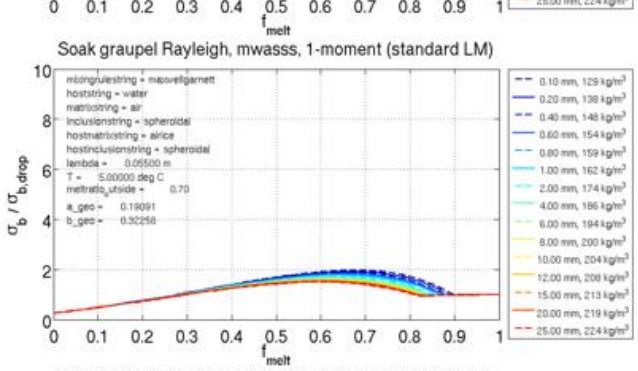
Soak graupel Rayleigh, mnisms, 1-moment (standard LM)



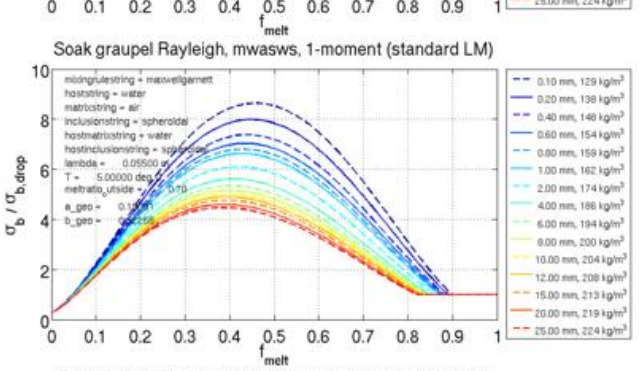
Soak graupel Rayleigh, mnwsms, 1-moment (standard LM)



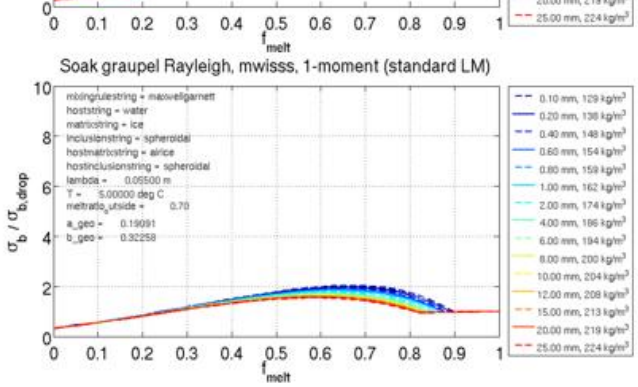
Soak graupel Rayleigh, mwasss, 1-moment (standard LM)



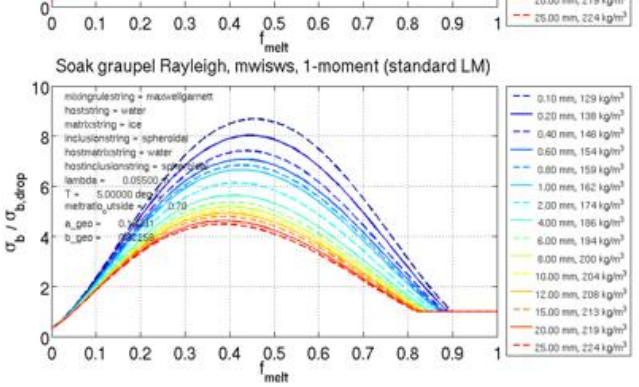
Soak graupel Rayleigh, mwasws, 1-moment (standard LM)

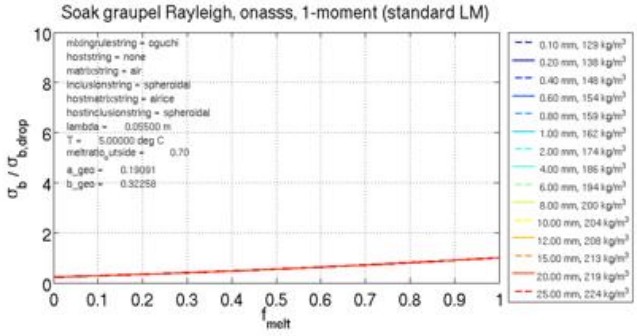


Soak graupel Rayleigh, mwisss, 1-moment (standard LM)



Soak graupel Rayleigh, mwisws, 1-moment (standard LM)

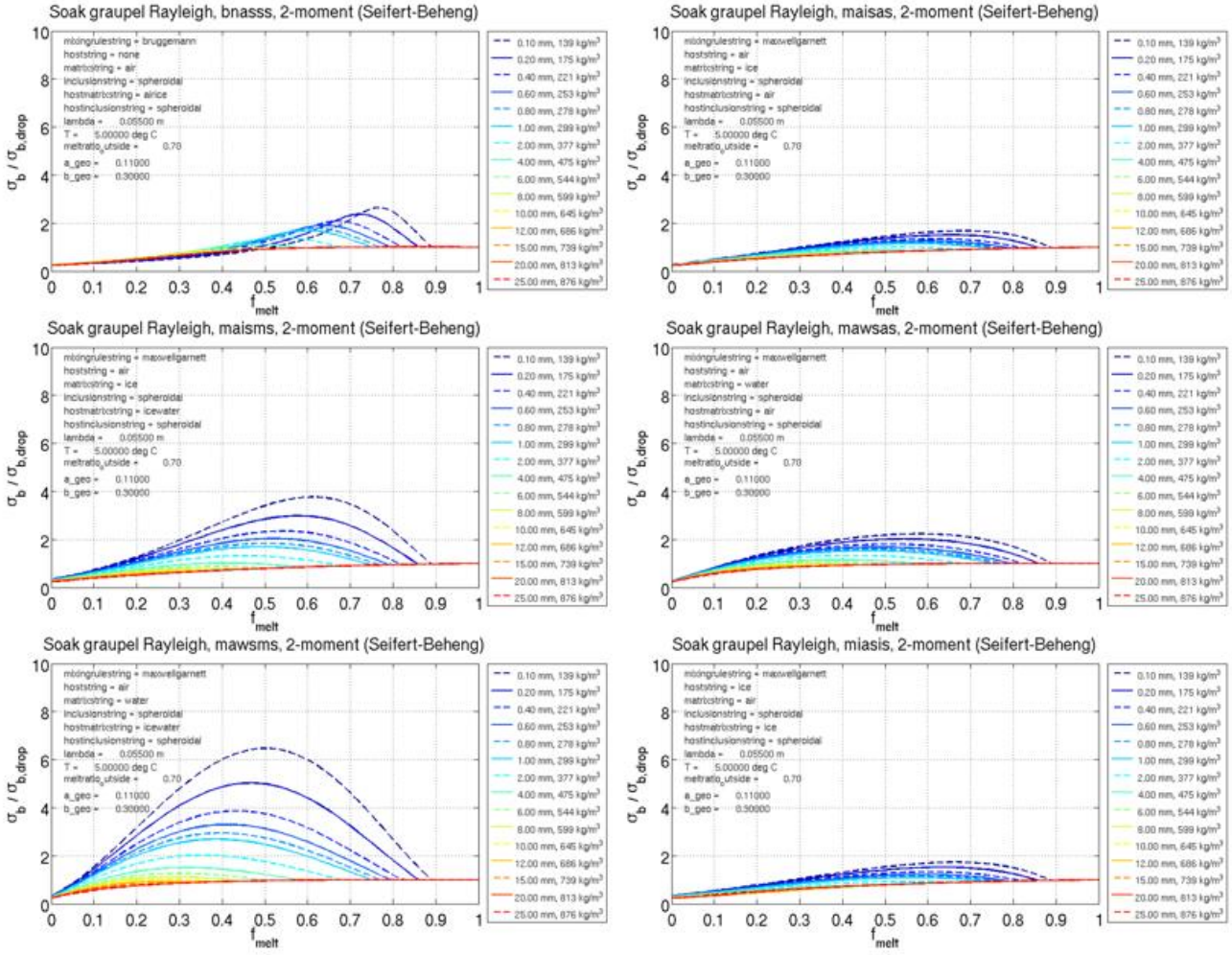



Soak graupel Rayleigh, onasss, 1-moment (standard LM)
mixingrulestring = oguchi
hoststring = none
matrixstring = air
inclusionstring = spheroidal
hostmatrixstring = airice
hostinclusionstring = spheroidal
lambda = 0.09500 m
T = 5.00000 deg C
meltratio_outside = 0.70
a_geo = 0.19091
b_geo = 0.32258
0.10 mm, 129 kg/m³
0.20 mm, 138 kg/m³
0.40 mm, 148 kg/m³
0.60 mm, 154 kg/m³
0.80 mm, 159 kg/m³
1.00 mm, 162 kg/m³
2.00 mm, 174 kg/m³
4.00 mm, 186 kg/m³
6.00 mm, 194 kg/m³
8.00 mm, 200 kg/m³
10.00 mm, 204 kg/m³
12.00 mm, 208 kg/m³
15.00 mm, 213 kg/m³
20.00 mm, 219 kg/m³
25.00 mm, 224 kg/m³
σb / σb,drop
fmelt
0
2
4
6
8
10
0 0.1 0.2 0.3 0.4 0.5 0.6 0.7 0.8 0.9 1

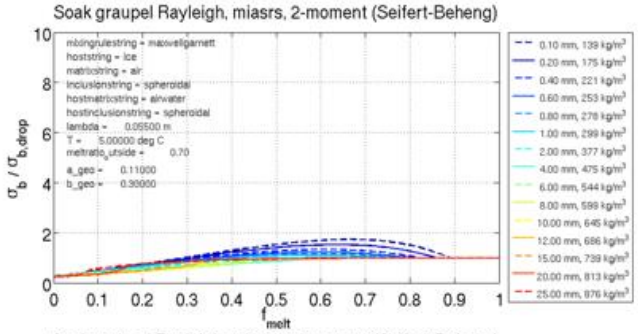
8.2 Rayleigh: soaked wet graupel, Seifert/Beheng-scheme

Similar to Subsection 8.1, results are shown for calculations of the backscattering cross section σ_b with subroutine `RAYLEIGH_SOAK_WETGRAUPEL()` (Rayleigh approximation), see subsubsection 5.3.12 on Page 50, but this time the particle bulk density as function of size is determined by equation (37) on Page 69. A depiciton of the resulting bulk density as function of particle size can be found in Figure 10 (red solid line). The following figures show the ratio of $\sigma_b/\sigma_{b,drop}$ as function of f_{melt} and the unmelted particle diameter for different EMA-formulations of the particles effective refractive index m_{eff}.

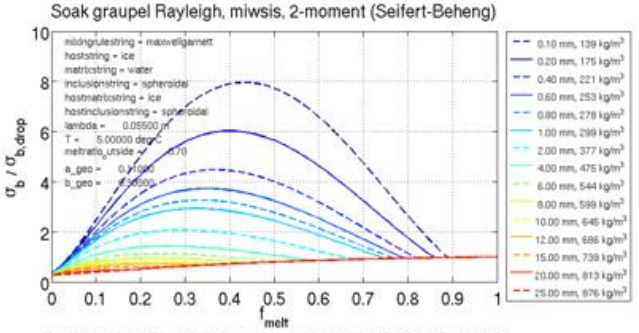
Again, every figure represents one particular EMA-formulation for m_{eff}, which is obtained by using function `get_m_mix_nested()` (subsubsection 5.2.5 on Page 28). The input parameter set for `get_m_mix_nested()` can be found in the text annotation within each graph. For users of the LM, the corresponding setting of the namelist-parameter `ctype_wetgraupel_ray` can be found as 6-character code in the figures title. For explanation of this code, see Table 40. The results of this section apply to the LM for graupel, snow and hail particles in case of application of the Seifert and Beheng (2006) two-moment bulk microphysical scheme (namelist-parameter `itype_gscp` ≥ 100) together with `itype_refl` $= 2$.



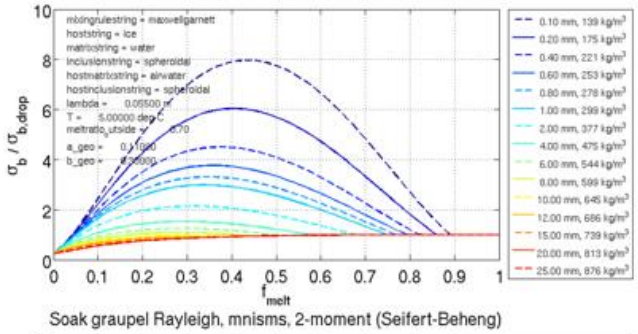
Soak graupel Rayleigh, miasrs, 2-moment (Seifert-Beheng)



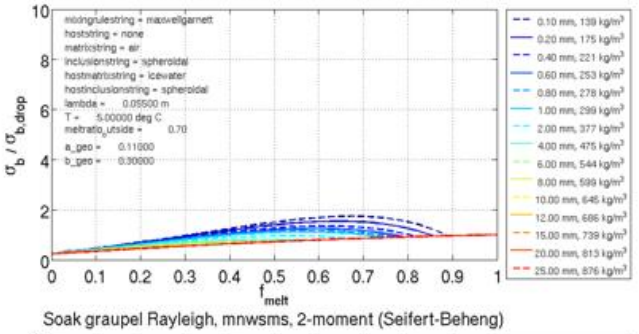
Soak graupel Rayleigh, miwsis, 2-moment (Seifert-Beheng)



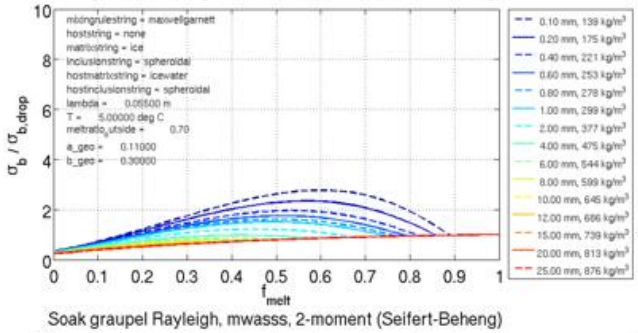
Soak graupel Rayleigh, miwsrs, 2-moment (Seifert-Beheng)



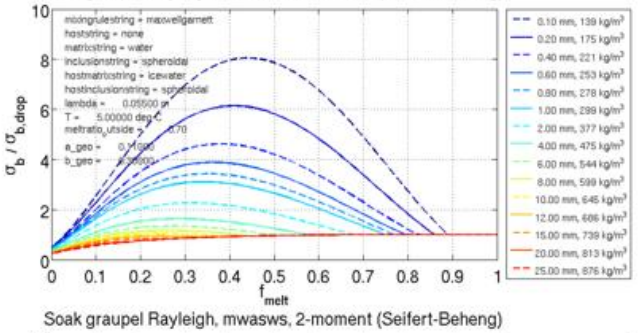
Soak graupel Rayleigh, mnasms, 2-moment (Seifert-Beheng)



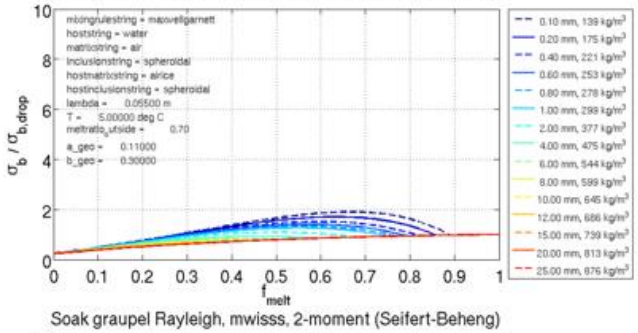
Soak graupel Rayleigh, mnisms, 2-moment (Seifert-Beheng)



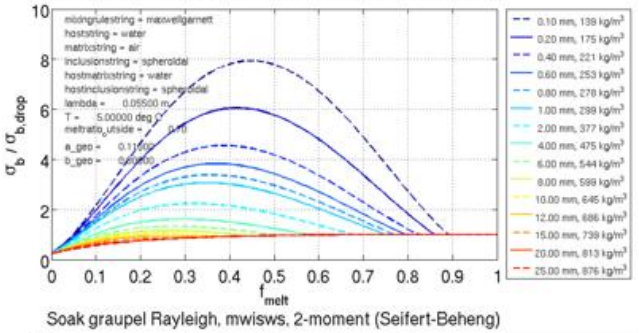
Soak graupel Rayleigh, mnwsms, 2-moment (Seifert-Beheng)



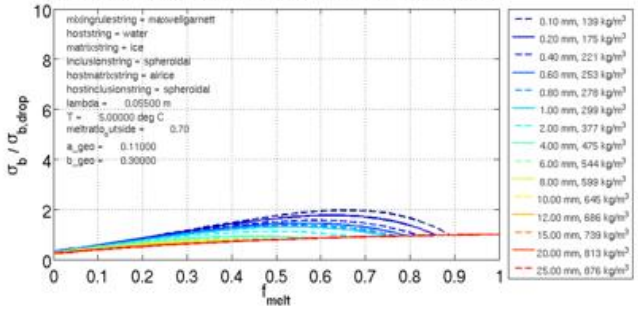
Soak graupel Rayleigh, mwasss, 2-moment (Seifert-Beheng)



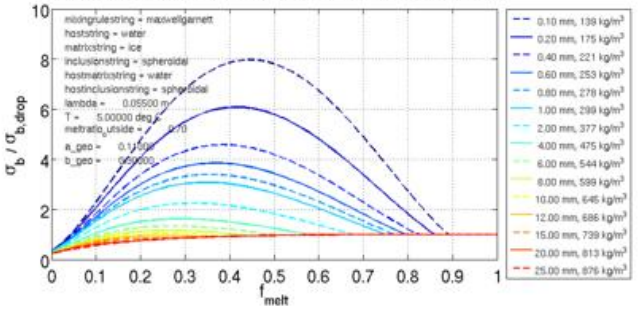
Soak graupel Rayleigh, mwasws, 2-moment (Seifert-Beheng)

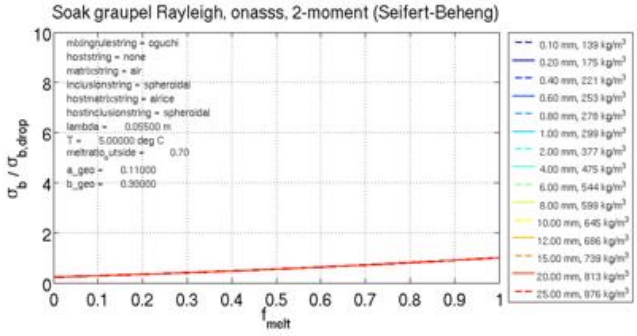


Soak graupel Rayleigh, mwisss, 2-moment (Seifert-Beheng)



Soak graupel Rayleigh, mwisws, 2-moment (Seifert-Beheng)

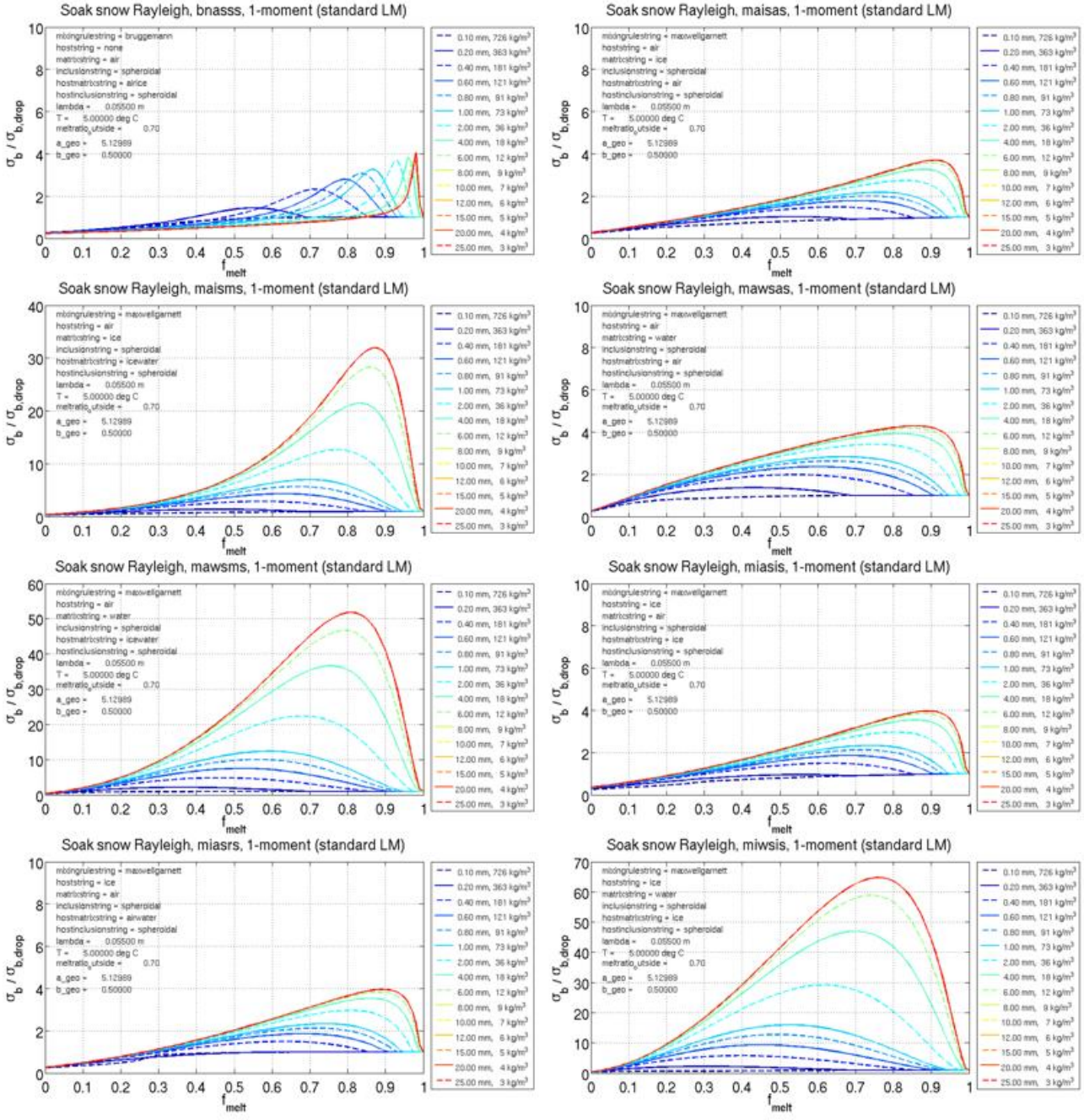


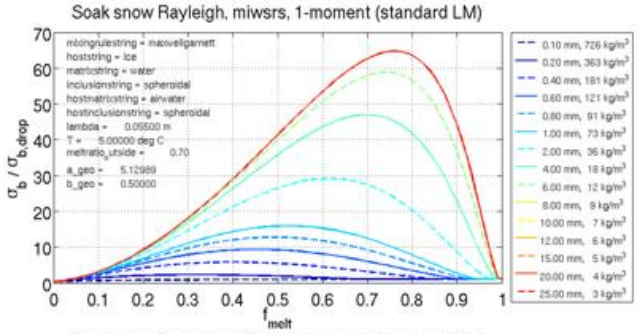

Soak graupel Rayleigh, onasss, 2-moment (Seifert-Beheng)
mixingrulestring = oguchi
hoststring = none
matrixstring = air
inclusionstring = spheroidal
hostmatrixstring = airice
hostinclusionstring = spheroidal
lambda = 0.09500 m
T = 5.00000 deg C
meltratio_outside = 0.70
a_geo = 0.11000
b_geo = 0.30000
0.10 mm, 139 kg/m³
0.20 mm, 175 kg/m³
0.40 mm, 221 kg/m³
0.60 mm, 253 kg/m³
0.80 mm, 278 kg/m³
1.00 mm, 299 kg/m³
2.00 mm, 377 kg/m³
4.00 mm, 475 kg/m³
6.00 mm, 544 kg/m³
8.00 mm, 599 kg/m³
10.00 mm, 645 kg/m³
12.00 mm, 686 kg/m³
15.00 mm, 739 kg/m³
20.00 mm, 813 kg/m³
25.00 mm, 876 kg/m³
σb / σb,drop
fmelt
0
2
4
6
8
10
0.1
0.2
0.3
0.4
0.5
0.6
0.7
0.8
0.9
1

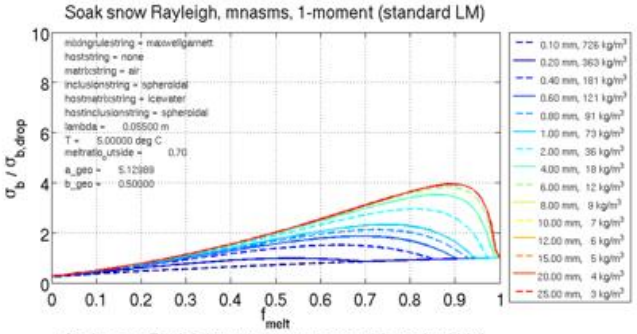
8.3 Rayleigh: soaked wet snow, LM-scheme

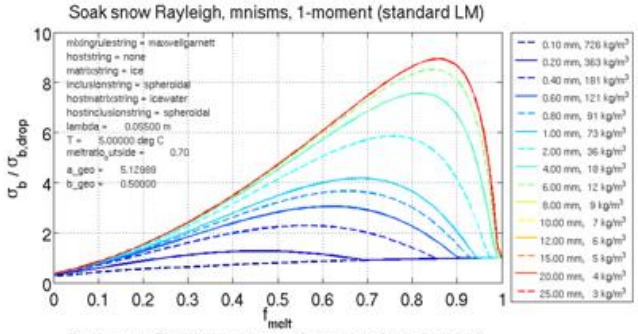
Similar to Subsection 8.1, results are shown for calculations of the backscattering cross section σ_b with subroutine `RAYLEIGH_SOAK_WETGRAUPEL()` (Rayleigh approximation), see subsubsection 5.3.12 on Page 50, but this time the particle bulk density as function of size is determined by equation (38) on Page 69. A depiciton of the resulting bulk density as function of particle size can be found in Figure 10 (blue solid line). The following figures show the ratio of $\sigma_b/\sigma_{b,drop}$ as function of f_{melt} and the unmelted particle diameter for different EMA-formulations of the particles effective refractive index m_{eff}.

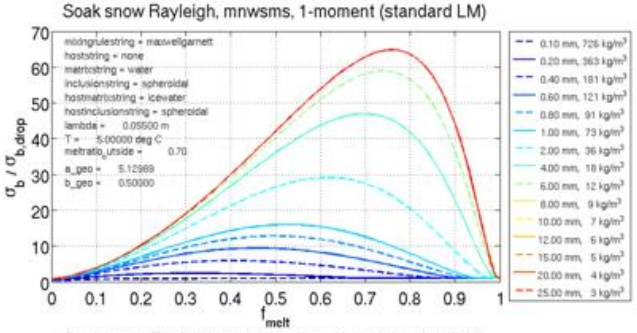
Again, every figure represents one particular EMA-formulation for m_{eff}, which is obtained by using function `get_m_mix_nested()` (subsubsection 5.2.5 on Page 28). The input parameter set for `get_m_mix_nested()` can be found in the text annotation within each graph. Although not beeing implemented into the LM interface functions for snow, the corresponding setting of the namelist-parameter `ctype_wetsnow_ray` (in analogy to `ctype_wetgraupel_ray`) can be found as 6-character code in the figures title. For explanation of this code, see Table 40.

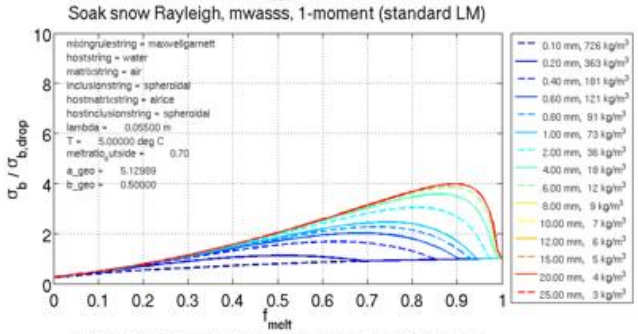


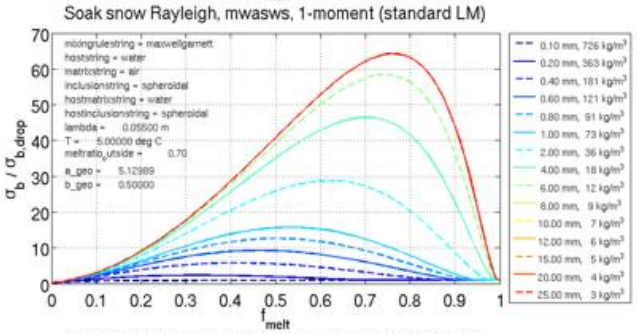

Soak snow Rayleigh, miwsrs, 1-moment (standard LM)
mixingrulestring = maxwellgarnett
hoststring = ice
matrixstring = water
inclusionstring = spheroidal
hostmatrixstring = airwater
hostinclusionstring = spheroidal
lambda = 0.05500 m
T = 5.00000 deg C
meltratio_outside = 0.70
a_geo = 5.12989
b_geo = 0.50000
0.10 mm, 726 kg/m³
0.20 mm, 363 kg/m³
0.40 mm, 181 kg/m³
0.60 mm, 121 kg/m³
0.80 mm, 91 kg/m³
1.00 mm, 73 kg/m³
2.00 mm, 36 kg/m³
4.00 mm, 18 kg/m³
6.00 mm, 12 kg/m³
8.00 mm, 9 kg/m³
10.00 mm, 7 kg/m³
12.00 mm, 6 kg/m³
15.00 mm, 5 kg/m³
20.00 mm, 4 kg/m³
25.00 mm, 3 kg/m³
σb / σb,drop
fmelt

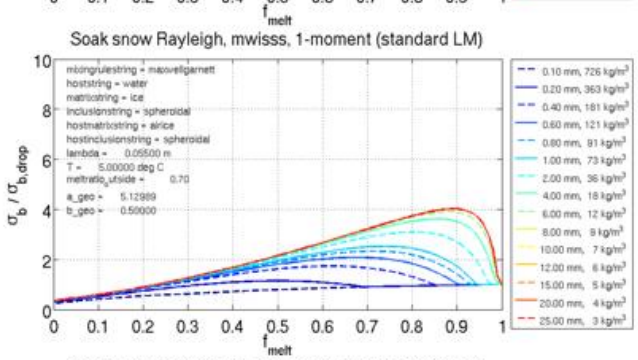

Soak snow Rayleigh, mnasms, 1-moment (standard LM)
mixingrulestring = maxwellgarnett
hoststring = none
matrixstring = air
inclusionstring = spheroidal
hostmatrixstring = icewater
hostinclusionstring = spheroidal
lambda = 0.05500 m
T = 5.00000 deg C
meltratio_outside = 0.70
a_geo = 5.12989
b_geo = 0.50000
0.10 mm, 726 kg/m³
0.20 mm, 363 kg/m³
0.40 mm, 181 kg/m³
0.60 mm, 121 kg/m³
0.80 mm, 91 kg/m³
1.00 mm, 73 kg/m³
2.00 mm, 36 kg/m³
4.00 mm, 18 kg/m³
6.00 mm, 12 kg/m³
8.00 mm, 9 kg/m³
10.00 mm, 7 kg/m³
12.00 mm, 6 kg/m³
15.00 mm, 5 kg/m³
20.00 mm, 4 kg/m³
25.00 mm, 3 kg/m³
σb / σb,drop
fmelt

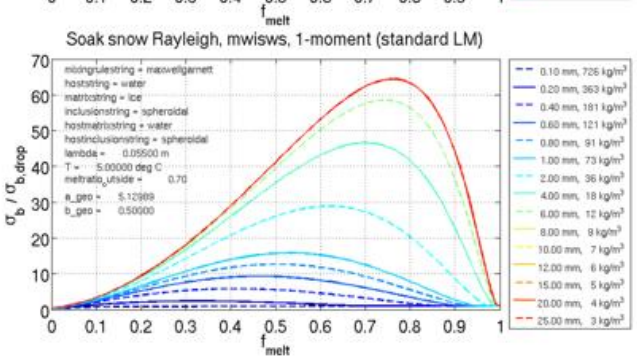

Soak snow Rayleigh, mnisms, 1-moment (standard LM)
mixingrulestring = maxwellgarnett
hoststring = none
matrixstring = ice
inclusionstring = spheroidal
hostmatrixstring = icewater
hostinclusionstring = spheroidal
lambda = 0.05500 m
T = 5.00000 deg C
meltratio_outside = 0.70
a_geo = 5.12989
b_geo = 0.50000
0.10 mm, 726 kg/m³
0.20 mm, 363 kg/m³
0.40 mm, 181 kg/m³
0.60 mm, 121 kg/m³
0.80 mm, 91 kg/m³
1.00 mm, 73 kg/m³
2.00 mm, 36 kg/m³
4.00 mm, 18 kg/m³
6.00 mm, 12 kg/m³
8.00 mm, 9 kg/m³
10.00 mm, 7 kg/m³
12.00 mm, 6 kg/m³
15.00 mm, 5 kg/m³
20.00 mm, 4 kg/m³
25.00 mm, 3 kg/m³
σb / σb,drop
fmelt

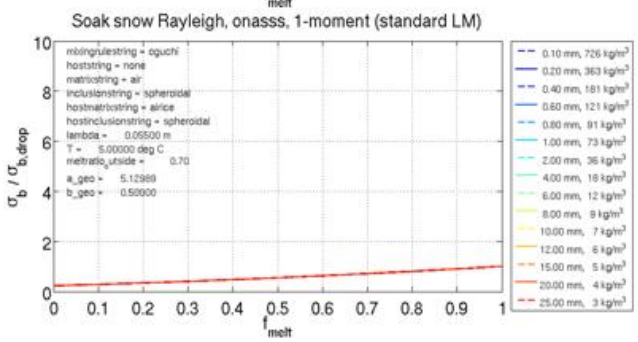

Soak snow Rayleigh, mnwsms, 1-moment (standard LM)
mixingrulestring = maxwellgarnett
hoststring = none
matrixstring = water
inclusionstring = spheroidal
hostmatrixstring = icewater
hostinclusionstring = spheroidal
lambda = 0.05500 m
T = 5.00000 deg C
meltratio_outside = 0.70
a_geo = 5.12989
b_geo = 0.50000
0.10 mm, 726 kg/m³
0.20 mm, 363 kg/m³
0.40 mm, 181 kg/m³
0.60 mm, 121 kg/m³
0.80 mm, 91 kg/m³
1.00 mm, 73 kg/m³
2.00 mm, 36 kg/m³
4.00 mm, 18 kg/m³
6.00 mm, 12 kg/m³
8.00 mm, 9 kg/m³
10.00 mm, 7 kg/m³
12.00 mm, 6 kg/m³
15.00 mm, 5 kg/m³
20.00 mm, 4 kg/m³
25.00 mm, 3 kg/m³
σb / σb,drop
fmelt


Soak snow Rayleigh, mwasss, 1-moment (standard LM)
mixingrulestring = maxwellgarnett
hoststring = water
matrixstring = air
inclusionstring = spheroidal
hostmatrixstring = airice
hostinclusionstring = spheroidal
lambda = 0.05500 m
T = 5.00000 deg C
meltratio_outside = 0.70
a_geo = 5.12989
b_geo = 0.50000
0.10 mm, 726 kg/m³
0.20 mm, 363 kg/m³
0.40 mm, 181 kg/m³
0.60 mm, 121 kg/m³
0.80 mm, 91 kg/m³
1.00 mm, 73 kg/m³
2.00 mm, 36 kg/m³
4.00 mm, 18 kg/m³
6.00 mm, 12 kg/m³
8.00 mm, 9 kg/m³
10.00 mm, 7 kg/m³
12.00 mm, 6 kg/m³
15.00 mm, 5 kg/m³
20.00 mm, 4 kg/m³
25.00 mm, 3 kg/m³
σb / σb,drop
fmelt


Soak snow Rayleigh, mwasws, 1-moment (standard LM)
mixingrulestring = maxwellgarnett
hoststring = water
matrixstring = air
inclusionstring = spheroidal
hostmatrixstring = water
hostinclusionstring = spheroidal
lambda = 0.05500 m
T = 5.00000 deg C
meltratio_outside = 0.70
a_geo = 5.12989
b_geo = 0.50000
0.10 mm, 726 kg/m³
0.20 mm, 363 kg/m³
0.40 mm, 181 kg/m³
0.60 mm, 121 kg/m³
0.80 mm, 91 kg/m³
1.00 mm, 73 kg/m³
2.00 mm, 36 kg/m³
4.00 mm, 18 kg/m³
6.00 mm, 12 kg/m³
8.00 mm, 9 kg/m³
10.00 mm, 7 kg/m³
12.00 mm, 6 kg/m³
15.00 mm, 5 kg/m³
20.00 mm, 4 kg/m³
25.00 mm, 3 kg/m³
σb / σb,drop
fmelt


Soak snow Rayleigh, mwisss, 1-moment (standard LM)
mixingrulestring = maxwellgarnett
hoststring = water
matrixstring = ice
inclusionstring = spheroidal
hostmatrixstring = airice
hostinclusionstring = spheroidal
lambda = 0.05500 m
T = 5.00000 deg C
meltratio_outside = 0.70
a_geo = 5.12989
b_geo = 0.50000
0.10 mm, 726 kg/m³
0.20 mm, 363 kg/m³
0.40 mm, 181 kg/m³
0.60 mm, 121 kg/m³
0.80 mm, 91 kg/m³
1.00 mm, 73 kg/m³
2.00 mm, 36 kg/m³
4.00 mm, 18 kg/m³
6.00 mm, 12 kg/m³
8.00 mm, 9 kg/m³
10.00 mm, 7 kg/m³
12.00 mm, 6 kg/m³
15.00 mm, 5 kg/m³
20.00 mm, 4 kg/m³
25.00 mm, 3 kg/m³
σb / σb,drop
fmelt

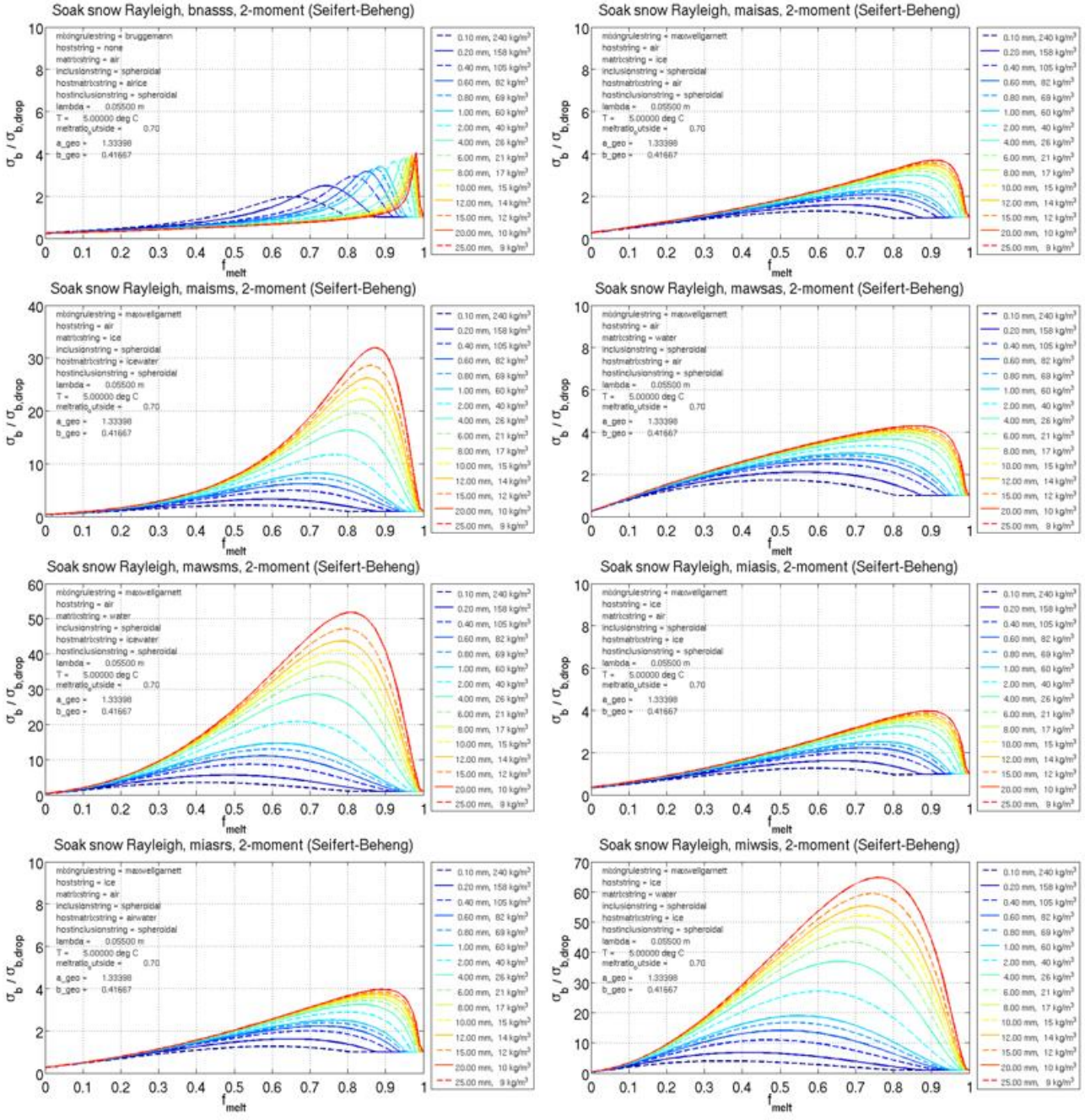

Soak snow Rayleigh, mwisws, 1-moment (standard LM)
mixingrulestring = maxwellgarnett
hoststring = water
matrixstring = ice
inclusionstring = spheroidal
hostmatrixstring = water
hostinclusionstring = spheroidal
lambda = 0.05500 m
T = 5.00000 deg C
meltratio_outside = 0.70
a_geo = 5.12989
b_geo = 0.50000
0.10 mm, 726 kg/m³
0.20 mm, 363 kg/m³
0.40 mm, 181 kg/m³
0.60 mm, 121 kg/m³
0.80 mm, 91 kg/m³
1.00 mm, 73 kg/m³
2.00 mm, 36 kg/m³
4.00 mm, 18 kg/m³
6.00 mm, 12 kg/m³
8.00 mm, 9 kg/m³
10.00 mm, 7 kg/m³
12.00 mm, 6 kg/m³
15.00 mm, 5 kg/m³
20.00 mm, 4 kg/m³
25.00 mm, 3 kg/m³
σb / σb,drop
fmelt


Soak snow Rayleigh, onasss, 1-moment (standard LM)
mixingrulestring = oguchi
hoststring = none
matrixstring = air
inclusionstring = spheroidal
hostmatrixstring = airice
hostinclusionstring = spheroidal
lambda = 0.05500 m
T = 5.00000 deg C
meltratio_outside = 0.70
a_geo = 5.12989
b_geo = 0.50000
0.10 mm, 726 kg/m³
0.20 mm, 363 kg/m³
0.40 mm, 181 kg/m³
0.60 mm, 121 kg/m³
0.80 mm, 91 kg/m³
1.00 mm, 73 kg/m³
2.00 mm, 36 kg/m³
4.00 mm, 18 kg/m³
6.00 mm, 12 kg/m³
8.00 mm, 9 kg/m³
10.00 mm, 7 kg/m³
12.00 mm, 6 kg/m³
15.00 mm, 5 kg/m³
20.00 mm, 4 kg/m³
25.00 mm, 3 kg/m³
σb / σb,drop
fmelt

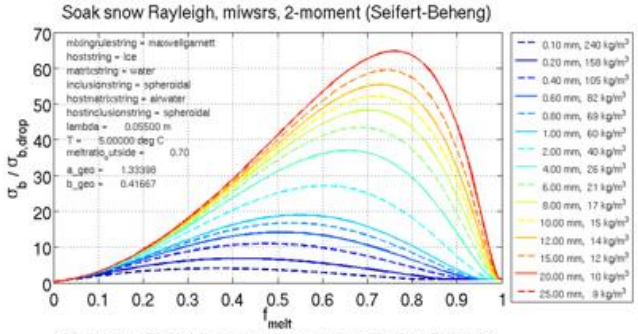
8.4 Rayleigh: soaked wet snow, Seifert/Beheng-scheme

Similar to Subsection 8.1, results are shown for calculations of the backscattering cross section σ_b with subroutine `RAYLEIGH_SOAK_WETGRAUPEL()` (Rayleigh approximation), see subsubsection 5.3.12 on Page 50, but this time the particle bulk density as function of size is determined by equation (39) on Page 69. A depiciton of the resulting bulk density as function of particle size can be found in Figure 10 (green solid line). The following figures show the ratio of $\sigma_b/\sigma_{b,drop}$ as function of f_{melt} and the unmelted particle diameter for different EMA-formulations of the particles effective refractive index m_{eff}.

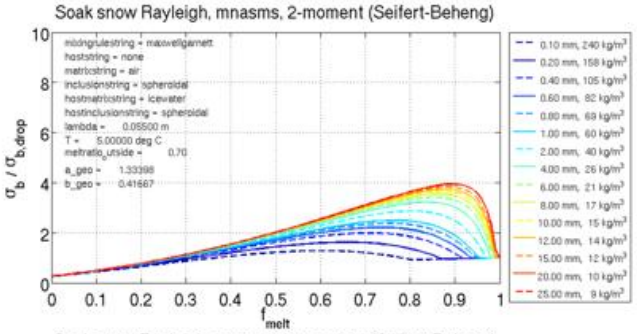
Again, every figure represents one particular EMA-formulation for m_{eff}, which is obtained by using function `get_m_mix_nested()` (subsubsection 5.2.5 on Page 28). The input parameter set for `get_m_mix_nested()` can be found in the text annotation within each graph. Although not beeing implemented into the LM interface functions for snow, the corresponding setting of the namelist-parameter `ctype_wetsnow_ray` (in analogy to `ctype_wetgraupel_ray`) can be found as 6-character code in the figures title. For explanation of this code, see Table 40.



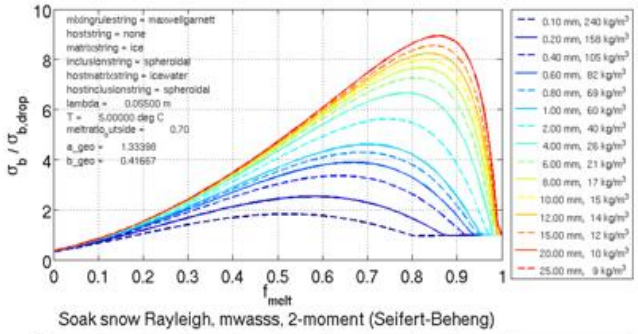
Soak snow Rayleigh, miwsrs, 2-moment (Seifert-Beheng)



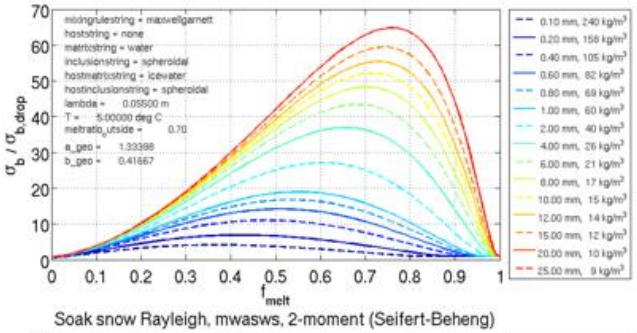
Soak snow Rayleigh, mnasms, 2-moment (Seifert-Beheng)



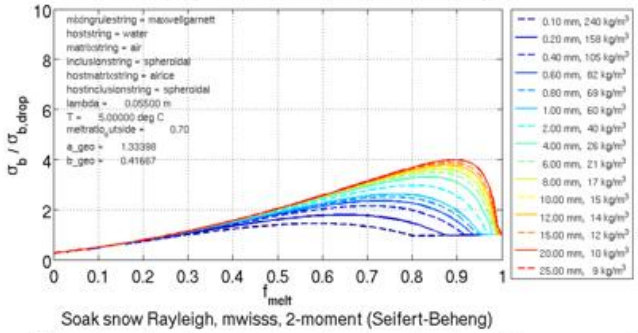
Soak snow Rayleigh, mnisms, 2-moment (Seifert-Beheng)



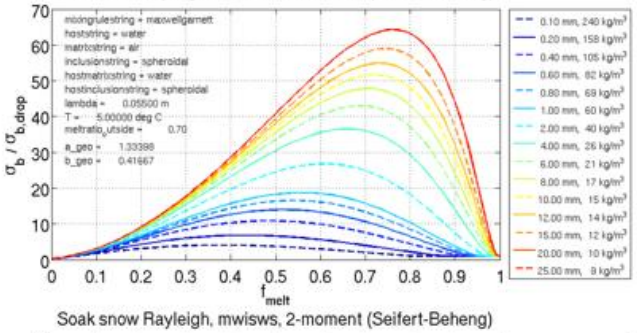
Soak snow Rayleigh, mnwsms, 2-moment (Seifert-Beheng)



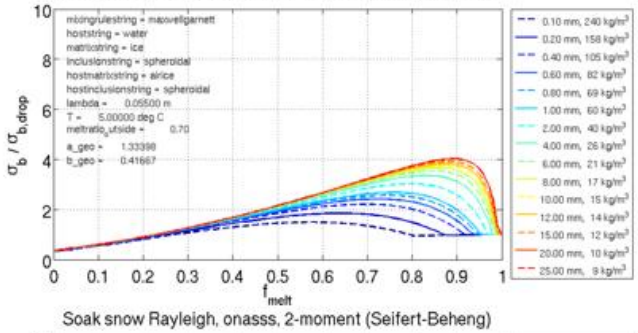
Soak snow Rayleigh, mwasss, 2-moment (Seifert-Beheng)



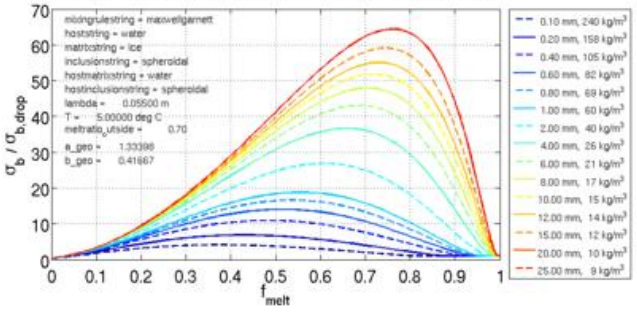
Soak snow Rayleigh, mwasws, 2-moment (Seifert-Beheng)



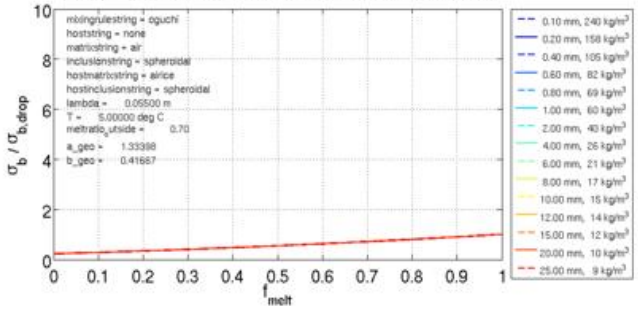
Soak snow Rayleigh, mwisss, 2-moment (Seifert-Beheng)



Soak snow Rayleigh, mwisws, 2-moment (Seifert-Beheng)



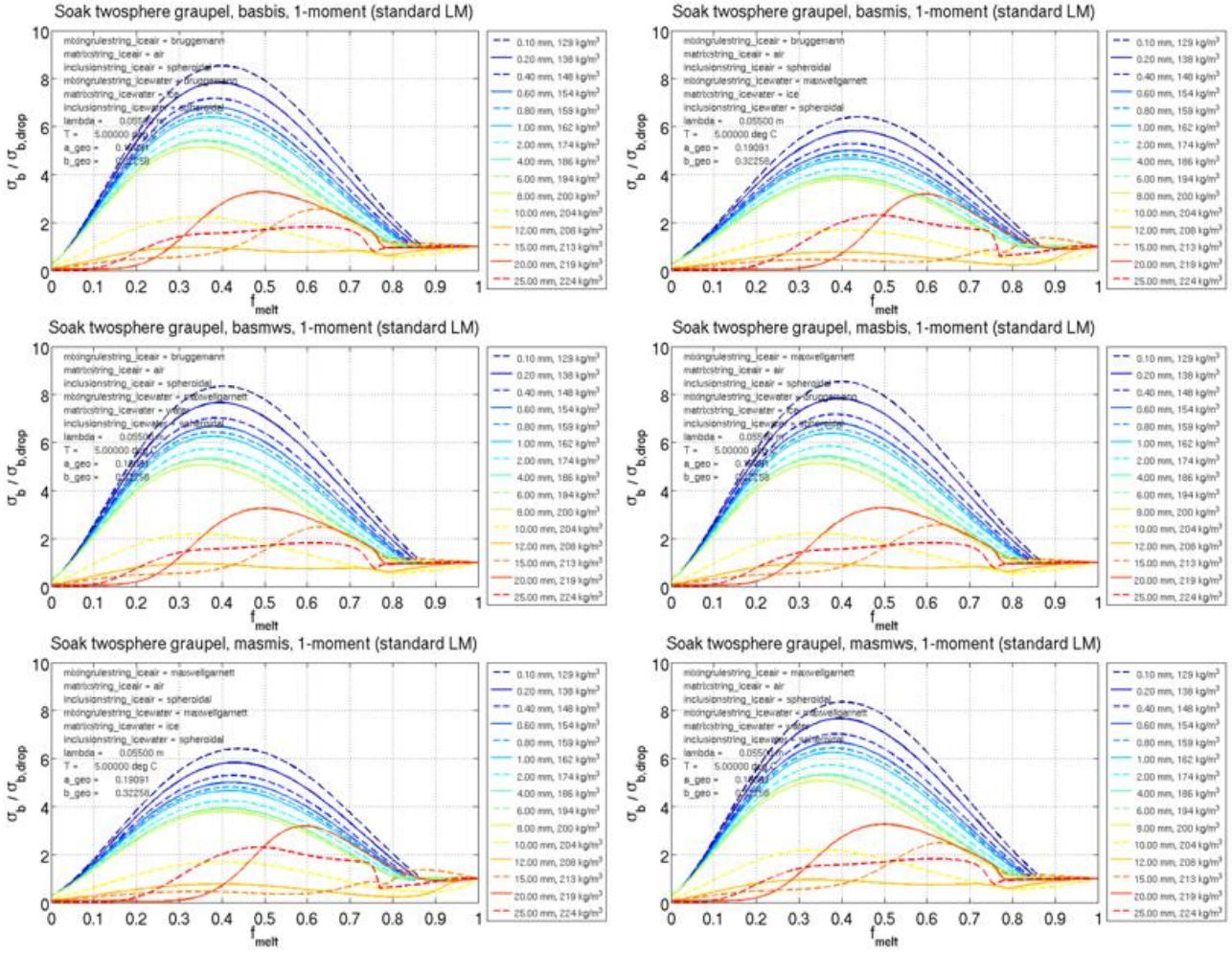
Soak snow Rayleigh, onasss, 2-moment (Seifert-Beheng)

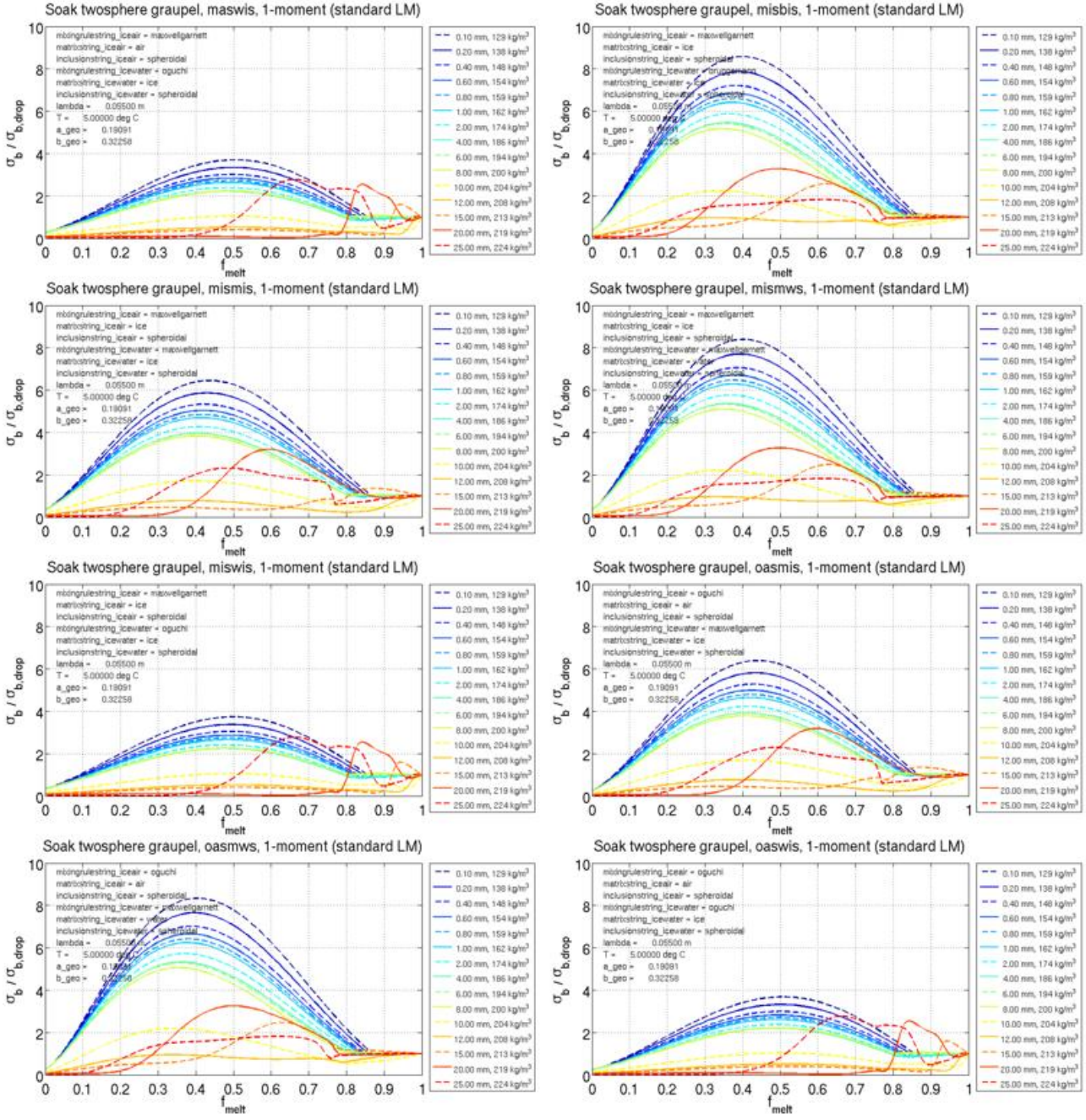


8.5 Mie: soaked twosphere wet graupel, LM-scheme

Similar to Subsection 8.1, results are shown for calculations of the backscattering cross section σ_b with subroutine `MIE_SOAK_TWOSPHERE_WETGRAUPEL()` (Mie scattering, two-layered sphere), see subsubsection 5.3.9 on Page 45. The following figures show the ratio of $\sigma_b/\sigma_{b,drop}$ as function of f_{melt} and the unmelted particle diameter for different EMA-formulations of the particles effective refractive indices m_{eff} of core and shell. The particle bulk density as function of size is determined by equation (36) on Page 69. A depiciton of the resulting bulk density as function of particle size can be found in Figure 10 (black solid line).

Again, every figure represents one particular EMA-formulation combination for m_{eff} of core and shell, which both are obtained by using function `get_m_mix()`, applied for two-component mixture materials (subsubsection 5.2.4 on Page 26). The input parameter sets for `get_m_mix()` can be found in the text annotation within each graph, discriminating ice-air core and ice-water shell. For users of the LM, the corresponding setting of the namelist-parameter `ctype_wetgraupel` can be found in the figures title as a combination of two 3-character codes. For explanation of this code, see Table 41. The results of this section apply to the LM for graupel particles in case of application of the standard one-moment bulk microphysical scheme (namelist-parameter `itype_gscp` < 100) together with namelist-parameters `itype_refl` $= 1$ and `igraupel_type` $= 2$.

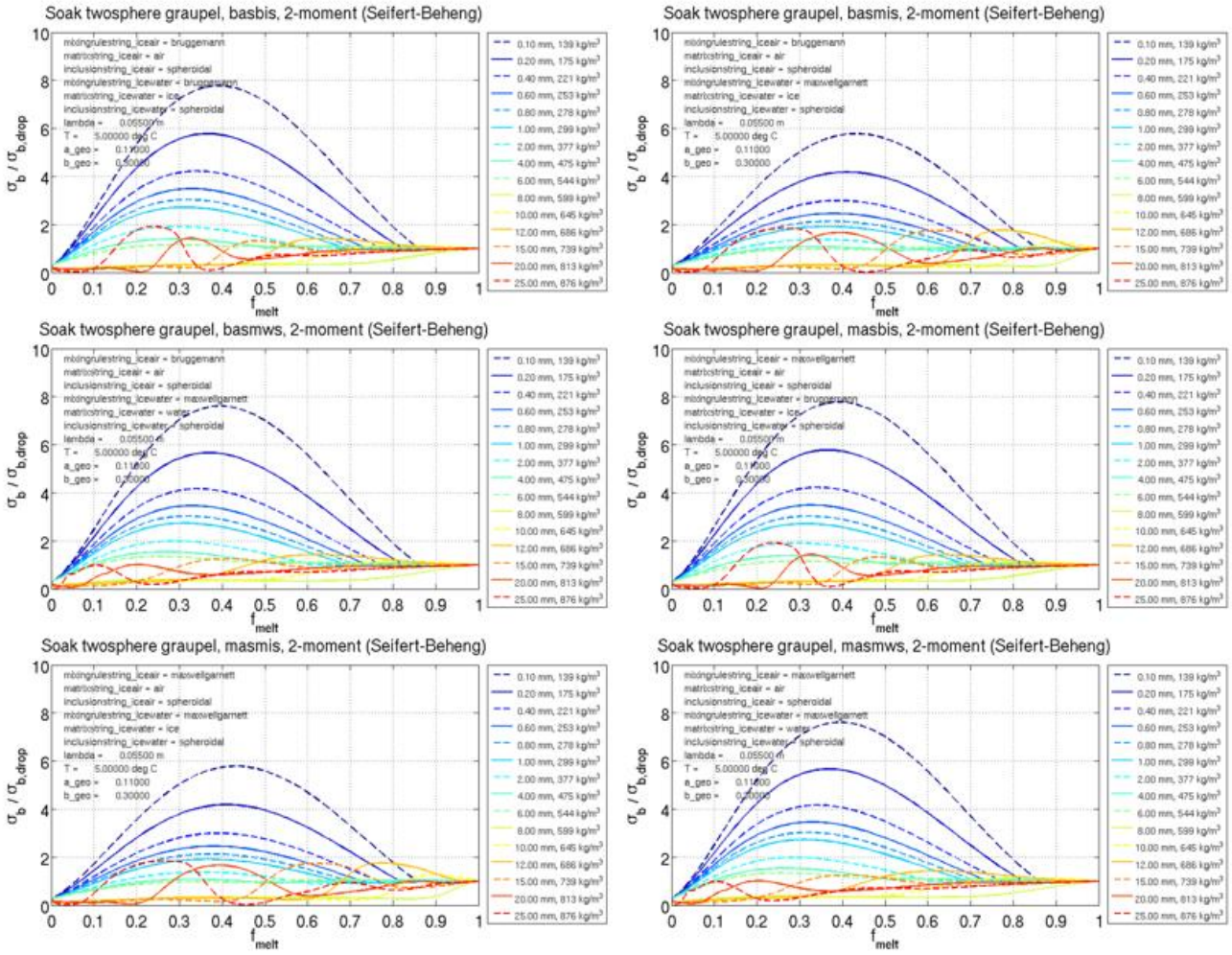



Soak twosphere graupel, maswis, 1-moment (standard LM)
Soak twosphere graupel, misbis, 1-moment (standard LM)
Soak twosphere graupel, mismis, 1-moment (standard LM)
Soak twosphere graupel, mismws, 1-moment (standard LM)
Soak twosphere graupel, miswis, 1-moment (standard LM)
Soak twosphere graupel, oasmis, 1-moment (standard LM)
Soak twosphere graupel, oasmws, 1-moment (standard LM)
Soak twosphere graupel, oaswis, 1-moment (standard LM)
σb / σb,drop
fmelt

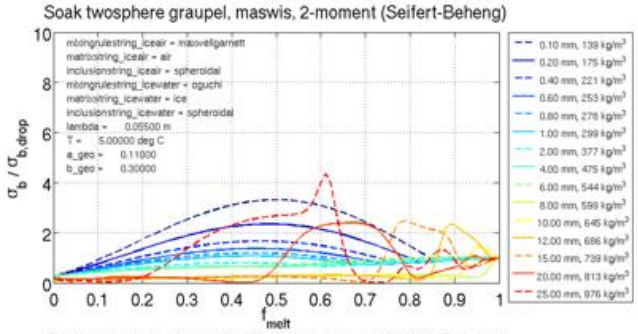
8.6 Mie: soaked twosphere wet graupel, Seifert/Beheng-scheme

Similar to Subsection 8.5, results are shown for calculations of the backscattering cross section σ_b with subroutine `MIE_SOAK_TWOSPHERE_WETGRAUPEL()` (Mie scattering, two-layered sphere), see subsubsection 5.3.9 on Page 45. But this time, the particle bulk density as function of size is determined by equation (37) on Page 69. A depiciton of the resulting bulk density as function of particle size can be found in Figure 10 (red solid line). The following figures show the ratio of $\sigma_b/\sigma_{b,drop}$ as function of f_{melt} and the unmelted particle diameter for different EMA-formulations of the particles effective refractive indices m_{eff} of core and shell.

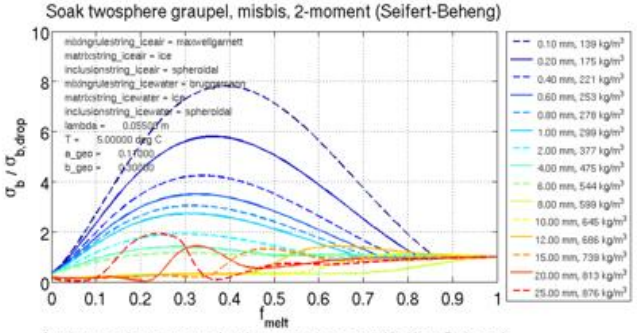
Again, every figure represents one particular EMA-formulation combination for m_{eff} of core and shell, which both are obtained by using function `get_m_mix()`, applied for two-component mixture materials (subsubsection 5.2.4 on Page 26). The input parameter sets for `get_m_mix()` can be found in the text annotation within each graph, discriminating ice-air core and ice-water shell. For users of the LM, the corresponding setting of the namelist-parameter `ctype_wetgraupel` can be found in the figures title as a combination of two 3-character codes. For explanation of this code, see Table 41. The results of this section apply to the LM for graupel particles in case of application of the Seifert and Beheng (2006) two-moment bulk microphysical scheme (namelist-parameter `itype_gscp` ≥ 100) together with namelist-parameters `itype_refl` $= 1$ and `igraupel_type` $= 2$.



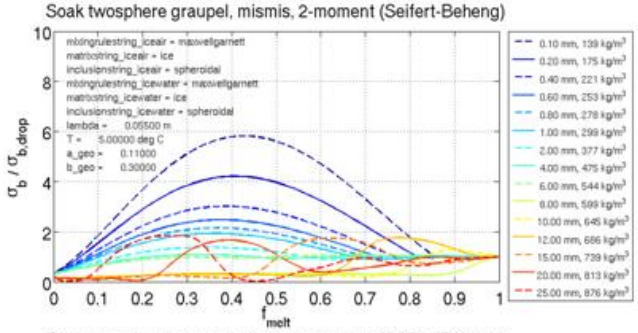
Soak twosphere graupel, maswis, 2-moment (Seifert-Beheng)



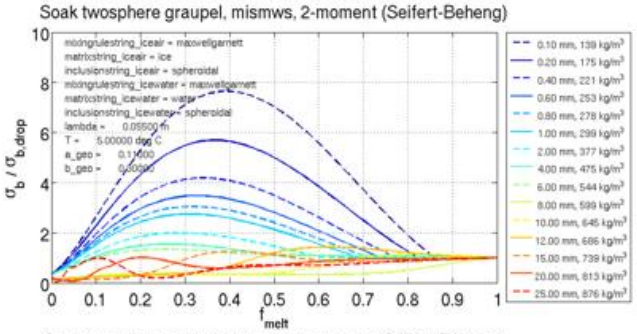
Soak twosphere graupel, misbis, 2-moment (Seifert-Beheng)



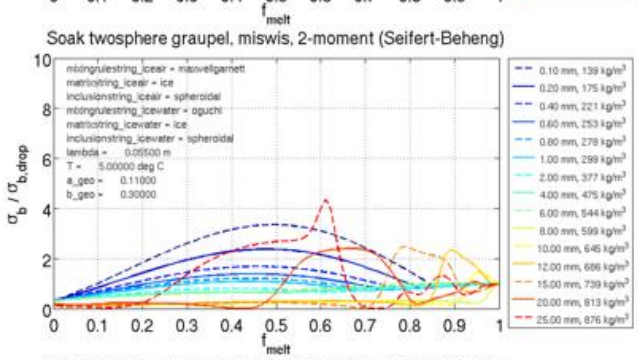
Soak twosphere graupel, mismis, 2-moment (Seifert-Beheng)



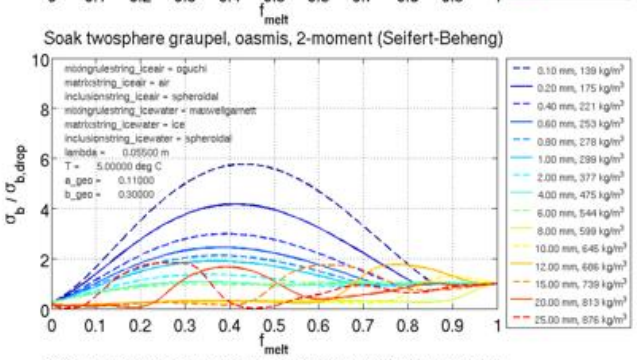
Soak twosphere graupel, mismws, 2-moment (Seifert-Beheng)



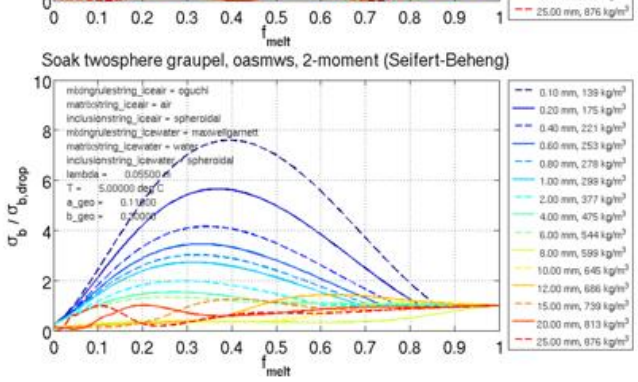
Soak twosphere graupel, miswis, 2-moment (Seifert-Beheng)



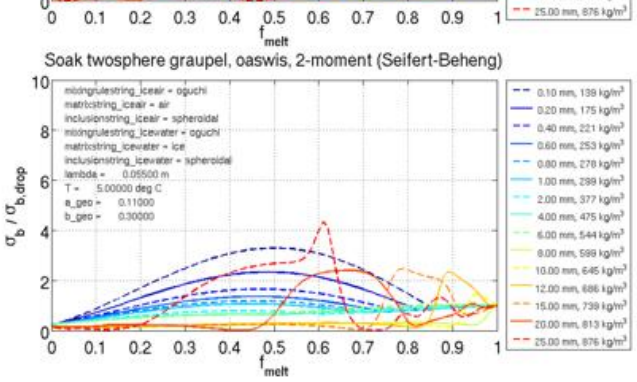
Soak twosphere graupel, oasmis, 2-moment (Seifert-Beheng)



Soak twosphere graupel, oasmws, 2-moment (Seifert-Beheng)



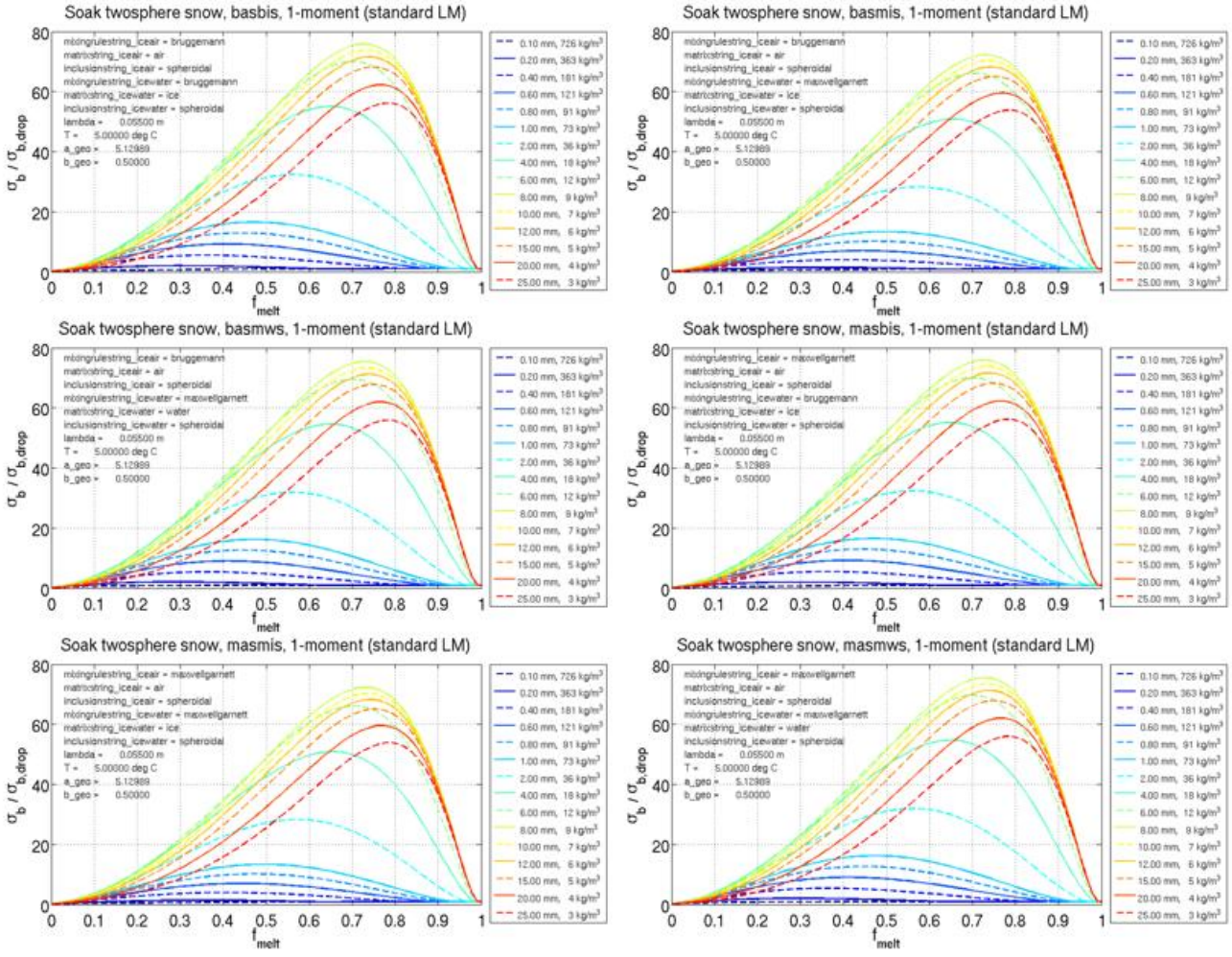
Soak twosphere graupel, oaswis, 2-moment (Seifert-Beheng)

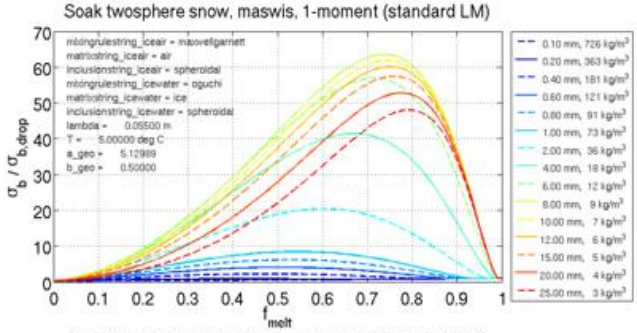


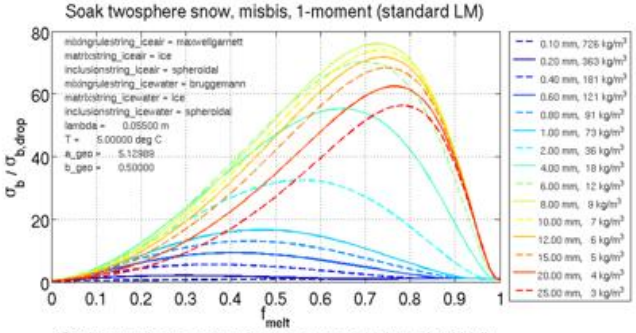
8.7 Mie: soaked twosphere wet snow, LM-scheme

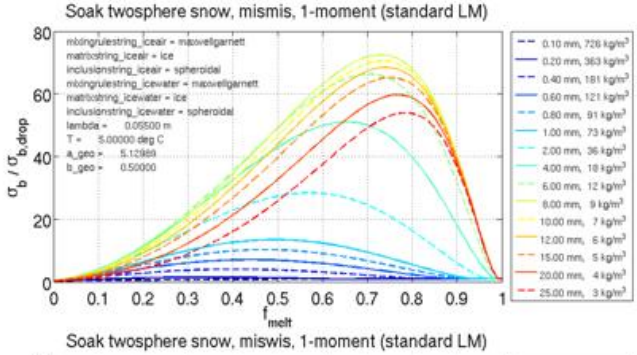
Similar to Subsection 8.5, results are shown for calculations of the backscattering cross section σ_b with subroutine `MIE_SOAK_TWOSPHERE_WETGRAUPEL()` (Mie scattering, two-layered sphere), see subsubsection 5.3.9 on Page 45. But this time, the particle bulk density as function of size is determined by equation (38) on Page 69. A depiciton of the resulting bulk density as function of particle size can be found in Figure 10 (blue solid line). The following figures show the ratio of $\sigma_b/\sigma_{b,drop}$ as function of f_{melt} and the unmelted particle diameter for different EMA-formulations of the particles effective refractive indices m_{eff} of core and shell.

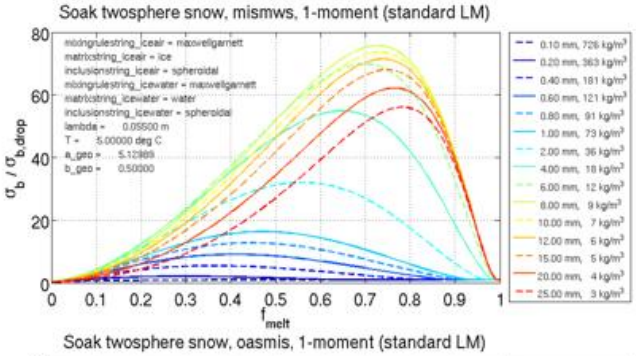
Again, every figure represents one particular EMA-formulation combination for m_{eff} of core and shell, which both are obtained by using function `get_m_mix()`, applied for two-component mixture materials (subsubsection 5.2.4 on Page 26). The input parameter sets for `get_m_mix()` can be found in the text annotation within each graph, discriminating ice-air core and ice-water shell. Although not beeing implemented into the LM interface functions for snow, the corresponding setting of the (nonexisting) namelist-parameter `ctype_wetsnow` (in analogy to `ctype_wetgraupel`) can be found in the figures title as a combination of two 3-character codes. For explanation of this code, see Table 41.

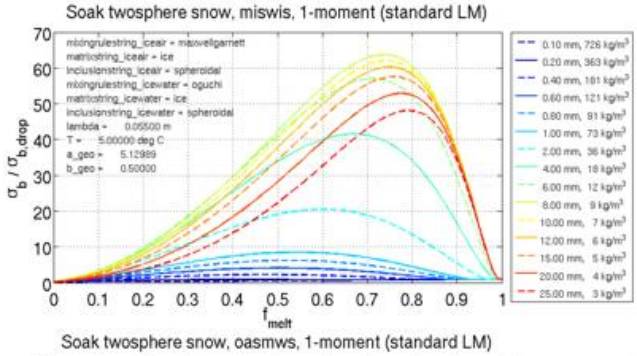


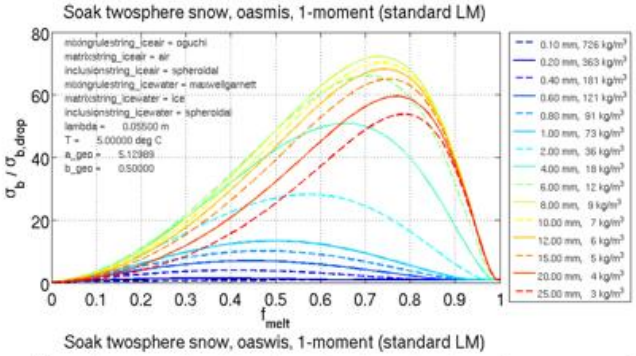

Soak twosphere snow, maswis, 1-moment (standard LM)
mixingrulestring_icewater = maxwellgarnett
matrixstring_icewater = ice
inclusionstring_icewater = spheroidal
lambda = 0.05500 m
T = 5.00000 deg C
a_geo = 5.12989
b_geo = 0.50000
σb / σb,drop
fmelt

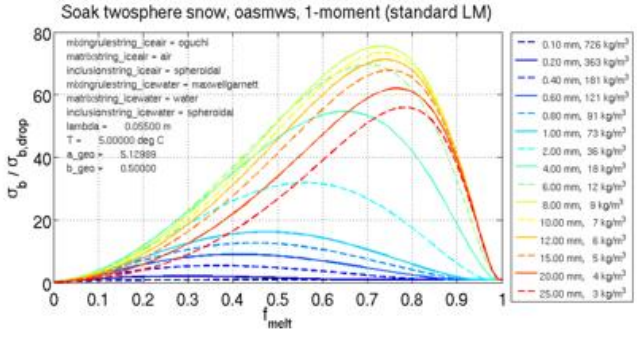

Soak twosphere snow, misbis, 1-moment (standard LM)
mixingrulestring_icewater = bruggemann
matrixstring_icewater = ice
inclusionstring_icewater = spheroidal
lambda = 0.05500 m
T = 5.00000 deg C
a_geo = 5.12989
b_geo = 0.50000
σb / σb,drop
fmelt

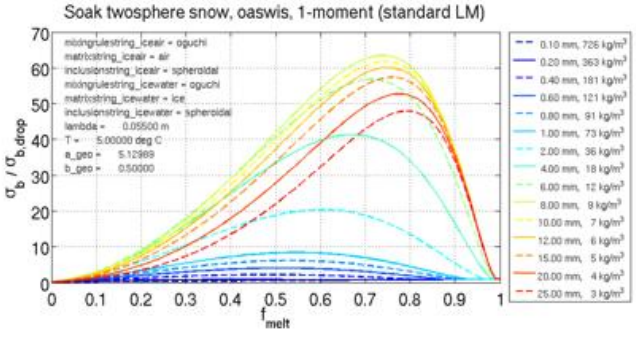

Soak twosphere snow, mismis, 1-moment (standard LM)
mixingrulestring_icewater = maxwellgarnett
matrixstring_icewater = ice
inclusionstring_icewater = spheroidal
lambda = 0.05500 m
T = 5.00000 deg C
a_geo = 5.12989
b_geo = 0.50000
σb / σb,drop
fmelt


Soak twosphere snow, mismws, 1-moment (standard LM)
mixingrulestring_icewater = maxwellgarnett
matrixstring_icewater = water
inclusionstring_icewater = spheroidal
lambda = 0.05500 m
T = 5.00000 deg C
a_geo = 5.12989
b_geo = 0.50000
σb / σb,drop
fmelt


Soak twosphere snow, miswis, 1-moment (standard LM)
mixingrulestring_icewater = maxwellgarnett
matrixstring_icewater = ice
inclusionstring_icewater = spheroidal
lambda = 0.05500 m
T = 5.00000 deg C
a_geo = 5.12989
b_geo = 0.50000
σb / σb,drop
fmelt


Soak twosphere snow, oasmis, 1-moment (standard LM)
mixingrulestring_icewater = maxwellgarnett
matrixstring_icewater = ice
inclusionstring_icewater = spheroidal
lambda = 0.05500 m
T = 5.00000 deg C
a_geo = 5.12989
b_geo = 0.50000
σb / σb,drop
fmelt

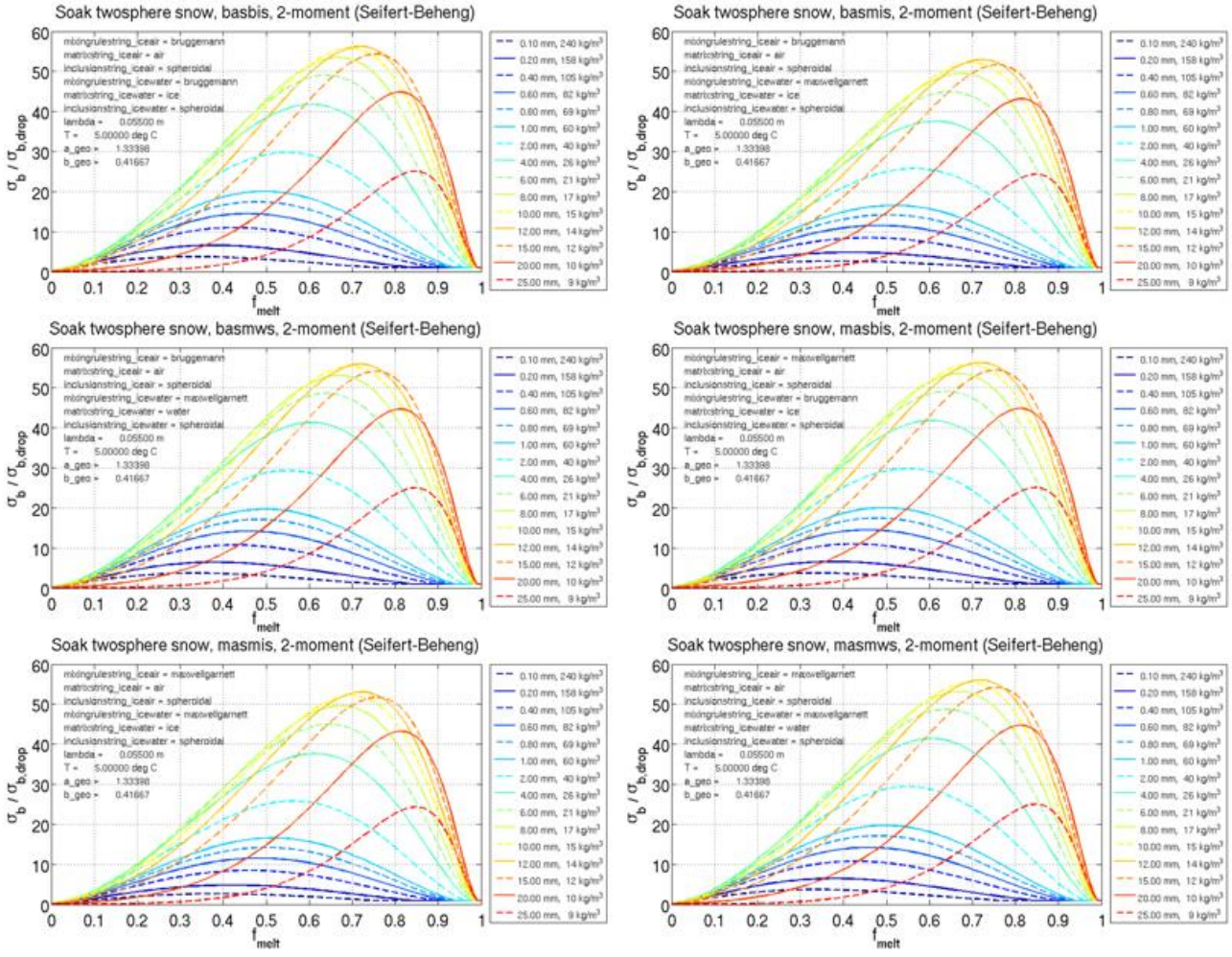

Soak twosphere snow, oasmws, 1-moment (standard LM)
mixingrulestring_icewater = maxwellgarnett
matrixstring_icewater = water
inclusionstring_icewater = spheroidal
lambda = 0.05500 m
T = 5.00000 deg C
a_geo = 5.12989
b_geo = 0.50000
σb / σb,drop
fmelt


Soak twosphere snow, oaswis, 1-moment (standard LM)
mixingrulestring_icewater = oguchi
matrixstring_icewater = ice
inclusionstring_icewater = spheroidal
lambda = 0.05500 m
T = 5.00000 deg C
a_geo = 5.12989
b_geo = 0.50000
σb / σb,drop
fmelt

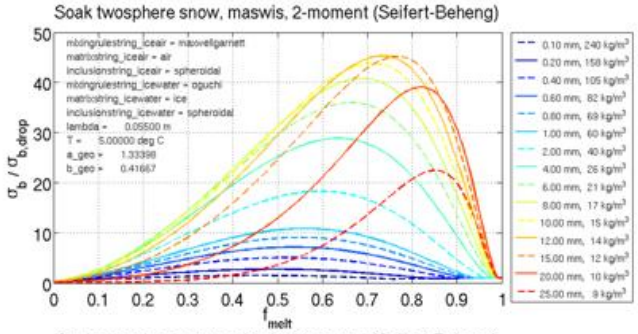
8.8 Mie: soaked twosphere wet snow, Seifert/Beheng-scheme

Similar to Subsection 8.5, results are shown for calculations of the backscattering cross section σ_b with subroutine `MIE_SOAK_TWOSPHERE_WETGRAUPEL()` (Mie scattering, two-layered sphere), see subsubsection 5.3.9 on Page 45. But this time, the particle bulk density as function of size is determined by equation (39) on Page 69. A depiciton of the resulting bulk density as function of particle size can be found in Figure 10 (green solid line). The following figures show the ratio of $\sigma_b/\sigma_{b,drop}$ as function of f_{melt} and the unmelted particle diameter for different EMA-formulations of the particles effective refractive indices m_{eff} of core and shell.

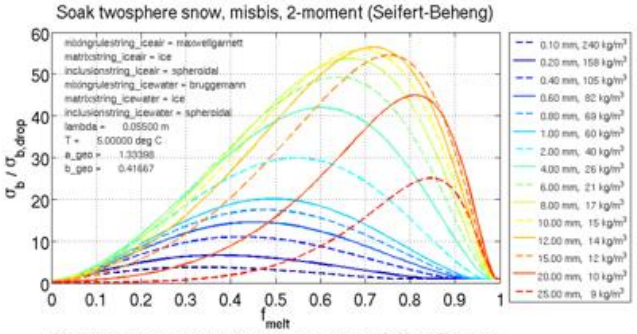
Again, every figure represents one particular EMA-formulation combination for m_{eff} of core and shell, which both are obtained by using function `get_m_mix()`, applied for two-component mixture materials (subsubsection 5.2.4 on Page 26). The input parameter sets for `get_m_mix()` can be found in the text annotation within each graph, discriminating ice-air core and ice-water shell. Although not beeing implemented into the LM interface functions for snow, the corresponding setting of the (nonexisting) namelist-parameter `ctype_wetsnow` (in analogy to `ctype_wetgraupel`) can be found in the figures title as a combination of two 3-character codes. For explanation of this code, see Table 41.



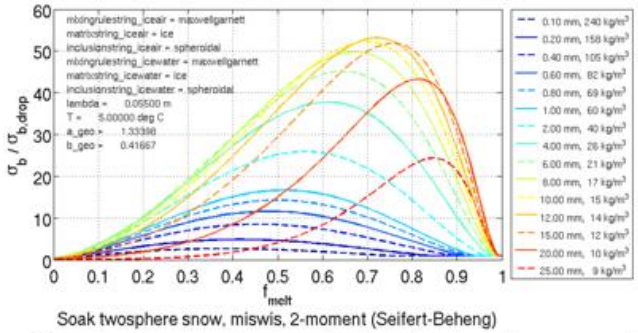
Soak twosphere snow, maswis, 2-moment (Seifert-Beheng)



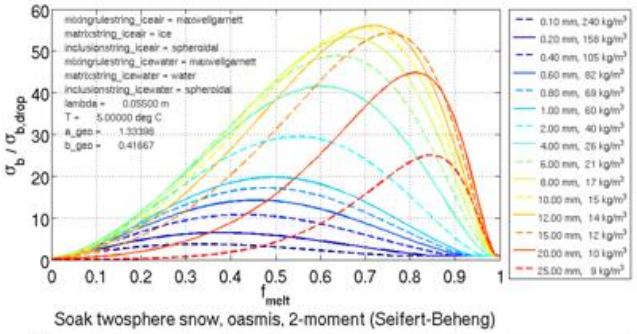
Soak twosphere snow, misbis, 2-moment (Seifert-Beheng)



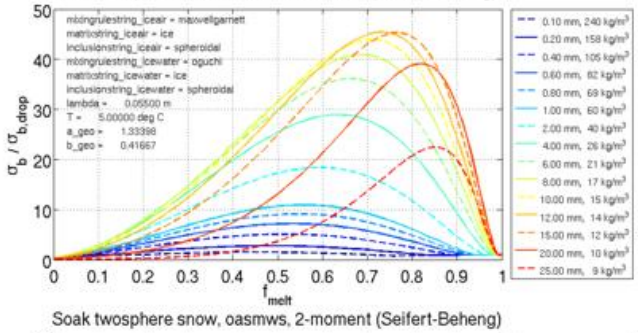
Soak twosphere snow, mismis, 2-moment (Seifert-Beheng)



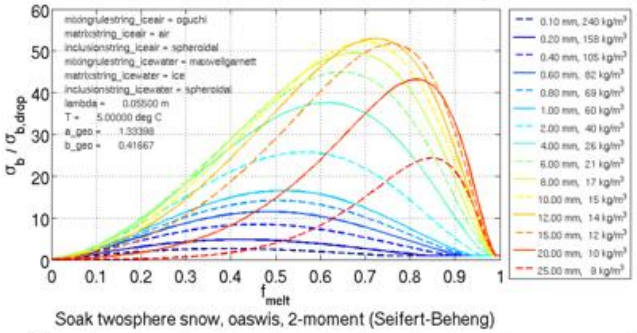
Soak twosphere snow, mismws, 2-moment (Seifert-Beheng)



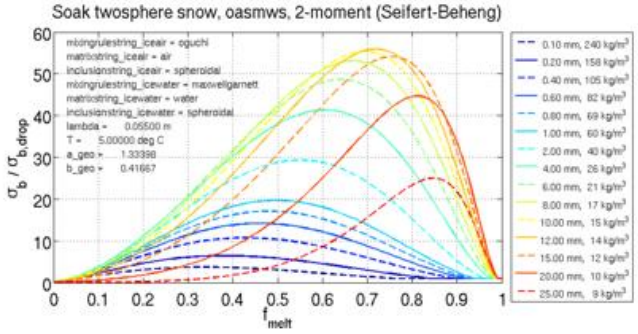
Soak twosphere snow, miswis, 2-moment (Seifert-Beheng)



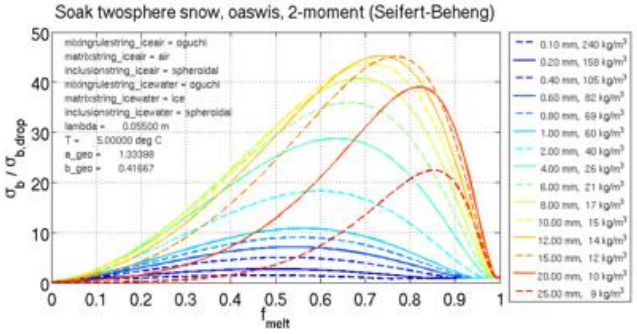
Soak twosphere snow, oasmis, 2-moment (Seifert-Beheng)



Soak twosphere snow, oasmws, 2-moment (Seifert-Beheng)



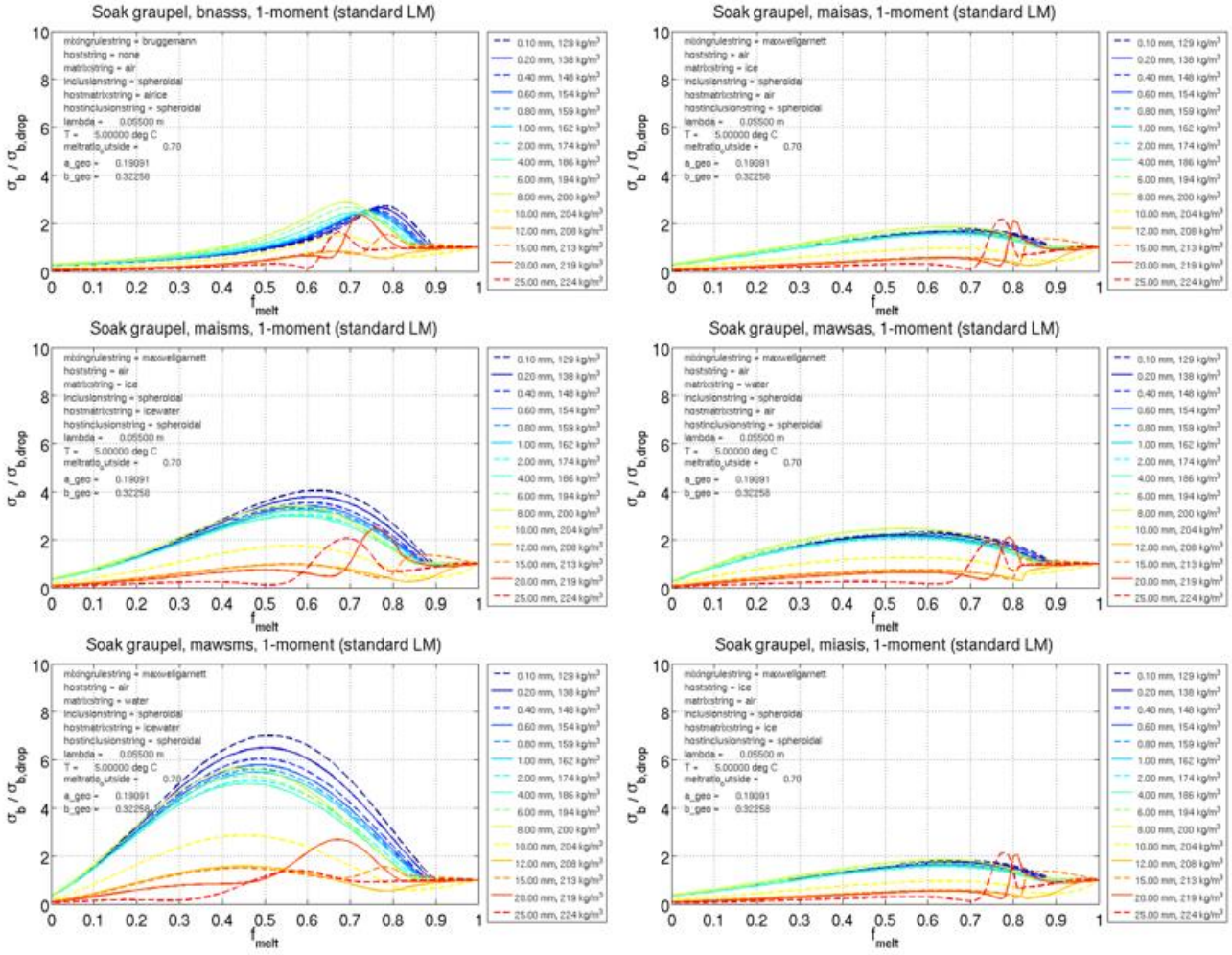
Soak twosphere snow, oaswis, 2-moment (Seifert-Beheng)

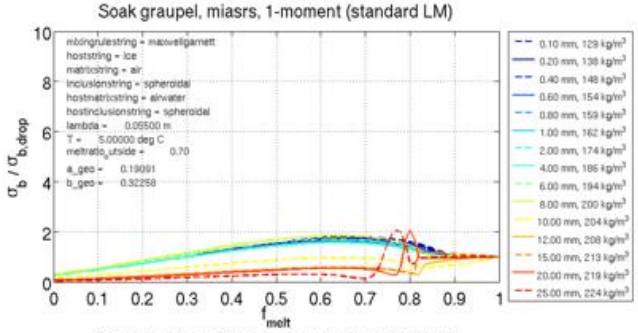


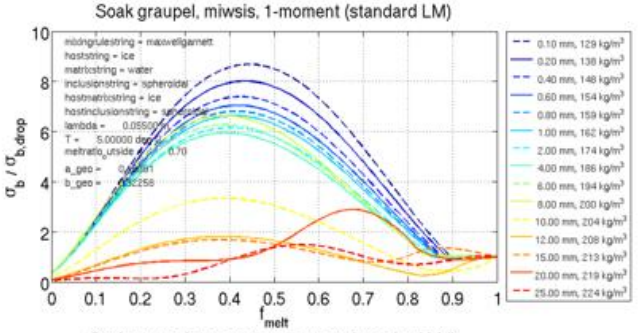
8.9 Mie: soaked wet graupel, LM-scheme

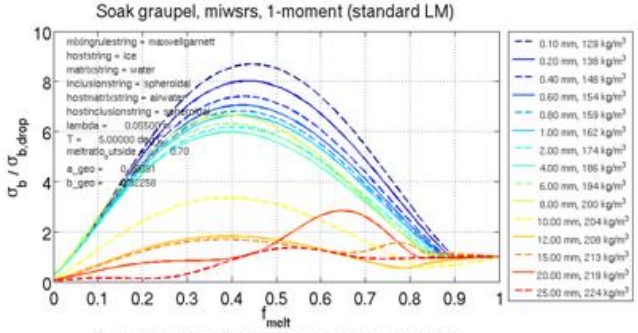
Similar to Subsection 8.1, results are shown for calculations of the backscattering cross section σ_b with subroutine `MIE_SOAK_WETGRAUPEL()` (Mie scattering), see subsubsection 5.3.11 on Page 48. The following figures show the ratio of $\sigma_b/\sigma_{b,drop}$ as function of f_{melt} and the unmelted particle diameter for different EMA-formulations of the particles effective refractive index m_{eff}. The particle bulk density as function of size is determined by equation (36) on Page 69. A depiciton of the resulting bulk density as function of particle size can be found in Figure 10 (black solid line).

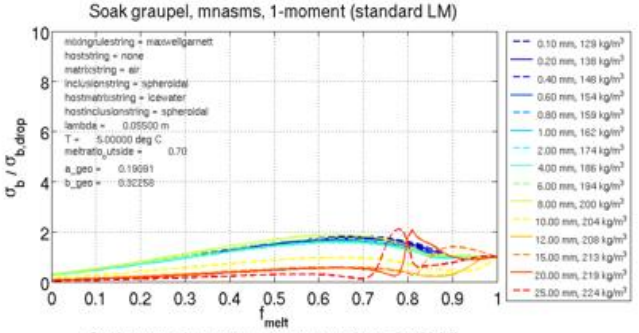
Again, every figure represents one particular EMA-formulation for m_{eff}, which is obtained by using function `get_m_mix_nested()` (subsubsection 5.2.5 on Page 28). The input parameter set for `get_m_mix_nested()` can be found in the text annotation within each graph. For users of the LM, the corresponding setting of the namelist-parameter `ctype_wetgraupel` can be found as 6-character code in the figures title. For explanation of this code, see Table 40. The results of this section apply to the LM for graupel particles in case of application of the standard LM one-moment bulk microphysical schemes (namelist-parameter `itype_gscp` $<$ 100) together with `itype_refl` $= 1$ and `igraupel_type` $= 1$.

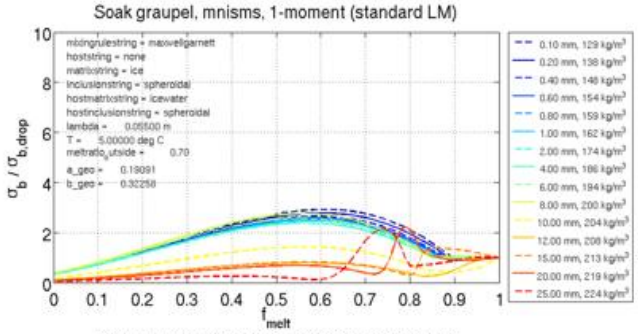


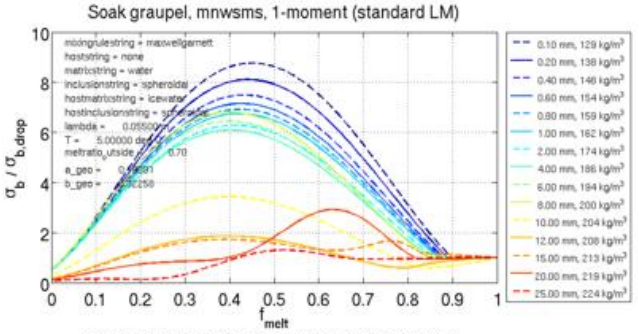

Soak graupel, miasrs, 1-moment (standard LM)
mixingrulestring = maxwellgarnett
hoststring = ice
matrixstring = air
inclusionstring = spheroidal
hostmatrixstring = airwater
hostinclusionstring = spheroidal
lambda = 0.05500 m
T = 5.00000 deg C
meltratio_utside = 0.70
a_geo = 0.19091
b_geo = 0.32258
σb / σb,drop
fmelt

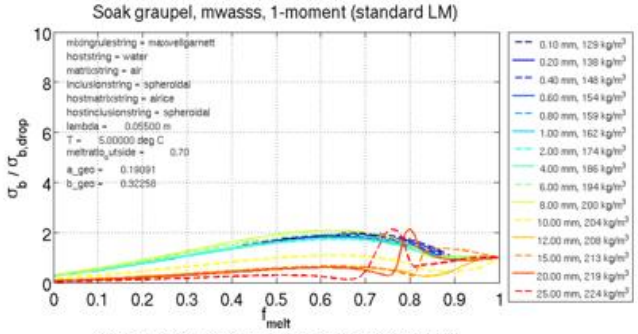

Soak graupel, miwsis, 1-moment (standard LM)
mixingrulestring = maxwellgarnett
hoststring = ice
matrixstring = water
inclusionstring = spheroidal
hostmatrixstring = ice
hostinclusionstring = spheroidal
lambda = 0.05500 m
T = 5.00000 deg C
meltratio_utside = 0.70
a_geo = 0.19091
b_geo = 0.32258
σb / σb,drop
fmelt

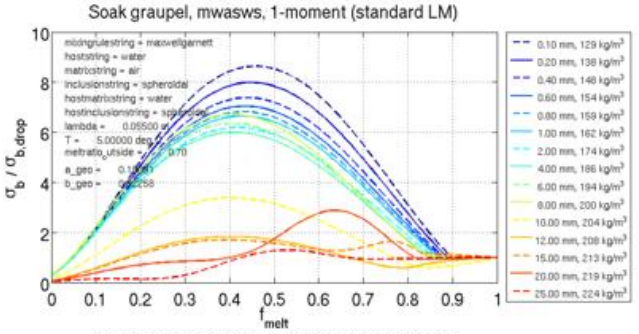

Soak graupel, miwsrs, 1-moment (standard LM)
mixingrulestring = maxwellgarnett
hoststring = ice
matrixstring = water
inclusionstring = spheroidal
hostmatrixstring = airwater
hostinclusionstring = spheroidal
lambda = 0.05500 m
T = 5.00000 deg C
meltratio_utside = 0.70
a_geo = 0.19091
b_geo = 0.32258
σb / σb,drop
fmelt

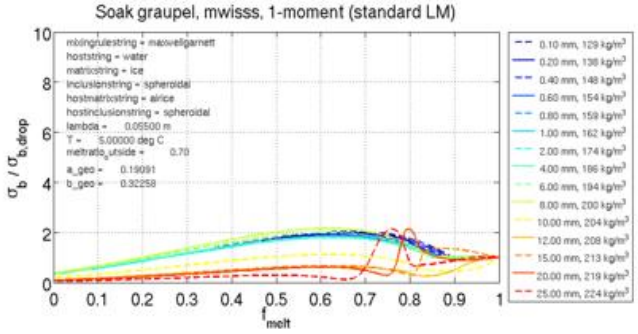

Soak graupel, mnasms, 1-moment (standard LM)
mixingrulestring = maxwellgarnett
hoststring = none
matrixstring = air
inclusionstring = spheroidal
hostmatrixstring = icewater
hostinclusionstring = spheroidal
lambda = 0.05500 m
T = 5.00000 deg C
meltratio_utside = 0.70
a_geo = 0.19091
b_geo = 0.32258
σb / σb,drop
fmelt

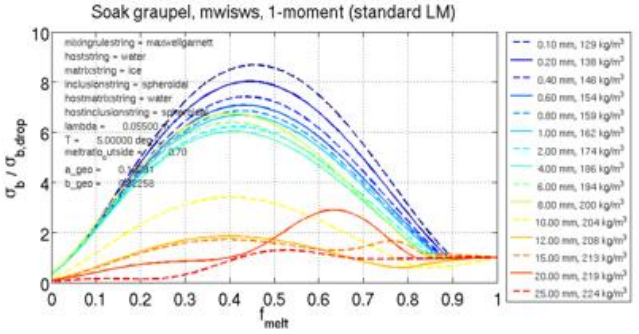

Soak graupel, mnisms, 1-moment (standard LM)
mixingrulestring = maxwellgarnett
hoststring = none
matrixstring = ice
inclusionstring = spheroidal
hostmatrixstring = icewater
hostinclusionstring = spheroidal
lambda = 0.05500 m
T = 5.00000 deg C
meltratio_utside = 0.70
a_geo = 0.19091
b_geo = 0.32258
σb / σb,drop
fmelt

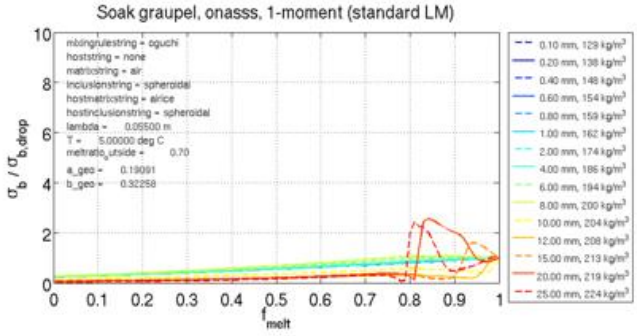

Soak graupel, mnwsms, 1-moment (standard LM)
mixingrulestring = maxwellgarnett
hoststring = none
matrixstring = water
inclusionstring = spheroidal
hostmatrixstring = icewater
hostinclusionstring = spheroidal
lambda = 0.05500 m
T = 5.00000 deg C
meltratio_utside = 0.70
a_geo = 0.19091
b_geo = 0.32258
σb / σb,drop
fmelt


Soak graupel, mwasss, 1-moment (standard LM)
mixingrulestring = maxwellgarnett
hoststring = water
matrixstring = air
inclusionstring = spheroidal
hostmatrixstring = airice
hostinclusionstring = spheroidal
lambda = 0.05500 m
T = 5.00000 deg C
meltratio_utside = 0.70
a_geo = 0.19091
b_geo = 0.32258
σb / σb,drop
fmelt


Soak graupel, mwasws, 1-moment (standard LM)
mixingrulestring = maxwellgarnett
hoststring = water
matrixstring = air
inclusionstring = spheroidal
hostmatrixstring = water
hostinclusionstring = spheroidal
lambda = 0.05500 m
T = 5.00000 deg C
meltratio_utside = 0.70
a_geo = 0.19091
b_geo = 0.32258
σb / σb,drop
fmelt


Soak graupel, mwisss, 1-moment (standard LM)
mixingrulestring = maxwellgarnett
hoststring = water
matrixstring = ice
inclusionstring = spheroidal
hostmatrixstring = airice
hostinclusionstring = spheroidal
lambda = 0.05500 m
T = 5.00000 deg C
meltratio_utside = 0.70
a_geo = 0.19091
b_geo = 0.32258
σb / σb,drop
fmelt

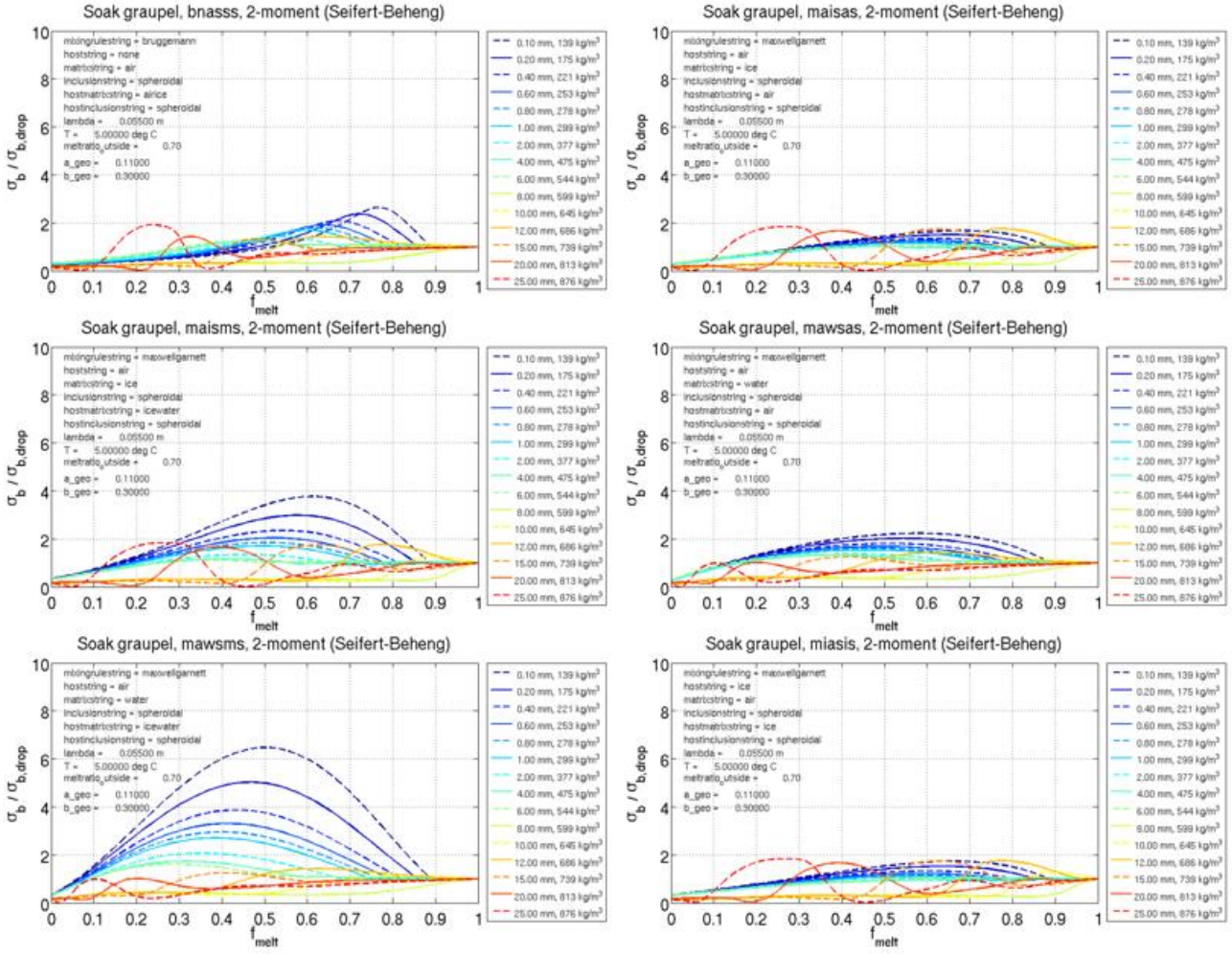

Soak graupel, mwisws, 1-moment (standard LM)
mixingrulestring = maxwellgarnett
hoststring = water
matrixstring = ice
inclusionstring = spheroidal
hostmatrixstring = water
hostinclusionstring = spheroidal
lambda = 0.05500 m
T = 5.00000 deg C
meltratio_utside = 0.70
a_geo = 0.19091
b_geo = 0.32258
σb / σb,drop
fmelt

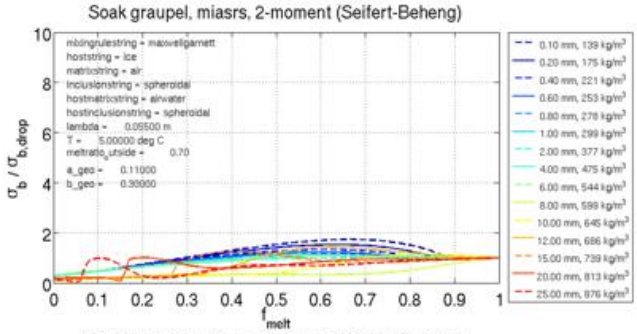

Soak graupel, onasss, 1-moment (standard LM)
meltstring = oguchi
hoststring = none
matrixstring = air
inclusionstring = spheroidal
hostmatrixstring = airice
hostinclusionstring = spheroidal
lambda = 0.09500 m
T = 5.00000 deg C
meltratio_outside = 0.70
a_geo = 0.19091
b_geo = 0.32258
0.10 mm, 129 kg/m³
0.20 mm, 138 kg/m³
0.40 mm, 148 kg/m³
0.60 mm, 154 kg/m³
0.80 mm, 159 kg/m³
1.00 mm, 162 kg/m³
2.00 mm, 174 kg/m³
4.00 mm, 186 kg/m³
6.00 mm, 194 kg/m³
8.00 mm, 200 kg/m³
10.00 mm, 204 kg/m³
12.00 mm, 208 kg/m³
15.00 mm, 213 kg/m³
20.00 mm, 219 kg/m³
25.00 mm, 224 kg/m³
σb / σb,drop
fmelt

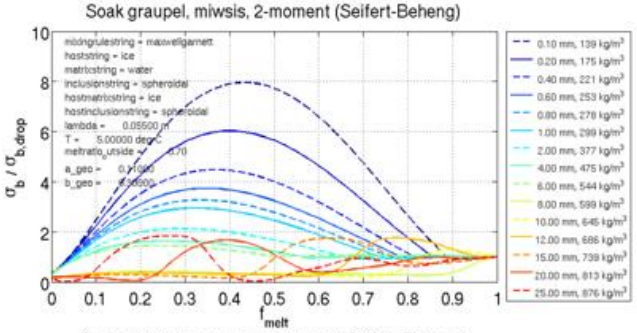
8.10 Mie: soaked wet graupel, Seifert/Beheng-scheme

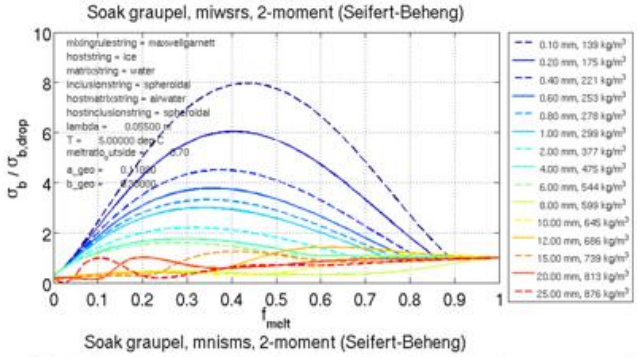
Similar to Subsection 8.9, results are shown for calculations of the backscattering cross section σ_b with subroutine `MIE_SOAK_WETGRAUPEL()` (Mie scattering), see subsubsection 5.3.11 on Page 48. But this time, the particle bulk density as function of size is determined by equation (37) on Page 69. A depiciton of the resulting bulk density as function of particle size can be found in Figure 10 (red solid line). The following figures show the ratio of $\sigma_b/\sigma_{b,drop}$ as function of f_{melt} and the unmelted particle diameter for different EMA-formulations of the particles effective refractive index m_{eff}.

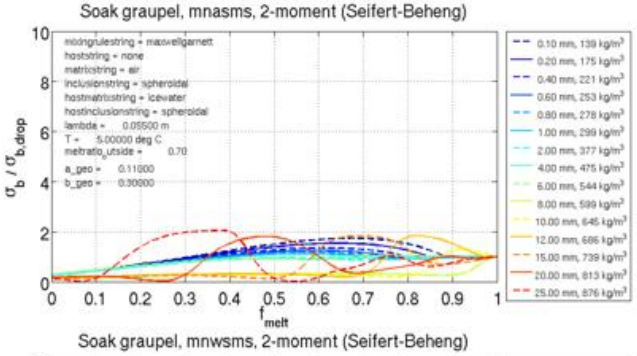
Again, every figure represents one particular EMA-formulation for m_{eff}, which is obtained by using function `get_m_mix_nested()` (subsubsection 5.2.5 on Page 28). The input parameter set for `get_m_mix_nested()` can be found in the text annotation within each graph. For users of the LM, the corresponding setting of the namelist-parameter `ctype_wetgraupel` can be found as 6-character code in the figures title. For explanation of this code, see Table 40. The results of this section apply to the LM for graupel particles in case of application of the Seifert and Beheng (2006) two-moment bulk microphysical scheme (namelist-parameter `itype_gscp` ≥ 100) together with `itype_refl` $= 1$ and `igraupel_type` $= 1$.

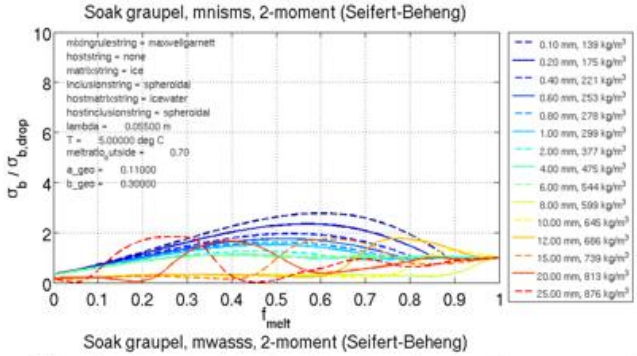


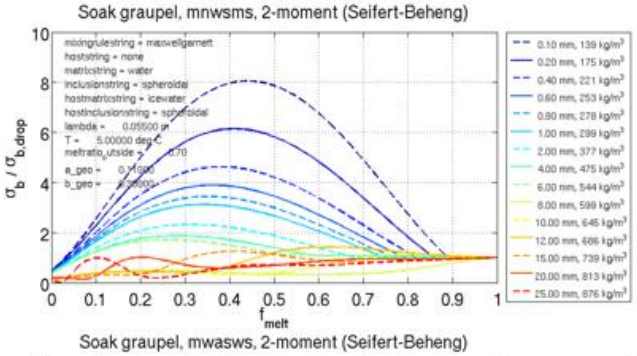

Soak graupel, miasrs, 2-moment (Seifert-Beheng)
mixingrulestring = maxwellgarnett
hoststring = ice
matrixstring = air
inclusionstring = spheroidal
hostmatrixstring = airwater
hostinclusionstring = spheroidal
lambda = 0.05500 m
T = 5.00000 deg C
meltratio_utside = 0.70
a_geo = 0.11000
b_geo = 0.30000
σb / σb,drop
fmelt

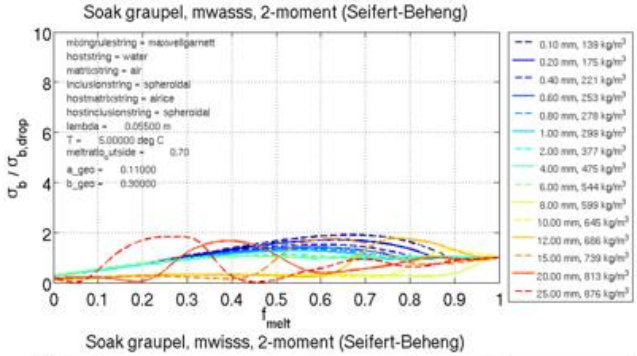

Soak graupel, miwsis, 2-moment (Seifert-Beheng)
mixingrulestring = maxwellgarnett
hoststring = ice
matrixstring = water
inclusionstring = spheroidal
hostmatrixstring = ice
hostinclusionstring = spheroidal
lambda = 0.05500 m
T = 5.00000 deg C
meltratio_utside = 0.70
a_geo = 0.11000
b_geo = 0.30000
σb / σb,drop
fmelt

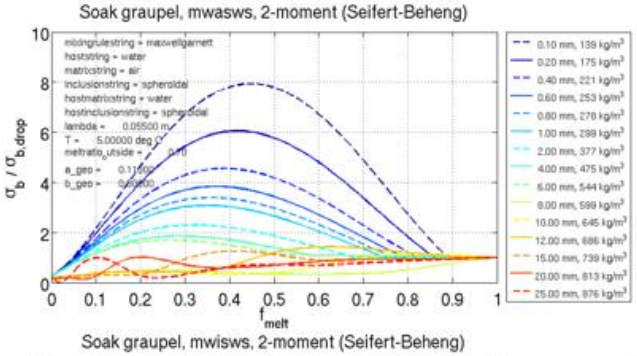

Soak graupel, miwsrs, 2-moment (Seifert-Beheng)
mixingrulestring = maxwellgarnett
hoststring = ice
matrixstring = water
inclusionstring = spheroidal
hostmatrixstring = airwater
hostinclusionstring = spheroidal
lambda = 0.05500 m
T = 5.00000 deg C
meltratio_utside = 0.70
a_geo = 0.11000
b_geo = 0.30000
σb / σb,drop
fmelt

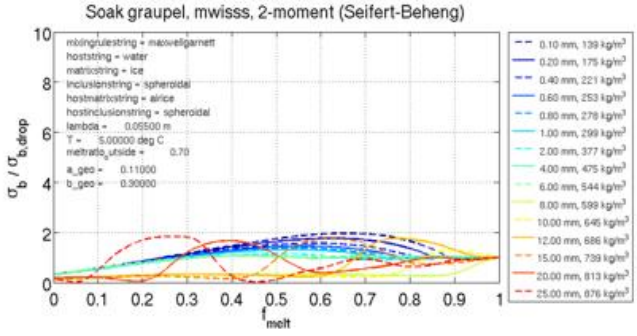

Soak graupel, mnasms, 2-moment (Seifert-Beheng)
mixingrulestring = maxwellgarnett
hoststring = none
matrixstring = air
inclusionstring = spheroidal
hostmatrixstring = icewater
hostinclusionstring = spheroidal
lambda = 0.05500 m
T = 5.00000 deg C
meltratio_utside = 0.70
a_geo = 0.11000
b_geo = 0.30000
σb / σb,drop
fmelt

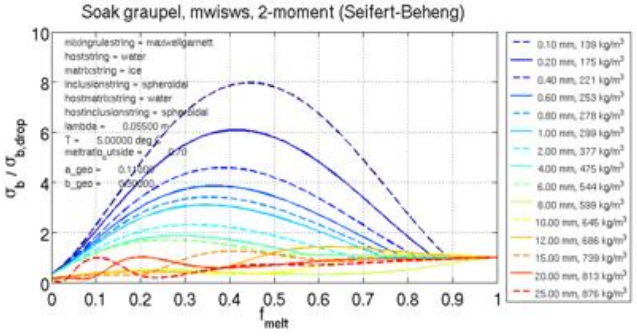

Soak graupel, mnisms, 2-moment (Seifert-Beheng)
mixingrulestring = maxwellgarnett
hoststring = none
matrixstring = ice
inclusionstring = spheroidal
hostmatrixstring = icewater
hostinclusionstring = spheroidal
lambda = 0.05500 m
T = 5.00000 deg C
meltratio_utside = 0.70
a_geo = 0.11000
b_geo = 0.30000
σb / σb,drop
fmelt

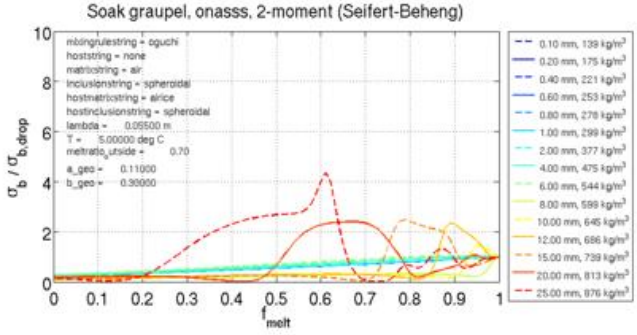

Soak graupel, mnwsms, 2-moment (Seifert-Beheng)
mixingrulestring = maxwellgarnett
hoststring = none
matrixstring = water
inclusionstring = spheroidal
hostmatrixstring = icewater
hostinclusionstring = spheroidal
lambda = 0.05500 m
T = 5.00000 deg C
meltratio_utside = 0.70
a_geo = 0.11000
b_geo = 0.30000
σb / σb,drop
fmelt


Soak graupel, mwasss, 2-moment (Seifert-Beheng)
mixingrulestring = maxwellgarnett
hoststring = water
matrixstring = air
inclusionstring = spheroidal
hostmatrixstring = airice
hostinclusionstring = spheroidal
lambda = 0.05500 m
T = 5.00000 deg C
meltratio_utside = 0.70
a_geo = 0.11000
b_geo = 0.30000
σb / σb,drop
fmelt


Soak graupel, mwasws, 2-moment (Seifert-Beheng)
mixingrulestring = maxwellgarnett
hoststring = water
matrixstring = air
inclusionstring = spheroidal
hostmatrixstring = water
hostinclusionstring = spheroidal
lambda = 0.05500 m
T = 5.00000 deg C
meltratio_utside = 0.70
a_geo = 0.11000
b_geo = 0.30000
σb / σb,drop
fmelt


Soak graupel, mwisss, 2-moment (Seifert-Beheng)
mixingrulestring = maxwellgarnett
hoststring = water
matrixstring = ice
inclusionstring = spheroidal
hostmatrixstring = airice
hostinclusionstring = spheroidal
lambda = 0.05500 m
T = 5.00000 deg C
meltratio_utside = 0.70
a_geo = 0.11000
b_geo = 0.30000
σb / σb,drop
fmelt

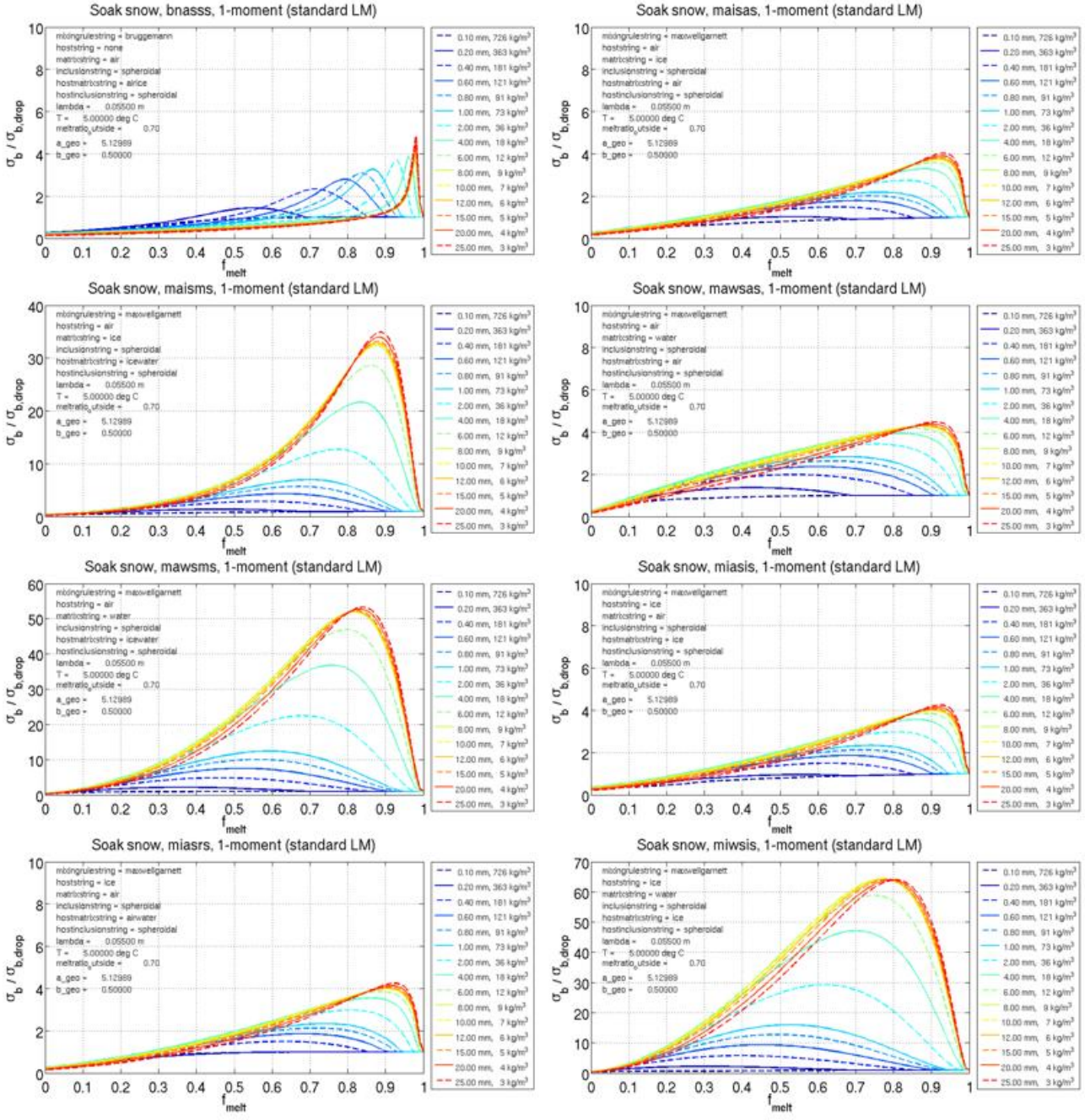

Soak graupel, mwisws, 2-moment (Seifert-Beheng)
mixingrulestring = maxwellgarnett
hoststring = water
matrixstring = ice
inclusionstring = spheroidal
hostmatrixstring = water
hostinclusionstring = spheroidal
lambda = 0.05500 m
T = 5.00000 deg C
meltratio_utside = 0.70
a_geo = 0.11000
b_geo = 0.30000
σb / σb,drop
fmelt


Soak graupel, onasss, 2-moment (Seifert-Beheng)
mixingrulestring = oguchi
hoststring = none
matrixstring = air
inclusionstring = spheroidal
hostmatrixstring = airice
hostinclusionstring = spheroidal
lambda = 0.09500 m
T = 5.00000 deg C
meltratio_outside = 0.70
a_geo = 0.11000
b_geo = 0.30000
0.10 mm, 139 kg/m³
0.20 mm, 175 kg/m³
0.40 mm, 221 kg/m³
0.60 mm, 253 kg/m³
0.80 mm, 278 kg/m³
1.00 mm, 299 kg/m³
2.00 mm, 377 kg/m³
4.00 mm, 475 kg/m³
6.00 mm, 544 kg/m³
8.00 mm, 599 kg/m³
10.00 mm, 645 kg/m³
12.00 mm, 686 kg/m³
15.00 mm, 739 kg/m³
20.00 mm, 813 kg/m³
25.00 mm, 876 kg/m³
σb / σb,drop
fmelt

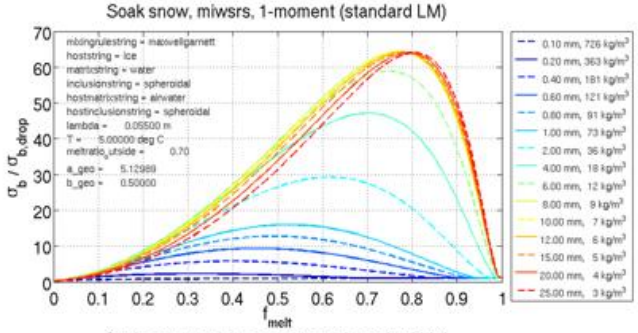
8.11 Mie: soaked wet snow, LM-scheme

Similar to Subsection 8.9, results are shown for calculations of the backscattering cross section σ_b with subroutine `MIE_SOAK_WETGRAUPEL()` (Mie scattering), see subsubsection 5.3.11 on Page 48. But this time, the particle bulk density as function of size is determined by equation (38) on Page 69. A depiciton of the resulting bulk density as function of particle size can be found in Figure 10 (blue solid line). The following figures show the ratio of $\sigma_b/\sigma_{b,drop}$ as function of f_{melt} and the unmelted particle diameter for different EMA-formulations of the particles effective refractive index m_{eff}.

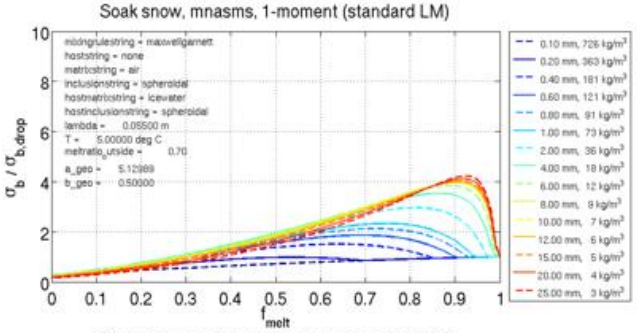
Again, every figure represents one particular EMA-formulation for m_{eff}, which is obtained by using function `get_m_mix_nested()` (subsubsection 5.2.5 on Page 28). The input parameter set for `get_m_mix_nested()` can be found in the text annotation within each graph. Although not beeing implemented into the LM interface functions for snow, the corresponding setting of the (nonexisting) namelist-parameter `ctype_wetsnow` (in analogy to `ctype_wetgraupel`) can be found as 6-character code in the figures title. For explanation of this code, see Table 40.



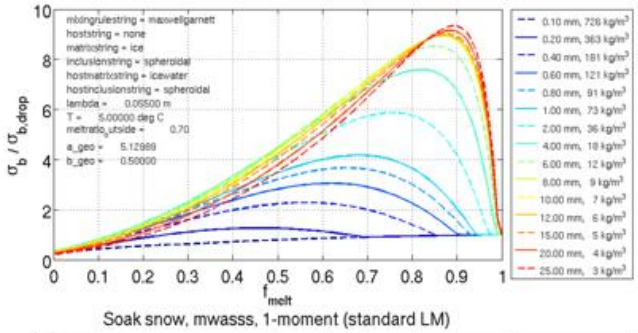
Soak snow, miwsrs, 1-moment (standard LM)



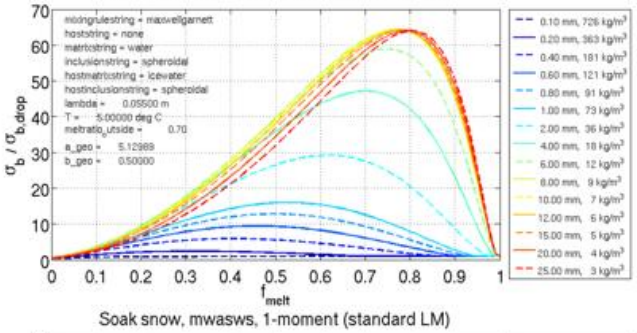
Soak snow, mnasms, 1-moment (standard LM)



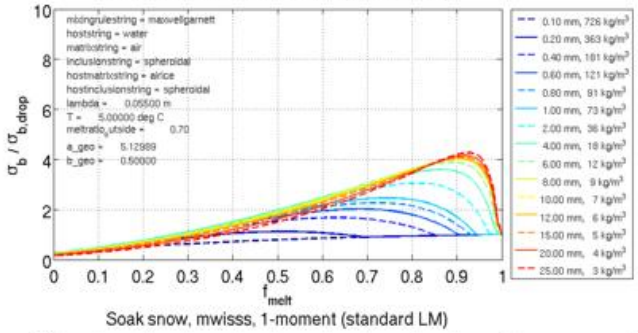
Soak snow, mnisms, 1-moment (standard LM)



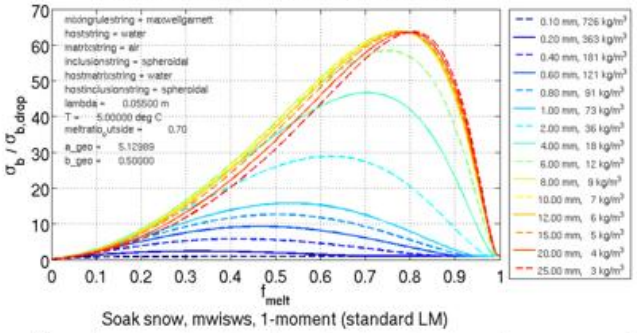
Soak snow, mnwsms, 1-moment (standard LM)



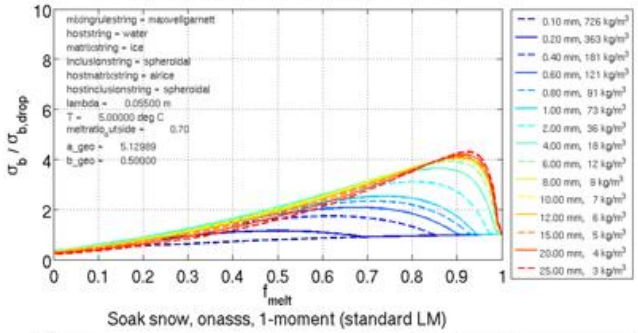
Soak snow, mwasss, 1-moment (standard LM)



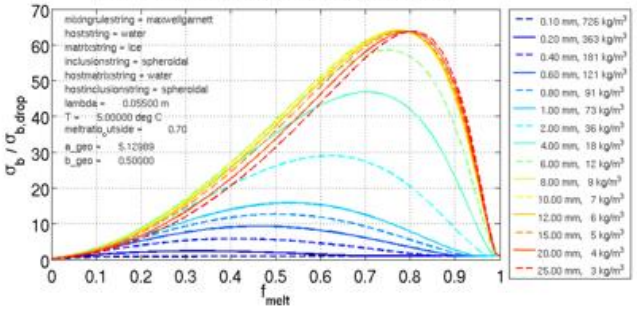
Soak snow, mwasws, 1-moment (standard LM)



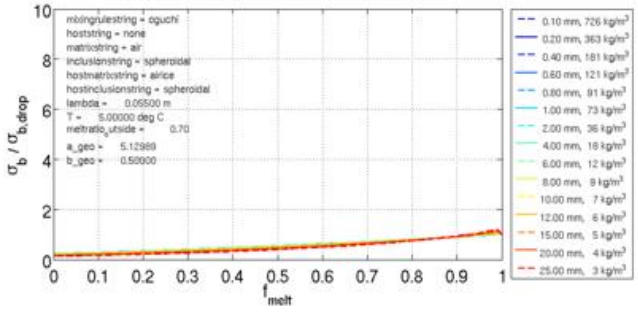
Soak snow, mwisss, 1-moment (standard LM)



Soak snow, mwisws, 1-moment (standard LM)



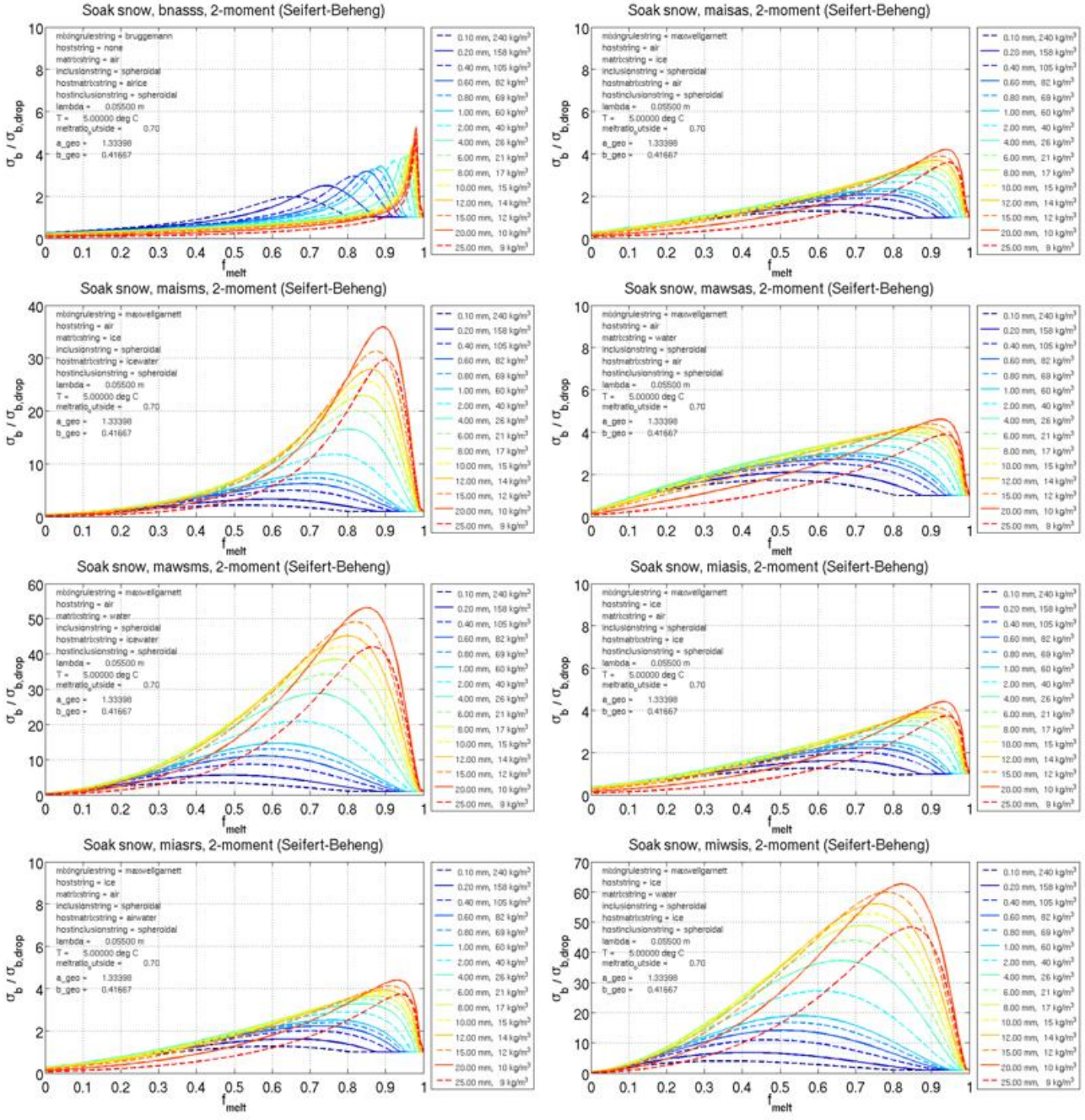
Soak snow, onasss, 1-moment (standard LM)



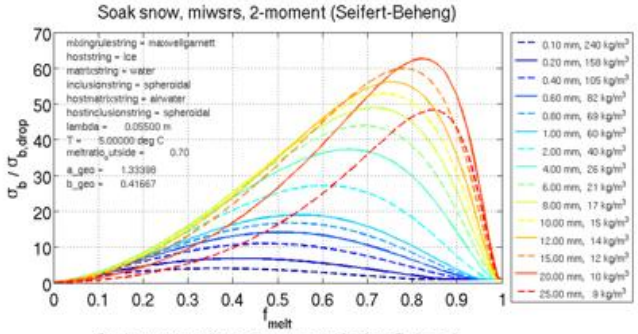
8.12 Mie: soaked wet snow, Seifert/Beheng-scheme

Similar to Subsection 8.9, results are shown for calculations of the backscattering cross section σ_b with subroutine `MIE_SOAK_WETGRAUPEL()` (Mie scattering), see subsubsection 5.3.11 on Page 48. But this time, the particle bulk density as function of size is determined by equation (39) on Page 69. A depiciton of the resulting bulk density as function of particle size can be found in Figure 10 (green solid line). The following figures show the ratio of $\sigma_b/\sigma_{b,drop}$ as function of f_{melt} and the unmelted particle diameter for different EMA-formulations of the particles effective refractive index m_{eff}.

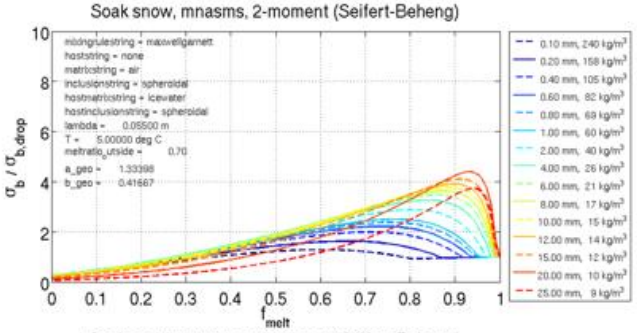
Again, every figure represents one particular EMA-formulation for m_{eff}, which is obtained by using function `get_m_mix_nested()` (subsubsection 5.2.5 on Page 28). The input parameter set for `get_m_mix_nested()` can be found in the text annotation within each graph. Although not beeing implemented into the LM interface functions for snow, the corresponding setting of the (provisional) namelist-parameter `ctype_wetsnow` (in analogy to `ctype_wetgraupel`) can be found as 6-character code in the figures title. For explanation of this code, see Table 40.



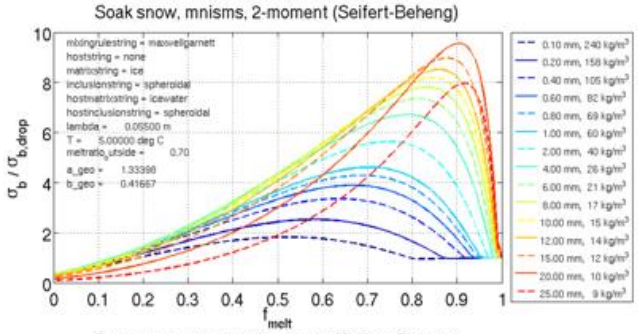
Soak snow, miwsrs, 2-moment (Seifert-Beheng)



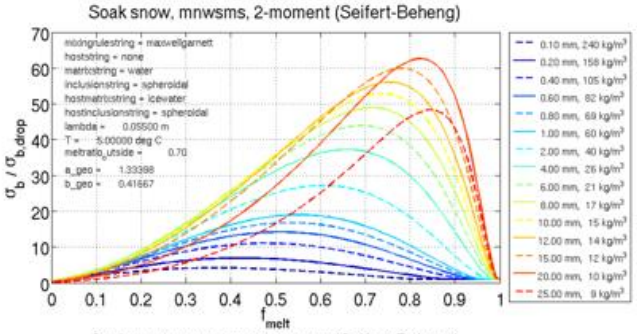
Soak snow, mnasms, 2-moment (Seifert-Beheng)



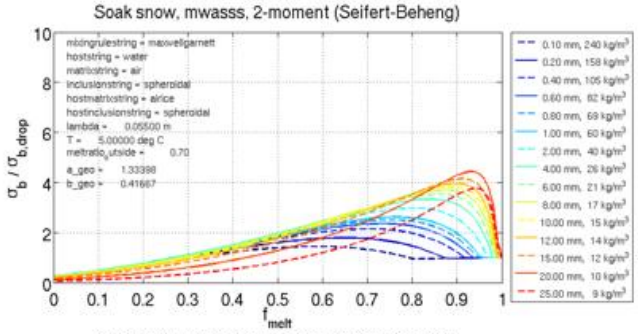
Soak snow, mnisms, 2-moment (Seifert-Beheng)



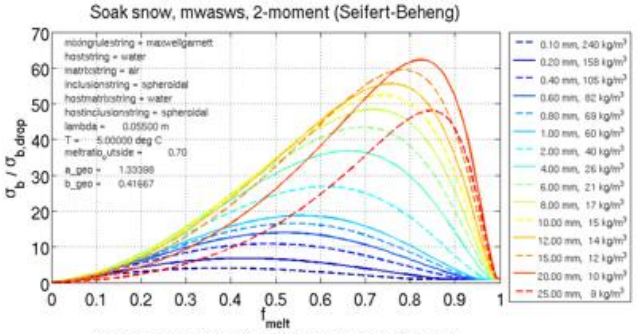
Soak snow, mnwsms, 2-moment (Seifert-Beheng)



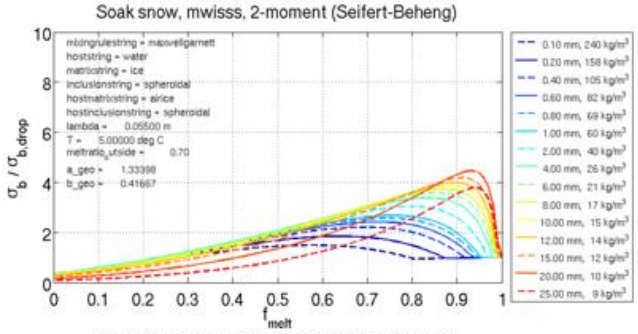
Soak snow, mwasss, 2-moment (Seifert-Beheng)



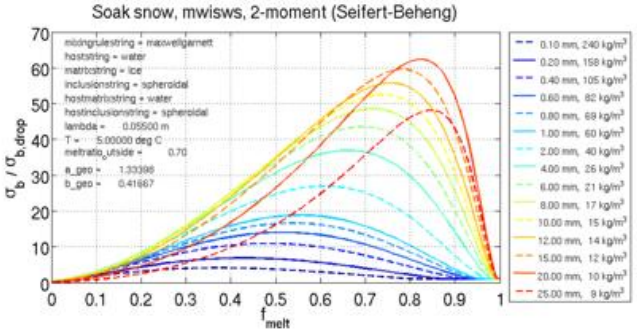
Soak snow, mwasws, 2-moment (Seifert-Beheng)



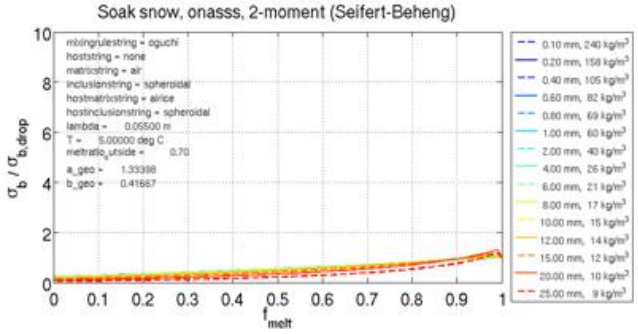
Soak snow, mwisss, 2-moment (Seifert-Beheng)



Soak snow, mwisws, 2-moment (Seifert-Beheng)



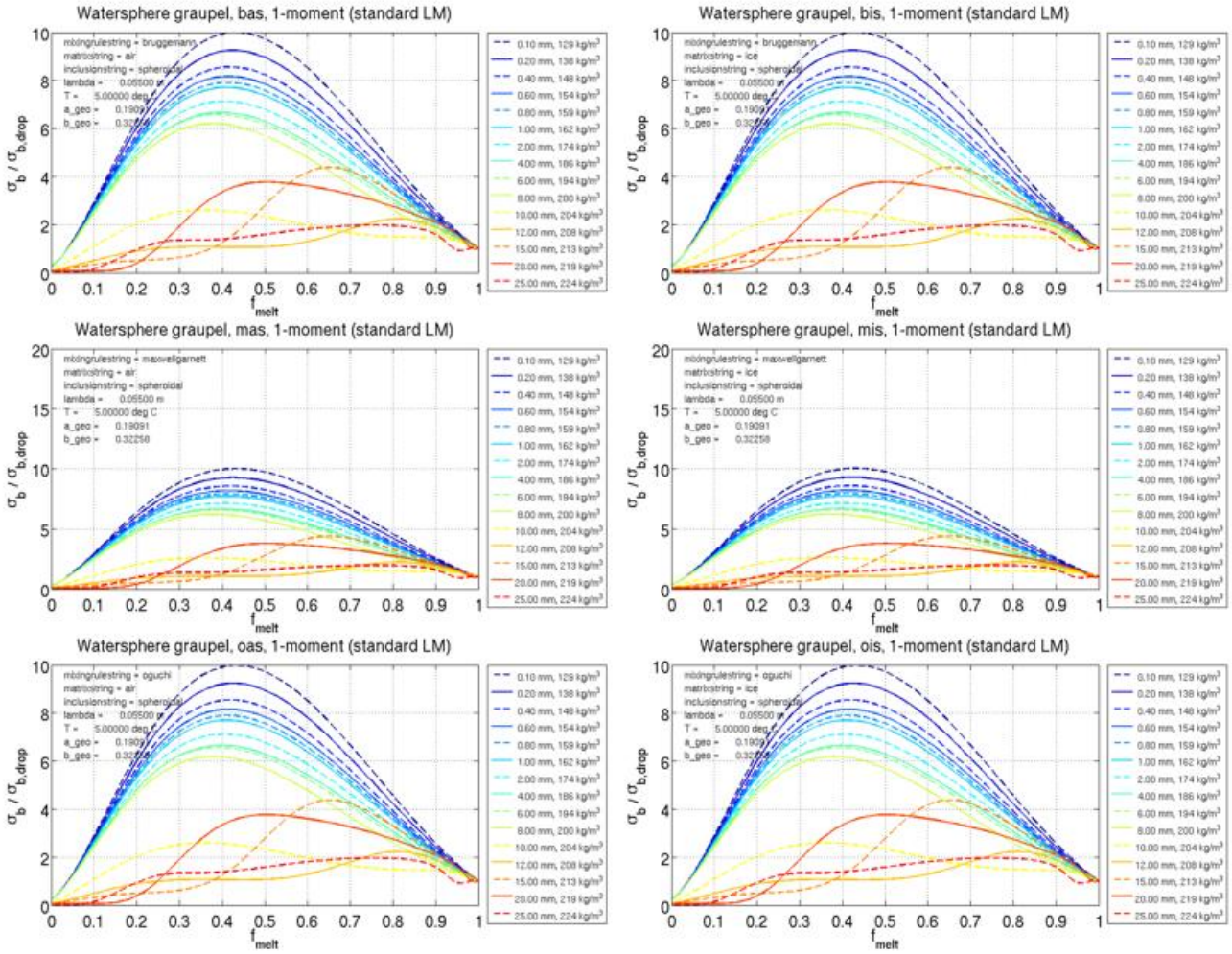
Soak snow, onasss, 2-moment (Seifert-Beheng)



8.13 Mie: watersphere wet graupel, LM-scheme

Similar to Subsection 8.1, results are shown for calculations of the backscattering cross section σ_b with subroutine `MIE_WATERSPHERE_WETGRAUPEL()` (Mie scattering, two-layered sphere), see subsubsection 5.3.8 on Page 43. The following figures show the ratio of $\sigma_b/\sigma_{b,drop}$ as function of f_{melt} and the unmelted particle diameter for different EMA-formulations of the particles core effective refractive index m_{eff}. The particle bulk density as function of size is determined by equation (36) on Page 69. A depiciton of the resulting bulk density as function of particle size can be found in Figure 10 (black solid line).

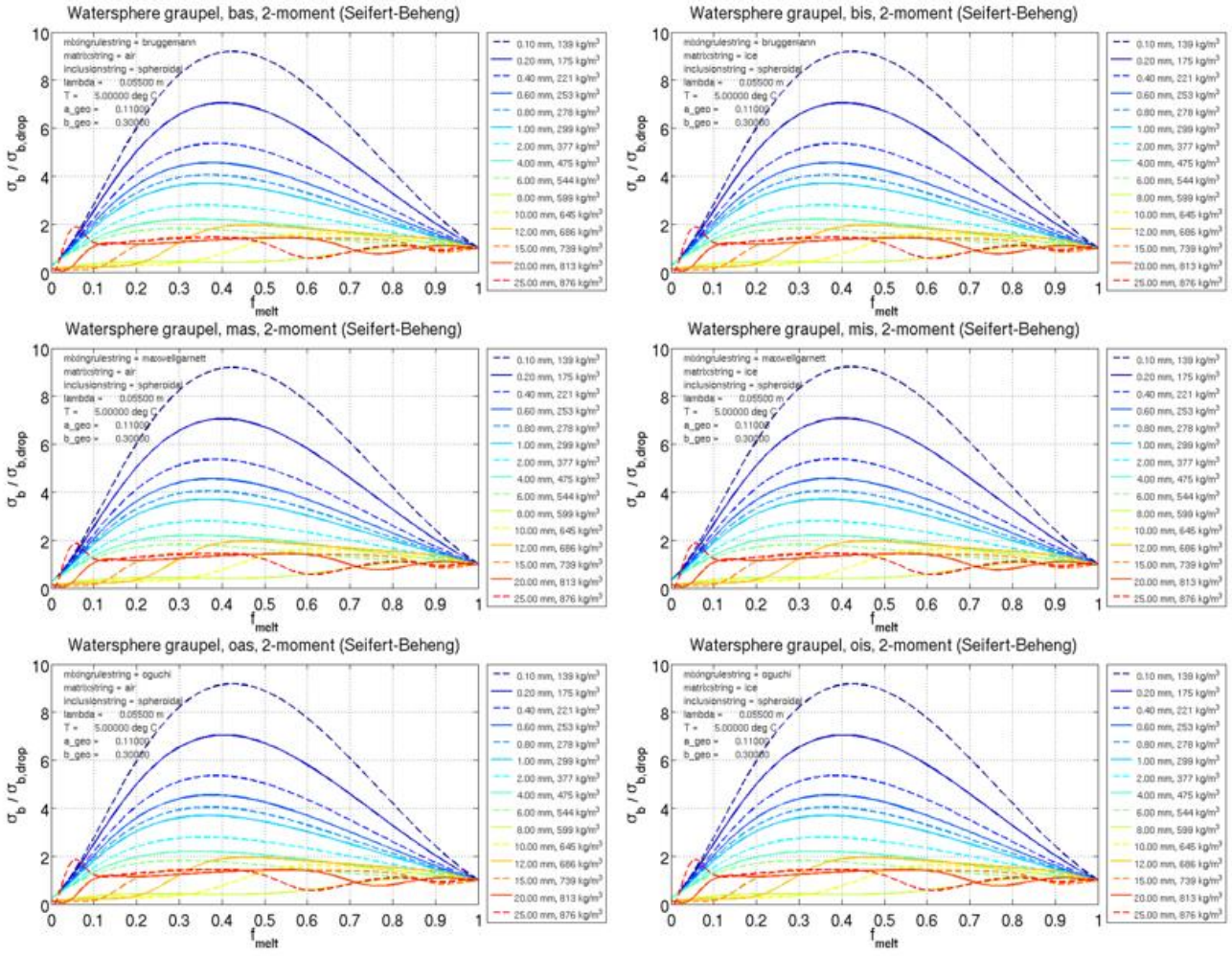
Again, every figure represents one particular EMA-formulation for m_{eff} of the particles ice-air core (the shell is composed of pure water), which is obtained by using function `get_m_mix()` (subsubsection 5.2.4 on Page 26). The input parameter set for `get_m_mix()` can be found in the text annotation within each graph. For users of the LM, the corresponding setting of the namelist-parameter `ctype_wetgraupel` can be found as 3-character code in the figures title. For explanation of this code, see Table 38. The results of this section apply to the LM for graupel particles in case of application of the standard LM one-moment bulk microphysical schemes (namelist-parameter `itype_gscp` < 100) together with `itype_refl` $= 1$ and `igraupel_type` $= 3$.



8.14 Mie: watersphere wet graupel, Seifert/Beheng-scheme

Similar to Subsection 8.13, results are shown for calculations of the backscattering cross section σ_b with subroutine `MIE_SOAK_WETGRAUPEL()` (Mie scattering, two-layered sphere), see subsubsection 5.3.8 on Page 43. But this time, the particle bulk density as function of size is determined by equation (37) on Page 69. A depiciton of the resulting bulk density as function of particle size can be found in Figure 10 (red solid line). The following figures show the ratio of $\sigma_b/\sigma_{b,drop}$ as function of f_{melt} and the unmelted particle diameter for different EMA-formulations of the particles core effective refractive index m_{eff}.

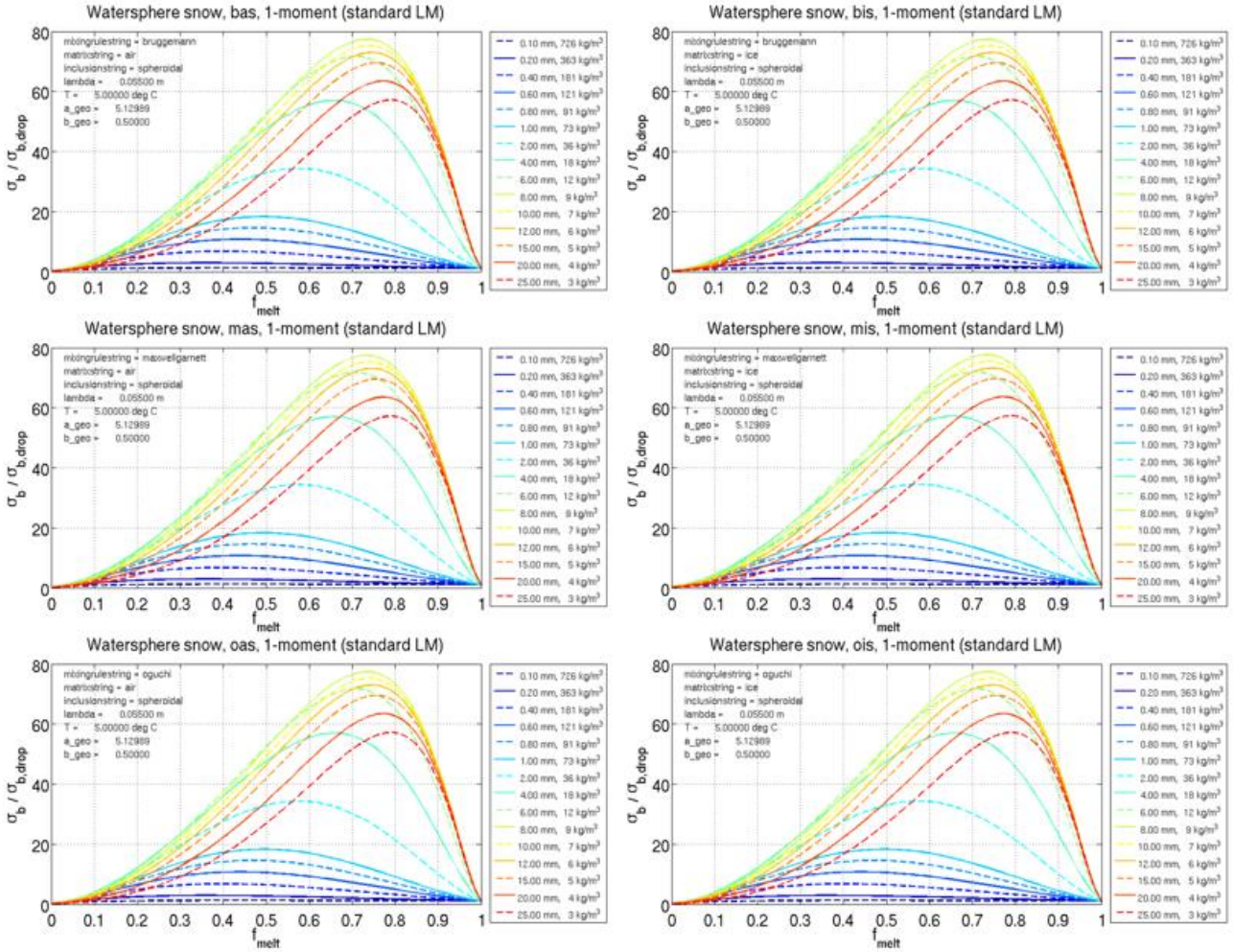
Again, every figure represents one particular EMA-formulation for m_{eff} of the particles ice-air core (the shell is composed of pure water), which is obtained by using function `get_m_mix()` (subsubsection 5.2.4 on Page 26). The input parameter set for `get_m_mix()` can be found in the text annotation within each graph. For users of the LM, the corresponding setting of the namelist-parameter `ctype_wetgraupel` can be found as 3-character code in the figures title. For explanation of this code, see Table 38. The results of this section apply to the LM for graupel particles in case of application of the Seifert and Beheng (2006) two-moment bulk microphysical scheme (namelist-parameter `itype_gscp` ≥ 100) together with `itype_refl` $= 1$ and `igraupel_type` $= 3$.



8.15 Mie: watersphere wet snow, LM-scheme

Similar to Subsection 8.13, results are shown for calculations of the backscattering cross section σ_b with subroutine `MIE_SOAK_WETGRAUPEL()` (Mie scattering, two-layered sphere), see subsubsection 5.3.8 on Page 43. But this time, the particle bulk density as function of size is determined by equation (38) on Page 69. A depiciton of the resulting bulk density as function of particle size can be found in Figure 10 (blue solid line). The following figures show the ratio of $\sigma_b/\sigma_{b,drop}$ as function of f_{melt} and the unmelted particle diameter for different EMA-formulations of the particles core effective refractive index m_{eff}.

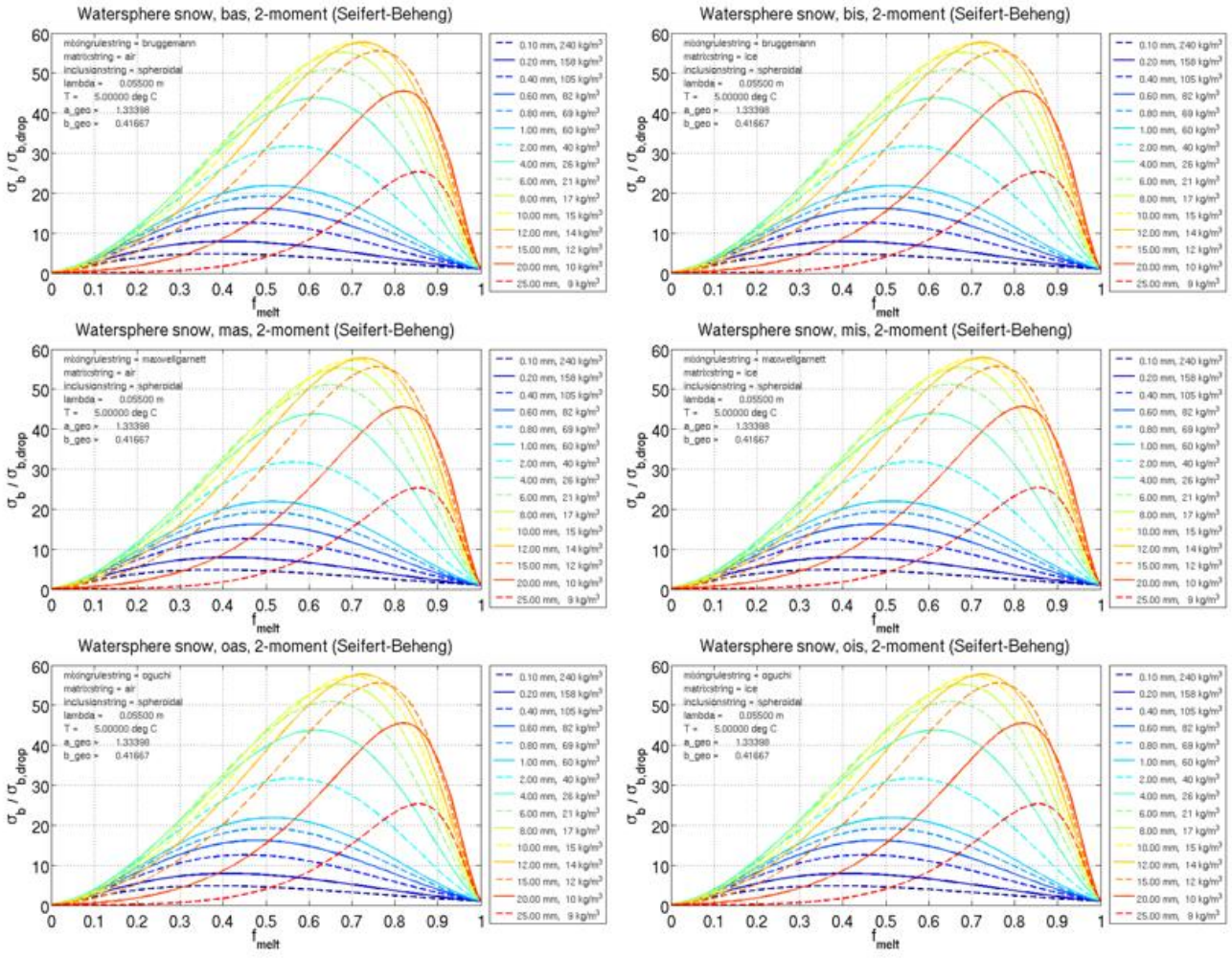
Again, every figure represents one particular EMA-formulation for m_{eff} of the particles ice-air core (the shell is composed of pure water), which is obtained by using function `get_m_mix()` (subsubsection 5.2.4 on Page 26). The input parameter set for `get_m_mix()` can be found in the text annotation within each graph. Although not beeing implemented into the LM interface functions for snow, the corresponding setting of the (provisional) namelist-parameter `ctype_wetsnow` (in analogy to `ctype_wetgraupel`) can be found as 3-character code in the figures title. For explanation of this code, see Table 38.



8.16 Mie: watersphere wet snow, Seifert/Beheng-scheme

Similar to Subsection 8.13, results are shown for calculations of the backscattering cross section σ_b with subroutine `MIE_SOAK_WETGRAUPEL()` (Mie scattering, two-layered sphere), see subsubsection 5.3.8 on Page 43. But this time, the particle bulk density as function of size is determined by equation (39) on Page 69. A depiciton of the resulting bulk density as function of particle size can be found in Figure 10 (green solid line). The following figures show the ratio of $\sigma_b/\sigma_{b,drop}$ as function of f_{melt} and the unmelted particle diameter for different EMA-formulations of the particles core effective refractive index m_{eff}.

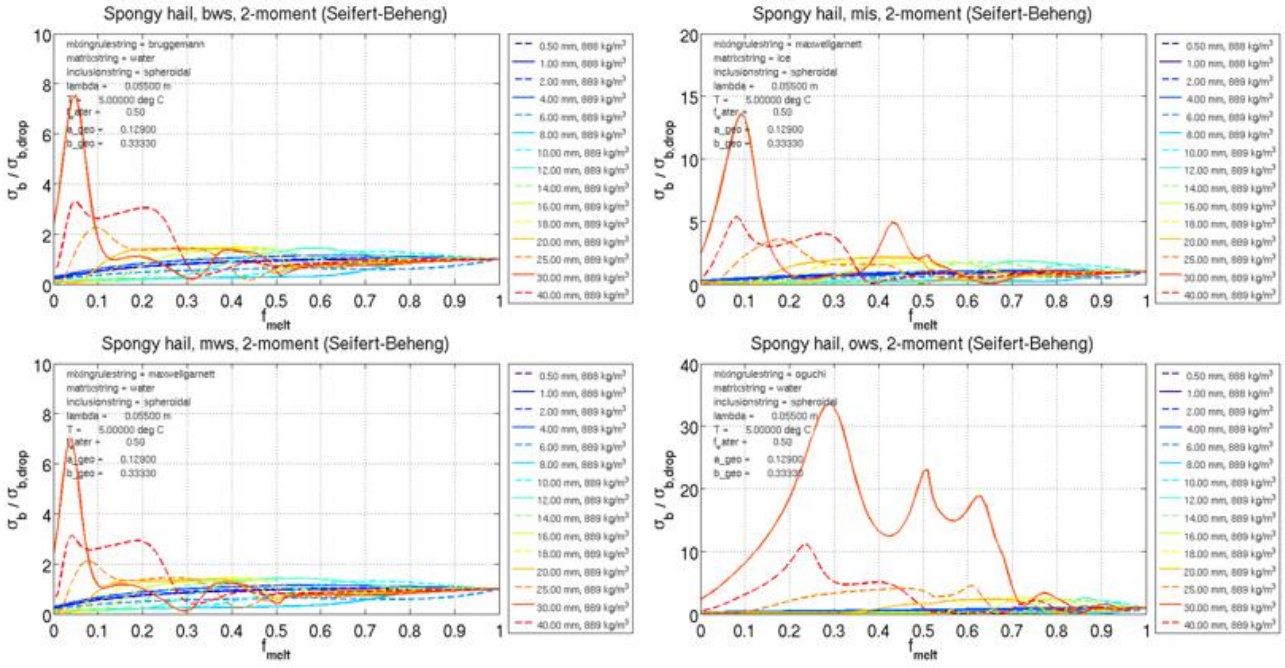
Again, every figure represents one particular EMA-formulation for m_{eff} of the particles ice-air core (the shell is composed of pure water), which is obtained by using function `get_m_mix()` (subsubsection 5.2.4 on Page 26). The input parameter set for `get_m_mix()` can be found in the text annotation within each graph. Although not beeing implemented into the LM interface functions for snow, the corresponding setting of the (provisional) namelist-parameter `ctype_wetsnow` (in analogy to `ctype_wetgraupel`) can be found as 3-character code in the figures title. For explanation of this code, see Table 38.



8.17 Mie: spongy wet hail, Seifert/Beheng-scheme

Similar to Subsection 8.1, results are shown for calculations of the backscattering cross section σ_b with subroutine `MIE_SPONGY_WETHAIL()` (Mie scattering, two-layered sphere), see subsubsection 5.3.7 on Page 41. The following figures show the ratio of $\sigma_b/\sigma_{b,drop}$ as function of f_{melt} and the unmelted particle diameter for different EMA-formulations of the particles ice-water shell effective refractive index m_{eff}. The unmelted particle bulk density does not depend on size here and is that of pure ice. The input parameter `f_water` (melt fraction within the ice-water shell) was set to 0.5, independent of size and f_{melt}.

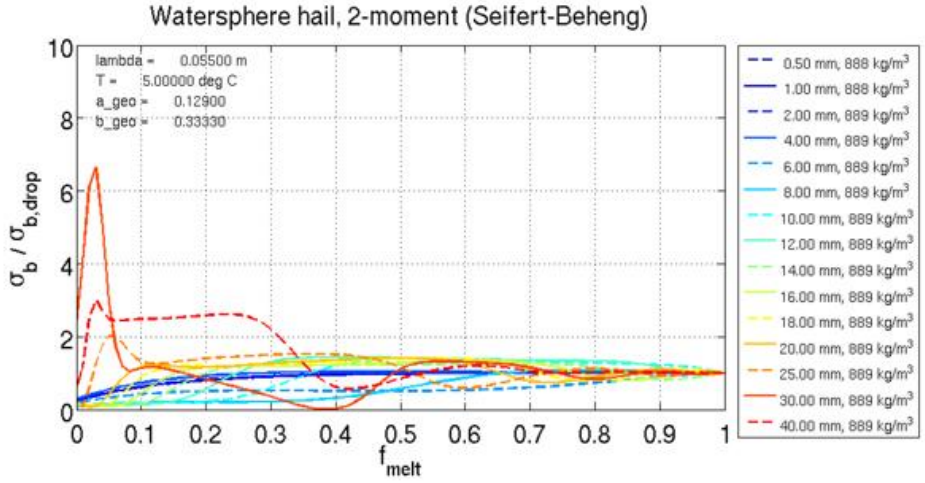
Again, every figure represents one particular EMA-formulation for m_{eff} of the particles ice-water shell (the core is composed of solid ice), which is obtained by using function `get_m_mix()` (subsubsection 5.2.4 on Page 26). The input parameter set for `get_m_mix()` can be found in the text annotation within each graph. For users of the LM, the corresponding setting of the namelist-parameter `ctype_wethail` can be found as 3-character code in the figures title. For explanation of this code, see Table 39. The results of this section apply to the LM for hail particles in case of application of the Seifert and Beheng (2006) two-moment bulk microphysical scheme (namelist-parameter `itype_gscp` ≥ 100) together with `itype_refl` $= 1$.



8.18 Mie: watersphere wet hail, Seifert/Beheng-scheme

Similar to Subsection 8.17, results are shown for calculations of the backscattering cross section σ_b with subroutine `MIE_WATERSPHERE_WETHAIL()` (Mie scattering, two-layered sphere), see subsubsection 5.3.6 on Page 40. The following figure shows the ratio of $\sigma_b/\sigma_{b,drop}$ as function of f_{melt} and the unmelted particle diameter. Since the core is composed of pure ice and the shell is assumed to be water, no effective medium approximation for m_{eff} of mixture materials is needed here. Therefore, only one figure is sufficient in the following.

`MIE_WATERSPHERE_WETHAIL()` is not implemented into the interface subroutines for the LM, but would be a possible choice in case of application of the Seifert and Beheng (2006) two-moment bulk microphysical scheme (namelist-parameter `itype_gscp` ≥ 100), together with `itype_refl` $= 1$.

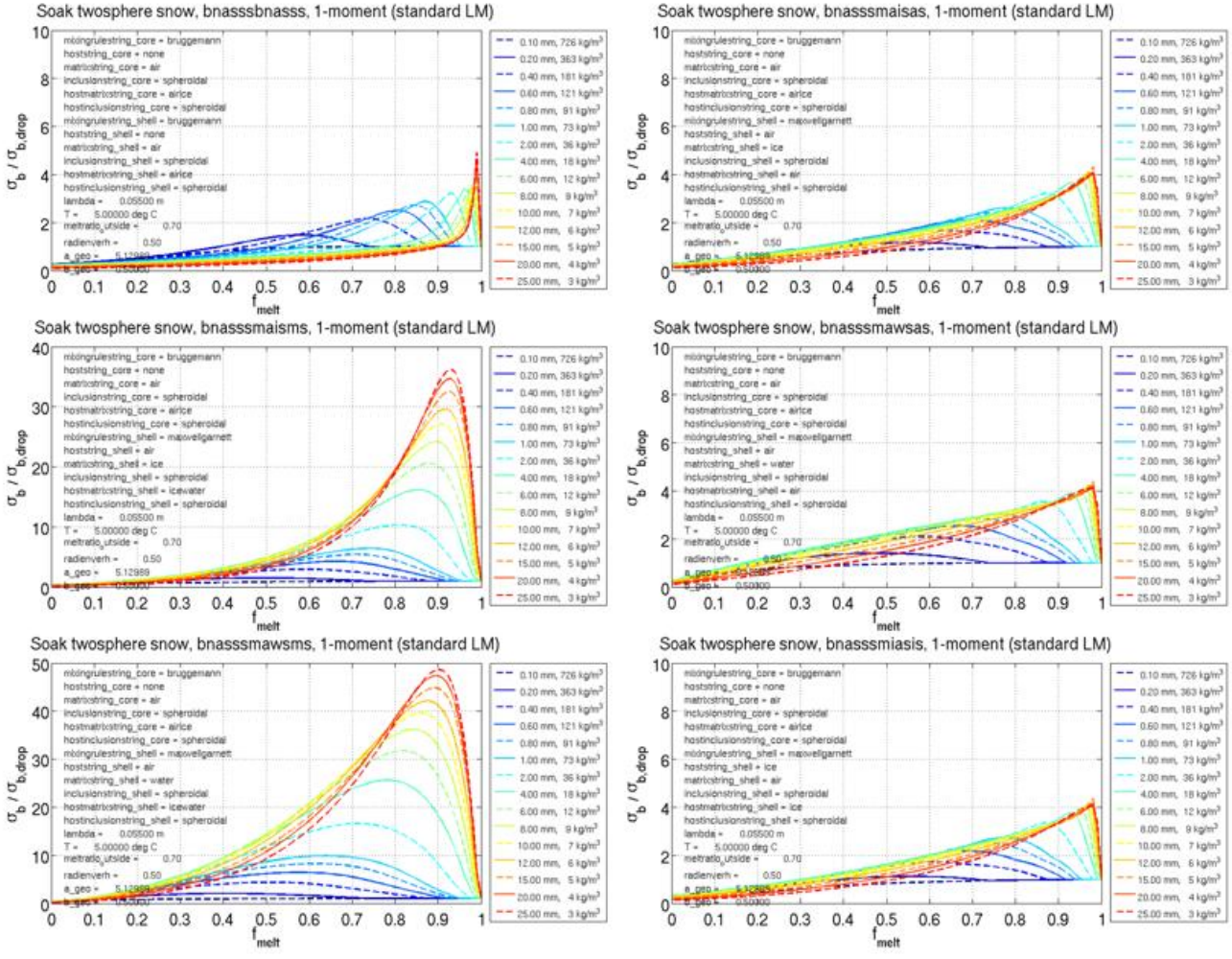


8.19 Mie: twosphere soaked wet snow, LM-scheme

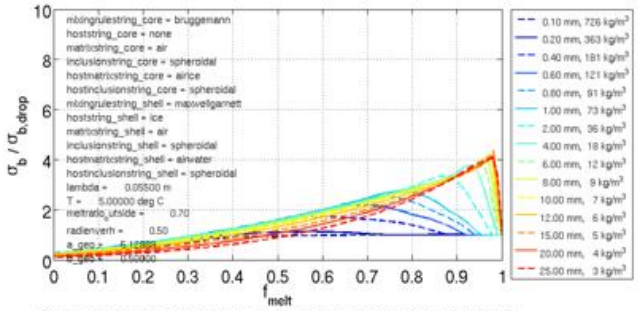
Similar to Subsection 8.1, results are shown for calculations of the backscattering cross section σ_b with subroutine `MIE_WETSNOW_TWOSPHERE()` (Mie scattering, two-layered sphere), see subsubsection 5.3.13 on Page 51. The following figures show the ratio of $\sigma_b/\sigma_{b,drop}$ as function of f_{melt} and the unmelted particle diameter for different EMA-formulations of the particles core and shell effective refractive indices m_{eff}. The particle bulk density as function of size is determined by equation (38) on Page 69. A depiciton of the resulting bulk density as function of particle size can be found in Figure 10 (blue solid line).

The input parameter `meltingratio_outside` (see subsubsection 5.3.13 on Page 51) is set to 0.7, and `radienverh` (inner to outer sphere radius) is set to 0.5, independent of size and f_{melt}.

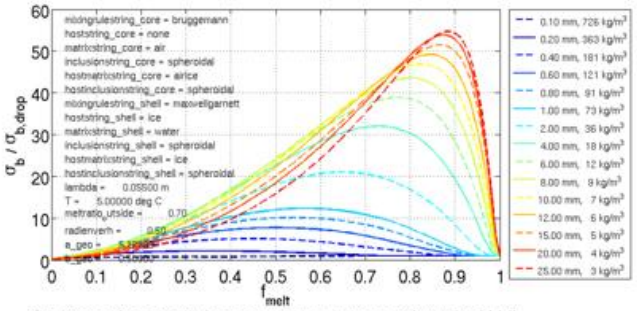
Again, every figure represents one particular EMA-formulation for m_{eff} of the particles ice-water-air core and ice-water-air shell, which both are obtained by using function `get_m_mix_nested()` (subsubsection 5.2.5 on Page 28). The input parameter sets of `get_m_mix_nested()` for core and shell can be found in the text annotation within each graph. For users of the LM, the corresponding setting of the namelist-parameter `ctype_wetsnow` can be found as 12-character code in the figures title. For explanation of the two 6-character parts of this code, see Table 40. The first 6-character sequence corresponds to the core material, the second 6-character sequence to the shell material. The results of this section apply to the LM for snow particles in case of application of the standard LM one-moment bulk microphysical schemes (namelist-parameter `itype_gscp` < 100) together with `itype_refl` $= 1$.



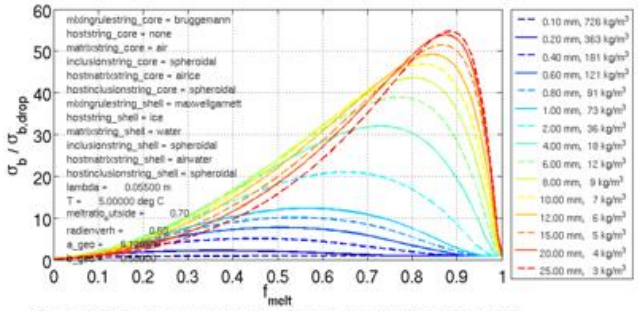
Soak twosphere snow, bnasssmiasrs, 1-moment (standard LM)



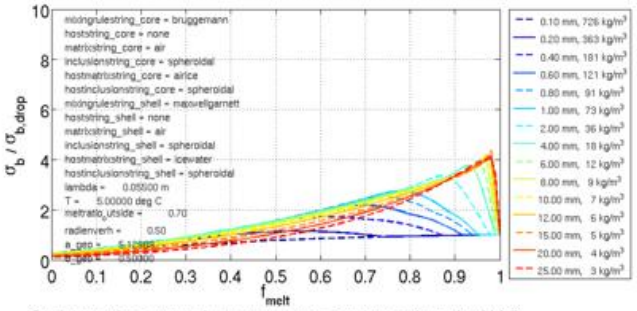
Soak twosphere snow, bnasssmiwsis, 1-moment (standard LM)



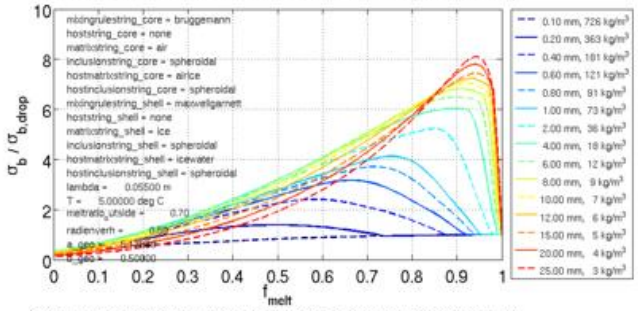
Soak twosphere snow, bnasssmiwsrs, 1-moment (standard LM)



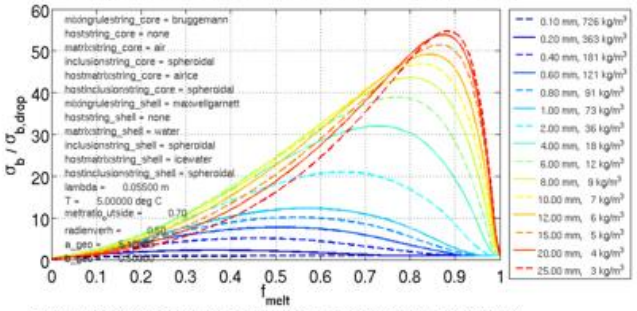
Soak twosphere snow, bnasssmnasms, 1-moment (standard LM)



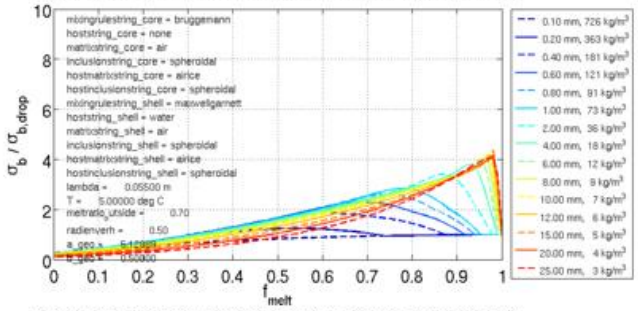
Soak twosphere snow, bnasssmnisms, 1-moment (standard LM)



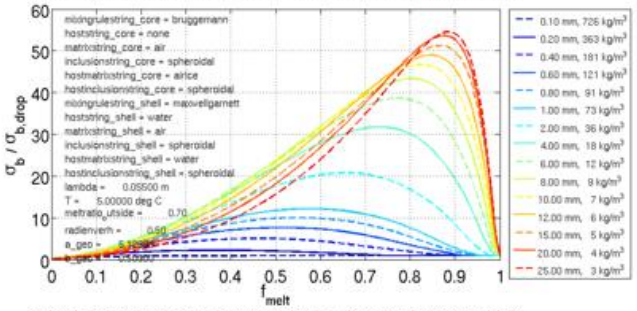
Soak twosphere snow, bnasssmnwsms, 1-moment (standard LM)



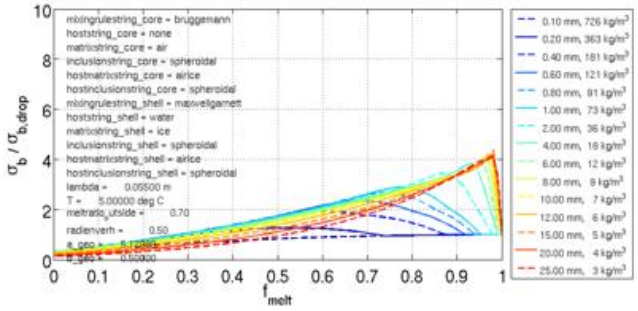
Soak twosphere snow, bnasssmwasss, 1-moment (standard LM)



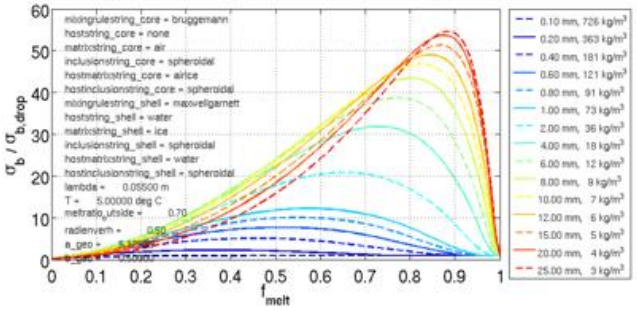
Soak twosphere snow, bnasssmwasws, 1-moment (standard LM)

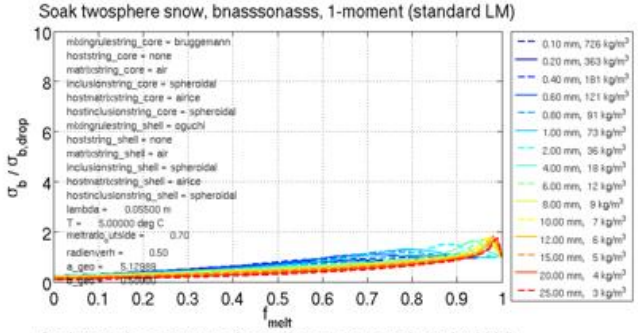


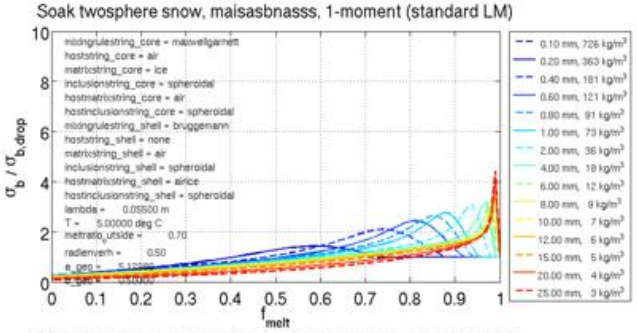
Soak twosphere snow, bnasssmwisss, 1-moment (standard LM)

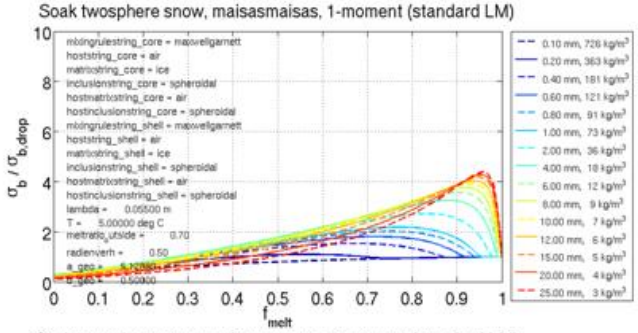


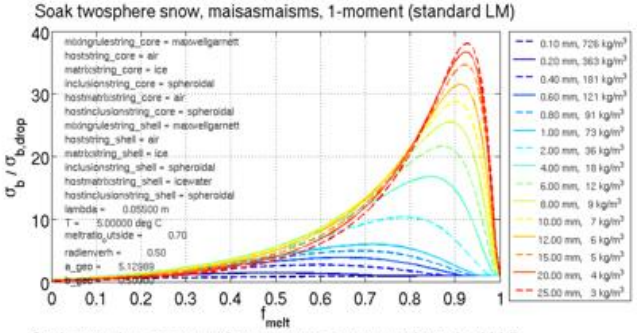
Soak twosphere snow, bnasssmwisws, 1-moment (standard LM)

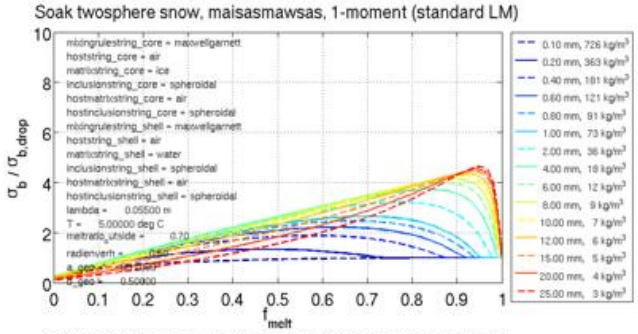


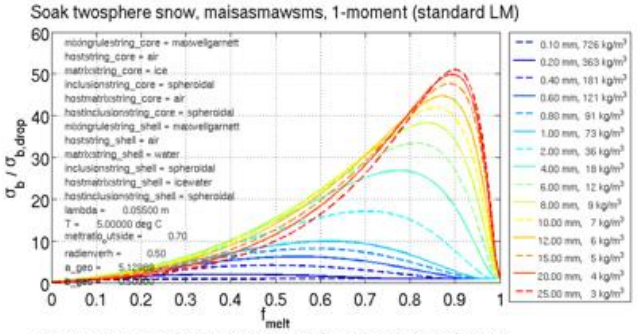

Soak twosphere snow, bnasssonasss, 1-moment (standard LM)
mixingrulestring_core = bruggemann
hoststring_core = none
matrixstring_core = air
inclusionstring_core = spheroidal
hostmatrixstring_core = airice
hostinclusionstring_core = spheroidal
mixingrulestring_shell = oguchi
hoststring_shell = none
matrixstring_shell = air
inclusionstring_shell = spheroidal
hostmatrixstring_shell = airice
hostinclusionstring_shell = spheroidal
lambda = 0.05500 m
T = 5.00000 deg C
meltratio_utside = 0.70
radienverh = 0.50
a_geo = 5.12989
b_geo = 0.50000
0.10 mm, 726 kg/m³
0.20 mm, 363 kg/m³
0.40 mm, 181 kg/m³
0.60 mm, 121 kg/m³
0.80 mm, 91 kg/m³
1.00 mm, 73 kg/m³
2.00 mm, 36 kg/m³
4.00 mm, 18 kg/m³
6.00 mm, 12 kg/m³
8.00 mm, 9 kg/m³
10.00 mm, 7 kg/m³
12.00 mm, 6 kg/m³
15.00 mm, 5 kg/m³
20.00 mm, 4 kg/m³
25.00 mm, 3 kg/m³
σb / σb,drop
fmelt

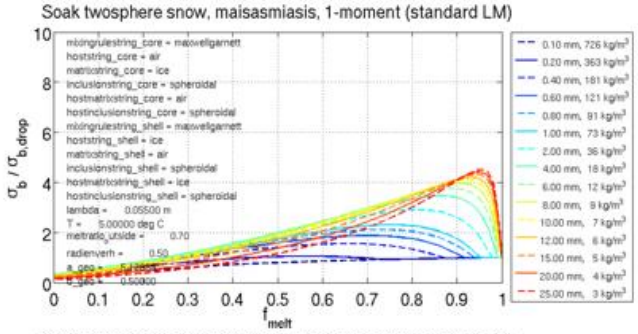

Soak twosphere snow, maisasbnasss, 1-moment (standard LM)
mixingrulestring_core = maxwellgarnett
hoststring_core = air
matrixstring_core = ice
inclusionstring_core = spheroidal
hostmatrixstring_core = air
hostinclusionstring_core = spheroidal
mixingrulestring_shell = bruggemann
hoststring_shell = none
matrixstring_shell = air
inclusionstring_shell = spheroidal
hostmatrixstring_shell = airice
hostinclusionstring_shell = spheroidal
lambda = 0.05500 m
T = 5.00000 deg C
meltratio_utside = 0.70
radienverh = 0.50
0.10 mm, 726 kg/m³
0.20 mm, 363 kg/m³
0.40 mm, 181 kg/m³
0.60 mm, 121 kg/m³
0.80 mm, 91 kg/m³
1.00 mm, 73 kg/m³
2.00 mm, 36 kg/m³
4.00 mm, 18 kg/m³
6.00 mm, 12 kg/m³
8.00 mm, 9 kg/m³
10.00 mm, 7 kg/m³
12.00 mm, 6 kg/m³
15.00 mm, 5 kg/m³
20.00 mm, 4 kg/m³
25.00 mm, 3 kg/m³
σb / σb,drop
fmelt

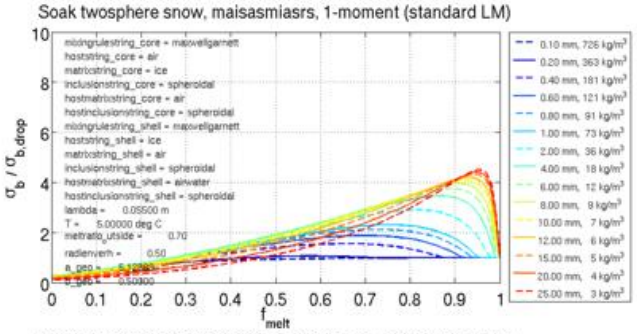

Soak twosphere snow, maisasmaisas, 1-moment (standard LM)
mixingrulestring_core = maxwellgarnett
hoststring_core = air
matrixstring_core = ice
inclusionstring_core = spheroidal
hostmatrixstring_core = air
hostinclusionstring_core = spheroidal
mixingrulestring_shell = maxwellgarnett
hoststring_shell = air
matrixstring_shell = ice
inclusionstring_shell = spheroidal
hostmatrixstring_shell = air
hostinclusionstring_shell = spheroidal
lambda = 0.05500 m
T = 5.00000 deg C
meltratio_utside = 0.70
radienverh = 0.50
0.10 mm, 726 kg/m³
0.20 mm, 363 kg/m³
0.40 mm, 181 kg/m³
0.60 mm, 121 kg/m³
0.80 mm, 91 kg/m³
1.00 mm, 73 kg/m³
2.00 mm, 36 kg/m³
4.00 mm, 18 kg/m³
6.00 mm, 12 kg/m³
8.00 mm, 9 kg/m³
10.00 mm, 7 kg/m³
12.00 mm, 6 kg/m³
15.00 mm, 5 kg/m³
20.00 mm, 4 kg/m³
25.00 mm, 3 kg/m³
σb / σb,drop
fmelt

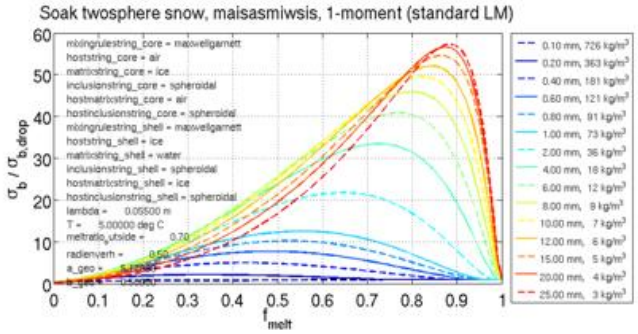

Soak twosphere snow, maisasmaisms, 1-moment (standard LM)
mixingrulestring_core = maxwellgarnett
hoststring_core = air
matrixstring_core = ice
inclusionstring_core = spheroidal
hostmatrixstring_core = air
hostinclusionstring_core = spheroidal
mixingrulestring_shell = maxwellgarnett
hoststring_shell = air
matrixstring_shell = ice
inclusionstring_shell = spheroidal
hostmatrixstring_shell = icewater
hostinclusionstring_shell = spheroidal
lambda = 0.05500 m
T = 5.00000 deg C
meltratio_utside = 0.70
radienverh = 0.50
a_geo = 5.12989
0.10 mm, 726 kg/m³
0.20 mm, 363 kg/m³
0.40 mm, 181 kg/m³
0.60 mm, 121 kg/m³
0.80 mm, 91 kg/m³
1.00 mm, 73 kg/m³
2.00 mm, 36 kg/m³
4.00 mm, 18 kg/m³
6.00 mm, 12 kg/m³
8.00 mm, 9 kg/m³
10.00 mm, 7 kg/m³
12.00 mm, 6 kg/m³
15.00 mm, 5 kg/m³
20.00 mm, 4 kg/m³
25.00 mm, 3 kg/m³
σb / σb,drop
fmelt

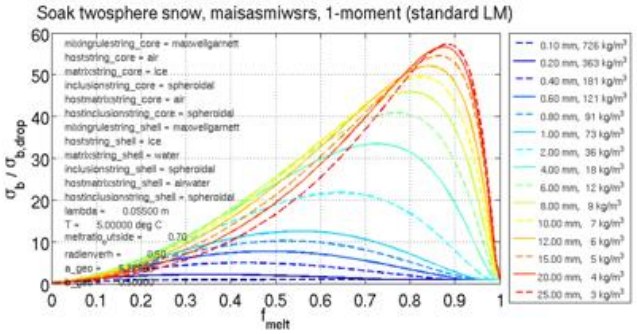

Soak twosphere snow, maisasmawsas, 1-moment (standard LM)
mixingrulestring_core = maxwellgarnett
hoststring_core = air
matrixstring_core = ice
inclusionstring_core = spheroidal
hostmatrixstring_core = air
hostinclusionstring_core = spheroidal
mixingrulestring_shell = maxwellgarnett
hoststring_shell = air
matrixstring_shell = water
inclusionstring_shell = spheroidal
hostmatrixstring_shell = air
hostinclusionstring_shell = spheroidal
lambda = 0.05500 m
T = 5.00000 deg C
meltratio_utside = 0.70
radienverh = 0.50
0.10 mm, 726 kg/m³
0.20 mm, 363 kg/m³
0.40 mm, 181 kg/m³
0.60 mm, 121 kg/m³
0.80 mm, 91 kg/m³
1.00 mm, 73 kg/m³
2.00 mm, 36 kg/m³
4.00 mm, 18 kg/m³
6.00 mm, 12 kg/m³
8.00 mm, 9 kg/m³
10.00 mm, 7 kg/m³
12.00 mm, 6 kg/m³
15.00 mm, 5 kg/m³
20.00 mm, 4 kg/m³
25.00 mm, 3 kg/m³
σb / σb,drop
fmelt


Soak twosphere snow, maisasmawsms, 1-moment (standard LM)
mixingrulestring_core = maxwellgarnett
hoststring_core = air
matrixstring_core = ice
inclusionstring_core = spheroidal
hostmatrixstring_core = air
hostinclusionstring_core = spheroidal
mixingrulestring_shell = maxwellgarnett
hoststring_shell = air
matrixstring_shell = water
inclusionstring_shell = spheroidal
hostmatrixstring_shell = icewater
hostinclusionstring_shell = spheroidal
lambda = 0.05500 m
T = 5.00000 deg C
meltratio_utside = 0.70
radienverh = 0.50
a_geo = 5.12989
0.10 mm, 726 kg/m³
0.20 mm, 363 kg/m³
0.40 mm, 181 kg/m³
0.60 mm, 121 kg/m³
0.80 mm, 91 kg/m³
1.00 mm, 73 kg/m³
2.00 mm, 36 kg/m³
4.00 mm, 18 kg/m³
6.00 mm, 12 kg/m³
8.00 mm, 9 kg/m³
10.00 mm, 7 kg/m³
12.00 mm, 6 kg/m³
15.00 mm, 5 kg/m³
20.00 mm, 4 kg/m³
25.00 mm, 3 kg/m³
σb / σb,drop
fmelt

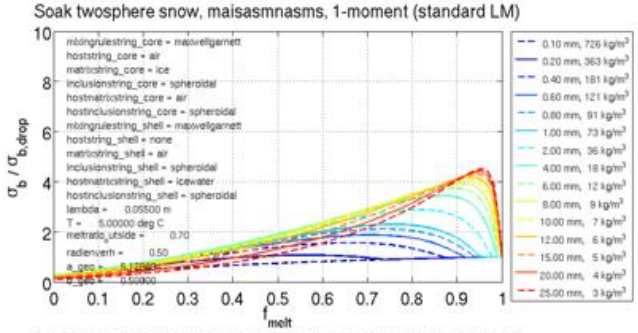

Soak twosphere snow, maisasmiasis, 1-moment (standard LM)
mixingrulestring_core = maxwellgarnett
hoststring_core = air
matrixstring_core = ice
inclusionstring_core = spheroidal
hostmatrixstring_core = air
hostinclusionstring_core = spheroidal
mixingrulestring_shell = maxwellgarnett
hoststring_shell = ice
matrixstring_shell = air
inclusionstring_shell = spheroidal
hostmatrixstring_shell = ice
hostinclusionstring_shell = spheroidal
lambda = 0.05500 m
T = 5.00000 deg C
meltratio_utside = 0.70
radienverh = 0.50
0.10 mm, 726 kg/m³
0.20 mm, 363 kg/m³
0.40 mm, 181 kg/m³
0.60 mm, 121 kg/m³
0.80 mm, 91 kg/m³
1.00 mm, 73 kg/m³
2.00 mm, 36 kg/m³
4.00 mm, 18 kg/m³
6.00 mm, 12 kg/m³
8.00 mm, 9 kg/m³
10.00 mm, 7 kg/m³
12.00 mm, 6 kg/m³
15.00 mm, 5 kg/m³
20.00 mm, 4 kg/m³
25.00 mm, 3 kg/m³
σb / σb,drop
fmelt


Soak twosphere snow, maisasmiasrs, 1-moment (standard LM)
mixingrulestring_core = maxwellgarnett
hoststring_core = air
matrixstring_core = ice
inclusionstring_core = spheroidal
hostmatrixstring_core = air
hostinclusionstring_core = spheroidal
mixingrulestring_shell = maxwellgarnett
hoststring_shell = ice
matrixstring_shell = air
inclusionstring_shell = spheroidal
hostmatrixstring_shell = airwater
hostinclusionstring_shell = spheroidal
lambda = 0.05500 m
T = 5.00000 deg C
meltratio_utside = 0.70
radienverh = 0.50
0.10 mm, 726 kg/m³
0.20 mm, 363 kg/m³
0.40 mm, 181 kg/m³
0.60 mm, 121 kg/m³
0.80 mm, 91 kg/m³
1.00 mm, 73 kg/m³
2.00 mm, 36 kg/m³
4.00 mm, 18 kg/m³
6.00 mm, 12 kg/m³
8.00 mm, 9 kg/m³
10.00 mm, 7 kg/m³
12.00 mm, 6 kg/m³
15.00 mm, 5 kg/m³
20.00 mm, 4 kg/m³
25.00 mm, 3 kg/m³
σb / σb,drop
fmelt

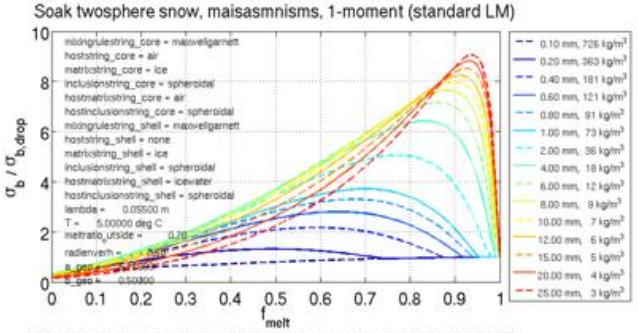

Soak twosphere snow, maisasmiwsis, 1-moment (standard LM)
mixingrulestring_core = maxwellgarnett
hoststring_core = air
matrixstring_core = ice
inclusionstring_core = spheroidal
hostmatrixstring_core = air
hostinclusionstring_core = spheroidal
mixingrulestring_shell = maxwellgarnett
hoststring_shell = ice
matrixstring_shell = water
inclusionstring_shell = spheroidal
hostmatrixstring_shell = ice
hostinclusionstring_shell = spheroidal
lambda = 0.05500 m
T = 5.00000 deg C
meltratio_utside = 0.70
radienverh = 0.50
0.10 mm, 726 kg/m³
0.20 mm, 363 kg/m³
0.40 mm, 181 kg/m³
0.60 mm, 121 kg/m³
0.80 mm, 91 kg/m³
1.00 mm, 73 kg/m³
2.00 mm, 36 kg/m³
4.00 mm, 18 kg/m³
6.00 mm, 12 kg/m³
8.00 mm, 9 kg/m³
10.00 mm, 7 kg/m³
12.00 mm, 6 kg/m³
15.00 mm, 5 kg/m³
20.00 mm, 4 kg/m³
25.00 mm, 3 kg/m³
σb / σb,drop
fmelt


Soak twosphere snow, maisasmiwsrs, 1-moment (standard LM)
mixingrulestring_core = maxwellgarnett
hoststring_core = air
matrixstring_core = ice
inclusionstring_core = spheroidal
hostmatrixstring_core = air
hostinclusionstring_core = spheroidal
mixingrulestring_shell = maxwellgarnett
hoststring_shell = ice
matrixstring_shell = water
inclusionstring_shell = spheroidal
hostmatrixstring_shell = airwater
hostinclusionstring_shell = spheroidal
lambda = 0.05500 m
T = 5.00000 deg C
meltratio_utside = 0.70
radienverh = 0.50
0.10 mm, 726 kg/m³
0.20 mm, 363 kg/m³
0.40 mm, 181 kg/m³
0.60 mm, 121 kg/m³
0.80 mm, 91 kg/m³
1.00 mm, 73 kg/m³
2.00 mm, 36 kg/m³
4.00 mm, 18 kg/m³
6.00 mm, 12 kg/m³
8.00 mm, 9 kg/m³
10.00 mm, 7 kg/m³
12.00 mm, 6 kg/m³
15.00 mm, 5 kg/m³
20.00 mm, 4 kg/m³
25.00 mm, 3 kg/m³
σb / σb,drop
fmelt

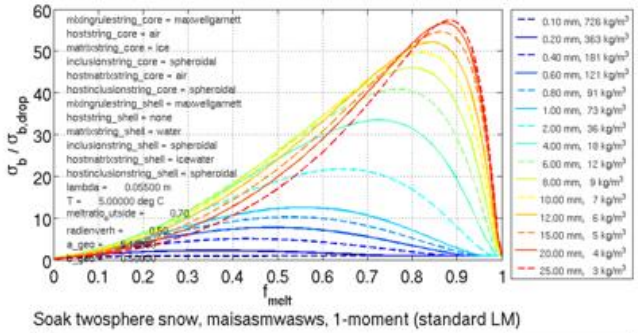
Soak twosphere snow, maisasmnasms, 1-moment (standard LM)



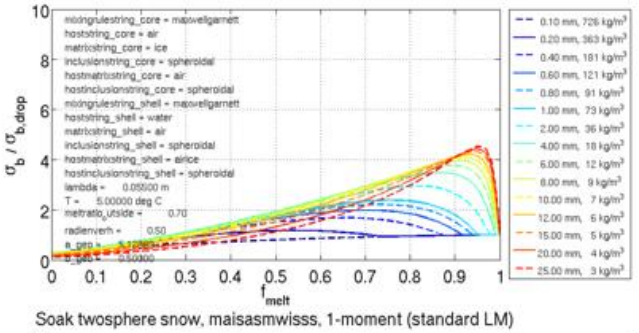
Soak twosphere snow, maisasmnisms, 1-moment (standard LM)



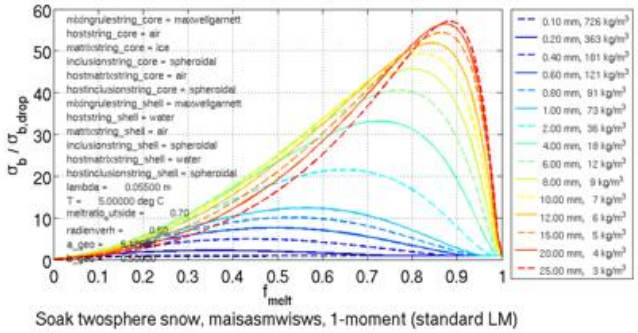
Soak twosphere snow, maisasmnwsms, 1-moment (standard LM)



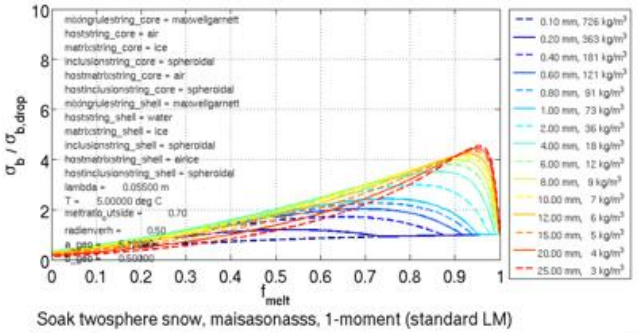
Soak twosphere snow, maisasmwasss, 1-moment (standard LM)



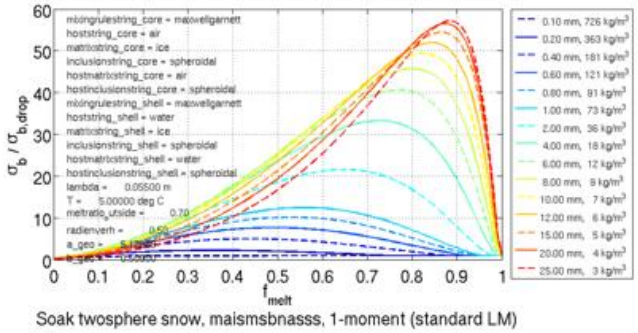
Soak twosphere snow, maisasmwasws, 1-moment (standard LM)



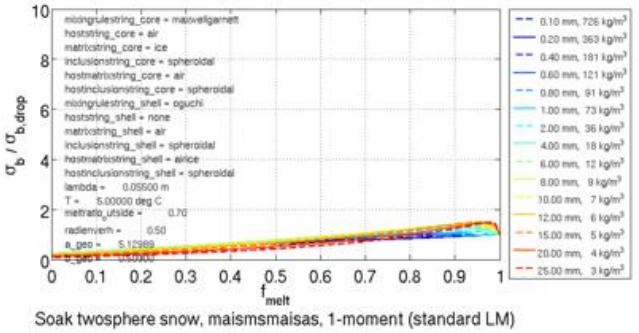
Soak twosphere snow, maisasmwisss, 1-moment (standard LM)



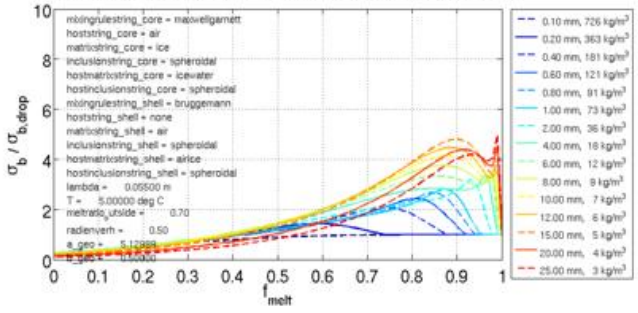
Soak twosphere snow, maisasmwisws, 1-moment (standard LM)



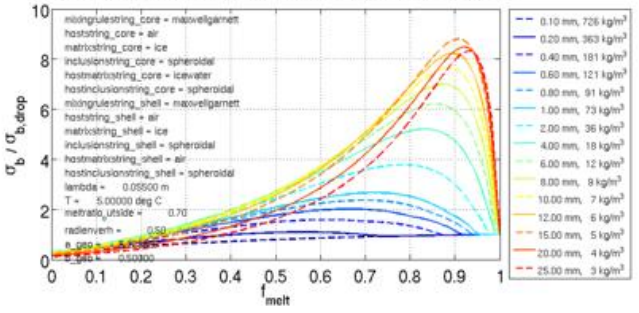
Soak twosphere snow, maisasonasss, 1-moment (standard LM)



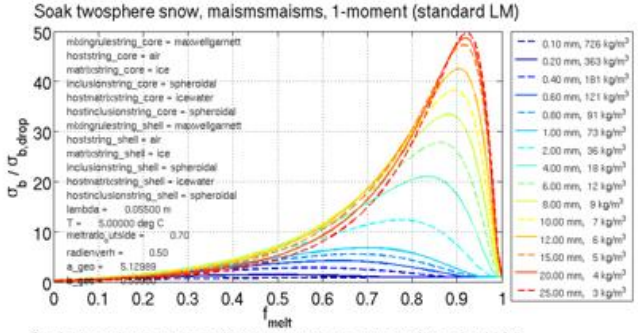
Soak twosphere snow, maismsbnasss, 1-moment (standard LM)



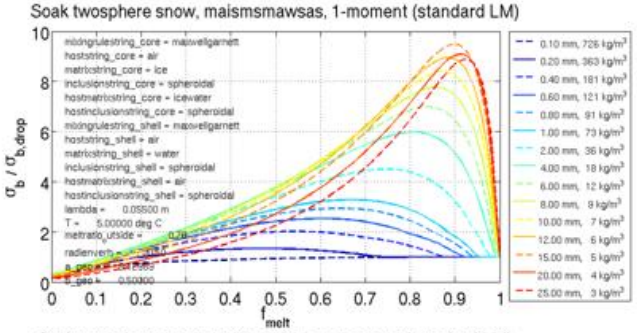
Soak twosphere snow, maismsmaisas, 1-moment (standard LM)



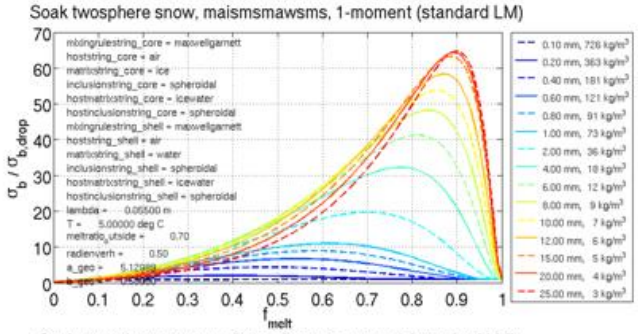
Soak twosphere snow, maismsmaisms, 1-moment (standard LM)



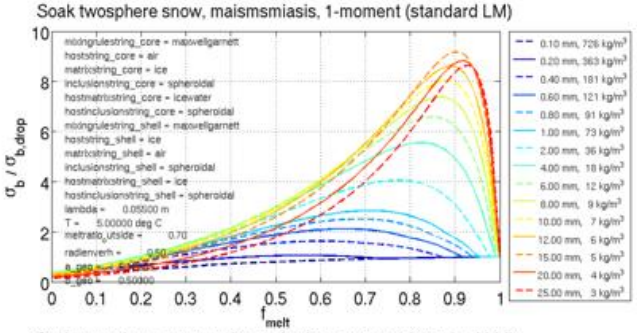
Soak twosphere snow, maismsmawsas, 1-moment (standard LM)



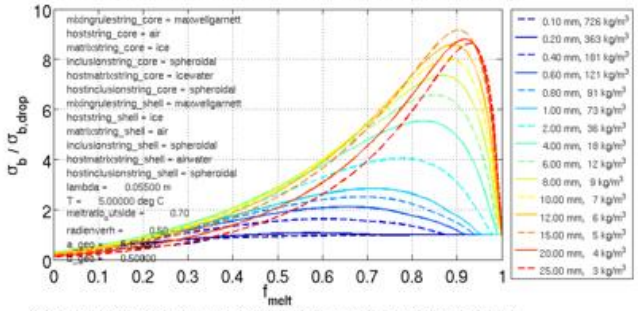
Soak twosphere snow, maismsmawsms, 1-moment (standard LM)



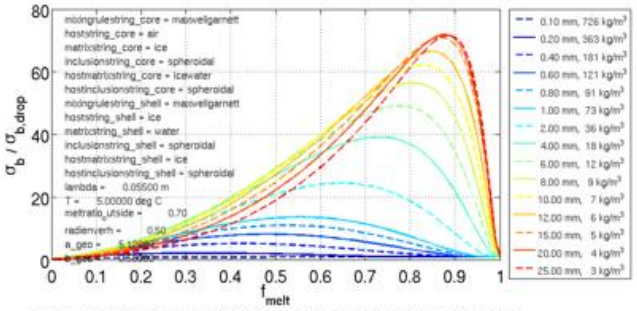
Soak twosphere snow, maismsmiasis, 1-moment (standard LM)



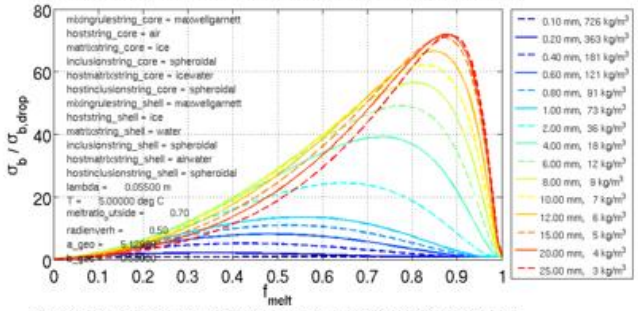
Soak twosphere snow, maismsmiasrs, 1-moment (standard LM)



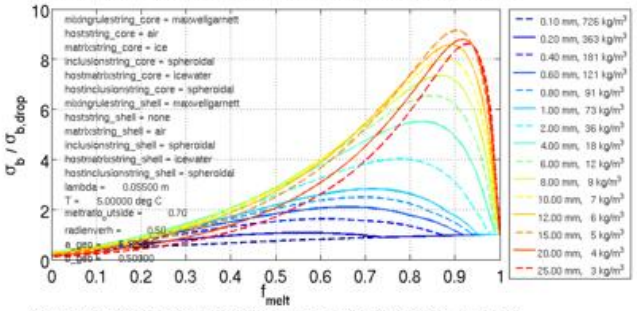
Soak twosphere snow, maismsmiwsis, 1-moment (standard LM)



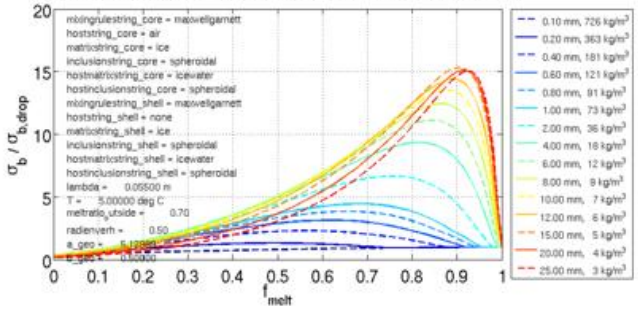
Soak twosphere snow, maismsmiwsrs, 1-moment (standard LM)



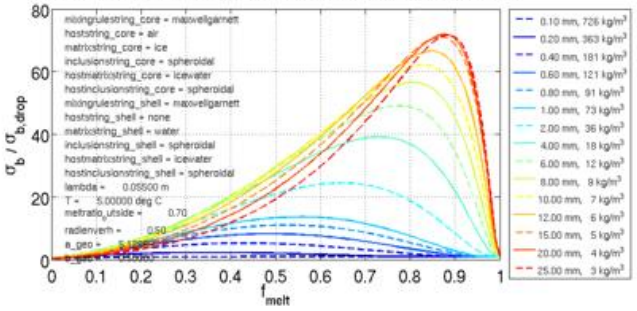
Soak twosphere snow, maismsmnasms, 1-moment (standard LM)



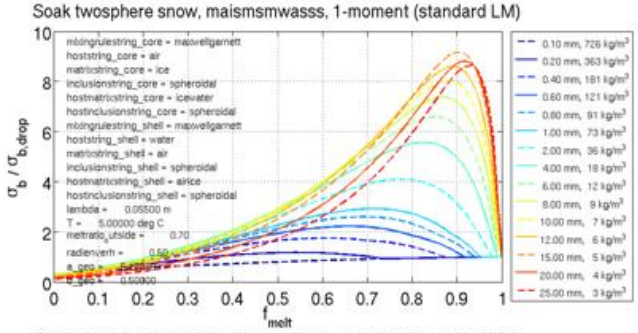
Soak twosphere snow, maismsmnisms, 1-moment (standard LM)



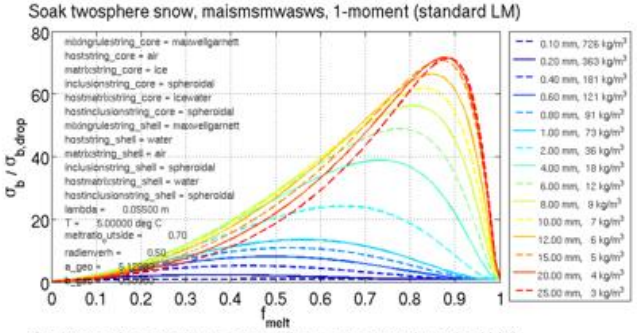
Soak twosphere snow, maismsmnwsms, 1-moment (standard LM)



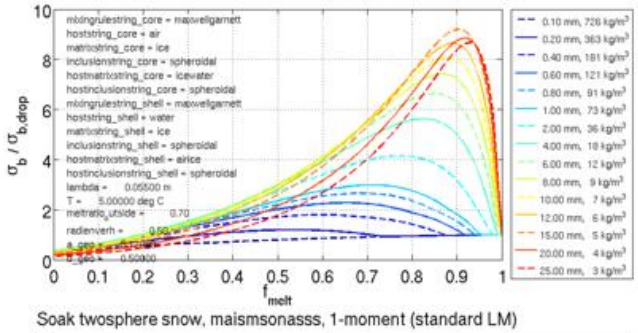
Soak twosphere snow, maismsmwasss, 1-moment (standard LM)



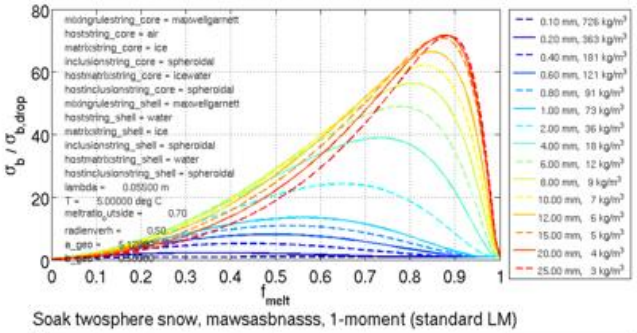
Soak twosphere snow, maismsmwasws, 1-moment (standard LM)



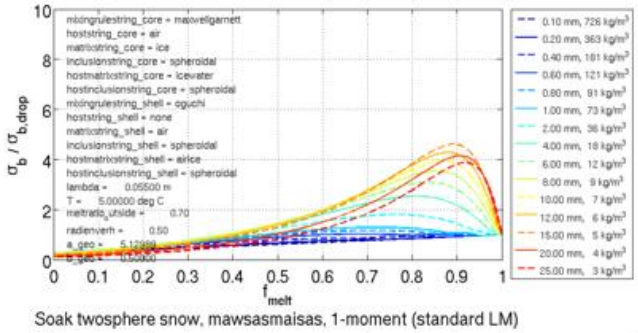
Soak twosphere snow, maismsmwisss, 1-moment (standard LM)



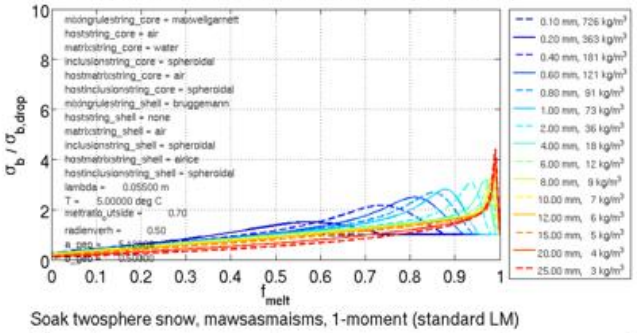
Soak twosphere snow, maismsmwisws, 1-moment (standard LM)



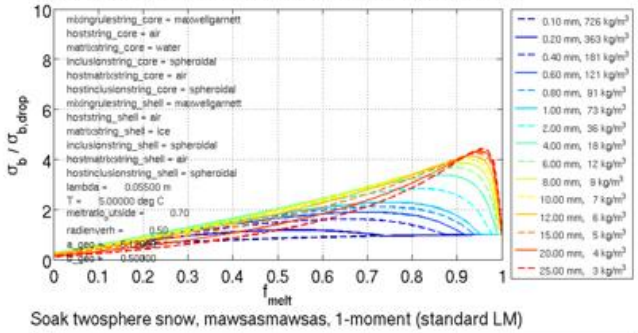
Soak twosphere snow, maismsonasss, 1-moment (standard LM)



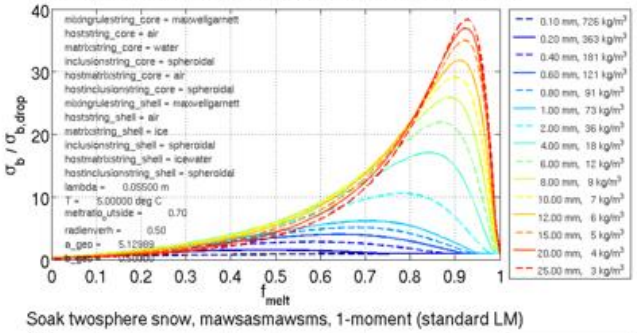
Soak twosphere snow, mawsasbnasss, 1-moment (standard LM)



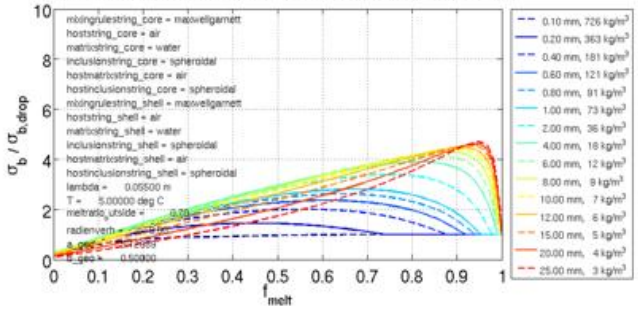
Soak twosphere snow, mawsasmaisas, 1-moment (standard LM)



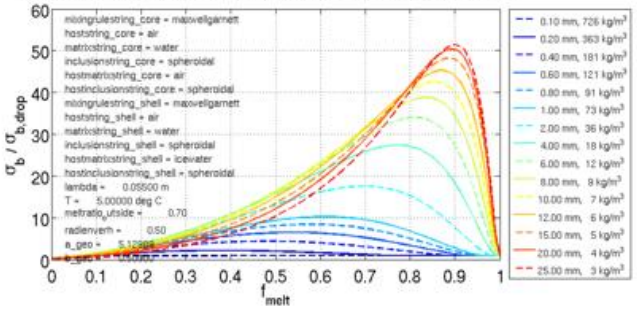
Soak twosphere snow, mawsasmaisms, 1-moment (standard LM)



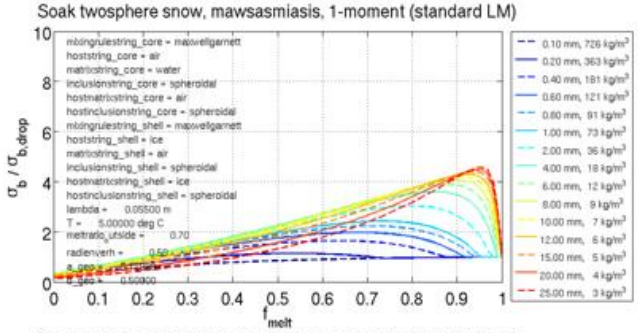
Soak twosphere snow, mawsasmawsas, 1-moment (standard LM)



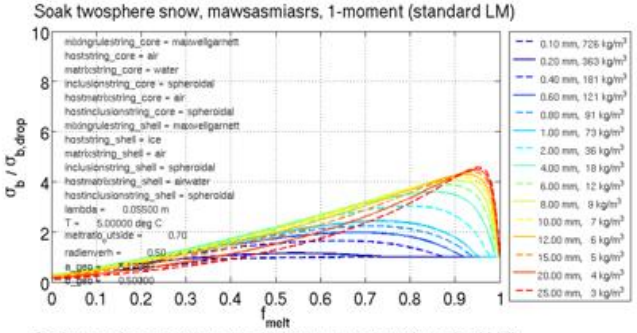
Soak twosphere snow, mawsasmawsms, 1-moment (standard LM)



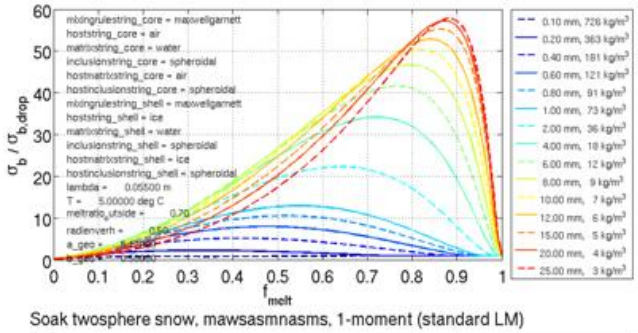
Soak twosphere snow, mawsasmiasis, 1-moment (standard LM)



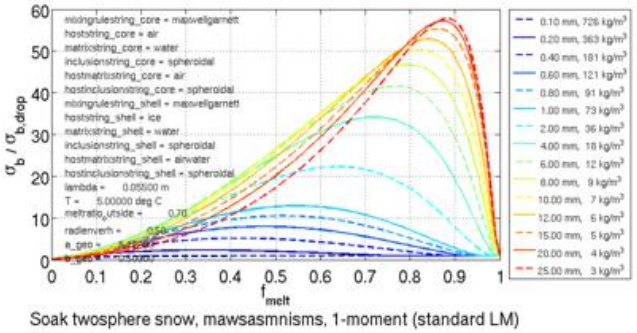
Soak twosphere snow, mawsasmiasrs, 1-moment (standard LM)



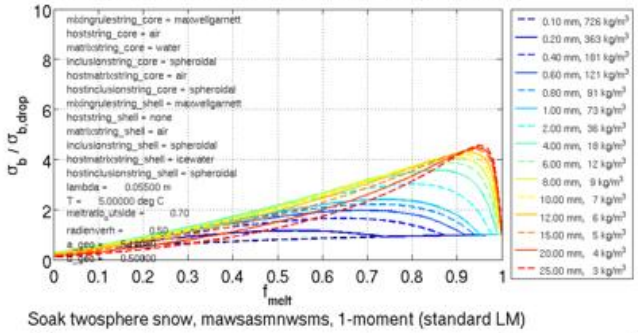
Soak twosphere snow, mawsasmiwsis, 1-moment (standard LM)



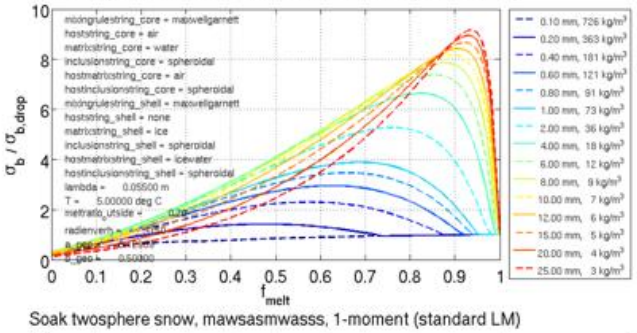
Soak twosphere snow, mawsasmiwsrs, 1-moment (standard LM)



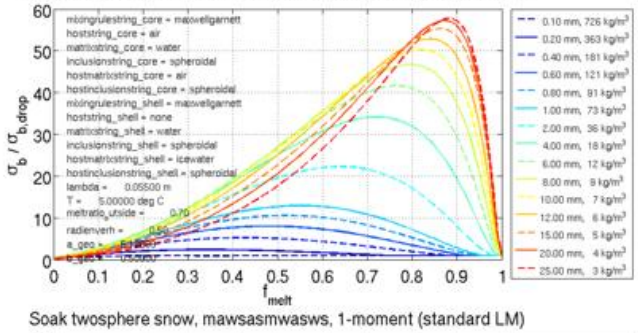
Soak twosphere snow, mawsasmnasms, 1-moment (standard LM)



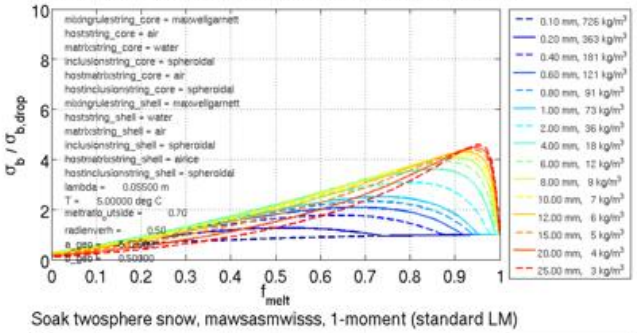
Soak twosphere snow, mawsasmnisms, 1-moment (standard LM)



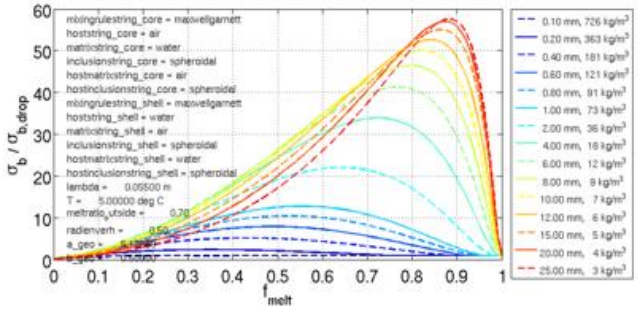
Soak twosphere snow, mawsasmnwsms, 1-moment (standard LM)



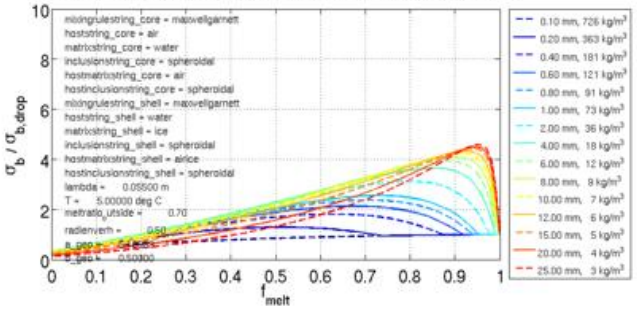
Soak twosphere snow, mawsasmwasss, 1-moment (standard LM)



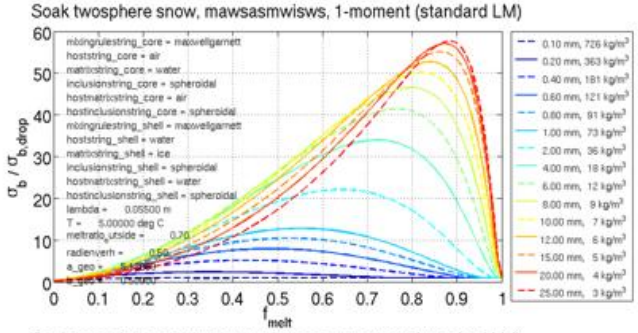
Soak twosphere snow, mawsasmwasws, 1-moment (standard LM)



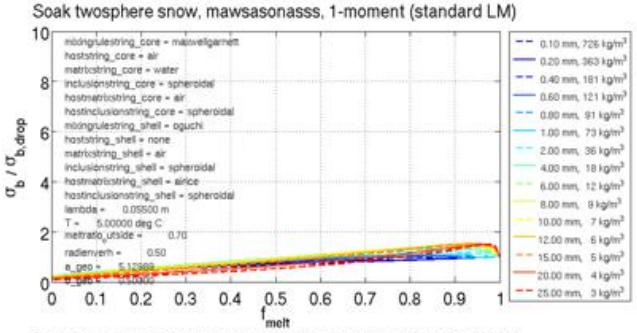
Soak twosphere snow, mawsasmwisss, 1-moment (standard LM)



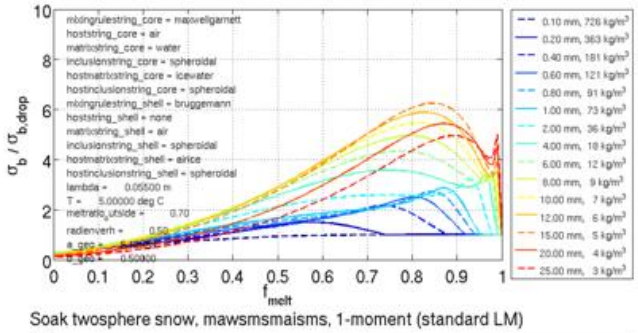
Soak twosphere snow, mawsasmwisws, 1-moment (standard LM)



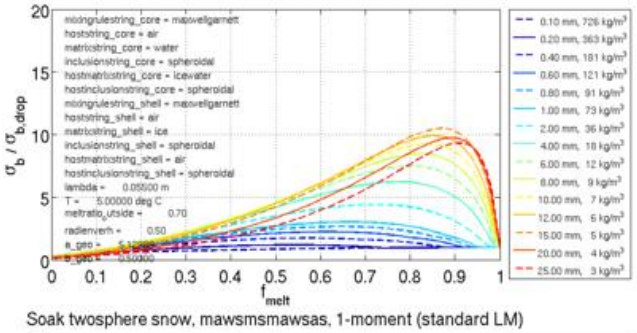
Soak twosphere snow, mawsasonasss, 1-moment (standard LM)



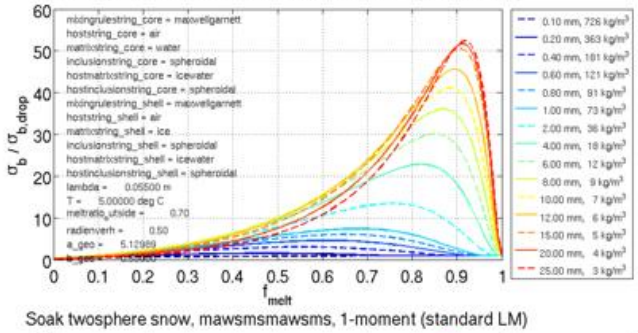
Soak twosphere snow, mawsmsbnasss, 1-moment (standard LM)



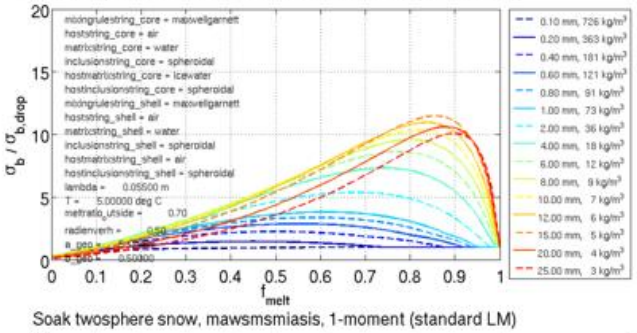
Soak twosphere snow, mawsmsmaisas, 1-moment (standard LM)



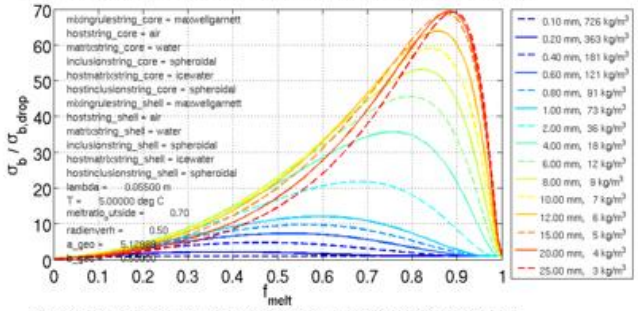
Soak twosphere snow, mawsmsmaisms, 1-moment (standard LM)



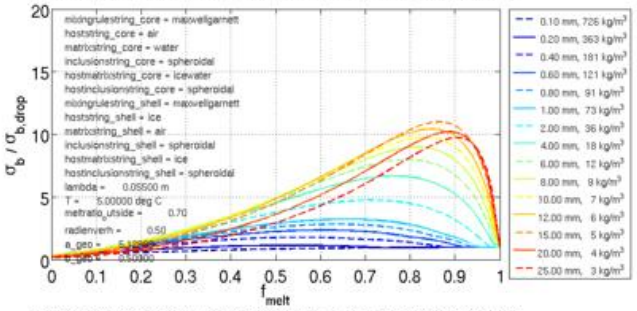
Soak twosphere snow, mawsmsmawsas, 1-moment (standard LM)



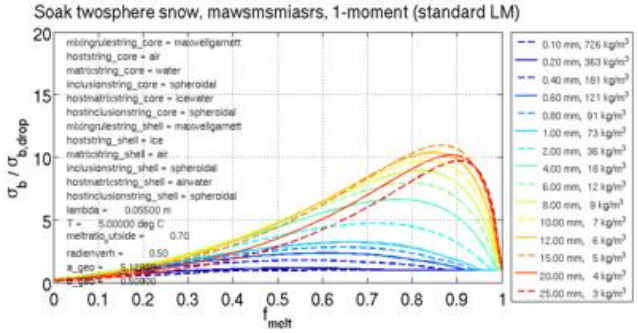
Soak twosphere snow, mawsmsmawsms, 1-moment (standard LM)



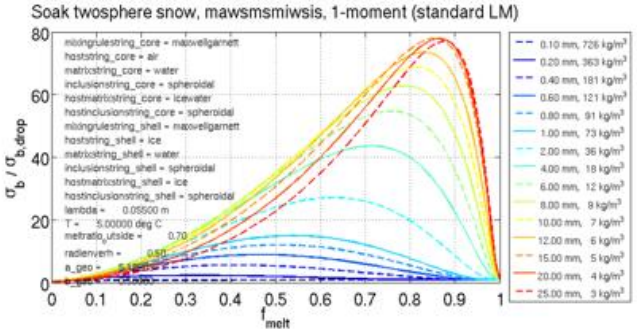
Soak twosphere snow, mawsmsmiasis, 1-moment (standard LM)



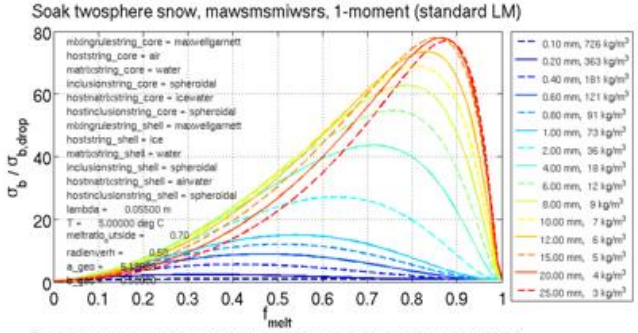
Soak twosphere snow, mawsmsmiasrs, 1-moment (standard LM)



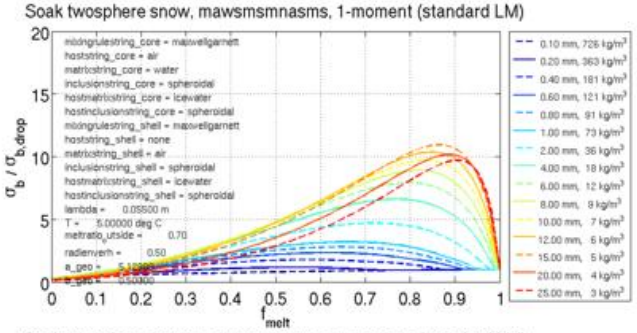
Soak twosphere snow, mawsmsmiwsis, 1-moment (standard LM)



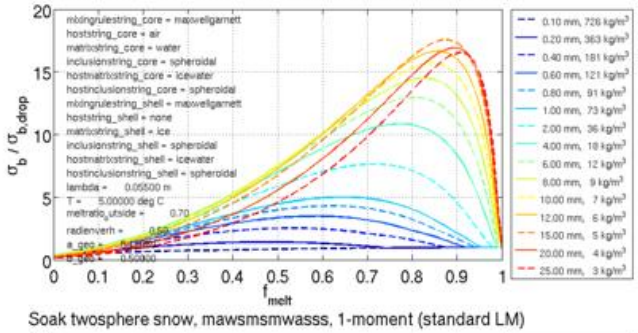
Soak twosphere snow, mawsmsmiwsrs, 1-moment (standard LM)



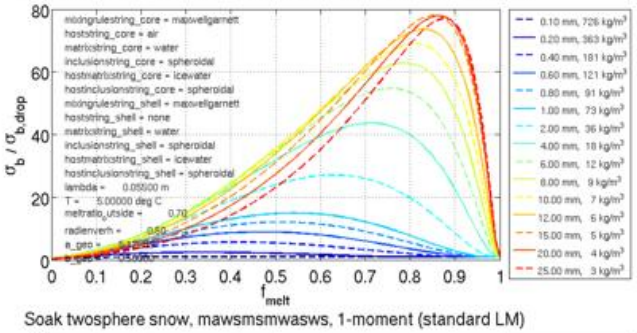
Soak twosphere snow, mawsmsmnasms, 1-moment (standard LM)



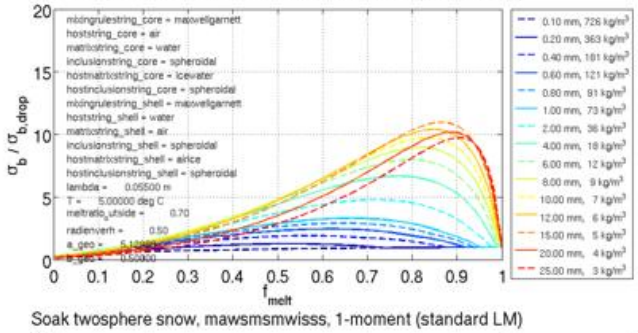
Soak twosphere snow, mawsmsmnisms, 1-moment (standard LM)



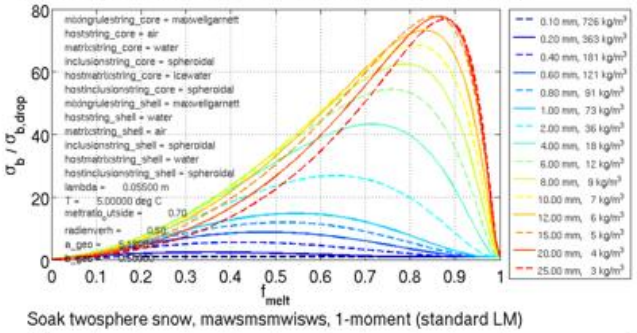
Soak twosphere snow, mawsmsmnwsms, 1-moment (standard LM)



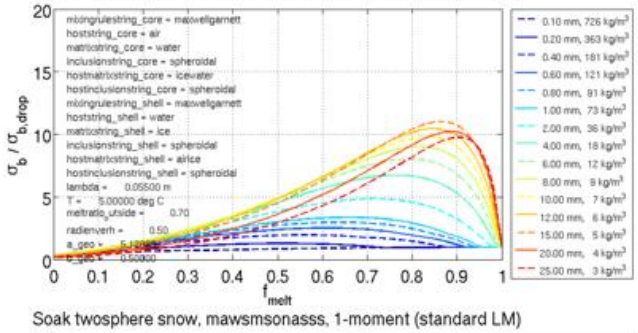
Soak twosphere snow, mawsmsmwasss, 1-moment (standard LM)



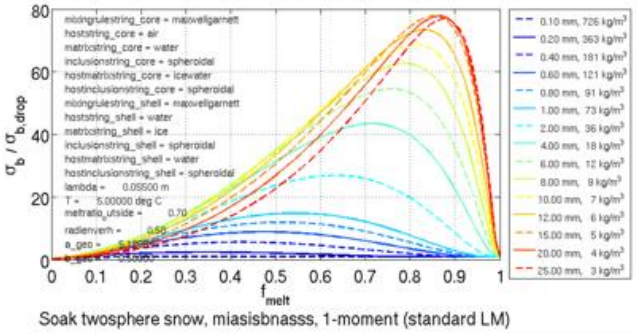
Soak twosphere snow, mawsmsmwasws, 1-moment (standard LM)



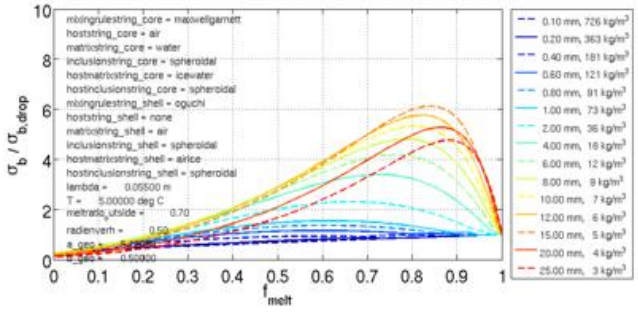
Soak twosphere snow, mawsmsmwisss, 1-moment (standard LM)



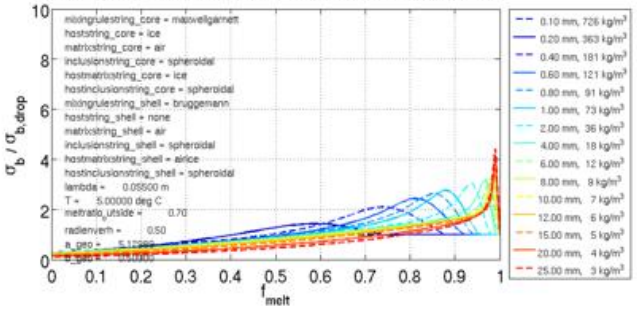
Soak twosphere snow, mawsmsmwisws, 1-moment (standard LM)



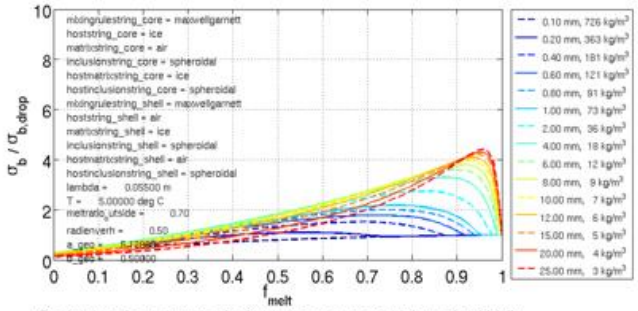
Soak twosphere snow, mawsmsonasss, 1-moment (standard LM)



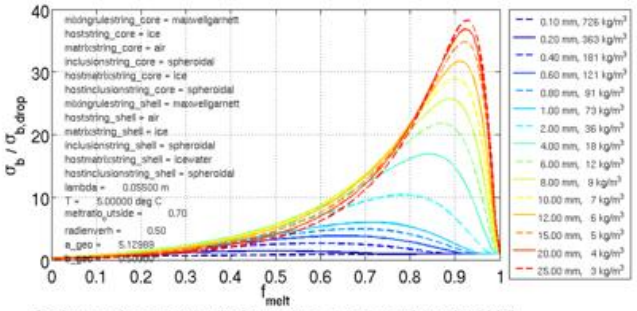
Soak twosphere snow, miasisbnasss, 1-moment (standard LM)



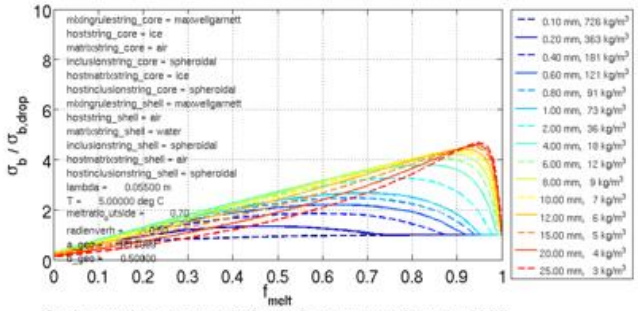
Soak twosphere snow, miasismaisas, 1-moment (standard LM)



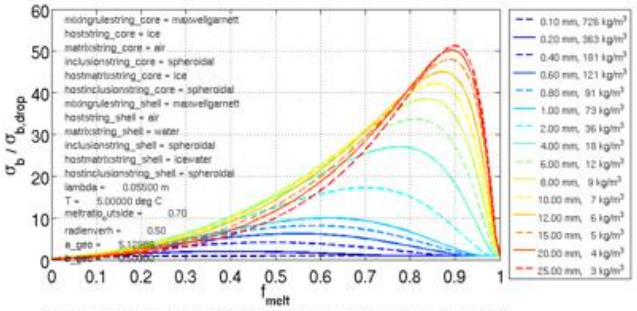
Soak twosphere snow, miasismaisms, 1-moment (standard LM)



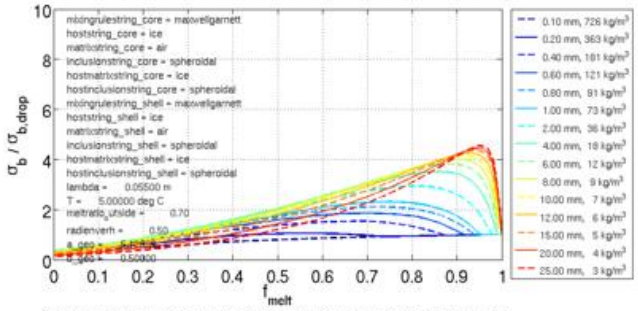
Soak twosphere snow, miasismawsas, 1-moment (standard LM)



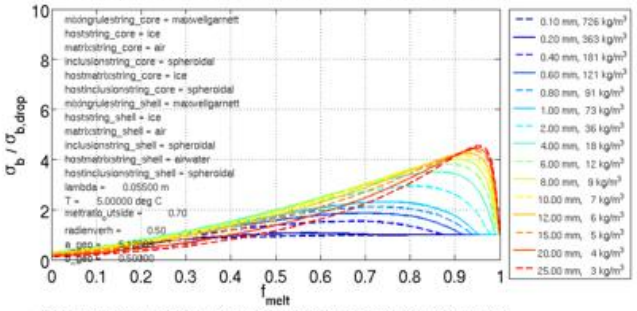
Soak twosphere snow, miasismawsms, 1-moment (standard LM)



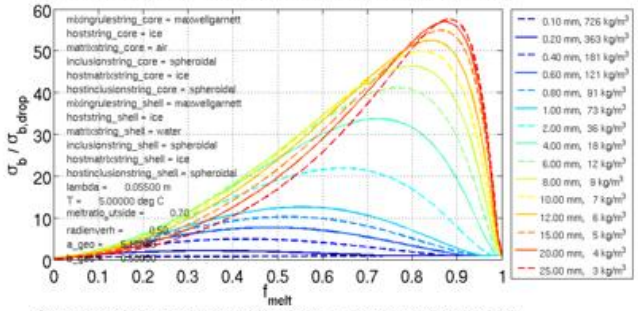
Soak twosphere snow, miasismiasis, 1-moment (standard LM)



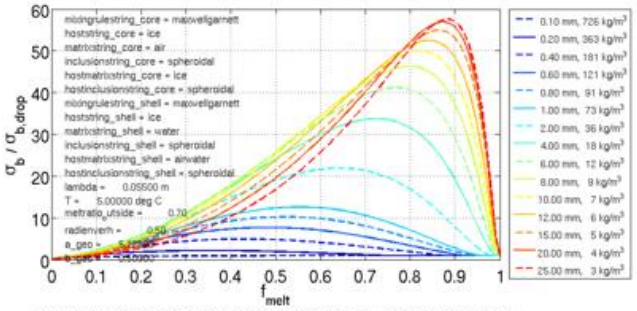
Soak twosphere snow, miasismiasrs, 1-moment (standard LM)



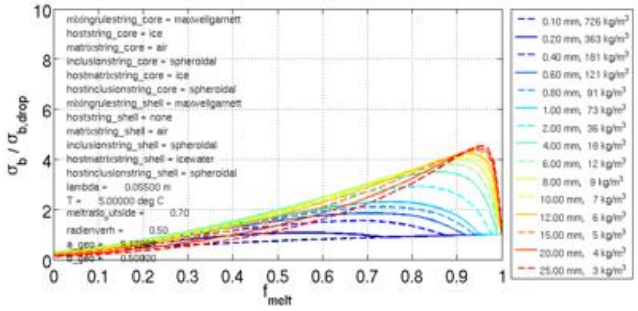
Soak twosphere snow, miasismiwsis, 1-moment (standard LM)



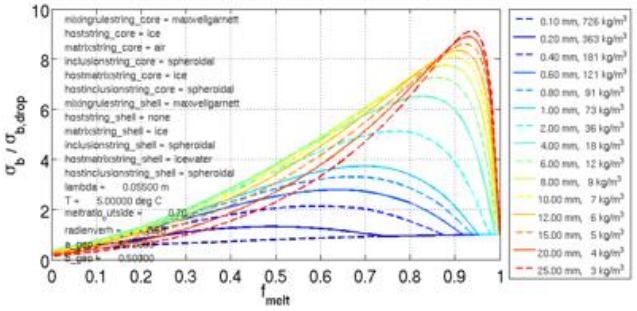
Soak twosphere snow, miasismiwsrs, 1-moment (standard LM)



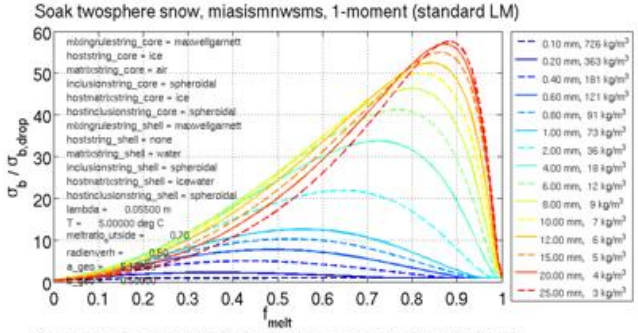
Soak twosphere snow, miasismnasms, 1-moment (standard LM)



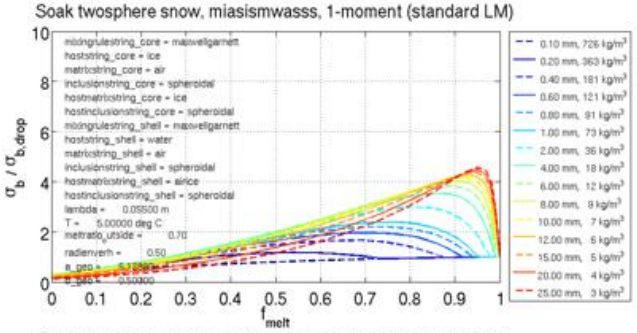
Soak twosphere snow, miasismnisms, 1-moment (standard LM)



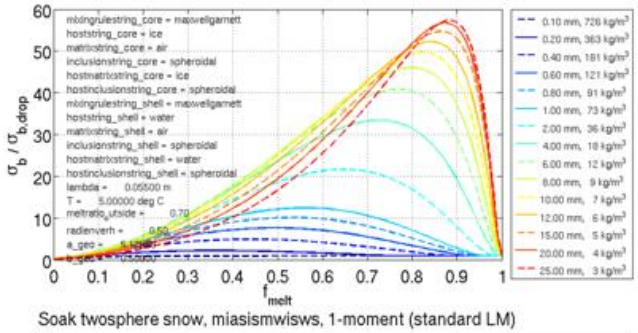
Soak twosphere snow, miasismnwsms, 1-moment (standard LM)



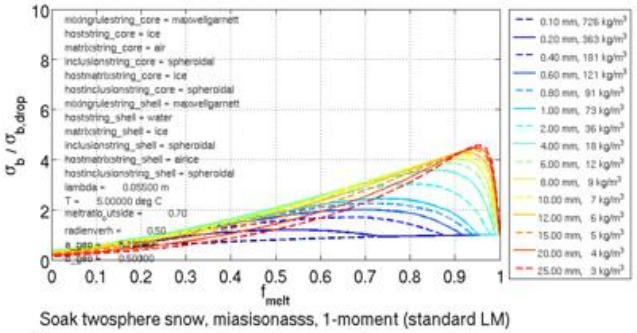
Soak twosphere snow, miasismwasss, 1-moment (standard LM)



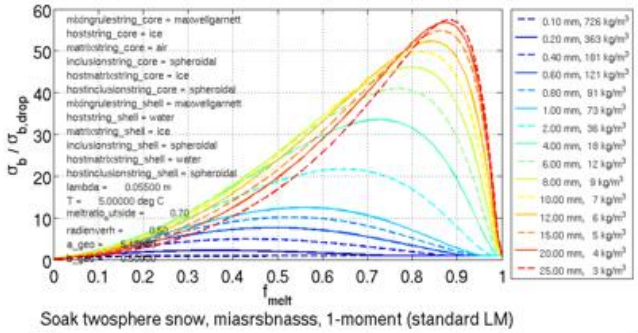
Soak twosphere snow, miasismwasws, 1-moment (standard LM)



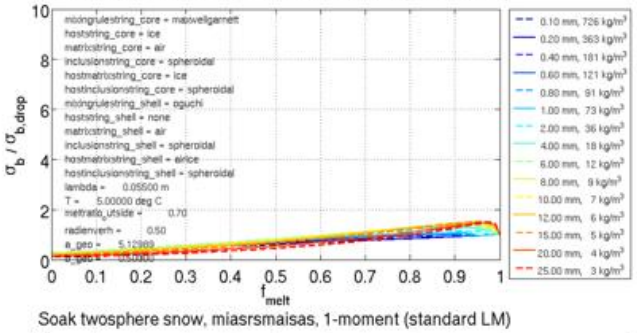
Soak twosphere snow, miasismwisss, 1-moment (standard LM)



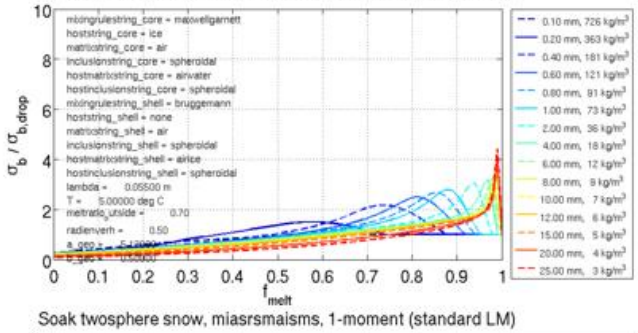
Soak twosphere snow, miasismwisws, 1-moment (standard LM)



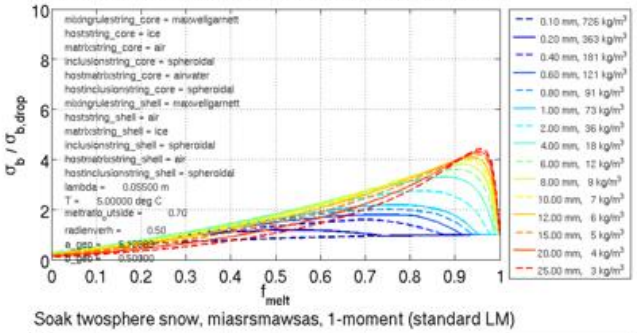
Soak twosphere snow, miasisonasss, 1-moment (standard LM)



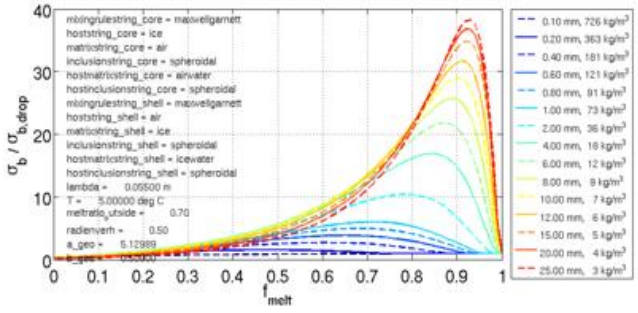
Soak twosphere snow, miasrsbnasss, 1-moment (standard LM)



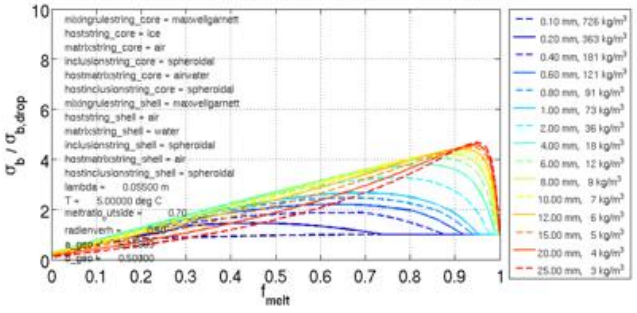
Soak twosphere snow, miasrsmaisas, 1-moment (standard LM)



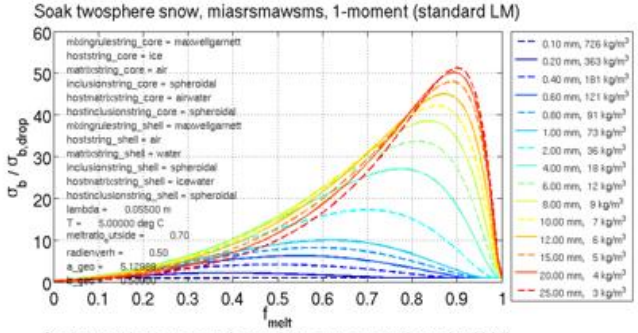
Soak twosphere snow, miasrsmaisms, 1-moment (standard LM)



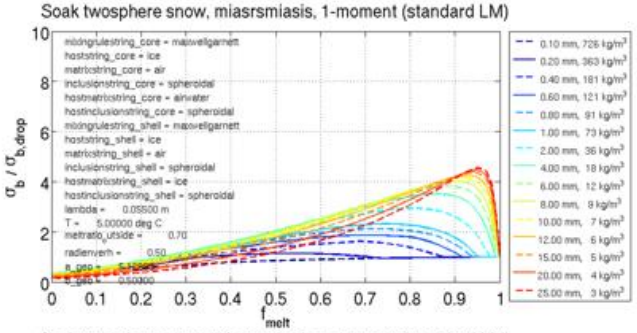
Soak twosphere snow, miasrsmawsas, 1-moment (standard LM)



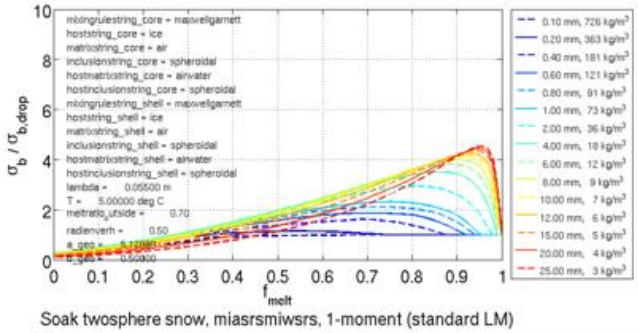
Soak twosphere snow, miasrsmawsms, 1-moment (standard LM)



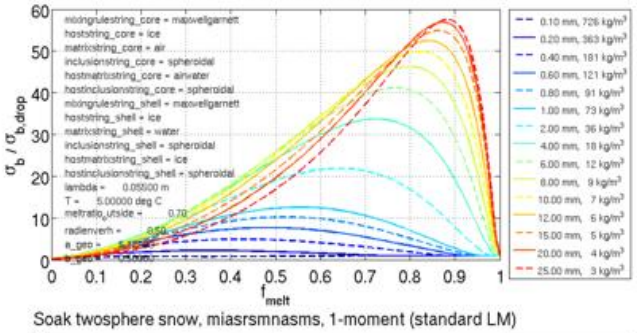
Soak twosphere snow, miasrsmiasis, 1-moment (standard LM)



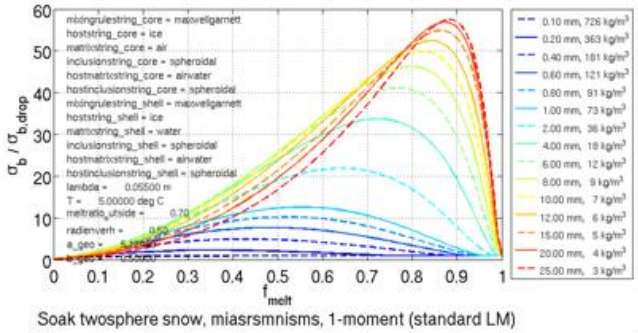
Soak twosphere snow, miasrsmiasrs, 1-moment (standard LM)



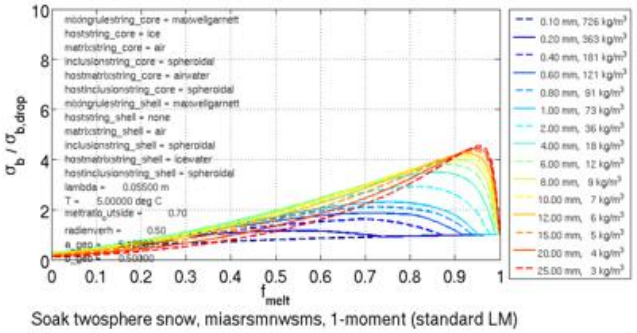
Soak twosphere snow, miasrsmiwsis, 1-moment (standard LM)



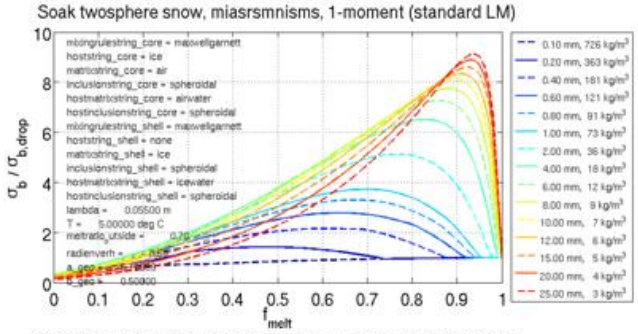
Soak twosphere snow, miasrsmiwsrs, 1-moment (standard LM)



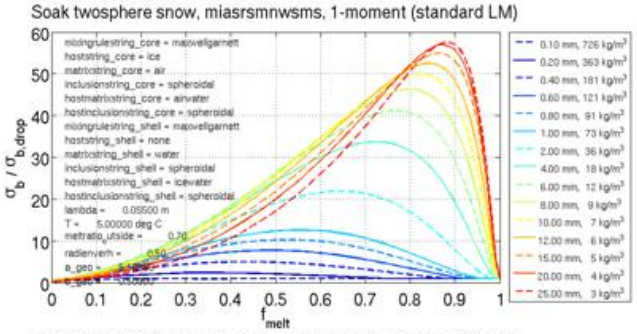
Soak twosphere snow, miasrsmnasms, 1-moment (standard LM)



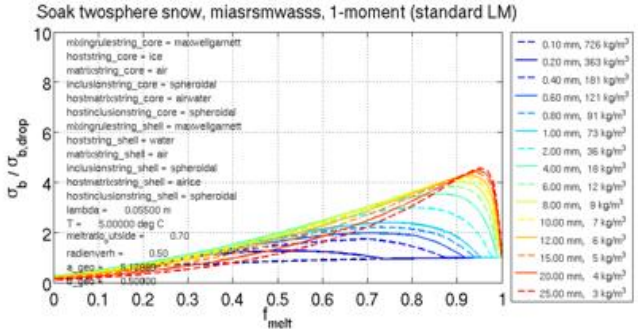
Soak twosphere snow, miasrsmnisms, 1-moment (standard LM)



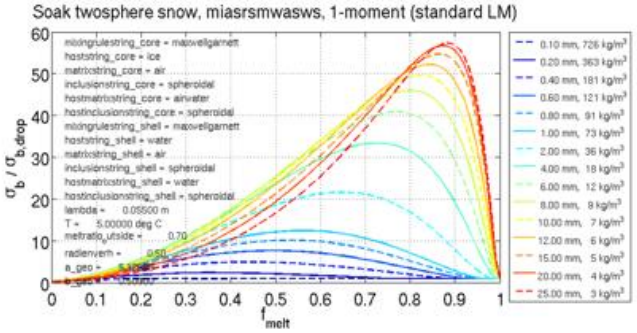
Soak twosphere snow, miasrsmnwsms, 1-moment (standard LM)



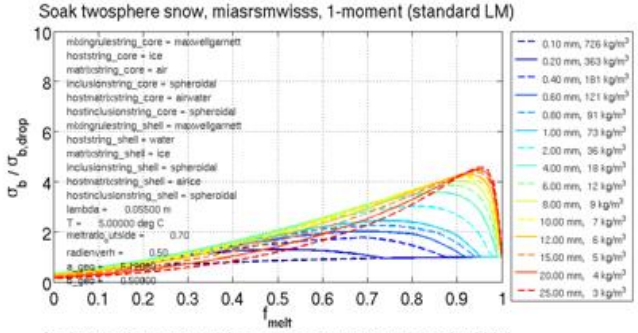
Soak twosphere snow, miasrsmwasss, 1-moment (standard LM)



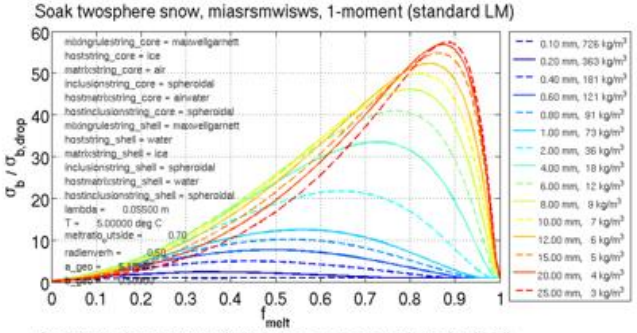
Soak twosphere snow, miasrsmwasws, 1-moment (standard LM)



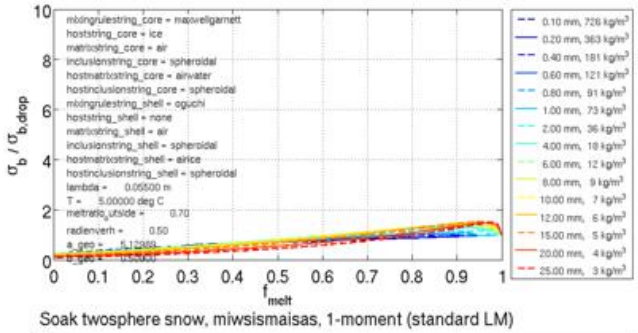
Soak twosphere snow, miasrsmwisss, 1-moment (standard LM)



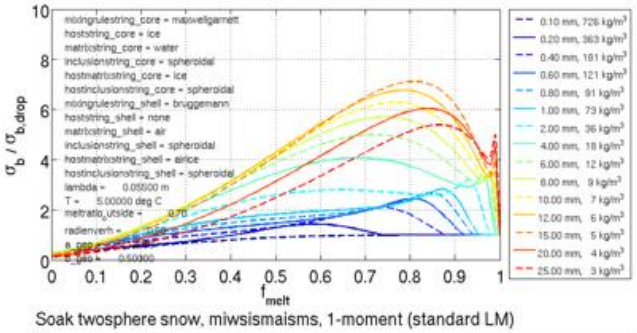
Soak twosphere snow, miasrsmwisws, 1-moment (standard LM)



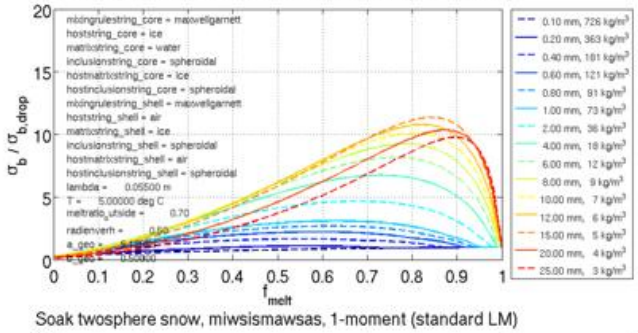
Soak twosphere snow, miasrsonasss, 1-moment (standard LM)



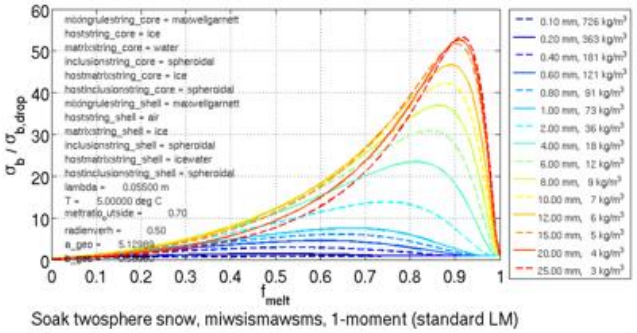
Soak twosphere snow, miwsisbnasss, 1-moment (standard LM)



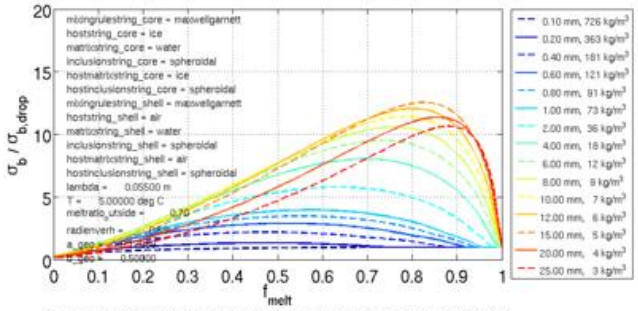
Soak twosphere snow, miwsismaisas, 1-moment (standard LM)



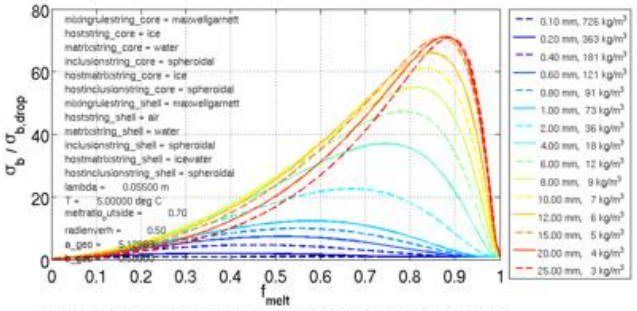
Soak twosphere snow, miwsismaisms, 1-moment (standard LM)



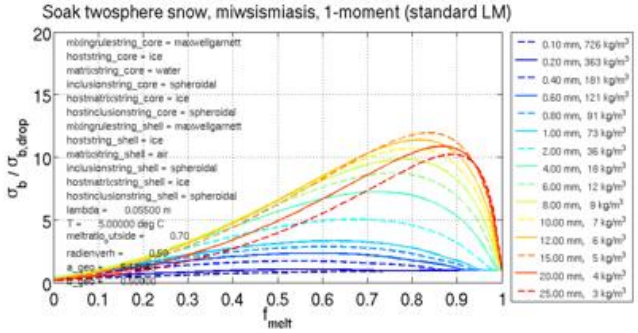
Soak twosphere snow, miwsismawsas, 1-moment (standard LM)



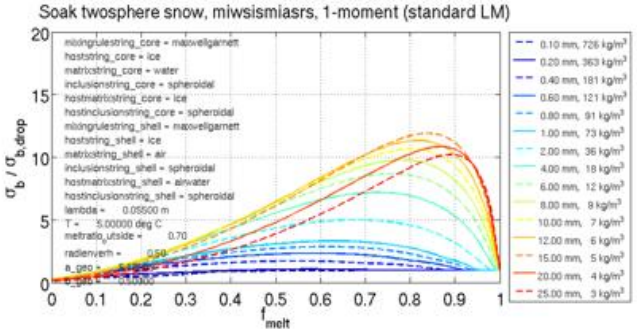
Soak twosphere snow, miwsismawsms, 1-moment (standard LM)



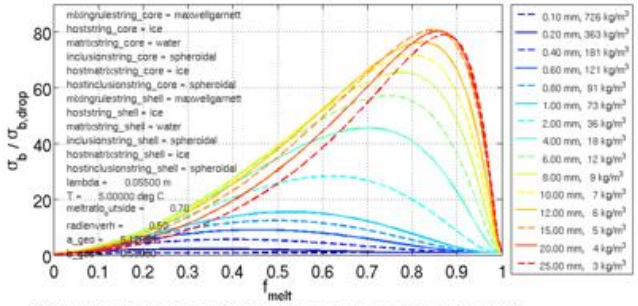
Soak twosphere snow, miwsismiasis, 1-moment (standard LM)



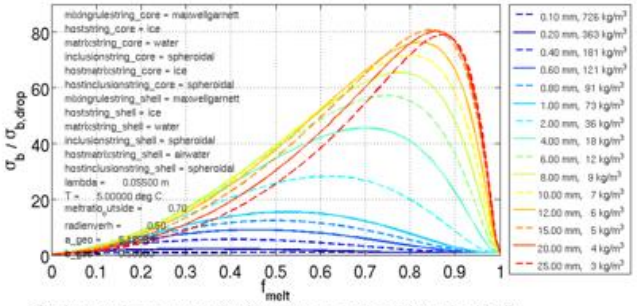
Soak twosphere snow, miwsismiasrs, 1-moment (standard LM)



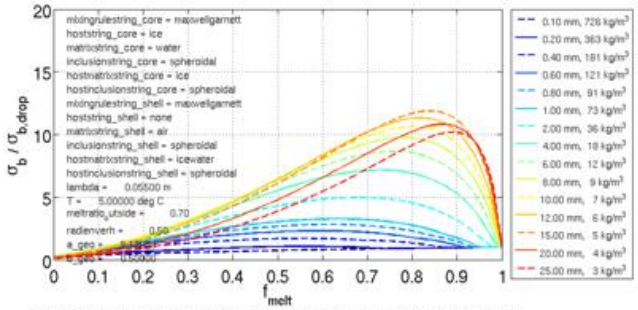
Soak twosphere snow, miwsismiwsis, 1-moment (standard LM)



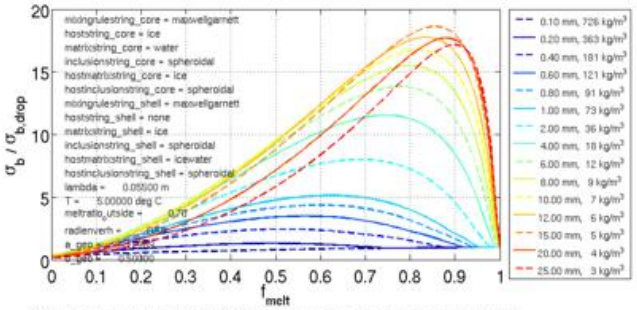
Soak twosphere snow, miwsismiwsrs, 1-moment (standard LM)



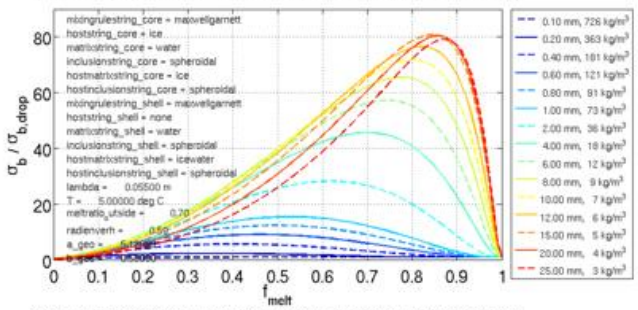
Soak twosphere snow, miwsismnasms, 1-moment (standard LM)



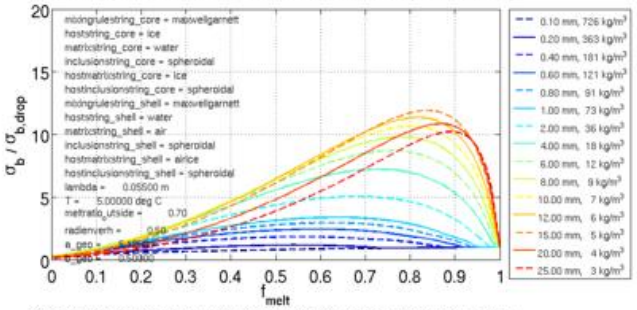
Soak twosphere snow, miwsismnisms, 1-moment (standard LM)



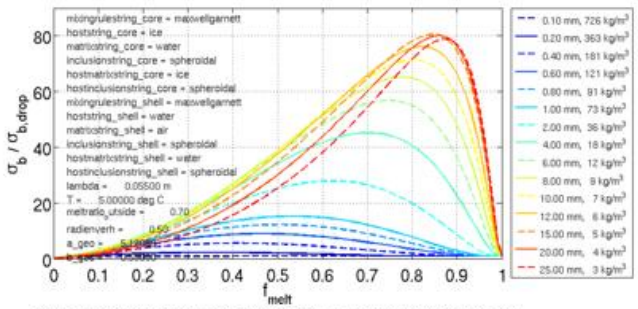
Soak twosphere snow, miwsismnwsms, 1-moment (standard LM)



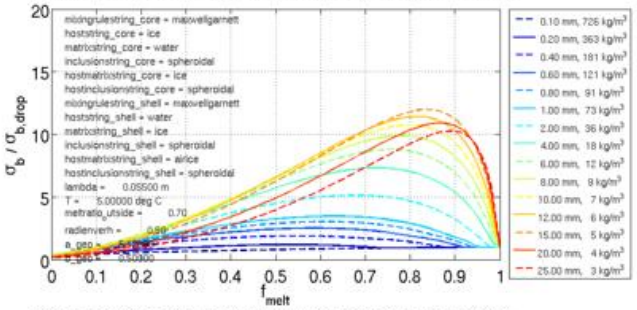
Soak twosphere snow, miwsismwasss, 1-moment (standard LM)



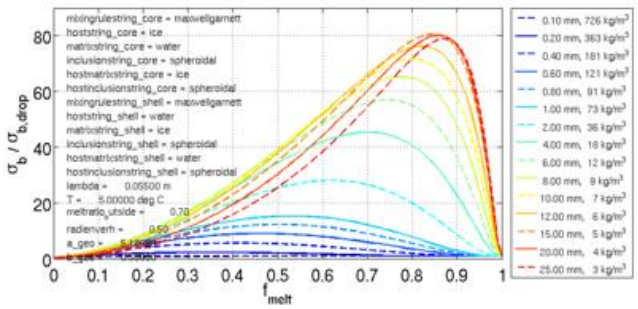
Soak twosphere snow, miwsismwasws, 1-moment (standard LM)



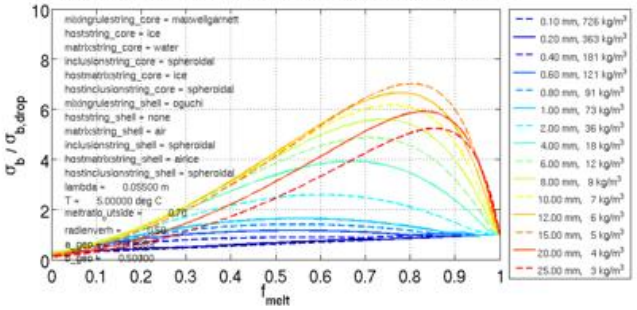
Soak twosphere snow, miwsismwisss, 1-moment (standard LM)



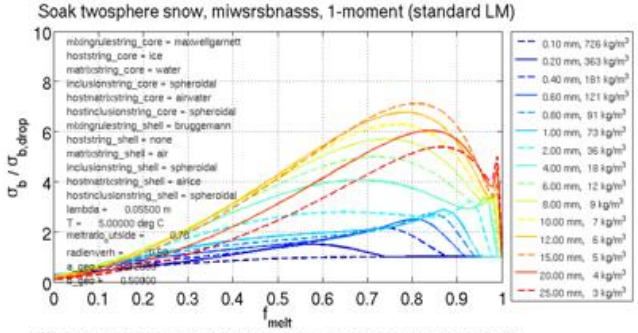
Soak twosphere snow, miwsismwisws, 1-moment (standard LM)



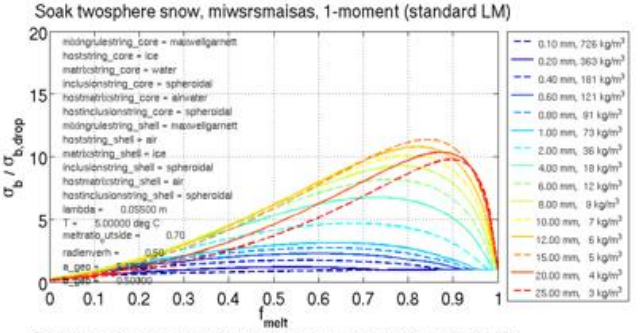
Soak twosphere snow, miwsisonasss, 1-moment (standard LM)



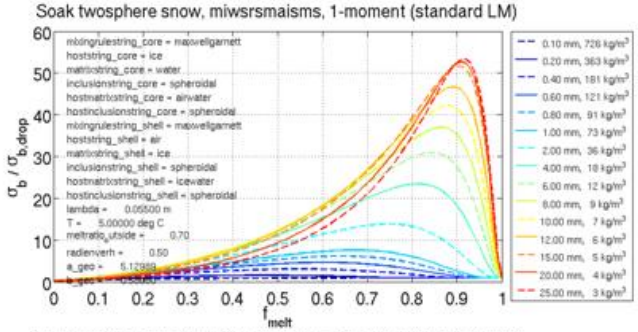
Soak twosphere snow, miwsrsbnasss, 1-moment (standard LM)



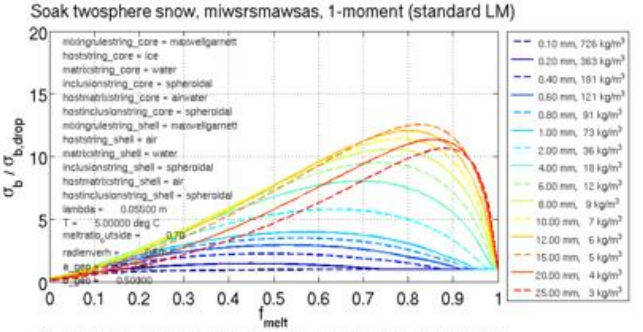
Soak twosphere snow, miwsrsmaisas, 1-moment (standard LM)



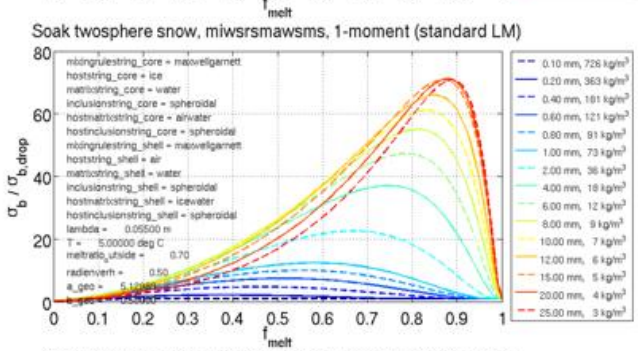
Soak twosphere snow, miwsrsmaisms, 1-moment (standard LM)



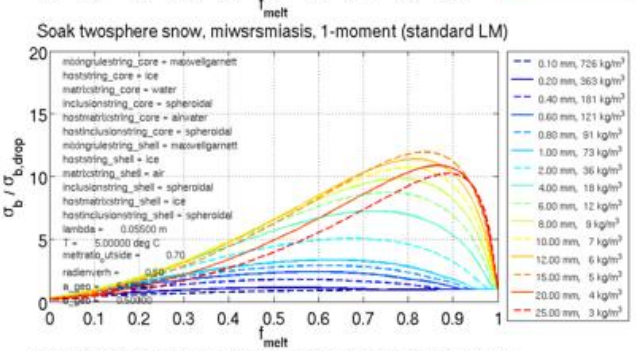
Soak twosphere snow, miwsrsmawsas, 1-moment (standard LM)



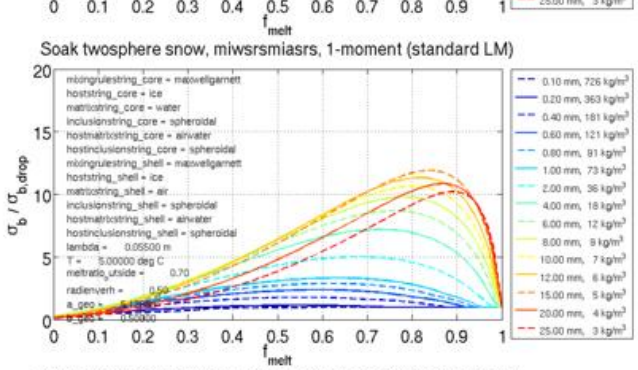
Soak twosphere snow, miwsrsmawsms, 1-moment (standard LM)



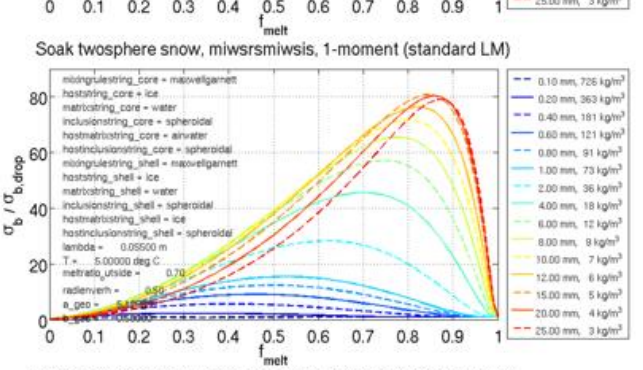
Soak twosphere snow, miwsrsmiasis, 1-moment (standard LM)



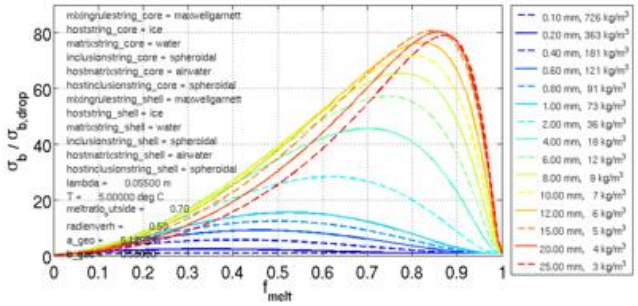
Soak twosphere snow, miwsrsmiasrs, 1-moment (standard LM)



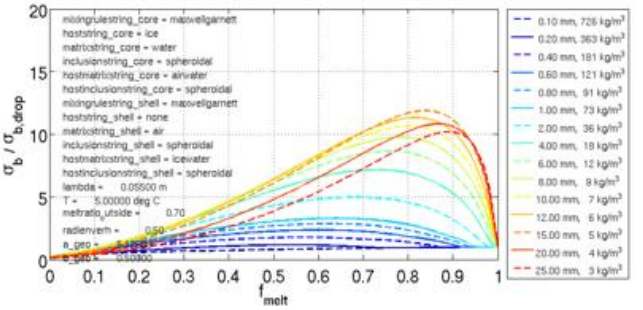
Soak twosphere snow, miwsrsmiwsis, 1-moment (standard LM)



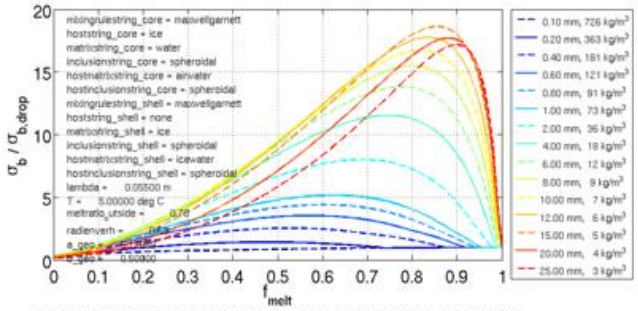
Soak twosphere snow, miwsrsmiwsrs, 1-moment (standard LM)



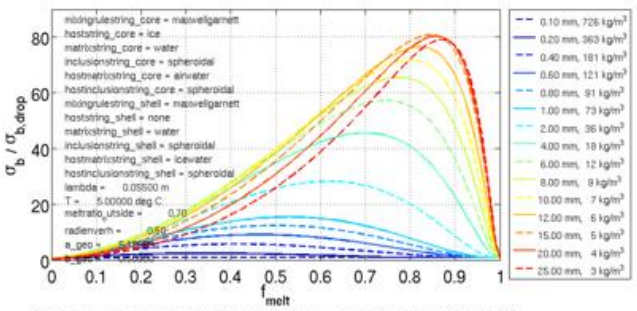
Soak twosphere snow, miwsrsmnasms, 1-moment (standard LM)



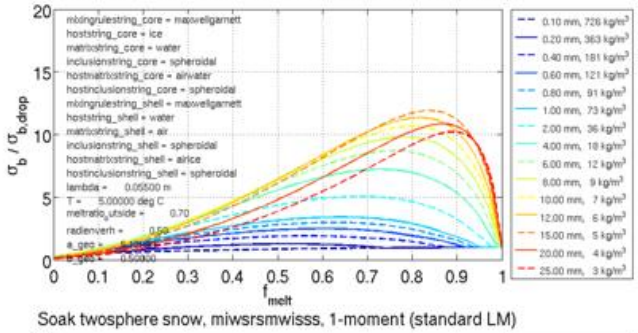
Soak twosphere snow, miwsrsmnisms, 1-moment (standard LM)



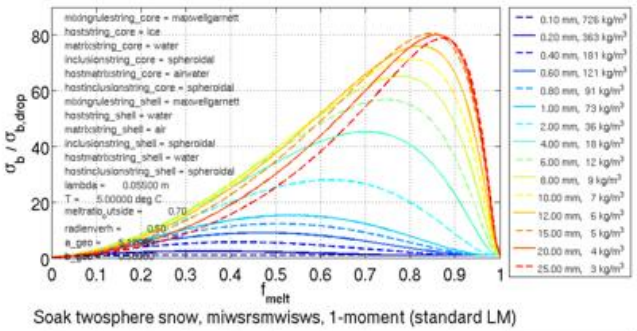
Soak twosphere snow, miwsrsmnwsms, 1-moment (standard LM)



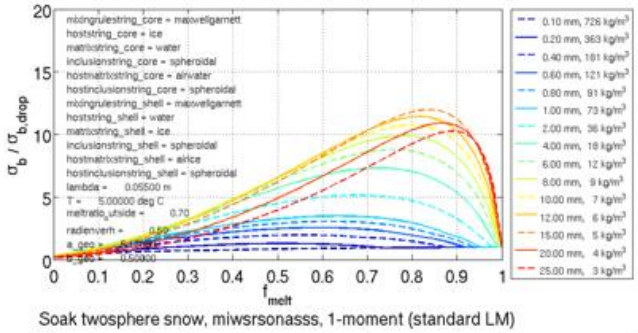
Soak twosphere snow, miwsrsmwasss, 1-moment (standard LM)



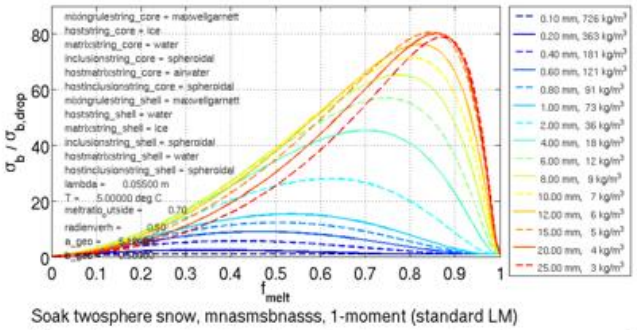
Soak twosphere snow, miwsrsmwasws, 1-moment (standard LM)



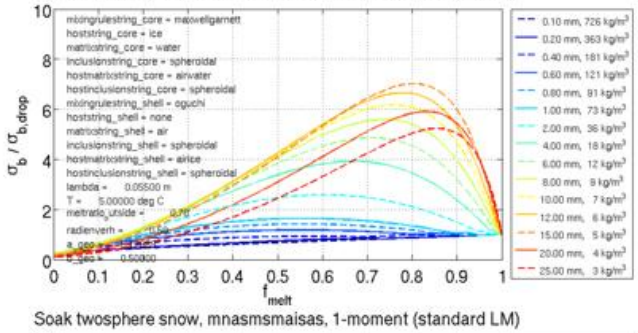
Soak twosphere snow, miwsrsmwisss, 1-moment (standard LM)



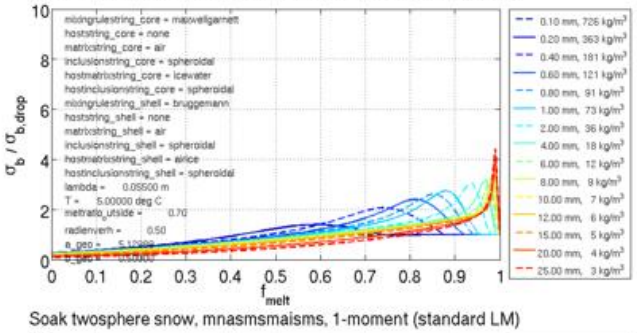
Soak twosphere snow, miwsrsmwisws, 1-moment (standard LM)



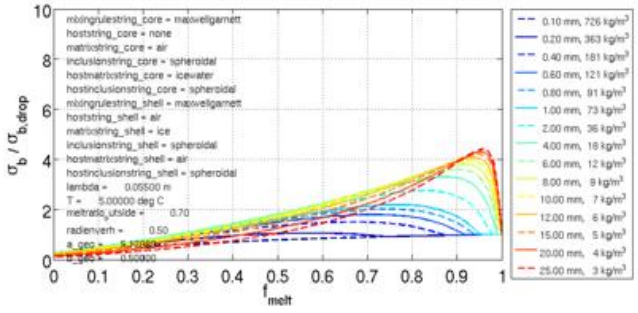
Soak twosphere snow, miwsrsonasss, 1-moment (standard LM)



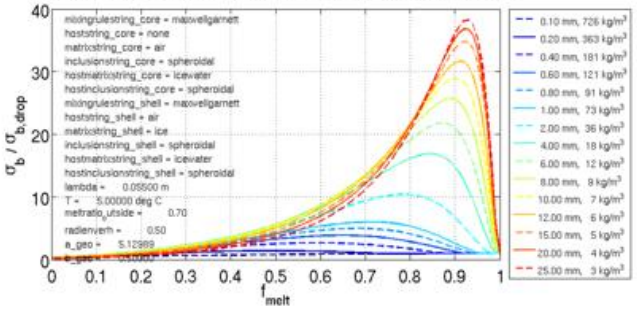
Soak twosphere snow, mnasmsbnasss, 1-moment (standard LM)



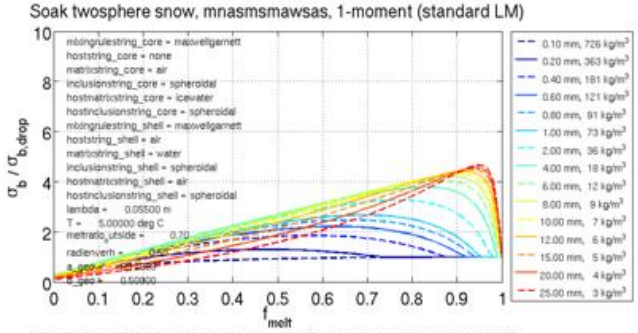
Soak twosphere snow, mnasmsmaisas, 1-moment (standard LM)



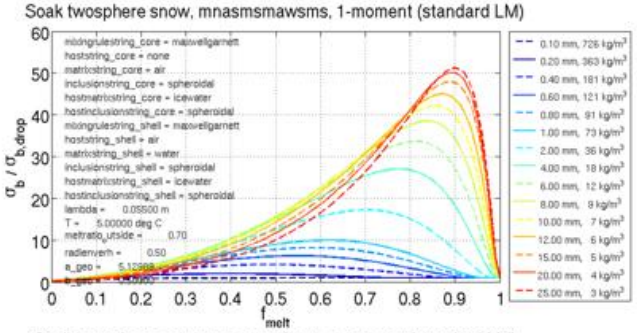
Soak twosphere snow, mnasmsmaisms, 1-moment (standard LM)



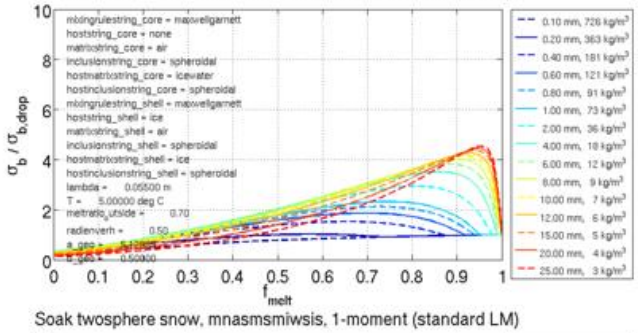
Soak twosphere snow, mnasmsmawsas, 1-moment (standard LM)



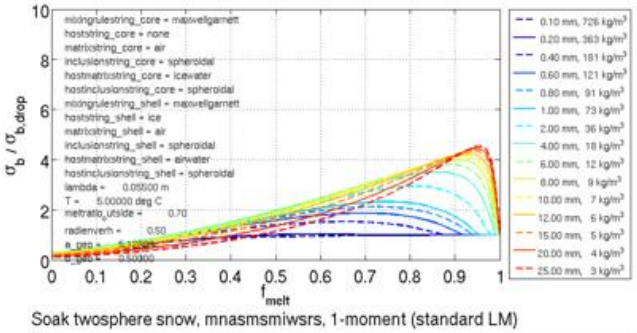
Soak twosphere snow, mnasmsmawsms, 1-moment (standard LM)



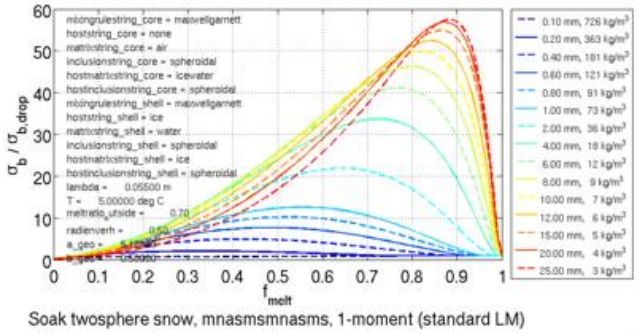
Soak twosphere snow, mnasmsmiasis, 1-moment (standard LM)



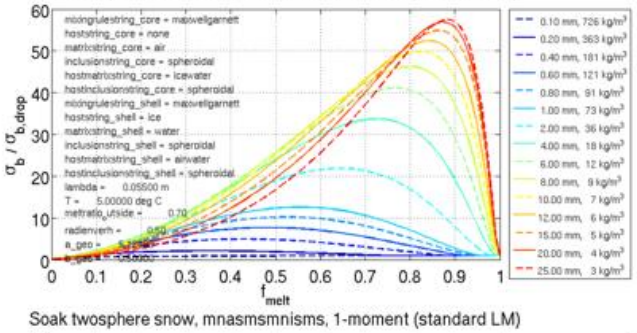
Soak twosphere snow, mnasmsmiasrs, 1-moment (standard LM)



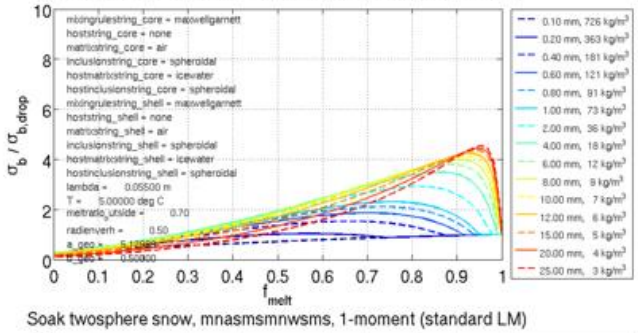
Soak twosphere snow, mnasmsmiwsis, 1-moment (standard LM)



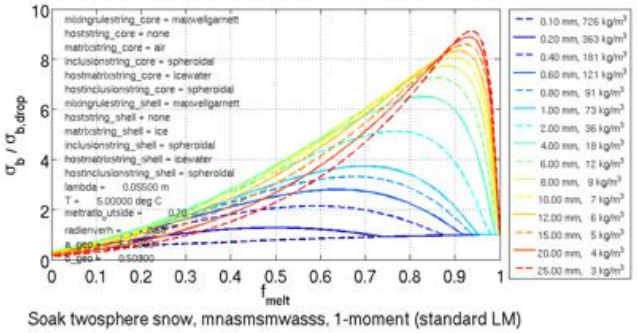
Soak twosphere snow, mnasmsmiwsrs, 1-moment (standard LM)



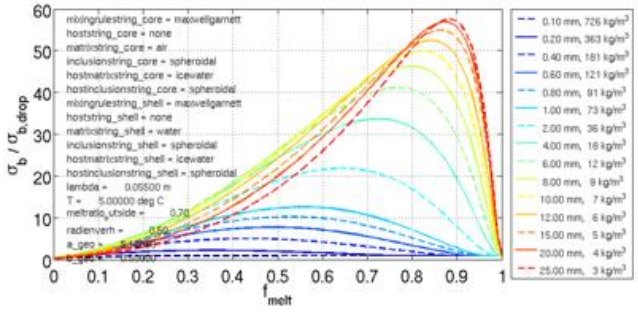
Soak twosphere snow, mnasmsmnasms, 1-moment (standard LM)



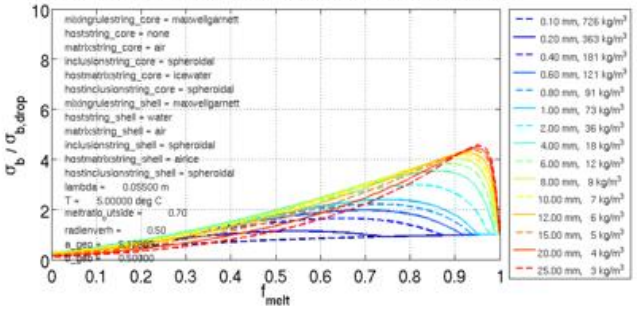
Soak twosphere snow, mnasmsmnisms, 1-moment (standard LM)



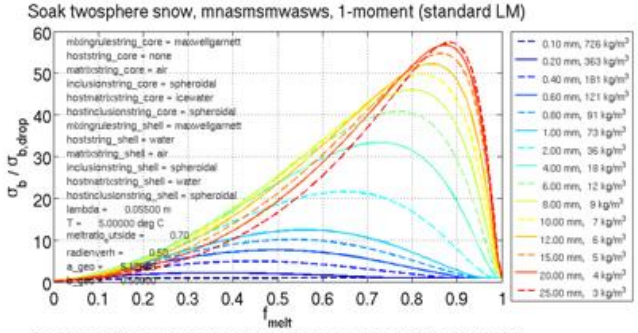
Soak twosphere snow, mnasmsmnwsms, 1-moment (standard LM)



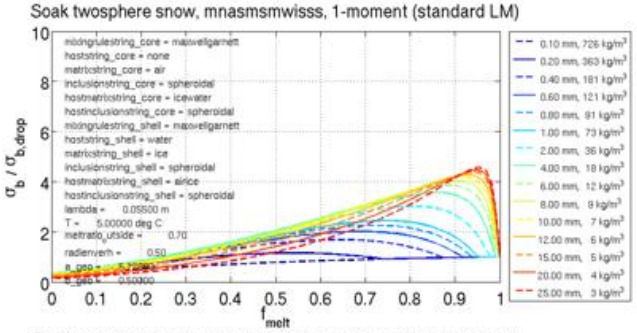
Soak twosphere snow, mnasmsmwasss, 1-moment (standard LM)



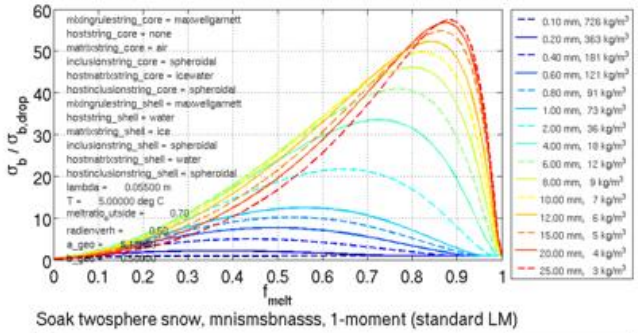
Soak twosphere snow, mnasmsmwasws, 1-moment (standard LM)



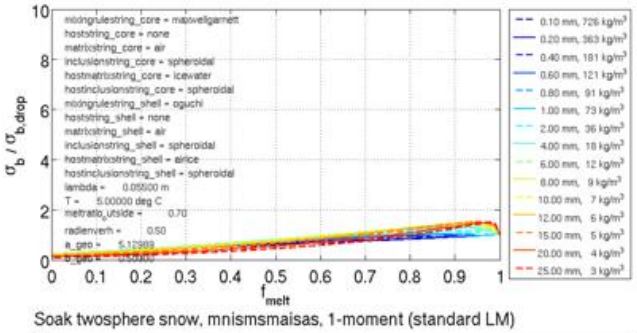
Soak twosphere snow, mnasmsmwisss, 1-moment (standard LM)



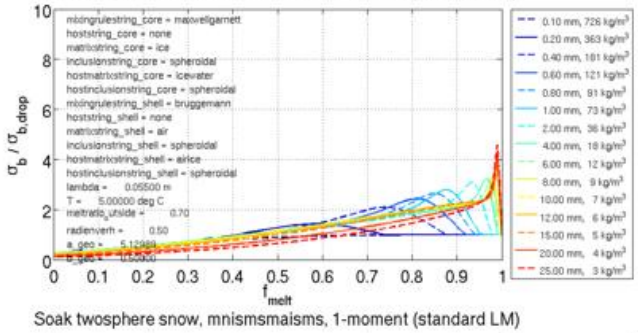
Soak twosphere snow, mnasmsmwisws, 1-moment (standard LM)



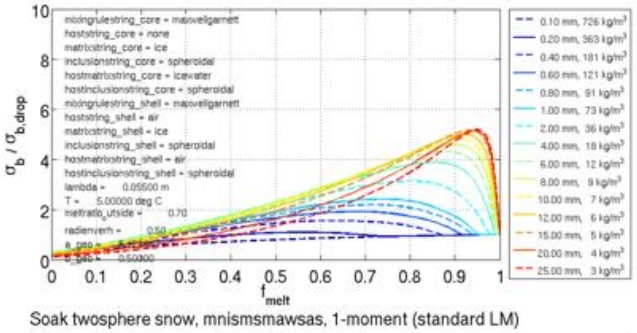
Soak twosphere snow, mnasmsonasss, 1-moment (standard LM)



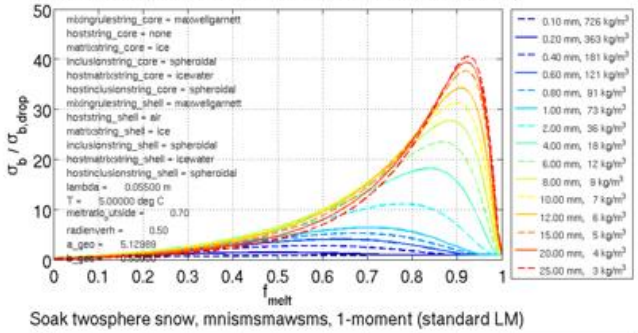
Soak twosphere snow, mnismsbnasss, 1-moment (standard LM)



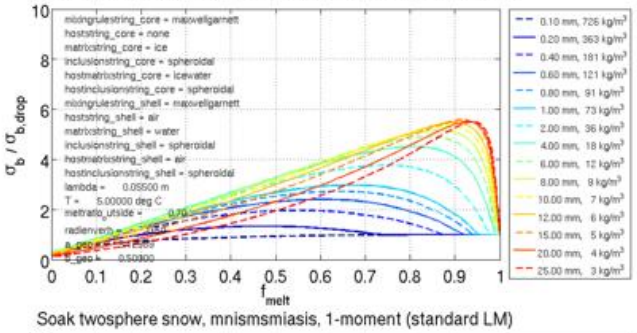
Soak twosphere snow, mnismsmaisas, 1-moment (standard LM)



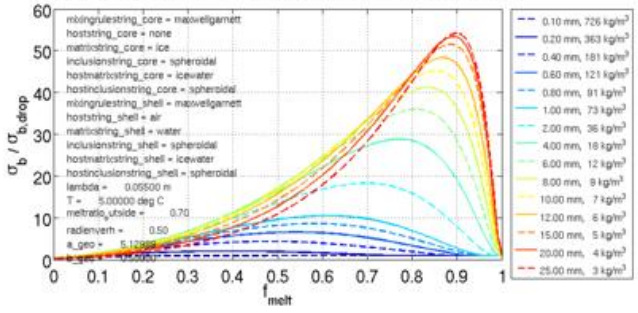
Soak twosphere snow, mnismsmaisms, 1-moment (standard LM)



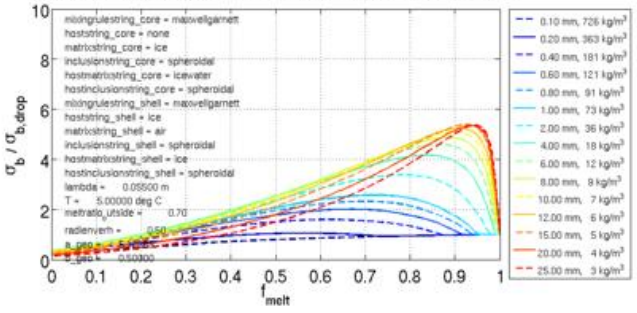
Soak twosphere snow, mnismsmawsas, 1-moment (standard LM)



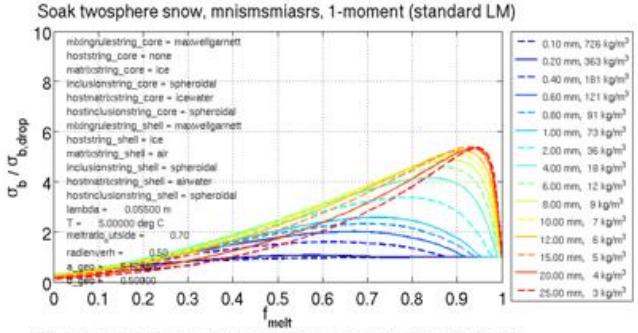
Soak twosphere snow, mnismsmawsms, 1-moment (standard LM)



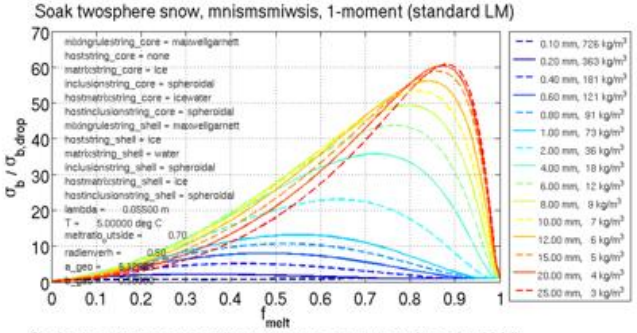
Soak twosphere snow, mnismsmiasis, 1-moment (standard LM)



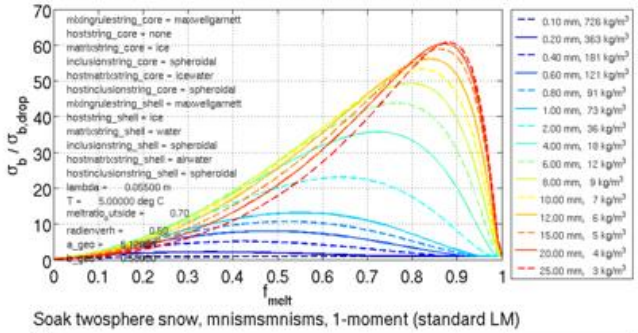
Soak twosphere snow, mnismsmiasrs, 1-moment (standard LM)



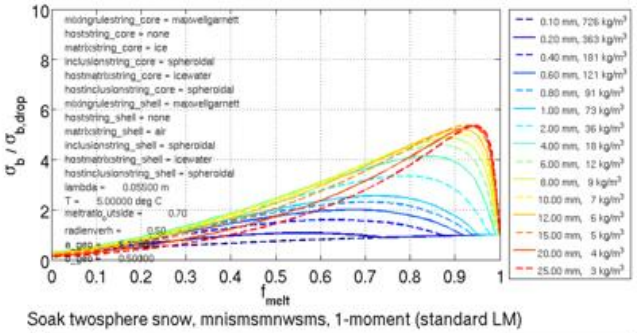
Soak twosphere snow, mnismsmiwsis, 1-moment (standard LM)



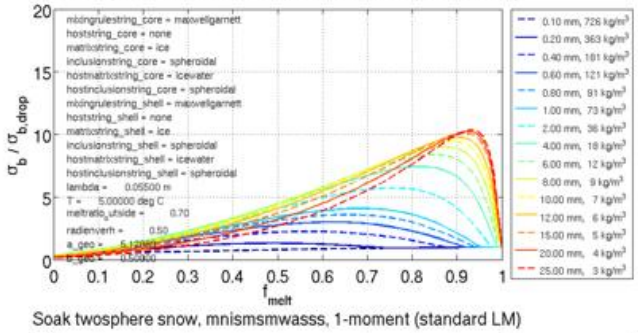
Soak twosphere snow, mnismsmiwsrs, 1-moment (standard LM)



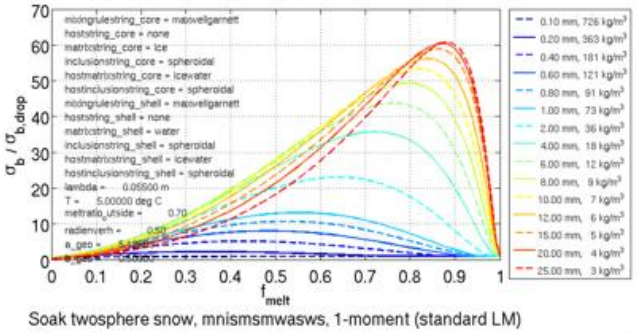
Soak twosphere snow, mnismsmnasms, 1-moment (standard LM)



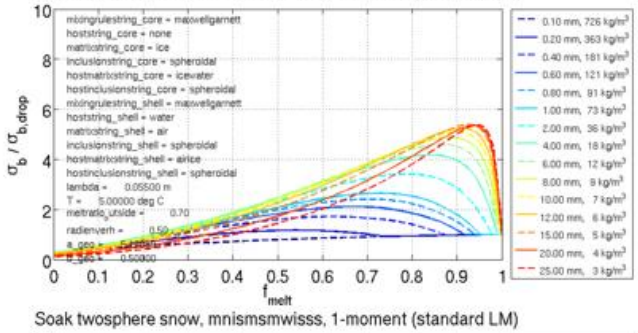
Soak twosphere snow, mnismsmnisms, 1-moment (standard LM)



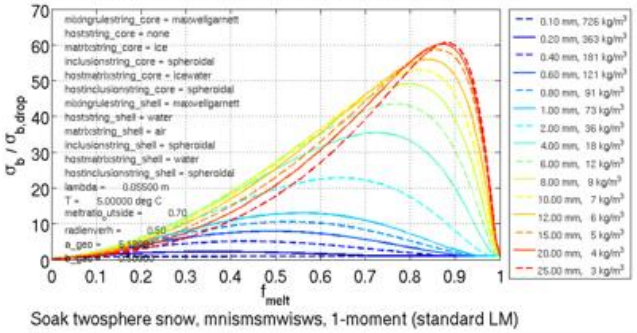
Soak twosphere snow, mnismsmnwsms, 1-moment (standard LM)



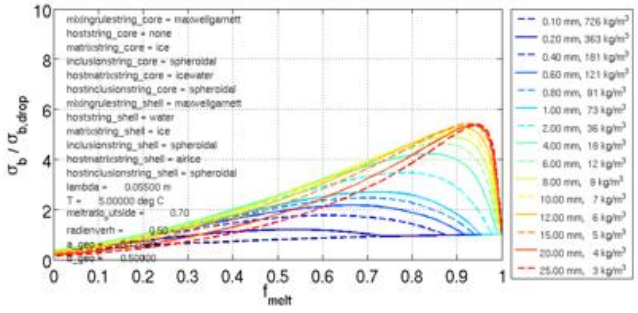
Soak twosphere snow, mnismsmwasss, 1-moment (standard LM)



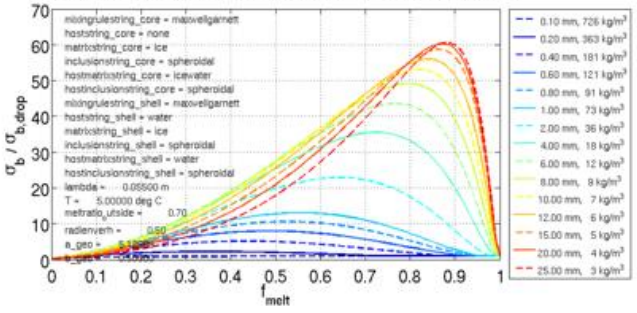
Soak twosphere snow, mnismsmwasws, 1-moment (standard LM)



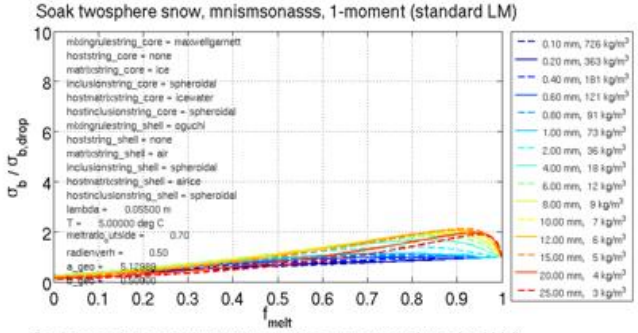
Soak twosphere snow, mnismsmwisss, 1-moment (standard LM)



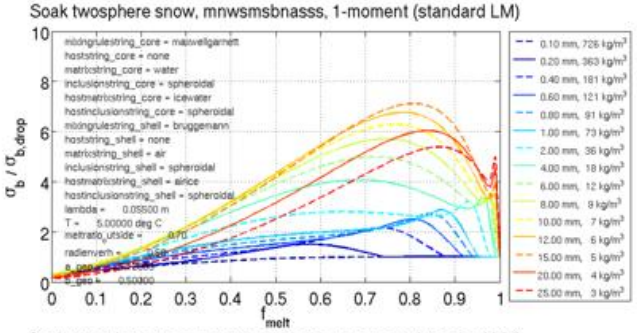
Soak twosphere snow, mnismsmwisws, 1-moment (standard LM)



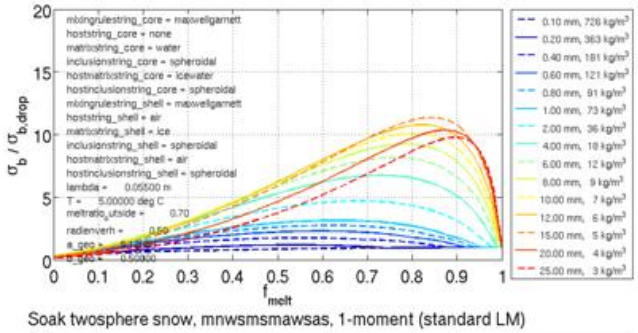
Soak twosphere snow, mnismsonasss, 1-moment (standard LM)



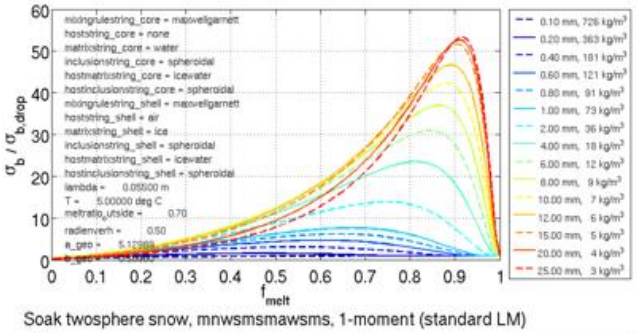
Soak twosphere snow, mnwsmsbnasss, 1-moment (standard LM)



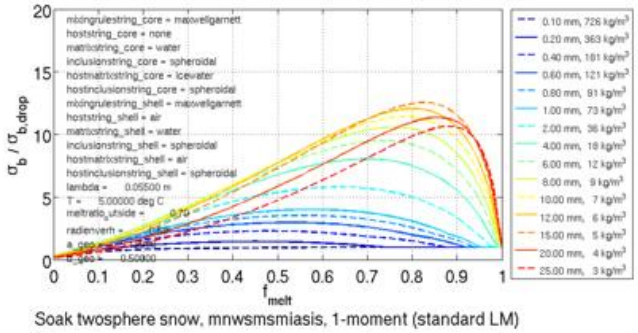
Soak twosphere snow, mnwsmsmaisas, 1-moment (standard LM)



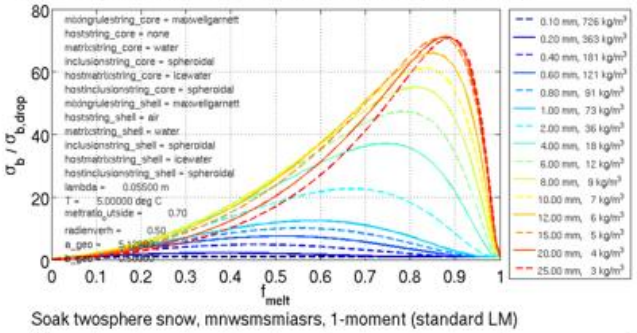
Soak twosphere snow, mnwsmsmaisms, 1-moment (standard LM)



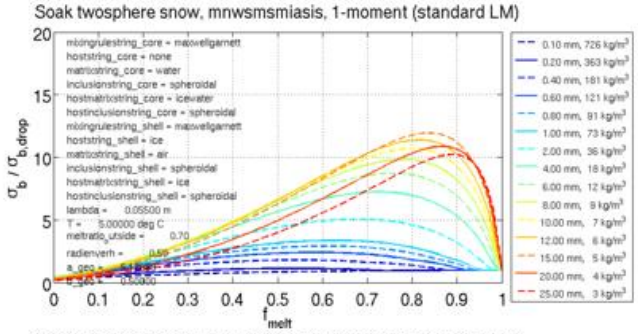
Soak twosphere snow, mnwsmsmawsas, 1-moment (standard LM)



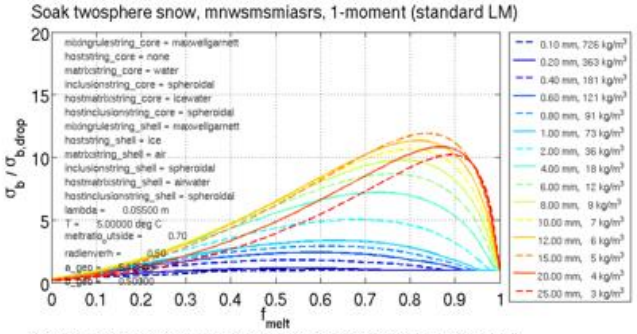
Soak twosphere snow, mnwsmsmawsms, 1-moment (standard LM)



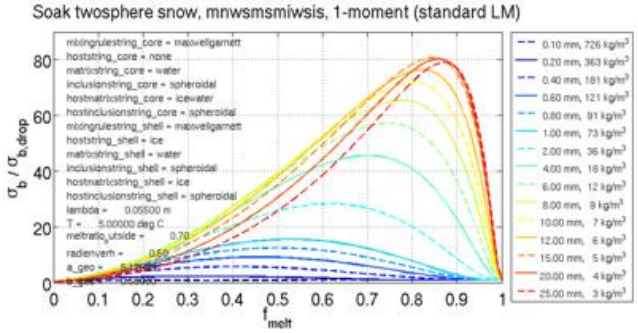
Soak twosphere snow, mnwsmsmiasis, 1-moment (standard LM)



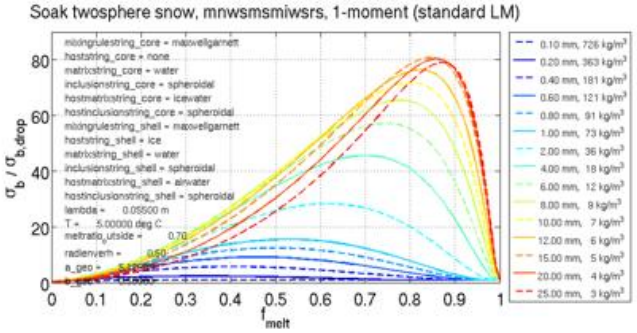
Soak twosphere snow, mnwsmsmiasrs, 1-moment (standard LM)



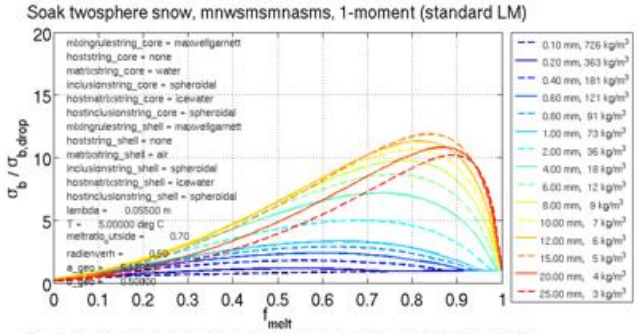
Soak twosphere snow, mnwsmsmiwsis, 1-moment (standard LM)



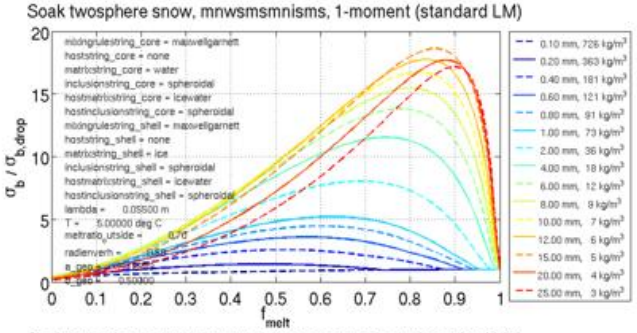
Soak twosphere snow, mnwsmsmiwsrs, 1-moment (standard LM)



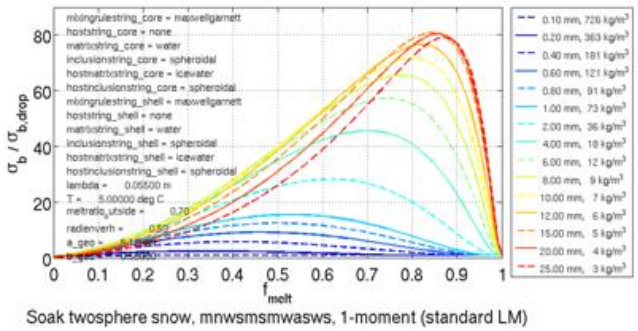
Soak twosphere snow, mnwsmsmnasms, 1-moment (standard LM)



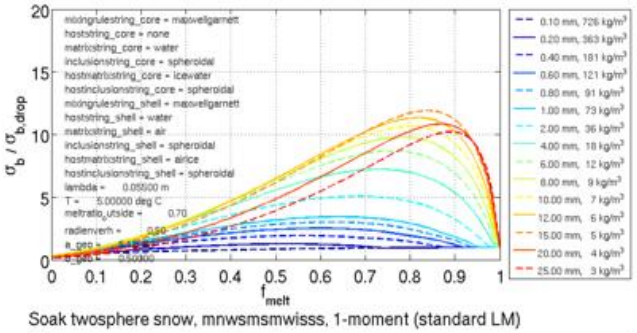
Soak twosphere snow, mnwsmsmnisms, 1-moment (standard LM)



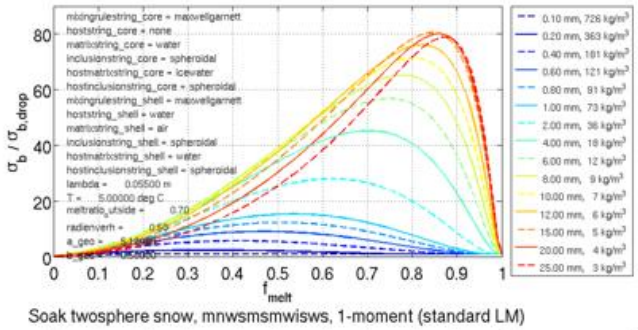
Soak twosphere snow, mnwsmsmnwsms, 1-moment (standard LM)



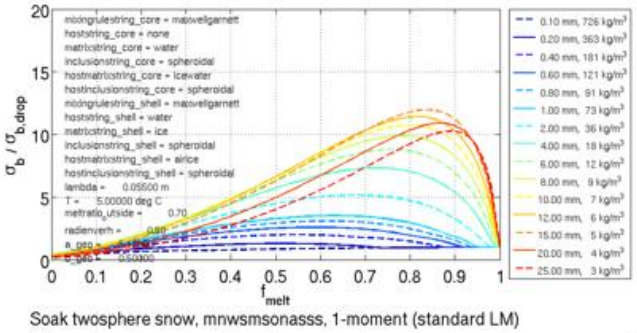
Soak twosphere snow, mnwsmsmwasss, 1-moment (standard LM)



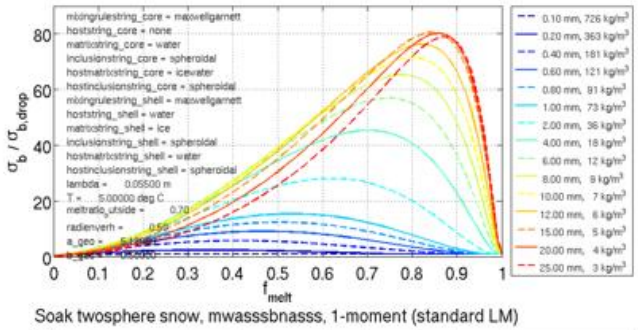
Soak twosphere snow, mnwsmsmwasws, 1-moment (standard LM)



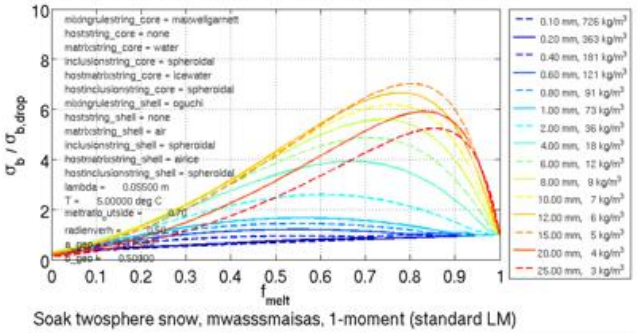
Soak twosphere snow, mnwsmsmwisss, 1-moment (standard LM)



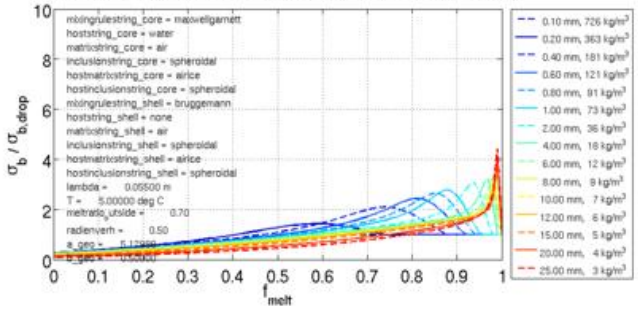
Soak twosphere snow, mnwsmsmwisws, 1-moment (standard LM)



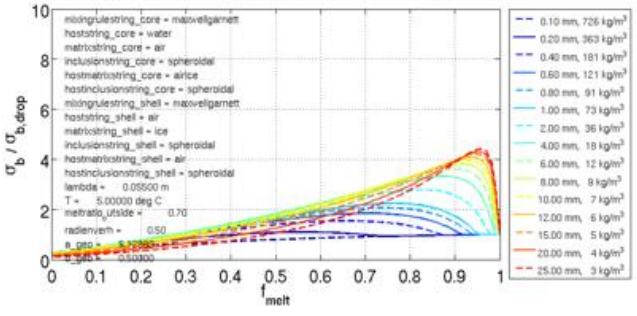
Soak twosphere snow, mnwsmsonasss, 1-moment (standard LM)



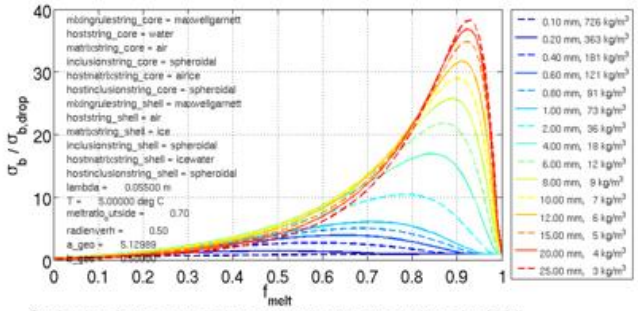
Soak twosphere snow, mwasssbnasss, 1-moment (standard LM)



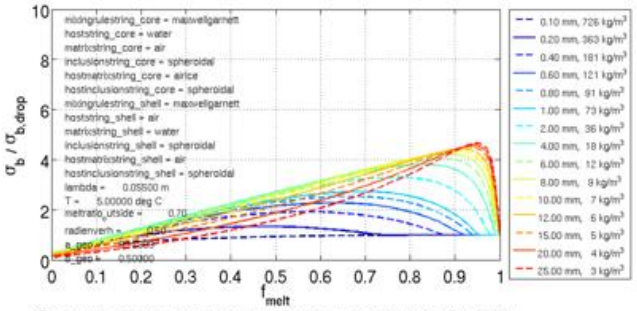
Soak twosphere snow, mwasssmaisas, 1-moment (standard LM)



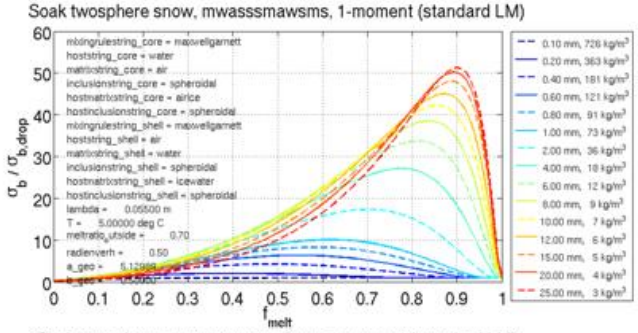
Soak twosphere snow, mwasssmaisms, 1-moment (standard LM)



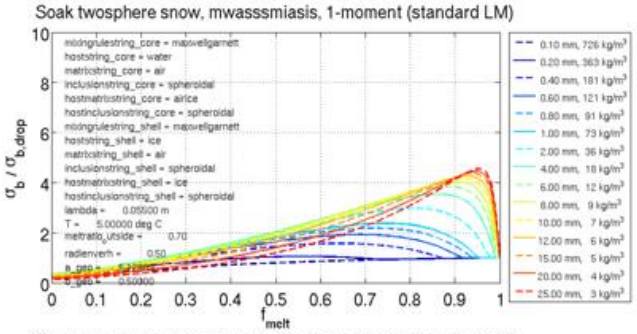
Soak twosphere snow, mwasssmawsas, 1-moment (standard LM)



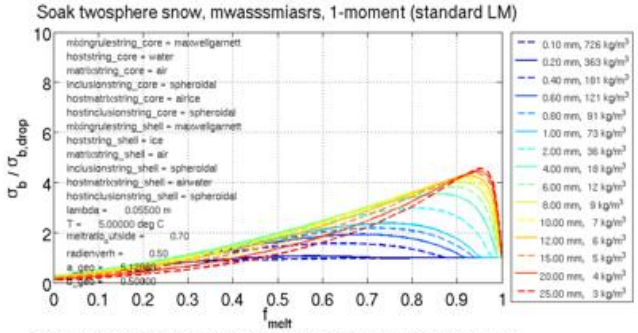
Soak twosphere snow, mwasssmawsms, 1-moment (standard LM)



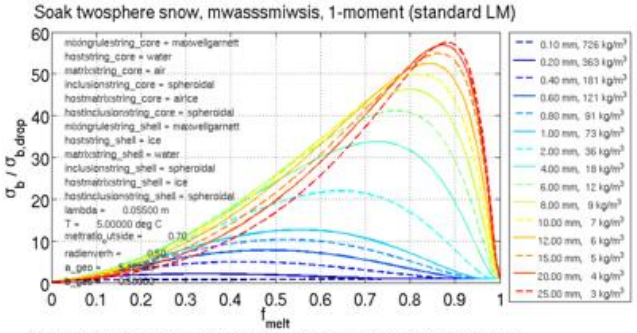
Soak twosphere snow, mwasssmiasis, 1-moment (standard LM)



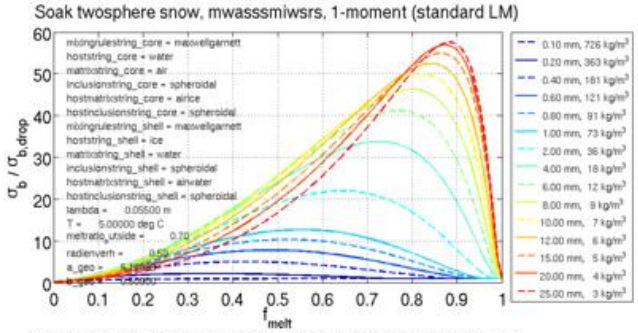
Soak twosphere snow, mwasssmiasrs, 1-moment (standard LM)



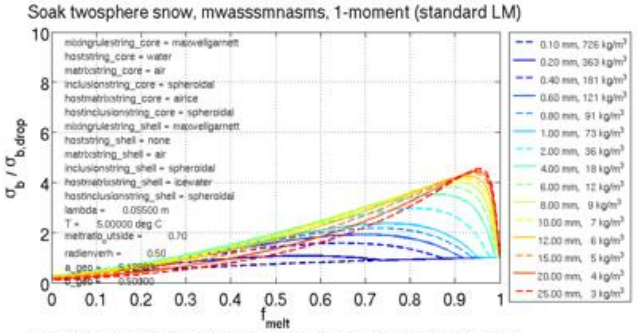
Soak twosphere snow, mwasssmiwsis, 1-moment (standard LM)



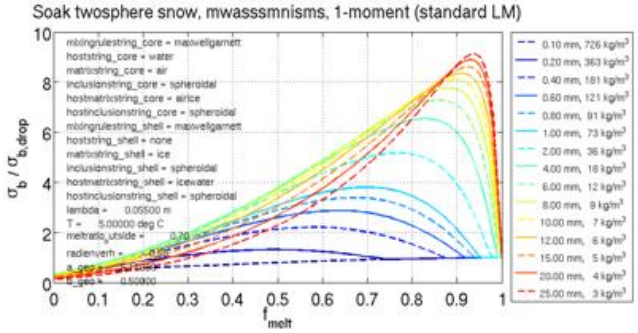
Soak twosphere snow, mwasssmiwsrs, 1-moment (standard LM)



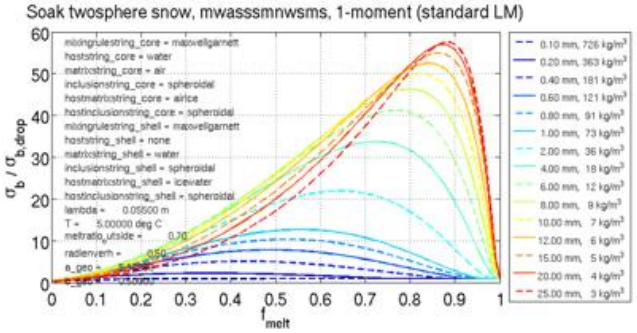
Soak twosphere snow, mwasssmnasms, 1-moment (standard LM)



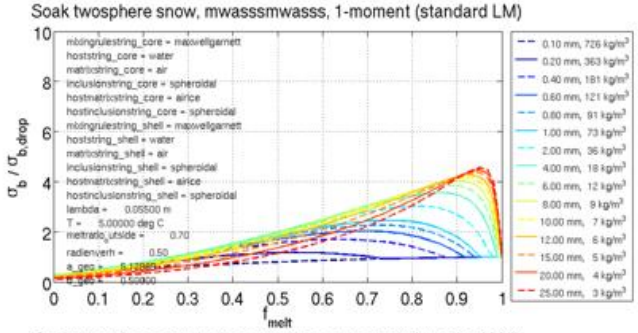
Soak twosphere snow, mwasssmnisms, 1-moment (standard LM)



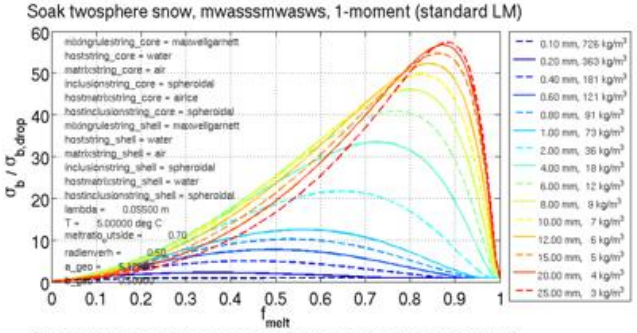
Soak twosphere snow, mwasssmnwsms, 1-moment (standard LM)



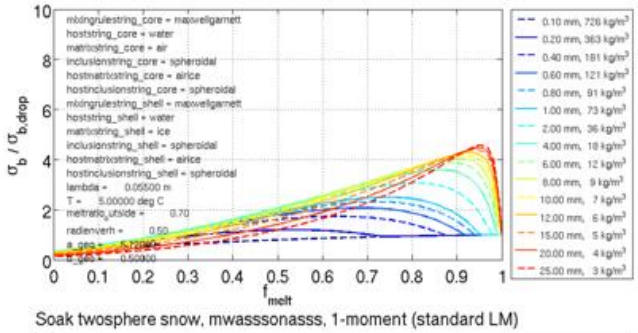
Soak twosphere snow, mwasssmwasss, 1-moment (standard LM)



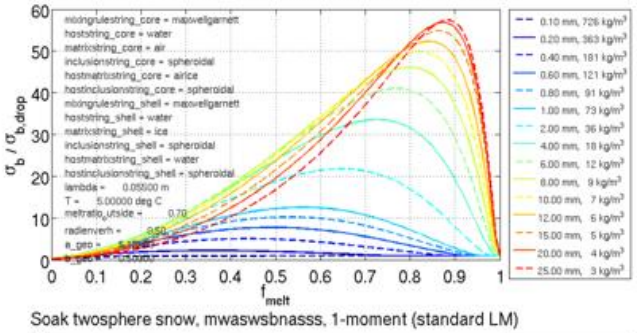
Soak twosphere snow, mwasssmwasws, 1-moment (standard LM)



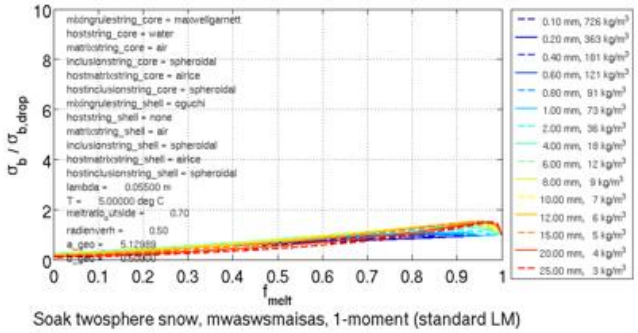
Soak twosphere snow, mwasssmwisss, 1-moment (standard LM)



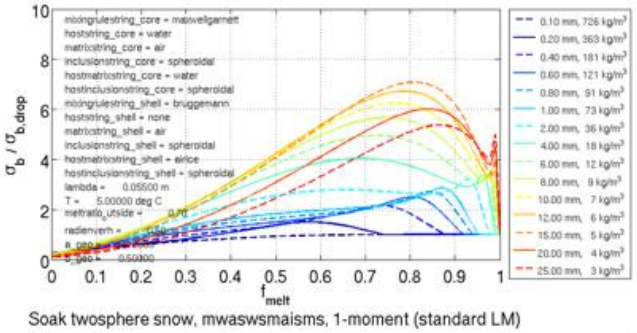
Soak twosphere snow, mwasssmwisws, 1-moment (standard LM)



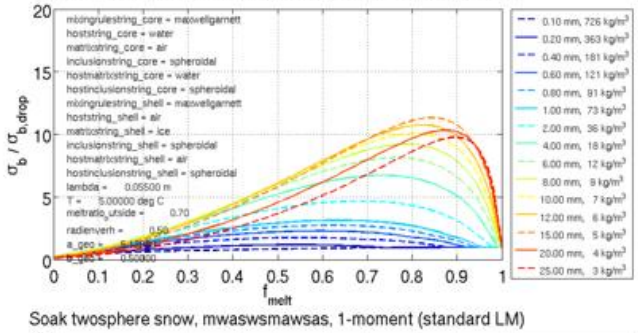
Soak twosphere snow, mwasssonasss, 1-moment (standard LM)



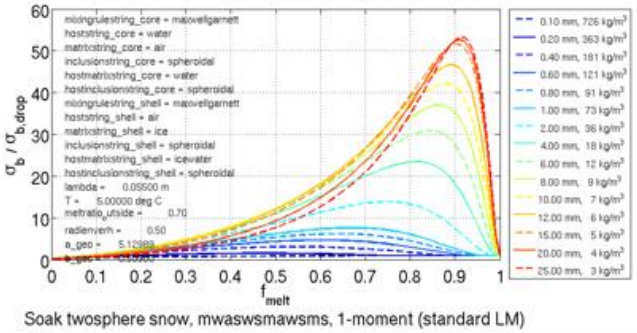
Soak twosphere snow, mwaswsbnasss, 1-moment (standard LM)



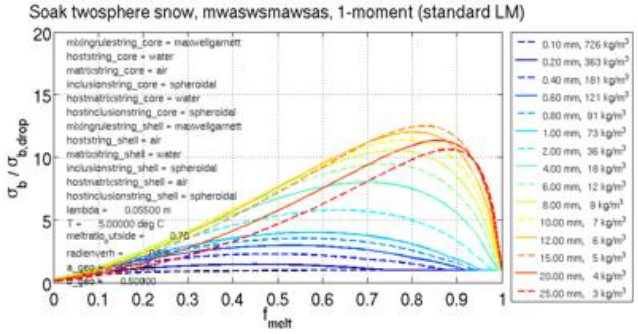
Soak twosphere snow, mwaswsmaisas, 1-moment (standard LM)



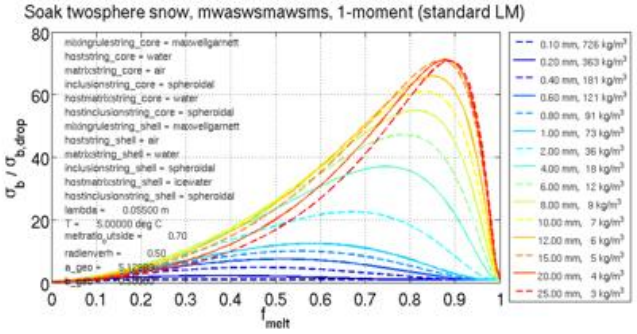
Soak twosphere snow, mwaswsmaisms, 1-moment (standard LM)



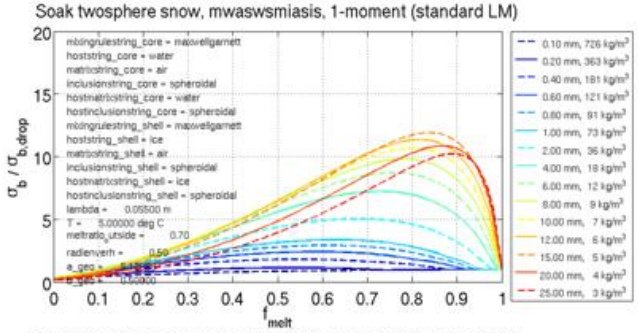
Soak twosphere snow, mwaswsmawsas, 1-moment (standard LM)



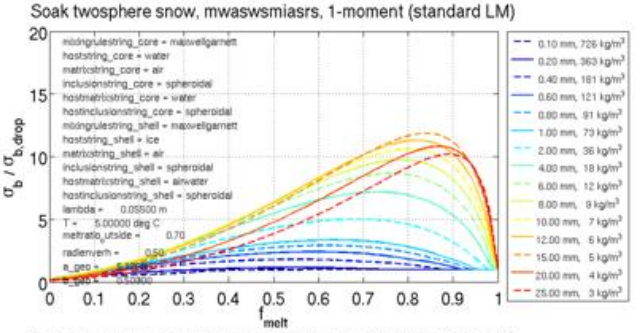
Soak twosphere snow, mwaswsmawsms, 1-moment (standard LM)



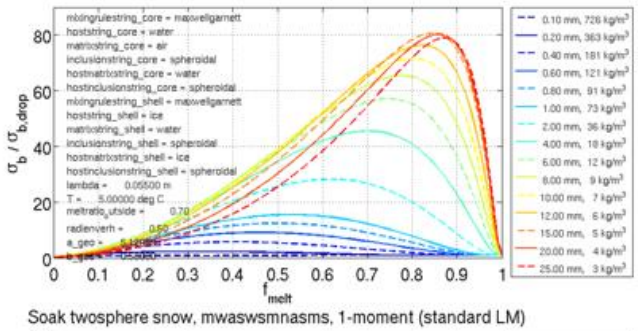
Soak twosphere snow, mwaswsmiasis, 1-moment (standard LM)



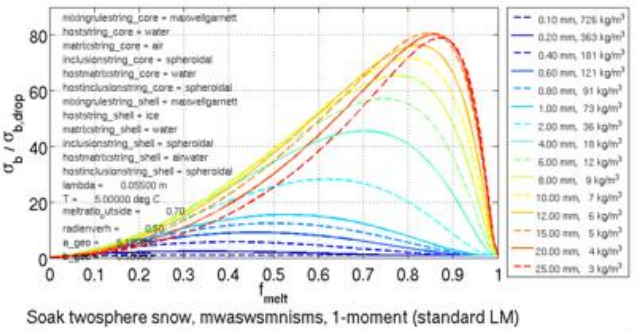
Soak twosphere snow, mwaswsmiasrs, 1-moment (standard LM)



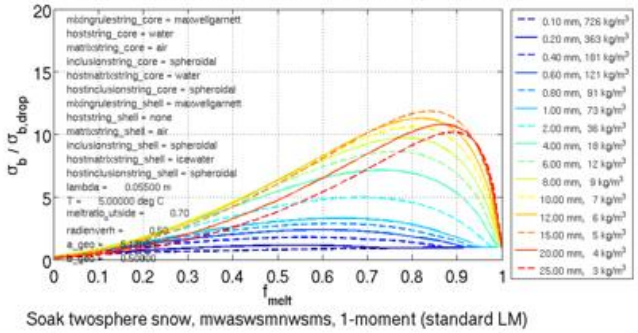
Soak twosphere snow, mwaswsmiwsis, 1-moment (standard LM)



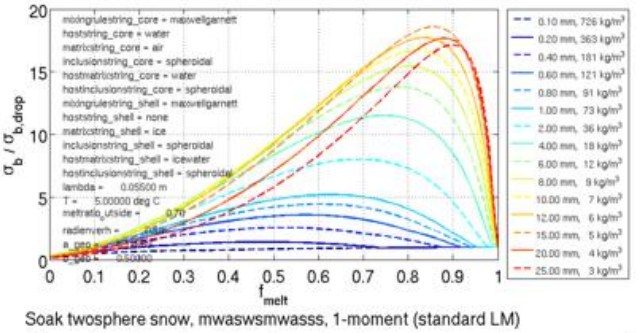
Soak twosphere snow, mwaswsmiwsrs, 1-moment (standard LM)



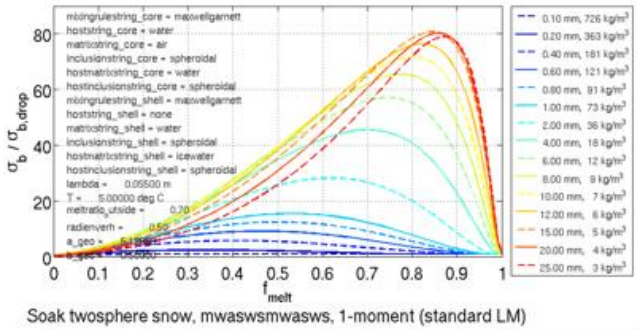
Soak twosphere snow, mwaswsmnasms, 1-moment (standard LM)



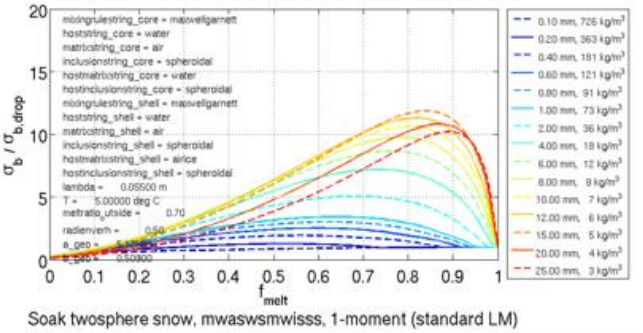
Soak twosphere snow, mwaswsmnisms, 1-moment (standard LM)



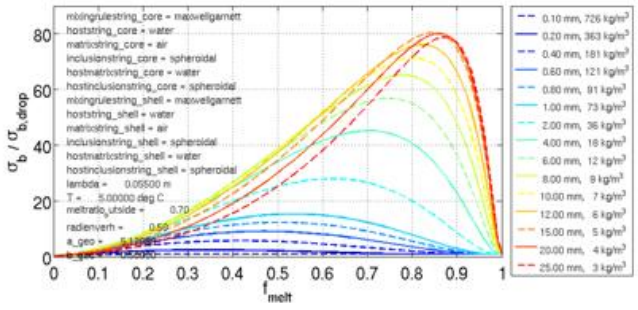
Soak twosphere snow, mwaswsmnwsms, 1-moment (standard LM)



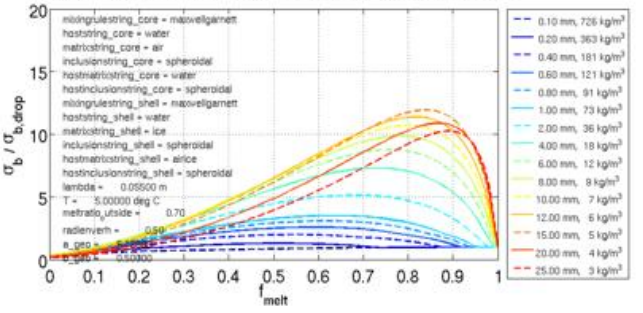
Soak twosphere snow, mwaswsmwasss, 1-moment (standard LM)



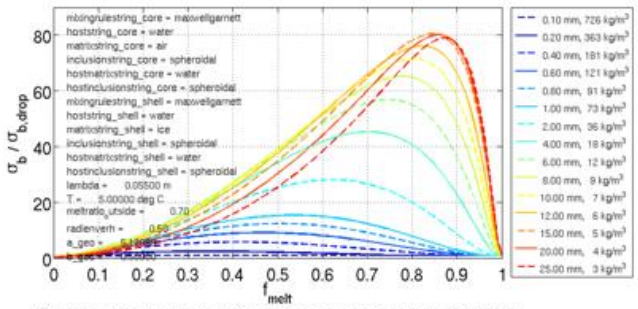
Soak twosphere snow, mwaswsmwasws, 1-moment (standard LM)



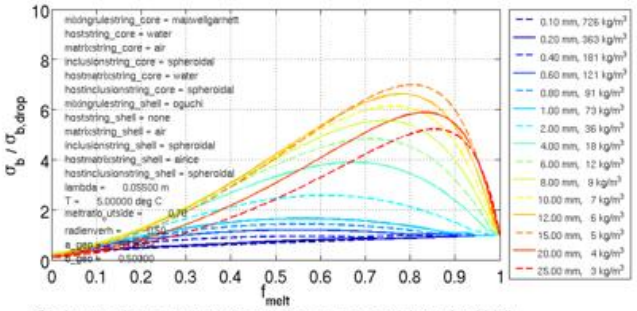
Soak twosphere snow, mwaswsmwisss, 1-moment (standard LM)



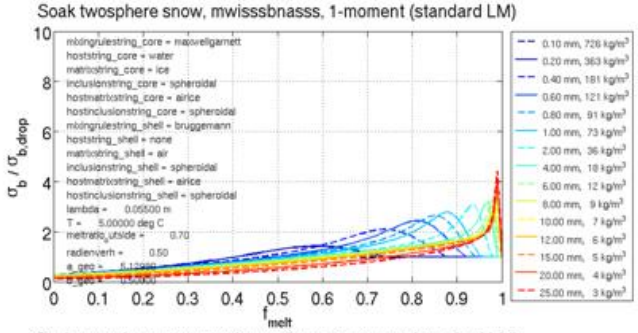
Soak twosphere snow, mwaswsmwisws, 1-moment (standard LM)



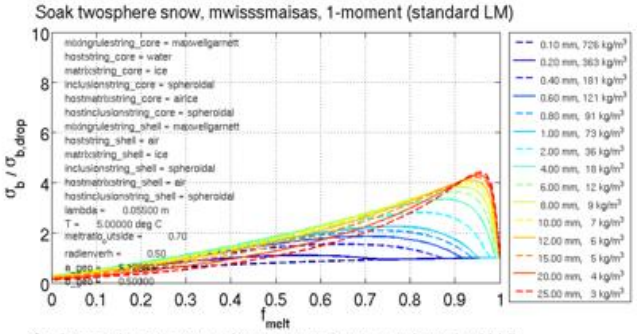
Soak twosphere snow, mwaswsonasss, 1-moment (standard LM)



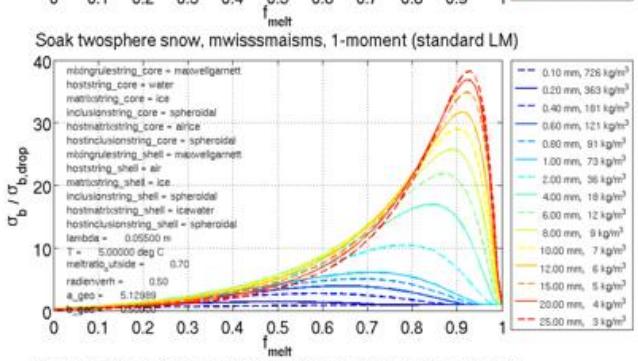
Soak twosphere snow, mwisssbnasss, 1-moment (standard LM)



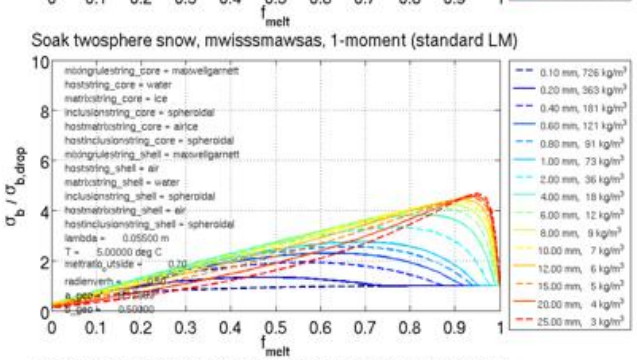
Soak twosphere snow, mwisssmaisas, 1-moment (standard LM)



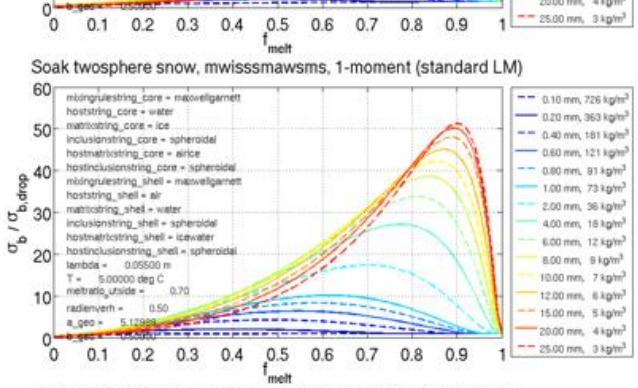
Soak twosphere snow, mwisssmaisms, 1-moment (standard LM)



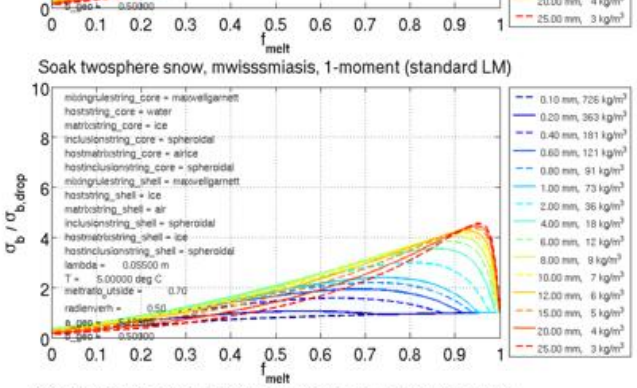
Soak twosphere snow, mwisssmawsas, 1-moment (standard LM)



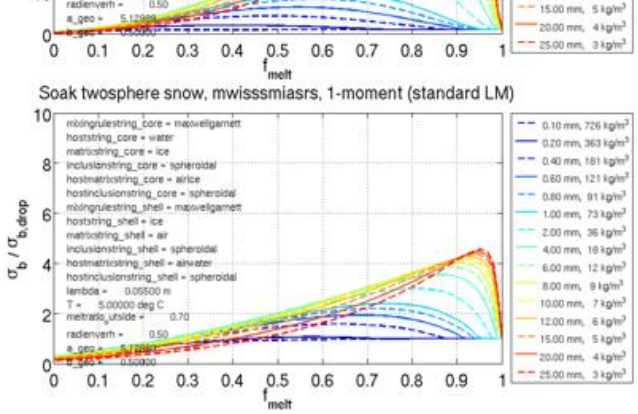
Soak twosphere snow, mwisssmawsms, 1-moment (standard LM)



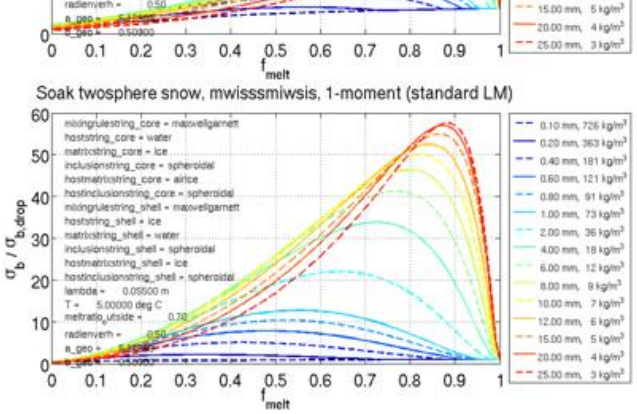
Soak twosphere snow, mwisssmiasis, 1-moment (standard LM)



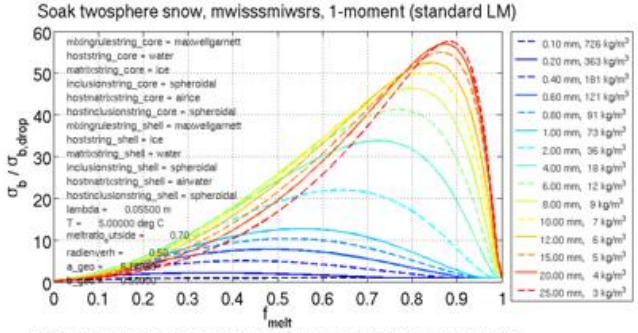
Soak twosphere snow, mwisssmiasrs, 1-moment (standard LM)



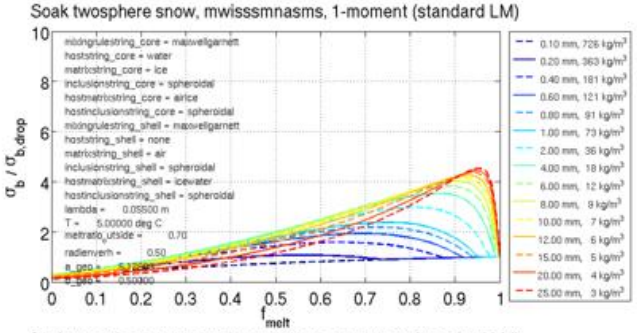
Soak twosphere snow, mwisssmiwsis, 1-moment (standard LM)



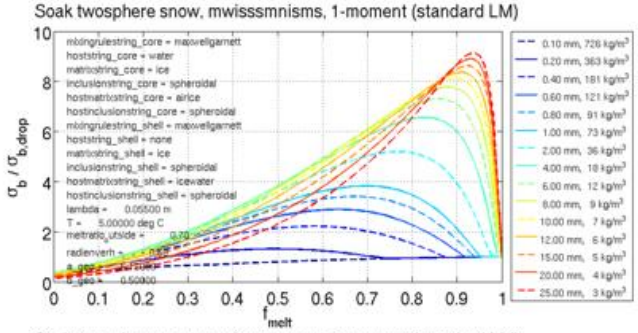
Soak twosphere snow, mwisssmiwsrs, 1-moment (standard LM)



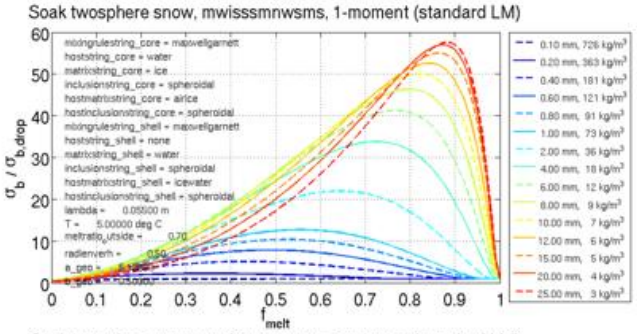
Soak twosphere snow, mwisssmnasms, 1-moment (standard LM)



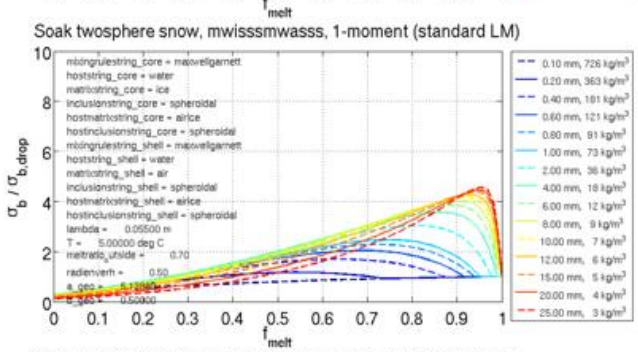
Soak twosphere snow, mwisssmnisms, 1-moment (standard LM)



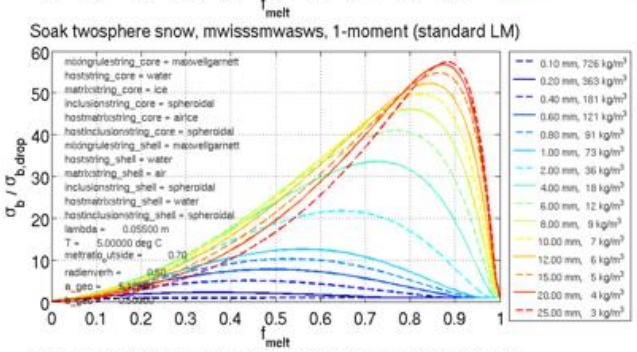
Soak twosphere snow, mwisssmnwsms, 1-moment (standard LM)



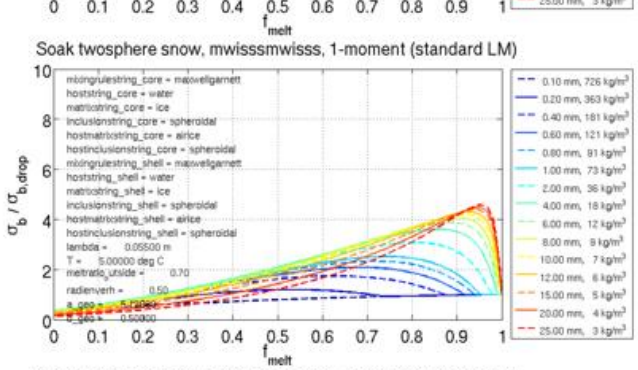
Soak twosphere snow, mwisssmwasss, 1-moment (standard LM)



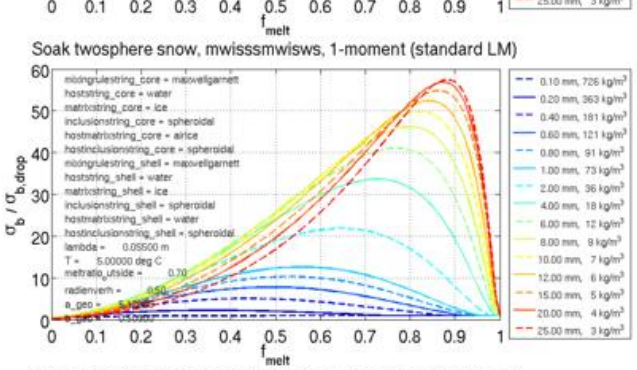
Soak twosphere snow, mwisssmwasws, 1-moment (standard LM)



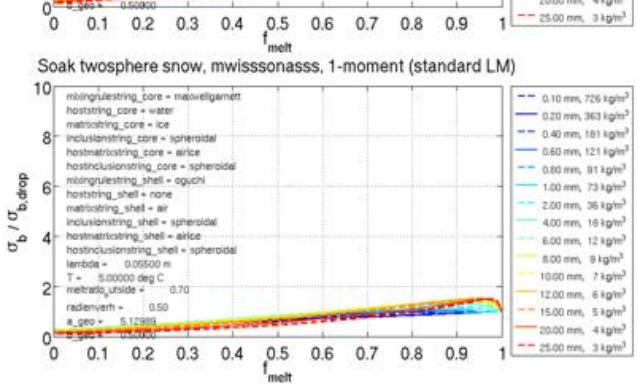
Soak twosphere snow, mwisssmwisss, 1-moment (standard LM)



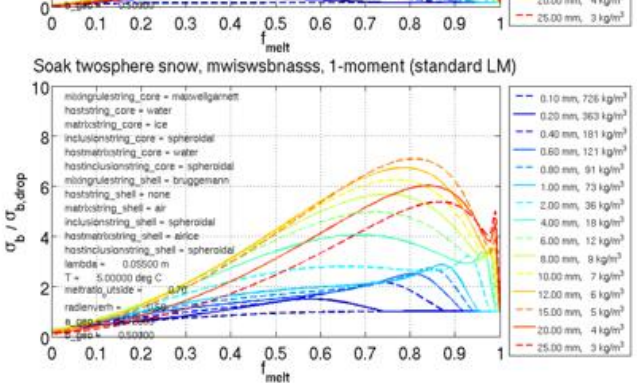
Soak twosphere snow, mwisssmwisws, 1-moment (standard LM)



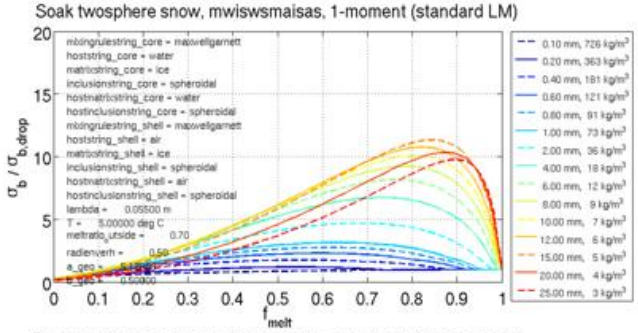
Soak twosphere snow, mwisssonasss, 1-moment (standard LM)



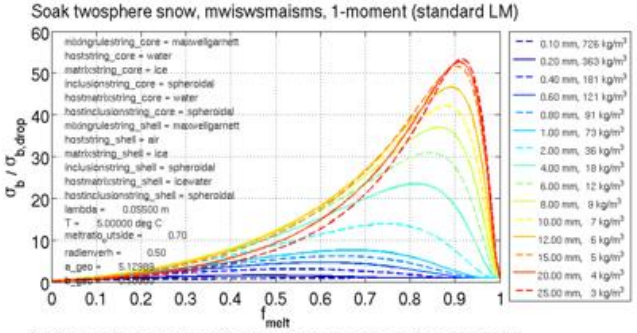
Soak twosphere snow, mwiswsbnasss, 1-moment (standard LM)



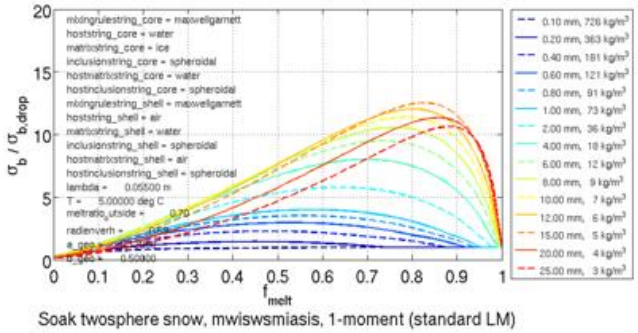
Soak twosphere snow, mwiswsmaisas, 1-moment (standard LM)



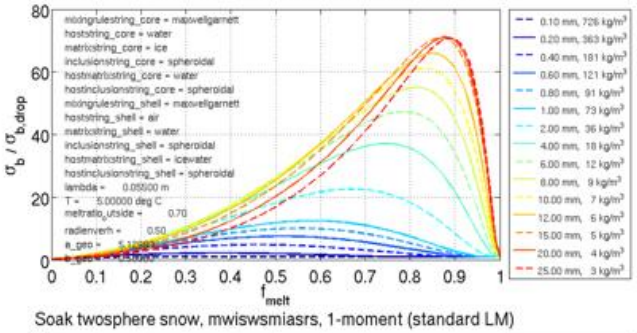
Soak twosphere snow, mwiswsmaisms, 1-moment (standard LM)



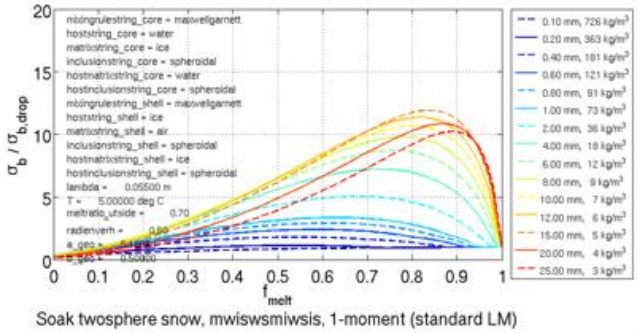
Soak twosphere snow, mwiswsmawsas, 1-moment (standard LM)



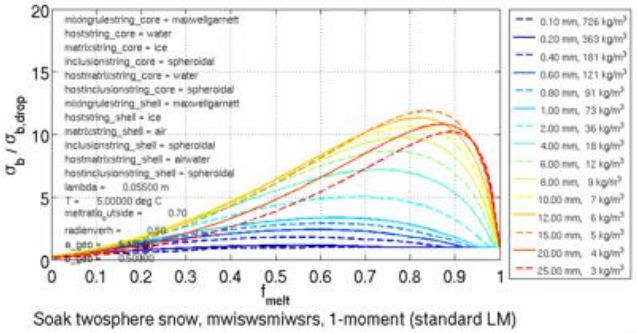
Soak twosphere snow, mwiswsmawsms, 1-moment (standard LM)



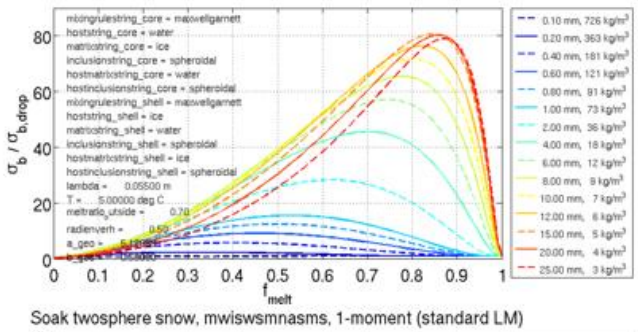
Soak twosphere snow, mwiswsmiasis, 1-moment (standard LM)



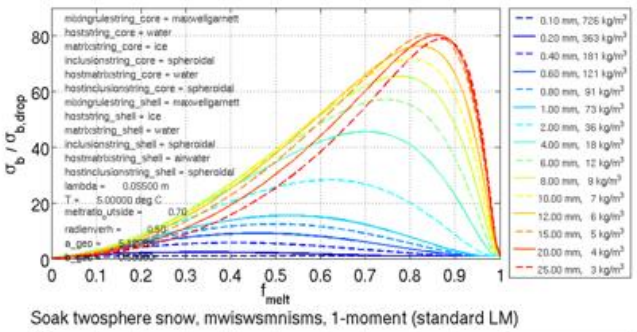
Soak twosphere snow, mwiswsmiasrs, 1-moment (standard LM)



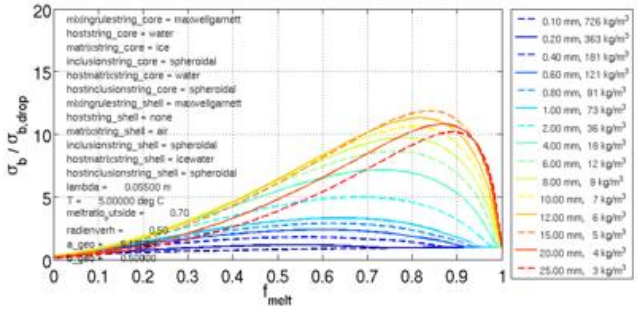
Soak twosphere snow, mwiswsmiwsis, 1-moment (standard LM)



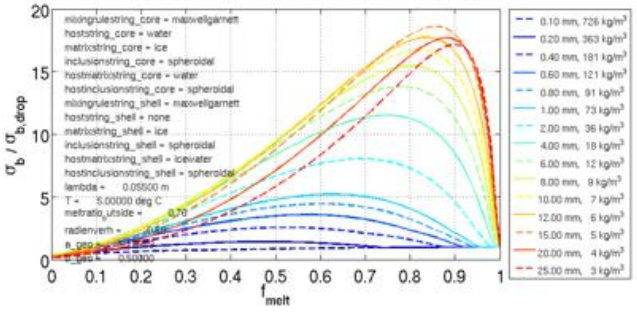
Soak twosphere snow, mwiswsmiwsrs, 1-moment (standard LM)



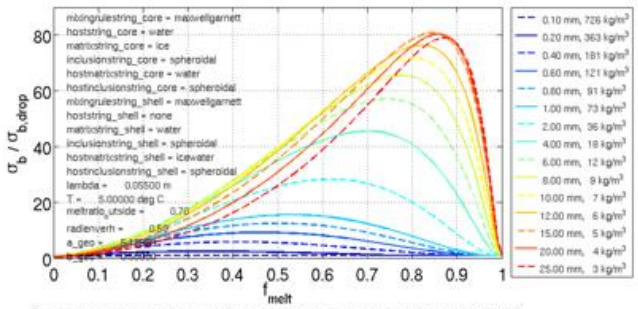
Soak twosphere snow, mwiswsmnasms, 1-moment (standard LM)



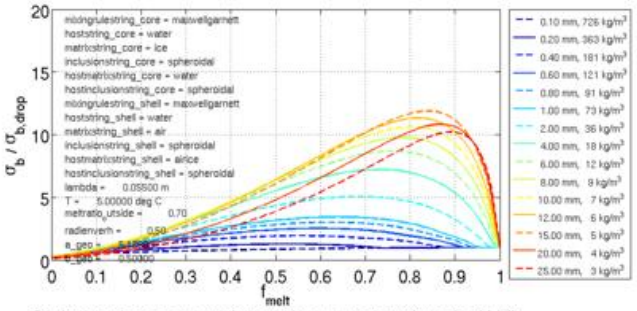
Soak twosphere snow, mwiswsmnisms, 1-moment (standard LM)



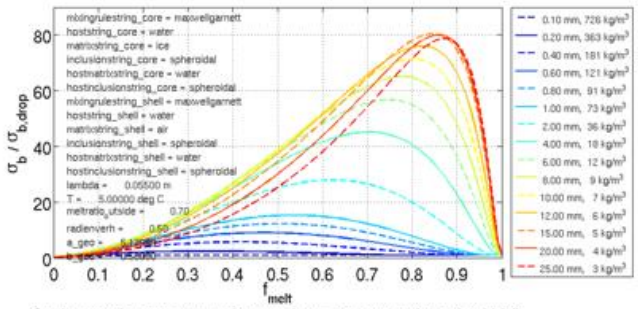
Soak twosphere snow, mwiswsmnwsms, 1-moment (standard LM)



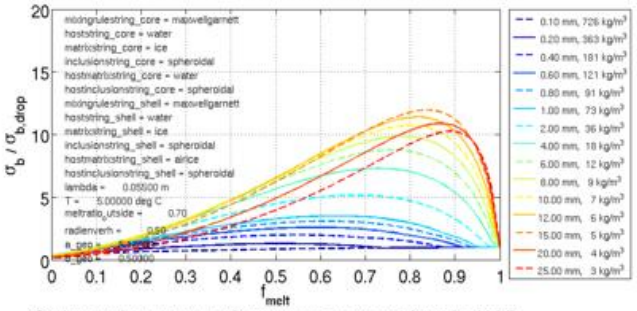
Soak twosphere snow, mwiswsmwasss, 1-moment (standard LM)



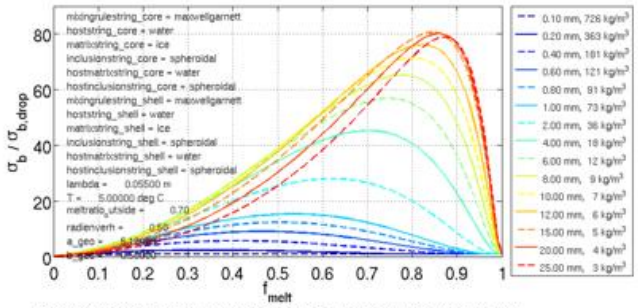
Soak twosphere snow, mwiswsmwasws, 1-moment (standard LM)



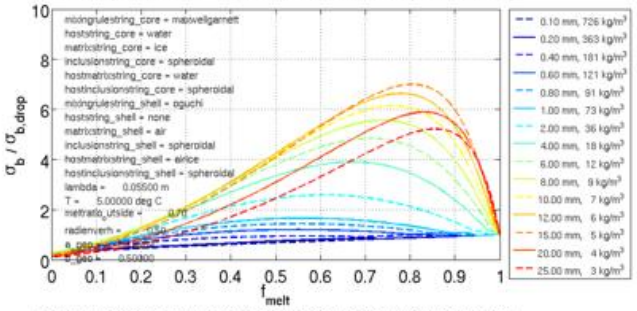
Soak twosphere snow, mwiswsmwisss, 1-moment (standard LM)



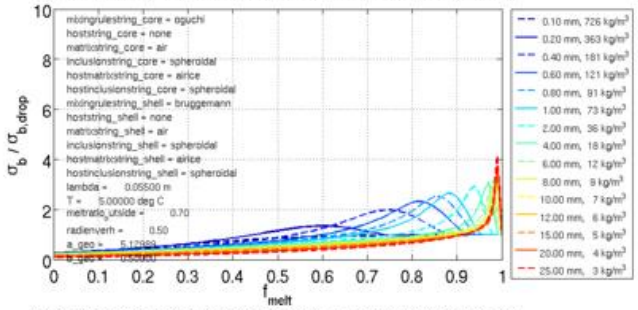
Soak twosphere snow, mwiswsmwisws, 1-moment (standard LM)



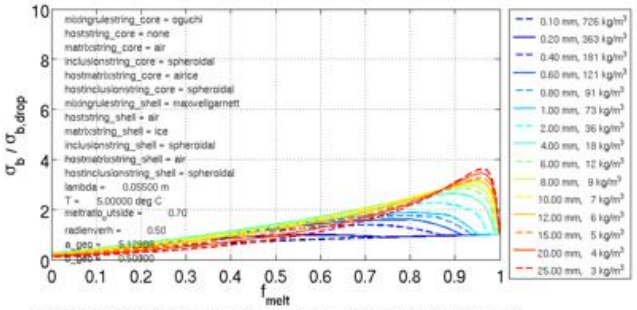
Soak twosphere snow, mwiswsonasss, 1-moment (standard LM)



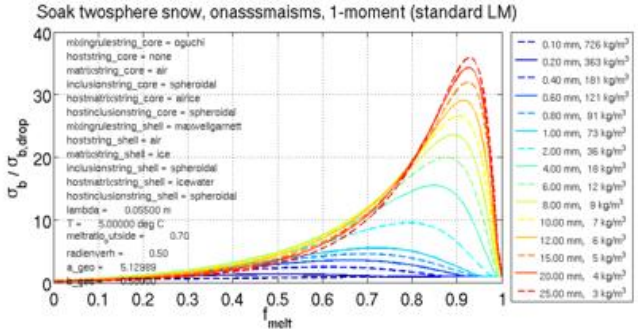
Soak twosphere snow, onasssbnasss, 1-moment (standard LM)



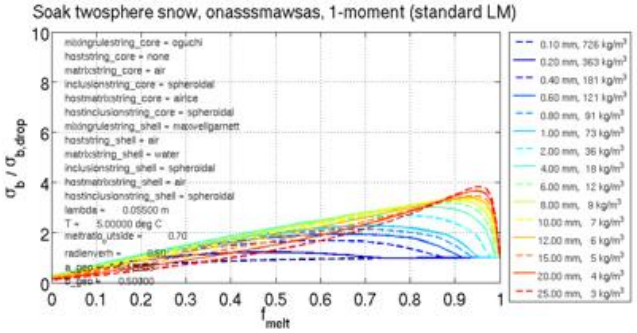
Soak twosphere snow, onasssmaisas, 1-moment (standard LM)



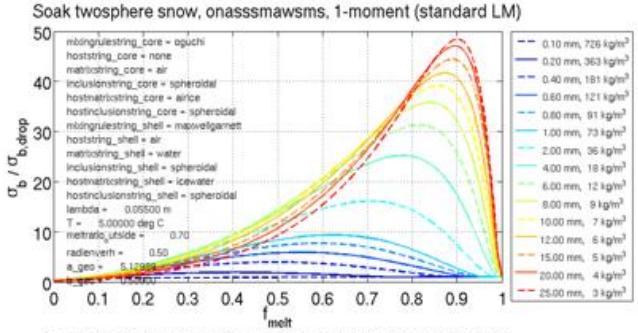
Soak twosphere snow, onasssmaisms, 1-moment (standard LM)



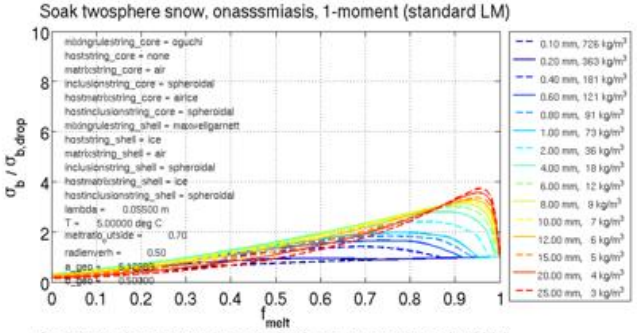
Soak twosphere snow, onasssmawsas, 1-moment (standard LM)



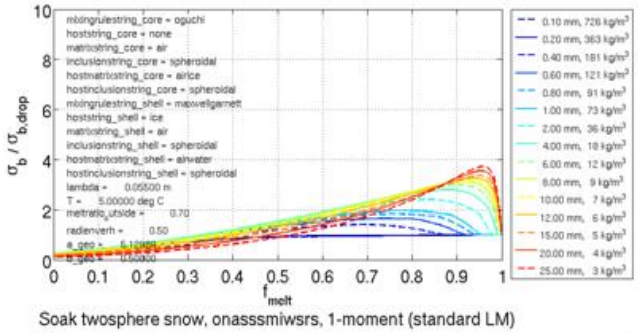
Soak twosphere snow, onasssmawsms, 1-moment (standard LM)



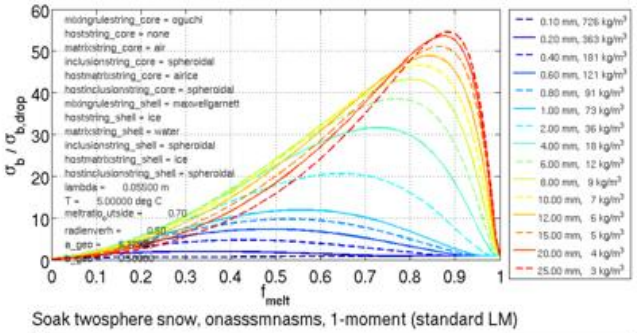
Soak twosphere snow, onasssmiasis, 1-moment (standard LM)



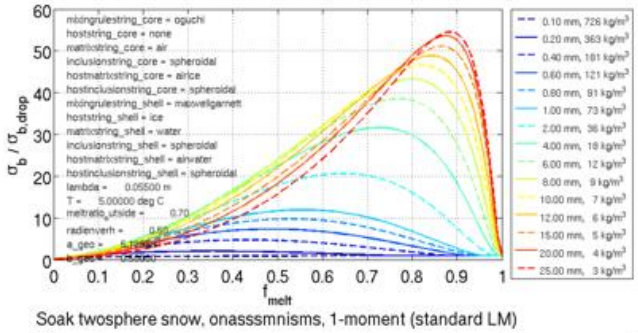
Soak twosphere snow, onasssmiasrs, 1-moment (standard LM)



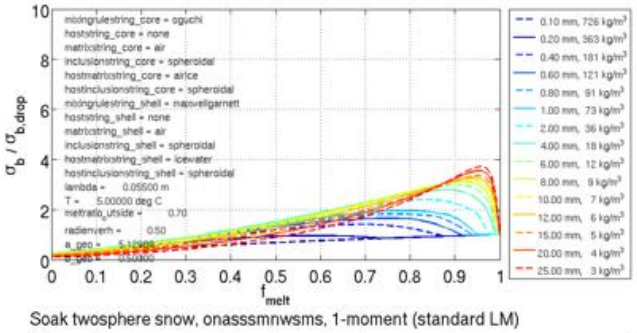
Soak twosphere snow, onasssmiwsis, 1-moment (standard LM)



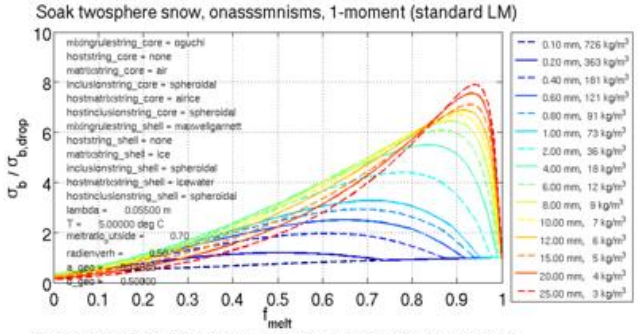
Soak twosphere snow, onasssmiwsrs, 1-moment (standard LM)



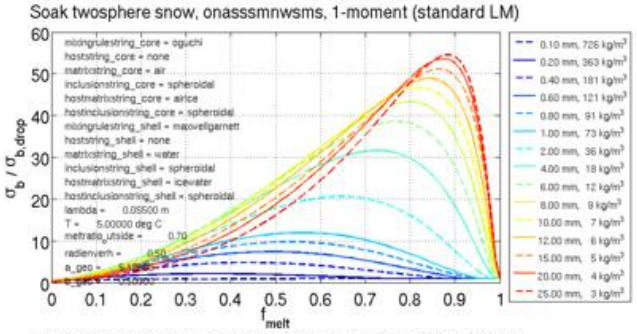
Soak twosphere snow, onasssmnasms, 1-moment (standard LM)



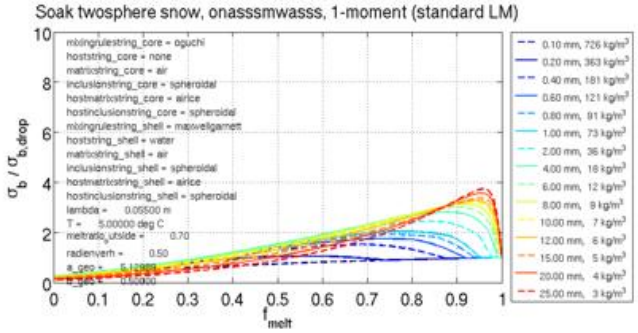
Soak twosphere snow, onasssmnisms, 1-moment (standard LM)



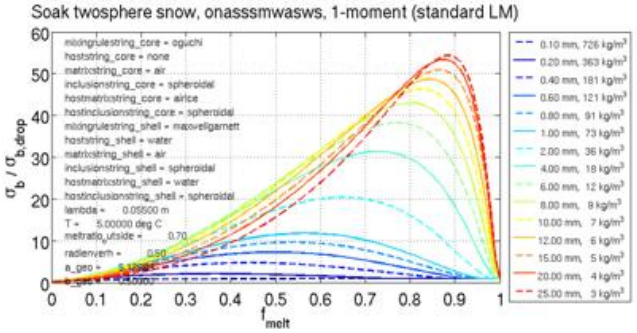
Soak twosphere snow, onasssmnwsms, 1-moment (standard LM)



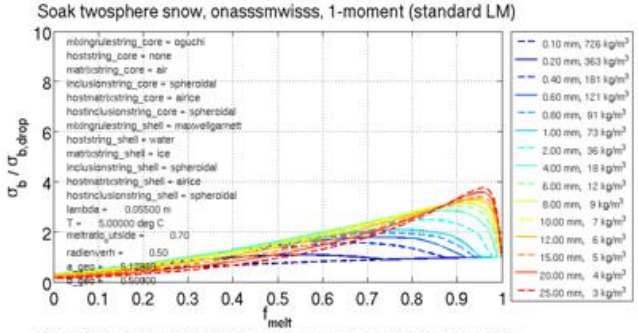
Soak twosphere snow, onasssmwasss, 1-moment (standard LM)



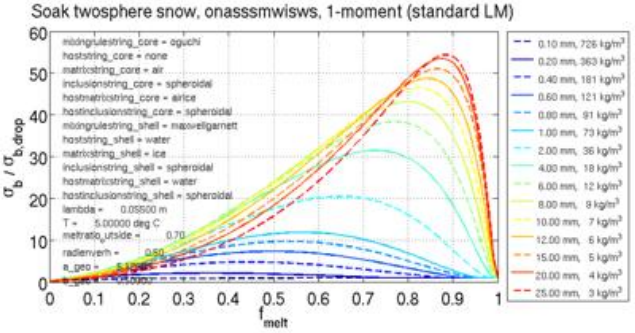
Soak twosphere snow, onasssmwasws, 1-moment (standard LM)



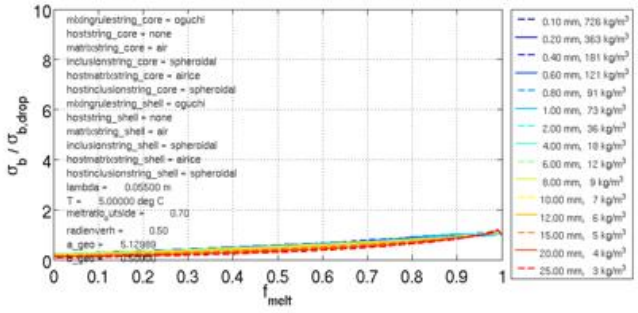
Soak twosphere snow, onasssmwisss, 1-moment (standard LM)



Soak twosphere snow, onasssmwisws, 1-moment (standard LM)



Soak twosphere snow, onasssonasss, 1-moment (standard LM)

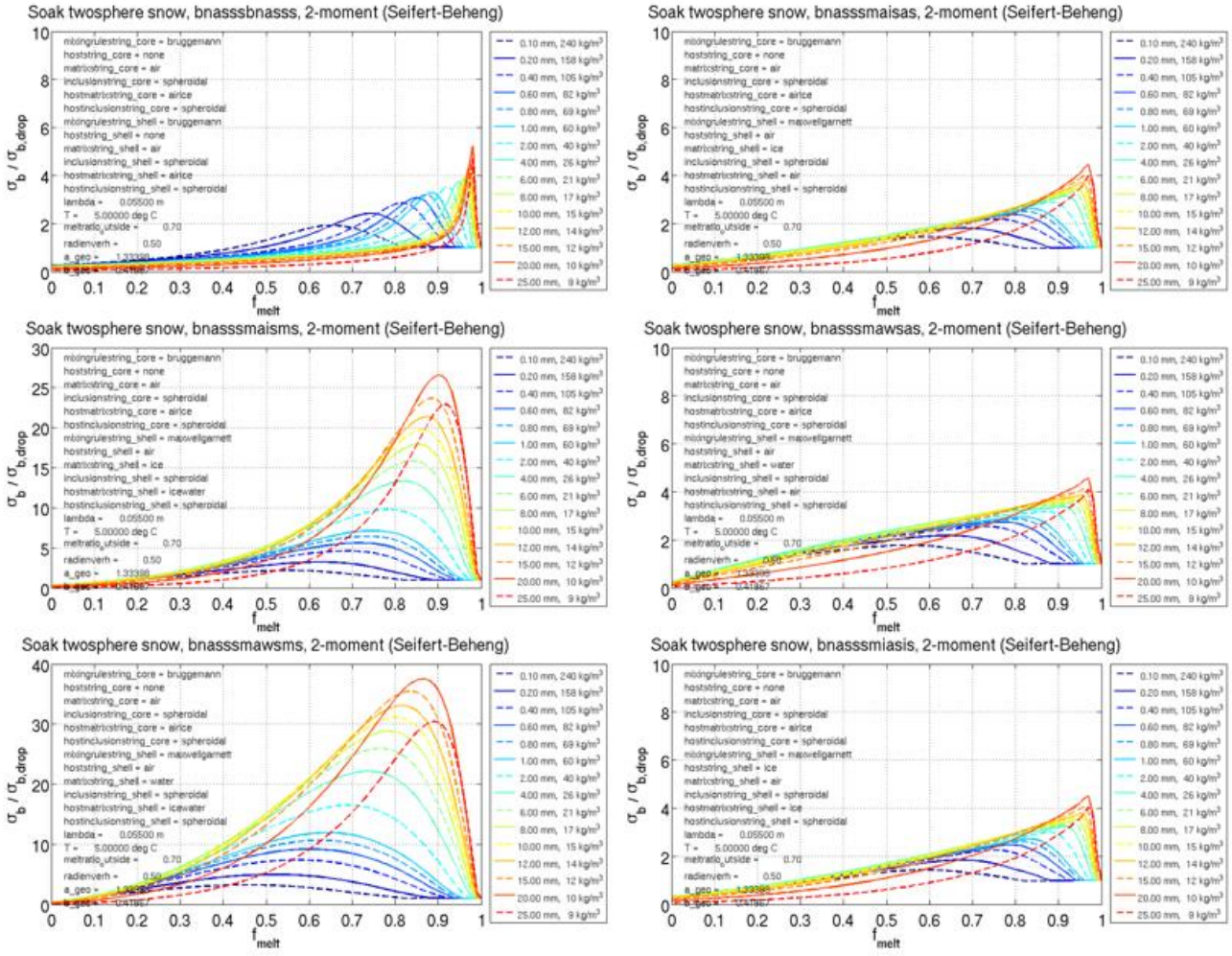


8.20 Mie: twosphere soaked wet snow, Seifert/Beheng-scheme

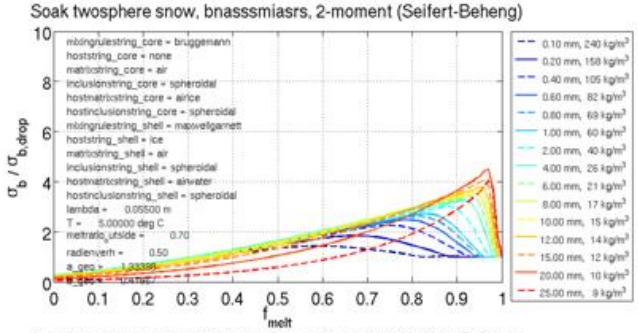
Similar to Subsection 8.19, results are shown for calculations of the backscattering cross section σ_b with subroutine `MIE_WETSNOW_TWOSPHERE()` (Mie scattering, two-layered sphere), see subsubsection 5.3.13 on Page 51. But this time, the particle bulk density as function of size is determined by equation (39) on Page 69. A depiciton of the resulting bulk density as function of particle size can be found in Figure 10 (green solid line). The following figures show the ratio of $\sigma_b/\sigma_{b,drop}$ as function of f_{melt} and the unmelted particle diameter for different EMA-formulations of the particles core and shell effective refractive indices m_{eff}.

The input parameter `meltingratio_outside` (see subsubsection 5.3.13 on Page 51) is set to 0.7, and `radienverh` (inner to outer sphere radius) is set to 0.5, independent of size and f_{melt}.

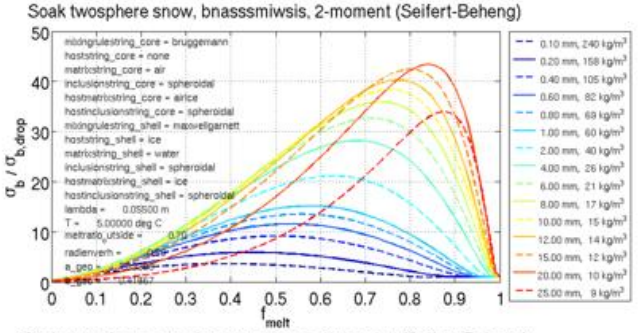
Again, every figure represents one particular EMA-formulation for m_{eff} of the particles ice-water-air core and ice-water-air shell, which both are obtained by using function `get_m_mix_nested()` (subsubsection 5.2.5 on Page 28). The input parameter sets of `get_m_mix_nested()` for core and shell can be found in the text annotation within each graph. For users of the LM, the corresponding setting of the namelist-parameter `ctype_wetsnow` can be found as 12-character code in the figures title. For explanation of the two 6-character parts of this code, see Table 40. The first 6-character sequence corresponds to the core material, the second 6-character sequence to the shell material. The results of this section apply to the LM for snow particles in case of application of the Seifert and Beheng (2006) two-moment bulk microphysical scheme (namelist-parameter `itype_gscp` ≥ 100) together with `itype_refl` $= 1$.



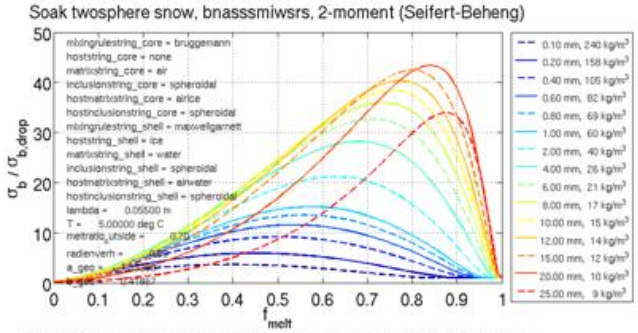
Soak twosphere snow, bnasssmiasrs, 2-moment (Seifert-Beheng)



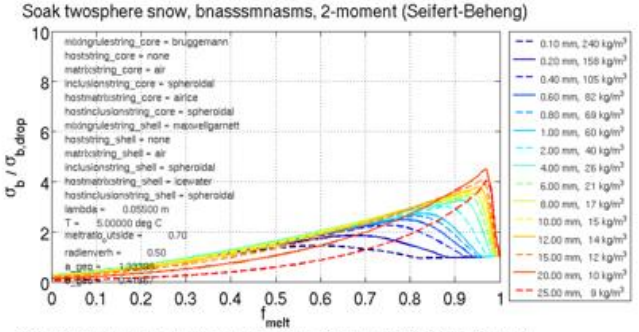
Soak twosphere snow, bnasssmiwsis, 2-moment (Seifert-Beheng)



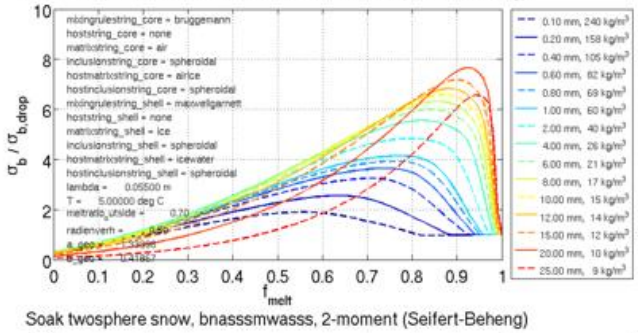
Soak twosphere snow, bnasssmiwsrs, 2-moment (Seifert-Beheng)



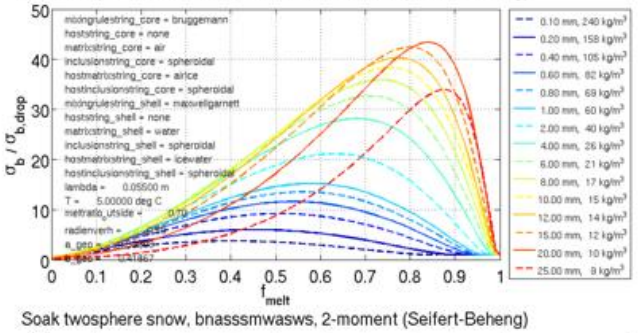
Soak twosphere snow, bnasssmnasms, 2-moment (Seifert-Beheng)



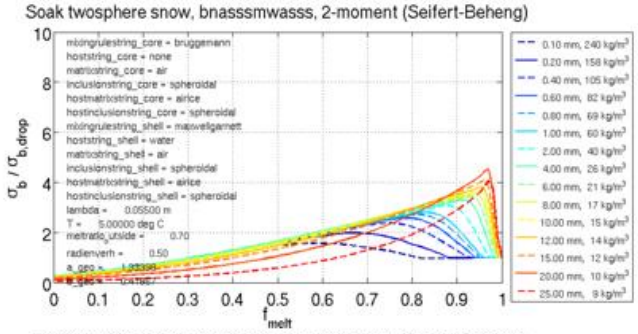
Soak twosphere snow, bnasssmnisms, 2-moment (Seifert-Beheng)



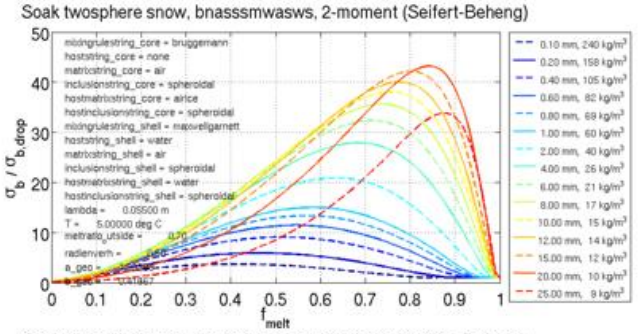
Soak twosphere snow, bnasssmnwsms, 2-moment (Seifert-Beheng)



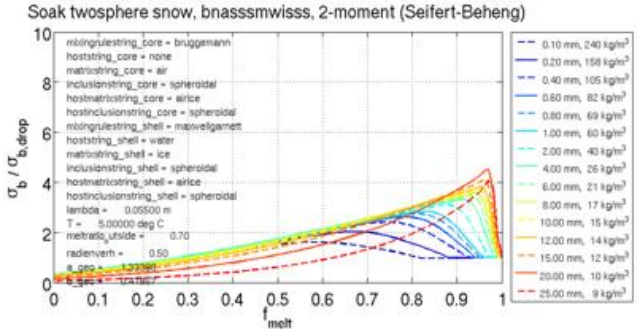
Soak twosphere snow, bnasssmwasss, 2-moment (Seifert-Beheng)



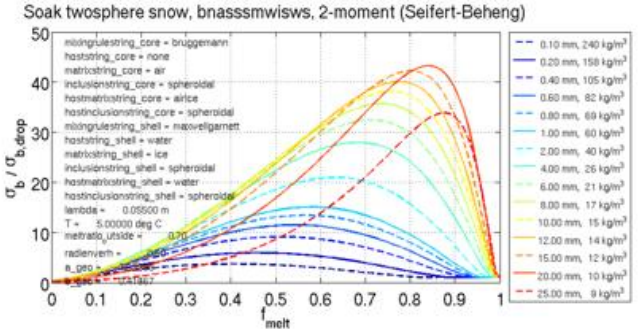
Soak twosphere snow, bnasssmwasws, 2-moment (Seifert-Beheng)



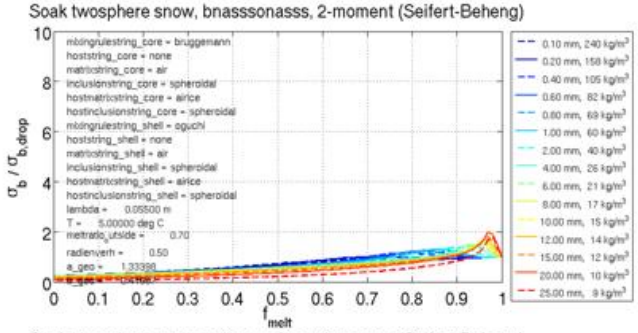
Soak twosphere snow, bnasssmwisss, 2-moment (Seifert-Beheng)



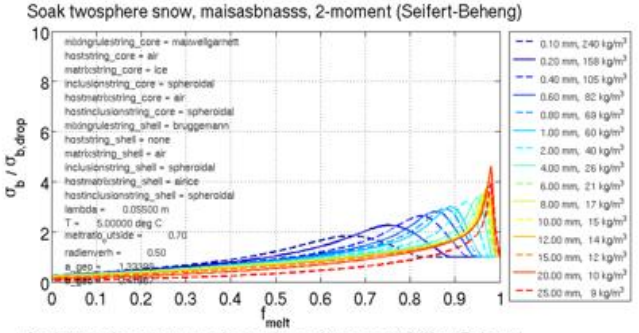
Soak twosphere snow, bnasssmwisws, 2-moment (Seifert-Beheng)



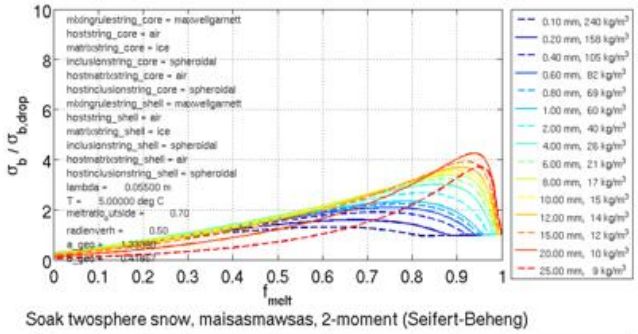
Soak twosphere snow, bnasssonasss, 2-moment (Seifert-Beheng)



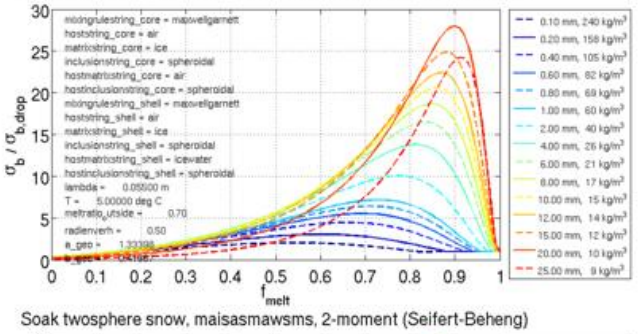
Soak twosphere snow, maisasbnasss, 2-moment (Seifert-Beheng)



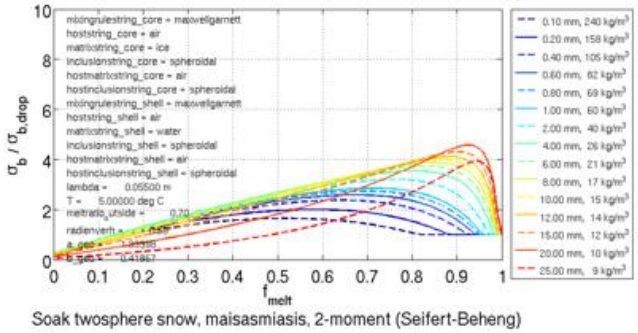
Soak twosphere snow, maisasmaisas, 2-moment (Seifert-Beheng)



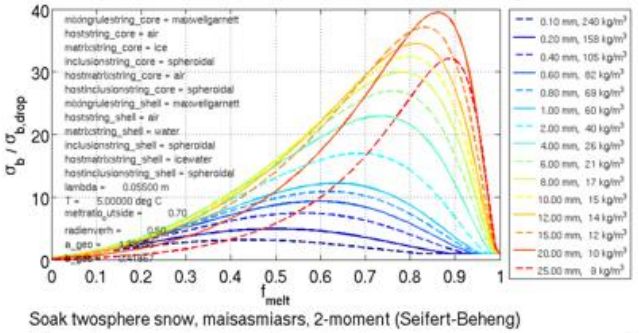
Soak twosphere snow, maisasmaisms, 2-moment (Seifert-Beheng)



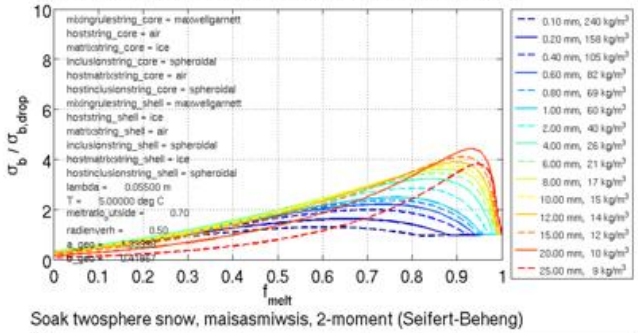
Soak twosphere snow, maisasmawsas, 2-moment (Seifert-Beheng)



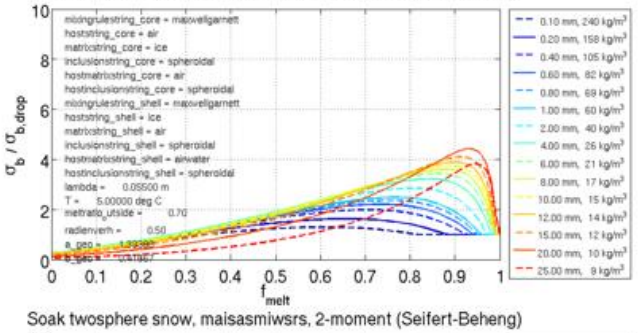
Soak twosphere snow, maisasmawsms, 2-moment (Seifert-Beheng)



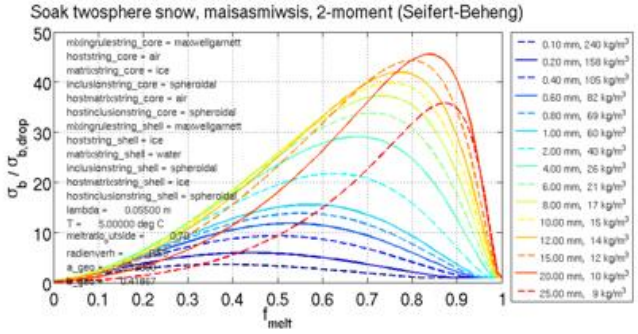
Soak twosphere snow, maisasmiasis, 2-moment (Seifert-Beheng)



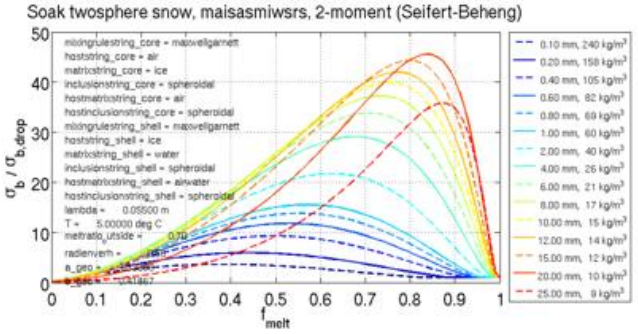
Soak twosphere snow, maisasmiasrs, 2-moment (Seifert-Beheng)



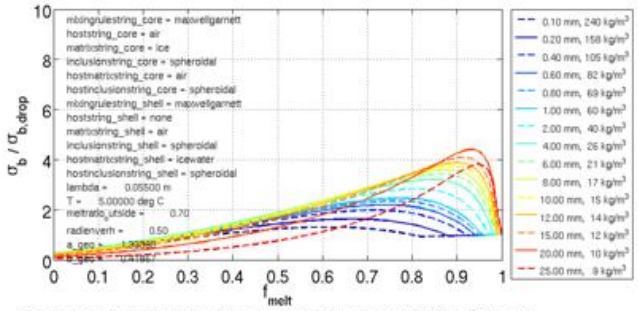
Soak twosphere snow, maisasmiwsis, 2-moment (Seifert-Beheng)



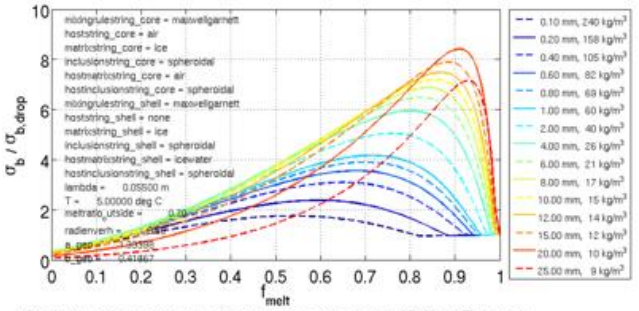
Soak twosphere snow, maisasmiwsrs, 2-moment (Seifert-Beheng)



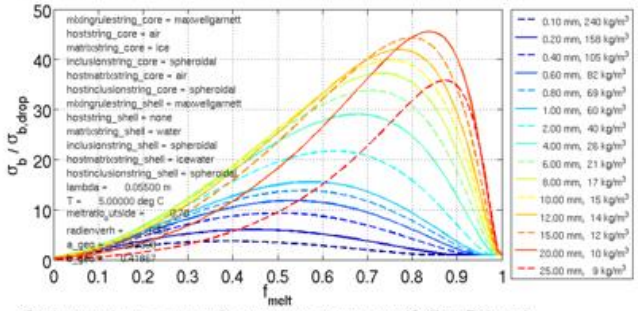
Soak twosphere snow, maisasmnasms, 2-moment (Seifert-Beheng)



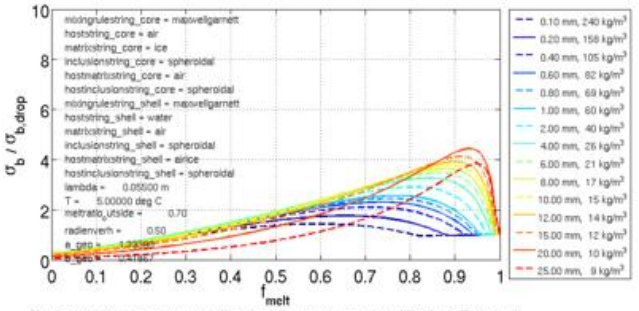
Soak twosphere snow, maisasmnisms, 2-moment (Seifert-Beheng)



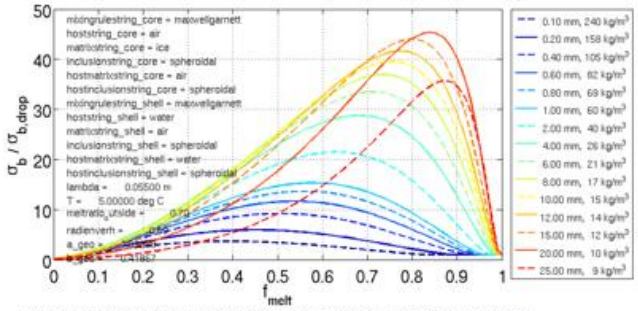
Soak twosphere snow, maisasmnwsms, 2-moment (Seifert-Beheng)



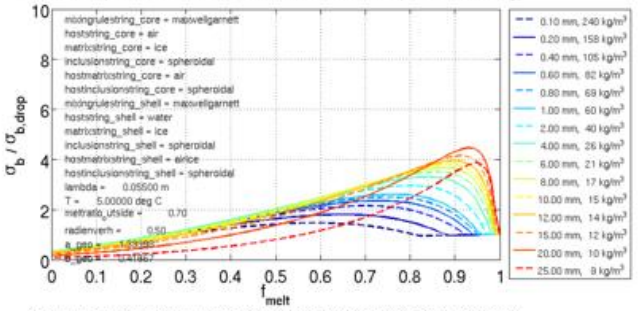
Soak twosphere snow, maisasmwasss, 2-moment (Seifert-Beheng)



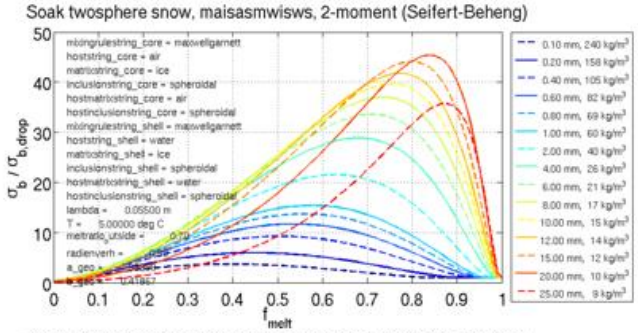
Soak twosphere snow, maisasmwasws, 2-moment (Seifert-Beheng)



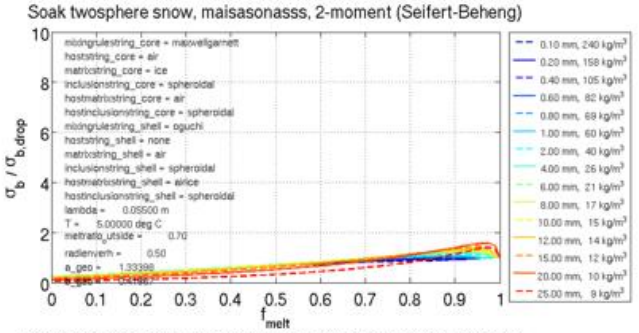
Soak twosphere snow, maisasmwisss, 2-moment (Seifert-Beheng)



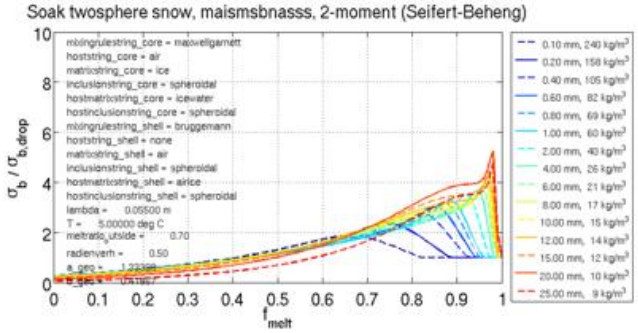
Soak twosphere snow, maisasmwisws, 2-moment (Seifert-Beheng)



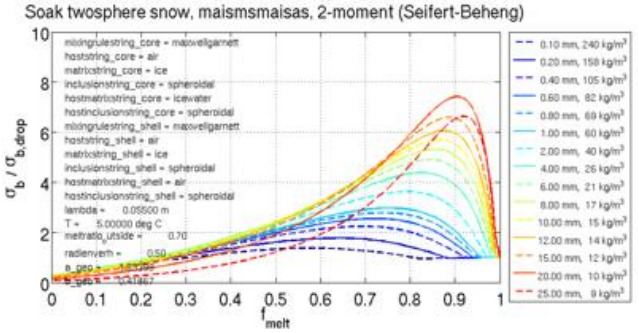
Soak twosphere snow, maisasonasss, 2-moment (Seifert-Beheng)



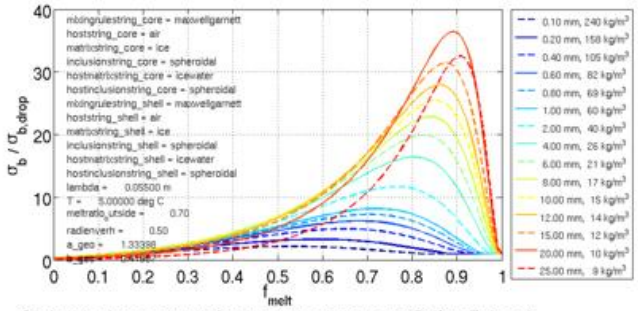
Soak twosphere snow, maismsbnasss, 2-moment (Seifert-Beheng)



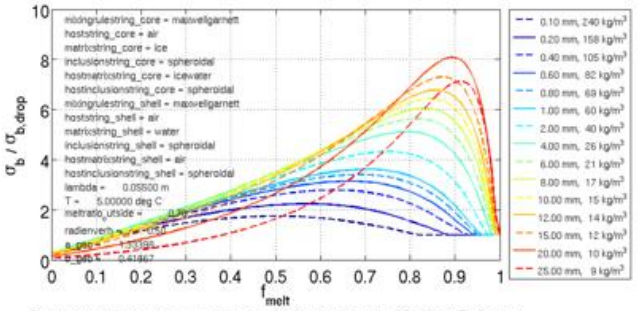
Soak twosphere snow, maismsmaisas, 2-moment (Seifert-Beheng)



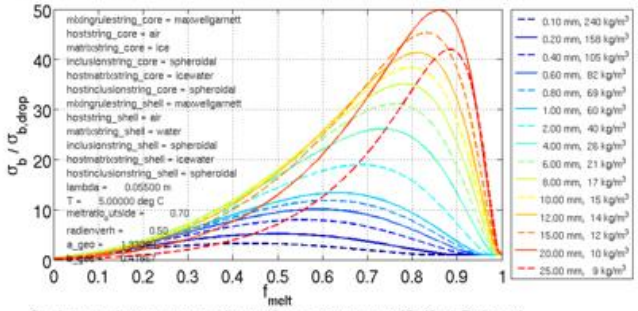
Soak twosphere snow, maismsmaisms, 2-moment (Seifert-Beheng)



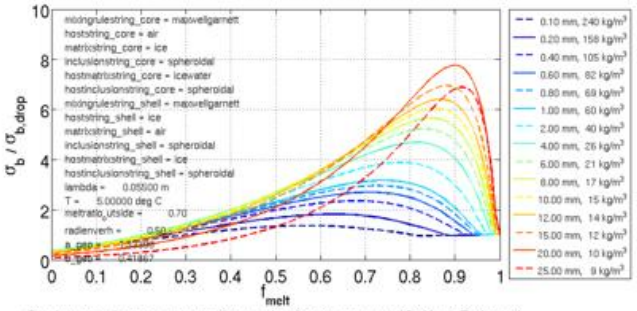
Soak twosphere snow, maismsmawsas, 2-moment (Seifert-Beheng)



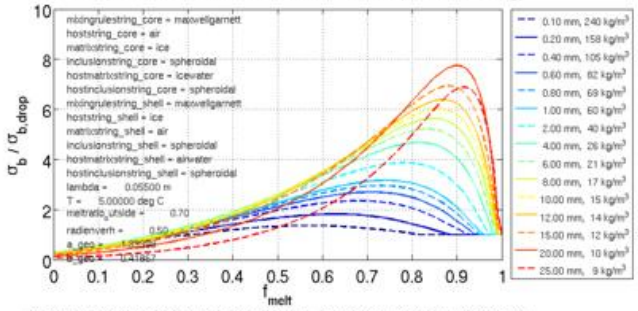
Soak twosphere snow, maismsmawsms, 2-moment (Seifert-Beheng)



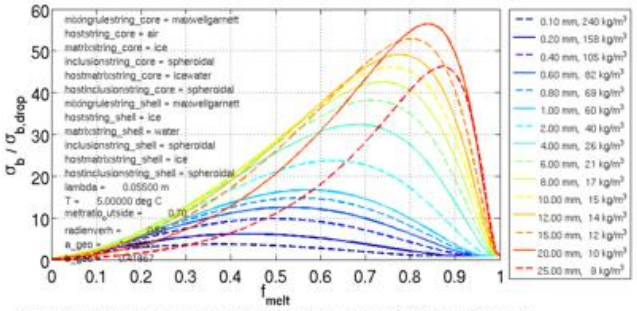
Soak twosphere snow, maismsmiasis, 2-moment (Seifert-Beheng)



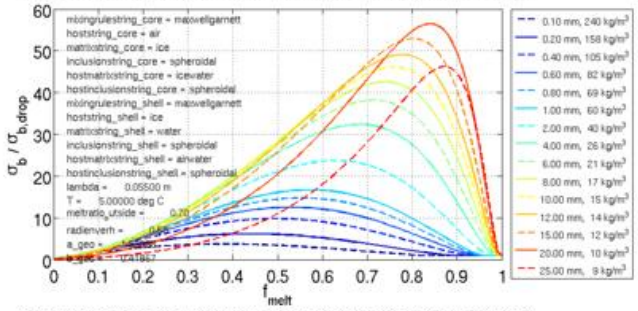
Soak twosphere snow, maismsmiasrs, 2-moment (Seifert-Beheng)



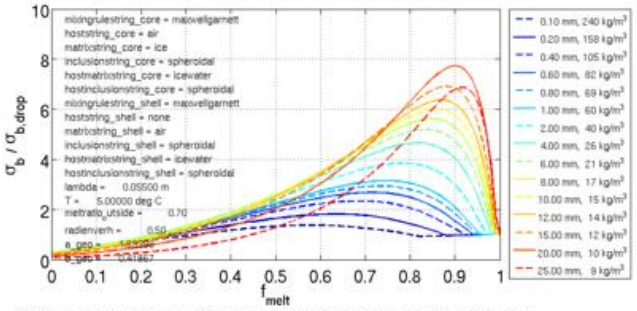
Soak twosphere snow, maismsmiwsis, 2-moment (Seifert-Beheng)



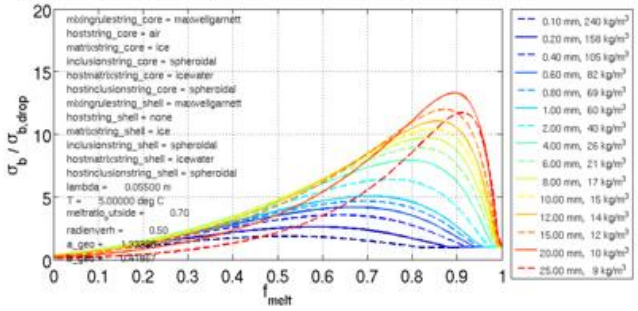
Soak twosphere snow, maismsmiwsrs, 2-moment (Seifert-Beheng)



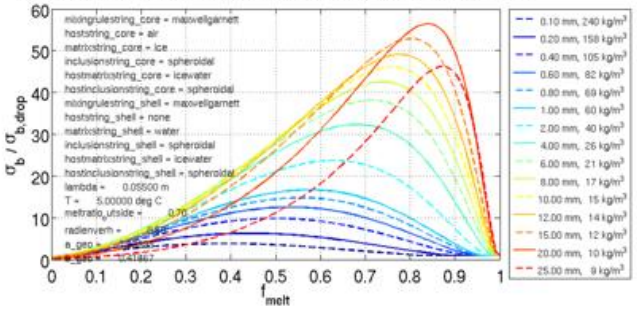
Soak twosphere snow, maismsmnasms, 2-moment (Seifert-Beheng)



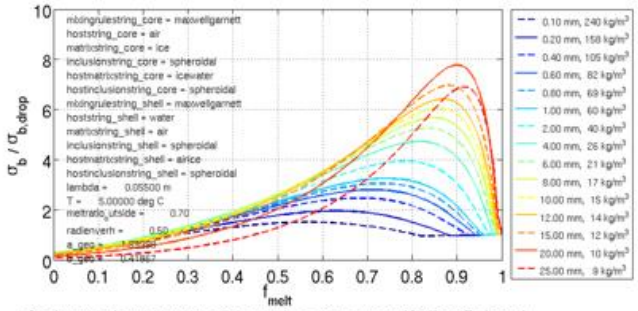
Soak twosphere snow, maismsmnisms, 2-moment (Seifert-Beheng)



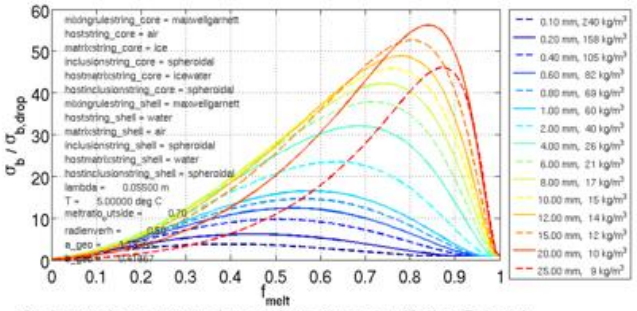
Soak twosphere snow, maismsmnwsms, 2-moment (Seifert-Beheng)



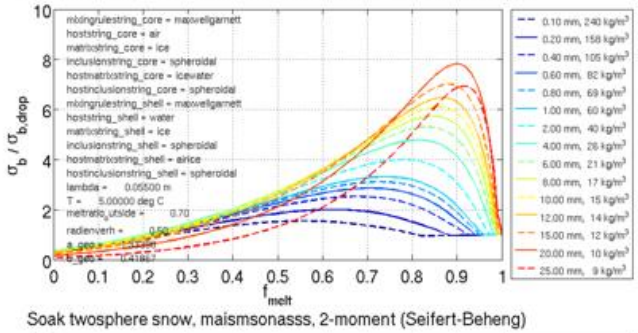
Soak twosphere snow, maismsmwasss, 2-moment (Seifert-Beheng)



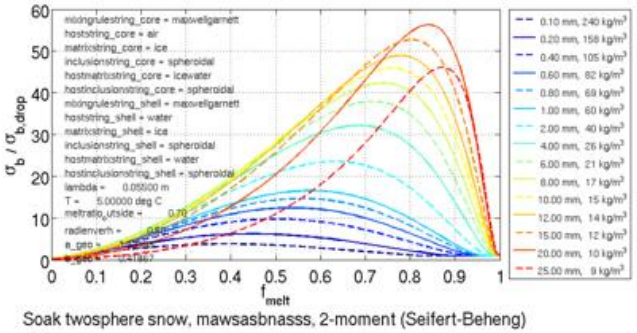
Soak twosphere snow, maismsmwasws, 2-moment (Seifert-Beheng)



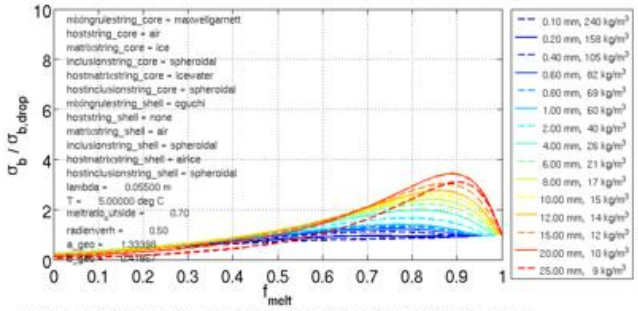
Soak twosphere snow, maismsmwisss, 2-moment (Seifert-Beheng)



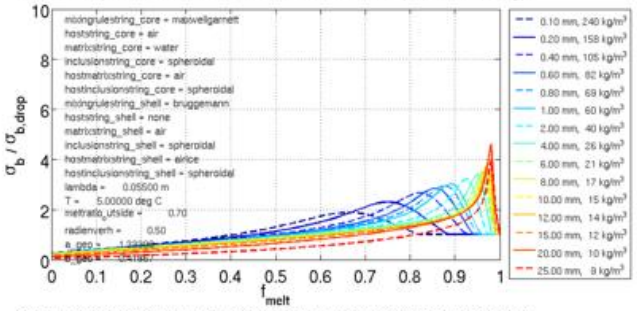
Soak twosphere snow, maismsmwisws, 2-moment (Seifert-Beheng)



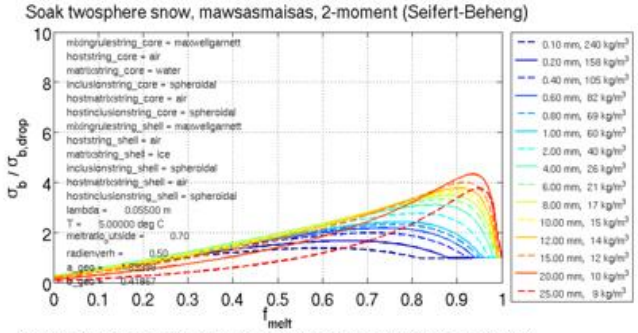
Soak twosphere snow, maismsonasss, 2-moment (Seifert-Beheng)



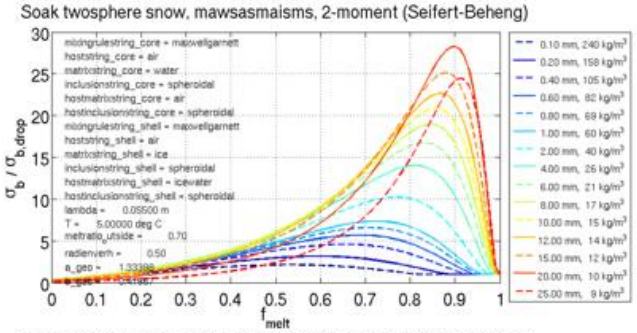
Soak twosphere snow, mawsasbnasss, 2-moment (Seifert-Beheng)



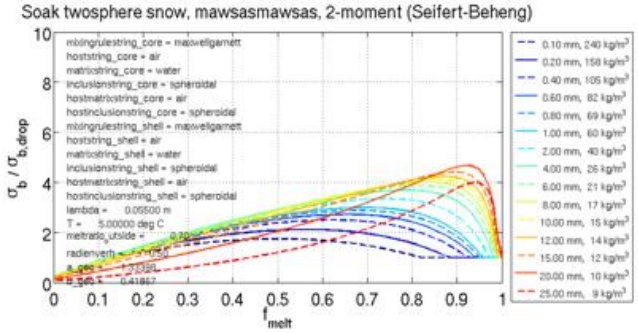
Soak twosphere snow, mawsasmaisas, 2-moment (Seifert-Beheng)



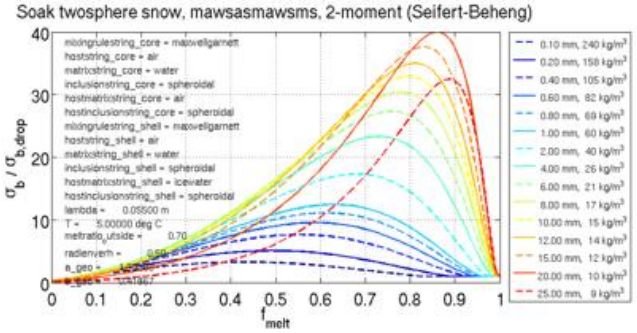
Soak twosphere snow, mawsasmaisms, 2-moment (Seifert-Beheng)



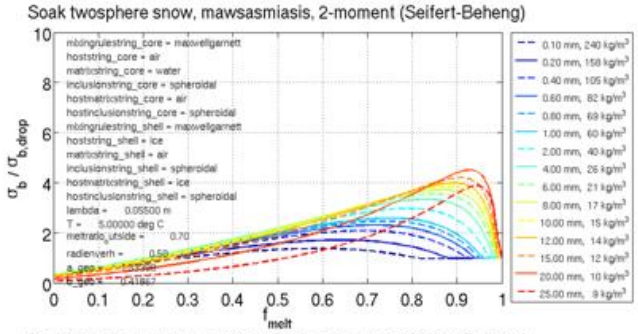
Soak twosphere snow, mawsasmawsas, 2-moment (Seifert-Beheng)



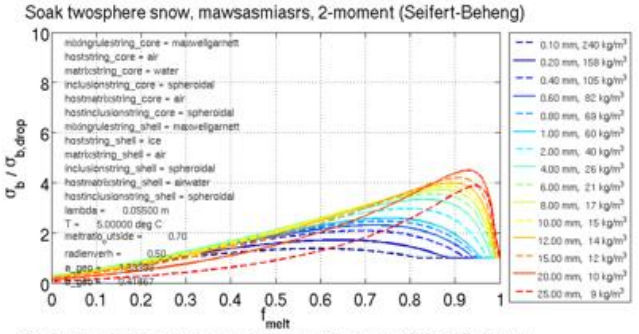
Soak twosphere snow, mawsasmawsms, 2-moment (Seifert-Beheng)



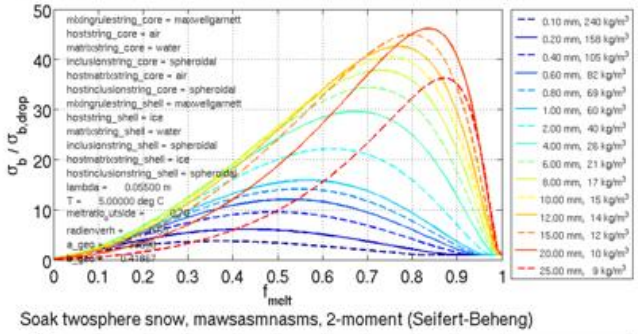
Soak twosphere snow, mawsasmiasis, 2-moment (Seifert-Beheng)



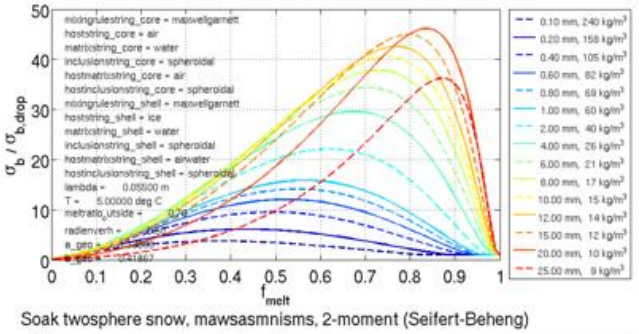
Soak twosphere snow, mawsasmiasrs, 2-moment (Seifert-Beheng)



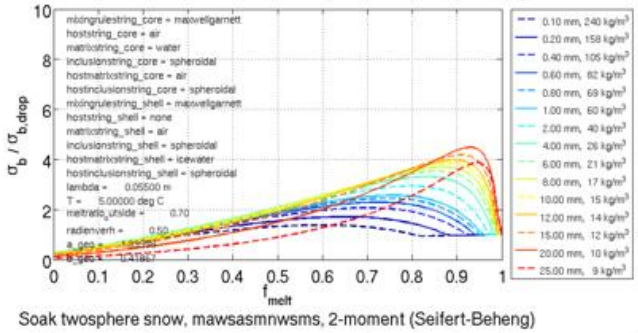
Soak twosphere snow, mawsasmiwsis, 2-moment (Seifert-Beheng)



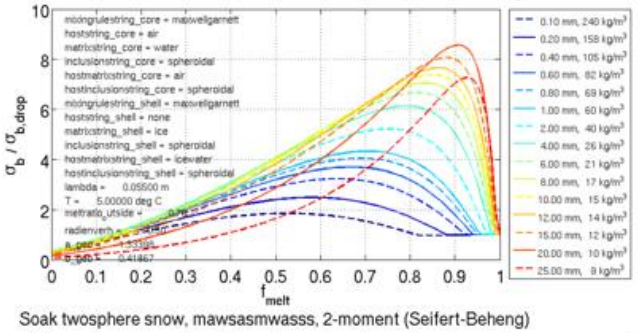
Soak twosphere snow, mawsasmiwsrs, 2-moment (Seifert-Beheng)



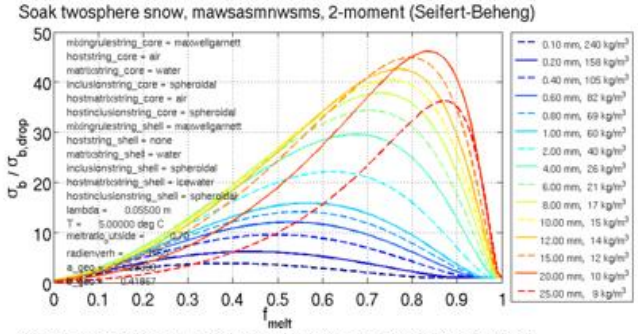
Soak twosphere snow, mawsasmnasms, 2-moment (Seifert-Beheng)



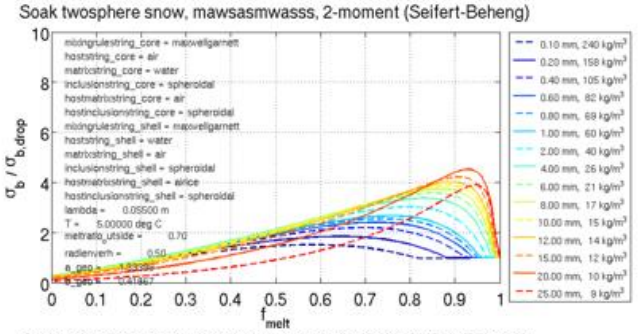
Soak twosphere snow, mawsasmnisms, 2-moment (Seifert-Beheng)



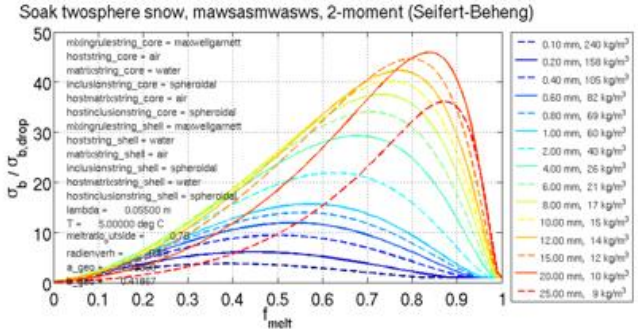
Soak twosphere snow, mawsasmnwsms, 2-moment (Seifert-Beheng)



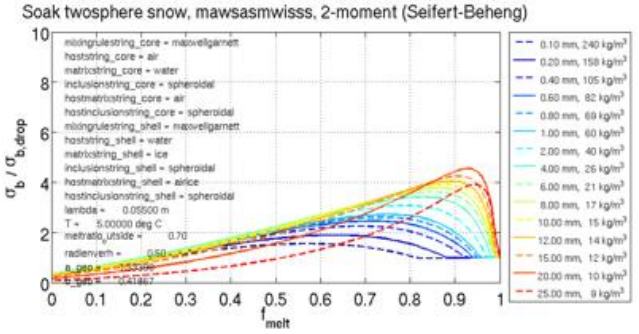
Soak twosphere snow, mawsasmwasss, 2-moment (Seifert-Beheng)



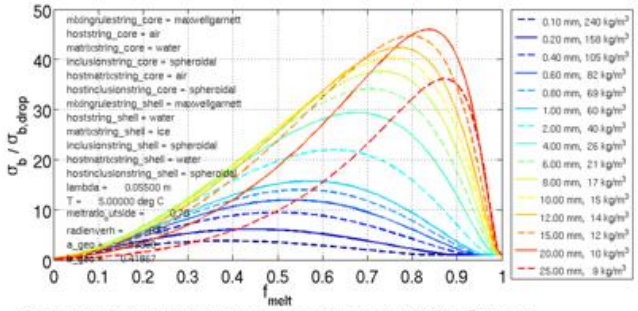
Soak twosphere snow, mawsasmwasws, 2-moment (Seifert-Beheng)



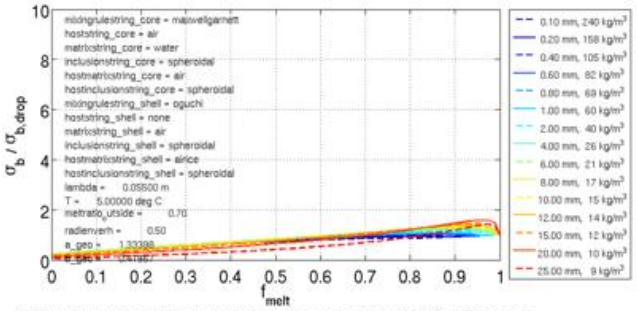
Soak twosphere snow, mawsasmwisss, 2-moment (Seifert-Beheng)



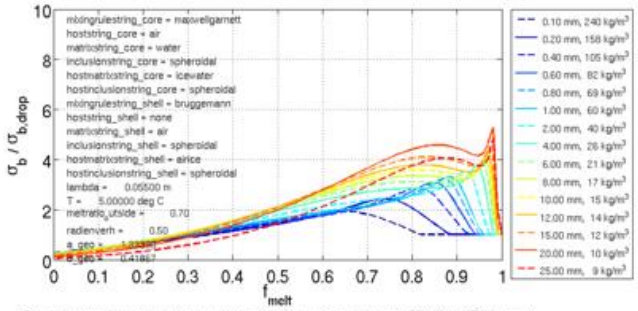
Soak twosphere snow, mawsasmwisws, 2-moment (Seifert-Beheng)



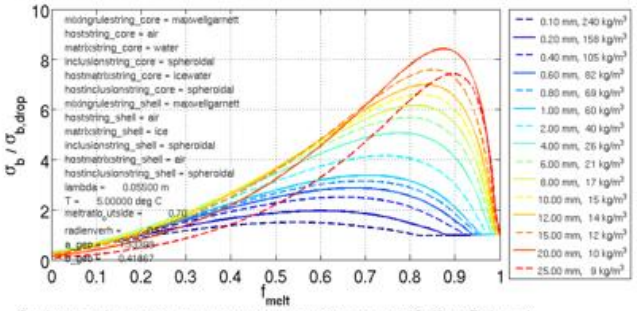
Soak twosphere snow, mawsasonasss, 2-moment (Seifert-Beheng)



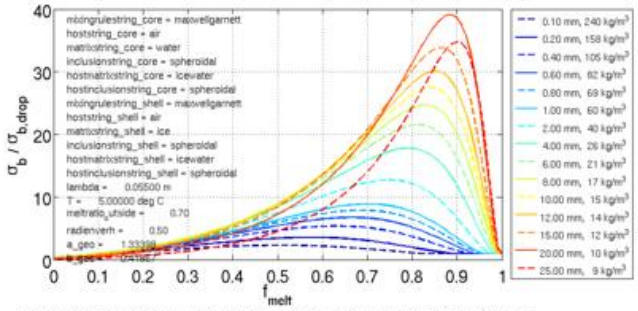
Soak twosphere snow, mawsmsbnasss, 2-moment (Seifert-Beheng)



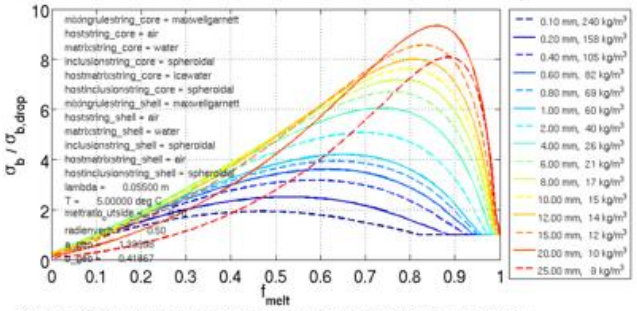
Soak twosphere snow, mawsmsmaisas, 2-moment (Seifert-Beheng)



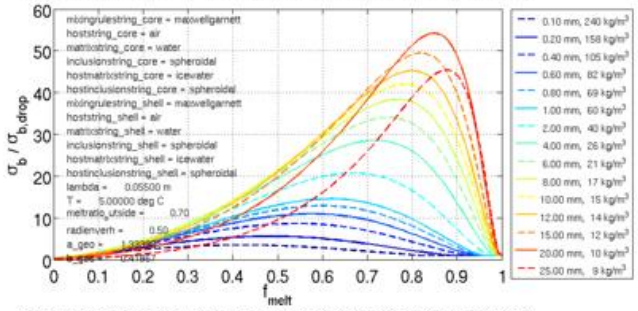
Soak twosphere snow, mawsmsmaisms, 2-moment (Seifert-Beheng)



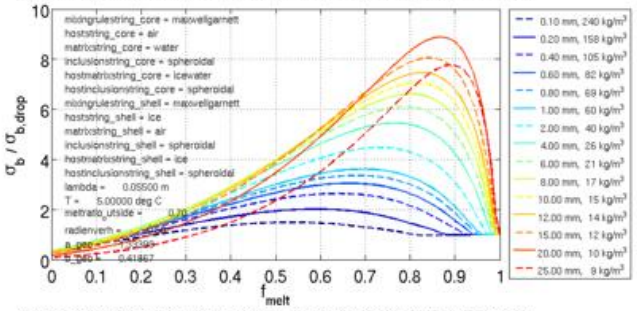
Soak twosphere snow, mawsmsmawsas, 2-moment (Seifert-Beheng)



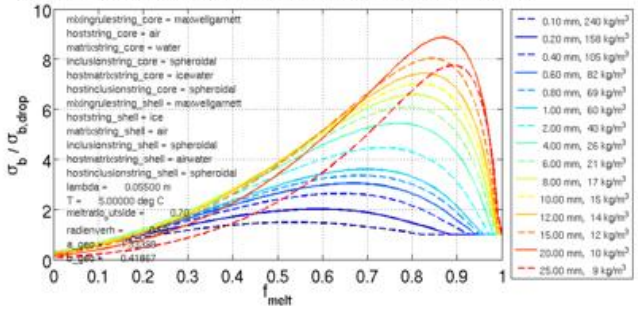
Soak twosphere snow, mawsmsmawsms, 2-moment (Seifert-Beheng)



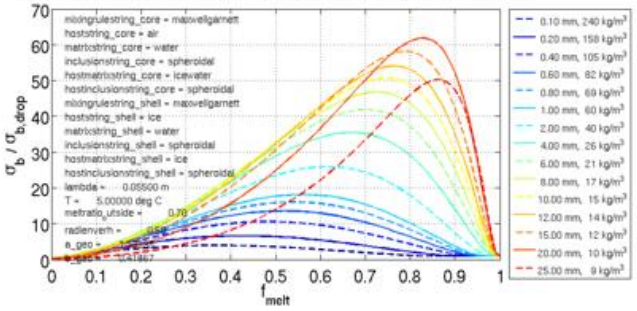
Soak twosphere snow, mawsmsmiasis, 2-moment (Seifert-Beheng)



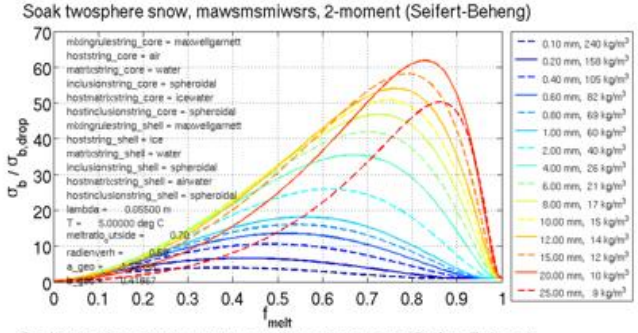
Soak twosphere snow, mawsmsmiasrs, 2-moment (Seifert-Beheng)



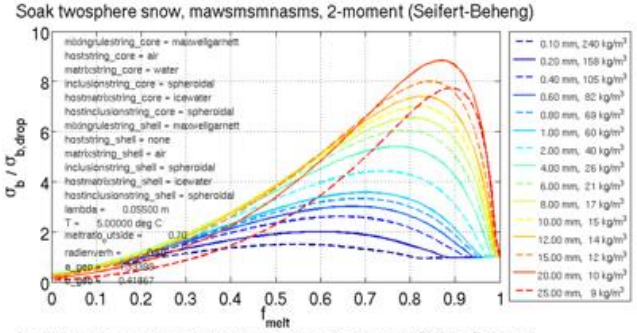
Soak twosphere snow, mawsmsmiwsis, 2-moment (Seifert-Beheng)



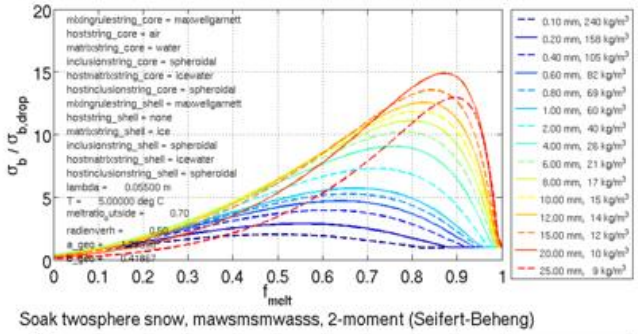
Soak twosphere snow, mawsmsmiwsrs, 2-moment (Seifert-Beheng)



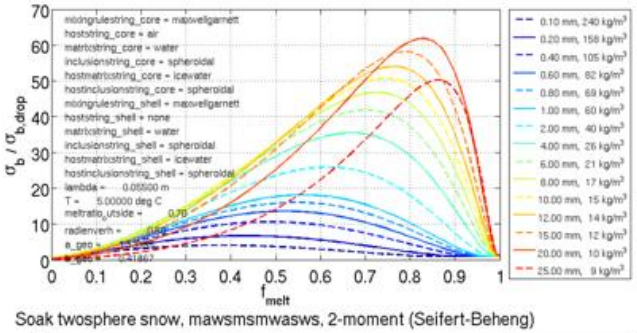
Soak twosphere snow, mawsmsmnasms, 2-moment (Seifert-Beheng)



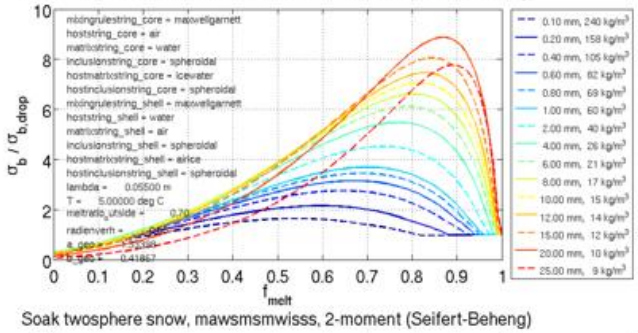
Soak twosphere snow, mawsmsmnisms, 2-moment (Seifert-Beheng)



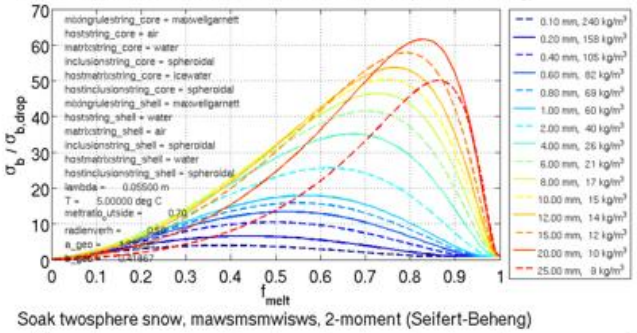
Soak twosphere snow, mawsmsmnwsms, 2-moment (Seifert-Beheng)



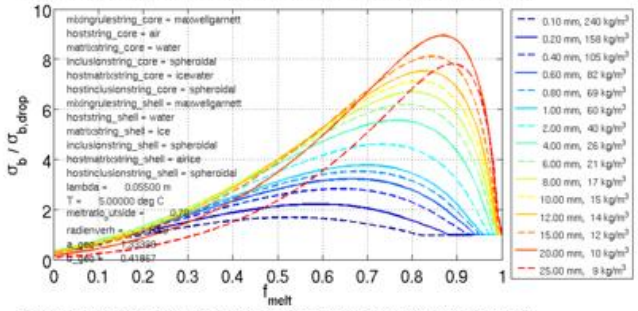
Soak twosphere snow, mawsmsmwasss, 2-moment (Seifert-Beheng)



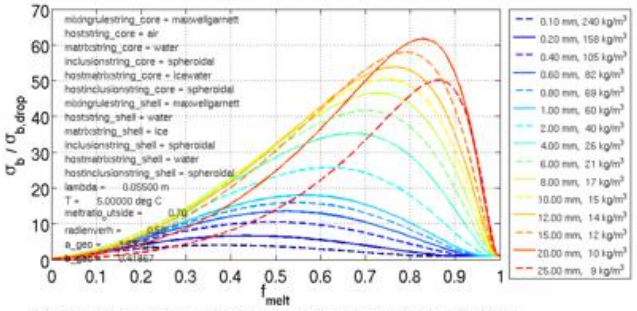
Soak twosphere snow, mawsmsmwasws, 2-moment (Seifert-Beheng)



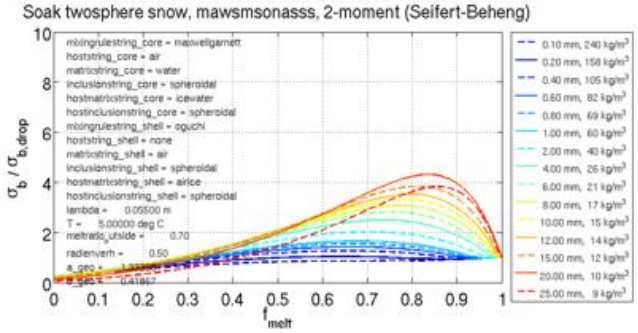
Soak twosphere snow, mawsmsmwisss, 2-moment (Seifert-Beheng)



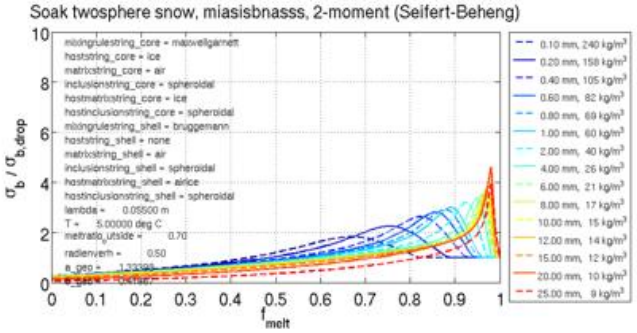
Soak twosphere snow, mawsmsmwisws, 2-moment (Seifert-Beheng)



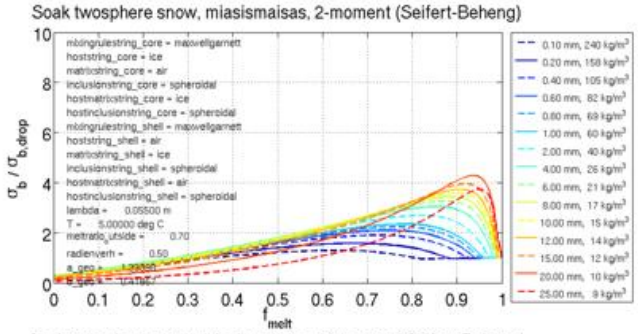
Soak twosphere snow, mawsmsonasss, 2-moment (Seifert-Beheng)



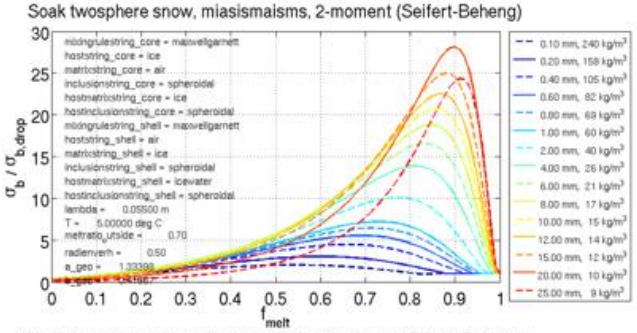
Soak twosphere snow, miasisbnasss, 2-moment (Seifert-Beheng)



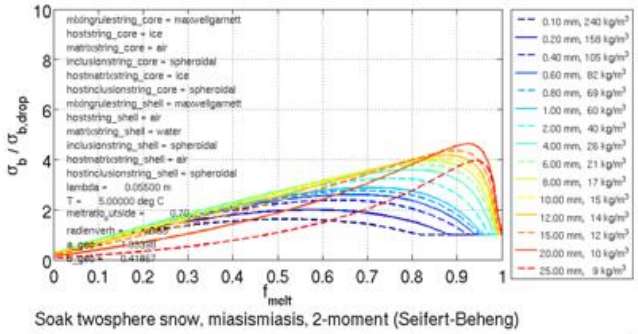
Soak twosphere snow, miasismaisas, 2-moment (Seifert-Beheng)



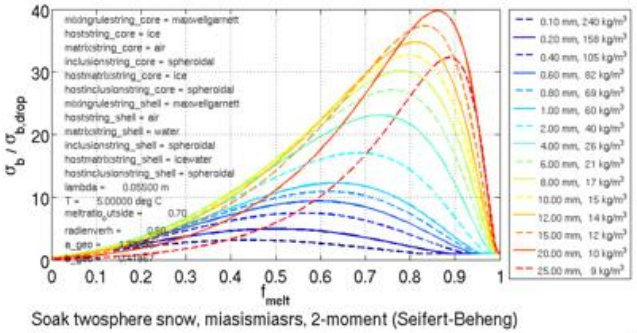
Soak twosphere snow, miasismaisms, 2-moment (Seifert-Beheng)



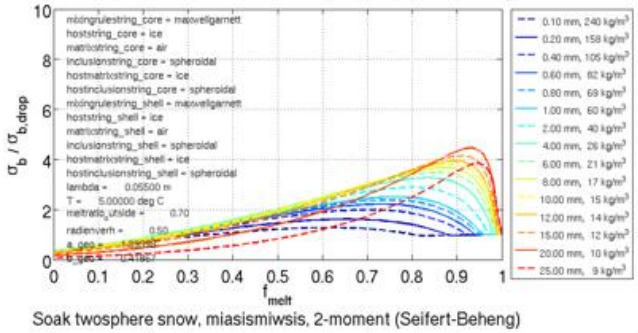
Soak twosphere snow, miasismawsas, 2-moment (Seifert-Beheng)



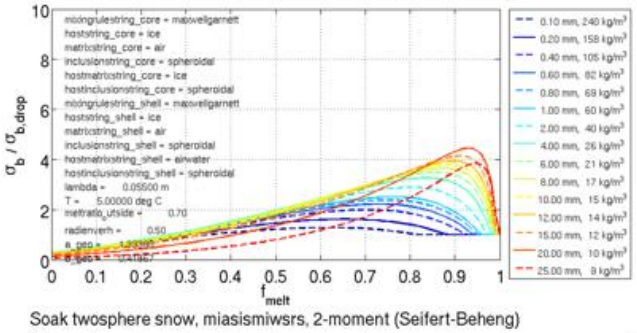
Soak twosphere snow, miasismawsms, 2-moment (Seifert-Beheng)



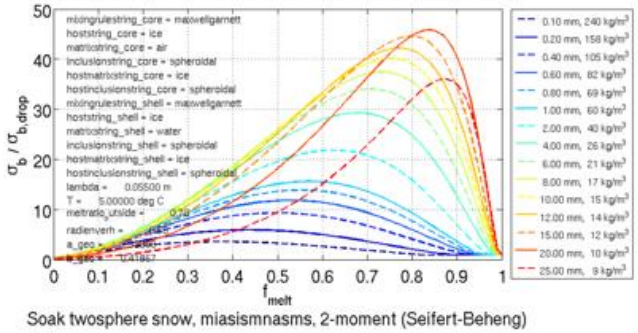
Soak twosphere snow, miasismiasis, 2-moment (Seifert-Beheng)



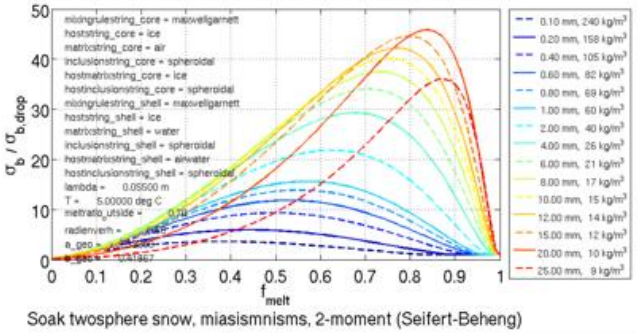
Soak twosphere snow, miasismiasrs, 2-moment (Seifert-Beheng)



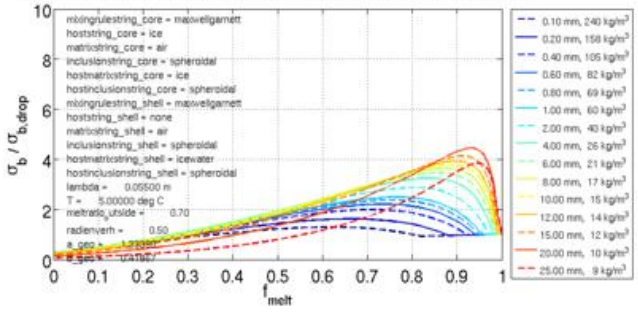
Soak twosphere snow, miasismiwsis, 2-moment (Seifert-Beheng)



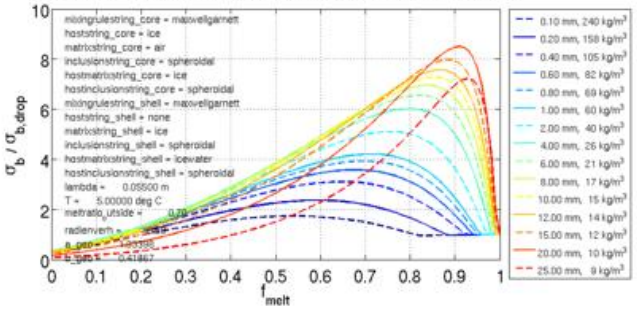
Soak twosphere snow, miasismiwsrs, 2-moment (Seifert-Beheng)



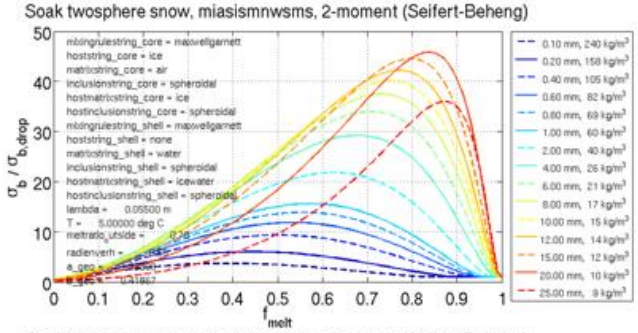
Soak twosphere snow, miasismnasms, 2-moment (Seifert-Beheng)



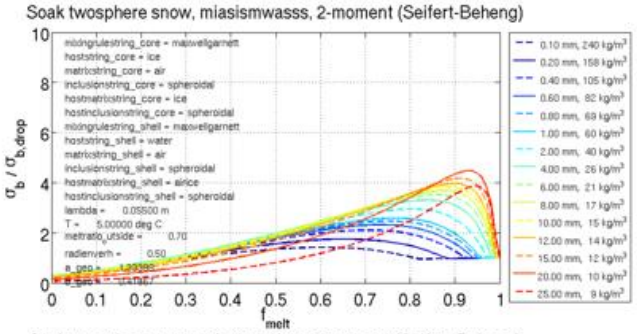
Soak twosphere snow, miasismnisms, 2-moment (Seifert-Beheng)



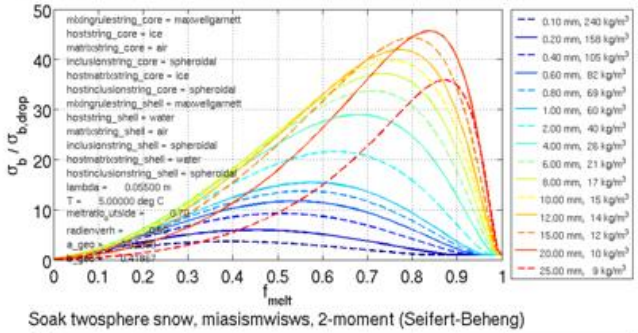
Soak twosphere snow, miasismnwsms, 2-moment (Seifert-Beheng)



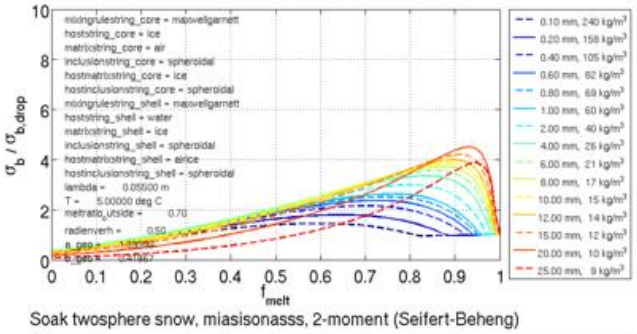
Soak twosphere snow, miasismwasss, 2-moment (Seifert-Beheng)



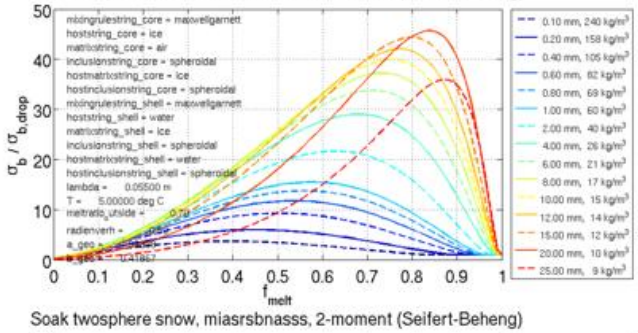
Soak twosphere snow, miasismwasws, 2-moment (Seifert-Beheng)



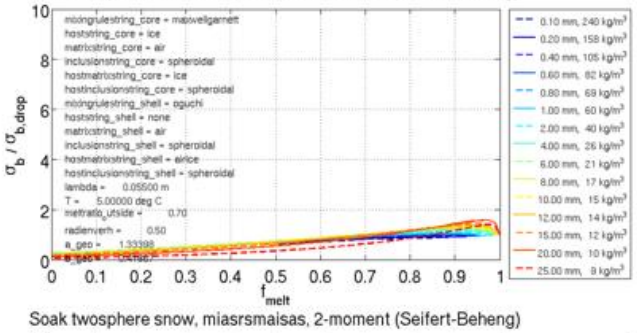
Soak twosphere snow, miasismwisss, 2-moment (Seifert-Beheng)



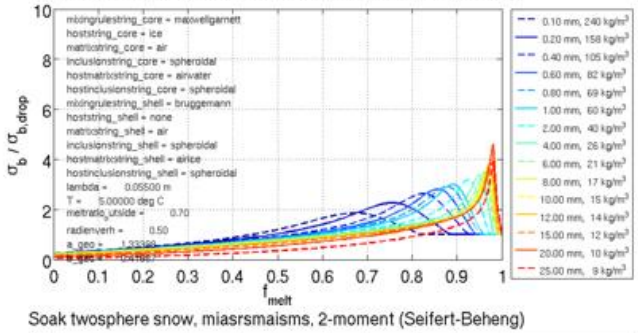
Soak twosphere snow, miasismwisws, 2-moment (Seifert-Beheng)



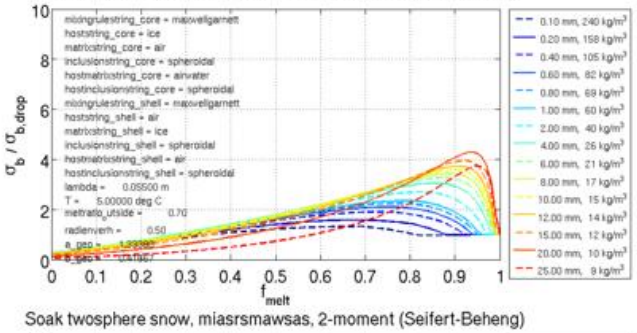
Soak twosphere snow, miasisonasss, 2-moment (Seifert-Beheng)



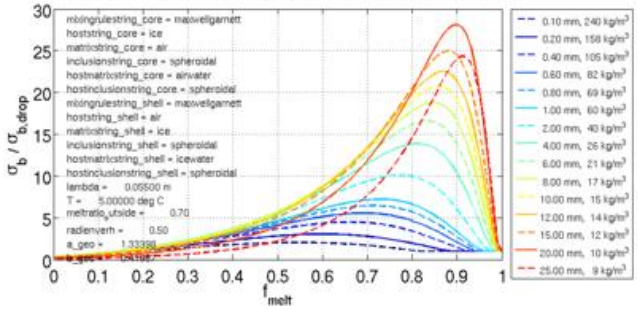
Soak twosphere snow, miasrsbnasss, 2-moment (Seifert-Beheng)



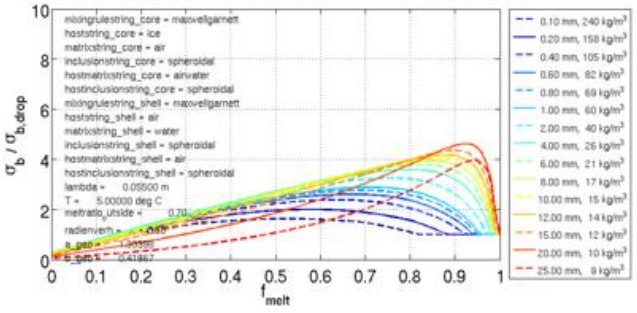
Soak twosphere snow, miasrsmaisas, 2-moment (Seifert-Beheng)



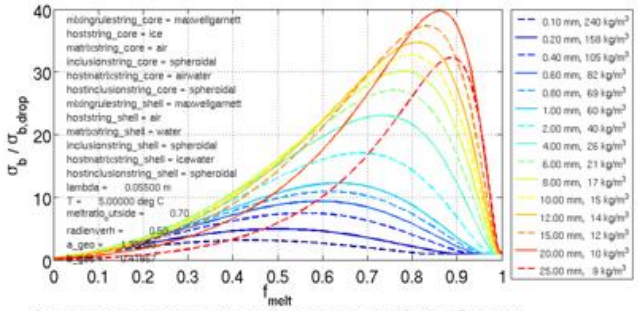
Soak twosphere snow, miasrsmaisms, 2-moment (Seifert-Beheng)



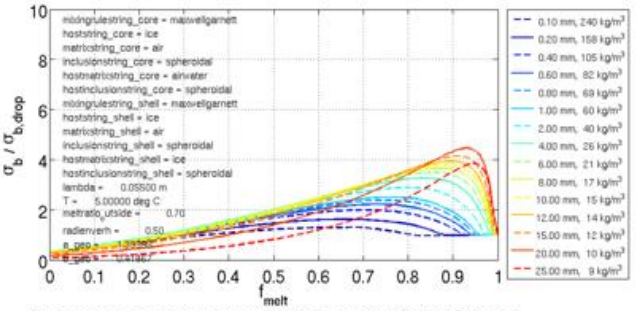
Soak twosphere snow, miasrsmawsas, 2-moment (Seifert-Beheng)



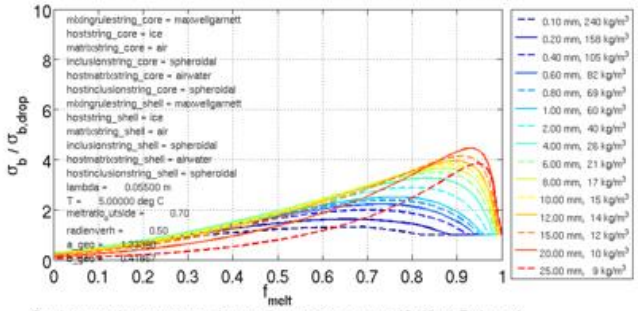
Soak twosphere snow, miasrsmawsms, 2-moment (Seifert-Beheng)



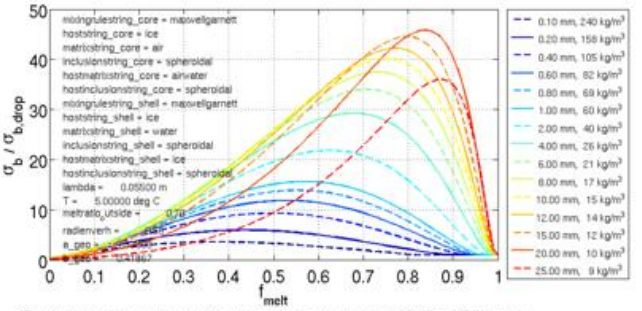
Soak twosphere snow, miasrsmiasis, 2-moment (Seifert-Beheng)



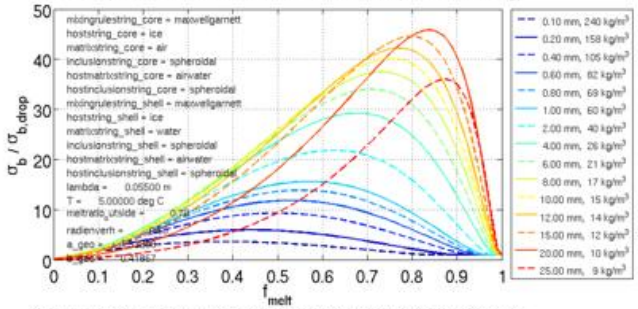
Soak twosphere snow, miasrsmiasrs, 2-moment (Seifert-Beheng)



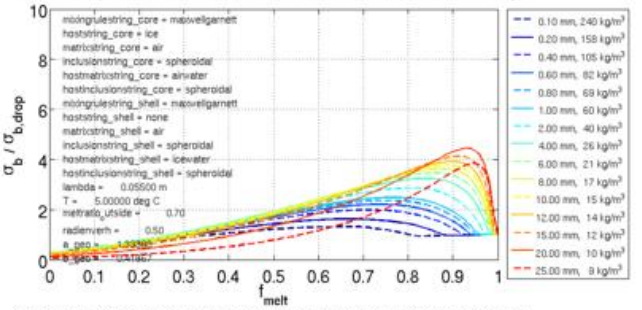
Soak twosphere snow, miasrsmiwsis, 2-moment (Seifert-Beheng)



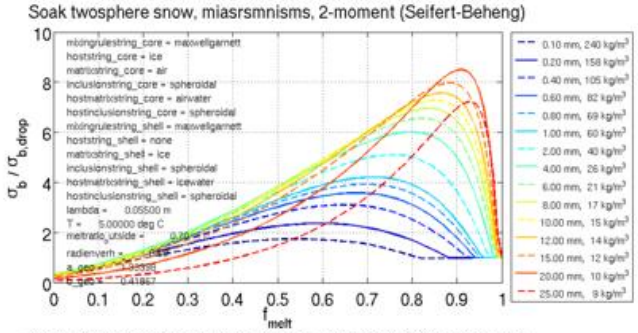
Soak twosphere snow, miasrsmiwsrs, 2-moment (Seifert-Beheng)



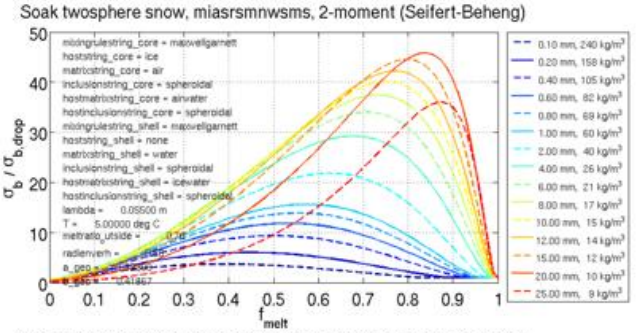
Soak twosphere snow, miasrsmnasms, 2-moment (Seifert-Beheng)



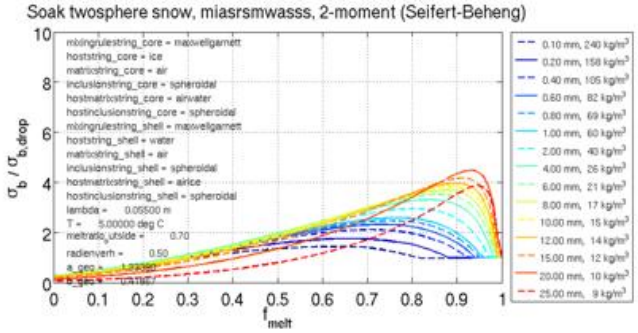
Soak twosphere snow, miasrsmnisms, 2-moment (Seifert-Beheng)



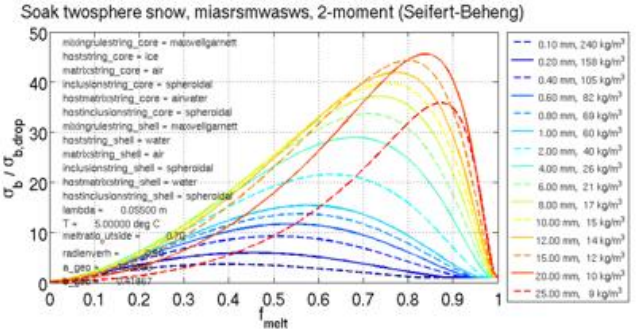
Soak twosphere snow, miasrsmnwsms, 2-moment (Seifert-Beheng)



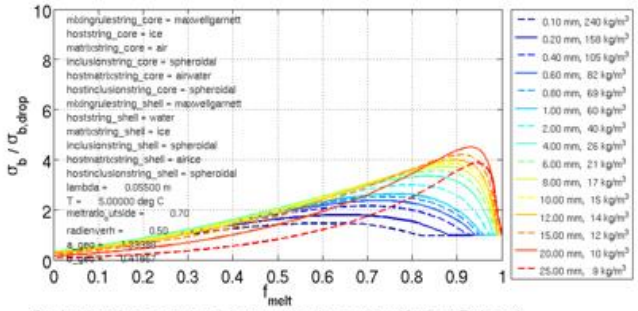
Soak twosphere snow, miasrsmwasss, 2-moment (Seifert-Beheng)



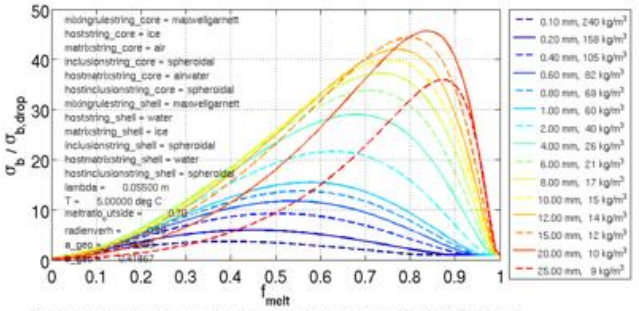
Soak twosphere snow, miasrsmwasws, 2-moment (Seifert-Beheng)



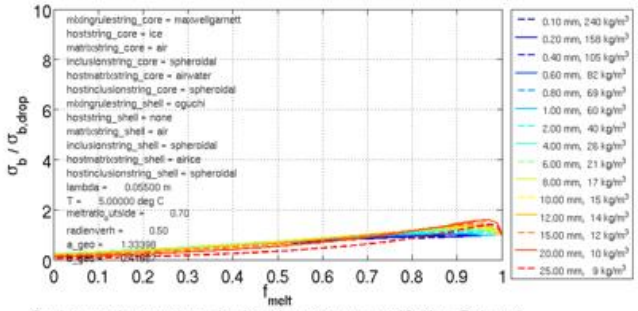
Soak twosphere snow, miasrsmwisss, 2-moment (Seifert-Beheng)



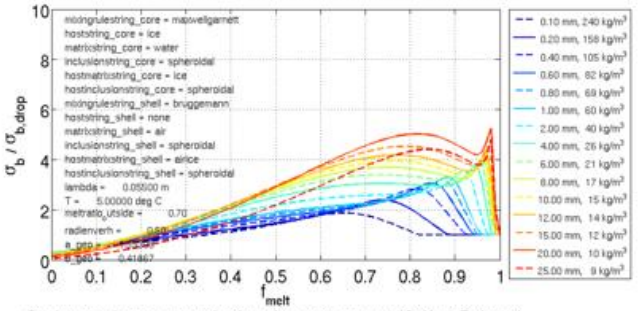
Soak twosphere snow, miasrsmwisws, 2-moment (Seifert-Beheng)



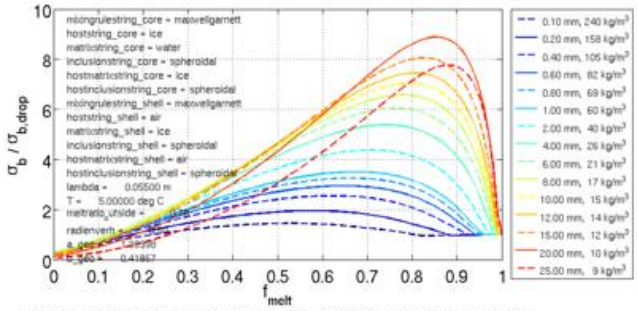
Soak twosphere snow, miasrsonasss, 2-moment (Seifert-Beheng)



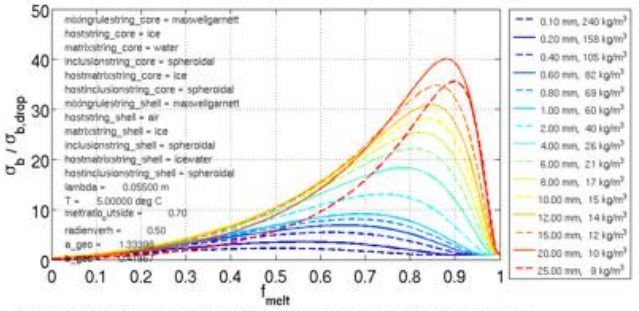
Soak twosphere snow, miwsisbnasss, 2-moment (Seifert-Beheng)



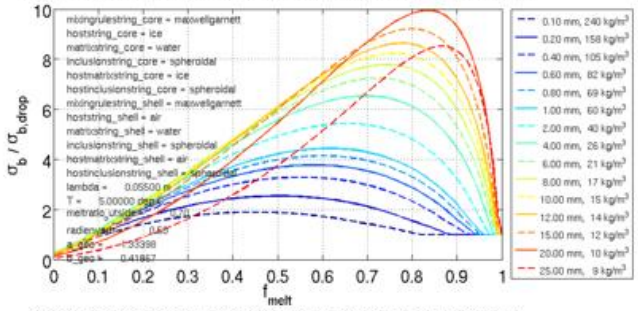
Soak twosphere snow, miwsismaisas, 2-moment (Seifert-Beheng)



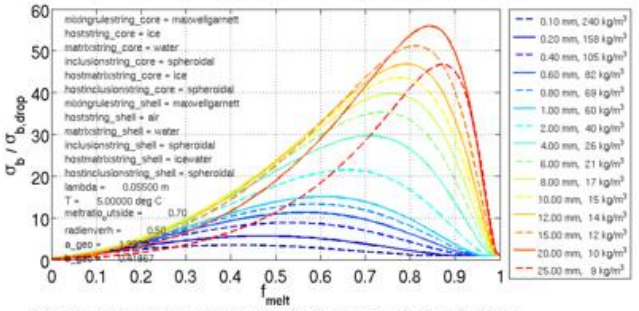
Soak twosphere snow, miwsismaisms, 2-moment (Seifert-Beheng)



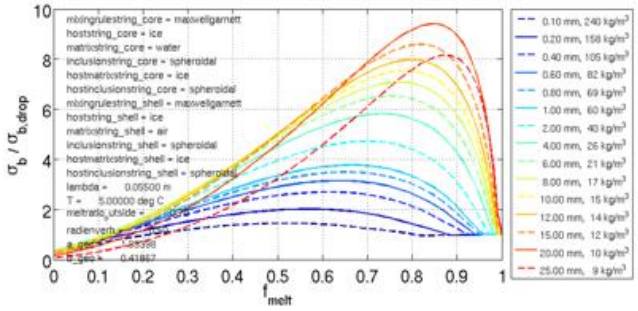
Soak twosphere snow, miwsismawsas, 2-moment (Seifert-Beheng)



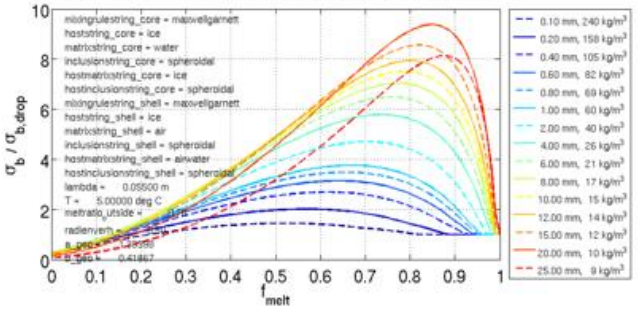
Soak twosphere snow, miwsismawsms, 2-moment (Seifert-Beheng)



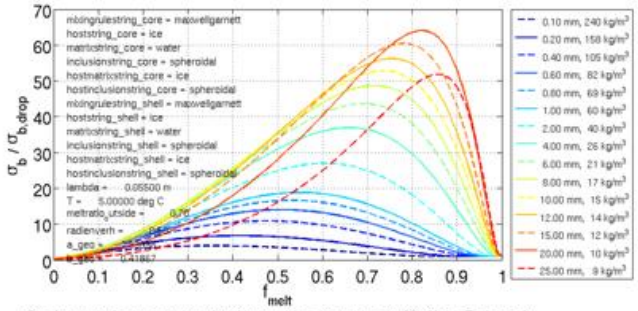
Soak twosphere snow, miwsismiasis, 2-moment (Seifert-Beheng)



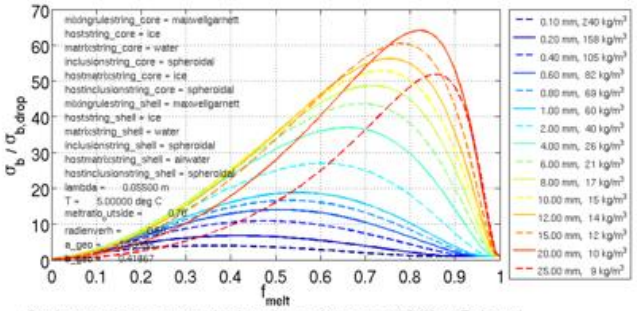
Soak twosphere snow, miwsismiasrs, 2-moment (Seifert-Beheng)



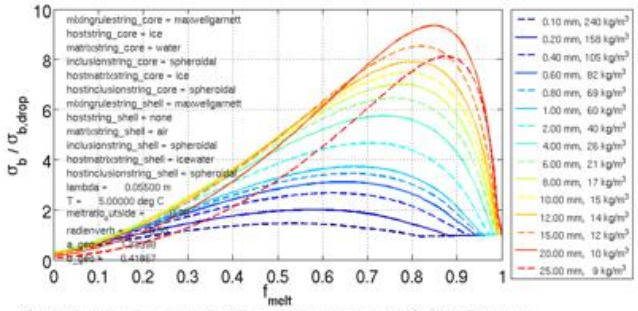
Soak twosphere snow, miwsismiwsis, 2-moment (Seifert-Beheng)



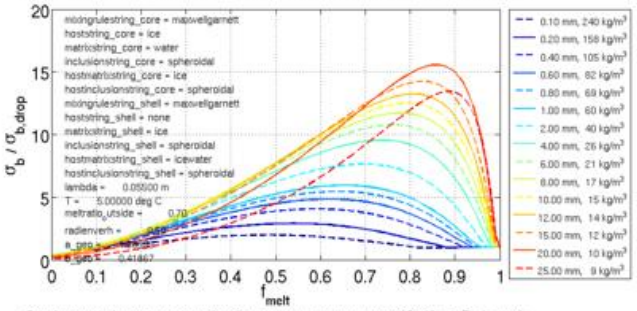
Soak twosphere snow, miwsismiwsrs, 2-moment (Seifert-Beheng)



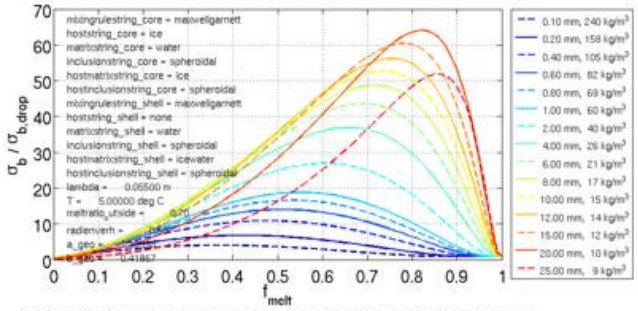
Soak twosphere snow, miwsismnasms, 2-moment (Seifert-Beheng)



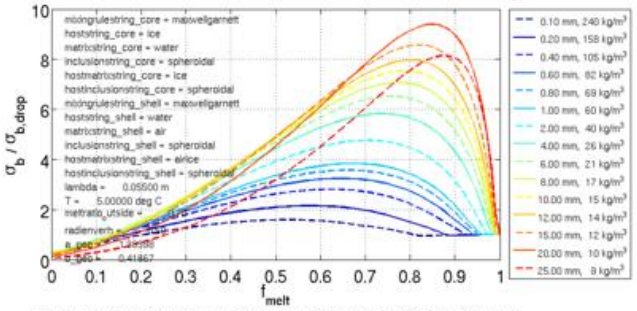
Soak twosphere snow, miwsismnisms, 2-moment (Seifert-Beheng)



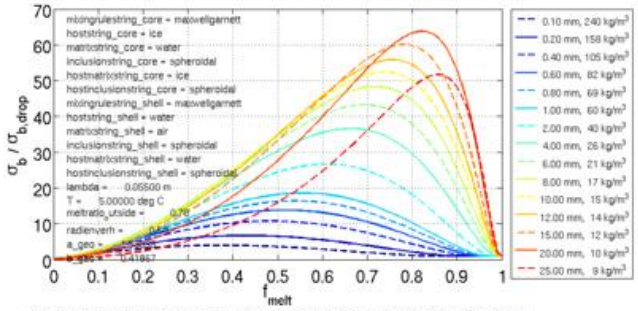
Soak twosphere snow, miwsismnwsms, 2-moment (Seifert-Beheng)



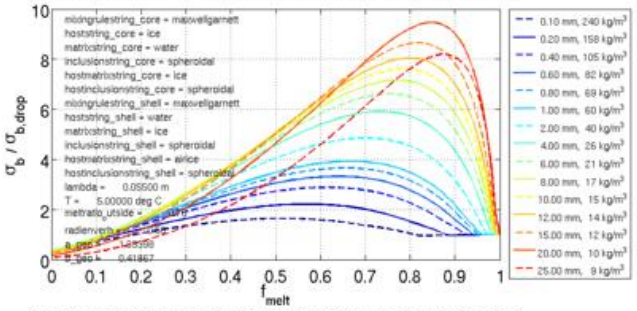
Soak twosphere snow, miwsismwasss, 2-moment (Seifert-Beheng)



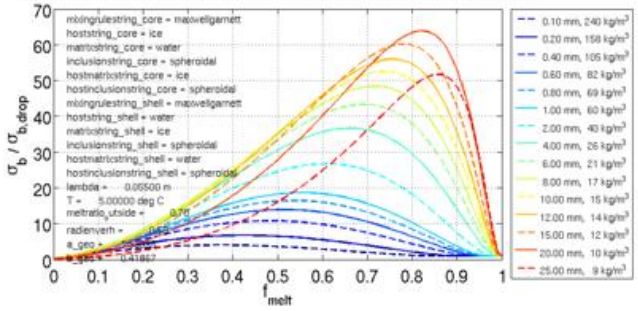
Soak twosphere snow, miwsismwasws, 2-moment (Seifert-Beheng)



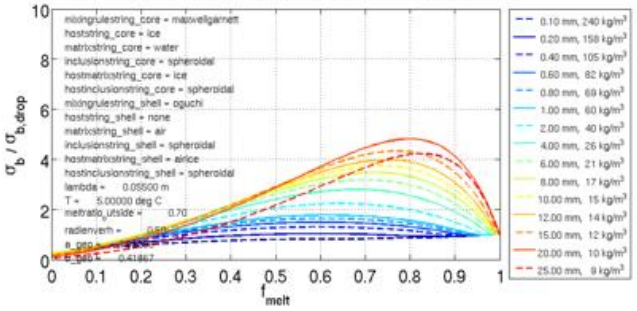
Soak twosphere snow, miwsismwisss, 2-moment (Seifert-Beheng)



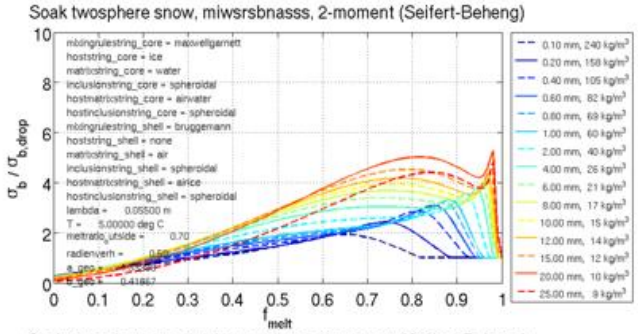
Soak twosphere snow, miwsismwisws, 2-moment (Seifert-Beheng)



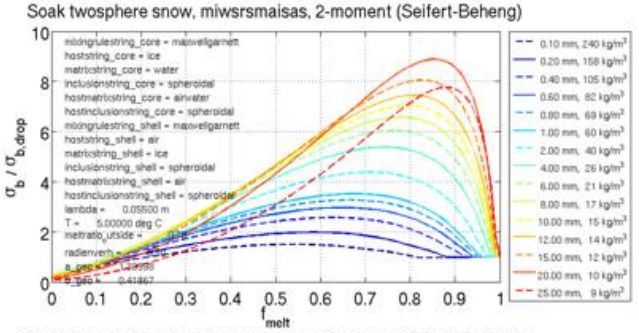
Soak twosphere snow, miwsisonasss, 2-moment (Seifert-Beheng)



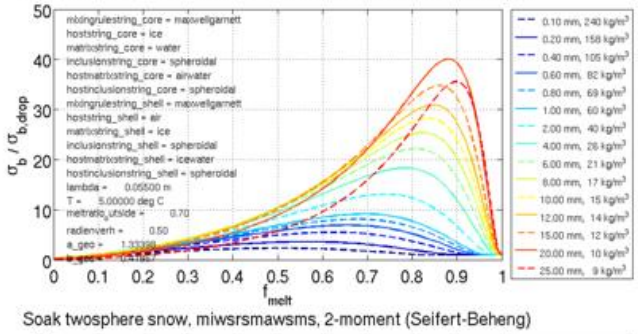
Soak twosphere snow, miwsrsbnasss, 2-moment (Seifert-Beheng)



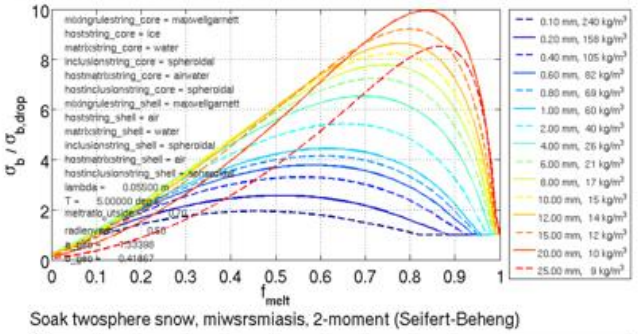
Soak twosphere snow, miwsrsmaisas, 2-moment (Seifert-Beheng)



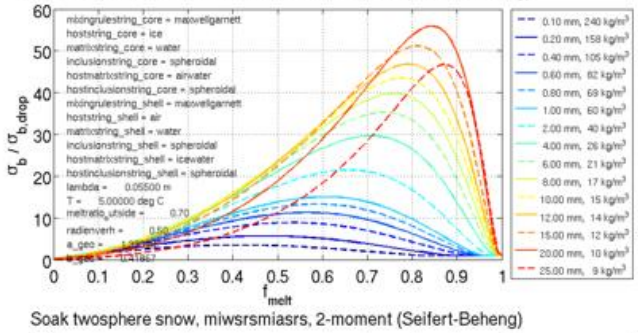
Soak twosphere snow, miwsrsmaisms, 2-moment (Seifert-Beheng)



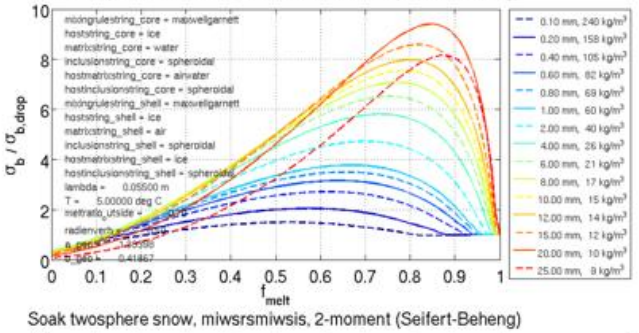
Soak twosphere snow, miwsrsmawsas, 2-moment (Seifert-Beheng)



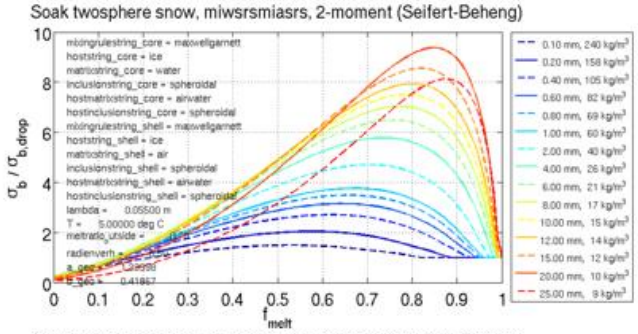
Soak twosphere snow, miwsrsmawsms, 2-moment (Seifert-Beheng)



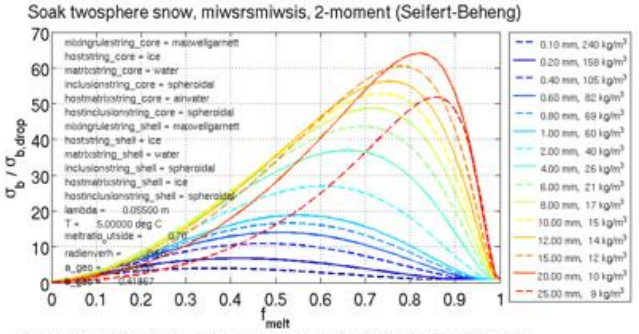
Soak twosphere snow, miwsrsmiasis, 2-moment (Seifert-Beheng)



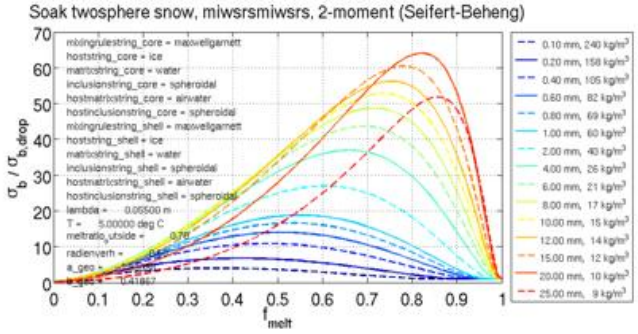
Soak twosphere snow, miwsrsmiasrs, 2-moment (Seifert-Beheng)



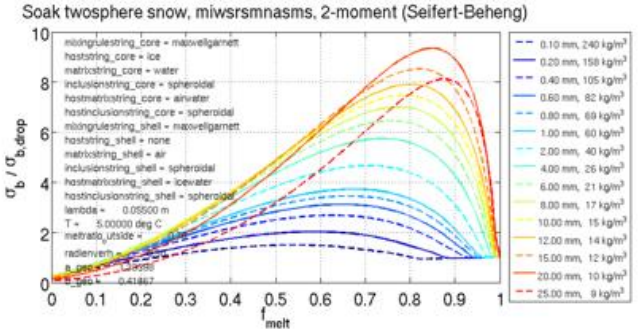
Soak twosphere snow, miwsrsmiwsis, 2-moment (Seifert-Beheng)



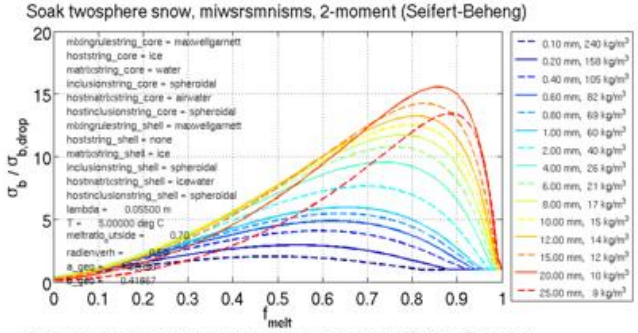
Soak twosphere snow, miwsrsmiwsrs, 2-moment (Seifert-Beheng)



Soak twosphere snow, miwsrsmnasms, 2-moment (Seifert-Beheng)



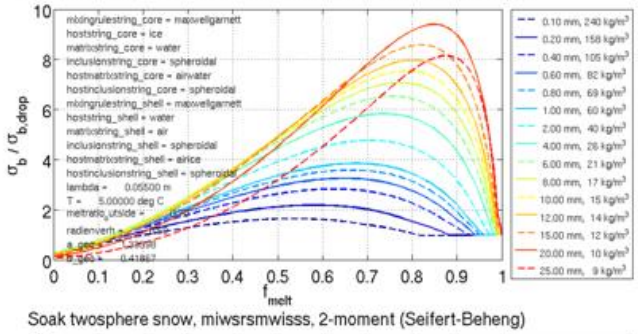
Soak twosphere snow, miwsrsmnisms, 2-moment (Seifert-Beheng)



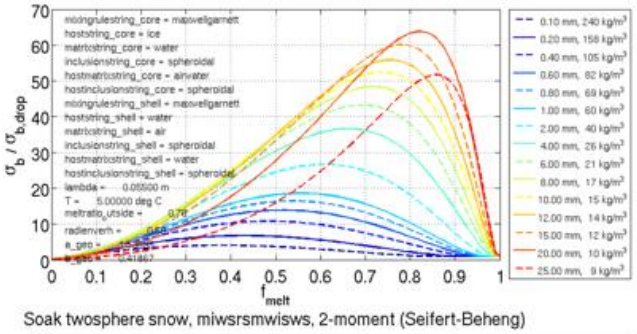
Soak twosphere snow, miwsrsmnwsms, 2-moment (Seifert-Beheng)



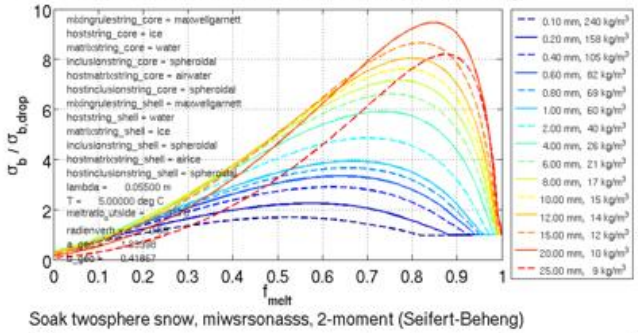
Soak twosphere snow, miwsrsmwasss, 2-moment (Seifert-Beheng)



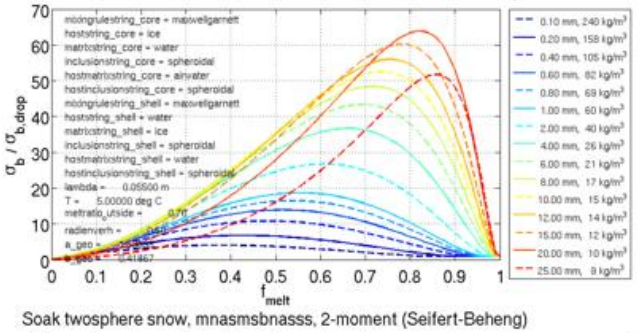
Soak twosphere snow, miwsrsmwasws, 2-moment (Seifert-Beheng)



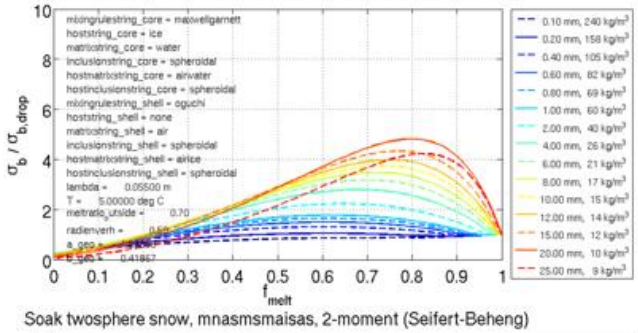
Soak twosphere snow, miwsrsmwisss, 2-moment (Seifert-Beheng)



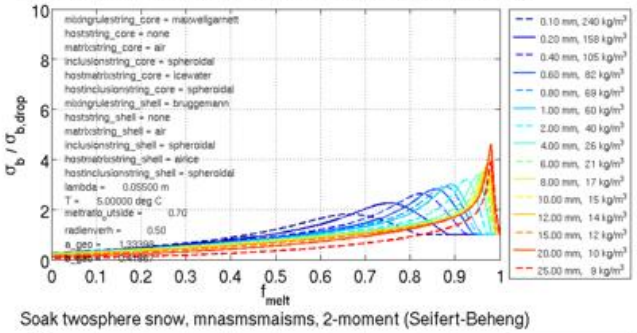
Soak twosphere snow, miwsrsmwisws, 2-moment (Seifert-Beheng)



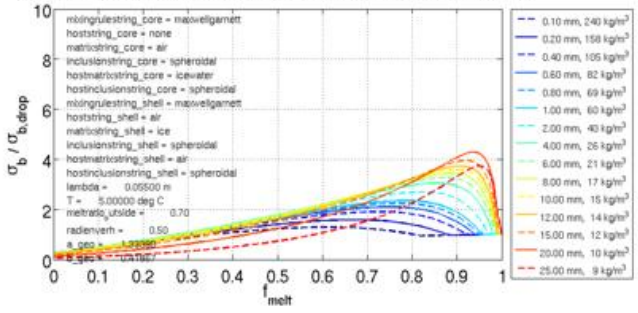
Soak twosphere snow, miwsrsonasss, 2-moment (Seifert-Beheng)



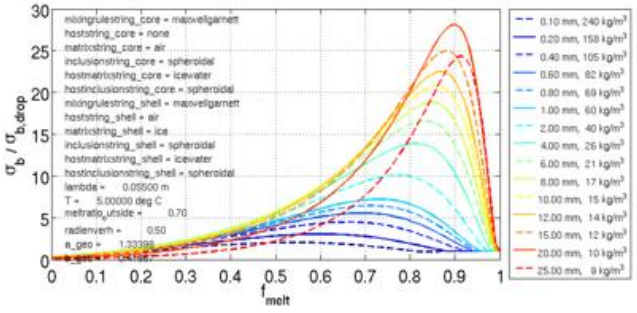
Soak twosphere snow, mnasmsbnasss, 2-moment (Seifert-Beheng)



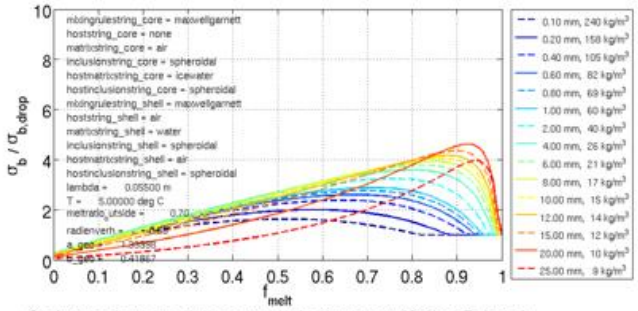
Soak twosphere snow, mnasmsmaisas, 2-moment (Seifert-Beheng)



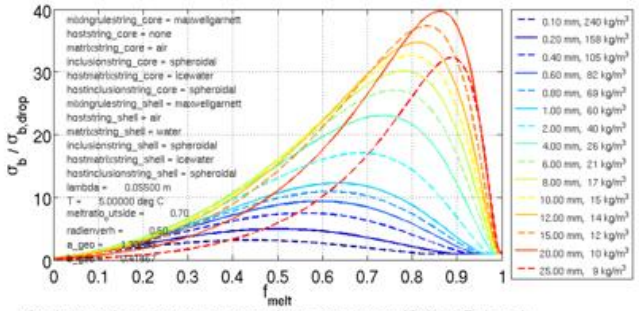
Soak twosphere snow, mnasmsmaisms, 2-moment (Seifert-Beheng)



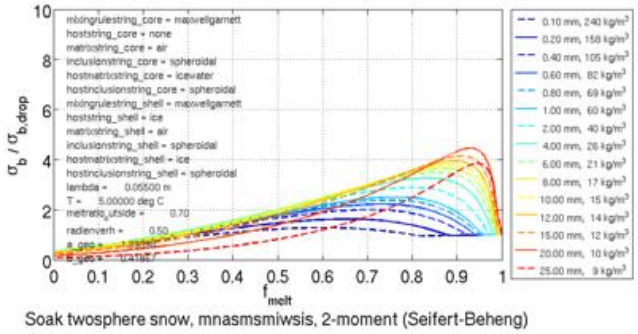
Soak twosphere snow, mnasmsmawsas, 2-moment (Seifert-Beheng)



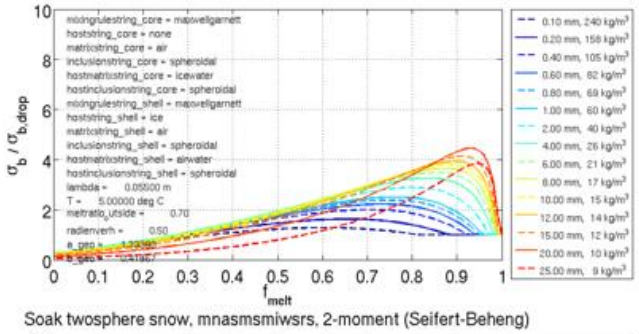
Soak twosphere snow, mnasmsmawsms, 2-moment (Seifert-Beheng)



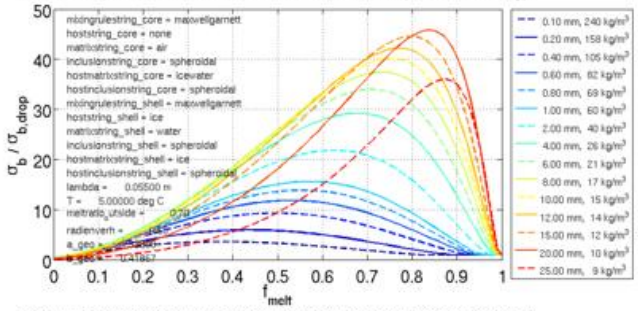
Soak twosphere snow, mnasmsmiasis, 2-moment (Seifert-Beheng)



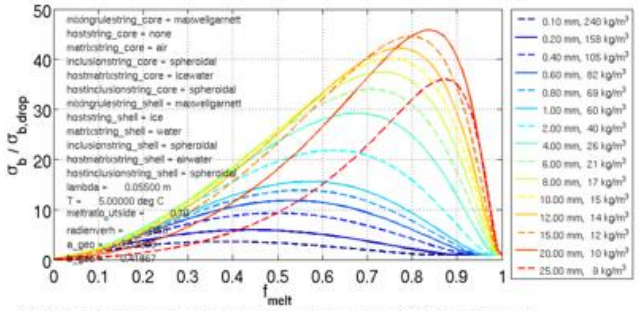
Soak twosphere snow, mnasmsmiasrs, 2-moment (Seifert-Beheng)



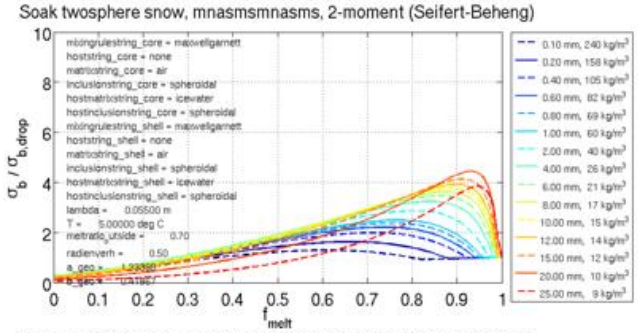
Soak twosphere snow, mnasmsmiwsis, 2-moment (Seifert-Beheng)



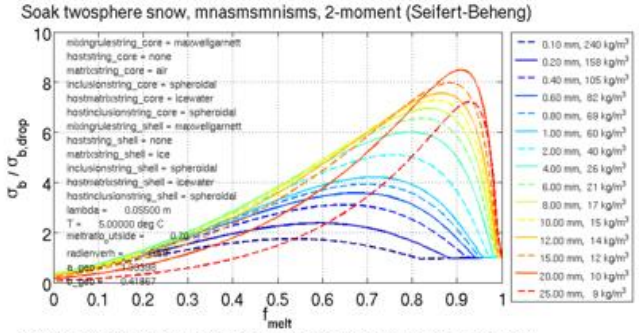
Soak twosphere snow, mnasmsmiwsrs, 2-moment (Seifert-Beheng)



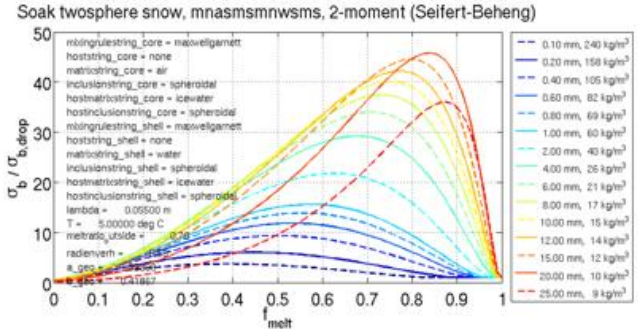
Soak twosphere snow, mnasmsmnasms, 2-moment (Seifert-Beheng)



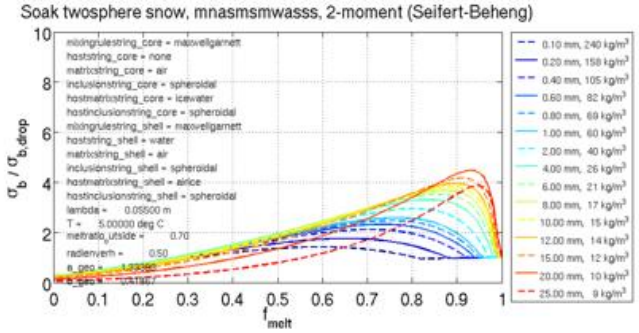
Soak twosphere snow, mnasmsmnisms, 2-moment (Seifert-Beheng)



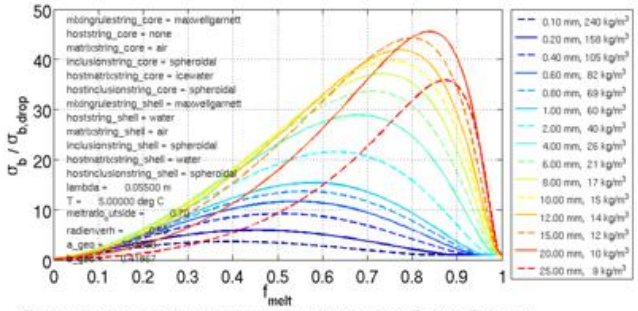
Soak twosphere snow, mnasmsmnwsms, 2-moment (Seifert-Beheng)



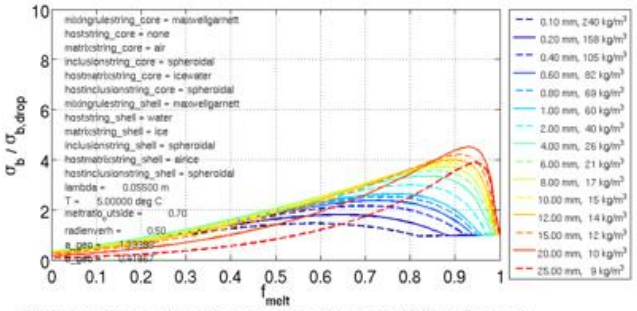
Soak twosphere snow, mnasmsmwasss, 2-moment (Seifert-Beheng)



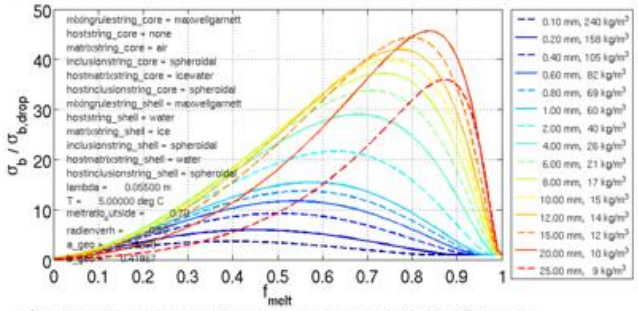
Soak twosphere snow, mnasmsmwasws, 2-moment (Seifert-Beheng)



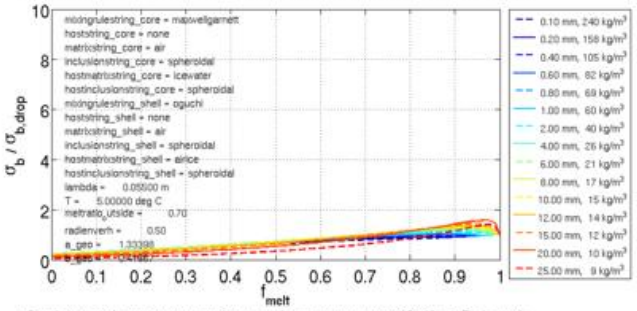
Soak twosphere snow, mnasmsmwisss, 2-moment (Seifert-Beheng)



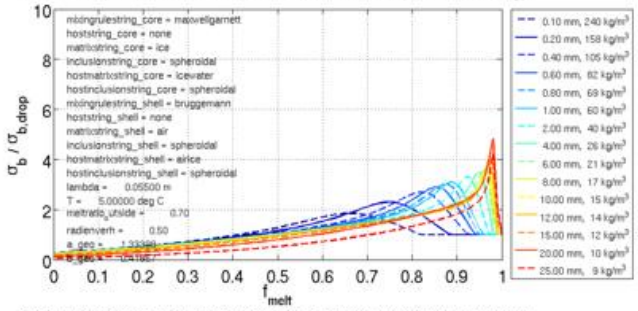
Soak twosphere snow, mnasmsmwisws, 2-moment (Seifert-Beheng)



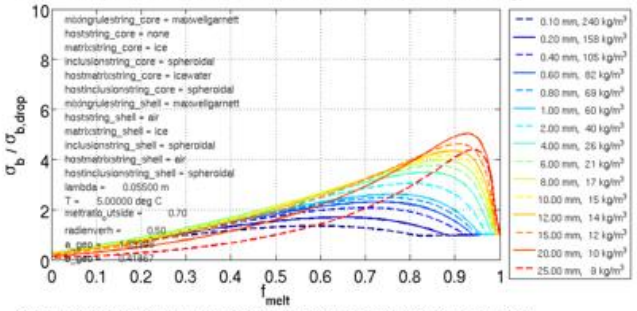
Soak twosphere snow, mnasmsonasss, 2-moment (Seifert-Beheng)



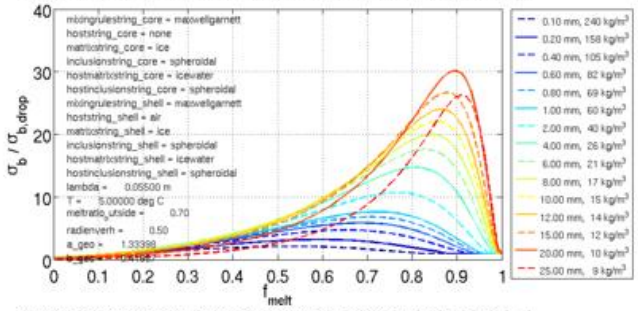
Soak twosphere snow, mnismsbnasss, 2-moment (Seifert-Beheng)



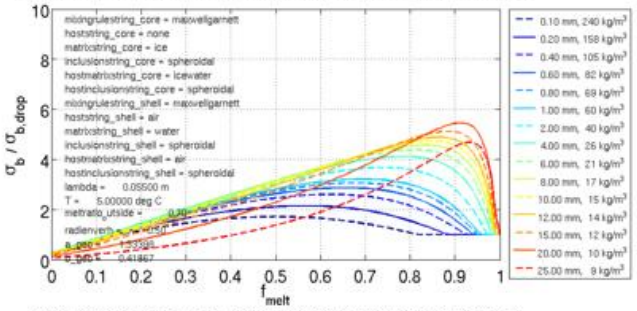
Soak twosphere snow, mnismsmaisas, 2-moment (Seifert-Beheng)



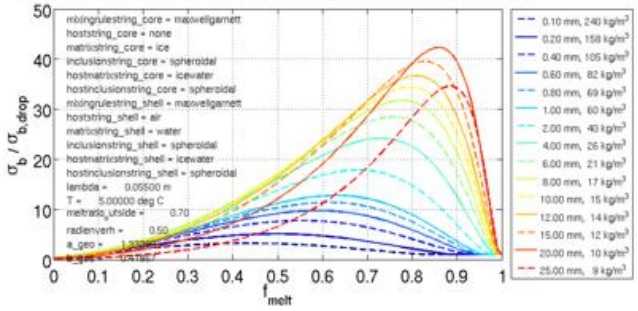
Soak twosphere snow, mnismsmaisms, 2-moment (Seifert-Beheng)



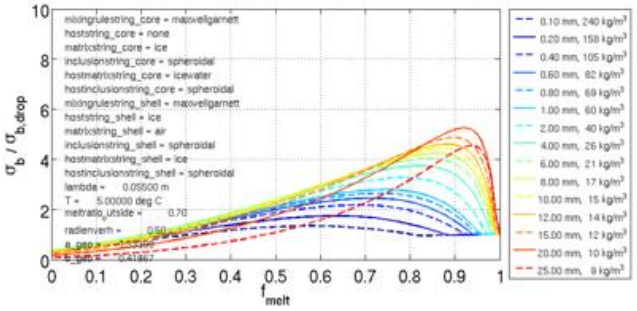
Soak twosphere snow, mnismsmawsas, 2-moment (Seifert-Beheng)



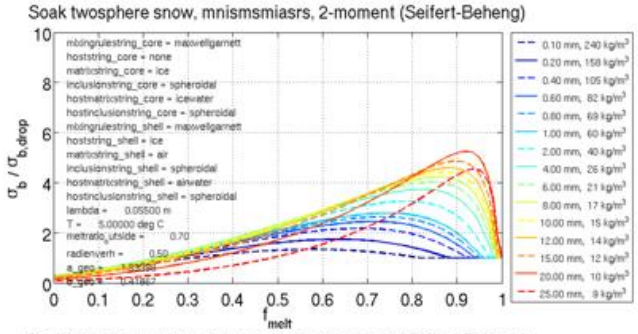
Soak twosphere snow, mnismsmawsms, 2-moment (Seifert-Beheng)



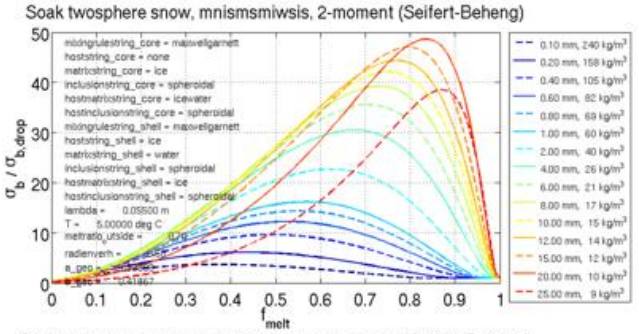
Soak twosphere snow, mnismsmiasis, 2-moment (Seifert-Beheng)



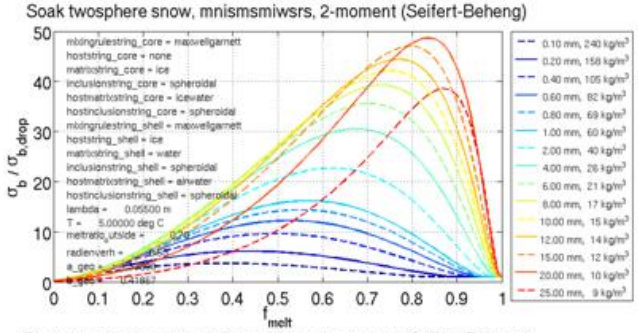
Soak twosphere snow, mnismsmiasrs, 2-moment (Seifert-Beheng)



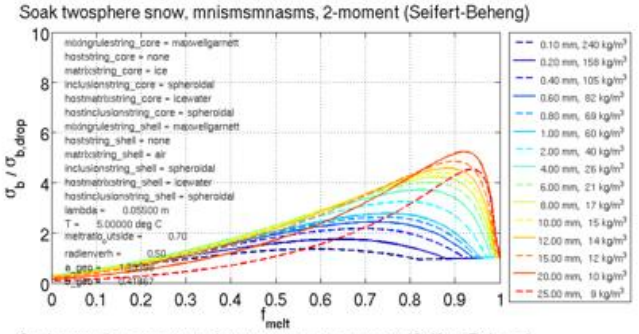
Soak twosphere snow, mnismsmiwsis, 2-moment (Seifert-Beheng)



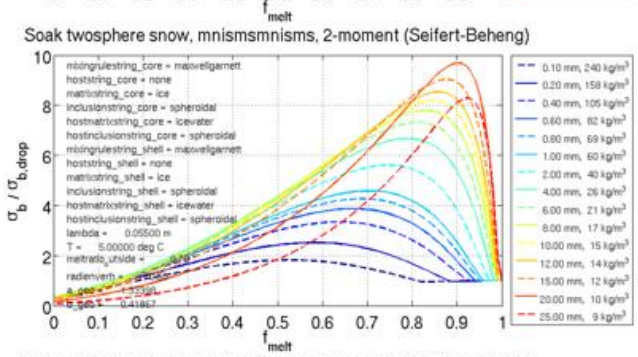
Soak twosphere snow, mnismsmiwsrs, 2-moment (Seifert-Beheng)



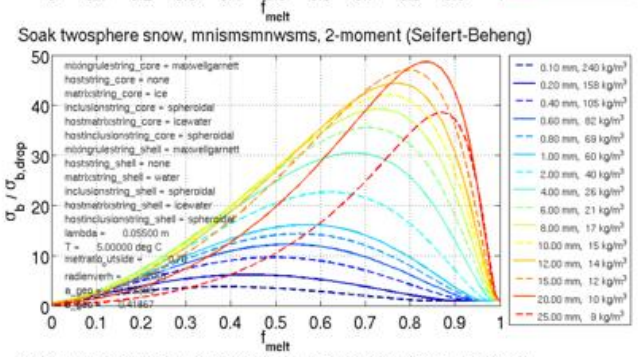
Soak twosphere snow, mnismsmnasms, 2-moment (Seifert-Beheng)



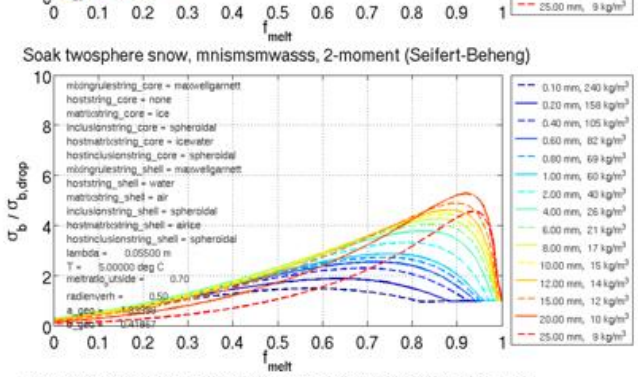
Soak twosphere snow, mnismsmnisms, 2-moment (Seifert-Beheng)



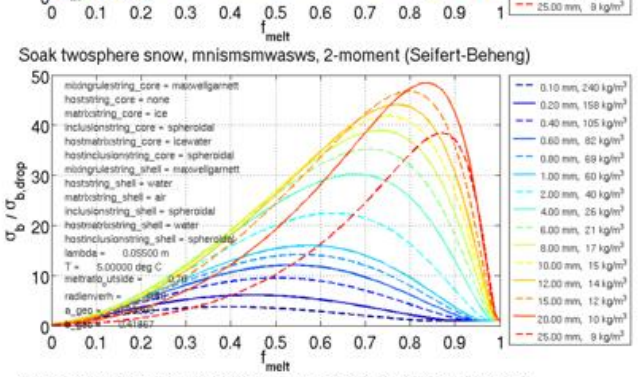
Soak twosphere snow, mnismsmnwsms, 2-moment (Seifert-Beheng)



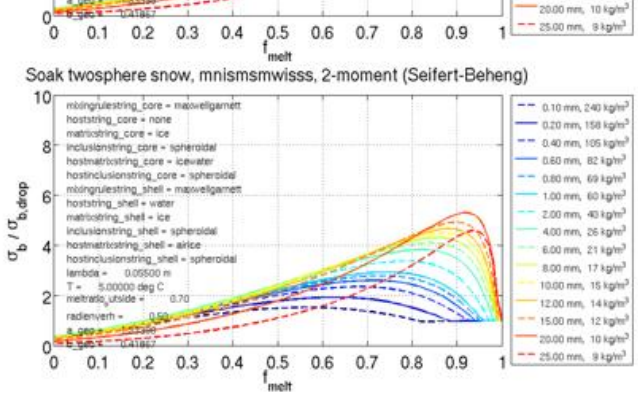
Soak twosphere snow, mnismsmwasss, 2-moment (Seifert-Beheng)



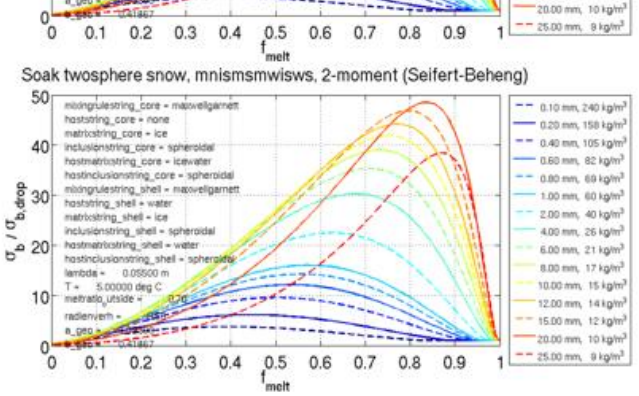
Soak twosphere snow, mnismsmwasws, 2-moment (Seifert-Beheng)



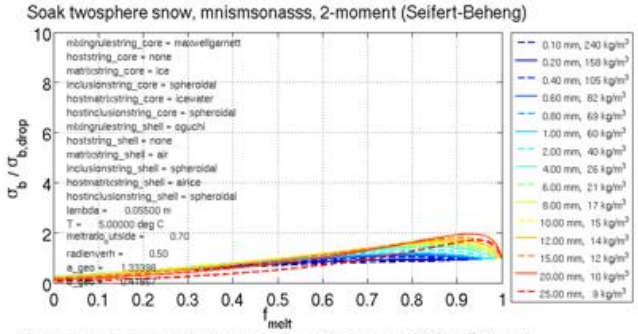
Soak twosphere snow, mnismsmwisss, 2-moment (Seifert-Beheng)



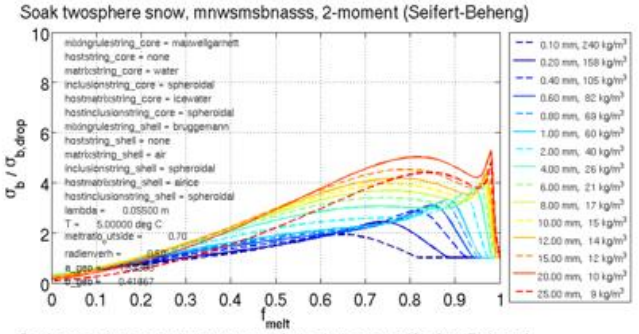
Soak twosphere snow, mnismsmwisws, 2-moment (Seifert-Beheng)



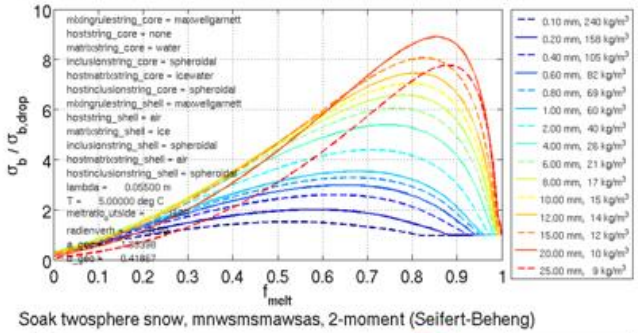
Soak twosphere snow, mnismsonasss, 2-moment (Seifert-Beheng)



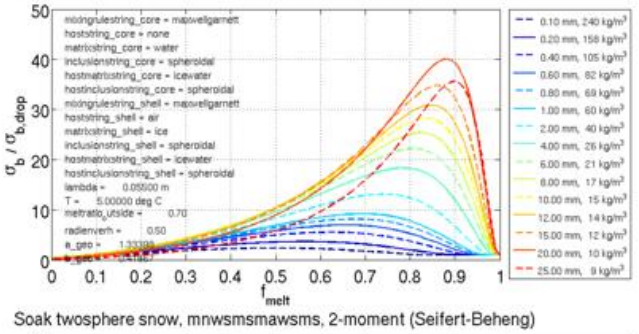
Soak twosphere snow, mnwsmsbnasss, 2-moment (Seifert-Beheng)



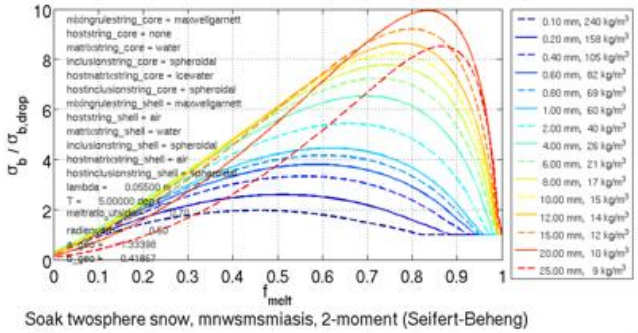
Soak twosphere snow, mnwsmsmaisas, 2-moment (Seifert-Beheng)



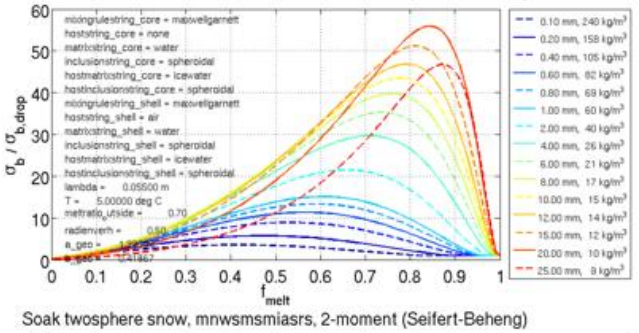
Soak twosphere snow, mnwsmsmaisms, 2-moment (Seifert-Beheng)



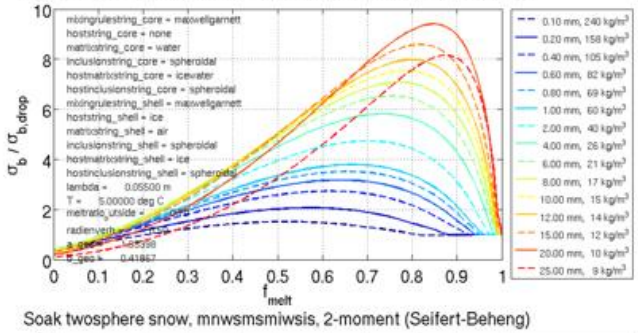
Soak twosphere snow, mnwsmsmawsas, 2-moment (Seifert-Beheng)



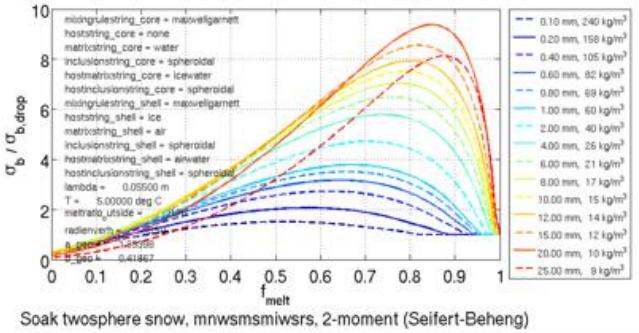
Soak twosphere snow, mnwsmsmawsms, 2-moment (Seifert-Beheng)



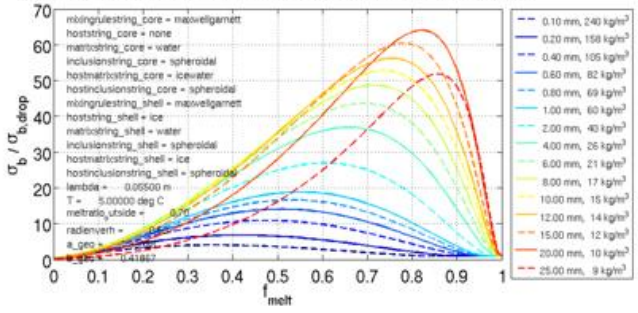
Soak twosphere snow, mnwsmsmiasis, 2-moment (Seifert-Beheng)



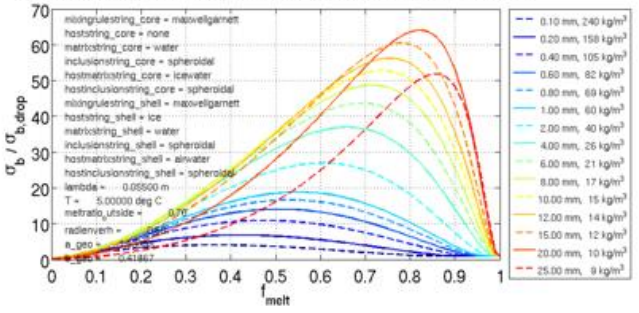
Soak twosphere snow, mnwsmsmiasrs, 2-moment (Seifert-Beheng)



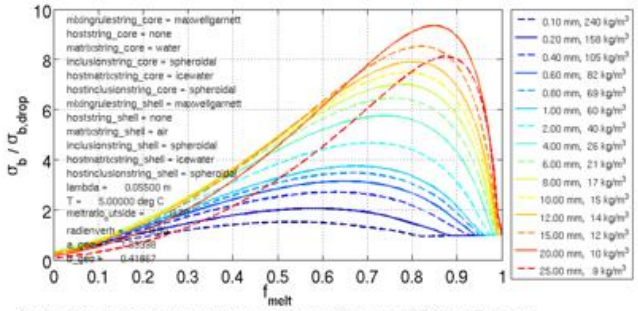
Soak twosphere snow, mnwsmsmiwsis, 2-moment (Seifert-Beheng)



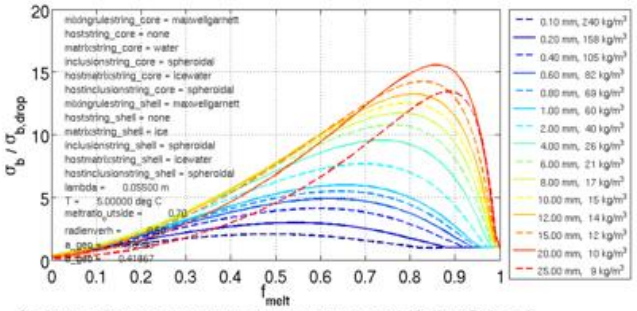
Soak twosphere snow, mnwsmsmiwsrs, 2-moment (Seifert-Beheng)



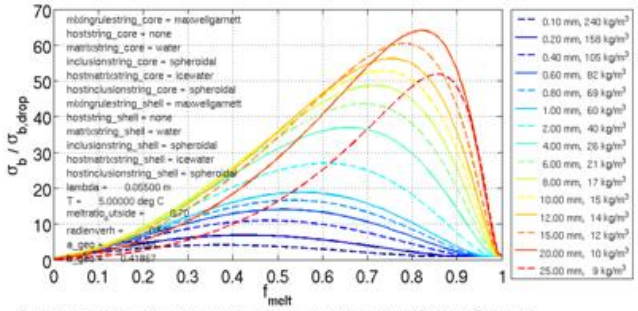
Soak twosphere snow, mnwsmsmnasms, 2-moment (Seifert-Beheng)



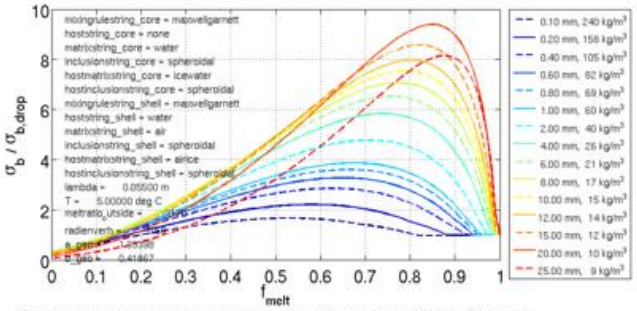
Soak twosphere snow, mnwsmsmnisms, 2-moment (Seifert-Beheng)



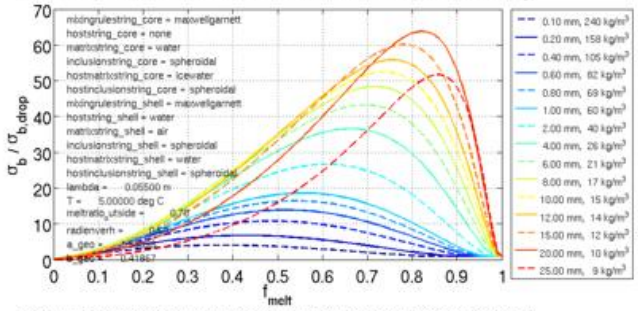
Soak twosphere snow, mnwsmsmnwsms, 2-moment (Seifert-Beheng)



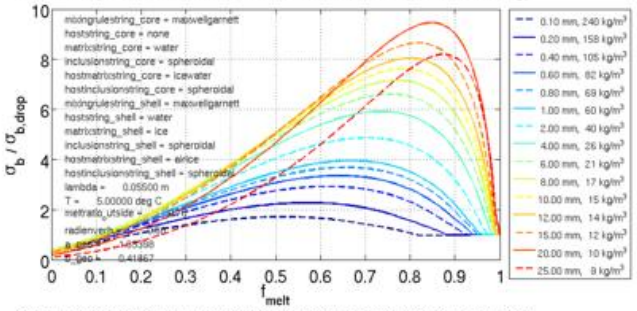
Soak twosphere snow, mnwsmsmwasss, 2-moment (Seifert-Beheng)



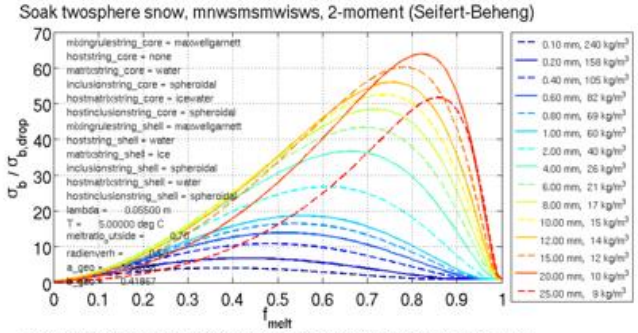
Soak twosphere snow, mnwsmsmwasws, 2-moment (Seifert-Beheng)



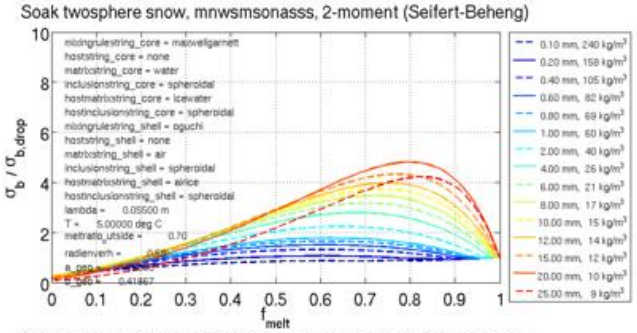
Soak twosphere snow, mnwsmsmwisss, 2-moment (Seifert-Beheng)



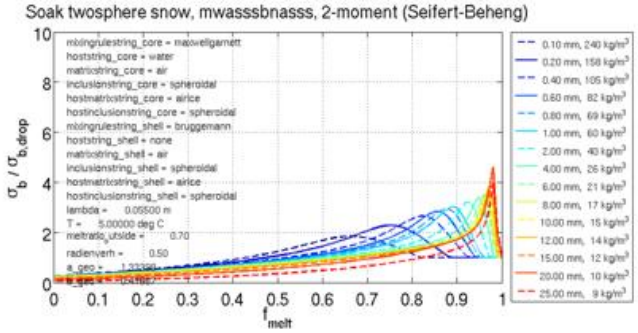
Soak twosphere snow, mnwsmsmwisws, 2-moment (Seifert-Beheng)



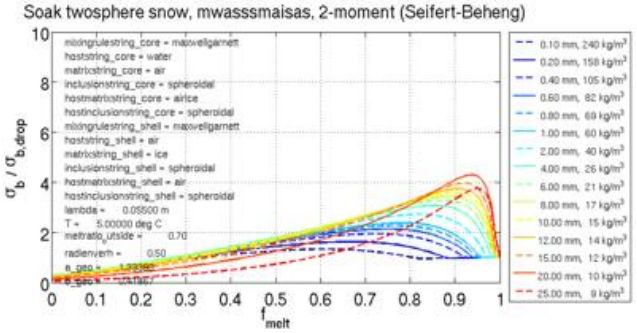
Soak twosphere snow, mnwsmsonasss, 2-moment (Seifert-Beheng)



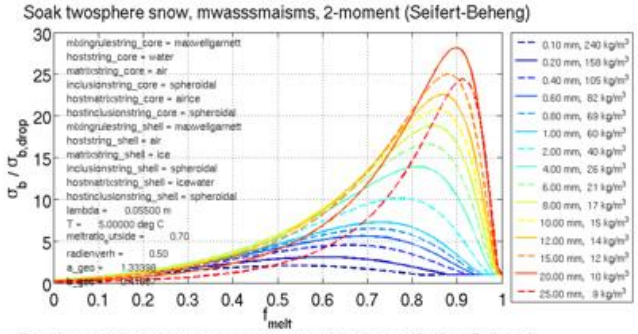
Soak twosphere snow, mwasssbnasss, 2-moment (Seifert-Beheng)



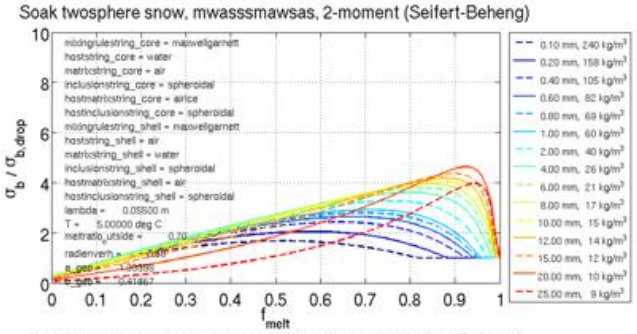
Soak twosphere snow, mwasssmaisas, 2-moment (Seifert-Beheng)



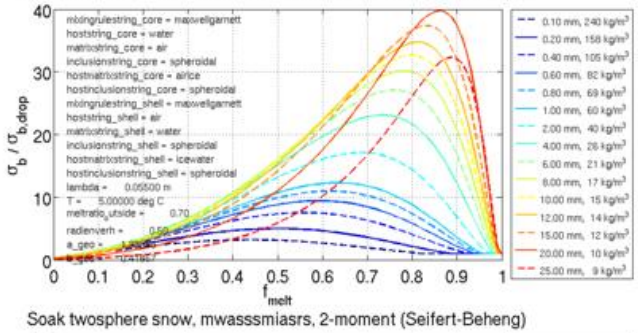
Soak twosphere snow, mwasssmaisms, 2-moment (Seifert-Beheng)



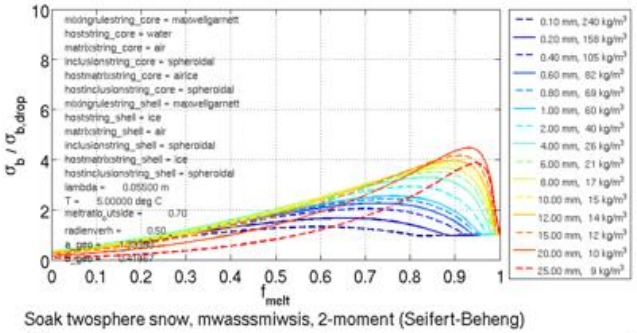
Soak twosphere snow, mwasssmawsas, 2-moment (Seifert-Beheng)



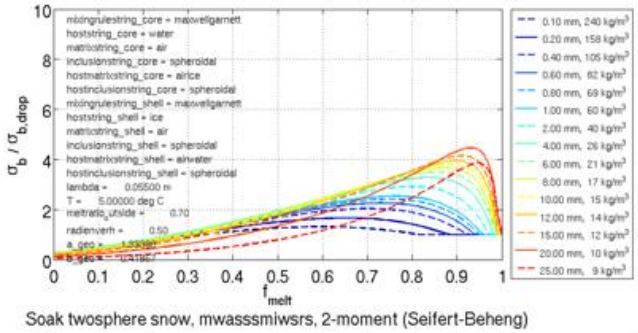
Soak twosphere snow, mwasssmawsms, 2-moment (Seifert-Beheng)



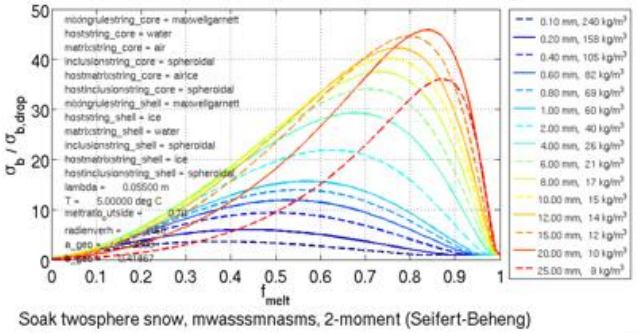
Soak twosphere snow, mwasssmiasis, 2-moment (Seifert-Beheng)



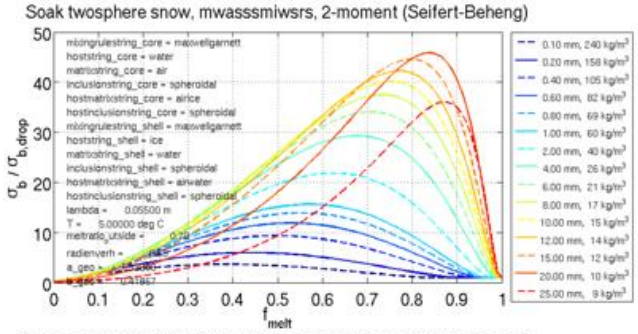
Soak twosphere snow, mwasssmiasrs, 2-moment (Seifert-Beheng)



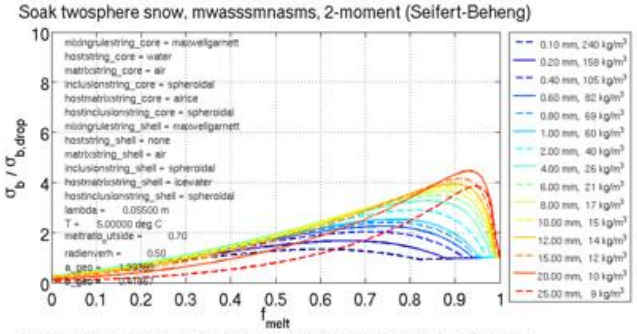
Soak twosphere snow, mwasssmiwsis, 2-moment (Seifert-Beheng)



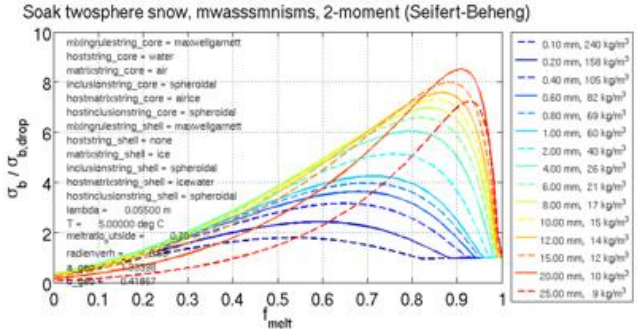
Soak twosphere snow, mwasssmiwsrs, 2-moment (Seifert-Beheng)



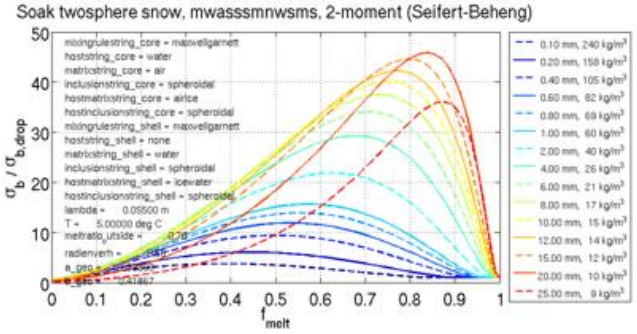
Soak twosphere snow, mwasssmnasms, 2-moment (Seifert-Beheng)



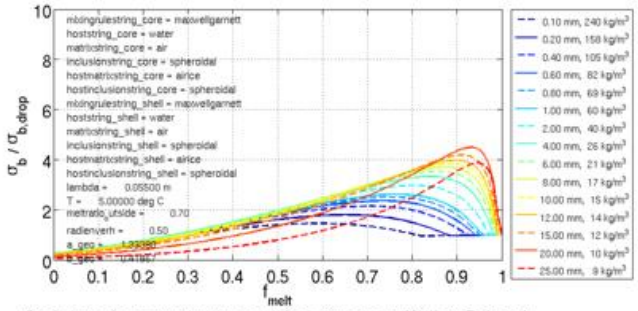
Soak twosphere snow, mwasssmnisms, 2-moment (Seifert-Beheng)



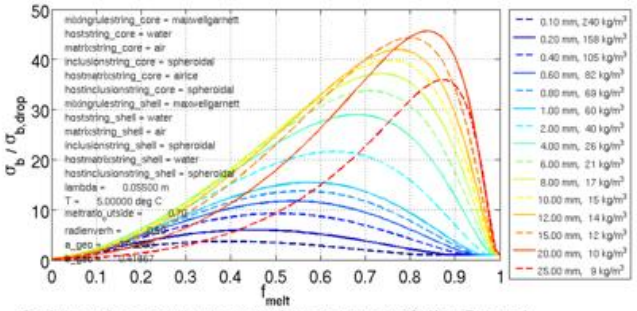
Soak twosphere snow, mwasssmnwsms, 2-moment (Seifert-Beheng)



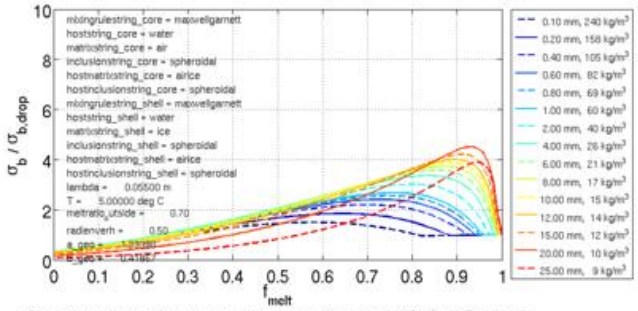
Soak twosphere snow, mwasssmwasss, 2-moment (Seifert-Beheng)



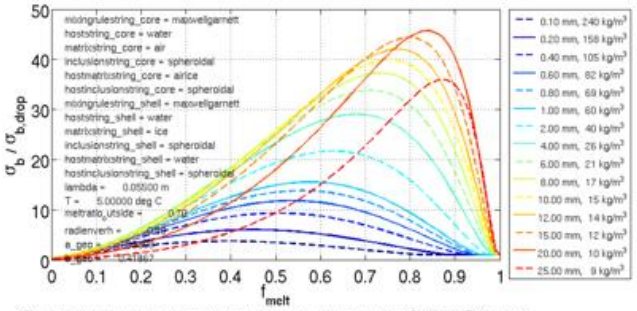
Soak twosphere snow, mwasssmwasws, 2-moment (Seifert-Beheng)



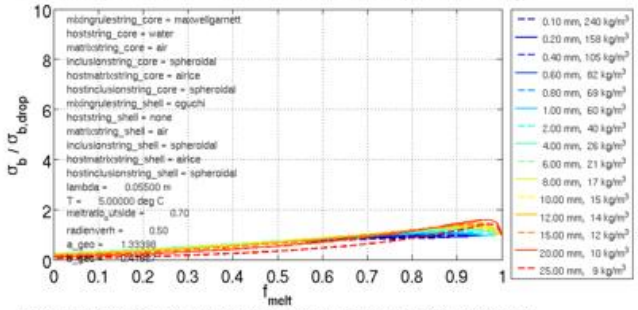
Soak twosphere snow, mwasssmwisss, 2-moment (Seifert-Beheng)



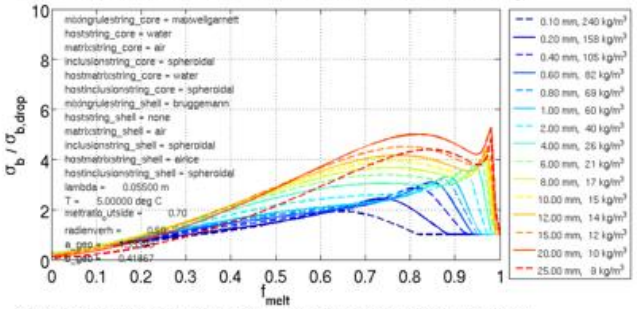
Soak twosphere snow, mwasswsmwisws, 2-moment (Seifert-Beheng)



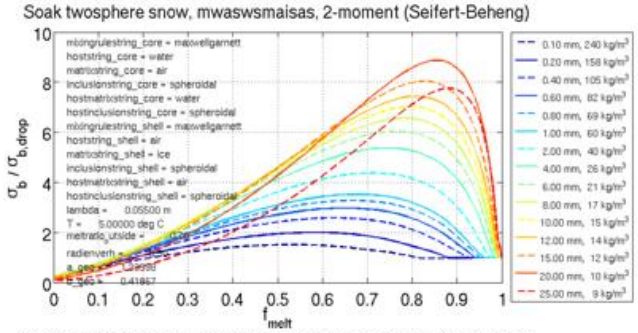
Soak twosphere snow, mwasssonasss, 2-moment (Seifert-Beheng)



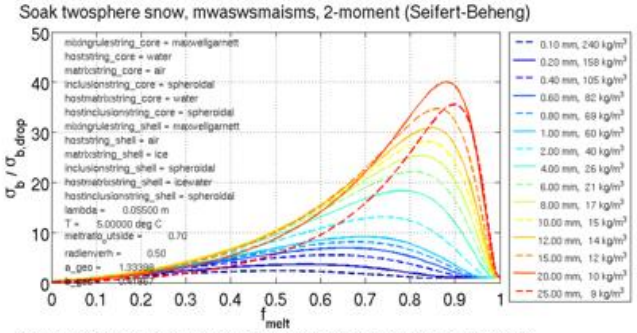
Soak twosphere snow, mwaswsbnasss, 2-moment (Seifert-Beheng)



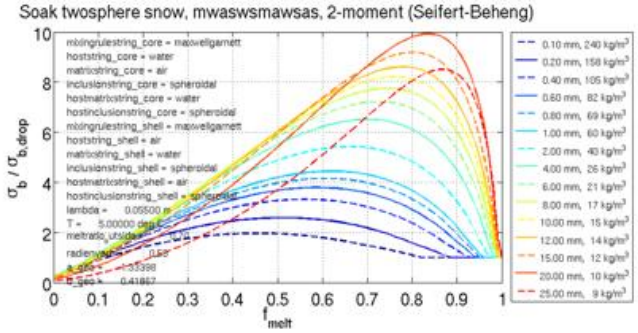
Soak twosphere snow, mwaswsmaisas, 2-moment (Seifert-Beheng)



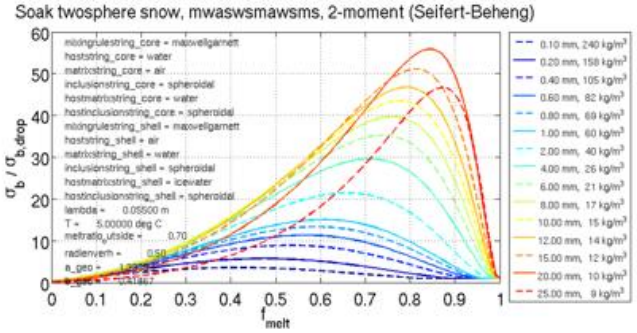
Soak twosphere snow, mwaswsmaisms, 2-moment (Seifert-Beheng)



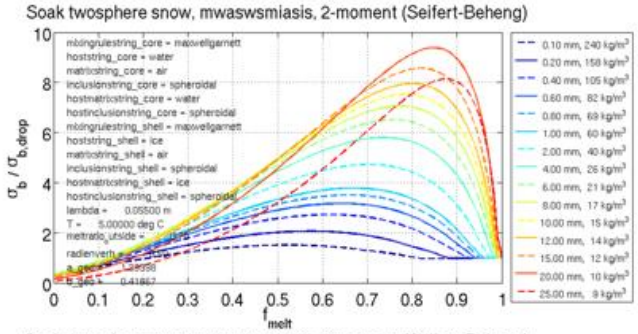
Soak twosphere snow, mwaswsmawsas, 2-moment (Seifert-Beheng)



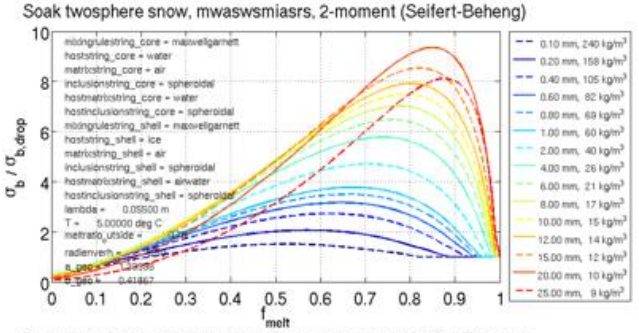
Soak twosphere snow, mwaswsmawsms, 2-moment (Seifert-Beheng)



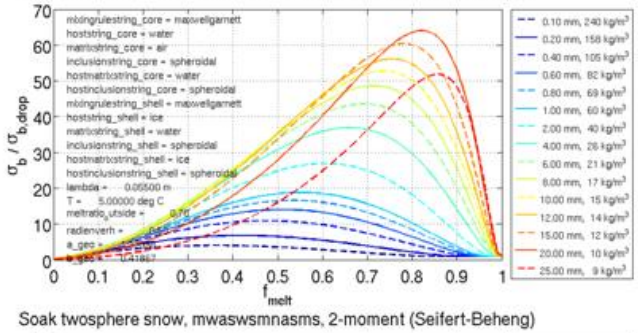
Soak twosphere snow, mwaswsmiasis, 2-moment (Seifert-Beheng)



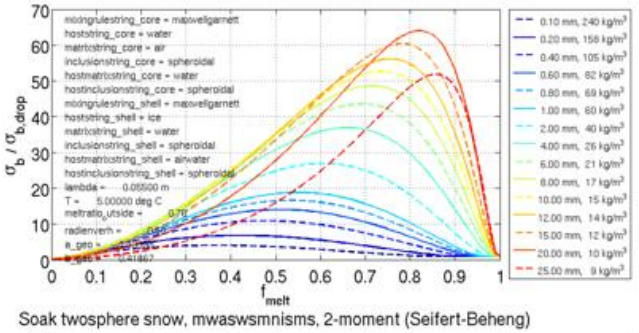
Soak twosphere snow, mwaswsmiasrs, 2-moment (Seifert-Beheng)



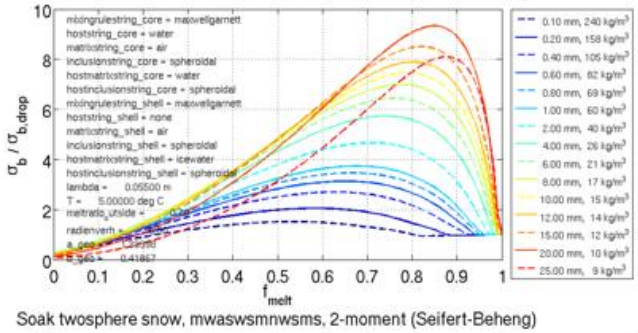
Soak twosphere snow, mwaswsmiwsis, 2-moment (Seifert-Beheng)



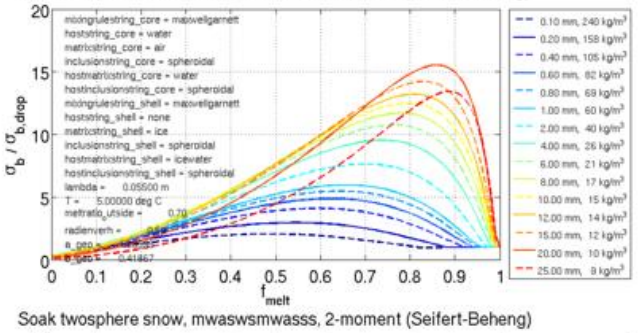
Soak twosphere snow, mwaswsmiwsrs, 2-moment (Seifert-Beheng)



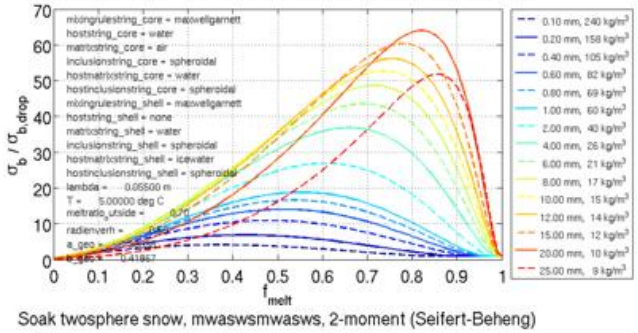
Soak twosphere snow, mwaswsmnasms, 2-moment (Seifert-Beheng)



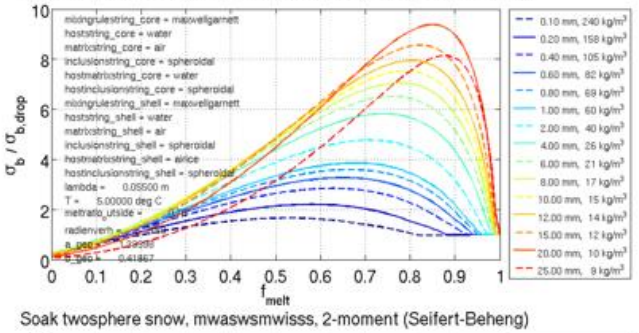
Soak twosphere snow, mwaswsmnisms, 2-moment (Seifert-Beheng)



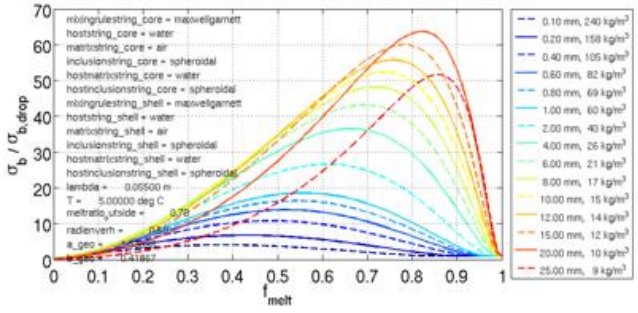
Soak twosphere snow, mwaswsmnwsms, 2-moment (Seifert-Beheng)



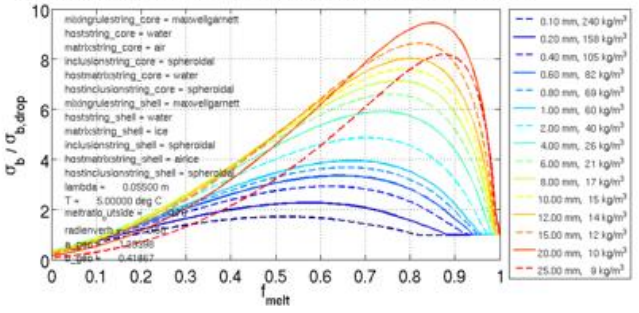
Soak twosphere snow, mwaswsmwasss, 2-moment (Seifert-Beheng)



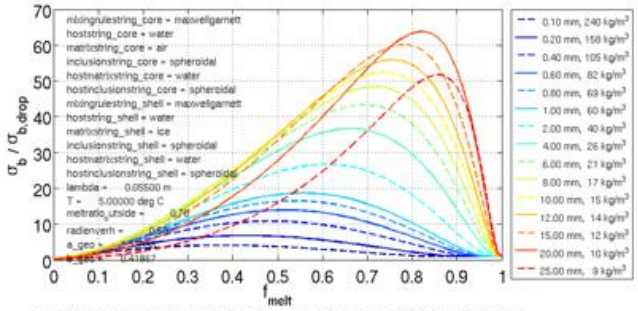
Soak twosphere snow, mwaswsmwasws, 2-moment (Seifert-Beheng)



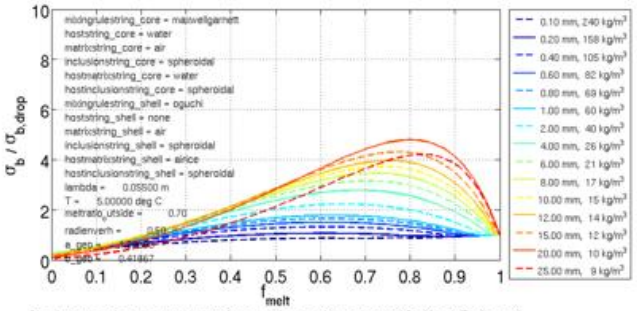
Soak twosphere snow, mwaswsmwisss, 2-moment (Seifert-Beheng)



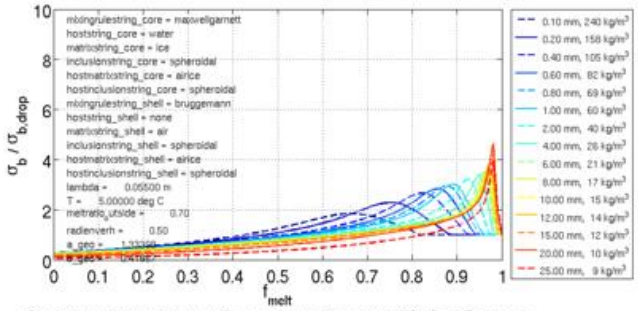
Soak twosphere snow, mwaswsmwisws, 2-moment (Seifert-Beheng)



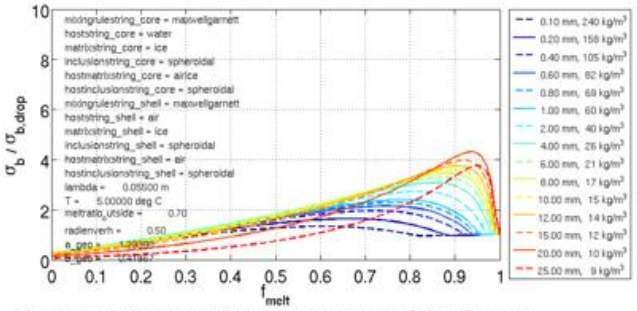
Soak twosphere snow, mwaswsonasss, 2-moment (Seifert-Beheng)



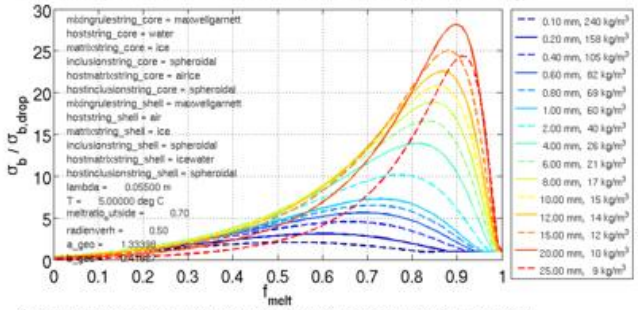
Soak twosphere snow, mwisssbnasss, 2-moment (Seifert-Beheng)



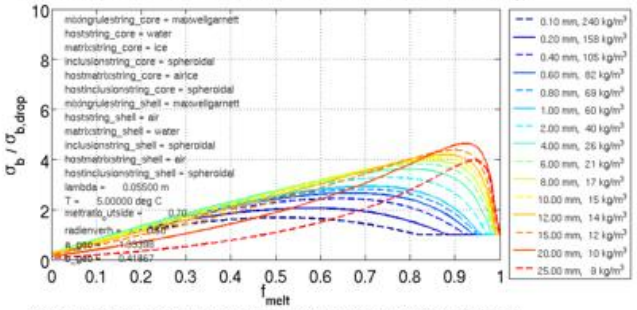
Soak twosphere snow, mwisssmaisas, 2-moment (Seifert-Beheng)



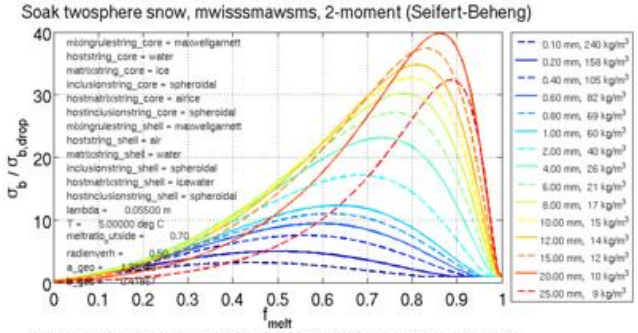
Soak twosphere snow, mwisssmaisms, 2-moment (Seifert-Beheng)



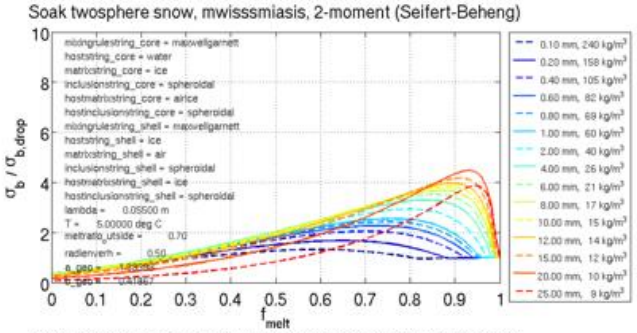
Soak twosphere snow, mwisssmawsas, 2-moment (Seifert-Beheng)



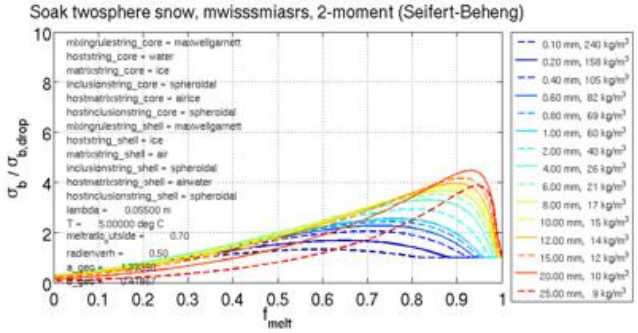
Soak twosphere snow, mwisssmawsms, 2-moment (Seifert-Beheng)



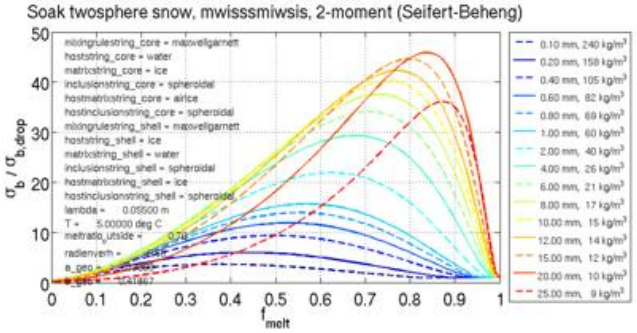
Soak twosphere snow, mwisssmiasis, 2-moment (Seifert-Beheng)



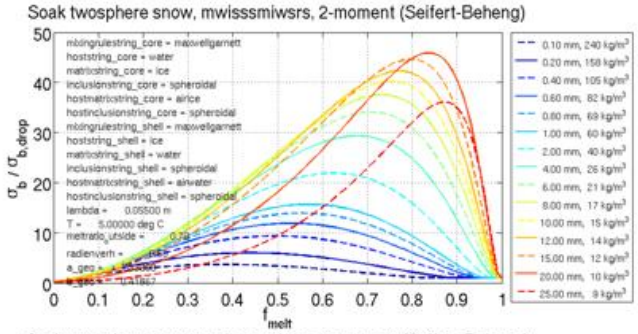
Soak twosphere snow, mwisssmiasrs, 2-moment (Seifert-Beheng)



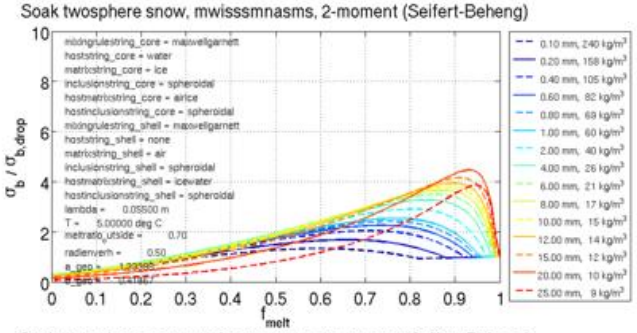
Soak twosphere snow, mwisssmiswis, 2-moment (Seifert-Beheng)



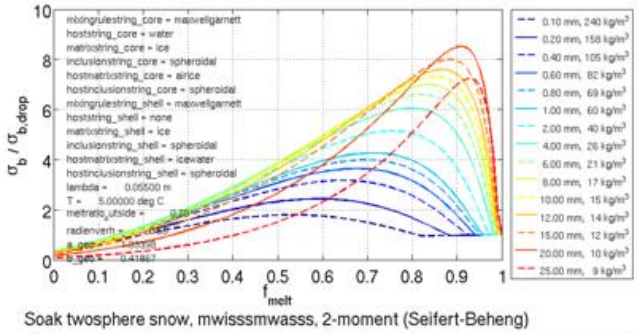
Soak twosphere snow, mwisssmiwsrs, 2-moment (Seifert-Beheng)



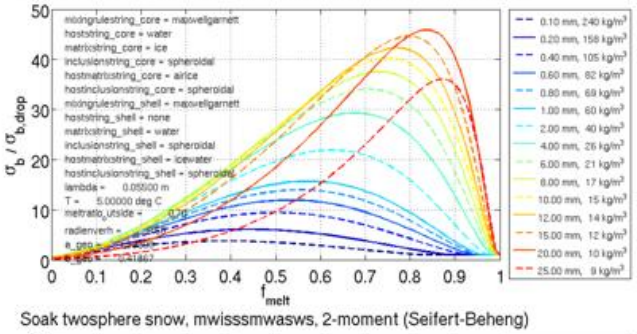
Soak twosphere snow, mwisssmnasms, 2-moment (Seifert-Beheng)



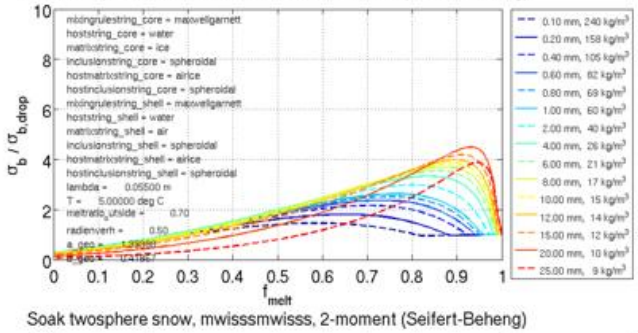
Soak twosphere snow, mwisssmnisms, 2-moment (Seifert-Beheng)



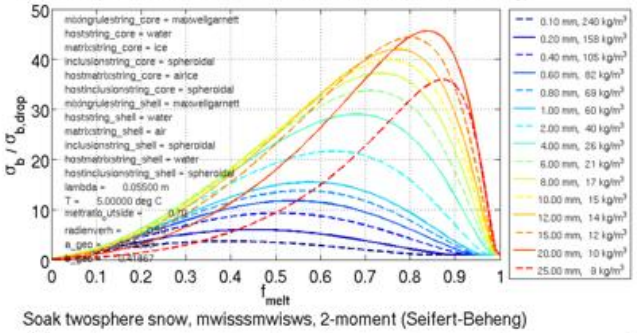
Soak twosphere snow, mwisssmnwsms, 2-moment (Seifert-Beheng)



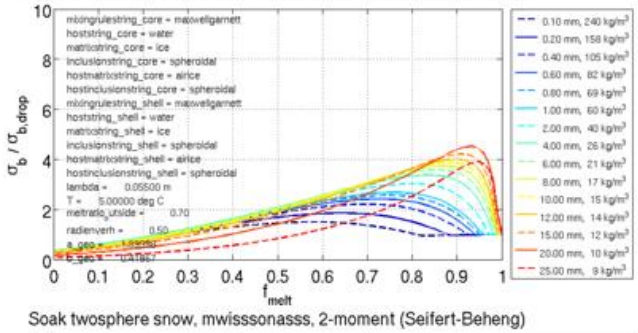
Soak twosphere snow, mwisssmwasss, 2-moment (Seifert-Beheng)



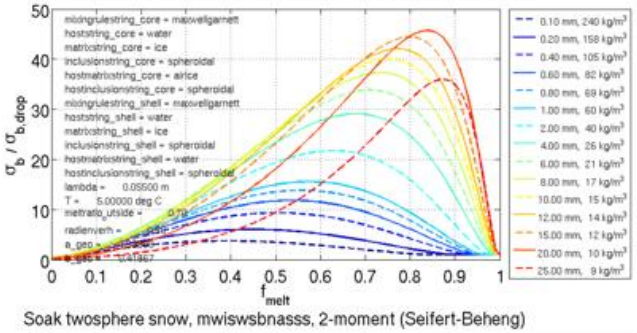
Soak twosphere snow, mwisssmwasws, 2-moment (Seifert-Beheng)



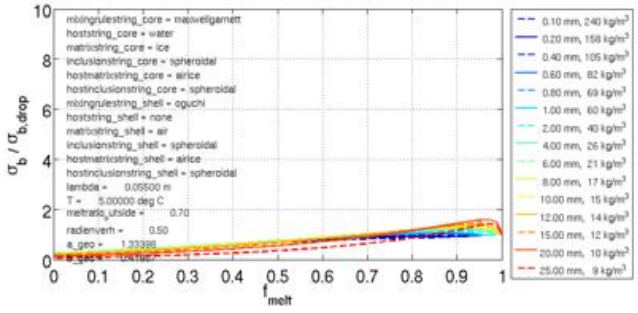
Soak twosphere snow, mwisssmwisss, 2-moment (Seifert-Beheng)



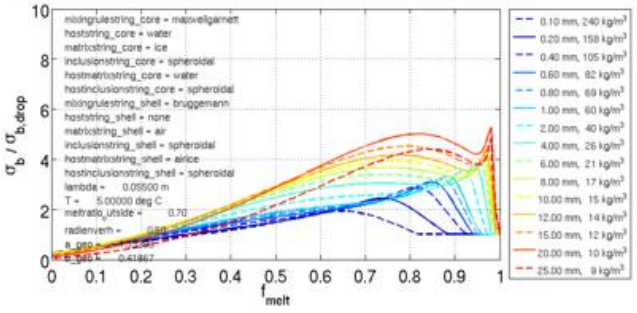
Soak twosphere snow, mwisssmwisws, 2-moment (Seifert-Beheng)



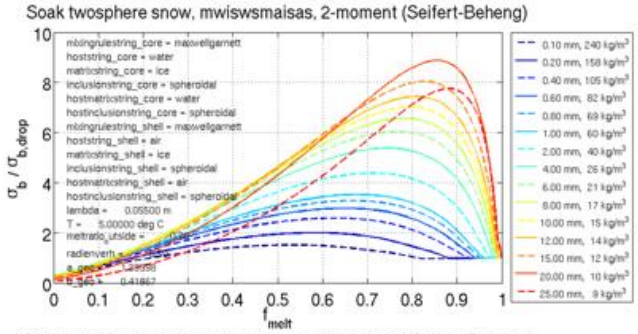
Soak twosphere snow, mwisssonasss, 2-moment (Seifert-Beheng)



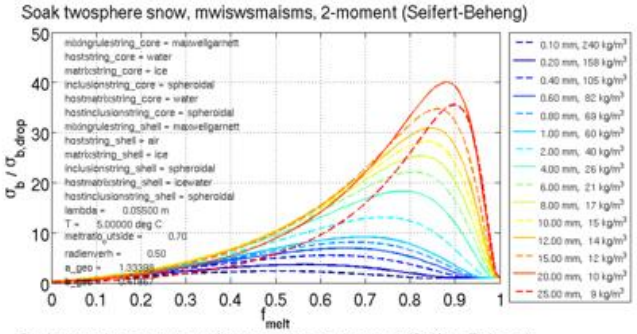
Soak twosphere snow, mwiswsbnasss, 2-moment (Seifert-Beheng)



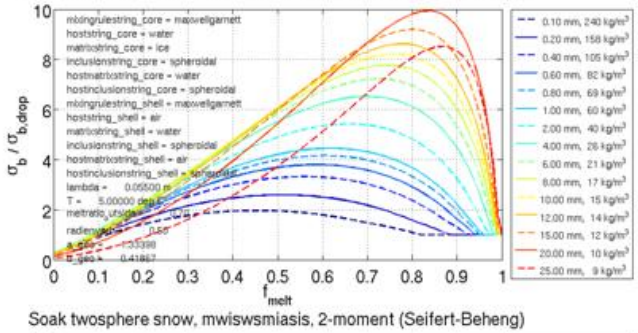
Soak twosphere snow, mwiswsmaisas, 2-moment (Seifert-Beheng)



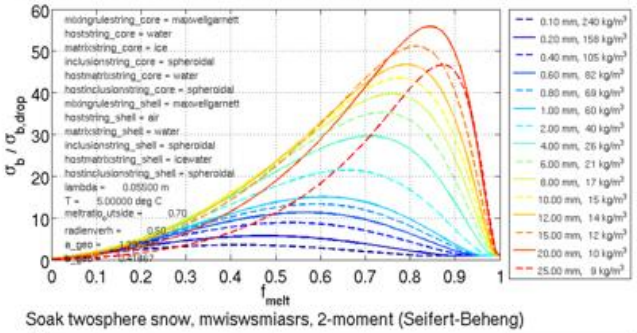
Soak twosphere snow, mwiswsmaisms, 2-moment (Seifert-Beheng)



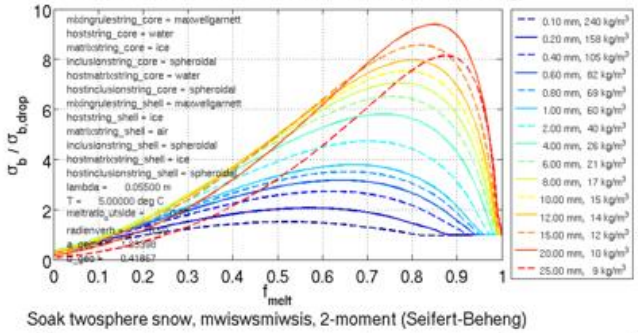
Soak twosphere snow, mwiswsmawsas, 2-moment (Seifert-Beheng)



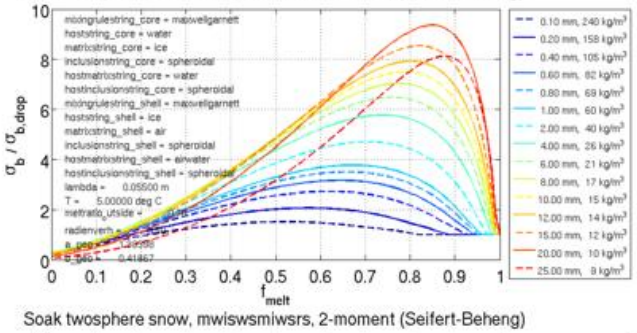
Soak twosphere snow, mwiswsmawsms, 2-moment (Seifert-Beheng)



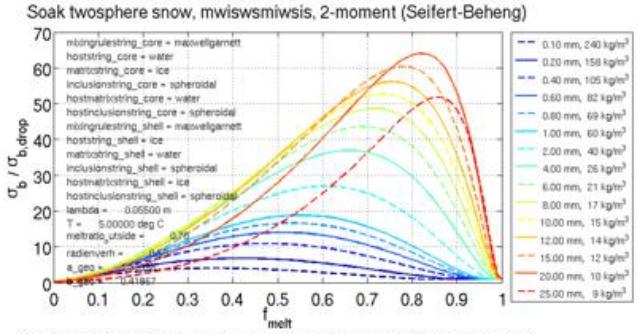
Soak twosphere snow, mwiswsmiasis, 2-moment (Seifert-Beheng)



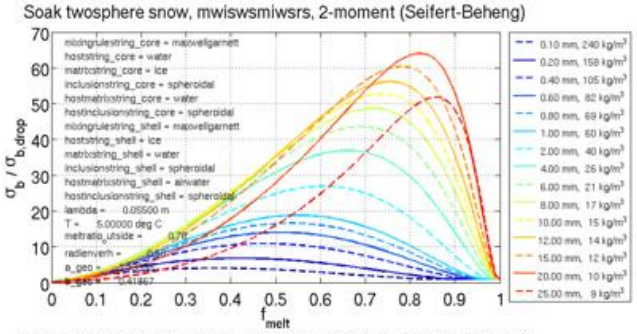
Soak twosphere snow, mwiswsmiasrs, 2-moment (Seifert-Beheng)



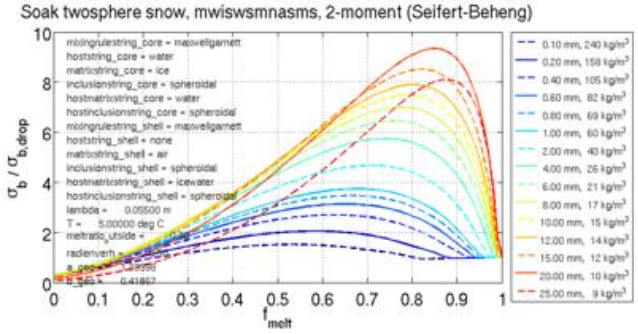
Soak twosphere snow, mwiswsmiwsis, 2-moment (Seifert-Beheng)



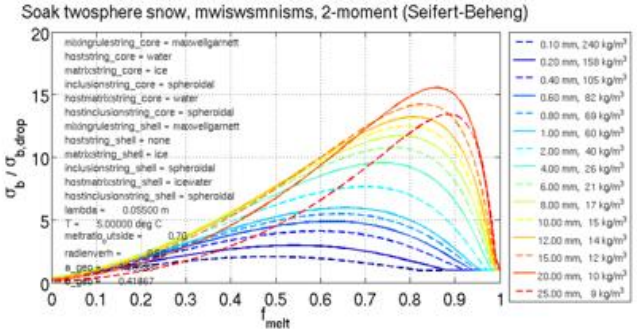
Soak twosphere snow, mwiswsmiwsrs, 2-moment (Seifert-Beheng)



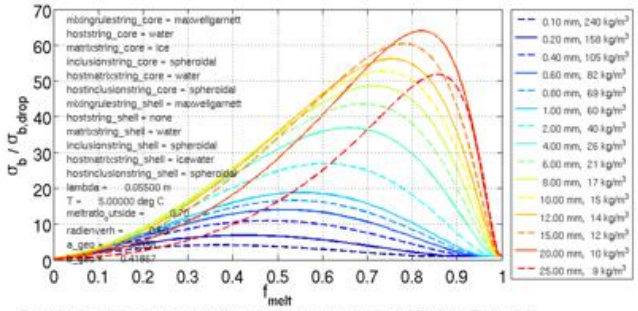
Soak twosphere snow, mwiswsmnasms, 2-moment (Seifert-Beheng)



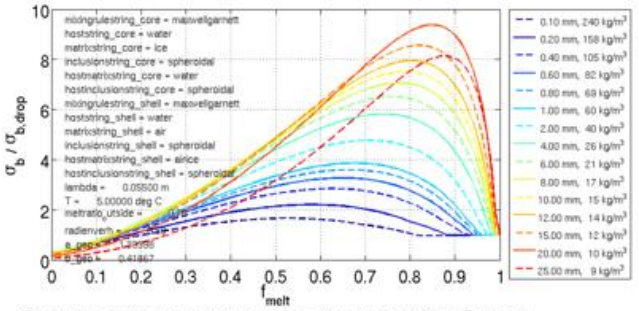
Soak twosphere snow, mwiswsmnisms, 2-moment (Seifert-Beheng)



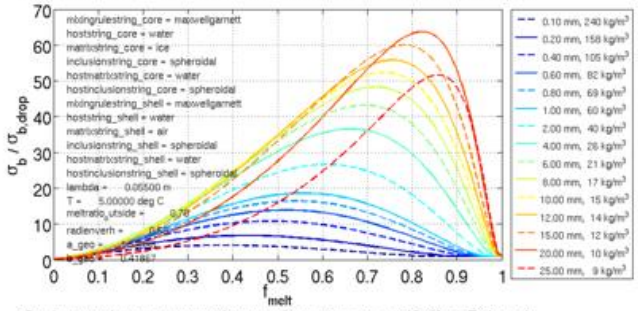
Soak twosphere snow, mwiswsmnwsms, 2-moment (Seifert-Beheng)



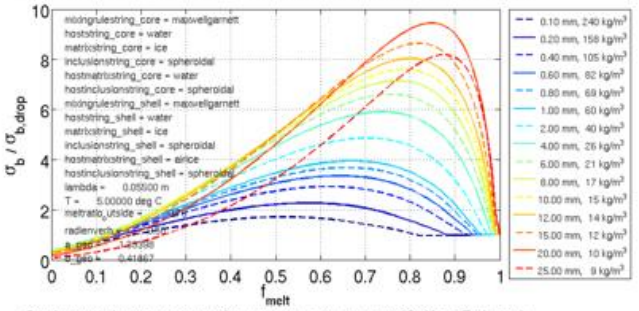
Soak twosphere snow, mwiswsmwasss, 2-moment (Seifert-Beheng)



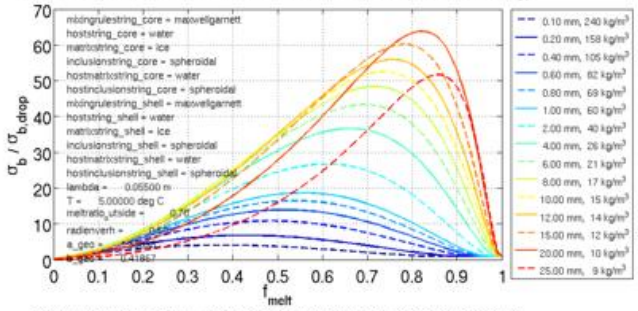
Soak twosphere snow, mwiswsmwasws, 2-moment (Seifert-Beheng)



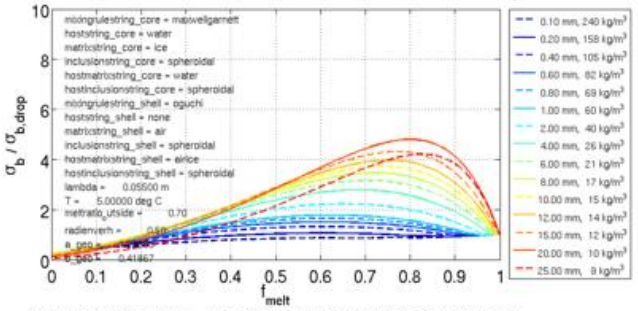
Soak twosphere snow, mwiswsmwisss, 2-moment (Seifert-Beheng)



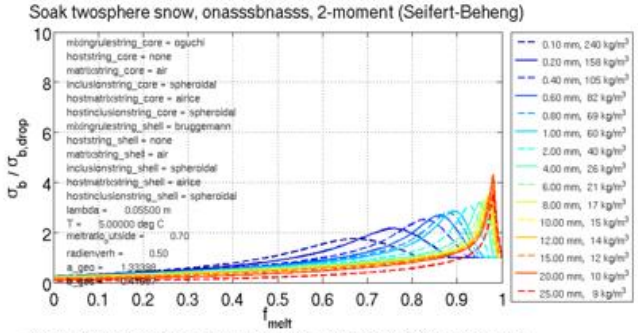
Soak twosphere snow, mwiswsmwisws, 2-moment (Seifert-Beheng)



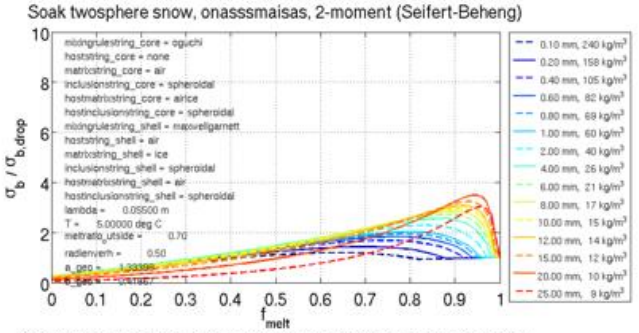
Soak twosphere snow, mwiswsonasss, 2-moment (Seifert-Beheng)



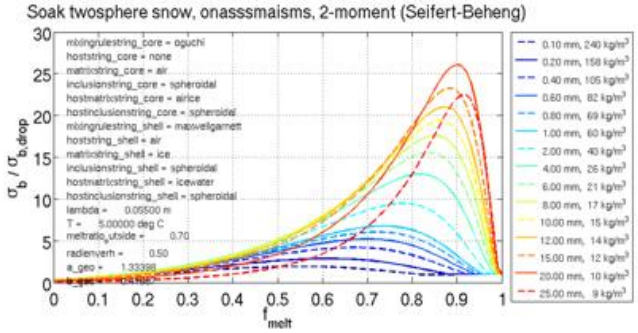
Soak twosphere snow, onasssbnasss, 2-moment (Seifert-Beheng)



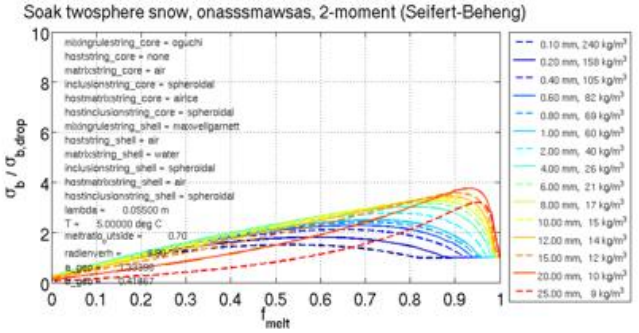
Soak twosphere snow, onasssmaisas, 2-moment (Seifert-Beheng)



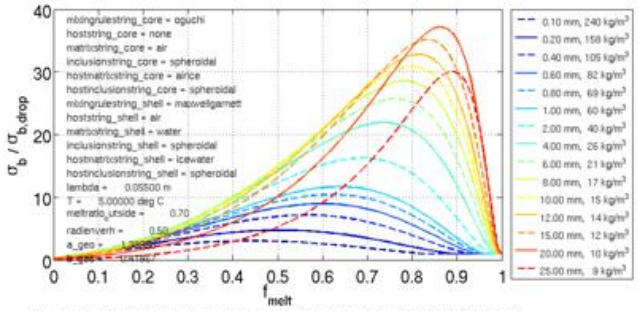
Soak twosphere snow, onasssmaisms, 2-moment (Seifert-Beheng)



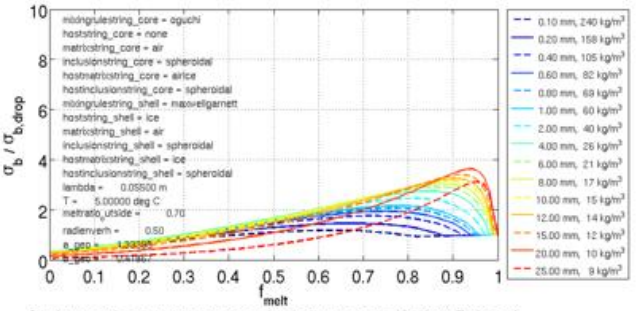
Soak twosphere snow, onasssmawsas, 2-moment (Seifert-Beheng)



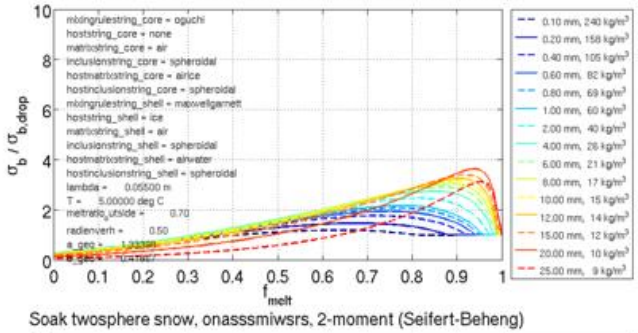
Soak twosphere snow, onasssmawsms, 2-moment (Seifert-Beheng)



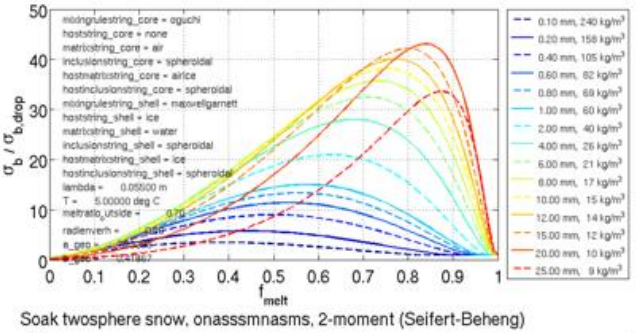
Soak twosphere snow, onasssmiasis, 2-moment (Seifert-Beheng)



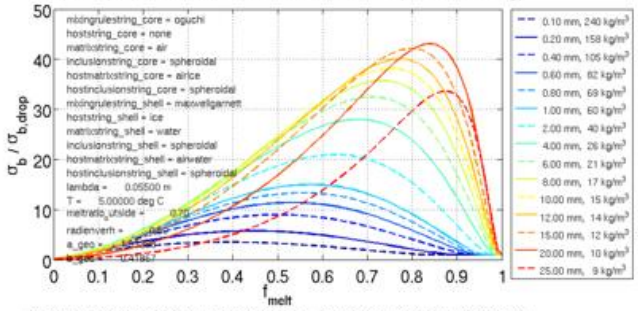
Soak twosphere snow, onasssmiasrs, 2-moment (Seifert-Beheng)



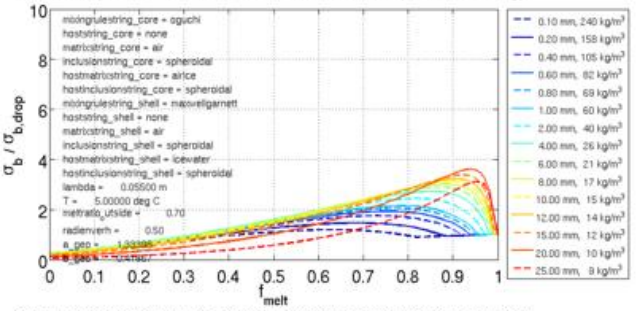
Soak twosphere snow, onasssmiwsis, 2-moment (Seifert-Beheng)



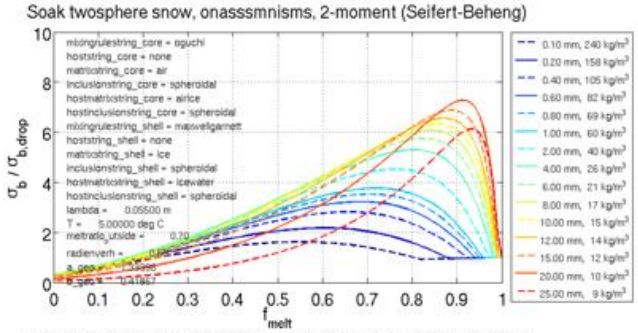
Soak twosphere snow, onasssmiwsrs, 2-moment (Seifert-Beheng)



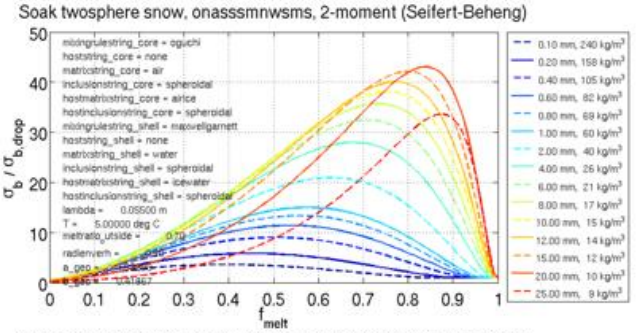
Soak twosphere snow, onasssmnasms, 2-moment (Seifert-Beheng)



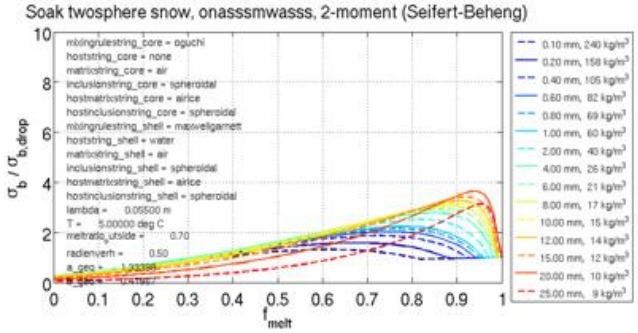
Soak twosphere snow, onasssmnisms, 2-moment (Seifert-Beheng)



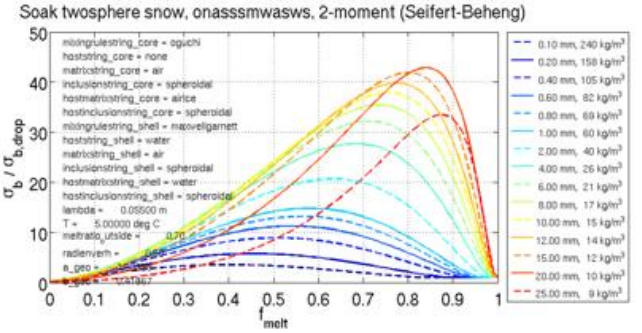
Soak twosphere snow, onasssmnwsms, 2-moment (Seifert-Beheng)



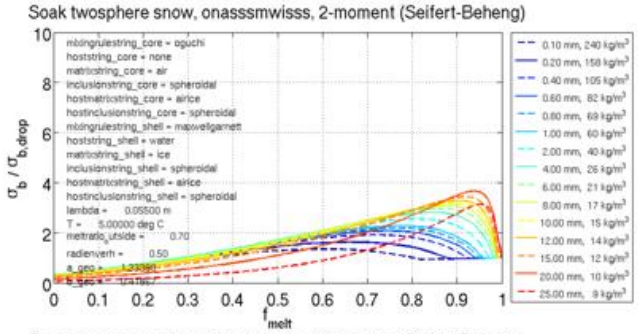
Soak twosphere snow, onasssmwasss, 2-moment (Seifert-Beheng)



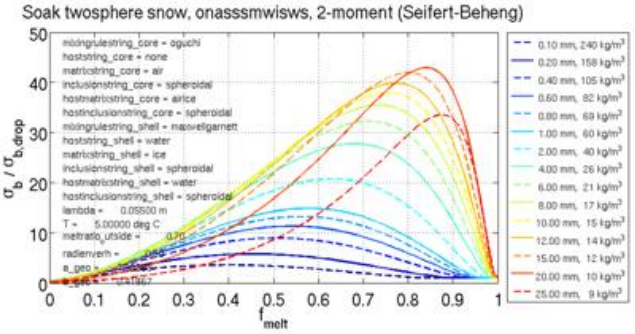
Soak twosphere snow, onasssmwasws, 2-moment (Seifert-Beheng)



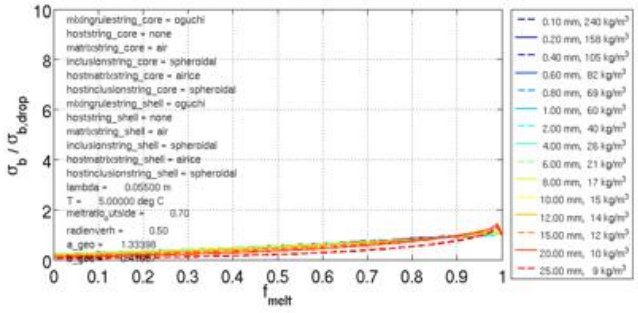
Soak twosphere snow, onasssmwisss, 2-moment (Seifert-Beheng)



Soak twosphere snow, onasssmwisws, 2-moment (Seifert-Beheng)



Soak twosphere snow, onasssonasss, 2-moment (Seifert-Beheng)



9 Index of the Figures of Section 8

9.1 Rayleigh: soaked wet graupel, LM-scheme

bnasss	74	miasrs	75	mwasss	75
maisas	74	miwsis	75	mwasws	75
maisms	74	miwsrs	75	mwisss	75
mawsas	74	mnasms	75	mwisws	75
mawsms	74	mnisms	75	onasss	76
miasis	74	mnwsms	75		

9.2 Rayleigh: soaked wet graupel, Seifert/Beheng-scheme

bnasss	77	miasrs	78	mwasss	78
maisas	77	miwsis	78	mwasws	78
maisms	77	miwsrs	78	mwisss	78
mawsas	77	mnasms	78	mwisws	78
mawsms	77	mnisms	78	onasss	79
miasis	77	mnwsms	78		

9.3 Rayleigh: soaked wet snow, LM-scheme

bnasss	80	miasrs	80	mwasss	81
maisas	80	miwsis	80	mwasws	81
maisms	80	miwsrs	81	mwisss	81
mawsas	80	mnasms	81	mwisws	81
mawsms	80	mnisms	81	onasss	81
miasis	80	mnwsms	81		

9.4 Rayleigh: soaked wet snow, Seifert/Beheng-scheme

bnasss	82	miasrs	82	mwasss	83
maisas	82	miwsis	82	mwasws	83
maisms	82	miwsrs	83	mwisss	83
mawsas	82	mnasms	83	mwisws	83
mawsms	82	mnisms	83	onasss	83
miasis	82	mnwsms	83		

9.5 Mie: soaked twosphere wet graupel, LM-scheme

basbis	84	masmws	84	miswis	85
basmis	84	maswis	85	oasmis	85
basmws	84	misbis	85	oasmws	85
masbis	84	mismis	85	oaswis	85
masmis	84	mismws	85		

9.6 Mie: soaked twosphere wet graupel, Seifert/Beheng-scheme

basbis	86	masmws	86	miswis	87
basmis	86	maswis	87	oasmis	87
basmws	86	misbis	87	oasmws	87
masbis	86	mismis	87	oaswis	87
masmis	86	mismws	87		

9.7 Mie: soaked twosphere wet snow, LM-scheme

basbis	88	masmws	88	miswis	89
basmis	88	maswis	89	oasmis	89
basmws	88	misbis	89	oasmws	89
masbis	88	mismis	89	oaswis	89
masmis	88	mismws	89		

9.8 Mie: soaked twosphere wet snow, Seifert/Beheng-scheme

basbis	90	masmws	90	miswis	91
basmis	90	maswis	91	oasmis	91
basmws	90	misbis	91	oasmws	91
masbis	90	mismis	91	oaswis	91
masmis	90	mismws	91		

9.9 Mie: soaked wet graupel, LM-scheme

bnasss	92	miasrs	93	mwasss	93
maisas	92	miwsis	93	mwasws	93
maisms	92	miwsrs	93	mwisss	93
mawsas	92	mnasms	93	mwisws	93
mawsms	92	mnisms	93	onasss	94
miasis	92	mnwsms	93		

9.10 Mie: soaked wet graupel, Seifert/Beheng-scheme

bnasss	95	miasrs	96	mwasss	96
maisas	95	miwsis	96	mwasws	96
maisms	95	miwsrs	96	mwisss	96
mawsas	95	mnasms	96	mwisws	96
mawsms	95	mnisms	96	onasss	97
miasis	95	mnwsms	96		

9.11 Mie: soaked wet snow, LM-scheme

bnasss	98	miasrs	98	mwasss	99
maisas	98	miwsis	98	mwasws	99
maisms	98	miwsrs	99	mwisss	99
mawsas	98	mnasms	99	mwisws	99
mawsms	98	mnisms	99	onasss	99
miasis	98	mnwsms	99		

9.12 Mie: soaked wet snow, Seifert/Beheng-scheme

bnasss	100	miasrs	100	mwasss	101
maisas	100	miwsis	100	mwasws	101
maisms	100	miwsrs	101	mwisss	101
mawsas	100	mnasms	101	mwisws	101
mawsms	100	mnisms	101	onasss	101
miasis	100	mnwsms	101		

9.13 Mie: watersphere wet graupel, LM-scheme

bas	102	mis	102	ois	102
bis	102	oas	102		
mas	102				

9.14 Mie: watersphere wet graupel, Seifert/Beheng-scheme

bas	103	mis	103	ois	103
bis	103	oas	103		
mas	103				

9.15 Mie: watersphere wet snow, LM-scheme

bas	104	mis	104	ois	104
bis	104	oas	104		
mas	104				

9.16 Mie: watersphere wet snow, Seifert/Beheng-scheme

bas	105	mis	105	ois	105
bis	105	oas	105		
mas	105				

9.17 Mie: spongy wet hail, Seifert/Beheng-scheme

bws 106 mws 106 ows 106
mis 106

9.18 Mie: watersphere wet hail, Seifert/Beheng-scheme

figure 107

9.19 Mie: twosphere soaked wet snow, LM-scheme

bnasssbnasss 108
bnasssmaisas 108
bnasssmaisms 108
bnasssmawsas 108
bnasssmawsms 108
bnasssmiasis 108
bnasssmiasrs 109
bnasssmiwsis 109
bnasssmiwsrs 109
bnasssmnasms 109
bnasssmnisms 109
bnasssmnwsms 109
bnasssmwasss 109
bnasssmwasws 109
bnasssmwisss 109
bnasssmwisws 109
bnasssonasss 110
maisasbnasss 110
maisasmaisas 110
maisasmaisms 110
maisasmawsas 110
maisasmawsms 110
maisasmiasis 110
maisasmiasrs 110
maisasmiwsis 110
maisasmiwsrs 110
maisasmnasms 111
maisasmnisms 111
maisasmnwsms 111
maisasmwasss 111
maisasmwasws 111
maisasmwisss 111
maisasmwisws 111
maisasonasss 111
maismsbnasss 111
maismsmaisas 111
maismsmaisms 112
maismsmawsas 112
maismsmawsms 112
maismsmiasis 112
maismsmiasrs 112
maismsmiwsis 112
maismsmiwsrs 112
maismsmnasms 112
maismsmnisms 112
maismsmnwsms 112
maismsmwasss 113
maismsmwasws 113
maismsmwisss 113
maismsmwisws 113
maismsonasss 113
mawsasbnasss 113
mawsasmaisas 113
mawsasmaisms 113
mawsasmawsas 113
mawsasmawsms 113
mawsasmiasis 114
mawsasmiasrs 114
mawsasmiwsis 114
mawsasmiwsrs 114
mawsasmnasms 114
mawsasmnisms 114
mawsasmnwsms 114
mawsasmwasss 114
mawsasmwasws 114
mawsasmwisss 114
mawsasmwisws 115
mawsasonasss 115
mawsmsbnasss 115
mawsmsmaisas 115
mawsmsmaisms 115
mawsmsmawsas 115
mawsmsmawsms 115
mawsmsmiasis 115
mawsmsmiasrs 115
mawsmsmiwsis 115
mawsmsmiwsrs 116
mawsmsmnasms 116
mawsmsmnisms 116
mawsmsmnwsms 116
mawsmsmwasss 116
mawsmsmwasws 116
mawsmsmwisss 116
mawsmsmwisws 116
mawsmsonasss 116
miasisbnasss 116
miasismaisas 117
miasismaisms 117
miasismawsas 117
miasismawsms 117
miasismiasis 117
miasismiasrs 117
miasismiwsis 117
miasismiwsrs 117
miasismnasms 117
miasismnisms 117
miasismnwsms 118
miasismwasss 118
miasismwasws 118
miasismwisss 118
miasismwisws 118
miasisonasss 118
miasrsbnasss 118
miasrsmaisas 118
miasrsmaisms 118
miasrsmawsas 118
miasrsmawsms 119
miasrsmiasis 119
miasrsmiasrs 119
miasrsmiwsis 119
miasrsmiwsrs 119
miasrsmnasms 119
miasrsmnisms 119
miasrsmnwsms 119

miasrsmwasss	119	mnasmsmwasss	124	mwasssmwasss	130
miasrsmwasws	119	mnasmsmwasws	125	mwasssmwasws	130
miasrsmwisss	120	mnasmsmwisss	125	mwasssmwisss	130
miasrsmwisws	120	mnasmsmwisws	125	mwasssmwisws	130
miasrsonasss	120	mnasmsonasss	125	mwasssonasss	130
miwsisbnasss	120	mnismsbnasss	125	mwaswsbnasss	130
miwsismaisas	120	mnismsmaisas	125	mwaswsmaisas	130
miwsismaisms	120	mnismsmaisms	125	mwaswsmaisms	130
miwsismawsas	120	mnismsmawsas	125	mwaswsmawsas	130
miwsismawsms	120	mnismsmawsms	125	mwaswsmawsms	130
miwsismiasis	120	mnismsmiasis	125	mwaswsmiasis	131
miwsismiasrs	120	mnismsmiasrs	126	mwaswsmiasrs	131
miwsismiwsis	121	mnismsmiwsis	126	mwaswsmiwsis	131
miwsismiwsrs	121	mnismsmiwsrs	126	mwaswsmiwsrs	131
miwsismnasms	121	mnismsmnasms	126	mwaswsmnasms	131
miwsismnisms	121	mnismsmnisms	126	mwaswsmnisms	131
miwsismnwsms	121	mnismsmnwsms	126	mwaswsmnwsms	131
miwsismwasss	121	mnismsmwasss	126	mwaswsmwasss	131
miwsismwasws	121	mnismsmwasws	126	mwaswsmwasws	131
miwsismwisss	121	mnismsmwisss	126	mwaswsmwisss	131
miwsismwisws	121	mnismsmwisws	126	mwaswsmwisws	132
miwsisonasss	121	mnismsonasss	127	mwaswsonasss	132
miwsrsbnasss	122	mnwsmsbnasss	127	mwisssbnasss	132
miwsrsmaisas	122	mnwsmsmaisas	127	mwisssmaisas	132
miwsrsmaisms	122	mnwsmsmaisms	127	mwisssmaisms	132
miwsrsmawsas	122	mnwsmsmawsas	127	mwisssmawsas	132
miwsrsmawsms	122	mnwsmsmawsms	127	mwisssmawsms	132
miwsrsmiasis	122	mnwsmsmiasis	127	mwisssmiasis	132
miwsrsmiasrs	122	mnwsmsmiasrs	127	mwisssmiasrs	132
miwsrsmiwsis	122	mnwsmsmiwsis	127	mwisssmiwsis	132
miwsrsmiwsrs	122	mnwsmsmiwsrs	127	mwisssmiwsrs	133
miwsrsmnasms	122	mnwsmsmnasms	128	mwisssmnasms	133
miwsrsmnisms	123	mnwsmsmnisms	128	mwisssmnisms	133
miwsrsmnwsms	123	mnwsmsmnwsms	128	mwisssmnwsms	133
miwsrsmwasss	123	mnwsmsmwasss	128	mwisssmwasss	133
miwsrsmwasws	123	mnwsmsmwasws	128	mwisssmwasws	133
miwsrsmwisss	123	mnwsmsmwisss	128	mwisssmwisss	133
miwsrsmwisws	123	mnwsmsmwisws	128	mwisssmwisws	133
miwsrsonasss	123	mnwsmsonasss	128	mwisssonasss	133
mnasmsbnasss	123	mwasssbnasss	128	mwiswsbnasss	133
mnasmsmaisas	123	mwasssmaisas	128	mwiswsmaisas	134
mnasmsmaisms	123	mwasssmaisms	129	mwiswsmaisms	134
mnasmsmawsas	124	mwasssmawsas	129	mwiswsmawsas	134
mnasmsmawsms	124	mwasssmawsms	129	mwiswsmawsms	134
mnasmsmiasis	124	mwasssmiasis	129	mwiswsmiasis	134
mnasmsmiasrs	124	mwasssmiasrs	129	mwiswsmiasrs	134
mnasmsmiwsis	124	mwasssmiwsis	129	mwiswsmiwsis	134
mnasmsmiwsrs	124	mwasssmiwsrs	129	mwiswsmiwsrs	134
mnasmsmnasms	124	mwasssmnasms	129	mwiswsmnasms	134
mnasmsmnisms	124	mwasssmnisms	129	mwiswsmnisms	134
mnasmsmnwsms	124	mwasssmnwsms	129	mwiswsmnwsms	135

mwiswsmwasss 135
mwiswsmwasws 135
mwiswsmwisss 135
mwiswsmwisws 135
mwiswsonasss 135
onasssbnasss 135
onasssmaisas 135
onasssmaisms 135
onasssmawsas 135
onasssmawsms 136
onasssmiasis 136
onasssmiasrs 136
onasssmiwsis 136
onasssmiwsrs 136
onasssmnasms 136
onasssmnisms 136
onasssmnwsms 136
onasssmwasss 136
onasssmwasws 136
onasssmwisss 137
onasssmwisws 137
onasssonasss 137

9.20 Mie: twosphere soaked wet snow, Seifert/Beheng-scheme

bnasssbnasss 138
bnasssmaisas 138
bnasssmaisms 138
bnasssmawsas 138
bnasssmawsms 138
bnasssmiasis 138
bnasssmiasrs 139
bnasssmiwsis 139
bnasssmiwsrs 139
bnasssmnasms 139
bnasssmnisms 139
bnasssmnwsms 139
bnasssmwasss 139
bnasssmwasws 139
bnasssmwisss 139
bnasssmwisws 139
bnasssonasss 140
maisasbnasss 140
maisasmaisas 140
maisasmaisms 140
maisasmawsas 140
maisasmawsms 140
maisasmiasis 140
maisasmiasrs 140
maisasmiwsis 140
maisasmiwsrs 140
maisasmnasms 141
maisasmnisms 141
maisasmnwsms 141
maisasmwasss 141
maisasmwasws 141
maisasmwisss 141
maisasmwisws 141
maisasonasss 141
maismsbnasss 141
maismsmaisas 141
maismsmaisms 142
maismsmawsas 142
maismsmawsms 142
maismsmiasis 142
maismsmiasrs 142
maismsmiwsis 142
maismsmiwsrs 142
maismsmnasms 142
maismsmnisms 142
maismsmnwsms 142
maismsmwasss 143
maismsmwasws 143
maismsmwisss 143
maismsmwisws 143
maismsonasss 143
mawsasbnasss 143
mawsasmaisas 143
mawsasmaisms 143
mawsasmawsas 143
mawsasmawsms 143
mawsasmiasis 144
mawsasmiasrs 144
mawsasmiwsis 144
mawsasmiwsrs 144
mawsasmnasms 144
mawsasmnisms 144
mawsasmnwsms 144
mawsasmwasss 144
mawsasmwasws 144
mawsasmwisss 144
mawsasmwisws 145
mawsasonasss 145
mawsmsbnasss 145
mawsmsmaisas 145
mawsmsmaisms 145
mawsmsmawsas 145
mawsmsmawsms 145
mawsmsmiasis 145
mawsmsmiasrs 145
mawsmsmiwsis 145
mawsmsmiwsrs 146
mawsmsmnasms 146
mawsmsmnisms 146
mawsmsmnwsms 146
mawsmsmwasss 146
mawsmsmwasws 146
mawsmsmwisss 146
mawsmsmwisws 146
mawsmsonasss 146
miasisbnasss 146
miasismaisas 147
miasismaisms 147
miasismawsas 147
miasismawsms 147
miasismiasis 147
miasismiasrs 147
miasismiwsis 147
miasismiwsrs 147
miasismnasms 147
miasismnisms 147
miasismnwsms 148
miasismwasss 148
miasismwasws 148
miasismwisss 148
miasismwisws 148
miasisonasss 148
miasrsbnasss 148
miasrsmaisas 148
miasrsmaisms 148
miasrsmawsas 148
miasrsmawsms 149
miasrsmiasis 149
miasrsmiasrs 149
miasrsmiwsis 149
miasrsmiwsrs 149
miasrsmnasms 149
miasrsmnisms 149
miasrsmnwsms 149
miasrsmwasss 149
miasrsmwasws 149
miasrsmwisss 150

miasrsmwisws	150	mnasmsmwisws	155	mwasssmwisws	160
miasrsonasss	150	mnasmsonasss	155	mwasssonasss	160
miwsisbnasss	150	mnismsbnasss	155	mwaswsbnasss	160
miwsismaisas	150	mnismsmaisas	155	mwaswsmaisas	160
miwsismaisms	150	mnismsmaisms	155	mwaswsmaisms	160
miwsismawsas	150	mnismsmawsas	155	mwaswsmawsas	160
miwsismawsms	150	mnismsmawsms	155	mwaswsmawsms	160
miwsismiasis	150	mnismsmiasis	155	mwaswsmiasis	161
miwsismiasrs	150	mnismsmiasrs	156	mwaswsmiasrs	161
miwsismiwsis	151	mnismsmiwsis	156	mwaswsmiwsis	161
miwsismiwsrs	151	mnismsmiwsrs	156	mwaswsmiwsrs	161
miwsismnasms	151	mnismsmnasms	156	mwaswsmnasms	161
miwsismnisms	151	mnismsmnisms	156	mwaswsmnisms	161
miwsismnwsms	151	mnismsmnwsms	156	mwaswsmnwsms	161
miwsismwasss	151	mnismsmwasss	156	mwaswsmwasss	161
miwsismwasws	151	mnismsmwasws	156	mwaswsmwasws	161
miwsismwisss	151	mnismsmwisss	156	mwaswsmwisss	161
miwsismwisws	151	mnismsmwisws	156	mwaswsmwisws	162
miwsisonasss	151	mnismsonasss	157	mwaswsonasss	162
miwsrsbnasss	152	mnwsmsbnasss	157	mwisssbnasss	162
miwsrsmaisas	152	mnwsmsmaisas	157	mwisssmaisas	162
miwsrsmaisms	152	mnwsmsmaisms	157	mwisssmaisms	162
miwsrsmawsas	152	mnwsmsmawsas	157	mwisssmawsas	162
miwsrsmawsms	152	mnwsmsmawsms	157	mwisssmawsms	162
miwsrsmiasis	152	mnwsmsmiasis	157	mwisssmiasis	162
miwsrsmiasrs	152	mnwsmsmiasrs	157	mwisssmiasrs	162
miwsrsmiwsis	152	mnwsmsmiwsis	157	mwisssmiwsis	162
miwsrsmiwsrs	152	mnwsmsmiwsrs	157	mwisssmiwsrs	163
miwsrsmnasms	152	mnwsmsmnasms	158	mwisssmnasms	163
miwsrsmnisms	153	mnwsmsmnisms	158	mwisssmnisms	163
miwsrsmnwsms	153	mnwsmsmnwsms	158	mwisssmnwsms	163
miwsrsmwasss	153	mnwsmsmwasss	158	mwisssmwasss	163
miwsrsmwasws	153	mnwsmsmwasws	158	mwisssmwasws	163
miwsrsmwisss	153	mnwsmsmwisss	158	mwisssmwisss	163
miwsrsmwisws	153	mnwsmsmwisws	158	mwisssmwisws	163
miwsrsonasss	153	mnwsmsonasss	158	mwisssonasss	163
mnasmsbnasss	153	mwasssbnasss	158	mwiswsbnasss	163
mnasmsmaisas	153	mwasssmaisas	158	mwiswsmaisas	164
mnasmsmaisms	153	mwasssmaisms	159	mwiswsmaisms	164
mnasmsmawsas	154	mwasssmawsas	159	mwiswsmawsas	164
mnasmsmawsms	154	mwasssmawsms	159	mwiswsmawsms	164
mnasmsmiasis	154	mwasssmiasis	159	mwiswsmiasis	164
mnasmsmiasrs	154	mwasssmiasrs	159	mwiswsmiasrs	164
mnasmsmiwsis	154	mwasssmiwsis	159	mwiswsmiwsis	164
mnasmsmiwsrs	154	mwasssmiwsrs	159	mwiswsmiwsrs	164
mnasmsmnasms	154	mwasssmnasms	159	mwiswsmnasms	164
mnasmsmnisms	154	mwasssmnisms	159	mwiswsmnisms	164
mnasmsmnwsms	154	mwasssmnwsms	159	mwiswsmnwsms	165
mnasmsmwasss	154	mwasssmwasss	160	mwiswsmwasss	165
mnasmsmwasws	155	mwasssmwasws	160	mwiswsmwasws	165
mnasmsmwisss	155	mwasssmwisss	160	mwiswsmwisss	165

mwiswsmwisws 165
mwiswsonasss 165
onasssbnasss 165
onasssmaisas 165
onasssmaisms 165
onasssmawsas 165
onasssmawsms 166
onasssmiasis 166
onasssmiasrs 166
onasssmiwsis 166
onasssmiwsrs 166
onasssmnasms 166
onasssmnisms 166
onasssmnwsms 166
onasssmwasss 166
onasssmwasws 166
onasssmwisss 167
onasssmwisws 167
onasssonasss 167

References

Battan, L. J., *Radar Observations of the Atmosphere*, The University of Chicago Press, Chicago, 1973.

Bohren, C. F. and L. J. Battan, 1982: Radar backscattering of microwaves by spongy ice spheres, *J. Atmos. Sci.*, **39**, 2623–2628.

Bohren, C. F. and D. R. Huffman, *Absorption and Scattering of Light by Small Particles*, John Wiley and Sons, Inc., 1983.

Bruggemann, D. A. G., 1935: Berechnung verschiedener physikalischer Konstanten von heterogenen Substanzen. I. Dielektrizitätskonstanten und Leitfähigkeiten der Mischkörper aus isotropen Substanzen, *Ann. Phys.*, **24**, 636–679.

Chýlek, P. and V. Srivastava, 1983: Dielectric constant of a composite inhomogeneous medium, *Phys. Rev. B*, **27**(8), 5098–5106.

Debye, P., *Polar Molecules*, New York (The Chemical Catalogue), 1929.

Deirmendjian, D., *Electromagnetic Scattering on Spherical Polydispersions*, American Elsevier Publishing Company, New York, 1969.

Fabry, F. and W. Szyrmer, 1999: Modeling of the melting layer. Part II: Electromagnetic, *J. Atmos. Sci.*, **56**, 3593–3600.

Joss, J. and A. N. Aufdermaur, 1965: Experimental determination of the radar cross sections of artificial hailstones containing water, *J. Appl. Meteor.*, **4**, 723–726.

Kerker, M., *The Scattering of Light and Other Electromagnetic Radiation*, Academic Press, New York, San Francisco, London, 1969.

Lichtenecker, A., 1926: Die Dielektrizitätskonstante natürlicher und künstlicher Mischkörper, *Phys. Z.*, **27**, 115–158.

Liebe, H. J., G. A. Hufford and T. Manabe, 1991: A model for the complex permittivity of water at frequencies below 1 THz, *Int. J. Infrared Millim. Waves*, **12**, 659–675.

Mätzler, C., Microwave properties of ice and snow, in: B. Schmitt et al. (editor), *Solar System Ices*, volume 227 of *Astrophysics and Space Science Library*, Kluwer Academic Publishers, Dordrecht, 1998, pp. 241–257.

Maxwell Garnett, J. C., 1904: Colors in metal glasses and in metallic films, *Phil. Trans. Roy. Soc. London*, **A203**, 385–420.

Oguchi, T., 1983: Electromagnetic wave propagation and scattering in rain and other hydrometeors, *Proc. IEEE*, **71**(9), 1029–1078.

Press, W. H., S. A. Teukolsky, W. T. Vetterling and B. P. Flannery, *Numerical Recipes in Fortran 77: The Art of Scientific Computing*, Cambridge University Press, 2001, 2. edition.

Ray, P. S., 1972: Broadband complex refractive indices of ice and water, *Appl. Opt.*, **11**, 1836–1844.

Segelstein, D. J., 1981: *The Complex Refractive Index of Water*, Master's thesis, Department of Physics, University of Missouri, Kansas City.

Seifert, A. and K. D. Beheng, 2006: A two-moment cloud microphysics parameterization for mixed-phase clouds. Part I: Model description, *Meteorol. Atmos. Phys.*, **92**, 45–66.

Stroud, D., 1975: Generalized effective-medium approach to the conductivity of an inhomogeneous material, *Phys. Rev. B*, **12**(8), 3368–3373.

Warren, S. G., 1984: Optical constants of ice from the ultraviolet to the microwave, *Appl. Opt.*, **23**(8), 1206–1225.

Wiener, O., 1912: Die Theorie des Mischk"orpers f"ur das Feld der station"aren Str"omung. Erste Abhandlung. Die Mittelwerts"atze f"ur Kraft, Polarisation und Energie, *32. Band der Abhandlungen der mathematisch-physikalischen Klasse der K"onigl. S"achsischen Gesellschaft der Wissenschaften*, (509–604).

Zhang, S. and J. Jin, *Computation of Special Functions*, John Wiley and sons, 1996.

List of COSMO Newsletters and Technical Reports

(available for download from the COSMO Website: www.cosmo-model.org)

COSMO Newsletters

No. 1: February 2001.

No. 2: February 2002.

No. 3: February 2003.

No. 4: February 2004.

No. 5: April 2005.

No. 6: July 2006.

No. 7: April 2008; Proceedings from the 8th COSMO General Meeting in Bucharest, 2006.

No. 8: September 2008; Proceedings from the 9th COSMO General Meeting in Athens, 2007.

No. 9: December 2008.

No. 10: March 2010.

No. 11: April 2011.

No. 12: April 2012.

No. 13: April 2013.

No. 14: April 2014.

No. 15: July 2015.

COSMO Technical Reports

No. 1: Dmitrii Mironov and Matthias Raschendorfer (2001):
Evaluation of Empirical Parameters of the New LM Surface-Layer Parameterization Scheme. Results from Numerical Experiments Including the Soil Moisture Analysis.

No. 2: Reinhold Schrodin and Erdmann Heise (2001):
The Multi-Layer Version of the DWD Soil Model TERRA_LM.

No. 3: Günther Doms (2001):
A Scheme for Monotonic Numerical Diffusion in the LM.

No. 4: Hans-Joachim Herzog, Ursula Schubert, Gerd Vogel, Adelheid Fiedler and Roswitha Kirchner (2002):
LLM ¯ the High-Resolving Nonhydrostatic Simulation Model in the DWD-Project LITFASS.
Part I: Modelling Technique and Simulation Method.

No. 5: Jean-Marie Bettems (2002):
EUCOS Impact Study Using the Limited-Area Non-Hydrostatic NWP Model in Operational Use at MeteoSwiss.

No. 6: Heinz-Werner Bitzer and Jürgen Steppeler (2004):
Documentation of the Z-Coordinate Dynamical Core of LM.

No. 7: Hans-Joachim Herzog, Almut Gassmann (2005):
Lorenz- and Charney-Phillips vertical grid experimentation using a compressible nonhydrostatic toy-model relevant to the fast-mode part of the 'Lokal-Modell'.

No. 8: Chiara Marsigli, Andrea Montani, Tiziana Paccagnella, Davide Sacchetti, André Walser, Marco Arpagaus, Thomas Schumann (2005):
Evaluation of the Performance of the COSMO-LEPS System.

No. 9: Erdmann Heise, Bodo Ritter, Reinhold Schrodin (2006):
Operational Implementation of the Multilayer Soil Model.

No. 10: M.D. Tsyrulnikov (2007):
Is the particle filtering approach appropriate for meso-scale data assimilation ?

No. 11: Dmitrii V. Mironov (2008):
Parameterization of Lakes in Numerical Weather Prediction. Description of a Lake Model.

No. 12: Adriano Raspanti (2009):
COSMO Priority Project "VERification System Unified Survey" (VERSUS): Final Report.

No. 13: Chiara Marsigli (2009):
COSMO Priority Project "Short Range Ensemble Prediction System" (SREPS): Final Report.

No. 14: Michael Baldauf (2009):
COSMO Priority Project "Further Developments of the Runge-Kutta Time Integration Scheme" (RK): Final Report.

No. 15: Silke Dierer (2009):
COSMO Priority Project "Tackle deficiencies in quantitative precipitation forecast" (QPF): Final Report.

No. 16: Pierre Eckert (2009):
COSMO Priority Project "INTERP": Final Report.

No. 17: D. Leuenberger, M. Stoll and A. Roches (2010):
Description of some convective indices implemented in the COSMO model.

No. 18: Daniel Leuenberger (2010):
Statistical analysis of high-resolution COSMO Ensemble forecasts in view of Data Assimilation.

No. 19: A. Montani, D. Cesari, C. Marsigli, T. Paccagnella (2010):
Seven years of activity in the field of mesoscale ensemble forecasting by the COSMO–LEPS system: main achievements and open challenges.

No. 20: A. Roches, O. Fuhrer (2012):
Tracer module in the COSMO model.

No. 21: Michael Baldauf (2013):
A new fast-waves solver for the Runge-Kutta dynamical core.

No. 22: C. Marsigli, T. Diomede, A. Montani, T. Paccagnella, P. Louka, F. Gofa, A. Corigliano (2013):
The CONSENS Priority Project.

No. 23: M. Baldauf, O. Fuhrer, M. J. Kurowski, G. de Morsier, M. Müllner, Z. P. Piotrowski, B. Rosa, P. L. Vitagliano, D. Wójcik, M. Ziemiański (2013):
The COSMO Priority Project 'Conservative Dynamical Core' Final Report.

No. 24: A. K. Miltenberger, A. Roches, S. Pfahl, H. Wernli (2014):
Online Trajectory Module in COSMO: a short user guide.

No. 25: P. Khain, I. Carmona, A. Voudouri, E. Avgoustoglou, J.-M. Bettems, F. Grazzini (2015):
The Proof of the Parameters Calibration Method: CALMO Progress Report.

No. 26: D. Mironov, E. Machulskaya, B. Szintai, M. Raschendorfer, V. Perov, M. Chumakov, E. Avgoustoglou (2015):
The COSMO Priority Project 'UTCS' Final Report.

No. 27: J-M. Bettems (2015):
The COSMO Priority Project 'COLOBOC': Final Report.

COSMO Technical Reports

Issues of the COSMO Technical Reports series are published by the *COnsortium for Small-scale MOdelling* at non-regular intervals. COSMO is a European group for numerical weather prediction with participating meteorological services from Germany (DWD, AWGeophys), Greece (HNMS), Italy (USAM, ARPA-SIMC, ARPA Piemonte), Switzerland (MeteoSwiss), Poland (IMGW), Romania (NMA) and Russia (RHM). The general goal is to develop, improve and maintain a non-hydrostatic limited area modelling system to be used for both operational and research applications by the members of COSMO. This system is initially based on the COSMO-Model (previously known as LM) of DWD with its corresponding data assimilation system.

The Technical Reports are intended

- for scientific contributions and a documentation of research activities,
- to present and discuss results obtained from the model system,
- to present and discuss verification results and interpretation methods,
- for a documentation of technical changes to the model system,
- to give an overview of new components of the model system.

The purpose of these reports is to communicate results, changes and progress related to the LM model system relatively fast within the COSMO consortium, and also to inform other NWP groups on our current research activities. In this way the discussion on a specific topic can be stimulated at an early stage. In order to publish a report very soon after the completion of the manuscript, we have decided to omit a thorough reviewing procedure and only a rough check is done by the editors and a third reviewer. We apologize for typographical and other errors or inconsistencies which may still be present.

At present, the Technical Reports are available for download from the COSMO web site (www.cosmo-model.org). If required, the member meteorological centres can produce hard-copies by their own for distribution within their service. All members of the consortium will be informed about new issues by email.

For any comments and questions, please contact the editor:

Massimo Milelli

Massimo.Milelli@arpa.piemonte.it

Consortium for Small-Scale Modelling

Technical Report No. 19

Seven years of activity in the field of mesoscale ensemble forecasting by the COSMO-LEPS system: main achievements and open challenges

June 2010

DOI: 10.5676/DWD_pub/nwv/cosmo-tr_19

Deutscher Wetterdienst

MeteoSwiss

Ufficio Generale Spazio Aereo e Meteorologia

ΕΘΝΙΚΗ ΜΕΤΕΩΡΟΛΟΓΙΚΗ ΥΠΗΡΕΣΙΑ

Instytucie Meteorogii i Gospodarki Wodnej

Administratia Nationala de Meteorologie

Agenzia Regionale per la Protezione Ambientale del Piemonte

Agenzia Regionale per la Protezione Ambientale dell' Emilia-Romagna: Servizio Idro Meteo

Centro Italiano Ricerche Aerospaziali

Amt für GeoInformationswesen der Bundeswehr

www.cosmo-model.org

Editor: Massimo Milelli, ARPA Piemonte
Printed at Deutscher Wetterdienst, P.O. Box 100465, 63004 Offenbach am Main

Seven years of activity in the field of mesoscale ensemble forecasting by the COSMO-LEPS system: main achievements and open challenges

A. Montani, D. Cesari, C. Marsigli

and T. Paccagnella

ARPA-SIMC
Viale Silvani 6
Bologna
Italy

Contents

1 Abstract **3**

2 Introduction **3**

3 Description of COSMO-LEPS operational system **4**

4 Methodology of verification **6**

5 Time–series results **9**

5.1 ROC Area 9

5.2 Brier Skill Score 11

5.3 Ranked Probability Skill Score 15

5.4 Percentage of Outliers 17

6 Seasonal scores **17**

6.1 Scores in autumn 18

6.2 Scores in summer 20

7 Conclusions **21**

8 Acknowledgments **22**

9 References **23**

1 Abstract

In this work, the main characteristics of COSMO–LEPS, the Limited–area Ensemble Prediction System developed in the framework of the COnsortium for Small-scale MOdelling, are presented. The present status of the system is shown with the description of the methodology and of the main upgrades which took place during its years of activity. The performance of COSMO–LEPS for the probabilistic prediction of precipitation is assessed in terms of both time–series and seasonal scores over a 7–year period. A fixed number of stations is selected and observations are compared to short and early–medium–range forecasts. Different verification indices are used to assess the skill of COSMO–LEPS and to identify the impact of system modifications on forecast skill. The different system upgrades are found to impact positively on COSMO–LEPS performance, with a gain of two days of predictability in the last four years of operational forecasts. This holds when the skill of the system is assessed both for single events (e.g. precipitation surpassing a fixed threshold) and for multi–event situations. Scores for fixed forecast ranges but varying thresholds confirm increasingly better performance of the system. Finally, the main stream of development for COSMO–LEPS system are discussed with future possible upgrades and methodology modifications.

2 Introduction

One of the main challenges for numerical weather prediction (NWP) is still recognised as quantitative precipitation forecasting. Computer power resources have greatly increased in the last years, thus allowing the generation of more and more sophisticated NWP model with accurate parametrisation of physical processes supported by high horizontal and vertical resolution. Nevertheless, the accurate forecast of high–impact weather still remains difficult beyond day 2 and sometimes, also for shorter ranges (Mullen and Buizza, 2001; Tibaldi et al., 2006). Several factors contribute to forecast failures and can be usually related to shortcomings in the definition of the initial conditions of the integrations, to model errors of different types and, last but not least, to the intrinsic low predictability of the physical phenomena under investigation. The use of the probabilistic approach via the ensemble forecasting has now become commonplace to tackle the chaotic behaviour of the atmosphere and to support forecasters in the management of alert procedures for events with little deterministic predictability. Several national and international weather centres, like the European Centre for Medium–Range Weather Forecasts (ECMWF), the Canadian Meteorological Centre (CMC), the National Centers for Environmental Prediction (NCEP) and the UK Meteorological Office, provide valuable operational ensemble prediction at a global scale (Tracton and Kalnay, 1993; Houtekamer et al., 1996; Molteni et al., 1996; Buizza et al., 2007; Bowler et al., 2008). In addition to them, many limited–area ensemble prediction systems have been recently developed, either in research or in operational mode, so as to address the need of detailing high–impact weather forecasts at higher and higher resolution and to support the reliability of the deterministic forecast beyond the very short range.

As far as operational implementations are concerned, the Consortium for Small–Scale MOdelling Limited–area Ensemble Prediction System (COSMO–LEPS) was the first mesoscale ensemble application running on a daily basis in Europe[1]. This system, initially developed and implemented by the HydroMeteoClimate Regional Service of Emilia-Romagna, in Bologna, Italy (ARPA–SIMC), has been running at ECMWF since November 2002 (Montani et al., 2003a) thanks to the ECMWF computer resources provided by the COSMO

[1]Information about the activities of the COSMO consortium can be found at http://www.cosmo-model.org.

countries which are ECMWF Member states. Nowadays, COSMO–LEPS is based on 16 integrations of the non–hydrostatic mesoscale model COSMO, formerly known as the Lokal Modell (Steppeler et al., 2003). The methodology (described more thoroughly in the next section) aims at combining the advantages of the probabilistic approach by global ensemble systems with the high–resolution details gained in the mesoscale integrations. In the construction of COSMO–LEPS, an algorithm selects a number of members (referred to as Representative Members, RMs) by a global ensemble system (Marsigli et al., 2001; Molteni et al., 2001). This intermediate step, referred to as "ensemble–size reduction", is required to keep the computational load operationally affordable, since it is not presently feasible to nest the limited-area model on each individual member of a highly–populated global ensemble. After the "ensemble–size reduction", the selected RMs are used to provide both initial and boundary conditions to the integrations with the COSMO model, which is run once for each RM. Therefore, COSMO–LEPS performs a sort of dynamical downscaling of a global–model probabilistic system, limiting to a certain extent the computation investment (Tibaldi et al., 2006).

In this work, the progresses in the development of COSMO–LEPS are reviewed, focusing on past and recent system upgrades and on the impact on its forecast skill. It is aimed to quantify the improvements of COSMO–LEPS in terms of probabilistic prediction of light and heavy precipitation events in the short and early–medium range. This will enable to indicate both strengths and weaknesses of the system, to highlight the open challenges and to suggest the main streams of future developments.
The rest of the paper is organised as follows: section 3 describes the main characteristics of the COSMO–LEPS system, while, in section 4, the features of the verification procedure are reported. Results in terms of both time–series and seasonal scores are presented in sections 5 and 6, respectively. Finally, conclusions are drawn in section 7.

3 Description of COSMO-LEPS operational system

As previously mentioned, the "core" of COSMO–LEPS methodology lies in the idea of reducing the number of global–ensemble elements driving the limited–area runs, still retaining a large fraction of the driving–ensemble information. In its first experimental–operational implementation which dates November 2002, the set–up of COSMO–LEPS can be described as follows (Montani et al., 2003b):

1. three successive runs of ECMWF Ensemble Prediction System (EPS), starting at 12UTC at day *d-1*, at 00UTC and 12UTC of day *d* are joined together, thus generating a 153–member lagged–ensemble, since each EPS is made up of one control run plus 50 perturbed members (Buizza, 2005);

2. EPS members are grouped into 5 clusters, the discriminating variable being a combination of four variables at three pressure levels and at 2 forecast steps: the two horizontal wind components, the geopotential height and the specific humidity at 500, 700, 850 hPa and at the ranges of 96 and 120 hours (the ranges are relative to the "youngest" ensemble, run at 12UTC of day *d*);

3. for each variable at each forecast step, the mean over the clustering area is calculated and, then, subtracted from any grid-point value. Hence, the result is divided by the standard deviation, thus obtaining a non–dimensional field;

4. the quadratic distances among the EPS members are computed for all variables at all levels at all steps and, then, space–averaged;

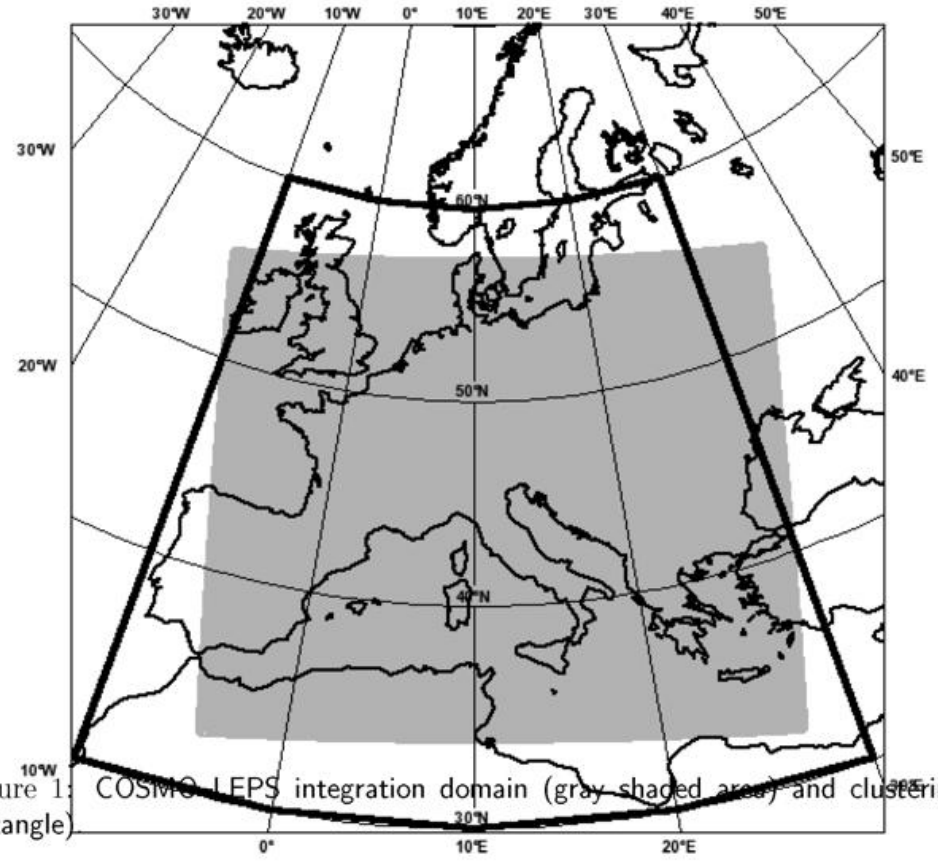


Figure 1: COSMO–LEPS integration domain (gray shaded area) and clustering area (black rectangle)

5. the cluster analysis is performed over the following area: 40N–60N, 10W–30E (denoted by the black rectangle of Fig. 1); the clusters are constructed using the complete–linkage algorithm (Wilks, 1995);

6. within each cluster (with different populations), one RM is selected, using the same discriminating variables as before; the RM is that cluster element which minimises the ratio between its distance from the other members of its own cluster and its distance from the members of the other clusters;

7. the so–selected RMs provide both initial and boundary conditions for the integrations with the COSMO model, which is run once for each RM over a domain covering Central and Southern Europe (shaded area in Fig. 1);

8. the 5 COSMO integrations which generate the COSMO–LEPS system, start at 12UTC of day d, with a horizontal resolution of 10 km, 32 vertical levels and a forecast length of 120 hours;

9. post–processed products (e.g. the probability of exceeding a threshold) are generated, assuming a relationship between cluster population and the probability of occurrence of its associated RM; hence each COSMO integration is given a weight proportional to the population of the cluster from which the RM (providing initial and boundary conditions) was selected.

In the course of its operational activity, the COSMO–LEPS system has undergone many changes. Without accounting for the model upgrades with bug fixes and more sophisti-

cated and precise parametrisation, the main milestones of COSMO–LEPS history can be summarised as follows:

- 4 November 2002: beginning of COSMO–LEPS activity in the above–described configuration;
- 1 June 2004 ([**A**]): ensemble population increased to 10 members; the RMs are selected out of 102 EPS members (only 2 successive EPS runs starting at 00UTC and 12UTC of day d are used); random procedure for the choice of either Kain-Fritsch or Tiedtke convection scheme with each COSMO–LEPS run;
- 1 July 2005: the forecast range of COSMO–LEPS integrations is increased from 120 to 132 hours;
- December 2005; COSMO–LEPS application becomes an "*ECMWF Member State time–critical application*" managed by ARPA–SIMC and monitored by ECMWF operators;
- 2 February 2006 ([**B**]); ensemble size increased from 10 to 16 members; vertical resolution increased from 32 to 40 model levels;
- 1 December 2007 ([**C**]); change of the numerical scheme in COSMO–LEPS integrations; introduction of new perturbations in the model parametrisations.

In this list, a number of changes are labelled with letters **[A], [B], [C]**: they represent those system upgrades with direct consequences on the performance of the COSMO–LEPS forecast skill, as will be shown later on.
It is worth pointing out that, both in the first years of activity as well as more recently, Marsigli et al. (2005a, 2005b and 2008), Montani et al. (2008a and 2008b) and Walser (2006) showed that COSMO–LEPS provided high–quality probabilistic quantitative prediction of heavy precipitation events. Over a number of case studies as well as over continuous verification periods, COSMO–LEPS was shown to perform usually better than ECMWF EPS in terms of geographical localisations of the regions most likely to be affected by the events as well as in terms of more realistic rainfall patterns. The above works used different verification techniques and different observational datasets; hence, they cannot provide exhaustive information on the evolution of the skill of the system. In order to shed light on the progresses of COSMO–LEPS, a comprehensive verification over the full history of the system is undertaken with the features described in the next section.

4 Methodology of verification

The performance of COSMO–LEPS system is analysed considering the probabilistic prediction of 12–hour accumulated precipitation exceeding a number of thresholds for several forecast ranges. Instead of the "more traditional" 24–hour accumulation period, it was decided to focus the attention on 12–hour precipitation (accumulated from 18 to 6 UTC and from 6 to 18 UTC) in order to investigate the performance of the system for both day–time and night–time precipitation forecasts. This should allow the possibility to isolate possible biases and/or systematic errors in the diurnal cycle of COSMO-LEPS model integrations, which would be otherwise masked if verification were performed over a 24–hour window.

As for observations, it is clear that a high–resolution network would be very desirable in order to assess the predictive skill of a mesoscale ensemble system. Since precipitation has a high-spatial variability, this network would provide better estimates of precipitation at

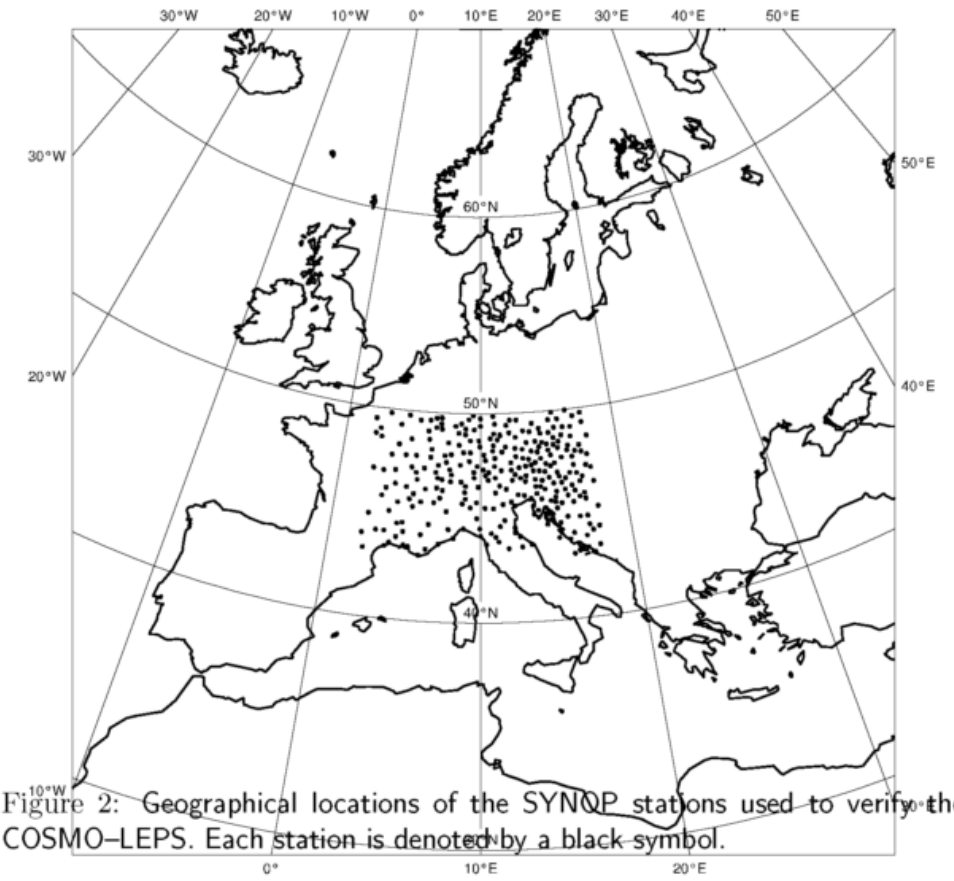


Figure 2: Geographical locations of the SYNOP stations used to verify the performance of COSMO–LEPS. Each station is denoted by a black symbol.

high resolution. Unfortunately, this type of network, like the high–density network adopted by Marsigli et al. (2008), is not available with continuity in the period 2002–2009, as it presents several "gaps", this making impossible a detailed evaluation of how the performance of COSMO–LEPS evolved in the years. For this reason, it has been decided to use the data obtained from the SYNOP reports available on the Global Telecommunication System (GTS), since this is recognised to be a homogeneous and stable dataset throughout the years 2002–2009.

In order to assess the skill of the system over complex topography, verification is performed in the domain ranging from 43N to 50N and from 2N to 18E. This domain, sometimes referred to as MAP D-PHASE area (Mesoscale Alpine Programme, Demonstration of Probabilistic Hydrological and Atmospheric Simulation of flood Events in the alpine region), is the common terrain of investigation for the Forecast Demonstration Project which took place during the Operation Period of D-PHASE (Zappa et al., 2008; Rotach et al., 2009). Within this domain, a fixed list of 412 SYNOP stations is considered and the relative reports in terms of total precipitation are used to evaluate the COSMO–LEPS skill.

Fig. 2 reports the locations of the stations used for the verification. The SYNOP reports have undergone a simple quality control firstly based on the "surpassing" of a confidence level (provided in the data retrieved by ECMWF archive) for the full report. In addition to this, for cases of very high precipitation records, the values are compared, whenever possible, to those taken from nearby non–GTS stations. In case of discrepancy between non–GTS and SYNOP reports, the latter is discarded and the relative data not used in the computation of the scores.

As for the comparison of model forecasts against SYNOP reports, we select the grid point

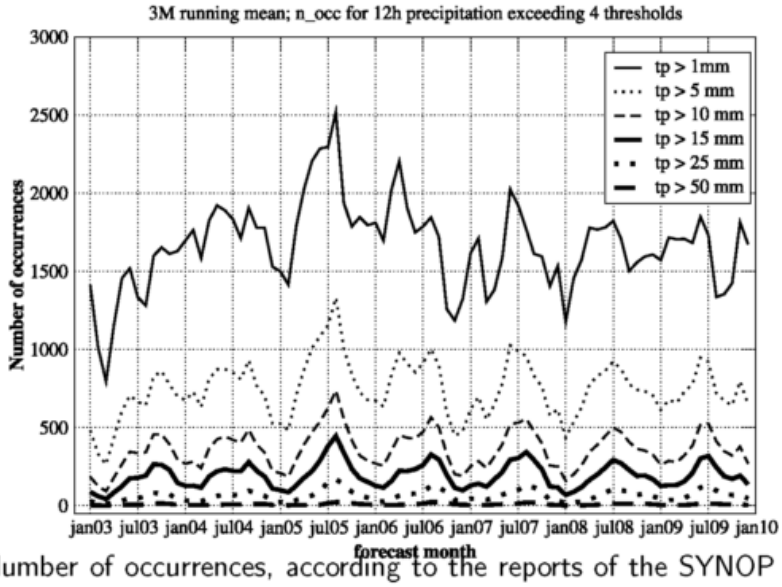


Figure 3: Number of occurrences, according to the reports of the SYNOP stations of Fig. 2, for 12–hour observed precipitation exceeding 4 different thresholds: 1mm/12h (thin–solid line), 5mm/12h (dotted), 10mm/12h (dashed), 15mm/12h (thick–solid), 25mm/12h (thick–dotted) and 50 mm/12h (thick–dashed). A 3–month running mean is applied to improve the readability of the plots.

closest to the observation. Little sensitivity to the results is found when, instead of the nearest grid point, a bi-linear interpolation using the 4 nearest points to the station location, is used to generate the model forecasts. Therefore, the results shown hereafter will be relative only to the nearest grid-point method.
The performance of COSMO–LEPS is examined for 6 different thresholds: 1, 5, 10, 15, 25 and 50 mm/12h.

Fig. 3 shows the overall number of occurrences for each threshold and for each month, from December 2002 to November 2009, according to the reports of the stations of Fig. 2. As the occurrences have a strong marked month–to–month variability (and for ease of comparison with the future plots), a 3–month running mean was applied to improve the readability of the figure. The high values for precipitation observed in July–August 2005 stand out, with about 500 events of rainfall exceeding 15 mm in 12 hours. In addition to that, other shifts between dry and wet periods are also evident. It is immediately worth pointing out that, when considering the two highest thresholds (thick–dotted and thick–dashed lines, relative to the 25 and 50 mm/12h values, respectively), a low number of occurrences, often below 10, is found for several seasons (especially in winters). This may cast some doubts on the statistical solidity of the results for these types of events over a long verification period. Good (poor) performance over specific seasons could be due to the fact that COSMO–LEPS predictions captured (did not capture) those few heavy precipitation events, this not allowing any solid conclusions on the effective performance of the system for the highest thresholds. On the other hand, large numbers of occurrences are often found for the other thresholds, including the event “15 mm of precipitation over 12 hours” (thick–solid line in Fig. 3), which is already a quite substantial amount. Therefore, the results relative to the two highest thresholds (25 and 50 mm/12h) will not be shown and more emphasis will be given to the remaining thresholds (1, 5, 10, 15 mm/12h).
As already mentioned, verification was performed over a 7-year period, from December 2002 to November 2009. For each month as well as for each season, the following probabilistic

Table 1: Main features of the verification configuration.

variable:	12–hour accumulated precipitation (18–06, 06–18 UTC);
period:	from Dec 2002 to Nov 2009;
region:	43–50N, 2–18E (D–PHASE area);
method:	nearest grid–point;
observations:	SYNOP reports;
forecast ranges (h):	6-18, 18-30, 30-42, 42-54, 54-66, 66-78, 78-90, 90-102, 102-114, 114-126;
thresholds:	1, 5, 10, 15, 25, 50 mm/12h;
scores:	ROC area, BSS, RPSS, OUTL;

scores are computed: the Brier Skill Score (BSS), the Ranked Probability Skill Score (RPSS), the Relative Operating Characteristic Curve (ROC) area and the Percentage of Outliers (OUTL). For a description of these scores, the reader is referred to Wilks (1995) and to Marsigli et al. (2008). The main features of the verification exercise are summarised in Table 1.

5 Time–series results

In the following subsections, the results relative to the performance of COSMO–LEPS for particular types of weather events are presented in terms of time–series scores for the above–mentioned probabilistic indices.

5.1 ROC Area

The ROC area (Mason and Graham, 1999) ranges from 0 to 1, the higher the better, and the value of 0.5 is the limit from skill and no–skill. For a forecast system to be useful, the ROC area should exceed the value of 0.7 (Buizza et al., 1999).

Fig. 4 shows the performance of COSMO-LEPS in terms of time-series values of the ROC area for the 30–42h forecast range (that is, the precipitation accumulated over the 12–hour period ending at 42–hour forecast step). The score exhibits a marked month–to–month variability and a 3–month running mean was applied to improve the readability of the plots. The skill of COSMO–LEPS is shown for the first 4 thresholds of Table 1: it can be noticed that, in any case, the performance of the system has increased throughout the years of COSMO–LEPS activity. This is especially true for the 10mm/12h and 15mm/12h thresholds (dashed and thick–solid lines, respectively), since the scores increased from about 0.6, in the first months of 2003, to more than 0.8, since mid–2007. The letters [A], [B] and [C] in the lower part of the plot denote the major system upgrades among those described in the previous section. It can be noticed that the [A] upgrade, relative to the increase of COSMO–LEPS ensemble size had a positive impact on the performance of the system. As for the [B] upgrade, it has to be noticed that, in February 2006, not only did COSMO–LEPS increase both ensemble size and vertical resolution, but also ECMWF EPS decreased its horizontal grid size from 80 to about 50 km in the horizontal (Buizza et al., 2007), thus improving the quality of both initial and boundary conditions provided to the limited–area runs. Despite these system upgrades, the performance of COSMO–LEPS was not as good as could be expected in the following months (Spring to Summer 2006), with scores below 0.8 for the 10 and 15 mm thresholds. On the other hand, some recovery in the performance of the system

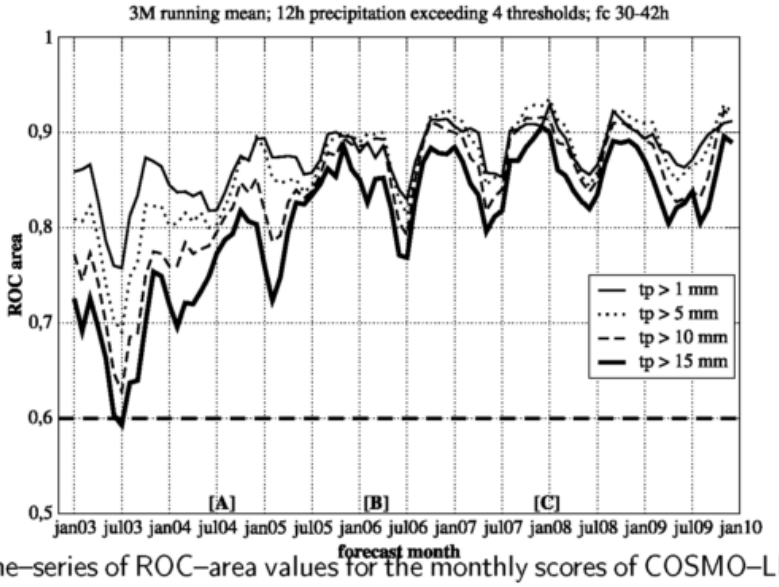


Figure 4: Time–series of ROC–area values for the monthly scores of COSMO–LEPS for 4 different thresholds: 1mm/12h (thin–solid line), 5mm/12h (dotted), 10mm/12h (dashed) and 15mm/12h (thick–solid). The forecast range is 30–42h. A 3–month running mean is applied to improve the readability of the plots. For the meaning of letters [A], [B], [C], refer to the text.

can be noticed in the following seasons. Hence, the drop in skill seems circumscribed to just a few months and cannot be ascribed to wrong implementations and/or faulty system upgrades. As for the [C] upgrade, the impact seems initially neutral with ROC area scores peaking up again in late 2009; a more detailed analysis (in next sections) will show some positive impact on the skill of the system also for 2008.
If the attention is focused on a longer forecast range, most of the above–mentioned results are confirmed.

Fig. 5 shows the ROC area values for the 78–90h range: it is clear that the absolute values of the scores are lower than before, since the prediction range has increased. In the first two years of activity of COSMO-LEPS (up to about February 2005), the scores relative to the 10 and 15 mm/12h thresholds fell below 0.7, which is generally considered the lower boundary for a prediction system to be useful. In the following months (and years), the improvement of performance is well detectable for all thresholds. The limited skill of the system after the [B] upgrade is confirmed for all thresholds, as well as the recovery of COSMO–LEPS in the subsequent months. Particularly high is the skill of the system during autumn and winter 2007, with ROC area value close, or slightly above, 0.9. It can be noticed that, for these seasons, the skill of the system is very similar for both the 30–42h and the 78–90h forecast range, this indicating a slow degrade of the prediction skill with the forecast range.
In addition to these comments, some dependence of the scores on the season can also be noticed. Both Figs. 4 and 5 indicate that ROC area values tend to be higher (lower) in autumns (summers). This may be related to the different types of atmospheric forcing for the precipitation events. In summer, precipitation is more related to convective–type of events, while in autumn large–scale forcing usually prevails. The former type of forcing tends to be less predictable by global–model ensemble systems (Buizza et al., 1999), which may provide less accurate initial and boundary conditions to COSMO–LEPS runs. In addition to this, convection is explicitly resolved by neither global nor limited–area integrations and this adds limitations to the system capability of simulating properly convective–type events. On the other hand, large–scale forcing is usually well captured by global–model systems,

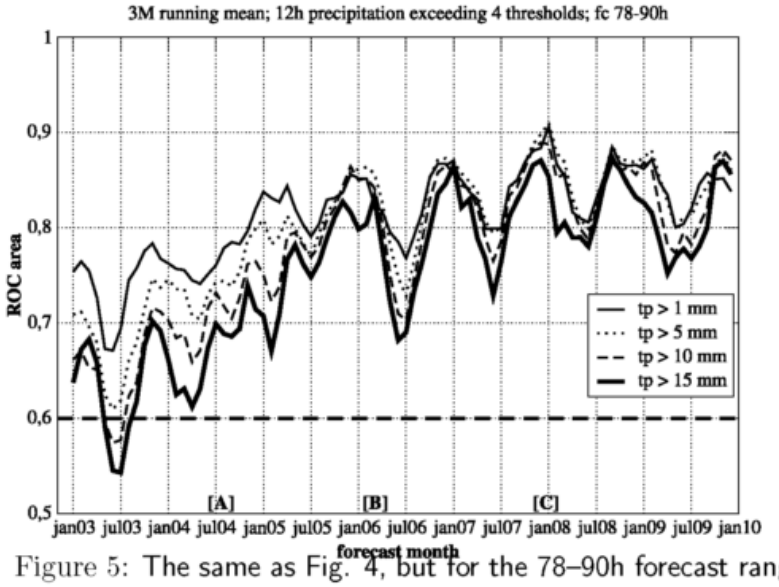


Figure 5: The same as Fig. 4, but for the 78–90h forecast range.

which provide higher quality boundaries for the dynamical downscaling by limited–area ensemble systems. On their turn, the added value of higher resolution and the more accurate description of mesoscale features, like the interaction of flow with orography, contributes to the better performance of COSMO–LEPS during the autumn season.

5.2 Brier Skill Score

Now, the attention is focused on the performance of COSMO–LEPS in terms of BSS (Wilks, 1995). This score ranges from minus infinity to 1 and, for a forecast system to be more useful than climatology (in this case, the reference climatology is given by the sample climate), has to be positive. Fig. 6 shows the time–series evolution of COSMO–LEPS performance for the 30–42h forecast range: despite a 3–month running mean is applied to the score values so as to increase the readability of the plot, the month–to–month variability is larger than in the case of the ROC area and the increase in forecast skill throughout the years of COSMO–LEPS activity is less evident. It is difficult to detect a clear benefit by any of the above–mentioned upgrades and, depending on the threshold, periods of relative high (low) skill alternate. Nevertheless, it can be noticed that the BSS has been positive for all thresholds since April 2009, possibly a consequence of the most recent forecast improvements.

In order to detect trends in the score, it was decided to apply a 12–month running mean[2] to the monthly BSS scores, as in Fig. 7. In this figure, the shapes of the profiles are much smoother than before, but longer–term trends can be identified. Depending on the threshold, the following considerations can be presented:

- the quality of the forecast progressed quite slowly for the 1mm/12h and 5mm/12h events (thin–solid and dotted lines, respectively); BSS is nearly always positive indicating a performance of the system better than climatology; the system upgrades do not seem to have had a large impact on the performance of COSMO–LEPS for the

[2]The BSS value for a particular month is given by the average of the score for the preceding 6 months and for the following 6 month values. Hence, BSS values cannot be computed for the first 6 months and for the last 6 month of the time–series.

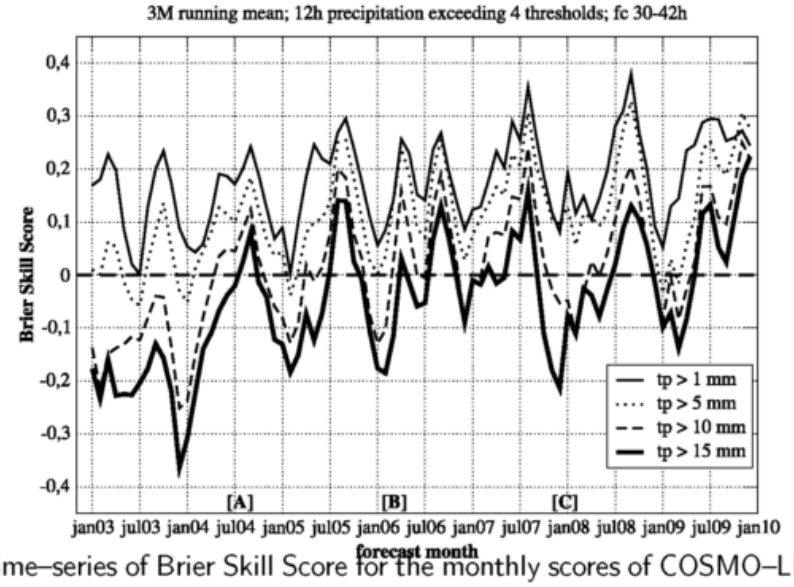


Figure 6: Time–series of Brier Skill Score for the monthly scores of COSMO–LEPS for 4 different thresholds: 1mm/12h (thin–solid line), 5mm/12h (dotted), 10mm/12h (dashed) and 15mm/12h (thick–solid). The forecast range is 30–42h. A 3–month running mean is applied to improve the readability of the plots. For the meaning of letters [A], [B], [C], refer to the text.

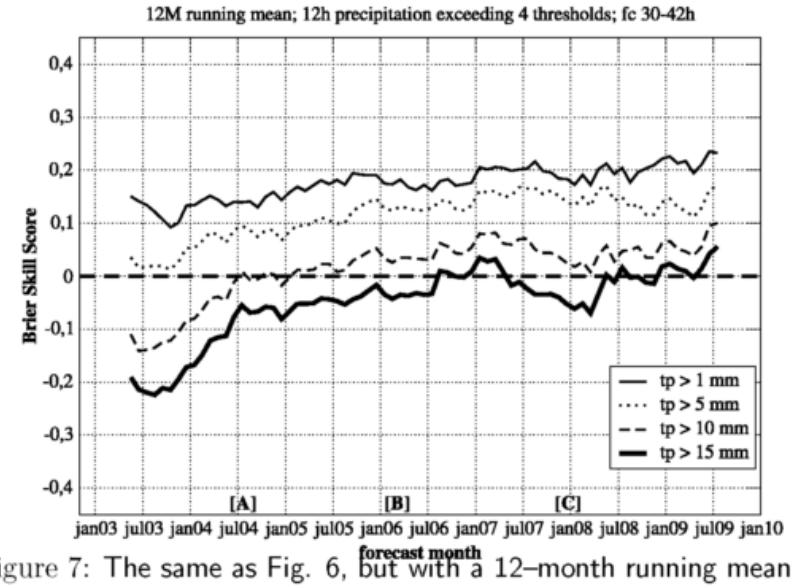


Figure 7: The same as Fig. 6, but with a 12–month running mean applied.

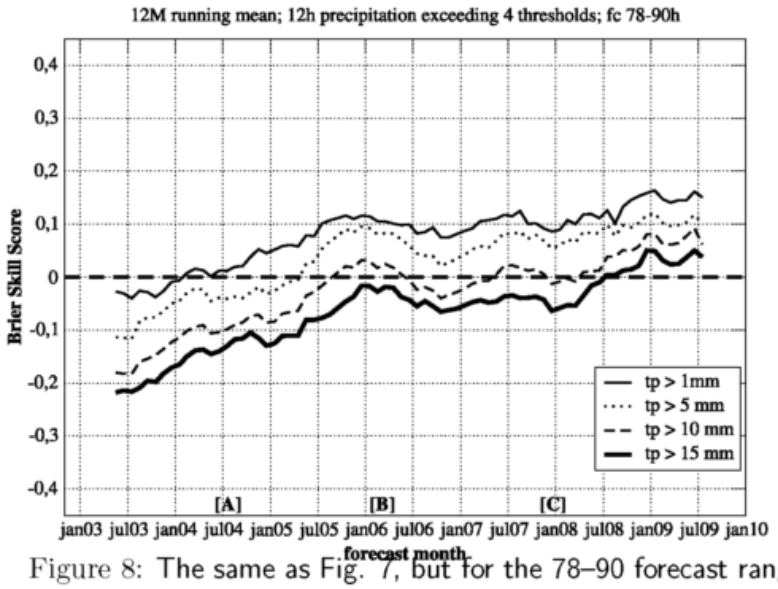


Figure 8: The same as Fig. 7, but for the 78–90 forecast range.

prediction of this type of events;

- the improvement is more evident for the two highest thresholds (dashed and thick–solid lines, respectively) throughout the years; BSS is systematically negative in the first years of activity, while it has been above zero for the 10mm/12h threshold since July 2005; as for the 15 mm/12h threshold, a good trend is evident up to January 2006, then the quality for the prediction of this type of events decreases up to mid–2008; since then, the skill of the system has started to increase again, although very close to the zero line. This is a very encouraging result, since it shows the improvement of the system performance for events of moderate–to–heavy precipitation in the early–medium range, the "hunting ground" of COSMO–LEPS;

- the dependence of the forecast skill on the threshold value has been reduced during the years of COSMO–LEPS activity. In 2003, the values of the BSS ranged roughly from -0.2 to 0.15 when passing from the highest to the lowest threshold; during 2009, BSS variations are approximately limited to the interval $[0.05, 0.25]$.

If the same type of running mean is applied to the BSS relative to the 78–90h forecast range, a common behaviour is evident for all thresholds. Fig. 8 shows an increase in the skill of the system for all types of events from the beginning of the activity up to January 2006. Then, the performance of the system stays stable for about 2 years and, finally, picks up again from July 2008 onwards. It can be seen that, for the 1mm (5mm) threshold, denoted with the solid (dotted) line of Fig. 8, the BSS has been positive since July 2004 (July 2005). As for the 10mm/12h and 15mm/12h thresholds (dashed and thick–solid lines, respectively), a positive trend on the forecast skill after the [C] upgrade can be noticed starting from July 2008. It is worth pointing out that we are assessing the possibility to predict 12–hourly accumulated precipitation after almost 4 days of integration (78–90 prediction range), which is a very "severe" test for any ensemble system. These results indicate the progresses of COSMO–LEPS forecasts in the early detection of severe and localised weather events. A quick comparison relative to the performance of the system for the highest thresholds (thick–solid lines of Figs. 7 and 8) indicates almost identical scores for both the shorter and the longer forecast range. This seems in apparent contradiction with the usual degrade of the

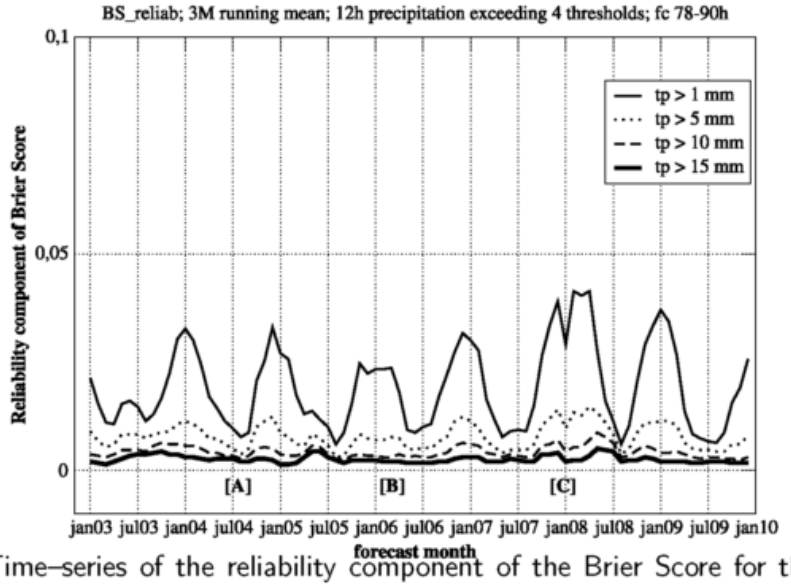


Figure 9: Time–series of the reliability component of the Brier Score for the monthly scores of COSMO–LEPS for 4 different thresholds: 1mm/12h (thin–solid line), 5mm/12h (dotted), 10mm/12h (dashed) and 15mm/12h (thick–solid). The forecast range is 78–90h. A 3–month running mean is applied to improve the readability of the plots. For the meaning of letters [A], [B], [C], refer to the text.

forecast skill with increasing forecast range, but is actually a feature of COSMO–LEPS system, which is mainly targeted for the early–medium range and is driven by those selected EPS members which should provide better guidance after the short range.

The reasons for the different results between the BSS and the ROC area can be found in the different type of information conveyed by the two indices (Marsigli et al., 2008). On the one hand, the BSS (and the RPSS) gives information about both the reliability and the resolution of the forecast system. The former one indicates how well the forecast probabilities by the ensemble system match the observed frequencies; the latter one highlights the extent to which the system can discriminate among events in different categories. A more thorough investigation on these two components, in their formulation used to compute the Brier Score (BS, not the BSS), shows the following:

- reliability component: the time–series of this quantity, which should be low (to contribute to a low BS and, hence, to a high BSS) is shown in Fig. 9 for the forecast range 78–90h, relative to the four thresholds in the previous figures. The time–series scores indicate little progress (if any) as for the reduction of the reliability component throughout the years of COSMO–LEPS activity. As for the 1mm/12h and 5mm/12h thresholds (thin–solid and dotted lines, respectively), a yearly cycle with almost constant amplitude is evident with higher values in winter; on the other hand, stable values can be noticed for the other thresholds. The reliability component could be modified by a change in the methodology used to construct the driving ensemble (ECWMF EPS) and/or COSMO–LEPS, which did not occur in these years;

- resolution component: this quantity should be high so as to provide a lower BS and a higher BSS. The time–series of this term (shown in Fig. 10 for the range 78–90h) indicates an increase of the values especially for the two lowest thresholds, indicating a greater capability of the system to distinguish among events in different categories.

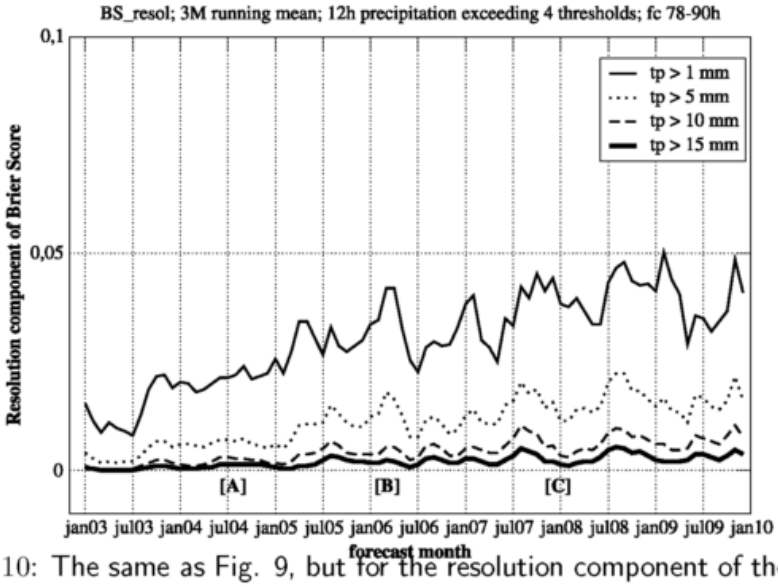


Figure 10: The same as Fig. 9, but for the resolution component of the Brier Score.

Therefore, the less marked improvement in terms of BSS is related to the behaviour of these two terms and on their relative weight in the generation of the score.
On the other hand, the ROC area provides information about the resolution component, which was shown to increase. For this reason, the improvement in terms of the ROC area is more evident, as was shown by Figs. 4 and 5.

5.3 Ranked Probability Skill Score

The RPSS (Epstein, 1969) is an extension of the BSS to a situation with many events, in this case those represented by the list of thresholds of Table 1. As before, the score ranges from minus infinity to 1 and a forecast system providing more useful information than the climatology (as before, given by the sample climate) would have a positive RPSS. If the RPSS is calculated for each month and for the different forecast ranges of Table 1, it turns out that the month–to–month variability of the score is extremely high (not shown). Therefore, in order to detect long–term behaviour for the value of this score, a 12–month running mean was again applied, like for the BSS. Fig. 11 shows the performance of the RPSS for different ranges, representative of COSMO–LEPS quality throughout the full integration period: 30–42h (solid), 54–66h (dotted), 78–90h (dashed) and 102–114 (thick–solid). The increase of the quality of COSMO–LEPS forecasts in the years is evident, although the pace of improvement is different depending on the forecast range. Periods of almost "monotonic growth" (e.g. the Jul05–Jan06 period for the 78–90h range) alternate with others of steady or slightly decaying performance. As an overall comment, the RPSS has been always positive for all forecast intervals, since the [B] upgrade, with particularly high scores in the last 12 months. The improvements concern all forecast ranges, the RPSS growing especially for the longest ones. In addition to that, those RPSS values reached around January 2004 in the early range (30–42h forecast, solid line in Fig. 11) are recently obtained for the 102–114 prediction range, with a gain of predictability of about 3 days in 5 years of system upgrades.

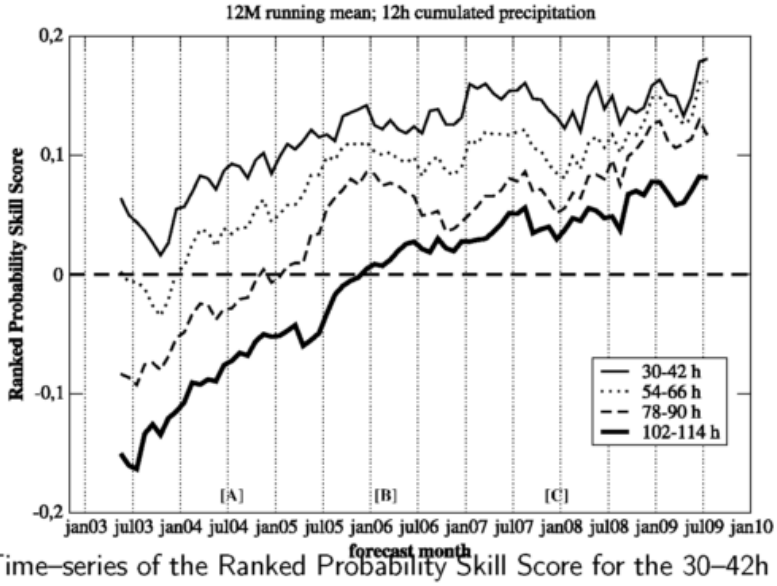


Figure 11: Time–series of the Ranked Probability Skill Score for the 30–42h (solid line), 54-66h (dotted line), 78–90h (dashed–line) and 102–114h (thick–solid line) forecast ranges. A 12–month running mean is applied to improve the readability of the plots. For the meaning of letters [A], [B], [C], refer to the text.

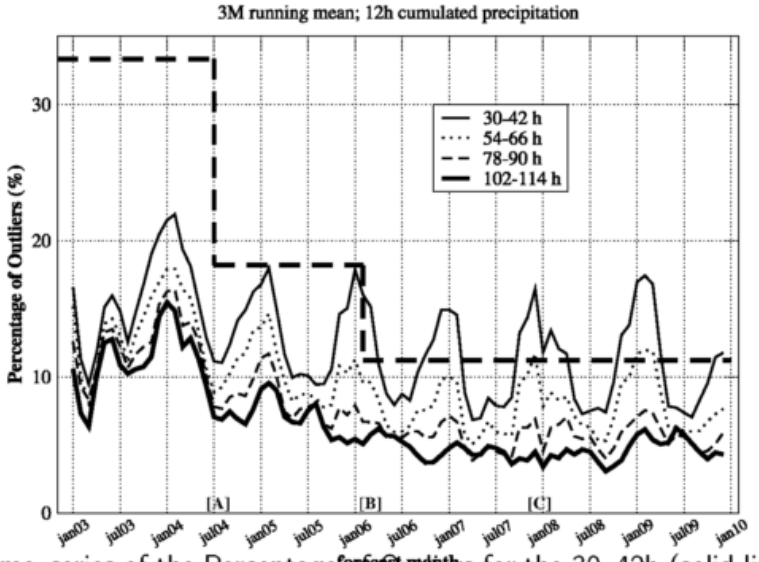


Figure 12: Time–series of the Percentage of Outliers for the 30–42h (solid line), 54-66h (dotted line), 78–90h (dashed–line) and 102–114h (thick–solid line) forecast ranges. A 3–month running mean is applied to improve the readability of the plots. The thick–dashed line indicates the theoretical values of the OUTL. For the meaning of letters [A], [B], [C], refer to the text.

5.4 Percentage of Outliers

The OUTL measures the percentage of times the observation stays outside the interval spanned by the values predicted by the ensemble members. For an ensemble of size N, its theoretical value is given by $2/(N+1)$ (Talagrand et al., 1999) and for a real ensemble system, it should be below this value. As for COSMO–LEPS, this value has changed during the years of the system activity: more precisely, it was 33.3% from November 2002 to July 2004 (up to the [A] upgrade); then, 18.2% for the 10–member ensemble (up to the [B] upgrade); finally, 11.2% for the 16–member size.
Fig. 12 shows the time–series evolution for OUTL at four different forecast ranges: 30–42h (solid), 54–66h (dotted), 78–90h (dashed) and 102–114 (thick–solid). For reference, the thick–dashed line indicates the theoretical value not to be exceeded. As for the previous scores, a 3–month running mean was applied to highlight the main results of the verification, which can be summarised as follows:

- a seasonal cycle of the score can be identified for all forecast ranges; OUTL tends to be higher in winters, especially for shorter forecast ranges, and lower in summers. This is due to an overestimation of little precipitation amounts during the cold season by the model runs; in fact, a partitioning of the OUTL into outl_max (observed value larger than all forecast ones) and outl_min (observed value smaller than all forecast ones) indicates that the latter contribution is well dominant for shorter ranges;

- for a fixed forecast range, it is shown an overall reduction of OUTL throughout the years of COSMO–LEPS activity from 2003 up to mid–2007, when, for any forecast range, OUTL was less than 10%, well below the theoretical value for a 16–member ensemble.

- from mid–2007 to early 2009, the OUTL has remained stable or has slightly grown for any range; in this period, the OUTL for shorter ranges exceeded the theoretical value;

- during 2009, a new reduction of OUTL takes place, with values of the same order (or below) those attained in 2007. For any forecast range but the first one, OUTL stays below the theoretical value. The excessive amount of OUTL for the shortest range is related to a lack of spread among COSMO–LEPS members in the early forecast intervals; this is possibly a consequence of the driving ensemble, which is specifically targeted to have sufficient spread in the medium range.

When the population of a small–size ensemble is increased, the reduction of OUTL is almost a natural consequence, since the probabilistic system can now access a wider fraction of the atmospheric phase space and account for a larger percentage of possible evolution weather scenario. Therefore, the OUTL reduction relative to upgrades [A] and [B] were not unexpected. On the other hand, the 2009–reduction is more likely due to the better performance of the individual COSMO–LEPS runs, related to model upgrades and refinements.

6 Seasonal scores

The results obtained in the previous section indicate that, on the basis of a number of probabilistic indices, the forecast skill of COSMO–LEPS has improved in many respects, in the past as well as recently. In this section, the performance of the system is studied in greater detail, investigating the COSMO–LEPS behaviour over specific periods and for particular types of weather events. More precisely, the attention is focused on the skill of

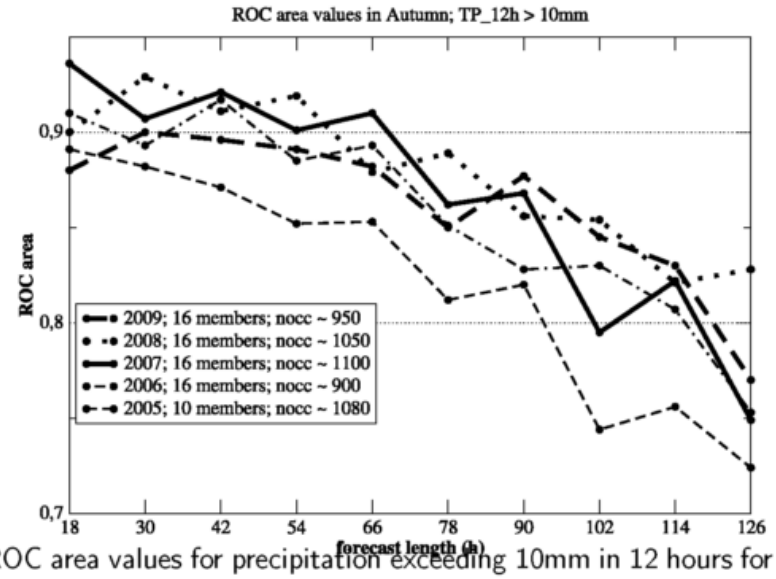


Figure 13: ROC area values for precipitation exceeding 10mm in 12 hours for the forecast ranges of Table 1 and for 5 successive autumns: 2005 (dashed), 2006 (dot–dashed), 2007 (thick–solid), 2008 (thick–dotted) and 2009 (thick–dashed).

the system during the two most rainy seasons in the Alpine area: autumn, defined as the 3–month period covering September, October and November (SON) and summer (June, July and August; JJA).
It has to be pointed out that, when comparing different seasons, the variations in the scores from one season to the other may depend on the fact that more occurrences took place during one season rather than during another one. In other words, if one autumn is more rainy than the previous one and also with a prevailing forcing better captured by the limited–area–model runs, then the ROC area values would be higher than for the other one. This may be probably due the different statistics of the two seasons under consideration and may not necessarily reflect an absolute improvement in forecast skill because of, e.g., model refinement or new ensemble strategies. Nevertheless, this type of verification, when applied to more and more seasons, enables to identify the improvements of the forecast system as well as of particular periods of good (or bad) performance.

6.1 Scores in autumn

For the autumn season, it is investigated the capability of the system to predict the event "precipitation exceeding 10mm over 12 hours". Fig. 13 shows the evolution of COSMO–LEPS performance in terms of ROC area for the forecast of this event. In order to limit the number of lines per plot, the scores of the system are reported only for the last 5 autumns (from 2005 to 2009). It can be noticed that the ROC area values relative to autumn 2005 (dashed line) are lower than those obtained in the following years for almost all forecast ranges. This may be related to the fact that in 2005 COSMO–LEPS still had a population of 10 members, the ensemble size being 16 in the other years. As for years 2006–2009, the performance of the system is quite stable: for shorter forecast ranges, COSMO-LEPS has slightly better performance in autumn 2007 (thick–solid line of Fig. 13), while higher ROC area values for longer ranges can be noticed in 2009 (thick–dashed line). For reference, the legend of Fig. 13 also reports, for each autumn, the number of occurrences, that is the number of times precipitation actually surpassed the 10mm threshold in 12 hours, according

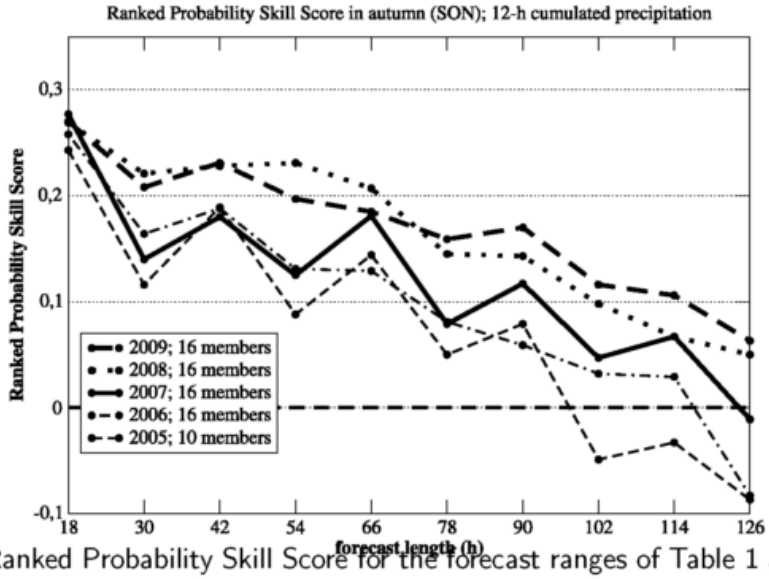


Figure 14: Ranked Probability Skill Score for the forecast ranges of Table 1 and for 5 successive autumns: 2005 (dashed), 2006 (dot–dashed), 2007 (thick–solid), 2008 (thick–dotted) and 2009 (thick–dashed).

to all reports of the SYNOP stations of Fig. 2.
As a further example of the behaviour of the probabilistic indices for the same season but in different years, the attention is focused on a score describing the COSMO–LEPS skill for multi–event situations. Fig. 14 shows the behaviour of the RPSS for the last 5 autumns as a function of the forecast step. The highest values are obtained in the last 2 years, the RPSS being positive for all forecast ranges (thick–dotted and thick–dashed lines for 2008 and 2009, respectively). In addition to that, Fig. 14 also indicates that, in the first years of activity, RPSS values had a marked semi–diurnal cycle. The system provides better guidance for "night–time" precipitation, that is for rainfall observed between 18UTC and 6UTC (and corresponding to the ranges 6–18h, 30–42h, 54–66h, 78–90h, 102–114h). As for "day–time" precipitation (observed from 6UTC to 18UTC), the model runs had a worse performance due to a systematic overestimation of rainfall (linked with a too rapid onset of convection). This is a general feature of the model, as pointed out by Oberto and Turco (2008) for runs of COSMO in "deterministic mode". This behaviour is evident throughout the full forecast range in 2005 and 2007 (dashed and thick–solid line, respectively). As for the last 2 years, the cycle in the score is still present, but its amplitude is reduced. It has to be pointed out that this type of model (mis)–behaviour shows up because of the decision to verify 12–hour accumulated precipitation. If the performance of COSMO–LEPS were evaluated over a 24–hour period, the problems relative to the semi–diurnal cycle would be masked and it would be more difficult to highlight the improvements in forecast performance under that aspect. Nevertheless, it can be noticed that, while the RPSS dropped definitely below 0.1 after about 72 hours of forecast in 2005, it does the same in 2009 but after 114 hours, with a gain of predictability of almost 2 days in 4 years.

Finally, it is presented the COSMO–LEPS performance at different forecast ranges in terms of Percentage of Outliers. The attention is focused, as before, on the last 5 autumns and Fig. 15 indicates that the best performance of the system is achieved in autumn 2009 (thick–dashed line), with OUTL below 10% after about 42 forecast hours. It has to be noticed that, during autumn 2007, the performance of the system was less satisfactory than in the other seasons up to day 4 (thick–solid line in the figure). This was due to a large

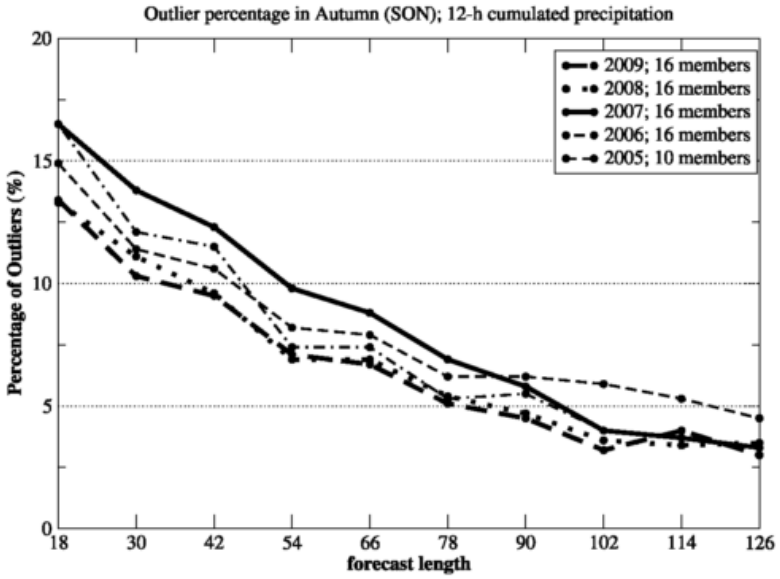


Figure 15: Percentage of Outliers for the forecast ranges of Table 1 and for 5 successive autumns: 2005 (dashed), 2006 (dot–dashed), 2007 (thick–solid), 2008 (thick–dotted) and 2009 (thick–dashed).

amount of outl_min, indicative of an overestimation of precipitation by COSMO–LEPS runs for several forecast ranges. As for 2005, the only season with a 10–member ensemble, a larger fraction of outliers is found for longer prediction ranges (dashed line), but the gap is not large. It is encouraging to notice that, as for the last autumns of activity, only in 5% of the cases is the observed precipitation outside the range spanned by the ensemble members from forecast–day 4 onwards.

6.2 Scores in summer

As for summer, the attention is limited to the COSMO–LEPS forecast skill in terms of RPSS for several prediction ranges. The 12–hourly cycle in the system performance, already shown for autumn by Fig. 14, is more evident during the warm season. Fig. 16 indicates that, for all summers under investigation (from 2005 to 2009), COSMO–LEPS has higher scores for "night–time" verification, while the skill is lower for precipitation observed between 6UTC to 18UTC and corresponding to the forecast ranges 18–30h, 42–54h, 66–78h, 90–102h and 114–126h [3]. As pointed out in the section 6.1, the sensitivity of the system performance to the time of verification is mainly due to an anticipation in the onset of convection by the model. This leads to precipitation occurring too early (morning or first hours of the afternoon) in the model runs. Obviously, this problem is amplified in summers, when the large–scale forcing is weaker than in autumns and the precipitation is mainly driven by convection processes. Due to the stronger role played by convection, the 12–hourly cycle in RPSS behaviour persists up to day 5 for all years but the last one. In fact, in 2009 (thick–dashed line), are not only the score values higher than in the past, but also the amplitude of the cycle is smaller for short forecast ranges and almost missing from day 3 onwards. This result seems to suggest that the model upgrades did bring benefit to the accuracy of COSMO–LEPS runs, which provide

[3]For a part of summer 2005, the forecast length was 120 hours, which means 12 hours shorter than in the other summers. Therefore, the score relative to this year (represented by the dashed line in Fig. 16) does not cover the last forecast range, but stops earlier.

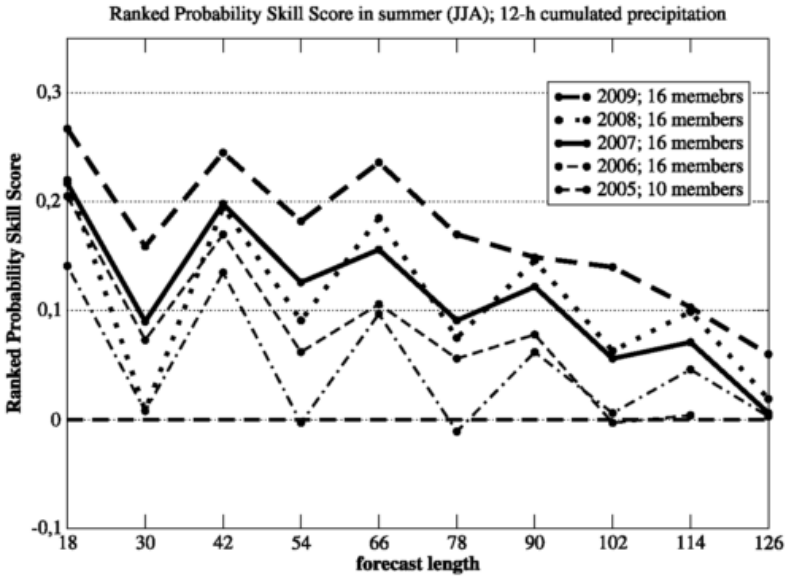


Figure 16: Ranked Probability Skill Score for the forecast ranges of Table 1 and for 5 successive summers: 2005 (dashed), 2006 (dot–dashed), 2007 (thick–solid), 2008 (thick–dotted) and 2009 (thick–dashed).

more and more valuable forecasts in the short and early–medium range. In fact, a quick comparison between the performances of 2005 and 2009 (dashed versus thick–dashed line in Fig. 16) shows that, with reference to the 0.1 value, the skill score obtained after 66 hours is now achieved after 114 hours, thus confirming the gain of about 2 days of predictability in 4 years of operational activity.

7 Conclusions

The main features of the mesoscale ensemble system COSMO–LEPS were presented. At the moment, the system is made up of 16 integrations of the non–hydrostatic COSMO model with a horizontal resolution of 10 km, 40 vertical levels and a forecast length of 132 hours, thus providing short and early–medium range ensemble forecast of high–impact weather with great spatial detail. COSMO–LEPS runs can be viewed as a dynamical downscaling of ECMWF EPS, where the number of global–ensemble members are reduced via an "ensemble–size reduction" technique.
The performance of COSMO–LEPS has been analysed in terms of probabilistic prediction of 12–hourly accumulated precipitation for a number of thresholds. The evolution of the skill of the system has been assessed over a 7–year period, namely from December 2002 up to November 2009. Observations of 12–hour accumulated precipitation were taken from the SYNOP reports over the Alpine area and compared to the nearest grid–point forecasts of the COSMO–LEPS members. A number of probabilistic indices has been used so as to evaluate both reliability and resolution of the system and to assess the extent to which the quality of COSMO–LEPS forecasts improved in recent times.
The main findings can be summarised as follows:

- time–series scores of the ROC area values for different thresholds indicate a clear improvement of COSMO–LEPS skill throughout the years, with an increase of this score up to 2006, then slower growth in the 2 following years and a resumption of

growth in the last part of 2009. This holds in the short as well as in the early–medium range;

- as for the BSS (and the RPSS), the month–to–month variability of the time–series scores is higher than for the ROC area and the positive impacts of system upgrades are more difficult to detect. If 12–month filters are applied to the scores, more insight is gained and forecast improvements with time become more detectable. As for an estimate of the improvement, RPSS values enables to quantify it as "2 days of predictability gained in the last 5 years";

- time–series of the OUTL indicate a decrease of Outliers up to early 2007 for various forecast ranges and a steady behaviour since then on. A new decrease is evident in 2009, with the OUTL below 10% from day 2;

- seasonal scores confirm to a large extent the previous results; they enable to highlight the progresses in the skill of the system over the same season but in different years. The improvements in skill are well noticeable in terms of RPSS during summer, where the gain in forecast skill can be estimated as about 2 days of predictability in the last 4 years of activity.

The reasons for the different results between the BSS and the ROC area were shown to be due to the different type of information conveyed by the two indices. On the one hand, the BSS (and the RPSS) gives information about both the reliability and the resolution of the forecast system (Marsigli et al., 2008). The former one indicates how well the forecast probabilities by the ensemble system match the observed frequencies. The latter one indicates the extent to which the system can discriminate among events in different categories. Reliability can be increased after a good calibration, which manages to match probabilities and frequencies; resolution cannot be improved by any statistical post-processing. On the other hand, the ROC area provides information only about the discrimination capability of the forecast system. As such, the ROC area scores show the COSMO–LEPS ability to detect between events and nonevents, despite the reliability, and represent the hypothetical skill of the system once it were properly calibrated. It was shown that the reliability component of COSMO–LEPS forecasts did not increase in the last years at the same pace as the resolution one, this explaining the better results obtained in terms of ROC area.

Work is in progress at both ARPA–SIMC and MeteoSwiss to provide calibrated COSMO–LEPS forecasts, thanks to the results obtained by the re–forecast exercise described in Fundel et al. (2009). This would improve the skill of COSMO–LEPS forecasts, making the system more reliable than it is now. As for the future, it is being tested the increase of the horizontal resolution of COSMO–LEPS runs so as to provide more detailed forecasts for the interaction of the flow with orography and to describe with a higher degree of accuracy mesoscale–related processes and local effects. This would have a positive impact on the prediction of a number of those surface fields still nowadays strongly influenced by local effects and not always properly represented in terms of their uncertainty by mesoscale ensemble systems.

8 Acknowledgments

The authors are indebted to the countries of the COSMO Consortium and to ECMWF for the possibility to run the COSMO–LEPS application. We are grateful to Manuel Fuentes, Umberto Modigliani and Paolo Patruno for technical assistance and continuous support. We also thank André Walser, Carlo Cacciamani and Stefano Tibaldi for useful discussions.

9 References

Bowler, N.E., Arribas, A., Mylne, K.R., Robertson, K.B. and Beare, S.E., 2008. The MOGREPS short–range ensemble prediction system. *Q. J. Roy. Meteorol. Soc.* **134**, 703–722.

Buizza, R., Hollingsworth, A., Lalaurette, F.and Ghelli, A., 1999. Probabilistic predictions of precipitation using the ECMWF Ensemble Prediction System. *Wea. Forecasting* **14**, 168–189.

Buizza, R., 2005. The ECMWF Ensemble Prediction System. In: *Predictability of weather and climate,* (eds. T. Palmer and R. Hagedorn), Cambridge University Press, Cambridge, 459–488.

Buizza, R., Bidlot, J.-R., Wedi, N., Fuentes, M., Hamrud, M., Holt, G. and Vitard, F., 2007. The new ECMWF VAREPS (Variable Resolution Ensemble Prediction System). *Q. J. Roy. Meteorol. Soc.* **133**, 681–695.

Epstein, E.S., 1969. A scoring system for probabilities of ranked categories. *J. Appl. Meteor.* **8**, 985–987.

Fundel, F., Walser, A., Liniger, M.A., Frei, C. and Appenzeller, C., 2009. Calibrated Precipitation Forecasts for a Limited-Area Ensemble Forecast System Using Reforecasts. *Mon. Wea. Rev.* **138**, 176–189.
DOI: 10.1175/2009MWR2977.1

Houtekamer, P.L., Derome, J., Ritchie, H. and Mitchell, H.L., 1996. A system simulation approach to ensemble prediction. *Mon. Wea. Rev.* **124**, 1225–1242.

Marsigli, C., Montani, A., Nerozzi, F., Paccagnella, T., Tibaldi, S., Molteni, F. and Buizza, R., 2001. A strategy for High–Resolution Ensemble Prediction. Part II: Limited–area experiments in four Alpine flood events. *Q. J. Roy. Meteorol. Soc.* **127**, 2095–2115.

Marsigli, C., Boccanera, F., Montani, A. and Paccagnella, T., 2005a. The COSMO–LEPS ensemble system: validation of the methodology and verification. *Nonlin. Proc. in Geophys.* **12**, 527–536.

Marsigli, C., Montani, A., Paccagnella, T., Sacchetti, D., Walser, A. and Schumann, T., 2005b. Evaluation of the performance of the COSMO–LEPS system. *COSMO Technical Report* no **8**, 40. Available at http://www.cosmo-model.org/.

Marsigli, C., Montani, A. and Paccagnella, T., 2008. A spatial verification method applied to the evaluation of high–resolution ensemble forecasts. *Met. Appl.* **15**, 125–143.

Mason, S.J. and Graham, N.E., 1999. Conditional probabilities, relative operating characteristics and relative operating levels. *Wea. Forecasting* **14**, 713–725.

Molteni, F., Buizza, R., Palmer, T.N. and Petroliagis, T., 1996. The ECMWF ensemble prediction system: methodology and validation. *Q. J. Roy. Meteorol. Soc.* **122**, 73–119.

Molteni, F., Buizza, R., Marsigli, C., Montani, A., Nerozzi, F. and Paccagnella, T., 2001. A strategy for High–Resolution Ensemble Prediction. Part I: Limited–area experiments in

four Alpine flood events. *Q. J. Roy. Meteorol. Soc.* **127**, 2069–2094.

Montani, A., Capaldo, M., Cesari, D., Marsigli, C., Modigliani, U., Nerozzi, F., Paccagnella, T., Patruno, P. and Tibaldi, S., 2003a. Operational limited–area ensemble forecasts based on the Lokal Modell. *ECMWF Newsletter* no **98**, 2–7. Available at: http://www.ecmwf.int/publications/.

Montani, A., Marsigli, C., Nerozzi, F., Paccagnella, T., Tibaldi S. and Buizza, R., 2003b. The Soverato flood in Southern Italy: performance of global and limited-area ensemble forecasts. *Nonlin. Proc. Geophys.* **10**, 261–274.

Montani, A., Marsigli, C. and Paccagnella, T., 2008a. Five Years of Limited–Area Ensemble Activities at ARPA–SIM: The COSMO–LEPS system. *COSMO newsletter* no **8**, 23–26. Available at: http://www.cosmo-model.org/.

Montani A., Marsigli, C. and Paccagnella, T., 2008b. Performance of COSMO–LEPS system during the D–PHASE Operations Period. *COSMO newsletter* no **9**, 50–53. Available at: http://www.cosmo-model.org/.

Mullen, S.L. and Buizza, R., 2001. Quantitative precipitation forecast over the United States by the ECMWF Ensemble Prediction System. *Mon. Wea. Rev.* **129**, 638–663.

Oberto, E. and Turco, M., 2008. Report about the Latest Results of Precipitation Verification over Italy. *COSMO newsletter* no **8**, 37–44. Available at: http://www.cosmo-model.org/.

Rotach, M.W., Ambrosetti, P., Ament, F., Appenzeller, C., Arpagaus, M., Bauer, H.-S., Behrendt, A., Bouttier, F., Buzzi, A., Corazza, M., Davolio, S., Denhard, M., Dorninger, M., Fontannaz, L., Frick, J., Fundel, F., Germann, U., Gorgas, T., Hegg, C., Hering, A., Keil, C., Liniger, M.A., Marsigli, C., McTaggart-Cowan, R., Montani, A., Mylne, K., Ranzi, R., Richard, E., Rossa, A., Santos-Muoz, D., Schr, C., Seity, Y., Staudinger, M., Stoll, M., Volkert, H., Walser, A., Wang, Y., Werhahn, J., Wulfmeyer, V. and Zappa, M., 2009. MAP D-PHASE: Real-time Demonstration of Weather Forecast Quality in the Alpine Region, *Bull. Amer. Meteor. Soc* **90** (9), 13211336, DOI:10.1175/2009BAMS2776.1

Steppeler, J., Doms, G., Schattler, U., Bitzer, H.W., Gassmann, A., Damrath, U. and Gregoric, G., 2003. Meso–gamma scale forecasts using the nonhydrostatic model LM. *Meteor. and Atmos. Phys.* **82**, 75–96.

Talagrand, O., Vautard, R. and Strauss, B., 1999. Evaluation of probabilistic prediction systems. *Proceedings of the ECMWF Workshop on Predictability*, Reading, 20–22 October 1997, 372. Available at:
http://www.ecmwf.int/publications/.

Tibaldi, S., Paccagnella, T., Marsigli, C., Montani, A. and Nerozzi, F., 2006. Limited–area ensemble forecasting: the COSMO–LEPS system. In: *Predictability of weather and climate*, (eds. T. Palmer and R. Hagedorn), Cambridge University Press, Cambridge, 489–513.

Tracton, M.S. and Kalnay, E., 1993. Operational ensemble prediction at the National Meteorological Centre: Practical Aspects. *Wea. and Forecasting* **8**, 379–398.

Walser, A., 2006. COSMO-LEPS Forecasts for the August 2005 Floods in Switzerland. *COSMO newsletter* no **6** , 142–145. Available at: http://www.cosmo-model.org/.

Wilks, D.S., 1995. Statistical Methods in the Atmospheric Sciences. Academic Press, New York, 467.

Zappa, M., Rotach, M.W., Arpagaus, M., Dorninger, M., Hegg, C., Montani, A., Ranzi, R., Ament, F., Germann, U., Grossi, G., Jaun, S., Rossa, A., Vogt, S., Walser, A., Wehrhan, J. and Wunram C., 2008. MAP D–PHASE: real–time demonstration of hydrological ensemble prediction systems. *Atmos. Sci. Let.* **9**, 80–87. DOI 10.1002/asl.183.

List of COSMO Newsletters and Technical Reports

(available for download from the COSMO Website: www.cosmo-model.org)

COSMO Newsletters

No. 1: February 2001.

No. 2: February 2002.

No. 3: February 2003.

No. 4: February 2004.

No. 5: April 2005.

No. 6: July 2006.

No. 7: April 2008; Proceedings from the 8th COSMO General Meeting in Bucharest, 2006.

No. 8: September 2008; Proceedings from the 9th COSMO General Meeting in Athens, 2007.

No. 9: December 2008

No. 10: March 2010.

COSMO Technical Reports

No. 1: Dmitrii Mironov and Matthias Raschendorfer (2001):
Evaluation of Empirical Parameters of the New LM Surface-Layer Parameterization Scheme. Results from Numerical Experiments Including the Soil Moisture Analysis.

No. 2: Reinhold Schrodin and Erdmann Heise (2001):
The Multi-Layer Version of the DWD Soil Model TERRA_LM.

No. 3: Günther Doms (2001):
A Scheme for Monotonic Numerical Diffusion in the LM.

No. 4: Hans-Joachim Herzog, Ursula Schubert, Gerd Vogel, Adelheid Fiedler and Roswitha Kirchner (2002):
LLM ¯ the High-Resolving Nonhydrostatic Simulation Model in the DWD-Project LITFASS.
Part I: Modelling Technique and Simulation Method.

No. 5: Jean-Marie Bettems (2002):
EUCOS Impact Study Using the Limited-Area Non-Hydrostatic NWP Model in Operational Use at MeteoSwiss.

No. 6: Heinz-Werner Bitzer and Jürgen Steppeler (2004):
Documentation of the Z-Coordinate Dynamical Core of LM.

No. 7: Hans-Joachim Herzog, Almut Gassmann (2005):
Lorenz- and Charney-Phillips vertical grid experimentation using a compressible nonhydrostatic toy-model relevant to the fast-mode part of the 'Lokal-Modell'.

No. 8: Chiara Marsigli, Andrea Montani, Tiziana Paccagnella, Davide Sacchetti, André Walser, Marco Arpagaus, Thomas Schumann (2005):
Evaluation of the Performance of the COSMO-LEPS System.

No. 9: Erdmann Heise, Bodo Ritter, Reinhold Schrodin (2006):
Operational Implementation of the Multilayer Soil Model.

No. 10: M.D. Tsyrulnikov (2007):
Is the particle filtering approach appropriate for meso-scale data assimilation ?

No. 11: Dmitrii V. Mironov (2008):
Parameterization of Lakes in Numerical Weather Prediction. Description of a Lake Model.

No. 12: Adriano Raspanti (2009):
COSMO Priority Project "VERification System Unified Survey" (VERSUS): Final Report.

No. 13: Chiara Marsigli (2009):
COSMO Priority Project "Short Range Ensemble Prediction System" (SREPS): Final Report.

No. 14: Michael Baldauf (2009):
COSMO Priority Project "Further Developments of the Runge-Kutta Time Integration Scheme" (RK): Final Report.

No. 15: Silke Dierer (2009):
COSMO Priority Project "Tackle deficiencies in quantitative precipitation forecast" (QPF): Final Report.

No. 16: Pierre Eckert (2009):
COSMO Priority Project "INTERP": Final Report.

No. 17: D. Leuenberger, M. Stoll and A. Roches (2010):
Description of some convective indices implemented in the COSMO model.

No. 18: Daniel Leuenberger (2010):
Statistical analysis of high-resolution COSMO Ensemble forecasts in view of Data Assimilation.

No. 19: A. Montani, D. Cesari, C. Marsigli, T. Paccagnella (2010):
Seven years of activity in the field of mesoscale ensemble forecasting by the COSMO–LEPS system: main achievements and open challenges.

COSMO Technical Reports

Issues of the COSMO Technical Reports series are published by the *COnsortium for Small-scale MOdelling* at non-regular intervals. COSMO is a European group for numerical weather prediction with participating meteorological services from Germany (DWD, AWGeophys), Greece (HNMS), Italy (USAM, ARPA-SIMC, ARPA Piemonte), Switzerland (MeteoSwiss), Poland (IMGW) and Romania (NMA). The general goal is to develop, improve and maintain a non-hydrostatic limited area modelling system to be used for both operational and research applications by the members of COSMO. This system is initially based on the COSMO-Model (previously known as LM) of DWD with its corresponding data assimilation system.

The Technical Reports are intended

- for scientific contributions and a documentation of research activities,
- to present and discuss results obtained from the model system,
- to present and discuss verification results and interpretation methods,
- for a documentation of technical changes to the model system,
- to give an overview of new components of the model system.

The purpose of these reports is to communicate results, changes and progress related to the LM model system relatively fast within the COSMO consortium, and also to inform other NWP groups on our current research activities. In this way the discussion on a specific topic can be stimulated at an early stage. In order to publish a report very soon after the completion of the manuscript, we have decided to omit a thorough reviewing procedure and only a rough check is done by the editors and a third reviewer. We apologize for typographical and other errors or inconsistencies which may still be present.

At present, the Technical Reports are available for download from the COSMO web site (www.cosmo-model.org). If required, the member meteorological centres can produce hard-copies by their own for distribution within their service. All members of the consortium will be informed about new issues by email.

For any comments and questions, please contact the editors:

Massimo Milelli
Massimo.Milelli@arpa.piemonte.it

Ulrich Schättler
Ulrich.Schaettler@dwd.de

Consortium for Small-Scale Modelling

Technical Report No. 18

Statistical analysis of high-resolution COSMO Ensemble forecasts in view of Data Assimilation

April 2010

DOI: 10.5676/DWD_pub/nwv/cosmo-tr_18

Deutscher Wetterdienst

MeteoSwiss

Ufficio Generale Spazio Aereo e Meteorologia

ΕΘΝΙΚΗ ΜΕΤΕΩΡΟΛΟΓΙΚΗ ΥΠΗΡΕΣΙΑ

Instytucie Meteorogii i Gospodarki Wodnej

Administratia Nationala de Meteorologie

Agenzia Regionale per la Protezione Ambientale del Piemonte

Agenzia Regionale per la Protezione Ambientale dell' Emilia-Romagna: Servizio Idro Meteo

Centro Italiano Ricerche Aerospaziali

Amt für GeoInformationswesen der Bundeswehr

www.cosmo-model.org

Editor: Massimo Milelli, ARPA Piemonte
Printed at Deutscher Wetterdienst, P.O. Box 100465, 63004 Offenbach am Main

Statistical analysis of high-resolution COSMO Ensemble forecasts in view of Data Assimilation

Daniel Leuenberger

MeteoSwiss
Krähbühlstrasse 58
8044 Zürich
Switzerland

Contents

1 Introduction **5**

2 Data and Evaluation Method **7**

2.1 Data 7

2.1.1 Forecast Departures 7

2.1.2 Ensemble Background Anomalies 7

2.2 Evaluation Method 9

3 Forecast Departure Statistics **11**

3.1 Near surface 11

3.1.1 Surface Pressure 11

3.1.2 2m Temperature 11

3.1.3 10m Wind 12

3.1.4 2m Humidity 13

3.1.5 Rainfall 13

3.2 Upper atmosphere 14

3.2.1 Temperature 14

3.2.2 Wind 14

3.2.3 Humidity 16

3.3 Sensitivity studies 19

3.3.1 Dependency on Humidity variable 19

3.3.2 Dependency on Model Resolution 23

3.3.3 Dependency on Weather Regime 24

4 Ensemble Anomaly Statistics **25**

4.1 Near surface 25

4.1.1 Temperature 25

4.1.2 Wind 27

4.1.3 Precipitation 29

4.2 Upper atmosphere 30

4.2.1 Temperature 30

4.2.2 Wind 31

5 Further Results **32**

5.1 Temperature from radiosondes 32
5.2 Zonal wind from radiosondes and windprofiler 34
5.3 Meridional wind from aircrafts, radiosondes and windprofiler 37

6 Summary and conclusions **42**

Abstract

Data assimilation techniques based on the statistical least squares theory or the best linear unbiased estimate (BLUE), such as variational or ensemble Kalman filter methods rely on the assumption that the model first guess and the observations are bias free and its errors are normally distributed with known variances and covariances. Nonlinearities, resulting from strong dynamical instabilities can result in non-Gaussian error distributions and thus potentially cause problems in data assimilation.
In this study, error distributions of the non-hydrostatic COSMO model in a convection-permitting deterministic and ensemble configuration are investigated. Forecast departures and ensemble background anomalies of varying lead time and different variables are considered for this purpose.
The forecast departures of most of the investigated variables show a reasonable Gaussian behaviour around the median, but exhibit more larger departures (both negative and positive) than described by a normal distribution ("fat tails"). Near-surface variables tend to be closer to normality than upper-level variables. Humidity and rainfall show a rather exponential than Gaussian behaviour.
Ensemble background anomalies at short lead times can deviate significantly from normality. Especially low-level temperature has been found to have multiple modes in their distribution. At longer lead times the anomaly distributions are much closer to normality. Upper level distributions are close to Gaussian. The large deviations from normality at short lead times are largely due to the physical perturbations employed in the current COSMO ensemble system to introduce spread.
Overall, the results of this study suggest that, ensemble data assimilation systems relying on the BLUE theory may well be feasible for the use with the high-resolution COSMO model, given that appropriate (i.e. more random) physics parametrisation perturbations are applied.

1 Introduction

Ensemble Kalman filter based assimilation methods for numerical weather prediction models currently receive considerable attention in the scientific community. While first implementations for global models are already operationally employed, the development of such schemes for regional [mesh size O(10km)] and convection permitting scale [mesh size O(1km)] models is still in its infancy. The COSMO consortium (http://www.cosmo-model.org) is currently developing a new ensemble assimilation system for its convection permitting NWP model. The Local Ensemble Transform Kalman Filter (LETKF, Hunt et al., 2007) is an ensemble Kalman filter method based on the statistical least squares theory or the best linear unbiased estimate (BLUE). Assimilation methods based on this theory (e.g. variational methods, ensemble Kalman filter methods) allow an optimal combination of model and observations, given that the basic assumptions of the BLUE theory are met, namely that the model first guess and the observations are bias free and its errors are normally distributed with known variances and covariances. The violation of the Gaussian assumption has found to be of concern in non-mean-preserving deterministic square-root filters (Sakov and Oke, 2008), where the ensemble can show a tendency to develop markedly non-Gaussian error distributions (Lawson and Hansen, 2004; Leeuwenburgh et al., 2005; Mitchell and Houtekamer, 2009). In these studies, the stochastic ensemble Kalman filter with perturbed observations seemed largely immune to this problem, even in strongly nonlinear applications. On the other hand, Bonavita et al. (2010) demonstrated that the LETKF works reasonable in a regional NWP system with distributions that slightly deviate from Normality. Yang and Kalnay (2009) and Kalnay and Yang (2009) proposed ways to deal with strong non-linearities and non-Gaussianity using the LETKF in iterative ways.

In an ensemble Kalman filter approach, the optimal combination of model forecast and observations, called analysis, can formally be determined by finding the minimum of the cost function

$$J(\mathbf{x}) = \left(\mathbf{x} - \bar{\mathbf{x}}^{\mathbf{b}}\right)^T \left(\mathbf{P}^b\right)^{-1} \left(\mathbf{x} - \bar{\mathbf{x}}^{\mathbf{b}}\right) + \left[\mathbf{y_o} - H(\mathbf{x})\right]^T \mathbf{R}^{-1} \left[\mathbf{y_o} - H(\mathbf{x})\right] \tag{1}$$

$\mathbf{x}$ is the multidimensional model state vector, $\bar{\mathbf{x}}^{\mathbf{b}}$ is the ensemble mean of the model background, defined by the average of all ensemble members $\mathbf{x}^{b(i)}, i = 1..k$

$$\bar{\mathbf{x}}^{\mathbf{b}} = k^{-1} \sum_{i=1}^{k} \mathbf{x}^{b(i)} \tag{2}$$

$\mathbf{P}^b$ is the background error covariance matrix, $\mathbf{y_o}$ is the observation vector, H is the observation operator and $\mathbf{R}$ is the observation error covariance matrix. The forecast departures $\mathbf{d} = \mathbf{y_o} - H(\mathbf{x})$ measure the difference between observations and model equivalents. The ensemble background anomaly (EBA) $\mathbf{a}_i$ is defined by the difference of a particular ensemble member and the ensemble mean $\mathbf{a}_i = \mathbf{x}^{b(i)} - \bar{\mathbf{x}}^{\mathbf{b}}$.

Even though the LETKF is by construction a mean-preserving ensemble square-root filter and thus should be less prone to problems with non-Gaussianity it is worth looking at how well the convection permitting COSMO model meets the assumption of the BLUE theory, namely how well the forecast departure statistics and the ensemble background anomalies can be approximated by a Gaussian distribution. The questions to be answered are

- What form take the distributions of forecast departures and EBA from a short-range high-resolution (ensemble) COSMO forecast ?
- How does the distribution changes with forecast lead time ?

- Are there differences in the distribution between summer and winter ?

The results are expected to give a hint if the LETKF is feasible to be used with the convection permitting COSMO model.

2 Data and Evaluation Method

2.1 Data

2.1.1 Forecast Departures

The forecast departure statistics considered in this study are based on operational DWD convection permitting COSMO-DE (mesh size of 2.8 km, without parametrized deep convection, covering Germany and surroundings) and regional COSMO-EU (mesh size of 7 km, with deep convection parametrization, covering whole Europe) forecasts from two periods:

- Winter: 12/2007 - 02/2008 (91 days, 364 forecasts)
- Summer: 06/2008 - 08/2008 (92 days, 368 forecasts)

Since we are interested in short-range forecasts we consider departures for forecast lead times from +3h to +6h. In order to see how the statistics change with evolving forecast time, we compare them with departures for leadtimes from +9 to +12h. Forecast departures are calculated for all conventional observations that are routinely assimilated in the COSMO model at DWD, namely

- SYNOP (p_s,T,u/v,RH, and pp)
- Radiosondes (T,u/v and RH at 940, 850, 500 and 300 hPa)
- Aircraft data (T and u/v at 940, 850, 500 and 300 hPa)
- Wind profiler (u/v at 940, 850, 500 and 300 hPa)

All observations from the above list are actively assimilated, except surface precipitation (pp) from SYNOP stations, which is only used for the calculation of the departures.

For ease of comparison of COSMO-DE and COSMO-EU, only departures from observations inside the COSMO-DE domain are taken into account.

2.1.2 Ensemble Background Anomalies

The ensemble background anomalies are calculated from forecasts of the pre-operational high resolution German COSMO-DE EPS, running in a similar configuration as the COSMO-DE deterministic forecast. The 20 ensemble forecast members are initialized at 00 UTC from a regional EPS (COSMO-SREPS) driven by different global models and using different physical parametrization settings and are integrated out to 24 hours. The configuration of the boundary conditions and of the physical parametrisations are summarized in Table 1.

- Ensemble forecast from a summer period (8.8.2007 - 16.8.2007) are considered.
- Forecast lead times of +3h and +24h are compared
- The following variables are looked at
  - T and u at the terrain-following model levels at approximately 10 m, and 5500 m above surface.
  - pp at the surface

Ensemble members	Driving global model	
01-05	ECMWF	
06-10	GME	
11-15	NCEP	
16-20	UKMO	
Ensemble members	Physical parameter perturbation	Default value
01, 06, 11, 16	entrscv=0.002	entrscv=0.0003
02, 07, 12, 17	clc_diag=0.75	clc_diag=0.5
03, 08, 13, 18	rlam_heat=50	rlam_heat=1
04, 09, 14, 19	rlam_heat=0.1	rlam_heat=1
05, 10, 15, 20	tur_len=150	tur_len=500

Table 1: Configuration of the COSMO-DE EPS in terms of boundary conditions and physical parametrisation tuning values.

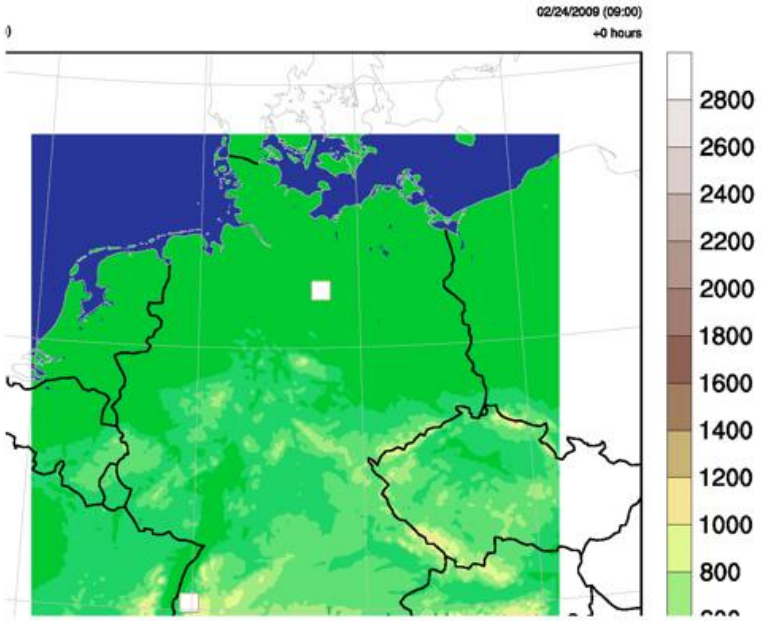


Figure 1: Computational domain of COSMO-DE and COSMO-DE EPS. The coloured domain depicts the plotting domain for the stamp maps in Section 4 and the two white squares marks the two verification domains South Germany and North Germany used for the calculation of the ensemble anomaly statistics.

2.2 Evaluation Method

In order to judge, how well the forecast departure and EBA distributions are approximated by the Gaussian distribution, we compare them, both qualitatively and more quantitatively with Gaussian pdf's fitted to the data. The forecast departure d_l of a single observation is

$$d_l = y_{o,l} - H(\mathbf{x})_l \tag{3}$$

where y_0 denote the observation and $H(\mathbf{x})_l$ the corresponding model equivalent obtained by the application of the observation operator H to the model state $\mathbf{x}$. $l = 1..N_l$ is the index specifying a particular observation from all N_l observations.

For the ensemble background anomalies we consider all k ensemble members and compute the distribution from all anomalies $a_{(i,j)}$, $i = 1..k$, $j = 1..N_j$, where N_j is the number of gridpoints of a 2d model field in a specified verification domain and at a certain terrain-following level.

The probability distribution $p(x)$ over a set of indices i (e.g. all temperature observations from radiosondes at $850 \pm 10hPa$ within a leadtime range of +3h to +6h using COSMO-DE forecasts in the summer period) is considered (near-)Gaussian if it approximates the Gaussian distribution

$$\tilde{p}(x) = N(\bar{x}, \sigma) = \frac{1}{\sqrt{2\pi}\sigma} e^{-\left(\frac{x-\bar{x}}{\sigma}\right)^2} \tag{4}$$

The mean $\bar{x}$ and the standard deviation σ of the distributions are calculated by

$$\bar{x} = \frac{1}{N}\sum_{i=1}^{N} x_i \tag{5}$$

$$\sigma = \sqrt{\frac{1}{N}\sum_{i=1}^{N}\left(x_i - \bar{x}\right)^2} \tag{6}$$

where N is the number of data in the considered set.

In the case of the forecast departures, $x = d, i = l$ and $N = N_l$. In the case of the ensemble background anomalies, $x = \mathbf{a}$ and $N = N_j \cdot k$. The qualitative evaluation of the Gaussianity of $p(x)$ is done graphically by plotting the pdf and its Gaussian approximation $\tilde{p}(x)$ calculated from (4) using (5) and (6). Figure 2 (upper panel) shows an example for a forecast departure distribution: the bold line represents the pdf $p(d)$ and the thin line its approximation $\tilde{p}(d)$. Note that in the semilogarithmic representation the normal pdf takes a parabolic form.

It is useful to not only estimate if the Gaussian approximation is fulfilled, but to estimate how well it is approximated. To this end we define the term "normrange" by the range of probabilities over which the Gaussian approximation is reasonable. A perfect Gaussian fit has a normrange of 100%. To calculate the normrange, a normal probability plot is drawn of $p(x)$. In this graph, the cumulative distribution function of $p(x)$ is transformed in a way that a Gaussian distribution represents a straight line. Any deviation from this line suggests non-Gaussianity. The reference Gaussian distribution, against $p(x)$ is compared, is obtained from the 25% and the 75% quantile of $p(x)$. It appears as the dash-dotted straight lines on the normal probability plots. The normrange is then calculated as the range, where $p(x)$ is close to the line. "Close" is defined such that $p(x)$ does not differ from the straight line by more than a threshold, defined by the difference of the 25% and the 75% quantile divided by 12 (subjective choice). Figure 2 (lower panel) shows an example of a normal probability plot. The crosses borders the normrange, i.e. the region where $p(x)$ can be reasonably approximated by the normal distribution.

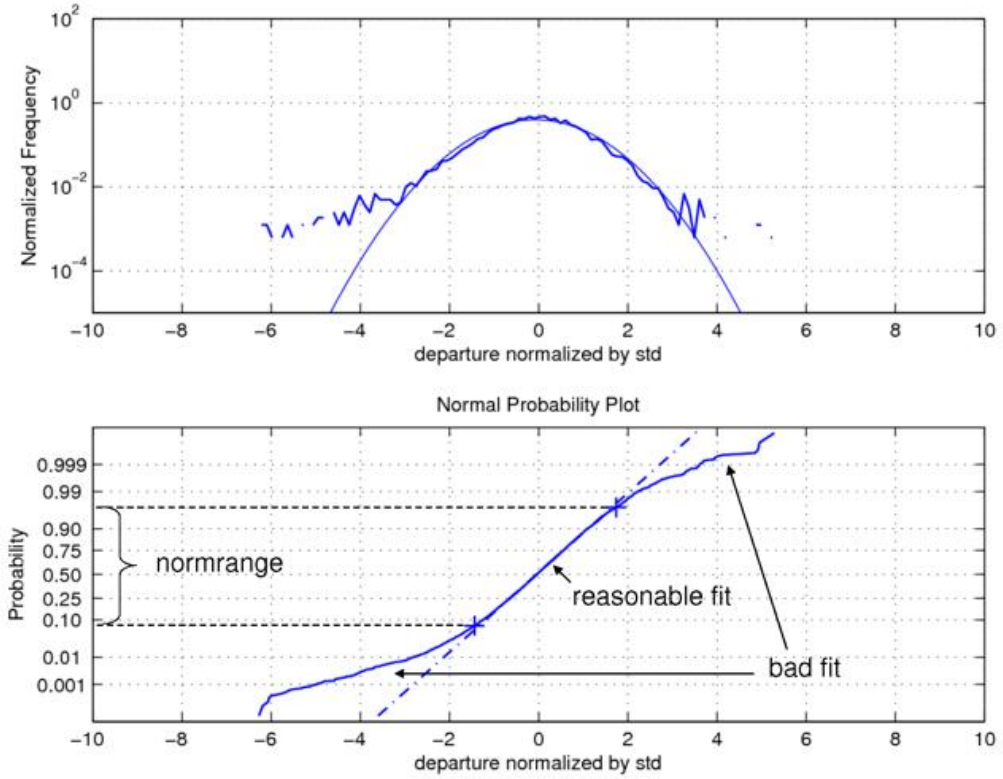


Figure 2: Example of the evaluation method used in this study. Upper panel: semilogarithmic representation of the departure distribution $p(d)$ (bold line) and its reference normal distribution $\tilde{p}(d)$ (thin line). Lower panel: normal probability plot and definition of normrange (see also text).

3 Forecast Departure Statistics

In this section we present COSMO-DE forecast departure distributions from all observations in the model domain mentioned in Section 2.1.

3.1 Near surface

3.1.1 Surface Pressure

Figure 3 shows the results for surface pressure. The distribution is near-Gaussian around the median and within approximatively ± 3 standard deviations, which corresponds to roughly ± 2.7 hPa, irrespective of the forecast lead time. At the end (tails) of the distributions, the departure distribution deviates from normality, i.e. there are more large deviations than what would be described by a Gaussian distribution. The distribution is slightly asymmetric at the tails, i.e. there are more large positive departures than large negative departures, meaning that the model more often largely underestimates pressure than largely overestimates it.

The negative pressure bias (i.e. in the mean, the model overestimates the pressure) increases by 17% in summer (26% in winter) with lead time (upper panels). The normranges amount to roughly 94% in summer and 87% in winter (lower panels) and do not change significantly during the first 12h of the forecast.

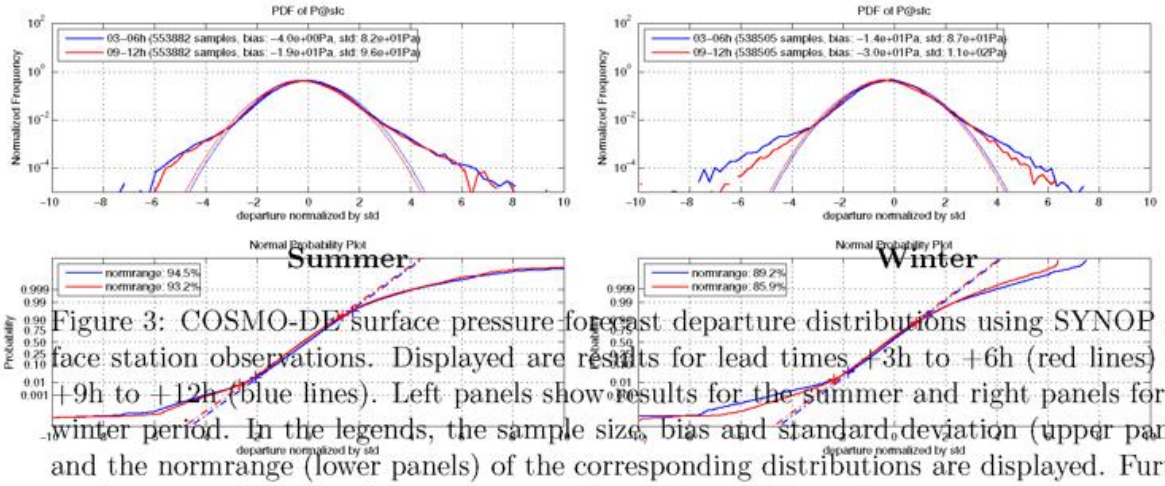


Figure 3: COSMO-DE surface pressure forecast departure distributions using SYNOP surface station observations. Displayed are results for lead times +3h to +6h (red lines) and +9h to +12h (blue lines). Left panels show results for the summer and right panels for the winter period. In the legends, the sample size, bias and standard deviation (upper panels) and the normrange (lower panels) of the corresponding distributions are displayed. Further explanations about the plots are given in Section 2 and Figure 2.

3.1.2 2m Temperature

The 2m temperature distributions differ from the surface pressure distributions in that they are less good approximated by a normal distribution (Figure 4). This is particularly obvious in winter (right upper panel), but to a less degree also in summer (left upper panel). The

lognormal curves have a more linear than parabolic shape, suggesting a more exponential than Gaussian nature. This behaviour is reflected in normranges of approx. 83% in summer and 75% in winter. The bias are below one degree and the standard deviations around 1.8 degrees. Both bias and standard deviation are nearly leadtime independent up to 12h.

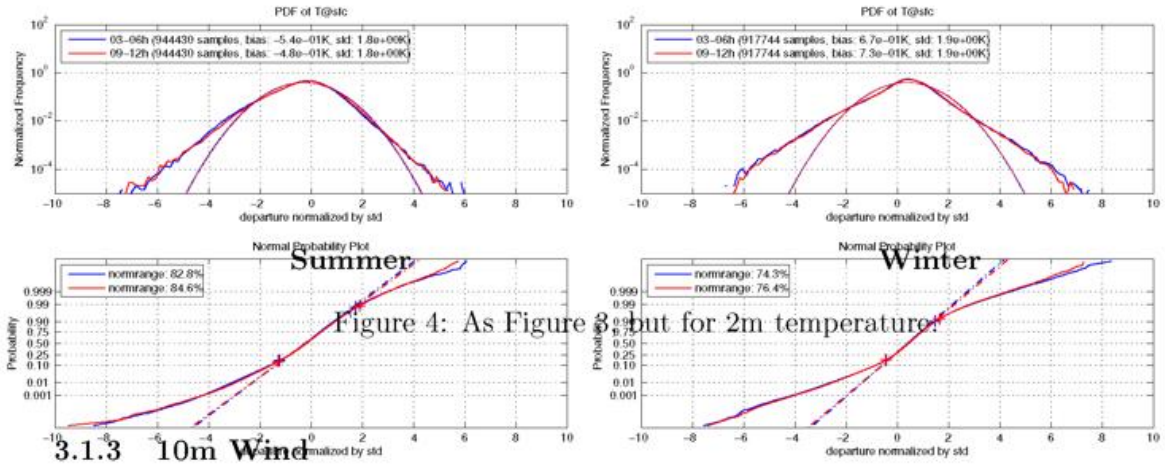


Figure 4: As Figure 3, but for 2m temperature.

3.1.3 10m Wind

The distributions of 10m wind are better Gaussian approximated than those of 2m temperature (Fig. 5). Normranges are about 89% in summer and 84% in winter.

The bias is around -0.1 m/s and the standard deviation around 1.8 m/s and nearly independent from lead time and season. Zonal and meridional components behave almost identically, therefore only the zonal wind speed is shown.

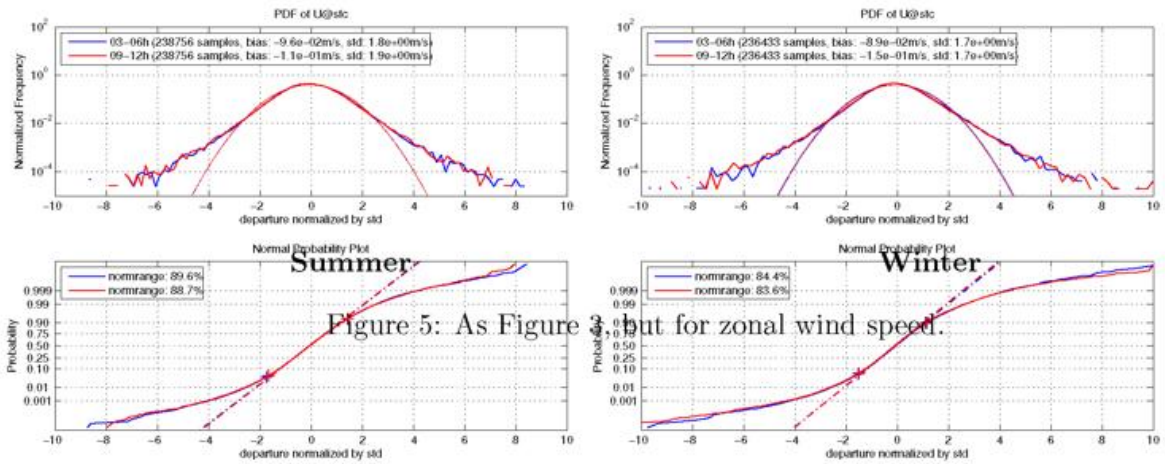
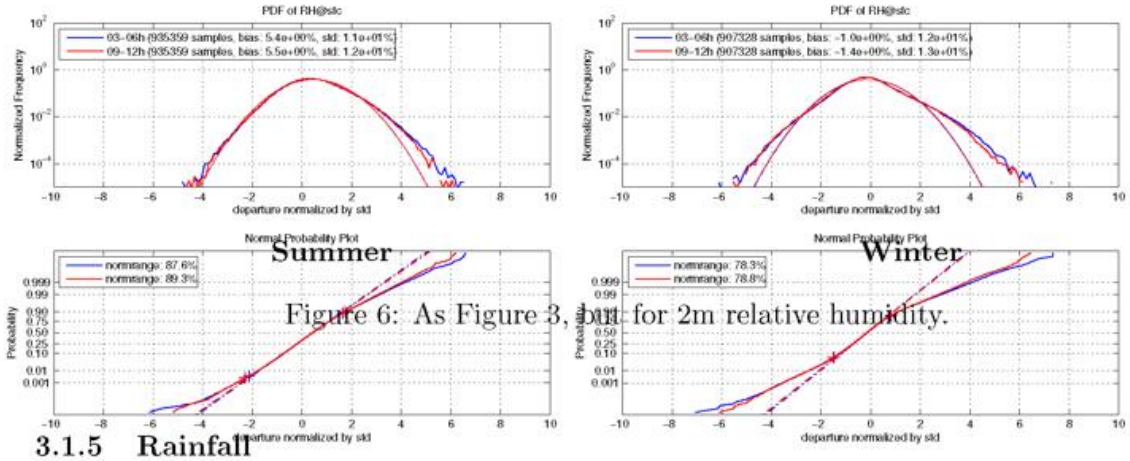


Figure 5: As Figure 3, but for zonal wind speed.

3.1.4 2m Humidity

The 2m relative humidity forecast departure distribution (Fig. 6) differs substantially between summer and winter. In summer the distribution is very close to normal, even the negative "fat tail" is absent, resulting in a high normrange of 88%. In winter the distribution is more exponential than Gaussian and thus the normrange does not exceed 79%. The distributions are nearly independent on lead time.

Also the bias is dependent on season and amounts 5.4% (-1%) in summer (winter). The standard deviation is in both seasons 11%.



Summer **Winter**

Figure 6: As Figure 3, but for 2m relative humidity.

3.1.5 Rainfall

Surface rainfall as observed by SYNOP stations is not actively assimilated in the model, but merely used to compute forecast departures. The distribution turns out to be far away from Gaussian both, in summer and winter (Figure 7). The normrange calculation is not reliably applicable for this type of distribution and is therefore omitted.

Summer **Winter**

Figure 7: As Figure 3, but for rainfall observed by SYNOP.

Forecast departures from radar rainfall have been computed using model output from the Swiss COSMO-2 (mesh size of 2.2 km, without parametrized deep convection) which runs in a similar configuration as the COSMO-DE model and from radar derived surface rainfall from the Swiss Radar Network (SRN). The model data is taken from 13 12UTC forecasts (same lead times as before) during the period from 1.6.2008 to 13.6.2008. A domain of 70x40 km with a very good radar visibility in the Swiss plateau has been chosen, in order to

obtain high quality observations. The departures are calculated gridpoint by gridpoint from hourly sums after a 3x3 gridbox filter application. Radar rainfall is assimilated in the high resolution COSMO-DE and the Swiss COSMO-2 using the latent heat nudging scheme.

As for SYNOP rainfall, the departures using radar rainfall (Figure 8) can not be approximated with a Gaussian distribution. A distinct peak at zero departure suggests the occurrence of many situations where rain is neither observed nor forecast. Beyond standard deviations of 1 (-1) the distribution shows an exponential rather than a Gaussian behaviour. Moreover the distribution is asymmetric and exhibits more large positive departures (i.e. underestimation by the model).

Figure 8: As Figure 7, but for Swiss summer rainfall derived from radar data.

3.2 Upper atmosphere

Upper air measurements are classified according to the pressure level, on which they are observed. Main pressure levels of 940, 850, 500 and 300 hPa are considered in this study. For the sake of increasing the sample size, observations within a pressure layer with thickness of 20 hPa centered around the main pressure level are also taken into account. Forecast departures have been calculated from radiosonde, aircraft and windprofiler observations. The distributions are of similar structure between corresponding observations, though they slightly differ in bias and standard deviation. Therefore, only the observations with the largest sample size are shown here (aircraft data for temperature and wind and radiosonde data for humidity), the rest of the results are shown in Section 5.

3.2.1 Temperature

Upper air temperature forecast departures can generally be well approximated by Gaussian distributions (Figures 9 - 12 and 38 - 41). Only in the winterly boundary layer (at 940 hPa and 850 hPa), deviations between 0 and -2 standard deviations are apparent. Normranges reach values of 86%-96% in summer and 79%-90% in winter. Values in the boundary layer are generally lower than in the middle and upper atmosphere.

Biases are well below 0.2 K and standard deviations below 1.5 K. Departures are larger in winter and in the boundary layer than in summer and in the mid/upper atmosphere.

3.2.2 Wind

Wind departures are found to be also very nearly Gaussian (Figures 13 - 16 and 42 - 61). Normranges are between 79% and 88%, generally higher in summer than in winter, but there is no clear dependence on height.

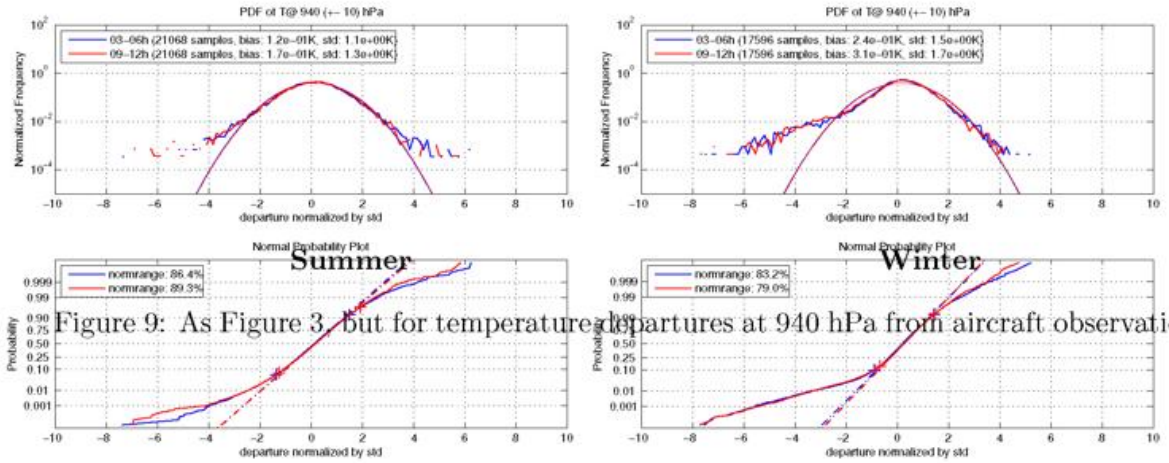


Figure 9: As Figure 3, but for temperature departures at 940 hPa from aircraft observations.

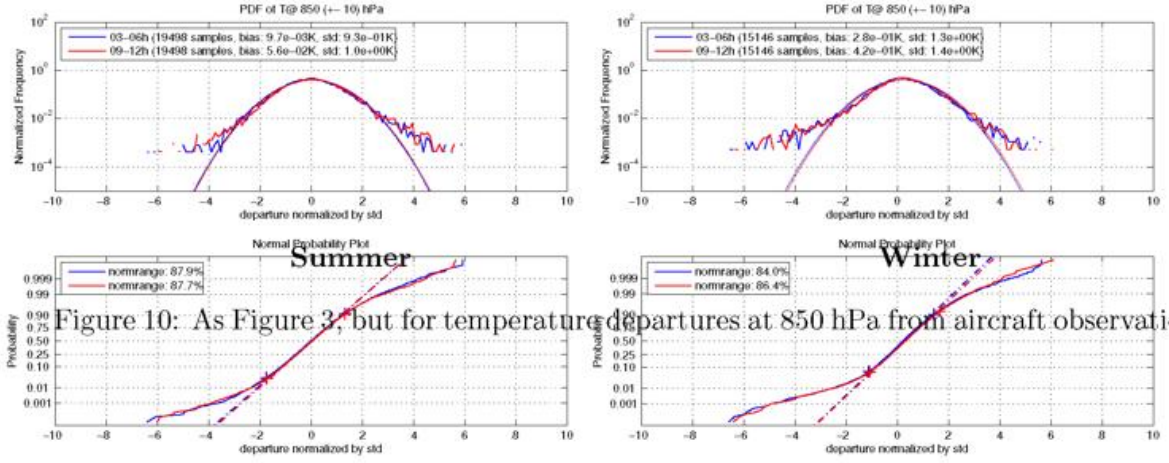


Figure 10: As Figure 3, but for temperature departures at 850 hPa from aircraft observations.

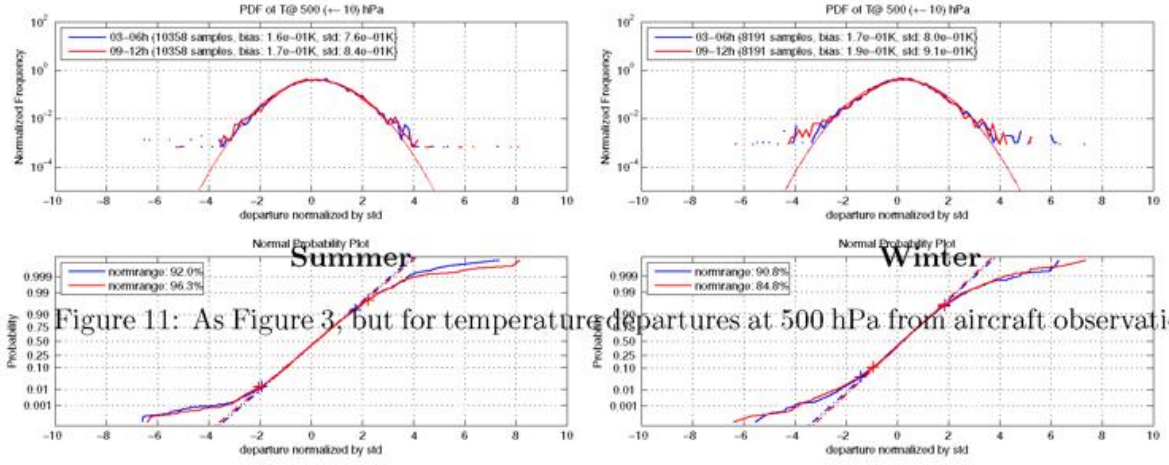


Figure 11: As Figure 3, but for temperature departures at 500 hPa from aircraft observations.

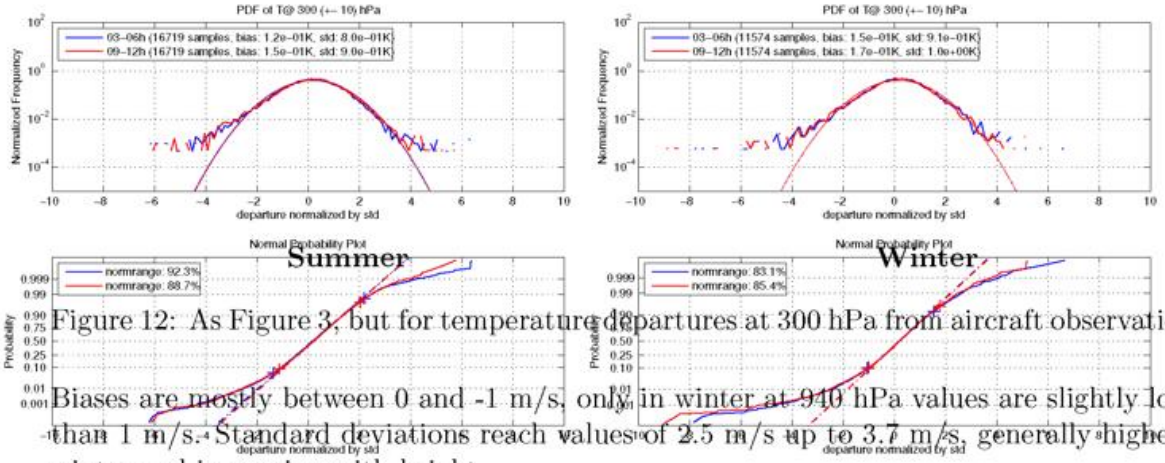


Figure 12: As Figure 3, but for temperature departures at 300 hPa from aircraft observations.

Biases are mostly between 0 and -1 m/s, only in winter at 940 hPa values are slightly lower than 1 m/s. Standard deviations reach values of 2.5 m/s up to 3.7 m/s, generally higher in winter and increasing with height.

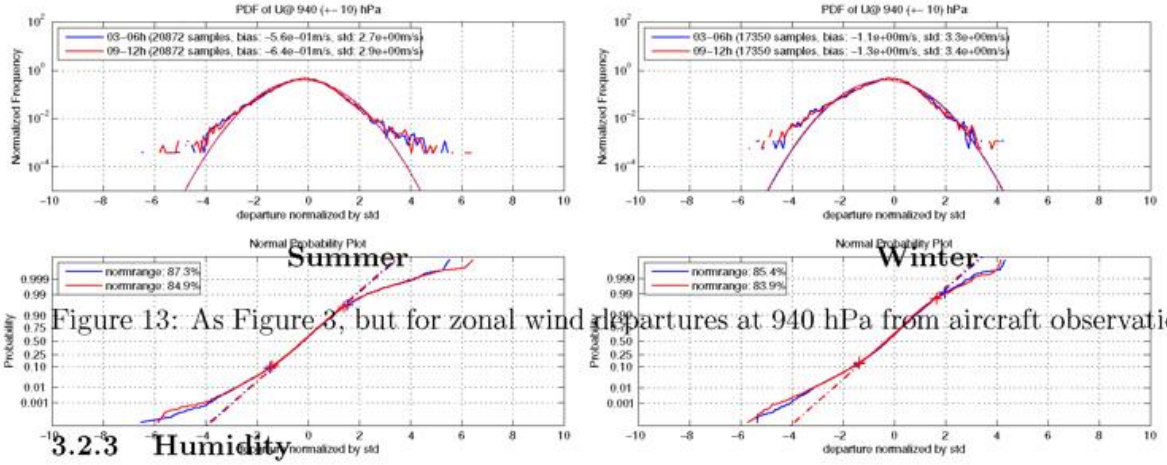


Figure 13: As Figure 3, but for zonal wind departures at 940 hPa from aircraft observations.

3.2.3 Humidity

Forecast departures of relative humidity can not be well approximated by a normal distribution (Figures 17 - 20). Especially in winter a distinct peak in the pdf is visible for zero departures in the boundary layer (940 hPa and 850 hPa, Figures 17 and 18). This peak origins from many winterly stratus situations, where both model and observations are saturated, resulting in zero departures (not shown). This peak is not apparent in summer and in the upper atmosphere. Winter distributions generally show a rather exponential, than Gaussian shape, resulting in generally low normranges, where summer distributions are more Gaussian.

Biases increase with height from less than 2% (940 hPa) to roughly -9% (300 hPa) in summer and 3% (940 hPa) to roughly -7% (300 hPa) in winter. Standard deviations are less height-

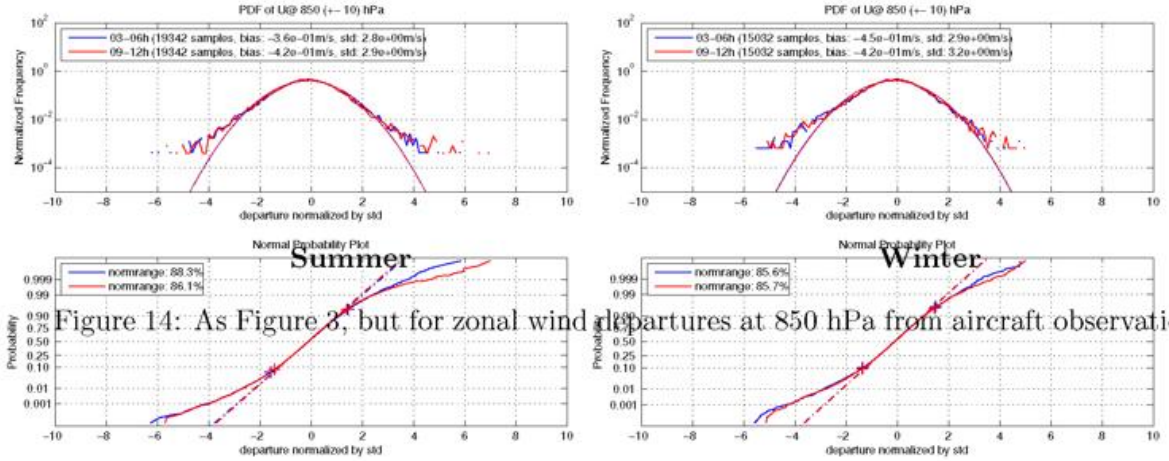


Figure 14: As Figure 3, but for zonal wind departures at 850 hPa from aircraft observations.

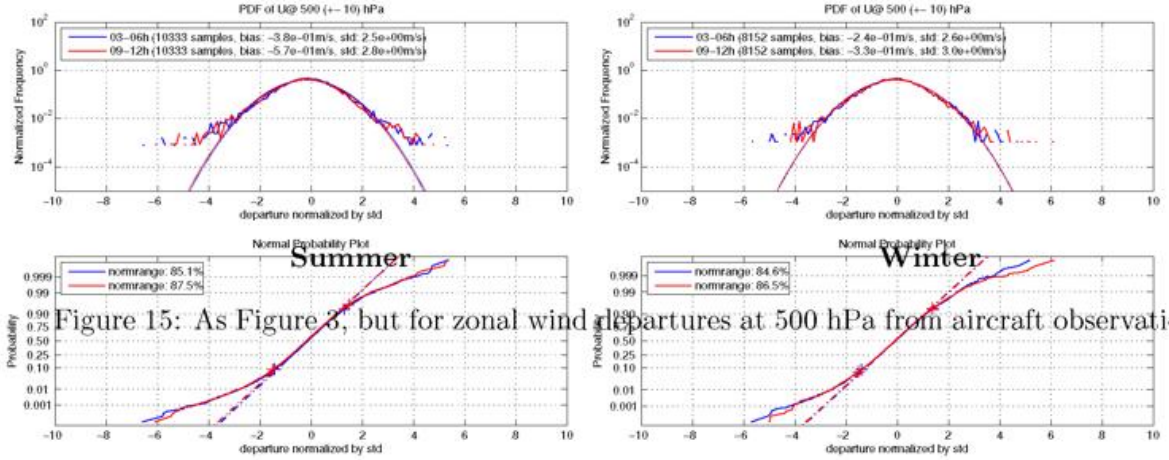


Figure 15: As Figure 3, but for zonal wind departures at 500 hPa from aircraft observations.

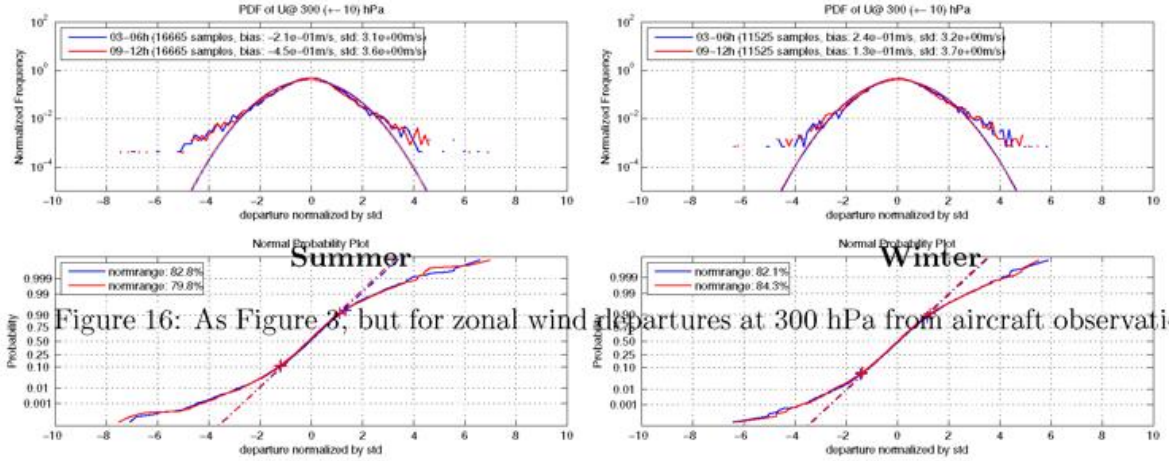


Figure 16: As Figure 3, but for zonal wind departures at 300 hPa from aircraft observations.

dependent and reach values of 15%-20% both in summer and winter. The errors only slightly increase in the first 12h.

Summer **Winter**

Figure 17: As Figure 3, but for relative humidity departures at 940 hPa from radiosonde observations.

Summer **Winter**

Figure 18: As Figure 3, but for relative humidity departures at 850 hPa from radiosonde observations.

Summer **Winter**

Figure 19: As Figure 3, but for relative humidity departures at 500 hPa from radiosonde observations.

Summer **Winter**

Figure 20: As Figure 3, but for relative humidity departures at 300 hPa from radiosonde observations.

3.3 Sensitivity studies

3.3.1 Dependency on Humidity variable

The forecast departure distributions of humidity and rainfall turned out to be the least Gaussian of all model variables. In this section other forms of humidity are investigated, namely specific humidity, the logarithm of specific humidity, a normalized relative humidity (Holm et al., 2002) and the logarithm of rainfall.

Humidity In this section, alternative humidity representations to the relative humidity are looked at. Holm et al. (2002) looked at different humidity variables for the assimilation in the ECMWF IFS model and proposed a normalized relative humidity (NRH) with appealing properties for the assimilation:

- the bias $\bar{d}$ is effectively eliminated, a prerequisite for a successful assimilation
- Forecast departure distributions are near-Gaussian over the whole range of relative humidity values, especially near saturation and in very dry situations, which is not the case for relative humidity departures

The normalized relative humidity departure (d_{NRH}) is calculated following Holm et al. (2002)

$$d_{NRH} = \frac{d_{RH}}{\sigma\left(RH_m + d_{RH}/2\right)}, \tag{7}$$

where the numerator is the standard relative humidity departure (d_{RH}) and the denominator is the standard deviation of the sum of model value (RH_m) and relative humidity departure divided by two.

Figure 21 shows results of COSMO-DE forecast departures using different representations of humidity observations from radiosondes at 850 hPa. Displayed are results for lead times +3h to +6h (red lines) and +9h to +12h (blue lines). Left panels show results for the summer and right panels for the winter period. Obviously, departures of specific humidity (first row) and its logarithm (second row) are less Gaussian than relative humidity (third row), particularly in summer (left panels). Departures of NRH (lowest row) show a similar Gaussian approximation but both bias and standard deviation are reduced by more than an order of magnitude as compared to those using relative humidity.

In order to see how the distributions behave in near saturated or very dry situations, forecast departures have been calculated conditional to the modelled relative humidity. Due to small sample sizes in summer, only the results of the winter period are shown. The upper panels

of Figure 22 show departures of relative humidity for situations where model values exceed 85% (blue lines) and very dry situations (relative humidity below 15%, red lines). Both distributions show a rather exponential than a Gaussian behaviour. Moreover, both, bias and standard deviation are clearly dependent on the modelled relative humidity. In the near saturated situations the model overestimates humidity by roughly 5% (std of 13%) , whereas in dry situations the model underestimates humidity by roughly 2% (std of 1%). Note that the peak at zero departure only appears in the near saturated situations.

When using NRH as variable both biases and standard deviations are reduced by an order of magnitude (right panel of Figure 22). Moreover, the distributions of both wet and dry situations appear to be near-Gaussian.

These results confirm the findings of Holm et al. (2002) and suggest that the normalized relative humidity should have superior properties for the assimilation than the relative humidity.

Summer **Winter**

Figure 21: COSMO-DE forecast departure distributions using different representations of humidity observations from radiosondes at 850 hPa. Displayed are results for lead times +3h to +6h (red lines) and +9h to +12h (blue lines). Left panels show results for the summer and right panels for the winter period. First row: specific humidity (q_v), second row: $\log(q_v)$, third row: relative humidity (same as Figure 18) and fourth row: normalized relative humidity.

Figure 22: COSMO-DE winterly forecast departure distributions of relative humidity (left panels) and normalized relative humidity (right panel) from radiosondes at 850 hPa and forecast leadtimes from +3h to +6h. Blue lines: departures for model (normalized) relative humidity above 85% (blue lines) and departures for model (normalized) relative humidity below 15% (red lines).

Rainfall Since rainfall amounts are nearly logarithmically distributed it is obvious to look at departures of the logarithm of rainfall. Figure 23 shows the resulting distributions for rainfall (upper panels, same as Figure 7) and the logarithm of rainfall (lower panels). The forecast departures of the logarithm of rainfall are clearly much more Gaussian than those of rainfall.

The same holds true for the departures using radar-derived rainfall (Figure 24). Since the logarithm of zero is not defined, only departures with non-zero observations and model forecasts are considered. Note that in situations where only a part of the domain shows rainfall in either the observations or the model forecasts, this can reduce the sample size of the departures by orders of magnitude. Also here the distribution using the logarithm of rainfall is much more Gaussian than that using rainfall.

Summer **Winter**

Figure 23: COSMO-DE rainfall forecast departure distributions using SYNOP surface station observations. Displayed are results for lead times +3h to +6h (red lines) and +9h to +12h (blue lines). Left panels show results for the summer and right panels for the winter period. Upper panels show distributions using rainfall (same as Figure 7) and lower panels using the logarithm of rainfall.

Figure 24: Same as Figure 23 but for COSMO-2 rainfall forecast departure distributions from radar observations. Only those departures are considered where both observations and forecasts are non-zero.

3.3.2 Dependency on Model Resolution

After having investigated the forecast departures of COSMO-DE model, we are interested in how the results differ from those of the regional model COSMO-EU with a model mesh width of 7 km. The largest difference between COSMO-DE and COSMO-EU, beside their resolution, is that in COSMO-EU deep convection is parametrized, where in COSMO-DE only the shallow convection is parametrized, but deep convetion is simulated explicitly. As a result of the better resolved topography in COSMO-DE, we expect the departures to differ mostly in the boundary layer. Therefore we compare the results of the forecast departures exemplarily on the 850 hPa pressure level.

When comparing the results of COSMO-DE and COSMO-EU it gets rapidly clear that the differences in the distributions are minor in all variables and independent on season (Figures 25 - 27). Normranges do not differ by more than 3%, whereas biases and standard deviations can vary considerably depending on model parameter. The same holds true for the other observation types and differences between the two models are even smaller in the upper atmosphere (not shown).

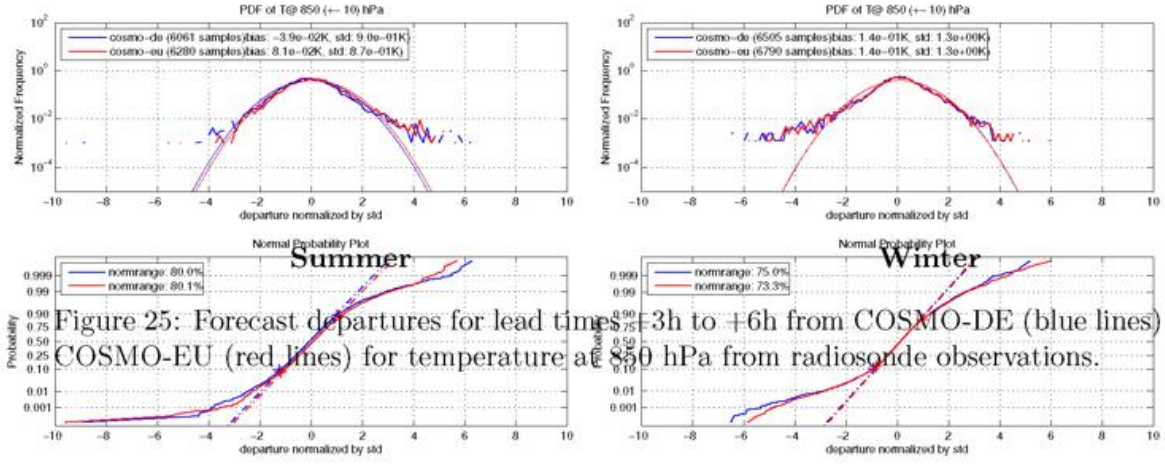


Figure 25: Forecast departures for lead times +3h to +6h from COSMO-DE (blue lines) and COSMO-EU (red lines) for temperature at 850 hPa from radiosonde observations.

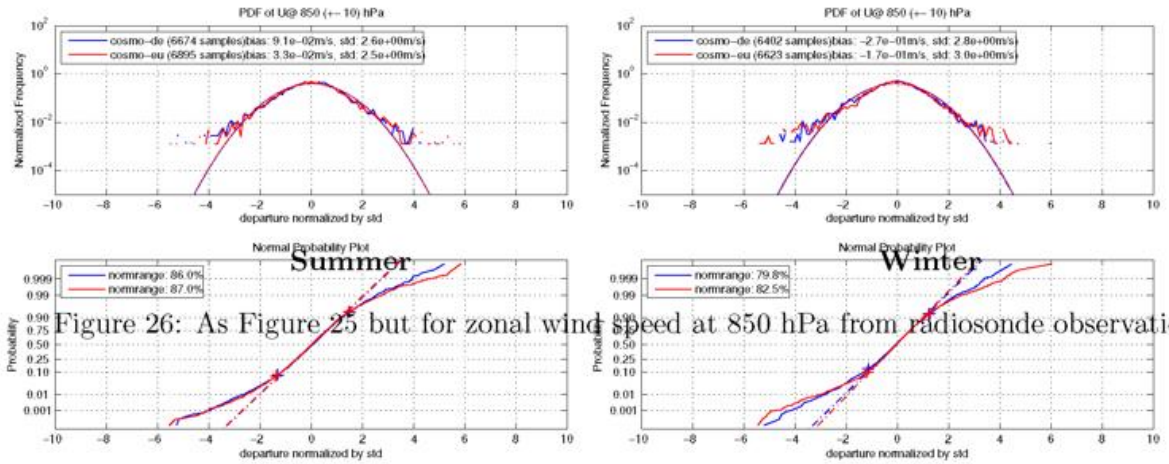


Figure 26: As Figure 25 but for zonal wind speed at 850 hPa from radiosonde observations.

Summer **Winter**

Figure 27: As Figure 25 but for relative humidity at 850 hPa from radiosonde observations.

3.3.3 Dependency on Weather Regime

All results presented so far were compiled using the whole summer (winter) period. In a sensitivity study, we stratified time according to the weather situation, i.e. we looked at the forecast departure distributions where only rainy days have been considered. We defined a rainy day as a day where a large part of the COSMO-DE domain was affected by precipitation. For this end daily accumulations from gridded raingauges have been used and a subjective separation has been made.

The resulting distributions were found to be slightly less Gaussian than those using all days for the statistics (not shown).

4 Ensemble Anomaly Statistics

In this section distributions of the ensemble background anomalies from COSMO-DE ensemble forecasts are presented. All distributions are calculated from gridpoint values of temperature and zonal wind speed at 10 m and 5400 m above surface and averaged spatially over 10x10 gridpoints of two verification domains (North and South Germany, see Figure 1) and temporally over the 9 days from 8 to 16 August 2007. Lead times of +3h and +24h are compared.

4.1 Near surface

4.1.1 Temperature

Figure 28 shows the ensemble background anomaly distribution of temperature at the lowest model level ($\approx$ 10m above surface) of the South Germany (left panel) and North Germany (right panel) verification domain. The +3h lead time distributions (blue lines) clearly show a significant deviation from normality (normrange well below 80%) for both domains. Beside the maximum around zero anomaly there is a second maximum around +2 (South Germany) and +3 (North Germany) standard deviations. On the other hand, the +24h lead time distributions (red lines) are much closer to normality (normrange above 90%) for both domains.

A closer look at the background anomalies of each ensemble member valid at 15 August 2007 03UTC (16 August 2007 00UTC) in Figure 29 (Figure 30) reveals the reason for the different distributions at +3h (+24h). At +3h (Figure 29) most members have small temperature anomalies due to the common analysis of all members. The anomalies are largely caused by the different physical parametrisations. Members 4, 9, 14, and 19 have much larger temperature anomalies than all other members. These members use a physical parametrisation tuning parameter rlam_heat = 0.1 instead of 1.0. This parameter influences the sensible heat fluxes from the surface and thus has an immediate impact on the near-surface temperature. At +24h the influence of the different boundary conditions of the driving global models on the anomalies has increased considerably (Figure 30). The amplitude of the anomalies are much larger and show more variation. The members 4, 9, 14 and 19 still show a clearly different anomaly distribution but the differences are smaller than at +3h. A similar behaviour can be found at the other days, leading to the systematic deviation from normality for the low level temperature at early lead times.

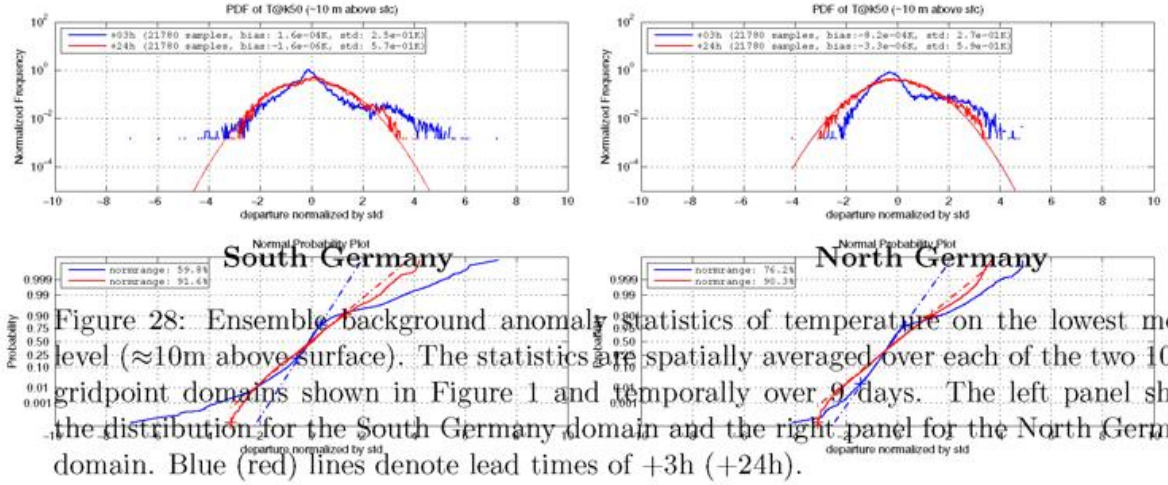


Figure 28: Ensemble background anomaly statistics of temperature on the lowest model level (≈10m above surface). The statistics are spatially averaged over each of the two 10x10 gridpoint domains shown in Figure 1 and temporally over 9 days. The left panel shows the distribution for the South Germany domain and the right panel for the North Germany domain. Blue (red) lines denote lead times of +3h (+24h).

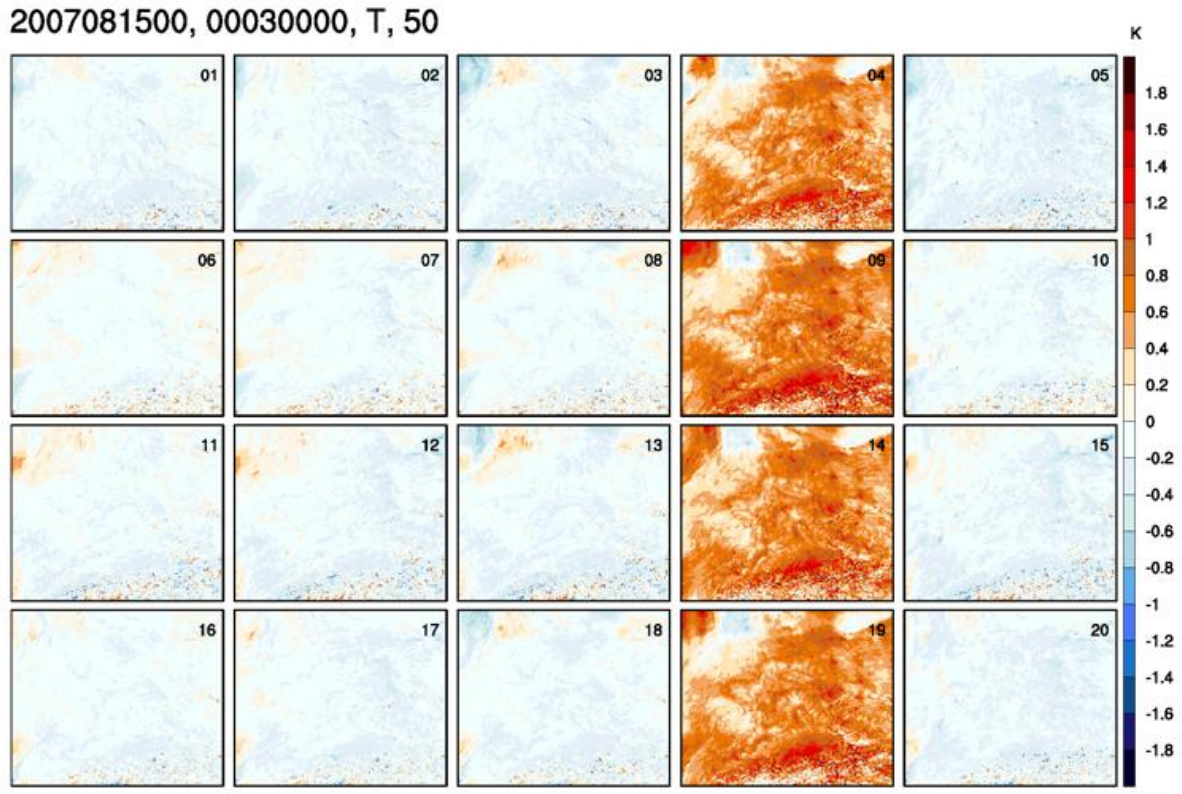


Figure 29: Stamp map of ensemble background anomalies of temperature at the lowest model level (≈10m above surface) valid at 15 August 2007 03UTC (i.e. at +3h). The domain corresponds to the coloured domain in Figure 1.

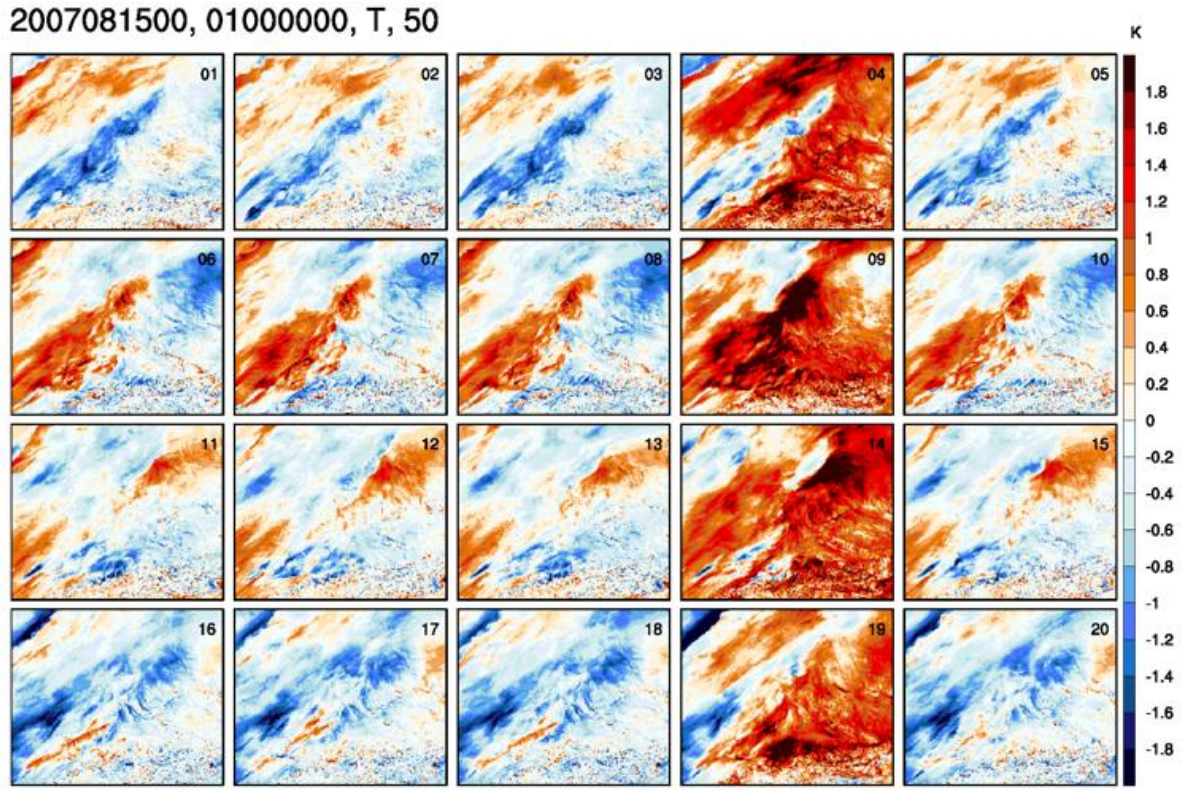


Figure 30: As Figure 29 but valid at 16 August 2007 00UTC (i.e. at +24h).

4.1.2 Wind

Figure 31 shows the distribution of zonal wind speed U at the lowest model level. The distributions at +3h and +24h are much more similar than for temperature in both domains. However, in the South Germany region, where topography is complex, the distributions show more deviations from normality than in the North Germany domain, which is essentially flat. The stamp maps in Figures 32 and 33 confirm that the anomalies are more evenly distributed in the two verification domains and all physical parametrisation settings show similar results in the wind speed.

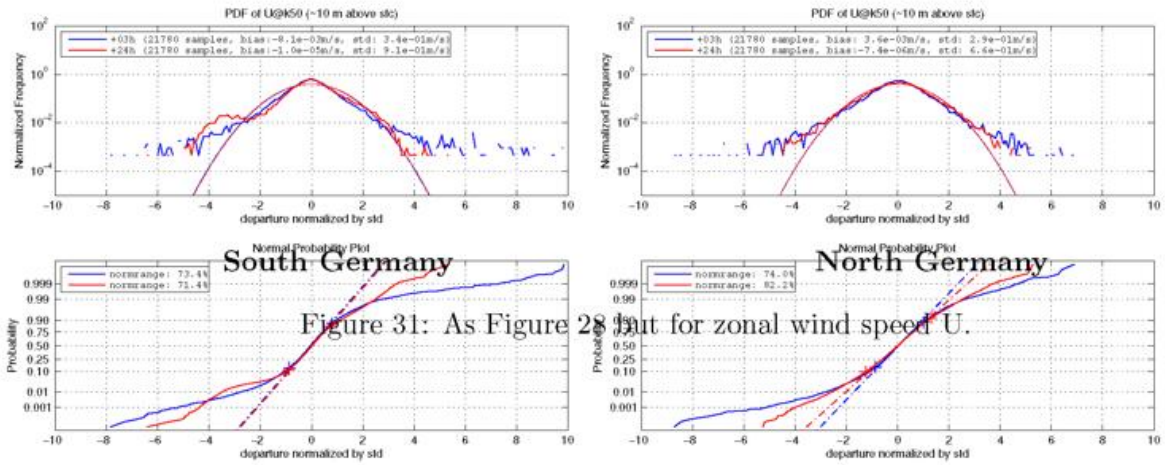


Figure 31: As Figure 28 but for zonal wind speed U.

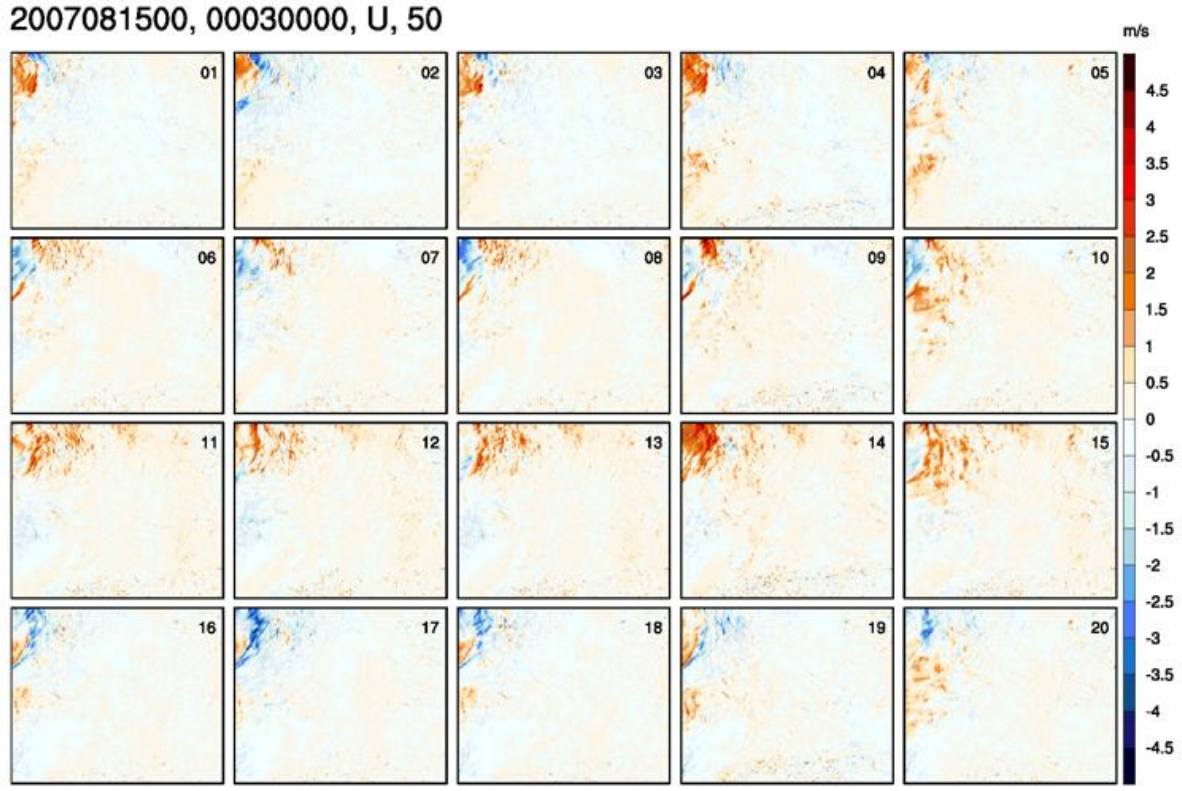


Figure 32: Stamp map of ensemble background anomalies of zonal wind speed valid at 15 August 2007 03UTC (i.e. at +3h). The domain corresponds to the coloured domain in Figure 1.

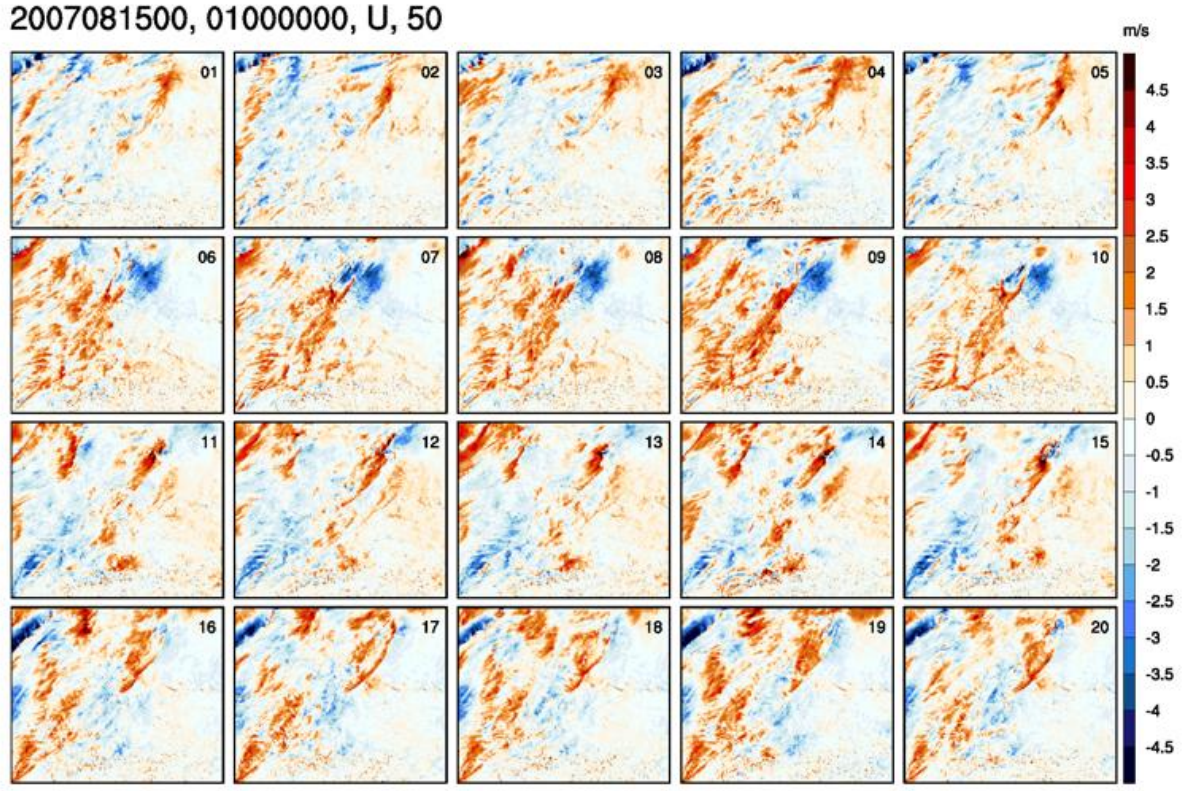


Figure 33: As Figure 29 but valid at 16 August 2007 0UTC (i.e. at +24h).

4.1.3 Precipitation

Figure 34 shows the distributions of hourly precipitation sums at lead times +2-3h and +23-24h. The distributions are clearly completely non-Gaussian at both lead times and verification domains. The stamp map in Figure 35 at +3h lead time valid at 15. August 2007 03UTC shows the reason for this. Most parts of the domain is precipitation-free and therefore anomalies are zero. In the sparse precipitation areas the anomalies take on large values, leading to a non-Gaussian distribution.

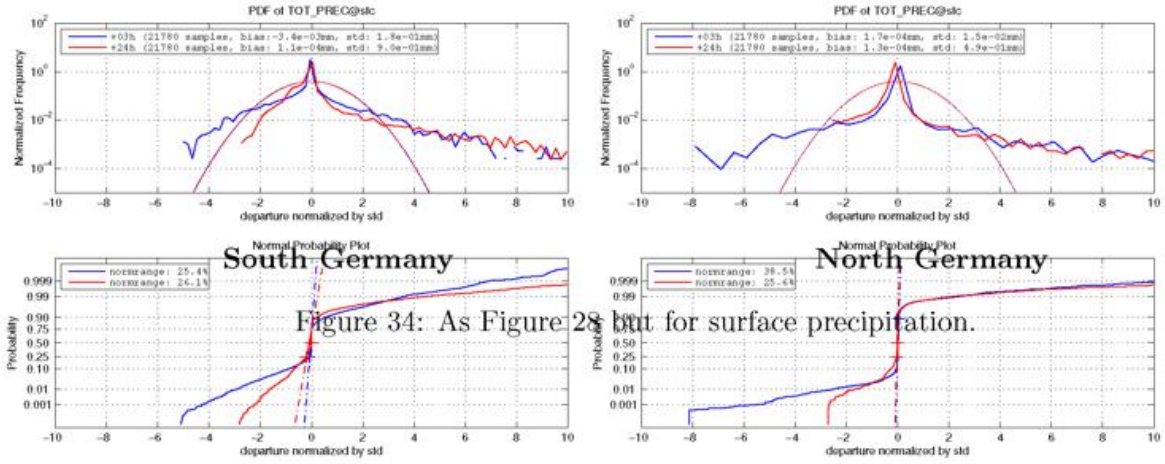


Figure 34: As Figure 28 but for surface precipitation.

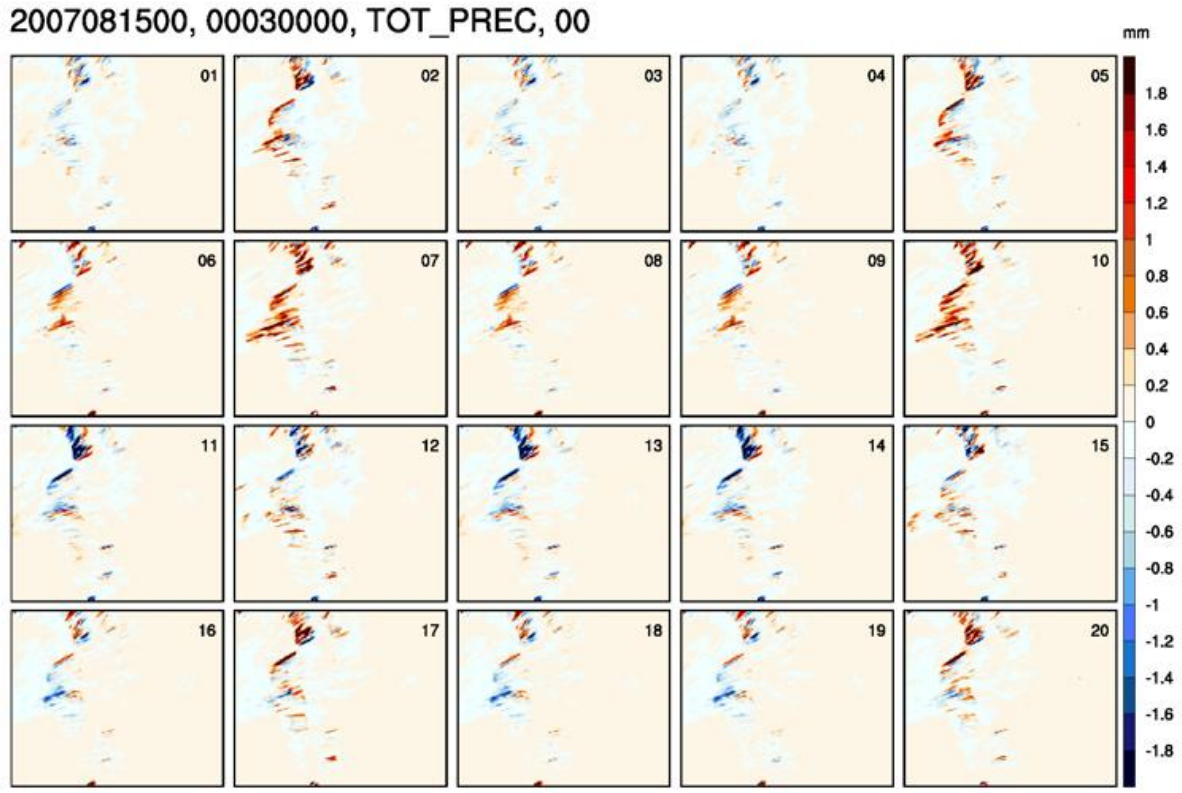


Figure 35: Stamp map of ensemble background anomalies of surface precipitation valid at 15 August 2007 03UTC (i.e. at +3h). The domain corresponds to the coloured domain in Figure 1.

4.2 Upper atmosphere

4.2.1 Temperature

Figure 36 shows the anomaly distributions for temperature on model level 24 ($\approx$ 5400 m above surface). The distributions are close to normality, both at +3h and +24 and in both verification domains. Obviously the physical parametrisation parameter affects the upper level temperature in a systematic way, as was the case in the low-level temperature.

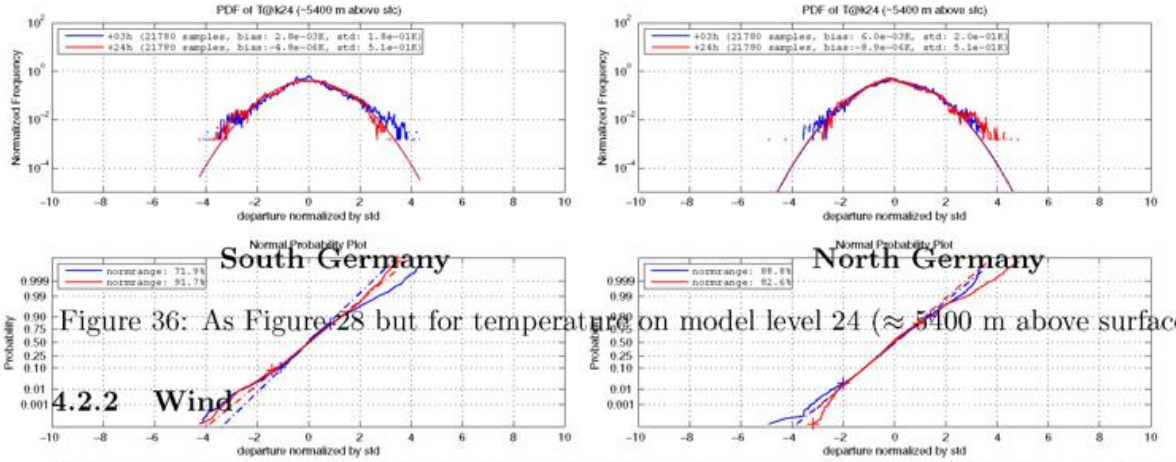


Figure 36: As Figure 28 but for temperature on model level 24 (≈ 5400 m above surface).

4.2.2 Wind

Figure 37 shows the anomaly distributions for zonal wind speed on model level 24 (≈ 5400 m above surface). The distributions are close to normality, both at +3h and +24. The distributions in the South Germany domain exhibits a slight deviation from normality, probably due to the more complex terrain which influences mid- and upper-level winds in a more systematic way than flat terrain.

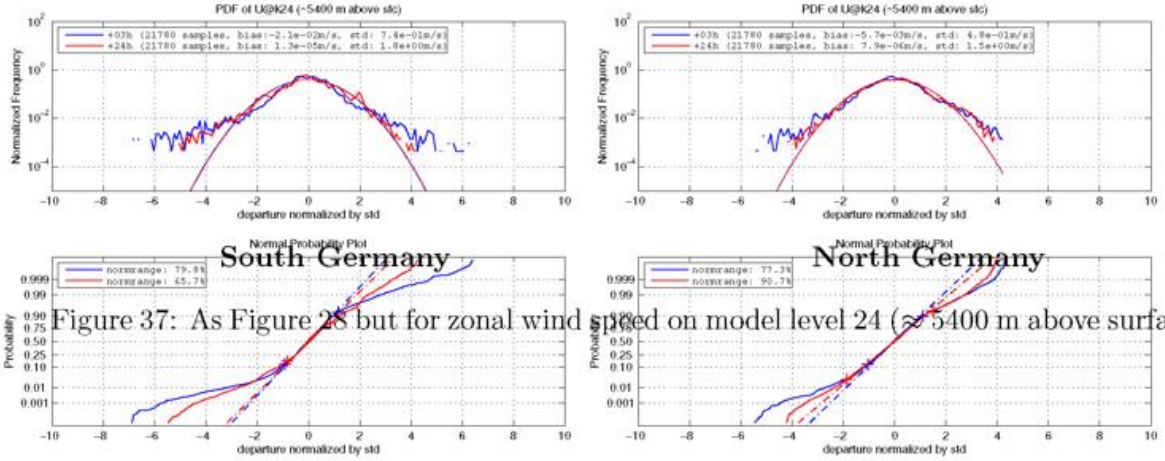


Figure 37: As Figure 28 but for zonal wind speed on model level 24 (≈ 5400 m above surface).

5 Further Results

In this section we list further results from forecast departure distributions of the COSMO-DE, which are not shown in Section 3.

5.1 Temperature from radiosondes

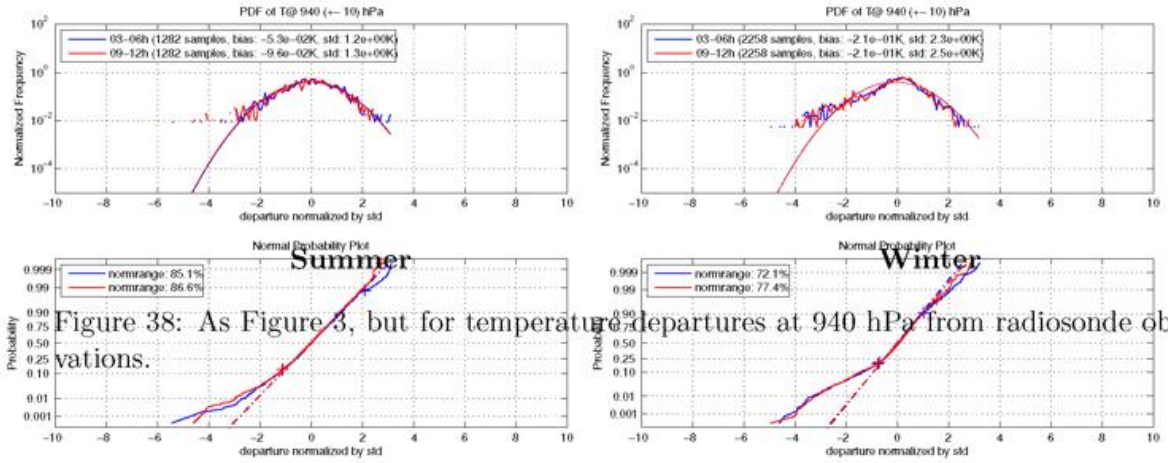


Figure 38: As Figure 3, but for temperature departures at 940 hPa from radiosonde observations.

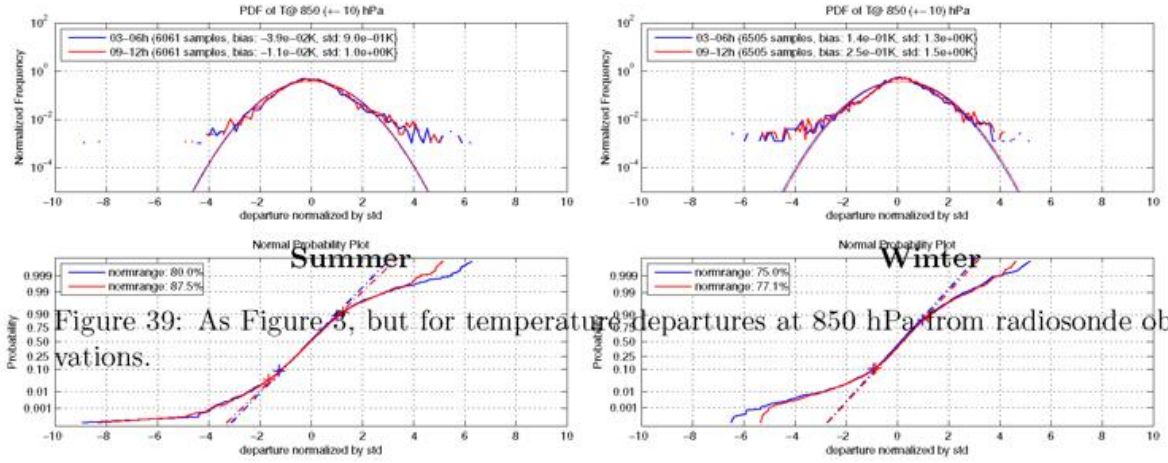


Figure 39: As Figure 3, but for temperature departures at 850 hPa from radiosonde observations.

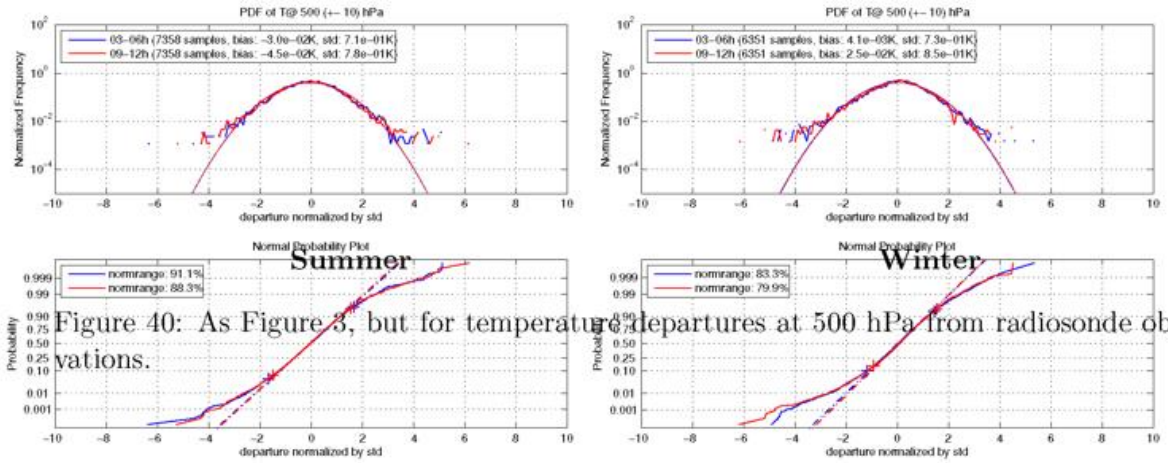


Figure 40: As Figure 3, but for temperature departures at 500 hPa from radiosonde observations.

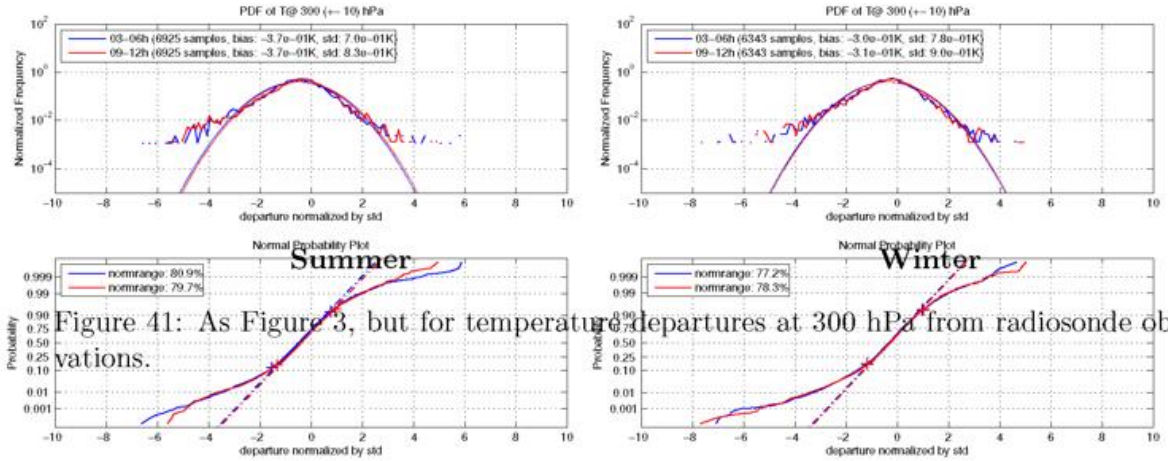


Figure 41: As Figure 3, but for temperature departures at 300 hPa from radiosonde observations.

5.2 Zonal wind from radiosondes and windprofiler

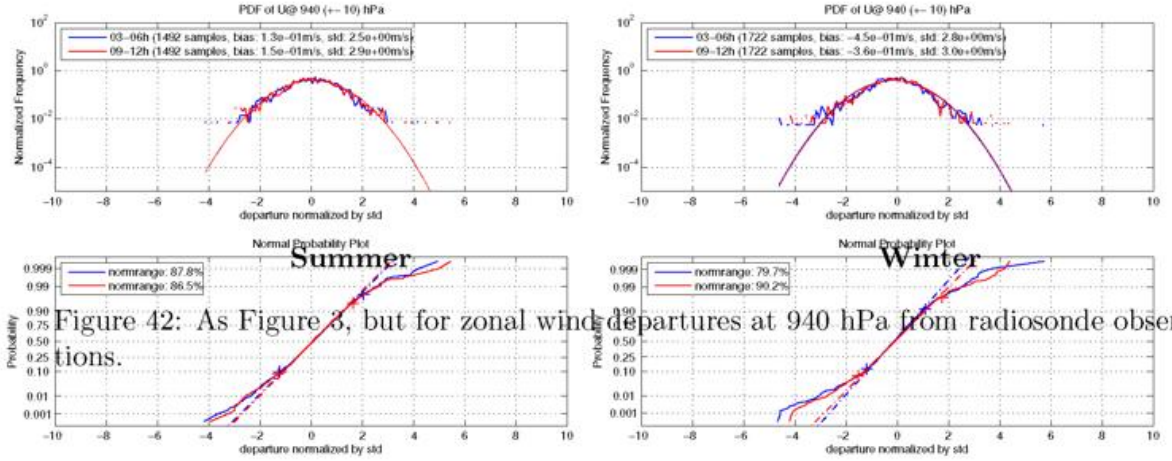


Figure 42: As Figure 3, but for zonal wind departures at 940 hPa from radiosonde observations.

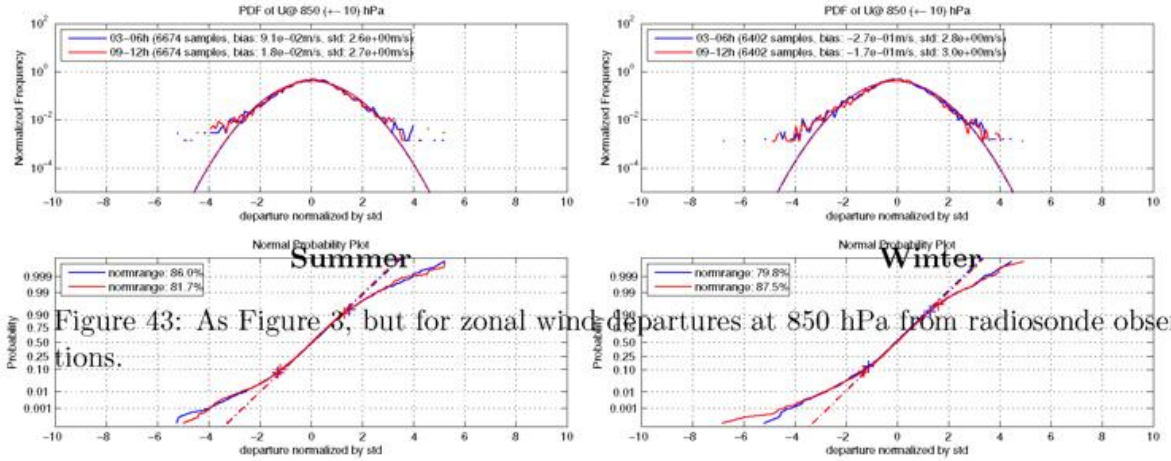


Figure 43: As Figure 3, but for zonal wind departures at 850 hPa from radiosonde observations.

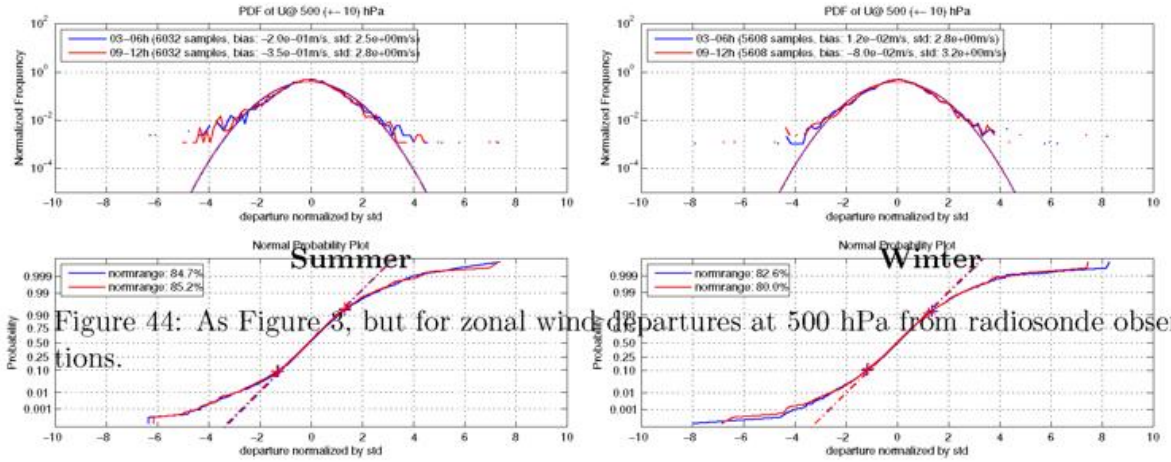


Figure 44: As Figure 3, but for zonal wind departures at 500 hPa from radiosonde observations.

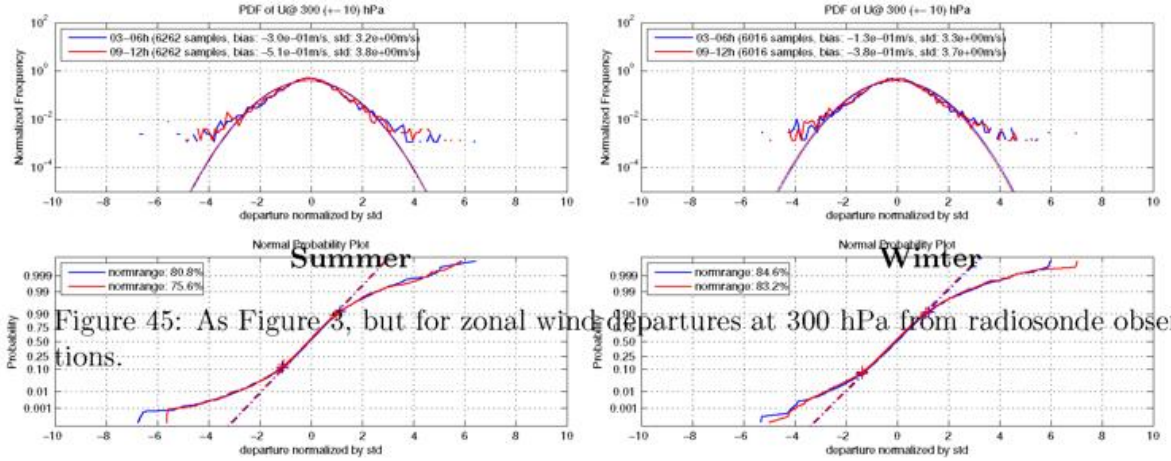


Figure 45: As Figure 3, but for zonal wind departures at 300 hPa from radiosonde observations.

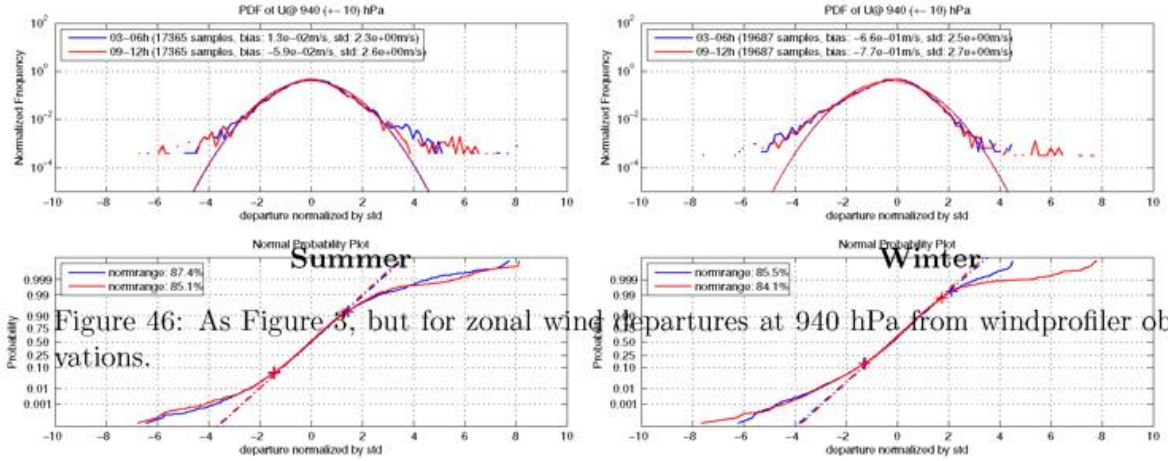


Figure 46: As Figure 3, but for zonal wind departures at 940 hPa from windprofiler observations.

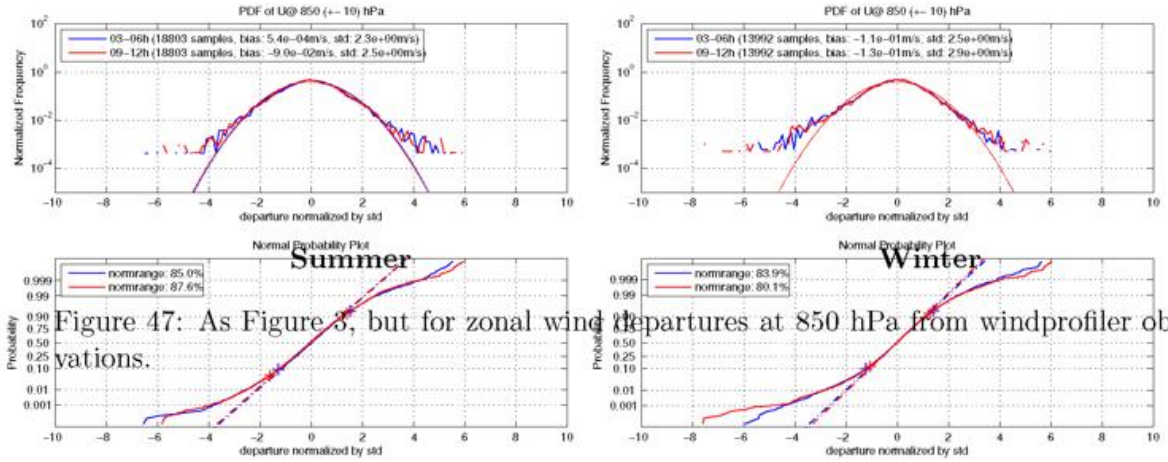


Figure 47: As Figure 3, but for zonal wind departures at 850 hPa from windprofiler observations.

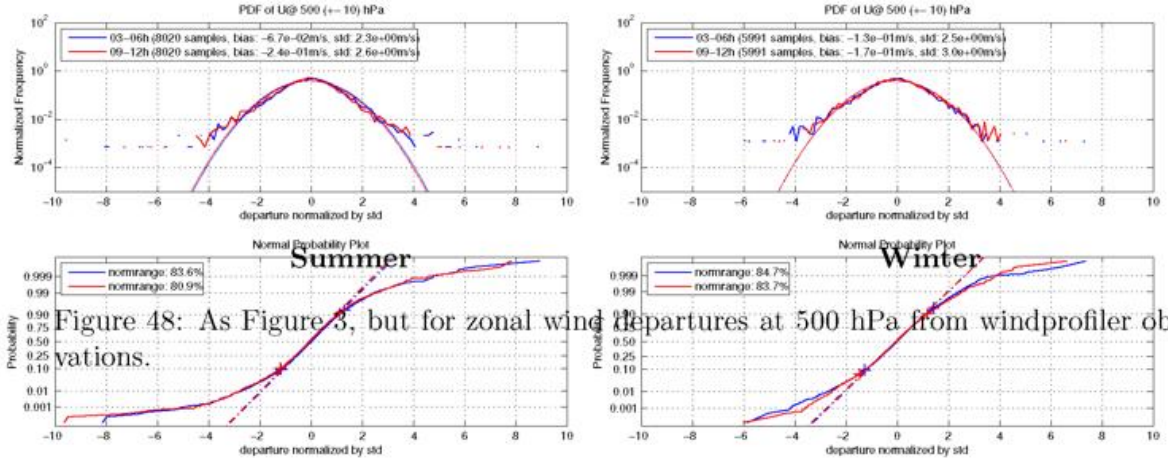


Figure 48: As Figure 3, but for zonal wind departures at 500 hPa from windprofiler observations.

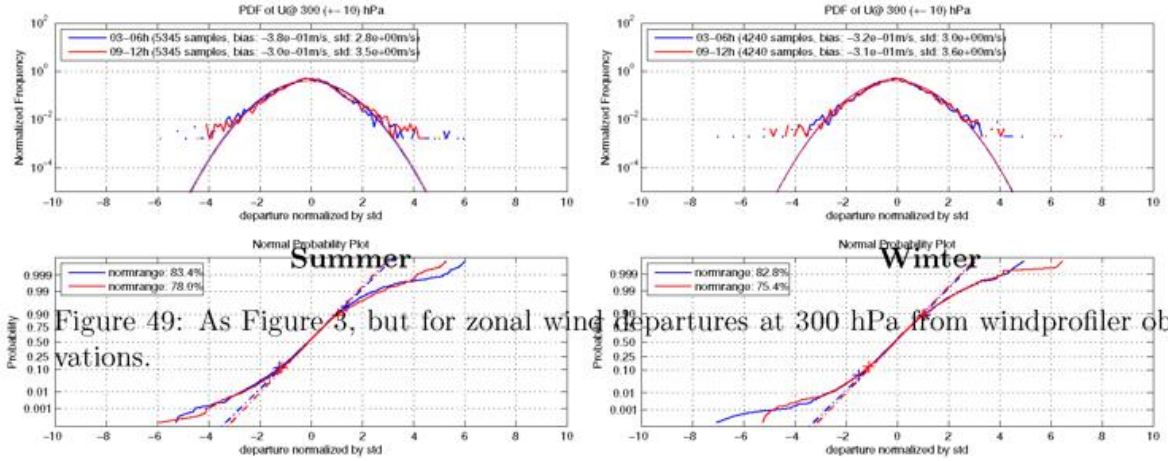


Figure 49: As Figure 3, but for zonal wind departures at 300 hPa from windprofiler observations.

5.3 Meridional wind from aircrafts, radiosondes and windprofiler

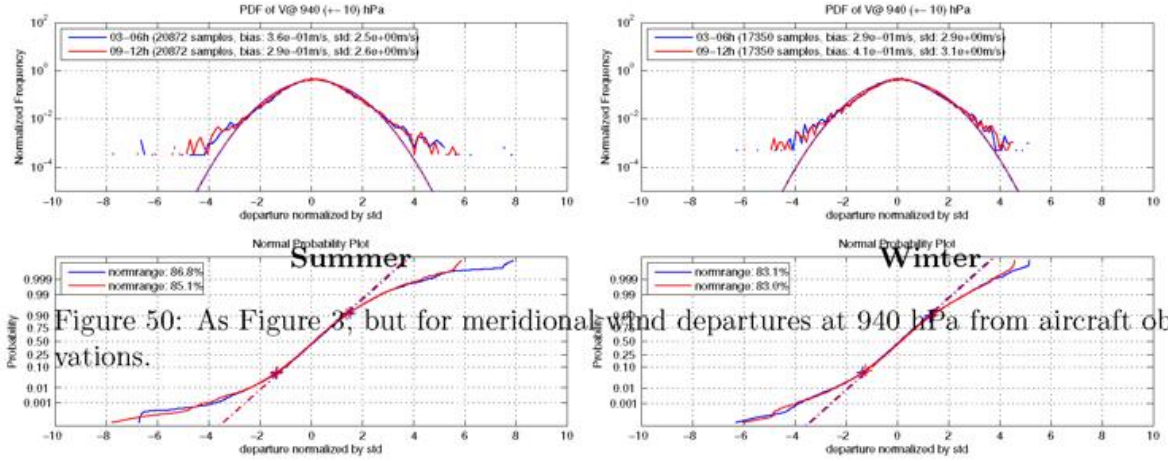


Figure 50: As Figure 3, but for meridional wind departures at 940 hPa from aircraft observations.

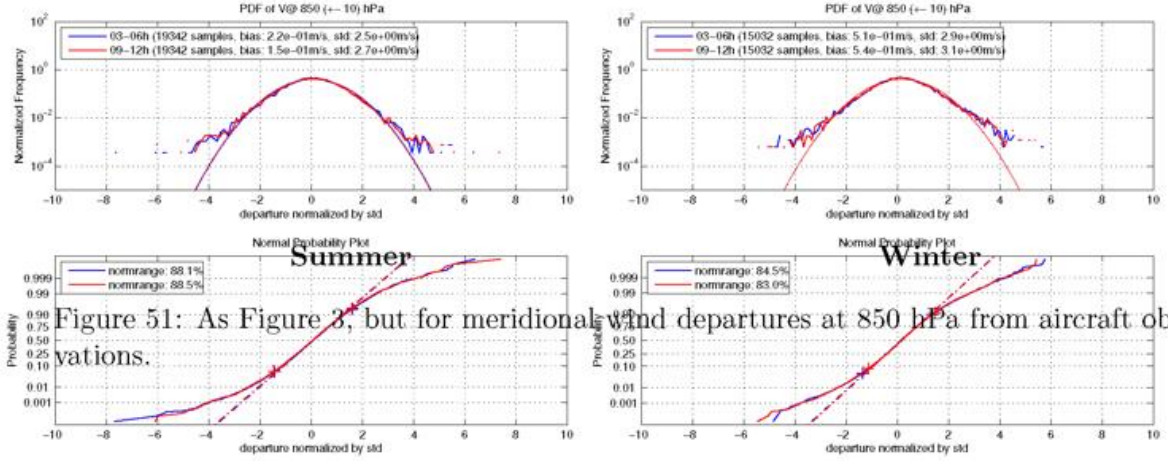


Figure 51: As Figure 3, but for meridional wind departures at 850 hPa from aircraft observations.

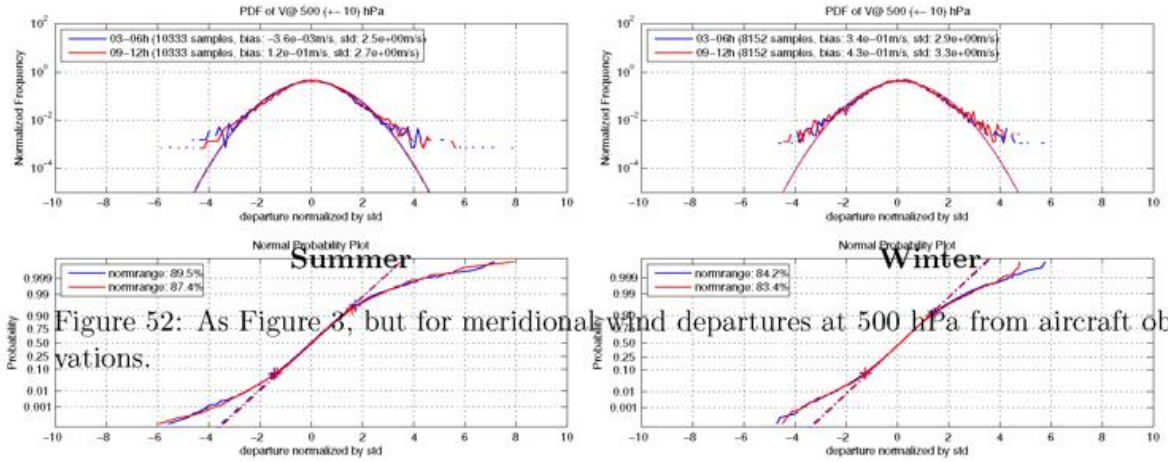


Figure 52: As Figure 3, but for meridional wind departures at 500 hPa from aircraft observations.

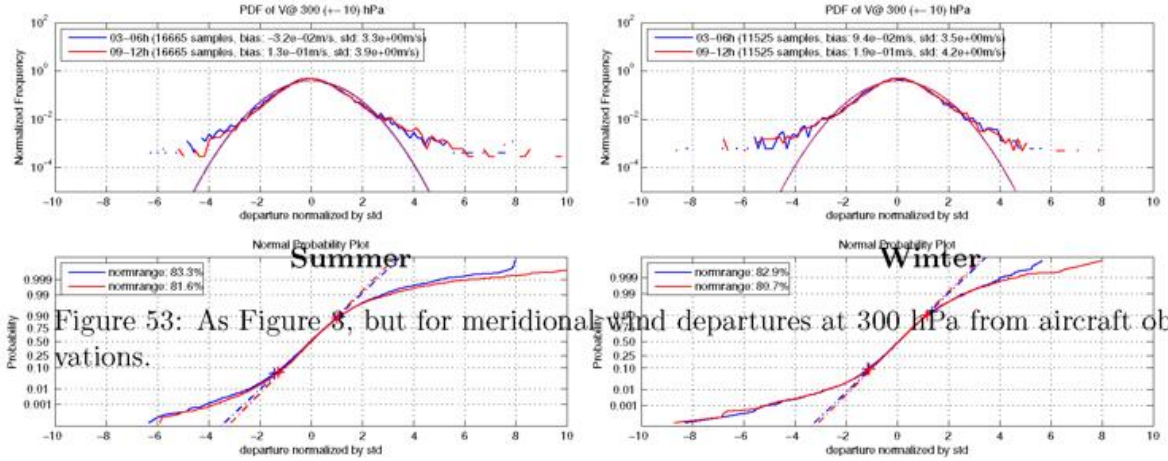


Figure 53: As Figure 3, but for meridional wind departures at 300 hPa from aircraft observations.

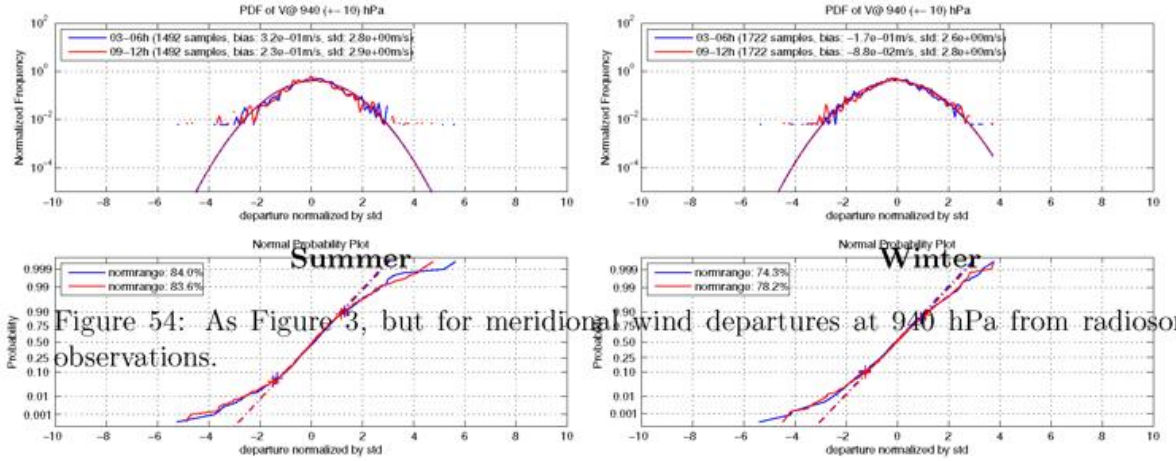


Figure 54: As Figure 3, but for meridional wind departures at 940 hPa from radiosonde observations.

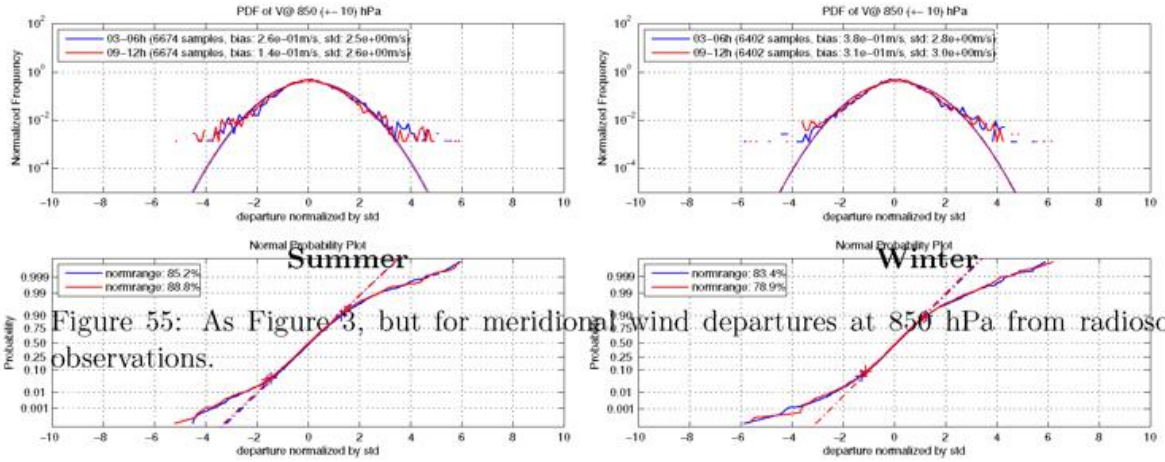


Figure 55: As Figure 3, but for meridional wind departures at 850 hPa from radiosonde observations.

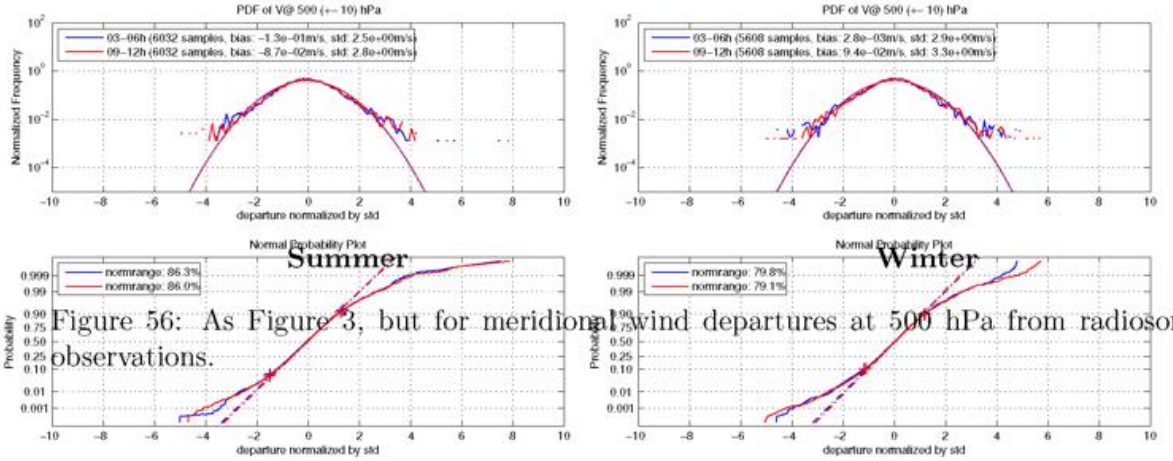


Figure 56: As Figure 3, but for meridional wind departures at 500 hPa from radiosonde observations.

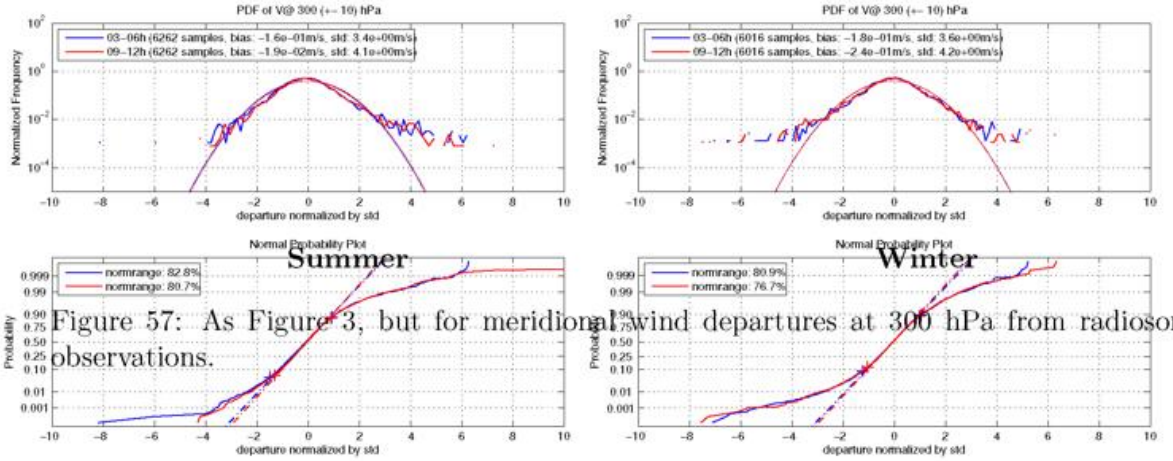


Figure 57: As Figure 3, but for meridional wind departures at 300 hPa from radiosonde observations.

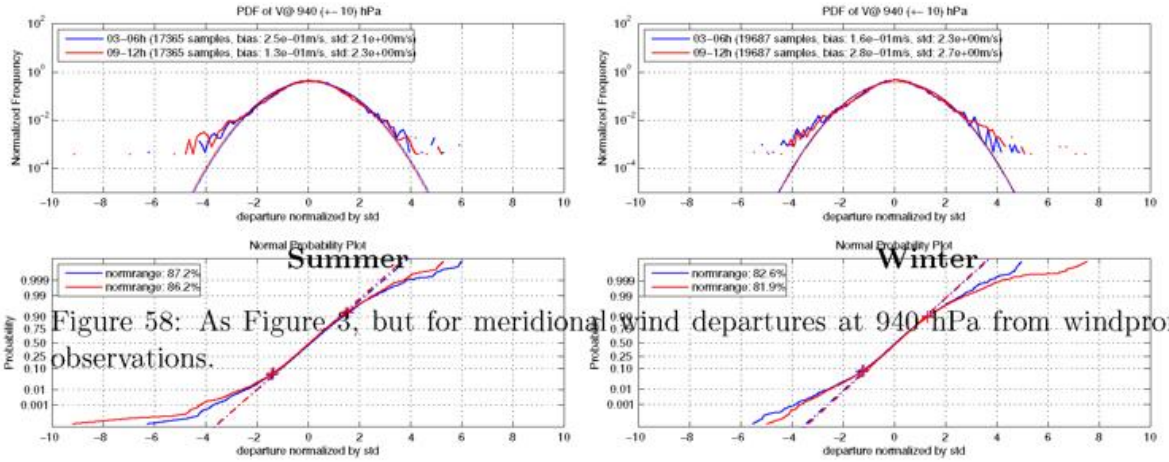


Figure 58: As Figure 3, but for meridional wind departures at 940 hPa from windprofiler observations.

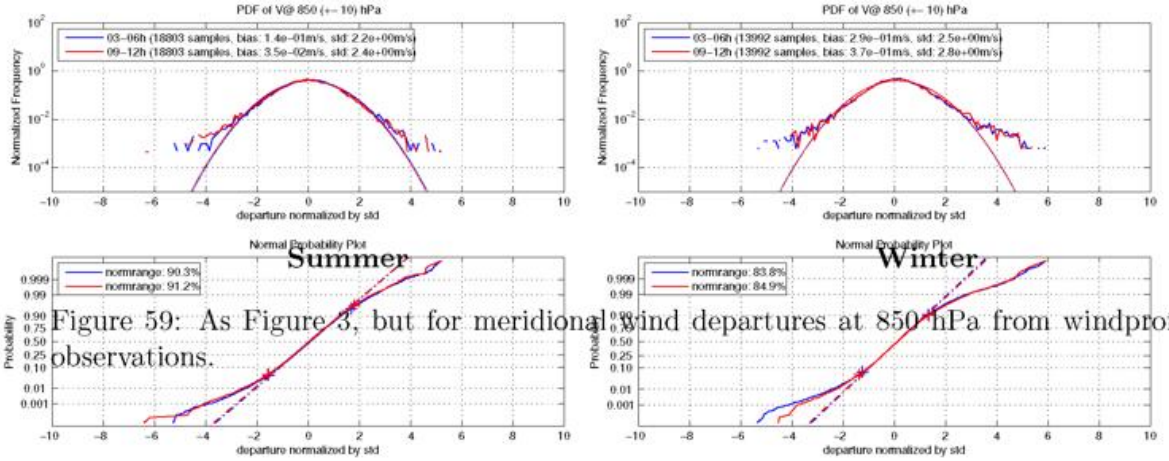


Figure 59: As Figure 3, but for meridional wind departures at 850 hPa from windprofiler observations.

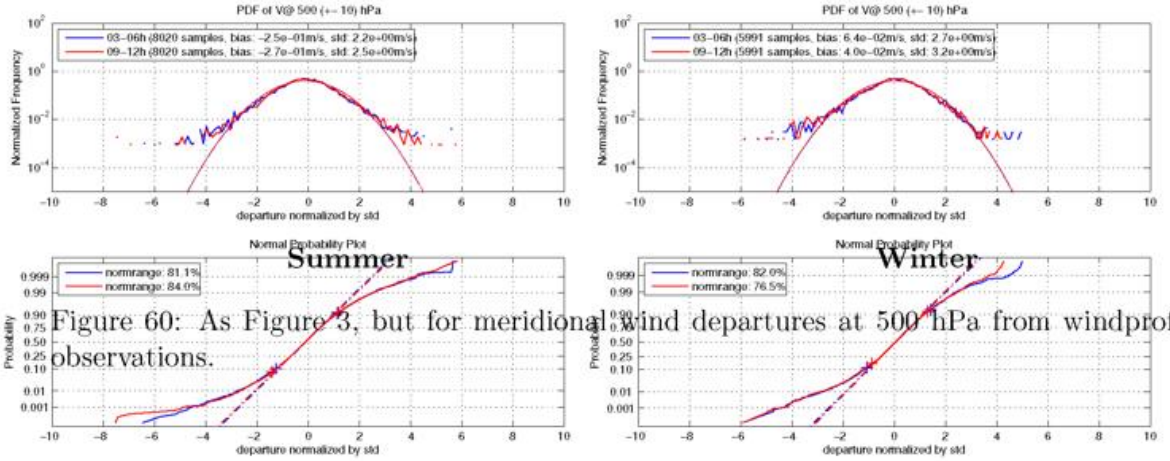


Figure 60: As Figure 3, but for meridional wind departures at 500 hPa from windprofiler observations.

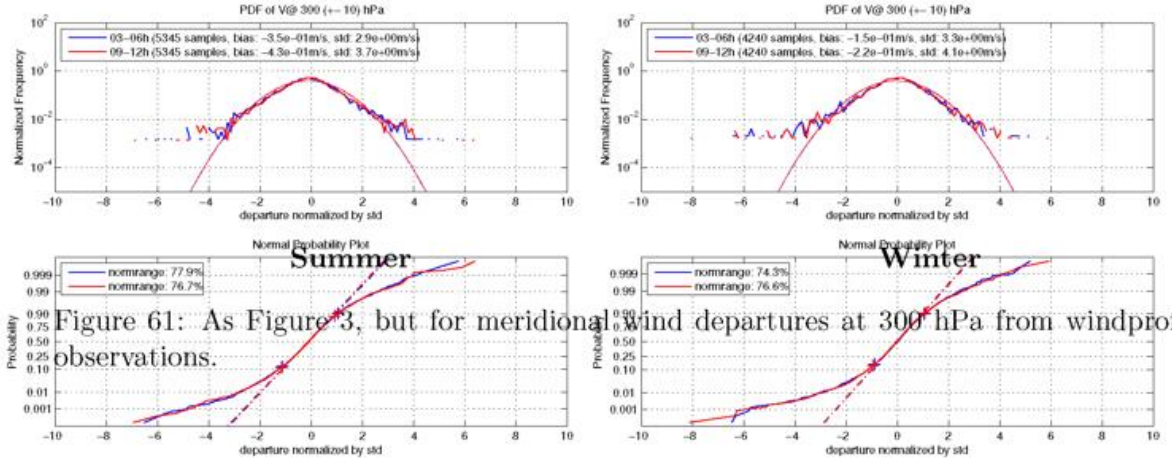


Figure 61: As Figure 3, but for meridional wind departures at 300 hPa from windprofiler observations.

6 Summary and conclusions

In this study we have investigated forecast departure distributions and ensemble background anomalies from the convection permitting COSMO model in view of the new ensemble data assimilation system for COSMO, being currently developed. Emphasis was put on how close the distributions are to the normal distribution.

Overall, the departures of most of the investigated variables show a reasonable Gaussian behaviour around the median, but exhibit more larger departures (both negative and positive) than described by a normal distribution. This behaviour (known as "fat tails") is well known in NWP data assimilation (e.g. Andersson and Järvinen, 1999; Seaman, 2008) and can be interpreted as follows: the departures belong to either of two populations, one which follows the normal Gaussian distribution, representing random errors and one which is modelled by a flat distribution, representing the population of data affected by gross errors (Andersson and Järvinen, 1999)

The main results of the study are summarized and discussed in the two following paragraphs for the forecast departures and the ensemble background anomalies, respectively.

Forecast departures

- The forecast departures of temperature, surface pressure and wind can be reasonably approximated by normal distributions. Normranges are mostly above 80%. Results among different observation systems (radiosondes, aircraft observations and windprofiler) are very similar.
- Humidity departures show a rather exponential than Gaussian distribution, relative humidity departures are more Gaussian than specific humidity departures. Normalized relative humidity departures have a much reduced bias and standard deviation and their distributions are much less dependent on the humidity itself, as compared to relative humidity.
- Surface rainfall departure distributions show a rather exponential than Gaussian shape. Departures of the logarithm of rainfall can be much better approximated by normal distributions.
- Generally, distributions are less Gaussian near the surface and in the boundary layer than in the middle and upper atmosphere.
- There is a generally slightly better Gaussian fit in summer than in winter.
- Large deviations from the Gaussian shape are found in winterly boundary layer relative humidity as a result of many near-saturated situations (stratus).
- The distributions only slightly change during the first 12 hours of forecast with the exception of surface pressure, where an increase in the bias and standard deviation is already obvious.
- The results from the convection permitting COSMO-DE model are similar to those of the regional COSMO-EU model.

One reason for the good Gaussian fit of most of the variables may be found in the fact, that the departure distributions rely on a large statistics covering all sorts of weather conditions.

A sensitivity study considering only rainy days indeed indicated that the distributions are slightly less Gaussian. However, the main findings of this study are still valid for this subsample of days.

Overall, temperature, wind and surface pressure forecast departures distributions from the convection permitting COSMO model are reasonably Gaussian out to 12 hours forecast, both in summer and winter. Humidity and rainfall are less Gaussian, but using appropriate transformations, derived humidity and rainfall variables can be found with more Gaussian distributions (e.g. normalized relative humidity and logarithm of rainfall).

Ensemble background anomalies

- At short lead times (+3h) the ensemble background anomaly distributions can deviate significantly from normality. Especially low-level temperature has been found to have multiple modes.
- Precipitation shows the similar exponential distribution as the forecast departures.
- At longer lead times (+24h) the anomaly distributions are close to normality for both, temperature and wind.
- Upper-level variables are more Gaussian than their low-level counterparts.
- The shape of the distributions are dependent on the domain under consideration. Distributions over flat terrain have been found to be closer to normality than those over more complex terrain.

The large deviations from normality at short lead times are largely due to the way the current COSMO-DE-EPS is designed. Starting from identical initial conditions (zero anomalies at the start of the forecast) the growth of the anomalies with time is first dominated by the physical parametrisation perturbations, at later times the different boundary conditions and the internal model errors start to dominate the anomaly growth. Some of the model switches systematically influence certain ensemble members, leading to a non-normal anomaly distribution at short lead times in some variables and some regions of the model domain. Therefore, in the light of an ensemble assimilation, care should be taken in the design of the physical model perturbations. The use of boundary conditions from different global models is judged as a suitable method to perturb the boundaries of the COSMO-DE-EPS in view of data assimilation, since at longer lead times, the anomaly distributions appear to be close to normality.

The error distributions found in this study closely resemble those found by Bonavita et al. (2010) using the LETKF in a regional NWP system. In particular, their distributions showed similar "fat tails" as those of the COSMO model. This slight deviation from Normality did not seem to strongly affect the performance of their application. However, as pointed out by the authors, their results did not reflect situations with strong non-linearities, such as convection. It remains to be proven that the LETKF also works in strongly convective situations. Recently, Yang and Kalnay (2009) and Kalnay and Yang (2009) proposed ways to deal with non-linearity and non-Gaussianity using the LETKF. Although they are computationally more expensive that the standard LETKF they proved to reduce the spin-up of the LETKF in highly non-linear applications and improve the Gaussianity of the errors.

Overall, the results of this study suggest that, ensemble data assimilation systems relying on the BLUE theory may well be feasible for the use with the high-resolution COSMO

model, given that more suitable (i.e. more random) physics parametrisation perturbations are applied.

References

Andersson, E., and H. Järvinen, 1999: Variational Quality Control,. *Quart. J. Roy. Meteor. Soc.*, **125**, 697–722.

Bonavita, M., L. Torrisi, and F. Marcucci, 2010: Ensemble Data Assimilation with the CNMCA Regional Forecasting System. *Quart. J. Roy. Meteor. Soc.*, accepted.

Holm, E., E. Andresson, A. Beljaars, P. Lopez, J.-F. Mahfouf, A. Simmons, and J.-N. Thépaut, 2002: Assimilation and Modelling of the Hydrological Cycle: ECMWF's Status and Plans. [ECMWF Technical Memorandum No. 383].

Hunt, B., E. Kostelich, and I. Szunyogh, 2007: Efficient data assimilation for spatiotemporal chaos: A local ensemble transform Kalman Filter. *Physica D*, **230**, 112–126.

Kalnay, E., and S.-C. Yang, 2009: Accelerating the spin-up of Ensemble Kalman Filtering. *Quart. J. Roy. Meteor. Soc.*, submitted.

Lawson, W., and J. Hansen, 2004: Implicatios of stochastic and deterministic filters as ensemble-based data assimilation methods in varying regimes of error growth. *Mon. Wea. Rev.*, **132**, 1966–1981.

Leeuwenburgh, O., G. Evensen, and L. Bertino, 2005: The impact of ensemble filter definition on the assimilation of temperature profiles in the tropical Pacific. *Quart. J. Roy. Meteor. Soc.*, **131**, 3291–3300.

Mitchell, H., and P. Houtekamer, 2009: Ensemble Kalman filter configurations and performance with the logistic map. *Mon. Wea. Rev.*, accepted.

Sakov, P., and P. Oke, 2008: Implications of the form of the ensemble transformation in the ensemble square root filter. *Mon. Wea. Rev.*, **136**, 1042–1053.

Seaman, R., 2008: The probability distribution of obeserved minus expected sea-level pressure; a quality control perspective. *Aust. Met. Mag.*, **57**, 37–43.

Yang, S.-C., and E. Kalnay, 2009: Handling Nonlinearity and Non-Gaussianity in Ensemble Kalman Filter, submitted.

List of COSMO Newsletters and Technical Reports

(available for download from the COSMO Website: www.cosmo-model.org)

COSMO Newsletters

No. 1: February 2001.

No. 2: February 2002.

No. 3: February 2003.

No. 4: February 2004.

No. 5: April 2005.

No. 6: July 2006.

No. 7: April 2008; Proceedings from the 8th COSMO General Meeting in Bucharest, 2006.

No. 8: September 2008; Proceedings from the 9th COSMO General Meeting in Athens, 2007.

No. 9: December 2008

No. 10: March 2010.

COSMO Technical Reports

No. 1: Dmitrii Mironov and Matthias Raschendorfer (2001):
Evaluation of Empirical Parameters of the New LM Surface-Layer Parameterization Scheme. Results from Numerical Experiments Including the Soil Moisture Analysis.

No. 2: Reinhold Schrodin and Erdmann Heise (2001):
The Multi-Layer Version of the DWD Soil Model TERRA_LM.

No. 3: Günther Doms (2001):
A Scheme for Monotonic Numerical Diffusion in the LM.

No. 4: Hans-Joachim Herzog, Ursula Schubert, Gerd Vogel, Adelheid Fiedler and Roswitha Kirchner (2002):
LLM ¯ the High-Resolving Nonhydrostatic Simulation Model in the DWD-Project LITFASS.
Part I: Modelling Technique and Simulation Method.

No. 5: Jean-Marie Bettems (2002):
EUCOS Impact Study Using the Limited-Area Non-Hydrostatic NWP Model in Operational Use at MeteoSwiss.

No. 6: Heinz-Werner Bitzer and Jürgen Steppeler (2004):
Documentation of the Z-Coordinate Dynamical Core of LM.

No. 7: Hans-Joachim Herzog, Almut Gassmann (2005):
Lorenz- and Charney-Phillips vertical grid experimentation using a compressible nonhydrostatic toy-model relevant to the fast-mode part of the 'Lokal-Modell'.

No. 8: Chiara Marsigli, Andrea Montani, Tiziana Paccagnella, Davide Sacchetti, André Walser, Marco Arpagaus, Thomas Schumann (2005):
Evaluation of the Performance of the COSMO-LEPS System.

No. 9: Erdmann Heise, Bodo Ritter, Reinhold Schrodin (2006):
Operational Implementation of the Multilayer Soil Model.

No. 10: M.D. Tsyrulnikov (2007):
Is the particle filtering approach appropriate for meso-scale data assimilation ?

No. 11: Dmitrii V. Mironov (2008):
Parameterization of Lakes in Numerical Weather Prediction. Description of a Lake Model.

No. 12: Adriano Raspanti (2009):
COSMO Priority Project "VERification System Unified Survey" (VERSUS): Final Report.

No. 13: Chiara Marsigli (2009):
COSMO Priority Project "Short Range Ensemble Prediction System" (SREPS): Final Report.

No. 14: Michael Baldauf (2009):
COSMO Priority Project "Further Developments of the Runge-Kutta Time Integration Scheme" (RK): Final Report.

No. 15: Silke Dierer (2009):
COSMO Priority Project "Tackle deficiencies in quantitative precipitation forecast" (QPF): Final Report.

No. 16: Pierre Eckert (2009):
COSMO Priority Project "INTERP": Final Report.

No. 17: D. Leuenberger, M. Stoll and A. Roches (2010):
Description of some convective indices implemented in the COSMO model.

No. 18: Daniel Leuenberger (2010):
Statistical analysis of high-resolution COSMO Ensemble forecasts in view of Data Assimilation.

COSMO Technical Reports

Issues of the COSMO Technical Reports series are published by the *COnsortium for Small-scale MOdelling* at non-regular intervals. COSMO is a European group for numerical weather prediction with participating meteorological services from Germany (DWD, AWGeophys), Greece (HNMS), Italy (USAM, ARPA-SIMC, ARPA Piemonte), Switzerland (MeteoSwiss), Poland (IMGW) and Romania (NMA). The general goal is to develop, improve and maintain a non-hydrostatic limited area modelling system to be used for both operational and research applications by the members of COSMO. This system is initially based on the COSMO-Model (previously known as LM) of DWD with its corresponding data assimilation system.

The Technical Reports are intended

- for scientific contributions and a documentation of research activities,
- to present and discuss results obtained from the model system,
- to present and discuss verification results and interpretation methods,
- for a documentation of technical changes to the model system,
- to give an overview of new components of the model system.

The purpose of these reports is to communicate results, changes and progress related to the LM model system relatively fast within the COSMO consortium, and also to inform other NWP groups on our current research activities. In this way the discussion on a specific topic can be stimulated at an early stage. In order to publish a report very soon after the completion of the manuscript, we have decided to omit a thorough reviewing procedure and only a rough check is done by the editors and a third reviewer. We apologize for typographical and other errors or inconsistencies which may still be present.

At present, the Technical Reports are available for download from the COSMO web site (www.cosmo-model.org). If required, the member meteorological centres can produce hard-copies by their own for distribution within their service. All members of the consortium will be informed about new issues by email.

For any comments and questions, please contact the editors:

Massimo Milelli
Massimo.Milelli@arpa.piemonte.it

Ulrich Schättler
Ulrich.Schaettler@dwd.de

Consortium

for

Small-Scale Modelling

Technical Report No. 39

Studying Perturbations for the Representation of modeling uncertainties in Ensemble Development (SPRED Final Report)

May 2019

DOI: 10.5676/DWD_pub/nwv/cosmo-tr_39

Deutscher Wetterdienst
MeteoSwiss
Ufficio Generale Spazio Aereo e Meteorologia
ΕΘΝΙΚΗ ΜΕΤΕΩΡΟΛΟΓΙΚΗ ΥΠΗΡΕΣΙΑ
Instytucie Meteorogii i Gospodarki Wodnej
Administratia Nationala de Meteorologie
ROSHYDROMET
Agenzia Regionale Protezione Ambiente Piemonte
Agenzia Regionale Prevenzione Ambiente Energia Emilia Romagna
Centro Italiano Ricerche Aerospaziali
Amt für GeoInformationswesen der Bundeswehr
Israel Meteorological Service

www.cosmo-model.org

Editor: Massimo Milelli, ARPA Piemonte

Studying Perturbations for the Representation of modeling uncertainties in Ensemble Development (SPRED Final Report)

Project participants:

***C. Marsigli*[1] ‡, *D. Alferov*[2], *E. Astakhova*[2],**

***G. Duniec*[3], *D. Gayfulin*[2], *C. Gebhardt*[1],**

***W. Interewicz*[3], *N. Loglisci*[4], *F. Marcucci*[5],**

***A. Mazur*[3], *A. Montani*[6], *M. Tsyrulnikov*[2], *A. Walser*[7].**

‡ Project Leader

[1] DWD

[2] Roshydromet

[3] IMGW

[4] ArpaP

[5] ItAF-ReMet

[6] ArpaE

[7] MCH

Contents

1 Introduction **3**

2 What we know (and what we do not know) about the spread/skill relation of our ensembles. **3**

2.1 DWD contribution 3

2.2 MeteoSwiss contribution 5

2.3 Arpae contribution 6

2.3.1 Convection-parametrised ensemble (COSMO-LEPS) 6

2.3.2 Convection-permitting ensemble (COSMO-2I-EPS) 8

2.4 IMGW contribution 11

2.5 RHM contribution 17

2.6 Remarks from the discussion of the results 21

3 Test and development of model perturbation **21**

3.1 EM-scheme and Parameter Perturbation at DWD 21

3.2 SPPT and BLPERT schemes at MeteoSwiss 21

3.3 Stochastic pattern Generator for model perturbation at RHM 22

4 Test and development of perturbation for the model lower boundary **27**

4.1 Soil moisture perturbation in a complete ensemble set-up (ARPA Piemonte) . 27

4.2 Soil parameters and soil temperature perturbation (IMGW) 28

5 Ensemble post-processing **32**

5.1 Development of probabilistic products at COMET 32

5.2 Calibration of ensemble output at IMGW 34

6 Initial Conditions for the CP ensembles **40**

6.1 Test of Initial Conditions from KENDA (DWD) 41

6.2 Test of Initial Conditions from KENDA (Arpae) 41

6.3 Clustering of ensemble members for Lateral Boundary Conditions at MeteoSwiss 45

1 Introduction

This document reports about the activities carried out in the SPRED Priority Project. The Project lasted from September 2015 to February 2018. The project was organized in 5 Tasks, with cross-cutting issues. The report reflects the structure of the Project, consisting of 5 sections. In Section 2, the work aimed at investigating the spread/skill relation of the ensembles run by the COSMO members is described. In Section 3, work on model physics perturbation is shown, while Section 4 deals with lower boundary perturbation. In Section 5, the activities carried out in the post-processing and calibration of the ensemble outputs are presented, also included in the SRNWP-EPS II Project of EUMETNET. Finally, in Section 6 is described the work on initial condition for the convection-permitting ensembles. Each Section is structured in subsections describing the contribution of the different COSMO members.

2 What we know (and what we do not know) about the spread/skill relation of our ensembles.

The spread/skill relation computed for the different COSMO ensembles highlights a common deficiency: the underdispersiveness of the ensembles for the surface weather parameters. Therefore it was decided to analyse this relation in greater detail, trying to provide indications about how to cure the problem. The general aim of this coordinated activity was to understand which factors determine the lack of spread for near-surface weather parameters and to propose solutions in terms of which elements of the modeling system should be perturbed to account for this uncertainty.

2.1 DWD contribution

During the PP, DWD was running operationally COSMO-DE-EPS, a 20 member ensemble based on the COSMO model run at 2.8 km horizontal resolution. At the beginning of PP SPRED, both the boundary and initial conditions of COSMO-DE-EPS were based on forecasts of four global models (ICON of DWD, IFS of ECMWF, GFS of NCEP, GSM of JMA) dynamically downscaled with a COSMO model to 7 km grid spacing. These four COSMO runs (called BC-EPS) were used as boundary conditions for COSMO-DE-EPS and contributed to the perturbation of the initial conditions. The deterministic operational analysis of COSMO-DE was perturbed with anomaly fields of BC-EPS runs with respect to 3h-forecasts of the operational COSMO-EU (ICON-EU since July 2016) resulting in the IC perturbations. For perturbation of model physics, a non-stochastic approach with perturbed parameters was used. Different model configurations were defined by setting one of 5 (later 7) parameters to non-default values. This set of perturbed parameters did not change during the forecast lead time and was identical for all forecast runs, i.e. each member of COSMO-DE-EPS was characterized by a specific parameter set-up being identical for all forecasts. More details (including the soil moisture perturbations) of the member generation of COSMO-DE-EPS at the beginning of PP SPRED are described in Peralta et al. (2012). During the SPRED PP, several improvements were applied to the member generation. In November 2016, the parameter perturbation method was enhanced by including additional parameters: thick_sc, radqi_fact, radqc_fact, a_stab, and c_diff. These new perturbations focus on the improvement of EPS forecasts for variables being relevant for renewable energy applications (wind at wind hub height, global radiation connected to cloud forecasts) and resulted in

a positive impact on the wind forecast. Furthermore, a randomization of the parameter selection methodically allowed for the inclusion of more parameters and lead to a slight increase in spread. Further improvements of the parameter perturbations during SPRED imposed that the value of rlam_heat x rat_sea is kept fixed in the parameter perturbation, otherwise a detrimental effect in 2m temperature was observed (too high spread over sea). In March 2017, the use of BC-EPS has been ceased in favour of IC perturbations based on KENDA (see Section 6.1) and boundary conditions provided by forecasts of the ICON-EPS calculated on the nested grid over Europe with approx. 20 km grid spacing. The use of Initial Conditions derived from KENDA analyses increases the spread of the ensemble, thereby improving the skill of relevant variables, keeping it constant. Results are briefly described in Section 6. The use of ICON-EPS mainly improved the spread of several parameters in particular for later lead times. A summary evaluation of the spread/skill relation for COSMO-DE-EPS in different configurations is shown in Fig. 1.

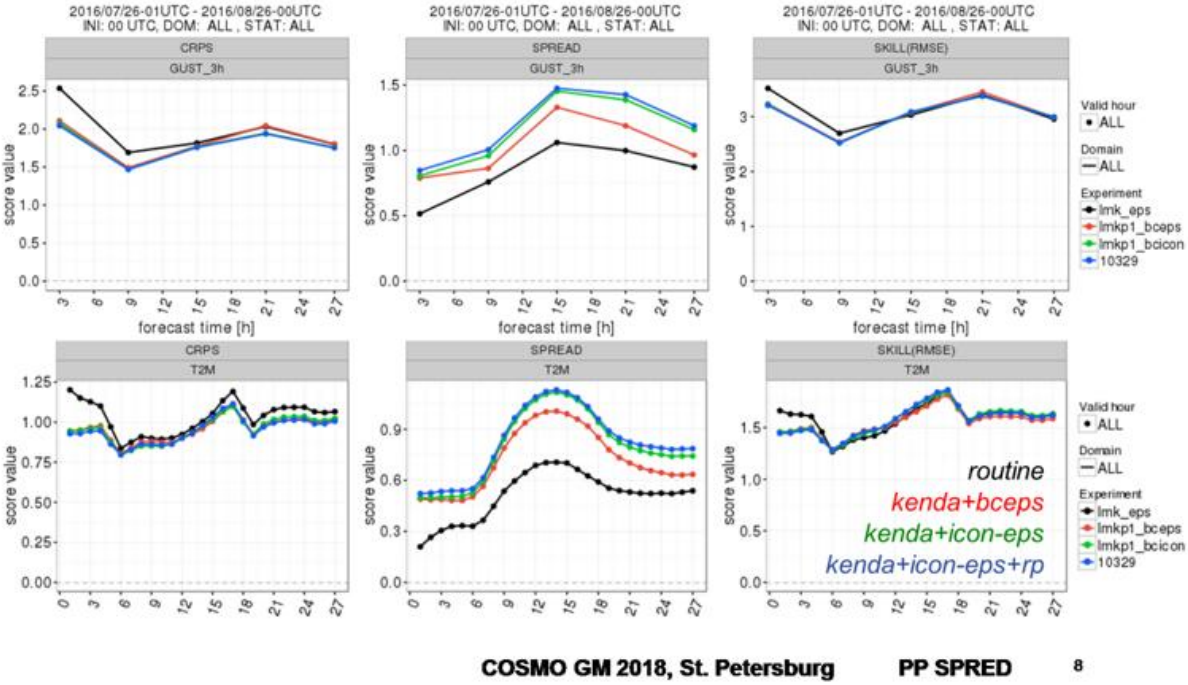


Figure 1: CRPS (left), spread (middle) and RMSE (right) of 4 different configurations of COSMO-DE-EPS, as a function of the forecast lead time, in terms of wind gusts (upper row) and 2m temperature (lower row). Black line: operational set-up before modifications; red line: use of KENDA for initial conditions, but BC-EPS for boundary conditions; green line: use of KENDA and ICON-EPS; blue line: use of KENDA, ICON-EPS and randomized physics perturbations.

The scheme for model error developed by Ekaterina Machulskaya (EM-scheme) has been tested (see presentation by Gebhardt et al. at WG7 parallel session during COSMO GM 2017, Jerusalem). It was found a bug in the code, the correction of this which led to a much smaller response of the model to perturbations as it should be. The point was that the diffusion of the model error, that is intended to represent spatial correlations, effectively (and artificially) decreases the noise level, the parameters of which are determined on the theoretical basis as if there were no spatial diffusion. This means that the effective parameters of the perturbations in the presence of the diffusion should differ from those that were determined according to the theory. The expressions for the effective values of the parameters were derived and

preliminary experiments (for selected days) were performed quite successfully.

2.2 MeteoSwiss contribution

MeteoSwiss was running operationally COSMO-E, a 21 member ensemble based on the COSMO model with 2.2 km grid-spacing. It was performed twice a day (00 and 12 UTC) and for a lead-time of 120 hours. Initial conditions are taken from a kilometer-scale ensemble data assimilation (KENDA) cycle running at the same resolution. Boundary conditions are taken from IFS-ENS control and the 20 first perturbed members. Model physics is perturbed with the SPPT scheme (Buizza et al., 1999; Palmer et al., 2009). COSMO-E is generally underdispersive in the lower troposphere, even though SPPT is effective in increasing the spread, except in winter when the physical tendencies are small. As shown in Fig. 2 taken from Klasa et al. (2018), the lack of spread is largest in winter, in particular for 2m temperature and 2m relative humidity (RH2m). In summer the ensemble is rather well dispersed or even overdispersive for RH2m when considering observation errors according to Saetra et al. (2004) with observation error estimates from Bouttier et al. (2016). Furthermore, as compared to ECMWF ENS, COSMO-E shows a better spread/error ratio, in particular for convective cases.

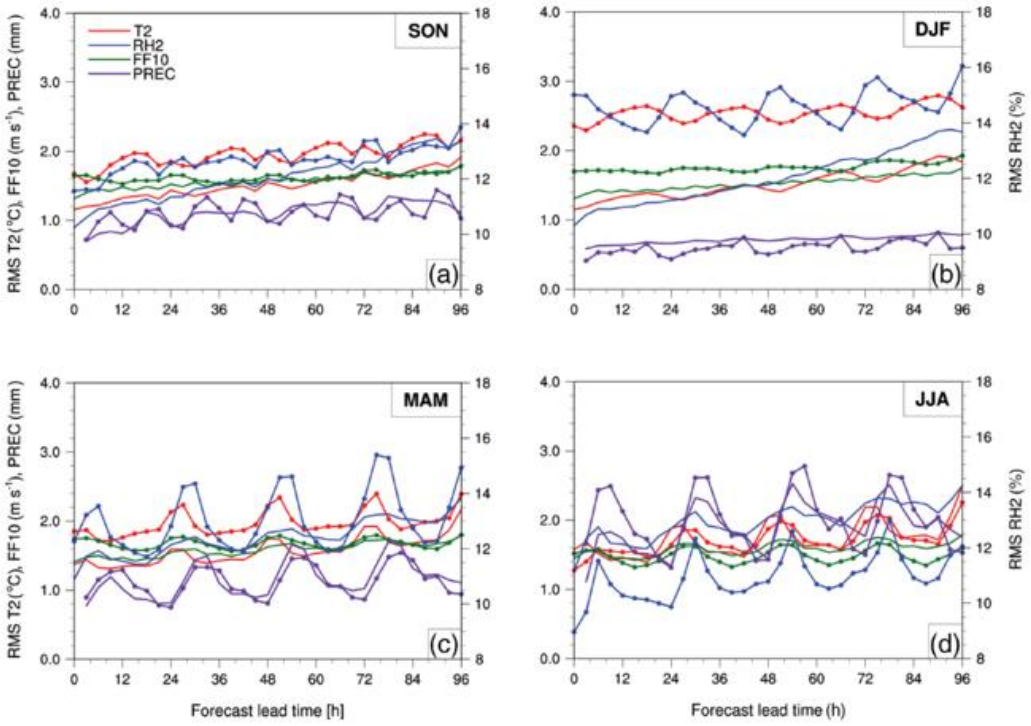


Figure 2: Unbiased forecast error (lines with symbols) and ensemble spread boosted by an observation-error estimate (lines without symbols) for the seasonal verification of COSMO-E forecasts initialized at 1200 UTC in 2016/2017 for Switzerland: 2m temperature (red), 2m relative humidity (blue), 10m wind speed (green), and 3 h accumulated precipitation (purple). Left-hand y-axes are for temperature, wind speed, and precipitation, while right-hand y-axes are for relative humidity. (Klasa et al., 2018).

In addition, dynamical processes determining the time evolution of difference kinetic energy (DKE) have been investigated (Klasa et al., 2019). DKE is quantified by means of ensemble

variance of the irrotational and nondivergent horizontal wind, respectively. Three case studies characterized by contrasting predictability levels of precipitation have been investigated with the convection permitting ensemble COSMO-E for a forecasting period of 4 days. The results suggest that the large-scale flow and diurnal solar forcing, associated with higher spatiotemporal predictability, determines the overall evolution of limited-area ensemble variance of the horizontal wind, which increases in the presence of moist convective activity or strong synoptic-scale forcing, and stagnates or decreases otherwise, rendering forecasts of convection-permitting ensembles valuable beyond the very short forecast range.

2.3 Arpae contribution

2.3.1 Convection-parametrised ensemble (COSMO-LEPS)

In the framework of enhancing the spread/skill relation for the COSMO-LEPS system, the use of SPPT was tested. For two sets of periods (from 22/11/2014 to 31/01/2015 and from 2/6/2015 to 20/7/2015), the operational COSMO-LEPS (referred to as OPER) was tested against a test version (referred to as SPPT_SNGL) characterized by the following features: use of SPPT and executable compiled in single-precision mode. Both systems ran at 7 km of horizontal resolution, 20 members, and with a forecast range of 132 hours. The performance of the two systems was analyzed in terms of 12-h cumulated precipitation as well as in terms of spread/skill relation of 2-metre temperature. The verification network included the SYNOP reports covering Central and Southern Europe, with an availability of about 1000 reports/day (see Fig. 3). Here, we consider the results relative to the summer period (June-July 2015). As for total precipitation, the 2 panels of Fig. 4 reports the probabilistic forecast skill of OPER and SPPT_SNGL in terms of the ROC area for total precipitation exceeding 1 and 10 mm over 12 hours (left and right panel, respectively).

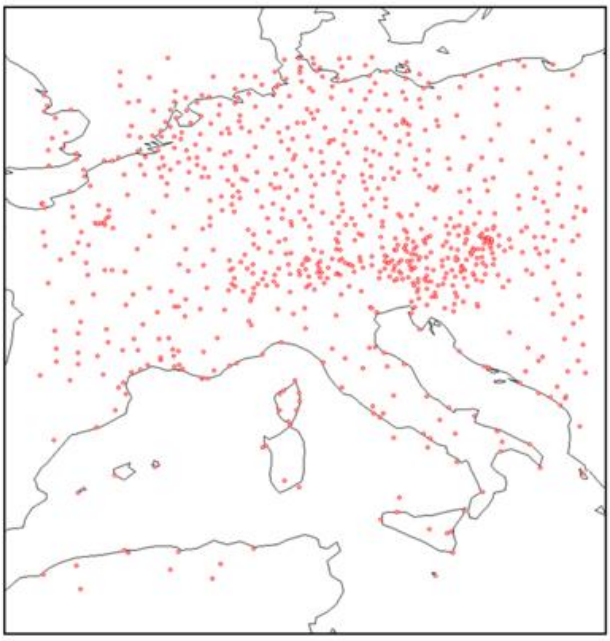


Figure 3: Verification network used for the intercomparison between OPER and SPPT_SNGL. Each red dot denotes a station.

It can be noticed that SPPT_SNGL provides a slight better performance than OPER for

both thresholds. This is especially true for in the short range, until, say, fc +72h. These results are confirmed also by other verification scores, either threshold oriented (e.g. Brier Score, Bier Skill Score) or not (e.g. Ranked Probability Score, Percentage of Outliers).

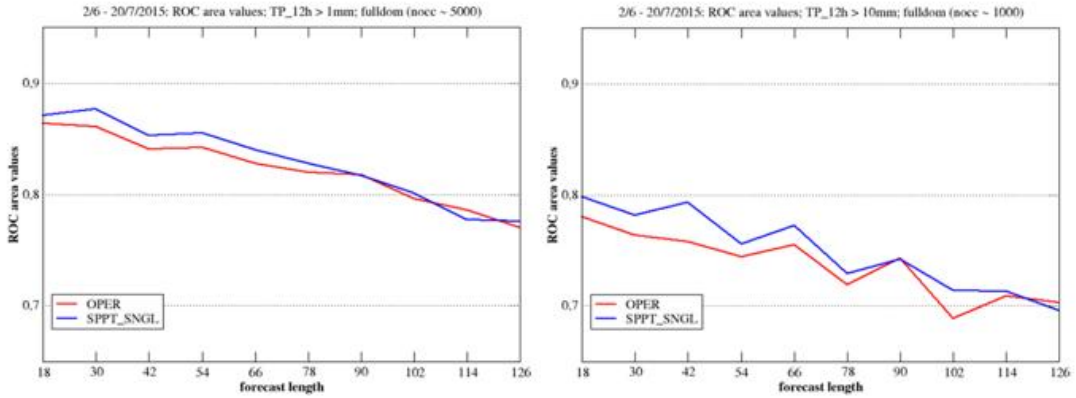


Figure 4: ROC area values for operational COSMO-LEPS (denoted with OPER, red lines) and test COSMO-LEPS (denoted with SPPT_SNGL, blue lines) for 12-hour precipitation exceeding 1 mm and 10 mm (left and right panel, respectively) as a function of the forecast range (in hours). Verification is performed over the station points of Fig. 3 and averaged over the verification period.

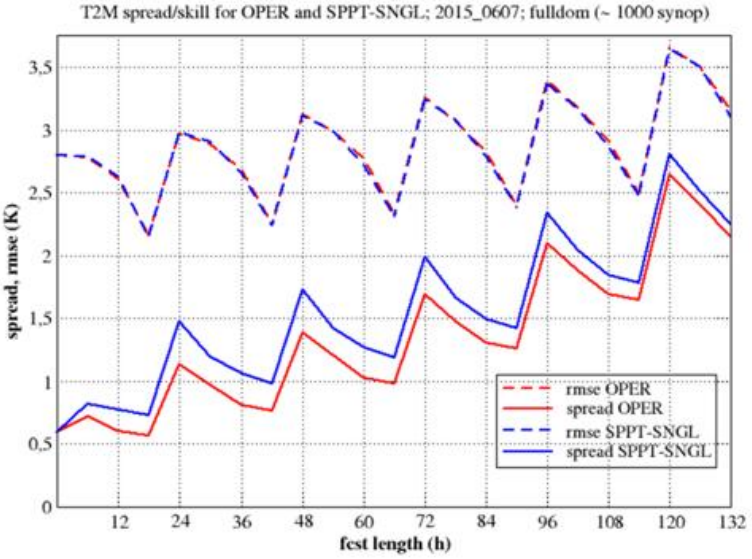


Figure 5: Root-mean-square error of the ensemble mean (dashed lines) and ensemble spread (solid lines) for operational COSMO-LEPS (denoted with "OPER", red lines) and test COSMO-LEPS (denoted with SPPT_SNGL, blue lines) for 2-metre temperature (in Kelvin) as a function of the forecast range (in hours). Verification is performed over the station points of Fig. 3 and averaged over the verification period.

As for 2-metre temperature, the results of the experimentation are summarized in Fig. 5, which reports the root-mean-square-error of the ensemble mean (dashed lines) and the ensemble spread (solid lines) for both OPER and SPPT_SNGL (read and blue, respectively). Both systems turn out to be under-dispersive, the ensemble-mean errors being about twice the

dispersion of the ensemble members. On the other hand, it can be noticed that SPPT_SNGL provides larger spread than OPER at all forecast ranges and especially for the shortest ones. This happens without a deterioration of the average skill of the system, as the forecast errors are approximately identical in both configuration (read and blue dashed lines). Although these results are relative to the summer experimentation, the outcome of the winter experimentation (NDJ2014-2015) provides the same findings and confirms the positive benefit of using SPPT in the description of model uncertainties.

2.3.2 Convection-permitting ensemble (COSMO-2I-EPS)

During the experimental phase of the COSMO-IT-EPS convection-permitting ensemble (now operational with the name COSMO-2I-EPS), the ensemble was run for selected periods in order to test the model perturbation methodology, assessing its spread/skill relation. COSMO-IT-EPS has been run for the month of October 2015, one run per day at 00 UTC, with Initial and Boundary Conditions from COSMO-ME-EPS, the 10-km ensemble of COMET, running over a Mediterranean domain. Model resolution was 2.8 km and the ensemble had 10 members. COSMO-IT-EPS was run in 3 different configurations:

- without model physics perturbation (ensemble CTRL);
- with SPPT (Stochastic Perturbation of Physical Tendencies) (ensemble SPPT);
- with SPPT and perturbation of dew parameters of the physics schemes (turbulence, microphysics, land surface) (ensemble SPPT-PP).

The spread/skill relation of the three configurations in terms of 2m temperature (above) and 6-h precipitation (below) is shown in Fig. 6.

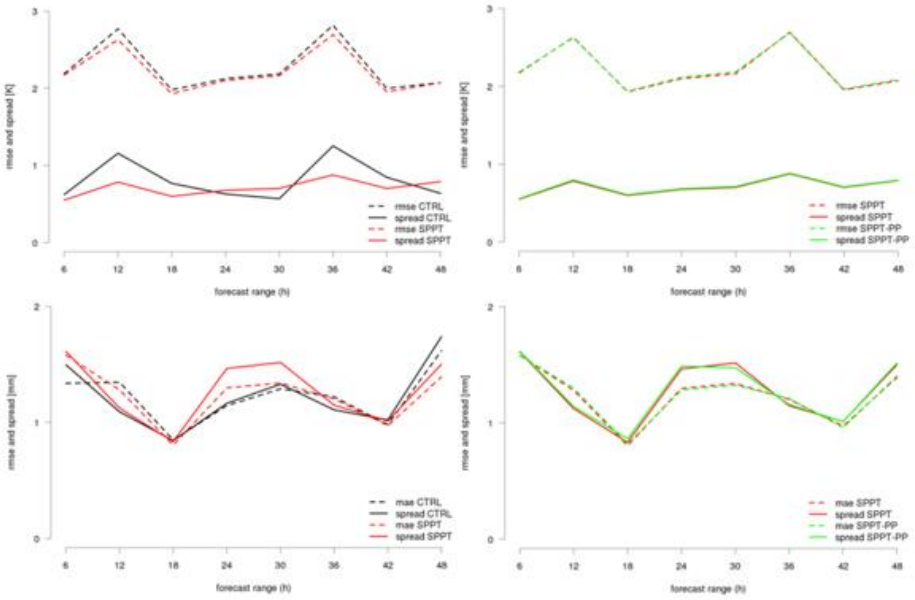


Figure 6: Error of the ensemble mean (dashed lines) and spread (solid lines), as a function of the forecast range, in terms of 2m temperature (upper row) and 6h precipitation (lower row), for the three experiments as indicated in legend. Error is RMSE for temperature and MAE for precipitation.

Temperature is compared against observed values at the SYNOP stations covering the Italian domain, while precipitation is compared against accumulated values recorded by the raingauges of a dense network covering Italy. In terms of 2mT, all configurations are underdispersive. Adding the SPPT does not yield an increase of the spread, in contrast with what was found in other configurations (e.g. COSMO-E). Adding parameter perturbations does not increase the spread and does not influence the error. In previous studies (Marsigli, 2009) it was noticed that parameter perturbation may have a highly localized impact, temporally and spatially, and dependent on the weather situation, therefore it is difficult to detect an impact in a statistical evaluation over a period. A spatial verification is applied to the precipitation fields, accumulated over 6 hour periods (Fig. 7). The verification method is the DIST method DIST (Marsigli et al, 2008). According to this method, the verification domain is first covered with boxes of selected size (here 0.2 x 0.2 deg). Then both forecasts (each ensemble member separately) and observations are aggregated in each box, by computing the average or the maximum (or other parameters of the precipitation distribution). Finally, common probabilistic verification scores are computed for both the average and maximum values belonging to each box and aggregated over the whole domain.

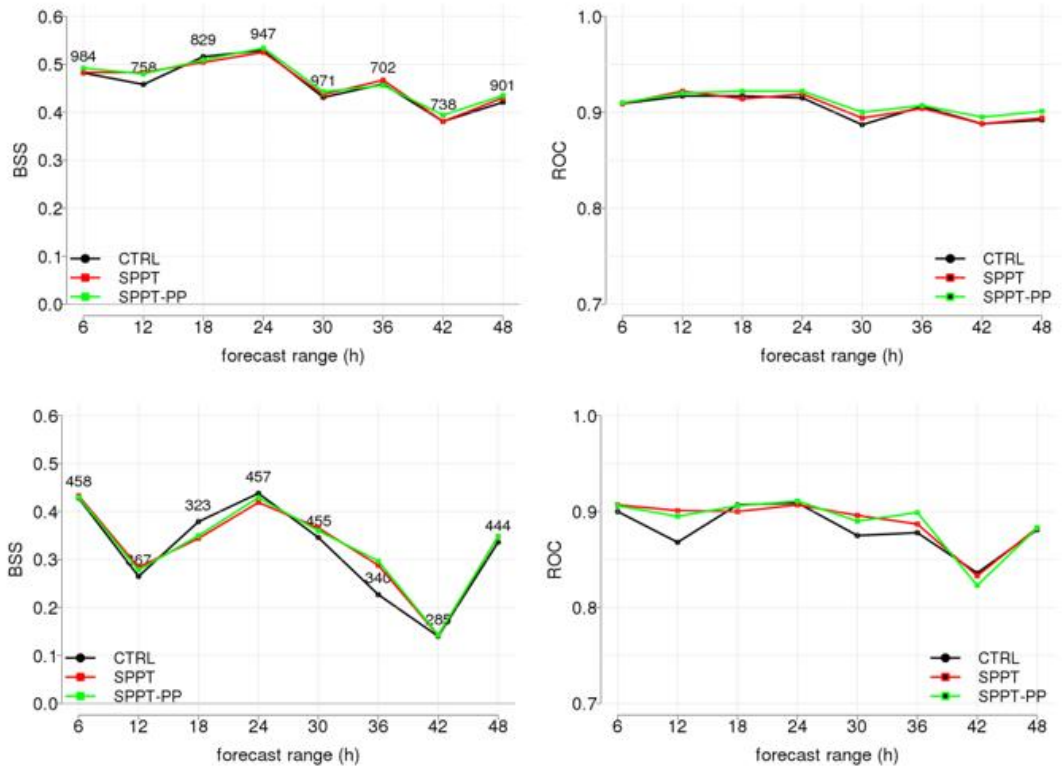


Figure 7: Brier Skill Score (left) and ROC area (right) as a function of the forecast range, for the 6h accumulated precipitation average values exceeding 1mm (top) and 5mm (bottom).

Results for average precipitation greater than 1mm/6h (upper row) and 5mm/6h (lower row) are shown in Fig. 7. While the ROC area indicates a better performance of the ensemble with perturbed physics, the Brier Skill Score shows mixed behavior. Parameter perturbation has a very little impact. How to assess the spread of the forecast in terms of precipitation is not straightforward, particularly for the convection-permitting scale. Following the development of spatial approaches for the verification of a high-resolution forecast, also the spread of the ensemble needs to be assessed in terms of spatial metrics. For this purpose, the methodology

proposed by Dey et al (2014) has been tested, where a dispersion Fraction Skill Score is computed as a measure of ensemble spread, evaluating the difference between couples of ensemble members in terms of FSS over boxes of increasing size. As an example, it is shown the mean over all couples of the dispersion FSS as a function of box size, for a case of intense precipitation occurred in the considered period (Fig. 8). The three experiments are compared, showing that the physics perturbations have an impact on the spread and that also the addition of Parameter Perturbation is able to increase the diversity of the members at all scales.

A different method has been also proposed in the Project for evaluating the ensemble spread: by computing its components using the SAL metric (Wernli et al 2008). The idea is that the different physics perturbations may address different components of the forecast uncertainty; therefore they may produce spread in different features of the resulting forecasted fields. The three component of the SAL (Structure, Amplitude and Localization) are computed for each couple of the ensemble members: 45 couples in a 10 member ensemble. The 45 dots are represented on a modified SAL-diagram in Fig. 9, where the Localisation is shown in the x axis, the Structure in the y axis and the Amplitude with the colour scale. This choice has been made to highlight the impact on the localization.

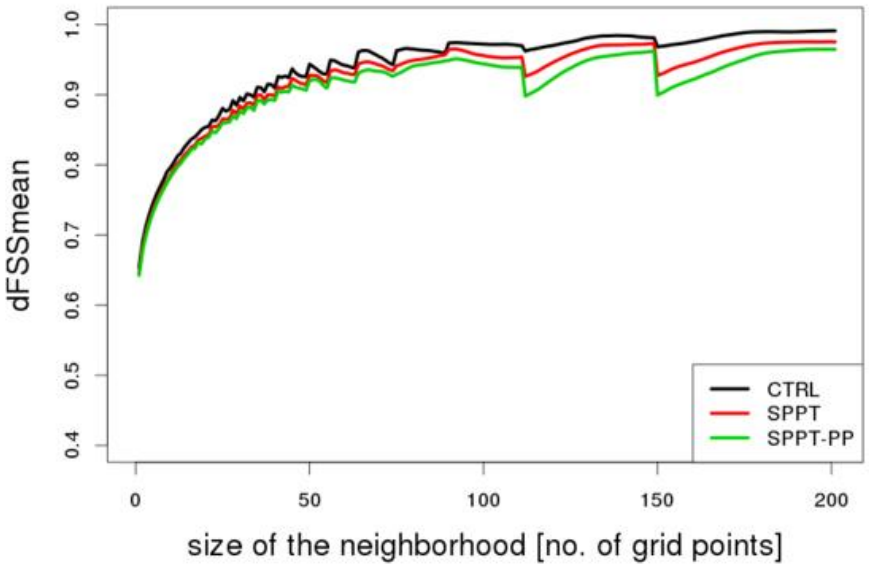


Figure 8: Mean value of the dispersion Fraction Skill Score a function of the forecast range, for the 24h accumulated precipitation for the even of the 31st October 2015.

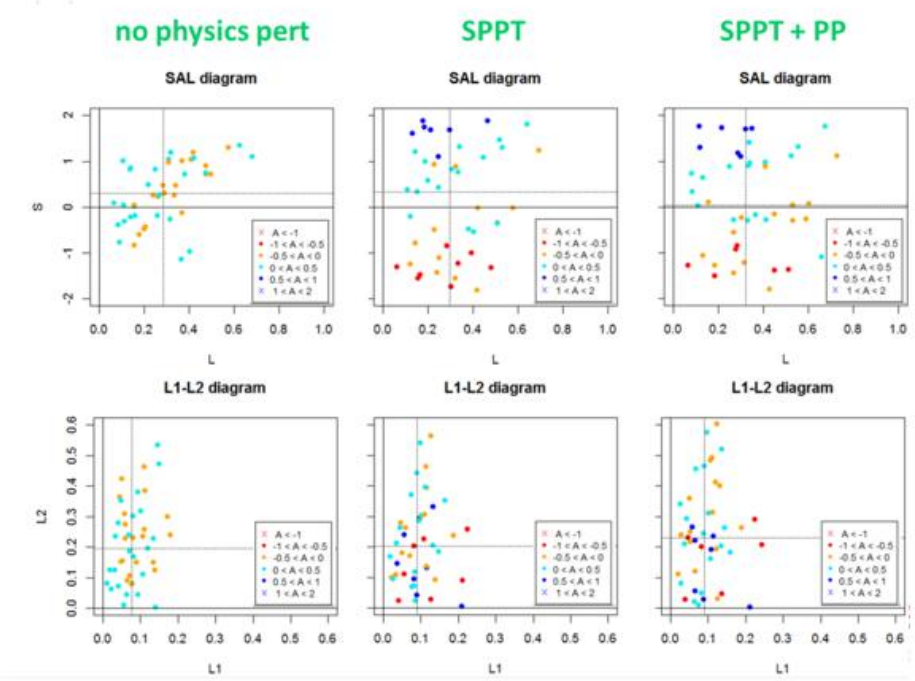


Figure 9: Dispersion of the members of the 3 ensembles (one in each column) represented as the three components of the SAL metric (top row), for the 24h accumulated precipitation for the event of the 10th October 2015. In the bottom row, the two sub-components of the L term are shown.

The impact of the physics perturbation in increasing the ensemble spread in terms of precipitation is now evident, and not only in Amplitude, but also in the Structure and in the Localization of the fields. It is now possible to detect an impact of the Parameter Perturbation, which determines more dispersion of the points in both L and S components. It is reminded that the L component consists of two terms: L1, measuring the distance of the centres of mass of the structures, and L2, measuring the difference in the degree of dispersion of each field around its centre of mass. How the increased dispersion is divided between these 2 components is shown in the bottom row, where an L1-L2 diagram is plotted. Introducing SPPT (central plot) both L1 and L2 are affected, and adding also the Parameter Perturbation (right plot), the spread in both components is further increased. This metric seems to be promising for the purpose of highlighting the contribution of a perturbation to the overall spread and to detail in which component this contribution takes place.

2.4 IMGW contribution

At IMGW, the COSMO model runs in a deterministic mode using initial and boundary conditions from the ICON global model, as shown in Fig. 10. The COSMO model with 7 km horizontal resolution (COSMO-7 km) applies nudging-based data assimilation to correct global model forecasts, ingesting the most recent set of meteorological data acquired from the GTS/WMO network. Forecast results from the COSMO-7 km are further used as IC/BCs for a nested instance of a COSMO model with a higher resolution of 2.8 km and 36-hour forecasts. A set of the deterministic COSMO-2.8 km forecasts define the basis for the operational configuration of an ensemble forecasting system.

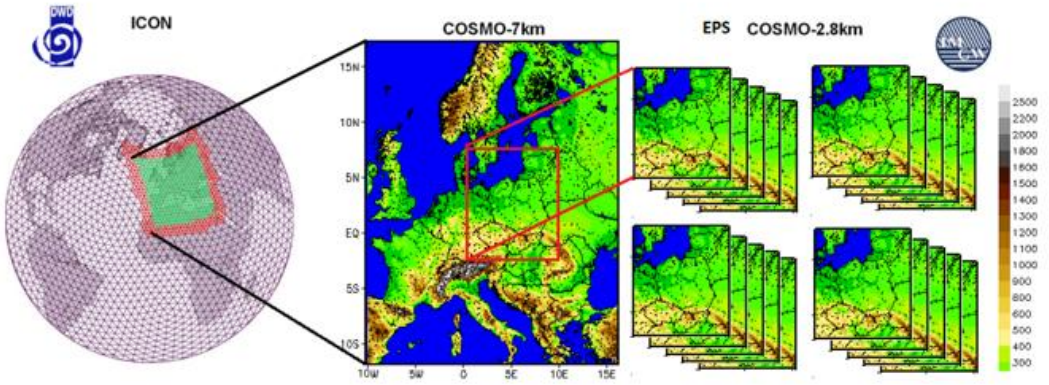


Figure 10: Operational configuration of deterministic COSMO-7 km model and 2.8 km resolution EPS runs at IMGW. From left to right domain of ICON global model, domain of COSMO-7 km model running at IMGW, and a set of nested COSMO-2.8 km domains.

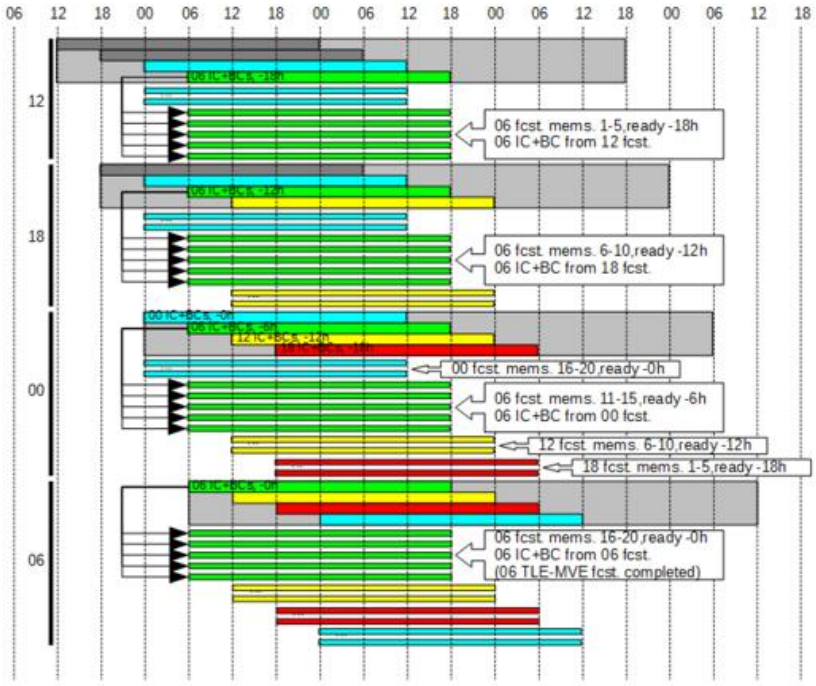


Figure 11: Operational setup of EPS based on Time-Lagged IC/BCs. X-axis lead time (UTC), Y-axis forecast individual initial time. The four different colours distinguish forecast nominal start time: blue 00 UTC, green 06 UTC, yellow 12 UTC, and red 18 UTC.

In the recently developed EPS configuration, twenty ensemble members were selected, based on the COSMO-2.8 km convection permitting (CP) forecasts. Every member of an ensemble applies perturbed lower boundary conditions, composed of the random noise of specified amplitude added to parameters of the soil-model physical parameterization (see e.g. Mazur and Duniec, 2015). In the basic EPS configuration, the whole set of IC/BC was nested from a single 78-hour run of a deterministic COSMO model with spatial resolution of 7 km, as shown in Fig. 11. In order to increase the spread of model parameters generated by forecasts, we have further adopted the concept of time-lagged IC/BCs (see e.g. Lu et al., 2007; Chen

et al., 2013), in which the set of deterministic CP forecasts is subdivided into groups starting at the consecutive time windows: 00, 06, 12, and 18 UTC.

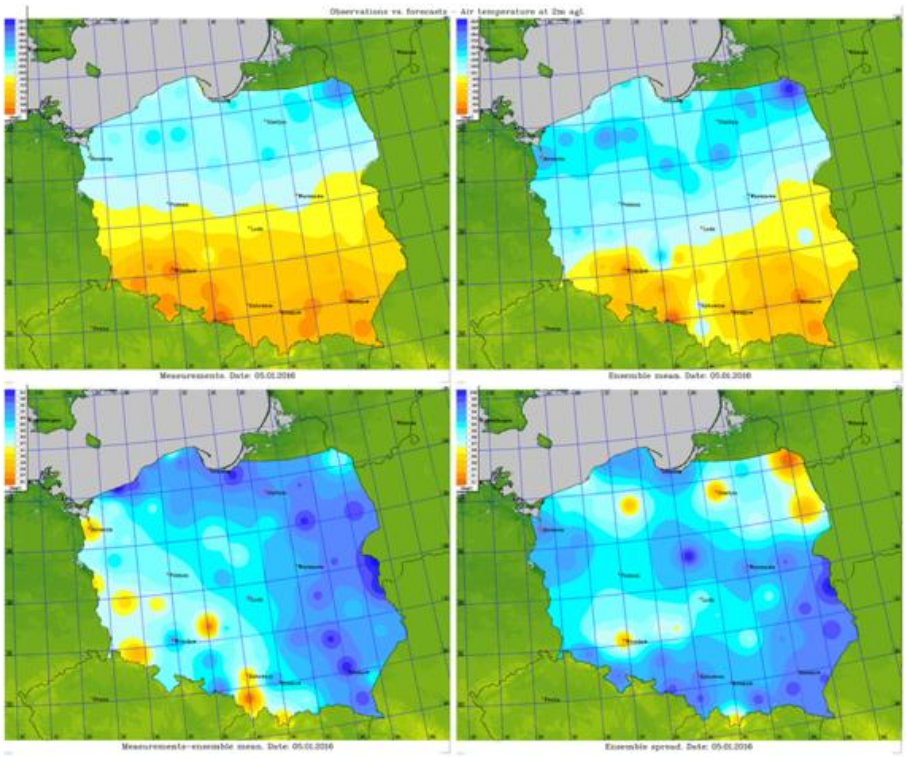


Figure 12: Comparison of the EPS derived temperature: ensemble mean (upper right), spread (lower right) with measurements (upper left), the absolute value of difference between measurement and ensemble mean (lower left).

The EPS results (in terms of EPS mean) are compared with observations collected from 61 Polish SYNOP stations. In Fig. 12 a representative analysis of the model generated temperature forecast averaged for the whole day of 5-01-2016 is presented, while Fig. 13 shows a similar verification for dew point temperature. In both cases, the EPS mean reproduces the main spatial features of the large-scale temperature distribution. The observed temperature is in a similar range (-20.7 ℃, -2.5 ℃) to the computed EPS mean (-20.8 ℃, -3.8 ℃). Similarly, the observed dew point temperature is in a similar range (-20.7 ℃, -2.0 ℃) to the EPS computed mean (-20.6 ℃, -1.6 ℃). In both cases, the model shows a bias when compared to observations with an absolute error of up to -6.1 ℃ for temperature and -5.7 ℃ for dew point temperature. For the temperature, larger error values (above 3 ℃) are well correlated with the air masses that came after the warm front crossing Poland during 5 January, 2016. Dew point temperature generally shows a small error - below 2 ℃ - except in the north-eastern part of Poland, where a persistent lack of cloud coverage can be observed for the selected date and in south-western areas, which may be correlated to a larger exceedance of precipitation intensity that started in the afternoon hours of 5-01-2016 and developed further during the night and the morning hours of the following day.

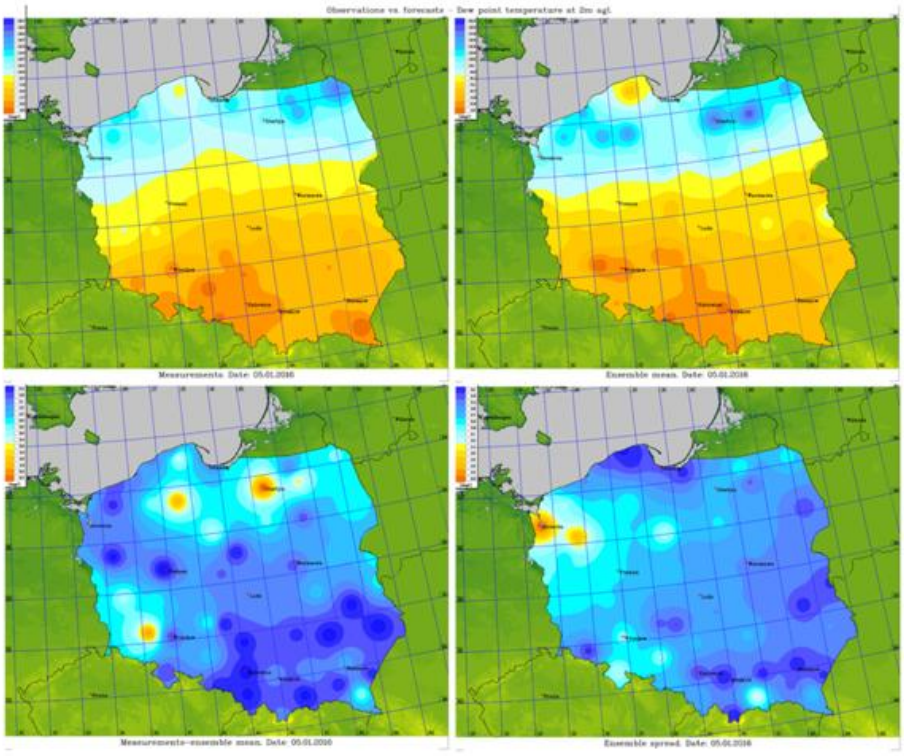


Figure 13: Same as in Fig. 12 but for dew point temperature.

A larger EPS spread implies more uncertainty in the forecast mean and hence in the ensemble members. The EPS spread is typically underestimated near the surface (Tennant and Beare, 2014) where the relations between prognostic parameters are controlled with higher fidelity parameterizations, not accounting enough for observation errors. Thus, in general EPS leads to overconfident forecasts of near-surface weather elements, especially in winter conditions where the natural variability of soil parameters is lower. In this approach, as shown in these examples, the perturbation of the evaporating fraction in the soil has a significant impact on the forecast due to the increased stimulation of energy exchange between the surface and atmosphere. The maximum spread for the temperature is 1.1 °C, with increased value covering the entire northern and western parts of Poland. For the dew point temperature, we observe a higher spread of the amplitude up to 2.0 °C, localized only in the north-western corner of the country. More advanced analysis of the EPS scores and the correlation between EPS error (skill) and spread is provided in the context of specific applications. First, selected parameters (air temperature, dew point temperature, wind speed and total precipitation) were studied for trimesters of 2016 and the entire year of 2016. The analysis was then carried out continuously in following periods. The quality of EPS forecasts, expressed in terms of skill and of spread in subsequent years seemed to improve, as shown in the following figures.

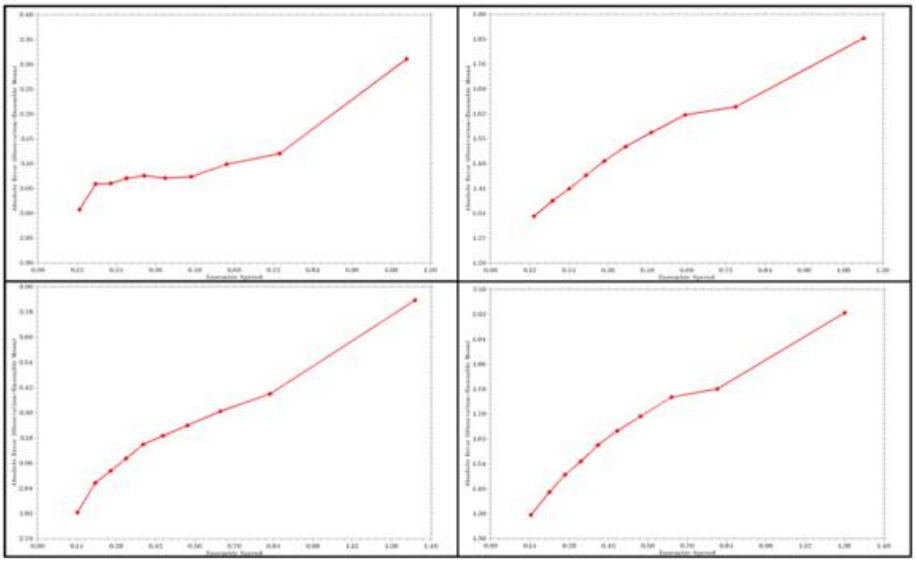


Figure 14: Left - skill-spread diagram for T2M, right - for U10M. Average values for the entire year 2016 (top row) and 2017 (bottom row).

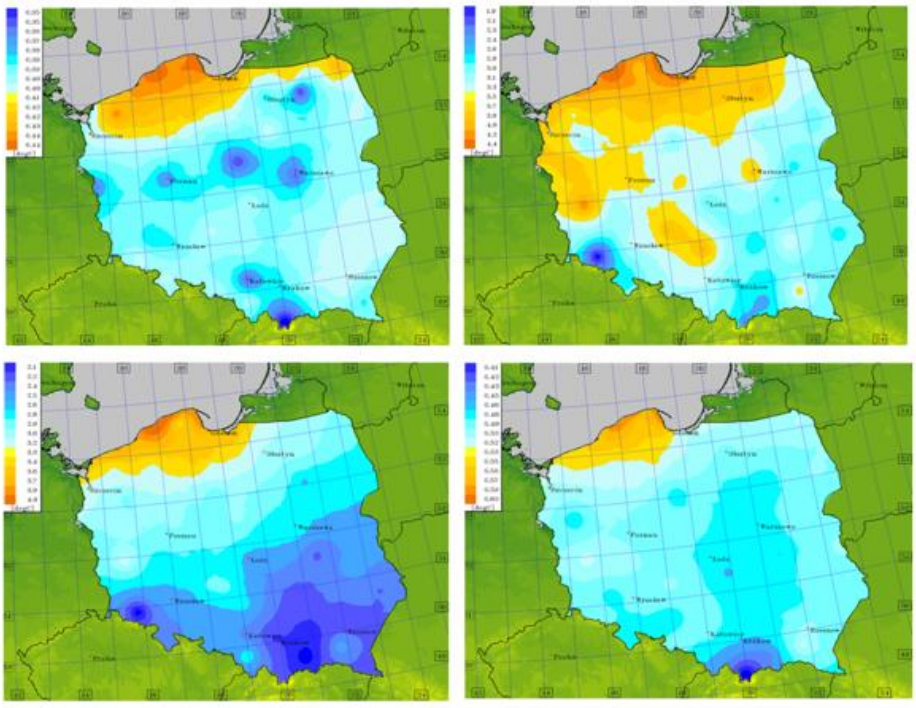


Figure 15: Spatial distribution of skill (left) and spread (right) for T2M (upper - average for year 2016; lower - for 2017).

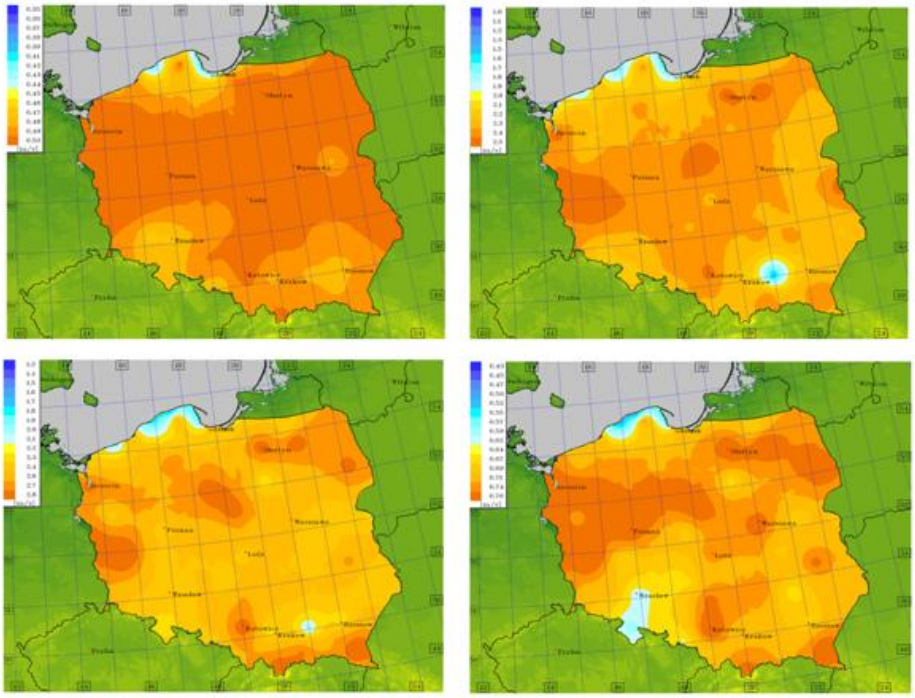


Figure 16: Same as Fig. 15, but for U10M.

The monthly analysis of skill/spread relation was done as well, starting from 2016. The representative results for the entire year 2016 are shown below.

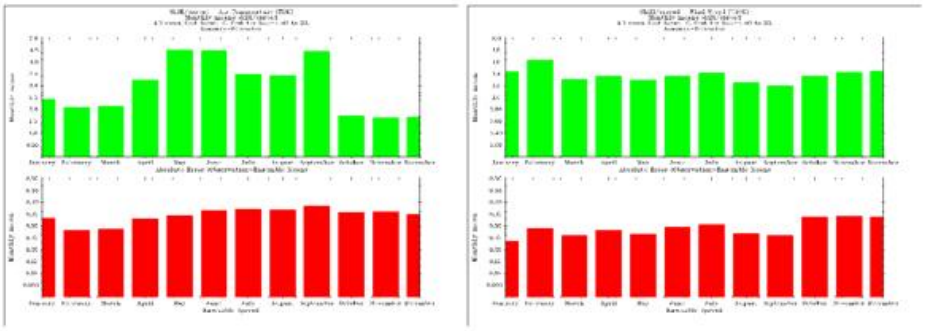


Figure 17: Monthly average skill (green) / spread (red) of T2M (left) and U10M (right). All runs/all stations, January to December 2016.

In conclusion to this part, it should be stated that skill/spread relation was studied thoroughly, using operational EPS results. Study has been carried out for months, seasons, entire year and, simultaneously, for runs (00, 06, 12, 18), forecast hours (0-36) and hours (0-23). Average spread is in general 2x to 10x lower than skill measured as MAE, which (as it was pointed out above) shows the under-dispersiveness of the system. As far as the spatial relations are concerned, one can observe that skill is in general better (i.e., smaller, as measured as MAE) for central and southern part of the domain. This is probably due to the way of generation EPS. Similarly, spread is bigger (meaning, better) in central and northern part of Poland. Similarly for time relation (monthly means) - skill is in general better (i.e., smaller) for warm months - probably due to EPS generation (perturbation of

lower boundary conditions - soil parameters - composed of the random noise of a specified amplitude added to parameters of the soil-model physical parameterization, as written above). Since it pertains to soil features, it may be less effective in winter (frozen ground) and more effective in warm and wet season. In turn, spread is been found in general bigger for warm months - again, probably due to the way the EPS members are prepared. Finally, another outcome of this part of Priority Project was a publication of paper at Meteorology Hydrology and Water Management - Research and Operational Applications (Grzegorz Duniec, Witold Interewicz, Andrzej Mazur, Andrzej Wyszogrodzki; MHWM recently became JCR journal), see: http://www.mhwm.pl/Operational-setup-of-the-soil-perturbed-time-lagged-Ensemble-Prediction-System-at,71048,0,2.html.

2.5 RHM contribution

Ideally, for a good ensemble, the behavior of the ensemble spread should follow that of the ensemble mean error and reflect the predictability of a meteorological situation. It is usually expected that a higher-resolution system has better skill (but in reality, it is not always so), thus theoretically the spread should decrease with resolution. However, the situation is not so straightforward when we are speaking about a pair "driving EPS-nested EPS" (as it is always the case with mesoscale EPSs), in which the spread at the lateral boundaries of the nested EPS is defined by the coarser-system spread.

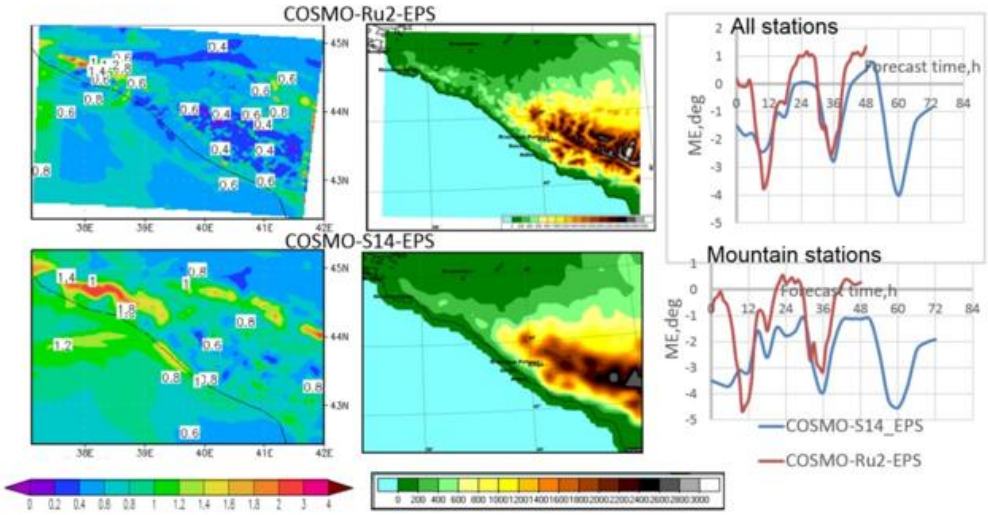


Figure 18: T2m ensemble spread (left) for 48h forecasts starting on 22 February, 2014 00UTC and orography (center) for COSMO-Ru2-EPS (top) and COSMO-S14-EPS (bottom). On the right: T2m mean error for the same date as a function of forecast lead-time for all stations in the region (top panel) and only for mountain stations (bottom panel).

Therefore, w decided to analyze the spread spatial distribution and temporal variations for two EPSs of different resolutions for the case when the higher-resolution system was nested to the coarser-resolution one. For this purpose, we applied the Sochi Olympics archive (Astakhova et al, 2016) and examined the runs of the 7-km COSMO-S14-EPS and the 2.2 km COSMO-Ru2-EPS (Montani et al, 2014). COSMO-Ru2-EPS was nested to COSMO-S14-EPS over a small region of about 350*300 km with a complex topography (containing mountain, valley, and sea points). For both systems, we considered 2-m temperature for the

1-month period from 1 to 28 February 2014 over the area corresponding to the integration domain of COSMO-Ru2-EPS. We considered both individual cases and monthly mean characteristics. Analysis of individual forecasts over the entire domain demonstrated that the higher-resolution EPS had less spread, however, its skill was not always convincingly better (see Fig. 18 for February 22, 2014). The geographical distribution of spread is correlated with orography, showing smaller spread over mountainous areas. Notably, the mean error decreased following the smaller spread over this high complex terrain (the Caucasus).

In fact, in a reliable forecast system we can expect a good spread-skill correspondence mostly for the results averaged over many forecasts ($\overline{Error^2} = \overline{Spread^2}$). Fig. 19 demonstrates the time evolution of T2m spread averaged over a month interval from February 1, 2014 to February 28, 2014 for two EPSs. As the forecasts were run twice a day (starting at 00 UTC and 12 UTC), the sample includes 56 forecasts. It can be seen that both systems start from approximately the same spread, but the spread of coarser-resolution forecasts grows with forecast time faster. The differences in spread between EPSs increase with lead time and are up to 0.8-1 deg. The smaller spread for the higher-resolution system corresponds to its smaller error (see Fig. 20 which shows the mean absolute error (wrt to all available station data in the region) of the two EPSs obtained using the FROST-2014 online verification tool for February 2014).

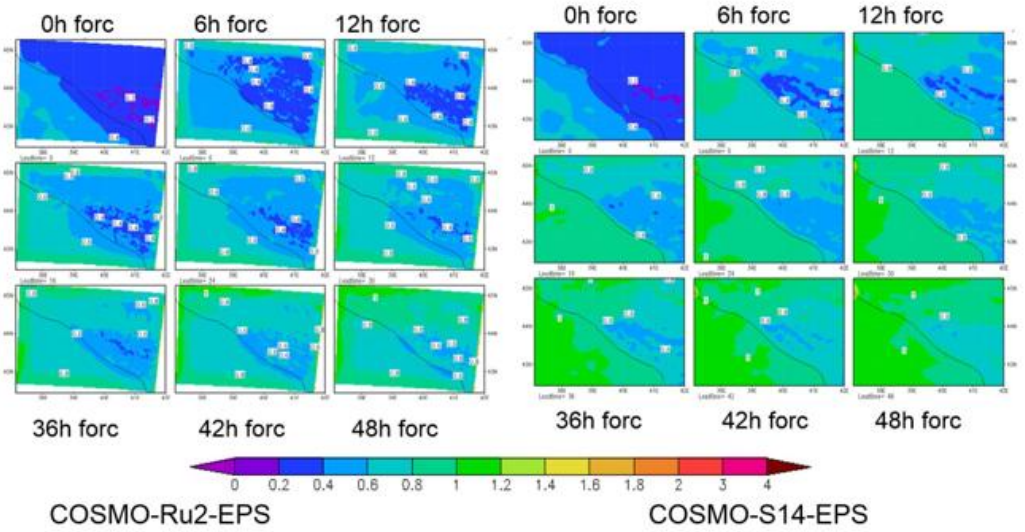


Figure 19: Evolution of 2m temperature spread with forecast time for two EPSs with different resolutions. Averaged over 56 forecasts in February 2014.

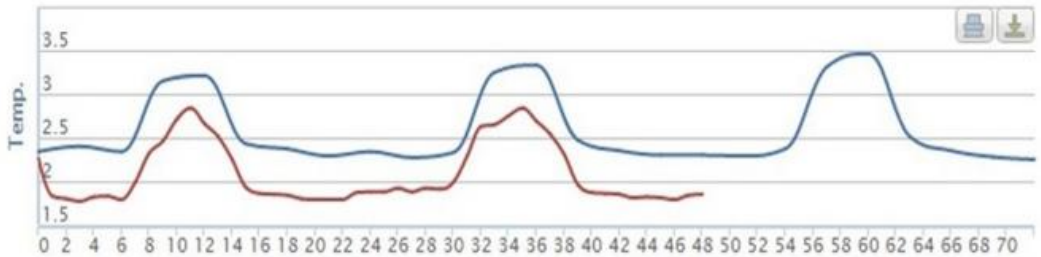


Figure 20: Mean absolute error of 2m temperature over the Sochi area averaged over 56 forecasts in February 2014. Red - COSMO-Ru2-EPS, blue - COSMO-S14-EPS.

It is also worth noting that for the T850 spread the differences between systems of different resolutions were much smaller (not shown). This indicates the important role of surface in forecast perturbations. We have examined EPSs not only with different resolutions but also with different integration domains. Looking at the spread fields in detail, we found that when regions with high T2m spread appeared near the lateral boundaries of COSMO-Ru2-EPS (near the borders of our post-stamp plots in Fig. 21), they occupied larger area and tended to propagate inside the domain in COSMO-S14-EPS being smaller and staying near the border in COSMO-Ru2-EPS. This indicates that the size of the EPS integration domain can also matter.

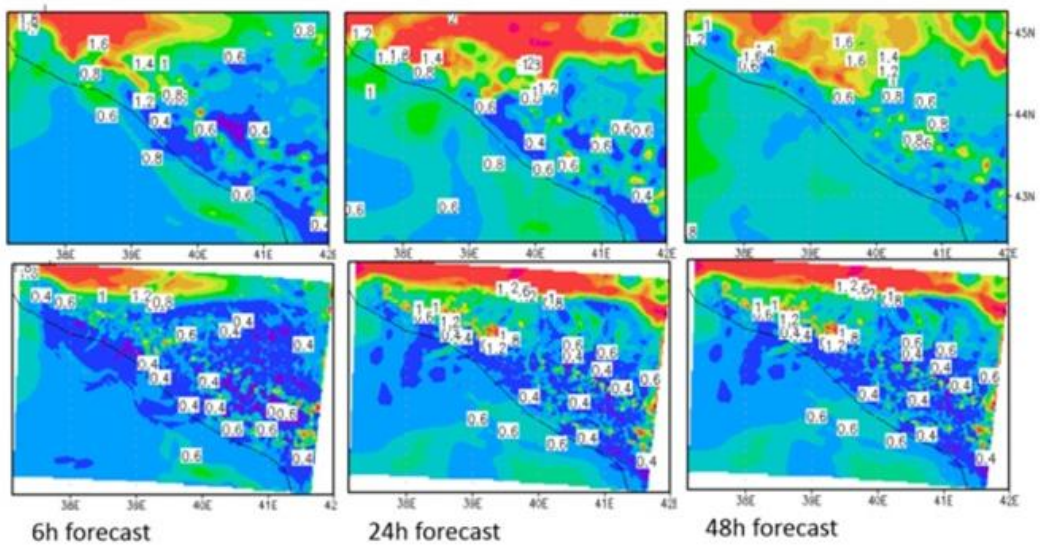


Figure 21: Evolution of the T2m spread with the forecast time in two EPSs. Upper panel: COSMO-S14-EPS; lower panel: COSMO-Ru2-EPS. Forecast from 22 February 2014 00UTC.

To explore this aspect, additional experiments were performed changing the size of the integration domain for COSMO-Ru2-EPS. The archive COSMO-Ru2-EPS data were obtained with model version 4.22 and with double precision. The new experiments were run with model 5.01 in single precision. Comparing the archive and the new results (with different model versions) we found non-zero differences in spread fields for one and the same date. Thus, we had to rerun the previous experiments for COSMO-Ru2-EPS. Finally, the experiment set was as presented in Fig. 22. The reruns of COSMO-Ru2-EPS were made for two different domains called LITTLE and BIG, while the COSMO-S14-EPS runs covered the domain S14. The comparison was made for the area, corresponding to the LITTLE domain. In addition to T2m temperature, the free atmosphere temperature was considered as well.

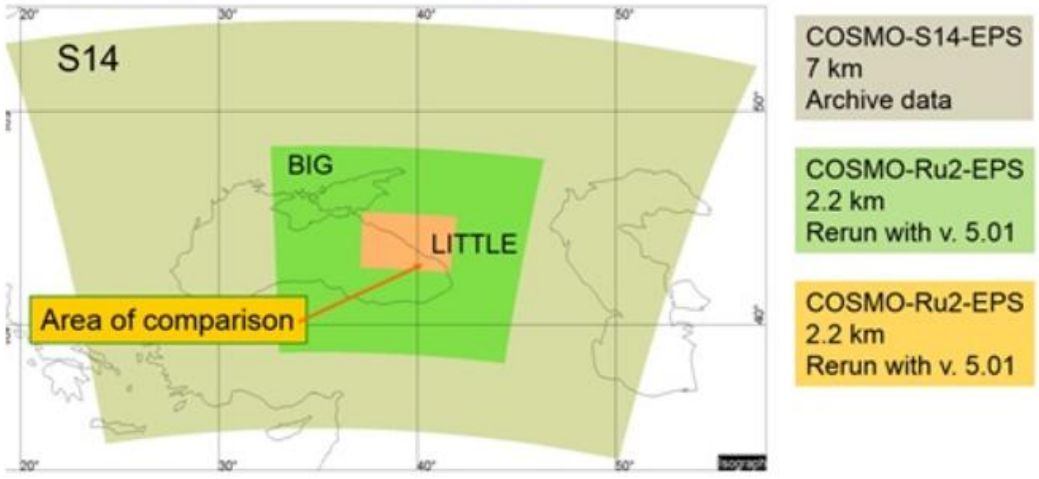


Figure 22: Experiment setting.

The resulting spread was found to depend on the size of the integration domain considerably (see Fig. 23). The effect is related to weather situation and is most pronounced near the surface and in regions with complex topography. The choice of integration domain can differently affect different prognostic realizations. Depending on location and air mass motions both ensemble mean and spread can be increased or decreased (in some cases - considerably) when the integration domain is changed. Choosing the integration domain for EPS, especially in mountain regions, one should be very careful and take into account the prevailing weather types and air mass motions.

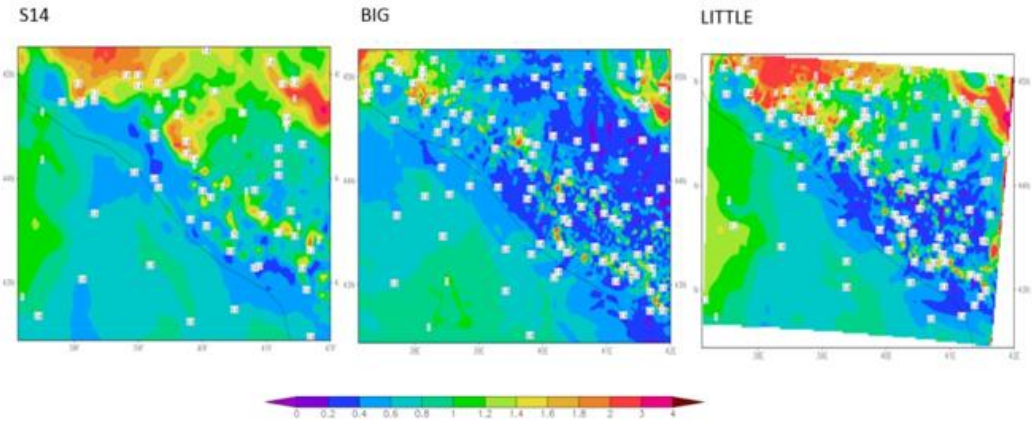


Figure 23: T2m spread fields obtained for integration domains S14, BIG and LITTLE (presented for LITTLE area). 48-h forecast starting from February 22, 2014 00 UTC.

We can conclude that generally the ensemble spread decreases for higher-resolution nested EPS but the effect depends on the size of the EPS integration domains and the dominating weather patterns.

2.6 Remarks from the discussion of the results

This Project activity has lead to a better shared understanding of the spread/skill relation of our ensembles, highlighting also the main deficiencies. Some conclusions have been drawn:

- it is important to consider also the day-by-day variation of the spread, which should follow the day-by-day variation of the error;
- it is suggested to investigate the impact of the Boundary Layer perturbations recently introduced in the COSMO model following the work by K. Kober (perturbations proportional to the variance of the tendencies coming from the turbulence scheme). Results are shown in Section 3.3;
- it is suggested to compute also the spread/skill relation on vertical profiles, to assess the vertical structure of the error and its representation in terms of spread
- it is highlighted the possibility of using Fraction Skill Score and SAL for computing the spread of the ensembles in a spatial verification sense;
- it is considered the work of Pirkka Ollinaho (ECMWF) on the introduction of parameter perturbations in their ensemble. This approach could be useful also for the COSMO Consortium but it requires strong link with the physics developers;
- it was mentioned that perturbation of parameters usually has a detectable impact on particular weather situations, therefore it is difficult to see an impact on a long statistics. Following this remark, it is suggested to perform also verification/evaluation on selected cases or collections of cases;
- it is suggested to compute also the spread/skill relation with respect to analysis, not only to observations, to reduce the influence of systematic model error;
- it is considered also how to include the observational error in the spread/skill evaluation. It is suggested to start from the literature and try the previous works of Neill Bowler and Marion Mittermaier.

3 Test and development of model perturbation

The methodologies available in the Consortium for model physics perturbations have been subjected to further study.

3.1 EM-scheme and Parameter Perturbation at DWD

The work has been described in Section 2.1.

3.2 SPPT and BLPERT schemes at MeteoSwiss

SPPT scheme

The SPPT scheme is used in the operational COSMO-E forecasts of MeteoSwiss. Several issues with SPPT could be solved within the SPRED priority project and a consolidated version of the scheme implemented by Lucio Torrisi (Italian Meteorological Service, Rome,

COMET) with support for GPUs is implemented in the official COSMO version 5.05. The main findings are:

- SPPT has significant impact only with large correlation lengths in space and time in the random pattern. COSMO-E thus uses 5deg and 6h, respectively. The sum of the parameterization tendencies for temperature and humidity are largest in summer and are then dominated by those of the turbulence scheme. This explains why SPPT enhances the spread mainly in summer, but hardly in winter;
- in order to avoid an effect on the total water content in the atmosphere by SPPT, all humidity variables (Qx) should be perturbed (itype_qxpert_rn=2). Other settings caused extensive precipitation in a few members during the test period;
- the COSMO advection scheme causes unphysical temperature anomalies in specific conditions and locations in complex topography. The model physics counteract against these anomalies. However, if SPPT reduces the physical tendencies the counteraction is weaker and thus less effective. Therefore, a new switch has been implemented in COSMO to switch off SPPT locally where temperature anomalies are diagnosed (ltargetdiff_mask=.true.).

BLPERT scheme

The boundary layer perturbation scheme (BLPERT) suggested by Kober and Craig (2016) includes stochastic perturbations related to turbulent fluctuations in kilometer-scale numerical weather prediction models. It has been implemented in a COSMO test version by Uli Blahak, DWD. Since COSMO-E shows a lack of convective precipitation in the Swiss Plateau, we tested whether the scheme is able to enhance the triggering of convection based on case studies for both strongly and weakly forced synoptic weather situations. The experiments confirmed the potential of the BLPERT scheme to improve forecasts in weakly forced cases by intensifying the triggering of convection as shown in Kober and Craig (2016). However, the factor that controls the amplitude of the perturbations, blpert_const, has been set to twice the value suggested by the authors to reveal a significantly positive impact in our case. More importantly, the scheme has a clearly negative impact on the convection characteristics in our cases with rather strong forcing. It produces too many small-scale unorganized cells with short lifetime and breaks up larger cells and squall lines, also with the recommended setup. Therefore, the benefit of the scheme in the current version is questionable for COSMO-E.

General remarks

Model perturbations by BLPERT or SPPT have an impact on the physical processes that keep a convective system alive and they can be disruptive. The chances that perturbations are disruptive are particularly high with BLPERT with new random numbers every 10 minutes, but it seems to be a general problem of stochastic model perturbation schemes in convection-resolving ensembles that are based on an additional term for prognostic model equations. Hence, the impact of new model perturbations on the convection characteristic or on physical processes in general, should be carefully investigated.

3.3 Stochastic pattern Generator for model perturbation at RHM

A Stochastic Pattern Generator (SPG) has been developed at the Hydrometcenter of Russia within the framework of PP KENDA (Tsyrulnikov, Gayfulin, 2016, 2017). The goal of this study was to try SPG for generation of model-error perturbations in the COSMO-Ru2-EPS.

SPG in a nutshell

The SPG produces Gaussian pseudo-random 3-D and 2-D spatio-temporal fields with realistic and tunable structure on a limited-area domain. The SPG benefits from the fact that it generates fields with realistic space-time interactions (the spatio-temporal covariances obey the "proportionality of scales" principle: larger (shorter) spatial scales are associated with larger (shorter) temporal scales (Tsyroulnikov, 2001). The SPG model is

$$(\frac{\partial}{\partial t} + \mu\sqrt{(1-\lambda^2\Delta)})^3\xi(t,s) = \sigma\alpha(t,s))$$

where $\xi(t,s)$ is the model-error random field to be generated, α is the white in space and time driving noise, t is time, s=(x,y,z) is the spatial vector, Δ is the spatial Laplacian, σ controls the variance, λ controls the spatial length scale, and μ controls the time scale. The SPG was first coded as a stand-alone version; it was later embedded in COSMO model versions 4.22 and 5.01. Modifications of the model code include the supplemental new modules mod_spsp.f90 and src_gen.f90; changes in some old modules, and introduction of additional tuning parameters in INPUT_ORG namelist. The SPG is easily tunable. Its main tuning parameters are defined in the namelist INPUT_ORG:

- the standard deviation of the random field (separate for u, v, T, qv: {u,v,T,qv}_rand_field_std);
- the distance in km at which the spatial correlation falls to 0.5 (separate for u, v, T, qv {u,v,T,qv}_L05);
- the time in sec when the temporal correlation falls to 0.2 (separate for u, v, T, qv: {u,v,T,qv}_t02).

In our experiments we varied these parameters to get a good spread/skill relation. The SPG was applied in the additive mode. The random field $\xi(t,s)$ was generated on an SPG coarse grid (with 64 grid points in x and y directions and 32 levels) and tri-linearly interpolated to the model grid. For each element F (i.e. u, v, T) its individual perturbation field rand_field on the model grid was recalculated every timeslice=1200s. The perturbations were added at each model timestep as follows

$F_{pert} = F_{unpert} + rand_field/timeslice.$

That is, the perturbations were smoothed in time and space and were different for each element and level. Humidity was not perturbed.

Experimental set up

Experiments were carried out with COSMO-Ru2-EPS system developed for the Sochi Olympics within the CORSO project (Montani et al, 2014). The following experimental set up was applied:

- Δx= 2.2 km, L50, 10 members;
- IC&BCs from COSMO-S14-EPS (a clone of COSMO-LEPS for Sochi region, Δx=7km, L40);
- forecast length 48h;
- period: February 1-7, 2014 (00UTC);

- domain: Sochi area (172*132 gridpoints);
- verification against observations (∼40 stations) using VERSUS;
- model version 5.01 (with SPG implemented);
- single precision runs.

Each set of experiments included reference experiments and experiments with different sets of the SPG parameters. There were two reference experiments:

- experiment NOPERT without model perturbations at all (both SPPT and SPG were switched off);
- experiment SPPTSW with SPPT turned on and the SPPT parameters recommended by MeteoSwiss (hinc_rn=6 h; dlat_rn=dlon_rn=5 deg; stdv_rn=1.0; range_rn=0.8; itype_qxpert_rn=2 ; tapering in the stratosphere, no tapering near the surface).

The focus was on the possibility of increasing the T2m spread with SPG-generated model perturbations. Temperature and wind spreads in the free atmosphere were considered as well. It was demonstrated that the SPG perturbation patterns were sensitive to pre-defined spatial and temporal correlations ({u,v,T}_ L05 and {u,v,T}_t02 parameters). However, no definite conclusions could be drawn from that analysis. Therefore, most experiments with SPG were run with fixed spatial and temporal correlations: we assumed that for random fields of all variables (T, u, v) the spatial correlation was 0.5 at a distance of 50 km ({u,v,T,qv}_ L05=50 km) and the temporal correlation becomes equal to 0.2 in 4800s {u,v,T,qv}_ t02=4800s). Then we varied the random field standard deviations, specifying them separately for temperature and wind fields. First experiments demonstrated that perturbations with standard deviations about 0.02-0.03 m/s per hour for wind and 0.01-0.02 K per hour for temperature had a negligible effect on the T2m ensemble spread. After some additional tests for individual dates, two versions of SPG setting were selected. The experiment SPGBIG2 was run with the standard deviations for wind u,v_std=0.15 m/s per hour and for temperatures T_std=0.045 K per hour. bit greater deviations were specified in the experiment SPGBG: u,v_std=0.21 m/s per hour, T_std=0.06 K/h.

Experimental set results

We ran the experiments NOPERT, SPPTSW, SPGBIG2 and SPGBG for 7 days and examined the behavior of ensemble mean and spread for temperature, wind, and mean sea level pressure. The application of both SPPT and SPG resulted in an increase of the ensemble spread. In the free atmosphere, the increase was much greater for SPG both in temperature (see Fig. 24) and wind (not shown). Fig. 24 demonstrates the high sensitivity of ensemble spread to the standard deviations of the random fields generated by SPG. This implies that tuning the SPG setup is a tricky task.

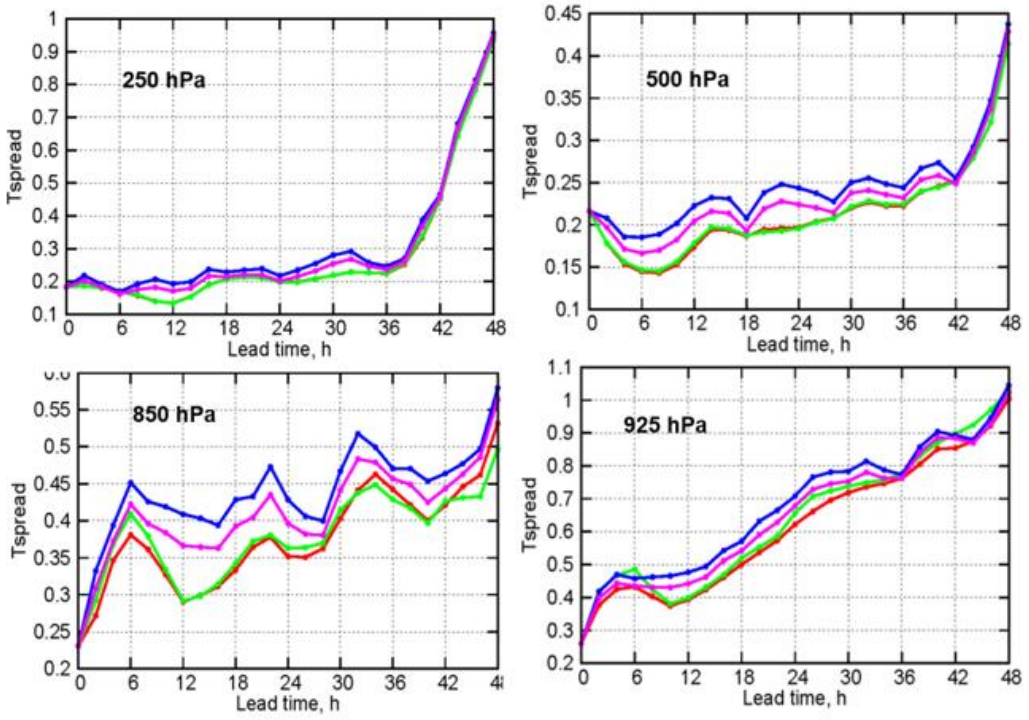


Figure 24: Temperature spread as a function of forecast time for experiments NOPERT (red), SPPTSW (green), SPGBIG2 (magenta), SPGBG (blue). Forecast start time is February 6, 2014 00UTC.

For individual days, the T2m spread with SPPT and SPG were comparable (see Fig. 25). The results of experiment SPGBG (with greater standard deviations of the SPG-generated random fields) seem to be superior.

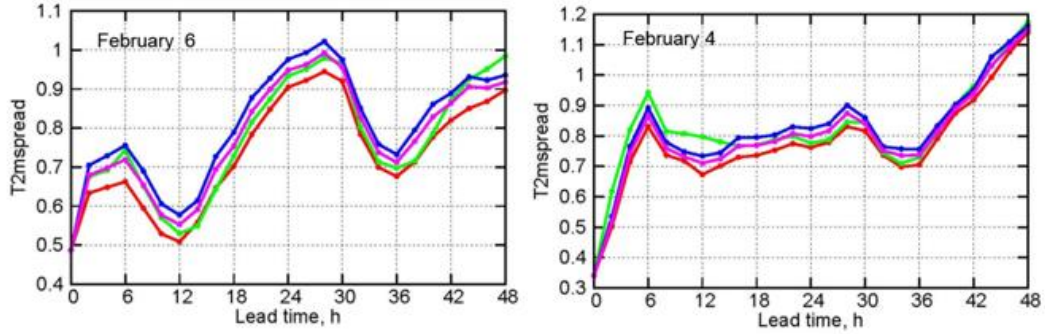


Figure 25: T2m spread as a function of forecast time for experiments NOPERT (red), SPPTSW (green), SPGBIG2 (magenta), SPGBG (blue) for forecasts starting on February 6, 2014 00UTC (left) and February 4, 2014 00UTC (right).

The ensemble forecasts of T2m were verified against the station data using VERSUS for the period of 7 days (February 1-7, 2014, 00UTC). In Fig. 26 the T2m spread for SPPT is slightly bigger than for SPG, while the latter slightly improved the T2m error. Note that all the above presented spread plots demonstrate the results of averaging over all grid points using the grib_api tools. On the other hand, VERSUS interpolates the forecasts to the points

of observations and the spread in Fig. 26 is averaged over observation points only.

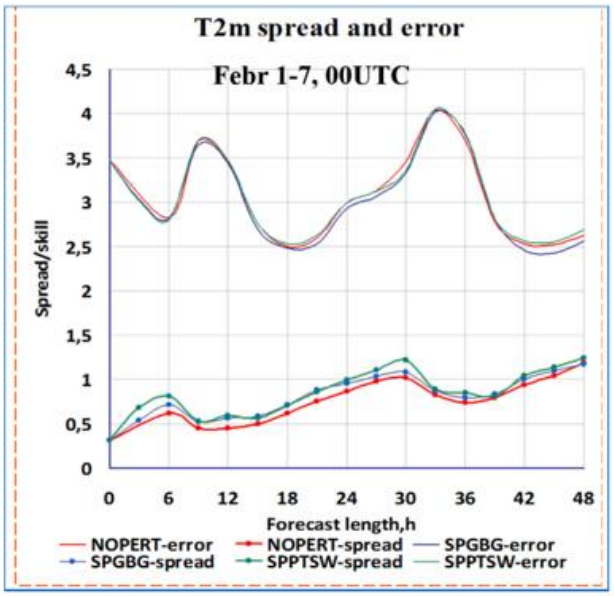


Figure 26: The error (upper curves) and the spread (lower curves) of T2m temperature for experiments NOPERT (red), SPPTSW (green) and SPGBG (blue) calculated for a 7-day period starting from February 1, 2014 00UTC. Sochi area.

Fig. 26 implies a possibility of a further increase of T_std and u,v_std in the SPG setup. An additional experiment with T_std=0.09 K/h and u,v_std= 0.3 m/s per hour was carried out. The T2m spread increased, but the effect on the free-atmosphere temperature spread was much greater, which does not look physically reliable. Thus, it was suggested to revise the way SPG is used for model perturbations and now the work continues within the APSU Priority Project.

Conclusions

- The application of SPG for perturbing model in COSMO-Ru2-EPS looks promising and results in increasing the ensemble spread;
- the application of SPG improves T2m forecasts;
- the ensemble spread is very sensitive to the SPG settings. Even a small increase in the standard deviation of the random fields leads to a spread growth. Variations in correlation lengths and times also have a visible effect but it is not so unequivocal and will be addressed later;
- in the free atmosphere, the temperature and wind spread is bigger with SPG than with SPPT;
- for T2m, the ensemble spreads in experiments with SPG and SPPT are comparable.

A new way of applying SPG (in which the number of parameters to be specified and tuned is reduced) will be considered in the Priority Project APSU.

4 Test and development of perturbation for the model lower boundary

The perturbation of the model lower boundary (surface/soil) has also been further developed, consolidating the methodologies developed in the COTEKINO PP.

4.1 Soil moisture perturbation in a complete ensemble set-up (ARPA Piemonte)

In the framework of the COTEKINO PP, a method for the perturbation of the soil moisture has been developed by Arpa Piemonte (Bonanno and Loglisci, 2018). The method is based on the Stochastic Pattern Generator developed by RHM (Tsyrulnikov and Gayfulin, 2016).

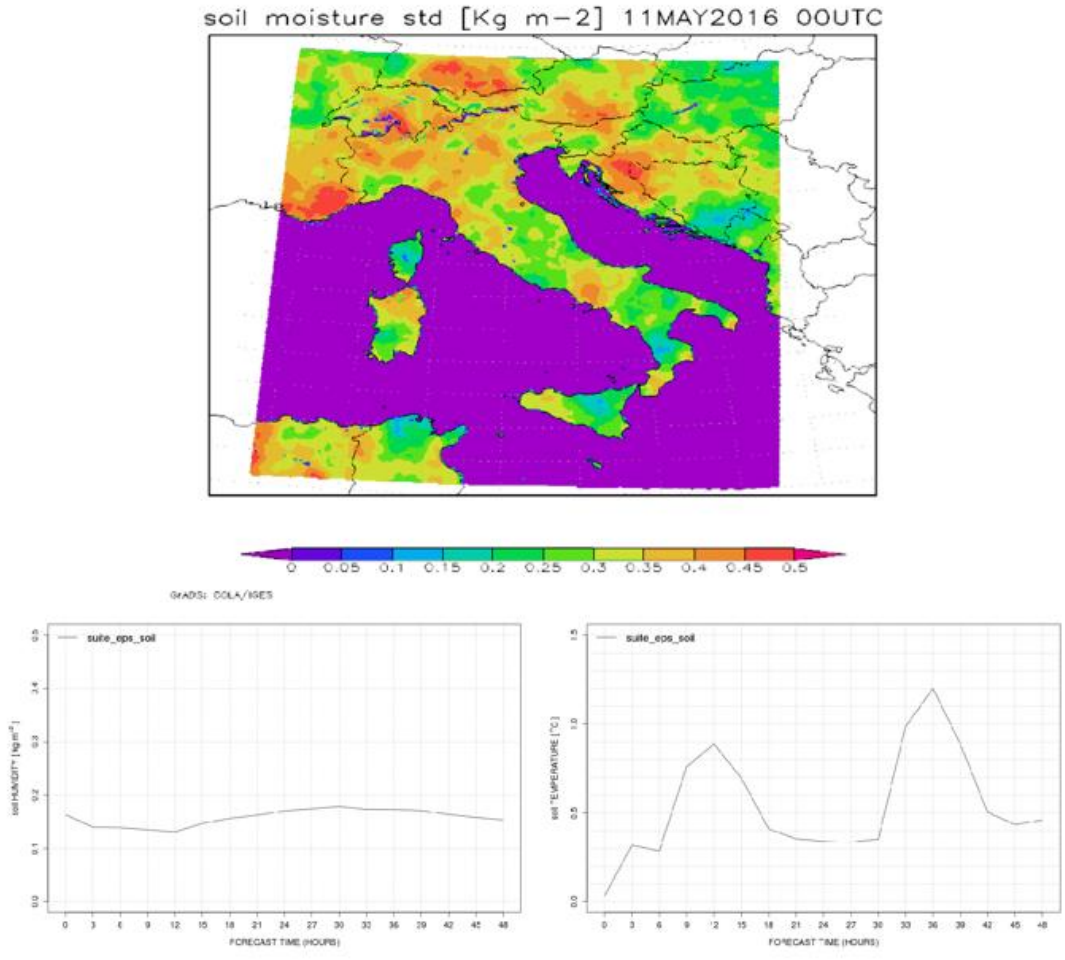


Figure 27: Soil mositure perturbation in the initial condition for the event of the 11 of May 2016 (top panel). Temporal evolution of the spread in terms of soil moisture (bottom left) and soil temperature (bottom right).

In the SPRED PP, the purpose of the task was to assess the benefit of the methodology by introducing the perturbation in an ensemble with "complete set-up", with perturbed Ini-

tial and Boundary Conditions, as well as physics perturbations. An experimental suite of COSMO-IT-EPS was created for this purpose. The ensemble was run in a complete ensemble set-up: Initial and Boundary Conditions from ECMWF ENS, SPPT and Parameter Perturbation applied to the COSMO model. The suite was run with and without soil moisture perturbation, for the month of May 2016. This period was selected due to the occurrence of several convective events over Italy. A statistical analysis of the results has not been completed due to a lack of resources. As an example of the perturbation applied, the field of the soil moisture perturbation is shown for the event on the 11 of May 2016 (top panel), together with the temporal evolution of the spread in terms of soil moisture (bottom left panel) and soil temperature (bottom right panel).

4.2 Soil parameters and soil temperature perturbation (IMGW)

At IMGW, the ensemble forecast was prepared in such a way that each member of the ensemble starts with a different value of the initial state of c_soil, the parameter describing the fraction of evaporating soil, and of soil surface temperature. The c_soil parameter is varied using the new random number generator. In addition to the variation of parameters that describe the state of soil surface, the collection efficiency coefficients (eff-coeff, see below) in the clouds were also perturbed to add perturbation in the physical parameterization of precipitation processes. The following perturbations were considered:

(a) *c_soil*: perturbation of a parameter describing evaporation from soil using RNG (described in Section 5.2);

(b) *eff-coeff*: perturbation of the collection efficiency coefficient;

(c) *eff-c_soil*: perturbation of the collection efficiency coefficient together with evaporation from the soil surface;

(d) *laf-pert*: perturbation of the surface temperature of the soil;

(e) *laf-c_soil*: perturbation of soil surface temperature in the set of initial conditions simultaneously with evaporation from the soil surface;

(f) *laf-eff*: perturbation of the soil surface temperature (as in (e)) together with a variation of the collection efficiency coefficient;

(g) *eps-all*: perturbation of all the above quantities (fields and parameters) at the same time.

The warm period (June-September) of 2013 was chosen for numerical simulations. The study was focused on ensemble forecasts of three meteorological fields: air temperature at 2 m above ground level (TE2M), dew point temperature at 2 m (TD2M), and wind speed at 10 m (U10M). For each meteorological field, the monthly average values of the spread (standard deviation of forecasts, calculated using all the members of the ensemble) and an indicator of skill S (mean absolute error, MAE, of the forecasts) were calculated (Jolliffe and Stephenson, 2012). In the next step the average values of spread and skill were compared with the average values of air temperature, the deviation of the average monthly air temperature in a given month in relation to the long-term average of 1971-2000 (Bulletin, 2013), the monthly precipitation sum and deviation of the monthly sum of atmospheric precipitation as a percentage of the long-term norm for 1971-2000 (Bulletin, ibid.). The results were cross-checked for correlation with the average values of spread and skill for the given type of soil that occurred in the analyzed area. The most effective perturbations (combinations) in

Period/Field	TD2m	T2m	U10m
June	eff-coeff	?	?(∼eff-c-soil)
July	c-soil	eff-coeff	?(∼laf-c-soil)
August	eff-coeff	eff-coeff	?(∼laf)
September	c-soil	eff-coeff	?
Jun-Sep	laf-c-soil	eff-coeff	?

Table 1: Most effective perturbations, see explanations in text above. Values averaged for June to August 2013. The ? means hard to establish, the ∼ means small tendency.

terms of skill and spread, averaged over the period of study, are presented in the following table.

The following figures present the most effective perturbation schemes in terms of skill (MAE) and spread on the period June-August 2013.

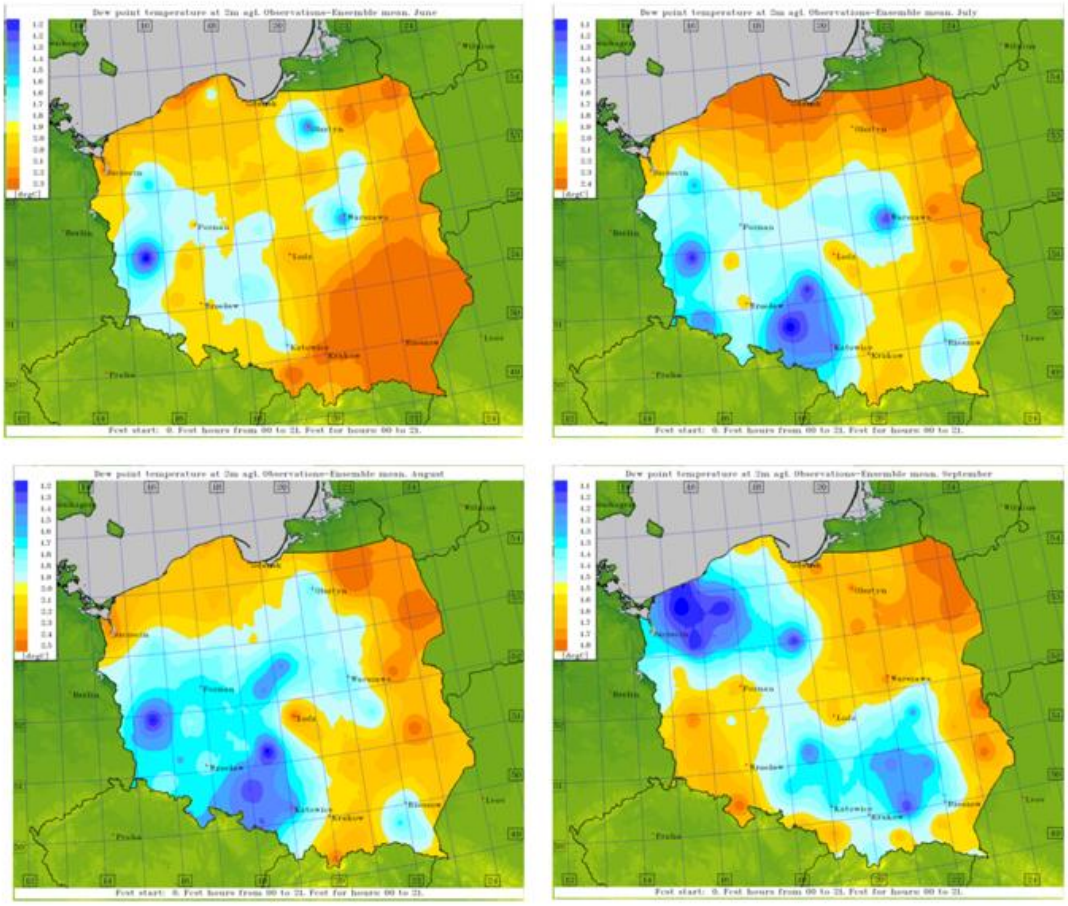


Figure 28: MAE (skill) spatial distribution for TD2M - most effective schemes. Upper left - June (eff-coef), upper right - July (c-soil), lower left - August (eff-coef), lower right - September(c-soil).

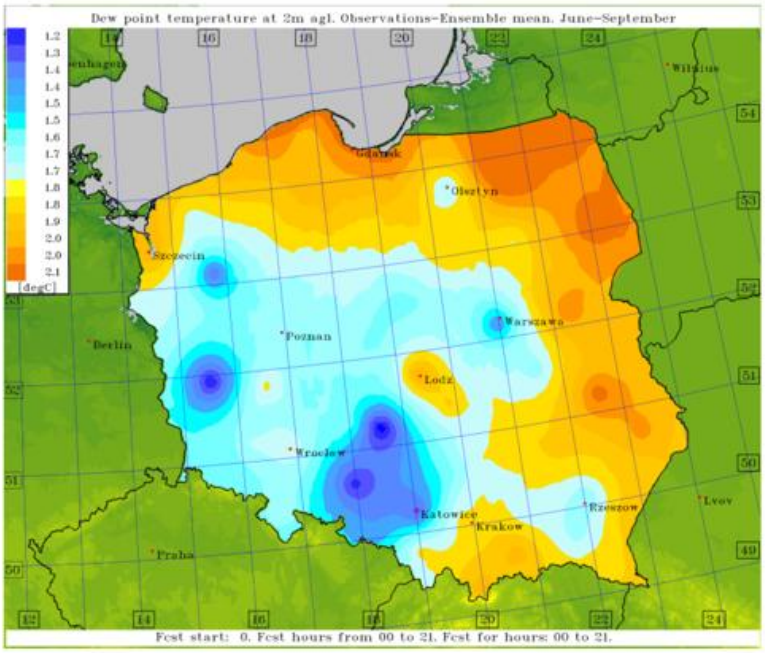


Figure 29: MAE (skill) spatial distribution for TD2M - most effective scheme for the entire period June-September 2013 - laf-c-soil.

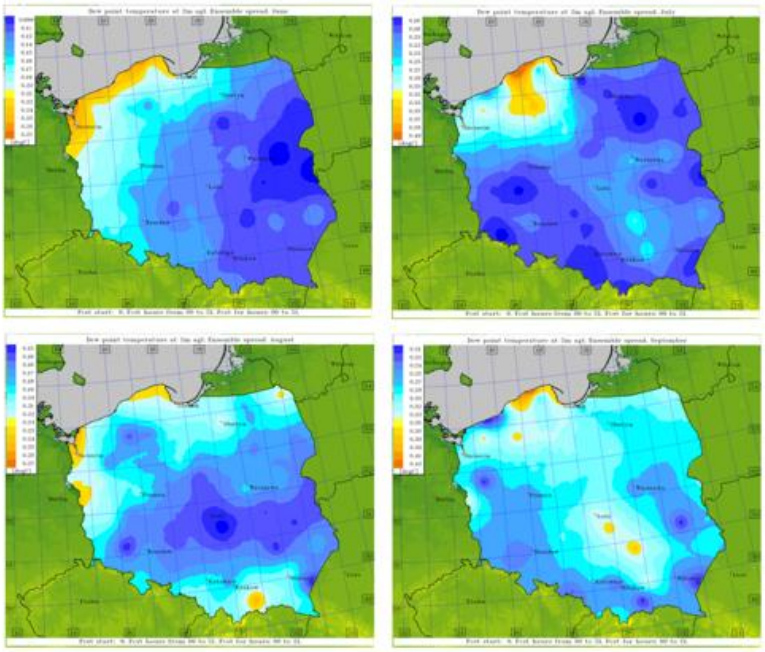


Figure 30: Spread spatial distribution for TD2M - most effective schemes. Upper left - June (eff-coef), upper right - July (c-soil), lower left - August (eff-coef), lower right - September(c-soil).

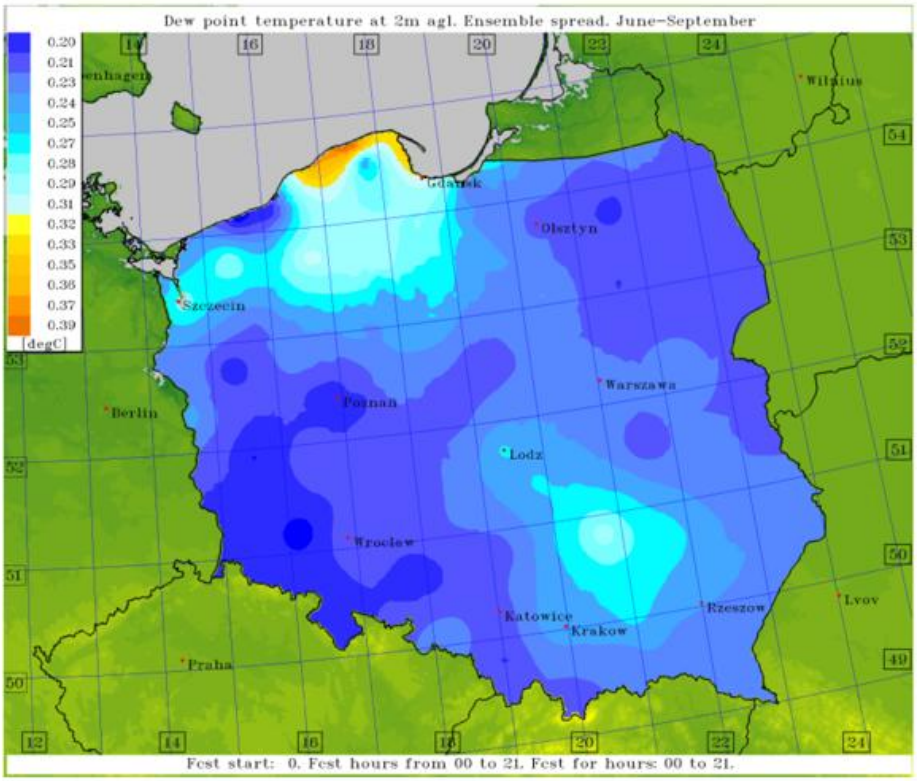


Figure 31: Spread spatial distribution for TD2M - most effective scheme for the entire period June-September 2013 - laf-c-soil.

Conclusions drawn from this part of study were as follows:

- values of spread/skill are in general independent on soil type;
- average values of spread of dew point temperature/air temperature/wind speed are inversely proportional to average monthly air temperature and to deviation of the mean monthly air temperature (T and ΔT) climatologically calculated for the period of 1971-2000;
- if long-term monthly sum of precipitation (P) is above a climatologically calculated average then the average values of spread of TD2M, T2M and U10M are low (EPS results are highly underdispersive);
- the correlations between the values of skill of TD2M, T2M, U10M and T, ΔT, P, and ΔP are similar to the ones between spread of TD2M, T2M, U10M and T, ΔT, P, and ΔP;
- average value of skill is independent on type of disturbed field or parameter. The distribution of the average values of skill is more or less similar to each other.

5 Ensemble post-processing

5.1 Development of probabilistic products at COMET

The work of generation of probabilistic products for the forecast of thunderstorms and fog is performed in the framework of the SRNWP-EPS II Project of EUMETNET. The main aim of the Project is to contribute to build very high-resolution ensemble systems in Europe, resolving the convection-permitting scale phenomena. First a review of literature on post-processing methods for prediction of fog and thunderstorms, with focus on ensembles, has been performed. Then the development of a software dedicated to this purpose has started, in particular a product for probabilistic prediction of fog has been implemented. The developed FORTRAN code provides surface visibility forecast starting from standard NWP models outputs. The following methods have been selected and implemented:

- "Zhou method" (Zhou, 2011). It is a new method, working properly for radiation and advection fog, based on the asymptotic liquid water content (LWC) vertical distribution. The asymptotic LWC distribution is a consequential balance among cooling, droplet gravitational settling and turbulence in the liquid water budget of radiation fog. Including the advection term, it is possible to write a partial differential equation as the governing equation for LWC [g/kg], with appropriate initial and boundary conditions for the one it is proposed an asymptotic solution that can be used to compute visibility through the Gultepe and Milbrandt (2007) formula;

- "Boudala method" (Boudala et al., 2012). This algorithm is based on the Stoelinga and Warner empirical equation that allows to compute visibility using information about relative humidity and dew point temperature;

- "LWC algorithm": it is the traditional approach that computes horizontal visibility using model forecastof specific cloud water content;

- "UPS method" (Baker et al., 2002). It is an empirical method proposed by UPS Airlines forecasters to forecast the radiation fog. It is based on the comparison of the low level atmospheric temperature and the so called crossover temperature, defined as the minimum of dew point during the warmest daytime hours. Following this approach it is possible to determine whether a station will radiatively cool enough for saturation. In a second step, in order to assess if boundary layer turbulence supports the fog formation process, a quantitative index of boundary layer turbulence mixing is used.

The code takes also into account the precipitation contribution to visibility reduction through an empirical formula.

Visibility forecast from different methods using deterministic COSMO-ME (5km hor. resolution) and COSMO-IT (2.8 km hor. resolution) model outputs have been compared with SYNOP observation over the Italian domain. The Zhou method seems to be the best candidate because it is able, in principle, to forecast both radiation and advection fog, but, as one of the trigger condition is the relative humidity from the NWP model output greater that 95 % (or other established threshold), results are highly influenced by this parameter. Looking at the results, the pattern of visibility seems to be much more reliable with Zhou with respect to the other methods, even if the visibility values seem to be underestimated (further tuning is needed through the configuration namelist). In order to overcome the sensitivity to the forecasted relative humidity (generally underestimated by the model), a combination of Boudala and Zhou methods has been proposed and used operationally at

the Italian AirForce Met Service. As an example, visibility forecasts with different methods applied to COSMO-ME deterministic model and COSMO-ME EPS (7 km resolution) probabilistic model, for a test case of 18 October 2017 06UTC (low visibility over Pratica di Mare airport), are shown in the figures below. Only Boudala and Zhou approaches forecast fog/mist in this region, in particular, Zhou approach has better correspondence with SYNOP observations.

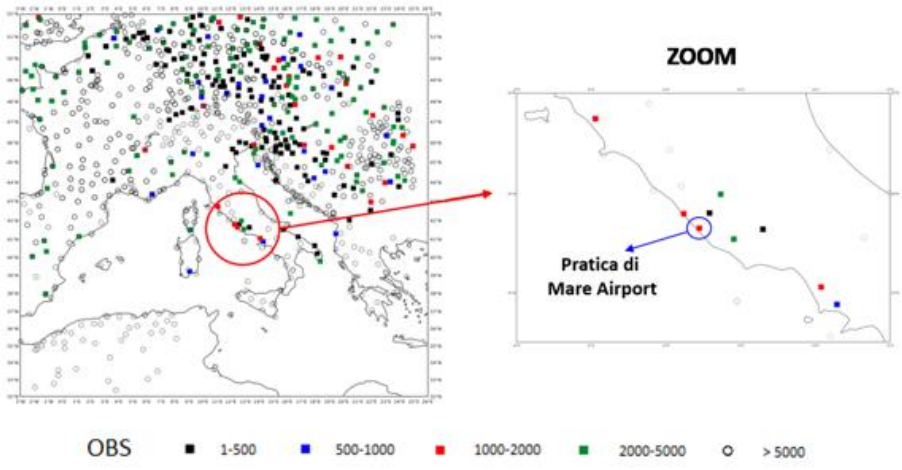


Figure 32: Test case of 18/10/2017 (intense fog event at Pratica di Mare airport): distribution of synop observations from 05 UTC to 07 UTC.

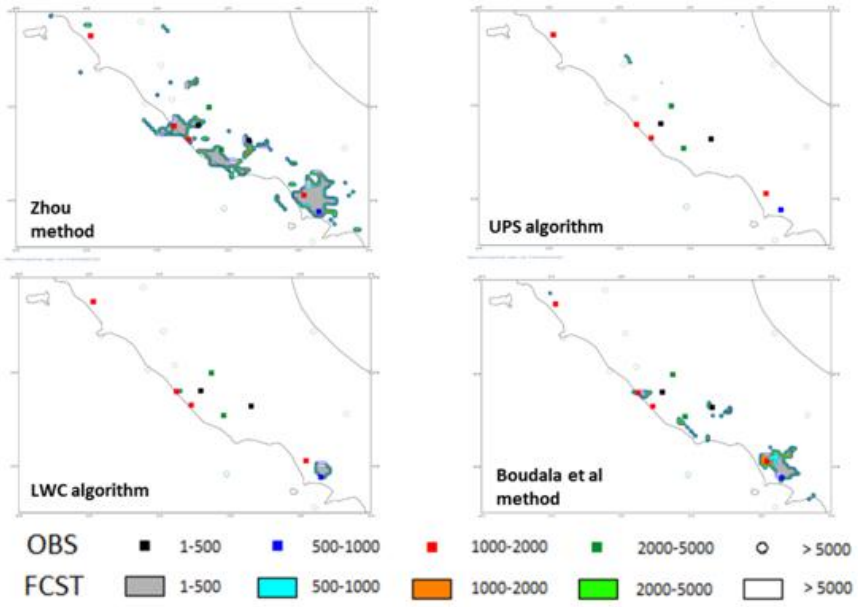


Figure 33: Test case of 18/10/2017 (intense fog event at Pratica di Mare airport): visibility forecast from different methods applied to the COSMO-ME (5 km) model outputs (run 00UTC of 18/10/2017, fc+6h).

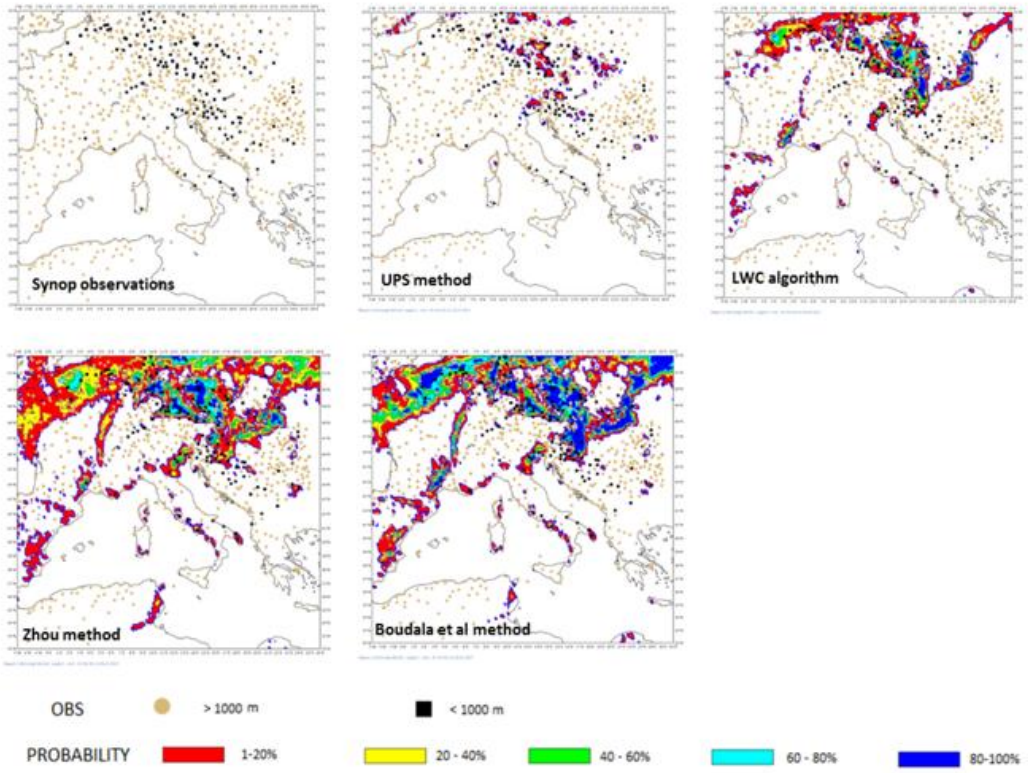


Figure 34: Test case of 18/10/2017: Forecasted probability of fog (visibility ¡ 1000 m) from different methods applied to the COSMO-ME-EPS (7 km) model outputs (run 00UTC of 18/10/2017, fc+6h).

Verification over an extended period has been planned together with the subjective verification from operational forecasters.

5.2 Calibration of ensemble output at IMGW

A review of literature concerning ensemble calibration methods and alternative perturbation patterns/random number generators has initially been performed. First, a new (alternative) Random Number Generator (RNG) has been introduced.

Alternative random number generator

Motivation for new (modified) initialization or seed of RNG was that seeding of RNG commonly is based on machine time (in general, milliseconds). This may results in seed(s) being identical for all processes (threads). This would lead to the situation, that with increasing number of parallel threads the probability of an occurrence of identical seeds would significantly increase. Having four hundred threads (like in case of IMGW EPS operational setup) vs. 999 milliseconds, it becomes more and more probable that some threats have an identical seed. This would results in an identical chain of RNG numbers generated, which in turn means a very poor stochasticity of EPS. One should also realize that using fast machines does not have 999 milliseconds, but much, much less. So, another initialization scheme has been selected combination of machine time with a thread ordinal number as in the figure below.

Spread values	*Ctrl (operational RNG)*	*Modified RNG*	*Ctrl (operational RNG)*	*Modified RNG*	*Ctrl (operational RNG)*	*Modified RNG*
	T2M (K)		**TD2M (K)**		**RH2M (%)**	
Mean	0.108191	0.238555	0.118675	0.272361	0.705627	2.120926
Max	2.262	2.458	3.284	3.536	12.261	14.758
	U10M (m/s)		**Surface pressure (hPa)**		**Total precipitation (mm)**	
Mean	0.139599	0.180653	0.023892	0.027456	0.286905	0.379897
Max	2.041	2.903	0.747	0.652	13.203	18.515

Table 2: Average spread values for June 2013, reference (operational RNG) vs. modified RNG.

```
type(random_state_t),intent(inout)::akrngs
integer::time(8),iseed
double precision::dprn1,dprn2
type(random_state_t)::krngs
! Init
! Get sys. time with non-zero millisecs. part
  time(8)=0
  do while ( time(8) .eq. 0 )
    call date_and_time(values=time)
  end do
! Calculate 1st seed based on milliseconds
  iseed = int( dble(time(8))... )
! Initialize temporary RNG  from mo_random
  call construct(krngs,iseed)
! Draw 1st RN  from mo_random
  call random_number(dprn1,krngs)
! Destroy temporary RNG  from mo_random
  call destruct(krngs)
! Calculate 2nd seed based on thread rank
  iseed = int( dble(icrnk+1) ... )
! Initialize temporary RNG  from mo_random
  call construct(krngs,iseed)
! Draw 2nd RN from mo_random
  call random_number(dprn2,krngs)
! Destroy temporary RNG from mo_random
  call destruct(krngs)
! Get 3rd RN: add 1st & 2nd RNs, normalize
  dprn1 = dprn1 + dprn2
  if(dprn1.gt.1.0d0) dprn1 = dprn1 - 1.0d0
! Calculate 3rd target seed based on 3rd RN
  iseed = int( dprn1... )
! Initialize target RNG using 3rd seed
  call construct(akrngs,iseed)
```

Figure 35: Block scheme of new seeding for RNG.

This procedure was tested first using archive data, with no time-lagged ICs/BCs to avoid influence from side effects other than change of seed. An average value of spread significantly increased as shown in the Table 2 below.

An example of spatial distribution of spread with/without new seeding scheme is shown in the Fig. 36.

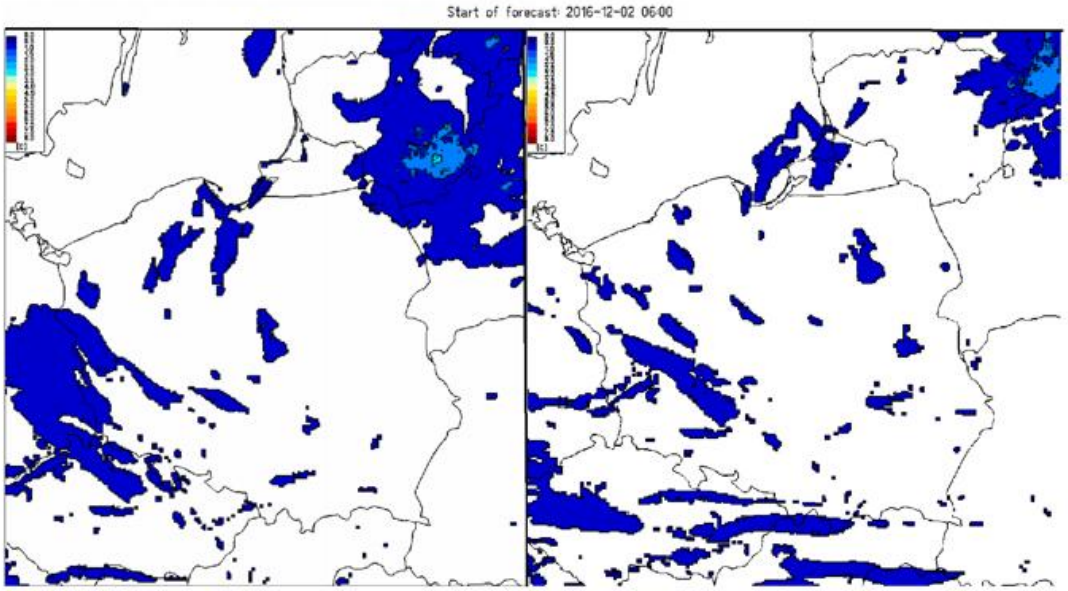


Figure 36: T2M spread for new (left) and old (right) seeding of RNG; 12 hour of forecast, December 2nd, 2916, 06:00 UTC.

This procedure is very efficient in terms of spread value (increasing average spread even 3 times comparing to "standard" RNG) especially on fast machines. It is also more realistic as far as spatio-temporal distribution of spread is concerned. At IMGW, it became operational in January 2017.

Post-processing multi-linear regression, logistic regression, Artificial Neural Networking

The most common procedure for calculating EPS mean is to use an arithmetic average as in the equation below (further Simple Mean):

$$\langle y \rangle = \frac{\sum_{i=1}^{m} x_i}{m}$$

An alternative approach can be described as (multi-)linear regression (MLR), where previously prepared forecasts from all members (X) of an EPS are compared with observations (learning phase). Then weights (β) of every member is computed to assess, how "important" for overall EPS-mean is a selected member (how big the contribution to EPS-mean from the member should be). The weights are calculated e.g. via least squares method, any potentially important factor(s) like geographical coordinates, terrain elevation etc. may also be considered. The following equation is a representation of the procedure, with an additional condition of normalization of weights to one. The "new" EPS mean y is calculated as a scalar product of vectors X and β:

$$\langle y \rangle = \vec{X} \cdot \vec{\beta}$$

Finally, an Artificial Neural Network (ANN) was studied to test if this approach could be a valid replacement for Simple Mean or MLR Mean. Basic idea is that the weights, with the same scheme as in MLR calculation, are calculated (learned) using a concept of layer of neurons, properly activated in learning phase. Basically, the representation of an ANN is presented in the following figures.

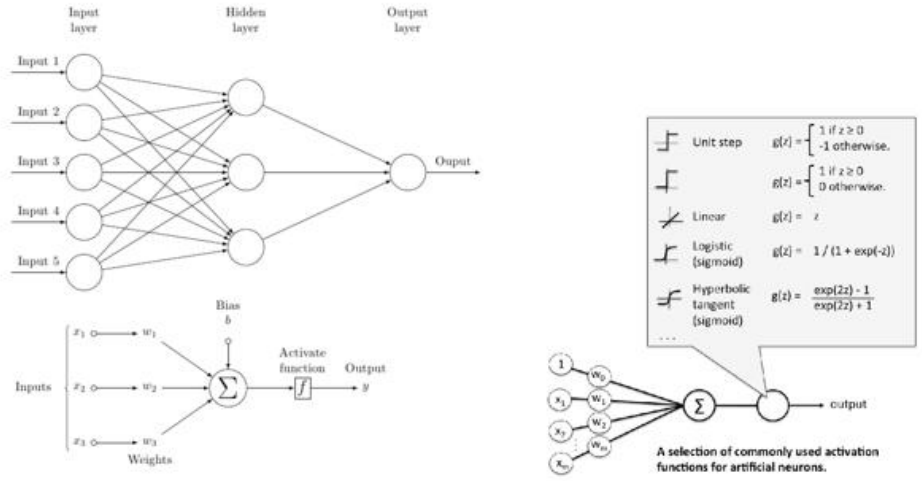


Figure 37: Basic concept of the Artificial Neural Network.

Pros and cons of the latest method are as follows: **Pros**:

1. ready-to-use dedicated software with source codes (FORTRAN);
2. sophisticated but elegant and intuitive concept;
3. improvement in preliminary case study observed;
4. forecasts are improving with the extension of learning period.

Cons (with answers to mitigate the cons):

1. complicated pre- and post-processing (answer: once the procedure is set-up and established, it can be further on done in an automatic way);
2. need for big data sets (archives), and for relatively huge computational resources (answer: this is a common feature of numerical forecasting - the need for huge volumes of data is a routine and a normal practice);
3. long computational time for training (answer: to avoid delays in operational post-processing, it can be done more or less frequently, with the acceptable quality of computations).

Results for case studies and for more extended periods (quasi-operational) are presented in the following tables and figures. First, case study for August 2017, with assorted number of predictors (input neurons) was analyzed. Learning period is July 1st, 2016 - July 31st, 2017, testing period is August 1st, 2017 - August 31st, 2017. The outcomes are presented in Table 3.

The spatial distribution of the average MAEs are presented in the Fig. 38.

Fields	Input Neurons* → / MAE ↓	24	22	20	Simple avg.**
U10m	Avg.	0.409	0.416	0.430	1.373
	Max	1.324	1.361	1.538	2.519
T2m	Avg.	0.266	0.275	0.451	2.606
	Max	0.924	1.144	1.302	3.628
Td2m	Avg.	0.268	0.305	0.365	1.736
	Max	0.906	0.999	1.238	2.006
PS	Avg.	2.398	2.405	2.595	2.864
	Max	11.683	11.464	9.708	11.786
TOT_PREC	Avg.	0.131	0.127	0.219	0.808
	Max	0.739	0.741	0.505	1.514

Table 3: ANN tests for August 2017, diversing number of neurons. * Input neurons: 20 - members (history, learning); 22 - 20 + geographical coordinates; 24 - 20 + geographical coordinates + forecast start + current hour. ** Simple averaging - 20 members mean (current forecast).

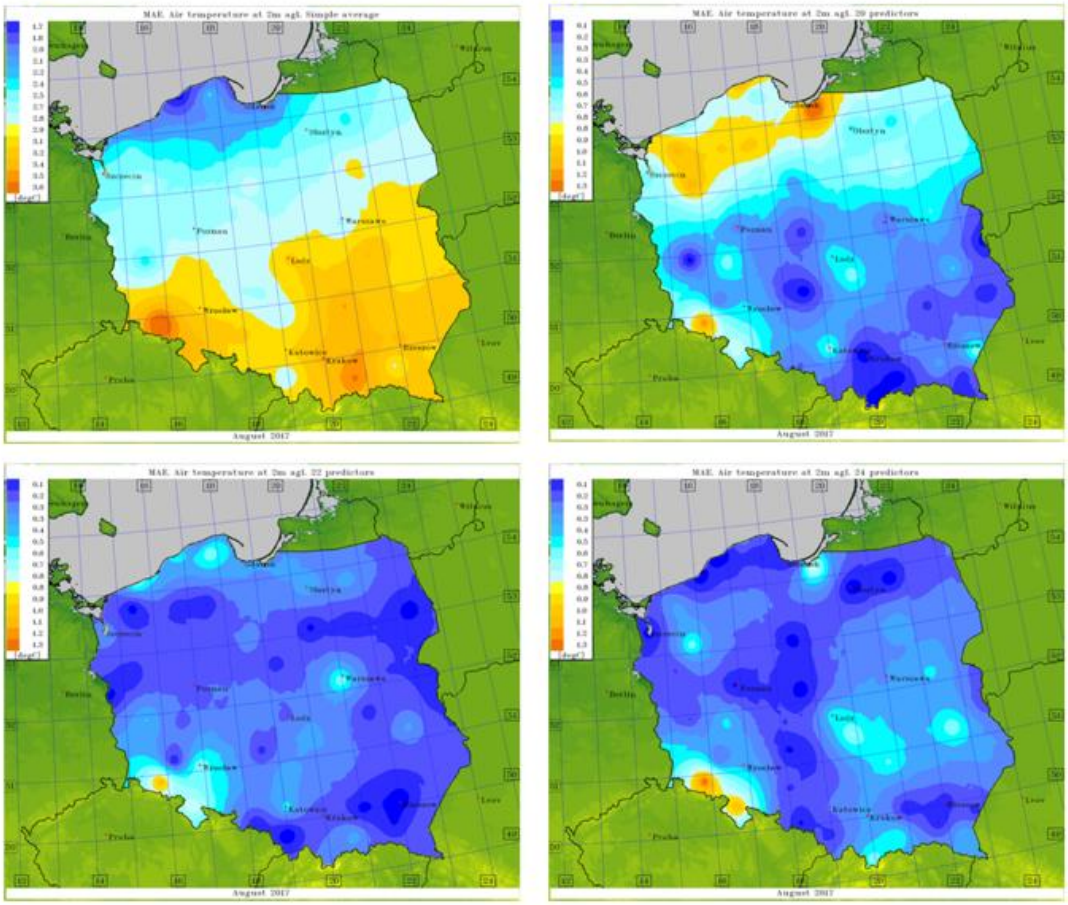


Figure 38: Results for different numbers of input neurons. Air temperature at 2m, mean absolute error, average values for August 2017. Upper left - reference (simple mean), upper right - ANN, 20 predictors, lower left - ANN, 22 predictors, lower right - ANN, 24 predictors.

Means	ME	MAE	RMSE	ME	MAE	RMSE	ME	MAE	RMSE
	Dew point			Air temp.			Wind speed		
Simple EPS	0.253	2.009	2.812	0.771	2.369	3.443	-0.618	1.737	2.297
MLR	-0.310	1.989	2.755	0.475	2.252	3.206	0.113	1.488	1.978
ANN	-0.244	1.981	2.750	0.066	2.214	3.135	-0.200	1.436	1.814

Table 4: ANN tests for April 2018, comparison with Simple Mean and MLR Mean.

For the further operational calculations the following setup has been chosen:

- 24 input neurons (20 members + λ, φ, ts, tc, with λ, φ - geographical coordinates, ts being start of forecast and tc - current hour of forecast in progress);
- 5 neurons in a single hidden layer (referring to 4 blocks of TL-ICs/BCs and spatial/temporal coordinates - blocked);
- every forecasted element, like temperature, wind speed, pressure, etc. is treated independently;
- activation function: hyperbolic tangent (symmetric with respect to 0,0, commonly used function);
- training method: backward propagation of errors (back-prop);
- optimization: gradient descent.

The following table and figures present an example results of EPS forecasts for April 2018, with the extended learning period (July 2016 - March 2018).

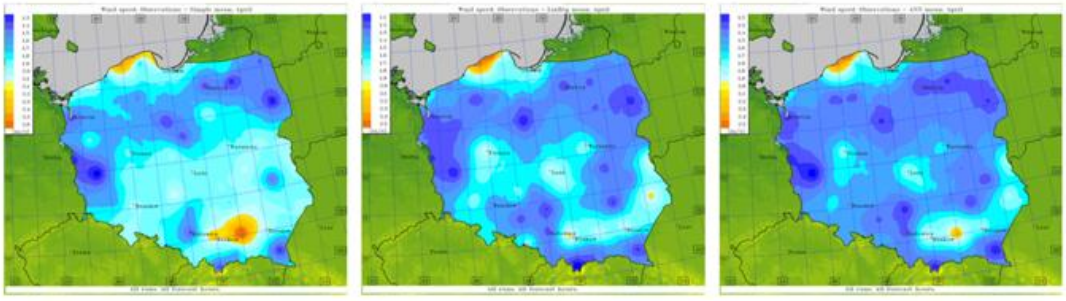


Figure 39: Results of different methods of computations of EPS mean. Left - observations vs. Simple Mean. Middle - observations vs. MLR mean. Right - observations vs. ANN mean. Wind speed forecasts, average values for April 2018.

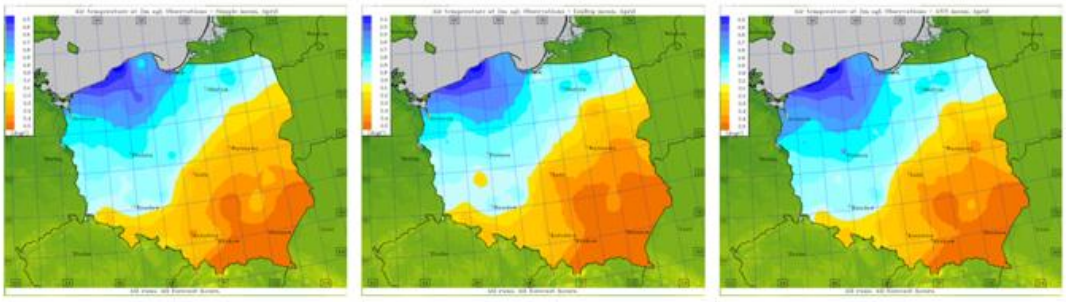


Figure 40: Results of different methods of computations of EPS mean. Left - observations vs. Simple Mean. Middle - observations vs. MLR mean. Right - observations vs. ANN mean. Air temperature forecasts, average values for April 2018.

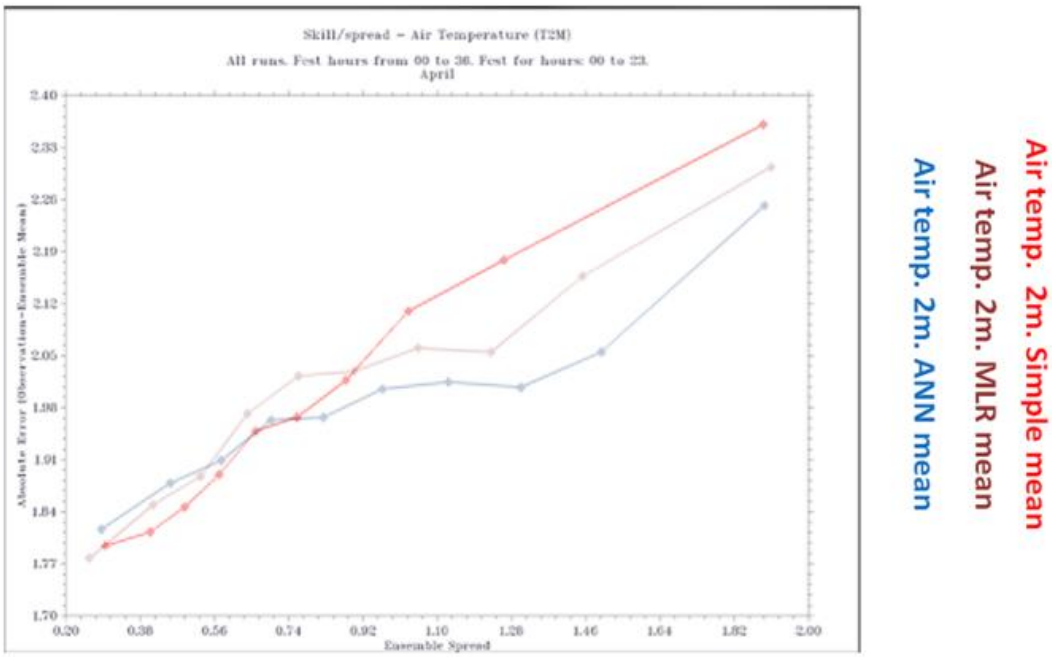


Figure 41: Skill-spread relation. Red - Simple Mean. Brown - MLR mean. Blue - ANN mean. Air temperature forecasts, average values for April 2018.

The general conclusions to be drawn from this study, was that significant improvement in forecasts (described in terms of EPS-mean vs. observations or forecast skill) can be seen. The longer learning period, the better forecasts are. Furthermore, the phrase "more predictors" - in general - means "better forecast", but also "longer calculations" - that is why some sort compromise should be established. ANN-based computation of EPS mean seems to be significantly better in comparison with Simple EPS Mean and with MLR mean, and that is why is has been chosen for further operational work.

6 Initial Conditions for the CP ensembles

The aim of this activity was to further study which methodology to follow to provide the ICs to the ensemble members. Experiments with ICs from KENDA compared with ICs from

cheaper options (downscaling) have been performed. It has also been performed a work on member selection from larger-scale ensembles.

6.1 Test of Initial Conditions from KENDA (DWD)

The KENDA-suite was running pre-operational providing initial perturbations for COSMO-DE-EPS. Two versions of BC perturbations are produced, with 20 members each (including physics perturbations): the known BCEPS multi-model approach and BCs from ICON-EPS (20 km grid size nest for Europe in a 40 km global EPS). Very preliminary results show an increase of spread together with a reduced RMSE of the ensemble mean for both 20 member setups. The resultingimproved spread-skill relation is still, but to a far less degree, underdispersive. The results have to be confirmed by longer verification periods and can be considered as first hints for improvement. The main results were an improvement in CRPS and partly RMSE of EPS mean for T_2M, gusts, and precipitation in summer and winter, particularly in the early forecast hours. An increase in spread for the variables lasts throughout the full forecast range of 27 hours. Improvements in thresholds-based BSS could be shown, where KENDA improved the resolution mainly. (Additionally, replacing BCEPS by ICON-EPS for the BCs improved mostly the reliability).

6.2 Test of Initial Conditions from KENDA (Arpae)

KENDA was tested for providing Initial Conditions to the deterministic and ensemble experimental chains with COSMO at 2.2 km over Italy. It is here shown the impact of the KENDA analyses as Initial Conditions to the members of the COSMO-IT-EPS ensemble for a period of May-June 2016 characterised by intense thunderstorms over different parts of Italy. The ensemble gets BCs from COSMO-ME-EPS and Parameter Perturbation is applied to the model. COSMO-IT-EPS with only parameter perturbations (PP experiment) and PP plus KENDA Initial Conditions (kendaIC_PP experiment) are compared in the following. An objective verification of the quality of the precipitation forecasted by the ensemble is carried out by comparing the forecasts with observations of precipitation estimated by radar and then adjusted with raingauge data. Both sets of data cover the entire Italian territory. Average and maximum over 0.2 deg boxes are considered.

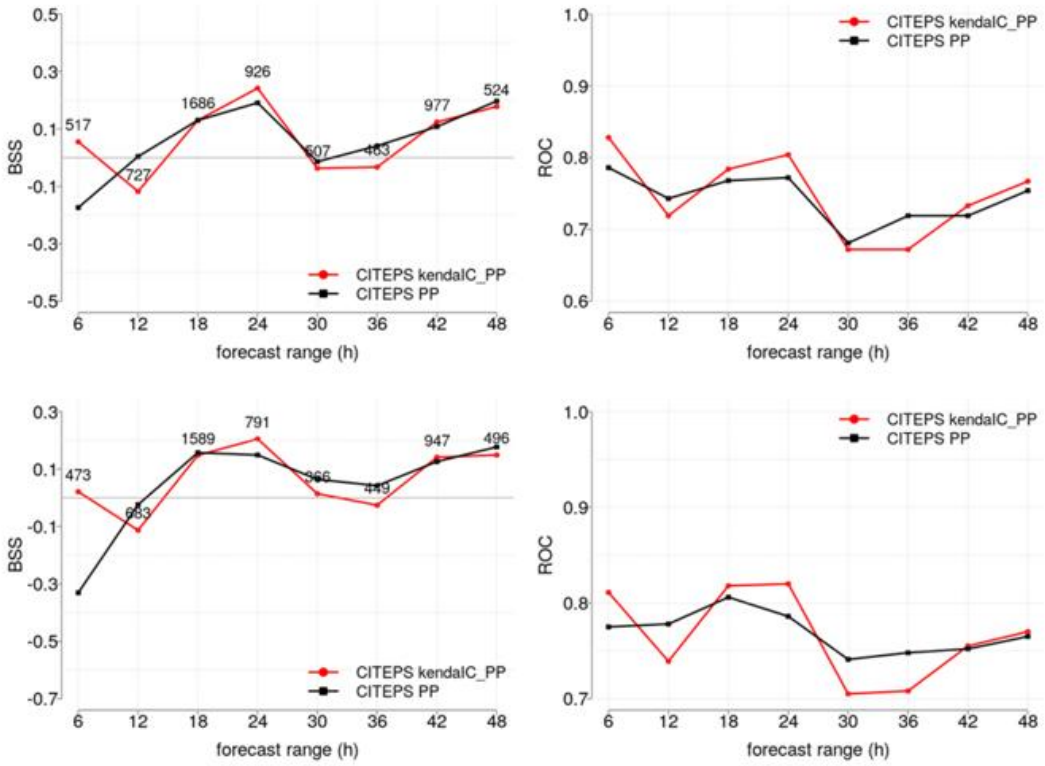


Figure 42: Brier Skill Score (left column) and the ROC area (right column) for average precipitation over each box exceeding 1 mm in 6 h (top row) and for maximum precipitation over each box exceeding 5 mm in 6 h (bottom row), computed against precipitation estimated from the Italian radar network, adjusted with raingauge values.

In all the plots of Fig. 42 is particularly evident the gain in skill in the first 6 hours of forecast determined by the use of Initial Conditions from the KENDA assimilation cycle. Generally, scores are not very high, showing the difficulty of forecasting thunderstorm events at high resolution (the verification boxes are of the order of 20 x 20 km). In order to show the quality of the ensemble members and how this is affected by the different initial conditions, a deterministic verification of the individual members is presented in Fig. 43.

The Frequency Bias (top rows, labelled Bias Score) indicates that the precipitation is generally underestimated by the ensembles, particularly for the lower threshold. It is interesting to notice that instead precipitation is overestimated for the first 6 hours for the 5 and 10 mm thresholds and that this bias is partly cured by the Initial Conditions from the KENDA analysis cycle. The other two scores do not vary much between the two ensemble configurations, with the exception of the first 6 hours as already noticed. In order to provide a clearer indication of what kind of events the 2.2 km ensemble is able to forecast in presence of thunderstorms, probability maps for selected cases are also shown.

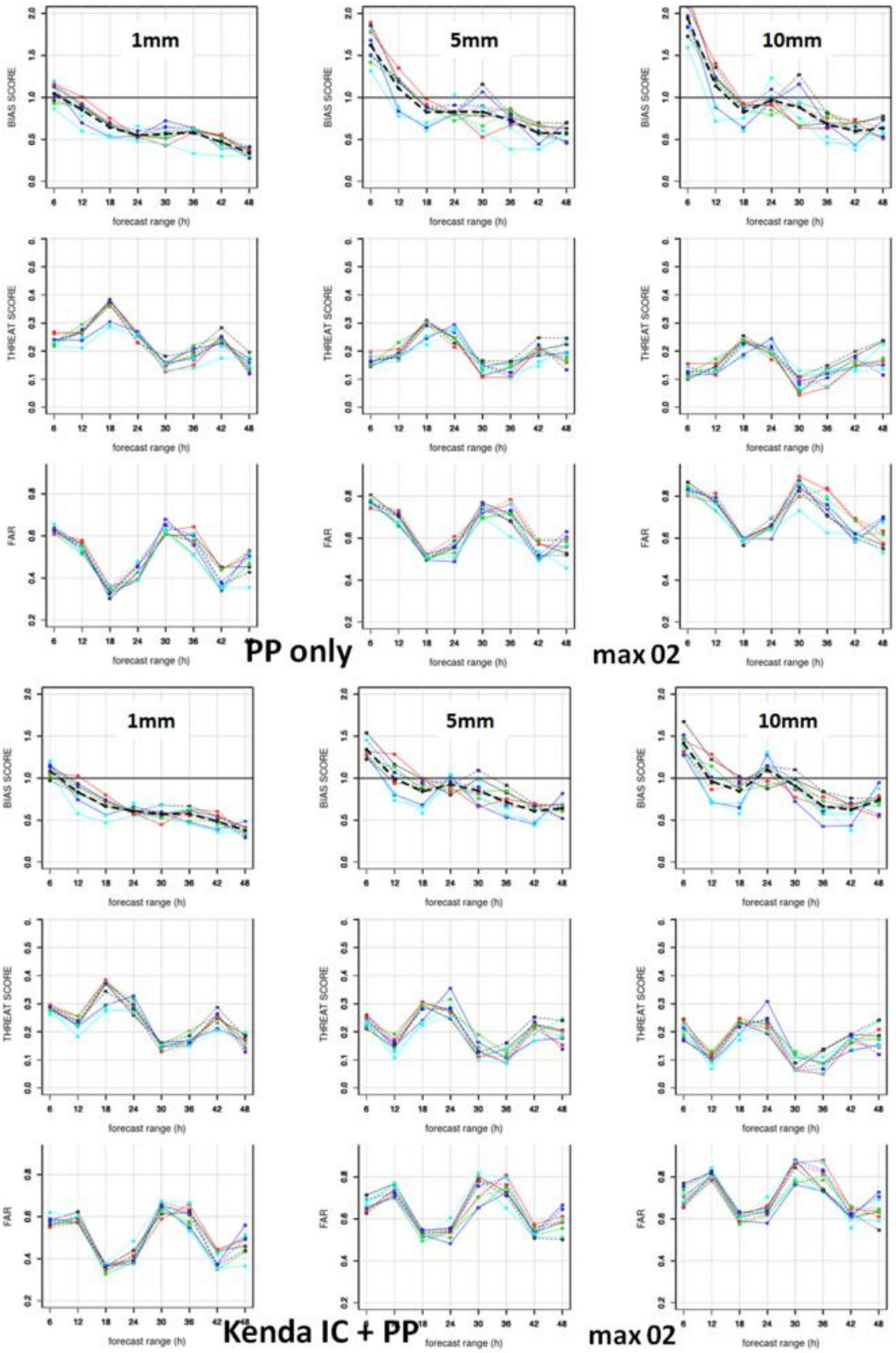


Figure 43: Frequency Bias (top row), Threat Score (middle row) and False Alarm Rate (bottom row) for the maxiumum precipitation over each box exceeding 1 mm in 6 h (left column), 5 mm in 6 h (central column) and 10 mm in 6 h (right row), computed against adjusted radar data for the PP (upper panels) and kendaIC_PP (lower panels) experiments.

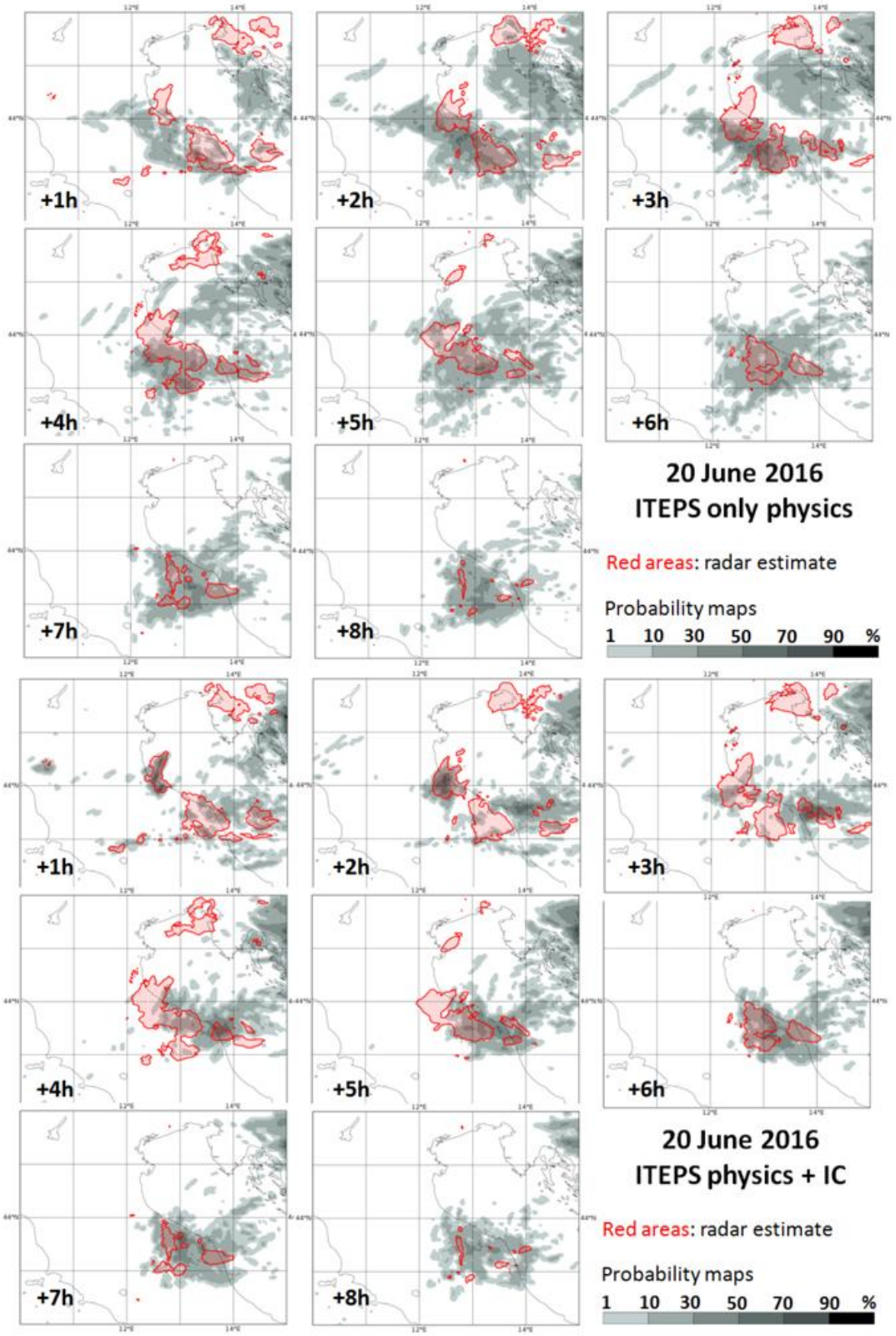


Figure 44: Probability maps (gray shaded) of precipitation exceeding 5 mm/1h generated by the ensemble, relative to the PP (upper panels) and kendalC_PP (lower panels) experiments, and filled contours (red areas) of precipitation estimated by radar exceeding 1mm/1h for the event of the 20th of June 2018, first 8 hours.

In Fig. 44, the probability of precipitation exceeding 5 mm in 1 hour as forecasted by the ensemble in the two different configurations (PP and kendaIC_PP) is plotted (as gray shaded) against the contour (red) relative to the precipitation exceeding 1mm in 1 hour as estimated by the radar network. It is possible to see that indeed the 2.2 km ensemble is generally able to indicated the probable occurrence of thunderstorms in the area where it was occurred. The level of spatial agreement between the forecast, issued in terms of probability and hence not really suitable for a one-to-one comparison with observations, is shown by the match or mismatch between the gray shaded areas and the red area. In this kind of evaluation, little can be said about the accuracy of the forecast of the precipitation amount, since the focus has been put on the capability of the ensemble to issue a forecast of thunderstorm at all, as a valuable tool to assist the forecasters in their daily task. On top, the level of spatial agreement or disagreement is what the forecaster should keep in mind for a profitable usage of the information provided by the ensemble. It is underlined that the different thresholds chosen for the probabilities and for the radar contouring are selected on purpose in order to take into account the tendency of the radar estimate to underestimate the precipitation amount (in analogy with what is done in a verification based on thresholds defined as percentiles instead of values). Considering the first 2-3 hours of forecast, it is evident that the data assimilation at 2.2 km with the KENDA cycle is able to provide initial conditions which greatly improve the position of the precipitation at the beginning of the forecast. This is believed to be partly due to the Latent Heat Nudging which is applied to each member of the KENDA ensemble, which had proven to increase the skill of the precipitation in the first few hours of the forecast. In this case, the forecast by the kendaIC_PP ensemble remains better than the PP one for the entire period shown.

6.3 Clustering of ensemble members for Lateral Boundary Conditions at MeteoSwiss

In the operational COSMO-E setup the perturbed members just use the first 20 members of KENDA and ECMWF ENS for the initial (ICs) and lateral boundary conditions (LBCs), respectively. Westerhuis (2016) investigated whether it is possible to enhance the COSMO-E forecast quality by using a smart selection. For COSMO-E it is found that:

- a sophisticated member selection like clustering for LBCs can improve COSMO-E forecasts significantly while a random member choice can result in significantly worse forecasts with bad luck;
- a clustering is able to decrease the outliers and increase the spread for near-surface variables which is probably the main reason for the better scores as show in Fig. 45;
- a sensitivity analysis of the clustering parameters demonstrates that the verification scores are very sensitive to the time steps used in the clustering analysis;
- the benefit of a better ICs selection is very limited due to the small spread.

Due to the positive results obtained with a member selection based on a clustering analysis, MeteoSwiss plans to implement such a member selection in the operational setup of COSMO-E.

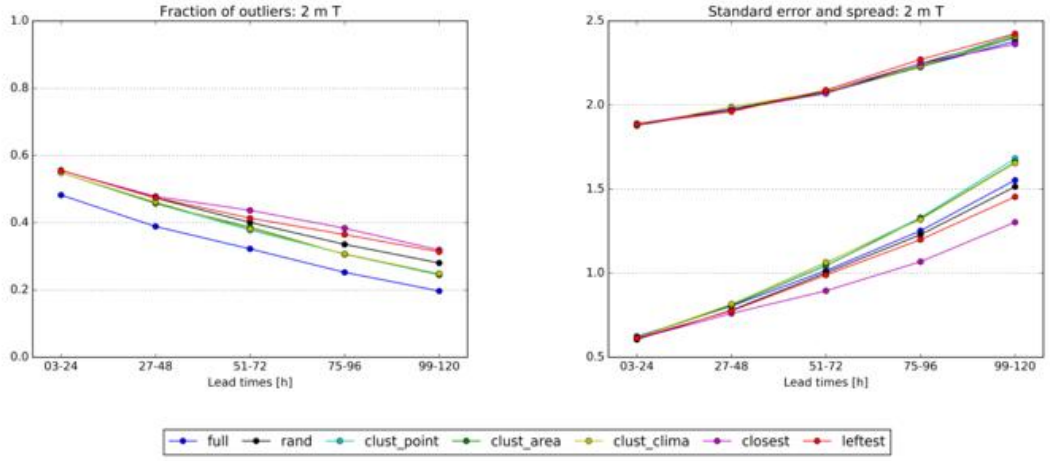


Figure 45: Fraction of outliers (left), standard deviation of error (upper lines in right panel) and ensemble spread (lower lines in right panel) for 2m temperature in COSMO-E forecasts from March 21 - April 8, 2015, for all stations in the model domain. The different lines show the scores obtained with different member selections methods: all 50 members (full), first 20 members (rand), clustering methods with different standardizations (clust), 20 members closest to ensemble mean (closest) and 20 driest members (leftest).

References

Astakhova, E. D., Montani, A., Alferov and Yu, D., 2015: Ensemble forecasts for the Sochi-2014 Olympic Games. *Russian meteorology and hydrology*, **40**, **8**, 531–539, DOI 10.3103/S1068373915080051

Astakhova, E. D., Montani, A., Kiktev, D., Smirnov, A., 2016: COSMO-based ensemble forecasting for Sochi-2014 Olympics: archiving the results. COSMO Newsletter No. 16, 40–45. Available online at http://cosmo-model.org/content/model/documentation/newsLetters/newsLetter16/cnl16_06.pdf

Baker, R. J., Cramer, Peters, J., 2002: Radiation fog: UPS Airlines conceptual models and forecast methods. Proc. 10th Conf. on Aviation, Range and Aerospace Meteorology, Portland, OR, *Amer. Meteor. Soc.*, 154–159

Bonnano, R., and Loglisci, N., 2018: Introducing lower boundary conditions perturbations in a convection-permitting ensemble system: sensitivity to soil moisture perturbation. *Meteorol. Atmos. Phys.*, **130**, **1**, 67–80

Boudala, F. S., Isaac, G. A., Crawford, R. W., and Reid, J., 2012: Parameterization of Runway Visual Range as a Function of Visibility: Implications for Numerical Weather Prediction Models. *Journal of Atmospheric and Oceanic Technology*, **29(2)**, 177–191

Bouttier, F., Raynaud, L., Nuissier, O., and Ménétrier, B., 2015: Sensitivity of the AROME ensemble to initial and surface perturbations during HyMeX. *Quarterly Journal of the Royal Meteorological Society*, **142**, 390–403. https://doi.org/10.1002/qj.2622

Buizza, R., Miller, M., and Palmer, T. N., 1999: Stochastic simulation of model uncertainties. *Quart. J. Roy. Meteorol. Soc.*, **125**, 2887–2908

Bulletin of the National Hydrological and Meteorological Service (referred as Bulletin) (2013), Institute of Meteorology and Water Management-National Research Institute, Poland

Chen, M., Wang, W., Kumar, A., 2013: Lagged Ensembles, Forecast Configuration, and Seasonal Predictions. *Monthly Weather Review*, **141**, 3477–3497. DOI: 10.1175/MWR-D-12-00184.1

Dey, S. R. A., Leoncini, G., Roberts, N. M., Plant, R. S., and Migliorini, S., 2014: A Spatial View of Ensemble Spread in Convection Permitting Ensembles. *Monthly Weather Review*, **142**, 4091–4107

Gultepe, I., and Milbrand, J., 2007: Microphysical observations and mesoscale model simulation of a warm fog case during FRAM project. *J. of Pure and Applied Geophy.*, Special issue on fog, edited by Gultepe I., **164**, 1161–1178

Jolliffe, I. T., and Stephenson, D. B., 2012: Forecast Verification - A Practitioners Guide in Atmospheric Science (second edition), Wiley & Sons, Chichester, UK, doi: 10.1002/9781119960003.ch7

Klasa, C., Arpagaus, M., Walser, A. and Wernli, H., 2018: An evaluation of the convection-permitting ensemble COSMO-E for three contrasting precipitation events in Switzerland. *Quart. J. Roy. Meteorol. Soc.*, **144**, 744–764, https://doi.org/10.1002/qj.3245

Klasa, C., Arpagaus, M., Walser, A., and Wernli, H., 2019: On the time evolution of limited-area ensemble variance: Case studies with the convection-permitting ensemble COSMO-E. *J. Atmos. Sci.*, **76**, 11–26, https://doi.org/10.1175/JAS-D-18-0013.1

Kober, K., and Craig, C., 2016: Physically Based Stochastic Perturbations (PSP) in the Boundary Layer to Represent Uncertainty in Convective Initiation, *J. Atmos. Sci.*, **73**, 2893–2911

Lu, C., Yuan, H., Schwartz, B. E., Benjamin, S. G., 2007: Short-range numerical weather prediction using time-lagged ensembles. *Weather and Forecasting*, **22**, 580–595. DOI: 10.1175/WAF999.1

Marsigli, C., 2009: COSMO Priority Project "Short Range Ensemble Prediction System" (SREPS): Final Report. COSMO Technical Report No. 13, available at http://www.cosmo-model.org/content/model/documentation/techReports/docs/techReport13.pdf.

Marsigli, C., Montani, A., and Paccagnella, T., 2008: A spatial verification method applied to the evaluation of high-resolution ensemble forecasts. *Meteorological Applications*, **15**, 125–143

Mazur, A., and Duniec, G., 2014a: Sensitivity test on the behavior of different COSMO suites to different lower boundary initial conditions. Presented during COSMO User Seminar, Offenbach, Germany, 2014

Mazur, A., and Duniec, G., 2014b: Soil state perturbations as an input for Ensemble Prediction System (EPS) forecast, 9th International Soil Science Congress on "The Soul of Soil and Civilization", Antalya/Turkey, 14-16 October, 2014. doi: 10.13140/2.1.1397.5840

Mazur, A., and Duniec, G., 2015: Ensemble Prediction System (EPS)-based forecast prepared from perturbation of soil conditions, COSMO Newsletter, **15**, 63–71

Montani, A., Alferov, D., Astakhova, E., Marsigli, C., and Paccagnella, T., 2014: Ensemble forecasting for Sochi-2014 Olympics: the COSMO-based ensemble prediction systems. COSMO Newsletter, **14**, 88–94, available online at http://cosmo-model.org/content/model/documentation/newsLetters/newsLetter14/cnl14_10.pdf

Palmer, T. N., Buizza, R., Doblas-Reyes, F., Jung, T., Leutbecher, M., Shutts, G. J., Steinheimer, M., and Weisheimer, A., 2009: Stochastic parametrization and model uncertainty. ECMWF Research Department Technical Memorandum, **598**, ECMWF, Shinfield Park, Reading RG2-9AX, UK, pp. 42

Peralta, C., Ben Bouallègue, Z., Theis, S. E., Gebhardt, C., and Buchhold, M., 2012: Accounting for initial condition uncertainties in COSMO-DE-EPS. *J. Geophys. Res.*, **117**, **D7**, doi:10.1029/2011JD016581

Sætra, Ø., Hersbach, H., Bidlot, J. R., and, Richardson, D. S., 2004: Effects of observation errors on the statistics for ensemble spread and reliability. *Monthly Weather Review*, **132**, 1487–1501

Tennant, W., and Beare, S., 2014: New schemes to perturb sea-surface temperature and soil moisture content in MOGREPS. *Quarterly Journal of the Royal Meteorological Society*, **140**, 1150–1160

Tsyrulnikov, M., and Gayfulin, D., 2016: A Stochastic Pattern Generator for ensemble applications. COSMO Technical Report, **29**, pp. 51

Tsyrulnikov, M., and Gayfulin, D., 2017: A limited-area spatio-temporal stochastic pattern generator for simulation of uncertainties in ensemble applications. *Meteorol. Zeitschrift*, **26**, **N5**, 549–566

Tsyrulnikov, M. D., 2001: Proportionality of scales: an isotropy-like property of geophysical fields. *Quarterly Journal of the Royal Meteorological Society*, **127**, **578**, 2741–2760

Wernli, H., Paulat, M., Hagen, M., and Frei, C., 2008: SAL - A novel quality measure for the verification of quantitative precipitation forecasts. *Mon. Wea. Rev.*, **136**, 4470–4487

Westerhuis, S., 2016: Ensemble member selection for COSMO-E initial and boundary conditions. Master thesis. Available at MeteoSwiss

Zhou, B., 2011: Introduction to A New Fog Diagnostic Scheme. NCEP Office Note 466, US Dept. of Commerce, NOAA, National Weather Service, NCEP, pp.43

List of COSMO Newsletters and Technical Reports

(available for download from the COSMO Website: www.cosmo-model.org)

COSMO Newsletters

No. 1: February 2001.

No. 2: February 2002.

No. 3: February 2003.

No. 4: February 2004.

No. 5: April 2005.

No. 6: July 2006.

No. 7: April 2008; Proceedings from the 8th COSMO General Meeting in Bucharest, 2006.

No. 8: September 2008; Proceedings from the 9th COSMO General Meeting in Athens, 2007.

No. 9: December 2008.

No. 10: March 2010.

No. 11: April 2011.

No. 12: April 2012.

No. 13: April 2013.

No. 14: April 2014.

No. 15: July 2015.

No. 16: July 2016.

No. 17: July 2017.

No. 18: November 2018.

COSMO Technical Reports

No. 1: Dmitrii Mironov and Matthias Raschendorfer (2001):
Evaluation of Empirical Parameters of the New LM Surface-Layer Parameterization Scheme. Results from Numerical Experiments Including the Soil Moisture Analysis.

No. 2: Reinhold Schrodin and Erdmann Heise (2001):
The Multi-Layer Version of the DWD Soil Model TERRA_LM.

No. 3: Günther Doms (2001):
A Scheme for Monotonic Numerical Diffusion in the LM.

No. 4: Hans-Joachim Herzog, Ursula Schubert, Gerd Vogel, Adelheid Fiedler and Roswitha Kirchner (2002):
LLM ¯ the High-Resolving Nonhydrostatic Simulation Model in the DWD-Project LITFASS.
Part I: Modelling Technique and Simulation Method.

No. 5: Jean-Marie Bettems (2002):
EUCOS Impact Study Using the Limited-Area Non-Hydrostatic NWP Model in Operational Use at MeteoSwiss.

No. 6: Heinz-Werner Bitzer and Jürgen Steppeler (2004):
Documentation of the Z-Coordinate Dynamical Core of LM.

No. 7: Hans-Joachim Herzog, Almut Gassmann (2005):
Lorenz- and Charney-Phillips vertical grid experimentation using a compressible nonhydrostatic toy-model relevant to the fast-mode part of the 'Lokal-Modell'.

No. 8: Chiara Marsigli, Andrea Montani, Tiziana Paccagnella, Davide Sacchetti, André Walser, Marco Arpagaus, Thomas Schumann (2005):
Evaluation of the Performance of the COSMO-LEPS System.

No. 9: Erdmann Heise, Bodo Ritter, Reinhold Schrodin (2006):
Operational Implementation of the Multilayer Soil Model.

No. 10: M.D. Tsyrulnikov (2007):
Is the particle filtering approach appropriate for meso-scale data assimilation ?

No. 11: Dmitrii V. Mironov (2008):
Parameterization of Lakes in Numerical Weather Prediction. Description of a Lake Model.

No. 12: Adriano Raspanti (2009):
COSMO Priority Project "VERification System Unified Survey" (VERSUS): Final Report.

No. 13: Chiara Marsigli (2009):
COSMO Priority Project "Short Range Ensemble Prediction System" (SREPS): Final Report.

No. 14: Michael Baldauf (2009):
COSMO Priority Project "Further Developments of the Runge-Kutta Time Integration Scheme" (RK): Final Report.

No. 15: Silke Dierer (2009):
COSMO Priority Project "Tackle deficiencies in quantitative precipitation forecast" (QPF): Final Report.

No. 16: Pierre Eckert (2009):
COSMO Priority Project "INTERP": Final Report.

No. 17: D. Leuenberger, M. Stoll and A. Roches (2010):
Description of some convective indices implemented in the COSMO model.

No. 18: Daniel Leuenberger (2010):
Statistical analysis of high-resolution COSMO Ensemble forecasts in view of Data Assimilation.

No. 19: A. Montani, D. Cesari, C. Marsigli, T. Paccagnella (2010):
Seven years of activity in the field of mesoscale ensemble forecasting by the COSMO–LEPS system: main achievements and open challenges.

No. 20: A. Roches, O. Fuhrer (2012):
Tracer module in the COSMO model.

No. 21: Michael Baldauf (2013):
A new fast-waves solver for the Runge-Kutta dynamical core.

No. 22: C. Marsigli, T. Diomede, A. Montani, T. Paccagnella, P. Louka, F. Gofa, A. Corigliano (2013):
The CONSENS Priority Project.

No. 23: M. Baldauf, O. Fuhrer, M. J. Kurowski, G. de Morsier, M. Müllner, Z. P. Piotrowski, B. Rosa, P. L. Vitagliano, D. Wójcik, M. Ziemiański (2013):
The COSMO Priority Project 'Conservative Dynamical Core' Final Report.

No. 24: A. K. Miltenberger, A. Roches, S. Pfahl, H. Wernli (2014):
Online Trajectory Module in COSMO: a short user guide.

No. 25: P. Khain, I. Carmona, A. Voudouri, E. Avgoustoglou, J.-M. Bettems, F. Grazzini (2015):
The Proof of the Parameters Calibration Method: CALMO Progress Report.

No. 26: D. Mironov, E. Machulskaya, B. Szintai, M. Raschendorfer, V. Perov, M. Chumakov, E. Avgoustoglou (2015):
The COSMO Priority Project 'UTCS' Final Report.

No. 27: J-M. Bettems (2015):
The COSMO Priority Project 'COLOBOC': Final Report.

No. 28: Ulrich Blahak (2016):
RADAR_MIE_LM and RADAR_MIELIB - Calculation of Radar Reflectivity from Model Output.

No. 29: M. Tsyrulnikov and D. Gayfulin (2016):
A Stochastic Pattern Generator for ensemble applications.

No. 30: D. Mironov and E. Machulskaya (2017):
A Turbulence Kinetic Energy – Scalar Variance Turbulence Parameterization Scheme.

No. 31: P. Khain, I. Carmona, A. Voudouri, E. Avgoustoglou, J.-M. Bettems, F. Grazzini, P. Kaufmann (2017):
CALMO - Progress Report.

No. 32: A. Voudouri, P. Khain, I. Carmona, E. Avgoustoglou, J.M. Bettems, F. Grazzini, O. Bellprat, P. Kaufmann and E. Bucchignani (2017):
Calibration of COSMO Model, Priority Project CALMO Final report

No. 33: N. Vela (2017):
VAST 2.0 - User Manual.

No. 34: C. Marsigli, D. Alferov, M. Arpagaus, E. Astakhova, R. Bonanno, G. Duniec, C. Gebhardt, W. Interewicz, N. Loglisci, A. Mazur, V. Maurer, A. Montani, A. Walser (2018):
COsmo Towards Ensembles at the Km-scale IN Our countries (COTEKINO), Priority Project final report.

No. 35: G. Rivin, I. Rozinkina, E. Astakhova, A. Montani, D. Alferov, M. Arpagaus, D. Blinov, A. Bundel, M. Chumakov, P. Eckert, A. Euripides, J. Förstner, J. Helmert, E. Kazakova, A. Kirsanov, V. Kopeikin, E. Kukanova, D. Majewski, C. Marsigli, G. de Morsier, A. Muravev, T. Paccagnella, U. Schättler, C. Schraff, M. Shatunova, A. Shcherbakov, P. Steiner, M. Zaichenko (2018):
The COSMO Priority Project CORSO Final Report.

No. 36: A. Raspanti, A. Celozzi, A. Troisi, A. Vocino, R. Bove, F. Batignani (2018):
The COSMO Priority Project VERSUS2 Final Report.

No. 37: A. Bundel, F. Gofa, D. Alferov, E. Astakhova, P. Baumann, D. Boucouvala, U. Damrath, P. Eckert, A. Kirsanov, X. Lapillonne, J. Linkowska, C. Marsigli, A. Montani, A. Muraviev, E. Oberto, M.S. Tesini, N. Vela, A. Wyszogrodzki, M. Zaichenko, A. Walser (2019):
The COSMO Priority Project INSPECT Final Report.

No. 38: G. Rivin, I. Rozinkina, E. Astakhova, A. Montani, J-M. Bettems, D. Alferov, D. Blinov, P. Eckert, A. Euripides, J. Helmert, M.Shatunova (2019):
The COSMO Priority Project CORSO-A Final Report.

COSMO Technical Reports

Issues of the COSMO Technical Reports series are published by the *COnsortium for Small-scale MOdelling* at non-regular intervals. COSMO is a European group for numerical weather prediction with participating meteorological services from Germany (DWD, AWGeophys), Greece (HNMS), Italy (USAM, ARPA-SIMC, ARPA Piemonte), Switzerland (MeteoSwiss), Poland (IMGW), Romania (NMA) and Russia (RHM). The general goal is to develop, improve and maintain a non-hydrostatic limited area modelling system to be used for both operational and research applications by the members of COSMO. This system is initially based on the COSMO-Model (previously known as LM) of DWD with its corresponding data assimilation system.

The Technical Reports are intended

- for scientific contributions and a documentation of research activities,
- to present and discuss results obtained from the model system,
- to present and discuss verification results and interpretation methods,
- for a documentation of technical changes to the model system,
- to give an overview of new components of the model system.

The purpose of these reports is to communicate results, changes and progress related to the LM model system relatively fast within the COSMO consortium, and also to inform other NWP groups on our current research activities. In this way the discussion on a specific topic can be stimulated at an early stage. In order to publish a report very soon after the completion of the manuscript, we have decided to omit a thorough reviewing procedure and only a rough check is done by the editors and a third reviewer. We apologize for typographical and other errors or inconsistencies which may still be present.

At present, the Technical Reports are available for download from the COSMO web site (www.cosmo-model.org). If required, the member meteorological centres can produce hard-copies by their own for distribution within their service. All members of the consortium will be informed about new issues by email.

For any comments and questions, please contact the editor:

Massimo Milelli
Massimo.Milelli@arpa.piemonte.it

Consortium for Small-Scale Modelling

Technical Report No. 22

The CONSENS Priority Project

July 2013

DOI: 10.5676/DWD_pub/nwv/cosmo-tr_22

Deutscher Wetterdienst
MeteoSwiss
Ufficio Generale Spazio Aereo e Meteorologia
ΕΘΝΙΚΗ ΜΕΤΕΩΡΟΛΟΓΙΚΗ ΥΠΗΡΕΣΙΑ
Instytucie Meteorogii i Gospodarki Wodnej
Administratia Nationala de Meteorologie
ROSHYDROMET
Agenzia Regionale per la Protezione Ambientale del Piemonte
Agenzia Regionale per la Protezione Ambientale dell'Emilia-Romagna
Centro Italiano Ricerche Aerospaziali
Amt für GeoInformationswesen der Bundeswehr



www.cosmo-model.org

Editor: Massimo Milelli, ARPA Piemonte

The CONSENS Priority Project

C. Marsigli [*], *T. Diomede* [*], *A. Montani* [*] *and T. Paccagnella* [*],

P. Louka [**] *and F. Gofa* [**],

A. Corigliano [***]

[*] ARPA-SIMC, Bologna, Italy
[**] HNMS, Athens, Greece
[***] University of Bologna, Bologna, Italy

Contents

1 Abstract **3**

2 Introduction **3**

3 Model perturbations **4**

3.1 Parameter perturbations 4

3.2 Soil moisture perturbation 6

4 Ensemble merging **13**

4.1 Clustering applied to a multi-ensemble 13

4.2 Multi-model vs single-model approach for IC and BC to ensemble 17

5 Calibration **20**

5.1 Comparison of the calibration methodologies in terms of precipitation forecast 20

5.2 Verification of the calibration process by coupling QPFS with an hydrological model 30

5.3 Comments and conclusions 37

6 Conclusions **38**

7 Acknowledgments **39**

8 References **39**

1 Abstract

This project was aimed at consolidating the COSMO ensemble forecasting systems for the mesoscale. The operational ensemble COSMO-LEPS and the experimental COSMO-SREPS system, both running at 7 km horizontal mesh-size, have been designed for different forecast ranges (day 3-5 and 1-2, respectively) and with different perturbation strategies. The aim of the project was to propose a solution for a unique "multi-perturbation-strategy" COSMO ensemble system, benefiting of perturbations which can produce appropriate spread for the entire forecast range (i.e., day 1-5), including a set of model perturbations which should guarantee a good description of the COSMO model error. Both perturbations of the mode physics parameters and perturbation of the soil moisture field had been considered. Furthermore, a calibration strategy was developed and applied to the QPF issued by the COSMO-LEPS ensemble. The project lasted for 3 years.

2 Introduction

Since November 2002, COSMO is running a Consortium ensemble, COSMO-LEPS (Montani et al., 2003). In the present configuration, COSMO-LEPS is a 16 member ensemble based on the COSMO model with a 7 km horizontal mesh-size and 40 vertical levels. The system is running at ECMWF using the Billing Units provided by the COSMO Countries which are also ECMWF member states (Germany, Greece, Italy, and Switzerland) and it is developed an maintained by ARPA-SIMC. COSMO-LEPS is a dynamical downscaling of the ECMWF EPS, taking initial and boundary conditions from 16 selected members of the EPS. COSMO-LEPS is mainly designed for the early medium range (day 3-5) and the forecast range is 5.5 days. Some perturbations to the model are included, following the outcomes of the SREPS and CONSENS PPs. The soil moisture analysis provided by DWD for COSMO-EU is also used (COSMO-LEPS is currently using the same grid as COSMO-EU, but for a smaller domain). For more detail, the reader is referred to Montani et al., 2011. In September 2006, COSMO started the SREPS Priority Project, aiming at the development of an ensemble system targeted for the short-range, COSMO-SREPS (Marsigli et al., 2009). Two different kind of perturbations are applied: initial and boundary conditions benefit of a multi-model approach, being provided by 4 different operational global models and the COSMO model itself is perturbed by changing the values of a set of physics parameters. The SREPS project ended in September 2008, delivering an ensemble system for the short-range based on the COSMO model with a 10 km horizontal mesh-size and 40 levels in the vertical. Initial and boundary conditions to the 10 km COSMO-SREPS runs were provided by 4 COSMO run at 25km hor. res. nested on IFS, GME, GFS, UM, performed by AEMET as part of their SREPS system. Then, a new COSMO-SREPS suite was implemented in 2010, with direct nesting of COSMO at 7 km on the 4 global model. The system was running quasi-regularly at ECMWF, using the Billing Units provided by some COSMO Countries. COSMO-SREPS provided initial and boundary conditions to the convection-resolving ensemble for Germany under development at DWD (COSMO-DE-EPS) and it was used to compute a flow-dependent B-matrix for a test version of the 1d-Var assimilation of satellite data under development at ARPA-SIMC. In order to avoid duplications, COSMO aimed at a confluence of the two 7 km ensemble systems into a unique COSMO ensemble, covering both the short and the medium range and based on the most appropriate perturbation strategy for the entire forecast range. This implies the development of a "multi-perturbation-strategy" ensemble system, with perturbations more appropriate for the short range in the beginning (day 1-2), and with perturbations more appropriate for the medium range thereafter, or

a combination of both. It should be reminded that the importance of such an ensemble system resides both in its inherent value as assistant to the 7-km operational runs and in its capability of providing boundary conditions for the convection-permitting ensemble system under development in the COSMO countries. The issue of ensemble merging and of multi-perturbation strategy design has been dealt in the Project and results are presented in Section 4. A satisfactory representation of the uncertainty affecting the mesoscale was still lacking. The quantification of the errors which are made by the model in the description of the meteorological phenomena at this scale needs to be improved. The development of mesoscale ensemble should then include 1) the perturbation of the lower boundary forcing and 2) the perturbation of the parametrised physical processes. The importance of further perturbing the physics parameters has been underlined by the outcome of the SREPS PP. Within COSMO it has also been suggested that adding perturbations in the soil parameters can be crucial in order to get a better representation of the model error in terms of surface variables. The issue of model perturbation was also addressed in the Project, and results are presented in Section 3. Within this work on the consolidation of the COSMO ensemble systems, attention has also been paid to the post-processing. Calibration of ensemble forecasts in terms of precipitation and surface temperature has been studied and applied widely in recent years (e.g. Hamill and Whitaker, 2006; Hagedorn et al., 2008; Hamill et al., 2008; Santos-Muñoz et al., 2007). As for the COSMO-LEPS ensemble, it has been recognised that a calibration for 24 h precipitation would be desirable to improve the forecast skill (Marsigli et al., 2008). Last year, work on COSMO-LEPS calibration has been carried out at MeteoSwiss (Felix Fundel et al., 2008). Thirty year of re-forecast of one member of COSMO-LEPS have been computed and stored at ECMWF, and they have been used for calibrating the COSMO-LEPS output over Switzerland. This work has shown the potential of using re-forecast to improve the forecast skill. Therefore, calibration of QPF, especially aimed at hydrological applications, was also addressed in the Project, and results are shown in Section 5.

3 Model perturbations

3.1 Parameter perturbations

On the basis of the work carried out in the SREPS Priority Project (COSMO Technical Report n. 13, 2009), further investigations on the perturbation of model parameters had been carried out. In CONSENS, it was decided to start by evaluating a set of parameters, already tested in SREPS, over a different season, JJA (summer 2008, 92 days). For this purpose, an ad hoc test suite have been set-up at ECMWF, CSPERT, where 16 runs of COSMO are performed, with the same configuration of the COSMOSREPS/LEPS runs, but with IC and BCs provided by the IFS deterministic forecast. The model domain is shown in Figure 1. The 16 runs have 16 different set-up of the physics parameters, as described in Figure 2. An analysis has been carried out in terms of 2m temperature and dew-point temperature, for both northern Italy and Greece (see Figure 3 and Figure 4 respectively). Results confirm what has been found for the autumn 2007 season:

- qc0: no detectable impact
- tur_len: small impact for tur_len=150
- c_soil, c_lnd and pat_len parameters: marked impact, even suspicious for c_soil and c_land

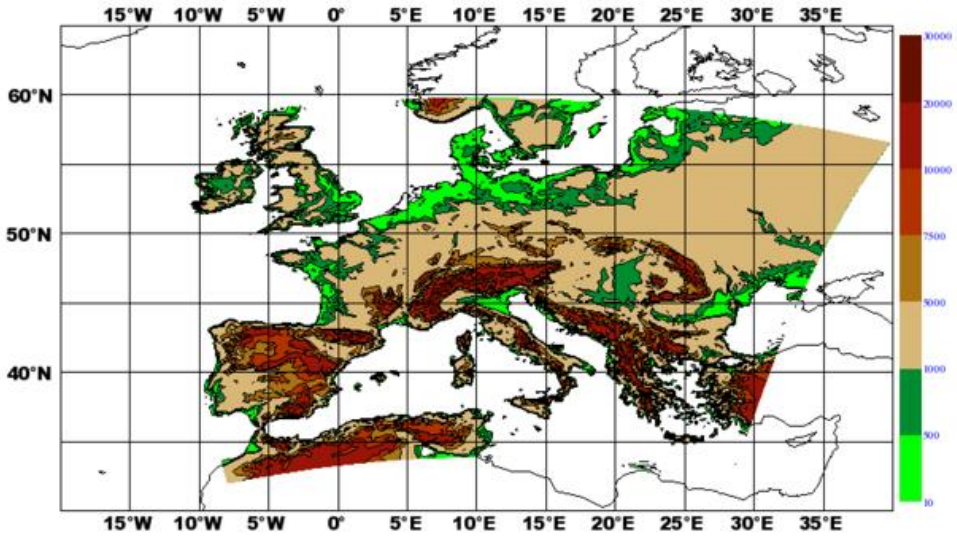


Figure 1: Orography of the model in the ensemble systems, showing the model domain.

- rlam_heat is an important parameter to perturb and it is sensitive to small changes, especially over Greece

On the basis of these results, and on the previous ones, it was decided to test other parameters or combinations of parameters in the CSPERT test suite (Figure 5). In this set up the new parameters considered are: cloud droplet number concentration (cloud), exponent of the raindrop size distribution (mu_rain) and switch on/off of the graupel scheme (gscp). These tests were run over MAM, JJA and SON 2009 and evaluation was performed in terms of precipitation over Northern Italy and Greece, then over Greece also for T, Td, and 10m wind. Some results of the evaluation are listed below:

- 2m temperature: patlen=10000 has strong detrimental effect over Greece ($\longrightarrow$ decision to switch to patlen=2000, also based on previous results); crsmin=200 has little positive impact
- 10 m wind: no strong effects (not expected, due to the perturbed parameters, at least for the horizontal wind)
- precipitation (very little precipitation in spring, though, especially over Greece):
  - crsmin=200 determines an increase the precipitation amount. Detrimental effect over Greece in terms of BSS
  - itype_gscp=3 determines a decrease of precipitation over Northern Italy
  - there is an impact of both perturbing cloud_num and mu_rain

In Figure 6 the scores in terms of 6h precipitation over Northern Italy are shown, for some parameter set-up for the spring 2009 season. The perturbation of the mu_rain parameter has an impact, increasing POD for intense precipitation and decreasing it for light precipitation,

run nr.	parameter name	parameter description	range	default	used
1	**ctrl**				ope
2	**lconv**	convection scheme	T or KF	T	KF
3	**tur_len**	maximal turbulent length scale	[100,1000] m	500	150
4	**tur_len**	maximal turbulent length scale	[100,1000] m	500	1000
5	**pat_len**	length scale of thermal surface patterns	[0,10000] m	500	10000
6	**rat_sea**	ratio of laminar scaling factors for heat over sea	[1,100]	20	1
7	**rat_sea**	ratio of laminar scaling factors for heat over sea	[1,100]	20	60
8	**qc0**	cloud water threshold for autoconversion	[0.,0.001]	0	0.001
9	**crsmin**	Minimal stomata resistance	[50,200] s/m	150	50
10	**crsmin**	Minimal stomata resistance	[50,200] s/m	150	200
11	**c_soil**	Surface area index of the evaporating soil	]0,c_lnd[	1	0
12	**c_soil**	Surface area index of the evaporating soil	]0,c_lnd[	1	2
13	**c_lnd**	surface area density of the roughness elements over land	[1,10]	2	1
14	**c_lnd**	surface area density of the roughness elements over land	[1,10]	2	10
15	**rlam_heat**	scaling factor of the laminar layer depth	[0.1,10]	1	0.1
16	**rlam_heat**	scaling factor of the laminar layer depth	[0.1,10]	1	10

Figure 2: Set up to the CSPERT suite for the 2007 and 2008 runs.

with almost no effect on the false alarm rate. Its association with the cloud_num perturbation gives detectable, though small, impact. The same scores are computed also for the autumn season (Figure 7), confirm that the impact of these 2 perturbations is detectable, especially for intense precipitation, and that they do not lead to a worsening of the forecast. On the basis of these results, a final set-up for the COSMO-SREPS perturbations (shown in Figure 8) has been implemented in 2011. The same perturbations have been adopted also in the COSMO-LEPS suite, but they can be combined differently.

3.2 Soil moisture perturbation

The interaction between the surface and the lower troposphere determines the development of fluxes close to the ground. Soil moisture is of primary importance in determining the partition of energy between surface heat fluxes, thus affecting surface temperature forecasts. The ensemble forecasts usually suffer of a lack of variability among the members, which is typically worse near the surface rather than higher in the troposphere. Therefore, the aim of this work is to ameliorate this deficiency by implementing a technique for perturbing soil moisture conditions and explore its impacts on the variability of the members for the different forecasted surface parameters (e.g. 2m air temperature, accumulative precipitation). The proposed technique is based on the method by Sutton and Hamill, 2004. The steps followed for its implementation are:

- use daily soil moisture data for a period with soil moisture variability for continuous years, in order to have a "climatology"
- calculate a 30-day running mean from this set of dataset
- subtract the running mean from the daily soil moisture data to calculate daily deviations
- apply an Empirical Orthogonal Function (EOF) analysis to calculate the perturbations in the variability categories appearing in the data

For the retrieval/archiving of soil moisture data, daily soil water content data were provided by DWD COSMO-EU surface analysis. The period selected for the dataset, is three months

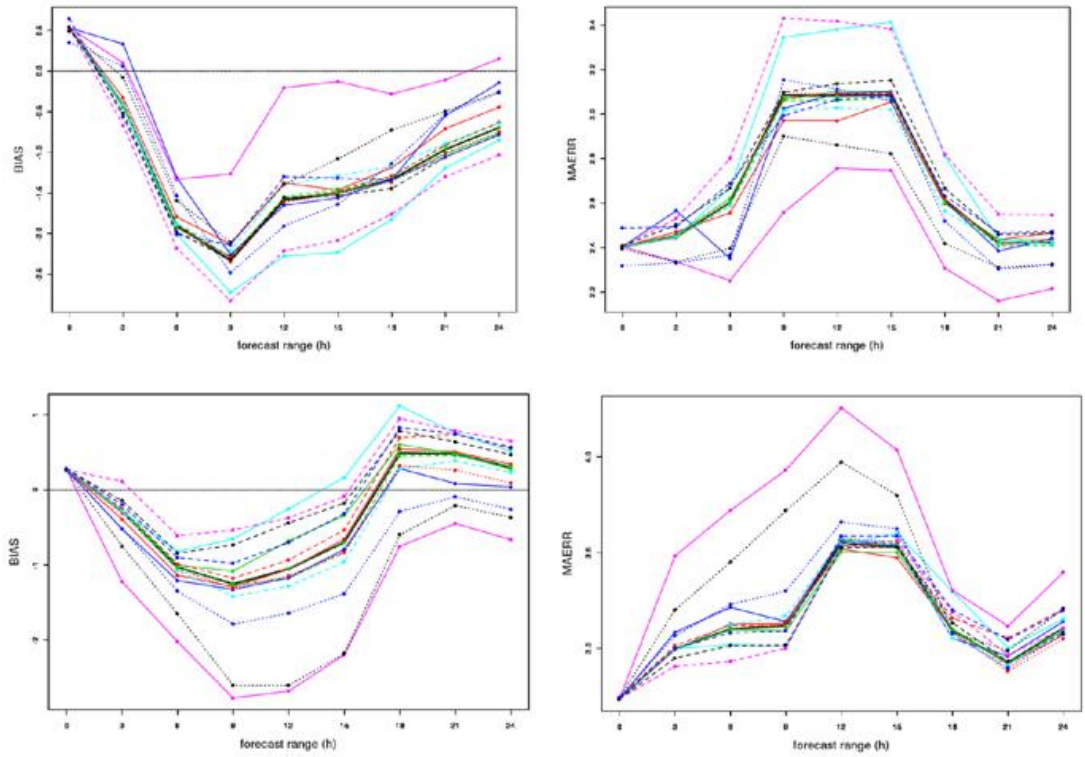


Figure 3: Bias and Mean Absolute Error of 2m T and Td for the CSPERT run, computed over Northern Italy against SYNOP station data, for JJA 2008.

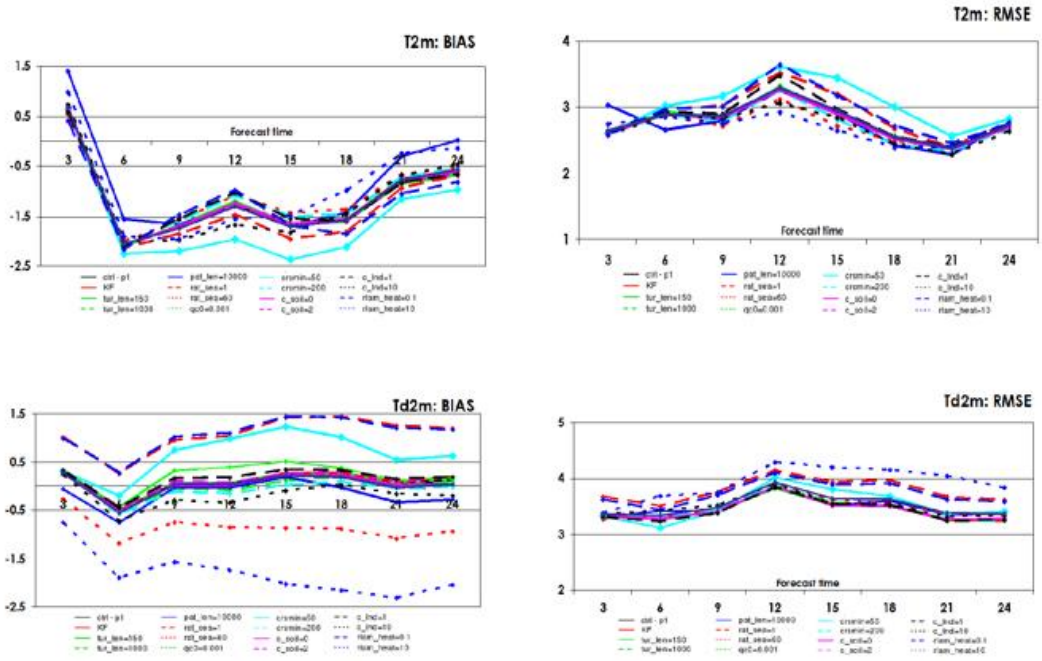


Figure 4: Bias and Mean Absolute Error of 2m T and Td for the CSPERT run, computed over Greece against SYNOP station data, for JJA 2008.

member	conv	pat_len	rlam_heat	rat_sea	crsmin	cloud	mu_rain	gscp
1	T	500	0.1	20	200	5.00e+08	0.5	4
2	KF	500	0.1	20	200	5.00e+08	0.5	4
3	T	500	1	1	200	5.00e+08	0.5	4
4	KF	500	1	1	200	5.00e+08	0.5	4
5	T	500	1	20	150	5.00e+07	0.5	4
6	KF	500	1	20	150	5.00e+07	0.5	4
7	T	500	1	20	150	5.00e+08	0	4
8	KF	500	1	20	150	5.00e+08	0	4
9	T	500	1	20	150	5.00e+08	0.5	3 (no gra)
10	KF	500	1	20	150	5.00e+08	0.5	3 (no gra)
11	T	10000	1	20	150	5.00e+07	0.5	4
12	KF	10000	1	20	150	5.00e+07	0.5	4
13	T	500	1	20	150	5.00e+07	0	4
14	KF	500	1	20	150	5.00e+07	0	4
15	T	500	1	20	150	5.00e+08	0.5	4
16	KF	500	1	20	150	5.00e+08	0.5	4

Figure 5: Set up to the CSPERT suite for the 2009 runs.

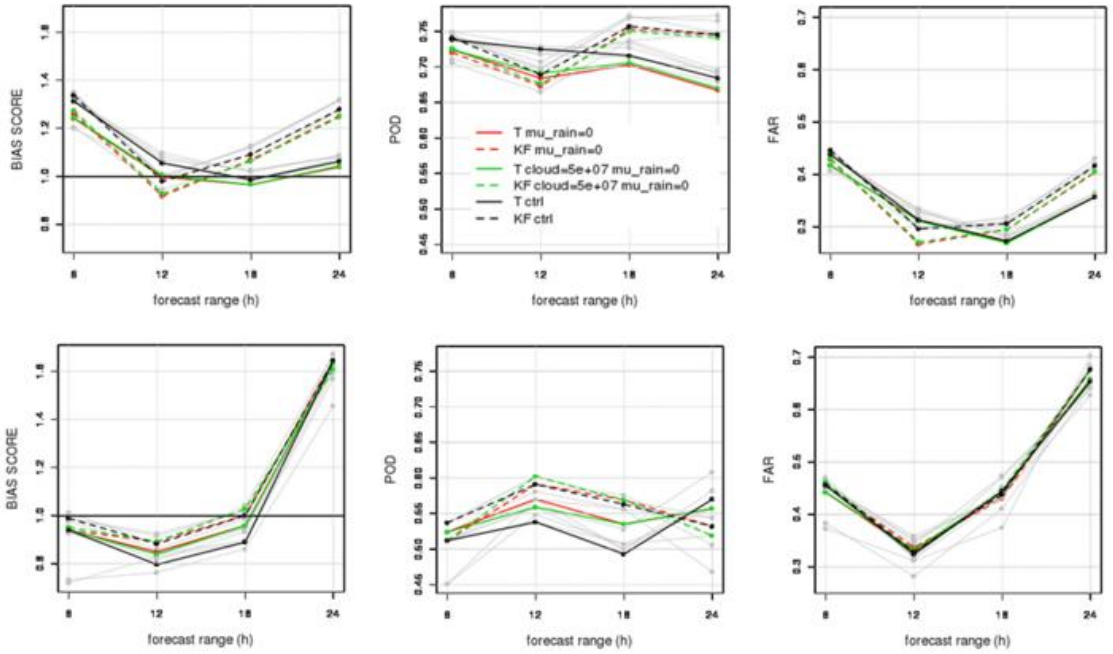


Figure 6: Bias Score, POD and FAR for the 6h-precipitation forecasted by some of the CSPERT runs, computed against high-resolution precipitation observations over Northern Italy, upscaled as average precipitation over boxes of 0.5 x 0.5 degrees exceeding 1 (top row) and 10 (bottom row) mm/6h. Scores are for spring 2009.

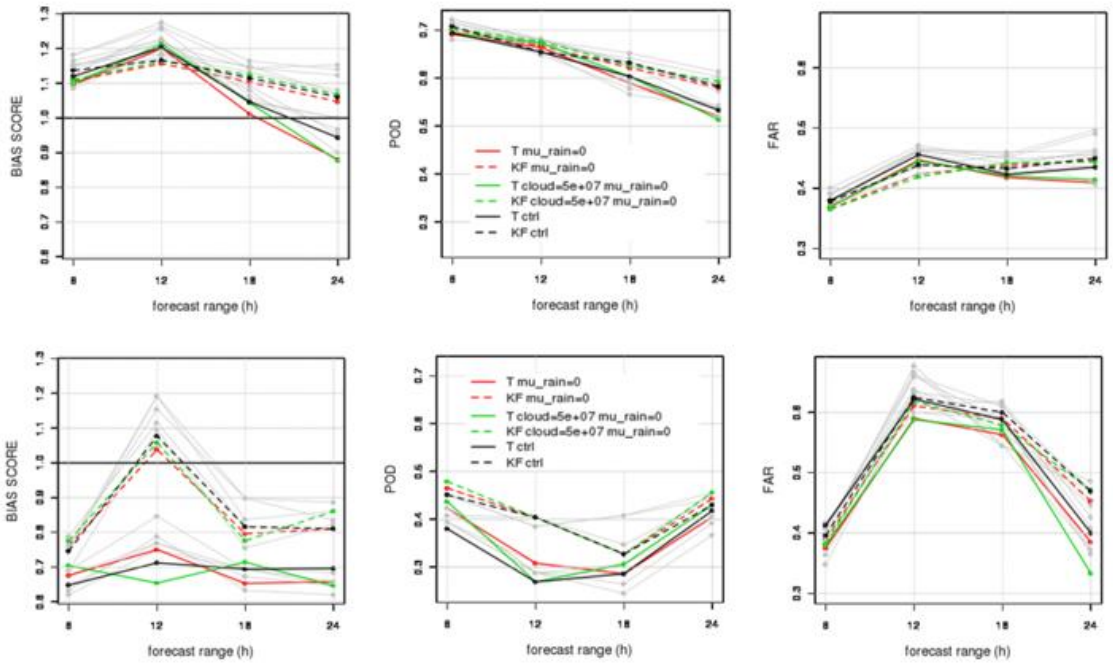


Figure 7: Bias Score, POD and FAR for the 6h-precipitation forecasted by some of the CSPERT runs, computed against high-resolution precipitation observations over Northern Italy, upscaled as average precipitation over boxes of 0.5 x 0.5 degrees exceeding 1 (top row) and 10 (bottom row) mm/6h. Scores are for autumn 2009.

member	father	itype_conv	tur_len	pat_len	rlam_heat	rat_sea	crsmin	cloud_num	mu_rain
1	ifs	0	150	500	1	20	150	5.00E+07	0.5
2	ifs	1	1000	500	1	20	150	5.00E+08	0.5
3	ifs	0	500	500	0.1	20	200	5.00E+08	0.5
4	ifs	1	500	500	1	1	150	5.00E+08	0.5
5	ifs	0	500	2000	1	20	150	5.00E+08	0.5
6	gme	0	500	500	0.1	20	150	5.00E+08	0.5
7	gme	0	500	500	1	1	200	5.00E+08	0.5
8	gme	0	500	500	5	20	150	5.00E+08	0
9	gme	0	1000	500	1	20	150	5.00E+07	0.5
10	gme	0	150	500	1	20	150	5.00E+08	0.5
11	gfs	0	500	500	5	20	150	5.00E+08	0.5
12	gfs	0	500	2000	1	20	150	5.00E+08	0.5
13	gfs	0	500	500	1	40	150	5.00E+08	0
14	gfs	0	500	500	1	40	50	5.00E+08	0.5
15	gfs	0	500	500	1	20	50	5.00E+08	0.5
16	ifs	0	500	500	1	20	150	5.00E+08	0.5

Figure 8: Final set up to the COSMO-SREPS suite.

(April to June) for three years (2007-2009). This spring-to-summer period can provide the necessary soil moisture variability in the data. These data (water content for each soil layer kg/m^2) are extracted at 8 different levels in the soil, namely 1, 2, 6, 18, 54, 162, 486, and 1458 cm. In this way, 241 deviation data files (=3years*3months*30days-29days=241 days) have been created, each of them containing 436,905 lines (grid points). Then an EOF analysis was developed and implemented to the daily soil water content data. The EOF analysis was implemented to the first soil layer from the surface. The perturbations are created through the following equation suggested by Houtekamer, 1993:

$$\varepsilon_j = \sum_{i=1}^{N=244} d_i \lambda_i \sigma_i \tag{1}$$

where, ε_j is the j-th perturbation, d_i a standard normally distributed random number, λ_i the square root of the eigenvalues and σ_i the corresponding eigenvectors. In order to solve the above equation a method for creating random numbers was used based on Press et al., 1992. Routines calculating EOFs have been found and selected the one by Ziemke J.R. (http://acdb-ext.gsfc.nasa.gov/People/Ziemke/) who has based his code on Kutzbach, 1967. This routine has been built to work for matrices with moderate size. Therefore, the main problem encountered with the available data is that the routine could not handle the extremely large data matrices (436,905 lines x 436,905 rows) as they require a very large stack memory. For this reason it was necessary to find solutions to overcome this problem. An efficient method was proposed by von Storch and Hannoschock, 1984 and Legler, 1984. They proposed to inverse the matrices, i.e. if initially there are M lines (grid points) and N days, with N $\ll$ M, it is possible to invert the problem and instead of creating MxM matrices to end up with NxN matrices that would lead to much less computationally intensive problem. Then, the input to the EOF analysis has been changed to an NxM data matrix in which there are N rows (corresponding to the available days) and M columns (corresponding to the grid points). After this change, the EOF analysis can run without stack memory problems. Then work has been performed on:

- adding the calculated "perturbations" to the initial soil water content file
- calculating the resulting fractional soil moisture
- constraining it to between 3% and 100% and then
- get the final perturbed soil moisture fields

The perturbations are calculated from:

$$P = d\Lambda c = \begin{pmatrix} \sum_{i=1}^{M} d_i c_{1,i} \\ \sum_{i=1}^{M} d_i c_{2,i} \\ \vdots \\ \sum_{i=1}^{M} d_i c_{M,i} \end{pmatrix} \tag{2}$$

where "d" are the random numbers , "c" are the space eigenvectors and "lambdas" are the space eigenvalues. Each line corresponds to each point in space and the sum is over the 244 EOF categories (if all are kept). In order to solve the equation a method for creating random numbers was used, based on Box-Muller method for generating random deviates with normal distribution (Press et al., 1992).

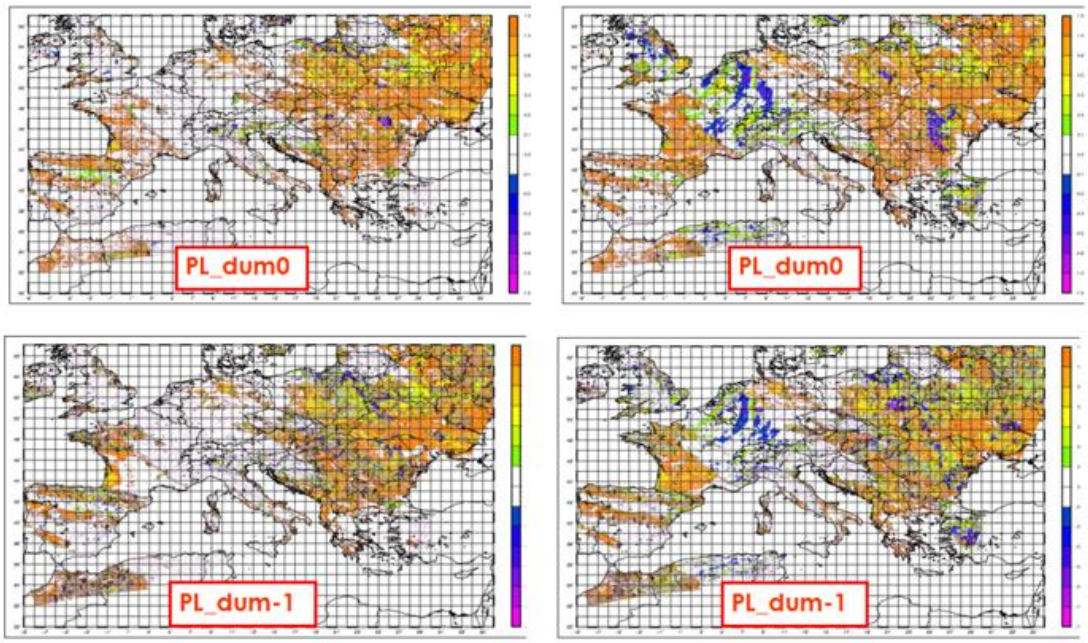


Figure 9: Differences of the soil moisture fields at the first level between perturbed runs (for different seeds, as indicated) and the control, at +24h (left) and +48h (right) forecast range.

Once the perturbed fields of soil moisture (on 7 levels) has been obtained, they have been tested in COSMO runs (Figure 9 and Figure 10). Different random seeds were used. The perturbations obtained (one set per each soil level) are added (the perturbations can be positive or negative) to the initial (original) soil moisture fields. A constraint is imposed: the perturbed value should not be more than 50% of the original value. Perturbations of the soil moisture is performed at all the soil levels (except the climatological level). COSMO was run on one case (9th June 2011) in the COSMO-SREPS configuration with perturbed soil moisture fields, for each perturbation set (no random number, seed=-1, seed=-5), at +48-hour. COSMO was also run with unperturbed soil moisture, for comparison (control run). Results have been presented at the COSMO GM 2011 (WG7 parallel session). As for the soil moisture difference, it is highlighted that positive values correspond to wetter soil layer for the CTRL run. The areas with positive values seem to be more than those with negative values at t+24h. For the particular date it seems that the method leads mostly to differences over East and some parts of West Europe although there are also differences in smaller areas elsewhere. At t+48h, the differences with the CTRL are greater and appear generally over the whole domain. There are also some changes among the results from the tests with various random numbers used (which could lead to different members of an ensemble). The control run is more wet in eastern Europe. Then, the control has more LHF than the perturbed, which is coherent with the fact that the control is wetter. For the SHF, this depends very much from the hour of the day. During the night (as it is at +24h, since the run starts at 00) it should be more from the ground towards the atmosphere, which means negative. Hence, since the difference it is positive, this may indicate that the SHF of the perturbed is stronger than that of the control, which is in agreement with the fact that in the perturbed the LHF is reduced, so the two are complementary. As for 2mT, the control is colder than the perturbed (and wetter in the soil and with more LHF and less SHF). The differences (positive or negative) between the CTRL run and the new runs in precipitation are larger at +48h, and they interest larger areas of the domain (Figure 11). This technique has not been implemented yet in an ensemble configuration for testing. Its applicability will be further investigated in the future.

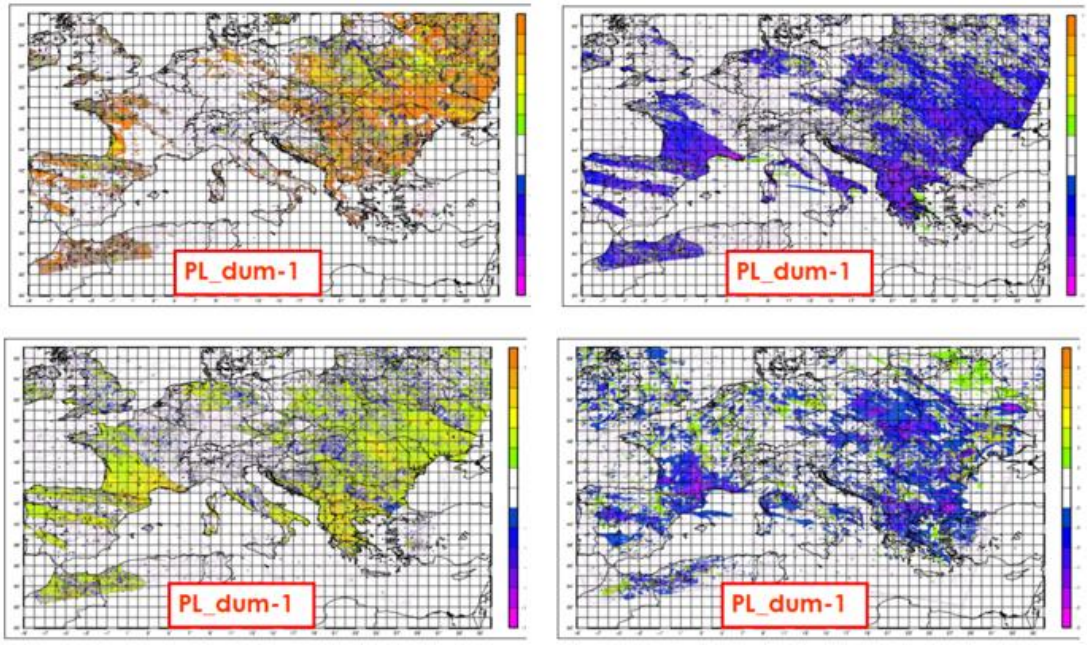


Figure 10: Difference between control and perturbed at +24h for: soil moisture (top left), latent heat flux (top right), sensible heat flux (bottom left) and 2m temperature (bottom right).

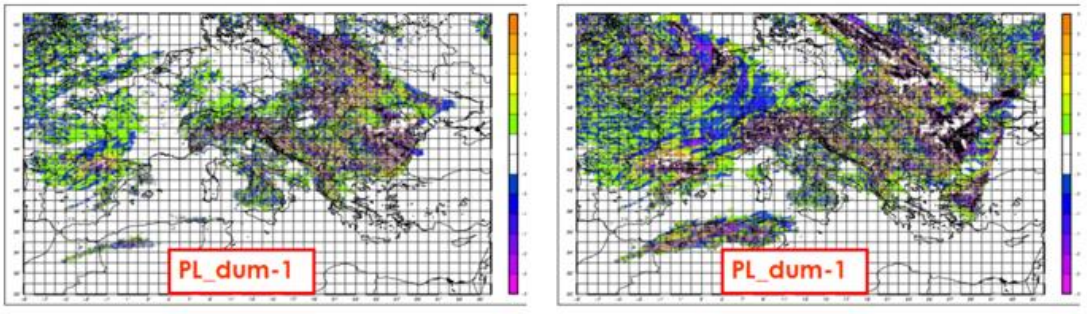


Figure 11: Difference in accumulated precipitation between the perturbed run and the control at 24h (left) and 48h (right) forecast range.

4 Ensemble merging

4.1 Clustering applied to a multi-ensemble

In the framework of the TIGGE-LAM coordination, it is proposed to analyse the possible benefit of a multi- ensemble for driving the limited area ensemble. More specifically, it is studied if a downscaling of a combination of more than one global ensemble can bring benefit with respect to downscaling a unique global ensemble. In this study, the member selection technique which is used to select the EPS members driving COSMO-LEPS (Molteni et al., 2001, Marsigli et al., 2001) is used to select members in the multi-ensemble made ECMWF EPS and the global MOGREPS ensemble of UKMO. The following global ensemble are considered:

- EPS (50+1): 51 members
- MOGREPS (23+1): 24 members
- MINI-MIX (EPS24 +MOGREPS24): 48 members
- MEGA-MIX (EPS51 +MOGREPS24): 75 members

For each of the above-mentioned ensembles, a 16-member cluster analysis and representative-member identification is performed. Then, 10-member global ensembles (EPS_REDU, MOGREPS_REDU, MINI_REDU, MEGA_REDU) are thus generated and the properties of the "REDU" ensembles are studied. It is worth pointing out that ECMWF EPS control run was always included in ECMWF24. More specifically, the following questions will be addressed:

- how many times do the 2 ensembles mix ?
- where do the best (and the worst) elements of "REDU" ensembles come from? How to they score depending on their "origin" ?
- how do "REDU" ensembles rank with respect to EPS, MOGEREPS, MINI-MIX and MEGA-MIX ?

The investigation was carried out over the period March to May 2009 (MAM09) for a total of 184 cases, considering both 00 and 12UTC runs of the two systems, as archived in TIGGE database. Z500 at fc+96h was used as clustering variable. As verifying analysis (at 00 and 12 UTC), a "consensus analysis" (average of UKMO and ECMWF high-resolution analyses) was taken. The performance of the MINIMIX48 ensemble was assessed in terms of root-mean-square error (RMSE) and anomaly correlation coefficient (ACC) of the geopotential height at 4-day forecast time (fc+96h), averaged over a domain covering Central and Southern Europe (30-60N, 10W-30E). The skill of MINIMIX24 is compared to that of UKMO24 and ECMWF24, using the common "consensus analysis". Figure 12 shows the time-series of the RMSE for the 3 ensembles means: a marked day-to-day variability is evident, with peaks of high (low) values of the score, indicative of particularly inaccurate (accurate) forecasts. It can also be noticed that ECMWF24 tends to outperform UKMO24, with lower values of RMSE for most of the days under investigation. As expected, the RMSE of the MINIMIX ensemble mean tends to stay somewhat in between the RMSE of the two other ensembles. It is worth pointing out that the use of MINIMIX turns out to be particularly useful in the days of failure of the more skilful ECMWF24. If we consider all 184 cases, the average RMSE of

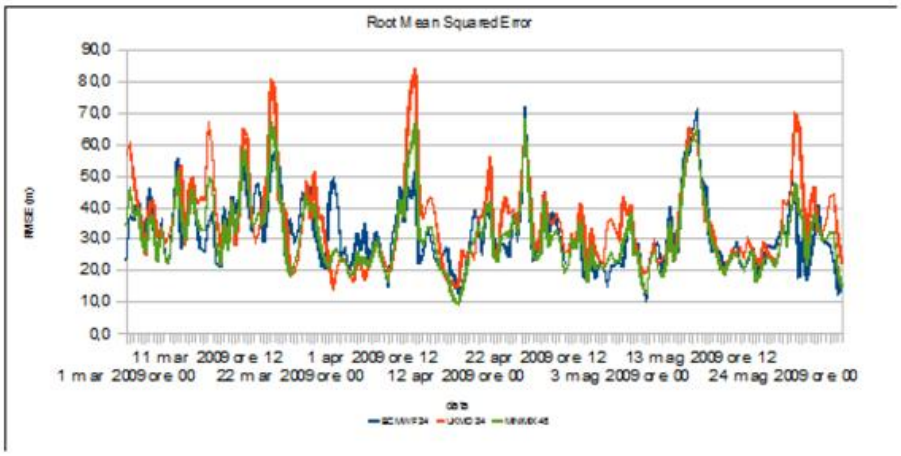


Figure 12: Time-series of the rmse (in metres) of the ensemble means for UKMO24 (red), ECMWF24 (blue) and MINIMIX48 (green) in terms of geopotential height at 500 hPa at fc+96h, averaged over the domain 30-60N, 10E-30W.

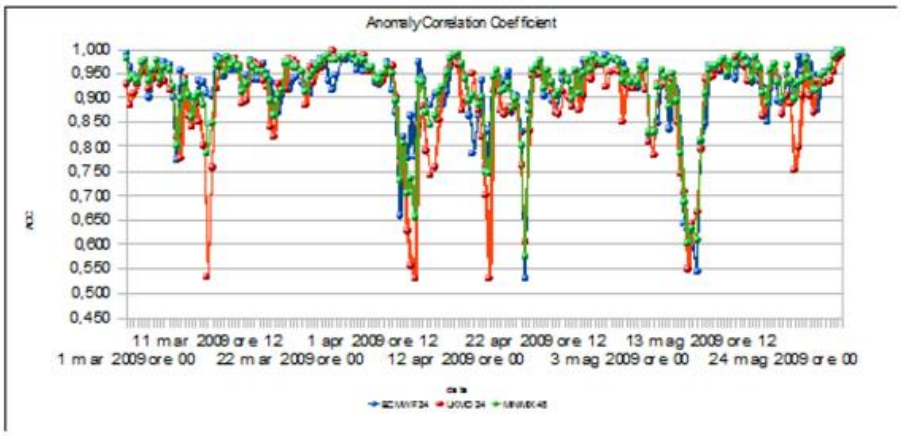


Figure 13: The same as Fig. 9, but for the anomaly correlation coefficient.

MINIMIX is slightly lower than ECMWF24, indicating the added value of multi-model even a low-population version of a very skilful global ensemble is used to generate a multi-model system.

Similar conclusions can be drawn if the ACC is considered (Figure 13). This score is sensitive to how the climate is computed. In fact, the ACC measures the correlation between the forecast and analysed deviations from climate. As an estimate of the climate, we used the three years of analyses present in TIGGE database and only the MAM season was considered. Also the ACC coefficient varies a lot from day to day and, as before, ECMWF24 tends to have better scores than UKMO 24, as shown by the higher values in ACC. It is again shown that the ACC of MINIMIX ensemble mean is, on average, slightly higher than that of ECMWF24, while UKMO24 has generally lower correlation coefficient. As a measure of the ensemble properties, we also considered the ensemble standard deviation (usually referred to as "spread") around the ensemble mean for the 3 ensembles. Figure 14 shows the time-series evolution of the spread for ECMWF24, UKMO24 and MINIMIX48. This quantity, rather than a pure verification score like RMSE and ACC, reflects the properties of the ensembles, more precisely the extent to which the different ensemble members get more and more differentiated as the forecast step increases. It is immediately evident that, at least for this

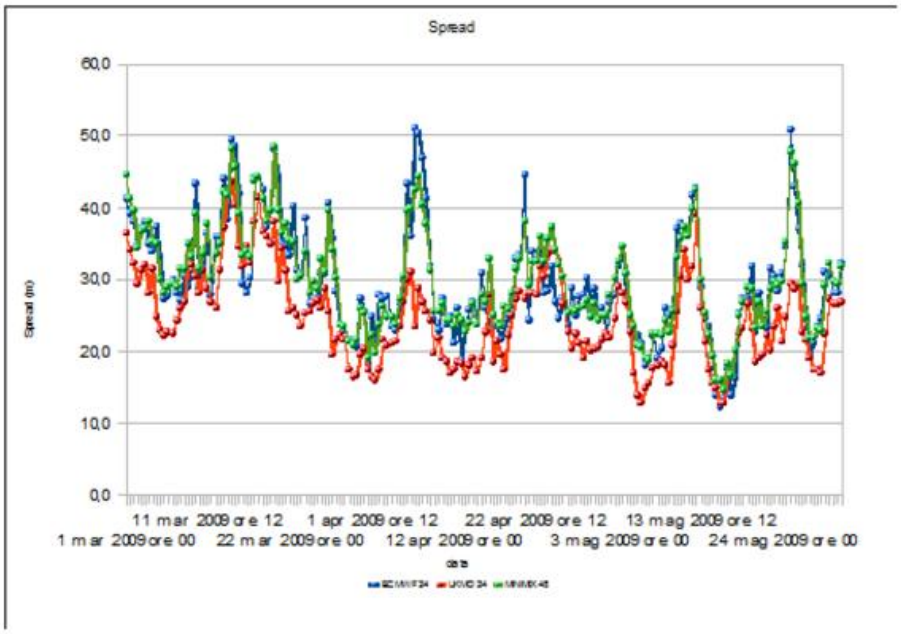


Figure 14: The same as Fig.9, but for the ensemble standard deviation (spread) among the members of the ensembles.



Figure 15: Synthesis of the performance for single-model and multi-model systems in terms of Z500 rmse and spread.

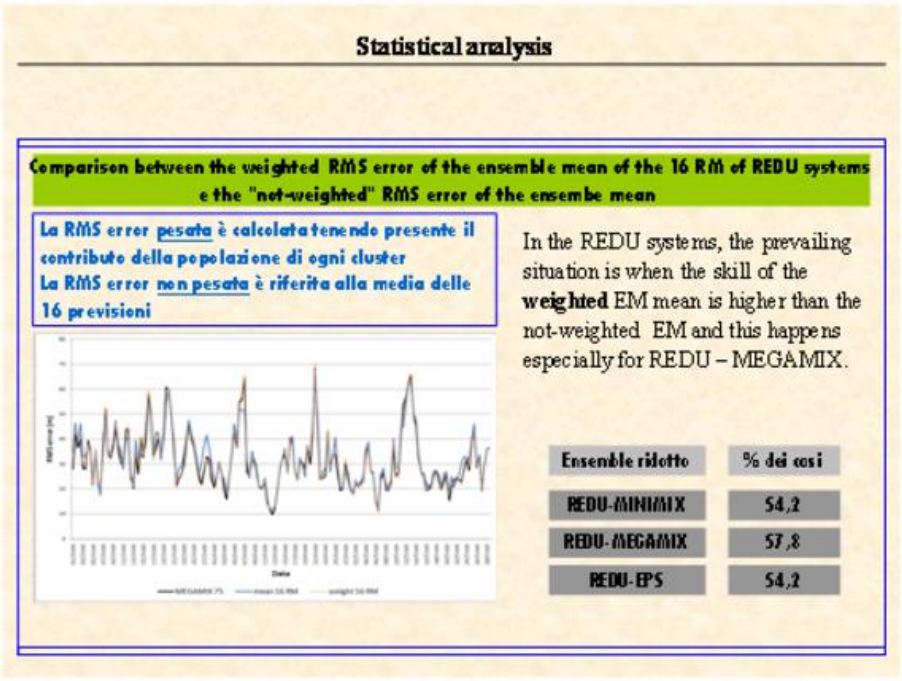


Figure 16: Synthesis of the performance for the REDU-ensembles.

forecast range, ECMWF24 has systematically larger spread than UKMO24. This is possibly related to the different strategies followed to generate the initial perturbations in the two ensembles (Singular Vectors for ECMWF24 versus Ensemble Transform Kalman Filter for UKMO24), although other interpretations are being put forward. As a further comment, it can be noticed that the MINIMIX48 ensemble has a spread very close to that of ECMWF24. In some cases, the MINIMIX48 spread is the largest one, suggesting that the use of a multi-model system allows the exploration of a wider region of the phase space of the atmosphere. If also the performances of EC-EPS51 (the full ECMWF-EPS system), MOGREPS24 (the full UKMO system) and MEGAMIX75 are considered, then the results indicate that the latter system outperforms all the others and that MINIMIX48 performs better than EC-EPS51 in terms of RMSE of the ensemble mean (see also Figure 15). As for the evaluation of the skill of the 16-member REDU ensembles, the attention is focus on the performance of the ensemble mean of these systems, calculated in the different ways: EM_w is the ensemble mean obtained weighting each member with the population of the cluster, while EM_now is the ensemble mean computed in the "classical way", that is without any weight. The attention is focussed of REDU-MINIMIX, REDU-MEGAMIX and REDU-EPS and results are summarised in Figure 16, which indicates a higher skill for the REDU systems where the ensemble mean is weighted according to the cluster population. This happens especially for the "best" system: REDU-MEGAMIX. Results can be summarized as follows:

- MINIMIX (48 members) performs better than EPS51 in terms of z500 RMSE of the ensemble means
- REDU-MEGAMIX outperforms the others ensembles in terms of "RMSE of the best element"
- REDU-MINIMIX performs slightly better than EPS51 in terms of "RMSE of the best element"
- for each of the 16-member ensembles, the weighted ensemble mean gives better score

member	father	itype_conv	tur_len	pat_len	rlam_heat	rat_sea	crsmin
1	ifs	0	150	500	1	20	150
2	ifs	1	1000	500	1	20	150
3	ifs	0	500	500	0.1	20	200
4	ifs	1	500	500	1	1	150
5	ifs	0	500	2000	1	20	150
6	gme	0	500	500	0.1	20	150
7	gme	0	500	500	1	1	200
8	gme	0	500	500	10	20	150
9	gme	0	1000	500	1	20	150
10	gme	0	150	500	1	20	150
11	gfs	0	500	500	10	20	150
12	gfs	0	500	2000	1	20	150
13	gfs	0	500	500	1	60	150
14	gfs	0	500	500	1	60	50
15	gfs	0	500	500	1	20	50
16	ifs	0	500	500	1	20	150

Figure 17: Set up of the COSMO-SREPS suite adopted for the comparison with COSMO-LEPS (winter 2010/2011 and spring 2011).

than the non-weighted one

4.2 Multi-model vs single-model approach for IC and BC to ensemble

The Consortium was running two mesoscale ensemble system, COSMO-LEPS, up to 6 days, mainly targeted for the early medium range, and COSMO-SREPS, which was developed for the aim of short-range forecasting (up to 48 h) in the last years (SREPS PP). One task of CONSENS was dedicated to decide what to do out of these two systems: - how is performing COSMO-SREPS for short-range forecasting, with respect to the already available COSMO-LEPS system? This also considering that recently the ECMWF EPS, on which COSMO-LEPS is based, has improved its spread-skill relation in the short-range, due to the introduction of the EDA.

- is it worth to run two separate systems at the same spatial scale, one for short-range only ?
- is it feasible to merge the two systems ? And if yes, how ?

The set-up of COSMO-SREPS is presented in Figure 17. An intercomparison of COSMO-LEPS and COSMO-SREPS in terms of short-range precipitation forecasting has been carried out, including also two combinations of the systems:

- a 20-member ensemble made up of the 16 COSMO-LEPS runs + 4 runs selected from COSMO-SREPS (mix20)
- a 16-member ensemble made up by the first 12 COSMO-LEPS runs + 4 runs selected from COSMO-SREPS (mix16)

The 4 runs selected from COSMO-SREPS are members 1 (nested on IFS), 6 (nested on GME), 11 (nested on GFS), 16 (control run). Verification is performed in terms of Probabilistic Quantitative Precipitation Forecast (PQPF), 6-hourly accumulated, over Northern Italy (more than 400 stations) for the winter 2010-2011 (20 Nov 2010 - 28 Feb 2011). The verification method is DIST (Marsigli et al., 2008), a distributional method. Some parameters

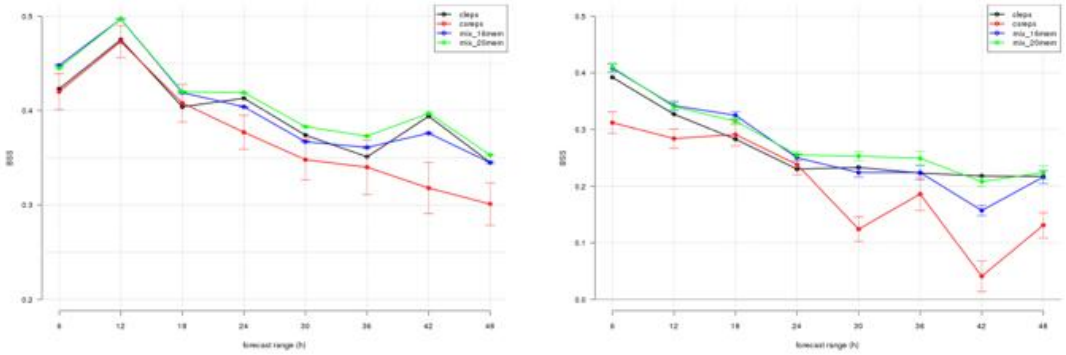


Figure 18: BSS as a function of the forecast range relative to the 4 ensemble systems for the event average precipitation exceeding 1 (left) and 5 (right) mm/6h.

of the distribution of both observed and forecasted precipitation are computed over boxes of 0.5 x 0.5 degrees size, then are compared. Results show that COSMO-LEPS performs better than COSMO-SREPS for almost all the forecast ranges, with some overlapping in the forecast range 18-24h (Figure 18). The mix16 ensemble outperforms COSMO-LEPS for the first 18 h in terms of BSS, while is comparable in terms of ROC area (not shown). For the higher threshold, mix16 performs better than COSMO-LEPS for the first 24. The mix20 ensemble performs better than COSMO-LEPS for almost the whole forecast range, especially for the higher precipitation threshold. Results are confirmed for different parameters of the precipitation distribution (not shown) and for a different season (spring 2011). It is shown that, for COSMO-SREPS, with only 3 global models providing initial and boundary conditions, the scores increase after 8 members is very limited (Figure 19). Therefore, it is not suggested to run an ensemble with more than 5-8 members with only 3 different perturbed initial and boundary conditions. Furthermore, the scores of both ensembles saturates around ensemble size 13-14. This implies that with a 16-member downscaling of the EPS we are already at the maximum skill attainable in the short-range, while there is some indication of room for improvement in the medium range. In summary, results (analysis of 6h precipitation over northern Italy for winter 2010/2011) indicates that:

- generally COSMO-LEPS outperforms COSMO-SREPS in terms of probabilistic indices
- the multi-model approach for i.c. and b.c. proves valuable even if model with different qualities are used
- comparing a 5-member COSMO-LEPS with a 5-member COSMO-SREPS (where all the 3 different i.c. and b.c. sets are included + 2 extra IFS-driven members), the two performs similarly
- comparing a 3-member COSMO-LEPS with a 3-member COSMO-SREPS (where the 3 members have the 3 different i.c. and b.c. sets), the reverse happens: COSMO-SREPS outperforms COSMO-LEPS
- hence, for the multi-model approach to be effective in providing i.c. and b.c., several models are needed to get a performance similar (or better) to a downscaling from a well constructed ensemble (like EPS)
- combining the 16 COSMO-LEPS members with 4 COSMO-SREPS members (taking 3 members with the 3 different i.c. and b.c. sets + the control), this 20-member ensemble outperforms both systems

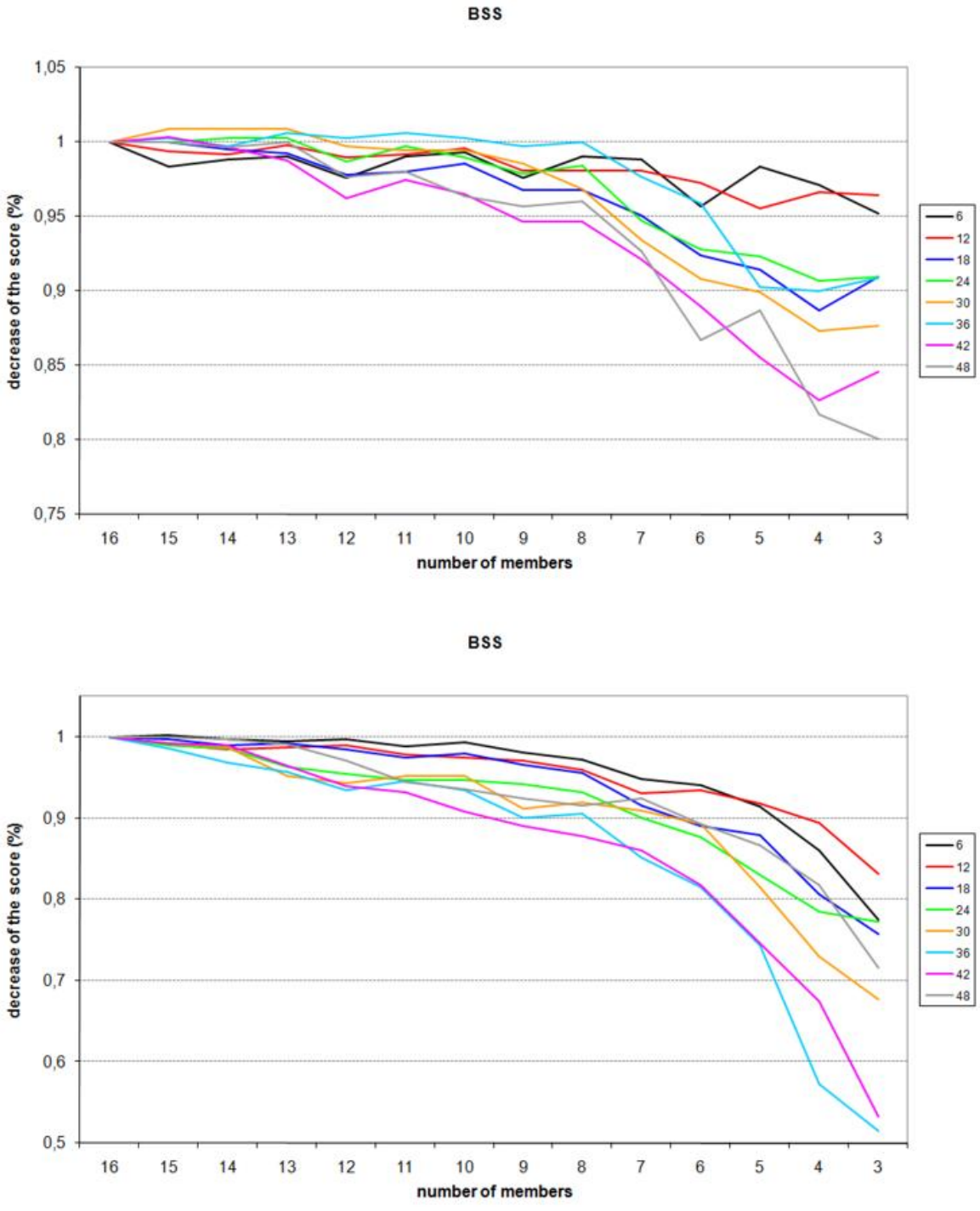


Figure 19: Dependence of the ensemble size of the BSS for COSMO-SREPS (top) and COSMO-LEPS (bottom).

- combining 12 COSMO-LEPS members with 4 COSMO-SREPS members (taking 3 members with the 3 different i.c. and b.c. sets + the control), this 16-member ensemble outperforms COSMO-LEPS for the first day (from 18 to 30 h)

A more comprehensive evaluation is described in Marsigli et al., 2013. On the basis of these results, it was decided to stop running the extra COSMO-SREPS members (nested on the same sets of IC and BC but with different physics), and to Keep only the COSMO-SREPS members which receive IC and BC by different global models, but prolonging the runs up to +132h, as COSMO-LEPS. Then, a new ensemble system has been created, COSMO-HYBEPS, by merging the 16 COSMO-LEPS runs with the 4 BC-EPS runs, creating an additional product which is currently under evaluation in a test suite.

5 Calibration

Three different calibration methods have been implemented and tested on 24h accumulated precipitation forecast issued by COSMO-LEPS. These techniques provide corrections based on: the cumulative distribution function (quantile-to-quantile mapping, hereafter, CDF), the linear regression (hereafter, LR) and analogs. The basic implementations of the CDF and LR methods were developed by generating a seasonal correction function for each model grid point. Each function was defined by using the historical data which were forecasted and observed for the considered grid point during each season. This approach generates correction functions that are location (i.e. grid point) specific. The analogs search was performed in terms of the similarity of the forecasted 24-h precipitation fields over the area under investigation (i.e. ER). The calibration strategy was based on historical forecast and observed rainfall data which were available over the area under investigation. Thirty years of reforecast of one member of COSMO-LEPS were run by MeteoSwiss. One reforecast run with a 90-h lead time was available every three days from 1971 to 2000. This model climatology is used to calibrate forecasts of all lead times, although forecasts of longer lead times might require a longer lead time reforecast data set. According to the model climatology, the climatological observed precipitation data were collected over the period 1971-2000 for ER and Switzerland; unfortunately, the observed data over Germany were available only for the period 1989-2000. Finally, the impact of the calibration process was also verified by performing the coupling of the ensemble QPFs with an hydrological model. This experiment was carried out only for a medium-sized catchment located in Emilia-Romagna, as other implementations of the meteo-hydrological coupled system were not available over the study areas under investigation.

5.1 Comparison of the calibration methodologies in terms of precipitation forecast

The impact of the calibration process on the 24-h QPFs operationally provided by COSMO-LEPS was verified for the years 2003-2007. Three study areas (Figure 20) have been analysed: the total area of Germany (about 357000 km^2), Switzerland (about 41000 km^2) and Emilia-Romagna (about 22000 km^2). Four different lead times were considered, ranging from day-2 to day-5.

According to the 24-h time window over which the observed rainfall amounts were available for each study area, these lead times correspond to, respectively, the 18-42, 42-66, 66-90 and 90-114 forecast hours for Germany and Switzerland and the 20-44, 44-68, 68-92 and 92-116

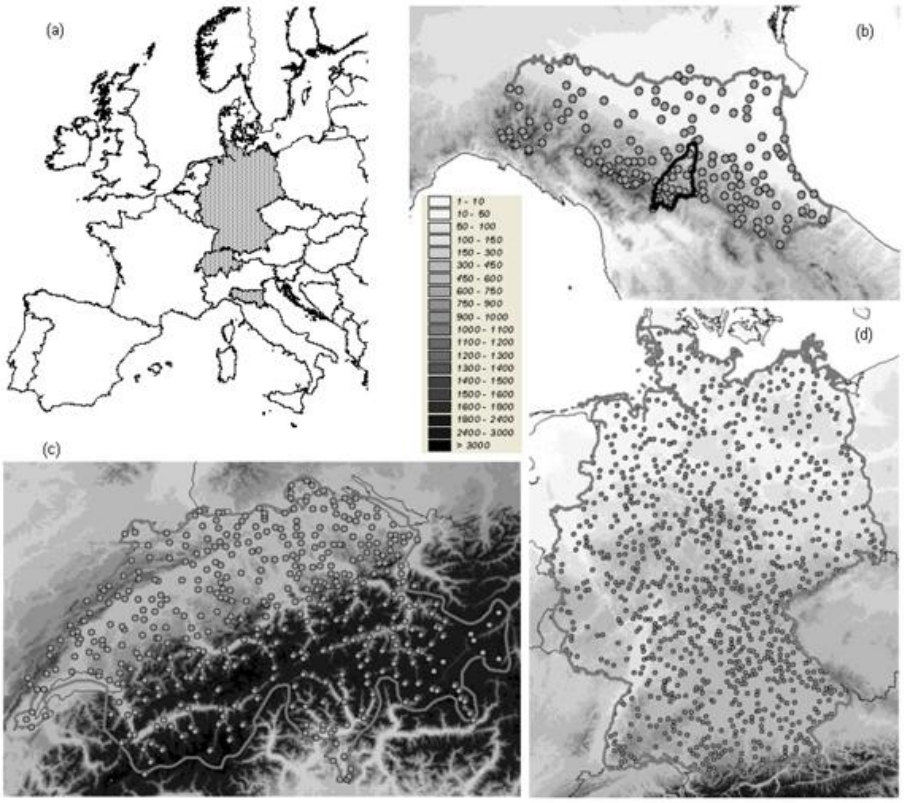


Figure 20: The three study areas localised in western Europe (a). Rain gauge locations (dots) of observed climatology and verification datasets for (b) Emilia-Romagna, northern Italy (in evidence the Reno river basin); (c) Switzerland and (d) Germany. The legend of the digital elevation model (in meters above sea) is common for the latter three panels.

forecast hours for Emilia-Romagna. The verification methods used here were the attributes diagram and the Brier Skill Score (BSS). The thresholds for the verified events were defined as percentiles of the climatological distribution of observed 24-h precipitation, different for each grid point. The use of percentiles of climatological distribution as thresholds guarantees that the sample points share the same climatological frequency of the event. This approach enables to avoid that chosen metrics might report unexpectedly large skill in some points due to the variation of the climatological event frequencies within the verification area. In the following of this Section, results are analysed for each study area separately. The forecast verification measures were first computed independently for each model grid point and were then averaged over the area under investigation. Attributes diagrams are shown for each season only at the day-2 lead time, considering the 80-th and the 95-th percentiles of 24-h climatological rainfall amount as verification thresholds. For brevity, we have chosen not to show attributes diagrams at other thresholds and lead times, as results do not depend strongly on the forecast range (forecasts show a slightly better reliability for the shorter lead times than for the longer lead times) and approximately shows a blend of the hereafter discussed diagrams, giving a little additional information only. Inset histograms for the frequency of usage were plotted on a log-10 scale, in order to provide a better visualization of the distribution in the tails. Results in terms of BSS are shown for each season, considering different forecast ranges (from day-2 up to day-5) and verification thresholds (the 80-th and 95-th percentiles of 24-h climatological rainfall amount). The observed climatology was used as the reference forecast for the computation of the BSS.

a Germany

1 ATTRIBUTES DIAGRAM
The raw ensemble provides poor performance at forecast probabilities lower than 60% in all the seasons; only forecasts of higher probabilities show reliability lines which lie above the no skill line, except for summer (Figure 21). The un-calibrated forecasts provided in autumn are better than forecasts provided in the remaining seasons. Generally, the calibration increases the forecast reliability at all the probabilities; the LR method is particularly effective in spring and summer. The best performances resulting from the forecast calibration are obtained in spring and winter. The improvement of the calibrated forecasts is somewhat less salient in summer, especially for probabilities greater than 60%. The calibrated forecasts show more reliability at lower probabilities for all the seasons. Generally, the raw and calibrated forecasts are overconfident; except for the forecast calibrated by the LR method which results underconfident at the lower probabilities of the higher threshold, especially in spring

2 BSS
The BSS values are always improved by calibrating the COSMO-LEPS system with the CDF method, for all the seasons and both the thresholds (Figure 22). The ANL and LR methods provide a less significant improvement, especially for the spring and summer seasons. The greatest amount of skill improvement is obtained in winter. Forecasts of lower precipitation events are slightly skilful than forecasts of higher precipitation events. Both the raw and calibrated forecasts show a remarkable decay of performance with lead time

b Switzerland

1 ATTRIBUTES DIAGRAM
The raw ensemble shows low reliability; un-calibrated forecasts for winter are particularly worse than forecasts for the other seasons (Figure 23), due to the

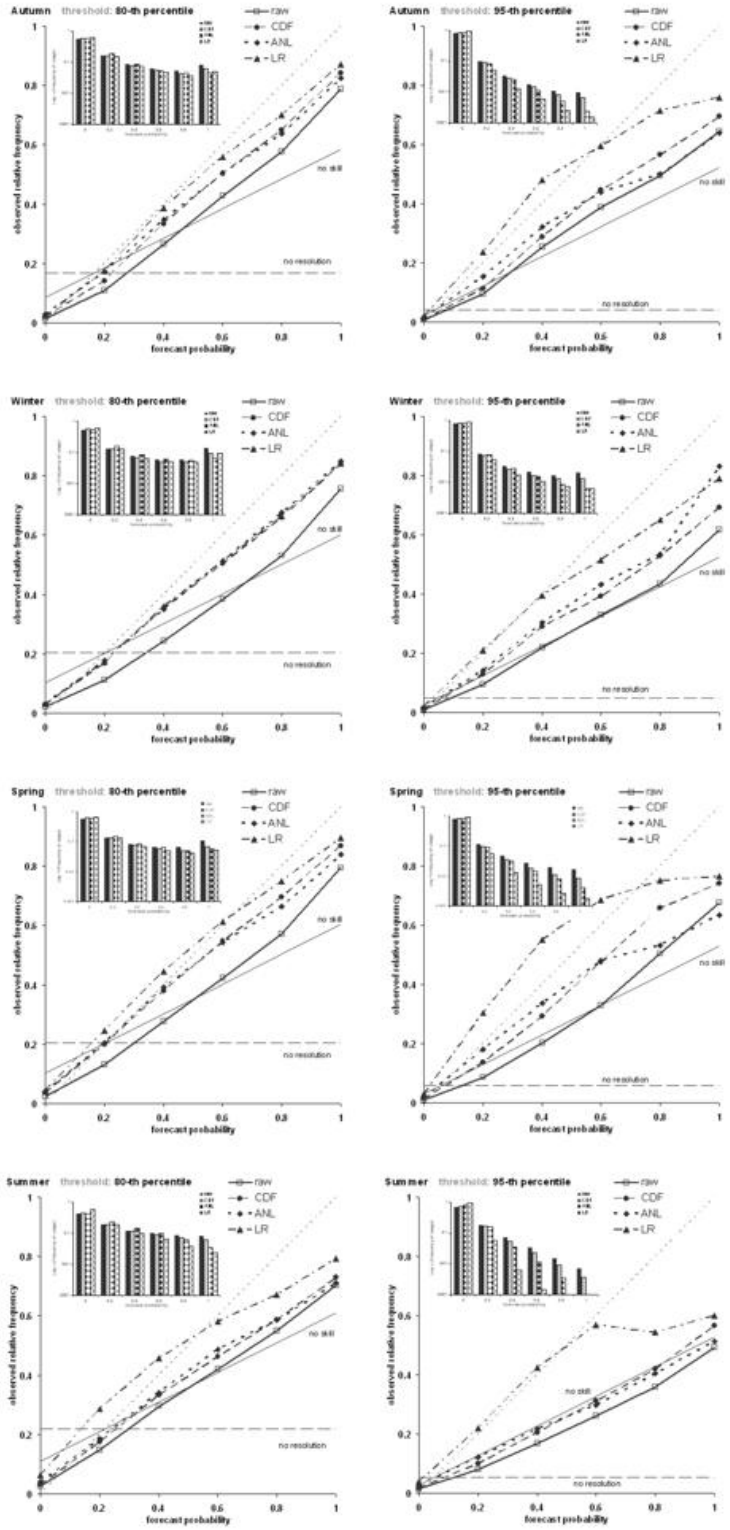


Figure 21: Attributes diagrams of the calibrated and raw forecasts over Germany at day2 lead time for the (left panels) 80-th and (right panels) 95-th percentile thresholds. The diagrams refer to (first row) autumn, (second row) winter, (third row) spring, (fourth row) summer. The inset histograms denote frequency of forecast usage of each probability bin.

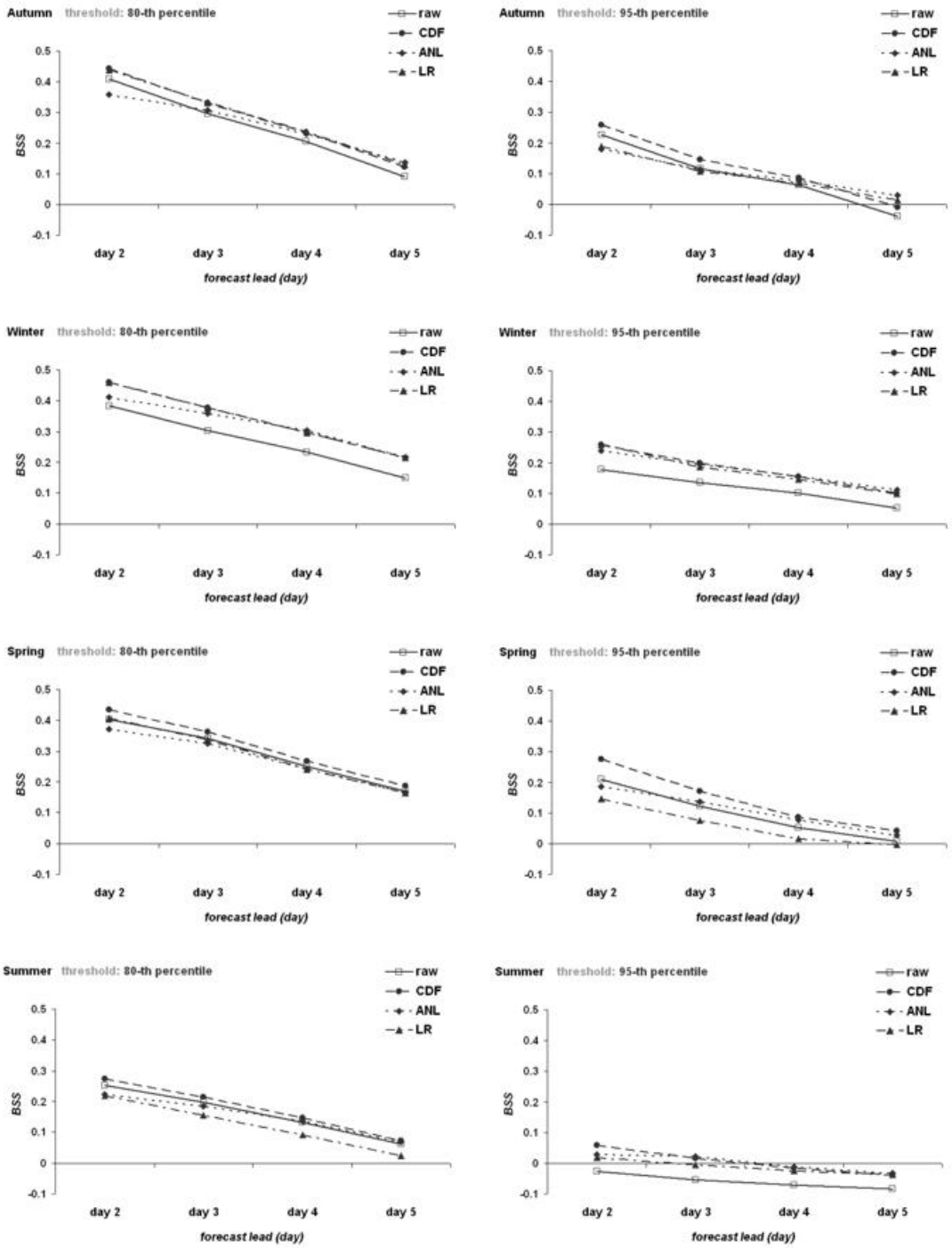


Figure 22: BSS at (left panels) 80-th and (right panels) 95-th percentile thresholds for the raw and calibrated ensembles over Germany in (first row) autumn, (second row) winter, (third row) spring, (fourth row) summer. The results refer to different forecast ranges, up to day5 lead time.

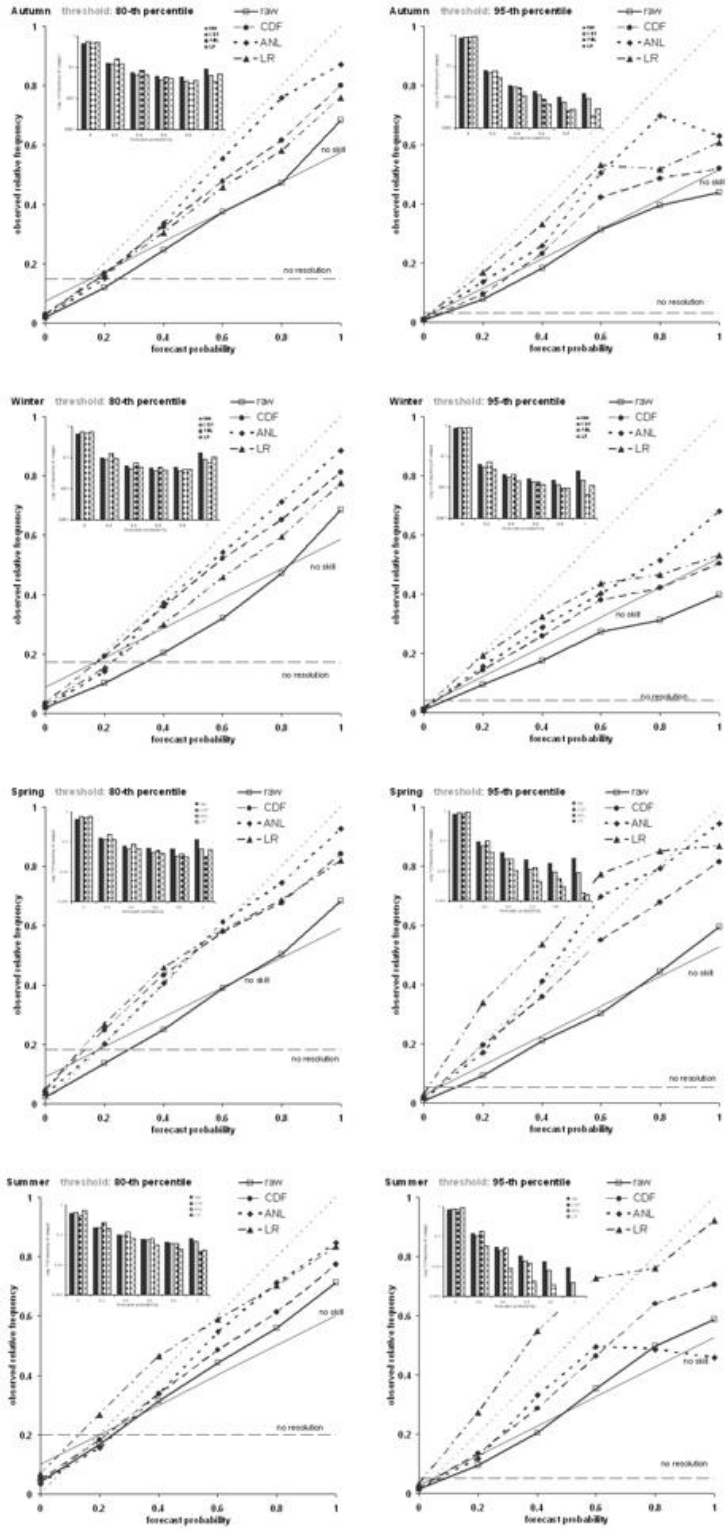


Figure 23: Same as Figure 21, but results refer to Switzerland.

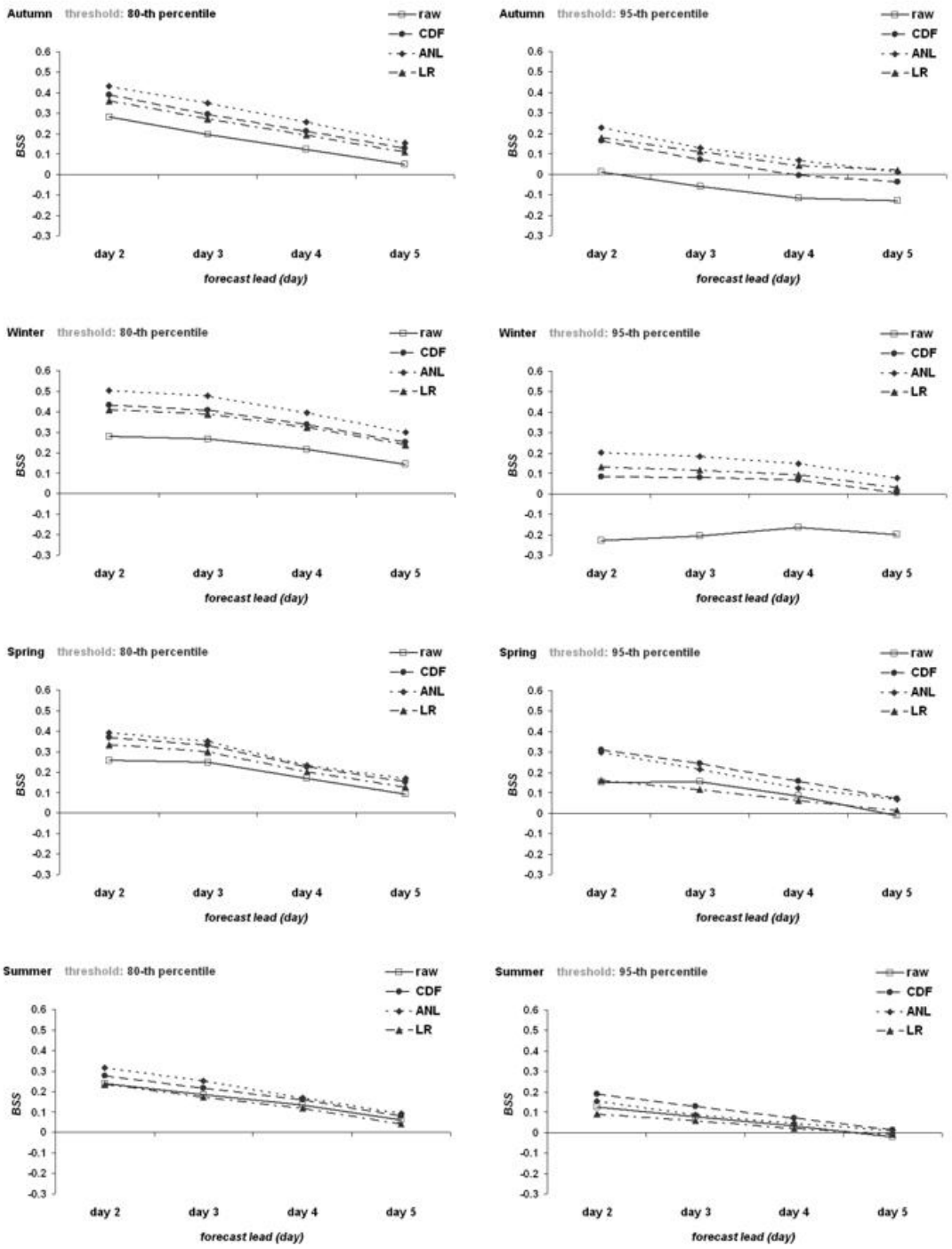


Figure 24: Same as Figure 22, but results refer to Switzerland.

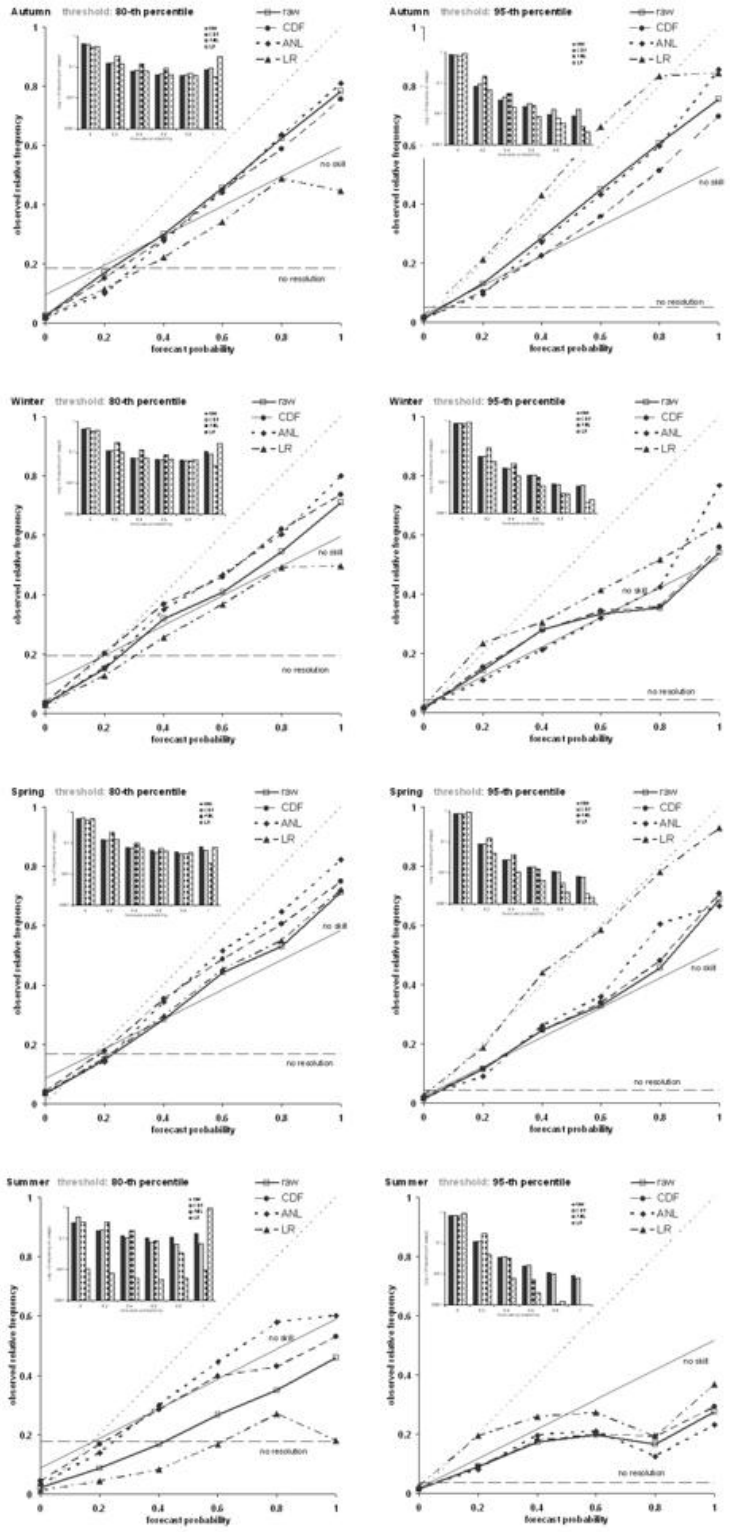


Figure 25: Same as Figure 21, but results refer to Emilia-Romagna.

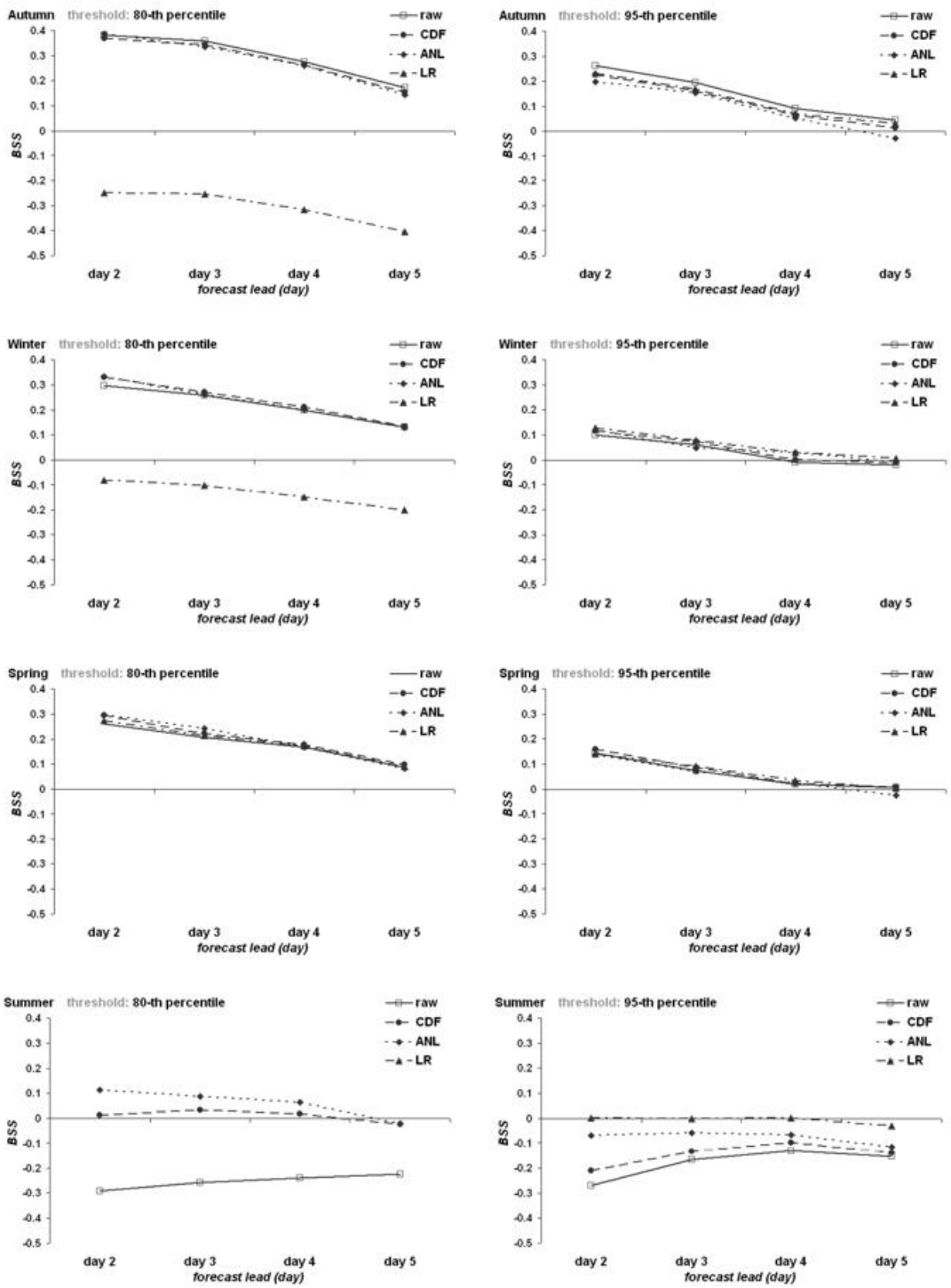


Figure 26: Same as Figure 22, but results refer to Emilia-Romagna.

larger systematic error which results in this season (Fundel et al. 2010). The calibration process enables to increase the reliability in all the seasons; generally, the ANL method performs better than the other methods (except for summer). Calibration is particularly effective in spring. The improvement of the calibrated forecasts is somewhat less salient in summer, as the raw forecasts have a relatively higher reliability. For all the seasons, the calibrated forecasts show more reliability at probabilities lower than 60%. Generally, both the raw and calibrated forecasts are overconfident in all the seasons, except for the forecasts calibrated by the LR method which result as underconfident in spring and summer at the lower probabilities

2 BSS
Generally, for all the seasons and both the thresholds, the BSS values are always improved by calibrating the COSMO-LEPS system with the CDF and ANL methods (Figure 24). The LR method proved to produce a less significant improvement, especially in spring and summer. A large amount of skill improvement is obtained in autumn and winter. Even, with respect to the higher threshold, unskilful raw forecasts for autumn and winter can be turned into skilful forecasts. The amount of skill improvement is smaller in spring and the smallest in summer. As explained in Fundel et al., 2010, the latter result can be due to the more convective and localized nature of precipitation events which occur in summer over Switzerland. During this season, systematic errors in the forecast system might be less important than spatial errors that cannot be corrected for with the proposed calibration methods. Forecasts of lower precipitation events are more skilful than forecasts of higher precipitation events. The decay of performance with lead time is quite evident for the raw and calibrated forecasts, especially for the lower threshold, and with a greater extent in autumn and spring

c Emilia-Romagna

1 ATTRIBUTES DIAGRAM
Generally, the raw and calibrated forecasts are overconfident in all the seasons (Figure 25). The raw ensemble has no good reliability; the un-calibrated forecasts provided in autumn are better than forecasts provided in the remaining seasons. This outcome can be ascribed to the higher predictability of precipitation in autumn, when precipitation events are more frequent and driven by large scale forcing. Raw forecasts for spring and winter show reliability lines which lie quite close to or under the no skill line; the higher threshold worsening this outcome. Even, raw forecasts for summer show reliability lines which lie quite under the no skill line. The results obtained by the forecast calibration process show high variability with respect to the season and the methods. The calibration does not substantially improve reliability in autumn, except for the LR technique at the higher threshold. However, a slight improvement is provided by the ANL method at the lower threshold for probabilities greater than 50%. Improvements are detectable in the winter and spring seasons at the lower threshold when the CDF or ANL calibration techniques are applied. At the higher threshold, only LR enables an increase of reliability, especially for spring. A little gain in reliability is obtained at the lower threshold for summer with the CDF and ANL methods, but results are still quite poor. As the performance of the calibration methods provide only slight improvements in such cases with respect to the raw forecast, a procedure based on a 1000-member block bootstrap sample was used, following Hamill, 1999, to test whether the possible benefits were statistically significant. Generally, the error bars showed a small magnitude, not overlapping to the raw

forecast line (not shown), revealing that the improvements can be evaluated as statistically significant, at a 95% level

2 BSS
The calibration process does not provide a clear beneficial impact on the ensemble QPFs (Figure 26), except for summer. For the autumn season, the values of BSS associated to the calibrated ensembles are lower than the BSS of the raw ensemble for all the lead times. For the winter and spring seasons, the BSSs associated to the calibrated ensembles are quite similar, sometimes slightly higher, with respect to the BSS of the raw ensemble. A clear improvement is obtained in summer, but the raw ensemble is quite unskilful and the calibrated ensembles perform similar to climatology. Generally, at the higher threshold, the calibration methods provide quite similar performances. Rather, at the lower threshold, the LR method provides very bad corrections with respect to the CDF and ANL methods (except for spring); even, very low negative BSS values (out of scale in the graph) result in summer. This outcome can be ascribed to the correction typical of the LR function. In particular, the value of the intercept strongly influences the calibrated value for lower QPF, providing a systematic increase of the raw forecast. Therefore, this aspect strongly penalizes the BSS when computed with respect to low QPF values as verification threshold, such as the 80-th percentile of observed climatology of Emilia-Romagna. Actually, this value is lower than 2.5 mm over the large part of Emilia-Romagna, especially in the plain areas. The scores for forecasts of lower precipitation events are slightly better than the scores of forecasts of higher precipitation events. The decay of performance with lead time is significant, except in summer

5.2 Verification of the calibration process by coupling QPFS with an hydrological model

The hydrological model used to generate simulated discharges is TOPKAPI (TOPographic Kine-matic Approximation and Integration), a physically-based distributed rainfall-runoff model. A detailed description of the model can be found in Liu and Todini, 2002. The performance of the meteo-hydrological coupled system has been evaluated over the Reno river basin (for a more detailed description of the basin refer to Diomede et al. 2008); in particular, the stream flow forecasts were evaluated at Casalecchio Chiusa, the closure section of its mountainous part which dimension is about 1000 km^2 (Figure 20 panel b). The stream flow forecast experiments covered the autumn and spring seasons in the period 2003-2008. Each hydrological run driven by COSMO-LEPS QPFs is 120-h long, starting at 1200 UTC on each day. Every hydrological forecast was run starting with basin initial conditions which were generated by running TOPKAPI in a continuous mode for the whole period 2003-2008 driven by observed precipitation and temperature data. Both QPF and rain gauge observations were downscaled to the hydrological model grid resolution (i.e., 500 x 500 m) by assigning to each cell, respectively, the QPF and the observed value provided on the nearest COSMO-LEPS grid point.

As the hydrological model runs with an hourly time step, hourly calibrated QPFs were used. For each grid point and 24-h lead time, the hourly calibrated QPFs were obtained from the hourly raw QPFs by using a scaling factor defined as the ratio of the calibrated and raw 24-h precipitation amounts. The hydrological simulations generated using rainfall observations were used as the reference measure, in order to assess the skill of the meteorological forecasts. Results of the meteo-hydrological coupling were investigated by statistical analyses. The analysis has firstly been carried out in terms of root-mean-square error (hereafter, RMSE). A

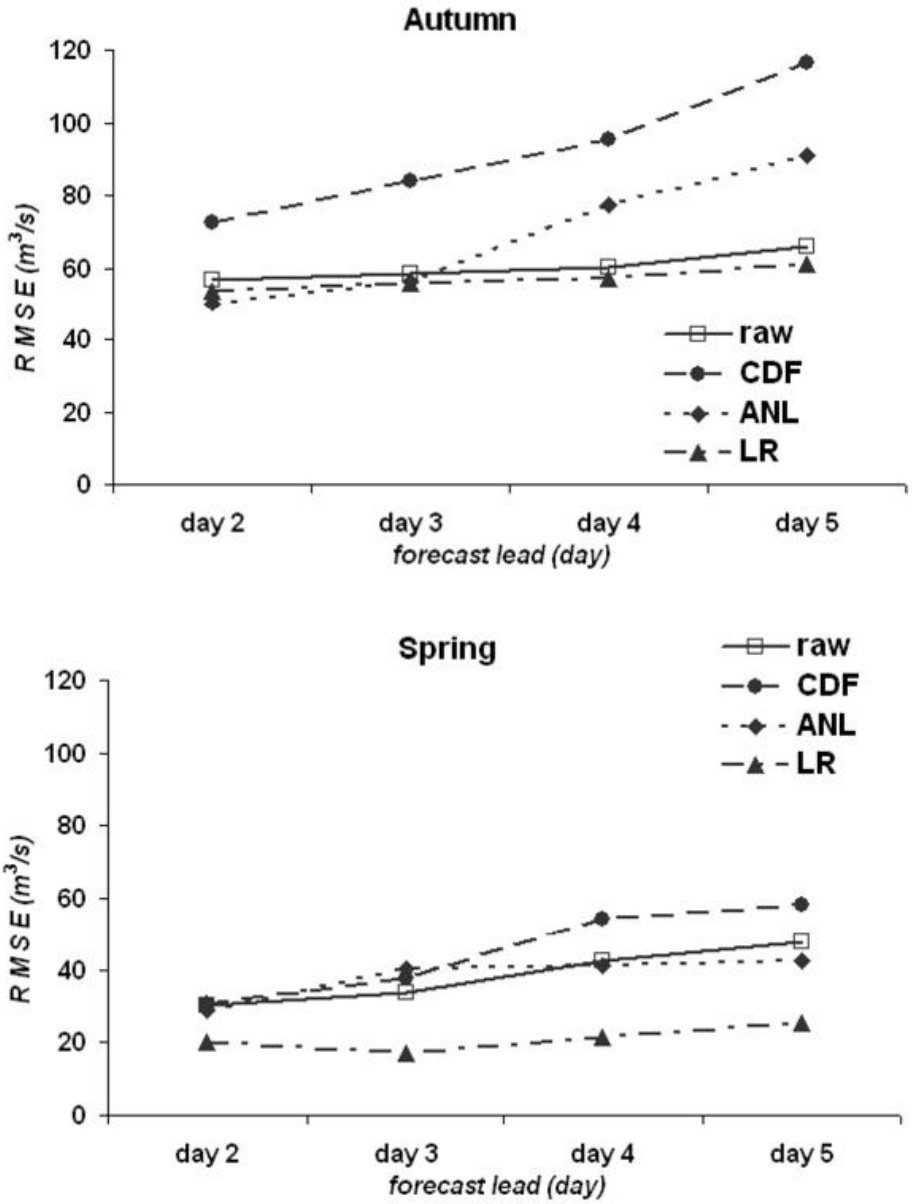


Figure 27: Root-mean-square error for the 95-th percentile of the ensemble of discharge forecasts provided at Casalecchio Chiusa in the autumn (panel a) and spring (panel b) seasons of the years 2003-2008. The discharge forecasts were driven by the QPFs provided by the raw ensemble (black line) and the ensemble calibrated by the CDF (dashed line with circles), ANL (dotted line with diamonds) and LR (dotted-dashed line with triangles) methods. The statistics are displayed as a function of the lead time of the forecast.

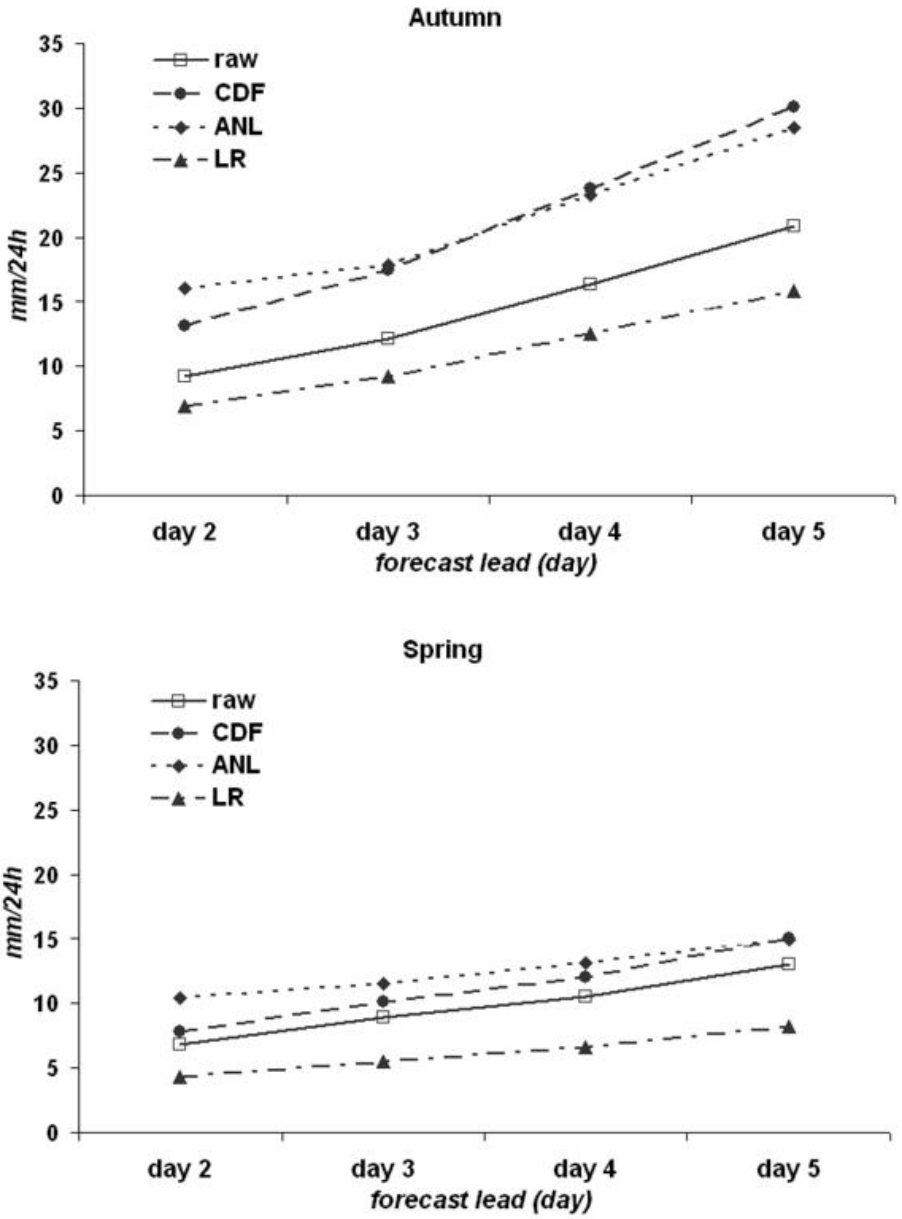


Figure 28: Spread of 24-h rainfall amount for the raw and calibrated ensembles, as a function of the lead time of the forecast. Results are shown for the autumn (panel a) and spring (panel b) seasons of the years 2003-2008.

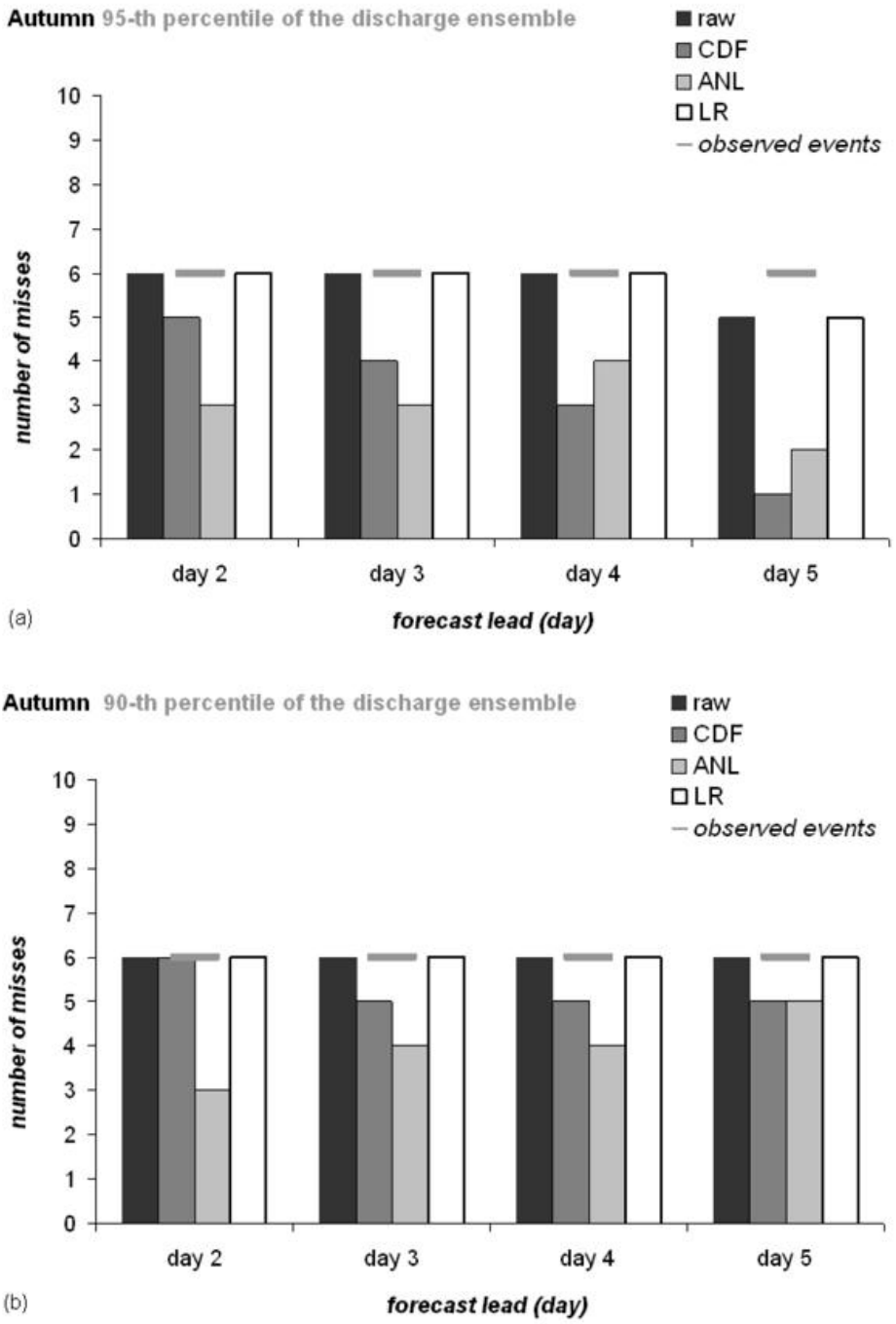


Figure 29: Number of missed events provided by the discharge forecasts driven by the raw and calibrated QPF ensembles for the autumn seasons in the years 2003-2008, as a function of the lead time. The statistics refer to the (panel a) 95-th and (panel b) 90-th percentiles of each discharge ensemble, with respect to the exceeding of the warning threshold at the Casalecchio Chiusa river section. The number of observed events (six) is displayed by the horizontal thick grey line.

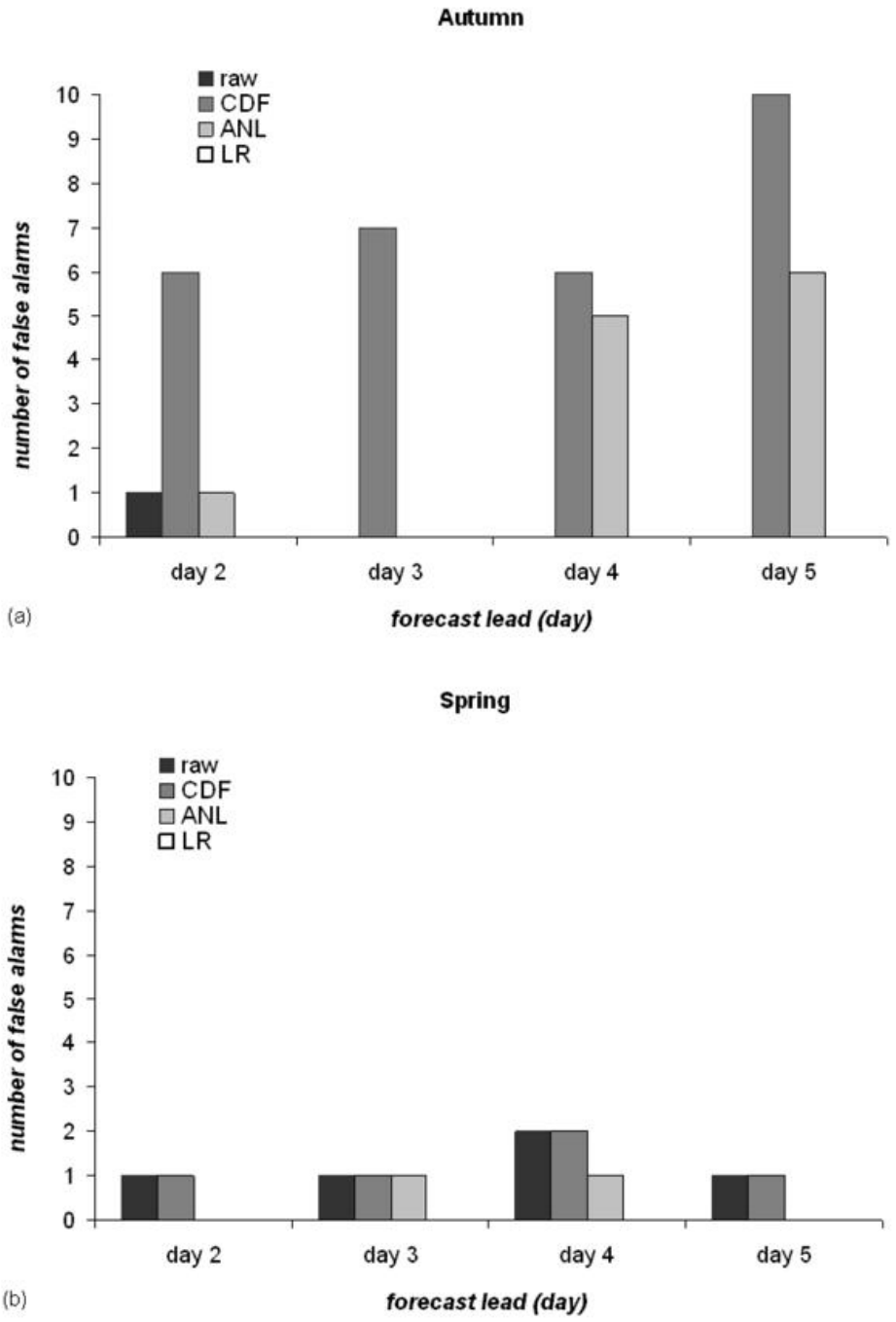


Figure 30: Number of false alarms provided by the discharge forecasts driven by the raw and calibrated QPF ensembles for the autumn (panel a) and spring (panel b) seasons in the years 2003-2008, as a function of the lead time. The statistics refer to the 95-th percentile of each discharge ensemble, with respect to the exceeding of the warning threshold at the Casalecchio Chiusa river section.

noteworthy outcome stands out by the calibration when the 95-th percentile of the discharge ensemble is considered. With respect to the raw ensemble, the CDF and ANL methods provided an increase of RMSE, especially in autumn for longer lead times; instead, the LR method provided a decrease of RMSE, more evident in spring (Figure 27). At the same time, for both autumn and spring, the RMSE values of the discharge ensemble mean driven by the raw and calibrated QPFs are quite similar (not shown). By the light of these outcomes, it seems that the CDF and ANL methods tend to increase the spread of the discharge ensemble. An additional investigation for the period 2003-2008 was then performed on the 24-h rainfall fields forecasted over the sub-area of Emilia-Romagna which includes the Reno river basin, in order to deeper investigate the impact of the calibration methodologies on the spread of the ensemble. This analysis confirms that the ANL and CDF methods tend to increase the spread of the ensemble (evaluated as the difference between the minimum and the maximum values of QPF provided by the ensemble members), especially in autumn (Figure 28). The increased spread associated to the ANL method can be due to the lower quality of analogs, namely very different situations which are not related to the current forecast are selected as analogs. Such a tendency to degrade the calibrated ensemble towards the climatology can also characterise the CDF method, which by construction does not correct for spread deficiencies (Hamill and Whitaker, 2006) and neglects the conditional relationship between observations and forecasts (Hopson and Webster, 2010). Instead, the reduced spread of the ensemble calibrated by the LR method could be explained by considering that in case of forecasts and observations are uncorrelated, this method is not able to remove the error systematically, providing a correction which could adjust all member forecasts to very close values (probably the climatological mean), regardless of their initial value (Hamill and Whitaker, 2006). Then, the impact of the calibration approach focussed on the verification of warning messages which would have been issued on the basis of the discharge scenarios driven by COSMO-LEPS. In particular, missed events and false alarms for the autumn and spring seasons in the years 2003-2008 have been investigated with respect to the exceeding of the warning threshold (i.e., the second level out of three levels of alert defined for the aims of civil protection) at Casalecchio Chiusa within each 24-h forecast period, up to day-5. Noteworthy outcomes were provided by the higher percentiles of the discharge ensemble. Considering the 95-th percentile, the impact of the calibration process in terms of reduction of misses for the autumn season is remarkable for the CDF and ANL methods (Figure 29, panel a). Actually, the discharge forecasts driven by the raw QPFs missed the six observed events totally for the lead times up to day-4; at day-5, five out of six events were missed. Rather, the discharge forecasts driven by the QPFs calibrated by the CDF and ANL methods reduced the missed events. In particular, the ANL method performs better up to day-3 (the number of misses is reduced by half), whereas the CDF method provides the best performance for longer lead times (one missed event only out of six cases at day-5). The LR method does not enable a reduction of misses with respect to the raw forecast. The positive impact provided by the CDF and ANL methods in terms of decrease of misses is reduced when the 90-th percentile of the discharge ensemble is considered (Figure 29, panel b). Nonetheless, the performance of the ANL method is quite similar up to day-4 for both the percentiles of the ensemble. No events occurred in the spring season in the period 2003-2008, thus no missed events result.

In terms of false alarms, when the 95-th percentile of the ensemble is considered, the discharge forecasts driven by QPFs calibrated by the CDF and ANL methods provide an increase of false alarms in the autumn season, with respect to the raw forecast (Figure 30, panel a). However, the worsening for the ANL method is evident only from day-4. The LR method does not provide any false alarm. When the 90-th percentile of the discharge ensemble is considered (not shown), only the CDF method still provides some (e.g., no more than four) false alarms. The number of false alarms provided by the 95-th percentile of the discharge ensemble is quite reduced (no more than two false alarms) in the spring season (Figure

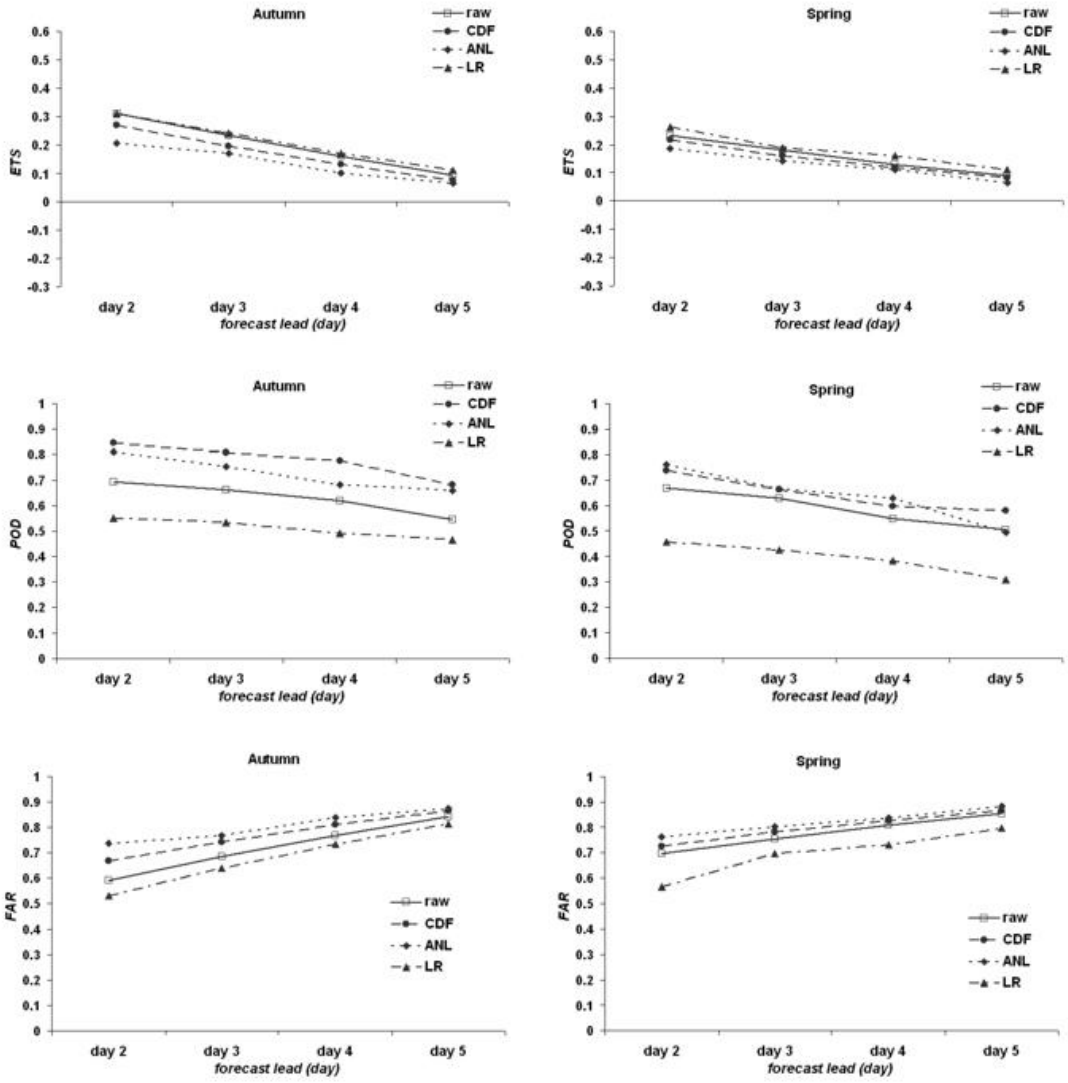


Figure 31: Equitable Threat Score, Probability Of Detection and False Alarm Rate at the 95-th percentile threshold of rainfall climatology for the 95-th percentile of QPFs of the raw and calibrated ensembles over the sub-area of Emilia-Romagna which includes the Reno river basin. The results refer to different forecast ranges, up to day 5 lead time, for the autumn (left panels) and spring (right panels) seasons in the years 2003-2008.

30, panel b). In particular, the discharge ensembles driven by QPFs calibrated with the CDF and ANL methods does not provide an increase of false alarms with respect to stream flow forecasts driven by the raw QPFs; even, the ANL method enables a reduction of false alarms. The LR method does not provide any false alarm. Similar results are obtained when the 90-th percentile of the discharge ensemble is considered (not shown). Summarising, the investigation over the Reno river basin shows that the calibration performed with the ANL and CDF methods enables to decrease the number of missed events, at the expenses of an increase of false alarms. Decision-makers have to evaluate (for instance, on the strength of a cost-loss analysis) which percentile of the discharge ensemble should be more suitable for supporting their activities. The noteworthy outcomes provided by the meteo-hydrological coupling suggested to perform an additional statistical analysis in terms of QPFs for the sub-area which includes the Reno river catchment, in order to investigate the ability of the calibrated ensembles to discriminate precipitation events. Actually, the calibration did not show a remarkable beneficial impact in terms of reliability and BSS on 24-h QPFs, especially in autumn . The attributes diagrams and the BSSs relative to the sub-area of the Reno river basin (not shown) provide results which are similar to those of the total area of Emilia-Romagna (shown in Figure 25 and Figure 26 respectively). The Equitable Threat Score (ETS), Probability Of Detection (POD) and False Alarm Rate (FAR) were thus computed for the autumn and spring seasons in the years 2003-2008. Figure 31 shows the forecast skills in terms of ETS, POD and FAR for the 95-th percentile of raw and calibrated ensembles, with respect to the 95-th percentile of rainfall climatology as verification threshold. The increase of POD and FAR for the ensembles calibrated by CDF and ANL with respect to the raw ensemble confirms the outcomes of the meteo-hydrological coupling. On the one hand, the improved QPF performance in terms of POD for the ensembles calibrated by CDF and ANL constitutes a real issue for the beneficial impact of calibration, as end-users are usually more concerned about missed events than by false alarms. On the other hand, these calibrated forecasts are characterised by an increase of FAR, even though not at a preoccupying rate. The ETS does not change significantly, due to the balance between the increases of both hits (influencing positively the ETS) and false alarms (influencing negatively the ETS).

5.3 Comments and conclusions

The direct model output of COSMO-LEPS is biased and shows deficiencies concerning both reliability and sharpness. Consequently, there is a need for calibration and post-processing techniques that address these issues and provide to the forecasters more reliable products for operational use. Here, the calibration approach utilized a 30-yr reforecast dataset produced by MeteoSwiss. In the recent past, several studies showed that reforecasts turn out to be useful for additional forecast improvement and diagnostic capability, making worth the extra computational resources required to produce them. In this work, the impact of the calibration approach was not so beneficial with respect to it had been reported in some comparable studies, in particular in terms of increase of reliability and skill. This can be due to the fact that in this study high resolution precipitation forecasts is dealt with. The paper investigated three methods for postprocessing the ensemble precipitation forecasts: quantile-to-quantile mapping, linear regression and analogs. The accuracy of calibrated QPFs was verified, with a particular focus on the use of such fields in hydrological applications. There appeared to be no single best forecast method for all applications and study areas, among the three tested. This study demonstrated that it is possible to improve raw ensemble forecasts of precipitation, but the improvements vary strongly from to site to site. It is reasonable to assume that this was more related to the non systematic model error than to the lack of capability of these methods to extract predictive information. The statistical analyses over Switzerland and

Germany revealed a positive impact of the calibration process. The calibrated ensembles increased the forecast reliability in all the seasons. The best performance over Switzerland was generally obtained with the ANL method, except for summer. Rather, the LR and CDF methods provided the best performances over Germany. No significant improvements resulted over Emilia-Romagna by the statistical analysis on the calibrated QPFs. But, the quality of these forecasts proved to be as improved for hydrological applications. Actually, the output of the hydrological model TOPKAPI driven by the calibrated QPFs revealed a beneficial impact of calibration for the discharge predictions over a medium-size catchment (i.e., the Reno river basin) selected as case study. In particular, the investigation on the hydrological runs covering the autumn and spring seasons of the years 2003-2008 showed that the calibration performed with the ANL and CDF methods enabled to obtain a decrease of missed events. But, an increase of false alarms resulted by the application of these two calibration methods, even though this trend was evident for the ANL method for longer lead times only. Decision-makers, who are usually more concerned by missed events than false alarms, have to evaluate which percentile of the discharge ensemble should be more suitable for supporting their activities. It seems clear that objective post-processing of ensemble forecasts will remain a critical component of the forecast process. The difficulty of accurately forecasting the intensity, location and timing of intense precipitation events at the spatial scale typical of small/medium-size catchments limits the ability of COSMO-LEPS to confidently and reliably capture observed intense peak discharges. Therefore, although calibrated forecasts do convey added-value in comparison to raw ones, precipitation forecasts need to be further improved to guarantee sufficiently reliable flood predictions over small/ medium-size catchments. The promising results of this study indicate that further research is merited. Whatever the case, there is definitely room for improvement in the calibration of ensemble systems. Reduction of errors that vary by weather element and flow configuration from ensemble precipitation forecasts is considered a necessary step to improving forecast quality and benefiting end users (Gneiting and Raftery, 2005; Yuan et al., 2007). There is a multitude of techniques that could be applied to regime-based calibration approach. Considering the techniques which were applied in the present study, a future improvement for the analog search could be obtained by a multi-variable approach, in order to find a better matching of the space-time evolution of the synoptic pattern. With respect to the CDF and LR methods, a solution could be the division of the training sample size according to some criteria which would allow to pool data which have similar model errors with respect to a certain meteorological situation.

6 Conclusions

The CONSENS PP has ended in 2011 and the work carried out within the Project has provided useful indications about the update and/or modification of the ensemble suites, together with suggestions about future works. The main outcomes are:

- the work on parameter perturbation has lead to the choice of a definite set of parameters and values which have been implemented in both the COSMO-SREPS and COSMO-LEPS ensembles. In the latter, though, perturbations can have different combinations with respect to those here analysed, since the combination is randomly selected day by days
- the soil moisture analysis perturbation technique has been developed and implemented, and it is available for further testing. This technique has not been implemented yet in an ensemble configuration for testing, but its applicability will be further investigated

in the future

- the work on multi-clustering has confirmed that the ensemble reduction methodology is able to retain a good fraction of the information contained in the original ensemble and that there is a relationship between cluster size and skill of the corresponding representative member of the large scale ensemble (for upper air variables). Therefore, the clustering methodology will be further developed and updated, aiming at improving also the short-range performances
- on the basis of the results of the COSMO-LEPS/COSMO-SREPS comparison, it was decided to stop running the extra COSMO-SREPS members (nested on the same sets of IC and BC but with different physics), and to keep only the COSMO-SREPS members which receive IC and BC by different global models, but prolonging the runs up to +132h, as COSMO-LEPS. These four extra runs (one nested on IFS with Tiedkte convection, one nested on IFS with Kain-Fritsch convection, one nested on GME and one nested on GFS) are now run as part of an experimental suite, which in combination with COSMO-LEPS constitutes the COSMO-HYBEPS 20 member ensemble, currently under evaluation
- an additional product of COSMO-LEPS has been made available, the 24h QPF calibrated with the CDF methodology over the 3 domains which have been considered in the study here presented

These results have lead to an effective consolidation of the mesoscale ensemble system of the Consortium and have provided useful indications about possible further improvements. Furthermore, the experience gained in the field of model perturbation techniques is useful for the development of the convection-permitting ensembles which is on-going in several COSMO Countries and which will be addressed in a forthcoming PP.

7 Acknowledgments

This project was carried out in the framework of the COSMO Consortium, therefore the authors would like to thank the COSMO colleagues for fruitful discussions and useful suggestions. We are also grateful for their help to Davide Cesari, Paolo Patruno and Fabrizio Nerozzi (ARPA-SIMC). The COSMO-LEPS and COSMO-SREPS ensembles have been run at ECMWF thanks to the Billing Units provided by the COSMO Countries which are also ECMWF members (Germany, Italy, Switzerland, Greece). The Italian institutions which provided observed data for the verification are also acknowledged.

8 References

Diomede, T., Nerozzi, F., Paccagnella, T. and E., Todini, 2008. The use of meteorological analogues to account for LAM QPF uncertainty. *Hydrol. Earth Syst. Sci.* **12**, 141-157.

Fundel, F., Walser, A., Liniger, M.A., Frei, C. and C., Appenzeller, 2010. Calibrated Precipitation Forecasts for a Limited Area Ensemble Forecast System Using Reforecasts. *Mon. Wea. Rev.* **138**, 176-189.

Gneiting, T. and A.E., Raftery, 2005. Weather forecasting with ensemble methods. *Science* **310**, 248-249.

Hamill, T.M. and J.S., Whitaker, 2006. Probabilistic quantitative precipitation forecasts based on reforecast analogs: theory and application. *Mon. Wea. Rev.* **134**, 3209-3229.

Hopson, T.M. and P.J., Webster, 2010. A 1-10-Day Ensemble Forecasting Scheme for the Major River Basins of Bangladesh: Forecasting Severe Floods of 2003-07. *J. Hydrometeor.* **11**, 618-641.

Houtekamer, P.L., 1993. Global and local skill forecasts. *Mon. Wea. Rev.* **121**, 1834-1846.

Kutzbach, J.E., 1967. Empirical eigenvectors of sea-level pressure, surface temperature and precipitation complexes over North America. *J. App. Meteorol.* **6**, 791-802.

Liu, Z. and E., Todini, 2002. Towards a comprehensive physically-based rainfall-runoff model. *Hydrol. Earth Syst. Sci.* **6**, 859-881.

Marsigli C., Montani A., Nerozzi F., Paccagnella T., Tibaldi S., Molteni F. and R., Buizza, 2001. A strategy for high-resolution ensemble prediction. Part II: Limited-area experiments in four Alpine flood events. *Q. J. R. Meteorol. Soc.* **127**, 2095-2115.

Marsigli, C., Montani A. and T., Paccagnella, 2008. A spatial verification method applied to the evaluation of high-resolution ensemble forecasts. *Meteorol. Appl.* **15**, 125-143.

Marsigli, C., 2009. Final report on priority project SREPS (Short Range Ensemble Prediction System). COSMO Technical Report N. 13, available at
http://www.cosmo-model.org/content/model/documentation/techReports/default.htm.

Marsigli C., Montani A. and T., Paccagnella, 2013. Perturbation of initial and boundary conditions for a limited-area ensemble: multi-model versus single-model approach. *Q. J. R. Meteorol. Soc.*, in press.

Molteni F., Buizza R., Marsigli C., Montani A., Nerozzi F. and T., Paccagnella, 2001. A strategy for high-resolution ensemble prediction. Part I: Definition of representative members and global model experiments. *Q. J. R. Meteorol. Soc.* **127**, 2069-2094.

Montani A., Capaldo M., Cesari D., Marsigli C., Modigliani U., Nerozzi F., Paccagnella T., Patruno P. and S., Tibaldi, 2003. Operational limited-area ensemble forecasts based on the Lokal Modell. *ECMWF Newsletter* **98**, 2-7.

Montani A., Cesari D., Marsigli C. and T., Paccagnella, 2011a. Seven years of activity in the field of mesoscale ensemble forecasting by the COSMO-LEPS system: Main achievements and open challenges. *Tellus* **63A**, 605-624.

Press, W.H., Teulosky S.A., Vetterling, W.T. and B.P., Flannery, 1992. Numerical Recipes in Fortran 77. 2nd ed. Cambridge Univ. Press, 280 pp.

Sutton, C. J. and T. M., Hamill, 2004. Impacts of perturbed soil moisture conditions on short-range ensemble variability. 16th NWP/20th W&F Conference, Seattle, American Meteorological Society.

von Storch, H. and G., Hannoschock, 1984. Comments on "Empirical Orthogonal Function Analysis of Wind Vectors over the Tropical Pacific Ocean". *Bulletin of the Meteorological Society of America* **65**, 162. (Appeared as a letter to the editor concerning: Legier, D.M.,

1983. Empirical Orthogonal Function Analysis of Wind Vectors over the Tropical Pacific Region. *Bulletin of the Meteorological Society of America* **64**, 234-241.)

Yuan, H., Gao, X., Mullen, S.L., Sorooshian, S., Du, J. and H-M. H., Juang, 2007. Calibration of Probabilistic Quantitative Precipitation Forecasts with an Artificial Neural Network. *Wea. Forecasting* **22**, 1287-1303.

Wilks, D.S., 2011. Statistical Methods in the Atmospheric Sciences. 3rd edn. Academic Press, New York, 676 pp.

List of COSMO Newsletters and Technical Reports

(available for download from the COSMO Website: www.cosmo-model.org)

COSMO Newsletters

No. 1: February 2001.

No. 2: February 2002.

No. 3: February 2003.

No. 4: February 2004.

No. 5: April 2005.

No. 6: July 2006.

No. 7: April 2008; Proceedings from the 8th COSMO General Meeting in Bucharest, 2006.

No. 8: September 2008; Proceedings from the 9th COSMO General Meeting in Athens, 2007.

No. 9: December 2008.

No. 10: March 2010.

No. 11: April 2011.

No. 12: April 2012.

No. 13: April 2013.

COSMO Technical Reports

No. 1: Dmitrii Mironov and Matthias Raschendorfer (2001):
Evaluation of Empirical Parameters of the New LM Surface-Layer Parameterization Scheme. Results from Numerical Experiments Including the Soil Moisture Analysis.

No. 2: Reinhold Schrodin and Erdmann Heise (2001):
The Multi-Layer Version of the DWD Soil Model TERRA_LM.

No. 3: Günther Doms (2001):
A Scheme for Monotonic Numerical Diffusion in the LM.

No. 4: Hans-Joachim Herzog, Ursula Schubert, Gerd Vogel, Adelheid Fiedler and Roswitha Kirchner (2002):
LLM ¯ the High-Resolving Nonhydrostatic Simulation Model in the DWD-Project LITFASS.
Part I: Modelling Technique and Simulation Method.

No. 5: Jean-Marie Bettems (2002):
EUCOS Impact Study Using the Limited-Area Non-Hydrostatic NWP Model in Operational Use at MeteoSwiss.

No. 6: Heinz-Werner Bitzer and Jürgen Steppeler (2004):
Documentation of the Z-Coordinate Dynamical Core of LM.

No. 7: Hans-Joachim Herzog, Almut Gassmann (2005):
Lorenz- and Charney-Phillips vertical grid experimentation using a compressible nonhydrostatic toy-model relevant to the fast-mode part of the 'Lokal-Modell'.

No. 8: Chiara Marsigli, Andrea Montani, Tiziana Paccagnella, Davide Sacchetti, André Walser, Marco Arpagaus, Thomas Schumann (2005):
Evaluation of the Performance of the COSMO-LEPS System.

No. 9: Erdmann Heise, Bodo Ritter, Reinhold Schrodin (2006):
Operational Implementation of the Multilayer Soil Model.

No. 10: M.D. Tsyrulnikov (2007):
Is the particle filtering approach appropriate for meso-scale data assimilation ?

No. 11: Dmitrii V. Mironov (2008):
Parameterization of Lakes in Numerical Weather Prediction. Description of a Lake Model.

No. 12: Adriano Raspanti (2009):
COSMO Priority Project "VERification System Unified Survey" (VERSUS): Final Report.

No. 13: Chiara Marsigli (2009):
COSMO Priority Project "Short Range Ensemble Prediction System" (SREPS): Final Report.

No. 14: Michael Baldauf (2009):
COSMO Priority Project "Further Developments of the Runge-Kutta Time Integration Scheme" (RK): Final Report.

No. 15: Silke Dierer (2009):
COSMO Priority Project "Tackle deficiencies in quantitative precipitation forecast" (QPF): Final Report.

No. 16: Pierre Eckert (2009):
COSMO Priority Project "INTERP": Final Report.

No. 17: D. Leuenberger, M. Stoll and A. Roches (2010):
Description of some convective indices implemented in the COSMO model.

No. 18: Daniel Leuenberger (2010):
Statistical analysis of high-resolution COSMO Ensemble forecasts in view of Data Assimilation.

No. 19: A. Montani, D. Cesari, C. Marsigli, T. Paccagnella (2010):
Seven years of activity in the field of mesoscale ensemble forecasting by the COSMO–LEPS system: main achievements and open challenges.

No. 20: A. Roches, O. Fuhrer (2012):
Tracer module in the COSMO model.

No. 21: Michael Baldauf (2013):
A new fast-waves solver for the Runge-Kutta dynamical core.

COSMO Technical Reports

Issues of the COSMO Technical Reports series are published by the *COnsortium for Small-scale MOdelling* at non-regular intervals. COSMO is a European group for numerical weather prediction with participating meteorological services from Germany (DWD, AWGeophys), Greece (HNMS), Italy (USAM, ARPA-SIMC, ARPA Piemonte), Switzerland (MeteoSwiss), Poland (IMGW), Romania (NMA) and Russia (RHM). The general goal is to develop, improve and maintain a non-hydrostatic limited area modelling system to be used for both operational and research applications by the members of COSMO. This system is initially based on the COSMO-Model (previously known as LM) of DWD with its corresponding data assimilation system.

The Technical Reports are intended

- for scientific contributions and a documentation of research activities,
- to present and discuss results obtained from the model system,
- to present and discuss verification results and interpretation methods,
- for a documentation of technical changes to the model system,
- to give an overview of new components of the model system.

The purpose of these reports is to communicate results, changes and progress related to the LM model system relatively fast within the COSMO consortium, and also to inform other NWP groups on our current research activities. In this way the discussion on a specific topic can be stimulated at an early stage. In order to publish a report very soon after the completion of the manuscript, we have decided to omit a thorough reviewing procedure and only a rough check is done by the editors and a third reviewer. We apologize for typographical and other errors or inconsistencies which may still be present.

At present, the Technical Reports are available for download from the COSMO web site (www.cosmo-model.org). If required, the member meteorological centres can produce hard-copies by their own for distribution within their service. All members of the consortium will be informed about new issues by email.

For any comments and questions, please contact the editor:

Massimo Milelli
Massimo.Milelli@arpa.piemonte.it

Consortium

for

Small-Scale Modelling

Technical Report No. 27

The COSMO Priority Project 'COLOBOC': Final Report

July 2015

DOI: 10.5676/DWD_pub/nwv/cosmo-tr_27

Deutscher Wetterdienst
MeteoSwiss
Ufficio Generale Spazio Aereo e Meteorologia
ΕΘΝΙΚΗ ΜΕΤΕΩΡΟΛΟΓΙΚΗ ΥΠΗΡΕΣΙΑ
Instytucie Meteorogii i Gospodarki Wodnej
Administratia Nationala de Meteorologie
ROSHYDROMET
Agenzia Regionale per la Protezione Ambientale del Piemonte
Agenzia Regionale per la Protezione Ambientale dell'Emilia-Romagna
Centro Italiano Ricerche Aerospaziali
Amt für GeoInformationswesen der Bundeswehr

www.cosmo-model.org

Editor: Massimo Milelli, ARPA Piemonte

The COSMO Priority Project 'COLOBOC': Final Report

Project participants:

J-M. Bettems[*], *H. Asensio, G. Bonafe, G. Duniec, O. Fuhrer, J. Helmert, C. Heret, E. Kazakova, M. Lange, E. Machulskaya, A. Mazur, G. de Morsier, G. Rianna, I. Rozinkina, B. Vieli, G. Vogel*

[*] Project coordinator:
Jean Marie Bettems
MeteoSchweiz
Kundendienst
OperationCenter 1
Postfach 257
CH-8058 Zürich-Flughafen
Switzerland

1 Introduction 4

2 State of the modelling system at the start of the project 4

3 Tasks and achievements 5

4 Experiments towards an unified soil-vegetation atmosphere transfer scheme TERRA for global and limited-area numerical weather prediction (J. Helmert, G. Vogel, H. Asensio, J. M. Bettems, M. Lange, F. Brenner, B. Ritter) 9

4.1 Introduction . . . 9
4.2 Model configuration . . . 10
4.3 Numerical experiments - Case study 10th April 2011 . . . 11
4.4 Long-term results . . . 21
4.5 Conclusions . . . 25
4.6 Summary and Outlook . . . 25
4.7 Appendix . . . 27

5 Documentation of a new multi-layers snow module (E. Machulskaya) 31

6 Implementation of the Martilli Urban Surface Parametrization in COSMO (O. Fuhrer, C. Muller, G. Fontannaz) 35

6.1 Introduction . . . 35
6.2 Bubble . . . 36
6.2.1 The Experiment . . . 36
6.2.2 Measurements of the UHI . . . 36
6.3 The COSMO Model . . . 37
6.3.1 Model Description . . . 37
6.3.2 MeteoSwiss Operational Implementation . . . 40
6.3.3 Model Setup . . . 41
6.4 COSMO vs. Measurements . . . 41
6.4.1 Increasing The Horizontal Resolution . . . 43
6.4.2 Increasing The Vertical Resolution . . . 43
6.5 BEP : *Building Effects Parametrization* . . . 45
6.5.1 Temperature at 2 mAGL . . . 46
6.6 Implementation of BEP in Cosmo . . . 48
6.6.1 First Method . . . 49
6.6.2 Second Method . . . 50

6.7 Simulation of the Basel UHI 51
6.7.1 Model Setup 51
6.7.2 Results 53
6.7.3 14 Days Simulation 57
6.8 Conclusion 58
6.9 Appendices 64
6.9.1 Bubble Measuring Stations 64
6.9.2 Meteorological Situation during the IOP 65
6.9.3 The Definition of Urban Categories for BEP 67

7 References **71**

1 Introduction

Atmospheric processes such as the development of the boundary layer, low level cloudiness, and the onset and intensity of convection are significantly influenced by the evolution of the lower boundary conditions. Consequently, an accurate representation of exchange processes between the soil and the atmosphere is essential to produce high quality NWP forecasts. At the time of the definition of the project, many activities concerning the lower boundary of the COSMO model had been undertaken, but most of these activities lacked some final efforts to bring them into operations and to make them accessible to the whole COSMO community. In 2008, the COSMO steering committee (STC) established a new Priority Project named Consolidation of Lower Boundary Conditions (COLOBOC), to finalize these developments and to incorporate them into well tested and documented software packages. The project was structured in 8 tasks, namely:

- Facilitate the access and usage of soil and surface observations (task 0)
- Consolidate an externalized TERRA module (task 1)
- Consolidate the software used to generate the external parameters (task 2)
- Consolidate and extend the external parameters database (task 3)
- Find and validate an optimal configuration of TERRA with its associated external parameters and look-up tables (task 4)
- Revise the snow model and the snow analysis (task 5)
- Deploy an urban module developed at EPFL/Switzerland (task 6)
- Consolidate the parameterization of land surface heterogeneity (task 7)

The project spanned the period 09.2008 to 09.2011; during these 3 years, about 8.5 FTE have been invested, with resources coming from 6 different institutions. Many discussions with colleagues of the CLM community took place during this project, resulting in the organization of regular COSMO / CLM meeting around this topic. Although not all tasks were successful (see chapter 3 for details), most of the developments done during this project have resulted in follow-up activities in the COSMO working group dedicated to soil and surface activities (see http://www.cosmo-model.org/content/tasks/workGroups/wg3b/default.htm).

2 State of the modelling system at the start of the project

The soil vegetation atmosphere transfer (SVAT) scheme TERRA and the associated external parameters provide the terrestrial lower boundary conditions for the atmospheric component of the COSMO model. TERRA is a multilayer model with a direct solution of the heat conduction equation and considers moisture transport due to hydraulic processes within the soil and the effects of transpiration by plants. Phase change processes of soil water (freezing/thawing of soil water/ice) are incorporated in the scheme both for their thermodynamic effect and for their impact on the hydraulic properties of the soil. In addition, the COSMO model employs a single layer snow module considering melting of a snow pack with prognostic snow density and time dependent snow albedo. Many uncertainties in the description and simulation of surface characteristics are partly caused by well-known problems. A critical

issue is the limited knowledge of the physical properties of the surface in the form of the so-called external parameters (e.g. soil type, root depth). These parameters play a vital role, e.g. in the simulation of the hydrological state, but both the quality of the raw databases and the methods used to derive the required model properties from these databases are not optimal. Moreover, the increase in horizontal resolution of current NWP models implies that some surface types previously neglected, such as lake and urban regions, are becoming more important. The simulation of the evolution of the soil is also hampered by inadequate knowledge of the initial state. Unrealistic drifts in soil moisture are ubiquitous in most NWP models, due to both incorrect representation of soil processes and the accumulation of precipitation errors (Scipal and Drusch, 2007). As demonstrated for the global model GME, an improvement may be achieved through a change in the root density distribution together with the introduction of seasonal vegetation parameters (Ritter, 2007). Due to the non-linear relations between surface parameters and fluxes, neglecting subgrid-scale land-surface heterogeneities by using average external parameters, may result in erroneous flux estimates. Studies have shown that, even with a grid spacing of only a few kilometres, considerable aggregation effects may indeed occur and must be corrected for. This can be tackled by introducing one of the so-called tile or mosaic approaches: the surface within a coarse scale atmospheric grid box is subdivided into patches with assumed homogeneous surface characteristics, fluxes are computed for each patch separately and then averaged. The current representation of the snow does not allow liquid water to stay within the snow pack, which is a severe limitation in spring when the freezing of trapped water during the night slows down the melting of the snow pack. Furthermore, many local effects such as snow transport by wind and influence of slope orientation make a correct representation of the snow cover particularly difficult.

3 Tasks and achievements

A summary of the different project tasks and of the achieved results are presented in this chapter. More details on some of these developments can be found in the following chapters.

Task 0: Facilitate the access and usage of soil and surface observations.

Goals: convenient access to recent operational high quality observations, representative for different climate and different type of soils.

Achievements: an action started in October 2009 with an official letter sent to a selection of NMS directors. Soil and surface data from 9 European observatories is now available on-line, in a common ASCII format (see http://www.cosmo-model.org/srnwp/content/default.htm). Time series starts in 2006; recent data is added each year, with 6 months time lag. The DWD has agreed to support this action in the future (C.Heret, F.Beyrich). This action is also supported by the C-SRNWP Programme of EUMETNET.

Open issues: only 5 sites are regularly updated (Cabauw, Lindenberg, Payerne, SP Capofiume, Sodankyla). Users community is small.

Task 1: Consolidate an externalized TERRA module.

TERRA standalone is the isolated terrestrial surface module of COSMO driven by external atmospheric fields, taken either from observations or from model runs. This tool provides a computationally efficient way to generate balanced soil conditions for the whole integration domain by computing multi-years TERRA integrations; it is also a useful tool to experiment with the soil model and the external parameters. It has been originally developed by F. Ament.

Goals: clean-up and consolidate the TERRA standalone code.

Achievements: a consolidated package, based on COSMO release 4.13, including documentation, is available on the COSMO web site (see http://www.cosmo-model.org/content/support/software/default.htm).

Open issues: the code is not compliant with the COSMO standard. The TERRA standalone code is not integrated in the COSMO software, making the synchronization with the model development difficult. No COSMO resource is available to further support this code, in particular to coordinate multiple developments taking place in the CLM community (the situation has changed at the time of writing of this report, IMS being interested taking over this duty).

Task 2: Consolidate the software used to generate the external parameters for the COSMO model.

Goals: the software infrastructure should be flexible and modular in order to support various raw datasets and to allow for experimentation with new aggregation algorithms or different look-up tables. It should be easily extensible to support future external parameters. It should support the needs of COSMO, COSMO-CLM, ICON, and GME.

Achievements: a software, called EXTPAR, fulfilling the stated goals and well documented, has been developed (see the Extpar user and implementation manual at http://www.cosmo-model.org/content/model/modules). At the time of writing of this report, this software is an official COSMO software, kept on a centralized repository at CSCS, with D. Lüthi as source code administrator; EXTPAR can now be activated through a web interface hosted on the CLM web site (http://www.clm-community.eu/index.php?menuid=221).

Open issues: none.

Task 3: Consolidate and extend the external parameters database.

Goals: a survey of external parameter fields and raw data sources used within the COSMO and the COSMO-CLM community will be performed. Where appropriate, replace older data sets by newer ones. Adapt work done for the GME. Consolidate external parameters required for new extensions of TERRA.

Achievements: the databases used for the external parameters have been updated according to the stated goals (see http://www.cosmo-model.org/content/model/modules/externalParams/default.htm).

In particular, a total of 15 new external parameters have been added: (vegetation characteristics) NDVI, NDVI_MX, NDVI_RATIO, RSMIN, (surface characteristics) EMISS_RAD, (deep soil) T2M_CL, (topo corrected radiation) SLOPE_ASP, SLOPE_ANG, HORIZON, SKYVIEW, (urban fraction) URBAN, (lake model) FR_LAKE, DEPTH_LK, (aerosols) AER_BC, AER_DUST, AER_SO4, AER_SS.

Open issues: the need to update the external parameters will always be present, e.g. for higher resolution applications or when new parameters are required for newly developed model parameterizations.

Task 4: Find and validate an optimal configuration of TERRA with its associated external parameters and look-up tables.

Goals: (1) gather and integrate tested developments of TERRA in official COSMO code, (2) define a consolidated set of look-up tables, (3) find and validate an optimal reference configuration of TERRA, using the external parameters and the consolidated look-up tables

developed within task 3.

Achievements: many experiments have been done to evaluate the impact of improved parameterizations, new external parameters and updated look-up tables. A new unified consolidated configuration, based on COSMO release 4.11, used both for the global scale in GME and for the regional scale in COSMO, has been defined. Experiments at MeteoSwiss and at DWD with this consolidated configuration showed mixed, neutral impact on verification scores; however, this consolidated configuration provides a physically sound basis for further developments. More details are available in chapter 4 of this report.

Open issues: compensating errors in different parts of the model hinders the development of TERRA.

Task 5: Revise the snow model and the snow analysis.

Goals: (1) Finalize and deploy a new multi-layer snow model supporting change of phases within the snow pack, (2) combine and improve a snow analysis approach based on in-situ observations and MSG derived snow mask.

Achievements: a detailed analysis of the performance of COSMO-RU has shown very large T2m errors in spring, up to 12 deg, at the boundary of the snow pack; these errors could be related to inadequate values of the snow water equivalent provided by the global snow analysis cycle. Different approaches have been proposed by our Russian colleagues to circumvent this issue (new parameterization of the snow density, observation driven 1D snow model). The work on the snow model has resulted in a revised parameterization of the snow albedo (incl. ageing), in a revised parameterization of the partial snow cover (height instead of snow water equivalent based), and in an experimental implementation of the multi-layers snow model in release 4.11 of COSMO (see chapter 5 for a description of this new snow model). The snow analysis software used at DWD (sfcana) has been adapted to support the use of the MSG derived snow mask.

Open issues: the multi-layers snow model has still some stability issues, in particular for very shallow snow layers, and needs more testing (at the time of writing of this report, the development of the multi-layers snow model has been transferred in ICON but is still not finalized). More generally, snow analysis and modelling still requires more work, in particular in complex terrain, during the snow melting period, or when going to finer resolution.

Task 6: Deploy an urban module developed at EPFL/Switzerland.

Goals: Consolidate and transfer an urban model developed at EPFL/Switzerland, based on the Buildings Effects Parametrization (BEP), into the latest COSMO release.

Achievements: an implementation of BEP, including some documentation, is available in a COSMO private release at MeteoSwiss (based on COSMO release 4.7). The description of the BEP implementation in COSMO, and of its impact, is available in chapter 6 of this report.

Open issues: no code responsible has been found. Furthermore, due to the complexity of this urban model, possibly not suited for general NWP applications, the decision to take it in the official COSMO release is pending (at the time of writing of this report, the choice of a simpler urban parameterization for the official COSMO release has been made).

Task 7: Consolidate the parameterization of land surface heterogeneity.

Goals: Finalize and deploy an implementation of the tile/mosaic approach, using the developments of Ament, 2006, implemented in a COSMO private release at MeteoSwiss.

Achievements: these developments have been consolidated and transferred in COSMO release 4.16. Dynamic snow tile has been introduced. Sensitivity studies have been performed, without conclusive results about the impact of this parameterization.

Open issues: code implementation is still experimental and has not been validated by COSMO Source Code Administrator (at the time of writing of this report, the COLOBOC implementation has been discarded and a new tile parameterization has been fully re-implemented in the ICON model).

4 Experiments towards an unified soil-vegetation atmosphere transfer scheme TERRA for global and limited-area numerical weather prediction (J. Helmert, G. Vogel, H. Asensio, J. M. Bettems, M. Lange, F. Brenner, B. Ritter)

4.1 Introduction

One of the critical issues in the description and simulation of surface characteristics in atmospheric models is due to physical surface properties in the form of the so-called external parameters (e.g. soil type, vegetation state, root depth, plant physiological parameters). These parameters play a crucial role, e.g. in the simulation of the hydrological state, but both, the variable quality of the raw databases and the used methods to retrieve the required model properties from these databases contribute to uncertainties in NWP model forecasts.

Together with the external parameters the soil vegetation atmosphere transfer (SVAT) scheme TERRA provides the terrestrial lower boundary conditions for the atmospheric component of the global GME model and the limited-area COSMO model. Driven by radiation fluxes, the evolution of the lower boundary conditions influence the exchange of heat, moisture, and momentum between the surface and the atmosphere and has a large impact on the simulation of screen level variables and atmospheric processes, such as the development of the boundary layer, low level cloudiness, and the onset and intensity of convection.

The SVAT model TERRA is a multilayer model with a direct solution of the heat conduction equation and considers moisture transport due to hydraulic processes within the soil and the effects of transpiration by plants. Phase change processes of soil water (freezing/thawing of soil water/ice) are incorporated in the scheme both for their thermodynamic effect and for their impact on the hydraulic properties of the soil. A snow module (single or multilayer) is employed considering melting of a snow pack with prognostic snow density and time dependent snow albedo. However, there is a need to employ also a canopy layer for vegetation in TERRA to improve the surface energy budget in COSMO.

Although the global GME and the limited-are COSMO model share the SVAT model TERRA in large parts it is reasonable to test new developments first on the global scale. Therefore a number of changes in external parameters and modifications of TERRA are used in operational GME, that are still experimental in COSMO. To fill this gap in the SVAT model between GME and COSMO a unified configuration for TERRA that further improves the lower boundary condition of NWP models at global and regional scale is proposed. For soil moisture analysis (SMA), employed to minimize the difference between diagnosed 2m-temperature and observations this unification between COSMO and GME is now achieved (Lange, 2011).

The report starts with the operational and experimental configuration of GME and COSMO-EU, both models with SMA, then show a case study at 10th April 2011 to illustrate the sensitivity of the results on the applied configuration. Long-term simulations of GME and COSMO-EU are evaluated from soil-moisture analyis monitoring and objective verification followed by a summary and an outlook. The appendix contains figures that refers to changes in external parameters.

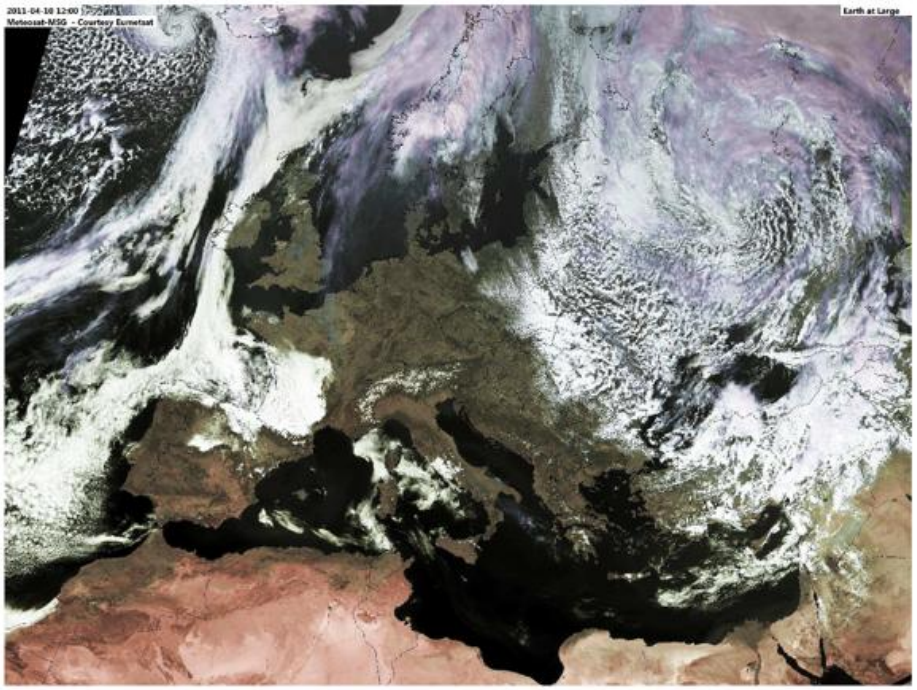


Figure 1: Meteosat VIS image of Europe on 10th April 2011 12 UTC

4.2 Model configuration

The differences in model configuration with impact on the energy budget at surface between GME and COSMO include the aerosol distribution, surface emissivity, vegetation albedo, vegetation climatology, root density profile, and minimum stomatal resistance (Tab. 1).

The radiation budget at Earth surface forces the energy fluxes into the atmosphere and to the ground. The magnitude of these fluxes depends on the amount of incoming global radiation, which is altered primarily by clouds and aerosols. While the global model GME uses a aerosol climatology from Tegen et al. (1997), the COSMO model employs a constant distribution of aerosols according to Tanre et al. (1984) with a known overestimation of desert dust aerosol in Europe (e.g. Hohenegger et al., 2005). In order to obtain a similar surface radiation budget in COSMO in comparison with GME, the aerosol climatology from Tegen et al. (1997) was applied in the COSMO experiment that used similar to the GME the land-use dependent surface emissivity.

In addition to the incoming radiation, the surface radiation budget of vegetation covered areas depends also on the vegetation albedo. The approach of a constant vegetation albedo of 15 % is enhanced in the numerical experiments of GME and COSMO, following e.g. Moody et al. (2008) by taking into account the land-use by distinction of evergreen (10 %), deciduous (15 %) , and non-forest (20 %). Given the radiation budget at surface, the partition of energy fluxes is influenced by the evapotranspiration depending on plant physiological parameters. The prescribed annual cycle of vegetation parameters (e.g leaf-area index (LAI) and vegetation fraction) in the outer-tropics depending on latitude and height (Doms et al., 2005) was modified in the GME and the COSMO experiments by employing an annual cycle from the climatology (1998-2003) of the normalized differential vegetation index (NDVI).

The partition of energy fluxes at the surface depends also on a large extent on the soil moisture (Balsamo et al., 2009), that has therefore a large impact on the Bowen ratio.

	GME	COSMO-EU	GME EXP	COSMO-EU EXP
Model status	operational	operational	109/1009	8474
Aerosol distribution	climatology	fixed	climatology	climatology
Emissivity	land-use	const	land-use	land-use
Vegetation albedo	const	const	land-use	land-use
Vegetation climatology	NDVI	analytical	NDVI	NDVI
Root density profile	exponential	uniform	exponential	exponential
Min. stomatal resistance	GLC2000	const	ECOCLIMAP	ECOCLIMAP

Table 1: Configuration of GME and COSMO routine and numerical experiments.

However, the simulation of the evolution of the soil is hampered by inadequate knowledge of the initial state. Unrealistic drifts in soil moisture are ubiquitous in most NWP models, due to both incorrect representation of soil processes and the accumulation of precipitation errors (Scipal and Drusch, 2008). As already demonstrated for the global model GME, an improvement may be achieved through the introduction of the NDVI-based annual cycle of vegetation together with a change in the root density distribution (Ritter, 2007). The exponential root density profile used in GME was employed also in the COSMO model and applied in the limited-area experiments.

The maximum possible evapotranspiration of plants is connected with a minimum stomatal resistance r_{min}. The constant value of this parameter of 150 sm^{-}1 in the COSMO model was replaced by a land-use dependent formulation from GME. However it was found in GME that large uncertainties in the value of r_{min} for individual land-use classes exist that leads to a domain averaged overestimation of r_{min}. In connection with the soil-moisture analysis (SMA) that was adapted from COSMO to the GME to minimize the difference between diagnosed 2m-temperature and observations (Lange, 2011), an overestimation of r_{min} results in an accumulation of soil moisture. To further improve the SMA in GME and COSMO the relationship between land-use classes and r_{min} was adapted from ECOCLIMAP Masson et al. (2003) and applied in numerical experiments of GME and COSMO. From the observed reduction of domain averaged r_{min}, a more realistic annual cycle of soil moisture with reduced SMA increments was expected.

4.3 Numerical experiments - Case study 10th April 2011

The soil-moisture analysis was introduced in the operational GME at 9th March 2011 for the 00 UTC analysis. The accompanying numerical GME experiment (experiment code 109/1009) was initialized at 12th March 2011 00 UTC, which applies the land-use based vegetation albedo and minimal stomatal resistance from land-use classes of ECOCLIMAP. In order to allow for a spin-up of the GME experiment the numerical COSMO experiment (experiment code 8474) was initialized at 1st April 2011 00 UTC. This spin-up is considered as sufficient for atmospheric processes and processes of the upper soil. It used the boundary conditions from 109/1009 and shares the configuration of the external parameters and the SVAT scheme with the global model experiment.

As a case study the sensitivity of the COSMO-EU 36 hour forecast on the used configuration was investigated for a clear-sky situation in central Europe on the 10th April 2011 12 UTC. Figure 1 shows the visible satellite image on this date with a large cloud-free area in central

Europe.

As shown in Tab. 1, the GME experiment 109/1009 uses the same configuration setup as the COSMO experiment 8474. Therefore, the following figures show the absolute values for the GME experiment and the difference between operational COSMO-EU and the COSMO experiment 8474 assuming a much smaller difference between GME experiment 109/1009 and the COSMO experiment 8474. The 36 hour forecast of the averaged net radiation budget at surface from the GME experiment (Fig. 2 top) shows small values in North-Scandinavia due to the snow pack with high albedo compared to the snow free regions in central Europe. The difference of the averaged net radiation budget at surface between operational COSMO-EU and COSMO-EU experiment 8474 reveals the changes in aerosol optical depth, vegetation albedo, and surface emissivity. The dominant effect of the reduced desert dust aerosol optical depth leads to the expected increase of the averaged net radiation budget at surface in the domain mean.

The surface albedo (Fig. 14 top) is dominated by snow in northern Europe and the mountains but the difference in the snow free regions refers to the changes in annual cycle of vegetation and formulation of the vegetation albedo (Fig. 14, bottom). The modified albedo of evergreen forest (set to 10 % in the experiment) is visible for the low-mountain range of central Europe. An additional contribution to the difference in vegetation albedo comes from the vegetation coverage (Fig. 15, top). Replacing the analytical function by a NDVI-based climatology leads to a significant higher vegetation coverage in south-west and central Europe and a decrease north-east after the first third of April (Fig. 15, bottom) .

As expected this is also the case for the leaf ara index LAI (Fig. 16). The GME experiment (Fig. 16, top) refers the LAI to the NDVI climatology and shows therefore realistic maximum values in south-western Europe. The comparison to the operational COSMO-EU (Fig. 16, bottom) shows that the difference to the empirical relationship in this region is increased.

For the plant evapotranspiration, in addition to the LAI, the minimum stomatal resistance r_{min} is one important vegetation parameter (Fig. 17, top) . The impact of the relationship of the land-use classes to r_{min} based on ECOCLIMAP is large, exceeding 30 sm^{-1} in domain average (Fig. 17, bottom). Only for the low-mountain range and Scandinavia the difference is below 15 sm^{-1}.

In the average over the forecast time, a sensitivity of the heat fluxes on the differences in external parameters and SVAT model is expected. Figure 3 (top) shows the averaged sensible heat flux (positive downward) those difference for COSMO is a result of changes in surface radiation budget (Fig. 2) and differences in partition of energy at the surface. Positive values of the sensible heat flux averaged over forecast time reveals the cooling over the snow (Fig. 3, top) but the mean value over the domain increased by about 8 Wm^{-2} for the COSMO-EU experiment that is larger than the increase in averaged latent heat flux (Fig. 4) of below 4 Wm^{-2}. However, even regions in western and central Europe and northern Africa with different vegetation properties (higher vegetation coverage, LAI, smaller minimum stomatal resistance, different root density profile) in the COSMO-EU experiment compared to the operational COSMO-EU exceeds this value clearly. Considering the change in the Bowen ratio based on sensible and latent heat flux averaged over the forecast time, Fig. 5 supports this result since regions in western Europe with positive Bowen ratio below one, i.e. less sensitive heat flux than latent heat flux with same sign, show a positive difference to the operational COSMO-EU. It could be expected that the increased latent heat flux in the COSMO-EU experiment is correlated with a decrease in soil moisture and Fig. 6 confirms this assumption. Due to the exponential root density profile in the experiment the impact of the upper soil levels on the evapotranspiration is increased that leads to 10 % dryer upper soil in parts of western Europe and northern Africa (Fig. 6, top). Here, the correlation of

this pattern to the changes in vegetation parameters is obvious. The modified root water uptake leads as expected to a soil moisture increase in the soil layers 54 cm and 162 cm (Fig. 6, center). However due to the large time scales in the deeper soil after 10 days of the numerical experiment the change in this case study is just small and below 5 %. This is also the case for considering all six hydraulic active layers in TERRA (Fig. 6, bottom), where the soil moisture increase for the experiment in domain average is 0.15 %.

Although feedback effects of changes in the SVAT scheme on precipitation could be assumed, their identification within one case study is difficult. This is confirmed by considering the accumulated precipitation fractions over 36 hours forecast time (Fig. 7). In this situation the increase in domain average is 0.05 kgm^{-2} for grid-scale and for convective precipitation with a small increase of the convective fraction on total precipitation in the COSMO-EU experiment.

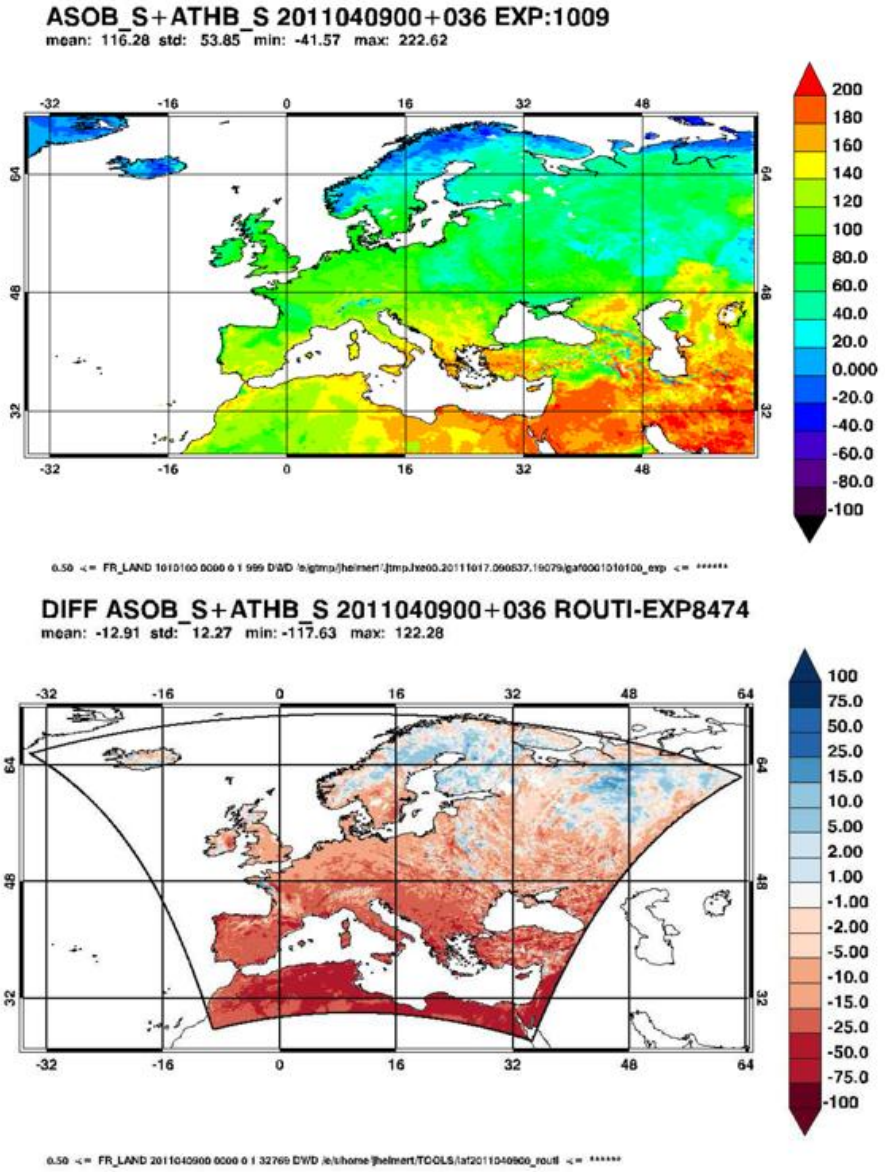


Figure 2: Averaged fluxes of solar and thermal radiation at surface (W/m^{-2}) at 10th April 2011 12 UTC for 36 hours forecast of the GME experiment 109/1009 (top) and difference between COSMO-EU routine and experiment 8474 (bottom)

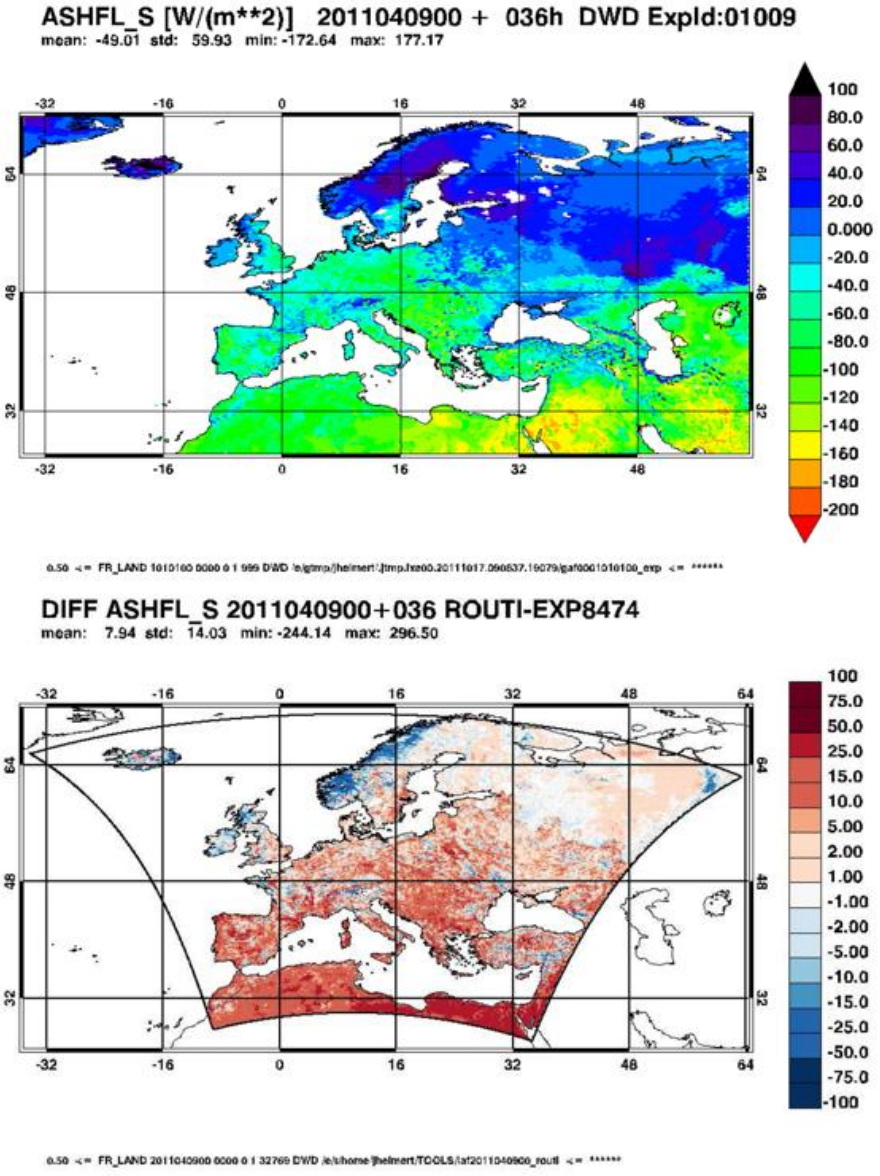


Figure 3: Flux of sensible heat (Wm^{-2}) averaged over 36 hours forecast time at 10th April 2011 12 UTC of the GME experiment 109/1009 (top) and difference between COSMO-EU routine and experiment 8474 (bottom).

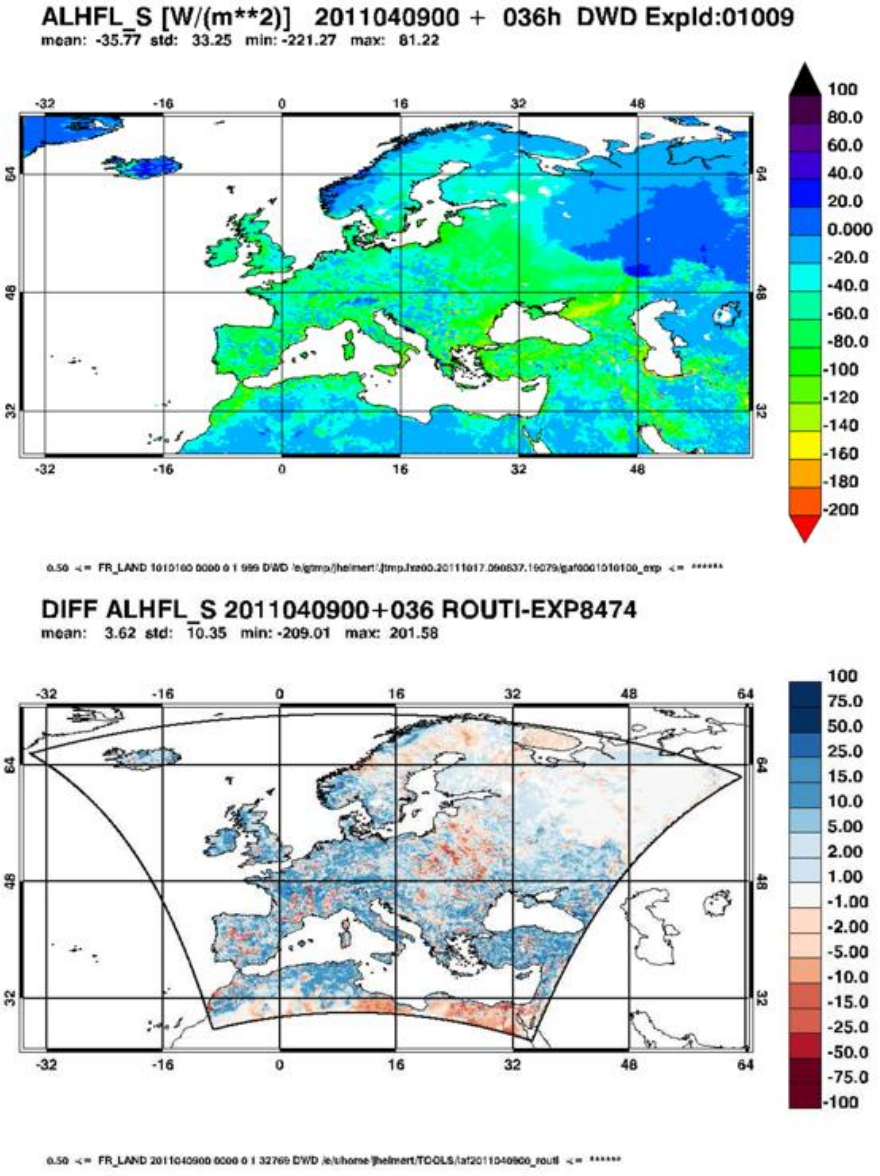


Figure 4: Flux of latent heat (Wm^{-2}) averaged over 36 hours forecast time at 10th April 2011 12 UTC of the GME experiment 109/1009 (top) and difference between COSMO-EU routine and experiment 8474 (bottom).

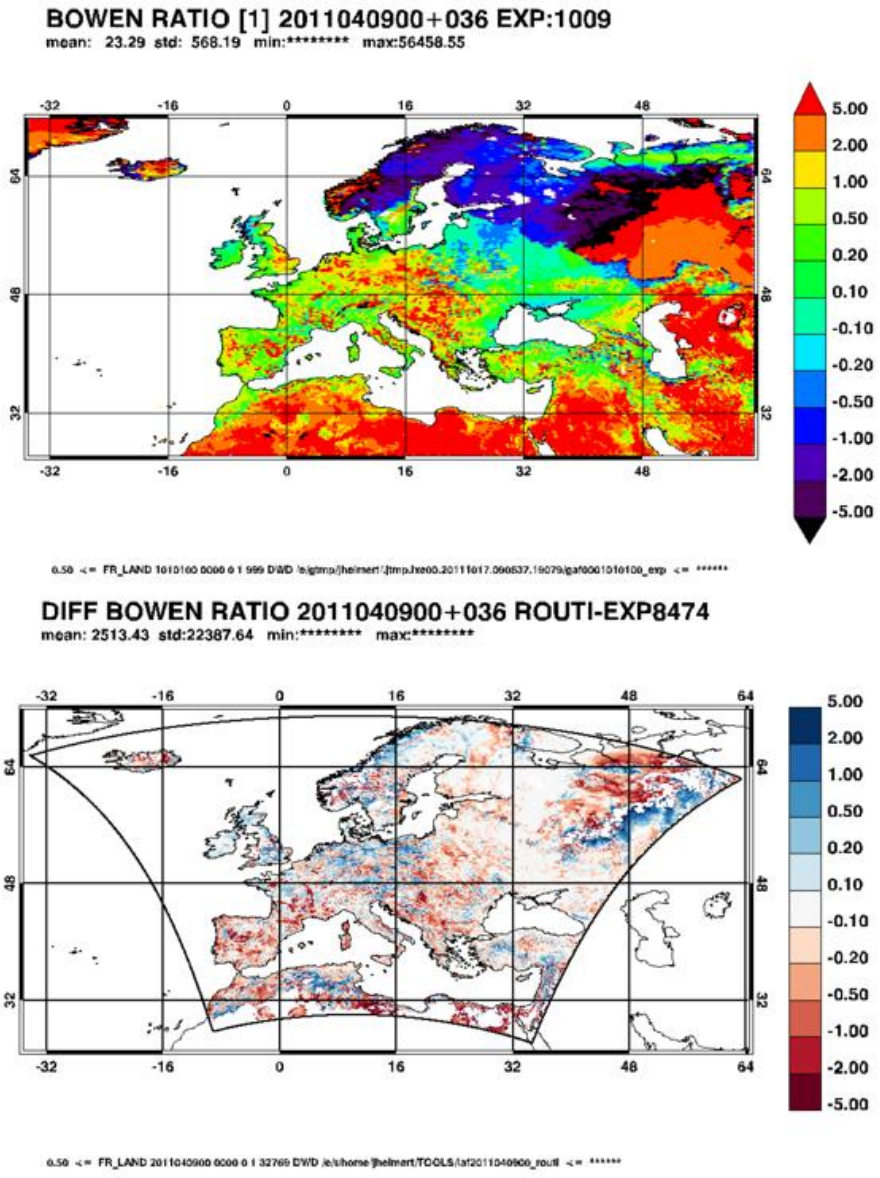


Figure 5: Bowen ratio based on flux of sensible and latent heat averaged over 36 hours forecast time at 10th April 2011 12 UTC of the GME experiment 109/1009 (top) and difference between COSMO-EU routine and experiment 8474 (bottom).

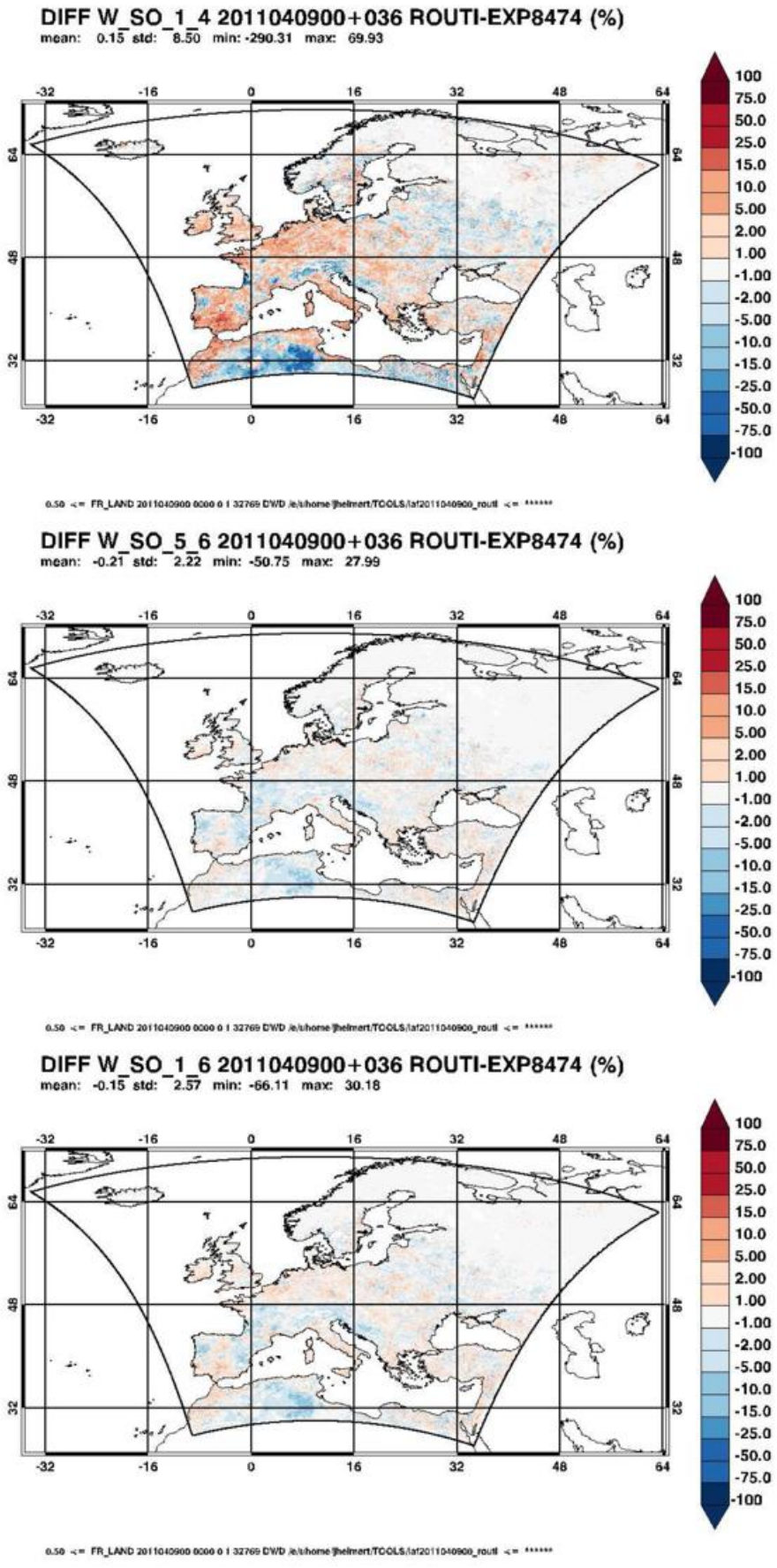


Figure 6: Difference between COSMO-EU routine and experiment 8474 for soil moisture including upper soil levels 1,2,6,18 cm (a), deeper soil levels 54 cm and 162 cm (b), and soil levels 1,2,6,18,54, and 162 cm (c). Shown is the deviation (%) in comparison to the COSMO-EU routine.

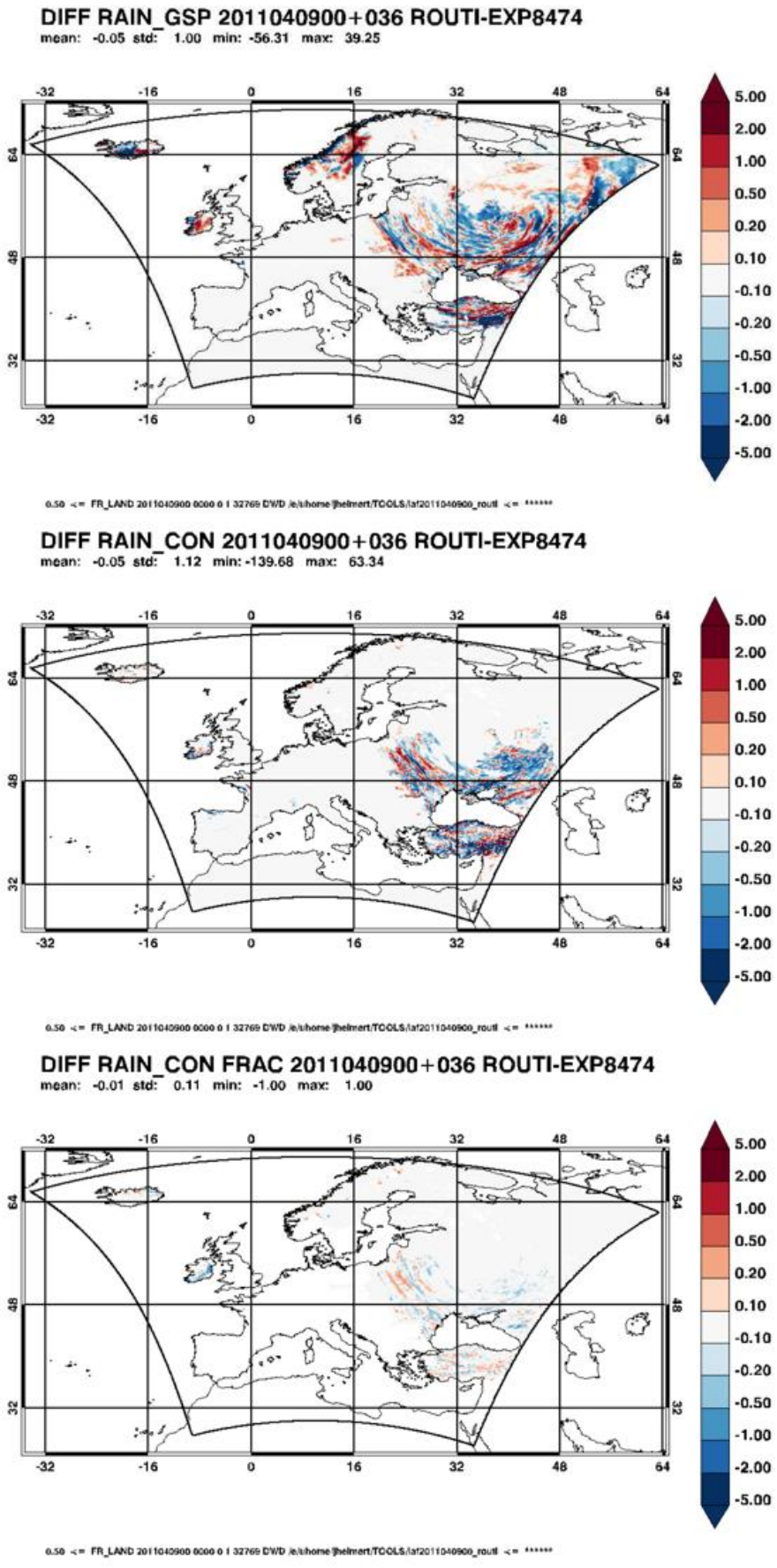


Figure 7: Difference between COSMO-EU routine and experiment 8474 for accumulated precipitation (kgm^{-2}) of grid-scale component (top), convective component (center), and fraction of convective component on total precipitation (grid-scale + convective) (bottom).

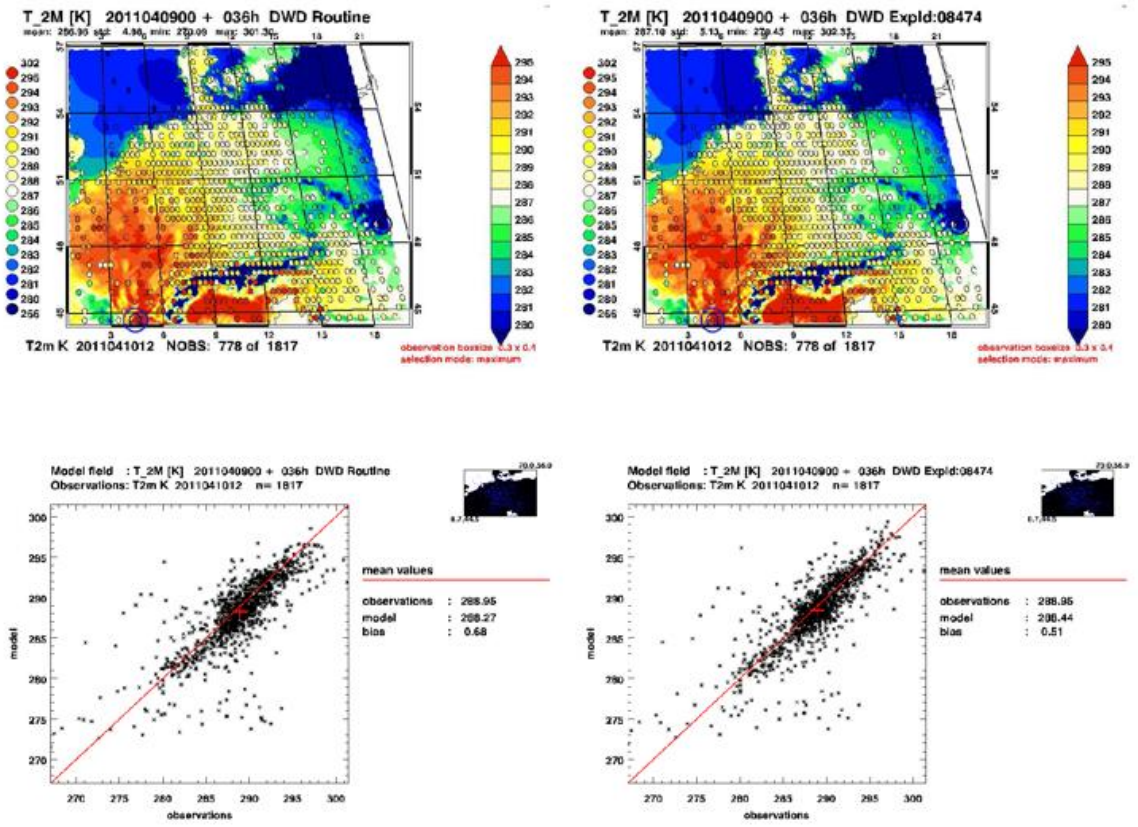


Figure 8: Comparison of 2m-temperature observations at 2011041012 and 36 hours forecast from 2011040900 of COSMO-EU routine (a) and experiment 8474 (b).

To exclude the impact of different cloud conditions in observation and model simulation, the clear sky region in central Europe was used for a validation of the COSMO-EU results with measurements at SYNOP stations. Figure 8 (top) shows that the difference in 2 m-temperature between operational COSMO and COSMO experiment is small, below 0.2 K in the area mean, but some measurements in northern Italy and France are in better agreement with the experiment. The statistical analysis (Fig. 8, bottom) confirms that considering 1817 observations the cold bias of 2 m-temperature of 0.68 K in the operational COSMO decreased in the experiment by 0.17 K that is mainly due to a better representation of 2 m-temperatures above 290 K in the experiment. This behaviour can be related to the impact of the aerosol climatology from Tegen et al. (1997).

Due to the changes in external parameters and in the SVAT scheme a feedback on the 2 m-dew point temperature can be assumed. Figure 9 (top) reveals that in area mean the difference in 2 m-dew point temperature of more than 0.4 K between operational COSMO-EU and experiment exceeds the difference in 2 m-temperature and by eye a better agreement with observations in the western region of the selected area can be found. For the 1869 observations the operational COSMO model bias of 2 m-dew point temperature was decreased from 3.10 K by 0.86 K in the experiment. The comparison of the model field with observations (Fig. 9, bottom) shows that a better capture of 2 m-dew point temperature in the range of 270 K to 280 K in the experiment is responsible for this improvement.

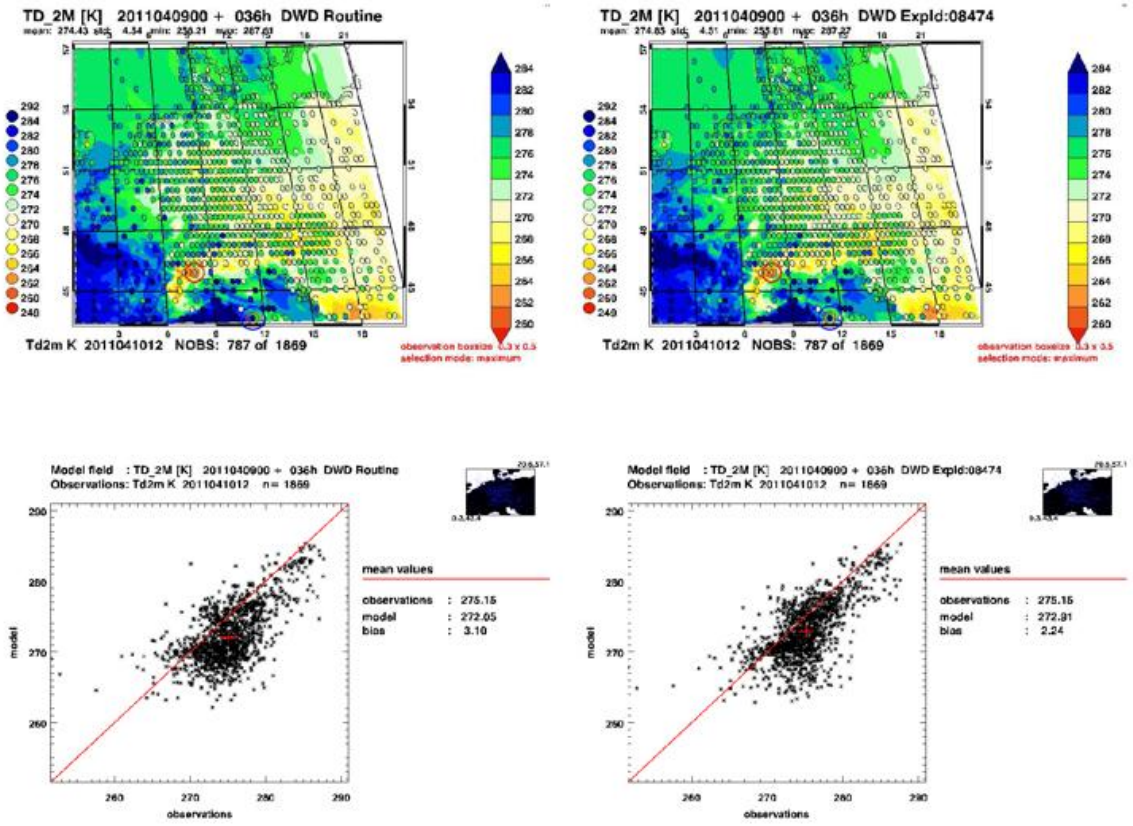


Figure 9: Comparison of 2m-dew point temperature observations at 2011041012 and 36 hours forecast from 2011040900 of COSMO-EU routine (a) and experiment 8474 (b).

4.4 Long-term results

A long-term comparison of the behavior of TERRA in the operational setup and with the new configuration in the soil-moisture analysis environment is available for the global model GME. Based on 24 hours forecasts Fig. 10 shows that the 2 m-temperature bias of GME in Europe (operational and experiment) changes its sign during April to the warm side for summer. Whereas the GME experiment 109/1009 shows similar RMSE values of 2 m-temperature as the operational simulations, the temperature bias in summer, when evapotranspiration of plants is most active in Europe is significantly reduced. Since the SMA diminishes their activity for the experiment by reduced soil water increments in top and bottom SMA layers it could be assumed that this is due to a more realistic behavior of TERRA in the experimental configuration. This assumption is further supported by the comparison of the soil moisture evolution in operational GME and experiment. The unrealistic nearly constant soil moisture in bottom SMA layer is improved by the experiment, which shows a decrease of soil moisture during summer that is confirmed by observations.

For the COSMO simulations an objective verification of the forecasts up to 72 hours against SYNOP stations in the COSMO-EU domain between 1st April 2011 and 30th June 2011 (Fig. 11 and 12) shows as expected largest changes in model bias of 2 m-temperature (TT) and 2 m-dew point temperature difference (TD) and surface pressure (P). However, verification shows a mixed picture. The bias and RMSE of 2 m-temperature and 2 m-dew point temperature difference increased but for surface pressure and 2-m minimum temperature (Tmin) an improvement was observed. In the global skill the experimental setup of COSMO-EU increased by 0.55 % compared to the operational setup.

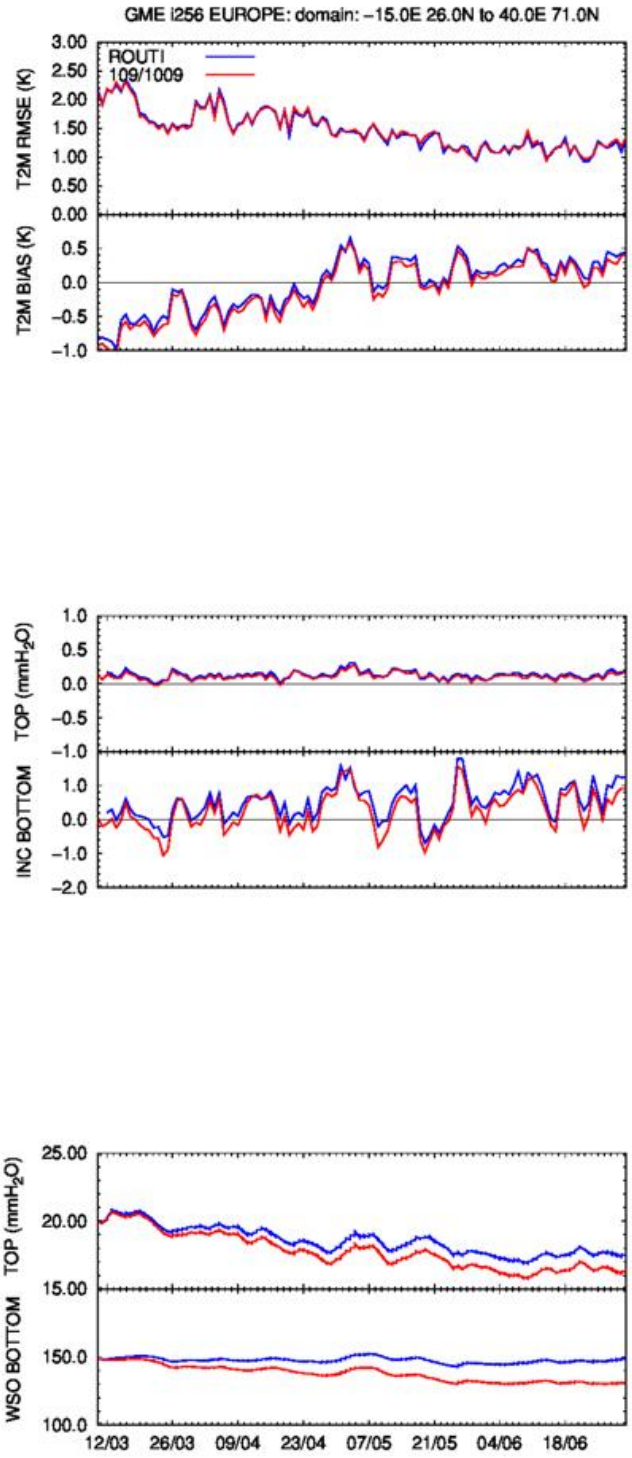


Figure 10: Comparison of operational GME (blue) and GME experiment 109/1009 (red) from soil-moisture analysis monitoring for Europe between 12th March 2011 and 1st July 2011. Shown are RMSE and bias of 2 m temperature (top), soil moisture analysis increments in top and bottom layers (center), and soil moisture evolution for top and bottom layers (bottom).

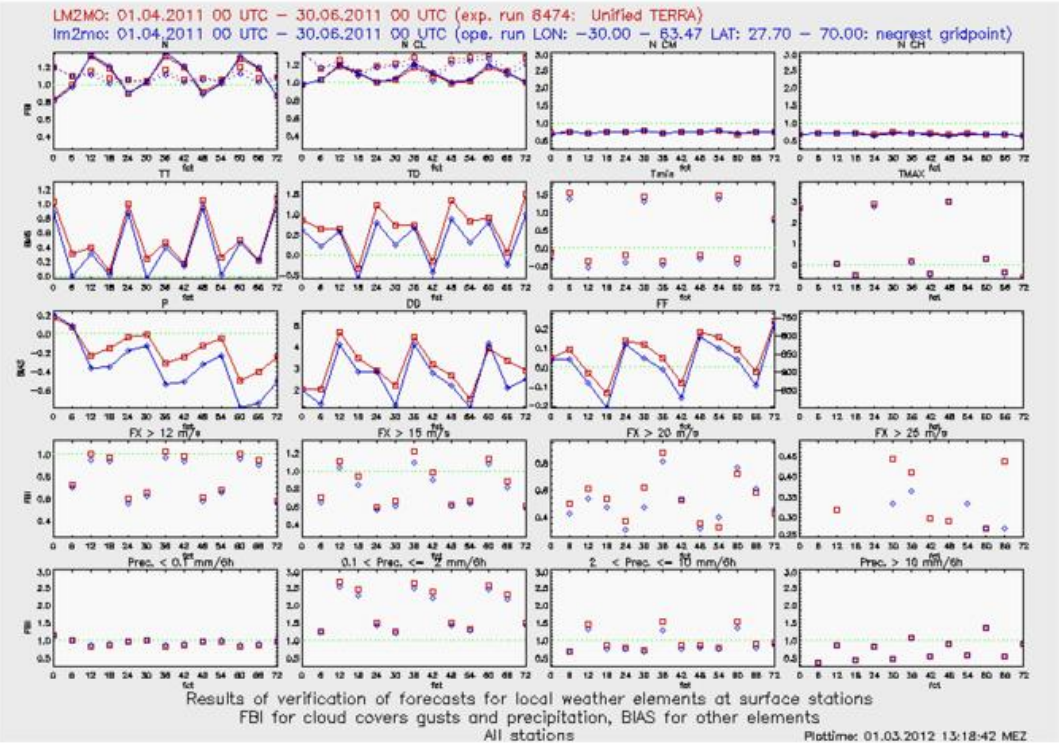


Figure 11: Objective verification up to 72 hours forecast between 1st April 2011 00 UTC and 30th June 2011 00 UTC in the model domain of operational COSMO-EU (blue) and numerical experiment 8474 (red). The verification is based on 00 UTC forecasts and considers FBI of cloud coverage (top row), bias of 2 m-temperature, 2 m-dew point temperature, minimum and maximum temperature (second row), surface pressure, wind direction, wind speed, and vector wind (center row), FBI for wind gusts of different threshold (fourth row), FBI for precipitation of different threshold (bottom row).

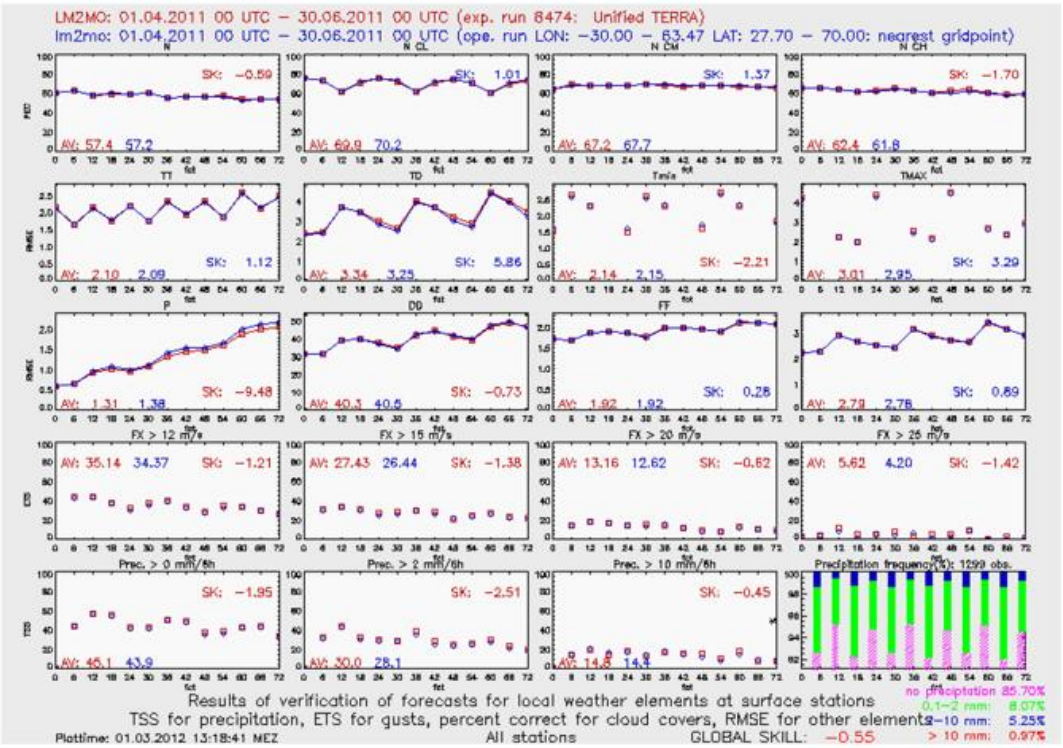


Figure 12: Objective verification up to 72 hours forecast between 1st April 2011 00 UTC and 30th June 2011 00 UTC in the model domain of operational COSMO-EU (blue) and numerical experiment 8474 (red). The verification is based on 00 UTC forecasts and considers PEC of cloud coverage (top row), RMSE of 2 m-temperature, 2 m-dew point temperature, minimum and maximum temperature (second row), surface pressure, wind direction, wind speed, and vector wind (center row), ETS for wind gusts of different threshold (fourth row), ETS for precipitation of different threshold (bottom row).

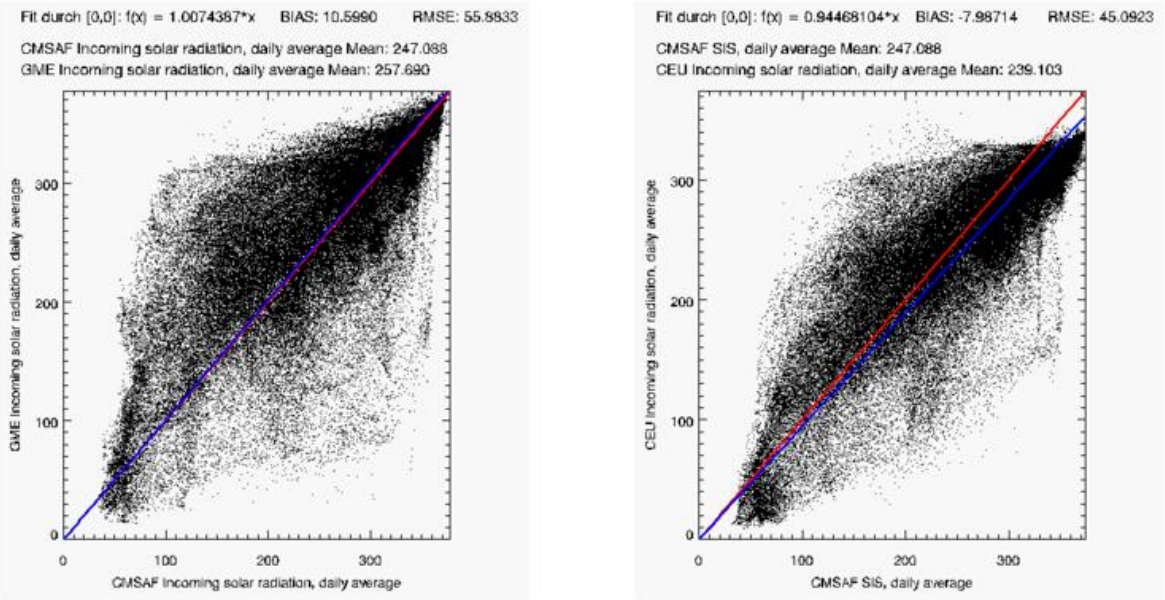


Figure 13: Comparison of the daily averaged solar incoming radiation at surface from the satellite retrieval of CMSAF with GME (left) and COSMO-EU (right) for the 1st June 2013.

4.5 Conclusions

The long-term objective verification over 3 months indicates that considering the global skill the experimental setup improves the operational COSMO-EU in various parameters. However, the question of the increased 2 m-temperature bias and RMSE of the experiment compared to the operational setup remains.

A recent comparison of the satellite retrieval of daily averaged short-wave incoming radiation at surface with COSMO-EU (Fig. 13, right) showed for the operational setup the expected underestimation of incoming solar radiation for cloud-free conditions, i.e. high values of solar radiation, and confirms the conclusions from results of the case study for the 10th April 2011 (Fig. 2, bottom). The comparison with GME supports the application of the aerosol climatology since GME's incoming surface fits better to the satellite retrieval in cloud-free conditions. However an overestimation of solar radiation by COSMO-EU occurs in the intermediate range of incoming solar radiation, corresponding to cloudy conditions. The application of the aerosol climatology with decreased aerosol optical depth in that radiation regime is counterproductive, since it enforces the solar radiation at surface and results in increased 2 m-temperature bias in the experimental setup. Therefore, further investigations are needed to improve the model solar radiation at surface in cloudy conditions.

4.6 Summary and Outlook

This study investigated current uncertainties in the description and simulation of surface characteristics that exist for global and limited area models. The critical issue of the limited knowledge of the external parameters and differences in the soil-vegetation atmosphere transfer model TERRA was considered in numerical experiments with GME and COSMO-EU. These experiments at global and regional scale employed a unified configuration of TERRA. A case study of 36 hours forecasts at 10th April 2011, 12 UTC was used to show the interrelationship between external parameters (e.g. vegetation, aerosol optical depth), surface

radiation budget, fluxes of sensible and latent heat, soil moisture, and screen level (dew point) temperature. For clear-sky conditions it was shown that COSMO-EU with the new configuration improves the agreement with SYNOP measurements compared to the operational setup. Based on 24 hours forecasts of soil-moisture analysis monitoring in Europe a long-term comparison of the behavior of TERRA in spring and summer with the new configuration was performed for the global model GME. It was shown that in connection with a decreased warm 2 m-temperature bias in summer, the SMA diminishes their activity for the experiment by reducing the soil water increments in top and bottom SMA layers, while the soil moisture shows the expected decrease in summer. This improvement on the global scale was traced back to a more realistic behavior of TERRA in the experimental configuration and it is expected that this remains valid in the COSMO-EU. The long-term verification of the COSMO experiment showed an improved global skill compared to the operational setup but further progress is expected after improvement of the surface solar radiation forcing in COSMO for cloudy conditions.

References

Tegen, I., Hollrig, P., Chin, M., Fung, I., Jacob, D., and J. Penner, 1997. Contribution of different aerosol species to the global aerosol extinction optical thickness: Estimates from model results. *J. Geophys. Res.*, **102**, 23895–23915.

Tanre, D., J. F. Geleyn, and J. Slingo, 1984. First results of the introduction of an advanced aerosol-radiation interaction in the ECMWF low resolution global model, in Aerosols and Their Climatic Effects. *Proceedings of the Meetings of Experts, Williamsburg, Va., 28-30 March 1983, edited by H. E. Gerber and A. Deepak, A. Deepak, Hampton, Va*, 133–177.

Hohenegger, C., and P. L. Vidale, 2005. Sensitivity of the European climate to aerosol forcing as simulated with a regional climate model. *J. Geophys. Res.*, **110**, D06201.

Moody, E. G., King, M. D., Schaaf, C. B., and S. Platnick, 2008. MODIS-Derived Spatially Complete Surface Albedo Products: Spatial and Temporal Pixel Distribution and Zonal Averages. *Journal of Applied Meteorology and Climatology*, **47(11)**, 2879–2894.

Balsamo, G., Viterbo, P., Beljaars, A., van den Hurk, B., Hirschi, M., Betts, A. K., and K. Scipal, 2009. A Revised Hydrology for the ECMWF Model: Verification from Field Site to Terrestrial Water Storage and Impact in the Integrated Forecast System. *J. Hydrometeor.*, **10**, 623–643.

Lange, M., 2011. Einführung der Bodenfeuchteanalyse (SMA) für GME. Änderungsmitteilung operationelles NWV-System, Deutscher Wetterdienst, Offenbach.

Ritter, B., 2007. Einführung GME-Version 2.13. Änderungsmitteilung operationelles NWV-System Deutscher Wetterdienst, Offenbach.

Scipal, K., Drusch, M., Wagner, W., 2008. Assimilation of a ERS scatterometer derived soil moisture index in the ECMWF numerical weather prediction system. *Advances in Water Resources*, **31**, 1101–1112.

Masson, V., Champeaux, J.-L., Chauvin, F., Meriguet, Ch., and R. Lacaze, 2003. A Global Database of Land Surface Parameters at 1-km Resolution in Meteorological and Climate Models. *J. Climate*, **16**, 1261–1282.

Doms, G., Förstner, J., Heise, E., Herzog, H.-J., Raschendorfer, M., Schrodin, R., Reinhardt, Th., and G. Vogel, 2005. A description of the Nonhydrostatic Regional Model LM, Part II: Physical parameterization. See: www.cosmo-model.org

4.7 Appendix

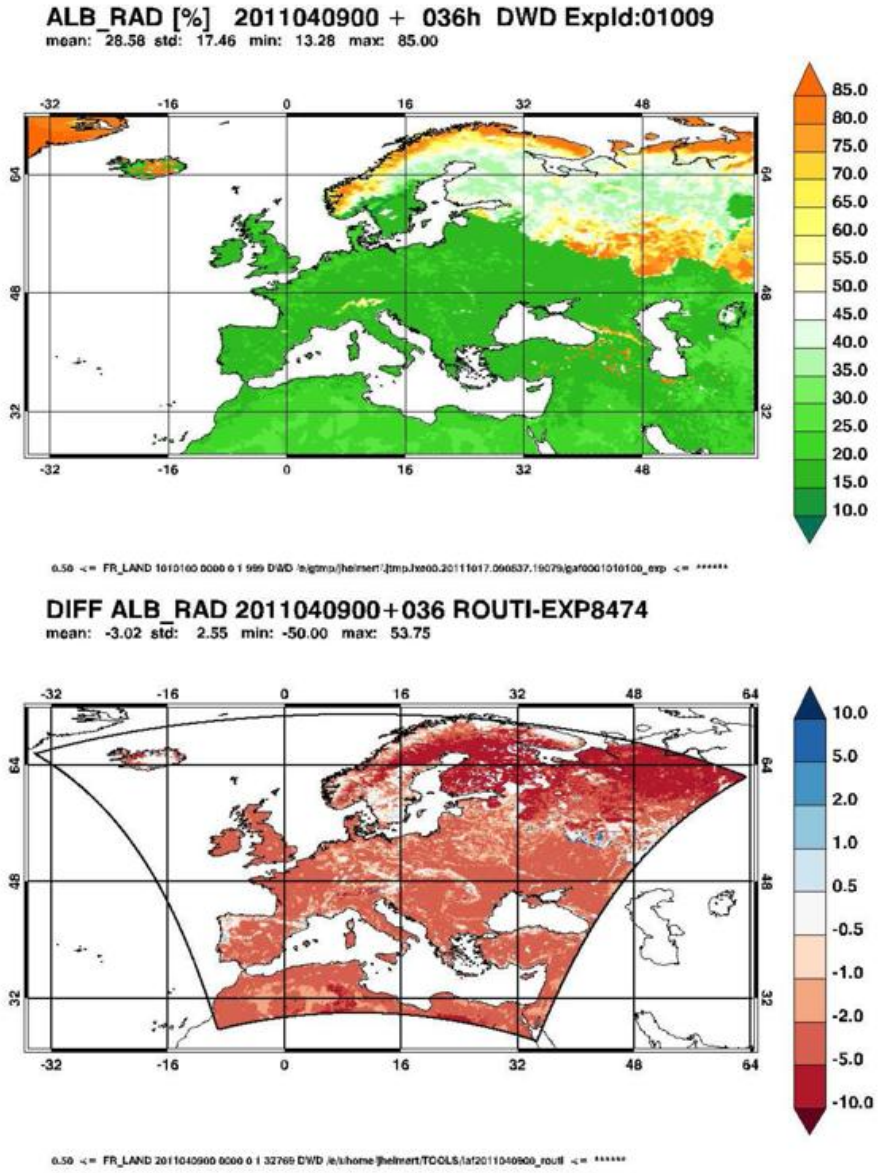


Figure 14: Surface albedo (%) at 10th April 2011 12 UTC for 36 hours forecast of the GME experiment 109/1009 (top) and difference between COSMO-EU routine and experiment 8474 (bottom).

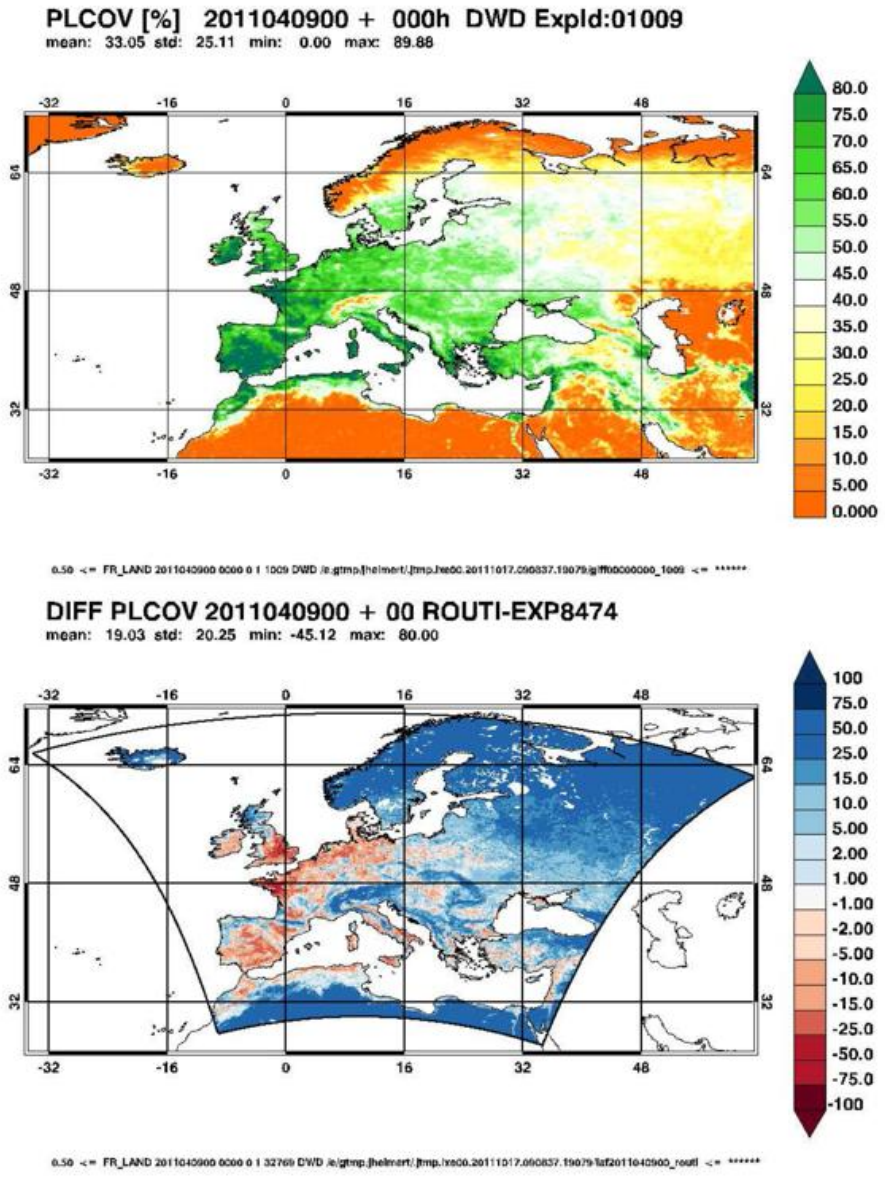


Figure 15: Vegetation coverage (%) at 9th April 2011 00 UTC of the GME experiment 109/1009 (top) and difference between COSMO-EU routine and experiment 8474 (bottom).

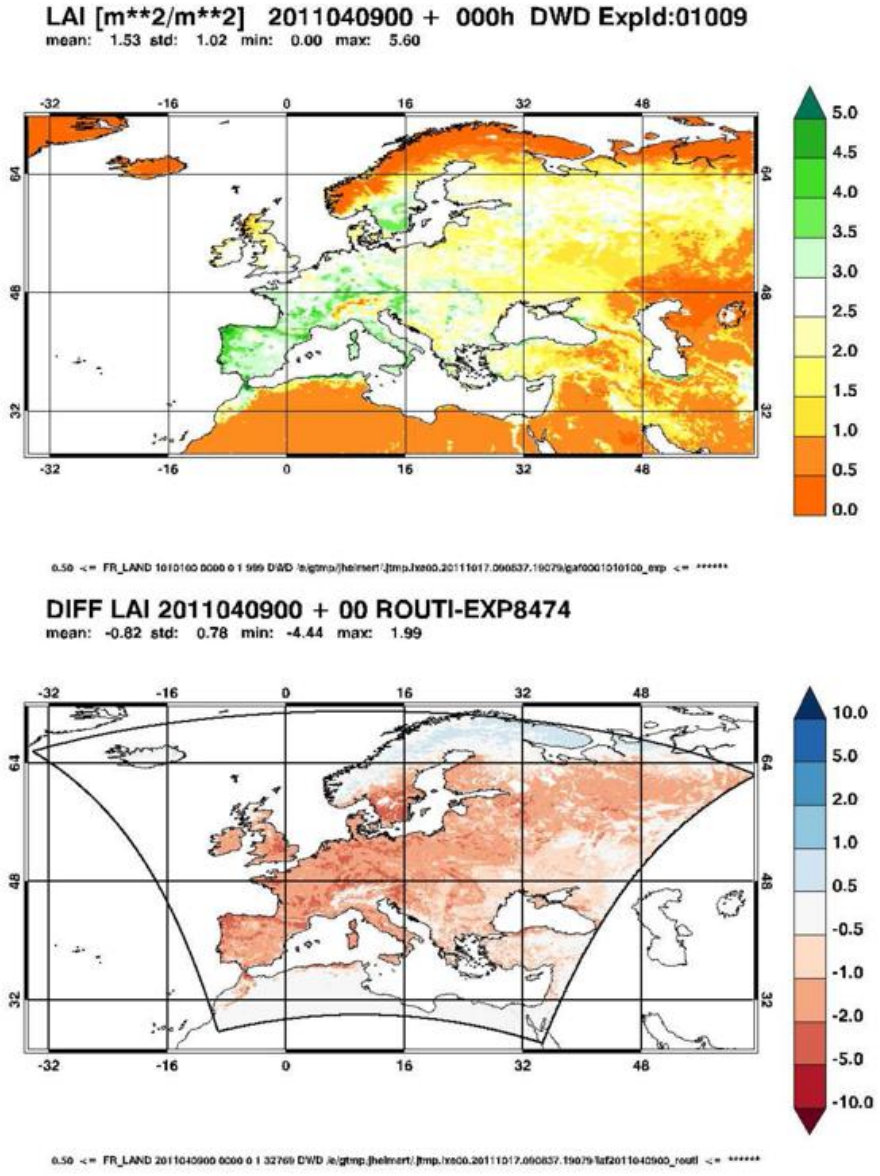


Figure 16: Leaf area index at 9th April 2011 00 UTC of the GME experiment 109/1009 (top) and difference between COSMO-EU routine and experiment 8474 (bottom).

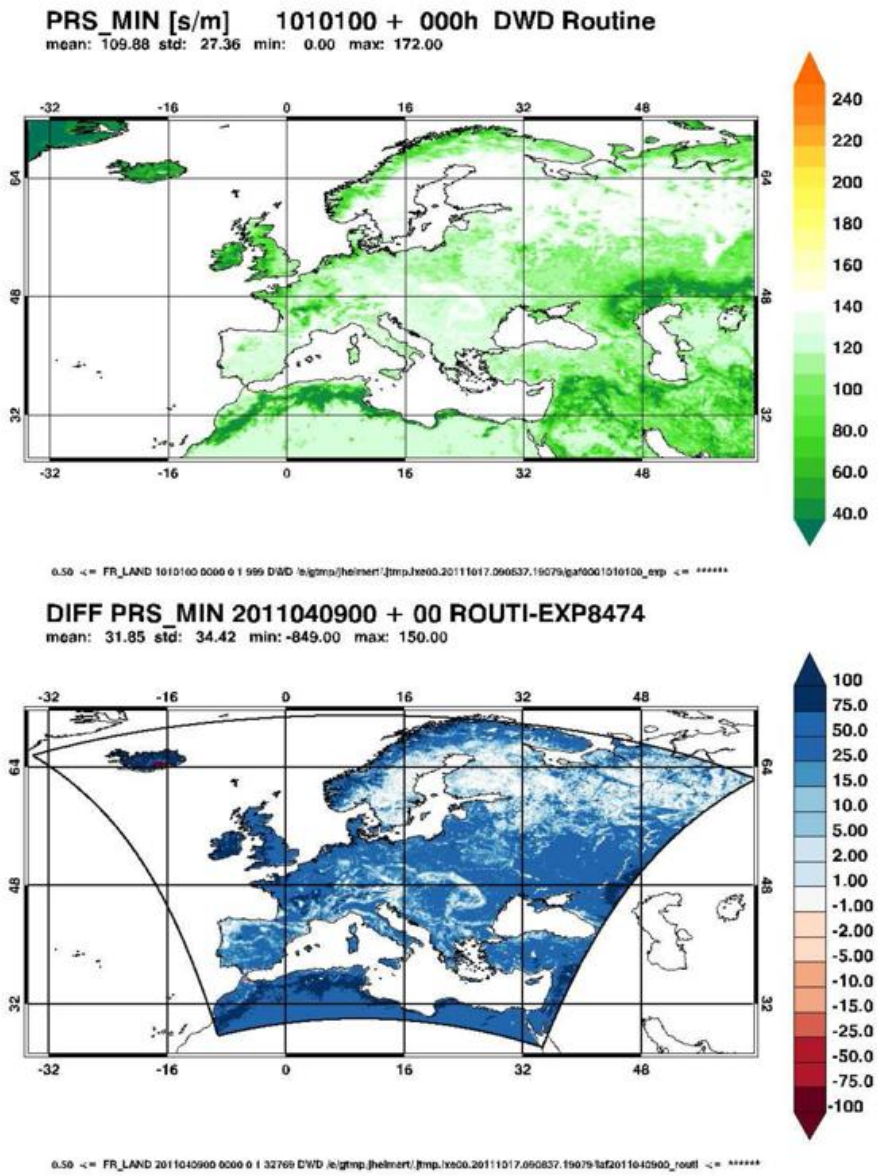


Figure 17: Minimum stomatal resistance ($sm^{-}1$) of the GME experiment 109/1009 (top) and difference at 9th April 2011 00 UTC between COSMO-EU routine and experiment 8474 (bottom).

5 Documentation of a new multi-layers snow module (E. Machulskaya)

The snow model that is presented here is a one-dimensional parameterization scheme for the heat and moisture transfer through the snowpack. Two main features of the scheme distinguish it from the snow parameterization scheme that is currently operational in COSMO. First, it allows the water to be in the liquid state within snowpack. Second, the new scheme is multi-layered, i.e. the vertical profiles of temperature, total and liquid water content, and density are explicitly resolved.

The heat and moisture transport through the snowpack is governed by the following set of equations

$$\begin{aligned}
\rho_{sn} C_{sn} \frac{\partial T_{sn}}{\partial t} &= \frac{\partial}{\partial z} \lambda_{sn} \frac{\partial T_{sn}}{\partial z} + L_f (F - M) - \frac{\partial R}{\partial z} \\
\frac{\partial W_{liq}}{\partial t} &= M - F - \frac{\partial q}{\partial z} \\
\frac{\partial W_{tot}}{\partial t} &= -\frac{\partial q}{\partial z} \\
\frac{\partial \rho_{sn}}{\partial t} &= \frac{\rho_{sn}}{W_{tot}} \left(-\frac{\partial q}{\partial z} \left(1 - \frac{\rho_{sn}}{\rho_w} \right) + \rho_{sn} \frac{\rho_w - \rho_i}{\rho_w \rho_i} (M - F) \right) + \sigma(t),
\end{aligned} \tag{1}$$

where T_{sn} is snow temperature, W_{liq} is specific liquid water content, W_{tot} is specific total water (liquid + solid) content, C_{sn} is specific heat capacity of snow, ρ_{sn}, ρ_w and ρ_i are densities of snow, water and ice, respectively, λ_{sn} is snow heat conductivity, L_f is latent heat of freezing, M and F are melting and refreezing rates, respectively, q is the liquid water flux, R is radiative heat flux, and $\sigma(t)$ characterizes the impact of gravitational compaction and metamorphism on snow density.

The first equation is an expression for the energy conservation law. As can be seen, snow temperature changes may be caused by the heat diffusion, latent heat release due to water phase changes (melting of solid part and refreezing of liquid part), and solar radiative heating that can occur not only at the upper snow surface, but also below it. The second equation is the expession for the liquid water balance; the liquid water content may change because of phase changes and percolation of water. The third equation is the total snow water-equivalent balance equation. The fourth equation describes the changes in the snow density. The first and the second terms on the right-hand side of this equation describe the change in snow density due to the changes of the ratio of the solid part (of the ice density) to the liquid part (of the water density). It may occur either because some amount of water is percolated from above (the first term) or because of phase changes (second term). The third term describes the densification of the snowpack due to the weight of the overlying layers and due to internal metamorphism.

Snow heat capacity C_{sn} is computed as

$$C_{sn} = W_{liq} \rho_w C_w + (W_{tot} - W_{liq}) \rho_{dry} C_i,$$

accounting for liquid water content. Here, ρ_{dry} is the density of the solid part of a snow layer and it is equal to

$$\rho_{dry} = \frac{W_{tot} - W_{liq}}{\frac{\rho_w}{\rho_{sn}} W_{tot} - W_{liq}} \rho_w.$$

Snow heat conductivity λ_{sn} depends on snow density and varies therefore with height and time. It is calculated by means of an empirical formula

$$\lambda_{sn} = 2.22 \left(\frac{\rho_{sn}}{\rho_i} \right)^{1.88}.$$

The liquid water flux q consists of precipitation flux at the upper boundary of snow which is provided by the host atmospheric model as an upper boundary condition, and of the flux due to the internal percolation of liquid water within the snowpack. Percolation flux is calculated according to (Colbeck, 1978) as

$$q = \rho_w h \max \left(\left(\frac{W_{liq}/\rho_w - W_{hc}}{\Pi - W_{hc}} \right)^3, 0.0 \right),$$

where $W_{hc} = 0.04$ m^3/m^3 is the volumetric water holding capacity of snow, $h = 0.01$ m/s is snow hydraulic conductivity by maximal liquid water content W_{hc}, and

$$\Pi = 1 - \frac{W_{liq}}{\rho_w} - \frac{W_{tot} - W_{liq}}{\rho_i}$$

is the snow porosity. The percolation flux through the lower boundary of the snowpack is regarded as net snow melting rate and it is used as the upper boundary condition for soil moisture by the soil model.

Radiative heat flux is calculated according to exponential extinction law

$$R(z) = R_0 e^{-\beta z},$$

where R_0 is the net solar radiation flux at the snow-air interface and β is the extinction coefficient. The latter is assumed to be dependent on snow density. A simple linear dependence was constructed based on the data reported in literature

$$\beta = b_1 \rho_{sn} + b_2,$$

where $b_1 = 0.13$ and $b_2 = 3.4$, so that $\beta = 10$ m^{-1} if snow density is 50 kg/m^3 and $\beta = 70$ m^{-1} if snow density is 500 kg/m^3 (fresh snow is more penetrable to sunlight).

Gravitational compaction and compaction due to metamorphism are described by means of the following semi-empirical law:

$$\sigma(z,t) = \frac{\rho_{sn}(z,t)}{\eta(z,t)} \left(\sigma_g(z,t) + \sigma_m(z,t) \right).$$

Here, σ_g describes the effect of gravity and it is equal to the total weight of the overlying layers

$$\sigma_g(z,t) = \int_0^z \rho_{sn}(z') g dz'.$$

The term σ_m describes the compaction due to metamorphism. It is set to a constant value $\sigma_m(z,t) = 75$ Pa.

The factor $\eta(z,t)$ is the compactive viscosity of snow that characterizes the proneness of the snowpack to the deformations due to both abovementioned processes. It is equal to

$$\eta(z,t) = A_1 \exp \left(A_2 \frac{\rho_{sn}(z,t)}{\rho_i} - a W_{liq}(z,t) + \frac{E}{R T_{sn}(z,t)} \right),$$

where $A_1 = 6.6 \cdot 10^{-7}$ Pa $\cdot$ s, $A_2 = 19.3$, $a = 70.0$, $E = 67300$ J/mol is the activation energy and $R = 8.31$ J/(mol K) is the universal gas constant. As can be seen, three characteristics of the snowpack determine its ability to densify: the snow density, liquid water content and snow temperature. The incompacter, warmer, and moister the snowpack is, the easier it shrinks.

Boundary conditions. Since the equation for temperature is of the second order and all other equations of the first order, the first equation requires two boundary conditions, and all other one boundary condition. The upper boundary condition for the temperature transport equation is the heat flux at the snow-air interface, as in the single-layer snow model. The total heat flux is the sum of net solar and infrared radiation, sensible and latent heat fluxes, heat conduction flux into snowpack and the flux of heat which is released by the freezing rain that falls onto the snow surface. Note that the latter flux is not present in the total heat balance in the single-layer snow model.

The upper boundary condition for the total water content also appears in the flux form. It is the precipitation flux, either in the form of snow or in the form of rain. The latter serves also as the upper boundary condition for the equation for liquid water content.

The lower boundary condition for temperature is the conductive heat flux through the soil-snow interface.

The density of the upper surface of the snowpack is determined by the falling snow density. This fresh snow density is calculated as in the single-layer snow model, namely

$$\rho_{fr} = \rho_{frmin} + (\rho_{frmax} - \rho_{frmin}) \frac{T_{air} - T_{min}}{T_0 - T_{min}},$$

where $\rho_{frmin} = 50$ kg/m^3, $\rho_{frmax} = 150$ kg/m^3, $T_{min} = 258.15$ K $= 273.15$ - 15.0 K, $T_0 =$ 273.15K. It is an increasing function of temperature that emulates heavy "moist snow" if the air temperature is close to the melting point.

Numerical implementation. Time discretization. The equation system (1) is solved by means of splitting up method. At the first half time step the heat diffusion is calculated (implicitly), at the second half time step the adjustment is made due to the presence of sources and sinks (explicitly).

The adjustment of the snow temperature and total and liquid water content profiles due to phase changes is made in the one-iteration way. Specifically, if after the temperature diffusion half-step snow temperature T^*_{sn} becomes greater than the melting point $T_0 = 273.15$K, melting is detected ($M > 0$). In this case, if the heat storage excess that should be spent on melting $E = C_i W_{tot}(T^*_{sn} - T_0)\rho_w$ is enough to melt the entire solid part of the layer $W_{tot} - W_{liq}$ (i.e. $E \geq L_f \rho_w (W_{tot} - W_{liq})$), then the melting rate is $M = (W_{tot} - W_{liq})/dt$, the whole layer becomes liquid ($W_{liq} = W_{tot}$), and the rest of energy is transferred into the underlying layer. Otherwise, if the heat stored in the layer is not enough to melt the entire solid part of the layer, it is spent to melt a part of it, the melting rate is then $M = C_i W_{tot}(T^*_{sn} - T_0)/(L_f dt)$ and liquid water content increases by $W_{liq} = W_{liq} + C_i W_{tot}(T^*_{sn} - T_0)/L_f$. In both cases, the temperature of the layer is set to $T^{new}_{sn} = T_0$.

Refreezing rate F is calculated in a similar way. $F > 0$ if the temperature of a layer T^*_{sn} after the diffusion half-step becomes less than the melting point T_0 but some amount of liquid water is present. In this case, if T^*_{sn} is low enough that the whole amount of liquid water can refreeze (i.e. $E = C_i W_{tot}(T_0 - T^*_{sn})\rho_w \geq L\rho_w W_{liq}$), then the new liquid water content is $W^{new}_{liq} = 0$ and temperature of the layer increases by latent heat release as $T^{new}_{sn} = T^*_{sn} + W_{liq} L_f/(W_{tot} C_i)$. Otherwise, if not all the liquid water can freeze, then a part

of it freezes, namely, W_{liq} becomes $W_{liq}^{new} = W_{liq} - C_i W_{tot}(T_0 - T_{sn}^*)/L_f$ and temperature T_{sn}^{new} is set to T_0.

Space discretization. The vertical grid consists of a constant number of layers that is fixed by user with setting the name-list variable *ke_snow*. At each time step the thickness of a layer can change:

1) due to changes in snow density of the layer whereas the total mass of the layer conserves but phase changes occur;

2) due to mass flux as some amount of water percolates from the overlying layer and/or into the underlying layer;

3) the thickness of the uppermost layer can increase if fresh snow has fallen.

Due to these processes the vertical grid becomes irregular even if it is regular at the initial time step. Thus, at the end of the time step a regularization is performed in order to return the grid to the regular one. This procedure sets new equidistant heights of layers and linearly interpolates snow temperature, density, total water and liquid water content values from the old grid to the new one.

To switch between the single-layer and multi-layer snow model the name-list logical variable *lmulti_snow* is used.

6 Implementation of the Martilli Urban Surface Parametrization in COSMO (O. Fuhrer, C. Muller, G. Fontannaz)

6.1 Introduction

Meteorological information has become more and more important in our society, as many activities and life being are largely influenced by the weather. For example, air and maritime transport security, air quality control, global change study, natural disaster forecast, water resources management or simply freetime activities require meteorological forecast and/or analysis. Our capacity to forecast the weather has hence became a great issue. Today half of the worlds' population lives in urban areas, where a wide variety of human activities takes place. Meteorological forecast needs are very important for urban area even if it represents only 0.05 % of the Earth's surface. In order to answer at best to these needs, the numerical forecast models are used. The quality of the information delivered by such models are strongly dependent on their resolution. During the last decade, computers performances have strongly increased, making it possible to constantly improve the model resolution. Being able to take into account finer scale and hence smaller geomorphological features, we could expect an improvement of the model results accuracy. However, results are only improved when different parametrizations, which take into account subgrid effects and the Earth's surface representation (landuse), are regularly updated to fit with the increasing resolution.

Concerning the Earth's surface fluxes exchanged with the atmosphere, increase of the model resolution have led to the adaptation of surface exchange parametrizations to take into account urbanized areas reproduced in mesoscale models by high resolution landuse database. Different solutions are available in order to parametrize the urban area in weather forecast models. The most common is based on the Monin-Obukhov Similarity Theory (MOST), which assumes that a stable surface layer develops above the ground and where turbulence is constant in time and space. A more sophisticated solution is to use Urban Canopy Models (UCM), where the surface fluxes are solved by taking into account buildings, different surfaces of city (roof, road and wall) and their interactions with the atmosphere (Martilli et al., 2002; Masson, 2000). In this study, we investigate the capacity of two parametrization (a MOST based scheme and an UCM) to reproduce the urban area effects in a Numerical Weather Prediction (NWP) model. We focus on the Urban Heat Island (UHI) which is a typically phenomenon for urban areas and relatively easy to measure and quantify. For this purpose, the model of the Swiss Federal Office of Meteorology and Climatology (MeteoSwiss) is used. This mesoscale model called Local Model (LM) uses a traditional urban area parametrization (dry soil and adapted surface roughness) based on MOST. It is used for operational numerical weather prediction since 2001 with a horizontal resolution of 7 km on a domain covering most of western Europe.

In order to see if LM is able to reproduce the urban effect, it is applied to the City of Basel, a mid-size city situated in Switzerland, where an extensive meteorological measurement campaign has been conducted in the city of Basel under the BUBBLE project (Basel UrBan Boundary Layer Experiment) (Rotach et al., 2005) from summer 2001 to summer 2002. This experiment investigates in detail the boundary layer structure over a city. Different modeling studies have been conducted in relation with this experiment (Roulet, 2004; Hamdi, 2005), but none of them with an operational model able to take into account numerous phenomenon, *i.e.* clouds, rain, snow, etc. In this report, the ability of LM to reproduce urban effects, and more particularly the UHI, is evaluated using BUBBLE measurement data as reference, first with the operational configuration of the model, and then with a finer horizontal and vertical resolution. In a second step, we focus on an urban canopy model developed by Martilli et

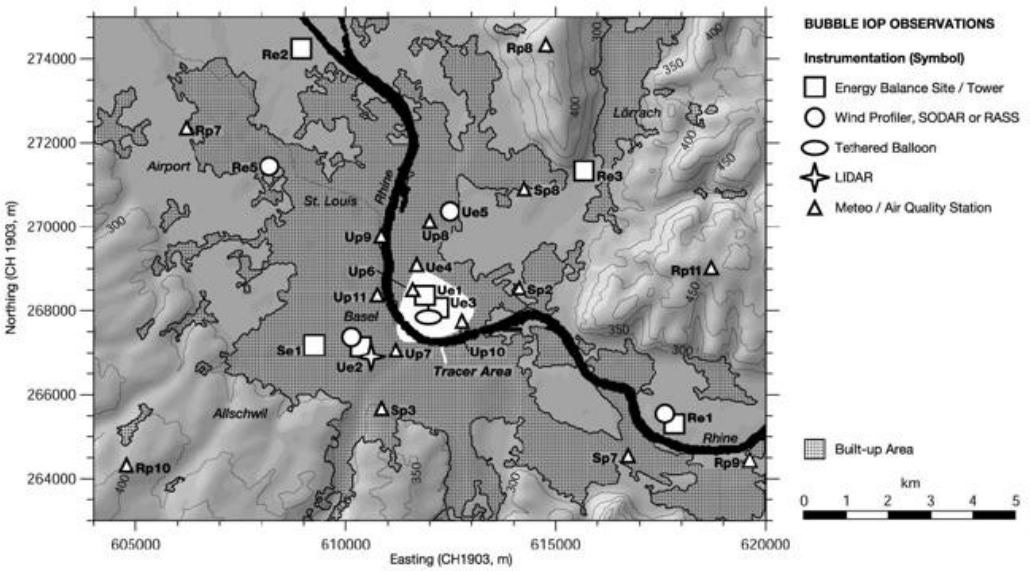


Figure 18: Map of the greater area of the city of Basel with an overview of all sites operated during the BUBBLE IOP in June/July 2002. The thick black line denotes the river Rhine. A complete list of the measuring stations can be found in Appendix 6.9.1

al. (2002). This Urban Effects Parametrization (BEP) is presented and implemented into LM. This implementation and its ability to reproduce the urban effects in LM for the case of Basel city are then evaluated and discussed.

6.2 Bubble

6.2.1 The Experiment

The City of Basel is located in the North-Western part of Switzerland and borders both France and Germany. It is the Switzerland's third most populous city with 190,000 inhabitants. It is situated on the Rhine river, at an altitude of about 260 m and surrounded by gentle but non-negligible topography (750m).

The Basel UrBan Boundary Layer Experiment (BUBBLE) took place from August 2001 to July 2002. Its main goal is to study boundary-layer and surface-exchange processes over different types of surfaces (*i.e.* urban, sub-urban and rural) and their role in the transport and diffusion of air pollution. A more complete description of BUBBLE can be found in Rotach et al. (2005) and on the BUBBLE website. For that purpose, two meteorological towers for turbulence measurements, a Lidar and wind profiler were operated. An Intensive Observation Period (IOP) took place from 15 June and 12 July 2002, with additional surface towers, sodars and tethered balloons (Fig. 18).

6.2.2 Measurements of the UHI

In contrast to rural area, a city represents a dry surface with obstacle (buildings) and a source of anthropogenic heat. The urban area modifies the energy budget, thus creating meteorological differences between urban and rural area. These dissimilarities can be formulated as the differences between urban and rural air temperatures, the first one being usually higher. This phenomenon is called the Urban Heat Island (UHI). As a UHI indicator, averaged and height corrected surface temperature observations within the city are

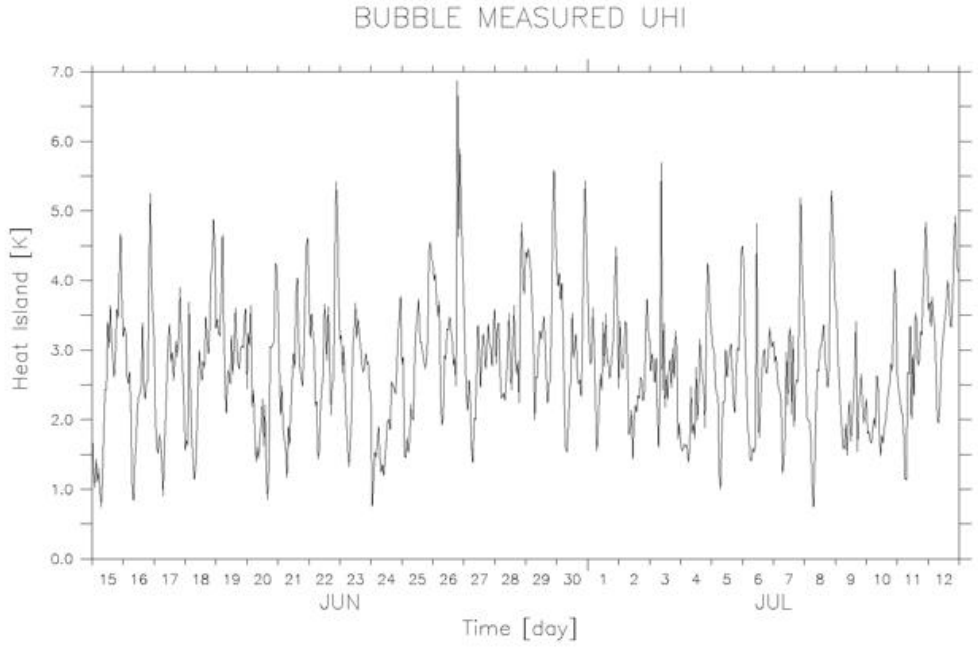


Figure 19: The UHI measured for the city of Basel at 2mAGL during the BUBBLE IOP in June/July 2002

compared with measurements from surroundings rural areas. The BUBBLE campaign provide temperature measurements at 2 m height on several representative sites for urban or rural conditions. Averaging temperature in both areas (urban and rural) allow to obtain a temperature difference between the city and its surroundings, which can be assimilated to the UHI. Figure 19 shows this averaged temperature difference between urban and rural area measured during the IOP. It is always positive and varies from 0.7 to 6.9 °C with an average of 2.8 °C. If we look at the weather bulletin (Appendix 6.9.2) during the IOP, the period from 25 to 27 June is characterized by a very constant meteorological situation and strong daily cycle. The mean UHI over this episode is representative for the IOP with an average of 3.0 °C. This episode is used to study UHI formation over Basel. Furthermore, it corresponds to the period studied by Roulet (2004).

In the following, an in-depth analysis of this UHI episode using measurements and numerical simulations is presented.

6.3 The COSMO Model

6.3.1 Model Description

The LM (Lokal-Modell[1]) is developed within the framework of the COnsortium for Small-Scale MOdeling (COSMO) bringing together the National Weather Services from Switzerland, Italy, Poland and Greece under the lead of the National Weather Service of Germany (DWD). LM is a nonhydrostatic fully compressible limited-area atmospheric model. It has been designed for both operational Numerical Weather Prediction (NWP) and various scientific applications on the meso-β and meso-γ scales (scales from which the nonhydrostatic effects begin to play an important role on the behavior of the atmospheric fluxes (Orlanski, 1975). The LM prognostic variables are horizontal and vertical cartesian wind compo-

[1]A more detailed description of the LM can be found on the COSMO website.

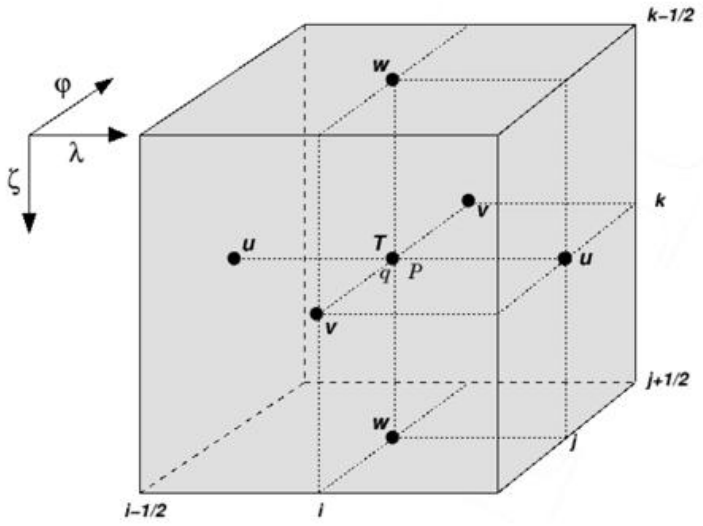


Figure 20: A grid box volume $\Delta V = \Delta\lambda\Delta\phi\Delta\zeta$ showing the *Arakawa-C/Lorenz* staggering of the dependent model variables. The scalar variables T, P and q are defined at the centre (i, j, k) of the box, whereas the normal velocity components are defined on the corresponding box faces $(i \pm 1/2, j \pm 1/2, k \pm 1/2)$.

nents, temperature, pressure perturbations, specific humidity, as well as different cloud water species and turbulence quantities according to the parametrizations chosen for the phenomena. The model is based on the primitive thermo-hydrodynamical equations describing a compressible flow in a moist atmosphere. The model equations are formulated horizontally in rotated geographical coordinates (λ, ϕ) and vertically in a generalized terrain following height coordinate (ζ). These equations are solved numerically using finite difference methods in an Arakawa-C/Lorenz grid (Figure 20 shows a grid box volume). Constant increments $\Delta\lambda, \Delta\phi, \Delta\zeta$ are used to set up the computational grid and the domain is represented by a finite number of grid points (i, j, k). Each of these points is the center of a rectangular grid box volume $\Delta V = \Delta\lambda\Delta\phi\Delta\zeta$.

NUMERICAL INTEGRATION

(a) The Time Integration Scheme

To illustrate the integration used in LM, let consider the model equations in the generic form

$$\frac{\partial\psi}{\partial t} = s_\psi + f_\psi, \tag{2}$$

where ψ denotes a prognostic model variable (u, v, w, T, p' or q), f_ψ the forcing terms due to the slow modes and s_ψ the source terms related to the acoustic and gravity wave modes. Equation 2 is solved using a Kemp-Wilhelmson time-splitting algorithm, where terms related to the slow modes are solved using a large time step dt, whereas the acoustic and gravity waves modes are solved using a small time step $d\tau$. The slow-mode forcing f_ψ is evaluated only once every large time step and kept constant throughout the small time steps, whereas the fast-mode terms contained in s_ψ are calculated for each small time step.

We focus on the turbulent fluxes of heat and momentum which are contained in the slow mode term f_ψ. Horizontal advection is treated explicitly and evaluated at mid-time level n, whereas diffusion evaluated at time level n would be unstable with respect to explicit *Leapfrog* integration scheme. Thus, the computational mixing terms are formulated following a simple forward scheme, *i.e.* they are evaluated at the time level $n-1$. Vertical advection and vertical

turbulent diffusion are treated implicitly using the *Crank-Nicolson* scheme involving the time levels $n-1$ and $n+1$. This results in a vertically coupled set of equations, abbreviated by

$$\frac{\psi^{n+1}-\psi^{n-1}}{2\Delta t} = f_\psi^n = f_\psi(\psi^{n-1}, \psi^n, \psi^{n+1}) \tag{3}$$

Finally for the slow mode tendency $\tilde{\psi}^{n+1}$, evaluating the finite difference equations for u, v, w, T, $p^{'}$ and q from (3) enables to obtain a linear tridiagonal equations system, which may be written in the general form

$$A_k\tilde{\psi}_{k-1}^{n+1} + B_k\tilde{\psi}_k^{n+1} + C_k\tilde{\psi}_{k+1}^{n+1} = D_k(\psi^n, ...), \tag{4}$$

for variables defined on main levels by k ($k = 1, ..., N_\zeta$). Boundary conditions are included in the inhomogeneous term D_k. Thus, we end up with a tridiagonal matrix of dimension $(N_\zeta) \times (N_\zeta)$, which can be solved by Gaussian elimination in LM.[2]

(b) Land-Surface Scheme

The turbulent mixing terms for temperature, moisture variables and horizontal momentum (in both directions u and v) are related respectively to the turbulent fluxes of sensible heat ($\hat{H}^3$), moisture (F_q^3) and momentum (τ^{13} and τ^{23}) respectively. These fluxes are defined at model half levels and at the horizontal position corresponding to the transported quantity. The calculation of the mixing terms requires boundary conditions for turbulent fluxes at the top ($\zeta = 1/2$) and at the bottom ($\zeta = N_\zeta + 1/2$) half level of the model , where N_ζ is the number of vertical levels. At the upper boundary, zero flux conditions are specified:

$$\begin{aligned} (\tau^{13})_{\zeta=1/2} = (\tau^{23})_{\zeta=1/2} &= 0, \\ (\hat{H}^3)_{\zeta=1/2} = (F_q^3)_{\zeta=1/2} &= 0 \end{aligned} \tag{5}$$

At the lower boundary, the turbulent fluxes are specified which a standard bulk-transfer scheme using a drag-law formulation [3]:

$$\begin{aligned} (\tau^{13})_{\zeta=N_\zeta+1/2} &= \tau_{sfc}^{13} = -\rho C_m^d |\vec{v}_h| u, \\ (\tau^{23})_{\zeta=N_\zeta+1/2} &= \tau_{sfc}^{23} = -\rho C_m^d |\vec{v}_h| v, \\ (\hat{H}^3)_{\zeta=N_\zeta+1/2} &= \hat{H}_{sfc}^3 = -\rho C_h^d |\vec{v}_h| (\theta\pi_{sfc} - T_{sfc}), \\ (F_{q^v}^3)_{\zeta=N_\zeta+1/2} &= (F_{q^v}^3)_{sfc} = -\rho C_h^d |\vec{v}_h| (q^v - q_{sfc}^v), \end{aligned} \tag{6}$$

where u, v, θ and q^v are the horizontal velocity components, the potential temperature and the specific humidity at the lowest grid level above the surface ($\zeta = N_\zeta$). $|\vec{v}_h|$ is the absolute horizontal wind speed at the same level. C_m^d denotes the drag coefficient for momentum exchanges at the ground and C_h^d is the bulk-aerodynamical transfer coefficient for turbulent heat. The transfer coefficient for moisture is assumed to be equal to the one for heat in LM. The air density ρ is evaluated from the surface values for temperature, pressure and humidity. Temperature and specific humidity at the ground are either provided by the soil model or externally specified, whereas the surface pressure is determined by hydrostatic extrapolation of the total pressure $p = p_0 + p^{'}$ at the first layer above the ground. The transfer coefficients C_m^d and C_h^d are calculated diagnostically and derived from the Monin-Obukhov Similarity Theory (MOST). Similarity theories are empirical relationships for variables of interest when our knowledge of the governing physics is insufficient to derive laws based on first principles (Stull, 1988). MOST is a first order approximation usually applied to the surface layer and assumes constant fluxes. Thus, in order to apply MOST for surface fluxes parametrization,

[2]The matrix diagonal terms A_k, B_k and C_k, as well as the D_k-term are derived in Doms et al. (2002a).
[3]As described in the Part II of the LM documentation (Doms et al., 2002b).

Table 2: Characteristic parameters for urban and built up areas in TERRA_LM: z_0 is the surface roughness.

Land use class	z_0 [m]	root depth [m]	plant cover		leaf area index	
			Max	Min	Max [-]	Min [-]
urban and built up land	1.00	0.60	10%	5%	4.70	0.10

the lowest grid layer of the model must be within the constant-flux layer. Usually, the top of the surface layer in rural areas is in the range of 10m to 30m.

THE SOIL AND VEGETATION MODEL

Surface fluxes represent the lower boundary conditions for the atmospheric part of the model. Their calculation requires temperature and specific humidity as input in the first soil layer predicted by the soil model. For land surfaces, the multi-layer soil model TERRA_LM (Doms et al., 2002b) provides surface temperature and specific humidity at the ground to the LM model. Most parameters of the soil model (heat capacity, water storage capacity, volume of voids, etc.) strongly depend on soil texture. Five different types are distinguished: sand, sandy loam, loam, loamy clay and clay. Three special soil types are considered additionally: ice, rock and peat. The ground temperature is calculated by the equation of heat conduction which is solved in an optimized two-layer model, to which a third layer called the climatological layer, characterized by constant temperature, is added. The urban and built-up land are described as a loam-clay soil with specific parameters described in Table 2. The temperature at 2 m Above Ground Level (AGL) is computed diagnostically from the ground surface temperature and the temperature in the first model layer according to the land-surface scheme *i.e.*, the Monin-Obukhov Similarity Theory.

6.3.2 MeteoSwiss Operational Implementation

Since April 2001, a nonhydrostatic mesoscale model (COSMO), is used at MeteoSwiss for operational Numerical Weather Prediction (NWP). The current (fall 2006) Swiss version of the model has a horizontal resolution of about 7 km. The domain covers most of western Europe. A terrain following vertical coordinate system is used, with 45 vertical layers and about 50 to 100 m vertical resolution in the lowest 2 km of the atmosphere, and an upper level at a geopotential height of 20 hPa. The 2 mAGL temperature is computed according to MOST using the temperature of the first layer and the surface temperature in the model. The operational run of COSMO at MeteoSwiss is performed twice daily, at 1:30 am and 1:30 pm GMT. Calculations are performed on a NEC-SX/5 supercomputer at the Swiss National Supercomputing Center (CSCS) in Manno (TI). A 72 hour forecast takes roughly 70 minutes real-time. Accurate initial conditions are generated with an additional assimilation system, using observations within the model domain (*e.g.* wind profiler). Boundary conditions are taken from the global model of the European Center for Medium-Range Weather Forecasts (ECMWF) in Reading (UK). A new version, called COSMO2, is currently being developed and tested at MeteoSwiss. It will use a horizontal grid-size of roughly 2 km, a more accurate vertical resolution and is planned to become operational at the beginning of 2008.

Table 3: The main model input parameters are: nx and ny the number of urban grid point in each horizontal direction, ny the number of layer on the grid, dx and dy the horizontal grid resolution, dz_{ground} the lowest layer depth and dt the slow modes time step

The main model input parameters	
nx	13
ny	13
nz	45
dx dy	7 km
dz_{groud}	60 m
dt	12 min
episode	25 to 27 June 2002 (72h)

6.3.3 Model Setup

For this study, the operational COSMO configuration is used, with a domain size limited to the Basel area. The computed domain centered on the city of Basel is 13 by 13 grid point for a total surface of 8281 km^2 with a 7 km horizontal resolution. The vertical resolution is 60 m for the lowest model layer. Boundary conditions are taken from the hourly analysis of COSMO computed by MeteoSwiss and are interpolated to our domain. The run lasts 72 hours and covers the 3 days described above, *i.e.* 25 to 27 June, 2002. The main model configuration parameters are summarized in Table 3.

6.4 COSMO vs. Measurements

A general overview of the model performance for the selected episode is presented in this section. In general, the model shows good agreement with the observed meteorological conditions. As the model is driven using analysis for boundary conditions, this is to be expected. In the following, the computed surface fields over the target area, *i.e.* the city of Basel and its immediate rural surroundings, are analyzed and compared to observations. The computed temperature is generally in good agreement with the measurements in rural area. Figure 21 shows the measured temperature averaged over several rural measuring sites (cf. map in Fig. 18) and the computed temperature averaged over the corresponding grid points. The computed maximum temperature at 2 mAGL in rural area occurs one hour earlier and is 0.5°C lower compared to the measurements for the first two days. During nighttime the simulated temperature fits very well to the measurements. However simulated temperature in urban area are too low by 1.5 to 3.0 °C (Fig. 22). The difference between the urban and rural temperature corresponds to the UHI. Figure 23 shows the measured and computed UHI over the city. The averaged computed UHI is 0.14 °C, hence showing no significant temperature difference between urban and rural areas. The temperature in the city is even regularly lower than the temperature in the rural area, particularly during nighttime. As a conclusion, COSMO with the operational configuration is not able to reproduce the UHI and underestimates the magnitude of the urban-rural temperature difference. One possible reason is a too low horizontal and vertical resolution:

- With a 7 km **horizontal resolution**, the city of Basel fills only one grid point; a finer horizontal resolution would allow to represent the city more accurately.
- The COSMO **vertical resolution** used is too low. An accurate representation of

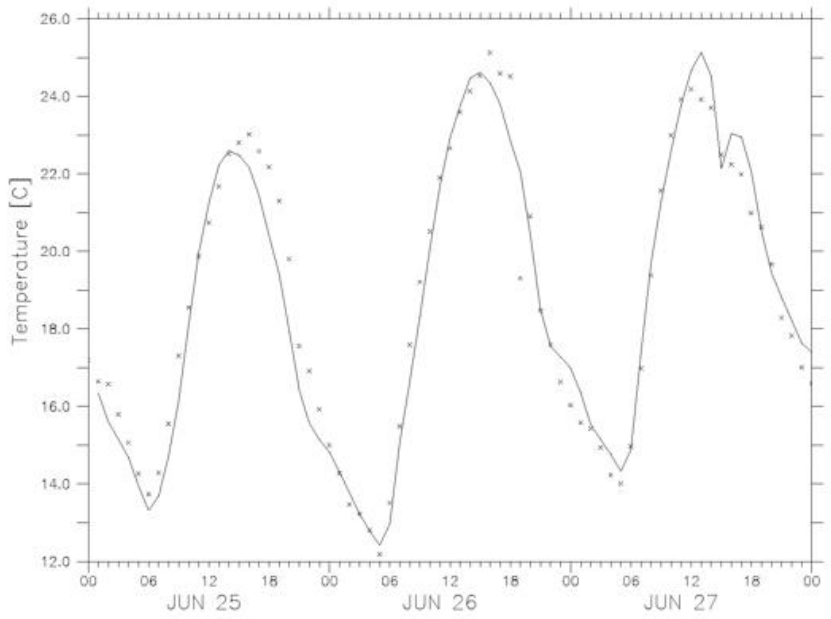


Figure 21: temperature at 2mAGL in rural areas for the period June 25 to 27, measured (crosses) and computed by COSMO (solid line) with the operational configuration.

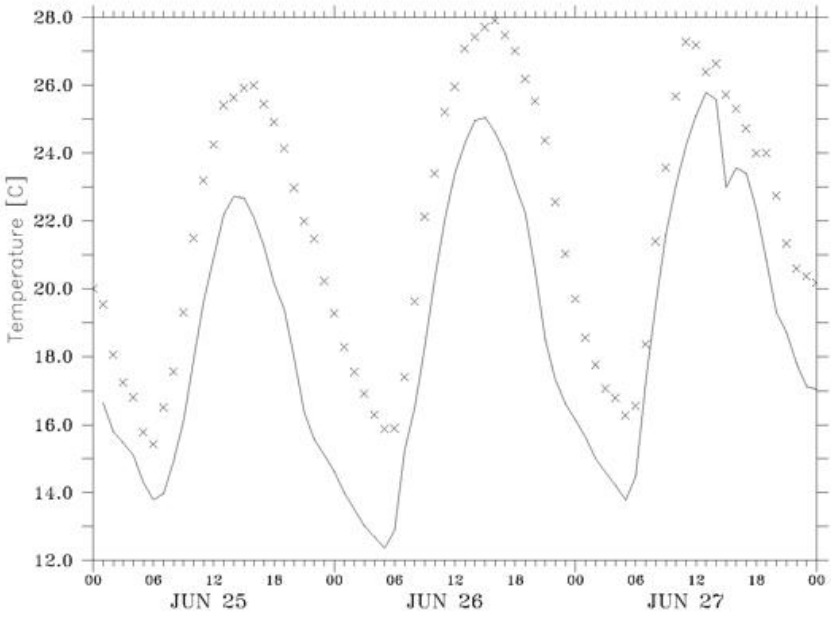


Figure 22: Temperature at 2mAGL in urban areas for a the period June 25 to 27, measured (crosses) and computed by COSMO (solid line) with the operational configuration.

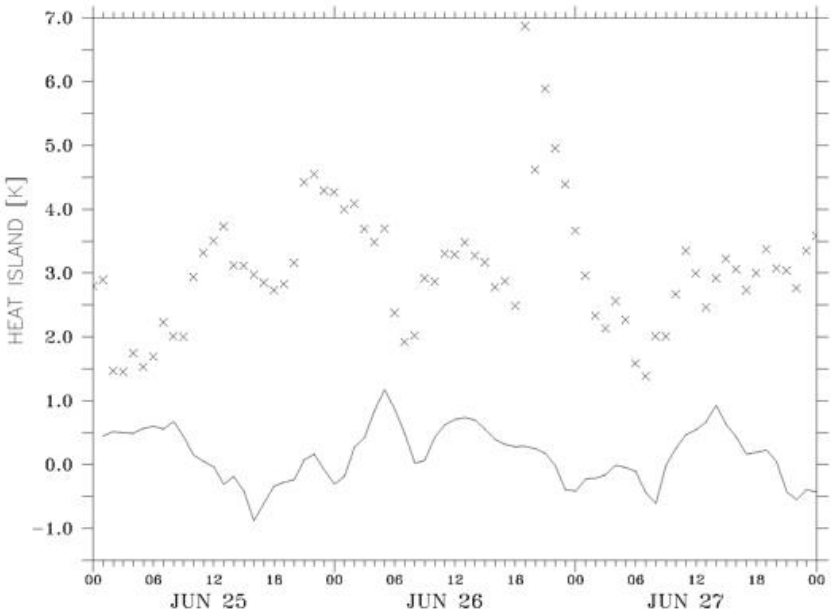


Figure 23: The Urban Heat Island (UHI) at 2mAGL for a three day period (June 25 to 27) measured (crosses) and computed by COSMO (solid line) with the operational configuration.

the boundary layer structure is of crucial importance in order to capture the physics leading to the UHI development.

6.4.1 Increasing The Horizontal Resolution

In order to investigate if the model is able to reproduce the UHI with an increased horizontal resolution, a simulation with the same model setup, and a finer horizontal grid spacing of 2.2 km is performed. This corresponds to the horizontal resolution of the COSMO2 configuration. As with the 7 km resolution, the 2 mAGL temperature in rural area is in good agreement with the measurements (not shown). For urban areas, the temperature is still too low and the UHI is not reproduced (Fig. 24). The average UHI is with 0.1 °C even lower than with a 7 km horizontal resolution. In this case, increasing the horizontal resolution of COSMO has no positive influence on the UHI simulation.

6.4.2 Increasing The Vertical Resolution

In this section, the vertical resolution is increased, applying heights of 20, 26 and 31 m respectively to the first three model layers. The horizontal resolution is kept at 2.2 km, this configuration corresponding to the model setups of COSMO2. As for the simulations with a lower vertical and horizontal resolution, COSMO is not able to reproduce an UHI (Fig. 25). As a conclusion, the ground surface temperature computed by the soil model TERRA_LM and use of the MOST land-surface scheme does not allow to take into account the modifications of the Planetary Boundary Layer (PBL) flow fields induced by the presence of a city. The street canyon geometry reduces sky view factor and wind speed and increases surface area and multiple reflection. Moreover, buildings characteristics modify the energy budget in the city. These factors affect the exchange surfaces-atmosphere from sensible heat and trapping radiation, and cannot be neglected (Oke, 1987). It is necessary to use an adapted parametrization in order to take into account the presence and the effect of a city in the model. For that purpose, the Building Effects Parametrization (BEP), developed by

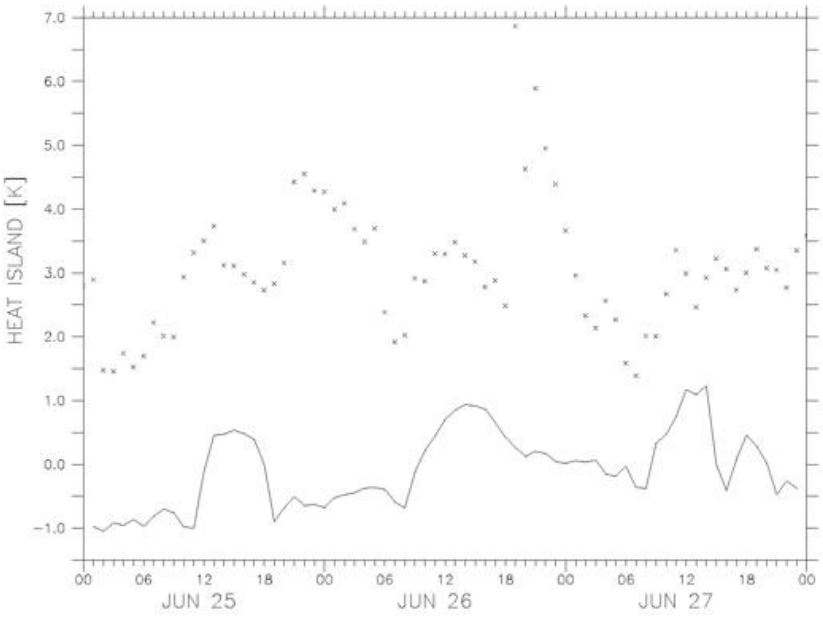


Figure 24: The Urban Heat Island (UHI) at 2m for a three day period (June 25 to 27) measured (crosses) and computed by COSMO (solid line) with an increasing horizontal resolution of 2.2 km.

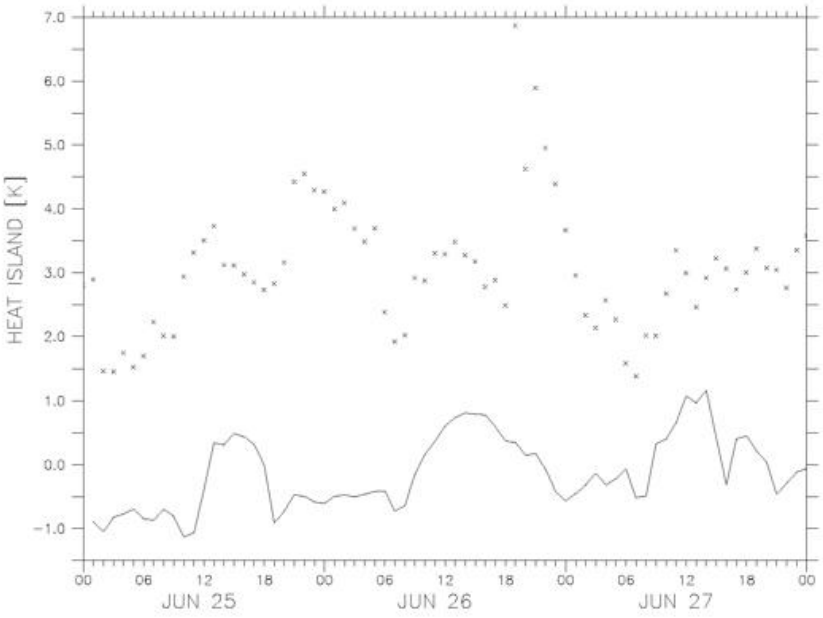


Figure 25: Urban Heat Island (UHI) at 2mAGL for 25 to 27 June, measured (crosses) and computed by COSMO (solid line) with the COSMO2 configuration.

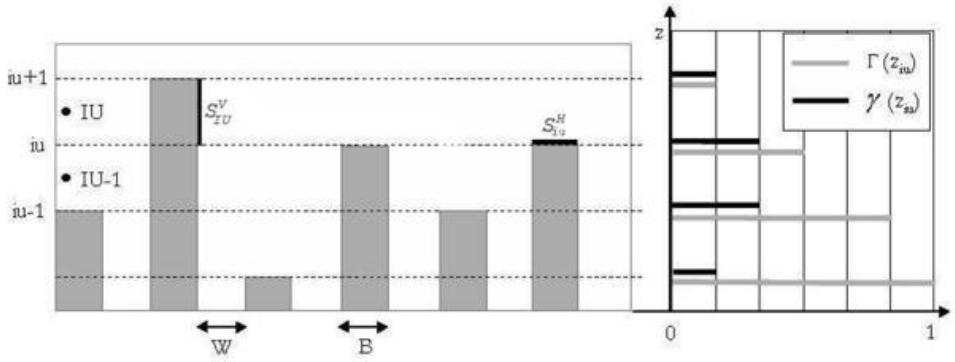


Figure 26: Schematic representation of the city in the urban grid of BEP and the buildings vertical distribution of density $\Gamma(z)$ and probability $\gamma(z)$ (Martilli, 2001).

Martilli et al. (2002) is implemented into the COSMO model.

6.5 BEP : *Building Effects Parametrization*

Results from the last section indicate that there is a clear need to better represent the physical processes of typical urban environments in order to improve the representation of these regions in mesoscale models. In this study we will use the parametrization developed by Martilli (2001) called the Building Effects Parametrization (BEP). It has initially been developed for the mesoscale model FVM and tested extensively on several situation (Martilli, 2002; Roulet et al., 2005) and applied to different cities (Athens (Martilli et al., 2003), Basel (Roulet, 2004), Bogota (Zrate et al., 2006) and Mexico (present work)). This section contains a description of BEP. The next two sections present the implementation of BEP in COSMO and the tests over the city of Basel. BEP takes into account the main characteristics of the urban environment: *(i)* vertical and horizontal surfaces (wall, canyon floor and roofs), *(ii)* shadowing and radiative trapping effects of the buildings, *(iii)* anthropogenic heat fluxes through the buildings wall and roof. In this parametrization the city is represented as a combination of several urban classes. Each class is characterized by an array of buildings (Fig. 26) of the same width B located at the same distance from each other W (canyon width), but with different heights (with a probability $\gamma(z)$ to have a building with height z and a density function $\Gamma(z)$ of buildings with height z or higher). To simplify the formulation we assume that the length of the street canyons is equal to the horizontal grid size. BEP computes urban effects on its own grid. The horizontal resolution is identical to the resolution of the mesoscale grid, while the vertical resolution is generally finer than the mesoscale resolution, and is usually set to 5 meters. Vertically the BEP grid extends up to one layer above the highest buildings. In this parametrization, the fluxes contributions of every urban surface type (canyon floor, roofs and walls) on the momentum, heat and turbulent kinetic energy (TKE) equations are computed separately. Firstly, the contributions of the horizontal surfaces (canyon floor and roofs) are calculated using the formulation of Louis (1979) based on MOST. The roughness lengths used for this calculation are representative for the local roughness of the specific surface types (roofs or canyon floor). Secondly, the exchange of momentum and TKE on the vertical surfaces (walls) are parametrized as the effect of pressure and drag forces induced by the buildings. The temperature fluxes from the walls are a function of the difference between air and wall temperature. They are parametrized using the formulation of Clark (1985) proposed by Arnfield and Grimmond (1998) in their urban energy budget model. The energy budget is computed for every mentioned surface (canyon floor, roofs and walls). Firstly, the direct and infrared radiation at the surfaces are calculated

to take into account the shadowing and radiative trapping effects of the buildings. Then, the surface temperatures for roofs, walls and canyon floor are solved by heat diffusion equation in several layers within the material (concrete or asphalt). After their calculation in the urban grid, the fluxes are vertically interpolated into the mesoscale grid. We will now consider the input parameters that are needed by BEP for each urban class:

Thermal parameters The material thermal diffusivity K_s $[m^2 s^{-1}]$ and specific heat C_s $[Jm^{-3}K^{-1}]$ for each urban surface (roof, canyon floor and wall), as well as building inside temperature T_{int} $[K]$.

Radiation parameters The surface albedo α and emissivity ε for each urban surface (roof, canyon floor and wall).

Roughness parameter The roughness length z_0 $[m]$ for the horizontal surfaces (roof and canyon floor).

Geometrical parameters The street direction, length and width, the buildings height and width, as well as the probability $\gamma(h)$ to have buildings of height h.

Meteorological variables The wind components (u and v), temperature and solar radiation (angle and intensity) from the mesoscale models.

Urban fraction parameter $u_{fraction}(i, j, iurb) \in [0 : 1]$ gives the urban fraction in each cell covering the city.

BEP is then able to compute new surface temperature, momentum, heat and TKE fluxes for each layer of the mesoscale grid influenced by the city.

6.5.1 Temperature at 2 mAGL

The temperatures available for model validation are generally measured at 2 m above the ground. So the model needs to compute the temperature at this height. In COSMO, it is computed as a prognostic variable using MOST, which is based on constant-flux layer approximation in the surface layer. Rotach (1993a,b) shows that the turbulent fluxes are not constant with height in the urban roughness sublayer (1-3 time mean building height) and that similarity theory cannot therefore be applied. As BEP takes into account the presence of a city, its computed fluxes can be used to specify the temperature at 2 m height. For that purpose modifications are implemented in BEP, that will allow to compute diagnostic variables (typically 2 m temperature, 10 m wind) consistent with the land-surface scheme assumptions. The temperature at 2 mAGL corresponds to the temperature simulated in the urban grid, in so far as the first layer near the ground remains thin enough for being considered as the temperature at 2 m. The energy budget equations for sensible heat, momentum and TKE are hence solved in the urban grid. With low horizontal resolution (here 2 km) compared to the high vertical resolution (5 m), vertical fluxes dominate the horizontal fluxes and represent the main source term in the energy budget equation. Therefore the horizontal fluxes can be neglected as shown by Masson et al. (2002) with measurements. The vertical turbulent exchanges balance the fluxes coming from the buildings and the ground, thus the equations for sensible heat, momentum and TKE are parametrized for each layer in the urban grid as follows:

$$\frac{\partial}{\partial z}\left(K_z \frac{\partial \theta}{\partial z}\right) = a_\theta \theta + b_\theta \tag{7}$$

$$\frac{\partial}{\partial z}\left(K_z \frac{\partial U_i}{\partial z}\right) = a_{U_i} U_i + b_{U_i} \tag{8}$$

$$\frac{\partial}{\partial z}\left(K_z \frac{\partial E}{\partial z}\right) = a_E E + b_E + \rho K_z \left[\left(\frac{\partial U_x}{\partial z}\right)^2 + \left(\frac{\partial U_y}{\partial z}\right)^2\right] - \frac{g}{\theta_0}\rho K_z \frac{\partial \theta}{\partial z} - \rho C_\varepsilon \frac{E^{3/2}}{l_\varepsilon} \tag{9}$$

Equations 7 and 8 parametrize respectively the temperature θ and the wind speed U_i for each direction in accordance with Pielke (1984). a_ψ and b_ψ are the flux source terms computed by BEP and K_z $[\frac{m^2}{s}]$ are the vertical diffusion coefficients. Equation 9 $[\frac{m^2}{s^2}]$ is the prognostic equation for the turbulent kinetic energy E according to Bougeault and Lacarrere (1989) with a $k-1$ closure. In this equation, $\rho K_z \left[\left(\frac{\partial U_x}{\partial z}\right)^2 + \left(\frac{\partial U_y}{\partial z}\right)^2\right]$ and $\frac{g}{\theta_0}\rho K_z \frac{\partial \theta}{\partial z}$ are the production terms representing the shear and the buoyancy respectively. The $\rho C_\varepsilon \frac{E^{3/2}}{l_\varepsilon}$ term is the dissipation rate where l_ε is a characteristic length of the energy-containing eddies, and computed as the root square of l_k multiplied by the street width. l_k $[m]$ is a characteristic length for eddies determined as the minimum between street width and height where l_k is computed. C_ε is a numerical coefficient set to 0.71 (Bougeault and Lacarrere, 1989). The system of 4 equations is characterized by 5 unknowns (θ ,U_x, U_y, E and K_z) for each layer of the urban grid. In order to close the system, K_z is defined as a function of E (Bougeault and Lacarrere, 1989) and is written:

$$K_z = C_k l_k E^{1/2}, \tag{10}$$

where C_k is a numerical coefficient set to 0.4 (Bougeault and Lacarrere, 1989).

In BEP, this system is solved by iteration once the flux source terms a_ψ and b_ψ are computed. Firstly TKE is estimated for computing K_z according to equation 10. Then temperature and wind speed are computed with equations 7 and 8, and TKE can be computed with (9). A new K_z is then calculated using the new TKE value, and iterations are made until TKE converge. The energy profile in the urban grid is used to initialize K_z for the next time step. It is necessary to determine the upper-boundary conditions in the urban grid. For wind, they are directly given by the mesoscale models at the height of the urban grid top. For TKE and temperature at the top of the urban grid (above the buildings), it is assumed that a neutral surface layer is developing above the roughness layer (Roth, 2000), which is virtually starting from the zero plane displacement (Oke, 1987) situated in the roughness layer (Fig. 27). In the surface layer, the vertical turbulent fluxes of momentum and heat are assumed to remain constant (Seinfeld and Pandis, 1998). In this case, only the production (shear and buoyancy) and the dissipation terms remain in the prognostic equation for E, *i.e.*

$$\rho C_\varepsilon \frac{E^{3/2}}{l_\varepsilon} = \rho K_z \left[\left(\frac{\partial U_x}{\partial z}\right)^2 + \left(\frac{\partial_U y}{\partial z}\right)^2\right] - \frac{g}{\theta_0}\rho K_z \frac{\partial \theta}{\partial z} \tag{11}$$

In accordance with the assumed surface layer properties, shear is defined as:

$$\rho \frac{U_*^3}{\kappa(z - z_d)}\phi, \tag{12}$$

Where κ is the von Karman constant set to 0.40, under neutral conditions and ϕ is equal to 1 (Businger et al., 1971). U_* is the friction velocity and z_d the zero plan height define as $0.67 * \textit{building height}$ (Grimmond and Oke, 1999). The buoyancy in the surface layer is defined as:

$$\frac{g}{\theta_0}\rho U_* \theta_* \tag{13}$$

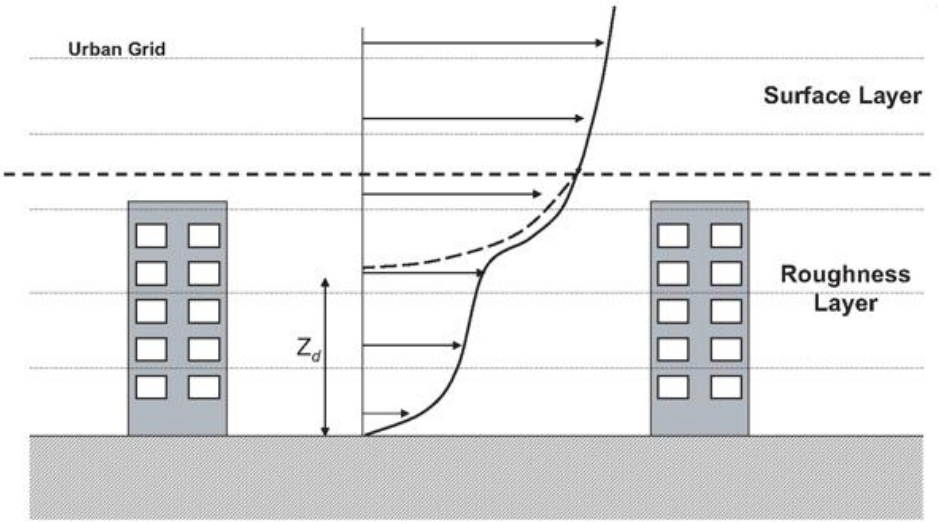


Figure 27: Schematic representation of a wind profile in the roughness layer and in the surface layer. It assumes that a surface layer has developed above the urban canopy and virtually starts at the zero plane displacement height Z_d.

Where θ_* is a potential temperature scale. U_*^2 is the total momentum flux and $U_*\theta_*$ the total heat flux:

$$U_*^2 = \sqrt{(A_{u_x}U_x + B_{u_x})^2 + (A_{u_y}U_y + B_{u_y})^2} \tag{14}$$

$$U_*\theta_* = A_\theta\theta + B_\theta \tag{15}$$

Where A_ψ and B_ψ represent the total source term in the urban grid. Based on (11) and using equations 12 to 15, TKE at the top of the urban grid is estimated as:

$$E_{top} = \left[\frac{1}{C_\varepsilon}\left(\frac{U_*^3}{\kappa} - \frac{g(z-z_d)}{\theta_0}U_*\theta_*\right)\right]^{2/3} \tag{16}$$

The upper-boundary condition for temperature is parametrized with a logarithmic profile (Pielke, 1984),

$$\theta_* = \frac{\kappa(\theta_z - \theta z_d)}{0.74[\ln(z/z_0) - \psi_H(z/L)]} \tag{17}$$

As explained before, the flux θ_* remains constant within the neutral surface layer. A further assumption is to neglect perturbation terms $\psi_H(z/L)$. Temperature $\theta_{z_{top}}$ at the top of the urban grid (z_{top}) can then be expressed as a function of the temperature at the first mesoscale model layer above the urban grid $\theta_{z_{meso}}$:

$$\theta_{z_{top}} = \theta_{z_{meso}} - 0.74\frac{\theta_*}{\kappa}\ln\left(\frac{z_{top} - z_d}{z_{meso} - z_d}\right) \tag{18}$$

The temperature at the urban grid top, $\theta_{z_{top}}$, is linked both to the mesoscale model, by the value above the urban grid $\theta_{z_{meso}}$ and to the urban parametrization, by the potential temperature scale θ_*. This method also solves wind speed and TKE in the urban grid.

6.6 Implementation of BEP in Cosmo

BEP outputs consist of a ground surface temperature and of momentum and heat fluxes profiles calculated over the entire height of the urban grid. In the original version of COSMO, surfaces fluxes are implicitly calculated by the soil module, using the formulations given in equation 6. In the modified version, BEP is implemented in COSMO and runs after the soil module. In the following, two implementation methods are presented.

6.6.1 First Method

The first method is based on the re-computation of the transfer coefficients C_m^d and C_h^d in order to impose surface variable tendencies corresponding to the ones computed in BEP. It is then necessary to find a formulation for the coefficients depending on the tendencies calculated by BEP, (*i.e.* u_{flux}, v_{flux} and t_{flux}). Beginning with the first two equations of system (6):

$$(\tau^{13})_{\zeta=N_\zeta+1/2} = \tau^{13}_{sfc} = -\rho C_m^d |\vec{v}_h| u = -\rho C_m^d \sqrt{u^2+v^2}\, u, \tag{19}$$

$$(\tau^{23})_{\zeta=N_\zeta+1/2} = \tau^{23}_{sfc} = -\rho C_m^d |\vec{v}_h| v = -\rho C_m^d \sqrt{u^2+v^2}\, v, \tag{20}$$

and introducing two new coefficients $C^d_{m,u}$ and $C^d_{m,v}$ to take into account both wind directions u and v:

$$\tau^{13}_{sfc} = -\rho C^d_{m,u} \sqrt{u^2+v^2}\, u, \tag{21}$$

$$\tau^{23}_{sfc} = -\rho C^d_{m,v} \sqrt{u^2+v^2}\, v, \tag{22}$$

with units $[\frac{kg}{ms^2}]$.

BEP module gives the tendencies u_{flux} and v_{flux} with units $[\frac{m}{s^2}]$, coming from wind speed temporal derivative, *i.e.* $\frac{\partial}{\partial t}[\frac{m}{s}]$. Thus, it is possible to find a relation between the tendencies of BEP and the surface fluxes of COSMO. In the following, this relation is derivated for the u-direction:

$$\tau^{13} = \Delta z \rho u_{flux}, \tag{23}$$

where Δz is the height of the first mesoscale layer and ρ is the density. Replacing τ^{13} by (21) and simplifying the density terms, we have:

$$-C^d_{m,u} \sqrt{u^2+v^2}\, u = \Delta z u_{flux}, \tag{24}$$

Finally, resolving for $C^d_{m,u}$ and similarly for the v-direction, we obtain the equations linking the momentum transfer coefficients with the fluxes within BEP:

$$C^d_{m,u,BEP} = -\Delta z \frac{u_{flux}}{u\sqrt{u^2+v^2}},$$

$$C^d_{m,v,BEP} = -\Delta z \frac{v_{flux}}{v\sqrt{u^2+v^2}}, \tag{25}$$

Following a similar approach, we can find a relation between the transfer coefficient C_h^d and the heat flux tendency t_{flux}, with units $[\frac{K}{s}]$. The third equation of (6) becomes:

$$(\hat{H}^3)_{\zeta=N_\zeta+1/2} = \hat{H}^3_{sfc} = -\rho C_h^d |\vec{v}_h| (\theta\pi_{sfc} - T_{sfc})$$

$$= \rho C_h^d \sqrt{u^2+v^2} (T_{sfc} - T_{\zeta=N_\zeta}), \tag{26}$$

with units $[\frac{kgK}{sm^2}]$. We have then to divide $\hat{H}^3_{sfc}$ by a density term ρ and a length term Δz to obtain $[\frac{K}{s}]$. Thus:

$$t_{flux} = \frac{\hat{H}^3_{sfc}}{\rho \Delta z} = \frac{\rho C_h^d \sqrt{u^2+v^2}(T_{sfc} - T_{\zeta=N_\zeta})}{\rho \Delta z}, \tag{27}$$

Again, simplifying the density terms and resolving for C_h^d, lead to an expression linking the transfer coefficient for sensible heat with the tendency given by BEP:

$$C^d_{h,BEP} = \Delta z \frac{t_{flux}}{\sqrt{u^2+v^2}(T_{sfc} - T_{\zeta=N_\zeta})}, \tag{28}$$

These three coefficients calculated by BEP are then used to create the final coefficients for input into COSMO, following a linear combination between BEP's and COSMO's coefficients:

$$\begin{aligned} C^d_{m,i,final} &= u_{fraction} C^d_{m,i,BEP} + (1 - u_{fraction}) C^d_{m,LM}, \\ C^d_{h,sensible,final} &= u_{fraction} C^d_{h,BEP} + (1 - u_{fraction}) C^d_{h,LM}, \end{aligned} \tag{29}$$

where $i = u, v$ and $u_{fraction} \in [0 : 1]$ defines the urban fraction in a mesoscale cell and depends on the landuse type.

We have now to consider the fact that BEP consider urban areas as a set of totally dry surfaces. Thus, the module does not calculate any tendencies for latent heat fluxes. A final coefficient for the latent heat is nevertheless calculated, using the following combination:

$$C^d_{h,latent,final} = (1 - u_{fraction}) C^d_{h,LM}, \tag{30}$$

so that the moisture exchanges at the surface are characterized by the rural fraction $(1 - u_{fraction})$ affected to each urban cell.

As already mentioned, BEP also calculates a street surface temperature tgs_u. The module is defined with three soil layers, the deepest having a constant temperature. At time $t = t_0$, the constant temperature of COSMO is used to initialize the temperature in every soil layers of BEP. Then, the module calculate a thermal gradient over all layers at each time step and gives tgs_u. As for (29) and (30), the final ground surface temperature is calculated with a linear combination between tgs_u from BEP and t_s from COSMO:

$$t_s_{final} = u_{fraction} tgs_u + (1 - u_{fraction}) t_s \tag{31}$$

This temperature finally replaces COSMO's ground surface temperature t_s at each time step.

The advantage of this implementation method of BEP into COSMO is that it requires no knowledge about the code solver and that the model code does not need to be modified. Nevertheless, it is not optimal for several reasons. With such an implementation, only the first mesoscale layer can be influenced by BEP. This means that it is not possible to consider buildings higher than the first mesoscale level. Moreover, terms 25, 25 and 28 show that for low wind speeds the recomputed exchange coefficient may numerically diverge. Thus, it is necessary to control and to limit the transfer coefficients for the low wind speed situations. This implementation method has some limits. Therefore a second method to implement BEP and to take into account the source flux terms above the first layer of the mesoscale model is presented in the next section.

6.6.2 Second Method

The first method is more complex but does not modify the LM code. This second method is simpler and more powerful but modifications must be applied to the implicit LM solver. To avoid the limitations of the first implementation method, a more direct method is presented that needs less modifications in BEP and LM code and acts on each vertical mesoscale layer influenced by urban areas. It relies on the use of tendencies ψ_{flux} and source terms a_ψ and b_ψ, where $\psi = u, v, t$. BEP calculates the tendency u_{flux} using the source terms, as follows

$$u_{flux} = \rho \Delta z (a_u u + b_u), \tag{32}$$

This can be generalized by:

$$\psi_{flux} = \rho \Delta z (a_\psi \psi + b_\psi), \tag{33}$$

where a_ψ and b_ψ are the implicit and explicit source terms respectively and $\rho\Delta z$ a conversion factor from BEP's tendencies and COSMO's fluxes. Now, if we look at equation (33) in term of temporal derivative, we have:

$$\frac{\psi^{n+1} - \psi^n}{\Delta t} = \rho\Delta z(a_\psi \psi^{n+1} + b_\psi), \tag{34}$$

The step is now to implement the tendencies and the source terms in COSMO through equation (4) for k-level only, which means:

$$B_k \psi_k^{n+1} = D_k(\psi^n, ...), \tag{35}$$

Finally, if we take the implicit and explicit terms of (34) and (35), it is possible, by analogy, to connect BEP to COSMO through the source terms:

$$\begin{aligned} B_k &\longrightarrow B_k - a_\psi, \\ D_k &\longrightarrow D_k + b_\psi \end{aligned} \tag{36}$$

Two valuable methods to implement BEP in COSMO have been presented. The choice of the implementation method depends on the user's knowledge of the mesoscale code and on the possibility to modify it. With some adaptations, but keeping the same implementation philosophy, these two methods allow to implement BEP in numerous mesoscale models. Having the possibility to change the implicit solver of LM, the second method is used in this study, which allows to take into account the urban source terms in each layer of the mesoscale grid influenced by the urban canopy.

6.7 Simulation of the Basel UHI

6.7.1 Model Setup

In this part, we keep the same simulation domain over Basel and its surroundings (cf. section 6.3.3) with the COSMO2 configuration *i.e.*, a 2.2 km horizontal resolution, a first layer thickness of 20 m and a 3 day simulation period from June 25 to 27. The characteristics and the fraction of urban area in each cell is determined from the KABA data base (Fehrenbach, 1999). Two city categories are defined:

- *City center*: high density of buildings (15 m high), narrow street and 80% of urban area[4]. Represented by 7 grid points.
- *Sub-urban areas*: smaller density of small buildings (7 m high) and 60% of urban area. Represented by 17 grid points.

Figure 28 shows the simulated domain with cells considered as urban and sub-urban. The properties for both urban and sub-urban categories are determined according to KABA and Roulet (2004) and are presented in Appendix 6.9.3. For the cells containing urban area, the parameters of the rural part have been changed in order to represent park and green area. The main model input parameters are summarized in Table 4.

[4]It means that 80% of the area of the grid cell fluxes are computed by the urban parametrization (BEP) and the rest is handled by the traditional LM parametrization with values for rural area.

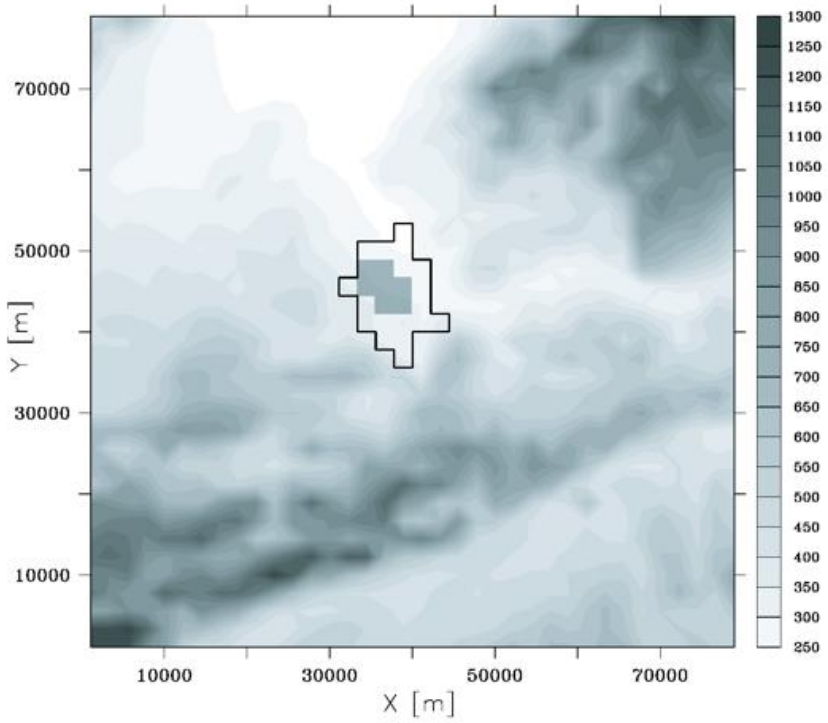


Figure 28: Topography [mASL] of the simulation domain (2.2 km horizontal resolution) over the city of Basel and the urban (gray squares) and sub-urban cells (black shape).

Table 4: The main model input parameters are: nx and ny the number of model grid points in each horizontal direction, nz the number of vertical layers, dx and dy the horizontal grid spacing, dz_{ground} the lowest layer depth and dt the slow modes time step

The main model input parameters	
nx	36
ny	36
nz	60
dx dy	2.2 km
dz_{groud}	20 m
dt	12 min
period	25 to 27 June 2002 (72h)

6.7.2 Results

In this section, we compare results from the mesoscale model calculated both with and without BEP, and give a general overview of the model performance with BEP for the selected episode.

WIND

The wind pattern (Fig. 29 and Fig. 30) is very typical for Basel area with strong inflow from the Rhine valley in the North and going up along the slopes of the terrain. The comparison between simulations with and without BEP shows only slight differences in the wind fields. A small decrease of wind speed over the city is observed with BEP. The air flow simulated without BEP (Fig. 29) is not modified above the city. However, the simulation with BEP (Fig. 30) shows a divergence-convergence system around the city. The simulation shows a divergence and a decrease of the wind speed upstream the city due to drag effect of the buildings. The wind accelerates around the city. Wind speed decreases drastically downstream as a combined effects of drag force and buoyancy due to temperature increase in the city. A convergence is observed south of the city. BEP impacts the air flow up to 7 km upwind and downwind the urban area. Looking hour by hour, we observe that the effect on wind flow increases with wind speed *i.e*, the impact of BEP increases with increasing wind speed.

TEMPERATURE

The simulated temperature at 2 m shows warmer temperature in the urban area with BEP than without. The computed UHI (Fig. 31) is always stronger in the simulations with BEP by 0.7 to 4 °C. The averaged UHI simulated with BEP reaches 2.3 °C, which is in agreement with the measurements (average UHI of 3 °C, Fig. 31). Furthermore, the simulated UHI is late by around 3 hours during the morning and too weak from 18LT to 00LT. We also observed a peak in the measurements at 18 LT on June 26 that the simulation is not able to reproduce. It is instructive to look at absolute temperature values and not differences in order to explain the observed inconsistencies. Figure 32 shows that the city is warmer with BEP particularly during nighttime. The morning temperature increase simulated with BEP comes with a delay, which explains the phase shift of the UHI observed above. Even if the maximum of temperature is too low the first day, it is generally well reproduced with the BEP simulation and the UHI during daytime is well reproduced. The temperature decrease in the afternoon and evening occurs earlier with BEP than in the measurements and a maximum difference between simulation and measurement is reached at sunset (20 LT). This explains the strong UHI anomaly at the end of the day and beginning of the night (cf. Fig. 31). The maximum of measured UHI reached at 18 LT on June 26 is not observed in the urban temperature. This maximum is due to a decrease of the temperature in the rural area (not shown).

Numerous tests have been conducted on the input parameters of BEP used to describe the city. Using typical values found in the literature (Oke, 1987; Masson et al., 2002; Dupont et al., 2004), the following parameters have been varied and sensitivity of the results studied:

- The *Thermal Parameters* of the materials, *i.e.* the thermal diffusivity and the specific heat for roof, wall and ground.
- The *Radiation Parameters* of the surfaces, *i.e.* the albedo and the emissivity of roof, wall and ground.
- The *Roughness Length* of horizontal surfaces (ground and roof).

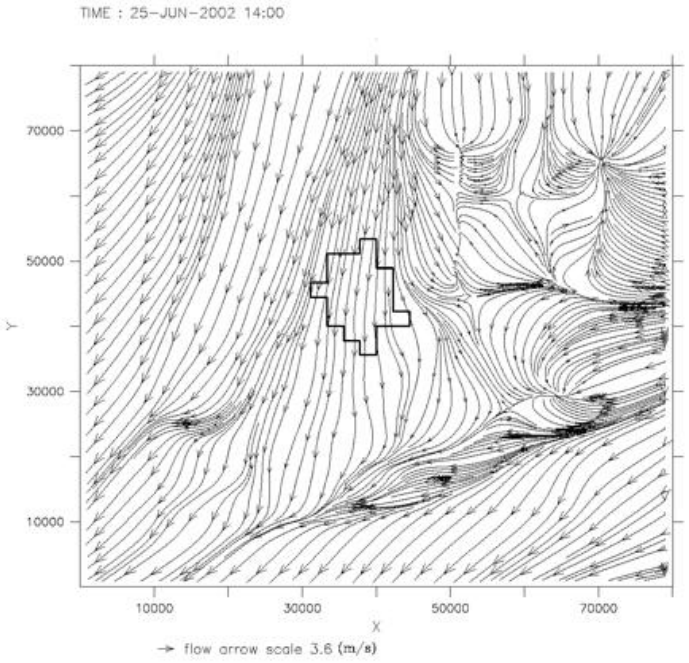


Figure 29: Simulated wind streamline (the size of the arrows indicates the wind speed strength) with COSMO, June 25 at 14LT in the first layer (20 meters height) above and around the city of Basel (black shape).

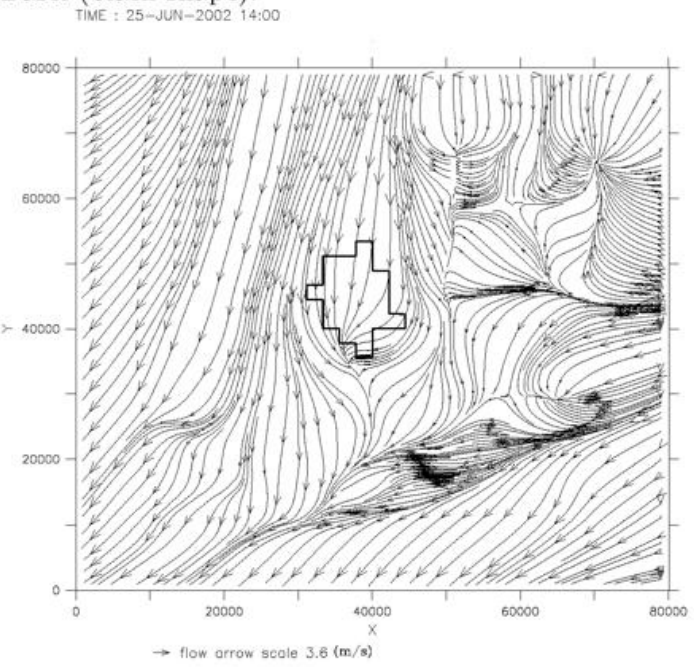


Figure 30: Simulated wind streamline with COSMO/BEP, June 25 at 14LT in the first layer (20 meters height) above and around the city of Basel (black shape).

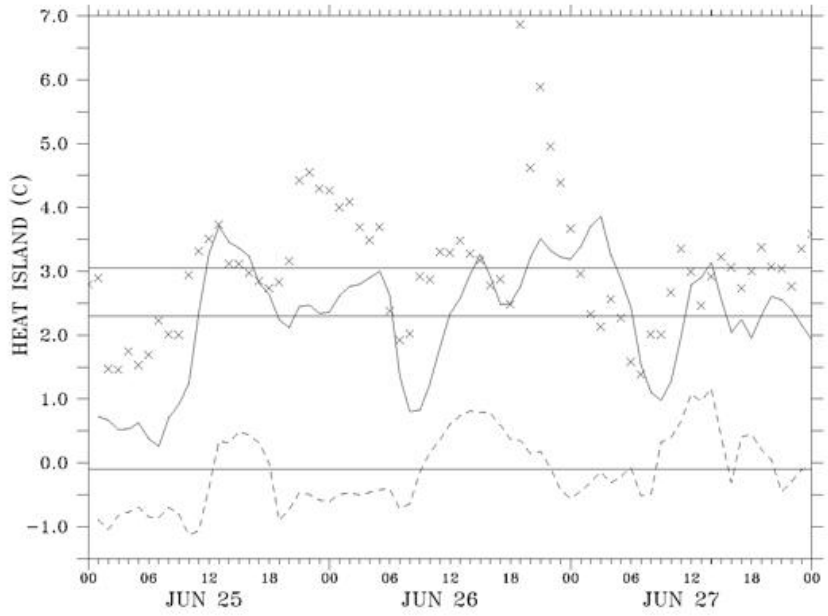


Figure 31: The Urban Heat Island (UHI) at 2m for a three day period (June 25 to 27) measured (crosses) and computed by COSMO with BEP (solid line) and without BEP (dashed line) with an horizontal resolution of 2.2 km

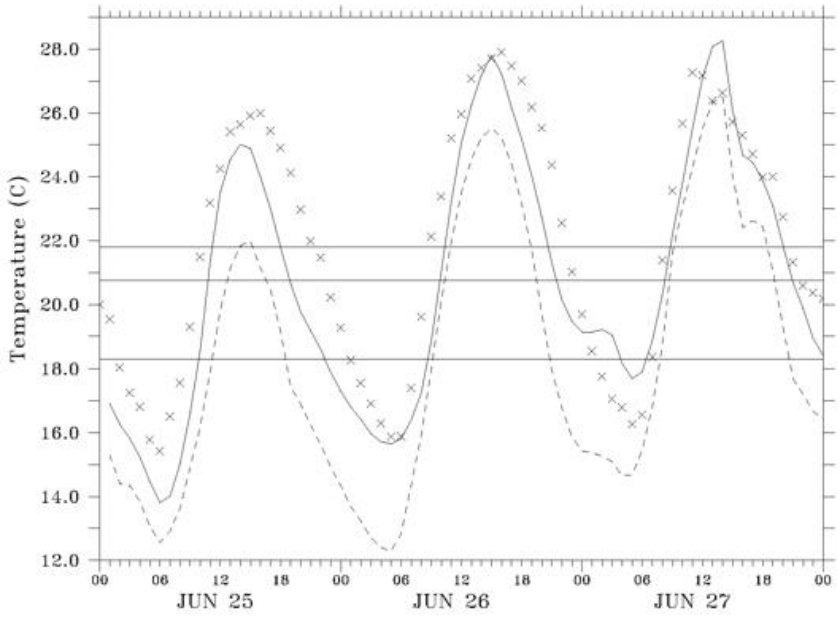


Figure 32: Average temperature at 2 m in the city of Basel, measured (crosses), simulated in COSMO without BEP (dashed line) and with BEP (solid line).

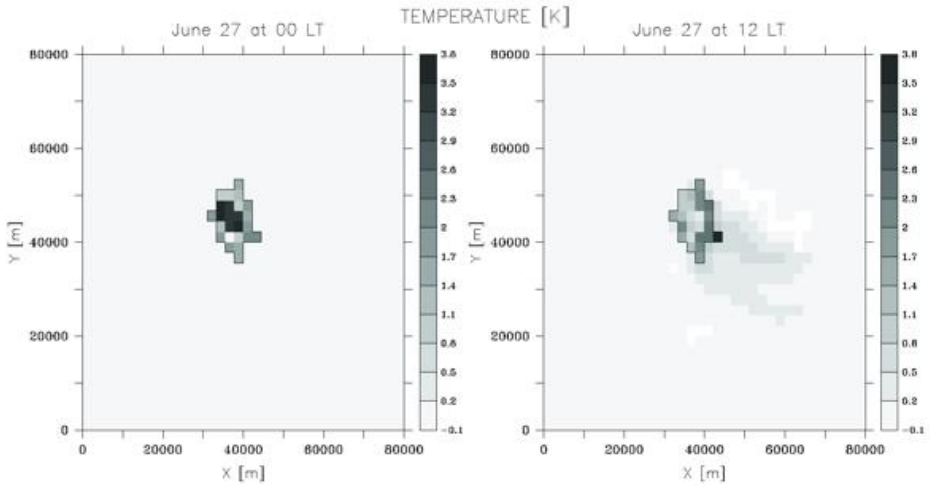


Figure 33: Temperature differences at 2 mAGL [°C] between an COSMO simulation with BEP and without BEP over the city of Basel (black shape) for 27 June, 2002 at midnight (left) and 27 June, 2002 at noon (right)

- The *Geometrical Parameters* of the city, *i.e.* street direction and width, buildings height and width and their repartition.

An impact on the average and on the amplitude of the temperature curve is observed when these parameters are modified. However the shape of the curve is not modified, *i.e.* the morning increase temperature is always late and the temperature decreases too early in the afternoon. Furthermore, modifying the parameters in the range proposed by the literature produces weak impacts (not shown) on the temperature, of around 0.6 °C on the amplitude and 0.3 °C degrees on the average. The results presented above have been computed with the set of parameters that provide the best fit between simulation and measurements. To summarize, the results show that a parametrization of heat and momentum fluxes over urban areas clearly improve mesoscale simulations using an horizontal resolution of 2.2 km. Results with BEP show a much better representation of the UHI as well as the general temperature evolution over an urban area such as Basel. Remaining differences between measured and simulated urban temperatures are dominated by a phase shift in the morning increase and evening decrease. This effect does not show any sensitivity to changes in BEP's input parameters. If measurements are considered representative of the urban environment, this gives an indication that the processes considered in BEP are not complete and some physical mechanisms determining the temperature are not or not well represented.

UHI DISPERSION

Figure 33 shows the difference of temperature at 2 mAGL between a simulation with and without BEP. Two behaviors are observed:

- During nighttime (left panel of Figure 33), the simulation using BEP is clearly warmer above the city by 3.0 to 3.8 °C for the city center and by 1.5 to 2.0 °C for the sub-urban area. During this period, the wind is weak and temperature increase is observed only in the urban cells.

- During daytime (right panel of Figure 33), temperature increase above the city with BEP is weaker than during nighttime (1.5 to 2.5 °C in the city center), however a maximum of 3.4 °C is reached in the east- and southeast-part of the sub-urban area. The wind is stronger during daytime and blows to south east. It creates a displacement

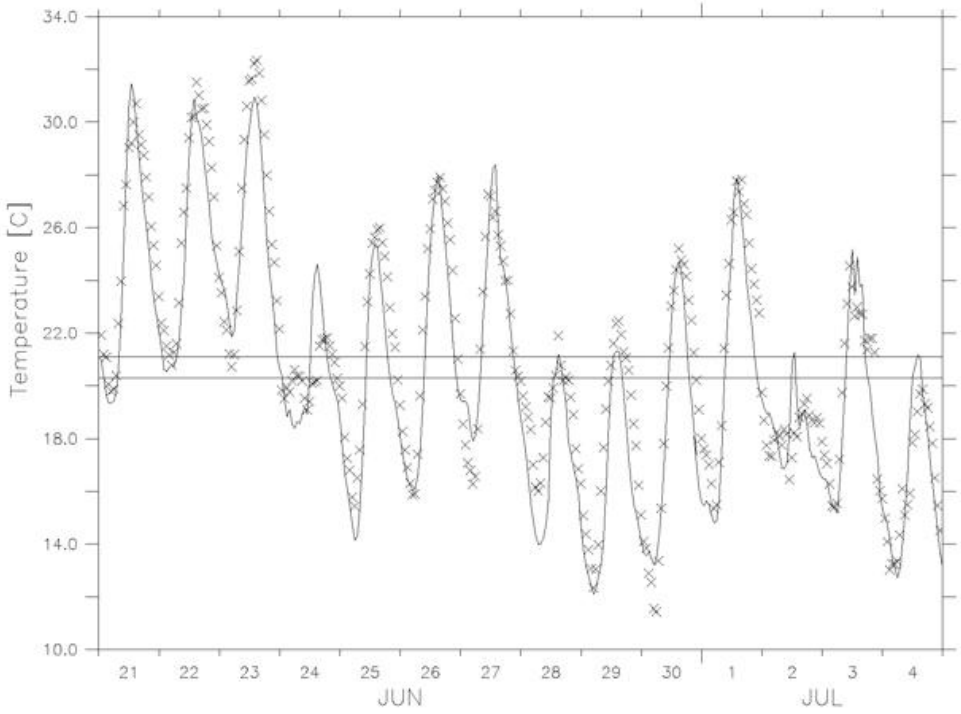


Figure 34: Urban temperature at 2m for a 14 days period (June 21 to July 4, 2002) measured (crosses) and simulated by COSMO with BEP (solid line) with a horizontal resolution of 2.2 km. The horizontal lines are the average of the measured temperature (21.1 °C) and the average of the computed temperature (20.3 °C).

of the maximum and a temperature "plume" which is observed south-east of the city and reaches 0.5 to 1.0 °C.

In both situations BEP increases the temperature in the city. The intensity and diffusion of this temperature increase are strongly dependent on the wind speed, so that BEP modifies not only the urban area but also the nearby area, up to 20 km downwind in the presented case.

6.7.3 14 Days Simulation

Up to now, BEP has only been tested on 2 to 4 day episodes. The implementation of BEP in an operational forecast model gives the opportunity to test it for longer periods (weeks or months) and different kinds of meteorological situations (days with strong cloudiness and/or precipitation). In this section we present a 14 days simulation during the BUBBLE IOP from June 21 to July 4 2002. Figure 34 shows the temperature simulated with COSMO/BEP in the urban area. No tendency being observed, BEP does not accumulate or lose heat during this 14 days period. Thus, BEP is able to compute the urban heat and momentum fluxes for longer period than 3 days. The mean temperature reaches 21.1 °C for measurements, 20.3 °C for the simulation with BEP and 18.3 °C for the simulation without BEP (not shown). The mean temperature is well reproduced with BEP as well as the general temperature behavior. The same tendencies are observed than during the 3 day simulations, which showed a warmer city by 2.4 °C with BEP. During nighttime of 23, 27 and 30 June, BEP slightly overestimates the temperature. The average of the computed UHI (Fig. 35) is 1.6 °C whereas it is around 2.8 °C in the measurements. The difference between measurements and simulation for the UHI is larger than the difference in the urban area temperature

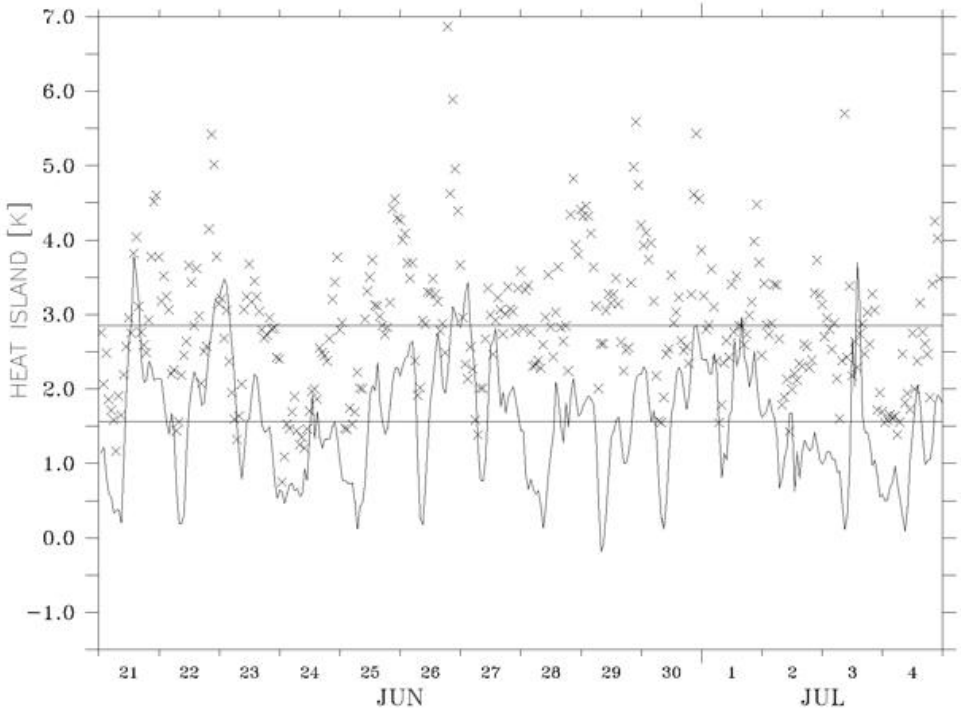


Figure 35: Urban Heat Island (UHI) at 2m for a 14 days period (June 21 to July 4, 2002) measured (crosses) and computed by COSMO with BEP (solid line) with a horizontal resolution of 2.2 km. The horizontal line are the average of the measured and of the computed UHI.

because, in the average, COSMO overestimates the temperature in rural area by 0.4 °C. If we focus on the temperature at 2 mAGL on June 24 when an important rainfall episode occurs form 01LT to 12 LT (Appendix 6.9.2), we observe that the simulation underestimates the temperature during nighttime and overestimates it during daytime. This phenomenon is also observed in the simulation without BEP (not shown), and is probably due to a too weak cloud cover in the simulation. The ground loses too much energy during nighttime by radiative effects and receives too much energy due to incoming solar radiation during daytime. The same phenomenon is observed on July 2 while very weak rainfall is observed during nighttime. However important rainfalls are observed during nighttime from 3 to 4 July and the simulation during this period fits very well to the measurement (Fig. 34). Even if BEP does not take into account latent heat flux, water storage or urban rainfall runoff, the rainfall episode does not deteriorate the results of temperature simulation. Nevertheless, taking into account water budget and latent heat flux in BEP could improve the urban energy balance and the temperature simulation which have shown a too fast cooling at the end of the day (section 6.7.2).

6.8 Conclusion

The presence of a city modifies the fluxes between the atmosphere and the Earth's surface. From August 2001 to July 2002, a year-long measurement campaign (BUBBLE) has been conducted in the city of Basel (Switzerland) and its surroundings with the aim of investigating in details the boundary layer structure in an urban area. During the intensive observation period (IOP), form June 15 to July 12 2002, an Urban Heat Island (UHI) has been underlined by temperature measurements at 2 mAGL inside and outside the city (Table 5). In order to investigate the ability of mesoscale models to take into account the effect of urban areas

Table 5: Average Urban Heat Island (UHI) in °C for the period of June 25 at 00 LT to June 27 at 23LT, for the BUBBLE measurements (left column), an COSMO simulation with 2.2 km horizontal resolution and 20 m vertical resolution for the first layer (center column) and an COSMO simulation and the urban parametrization BEP with the same configuration (right column).

UHI average for June 25 to 27 2002		
Measurement	COSMO	COSMO - BEP
3.0 °C	-0.1 °C	2.3 °C

on atmospheric flow fields and to reproduce the UHI, we have selected a three day episode during the IOP for simulation with the COSMO mesoscale model. COSMO is the operational numerical weather prediction model of MeteoSwiss. It is used on a domain covering most of western Europe with a horizontal resolution of 7 km and a vertical resolution with a 60 m depth for the first layer above the ground. The results obtained with COSMO over the city of Basel and its surroundings shows no UHI. With a 7 km horizontal resolution and a 60 m vertical resolution, the city of Basel and the urban boundary layer are not represented with enough accuracy. In order to investigate if a better resolution allows COSMO to reproduce the measured UHI over Basel, the horizontal resolution has been increased to 2.2 km and the vertical resolution to 20 m for the first layer. The results show that a finer resolution has no impact on the UHI simulation by COSMO (Table 5). As a conclusion, the surface scheme in COSMO based on the similarity theory is not adapted to the urban areas. In order to take into account the presence of a city with a more accurate surface scheme, the Buildings Effects Parametrization (BEP) has been implemented in COSMO. BEP has been modified in order to compute the temperature at 2 mAGL inside the urban canopy. Results show that the implementation is successful and works as expected. The results obtained with BEP show that the urban parametrization modifies the wind flow above and around the city. The wind speed decreases above the city and a system of divergence-convergence is observed around it. Wind divergence-convergence systems are particularly important in air pollution study as they generally lead to a pollution maximum. The temperature is reproduced with a good accuracy in the urban area. Thus, COSMO with BEP is able to reproduce an UHI in the city of Basel (Tab. 5). We have underlined that the temperature increase does not stay confined in the urban area, but extends around the city up to 15 to 20 km. Nevertheless, the UHI computed with BEP is generally too weak (Tab. 5) and even with tuning the urban parameters, BEP is not able to reach the measured values. Sometime, a phase shift is also observed between the measured and simulated temperature. BEP is based on a simplified representation of the urban area and several phenomenon are neglected. The urban parametrization could be adapted in order to take into account different phenomenon, which should modify the urban energy balance:

- The vertical surfaces in BEP are uniform and opaque. Take into account the **windows** will modifying the radiative budget at wall surfaces and in the buildings.
- The **temperature inside the buildings** is maintained constant during the simulation. It will be necessary to take into account its variations in order to represent the buildings energy budget more realistically.
- The **natural ventilation** is the air exchange between inside and outside the buildings (windows opened, ventilation, ...). Koutrakis et al. (1992) estimated that more than 50% of the buildings volume of air can directly be exchanged with the outdoor each

hour.

- The **air conditioning** cools down the air inside and rejects heat in the urban atmosphere. It modifies the balance between inside and outside buildings, and is an important source of heat due to its energy consumption.
- No **urban water budget** is computed in BEP. It doesn't take into account precipitation, pipped water supply of the city and water vapor released due to anthropogenic activities, such as combustion.

A 14 days period has been simulated with COSMO/BEP. It is the first time that BEP is applied for a such long period. That allows to verify that BEP does not accumulate or lose energy and that it can be used for long term simulations. Rainfall episodes are included in these 14 days. BEP does not take into account latent heat flux, water storage and urban rainfall runoff. Nevertheless, the simulation with BEP are in good agreement with the measurements. The results show the importance to have an adapted parametrization for urban areas in order to take into account the modification of the atmospheric flow fields induced by the presence of a city. The increase of horizontal and vertical resolution in COSMO2 is not sufficient to take into account the presence of a city, the use of an adapted parametrization is necessary. BEP implementation in COSMO is a distinct enhancement for the simulation above urbanized region. We have focused our study on the 2 m observations for temperature, 10 m observations for the wind and the horizontal dispersion of the UHI. The urban effects are also present in the vertical direction. It is important to investigate the impact of BEP on the vertical structure of the atmosphere and its capacity to be used with a low resolution mesoscale model for operational forecast purposes.

References

Arnfield, A. J. and Grimmond, C. S. B., 1998. An Urban Canyon Energy Budget Model and its Application to Urban Storage Heat Flux Modelling, *Energ. Buildings*, **27**, 61–68.

Bougeault, P. and Lacarrere, P., 1989. Parameterisation of Orography-Induced Turbulence in a Mesobeta-Scale Model, *Mon. Wea. Rev.*, **117**, 1872–1890.

BUBBLE. *http://pages.unibas.ch/geo/mcr/Projects/BUBBLE.*

Businger, J. A., Wyngaard, J. C., Izumi, Y., Bradley, E. F., 1971. Flux-Profile Relationships in the Atmospheric Surface Layer, *J. Atmos. Sci.*, **28**, 181–189.

Clarke, J. A., 1985. *Energy Simulation in Building Design*, Adam Hilger, Bristol, 362 pp.

COSMO. *http://www.cosmo-model.org/public/documentation.htm.*

Doms, G., Fäurstner, J., Heise, E., Herzog, H.-J., Raschendorfer, M., Schrodin, R., Reinhardt, T., Vogel, G., 2002. A Description of the Nonhydrostatic Regional Model LM, Part I: Dynamics and Numerics, *Documentation of the LM Package*, 2nd version.

Doms, G., Fäurstner, J., Heise, E., Herzog, H.-J., Raschendorfer, M., Schrodin, R.,Reinhardt, T., Vogel, G., 2002. A Description of the Nonhydrostatic Regional Model LM, Part II: Physical Parameterization, *Documentation of the LM Package*, 2nd version.

Dupont, S., Otte, T.L. and Ching, J.K.S., 2004. Simulation of meteorological fields within and above urban and rural canopies with a mesoscale model, *Boundary-Layer Meteorol.*, **113** (1), 11–158.

Fehrenbach, U., 1999. Analyse und Bewertung lokal- und regional-klimatisch wirksamer Faktoren in der Region Basel, Diss. Phil.-Nat. Fak., Univ. Basel, ISBN 3-85977-245-7.

Grimmond, C. S. B., Oke, T. R., 1999. Aerodynamic Properties of Urban Areas Derived from Analysis of Surface Form, *J. Appl. Meteorol.*, **38**, 1262–1292.

Koutrakis, P., Briggs, S.L.K., Leaderer, B. P., 1992. Source Apportionment of Indoor Aerosols in Suffolk and Onondag Counties, New York, *Environ. Sci. Technol.*, **26**, 521–527.

Hamdi, R., 2005. Validation for the cities of Basel and Marseilles, *PhD Thesis*. Université catholique de Louvain, Belgium.

Louis, J.-F., 1979. A parametric model of vertical eddy fluxes in the atmosphere, *Bound.-Layer Meteor.*, **17**, 187–202.

Martilli, A., 2001. Development of an urban turbulence parameterisation for mesoscale atmospheric models, *PhD Thesis N° 2445*. Federal Institute of Technology (EPFL), Lausanne, Switzerland.

Martilli, A., Clappier, A., Rotach, M. W., 2002. An urban surfaces exchange parameterisation for mesoscale models, *Bound.-Layer Meteor.*, **104**, 261–304.

Martilli, A., 2002. Numerical study of urban impact on the boundary layer structure: sensitivity to wind speed and urban morphology, and rural soil moisture, *J. Appl. Meteorol.*, **41**, 1247–1267.

Martilli, A., Roulet, Y.-A., Junier, J., Kirchner, F., Rotach, M. W., Clappier, A., 2003. On the impact of urban surface exchange parameterisations on air quality simulations: the Athens case, *Atmos. Environ.*, **37**, 4217–4231.

Masson, V., 2000. A Physically-Based Scheme For The Urban Energy Budget In Atmospheric Models, *Bound.-Layer Meteor*, **94**, 357–397.

Masson, V., Grimmond, C.S.B, Oke, T.R., 2002. Evaluation of the Town Energy Balance (TEB) scheme with direct measurements from dry districts in two cities, *J. Applied Meteorol.*, **41**, 1011–1026.

Oke, T.R, 1987. Boundary Layer Climates, 2nd edn. London: Methuen, 435 pp.

Orlanski, L., 1975. A rational subdivision of scales for atmospheric processes, *Bull. Amer. Meteor. Soc.*, **56**, 527–534.

Pielke, R., 1984. *Mesoscale Meteorological Modeling*, Academic Press, San Diego, pp 612.

Rotach, M. W., 1993. Turbulence close to a rough urban surface. Part I: Reynolds stress, *Bound.-Layer Meteor.*, **65**, 1–28.

Rotach, M. W., 1993. Turbulence close to a rough urban surface Part II: variances and gradients, *Bound.-Layer Meteor.*, **66**, 75–92.

Rotach, M. W., Vogt, R., Bernhofer, C., Batchvarova, E., Christen, A., Clappier, A., Feddersen, B., Gryning, S.-E., Martucci, G., Mayer, H., Mitev, V., Oke, T. R., Parlow, E., Richner, H., Roth, M., Roulet, Y.-A., Ruffieux, D., Salmond, J. A., Schatzmann M., Voogt, J. A., 2005. BUBBLE - an Urban Boundary Layer Meteorology Project, *Theor. Appl. Climatol.*, **81**, 231–261.

Roth, M., 2000. Review of atmospheric turbulence over cities, *Q. J. R. Meteorol. Soc.*, **126**, 941–990.

Roulet, Y.-A., 2004. Validation and Application of an urban turbulence parameterisation scheme for mesoscale atmospheric models, *PhD Thesis N°*. **3032**, Swiss Federal Institute of Technology, Lausanne.

Roulet, Y.-A., Martilli, A., Rotach, M. W., Clappier, A., 2005. Validation of an urban surface exchange parameterization for mesoscale models - 1D case in a street canyon, *J. of App. Meteorol.*, **44**, 1484–1498.

Seinfeld, J. H., Pandis, S. N., 1998. Atmospheric Chemistry and Physics, *Wiley Interscience publication*, New-York, pp 1326.

Stull, R.B., 1988. An Introduction to Boundary Layer Meteorology, Kluwer Academic Publisher, Dordrecht, pp 670.

Zarate, E., Clappier, A., Belalcazar, L. C., 2006. A study of the photochemical plume formed in Bogota (Colombia) using numerical simulations, *submitted to J. Environ. Manage.*

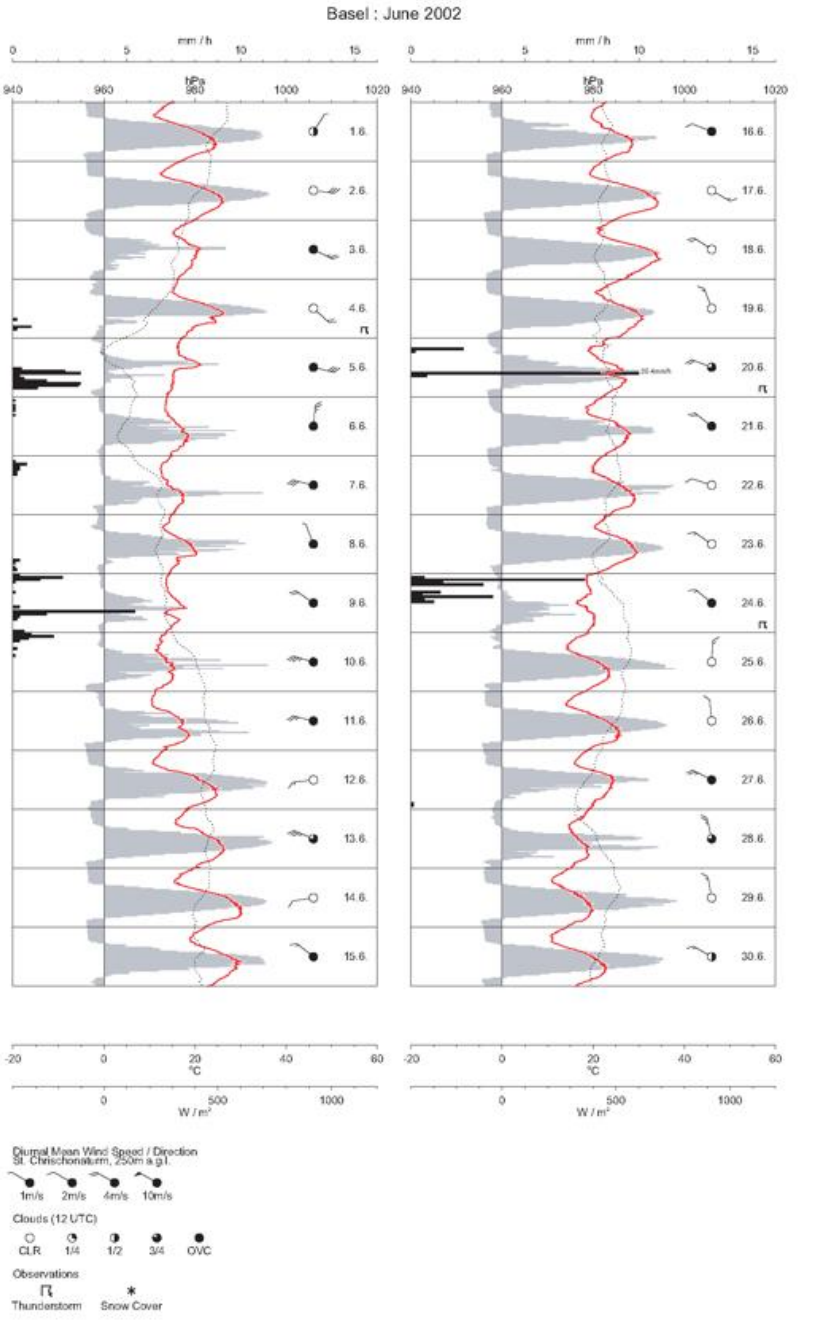
6.9 Appendices

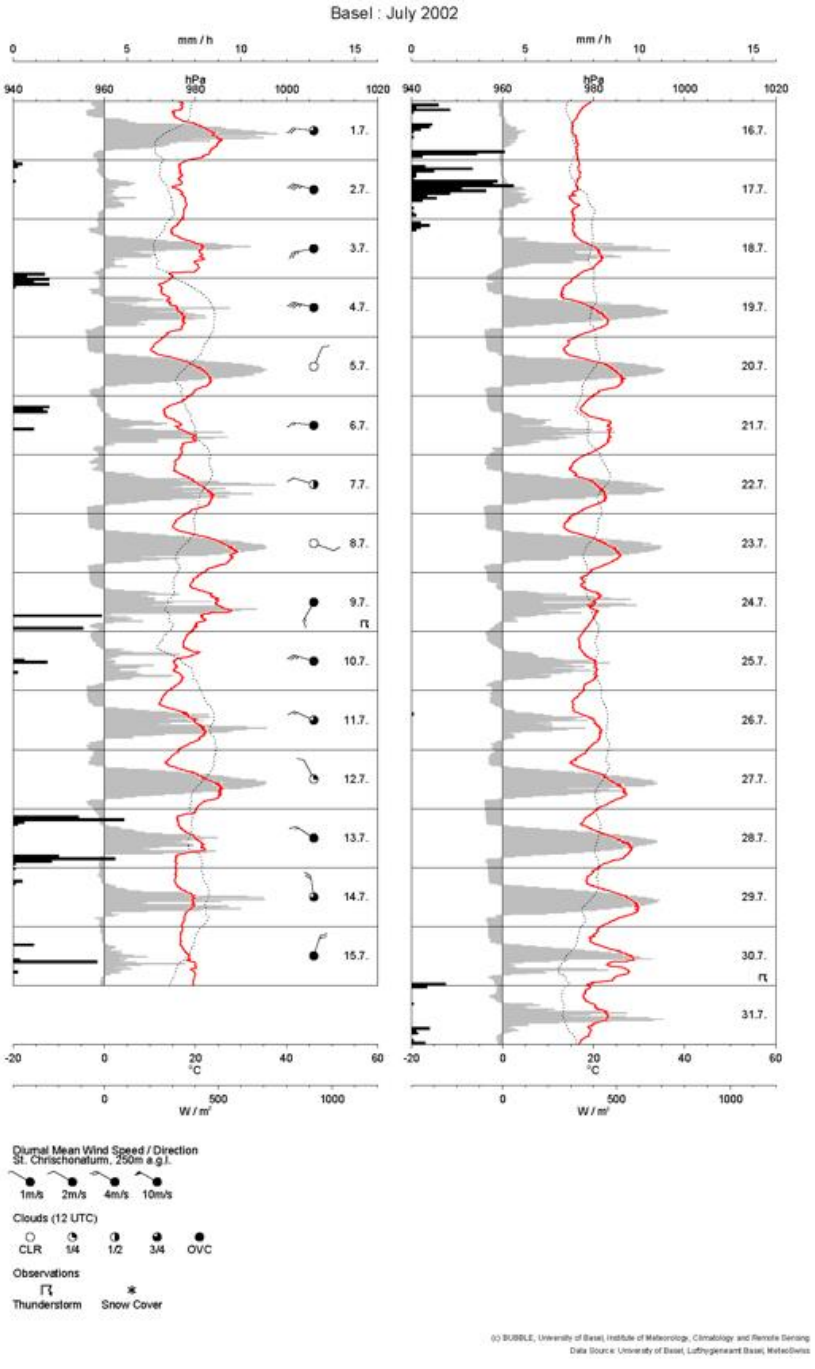
6.9.1 Bubble Measuring Stations

List of the measuring stations available during the BUBBLE IOP. The first letter of the station code correspond to the situation of the station (U for Urban area, S for Sub-Urban area and R for Rural area).

Code on map (Fig. 18)	Station Name	Height [mASL]
Rp6	Aesch Schlatthof	353
Se1	Allschwil	277
Rp7	Airport Basel-Mulhouse	
Sp2	Basel - Bumlihof	289
Sp3	Basel - Binningen (ANETZ, NABEL)	316
Up6	Basel - Feldbergstrasse	255
Ue4	Basel - Horburg	254
Re3	Basel - Lange Erlen	275
Up7	Basel - Leonhard	273
Ue5	Basel - Kleinhningen	265
Up8	Basel - Novartis Klybeck	255
Ue3	Basel - Messe	255
Up9	Basel - Novartis St.Johann	257
Up10	Basel - Roche	255
Ue2	Basel - Spalenring	278
Ue1	Basel- Sperrstrasse	255
Up11	Basel- St. Johann	260
Rp11	St. Chrischonaturm	490
Sp4	Dornach	325
Re4	Gempen	710
Re1	Grenzach	265
Sp5	Liestal LHA	320
Rp8	Oetlingen	450
Rp9	Pratteln Hardwasser	272
Sp6	Rheinfelden	285
Rp10	Schnenbuch	400
Sp7	Schweizerhalle	270
Re5	St. Louis	250
Re2	Village Neuf	240
Sp8	Weil am Rhein	250

6.9.2 Meteorological Situation during the IOP





(c) SUBBLE, University of Basel, Institute of Meteorology, Climatology and Remote Sensing
Data Source: University of Basel, Luftmygienearit Basel, MeteoSwiss

6.9.3 The Definition of Urban Categories for BEP

The urban properties as they are described in COSMO for the city of Basel

```
URBAN CATEGORY


!     Building parameters
! Ground thermal diffusivity [m^[m^2 s^-1]
      alag_u(1)=0.3e-06,
! Wall thermal diffusivity [m^2 s^-1]
      alaw_u(1)=0.2e-06,
! Roof thermal diffusivity [m^2 s^-1]
      alar_u(1)=0.2e-06,
! Specific heat of the ground material [J m^3 K^-1]
      csg_u(1)=1.4e+6,
! Specific heat of the wall material [J m^3 K^-1]
      csw_u(1)=0.2e+6,
! Specific heat of the roof material [J m^3 K^-1]
      csr_u(1)=0.2e+6,
! Temperature inside the buildings behind the wall [K]
      twini_u(1)=295.,
! Temperature inside the buildings behind the roof [K]
      trini_u(1)=295.,
!     Radiation parameters
! Albedo of the ground
      albg_u(1)=0.2,
! Albedo of the wall
      albw_u(1)=0.2,
! Albedo of the roof
      albr_u(1)=0.2,
! Emissivity of ground
      emg_u(1)=0.95,
! Emissivity of wall
```

```
      emw_u(1)=0.9,
! Emissivity of roof
      emr_u(1)=0.9,
!     Roughness parameters
! The ground's roughness length
      z0g_u(1)=0.0005,
! The roof's roughness length
      z0r_u(1)=0.0005,
!     Street configuration parameters
! Number of street direction
for each urban class
      nd_u(1)=2,
! Street direction [radian]
      drst_u(1,1)=0.7854, !45.*pi/180.
      drst_u(2,1)=2.3562, !135.*pi/180.
! Street width [m]
      ws_u(1,1)=15.,
      ws_u(2,1)=15.,
! Building width [m]
      bs_u(1,1)=22.,
      bs_u(2,1)=22.,
! Bulding's heights [m]
      h_b(1,1)=10.,
      h_b(2,1)=15.,
      h_b(3,1)=17.,
! The probability that a building has an height h_b
      d_b(1,1)=20.,
      d_b(2,1)=55.,
      d_b(3,1)=25.,
```

```
SUB-URBAN CATEGORY


!     Building parameters
! Ground thermal diffusivity [m^2 s^-1]
      alag_u(2)=0.47e-6,
! Wall thermal diffusivity [m^2 s^-1]
      alaw_u(2)=0.37e-06,
! Roof thermal diffusivity [m^2 s^-1]
      alar_u(2)=0.42e-06,
! Specific heat of the ground material [J m^3 K^-1]
      csg_u(2)=1.75e+6,
! Specific heat of the wall material [J m^3 K^-1]
      csw_u(2)=0.5e+6,
! Specific heat of the roof material [J m^3 K^-1]
      csr_u(2)=0.5e+6,
! Temperature inside the buildings behind the wall [K]
      twini_u(2)=293.,
! Temperature inside the buildings behind the roof [K]
      trini_u(2)=293.,
!     Radiation parameters
! Albedo of the ground
      albg_u(2)=0.2,
! Albedo of the wall
      albw_u(2)=0.2,
! Albedo of the roof
      albr_u(2)=0.2,
! Emissivity of ground
      emg_u(2)=0.95,
! Emissivity of wall
      emw_u(2)=0.9,
! Emissivity of roof
      emr_u(2)=0.9,
```

```
!     Roughness parameters
! The ground's roughness length
      z0g_u(2)=0.005,
! The roof's roughness length
      z0r_u(2)=0.005,
!     Street configuration parameters
! Number of street direction
for each urban class
      nd_u(2)=2,
! Street direction [radian]
      drst_u(1,2)=0.7854, !.45.*pi/180.
      drst_u(2,2)=2.3562, !135.*pi/180.
! Street width [m]
      ws_u(1,2)=25.,
      ws_u(2,2)=25.,
! Building width [m]
      bs_u(1,2)=17.,
      bs_u(2,2)=17.,
! Building's heights [m]
      h_b(2,2)=6.,
      h_b(3,2)=9.,
! The probability that a building has an height h_b
      d_b(1,2)=75.,
      d_b(2,2)=25.,
```

7 References

Ament, F. and Simmer, C., 2006. Improved Representation of Land-Surface Heterogeneity in a Non-Hydrostatic Numerical Weather Prediction Model. *Boundary-Layer Meteorology*, **121**, 153–174.

Colbeck, S.C., 1978. The physical aspects of water flow through snow. *Adv. Hydrosci.*, **11**, 165–206.

Heinemann, G. and Kerschgens, M., 2005. Comparison of methods for area-averaging surface energy fluxes over heterogeneous land surfaces using high-resolution non-hydrostatic simulations. *Int. J. Clim.*, **25**, 379–403.

Ritter, B., 2007. Einführung GME-Version 2.13. Änderungsmitteilung operationelles NWV-System, Deutscher Wetterdienst, Offenbach.

List of COSMO Newsletters and Technical Reports

(available for download from the COSMO Website: www.cosmo-model.org)

COSMO Newsletters

No. 1: February 2001.

No. 2: February 2002.

No. 3: February 2003.

No. 4: February 2004.

No. 5: April 2005.

No. 6: July 2006.

No. 7: April 2008; Proceedings from the 8th COSMO General Meeting in Bucharest, 2006.

No. 8: September 2008; Proceedings from the 9th COSMO General Meeting in Athens, 2007.

No. 9: December 2008.

No. 10: March 2010.

No. 11: April 2011.

No. 12: April 2012.

No. 13: April 2013.

No. 14: April 2014.

No. 15: July 2015.

COSMO Technical Reports

No. 1: Dmitrii Mironov and Matthias Raschendorfer (2001):
Evaluation of Empirical Parameters of the New LM Surface-Layer Parameterization Scheme. Results from Numerical Experiments Including the Soil Moisture Analysis.

No. 2: Reinhold Schrodin and Erdmann Heise (2001):
The Multi-Layer Version of the DWD Soil Model TERRA_LM.

No. 3: Günther Doms (2001):
A Scheme for Monotonic Numerical Diffusion in the LM.

No. 4: Hans-Joachim Herzog, Ursula Schubert, Gerd Vogel, Adelheid Fiedler and Roswitha Kirchner (2002):
LLM – the High-Resolving Nonhydrostatic Simulation Model in the DWD-Project LITFASS.
Part I: Modelling Technique and Simulation Method.

No. 5: Jean-Marie Bettems (2002):
EUCOS Impact Study Using the Limited-Area Non-Hydrostatic NWP Model in Operational Use at MeteoSwiss.

No. 6: Heinz-Werner Bitzer and Jürgen Steppeler (2004):
Documentation of the Z-Coordinate Dynamical Core of LM.

No. 7: Hans-Joachim Herzog, Almut Gassmann (2005):
Lorenz- and Charney-Phillips vertical grid experimentation using a compressible nonhydrostatic toy-model relevant to the fast-mode part of the 'Lokal-Modell'.

No. 8: Chiara Marsigli, Andrea Montani, Tiziana Paccagnella, Davide Sacchetti, André Walser, Marco Arpagaus, Thomas Schumann (2005):
Evaluation of the Performance of the COSMO-LEPS System.

No. 9: Erdmann Heise, Bodo Ritter, Reinhold Schrodin (2006):
Operational Implementation of the Multilayer Soil Model.

No. 10: M.D. Tsyrulnikov (2007):
Is the particle filtering approach appropriate for meso-scale data assimilation ?

No. 11: Dmitrii V. Mironov (2008):
Parameterization of Lakes in Numerical Weather Prediction. Description of a Lake Model.

No. 12: Adriano Raspanti (2009):
COSMO Priority Project "VERification System Unified Survey" (VERSUS): Final Report.

No. 13: Chiara Marsigli (2009):
COSMO Priority Project "Short Range Ensemble Prediction System" (SREPS): Final Report.

No. 14: Michael Baldauf (2009):
COSMO Priority Project "Further Developments of the Runge-Kutta Time Integration Scheme" (RK): Final Report.

No. 15: Silke Dierer (2009):
COSMO Priority Project "Tackle deficiencies in quantitative precipitation forecast" (QPF): Final Report.

No. 16: Pierre Eckert (2009):
COSMO Priority Project "INTERP": Final Report.

No. 17: D. Leuenberger, M. Stoll and A. Roches (2010):
Description of some convective indices implemented in the COSMO model.

No. 18: Daniel Leuenberger (2010):
Statistical analysis of high-resolution COSMO Ensemble forecasts in view of Data Assimilation.

No. 19: A. Montani, D. Cesari, C. Marsigli, T. Paccagnella (2010):
Seven years of activity in the field of mesoscale ensemble forecasting by the COSMO–LEPS system: main achievements and open challenges.

No. 20: A. Roches, O. Fuhrer (2012):
Tracer module in the COSMO model.

No. 21: Michael Baldauf (2013):
A new fast-waves solver for the Runge-Kutta dynamical core.

No. 22: C. Marsigli, T. Diomede, A. Montani, T. Paccagnella, P. Louka, F. Gofa, A. Corigliano (2013):
The CONSENS Priority Project.

No. 23: M. Baldauf, O. Fuhrer, M. J. Kurowski, G. de Morsier, M. Müllner, Z. P. Piotrowski, B. Rosa, P. L. Vitagliano, D. Wójcik, M. Ziemiański (2013):
The COSMO Priority Project 'Conservative Dynamical Core' Final Report.

No. 24: A. K. Miltenberger, A. Roches, S. Pfahl, H. Wernli (2014):
Online Trajectory Module in COSMO: a short user guide.

No. 25: P. Khain, I. Carmona, A. Voudouri, E. Avgoustoglou, J.-M. Bettems, F. Grazzini (2015):
The Proof of the Parameters Calibration Method: CALMO Progress Report.

No. 26: D. Mironov, E. Machulskaya, B. Szintai, M. Raschendorfer, V. Perov, M. Chumakov, E. Avgoustoglou (2015):
The COSMO Priority Project 'UTCS' Final Report.

COSMO Technical Reports

Issues of the COSMO Technical Reports series are published by the *COnsortium for Small-scale MOdelling* at non-regular intervals. COSMO is a European group for numerical weather prediction with participating meteorological services from Germany (DWD, AWGeophys), Greece (HNMS), Italy (USAM, ARPA-SIMC, ARPA Piemonte), Switzerland (MeteoSwiss), Poland (IMGW), Romania (NMA) and Russia (RHM). The general goal is to develop, improve and maintain a non-hydrostatic limited area modelling system to be used for both operational and research applications by the members of COSMO. This system is initially based on the COSMO-Model (previously known as LM) of DWD with its corresponding data assimilation system.

The Technical Reports are intended

- for scientific contributions and a documentation of research activities,
- to present and discuss results obtained from the model system,
- to present and discuss verification results and interpretation methods,
- for a documentation of technical changes to the model system,
- to give an overview of new components of the model system.

The purpose of these reports is to communicate results, changes and progress related to the LM model system relatively fast within the COSMO consortium, and also to inform other NWP groups on our current research activities. In this way the discussion on a specific topic can be stimulated at an early stage. In order to publish a report very soon after the completion of the manuscript, we have decided to omit a thorough reviewing procedure and only a rough check is done by the editors and a third reviewer. We apologize for typographical and other errors or inconsistencies which may still be present.

At present, the Technical Reports are available for download from the COSMO web site (www.cosmo-model.org). If required, the member meteorological centres can produce hard-copies by their own for distribution within their service. All members of the consortium will be informed about new issues by email.

For any comments and questions, please contact the editor:

Massimo Milelli
Massimo.Milelli@arpa.piemonte.it

Consortium

for

Small-Scale Modelling

Technical Report No. 26

The COSMO Priority Project
'UTCS'
Final Report

June 2015

DOI: 10.5676/DWD_pub/nwv/cosmo-tr_26

Deutscher Wetterdienst
MeteoSwiss
Ufficio Generale Spazio Aereo e Meteorologia
ΕΘΝΙΚΗ ΜΕΤΕΩΡΟΛΟΓΙΚΗ ΥΠΗΡΕΣΙΑ
Instytucie Meteorogii i Gospodarki Wodnej
Administratia Nationala de Meteorologie
ROSHYDROMET
Agenzia Regionale per la Protezione Ambientale del Piemonte
Agenzia Regionale per la Protezione Ambientale dell'Emilia-Romagna
Centro Italiano Ricerche Aerospaziali
Amt für GeoInformationswesen der Bundeswehr

www.cosmo-model.org

Editor: Massimo Milelli, ARPA Piemonte

The COSMO Priority Project

'UTCS'

Final Report

Project participants:

D. Mironov *, E. Machulskaya, B. Szintai, M. Raschendorfer,

V. Perov, M. Chumakov, E. Avgoustoglou

* corresponding author:
Dr. Dmitrii Mironov
Deutscher Wetterdienst
Frankfurter Str. 135
63067 Offenbach am Main
Germany

1 Introduction **3**

2 Development and testing of the TKE-Scalar Variance mixing scheme for the COSMO model (Ekaterina Machulskaya and Dmitrii Mironov) **3**

3 Comprehensive testing and further development of the current COSMO-model turbulence scheme, including the surface-layer transfer scheme **5**

3.1 Comprehensive testing of the COSMO-model TKE turbulence scheme (Balazs Szintai) 5

3.2 Detailed investigation of diurnal cycle of the near surface quantities, revision of the surface-layer transfer formulation (Matthias Raschendorfer) 6

3.3 Generalization of non-local formulation of the turbulence length scale to account for moist processes (Veniamin Perov and Mikhail Chumakov) 7

3.4 Development of a unified turbulence scheme for COSMO, COSMO-SCM and ICON (Matthias Raschendorfer) 7

4 Evaluation of SGS cloud schemes against satellite data and data from measurements in the surface air layer (Euripides Avgoustoglou) **10**

5 References **12**

1 Introduction

The PP UTCS was completed in September 2012. The interim reports of the project participants are available at the COSMO web page. A summary of the project results as of September 2012 are given below. Results from the efforts, that are initiated within the framework of the PP UTCS but are completed (or still ongoing) past the official end of the project in September 2012, are reported to COSMO through the Working Group 3a. In what follows, the authors of the respective section are given in parentheses.

2 Development and testing of the TKE-Scalar Variance mixing scheme for the COSMO model (Ekaterina Machulskaya and Dmitrii Mironov)

The TKE-Scalar Variance (TKESV) scheme for the COSMO model is developed. The scheme carries prognostic equations for the turbulence kinetic energy (TKE), the liquid water potential temperature variance, the total water specific humidity variance, and the temperature-humidity covariance. These prognostic second-moment equations include the turbulent diffusion terms (divergence of the velocity-velocity and velocity-scalar triple correlations) that are parameterized through the down-gradient approximations. The other second-order moments, viz., the Reynolds stress and the scalar fluxes, are determined through the algebraic diagnostic expressions. The expressions for the scalar fluxes include non-gradient terms that are parameterized with due regard for the turbulence anisotropy. The formulation for the turbulence length (time) scale accounts for the effect of static stability. Recall that within the framework of the current COSMO-model turbulence scheme (one-equation TKE scheme), the time-rate-of-change and the turbulent diffusion terms are retained in the TKE equation only, whereas all other second-order moments, including scalar variances, are determined from the algebraic diagnostic expressions. The expressions for the scalar fluxes do not include non-gradient terms (among other things, this does not allow for up-gradient scalar transfer), and a Blackadar-type turbulence length scale formulation independent of static stability is used.

The TKESV scheme is tested through single-column numerical experiments. Results of simulations with the TKESV and the TKE schemes are compared with observational and numerical large-eddy simulation (LES) data from dry convective planetary boundary layer (PBL) and from cloudy PBLs (BOMEX and ARM shallow cumulus test cases and DYCOMS-II stratocumulus case). The TKESV scheme clearly outperforms the TKE scheme in dry convective PBL. Vertical profiles of the scalar variances and of the TKE computed with the TKESV scheme show better agreement with data. The PBL is better mixed with respect to potential temperature. An up-gradient heat transfer that is known to occur in the upper part of the dry convectively-mixed layer is well reproduced by the TKESV scheme. This is not possible with the TKE scheme, where the down-gradient formulations for the scalar fluxes are used. For cloudy PBLs, the application of the TKESV scheme leads to a better prediction of the scalar variances and TKE and to slight improvements with respect to the vertical buoyancy flux and the mean temperature and humidity. Both schemes tend to overestimate fractional cloud cover in the cumulus-topped PBL. This error is attributed primarily to the shortcoming of quasi-Gaussian statistical cloud parameterization scheme used by both TKESV and TKE schemes to determine fractional cloudiness (which in term strongly affects the buoyancy flux). A detailed analysis of simulation results suggests that a quasi-Gaussian cloud scheme is unable to accurately describe fractional cloudiness in the

cumulus regime even though the characteristics of turbulence (first of all, scalar variances that serve as input to the cloud scheme) may be predicted perfectly. A somewhat more sophisticated cloud scheme that accounts of non-Gaussian effects is required.

The TKESV scheme is implemented into the COSMO model and tested through a series of parallel experiments including the entire COSMO-model data assimilation cycle. Both COSMO-EU and COSMO-DE model configurations operational at DWD are used (the horizontal mesh size of these configurations is ca. 7 km and ca. 2.8 km, respectively). Results from parallel experiments with the TKESV scheme performed to date look promising. Verification of results against observational data indicates improvements as to some scores, e.g. fractional cloud cover and 2m temperature and humidity. Further analysis of the new TKESV scheme performance within COSMO is underway.

Reduced minimum (background) diffusion coefficients of 0.1 m^2/s are used in some parallel experiments. Recall that in the current operational COSMO-model configurations a large value of 1 m^2/s is utilized for both momentum and scalars, which is often detrimental for stably stratified boundary layers and for the inversions capping convective boundary layers (this is a long-standing problem of the COSMO model). It is worth noting that some improvements in terms of verification scores can be achieved by just reducing the minimum diffusion coefficients, without the use of the new TKESV scheme. However, the application of the TKESV scheme and the reduced minimum diffusion coefficients leads to a better overall COSMO-model performance as compared to the model configuration with the reduced coefficients only. Furthermore, minimum diffusion coefficients are insensitive to the mixing regime. That is, a reduction of minimum diffusion coefficients is desirable in stably-stratified parts of the flow, but relatively large diffusion coefficients may be needed in other parts of the flow as a (unphysical) proxy for unaccounted mixing processes. This is impossible to achieve with constant minimum diffusion coefficients. On the contrary, the TKESV scheme is selective in terms of mixing regimes. Importantly, it does not produce excessive unphysical mixing in the stably-stratified PBL and in the capping inversion. A combination of the TKESV scheme and reduced minimum diffusion coefficients is a promising option for the COSMO model.

As the results from the LES study of Mironov and Sullivan (2010) demonstrate, the stably-stratified PBL should be parameterized with due regard for the heterogeneity of the underlying surface (first of all, with respect to the temperature). This can be achieved through the application of a tile approach to compute surface fluxes. The use of tiled surface scheme allows to account for the enhanced mixing in the SBL over heterogeneous surfaces in a physically plausible way (cf. large background diffusivity discussed above), and to prevent the PBL turbulence from dying out entirely as the (grid-box mean) static stability increases. The idea is successfully tested through single-column numerical experiments. The number of tiles should not necessarily be large (otherwise the tiled scheme becomes computationally expensive) but the tiles with the largest difference in terms of thermal inertia should be accounted for. In this regard, the treatment of the sub-grid scale (SGS) water bodies is crucial. As the thermal inertia of water is (much) larger than the inertia of most other land types, the inclusion of SGS water allows to maintain the temperature difference between tiles and hence to account for the enhanced mixing due to surface heterogeneity. The implementation of tile approach into the COSMO model is underway at DWD, where the mosaic approach implemented by Felix Ament is taken as a starting point. A parallel COSMO-EU experiment with a two-tile surface scheme is performed, where a land tile with the land-use type the same as in the operational COSMO model and inland water tile (lake) are considered in each COSMO-model grid box. The surface temperature of the inland-water tile is computed with the lake parameterization scheme FLake. Recall that in the operational COSMO configurations, only the grid boxes with the inland-water fraction in excess of 0.5 are treated as the

inland-water-type grid boxes whereas the SGS water bodies with fractional area coverage less than 0.5 are entirely ignored. Results from the parallel experiment indicate some improvements of the COSMO-model performance, e.g. warm bias of the near-surface temperature during summer is slightly reduced.

In summary, the TKESV scheme holds considerable promise in terms of the improvement of the COSMO-model performance. The TKESV scheme is currently not coded as a separate module. Changes associated with the TKESV scheme are implemented into the current COSMO-model TKE scheme developed by Matthias Raschendorfer. Since massive modifications to the current TKE scheme (many of them being of technical and re-organizational order) are prepared by Matthias Raschendorfer and should soon be included into the official COSMO code, modifications associated with the TKESV scheme will be implemented into the COSMO version following the version with Matthias changes. The implementation process will be controlled by the COSMO source code administrator. Every effort will be made to complete the implementation and testing of the tile approach. To this end, the software to generate external-parameter fields (e.g. the field of lake depth) should be modified. This may require considerable effort and take much time. A deadline for the tile approach implementation cannot be set at the time being.

A brief outline of the TKESV scheme, a discussion of the scheme performance in various clear and cloudy boundary-layer regimes as revealed by off-line single-column tests, details of the implementation of the new scheme into COSMO, and some results from numerical experiments with the full-edged COSMO model are given in Machulskaya and Mironov (2013). Documentation of the scheme is in preparation.

3 Comprehensive testing and further development of the current COSMO-model turbulence scheme, including the surface-layer transfer scheme

3.1 Comprehensive testing of the COSMO-model TKE turbulence scheme (Balazs Szintai)

The performance of the COSMO model was evaluated in the Planetary Boundary Layer for different conditions. Next to the mean prognostic variables, the turbulence characteristics of the model were also verified. The following conclusions can be drawn from the experiments.

It has been shown that the COSMO model is able to reproduce the main evolution of the boundary layer in dry convective situations with the operational parameter setting if the external parameters are realistic and if the initial conditions are adequate. However, it has been found that the COSMO model tends to simulate a too moist and too cold PBL, with shallower PBL heights than observed. During stable conditions the operational parameter setting has to be modified significantly (e.g. the minimum diffusion coefficient) to obtain a good model performance.

The reasons for the inadequate temperature and humidity profiles in convective conditions have been investigated with the component testing approach. The budget terms in the TKE equation have been validated separately against LES data and turbulence measurements. The turbulent transport term (third order moment) has been found to be significantly underestimated by the COSMO model. This results in inaccurate TKE profiles and thus missing entrainment fluxes at the top of the PBL. A solution to increase the TKE transport in the PBL was proposed, resulting in a more realistic TKE profile and higher entrainment fluxes.

This modification of the turbulence scheme has also been tested in a parallel experiment over a one-month period. Results show only minor impacts on the operationally verified fields.

The impact of the horizontal resolution on the simulation results has also been studied. It was shown that the three-dimensional structure of the PBL is significantly different in the 1 km simulation than in the 2.2 km run, and the former shows great sensitivity towards the horizontal diffusion. The standard isotropic three-dimensional turbulence scheme was compared to the fourth-order numerical diffusion and to the newly implemented first-order Smagorinsky closure. It can be concluded that without horizontal diffusion the 1 km simulation exhibits unrealistically strong waves in the PBL. Based on these findings, it is recommended to use the three-dimensional turbulent diffusion scheme with horizontal mesh sizes on the order of 1 km, because it is more physically based than the fourth-order numerical filter. For flat convective conditions with very low horizontal wind field deformation the Smagorinsky closure in its classical formulation generates too low mixing, however, the extension of the scheme to include the horizontal shear of vertical wind might be beneficial for these cases.

3.2 Detailed investigation of diurnal cycle of the near surface quantities, revision of the surface-layer transfer formulation (Matthias Raschendorfer)

A final COSMO-SC (single column) version adapted to COSMO version 4.24 has been composed including the recent running developments of Task 2.1 and 2.3 and being ready for component testing.

The new COSMO-SC version includes a couple of bug fixes and extensions and the possibility of forcing with measured surface fluxes, which caused related modifications not only in the SC framework and the turbulence code (MODULE src_turbdiff) but also in that for soil processes (MODULE src_soil_multlay, with particular difficulties in relation to forcing the soil moisture calculation with measured evaporation) and in that for implicit vertical diffusion (MODULE slow_tendencies, which is going to become obsolete due to the development of a new universal code, see Task 2.3).

Some component tests have been performed with COSMO-SC attendant to the current model development.

A revised formulation of the complete transfer resistance in the surface-to-atmosphere transfer scheme has been developed, but not yet implemented. However as a first step, the code structure has been modified in order to allow for an easier implementation of the new formulation. As a second step an adopted profile function for stable stratification has been implemented in the current test version as an option that needs to be tested soon.

Future plans for a pending priority task (ConSAT):

- detailed investigation of the problems with daily cycle of near surface variables using measurements and COSMO-SC;
- implementation and verification of the full revised transfer formulation.

Future plans for later years:

- implementation of a canopy/skin layer.

3.3 Generalization of non-local formulation of the turbulence length scale to account for moist processes (Veniamin Perov and Mikhail Chumakov)

The new formulation for turbulence length scale based on the Bougeault and Lacarrere (BL89) proposal have been developed and implemented in 3-D COSMO model. We use a postulate proposed by BL89 that for each level in the atmosphere turbulence length scale l can be related to the distance that a parcel of originating from this level and having an initial kinetic energy equal to the mean TKE of the layer, can travel upward and downward before being stopped by buoyancy effects. More precisely, if we define l_up and l_down then l must be related to some average value between l_up and l_down. The main advantage of the method is to allow for remote effects of stable zones on the definition of the turbulence length scale. For instance, using l_up, the vertical depth of an unstable layer capped by a strong inversion is automatically selected as the length scale for turbulence.

The non-local length scale algorithm was generalized for cloudy boundary layers, in order to consider the influence of moist processes and phase transition of moisture on the scale of turbulence. The new algorithm uses a turbulent kinetic energy equation in conservative variables for non-precipitating processes. The new algorithm was tested for stratocumulus-capped boundary layers. From the results we can conclude that the new mixing length gives more realistic results, because the reference mixing length formulation gives an anomalously high dissipation inside the cloud, near the inversion.

The new algorithm was implemented in the module TURBDIFF of COSMO. Convective summer cases were analysed. Firstly, we have found a significant difference in change with height of a local (reference scheme) and nonlocal (new scheme) turbulence length scale. The nonlocal l results in a strong damping of turbulence as soon as stable conditions (inversion at the top of convective layer) are encountered, while local l results a monotonic increase with height. The results suggest that boundary layer (BL) with reference length scale underestimates surface temperature T_s and generate a colder and shallow convective mixed layer. The BL scheme with the new length scale yields better T_s and improved vertical profiles of temperature and humidity. Thus, the height of the boundary layer was 20 percent higher, the temperature of convective layer has increased by 1.5-2.0 °C. In conclusion, we assume that the new mixing length algorithm is preferred when the turbulent structure of atmospheric boundary layer is not known in advance.

Proposals for the future work:

- Use the new algorithm for cases with a stable boundary layer. The goal is to reduce a negative bias of T2m (2-4 °C), which is often observed in COSMO-RU in winter;
- Develop a new boundary-layer scheme over mountainous terrain.

3.4 Development of a unified turbulence scheme for COSMO, COSMO-SCM and ICON (Matthias Raschendorfer)

The code of MODULE src_turbdiff has been revised, reorganized and reformulated in large parts in order to achieve a better modularization, as well as a numerically and conceptually better representation of the whole system of 2-nd order equations, including sub grid scale condensation, TKE diffusion and the integration of scale interaction. A special focus was turned on artificial security measures to guarantee realizability, that is to avoid singularities. A further intention was to unify the formulation of implicit vertical diffusion and to gain

more flexibility with respect to grid structure, time step organization and so on, in order to use the MODULE also in ICON. Some modifications have also been done in order to allow a better vectorization of the code.

A lot of modifications refer to the solution of second order equations (TKE equation and stability functions) as well as to the description of moist physics. Each of both tasks is now treated as a specific SUBROUTINE that is called from both, the turbulence model (turbdiff) and the scheme for surface-to-atmosphere-transfer (turbtran). In the prior code, for both sub-models these tasks are formulated explicitly, each with specific modifications.

The positive definite solution of TKE equation has been modified, allowing less serious restrictions for realizability. These restrictions can now be selected and modified by NAMELIST-input in order to test their effect in detail, in particular for stable stratification.

Numerics of solving for the stability functions have been changed, introducing a matrix preconditioning and the possibility to better control how far TKE can be apart from equilibrium without generating singularities in the solution.

Since all aspects of moist physics, in particular the calculation of conservative variables and the local saturation adjustment, are treated now in a single SUBROUTINE, these aspects are now treated consistently in turbdiff and turbtran, and - since conservative variables and not the model variables should be interpolated onto the 2m level - are applied even to 2m-diagnostics. This modularization further allows for a better control in case of modifications Thus, the mixed water-ice phase that already exists in an earlier sub version of the code (used by E. Avgoustoglou) can now be implemented here again with less modification effort.

Despite their formulation based on conservative scalar variables, sub grid scale variations of condensation need to be considered in our turbulence scheme as well, not at least because the buoyancy source term for TKE is dependent on it. By means of our statistical saturation adjustment assuming a Gaussian distribution function of local oversaturation this issue has already been implemented before. However, due to condensation coupling the turbulent vertical fluxes of scalar model variables are linear combinations of the respective fluxes in conserved variables and hence have no strict flux gradient representation being a prerequisite of our implicit solution for vertical diffusion. Although analytical inspection showed that we can apply vertical diffusion simply with the flux gradient form as long as a grid scale saturation adjustment is applied at the end of each time step, we invented a general method of gradient correction in order to gain a 3-diagonal linear system for the implicit diffusion equation even in the case of non gradient fluxes. This case had to be treated by an explicit (moist) diffusion correction before. As an alternative it is also possible to apply vertical diffusion to the conserved thermodynamic variables followed by subsequent transformation of the updated variables into the model variables by means of statistical saturation adjustment. So far it is a question of model configuration and numerical accuracy or efficiency what option should be used.

The TKE diffusion is now calculated by means of a common SUBROUTINE for semi-implicit vertical diffusion applicable to all variables to be diffused including passive tracers. This routine contains options as to how to consider explicit tendencies or corrections of vertical gradients, where the latter option enables expressing non gradient fluxes by effective vertical gradients.

This new scheme for semi-implicit vertical diffusion is going to substitute the current code for that purpose being a part of the numerical core in COSMO, where similar code is written explicitly for each diffused variable, in particular for each passive tracer. The lower boundary condition can be chosen by NAMELIST input (either concentration condition or flux

condition), and in case of a flux condition, the surface fluxes can be specified. Otherwise the resulting surface flux has an implicit part as well depending on the degree of implicitness.

The current representation of the circulation term, still expressed in terms of a flux divergence, is treated as a gradient correction as well, avoiding an extra explicit formulation for it. Nevertheless, this current representation of the circulation term is going to be changed into a thermal SSO term, what unfortunately had to be delayed again.

All the above mentioned development is present in a still private test version based on COSMO version 4.24. Due to the quite fundamental modifications of the code, it was not yet possible to test the code sufficiently and to provide an optimal parameter setup. Nevertheless, the code is already running and provides reasonable results. But final tuning and consolidation as well as formal adoptions to the official COSMO version may take some more time.

A stability correction of turbulent master length scale according to Deardorff has been implemented into the official code, which might currently be missing.

In order to gain a theoretical framework for a comprehensive and consistent parameterization of sub-grid scale processes, a concept of scale separation has been developed and described in an internal still growing document. This concept takes into account the fact that generally valid closure assumptions cannot exist in principle and that consequently the full generality of sub grid scale processes needs to be split somehow into separated regimes valid for the application of specific closure assumptions. In this sense turbulence is a regime defined by the fundamental closure assumptions allowing a quite consistent solution of the 2-nd order budget equations. Since the separator has been related to the filter operator associated with discretization, a separated treatment of turbulence automatically generates additional interaction terms in the 2-nd order equations for turbulence that formally will make the scheme applicable, if non turbulent sub-grid scale processes are present as well and may be of particular importance when a solution without interaction terms is not possible and thus requires artificial manipulation (like in the strongly stable boundary layer) for the lack of missing physics.

According to the concept of scale separation three scale interaction terms have been introduced into our prognostic TKE equation, representing a transfer of sub grid scale kinetic energy towards turbulent scales by the action of shear generated by related non-turbulent sub-grid scale flow patterns. These are production terms by SSO wakes, convective plumes, and separated horizontal shear eddies. The SSO term is expressed using the SSO tendencies of momentum and the convection term is buoyant convective kinetic energy production derived form the convection scheme (Tiedke and shallow convection). The horizontal shear term is the horizontal shear production with respect to a special non isotropic length scale. All the 3 additional terms are based on an assumed equilibrium of production and scale transfer being treated like a dissipation term. They are implemented in the official code and can be switched on by NAMELIST input. At DWD the SSO source term has been already switched on in the operational code, the others need to be verified. However, these source terms are already used as important predictors of atmospheric turbulence for aviation purpose. Their effect is being tested in more detail by our aviation department using the package TMOS (turbulence model output statistics) developed during an internal DWD project parallel to UTCS.

A crucial problem of an UTCS is the consistent representation of sub-grid scale variation in terms of moist physics. In the framework of a single set of 2-nd order equations this can be tried by means of a statistical saturation adjustment, as we do it in our moist turbulence scheme, at which this procedure requires the existence of saturation equilibrium and the

knowledge of the distribution function of oversaturation. However, as far as the whole sub grid scale variability is represented by each of the governing statistical moments, the ice phase and precipitation cannot be neglected, in particular if deep convection is included. Since both of these condensates are known not to be in saturation equilibrium and since the overall distribution functions may be rather arbitrary, attempts in that direction are very likely to fail. Thus some analytical work has been done in order to treat this problem in the framework of scale separation, what is necessary anyway according to the previous arguments. The main result of this analysis is the finding that a modified mass flux approach can be a solution, if simplified averaged budget equations are considered for convective sub-domains. Considering the necessary construction constraints for these sub-domains, estimates of their volume fraction can be provided and the full model microphysics can be applied to these sub domains. In this approach turbulence is assumed to be either a sub grid scale process with respect to the sub domains maintaining lateral mixing, or it provides initial convective sub domains. Thus turbulence and convection would really be interacting and the governing scales of convection would develop by the governing physics. Finally a separation to resolved scales can be formulated for convection as well. The concept has been worked out only in a manuscript yet and an excerpt of it has been compiled as PPT file.

Future plans for related work after the PP UTCS:

- generation of an official well-tested code valid for COSMO, SCM and ICON, ready for operational forecast, containing all the development present in the private test code being active, in particular the new routine for vertical diffusion;
- finding an optimal mode for vertical diffusion with respect to the lower boundary condition, the consideration of explicit tendencies and of moist corrections;
- switching on the implemented scale interaction terms after verification against SYNOP data (operational verification).

Future plans for a medium range prospect:

- reformulation of the current circulation term to be a thermal SSO source term for TKE;
- implementation of SSO/roughness layer terms based on an extended boundary layer approximation in a vertically resolved roughness layer;
- consideration of missing mixing by non-turbulent sub-grid scale motions themselves (in case of SSO wakes and horizontal shear eddes).

Future plans for later years:

- implementation of a scale separated mass-flux convection interacting with turbulence and providing volume fractions of convective sub-domains (final step of a scale separated UTCS).

4 Evaluation of SGS cloud schemes against satellite data and data from measurements in the surface air layer (Euripides Avgoustoglou)

COSMO model uses operationally two sub-grid schemes for stratus clouds. A semi-empirical one based on relative humidity used in the radiation module, denoted as RH scheme, and

a parameterizable statistical one used in the turbulence module, denoted as SGSLI scheme. The main objective of the work was to show whether SGSLI could be operationally implemented in the radiation module.

Although the task looked straightforward, several issues needed to be settled as the work was progressing.

The main issues of consideration were:

- the availability of a code version that could properly include the cloud-ice content into the statistical scheme;
- the proper boundary conditions;
- the availability and comparison with real time data;
- the selection of the test cases.

The test version was provided by Matthias Raschendorfer and is based on COSMO version 4.6. Although this version is relatively old, any comparative tests that were made with newer versions did not change the diagnostics.

The domain was centred around the Hellenic geographical area characterized by equal sea and land partitions. This choice gives rise to the strong mixing of continental as well as marine clouds which is one of the most challenging features regarding the operational use of numerical weather prediction models by the Hellenic Meteorological Service.

The choice of the initial and boundary conditions was considered an issue because the main synoptic features are carried by the global model used. Over the first diagnostic tests, GME as well as ECMWF forecasts were used without any important differences between them. However our main evaluations were delivered through GME analysis mode over 3-hour intervals of 36 or 48-hour spans provided by DWD.

The default parameterization of the SGSLI scheme was mainly used, however several other diagnostics were performed either through different parameterization of SGSLI or mixing of SGSLI and RH.

The main strategy regarding the choice of the considered test cases was to have synoptic conditions that favour stratus clouds over the domain under consideration without any significant convection and over the full seasonal span.

Over the fist stages of the project, direct heuristic comparisons of the model total cloud cover with MSG satellite images at the 10.8 and 8.7 micron channels were performed. The main outcome of these comparisons was that the implementation of the SGSLI scheme was realistic but not conclusive. Further comparisons were made regarding 2-meter minimum and maximum daily temperatures as well as daily 2-m temperature variations for about 50 synoptic Hellenic meteorological stations. The revealed feature was that the 2-meter minimum temperature was better simulated when the SGSLI scheme was implemented in the radiation module while the 2-meter maximum temperature was better simulated when the default RH scheme was implemented in the radiation module.

An important boost towards the relative impact of the cloud schemes came from a close comparison of artificial satellite images provided by the model with the real ones provided directly at the Hellenic Meteorological Service by MSG. These comparisons were accomplished via the CineSat software and became possible by the Remote Sensing Division of the Hellenic National Meteorological Service that provided access to the available tools and

database structure in order to create the necessary look-up tables and perform the statistics. It became clear from these direct comparisons that the implementation of the SGSLI scheme leads to an underestimation of low cloud cover by the model in contrast to the implementation of the default RH scheme. However, another important feature was that the implementation of the SGSLI scheme leads to a relatively better simulation for medium cloud-cover. Nevertheless, the total cloud cover is better estimated by the default relative humidity scheme, and so are the radiation temperatures in the 10.8, 3.9, 6.2 and 7.3 μm.

Although the SGSLI scheme cannot in its present form replace the RH scheme in the radiation module, it is an important asset to COSMO model that can be used as a reference to support the ongoing research in this crucial area of atmospheric physics.

A further investigation of the cloud schemes associated with different COSMO parameterizations in an updated model version (like changing the default values of vertical turbulent diffusion coefficients) in the fashion of QPF Project could be considered as an extension to the project.

5 References

Avgoustoglou, E., Tzeferi, T. and Papageorgiou, I., 2006. Implementations of the statistical cloud scheme option: preliminary tetst. *COSMO Newsletter*, **6**, 88–93.

Avgoustoglou, E., 2011. Various implementations of a statistical cloud scheme in COSMO model. *COSMO Newsletter*, **11**, 61–68.

Avgoustoglou, E., 2012. A note on the direct comparison of synthetic satellite images from COSMO model with MSG products. *COSMO Newsletter*, **12**, 52–55.

Avgoustoglou, E., 2013. On the direct comparison of COSMO model sub-grid stratiform cloud schemes with satellite images. *COSMO Newsletter*, **13**, 34–38.

Bougeault, P. and Lacarrere, P., 1989. Parameterization of orography-induced turbulence in a mesobeta-scale model. *Monthly Weather Review*, **117(8)**, 1872–1890.

Machulskaya, E. and Mironov, D., 2013. Implementation of TKE-Scalar Variance mixing scheme into COSMO. *COSMO Newsletter*, **13**, 25–33.

Mironov, D. and Sullivan, P., 2010. Effect of horizontal surface temperature heterogeneity on turbulent mixing in the stably stratified atmospheric boundary layer. *19th Conference on Boundary Layer and Turbulence, Keystone, CO.*

Szintai, B. and Kaufmann, P., 2008. TKE as a measure of turbulence. *COSMO Newsletter*, **8**, 2–9.

Szintai, B. and Fuhrer, O., 2008. Component testing of the COSMO model's turbulent diusion scheme. *COSMO Newsletter*, **9**, 37–41.

Szintai, B., 2010. Improving the Turbulence Coupling between High Resolution Numerical Weather Prediction Models and Lagrangian Particle Dispersion Models. *Ph.D. Thesis, École Polytechnique Fédérale de Lausanne, Lausanne, Switzerland*, 142 pp.

List of COSMO Newsletters and Technical Reports

(available for download from the COSMO Website: www.cosmo-model.org)

COSMO Newsletters

No. 1: February 2001.

No. 2: February 2002.

No. 3: February 2003.

No. 4: February 2004.

No. 5: April 2005.

No. 6: July 2006.

No. 7: April 2008; Proceedings from the 8th COSMO General Meeting in Bucharest, 2006.

No. 8: September 2008; Proceedings from the 9th COSMO General Meeting in Athens, 2007.

No. 9: December 2008.

No. 10: March 2010.

No. 11: April 2011.

No. 12: April 2012.

No. 13: April 2013.

No. 14: April 2014.

COSMO Technical Reports

No. 1: Dmitrii Mironov and Matthias Raschendorfer (2001):
Evaluation of Empirical Parameters of the New LM Surface-Layer Parameterization Scheme. Results from Numerical Experiments Including the Soil Moisture Analysis.

No. 2: Reinhold Schrodin and Erdmann Heise (2001):
The Multi-Layer Version of the DWD Soil Model TERRA_LM.

No. 3: Günther Doms (2001):
A Scheme for Monotonic Numerical Diffusion in the LM.

No. 4: Hans-Joachim Herzog, Ursula Schubert, Gerd Vogel, Adelheid Fiedler and Roswitha Kirchner (2002):
LLM ¯ the High-Resolving Nonhydrostatic Simulation Model in the DWD-Project LITFASS.
Part I: Modelling Technique and Simulation Method.

No. 5: Jean-Marie Bettems (2002):
EUCOS Impact Study Using the Limited-Area Non-Hydrostatic NWP Model in Operational Use at MeteoSwiss.

No. 6: Heinz-Werner Bitzer and Jürgen Steppeler (2004):
Documentation of the Z-Coordinate Dynamical Core of LM.

No. 7: Hans-Joachim Herzog, Almut Gassmann (2005):
Lorenz- and Charney-Phillips vertical grid experimentation using a compressible nonhydrostatic toy-model relevant to the fast-mode part of the 'Lokal-Modell'.

No. 8: Chiara Marsigli, Andrea Montani, Tiziana Paccagnella, Davide Sacchetti, André Walser, Marco Arpagaus, Thomas Schumann (2005):
Evaluation of the Performance of the COSMO-LEPS System.

No. 9: Erdmann Heise, Bodo Ritter, Reinhold Schrodin (2006):
Operational Implementation of the Multilayer Soil Model.

No. 10: M.D. Tsyrulnikov (2007):
Is the particle filtering approach appropriate for meso-scale data assimilation ?

No. 11: Dmitrii V. Mironov (2008):
Parameterization of Lakes in Numerical Weather Prediction. Description of a Lake Model.

No. 12: Adriano Raspanti (2009):
COSMO Priority Project "VERification System Unified Survey" (VERSUS): Final Report.

No. 13: Chiara Marsigli (2009):
COSMO Priority Project "Short Range Ensemble Prediction System" (SREPS): Final Report.

No. 14: Michael Baldauf (2009):
COSMO Priority Project "Further Developments of the Runge-Kutta Time Integration Scheme" (RK): Final Report.

No. 15: Silke Dierer (2009):
COSMO Priority Project "Tackle deficiencies in quantitative precipitation forecast" (QPF): Final Report.

No. 16: Pierre Eckert (2009):
COSMO Priority Project "INTERP": Final Report.

No. 17: D. Leuenberger, M. Stoll and A. Roches (2010):
Description of some convective indices implemented in the COSMO model.

No. 18: Daniel Leuenberger (2010):
Statistical analysis of high-resolution COSMO Ensemble forecasts in view of Data Assimilation.

No. 19: A. Montani, D. Cesari, C. Marsigli, T. Paccagnella (2010):
Seven years of activity in the field of mesoscale ensemble forecasting by the COSMO–LEPS system: main achievements and open challenges.

No. 20: A. Roches, O. Fuhrer (2012):
Tracer module in the COSMO model.

No. 21: Michael Baldauf (2013):
A new fast-waves solver for the Runge-Kutta dynamical core.

No. 22: C. Marsigli, T. Diomede, A. Montani, T. Paccagnella, P. Louka, F. Gofa, A. Corigliano (2013):
The CONSENS Priority Project.

No. 23: M. Baldauf, O. Fuhrer, M. J. Kurowski, G. de Morsier, M. Müllner, Z. P. Piotrowski, B. Rosa, P. L. Vitagliano, D. Wójcik, M. Ziemiański (2013):
The COSMO Priority Project 'Conservative Dynamical Core' Final Report.

No. 24: A. K. Miltenberger, A. Roches, S. Pfahl, H. Wernli (2014):
Online Trajectory Module in COSMO: a short user guide.

No. 25: P. Khain, I. Carmona, A. Voudouri, E. Avgoustoglou, J.-M. Bettems, F. Grazzini (2015):
The Proof of the Parameters Calibration Method: CALMO Progress Report.

COSMO Technical Reports

Issues of the COSMO Technical Reports series are published by the *COnsortium for Small-scale MOdelling* at non-regular intervals. COSMO is a European group for numerical weather prediction with participating meteorological services from Germany (DWD, AWGeophys), Greece (HNMS), Italy (USAM, ARPA-SIMC, ARPA Piemonte), Switzerland (MeteoSwiss), Poland (IMGW), Romania (NMA) and Russia (RHM). The general goal is to develop, improve and maintain a non-hydrostatic limited area modelling system to be used for both operational and research applications by the members of COSMO. This system is initially based on the COSMO-Model (previously known as LM) of DWD with its corresponding data assimilation system.

The Technical Reports are intended

- for scientific contributions and a documentation of research activities,
- to present and discuss results obtained from the model system,
- to present and discuss verification results and interpretation methods,
- for a documentation of technical changes to the model system,
- to give an overview of new components of the model system.

The purpose of these reports is to communicate results, changes and progress related to the LM model system relatively fast within the COSMO consortium, and also to inform other NWP groups on our current research activities. In this way the discussion on a specific topic can be stimulated at an early stage. In order to publish a report very soon after the completion of the manuscript, we have decided to omit a thorough reviewing procedure and only a rough check is done by the editors and a third reviewer. We apologize for typographical and other errors or inconsistencies which may still be present.

At present, the Technical Reports are available for download from the COSMO web site (www.cosmo-model.org). If required, the member meteorological centres can produce hard-copies by their own for distribution within their service. All members of the consortium will be informed about new issues by email.

For any comments and questions, please contact the editor:

Massimo Milelli
Massimo.Milelli@arpa.piemonte.it

Consortium for Small-Scale Modelling

Technical Report No. 45

The COSMO Priority Project APSU: Final Report

February 2022

DOI: 10.5676/DWD_pub/nwv/cosmo-tr_45

Deutscher Wetterdienst
MeteoSwiss
Ufficio Generale Spazio Aereo e Meteorologia
ΕΘΝΙΚΗ ΜΕΤΕΩΡΟΛΟΓΙΚΗ ΥΠΗΡΕΣΙΑ
Instytut Meteorologii i Gospodarki Wodnej
Administratia Nationala de Meteorologie
ROSHYDROMET
Agenzia Regionale Protezione Ambiente Piemonte
Agenzia Regionale Prevenzione Ambiente Energia Emilia Romagna
Centro Italiano Ricerche Aerospaziali
Amt für GeoInformationswesen der Bundeswehr
Israel Meteorological Service

www.cosmo-model.org

Editor: Massimo Milelli, CIMA Foundation

The COSMO Priority Project APSU: Final Report

***Marsigli C.*[1]*, *Astakhova E.*[2], *Duniec G.*[3], *Füzer L.*[5], *Gayfulin D.*[2], *Gebhardt C.*[1], *Golino R.*[4], *Heppelmann T.*[1], *Interewicz W.*[3], *Marcucci F.*[4], *Mazur A.*[3], *Sprengel M.*[1], *Tsyrulnikov M.*[2], *Walser A.*[5]**

* Project coordinator
[1] Deutscher Wetterdienst - DWD
[2] HydroMetCenter of Russia - RHM
[3] Instytut Meteorologii i Gospodarki Wodnej - IMGW
[4] ItAF-ReMet - COMET
[5] MeteoSwiss - MCH

Contents

1 Abstract **4**

2 Introduction **4**

3 New model perturbation methods **5**

3.1 SMME: Stochastic model of the model error (M. Sprengel, T. Heppelmann, C. Gebhardt, DWD) . . . 5

3.1.1 Method . . . 5

3.1.2 Parameter estimation . . . 7

3.1.3 Experiments and verification results . . . 10

3.1.4 Bulk Richardson number as additional predictor . . . 12

3.2 AMPT: Additive Model-error perturbations scaled by Physical Tendencies (M. Tsyrulnikov, D. Gayfulin, E. Astakhova, RHM) . . . 14

3.2.1 SPPT in a nutshell . . . 14

3.2.2 AMPT . . . 14

3.2.3 AMPT model-error perturbations: "Gaussian" atmospheric variables . 16

3.2.4 AMPT model-error perturbations: Humidity and hydrometeor fields . 16

3.2.5 AMPT model-error perturbations: Soil fields . . . 17

3.2.6 Initial soil perturbations . . . 18

3.2.7 Stability . . . 19

3.2.8 Experimental setup . . . 19

3.2.9 Unperturbed T_{so}, W_{so} total tendencies . . . 21

3.2.10 Testing AMPT in an ensemble prediction system . . . 21

3.2.11 Discussion on AMPT . . . 25

3.2.12 Conclusions on AMPT . . . 27

3.3 Model perturbations at IMGW (A. Mazur and G. Duniec, IMGW) . . . 29

3.3.1 Perturbations based on adapted Random Number Generator. . . . 29

3.3.2 Perturbation of soil surface temperature in combination with upper air perturbation . . . 31

3.4 Perturbations based on SPPT with independent pattern (iSPPT) (André Walser and Linda Füzér, MCH) . . . 33

3.5 Perturbations based on analysis increments (André Walser and Linda Füzér, MCH) . . . 33

4 Post-processing and interpretation of ensembles **34**

4.1 Calibration (A. Mazur, W. Interewicz, IMGW) 34
4.2 Specific products from ensemble outputs (R. Golino, F. Marcucci, COMET) . 37
4.3 Specific products from ensemble outputs (A. Mazur, G. Duniec, IMGW) . . . 39

5 Transition to ICON-LAM **41**
5.1 Randomly perturbed parameters in ICON-D2-EPS (C. Gebhardt, DWD) . . 42

6 Conclusions **49**

7 Acknowledgements **50**

8 References **50**

1 Abstract

The APSU Priority Project focussed on the improvement of the ensemble forecast systems run by the COSMO members, developing both the perturbation methodology and the post-processing. The aim was to improve the forecast issued by the convection-permitting (CP) scale modelling system, particularly for severe and high-impact weather events. The research and development work covered three main areas:

- development of model perturbation methodologies, including new methods and the development of surface/soil perturbations;
- development of post-processing methods for the convection-permitting ensembles, especially focused on the forecast of selected severe weather phenomena;
- better use of the KENDA analyses as Initial Conditions (ICs) to initialize the CP ensembles and improvement of the perturbed Boundary Conditions (BCs).

The project provided also the occasion to discuss and plan the transition of the ensembles to the ICON-LAM model.

2 Introduction

The APSU Priority Project was initiated due to the need of improving the ensemble systems run by the members of the COSMO Consortium, in particular for the prediction of near-surface weather parameters at high spatio-temporal resolution.

During the WG7 meeting held in Offenbach in March 2017, it was recognised that the perturbations applied to the model in the ensemble configurations do not provide yet a satisfactory representation of the model error, as evidenced by the spread-skill relation for near-surface parameters (Marsigli et al., 2019). The shared opinion was that the spread of the ensembles in terms of near-surface parameters (temperature, wind) should be increased, in order to better match the forecast error. This should be done with care, since it is recognised that the ensemble spread cannot be increased up to exactly reaching the forecast error, because the latter includes also the systematic error, which should be tackled by improving the model, not by increasing the spread. On top, observation error should be considered in the computation of the forecast error (Ben Bouallegue et al., 2020). What should be better represented in the ensembles is that part of the error which depends on the uncertainties in the determination of initial and boundary conditions as well as in the description of the physical processes in the model, which are mainly due to the variability of the model performance in dependence of the meteorological situation, usually called "error of the day" or flow-dependent error (see for example Leutbecher et al., 2017). To reach this goal, it is needed to work on a better representation of the model error. The strategy proposed in APSU is based on testing new approaches for model perturbation which have been recently developed or made available to the COSMO model, and to review and improve the already existing ones. More specifically:

- further develop and test the new stochastic approach to model the model error developed at DWD
- develop an additive perturbation method based on the Stochastic Pattern Generator (Tsyrulnikov and Gayfulin, 2017)

- test of two new available methods for model perturbations: iSPPT (independent SPPT, Christensen et al., 2017) and the perturbations based on analysis increments (Piccolo et al., 2018)
- develop perturbations of the soil/surface and test the combination of the different perturbations

It was also noted that the potential of the ensembles is not fully exploited for the operational duties, in particular for high spatial and temporal resolution forecasts, therefore it was identified the need to continue working on ensemble post-processing and interpretation. In particular it is needed to:

- develop suitable probabilistic products for operational applications. In order to benefit from the link with the SRNWP-EPS Project of EUMETNET, the focus was on products for thunderstorms and fog;
- further develop suitable calibration procedures for the CP ensembles.

This activity has a strong link with the activities carried out in WG4.

On top of these development areas, the transition from the COSMO to the ICON model implies also a transition of the ensemble systems. To make this possible, a planning of the needed activities was started in the APSU PP. A first concrete task was performed at DWD, where the Parameter Perturbation methodology was transferred and tested in the new ICON-LAM ensemble.

3 New model perturbation methods

New methodologies for model perturbations have been tested in the APSU PP, and further developed.

3.1 SMME: Stochastic model of the model error (M. Sprengel, T. Heppelmann, C. Gebhardt, DWD)

3.1.1 Method

At DWD, a prognostic stochastic model of the model error ("EM-scheme", Ekaterina Machulskaya) has been developed. The concepts of the EM scheme have been the basis for the development of an improved framework called "stochastic model of the model error" (SMME). The development of SMME is carried out within the project Gridcast and its precursor EweLine which both are collaborative research projects of the DWD with the Fraunhofer IEE and the German transmission system operators (TSOs) in the context of renewable energies. The growing share of renewable energy in power generation increases the impact of the weather on the stability of the electrical power grid. Especially prior to severe weather events, not only high-quality weather forecasts but also information about forecast uncertainties is needed by the TSOs to prepare stability provisions. Improving the description of the inherent model error is therefore one of the goals of the research project Gridcast. Even if this development is focused on optimizing the use of renewable energies, it can be beneficial for NWP model development in general and therefore fits well as a contribution to PP APSU.

The EM-scheme and the SMME have in common that the errors of the tendencies of different model variables are assumed to obey the Langevin-type stochastic differential equation being correlated in space and time and stochastically driven by Gaussian noise as in equation (1).

$$\frac{\partial \eta_X(x,t)}{\partial t} = -\gamma(\tau_X)\eta_X(x,t) + \gamma(\tau_X)\nabla \cdot \left(\lambda^2(\tau_X)\nabla\eta_X(x,t)\right) + \sigma(\tau_X)\xi(x,t), \tag{1}$$

where

- $\tau_X = \tau_X(x,t)$ is the tendency of the predictor variable X,
- γ is the damping,
- diffusion λ guarantees spatial correlation,
- ξ is a standard normal random field with standard deviation σ.

The weather-dependent values of the parameters γ, λ, and σ of this equation are determined by predictors, whereas the dependencies of the parameters on the predictors are inferred from past data. The solution η_X of eq. 1 is our model of the model error and is added to the dynamic equations of the model to correct the tendencies from the NWP online for a set of variables X:

$$\frac{\Delta X}{\Delta t}(x,t) = \left[\frac{\Delta X}{\Delta t}(x,t)\right]_{\text{phys}} - \eta_X(x,t).$$

The method is applied to temperature and zonal and meridional wind as prognostic variables with the tendency τ_X of each variable X acting as predictor for the respective error model parameters.

Going from the EM-scheme to the SMME, the method for estimating the parameters has been re-developed from scratch by taking the spatial diffusion term into account from the very beginning of the development. This approach enabled us to have a consistent framework for all three parameters γ, λ, and σ that includes the spatial diffusion without the need for a separate treatment.

As first COSMO-D2-EPS experiments with the method showed an increased forecast spread but at the expense of a substantial degradation of the RMSE (see later in section 3.1.3), a new method for estimating γ has been developed based on results of (García-Ojalvo et al., 1992):

Assuming spatially constant coefficients, we can discretize the stochastic partial differential equation eq. 1 in space and perform a spatial Fourier transform to obtain a system of stochastic ordinary differential equations. For these equations certain expectation values and correlations can be derived analytically. For example for the stationary correlation function at different times t and t' and Fourier modes k and k' one finds

$$\left\langle \eta_k(t)\eta_{k'}(t')\right\rangle^{st} = \frac{\sigma^2 N_x \Delta x N_y \Delta y}{2\gamma c_k} e^{-\gamma c_k |t-t'|}\delta_{k,-k'} \tag{2}$$

where Δx and Δy denote the horizontal grid spacing, N_x and N_y are the number of grid points, and c_k is the Fourier transform of the differential operator. For the Fourier modes $k = k' = 0$ this further simplifies and we can take the quotient at different times $t' = t + \Delta t$ and $t' = t + 2\Delta t$ to obtain

$$\frac{\left\langle \eta_k(t)\eta_{k'}(t+\Delta t)\right\rangle^{st}}{\left\langle \eta_k(t)\eta_{k'}(t+2\Delta t)\right\rangle^{st}} \overset{k=k'=0}{=} e^{\gamma \Delta t}. \tag{3}$$

This method resulted in a much better RMSE (see later in section 3.1.3).

3.1.2 Parameter estimation

The estimation of the parameters γ, λ, and σ from past data requires the estimation of the model error tendencies on the left-hand side of eq. 1 which in turn requires an approximation of the truth to be compared with model forecast. For SMME, the truth is approximated by analysis fields of KENDA for COSMO-D2 and the model error is defined as the deviation of short-range forecasts of COSMO-D2 from these analyses. Other approaches exist to estimate the model error tendencies by comparing forecasts only (see for example Tsyrulnikov and Gayfulin, 2019 and Christensen, 2020).
This section exemplifies important aspects of the dependencies of the estimated parameters γ, λ, and σ on their predictors, on the forecast time and the time of the day as well as on the vertical model level. The training period for the parameter estimation is 5 months in autumn 2018 and 2019 with the exclusion of the application month October 2018. The training data are the operational COSMO-D2 forecasts started at 03 UTC up to 45 hours of forecast time and the operational analyses for the same period. Fig. 1 shows the changes of the damping parameter γ with forecast time for temperature at ca. 300m above ground.

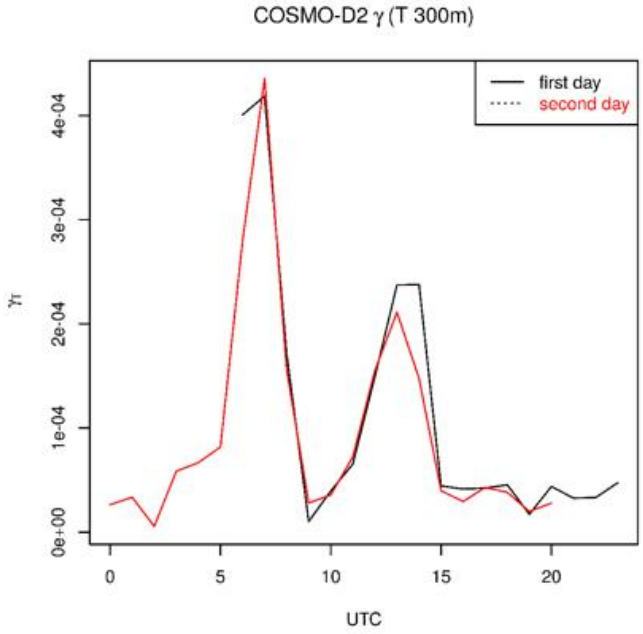


Figure 1: Estimated γ for temperature at ca. 300m as a function of the time of the day for lead times 1h to 45h (first day in black, second day in red, forecast start is 03 UTC).

There is a clear dependence on the time of the day without a significant difference between day 1 and day 2. The dependence on the time of the day decreases with increasing height of the vertical model level (not shown). The parameter γ depends on the prognostic variable X but hardly on the size of its tendency τ_X (not shown). However, there is a clear dependence of the diffusion parameter λ on the predictor tendency τ_X (Fig. 2).

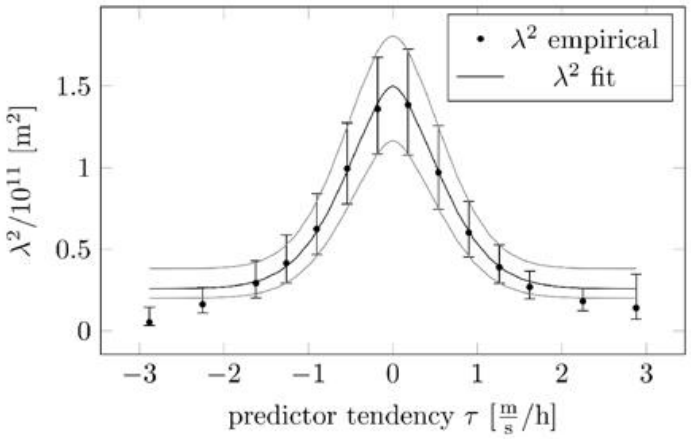


Figure 2: Estimated λ for the zonal wind at 97m above ground and fitted to a function of type $\lambda(\tau) = \lambda_a e^{-(|\tau|/\lambda_b)^{\lambda_c}} + \lambda_d$. The error bars are the 95%-confidence intervals estimated from the sample of days for training. The black line is the fit to the empirical values of λ and the grey lines fit to the limits of the confidence intervals.

The tendencies have been arranged in equally populated bins for the parameter estimation. A parametrized function can be nicely fitted to the empirical values.

Fig. 3 shows the combined effect of forecast time, time of the day and atmospheric height on λ for temperature.

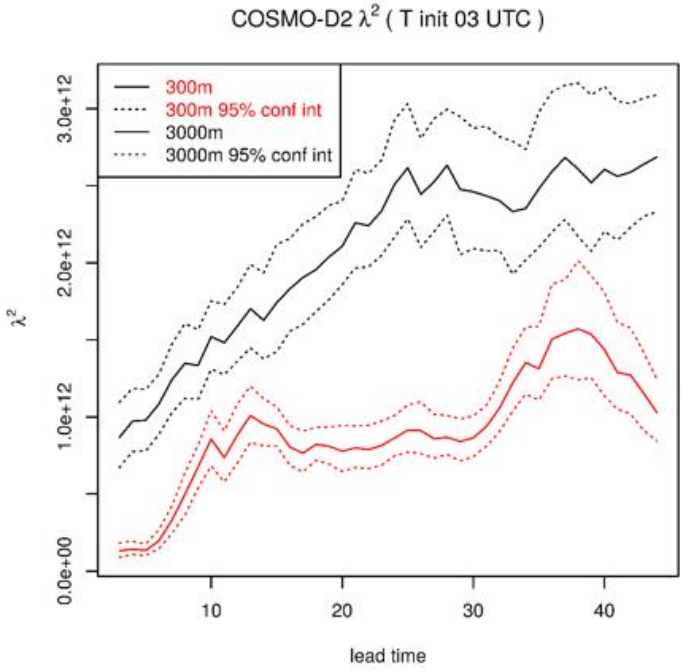


Figure 3: Estimated λ for temperature (solid line) at two atmospheric heights (300m in red, 3000m in black) as function of forecast lead time. The dashed lines are the 95%-confidence intervals estimated from the sample of days for training.

The values of λ are larger for higher altitudes and a given forecast lead time. There is a general trend of increasing λ with increasing lead time which is modulated by a daily cycle in the boundary layer. This dependence on the time of the day shows an increase of λ starting

after dawn with the onset of boundary layer mixing with a moderate decrease in the evening and a quasi-plateau during the night. In general, the characteristics of λ for temperature apply to the horizontal wind components as well.

Since the parameter σ is calculated on the basis of the estimated γ and λ it basically inherits the dependencies on time and height from those parameters. In Fig. 4, the dependence of σ on model level and predictor tendency for zonal wind is shown.

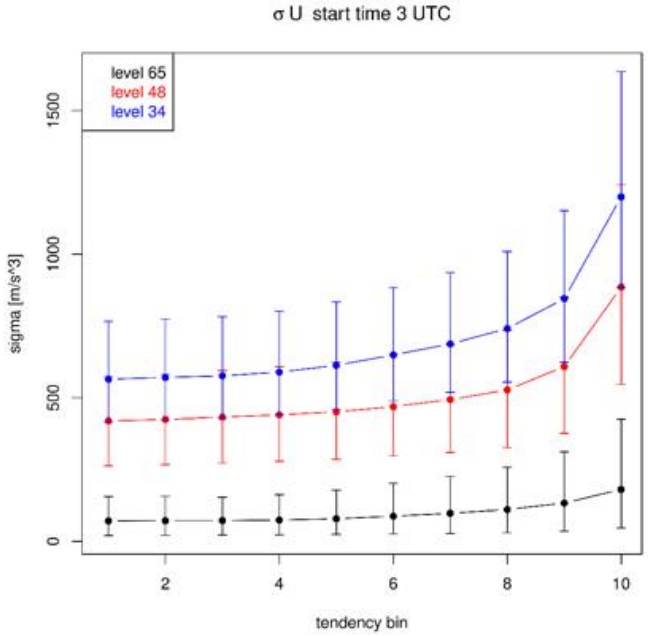


Figure 4: Estimated σ for zonal wind at different atmospheric heights (different colours) as function of tendency bin τ_U, i.e. numbers on the abscissa are bin counts. The error bars are the 95%-confidence intervals estimated from the sample of days for training. The levels 65, 48, and 34 correspond to the heights 10m, 757m, and 3000m, respectively.

There is an increase of σ with height as well as with the magnitude of τ_U, the latter being negligible to moderate for lower values of the tendency. The increase of σ with τ_U is larger higher up in the atmosphere.

In practice, the parameters γ, λ, and σ are estimated for distinct model levels only (at 10m, 757m, and 3000m for U and V; and 300m, 757m, and 3000m for T). Accordingly in the application, the model error η is calculated for these three levels and linearly interpolated vertically between those levels. Above the highest level $k_{max} = 34$ at 3000m (and for T below $k_{min} = 55$ at 300m) η is exponentially damped towards zero (recall that smaller k correspond to greater height):

$$\eta_X^k(x,t) = \eta_X^{k_{max}}(x,t)e^{-(k_{max}-k)} \quad \text{for } k = k_{max}-1,\ldots,k_{max}-4,$$

and similarly for T at $k = k_{min}+1,\ldots,k_{min}+4$.

Investigations about the model of the model error in the global ICON-EPS within the project Gridcast have shown further dependencies of the parameters (land/sea grid points, geographical latitude) which can be neglected for the application of SMME to the limited domain of COSMO-D2.

3.1.3 Experiments and verification results

Based on the parameters γ, λ, and σ as estimated from a training data set of the operational COSMO-D2 forecasts and analyses for autumn 2018 and 2019, two experiments were performed for October 2018 with the operational COSMO-D2-EPS settings. All forecasts start at 03 UTC and run for 45 hours. Verification shown in this section is against SYNOP observations.
The first experiment resulted in an increased spread for several prognostic variables, but there was a significant increase in the forecast error as well (e.g. for 10m wind speed, see Fig. 5).

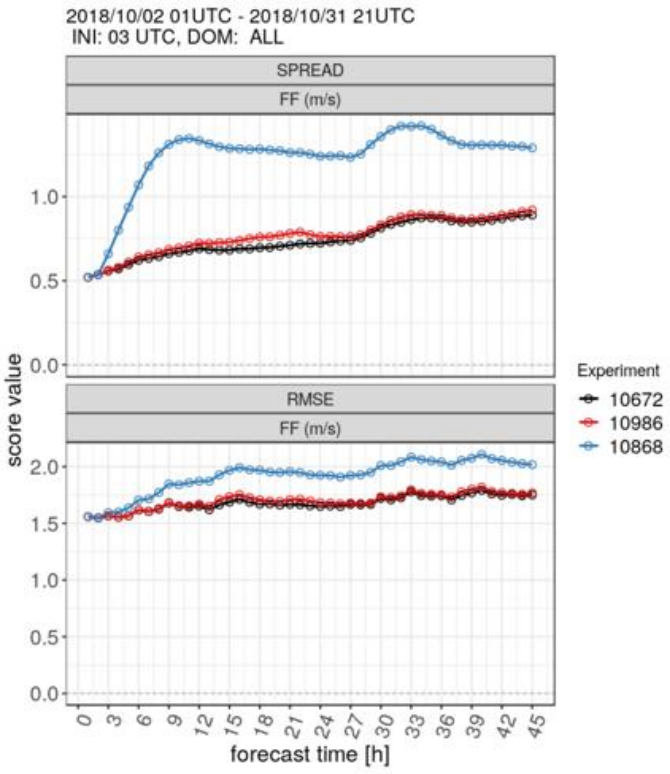


Figure 5: EPS spread (top) and root mean squared error (bottom) of the ensemble mean for 10m wind speed as function of forecast lead time for the first experiment with the model of the model error (blue, experiment 10868), the modified SMME experiment (red, 10968), and a reference run with operational settings but without model error (black, 10672).

These results initiated the changes in the estimation method for the damping parameter γ following García-Ojalvo et al. (1992) as mentioned in section 3.1.1. The effect of this methodological change in comparison to the first experiment can be seen in Fig. 5 as well. The results are mostly neutral compared to the reference, with a slight increase of the spread for wind speed in the afternoon hours of the first forecast day.

The new experiment incorporated a further methodological adjustment. The model tendencies acting as predictors for the parameters in the application of SMME are calculated during the forecast as changes with respect to the model time step. However, the estimation of the tendency-parameter relation from the training data has to refer to the output frequency of the model data, i.e. hourly steps being much larger than the model time step. This leads to a more frequent occurrence of relatively large tendencies in the application compared to the training of the parameters. To account for this effect, the properties of the tendency

distributions are harmonized between the two different time scales by applying a factor of 0.43–0.58 to the variance of the tendency distribution during the model forecast.

Fig. 6 shows several verification scores for 10m wind speed and 2m temperature for the experiment with SMME based on the improved estimation method in comparison to the operational set-up.

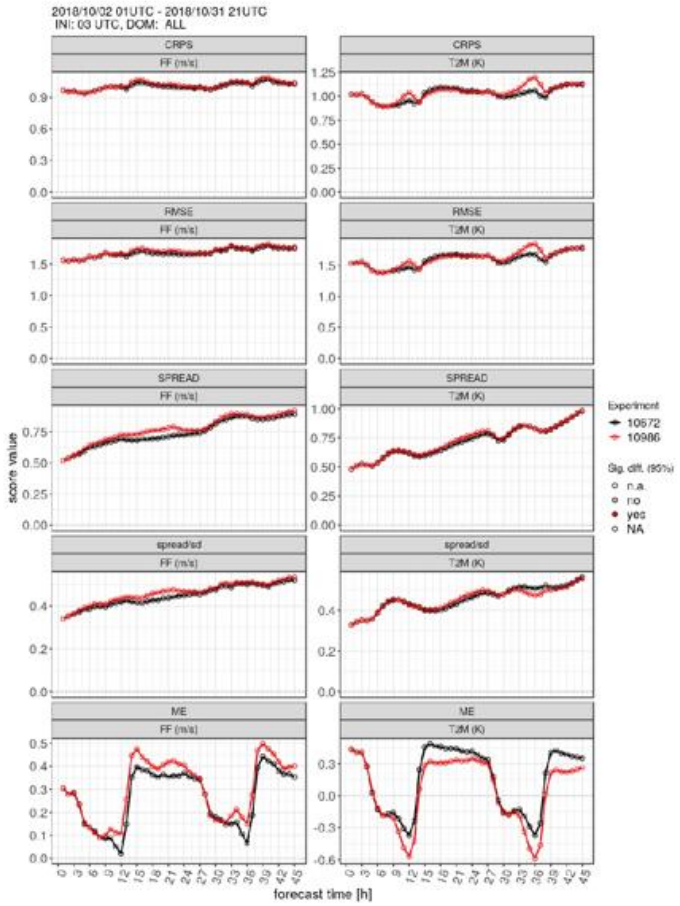


Figure 6: Continuous ranked probability score (CRPS), RMSE, EPS spread, ratio of spread to the standard deviation of forecast errors and mean error of the ensemble mean (from top to bottom) for 10m wind speed (left) and 2m temperature (right) as a function of forecast lead time for the modified SMME experiment (red, experiment 10968) and a reference run with operational settings but without SMME (black, 10672).

The results are mostly neutral compared to the operational set-up. There are slight increases in CRPS and RMSE for 2m temperature around 15 UTC day time, but the differences are not significant (as indicated by the non-filled circles in the plot). There is an increase of spread for wind speed during the first forecast day which is also not significant.

Most obvious differences occur in the mean error of the EPS mean for both variables. The SMME run produces consistently an EPS mean of 10m wind with a slightly larger bias than the reference run which itself has a positive bias. The 2m temperature bias shows qualitatively the same daily cycle with slightly colder temperatures in SMME. Note that the SMME is effective only from 2.5 forecast hours onward to allow for the spin-down of forecast tendencies resulting from minor deviations of analysis fields from the balance properties of the model dynamics. This leads to almost identical mean errors of the SMME and the reference run in the first forecast hours.

In general, the SMME in its current set-up leads to neutral results and the methodological changes were successful in avoiding the forecast deterioration seen in the first experiments. This neutral implementation of the SMME into the COSMO-D2 is a promising starting point for further improvements. A first step for improvements is described in the next section.

3.1.4 Bulk Richardson number as additional predictor

Fig. 7 shows the time series of the mean error of the 24 hours EPS mean forecast of 10m wind speed for the SMME and the reference run.

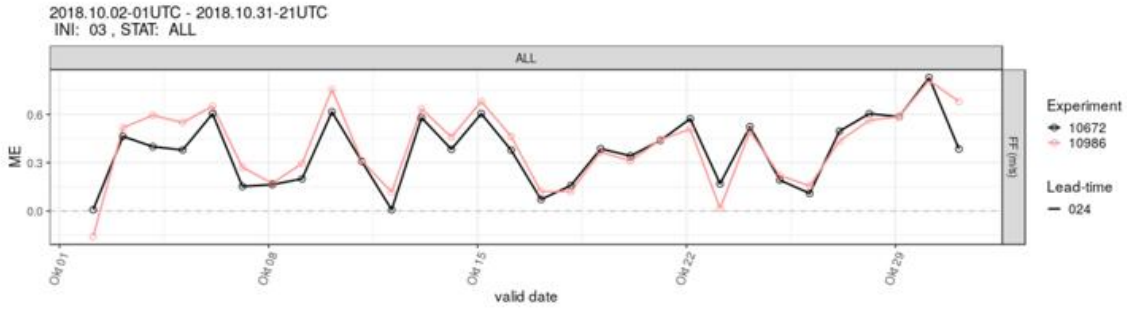


Figure 7: Time series of the mean error of the 24 hours EPS mean forecast of 10m wind speed for the SMME (experiment 10986) and the reference run (experiment 10672).

There are periods with an increased bias in the SMME run, but also periods with neutral results by the SMME approach. A conditional verification showed that the SMME increases the error particularly in nights with stable PBLs. This leads to further investigating how to include knowledge about the stability of the PBL into the SMME. The suggestion is to introduce the bulk Richardson number as a further predictor in addition to the tendency of the respective variable.

We chose to discriminate three cases: stable, unstable, and neutral PBL. To this end, we calculate the bulk Richardson number

$$R_B = \frac{(g/T_v)\Delta\theta_v \Delta z}{(\Delta U)^2 + (\Delta V)^2} \tag{4}$$

for a bulk layer of levels 65–55 (10m–300m) and perform a horizontal smoothing over 7×7 grid points. In eq. 4 we use the following definitions:

- g gravitational constant,
- absolute T_v virtual temperature,
- Δz layer thickness,
- $\Delta\theta_v$ change in virtual potential temperature across layer,
- ΔU, ΔV change in wind speed across same layer.

Our thresholds for the three cases are

$$R = \begin{cases} \text{stable} & R_B >= 1.5 \\ \text{neutral} & R_B \in (0.25, 1.5) \\ \text{unstable} & R_B <= 0.25. \end{cases} \tag{5}$$

Fig. 8 provides the fields of the bulk Richardson number for a stable (14th October) and an unstable (24th October) case.

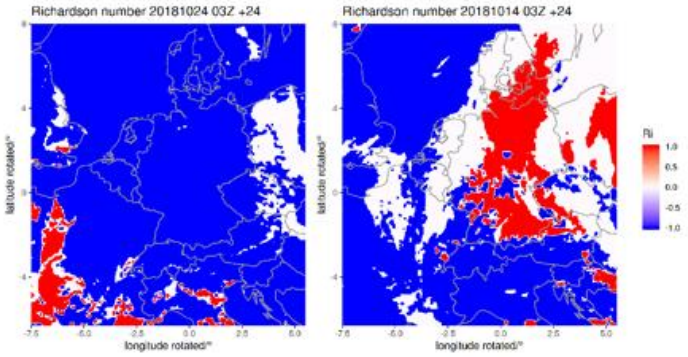


Figure 8: Bulk Richardson number for an unstable (24th October) and a stable (14th October) case.

These fields together with Fig. 7 exemplify the link between nocturnal stable/unstable conditions and their effect on the wind forecast of the COSMO-D2-EPS using the SMME method. The stratification along the three cases stable, unstable, and neutral boundary layer according to R_B leads to differences in the estimated parameters as can be seen in Fig. 9 for the diffusion parameter λ. The stratification of the estimation of the parameters γ, λ, and σ by the bulk Richardson number and the use of R_B as an additional predictor will be adopted in further experiments with SMME.

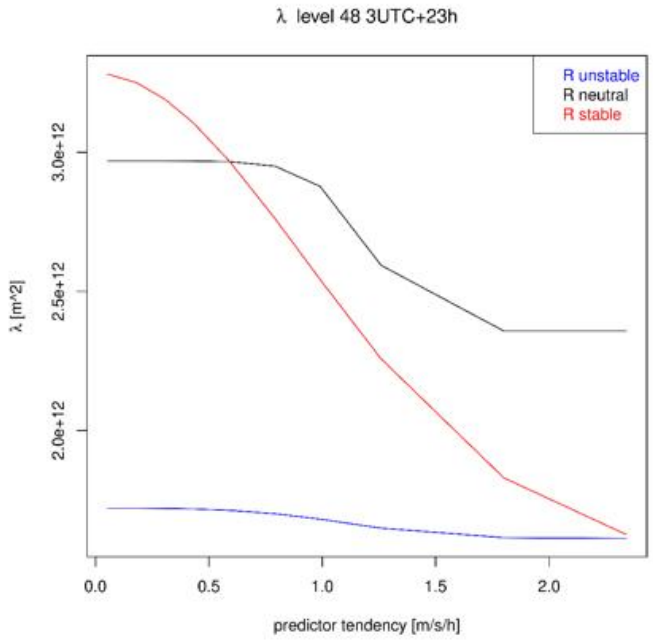


Figure 9: Diffusion parameter λ for zonal wind at 757m at 2 UTC during the night for stable (red), neutral (black), and unstable(blue) conditions.

The next steps in the development of the SMME will be its application to ICON-D2-EPS in its current state, analysing potentials for further improvements of the methodology, and speed-up of the method from a computational point of view.

3.2 AMPT: Additive Model-error perturbations scaled by Physical Tendencies (M. Tsyrulnikov, D. Gayfulin, E. Astakhova, RHM)

In this section, we introduce a new ad-hoc approach to generation of model-error perturbations. The idea is to generate additive perturbations as four-dimensional random fields whose magnitude is determined by the area-averaged modulus of physical tendency. The AMPT (Additive Model-error perturbations scaled by Physical Tendencies) scheme is applied to both atmosphere and soil. Nearly-Gaussian and significantly non-Gaussian fields are treated. Results of numerical experiments with a COSMO-model ensemble prediction system are given.

3.2.1 SPPT in a nutshell

To facilitate the presentation of the new AMPT scheme, we first outline Stochastic Perturbation of Physical Tendency (Buizza et al., 1999), the very popular technique to represent errors in physical parametrizations. This simple and effective technique relies on the assumption that the magnitude of error in physical tendency is proportional to the magnitude of physical tendency itself. There is also a flavour of SPPT called iSPPT in which tendencies from different physical parametrizations are perturbed independently (Christensen et al., 2017).

By $\mathbf{P}(x,y,\zeta,t) = (P_1(x,y,\zeta,t),\dots,P_{n_{\text{fields}}}(x,y,\zeta,t))$ we denote the vector valued physical tendency (sometimes called the *net* physical tendency, generated by all physical parametrizations combined) at the spatial grid point with the horizontal coordinates (x,y), the vertical coordinate ζ, and the time step t. Here $P_i(x,y,\zeta,t)$ is the component of $\mathbf{P}(x,y,\zeta,t)$ in the i-th model field (variable) X_i, and n_{fields} is the number of model fields selected to be perturbed, normally, temperature, winds, and humidity.

In SPPT, the perturbed physical tendency $\mathbf{P}^*$ is postulated to be

$$\mathbf{P}^*(x,y,\zeta,t) = (1+\epsilon\,\xi(x,y,t))\cdot\mathbf{P}(x,y,\zeta,t), \tag{6}$$

where $\xi(x,y,t)$ is a *scalar* (i.e. common for all physical tendency components) zero mean and unit variance spatio-temporal random field and ϵ the parameter that controls the magnitude of the perturbation (normally, 0.4–0.8). For stability reasons, the point wise probability distribution of $\xi(x,y,t)$ is specified in such a way that $1+\epsilon\,\xi(x,y,t)>0$, that is, avoiding sign reversal of the physical tendency (Leutbecher et al., 2017). Note that in SPPT the random pattern ξ is two-dimensional in space.

From eq. 6, the SPPT perturbation is seen to be multiplicative:

$$\delta\mathbf{P} = \mathbf{P}^*(x,y,\zeta,t) - \mathbf{P}(x,y,\zeta,t) = \epsilon\,\xi(x,y,t)\,\mathbf{P}(x,y,\zeta,t). \tag{7}$$

Here and elsewhere δ denotes a perturbation.

3.2.2 AMPT

Motivation

The following three deficiencies of SPPT led us to propose the new approach.

1. In SPPT, perturbations are large when and where the physical parametrizations generate a *large* physical tendency $\mathbf{P}$. This formulation gives rise to a meaningful scaling

of perturbations in situations when the model predicts high subgrid-scale variability and produces a large physical tendency. But it cannot cover situations in which the model error magnitude is large whereas the magnitude of the physical tendency is small. This occurs, for example, if in some grid cell convection is initiated in nature whilst a convective parametrization fails to be activated.

2. In SPPT, the *multivariate* perturbation vector $\delta\mathbf{P}(x, y, \zeta, t)$ is strictly proportional to the physical tendency vector $\mathbf{P}(x, y, \zeta, t)$ (see eq. 7). This implies that *SPPT tacitly assumes that the model error is only in the magnitude* of the vector $\mathbf{P}$, whilst the *ratios* between the physical tendencies in different variables (i.e. between $\delta P_i(x, y, \zeta, t)$ for different variables labelled by i at the same grid point x, y, ζ, t) are *error-free*, which is highly unlikely. Indeed, eq. 7 implies that the relationship between any two components of $\mathbf{P}$, say, those that correspond to temperature T and zonal wind u, i.e. P_T and P_u, is the same before and after the perturbation:

$$\frac{P^*_\mathrm{T}}{P^*_u} = \frac{P_\mathrm{T}}{P_u}. \tag{8}$$

   The *ratios* of the components of the physical tendency vector are, thus, not perturbed in SPPT (in iSPPT, this is the case for each individual physical parametrization).

3. Similarly, as the SPPT random pattern ξ does not depend on the vertical coordinate ζ, the ratios of physical tendencies at different *vertical levels* are not perturbed:

$$\frac{P^*_i(x, y, \zeta_k, t)}{P^*_{i'}(x, y, \zeta_{k'}, t)} = \frac{P_i(x, y, \zeta_k, t)}{P_{i'}(x, y, \zeta_{k'}, t)} \tag{9}$$

   for any two variables i, i' and any two vertical levels k, k'. This implies that there are *no errors* in those ratios, which, again, is unlikely.

Approach

We propose to address the above deficiencies of SPPT in our AMPT scheme as follows.

1. In SPPT, as it follows from eq. 7, the standard deviation of the perturbation in the i-th prognostic field (given $\mathbf{P}$) is $\epsilon|P_i|$ so that the standard deviation of the multivariate (vector) perturbation is proportional to the modulus of the physical tendency: $\mathrm{SD}(\delta\mathbf{P}|\mathbf{P}) = \epsilon|\mathbf{P}|$. In AMPT, we retain this linear dependency of the magnitude (standard deviation) of model-error perturbations on the modulus of physical tendency. But we define this dependency to be more general than just *point wise*.

   Specifically, we propose to generate model-error perturbations in the *additive* (rather than multiplicative as in SPPT) way and postulate their magnitude to be proportional to an *area-averaged* (rather than point wise as in SPPT) $|\mathbf{P}|$ in the horizontal. This allows AMPT to generate non-zero perturbations even at grid points with zero physical tendency — if there are nearby points with non-zero physical tendency.

2. We allow for errors in the relationships between physical tendencies in different model variables by introducing *independent* driving random fields for different model variables.

3. We allow for errors in the relationships between physical tendencies at different model levels by making ξ a *four-dimensional* random field $\xi(x, y, \zeta, t)$ rather the three-dimensional field $\xi(x, y, t)$ as in SPPT.

It is worth remarking that the SPPT perturbations at any given horizontal-grid point and time step are perfectly correlated between different variables and different levels, whereas the AMPT perturbations are uncorrelated between different variables and partly correlated in the vertical. This suggests that a hybrid SPPT+AMPT scheme might be considered. In this study we focus on the pure AMPT.

3.2.3 AMPT model-error perturbations: "Gaussian" atmospheric variables

In the context of limited-area modelling, we define the area-averaged magnitude of physical tendency for nearly Gaussian distributed fields such as temperature T and the two wind components u, v (T, u, v are denoted generically as Y in this section) through averaging over the *whole domain* in the horizontal:

$$\mathcal{P}_{\mathrm{Y}}(z,t) = \widehat{\mathbb{E}}|P_{\mathrm{Y}}(x,y,\zeta,t)|, \tag{10}$$

where ζ stands for the vertical coordinate, P_{Y} is the tendency in Y due to all physical parametrizations, and $\widehat{\mathbb{E}}$ is the horizontal averaging operator on the model grid. Then, the perturbation is defined to be

$$\delta Y(x,y,\zeta,t) = \epsilon_{\mathrm{Y}} \cdot \mathcal{P}_{\mathrm{Y}}(\zeta,t) \cdot \xi_{\mathrm{Y}}(x,y,\zeta,t), \tag{11}$$

where the multiplier ϵ_{Y} is the external parameter that controls the overall magnitude of the perturbation and $\xi_{\mathrm{Y}}(x,y,\zeta,t)$ is the Gaussian pseudo-random field with zero mean, unity variance and the tunable spatio-temporal structure (that is, spatial and time scales). The four-dimensional pseudo-random fields ξ are to be generated "online", that is, in the course of the forecast model's time integration. In this study we used the Stochastic Pattern Generator (Tsyrulnikov et al., 2017) for this purpose. The perturbations $\delta T(x,y,\zeta,t), \delta u(x,y,\zeta,t), \delta v(x,y,\zeta,t)$ (and any other perturbations referenced below) are computed and added to the model state at each time step.

Note that theoretically, specifying mutually uncorrelated random stream function and velocity potential fields instead of specifying uncorrelated random u and v wind components is to be preferred. The reason is that the former approach allows for *isotropic* vector-wind perturbations (Monin et al., 2013), unlike the latter approach. However, in practical terms, we were not able to identify any significant flaw in the vector field composed of two independent u and v fields. For this reason and due to the almost complete lack of evidence on the actual structure of model errors, we stick to the simpler formulation of AMPT with mutually *independent* $\delta u(x,y,\zeta,t)$ and $\delta v(x,y,\zeta,t)$ in this study.

From $\delta T(x,y,\zeta,t)$, we compute the pressure perturbation $\delta p(x,y,\zeta,t)$ integrating the hydrostatic equation (in which δq is neglected as a small contribution to a small perturbation). The integration goes from the model's top pressure downwards.

3.2.4 AMPT model-error perturbations: Humidity and hydrometeor fields

In contrast to roughly Gaussian distributed physical tendencies for T, u, v, physical tendencies for specific humidity q_{v}, cloud water content q_{c}, and cloud ice content q_{i} are highly non-Gaussian. Specifically, there are areas of high physical tendencies (related, mainly, to precipitation) and there are much (orders of magnitude) lower tendencies in non-precipitating areas (not shown). To simplify notation, we denote in this subsection any of these fields generically by Z in this section.

The highly variable magnitude of the physical tendency for non-Gaussian fields in different areas across the forecast domain makes the above whole-domain averaging (eq. 10) not meaningful. For these fields, we propose the *local-area* (moving-window) averaging as a means to compute the *local* (instead of global) area-averaged magnitude of physical tendency:

$$\mathcal{P}_{\mathrm{Z}}(x,y,\zeta,t) = \frac{\iint_G h_A(x-x',y-y')\cdot|P_{\mathrm{Z}}(x',y',\zeta,t)|\,\mathrm{d}x'\mathrm{d}y'}{\iint_G h_A(x-x',y-y')\,\mathrm{d}x'\mathrm{d}y'}, \tag{12}$$

where G is the model domain and h_A is the averaging kernel chosen to have the simplest "boxcar" shape:

$$h_A(x,y) = \frac{1}{A^2} \qquad \text{if } |x| < \frac{A}{2} \text{ and } |y| < \frac{A}{2} \qquad \text{and 0 otherwise} \tag{13}$$

(A is the averaging radius). The *local* averaging of the absolute (i.e. the absolute value or modulus of the) physical tendency, eq. 12, allows us to model the non-Gaussian perturbation field δZ still using the Gaussian SPG random pattern ξ_{Z}:

$$\delta Z(x,y,\zeta,t) = \epsilon_{\mathrm{Z}}\cdot\mathcal{P}_{\mathrm{Z}}(x,y,\zeta,t)\cdot\xi_{\mathrm{Z}}(x,y,\zeta,t), \tag{14}$$

where ϵ_{Z} is the external parameter (like ϵ_{Y} in eq. 11). In mathematical terms, eq. 14 implies that δZ is conditionally Gaussian given $\mathcal{P}_{\mathrm{Z}}$ and thus unconditionally non-Gaussian due to the random nature of the $\mathcal{P}_{\mathrm{Z}}$ field.

After the perturbation δZ is added to the model state at the current time step, $Z^* = Z + \delta Z$, we limit the perturbed humidity and hydrometeor fields below by nullifying negative $Z^*(x,y,\zeta,t)$. We do *not* apply a humidity supersaturation limiter (because otherwise the perturbations led to biases in perturbed forecasts).

Note that if the local averaging radius A is big enough, the moving-window scheme becomes equivalent to the formulation of AMPT with the whole-domain averaged magnitude of physical tendency. Therefore, we will assume by default that the AMPT scheme is formulated with the *moving-window-averaged* area-averaged magnitude of physical tendency $\mathcal{P}$ (as described in this section). Thus, for the i-th field, we specify its own averaging radius A_i, larger for Gaussian and smaller for non-Gaussian model variables (see section 3.2.8 for the actual choices we made).

Note that the local-averaging formulation of AMPT is applicable for the global domain as well as for the local (regional) domain.

3.2.5 AMPT model-error perturbations: Soil fields

In the land-surface model, tendencies of the two prognostic fields are perturbed: soil temperature T_{so} and soil moisture (more specifically, soil water content W_{so}), at n_{z} levels in the soil (which are counted downwards).

Due to the lack of reliable error statistics in the soil, we set up a scheme which is (i) as simple as possible, (2) consistent with statistics of the soil fields, and (iii) provides a reasonable forecast spread both in the soil and just above the land surface in the atmosphere.

The approach is to apply the above AMPT scheme. The differences with the atmospheric AMPT are:

1. In the soil AMPT, we perturb the *total* (not physical) tendency, assuming that all processes in the soil that contribute to the total tendency are modelled with substantial uncertainty.

2. The area-averaged absolute tendencies, $\mathcal{P}_{T_{\rm so}}$ and $\mathcal{P}_{W_{\rm so}}$, are computed using grid points over land only.

3. The perturbation patterns (SPG random fields) in the soil, $\xi_{T_{\rm so}}(x,y,t)$ and $\xi_{W_{\rm so}}(x,y,t)$, are two-dimensional (not three-dimensional as in the atmosphere).

4. The range of $W_{\rm so}$ is limited so that the volumetric soil water content

$$\eta_{\rm so}(x,y,z,t) = \frac{W_{\rm so}(x,y,z,t)}{\Delta_z} \tag{15}$$

(where Δ_z is the thickness of the z-th soil layer) lies between the wilting-point $\eta_{\rm wp}$ and field capacity $\eta_{\rm fc}$:

$$\eta_{\rm wp} \leqslant \eta_{\rm so}(x,y,z,t) \leqslant \eta_{\rm fc}. \tag{16}$$

If the perturbed soil water content $W_{\rm so}(x,y,z,t)$ (at any spatial grid point and any model time step) does not satisfy the constraint eq. 16, it is truncated accordingly.

For $T_{\rm so}$, the *domain* averaging is used to compute the area-averaged tendency $\mathcal{P}_{T_{\rm so}}$ (as in eq. 10). For $W_{\rm so}$, the *moving-window* averaging is employed to compute $\mathcal{P}_{W_{\rm so}}$ (as in eq. 12). These choices are motivated below in section 3.2.9.

3.2.6 Initial soil perturbations

In the soil, processes have much longer time scales than in the atmosphere, therefore weeks of cycling are needed to reach equilibrium in the ensemble statistics there. To avoid long cycling, we developed a generator of *initial* $T_{\rm so}$ and $W_{\rm so}$ perturbations.

The initial soil *temperature* perturbation is specified to be

$$\delta T_{\rm so}^{\rm ini}(x,y,z) = \sigma_{T_{\rm so}}^{\rm ini} \cdot \varkappa_{T_{\rm so}}^{1-z} \cdot \xi(x,y), \tag{17}$$

where $\sigma_{T_{\rm so}}^{\rm ini}$ is the external parameter that defines the magnitude of the perturbation at the uppermost level, $\varkappa_{T_{\rm so}} > 1$ is the vertical-decay external parameter, $z = 1, 2, \ldots, n_{\rm z}$ labels the vertical level, and $\xi(x,y)$ is the 2D SPG pseudo-random field. Note that the perturbation pattern ξ is the same for all vertical levels, whilst the magnitude of the perturbation exponentially decreases downwards (the decrease was motivated by the experimental results given below in section 3.2.9).

With the soil moisture $W_{\rm so}$, the technique is to perturb the Soil Moisture Index

$$S = \frac{\eta_{\rm so} - \eta_{\rm wp}}{\eta_{\rm fc} - \eta_{\rm wp}} \tag{18}$$

as follows:

$$\delta S^{\rm ini}(x,y,z) = \sigma_{S}^{\rm ini} \cdot \varkappa_{W_{\rm so}}^{1-z} \cdot \xi(x,y), \tag{19}$$

where $\sigma_{S}^{\rm ini}$ is the magnitude parameter like $\sigma_{T_{\rm so}}^{\rm ini}$ in eq. 17 and $\varkappa_{W_{\rm so}}$ is the vertical-decay parameter. If at some grid point the perturbed S appears to lie outside the meaningful range $[0,1]$, the perturbation $\delta S^{\rm ini}$ is truncated accordingly.

Using equations(18) and (14), we finally convert the perturbation $\delta S^{\rm ini}(x,y,z)$ into the perturbation of $W_{\rm so}$:

$$\delta W_{\rm so}^{\rm ini}(x,y,z) = \Delta_z \cdot [\eta_{\rm wp} + \delta S^{\rm ini}(x,y,z)(\eta_{\rm fc} - \eta_{\rm wp})]. \tag{20}$$

3.2.7 Stability

Stochastic-dynamic schemes in which the magnitude of forcing depends on the current state of the system can be unstable due to the positive feedback loop: a larger perturbation at the current time step may lead to a greater deviation of the state from its time-mean value, which may result in a larger physical tendency at the next time step, which would give rise to a larger perturbation, etc. until explosion.

To break this vicious circle, we considered two strategies. A technically simpler one, which we adopted in this study, is to update $\mathcal{P}_i$ not at every time step, but less frequently, once per $\mathcal{T}_{\mathcal{P}_i}^{\text{update}}$ lead time, where $\mathcal{T}_{\mathcal{P}_i}^{\text{update}}$ is the external parameter defined below in section 3.2.8.

A somewhat more involved but potentially more powerful approach (which we left for future research) is to calculate $\mathcal{P}(x, y, \zeta, t)$ from the *unperturbed* (control) model run (possibly, on a coarse spatio-temporal grid) and then use it to compute AMPT perturbations for all ensemble members. This will completely destroy the harmful positive feedback.

3.2.8 Experimental setup

The domain is shown in Fig. 10 (the Sochi Olympics-2014 area). Note the complexity of the area, which contains high mountains adjoining the sea and the valleys. The centre of the domain is located nearly at 44° N. The climate at the sea level is humid subtropical. Numerical experiments were carried out in this study mostly for the winter-spring season: in February and March, for which we had access to all data needed to run and verify an EPS. Some sensitivity experiments were also conducted for May cases.

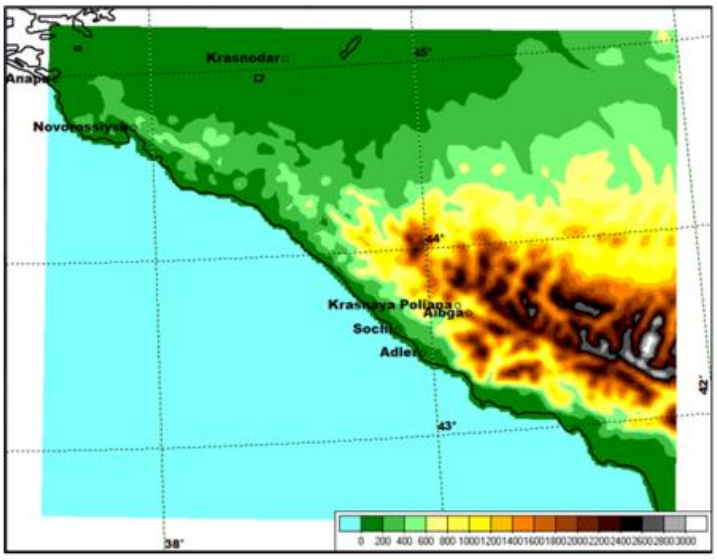


Figure 10: Model domain and orography.

The COSMO model (Baldauf et al., 2011) (version 5.01) in the convection permitting configuration with the horizontal grid spacing of 2.2 km, with the grid of 172*132 points in the horizontal, and 50 vertical levels was used for numerical experiments in this study. The model integration time step was 20 s. All calculations were performed in a single precision mode. The model's vertical coordinate was the height-based hybrid (Gal-Chen) coordinate (Gal-Chen et al., 1975).

The following AMPT parameters were selected for numerical experiments. The horizontal

length scale L_i of the SPG driving random fields ξ_i (where i labels the perturbed fields) was equal to 50 km (i.e. 20–25 horizontal mesh sizes) for T, u, v, 70% of this value (i.e. 35 km) for q_v, and 50% (25 km) for the cloud fields.

The time scales $\mathcal{T}_i$ of the atmospheric random fields ξ_i were specified as L_i/U , where U is the characteristic velocity. By trial and error, we found that $U = 15$ m/s worked well (and is physically meaningful). For both soil fields, i.e. T_so and W_so, the common time scale $\mathcal{T}_\mathrm{so}$ was specified as the time scale for atmospheric temperature, $\mathcal{T}_\mathrm{T}$, multiplied by a factor $\tau_\mathrm{so} > 1$ that reflects a much greater inertia of the soil as compared to the atmospheric air, so that $\mathcal{T}_\mathrm{so} = \tau_\mathrm{so} \cdot \mathcal{T}_\mathrm{T}$. The optimally tuned value of the soil inertia factor τ_so was 12 (i.e. the time scales were, roughly, 1 h in the atmosphere and 12 h in the soil).

The time-update interval $\mathcal{T}_{\mathcal{P}_i}^{\mathrm{update}}$ (see section 3.2.7) for the model field X_i was set equal to the time scale $\mathcal{T}_i$ of the respective random pattern ξ_i. Note that with $\mathcal{T}_{\mathcal{P}_i}^{\mathrm{update}}$ much lower than $\mathcal{T}_i$, the perturbed model may become unstable (see section 3.2.7), whereas with $\mathcal{T}_{\mathcal{P}_i}^{\mathrm{update}}$ much greater than $\mathcal{T}_i$, the resulting area-averaged $\mathcal{P}_i$ may become irrelevant in a rapidly developing meteorological situation.

The magnitude parameter of the initial T_so perturbation, $\sigma_{T_\mathrm{so}}^{\mathrm{ini}}$, was set to 1 K. The magnitude parameter of the initial soil moisture index perturbation, σ_S^{ini} was set to 0.01 (larger values led to unrealistically large model tendencies in T_so).

After some experimentation, the model-error multipliers ϵ_i were specified equal to 0.75 for T, u, v, T_so, and W_so, and 0.5 for q_v, q_c, and q_i.

The absolute-physical-tendency averaging length scale A_i (see section 3.2.4) was specified equal to the length scale L_i of the respective SPG random field ξ_i for q_v, q_c, q_i, and W_so. For the nearly Gaussian fields T, u, v, the respective A_i were selected large enough to ensure the whole-domain averaging of $|P_i|$.

In the ensemble prediction experiments presented below, we actually perturbed only temperature and winds because this configuration produced stable and positive results. As for humidity and cloud fields perturbations, they led to mixed results in EPS verification scores and so were not included in the model-error perturbation scheme.

We also compared AMPT with SPPT, implemented in the COSMO model by L. Torrisi and tuned by Maurer et al., 2014. In the SPPT, the standard deviation of the random field was set to 0.8, the spatial scale to 5° (i.e. some 500 km), and the time scale to 6 h. Temperature, wind, and humidity were perturbed.

Tapering, that is, a gradual reduction of the perturbation magnitude (1) in the lower troposphere towards the surface and (2) in the stratosphere from the tropopause upwards, was handled in the SPPT as follows. The stratospheric tapering was always active in our experiments because it is believed that the radiation tendency, which is dominant in the stratosphere, is quite accurate in clear-sky conditions (e.g. Leutbecher et al., 2017). As for the lower-tropospheric tapering, which is intended to prevent instabilities due to inconsistencies of perturbed physical tendencies and unperturbed surface fluxes (Wastl et al., 2019), we found that the SPPT worked better without it. Specifically, our experiments showed that, on the one hand, the SPPT without tapering was stable in the boundary layer. On the other hand, with tapering, SPPT led to an unacceptably small ensemble spread in the near-surface fields, so we switched off the lower-tropospheric tapering in the SPPT. In AMPT, tapering was switched off in the experiments described below.

Note that the above spatial and time scales employed in AMPT were an order of magnitude less than those in the SPPT (50 km vs. 500 km and 1 h vs. 6 h). This is reasonable because

in SPPT, the perturbation is *multiplicative*, i.e. the random field (pattern), $\xi(x, y, t)$, is multiplied by the physical tendency, $\mathbf{P}(x, y, \zeta, t)$, which is a rather small-scale random field itself, so that the perturbation, $\xi(x, y, t) \cdot \mathbf{P}(x, y, \zeta, t)$, appears to be a reasonably small-scale field even if $\xi(x, y, t)$ is large-scale. If $\xi(x, y, t)$ were small-scale in SPPT, the product $\xi \cdot \mathbf{P}$ would be too patchy, which would reduce the effect on the forecast. In contrast, AMPT introduces an *additive* perturbation, which needs to be small-scale in order to represent the errors in parametrizations of *subgrid-scale* processes.

To find out if this argument is reasonable, we ran the SPPT with the smaller time scale of 1 h and the spatial scales of 50 and 100 km. The resulting spread in the ensemble forecast was very small, confirming the conclusions of Maurer et al., 2014 (made for a different domain, orography, physiography, etc.) and justifying the choice of the SPPT parameters for our domain (the setup was also consistent with that employed in AROME-EPS, (Bouttier et al., 2012)). For the set-up of SPPT in COSMO, see also Klasa et al. (2018).

Note that in what follows, by "model perturbations" we mean model-error perturbations generated by AMPT and SPPT in the atmosphere and also the initial and model-error perturbations generated by AMPT in the soil.

3.2.9 Unperturbed T_{so}, W_{so} total tendencies

Fig. 11 shows the unperturbed tendencies for T_{so} and W_{so} at the soil level $z = 2$ and lead time 2 h (the forecast started at 00 UTC on the 1st of May 2014). The tendencies were computed as one-time-step differences and recalculated w.r.t. 1 h (so that the T_{so} tendency is measured in K/h).

The T_{so} tendencies (left panel in Fig. 11) look more or less uniform (albeit with a few isolated outliers) and thus not far from Gaussian. For this reason, the AMPT perturbation scheme for T_{so} model-error perturbations was selected to involve whole-domain (not moving-window) averaging of the modulus of the tendency.

The W_{so} tendencies on the contrary (right panel in Fig. 11), are highly inhomogeneous and thus non-Gaussian. This motivated the use in the AMPT perturbation scheme for W_{so} of a *moving-window* averaging of the modulus of the tendency to scale the model-error perturbation of W_{so}.

In the vertical, the mean absolute tendency in $\mathrm{T_{so}}$ roughly halved when going one level down in the soil (not shown). So did (again, roughly) the maximal absolute tendency in $\mathrm{W_{so}}$[1].

We found no significant dependencies in the magnitude and spatial structure of soil tendencies on the soil type (there were only two soil types in the COSMO model across the domain, not shown).

One can see a signature of orography (Fig. 10) in the soil tendency fields (Fig. 11).

3.2.10 Testing AMPT in an ensemble prediction system

Numerical experiments were carried out to study the effect of AMPT model perturbations in COSMO-Ru2-EPS (Montani et al., 2014 and Astakhova et al., 2015), the ensemble prediction

[1]The *maximal* absolute tendency looks more appropriate to measure the magnitude of the tendency in $\mathrm{W_{so}}$ than the *mean* absolute tendency — because the magnitude of the soil moisture tendency exhibits very big changes over the model domain (see Fig. 11, right panel) so that the averaged value is irrelevant for areas of both big and small model tendencies (that is, almost everywhere).

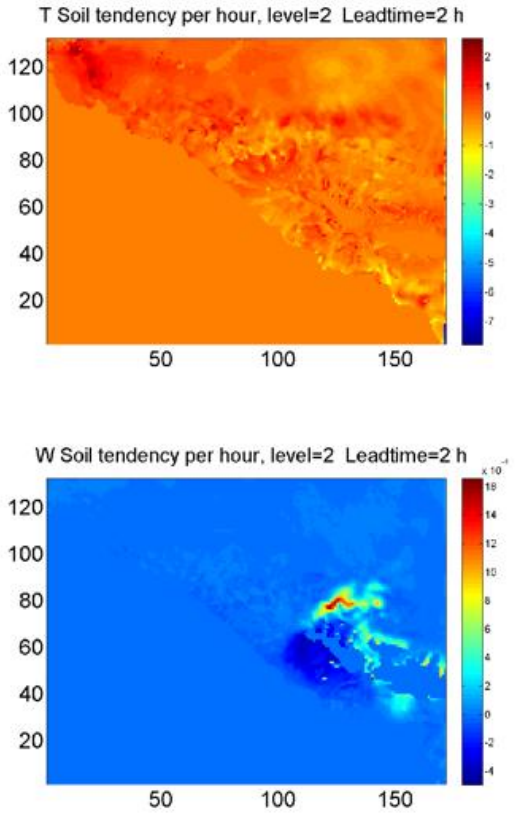


Figure 11: Total tendency of T_{so} (left, K/h) and W_{so} (right, W_{so} units per hour) at level 2, forecast lead time 2h. The forecasts were initialized at 00 UTC 1 May 2014. Tick labels are grid points in the longitudinal (x-axis) an latitudinal (y-axis) directions

system developed within the FROST-2014 project (Kiktev et al., 2017) and CORSO priority project of the COSMO consortium (Rivin et al., 2018). For the COSMO model set-up used in the ensemble prediction system, see above section 3.2.8. The ensemble size was 10. COSMO-Ru2-EPS performed a dynamical downscaling of the forecasts of the driving COSMO-S14-EPS system developed by ARPA-SIMC for the Sochi Olympics (Montani et al., 2013). Thus, both initial and lateral boundary conditions for the control forecast and the ensemble members were provided by COSMO-S14-EPS. In turn, COSMO-S14-EPS was a clone of the consortium ensemble prediction system COSMO-LEPS (Montani et al., 2011) with a smaller ensemble size and shifted to the area of the Sochi Olympics. COSMO-S14-EPS had the horizontal grid spacing of 7 km and 40 levels in the vertical.

Experiments setup

A continuous series of experiments was performed with COSMO-Ru2-EPS for the two-month period of February-March 2014 without model perturbations as well as using AMPT and SPPT with the parameters indicated above (section 3.2.8). The forecasts were initialized every day at 00 UTC. The local time for the region considered was UTC+3 h. The results were verified against near-surface observations (about 40 stations) using the COSMO unified verification system VERSUS (Raspanti, 2009). Ensemble forecasts in the free atmosphere were verified against zero-lead-time ECMWF forecasts (with the horizontal resolution of about 16 km).

Below we show verification scores for the whole two-month period. Similar results were obtained for each of the two months separately (not shown).

We concentrate on the impact of model perturbations on probabilistic forecasts of $T_{2\mathrm{m}}$ and precipitation.

The list of experiments and their basic features are presented in Table 1.

Table 1: List of experiments with COSMO-Ru2-EPS

Experiment	Model perturbations in addition to initial and lateral-boundary ones
NOPERT	None
SPPT	SPPT model-error perturbations in the atmosphere
AMPT-NOSOIL	AMPT model-error perturbations in the atmosphere
AMPT-SOIL	AMPT perturbations: atmosphere + soil

Deterministic verification

Fig. 12 shows the root-mean-square error (RMSE) of the $T_{2\mathrm{m}}$ *ensemble mean* forecast (the upper bunch of curves). One can see that, excluding the initial transient (spinup) period of some 3 h (likely, due to imbalances in the initial perturbations), the RMSE had a prominent diurnal cycle with a broad minimum at night and a narrower maximum shortly after midday. This corresponds to the known systematic error in $T_{2\mathrm{m}}$ in the COSMO model (Fig. 2 in Kirsanov et al., 2020).

Fig. 13 displays the normalized ensemble-mean RMSE reduction w.r.t. NOPERT (to highlight the barely seen in Fig. 12 differences between the experiments), that is, $(RMSE_{NOPERT} - RMSE)/RMSE_{NOPERT}$. SPPT led to a persistent slight reduction in RMSE. AMPT model perturbations gave rise to a more significant decrease in the $T_{2\mathrm{m}}$ RMSE most of the time except for the rather short time periods in the afternoon, when the ensemble-mean forecast deteriorated. Soil perturbations added skill to the ensemble mean forecast: the RMSE reduction is higher in the experiment AMPT-SOIL than in AMPT-NOSOIL.

Reliability

The lower bunch of curves in Fig. 12 shows the ensemble spread, which was a bit too low with both SPPT and AMPT. This implies that the ensemble forecast was lacking reliability, though AMPT perturbations increased the spread to a much greater extent than SPPT perturbations. The effect of the AMPT perturbations on the spread was nearly the same for all lead times. The gradual overall growth of the spread with time was, likely, caused by the lateral boundary perturbations as they propagated from the boundaries to the domain interior. This explanation is consistent with the gradual reduction in the differences between the experiments (since they had the same lateral boundary perturbations).

Higher in the atmosphere, the RMSE of temperature and wind speed was negligibly affected by AMPT perturbations while the related spread grew most efficiently near the surface and fell with height.

For temperature, the AMPT atmospheric perturbations resulted in a spread growth by 0.3 K at 20 m, 0.25 K at 150 m, and 0.1 K at 1000 m. The soil perturbations added only about 0.08 K to the spread below 150 m and their effect vanished towards the top of the boundary layer.

For wind speed, the spread gain due to the AMPT purely atmospheric perturbations was

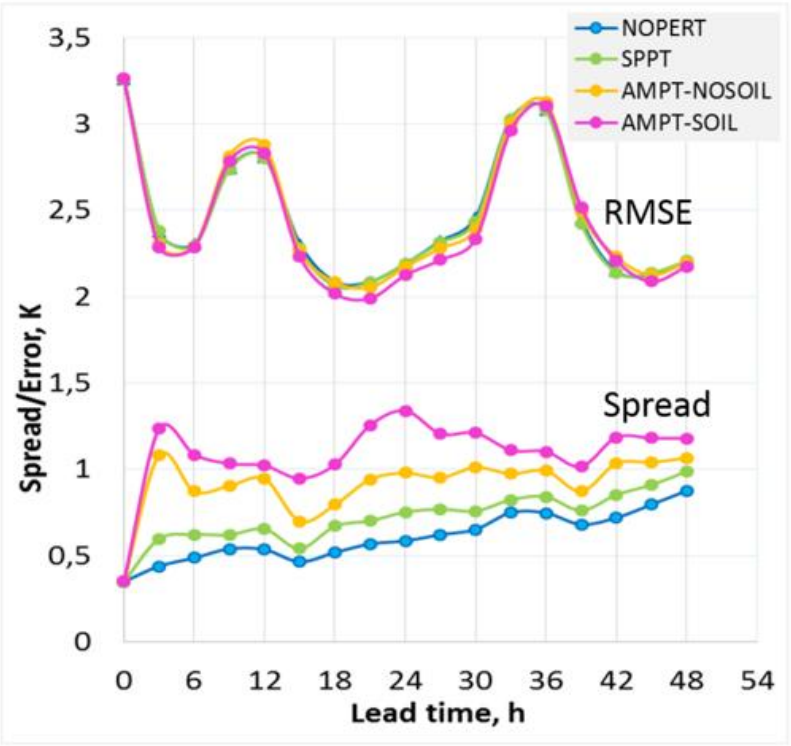


Figure 12: RMSE of T_{2m} ensemble mean and spread. Experiments NOPERT (blue), SPPT(green), AMPT-NOSOIL (orange), and AMPT-SOIL (magenta).

about 0.3-0.4 m/s below 150 m and reduced to 0.2 m/s at 1000 m. The impact of soil perturbations on the wind speed was rather weak. Even at the lowest model level (20 m) the spread difference between AMPT-NOSOIL and AMPT-SOIL was only 0.01 m/s.

AMPT perturbations of humidity and cloud fields generated significant spread in precipitation and in the upper-air temperature during precipitating events but the effect of those perturbations on the ensemble prediction performance scores was mixed (not shown). Further experiments are needed to reach more conclusive results.

Probabilistic verification

Standard probabilistic scores for near-surface variables were calculated for all experiments. The continuous ranked probability score (CRPS), which generalizes the mean absolute error to the case of probabilistic forecasts, is presented in Fig. 14 for T_{2m}. CRPS measures the difference between the predicted and occurred cumulative probability distributions. Both SPPT and AMPT improved CRPS but AMPT was undoubtedly more successful, especially with additional soil perturbations.

The advantage of AMPT over SPPT for T_{2m} is also supported by the analysis of the Brier score, which characterizes the magnitude of the probability forecast error, see Fig. 15. In fact, this result could be expected as CRPS is usually interpreted as the integral of the Brier score over all possible threshold values (Hersbach,2000).

We also examined the ability of our EPS with different model perturbations to discriminate between two alternative outcomes (say, "T is below a threshold" and "T is above the threshold"). The relative operating characteristic (ROC) is normally used to assess the discrimination ability of an EPS. Fig. 16 shows the area below the ROC curve (ROCA) for two thresholds. Note that the perfect value for ROCA is 1 and the value less than 0.5 indicates

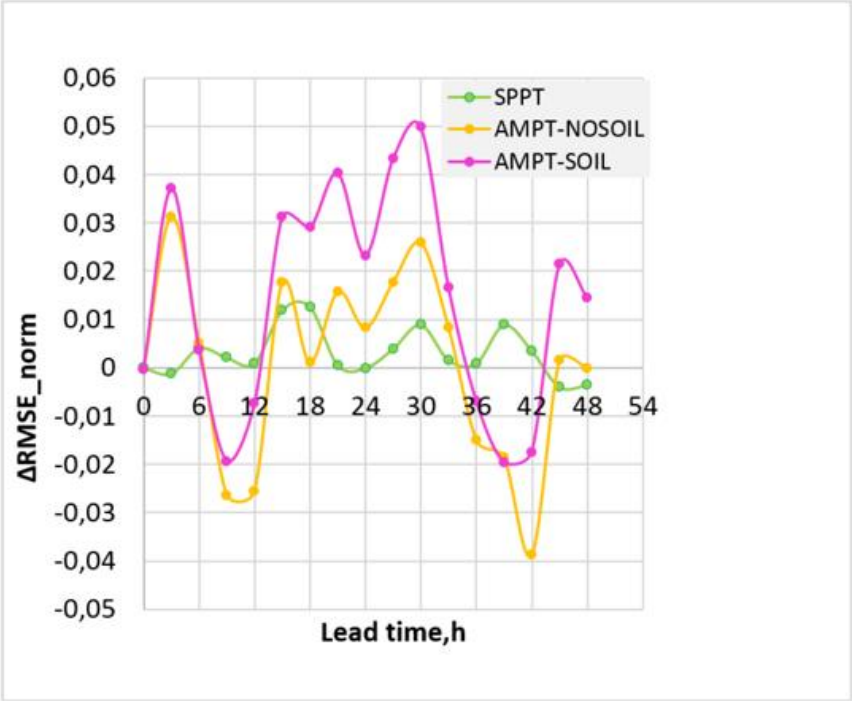


Figure 13: Normalized $T_{2\mathrm{m}}$ ensemble-mean RMSE reduction (the greater the better).

no skill. Actually, ROCA in Fig. 16 is quite high, indicating that the EPS was skillful. Like the previously mentioned probabilistic scores, ROCA demonstrates the advantage of the EPS configuration AMPT-SOIL for both thresholds indicated in Fig. 16 and for the majority of other thresholds we tested (not shown).

The effect of T, u, v perturbations on precipitation was rather ambiguous (see Fig. 17)), perhaps because the time period considered was rather dry (Vasil, 2015). The first half of February 2014 was characterized by an anticyclonic weather, that favoured the precipitation deficit. Only during the second ten-day period of March 2014 considerable amounts of precipitation were observed. Further experiments are needed and will be conducted after this study.

3.2.11 Discussion on AMPT

Limitations of the experimental setup

1. The initial and lateral-boundary (driving) ensemble was under dispersive. This factor might lead to an overestimation of the tuned AMPT *model-error* parameters (the model-error perturbations might be forced to, partly, do the job of initial and lateral-boundary perturbations).

2. The study is conducted on a small model integration domain and for a time period of only one season, which may imply that additional experiments with AMPT on a domain in a different climate zone, different orography and physiography in different seasons and weather conditions need to be conducted to get more conclusive results.

3. In particular, the period of February-March 2014 was rather dry, so it was hard to justify the effect of AMPT perturbations on precipitation. However, sensitivity exper-

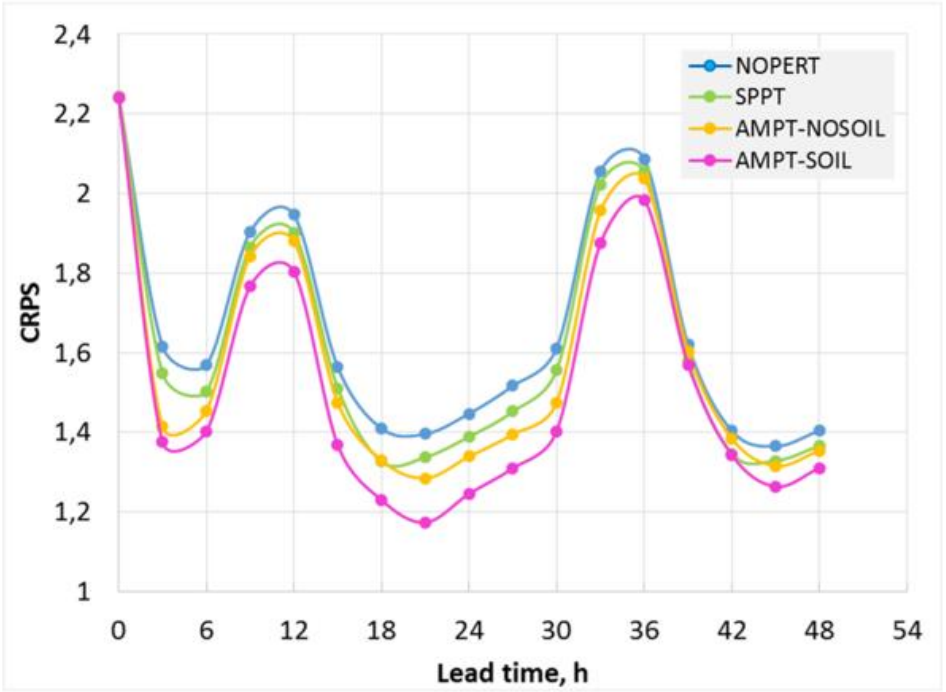


Figure 14: CRPS for $T_{2\mathrm{m}}$. The lower the better.

iments for May 2014, not presented in this report, suggest that AMPT humidity and cloud-fields perturbations can be important during periods with convective events.

4. For the same reason, we do not present here results of experiments with humidity perturbations. Only perturbations of temperature, wind, and soil were introduced in the above experiments.

Advantages and limitations of AMPT

Theoretically, potential advantages of AMPT w.r.t. SPPT are:

- AMPT generates *additive* model-error perturbations, which can represent errors in physical parametrization schemes when they produce an erroneously small physical tendency. SPPT cannot do that because its perturbations are multiplicative.
- AMPT can account for errors in the *relationships* between errors in different variables and at different model levels. In SPPT, these relationships are, effectively, assumed to be error free.

A potential disadvantage of AMPT w.r.t. SPPT is:

- AMPT produces, likely, less balanced perturbations than SPPT because the latter preserves the relationships between different variables and between different model levels. But model-error perturbations (imposed at every model time step) are very small and so are the imbalances. In our numerical experiments we found no evidence of problems related to the imbalances, unless the AMPT perturbations were "too big" (i.e. having an excessive magnitude and/or spatial or time scale). For "not too big" AMPT perturbations, the model was able to cope with the small imbalances without any indication of spinup-like behaviour.

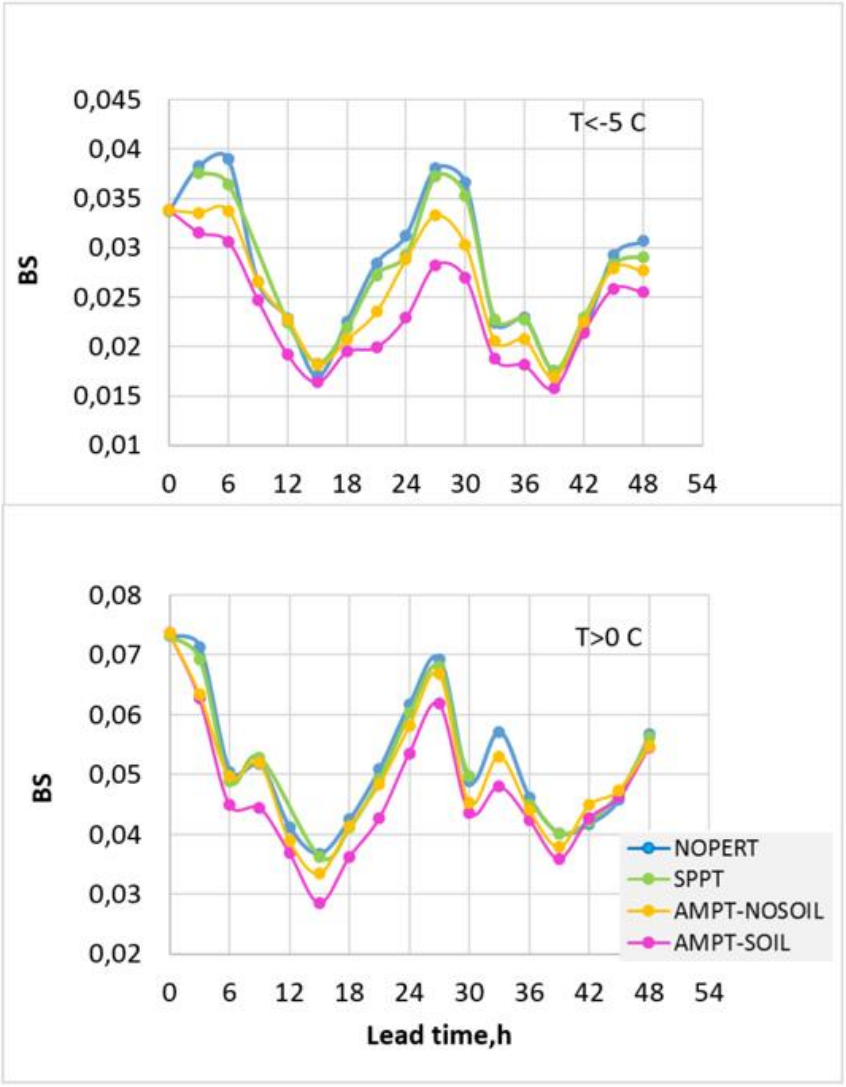


Figure 15: The same as Fig. 14 but for the Brier score for the events $T_{2\mathrm{m}} > 0$ C (the upper panel) and $T_{2\mathrm{m}} < -5$ C (the lower panel). The lower the better.

3.2.12 Conclusions on AMPT

- A new technique called Additive Model-error Perturbations scaled by physical Tendency (AMPT) is proposed. AMPT employs the Stochastic Pattern Generator (Tsyrulnikov et al., 2017) to generate four-dimensional random fields with tunable spatio-temporal correlations. The SPG random fields in AMPT are independent for different model fields. They are scaled by an area-averaged modulus of physical tendency and added to the model fields at every model time step. Gaussian and non-Gaussian fields are treated by AMPT.
- Three-dimensional model fields of temperature and winds were perturbed.
- Three-dimensional soil fields (temperature and moisture) are perturbed as well.
- In ensemble experiments, it was found that AMPT perturbations were very effective in generating spread in the ensemble.

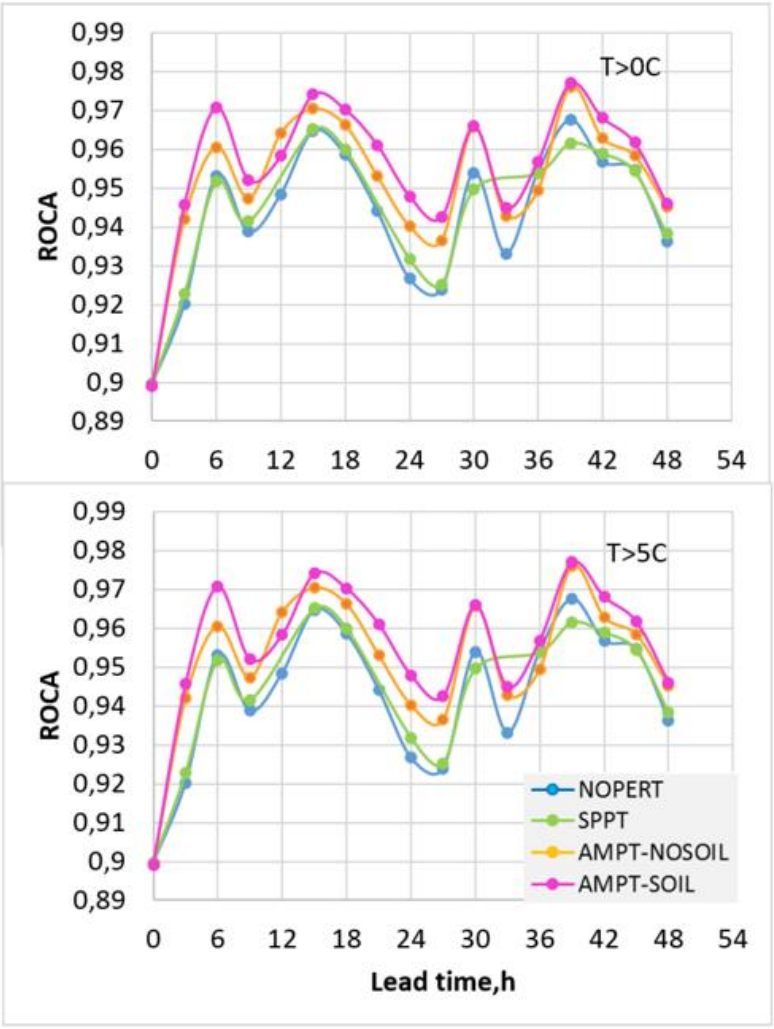


Figure 16: The same as Fig. 14 but for ROCA for $T_{2\mathrm{m}}$ for the events "$T > 0$ C" and "$T > 5$ C". The higher the better.

- Perturbing humidity and cloud fields generated significant spread in precipitation and upper-air temperature during precipitating events (not shown).
- Soil perturbations contributed significantly to the spread of near-surface fields.
- AMPT was able to reduce the average root-mean-square error (RMSE) of the ensemble mean w.r.t. no model perturbations and w.r.t. SPPT, however sometimes RMSE was degraded.
- Probabilistic ensemble verification scores (CRPS, Brier score, and ROC area) for near-surface temperature and wind speed were improved due to AMPT model perturbations in the atmosphere w.r.t. no model perturbations and w.r.t. SPPT.
- AMPT soil perturbations further improved the probabilistic verification scores.
- Probabilistic verification of precipitation gave mixed results, perhaps due to the insufficient number of precipitating events during the time period examined.

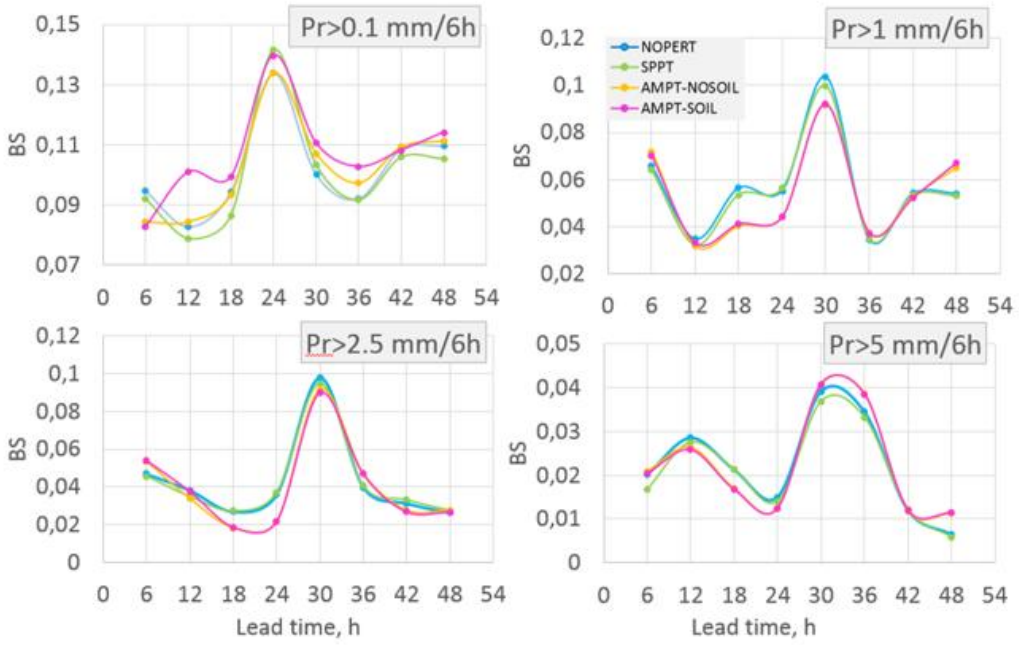


Figure 17: Brier score for total precipitation for the various thresholds indicated in the panels. The lower the better.

3.3 Model perturbations at IMGW (A. Mazur and G. Duniec, IMGW)

At IMGW, the basic instance of the COSMO model runs in a deterministic mode, using the initial (IC) and boundary (BC) conditions from the global ICON model. ICON generates a sets of IC/BC for 78-hour mesoscale COSMO forecasts. In turn, COSMO model with a horizontal resolution of 7 km (COSMO-7) uses nudging-based data assimilation to correct the forecasts of the global model by retrieving the latest data from the WMO network. The forecast results with a resolution of 7 km are further used as sets of IC/BCs for a nested COSMO model instance with a higher resolution of 2.8 km, and 48-hour forecasts. These deterministic COSMO-2.8 km forecasts define the basis for the operational configuration of the Ensemble Prediction System (EPS). In the final configuration of the operational EPS at IMGW, the set of twenty ensemble members is grouped into four packages, staggered in time by 6 hours from one another, obtained from previous model runs. Each package contains five members (Mazur and Duniec, 2015). All forecast (ensemble) results are then processed to provide the selected statistics (ensemble mean, spread, probability of exceedance of selected thresholds, etc.) in a graphical form. Model perturbations are added, by perturbing the parameter describing evaporation from the soil (c_soil).

3.3.1 Perturbations based on adapted Random Number Generator.

Computer-generated random numbers are called "pseudo-random" numbers as they are designed to mimic randomness but they are determined in a deterministic, though often very complex, way. Due to the ever-growing demand for good pseudo-random numbers, the literature describes many ways to generate them, and many people are still working on new methods. To generate numbers from the uniform distribution are used, among others, the following algorithms: Wichmann-Hill (Wichamnn and Hill, 1982), Marsaglia (Marsaglia,

2003), Knuth (Knuth, 1981). In general, a Random Number Generators (RNG) is a deterministic function. It uses the so-called "seed" that completely determines the values of the subsequent pseudorandom numbers. The seed is the value on the basis of which successive random numbers will be constructed. For a permanent generator and seed, identical random numbers will be generated regardless of the operating system or computer type. This property can be easily exploited. By controlling the selection of the seed, it is possible to obtain identical sequences of random numbers on different computers. In this way, one can repeat the simulation results, reproducing these results on other computers, or continuing calculations interrupted by some error. However, the basic selection of seed has its weaknesses. The seed on most computers is based on machine time (generally milliseconds). On high-speed machines, seeds can be identical for many, if not all, processes (threads). This problem is illustrated in the Fig. 18. More threads means more likelihood to have identical seeds. With an exemplary operating configuration of 400 threads versus 999 milliseconds, one will not get 999 ms (and, hence, 999 values of seed) on high-speed machines, but much less. This increases the probability that multiple threads (the blue diamonds) will have the same grain (red rectangles). The basics of the new RNG have already been presented in the framework of the Priority Project SPRED. Here, therefore, just to reminder is provided: the basic scheme of the new RNG assumes a sequence (in particular, even several stages) of generating seed values. That is, the first operation in a sequence generates a (pseudo-random) number which is the input to the next operation, and so on (see Fig. 18). Ultimately, the final seed value suitable for the RNG is obtained. At the expense of a slight extension in time, significantly randomized seed values are obtained.

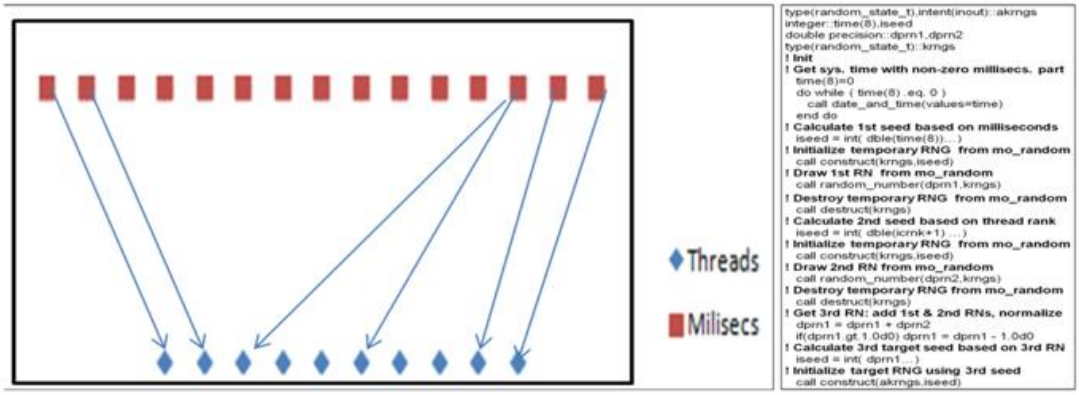


Figure 18: Left (a): Problem with parallel threads of stochastic computations - seeding RNG with machine time (milliseconds). Right (b): Block scheme of new seeding for RNG

Changing the RNG to the proposed one causes (may cause) a problem related to the loss of reproducibility of the results, mentioned in the introduction. However, from a mathematical point of view, the reproducibility requirement cannot be applied to single samples of partially or wholly nondeterministic phenomena, although it still applies to a probabilistic description of these phenomena, with the error tolerance defined by the probability theory. Apart from repeatability for technical or comparative tests, however, it is difficult to see too many arguments in favour of choosing permanent seeds. Perturbations based on an adapted Random Number Generator (RNG) were prepared for the years 2011-2015 (archive data).

This part of the report presents a comparison between a "new" RNG vs. a standard one. Essentially, the "new" RNG has been operating in operational mode since 2019, replacing the "old" one. The modification was made when the perturbed parameter (c_soil) was defined in the code. The main reason for choosing where to introduce the random variation was code maintenance. By introducing variations in the original position (defining the field of the

disturbed parameter) on all nodes, it is possible to avoid excessive communication between the processors during the redistribution of the field. The use of machine time was due to the fact that initialization is performed only once (i.e. at the beginning of the model launch). The disturbed parameter is used only in the soil model (only once after the model started), and further during computations the distribution is no longer needed. The procedure does not repeat afterwards and does not affect efficiency in any way, but it seems to be one of the best sources of stochastic initiation. The results of the initial application of the new RNG were presented in PP SPRED, while further results of the RNG use tests are shown here. The influence of the RNG on the air temperature and dew point at 2m, wind speed at 10m and relative humidity at 2m is shown (Table 19 and Fig. 20, compared to values obtained with the standard "old" generator.

Spread values	Reference (standard RNG)	Modified RNG (operational)	Reference (standard RNG)	Modified RNG (operational)
	T2M (K)		TD2M (K)	
Mean	0.1218173	0.250191	0.13452	0.282912
Max	2.813	3.212	3.541	4.189
	U10M (m/s)		RH2M (%)	
Mean	0.17813	0.22381	0.965178	2.694192
Max	2.412	3.258	12.419	16.617

Figure 19: Average spread values for T2m and Td2m for years 2011-2015, modified RNG (left) and standard RNG (right). Tests with perturbations included, lagged members excluded.

Upon completion of the tests, the standard RNG was turned off. Currently, taking into account the quality from the new RNG, a new method of seed generation is operationally used for perturbations.

3.3.2 Perturbation of soil surface temperature in combination with upper air perturbation

The usage of other types of model perturbations has been tested and the results are here presented. Perturbations include soil surface temperature, coefficient of performance and combinations thereof. The following cases were considered:

a. operational set-up: perturbation of the parameter describing evaporation from the soil (c_soil);

b. eff-coeff: perturbation of the collection efficiency coefficient;

c. laf-pert: perturbation in soil surface temperature (initial values, with the amplitude of perturbation depending on the type of soil, see Duniec and Mazur, 2020);

d. combination of b) and c)

The general perturbation scheme have the following form:

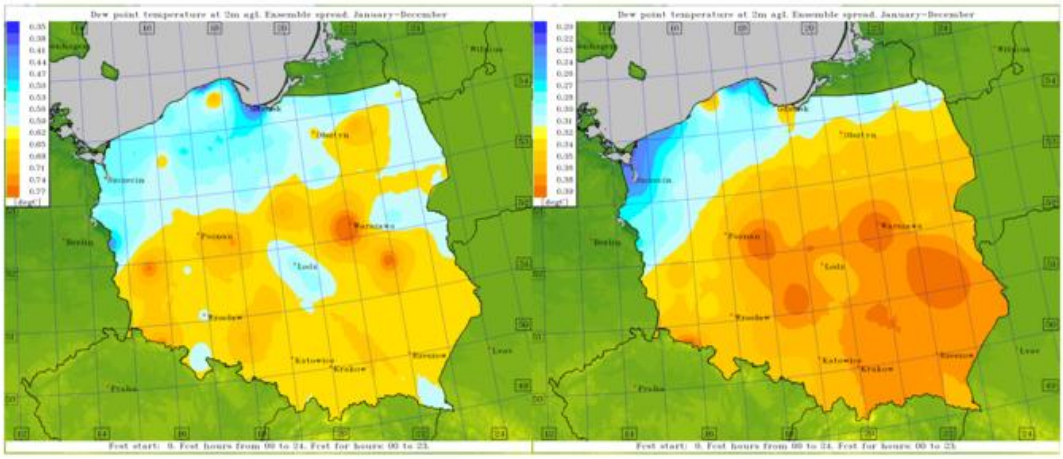


Figure 20: TD2M average spread values for years 2011-2015, modified RNG (left) and standard RNG (right). Tests with perturbations included, lagged members excluded.

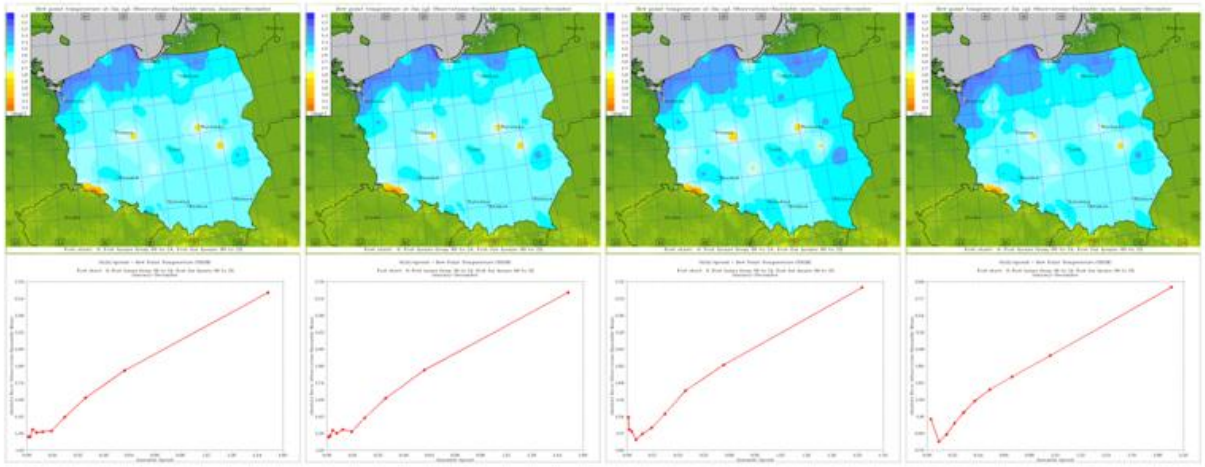


Figure 21: Upper panels: observations minus ensemble means, lower panels: spread-skill diagrams. Left to right are shown the 4 configurations of the ensemble: (a), (b), (c), (d) (see explanations in the text). Averaged values for the years 2011-2015.

perturbed_value=basic_value * [1+(random_number -0.5) * amplitude]

where the "random_number" (obtained from a computing dependent pseudorandom number generator, see section 3.3.1) varies from 0 to 1. In the laf-pert perturbation it is assumed that the ability to transfer heat and water is related to the compactness of the soil. If the soil is coarse (like sand), the amplitude of the disturbance is one, and the more compact the soil texture, such as peat or clay, the smaller is the disturbance amplitude. For example, for sand the amplitude was set to 1.0, for clay it was set to 0.6 and for peat it was set to 0.5. Thus, for sand, the perturbation ranged from 0.5 to 1.5 of the original (undisturbed) value. A climatological analysis for the warm period of a selected year was presented in Duniec and Mazur (2015). The overall results were also presented at the ICCARUS 2020 seminar. In Fig. 21 are reported only the most significant results, a comparison of different perturbation methods vs. measurements at SYNOP stations in Poland.

Research results essentially confirmed that:

1. the influence of the perturbation of the efficiency coefficient is, as expected, significant only in the case of precipitation;

2. the combination of different types of perturbations does not necessarily have a linear effect on the spread value and, moreover, on the quality of the forecasts. In some cases, the size of the spread produced by the perturbation combination was significantly greater than the algebraic sum of the spread produced by the perturbations applied separately;

3. compared to the operational EPS setup, new types of perturbation improve the quality of the forecasts in terms of skill and spread. The most effective perturbation scheme in terms of MAE and spread, averaged over the period 2011-2015, was the combination of perturbation types, with the mentioned restriction concerning point (1).

3.4 Perturbations based on SPPT with independent pattern (iSPPT) (André Walser and Linda Füzér, MCH)

The operational ensemble prediction system (EPS) of MeteoSwiss, COSMO-E, is underdispersive, i.e. the forecast shows a lack in the ensemble spread near surface, particularly in the short-range during the winter season. Stochastic perturbation of physical tendencies (SPPT) is operationally used in COSMO-E to represent model errors by perturbing the sum of the physical tendencies from the parametrization schemes. Although SPPT increases the spread significantly, there are still opportunities for further improvements. Christensen et al. (2017) suggest a modified version of SPPT called independent stochastically perturbed physical tendencies (iSPPT) which allows more flexibility in the perturbation setup and yields a better spread-error relationship in a global ensemble prediction system. For this reason, we have implemented iSPPT in the COSMO code in a test branch and investigated whether an iSPPT scheme can improve COSMO-E forecasts.

The results of the iSPPT experiments are shown in detail in Füzér (2018). In summary, iSPPT does not reveal a consistent improvement of the COSMO-E forecast spread-error relationship as compared to SPPT experiments. The ensemble mean error of the forecast is hardly sensitive to iSPPT, and a positive effect on the spread is found for wind speed and humidity and in some setups only while the spread for temperature could not be increased. The flexibility provided by iSPPT to perturb the individual physical tendencies differently is not helpful to achieve better scores for COSMO-E. Best results with iSPPT are achieved with the same random number setup as for SPPT applied to all physical tendencies.

3.5 Perturbations based on analysis increments (André Walser and Linda Füzér, MCH)

Perturbations from both SPPT and iSPPT do not account for model errors different than the ones arising from the parametrization schemes. For a global EPS, Piccolo et al. (2018) thus propose model perturbations using analysis increments (AIs) of the data assimilation cycle, as they are not random quantities but rather include possible sources of forecast errors. Such perturbations could also be beneficial for a limited-area EPS like COSMO-E. However, the characteristics of the AIs from the KENDA system, which provides the initial conditions for COSMO-E, has not been investigated yet and is thus unknown.

Füzér (2018) shows a detailed analysis of the AIs from the operational KENDA system of MeteoSwiss. The considered time period is 1st June 2017 to 31st August 2018 to cover all seasons and to be able to compare the summer of two different years. In summary, the AI

dataset only shows notable biases for summer temperature and humidity. Between 8 and 16 UTC, a negative temperature bias of up to -1.5 K can be found in the lowest model levels. During the other seasons and variables, regional biases are visible. Both the absolute mean AIs and standard deviation show clear variability among the seasons and have a diurnal cycle that also varies with the seasons. The magnitude and variability of the AIs increase throughout the course of the day and reach a maximum at 12 UTC and a minimum at night time. The most pronounced diurnal cycle is visible for summer, followed by spring and autumn. A comparison of summer 2017 and 2018 leads to the conclusion that the AIs analysed in this thesis are representative for the respective seasons because the two years show very similar characteristics although they were different in terms of meteorology. The comparison of AIs and model verifications against radiosondes reveals that the magnitude of the AIs is in good agreement with the model first guess mean error. Additionally, as expected, the AIs have opposite signs compared to the mean error of the FG ensemble mean.

The results of the analysis point towards a possible suitability of the AIs as model perturbations. There is a variability within the data, therefore the individual members of the ensemble prediction system would be perturbed differently and lead to an enhanced spread in the result. The AI fields should be grouped by season and time of the day and drawn from the corresponding group when the perturbations are applied. As the AIs are in good agreement with the bias of the FG ensemble mean, perturbations generated using AIs have the potential of reducing the model error and local biases. Before using the AIs as model perturbations, the outliers in the AI data set should be further investigated. It might be useful to set a range for the AIs in order to avoid disproportionally large perturbations.

Even though the study confirms that model perturbations with analysis increments have a large potential to be beneficial for a high-resolution EPS too, it has not been implemented and tested yet due to missing resources.

4 Post-processing and interpretation of ensembles

4.1 Calibration (A. Mazur, W. Interewicz, IMGW)

The development and application of calibration methods at IMGW were initiated in the previous Priority Project SPRED, and here only the results and conclusions from the continuation of the research and method(s) development are presented. The research essentially focused on three basic methods of determining the ensemble mean.

- The most common procedure for calculating the ensemble mean is to use the arithmetic mean of values obtained for all particular members, here called "Simple" Average. Values obtained from the members affect the ensemble mean with the same weight. The simplicity of the method implies that no additional procedures or assumptions are required.
- An alternative approach can be described as (multi-) linear regression (MLR), where pre-made predictions of all (X) EPS members are compared with the observations during a learning phase. The weights of each member are then calculated to judge how "important" the selected member should be in the overall EPS average (or how large a member's share in the EPS average should be). The least squares method used for the computation of the weights can also take into account all potentially important factors such as geographic coordinates, altitude, hour of forecast start, current forecast hour etc. An additional condition is the normalization of weights to one.

- Finally, an artificial neural network (ANN) was investigated to see if this approach could be a valid substitute for a Simple Average or MLR Mean. The basic idea is that the weights, according to the same scheme as in the MLR calculation, are calculated (learned) using the concept of the neuron layer(s), appropriately activated during the learning phase. This approach uses the commonly used ANN back-prop method combined with the activation function of a hyperbolic tangent. During the research (and later in the operational application of the method), a system with two layers of neurons (input and hidden) was used. The first (input) layer contains six neurons, the second, hidden layer contains two neurons. Such a scheme is due to the fact that the EPS creates four sets of five members, corresponding to four neurons, while the other two input neurons are related to spatial (geographic coordinates, terrain height) and time constants (forecasts leadtime). In the hidden layer, two neurons are assigned to variables (forecast members) and constants.

The effectiveness and superiority of the ANN method compared to the Simple Average and MLR were proven (Fig. 22). After the tests and this comparison the ANN method was implemented in an operational mode.

Another calibration technique applied and tested was the VOD (Vector Of Displacement) procedure. The method based on the space-lagged (cross-) correlation technique was used in this respect.

The basic principle of the method is based on the assumption that the forecast value field (including the ensemble mean forecast) can be spatially shifted relative to the actual value field, maintaining the spatial "shape". To determine the size of this shift (i.e. VOD - Vector Of Displacement), these steps are followed:

1. Calculate the "centre of mass" of the two-dimensional field of forecast values
2. Calculate the "centre of mass" of the two-dimensional field of measured values
3. Define VOD as the vector connecting these two points
4. "Shift" the forecast field by the VOD vector

An example of the result of using this procedure is shown in the figure 23.

As the number of SYNOP stations in Poland is not quite large (61), the procedure has been modified for the elements measured at the stations. Instead of calculating the "centres of mass" of continuous fields, the procedure is as follows:

1. at each SYNOP station, find the grid point (in a specific vicinity) with the forecast value closest to the one measured at station;
2. calculate the displacement vector for single station as the difference between the station location and the location of this point in the forecast field;
3. calculate an overall VOD as the average over all the stations
4. displace every value of forecasts by the vector of displacement

An example of the result of using this procedure is shown in figure 24.

After finding an improvement in the quality of the forecasts, this procedure was also applied operationally. In the operational mode, VOD is being determined at the beginning of each calculation cycle for each forecasted meteorological element. It is assumed, that this value does not change in the current calculation cycle, but it is updated at the next model run.

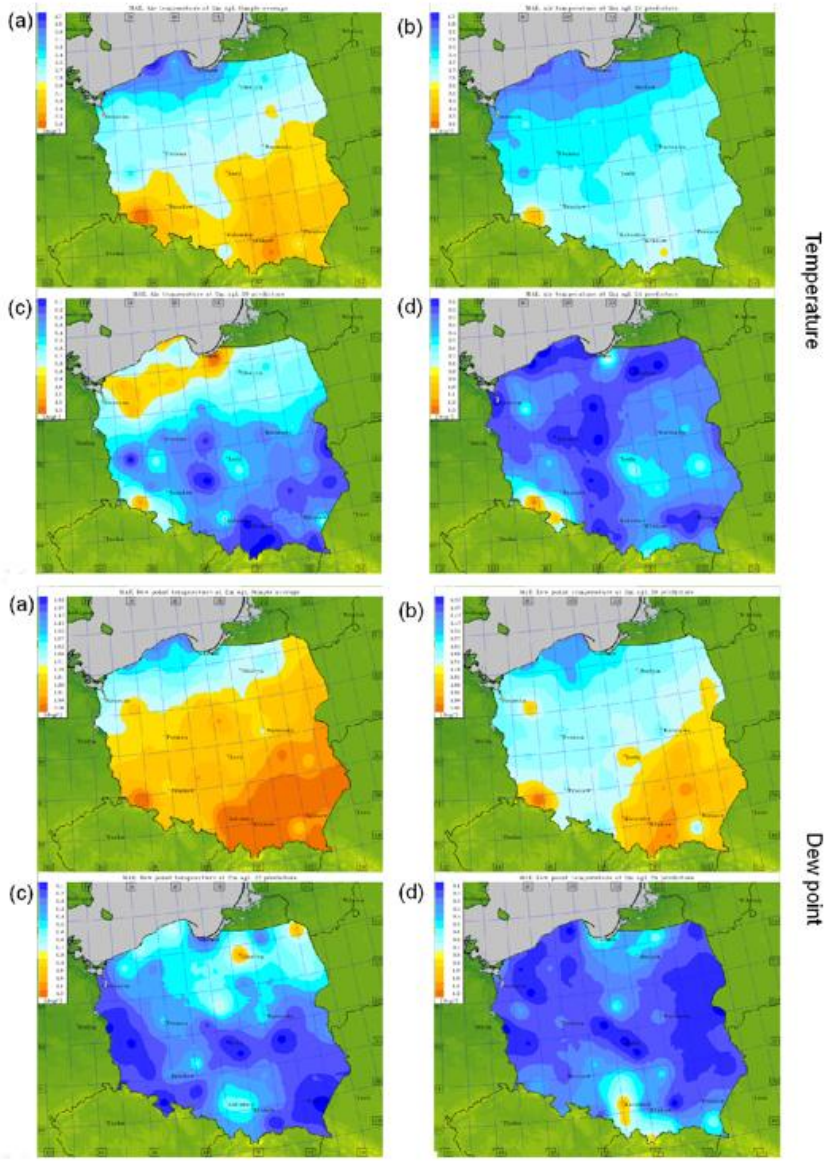


Figure 22: Skill comparison for different calibration methods, in terms of 2m air temperature (upper four panels) and dew point temperature (lower four panels). Panel (a) Simple average, (b) Multiline Regression (MLR), 24 predictors, (c) ANN, 20 predictors (ensemble values only), (d) ANN, 24 predictors (ensemble values + spatiotemporal coordinates). Results are for the years 2011-2015.

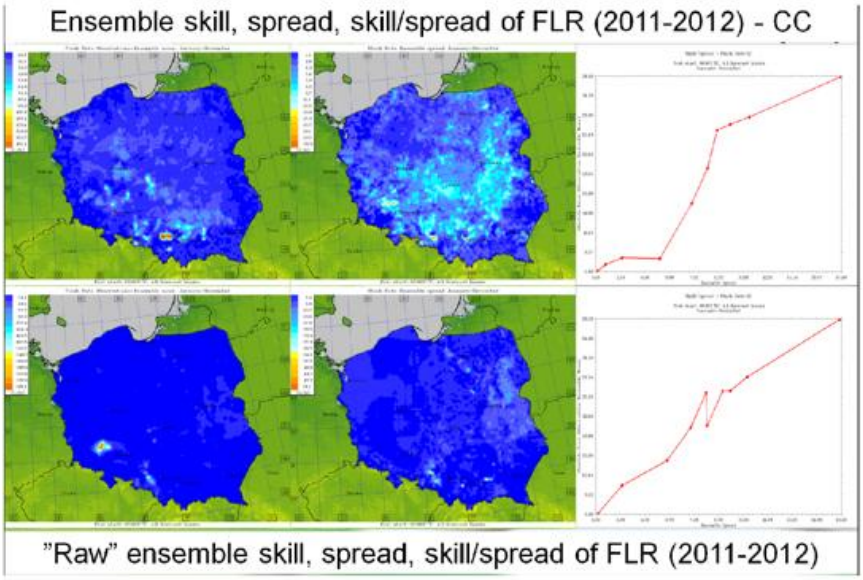


Figure 23: 2011-2012 average skill, spread and skill-spread relation for Flashrate (FLR) frequencies using the VOD procedure (upper panel) against the "raw" scores (lower panel).

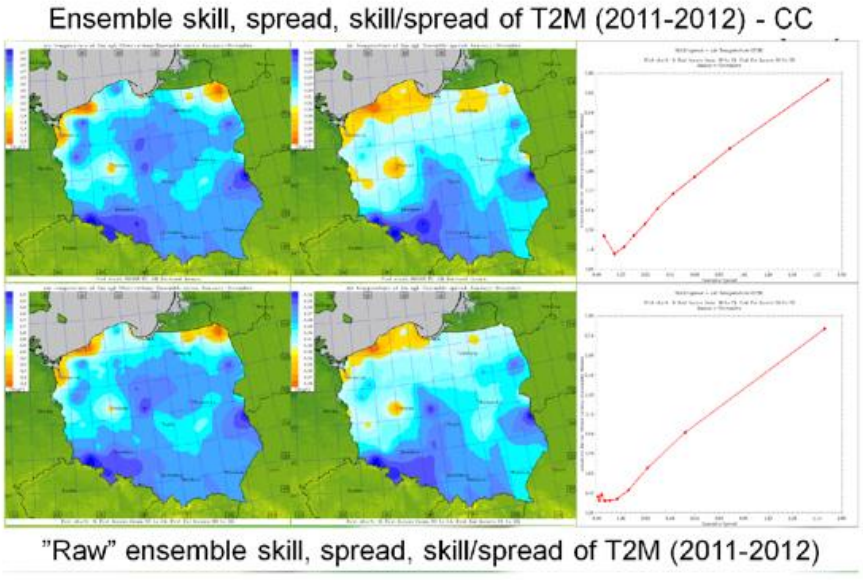


Figure 24: Same as Fig. 23 but for air temperature at 2m.

4.2 Specific products from ensemble outputs (R. Golino, F. Marcucci, COMET)

In the framework of the EUMETNET SRNWP-EPS project, a tool for thunderstorm forecasting has been developed. The algorithm combines different indices following the decision tree in Fig. 25 and evaluates for each grid point the suitable weather phenomenon according to the WMO table 4678.

The most important indices used in the code are: Cape, Cin, Total total index (TT), Showalter Index (SI), Updraft Helicy (UH), Lighting Potential Index (LPI), Integrated Graupel (QG), Cloud Physics Thunder Parameter (CPTP). Indices can be computed internally if

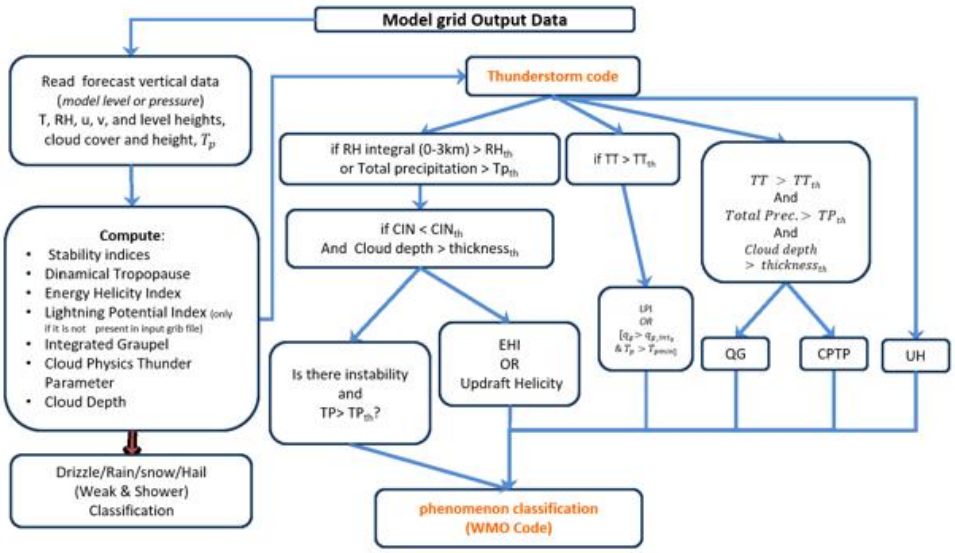


Figure 25: A schematic overview of the algorithm decision tree to evaluate the phenomenon assigned to a specific grid point.

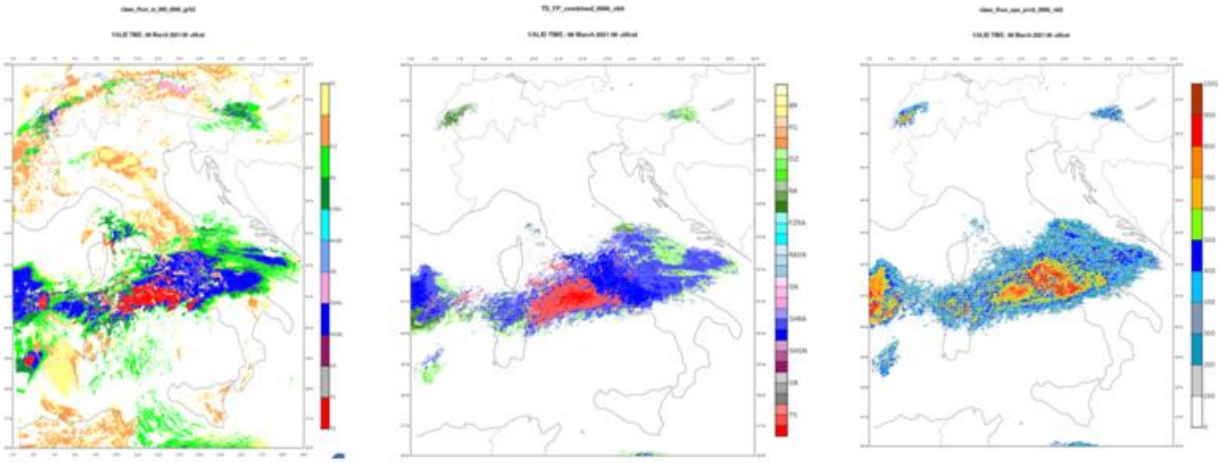


Figure 26: Output of the algorithm applied to deterministic COSMO-IT (left). Most probable phenomenon computed using the 20 outputs of the algorithm applied to the COSMO-IT EPS ensemble members (centre) and related probability (right). All pictures are referred to the 00UTC run of 08 March 2021, forecast step +6h.

not available as model output. The algorithm has been applied to deterministic outputs of COSMO-IT model and also to the 20 forecast members of the ensemble convection permitting system COSMO-IT EPS. In order to have a synthetic picture of the scenario predicted by the ensemble, the EPS outputs can be post-processed to obtain a single field (grib format) that represents the most probable phenomenon. For each grid point, the phenomena predicted by all the members are collected and clustered, then the most populated cluster is considered to decide the suitable phenomenon. The associated probability is computed taking also into account events from the most severe group. Low-probability phenomena (less than 20%) are discarded. An example of the algorithms output from different models (deterministic COSMO-IT and ensemble COSMO-IT EPS) is given in Fig. 26. In the ensemble outputs (two rightmost pictures) fog/mist events (BR/FG - yellow/orange in the colorbar) are not

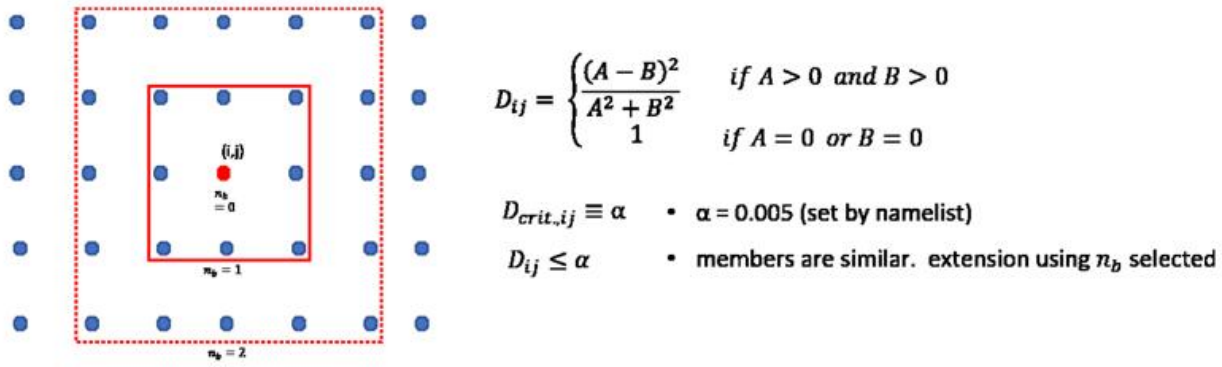


Figure 27: A schematic overview of the method proposed by Dey et al (2016).

considered. To enlarge the sample, a nearest neighbour post processing is applied using the similarity criterion proposed by Dey et al (2016). Namely, for each single grid point (i,j) the values of the EPS members are considered in pairs (190 independent comparison with 20 members) in order to assess if there is an agreement among the ensemble members. The value Dij is computed for all the pairs as shown in Fig. 27, where A and B are the values of the 2 chosen members at the grid point (i,j). If the averaged value Dij is greater than a given parameter (= 0.05 by default), there is no similarity and the agreement is further verified increasing the scale (stopping at nb-order of neighbourhood, 1 by default resulting in 3x3 box and 9x20 values to be compared). Finally, the most representative phenomenon is assigned to the (i,j) grid point. The similarity criterion, currently under evaluation, is expected to be able to filter out showers and drizzle if more significant weather is predicted by other members/neighbours, thus producing a more realistic output.

4.3 Specific products from ensemble outputs (A. Mazur, G. Duniec, IMGW)

Flashrate (as a storm indicator) and visibility range or visibility limitations (caused by fog, but also precipitation) are derived as non-standard products from the EPS.

Forecasts of visibility range were calculated from direct model output using an algorithm based on the forecast of the extinction parameter ext (calculated as a function of water/ice amount in the air, see Stoelinga and Warner, 1999, or Gultepe et al., 2006):

$$VIS = \frac{-\ln(0.02)}{\beta_{ext}}$$

Figure 28: Visibility range from extinction parameter.

These forecasts were verified against measurements at Polish SYNOP stations (see Fig. 29.

Overall conclusions drawn from this research were as follows:

- the average spread is two to ten times lower than the error measured as MAE: the ensemble FVIS is strongly under-dispersive;
- as far ad the spatial relations are concerned, the error is smaller for central and southern Poland, while spread is bigger in the southern and northern part of Poland;

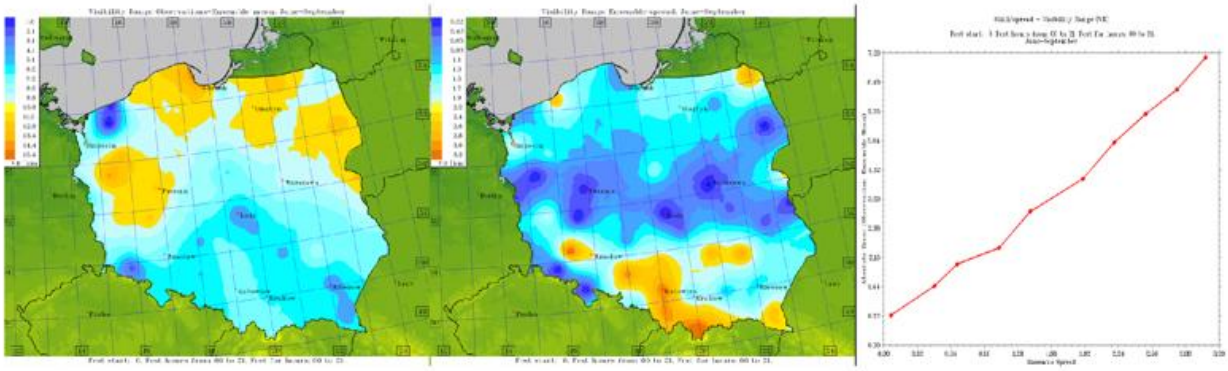


Figure 29: An example of skill (left), spread (middle) and skill-spread relation (right) of the VIS forecasts. Averaged values for June to September, 2011-2015.

- skill and spread are in general better (i.e., smaller and bigger, respectively) for "dry" months (June and September).

In the FLR calculation it is assumed that there is a relationship between the CAPE (from which the maximum updraft velocity W is calculated), the cloud top/base temperatures (CTT/CBT respectively) and the lightning frequency (FR, 1/minutes):

$$W = 0.3 \cdot \sqrt{2 \cdot CAPE}$$

$$FR = \left(\frac{W}{14.66} \right)^{4.54}$$

$$if \quad CTT > -15°C \quad FR = FR \cdot \left[\max\left(\frac{-CTT}{15}, 0.01 \right) \right]$$

$$if \quad CBT < -5°C \quad FR = FR \cdot \left[\max\left(\frac{CBT + 15}{10}, 0.01 \right) \right]$$

Figure 30: Flashrate forecasts calculated from CAPE and cloud top/base temperatures.

Additional filters were used to improve the quality of forecasts (see e.g. Wong et al., 2013).

Forecasts were verified against measurements at Polish lightning detection network PERUN (Fig. 31).

A general conclusion drawn from this part of the study was that the CAPE-based forecasts of flashrate intensity produce good skill values for central and north-western Poland, with the spread being bigger in central and western Poland. This algorithm, however, significantly overestimates flashrate intensity. A precipitation filter is applied, that is, it is assumed that flashrate intensity is zero in the absence of rainfall.

The Universal Tornadic Index (UTI, Taszarek and Kolendowicz, 2013) was a possible candidate for thunderstorm recognition and forecasts, to be verified against data from the lightning detection network:

In the above formula, CAPE is the surface based Convective Available Potential Energy, CAPE3km the Surface based CAPE released below 3 km, LCL the Surface based lifting condensation level height, AMR500 the Average mixing ratio below 500 m, LLS the 0-1 km wind shear, DLS the 0-6 km wind shear (magnitude of vector difference) and SRH1km the 0-1 km storm relative helicity. It is also assumed that SRH1kmis non-negative, and if

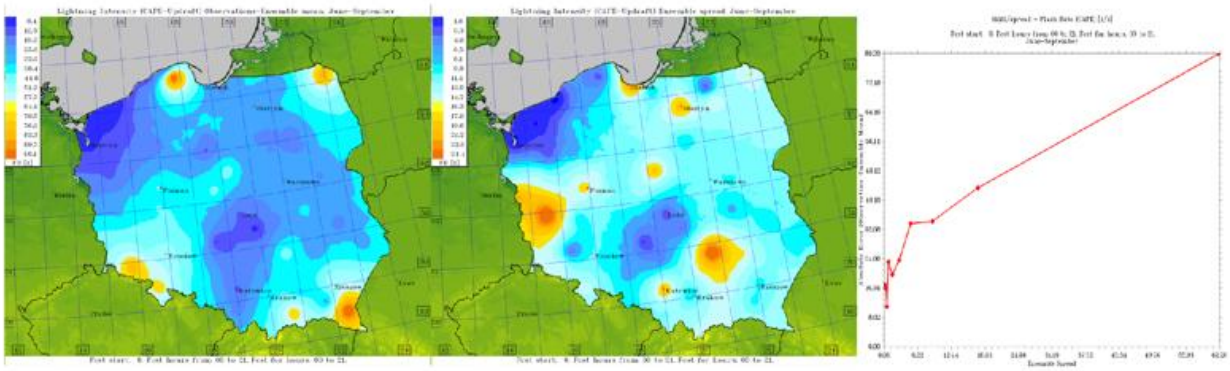


Figure 31: An example of skill (left), spread (middle) and skill-spread relation (right) of the FLR forecasts. Averaged values for June to September, 2011-2015.

$$UTI = \frac{CAPE \cdot SRH_{1km}}{200} \cdot \frac{5 \cdot (DLS - 20) + \left(\frac{200 - LCL}{10}\right)}{100} + CAPE_{3km} + \frac{SRH_{1km}}{4} \cdot \frac{LLS}{12} \cdot \frac{AMR_{500}}{100}$$

Figure 32: Universal Tornadic Index as a possible indicator of thunderstorm occurrence.

LCL is greater than 1500m or CAPE is equal to zero or convection precipitation is less than 2mm/h, then UTI becomes zero. UTI increases with the probability for a significant tornado. For Poland, the operational significance of UTI should attract attention when greater than 0.5-1.0. It should however be kept in mind, that these (climatologically obtained) values do not guarantee that if a forecaster uses threshold values in real-time data, he will be able to specify whether a tornado will occur. Results rather suggest that tornadoes can (may) be formed at all. Universal Tornadic Index was assumed as an indicator of the occurrence of a extreme convective phenomenon. Since it contains many factors (CAPE, storm relative helicity, convective precipitation, wind shear etc.), it may be useful in forecasting not only tornadoes, but also thunderstorms or squall lines. The ensemble mean value of the UTI is comparable to the one calculated in a deterministic run, however significantly less amount of "noise signal" is observed. Further research was carried out to determine any climatological connection between UTI and FLR values. Still, this index did not meet the expectations, in the sense that no significant correlation of this kind was detected. It was perhaps due to a different spatial range of the predicted convective phenomena, namely tornadoes (basic scale of tens to hundreds of meters) vs. "regular" thunderstorms (hundreds of meters to few kilometres).

5 Transition to ICON-LAM

The COSMO Consortium is moving towards the model ICON. This means that the convection-permitting ensemble systems must be converted to the ICON-LAM model. In order to be able to perform a transition to ICON-LAM in the current ensemble configurations, two ingredients are needed: (i) data assimilation for ICON-LAM based on LETKF and (ii) a model perturbation method for ICON-LAM. The first issue is addressed by the data assimilation projects and plans, the second is addressed in the present PP.

For tackling the issue of model perturbation with ICON-LAM, in addition to the technical

adaptations, it has to be examined whether the previous approaches to the representation of the model uncertainties can also be used with ICON-LAM. Due to the change in the characteristics of the model, modifications of the applied methods are likely to be required. The migration of the CP ensemble systems to ICON-LAM will require: forecast experiments for different test periods to explore the properties of the new systems, identification of further development requirements, adaptation of ensemble generation methods.

During the APSU Priority Project, all the ensembles were still running based on the COSMO model, and the model perturbation methods were developed in COSMO. The only exception was DWD, where the transition was more advanced. Here, experiments on the Parameter Perturbation in ICON-LAM (ICON-D2-EPS configuration) were carried out. This work is described in the next subsection.

At the time of writing, a new Priority Project on ensemble development is ongoing (PROPHECY), where model perturbation methods are developed, implemented and tested in ICON in several COSMO members.

5.1 Randomly perturbed parameters in ICON-D2-EPS (C. Gebhardt, DWD)

Coinciding with the lifetime of PP APSU, the ICON-D2-EPS has been prepared as operational EPS application of the ICON limited area mode at DWD. ICON-D2-EPS replaces COSMO-D2-EPS as ensemble prediction system on the convection-permitting scale.
On the one hand, the general methodological approach for member generation in COSMO-D2-EPS is transferred to ICON-D2-EPS, i.e. local ensemble transform Kalman filter for the initial conditions, forecasts of ICON-EU-EPS as lateral boundaries, and randomly perturbed parameters representing model uncertainties. The EPS set-up is identical for the first phase after the transition, with 20 members running every 3 hours for up to 27 hours lead time (45 hours for the 03 UTC run) on a similar domain with a grid spacing of ca. 2.1km.
On the other hand, some of these methods require adjustments to fit to the characteristics of the ICON model in a beneficial manner. Within the PP APSU, the adjustments and the effects of the method of randomly perturbed parameters (RPP) in ICON-D2-EPS are of particular interest and can provide valuable information for the COSMO community. This section reports about the adjustments made to both the range of perturbed values of certain parameters as well as to the technical implementation of the perturbation approach. This implementation is now fully controlled via the ICON namelists and applied within the model. There is no need for preparatory processing scripts in contrast to the procedure for COSMO-D2-EPS.
The general approach remains the same, i.e. for each parameter to be perturbed a value is selected randomly from the default and one or two pre-defined perturbed values in each member. This selection is done at forecast start and the selected parameter values are fixed for the entire forecast range of an EPS run. This selection from a *limited number* of possible values is different from approaches with a random choice of *any* parameter value within the given range.

Most aspects of the physics parametrizations do not substantially change between COSMO-D2 and ICON-D2, which means that many parameters of RPP for COSMO-D2-EPS can be perturbed analogously in ICON-D2-EPS, subject to minor re-tuning. Some parameters have to be adjusted to changes in the parametrization (i.e. the dependence of the vertical diffusion on the Richardson number affects the appropriate range of values for `tkhmin` / `tkmmin`). There are a few replacements (i.e. `radqc_fact` vs. `box_liq` for radiation/cloud cover) and some new parameters are added. More details are listed in Table 2 together with the default values and perturbation ranges for ICON-D2-EPS resulting from preparatory

sensitivity studies.

For the sensitivity studies, 14 days of deterministic ICON-D2 00 UTC runs are performed for each potential perturbation of a parameter with only this perturbation applied for the entire forecast range of 24 hours and all other parameters set to the default value. This procedure is, of course, different from the application in the EPS with its daily randomized mixture of perturbations, but it turned out to be very efficient in detecting which perturbations have a potential for leading to outliers in terms of verification scores. The sensitivity studies aim at a selection of parameter perturbations leading to similar forecast quality without outliers (neither 'better' nor 'worse'). The starting point for the perturbation ranges for ICON-D2 are based on experiences with perturbations for COSMO-D2-EPS (acting on the same scale) and for the global ICON-EPS (using the same model). Note that differences in the scale can lead to differences in the appropriate perturbation ranges between ICON global/EU and ICON-D2. Fig. 33 exemplifies the results of the sensitivity study for the initial set of perturbations for selected variables and for mean error only (other scores were tested as well but they are not shown).

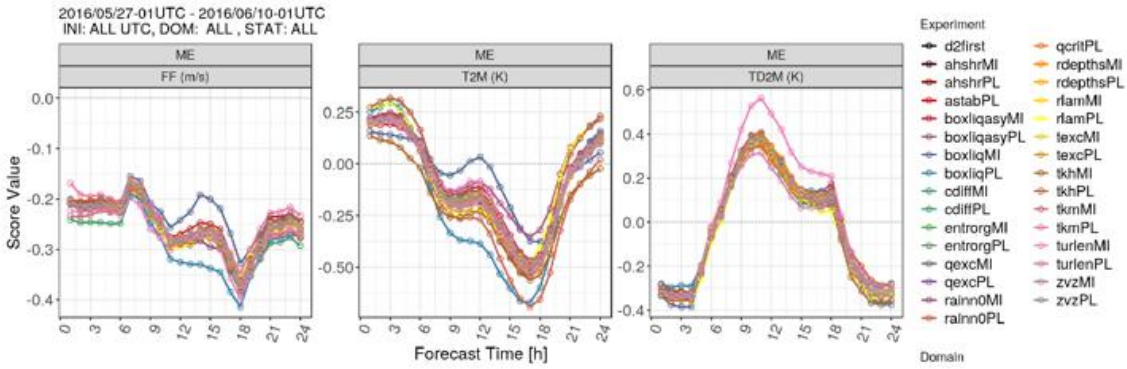


Figure 33: Mean error of 10m wind speed (left), 2m temperature (middle), and 2m dewpoint temperature (right) as a function of the forecast lead time averaged over 14 days of 00 UTC deterministic ICON-D2 runs. Each coloured line corresponds to exactly one parameter being perturbed in just one direction (see legend with 'PL' for 'increased' and 'MI' for 'decreased') keeping all other parameters at their default values. The fully unperturbed run ('d2first') is contained as well but overlaid by the other runs.

Most of the mean errors are very similar among the different runs for the three variables 10m wind speed, 2m temperature, and 2m dewpoint temperature. Just a few parameter perturbations are considered to produce outliers, e.g. the perturbation in both directions of `box_liq` (blueish lines) for wind speed and 2m temperature and `rain_n0_factor` for 2m temperature or the reduction of `tur_len` for the 2m dewpoint temperature. The parameter perturbations pointing at possible outliers with this quite conservative test have been adjusted for the first experiments with ICON-D2-EPS and table 2 lists the accordingly selected perturbation set-up.

Note that these perturbation ranges are subject to change in light of further developments of the parametrizations and of the ICON-D2-EPS. An up-to-date list of perturbations used in operational set-up can be found online in the ICON database reference manual (Reinert et al., 2021, latest version).

In the following, verification results of the pre-operational ICON-D2-EPS in comparison to the operational COSMO-D2-EPS are presented for a winter (December 2019 to February 2020) and summer (June to August 2020) period. Fig. 34 shows verification scores of the winter period for 2m temperature, 2m dewpoint temperature, hourly precipitation, and

CD2	ID2	meaning	def-	−	+
a_stab	a_stab	stability correction of turbulent length scale	0	none	1
c_diff	c_diff	length scale factor for vertical diffusion of TKE	0.2	0.1	0.4
q_crit	q_crit	critical value for normalized super-saturation	2	none	3.5
tur_len	tur_len	asymptotic maximal turbulent distance	300	250	350
rlam_heat	rlam_heat	scaling factor of the laminar boundary layer for heat (rlam_heat × rat_sea = 8.)	10	7.5	12.5
thick_sc	tune_rdepths	maximum allowed depth of shallow convection	2 $*10^4$	1.5 $*10^4$	2.5 $*10^4$
entr_sc	tune_entrorg	Entrainment parameter valid for dx=20 km	1.95 $*10^{-3}$	1.75 $*10^{-3}$	2.15 $*10^{-3}$
radqc_fact	tune_box_liq tune_box_liq_asy	box width for liquid cloud diagnostic in cloud cover scheme & asymmetry factor	0.05 3.25	0.05 3.0	0.06 3.5
radqi_fact	none	-	-	-	-
tkhmin	tkhmin	scaling factor for minimum vertical diffusion coefficient for heat and moisture	0.5	0.4	0.6
tkmmin	tkmmin	... for momentum	0.75	0.6	0.9
none	tkred_sfc	reduction of minimum diffusion coefficients near the surface	1	0.25	4.0
none	rain_n0_factor	tuning factor for intercept parameter of raindrop size distribution	0.1	0.05	0.2
none	a_hshr	length scale factor for the separated horizontal shear mode	2	1	3
none	tune_zvz0i	terminal fall velocity of ice	1.25	1	1.5
none	tune_texc	excess value for temperature used in test parcel ascent	0.125	0.075	0.175
none	tune_qexc	excess fraction of grid-scale QV used in test parcel ascent	0.125	0.075	0.175

Table 2: Perturbed parameters in COSMO-D2-EPS (**CD2**) and in first experiments with ICON-D2-EPS (**ID2**). The default (**def.**) and perturbed values (decreased: −; increased +) refer to ICON-D2-EPS. The updates to operationally used parameters, default values, and perturbation ranges in ICON-D2-EPS are available online (Reinert et al., 2021) together with information about the perturbation being additive or multiplicative for a given parameter (e.g. rlam_heat changes from multiplicative to additive with ICON-D2-EPS).

hourly 10m wind gusts as a function of the forecast lead time for 00 and 12 UTC runs combined.

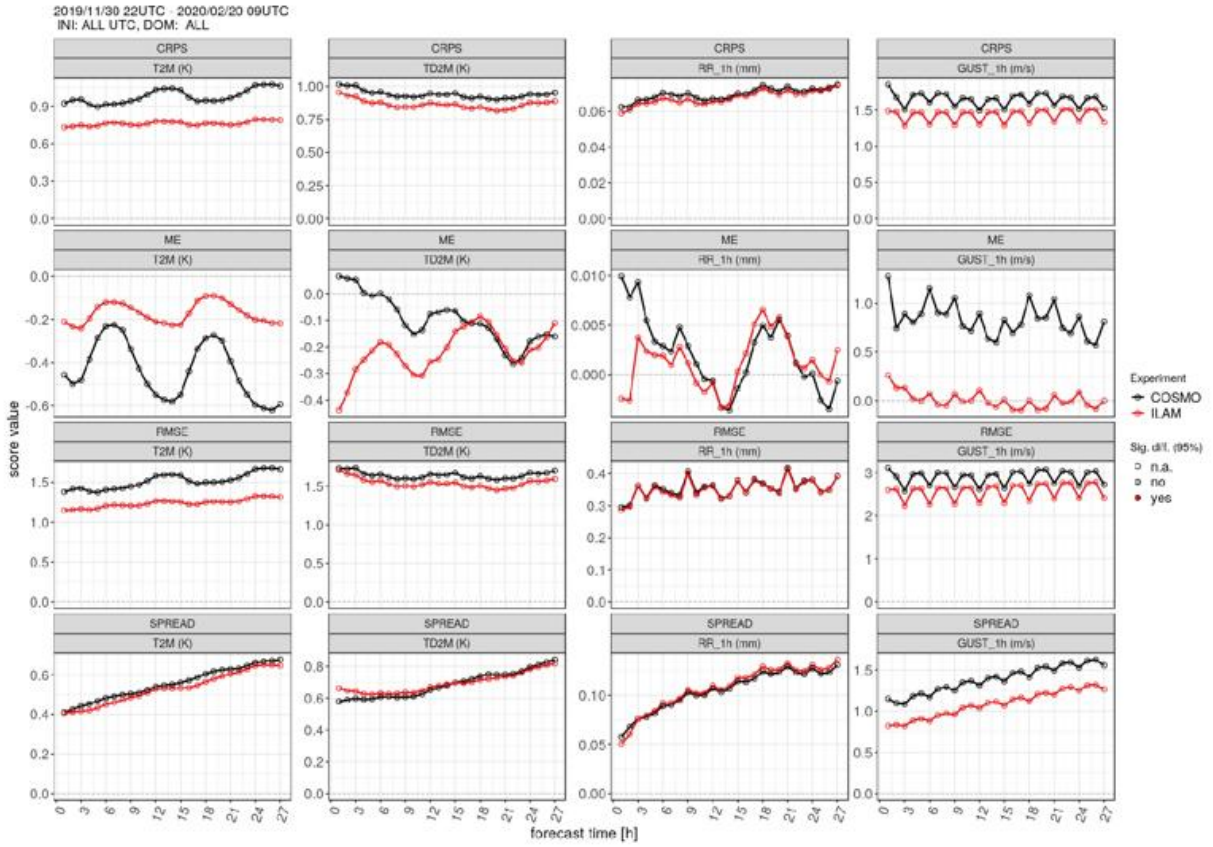


Figure 34: Continuous ranked probability score (CRPS), mean error and root mean squared error of the EPS mean, and EPS spread (from top to bottom) for 2m temperature, 2m dewpoint temperature, hourly precipitation, and hourly 10m wind gusts (from left to right) as a function of the forecast lead time of the pre-operational ICON-D2-EPS (red) and the operational COSMO-D2-EPS (black) for winter 2019/2020. Scores of 00 and 12 UTC runs are combined.

Comparing ICON-D2-EPS with COSMO-D2-EPS an improvement of CRPS is evident for all variables. The mean error for 2m temperature is clearly improved both in terms of magnitude as well as reduced daily cycle. The reduction of the daily cycle of the bias supports the beneficial use of ICON-D2 compared to COSMO-D2 in forecasting. It is observed for other variables as well (not shown, e.g. 10m wind speed). The dewpoint temperature shows a dry bias at forecast start of ICON-D2-EPS compared to COSMO-D2-EPS which extends up to forecast hour 15. This problem has been overcome in the further development of the system by different measures, of which the most important is the incorporation of 2m temperature and 2m relative humidity observations in the data assimilation.
The bias of the hourly precipitation in the early forecast hours is reduced in ICON-D2-EPS. Very remarkable is the reduction of the mean error for 10m wind gusts to nearly 0 m/s over most parts of the forecast range.
The RMSE of the EPS mean is reduced by ICON-D2 for most variables and neutral otherwise (hourly precipitation) and is similar to changes in CRPS. It should be noted here, that changes in mean error and RMSE for winter and summer for the variables shown here, as well as for other variables, closely follow the changes of the deterministic run from COSMO-D2 to ICON-D2 (not shown).

The EPS spread does hardly change from COSMO-D2-EPS to ICON-D2-EPS except for a reduction for the 10m wind gusts (as well as mean wind, not shown). The reason for this reduced spread is not clear yet and subject to further research. Overall, the threshold-based forecast of 10m wind gusts benefits from the step to ICON-D2-EPS according to the Brier skill score plotted in Fig. 35 for different thresholds. The improvement affects both the reliability as well as the resolution component of the Brier score (not shown).

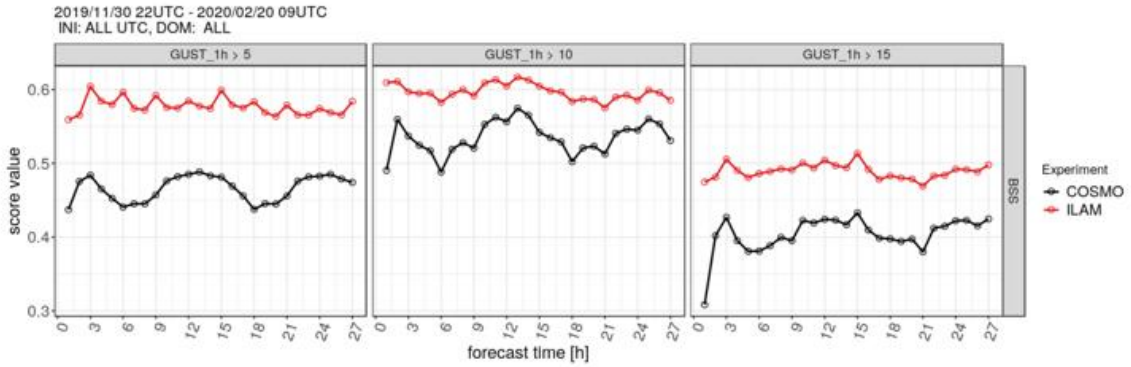


Figure 35: Brier skill score of hourly 10m wind gusts for thresholds of 5 m/s, 10 m/s, and 15 m/s (from left to right) as a function of the forecast lead time for the pre-operational ICON-D2-EPS (red) and the operational COSMO-D2-EPS (black) for winter 2019/2020. Scores of 00 and 12 UTC runs are combined.

The selection of verification scores for the summer period is shown in Fig. 36 in analogy to the scores for the winter period.

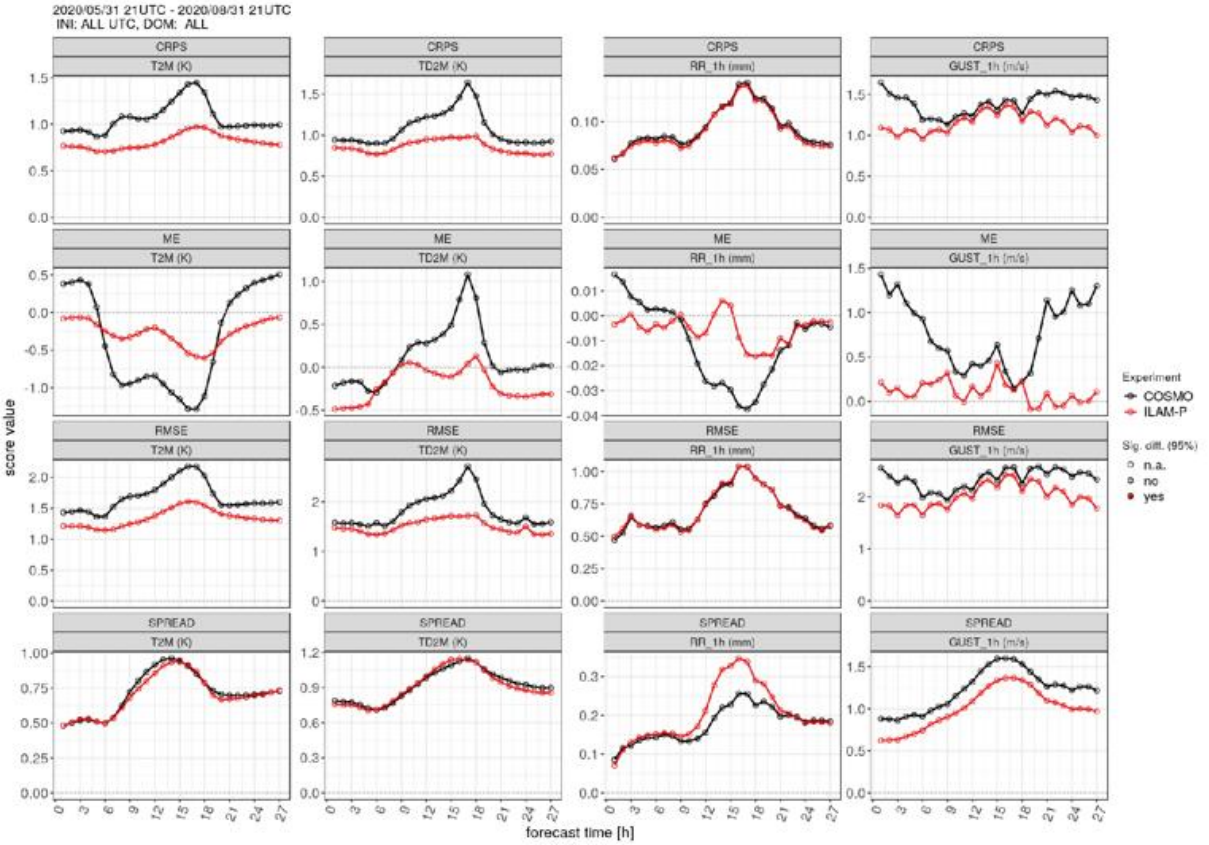


Figure 36: Continuous ranked probability score, mean error and root mean squared error of the EPS mean, and EPS spread (from top to bottom) for 2m temperature, 2m dewpoint temperature, hourly precipitation, and hourly 10m wind gusts (from left to right) as a function of the forecast lead time of the pre-operational ICON-D2-EPS (red) and the operational COSMO-D2-EPS (black) for summer 2020. Scores of 00 and 12 UTC runs are combined.

The main features seen for winter also hold for the summer period. Main differences are the remarkable quality gain by ICON-D2-EPS in the mean error of 2m dewpoint temperature and hourly precipitation and the more pronounced reduction of RMSE for 2m (dewpoint) temperature around mid-day as compared to the winter period. For 10m wind gusts, the quality of ICON-D2-EPS in summer and winter is similar. This in turn results in a moderate improvement in summer around mid-day compared to COSMO-D2-EPS, which itself shows better scores for the wind gusts in summer than in winter. The improvement in Brier skill score by ICON-D2-EPS in summer is qualitatively similar to the results for winter and is not shown here.
One effect to mention here is the increased spread of hourly precipitation during mid-day in summer which is not observed for winter. However, it should be kept in mind that increased spread of precipitation tends to be linked to increased mean values. A threshold-based verification with the Brier skill score for hourly precipitation in summer points at moderate improvements when using ICON-D2-EPS (Fig. 37).

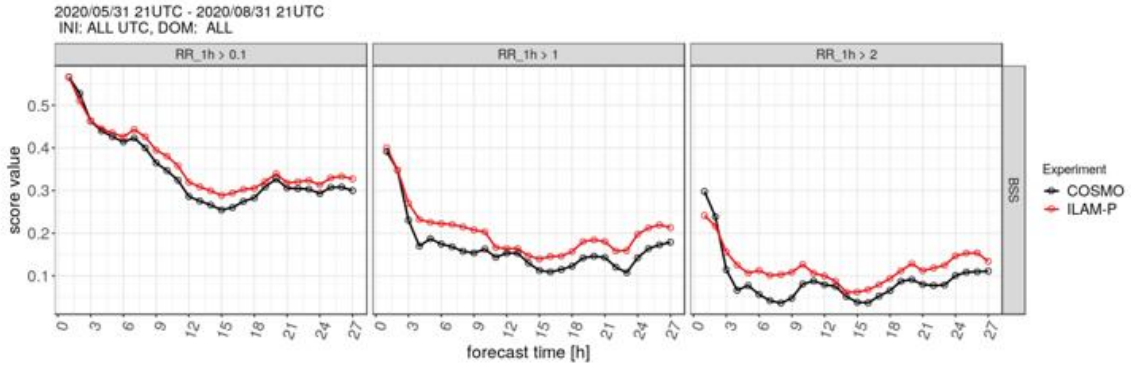


Figure 37: Brier skill score of hourly precipitation for the thresholds 0.1 mm/h, 1 mm/h, and 2 mm/h (from left to right) as a function of the forecast lead time for the pre-operational ICON-D2-EPS (red) and the operational COSMO-D2-EPS (black) for summer 2020. Scores of 00 and 12 UTC runs are combined.

The last part of this section covers the technical implementation of the parameter perturbations in ICON-D2-EPS. While the perturbation approach for COSMO-D2-EPS requires the perturbed parameter values to be set explicitly in the namelist for each member separately as a pre-processing step, including the randomization, the ICON-D2-EPS just needs general information about the parameters to be perturbed and the relevant ranges provided via the namelist. The randomization is done during the model run and there are additional namelist parameters to control a few options of the randomization and parameter selection.
Fig. 38 is a flow chart of the procedure.

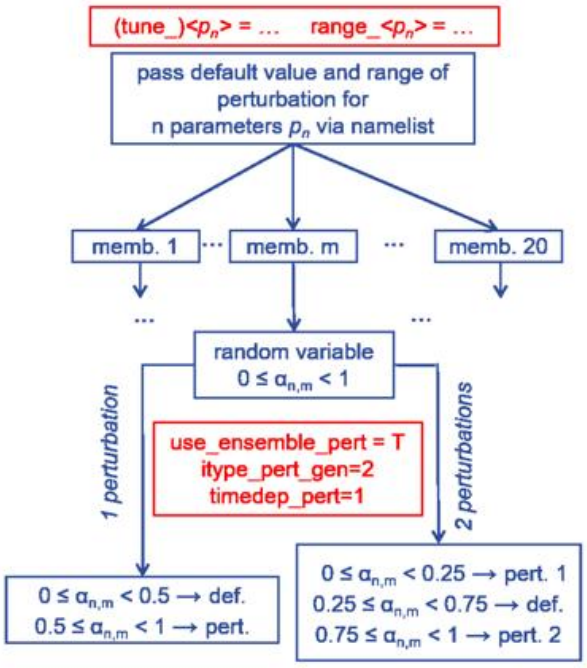


Figure 38: Technical implementation of the parameter perturbations in ICON-D2-EPS.

The default values of the parameters (tune_)$< p_n >$ are set in their respective namelists as for the deterministic run. A range for perturbations is set as (range_)$< p_n >$ in the ICON namelist `ensemble_pert_nml`. There is only one entry for the range which has to be given

as deviation from the default value. Therefore, only symmetric perturbations (in an additive or multiplicative sense depending on p_n) are possible in ICON-D2-EPS. There are also restrictions for a few parameters to be perturbed only in one direction.
The namelist `ensemble_pert_nml` contains the important switch `use_ensemble_pert` to be set to `.TRUE.` to activate the parameter perturbation. A random variable $\alpha_{n,m}$ is then generated in ICON from a uniform distribution between 0 and 1 for each parameter p_n and member m. By setting the parameter `itype_pert_gen=2` in `ensemble_pert_nml`, the random variable $\alpha_{n,m}$ leads to the value of p_n being one of default or perturbed value, as indicated in Fig. 38. A choice of `itype_pert_gen=1` would lead to a perturbed value somewhere within the perturbation range according to $\alpha_{n,m}$ taken at face value as implemented for the global ICON-EPS and its nest over Europe.
Another important control switch for the perturbation procedure is the namelist entry `timedep_pert` in `ensemble_pert_nml`. A value of 1 causes the randomization to depend on forecast start time as it is done in ICON-D2-EPS. The global ICON-EPS uses a value of 0 leading to a dependence on the member ID only. Some details about these namelist entries can be found in Reinert et al. as well. They provide for more options to generate EPS members than just in the way it is presented here for ICON-D2-EPS.
There might be slight drawbacks in the described implementation of the perturbation procedure in ICON-D2-EPS compared to COSMO-D2-EPS, like the symmetric perturbation ranges and the methodological aspect that each parameter is no longer perturbed exactly in 50% of the members of a model run, but only statistically. However, the namelist-based approach makes it more feasible to run the RPP and makes the approach more portable between different machines and exchangeable among COSMO partners compared to COSMO-D2-EPS.

6 Conclusions

Like most of the WG7 Priority Projects, the activities of APSU covered a quite broad range of ensemble development topics. This allows us to carry out ensemble development in a coordinated way between the different COSMO partners, while preserving the specificity of the different ensemble implementations and needs (different domains, focus on somehow different weather phenomena, different computing capabilities and human resources). However, thanks to the APSU Priority Project, the activities about ensemble development of the different COSMO members were focused on specific high-priority themes, benefiting from each others' work and avoiding duplications and dispersion of efforts.

Some conclusions can be drawn from this work, highlighting the impact of the Project activities on the ensemble development and operational usage, and identifying the next steps needed to perform the transition of the ensembles to the ICON model.

- The new stochastic approaches to model the model error (SMME and AMPT) are promising methods to describe the model error and incorporate it into ensemble design. However, their complexity and the difficulty of objectively representing the model error require a long development phase, which is not concluded in the time frame of APSU. It is important to keep these developments linked to each other, in order to benefit from each others' results and experiences. Due to the transition of the Consortium to the ICON model, it is now suggested to implement the two methods in ICON and continue their development in the new model.
- The SPPT method is successfully used at MCH as operational model perturbation method. Therefore MCH will invest resources in implementing SPPT in ICON, in

view of the future transition to the ICON model for their ensembles. The proposed iSPPT variant, even if it did not prove to be more beneficial than the classical SPPT in COSMO, will be considered for implementation, in order to permit its usage and further assessment in the new model framework. The study performed on the analysis increments, to be possibly used as source of model perturbation, lead to positive results. However, the development of this method would require time and resources, and this has to be taken in account in planning future actions.

- The implementation of model perturbation methods in ICON will also permit to the COSMO partners to start working on the new model system and to contribute to the development of the ICON model
- The application of soil/surface perturbations proved to be successful and lead, in combination to the perturbation of the atmospheric fields, to promising results. Therefore these perturbations will also be adopted in the ICON-based ensembles.
- In order to apply the parameter perturbation method in ICON it is needed to study the sensitivity of the ICON model to its parameters, as it was done at DWD during APSU. Therefore this activity will be repeated for the other domains where ICON-based ensembles need to be developed. This will also permit to gain a deeper knowledge of the model and its behaviour, which is in the interest of all the COSMO partners.
- The tasks related to the development of new ensemble products and ensemble output calibration lead to an operational usage of the new products and of the calibrated outputs. Therefore this task will be continued in the future, by expanding to new products and improving the calibration methodology.

Concluding with a poetic note, the APSU PP was like the underground fresh water reservoir of the Sumerian and Accadic culture, after which the project is named, from which fertilising quality the future work will benefit.

7 Acknowledgements

We are grateful to the COSMO Consortium, which gives us the opportunity to work together and benefit from mutual exchanges and discussions. The Project leader would like to thank the members of Working Group 7 for their continuous and active engagement.

8 References

Astakhova, E. D., Montani, A., Alferov, D. Yu., 2015. Ensemble forecasts for the Sochi-2014 Olympic Games. *Russian meteorology and hydrology* **40**, 8, 531-539.

Alferov, D. Yu., Astakhova, E. D., Rivin, G. S., Rozinkina, I. A., 2014. Development of High-resolution Ensemble Prediction System for the Region of Sochi-2014 Winter Olympics. *Proceedings of Hydrometcenter of Russia* No. 352, 5-20.

Baldauf, M., Seifert, A., Förstner, J., Majewski, D., Raschendorfer, M. and Reinhardt, T., 2011. Operational convective-scale numerical weather prediction with the COSMO model: description and sensitivities *Mon. Weather Rev.* **139**, 12, 3887-3905.

Ben Bouallegue, Z., Haiden, T., Weber, N. J., Hamill, T. M., and Richardson, D. S., 2020. Accounting for Representativeness in the Verification of Ensemble Precipitation Forecasts. *Mon. Weather Rev.* **148**, 2049-2062. doi:10.1175/MWR-D-19-0323.1, 2020.

Berner, J., Ha, S.-Y., Hacker, J. P., Fournier, A. and Snyder, C., 2011. Model uncertainty in a mesoscale ensemble prediction system: Stochastic versus multiphysics representations. *Mon. Weather Rev.* **139**, 6, 1972-1995.

Berner, J., Shutts, G. J., Leutbecher, M. and Palmer, T. N., 2009. A spectral stochastic kinetic energy backscatter scheme and its impact on flow-dependent predictability in the ECMWF ensemble prediction system. *J. Atmos. Sci.* **66**, 3, 603-626.

Bouttier, F., Vié, B., Nuissier, O. and Raynaud, L., 2012. Impact of stochastic physics in a convection-permitting ensemble. *Mon. Weather Rev.* **140**, 11, 3706-3721.

Buizza, R., Miller, M. and Palmer, T. N., 1999. Stochastic representation of model uncertainties in the ECMWF ensemble prediction system. *Q. J. R. Meteorol. Soc* **125**, 560, 2887-2908.

Christensen, H. M., Lock, S. J., Moroz, I. M. and Palmer, T. N., 2017. Introducing independent patterns into the Stochastically Perturbed Parametrization Tendencies (SPPT) scheme. *Q. J. R. Meteorol. Soc* **143**, 2168-2181. doi:10.1002/qj.3075

Christensen, H. M., Moroz, I. M. and Palmer, T. N., 2015. Stochastic and Perturbed Parameter Representations of Model Uncertainty in Convection Parameterization. *J. Atmos. Sci.* **72**, 6, 2525-2544.

Christensen, H.M., 2020. Constraining stochastic parametrisation schemes using high-resolution simulations. *Q. J. R. Meteorol. Soc* **146**, 938-962.

Dey, S.R.A., Roberts, N.M., Plant, R.S. and Migliorini, S., 2016. A new method for the characterization and verification of local spatial predictability for convective-scale ensembles. *Q.J.R. Meteorol. Soc.* **142**, 1982-1996.

Duniec, G., Mazur, A., 2020. Dependence of skill and spread of the ensemble forecasts on the type of perturbation and its relationship with long-term norms of precipitation and temperature. *Acta Geophys.* **68**, 1505-1528. https://doi.org/10.1007/s11600-020-00467-4

Füzér, L., 2018. Analysing new approaches for model perturbations in COSMO-E. ETH Zürich.

Gal-Chen, T. and Somerville, R. C. J., 1975. On the use of a coordinate transformation for the solution of the Navier-Stokes equations. *Journal of Computational Physics* **17**, 2, 209-228.

García-Ojalvo, J. and Sancho, J. M. and Ramírez-Piscina, L., 1992. Generation of spatiotemporal colored noise. *Physical Review A* **46** 4670–4675.

Gultepe et al., 2006. A New Visibility Parameterization for Warm-Fog Applications in Numerical Weather Prediction Models. *JAMC* **45**, 1469-1480.

Hersbach, H., 2000. Decomposition of the continuous ranked probability score for ensemble

prediction systems. *Wea. and Forecasting* **15**, 5, 559–570.

Kiktev, D., Joe, P., Isaac, G. A., Montani, A., Frogner, I.-L., Nurmi, P., Bica, B., Milbrandt, J., Tsyrulnikov, M., Astakhova, E., Bundel, A. and others, 2017. FROST-2014: The Sochi winter Olympics international project. *Bull. Amer. Meteor.* **98**, 9, 1908-1929.

Kirsanov, A., Gofa, F., Boucouvala, D., Batignani, F., Bogdan, M., Linkowska, J., Pflüger, U., Tesini, M.S. and Bundel, A., 2020. Common Verification Activity during JJA 2018 – MAM 2019: Main Results. *COSMO Newsletter* **20**, 10-17.

Klasa, C., Arpagaus, M., Walser, A., Wernli, H., 2018. An evaluation of the convection-permitting ensemble COSMO-E for three contrasting precipitation events in Switzerland. *Q. J. R. Meteorol. Soc.* **144**, 744–764. https://doi.org/10.1002/qj.3245

Knuth, D. E., 1981. Generating Uniform Random Numbers. In: Seminumerical Algorithms, 2nd ed., Reading, MA, Addison-Wesley Pub.2, 9-38. Print.: The Art of Computer Programming.

Leutbecher, M., Lock, S.-J., Ollinaho, P., Lang, S.T.K., Balsamo, G., Bechtold, P., Bonavita, M., Christensen, H.M., Diamantakis, M., Dutra, E., English, S., Fisher, M., Forbes, R.M., Goddard, J., Haiden, T., Hogan, R.J., Juricke, S., Lawrence, H., MacLeod, D., Magnusson, L., Malardel, S., Massart, S., Sandu, I., Smolarkiewicz, P.K., Subramanian, A., Vitart, F., Wedi, N. and Weisheimer, A., 2017. Stochastic representations of model uncertainties at ECMWF: state of the art and future vision. *Q.J.R. Meteorol. Soc* **143**, 2315-2339. https://doi.org/10.1002/qj.3094

Machulskaya, E. and Seifert, A., 2019. Stochastic differential equations for the variability of atmospheric convection fluctuating around the equilibrium. *Journal of Advances in Modeling Earth Systems* **11**, 8, 2708-2727.

Marsaglia, G., 2003. Random number generators. *Journal of Modern Applied Statistical Methods* **2**, 1, 2-13. doi:10.22237/jmasm/1051747320.

Marsigli, C., D. Alferov, E. Astakhova, G. Duniec, D. Gayfulin, C. Gebhardt, W. Interewicz, N. Loglisci, F. Marcucci, A. Mazur, A. Montani, M. Tsyrulnikov, A. Walser, 2019. Studying perturbations for the representation of modeling uncertainties in Ensemble development (SPRED Priority Project): Final Report. *COSMO Technical Report* **No. 39**, 55 pp.

Maurer, D., Walser, A. and Arpagaus, M., 2014. First COSMO-E experiments with the Stochastically Perturbed Parametrization Tendencies (SPPT) scheme. *COSMO Newsletter* **14**, 19-27.

Mazur, A., Duniec G., 2015. Ensemble Prediction System (EPS)-based forecast prepared from perturbation of soil conditions. *COSMO Newsletter* **15**, 63-71.

Monin, A. S. and Yaglom, A. M., 2013. Statistical fluid mechanics, volume II: Mechanics of turbulence. Edited by Courier Corporation.

Montani, A., Cesari, D., Marsigli, C. and Paccagnella, T., 2011. Seven years of activity in the field of mesoscale ensemble forecasting by the COSMO-LEPS system: main achievements and open challenges. *Tellus A: Dynamic Meteorology and Oceanography* **63**, 3, 605-624.

Montani, A., Marsigli, C. and Paccagnella, T., 2013. Development of a COSMO-based limited-area ensemble system for the 2014 Winter Olympic Games. *COSMO Newsletter* **13**, 93-99.

Montani, A., Alferov, D., Astakhova, E., Marsigli, C. and Paccagnella, T., 2014. Development of a COSMO-based limited-area ensemble system for the 2014 Winter Olympic Games. *COSMO Newsletter* **14**, 88-94.

Piccolo, C., Cullen, M., Tennant, W. J. and Semple, A. T., 2018. Comparison of different representations of model error in ensemble forecasts. *Q. J. R. Meteorol. Soc* **145**, 15-27. doi:10.1002/qj.3348

Raspanti, A., 2009. VERification System Unified Survey (VERSUS): Final Report. *COSMO Technical Report* **12**, pp 12.

Rivin, G., Rozinkina, I., Astakhova, E. and Coauthors, 2018. The COSMO Priority Project CORSO (Consolidation of Operational and Research Results for the Sochi Olympic Games). Final Report. *COSMO Technical Report* **35**, pp 70.

Reinert, D., Prill, F., Frank, H., Denhard, M., Baldauf, M., Schraff, C., Gebhardt, C., Marsigli, C., and Zängl, G., 2021. DWD Database reference manual for global and regional ICON and ICON-EPS forecasting system.
https://www.dwd.de/SharedDocs/downloads/DE/modelldokumentationen/nwv/icon/icon_dbbeschr_aktuell.html

Stoelinga, M. T., and T. T. Warner, 1999. Nonhydrostatic, mesobeta-scale model simulations of cloud ceiling and visibility for an East Coast winter precipitation event. *J. Appl. Meteor.* **38**, 385-404.

Taszarek, M. and L. Kolendowicz, 2013. Sounding-derived parameters associated with tornado occurrence in Poland and Universal Tornadic Index. *Atmos. Res.* **134**, 186-197.

Tsyrulnikov, M. and Gayfulin, D., 2019. Estimation of model errors on convective scales: a coarse-graining study (preliminary stage results). *COSMO Newsletter* **19**, 12-22.

Tsyrulnikov, M. and Gayfulin, D., 2017. A limited-area spatio-temporal stochastic pattern generator for simulation of uncertainties in ensemble applications. *Meteorol. Zeitschrift* **26**, 5, 549-566.

Wastl, C., Wang, Y., Atencia, A. and Wittmann, C., 2019. A hybrid stochastically perturbed parametrization scheme in a convection-permitting ensemble. *Mon. Weather Rev.* **147**, 6, 2217-2230.

Wichmann, B. A., Hill, I. D., 1982. Algorithm AS 183: An Efficient and Portable Pseudo-Random Number Generator. *Journal of the Royal Statistical Society.* Series C (Applied Statistics). **31**, 2, 188-190. doi:10.2307/2347988

Wong et al., 2013. Evaluating a lightning parameterization based on cloud-top height for mesoscale numerical model simulations. *Geosci. Model Dev.* **6**, 429-443.

List of COSMO Newsletters and Technical Reports

(available for download from the COSMO Website: www.cosmo-model.org)

COSMO Newsletters

No. 1: February 2001.

No. 2: February 2002.

No. 3: February 2003.

No. 4: February 2004.

No. 5: April 2005.

No. 6: July 2006.

No. 7: April 2008; Proceedings from the 8th COSMO General Meeting in Bucharest, 2006.

No. 8: September 2008; Proceedings from the 9th COSMO General Meeting in Athens, 2007.

No. 9: December 2008.

No. 10: March 2010.

No. 11: April 2011.

No. 12: April 2012.

No. 13: April 2013.

No. 14: April 2014.

No. 15: July 2015.

No. 16: July 2016.

No. 17: July 2017.

No. 18: November 2018.

No. 19: October 2019.

No. 20: December 2020.

COSMO Technical Reports

No. 1: Dmitrii Mironov and Matthias Raschendorfer (2001):
Evaluation of Empirical Parameters of the New LM Surface-Layer Parameterization Scheme. Results from Numerical Experiments Including the Soil Moisture Analysis.

No. 2: Reinhold Schrodin and Erdmann Heise (2001):
The Multi-Layer Version of the DWD Soil Model TERRA_LM.

No. 3: Günther Doms (2001):
A Scheme for Monotonic Numerical Diffusion in the LM.

No. 4: Hans-Joachim Herzog, Ursula Schubert, Gerd Vogel, Adelheid Fiedler and Roswitha Kirchner (2002):
LLM ¯ the High-Resolving Nonhydrostatic Simulation Model in the DWD-Project LITFASS.
Part I: Modelling Technique and Simulation Method.

No. 5: Jean-Marie Bettems (2002):
EUCOS Impact Study Using the Limited-Area Non-Hydrostatic NWP Model in Operational Use at MeteoSwiss.

No. 6: Heinz-Werner Bitzer and Jürgen Steppeler (2004):
Documentation of the Z-Coordinate Dynamical Core of LM.

No. 7: Hans-Joachim Herzog, Almut Gassmann (2005):
Lorenz- and Charney-Phillips vertical grid experimentation using a compressible nonhydrostatic toy-model relevant to the fast-mode part of the 'Lokal-Modell'.

No. 8: Chiara Marsigli, Andrea Montani, Tiziana Paccagnella, Davide Sacchetti, André Walser, Marco Arpagaus, Thomas Schumann (2005):
Evaluation of the Performance of the COSMO-LEPS System.

No. 9: Erdmann Heise, Bodo Ritter, Reinhold Schrodin (2006):
Operational Implementation of the Multilayer Soil Model.

No. 10: M.D. Tsyrulnikov (2007):
Is the particle filtering approach appropriate for meso-scale data assimilation ?

No. 11: Dmitrii V. Mironov (2008):
Parameterization of Lakes in Numerical Weather Prediction. Description of a Lake Model.

No. 12: Adriano Raspanti (2009):
COSMO Priority Project "VERification System Unified Survey" (VERSUS): Final Report.

No. 13: Chiara Marsigli (2009):
COSMO Priority Project "Short Range Ensemble Prediction System" (SREPS): Final Report.

No. 14: Michael Baldauf (2009):
COSMO Priority Project "Further Developments of the Runge-Kutta Time Integration Scheme" (RK): Final Report.

No. 15: Silke Dierer (2009):
COSMO Priority Project "Tackle deficiencies in quantitative precipitation forecast" (QPF): Final Report.

No. 16: Pierre Eckert (2009):
COSMO Priority Project "INTERP": Final Report.

No. 17: D. Leuenberger, M. Stoll and A. Roches (2010):
Description of some convective indices implemented in the COSMO model.

No. 18: Daniel Leuenberger (2010):
Statistical analysis of high-resolution COSMO Ensemble forecasts in view of Data Assimilation.

No. 19: A. Montani, D. Cesari, C. Marsigli, T. Paccagnella (2010):
Seven years of activity in the field of mesoscale ensemble forecasting by the COSMO–LEPS system: main achievements and open challenges.

No. 20: A. Roches, O. Fuhrer (2012):
Tracer module in the COSMO model.

No. 21: Michael Baldauf (2013):
A new fast-waves solver for the Runge-Kutta dynamical core.
DOI: 10.5676/DWD_pub/nwv/cosmo-tr_21

No. 22: C. Marsigli, T. Diomede, A. Montani, T. Paccagnella, P. Louka, F. Gofa, A. Corigliano (2013):
The CONSENS Priority Project.
DOI: 10.5676/DWD_pub/nwv/cosmo-tr_22

No. 23: M. Baldauf, O. Fuhrer, M. J. Kurowski, G. de Morsier, M. Müllner, Z. P. Piotrowski, B. Rosa, P. L. Vitagliano, D. Wójcik, M. Ziemiański (2013):
The COSMO Priority Project 'Conservative Dynamical Core' Final Report.
DOI: 10.5676/DWD_pub/nwv/cosmo-tr_23

No. 24: A. K. Miltenberger, A. Roches, S. Pfahl, H. Wernli (2014):
Online Trajectory Module in COSMO: a short user guide.
DOI: 10.5676/DWD_pub/nwv/cosmo-tr_24

No. 25: P. Khain, I. Carmona, A. Voudouri, E. Avgoustoglou, J.-M. Bettems, F. Grazzini (2015):
The Proof of the Parameters Calibration Method: CALMO Progress Report.
DOI: 10.5676/DWD_pub/nwv/cosmo-tr_25

No. 26: D. Mironov, E. Machulskaya, B. Szintai, M. Raschendorfer, V. Perov, M. Chumakov, E. Avgoustoglou (2015):
The COSMO Priority Project 'UTCS' Final Report.
DOI: 10.5676/DWD_pub/nwv/cosmo-tr_26

No. 27: J-M. Bettems (2015):
The COSMO Priority Project 'COLOBOC': Final Report.
DOI: 10.5676/DWD_pub/nwv/cosmo-tr_27

No. 28: Ulrich Blahak (2016):
RADAR_MIE_LM and RADAR_MIELIB - Calculation of Radar Reflectivity from Model Output.
DOI: 10.5676/DWD_pub/nwv/cosmo-tr_28

No. 29: M. Tsyrulnikov and D. Gayfulin (2016):
A Stochastic Pattern Generator for ensemble applications.
DOI: 10.5676/DWD_pub/nwv/cosmo-tr_29

No. 30: D. Mironov and E. Machulskaya (2017):
A Turbulence Kinetic Energy – Scalar Variance Turbulence Parameterization Scheme.
DOI: 10.5676/DWD_pub/nwv/cosmo-tr_30

No. 31: P. Khain, I. Carmona, A. Voudouri, E. Avgoustoglou, J.-M. Bettems, F. Grazzini, P. Kaufmann (2017):
CALMO - Progress Report.
DOI: 10.5676/DWD_pub/nwv/cosmo-tr_31

No. 32: A. Voudouri, P. Khain, I. Carmona, E. Avgoustoglou, J.M. Bettems, F. Grazzini, O. Bellprat, P. Kaufmann and E. Bucchignani (2017):
Calibration of COSMO Model, Priority Project CALMO Final report.
DOI: 10.5676/DWD_pub/nwv/cosmo-tr_32

No. 33: N. Vela (2017):
VAST 2.0 - User Manual.
DOI: 10.5676/DWD_pub/nwv/cosmo-tr_33

No. 34: C. Marsigli, D. Alferov, M. Arpagaus, E. Astakhova, R. Bonanno, G. Duniec, C. Gebhardt, W. Interewicz, N. Loglisci, A. Mazur, V. Maurer, A. Montani, A. Walser (2018):
COsmo Towards Ensembles at the Km-scale IN Our countries" (COTEKINO), Priority Project final report.
DOI: 10.5676/DWD_pub/nwv/cosmo-tr_34

No. 35: G. Rivin, I. Rozinkina, E. Astakhova, A. Montani, D. Alferov, M. Arpagaus, D. Blinov, A. Bundel, M. Chumakov, P. Eckert, A. Euripides, J. Förstner, J. Helmert, E. Kazakova, A. Kirsanov, V. Kopeikin, E. Kukanova, D. Majewski, C. Marsigli, G. de Morsier, A. Muravev, T. Paccagnella, U. Schättler, C. Schraff, M. Shatunova, A. Shcherbakov, P. Steiner, M. Zaichenko (2018):
The COSMO Priority Project CORSO Final Report.
DOI: 10.5676/DWD_pub/nwv/cosmo-tr_35

No. 36: A. Raspanti, A. Celozzi, A. Troisi, A. Vocino, R. Bove, F. Batignani (2018):
The COSMO Priority Project VERSUS2 Final Report.
DOI: 10.5676/DWD_pub/nwv/cosmo-tr_36

No. 37: A. Bundel, F. Gofa, D. Alferov, E. Astakhova, P. Baumann, D. Boucouvala, U. Damrath, P. Eckert, A. Kirsanov, X. Lapillonne, J. Linkowska, C. Marsigli, A. Montani, A. Muraviev, E. Oberto, M.S. Tesini, N. Vela, A. Wyszogrodzki, M. Zaichenko, A. Walser (2019):
The COSMO Priority Project INSPECT Final Report.
DOI: 10.5676/DWD_pub/nwv/cosmo-tr_37

No. 38: G. Rivin, I. Rozinkina, E. Astakhova, A. Montani, J-M. Bettems, D. Alferov, D. Blinov, P. Eckert, A. Euripides, J. Helmert, M.Shatunova (2019):
The COSMO Priority Project CORSO-A Final Report.
DOI: 10.5676/DWD_pub/nwv/cosmo-tr_38

No. 39: C. Marsigli, D. Alferov, E. Astakhova, G. Duniec, D. Gayfulin, C. Gebhardt, W. Interewicz, N. Loglisci, F. Marcucci, A. Mazur, A. Montani, M. Tsyrulnikov, A. Walser (2019):
Studying perturbations for the representation of modeling uncertainties in Ensemble development (SPRED Priority Project): Final Report.
DOI: 10.5676/DWD_pub/nwv/cosmo-tr_39

No. 40: E. Bucchignani, P. Mercogliano, V. Garbero, M. Milelli, M. Varentsov, I. Rozinkina, G. Rivin, D. Blinov, A. Kirsanov, H. Wouters, J.-P. Schulz, U. Schättler (2019):

Analysis and Evaluation of TERRA_URB Scheme: PT AEVUS Final Report.
DOI: 10.5676/DWD_pub/nwv/cosmo-tr_40

No. 41: X. Lapillonne, O. Fuhrer (2020):
Performance On Massively Parallel Architectures (POMPA): Final report.
DOI: 10.5676/DWD_pub/nwv/cosmo-tr_41

No. 42: E. Avgoustoglou, A. Voudouri, I Carmona, E. Bucchignani, Y. Levy, J. -M. Bettems (2020):
A methodology towards the hierarchy of COSMO parameter calibration tests via the domain sensitivity over the Mediterranean area.
DOI: 10.5676/DWD_pub/nwv/cosmo-tr_42

No. 43: H. Muskatel, U. Blahak, P. Khain, A. Shtivelman, M. Raschendorfer, M. Kohler, D. Rieger, O. Fuhrer, X. Lapillonne, G. Rivin, N. Chubarova, M. Shatunova, A. Poliukhov, A. Kirsanov, T. Andreadis, S. Gruber (2021):
The COSMO Priority Project $T^2(RC)^2$: Testing and Tuning of Revised Cloud Radiation Coupling, Final Report
DOI: 10.5676/DWD_pub/nwv/cosmo-tr_43

No. 44: M. Baldauf, D. Wojcik, F. Prill, D. Reinert, R. Dumitrache, A. Iriza, G. deMorsier, M. Shatunova, G. Zaengl, U. Schaettler (2021):
The COSMO Priority Project CDIC: Comparison of the dynamical cores of ICON and COSMO, Final Report
DOI: 10.5676/DWD_pub/nwv/cosmo-tr_44

COSMO Technical Reports

Issues of the COSMO Technical Reports series are published by the *COnsortium for Small-scale MOdelling* at non-regular intervals. COSMO is a European group for numerical weather prediction with participating meteorological services from Germany (DWD, AWGeophys), Greece (HNMS), Italy (USAM, ARPA-SIMC, ARPA Piemonte), Switzerland (MeteoSwiss), Poland (IMGW), Romania (NMA) and Russia (RHM). The general goal is to develop, improve and maintain a non-hydrostatic limited area modelling system to be used for both operational and research applications by the members of COSMO. This system is initially based on the COSMO-Model (previously known as LM) of DWD with its corresponding data assimilation system.

The Technical Reports are intended

- for scientific contributions and a documentation of research activities,
- to present and discuss results obtained from the model system,
- to present and discuss verification results and interpretation methods,
- for a documentation of technical changes to the model system,
- to give an overview of new components of the model system.

The purpose of these reports is to communicate results, changes and progress related to the LM model system relatively fast within the COSMO consortium, and also to inform other NWP groups on our current research activities. In this way the discussion on a specific topic can be stimulated at an early stage. In order to publish a report very soon after the completion of the manuscript, we have decided to omit a thorough reviewing procedure and only a rough check is done by the editors and a third reviewer. We apologize for typographical and other errors or inconsistencies which may still be present.

At present, the Technical Reports are available for download from the COSMO web site (www.cosmo-model.org). If required, the member meteorological centres can produce hard-copies by their own for distribution within their service. All members of the consortium will be informed about new issues by email.

For any comments and questions, please contact the editor:

Massimo Milelli
massimo.milelli@cimafoundation.org

Consortium

for

Small-Scale Modelling

Technical Report No. 46

The COSMO Priority Project CARMA: Common Area with Rfdbk/MEC Application Final Report

May 2022

Deutscher Wetterdienst
MeteoSwiss
Ufficio Generale Spazio Aereo e Meteorologia
ΕΘΝΙΚΗ ΜΕΤΕΩΡΟΛΟΓΙΚΗ ΥΠΗΡΕΣΙΑ
Instytut Meteorologii i Gospodarki Wodnej
Administratia Nationala de Meteorologie
ROSHYDROMET
Agenzia Regionale Protezione Ambiente Piemonte
Agenzia Regionale Prevenzione Ambiente Energia Emilia Romagna
Centro Italiano Ricerche Aerospaziali
Amt fr GeoInformationswesen der Bundeswehr
Israel Meteorological Service
Centro Euro-Mediterraneo sui Cambiamenti Climatici
CIMA Foundation

www.cosmo-model.org

Editor: Massimo Milelli, ARPA Piemonte

The COSMO Priority Project CARMA: Common Area with Rfdbk/MEC Application Final Report

Amalia Iriza-Burca[*,1], ***Flora Gofa***[2], ***Dimitra Boucouvala***[2], ***Theodore Andreadis***[2], ***Joanna Linkowska***[3], ***Pavel Khain***[4], ***Alon Shtivelman***[4], ***Francesco Batignani***[5], ***Andreas Pauling***[6], ***Alexander Kirsanov***[7], ***Thomas Gastaldo***[8], ***Bogdan Maco***[1], ***Mihaela Bogdan***[1] ***Felix Fundel***[9]

[*]Project Coordinator[1]National Meteorological Administration - NMA
[2]Hellenic National Meteorological Service - HNMS
[3]Instytut Meteorologii i Gospodarki Wodnej - IMGW-PIB
[4]Israel Meteorological Service - IMS
[5]Aeronautica Militare-Reparto per la Meteorologia - COMET
[6]MeteoSwiss - MCH
[7]HydroMetCenter of Russia - RHM
[8]Agenzia Regionale Prevenzione Ambiente Energia Emilia Romagna, Struttura Idro-Meteo-Clima - Arpae-SIMC
[9]Deutscher Wetterdienst - DWD

Contents

1 Introduction **4**

1.1 Goal of PP 4

1.2 Brief Description of System Design 5

1.2.1 The Model Equivalent Calculator (MEC) 6

1.2.2 The Rfdbk package 7

1.2.3 R Shiny web server 8

1.3 Overview of System Implementation 8

2 Description of Tasks **9**

2.1 Task 1: First Level Support Implementation and Training 9

2.1.1 Subtasks 9

2.1.2 Deliverables and Preliminary Results 10

2.2 Task 2: Second Level Implementation and support+ 10

2.2.1 Subtasks 10

2.2.2 Deliverables and Preliminary Results 10

2.3 Task 3: Cross-validation of implementation 11

2.3.1 Subtasks 11

2.3.2 Deliverables and Preliminary Results 11

2.4 Task 4 Elaboration of guidelines for CARMA (MEC-Rfdbk) system use . . . 12

2.4.1 Deliverables and Preliminary Results 12

2.5 Overview of Issues and Remaining Discussion Points 12

3 Timeline of Activities and Results **12**

3.1 MAM 2020: First Results 15

3.2 SON2020: Verification of ICON in Limited Area Mode at COSMO National Meteorological Services 15

3.3 DJF2021: First Common Activity Applications 16

3.4 MAM2021: Extended Common Area Activities 17

3.5 JJA2021: Ongoing Activities 19

4 Conclusions and Outlook **19**

5 Meetings **20**

6 Documentation **20**

7 Acknowledgments **21**

1 Introduction

In 2006, the STC approved the development of a common, unified verification 'library' through the VERSUS project, which was followed by the PP-VERSUS2 in 2009. The objective of this strategic decision was to develop a common COSMO verification software package that would enable the production of homogeneous and comparable statistical results. In recent years, partly due to technical limitations of VERSUS and the ceasing of further development, the WG5 members considered the possibility of utilizing multiple verification modules that would not necessarily be linked to one software package (e.g. VAST software for spatial methods). For the CP activity, it is essential to maintain a software as a common tool for their production as this will ensure the adoption of the same verification practices that will allow for the easier long-term monitoring of the derived results.

Before the start of PP CARMA, Common Plot verification activities were carried out using the VERSUS verification software environment. Because of the technical limitations of VERSUS and lack of further development, it has been decided within the consortium that this should be replaced with the MEC-Rfdbk software. The MEC-Rfdbk system uses small files for fast calculation of verification scores, while the results can be browsed interactively online. The verification is based on the use of feedback files (FF), that hold information on observations (including meta-data) and their usage in data assimilation, as well as the corresponding model analysis, first-guess and past forecasts, in NetCDF format. These files are relatively small, being produced for each valid time / observation type and can be used for various verification tasks.

The Model Equivalent Calculator (MEC) software for the production of Feedback Files, and verification scripts based on the R package Rfdbk, are tools that were developed and are in operational use at DWD for the verification of both COSMO and ICON model chains.

1.1 Goal of PP

The goal of the CARMA Priority Project (2018-2021) was to replace the existing VERSUS verification software environment with the MEC-Rfdbk software developed by DWD, as a Common Verification Software (CVS), in order to perform part of the verification activities in the consortium. The main use of the new CVS is be the production of the Common Plot (CP) verification while spatial verification should rather be performed with other available tools (VAST, etc.) in each service. MEC-Rfdbk is also suitable for EPS verification, but this type of application was not be included in the current project as EPS verification is not part of CP activity, but can be considered in a next phase. The CVS that is based on MEC-Rfdbk is chosen with the intention of being a useful user-friendly tool for the entire COSMO community. It addresses the need to perform traditional point verification both for the surface and the upper air using conventional methods, which arise from operational and research activities. Moreover, a centralized transfer and visualization of CP statistics on COSMO web server will facilitate the easier analysis of the outcome of this activity and is one of the main goals of this project.

The most striking advantages of the new verification system adopted for CP preparation activity, are the shortfall of data pre-processing (all data in one place, observation and forecast correctly assigned to each other, quality control done by data assimilation, small files), the fast and simple calculation of standard verification scores and the interactive visualisation and online production of results.

PP CARMA was also linked with the following COSMO tasks:

- Support Activities – NWP Test Suite: the MEC-Rfdbk system is currently installed and used on the ECMWF platform for the evaluation of new model versions before they are officially released.
- PP C2I Task 3 for the evaluation and comparison of COSMO and ICON-LAM forecasts: the MEC+Rfdbk system was used to produce verification results included in the ICON Report "Verification of ICON in Limited Area Mode at COSMO National Meteorological Services" (Rieger et al., 2021) published as part of the Priority Project
- Support Activities – Common Plot verification (SPRT).

1.2 Brief Description of System Design

The MEC-Rfdbk verification system is based on the use of feedback files (FF) that hold information on observations and their usage in the data assimilation (DA) system. FF and are available for each observation system used in DA and contain information regarding the observations (including meta-data) and corresponding model analysis, first-guess and past forecast (also ensemble) in the NetCDF format. These files have a relatively small size (e.g. 4.8Mb SYNOP for COSMO-7km run for the NWP Test Suite domain covering the entire Europe) and are produced as one file for each valid-time (time window), model and observation system. A detailed description of FF can be found here (http://cosmo-model.org/content/model/documentation/core/default.htm).

The FF are produced by the Model Equivalent Calculator (MEC; Potthast, 2019) within the data assimilation system or as stand-alone. Information from FF can be used for verification tasks (e.g. name, location, level, weight in DA, ensemble spread, Talagrand index and so on). Further on, these files are used by the Rfdbk (Fundel, 2021) package to perform some convenience functions like data adjustment, re-labelling, binning etc. and then calculate the verification scores. Finally, the verification scores in Rdata format are visualized on the dedicated COSMO web page, using the R shiny server (Chang et al., 2020).

A schematic diagram of the system is presented in Fig. 1, followed by short descriptions of the main system components. **For more detailed presentations of the MEC-Rfdbk system and its components, including information regarding installation and use, please check the dedicated documents referenced in Section 6.**

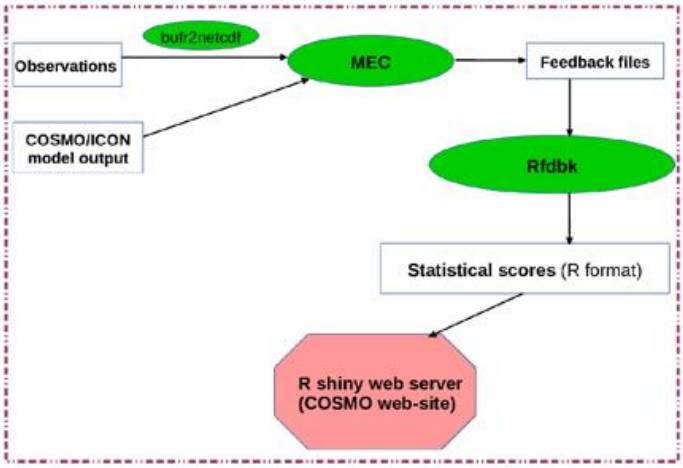


Figure 1: Schematic representation of the MEC-Rfdbk system.

1.2.1 The Model Equivalent Calculator (MEC)

MEC applies the observation operators from the data assimilation scheme (Nudging, 3Dvar, Ensemble Kalman Filter) to model forecasts (COSMO, ICON) and stores the results in verification files (NetCDF feedback file format). The software can use as input observations, model runs (deterministic or ensemble), analysis runs or even another MEC run, depending on the user needs and can be applied to interpolate between two or more time periods. Observation operators are either those implemented in the DWD global data assimilation code (3dvar/EnVar/LETKF) or those implemented in the COSMO model, as used in the nudging and the KENDA/LETKF data assimilation scheme. Alternatively, the fof-files (feedback file format as well) written by COSMO (in the nudging mode or in the first guess run for KENDA) may be taken as input for MEC. A further option is to use the original observational data (CDFIN, i.e. BUFR format converted to NetCDF). In these cases verification files will be generated separately for each observation type (TEMP, PILOT, SYNOP, etc).

For this project (as well as for the permanent Common Plot Activity), this second approach was adopted by using a common set of observations retrieved in bufr format from the MARS archive. These observations are converted in NetCDF format with the bufr2netcdf software (Patruno and Cesari, 2011) and used as input in MEC. The results of MEC are stored in the NetCDF feedback file format.

The advantages of using the MEC software as part of the verification system for CP activities are related to data pre-processing (all data in one place) and ensuring observation and forecasts are correctly assigned to each other, with quality control done by data assimilation.

MEC characteristics and requirements:

- produces feedback files
- namelist based

Installation

- Sources: Fortran 2003/2008 and C (Makefile for gfortran provided)
- Dependencies: NetCDF, CGRIBEX (MPI Hamburg), GRIP-API (ECMWF), (MPI recommended), Fortran compiler, C compiler
- Sufficient memory to hold one model state (1 ensemble state)

IO specifications

- model in Grib2 format – COSMO or ICON-LAM
- parameters - PS, T, U, V, P, Q (mandatory, all model levels); T2M, TD2M, CLC, CLCT, CLCL, CLCM, CLCH, CLC, H_SNOW, TOT_PREC, VMAX_10, TMIN_2M, TMAX_2M
- observations (CDFIN: BUFR converted by bufrx2netcdf to NetCDF)
- output: ver-files, NetCDF feedback files including past forecasts

MEC can produce feedback-files for any model, which can then be used as input to produce verification statistics using Rfdbk. Some mandatory parameters from the model of interest must be available on all model levels: PS, T, U, V, P, Q, while others are optional, depending on the available observations and user needs (T2M, TD2M, PS, N, FF, DD, Gust, RR, etc).

The production of IFS FF using the Common Plot set of observations (cdfin files) is at the moment on-going, due to some limitations of the MEC software that need further investigation. This activity is included in the COSMO-SPRT Common Plot one for 2021-2022.

1.2.2 The Rfdbk package

This is an R interface that aims to exploit the information contained in the feedback files and can be used to perform feedback file-based verification. Rfdbk uses as input the feedback files obtained from MEC (one file for each validity date and observation type) and outputs score files (again, for each validity date and observation type). Rfdbk exploits the functionality of the R data.table format and can therefore handle huge data tables efficiently with a concise syntax that allows to apply functions on sub-categories. Rfdbk itself is not a verification package but an assortment of R functions (libraries). Based on Rfdbk libraries, R scripts exist to quickly and reliably produce verification results. These scripts can be modified and adjusted according to the needs of each particular system that will be linked to.

Rfdbk characteristics and requirements:

- R interface for COSMO feedback files
- main purpose is to load feedback file content with R
- additional functionalities useful for verification implemented as well
- namelist based verification scripts using Rfdbk do the verification

Installation

- Sources: R language
- Dependencies: NetCDF library and R with additional R packages: RNetCDF, data.table, parallel, strings, survival, grid, verification, reshape2, pcaPPIO specifications
- input - feedback files obtained previously with MEC - one file for each validity date and observation type
- output - score files for each validity date and observation type

Verification can be done for various types of observations (SYNOP, radiosondes, radio occultation, aircraft, wind profiler and so on). Continuous scores are computed for various types of observations, while categorical scores are also available for SYNOP observations. Verification can be performed for deterministic runs (forecast or hindcast) or ensemble, for any model (COSMO, ICON, IFS, etc.), while cross model verification (e.g. COSMO vs. ICON vs. IFS) is also possible. The package allows the handling of large data tables that facilitate the loading of feedback file content, data adjustment, binning, calculation of basic verification scores and so on. Rfdbk -based scripts can be used for:

- domain average verification (function of forecast lead-time for a user defined verification period), including domain stratification,
- time series (function of valid time in the verification period or as a function of the forecast lead-time)
- station based verification (function of observation station).
- aggregation on sub-domains, height bins, levels or periods

Rfdbk is a user-friendly package that can be employed in R-based scripts in order to perform point verification for either surface or upper air parameters using various types of observations and model runs. The advantage of using Rfdbk based verification scripts is their flexibility, which means they can be modified and adjusted according to the needs of each user and (UNIX) system.

1.2.3 R Shiny web server

On top, an interactive (R based) tool for the online visualization of verification results has been developed and will be also adopted in this project. This is based on the R Shiny web server that is currently setup on the COSMO web-site for the NWP Test suite needs. Through this capability it is possible to have on demand interactive plot web browser application, plot and arrange scores, summary score charts and browse data, with separate web-based apps for each observation and verification type.

This centralized, online and interactive visualization of the results on the COSMO web-site using the R Shiny server is meant to enable an easier evaluation of the results.

1.3 Overview of System Implementation

PP CARMA has obtained the successful results. The main outcome was the implementation of the new CVS in most countries of the COSMO consortium, with the system already in use for various operational implementations of both COSMO and ICON, as can be seen from tables 1 and 2.

	IMPLEMENTATION		**PRODUCTION**		**Visualization**
	DACE/MEC	**Rfdbk**	**FF**	**SCORES**	**(optional)**
NMA	yes	yes	yes	yes	yes
HNMS	yes	yes	yes	yes	-
DWD	*(yes)	*(yes)	*(yes)	*(yes)	*(yes)
MCH	*(yes)	*(yes)	on-going	on-going	
COMET	yes	yes	yes	yes	
IMGW-PIB	yes	yes	yes	yes	yes
RHM	yes	yes	on-going		
IMS	yes	yes	yes	yes	yes
ArpaE-SIMC	yes	on-going			

Table 1: Status of implementations for the MEC+Rfdbk system in each centre. *denotes that the system was installed and in use before the start of the project.

	NMA	HNMS	DWD	IMGW-PIB	COMET	MCH	RHM	IMS	ArpaE-SIMC
COSMO	x	-	x	x	x	x	-	-	x
ICON	x	x	x	x	x	-	x	x	-

Table 2: Overview of models verified by each centre using the MEC+Rfdbk software.

First results using the MEC+Rfdbk output for some CP activities started in the 2020 spring season (MAM 2020). The number of model scores computed with the new CVS has gradually increased until present (15 models expected for JJA2021), as will be shown in Section 3, dedicated to presenting the PP results.

2 Description of Tasks

2.1 Task 1: First Level Support Implementation and Training

Goal: The first level support implementation and training of the Project Support Team (PST) were included. In turn, the PST ensured and supported the implementation of the system for all the other partners.

2.1.1 Subtasks

1.1 Documentation review (MEC-Rfdbk), analysis of resources required. Preparation of a document for verification task specifications (common areas, models, parameters, statistical indices, representation) included in CP activity.

1.2 Documentation preparation (MEC-Rfdbk) with all the necessary installation and use notes for the PST training.

1.3 Preparation of a complete example set of data (one season, one model) to be used during the training and testing period. Model output as a test bed, including parameters that are part of CP requirements prepared. Adaptation of observations in NetCDF format (with bufr2netcdf COSMO software).

1.4 Training provided by DWD experts for first level support to the PST. During this training, a "clean" installation of MEC, Rfdbk and Shiny routines for visualization of results will be performed on a test machine. A complete cycle of model evaluation for a test case (outcome of Task 1.3) over CP area will be performed (observation preparation, run of MEC for Feedback files preparation, run of Rfdbk for extraction of statistical indices for both continuous and dichotomic parameters, visualization of results with Shiny).

1.5 Implementation of the MEC-Rfdbk system at NMA and HNMS (PST), in order to set up the MEC+Rfdbk system in all participating countries (with support from DWD experts where necessary).

1.6 Adaptation of scripts to produce the necessary statistical information for the production of the CP requirements, on a seasonal basis. Preparation and testing of scripts for semi-automatic use of the system.

1.7 Setup of web interface with the use of Shiny R routines on COSMO server to host CP activity outputs once the system becomes operational.

2.1.2 Deliverables and Preliminary Results

- Written instructions for installation and use of MEC-Rfdbk system.
- Installation of the MEC-Rfdbk system at NMA and HMNS (PST) and first tests of the implementation.
- Scripts for semi-automatic use of the system, available to project participants through common WG5 repository.
- Dataset (forecast/observation) to be used for test period of MEC-Rfdbk system.
- Completion of test period experiment and production of statistics (PST).
- Web interface to host Common Area plots for all countries.

The observations necessary for CP activity are prepared and disseminated to the participants operationally, on a daily basis.

Together with the daily observations, three sets of scripts are available for:

- production of FF with MEC from various model specifications (COSMO, ICON-LAM native or regular grid), on different platforms (local machine, ECMWF)
- production of scores using Rfdbk
- templates for plotting the results using the shiny server

The web interface to host Common Area plots for all countries is available on the COSMO web-site: http://www.cosmo-model.org/shiny/apps/carma/.

2.2 Task 2: Second Level Implementation and support+

Goal: Implementation of the MEC-Rfdbk system by all the member countries in the consortium, with support from PST (DWD support provided only when necessary and always through the PST).

2.2.1 Subtasks

2.1 Remote training PST for users from each centre. Dissemination of instructions, mailing list creation for problems solving, videoconferences, etc.

2.2 Implementation of MEC-Rfdbk system in each participating centre with support of PST

2.2.2 Deliverables and Preliminary Results

MEC-Rfdbk system installed by all project participants with support from PST. An overview of implementation status for each system component was shown in tables 1 and 2 (Section 1.3).

2.3 Task 3: Cross-validation of implementation

Goal: Testing of the verification system implementation and training through practical use.

Requirements from the participating scientists with regards to their verification needs led to the necessity of shifting the initially main task of the project from COSMO to ICON, in the view of the COSMO to ICON migration. As a consequence, two additional sub-tasks were included after the start of the project. The first additional sub-task was directly related to the COSMO to ICON migration and the need to test the new verification system for ICON-LAM implementations, rather than continue to invest much effort in adapting it for COSMO needs. Apart from this, an optional sub-task was also proposed, which was not foreseen at the beginning of the project. With the shiny server (COSMO web) used for both CP activities and the NWP Test Suite verification platform and due to the interest of the participants to use the MEC+Rfdbk system for verification requirements additional to CP activities, set-up of individual shiny servers was advised, in order to avoid loading the COSMO shiny server unnecessarily.

2.3.1 Subtasks

3.1 Performance of a test with all the necessary output for the CP reports. This task included development/adaptation of automatic procedures (scripts adaptation to local DBs) for seasonal CP activities based on the MEC-Rfdbk system by all services. Preparation of MEC output files for seasonal CP.

3.2 Transfer to statistical output to COSMO web server and visualization of results through installation of Shiny server (capability developed in Task 1.6) for comparison purposes.

3.3 Optional comparison of test output with VERSUS system or any other "home" verification system.

3.4 Set-up and testing of MEC+Rfdbk capabilities for ICON-LAM
Set-up of system and performance of a test with all the necessary output of ICON-LAM for the CP reports. This task was added due to the requirements of the participants, in view of the new ICON implementations. Some centres were unable to verify COSMO because of MEC model data requirements and lack of storage resources (e.g. not all required model data are archived). This additional sub-task also took into consideration the migration from COSMO to ICON.

3.5 (optional) Set-up of individual shiny server for visualization
At the start of the project, the shiny server on the COSMO web-site was used for visualization of results from Rfdbk (CP verification as well as NWP test suite). However, this can only be a solution for the CP activities, since verification activities of the users from the MEC+Rfdbk system vary and also include other type of individual verification. For future use (optimal) of the MEC+Rfdbk system, the set-up of individual shiny servers for each interested centre was suggested, to facilitate the visualization of the verification results. Similar to the implementation of the MEC+Rfdbk system, the shiny server was first set-up for the PST team who would, in turn help the other participants set-up their own systems.

2.3.2 Deliverables and Preliminary Results

- Evaluation of MEC-Rfdbk system for CP production based on an example dataset. Comparison with results from other verification software.

- Implementation of CP seasonal output with the MEC-Rfdbk system.

2.4 Task 4 Elaboration of guidelines for CARMA (MEC-Rfdbk) system use

Goal Preparation of documentation on the use of the MEC-Rfdbk system (including CP activities specifications).

2.4.1 Deliverables and Preliminary Results

Guidelines on the implementation, use and application of the MEC-Rfdbk system for CP production. ***An overview of the PP documentation (including Guidelines) is available in Section 6.***

2.5 Overview of Issues and Remaining Discussion Points

Remaining Discussion Points
Following the finalization of the project, a few remaining issues are at the moment still on-going, due to some limitations either of the software or specific problems of some users. These activities are included in the COSMO-SPRT Common Plot activities for 2021-2022 and refer to:

- IFS based FF
- installation and user support
- inclusion of all models in the new verification system

As Common Plot activities are a continuous and evolving task, some features of the current requirements might differ to the ones envisioned at the beginning of the project. As a consequence, follow up activities will also aim to incorporate the new requirements included in this year guidelines of the CP activity, such as:

- upper air verification
- 6h precipitation in all time intervals
- conditional verification
- update of the system with new versions of Rfdbk and distribution of new MEC versions for FF production

3 Timeline of Activities and Results

For the various results presented in the sections bellow, the following models were employed:

ICON GLOBAL (DWD)
ICON-EU (DWD)
COSMOPL7 / COSMO-PL(IMGW-PIB)
COSMO_ME (COMET)

ICON-D2 (DWD)
ICON_IT2 (COMET)
ICONGR (HNMS)
ICON_IMS / ICON-IL2p5 (IMS)
ICONPL (IMGW-PIB)
COSMO-CE-PL (IMGW-PIB)
COSMO_IT2 (COMET)
COSMO-1E (MCH)
COSMO-2E (MCH)
COSMO-RO_2p8 (NMA)
ICON-RO_2p8 (NMA)
COSMO-D2 (DWD)
COSMOP2k8 (IMGW-PIB)
COSMO-RO (NMA)

Standard Verification (seasonal) is generally performed for the following continuous parameters: 2-meter temperature – T2M (deg K), 2-meter dew point temperature - TD2M (deg K), surface pressure - PS (Pa), total cloud cover - N (octa), 10-meter wind speed - FF (m/s), wind direction - DD (deg) and wind gust - Gust (1 hour, m/s). Categorical scores are also computed, for the following parameters: 6 hour accumulated precipitation - RR_6h (thresholds: 0.2, 1, 5, 10, 15, 20 mm/6h), total cloud cover (thresholds >= 1, >= 4 and >= 7) and 10-meter wind gust (thresholds: >= 12.5, >= 15, >= 20 m/s).

Scores for continuous parameters include the mean error (ME) and root mean squared error (RMSE), mean absolute error (MAE), standard deviation (SD) and so on (only ME and RMSE will be discussed in the following examples). Dichotomic scores include the probability of detection (POD), false alarm rate (FAR), equitable threat score (ETS), frequency bias (FBI). Other scores based on the number of hits, misses, false alarms and correct negatives respectively are also available, but will not be shown. For all scores, the number of observations used in computations (LEN) is also available.

For the purpose of the project and future Common Plot Activities, scores were performed either for national domains or for the two domains used in the Common Area Verification Activities (see Figs. 2, 3 and Table 3).

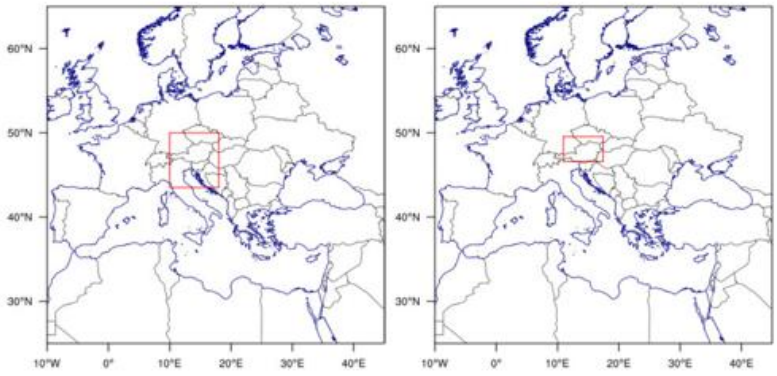


Figure 2: Common Areas: CA1 (left) and CA2 (right) used for the verification.

The two common areas for which the scores are computed include parts of Northern Italy, Austria, Slovenia, Croatia, Germany, Bosnia and Herzegovina, Hungary, Slovakia, and the Czech Republic. For Common Area 1, 96 stations were selected, with altitudes between 0m and 753 meters. Although slightly more restricted geographically, Common Area 2

included a larger number of stations than CA1. The stations in CA2 also cover a greater range of altitudes compared to CA1 (maximum altitude 3114m in CA2 compared to 753m in CA1). Table 3 offers an overview of station distribution for the two areas. The two areas were defined according to the list of stations previously used in verification activities with VERSUS. The results are computed taking into account all stations of interest. However, results are also available stratified by station altitude.

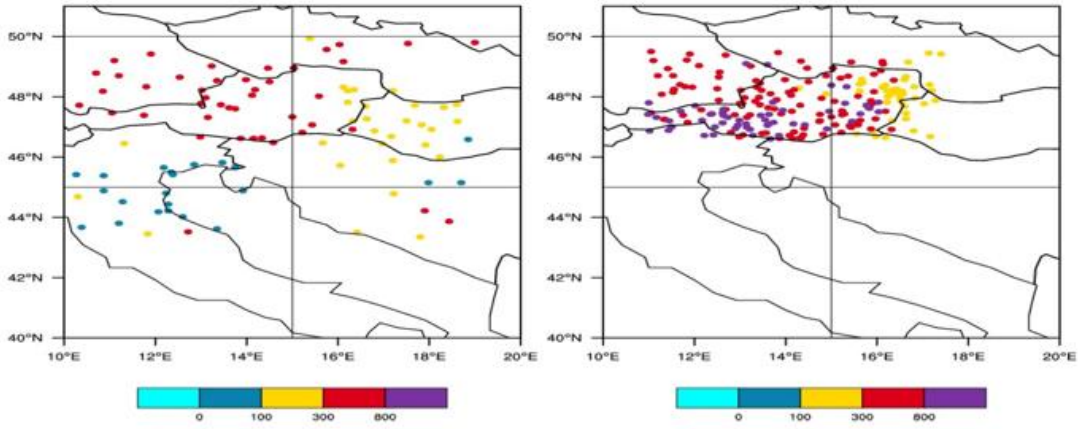


Figure 3: Location and altitude of synoptic stations in CA1 (left) and CA2 (right) used for the verification.

Common Area	Number of stations					Altitude	
	Total	$alt < 100m$	$100m < alt < 300m$	$300m < alt < 800m$	$alt > 800m$	Min	Max
CA1	96	23	30	43	0	0m	753 m
CA2	205	2	41	107	55	0m	3114m

Table 3: Overview of stations distribution for the 2 Common Areas, depending on altitude.

The verification results presented in the following sections are a sample of the derived statistics that were gradually obtained following the implementation of the MEC+Rfdbk system in more participating institutes. Complete sets of statistical scores obtained with the MEC-Rfdbk verification system for the models considered here are either available on the COSMO shiny server (http://www.cosmo-model.org/shiny/apps/carma/) or detailed in various papers referenced hereafter, including the Common plot annual reports available on the COSMO web site (http://cosmo-model.org/content/tasks/verification.priv/default.htm). For a detailed description of the Common Area Verification Activities, we refer to the document by

The following type of graphs produced with the MEC-Rfdbk system are exemplified below:

- Categorical scores for Gust (Fig. 4), RR_6h (figure 6) and N (figure 8);
- Scores for continuous parameters (Figs. 5 and 7);
- Scores for upper air parameters (figure 9);
- Comparison between two models showing reduction in ME and RMSE (Fig. 5).

3.1 MAM 2020: First Results

The first results of a cross model verification (with the MEC-Rfdbk software) for the Common Plot activities were performed for the 2020 spring season (MAM 2020) and detailed in Iriza-Burcă, Linkowska, and Fundel (2020). For these results, a set of three COSMO model runs were considered: COSMO-D2 (DWD), COSMO-PL (IMGW) and COSMO-RO (NMA). Only COSMO 00 UTC model runs were evaluated, with forecast step every 3 hours. The integration domains for COSMO-D2 and COSMO-PL were the operational ones (also included in the official Common Plots activities), while the COSMO-RO integration domain differed from the operational set-up of the model employed in NMA (in order to cover the Common Areas). The scores were computed for the two common areas presented before. Selective results obtained with the MEC+Rfdbk system for CA1 are presented below.

Categorical scores for 10-meter wind gust (1 hour) computed for CA1 (exemplified in Fig. 4) show a generally higher probability of detection for the 12.5m/s threshold than for the 15m/s one. For the first threshold, highest POD values are obtained during the day, with lower values starting with +21 hours anticipation, especially for COSMO-D2. A high false alarm rate from all three models can be seen for the 15m/s threshold, especially from COSMO-RO for CA1 in the second part of the considered forecast interval. For this threshold, a slightly better behaviour is exhibited by COSMO-RO for the first hours of forecast, while for the 12.5m/s threshold, the behaviour of the three models is similar for both areas. For both areas, the behaviour of the model (mainly for the 12.5 m/s threshold) is more similar between COSMO-D2 and COSMO-RO. For a detailed analysis of all the results for MAM 2020, we refer to the paper by Iriza-Burcă, Linkowska, and Fundel (2020).

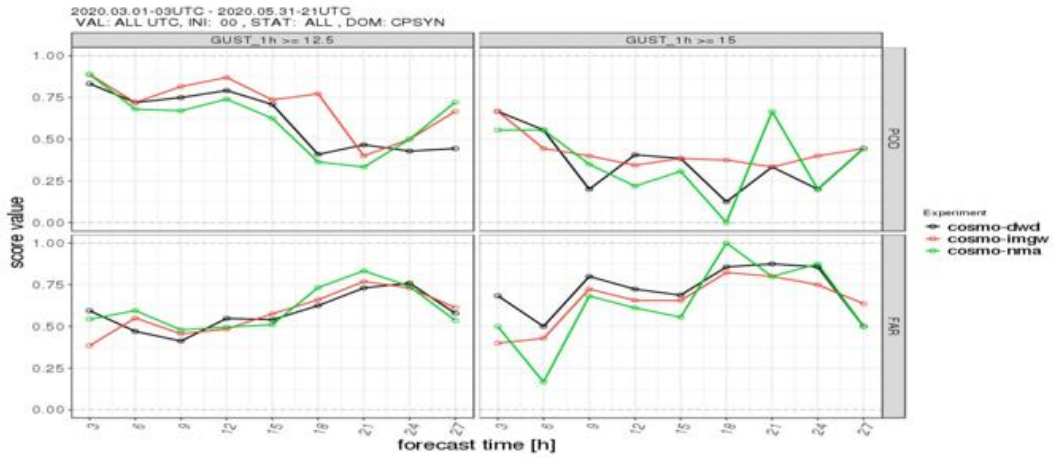


Figure 4: MAM2020 - Categorical scores for Gust (CA1); POD (top) and FAR (bottom): threshold >= 12.5 (left) and >= 15 (right). COSMO-D2 (black), COSMO-PL (red) and COSMO-RO (green).

3.2 SON2020: Verification of ICON in Limited Area Mode at COSMO National Meteorological Services

Some verification results using the MEC+Rfdbk system were included in the ICON Report "Verification of ICON in Limited Area Mode at COSMO National Meteorological Services (Rieger et al., 2021) published as part of the Priority Project 'Transition of COSMO to ICON' (PP C2I). The aim of the project was to ensure a smooth transition for the COSMO national meteorological services to the ICON model and the report offered the first published

verification results on this subject. For this report, verification results were obtained either entirely using the MEC+Rfdbk system (e.g. COSMO-RO_2p8 vs. ICON-RO_2p8) or with the VERSUS verification software and translated to Rdata in order to visualize them using Rfdbk/Shiny server (COSMO-CE-PL vs. ICON-PL and Common Area Verification Results).

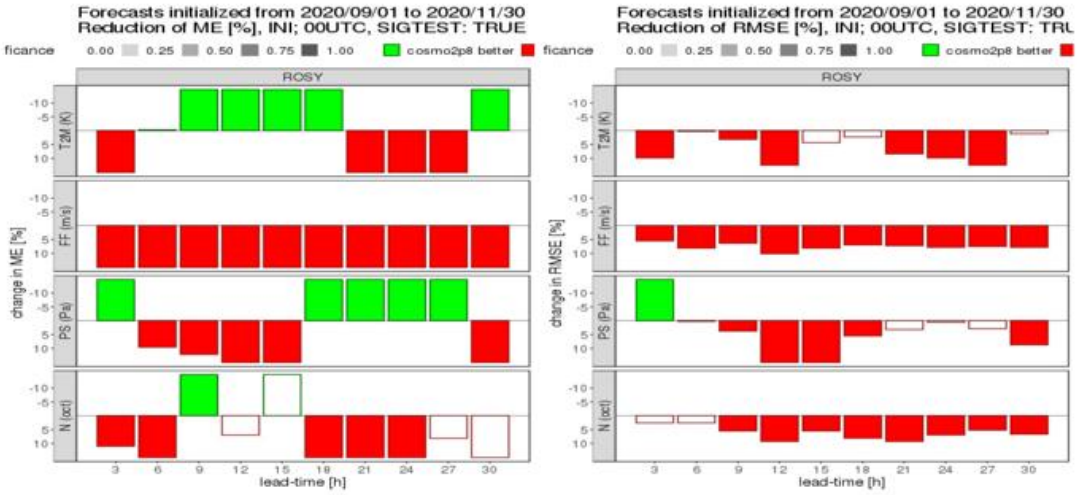


Figure 5: SON2020 - Comparison between ICON-RO-2.8km and COSMO-RO-2.8km: changes in ME (left) and RMSE (right) for all Romanian synop stations; top to bottom: T2M (K), FF (m/s), PS (Pa), N (octa); green - COSMO-RO-2.8km better, red - ICON-RO-2.8km better.

Comparison between ICON-RO-2.8km and COSMO-RO-2.8km **showing reduction in ME and RMSE** is exemplified in Fig. 5. The results obtained with MEC+Rfdbk suggested a good performance of the ICON-LAM model integrated for Romanian territory for the season of interest (up to 78 hours), with a small systematic increase in errors for the later forecast times (+60 hours) for T2M, FF, PS and N (Fig. 5). The comparison between COSMO-RO-2.8km and ICON-RO-2.8km showed a better performance from ICON for most continuous parameters, for the first 30 hours of forecast, visible especially from the reduction in the amplitude of errors.

3.3 DJF2021: First Common Activity Applications

Starting with the 2021 winter season (2021), the first results obtained with MEC+Rfdbk were included in the Common Verification Results (Fig. 6). For the DJF2021 season, FF were produced from the following models:

CA1: ICON-EU, COSMOPL7, COSMO_ME
CA2: ICON-D2, ICON_IMS / ICON-IL2p5, ICONGR, ICONPL, COSMO-1E, COSMO-2E, COSMO-D2, COSMOP2k8
National domains: ICON-RO_2p8, COSMO-RO_2p8

Selective Results for CA2 are shown in Fig. 6 (categorical scores RR_6h). ETS (Equitable Threat Score) and FBI (Frequency Bias) computed for 4 thresholds ($>= 0.2mm/6h$, $>= 1mm/6h$, $>= 10mm/6h$ *and* $>= 20mm/6h$). Results suggest a better performance of the models for the lower thresholds ($>= 0.2\ mm/6h$, $>= 1mm/6h$), with a general tendency to over-forecast. For the higher thresholds, this tendency is mostly shown by COSMOP2k8 and ICONPL.

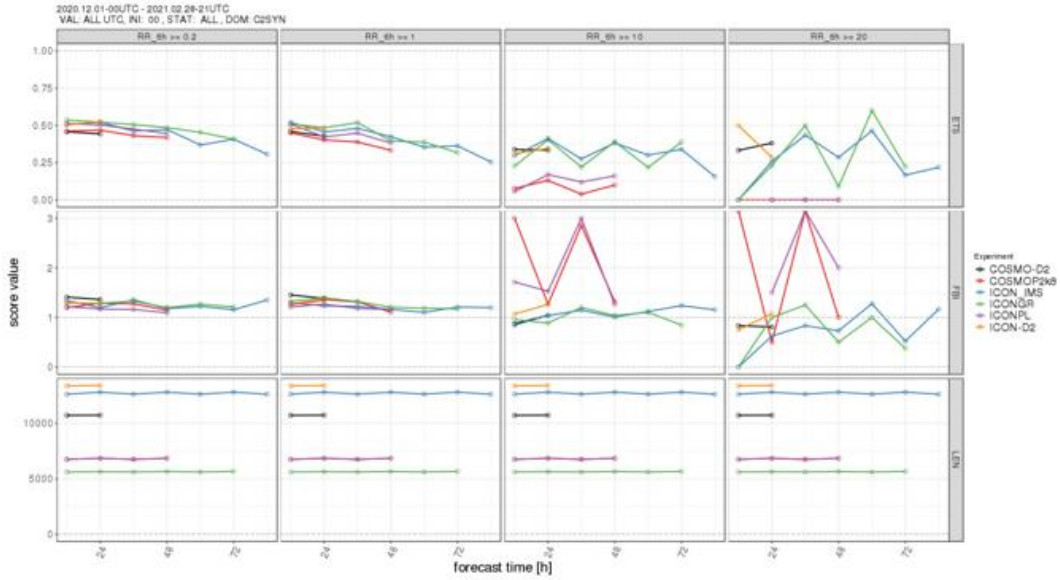


Figure 6: DJF2021 - Categorical scores for RR_6h (CA2): ETS (top), FBI (middle) and number of observations (bottom) values for CA2; thresholds (left to right): $>= 0.2mm/6h$, $>= 1mm/6h$, $>= 10mm/6h$ *and* $>= 20mm/6h$. COSMO-D2 (black), COSMOPk28 (red), ICON_IMS / ICON-IL2p5 (blue), ICONGR (green), ICONPL (purple) and ICON-D2 (orange).

3.4 MAM2021: Extended Common Area Activities

For the MAM2021 season, FF were produced from the following models:

CA1: ICON-GLOBAL, ICON-EU, COSMO_ME, COSMOPL7
CA2: ICON-D2, ICON_IMS / ICON-IL2p5, ICONPL, ICONGR, ICON_IT2, COSMO-CE-PL, COSMO-1E, COSMO-2E, COSMO_IT2
National domains: ICON-RO_2p8, COSMO-RO_2p8

Selective Results for CA1 are presented in Fig. 7, exemplifying scores computed for continuous parameters. For this season and area, in general, lowest ME values are obtained from ICON-EU, that also displays the smaller amplitude of errors for all parameters. The difference in number of observations is given by the fact that ICON-EU is only integrated for a period of 48 hours.

Selective Results for National Domains can be seen in Fig. 8. **Categorical scores for cloud cover** are computed for 3 thresholds (in octa): $N >= 1$, $>= 4$ *and* $>= 7$), taking into account all Italian stations (**national domain**). These results show a similar behaviour of all three evaluated models (COSMO_ME, COSMO_IT2 and ICON_IT2), especially for the first two thresholds, with high POD and a relatively small FAR. Slightly larger values of FAR can be seen for the highest threshold.

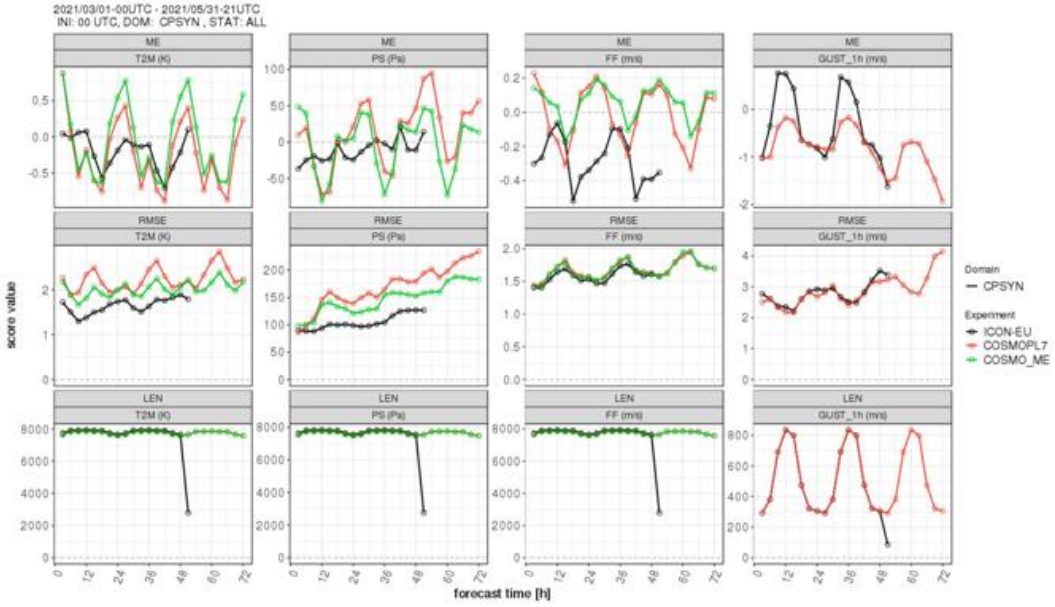


Figure 7: MAM2021 - ME (top), RMSE (middle) and number of observations (bottom) values for CA1; left to right: T2M, PS, FF and GUST (1h). ICON-EU (black) (black), COSMO-PL7 (red) and COSMO_ME (green).

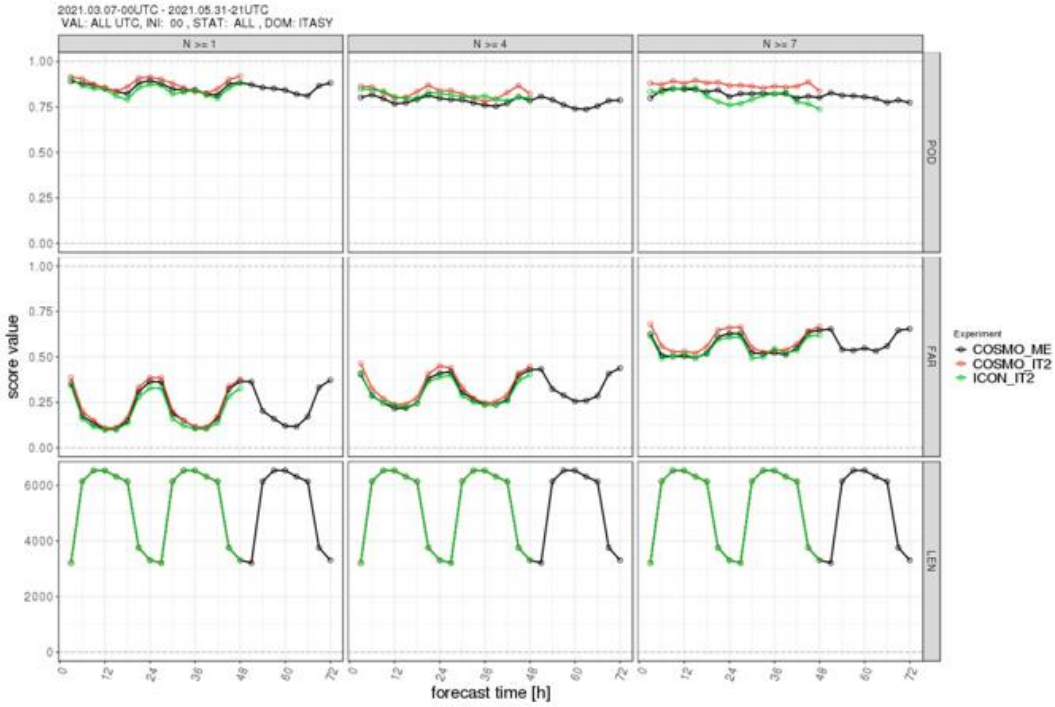


Figure 8: MAM2021 - Categorical scores for Cloud Cover: POD (top) and FAR (bottom) values from: COSMO_ME (black), COSMO_IT2 (red) and ICON_IT2 (green) for Italy national domain (all Italian stations); thresholds (left to right): $>= 1$, $>= 4$ *and* $>= 7$ (octa).

3.5 JJA2021: Ongoing Activities

Compared to the previous season, starting with JJA 2021, it was decided to employ a polygon description for the verification area instead of the previously used station lists. Also starting with the JJA2021 season, TEMP verification scores obtained with the MEC+Rfdbk verification system will be gradually included in the Common Plot activities. An example of the derived statistics obtained for upper air parameters is presented in Fig. 9.

For the JJA2021 season, FF are expected to be produced from the following models:

CA1: ICON-GLOBAL, ICON-EU, COSMO_ME, COSMOPL7
CA2: ICON-D2, ICONGR, ICON_IMS / ICON-IL2p5, ICON_IT2, ICONPL, COSMO_IT2, COSMO-CE-PL, COSMO-1E, COSMO-2E
National domains: All as CA1 and CA2, ICON-RO_2p8, COSMO-RO_2p8

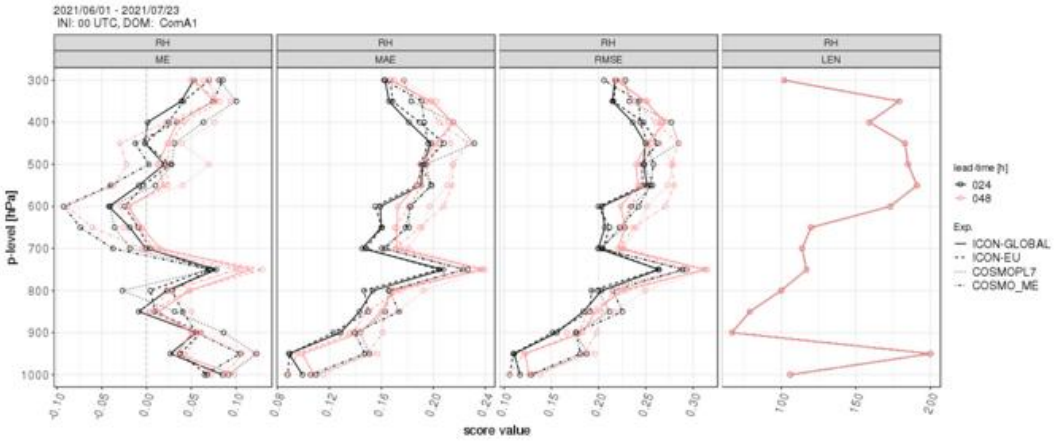


Figure 9: JJA2021 – Upper air relative humidity: ME, MAE, RMSE and LEN (left to right), values from: ICON-GLOBAL (continuous line), ICON-EU (dashed line), COSMOPL7 (dotted line) and COSMO_ME (dotted and dashed line), for +24 h (black) and 48 h (pink) lead time; scores computed for CA1.

4 Conclusions and Outlook

Following the finalization of the project, the MEC-Rfdbk system is implemented and runs operationally in IMGW-PIB, IMS, NMA, HNMS and COMET for various configurations of the ICON and COSMO models. As previously mentioned, the system was already in use before the start of the project in MCH (surface verification only) and DWD.

The following type of graphs can be produced with the MEC-Rfdbk system for Common Plot Activities:

- Categorical scores for Gust, RR_6h and N;
- Scores for continuous parameters;
- Scores for upper air parameters;
- Comparison between two models showing reduction in different scores.

All the remaining open issues that concern MEC-Rfdbk adaptation in some services and implementation of new features, will be performed through WG5 SPRT Common Plot activity.

Detailed documentation and templates for the use of the MEC-Rfdbk system are available for usage both for CP and national verification activities.

For more detailed presentations of the MEC-Rfdbk system and its components, including information regarding installation and use, documentation is available in the COSMO repository (PP CARMA Branch): http://cosmo-model.org/view/repository/wg5/PP-CARMA .

5 Meetings

- 20th COSMO General Meeting, Saint Petersburg (Russia), 3-7 September 2018
- ICCARUS 2019 (ICON/COSMO/CLM/ART USER SEMINAR), Offenbach, Germany, 18 – 22 March 2019
- COSMO-CARMA TRAINING for PST, Offenbach, Germany, 9 – 11 April 2019
- 21st COSMO General Meeting, Rome (Italy), 9-13 September 2019
- ICCARUS 2020 (ICON/COSMO/CLM/ART User Seminar), 2 – 6 March 2020 / PP CARMA web-meeting, 1st April 2020 (Minutes)
- 22nd COSMO General Meeting, 1-11 September 2020, teleconferences
- ICON/COSMO/CLM/ART User Seminar (ICCARUS) 2021, virtual seminar 8 – 19 March 2021 (Minutes)
- PP CARMA virtual discussion (PL and WG5c, 1st July 2021 (Minutes)
- 23rd COSMO General Meeting, 14-17 September 2021, teleconference

6 Documentation

The documentation for the installation and use of the MEC+Rfdbk verification system is available in the COSMO repository (PP CARMA Branch):
http://cosmo-model.org/view/repository/wg5/PP-CARMA

How to install (COSMO repository)
http://cosmo-model.org/repository/wg5/PP-CARMA/Task1/Install_notes_CARMA_v1.5.pdf

How to use (example based on NWP Test Suite @ECMWF; COSMO Repository)
NWPTest-Suite_Doc4CARMA.docx

About RFDBK
Ffverificationsuite[at]DWD.docx (COSMO Repository)
http://www.cosmo-model.org/shiny/users/fdbk/RfdbkVeriDoku.html

About feedback files
cosmoFeedbackFileDefinition.pdf
http://cosmo-model.org/content/model/documentation/core/default.htm

General Guidelines (COSMO repository)
http://cosmo-model.org/repository/wg5/PP-CARMA/Task1/CARMA_guidelines.pdf

7 Acknowledgments

We are grateful to our DWD colleagues (esp. Harald Anlauf, Roland Potthast and Hendrik Reich) for their support. The Project leader would like to thank all those involved for their continuous and active contributions. We also thank the Editor for his help in drafting this report.

References

W. Chang, J. Cheng, J.J. Allaire, Y. Xie, and J. McPherson. shiny: Web Application Framework for R. R package version 1.5.0. Available online at http://CRAN.R-project.org/package=shiny, 2020.

F. Fundel. Feedback File Verification Suite at DWD. Available online at http://www.cosmo-model.org/shiny/users/fdbk/RfdbkVeriDoku.html, 2021.

A. Iriza-Burcă, J. Linkowska, and F. Fundel. Common Area Verification Activity with Rfdbk/MEC Application: MAM 2020 First Results. *COSMO Newsletter*, 20:18–30, 2020. doi: doi:10.5676/dwd_pub/nwv/cosmo-nl_20_04.

P. Patruno and D. Cesari. Wreport-bufr2netcdf: a free library and tools for decoding BUFR reports and creating input files for COSMO-Model assimilation. In *13th COSMO General Meeting, 5-9 September 2011, Rome, Italy, Parallel session: WG1 and PP KENDA*, 2011. Available on-line at: http://cosmo-model.org/content/consortium/generalMeetings/general2011/wg1.htm.

R. Potthast. Model Equivalent Calculator (MEC) overview. In *21st COSMO General Meeting, 9-13 September 2019, Rome, Italy*, 2019. Available on-line at: http://cosmo-model.org/content/consortium/generalMeetings/general2019/default.htm.

D. Rieger, M. Milelli, D. Boucouvala, F. Gofa, A. Iriza-Burcă, P. Khain, A. Kirsanov, J. Linkowska, F. Marcucci, and the C2I team. Verification of ICON in Limited Area Mode at COSMO National Meteorological Services. *Reports on ICON*, 006, 2021. doi: https://doi.org/10.5676/dwd_pub/nwv/icon_006.

List of COSMO Newsletters and Technical Reports

(available for download from the COSMO Website: www.cosmo-model.org)

COSMO Newsletters

No. 1: February 2001.

No. 2: February 2002.

No. 3: February 2003.

No. 4: February 2004.

No. 5: April 2005.

No. 6: July 2006.

No. 7: April 2008; Proceedings from the 8th COSMO General Meeting in Bucharest, 2006.

No. 8: September 2008; Proceedings from the 9th COSMO General Meeting in Athens, 2007.

No. 9: December 2008.

No. 10: March 2010.

No. 11: April 2011.

No. 12: April 2012.

No. 13: April 2013.

No. 14: April 2014.

No. 15: July 2015.

No. 16: July 2016.

No. 17: July 2017.

No. 18: November 2018.

No. 19: October 2019.

No. 20: December 2020.

COSMO Technical Reports

No. 1: Dmitrii Mironov and Matthias Raschendorfer (2001):
Evaluation of Empirical Parameters of the New LM Surface-Layer Parameterization Scheme. Results from Numerical Experiments Including the Soil Moisture Analysis.

No. 2: Reinhold Schrodin and Erdmann Heise (2001):
The Multi-Layer Version of the DWD Soil Model TERRA_LM.

No. 3: Günther Doms (2001):
A Scheme for Monotonic Numerical Diffusion in the LM.

No. 4: Hans-Joachim Herzog, Ursula Schubert, Gerd Vogel, Adelheid Fiedler and Roswitha Kirchner (2002):
LLM — the High-Resolving Nonhydrostatic Simulation Model in the DWD-Project LITFASS.
Part I: Modelling Technique and Simulation Method.

No. 5: Jean-Marie Bettems (2002):
EUCOS Impact Study Using the Limited-Area Non-Hydrostatic NWP Model in Operational Use at MeteoSwiss.

No. 6: Heinz-Werner Bitzer and Jürgen Steppeler (2004):
Documentation of the Z-Coordinate Dynamical Core of LM.

No. 7: Hans-Joachim Herzog, Almut Gassmann (2005):
Lorenz- and Charney-Phillips vertical grid experimentation using a compressible nonhydrostatic toy-model relevant to the fast-mode part of the 'Lokal-Modell'.

No. 8: Chiara Marsigli, Andrea Montani, Tiziana Paccagnella, Davide Sacchetti, André Walser, Marco Arpagaus, Thomas Schumann (2005):
Evaluation of the Performance of the COSMO-LEPS System.

No. 9: Erdmann Heise, Bodo Ritter, Reinhold Schrodin (2006):
Operational Implementation of the Multilayer Soil Model.

No. 10: M.D. Tsyrulnikov (2007):
Is the particle filtering approach appropriate for meso-scale data assimilation ?

No. 11: Dmitrii V. Mironov (2008):
Parameterization of Lakes in Numerical Weather Prediction. Description of a Lake Model.

No. 12: Adriano Raspanti (2009):
COSMO Priority Project "VERification System Unified Survey" (VERSUS): Final Report.

No. 13: Chiara Marsigli (2009):
COSMO Priority Project "Short Range Ensemble Prediction System" (SREPS): Final Report.

No. 14: Michael Baldauf (2009):
COSMO Priority Project "Further Developments of the Runge-Kutta Time Integration Scheme" (RK): Final Report.

No. 15: Silke Dierer (2009):
COSMO Priority Project "Tackle deficiencies in quantitative precipitation forecast" (QPF): Final Report.

No. 16: Pierre Eckert (2009):
COSMO Priority Project "INTERP": Final Report.

No. 17: D. Leuenberger, M. Stoll and A. Roches (2010):
Description of some convective indices implemented in the COSMO model.

No. 18: Daniel Leuenberger (2010):
Statistical analysis of high-resolution COSMO Ensemble forecasts in view of Data Assimilation.

No. 19: A. Montani, D. Cesari, C. Marsigli, T. Paccagnella (2010):
Seven years of activity in the field of mesoscale ensemble forecasting by the COSMO–LEPS system: main achievements and open challenges.

No. 20: A. Roches, O. Fuhrer (2012):
Tracer module in the COSMO model.

No. 21: Michael Baldauf (2013):
A new fast-waves solver for the Runge-Kutta dynamical core.
DOI: 10.5676/DWD_pub/nwv/cosmo-tr_21

No. 22: C. Marsigli, T. Diomede, A. Montani, T. Paccagnella, P. Louka, F. Gofa, A. Corigliano (2013):
The CONSENS Priority Project.
DOI: 10.5676/DWD_pub/nwv/cosmo-tr_22

No. 23: M. Baldauf, O. Fuhrer, M. J. Kurowski, G. de Morsier, M. Müllner, Z. P. Piotrowski, B. Rosa, P. L. Vitagliano, D. Wójcik, M. Ziemiański (2013):
The COSMO Priority Project 'Conservative Dynamical Core' Final Report.
DOI: 10.5676/DWD_pub/nwv/cosmo-tr_23

No. 24: A. K. Miltenberger, A. Roches, S. Pfahl, H. Wernli (2014):
Online Trajectory Module in COSMO: a short user guide.
DOI: 10.5676/DWD_pub/nwv/cosmo-tr_24

No. 25: P. Khain, I. Carmona, A. Voudouri, E. Avgoustoglou, J.-M. Bettems, F. Grazzini (2015):
The Proof of the Parameters Calibration Method: CALMO Progress Report.
DOI: 10.5676/DWD_pub/nwv/cosmo-tr_25

No. 26: D. Mironov, E. Machulskaya, B. Szintai, M. Raschendorfer, V. Perov, M. Chumakov, E. Avgoustoglou (2015):
The COSMO Priority Project 'UTCS' Final Report.
DOI: 10.5676/DWD_pub/nwv/cosmo-tr_26

No. 27: J-M. Bettems (2015):
The COSMO Priority Project 'COLOBOC': Final Report.
DOI: 10.5676/DWD_pub/nwv/cosmo-tr_27

No. 28: Ulrich Blahak (2016):
RADAR_MIE_LM and RADAR_MIELIB - Calculation of Radar Reflectivity from Model Output.
DOI: 10.5676/DWD_pub/nwv/cosmo-tr_28

No. 29: M. Tsyrulnikov and D. Gayfulin (2016):
A Stochastic Pattern Generator for ensemble applications.
DOI: 10.5676/DWD_pub/nwv/cosmo-tr_29

No. 30: D. Mironov and E. Machulskaya (2017):
A Turbulence Kinetic Energy – Scalar Variance Turbulence Parameterization Scheme.
DOI: 10.5676/DWD_pub/nwv/cosmo-tr_30

No. 31: P. Khain, I. Carmona, A. Voudouri, E. Avgoustoglou, J.-M. Bettems, F. Grazzini, P. Kaufmann (2017):
CALMO - Progress Report.
DOI: 10.5676/DWD_pub/nwv/cosmo-tr_31

No. 32: A. Voudouri, P. Khain, I. Carmona, E. Avgoustoglou, J.M. Bettems, F. Grazzini, O. Bellprat, P. Kaufmann and E. Bucchignani (2017):
Calibration of COSMO Model, Priority Project CALMO Final report.
DOI: 10.5676/DWD_pub/nwv/cosmo-tr_32

No. 33: N. Vela (2017):
VAST 2.0 - User Manual.
DOI: 10.5676/DWD_pub/nwv/cosmo-tr_33

No. 34: C. Marsigli, D. Alferov, M. Arpagaus, E. Astakhova, R. Bonanno, G. Duniec, C. Gebhardt, W. Interewicz, N. Loglisci, A. Mazur, V. Maurer, A. Montani, A. Walser (2018):
COsmo Towards Ensembles at the Km-scale IN Our countries (COTEKINO), Priority Project final report.
DOI: 10.5676/DWD_pub/nwv/cosmo-tr_34

No. 35: G. Rivin, I. Rozinkina, E. Astakhova, A. Montani, D. Alferov, M. Arpagaus, D. Blinov, A. Bundel, M. Chumakov, P. Eckert, A. Euripides, J. Förstner, J. Helmert, E. Kazakova, A. Kirsanov, V. Kopeikin, E. Kukanova, D. Majewski, C. Marsigli, G. de Morsier, A. Muravev, T. Paccagnella, U. Schättler, C. Schraff, M. Shatunova, A. Shcherbakov, P. Steiner, M. Zaichenko (2018):
The COSMO Priority Project CORSO Final Report.
DOI: 10.5676/DWD_pub/nwv/cosmo-tr_35

No. 36: A. Raspanti, A. Celozzi, A. Troisi, A. Vocino, R. Bove, F. Batignani (2018):
The COSMO Priority Project VERSUS2 Final Report.
DOI: 10.5676/DWD_pub/nwv/cosmo-tr_36

No. 37: A. Bundel, F. Gofa, D. Alferov, E. Astakhova, P. Baumann, D. Boucouvala, U. Damrath, P. Eckert, A. Kirsanov, X. Lapillonne, J. Linkowska, C. Marsigli, A. Montani, A. Muraviev, E. Oberto, M.S. Tesini, N. Vela, A. Wyszogrodzki, M. Zaichenko, A. Walser (2019):
The COSMO Priority Project INSPECT Final Report.
DOI: 10.5676/DWD_pub/nwv/cosmo-tr_37

No. 38: G. Rivin, I. Rozinkina, E. Astakhova, A. Montani, J-M. Bettems, D. Alferov, D. Blinov, P. Eckert, A. Euripides, J. Helmert, M.Shatunova (2019):
The COSMO Priority Project CORSO-A Final Report.
DOI: 10.5676/DWD_pub/nwv/cosmo-tr_38

No. 39: C. Marsigli, D. Alferov, E. Astakhova, G. Duniec, D. Gayfulin, C. Gebhardt, W. Interewicz, N. Loglisci, F. Marcucci, A. Mazur, A. Montani, M. Tsyrulnikov, A. Walser (2019):
Studying perturbations for the representation of modeling uncertainties in Ensemble development (SPRED Priority Project): Final Report.
DOI: 10.5676/DWD_pub/nwv/cosmo-tr_39

No. 40: E. Bucchignani, P. Mercogliano, V. Garbero, M. Milelli, M. Varentsov, I. Rozinkina, G. Rivin, D. Blinov, A. Kirsanov, H. Wouters, J.-P. Schulz, U. Schättler (2019):

Analysis and Evaluation of TERRA_URB Scheme: PT AEVUS Final Report.
DOI: 10.5676/DWD_pub/nwv/cosmo-tr_40

No. 41: X. Lapillonne, O. Fuhrer (2020):
Performance On Massively Parallel Architectures (POMPA): Final report.
DOI: 10.5676/DWD_pub/nwv/cosmo-tr_41

No. 42: E. Avgoustoglou, A. Voudouri, I Carmona, E. Bucchignani, Y. Levy, J. -M. Bettems (2020):
A methodology towards the hierarchy of COSMO parameter calibration tests via the domain sensitivity over the Mediterranean area.
DOI: 10.5676/DWD_pub/nwv/cosmo-tr_42

No. 43: H. Muskatel, U. Blahak, P. Khain, A. Shtivelman, M. Raschendorfer, M. Kohler, D. Rieger, O. Fuhrer, X. Lapillonne, G. Rivin, N. Chubarova, M. Shatunova, A. Poliukhov, A. Kirsanov, T. Andreadis, S. Gruber (2021):
The COSMO Priority Project $T^2(RC)^2$: Testing and Tuning of Revised Cloud Radiation Coupling, Final Report
DOI: 10.5676/DWD_pub/nwv/cosmo-tr_43

No. 44: M. Baldauf, D. Wojcik, F. Prill, D. Reinert, R. Dumitrache, A. Iriza, G. deMorsier, M. Shatunova, G. Zaengl, U. Schaettler (2021):
The COSMO Priority Project CDIC: Comparison of the dynamical cores of ICON and COSMO, Final Report
DOI: 10.5676/DWD_pub/nwv/cosmo-tr_44

No. 45: Marsigli C., Astakhova E., Duniec G., Fuezer L., Gayfulin D., Gebhardt C., Golino R., Heppelmann T., Interewicz W., Marcucci F., Mazur A., Sprengel M., Tsyrulnikov M., Walser A. (2022):
The COSMO Priority Project APSU: Final Report
DOI: 10.5676/DWD_pub/nwv/cosmo-tr_45

COSMO Technical Reports

Issues of the COSMO Technical Reports series are published by the *COnsortium for Small-scale MOdelling* at non-regular intervals. COSMO is a European group for numerical weather prediction with participating meteorological services from Germany (DWD, AWGeophys), Greece (HNMS), Italy (USAM, ARPA-SIMC, ARPA Piemonte), Switzerland (MeteoSwiss), Poland (IMGW), Romania (NMA) and Russia (RHM). The general goal is to develop, improve and maintain a non-hydrostatic limited area modelling system to be used for both operational and research applications by the members of COSMO. This system is initially based on the COSMO-Model (previously known as LM) of DWD with its corresponding data assimilation system.

The Technical Reports are intended

- for scientific contributions and a documentation of research activities,
- to present and discuss results obtained from the model system,
- to present and discuss verification results and interpretation methods,
- for a documentation of technical changes to the model system,
- to give an overview of new components of the model system.

The purpose of these reports is to communicate results, changes and progress related to the LM model system relatively fast within the COSMO consortium, and also to inform other NWP groups on our current research activities. In this way the discussion on a specific topic can be stimulated at an early stage. In order to publish a report very soon after the completion of the manuscript, we have decided to omit a thorough reviewing procedure and only a rough check is done by the editors and a third reviewer. We apologize for typographical and other errors or inconsistencies which may still be present.

At present, the Technical Reports are available for download from the COSMO web site (www.cosmo-model.org). If required, the member meteorological centres can produce hard-copies by their own for distribution within their service. All members of the consortium will be informed about new issues by email.

For any comments and questions, please contact the editor:

Massimo Milelli
Massimo.Milelli@arpa.piemonte.it

Consortium

for

Small-Scale Modelling

Technical Report No. 44

The COSMO Priority Project CDIC: Comparison of the dynamical cores of ICON and COSMO, Final Report

October 2021

DOI: 10.5676/DWD_pub/nwv/cosmo-tr_44

Deutscher Wetterdienst
MeteoSwiss
Ufficio Generale Spazio Aereo e Meteorologia
ΕΘΝΙΚΗ ΜΕΤΕΩΡΟΛΟΓΙΚΗ ΥΠΗΡΕΣΙΑ
Instytut Meteorologii i Gospodarki Wodnej
Administratia Nationala de Meteorologie
ROSHYDROMET
Agenzia Regionale Protezione Ambiente Piemonte
Agenzia Regionale Prevenzione Ambiente Energia Emilia Romagna
Centro Italiano Ricerche Aerospaziali
Amt für GeoInformationswesen der Bundeswehr
Israel Meteorological Service

www.cosmo-model.org

Editor: Massimo Milelli, ARPA Piemonte

The COSMO Priority Project CDIC: Comparison of the dynamical cores of ICON and COSMO, Final Report

Michael Baldauf[1 *], *Damian Wojcik*[2], *Florian Prill*[1], *Daniel Reinert*[1], *Rodica Dumitrache*[3], *Amalia Iriza*[3], *Guy deMorsier*[4], *Marina Shatunova*[5], *Günther Zängl*[1], *Ulrich Schättler*[1]

[*] Project coordinator
[1] Deutscher Wetterdienst - DWD
[2] Instytut Meteorologii i Gospodarki Wodnej - IMGW
[3] Administratia Nationala de Meteorologie - NMA
[4] MeteoSwiss - MCH
[5] HydroMetCenter of Russia - RHM

Contents

1 Introduction **3**

2 Brief overview and comparison of the dynamical core formulations of ICON and COSMO **3**

3 Idealized test cases **5**

3.1 Linear gravity and sound wave expansion 6

3.1.1 Small scale test 6

3.1.2 Large scale test. 7

3.2 Atmosphere at rest 10

3.3 Linear flow over mountains 12

3.3.1 2-dimensional flow 12

3.3.2 3-dimensional flow 12

3.4 Nonlinear flow over steep mountains 15

3.5 Falling cold bubble 18

3.6 The Weisman and Klemp (1982) test case 20

3.6.1 Experimental setup 20

3.6.2 Results of simulations 21

3.6.3 Summary 23

4 Scalability aspects **26**

5 Application for special purposes (Climate, environmental appl.) **28**

6 Conclusions **29**

1 Introduction

The ICON model development originally was a joint effort between the Deutscher Wetterdienst (DWD, Offenbach) and the Max-Planck Institute for Meteorology (MPI, Hamburg) with the aim to get a common modeling framework for global weather forecast and climate simulations. Later on, the Deutsches Klimarechenzentrum (DKRZ, Hamburg) and the Karlsruhe Institute for Technology (KIT, Karlsruhe) joined this model development. ICON became operational as a global model for NWP at DWD at 20 January 2015.

Although being a global model, ICON (Zängl et al., 2015) should be able to do simulations on the regional scale, too, first by two-way nesting (at 21 July 2015, the ICON-EU nest replaced the former COSMO-EU at DWD), and later on as an externally coupled limited-area model. In consequence, currently and in the following years the COSMO-Consortium (Consortium for Small-Scale Modelling) also joins the ICON-model development and the member states will replace the regional model COSMO (www.cosmo-model.org) (Doms and Baldauf, 2018; Baldauf et al., 2011) by the limited-area setup of ICON during the next years. The same holds for the COSMO licensee countries.

To support and to supervise this migration process and to maintain quality assurance at the several weather services for the replacement of a regional-scale NWP model, a few priority projects have been defined in the COSMO consortium. The goal of the priority project 'Comparison of the dynamical cores of ICON and COSMO' (PP CDIC) is an objective as possible assessment of the dynamical cores of both models. It was carried out mainly during the two year period 2016-2017. The need for such a comparison stems from the fact that it is not a priori clear if the triangle grid of ICON and some properties of its dynamical core (e.g. there is no time-splitting between slow and fast processes in the pure non-hydrostatic Euler equations), although being beneficial on the global scale, will be beneficial on the small (or regional) scale, too.

Section 2 gives a brief overview and comparison of the main properties of the dynamical cores of ICON and COSMO. Their assessment is mainly done by the evaluation of several (idealized) test cases that are typical for limited area models. Physical parameterizations are switched off as much as possible. These idealized test cases and their comparison of ICON and COSMO are discussed in section 3. Strong scaling properties on massively parallel computers are presented in section 4.

2 Brief overview and comparison of the dynamical core formulations of ICON and COSMO

In this section, a brief comparison between the dynamical cores of COSMO and ICON is given, more details can be found in Doms and Baldauf (2018) and Zängl et al. (2015), respectively. The dynamical cores of both models are based on the compressible, non-hydrostatic Euler equations (this holds for the new COSMO-EULAG development (Kurowski et al., 2016; Ziemiański et al., 2021), too. However, in the following only the operationally used so-called 'Runge-Kutta-version' of COSMO is considered). For operational setups, both models use the shallow atmosphere approximation (together with the traditional approximation for some Coriolis and spherical metric terms in the advection).

The prognostic variables of COSMO are pressure p', temperature T' (both perturbations from a reference state) and the 3 spherical velocity components u, v, w. ICON uses density ρ, either density weighted virtual potential temperature $\rho\Theta_v$ or Exner pressure Π (the latter for

easier vertically implicit time integration), vertical velocity w and the triangle edge normal component of the horizontal velocity v_n as prognostic variables (of course u and v can be diagnosed from v_n for each triangle and vice versa). To increase numerical accuracy, ICON again uses the deviations from a reference state of the thermodynamic variables (ρ', $(\rho\Theta_v)'$, or Π') in the dynamical core.

A basic difference between ICON and COSMO lies in the horizontal grid and the related discretizations. COSMO uses a structured (i.e. a rotated lat-lon) grid, whereas ICON uses a triangular grid based on successive subdivision of the triangles of an icosahedron. Horizontal discretizations use a staggered C-grid and vertically a Lorenz-grid: scalar variables (like ρ, T, p, ...) are positioned in the cell center; in the center of a cuboid in COSMO and in the center of a prism in ICON (more precise: this center is determined as the circumcentre of a triangle). In contrast, each edge normal velocity component sits in the center of the edge face. In spite of this formal similarity in the staggering, though one can apply simple finite-difference formulas in the case of COSMO, the discretizations in ICON merely must be constructed via the integral theorems of Gauss and Stokes. However, the application of the Gauss theorem in the continuity equation (i.e. a finite-volume approach) allows exact mass conservation in ICON. This is not possible in COSMO, since ρ is not a prognostic variable there.

In particular for the advection of these 'dynamic' variables, COSMO can use higher order schemes (although one-dimensional, direction-split) in the horizontal direction due to the simple finite-difference approach. In the convection-permitting setups, usually a fifth order scheme (Wicker and Skamarock, 2002) is used. In contrast, ICON has to use again second order discretizations. However, this is at least consistent to the other second order discretizations.

Concerning the time integration of the Euler equations, both dynamical cores use the horizontally explicit, vertically implicit (HEVI) approach. This treats the fast vertically expanding sound and gravity waves in an implicit manner, to avoid too small time steps. However, COSMO uses a split-explicit scheme to treat the remaining horizontal directions: the fast waves (sound and gravity waves) are integrated with a small time step, whereas the slower advection terms are treated with a larger time step. Both processes are combined by so-called partial operator splitting, which couples these processes better than complete operator splitting (Skamarock and Klemp, 1992) and to achieve at least second order in time a 3-stage Runge-Kutta scheme is used. This approach was first developed for the WRF model by Wicker and Skamarock (2002), and its stability properties for COSMO have been proven in Baldauf (2010). In contrast, ICON avoids the split-explicit method but integrates both the fast waves and the advection of the above mentioned dynamic variables with the same small time step (Zängl et al., 2015). The motivation stems from the fact that in a global model with higher model tops, the maximum advection velocities are not so far away from sound velocity, therefore, a split-explicit approach is obviously less advantageous for a global model than for a pure limited-area model like COSMO. To achieve second order in time a two-time-level predictor-corrector scheme is applied.

Apart from these fundamental discretization approaches, each dynamical core needs more or less additional measures for stabilization. For the vertically implicit integration both dynamical cores use some off-centering in the coefficients weighting the previous and the actual time level. In COSMO, quasi-3D divergence damping is indispensable to stabilize the split-explicit approach. In contrast, divergence damping is not essential for stability in ICON (however, to calculate diffusion on the longer fast physics time step, a weak 3D and 2D divergence damping is used, too). On the other hand, ICON needs a mechanism to stabilize artificial modes that arise due to the C-grid discretization on triangles. Here, a higher order

velocity reconstruction solves the problem (Zängl et al., 2015). Furthermore, additional fourth order hyperdiffusion and Smagorinsky diffusion are applied in both models mainly to suppress non-linear instabilities. However, the detailed strength of these mechanisms may be differently implemented in both models.

Finally, although not directly part of the Euler solver, the tracer advection schemes should be compared. COSMO uses the second order Bott (1989) scheme for the transport of the water variables and turbulent kinetic energy (Förstner et al., 2006), and potentially also for other variables e.g. arising in the ART module. Although this scheme is mass-conserving, this property is unfortunately slightly weakened due to a mass-consistency fix, which is needed for a proper moisture treatment (see also the discussion in Baldauf (2019)). ICON uses the third order scheme by Miura (2007) for the transport of water vapour ρ_v, and the corresponding second order variant for the other tracers. This scheme is mass-conserving, too, for every single tracer. The additional mass-consistency does not destroy mass-conservation because ICON itself is already mass-conserving.

These whole bundles of different discretization strategies make it quite difficult to answer in advance which dynamical core is superior over the other. Only a comprehensive simulation study with several tests can try to assess and compare these approaches.

3 Idealized test cases

In this main section, several idealized test cases that are relevant for small-scale models are performed. During the last decades, a certain set of such standard test cases for the non-hydrostatic flow regime has been established in the community of dynamical core developers for atmospheric models. These include linear wave expansion, linear and nonlinear flows over mountains, and highly nonlinear falling or rising of bubbles to test the solver for the Euler equations. These tests are designed to indicate e.g. possible problems with the terrain-following coordinate or with well-balancing properties. Additionally, there exist several test cases for the pure tracer advection.

Since the focus of the project lies on the capability of limited-area modeling, all tests use flat domains (i.e. they are not defined on a sphere). Technically, mainly the use of the alternative torus grid generator (by Leonidas Linardakis) instead of the standard ICON grid generator is a new aspect. It allows the use of either single periodic BCs (in y-direction only) of of double periodic BCs (in both x- and y-direction). Most of the test cases use a 2D $x-z-$ vertical slice setup. To this purpose four (double) rows of triangles with periodicity in y-direction have been placed along the 'equator' (along the x-axis) of the torus grid (side remark: two (double) rows of triangles should be sufficient to achieve periodicity, but a few internal calculations of metric coefficients require a larger grid).

A comparison by idealized test cases seems to be a very objective evaluation method. Nevertheless, some ambiguities remain; some broader discussion about such an evaluation can be found in Theis and Baldauf (2019). In the case of ICON and COSMO especially the different horizontal grids (triangle and quadrilateral, respectively) complicates the comparison of accuracy and efficiency. Whereas in COSMO Δx, Δy and Δz are just given by the quadrilateral dimensions of each grid cell, we use here for ICON Δx as the length of those triangle edge that goes around the 'equator' of the torus grid. Note, that in contrast Zängl et al. (2015) define the ICON grid spacing as the square root of the average grid cell area $\Delta x_A = \sqrt{A}$. The difference is just $\sqrt{A} \approx 0.658 \Delta x$. In COSMO, the time step Δt means the advective time step, whereas the fast waves time step is a factor of 6 smaller. In ICON, Δt denotes the 'fast-physics' time step, whereas the dynamics time step is a factor of 5 smaller.

For most of the idealized tests the COSMO version 5.4b.1 from 18 July 2016 was used and for ICON a version around September 2016. At this time the ICON dynamical core was settled enough and didn't changed since then. Nearly all tests have been performed on the Cray XC40 (Broadwell) at DWD, with the exception of the Weisman, Klemp-Test of section 3.6 performed on the operational Linux cluster (Sandy Bridge) at IMGW.

3.1 Linear gravity and sound wave expansion

This test case considers the expansion of gravity and sound waves, which are generated by the small vertical oscillations of a weak warm bubble in a stably stratified atmosphere, possibly with a horizontal background flow of constant velocity. The whole configuration is limited to a 2D channel with the horizontal length L and the height $H = 10$ km. Consequently, the test exercises every term of the Euler equations (but with the exception of all terrain-following metric correction terms) together with the time integration scheme. This setup was originally proposed by Skamarock and Klemp (1994), who delivered an approximated analytic solution. Later on, the test was slightly modified by Baldauf and Brdar (2013), in particular by using an isothermal background atmosphere with constant T_0, with the goal to deliver an (apart from linearization) unapproximated analytic solution. With such an analytic solution convergence properties can be investigated.

The test is performed in two setups: a 'small scale' setup with channel length $L = 300$ km, where all Coriolis terms have been switched off, and a 'large scale' setup with $L = 6000$ km and with Coriolis terms. Both tests use a background temperature of $T_0 = 250$ K.

3.1.1 Small scale test

Fig. 1 demonstrates the expansion of the wave pattern after 30 min. for the variables $T - T_0$ and w. The bubble initially was set in $x = 100$ km, and the whole field is advected by a constant background velocity of 10 m/s to the right. The comparison with the analytic solution of Baldauf and Brdar (2013) (blue lines) shows a good agreement already for the coarse horizontal grid spacing of $\Delta x = 1000$ m and an even better one for the finer grid spacing $\Delta x = 250$ m.

This convergence behavior is further examined in a dedicated convergence study shown in Fig. 2, which compares the standard error measures L_1, L_2, and L_∞ of the simulation against the analytic solution. Simulations with grid spacings of $\Delta x = \Delta z = 2000, 1000, 500, 250, 125$ m have been performed. COSMO used time steps of $\Delta t = 10, 5, 2.5, 1.25, 0.625$ s, respectively, and ICON used $\Delta t = 6, 3, 1.5, 0.75, 0.375$ s, respectively. Both models converge in all measures and both variables $T - T_0$ and w, however the convergence rate of COSMO is clearly below second order for w, and nearly second order for T only for coarser resolutions. In contrast, ICON shows an almost perfect second order convergence. An explanation for the slightly reduced convergence of COSMO due to the split-explicit approach is given in Baldauf (2010) (as a side remark: the convergence rate of COSMO shown in Baldauf and Brdar (2013) is even smaller. The reason was, that the distance for the application of periodic BCs was unfortunately chosen slightly smaller than $L = 300$ km; this happened due to the special treatment of periodic BCs in COSMO).

One should mention, that the second order convergence of ICON is only achievable, if the off-centering parameters in the vertically implicit integration are set to zero (i.e. a purely centered Crank-Nicholson scheme). This is not possible in the combination with physical parameterizations due to stability problems.

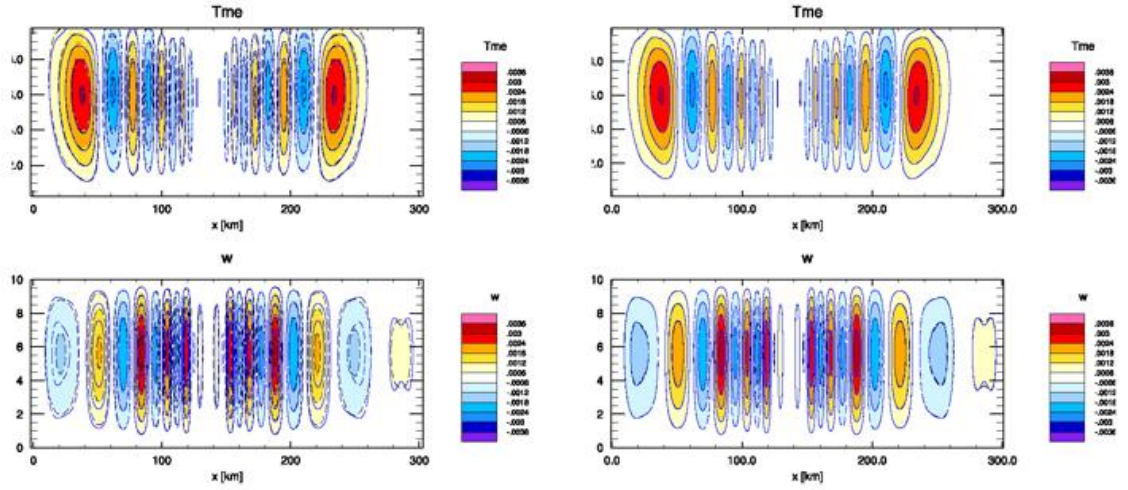


Figure 1: Linear gravity and sound wave expansion test. Small scale setup. COSMO simulation (colors and dashed, black, lines) after $t = 30$ min. Temperature deviation T' from background state (top) and vertical velocity w (bottom) for the grid spacing $\Delta x = \Delta z = 1000$ m (left) and $\Delta x = \Delta z = 250$ m (right). Analytic solution in blue lines.

3.1.2 Large scale test.

In the large scale test, the background velocity is set to zero; this is necessary for the proper comparison with the analytic solution in the case of a non-vanishing Coriolis force. Fig. 3 shows the wave pattern after 8 hours for the variables $T - T_0$ and w. In this large scale setup both models show a proper second oder convergence (Fig. 4), with slightly smaller errors for ICON (however, this also depends on a proper definition of grid spacing in ICON, see above).

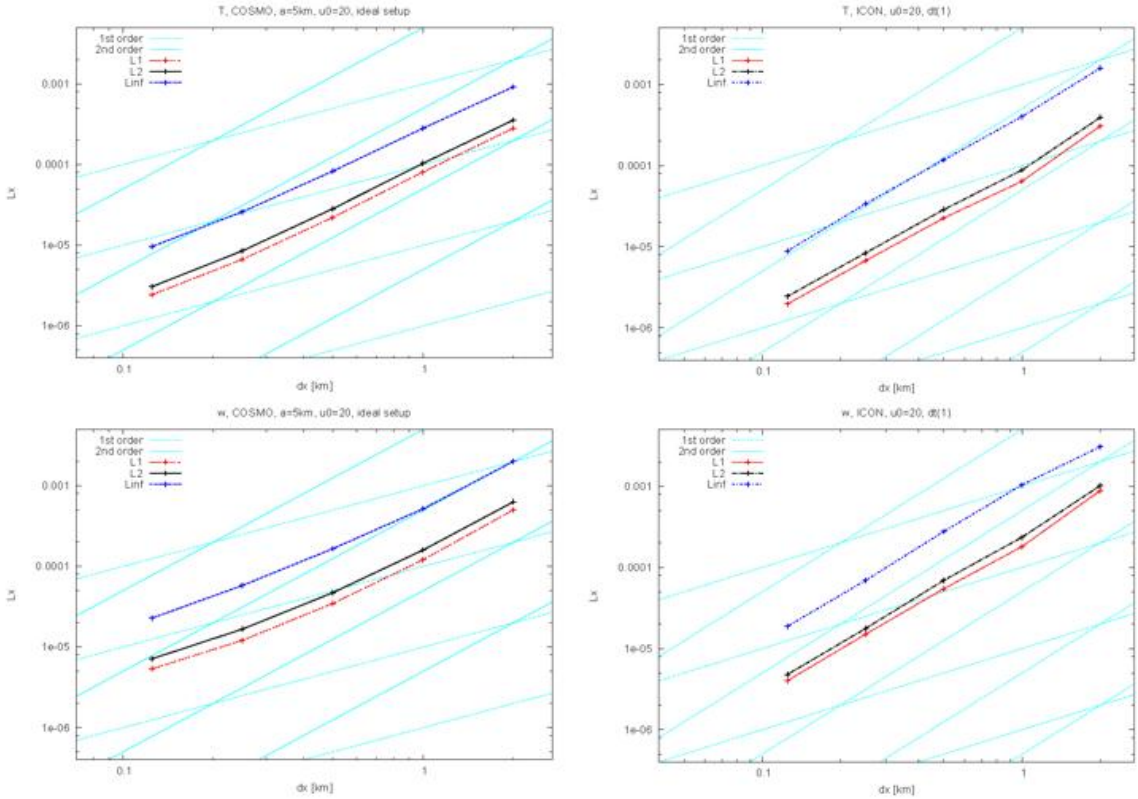


Figure 2: Linear gravity and sound wave expansion test. Small scale setup. Error measures L_1 , L_2 and L_∞ over the grid spacing for temperature deviation T' from background state (top) and vertical velocity w (bottom). Comparison between COSMO (left) and ICON (right).

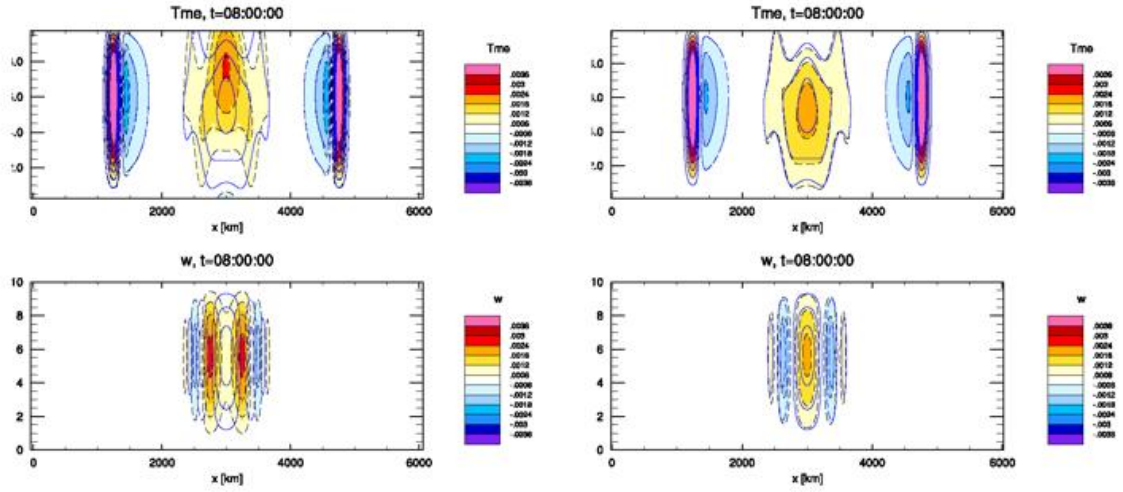


Figure 3: Linear gravity and sound wave expansion test. Large scale setup. COSMO simulation (colors and black, dashed lines) after $t = 8$ h. Temperature deviation T' from background state (top) and vertical velocity w (bottom) for the grid spacing $\Delta x = 20$ km (left) and $\Delta x = 5$ km (right), and $\Delta z = \Delta x/40$. Analytic solution in blue lines.

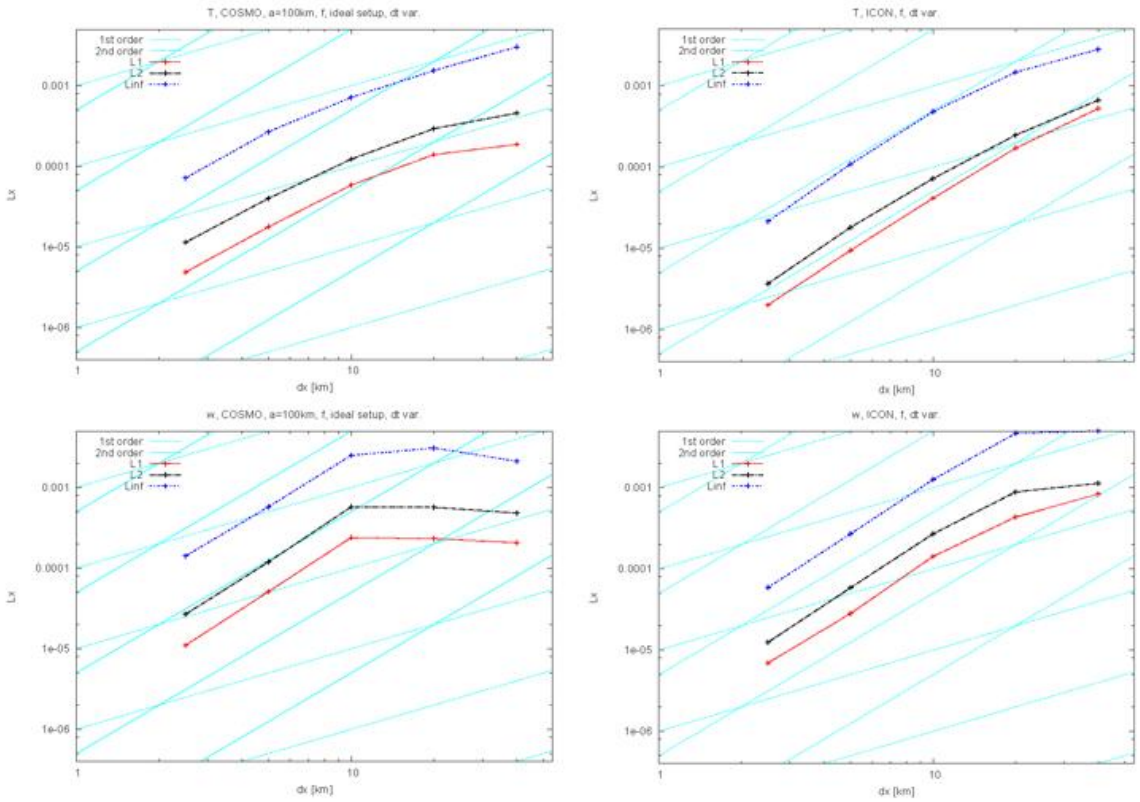


Figure 4: Linear gravity and sound wave expansion test. Large scale setup. Error measures L_1 , L_2 and L_∞ over the grid spacing for temperature deviation T' from background state (top) and vertical velocity w (bottom). Comparison between COSMO (left) and ICON (right).

3.2 Atmosphere at rest

This test consists of a single mountain of Gaussian shape with a maximum height of 1000 m and a half width of 5000 m analogous to Zängl et al. (2004). The atmosphere is at rest with a prescribed stratification with constant Brunt-Vaisala frequency of $N = 0.01$ 1/s and a temperature of $T = 288$ K at mean sea level. The other thermodynamic variables are in hydrostatic balance. Such a configuration should remain stationary for arbitrarily long times. However, at least for models that use terrain-following coordinates, a numerical imbalance between differently discretized terms will induce a flow after some time. Obviously, as smaller these disturbances are, as better the model formulation. In principle, this test cases inspects two properties of the model: first, the accuracy of the pressure gradient in vertical direction and along coordinate surfaces and its balance with the buoyancy term. Second, it tests the accuracy of the initial hydrostatic balance (a piecewise polytropic atmosphere was initialized and the new exponential reference atmosphere was used in both models). A further discussion about this test case can be found in Zängl et al. (2004).

Figure 5 demonstrates that ICON (bottom) induces much less disturbances than the standard setup of COSMO (top): COSMO induces vertical velocities w that reach about ± 4 m/s, whereas ICON induces maximum values of less than ± 1 m/s and spatially more limited to the vicinity of the mountain. Both models use the same vertical grid spacing, relatively close to operational settings ($\Delta z \approx 19.8$ m near the bottom until 780 m at the model top). After about 17 hours, the COSMO run broke. One can reduce the disturbances of COSMO and prevent the model crash by using third order implicit vertical advection. However, this version decouples the vertical advection process a bit more from the other dynamical processes and therefore was never used operationally.

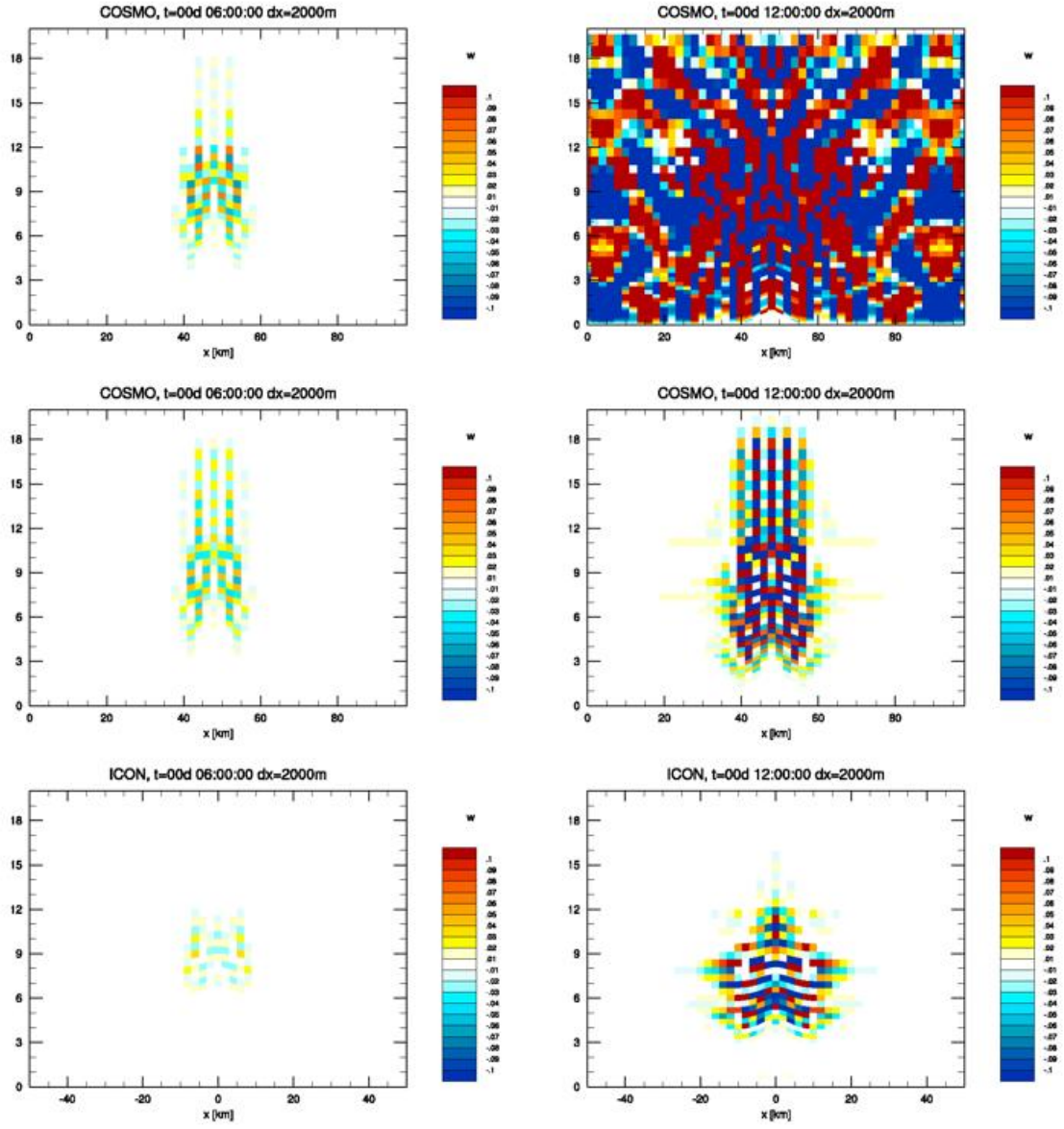


Figure 5: Atmosphere at rest. COSMO with operational setting (top), COSMO with third order vertical implicit advection (middle), and ICON (bottom). w after $t = 6$ h (left) and 12 h (right).

3.3 Linear flow over mountains

A further standard test case is the linear flow over flat mountains. Such a test investigates many of the spatial discretizations of a model including the metric terms of the terrain-following coordinate formulation. Their correct implementation and numerical behavior again can be assessed by the comparison with the linearized analytic solution, which is applicable due to the quasi-linearity of the setup. Here, the analytic solution of Baldauf (2008) is used, which is virtually identical to the slightly more approximated solution by Smith (1980).

The whole setup is adapted from Schär et al. (2002) (section 5b), which defines a series of mountains with the orography function

$$h(x) = H_0\, e^{-x^2/a_e^2}\, \cos^2 \pi \frac{x}{a_c}$$

with the two length scales $a_e = 5$ km and $a_c = 4$ km. The inflow velocity is $u_0 = 10$ m/s, the temperature is stably stratified with a constant Brunt-Vaisala frequency of $N = 0.01$ 1/s, and the surface temperature is $T_s = 288$ K.

3.3.1 2-dimensional flow

The vertical grid is chosen as equidistant. The maximum mountain height is $H_0 = 25$ m, which results in a vertical Froude-number of $Fr_H = u_0/(NH_0) = 40 \gg 1$. Therefore, this setup can be considered as linear in a good approximation. The horizontal Froude-number $Fr_a = u_0/(NL)$ lies in the range 0.1...0.5, i.e. in the range of almost hydrostatic to nearly non-hydrostatic flow over mountains. As can be seen in Fig. 6, both models reproduce the analytic solution quite well, perhaps with a minimal advantage for ICON. Note, that a proper convergence study is difficult due to the influence of the artificial damping layers and therefore was not performed (this problem does not exist in the test case of section 3.1). Beyond this, both models use different formulations: whereas COSMO uses a relaxation scheme towards the large scale values for all prognostic variables, ICON uses the damping layer formulation for w alone by Klemp et al. (2008). At least, a comparable damping height starting in about $z = 14$ km was used both in COSMO and ICON.

3.3.2 3-dimensional flow

The setup for the 3D flow uses a vertically stretched grid with a cell thickness of 24.7 m near the ground and 976 m at the model top. This vertical grid spacing and the background temperature profile is shown in Fig. 7. For the horizontal grid spacing the coarser value $\Delta x = 500$ m has been chosen for these 3D simulations. Now a circular symmetric Gaussian mountain $h(x, y) = H_0\ 2^{-(x^2+y^2)/a^2}$ is used with $H_0 = 1$ m (leading to $Fr_H = 2000$) and $a = 5$ km (leading to $Fr_a = 0.4$). The inflow velocity is $u_0 = 20$ m/s and the stratification again uses a constant $N = 0.01$ 1/s. The damping layers are chosen as for the 2D case, and Fig. 8 demonstrates that both damping layers behave relatively similar near the model top. Both models reproduce the analytic solution quite well (Fig. 9), now perhaps with a minimal advantage of COSMO. This demonstrated in particular that all metric correction terms are correctly implemented in both models.

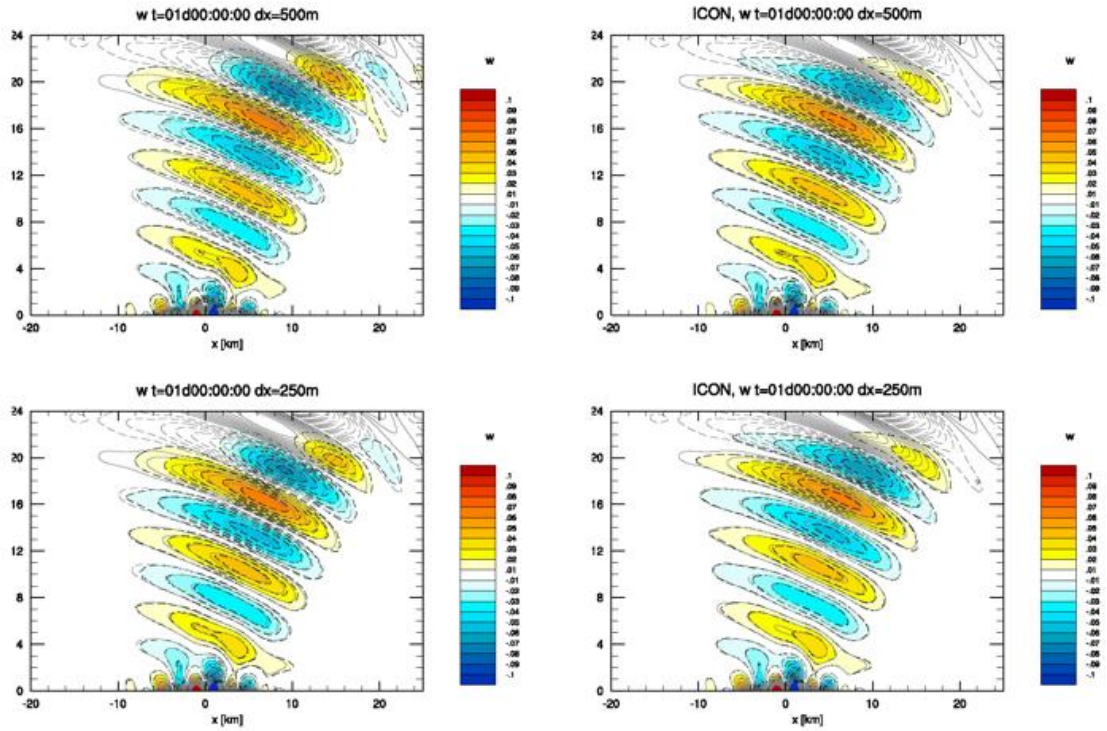


Figure 6: 2D linear flow over mountains. Vertical velocity w of COSMO (left) and ICON (right) for the two resolutions $dx = 500$ m (top) and $dx = 250$ m (bottom). Colors and dashed, black lines: simulation; grey lines: analytic solution.

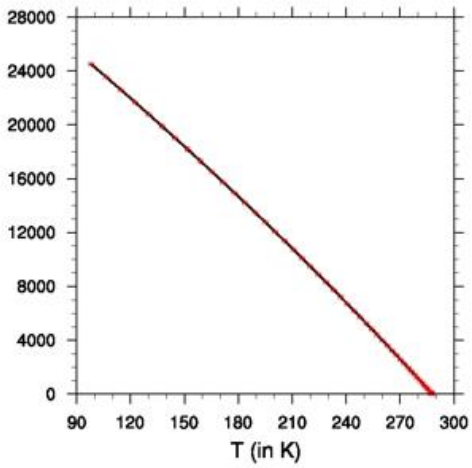


Figure 7: 3D linear flow over mountains. Initial temperature profile and vertical grid spacing (stars).

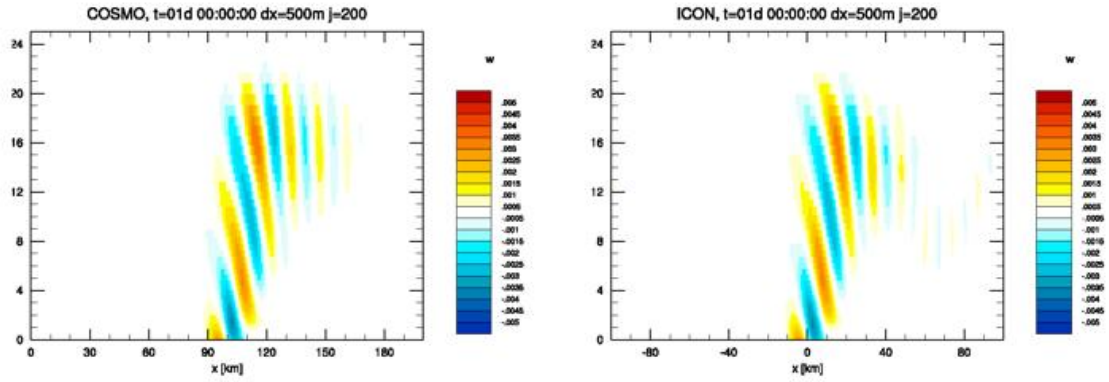


Figure 8: 3D linear flow over mountains. COSMO (left) and ICON (right). Vertical cross section of vertical velocity w through the symmetry axis.

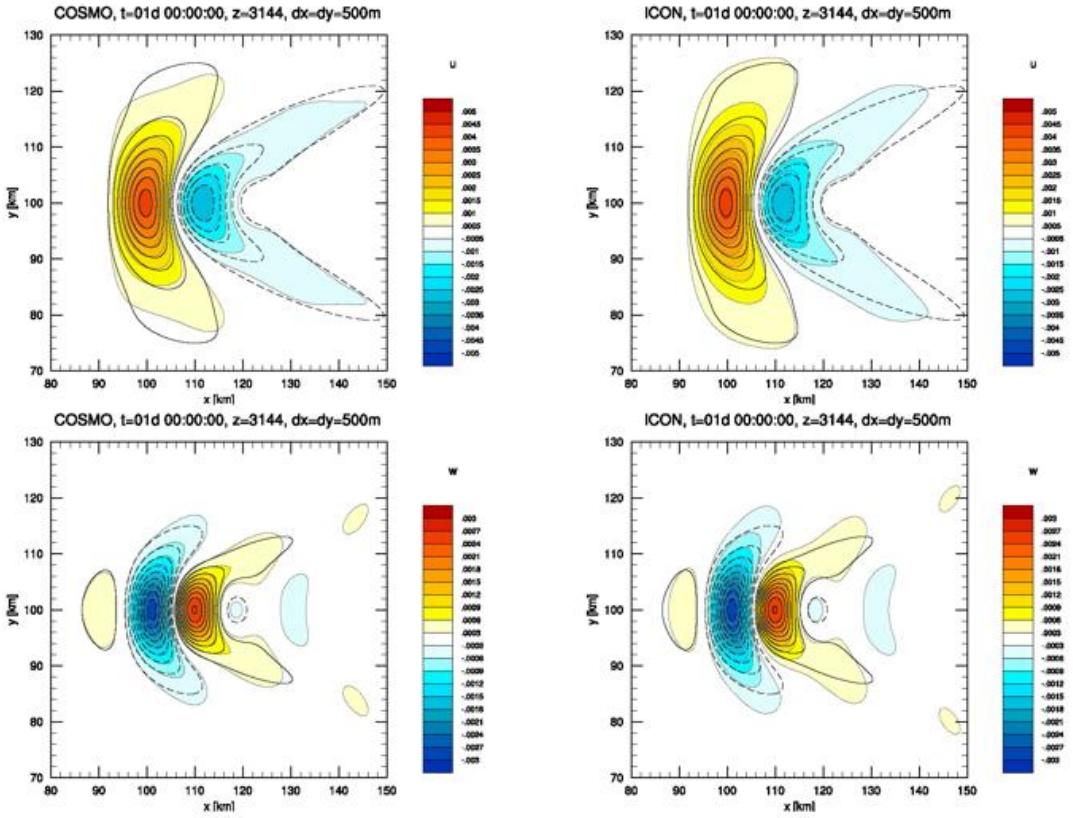


Figure 9: 3D linear flow over mountains. COSMO (left) and ICON (right). Horizontal cross sections of horizontal velocity u (top) and vertical velocity w (bottom) at height $z = 3144$ m above MSL. Colors and grey lines: simulations; black lines: analytic solution.

Table 1: Some characteristic values for the Gaussian mountain $h(x, y) = H_0\ 2^{-(x^2+y^2)/a^2}$ with $a = 3$ km in the 3D non-linear case: the maximum mountain height H_0, the maximum orography step max Δh between two neighboring grid cells, and the maximum slope angle max α.

H_0	max Δh	max α
1000 m	234.9 m	13.2°
3000 m	704.7 m	35.2°
4000 m	939.6 m	43.2°
4500 m	1057 m	46.8°
4700 m	1104 m	48.0°
5000 m	1174 m	49.6°
6000 m	1409 m	54.8°
7000 m	1644 m	58.9°
8000 m	1879 m	62.0°

3.4 Nonlinear flow over steep mountains

We use the same setup as for the linear 3D flow in section 3.3.2, with the exception that the Gaussian mountain is bit narrower ($a = 3$ km) and the mountain heights H_0 are much higher to reach the strongly non-linear regime with steep mountains. Furthermore, an even coarser horizontal grid spacing of $\Delta x = 1000$ m has been chosen to again increase the height step Δh between two neighboring grid points (the vertical grid stretching is the same as in section 3.3.2). Additional to the slope angle, Δh has a stability limiting influence, too. Table 1 gives some characteristic properties for these mountains and the setup. To prevent model breaks by unphysical gravity wave breaking, turbulent diffusion was switched on (each model uses its 'standard' turbulence scheme for this purpose).

Fig. 10 shows the comparison between COSMO and ICON for relatively moderate mountain heights up to $H_0 = 3000$ m. To keep the model domain small enough to perform larger series of tests, a periodic boundary condition has been chosen. Its effect is visible by the entrance of the mountain lee wave again on the left side of the domain. This might have a certain influence to the mountain inflow (e.g. some sort of blocking), however, these effects seem tolerable for this more qualitative study.

Fig. 11 shows the COSMO model for the maximum heights $H_0 = 4000$ m (in comparison with ICON), and 4500 and 4700 m. These COSMO simulations are only stable with the Mahrer discretization of the pressure gradient term (Baldauf, 2013).

Fig. 12 shows the ICON model for mountain heights H_0 between 5 km and 8 km; COSMO is no longer stable for such high values of H_0, whereas ICON tolerates very steep mountains. This very positive property is due to a modified version of the Mahrer discretization by Zängl (2012).

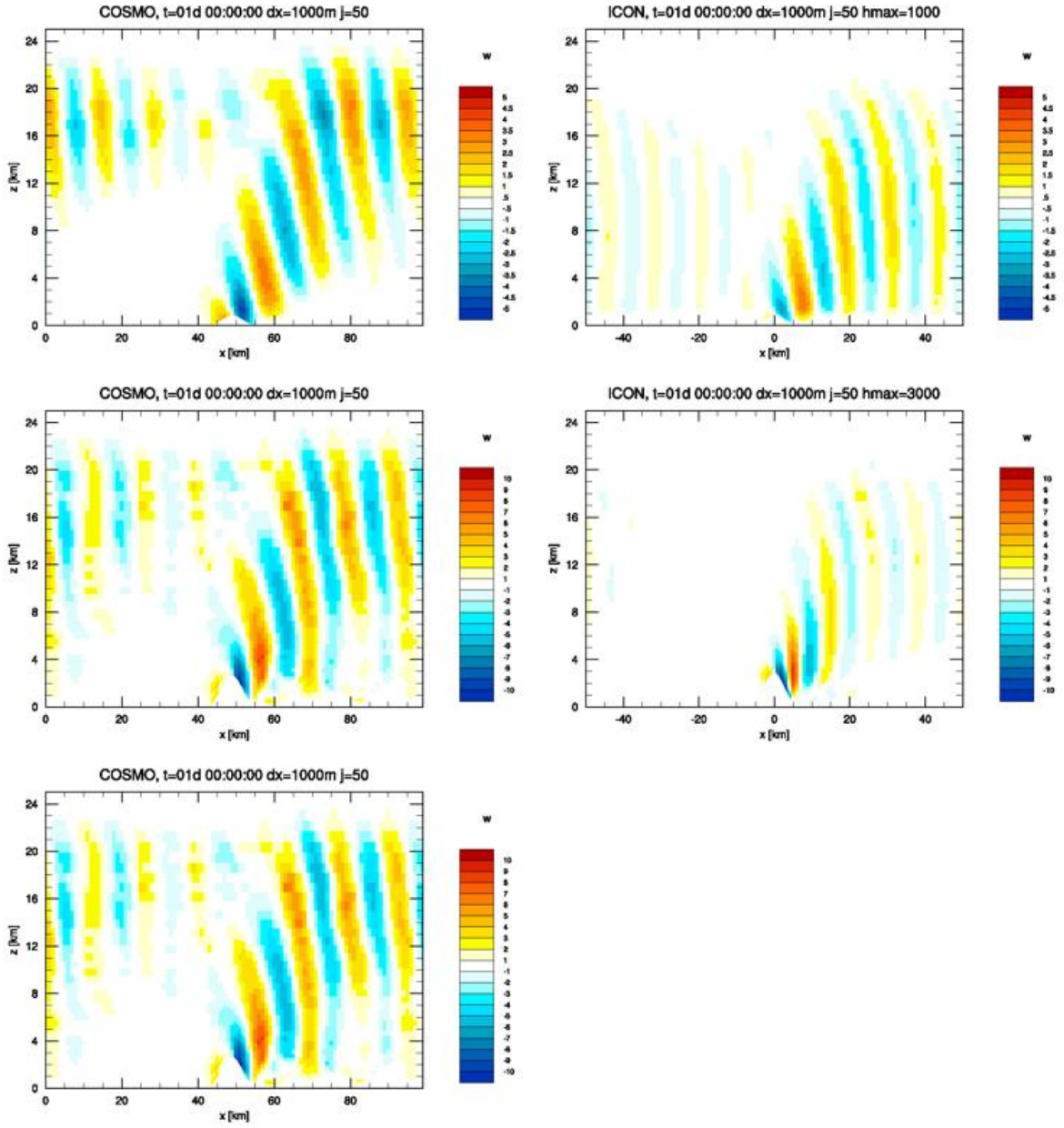


Figure 10: 3D flow over steep mountains. Cross section through the symmetry axis of COSMO (left) and ICON (right) for maximum mountain heights $H_0 = 1000$ (top) and $H_0 = 3000$ m. The bottom figure shows COSMO but with the alternative Mahrer-discretization in the fast waves solver.

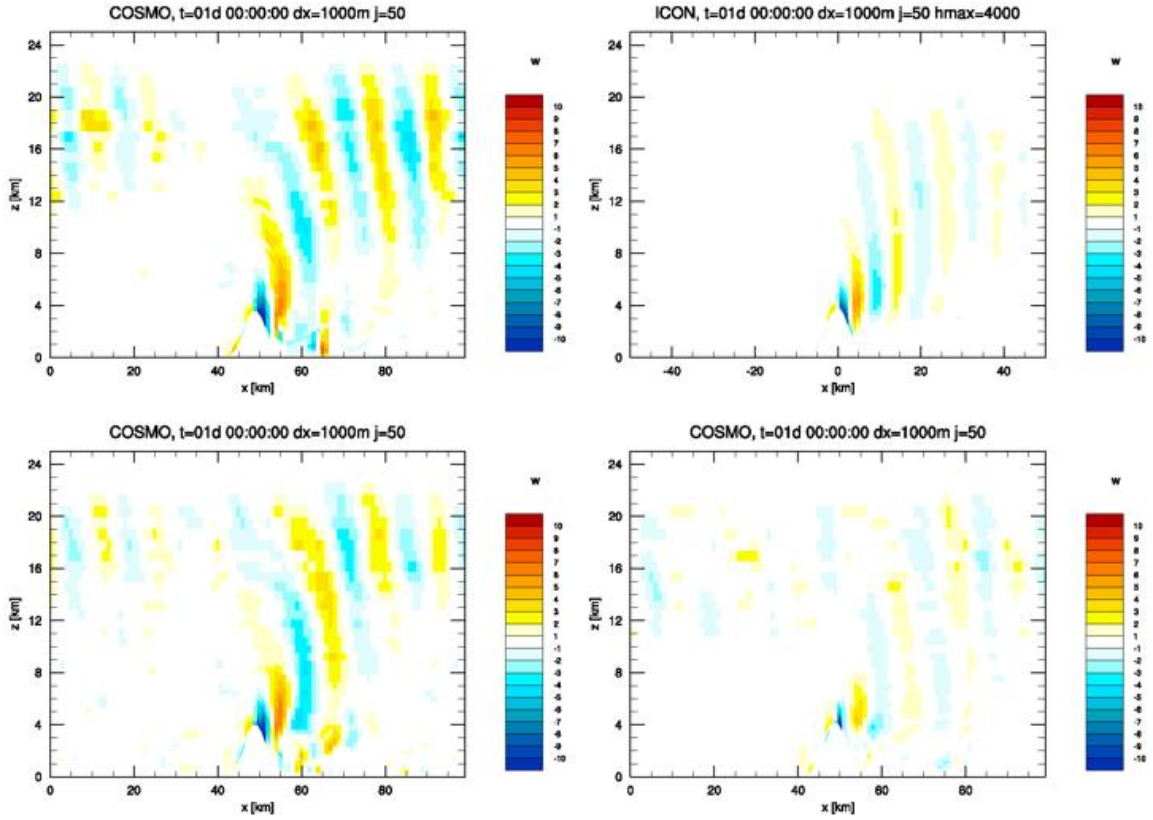


Figure 11: 3D flow over steep mountains, COSMO and ICON for maximum mountain heigh $H_0 = 4000$ (top row). COSMO for $H_0 = 4500, 4700$ m (bottom row).

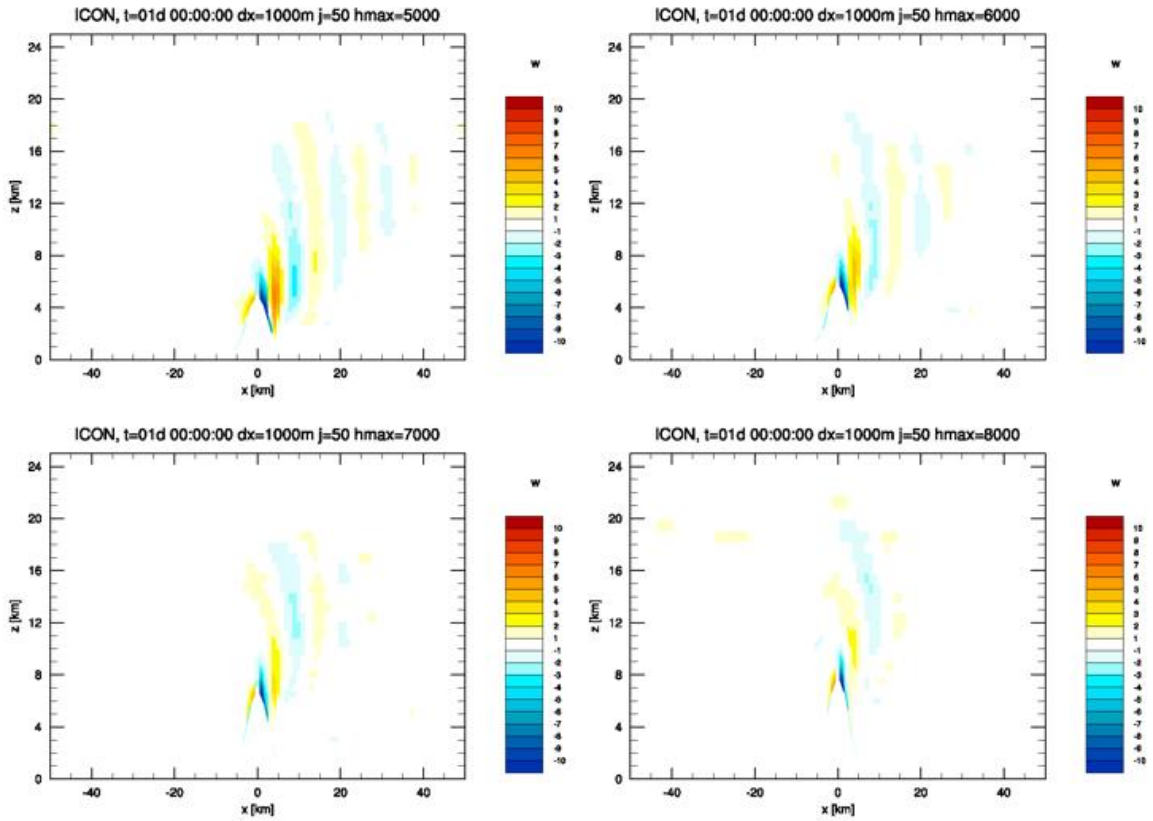


Figure 12: 3D flow over steep mountains with the ICON model for maximum mountain heights $H_0 = 5000$, 6000, 7000 and 8000 m (top, left to bottom, right).

3.5 Falling cold bubble

This highly non-linear test case is defined in Straka et al. (1993). A bubble that is up to 15 K colder than the neutrally stratified surrounding atmosphere is set 3 km above the ground in a 6.4 km high and 51.2 km wide 2D channel. This initial situation is shown in the left, upper panel in Fig. 13 (only a part of the right half of this horizontally symmetric setup is shown) The bubble falls down and after hitting the ground, bow fronts on both sides evolve. Due to a Kelvin-Helmholtz instability, several vortices are generated. To prevent the simulation to develop too fine-scale structures and to allow convergence, diffusion with a constant diffusion coefficient of $K = 75m^2/s$ is used both for heat and momentum. Coriolis force is switched off.

Fig. 13 shows the evolution of the potential temperature for the grid spacing $\Delta x = \Delta z = 25$ m with the COSMO model. For this fine resolution one can expect an almost converged solution; in fact the agreement with the reference solution given in Straka et al. (1993) (their Fig. 1) is very good (note that Fig. 13 and 14 use the same isolines as this reference figure).

Fig. 14 shows a comparison between COSMO and ICON for the different grid spacings $\Delta x = \Delta z = 200, 100, 50, 25$ m, where for COSMO time steps of $\Delta t = 2.0, 1.0, 0.5, 0.25$ sec. have been used, and for ICON $\Delta t = 1.44, 0.72, 0.36, 0.18$ sec., respectively. One easily recognizes the convergence of both models for finer resolutions. However, the final state of ICON (i.e. after 15 min.) is not exactly identical to the reference solution of Straka et al. (1993). (e.g. the second vortex overlaps the third one a bit more). Until now, the reason for this behavior is not yet clear. One only can speculate that the diffusion might work slightly different, but further investigation seems to be necessary.

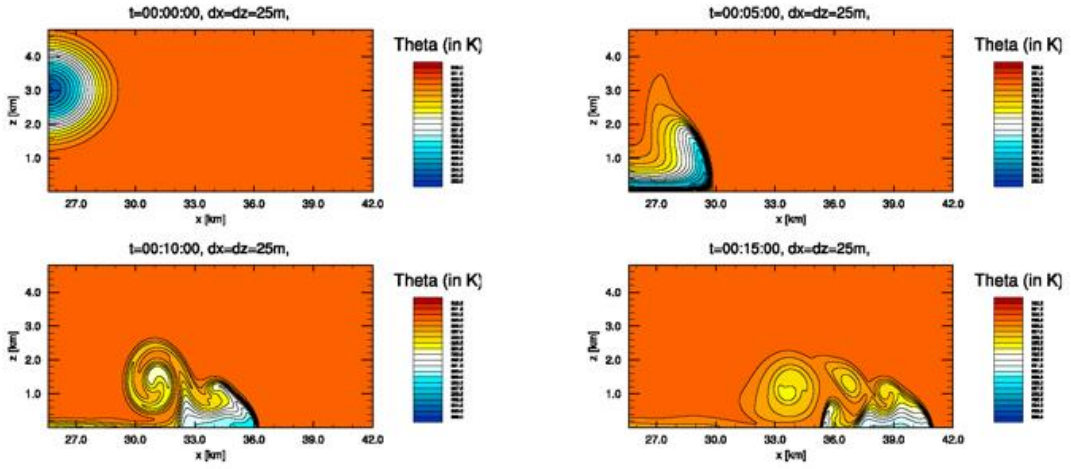


Figure 13: Falling cold bubble test. COSMO, $\Delta x = \Delta z = 25$ m, Θ after t=0, 5, 10, 15 min., `y_vert_adv_dyn='impl2'`. Only parts of the right half of the domain is shown.

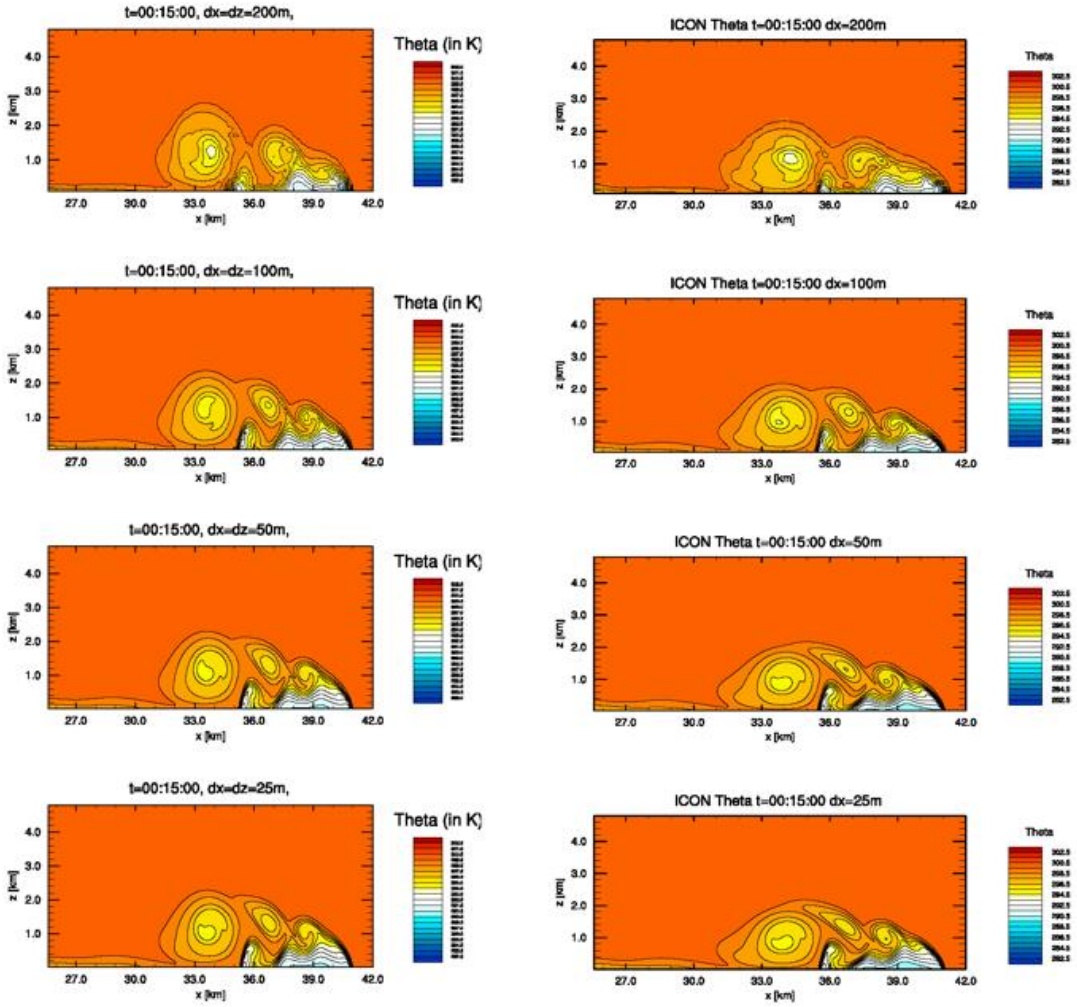


Figure 14: Falling cold bubble test. Θ after t=15 min., comparison between COSMO (left) and ICON (right) for different grid spacings $\Delta x = \Delta z = 200, 100, 50, 25$ m.

3.6 The Weisman and Klemp (1982) test case

This section reports results from the idealized moist deep convection test case of Weisman and Klemp (1982) carried out for the ICON model. The test requires from the model a capability to handle nonhydrostatic flows, triggered by latent heat release and rain water evaporation. The ICON model results are compared with references provided by the COSMO model (Baldauf et al., 2011) and Weisman and Klemp (1982) model. Symmetry of solutions allows limiting comparisons to the southern part of the computational domains.

3.6.1 Experimental setup

Definition of the environmental atmospheric profiles of potential temperature, moisture, and wind predominantly follows the setup of Weisman and Klemp (1982) (theirs Equations 1, 2, and 4). The qv_0 parameter of the moisture profile is set to 14 g/kg. Subsequent simulations differ by the environmental wind shear parameter U_S, while the other parameters are kept unchanged. A constant wind profile is added to the original environmental wind profile in the ICON simulations ($0.45 \cdot U_S$) to keep developing convective systems near the centre of the computational domain. Convection is initiated by an ellipsoidal thermal having the horizontal radius $r_h = 10$ km, vertical radius $r_v = 1.4$ km, and maximum temperature excess $+6°$C.

The computational domain of the ICON model utilizes a horizontally-unstructured grid equivalent to a cartesian 100 x 100 grid points periodic grid with the grid length equal 2 km. The vertically-structured grid has 90 levels, with stretching, and spans up to 40 km height above the surface. The sponge layer is between 25 km height and the top of domain. The simulations are carried out using a 3-category ice Kessler-like microphysical scheme, with snow, cloud ice, and graupel. The turbulence parameterization utilizes a TKE-based mixing scheme. The integration time is limited to 120 minutes. The Coriolis force is not included in the model equation set.

Configuration of the reference COSMO simulations is based on the ARTIFCTL module of Blahak (2015) and approximately follows the ICON model test case configuration. A few important differences are listed below:

- the horizontal grid of the COSMO model is structured,
- the original environmental wind profiles are used,
- the COSMO domain is elongated to 300 km in the X-direction,
- the vertically-structured grid has 74 levels between the surface and 25 km height, sponge layer starts at 15 km height, and levels are colocated with the ICON levels.

Data visualisation is based on the NCL environment[1]. The ICON native-output data were used for visualisation. Data regridding to the cartesian grid was carried out using tools the Earth System Modeling Framework[2] tools.

[1] www.ncl.ucar.edu

[2] www.earthsystemcog.org/projects/esmf/

3.6.2 Results of simulations

Three types of experiments were performed with the wind shear parameters (U_S) equal 15, 25, and 35 m/s. A few principal convective phenomena are observed in each simulation: (i) formation of an updraft in result of the convection initiation, (ii) formation of rain shafts, (iii) subsequent formation of precipitation-driven downdrafts, and (iv) a cold pool growth at the surface. For example, all these phenomena are observed in the ICON $U_S = 15$ m/s simulation (Figure 15), as well as in the reference Weisman and Klemp (1982) (Figure 16) and COSMO (Figure 17) simulations.

Growth of 4 convective cells is observed in the low-shear ICON simulation ($U_S = 15$ m/s; Figure 15). Those cells live relatively short and feature relatively moderate vertical velocities and vorticity within the mid-tropospheric updrafts (Figure 15 and Figure 18, left). That suggests that those cells are likely not supercellular.

Convective cells that develop at the gust front in the ICON simulation with $U_S = 15$ m/s (e.g., cell II) tend to move slower than the gust front and are prone to decay once cut off from CAPE-rich air. A qualitatively similar solution is observed in Weisman and Klemp (1982) (Figure 16). A rather contrasting solution is observed in the COSMO simulation (Figure 17). In that simulation, a long-lived cell develops with a stronger updraft encompassing increased vertical vorticity (around 0.006 s^{-1} in the COSMO versus 0.004 s^{-1} in the ICON; Figure 19, left), and that cell sticks to the gust front.

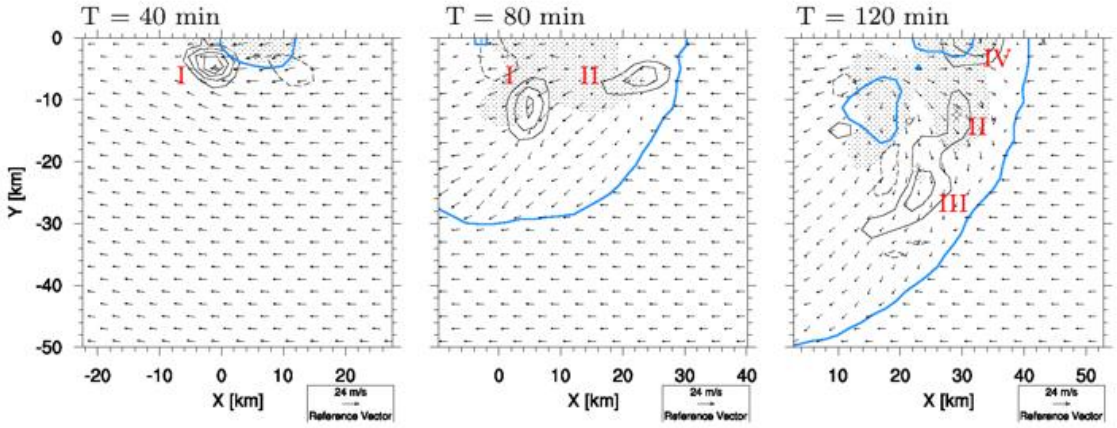


Figure 15: Convective cells and low-level flow field developing in the ICON simulation with $U_S = 15$ m/s. The arrows denote approximately storm-relative flow at 147 m height above the surface ($\overline{U} = 12$ m/s was subtracted from the flow field). The blue line denotes the meso-cold front position at 10 m height. The contours denote vertical wind speed at 4677 m height (contours shown for -8, -6, -4, -2, 5, 10, 15, 20, 25, 30 and 35 m/s; negative values dashed). The shading (hatching) denotes the rain water mixing ratio exceeding 1 g/kg (4 g/kg) at 10 m height. Individual convective cells are marked with the red roman numbers.

The ICON simulation with $U_S = 25$ m/s is shown in Figure 20. Here, two convective cells develop by 80 minute of simulation and subsequently merge around 120 minute. At least three differences arise in comparison to the previous ICON simulation. First, the mid-level vertical vorticity within the first cell (I) reaches around 0.008 s^{-1} (Figure 18, middle), that is, a value close to the threshold defining the mid-level supercellular mesocyclone (0.01 s^{-1}). Second, the cell I is long-lived and has a rather compact updraft. Finally, the cell I propagates around 36 km to the south after 120 minutes of simulation. Those observations suggest that the cell I represents to some extent the supercellular convection. A quite similar convective

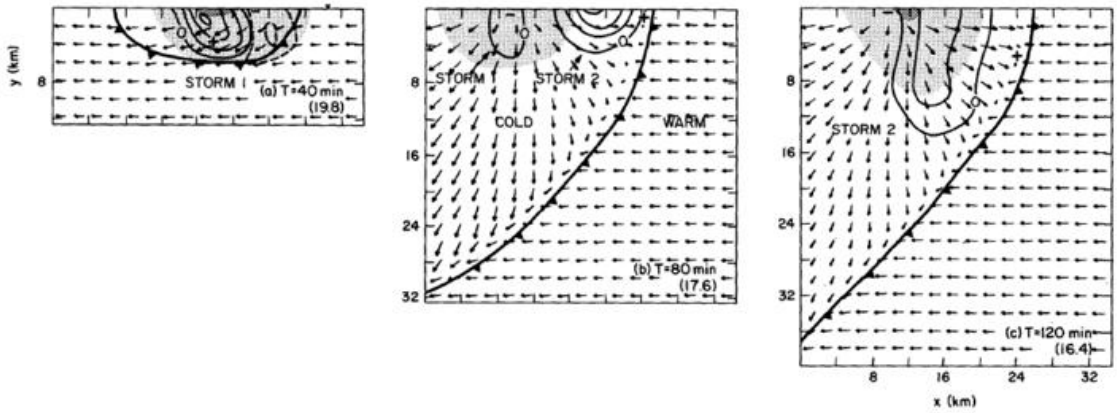


Figure 16: The reference Weisman and Klemp (1982) simulation for $U_S = 15$ m/s (theirs Figure 4).

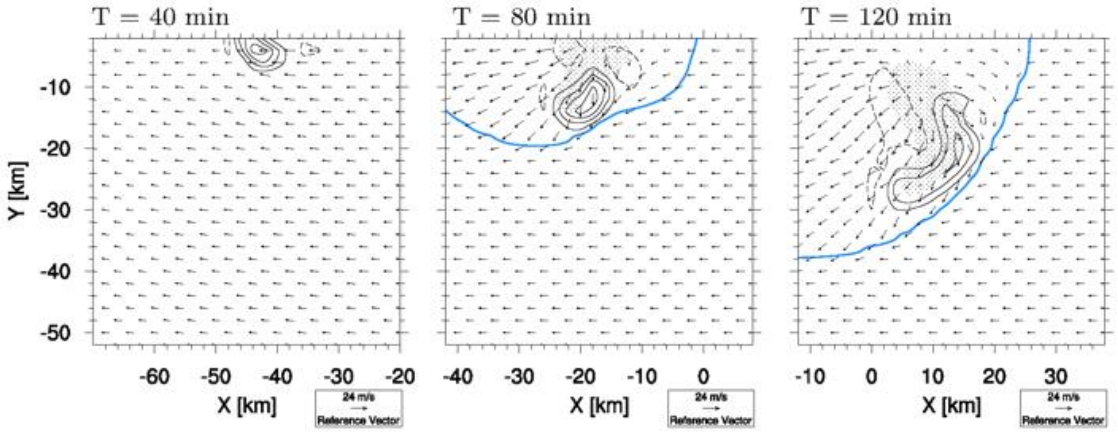


Figure 17: The reference COSMO simulation with $U_S = 15$ m/s, and $\overline{U} = 12$ m/s. Data is depicted as in Figure 15.

cell with the vertical vorticity of around 0.008 s^{-1} (Figure 19, middle) is observed in the COSMO simulation as well (Figure 21).

Figure 22 shows a convective cell developing in the ICON simulation with the strongest environmental wind shear ($U_S = 35$ m/s). At 80 minute, the maximum mid-level vertical vorticity of the cell exceeds 0.012 s^{-1} (Figure 18, right), a value in the range of supercellular mesocyclones. The cell moves to the right of the environmental winds and departs around 42 km to the south (120 minute), while remaining in proximity of the gust front. The updraft and precipitation shafts seem to be almost separated. Therefore, that cell likely represents the supercellular convection. The reference COSMO (Figure 23 and Figure 19, right) and Weisman and Klemp (1982) simulations (Figure 24) show development of quite similar supercellular storms. In those simulations, the maximum vertical vorticity is slightly weaker (around 0.008 s^{-1} and 0.01 s^{-1}, respectively).

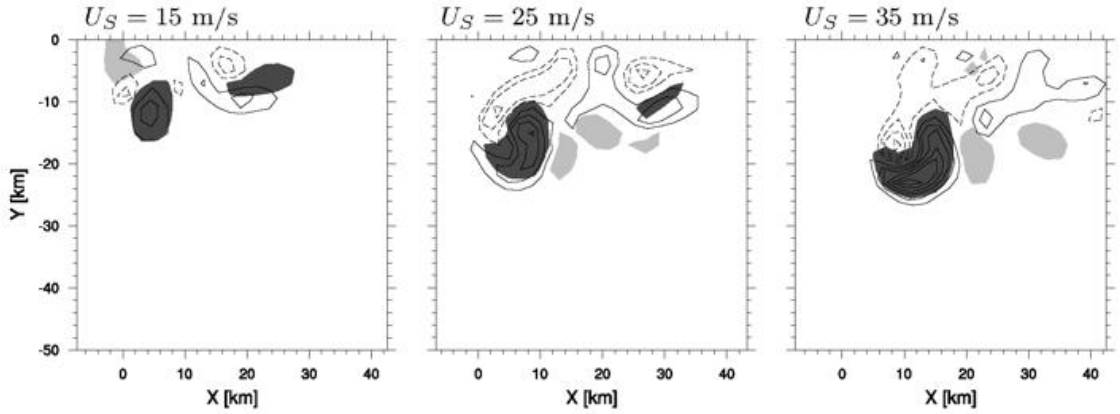


Figure 18: Vertical vorticity at 4677 m height (negative values dashed; contour interval 0.002 s^{-1}; the zero contour not shown) after 80 minutes of the ICON simulations. Light (dark) shading denotes vertical velocities lower than −2 m/s (larger than 5 m/s) at the same height.

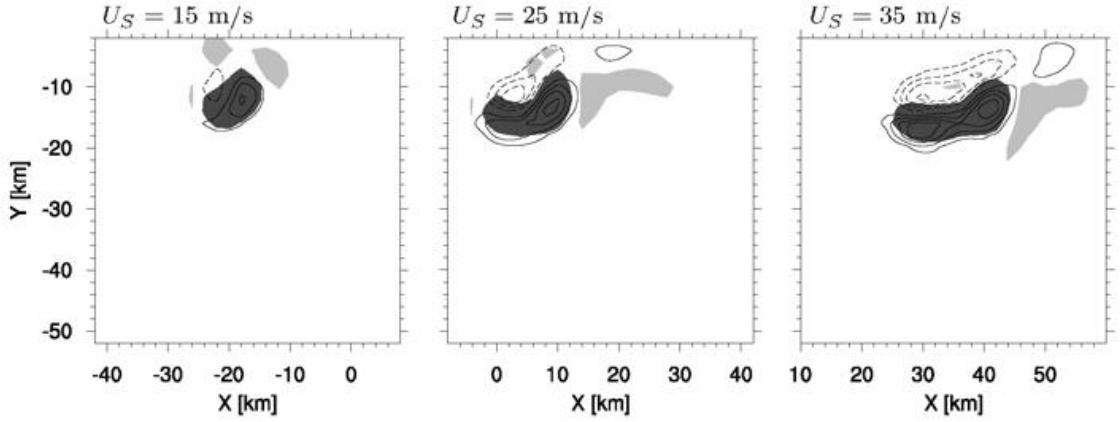


Figure 19: Vertical vorticity at 4677 m height (negative values dashed; contour interval 0.002 s^{-1}; the zero contour not shown) after 80 minutes of the COSMO simulations. Light (dark) shading denotes vertical velocities lower than −2 m/s (larger than 5 m/s) at the same height.

3.6.3 Summary

This experiment was intended to verify whether the nonhydrostatic ICON model is capable to simulate deep moist convective flows, and in particular the supercellular convection. Although the scope of analysis was limited, results indicate that this model consistently simulates convective flows in differently-sheared environments. The long-lived supercellular convection begins to develop in the moderate-shear environment and is further enhanced in the large-shear environment. When evolution of morphological flow features is concerned, convection observed in the ICON simulations is more similar to the one in the Weisman and Klemp (1982) simulations than in the COSMO simulation (especially for the low-shear experiment). The results do not indicate presence of any basic error in the coupling between the ICON nonhydrostatic dynamical core, saturation adjustment scheme, and parameterizations of the moist and turbulent processes.

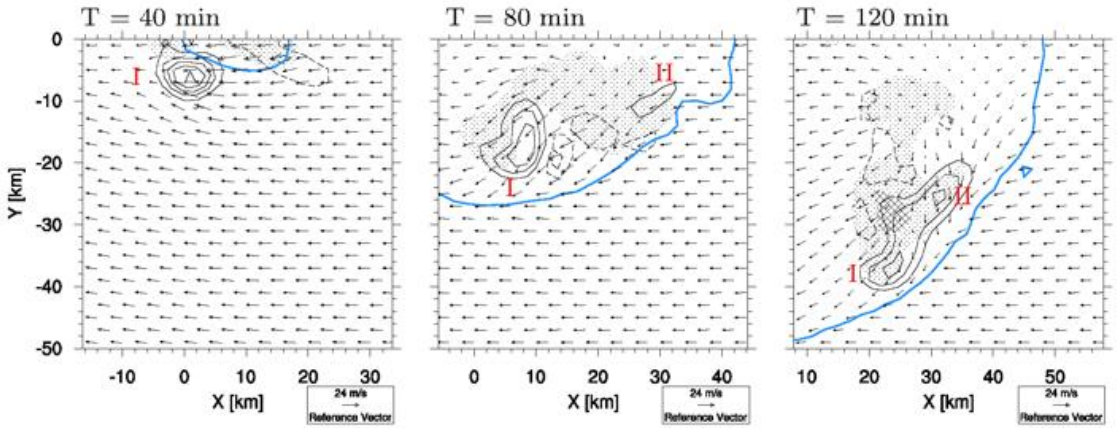


Figure 20: As Figure 15 but for the $U_S = 25$ m/s, and $\overline{U} = 19$ m/s.

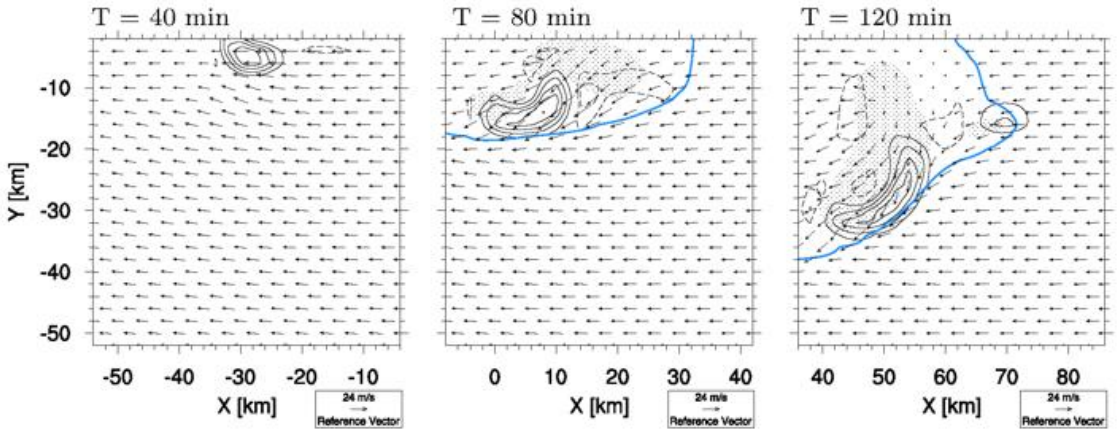


Figure 21: As Figure 17 but for the $U_S = 25$ m/s, and $\overline{U} = 19$ m/s.

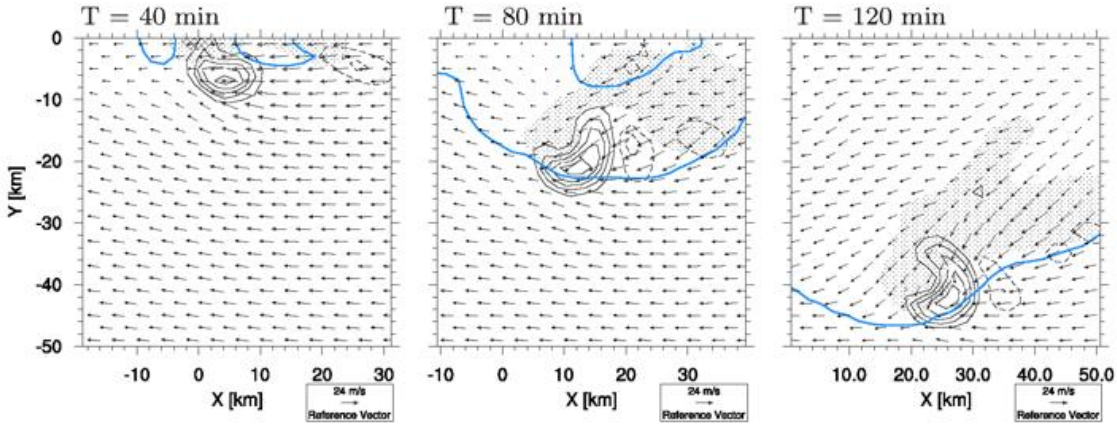


Figure 22: As Figure 15 but for the $U_S = 35$ m/s, and $\overline{U} = 22.5$ m/s.

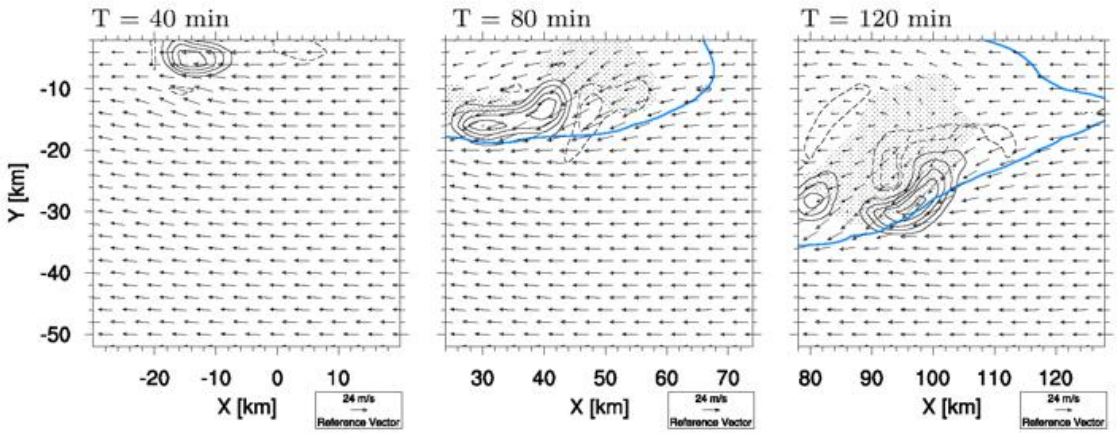


Figure 23: The reference COSMO simulation with $U_S = 35$ m/s, and $\overline{U} = 22.5$ m/s. Data is depicted as in Figure 15.

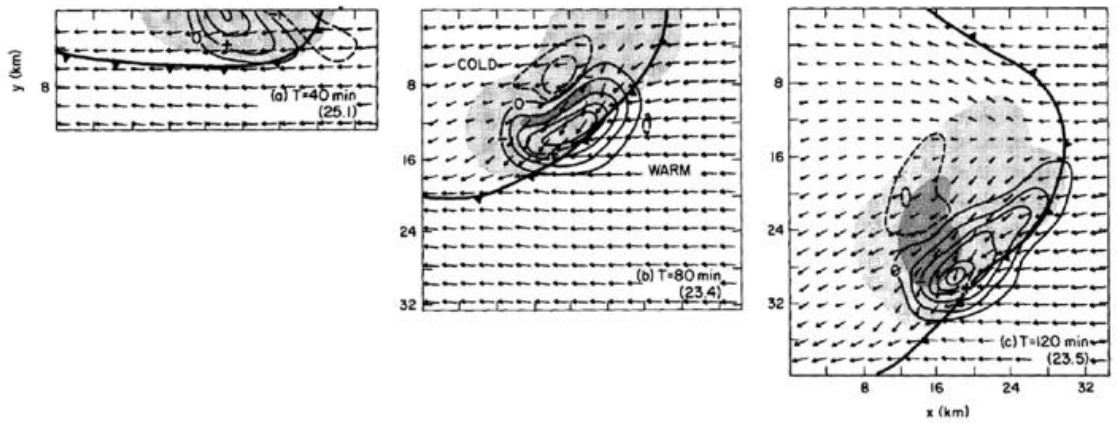


Figure 24: The reference Weisman and Klemp (1982) simulation for $U_S = 35$ m/s (theirs Figure 6).

4 Scalability aspects

In such a basic comparison between two models, computational efficiency of course also plays a big role. In general, one can say, that ICON runs definitely faster than COSMO on most platforms. In this section, we want to investigate in particular the scaling behaviour of both models for larger numbers of processors on massively parallel computers. Here we concentrate on the strong scaling properties, i.e. the reduction of wall-clock time by running on an increasing number of processors for *the same* simulation setup (i.e. same domain, same number of grid points, same time step, ...). The strong scaling property is important to assess how large a machine must be to tackle a given problem (by the way, strong scaling is a bit easier to investigate than weak scaling with different setups for different processor numbers). We have investigated only CPU based machines, more precise the experiments for both COSMO and ICON have been run on the Cray XC40 (Broadwell) of DWD (i.e. neither GPU based computers nor vector computers have been used).

It is important to mention a difference in the parallelization strategy: COSMO uses only distributed memory parallelization based on the MPI library, In contrast, ICON uses both distributed memory (with MPI) and shared memory parallelization (using openMP).

Fig. 25 shows the strong scaling behavior of COSMO for a COSMO-D2 setup: a simulation over 27 h covering the area of Germany and parts of the surrounding countries. The experiment was carried out with COSMO version 5.4d.4 from 29 May 2017. The strong scaling behavior of the dynamical core (green line) and the physical parameterizations (light blue line) is almost perfect (i.e. linear decrease of wall-cock time) up to about 1000 processors and is still satisfactory at least up to about 10000 processors. The bad scaling of the 'additional computations' is mostly due to the RTTOV library (remark: U. Schättler could cure this problem later on, so that the scaling of these computations now is also quite good). Both the input as also the output don't scale at all: wall-clock times even slightly increase with increasing number of processors.

Fig. 26 shows the analogous strong scaling behavior of ICON for an ICON-D2 setup: it is quite similar to the COSMO-D2 setup, it also runs over 27h and covers roughly the same domain (the output on the regular lat-lon grid is exactly the same horizontally, however the triangle grid covers a slightly larger area). The experiment was carried out with an ICON version from May 2017. As for COSMO, the scaling for the dynamical core and the parameterizations is perfect for up to about 1000 processors. Note that the absolute wall-clock time for the sum of dynamics and physics calculations is smaller than for COSMO. The scaling becomes worse for higher numbers of processors, which is mainly caused by the input of boundary data. Remark: this problem could be largely improved in the meanwhile, in particular by reducing latency by collecting all levels before communication. Moreover, it is worth to mention that ICON allows to optimize the use of the cache by the choice of the so-called `nproma` parameter, i.e. to adapt the length of data blocks to the size of the cache. However, in these tests the value of `nproma` was not changed.

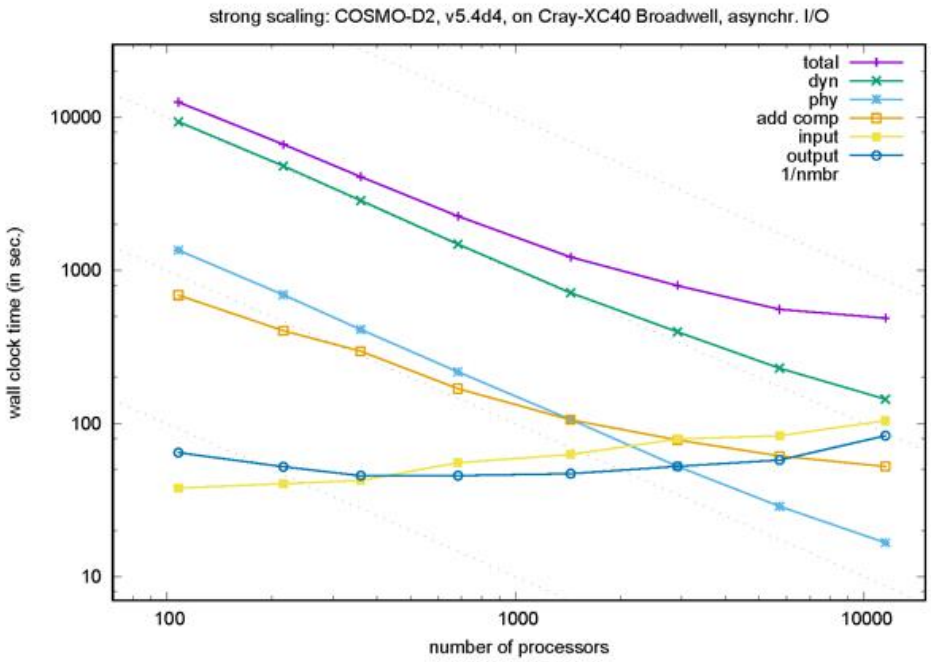


Figure 25: Strong scaling test for COSMO with a COSMO-D2 setup.

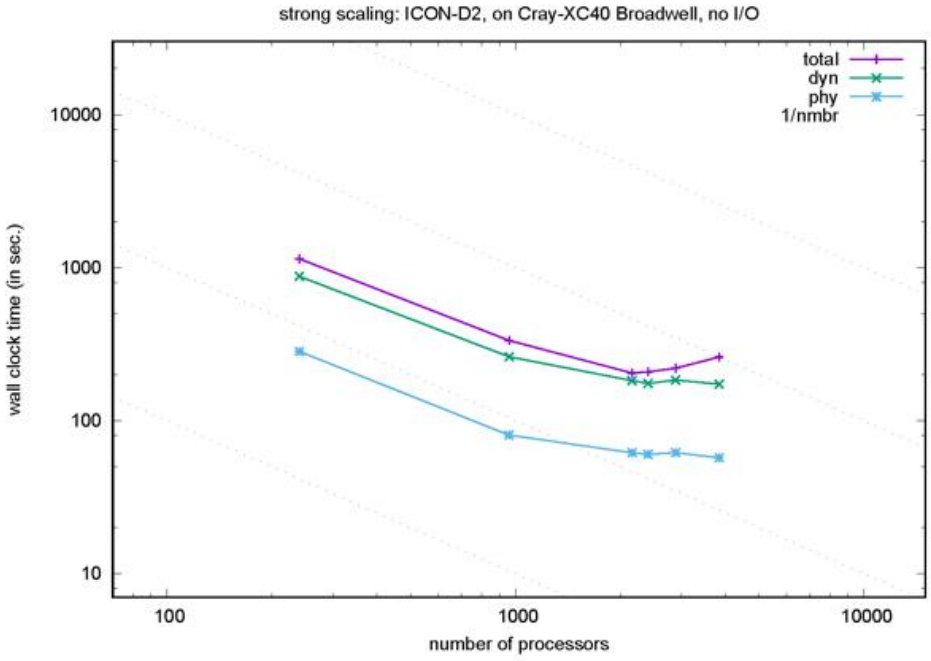


Figure 26: Strong scaling test for ICON with an ICON-D2 setup.

Table 2: List of requirements to the ICON model from climate modelers at DWD.

Issues	Status (around 2017)
Read in LBC Data from frame grid for ICON-LAM does not work yet with NCDF files.	Daniel Reinert and Günther Zängl were already informed.
After restarting, ICON still read the LBC data from the first month.	Already solved in new version.
ICON creates itself a symbolic link to the restart file.	This does not hurt. But just does not look nice and not necessary for us because we have different directories to store data and run the model. One can create the link by a run script and link to wherever
Need to decide a standard input data that iconremap can treat. All GCM data should be transformed to this format.	Task for CLM community.
Soil must be deep enough ($>$ 12 m) that the temperature at the bottom is constant throughout the year (should be the case in Terra).	Will be checked in our long simulation.
Less frequently updated SST.	(addendum: higher frequent updates are now implemented)

5 Application for special purposes (Climate, environmental appl.)

One task in the project was to identify possible obstacles for the use of ICON for other limited-area applications besides pure NWP. First, these are all kind of environmental simulations for several sort of pollutants like pollen, volcanic ash, and radioactive substances. Furthermore, the transport of aerosol or mineral dust in particular for the estimation of the mitigation of solar irradiation for renewable power generation is of interest. In the meanwhile the ART module is well established, so that the applicability of ICON for these purposes is out of question.

Another large application is regional climate simulation. During the project, mainly technical problems have been reported by the climate modelers listed in table 2 (reported by Christian Steger and Trang Van Pham (DWD)). These were mainly assessed as of minor priority, have already been solved in the meanwhile or probably can be solved with relatively low effort. In any case, no basic obstacle could be named for the application of ICON in this field.

6 Conclusions

To assess the ability of the dynamical core of ICON to be applicable for limited-area modeling and to possibly replace the COSMO model, a series of idealized test cases have been performed for both models. These test cases in particular are designed for small scale applications. It may be summarized that ICON delivers in most cases solutions that have similar or even slightly better quality (compared either to analytic solutions or at least to established reference solutions) as COSMO. The only exception is the Straka test case, where ICON delivers a slightly weaker solution; a fact that should be inspected further.

One main strength of ICON is its tolerance of much steeper mountains than COSMO without an additional orography smoothing. Furthermore, it is exactly mass-conserving both for the dry dynamical core and also for the tracers.

The scaling experiments show that ICON runs well on current parallel computers (at least CPU based ones) and its parallelization strategy and implementation is well suited for future massively parallel computers. In practical applications the wall-cock time of ICON is smaller than of COSMO. Remark: more recent results show also an efficient behavior of ICON on vector computers (here in particular on NEC SX Aurora). A GPU port, mainly done at MeteoSwiss, CSCS (Swiss National Supercomputing Centre) and at the DKRZ is widely advanced, too. This efficiency advantage of ICON towards COSMO should also be seen as an indicator, beyond this pure comparison of two particular models, that the split-explicit approach might be less superior to a pure 'single time step' approach than expected.

To summarize, from the viewpoint of the dynamical core, there is no visible obstacle for the replacement of the COSMO model by the ICON model.

References

Baldauf, M., 2008: A linear solution for flow over mountains and its comparison with the COSMO model. *COSMO-Newsletter*, **9**, 19–24, http://www.cosmo-model.org/content/model/documentation/newsLetters/.

Baldauf, M., 2010: Linear stability analysis of Runge-Kutta based partial time-splitting schemes for the Euler equations. *Mon. Wea. Rev.*, **138**, 4475–4496.

Baldauf, M., 2013: A new fast-waves solver for the Runge-Kutta dynamical core. Tech. Rep. 21, Consortium for Small-Scale Modelling (COSMO), 46 pp., http://www.cosmo-model.org/content/model/documentation/techReports/default.htm. doi:10.5676/DWD_pub/nwv/cosmo-tr_21.

Baldauf, M., 2019: Local time stepping for a mass-consistent and time-split advection scheme. *Quart. J. Roy. Met. Soc.*, **145**, 337–346.

Baldauf, M. and S. Brdar, 2013: An analytic solution for linear gravity waves in a channel as a test for numerical models using the non-hydrostatic, compressible Euler equations. *Quart. J. Royal Met. Soc.*, **139**, 1977–1989.

Baldauf, M., A. Seifert, J. Förstner, D. Majewski, M. Raschendorfer, and T. Reinhardt, 2011: Operational Convective-Scale Numerical Weather Prediction with the COSMO Model: Description and Sensitivities. *Monthly Weather Review*, **139**, 3887–3905.

Blahak, U., 2015: Simulating idealized cases with the COSMO-model. *COSMO*.

Bott, A., 1989: A Positive Definite Advection Scheme Obtained by Nonlinear Renormalization of the Advective Fluxes. *Mon. Wea. Rev.*, **117 (5)**, 1006–1015.

Doms, G. and M. Baldauf, 2018: *A Description of the Nonhydrostatic Regional COSMO-Model, Part I: Dynamics and Numerics, v5.05*. Offenbach, Germany, Deutscher Wetterdienst, doi:10.5676/DWD_pub/nwv/cosmo-doc_5.05_I.

Förstner, J., M. Baldauf, and A. Seifert, 2006: Courant Number Independent Advection of the Moisture Quantities for the LMK. *COSMO-Newsletter*, **6**, 51–64, http://www.cosmo-model.org/content/model/documentation/newsLetters/.

Klemp, J. B., J. Dudhia, and A. D. Hassiotis, 2008: An Upper Gravity-Wave Absorbing Layer for NWP Applications. *Mon. Wea. Rev.*, **136**, 3987–4004.

Kurowski, M., D. Wojcik, M. Ziemianski, B. Rosa, and Z. Piotrowski, 2016: Convection-Permitting Regional Weather Modeling with COSMO-EULAG: Compressible and Anelastic Solutions for a Typical Westerly Flow over the Alps. *Mon. Wea. Rev.*, **144**, 1961–1982.

Miura, H., 2007: An Upwind-Biased Conservative Advection Scheme for Spherical Hexagonal-Pentagonal Grids. *Mon. Wea. Rev.*, **135**, 4038–4044.

Schär, C., D. Leuenberger, O. Fuhrer, D. Lüthi, and C. Girard, 2002: A New Terrain-Following Vertical Coordinate Formulation for Atmospheric Prediction Models. *Mon. Wea. Rev.*, **130 (10)**, 2459–2480.

Skamarock, W. C. and J. B. Klemp, 1992: The stability of Time-Split Numerical methods for the Hydrostatic and the Nonhydrostatic Elastic Equations. *Mon. Wea. Rev.*, **120**, 2109–2127.

Skamarock, W. C. and J. B. Klemp, 1994: Efficiency and accuracy of the Klemp-Wilhelmson Time-Splitting scheme. *Mon. Wea. Rev.*, **122**, 2623–2630.

Smith, R. B., 1980: Linear theory of stratified hydrostatic flow past an isolated mountain. *Tellus*, **32**, 348–364.

Straka, J. M., R. B. Wilhelmson, L. J. Wicker, J. R. Anderson, and K. K. Droegemeier, 1993: Numerical solutions of a non-linear density current: a benchmark solution and comparisons. *Int. J. Num. Meth. Fluids*, **17**, 1–22.

Theis, S. and M. Baldauf, 2019: Validation in weather forecasting. *Computer Simulation Validation. Simulation Foundations, Methods and Applications*, C. Beisbart and N. J. Saam, Eds., Springer, Cham, Simulation Foundations, Methods and Applications, 711–736, doi:10.1007/978-3-319-70766-2_29, online ISBN: 978-3-319-70766-2, Print ISBN: 978-3-319-70765-5.

Weisman, M. L. and J. B. Klemp, 1982: The Dependence of Numerically Simulated Convective Storms on Vertical Wind Shear and Buoyancy. *Monthly Weather Review*, **110 (6)**, 504–520.

Wicker, L. J. and W. C. Skamarock, 2002: Time Splitting Methods for Elastic Models using Forward Time Schemes. *Mon. Wea. Rev.*, **130**, 2088–2097.

Zängl, G., 2012: Extending the Numerical Stability Limit of Terrain-Following Coordinate Models over Steep Slopes. *Mon. Wea. Rev.*, **140 (11)**, 3722–3733.

Zängl, G., L. Ganthner, G. Hartjenstein, and H. Noppel, 2004: Numerical errors above steep topography: A model intercomparison. *MetZ*, **13 (2)**, 69–76.

Zängl, G., D. Reinert, P. Ripodas, and M. Baldauf, 2015: The ICON (ICOsahedral Non-hydrostatic) modelling framework of DWD and MPI-M: Description of the non-hydrostatic dynamical core. *Quart. J. Royal Met. Soc.*, **141**, 563–579.

Ziemiański, M. Z., D. K. Wójcik, B. Rosa, and Z. P. Piotrowski, 2021: Compressible EULAG dynamical core in COSMO: convective-scale Alpine weather forecasts. *Mon. Wea. Rev.*, doi:10.1175/MWR-D-20-0317.1.

List of COSMO Newsletters and Technical Reports

(available for download from the COSMO Website: www.cosmo-model.org)

COSMO Newsletters

No. 1: February 2001.

No. 2: February 2002.

No. 3: February 2003.

No. 4: February 2004.

No. 5: April 2005.

No. 6: July 2006.

No. 7: April 2008; Proceedings from the 8th COSMO General Meeting in Bucharest, 2006.

No. 8: September 2008; Proceedings from the 9th COSMO General Meeting in Athens, 2007.

No. 9: December 2008.

No. 10: March 2010.

No. 11: April 2011.

No. 12: April 2012.

No. 13: April 2013.

No. 14: April 2014.

No. 15: July 2015.

No. 16: July 2016.

No. 17: July 2017.

No. 18: November 2018.

No. 19: October 2019.

No. 20: December 2020.

COSMO Technical Reports

No. 1: Dmitrii Mironov and Matthias Raschendorfer (2001):
Evaluation of Empirical Parameters of the New LM Surface-Layer Parameterization Scheme. Results from Numerical Experiments Including the Soil Moisture Analysis.
DOI: 10.5676/DWD_pub/nwv/cosmo-tr_1

No. 2: Reinhold Schrodin and Erdmann Heise (2001):
The Multi-Layer Version of the DWD Soil Model TERRA_LM.
DOI: 10.5676/DWD_pub/nwv/cosmo-tr_2

No. 3: Günther Doms (2001):
A Scheme for Monotonic Numerical Diffusion in the LM.
DOI: 10.5676/DWD_pub/nwv/cosmo-tr_3

No. 4: Hans-Joachim Herzog, Ursula Schubert, Gerd Vogel, Adelheid Fiedler and Roswitha Kirchner (2002):
LLM ¯ the High-Resolving Nonhydrostatic Simulation Model in the DWD-Project LITFASS. Part I: Modelling Technique and Simulation Method.
DOI: 10.5676/DWD_pub/nwv/cosmo-tr_4

No. 5: Jean-Marie Bettems (2002):
EUCOS Impact Study Using the Limited-Area Non-Hydrostatic NWP Model in Operational Use at MeteoSwiss.
DOI: 10.5676/DWD_pub/nwv/cosmo-tr_5

No. 6: Heinz-Werner Bitzer and Jürgen Steppeler (2004):
Documentation of the Z-Coordinate Dynamical Core of LM.
DOI: 10.5676/DWD_pub/nwv/cosmo-tr_6

No. 7: Hans-Joachim Herzog, Almut Gassmann (2005):
Lorenz- and Charney-Phillips vertical grid experimentation using a compressible nonhydrostatic toy-model relevant to the fast-mode part of the 'Lokal-Modell'.
DOI: 10.5676/DWD_pub/nwv/cosmo-tr_7

No. 8: Chiara Marsigli, Andrea Montani, Tiziana Paccagnella, Davide Sacchetti, André Walser, Marco Arpagaus, Thomas Schumann (2005):
Evaluation of the Performance of the COSMO-LEPS System.
DOI: 10.5676/DWD_pub/nwv/cosmo-tr_8

No. 9: Erdmann Heise, Bodo Ritter, Reinhold Schrodin (2006):
Operational Implementation of the Multilayer Soil Model.
DOI: 10.5676/DWD_pub/nwv/cosmo-tr_9

No. 10: M.D. Tsyrulnikov (2007):
Is the particle filtering approach appropriate for meso-scale data assimilation ?
DOI: 10.5676/DWD_pub/nwv/cosmo-tr_10

No. 11: Dmitrii V. Mironov (2008):
Parameterization of Lakes in Numerical Weather Prediction. Description of a Lake Model.
DOI: 10.5676/DWD_pub/nwv/cosmo-tr_11

No. 12: Adriano Raspanti (2009):
COSMO Priority Project "VERification System Unified Survey" (VERSUS): Final Report.
DOI: 10.5676/DWD_pub/nwv/cosmo-tr_12

No. 13: Chiara Marsigli (2009):
COSMO Priority Project "Short Range Ensemble Prediction System" (SREPS): Final Report.
DOI: 10.5676/DWD_pub/nwv/cosmo-tr_13

No. 14: Michael Baldauf (2009):
COSMO Priority Project "Further Developments of the Runge-Kutta Time Integration Scheme" (RK): Final Report.
DOI: 10.5676/DWD_pub/nwv/cosmo-tr_14

No. 15: Silke Dierer (2009):
COSMO Priority Project "Tackle deficiencies in quantitative precipitation forecast" (QPF): Final Report.
DOI: 10.5676/DWD_pub/nwv/cosmo-tr_15

No. 16: Pierre Eckert (2009):
COSMO Priority Project "INTERP": Final Report.
DOI: 10.5676/DWD_pub/nwv/cosmo-tr_16

No. 17: D. Leuenberger, M. Stoll and A. Roches (2010):
Description of some convective indices implemented in the COSMO model.
DOI: 10.5676/DWD_pub/nwv/cosmo-tr_17

No. 18: Daniel Leuenberger (2010):
Statistical analysis of high-resolution COSMO Ensemble forecasts in view of Data Assimilation.
DOI: 10.5676/DWD_pub/nwv/cosmo-tr_18

No. 19: A. Montani, D. Cesari, C. Marsigli, T. Paccagnella (2010):
Seven years of activity in the field of mesoscale ensemble forecasting by the COSMO–LEPS system: main achievements and open challenges.
DOI: 10.5676/DWD_pub/nwv/cosmo-tr_19

No. 20: A. Roches, O. Fuhrer (2012):
Tracer module in the COSMO model.
DOI: 10.5676/DWD_pub/nwv/cosmo-tr_20

No. 21: Michael Baldauf (2013):
A new fast-waves solver for the Runge-Kutta dynamical core.
DOI: 10.5676/DWD_pub/nwv/cosmo-tr_21

No. 22: C. Marsigli, T. Diomede, A. Montani, T. Paccagnella, P. Louka, F. Gofa, A. Corigliano (2013):
The CONSENS Priority Project.
DOI: 10.5676/DWD_pub/nwv/cosmo-tr_22

No. 23: M. Baldauf, O. Fuhrer, M. J. Kurowski, G. de Morsier, M. Müllner, Z. P. Piotrowski, B. Rosa, P. L. Vitagliano, D. Wójcik, M. Ziemiański (2013):
The COSMO Priority Project 'Conservative Dynamical Core' Final Report.
DOI: 10.5676/DWD_pub/nwv/cosmo-tr_23

No. 24: A. K. Miltenberger, A. Roches, S. Pfahl, H. Wernli (2014):
Online Trajectory Module in COSMO: a short user guide.
DOI: 10.5676/DWD_pub/nwv/cosmo-tr_24

No. 25: P. Khain, I. Carmona, A. Voudouri, E. Avgoustoglou, J.-M. Bettems, F. Grazzini (2015):
The Proof of the Parameters Calibration Method: CALMO Progress Report.
DOI: 10.5676/DWD_pub/nwv/cosmo-tr_25

No. 26: D. Mironov, E. Machulskaya, B. Szintai, M. Raschendorfer, V. Perov, M. Chumakov, E. Avgoustoglou (2015):
The COSMO Priority Project 'UTCS' Final Report.
DOI: 10.5676/DWD_pub/nwv/cosmo-tr_26

No. 27: J-M. Bettems (2015):
The COSMO Priority Project 'COLOBOC': Final Report.
DOI: 10.5676/DWD_pub/nwv/cosmo-tr_27

No. 28: Ulrich Blahak (2016):
RADAR_MIE_LM and RADAR_MIELIB - Calculation of Radar Reflectivity from Model Output.
DOI: 10.5676/DWD_pub/nwv/cosmo-tr_28

No. 29: M. Tsyrulnikov and D. Gayfulin (2016):
A Stochastic Pattern Generator for ensemble applications.
DOI: 10.5676/DWD_pub/nwv/cosmo-tr_29

No. 30: D. Mironov and E. Machulskaya (2017):
A Turbulence Kinetic Energy – Scalar Variance Turbulence Parameterization Scheme.
DOI: 10.5676/DWD_pub/nwv/cosmo-tr_30

No. 31: P. Khain, I. Carmona, A. Voudouri, E. Avgoustoglou, J.-M. Bettems, F. Grazzini, P. Kaufmann (2017):
CALMO - Progress Report.
DOI: 10.5676/DWD_pub/nwv/cosmo-tr_31

No. 32: A. Voudouri, P. Khain, I. Carmona, E. Avgoustoglou, J.M. Bettems, F. Grazzini, O. Bellprat, P. Kaufmann and E. Bucchignani (2017):
Calibration of COSMO Model, Priority Project CALMO Final report.
DOI: 10.5676/DWD_pub/nwv/cosmo-tr_32

No. 33: N. Vela (2017):
VAST 2.0 - User Manual.
DOI: 10.5676/DWD_pub/nwv/cosmo-tr_33

No. 34: C. Marsigli, D. Alferov, M. Arpagaus, E. Astakhova, R. Bonanno, G. Duniec, C. Gebhardt, W. Interewicz, N. Loglisci, A. Mazur, V. Maurer, A. Montani, A. Walser (2018):
COsmo Towards Ensembles at the Km-scale IN Our countries" (COTEKINO), Priority Project final report.
DOI: 10.5676/DWD_pub/nwv/cosmo-tr_34

No. 35: G. Rivin, I. Rozinkina, E. Astakhova, A. Montani, D. Alferov, M. Arpagaus, D. Blinov, A. Bundel, M. Chumakov, P. Eckert, A. Euripides, J. Förstner, J. Helmert, E. Kazakova, A. Kirsanov, V. Kopeikin, E. Kukanova, D. Majewski, C. Marsigli, G. de Morsier, A. Muravev, T. Paccagnella, U. Schättler, C. Schraff, M. Shatunova, A. Shcherbakov, P. Steiner, M. Zaichenko (2018):
The COSMO Priority Project CORSO Final Report.
DOI: 10.5676/DWD_pub/nwv/cosmo-tr_35

No. 36: A. Raspanti, A. Celozzi, A. Troisi, A. Vocino, R. Bove, F. Batignani (2018):
The COSMO Priority Project VERSUS2 Final Report.
DOI: 10.5676/DWD_pub/nwv/cosmo-tr_36

No. 37: A. Bundel, F. Gofa, D. Alferov, E. Astakhova, P. Baumann, D. Boucouvala, U. Damrath, P. Eckert, A. Kirsanov, X. Lapillonne, J. Linkowska, C. Marsigli, A. Montani, A. Muraviev, E. Oberto, M.S. Tesini, N. Vela, A. Wyszogrodzki, M. Zaichenko, A. Walser (2019):
The COSMO Priority Project INSPECT Final Report.
DOI: 10.5676/DWD_pub/nwv/cosmo-tr_37

No. 38: G. Rivin, I. Rozinkina, E. Astakhova, A. Montani, J-M. Bettems, D. Alferov, D. Blinov, P. Eckert, A. Euripides, J. Helmert, M.Shatunova (2019):
The COSMO Priority Project CORSO-A Final Report.
DOI: 10.5676/DWD_pub/nwv/cosmo-tr_38

No. 39: C. Marsigli, D. Alferov, E. Astakhova, G. Duniec, D. Gayfulin, C. Gebhardt, W. Interewicz, N. Loglisci, F. Marcucci, A. Mazur, A. Montani, M. Tsyrulnikov, A. Walser (2019):
Studying perturbations for the representation of modeling uncertainties in Ensemble development (SPRED Priority Project): Final Report.
DOI: 10.5676/DWD_pub/nwv/cosmo-tr_39

No. 40: E. Bucchignani, P. Mercogliano, V. Garbero, M. Milelli, M. Varentsov, I. Rozinkina, G. Rivin, D. Blinov, A. Kirsanov, H. Wouters, J.-P. Schulz, U. Schättler (2019):
Analysis and Evaluation of TERRA_URB Scheme: PT AEVUS Final Report.
DOI: 10.5676/DWD_pub/nwv/cosmo-tr_40

No. 41: X. Lapillonne, O. Fuhrer (2020):
Performance On Massively Parallel Architectures (POMPA): Final report.
DOI: 10.5676/DWD_pub/nwv/cosmo-tr_41

No. 42: E. Avgoustoglou, A. Voudouri, I Carmona, E. Bucchignani, Y. Levy, J. -M. Bettems (2020):
A methodology towards the hierarchy of COSMO parameter calibration tests via the domain sensitivity over the Mediterranean area.
DOI: 10.5676/DWD_pub/nwv/cosmo-tr_42

No. 43: H. Muskatel, U. Blahak, P. Khain, A. Shtivelman, M. Raschendorfer, M. Kohler, D. Rieger, O. Fuhrer, X. Lapillonne, G. Rivin, N. Chubarova, M. Shatunova, A. Poliukhov, A. Kirsanov, T. Andreadis, S. Gruber (2021):
The COSMO Priority Project $T^2(RC)^2$: Testing and Tuning of Revised Cloud Radiation Coupling, Final Report
DOI: 10.5676/DWD_pub/nwv/cosmo-tr_43

COSMO Technical Reports

Issues of the COSMO Technical Reports series are published by the *COnsortium for Small-scale MOdelling* at non-regular intervals. COSMO is a European group for numerical weather prediction with participating meteorological services from Germany (DWD, AWGeophys), Greece (HNMS), Italy (USAM, ARPA-SIMC, ARPA Piemonte), Switzerland (MeteoSwiss), Poland (IMGW), Romania (NMA) and Russia (RHM). The general goal is to develop, improve and maintain a non-hydrostatic limited area modelling system to be used for both operational and research applications by the members of COSMO. This system is initially based on the COSMO-Model (previously known as LM) of DWD with its corresponding data assimilation system.

The Technical Reports are intended

- for scientific contributions and a documentation of research activities,
- to present and discuss results obtained from the model system,
- to present and discuss verification results and interpretation methods,
- for a documentation of technical changes to the model system,
- to give an overview of new components of the model system.

The purpose of these reports is to communicate results, changes and progress related to the LM model system relatively fast within the COSMO consortium, and also to inform other NWP groups on our current research activities. In this way the discussion on a specific topic can be stimulated at an early stage. In order to publish a report very soon after the completion of the manuscript, we have decided to omit a thorough reviewing procedure and only a rough check is done by the editors and a third reviewer. We apologize for typographical and other errors or inconsistencies which may still be present.

At present, the Technical Reports are available for download from the COSMO web site (www.cosmo-model.org). If required, the member meteorological centres can produce hard-copies by their own for distribution within their service. All members of the consortium will be informed about new issues by email.

For any comments and questions, please contact the editor:

Massimo Milelli
Massimo.Milelli@arpa.piemonte.it

Consortium

for

Small-Scale Modelling

Technical Report No. 23

The COSMO Priority Project 'Conservative Dynamical Core' Final Report

October 2013

DOI: 10.5676/DWD_pub/nwv/cosmo-tr_23

Deutscher Wetterdienst
MeteoSwiss
Ufficio Generale Spazio Aereo e Meteorologia
ΕΘΝΙΚΗ ΜΕΤΕΩΡΟΛΟΓΙΚΗ ΥΠΗΡΕΣΙΑ
Instytucie Meteorogii i Gospodarki Wodnej
Administratia Nationala de Meteorologie
ROSHYDROMET
Agenzia Regionale per la Protezione Ambientale del Piemonte
Agenzia Regionale per la Protezione Ambientale dell'Emilia-Romagna
Centro Italiano Ricerche Aerospaziali
Amt für GeoInformationswesen der Bundeswehr



www.cosmo-model.org

Editor: Massimo Milelli, ARPA Piemonte

The COSMO Priority Project 'Conservative Dynamical Core' Final Report

M. Baldauf *, O. Fuhrer, M. J. Kurowski, G. de Morsier, M. Müllner, Z. P. Piotrowski, B. Rosa, P. L. Vitagliano, D. Wójcik, M. Ziemiański

* corresponding author:
Dr. Michael Baldauf
Deutscher Wetterdienst
Frankfurter Str. 135
63067 Offenbach am Main
Germany

Contents

1 Introduction **5**

2 Dry benchmark experiments with the anelastic EULAG model **7**

2.1 Introduction 7

2.2 Cold density current test 7

2.2.1 Experiment setup 7

2.2.2 Results 8

2.3 Bubble convection test 12

2.4 Numerical modeling of inertia-gravity waves 12

2.4.1 Experiment setup 13

2.4.2 Short channel 14

2.4.3 Long channel 15

2.5 Modeling of mountain gravity waves 15

2.5.1 Experiment setup 17

2.5.2 Linear hydrostatic regime 17

2.5.3 Linear nonhydrostatic regime 17

2.5.4 Nonlinear hydrostatic regime 18

2.5.5 Nonlinear nonhydrostatic regime 19

2.6 Summary and conclusions 20

3 Moist benchmark experiments with the anelastic EULAG model **23**

3.1 Introduction 23

3.2 General model setup 23

3.3 Klemp and Wilhelmson (1978) experiment 24

3.3.1 Setup details 24

3.3.2 Atmosphere-at-rest case 25

3.3.3 Shear flow case 26

3.3.4 Veering wind case 30

3.3.5 Sensitivity tests 31

3.4 Weisman and Klemp (1982) experiment 32

3.4.1 Setup details 32

3.4.2 Shear flow case 32

3.5 Summary and further development 38

4 Semi-realistic flow over the Alps with the anelastic EULAG model 40

4.1 The experiment setup 40

4.2 Results 42

4.3 Summary and conclusions 52

5 Semi-realistic flow over the Alps with the COSMO-EULAG model 56

5.1 Introduction 56

5.2 The COSMO-EULAG prototype 56

5.3 The experiment setup 57

5.4 Results 59

5.5 Summary and conclusions 66

6 MPDATA as an alternative tracer advection scheme 69

6.1 Introduction 69

6.2 Advection of prognostic fields 69

6.3 Positive definite advection 70

6.4 MPDATA in 3-dimensions 70

6.5 Non-oscillating option 73

6.6 Illustration in a one dimensional case 75

6.7 Advection tests 77

6.8 Deformation flow tests 81

6.9 Conclusions 82

7 Normal mode analysis of anelastic and compressible equation sets 86

7.1 Introduction 86

7.2 Derivation of the dispersion relations 86

7.3 Discussion of the results 89

7.4 Summary 94

8 The finite volume implicit solver CONSOL 96

8.1 Introduction 96

8.2 Mathematical formulation 96

8.3 Finite volume scheme and time integration 98

8.4 Atmosphere at rest 99

8.5 Pressure gradient correction 103

8.6 Gravity wave 104

8.7 Density current 105
8.8 Advection 106
8.9 Hydrostatic mountain flow 107
8.10 Conclusions 108
8.11 Implementation of a time integration procedure based upon dual time stepping in COSMO 108

9 Acknowledgement **113**

1 Introduction

In 2008, the COSMO steering committee (STC) established a new Priority Project named 'Conservative Dynamical Core' (CDC). The motivation for such a project stems from the fact that the three currently available dynamical cores of COSMO (called 'leapfrog', 'Runge-Kutta' and 'semi-implicit') don't have any conservation properties concerning the dynamical variables mass, energy or momentum. However, conservation of these variables is one of the fundamental guiding principles in the development of dynamical cores in many branches of fluid dynamics. The aim of the project was to investigate possible candidates for a new dynamical core with conservation properties (at least mass conservation) and to deliver prototypes that are already implemented into the COSMO model.

Considering the different proposed dynamical core formulations of the first draft project plan, the STC decided to concentrate the project on two branches: on the one hand to the EULAG model ('anelastic branch'), which is already well established in the fluid dynamics community, and on the other hand to the CONSOL solver ('compressible branch'), which stems from the aerodynamics community. EULAG is based on an anelastic approximation of the Euler equations. It uses a finite volume approach, which per se guarantees certain conservation properties. CONSOL is based on the compressible Euler equations and also uses a finite volume approach. Both solvers use implicit time integration methods: CONSOL for the whole dynamical core, EULAG at least for the fast, quasi-linear processes. This solution strategy in general helps in solving another issue which should be tackled by the project, namely to improve the ability of the dynamical core to be stable in steep terrain. This requirement is caused by the future applications of COSMO which will cover more and more horizontal resolutions of 1 km and less, where one can expect increasingly steeper slopes.

During the project, the properties of the two proposed solvers should be inspected. For this purpose, a 'decision tree' was defined at the beginning starting from a set of well accepted idealized tests until more complex semi-realistic tests which should be simulated by the prototypes.

Therefore, the first 2 papers (sections 2 and 3) deal with idealized tests consisting of stationary flow over mountains, expansion of linear gravity waves, strongly nonlinear and unstationary falling bubbles, and convection containing cloud microphysics, simulated with the EULAG model. The ability of the EULAG dynamical core to simulate meteorologically relevant flow fields is demonstrated in section 4. Finally the functionality of the COSMO-prototype with the implemented EULAG dynamical core is demonstrated with semi-realistic model setups in section 5.

Whereas the EULAG model has been used for some meteorological simulations before, this was not the case for CONSOL, for which a great challenge was the introduction of the buoyancy term into the existing pure hydrodynamical solver. Therefore, only a reduced test set could be inspected with this solver. Section 8 describes the solver and the idealized tests performed with it.

Apart from the pure dynamical core (the solver of the EULER equations), tracer advection is an important aspect of the numerics of a model, too. Section 6 investigates the basic advection scheme of EULAG, the MPDATA, for its usability as an alternative tracer transport scheme in COSMO.

The accompanying section 7 compares wave expansion properties of the several anelastic approximations with the compressible equations and the basic divergence damping mechanism used in the current COSMO dynamical core.

After a lifetime of about four years (end of 2012), the overall status of the project is an available prototype of COSMO-EULAG, ready for further testing in real case applications. Due to constraints in man power resources, the CONSOL solver couldn't achieve a similar stage. Therefore, the COSMO Science Management Committee and STC decided to finish the CDC project and to establish a folluw-up project, which concentrates on the 'COSMO-EULAG operationalization' (CELO).

M. Baldauf
Deutscher Wetterdienst

2 Dry benchmark experiments with the anelastic EULAG model

Bogdan Rosa, Marcin J. Kurowski, Michał Z. Ziemiański

Institute of Meteorology and Water Management - National Research Institute, Poland

2.1 Introduction

This chapter describes results from dry idealized benchmark experiments performed with the anelastic model EULAG. The goal of the study is to test the feasibility of an anelastic approach for very high-resolution (kilometer and sub-kilometer) operational numerical weather prediction. The choice of tests draws on experiences with analogous problems Skamarock et al. (2004) and is based on widely accepted benchmark solutions. The experiments were performed in the framework of the COSMO Priority Project Conservative Dynamical Core.

The first experiment concerns the evolution of a two-dimensional density current induced by a large bubble of cold air descending to the ground Straka et al. (1993). The second experiment considers two interacting bubbles with different temperatures Robert (1993). Both problems are strongly non-linear and do not have analytical solutions. The third test examines the propagation of inertia-gravity waves in a periodic channel (Skamarock and Klemp, 1994) of different length. The last problem regards the evolution of gravity waves generated by a flow over a single Agnesi mountain (Bonaventura, 2000). Several flow regimes (linear / nonlinear hydrostatic and linear / nonlinear non-hydrostatic), are examined. The results are validated against the reference solutions obtained using compressible models.

2.2 Cold density current test

The simulations of a cold density current are based on a setup described in Straka et al. (1993). This experiment is one of the well-known benchmarks often employed for testing numerical models.

2.2.1 Experiment setup

As defined in Straka et al. (1993), the two-dimensional density current is initiated as a cold bubble of air that subsequently descends to the ground in a homogenous and isentropic atmosphere. After reaching the ground, the bubble spreads laterally and rotors induced by a Kelvin-Helmholtz instability form on its upper boundary. The basic set of parameters and configuration of the model are as in Straka et al. (1993). This involves constant potential temperature of the basic hydrostatic state $\theta_0 = 300$ K and diffusion coefficient $K = 75$ m^{2}s^{-1}. The appropriate environmental density profile is given by the Ogura-Philips formula Ogura and Phillips (1962). The bubble is located at the center of the model domain which extends from $x = -25.6$ km to $x = 25.6$ km. The vertical domain size is $z = 6.4$ km. In the original experiment Straka et al. (1993) the lateral boundary conditions were set as $u = w_x = p_x = \theta_x = 0$ and similarly the vertical ones, namely $w = u_z = p_z = \theta_z = 0$ Here, the lateral boundary conditions are periodic. A free-slip and rigid boundary conditions are imposed at the ground and at the top of the computational domain, respectively. The numerical calculations in Straka et al. (1993) exploit the symmetry of the problem about the vertical line $x = 0$, which is not the case for the current simulations.

2.2.2 Results

The study, following Straka et al. (1993), is focused on the first 15 minutes of the evolution of the density current. Time evolution of potential temperature field and a process of formation of the vortical structures is presented in Rosa et al. (2011). Because the problem is symmetric with respect to the vertical axis it is sufficient to visualize and analyze evolution in only half of the domain. The symmetry of the solution was monitored during the experiment but no significant deviations have been observed. In order to verify the grid-convergence of the EULAG solution, a set of experiments employing various spatial resolutions was performed. Four different spatial resolutions were used, with the grid distances of 200, 100, 50 and 25 m, the same in horizontal and vertical directions. The snapshots of the potential temperature field after 15 minutes of evolution, obtained with different grid resolutions are presented in Fig. 1.

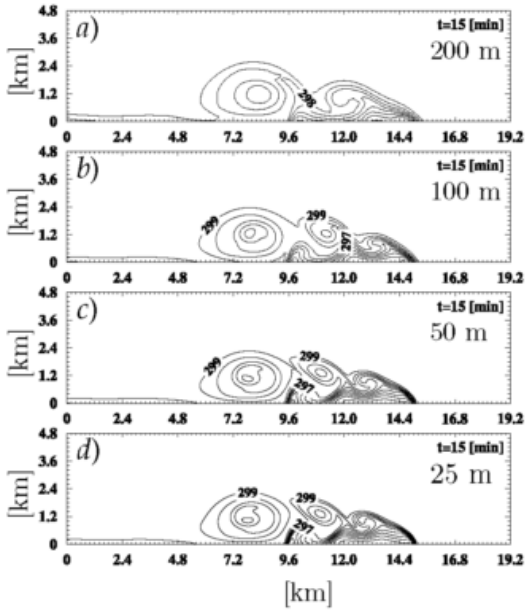


Figure 1: Plots of the potential temperature θ at 15 min for four different grid resolutions a) 200 m, b) 100 m, c) 50 m, d) 25 m computed using the EULAG model. Contour interval of the isentropes is 1 K.

It is seen, that there are no significant differences between potential temperature distribution obtained at resolutions between 25 m and 100 m. They all allow to identify the basic three-rotor structure of the flow, with a very small differences between the solutions obtained with 25 and 50 m resolutions. It shows that the EULAG simulation is grid-convergent and the simulation with the spatial resolution of 25 m can be regarded as the reference one, sufficiently resolving all scales of the flow, as is the case for the reference solution of Straka et al. (1993) employing also the grid size of 25 m.

Apparently, for the lowest grid resolution, applied (200 m), the flow is underresolved as after 15 minutes of the evolution only two well developed rotors are visible. This is similar to Straka et al. (1993) where 100 m spatial resolution was necessary to start capturing the three-rotor structure. On the other hand, solution provided by EULAG at 200 m has no numerical noise on the contrary to respective solution from Straka et al. (1993). Such robustness of the model is advantageous in NWP applications, where underresolved flow structures are unavoidable.

The quantitative comparison of the results of the EULAG simulation with the reference results from Straka et al. (1993) are presented in Table 1. They concern extreme values of

Table 1: Comparison of maxima and minima of p'-pressure perturbation, θ'-potential temperature perturbation, u-horizontal component of velocity and w-vertical component of velocity at 900 s for EULAG and Straka et al. (1993): REFC - the compressible model using unstaggered grid (resolution 25 m), REFS - the compressible model using a staggered grid (resolution 25 m), REFQ - the quasi-compressible model with unstaggered grid (resolution 25 m), for EULAG the grid size employed is shown. In the last row, location of the density current front (the $\theta' = -1^oC$ contour) from the EULAG simulations performed at four different grid resolution is given. REFC, REFS and REFQ values taken from Straka et al. (1993).

				EULAG			
Variable	REFC	REFS	REFQ	25 [m]	50 [m]	100 [m]	200 [m]
$p'_{max}(mb)$	2.87	2.49	1.74	1.67	1.66	1.47	1.49
$p'_{min}(mb)$	-5.14	-5.55	-5.21	-5.40	-5.34	-5.18	-5.04
$\theta'_{max}(K)$	0.00	0.00	0.00	0.00	0.00	0.00	0.00
$\theta'_{min}(K)$	-9.77	-9.77	-10.00	-9.96	-9.52	-9.24	-8.26
$u_{max}(m/s)$	36.46	35.02	34.72	35.06	35.26	35.26	33.48
$u_{min}(m/s)$	-15.19	-16.32	-15.31	-15.29	-15.11	-14.60	-13.68
$w_{max}(m/s)$	12.93	13.28	13.04	13.07	12.96	12.56	14.04
$w_{min}(m/s)$	-15.95	-16.11	-16.89	-15.94	-15.78	-15.41	-15.14
Front location (km) after 15 min	-	-	-	15.16	15.17	15.26	15.55

pressure perturbation, potential temperature perturbation and both components of velocity, after 15 minutes of the flow evolution. The names of the reference models presented in the current paper are consistent with the original notation used in Straka et al. (1993). The reference model simulations from Straka et al. (1993) are: compressible with unstaggered grid (REFC), compressible with staggered C-grid (REFS) and quasi-compressible with unstaggered grid (REFQ), each operating at 25 m resolution. EULAG results are presented for grid size ranging from 200 m to 25 m.

For most of the parameters, the EULAG simulation with 25 m resolution gives their values inside the interval defined by the values obtained with the reference compressible simulations employing staggered or unstaggered grid (it concerns minimum pressure perturbation (p), minimum and maximum wind (u), maximum vertical velocity (w); minimum (w) differs from the reference value from Straka by 0.01 m/s). The difference of the maximum potential temperature perturbation between EULAG and the reference compressible model from Straka et al. (1993) Straka is very small (in the range of 2%). The largest difference between compressible and EULAG solution concerns the maximum pressure perturbation being in the range of 1.2 hPa. To some degree it can result from the anelastic approximation of EULAG. On the other hand, the difference between the staggered and unstaggered compressible simulation reaches about 0.4 hPa.

Another quantitative analysis of model accuracy is based on comparison of the location of a cold front perturbation (after 15 minutes evolution of the current). A front location is defined as the place near the edge of the current where the perturbation potential temperature at the ground reaches 1 K. It is represented by the value of the x-coordinate at the location. In Fig. 2a, a front location from EULAG simulations are compared with the results of Straka et al. Straka et al. (1993). The reference data are taken from Table IV of Straka et al. (1993) and concern the simulations performed with the resolution of 200 m, except the results of fully compressible and quasi-compressible models REFC25, REFQ25,

computed with the grid size of 25 m. The EULAG results are presented for four different grid resolutions and are labeled as follows: 200 m – EULAG200, 100 m – EULAG100, 50 m – EULAG50 and 25 m – EULAG25. Additionally, the extreme values of potential temperature perturbation are plotted in Figs. 2b and 2c, for its minimum and maximum values, respectively. The differences between the solutions of different models, illustrated in Fig. 2,

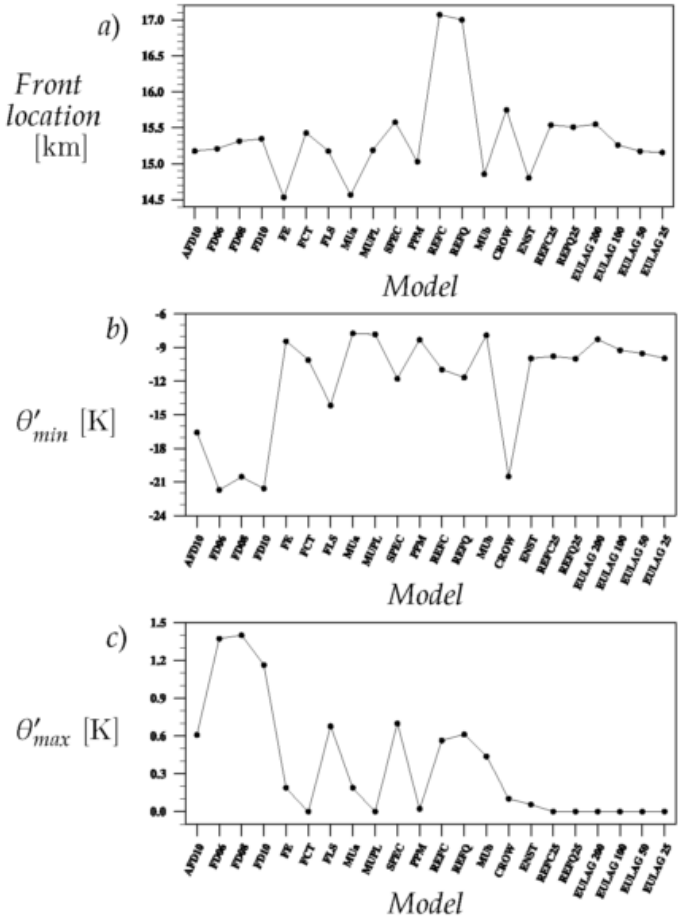


Figure 2: Quantitative comparison of front location and extreme values of potential temperature perturbation at t =15 min. Names of the models corresponds to acronyms used by Straka et al. (1993).

result both from differences in their analytical formulations and in their numerical design. However, analysis of Fig. 2a, showing the cold front location, leads to a general conclusion, that the differences resulting from analytical formulations of the models (compressible, anelastic, quasi-compressible) influence the solutions much less than the differences in the numerical schemes, employed. Note, that the majority of the models calculated with 200 m resolution (of all three analytical types, considered, including EULAG) give similar results in the range 14.5 km to 15.5 km, while the two outliers (giving very similar results of about 17.0 km) result from analytically differing compressible and quasi-compressible models. The detailed comparison of the simulations employing 200 m resolution with the reference, grid-convergent solution REFC25 (employing 25 m resolution and representing the 'true' value of about 15.5 km), confirms the above. Front positions similar to the reference one were achieved by both compressible (FCT) and anelastic models (both SPEC and EULAG). On the other hand, the results of the compressible model REFC and of the quasi-compressible model REFQ, calculated with 200 m resolution, differ significantly from the reference result. For both models, a relatively large error was a result of the under-resolving setup. This is not

the case for EULAG, as the difference between the solutions obtained with the 200 m and 25 m resolutions is relatively small. It shows reliable numerical properties of the model and confirms a grid-convergence of the solution that is very close to the reference compressible result.

The analysis of Fig. 2b, showing the minimum potential temperature perturbation after 15 minutes of evolution, leads to a similar conclusion. The majority of models using different analytical formulations give similar results being in the range of -14 K to -8 K (in a general agreement with the reference solution of -9.77 K). There are also outliers, resulting from quasi-compressible models, with much smaller values of the parameter. However, as not all quasi-compressible models are outliers, such a difference is a consequence of the numerics rather than of the analytical formulation. It is worth noting, also, that the outliers give reasonably good solutions for the front locations. This shows that the model comparison should not be limited to a single parameter only. Concerning EULAG simulations we observe both a good agreement with the reference solution from Straka et al. (1993) (-9.96 K for EULAG) and a grid-convergence to the EULAG reference solution employing 25 m grid size (see Tab. 1).

The analysis of Fig. 2c, showing the maximum potential temperature perturbation, allows for another quantitative comparison of the models. For this parameter the correct solution is known, as due to the adiabaticity of the process the actual value of the parameter is zero. Note, that the majority of the simulations performed with 200 m resolution gives incorrect results, including the compressible REFC model. However, as discussed above, these models give basically credible results for the front location and minimum θ'. The maximum potential temperature perturbation was correctly reproduced only by EULAG (anelastic), FCT (compressible), MUPL (quasi-compressible high-order accurate) and PPM (compressible high-order accurate).

The above analysis leads to the conclusion that for the problem at hand, the analytical formulation of the model equations does not have a significant impact on the simulation results, on the contrary to the numerics. The anelastic approximation allows for a correct representation of the dynamics of the system, provided the appropriate numerical design of the model, as is the case for EULAG. This result is in a general agreement with the analysis by Cullen et al. (2000) of the simulations of realistic mesoscale flow over the Scandinavian topography.

Optimal size of a time step for model integration is of great importance as it may significantly affect computational efficiency. The EULAG solutions presented above were obtained employing the same time step size as in Straka et al. (1993), i.e. 0.125 s. Additionally, several experiments with time steps increased by a factor of 2 up to 8 were performed. The tests were conducted at 100 m resolution and the results are presented in Rosa et al. (2011) Qualitative comparison of potential temperature field between solutions obtained for the original time step and the one being 8 times greater does not reveal any significant differences Rosa et al. (2011). A quantitative comparison in terms of a cold front location is presented in Table 2. The differences between the simulations for Courant numbers ranging from 0.045 to 0.36 are smaller than the grid spacing and the maximum relative difference between the solutions does not exceed 0.2 %. The presented results confirm that EULAG is not sensitive to such an increase of the Courant number.

Table 2: Front location at t=15 min and Courant number (CFL) for different time steps. Resolution is fixed at 100 m.

Time step size	CFL ($V_{max} = 36m/s$)	Front location [m]
$dt_{Straka} = 0.125\ s$	0.045	15279
$2dt_{Straka} = 0.25\ s$	0.09	15276
$4dt_{Straka} = 0.5\ s$	0.18	15269
$8dt_{Straka} = 1\ s$	0.36	15260

2.3 Bubble convection test

The goal of the second experiment is to test the feasibility of the anelastic approach for modeling a system of two interacting density currents (warm and cold). Configuration of the experiment follows the setup proposed originally by Robert (1993). The original experiment was performed employing fully compressible model, defining a suitable benchmark for the EULAG anelastic solution.

In the experiment the atmosphere is isentropic, thus the potential temperature of the reference state is $\theta = 300$ K. The reference profile of density for the EULAG simulations is the same as used for the cold density current (Straka test). Moist processes such as condensation, evaporation or rain formation are not considered. The initial conditions are set similarly to the Robert's experiment Robert (1993). The two bubbles are defined as perturbations of potential temperature with a Gaussian profile. The maximum values of temperature perturbation are 0.5 K for the warm bubble and -0.15 K for the cold one. Domain covers an area of 1 km $\times$ 1 km. Simulations are performed at three different resolutions 16×16, 8×8 and 4×4 m^2. Free-slip, rigid boundary condition are imposed on each side of the computational domain. The time step is set to $\Delta t = 1$ s. Pure Eulerian set of governing equations is used without any sub-grid scale model for viscosity. There is no external flow so that dynamics is governed only by density currents.

Figure 3 presents results of the EULAG simulation performed at the resolution 8×8 m^2, as results employing two other resolutions do not reveal substantial differences, during the 10 minutes of simulations. Robert (1993) performed the original experiment at the resolutions of 10×10 and 5×5 m^2. Comparing Fig. 3 with the benchmark results from Robert (1993) (Figs. 8 and 9 therein) we conclude that the differences between fully compressible and anelastic models are visually hardly to notice, which confirms the EULAG abilities to correctly represent the complicated and highly nonlinear processes.

2.4 Numerical modeling of inertia-gravity waves

In this section we demonstrate EULAG capabilities for simulating two-dimensional inertia-gravity waves. The waves are excited in air flowing through a long, periodic channel via an initial perturbation of potential temperature. The experiment was proposed by Skamarock and Klemp (1994) and is widely used for testing numerical schemes of the meteorological models.

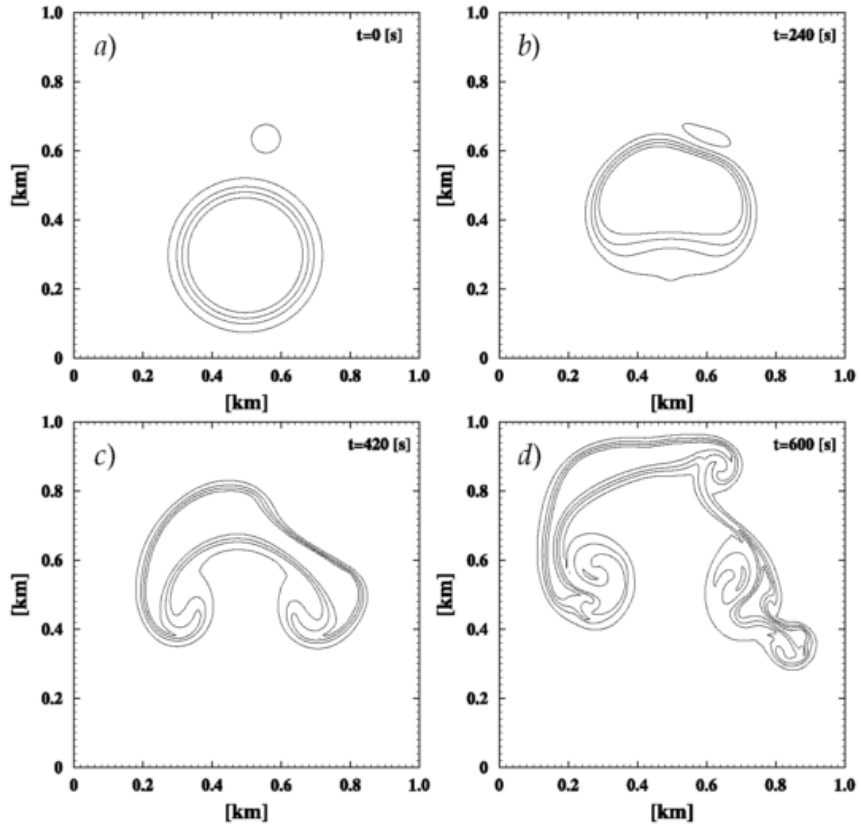


Figure 3: Time evolution of potential temperature perturbation θ' at $t = 0, 240, 420$ and 600 s. The initial distribution is depicted in panel *a*. The flow is induced by a rising large warm bubble and a descending small cold bubble. The asymmetry results from initial horizontal displacement between centers of the two bubbles.

2.4.1 Experiment setup

The computational domain is a periodic flat channel with solid, free-slip upper and lower boundaries. The simulations are performed for two different lengths of the channel, namely 300 km and 6000 km, and the same domain height of 10 km. The atmosphere inside the channel is uniformly stratified with a Brunt-Väisälä frequency equal to 0.01 s^{-1}. Constant horizontal ambient flow at an inlet is set to 20 m/s. The spatial distribution of the potential temperature perturbation, which leads to excitation of the gravity waves is defined as

$$\theta'(x, z, t = 0) = \Delta\theta_0 \frac{sin(\pi z/H)}{1 + (x - x_c)^2 / a^2}, \tag{1}$$

where $H = 10$ km is a domain height and $\Delta\theta_0 = 10^{-2}$ K is small amplitude of initial perturbation. The center of the initial perturbation x_c depends on the length of the channel and is 100 km for the short (300 km) and 2000 km for the long (6000 km) one.The half-width of the initial perturbation a also depends on the domain length and is $a = 5$ km and 100 km for the short and the long channel respectively. For the short channel, the resolution of computational grid in horizontal and vertical direction is the same. Simulation in a long channel is performed on a grid with an aspect ratio $\Delta x/\Delta z = 20$. Coriolis force is considered in both simulations, but its significant contribution to the flow dynamics is observed only for the long channel. Similarly to the previous experiments, there is no surface friction nor viscosity. More details about the experiment setup can be found in Skamarock and Klemp (1994).

2.4.2 Short channel

First, we analyze EULAG results for simulations performed for the short channel and the Boussinesq set of governing equations. In order to test the grid convergence of the solution, three different grid resolutions, namely $\Delta x = \Delta z = 1$ km, 0.5 km and 0.25 km are used. Figure 4 compares the perturbation of potential temperature at t = 50 min for the analytical solution (*a*) with numerical results ($b - d$), computed at the three grid resolutions. It is seen, that the numerical solutions converge to the analytical one with decreasing grid sizes.

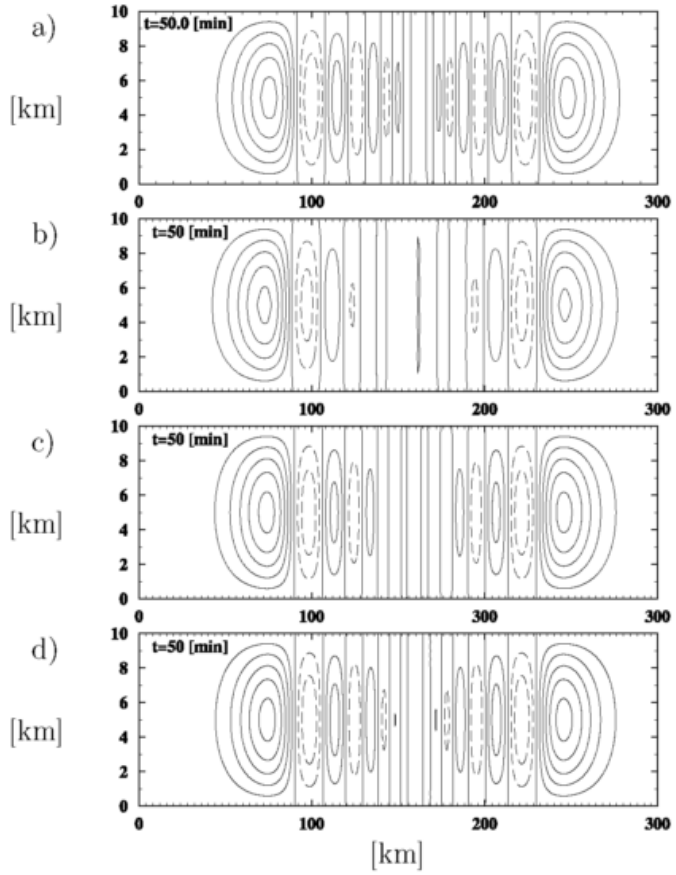


Figure 4: Spatial distribution of the potential temperature perturbation θ' after $t = 50$ min plotted (using contour values between −0.0015 K and 0.003 K) with a contour interval of 0.0005 K. Comparison of analytical solution *a*), with numerical solutions based on Boussinesq approximation computed using three different grid resolutions *b*) $\Delta x = \Delta z = 1$ km, *c*) $\Delta x = \Delta z = 0.5$ km, *d*) $\Delta x = \Delta z = 0.25$ km; negative values dashed.

In the original numerical experiment by Skamarock and Klemp (1994), the grid size was fixed to $\Delta x = \Delta z = 1$ km. Our result at this resolution (Fig. 4c) is very similar to that benchmark (see their Fig. 1c). Nevertheless, such grid size still does not allow to fully resolve the flow, which motivated us to apply higher resolutions, as described above.

Additionally, Fig. 5 compares the analytical solution for the potential temperature perturbation at constant height of 5 km above the surface (red line), with the EULAG results at three grid sizes, employed (black lines). Although small differences between numerical and analytical solutions are noticeable, the convergence to the analytical one is clearly visible. As the resolution of computational grid increases, the differences between numerical and analytical solutions diminish quickly, except the most central part of the wave-train, where 0.25 km grid size still underresolves the flow.

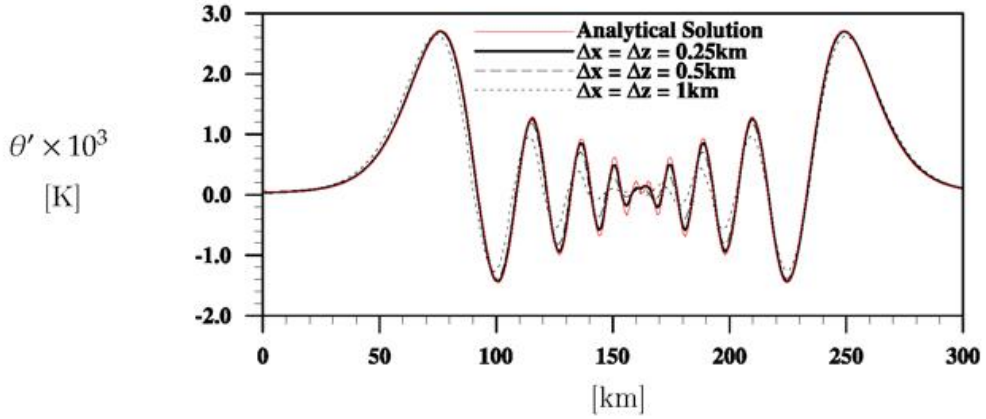


Figure 5: Profiles of potential temperature perturbation θ' along 5000 m height for the analytical solution and three different grid resolutions presented in Fig. 4.

2.4.3 Long channel

For the experiment involving 6000 km domain we used longer time step $t = 200$ s (previously 1 s), longer simulation time equal 1000 min, and different initial location of temperature perturbation ($x_c = 2000$ km). The computational grid has the same number of nodes in every direction, what implies a relatively large aspect ratio $\Delta x/\Delta z = 20$. As discussed in Skamarock and Klemp (1994), simulating atmospheric flows on grids with such high aspect ratio could be challenging for compressible models based on explicit numerical schemes. For such models, vertically propagating acoustic modes are disruptive for the slower modes of physical interest. Here, we intend to show that the numerics of EULAG provide a stable and accurate solution.

Figure 6 presents a comparison between the analytical and EULAG's numerical solutions for the potential temperature perturbation at 1000 min computed on grids with sizes of (20 km × 1 km, 10 km × 0.5 km and 5 km × 0.25 km), in horizontal and vertical directions, respectively. For different resolutions, the general pattern is similar but some differences in temperature gradients on the lateral sides of the perturbation are noticeable. With increasing resolution, the differences between the analytical and numerical solutions diminish significantly and we can conclude that the EULAG numerical solution is grid-convergent to the analytical formula. Similar to the short channel experiment, the highest resolution employed locally underresolves the potential temperature distribution, this time at the sides of the wave-train.

It is also interesting to analyze the grid convergence more quantitatively. Figure 7 presents the distribution of the potential temperature perturbation along the horizontal line at 5 km height. It confirms the grid-convergence of the numerical solutions, showing also that the largest differences between the analytic and numerical solutions can be found in the regions of high horizontal gradients of θ'.

Additional results from EULAG simulations performed using linearized version of the governing equations and pseudo-incompressible system of Durran (1989) one can find in Rosa et al. (2011).

2.5 Modeling of mountain gravity waves

The aim of that class of experiments is a comparison of the anelastic EULAG simulations of mountain flows with results of compressible models by Bonaventura (2000) and Pinty et al.

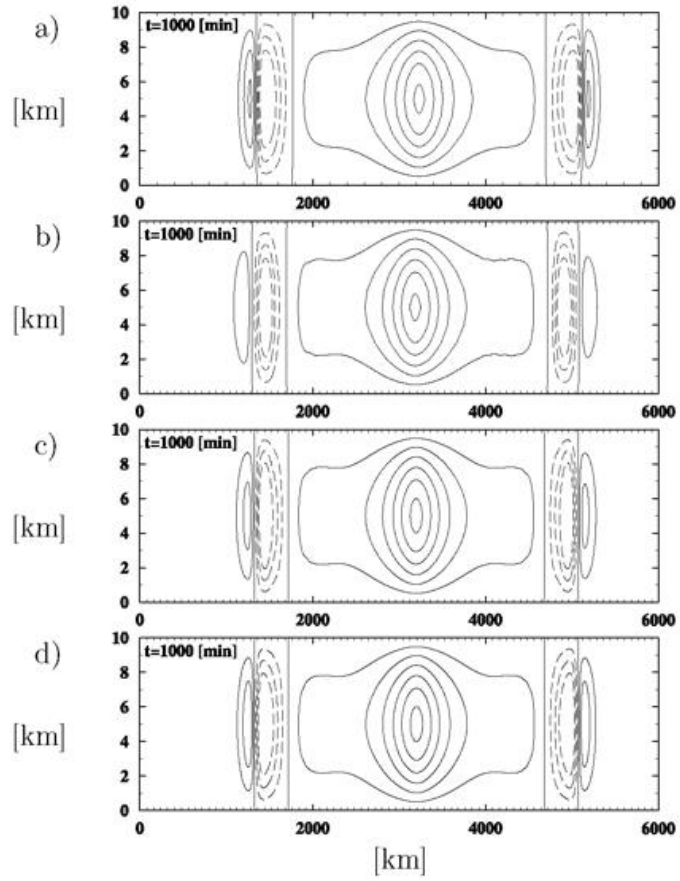


Figure 6: Spatial distribution of the perturbation of potential temperature θ' after t = 1000 min plotted with a contour interval of 0.0005 K. Comparison of analytical solution *a*) with the numerical solution based on Boussinesq approximation computed with three different grid resolutions *b*) Δx = 20 km, Δz = 1 km, *c*) Δx = 10 km Δz = 0.5 km, *d*) Δx = 5 km Δz = 0.25 km; negative values dashed.

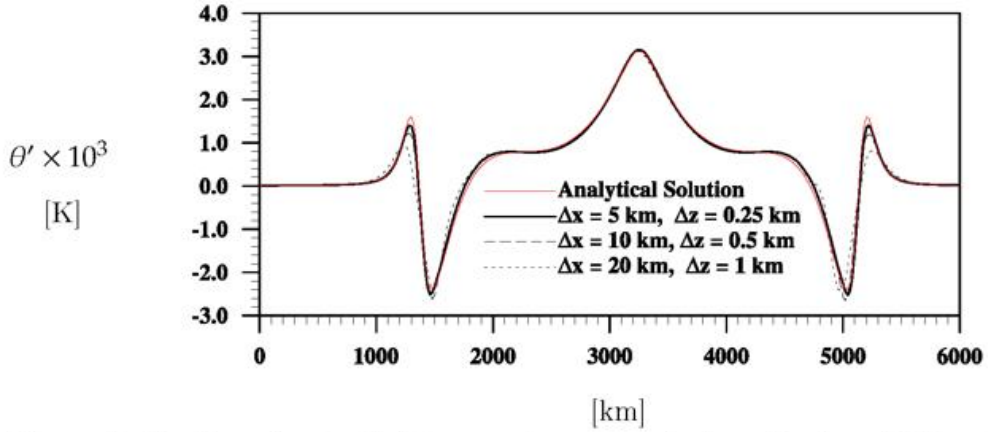


Figure 7: Profiles of potential temperature perturbation θ' along 5000 m height for the analytical solution and three different grid resolutions presented in Fig. 6.

(1995). The experiments are performed for different flow regimes, such as linear hydrostatic, linear nonhydrostatic, nonlinear hydrostatic and nonlinear nonhydrostatic.

2.5.1 Experiment setup

The flow configurations are based on Bonaventura (2000) and Pinty et al. (1995). The shape of the hill is defined by the Agnesi formula:

$$h(x) = \frac{h_0}{1 + [(x - x_0)/a]^2}, \qquad 0 \le x \le L, \tag{2}$$

where h_0, x_0 and a are height, center location and half width of the hill, correspondingly. The parameters defining shape of the hill define also a flow regime, so they differ between the simulations.

For all simulations, the reference potential temperature is given by the Clark-Farley formula. Height of the computational domain is 25 km, while its length depends on the particular flow regime. In order to avoid reflections of the gravity waves from the upper and lateral boundaries, absorbing layers are applied. Thickness and strength of the lateral damping layer depends on the flow regime. In vertical direction, the absorbing layer is the same for each experiment and covers the whole domain above 10 km height. There is no Coriolis force, nor explicit viscosity nor surface friction in the simulations.

2.5.2 Linear hydrostatic regime

The linear hydrostatic regime is characterized by the nondimensional parameter $aN/U \approx 10$ and a very small aspect ratio of h_0/a. An initial horizontal velocity U is 32 m/s. Height and half width of the hill are $h_0 = 1$ m and $a = 16$ km, correspondingly. Computational grid has significant anisotropy. Its size in the horizontal direction is $\Delta x = 3$ km while in the vertical direction it is $\Delta z = 250$ m. While the grid size in the vertical direction is much larger then the height of the hill, its presence is defined via terrain following coordinates. Brunt-Vaisala frequency is set to $N = 0.0187$ s^{-1} and the time step $\Delta t = 40$ s.

An analytical stationary solution for the wind perturbation for linear hydrostatic wave regime was developed by Klemp and Lilly (1978), for compressible atmosphere. Therefore, accuracy of the numerical solution can be directly verified against this result. Figure 8 shows a comparison of EULAG horizontal wind after 11.11 hours integration with that analytical solution. The general agreement between the solutions is apparent and is seen especially in the velocity pattern. The small differences concern mainly wave amplitudes, which are about 5% smaller for EULAG, in the areas outside the absorber. While Pinty and Bonaventura did not present a direct comparison of their simulation results with the analytical solution, we can conclude that the EULAG velocity distribution is in a close agreement with their compressible solutions.

2.5.3 Linear nonhydrostatic regime

For the linear nonhydrostatic flow regime we chose the nondimensional parameter aN/U to be of the order of 1, and the hill aspect ratio slightly smaller than 1. Thus, the hill shape parameters are $a = 500$ m and $h_0 = 100$ m for $N = 0.0187$ s^{-1} and $U = 14$ m/s. Resolution of computational grid is $\Delta x = 100$ m in horizontal and $\Delta z = 250$ m in vertical direction, to follow possibly closely a configuration applied by Bonaventura (2000). Time step used for the integration is $\Delta t = 4$ s. Distribution of the velocity and vertical momentum flux is analyzed after 1.2 h. In normalized time scale it corresponds to $t^* = Ut/a = 120$ and we can expect that they are close to the stationary solutions.

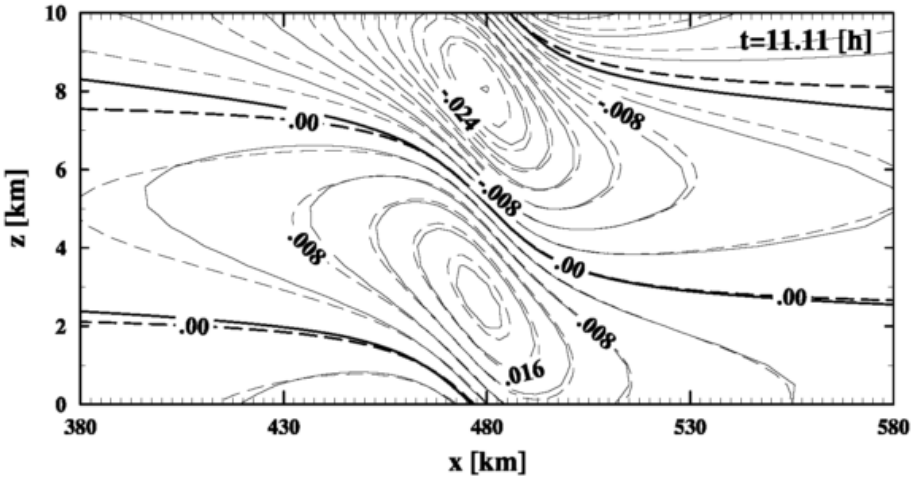


Figure 8: Perturbation of horizontal component of velocity after 11.11 hours. Comparison of numerical EULAG's solution (solid lines) with analytical solutions (dashed lines).

Vertical and horizontal components of velocity from EULAG are plotted in Figs. 9a and 9b. Their comparison with the compressible results from Bonaventura (2000) (Fig. 5 therein) shows that the characteristic features of the flow are properly reproduced and this concerns especially the pattern amplitude of the vertical velocity distribution. The small difference between the anelastic and compressible solution by Bonaventura is noticeable in the direction of the wave propagation, as in the EULAG solution, the waves propagate more steeply. Precise determination of this difference is somehow problematic due to limited resolution of Bonaventura's figure. Nevertheless, it can be said that the difference in the direction of the wave propagation does not exceed 5 degrees.

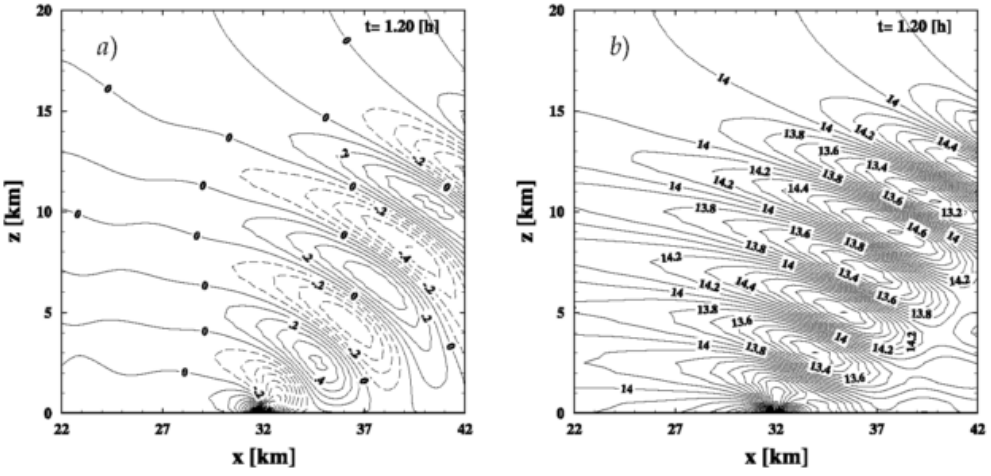


Figure 9: Velocity flow field in linear nonhydrostatic regime. Vertical *a*) and horizontal *b*) component of velocity (after 1.2 hour) computed using EULAG code, contours every 0.1 m/s.

2.5.4 Nonlinear hydrostatic regime

Nondimensional parameter aN/U for this test is equal 10. The mountain shape parameters are $a = 16$ km and $h_0 = 800$ m, while $U = 32$ m/s. Brunt-Vaisala frequency for this simulation is slightly increased $N = 0.02$ s^{-1}. Grid size is $\Delta x = 2.8$ km in the horizontal and $\Delta z = 200$ m

in the vertical direction. The whole domain covers the area of 1728 × 25 km. The equations are integrated over 23.9 h with the time step $\Delta t = 30$ s.

Figure 10 presents EULAG results for vertical and horizontal components of velocity perturbation. The comparison of the vertical velocity perturbation (Fig. 10b) with corresponding results from Pinty et al. (1995) (see their Fig. 8b) shows that both solutions are characterized by similar velocity pattern, as well as positions and magnitudes of the velocity extrema. This is also the case for the horizontal velocity perturbations, as both models place its first maximum at 8 km height with maximum value of about −3.5 m/s and the first minimum at ~ 9 km height with value −25 m/s for EULAG and ~ −26 m/s for Pinty et al. (1995). Also, the EULAG solution is more smooth in the upper part of the domain.

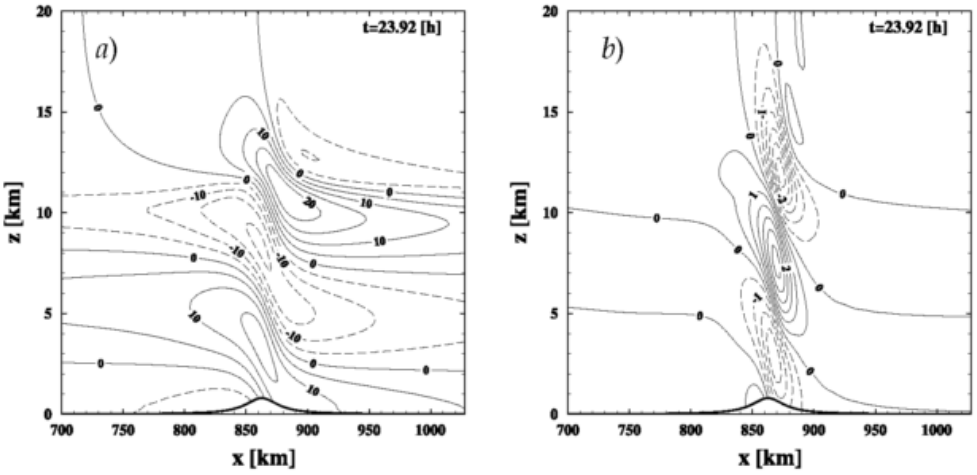


Figure 10: Spatial distribution of velocity perturbation in the hydrostatic nonlinear regime *a*) horizontal component with contour interval every 5 ms^{-1}, *b*) vertical component with contour intervals every 50 cms^{-1}. The dashed line indicate negative values.

2.5.5 Nonlinear nonhydrostatic regime

The nonlinear, nonhydrostatic flow regime is characterized by nondimensional parameter aN/U equal 1.5. Complexity of the flow results from the high steepness of the hill characterized by $a = 1000$ m and $h_0 = 900$ m giving a relatively high aspect ratio $h_0/a = 0.9$. Initial velocity at the inlet is set to $U = 13.28$ m/s. Brunt-Väisälä frequency is $N = 0.02$ s^{-1}. Resolution of the computational grid is $\Delta x = 200$ m in horizontal and $\Delta z = 100$ m in vertical direction. Size of the domain is 127.8 × 25 km. The experiment is run for 2400 s with the time step of 4 s. In EULAG simulations the hill is represented using the terrain following coordinates, while the Bonaventura's model uses Cartesian rectangular coordinates with step-like representation of the orography.

Figure 11 shows the EULAG solutions for vertical and horizontal components of velocity after 2400 s of calculations and, similarly to Bonaventura, focuses the analysis on the lee-side of the hill. The comparison with the compressible model of Bonaventura (2000) shows that even for this highly complicated flow regime and differing representations of orography, the main characteristic features of the flow are the same for both models. For horizontal velocity, they show similar spatial perturbation structure, with the area of positive perturbation elongated just above the lee-side slope. In EULAG solution, center-line of the area is closer to the ground comparing with the Bonaventura's solution and the difference may result from different representations of orography pattern. Maximum value of the horizontal wind inside the perturbation area and located close to the mountain peak is 25 m/s in EULAG and

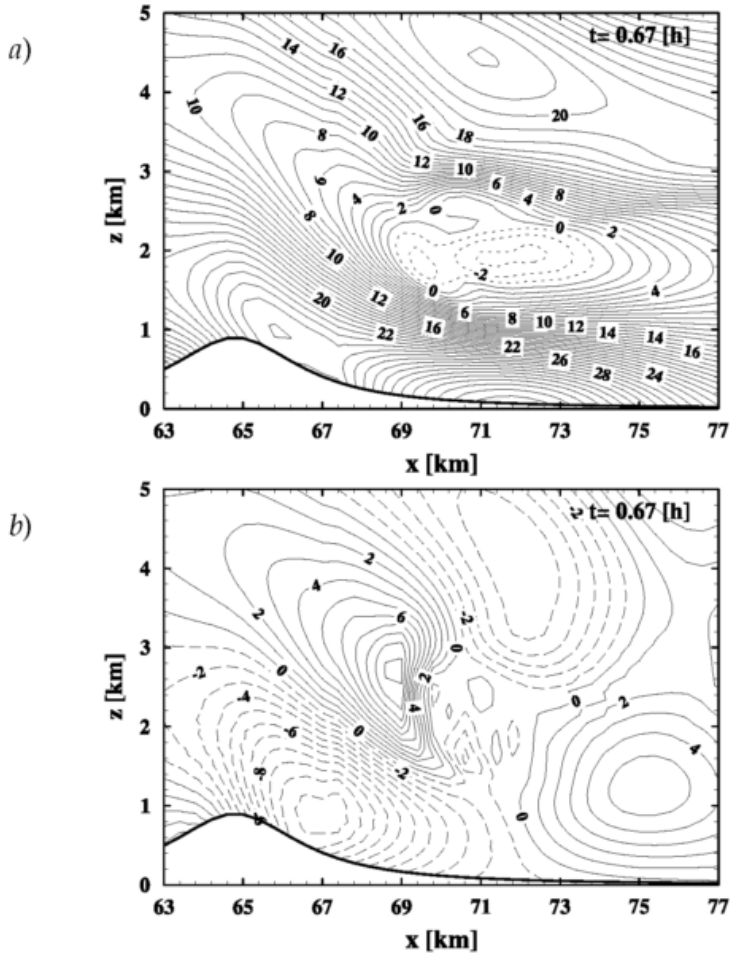


Figure 11: Velocity flow field in nonhydrostatic nonlinear regime *a*) EULAG - horizontal wind perturbation with contour interval 1 m/s, *b*) EULAG - vertical velocity with contour interval of 1 cm/s.

27.9 m/s in Bonaventura's solution. Region of negative horizontal velocity is also similar in location and shape with the corresponding region in the Bonaventura's solution Bonaventura (2000)(Fig. 15 therein). The minimum value of the horizontal velocity in EULAG is ~ -3 m/s while in the Bonaventura's solution is slightly smaller and equal ~ -5 m/s.

Vertical velocity field on the lee side of the hill (Fig. 11) is organized into a quadrupole structure. The flow pattern, as well as the position of minima and maxima are consistent with results obtained with compressible model (see Fig. 16 in Bonaventura (2000)).

In summary, the results show that anelastic approximation does not impose any significant limit for accurate modeling of the mountain gravity waves for tested flow regimes, including the nonlinear nonhydrostatic one, featuring also a strong wave-breaking process.

2.6 Summary and conclusions

The paper presents results of the study aimed at testing the anelastic dynamical core of the multiscale research flow model EULAG. The study is focused on the two-dimensional dry flows, free of phase transitions of water vapor. All the tests show that the results obtained using the anelastic EULAG core agree to a high degree with the benchmark compressible solutions, for all analyzed classes of the flow. This is also the case for comparisons with the

analytical solutions, where they are obtainable, that is for the inertia gravity waves, as well as for the orographic waves in the linear and hydrostatic flow regime. Additionally, the tests confirm the robustness of the EULAG numerical design.

The test of Straka et al. (1993) allows to thoroughly analyze the properties of EULAG via comparison of its solutions with results of an ensemble of fluid models of different analytic and numerical designs. The analysis confirms that the differences between the reference compressible benchmark solution and results of other simulations depend rather on their numerical designs and not significantly on their analytical formulations, with the anelastic EULAG solutions being very close to the benchmarks ones. In this sense, the experiment confirms findings by Cullen et al. (2000) concerning an influence of numerical model design on realistic representations of mesoscale flows over Scandinavian Peninsula. Our analysis shows also that EULAG solutions well represent the flow structure, even underresolved by the model. That virtue characterizes a small minority of the tested models, not even the benchmark one of Straka et al. (1993).

In summary, the analysis of EULAG results and its comparison with the benchmark solutions confirms that the model has a number of characteristics desirable from the view point of mesoscale NWP applications. They involve the high degree of conformity with the benchmark results, as well as consistent and smooth representation of subscale process, always present in NWP applications.

References

W. C. Skamarock, J. Doyle, P. Clark, and N. Wood. A standard test set for nonhydrostatic dynamical cores of NWP models. *16th Conference on Numerical Weather Prediction, Seattle WA*, P2.17, 2004.

J. M. Straka, R. B. Wilhelmson, L. J. Wicker, J. R. Anderson, and K. K. Droegemeier. Numerical-solutions of a nonlinear density-current - A benchmark solution and comparisons. *International Journal for Numerical Methods in Fluids*, 17(1):1–22, 1993.

A. Robert. Bubble convection experiments with a semi-implicit formulation of Euler equations. *Journal of the Atmospheric Sciences*, 50(13):1865–1873, 1993.

W. C. Skamarock and J. B. Klemp. Efficiency and accuracy of the Klemp-Wilhelmson time-splitting technique. *Monthly Weather Review*, 122(11):2623–2630, 1994.

L. Bonaventura. A semi-implicit semi-Lagrangian scheme using the height coordinate for a nonhydrostatic and fully elastic model of atmospheric flows. *Journal of Computational Physics*, 158(2):186–213, 2000.

Y. Ogura and N. A. Phillips. Scale analysis of deep and shallow convection in the atmosphere. *Journal of the atmospheric sciences*, 19:173–179, 1962.

B Rosa, M. J. Kurowski, and M. Ziemianski. Testing the anelastic nonhydrostatic model EULAG as a prospective dynamical core of a numerical weather prediction model. Part I - dey benchmarks. *Acta Geophys.*, 59:1236–1266, 2011.

M. Cullen, D. Salmond, and P. K. Smolarkiewicz. Key numerical issues for the future development of the ECMWF model. *Proc. 2000 Workshop on developments in numericsal methods for very high resolution global models*, pages 183–206, 2000.

D. R. Durran. Improving the anelastic approximation. *J. Atmos. Sci.*, 46:1453–1461, 1989.

J. P. Pinty, R. Benoit, E. Richard, and R. Laprise. Simple tests of a semiimplicit semi-lagrangian model on 2d mountain wave problems. *Monthly Weather Review*, 123(10):3042–3058, 1995.

J. B. Klemp and D. K. Lilly. Numerical-simulation of hydrostatic mountain waves. *Journal of the Atmospheric Sciences*, 35(1):78–107, 1978.

3 Moist benchmark experiments with the anelastic EULAG model

Marcin J. Kurowski, Bogdan Rosa, Michał Z. Ziemiański

Institute of Meteorology and Water Management - National Research Institute, Poland

3.1 Introduction

In this section, the results of two moist benchmark tests (Klemp and Wilhelmson 1978, hereafter KW78; and Weisman and Klemp 1982, hereafter WK82) performed by the EULAG model for convection-permitting scales are documented. The both experiments consider development and evolution of a three-dimensional supercell over a flat terrain. Our strategy follows the idea of Skamarock et al. (2004), in which supercell experiments define one of the tests regarding standard verification of nonhydrostatic dynamical cores. Since the problem is strongly nonlinear and moist processes are coupled with three-dimensional dynamics, the supercell simulations are considered one of the most complex cases proposed in the test set. This is also because supercell formation involves a variety of coupled microphysical and dynamical aspects, including ice processes, gust fronts and cold pool dynamics, mesocyclone formation, forward and rear downdrafts, storm splitting, surface inflow, and multi-phase precipitation. However, a basic requirement of the test is to reduce relevant physics in order to facilitate evaluation of the results. In consequence, a set of simplifications was imposed on the experimental setup, e.g., moist physics is limited to bulk parameterization allowing only for warm rain formation. Nonetheless, the simplified setup is suitable for studying supercell development and to qualitatively reconstruct the most typical storm features, as shown in KW78 and WK82. The results of severe convection simulations presented in this report along with a set of additional sensitivity studies performed by EULAG were already published in the scientific literature (Kurowski et al. 2011).

3.2 General model setup

The two experiments presented in this report (i.e., KW78 and WK82) use a highly consistent numerical setup but different initial and boundary conditions. All simulations are carried out in a horizontally homogeneous environment and in the absence of orography. The reference profiles are based on observations and represent realistic conditions for severe storm development. The moist framework of EULAG is based on the Lipps and Hemler (1982) approach. The EULAG's reference (environmental) state is defined by the profiles of temperature and potential temperature (what allows for a derivation of reference pressure used in the moist thermodynamics), water vapor mixing ratio and both components of horizontal velocity. The initial perturbation of the potential temperature has a form of bubble with positive temperature excess in the center gradually decreasing to zero at its edge. It is placed near the ground in order to initiate convection. The Coriolis effect is not taken into account.

The bulk moist thermodynamics is represented in the model by three prognostic variables: water vapor (q_v), cloud (q_c) and rain (q_r) mixing ratios (cf. eqs. 1b, 1c and 1d from Grabowski and Smolarkiewicz, 2002). Condensation and evaporation processes are based on an instantaneous saturation adjustment (i.e., no supersaturation) while rain development is represented through a Kessler scheme. Respective mathematical formulas describing the processes of autoconversion, accretion, evaporation and rain subsidence along with a set of accompanying parameters follow KW78.

The subgrid-scale (SGS) mixing scheme (Margolin et al., 1999) is based on the prognostic equation of a volume averaged turbulent kinetic energy (TKE), which is subsequently used to prescribe the subgrid-scale turbulent mixing coefficient for momentum: $Km = c_m TKE^{1/2}(\Delta x \Delta y \Delta z)^{1/3}$, where c_m is a constant. As in KW78, the Prandtl number (i.e. $Pr = K_m/K_h$, where K_h is the subgrid-scale mixing coefficient for scalars) is 0.33. Because some of the SGS parameters of the KW78 scheme are not given explicitly, the subgrid-scale model used in KW78 may differ from the model employed in EULAG.

Rigid and free-slip boundary conditions are imposed at the top and bottom of the domain. The model's lateral boundaries are defined as follows: each explicit variable (i.e. the potential temperature, momentum, mixing ratio, etc.) has an inflow boundary value which is defined by a constant in time environmental profile; processes taking place within the domain do not affect the inflow conditions; the actual state of the flow is a superposition of the reference state and a perturbation; the perturbations are advected out of the domain at the outflow boundary by a prescribed environmental flow. We will further refer to this type of boundary condition as open. When absorber of the Davies type (Davies, 1976; Smolarkiewicz and Margolin, 1997; see discussion after eq. 9 and eqs. 17a-17d) is applied then the perturbations are attenuated to zero in this region. It helps to control an excess and propagation of gravity waves in a stably stratified atmosphere. If not otherwise stated, the sponge layer is not applied. This is because the effects of gravity wave propagation were found to be insignificant for the short-term integration time. We also tested periodic boundary conditions, and, as will be shown further, the choice between open and periodic b.c. is of negligible importance to the EULAG's solutions.

3.3 Klemp and Wilhelmson (1978) experiment

3.3.1 Setup details

The KW78 experiment represents a classic study on a supercell formation, however, it does not provide the details of initial soundings applied in the model. The approximate profiles subjectively reproduced from a skew-T diagram (cf. Fig. 1 in KW78) are given in Table 3. A well-mixed boundary layer extends in the lowest part of the atmosphere (up to 1600 m), with two layers of different stability aloft, having an interface at about 6 km. Convective available potential energy (CAPE) is about 1400 J with the lifted condensation level located at 870 mb. It should be stressed that skew-T representation is a source of insufficient information and a small modification of the initial conditions significantly affects CAPE. For instance, an ensemble of a few profiles within an envelope not exceeding 0.3 K, with respect to the values given in Table 3, changes CAPE by about 5%. The initial perturbation of the potential temperature is defined in the same way as in KW78 (cf. eq. 4.1 and 4.2 therein) and is placed near the ground in the center of the domain. Moist initial fields are not affected by this perturbation and water vapor mixing ratio changes only according to the sounding. Surface pressure is 965 hPa. The model timestep is 10 s and a total integration time is 24 min for a case with no external flow, 36 min for the simulation with a shear flow and 40 min for a case with a veering wind profile. Two sets of simulations are reported here. One does not include any explicit turbulent diffusion (NSG). The other uses the SGS scheme. Basic domain size is 24 km × 24 km × 10 km with a uniform grid spacing $\Delta x = \Delta y = 1$ km and $\Delta z = 500m$. Since the size of a developing supercell is relatively large compared to the domain, we also performed sensitivity study for domains of 36 km × 36 km × 10 km and 256 km × 256 km × 10 km with the same spatial resolution as for the basic simulations. This is to verify how convective development depends on the proximity of lateral boundaries and on the volume of the surrounding where subsiding air may differently respond to the strong

convective updraft.

Table 3: Initial profiles of height (z), pressure (p), potential temperature (θ), temperature (T), dew point temperature (Td) and water vapor mixing ratio (qv) used in KW78 experiment. Surface pressure is $965hPa$.

z [m]	p [Pa]	θ [K]	Td [K]	qv [g/kg]
0	965	300.19	290.15	$1.32 \cdot 10^{1}$
137	950	300.22	289.45	$1.28 \cdot 10^{1}$
600	900	300.25	287.05	$1.14 \cdot 10^{1}$
1083	850	300.17	284.25	$9.99 \cdot 10^{0}$
1587	800	300.83	281.05	$8.48 \cdot 10^{0}$
2116	750	302.85	276.95	$6.76 \cdot 10^{0}$
2675	700	305.44	271.25	$4.77 \cdot 10^{0}$
3267	650	308.36	256.15	$1.84 \cdot 10^{0}$
3897	600	311.44	244.85	$6.26 \cdot 10^{-1}$
4574	550	314.89	230.35	$1.66 \cdot 10^{-1}$
5303	500	318.83	215.95	$3.73 \cdot 10^{-2}$
6097	450	323.3	201.65	$6.83 \cdot 10^{-3}$
6968	400	328.52	187.25	$9.47 \cdot 10^{-4}$
7937	350	334.41	172.85	$9.41 \cdot 10^{-5}$
9029	300	341.43	158.35	$5.99 \cdot 10^{-6}$
10285	250	351.73	142.15	$1.38 \cdot 10^{-7}$

3.3.2 Atmosphere-at-rest case

Comparison of EULAG's results for simulations with and without explicit subgrid-scale mixing is presented in Fig. 12 and should be compared with Fig. 2 from KW78. Note that zero isoline is not plotted for positive defined fields such as cloud and rain mixing ratios in contrast to the plots from KW78. The results of the simulations are in qualitative agreement with KW78, that is, the dynamic and thermodynamic fields have similar patterns. A general picture of the process compares well with the reference experiment, however, some differences can be found in details. SGS model reduces the strength of convection and leads to suppressed cloud and rain development. This effect is physical and shows an influence of enhanced subgrid-scale diffusion on water species. A better consistency with KW78 is obtained when no sugbrid-scale diffusion is applied, however, the results still suggest a possible deficiency in the initial sounding. The EULAG's dynamical fields such as vertical velocity are similar to KW78, except that maximum updraft velocity is 24 m/s in KW78, 21 m/s and 18 m/s in NSG and SGS simulation, respectively. As for the moist fields, the vertical extent of convection as seen by the cloud top level (defined by the height of $q_c = 0.5$ g/kg isoline) reaches 6.5 km (SGS) or 7.5 km (NSG). These are smaller than about 8 km in KW78. Similarly to KW78, a vortical structure of cloud water is visible around the cloud base for NSG. Such a pattern is also present in SGS simulation, but for a smaller isoline interval than used in Fig. 12. The most significant differences regard maximum values of the rain field, which are strongly reduced especially for SGS case. This is a straightforward consequence of

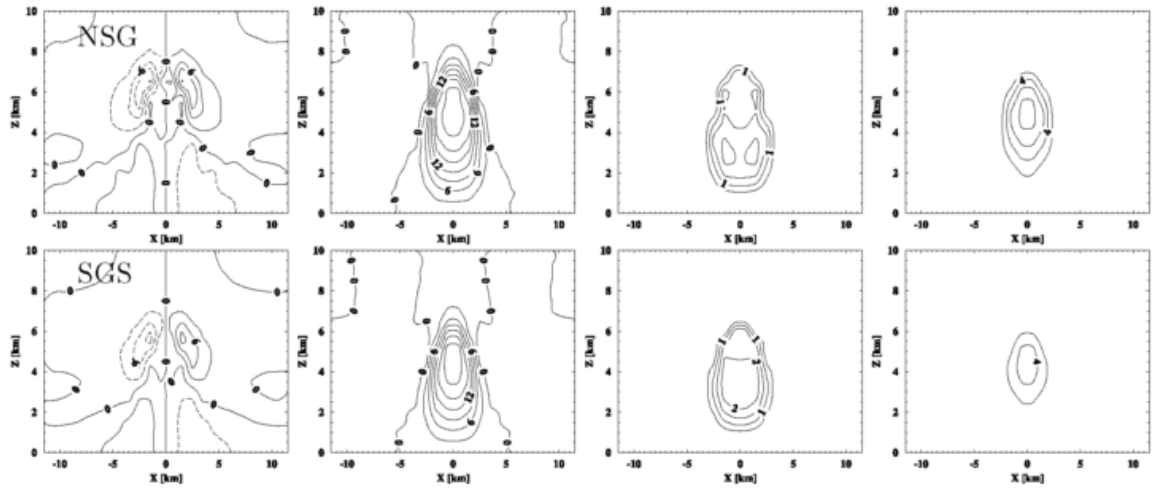


Figure 12: Starting from left column: vertical cross section of u (m/s), w (m/s), q_c (g/kg) and q_r (g/kg) at y = 0 for simulation in resting atmosphere. Results for NSG (upper row) and SGS (right column) are plotted at t = 24 min. Intervals between the isolines exactly correspond to those used in KW78. Negative values of velocity are dashed.

lower amount of cloud water converted into rain water, accordingly to the Kessler formula. Maximum isoline of q_r is 12 g/kg in KW78, 8 g/kg in NSG and 4 g/kg in SGS case.

A significant difference in the moist fields between SGS and NSG models illustrates an important role of diffusion in controlling the supercell formation. This is especially important for the large-gradient fields as narrow convective updraft that impinges upon the dry environment. The diffusion can reduce buoyancy of a rising thermal what in turn limits moisture supply. On the other hand, our sensitivity study shows that at 24 min the cell undergoes a vigorous development characterized by intensive growth of maximum updraft velocity and maximum values of water species. Therefore, even relatively small differences in model speed-up may lead to significant differences between models, at this moment. The comparison of the results at a more mature stage of the cloud development would be more illuminating, but KW78 does not offer such results for the atmosphere-at-rest case. Nonetheless, this example illustrates the complexity of a seemingly simple problem, where the coupling between dynamics and moist thermodynamics with precipitation may result in noticeable model-to-model differences in physically important fields such as cloud and rain water.

3.3.3 Shear flow case

A low-level shear is an essential component of a supercell formation as it is responsible for the storm splitting with subsequent separation of updraft and downdraft structures. This process is initiated when a vorticity tube associated with the low-level vertical shear flow is tilted up by a convective current and subsequently deformed into two separate horizontally counter-rotating branches of the air (e.g. Klemp, 1987). A low-level shear is a necessary prerequisite of the process but it also affects the vertical structure of the supercell, which may be torn apart when the shear is too strong (Weisman and Klemp, 1982). In the current simulations, a horizontal velocity in x-direction changes linearly from -5 m/s at z = 0 km to 5 m/s at 3.25 km and remains constant (5 m/s) above.

Horizontal cross sections of vertical and horizontal velocites, and cloud and rain water mixing ratios at 24 min and 36 min are presented in Fig. 13 and Fig. 14, respectively, and should be compared to Fig. 4 and 5 from KW78. Cloud water shown in Fig. 13 is replaced with the

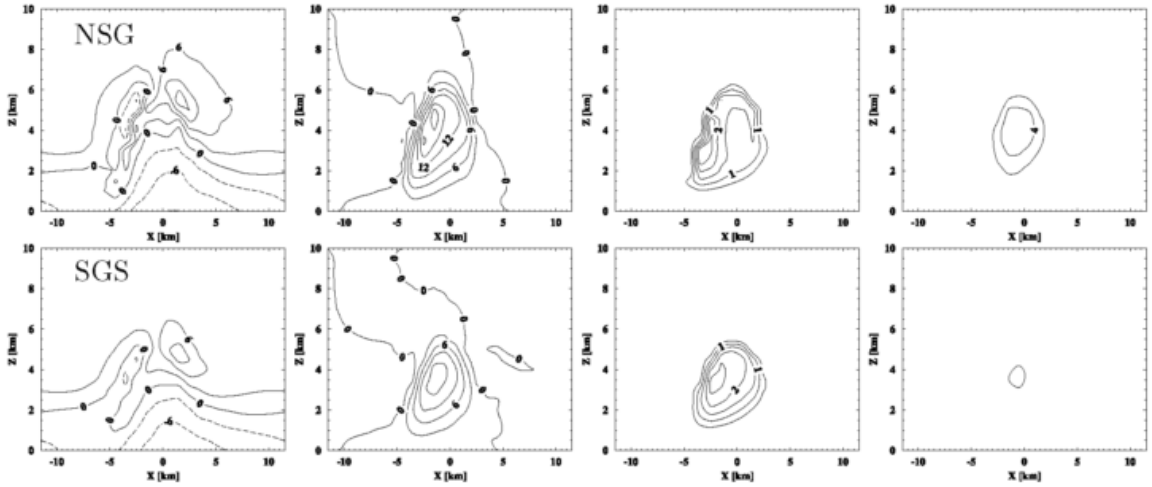


Figure 13: As in Fig. 12 but for sheared environment at 24 min.

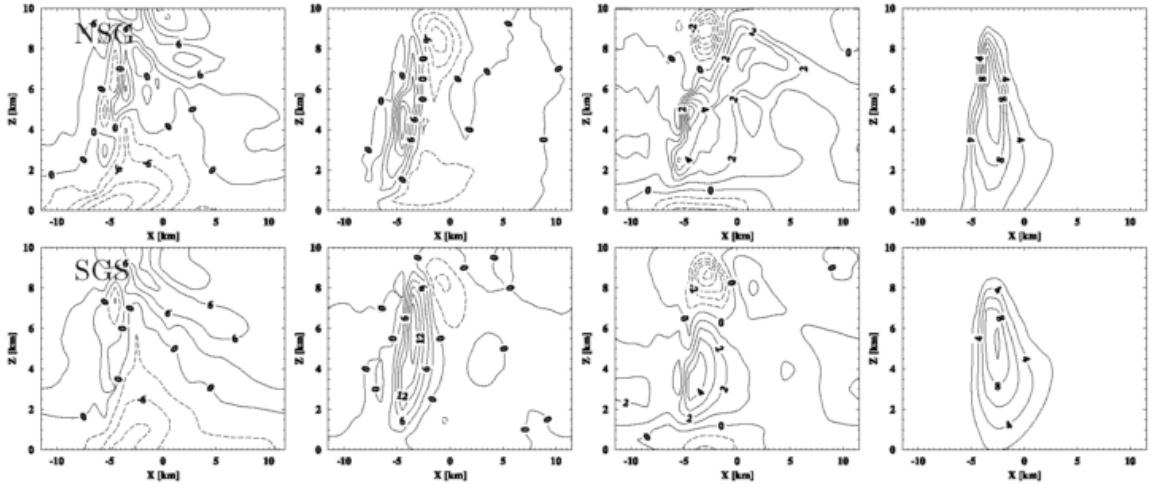


Figure 14: As in Fig. 13 except at 36 min and the third column is potential temperature perturbation (θ') in (K).

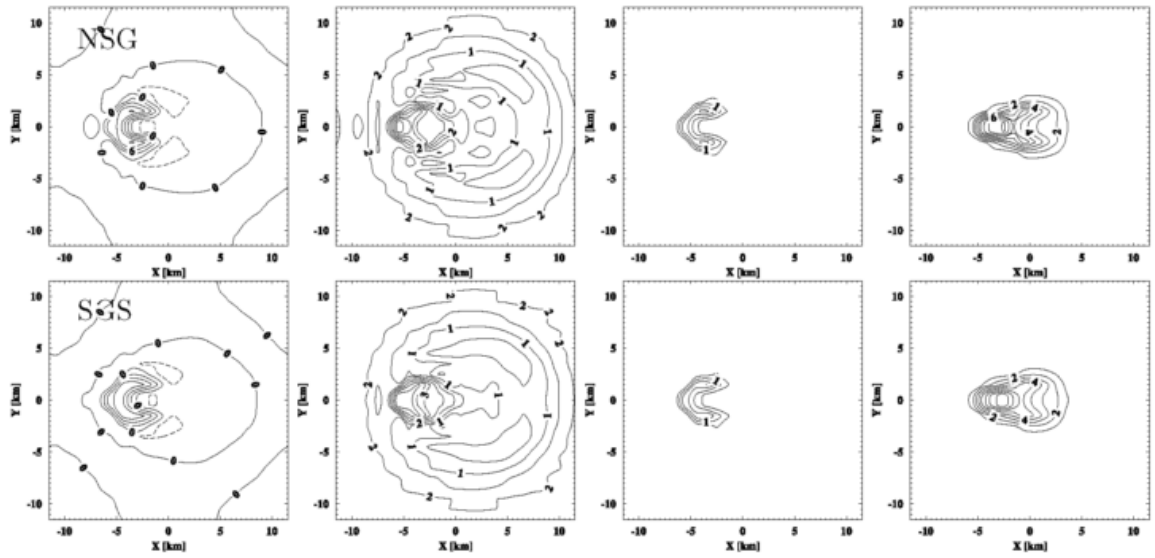


Figure 15: Horizontal cross sections at $z = 2.75$ km for one-directional shear simulations at 36 min. From left to right: vertical velocity, potential temperature perturbation, cloudy and rain water are presented for NSG (top row) and SGS (bottom row) model.

potential temperature fluctuation in Fig. 14, in agreement with Fig. 5 from KW78. Again, all the fields are in qualitative agreement with KW78 and a general picture of supercell formation in sheared environment is similar in both cases. The main differences regard the amount of rain water that is lower in the EULAG simulations. The rain water mixing ratio is especially reduced at 24 min for SGS case. This is associated with approximately 40% lower intensity of a convective updraft and thus lower moisture supply. At later times, the EULAG results compare better with KW78. For instance, after 36 min cloud and rain fields are very close to KW78. NSG model produces slightly more rain than is seen in the reference experiment as a small region of high rain water amount ($q_r > 12$ g/kg) is present in between 6 and 7 km. Rain water advected into upper parts of the supercell by a strong updraft overshoots the cloud top height (not shown) by about 2.5 km. Maximum potential temperature excess resulting from the latent heat release (4 K in EULAG simulations) compares well with KW78. As shown in Fig. 14, results of SGS model at 36 min are more consistent with KW78 than at 24 min, and only a slight delay of rain fallout is present (note that isoline of 4 g/kg have not yet reached the ground).

Horizontal cross sections of vertical velocity, potential temperature perturbation and cloud and rain mixing ratios at z = 2.75 km and at 36 min are depicted in Fig. 15 using the same intervals as in Fig. 6 from KW78. A characteristic horse-shoe-shaped deformation of an updraft region with the two nearly separate convective branches marks the beginning of the storm splitting. Rain water and potential temperature fields still have only one maximum, similarly to KW78. The rain water at 2.75 km, falling out between convective updrafts, covers larger horizontal area than the cloud water. As discussed above, the difference between EULAG and KW78 at 24 min can be due to different model spin-up. A longer integration time removes transient differences in moisture supply. In consequence, similar intensity of an updraft is achieved at later times and thus the cumulative total water amount is more consistent in both cases.

z [m]	u [m/s]	v [m/s]
0	-6.0	2.0
500	-3.5	1.7
1000	-1.3	1.0
1500	0.5	-0.5
2000	2.25	-2.4
2500	3.1	-4.2
3000	4.0	-6.0
3500	5.3	-5.1
4000	6.7	-2.5
4500	8.5	1.0
5000	10.3	4.8
5500	12.1	8.8
6000	13.8	12.5
6500	14.3	13.8
7000	14.8	15.0
7500	14.8	15.0
8000	14.8	15.0
8500	14.8	15.0
9000	14.8	15.0
9500	14.8	15.0
10000	14.8	15.0

Table 4: Numerical values of both components of horizontal velocity (u, v) as used in EULAG's simulation of the flow with a veering wind.

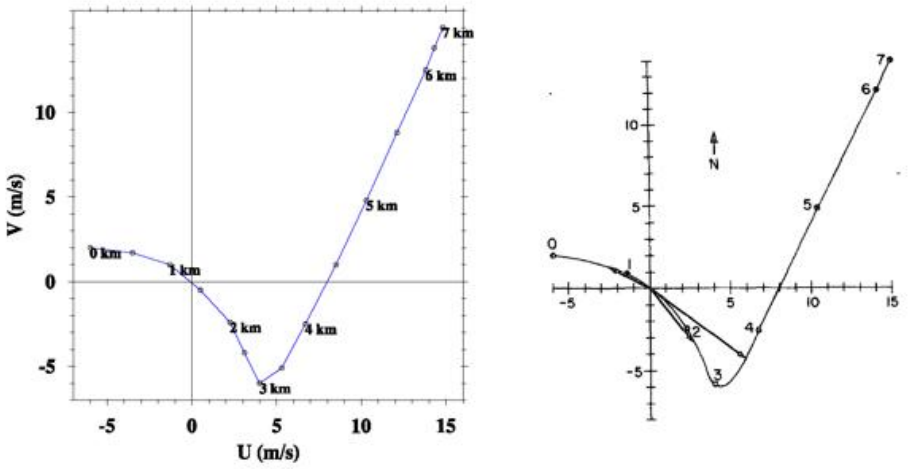


Figure 16: Hodograph of the horizontal velocity as used in EULAG's simulations (left panel) and that from the original KW78's setup (right panel). Empty circles on the left panel indicate the values exactly at model's vertical levels, i.e. the distance between adjacent points is $\Delta z = 0.5$ km.

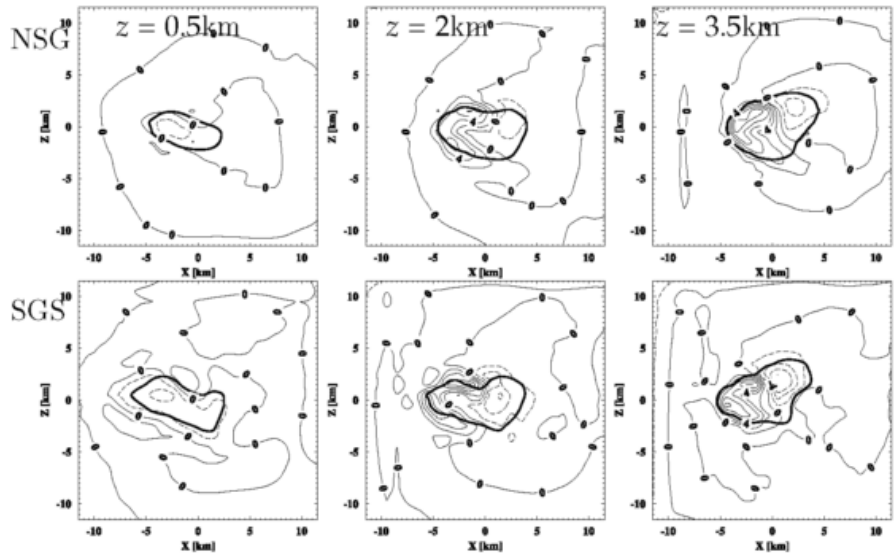


Figure 17: Horizontal cross sections of the vertical velocity w for veering wind simulation at three different levels: 0.5 km (left column), 2 km (middle) and 3.5 km (right) and after 40 min of simulation. Thick line denotes rain water contour of $q_r = 1$ g/kg.

3.3.4 Veering wind case

A case with a veering wind is the most complex out of the three presented in this study and most typical for severe storm formation (KW78). For a straight hodograph used in the previous case along with the Coriolis force omitted, supercell development is symmetric to the XZ plane at y = 0 and none of the branches is favored (cf. Fig. 15). Presence of veering wind, however, causes asymmetry in the supercell propagation and strongly affects evolution of its internal structure. This allows for a development of new characteristics that resemble supercell features observed in nature.

The environmental profile of horizontal velocity shown in Fig. 16 was reproduced from Fig. 12 in KW78 and appropriate numerical values used for the study are given in Table 3.3.4. Figure 17 presents horizontal cross sections of the vertical velocity and rain water fields after 40 minutes of simulation at three different levels: 0.5 km, 2 km and 3.5 km (using the same contour intervals as in KW78) for NSG and SGS simulations. The results were obtained for slightly larger horizontal domain size (i.e. 32 km × 32 km) in order to minimize boundary effects.

The structure at z = 0.5 km consists of two updrafts separated by rain-laden downdraft. The convective branches merge at upper levels where asymmetry of the structure is evident. The branch of stronger updraft borders upon the downdraft and the convection is more vigorous than at lower levels. The rain water contour of 1 g/kg at z = 0.5 km encloses only a region of the descending air. At upper levels, the region expands into an area where the updrafts are also present. Maximum value of the vertical velocity is similar to that from KW78, but about 25% lower for SGS model. YZ vertical cross sections of cloud and rain water as well as vertical velocity and potential temperature perturbation at x = -2 km are depicted in Fig. 18. The vertical velocity field has two updrafts in the lower part of the supercell which are merged together in the upper part. There is a region of negative velocity in between the convective branches, close to the ground, which is associated with a cold pool formation.

The potential temperature field is separated into three regions, as in KW78. The amplitude of its perturbation near the cloud top reaches -6 K in KW78 and -4 K in both EULAG

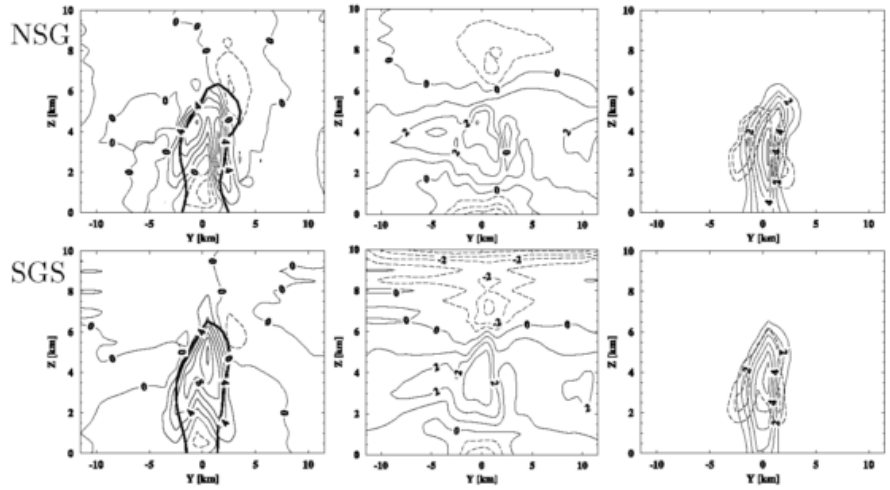


Figure 18: Vertical cross section along yz direction at $x = -2$ km after 40 min: w field (m/s) (left) with bold solid line enclosing the region of $q_r > 1$ g/kg, θ' (K) (middle), and water fields (g/kg) (right) where dashed line refers to q_c and the solid line to q_r.

simulations. The maximum positive temperature excess is 3 K in all cases. The cold pool at the bottom of supercell is characterized with temperature decrease to -4 K in KW78, -4 K for NSG and -3 K for the SGS model. The cloud and rain patterns have similar structure as in KW78 except that the maximum values of q_r are 8 g/kg in both EULAG simulations and 4 g/kg in KW78. The cloud top level reaches about 8.5 km in NSG, 8 km in SGS and 7 km in KW78 simulations.

3.3.5 Sensitivity tests

The influence of horizontal domain extent, the type of lateral boundary condition and spatial resolution were investigated in a series of sensitivity tests. As for the horizontal extend of the domain, the proximity of lateral boundaries noticeably suppresses vertical supercell development. This is evident for the maxima of rain water and updraft velocity, which are about 20% and 40% larger for 256 km × 256 km domain than for 24 km × 24 km one, at 24 and 36 minutes, respectively. The spread of the results for different domain sizes depends on the environmental flow and is generally the smallest for the veering wind where at 40 min of evolution the spread is about 20% for q_r and q_c and about 40% for maximum updraft velocity. The largest differences concern maximum updraft velocity for the atmosphere at rest, where w varies between 6 and 16 m/s at 40 min. The comparison suggests that in general terms the presence of external flow, allowing for convection organization, makes representation of convection less dependent on the model setup.

Changes in horizontal and vertical gridlength turned out to have a dominant impact on the supercell dynamics. According to the results, larger values of the extrema are generally obtained for a finer grid resolution. The strongest sensitivity is observed for maximum vertical velocity which increases from about 26 m/s for $\Delta x = 1$ km and $\Delta z = 500$ m to about 34 m/s for $\Delta x = 500m$ and $\Delta z = 170m$. Changes in resolution also affect the moist fields. Notice however, that doubling horizontal resolution (i.e. using $\Delta x = 500m$ instead of $\Delta x = 1$ km) leads to relatively small changes in the evolution of q_c and q_r extrema, whereas modification of the vertical grid has a significant impact on the fields. Another observed effect is earlier development of convection for finer grid resolution. This indicates that a simple comparison of instantaneous fields may lead to misleading conclusions, especially

when similarly evolving supercells are only shifted in time for different model setups.

The experiments with different types of boundary conditions show that the choice between open and periodic b.c. is of negligible importance to the EULAG results. The spread of results for the updraft velocity, cloud and rain mixing ratio for the most complex case (with a veering wind) is at least an order of magnitude smaller than that introduced by other modifications (i.e., resolution and domain size). For the atmosphere-at-rest case the differences between the two types of boundary conditions in terms of vertical velocity and water condensate did not exceed 0.1%.

3.4 Weisman and Klemp (1982) experiment

3.4.1 Setup details

Setup of the experiment is based on the analytic profiles of the potential temperature, relative humidity and uni-directional horizontal wind (cf. eq. 1, 2 and 4 from WK82) extending vertically up to 17.5 km. Horizontal and vertical gridlength is 2 km and 350 m, respectively. WK82 employs vertical stretching from 350 m near the ground to about 1 km at the top of the domain. This is the main difference from the EULAG's setup which employs a uniform grid. Based on the symmetry of the problem, WK82's horizontal domain was limited to one-half, in order to reduce computational cost. In contrary, we use a full domain with a horizontal size of 128 km $\times$ 128 km. This size was found to be optimal for representing propagation of supercell during the storm splitting without any noticeable interference with the lateral boundary effects. Initial perturbation of the potential temperature is similar to KW78 experiment, but the temperature excess is now 2 K. Open boundary conditions, a Kessler-type warm rain parametrization and a TKE-based subgrid-scale mixing scheme are employed in the experiment. EULAG's physics and numerics are the same as in the previous experiment. This is in contrast to WK82, where a modified version of KW78 model was used (cf. section 2 in WK82). Again, neither ice processes nor Coriolis effects are included. Total integration time is 120 min. It is worth mentioning that a SGS model is a necessary prerequisite for the simulations as the lack of subgrid-scale transport leads to disintegration of a well-organized internal supercell structure.

3.4.2 Shear flow case

The environmental horizontal shear flow employed in the simulations is defined as follows: $U(z) = U_s tanh(z/z_s)$, where z_s = 3 km, and U_s is a free parameter which changes in the range from 5 m/s to 45 m/s (see Fig. 2 in WK82 and its explanation in the text). We consider five cases, namely U_s = 5 m/s, 15 m/s, 25 m/s, 35 m/s and 45 m/s. A constant wind U of a different strength for different simulations is added as Galilean transformation to keep the supercell in the middle of the domain during the simulation. Its magnitude is chosen experimentally and depends on U_s. Using a constant U does not affect the solution since free-slip bottom boundary condition is imposed and no surface fluxes are applied.

Results of the simulations for this setup are presented in Figs. 19, 20 and 21 in a similar manner to WK82. Each figure shows the time evolution of the following fields: horizontal flow at 175 m height (black vectors), vertical velocity at 4900 m (black lines, dashed for negative values), surface precipitation (light blue lines) and a cold front defined as the edge of a cold pool ($\Delta\theta$ = -1K) at the surface (bold blue line). Dotted area marks region of q_r >2 g/kg at the ground. In addition, results from WK82 are plotted in the figures. Such representation of the storm development gives an insight into the supercell dynamics, however, WK82 does not

show any vertical cross sections of the storm structure, what precludes more comprehensive comparison of the results. Note that a mean horizontal flow ($\bar{U}$) of different magnitude was subtracted from EULAG and WK82 solutions, what affects representation of storm-relative low level flow (e.g. to keep the solution for U_s =15 m/s in the domain center, $\bar{U}$=9.15 and 12m/s were used in EULAG and WK82, respectively).

The storm system evolves in a similar way for three different values of U_s (Figs. 19, 20 and 21). After 40 min of simulations the storm splitting is already underway, but only one maximum of the surface precipitation is being formed. Apparently, horizontal extent of convective perturbations depends on the shear strength. For larger U_s the fields become more asymmetric in x and y directions. This reduces the maximum updraft velocity due to lower moisture supply. This in turn suppresses precipitation-laden downdraft and delays formation of a cold pool, as compared to the other cases. After 80 min, each supercell consists of two clearly separated convective cores with a precipitation area between them. Again, intensity and horizontal extent of the vertical velocity and rain water fields decreases with increasing U_s. After 120 min, the splitting of the surface precipitation is completed for U_s = 25 m/s and U_s = 35 m/s as the rain pattern no longer extends over a single area. A local circulation within each core induces a downdraft in its rear part which diverges near the ground away from the supercell center. The largest velocity of diverging flow is for U_s = 15 m/s. These velocity perturbations are superimposed on the external flow that results in larger western component of horizontal velocity for greater U_s. A cold pool develops on the rear side of the supercell with a cold front located near the leading edge of the convective structure during the whole simulation. One of the most characteristic features is that the distance between the two convective branches almost does not depend on the shear-strength. It differs less than a few percent for U_s ranging from 15 to 35 m/s. The shear mostly affects the supercell evolution through the intensity of convection.

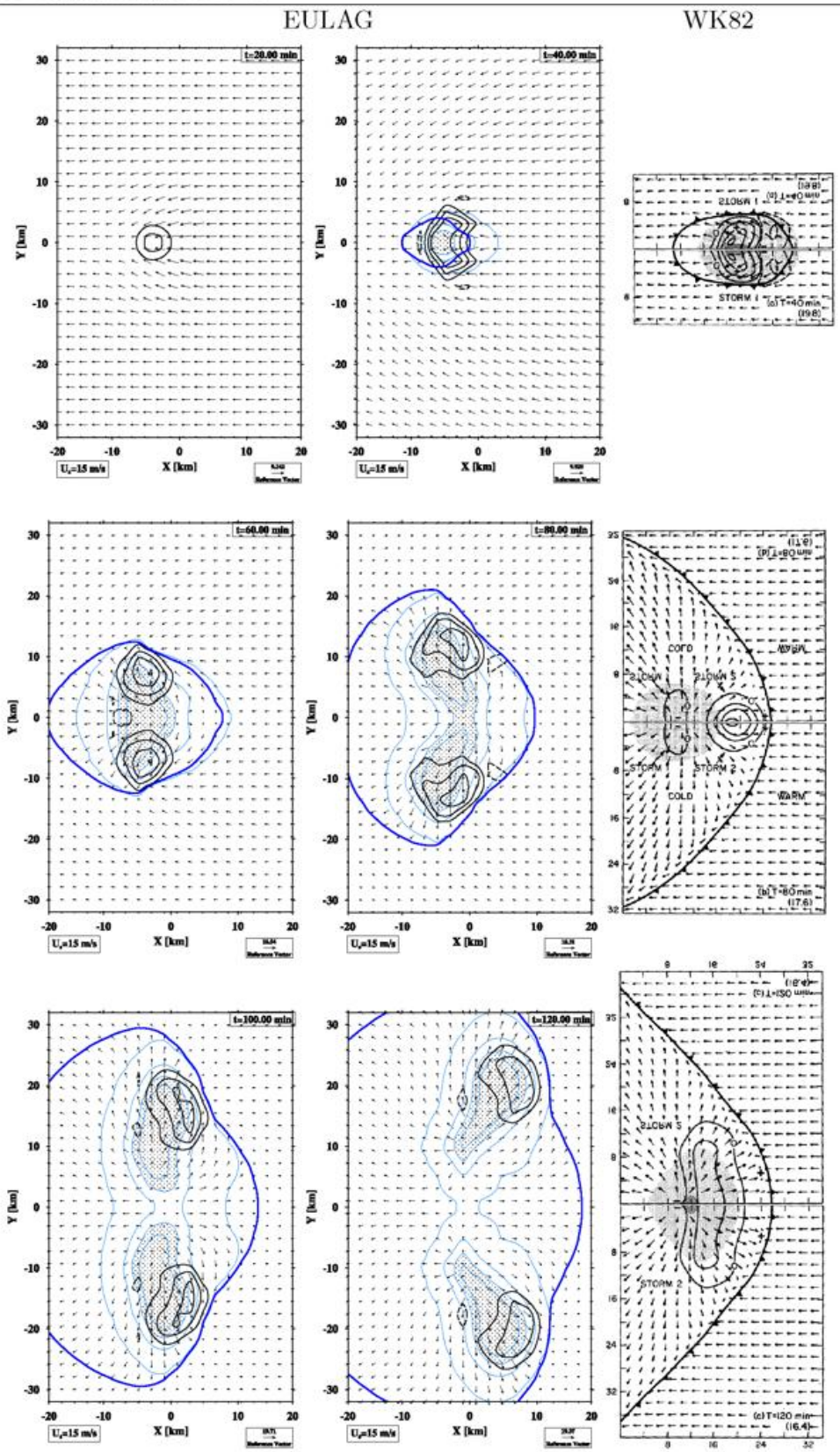


Figure 19: Time evolution of horizontal flow at 175 m (black vectors), vertical velocity at 4900 m (black lines, dashed for negative values), surface precipitation (light blue lines) and a cold front defined as the edge of a cold pool ($\Delta\theta$ = -1K) at the surface (bold blue line). Dotted area marks region of q_r ¿ 2 g/kg at the ground. Vertical velocity is contoured every 5 m/s for positive values and 2 m/s for negative values. Surface precipitation is contoured every 1 g/kg. The results are plotted for U_s = 15 m/s. Right column represents the results from WK82 experiment).

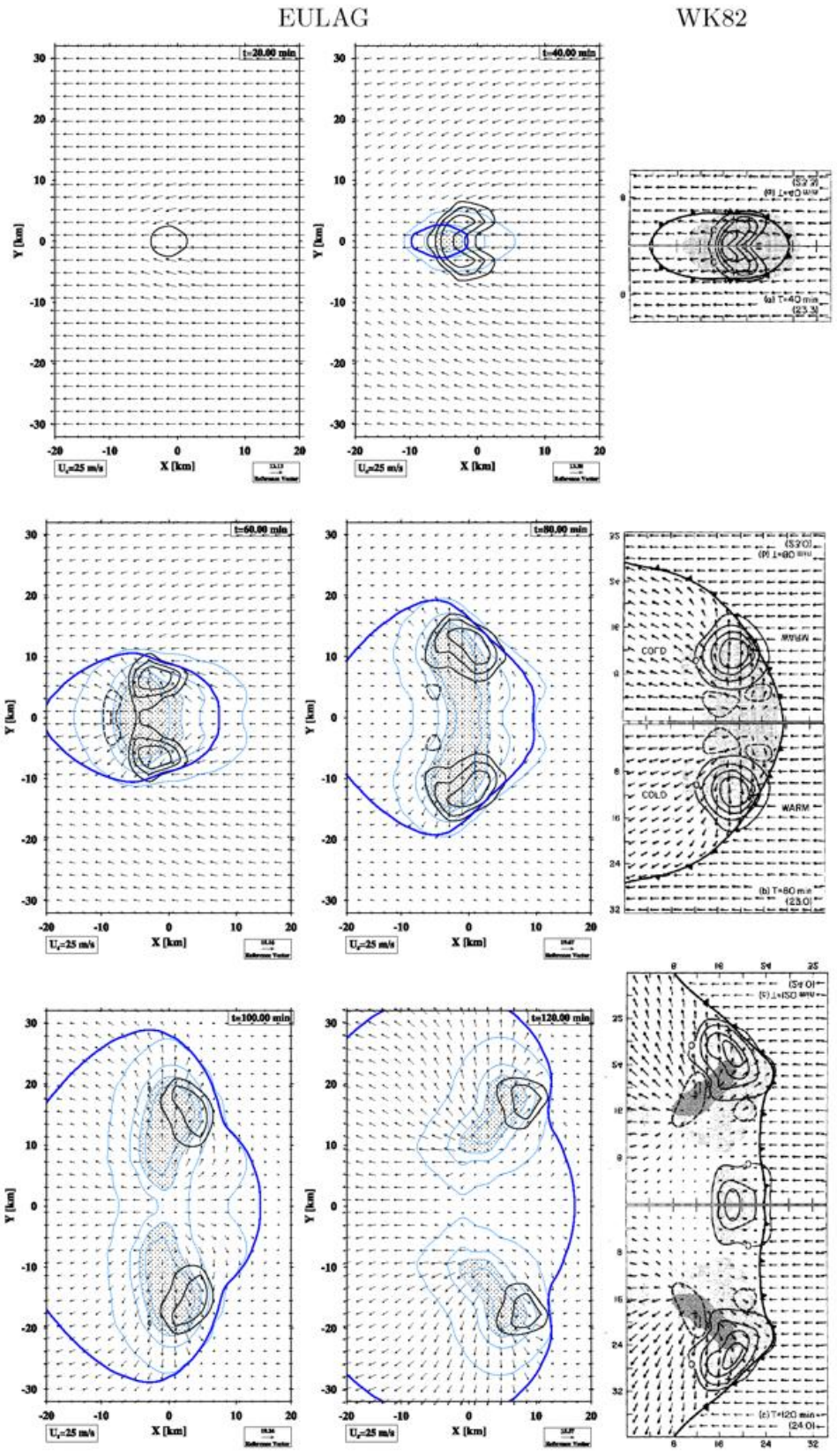


Figure 20: Same as in Fig.19 but for $U_s = 25$ m/s

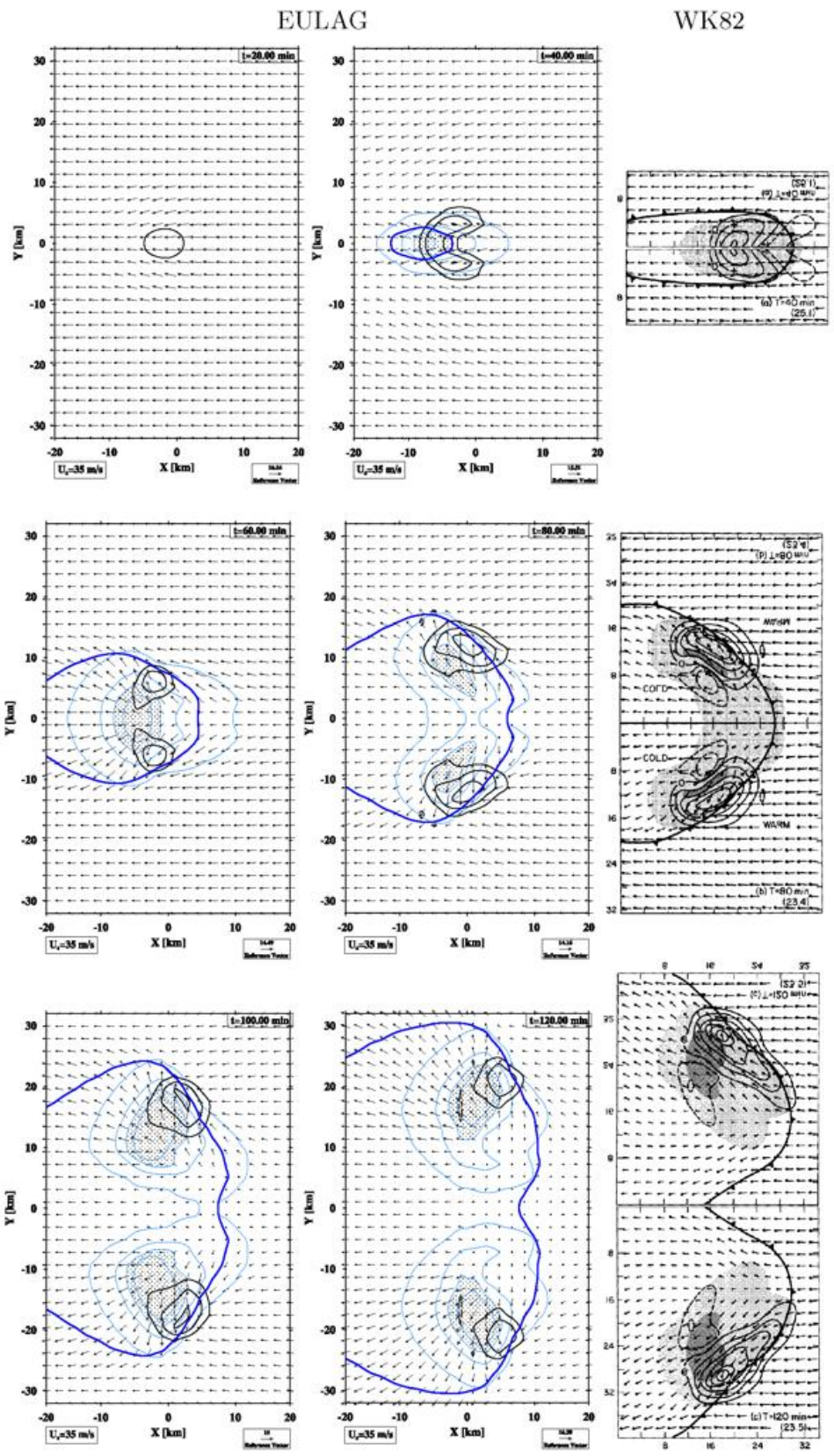


Figure 21: Same as in Fig.19 but for $U_s = 35$ m/s

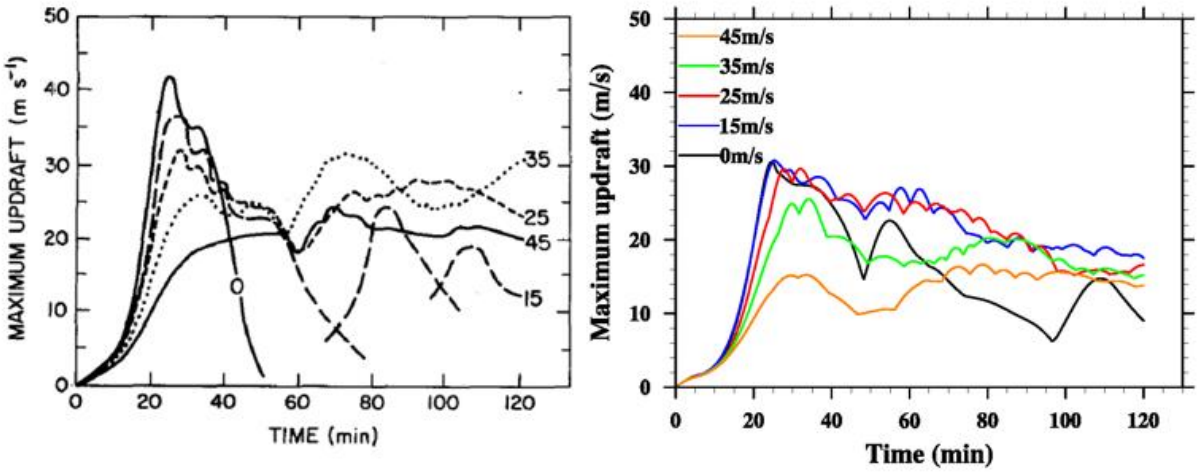


Figure 22: Comparison of the time series of maximum vertical velocity for simulations with different U_s. The results from WK82 (left) and EULAG (right) are shown.

Comparison of the results with WK82 shows that EULAG correctly reconstructs the convective process leading to formation of storm splitting and a cold pool. The main difference concerns buoyancy production that is lower in EULAG simulations. With lower strength of maximum updraft the EULAG simulations yield lower amount of surface precipitation. Additional sensitivity study indicates, however, relatively high sensitivity of convection characteristics to horizontal and vertical resolution. Reducing model's grid box size by a factor of 2 leads to about 40% increase in updraft intensity and about 50% and 10% enhancement for maximum amount of cloud and rain water, respectively. It should be underlined that, for this particular case, the improvement is stronger when horizontal resolution is refined rather than vertical one. The spread of the results is larger than for KW78 experiment, especially for water species. This suggests that we are in a flow regime where the problem is strongly underresolved. Thus a comparison between the models is somewhat burdened with possible susceptibility of the results to the details of numerics (see e.g. discussion in Rosa et al., 2011, on cold density current experiment according to Straka et al., 1998).

Detailed comparison of the storm splitting shows that the EULAG's representation of the process is similar to WK82 in terms of horizontal extent of the cells and the relative distance between them during the storm development. In both cases, formation of rear precipitation is observed in similar regions. The area of the cold pool depends directly on the distance between the cores and is larger for more mature supercells. The main difference between the models is that the storm splitting starts at lower shear strength for EULAG simulation and is already observed for $U_s = 15$ m/s, in contrary to $U_s = 25$ m/s for WK82.

Time evolution of maximum updraft velocity for different values of U_s is shown in Fig. 22. A supercell developing in a resting atmosphere ($U_s = 0$) decays quickly in WK82 but it is able to restore secondary circulations in EULAG simulation. Convection is also less vigorous in EULAG simulations since w_{max} reaches about 30 m/s in contrary to about 40 m/s in WK82. This parameter, however, is especially sensitive to the simulation details, as shown through sensitivity experiment for KW78 and WK82. Generally, the spin-up time is shorter in WK82 than in EULAG. The EULAG's spin-up time depends on the resolution in such a way that for smaller grid box sizes the convection starts earlier. The differences are relatively large as the model reaches first maximum of rain water mixing ratio after 38 min for basic resolution and at about 30 min for a doubled one. Such a time shift is also observed for maxima of cloud and rain water mixing ratios.

3.5 Summary and further development

This section documents the results of two moist benchmark experiments (KW78 and WK82) carried out by the EULAG model in order to verify its performance as a potential candidate for the future dynamical core of weather forecasting model. Both experiments concern formation of supercell in a deep atmosphere, which is unstable to moist convective motions. The results of EULAG simulations show that the model is capable to reconstruct main features of the supercell development, such as storm splitting and a cold pool formation. The EULAG solutions are realistic and compare well qualitatively with the reference solutions from KW78 and WK82 for a wide set of initial conditions (i.e., atmosphere at rest, unidirectional shear flow of different strength, veering wind). In general, the EULAG model yields less intense storm development, however, it is difficult to find the factors controling the results. Sensitivity studies indicate that convection-permitting NWP models operating at resolution of $O(1km)$ are in a strongly underresolved regime where relatively small modifications in resolution can significantly change the result (e.g., about 40% enhancement of the updraft strength for doubled vertical resolution). Moreover, the comparison between different numerical models does not allow for credible estimation/separation of the numerical and mathematical effects in the solution.

More recently, a compressible version of the EULAG model has been developed (see e.g., Kurowski et al., 2013). This created a new opportunity to compare the anelastic and compressible solutions using a highly unified numerical framework, and thus to limit the effects associated with different numerical design of the models. Currently, the model has been verified in a set of moist experiments regarding various scales of the atmosphere. First results of these experiments were already published (Kurowski et al., 2013). As for moist deep convection, the results obtained for Weisman and Klemp (1982) experiment have confirmed high consistency of anelastic and compressible solutions. It was also found that non-hydrostatic pressure perturbations are of negligible importance to the storm development. Concomitantly, sensitivity of the solutions to the numerical details (e.g., resolution) and/or physical parameterizations (e.g., subgrid-scale mixing) turned out to be at least one order of magnitude larger than for mathematical differences. Detailed results of these experiments are expected to be published soon.

References

Davies H. C., (1976), A lateral boundary formulation for multi-level prediction models, *Quart. J. R. Met. Soc.*, 102, 405-418.]

Klemp J. B. and R. B. Wilhelmson, (1978), The simulation of three-dimensional convective storm dynamics, *J. Atmos. Sci.*, 35, 1070-1090.

Lipps F. B., and R. S. Hemler, (1982), A scale analysis of deep moist convection and some related numerical calculations, *J. Atmos. Sci.*, 39, 2191-2210.

Kurowski M. J., Grabowski W. W., and P. K. Smolarkiewicz, 2013, Towards multiscale simulation of moist flows with soundproof equations, *J. Atmos. Sci.* (accepted, doi:10.1175/JAS-D-13-024.1)

Kurowski M. J., Rosa B., Ziemianski M., 2011, Testing the anelastic nonhydrostatic model EULAG as a prospective dynamical core of a numerical weather prediction model. Part II - simulations of supercell., *Acta Geophysica*, 59, 1267-1293

Skamarock W. C., J. D. Doyle, P. Clark, and N. Wood, (2004), A standard test set for nonhydrostatic dynamical cores of NWP models, *20th Conference on Weather Analysis and Forecasting/16th Conference on Numerical Weather Prediction, Seattle*

Weisman M. L. and J. B. Klemp, (1982), The dependence of numerically simulated convective storms on vertical wind shear and buoyancy, *Mon. Wea. Rev.*, 110, 504-520.

4 Semi-realistic flow over the Alps with the anelastic EULAG model

Michał Ziemiański, Marcin J. Kurowski, Zbigniew P. Piotrowski, Bogdan Rosa and Oliver Fuhrer

Institute of Meteorology and Water Management - National Research Institute, Poland, and MeteoSwiss, Switzerland

4.1 The experiment setup

The aim of the experiment was to test the EULAG dynamical core over realistic high-mountain orography for its robustness and for general physical viability of the solutions and their consistency for varying but very high horizontal resolutions (grid sizes of 2.2, 1.1 and 0.55 km). For such resolutions, the approximation of quasi-horizontal flows is no longer valid, as the models begin to resolve explicitly convective processes. Also, the model-represented inclinations of high-mountain slopes begin to resemble their actual steep values. In consequence, the dynamical cores for very-high-resolution NWP require reliable and robust solvers, which do not compromise the advantages of very high horizontal resolutions via, e.g., the introduction of a strong artificial smoothing of the orography or the simulated flow. The experiment allows also to investigate how increasing horizontal resolutions influence model-represented flow over high and diversified orographies, for horizontal grid sizes that allow a realistic representation of mountain slopes and heights. The detailed description of the experiment and its results can be found in Ziemiaski et al (2011).

The experiment employs the frictionless and adiabatic flow, which allows direct focus on the dynamical aspects of the flow, influenced only by the model-represented orography, independent of the impacts of the parameterized boundary layer physics or moist processes. An additional argument is that knowledge of mountain boundary layer physics is limited, which also concerns its parameterizations (see e.g., Rotach et al., 2008 and references therein). It was important also to employ relatively simple and easy-to-reproduce initial and boundary conditions. The idea of the experiment follows previous studies, where the numerical simulations of mountain flows were used to study varying spatial resolutions on mountain drag, e.g., Clark and Miller (1991), Hoinka and Clark (1991), Salvador et al., (1999), Rontu (2006) and Smith et al., (2006), or to study the influence of varying numerical schemes on the properties of the simulated flows, as in Cullen et al., (2000).

a. Domain

The experimental setup is based on the operational NWP COSMO model employing horizontal grid length of 2.2 km, used by MeteoSwiss (the COSMO-2 model, see description in Leuenberger et al., 2010). It concerns the experimental domain (see Fig. 23) which for 2.2 km horizontal grid spacing involves 520 by 350 grid points, so that the horizontal size of the domain is 1144 by 770 km, respectively. The locations (geographical coordinates) of the grid points for the experiment are the same as for the grid points of operational COSMO-2. For the experiment involving 1.1 km horizontal grid spacing, the locations of the grid points collocate with the grid points of COSMO-2, where possible, while the locations of the additional points are defined via halving the distances between the COSMO-2 grid points. Similarly, the additional grid points for the simulations with 0.55 km grid spacing are calculated by halving the distances between the grid points used for simulations employing the 1.1 km grid. As a consequence, the simulations at 1.1 km grid size employ a 1040 by 700 grid point

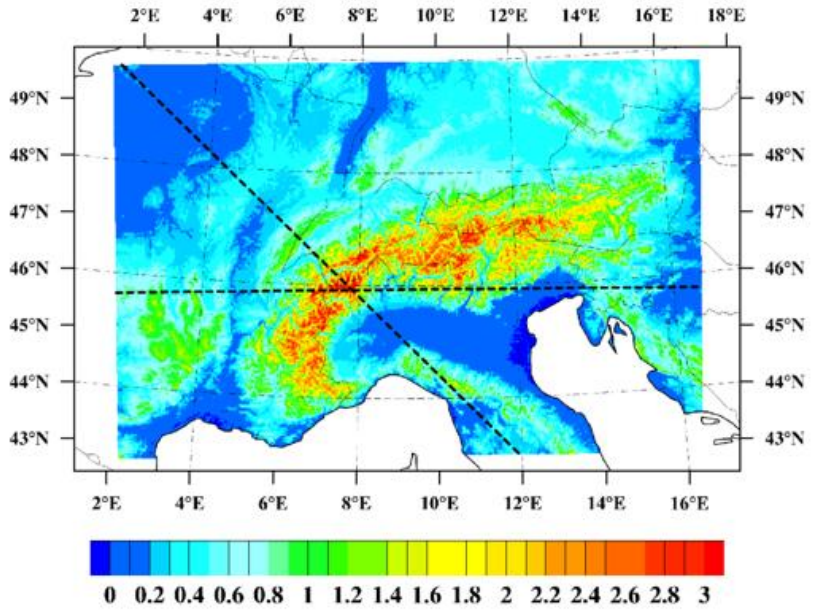


Figure 23: Model orography for 1.1 km grid size (in km, colors), illustrating the orientation of the model domain relative to the main geographic features of the area and political boundaries (thin lines). The thick dashed lines show positions of the cross sections discussed in the paper.

domain, and simulations at 0.55 km grid size employ a 2080 by 1400 grid point domain. The time steps used are 20, 12 and 6 s, for horizontal resolutions of 2.2, 1.1 and 0.55 km, respectively.

The orography for the 2.2 km grid length experiment is the same as the orography employed by COSMO-2. The orography for higher horizontal resolutions was calculated using the satellite SRTM data (Rabus et al., 2003) of approximately 90 m grid size, separate for experiments employing 1.1 and 0.55 km grid length. The satellite data were averaged over the target model grid cells, resulting in a model orography with increasing detail for decreasing grid spacing. No additional smoothing was applied for the data.

In the vertical, the model domain spans from the surface to a height of 23.5 km and employs terrain-following Gal-Chen coordinates (Gal-Chen and Somerville 1975) for the whole vertical extent of the domain using 61 grid levels. The definitions of the grid levels, except the lowest one, are as in the COSMO-2 model, with the vertical grid spacing ranging from about 10 m near the surface to about 500 m in the stratosphere, as is typical for NWP models having relatively high vertical resolution in the near-surface area of the boundary layer. The number and configuration of the vertical grid levels is the same for all the resolutions, employed.

b. The flow configuration

The model employs a free-slip boundary condition on its bottom and top levels, and there are no parameterizations of physical, subgrid-scale processes. The Coriolis force is incorporated into the simulation setup. To avoid the effects of gravity wave reflections from the top of the domain, an absorber was applied above 16 km altitude.

The ambient flow configuration of potential temperature and wind is possibly simple and defined as horizontally uniform. It is imposed by appropriate initial and constant in time boundary conditions. Such a flow configuration is commonly used for idealized simulations

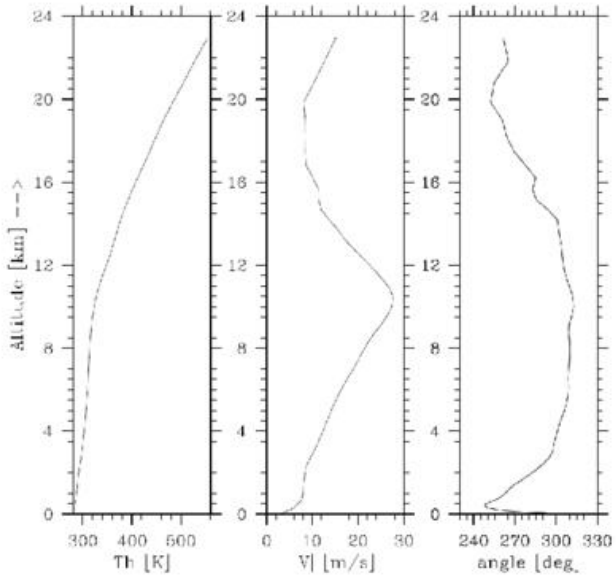


Figure 24: Profiles of the parameters of the ambient flow: potential temperature (left), wind velocity (middle), and wind direction (right).

of deep convective flows (e.g., Klemp and Wilhelmson 1978, Weisman and Klemp 1982, Rotunno and Klemp 1985, Bryan and Fritsch 2002) even though it does not formally preserve the thermal wind balance. It allows for a simple definition of the initial conditions for resolution-dependent configurations of orography.

To ensure that the wind and potential temperature profiles take typical atmospheric values, they are based on an actual meteorological situation in Central Europe on 12 November 2009 at 00.00 UTC. The profiles were calculated as horizontally-averaged wind and potential temperature coming from the operational COSMO-2 analysis of MeteoSwiss. The profiles (Fig. 24) indicate typical moderate north-westerly atmospheric flow of moderate stratification (the Brunt-Väisälä frequency for the lower half of the troposphere equals 0.013 s^{-1}), with a presence of a moderate jet stream characterized by maximum wind reaching 27.6 ms^{-1} at 10450 m above the sea level.

4.2 Results

The aim of the experiment is to analyze and compare the EULAG results for different horizontal resolutions when a quasi-stationary state of the flow is established. The analysis of time-dependent flow diagnostics (not shown) indicates that the flow fields of all simulations have reached a quasi steady-state after 24h of integration time.

a. Surface wind

Figure 25 compares the distribution of the horizontal wind on the second computational level (counting from the Earths surface) of EULAG (located about 10 m above the ground) for the tests using horizontal grids of 2.2, 1.1 and 0.55 km.

For all resolutions used, results have a very high level of consistency and realism. The large-scale flow pattern is practically the same for all resolutions, showing a westerly inflow on the Alpine ridge that divides the flow into two branches around the Alps from north and

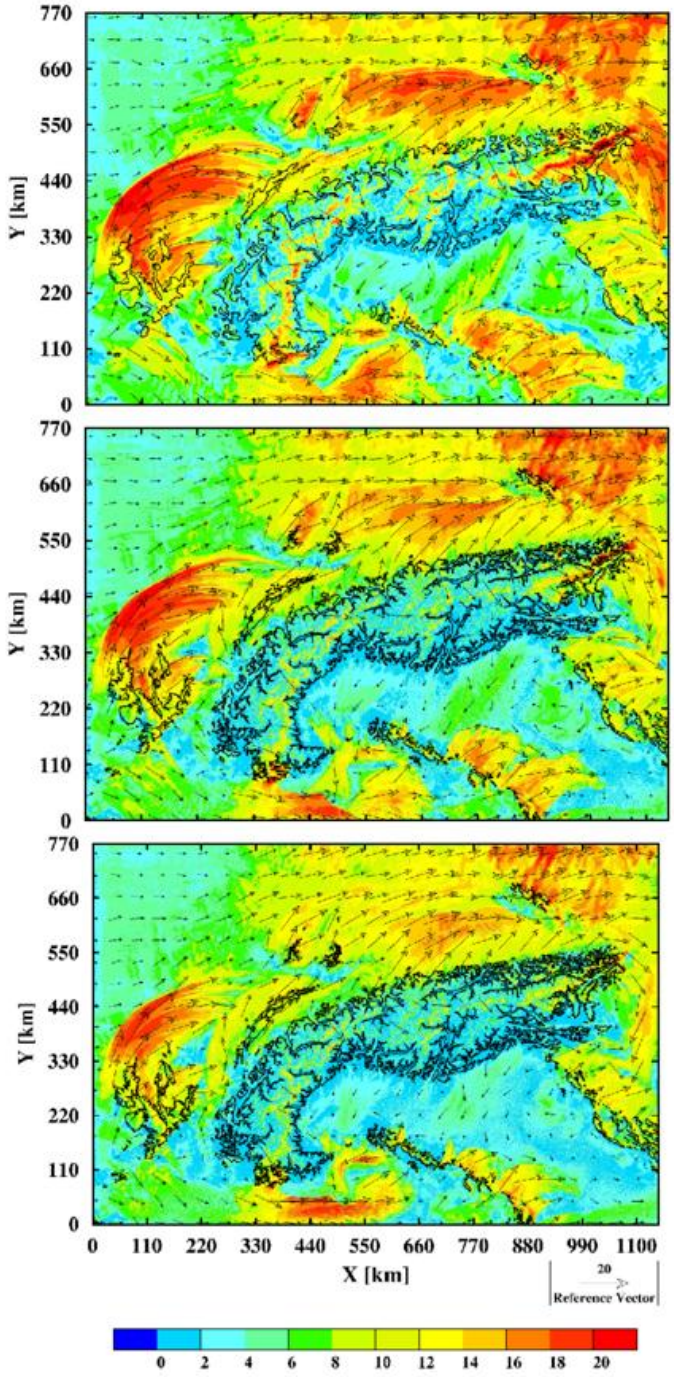


Figure 25: Distribution of the surface (10 m above the ground) wind (arrows) and its speed in m/s (colors) after 24-hours for grid sizes of 2.2 km (upper panel), 1.1 km (middle panel), and 0.55 km (lower panel).

south. The scenario agrees with a blocking condition, characterized by low Froude number (see e.g., Brighton (1978) for laboratory or Smolarkiewicz and Rotunno (1990) for numerical experiments). The Froude number is defined as $F = U/(NH)$, where U is the characteristic horizontal wind velocity, N is the Brunt-Väisälä frequency, and H is the characteristic mountain height. For the characteristic wind speed and stability defined by the ambient temperature profile, it is about 0.2. There is also a signature of an easterly circulation, opposite to the ambient wind, that turns into a southerly flow west of the windward slopes of the western Alps, consistent with the blocking condition. On the lee, southeastern side of the Alps (Po Valley), a weak-to-moderate easterly and northeasterly flow is also present. The Rossby number, assuming a half-width of the Alpine ridge ranging between 100 to 400 km and the wind speed in the lower troposphere in the range of 5 to 10 ms^{-1}, is less than 1 (for average values of the above parameters, its value is 0.3), indicating that Coriolis effects limit the spatial extent and strength of the return upstream circulation (Pierrehumbert and Wyman, 1985), in agreement with the simulation results.

All the experiments show the presence of many mesoscale (size of about 100 km) features of the wind distribution. They show the flow response to the topography and especially to its mesoscale features of sizes and elevations smaller than that of the Alps. Areas of enhanced flow are mainly located over and north-northwest of major terrain obstacles. This effect is particularly evident in the Massif Central, the western Alps and Jura, Vosges, and Schwarzwald. South of the Alps, such areas are located over the Ligurean Sea, south of the Gulf of Genoa, on the lee side of the Appenines, and on the lee side of the Dinaric Alps on the Balkan Peninsula. Areas of pronounced deceleration of the flow are the upper parts of the Saône and Rhine Valleys, and the area west of the Sumava Mountains. South of the Alps, two pronounced areas of relative deceleration are parts of the Gulf of Genoa and of the Adriatic Sea south of the Gulf of Venice.

The prominent difference between the simulations at different horizontal resolutions involves the flow magnitude. While the domain-averaged wind velocity on that level equals 9.09 ms^{-1} for 2.2 km grid size, it is 8.16 and 7.25 ms^{-1} for grid sizes of 1.1 and 0.55 km, respectively. As the simulations do not employ an explicit drag, the results show the influence of terrain-induced form drag of the explicitly represented orography (see e.g., Welch et al., 2001), which increases significantly at higher resolutions. This extends the findings of Clark and Miller (1991) and Smith et al., (2006) to higher resolutions.

Figure 26 shows that the patterns of wind speed differences between the simulations employing different resolutions span a range of scales from the smallest to hundreds of kilometers. The amplitudes of the differences are relatively high and reach -19 to 17 m/s for the difference between 1.1 and 2.2 km grid lengths, -20 to 19 m/s for the difference between 0.55 and 1.1 km grid lengths, and -24 to 17 m/s for the difference between 0.55 and 2.2 km grid lengths. Horizontally, the most extended difference patterns are located over the outskirts of the Alps and form elongated areas aligned with the wind direction (see Figure 3). The narrow streaks of extremum wind speed differences in such structures can be identified with differences in spatial extent of main mesoscale features of wind distribution, discussed above. There are also many features on a scale of about 100 kilometers, where the amplitudes of wind speed differences exceed 10 ms^{-1} and have both signs. They primarily occur in areas between or on the lee sides of main orographic features. Frequently, these flow features are systematic enough to be recognized on all the figures by their similar location and size, and they frequently have the same sign. Therefore, increasing the resolution to grid sizes of 1.1 and 0.55 km tends to have a similar effect on the mesoscale differences of the simulated flow. On the other hand, the differences between simulations with 0.55 and 1.1 km grid lengths tend to be smaller in terms of horizontal sizes and magnitudes. There is also an abundance of very small-scale differences in the wind speed pattern - of an amplitude of a few m/s -

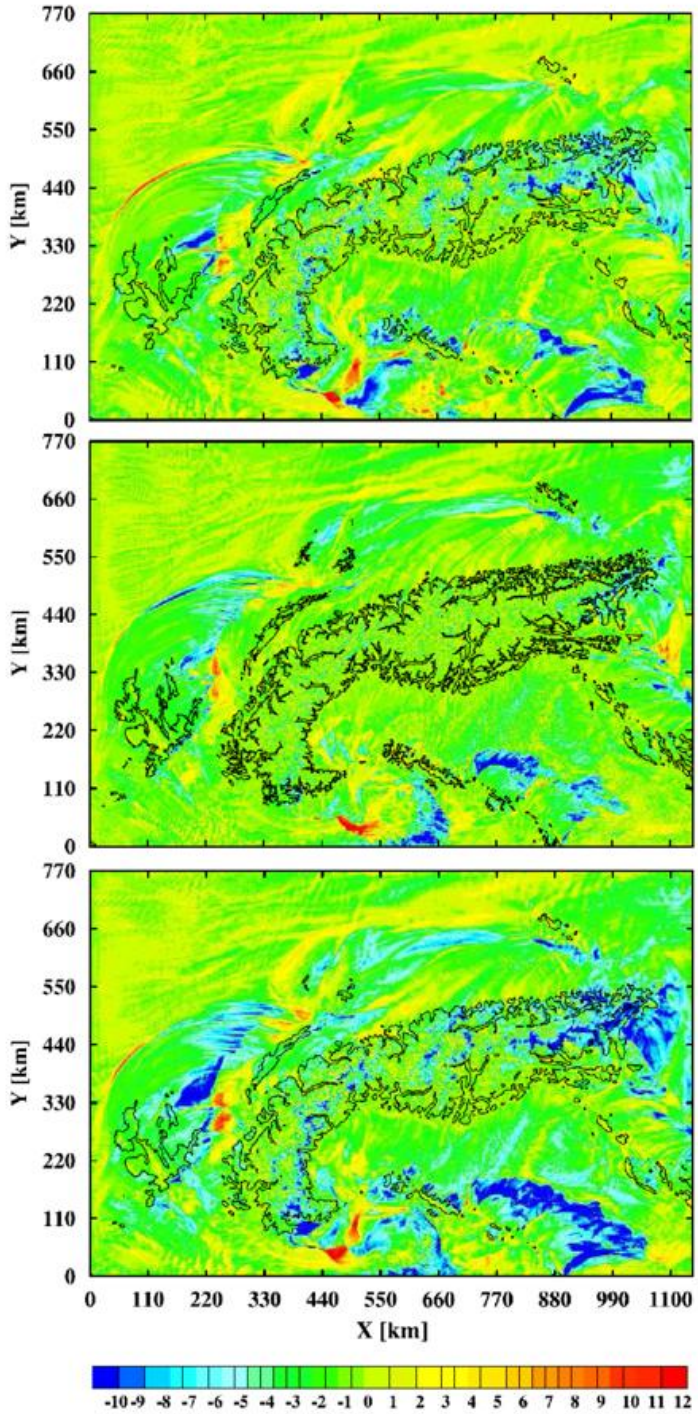


Figure 26: Distribution of the differences for surface (10 m above the ground) wind speeds in m/s (colors) after 24 hours. These difference plots compare the experiment using 1.1 km grid size (averaged to 2.2 km grid box) with the one using 2.2 km grid size (upper panel), the experiment using 0.55 km grid size (averaged to 1.1 km grid box) with the one using 1.1 km grid size (middle panel), and the experiment using 0.55 km grid size (averaged to 2.2 km grid box) with the one using 2.2 km grid size (lower panel).

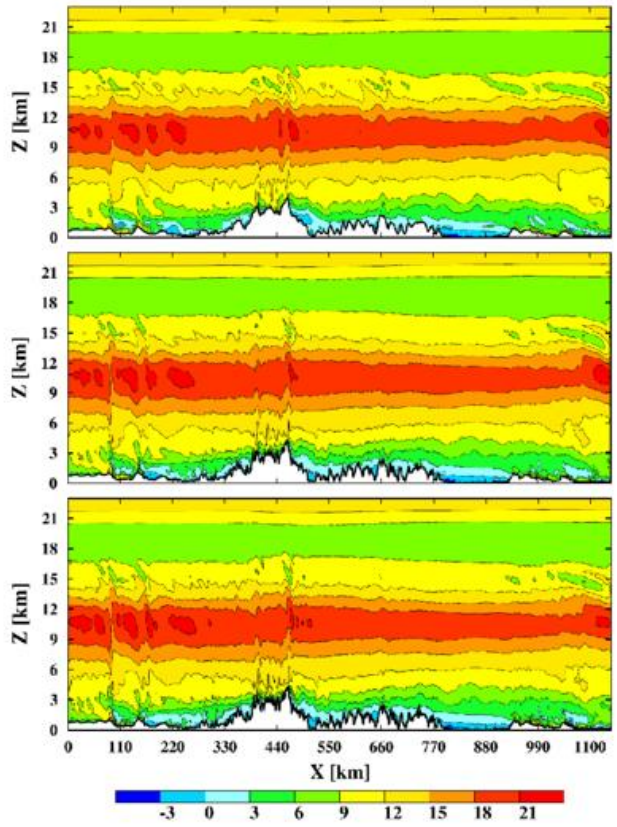


Figure 27: Vertical cross section through the u-component of wind (in ms^{-1}) after 24-hour simulations, for grid sizes of 2.2 km (upper panel), 1.1 km (middle panel), and 0.55 km (lower panel).

both over the relatively flat terrain (including sea surface) and over orographic features.

b. Vertical wind structure

Figure 27 shows west-east vertical cross sections of the u-component of wind velocity, along a line crossing the highest surface elevation represented by the model (Mt. Rosa). The general pattern of the flow is very similar for all the horizontal resolutions in the study. Its main feature is a moderate jet stream, and there are a number of mesoscale flow features over the whole domain. In the jet stream area, the locations and overall shapes of the mesoscale features are similar for all the simulations, which include e.g., pronounced acceleration areas above and in the lee of the Massif Central (left), over the Mt. Rosa area, and in the lee of the Dinaric Alps (right). Small-scale details differ between the simulations: very sharp horizontal wind gradients above the Massif Central and the Cevennes are especially pronounced, and they are reproduced with more detail and sharper gradients as the resolution increases.

The flow variability is closely related to mountain wave activity, which is abundant in the whole model domain and occurs on scales of about 50 km and smaller. All the simulations show similar flow features on the horizontal scales between 20 and 50 km (e.g., the structures over the Massif Central and the Cevennes, or over the Dinaric Alps). But there are also many smaller-scale features that differ significantly between the simulations.

Figures 28 shows the u-components of wind for a magnified part of the domain shown in Figure 27 located in the vicinity of the highest Alpine peaks (the x-coordinate is the same for

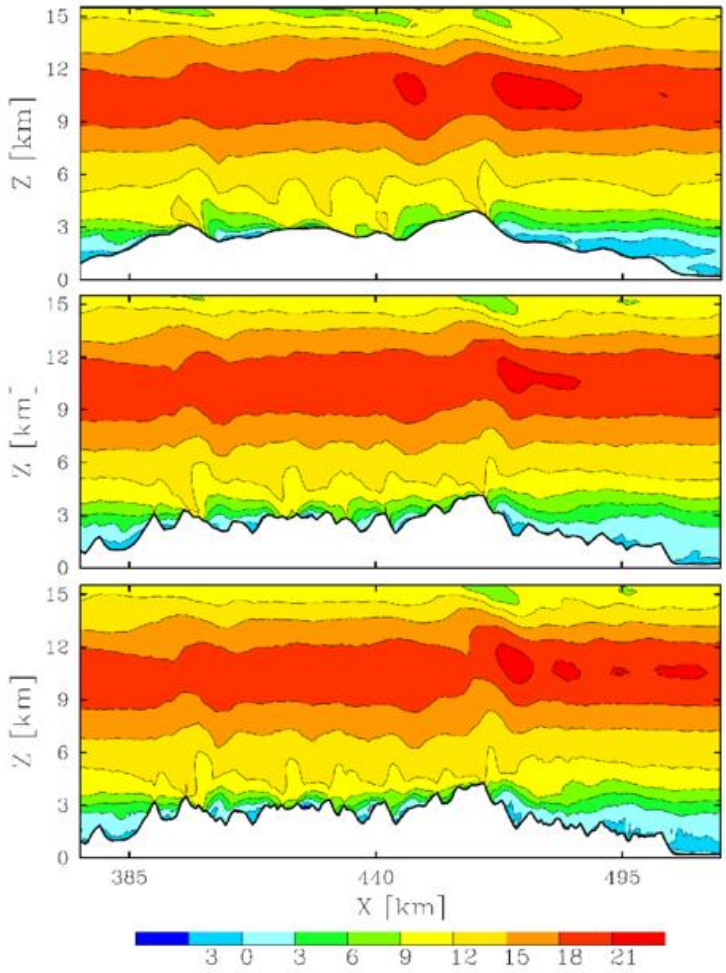


Figure 28: Closer view of the wind u-component (in m/s) over the highest Alpine peaks shown in Fig. 27 for a more detailed comparison as model resolution increases. Upper panel shows model output at 2.2 km grid size, middle shows 1.1 km grid size, and lower shows 0.55 km grid size.

all three figures). It confirms that the overall flow pattern is similar for all three resolutions. The differences are especially evident in many small-scale details of about 1 to 20 km in horizontal size for the u-component of the wind. They are seen in the jet stream area, particularly in the spatial structure of the maximum wind pattern. The largest differences appear, as expected, in the near-surface flows. Some of the differences represent circulations related to valleys, peaks, or ridges, represented only with very-high-resolution orography.

Qualitatively similar results are found for the v-component of the horizontal velocity (not shown).

Table 5 compares the RMS wind speed differences between simulations of different horizontal resolutions. It uses the 0.55 km simulation as the reference and compares data interpolated to a fixed height above ground (or above mean sea level). The comparison is done using grid point values and only grid points present in coarser resolution are used. To focus on the mountain regions, the comparison concerns areas of surface elevations exceeding 800 m above the mean sea level, for orography employing 0.55 km horizontal grid length. The table shows the wind differences on a few near-surface levels (at 20, 100, 500 and 2000 m above the ground) and on a few levels representing middle and upper troposphere (5, 6, 7 and 10 km

Altitude (m) above surface	RMS wind speed difference (m/s) between models of grid sizes (km):	
	0.55-2.2	0.55-1.1
20	3.92	1.83
100	3.80	1.64
500	2.87	1.10
2000	1.65	0.72
Altitude (m) above mean sea level	RMS wind speed difference (m/s) between models of grid sizes (km):	
	0.55-2.2	0.55-1.1
5 000	1.12	0.39
6 000	0.73	0.28
7 000	0.57	0.28
10 000	0.91	0.32

Table 5: RMS wind speed difference between simulations with 0.55 and 2.2 km grid sizes and between simulations with 0.55 and 1.1 km grid sizes, at selected altitudes above the surface and above mean sea levels. The differences are calculated only over the areas of surface elevation exceeding 800 m above mean sea level.

above the mean sea level). The table demonstrates larger differences between experiments with 0.55 km and 2.2 km grid sizes as compared to the differences between the experiments with 0.55 km and 1.1 km grid sizes. The largest differences between the experiments are located just above the surface, with values reaching almost 4 m/s for comparison between experiments with 0.55 and 2.2 km grid sizes. The differences diminish rapidly above 100 m height. The differences still decrease with height in the middle troposphere, but tend to increase near the tropopause.

c. Potential temperature

The general pattern of the potential temperature field is very similar for all three resolutions, and only small-scale details differ between the simulations (not shown). The differences are largest in the near-surface layer. They are due to both the ambient relation between the temperature and height, and the differences in the orographically induced flows. Also, the undulations of the isentropes in the near-surface layer of about 2 km depth above the Alpine ridge tend to have larger amplitudes for higher-resolution simulations. The differences between the simulations are hardly noticeable in the middle and upper troposphere.

Table 6, calculated analogously to Table 5, shows the RMS differences in the potential temperature between the simulations using interpolated values at the selected height levels. The table shows that the differences between simulations with 0.55 km and 2.2 km grid lengths are larger than the differences between experiments with 0.55 km and 1.1 km grid lengths. The largest differences are located in the near surface layer, and are in the range of 1 and 0.6 K for comparison with 2.2 km and 1.1 km grid simulations, respectively. In the middle troposphere the differences reach about one third of the surface values and increase in the tropopause area.

Altitude (m) above surface	RMS potential temperature difference (K) between models of grid sizes (km):	
	0.55-2.2	0.55-1.1
20	0.97	0.56
100	0.83	0.47
500	0.71	0.36
2000	0.52	0.25
Altitude (m) above mean sea level	RMS potential temperature difference (K) between models of grid sizes (km):	
	0.55-2.2	0.55-1.1
5 000	0.37	0.18
6 000	0.37	0.17
7 000	0.22	0.09
10 000	0.33	0.15

Table 6: RMS potential temperature difference between simulations with 0.55 and 2.2 km grid sizes and between simulations with 0.55 and 1.1 km grid sizes at selected altitudes above the surface and above mean sea levels. The differences are calculated only over the areas of surface elevation exceeding 800 m above mean sea level.

d. Vertical velocity

Figure 29 shows the horizontal distribution of the vertical velocity at level 40, located in the free atmosphere at a height of about 10400 m for all simulations. While the general pattern of the main features of the vertical velocity distribution is basically similar for all three resolutions, and while the regions of gravity wave activity do not change, significant small-scale differences are also present. In all simulations, it is common for the main patterns of the vertical velocity to be located in the vicinity of orographic features with the wave crests typically oriented perpendicular to the mean flow direction. This description generally applies to the Massif Central and the Cevennes, the Vosges Mountains and Schwarzwald, and the Sumava Mountains and the Alps. The amplitudes of the vertical velocity are in the range of 0.5 m/s, which is a realistic value.

For the area above the Alps, the pattern of the vertical velocity structure is generally similar for all the simulations in the sense that the main activity is located over the eastern slopes of the southwestern Alps and over the central crests of the eastern Alps. There are, however, clear differences. As the horizontal grid size of the model diminishes, the wave activity over the main Alpine body seems less pronounced as its spatial extent is also smaller and the wave amplitudes tend to be smaller in the area. In contrast, the wave activity over the areas south of the southwestern (Maritime) Alps and southeast of the eastern Alps seems to be at least as vigorous as for the coarser resolution simulation, but with a more complicated wave structure and many additional small-scale details.

Figure 30 presents vertical cross sections of vertical velocity, crossing the highest surface elevation of the model (Mt. Rosa), along the wind direction in the middle and upper troposphere and spanning the full model domain (see Figure 23 for the exact location of the cross-section). It shows similarity of the high-amplitude component of the wave distribution

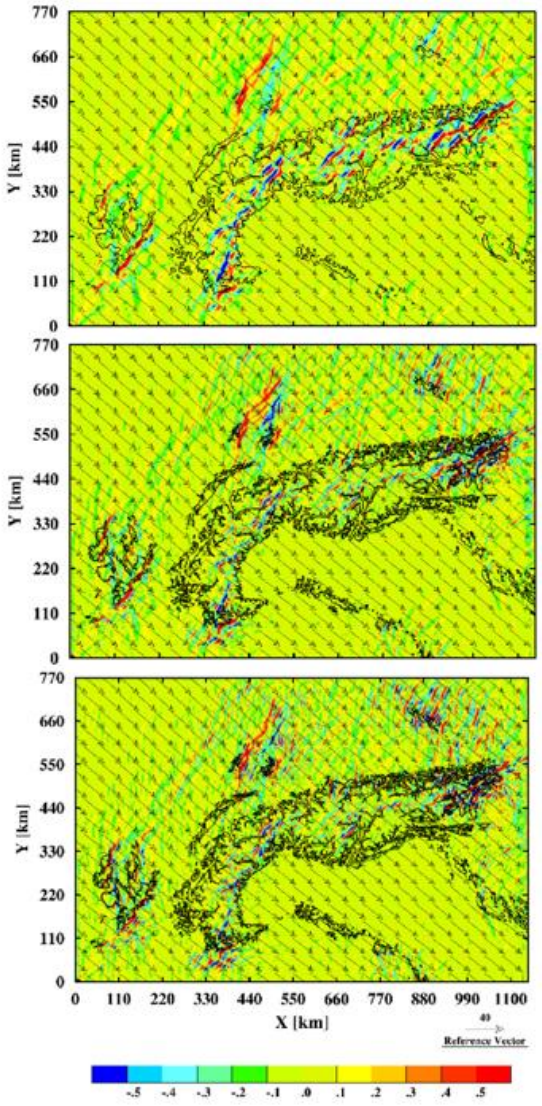


Figure 29: Horizontal distribution of wind (arrows) and the vertical velocity in ms^{-1} (colors) at 10400 m height after 24-hour simulations for grid sizes of 2.2 km (upper panel), 1.1 km (middle panel), and 0.55 km (lower panel).

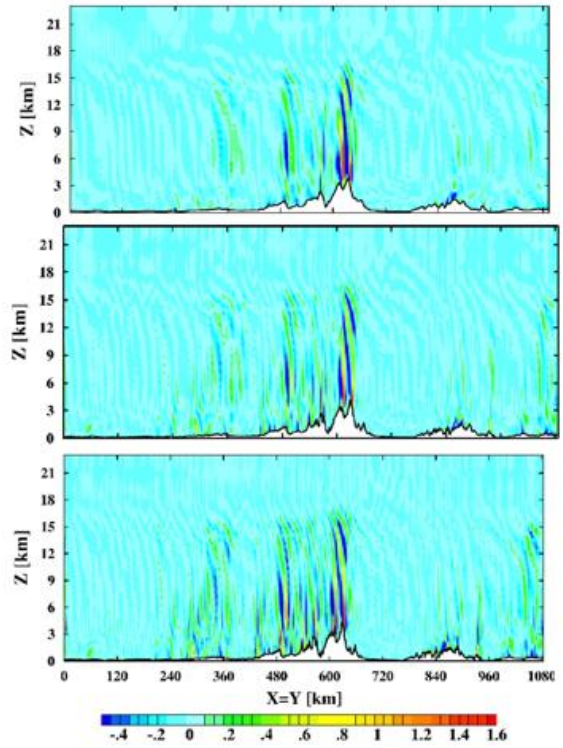


Figure 30: Vertical velocity distribution (colors in m/s) after 24 hours for simulations with grid sizes of 2.2 km (upper panel), 1.1 km (middle panel), and 0.55 km (lower panel). The cross section is oriented along the prevailing wind in the middle and upper atmosphere.

for different resolutions, but it confirms also the significant influence of horizontal model resolution on the simulated structure of vertical velocity. The differences appear in both the relatively low highlands, like the Plateau de Langres, where the 2.2 km grid shows the presence of only a single wave pattern in the middle and upper troposphere. In contrast, the higher resolution simulations show rich wave structures of slightly larger amplitudes in the middle troposphere and significantly higher amplitudes near the surface. The differences are also clearly seen above the higher mountains, especially in the area between the Jura and Mt. Rosa, where the higher-resolution simulations have significantly richer wave structures characterized by larger amplitudes.

Figure 30 shows a detail of Figure 29 over the Alps. The significant influence of the horizontal model resolution on the vertical velocity distribution is seen by the presence of the complicated wave pattern in the area west of the Rhone Valley (left), obtained with the highest-resolution simulation. For the common features, the 0.55 km grid size gives significantly higher amplitudes and more realistic wave structures for the wave triggered by the Jura (the western part of the figure) and the eastern parts of the Bernese Alps. The wave pattern and magnitudes of extremes triggered by the Pennine Alps, including Mt. Rosa, are similar at all three resolutions. However, the higher-resolution simulations show many small-scale details of the structure, especially in the near-surface layer, where small-scale terrain features play an important role in forming the shape of the wave pattern. For the area roughly 2 km above the surface, the influence of the larger scales prevails and the differences between the simulations become smaller.

The realism of the simulations can be further confirmed by noticing that the wave crests tend to change to a horizontal orientation in the upper part of the domain. This is a typical

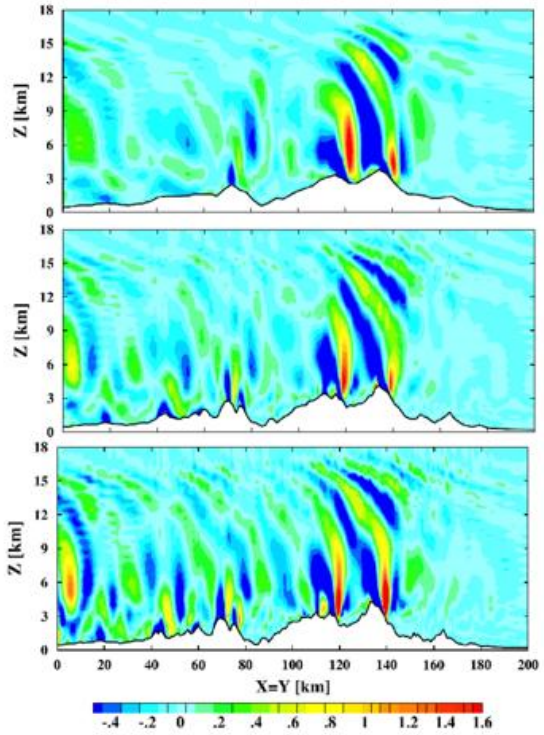


Figure 31: Enlarged picture of the flow over the Alps.

behavior for a gravity wave in the presence of the critical layer, where the phase velocity of the wave equals the flow velocity. For the Brunt-Väisälä frequency on the order of 0.013 s^{-1}, and the wavelength in the horizontal and vertical directions on the order of 10 km, estimates place the critical velocity in the range of 20 m/s which corresponds well to the typical wind speeds found in the upper troposphere. This suggests the presence of the critical layer in our simulations and confirms the physical consistency of the simulated gravity waves.

Table 7 shows the RMS differences of the vertical velocity between the simulations at selected levels, for the areas with surface elevations above 800 m and not averaged to the coarser grid. It shows that the differences between experiments with 0.55 km and 2.2 km grid lengths are larger than the differences between simulations with 0.55 km and 1.1 km grid lengths. While the differences between analyses of velocities and potential temperature presented in Figure 30 and Tables 5 and 6 are relatively small, they are larger for the vertical wind. Table 7 shows that the vertical velocity differences between the solutions over higher elevations are almost three times larger than average. This is confirmed by a qualitative analysis of Figures 29 to 30, suggesting that vertical velocity perturbations are spatially related to the areas of highest elevations, and that the horizontal resolutions significantly affect the vertical velocity pattern. Over the mountains, the RMS differences are highest in the near-surface layer, reaching almost 0.9 m/s for the comparison between the experiments with 0.55 and 2.2 km grid lengths. They decrease with height by about one third at 2000 m altitude. In the middle and upper troposphere the difference still diminishes with height, consistent with Figure 30a.

4.3 Summary and conclusions

The tests show the numerical robustness of the EULAG dynamical core, as no numerical problems were encountered during the simulations and no artificial measures, like flow or

Altitude (m) above surface	RMS vertical velocity difference (m/s) between models of grid sizes (km):	
	0.55-2.2	0.55-1.1
20	0.87	0.54
100	0.80	0.47
500	0.69	0.38
2000	0.59	0.35
Altitude (m) above mean sea level	RMS vertical velocity difference (m/s) between models of grid sizes (km):	
	0.55-2.2	0.55-1.1
5 000	0.49	0.29
6 000	0.42	0.24
7 000	0.33	0.28
10 000	0.20	0.11

Table 7: RMS of vertical velocity difference between simulations with 0.55 and 2.2 km grid sizes and between simulations with 0.55 and 1.1 km grid sizes, over areas of elevation exceeding 800 m above mean sea level, at selected altitudes.

orography smoothing, were applied to achieve the results. The scales of the values of the flows physical parameters are represented correctly. This concerns especially vertical velocity, magnitude of which is sensitive to possible problems in the model setups. This suggests that an anelastic dynamical core like EULAG has numerical robustness appropriate for NWP purposes at horizontal grid sizes of at least $O(1km)$.

The analysis of the results, especially of the spatial distribution of different parameters characterizing the flow and their comparison for varying horizontal resolutions, shows that the results are realistic and highly consistent. Results indicate a realistic low-level flow pattern characteristic of mountain blocking, and the presence of characteristic mesoscale features related to the flow over specific terrain features like large valleys, highlands, and mountains. The vertical flow structure shows that the orography significantly influences regional and local circulations, including low-level circulations like valley flows, but especially mountain waves, and the whole troposphere including the structure of the jet stream.

The flow structures are consistent between the three model resolutions, especially for flow features having characteristic sizes of 20 km and more. However, the differences between simulations involve a wide range of scales and are not limited solely to the barely resolved scales. The differences are seen especially clearly and abundantly in the near-surface tropospheric layer at a depth of about 1.5 to 3 km. For surface wind, differences between the three solutions have characteristic structures of horizontal sizes varying from hundreds of kilometers to the smallest resolved by the model, the amplitudes of the differences reach up to 20 m/s, and the RMS difference reaches 4 m/s. From the viewpoint of NWP, the near-surface area is highly important for a majority of the forecast users, including aviation.

References

Brighton, P.W.M. (1978), Strongly stratified flow past three-dimensional obstacles, *Q. J. Roy. Meteorol. Soc.* 104, 289-307.

Bryan, G. H., and J. M. Fritsch (2002), A benchmark simulation for moist nonhydrostatic numerical models, *Month. Wea. Rev.*, 1030, 2917-2928.

Clark, T.C., and M. Miller (1991), Pressure drag and momentum fluxes due to the Alps. II: Representation in large scale atmospheric models,*Quart. J. Roy. Meteor. Soc.* 117, 527-552.

Cullen, M., D. Salmond, and P.K. Smolarkiewicz (2000), Key numerical issues for the future development of the ECMWF model, *Proc. ECMWF Workshop on Developments in Numerical Methods for Very High Resolution Global Models*, Reading, ECMWF, pp. 183-206

Gal-Chen T., and R.C.J. Somerville (1975), On the use of a coordinate transformation for the solution of the Navier-Stokes equations,*J. Comput. Phys.* 17, 209-228.

Hoinka, K.P., and T.C. Clark (1991), Pressure drag and momentum fluxes due to the Alps. I: Comparison between numerical simulations and observations, *Quart. J. Roy. Meteor. Soc.* 117, 495-525.

Klemp, J. B., and R. B. Wilhelmson (1978), The simulation of three-dimensional convective storm dynamics, *J. Atmos. Sci.* 35, 1070-1096.

Leuenberger, D., M. Koller, O. Fuhrer, and C. Schaer (2010), A generalization of the SLEVE vertical coordinate, *Month. Wea. Rev.*, 138, 3683-3689.

Rabus, B., M. Eineder, A. Roth, and R. Bamler (2003), The shuttle radar topography mission (SRTM) - A new class of digital elevation models acquired by space borne radar, *ISPRS J. Photogramm. Remote Sens.* 57, 241-262.

Rontu, L. (2006), A study on parametrization of orography-related momentum fluxes in a synoptic-scale NWP model, *Tellus A* 58, 69-81.

Rotach, M.W., M. Andretta, P. Calanca, A.P. Weigl, and A. Weiss (2008), Boundary layer characteristics and turbulent exchange mechanisms in highly complex terrain, *Acta Geophysica* 56, 194-219.

Rotunno, R., and J.B. Klemp (1985), On the rotation and propagation of simulated supercell thunderstorms, *J. Atmos. Sci.* 42, 271-292.

Salvador, R., J. Calbo, and M.M. Millan (1999), Horizontal grid size selection and its influence on mesoscale model simulations, *J. Appl.Meteorol.* 38, 1311-1329.

Smith, S.A., J.D. Doyle, A.R. Brown, and S. Webster (2006), Sensitivity of resolved mountain drag to model resolution for MAP case-studies, *Quart. J. Roy. Meteor. Soc.* 132, 1467-1487.

Smolarkiewicz, P. K., and R. Rotunno (1990), Low Froude number flow past three-dimensional obstacles. Part II: Upwind flow reversal zone, *J. Atmos. Sci.* 47, 1498-1511.

Weisman, M. L., and J. B. Klemp (1982), The dependence of numerically simulated convective storms on vertical wind shear and buoyancy, *Monthly Weath. Rev.* 110, 504-520.

Welch, T.W., P.K. Smolarkiewicz, R. Rotunno, and B.A. Boville (2001), The large scale effects of flow over periodic mesoscale topography, *J. Atmos. Sci.* 58, 1477-1492.

Ziemianski, M.Z., M.J. Kurowski, Z.P. Piotrowski, B. Rosa, and O. Fuhrer (2011), Toward very high horizontal resolution NWP over the Alps: Influence of in-creasing model resolution on the flow pattern, *Acta Geophys.* 59, 6, DOI:10.2478/s11600-011-0054-9.

5 Semi-realistic flow over the Alps with the COSMO-EULAG model

Michał Ziemiański, Marcin J. Kurowski, Zbigniew P. Piotrowski, Bogdan Rosa, Damian Wójcik

Institute of Meteorology and Water Management - National Research Institute, Poland

5.1 Introduction

This section reports on semi-realistic simulations of weather for the Alpine region using a prototype COSMO model equipped with the anelastic dynamical core. The prototype couples the dynamical core of the EULAG model with a limited set of standard COSMO parameterizations. The report begins with a brief description of the implementation of the EULAG dynamic core into the operational software environment of the COSMO model. Next, it shows the results of testing the COSMO-EULAG prototype (CE) for a simulation of mesoscale weather for 24 hours forecast at three different horizontal resolutions i.e. with 2.2, 1.1 and 0.55 km horizontal grid size. The CE results for 2.2 km grid are compared with analogous results obtained using the COSMO model employing standard Runge-Kutta dynamical core and the same limited set of physical parameterizations (RK) to evaluate the viability, consistency and correctness of the CE results. The goal of the comparison is to assess whether the anelasticity of the CE dynamical core has noticeable detrimental effect on the simulation results. Also, the CE results for various resolutions are inter-compared and analyzed to assess whether they are consistent, realistic and robust.

Both model setups involve physical parameterizations of boundary layer effects with surface fluxes, radiation and moist processes. The experiment employs also realistic initial and changing in time boundary conditions for a selected actual weather situation, provided by MeteoSwiss and taken from its operational data. The experiment has, therefore, a higher degree of realism comparing with the one described in the previous section, but the model prototype is still not in a full and consistent NWP setup.

5.2 The COSMO-EULAG prototype

The implementation of the EULAG dynamical core into the COSMO operational environment required addressing a number of technical issues. First, the EULAG dynamical core has been translated from Fortran 77 to Fortran 90/95 which allowed the implementation of alternative programming structures required by the COSMO programming standards. Common blocks were replaced by modules, and the data structure in the translated code is based on explicit dynamic memory allocation. The MPI communication of the CE model was organized in a consistent way with COSMO framework. The key steps of the implementation and the relevant technical details regarding translation have been reported by Wojcik et al. (2012).

The coupling of the two codes (COSMO and EULAG) required a development of specially designed interface. Its main purpose was to allow a data communication between dynamical core and physical parameterizations applying different types of computational grids. The nodal points of the EULAG grids are non-staggered (A-grid) whereas algorithms of COSMO parameterizations have been developed for the staggered C-grid.

The interface is designed according to the rule that the COSMO mass levels and mass

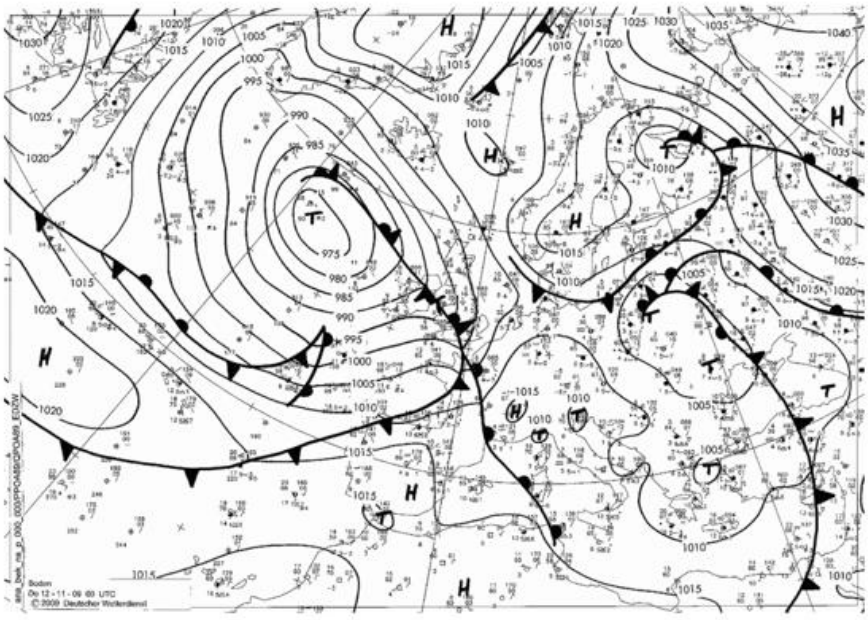


Figure 32: Surface synoptic chart of Europe for 12 November 2009, 00:00 UTC.

points collocate with the EULAG computational points and levels in order to avoid spatial interpolation of the mass-related flow parameters. In order to provide the bottom boundary conditions for the vertical component of velocity (w), an additional EULAG level is provided just at the ground. Its physical flow parameters are the same as the parameters on the next EULAG level collocated with the first COSMO mass level (counting from the surface) in order to ensure consistent values of the flow parameters from the finite-volume-wise view point (alteration of the physical parameters within the surface level would result in alteration of volume averaged values in the COSMO finite volumes around its lowest-lying mass points).

With such an approach, the interface requires interpolation of velocity values between grid A and C while providing information from the dynamical core to the parameterizations, and interpolation of their forcings, diagnosed by COSMO parameterizations, between grid C and A. It transforms also potential temperature of EULAG to temperature of COSMO, as well as temperature forcing from COSMO parameterizations to potential temperature forcing to be used by the dynamical core.

5.3 The experiment setup

The tests are based on 24-hour simulation of an Alpine flow using the COSMO model with the RK and CE setups, both using the same limited set of physical parameterizations. The employed parameterizations are:

- Vertical Turbulent Diffusion
- Surface Fluxes Louis (1979)
- Radiative Transfer Scheme Ritter, Geleyn (1992)
- Multilayer Soil Model
- Moist Microphysics with prognostic variables including rain, snow, ice and graupel.



Figure 33: Wind velocity (color scale and wind arrow length) and direction (wind arrow direction) on the 10 m model level for 12 hour (left panels) and 24 hour (right panel) forecast for the CE (upper panels) and RK (lower panels) model versions.

There was no special tuning of the physical parameterizations for the CE setup and their parameters took values tuned for the operational COSMO model using the RK dynamical core.

a. Domain

Similarly to the semi-realistic tests described in the previous section, the experiment setup is based on the COSMO-2 model of MeteoSwiss. Its domain (see Fig. 23 of the previous section), orography, vertical Gal-Chen coordinates and computational layers are configured as for the experiment described in the previous section. Only the size of the computational domain for the experiment employing 0.55 km resolution was limited and covers only a part of the full COSMO-2 domain (see Fig. 41) due to computational reasons.

b. The flow configuration

The experiment follows the actual operational COSMO forecast for 12 November 2009 and involves a 24-hour simulation starting at 00:00 UTC. The initial conditions are the same for RK and CE runs and are taken from operational data of MeteoSwiss. It concerns also the boundary conditions, which are interpolated linearly in time from the hourly data sets.

The synoptic situation, chosen, involves a moderately stratified westerly flow with a moderate



Figure 34: As in Figure 33 but for the 10th model level (approximately 500 m above the ground level).

jest stream. It features a relatively shallow low-pressure system with atmospheric fronts traversing the simulation domain (Fig. 32).

5.4 Results

An analysis of the simulation results is presented below. It compares the wind velocity distribution, cloud water and cumulative surface precipitation for the RK and CE models. Both models use 2.2 km grid size and their results are compared for 12 and 24 hour forecast. Also, the CE results after 12 and 24-hour forecasts are inter-compared for varying resolutions of 2.2, 1.1 and 0.55 km and analyzed.

RK and CE comparison

Figure 33 presents the wind velocity at 10 m above the ground (the first COSMO computational level) for 12 and 24 hour forecast for the CE (upper panels) and RK (lower panels) versions of the model. For both realizations, the general pattern of the flow is practically the same and follows the synoptic situation with weak to moderate south-westerly flow in the western part of the domain and relatively weak variable flow in the rest of the domain which is influenced by the anticyclonic pressure system. Moreover, both simulations very similarly represent the mesoscale structure of the flow with the same patterns of flow acceleration and deceleration(see for instance the pronounced flow patters over the Genoa Bay and Adriatic



Figure 35: As in Figure 33 but for the 26th model level (approximately 4600 m above the ground level).

Sea). Also the wind velocities are very similar for both model versions, with a tendency of the CE solution for slightly higher wind speeds. The effect is especially seen over the Alps. That may result from the lack of tuning of the parameterizations for the CE setup (note the diminishing surface wind velocities of the CE simulations for increasing resolutions, described below). The pattern of the flow areas with nearly zero wind velocities suggests also more patchy (spatially variable) structure of the CE velocity field within the smallest resolvable scales.

Figures 34, 35 and 36 present, respectively, the wind velocity on different computational model levels ranging from level 10 (approximately 500m above the ground), to 26 (approximately 4600 m above the ground) and 40 (approximately 10 km above the ground). Note that the levels are counted from the ground level up (that is opposite to standard COSMO level counting) and the approximate heights of the computational levels concern areas where the ground surface is located at the mean sea level. The results are for 12 (left panels) and 24 hour (right panels) forecast for the CE (upper panels) and RK (lower panels) versions of the model.

The figures show that both the synoptic and mesoscale patterns of the flow as well as wind velocities are to very high degree the same for both simulations and the similarity is even greater, comparing with the surface wind field, for the flow less or not affected by the friction. Only some differences are noticeable for wind velocities. For 10 and 26 model levels (lower and middle troposphere) CE gives slightly higher wind velocities in constrained, localized



Figure 36: As in Figure 33 but for the 40th model level (approximately 10 km above the ground level).

areas, especially immediately north of the Alpine ridge (see the 12 hour forecast at 10 level and 24 hour forecast at 26 level). For level 40 (near the tropopause) the situation is different: the CE solution brings slightly lower wind velocity at areas just over the Alpine ridge (for 12 and 24 hour forecast) and on the lee side of the Alps (for 24 hour forecast). That suggests generally stronger effects of the explicitly resolved orographically induced gravity wave drag in the CE representation of the flow.

Figure 37 presents the vertical cross section through the fragment of wind velocity field in the vicinity of Mt. Rosa. The orientation of the section line is from north-west to south-east (similar to Figure 27 of the previous section), for 12 hour (left panels) and 24 hour (right panel) forecast for the CE (upper panels) and RK (lower panels) model versions. The figure shows clear similarity of the general pattern of the flow but also some differences. The differences are located in the near surface layer where numerous differing very-small-scale details are superimposed within the same large-scale flow pattern. The localized differences are also present in the middle troposphere and have generally a signature of gravity wave structures. For the jet stream area larger-scale differences are seen especially over the mountains (12 hour forecast) and over their lee side (24 hour forecast) where CE wind velocities are smaller suggesting stronger gravity wave drag, in agreement with analysis of Fig. 36.

Figure 38 presents the vertical cross section through vertical velocity distribution in the vicinity of Mt. Rosa, in the area shown by Fig. 37. Also for the vertical velocity distribution the general pattern of the flow is similar for both realizations and for both instances.

Figure 37: Vertical cross section through wind velocity in the vicinity of Mt. Rosa, the north-west to south-east orientation of the section line for 12 hour (left panels) and 24 hour (right panel) forecast for the CE (upper panels) and RK (lower panels) model versions

It concerns especially the magnitudes of the amplitudes and general pattern of the most pronounced features. There are also noticeable differences between CE and RE simulations, which concern details of shape and extension as well as magnitudes of weaker flow features, but they are generally common for both representations.

Figure 38: Like in Figure 37 but for vertical cross section through vertical velocity field

The experiment involved also a simulation of moist processes. The results for CE and RK realizations are very similar. It is seen e.g. analyzing a 3-dimensional distribution of iso-surfaces of constant cloud condensate mixing ratio for which there are no significant differences between the realizations (not shown). A comparison of distribution of cloud water

mixing ratio is shown in Figure 39 presenting a vertical cross section through the field along the north to south oriented cutting line crossing the Western Alps for 6, 12 and 24 hour forecast. The figure demonstrates very similar cloud pattern for CE and RK simulations, especially for relatively dense cloud structures, with some differences concerning smaller scale details and the parameter's amplitudes. For less dense clouds the differences are more significant and in places concern also more general cloud patter. Nevertheless, the similarity of the solutions is significant.

Figure 39: Vertical cross section through the cloud water mixing ratio along the north to south oriented cutting line crossing the Western Alps for 6 (upper panel), 12 (middle panel) and 24 hour forecast; RK results on the left panel, CE on the right.

A good general indication of the consistency of simulations involving representation of moist processes comes from analysis of the resulting precipitation distribution. Figure 40 shows the precipitation accumulated within 12 (left panel) and 24 hours (right panel) periods. The figure confirms a very high degree of similarity of the precipitation pattern for the RK and CE realizations, for both instants. Also the precipitation amounts are similar, especially during the first 12 hours of forecast. Later, for the 24 hour accumulation of precipitation, the locations of maxima are still very similar for both model versions but CE tends to generally produce higher precipitation maxima.

Overall, the consistency of the RK and CE results involving the parameterizations tuned for the RK operational setup and simply implemented to the CE setup can be regarded as significant

CE inter-comparison for increasing horizontal resolution



Figure 40: Accumulated precipitation (color scale) and direction on the surface for 12 hour (left panels) and 24 hour (right panel) forecast for the CE (upper panels) and RK (lower panels) model versions.

Figure 41 presents an inter-comparison of surface wind (on the computational level 10m above the surface) obtained with the CE model for 2.2, 1.1 and 0.55 km horizontal grid size. The figures show consistently the same synoptic and mesoscale velocity pattern, discussed above, for all the resolutions. The differences concern mainly small scale details of the flow field and a general tendency for lower wind velocities for increasing horizontal resolution of the simulation, especially over the Alps, suggesting an influence of explicitly resolved orography drag, increasing with increasing model and orography resolutions.

Similarly, Figure 42 compares the wind on 10-th computational level (about 500 m above the surface) for the CE forecast with 2.2, 1.1 and 0.55 km horizontal grid size. The figures show very high consistency of the flow pattern, for all the resolutions. The differences concern mainly small-scale details of the flow field, especially in the immediate vicinity of high mountains. A general tendency for lower wind velocities for higher horizontal resolution is also seen over the Alps, especially while comparing the results for 2.2 and 0.55 km grid size.

Figure 43 (left panels) compares the vertical cross sections through a fragment of the wind velocity field obtained with horizontal grid sizes of 2.2, 1.1 and 0.55 km for the Mt. Rosa vicinity in location close to the one in Fig. 37. The figure allows analyzing in more details the differences in the forecasted velocity field as well as in the orography pattern for different resolutions. It shows that while the results keep consistency of the general flow pattern,

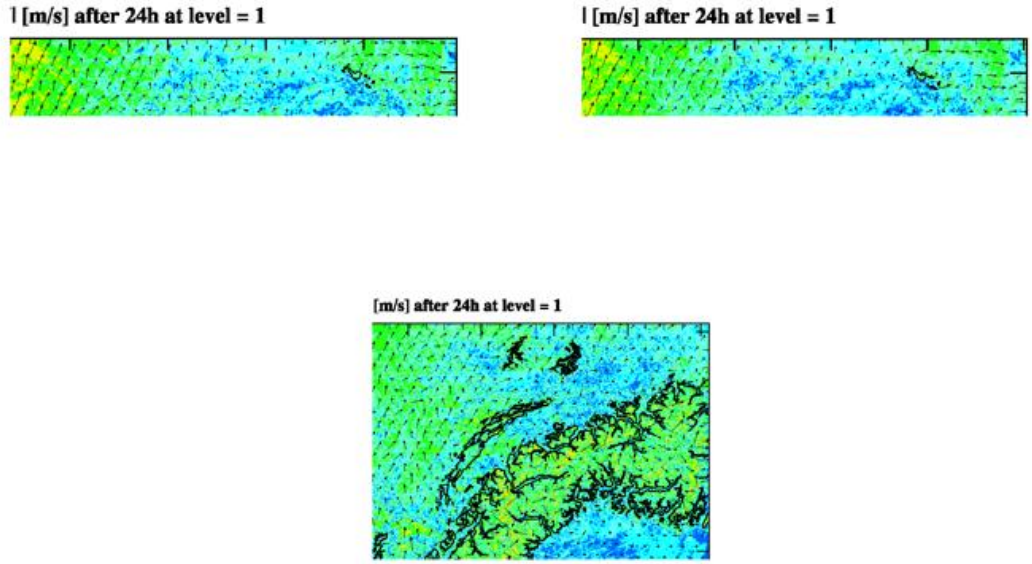


Figure 41: Wind velocity (color scale and wind arrow length) and direction (wind arrow direction) on the 10m model level for 24 hour forecast with the CE model version using horizontal grid size of 2.2 km (left, upper panel), 1.1 km (right panel) and 0.55 km (left lower panel).

the differences concern whole depth of the troposphere and are pronounced especially in the near-surface and the jet stream area. For increasing resolution, in the near-surface area there is more variability in the flow for the smallest scales, which results both from the increased variability of the resolved orographic forcing and of the model resolved scales. In the jet stream area, the differences concern mainly mesoscale patterns of the sizes of tens of kilometers. The general tendency is diminishing strength of the jet stream with increasing resolution, suggesting an increasing drag of explicitly resolved mountain waves. There is no grid-convergence of the simulated flow due to the resolution dependent orography pattern.

Figure 43 (right panels) compares also the vertical cross sections through the CE vertical velocity field obtained with grid sizes of 2.2, 1.1 and 0.55 km for the Mt. Rosa vicinity in the location shown in Figure 42. The wave features forecasted with the 2.2 km resolution and especially the most pronounced wave patterns are also clearly present in simulations with higher resolutions. The features have also similar amplitudes. On the other hand, the simulations with higher resolutions show a presence of increasingly complicated wave patterns with additional or significantly amplified features comparing with 2.2 km grid simulations. Such features are present not only in the vicinity of the surface but also in the middle and upper troposphere and in places reach magnitudes of the main wave features obtained with

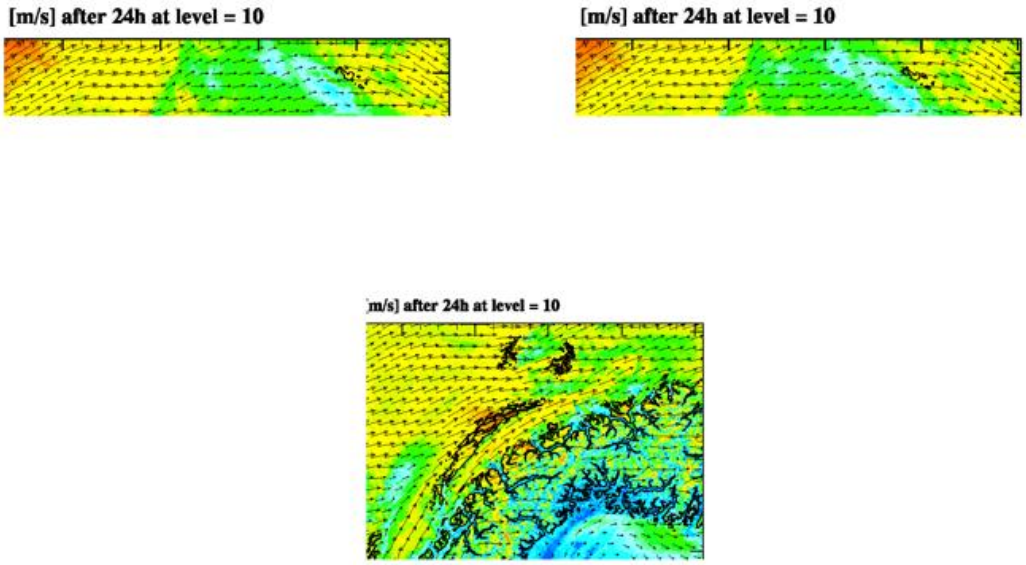


Figure 42: As in Figure 41 but for 10th model level above the ground.

2.2 km grid.

Finally, Fig. 44 compares vertically integrated cloud water for the CE forecast for 12 hours for 2.2 km (left panel) and 0.55 km (right panel) grid sizes. It presents high similarity of the obtained cloud fields, concerning both the cloud pattern and the amount of the condensate. The high-resolution simulation shows, however, a general presence of many very small-scale details absent in the lower-resolution simulations.

5.5 Summary and conclusions

The COSMO-EULAG prototype with EULAG dynamical core implemented into the software structure of the COSMO model and linked with basic physical parameterizations was successfully developed. The prototype was tested comparing its results with analogous COSMO model based on the compressible Runge-Kutta dynamical core for high-resolution 2.2 km horizontal grid sizes, for semi-realistic 24 hour forecast of the flow over Alps and its vicinity.

The tests have shown that the realistic CE results are similar to and consistent with the results of COSMO with RK dynamical core. It concerns not only basic parameters of the flow like wind and potential temperature distribution (the latter not shown) but also moist parameters like cloud condensate distribution and cumulative surface precipitation. Interesting differences between the models concern mountain gravity waves. While their distribution

Figure 43: Vertical cross section through wind velocity (left panels) and vertical velocity (right panels) for 24 hour forecast in the vicinity of Mt. Rosa with the CE model using horizontal grid size of 2.2 km (left, upper panel), 1.1 km (right panel) and 0.55 km (left lower panel).

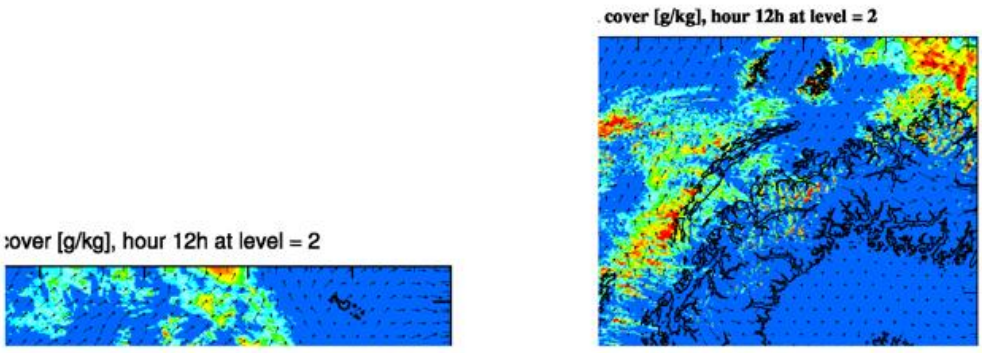


Figure 44: Vertically integrated cloud water (g/kg) for the CE forecast for 12 hours using 2.2 km (left panel) and 0.55 km (right panel) grid size.

is generally similar for both models, they differently influence the upper flow pattern leading to noticeable differences of the wind velocity in the jet stream area, while preserving similar general flow pattern. In general, no discrepancies of the CE simulations were found which would prove unsuitability of the EULAG dynamical core as well as of the anelastic approach for the very-high resolution regional NWP applications.

Finally, the CE prototype was tested for the varying horizontal resolutions with grid sizes of 2.2, 1.1 and 0.55 km. The simulations show a high degree of consistency of the results as well as the desirable robustness of the CE prototype. It was shown that with the increasing grid resolution the small scale variability of the flow increases with appearance of many small scale details especially in the near surface layer and gravity wave pattern. There are also resolution dependent differences in the jet stream velocity distribution suggesting effects of explicitly resolved gravity wave drag. There is no grid convergence of the solution for the orography significantly varying between the simulations.

References

Wojcik, D., K. Kurowski, B. Rosa and M. Ziemianski, 2012: A study on parallel performance of the EULAG F90/95 code. *Lecture Notes in Computer Science*, **7204**, 419–427.

Louis, J.-F., 1979: A parametric model of vertical eddy fluxes in the atmosphere. *Bound. Layer Meteor.* **17**, 187–202.

Ritter, B. and J.-F. Geleyn, 1992: A comprehensive radiation scheme for numerical weather prediction models with potential applications in climate simulations. *Mon. Wea. Rev.*, **120**, 303–325.

6 MPDATA as an alternative tracer advection scheme

Guy de Morsier and Marie Müllner

MeteoSwiss, Krähbühlstrasse 58, 8044 Zürich, Switzerland

6.1 Introduction

The results shown here were achieved during a 6 month diploma work done by Marie Müllner at MeteoSwiss in 2010 and for the full details see the original work by Muellner (2010) (in German).
In the current COSMO model the advection of the prognostic variables is done with an upwind scheme[1]. This scheme is efficient and therefore well adapted for a fast operational model but it is not monotone and not conservative. For the advection of positive definite variables such as scalar tracer fields, i.e. all water constituents, possible aerosol particles and gaseous substances or turbulent kinetic energy, finite volume schemes are more appropriate. For the tracer transport the model provides already different formulations but all of them have some drawbacks.
The aim of this work is to implement, evaluate and test a fully three dimensional advection scheme for the COSMO model. The proposed advection scheme is MPDATA (multidimensional positive definite advection transport algorithm, see Smolarkiewicz and Margolin (1998)) which is used in the EULAG (Eulerian/Semi-Lagrangian fluid solver, see Prusa et al. (2008)) numerical model. The code used for the implementation is from Piotr K. Smolarkiewicz and it can be found in the appendix of Muellner (2010).

6.2 Advection of prognostic fields

In COSMO the advection of the wind components, the temperature and the pressure is operated with an upwind scheme of the 5th order. The upwind scheme is a numerical discretization for hyperbolic partial differential equations.
We take the following advection equation

$$\frac{\partial u}{\partial t} + a\frac{\partial u}{\partial x} = 0 \tag{3}$$

A solution of this equation is a wave that travels along the x-direction with the speed a. For a numerical approximation of $\partial u/\partial t$ we use

$$\frac{\partial u}{\partial t} = \frac{u_i^{n+1} - u_i^n}{\Delta t}$$

and for the approximation of $\partial u/\partial x$ we use the backward difference if $a > 0$

$$\frac{\partial u}{\partial x} = \frac{u_i^n - u_{i-1}^n}{\Delta x} \tag{4}$$

and the forward difference if $a < 0$

$$\frac{\partial u}{\partial x} = \frac{u_{i+1}^n - u_i^n}{\Delta x} \tag{5}$$

[1] upwind scheme of 5th order is used (Wicker and Skamarock, 2002); more general operators are described in (Doms et al., 2011, section 8.1.2) .

After replacement in (3) and depending on a we obtain

$$\frac{u_i^{n+1} - u_i^n}{\Delta t} + a\frac{u_i^n - u_{i-1}^n}{\Delta x} = 0$$

or

$$\frac{u_i^{n+1} - u_i^n}{\Delta t} + a\frac{u_{i+1}^n - u_i^n}{\Delta x} = 0$$

By defining $a^+ = \max(a,0)$, $a^- = \min(a,0)$, $u_x^- = \frac{u_i^n - u_{i-1}^n}{\Delta x}$ and $u_x^+ = \frac{u_{i+1}^n - u_i^n}{\Delta x}$ we can put the 2 cases together to

$$u_i^{n+1} = u_i^n - \Delta t(a^+ u_x^- + a^- u_x^+)$$

or

$$u_i^{n+1} = u_i^n - C(u_i^n - u_{i-1}^n)$$

where C is the Courant-Friedrichs-Lewy number (CFL) which is defined by

$$C = \left|\frac{a\Delta t}{\Delta x}\right|$$

This upstream scheme is of the first order and is only stable if $C \leq 1$.

6.3 Positive definite advection

For the advection of tracers the model provides a semi-Lagrangian scheme (SL) and direction splitted finite volume schemes. For the latter, several flux formulations exist under which the flux calculation by Bott (1989) is the standard one and the others are the vanLeer-scheme and a piecewise parabolic method (PPM). The different methods should satisfy the following conditions so that the physical properties are fulfilled:

- conservation of mass
- computation of the fluxes in upstream direction
- no production of new maxima or minima
- conservation of tracer relationships during the advection
- efficient computation in spherical coordinates

The Bott-scheme is a one-dimensional scheme which is used in split mode for the different directions. The advection is done in 2 steps. After weighting the advective fluxes, corrections are applied to make the scheme positive definite. These corrections gives the scheme a precision of the second or forth order. The second order is usually used for operational applications and is hereafter referred to as Bott_2. The SL-scheme is a fully 3-dimensional but it does not conserve the mass. More details about these schemes can be found in the chapter 8.3 of Doms et al. (2011).

6.4 MPDATA in 3-dimensions

MPDATA is a finite difference scheme which is positive definite, mass conserving and efficient. Moreover through a flux correction it can be made monotonous. It is an iterative scheme. In a first step a donor cell approximation (also called upstream method, positive definite but

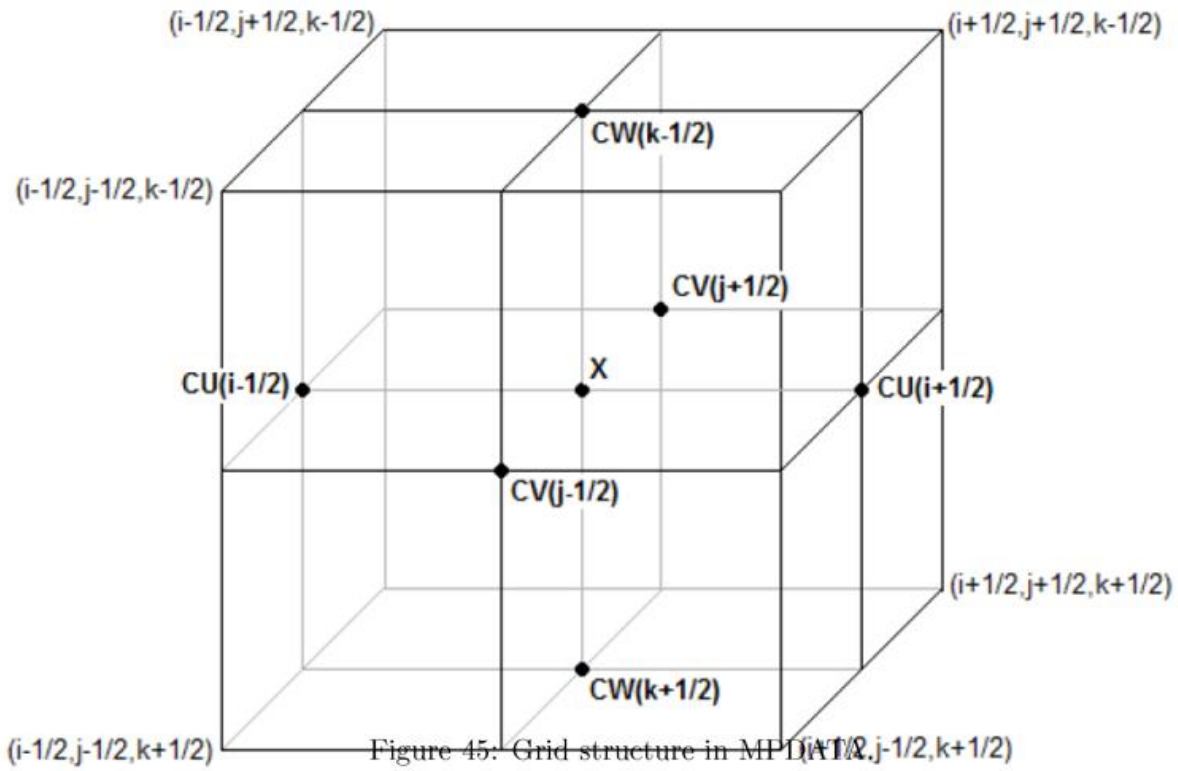


Figure 45: Grid structure in MPDATA

only of first order accuracy) is made. In the second step which can be repeated, corrections are applied to make the scheme more accurate (second order in time and space). In the first step, the physical velocities are used but in the iterations, the velocities are computed from the advection fields and we call them diffusive velocities.
The grid used in MPDATA is basically composed of two set of grids which are shifted by half a grid length in all directions so that the center of the cells are whole numbers i (i.e. the contribution of the first grid) and the grid summits (contribution of the second grid) with half valued indexes $i \pm 1/2$, see Figure 45. The **X** sign marks in the figure the position of the quantity to be advected, $\mathbf{CU(i-1/2)}$ and $\mathbf{CU(i+1/2)}$ are the Courant numbers in the x direction, $\mathbf{CV(j-1/2)}$ and $\mathbf{CV(j+1/2)}$ are the Courant numbers in the y direction and $\mathbf{CW(k-1/2)}$ and $\mathbf{CW(k+1/2)}$ are the Courant numbers in the z direction.
The equation of advection in 3-dimensions is

$$\frac{\partial \Psi}{\partial t} = -\frac{\partial}{\partial x}(u\Psi) - \frac{\partial}{\partial y}(v\Psi) - \frac{\partial}{\partial z}(w\Psi) \tag{6}$$

The equation for the donor cell approximation of (6) is then

$$\begin{aligned}\Psi^{n+1}_{i,j,k} = \Psi^{n}_{i,j,k} &- [F(\Psi^{n}_{i,j,k}, \Psi^{n}_{i+1,j,k}, U_{i+\frac{1}{2},j,k}) - F(\Psi^{n}_{i-1,j,k}, \Psi^{n}_{i,j,k}, U_{i-\frac{1}{2},j,k})] \\ &-[F(\Psi^{n}_{i,j,k}, \Psi^{n}_{i,j+1,k}, V_{i,j+\frac{1}{2},k}) - F(\Psi^{n}_{i,j-1,k}, \Psi^{n}_{i,j,k}, V_{i,j-\frac{1}{2},k})] \\ &-[F(\Psi^{n}_{i,j,k}, \Psi^{n}_{i,j,k+1}, W_{i,j,k+\frac{1}{2}}) - F(\Psi^{n}_{i,j,k-1}, \Psi^{n}_{i,j,k}, W_{i,j,k-\frac{1}{2}})]\end{aligned} \tag{7}$$

where the whole indexes correspond to the center and the half indexes are on the boundaries of the grid cells.
The Courant numbers U, V and W are $U \equiv u\delta t/\delta x, V \equiv v\delta t/\delta y$ and $W \equiv w\delta t/\delta z$ where the time step is δt and the grid space in x, y and z direction are $\delta x, \delta y$ and δz. The flux functions

are defined as

$$\begin{aligned} F(\Psi_L, \Psi_R, U) &\equiv [U]^+ \Psi_L + [U]^- \Psi_R \\ F(\Psi_L, \Psi_R, V) &\equiv [V]^+ \Psi_L + [V]^- \Psi_R \\ F(\Psi_L, \Psi_R, W) &\equiv [W]^+ \Psi_L + [W]^- \Psi_R \end{aligned} \tag{8}$$

with the Courant numbers

$$[U]^+ \equiv max(0, U),\ [U]^- \equiv min(0, U) \quad [V]^+ \equiv max(0, V),\ [V]^- \equiv min(0, V)$$

$$[W]^+ \equiv \mathrm{max}(0, W),\ [W]^- \equiv \mathrm{min}(0, W)$$

The $[U]^+$, $[V]^+$ and $[W]^+$ are the nonnegative, and $[U]^-$, $[V]^-$ and $[W]^-$ are the nonpositive parts of the Courant numbers. With a Taylor expansion and under the assumption that u, v and w are constant, we can again compute the donor cell approximation as:

$$\begin{aligned} \Psi^{n+1}_{i,j,k} &= \Psi^n_{i,j,k} + \delta t \frac{\partial \Psi}{\partial t} + \frac{(\delta t)^2}{2} \frac{\partial^2 \Psi}{\partial t^2} + \qquad O(\delta t^3) \\ &= \Psi^n_{i,j,k} + \delta t \frac{\partial \Psi}{\partial t} + \frac{(\delta t)^2}{2} u^2 \frac{\partial^2 \Psi}{\delta x^2} + \frac{(\delta t)^2}{2} v^2 \frac{\partial^2 \Psi}{\delta y^2} + \frac{(\delta t)^2}{2} w^2 \frac{\partial^2 \Psi}{\delta z^2} + \\ &\quad \frac{(\delta t)^2}{2} 2uv \frac{\partial^2 \Psi}{\partial x \partial y} + \frac{(\delta t)^2}{2} 2uw \frac{\partial^2 \Psi}{\partial x \partial z} + \frac{(\delta t)^2}{2} 2vw \frac{\partial^2 \Psi}{\partial y \partial z} + O(\delta t^3) \end{aligned}$$

$$\begin{aligned} \Psi^n_{i+1,j,k} &= \Psi^n_{i,j,k} + \delta x \frac{\partial \Psi}{\partial x} + \frac{(\delta x)^2}{2} \frac{\partial^2 \Psi}{\partial x^2} + O(\delta x^3) \\ \Psi^n_{i-1,j,k} &= \Psi^n_{i,j,k} - \delta x \frac{\partial \Psi}{\partial x} + \frac{(\delta x)^2}{2} \frac{\partial^2 \Psi}{\partial x^2} + O(\delta x^3) \\ \Psi^n_{i,j+1,k} &= \Psi^n_{i,j,k} + \delta y \frac{\partial \Psi}{\partial y} + \frac{(\delta y)^2}{2} \frac{\partial^2 \Psi}{\partial y^2} + O(\delta y^3) \\ \Psi^n_{i,j-1,k} &= \Psi^n_{i,j,k} - \delta y \frac{\partial \Psi}{\partial y} + \frac{(\delta y)^2}{2} \frac{\partial^2 \Psi}{\partial y^2} + O(\delta y^3) \\ \Psi^n_{i,j,k+1} &= \Psi^n_{i,j,k} + \delta z \frac{\partial \Psi}{\partial z} + \frac{(\delta z)^2}{2} \frac{\partial^2 \Psi}{\partial z^2} + O(\delta z^3) \\ \Psi^n_{i,j,k-1} &= \Psi^n_{i,j,k} - \delta z \frac{\partial \Psi}{\partial z} + \frac{(\delta z)^2}{2} \frac{\partial^2 \Psi}{\partial z^2} + O(\delta z^3) \end{aligned}$$

After putting this in (7) we get the following advection diffusion equation

$$\begin{aligned} \frac{\partial \Psi}{\partial t} &= -u \frac{\partial \Psi}{\partial x} - v \frac{\partial \Psi}{\partial y} - w \frac{\partial \Psi}{\partial z} + \\ &\quad (|U| - U^2) \frac{(\delta x)^2}{2 \delta t} \frac{\partial^2 \Psi}{\partial x^2} + (|V| - V^2) \frac{(\delta y)^2}{2 \delta t} \frac{\partial^2 \Psi}{\partial y^2} + (|W| - W^2) \frac{(\delta z)^2}{2 \delta t} \frac{\partial^2 \Psi}{\partial z^2} - \\ &\quad \frac{UV \delta x \delta v}{\delta t} \frac{\partial^2 \Psi}{\partial x \partial y} - \frac{UW \delta x \delta z}{\delta t} \frac{\partial^2 \Psi}{\partial x \partial z} - \frac{VW \delta y \delta z}{\delta t} \frac{\partial^2 \Psi}{\partial y \partial z} \end{aligned} \tag{9}$$

The error which arises from the diffusion term in (9) is estimated with a donor cell approximation and then subtracted from (7) to obtain a higher precision. The equation (9) is written with the diffusive velocities u_d, v_d and w_d as

$$\frac{\partial \Psi}{\partial t} = -\frac{\partial}{\partial x}(u\Psi) - \frac{\partial}{\partial y}(v\Psi) - \frac{\partial}{\partial z}(w\Psi) + \frac{\partial}{\partial x}(u^{(1)}_d \Psi) + \frac{\partial}{\partial y}(v^{(1)}_d \Psi) + \frac{\partial}{\partial z}(w^{(1)}_d \Psi) \tag{10}$$

with the following definitions:

$$
\begin{aligned}
u_d^{(1)} &\equiv (|U| - U^2)\frac{(\delta x)^2}{2\delta t}\frac{1}{\Psi}\frac{\partial \Psi}{\partial x} - r\frac{UV\delta x\delta y}{\delta t}\frac{1}{\Psi}\frac{\partial \Psi}{\partial y} - s\frac{UW\delta x\delta z}{\delta t}\frac{1}{\Psi}\frac{\partial \Psi}{\partial z} \\
v_d^{(1)} &\equiv (|V| - V^2)\frac{(\delta y)^2}{2\delta t}\frac{1}{\Psi}\frac{\partial \Psi}{\partial y} - (1-r)\frac{UV\delta x\delta y}{\delta t}\frac{1}{\Psi}\frac{\partial \Psi}{\partial x} - t\frac{VW\delta y\delta z}{\delta t}\frac{1}{\Psi}\frac{\partial \Psi}{\partial z} \\
w_d^{(1)} &\equiv (|W| - W^2)\frac{(\delta z)^2}{2\delta t}\frac{1}{\Psi}\frac{\partial \Psi}{\partial z} - (1-s)\frac{UW\delta x\delta z}{\delta t}\frac{1}{\Psi}\frac{\partial \Psi}{\partial x} - (1-t)\frac{VW\delta y\delta z}{\delta t}\frac{1}{\Psi}\frac{\partial \Psi}{\partial y}
\end{aligned}
\tag{11}
$$

with $r, s, t \in \mathbb{R}$ can be chosen arbitrarily. The implementation is independent of the choice for $r, s, t \in [0,1]$ and as default values we choose $r, s, t = 0.5$ The diffusive velocities must be built at the grid cell boundaries. The explicit form depends if the boundary is horizontal or vertical but they can be written in the following dimensionless form

$$
\begin{aligned}
U^{(1)} &\equiv \frac{u^{(1)}\delta t}{\delta x} = (|U| - U^2)A^{(1)} - 2rUVB^{(1)} - 2sUWC^{(1)} \\
V^{(1)} &\equiv \frac{v^{(1)}\delta t}{\delta y} = (|V| - V^2)B^{(1)} - 2(1-r)UVA^{(1)} - 2tVWC^{(1)} \\
W^{(1)} &\equiv \frac{w^{(1)}\delta t}{\delta z} = (|W| - W^2)C^{(1)} - 2(1-s)UWA^{(1)} - 2(1-t)VWB^{(1)}
\end{aligned}
\tag{12}
$$

with

$$
\begin{aligned}
A^{(1)} &\equiv \left[\frac{\delta x}{2\Psi}\frac{\partial \Psi}{\partial x}\right]_{i+1/2,j,k}^{n+1} = \frac{\Psi^{(1)}_{1+1,j,k} - \Psi^{(1)}_{i,j,k}}{\Psi^{(1)}_{1+1,j,k} + \Psi^{(1)}_{i,j,k}} \\
B^{(1)} &\equiv \left[\frac{\delta y}{2\Psi}\frac{\partial \Psi}{\partial y}\right]_{i+1/2,j,k}^{n+1} = \frac{1}{2}\frac{\Psi^{(1)}_{i+1,j+1,k} + \Psi^{(1)}_{i,j+1,k} - \Psi^{(1)}_{i+1,j-1,k} - \Psi^{(1)}_{i,j-1,k}}{\Psi^{(1)}_{i+1,j+1,k} + \Psi^{(1)}_{i,j+1,k} + \Psi^{(1)}_{i+1,j-1,k} + \Psi^{(1)}_{i,j-1,k}} \\
C^{(1)} &\equiv \left[\frac{\delta z}{2\Psi}\frac{\partial \Psi}{\partial z}\right]_{i+1/2,j,k}^{n+1} = \frac{1}{2}\frac{\Psi^{(1)}_{i,j,k+1} + \Psi^{(1)}_{i+1,j,k+1} - \Psi^{(1)}_{i,j,k-1} - \Psi^{(1)}_{i+1,j,k-1}}{\Psi^{(1)}_{i,j,k+1} + \Psi^{(1)}_{i+1,j,k+1} + \Psi^{(1)}_{i,j,k-1} + \Psi^{(1)}_{i+1,j,k-1}}
\end{aligned}
$$

6.5 Non-oscillating option

The algorithm described in the previous paragraph is positive definite but not monotone. The solution can show wrong extrema. The reasons for the oscillations in the numerical solution are that on one side some fluxes are overestimated and on the other an underestimation can arise from the first order accuracy of the fluxes. The flux-corrected transport (FCT) methodology enforces appropriate limits to the fluxes and removes these oscillations. The adopted method merges the FCT with the iterative formalism of MPDATA (Smolarkiewicz and Grabowski, 1990). The numerical diffusion of the advection is reduced by limiting the anti-diffusive fluxes so that no unphysical extrema occur in the solutions.

General form of the FCT methodology Starting with the conservation of a time dependent fluid variable (e.g. mass, momentum) Ψ can be written as

$$
\frac{\partial \Psi}{\partial t} + \nabla \cdot (\Psi \mathbf{u}) = S
$$

where $\mathbf{u}$ is the fluid velocity and S is a source term. First Ψ is advected. In the second FCT step Ψ is numerically diffused so that the solution is positive everywhere if the starting

profile Ψ^0 was positive. The source term S is added to obtain the low order value Ψ^l. In the next step the anti-diffusive fluxes are computed and we obtain a higher order approximation Ψ^h. The anti-diffusive fluxes are limited to not generate any new extrema and not to reduce any extrema of the start profile. Applying these fluxes to Ψ^l gives the new solution Ψ^n which is positive and monotone.

Limiters in MPDATA First the extrema Ψ^{min} and Ψ^{max} are computed

$$\Psi^{l,min}_{i,j,k} = \min(\Psi^l_{i,j,k}, \Psi^l_{i-1,j,k}, \Psi^l_{i+1,j,k}, \Psi^l_{i,j-1,k}, \Psi^l_{i,j+1,k}, \Psi^l_{i,j,k-1}, \Psi^l_{i,j,k+1})$$
$$\Psi^{l,max}_{i,j,k} = \max(\Psi^l_{i,j,k}, \Psi^l_{i-1,j,k}, \Psi^l_{i+1,j,k}, \Psi^l_{i,j-1,k}, \Psi^l_{i,j+1,k}, \Psi^l_{i,j,k-1}, \Psi^l_{i,j,k+1})$$

Then Ψ^h is computed using (7) and the new extrema Ψ^{min} and Ψ^{max} are found

$$\Psi^{h,min}_{i,j,k} = \min(\Psi^h_{i,j,k}, \Psi^h_{i-1,j,k}, \Psi^h_{i+1,j,k}, \Psi^h_{i,j-1,k}, \Psi^h_{i,j+1,k}, \Psi^h_{i,j,k-1}, \Psi^h_{i,j,k+1}, \Psi^{l,min}_{i,j,k})$$
$$\Psi^{h,max}_{i,j,k} = \max(\Psi^h_{i,j,k}, \Psi^h_{i-1,j,k}, \Psi^h_{i+1,j,k}, \Psi^h_{i,j-1,k}, \Psi^h_{i,j+1,k}, \Psi^h_{i,j,k-1}, \Psi^h_{i,j,k+1}, \Psi^{l,max}_{i,j,k})$$

The flux terms in (8) are computed and in the next step the total in- and outgoing anti-diffusive fluxes F^{in} and F^{out} of each cell can be computed as

$$F^{in}_i = \max(F_{i-1/2},0) - \min(F_{i+1/2},0)\ ,\ F^{out}_i = \max(F_{i+1/2},0) - \min(F_{i-1/2},0)$$
$$F^{in}_j = \max(F_{j-1/2},0) - \min(F_{j+1/2},0)\ ,\ F^{out}_j = \max(F_{j+1/2},0) - \min(F_{j-1/2},0)$$
$$F^{in}_k = \max(F_{k-1/2},0) - \min(F_{k+1/2},0)\ ,\ F^{out}_k = \max(F_{k+1/2},0) - \min(F_{k-1/2},0)$$

The partial in- and outgoing fluxes f^{in} and f^{out} which have to be applied to each grid cell are then

$$f^{in}_i = \frac{\Psi^{h,max}_{i,j,k} - \Psi^l_{i,j,k}}{F^{in}_i}\ ,\ f^{out}_i = \frac{\Psi^l_{i,j,k} - \Psi^{h,min}_{i,j,k}}{F^{out}_i}$$
$$f^{in}_j = \frac{\Psi^{h,max}_{i,j,k} - \Psi^l_{i,j,k}}{F^{in}_j}\ ,\ f^{out}_j = \frac{\Psi^l_{i,j,k} - \Psi^{h,min}_{i,j,k}}{F^{out}_j}$$
$$f^{in}_k = \frac{\Psi^{h,max}_{i,j,k} - \Psi^l_{i,j,k}}{F^{in}_k}\ ,\ f^{out}_k = \frac{\Psi^l_{i,j,k} - \Psi^{h,min}_{i,j,k}}{F^{out}_k}$$

Finally in the last step each of these partial anti-diffusive fluxes are limited so that no undershooting is produced at the exit and no overshooting at the entry of the grid cell. For the pseudo velocities u, v and w we use

$$u_{i+1/2,j,k} = \min(1, f^{out}_i, f^{in}_{i+1}) \max(0, u_{i+1/2,j,k}) + \min(1, f^{in}_i, f^{out}_{i+1}) \min(0, u_{i+1/2,j,k})$$
$$v_{i,j+1/2,k} = \min(1, f^{out}_j, f^{in}_{j+1}) \max(0, v_{i,j+1/2,k}) + \min(1, f^{in}_j, f^{out}_{j+1}) \min(0, v_{i,j+1/2,k})$$
$$w_{i,j,k+1/2} = \min(1, f^{out}_k, f^{in}_{k+1}) \max(0, w_{i,j,k+1/2}) + \min(1, f^{in}_k, f^{out}_{k+1}) \min(0, w_{i,j,k+1/2})$$

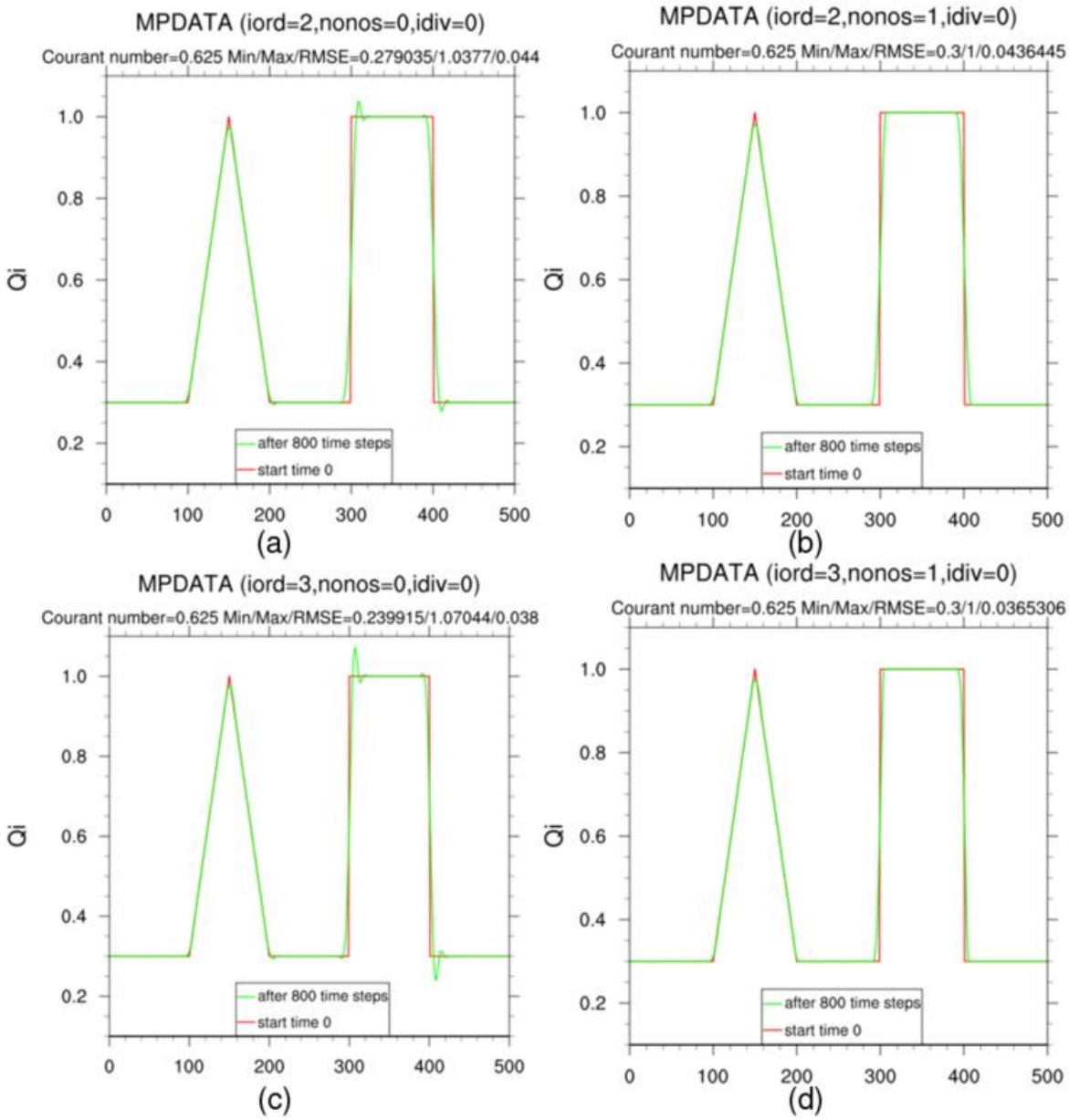


Figure 46: First example of MPDATA in one dimension, details see text.

6.6 Illustration in a one dimensional case

To show how MPDATA works a simple advection in one dimension is used here. The initial distributions of the tracer (Qi) are a triangle and a rectangular function with maximum value 1 and minimum value 0.3 over 100 grid points. These are shown in red in the Figure 46. A constant positive velocity (to the right) is applied to the tracer with a Courant number of 0.625 and periodic boundary conditions are used. After 800 time steps the distribution has passed over all the 500 grid points and is back at the initial position (in green in Figure 46) and the impact of the different advection options is visible. These options are the number of iterations (*iord*) used in the MPDATA algorithm, the non-oscillating option described in the previous section if *nonos* = 1 and a switch for non-divergent fields (*idiv* = 1 if the divergence of the velocity field is different than zero). For *iord* = 1 only the donor cell advection is operated and the scheme is very diffusive (not shown). With *iord* = 2 we have the basic

MPDATA scheme with only one anti-diffusive flux computed. This step can be repeated although for *iord* higher than 3 no significant improvement is obtained (not shown). On the top left of Figure 46 *iord* is equal 2 and on the left of the rectangular tracer there is a 4% overshooting and on the right an undershooting of 7%. This effect is totally absent in the part (b) of the figure where *nonos* = 1. With an extra iteration (*iord* = 3, lower left part c) the over- and undershooting are worse (respectively 7 and 20%) but the root mean square error (RMSE) of the overall distribution is reduced. The best results are obtained in the lower right corner in part (d) of the figure and one can also state that the triangular distribution does not seem to change much for any of the shown options. In a more stringent

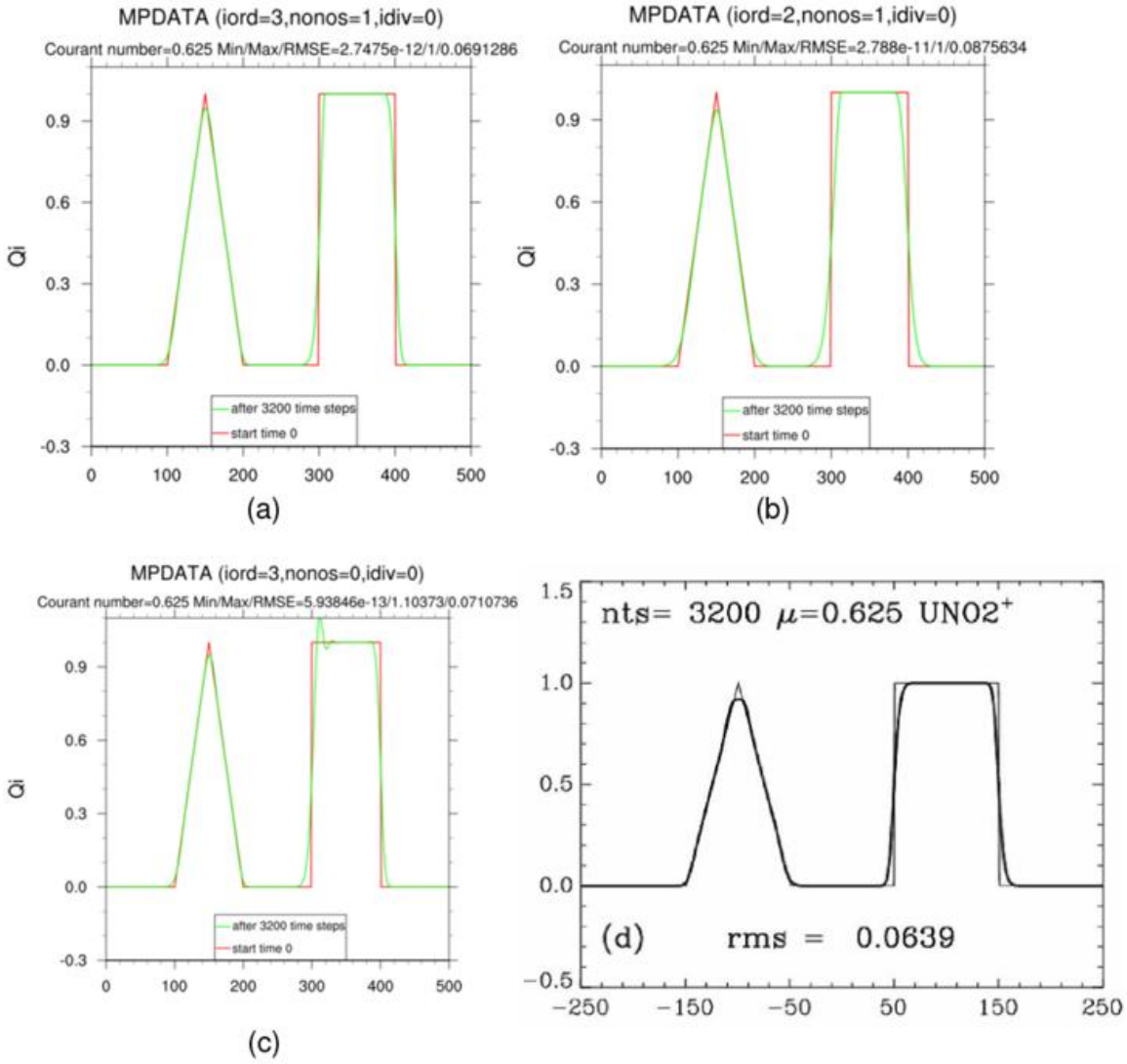


Figure 47: Second example of MPDATA in one dimension, details see text.

test the 2 previous distributions are compared after 3200 time steps which correspond to 4 complete rotations. In contrast to Figure 46 the starting distributions have a minimum of 0 and only three options are shown in Figure 47. In the lower right part an upstream non-oscillatory (UNO2+) solution from Li (2008) is displayed for comparison. The RMSE with the best MPDATA options (iord=3, nonos=1) is shown in the upper left part (a) and is similar to the UNO2+ method.

6.7 Advection tests

In a first configuration MPDATA was tested by conducting synthetic experiments with the module src_artifdata. This module permits to construct artificial initial and boundary data and all the usual settings of the model and then to do component testing while still using the whole COSMO model in its version 4.12 for the dynamics of the flow. MPDATA could therefore be easily compared to results obtained with Bott_2 or the semi-Lagrangian scheme (SL).
These so-called solid body rotation tests were computed on a domain of 80x80 grid points with an horizontal resolution of 2.2km. The time step used was 20s. There is no orography and the vertical extension of the model has no impact but permits to conduct different experiments on different model levels.

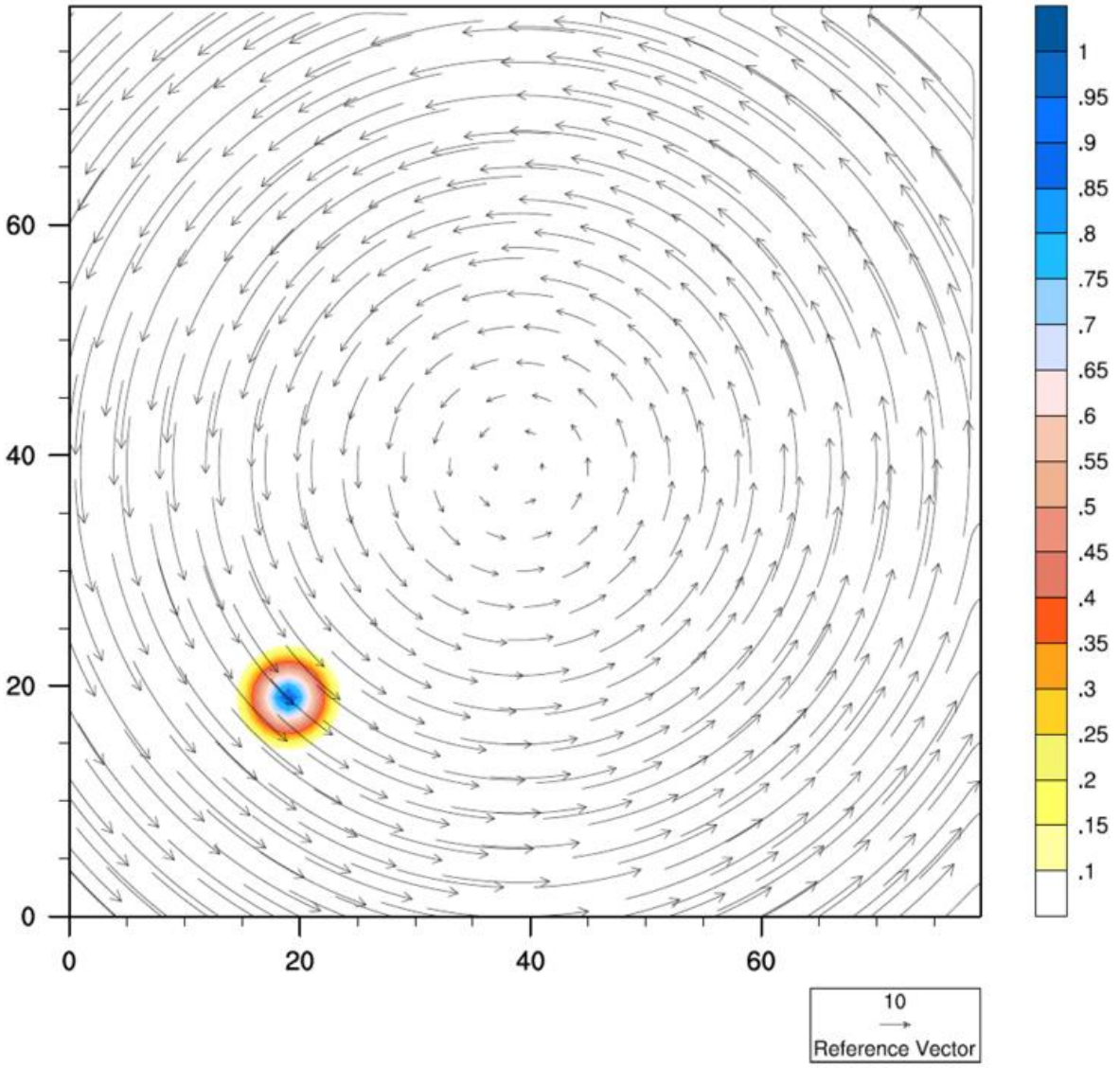


Figure 48: Rotating wind field in m/s over the whole computational domain with the starting tracer concentration (cone with base radius of 5 grid points) in colours centered at position (20,20).

Rotating cone test with 0 background As in the previous paragraph the specific cloud ice content q_i (in units of kg/kg) was used as a tracer and initialized to zero everywhere except

for a cone centered over the position $(i, j) = (20, 20)$ and with radius of 5 grid points and placed on the 10th level of the model so that we can write

$$q_i(i, j, 10) = \max(0.0, 1.0 - \sqrt{((i - i_{max})/5)^2 + ((j - j_{max})/5)^2})$$

where the maximum of q_i is 1 and is positioned on the grid point $(i_{max}, j_{max} = (20, 20)$. The rotating wind field is defined as

$$u(i, j, k) = -\omega(j - j_0) \quad v(i, j, k) = \omega(i - i_0) \quad w(i, j, k) = 0.0$$

where $\omega = 0.97m/s$, $u(i, j, k)$, $v(i, j, k)$ and $w(i, j, k)$ are the wind velocities in the i-, j- and k-direction and (i_0, j_0) is the mid point of the horizontal layer. The stationary winds and the distribution of the tracer at time 0 are shown in Figure 48.
The rotation period is 4h and the Courant number at the location of the tracer is about 0.3 but the maximum values are close to 0.5 in the corners of the domain.
The tracer should theoretically be transported without changing its shape and after 4h of computation it should be back in its starting position. To show the characteristics of the different schemes, the isolines of the tracer concentrations of the MPDATA method are drawn on top of the colored results of the Bott_2 scheme. Figure 49 displays 2 different settings of the MPDATA scheme. For MPDATA one can see that the maximum values have been reduced by 78% and 66% whereas Bott_2 has only been reduced by 50%. The results of the SL scheme are not shown but are very similar to the Bott_2 with a slightly better maximum value of 0.510. There is not only a reduction of the maximum but there is also a phase shift in the position of this value.

We compute the following statistical measures to quantify the results:

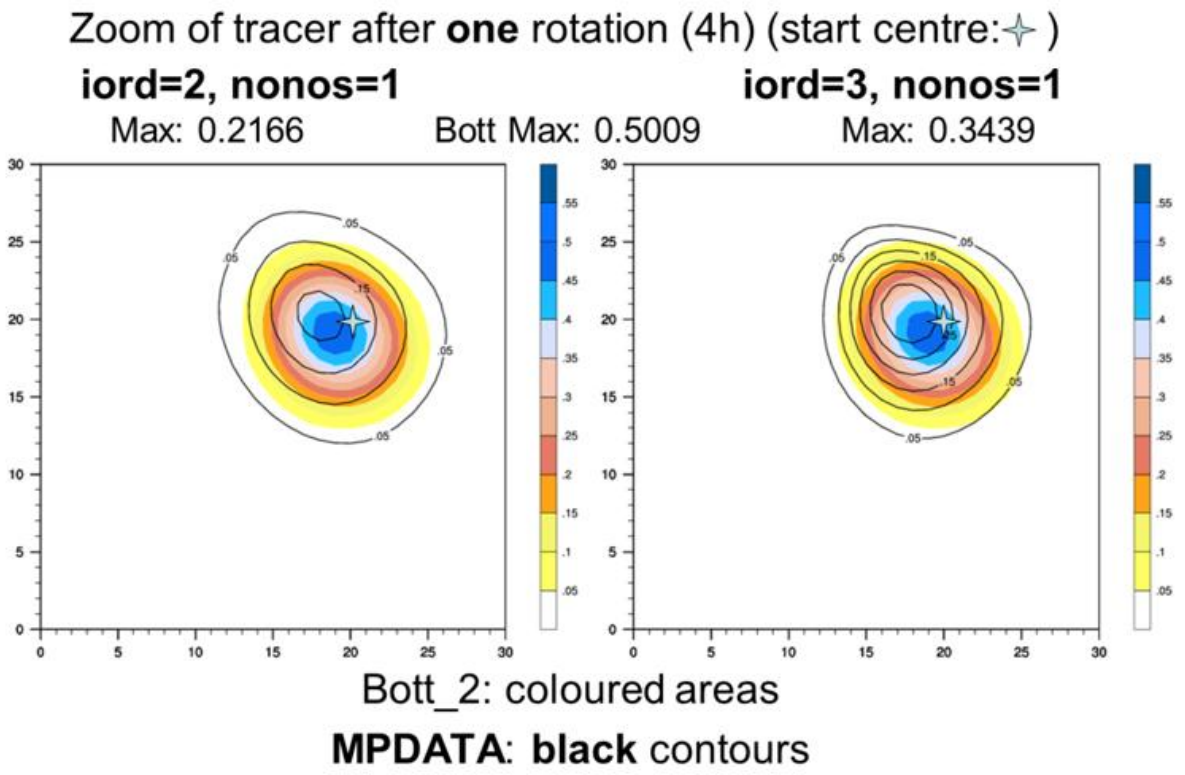


Figure 49: Zoom of the lower left domain with the tracer concentrations after one complete rotation of a cone with maximum of 1 and horizontal radius of 5 grid points centered at the position (20,20).

- the phase error E_{phase} is defined as the distance between the exact maximum position (i^{start}, j^{start}) and the computed one (i^{end}, j^{end}):

$$E_{phase} = \sqrt{(i^{start} - i^{end})^2 + (j^{start} - j^{end})^2} \tag{13}$$

- the diffusion error is

$$E_{diffusion} = \max(q_i^{start}) - max(q_i^{end}) \tag{14}$$

- the L2-norm is

$$E_{L2} = \sqrt{\sum_{i=1}^{N} A_i \cdot (q_i^{start} - q_i^{end})^2} \tag{15}$$

where N is the number of grid cells and A_i is the area of the grid cell.

Advection scheme after one rotation	L2-norm E_{L2}	Maximum value	E_{phase}	$E_{diffusion}$
Bott_2	3.068	0.501	1.414	0.499
Semi-Lagrange	3.147	0.510	1.414	0.490
MPDATA				
iord=2, nonos=0	5.798	0.219	2.000	0.781
iord=3, nonos=0	4.925	0.348	2.236	0.652
iord=2, nonos=1	5.795	0.217	2.000	0.783
iord=3, nonos=1	4.906	0.344	2.000	0.656

Table 8: Overview of the different schemes for the rotating cone test with 0 background.

All the results of the different experiments with the rotating cone are shown in Table 8. The smallest MPDATA diffusion error is given by the experiment with *iord* = 3 and *nonos* = 0 but its phase error is the largest and the overall smallest L2-norm is given by the Bott_2 scheme although its diffusion error is larger than the SL experiment.

Rotating cylinder test with non-zero background

In this test the tracer has a value of 0.3 over the whole domain and only in a radius of 5 grid points around the center position $(i, j) = (20, 20)$ does the tracer have a value of 1.0. The rotating wind field is the same as in the previous cone test. Figure 50 shows the same 2 settings of the MPDATA scheme on top of the Bott_2 solution as for the rotating cone test. Although we use the non-oscillating option for MPDATA local minima and maxima appear in the vicinity of the main tracer concentration. This is also the case for the Bott_2 but the trail behind the main concentration is much smaller than with MPDATA. For MPDATA one can see that the maximum values have been reduced by 37% and 26% whereas Bott_2 has only been reduced by 16%. This is much better than in the previous test but because of the local extrema the overall L2-norm is much larger in this experiment (see Table 9). The results of the SL scheme are not shown here because there is a boundary undershooting problem for this experiment.

All the results of the different experiments with the rotating cylinder are shown in Table 9. The smallest MPDATA diffusion error is again given by the experiment with *iord* = 3 and *nonos* = 0 with a maximum reduction of only 21% but its phase error is again the largest and the overall smallest L2-norm is again given by the Bott_2 scheme and its diffusion error is also the overall smallest.

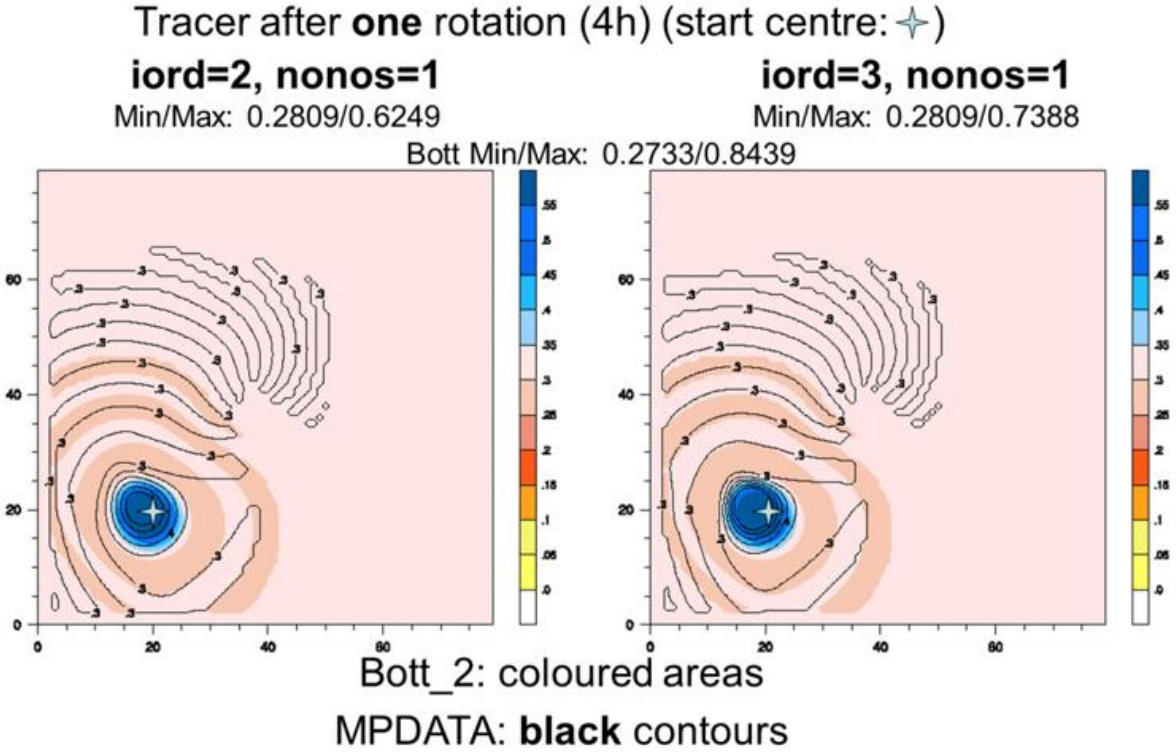


Figure 50: Tracer concentrations after one complete rotation (4h) of a cylinder of maximum 1 and horizontal radius of 5 grid points centered at the position (20,20) on top of a background value of 0.3.

Advection scheme after one rotation	L2-norm E_{L2}	Minimum value	Maximum value	Phase error	Diffusion error
Bott_2	5.233	0.273	0.844	1.414	0.156
Semi-Lagrange	12.574	0.125	0.843	1.414	0.157
MPDATA					
iord=2, nonos=0	6.907	0.261	0.633	2.000	0.367
iord=3, nonos=0	6.771	0.199	0.785	3.162	0.215
iord=2, nonos=1	6.882	0.281	0.625	2.000	0.375
iord=3, nonos=1	6.402	0.281	0.739	2.000	0.261

Table 9: Overview of the different schemes for the rotating cylinder test with non-zero background.

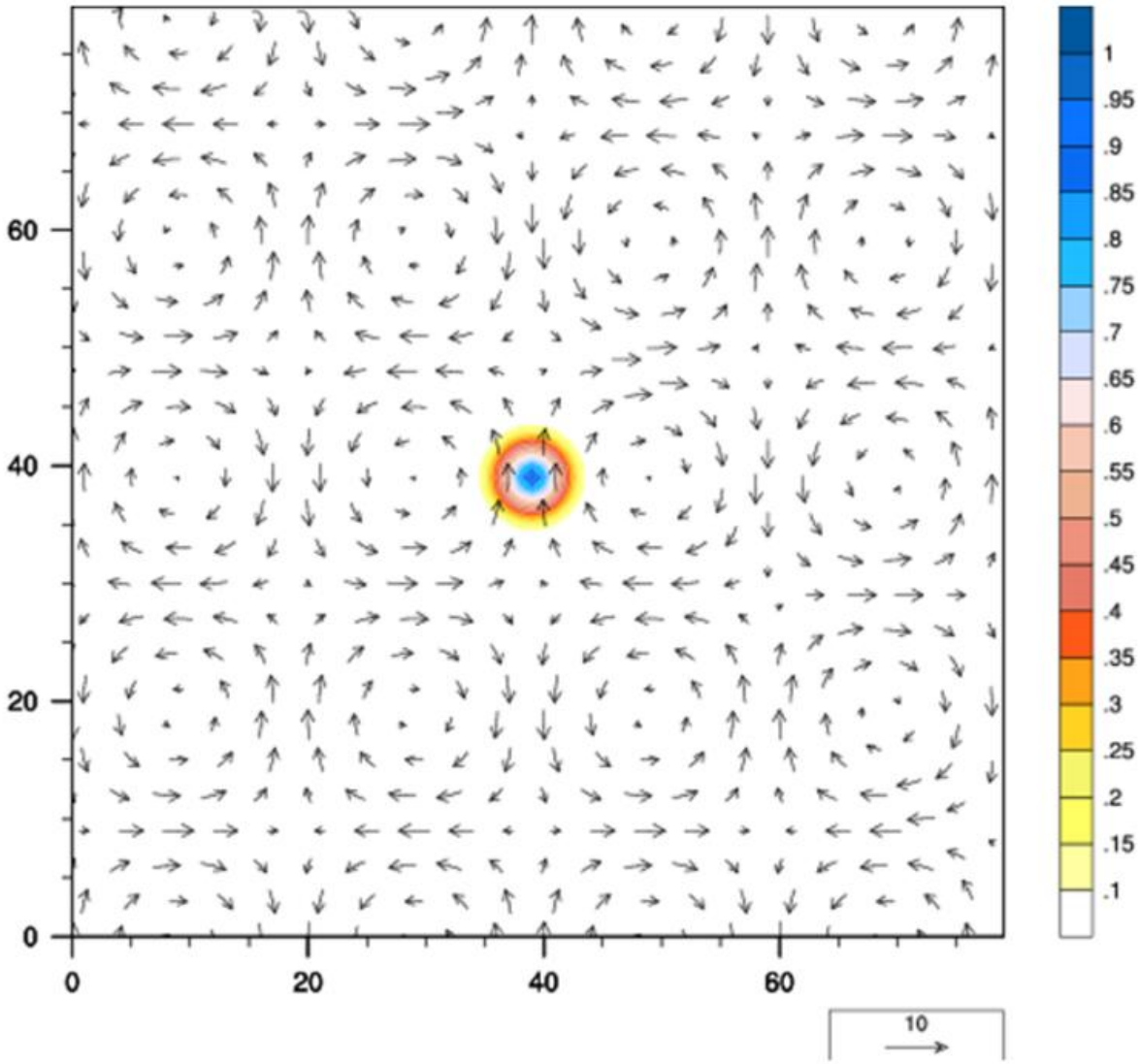


Figure 51: Wind field in m/s for the deformational flow test with the starting tracer concentration (cone with base radius of 5 grid points) in colours centered at position (40,40).

6.8 Deformation flow tests

The stability and the qualitative value of the different advection schemes can be best tested in this set-up because the splitting schemes have here the potential to fail. The wind field is now composed of series of symmetrical vortices with all neighbors rotating in opposite directions and the divergence is non-zero. Therefore the MPDATA switch $idiv = 1$ needs to be used for this test. The purely horizontal wind speed components ($w(i, j, 10) = 0$) are defined as follows

$$u(i, j, 10) = \frac{120.0 \cdot \pi}{80.0} \sin(\frac{4.0 \cdot \pi}{80.0} i) \sin(\frac{4.0 \cdot \pi}{80.0} j)$$
$$v(i, j, 10) = \frac{120.0 \cdot \pi}{80.0} \cos(\frac{4.0 \cdot \pi}{80.0} i) \cos(\frac{4.0 \cdot \pi}{80.0} j)$$

Similar to the first advection test, a cone tracer q_i of 5 grid point radius is placed on the 10th level at the centre of the domain $(i_{max}, j_{max}) = (40, 40)$ and every where else set to zero

$$q_i(i, j, 10) = \max(0.0, 1.0 - \sqrt{((i - i_{max})/5)^2 + ((j - j_{max})/5)^2})$$

The shear flow generated by the equations above is shown in Figure 51 where the initial distribution of the tracer at time 0 is exactly split in the middle by a counterclockwise and a clockwise rotating vortex. The tracer will therefore be transported first to the North reaching a strongly divergent zone (with a saddle point at the center of the top 4 complete vortices) where the tracer will be split in two parts, one going West and another going East. Near the tracer maximum the Courant number is 0.04. The time for the tracer to go round once depends on the starting position and as the fluid trajectories are not circles for a position close to the center of the domain the period can be analytically computed by $P_c = 2\pi/(k^2|A|) = L^2/(8\pi|A|)$ where L is the computational domain and A is the amplitude of the stream function which describes the wind field (see formula (12) in Staniforth et al. (1987)). This corresponds here to about 1500 time steps so that after 10 hours of simulation the tracer has gone round about 1.2 times.

Advection scheme	Maximum after 5h	Maximum after 10h
Bott_2	0.297	0.148
Semi-Lagrange	0.334	0.164
MPDATA		
iord=2, nonos=0	0.278	0.126
iord=3, nonos=0	0.299	0.149
iord=2, nonos=1	0.267	0.128
iord=3, nonos=1	0.287	0.146

Table 10: Maximum values of the cone tracer in a deformational flow field.

Figure 52 displays the tracer concentration with the Bott_2 and the SL scheme and they can be compared with 2 different settings of the MPDATA scheme in Figure 53. Although the setup is completely symmetric the results show some small asymmetry which can be perhaps explained by the Coriolis force which was not excluded. The maximum tracer values of the experiments are summarized in Table 10 and for the *iord* = 3 and *nonos* = 0 configuration of MPDATA the values are higher than for Bott_2 but the results for SL are overall best.

The test referred to in Smolarkiewicz (1982) and in Staniforth et al. (1987) is laid out in a larger domain with a square side of 100 grid points and starts with a cone with a radius of 15 grid points which interacts with six vortices. The amplitude of the stream function is also reduced from 30 to 8 so that the time needed to reach $3T/200$ ($T = 2637.6$) is of 32 hours. Three different advection schemes are shown in Figure 54 and can be compared to the analytical solution shown in Figure 4a of Staniforth et al. (1987). The overall symmetry of this setup is much higher than with the previous deformation flow test. The solution with the highest wall on the North side of the two central vortices and between these two vortices is the SL configuration. The MPDATA configuration maintains higher maximum values than the Bott_2 scheme and the advection of the tracer near the North saddle point produces far reaching 'horns' which are also in the analytical solution, but the southern tracer extension from the South saddle point is the smallest with MPDATA.

6.9 Conclusions

MPDATA is a 3-dimensional advection scheme which was introduced by Piotr Smolarkiewicz. It is based on the upstream scheme. The strong diffusion of the upstream scheme is reduced

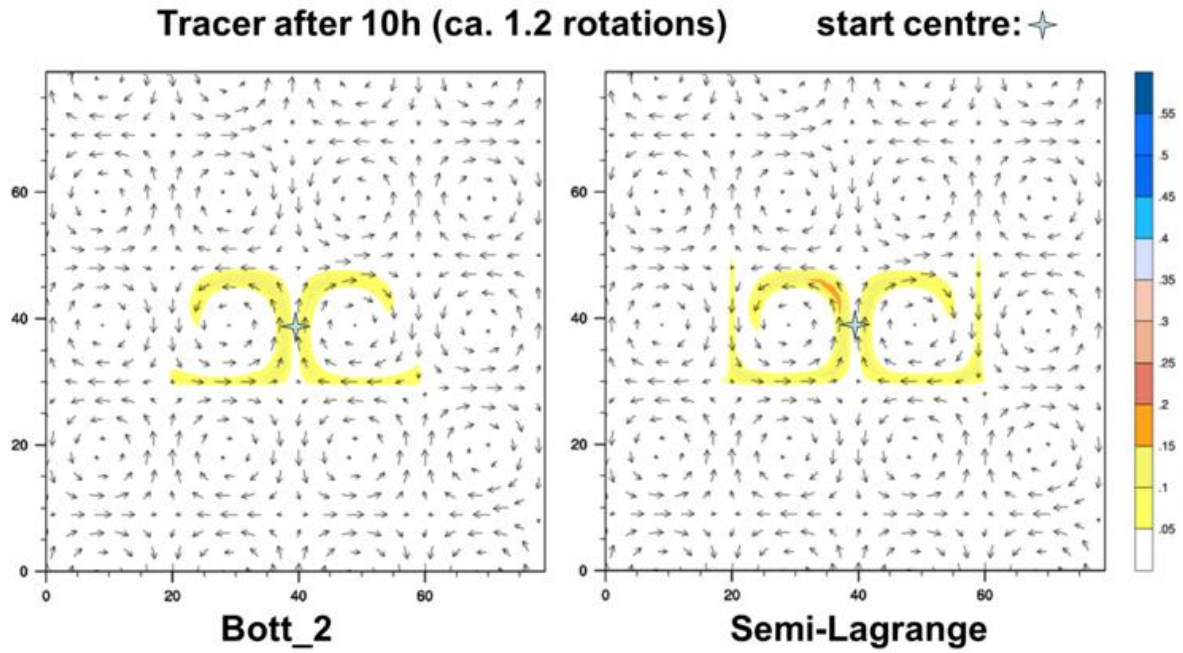


Figure 52: Tracer concentrations after more than a complete rotation of a cone with maximum of 1 and horizontal radius of 5 grid points centered in the middle of the domain for the Bott_2 (left) and semi-Lagrangian (right) advection scheme.

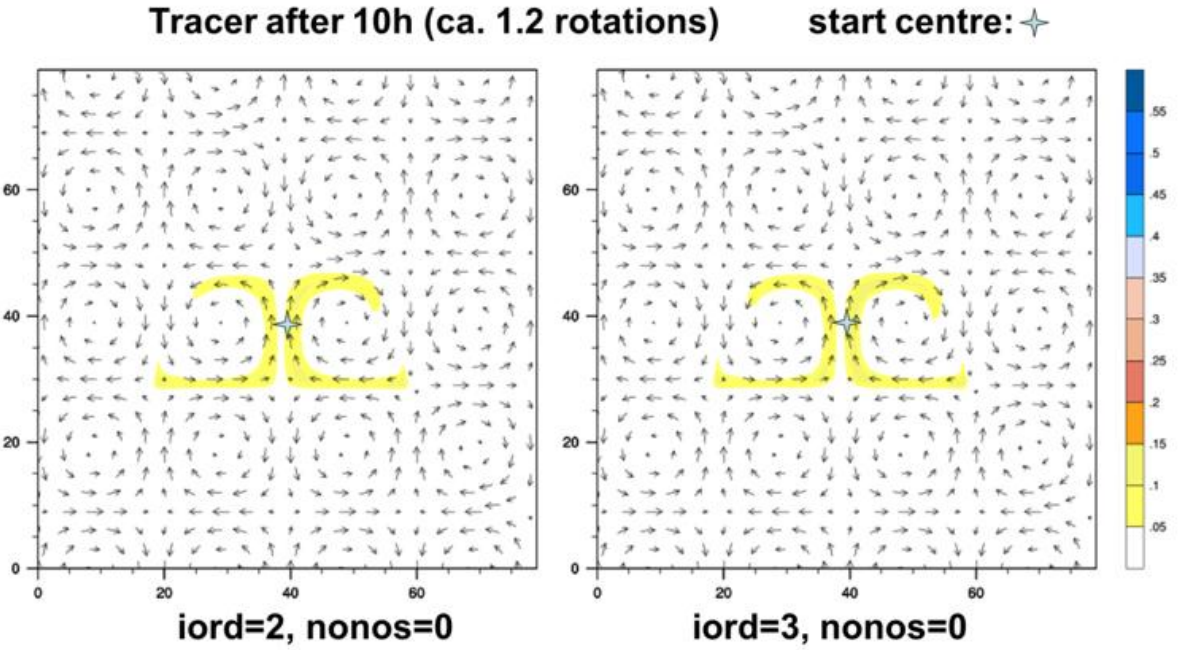


Figure 53: Same as Figure 52 but for 2 different settings of the MPDATA scheme.

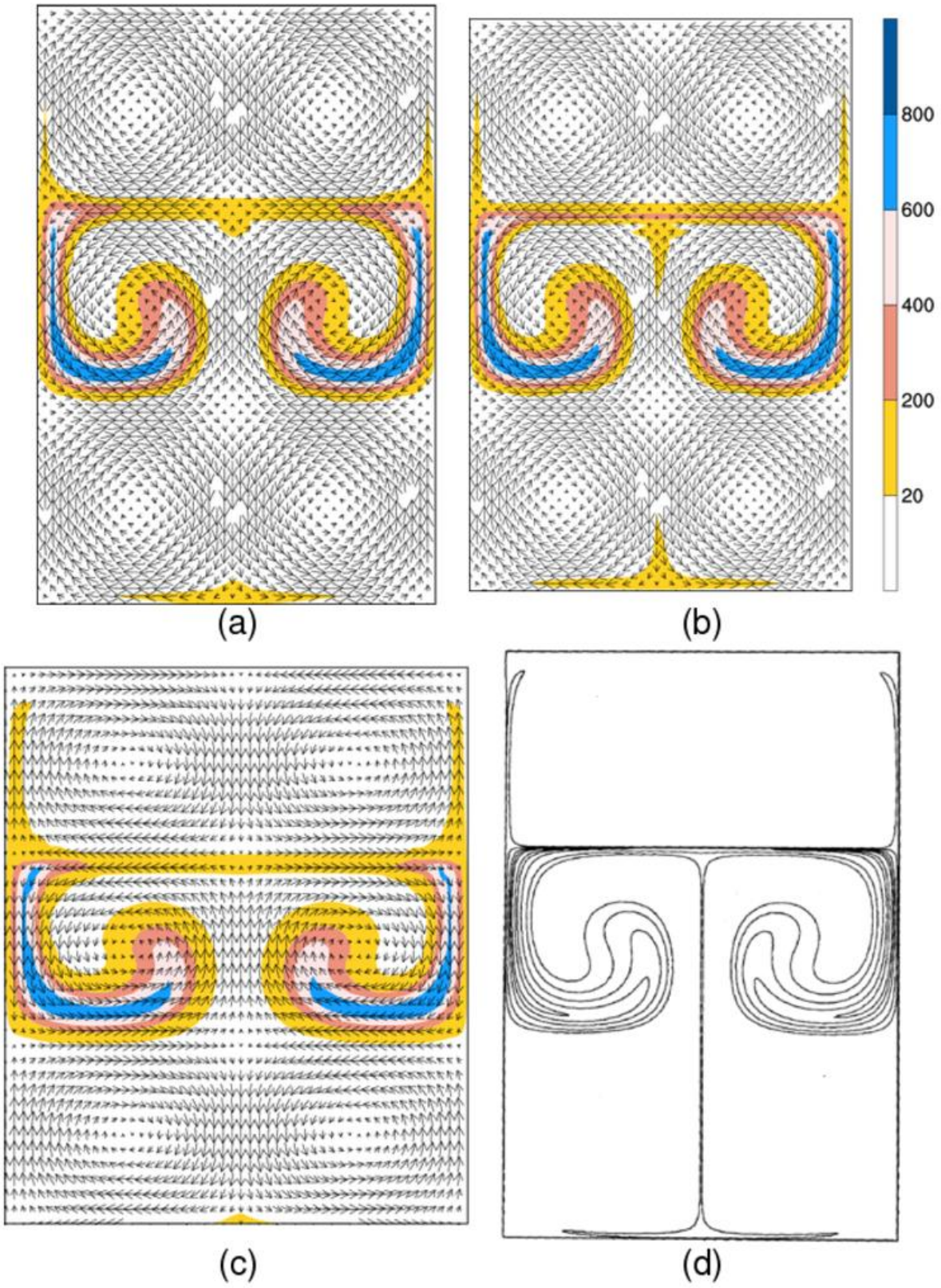


Figure 54: Tracer concentrations after 32 hours for (a) the Bott_2 scheme, (b) the SL scheme, (c) MPDATA scheme with *iord* = 3 and *nonos* = 1. (d) is the Fig. 4a of Staniforth et al. (1987) for $T/50$ with (T = 2637.6). All the isolines are 0.8 (not present in (a), (b) or (c)), 0.6, 0.4, 0.2, 0.02. Except for (d) the divergent flow field of the internal six vortices where the tracer is confined is also shown.

by iterating anti-diffusive steps.
Compared to splitted schemes, as the Bott-scheme, MPDATA has the advantage not to have the tendency to oscillate and is therefore more precise and as a fully 3-dimensional scheme it therefore can not empty a grid box in a single step. But MPDATA is more diffusive as the Bott_2 scheme or the 3-dimensional semi-Lagrangian scheme (SL). This was particularly the case in the solid body rotation tests because in the deformation flow tests the maximum values of MPDATA were better than for the Bott_2 scheme. To be fair a fully 3-dimensional test was not conducted so that the full advantage of MPDATA as a non-splitted scheme could not be completely compared to the Bott-scheme.
The computing time for MPDATA as used in this work is considerably larger than for Bott_2 or for the Semi-Lagrange scheme but no effort was undertaken to optimize the scheme as it is already done for the two other schemes which can be used for operations. For the moment MPDATA runs only on one processor and to operate weather forecasts one should consider to use a parallelised and optimized version of MPDATA and then to compare the results of the different advection schemes.

References

Bott A., 1989: A positive definite advection scheme obtained by nonlinear renormalization of the advective fluxes. *Monthly Weather Review*, **117**, 1006-1015.

Doms G. et al., 2011: A Description of the Nonhydrostatic Regional COSMO-Model. Part I: Dynamics and Numerics. Available at *http://www.cosmo-model.org*

Li J.-G., 2008: Upstream nonoscillatory advection schemes, *Monthly Weather Review*, **136**, 4709-4729.

Müllner M., 2010: Implementierung eines dreidimensionalen Advektionsschemas für den dynamischen COSMO Kern, Diplomarbeit bei der Fakultät für Mathematik der Technischen Universität Chemnitz, pp. 69.

Prusa J. M., P. K. Smolarkiewicz, A. A. Wyszogrodzki, 2008: EULAG, a computational model for multiscale flows. *Computer and Fluids*, **37**, 119-1207.

Smolarkiewicz P. K., 1982: The multi-dimensional Crowley advection scheme. *Monthly Weather Review*, **113**, 1050-1065.

Smolarkiewicz P. K. and W. W. Grabowski, 1990: The Multidimensional Positive Definite Advection Transport Algorithm: Nonoscillatory Option. *Journal of Computational Physics*, **86**, 355-375.

Smolarkiewicz P. K. and L.G. Margolin, 1998: MPDATA: a finite-difference solver for geophysical flows. *Journal of Computational Physics*, **140**, 459-480.

Staniforth A., J. Côté and J. Pudykiewicz, 1987: Comment on "Smolarkiewicz's deformational flow". *Monthly Weather Review*, **115**, 894-900.

Wicker, L. and W. Skamarock, 2002: Time-splitting methods for elastic models using forward time schemes. *Monthly Weather Review*, **130**, 2088-2097.

7 Normal mode analysis of anelastic and compressible equation sets

Michael Baldauf

Deutscher Wetterdienst, Germany

7.1 Introduction

Inspection of linear wave expansion properties is often one of the starting points in the investigation of a hyperbolic equation set. Such an analysis gives also a first impression about the accuracy of possible approximations made in an equation set. Here we will investigate the wave expansion properties of several anelastic approximations of the Euler equations. Such a study has already been done by Davies et al. (2003) and some of their results will be reproduced here. Contrariwise, the current COSMO model uses the fully compressible Euler equations with a split-explicit solver by Wicker and Skamarock (2002). This time-splitting approach needs a so-called divergence damping to be stable (Baldauf, 2010), which can be considered as an artificial additional term in the compressible Euler equations. It will be of interest in which manner such a term will change the wave expansion properties, too. In the frame of the CDC priority project, it is of particular interest to compare the divergence damping with the anelastic equations. This comparison is done here on the level of the analytic equations.

Such an investigation has been already performed by Baldauf (2011), where the anelastic approximation sets of Ogura and Phillips (1962), here denoted as 'OP62', Wilhelmson and Ogura (1972) ('WO72'), and Lipps and Hemler (1982) ('LH82') have been compared with a compressible equation set with the artificial 3-dimensional (3D) divergence damping. The equation set 'LH82' is used in the EULAG model (e.g. Smolarkiewicz and Prusa, 2005). This study extends those of Baldauf (2011) by considering additionally the anelastic equation set of Durran (1989) ('D89') and by comparing different versions (3D, 2D) of the divergence damping, too. The basic methodology again follows the normal mode analysis of Davies et al. (2003).

7.2 Derivation of the dispersion relations

In the following a steady atmosphere (no base flow $u_0 = 0$) is assumed for the base state. It is further hydrostatic ($\partial p_0/\partial z = -g\rho_0$) and fulfills the ideal gas law $p_0 = \rho_0 R T_0$. The sound velocity of the base state is $c_s = \sqrt{\frac{c_p}{c_v} R T_0}$.

We will use an equation for the pressure perturbation p' as in the COSMO-model, but a continuity equation to have a direct control about the anelastic approximations. The different anelastic equation sets are summarized e.g. in Nance and Durran (1994) and are therefore

not repeated here The linearization around the base state delivers

$$\frac{\partial u'}{\partial t} = -\frac{1}{\rho_0}\frac{\partial p'}{\partial x} + fv' + \alpha_D \frac{\partial D'}{\partial x}, \tag{16}$$

$$\frac{\partial v'}{\partial t} = -\frac{1}{\rho_0}\frac{\partial p'}{\partial y} - fu' + \alpha_D \frac{\partial D'}{\partial y}, \tag{17}$$

$$\frac{\partial w'}{\partial t} = -\frac{1}{\rho_0}\frac{\partial p'}{\partial z} - \sigma_{LH}\frac{1}{\rho_0}\frac{N^2}{g}p' - g\frac{\rho'}{\rho_0} + \alpha_{D,v}\frac{\partial D'}{\partial z} + \sigma_{dd2}\alpha_{D,v}D'\frac{1}{\rho_0}\frac{\partial \rho_0}{\partial z}, \tag{18}$$

$$\sigma_2\frac{\partial \rho'}{\partial t} + w'\frac{\partial \rho_0}{\partial z} = -\rho_0 D' - \sigma_{D89}\frac{\rho_0}{\Theta_0}\frac{\partial \Theta_0}{\partial z}w', \tag{19}$$

$$\frac{\partial p'}{\partial t} + \underbrace{w'\frac{\partial p_0}{\partial z}}_{=-g\rho_0 w'} = c_s^2\left(\frac{\partial \rho'}{\partial t} + w'\frac{\partial \rho_0}{\partial z}\right), \tag{20}$$

$$D' = \frac{\partial u'}{\partial x} + \frac{\partial v'}{\partial y} + \frac{\partial w'}{\partial z}. \tag{21}$$

Some switches $\sigma_{...}$ have been introduced whose values (0 or 1) are summarized in table 11. σ_{dd2} distinguishes two types of the artificial divergence damping in the 3D case: either the term $\alpha_D \partial D'/\partial z$ ('type 1', $\sigma_{dd2} = 0$) or the term $\alpha_D/\rho_0 \partial(\rho_0 D')/\partial z$ ('type 2', $\sigma_{dd2} = 1$). Type 2 is used in COSMO and MM5 because it can be coded more efficiently than type 1.
σ_2 is the main switch of the anelastic approximation. The additional term $\sim \sigma_{LH}$ only arises in the equation system of LH82. For its derivation one has to consider that LH82 are using $-c_p\nabla\Theta_0\pi' + \mathbf{g}\Theta'/\Theta_0$ for the pressure gradient and the buoyancy term instead of the correct term $-c_p\Theta\nabla\pi' + \mathbf{g}\Theta'/\Theta_0$ (Nance and Durran, 1994). In linear approximation the difference between these two terms is $-c_p\pi'\nabla\Theta_0$. Expressed by the variables used in the equation system above this can be approximated linearly by $-\frac{1}{\rho_0}\frac{N^2}{g}p'$. Alternatively, the D89 equation set uses $\nabla \cdot \rho_0\Theta_0\mathbf{v} = 0$ (for adiabatic processes) instead of $\nabla \cdot \rho_0\mathbf{v} = 0$ (used in OP62, WO72 and LH82). In linear approximation this delivers an additional term $\sim \sigma_{D89}$. The pressure equation is just the linearized adiabatic state equation $d\Theta/dt = 0$ which is used by all equation sets considered here. Furthermore, it should be mentioned that in this *linear* analysis there is no difference between the equation systems of OP62 and WO72.

equation system	σ_2	σ_{LH}	σ_{D89}	α_D	$\alpha_{D,v}$	σ_{dd2}
compressible	1	0	0	0	0	0
compressible, with 3D-div. damping, type 1	1	0	0	$\neq 0$	$= \alpha_D$	0
compressible, with 3D-div. damping, type 2	1	0	0	$\neq 0$	$= \alpha_D$	1
compressible, with 2D-div. damping	1	0	0	$\neq 0$	0	0
anelastic (OP62, WO72)	0	0	0	0	0	0
anelastic (LH82)	0	1	0	0	0	0
anelastic (D89)	0	0	1	0	0	0

Table 11: Switches for the different equation sets inspected in the normal mode analysis.

The coefficient functions of the linearized equations (16)-(21) are dependent on z. To reduce this z-dependency (the following Fourier transformation requires even constant coefficients) we perform a variable transformation by a function of the density according to Bretherton (1966, section 5):

$$\phi' = \left(\frac{\rho_0}{\rho_s}\right)^{\alpha} \cdot \phi_b. \tag{22}$$

where ρ_s is a constant reference value (e.g. at the bottom). The exponent is $\alpha = -1/2$ for the variables $\phi' = u, v, w, T'$ and $\alpha = +1/2$ for $\phi' = p', \rho'$. Insertion into eqns. (16)-(21) results in a quite similar system with additional terms proportional to the (inverse) scale height

$$\delta = -\frac{\partial}{\partial z}\left(\log\frac{\rho_0}{\rho_s}\right). \tag{23}$$

In the special case of an isothermal atmosphere ($T_0 = const.$) the density is purely exponential and therefore $\delta = g/(RT_0) = const.$ The result of this Bretherton transformation is that some coefficients (namely those $\sim 1/\rho_s$) become constant, whereas others like $\sim c_s^2$, $\sim T_0$, $\sim \delta$ remain dependent on z (they are only constant for an isothermal atmosphere). But this z-dependency is quite weak, therefore they can also be considered nearly as constant. This allows to extent the analysis to more realistic stratifications (see 'second stratification case' below).

It is convenient to introduce the acoustic cutoff frequency

$$\omega_a^2 = -\frac{g}{\rho_0}\frac{\partial\rho_0}{\partial z} \tag{24}$$

and therefore $\delta = \omega_a^2/g$, and the Brunt-Väisälä-frequency

$$N^2 = \frac{g}{\Theta_0}\frac{\partial\Theta_0}{\partial z} = \frac{g}{T_0}\left(\frac{\partial T_0}{\partial z} + \frac{g}{c_p}\right). \tag{25}$$

With the aid of the sound velocity, the ideal gas equation and the hydrostatic equation one can derive

$$\omega_a^2 = N^2 + \frac{g^2}{c_s^2}. \tag{26}$$

Now we can Fourier transform the equations by

$$\phi_b'(x,y,z,t) = \hat{\phi}_b(k_x,k_y,k_z,\omega)\, e^{i(k_x x + k_y y + k_z z - \omega t)}. \tag{27}$$

This leads to a system of the form $\mathbf{A}\cdot(\hat{u}_b,\hat{v}_b,\hat{w}_b,\hat{\rho}_b,\hat{p}_b)^T = 0$ with

$$\mathbf{A} = \begin{pmatrix} i\omega + \alpha_D(ik_x)^2 & f - \alpha_D k_x k_y & \alpha_D ik_x(ik_z + \frac{\delta}{2}) & 0 & -ik_x\frac{1}{\rho_s} \\ -f - \alpha_D k_x k_y & i\omega + \alpha_D(ik_y)^2 & \alpha_D ik_y(ik_z + \frac{\delta}{2}) & 0 & -ik_y\frac{1}{\rho_s} \\ \alpha_{D,v} ik_x K_d & \alpha_{D,v} ik_y K_d & i\omega + \alpha_{D,v}(ik_z + \frac{\delta}{2})K_d & -\frac{g}{\rho_s} & A_{35} \\ -ik_x\rho_s & -ik_y\rho_s & A_{43} & \sigma_2 i\omega & 0 \\ 0 & 0 & -\frac{\rho_s}{g}N^2 c_s^2 & -i\omega c_s^2 & i\omega \end{pmatrix} \tag{28}$$

and with the abbreviations

$$K_d = \left(ik_z + \frac{\delta}{2} - \sigma_{dd2}\frac{\omega_a^2}{g}\right), \tag{29}$$

$$A_{35} = -\frac{1}{\rho_s}\left(ik_z - \frac{\delta}{2}\right) - \sigma_{LH}\frac{1}{\rho_s}\frac{N^2}{g}, \tag{30}$$

$$A_{43} = -\rho_s(ik_z + \frac{\delta}{2}) + \rho_s\frac{\omega_a^2}{g} - \sigma_{D89}\rho_s\frac{N^2}{g}. \tag{31}$$

After an appropriate non-dimensionalization the requirement $\det A = 0$ leads to the characteristic equation for $\omega(\mathbf{k})$. This delivers the following dispersion relations:

The characteristic equation for the **non-hydrostatic, compressible equations** follows from the switches $\sigma_2 = 1$, $\sigma_{LH} = 0$, $\sigma_{D89} = 0$:

$$\begin{aligned}
&\omega^4 + \left[i\alpha_D(k_x^2 + k_y^2) + i\alpha_{D,v}\left(k_z - \frac{i}{2}\frac{\omega_a^2}{g}\right)^2 - \sigma_{dd2}\alpha_{D,v}\left(k_z - \frac{i}{2}\frac{\omega_a^2}{g}\right)\frac{\omega_a^2}{g} \right] \omega^3 \\
&- \left[c_s^2\left(k^2 + \frac{1}{4}\frac{\omega_a^4}{g^2}\right) + f^2 \right] \omega^2 \\
&+ \left[(k_x^2 + k_y^2)(\alpha_D - \alpha_{D,v})g\left(k_z - \frac{i}{2}\frac{\omega_a^2}{g}\right) - i\alpha_{D,v} f^2 \left(k_z - \frac{i}{2}\frac{\omega_a^2}{g}\right)^2 \right. \\
&\left. + \sigma_{dd2}\alpha_{D,v}\left(-i(k_x^2 + k_y^2)\omega_a^2 + f^2\left(k_z - \frac{i}{2}\frac{\omega_a^2}{g}\right)\frac{\omega_a^2}{g}\right) \right] \omega \\
&+ N^2 c_s^2 (k_x^2 + k_y^2) + f^2 c_s^2 \left(k_z^2 + \frac{1}{4}\frac{\omega_a^4}{g^2}\right) = 0.
\end{aligned} \tag{32}$$

For $\alpha_D = 0$ and $\alpha_{D,v} = 0$ we get the compressible solution (i.e. the 'true' solution), whereas the influence of the artificial divergence damping can be inspected by $\alpha_D, \alpha_{D,v} \neq 0$. Note, that this dispersion relation is identical to equations (15) and (18) of Gassmann and Herzog (2007), if the simplifications $f = 0$ and $\sigma_{dd2} = 0$ are made.

The different **anelastic approximations** follow from $\sigma_2 = 0$, $\alpha_D = \alpha_{D,v} = 0$ and the setting of the switches σ_{LH} and σ_{D89} (see table 11). This results in the dispersion relation

$$\left[c_s^2\left(k^2 + \frac{1}{4}\frac{\omega_a^2}{g}\right) + a_0 \right] \omega^2 - \left[c_s^2(k_x^2 + k_y^2)N^2 + f^2\left(c_s^2\left(k_z^2 + \frac{1}{4}\frac{\omega_a^2}{g}\right) + a_0 \right) \right] = 0 \tag{33}$$

with

$$a_0 = \begin{cases} \frac{N^2 c^2}{g}\left(ik_z - \frac{1}{2}\frac{\omega_a^2}{g}\right) & \text{for OP62, WO72,} \\ 0 & \text{for LH82,} \\ -N^2 & \text{for D89.} \end{cases} \tag{34}$$

All the anelastic approximations eliminates sound waves, only the two branches for gravity waves are contained.

In the following sections, we will evaluate and compare the dispersion relations (32) and (33) for several realistic parameters.

7.3 Discussion of the results

To get an impression about the behavior of waves we consider two stratifications. First an isothermal atmosphere with $T_0 = 260$ K. In this case the inverse scale height is $\delta \approx 1/7606.5$ 1/m, the sound velocity is $c_s \approx 323.2$ m/s, the Brunt-Väisälä-frequency is $N \approx 0.01919$ 1/s, and the acoustic cut-off frequency is $\omega_a \approx 0.03591$ 1/s. The second considered atmosphere also has a mean temperature of $T_0 = 260$ K but a Brunt-Väisälä frequency of $N = 0.01$ 1/s. We further consider wave expansion both in pure horizontal direction or in a direction which is tilted by 20 degrees against the horizontal.

For the compressible equations *with* divergence damping we choose values of $\alpha_D, \alpha_{D,v} = 50000$, 100000, or 150000 m^2/s, which are typical values for COSMO grid mesh sizes from about 2.8 km until about 10 km, respectively.

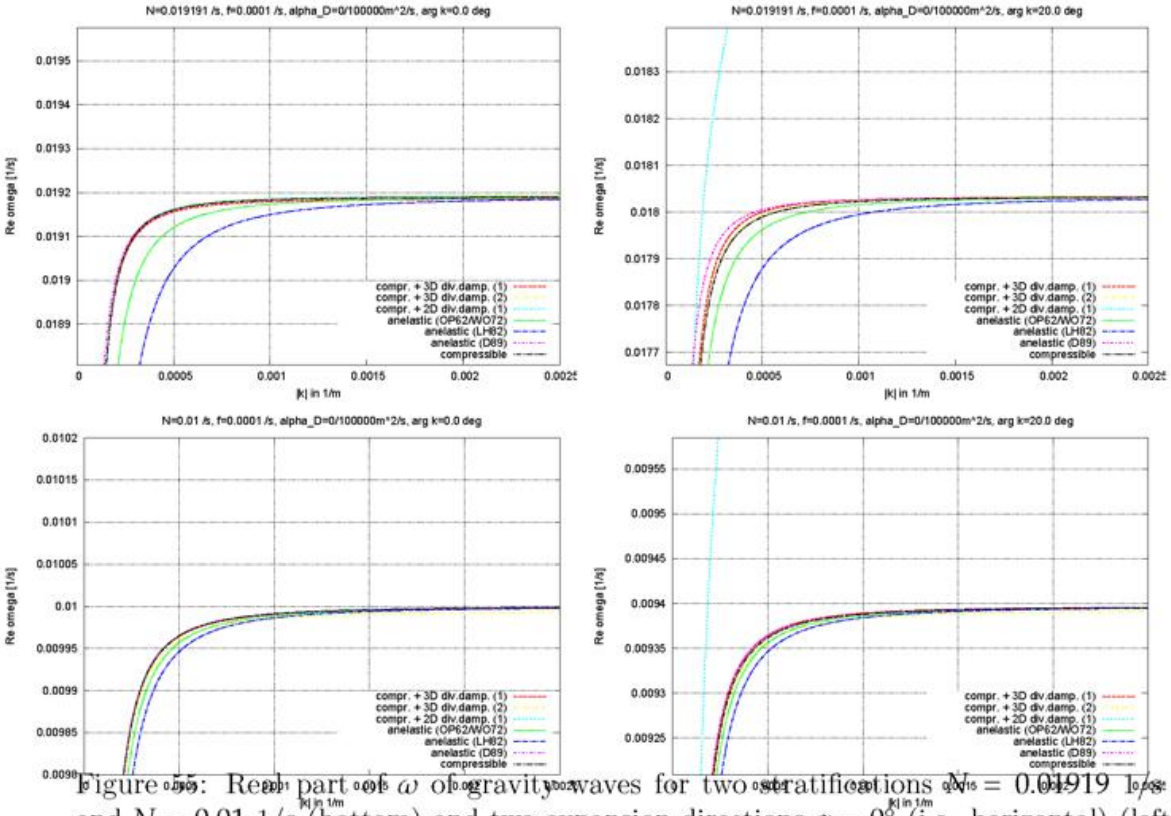


Figure 55: Real part of ω of gravity waves for two stratifications $N = 0.01919$ 1/s (top) and $N = 0.01$ 1/s (bottom) and two expansion directions $\alpha = 0°$ (i.e. horizontal) (left) and $\alpha = 20°$ (right). The different equation sets are distinguished by different colors and line types (see also table 11).

Short gravity waves. Figure 55 shows the positive real part of the gravity for the different equation sets. For very short gravity waves ($k = 0.003$ 1/m corresponds to a wavelength $\lambda = 2\pi/k \approx 2.1$ km) all equation sets show a quite good agreement with the 'truth', the dispersion relation of the compressible equations (black line). A closer examination shows that for the anelastic equation sets it holds indeed that $\omega \to \pm N$ for $k \to \infty$. The compressible 3D divergence damping versions do not exactly converge to the right value but the deviations are less than about 0.05 % and therefore are negligible. The 2D divergence damping has a quite strange behavior for tilted expansion, which is separately discussed below.

For longer waves (> 10 km) stronger deviations in the order of one percent are visible for the OP62 and WO72 system and even stronger for the LH82 system. In contrast, a remarkably good agreement with the compressible system is shown by the D89 equation set. The compressible sets *with* 3D-divergence damping are generally quite close to the compressible solution.

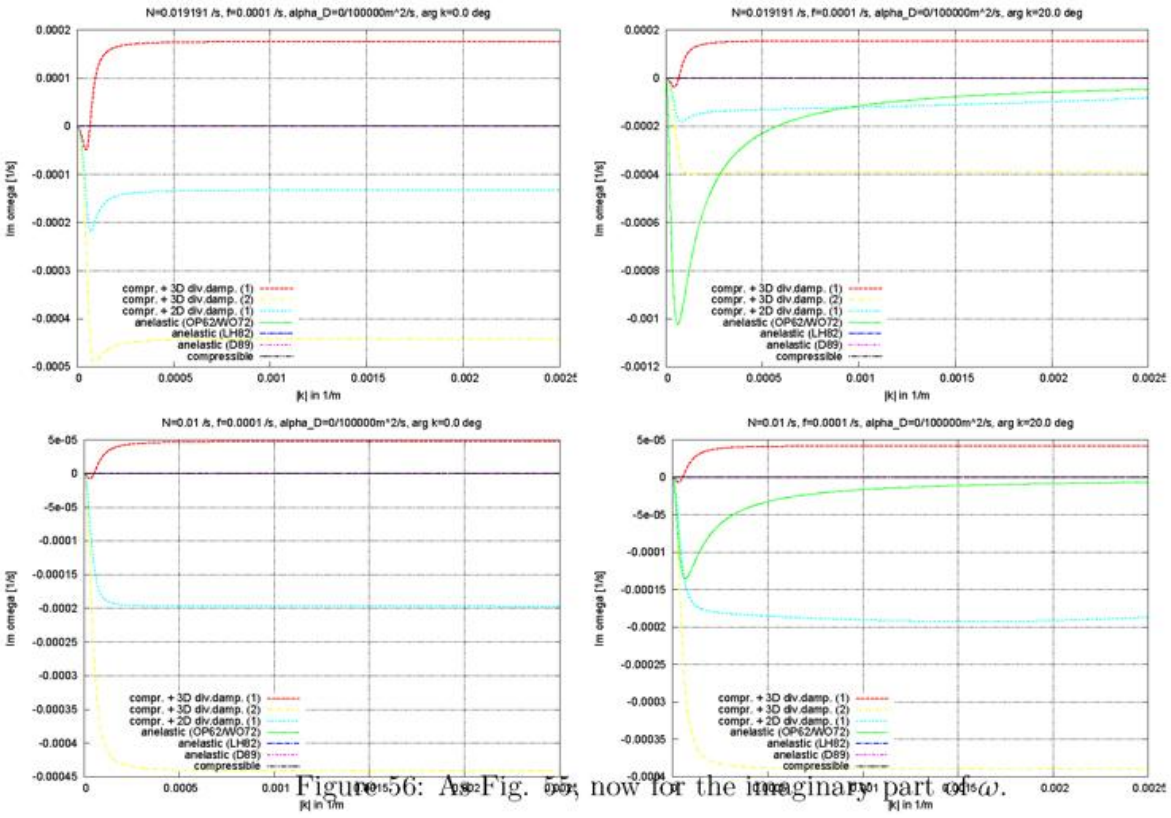


Figure 56: As Fig. 55, now for the imaginary part of ω.

The damping (i.e. the imaginary part of ω) is shown in Figure 56. The horizontal expansion of all anelastic sets has no damping. The same holds for tilted expansion in the cases LH82 and D89, however OP62 or WO72 show a certain damping for longer gravity waves. The compressible equations with 3D divergence damping type 2 show a damping of nearly all gravity waves. This is smaller for the 2D divergence damping. In contrast, type 1 even shows a weak amplification. This was also stated in Baldauf (2010, appendix), were it has been shown, too, that this behavior does not occur if the Bretherton-transformation is not performed.

Long gravity waves. The long gravity wave behavior is shown in Fig. 57 ($k = 0.0001$ 1/m corresponds to $\lambda \approx 63$ km). Obviously divergence damping has almost no influence to this wave type. The OP62 and WO72 systems are still relatively close to the compressible equations for wave lengths larger around 100 km. For even larger wave lengths the deviations become larger. A different behavior has LH82: here an intermediate range of long gravity waves show a larger deviation from the compressible solution, however, very long gravity waves ($\lambda > 300$ km) are well represented. Under all anelastic approximations considered here, such very long waves are worst represented by the D89 system. All these statements reduce in strength if the stratification becomes less stable. (lower figures in Fig. 57).

For the damping of long waves (Figs. 58) similar statements hold as for the shorter waves. For extremely long waves the influence of divergence damping decreases with increasing wave length.

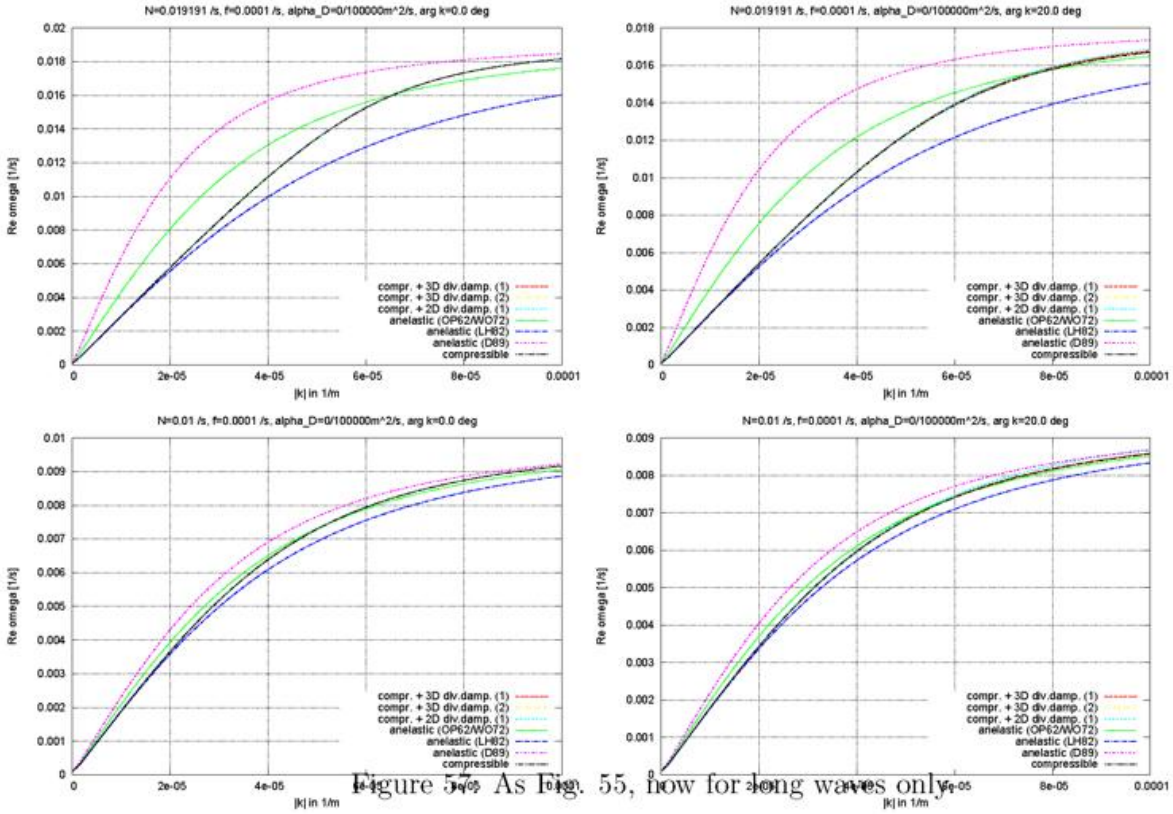


Figure 57: As Fig. 55, now for long waves only.

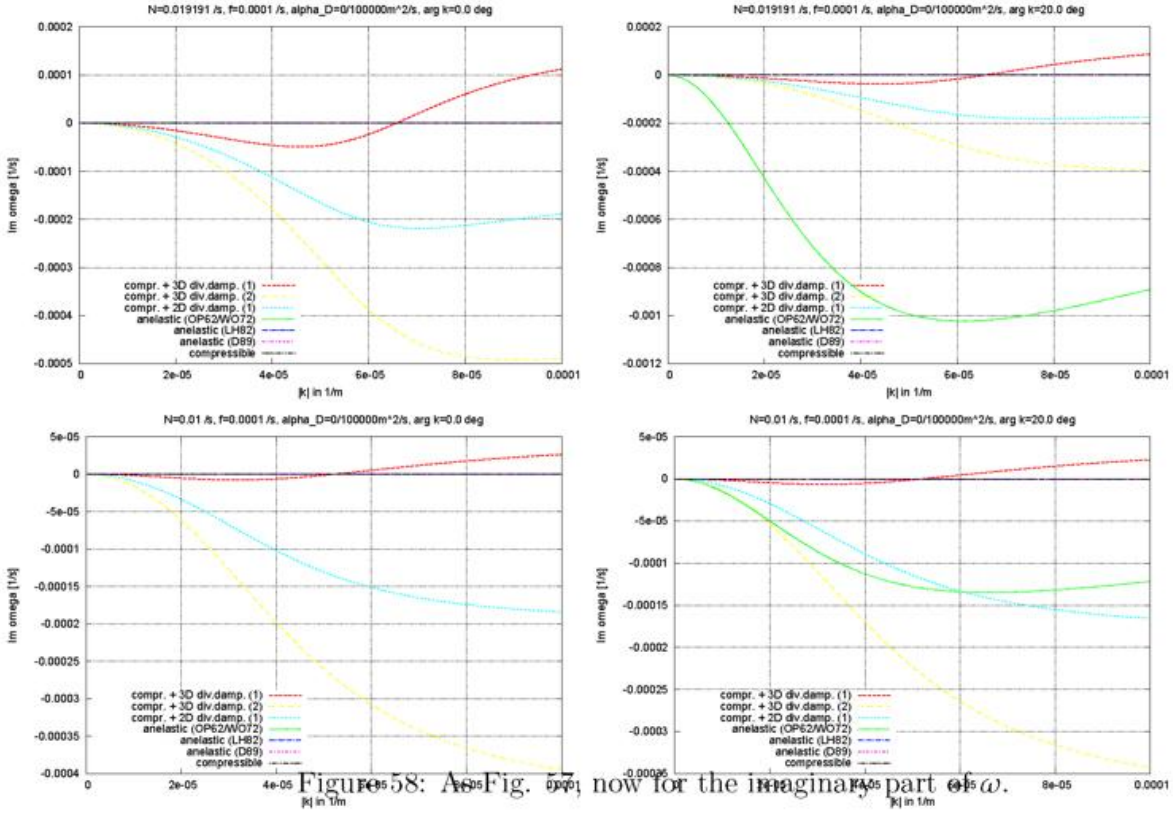


Figure 58: As Fig. 57, now for the imaginary part of ω.

Sound waves in the compressible systems. The compressible equations contain sound waves. The divergence damping increasingly reduces their phase velocity with decreasing wave length (Figure 59). However, for strong divergence damping the e-folding time is quite small, therefore only long sound waves will be simulated in the current COSMO dynamical core. In the case of tilted expansion (Figure 60), there is a small but relatively unimportant difference between the different types of divergence damping.

The temperature stratification has almost no influence to the expansion of sound waves. Therefore only results for $N = 0.01$ 1/s are shown.

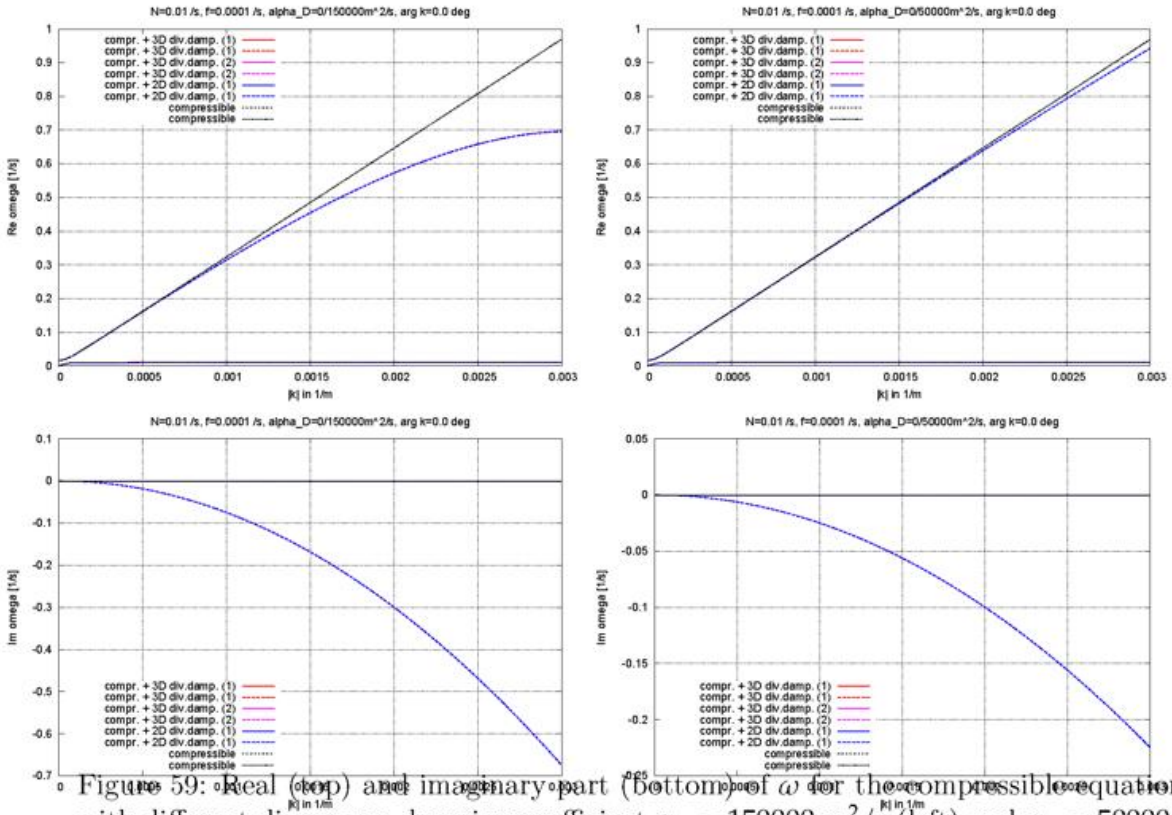


Figure 59: Real (top) and imaginary part (bottom) of ω for the compressible equation sets with different divergence damping coefficient $\alpha_D = 150000$ m^2/s (left) and $\alpha_D = 50000$ m^2/s (right). $N = 0.01$ 1/s, $\alpha = 0°$.

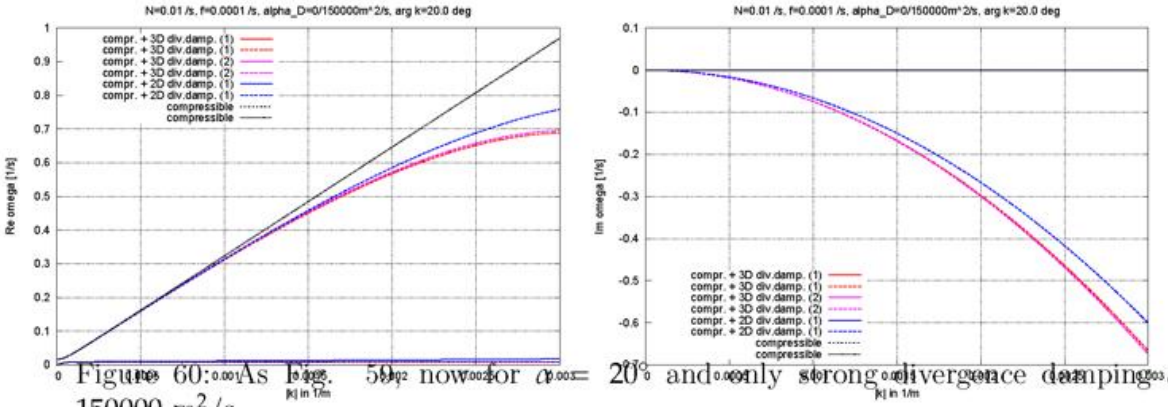


Figure 60: As Fig. 59, now for $\alpha = 20°$ and only strong divergence damping $\alpha_D = 150000\ \mathrm{m}^2/\mathrm{s}$.

Gravity waves in the compressible systems. In a section above we have already seen that the gravity waves are almost correctly treated by the 3D divergence damping. For the 2D divergence damping, this also holds only for purely horizontal expansion of gravity waves, whereas it shows a strange behavior for tilted expansion: the frequency obviously increases with decreasing wavelength instead of remaining constant. This behavior was already remarked by (Gassmann and Herzog, 2007, eq. (20)). Since in real case simulations and also in idealized tests this equation system behaves not so bad, a look to all the branches of the dispersion relation is advisable. Figure 61 shows that the positive frequencies ω are increasing with k. But the absolute values of the negative frequencies are *decreasing*. Physically this means that upward traveling gravity waves are faster then expected, whereas downward traveling gravity waves are slower than expected, so that their mean velocity is nearly the correct one.

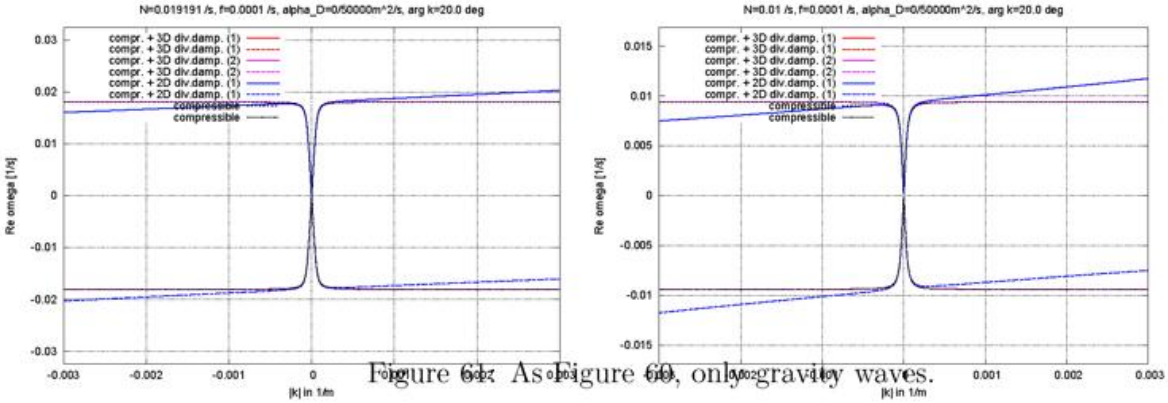


Figure 61: As Figure 60, only gravity waves.

7.4 Summary

The dispersion relations for several anelastic equation sets and compressible equations with several versions of the artificial divergence damping have been compared.

The general outcome is that the anelastic equation set is very well suited to simulate shorter gravity waves. The compressible systems with 'type 2' 3D-divergence damping treats the phase and group velocity of this wave type well, too, apart from a small damping. But

the 2D divergence damping, which is actually used in the COSMO model, exhibits a not completely satisfying behavior.

Concerning long gravity waves ($\lambda > 100$ km), the anelastic equation sets have some drawbacks. This probably reduces their applicability for global models a bit.

Sound waves are of course not contained in the anelastic equations, but also the shorter waves are heavily damped in the compressible equations by divergence damping. Only for rather long sound waves a reasonable realistic treatment can be expected.

References

Baldauf, M., 2010: Linear stability analysis of Runge-Kutta based partial time-splitting schemes for the Euler equations. *Mon. Wea. Rev.*, **138**, 4475–4496.

Baldauf, M., 2011: Non-hydrostatic modelling with the COSMO model. *ECMWF Workshop on Non-hydrostatic Modelling.*

Bretherton, F. P., 1966: The propagation of Groups of Internal Gravity Waves in a Shear Flow. *Quart. J. Roy. Met. Soc.*, **92**, 466–480.

Davies, T., A. Staniforth, N. Wood, and J. Thuburn, 2003: Validity of anelastic and other equation sets as inferred from normal-mode analysis. *Quart. J. Roy. Met. Soc.*, **129**, 2761–2775.

Durran, D. R., 1989: Improving the Anelastic Approximation. *J. Atmos. Sci.*, **46 (11)**, 1453.

Gassmann, A. and H.-J. Herzog, 2007: A Consistent Time-Split Numerical Scheme Applied to the Nonhydrostatic Compressible Equations. *Mon. Wea. Rev.*, **135**, 20–36.

Lipps, F. B. and R. S. Hemler, 1982: A scale-analysis of deep moist convection and some related numerical calculations. *J. Atmos. Sci.*, **39**, 2192–2210.

Nance, L. B. and D. R. Durran, 1994: A Comparison of the Accuracy of Three Anelastic Systems and the Pseudo-Incompressible System. *JAS*, **52 (24)**, 3549–3565.

Ogura, Y. and N. A. Phillips, 1962: Scale analysis of deep and shallow convection in the atmosphere. *J. Atmos. Sci.*, **19**, 173.

Smolarkiewicz, P. K. and J. M. Prusa, 2005: Towards mesh adaptivity for geophysical turbulence: continuous mapping approach. *Int. J. Numer. Meth. Fluids*, **47**, 789–801.

Wicker, L. J. and W. C. Skamarock, 2002: Time Splitting Methods for Elastic Models using Forward Time Schemes. *Mon. Wea. Rev.*, **130**, 2088–2097.

Wilhelmson, R. and Y. Ogura, 1972: The pressure perturbation and the numerical modeling of a cloud. *J. Atmos. Sci.*, **29**, 1295–1307.

8 The finite volume implicit solver CONSOL

Pier Luigi Vitagliano

CMCC, Centro Euro-Mediterraneo sui Cambiamenti Climatici

CIRA, Centro Italiano Ricerche Aerospaziali

Via Maiorise, 80143 Capua (CE), Italy

Summary

A flow solver for the Euler and Navier-Stokes equations in 3 dimensions has been written. Time integration is based on dual time stepping, spatial discretization on finite volumes. Second order central scheme with added artificial dissipation and fourth order scheme have been currently implemented. Convergence in dual time is improved by adopting residual averaging, local time stepping, preconditioning, multigrid. Tests with complex orography were carried out, they are meant to address the issues related with flow initialization, hydrostatic balance in the equations, inflow, outflow and upper boundary conditions. Some other test cases are reported, to demonstrate the capability of the present method to dial with typical basic phenomena.

8.1 Introduction

The general trend in numerical weather prediction is to increase the mesh resolution; consequences are the increase in amount of mesh cells, reduction of time step and steeper lower boundaries in regions with complex orography. In those regions mesh cells are more skewed, so horizontal and vertical components of velocity and pressure gradient (and numerical errors as well) are more strongly coupled.

Motivations for this work are the needs of improving numerical efficiency of the COSMO model, improving the conservation properties of the scheme and its capability to deal with steep orography.

Finite volume formulation has the capability of conserving the transported quantities, for this reason it is a good candidate for improving the conservation properties of the dynamical core. The dual time stepping procedure is very popular in the field of aerodynamics but it seems that was never tested for simulation of atmospheric flows. The aim of this work is to evaluate the performances of the scheme in comparison with the classical time splitting procedure, which is the standard time integration scheme of COSMO, in the perspective of using very small grid size and also very large time steps, those are required for climatological simulations. The main questions to answer are related to three aspects: equation set in conservative variables, the dual time stepping procedure and the finite volume schemes, whether they are suitable for numerical weather prediction.

8.2 Mathematical formulation

The unsteady Euler equations are cast in integral form for a region Ω with boundary $\partial\Omega$:

$$\frac{\partial}{\partial t}\int_{\Omega}\underline{\mathbf{W}}\,\mathrm{d}\Omega+\oint_{\partial\Omega}\underline{\underline{\mathbf{F}}}\cdot\underline{n}\,\mathrm{d}S=\int_{\Omega}\underline{\mathbf{B}}\,\mathrm{d}V \tag{35}$$

when the region Ω is fixed in time the above matrices are:

$$\underline{\mathbf{W}} = \begin{bmatrix} \rho \\ \rho u \\ \rho v \\ \rho w \\ \rho E \end{bmatrix}, \quad \underline{\underline{\mathbf{F}}} = \begin{bmatrix} \rho u & \rho v & \rho w \\ \rho u^2 + p & \rho uv & \rho uw \\ \rho uv & \rho v^2 + p & \rho w \\ \rho uw & \rho vw & \rho w^2 + p \\ \rho uH & \rho vH & \rho wH \end{bmatrix}, \quad \underline{\mathbf{B}} = \begin{bmatrix} 0 \\ 0 \\ 0 \\ \rho g \\ \rho gw \end{bmatrix}, \tag{36}$$

where $\underline{\mathbf{W}}$ is the vector of conserved quantities, $\underline{\underline{\mathbf{F}}}$ is the corresponding flux term, $\underline{\mathbf{B}}$ the source term, g the vertical component of the gravity vector $\underline{g}$ (usually the reference system z axis is oriented like -$\underline{g}$), $\underline{n}$ is the unit vector normal to the boundary surface and $\mathrm{d}S$ is the surface area element. We denote density and pressure as ρ and p, the velocity vector $\underline{\mathbf{u}}$=(u,v,w). For a perfect gas we can express the pressure from the total energy E

$$p = (\gamma - 1)\rho(E - \frac{\mathbf{u}^2}{2}) \tag{37}$$

the total enthalpy is defined by

$$H = E + \frac{p}{\rho}. \tag{38}$$

The integral form allows discontinuities in the flow field.

For computing the Navier-Stokes equations, viscous fluxes $\underline{\underline{\mathbf{G}}}$ are added to $\underline{\underline{\mathbf{F}}}$:

$$\underline{\underline{\mathbf{G}}} = -\begin{bmatrix} 0 & 0 & 0 \\ \sigma_{xx} & \sigma_{xy} & \sigma_{xz} \\ \sigma_{xy} & \sigma_{yy} & \sigma_{yz} \\ \sigma_{xz} & \sigma_{yz} & \sigma_{zz} \\ \underline{\mathbf{u}} \cdot \sigma_{ix} - \kappa\frac{\partial T}{\partial x} & \underline{\mathbf{u}} \cdot \sigma_{iy} - \kappa\frac{\partial T}{\partial y} & \underline{\mathbf{u}} \cdot \sigma_{iz} - \kappa\frac{\partial T}{\partial z} \end{bmatrix} \tag{39}$$

$\underline{\underline{\sigma}}$ is the stress tensor and its components are:

$$\begin{aligned} \sigma_{xx} &= \mu[2\frac{\partial u}{\partial x} - \tfrac{2}{3}(\frac{\partial u}{\partial x} + \frac{\partial v}{\partial y} + \frac{\partial w}{\partial z})] \\ \sigma_{xy} &= \mu(\frac{\partial u}{\partial y} + \frac{\partial v}{\partial x}) \end{aligned} \tag{40}$$

the other components are obtained by exchanging the velocity gradient derivatives. μ is the kinematic viscosity, the heat flux is given by the thermal diffusion coefficient κ multiplied by the temperature gradient. In case of turbulent fluxes the turbulent viscosity μ_{tur} and turbulent thermal diffusion κ_{tur} are modeled and added to the thermodynamical (laminar) coefficients. Turbulent viscous flows were not simulated in this work.

Boundary conditions are different in case of inflow, outflow and rigid wall. Inflow conditions allow to set four variables and extrapolate one variable from inside the flow field. Usually momentum and density are set, and pressure is extrapolated. Outflow conditions allow to set one variable (usually pressure or normal momentum component) and extrapolate the others. Boundary conditions on rigid walls fix normal momentum component to 0 and extrapolate tangential components and pressure. Artificial dissipation also requires boundary conditions: usually zero artificial fluxes are set at the boundaries. In case of viscous computations all the momentum components at the wall can be set to 0 (no-slip boundary condition), and wall enthalpy or heat flux (enthalpy gradient) can be assigned. In case of inviscid flow the heat flux at the wall could be added as an external source to the ground layer.

8.3 Finite volume scheme and time integration

The equations are discretized by sub-dividing the flow domain in sub-domains (mesh cells), assuming the conserved quantities $\underline{\mathbf{W}}$ are known at the center of each mesh cell. In our case the domain is sub-divided in structured form, which means that each cell is stored in a 3-dimensional array and can be addressed by a 3-d index (i,j,k). Its 6 neighbors can be simply addressed by the indices (i+1,j,k), (i-1,j,k), (i,j-1,k), (i,j+1,k), (i,j,k-1), (i,j,k+1). The structured mesh arrangement allows more efficient algorithms for computing advective and diffusive fluxes, and more efficient data storage, since it is not necessary to keep informations for addressing the neighbor cells. The semi-discretization for a sub-domain of volume V leads to the equation:

$$V\frac{\partial(\underline{\mathbf{W}})}{\partial t} + \underline{\mathbf{R}}(\underline{\mathbf{W}}) = 0 \tag{41}$$

where

$$\underline{\mathbf{R}}(\underline{\mathbf{W}}) = \underline{\mathbf{Q}} - \underline{\mathbf{D}} - \underline{\mathbf{B}}. \tag{42}$$

$\underline{\mathbf{R}}$ represents the sum of the net flux out of the sub-domain $\underline{\mathbf{Q}}$, the artificial dissipative flux -$\underline{\mathbf{D}}$ (that is required for numerical stability) and the source term -$\underline{\mathbf{B}}$, which are balanced by the rate of change of $\underline{\mathbf{W}}$. The net flux out of the cell m is given by the sum over the six cell faces k

$$\mathbf{Q}_{\mathrm{m}} = \sum_{\mathrm{k}=1}^{6} \underline{\underline{\mathbf{F}}}_{\mathrm{mk}} \cdot \underline{n} S_{\mathrm{mk}} \tag{43}$$

Fluxes $\underline{\underline{\mathbf{F}}}$ are approximated at the cell face centers by averaging the quantities between the cell m and its neighbors k,

$$\underline{\underline{\mathbf{F}}}_{\mathrm{mk}} = \frac{\underline{\underline{\mathbf{F}}}_{\mathrm{m}} + \underline{\underline{\mathbf{F}}}_{\mathrm{k}}}{2} \tag{44}$$

S_{mk} is the area of the face between cells m and k, and $\underline{n}$ the unit vector normal to the cell face pointing outward. The artificial dissipation $\underline{\mathbf{D}}$ is proportional to the fourth derivative of the conserved variables:

$$\underline{\mathbf{D}} = \nu\nabla^4(\underline{\mathbf{W}}). \tag{45}$$

It can be expressed in flux form as the sum of the third derivative over the cell faces, in order to keep the conservation properties of the scheme.

Time derivatives are discretized by a second order backward formula, where the upper index n indicates the current time step. Volume for our system is constant in time and can be taken out of the time derivative:

$$\frac{\partial(\underline{\mathbf{W}})}{\partial t} = \frac{3\underline{\mathbf{W}}^{n+1} - 4\underline{\mathbf{W}}^{n} + \underline{\mathbf{W}}^{n-1}}{2\Delta t} \tag{46}$$

This formula is implicit, as it contains the variables $\underline{\mathbf{W}}$ at the time step n+1. It is A-stable and damps the highest frequency. In principle there are no limitations to Δt due to numerical stability. The dual time stepping procedure (Jameson, 1992) consists in solving the following system by inner iterations which advance in pseudo-time τ to steady state:

$$\frac{\partial(\underline{\mathbf{W}}^{n+1})}{\partial \tau} + \underline{\mathbf{R}}^{*}(\underline{W}^{n+1}) = 0 \tag{47}$$

where

$$\underline{\mathbf{R}}^{*}(\underline{W}^{n+1}) = \frac{3\underline{\mathbf{W}}^{n+1} - 4\underline{\mathbf{W}}^{n} + \underline{\mathbf{W}}^{n-1}}{2\Delta t} + \underline{\mathbf{R}}(\underline{W}^{n+1}) \tag{48}$$

An explicit multistage Runge-Kutta time marching scheme with variable local $\Delta\tau$, residual averaging, preconditioning and multigrid is implemented to advance the system in dual time, until a norm of the dual time derivative is smaller than a given small value. It should be noted that the backward implicit time derivative is second order accurate only when the residuals of the dual time equations are driven to 0. A technique based on prediction can be adopted, in order to keep the second order accuracy also in case of non perfect convergence of the dual time iterations: the flow variables are initialized at the beginning of the dual time iterations by an appropriate prediction formula, second order accurate in time. It has been shown that the dual time iterations do not destroy the second order accuracy of the prediction formula.

The convergence rate of iterative solvers for compressible Euler or Navier-Stokes equations is limited in case of low Mach number flows, because of the large difference between the velocities of the advective fluxes and the pressure perturbations (acoustic waves). Usual technique is to modify the acoustic speed in order to make the local Mach number large enough almost everywhere in the flow domain. It has essentially two functions: the first one is to improve the convergence rate, the second one is to modify the relative influence of the artificial dissipation term, which would affect the physical solution for very small Mach numbers. The basic idea is to pre-multiply the time derivatives of the flow variables (without artificial dissipation) by an appropriate matrix, which performs the scaling of the acoustic speeds with respect to the flux velocities. More details are in Turkel et al. (1996). Preconditioning can only be applied when we are interested to obtain a steady solution, since it destroys the time accuracy of the governing equations. In our procedure the physical time derivatives are treated as source terms and they are concealed in the right hand side of the equations set, while the dual time derivatives are relaxation terms.

8.4 Atmosphere at rest

The test case with atmosphere at rest (i.e. zero velocity components and no fluxes from the boundaries) is useful to highlight the numerical issues related to the large vertical gradient of pressure and density in case of a deformed mesh. Discretization errors in the computation of the pressure gradient for tilted cells can produce non-zero horizontal components. Even the little displacement of a single mesh point in the interior of a perfectly regular rectangular mesh on flat orography can produce spurious velocity and disturbances in the flow solutions. When pressure is a function only of the vertical coordinate z, a density field exists that allows a steady solution with zero velocity. But the spatial discretization of the pressure gradient is affected by metric terms. The discrete Euler flow equations for a cell m in case of atmosphere at rest simplify to:

$$\frac{\partial \rho}{\partial t} = 0 \tag{49}$$

$$\frac{\partial \rho u}{\partial t} + \frac{1}{V}\sum_{k=1}^{6} p_{mk} n_x S_{mk} = 0 \tag{50}$$

$$\frac{\partial \rho v}{\partial t} + \frac{1}{V}\sum_{k=1}^{6} p_{mk} n_y S_{mk} = 0 \tag{51}$$

$$\frac{\partial \rho w}{\partial t} + \frac{1}{V}\sum_{k=1}^{6} p_{mk} n_z S_{mk} = \rho g \tag{52}$$

$$\frac{\partial \rho E}{\partial t} = 0 \tag{53}$$

p_{mk} is the pressure averaged at the face between the cells m and k:

$$p_{\mathrm{mk}} = \frac{p_{\mathrm{m}} + p_{\mathrm{k}}}{2} \tag{54}$$

n_x, n_y, n_z are the Cartesian components of the unit vector normal to the face, S_{mk} is the face area. The set of discrete equations in case of zero velocity is a system of $3\mathrm{N}_c$ linear equations in $2\mathrm{N}_c$ unknowns p, ρ, constant in time, where N_c is the total amount of mesh cells. So it is not possible to find discrete solution for the atmosphere at rest with generic 3 dimensional meshes: only additional constraints on mesh coordinates could allow a solution for the equilibrium of the horizontal pressure gradient components. The resulting horizontal accelerations produce spurious motions.

A reference pressure and density field p_{ref} , ρ_{ref} in hydrostatic equilibrium is subtracted from the momentum equation to reduce the amount of spurious accelerations. By assuming that:

$$\nabla p_{\mathrm{ref}} = \rho_{\mathrm{ref}} g \tag{55}$$

$$p' = p - p_{\mathrm{ref}} \tag{56}$$

$$\rho' = \rho - \rho_{\mathrm{ref}} \tag{57}$$

the momentum equations in discrete form can be written as follows:

$$\frac{\partial \rho u}{\partial t} + \frac{1}{V} \sum_{\mathrm{k}=1}^{6} p'_{\mathrm{mk}} n_x S_{\mathrm{mk}} = 0 \tag{58}$$

$$\frac{\partial \rho v}{\partial t} + \frac{1}{V} \sum_{\mathrm{k}=1}^{6} p'_{\mathrm{mk}} n_y S_{\mathrm{mk}} = 0 \tag{59}$$

$$\frac{\partial \rho w}{\partial t} + \frac{1}{V} \sum_{\mathrm{k}=1}^{6} p'_{\mathrm{mk}} n_z S_{\mathrm{mk}} = \rho' g \tag{60}$$

Since the pressure perturbation p' is usually 10 to 100 times smaller than full pressure, the spurious acceleration is also smaller. Pressure and density perturbations are adopted for computing the artificial dissipation terms. In order to evaluate the performances of the numerical scheme, a skewed mesh was produced on a simplified orography with highest mountain of 3 km (Fig. 62). The mesh contains 150 cells in horizontal direction and 160 in vertical direction, with Δx = 1 km and Δz= 125 m. The mesh levels are flat above 13.5 km.

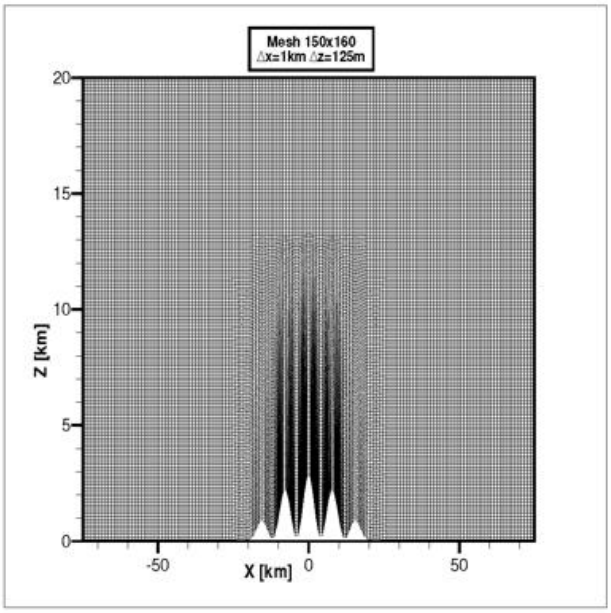
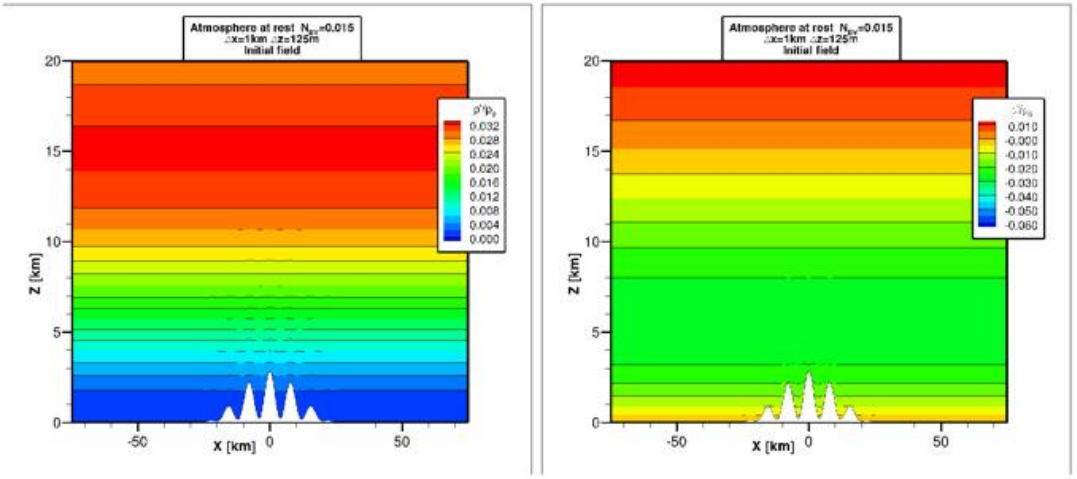


Figure 62: Mesh for testing the atmosphere at rest

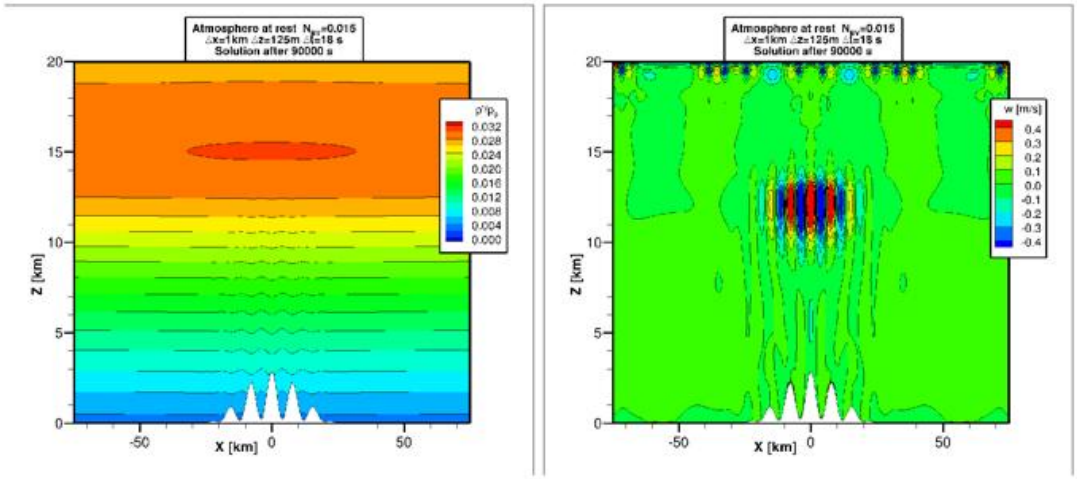
The reference pressure and density field is defined with constant Brunt-Väisälä frequency N_{BV}=0.01 1/s, and the initial field is defined with N_{BV}=0.015 1/s, so the initial pressure and density perturbations are computed as the difference between the two fields (Fig. 63). The flow field computed after 90000 seconds is shown in Fig. 64.



(a) Initial pressure perturbation

(b) Initial density perturbation

Figure 63: Initial perturbation field for atmosphere with N_{BV}=0.015 1/s

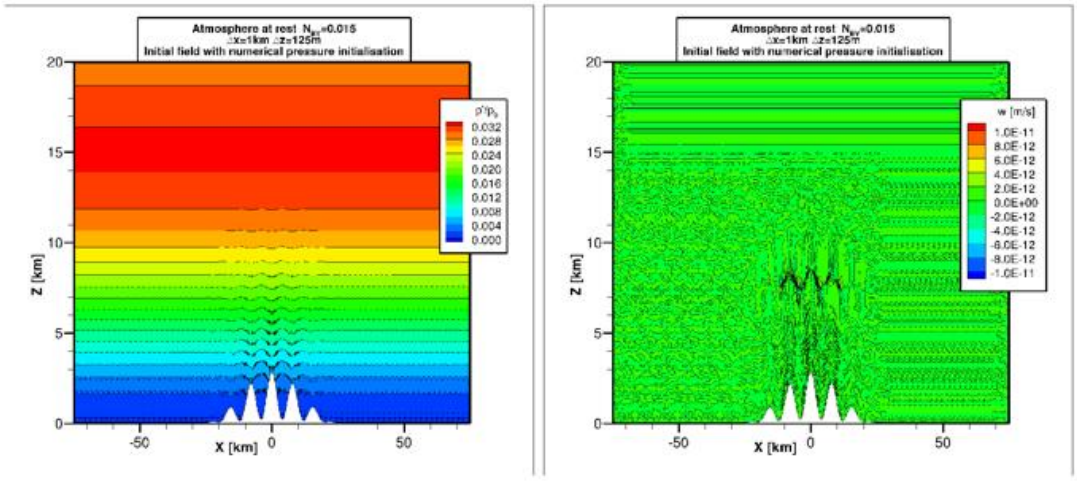


(a) Pressure perturbation (b) Vertical velocity component

Figure 64: Velocity components after 90000 s

The magnitude of the spurious velocity field is affected by the artificial viscosity ν: near the ground it damps the oscillations, at the higher levels the mesh stretching in vertical direction increases the artificial fluxes. This effect calls for a more appropriate formulation of the artificial dissipation and for a smoother mesh clustering in vertical direction.

An exact solution of the discrete equations for the atmosphere at rest can be obtained in 2D cases on generic meshes: the pressure field can be computed from the equation for the horizontal component (equilibrium of the horizontal component of the pressure forces acting on the four sides of each cell): the pressure depends upon the metric terms. After the pressure has been computed, the density field can be readily derived from the equilibrium in vertical direction. An example of such a 2D solution for a skewed mesh shown in Fig. 65.



(a) Pressure perturbation (b) Vertical velocity component

Figure 65: Exact solution of the discrete equations for 2D atmosphere at rest: pressure field computed from the equilibrium in horizontal direction

By comparing the numerical solution of pressure and density fields with the mathematical solution (horizontal stratification) the effect of a deformed mesh can be seen: it is clear that a mesh deformation induces disturbances in the field in such a way that pressure is increased where the mesh density decreases (i.e. in correspondence of the valleys). The resulting

velocity field is balanced.

8.5 Pressure gradient correction

A correction of the pressure gradient terms has been tested, in order to reduce the spurious velocity for the atmosphere at rest. This seems to improve the convergence rate of dual time iterations as well. The basic idea is to add a first order correction to the pressure averaged at the cell faces, by considering the vertical pressure gradient ρg, when the face center has different vertical coordinate from the cell center. Two different approaches were tested and compared. In the first case the density is considered to be constant inside a mesh cell. The averaged pressure at the face between cells m and k is computed as follows:

$$p'_{mk} = \frac{p'_m + (\frac{\partial p'}{\partial z})_m \delta z_m + p'_k + (\frac{\partial p'}{\partial z})_k \delta z_k}{2} \tag{61}$$

where δz_k is the difference between the z coordinate of the cell face center and the k cell center.

$$(\frac{\partial p'}{\partial z})_k = \rho'_k g \tag{62}$$

The second approach considers a vertical gradient of the density perturbation inside the cell, related to the pressure gradient by the isentropic relation:

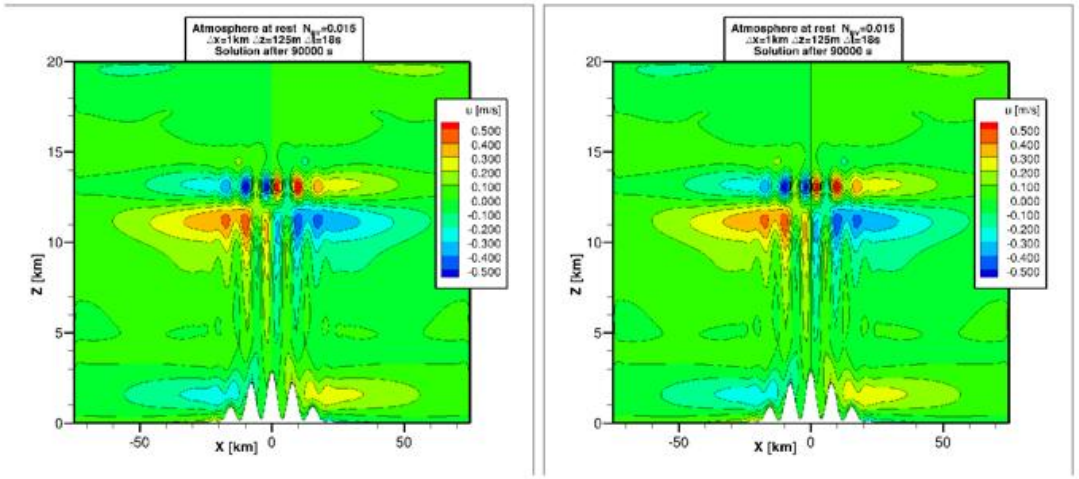
$$(\frac{\partial p'}{\partial \rho'}) = \gamma p/\rho = c^2 \tag{63}$$

It means that entropy is assumed to be constant inside a cell, rather than density. Both the averaged pressure and density are modified by adding the following corrections like in eq.(61):

$$(\frac{\partial p'}{\partial z})_k = \frac{\rho'_k g}{1 + \frac{\delta z_k}{c^2}} \tag{64}$$

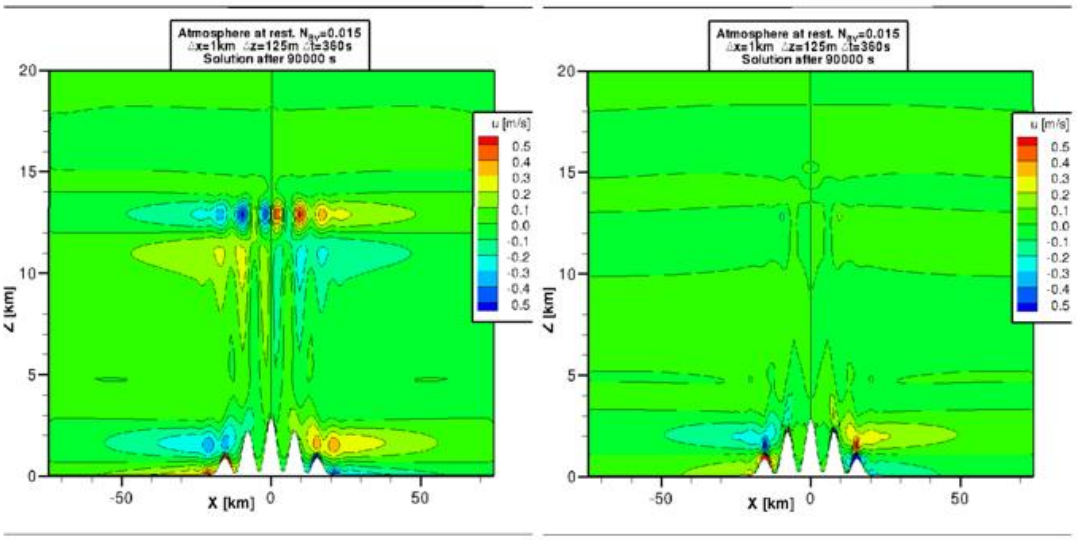
$$(\frac{\partial \rho'}{\partial z})_k = \frac{\rho'_k g}{c^2 + \delta z_k} \tag{65}$$

The perturbation fields after 90000 seconds are compared in Fig. 66 and show similar behavior, with smaller velocities near the ground. Finally, the effect of reducing the artificial viscosity is shown in Fig. 66(d). The flow computations of the atmosphere at rest were carried out with time steps ranging from 18 to 750 seconds, without significant differences in the results.



(a) Pressure correction approach 1

(b) Pressure correction approach 2



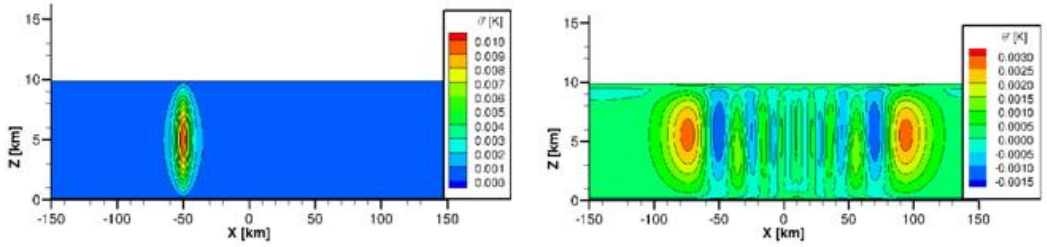
(c) No pressure correction

(d) Pressure correction and reduced artificial viscosity

Figure 66: Comparison of horizontal velocity components after 90000 s with different pressure correction approaches

8.6 Gravity wave

The test case is described in Skamarock and Klemp (1994), it shows the capability of the present scheme to simulate the time evolution of gravity waves produced by potential temperature perturbations. The flow field is initialized with constant Brunt Väisälä frequency N_{BV}=0.01 1/s in a channel of length 300 km and height 10 km, with rigid free-slip upper and lower boundaries. A small perturbation of potential temperature is located at x=-50 km (Fig. 67(a)). The wave is advected by a uniform stream of 20 m/s. The perturbation of total temperature is implemented as a perturbation of density. The mesh is made of 1200x40 cells, Δx=Δz=250m. Initial disturbance of potential temperature and solution computed after 3000 s are shown in Fig. 67. Time steps from 0.25 s to 50 s were tested, although details of the solution deteriorate when the time step is larger than 3 s.

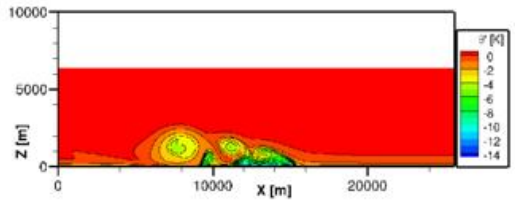


(a) Initial potential temperature perturbation (b) Potential temperature perturbation after 3000 s

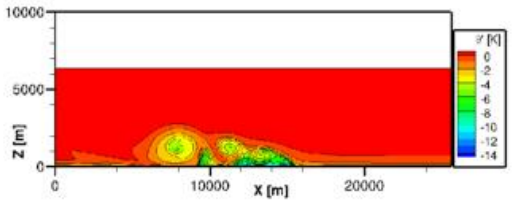
Figure 67: Gravity wave. Mesh with Δx=Δz=250 m, time step 1 s

8.7 Density current

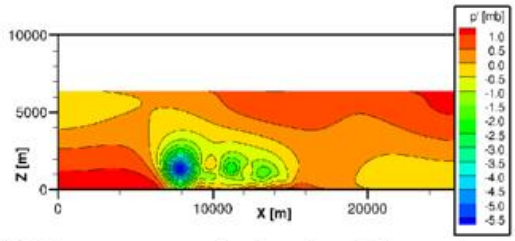
The test case is described in Straka et al. (1993). The equation set is completed by viscous fluxes (momentum and internal energy diffusion), with constant diffusion coefficient. Different mesh sizes (from Δx = Δz= 200m to 12.5m) and time steps between 0.25 and 10 seconds were tested. The complete flow field was simulated, without symmetric boundary condition in x=0. The solution is affected by the time step when Δt is larger than 1 second: it seems that larger time steps introduce a sort of viscosity, so that local maxima of the flow variables are smoothed and velocity is smaller. Mesh size below 50 m is sufficient to obtain grid-converged solutions. In Fig. 68 the solution obtained with the finest mesh is shown, together with a comparison of the potential temperature obtained with different mesh density and time step.



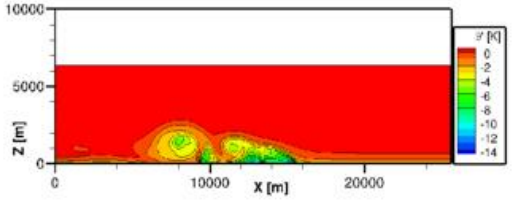
(a) Potential temperature Δx=12.5 m, Δt=1 s ν=1/160



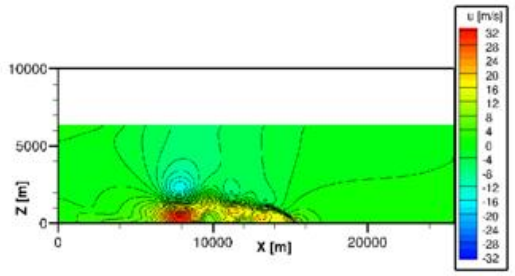
(b) Potential temperature Δx=50 m, Δt=1 s ν=1/160



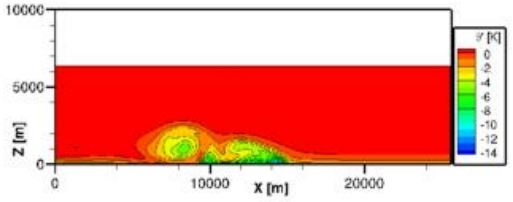
(c) Pressure perturbation Δx=12.5 m, Δt=1 s ν=1/160



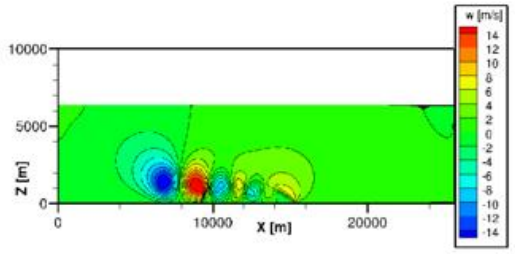
(d) Potential temperature Δx=100 m, Δt=1 s ν=1/160



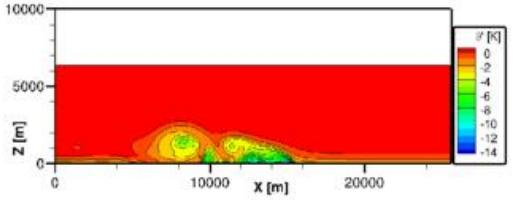
(e) Horizontal velocity Δx=12.5 m, Δt=1 s ν=1/160



(f) Potential temperature Δx=100 m, Δt=10 s ν=1/160



(g) Vertical velocity Δx=12.5 m, Δt=1 s ν=1/160

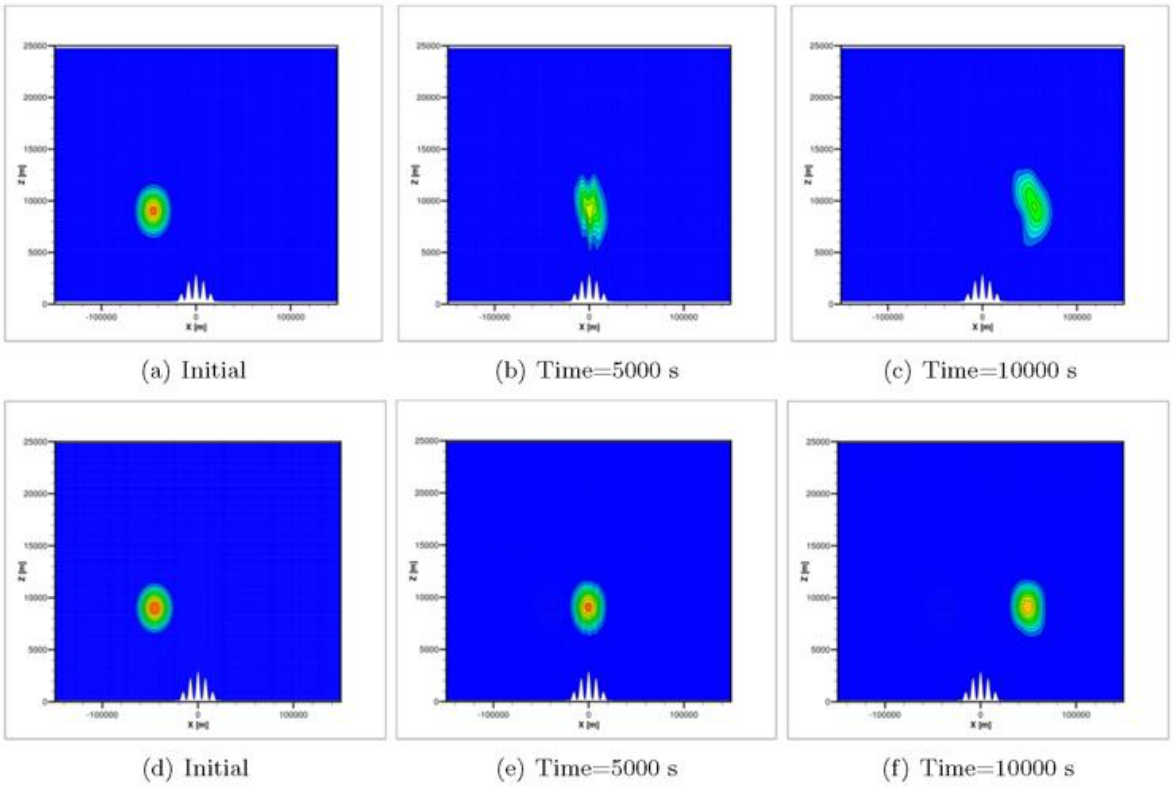


(h) Potential temperature Δx=100 m, Δt=1 s ν=1/80

Figure 68: Density current. Results after 900 s. Left: mesh with Δx=12.5 m. Right: effect of mesh density, time step, artificial dissipation ν

8.8 Advection

The test case is described in Schär et al. (2002). A scalar quantity contained in a circular bubble is advected accross a highly skewed mesh. The inflow velocity is 0 below the altitude of 4 km and rises smoothly to 10 m/s between 4 km and 5 km. Two different meshes were tested: the first one contains 300x50 cells with Δx=1 km and Δz=500 m, the second one has twice the number of cells in both directions with Δx=0.5 km and Δz=250 m (Fig. 69). A time step of 50 s was adopted in both computations. An attempt was made to implement and test the fourth order scheme described in Kok (2009), without significant improvements.



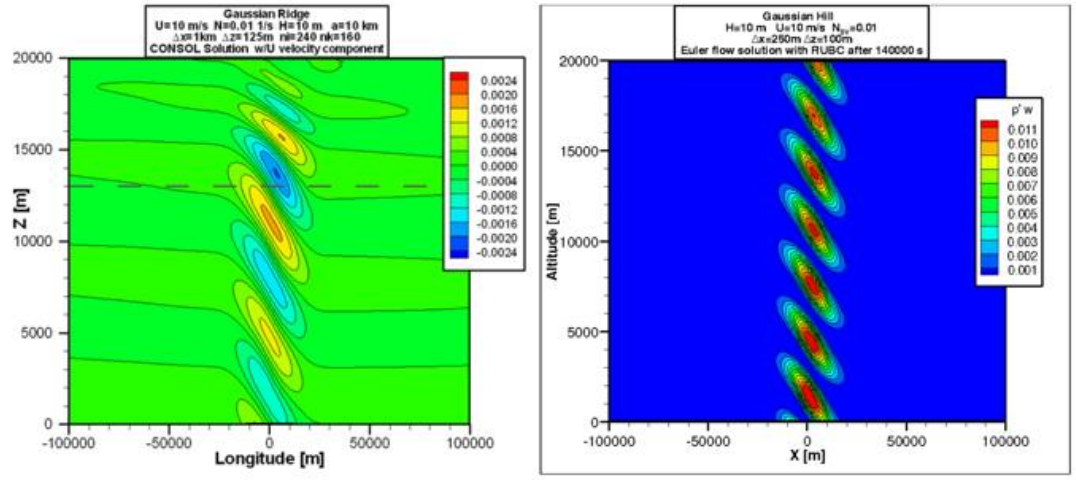
(a) Initial (b) Time=5000 s (c) Time=10000 s

(d) Initial (e) Time=5000 s (f) Time=10000 s

Figure 69: Advection of a conserved quantity in a deformed mesh. Above: coarse mesh 1. Below: mesh 2

8.9 Hydrostatic mountain flow

A classical hydrostatic test case is the flow simulation of a reference atmosphere with Brunt Väisälä frequency N_{BV}=0.01 1/s over a Gaussian shaped hill 10 m high, with free stream velocity of 10 m/s. The gravity waves produced above the mountain are stationary and momentum is transported in vertical direction. In order to avoid spurious reflection of the waves against the upper boundary, two techniques can be adopted: a damping layer in the upper atmosphere, where vertical velocities are smoothly damped, or a radiative upper boundary condition, that allows the wave energy to cross the boundary without reflection. In the first case (Fig. 70 a) about one third of the flow field is affected by an artificial damping term, that modifies the global momentum budget. In the second case (Fig. 70 b) the boundary condition has to be tuned to the local flow conditions, in order to be effective.



(a) Rayleigh damping: velocity field. The dashed line shows the lower side of the damping layer

(b) Radiative upper boundary condition: energy flux

Figure 70: Hydrostatic flow computed with different upper boundary conditions

8.10 Conclusions

The CONSOL flow solver, based upon second order central finite volume schemes and implicit time integration with dual time stepping, is capable to simulate the test cases considered in the present work. A wide range of time steps can be adopted, as it is not limited by numerical stability, that could be an advantage when time accuracy is not an issue. It is not possible at this moment to draw a conclusion about the numerical efficiency with respect to other schemes, since the solver is not optimized yet. More complex 3D test cases should be simulated.

8.11 Implementation of a time integration procedure based upon dual time stepping in COSMO

The time integration procedure based upon dual time stepping was implemented in a test version of COSMO, by replacing the Runge-Kutta scheme currently adopted. This preliminary study was meant to assess the possibility to use the scheme in the dynamical core of COSMO. It seems that the dual time stepping was never used in the field of numerical weather prediction, despite its popularity in aerodynamics. The idea was to keep the equations set with the spatial discretization schemes adopted in COSMO, and to replace only the time integration scheme. Main difference is that the time splitting procedure operates in physical time, by advancing the flow solution with smaller time steps for the fast processes and larger steps for slow processes. The dual time stepping computes all processes with the same time step, and iterates in order to improve the evaluation of the flow variables and the time derivatives using the 'dual' time as relaxation parameter. The dual time relaxation is a pseudo-steady problem, which does not require time accuracy and can be solved with any convergence acceleration technique, like local time stepping, implicit residual averaging and preconditioning. As the scheme is implicit, in theory there is no limitation to the physical time step due to stability.

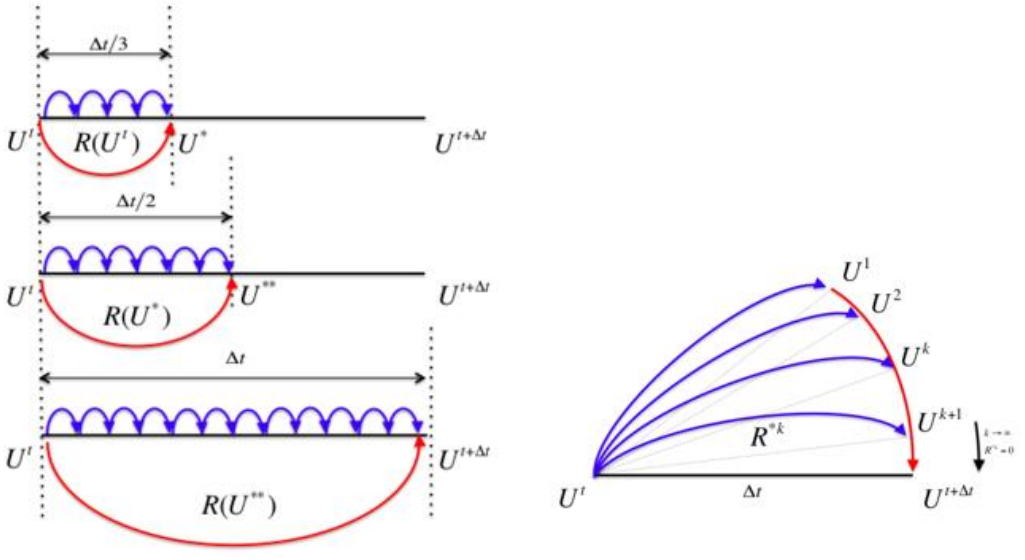
Defining the prognostic variables in the COSMO solver as $\underline{\mathbf{U}} = (u,v,w,p',T')$ and the model equations as

$$\frac{\partial \underline{\mathbf{U}}}{\partial t} = -R(\underline{\mathbf{U}}) \tag{66}$$

where $R(\underline{\mathbf{U}})$ denotes the right hand side of the model equation for $\underline{\mathbf{U}}$, the Runge Kutta integration takes the form of three steps to advance a solution $\underline{\mathbf{U}}(t)$ to $\underline{\mathbf{U}}(t + \Delta t)$:

$$\begin{aligned} \underline{\mathbf{U}}^{*} &= \underline{\mathbf{U}}^{t} - \frac{\Delta t}{3} R(\underline{\mathbf{U}}^{t}) \\ \underline{\mathbf{U}}^{**} &= \underline{\mathbf{U}}^{t} - \frac{\Delta t}{2} R(\underline{\mathbf{U}}^{*}), \\ \underline{\mathbf{U}}^{t+\Delta t} &= \underline{\mathbf{U}}^{t} - \Delta t R(\underline{\mathbf{U}}^{**}) \end{aligned} \tag{67}$$

where Δt is the time step for the slow-frequency modes (the model time step), and superscripts denote time levels. The time-splitting technique integrates fast modes with smaller time steps; terms associated with horizontally propagating modes are integrated explicitly, while terms associated with vertically propagating modes are integrated implicitly. The implicit integration component alleviates the severe Courant number restriction, arising from vertically propagating acoustic modes when using grids with large aspect ratios $\frac{\Delta x}{\Delta z}$, at the cost of a simple tridiagonal matrix inversion. The Figure 71a shows the three stages of the Runge-Kutta time integration procedure, where the blue arrows represent the small time steps used to advance the fast tendencies of the governing equations, while the slow tendencies are kept constant in each stage, represented by the red arrows.



(a) Runge-Kutta time integration

(b) Dual time stepping integration

Figure 71: Time integrations in COSMO: 3 stages Runge-Kutta and Dual time stepping

In the dual time stepping procedure (see equations 47 and 48) the residual at the dual iteration k is computed as follows:

$$\underline{\mathbf{R}}^{*k} = \underline{\mathbf{R}}(\underline{\mathbf{U}}^{k}) + \frac{3\underline{\mathbf{U}}^{k} - 4\underline{\mathbf{U}}^{t} + \underline{\mathbf{U}}^{t-\Delta t}}{2\Delta t} \tag{68}$$

we evaluate $\underline{\mathbf{R}}(\underline{\mathbf{U}}^k)$ using the spatial schemes already implemented in the dynamical core of COSMO for computing the time derivatives. The dual time derivative

$$\frac{\partial \underline{\mathbf{U}}^k}{\partial \tau} = -\underline{\mathbf{R}}^{*k} \tag{69}$$

is integrated to the steady state (see Fig. 71b). A flow chart of the implementation is shown in Fig. 72.

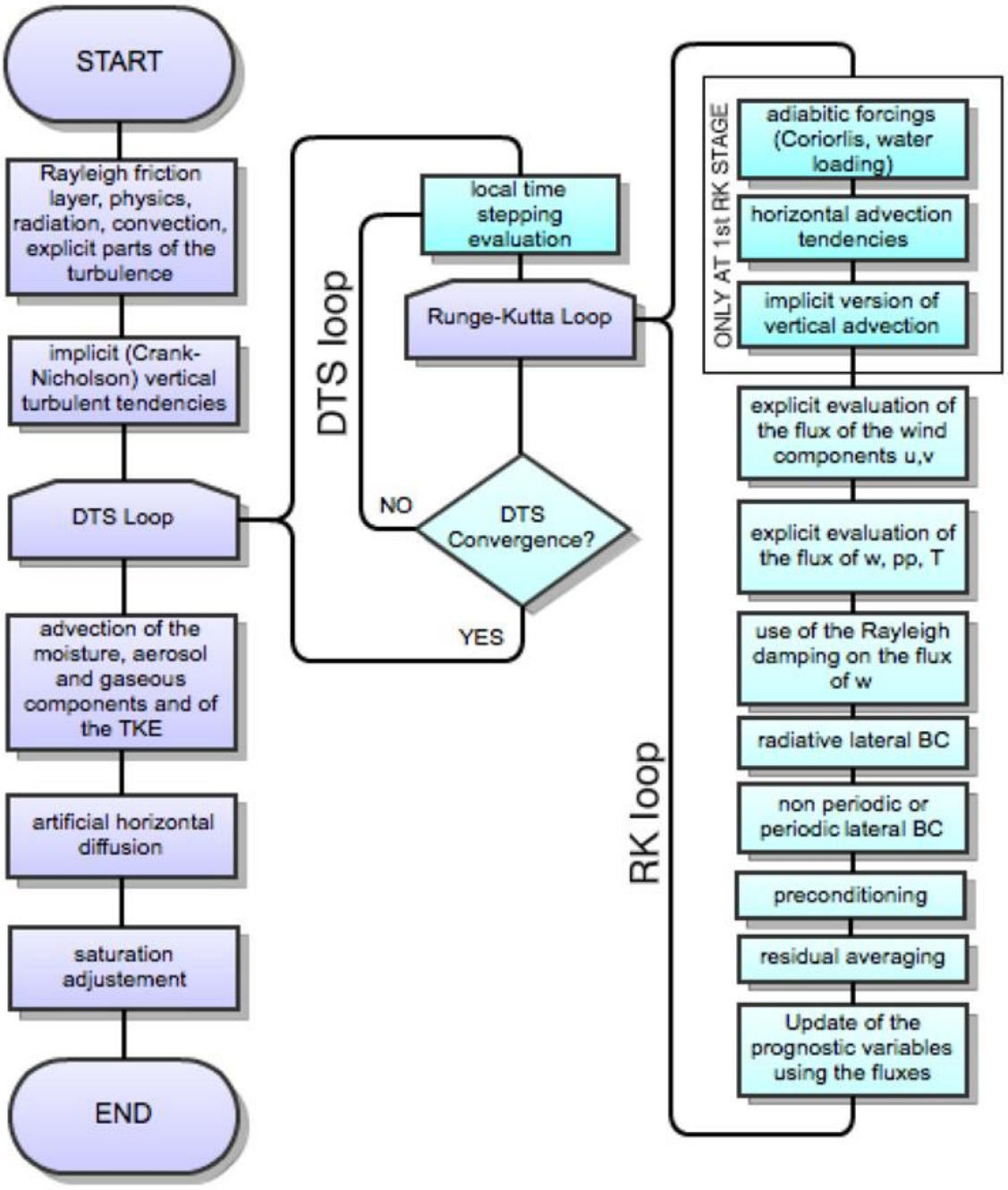


Figure 72: Flow chart of the Dual time stepping implementation in COSMO

Idealized test cases were computed, like mountain flow and inertia-gravity waves, which have

shown that the scheme is capable to give similar results to the original COSMO model, as reported in Petrone (2012). Larger time steps can be adopted. Applications to real test cases would require further work to be completed.

References

Baldauf, M., 2008: A linear solution for flow over mountains and its comparison with the COSMO model. *COSMO-Newsletter*,**9**, 19–24.

Baldauf, M., 2010: Linear stability analysis of Runge-Kutta based partial time-splitting schemes for the Euler equations. *Mon. Wea. Rev.*,**138**, 4475–4496.

Baldauf, M., and S. Brdar, 2013: An Analytic Solution for Linear Gravity Waves in a Channel as a Test for Numerical Models using the Non-Hydrostatic, Compressible Euler Equations. *Q. J. R. Meteorol. Soc.*, DOI:10.1002/qj.2105.

Botta, N., R. Klein, S. Langenberg, S. Lützenkirchen, 2004: Well balanced finite volume methods for nearly hydrostatic flows. *J. Comput. Phys.*,**196**, 539–565.

Choi, Y.-H. and C. L. Merkle, 1993: The application of preconditioning in viscous flows. *J. Comput. Phys.*, **105**, 207.

Giraldo, F. X., and M. Restelli, 2008: A study of spectral element and discontinuous Galerkin methods for the Navier-Stokes equations in nonhydrostatic mesoscale atmospheric modeling: equation sets and test cases. *J. Comput. Phys.*, **227**, 3849–3877.

Jameson, A., 1992: Time dependent calculations using multigrid with applications to unsteady flows past airfoils and wings. *AIAA Paper*, **91**, 1596.

Kok, J. C., 2009: A high-order low-dispersion symmetry-preserving finite-volume method for compressible flow on curvilinear grids. *J. Comput. Phys.*, **228**, 6811–6832.

Petrone, G., 2012: Implementation of a numerical scheme based on the dual time stepping in COSMO LM: idealized test cases. Research Papers Issues RP0146, CMCC.

Robert, A., 1993: Bubble convection experiments with a semi-implicit formulation of the Euler equations. *J. Atmos. Sci.*, **50**, No. 13, 1865–1873.

Schär, C., D. Leuenberger, O. Fuhrer, D. Lüthi, and C. Girard, 2002: A new terrain-following vertical coordinate formulation for atmospheric prediction models. *Mon. Wea. Rev.*, **130(10)**, 2459–2480.

Skamarock, W. C. and J. B. Klemp, 1992: The stability of time-split numerical methods for the hydrostatic and the nonhydrostatic elastic equations. *Mon. Wea. Rev.*, **120**, 2109–2127.

Skamarock, W. C. and J. B. Klemp, 1994: Efficiency and accuracy of the Klemp-Wilhelmson time-splitting scheme. *Mon. Wea. Rev.*, **122**, 2623–2630.

Straka, J. M., R. B. Wilhelmson, L. J. Wicker, J. R. Anderson, and K. K. Droegemeier, 1993: Numerical solutions of a non-linear density current: A benchmark solution and comparisons. *Int. J. Num. Meth. Fluids*, **17**, 1–22.

Turkel, E., V. N. Vatsa, and R. Radespiel, 1996: Preconditioning methods for low speed flows. *AIAA-96-2460-CP*, 650–660.

Turkel, E., 1999: Preconditioning techniques in computational fluid dynamics. *Annu. Rev. Fluid Mech.*, **31**, 385–416.

Weiss, J. M. and W. A. Smith, 1995: Preconditioning applied to variable and constant density flows. *AIAA Journal*, **33**, No. 11, 2050–2057.

Wicker, J. L. and W. C. Skamarock, 1998: A time-splitting scheme for elastic equations incorporating second-order Runge-Kutta time differencing. *Mon. Wea. Rev.*, **126**, 1992–1999.

Wicker, J. L. and W. C. Skamarock, 2002: Time-splitting method for elastic models using forward time schemes. *Mon. Wea. Rev.*, **130**, 2088–2097.

Wunderlich, S., 2004: A 2D well balanced finite volume non-hydrostatic atmospheric model. Hydrostatic balance and simulation of mountain waves. *Ph.D. thesis ETH Zürich.*

Zängl, G., L. Gantner, G. Hartjenstein, H. Noppel, 2004: Numerical errors above steep topography: a model intercomparison. *Meteorol. Z.*, **13**, No. 2, 69–76.

9 Acknowledgement

The authors of the anelastic branch of the Priority Project "Conservative Dynamical Core" (CDC) would like to express their sincere gratitude to Piotr Smolarkiewicz (NCAR, currently ECMWF), Wojciech Grabowski (NCAR) and Andrzej Wyszogrodzki (NCAR) for many discussions, comments and valuable suggestions which significantly helped in realization of the project. The use of computer resources at Swiss CSCS and NCAR is gratefully acknowledged.

List of COSMO Newsletters and Technical Reports

(available for download from the COSMO Website: www.cosmo-model.org)

COSMO Newsletters

No. 1: February 2001.

No. 2: February 2002.

No. 3: February 2003.

No. 4: February 2004.

No. 5: April 2005.

No. 6: July 2006.

No. 7: April 2008; Proceedings from the 8th COSMO General Meeting in Bucharest, 2006.

No. 8: September 2008; Proceedings from the 9th COSMO General Meeting in Athens, 2007.

No. 9: December 2008.

No. 10: March 2010.

No. 11: April 2011.

No. 12: April 2012.

No. 13: April 2013.

COSMO Technical Reports

No. 1: Dmitrii Mironov and Matthias Raschendorfer (2001):
Evaluation of Empirical Parameters of the New LM Surface-Layer Parameterization Scheme. Results from Numerical Experiments Including the Soil Moisture Analysis.

No. 2: Reinhold Schrodin and Erdmann Heise (2001):
The Multi-Layer Version of the DWD Soil Model TERRA_LM.

No. 3: Günther Doms (2001):
A Scheme for Monotonic Numerical Diffusion in the LM.

No. 4: Hans-Joachim Herzog, Ursula Schubert, Gerd Vogel, Adelheid Fiedler and Roswitha Kirchner (2002):
LLM ¯ the High-Resolving Nonhydrostatic Simulation Model in the DWD-Project LITFASS.
Part I: Modelling Technique and Simulation Method.

No. 5: Jean-Marie Bettems (2002):
EUCOS Impact Study Using the Limited-Area Non-Hydrostatic NWP Model in Operational Use at MeteoSwiss.

No. 6: Heinz-Werner Bitzer and Jürgen Steppeler (2004):
Documentation of the Z-Coordinate Dynamical Core of LM.

No. 7: Hans-Joachim Herzog, Almut Gassmann (2005):
Lorenz- and Charney-Phillips vertical grid experimentation using a compressible nonhydrostatic toy-model relevant to the fast-mode part of the 'Lokal-Modell'.

No. 8: Chiara Marsigli, Andrea Montani, Tiziana Paccagnella, Davide Sacchetti, André Walser, Marco Arpagaus, Thomas Schumann (2005):
Evaluation of the Performance of the COSMO-LEPS System.

No. 9: Erdmann Heise, Bodo Ritter, Reinhold Schrodin (2006):
Operational Implementation of the Multilayer Soil Model.

No. 10: M.D. Tsyrulnikov (2007):
Is the particle filtering approach appropriate for meso-scale data assimilation ?

No. 11: Dmitrii V. Mironov (2008):
Parameterization of Lakes in Numerical Weather Prediction. Description of a Lake Model.

No. 12: Adriano Raspanti (2009):
COSMO Priority Project "VERification System Unified Survey" (VERSUS): Final Report.

No. 13: Chiara Marsigli (2009):
COSMO Priority Project "Short Range Ensemble Prediction System" (SREPS): Final Report.

No. 14: Michael Baldauf (2009):
COSMO Priority Project "Further Developments of the Runge-Kutta Time Integration Scheme" (RK): Final Report.

No. 15: Silke Dierer (2009):
COSMO Priority Project "Tackle deficiencies in quantitative precipitation forecast" (QPF): Final Report.

No. 16: Pierre Eckert (2009):
COSMO Priority Project "INTERP": Final Report.

No. 17: D. Leuenberger, M. Stoll and A. Roches (2010):
Description of some convective indices implemented in the COSMO model.

No. 18: Daniel Leuenberger (2010):
Statistical analysis of high-resolution COSMO Ensemble forecasts in view of Data Assimilation.

No. 19: A. Montani, D. Cesari, C. Marsigli, T. Paccagnella (2010):
Seven years of activity in the field of mesoscale ensemble forecasting by the COSMO–LEPS system: main achievements and open challenges.

No. 20: A. Roches, O. Fuhrer (2012):
Tracer module in the COSMO model.

No. 21: Michael Baldauf (2013):
A new fast-waves solver for the Runge-Kutta dynamical core.

No. 22: C. Marsigli, T. Diomede, A. Montani, T. Paccagnella, P. Louka, F. Gofa, A. Corigliano (2013):
The CONSENS Priority Project.

COSMO Technical Reports

Issues of the COSMO Technical Reports series are published by the *COnsortium for Small-scale MOdelling* at non-regular intervals. COSMO is a European group for numerical weather prediction with participating meteorological services from Germany (DWD, AWGeophys), Greece (HNMS), Italy (USAM, ARPA-SIMC, ARPA Piemonte), Switzerland (MeteoSwiss), Poland (IMGW), Romania (NMA) and Russia (RHM). The general goal is to develop, improve and maintain a non-hydrostatic limited area modelling system to be used for both operational and research applications by the members of COSMO. This system is initially based on the COSMO-Model (previously known as LM) of DWD with its corresponding data assimilation system.

The Technical Reports are intended

- for scientific contributions and a documentation of research activities,
- to present and discuss results obtained from the model system,
- to present and discuss verification results and interpretation methods,
- for a documentation of technical changes to the model system,
- to give an overview of new components of the model system.

The purpose of these reports is to communicate results, changes and progress related to the LM model system relatively fast within the COSMO consortium, and also to inform other NWP groups on our current research activities. In this way the discussion on a specific topic can be stimulated at an early stage. In order to publish a report very soon after the completion of the manuscript, we have decided to omit a thorough reviewing procedure and only a rough check is done by the editors and a third reviewer. We apologize for typographical and other errors or inconsistencies which may still be present.

At present, the Technical Reports are available for download from the COSMO web site (www.cosmo-model.org). If required, the member meteorological centres can produce hard-copies by their own for distribution within their service. All members of the consortium will be informed about new issues by email.

For any comments and questions, please contact the editor:

Massimo Milelli
Massimo.Milelli@arpa.piemonte.it

Consortium for Small-Scale Modelling

Technical Report No. 35

The COSMO Priority Project CORSO Final Report

July 2018

DOI: 10.5676/DWD_pub/nwv/cosmo-tr_35

Deutscher Wetterdienst
MeteoSwiss
Ufficio Generale Spazio Aereo e Meteorologia
ΕΘΝΙΚΗ ΜΕΤΕΩΡΟΛΟΓΙΚΗ ΥΠΗΡΕΣΙΑ
Instytucie Meteorogii i Gospodarki Wodnej
Administratia Nationala de Meteorologie
ROSHYDROMET
Agenzia Regionale Protezione Ambiente Piemonte
Agenzia Regionale Prevenzione Ambiente Energia Emilia Romagna
Centro Italiano Ricerche Aerospaziali
Amt für GeoInformationswesen der Bundeswehr
Israel Meteorological Service

www.cosmo-model.org

Editor: Massimo Milelli, ARPA Piemonte

The COSMO Priority Project CORSO

Final Report

Project participants:

***G. Rivin*[1]‡, *I. Rozinkina*[1]‡, *E. Astakhova*[1], *A. Montani*[4],**

***D. Alferov*[1], *M. Arpagaus*[2], *D. Blinov*[1], *A. Bundel*[1],**

***M. Chumakov*[1], *P. Eckert*[2], *A. Euripides*[5], *J. Förstner*[3],**

***J. Helmert*[3], *E. Kazakova*[1], *A. Kirsanov*[1], *V. Kopeikin*[1],**

***E. Kukanova*[1], *D. Majewski*[3], *C. Marsigli*[4], *G. de Morsier*[2],**

***A. Muravev*[1], *T. Paccagnella*[4], *U. Schättler*[3], *C. Schraff*[3],**

***M. Shatunova*[1], *A. Shcherbakov*[1], *P. Steiner*[2], *M. Zaichenko*[1]**

[1] Roshydromet

[2] MeteoSwiss

[3] Deutscher Wetterdienst

[4] Agenzia Prevenzione Ambiente Energia Emilia Romagna

[5] Hellenic National Meteorological Service

‡ Project Coordinator

Contents

1 Introduction *(G. Rivin, I. Rozinkina)* **4**

2 Actions proposed *(G. Rivin, I. Rozinkina)* **5**

3 Tasks, brief description *(G. Rivin, I. Rozinkina, E. Astakhova, A. Montani)* **6**

4 Development of High resolution COSMO-modeling for mountainous regions *(G. Rivin, M. Shatunova, D. Blinov, D. Majewski, J. Förstner, J. Helmert, U. Schättler, C. Schraff, M. Arpagaus, G. de Morsier, P. Steiner)* **10**

4.1 Data assimilation system (DAS) based on the nudging scheme for the Sochi region *(G. Rivin, D. Blinov, C. Schraff)* 10

4.2 Development of High resolution COSMO-modeling for mountainous regions *(G. Rivin, M. Shatunova, D. Majewski, J. Förstner, J. Helmert, U. Schättler, D. Blinov, M. Arpagaus, G. de Morsier, P. Steiner)* 13

4.2.1 Model installation (and domain size selection) 13

4.2.2 COSMO-Ru1 model orography options 15

4.2.3 COSMO-Ru1 operational use and verification 16

4.2.4 Case study 21

5 Downscalling/post-processing for Sochi area and applications *(I. Rozinkina, E. Kazakova, M. Chumakov, A. Bundel, A. Muravev, D. Blinov, A. Kirsanov, P. Eckert, G. Rivin, A. Euripides, E. Kukanova)* **22**

5.1 T2m correction *(I. Rozinkina, D. Blinov, G. Rivin)* 22

5.2 Kalman filtering application for correction of T2m COSMO-Ru-So forecasts *(M. Chumakov, E. Kazakova, I. Rozinkina, P. Eckert)* 22

5.2.1 Description of the method 23

5.2.2 Operational results and verification 26

5.3 Fresh snow depth postprocessing example for COSMO-Ru-So *(E. Kazakova, M. Chumakov, I. Rozinkina)* 29

5.3.1 Description of fresh snow depth calculation algorithm and its testing . 30

5.3.2 COSMO-model fresh snow depth output 32

5.3.3 Results of fresh snow depth calculation implemented into COSMO-Ru system postprocessing 32

5.3.4 Conclusions 35

5.4 Verification of COSMO forecasts for the Sochi-2014 region *(A. Bundel, A. Muravev, D. Blinov, A. Kirsanov)* 35

5.4.1 Verification tools 35

5.4.2 Verification problems 35

5.4.3 Verification over the test periods and during the official evaluation period of the Games of 2014 36

5.4.4 Conclusions and prospect for the future 43

6 Development and adaptation of COSMO EPSs for the Sochi region *(D. Alferov, E. Astakhova, C. Marsigli, A. Montani, T. Paccagnella, G. Rivin, A. Shcherbakov)* **44**

6.1 Ensemble prediction system with a 7-km resolution 44

6.2 Ensemble prediction system with a 2.2-km resolution 45

6.3 Providing ensemble forecasts for the Sochi Olympics and preceding trial competition 46

6.4 Skill of ensemble forecasts *(E. Astakhova, A. Bundel, A. Muravev)* 49

6.4.1 Verification of COSMO-S14-EPS compared to ECMWF-EPS 49

6.4.2 Case studies 52

6.4.3 Verification of COSMO-S14-EPS and COSMO-Ru2-EPS for the Olympic and pre-Olympic periods 56

6.5 Conclusions 62

7 References **63**

1 Introduction

The latter Winter Olympic Games were hold in Sochi, Russia. Sochi–2014 region is very complicated for numerical modeling because of the mosaic surface properties determined by the close proximity of the Black Sea coast line combined with the mountainous terrestrial conditions. The local mesoscale circulation causes numerous weather phenomena at the differently oriented mountain slopes and valleys. It requires high resolution numerical model, particularly COSMO-Ru model, which was selected for meteorological support of the Games. The model should have to be able to predict meteorological conditions in the region with highly variable terrain. Specificity of physical variables had to be predicted for different sporting events on the basis of large amount of observational and forecasting data.

Annually registered number of weather hazards is very high in the Northern Caucasus, especially in winter. The high variability of local small-scale conditions (differently oriented slopes, valleys, significant high gradients) and proximity of non-freezing Black Sea generating medium-scale energy fluxes require the ensemble approach, improvement of model resolution to the scale of relief features, i.e. in the case of COSMO weather forecasting model the grid step had to be lesser than existing 2.2 km. It also required the improvement of the postprocessing methods of forecasting certain meteorological characteristics (wind, snow cover, visibility, humidity, etc.).

CORSO project was proposed to enhance and demonstrate the capability of COSMO-based systems of numerical weather prediction in winter conditions for mountainous terrain and to assess the effect of practical use of meteorological information in support of Sochi–2014 Olympic Games. The peculiarity of the Sochi region justified the development and adaptation of the available COSMO technologies. The insurance of the best performance of the COSMO system at the Sochi-2014 Olympics was required. It assumed a development of modeling techniques including. data assimilation for near-surface and land-surface parameters, model physics and dynamical core. Ensemble forecasting, applied post-processing and downscaling, comprehensive verification and other predictive components were crucially important for the enhancement of the Sochi-2014 meteorological services.

Significantly the PP CORSO for preparation and providing the meteorological services for Olympics Sochi-2014 is based on solving the tasks determined in the COSMO Science PLAN 2010-2014, where it stated (p. 11): "From the scale of the targeted processes it becomes clear that the mesh-size of the model system has to be of the order of 1–2.2 km. The COSMO Steering Committee decided to focus on the development of a model-system for the short to very short range forecasting considering convective-scale resolution".

In the region of the Sochi–2014 the additional observational network was developed since the end of 2011. It includes the automatic stations for near-surface measurements, meteorological radar, and aerological stations. This additional information could be used as a new source for data assimilation, model verification and for testing and adaptation of certain algorithms.

The improvements introduced to the COSMO system during this activity widened its applicability to regions with complex terrain characterized by frequent severe weather events, which could benefit COSMO as a whole.

CORSO project can be considered as a COSMO-related part of FROST–2014 project (FROST — Forecast and Research in the Olympic Sochi Testbed), initiated by WMO (Kiktev et al., 2017)..

2 Actions proposed

Development of the COSMO model version adjusted for the region with complex terrain, improvement of operational forecasts based on the COSMO-Ru7/So2 model and development of the version of this model with resolution approximately 1 km. Identification of the gaps, adaptation of data assimilation techniques, analysis of numerical aspects using the high resolution and modification of parameterization schemes (Task1).

Development and adaptation of approaches for post-processing downscaling and possible forecasters feedback (Task 2).

Adjustment of the COSMO EPS's techniques (COSMO-LEPS) for the Sochi area and to specific requirements of winter Olympics. Development of COSMO-RU-EPS system (Task 3).

All developed systems and technologies had to be validated and made available to forecasters during trials well before the Olympics. Forecast products were transferred to Olympic forecasters via web-based tools.

Available expertise within COSMO

COSMO-LEPS (ARPA–SIMC);
High-resolution modeling and post-processing for the Alps (DWD, MeteoSwiss, ARPA-SIMC);
Experience of MeteoSwiss and of DWD in meteo-support of winter sporting events in the mountains;
Developed tools ("nudging-process", Fieldextra, VERSUS);
Experience of Torino–2006 Olympics (ARPA Piemonte).

Links to other projects or work packages

Cooperation with all working groups will be required (as needed), during the lifetime of the project. Some activities are supposed to include expansion of actions considering the results and experience obtained within the framework of PP COLOBOC (external parameters, snow cover investigations), verification tools (VERSUS2), improvement of turbulence schemes (UTCS).

3 Tasks, brief description

3.1 TASK1 "High resolution COSMO-modeling for mountainous regions", *(TL G. Rivin)*

Motivation:

The pre-operational version of COSMO-RU07/So2 (resolution 2.2 km) for the North-Caucasian region was developed in Roshydromet in 2010–2011 (nested into OSMO-Ru07 (without regional DAS). OSMO-Ru07 is based on the use of the initial data, received from the GME modeling system (30 $\longrightarrow$ 20 km) of DWD and external parameters prepared as an output of the COSMO EXPAR system (2.2 km)).

Preliminary tests sometimes showed a presence of significant errors in meteorological fields predicted by the COSMO-RU07/So2 near land surface (primarily in air temperature, and as a consequence, conditions of boundary layer stability and the precipitation phase).

It was detected that certain inaccuracies in determining of initial values of T2m, snow-properties (the mask and water equivalent WE), as well as some external (geographic) parameters, such as mask and absolute height.

The goal of the starting actions of TASK1 is the identification of contribution of regional data assimilation for COSMO-RU07 forecasting based on comparison of skill scores of COSMO-RU and COSMO-EU (with assimilation) for the area of COSMO-RU, including the region of Sochi-2014. In parallel, inclusion of nudging continuous cycle using all available data for both (COSMO-RU7 and nested COSMO-RU/So2) is expected. It will be based on the standard network measurement and new additionally added observational network in the Sochi 2014 region. The techniques of correction of temperature in upper soil levels was based on T2m measurements. This technique was previously developed in Roshydromet. It should be coupled with nudging continuous cycle and corrected snow mask from satellite observations.

The more precise modeling of the near surface meteorological parameters taking into account the fractional relation of snow cover and stable and mosaic thermal stratification is one of the problems of numerical weather forecasting. It was obvious for Sochi-2014 weather forecasting support. Previously, based on a study of the COSMO-RU model forecasts for the large winter periods for the entire domain of COSMO-Ru07 it was revealed that the model produces the highest T2m errors in case of heating over the partial snow cover and some modification of TERRA was proposed and tested. TASK1 was expended to develop and test the modified algorithms of TERRA and to propose the modification of algorithms for turbulent diffuse parameterization scheme to improve the forecasts for certain cases.

The perspective plan of COSMO for 2014 stipulated the development of 1-km modeling techniques. Some results were obtained by DWD, MeteoSwiss and ARPA-SIMC. The united efforts of COSMO partners focus on the activities, which could potentially accelerate the development of 1-km COSMO techniques. The collaboration and coordination between DWD, MeteoSwiss, ARPA-SIMC, and Roshydromet is expected.

Task1 consists of two subtasks:

Subtask 1.1:"Improvement of technology of deterministic forecasting of weather conditions with model resolution 2.2 km for the North-Caucasian area (Sochi-2014), (including the operational support)",

Subtask 1.2: "Development of COSMO-So-1km"

Goals RDP:

Develop 1km version for Sochi-2014.

The strategy depends of available technical resources and results obtained by participants.

Deliverables:

Research technology COSMO-So1 with horizontal resolution ≈ 1 km (RDP).

3.2. TASK2 "Downscaling/post-processing for Sochi area and applications", *(TL I.Rozinkina)*

Motivation:

The local mesoscale circulation in the Sochi-2014 area causes multiple weather phenomena at the mountain slopes and valleys. The local values of meteoparameters for this region, including area of Olympics venues (coastal or mountainous clusters) may be identified considering the processes of the scales not modeled explicitly even at high resolution.

Forecasting for the Olympic Games may be complicated by the necessity to predict parameters, which are not explicitly included in the models output (i.e., visibility, wind chill, hill fog, katabatic winds). Furthermore it is requested that the exceeding of certain thresholds are accurately predicted (precipitation amount, fresh snow amount, visibility, wind, temperature, humidity, wind chill) in order to assess whether to confirm or to cancel open air competitions.

This implies the development and implementation of downscaling and post-processing methods. The goals are the following:

- Improve the skill of numerical forecasting and obtain reliable results for the specific points of the venues, the clusters, or the entire Sochi-2014 area;
- Target on the specific parameters needed for organizing committee and the assessment of the critical thresholds for different competitions.

In the Sochi-2014 region, the information from additional automatic stations for near-surface measurements of T, V, Q, precipitation, visibility, and snow parameters can be used as an additional source for development of algorithms for downscaling.

The following algorithms are presently available at Roshydromet: linear regression of COSMO-SIB-14 output for Altay mountains (trial period: 2 weeks), MOS on IFS/GFS (experimentally used also with COSMO-RU-7/WRF), trial period: 2 years, empirical rules based on manual weather classification for forecasting of significant weather phenomena. This experience allows to develop the new techniques for the region of interest with shorter (several days) training period, i.e Kalman Filter techniques firstly for improvement of T2m measurements at observational points. The experience of COSMO-countries in utilizing the Kalman-filter correction techniques with mountain weather conditions (Firstly, Switzerland) is very important. The data sets - rows "model – measurements"for some points for the area with similar geographical conditions (subtropical mountains near sea) are also useful to obtain the statistics for large variety of weather phenomena in stage of development and tuning of Kalman-filter algorithms. (In particular the data obtained in the Greek mountain areas could be useful for obtaining flexible algorithm).

The implementation of the automated weather classification systems together with climatological series of local observations can be used for forecasting relevant phenomena in the Sochi-2014 region. Furthermore, the project will take the opportunity to use the practical experience of the COSMO countries in their meteorological support to winter sports in

mountainous regions. The previous results obtained in WG4 in the domain of conditional verification and the interpretation of model results will also be used.

The collaboration with MeteoSwiss and HNMS is expected.

Task2 consists of two subtasks:

Subtask 2.1. (FDP): "Adapted downscaling techniques for winter conditions in the mountains and IOC requirements"

Subtask 2.2. ($FDP + RDP$): "Determination of typical COSMO model inaccuracies for typical climatological / synoptic situations"

3.3. TASK3 "Development and adaptation of COSMO EPSs for the Sochi region", *(TL E.Astakhova and A. Montani)*

Motivation:

Accurate assessment of probabilities of High-Impact Weather (HIW) events is the main challenge for regional ensemble prediction systems (EPS). For the winter Olympics, HIW are not necessarily linked with very intense or extreme meteorological phenomena. For outdoor sport events HIW forecasting also includes accurate representation of cross-zero temperature transitions (especially critical for cross-country skiing), precipitation phase and other sensible weather changes with respect to the prescribed decision-making thresholds. Development and demonstration of various HIW-related specific products is part of the ensemble component of the project CORSO.

COSMO-LEPS is an ensemble prediction system developed by the COSMO consortium. In the past years, COSMO-LEPS proved to be a valuable tool for the generation of probabilistic predictions of high-impact weather over complex topography and it is envisaged that it can be successfully used for the SOCHI region and provide useful support to bench forecasters during the Olympics. A 7-km COSMO-LEPS system for the Sochi region (COSMO-FROST-LEPS) is to be developed within the framework of the project and will be used for operational support of Sochi-2014 Olympics.

EPS with higher than 7-km resolution is desirable for better probabilistic prediction over the complex Caucasus terrain. Within the RDP part of Task 3 CORSO, the development and testing of COSMO-RU-LEPS 2.2 km is suggested.

COSMO-RU-SO-2.2 for the North-Caucasian region already runs operationally at Roshydromet. This technology is nested to OSMO-Ru07. On the other hand, COSMO-FROST-LEPS (also with 7-km resolution) will run daily during pre-trials, trials and Olympics and can provide initial and boundary conditions (ICs and BCs) for a higher-resolution ensemble system. This gives a possibility to develop a 2.2 km EPS based on COSMO-RU-SO-2.2 and ICs and BCs from SOCHMEL.

In collaboration and coordination with ARPA-SIMC

Task3 consists of two subtasks:

3.1. Adaptation of COSMO LEPS 7 km to the Sochi region and to specific requirements of winter Olympics. Operational ensemble forecasts during the Olympics (FDP)

3.2. Development and verification of COSMO-RU-LEPS 2.2 km for the Sochi region (with ICs and BCs from SOCHMEL7)

Goals:

Subtask 3.1 (FDP):

Development of a COSMO-LEPS system with a resolution of 7 km adapted to the Sochi region and to specific requirements of winter Olympics (SOCHMEL7) and operational support of the Sochi-2014 Olympics with COSMO-based 7-km ensemble forecasts:

- Adaptation of COSMO-LEPS 7 km to the Sochi region and to specific requirements of winter Olympics (SOCHMEL7). Organization of data transfer from ARPA -SIMC to RHMC.
- Development of visualization, interpretation and verification tools for SOCHMEL7. Coupling with post-processing techniques.
- COSMO-FROST-LEPS forecasts during the pre-trial (from 10 Dec 2011 to 31 Marh 2012) and trial (from 01 Dec 2012 to 31 Marh 2013) periods and their verification. Assessment of the effect of practical use of these forecasts.
- Operational ensemble forecasts during the Olympics and their verification. (The use of VERSUS with included EPS-verification tools is expected)

Deliverables (FDP):

A COSMO-LEPS system with 7 km resolution adapted to the Sochi region and to specific requirements of winter Olympics (SOCHMEL7). Operational ensemble forecasts during the Olympics. Technology of presentation and interpretation of the COSMO-FROST-LEPS results in operational mode.

Subtask 3.2 (RDP):

Investigation of the capability of high-resolution (2.2-km) ensemble system in forecasting over a complex terrain.

- Development of COSMO-RU-LEPS 2.2 km for the Sochi region (with ICs and BCs from SOCHMEL7)
- COSMO-RU-LEPS 2.2 km forecasts during trials and forecasts verification (if feasible).
- Comparison of capability of high-resolution (2.2-km) ensemble system with SOCHMEL7.
- COSMO-RU-LEPS 2.2 km forecasts during the Olympic Games (if feasible). Analysis of the results.

Deliverables (RDP):

COSMO-RU-LEPS 2.2 km for the Sochi region (with ICs and BCs from SOCHMEL7)

4 Development of High resolution COSMO-modeling for mountainous regions *(G. Rivin, M. Shatunova, D. Blinov, D. Majewski, J. Förstner, J. Helmert, U. Schättler, C. Schraff, M. Arpagaus, G. de Morsier, P. Steiner)*

4.1 Data assimilation system (DAS) based on the nudging scheme for the Sochi region *(G. Rivin, D. Blinov, C. Schraff)*

DAS activities

(a) **The new version of COSMO-Ru7/2 operational technology including the nudging- assimilation was developed for Caucasian and Central regions.** The analysis of skill of forecasts of T2m, Td2m, winds at 10m, PMSL showed the essential improving of models results **for the first 3–6 hours** for the version with nudging-assimilation (Fig.1)

(b) The realization of continuous model runs based on continuous assimilation cycles has allowed organizing the optimal time of starts of operational runs of COSMO-Ru1, nested into COSMO-Ru7/2, adapted to the timetable of work of Olympic Organizing Committee.

(c) RDP: The module of correction of initial values of T at the low model levels and of soil based on the T2m observations was realized and tested. After the coupling with COSMO-Ru domestic research version it was detected the more realistic results for the forecasts of vertical profiles of temperature during all period of short-range forecasts and the little decreasing of the models precipitations. **The module is ready for coupling with operational technology and for nudging-cycles**, but needs the further testing for accumulation of larger statistics of forecasts for different synoptic situations and seasons.

Table 1: The number of used observations from RHM database for data assimilation

	number of measurements for one station per day	number of available stations (maximal value)			
		Database RHM	domain COSMO-RU07	domain COSMO-Ru2 (South)	domain COSMO-Ru2 (North)
SYNOP	8	7800	2950	155	180
TEMP, PILOT, TEMPSHIP	2	600	120	5	12
Sochi AMS	8–288	50	50	50	0

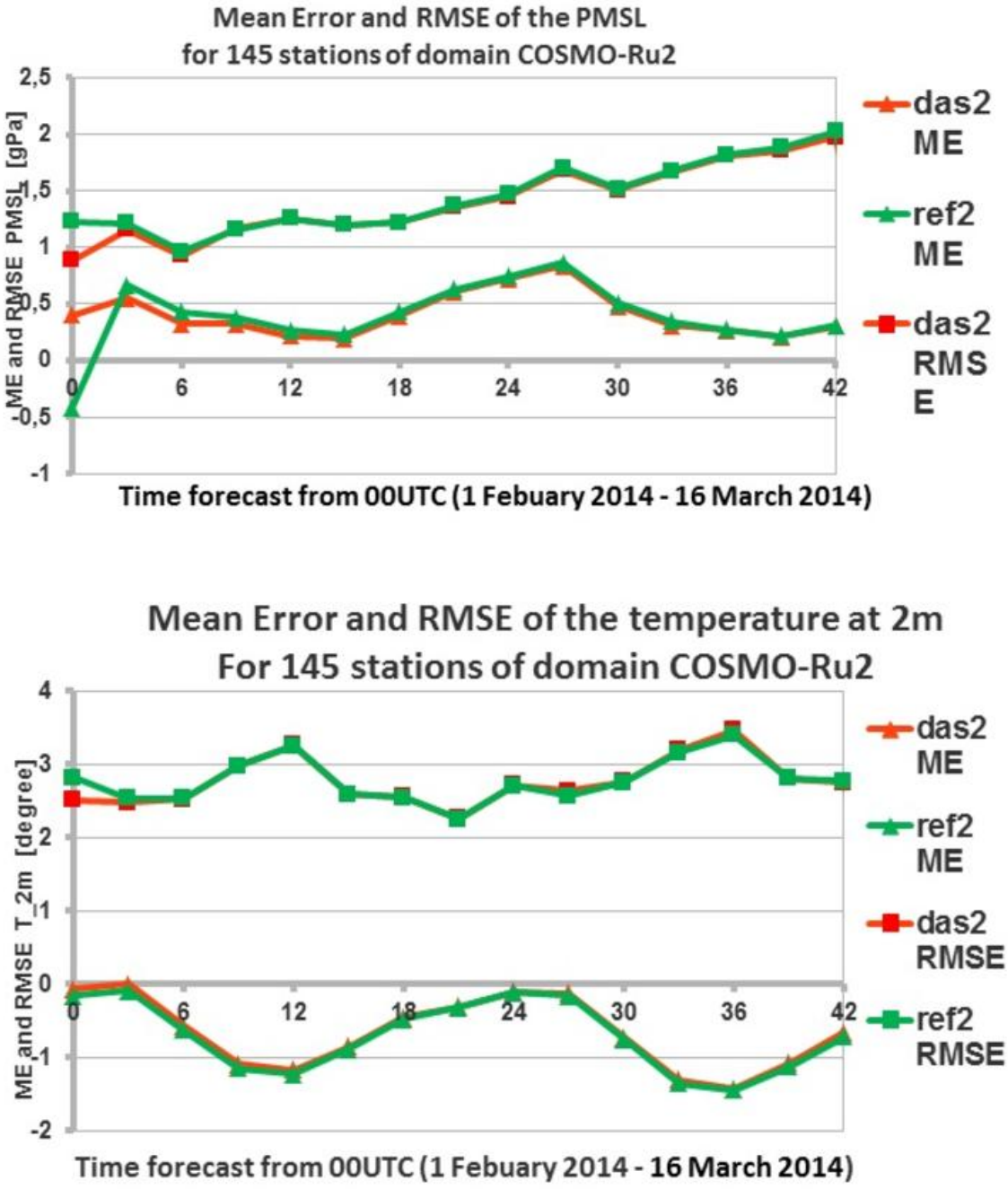
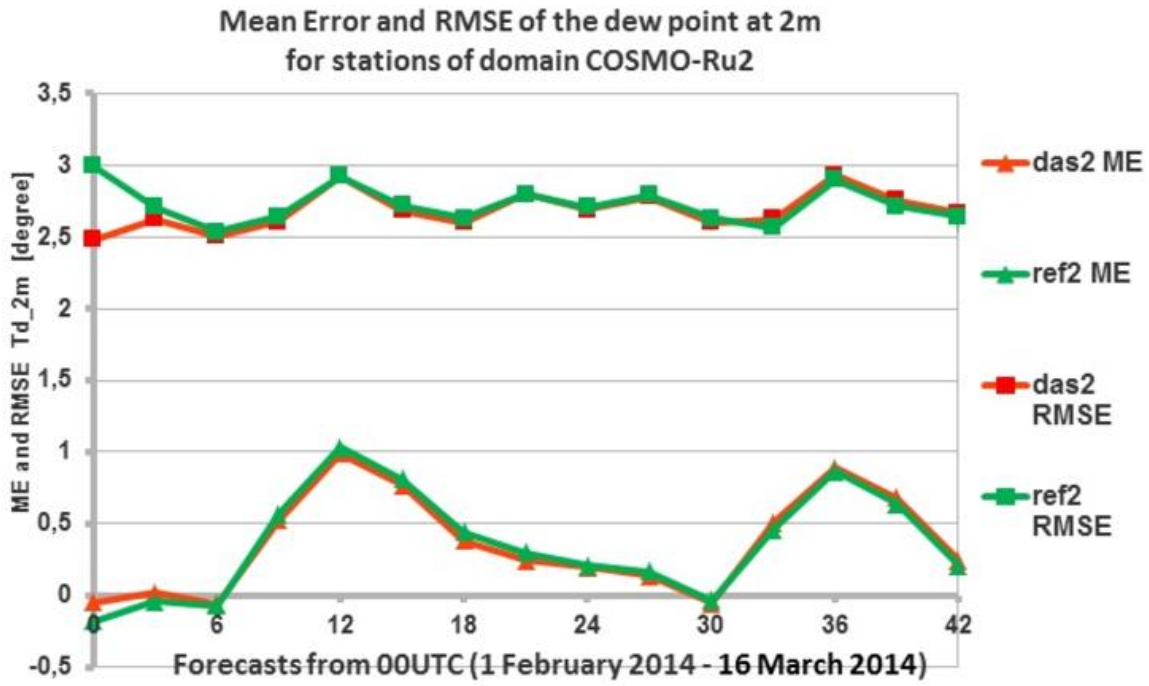
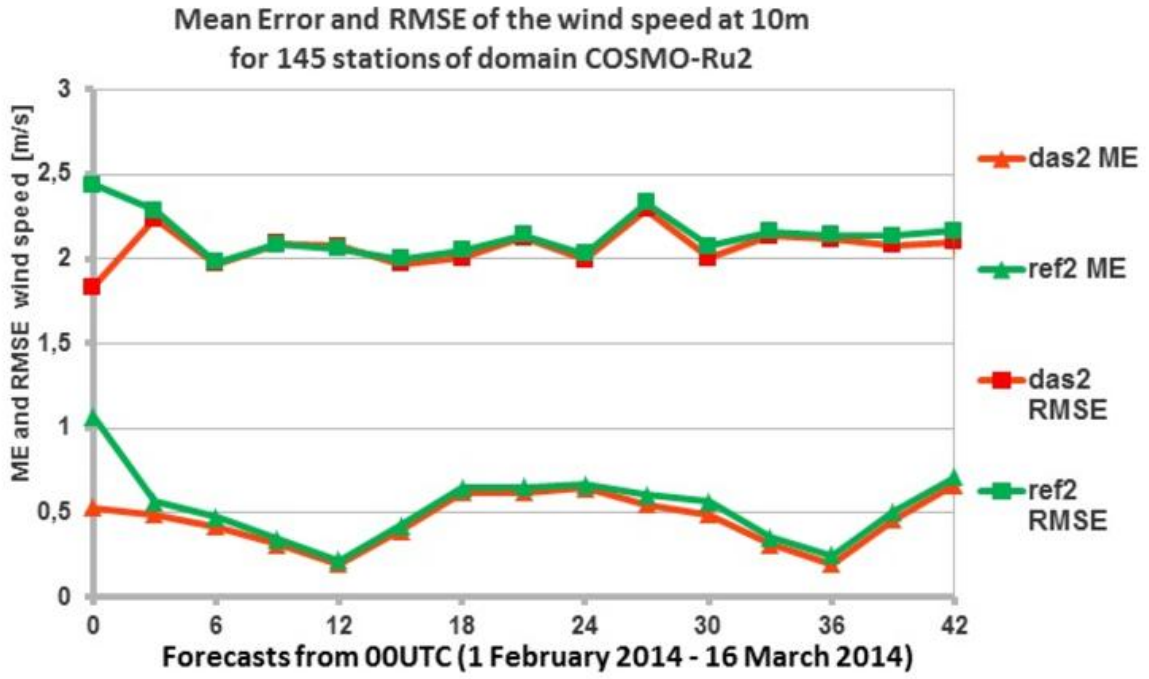


Figure 1: Mean error (ME) and Root Mean Square Errors (RMSE) of forecasts COSMO-Ru2 with DAS (red line) and without (green line) for PMSL, T_2m, Td_2m and wind speed respectively for Olimpic period 1 February – 16 March 2014

Cont. Fig.1.


Mean Error and RMSE of the dew point at 2m
for stations of domain COSMO-Ru2
ME and RMSE Td_2m [degree]
3,5
3
2,5
2
1,5
1
0,5
0
-0,5
0
6
12
18
24
30
36
42
Forecasts from 00UTC (1 February 2014 - 16 March 2014)
das2 ME
ref2 ME
das2 RMSE
ref2 RMSE


Mean Error and RMSE of the wind speed at 10m
for 145 stations of domain COSMO-Ru2
ME and RMSE wind speed [m/s]
3
2,5
2
1,5
1
0,5
0
0
6
12
18
24
30
36
42
Forecasts from 00UTC (1 February 2014 - 16 March 2014)
das2 ME
ref2 ME
das2 RMSE
ref2 RMSE

4.2 Development of High resolution COSMO-modeling for mountainous regions *(G. Rivin, M. Shatunova, D. Majewski, J. Förstner, J. Helmert, U. Schättler, D. Blinov, M. Arpagaus, G. de Morsier, P. Steiner)*

4.2.1 Model installation (and domain size selection)

Version of the COSMO model with horizontal resolution 1.1 km, named COSMO-Ru1, was installed on cluster-based architecture Tornado in Roshydromet. First COSMO-Ru1 version was released for domain size 450 x 450 grid points with lateral boundary conditions (LBC) from COSMO-Ru2SFO (with grid step 2.2 km for Southern Federal Region) for the same initial time run. COSMO-Ru1 is nested into COSMO-Ru2 but rotated grids of these models have different pole.

Model run time on cluster-based architecture Tornado for 24 hours forecast using 18 processors (244 cores) was approximately 50 min.

Because of limited computing resources and taking into account timing of the all COSMO-Ru models it was decided to reduce COSMO-Ru1 domain size for future operational use.

Forecasts for two versions of simulation domains were evaluated. Specifications of COSMO-Ru1 for experimental runs are presented in Table 2; positions of two domains are shown in Fig.2 along with COSMO-Ru2SFO domain.

Table 2: Specifications of COSMO-Ru1 experimental version

Domain size (grid points)	200 x 200 // 450 x 450
Horizontal grid spacing (degree / km)	0.01 / 1.1
Number of layers	50
Time step (seconds)	5-10
Forecast range (hours)	24-48
Initial time of model runs (UTC)	00, 06, 12, 18
Lateral Boundary conditions	COSMO-Ru2SFO
LBC update frequency (hours)	1
Initialization	none
COSMO version	4.27
Hardware	RSK Tornado
No. of cores used	224 (of 1152)

Assessment of the temperature at 2 m and precipitation forecasts showed that changes of domain size had greater effect on precipitation forecast than on temperature forecast. The difference in T2m forecast for two different domains would not exceed 0.5° (see Fig.3) while for precipitation forecast, especially for heavy precipitation cases, the difference varies from 30 % (for 24 h accumulated precipitation) to 100 % (for 1 h sums).

It is evident that change of the simulations domain size lead to changes in spatial (see Fig.4) and temporal (see Table 3) distribution of predicted precipitation. Assessment of results for two domains by comparison 3h and 24 h accumulated precipitation with observed values does not allow a definite conclusion about preferable domain.

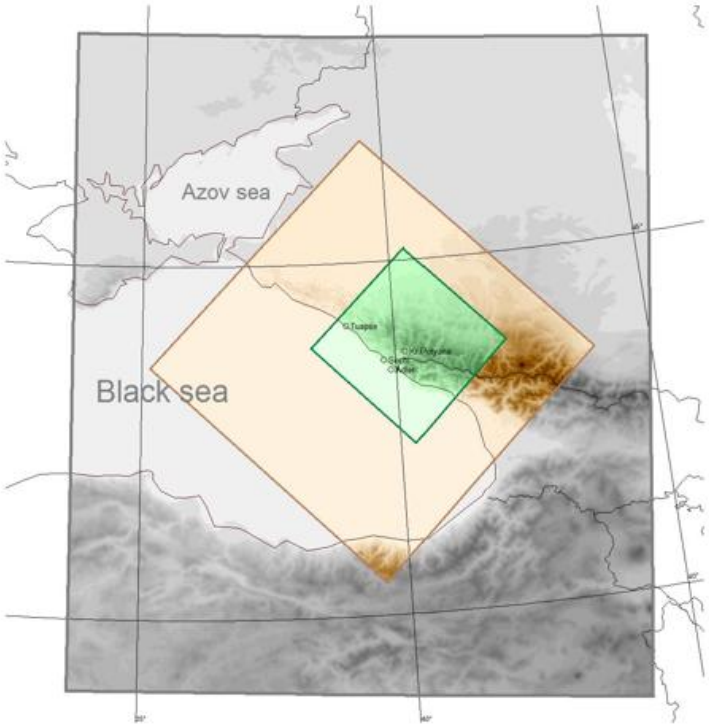


Figure 2: Location and size of COSMO-Ru2 domain (outer grey rectangle) and COSMO-Ru1 domains used in experiments: 450 x 450 grid points (brown-colored square) and 200 x 200 grid points (inner green-colored square)

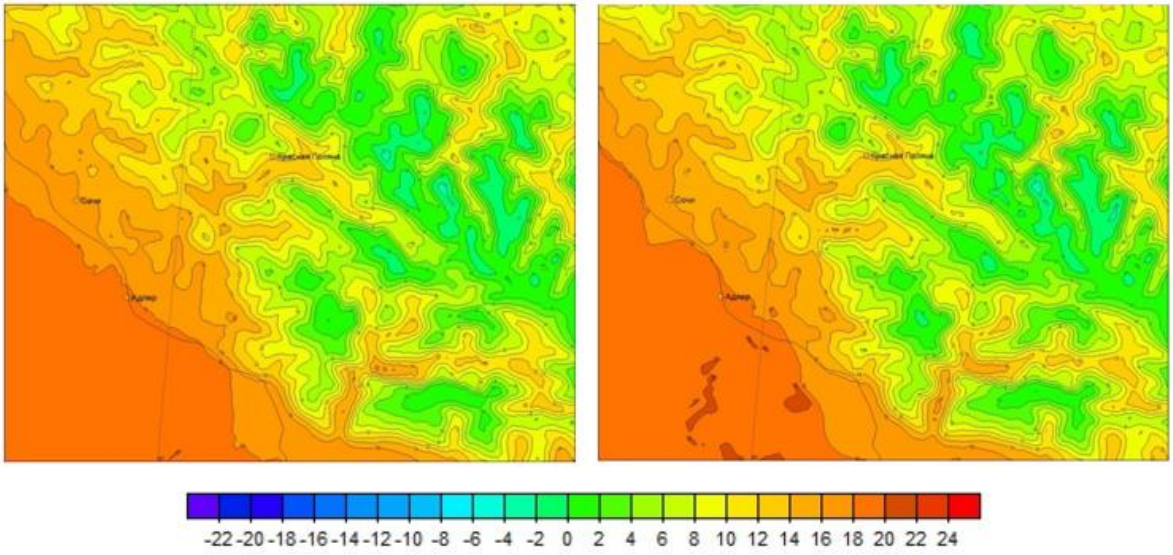


Figure 3: T2m 12 h forecasts from 24.09.2013, 00 UTC obtained in experiments with simulations domain 200 x 200 grid points (left) and 450 x 450 grid points (right)

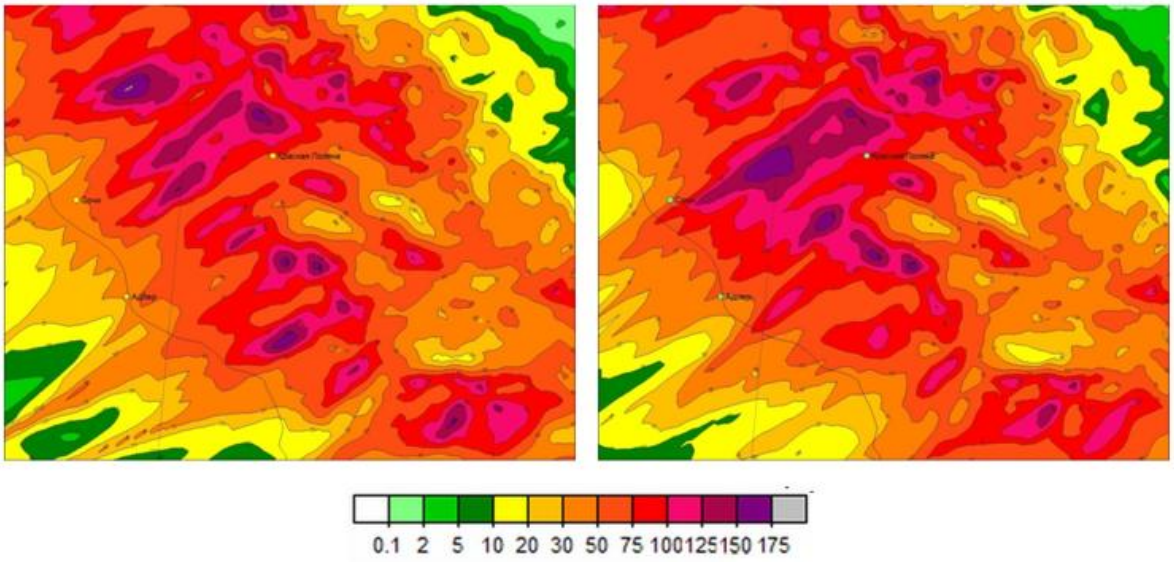


Figure 4: The same as figure 3 but for 12h precipitation sum

4.2.2 COSMO-Ru1 model orography options

Initially COSMO-Ru1 model orography was based on GLOBE *(The Global Land One-km Base Elevation Project)* data (NOAA/NGDC) (http://www.ngdc.noaa.gov/mgg/topo/globe.html). Great differences between height of observation points and height of the nearest model grid nodes forced us to check model orography by comparison with high-resolution ASTER *(Advanced Spaceborne Thermal Emission and Reflection Radiometer)* data (METI/NASA) (http://asterweb.jpl.nasa.gov/gdem.asp) that has resolution 1"($\sim 30\ m$). This comparison revealed a discrepancy between model orography and "real"one that reached 500 m for some nodes.

In December 2013, new orography data from EXTPAR based on ASTER GDEM2 became available and replaced COSMO-Ru1 model orography. The following orography filters were used: $ilow_pass_oro = 4$, $ilow_pass_xso = 5$, $rxso_mask = 625$.

Numerical experiments shown a positive effect of new orography data on the temperature, wind and precipitation forecast. Some errors in ASTER data locations discovered by EXTPAR developers later were insignificant for forecast quality.

Difference between observation site height and height of corresponding grid node became smaller. That lead to better agreement between observed and predicted values of T2m and wind speed (see Fig.5). For Gornaya Karusel height difference reduced to -32 m (previously -568 m), for Krasnaya Polyana 7 m (previously 248 m), for Aibga -194 m (previously -443 m). Improvement of T2m forecast was below 3° for some sites depending on weather conditions.

Model orography replacement affected also the predicted precipitation spatial and temporal distribution. Fig.6 shows forecasts with different model orography in comparison with observations for two sites: Gornaya Karusel-1500 and Krasnaya Polyana. Both sites are located within the mountain valley, height changes of the model grid node are mentioned above. Impact of new orography on forecasted accumulated precipitation can be seen better on the bottom graphs where differences "forecast – observation"for two variants of the model orography are presented. For Gornaya Karusel-1500 errors are the same: overestimation for the 4 first and the 4 last hours of the event and large underestimation of the accumulated precipitation at 2 (first maximum of the event) and 6 UTC 19.10. However, for the period

Table 3: Observed and predicted 3h precipitation sum for 24.09.2013

	Period, h								
	00–03	03–06	06–09	09–12	12–15	15–18	18–21	21–00	00–24
Krasnaya Polyana									
Observations	0.6	3.8	17.1	30.6	13.6	25.4	19.1	4.6	114.8
COSMO-Ru1 (200 x 200 g.p.)	13.0	29.1	11.9	12.1	31.9	28.9	3.8	0.8	131.5
COSMO-Ru1 (450 x 2450 g.p.)	12.5	30.4	22.7	22.6	26.5	11.9	2.9	0.1	129.5
COSMO-Ru2	4.7	41.5	21.7	11.3	40.4	12.4	4.4	1.8	138.1
Gornaya Karusel-1500									
Observations	0.5	10.5	28.7	34.6	16.6	20.1	20.2	1.7	132.9
COSMO-Ru1 (200 x 200 g.p.)	8.2	31.1	11.9	20.9	8.6	17.7	3.5	1.5	103.4
COSMO-Ru1 (450 x 2450 g.p.)	8.4	35.8	26.9	24.2	18.7	13.9	3.6	0.0	131.5
COSMO-Ru2	5.7	25.6	26.1	15.9	19.5	15.1	4.2	0.1	112.2
Roza Khutor-4									
Observations	0.5	9.7	19.0	33.0	31.8	29.6	26.4	4.4	154.4
COSMO-Ru1 (200 x 200 g.p.)	7.2	31.4	30.5	50.3	19.6	25.6	3.1	1.1	168.9
COSMO-Ru1 (450 x 2450 g.p.)	7.5	43.2	41.4	36.6	33.5	32.2	3.9	0.0	198.4
COSMO-Ru2	1.4	10.9	16.7	18.5	22.3	22.3	4.6	0.1	96.6
Roza Khutor-7									
Observations	0.3	10.5	25.9	34.1	26.1	28.0	25.0	5.0	154.9
COSMO-Ru1 (200 x 200 g.p.)	5.3	24.7	31.1	48.4	21.6	28.6	3.5	0.9	164.2
COSMO-Ru1 (450 x 2450 g.p.)	5.6	29.9	36.5	33.7	29.2	31.4	3.3	0.0	169.7
COSMO-Ru2	2.7	17.7	26.1	24.7	26.4	21.9	2.8	0.1	122.4

7-18 UTC forecast with new orography is better, errors have opposite sign. For Krasnaya Polayna forecast improvement is not obvious, errors are mostly the same or even greater.

4.2.3 COSMO-Ru1 operational use and verification

From January 29, 2014 COSMO-Ru1 run in operational mode is conducted 4 times a day. In order to perform forecast delivery schedule to forecasters COSMO-Ru1, COSMO-Ru2 and COSMO-Ru7 models run as priority tasks on additional cluster-based architecture ICE-X in Roshydromet during Olympics/Paralympics. Specifications of COSMO-Ru1 for operational use are presented in Table 4.

COSMO-Ru1 used initial and boundary conditions from COSMO-Ru2SFO from previous start-time (Fc-06h). The preliminary experiments demonstrated the capability of COSMO-Ru1 to produce satisfactory forecast with lead-time until 36 hours. It made possible to create operational forecast technology, which meets the requirements of forecasters, taking

into account time difference (UTC+4) and need to provide forecast for the current day to forecasters on 5 a.m. local time (1UTC).

COSMO-Ru1 forecast were used by forecasters along with COSMO-Ru2 during SOCHI-2014 Olympic Games. Model output parameters were produced in form of forecast charts of individual meteorological characteristics or combination of them and those produced in form of meteograms. Forecast charts were prepared for the three regions with varying order of detail: for whole simulations domain, for the Sochi coastal region and for mountain cluster (see examples in Fig.7).

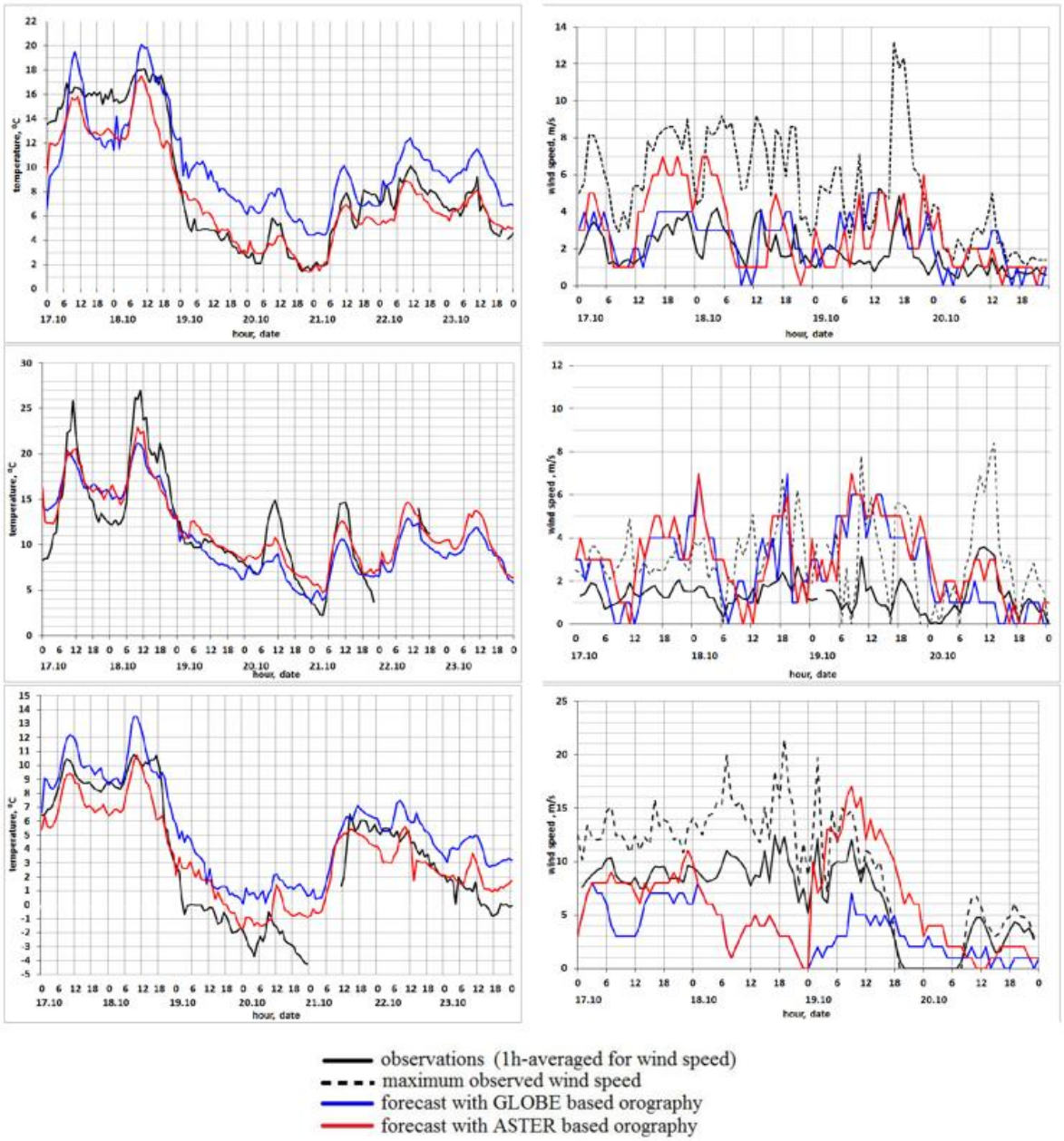


Figure 5: Series of 24 h forecasts for T2m (left) and wind speed at 10 m (right) from 00 UTC, for the period October, 17-23, 2013 (for T2m) and October, 17-20 (for wind) and observation data at Gornaya Karusel (top), Krasnaya Polyana (middle) and Aibga (bottom) for the same period

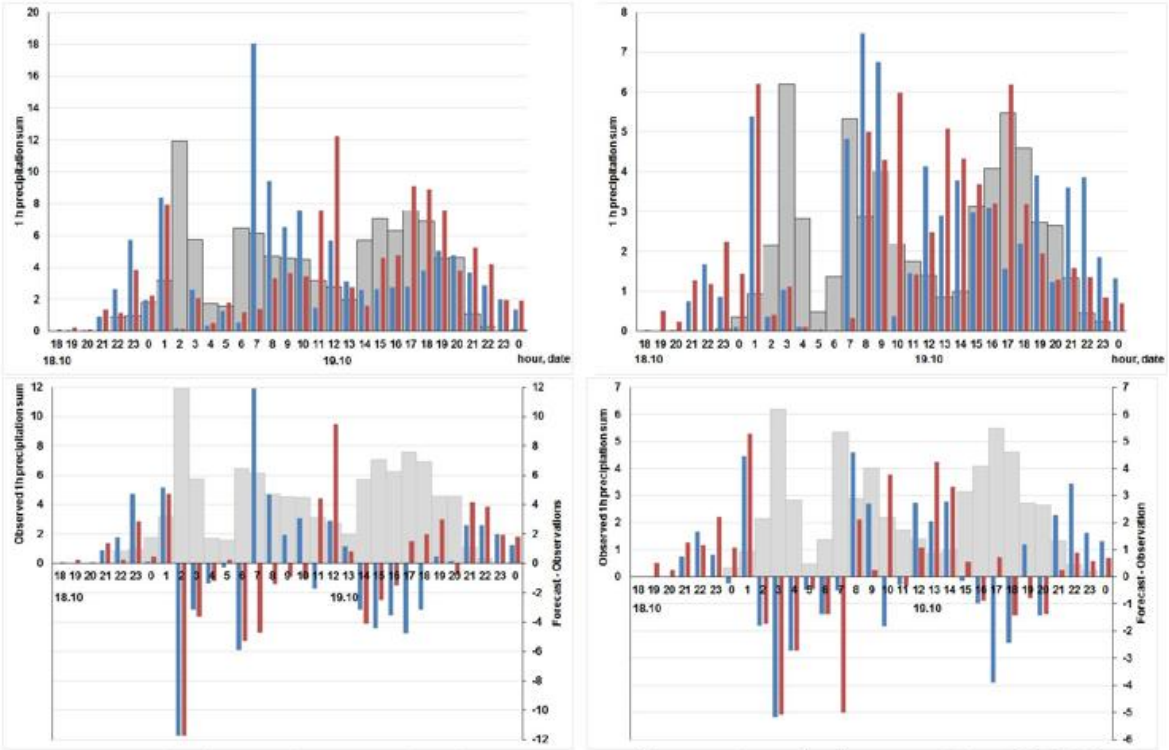


Figure 6: 1 h observed accumulated precipitation (grey column), forecasted by COSMO-Ru1 with different model orography: based on GLOBE data (blue) and ASTER data (red) for Gornaya Karusel-1500 (left) and Krasnaya Polyana (right). Comparison of 1h accumulated precipitation (top) and difference of two forecasts (bottom)

Table 4: Specifications of COSMO-Ru1 operational version during Olympics/Paralympics

Domain size (grid points)	190 x 190
Horizontal grid spacing (degree / km)	0.01 / 1.1
Number of layers	50
Time step (seconds)	5
Forecast range (hours)	36
Initial time of model runs (UTC)	00, 06, 12, 18
Lateral Boundary conditions	COSMO-Ru2SFO
LBC update frequency (hours)	1
Initialization	none
COSMO version	5.0
Hardware	SGI ICE-X
No. of cores used	660 (of 720)

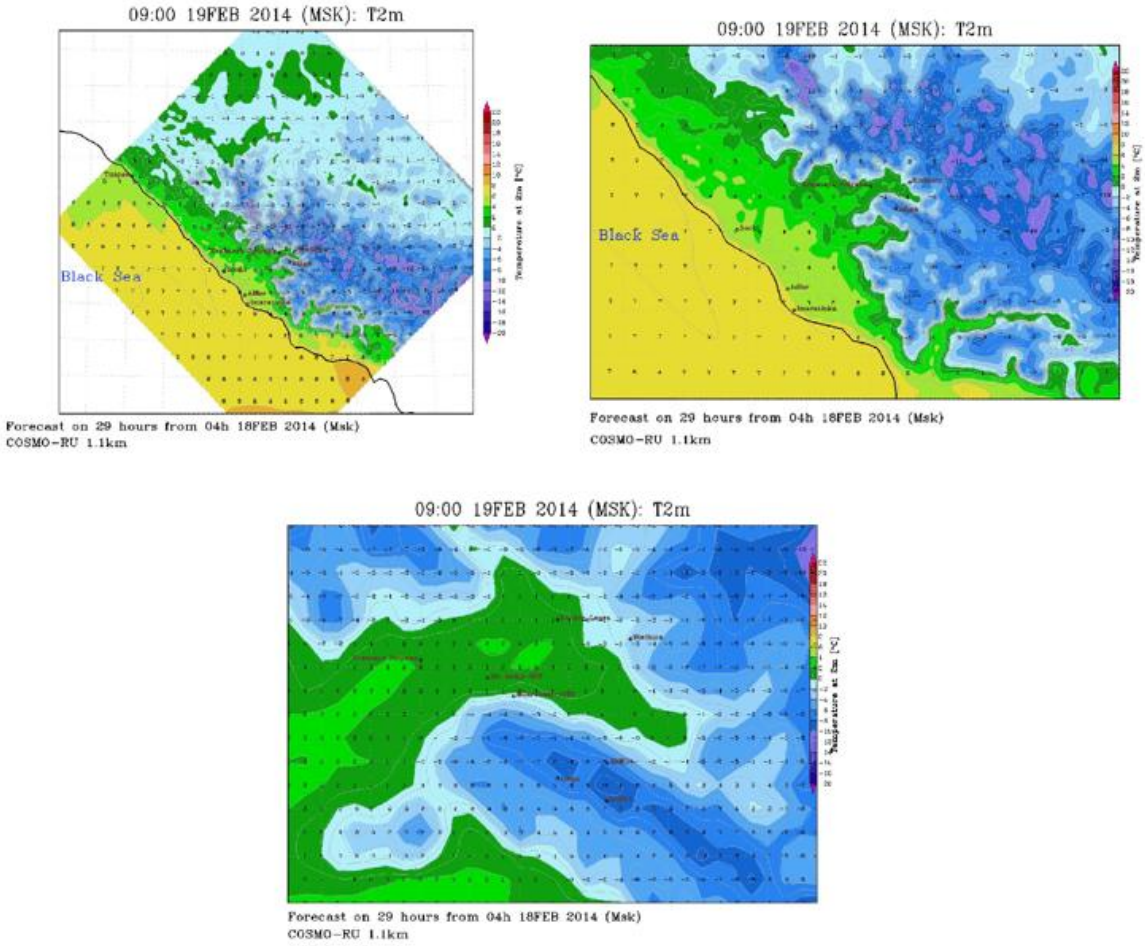


Figure 7: COSMO-Ru1 output presentation example. T2m forecast for the entire simulation domain (upper left), the Sochi region (upper right) and mountain cluster (bottom)

COSMO-Ru1 results were verified by VERSUS for the period of the Olympics/Paralympics along with COSMO-Ru2 and COSMO-Ru7. Some results for 00 UTC run are presented in Fig.8 *(by courtesy of Anastasia Bundel and Alexander Kirsanov)*. Verification made for 39 stations located at different altitudes in the mountain and coastal clusters for the period 29.01.2014 15.03.2014.

As for subjective verification, forecasters favored COSMO-Ru1 less than COSMO-Ru1 because COSMO-Ru1 began to run operationally just before the Olympics and they had no experience using products of this model. However COSMO-Ru1 forecasts for mountain cluster, such as combined charts "RH + streamlines", proved to be very popular and useful in the preparation of synoptic forecasts.

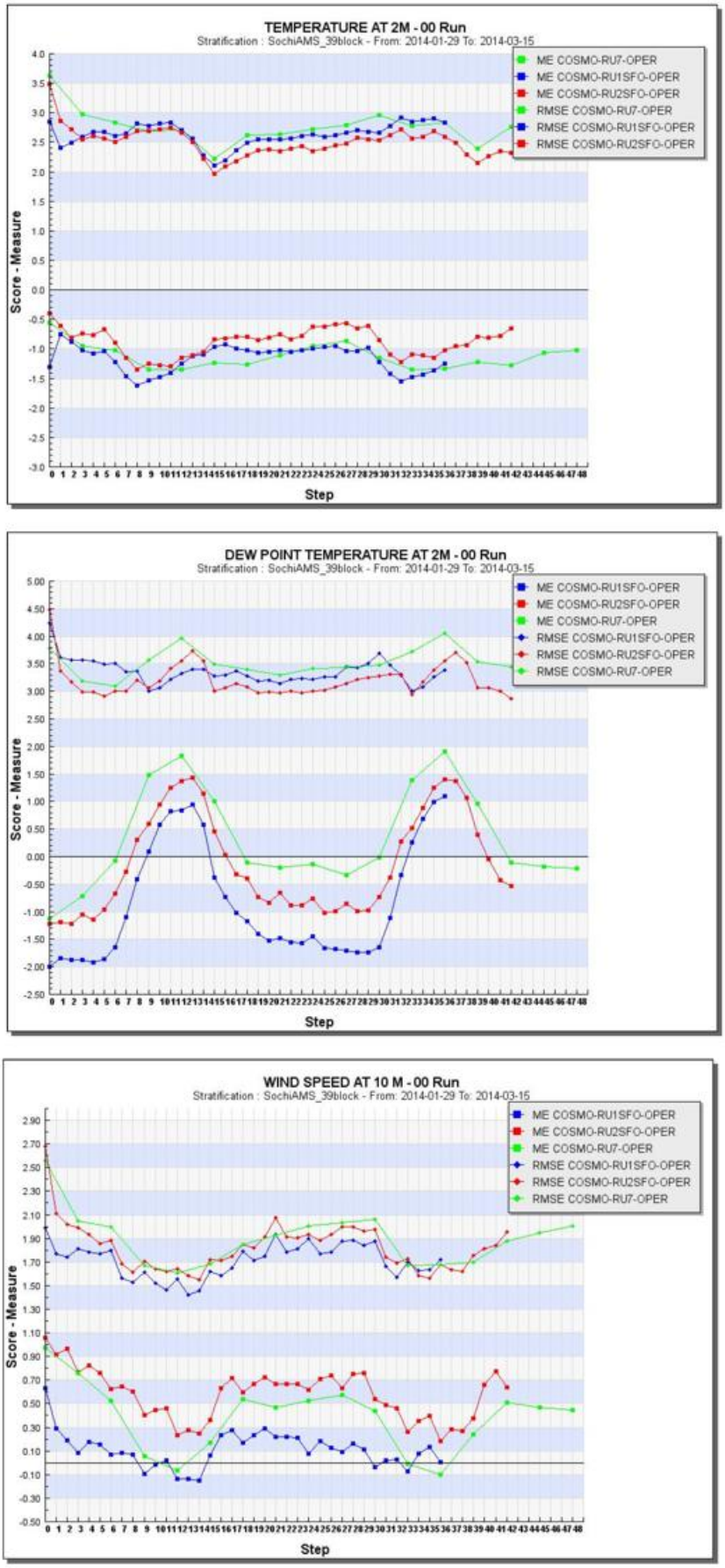


Figure 8: Verification COSMO-Ru1 (blue), COSMO-Ru2 (red) and COSMO-Ru7 (green) results for the 39 stations located at different altitudes in the mountain and coastal clusters for the period 29.01.2014 15.03.2014

4.2.4 Case study

The presence of observation data of different kinds and increasing of AMS numbers in the Sochi region during pre-Olympics period allowed to conduct several case studies. Satellite images, radars and profilers'data, as well as AMS data of high temporal resolution used to investigate COSMO-Ru1 model behavior in different synoptic conditions. List of weather events along with several NWP models behavior in appropriate situations was prepared by forecasters on the basis of their experience obtained during Sochi-2014 Olympics. Two events in the list related to low visibility cases have been studied. Detailed description of these cases is presented in (Shatunova, Rivin, Rozinkina, 2015).

5 Downscalling/post-processing for Sochi area and applications *(I. Rozinkina, E. Kazakova, M. Chumakov, A. Bundel, A. Muravev, D. Blinov, A. Kirsanov, P. Eckert, G. Rivin, A. Euripides, E. Kukanova)*

5.1 T2m correction *(I. Rozinkina, D. Blinov, G. Rivin)*

The goal: To realize the updated software of Fieldextra with inclusion of calculations of subgrid values of T2m based on the forecasts of vertical temperature gradient and to provide the software of 1-D correction of T2m forecasts based on the forecasts of vertical T gradient ("h-correction").

Method:

1. Determine the difference in heights of the model gridpoint and the height at the station Δh.
2. Find the vertical temperature gradient in the planetary boundary layer dT_{pbl}.
3. Find an amendment of temperature to the height as a product of the gradient and the difference in heights. The value of the amendments added to the model temperature at 2 meters. $T2m_hcorr = T2m + \Delta h \times dT_{pbl}$

Technology: The algorithm was tested in RHM and was operationally used during the Olympic Games in 2014. The vertical profiles of temperature from FieldExtra were used to find the vertical temperature gradients in PBL . As a result, the corrected temperature appears in the text and graphic 1D meteograms.

Outcome: Description of 1-D algorithm of h-correction of T2m.

The examples of results in using the proposed algorithm in COSMO-model are presented in the next sections of this chapter.

5.2 Kalman filtering application for correction of T2m COSMO-Ru-So forecasts *(M. Chumakov, E. Kazakova, I. Rozinkina, P. Eckert)*

It is a commonly acknowleged that Numerical Weather Prediction (NWP) models exhibit systematic errors in the forecasts of near surface weather parameters. This is a result not only of deficiencies of the physical parameterizations, but also of the inability of these models to handle successfully sub-grid phenomena. Furthermore, forecasts for the areas that are not in close proximity to the model grid points are usually based on interpolation of model output parameters, which also increases the 'noise' in the final forecast products.

Well known that the 2m-temperature, is one of the most commonly biased variable, where the magnitude of this bias depends, among other factors, on the geographical location and the season. So for better forecast result some correction algorithm should be used.

One of the most common approache to the above mentioned problems is the use of Kalman filtering (Kalman, 1960). This technique gives excellent results in the correction of systematic errors in any type of prediction, based on the recursive combination of recent forecasts and observations. The main advantage is the easy adaptation to any changes in the data being used (Galanis, Anadranistakis, 2002).

5.2.1 Description of the method

At Hydrometcenter of Russia Kalman filtering and height T2m correction algorithm (through vertical gradient) are implemented in COSMO-Ru2 (the Sochi region) (station locations are shown in the map in Fig.9). The technology works operationally since February 2015.

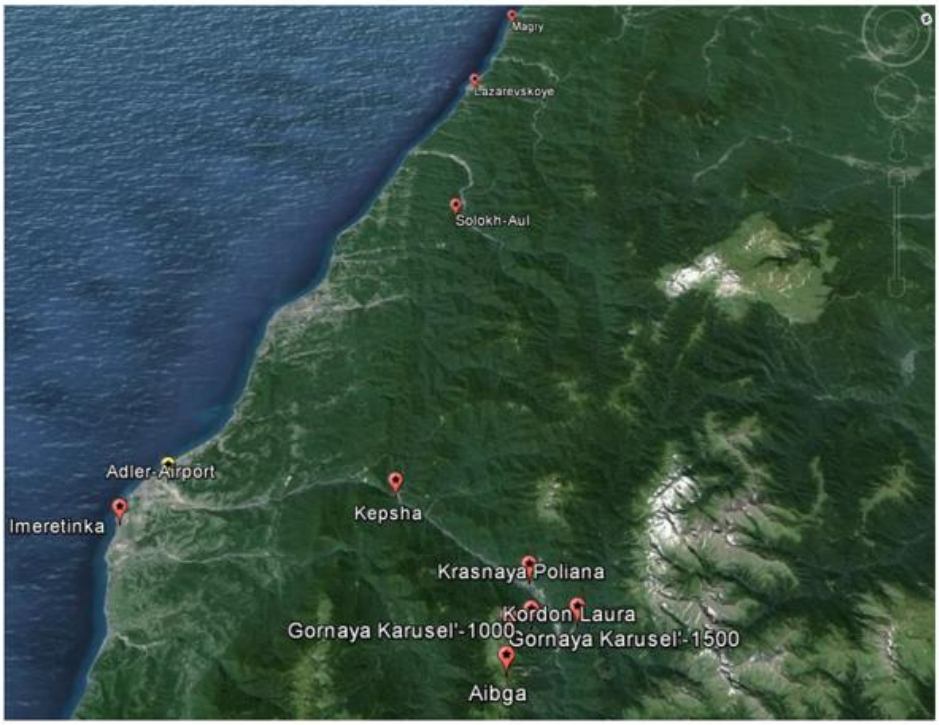


Figure 9: Station locations in the Sochi region

Describe briefly the main features of the implemented Kalman filtering. Suggest that there are two T2m observations T_1 and T_2 which can be represented as:

$T_1 = T_{true} + g_1$

$T_2 = T_{true} + g_2$

where T_{true} — true value of T2m, g_1, g_2 — stochastic variables (connected with measurement or forecast errors). As a rule, it is impossible to know exactly the value of T_{true}. But T_1, T_2 can be specified through reducing noise components g_1, g_2.

Consider that g_1, g_2 obey the normal distribution law and following conditions for mathematical expectation M and variance D are relevant:

$$\begin{aligned} M(g_1) = 0, M(g_2) = 0 \\ D(g_1) = \sigma_1^2, D(g_2) = \sigma_2^2. \end{aligned} \tag{1}$$

At this assumptions the best fit (best estimator), T_{cor}, of the true value of T2m would be written as:

$$T_{cor} = \alpha_1 T_1 + \alpha_2 T_2, \tag{2}$$

where α_1, α_2 are some unknown weight coefficients which has one important feature:

$$\alpha_1 + \alpha_2 = 1. \tag{3}$$

Take into account (3) we may rewrite (2) in following form:

$$T_{cor} = (1 - \alpha)T_1 + \alpha T_2, 0 \leq \alpha \leq 1. \tag{4}$$

In general case to assess the quality of it should be introduced some cost function $f(\varepsilon)$. Let the cost function has the form

$$f(\varepsilon) = \varepsilon^2 = (T_{true} - T_{cor})^2. \tag{5}$$

Such form of cost function is convenient for estimation of assessment quality since it has one minimum where derivative exists and equals to zero. This feature gives opportunity to find analytical form of T_{cor}.

Generally speaking function ε is a random variable as errors g_1, g_2 are changing from measurement to measurement, what lead to change of T_{cor} value at the same algorithm of measurements' processing. That's why quality criterion should be chosen in the way that algorithm gives minimum in average function $f(\varepsilon)$, i.e. assessment error variance P must tend to zero:

$$P = M\{(T_{true} - T_{cor})^2\} \longrightarrow 0. \tag{6}$$

Take into account (1) and (4) we obtain analytical formula for P:

$$P = (1 - \alpha)^2 D(g_1) + \alpha^2 D(g_2). \tag{7}$$

From the condition

$P = \frac{dP(\alpha)}{d\alpha} = 0$

we find optimal value of α, so Kalman filter is written as:

$$T_{cor1} = T_1 + K \cdot (T_2 - T_1), \tag{8}$$

where $K = \frac{P_1}{\sigma_2^2}$ — amplification factor. P_1 — variance of estimation which is calculated as:

$$P_1 = \frac{D(g_1) \cdot D(g_2)}{D(g_1) + D(g_2)} = 0. \tag{9}$$

This formula is easily extended to the case when there are more than two measurements.

It gives opportunity employ this algorithm for correction current forecast values using results of the preceding forecasts in assumption that variance of current forecast error is equal to value which was calculated using value of error during a few previous days.

Scheme of using COSMO-model (2.2 km) forecast series for the Sochi region is presented in Fig.10. This figure shown, for example, for correction result of 15-hour forecast T2m from 00 UTC of any day may be used forecast result for this time from 00, 06, 12 and 18 UTC of previous day.

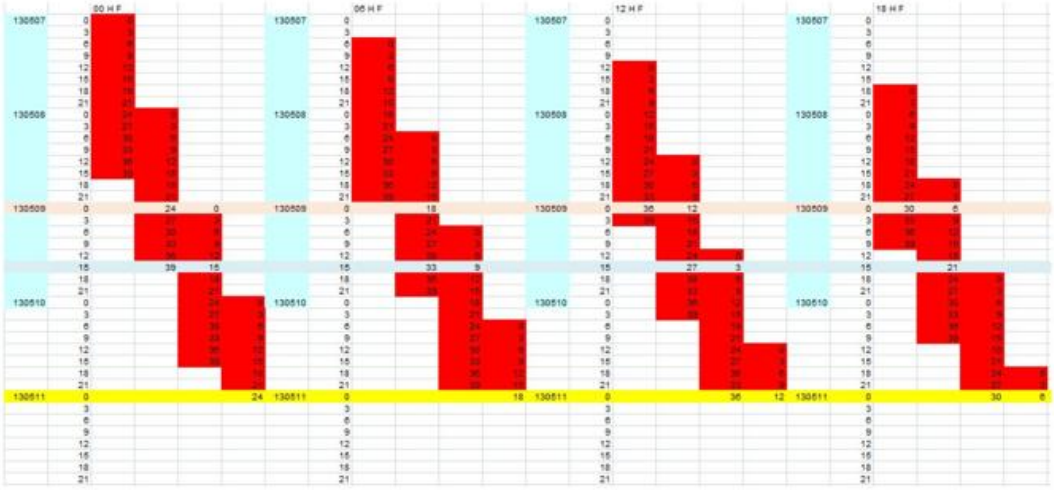


Figure 10: Scheme of COSMO-Ru2 forecast series for the Sochi region

Testing of the algorithm was done for station Adler (Sochi) for May 2013 with the use of COSMO-Ru2 version. Results are presented in Table 1. As can be seen, significant reduction of T2m RMSE values was observed for 3-hour, 9-hour and 15-hour lead time model forecasts starting from 06 UTC. It may be supposed that it is related to the quality of forecasted values, which were used in correction or statistical characteristics of forecast errors at this time.

It will be appreciated that only strict implementation of the conditions (1) ensures successful operation of Kalman filtering. Unfortunately forecast's values of T2m not always satisfy these conditions. As a result of studies it was determined that the Fourier coefficients are more relevant.

Thus, modification of Kalman filter algorithm application was done by using discrete Fourier transform. T2m forecast series on particular date can be treated as a real time-dependent function f. Thus suppose that we sample f at N equally spaced time intervals of length Δ seconds starting at moment t_0. Consequently:

$SEQ_i = f(t_0 + (i-1)\Delta) i = 1, ..., N.$

Table 5: RMSE values for T2m COSMO-Ru2 forecasts with Kalman filtering application for station Adler for period of May 2013

Forecast, hour	Start 00 h		Start 06 h		Start 12 h		Start 18 h	
	Filtered	Ref.	Filtered	Ref.	Filtered	Ref.	Filtered	Ref.
03	1.3	2.0	1.3	2.3	0.9	1.4	1.1	2.0
06	1.4	1.1	1.4	1.6	1.3	1.3	1.7	1.8
09	1.3	1.3	1.6	2.7	1.1	1.5	1.7	2.1
12	1.5	1.4	1.3	1.5	1.7	1.9	1.6	1.2
15	1.3	1.6	1.1	1.9	1.7	2.1	1.3	1.2
18	1.4	1.3	1.7	1.8	1.1	1.1	1.4	1.4
21	1.1	1.5	1.7	2.0	1.3	1.1	1.2	1.6
24	1.7	1.9	1.1	1.1	1.5	1.3	1.3	1.3

Note. In colors: orange improvement, red significant improvement, blue measurement error.

Discrete Fourier transform of this function can be written as:

$$SEQ_i = \frac{1}{N}[c_1 + 2\sum_{n=2}^{(N+1)/2} c_{2n-2}cos[\frac{2\pi(n-1)(i-1)}{N}] - 2\sum_{n=2}^{(N+1)/2} c_{2n-1}sin[\frac{2\pi(n-1)(i-1)}{N}]]. \tag{10}$$

For obtaining sufficient number of Fourier coefficients synoptic period (7 days) must be used. Each Fourier coefficient (c_i) can be represented as an independent temperature measurement. Accordingly Kalman filtering (KF) algorithm mentioned above can be applied to these coefficients.

5.2.2 Operational results and verification

Since the mid February 2014 Kalman filtering was implemented in operational mode for COSMO-Ru2 Sochi domain at Hydrometcentre of Russia. Meteograms were produced for 11 stations situated in the region, which sent standard regular SYNOP measurements (example is presented in Fig.11). Height corrected temperature forecasts (authors of the algorithm — I. Rozinkina, D. Blinov) were used as T2m COSMO-Ru2 forecasts.

Thus, Kalman filtering was applied to the value of corrected T2m COSMO-Ru2 forecasts and observations at meteorological stations. It could work for other COSMO-Ru domains and when using standard T2m COSMO-Ru forecasts.

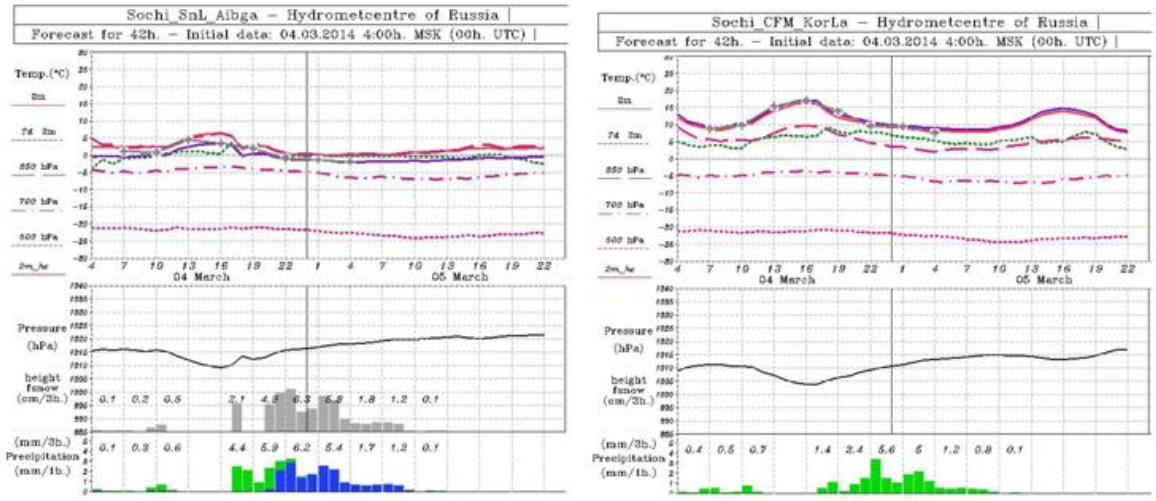


Figure 11: Example of meteograms obtained from integration of COSMO-Ru2 for station Aibga (left) and Kordon Laura (right). Start 00 UTC 4 March 2014. Height corrected temperature is presented by a violet curve, 2m temperature — pink line, result of KF application — gray dots. Grey columns show hourly accumulated depth of fresh snow, numbers above — its 3-hour sums. Blue columns indicate hourly accumulated precipitation in the form of snow, green — in the form of rain

Kalman filtering (with using corrected COSMO-Ru2 T2m forecasts) provides more accurate T2m forecast in mountain region rather than operational version of COSMO-Ru2 (improvement is about 2° C in RMSE) and in most cases — better than using only height correction algorithm for T2m (Fig.12-13). Improvement of T2m forecasts with the use of KF is observed not only for mountain areas, but also for the coastal stations. Comparison between T2m forecasts for the period up to 24 hours was done for these statiuons with start time 00

and 18 UTC — RMSE absolute values were close. The accuracy of KF and T2m corrected algorithm is comparable.

Sochi Adler (0 m)

forecast. hour	RMSE oper	RMSE cor	RMSE KF
3	1.8	1.9	1.5
6	1.8	1.8	1.5
9	2.0	2.0	2.1
12	1.9	1.9	1.9
15	1.6	1.6	1.7
18	1.5	1.5	1.8
21	2.0	2.0	2.2
24	1.4	1.5	1.9

Imeretinka (6 m)

forecast. hour	RMSE oper	RMSE cor	RMSE KF
3	3.0	3.1	2.8
6	3.1	3.1	3.0
9	3.8	3.8	3.9
12	3.7	3.7	3.6
15	1.7	1.6	1.6
18	2.0	2.1	2.3
21	2.0	2.0	2.3
24	2.3	2.3	2.6

Lazarevskoe (9 m)

forecast. hour	RMSE oper	RMSE cor	RMSE KF
3	2.0	2.1	1.8
6	2.0	2.0	2.1
9	3.0	3.0	2.6
12	3.1	3.1	2.5
15	2.4	3.3	2.4
18	1.6	1.6	2.0
21	1.6	1.6	1.5
24	2.0	1.9	1.7

Magri (50 m)

forecast. hour	RMSE oper	RMSE cor	RMSE KF
3	4.0	3.9	3.4
6	1.9	1.9	2.1
9	2.9	3.0	2.7
12	2.9	2.9	2.5
15	1.9	1.9	1.9
18	3.3	3.2	2.5
21	4.2	4.1	3.2
24	4.1	3.9	3.2

Kepsha (180 m)

forecast. hour	RMSE oper	RMSE cor	RMSE KF
3	2.8	3.1	2.8
6	2.8	3.4	2.8
9	4.2	4.2	4.0
12	5.0	4.7	4.4
15	3.4	3.5	3.6
18	1.5	2.1	1.6
21	1.4	1.6	1.7
24	1.6	1.6	1.9

Kalman filter is better/equal than operational version and T2m correction algorithm

Kalman filter is better than operational version

T2m correction algorithm is better than operational version

Solokh Aul (443 m)

forecast. hour	RMSE oper	RMSE cor	RMSE KF
3	1.8	1.6	1.3
6	1.8	1.7	1.8
9	2.6	2.5	2.5
12	2.9	2.8	2.7
15	2.7	2.6	2.7
18	1.6	1.3	1.3
21	1.7	1.4	1.3
24	2.6	2.5	2.5

Krasnaya Polyana (564 m)

forecast. hour	RMSE oper	RMSE cor	RMSE KF
3	1.7	1.5	1.3
6	1.9	2.0	1.7
9	2.7	2.3	2.3
12	3.3	2.7	2.3
15	2.5	2.0	2.0
18	2.0	1.8	2.1
21	1.7	1.5	1.8
24	1.6	1.5	1.6

Kordon Laura (570 m)

forecast. hour	RMSE oper	RMSE cor	RMSE KF
3	2.9	3.1	2.4
6	3.2	3.4	3.3
9	3.1	3.0	3.0
12	3.7	4.0	3.7
15	2.0	2.8	1.7
18	2.8	3.1	2.4
21	2.1	2.4	1.8
24	2.6	2.9	2.1

Gornaya Karusel (977 m)

forecast. hour	RMSE oper	RMSE cor	RMSE KF
3	2.3	2.3	2.1
6	2.9	2.7	2.7
9	2.3	2.0	2.0
12	3.0	2.6	2.7
15	3.1	2.9	3.1
18	1.7	1.5	1.6
21	1.6	1.5	1.5
24	1.4	1.3	1.6

Gornaya Karusel (1434 m)

forecast. hour	RMSE oper	RMSE cor	RMSE KF
3	2.0	2.1	2.2
6	2.2	2.2	2.2
9	2.4	2.4	2.4
12	3.0	3.0	3.1
15	1.6	1.6	1.8
18	1.3	1.3	1.8
21	1.4	1.4	1.7
24	1.3	1.3	1.6

Aibga (2225 m)

forecast. Hour	RMSE oper	RMSE cor	RMSE KF
3	2.5	1.3	1.4
6	3.0	1.3	1.4
9	3.5	1.7	1.7
12	4.1	2.5	2.3
15	3.0	1.4	1.3
18	3.2	1.4	1.9
21	2.8	1.1	1.1
24	7.4	1.5	2.3

Figure 12: RMSE for T2m COSMO-Ru2 forecasts for stations in the Sochi region. Start 00 UTC. 1 March — 30 June 2014

Sochi Adler (0 m)

forecast. hour	RMSE oper	RMSE cor	RMSE KF
3	2.0	2.0	1.9
6	1.6	1.6	1.5
9	1.5	1.5	1.5
12	1.9	1.9	1.7
15	2.2	2.2	2.3
18	2.0	2.0	2.4
21	1.7	1.7	1.8
24	1.4	1.4	1.7

Imeretinka (6 m)

forecast. hour	RMSE oper	RMSE cor	RMSE KF
3	2.0	2.1	2.0
6	2.4	2.4	2.3
9	2.8	2.9	2.7
12	3.2	3.2	3.0
15	3.0	3.0	3.1
18	3.5	3.5	3.8
21	1.7	1.6	1.7
24	2.2	2.3	2.5

Lazarevskoe (9 m)

forecast. hour	RMSE oper	RMSE cor	RMSE KF
3	1.5	1.5	1.4
6	1.8	1.9	1.6
9	2.2	2.2	1.8
12	2.3	2.2	2.3
15	3.3	3.2	2.7
18	3.4	3.3	2.8
21	2.4	2.4	2.5
24	1.7	1.7	2.1

Magri (50 m)

forecast. hour	RMSE oper	RMSE cor	RMSE KF
3	4.3	4.2	3.6
6	4.0	3.9	3.2
9	4.2	4.0	3.3
12	2.1	2.2	2.3
15	3.1	3.2	2.7
18	3.2	3.3	2.9
21	3.6	3.6	3.6
24	3.3	3.2	2.7

Kepsha (180 m)

forecast. hour	RMSE oper	RMSE cor	RMSE KF
3	1.8	1.9	1.5
6	2.1	1.9	1.8
9	2.7	2.8	2.8
12	2.8	3.3	2.7
15	4.2	4.3	3.9
18	4.7	4.5	4.6
21	2.2	2.4	2.4
24	1.5	1.9	1.6

Kalman filter is better/equal than operational version and T2m correction algorithm

Kalman filter is better than operational version

T2m correction algorithm is better than operational version

Solokh Aul (443 m)

forecast. hour	RMSE oper	RMSE cor	RMSE KF
3	1.4	1.2	1.2
6	2.6	2.5	2.3
9	2.8	2.6	2.4
12	3.0	2.8	3.0
15	3.6	3.5	3.6
18	3.8	3.7	4.0
21	1.7	1.6	1.7
24	1.6	1.4	1.5

Krasnaya Polyana (564 m)

forecast. hour	RMSE oper	RMSE cor	RMSE KF
3	2.1	1.8	1.6
6	1.9	1.7	1.5
9	1.7	1.5	1.3
12	1.9	2.0	1.7
15	2.7	2.5	2.7
18	3.2	2.7	2.7
21	2.5	2.1	2.0
24	2.1	1.9	2.2

Kordon Laura (570 m)

forecast. hour	RMSE oper	RMSE cor	RMSE KF
3	2.4	2.6	1.9
6	2.8	3.0	2.1
9	2.7	2.9	2.2
12	2.3	2.4	2.2
15	3.3	3.3	3.2
18	2.5	2.9	2.8
21	2.2	5.1	4.1
24	2.8	3.4	2.3

Gornaya Karusel (977 m)

forecast. hour	RMSE oper	RMSE cor	RMSE KF
3	1.8	2.0	1.6
6	1.8	1.9	1.4
9	1.9	2.0	1.5
12	2.3	2.1	2.1
15	2.5	2.1	2.0
18	3.0	2.6	2.9
21	2.3	2.1	2.2
24	1.8	1.6	1.8

Gornaya Karusel (1434 m)

forecast. hour	RMSE oper	RMSE cor	RMSE KF
3	1.5	1.5	1.4
6	1.5	1.5	1.3
9	2.1	2.1	2.2
12	2.1	2.1	2.3
15	2.5	2.5	2.4
18	3.0	2.9	3.4
21	1.7	1.7	1.8
24	1.4	1.4	1.8

Aibga (2225 m)

forecast. hour	RMSE oper	RMSE cor	RMSE KF
3	2.3	1.0	1.0
6	2.5	1.1	1.2
9	2.4	1.2	1.3
12	3.2	1.4	1.4
15	3.8	1.8	1.7
18	4.2	2.4	2.5
21	3.1	1.5	1.3
24	3.3	1.6	2.0

Figure 13: RMSE for T2m COSMO-Ru2 forecasts for stations in the Sochi region. Start 18 UTC. 1 March — 30 June 2014

According to Kalman filtering approach, most T2m picks during spring period in 2014 were predicted in a good correspondence with measurements (Fig.14).

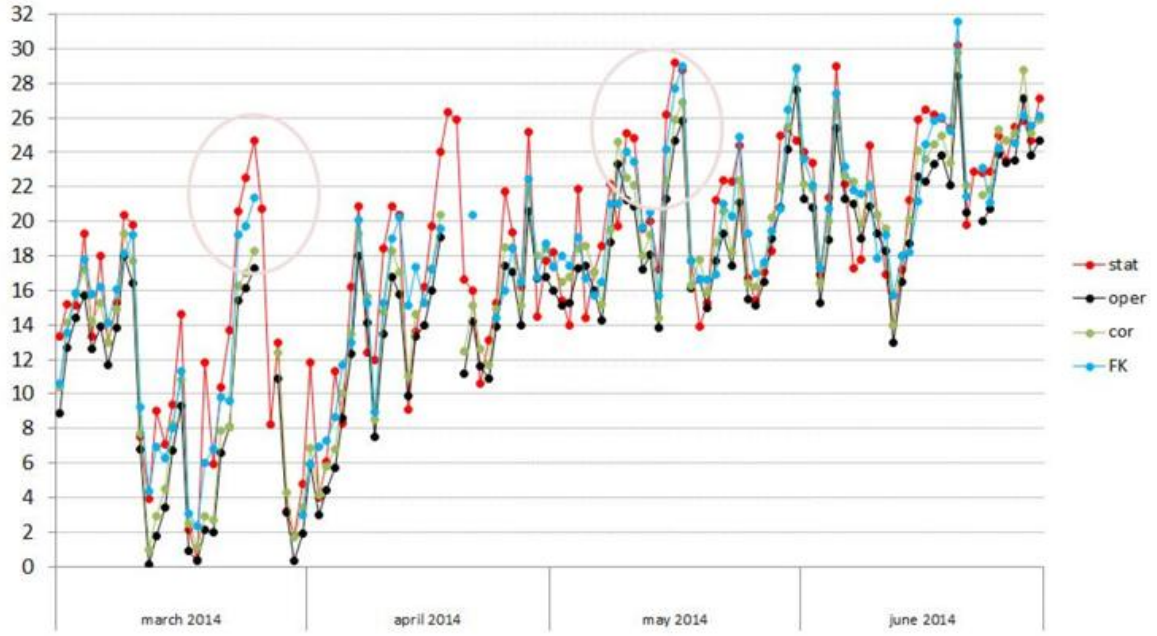


Figure 14: Example of T2m 12h forecasts by COSMO-Ru2 for station Krasnaya Polyana. Start 00 UTC. 1 March — 30 June 2014. Red line observations, black — operational forecast, green — T2m correction algorithm, blue — Kalman filtering

In future we plan to perform a series of experiments to develop the technology of using Kalman filtering in case of the partial absence of forecast data.

5.3 Fresh snow depth postprocessing example for COSMO-Ru-So *(E. Kazakova, M. Chumakov, I. Rozinkina)*

Model precipitation is considered to be a mass of water, which reached earth surface (taking into account its phase state) for given time period, i.e. accumulated water equivalent. According to WMO regulations, information about fallen precipitation is received from synoptic observational network in the same terms as the general-purpose weather forecasts are made.

Due to determined structure "data numerical forecast general-purpose weather forecast", in case of falling of solid or mixed precipitation, users (transportation, electricity supply networks, community facilities, organization of winter sports events, etc.) are not provided with greatly demanded information about depth of snow layer after snowfall which has already taken place or predicted.

As a rule, for fresh snow depth determination simple empirical dependences based on assumption of constant values of its density are used in operational synoptic practice. Use of more valid difficult dependencies should be provided on the basis of automated technology.

Snow depth measurements are held at hydrometeorological stations (HMS) and sent once a day through communication link to international exchange. Such a discreteness of measurements is not satisfactory for exact determination of snow depth in the train of snowfalls, since during this period of time snow cover could experience significant changes (snow could dense, melt, be blown by wind). In some regions there are automated meteorological stations (AMS), for example, in the Sochi region in Russia, which measure snow depth with high time

discreteness (once in 10 minutes). Yet, as the practical usefulness of these measurements has been demonstrated, these data should have pass quality control because reliability of these data is very sensitive to accuracy of setting, operation conditions and regularity of technical service of AMS. Thus the information about snow from AMS can't always be directly used in operational practice.

The main goal of the project was to provide users of mesoscale forecasting system COSMO-Ru output with a new type of information snow increment for several hours. In order to achieve this goal a number of algorithmic and technological issues needed to be resolved.

Forming of suggestions and testing of algorithm for fresh snow density calculation (hence, its layer thickness) referred to algorithmic tasks, combination of calculation of this characteristic from existing elements of postprocessing of COSMO-Ru operational system to technology application. Additional task was analyzing a success of fresh snow depth calculation received from direct COSMO-Ru forecasts (with the proposed algorithm included into its postprocessing) versus direct snow observations at AMS and HMS of North-Caucasian region during the period of winter Olympic Games Sochi-2014. Technological aspects consist of combining the calculations according to the proposed module with operationally functioning postprocessing systems of COSMO-Ru.

While forming meteograms, fresh snow depth could be calculated on the basis of elements' values included in the table. The peculiarity of technological changes during present work was the fact that in the framework of preparation of meteorological support for Sochi-2014 at Hydrometcenter of Russia algorithm of model air temperature (2 meters) correction for mountain region based on moving amendments connected with differences between model and actual relief heights (for points for which meteograms are prepared) was proposed and implemented. Its obvious that when big differences occur, such a temperature amendment should be taken into account in calculations of fresh snow depth, especially at temperatures close to zero.

For output processing in grid nodes the program module of universal postprocessing FieldExtra was developed in COSMO consortium. One of the tasks of the present work was to adapt and implement the proposed algorithm of fresh snow depth calculation based on air temperature data in FieldExtra tool, which in future could allow providing users with calculated information in form of maps.

5.3.1 Description of fresh snow depth calculation algorithm and its testing

Calculation of fresh snow depth is based on the formulas which are used in the snow model SMFE (see COSMO Newsletter, Kazakova, Chumakov, Rozinkina, 2013). For fresh snow depth $h_{s,f}$ (mm) calculations of accumulated precipitation (observed or prognostic) p_s (mm) and fresh snow density $\rho_{s,f}$ (kg/m^3) are needed:

$h_{s,f} = \frac{p_s \cdot \rho_w}{\rho_{s,f}}$,

where $\rho_w = 1000\ kg/m^3$ - water density.

For testing of the proposed method it was checked against several assumptions:

- linear dependence on air temperature at 700 hPa from (McGurk, Azuma, Kattelmann, 1988);
- formula for fresh snow density calculation in TERRA of the COSMO-model, depending on temperature of the model lowest atmospheric level (Doms et al., 2011);

– constant density value equal to 100 kg/m^3, which is mostly used in synoptic practice while making weather forecast for conversion of precipitation sums into snow depth.

For quality assessment of unique observations of several snowfalls in January 2013 at the station Gornaya Karusel (1500 m) was conducted (Fig.15). As shown, the proposed fresh snow depth calculation method gives a good approximation to the values measured at the station, which happened to be more accurate in comparison with other algorithms. Thus, RMSE of fresh snow depth in case of the proposed method is 1.1 cm and MAE is 2.9 cm, while relative error is equal to 8.3 %. Linear dependence on T700 could be used only for a limited temperature range. As a rule, use of constant value of 100 kg/m^3 and formula from TERRA lead to fresh snow depth underestimation.

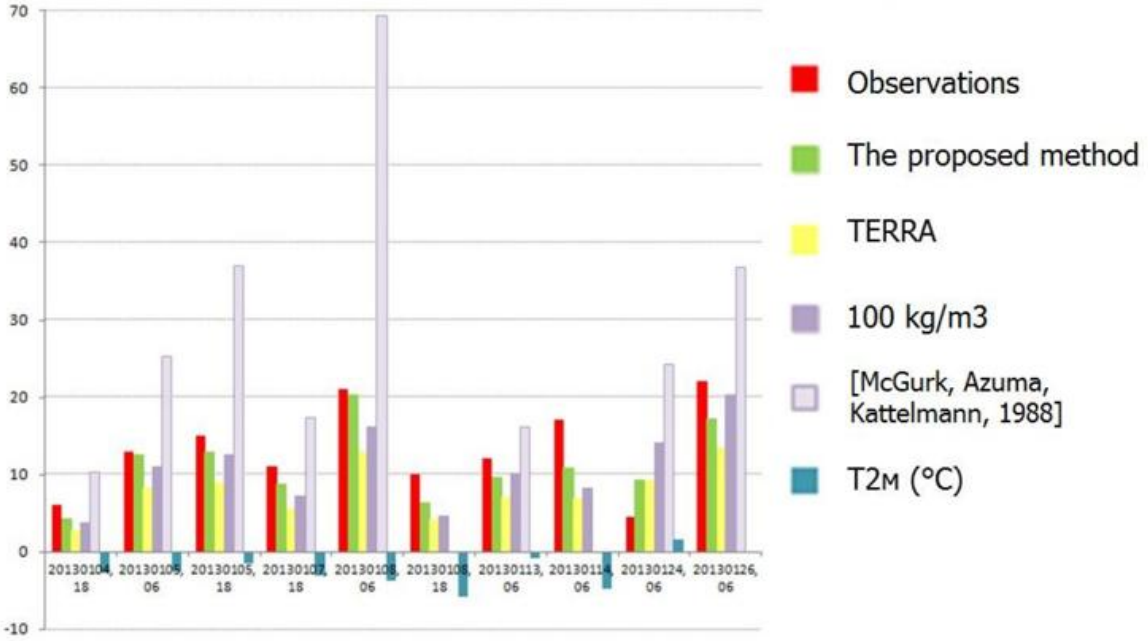


Figure 15: Fresh snow depth (cm) is coloured as: red observations at station Gornaya Karusel, light green results of proposed method using T2m (° C), yellow using formula from TERRA of the COSMO-model, violet under the assumption of the constant fresh snow density value of 100 kg/m^3, light violet according to linear dependency on T700. In blue T2m values (° C) are shown

From a network of observation stations and reports of road services in Moscow numerical experiments an assessment of the proposed method results in case of heavy snowfall in Central Russia at 3-4 February, 2013 was conducted. In particular, information of road services helped to take into account the increment of snow depth up to 25 cm, not recorded in the standard reports in SYNOP code. The latter indicated the snow depth growth only by 13 cm. Standard observations are done once a day, however, during this period snow had compacted. Calculated by COSMO-Ru7 prognostic values of accumulated snow were a little bit less than 12-hour observations (19.2 and 25.0 mm, respectively). According to the proposed method on the basis of observed 12-hour precipitation sums recalculation, fresh snow depth estimations of 25.2 cm were obtained (which corresponded the reports of road services). The research showed applicability of the method and its greater efficiency in case of using of accurate needed initial data of accumulated precipitation and air temperature when they were fallen.

5.3.2 COSMO-model fresh snow depth output

Prior to start of winter Olympic Games Sochi-2014, a prognostic maps of fresh snow depth were being produced since 3 February 2014 at Hydrometcenter of Russia on the basis of forecasts of accumulated precipitation provided by different versions of COSMO-Ru model with grid resolution of 7 km (COSMO-Ru7), 2.2 km (COSMO-Ru2) and 1.1 km (COSMO-Ru1). Maps were formed according to operational forecasts starting at 00, 06, 12 and 18 UTC.

Also values of fresh snow depth were recorded in meteograms for stations situated in North-Caucasian region. Prognostic values were calculated taking height-corrected air temperature into consideration.

The technological branch of fresh snow postprocessing and its output in the framework of COSMO-Ru system postprocessing are shown in Fig.16.

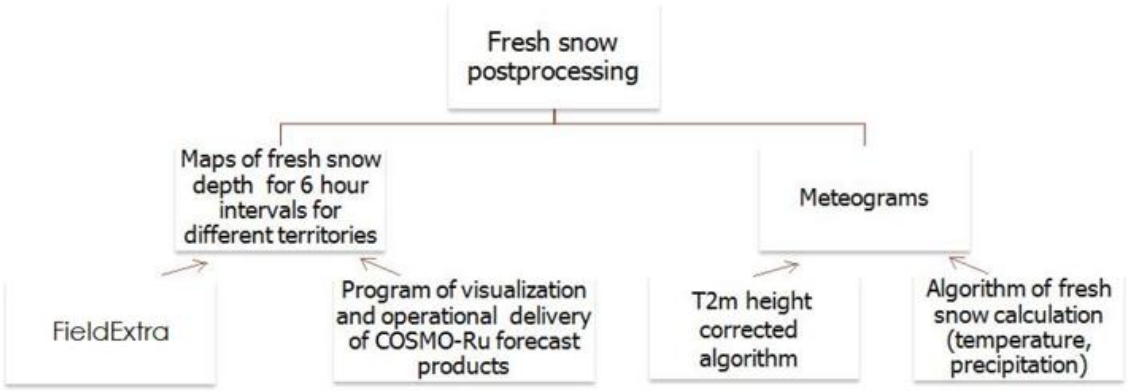


Figure 16: The scheme of fresh snow depth calculation at Hydrometcenter of Russia (based on mesoscale model COSMO-Ru)

Output in form of meteograms for stations and maps of fresh snow depth for 6-hour intervals prepared for versions COSMO-Ru7, COSMO-Ru2 and COSMO-Ru1 four times a day with the use of FieldExtra.

Fig.17 shows that there are significant differences in calculations using different COSMO-model versions.

The fact that relief detailing and its model heights for this region turned to be principle for precipitation phase prediction, large elevation and temperature extremes are observed. The relief is smoothed for coarser model resolution (COSMO-Ru7) and larger area with negative air temperatures occurred in comparison with more detailed modeling (COSMO-Ru2, COSMO-Ru1), where definition of relief led to more accurate description of extended valleys and relatively small highlands regions, for which snow falling was typical. In addition testing done in (Shatunova, Rivin, 2013) indicated to lower precipitation sums formed by COSMO-Ru1 in comparison with COSMO-Ru2.

5.3.3 Results of fresh snow depth calculation implemented into COSMO-Ru system postprocessing

Maps of fresh snow depth and meteograms were used for initial quality estimation of work of the proposed system as well as hourly measurements from AMS situated at different levels on

the mountain resort Roza Khutor and daily measurements from three HMS (Aibga, Kordon Laura, Gornaya Karusel-1500) located in the region of winter Olympic Games Sochi-2014.

Complexity of testing realization was determined by several factors: firstly, snowfalls were observed only several times during winter season 2013/2014; secondly, model data could be compared with measurements only at some stations.

During winter Olympic Games Sochi-2014 there were three cases with significant snowfalls: 17-19 February, 21 February and 26-28 February. The main peculiarities in fresh snow depth reproduced by COSMO-Ru in the region of winter Olympic Games Sochi-2014 are described below.

Preliminary results demonstrated significant variability of snowfall forecasts for the same period started at different time and the latest forecast was not always the best in comparison with forecasts started before. Based on quite detailed analysis of time-distribution intensities inside snowfall period its turned out to be impossible to conclude which forecast with what lead time is more successful, and which forecast is more accurate: obtained by model versions with resolution of 2.2 km or 1.1 km. Yet in general the best agreement with snowfall measurements was observed in case of all realizations averaging.

Comparison with similar calculations found at website www.snow-forecast.com (www.snow-forecast.com) showed systematic underestimation of represented fresh snow values and results are more close to reality calculated by COSMO-Ru1 and COSMO-Ru2 systems. Example of analysis of one snowfall case according to observations at Roza Khutor is shown in table 6.

Table 6: Fresh snow depth (cm) according to observations at AMS Roza Khutor 4, forecasts from COSMO-Ru2 and COSMO-Ru1 and data from publically available website, produced by WRF model, www.snow-forecast.com. 18 February 2014

Observations	Forecast start (day hour)						Website data
	mean	17 00	17 06	17 12	17 18	18 00	
	COSMO-Ru2						
28.2	27.6	30.0	39.5	22.1	25.4	21.3	12.0
	COSMO-Ru1						
28.2	23.8	17.0	24.9	40.8	19.9	16.8	12.0

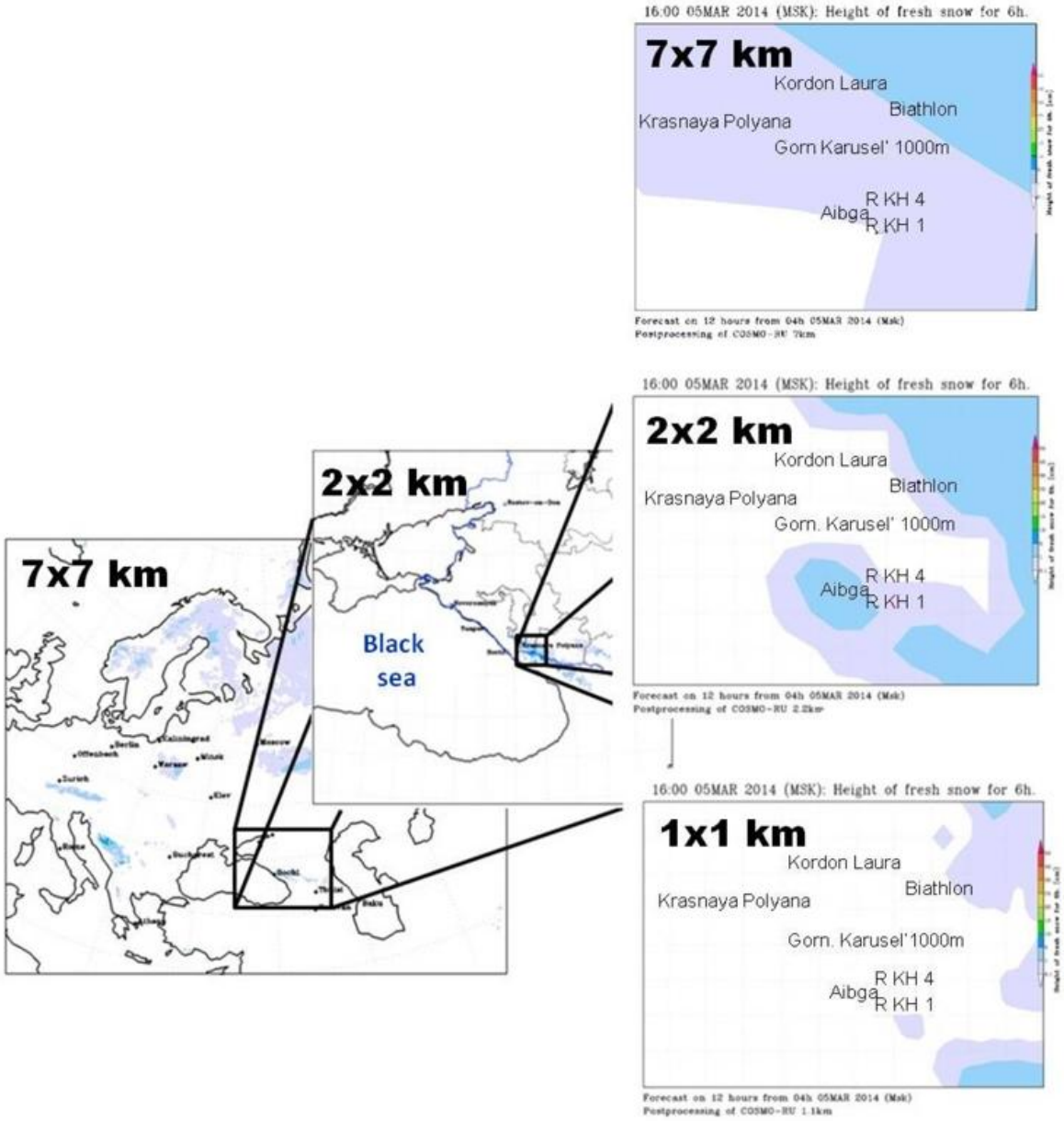


Figure 17: 12h-forecasts of fresh snow fallen for the last 6 hours according to COSMO-Ru7, COSMO-Ru2 and COSMO-Ru1. Start — 00 UTC 5 March 2014)

The proposed system gives more successful fresh snow depth forecast with account of height-corrected air temperature against the case of using air temperature received from standard version of COSMO-Ru model (the example is shown in Fig.11 (see Section 5.2.2 for station Aibga).

Maps of fresh snow depth can be created for any territory which coincides with the calculated grids of COSMO-Ru model versions (Fig.17). For example, it is true for the region, which include most part of the European territory of Russia. Meteograms containing fresh snow depth forecasts were prepared in January-March 2014 for North-Caucasian region for the purpose of specifying this meteorological element at points (stations). Analogous meteograms with fresh snow depth data can be obtained for stations located in other regions.

The testing showed that the developed system reproduces fresh snow depth quite realistically.

Note that COSMO-Ru provides the fact of precipitation falling in form of snow reliably, but quantitative estimations depend on forecast interval.

5.3.4 Conclusions

Thus, the system of prediction of fresh snow depth in the framework of COSMO-Ru post-processing is developed and realized at Hydrometcenter of Russia. The system includes preparation of fresh snow depth maps for 6-hour intervals four times a day according to model versions with the resolutions of 7, 2.2 and 1.1 km. Additionally, the fresh snow forecasts for stations are provided as meteodrams. Preliminary analysis of snowfalls occurred in North-Caucasian region in February 2014 showed that COSMO-Ru output connected with fresh snow characteristics could be used in weather forecasting. This output was used by weather forecasters in the framework of meteorological support of winter Olympic Games Sochi-2014, in particular for completion of daily bulletins and competitions planning.

5.4 Verification of COSMO forecasts for the Sochi-2014 region *(A. Bundel, A. Muravev, D. Blinov, A. Kirsanov)*

Verification of weather forecasts was one of the most important components of Sochi-2014 Winter Olympics and Paralympics meteorological support. The Sochi region has complex terrain with the Black Sea in close proximity. Information of high spatial and temporal resolution was required for competitions. These factors made more challenging both forecasting itself and verification and required development of new approaches.

5.4.1 Verification tools

Most of the scores were calculated in VERSUS (VERification System Unified Survey), an official COSMO verification tool. Several FROST online verification tools were used: FROST online monitoring of forecast quality only for stations, and FROST Point forecast and diagnostic data viewer. For some tasks, MET tool was used.

5.4.2 Verification problems

A dense observational network is needed for reliable verification. A number of automatic weather stations were installed in the regions of Games. However, their number was not sufficient for application of some verification methods. The stations are clustered. Even several 1-km grid points could be the nearest to certain station (Fig.18). For statistically reliable conclusions, long time series of data are necessary, while some models and verification tools became available just before the Games (for example, COSMO-Ru1 only at the end of January).

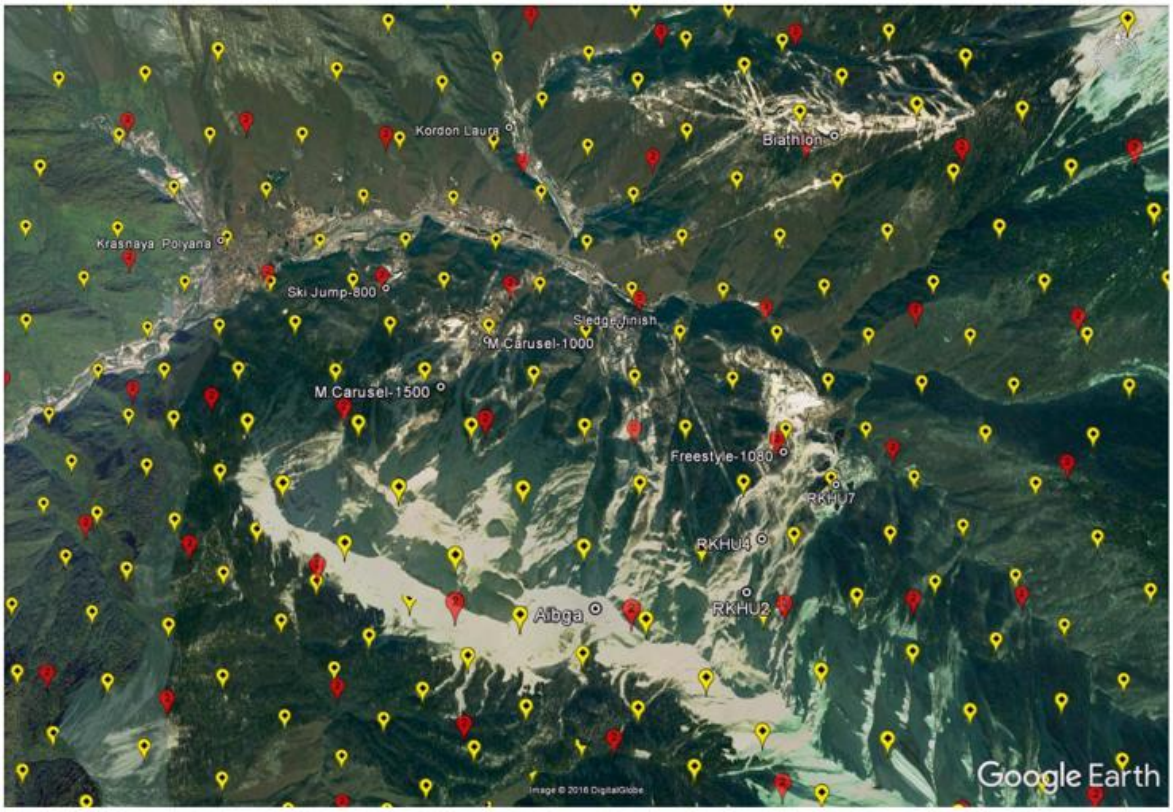


Figure 18: Nearest point approach: COSMO-RU2 (red lamps) and COSMO-Ru1 (yellow points) — models grid points and weather stations (superscripted)

5.4.3 Verification over the test periods and during the official evaluation period of the Games of 2014

Deterministic verification

Deterministic forecasts of COSMO-Ru7, COSMO-Ru2, COSMO-Ru1 systems were verified. The evaluation period was 15 January — 15 March, 2014. Various continuous and categorical metrics were applied to near-surface temperature, dew point temperature, relative humidity, wind speed, wind direction, wind gusts, and 3-hour accumulated precipitation.

Period of the Games was anomalously warm, the COSMO models, like most models providing forecasts for Sochi-2014, underestimated surface air temperature (in particular, during the daytime). The underestimation is more pronounced during the clear sky conditions compared to overcast ones. The likely cause of this behavior is insufficient soil warming in the sunny weather.

For the COSMO model family, the effect of resolution enhancement was especially notable for wind speed and gusts (Fig.19, Fig.20). COSMO-Ru7 is worse overall. T2m and dew point temperature were better in COSMO-RU2. Traditional scores aggregated over the Sochi region show overall prevalence of COSMO-Ru2 with relation to COSMO-Ru7 and COSMO-Ru1. However, some cases of intense precipitation and visibility were better predicted by COSMO-Ru1 during the period of Games. That coincides overall with subjective forecasters' opinion that among the five COSMO based models/ensembles, COSMO-Ru2 is perhaps the best.

The best precipitation forecasts were made during the late afternoon (16–19 h local time) according to the Pierce Skill score.

The spatial methods are needed to better analyze the effect of high resolution of precipitation (and some other variables, e.g., wind characteristics). These methods applied to the Sochi-2014 archive are explored within the relevant PP INSPECT tasks.

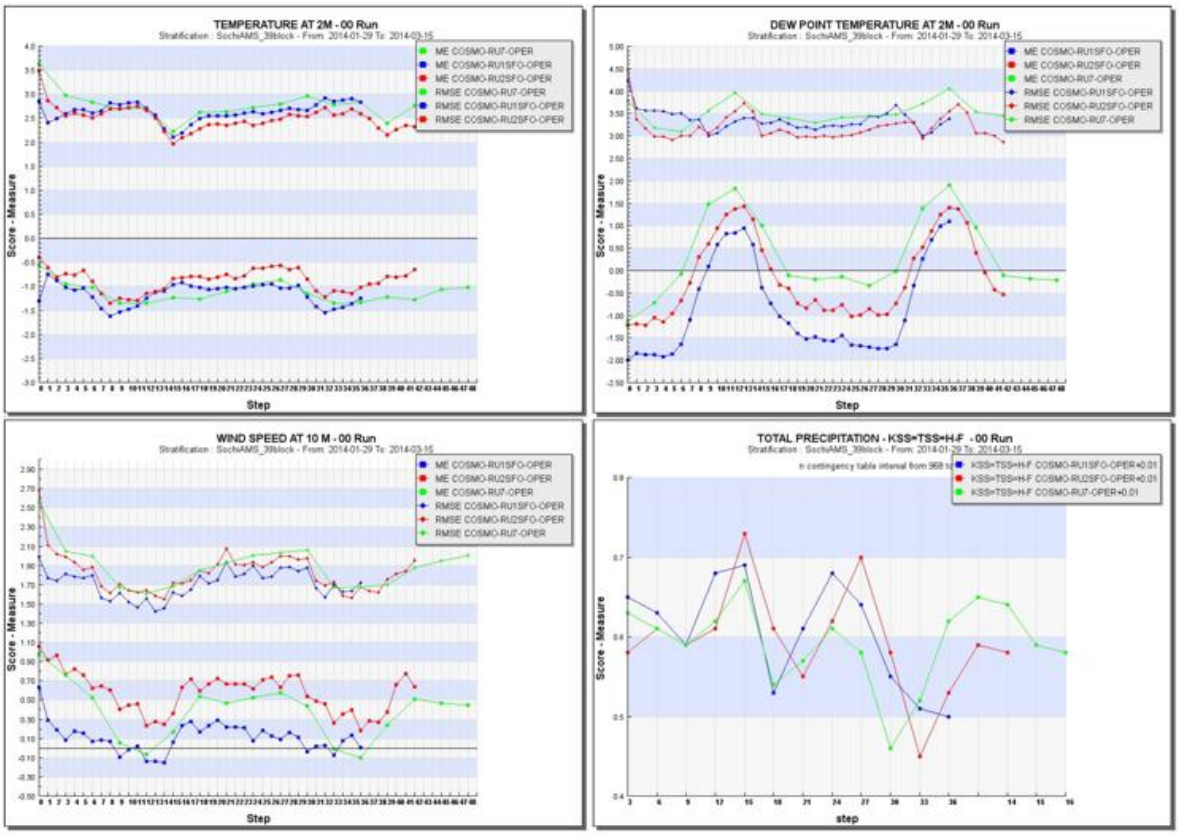


Figure 19: Scores for COSMO-Ru1, COSMO-Ru2, and COSMO-Ru7, 29 Jan–15 March 2014

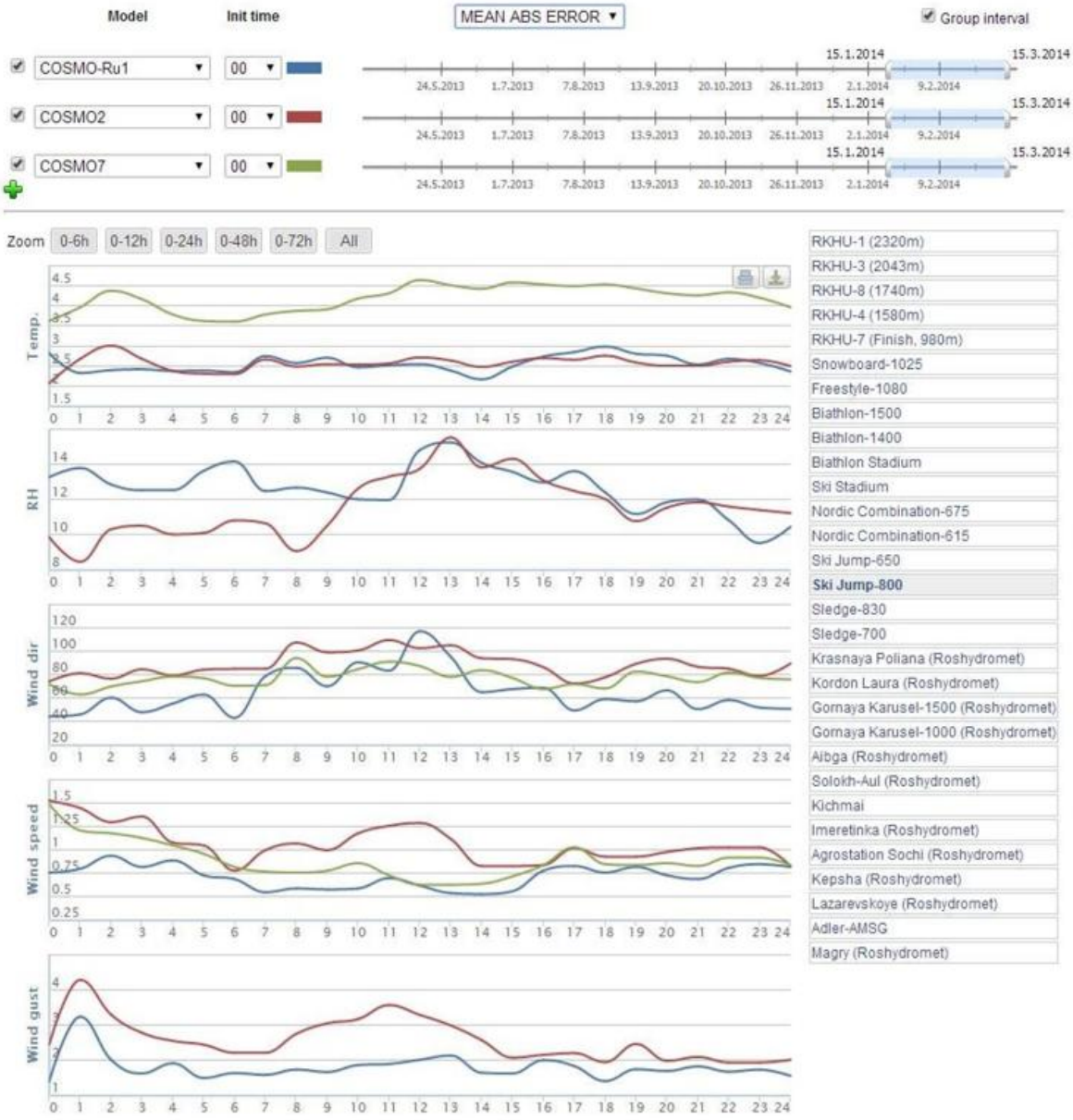


Figure 20: Effect of resolution, COSMO-Ru1, COSMO-Ru2, and COSMO-Ru7, 15 Jan–15 Mar 2014. Ski Jump-800 station

The dependence of COSMO forecast skill on the driving model (either ECMWF-IFS or DWD-GME) was found limited (study of Andrea Montani).

Analysis of test periods

Thorough verification of past seasons is important for the development of models and new methods. Analysis of COSMO-Ru performance during the previous test seasons revealed that the model bias could change its sign from one cold season to another depending on the prevailing weather regimes (Fig.21). It is still unclear, is it due to 2013 warm anomaly, or observation data distribution, amount, and quality? Therefore, it was found difficult to make model calibration.

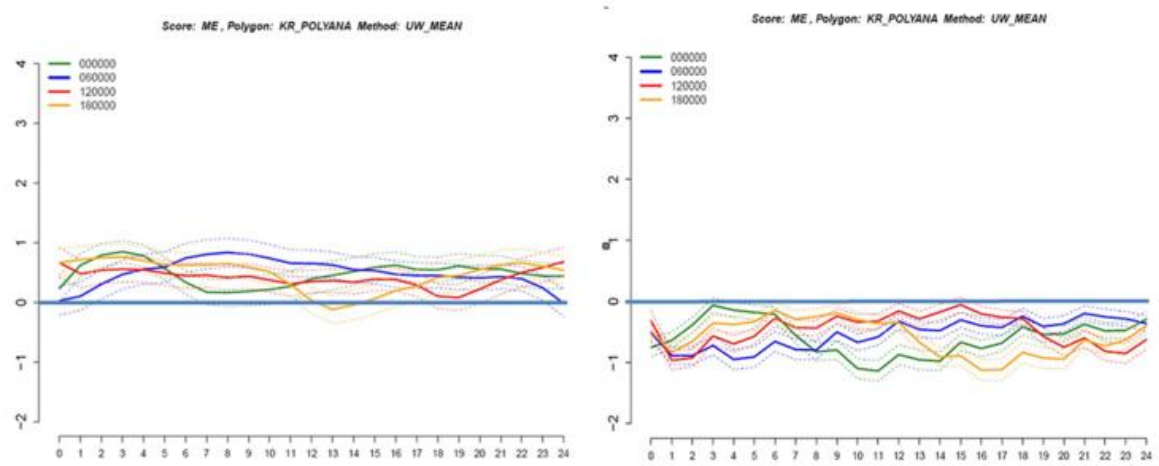


Figure 21: COSMO2Ru T2m mean error during the first test period (winter 2012–2013) (left panel) and the second test period (Jan–Feb 2014) (right panel) (all initial times) at Krasnaya Polyana station

Diagnostic verification

"It is advisable in verification projects to examine the data before computing the scores. This can be done by means of scatter plots and quantile-quantile plots, or, for categorical data, by histograms" (Recommendations of **"Suggested methods for the verification of precipitation forecasts against high resolution limited area observations"** by the JWGFVR for the WGNE (Laurie Wilson, Beth Ebert et al.)

A station-based diagnostic verification tool for thorough diagnostic analysis was created for the Sochi-2014 project. It is "diagnostic"in the sense that it focuses on the fundamental characteristics of the forecasts, the corresponding observations, and their relationships (A. Murphy, B. Brown, Y. Chen, 1989). Figure 22 shows an example of diagnostic verification plots. On the right-hand bottom plot, the red lines denote maximum, mean, and minimum observed value for each forecast bin. Green lines denote 75, 50, and 25 % quantiles for the bin sample volume of no less than 10 pairs (sample stability). Such plots were made for each variable, station, lead time, and method. They show the forecast errors in the whole variable range including the distribution tails, that is, extreme values important for decision making about the competitions; show the sample size in different categories and outliers. The interquantile range values are inversely related to forecast accuracy.

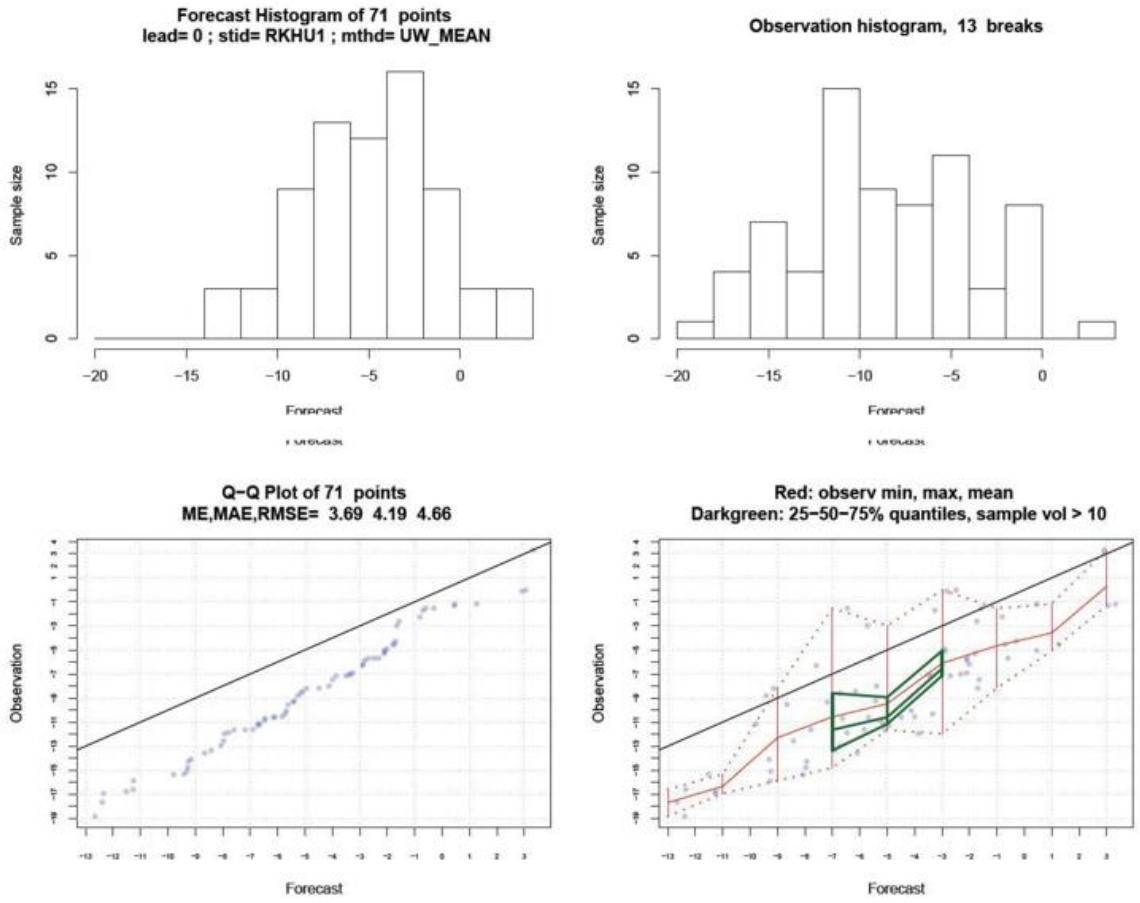


Figure 22: An example of diagnostic verification plots

High Impact Weather (HIW) verification

HIW definitions can be prescribed by value thresholds given by authorities or statistically determined by extreme values or distribution tail statistics.

Traditional scores become insensitive to changes in accuracy for low base rates (rare events) (base rate is the frequency of occurrence of the event in the verification sample). For example, the PSS becomes 0 with the base rate diminishing. There is increasing uncertainty about the quality (sample effect, jumping score values) *(J.Jolliffe, D.Stephenson)*. It was shown (Ferro and Stephenson 2011) that the extremal dependency index (EDI) and symmetric extremal dependency index (SEDI) are insensitive to base rate; they also are both formulated to use the hit rate (H) and false alarm rate (F) only, which links these scores to the Pierce Skill score (H-F) and the ROC curve frequently used in verification of probability forecasts.

$$EDI = (logF - logH)/(logF + logH)$$

The EDI is especially recommended for low base-rate thresholds, but it will give a good comparative estimate of accuracy for all thresholds. These scores were applied to the Sochi-2014 data. The dependence of EDI, PSS, and base rate on precipitation threshold is shown in Fig.23.

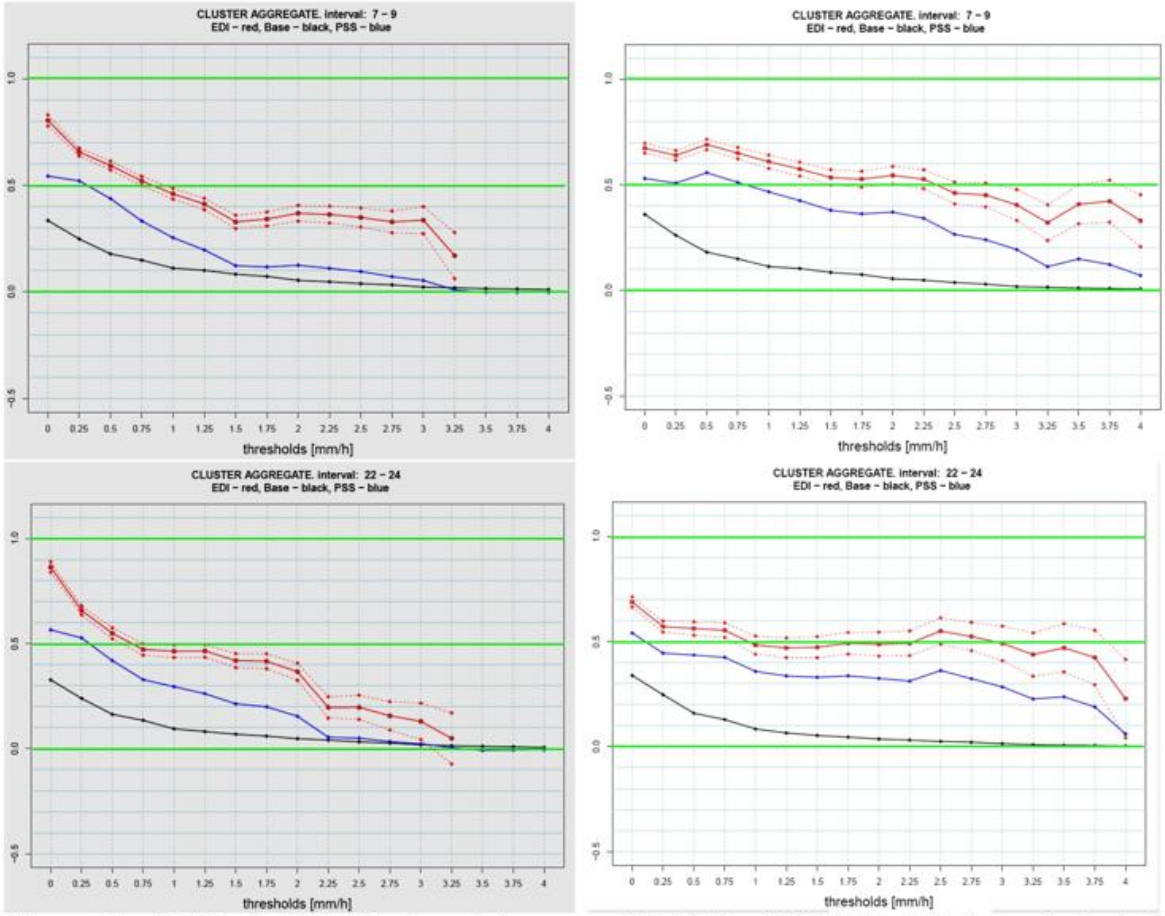


Figure 23: EDI (red), PSS (blue), and base rate (black) for COSMO-Ru2 (left panel, shaded) and NMMB (right panel) 3h precipitation, nearest point, Jan–March 2013, Mountain cluster

Figure 23 shows that:

- There are 10 % of events higher than 1 mm and 5 % , higher than 2 mm;
- $EDI > PSS$ (Pierce Skill Score);
- COSMO predicts better precipitation fact, NMMB predicts better more intense precipitation.

The similar graphs were made for temperature and wind speed.

The study on EDI application showed that:

- EDI is appropriate but not universally applicable (failure with wind speed);
- EDI does not always converge, often it reflects a combination of model, observation and sampling errors;
- EDI is generally not monotonic with relation to PSS (Fig.24);
- EDI is always greater than PSS for positive PSS (Fig.25).

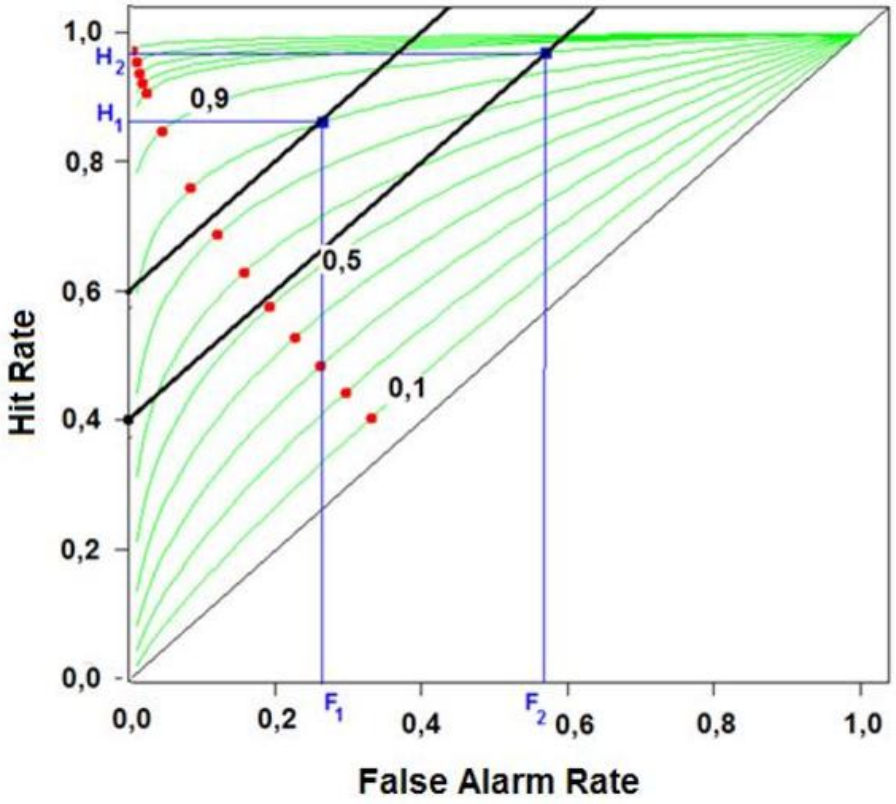


Figure 24: EDI (green) and PSS (black) isopleths; EDI for 0.1 – 0.9 and 0.95 – 0.99 with intervals 0.1 and 0.01; $PSS = H - F$ for 0.4 and 0.6 values; $H = F$ diagonal corresponds to $EDI = PSS = 0$.; Red points: EDI curves tangent to straight PSS lines (strict formulas). Blue squares at (F,H): the monotonic EDI and PSS relation breaks down: Nonlinear dependence — not STRICTLY monotonic: for $(F1, H1)$ and $(F2, H2)$ $PSS1 > PSS2$, but $EDI1 < EDI2$



Figure 25: Relation between EDI minimum value and PSS

5.4.4 Conclusions and prospect for the future

- Nearest point approach in the complex terrain
- Different seasons and model changes calibration difficulties
- Weather dependent verification much effort, but it turned out difficult to give exact instructions to forecasters because of insufficient data and calibration difficulties
- More Conditional verifications are needed

The spatial methods are needed to better analyze the effect of high resolution of precipitation (and some other variables, e.g., wind characteristics). These methods applied to the Sochi-2014 archive are explored within the relevant PP INSPECT tasks.

Overall, the findings of objective verification agree with subjective opinion of Sochi forecasters.

6 Development and adaptation of COSMO EPSs for the Sochi region *(D. Alferov, E. Astakhova, C. Marsigli, A. Montani, T. Paccagnella, G. Rivin, A. Shcherbakov)*

The Sochi region belongs to the moderately humid subtropical zone and is influenced by the non-freezing Black Sea and by the spurs of the Main Caucasus Range. The necessity of weather forecasting at Olympic venues located both in the coast and in the mountains, quite steep and intersected by multiple shallow canyons, made meteorological support of the Sochi-2014 Olympics rather complicated effort. A state-of-the-art approach to mountain weather forecasting implies the application of high-resolution modeling, nowcasting and ensemble technologies. Reasoning from this, the ensemble component was included to the CORSO project as task 3.

The goal of task 3 was to demonstrate the capabilities of ensemble systems in numerical weather prediction in a mountainous region with complex orography and to assess the effect of practical use of ensemble products during Sochi-2014 Olympic Games. To achieve this goal, two activities were planned:

- adaptation of COSMO-LEPS 7 km to the Sochi region and to specific requirements of winter Olympics; operational ensemble forecasts during the Olympics;
- development and verification of a convective-resolving EPS for the Sochi region (with ICs and BCs from the 7-km EPS).

As a result, the two ensemble prediction systems based on COSMO model were developed: COSMO-S14-EPS with a 7-km resolution (a relocation of COSMO-LEPS to the Sochi region) and COSMO-Ru2-EPS with a 2.2 km resolution (nested to COSMO-S14-EPS). Both systems ran in operational mode during the Olympics; the probabilistic products were regularly delivered to Sochi forecasters. Analysis of regular runs, their application, and case studies demonstrated that ensembles gave a valuable support to forecasters and the higher-resolution ensemble gave more detailed and precise forecasts.

The following sections give the description of the systems, survey their application during the Olympics and present the analysis of EPS performance.

6.1 Ensemble prediction system with a 7-km resolution

A system with a 7-km grid size named COSMO-S14-EPS (S14 stands for Sochi-2014) was created at ARPA-SIMC (Montani et al., 2013, 2014) and is a version of the COSMO-LEPS system displaced from the European area to the Sochi region. COSMO-LEPS has been operationally running for more than 10 years and demonstrated good results, in particular, for regions with complex orography (Marsigli et al, 2003; Montani et al., 2011).

Methods and approaches used in COSMO-LEPS and COSMO-S14-EPS are similar. The boundary and initial conditions came from the global ensemble system of the European Centre for Medium Range Forecasting (ECMWF-EPS, (Molteni et al, 1996)). The facts that the horizontal resolution should be higher in limited-area forecasts and the time for preparing operational forecasts should be minimal combined with usually limited computer resources lead to the necessity to reduce the ensemble size. It was done by selecting the most representative prognostic realizations of the global ECMWF-EPS via clustering (48-72 hour forecasts of geopotential, wind components, and humidity at 500, 700, and 850 hPa

were considered) (Molteni et al, 2001; Montani et al, 2013). The prognostic realizations of the global EPS chosen by this procedure were then interpolated to the grid of the mesoscale model COSMO (see http://www.cosmo-model.org) and served as initial and boundary conditions for limited-area forecasts. No additional regional perturbations were introduced. The most essential differences between the COSMO-S14-EPS and COSMO-LEPS systems were integration domains (the Sochi region or Europe) and ensemble sizes (10 or 16 members, respectively).

The lower boundary condition for all COSMO-S14-EPS members was taken from COSMO model runs in hindcast mode (short-range forecast nested on ECMWF analyses).

The model-related uncertainty was taken into account in COSMO-S14-EPS by using two different convection parameterization schemes (Tiedtke or Kain-Fritsch, random choice) in different members and also by varying tuning coefficients in parameterizations of sub-grid scale processes (in particular, turbulent).

The main characteristics of COSMO-S14-EPS are summarized in Table 7, which also reports some details relative to the global ensemble ECMWF-EPS.

Table 7: Main features of the present implementations of ECMWF-EPS, COSMO-S14-EPS, and COSMO-Ru2-EPS

	ECMWF-EPS	COSMO-S14-EPS	COSMO-Ru2-EPS
Hor. res. Vert. res.	$\sim 31\ km$ 62 ML	7 km 40 ML	2.2 km 50 ML
Forecast length	240h	72h	48h
Ensemble size	50+1	10	10
Initial time	00/12 UTC	00/12 UTC	00/12 UTC
Convection	Parameterized	Parameterized	Resolved
Running at	ECMWF	ECMWF	Roshydromet
ICs and BCs	SV ini pert + EDA	from selected ECMWF-EPS members	from COSMO-S14-EPS members
Model perturbations	Stochastic physical tendencies + backscatter	Physical parameterizations	

COSMO-S14-EPS was implemented on ECMWF supercomputers in November 2011 and ran on a regular basis from 19 December 2011 till mid-May 2014 thanks to the billing units provided by the ECMWF Special Project SPCOFROST.

6.2 Ensemble prediction system with a 2.2-km resolution

The experience of projects initiated by WWRP before the Olympic Games in Beijing in 2008 and Vancouver in 2010 (B08RDP and SNOW-V10) (Duan Y. et al, 2012; Isaac G. A., 2012), as well as of the MAP D-PHASE project (Rotach M. W. et al, 2009) demonstrated that good descriptions of meteorological processes and forecasts of severe events in the regions with complex mountainous relief can be achieved only with high-resolution models (with resolution not coarser than 2–3 km). This is because of more accurate orography data used in such models, fine resolution enabling to simulate local events, and switched off convective parameterization. It is worth to note that development of convection-permitting ensemble

prediction systems (with a grid size of 2–3 km) is in the mainstream now.

The ensemble prediction system COSMO-Ru2-EPS was created as a research tool and is based on the COSMO-Ru2 model version (Rivin et al, 2015) with a resolution of 2.2 km. The initial and boundary conditions were interpolated from COSMO-S14-EPS forecasts. The boundary conditions were refreshed every hour.

COSMO-Ru2-EPS and COSMO-S14-EPS had the same ensemble size. No additional model perturbations were introduced. Thus, COSMO-Ru2-EPS performed a dynamical downscaling of COSMO-S14-EPS increasing the forecast resolution both in horizontal (from 7 to 2.2 km) and in vertical (from 40 to 50 levels). The COSMO-Ru2-EPS system was implemented on a Roshydromet computer SGI Altix 4700.

The main features of COSMO-Ru2-EPS are summarized in Table 7 along with the features of ECMWF-EPS and COSMO-S14-EPS. The organization of COSMO-based ensemble forecasting for the Sochi region is sketched in Fig.26.

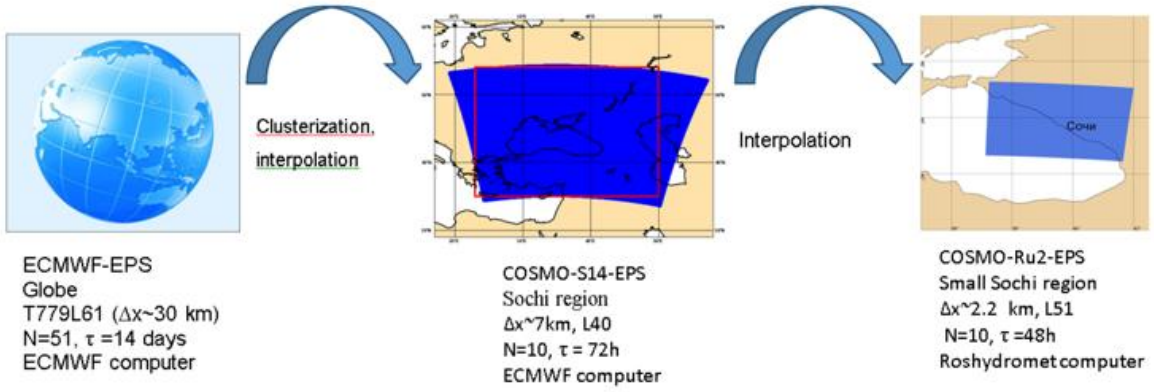


Figure 26: Organization of COSMO ensemble forecasting for the Sochi region. N is the ensemble size, τ is the forecast length, and L is the number of vertical levels

Figure 27 reports the orography for three systems of Table 7 and is meant to indicate the potential impact of increased horizontal resolution in the description of orographic and mesoscale-related processes.

The ECMWF-EPS orography (top-left panel) shows almost no evidence of the valley running for about 40 kilometres from Sochi-Adler, the coastal cluster of the winter Olympics 2014, where ice-sport competitions took place, towards Krasnaya Polyana, located in the mountain Olympic cluster where snow-sport competitions were held. COSMO-S14-EPS (top-right panel of Fig.27) already offers a better description of the complex topography of the area, although it has to be pointed out that only with the 2.2 km grid-size of COSMO-RU2-EPS (bottom panel) some important details of the geography (e.g. the eastward turn of the valley after Krasnaya Polyana) can emerge.

6.3 Providing ensemble forecasts for the Sochi Olympics and preceding trial competition

The COSMO-S14-EPS products were accessed by the Hydrometcenter of Russia since the end of 2011. These mesoscale ensemble forecasts for the Sochi region were the first for Russian forecasters. During the following three pre-Olympic years all technology problems were solved (in particular, the earlier time of forecast accessibility was achieved) and tools

for presenting the COSMO-S14-EPS probabilistic information were developed. The most important was that forecasters got a valuable experience of working with this information. Therefore, it is not surprising that COSMO-S14-EPS probabilistic forecasts were most widely applied among all ensemble forecasts prepared within the FROST-2014 project (the blended RDP/FDP project devoted to the Olympics 2014) and available to forecasters during the Olympic Games in Sochi.

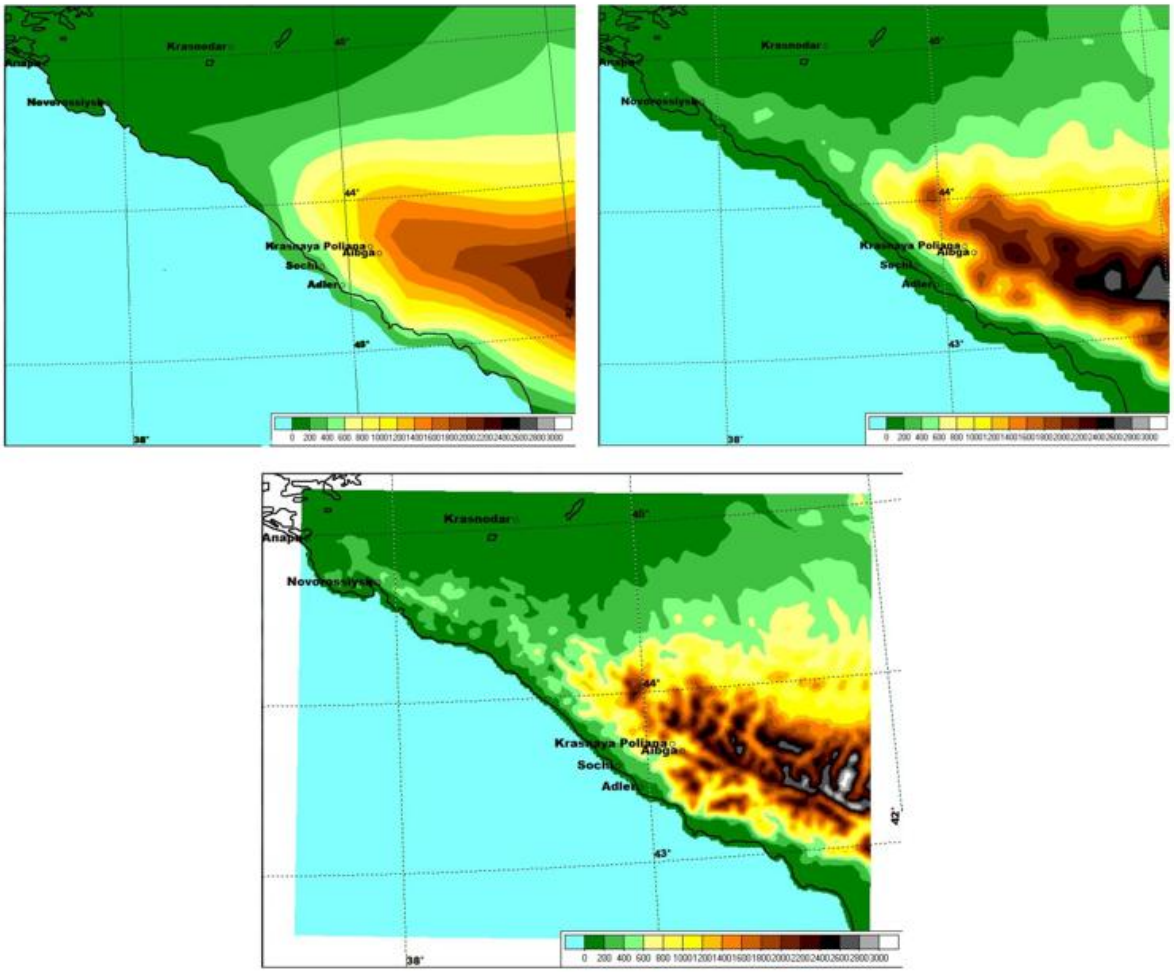


Figure 27: Model orography (in m) for ECMWF-EPS ($\Delta x = 31\ km$, top-left panel), COSMO-S14-EPS ($\Delta x = 7\ km$, top-right panel) and COSMO-RU2-EPS ($\Delta x = 2.2\ km$, bottom panel) in the Olympic region

COSMO-S14-EPS generated a set of standard probabilistic products, including probability of surpassing a threshold, ensemble mean and ensemble standard deviation for several surface and upper-air variables. These products were delivered in real time to the Hydrometcenter of Russia (Roshydromet), further disseminated to Sochi forecasters and presented at the FROST-2014 Web-site (http://frost2014.meteoinfo.ru, authorization required)). In addition to this, all forecast members for a specially defined area were transferred to Roshydromet where the epsgrams for predetermined points were prepared (see http://frost2014.meteoinfo.ru/forecast/arpa-new). Generation of different types of non-graphical products made use of Fieldextra, the official COSMO post-processing software (for information about Fieldextra, please refer to http://www.cosmo-model.org). The graphical products were prepared using the GRADS package.

In addition to the ensemble products, initial and hourly-boundary conditions (up to t+48h) were provided to Roshydromet for the experimentation with the convection-resolving ensem-

ble COSMO-Ru2-EPS (see below). Some examples of COSMO-S14-EPS products provided to Sochi forecasters during the Olympics are presented in figs.28 and 29. (Note that initially the system was named COSMO-FROST-EPS and this title was kept in the operational plots to avoid confusion).

In addition to the ensemble products, initial and hourly-boundary conditions (up to t+48h) were provided to Roshydromet for the experimentation with the convection-resolving ensemble COSMO-Ru2-EPS.

First it was not planned to use COSMO-Ru2-EPS for the meteorological support of the Olympics. However, the analysis of COSMO-Ru2-EPS skill during the winter of 2012/13 demonstrated the usefulness of the system and confirmed that the high resolution enables more detailed information (without loss of quality) to be achieved about the future state of the atmosphere. Thus it was decided to run COSMO-Ru2-EPS operationally in winter-spring 2014 and disseminate the prognostic results to the Olympic forecasters. COSMO-Ru2-EPS ensemble meteograms and plume diagrams were regularly posted at the FROST-2014 site and refreshed twice a day. A 2m temperature was corrected for the difference between the heights of model gridpoints and the real heights of the stations using the prognostic temperature lapse rate (see the description of CORSO task 2 for more details).

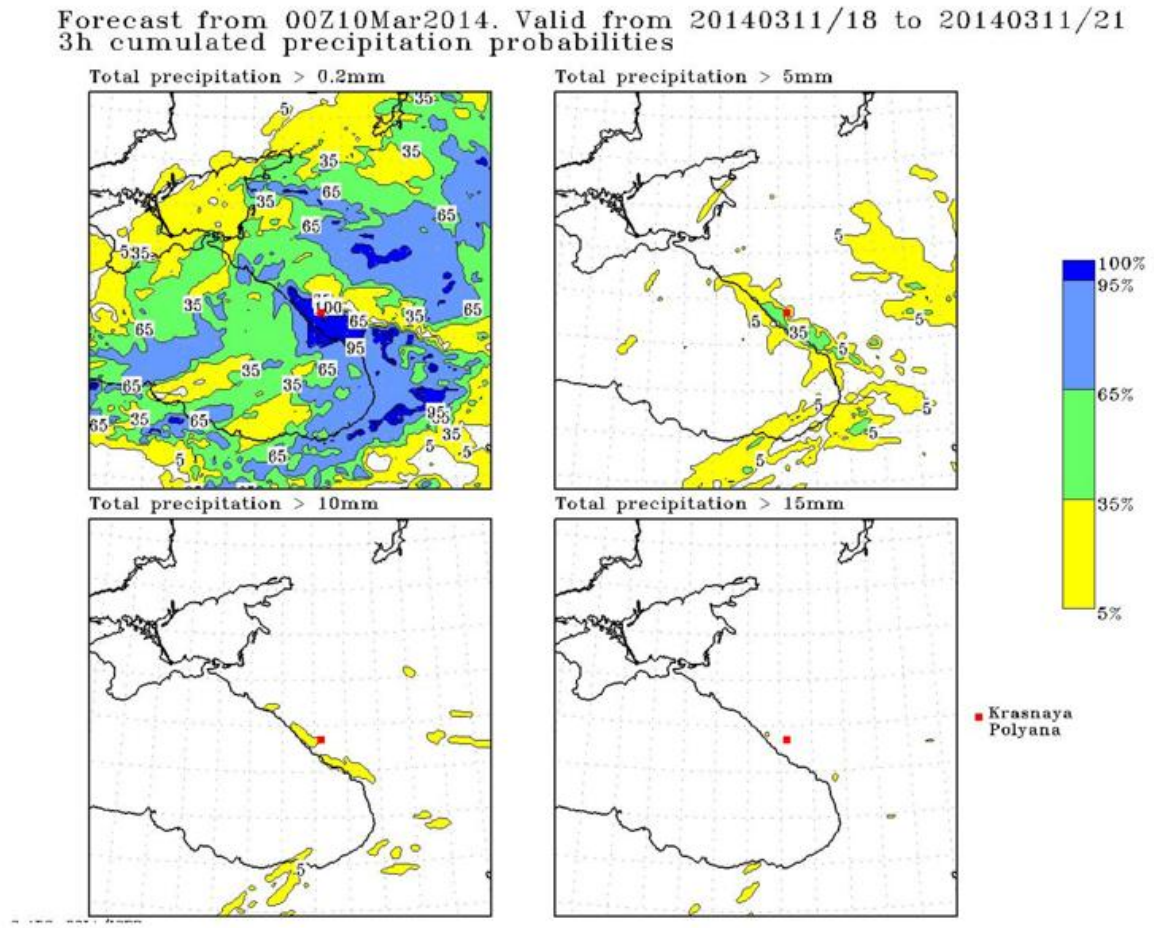


Figure 28: An example of COSMO-S14-EPS products operationally provided to the Olympic forecasters: probabilities of the events "3-h cumulated precipitation is more than 0.2 (upper left panel), 5 (upper right panel), 10 (lower left panel), and 15 mm (lower right panel)". COSMO-S14-EPS 45-h forecast starting from 10 March 2014, 00 UTC. A red square indicates the location of Krasnaya Polyana

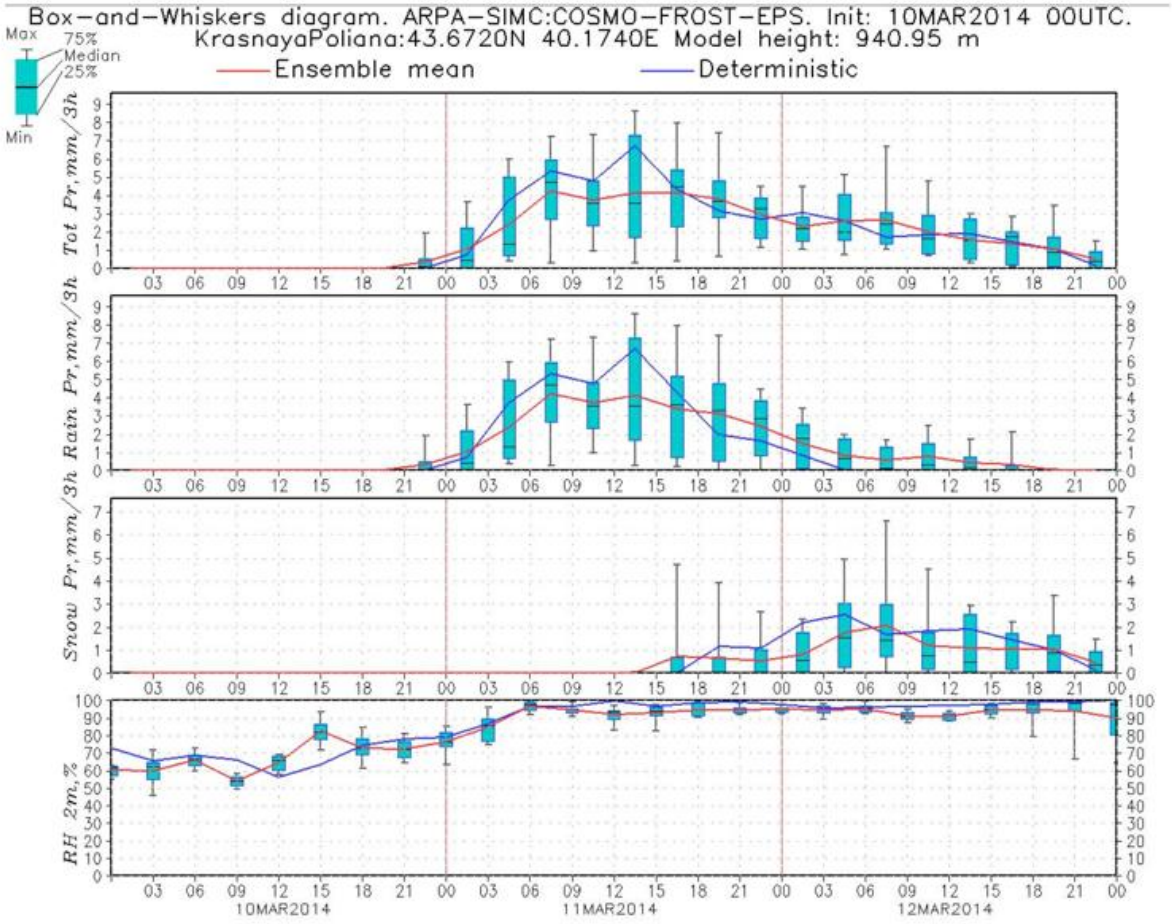


Figure 29: An example of COSMO-S14-EPS products operationally provided to the Olympic forecasters: the ensemble meteograms for total precipitation, rain, snow, and 2-m relative humidity for the Krasnaya Polyana station

6.4 Skill of ensemble forecasts *(E. Astakhova, A. Bundel, A. Muravev)*

The skill of the ensemble systems developed was analyzed step by step in several ways. First, the skill of COSMO-S14-EPS was compared to that of the driving ECMWF-EPS system and it was demonstrated that the mesoscale EPS outperforms the global system. Then several case studies with mesoscale EPSs of both resolutions were made showing the correct representation of near-surface temperature and precipitation patterns including the precipitation phase. Finally, probabilistic verification scores were calculated for month or longer periods. The details are given hereafter.

6.4.1 Verification of COSMO-S14-EPS compared to ECMWF-EPS

The skill of the mesoscale ensemble COSMO-S14-EPS was assessed over the period JanuaryMarch 2012 and compared to that of ECMWF EPS. For both systems, the probabilistic prediction of 12hour accumulated precipitation exceeding a number of thresholds for several forecast ranges was considered. Only forecasts starting at 12 UTC were examined.

As for observations, it was decided to use the data obtained from the SYNOP reports available on the Global Telecommunication System (GTS), since this was recognized to be a

homogeneous and stable dataset throughout the verification period. In order to quantify the skill of the system over complex topography, the verification was performed over the domain 40N50N, 35E45E. Within this domain, a xed list of 60 SYNOP stations was considered and the relative reports in terms of total precipitation were used to evaluate the COSMOS14EPS and ECMWF-EPS skill.

As for the comparison of model forecasts against SYNOP reports, the gridpoint closest to the observation was selected. Little sensitivity to the results was found when, instead of the nearest gridpoint, a bi-linear interpolation using the 4 nearest points to the station location, was used to generate the model forecasts. Therefore, the results shown hereafter will be relative only to the nearest gridpoint method. The performance of both systems was examined for 6 different thresholds: 1, 5, 10, 15, 25, and 50 mm/12 h.

The following probabilistic scores were computed over the verication period: the Brier Skill Score (BSS), the Ranked Probability Skill Score (RPSS), the Relative Operating Characteristic Curve (ROC) area and the Percentage of Outliers (OUTL). For a description of these scores, the reader is referred to Wilks (1995) and to Marsigli et al. (2008). The main features of the verification exercise are summarized in Table 8.

Table 8: Main features of the verification configuration

variable	12hour accumulated precipitation (18-06, 06-18 UTC)
period	from 1 January to 31 March 2012
region	40-50N, 35E-45E
method	nearest grid-point
observations	SYNOP reports
fcst ranges (h)	6-18, 18-30, 30-42, 42-54, 54-66
thresholds	1, 5, 10, 15, 25, 50 mm/12h
scores	ROC area, BSS, RPSS, OUTL

The skill of the two systems in terms of prediction of 12hour accumulated precipitation is summarized in Fig.30, where the Ranked Probability Skill Score (RPSS) is plotted against the forecast range for both COSMOS14EPS and ECMWF EPS. It can be noticed that COSMO-S14EPS has higher RPSS for all forecast ranges. The difference between the two systems is consistent throughout the full forecast range, with a larger gap for the first day of integration. This implies that, despite the larger ensemble size of ECMWF EPS, the higher resolution of COSMO-S14EPS contributes to provide more accurate probabilistic predictions of precipitation.

If the attention is now focused on the performance of both systems for a specic event, most of the above comments still hold. As an example, Fig.31 shows the scores of COSMO-S14-EPS and ECMWF EPS in terms of ROC area for the event "12hour accumulated precipitation exceeding 10 mm". COSMO-S14EPS outperforms ECMWF EPS for all forecast ranges, although both systems exhibit a semidiurnal cycle in the score and tend to provide better guidance for "night-time" precipitation, that is occurring between 18UTC and 6UTC (and corresponding to the ranges 6–18 h, 30–42 h and 54–66 h). As for COSMO, this is linked with a too rapid onset of convection, as pointed out by Oberto and Turco (2008) for runs of COSMO in "deterministic mode".

Finally, the attention is focused on the ability of COSMOS14EPS to reduce the number of outliers with respect to ECMWF EPS, thanks to the higher resolution and the better description of mesoscale and orographicrelated processes. Fig.32 shows that COSMOS14EPS has

fewer outliers than the global ensemble, with a clear added value of the mesoscale ensemble for short forecast ranges.

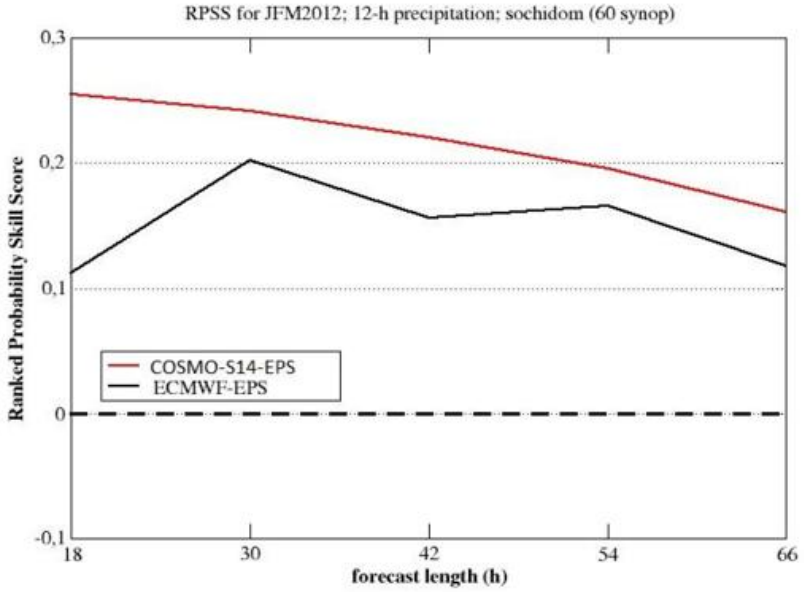


Figure 30: Ranked Probability Skill Score as a function of forecast length for COSMO-S14-EPS

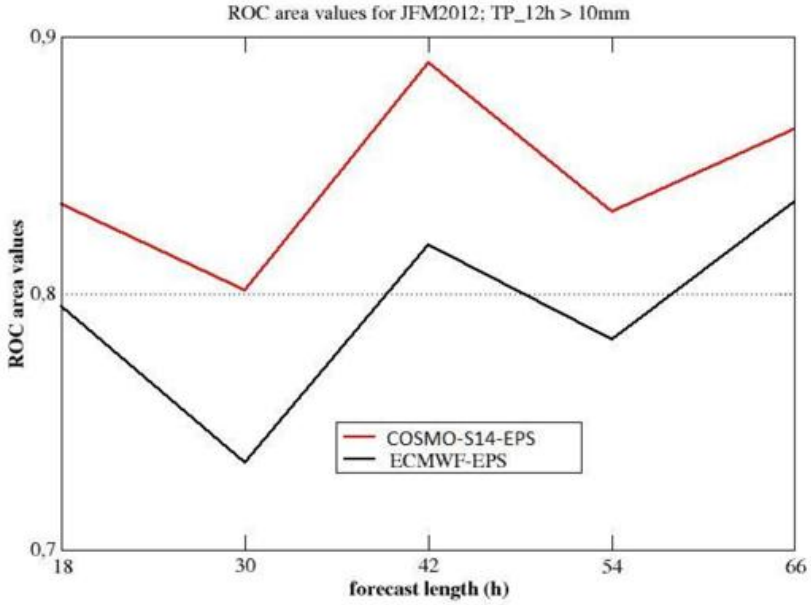


Figure 31: ROC area values for COSMO-S14-EPS (red) and ECMWF EPS (black) relative to the event "precipitation exceeding 10mm in 12 hours" for the forecast ranges of Table 8. Both scores are calculated over the 3-month period from January to March 2012

According to Talagrand et al. (1999), the value of outliers for a reliable ensemble of size N is given by $2/(N+1)$. These values should not be exceeded. The dashed lines of Fig.32 indicate these limits for both COSMO-S14-EPS (red, 18 %) and ECMWF EPS (black, 4 %). Therefore, it looks as if COSMO-S14-EPS approaches the theoretical value to larger extent than ECMWF EPS, which seems to have too many outliers in the short range.

Generally, it was concluded that the mesoscale COSMO-S14-EPS system, based on a relocation of COSMO-LEPS, provided added value with respect to the driving global ensemble

ECMWF EPS as for the probabilistic prediction of precipitation events.

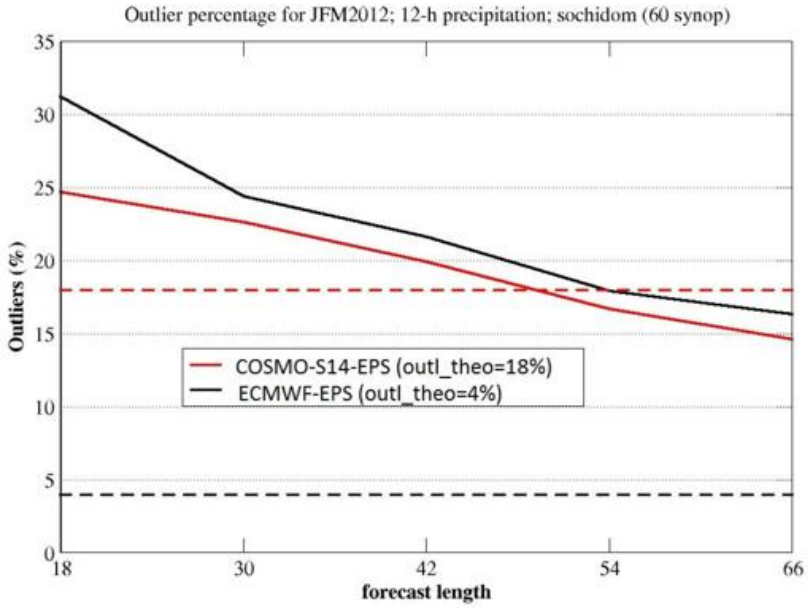


Figure 32: Percentage of Outliers for COSMO-S14-EPS (red) and ECMWF EPS (black), calculated over the 3-month period from January to March 2012. The red (black) dashed line indicates the theoretical limit of outliers for COSMO-S14-EPS (ECMWF EPS)

6.4.2 Case studies

The performance of COSMO-S14-EPS and COSMO-Ru2-EPS was analyzed in detail for several cases.

Hereafter, the attention is focused on two highimpact weather events:

- heavy precipitation event on 13 January 2013 with 21 mm of rain during the day on the coast (Sochi/Adler) and 33 mm of snow-water equivalent in the mountains (Krasnaya Polyana);
- Foehn event on 14-15 February 2013 with a sudden 14-degree warming.

Heavy precipitation event

Heavy precipitation was observed on the 13th of January 2013 in the Sochi region with mainly rain in the coastal cluster and snow in the mountain cluster. The corresponding SYNOP data are presented in Table 9.

Figure 33 reports the performance of COSMO-S14-EPS in terms of probabilistic prediction for two variables: probability of 12hourly accumulated rainfall exceeding 20 mm (left panel) and probability of 12hourly simulated snowfall exceeding 15 mm of equivalent water (right panel).

The ensemble runs start at 00 UTC of 11 January 2013 and the attention is focused on the 48-60 hour forecast range: it can be noticed that COSMO-S14-EPS provides quite accurate forecasts giving large probability of heavy precipitation. Despite the steepness of the orography and the length of the forecast range, the system is able to distinguish between the area more likely affected by rainfall (along the coast, left panel) and the region mainly affected

by snowfall (in the mountains, right panel). This is an interesting result, as the knowledge of the possibility of this weather event, with an advance of about 2 days, gives organizers the chance of taking counter measures and relieving the weather-related problems.

Table 9: 12-h accumulated precipitation observed in the Sochi region on January 11-14, 2013

Period (DDMM/HH UTC)	12-h prec, mm Sochi	12-h prec, mm Krasnaya Polyana
11.01/03 - 11.01/15	4	–
11.01/15 - 12.01/03	0	0
12.01/03 - 12.01/15	0	0.9
12.01/15 - 13.01/03	5	10
13.01/03 - 13.01/15	21	33
13.01/15 - 14.01/03	10	9
14.01/03 - 14.01/15	0	–

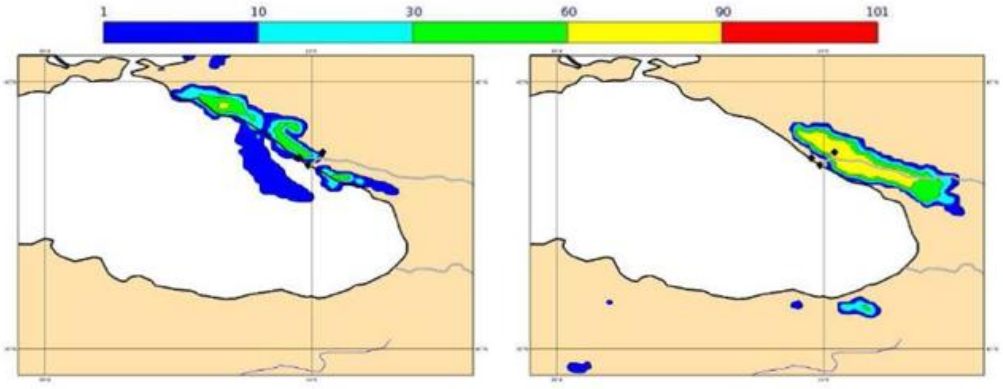


Figure 33: COSMO-S14-EPS run starting at 00UTC of 11 January 2013 (48-60 hour forecast range): probability of 12-hour rainfall exceeding 20 mm (left panel) and of 12-hour snowfall exceeding 15 mm of water equivalent (right panel). The black squares on the coast denote Sochi and Adler; the black square inland denotes Krasnaya Polyana

Let us compare the COSMO-S14-EPS forecasts to COSMO-Ru2-EPS ones. The attention is fixed on the ability of both systems to predict the possible occurrence of heavy snowfall inland. More precisely, we consider the predictability of the following event: "probability of 12h snowfall exceeding 15 mm of equivalent water". In Fig.34, the left column (right column) panels report the performance of COSMO-S14-EPS (COSMO-Ru2-EPS) for the forecast ranges 36-48 hour and 24-36 hour (top-row and bottom-row panels, respectively). It can be noticed that the signal by COSMO-S14-EPS forecasts (left column) is consistent for the different prediction ranges, with a probability of snowfall above 90 % in the area actually affected by the weather event. It is also worth pointing out that no snowfall is predicted along the coast at any forecast range (probabilities below 1 %), consistently with observations.

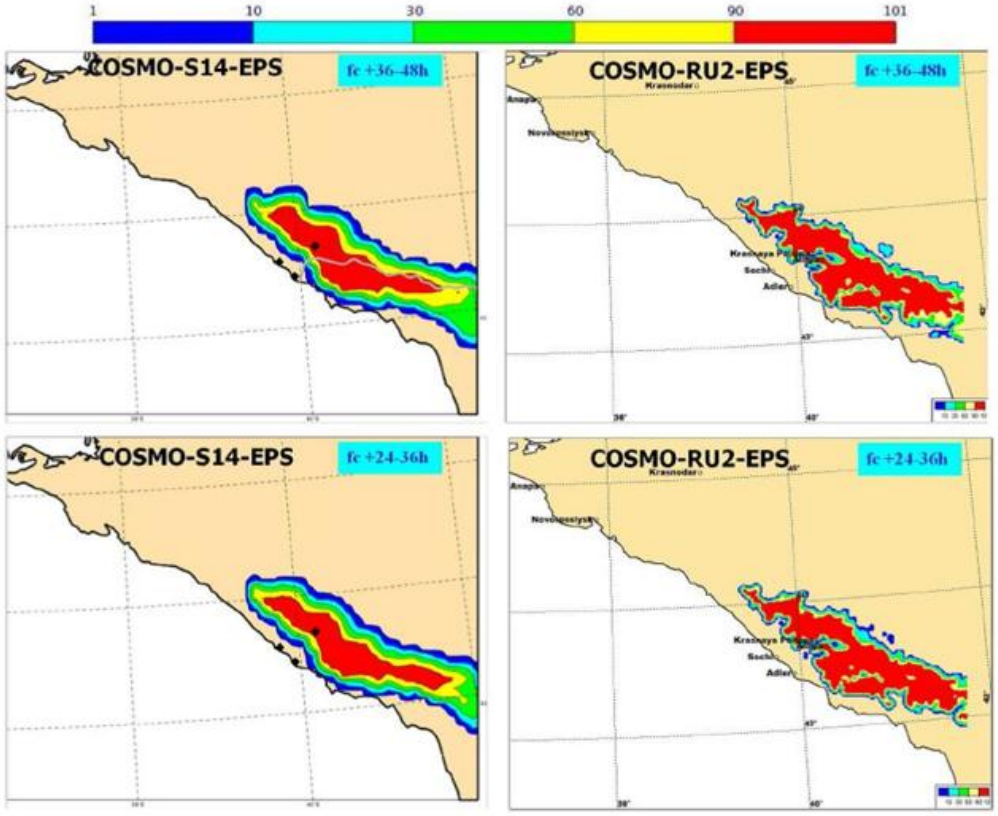


Figure 34: Probability of 12-hour snowfall exceeding 15 mm of equivalent water: COSMO-S14-EPS runs starting at 12 UTC of 11 January (top-left panel, t+36-48h) and at 00 UTC of 12 January (bottom-left panel, t+24-36h) and COSMO-Ru2-EPS runs starting at 12 UTC of 11 January (top-right panel, t+36-48h) and at 00 UTC of 12 January (bottom-right panel, t+24-36h). All forecasts verify at 12 UTC of 13 January 2013. As in Fig.33, the black squares in the left panels denote Sochi, Adler and Krasnaya Polyana.

A straight comparison of COSMO-S14-EPS against COSMO-Ru2-EPS forecasts indicates that the higher resolution ensemble (right column panels of Fig.34) provides more detailed information in terms of location of the regions affected or not by heavy snowfall. In the convective-resolving ensemble, the extent of the coastal region not interested by snowfall turns out to be more evident. At the same time, the higher-resolution ensemble is more confident in giving larger probabilities of snow in the mountainous region. Since more and more spatial and time details are usually required to the forecasts for shorter time ranges, COSMO-Ru2-EPS seems to have, on the basis of this case study, the potential to provide a larger amount of information to local forecasters and event organizers.

Foehn event

Sudden temperature changes in the Olympic areas are considered highimpact weather events possibly affecting outdoor competitions. Therefore, the prediction of this type of event is an important benchmark for the usefulness of ensemble prediction systems. Note that the event considered below was regarded as hardly predictable by local forecasters.

Table 10 shows the evolution of surface temperature in Krasnaya Polyana from 13 to 16 February 2013 (SYNOP data). Linked to the onset of Foehn winds, a marked increase took place between 13 and 15 February, affecting mainly daytime temperatures. On 14 and 15 February, the observed peaks amounted to 13 and 16.2° C, respectively. Ten-minute

observations of the automatic meteorological station located at the same point demonstrate even higher values (see Fig.35).

Table 10: Near-surface temperature (SYNOP T2m data) for Krasnaya Polyana during the Foehn event in February 2013

12.02/00	7.1
12.02/06	5.5
12.02/12	6.3
12.02/18	5.1
13.02/00	4.2
13.02/06	4.6
13.02/12	11.3
13.02/18	3.9
14.02/00	1
14.02/06	3.2
14.02/12	13
14.02/18	6.2
15.02/00	2.4
15.02/06	3.7
15.02/12	16.2
15.02/18	9.7
16.02/00	5.4

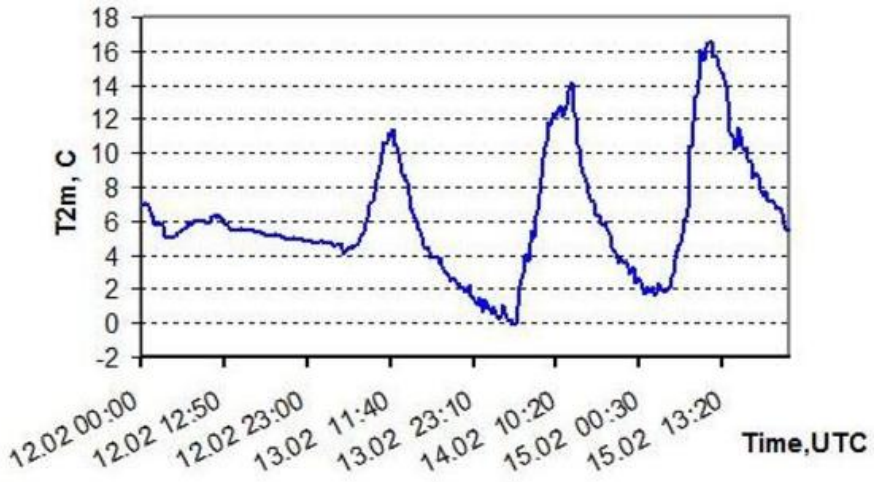


Figure 35: Behavior of 2-metre temperature in Krasnaya Polyana (10-min data of the automatic meteorological station)

As for the ability of COSMO-S14-EPS to predict this temperature increase, Fig.36 reports the meteograms computed over the station point of Krasnaya Polyana, in terms of 2-metre temperature, for different starting times. The top panel of the figure indicates that, already at the 72-hour range (forecasts starting at 12UTC of 12 February), the COSMO-S14-EPS members predict the temperature increase of 14 and 15 February, with peaks close to, or above, 10° C. In this panel, as well as in the others, some discrepancies between observed and predicted temperature are evident, but the differences are partly related to the model

orography, which locate Krasnaya Polyana at about 941 m, instead of 564 m.

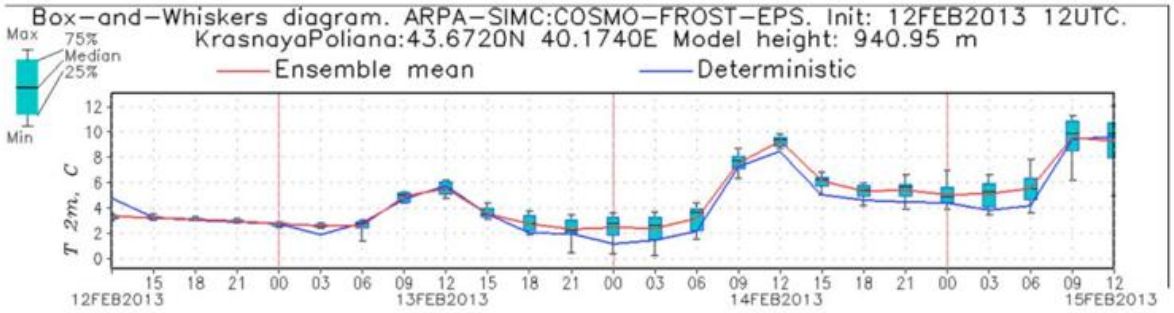
According to COSMO-Ru2-EPS orography, the model gridpoint nearest to Krasnaya Polyana lies at about 734 m above the sea level. This enables the higher-resolution system to describe the temperature peak on February 14 better giving about 12° C (see Fig.36e). However, similarly to COSMO-S14-EPS it fails to give strong enough increase in 2m temperature on February 15. Note that the ECMWF deterministic forecast presented in blue in the epsgrams shows even lower maximum on this date thus indicating that the mistake is possibly related to the weakness of the driving global system in this case.

Fig.37 demonstrates the ability of COSMO-Ru2-EPS to give reasonable probability fields. The probabilities of the event "3-h maximum of 2m temperature exceeds 5° C" are presented in the right panels and the temperature variations at two mountain stations, Aibga (upper curve) and Krasnaya Polyana (lower curve) are shown in the left panels. The vertical red bars in the left figures show two 3-h periods for which the probability fields are given on the right. The COSMO-Ru2-EPS forecast starts at 00 UTC on February 13, 2013 and the probability fields are valid for two 3-h intervals, 03-06 and 09-12 UTC on February 14. The figure obviously demonstrates the coincidence of the periods when 2m temperatures really exceeded 5° C in Krasnaya Polyana and the probability of this event was predicted as high. The temperature was less than 5° C during the entire period 12-16 February in Aibga. Note that the probabilities there are close to zero all the time considered.

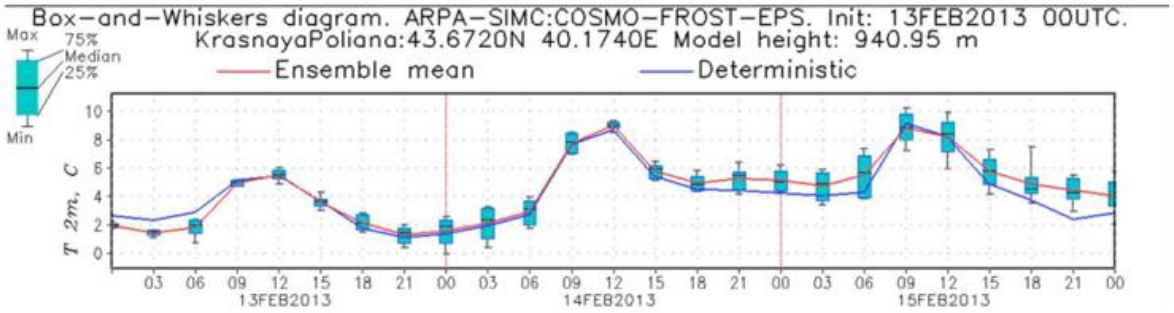
The ensemble forecasts were analyzed in detail for many other cases, mainly characterized by heavy precipitation, sudden temperature changes, or strong wind gusts. As a result of such case studies it was concluded that both COSMO mesoscale ensemble prediction systems (COSMO-S14-EPS and COSMO-Ru2-EPS) were good in simulating 2m temperature and precipitation (precipitation phase was predicted correctly as well) and that much more details can be found in COSMO-Ru2-EPS prognostic charts.

6.4.3 Verification of COSMO-S14-EPS and COSMO-Ru2-EPS for the Olympic and pre-Olympic periods

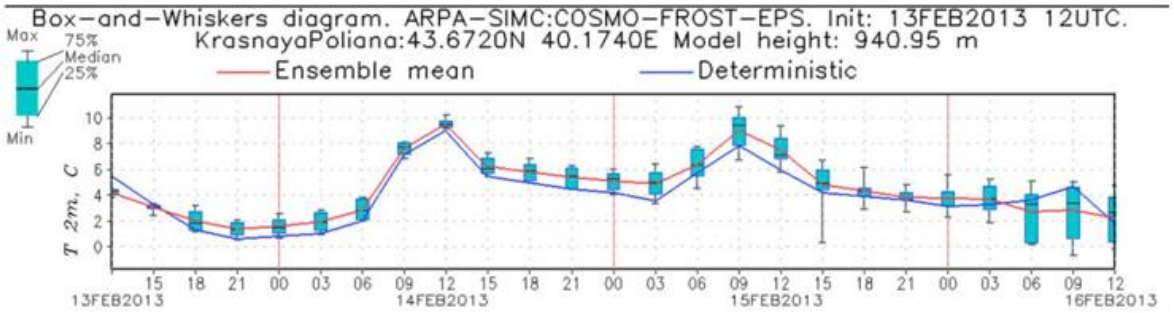
In this section, some verification results are presented; the skills of COSMO-S14-EPS and COSMO-Ru2-EPS are assessed over the period January-February 2013. For both systems, we considered the probabilistic prediction of 2-metre temperature exceeding a number of thresholds for several forecast ranges. As for observations, it was decided to use the data obtained from the SYNOP reports available on the Global Telecommunication System (GTS) as well as from all non-GTS stations in the region.



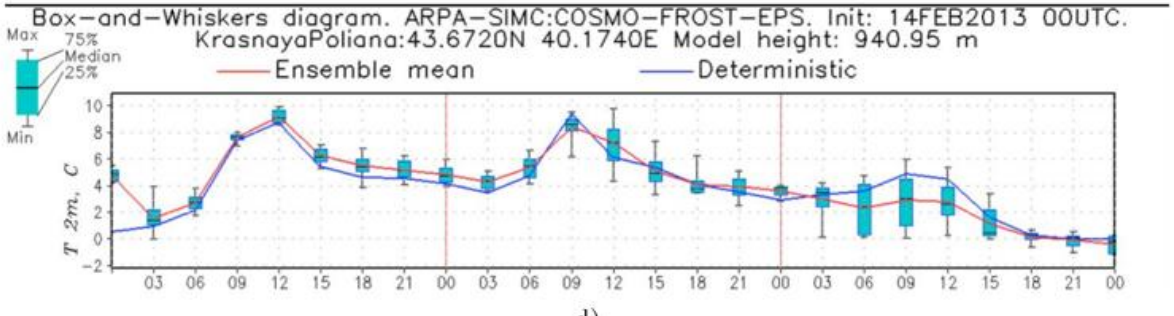
a)



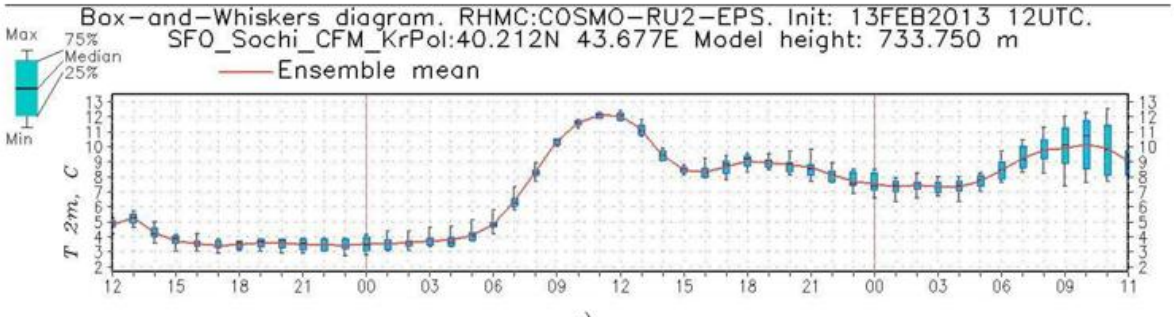
b)



c)



d)



e)

Figure 36: Point meteograms in terms of 2-metre temperature over Krasnaya Polyana based on COSMO-S14-EPS and starting at: (a) 12 UTC of 12 February, (b) 00 UTC of 13 February, (c) 12 UTC of 13 February and (d) 00 UTC of 14 February; and based on COSMO-Ru2-EPS and starting at 12 UTC of 13 February (e)

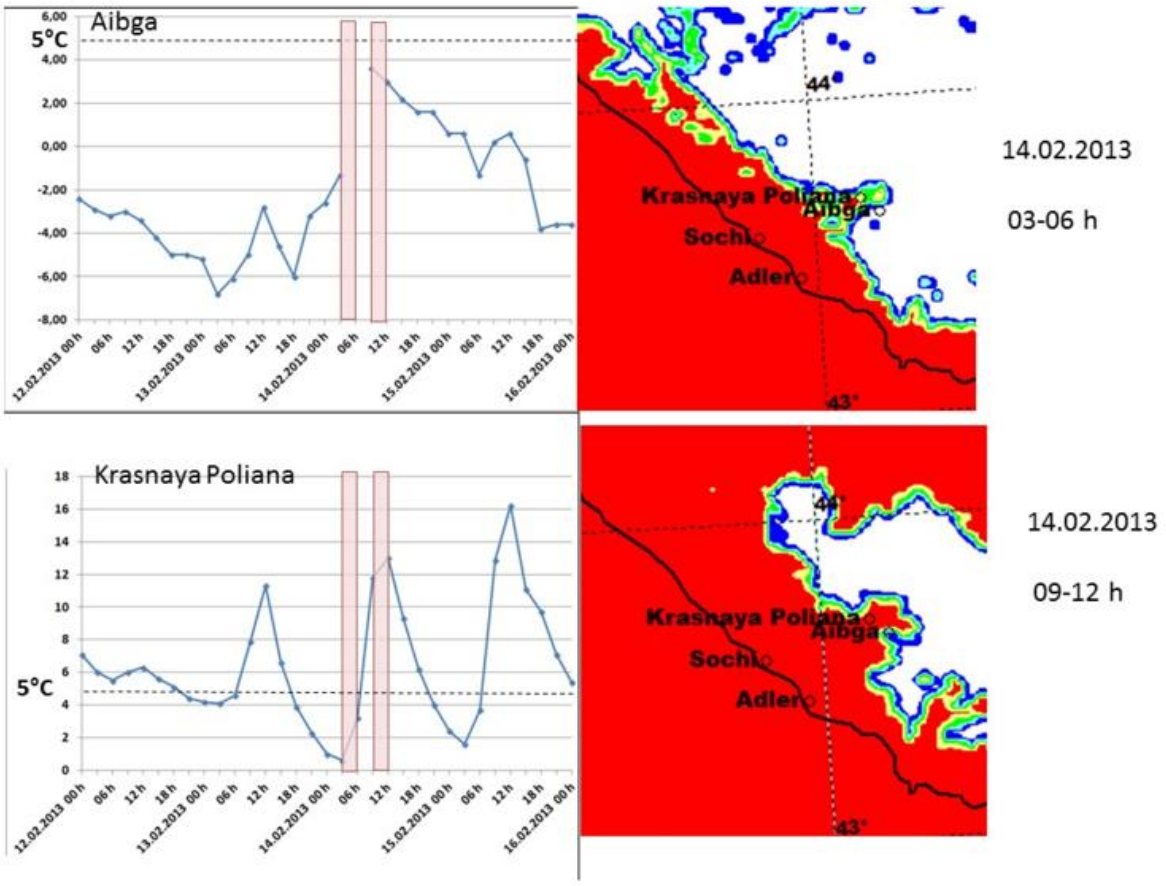


Figure 37: The probabilities of the event "3-h maximum of 2m temperature exceeds 50° C" (right panels) as predicted by COSMO-Ru2-EPS for two 3-h periods on February 14, 2013 and the observed temperature variations (left panels) at two mountain stations, Aibga (upper curve) and Krasnaya Polyana (lower curve). Red: 90-100 %, yellow: 60-90 %, green: 30-60 %, light blue: 10-30 %; blue: 0.1-10 %. See text for details

Table 11: Main features of the verification configuration

variable	2-metre temperature
starting time	12 UTC
period	from 1 January to 28 February 2013
region	42.5-45 N, 37.5-41.5 E
method	nearest 3D optimized grid-point; observations
observations	SYNOP reports + local stations (69 in total); fcst
fcst ranges (h)	from fc+3h to fc+72h every 3h
thresholds	-5, 0, +5, +10 ° C
scores	ROC area, BSS

This enabled the possibility to assess the performance of the systems over a relatively dense observation dataset (69 stations), since the verification domain was restricted to an area centered over the Olympic venue (42.5-45N, 37.5-41.5E). As for the comparison of model forecasts against observations, we selected the gridpoint closest (in 3D) to the observation. The performance of both systems was examined for 4 different thresholds: -5, 0, +5 and 10 ° C. Verification was performed using COSMO software VERSUS. The following probabilistic

scores were computed: the Brier Skill Score (BSS) and the Relative Operating Characteristic Curve (ROC) area. For a description of these scores, the reader is referred to Wilks (1995). The main features of the verification exercise are also summarized in Table 11.

The skill of two systems in terms of probabilistic prediction of 2-metre temperature is summarized in Fig.38, where the values of the ROC area are plotted against the forecast range for 4 different weather events: temperature below -5° C (top-left), above 0° C (top- right), above +5° C (bottom-left) and above +10° C (bottom-right). It can be noticed that the ROC area values are well above 0.8 for three out of the four thresholds, indicating that both COSMO-S14-EPS and COSMO-Ru2-EPS manage to discriminate these events. The performance of two systems is quite similar, with a slight predominance of COSMO-Ru2-EPS that has higher scores for most of the thresholds/forecast ranges. Worse scores are obtained by both systems for the highest threshold (bottom-right panel), where COSMO-S14-EPS outperforms COSMO-Ru2-EPS. It is worth pointing out that this is the rarest event with few observations; therefore, the statistical significance of this result needs to be confirmed by a more detailed investigation over a longer verification period.

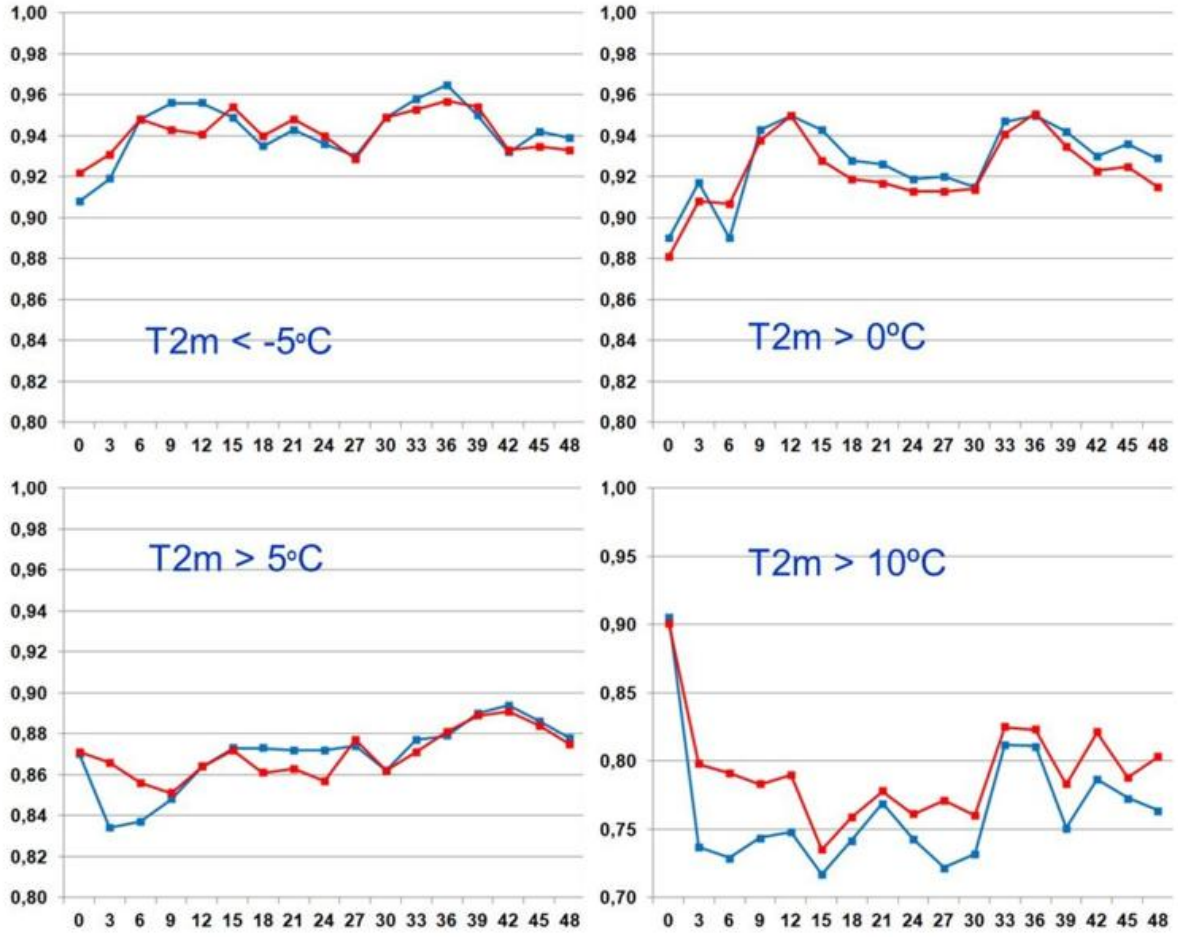


Figure 38: ROC area values as a function of forecast range for four different weather events: 2-metre temperature below -5° C (top-left panel), above 0° C (top right), above +5° C (bottom left) and above +10° C (bottom-right with different vertical scales). The scores are calculated over the period January-February 2013. Red (blue) lines refer to COSMO-S14-EPS (COSMO-Ru2-EPS)

Similar results are obtained when the attention is focused on the Brier Skill Score (BSS),

shown in Fig.39. Also with this score, the satisfactory performance of both systems is confirmed: the BSS is always positive for COSMO-S14-EPS and COSMO-Ru2-EPS, indicating a benefit of both systems with respect to climatology as regards the probabilistic prediction of 2-metre temperature for the thresholds of Table 11. Similarly to Fig.38, it can be noticed that COSMO-Ru2-EPS usually outperforms the lower-resolution ensemble, although the difference is not very marked. As for the +10° C threshold (bottom-left panel of Fig.38), the skill of the two ensembles is almost identical, with slightly higher scores for COSMO-S14-EPS.

Precipitation verification for January-February 2014 demonstrated rather high skill of both systems but only slight differences in ROCA and BSS (not shown).

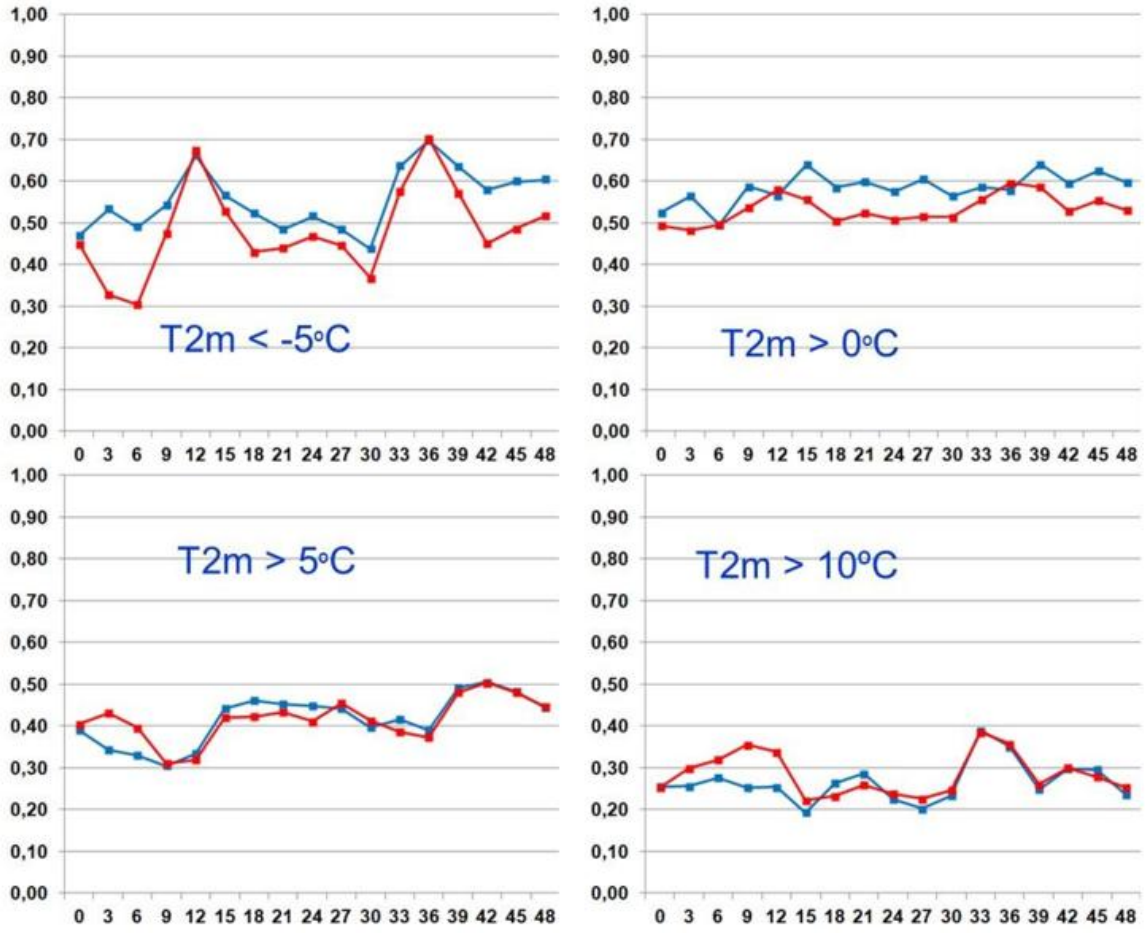


Figure 39: The same as Fig.38 but for the Brier Skill Score. The vertical scale is the same in all panels.

It is important to note that the scores strongly depend on the set of stations applied for verification. Unfortunately, the observation stations are very irregularly distributed over the Sochi region with their highest concentration in the Olympics mountain cluster. In this area, a model gridpoint is often matched (found to be the nearest) to several observation stations. The number of such gridpoints varies for different model resolutions. Additional difficulties are introduced by deviations of the model gridpoint heights from the real heights of meteorological stations. Figures 40a-f demonstrate the ensemble mean 2m temperature at 6 stations of the mountain cluster predicted by COSMO-S14-EPS and COSMO-Ru2-EPS starting from 00UTC February 18, 2014 analysis. The higher-resolution system obviously

outperforms. In Fig.40g-h the quantile-quantile plots are presented for 24-h forecasts of two systems from January 15 to March 15, 2014 and the corresponding observations at RKHU7 station. The COSMO-Ru2-EPS forecasts are clearly distributed more like observations for the entire two-month period (the blue line in Fig.40g almost coincides with the forecast-observation diagonal line). However, probably the advantage of high-resolution system mostly comes from a better gridpoint location: the RKHU7 station is 980 m above the sea level while the height of the nearest gridpoint of the COSMO model with resolutions of 7 and 2.2 km is 1460 and 941 m, respectively. This confirms the analysis of ROCA behavior in Fig.38. The scores presented there were calculated involving all stations in the Sochi region, located both in the coastal and mountain clusters. Though the COSMO-Ru2-EPS curves mainly lie higher thus indicating better forecast skill, the benefits from high-resolution are not great. Note that ROCA is not bias-sensitive.

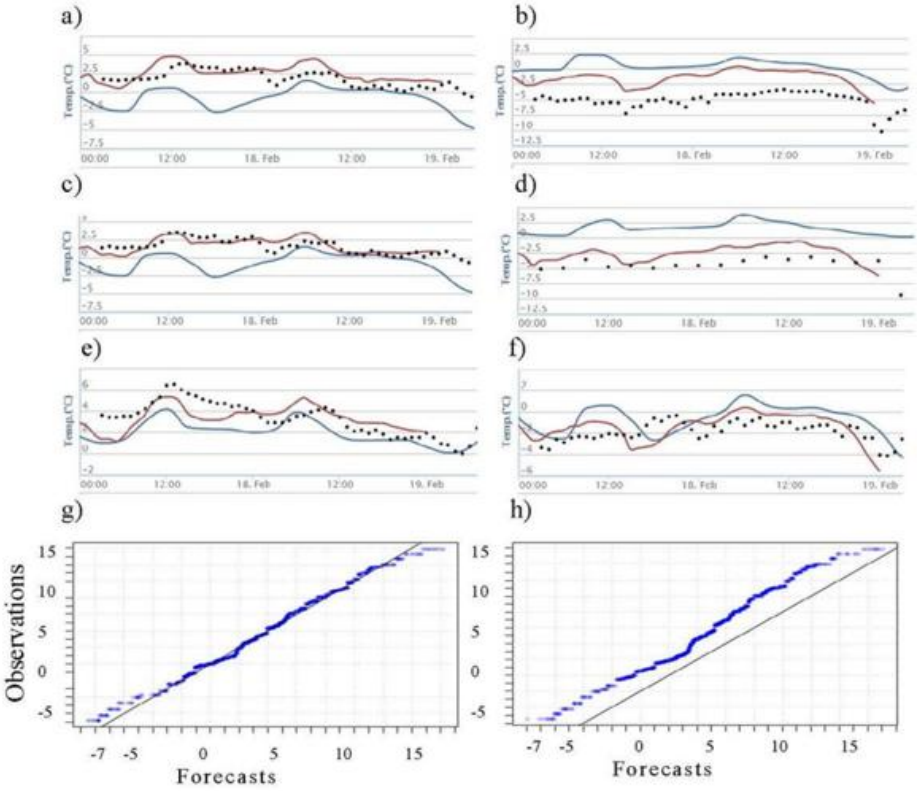


Figure 40: Ensemble mean 2-m temperature predicted by COSMO-Ru2-EPS (in red) and COSMO-S14-EPS (in blue) and observed (black dotted line) at mountain stations RKHU-7 (980 m) (a), RKHU-1 (2320 m) (b), Snowboard-1025 (1027 m) (c), Aibga (2225 m) (d), Sledge-700 (701 m) (e), Gornaya Karusel-1500 (1434 m) (f) using the analysis on 18 February 2014, 00 UTC; quantile-quantile plots for 24-h forecasts of COSMO-Ru2-EPS (g) and COSMO-S14-EPS (h) and observations at RKHU-7 station for the period from January 15 to March 15, 2014

On the whole, both EPS systems demonstrated good skill for 2m temperature, precipitation and wind. Higher-resolution system was slightly more skilful for temperature, but worse for wind. The verification exercises demonstrated the necessity of observations at high temporal and spatial resolution and application of spatial verification methods.

6.5 Conclusions

Two limited-area ensemble prediction systems, based on COSMO-model and referred to as COSMO-S14-EPS (convection-parameterized, 7-km resolution) and COSMO-Ru2-EPS (convection-permitting, 2.2 km resolution), were implemented and run on operational/quasi-operational basis during the pre-Olympic and Olympic seasons. The ensemble systems provided a good support to Sochi forecasters and their probabilistic products were highly appreciated.

The ensemble forecasts were verified by assessing the probabilistic skill of both systems in terms of 2-metre temperature and precipitation during the Olympic and pre-Olympic season (January- February 2013, 2014) over a region centered around Sochi.

Both COSMO-S14-EPS and COSMO-Ru2-EPS turned out to have an overall good performance with ability to discriminate different weather events. The added value of the higher resolution in COSMO-Ru2-EPS was confirmed for 2m temperature by the better probabilistic scores obtained by this system. Verification activity should be continued, including application of new approaches and observations, comparison with other FROST-2014 ensembles.

The forecasts and meteograms prepared during the Olympics were saved in a special archive along with the results of other ensemble systems that participated in FROST-2014 project. The archived information on forecasts, initial and boundary conditions for the higher-resolution system, and observations are valuable and new experiments can be performed within the Sochi testbed.

7 References

Alferov D.Yu, Astakhova E.D., Montani A., Rivin G.S., Rozinkina I.A., 2014. Development of high resolution ensemble prediction system for the region of Sochi-2014 Winter Olimpics. *Proc. of Hydrometcenter of Russia*, no. 352, pp. 5-20. Available at http://elibrary.ru/contents.asp?issueid=1350714 *(In Russian)*

Astakhova E.D., Montani A., Alferov D.Yu., 2014. Ensemble prediction systems for Sochi region based on COSMO model: developments of methods and provision of probabilistic forecasts for XXII Winter Olimpics. *Proc. of Hydrometcenter of Russia*, no. 352, pp. 21-36. Available at http://elibrary.ru/contents.asp?issueid=1350714 *(In Russian)*

Astakhova E.D., Montani A., Alferov D.Yu, 2015. Ensemble forecasts for Sochi-2014 Olympic Games. *Russian Meteorology and Hydrology*, Volume 40, Issue 8, pp 531-539. DOI: 10.3103/S1068373915080051.

Bundel A.Yu., Kirsanov A.A., Muraviev A.V., Rivin G.S., Rozinkina I.A., Blinov D.V., 2014. First verification results for COSMO-Ru mesoscale numerical weather forecasts issued for the Sochi-2014 Olimpics. *Proc. of Hydrometcenter of Russia*, no. 352, pp. 37-54. Available at http://elibrary.ru/contents.asp?issueid=1350714 *(In Russian)*

Doms et al., 2011. A Description of the Nonhydrostatic Regional COSMO Model, part 2: Physical Parameterization, 154 p.

Duan Y., Gong J., Du J., et al., 2012. An Overview of the Beijing 2008 Olympics Research and Development Project (B08RDP). *Bull. Amer. Meteor. Soc.*, vol. 93, iss. 3, pp. 381-404.

Ferro Christopher A. T. and David B. Stephenson, 2011. Extremal Dependence Indices: Improved Verification Measures for Deterministic Forecasts of Rare Binary Events.Wea. Forecasting,26, 699-713. doi:http://dx.doi.org/10.1175/WAF-D-10-05030.1.

General Description of the COSMO-Model. Available at http://www.cosmo-model.org.

Galanis G., Anadranistakis M., 2002. A one-dimensional Kalman filter for the correction of near surface temperature forecasts. *Meteorol. Appl.*, 9, pp. 437-441.

Isaac G. A., Joe P., Mailhot J., et al., 2012. Science of Nowcasting Olympic Weather for Vancouver 2010 (SNOW-10): A World Weather Research Programme project. *J. of Pure and Applied Geophysics*, DOI 10.1007/s00024-012-0579-0.

Jolliffe I. and D. Stephenson, 2012. Forecast Verification in Atmospheric Science. A Practitioner's Guide. Eds. John Wiley & Sons Ltd.

JWGFVR, 2013. Suggested methods for the verification of precipitation forecasts against high resolution limited area observations. Available on-line at http://wgne.meteoinfo.ru/wp-content/uploads/2018/03/WGNE

Kalman, R.E., 1960. A new approach to linear filtering and prediction problems. *Transactions of the American Society of Mechanical Engineers*, D 82, pp. 35-45.

Kazakova E.V., Chumakov M.M., Rozinkina I.A., 2013. Realization of the parametric snow

cover model SMFE for snow characteristics calculation according to standard net meteorological observations. *COSMO Newsletter*, No.13, . 39-49.

Kazakova E.V., Chumakov M.M., Rozinkina I.A., 2014. Fresh snow depth calculation via results of atmospheric modeling (exemplified for the use of the COSMO-Ru model). *Proc. of Hydrometcenter of Russia*, no. 352, pp. 74-84. Available at http://elibrary.ru/contents.asp?issueid=1350714 *(In Russian)*

Kiktev D., Astakhova E.D., Blinov D.V., Zaripov R.B., Muravev A.V., Rivin G.S., Rozinkina I.A., Smirnov A.V., Tsyrulnikov M D. 2013. Development of forecasting technologies for meteorological support of the Sochi-2014 Winter Olympic Games. *Russian Meteorology and Hydrology*, Volume 38, Issue 10, pp 653-660. DOI: 10.3103/S1068373913100014.

Kiktev D., Joe P., Isaac G., Montani A., Frogner I.-L., Nurmi P., Bica B., Milbrandt J., Tsyrulnikov M., Astakhova E., Bundel A., Belair S., Pyle M., Muravyev A., Rivin G., Rozinkina I., Paccagnella T., Wang Y., Reid J., Nipen T., Ahn K.-D., 2017. FROST-2014: the Sochi Winter Olympics International Project. Bulletin of the American Meteorological Society, no. 9, pp. 1908-1929. DOI: 10.1175/BAMS-D-15-00307.1.

Marsigli C., Montani A., Nerozzi F., Paccagnella T., 2003. Performance of COSMOLEPS over the Alpine region /In: Extended abstracts of International Conference on Alpine Meteorology and MAP-Meeting 2003. Publications of MeteoSwiss, vol.A, No.66. pp.294-297. Available at http://www.map.meteoswiss.ch/map-doc/icam2003/596.pdf.

Marsigli C., Montani A., Paccagnella T., 2008. A spatial verification method applied to the evaluation of highresolution ensemble forecasts. *Met. Appl.*, 15, 125-143.

McGurk B., Azuma D., Kattelmann R., 1988. Density of new snow in the Central Sierra Nevada. Proc. 56th Annual Meeting, Western Snow Conference. Kalispell, MT, p. 158-161.

Molteni F., Buizza R., Marsigli C., Montani A., Nerozzi F., Paccagnella T., 2001. A strategy for HighResolution Ensemble Prediction. Part I: Definition of Representative Members and Global Model Experiments. *Quart. J. Roy. Meteor. Soc.*, vol. 127, pp. 2069-2094.

Molteni F., Buizza R., Palmer T. N., Petroliagis T., 1996. The ECMWF ensemble prediction system: Methodology and validation. *Quart. J. Roy. Meteor. Soc.*, vol. 122, pp. 73-119.

Montani A., Alferov D., Astakhova E., Marsigli C. and Paccagnella T., 2014. Ensemble forecasting for Sochi-2014 Olympics: the COSMO-based ensemble prediction systems. *COSMO Newsletter*, No. 14, pp. 88-94.

Montani A., Cesari D., Marsigli C., Paccagnella T., 2011. Seven years of activity in the field of mesoscale ensemble forecasting by the COSMO-LEPS system: main achievements and open challenges. *Tellus A.*, vol. 63, pp. 605-624. DOI: 10.1111/j.1600-0870.2010.00499.

Montani A., Marsigli C., Paccagnella T., 2013. Development of a COSMO-based limited-area ensemble system for the 2014 Winter Olympic Games. *COSMO Newsletter*, No. 13. pp. 93-99.

Muravev A.V., Bundel A.Y., Kiktev D.B., Blinov D.V., Smirnov A.V., 2013. Verification of mesoscale forecasts in the 2014 Olympic Games region for the first test period. Part I: Verification techniques and polygonal quality assessments of the COSMO model

forecasts. *Russian Meteorology and Hydrology*. Vol. 38. No.11. pp. 723-734. DOI: 10.3103/S1068373913110010.

Muravev A.V., Bundel A.Y., Kiktev D.B., Smirnov A.V., 2013. Verification of mesoscale forecasts in the 2014 Olympic Games region. Part II: Preliminary results of diagnostic evaluation of quality and calibration of the forecasts by the Cosmo-Ru2 model. *Russian Meteorology and Hydrology*. Vol. 38. No.12. pp. 797-807. DOI: 10.3103/S1068373913120017.

Murphy, A., B. Brown and Y. Chen, 1989. Diagnostic Verification of Temperature Forecasts. Weather and Forecasting, Vol 4, pp 485-501.

Oberto, E. and Turco, M. 2008: Report about the latest results of precipitation verification over Italy. *COSMO Newsletter*, 8, 3744. Available at: http://www.cosmo-model.org/.

Rivin G., Rozinkina I. Priority Project "CORSO": Consolidation of Operation and Research results for the Sochi Olympic Games. Available at http://cosmo-model.org/content/tasks/priorityProjects/corso/default.htm.

Rivin G.S., Rozinkina I.A., Vilfand R.M., Alferov D.Yu, Astakhova E.D., Blinov D.V., Bundel A.Yu., Kazakova E.V., Kirsanov A.A., Nikitin M.A., Perov V.L., Surkova G.V., Revokatova A.P., Shatunova M.V., Chumakov M.M., 2015. COSMO-Ru system for nonhydrostatic hydrometeorological weather forecast at the Hydrometcenter of Russia: the second stage of realization and development. sl Russian Meteorology and Hydrology, Volume 40, Issue 6, pp. 440-450. DOI: 10.3103/S1068373915060060.

Rotach M. W., Ambrosetti P., Appenzeller C., et al., 2009. MAP D-PHASE: Real-Time Demonstration of Weather Forecast Quality in the Alpine Region. *Bull. Amer. Meteor. Soc.*, vol. 90, pp. 1321-1336.

Shatunova M.V., Rivin G.S., 2014. Model COSMO-Ru1 with high space resolution: influence of external parameters on modeling results. *Proc. of Hydrometcenter of Russia*, no. 352, pp. 150-167. Available at http://elibrary.ru/contents.asp?issueid=1350714 *(In Russian)*

Shatunova M.V., Rivin G.S., Rozinkina I.A., 2015. Visibility forecasting for February 16-18, 2014 for the region of the Sochi-2014 Olympic Games using the high-resolution COSMO-Ru1 model. *Russian Meteorology and Hydrology*, Volume 40, Issue 8, pp 523-530. DOI: 10.3103/S106837391508004X.

Talagrand, O., Vautard, R. and Strauss, B. 1999. Evaluation of probabilistic prediction systems. Proceedings of the ECMWF Workshop on Predictability, Reading, UK, 2022 October 1997, 372. Available at: http://www.ecmwf.int/publications/.

Wilks, D.S., 1995. Statistical Methods in the Atmospheric Sciences. Academic Press, New York, 467.

www.snow-forecast.com.

List of COSMO Newsletters and Technical Reports

(available for download from the COSMO Website: www.cosmo-model.org)

COSMO Newsletters

No. 1: February 2001.

No. 2: February 2002.

No. 3: February 2003.

No. 4: February 2004.

No. 5: April 2005.

No. 6: July 2006.

No. 7: April 2008; Proceedings from the 8th COSMO General Meeting in Bucharest, 2006.

No. 8: September 2008; Proceedings from the 9th COSMO General Meeting in Athens, 2007.

No. 9: December 2008.

No. 10: March 2010.

No. 11: April 2011.

No. 12: April 2012.

No. 13: April 2013.

No. 14: April 2014.

No. 15: July 2015.

No. 16: July 2016.

No. 17: July 2017.

COSMO Technical Reports

No. 1: Dmitrii Mironov and Matthias Raschendorfer (2001):
Evaluation of Empirical Parameters of the New LM Surface-Layer Parameterization Scheme. Results from Numerical Experiments Including the Soil Moisture Analysis.

No. 2: Reinhold Schrodin and Erdmann Heise (2001):
The Multi-Layer Version of the DWD Soil Model TERRA_LM.

No. 3: Günther Doms (2001):
A Scheme for Monotonic Numerical Diffusion in the LM.

No. 4: Hans-Joachim Herzog, Ursula Schubert, Gerd Vogel, Adelheid Fiedler and Roswitha Kirchner (2002):
LLM ¯ the High-Resolving Nonhydrostatic Simulation Model in the DWD-Project LITFASS.
Part I: Modelling Technique and Simulation Method.

No. 5: Jean-Marie Bettems (2002):
EUCOS Impact Study Using the Limited-Area Non-Hydrostatic NWP Model in Operational Use at MeteoSwiss.

No. 6: Heinz-Werner Bitzer and Jürgen Steppeler (2004):
Documentation of the Z-Coordinate Dynamical Core of LM.

No. 7: Hans-Joachim Herzog, Almut Gassmann (2005):
Lorenz- and Charney-Phillips vertical grid experimentation using a compressible nonhydrostatic toy-model relevant to the fast-mode part of the 'Lokal-Modell'.

No. 8: Chiara Marsigli, Andrea Montani, Tiziana Paccagnella, Davide Sacchetti, André Walser, Marco Arpagaus, Thomas Schumann (2005):
Evaluation of the Performance of the COSMO-LEPS System.

No. 9: Erdmann Heise, Bodo Ritter, Reinhold Schrodin (2006):
Operational Implementation of the Multilayer Soil Model.

No. 10: M.D. Tsyrulnikov (2007):
Is the particle filtering approach appropriate for meso-scale data assimilation ?

No. 11: Dmitrii V. Mironov (2008):
Parameterization of Lakes in Numerical Weather Prediction. Description of a Lake Model.

No. 12: Adriano Raspanti (2009):
COSMO Priority Project "VERification System Unified Survey" (VERSUS): Final Report.

No. 13: Chiara Marsigli (2009):
COSMO Priority Project "Short Range Ensemble Prediction System" (SREPS): Final Report.

No. 14: Michael Baldauf (2009):
COSMO Priority Project "Further Developments of the Runge-Kutta Time Integration Scheme" (RK): Final Report.

No. 15: Silke Dierer (2009):
COSMO Priority Project "Tackle deficiencies in quantitative precipitation forecast" (QPF): Final Report.

No. 16: Pierre Eckert (2009):
COSMO Priority Project "INTERP": Final Report.

No. 17: D. Leuenberger, M. Stoll and A. Roches (2010):
Description of some convective indices implemented in the COSMO model.

No. 18: Daniel Leuenberger (2010):
Statistical analysis of high-resolution COSMO Ensemble forecasts in view of Data Assimilation.

No. 19: A. Montani, D. Cesari, C. Marsigli, T. Paccagnella (2010):
Seven years of activity in the field of mesoscale ensemble forecasting by the COSMO–LEPS system: main achievements and open challenges.

No. 20: A. Roches, O. Fuhrer (2012):
Tracer module in the COSMO model.

No. 21: Michael Baldauf (2013):
A new fast-waves solver for the Runge-Kutta dynamical core.

No. 22: C. Marsigli, T. Diomede, A. Montani, T. Paccagnella, P. Louka, F. Gofa, A. Corigliano (2013):
The CONSENS Priority Project.

No. 23: M. Baldauf, O. Fuhrer, M. J. Kurowski, G. de Morsier, M. Müllner, Z. P. Piotrowski, B. Rosa, P. L. Vitagliano, D. Wójcik, M. Ziemiański (2013):
The COSMO Priority Project 'Conservative Dynamical Core' Final Report.

No. 24: A. K. Miltenberger, A. Roches, S. Pfahl, H. Wernli (2014):
Online Trajectory Module in COSMO: a short user guide.

No. 25: P. Khain, I. Carmona, A. Voudouri, E. Avgoustoglou, J.-M. Bettems, F. Grazzini (2015):
The Proof of the Parameters Calibration Method: CALMO Progress Report.

No. 26: D. Mironov, E. Machulskaya, B. Szintai, M. Raschendorfer, V. Perov, M. Chumakov, E. Avgoustoglou (2015):
The COSMO Priority Project 'UTCS' Final Report.

No. 27: J-M. Bettems (2015):
The COSMO Priority Project 'COLOBOC': Final Report.

No. 28: Ulrich Blahak (2016):
RADAR_MIE_LM and RADAR_MIELIB - Calculation of Radar Reflectivity from Model Output.

No. 29: M. Tsyrulnikov and D. Gayfulin (2016):
A Stochastic Pattern Generator for ensemble applications.

No. 30: D. Mironov and E. Machulskaya (2017):
A Turbulence Kinetic Energy – Scalar Variance Turbulence Parameterization Scheme.

No. 31: P. Khain, I. Carmona, A. Voudouri, E. Avgoustoglou, J.-M. Bettems, F. Grazzini, P. Kaufmann (2017):
CALMO - Progress Report.

No. 32: A. Voudouri, P. Khain, I. Carmona, E. Avgoustoglou, J.M. Bettems, F. Grazzini, O. Bellprat, P. Kaufmann and E. Bucchignani (2017):
Calibration of COSMO Model, Priority Project CALMO Final report

No. 33: N. Vela (2017):
VAST 2.0 - User Manual.

No. 34: C. Marsigli, D. Alferov, M. Arpagaus, E. Astakhova, R. Bonanno, G. Duniec, C. Gebhardt, W. Interewicz, N. Loglisci, A. Mazur, V. Maurer, A. Montani, A. Walser (2018):
COsmo Towards Ensembles at the Km-scale IN Our countries (COTEKINO), Priority Project final report.

COSMO Technical Reports

Issues of the COSMO Technical Reports series are published by the *COnsortium for Small-scale MOdelling* at non-regular intervals. COSMO is a European group for numerical weather prediction with participating meteorological services from Germany (DWD, AWGeophys), Greece (HNMS), Italy (USAM, ARPA-SIMC, ARPA Piemonte), Switzerland (MeteoSwiss), Poland (IMGW), Romania (NMA) and Russia (RHM). The general goal is to develop, improve and maintain a non-hydrostatic limited area modelling system to be used for both operational and research applications by the members of COSMO. This system is initially based on the COSMO-Model (previously known as LM) of DWD with its corresponding data assimilation system.

The Technical Reports are intended

- for scientific contributions and a documentation of research activities,
- to present and discuss results obtained from the model system,
- to present and discuss verification results and interpretation methods,
- for a documentation of technical changes to the model system,
- to give an overview of new components of the model system.

The purpose of these reports is to communicate results, changes and progress related to the LM model system relatively fast within the COSMO consortium, and also to inform other NWP groups on our current research activities. In this way the discussion on a specific topic can be stimulated at an early stage. In order to publish a report very soon after the completion of the manuscript, we have decided to omit a thorough reviewing procedure and only a rough check is done by the editors and a third reviewer. We apologize for typographical and other errors or inconsistencies which may still be present.

At present, the Technical Reports are available for download from the COSMO web site (www.cosmo-model.org). If required, the member meteorological centres can produce hard-copies by their own for distribution within their service. All members of the consortium will be informed about new issues by email.

For any comments and questions, please contact the editor:

Massimo Milelli
Massimo.Milelli@arpa.piemonte.it

Consortium for Small-Scale Modelling

Technical Report No. 38

The COSMO Priority Project CORSO-A Final Report

April 2019

DOI: 10.5676/DWD_pub/nwv/cosmo-tr_38

Deutscher Wetterdienst
MeteoSwiss
Ufficio Generale Spazio Aereo e Meteorologia
ΕΘΝΙΚΗ ΜΕΤΕΩΡΟΛΟΓΙΚΗ ΥΠΗΡΕΣΙΑ
Instytucie Meteorogii i Gospodarki Wodnej
Administratia Nationala de Meteorologie
ROSHYDROMET
Agenzia Regionale Protezione Ambiente Piemonte
Agenzia Regionale Prevenzione Ambiente Energia Emilia Romagna
Centro Italiano Ricerche Aerospaziali
Amt für GeoInformationswesen der Bundeswehr
Israel Meteorological Service

www.cosmo-model.org

Editor: Massimo Milelli, ARPA Piemonte

The COSMO Priority Project CORSO-A

Final Report

Project participants:

***G. Rivin*[1]‡, *I. Rozinkina*[1]‡, *E. Astakhova*[1], *A. Montani*[2],**

***J-M. Bettems*[3], *D. Alferov*[1], *D. Blinov*[1],**

***P. Eckert*[3], *A. Euripides*[4], *J. Helmert*[5], *M.Shatunova*[1].**

‡ Task Leaders
Federal Service for Hydrometeorology and Environmental Monitoring, Russia (Roshydromet)
Hydrometeorological Research Centre of Russian Federation (Hydrometcentre of Russia)
11-13, B. Predtechensky per., Moscow, 123242, Russia

[1] RHM

[2] ARPAE

[3] MCH

[4] HNMS

[5] DWD

Contents

1 Introduction **4**

1.1 The goal of PT 4

2 SubTasks, brief description **5**

2.1 SubTask 1 The guidance of the optimal domain's size selection for 1.1 km resolution of nested COSMO models for the regions with complex mountain relief (STL G. Rivin) 5

2.1.1 Motivation 5

2.1.2 Goal 5

2.2 SubTask 2 Development of algorithm of subgrid h-correction of T2m (due to the differences between models and real heights) based on COSMO- forecasts of vertical T-gradient (STL I. Rozinkina) 5

2.2.1 Motivation 5

2.2.2 Goal 6

2.3 SubTask 3 Preparing of archives of 7 km and 2.2 km EPSs forecasts for the Sochi-2014 modelling area applicable for research aimed at improving COSMO EPS systems and available for community (TL E. Astakhova, A. Montani) . . 6

2.3.1 Motivation 6

2.3.2 Goal 7

2.4 SubTask 4. Preparing of recommendations for forecasters The features of using and interpretation of the results of limited- area meso-scale modeling (TL I. Rozinkina) 7

2.4.1 Motivation 7

2.4.2 Goal 7

3 The guidance of the optimal domain's size selection for 1.1 km resolution of nested COSMO models for the regions with complex mountain relief (G. Rivin, M. Shatunova, J. Helmert) **8**

3.1 Introduction 8

3.2 Simulation domains 8

3.3 VERSUS verification results 10

3.4 Verification of heavy precipitation event forecast (case studies) 13

3.5 Conclusions 21

4 Development of algorithm of subgrid h-correction of T2m for mountains based on COSMO forecasts of local lapse rate (h-correction) (I. Rozinkina, J-M. Bettems, D. Blinov, A. Euripides) **22**

5 COSMO-BASED ENSEMBLE FORECASTING FOR SOCHI-2014 OLYMPICS: ARCHIVING THE RESULTS (E. Astakhova, A. Montani, D. Kiktev, D. Alferov, A. Smirnov) 23

5.1 Introduction . . . 23

5.2 Ensemble prediction systems developed in CORSO . . . 23

5.3 CORSO-A necessity and goal . . . 24

5.4 A Unified Sochi archive . . . 24

5.5 Conclusions . . . 27

6 PREPARING OF RECOMMENDATIONS FOR FORECASTERS ABOUT FEATURES OF INTERPRETATION OF THE RESULTS OF MESO-SCALE MODELING (How to use the LAM mesoscale NWP results for mountain terrain) (I. Rozinkina, P. Eckert, G. S. Rivin) 28

6.1 Introduction . . . 28

6.2 Key definitions . . . 28

6.3 Main statements of use of products of global / Limited area NWP Products for short-range and very-short range forecasting . . . 29

6.4 Stages of analysis of NWP products for local short- range forecasting . . . 31

6.4.1 Common recommends . . . 31

6.4.2 Experience of large-scale weather types before the analyze of HR products . . . 32

6.4.3 Recommended sequence of analysis, design and content of forecasters maps . . . 34

6.5 Analysis of Meteograms of deterministic LAM HR NWP . . . 39

6.5.1 Definitions and goals . . . 39

6.5.2 Key principles for technology of meteogram forming . . . 40

6.5.3 Forecasters analysis based on meteograms . . . 41

6.6 Conclusion . . . 43

7 Acknowledgements 43

A Appendix 44

1 Introduction

The PP CORSO (Consolidation of Operation and Research results for the Sochi Olympics) dedicated to development of high-resolution NWP meteosupport of Sochi2014 Olympics held in 2011-2014. PP CORSO was adopted with a goal to enhance and demonstrate the capabilities of COSMO-based systems of NWP in winter conditions for mountainous terrain and to assess the effect of practical use of this information during Sochi-2014 Olympic Games. There were 3 directions of activities concerning the development and implementation of:

a) high-resolution forecasting system (Task1),

b) the means of practical forecasting and down-scaling post-processing (Task2),

c) mesoscale EPS (Task3).

PP CORSO obtained the successful results. The main result of FDP part of PP CORSO was the implementation of high quality NWP system, which the forecasters of Organizing Committee and of sport venues have used as a basic. The COSMO experience and its possibilities were concentrated for obtain the renovated NWP system for SOCHI-2014 region with complex geographical terrain. Due to the cooperation of FDP and RDP activities of PP CORSO, the new level of modeling and of interpretation of results were obtained (The new COSMO-version with step 1.1km, the some down-scaling postprocessing algorithms, knowledge of feed-back from forecasters, the implementation of High-resolution EPS-system 2.2. km for mountain area). Some aspects obtained results could be further researched and could be useful for implementation and investigations in whole COSMO community. The obtained experience, accumulated data of measurements and of forecasts and new numeric experiments permit to adapt & develop and test of the proposed algorithms and technical solutions. The new PT CORSO-After (CORSO-A) should meet these developed challenges for implementation in COSMO technologies and investigations.

1.1 The goal of PT

To prepare the new COSMO tools and practical instructions for be available for COSMO-community related to:

- the implementation of versions COSMO-1km (SubTask1 The guidance of the optimal domain's size selection for 1.1 km resolution of nested COSMO models for the regions with complex mountain relief, TL G.Rivin),
- the realization of down-scaling postprocessing tools for mountain area, (SubTask2, Development of algorithm of subgrid h-correction of T2m (due to the differences between models and real heights) based on COSMO- forecasts of vertical T-gradient , STL I.Rozinkina),
- the development of archive for development of convective-resolution EPS (SubTask3 Preparing of archives of 7 km and 2.2 km EPS forecasts for the Sochi- 2014 modeling area applicable for research aimed at improving COSMO EPS systems and available for community. Their compliance with FROST2014 archives, STL E.Astakhova, A.Montani),

- the preparing of instructions for forecasters for use the results of meso-scale deterministic and EPS results (SubTask4 Preparing of recommendations for forecasters The features of using and interpretation of the results of limited- area meso-scale modeling STL I.Rozinkina).

2 SubTasks, brief description

2.1 SubTask 1 The guidance of the optimal domain's size selection for 1.1 km resolution of nested COSMO models for the regions with complex mountain relief (STL G. Rivin)

2.1.1 Motivation

The development and implementation of COSMO1 were obtained as result of RDP part of PP CORSO. As addition the participants managed to organize the operational runs of COSMO1 for Sochi2014 area during the Olympics 2014, and the positive experience of use of COSMO 1 for Sochi area was gained. The modeling with grid step about 1 km is significantly more realistic for mountain area and as sequence permit to provide for forecasters the additional important products as, e.g. flows of wind in bottom level, that determines the weather in hills and valleys. During the CORSO PP were obtained results shown the strong dependence of the predicted precipitation amount and spatial distribution on the models domain size. This problem need the more attentive examination, because the runs of COSMO1 as part of nested technologies are very expensive in point of view of computing time. The computing resources and the technological requirements of providing forecast by a certain time determine the model run timing. On the other hand it exists the requirements for the quality of the forecasts.

2.1.2 Goal

To formulate and to prove the selection of models domain size for COSMO1 model runs for disseminate this experience for create the similar technologies for detailed calculations on mountain domains in condition of limited computing resources.

2.2 SubTask 2 Development of algorithm of subgrid h-correction of T2m (due to the differences between models and real heights) based on COSMO- forecasts of vertical T-gradient (STL I. Rozinkina)

2.2.1 Motivation

In framework of PP CORSO were realized some approaches for subgrid correction of T2m, as the direct forecasts from COSMO-model of T2m for mountain region were not convenient. There are some causes because it. One of principal causes of this fact for mountain area is the simple discrepancy of local real and averaged of grid cells height. As traditional, T2m can be corrected by use standard adiabatic gradient, but in Sochi2014 region the real temperature profiles can be significantly different including inversions. Because of the variability of the vertical temperature profile depending on a large-scale weather forecasts the implementation of KF or MOS in lot of cases is inefficiently because there are non systematic errors. The CORSO participants proposed the algorithm of correction of local

values of T2m for mountains based the COSMO- models forecasts of T-profile of bottoms levels (H-corection). The implementation of this algorithm in meteogram tables permit to obtain the more realistic T2m forecasts for points before the possible subsequent correction tools (KF or MOS), due to improve the limitations of parameterization schemes. This proposed algorithm can be disseminate in two direction of implementation: a) by modified technology of forming of meteograms by including into FieldExtra for calculate the fields of subgrid variations of T2m (for min and max real height of cells).

2.2.2 Goal

To realize the updated software of Fieldextra with including of calculations of subgrid values of T2m based the forecasts of vertical T gradient. To provide the software of 1-D correction of T2m forecasts based the forecasts of vertical T gradient (h-correction).

2.3 SubTask 3 Preparing of archives of 7 km and 2.2 km EPSs forecasts for the Sochi-2014 modelling area applicable for research aimed at improving COSMO EPS systems and available for community (TL E. Astakhova, A. Montani)

2.3.1 Motivation

The two ensemble prediction systems were developed within the PP CORSO: COSMO-S14-EPS with a 7-km resolution and COSMO-Ru2-EPS with a 2.2 km resolution. The results of both ensembles were provided to Sochi forecasters during the Olympics and proved to give a valuable support to them. COSMO-S14-EPS (S14 stands for Sochi-2014) is a relocation of COSMO-LEPS to the area of Olympic Games and was generated rather similarly to COSMO-LEPS but with some changes introduced because of computer-time constraints and the interest towards the short-range. Initial and boundary conditions for COSMO-S14-EPS were taken from ECMWF EPS. The initial ensemble size was reduced to 10 members selected by a clustering procedure (Montani et al., 2011). The lower boundary condition for all COSMO-S14-EPS members was taken from COSMO model run in hindcast mode (short-range forecast nested on ECMWF analyses). COSMO-S14-EPS ran on a regular basis since 19 December 2011 on ECMWF supercomputers. COSMO-S14-EPS generated a set of standard probabilistic products (including probability of surpassing a threshold, ensemble mean, ensemble standard deviation, and ensemble meteograms for several surface and upper-air variables) which were delivered to Sochi forecasters in operational mode. COSMO-Ru2-EPS is a convective-permitting ensemble, based on initial and boundary conditions provided by COSMO-S14-EPS. The system ran on Roshydromet computers. The first winter of its regular runs (2012-2013) and case studies (2011-2013) showed that COSMO-Ru2-EPS gave rather precise and detailed forecasts and therefore could be useful for Sochi forecasters. Following this conclusion, COSMO-Ru2-EPS operationally ran twice a day (00 and 12 UTC) since November 2013 and during the Olympics. In course of CORSO project, the output results of the two EPSs were archived on Roshydromet computers. In total, the results of nearly six months of runs of the COSMO EPSs (both 7 and 2.2 km) are available (November 2013-April 2014). These are forecasts for a very specific area, where mountains with very steep slopes are in close vicinity to the sea and where high-resolution forecasting of high-impact events is a real challenge. The available COSMO-EPS forecasts can be also considered as a part of the FROST2014 archive. Roshydromet suggested that the FROST2014 archive be freely accessible to the entire meteorological community. In addition to the forecasts, available in the FROST2014 archive, the initial and boundary conditions generated by COSMO-S14-EPS

were stored at Roshydromet as well. The entire dataset available (COSMO EPSs forecasts + initial and boundary conditions for COSMO high-resolution EPS + FROST forecasts and observations) can be very useful for the international community and especially for COSMO community. Re-forecasts using a modified high-resolution EPS can be done to estimate the influence of different aspects of ensemble generation (e.g. model-related perturbations, soil perturbations, etc.) However, at present there are still some obstacles for using the COSMO-related data:

- there are some gaps in the data;
- the COSMO-Ru2-EPS forecasts are stored on different computers to which there is no external access;
- the entire outputs of COSMO models are stored for COSMO-Ru2-EPS while only a pre-specified set of variables should be archived according to the FROST rules;
- there is no manual;
- the data should be completed by a list of severe events and periods that are worth to examine.

2.3.2 Goal

To prepare an archive of COSMO ensemble forecasts (with 7 and 2.2 km resolutions) for the Sochi area accompanied by initial and boundary conditions for high-resolution ensembles and by a list of important weather events during the period considered. The archive must be provided according to TIGGE-LAM archiving standards, easily accessible and have a clear manual to provide COSMO-community a possibility of experiments over an area where steep mountains are in close vicinity to the sea and high-resolution forecasts of severe events are a challenge.

2.4 SubTask 4. Preparing of recommendations for forecasters The features of using and interpretation of the results of limited- area mesoscale modeling (TL I. Rozinkina)

2.4.1 Motivation

Due to the COSMO PP CORSO and the WMO DP Frost2014 the forecasters of Sochi 2014 region obtained the cascade of model outputs form deterministic and ensemble modern mesoscale NWP technologies at large window of spatial resolutions. The some synoptical trainings for understanding of possible limitations of models are realized d at 2011-2014. Sometime there are not evident forecasting rules for correct interpretation of it output. The study of experience of feedback form forecasters permitted to obtain the experience, useful for disseminate among the forecasters. This practical rules must be based the knowledge of technology and limitations of algorithms for more effective interpretation the main correction.

2.4.2 Goal

To prepare the recommendations for forecasters to formulate and disseminate the experience of feedback and trainings of period before and during the Sochi-2014 concerning the features of interpretation of limited- area mesoscale NWP Systems (based COSMO-Ru technologies).

3 The guidance of the optimal domain's size selection for 1.1 km resolution of nested COSMO models for the regions with complex mountain relief (G. Rivin, M. Shatunova, J. Helmert)

3.1 Introduction

The development and implementation of COSMO model with 1.1 km resolution for the Sochi region was a part of RDP works within the Priority Project CORSO (Consolidation of Operation and Research results for the Sochi Olympics). The RDP results shown the strong dependence of the predicted precipitation amount and its spatial distribution on the models domain size. This problem need the more attentive examination, because the run of COSMO-Ru1 as part of nested technologies is rather expensive in point of view of computational time. The computing resources and the technological requirements of providing forecast by a certain time determine the model run timing. On the other hand, there are requirements for the quality of the forecasts. Factors determining the weather in the region, e.g., predominant direction of air mass transfer, and regional orography define possible location and size of the simulation domain. Forecasts assessment for the area on interest, area of the Sochi Olympics 2014 in our case, allow designate preferable domain. We used data from the observation sites located for the most part near the sports venues in two clusters coastal and mountainous, for verification. Sites of the first cluster are located on the coastline of 95 km and at distance up to 12 km, at an altitude from 2 to 660 m. Mountainous sites are located within the Mzymta river valley and adjoined highlands at an altitude from 560 to 2225 m. Forecast verification was made for the whole region and for mountain valley separately considering distribution of the observation sites.

3.2 Simulation domains

Selection of the simulation domains size and location was made using the results of Subtask 2.2 of PP CORSO Compilation of significant weather climatology for the Sochi region, based on automated weather classification and taking into consideration influence of regional orography. Area of Sochi Olympics and surroundings presented on Fig. 1, where red rectangle indicates location of the Sochi2014 sport venues. Air masses coming from WSW and EN determined weather conditions in the area of Sochi2014 during the winter. Local cyclone formed over the eastern Black Sea basin affects weather also. While western (NW or SW) direction prevails in a large-scale air transport, warm and moisture air mass moves along the local cyclone periphery and along the coast in NE direction, shifts over land and inflows into the mountain valleys. Two mountain ridges Main Caucasian Ridge and East Pontic Mountains are a kind of natural border, preventing the penetration of air masses in the Sochi2014 area from the northeast and southeast. It seems reasonable that simulation domain covered the eastern Black Sea basin and be limited by mentioned mountain ridges. The following three variants were suggested: domain 1 (D1) has 300x300 grid points, domain 2 (D2) has 450x450 and domain 3 (D3) has 450x650, and grid points (see Fig. 2). The results obtained for these three domains were verified by VERSUS. An effect of the simulation domain size and location on precipitation forecast was investigated also for several cases of heavy precipitation. Additional simulations were performed for the one more domain D4 (750x750 grid points) for case studies. COSMO-Ru7 model (7 km grid spacing) provided initial and boundary conditions for COSMO-Ru1.

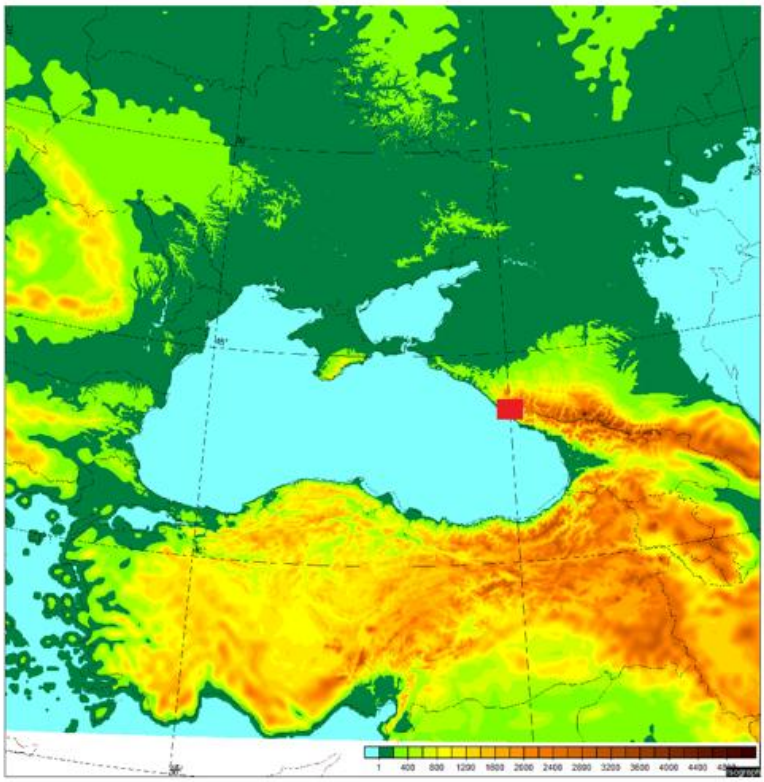


Figure 1: Geographical location of Sochi2014 region (red rectangle).

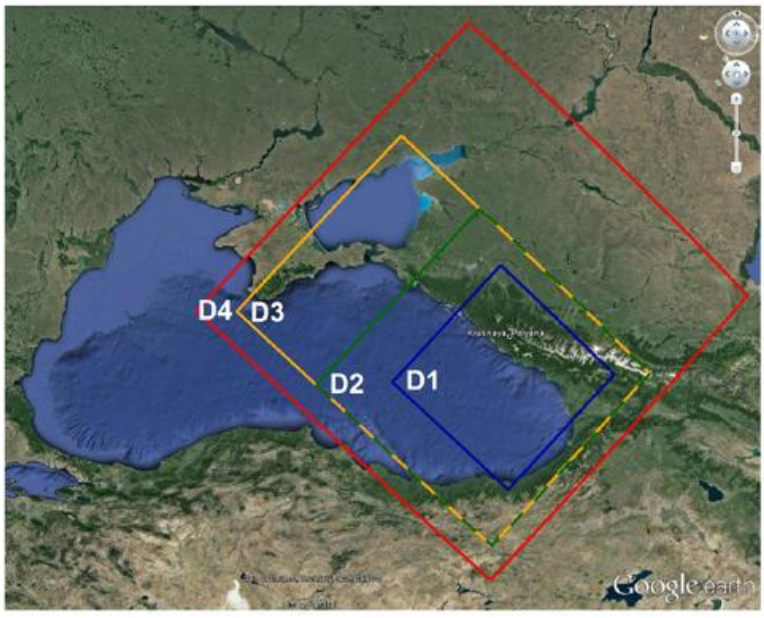


Figure 2: Simulation domains: D1 (blue rectangle) 300 x 300 grid points, D2 (green rectangle) 450 x 450 grid points, D3 (yellow rectangle) 450 x 650 grid points, D4 (red rectangle) 750 x 750 grid points.

3.3 VERSUS verification results

By means of VERSUS, 24 h forecasts for air temperature at 2 m, dew point temperature at 2 m, wind speed at 10 m and 3 h precipitation sum were verified. Two kind of VERSUS stratification were used. The first, Sochi39, includes 56 stations of which half is in the coastal zone and half is in the mountains. The second stratification, Sochi_Mount, includes 25 stations located in the mountain cluster of Sochi2014 within the upper and middle part of the Mzymta river valley. Nearest point 3D optimized method was chosen for verification. During February and March, 2014 local time was equivalent to UTC + 04 h. Verification results mean error (ME) and root mean square error (RMSE) of the 24 h forecast for the different domains are presented on Fig. 3. The results for all domains and two variant of stratification look rather similar but have some features:

- RMSE is less for the D1 for the daytime (04 14 UTC) for air temperature and wind speed forecasts. RMSE difference reaches 0.8 for T2m forecast and 0.3 for wind speed forecast;
- dew point temperature was predicted better for D1 for the most, difference between results for D1 and D2 and D3 became greater after 18 h and at 24 h lead time amounts 0.7-0.9 for mean error.

The difference between results for D2 and D3 is negligible. Thus, the expansion of the simulation domain in the NW direction has not given effect. Average difference between results for D1, D2 and D3 for air temperature is less 0.1 (for ME) and 0.1-0.2 (for RMSE), for dew point temperature is less 0.4 (for ME) and 0.4-0.6 (for RMSE), for wind speed is less 0.1 (for ME) and about 0.1 (for RMSE). Analysis of the results for two stratifications shows that wind speed is slightly better predicted for the mountain cluster, whereas air temperature and dew point temperature forecasts for mountain cluster have lesser score than for the whole assessment area. To assess accumulated precipitation several verification scores described below were calculated using 2x2 contingency table (Table 8) for different thresholds. These scores were calculated for 3h precipitation forecast and for all lead-time (Tables 9-13).

Bias is used to detect whether model overestimated precipitation event or underestimated it (Schirmer, Jamieson, 2015), $bias = (A + B)/(A + C)$.

Critical success index (CSI), also called the threat score (TS), $CSI = A/(A + B + C)$. This score indicates the relative worth of different forecasting techniques (Schaefer, 1990).

True skill statistic (TSS), $TSS = (A \cdot D - B \cdot C)/[(A + C)(B + D)]$; also known as Hanssen-Kuiper skill score is a verification measure of categorical forecast.

Heidke skill score (HSS), $HSS = (A + D - E)/(A + B + C + D - E)$, where E is the correct random forecasts. HSS score used for evaluating rare event forecast is suitable for heavy precipitation forecast assessment.

Equitable Threat Score (ETS), also called Gilbert skill score (GS), $ETS = (A - CH)/(A + B + C - CH)$, where $CH = (A + B)(A + C)/(A + B + C + D)$ is hit due to chance. ETS is commonly used for precipitation verification, in particular because correct no-event forecasts are not considered in this score.

Extremal Dependency Index (EDI), $EDI = (\log F - \log H)/(\log F + \log H)$, where $F = B/(B + D)$ is false alarm rate and $H = A/(A + C)$ is hit rate. EDI is an innovative

categorical measured, being independent from base rate $(A+C)/(A+B+C+D)$, used for rare dichotomic events verification.

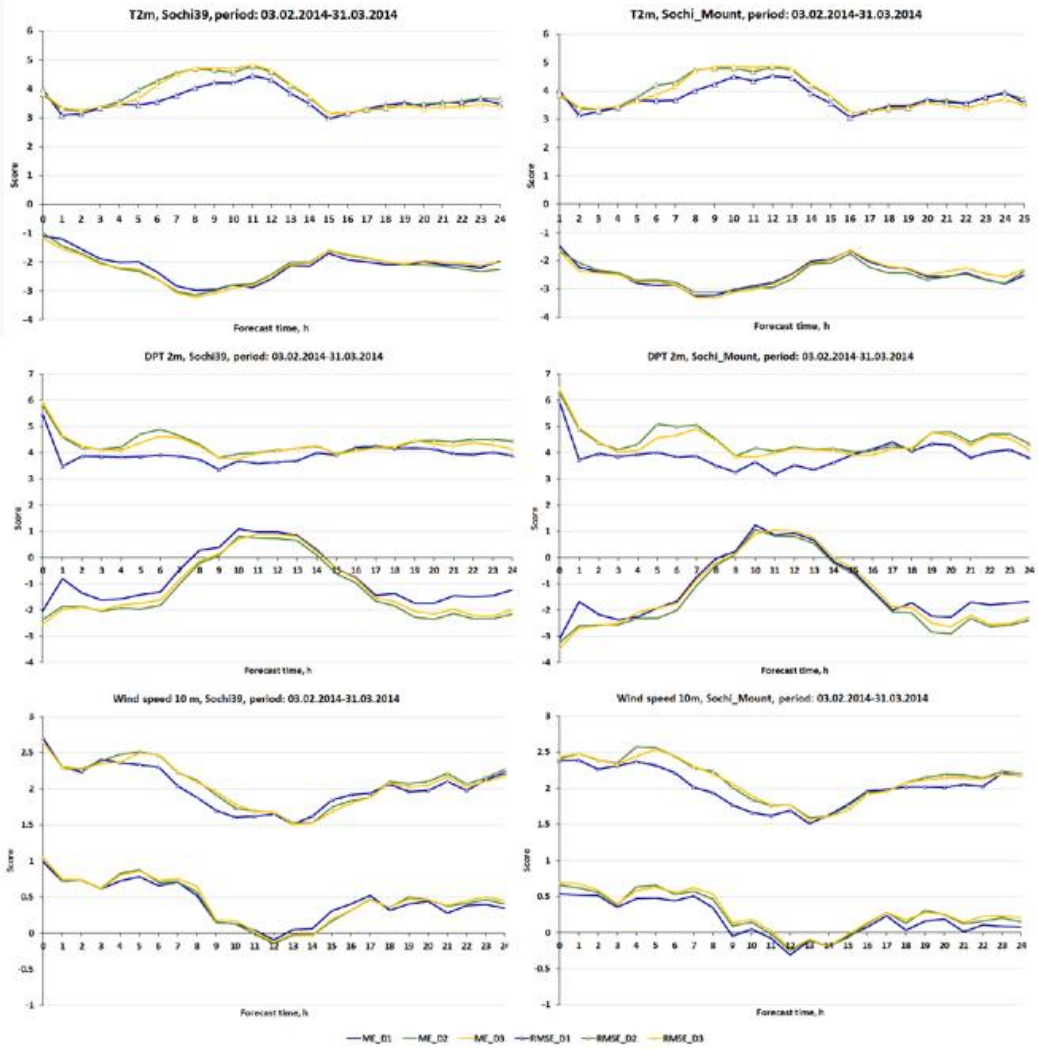


Figure 3: Mean error and RMSE of the air temperature at 2 m, dew point temperature at 2 m and wind speed at 10 m forecasts obtained for three domains.

Precipitation on February and March 2014 in Sochi2014 region usually occurred during daytime, 7-15 h local time (total number of cases indicated at the bottom of the column on Fig. 4). The most cases of heavy precipitation were observed within the 10-16 h local time. Secondary maximum of heavy precipitation (>5 mm/3h) was registered at 22-01 h local time. Bias values for precipitation threshold 0.1 mm/3h for different lead-time (Fig. 5a) show that model overestimates precipitation event for all lead-time regardless of the domain size. For moderate and heavy precipitation (1-5 mm/3h) there is a temporal shift shown on Fig. 5b: while precipitation for the period 9-12 UTC is overestimated, there is underestimation of the event for the previous 3 hours (6-9 UTC). Evaluation of the precipitation with the threshold 3, 5 and 10 mm/3h was made using sample large enough to obtain statistically significant scores.

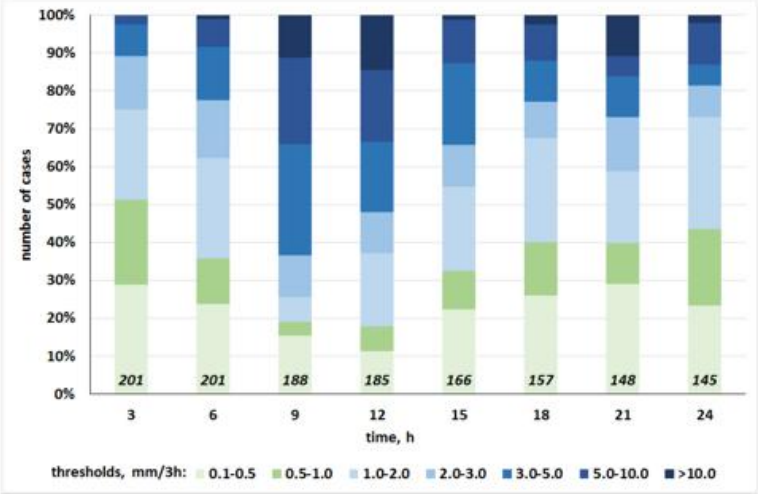


Figure 4: Number of observed precipitation cases for different threshold for 3-hour periods during the day.

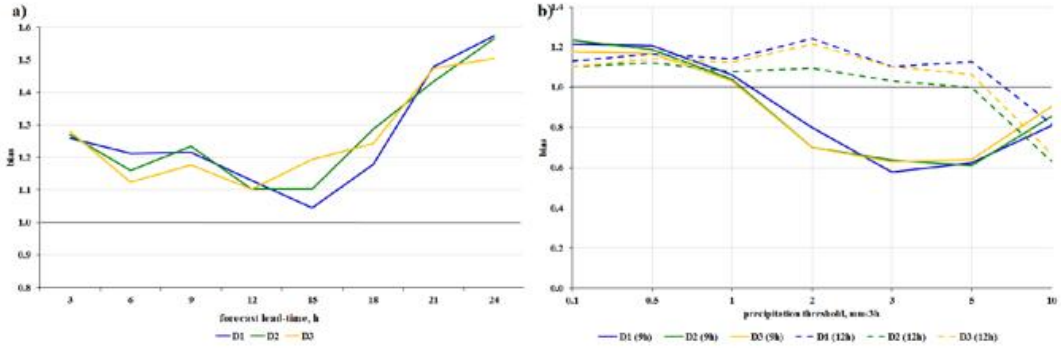


Figure 5: Bias for precipitation threshold 0.1 mm/3h for different lead-time (a) and for different thresholds for lead-time 9 and 12 h (b) for different simulation domains.

Analysis of the scores presented in Tables 9-12 shows that for the first 3 hours period for all domains forecast may be considered no more than satisfactory. Assessment increases for the next periods and for the 9-12 h period forecast has the highest scores for all domains and precipitation thresholds from 0.1 to 5 mm/3h. It is noted that model has rather high scores for forecast precipitation more 10 mm/3h with lead-time 21 h, when secondary maximum of heavy precipitation observed. Comparison of the results for different domains shows that scores for precipitation event forecast (0.1 mm/3h threshold) for D1 are slightly worse than that for D2 and D3. Based on ETS and HSS values that are most suitable for rare event assessment it can be conclude that D1 and D3 have some advantages in heavy precipitation forecasting. It is interesting to note that precipitation forecast for 10 mm/3h threshold is better for D1 for 12 h lead-time, while D3 has some advantages for longer lead-time 21 h. This is also confirmed by the EDI values. Verification by VERSUS shows that small domain can be used for precipitation simulation for the lead-time until 18 h, for greater lead-time it is better to make simulation for larger domain.

3.4 Verification of heavy precipitation event forecast (case studies)

Analysis of the several cases of heavy precipitation was performed to assess the effect of the domain size on the forecast of precipitation amount, its spatial and temporal distribution. The analysis was performed for 12 sites located in the central part of the Sochi2014 area (Fig. 6). Solokh-Aul, Lazarevskoe and Imeretinka are in the coastal cluster, but only the last two are on the seashore. Solokh-Aul is located in the hills at a distance of 12 km from the sea.



Figure 6: Location of the observation sites used in case studies.

Predicted precipitation daily amount for all domains in comparison with the observations are presented in Tables 1-5. The maximum difference between forecasts was nearly 10 mm/24h. Comparison of the results detects various situations, e.g.:

- results for all domains could be very close to each other and to observation (see Table 3 for G.Karusel-1500);
- difference between forecast and observation could be much greater than difference between forecasts for various domains (see Table 2 for Solokh-Aul);
- for the one domain predicted amount could have good agreement with observations while the difference between forecasts for various domains could be significant (see Table 1 for Kepsha).

Site	Obs.	Forecast			
		750x750	450x650	450x450	300x300
Coastal cluster					
Solokh-Aul	23.0	27.5	28.9	30.5	31.7
Lazarevskoe	19.7	10.8	14.5	7.8	14.2
Imeretinka	9.0	17.0	14.0	17.3	13.3
Mountain cluster (h<1000 m)					
Kepsha	33.5	33.7	29.3	28.6	24.1
Kr. Polyana	29.4	40.0	39.3	38.9	37.1
K. Laura	37.5	41.4	42.4	40.6	40.9
Sledge-700	24.1	28.4	26.8	27.4	25.1
Rosa Khutor-7	32.7	24.6	23.3	26.3	23.1
Sledge-830	24.1	22.8	21.0	22.7	18.4
Mountain cluster (h>1000 m)					
Rosa Khutor-4	38.4	25.9	24.4	26.2	23.1
Biathlon Std.	34.7	30.4	31.2	28.8	30.3
G. Karusel-1500	26.0	22.3	21.0	22.3	19.1

Table 1: Observed and forecasted accumulated precipitation for 24 h on February 18, 2014.

Precipitation temporal distribution presented on Fig. 7 for several sites allows detect domain size influence on the forecast. Variation of the hourly precipitation amount depending on domain could be estimated also. The precipitation on March 17 was caused by convection developed on the cold front and occurred in the morning with peak at 6-7 UTC on coastal sites and at 8-10 UTC on mountainous sites. Maximum hourly amount equal to 12.7 mm was observed at Kepsha. On March 18 precipitation was accompanied by the passage of the rather weak warm front and continued throughout the day. On coastal sites two peaks were observed at 7 and 12 UTC, while within the mountain valley precipitation was more evenly distributed in time. The same forecasted temporal distribution of the precipitation was obtained for all simulation domains. There is shift of the event start time that is about 1-2 hours, predicted precipitation starts earlier than observed. The difference between forecasts for D1-D4 is small for the first 3-5 hours of the forecast. Later it could reach 2-3 mm for hourly-accumulated amount and this was noted both for coastal and mountains sites.

Site	Obs.	Forecast			
		750x750	450x650	450x450	300x300
Coastal cluster					
Solokh-Aul	74.7	37.4	41.5	38.9	41.1
Lazarevskoe	39.0	24.4	26.7	24.6	24.5
Imeretinka	22.7	33.4	31.4	31.8	35.7
Mountain cluster (h<1000 m)					
Kepsha	28.9	31.5	34.4	34.0	35.8
Kr. Polyana	15.1	17.9	20.6	20.7	21.8
K. Laura	17.0	15.3	17.8	17.4	17.2
Sledge-700	15.8	14.2	17.2	16.6	15.3
Rosa Khutor-7	13.8	14.0	16.9	17.0	17.4
Sledge-830	18.8	15.7	16.9	18.8	17.3
Mountain cluster (h>1000 m)					
Rosa Khutor-4	13.9	16.7	19.2	18.9	20.0
Biathlon Std.	11.1	15.0	16.9	16.4	11.6
G. Karusel-1500	20.9	17.0	21.4	21.1	20.3

Table 2: Observed and forecasted accumulated precipitation for 24 h on March 11, 2014

Site	Obs.	Forecast			
		750x750	450x650	450x450	300x300
Coastal cluster					
Solokh-Aul	32.9	26.3	26.2	25.9	26.0
Lazarevskoe	24.2	13.8	15.6	14.7	14.6
Imeretinka	13.4	18.5	19.1	18.3	19.1
Mountain cluster (h<1000 m)					
Kepsha	26.4	17.8	18.3	18.7	18.7
Kr. Polyana	10.4	8.9	9.6	9.7	9.8
K. Laura	15.1	7.6	7.9	7.9	8.4
Sledge-700	12.9	10.6	10.9	10.8	11.5
Rosa Khutor-7	11.7	8.9	9.1	9.0	10.2
Sledge-830	14.2	10.3	10.7	10.6	11.5
Mountain cluster (h>1000 m)					
Rosa Khutor-4	13.8	9.9	10.0	10.1	11.2
Biathlon Std.	15.1	9.4	9.4	9.4	10.1
G. Karusel-1500	15.3	13.5	13.5	13.6	14.5

Table 3: Observed and forecasted accumulated precipitation for 24 h on March 12, 2014

Site	Obs.	Forecast			
		750x750	450x650	450x450	300x300
Coastal cluster					
Solokh-Aul	4.9	14.0	14.8	11.9	12.9
Lazarevskoe	9.2	3.6	3.3	2.5	3.5
Imeretinka	6.6	4.9	5.2	5.1	3.6
Mountain cluster (h<1000 m)					
Kepsha	34.3	29.8	30.4	29.6	31.3
Kr. Polyana	22.5	17.2	17.8	19.6	18.7
K. Laura	18.5	21.5	21.5	23.7	21.7
Sledge-700	14.3	26.8	25.7	25.1	25.3
Rosa Khutor-7	17.3	29.1	27.3	27.7	26.9
Sledge-830	16.7	27.8	26.6	26.8	26.9
Mountain cluster (h>1000 m)					
Rosa Khutor-4	22.2	34.8	32.8	33.3	32.2
Biathlon Std.	9.1	22.6	21.4	20.4	21.5
G. Karusel-1500	22.4	28.8	27.6	26.7	28.8

Table 4: Observed and forecasted accumulated precipitation for 24 h on March 17, 2014

Site	Obs.	Forecast			
		750x750	450x650	450x450	300x300
Coastal cluster					
Solokh-Aul	13.0	10.1	15.8	16.8	19.8
Lazarevskoe	21.3	7.0	15.6	10.3	15.5
Imeretinka	1.2	0.6	19.1	1.4	1.2
Mountain cluster (h<1000 m)					
Kepsha	13.9	4.2	5.5	6.0	7.4
Kr. Polyana	20.8	12.9	14.2	13.1	14.5
K. Laura	24.5	16.4	17.5	17.2	19.7
Sledge-700	15.3	11.0	11.7	11.3	13.6
Rosa Khutor-7	24.8	11.4	12.2	12.2	14.0
Sledge-830	14.3	11.0	11.4	11.0	13.6
Mountain cluster (h>1000 m)					
Rosa Khutor-4	25.6	15.1	16.2	15.7	18.5
Biathlon Std.	16.2	13.9	14.7	14.2	17.1
G. Karusel-1500	19.6	12.1	12.6	11.9	14.4

Table 5: Observed and forecasted accumulated precipitation for 24 h on March 18, 2014

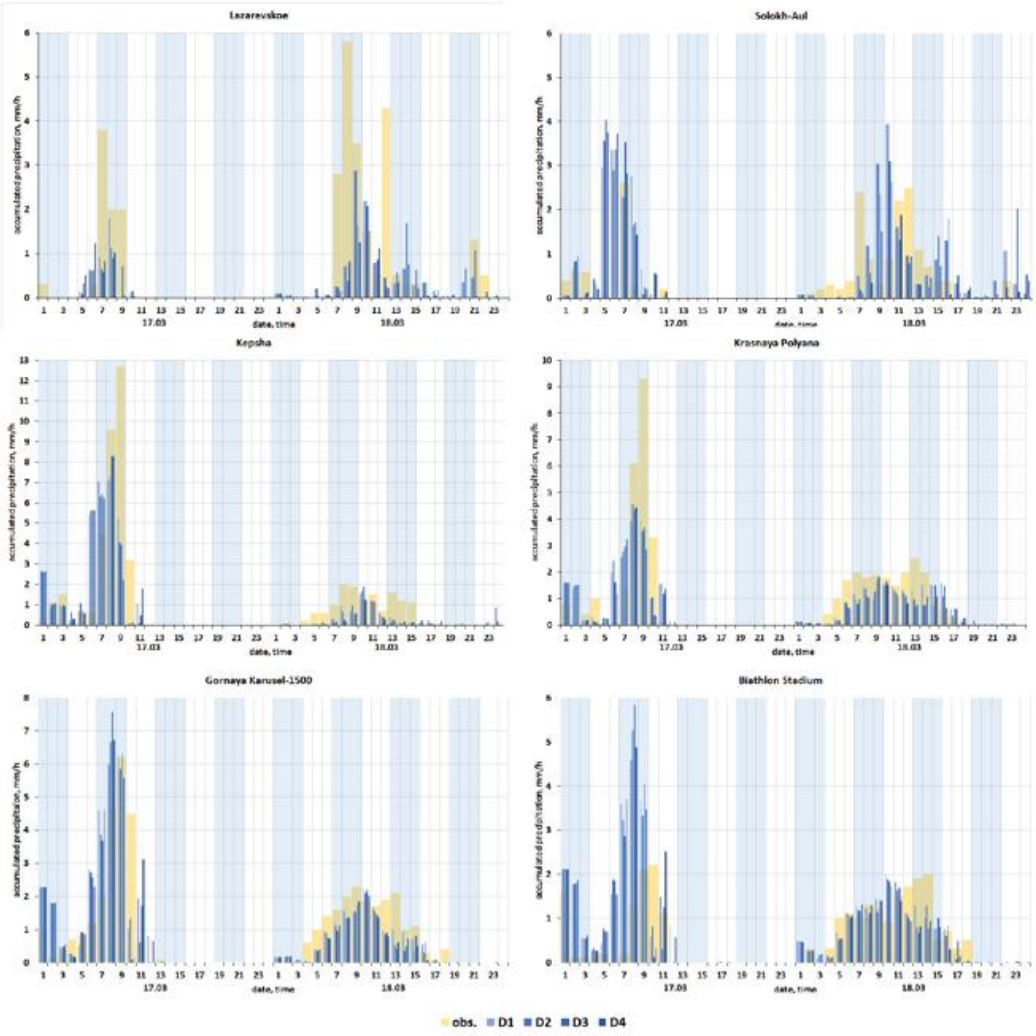


Figure 7: Hourly accumulated precipitation forecasts simulated for various domains in comparison with observation.

The most evident effect of the domain size in precipitation spatial distribution reveals near the domains boundary (Fig. 8 and 10). The difference between forecasts for two domains can reach 10 mm/day. Looking closer on the results for D1-D4 (Fig. 9 and 11), it is noted that the main structure of the precipitation spatial distribution is the same, but there are some variations. In particular, on March 17 precipitation amount increases within the Mzymta river valley (where the Olympic competition took place) with increasing domain size (Fig. 11). Comparison the results for different events shows that changes of the precipitation maximum location and amount could occurred in different direction. The interrelation of the direction of the air mass movement and local orography plays its role here.

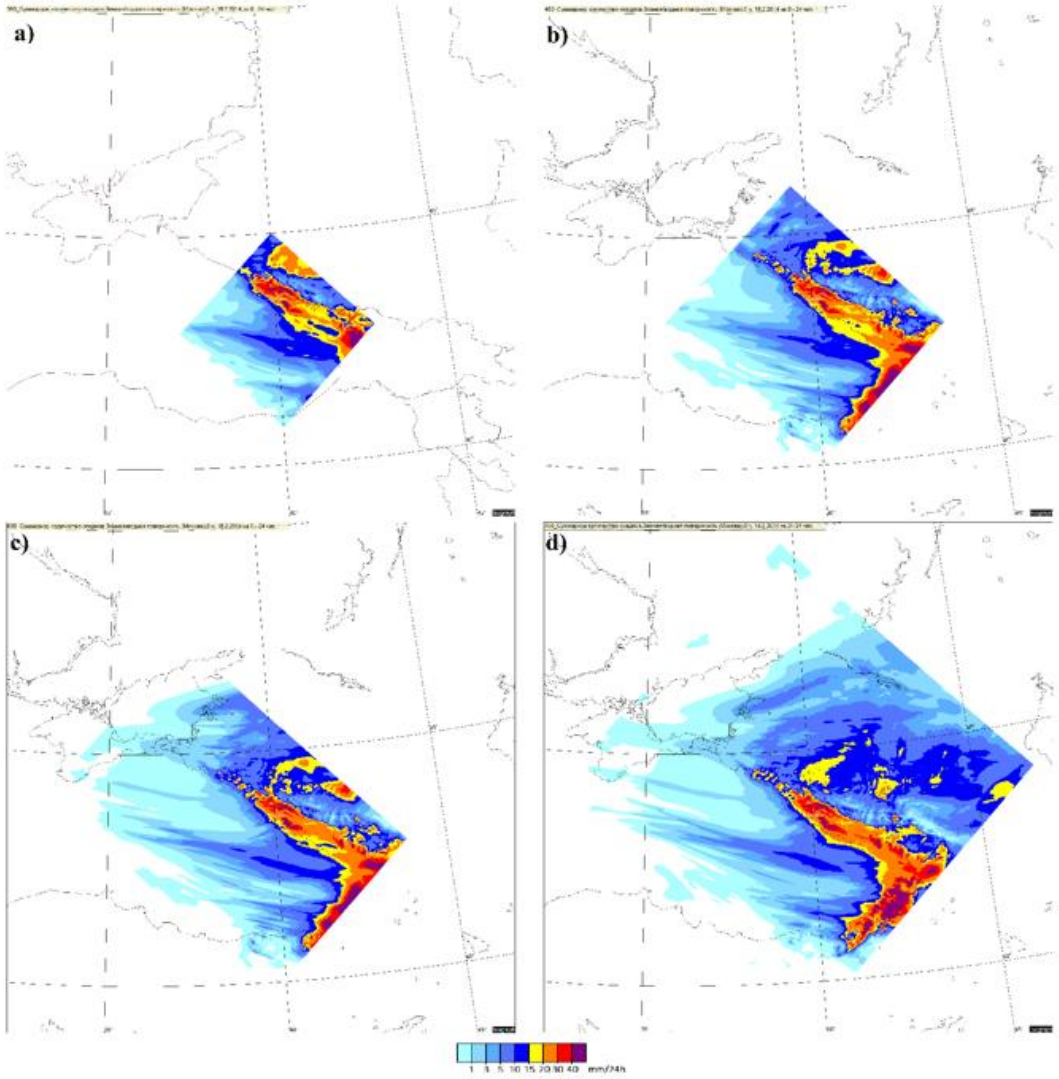


Figure 8: 24 hours accumulated precipitation predicted for various domains: D1 (a), D2 (b), D3 (c), D4 (d). Forecast start 18.02.2014, 00 UTC.

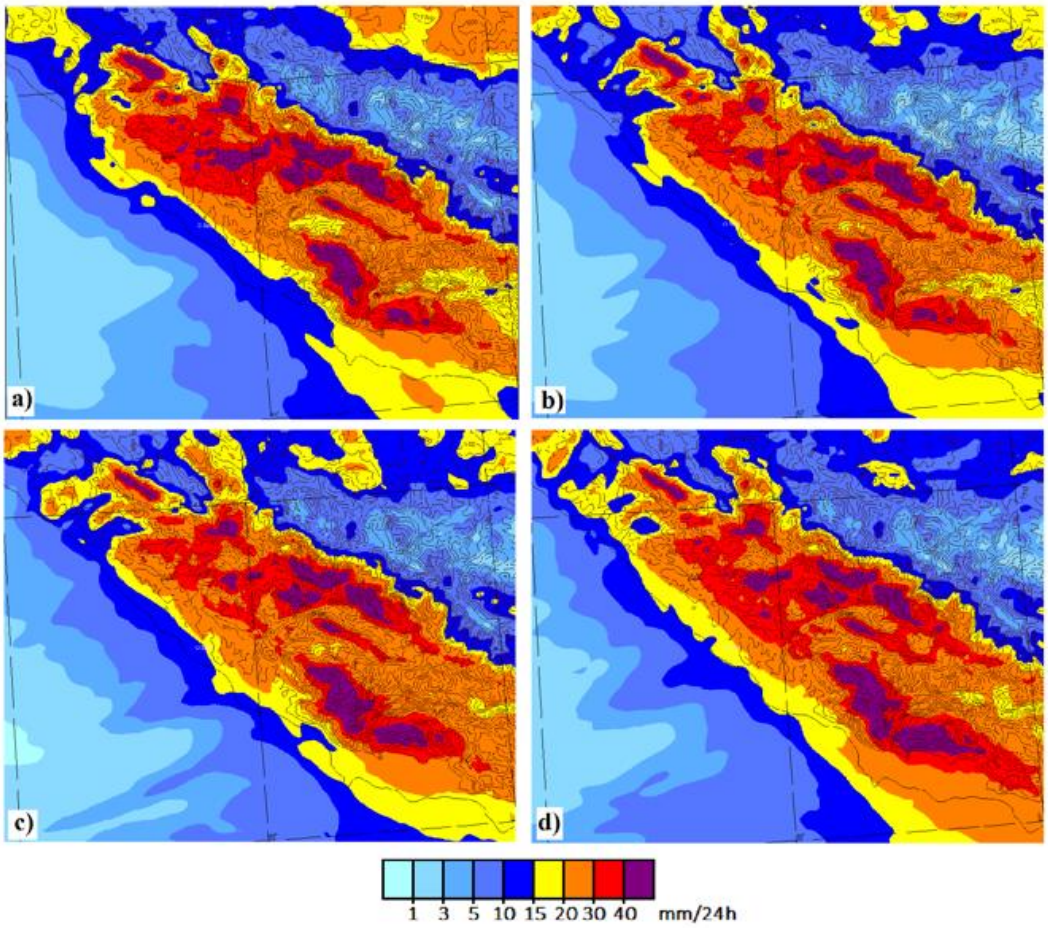


Figure 9: The same as Fig. 8 but for the Sochi region with model orography (isolines).

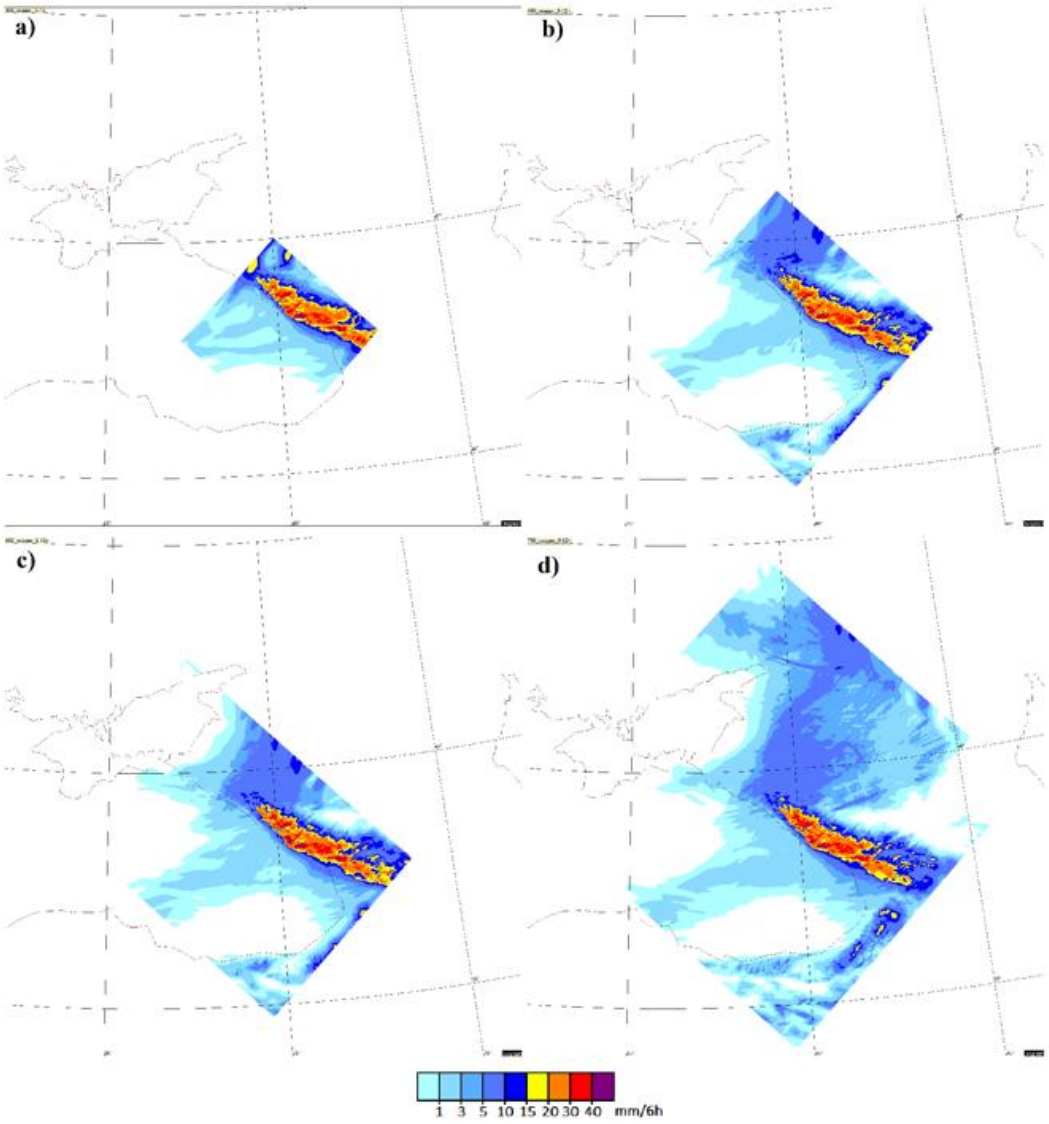


Figure 10: Accumulated precipitation for the period 06-12 UTC predicted for various domains: D1 (a), D2 (b), D3 (c), D4 (d). Forecast start from 17.03.2014, 00 UTC.

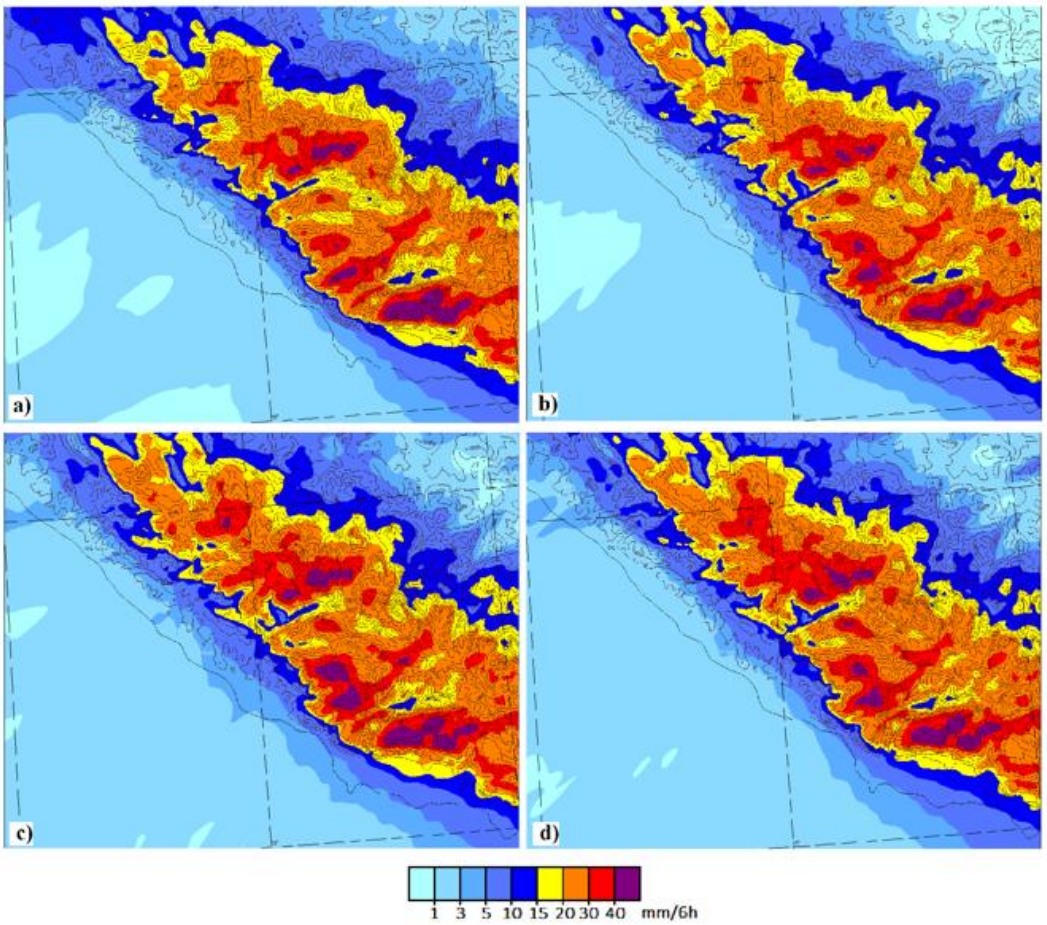


Figure 11: The same as Fig. 10 but for the Sochi region with model orography (isolines).

3.5 Conclusions

COSMO-Ru1 model simulations performed for different domains allow evaluate influence of domain size on the weather elements forecast. A large number of observations provided an assessment period from February 3 to March 31, 2014 for Sochi2014 region. Verification by VERSUS of the forecasts for air temperature at 2 m, dew point temperature at 2 m, wind speed at 10 m shown insignificant variations of the results for chosen domains. Verification shown that model overestimates precipitation event for all lead-time regardless of the domain size and indicated the presence of temporal shift in the forecast of the moderate and heavy precipitation. The difference between forecasts of heavy precipitation amount for various domains can reach 10 mm for daily amount and 2-3 mm for hourly-accumulated precipitation. Verification scores used traditionally for precipitation assessment demonstrate possibility to use rather small simulation domain (300x300 grid points) for the forecasts with lead-time until 18 h without loss of forecast quality.

4 Development of algorithm of subgrid h-correction of T2m for mountains based on COSMO forecasts of local lapse rate (h-correction) (I. Rozinkina, J-M. Bettems, D. Blinov, A. Euripides)

The mail idea of proposed technique is to forecast the lapse-rate of T and Td for the points and make the T2m and TD2m correction based these values. This could be useful in inversia-situations via hight- resolution modeling. In the framework of CORSO-A the proposed algorithm should to be included into FieldExtra.

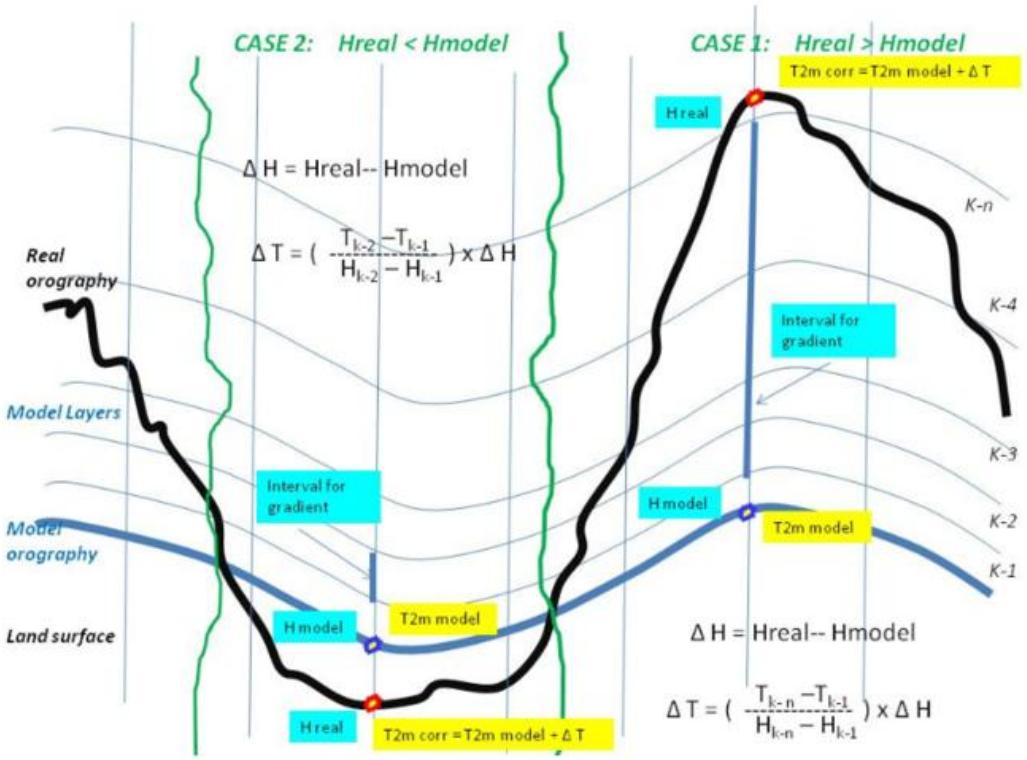


Figure 12: The description of tests and results is given in PP CORSO report.

The description of algorithm and proposals for FieldExtra extension are obtained. The realization of algorithm of FieldEextra (calculation of orography differences for points in FieldExtra and extension of software) + additional testing of 1-D version have been included The algorithm was formulated and included into FieldExtra Software (since 2016, FieldExtra 12.2.0, J-M Bettems).

5 COSMO-BASED ENSEMBLE FORECASTING FOR SOCHI-2014 OLYMPICS: ARCHIVING THE RESULTS (E. Astakhova, A. Montani, D. Kiktev, D. Alferov, A. Smirnov)

5.1 Introduction

The last winter Olympic/Paralympic Games were held in February-March 2014 in Sochi, Russia. The Russian Meteorological Service (Roshydromet) initiated a special international project FROST-2014 (FROST - Forecast and Research in the Olympic Sochi Testbed) related to these Games; it got a status of WMO World Weather Research Programme (WWRP) blended Forecast Demonstration and Research and Development Project (Kiktev et al., 2015a; Kiktev et al., 2015b) . The COSMO activity in FROST-2014 was integrated within a consortium priority project Consolidation of Operation and Research results for the Sochi Olympic Games (PP CORSO) (Rivin and Rozinkina, 2013). PP CORSO finished in 2014. Its results included a successful experience of high-resolution modeling in mountainous areas, improved downscaling/postprocessing procedures for the Sochi region, regular provision of probabilistic forecasts during the Games as well as research in ensemble modeling with different resolutions. It was realized in 2014 that some additional work was necessary to implement CORSO achievements to COSMO practice and to enable their better usage. That is why the priority task CORSO-A followed PP CORSO. Here only the ensemble component of CORSO and CORSO-A activity will be considered. We shall briefly remind CORSO results, overview the goal of CORSO-A, and summarize its results.

5.2 Ensemble prediction systems developed in CORSO

Two ensemble prediction systems (EPS) were developed within PP CORSO: COSMO-S14-EPS with a 7-km resolution and COSMO-Ru2-EPS with a 2.2 km resolution (Montani et al, 2013, 2014, 2015). COSMO-S14-EPS (S14 stands for Sochi2014) was created at ARPA-SIMC (Montani et al, 2013) and was a version of COSMO-LEPS system (Montani et al, 2011) displaced from the European area to the Sochi region. The system was driven by the ECMWF EPS, namely, by its most representative prognostic realizations which were selected by a clustering procedure. The lower boundary condition was a result of COSMO model run in hindcast mode (a short-range forecast nested on ECMWF analyses). The model-related uncertainties were taken into account in COSMO-S14-EPS by using two different convection parameterization schemes (Tiedtke or Kain-Fritsch, random choice) in different members and also by varying tuning coefficients in parameterizations of sub-grid scale processes (in particular, turbulent). The most essential differences between COSMO-S14-EPS and COSMO-LEPS systems were integration domains (Sochi region or Europe) and ensemble sizes (10 or 16 members, respectively). The system with a 2.2-km grid size named COSMO-Ru2-EPS ran at Roshydromet and performed a dynamical downscaling of COSMO-S14-EPS increasing the forecast resolution both in horizontal (from 7 to 2.2 km) and in vertical (from 40 to 50 levels). No additional perturbations were introduced neither to initial and boundary conditions nor to the model. The ensemble has the same size as in COSMO-S14-EPS and was composed of 10 perturbed members with no control. Both EPSs ran operationally during the Olympics/Paralympics, their results were provided to Sochi forecasters and proved to give a valuable support to them. In fact, the entire length of parallel runs of COSMO-S14-EPS and COSMO-Ru2-EPS was longer than the period of the Games and covered December 2013-April 2014. The forecast results were archived on Roshydromet servers along with initial and boundary conditions generated by COSMO-S14-EPS and later used by COSMO-Ru2-EPS.

5.3 CORSO-A necessity and goal

It is worth to note here that COSMO ensemble forecasts can be considered a part of a more extensive FROST-2014 archive that included the results of four more ensemble prediction systems (Kiktev et al, 2015; Astakhova et al, 2015). The two systems, GLAMEPS and HarmonEPS, were presented to FROST-2014 by the Norwegian Meteorological Institute, while ALADIN-LAEF and NMMB-EPS came from the Central Institution for Meteorology and Geodynamics (ZAMG), Austria, and the National Centers for Environmental Prediction (NCEP), USA, respectively. The EPS resolution was 7 to 11 km except for the convection permitting HarmonEPS with its 2.5 km horizontal step; the ensemble size varied from 7 to 54. Additionally, deterministic forecasts by 9 different systems, nowcasts from 6 systems, and a variety of observational data of different types, including station, radar, profiler data, operational meteorological bulletins, camera snapshots, etc., were aggregated at the FROST-2014 server and available via the project web-site http://frost2014.meteoinfo.ru. By no doubt, this huge amount of forecast and observation data could be very useful for research in the field of short-range limited-area deterministic and ensemble prediction. Remember that the Sochi area is a very complex region with steep mountains lying near the warm Black Sea and forecasting in mountainous regions is still a challenge for numerical weather prediction models. However, it became clear after the Olympic Games, that in research tasks it would be quite difficult and problematic to use the forecast data in the form presented on the FROST-2014 server because of different coding and organization of data files transferred to Roshydromet by various data providers. The application of the archive would be much easier if the forecast data were organized following some standard rules. A good idea is to follow TIGGE-LAM project and to prepare a Sochi unified archive using the coding standards and user interfaces adopted in TIGGE-LAM (Paccagnella et al., 2012). TIGGE and TIGGE-LAM data portals are well known and very popular in scientific community and a lot of research has been done using the data presented there. That is why one of CORSO-A goals was to implement a unified archive of COSMO ensemble forecasts (with 7 and 2.2 km resolutions) for the Sochi area. The archive was expected to be accompanied by the data on initial and boundary conditions for high-resolution ensembles and by a list of important weather events during Olympics and Paralympics.

5.4 A Unified Sochi archive

The Sochi unified archive covers the period from January 15, 2014 to March 16, 2014. This time interval coincides with the period adopted for verification in FROST-2014 (January 15 - March 15, 2014). The archive contains the ensemble forecasts by COSMO-S14-EPS and COSMO-Ru2-EPS starting at 00 UTC and 12 UTC on the dates within the above-mentioned two-month interval. The prognostic fields for all members are presented with a 3h time frequency on the original COSMO-model rotated latitude-longitude grid with resolutions 7 and 2.2 km for COSMO-S14-EPS and COSMO-Ru2-EPS, respectively. The accumulated parameters (precipitation and wind gusts at 10 m) are not archived at zero time step. The data are in WMO-GRIB2 format. The archived parameters and the corresponding coding information are listed in Table 6. The parameter set is slightly different from the TIGGE-LAM high-priority parameters. The Sochi archive does not contain large-scale precipitation, convective inhibition, and convective available potential energy. As static fields (land-sea mask and orography) did not change during the period, they were written to the archive only once.

Parameter	Abbreviation	Level	Units	GRIB2 specifics
10 meter U-velocity	10u	10m (103,10)	m/s	Instantaneous Product Discipline 0 Parameter Category 2 Parameter number 3 paramId 165
10 meter V-velocity	10v	10m (103,10)	m/s	Instantaneous Product Discipline 0 Parameter Category 2 Parameter number 2 paramId 166
Mean sea level pressure	msl	MSL (101)	Pa	Instantaneous Product Discipline 0 Parameter Category 3 Parameter number 0 paramId 151
Surface air temperature	2t	2m (103,2)	K	Instantaneous Product Discipline 0 Parameter Category 0 Parameter number 0 paramId 167
Surface air dew point temperature	2d	2m (103,2)	K	Instantaneous Product Discipline 0 Parameter Category 0 Parameter number 6 paramId 168
Acc. precipitation (liquid+frozen, convective+ large-scale)	Tp	surface (1)	kg/mˆ2	Accumulated from the beginning of the forecast Product Discipline 0 Parameter Category 1 Parameter number 52 paramId 228228
10 meter wind gust in the last 3 hours	10fg3	10m (103,10)	m/s	Product Discipline 0 Parameter Category 2 Parameter number 22 typeOfStatisticalProcessing 2 paramId 228028
Orography (geopotential height at the surface)	Orog	surface (1)	gpm	Instantaneous Control run Product Discipline 0 Parameter Category 3 Parameter number 5 paramId 228002
Land-sea mask	lsm	surface (1)	Proportion (0- 1)	Instantaneous Control run Product Discipline 2 Parameter Category 0 Parameter number 0 paramId 172

Table 6: Specification of Sochi archive.

Case	Meteorological process/ phenomenon	Models behavior	Impact on competitions
07.02	Foehn	Poor temperature forecast (underestimated by 1.4 ... 3.7 °C) by most models at Biathlon Stadium	
10-11.02	Dissipated precipitation	Precipitation in the Mountain Cluster predicted by the majority of systems, but not observed actually	
15.02		Poor forecast of maximum wind speed by most models at Krasnaya Polyana (underestimated by 3.5 ... 7 m/s)	
16.02	Low visibility		Postponed competitions at Laura and Extreme Park
18.02	Cold front	Good precipitation forecast by most models	
22.02	Foehn	Poor temperature forecast by most models (negative forecast errors: -2.4 ... -4.4 °C, mostly at 1500 m)	
11.03	Cold front. Low visibility	Bad description of the behavior of maximum temperature (Tmax) by most models (Tmax forecasted at noon, whereas in reality it was observed in the morning)	Postponed skiing competitions at Roza Khutor
13.03		Poor precipitation forecast by most models above 1500 m	
17.03	Cold front	Underestimation of maximum wind speed by most models above 1500 m	

Table 7: The most interesting cases during the Olympics/Paralympics.

The following ensemble meta-data information is included to the GRIB files:

- the ensemble size (GRIB key numberOfForecastsInEnsemble);
- the number of ensemble member (GRIB key perturbationNumber);
- the forecast type (GRIB key dataType = pf/cf, i.e. perturbed/control).

No data for mean sea level pressure is available for COSMO-S14-EPS. Initial and boundary conditions for high-resolution COSMO EPS are available on demand. All other FROST-2014 forecast data (both deterministic and ensemble) in the Sochi unified archive are coded

in the same way. The archive is available at http://frost2014.meteoinfo.ru (authorization required). To download the forecasts, you must switch to Forecasts (upper panel) -Export of gridded ensemble forecasts (right panel), and then select the necessary data using the interface similar to that of TIGGE-LAM data portal (Fig. 13). The necessary data will be prepared in compressed form, the corresponding reference will be sent by e-mail, and then the data can be downloaded. In addition to the prognostic fields, point forecasts (mean for ensembles) can be exported in csv format for more than 30 stations in the Sochi region. During the Olympics these forecasts were regularly presented at the multi-system page of the FROST-2014 site along with observation data and were considered very useful both by forecasters and researchers. To prepare these forecasts, the nearest grid-point approach was applied. A Web-tool to export observation data was also developed. For more details, please visit http:/frost2014.meteoinfo.ru, where you will also find a short description of all FROST-2014 numerical weather prediction systems. When research deals with the investigation of the skill of different weather prediction systems and of new ways to improve the forecast, it is important to have information about the synoptic situation in the analyzed domain and to select really essential events for case studies. To facilitate research in the field of short-range forecasting, Sochi forecasters prepared a list of cases recommended for detailed consideration. This list supplements the unified archive and is given in Table 7.

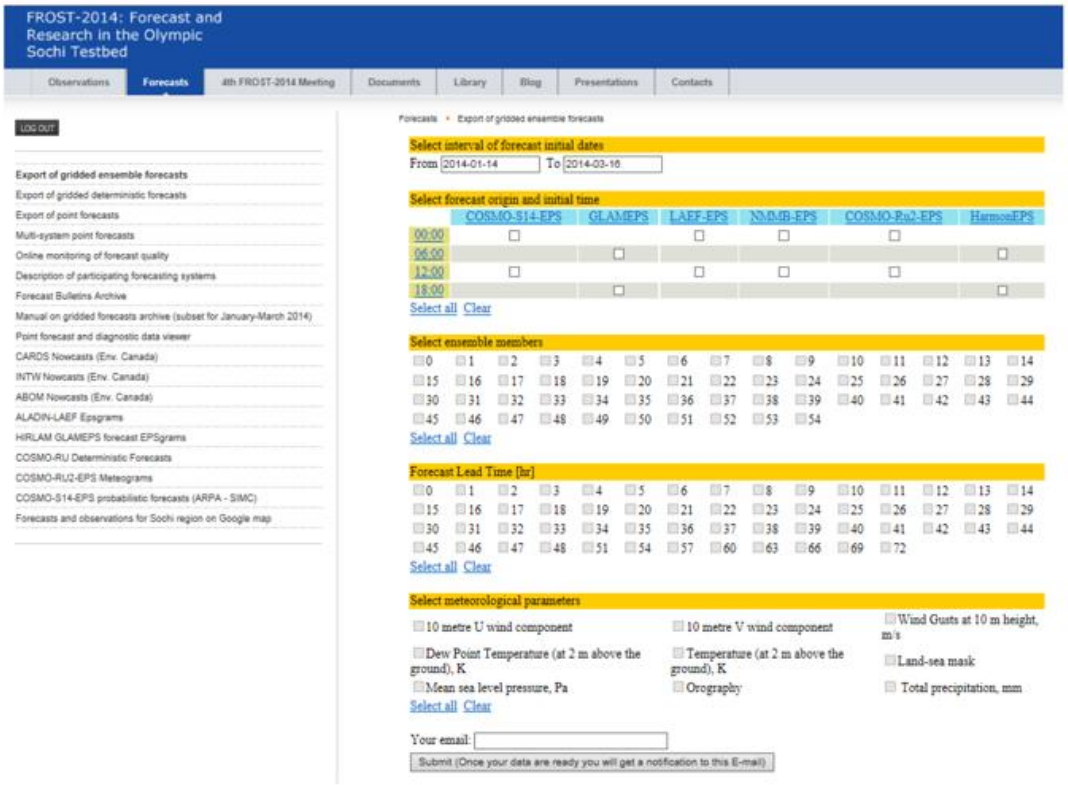


Figure 13: The FROST-2014 Web-interface used to download forecasts from the unified Sochi archive.

5.5 Conclusions

The unified Sochi archive containing forecasts for the area of Olympic Games 2014 for the period from January 15, 2014 to March 16, 2014 was prepared. The forecasts of two COSMO-based ensemble prediction systems, COSMO-S14-EPS and COSMO-Ru2-EPS with

resolutions 7 and 2.2 km respectively, are stored in the archive. The Web-tool to download the forecasts and observations as well as the list of interesting cases for research supplement the archive. The archive is organized in TIGGE-LAM style and is available at http://frost2014.meteoinfo.ru.

6 PREPARING OF RECOMMENDATIONS FOR FORECASTERS ABOUT FEATURES OF INTERPRETATION OF THE RESULTS OF MESO- SCALE MODELING (How to use the LAM mesoscale NWP results for mountain terrain) (I. Rozinkina, P. Eckert, G. S. Rivin)

The feed-back from forecasters of Sochi-team in domain of experience of use of numeric mesoscale products was studied. The Some recommendations for improving the further trainings were obtained.

6.1 Introduction

This document summarizes the lessons from experience of meteorological support of Sochi Trials 2011, 2012, 2014), Olympics and Paraolympics (2014), matters of trainings for forecasters team for Sochi2014 meteosupport (2011-2014) in part of use of High resolution NWP products based on COSMO-Ru output, the discussions of experts of the COSMO WG4 sessions during and after period of Sochi-2014 meteosupport and learning exercise. Some examples of NWP output of named learning period were upgraded. The complexity of the Sochi region (steep mountains located in close proximity to the wide warm Black Sea area) justifies the application of the high resolution for short-term numerical weather forecasting. Weather forecast for the "Sochi-2014" is yet a big challenge. This document is focused on the features of using Mesoscale NWP products for mountain terrain on example of COSMO-Ru model with resolution 2.2 km with 1.2 km nested domains. This document is prepared in framework of COSMO PT "CORSO-A" which had the goal to summarize the experience of using results obtained during the realization of Sochi meteosupport for dissemination among the COSMO participating countries. As part, it consists of fixation of certain experience obtained using the products of High-resolution mesoscale model.

6.2 Key definitions

- **Mesoscale atmospheric circulations** - in context of this document it is determined as the atmospheric processes of the spatial scale from several (first tens kilometers) to 100 - 500 km (as distinct from synoptic scale processes - from 100 - 500 to 5000 km). It should be considered that no defined distinction between these scales could be stated as absolute truth. All scales are cross-related and could be determined only specifically in context of specific synoptic situation. In terms of time scale the mesoscale processes could last from minutes to several hours. However these phenomena can generate the synoptic scale events, which could be viable for several days. The cyclones, including tropical cyclones are defined as synoptic objects. The earlier classifications (1970-th) limit the synoptic processes with much more rough scale 2000 km, latter (1980-th) - several hundred km, which partially was related to possibility identifying the circulation objects according the density of observation data.

- **Model grid step** - horizontal distance between the centers of adjacent grids. Size of atmospheric model grid step limits the lower edge of the synoptic objects, which could be identified by the certain model.

- **Resolution of modelled processes** - determines the dimension of reliably circumscribed by the model circulation objects. Normally these objects are of the size of 7 - 10 model grid sells. Accuracy of forecast of atmospheric phenomena related to these objects is of the same scale. For meteorological parameters near the surface, especially at the mountains, the accuracy of the detailed model results could be significantly closer to the size of grid sell due to local limited land surface forcing.

- **Mesoscale atmospheric models** - global or limited area models (LAM) with the grids allowing describe the different atmospheric processes of defined spatial and time intervals (1, 3).

- **Non-hydrostatic atmospheric models** are the models with such spatial resolution when the hydro-static approximation is non-correct, and is required the explicit consideration of vertical motion acceleration (based on vertical component of wind speed), where the hydrostatic approximation can not be used. Non-hydrostatic effects should be taken into account for the grids with the step lesser than 9 - 10 km. This is the typical characteristic of the contemporary models for the limited areas. At the same time, the non-hydrostatic approach is evolved in global modeling aspect.

- **Convective-resolving atmospheric models** - models of the atmosphere allowing (not using parameterizations) describe the large convective systems. Such models have the horizontal grid step of less than 3 km. However, a certain part of convective processes (depending on grid step) will remain in the under-grid scale and should be parameterized. The algorithms of remaining share of convective processes should adequately describe their scale.

6.3 Main statements of use of products of global / Limited area NWP Products for short-range and very-short range forecasting

For short-range weather prediction a forecaster should analyze the output of both kinds of NWP technologies: global and systems of the limited area modeling. The advance of LAMs against the global models is determined by combination of two factors: higher resolution / considering non-hydrostatic effects and the list of available output for forecasters of National meteorological centers, which develop LAM technology. The following statements explain the above.

Purposes for the use of the output of:

a) **Global modeling**

To determine the large-scale weather patterns of atmospheric processes, analyzing and forecasting of generation, evolution and trajectories of the cyclones and anticyclones in short- and medium-range forecasting (in medium-range forecasting the forecasts are based usually on global ensemble modeling). Grid resolution of advances operational global models allows reasonably accurately reproduce the baroclinic zones, jet streams in upper troposphere and stratosphere, processes of cyclones generation, forming and degradation of atmospheric fronts. The grid resolution of global models has a tendency to more and more increasing, and the new generation of Global NWP are usually use non-hydrostatic approach. However, frequently some limitations exist for providing the

full sets of products of Global NWP to local users - this is one of serious reasons why the LAM technologies become more and more popular in the National Meteorological Services.

b) **Limited-area modeling**

For forecasting of large variety of phenomena from synoptic to local (depending of dimension of calculation area and dimension/resolution of grid cells. Operational non-hydrostatic LAM might have a large range of grid dimensions - from hundreds meters to several or even first tens of kilometers. They can reasonably adequately reproduce the wide range of meteorological processes in different LAM, often, by "nested" technologies: from large-scale processes (generation, evolution and trajectories of the cyclones) to events of convective nature and/or hazard of appearance of local phenomena (wind gusts, heavy showers, blizzards), fogs, circulation in the mountains and in the coastal areas, influence of the urbanized territories on meteorological characteristics, genesis and development of small-scale, but extremely dangerous polar-lows, etc. Possibility of description of the processes of certain scales is limited to the dimension of LAM grid resolution and form one side and from another - to the dimension of calculation area. Products of LAM operating in the spacious areas of calculation could be used by forecasters along with the products of global systems in analysis of synoptic objects dynamics.

Centers operating the models:

a) **Global NWP models**

Global NWP systems are developed on their own in relatively small number of centers. These global centers have sufficient computational, technological and communicational resources, as well as a proper personnel skills. An important component of the global NWP producing is the development of comprehensive technologies of data assimilation and processing.

b) **Limited-area NWP systems**

The LAM systems are developing in more than 70 National meteorological centers of WMO. LAM systems are developing as a role, both in the centers of global modelling, and in the National meteorological centers, and in some local forecasting centers. LAM "cascade" technologies produce more and more detailed products from initial global model, using the more rough version to LAM versions with each step increasing resolution 3-4 times to hundreds meters comparing with the models, which are used for producing the initial and boundary conditions for LAMs normally having more rough resolution. These systems could be developed for weather forecasting in relatively small areas within the region of responsibility of National (district) meteorological services. Many NGMSs are using LAM models developed in other countries, which relates especially to international consortiums. The LAM systems are based on the operational access to the sets of initial data and boundary conditions for calculation area provided by centers of global NWP via Internet.

Features of Dissemination of NWP products for NHMS WMO weather forecasters

a) **Global NWP products:**

1 Information is provided via WMO WIS in standard code formats on the net - grids in correspondence with WMO regulations (if other is not envisaged by agreement of the country with producers of global forecasts). WMO WIS regulations are oriented on φ/λ grids and standard vertical levels. In the Global models grids of disseminated products are naturally more rough than computational grids. Therefore a part of information of the surface weather produced by global models are often additionally smoothed in the process of transmission of digital information.

2 Via specialized meteorological Internet sites as graphical products. At the same time, lists of the placed products are limited and it is practically impossible to satisfy all requirements connected with detailed visualization and maps design for zone of responsibility of each NHMS.

b) **LAM NWP products:**

Each NHMS can use maximally the LAM output with required details both in computational aspect and visualization for certain region via Internet-technologies.

6.4 Stages of analysis of NWP products for local short- range forecasting

6.4.1 Common recommends

The forecaster analysis of NWP products should have certain stages.

The main idea: To understand the genesis of meteorological processes (following, their properties and potential conditions for severe weather) for identified areas based on combination of synoptic analysis with more detailed data.

The daily operational forecaster discussions (briefing):

The discussion (synoptic briefing) have to be organized to coordinate forecasts for all venues of area of responsibility creating unified concept of understanding of different forecasters and forecasters groups of current and future weather processes. These briefings should be organized firstly in the each forecasters group (e.g. concrete venue or region) and after that via video-conference arranging participation of representatives of all groups at least once a day, but preferably - twice a day, before the issue of morning official forecast and in the evening. The main responsibility takes the main forecaster group, which issues the daily bulletin and controls the Web-site information The discussion have to contain the following items:

1 Analysis of processes from large to local space - scales

2 Proposals for 4-5 Day weather trends based on NWP of large-scale processes for about half/third of Hemisphere

3 Analysis of weather of previous day/night

4 Knowledge of current NWP forecast quality (typical errors for the last several days)

5 Proposals for short-range (from 12 until 72h: tomorrow, after-tomorrow) and very short-range (from 2 until 12 hours: today/tonight)

6 Threat assessment of severe weather events for each forecasting interval.

6.4.2 Experience of large-scale weather types before the analyze of HR products

Each forecasting center or leading forecasting group in specialized meteosupport should have a previous knowledge of relationship between large-scale circulation types and probable local weather phenomena. In framework of development of meteosupport Sochi2014 forecasters from Sochi Black and Azov-seas Branch of North Caucasian Department of Roshydromet prepared the description of typical for rainy/snowy weather situations for mountain cluster of Sochi-2014 area. The typical large-scale processes which lead to the mesoscale circulations with heavy precipitation in Sochi area were described with applicate pictures, examples. The most dangerous hazards for this region are the heavy precipitation events, which can lead to the avalanches, mudslides, floods, traffic jams, damages to electric networks and roads. The previous investigations of weather types were concentrated firstly on the forecasting of probable heavy precipitation and on its phase. Some typical large-scale patterns of processes were identified. In Fig. 14 one of these is shown. This situation can provide a forming of the local cyclones on the South-Eeast of the Black Sea. The cold advection from the North to the western parts of Mediterranean cyclones and cold advection to the central part of Black Sea can amplify the local cyclone forming. These cyclones often could not be well detected in the pressure fields, and sometimes the hazards arrive suddenly for forecasters.

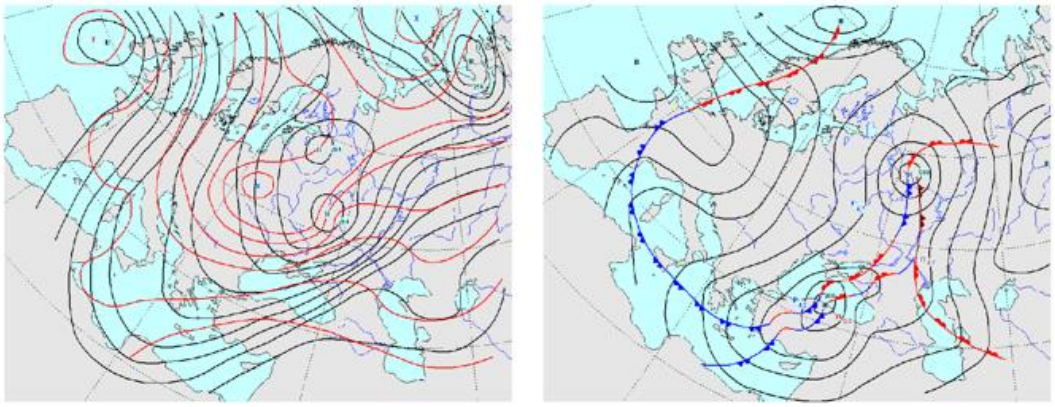


Figure 14: Example of one of typical large-scale situation providing the local cyclogenesis over Southeast of Black sea: H700 and H_{1000}^{500} are on the left, sea level pressure with frontal analysis is on the right.

This forming of little cyclone over the South-eastern coast of Black Sea, providing the transport of wet air to the Sochi mountain valleys in correspondence with orientation of mountain chains. These little cyclonic circulation is well presented on the maps of stream-lines for near-surface level, since the pressure minimums often are not sufficient for draw them. The high resolution information (stream-lines over Black Sea in COSMO realization) helped to detect these situations. The other approach had attempted to be realized for Sochi. Based on COST 733 facilities, the set of synoptic pictures for entire winter period of 2013 was analyzed. Forecasters had a lot of difficulties for join the concrete processes to certain circulation types in provided in COST 733 classifications. It appeared to be easier to do it for the types determined in classification GWT_27 (mainly attachment of every day real synoptic picture to the one of proposed types from GWT_27). It was surprising that the heavy precipitation were probable for a most part of provided large-scale types. It happened to identify only few situations with low probability of precipitation (NN8 and 20, picture 4) and corresponding to heavy rain events in mountain cluster 4 first (Fig. 15, the heavy rains in most cases) as well, 15, 16, 26 (heavy rain are probable in few cases). The formal use of typical patterns

from GWT_27, type 4 showed a good correspondence with process shown in Fig. 14, selected in independent mode via only forecasters experience.

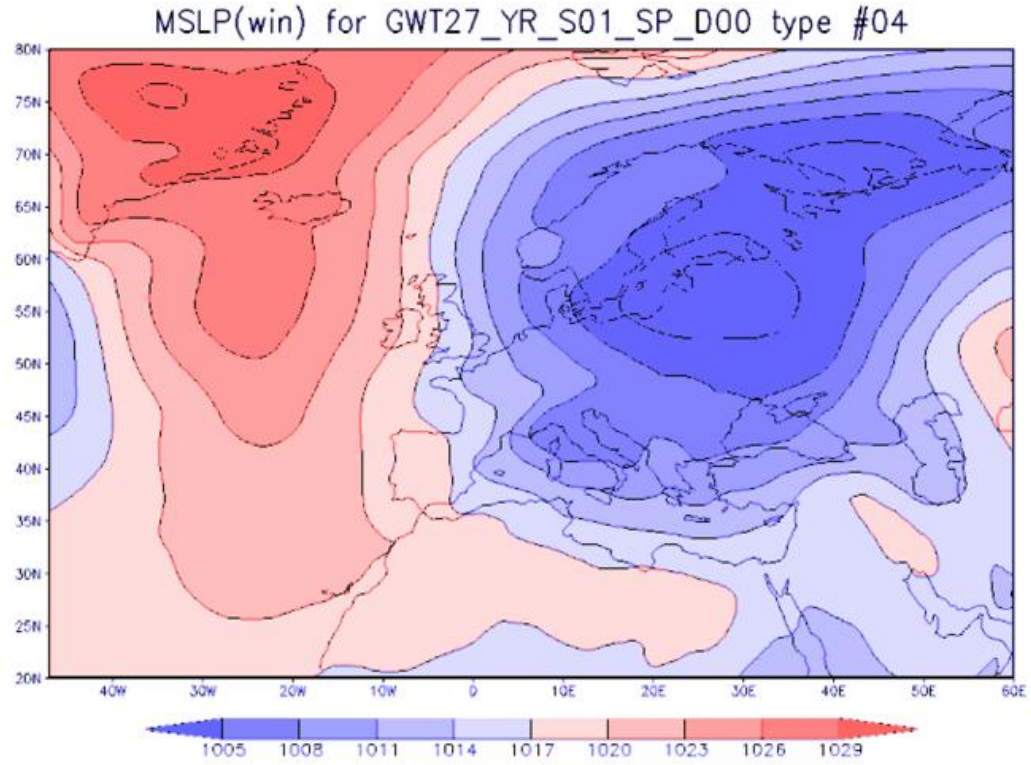


Figure 15: The Pattern N4 from GWT-27. ("wet" with lot of cases of heavy precipitations).

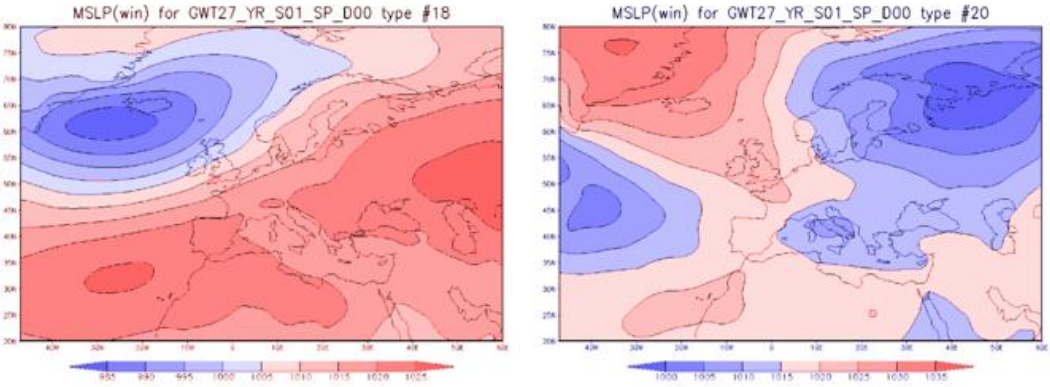


Figure 16: The Pattern N4 (left) and 20 (right) from GWT-27. ("dry" without precipitation).

Note, these "dry" cases are not depended form Ps values, but in both cases the advection of cold air to the middle Black sea is blocked. This below illustrates following conclusions:

- **A large scale synoptic analysis for this region has to establish the factors (cold advection from North or North-East, high humidity flows) to front**

forming near and over the area of forecasters responsibility. For certain days cold advection to the Black Sea has to be detected.

- **The combination with HR results is necessary for notify the forming of the regional circulation or to notify the large-scale synoptic circulation with passing of active fronts with additional advection from North-West.**

6.4.3 Recommended sequence of analysis, design and content of forecasters maps

A view of some - days forecast row of H500 pictures in parallel with P for further 3-4 days

A goal to detect the main atmospheric flow forming advection on area of responsibility, the velocity of processes moving and development, the lapse rates and resemblance to the typical large-scale patterns. The combining of H500 with T2m (or T850) and of P with Middle level clouds and 3-h precipitation amounts is recommended. The printing of these rows of maps is recommended for forecasters for compare the next day old and new forecast rows to discover tendencies of model errors in movement of synoptic objects and front development. The initial part of such forecast row (until 48 hours) by COSMO-Ru7 (step 7 km) is shown at Fig. 17). Figs 18 and 19 present more detailed an example of H500+T2m forecast map design.

Some remarks:

- *The time step for quick large- scale analysis can be 12 hours.*
- *The grid- step of modelling of 15 km is sufficient (If global products with similar grid-step are available, they can be used in similar visualization).*

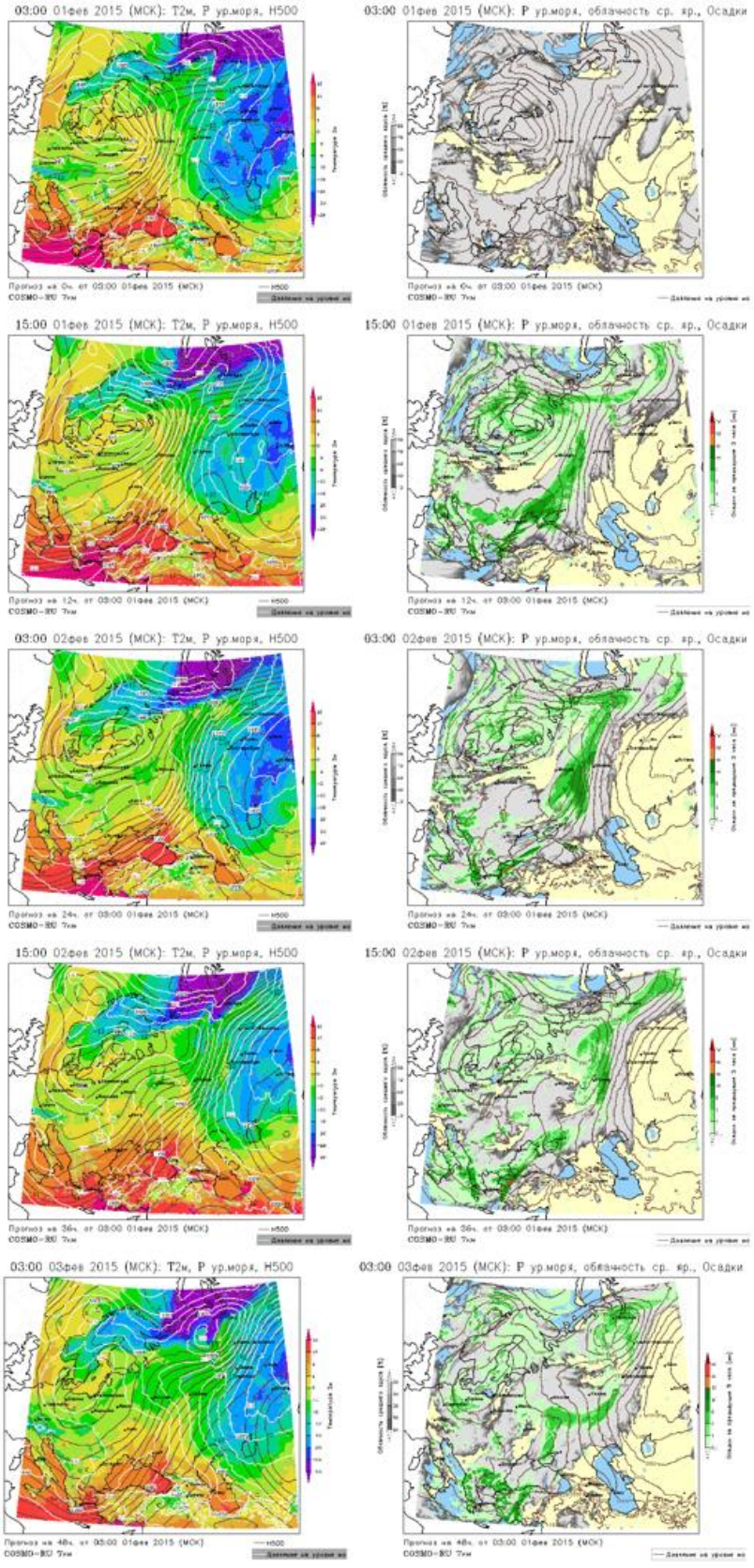


Figure 17: A row of forecasts: H500 and T2m on the left, PMSL, 3h accumulated precipitation and midlevel cloud on the right.

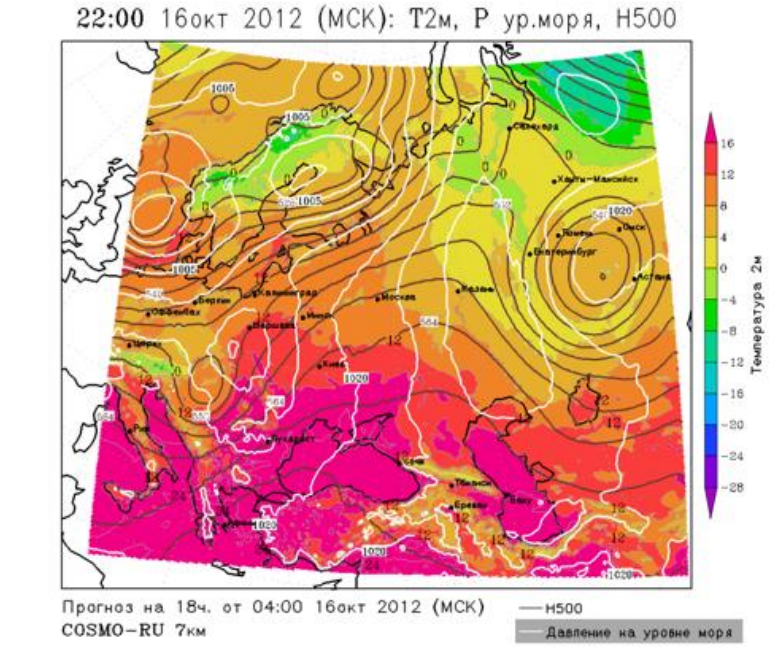


Figure 18: An example map design with H500 and T2m forecast. (Inscription in Russian: (Top) Forecast time and date, forecasted parameters; (Bottom) lead time and forecast start time, model and grid spacing; map legend: color scale for temperature, lines: black- , white: PMSL).

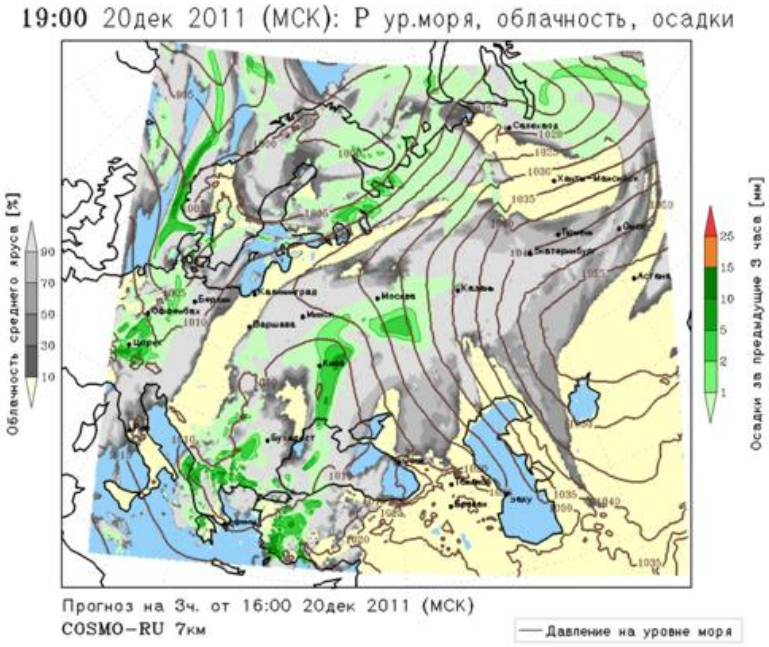


Figure 19: An example map design with PMSL, 3h accumulated precipitation and mid-level cloudiness forecast. (Inscription in Russian: (Top) Forecast time and date, forecasted parameters; (Bottom) lead time and forecast start time, model and grid spacing; map legend: color scale of 3h Precipitation, color scale of Clouds, lines: black: PMSL).

Analysis of maps series of PMSL, Cloudiness, Precipitation with 3h-temporal resolution until 78-84 hours lead time is recommended additionally. This permits to understand the genesis of cyclones and related precipitation. The Mid-level clouds correlate with the frontal area.

Analysis of map series of high- resolution output: COSMO-Ru2 (2.2.km)

Temporal resolution 1 hour, until 48 hours lead time, for entire Caucasian and Eastern Black Sea area:

- Low clouds
- PMSL+ Mid-level Clouds + 3h Precipitation /1h Precipitation (recommended time step of view maps is 3 hours)
- V10m and wing gusts
- T2m + T850
- Fresh snow accumulated for 3 hours and for 24 hours
- Stream lines + Relative humidity at the 900, 800, 750 hPa
- Stream lines + Relative humidity at the 900, 800, 750 hPa

Some design examples are shown in Figs. 20-22.

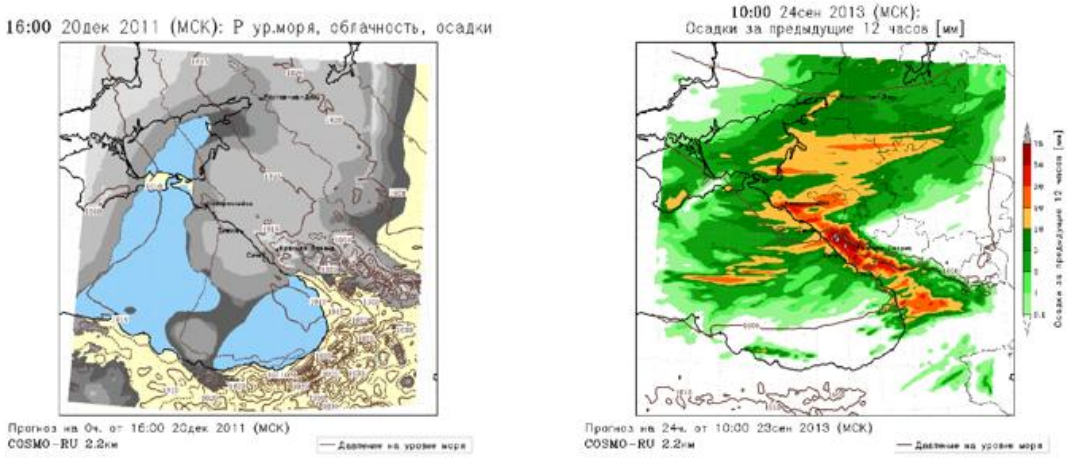


Figure 20: Design of COSMO-Ru2 forecast maps: PMSL, mid-level clouds, 1h precipitation (left) and 12 h accumulated precipitation (right).

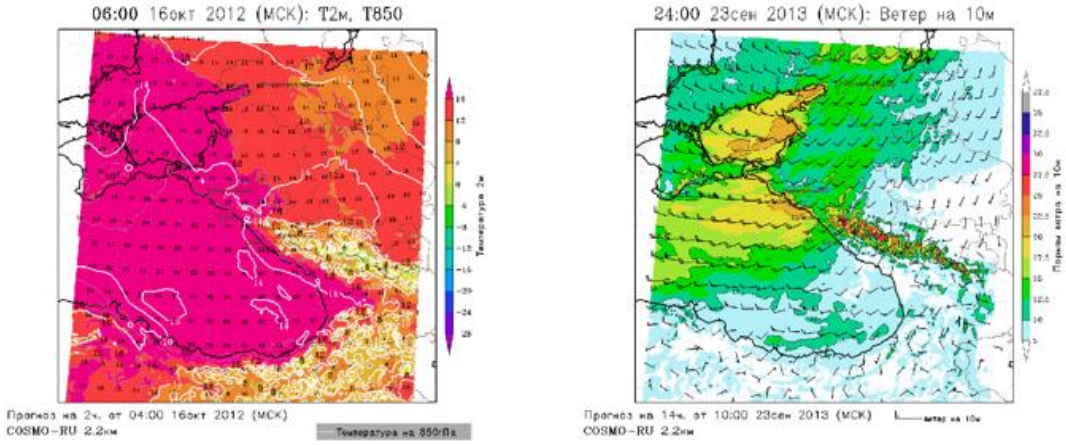


Figure 21: Design of COSMO-Ru2 forecast maps: T2m and T850 (left), wind speed and direction at 10m and wind gusts (right).

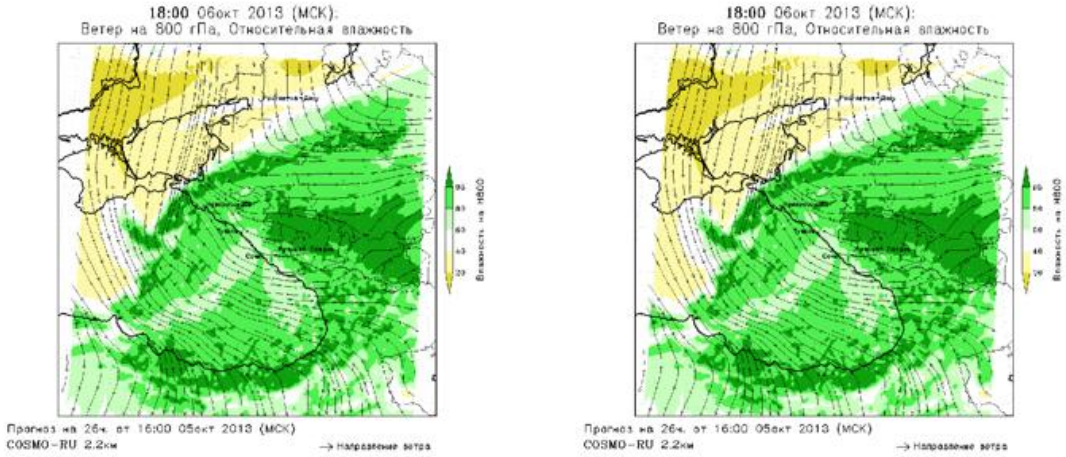


Figure 22: Design of COSMO-Ru2 forecast maps: Streamlines and relative humidity at 800 hPa (left) and at 700 hPa (right).

The Streamlines forecasting maps of HR NWP permits to determine the direction of air movement, the presence of convergence-divergence zones, mesovortices, to specify the time of passage of fronts. The combining with relative humidity helps to determine the change of different air masses (wet-dry), because the relative humidity is the good conservative characteristic of air mass. Sometimes the relative humidity pictures can more clearly indicate the front position (sometimes poorly detected in clouds or wind fields in mountain conditions).

Analysis of rows of maps of high- resolution output: COSMO-Ru1 (1.1.km)

Temporal resolution 1 hour, until 24-36 hours lead time, for Sochi, mountain cluster (minimal area size 200x200 km):

- Low clouds
- Mid-level clouds + 1 h Precipitation
- 12h Precipitation (recommended time step of view maps is 3 hours)

- V10m and wing gusts
- T2m + T850
- Fresh snow accumulated for 3 hours and for 24 hours
- Stream lines + Relative air humidity at the 900, 800, 750 hPa

The products of NWP technology with 1km grid step are the most important kind of NWP information for weather forecasting in the mountains. The most important forecast elements via NWP-1 km are wind and fresh snow fields. The forecasts reflect mountain chains and valleys most accurately (see Fig. 23).

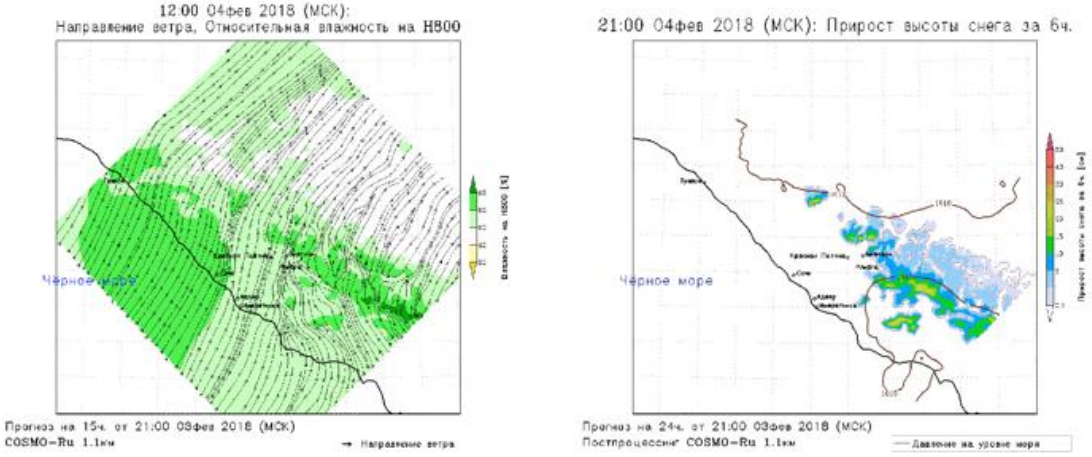


Figure 23: Design of COSMO-Ru1 forecast maps: Streamlines and relative humidity at 800 hPa (left) and fresh snow (right).

6.5 Analysis of Meteograms of deterministic LAM HR NWP

6.5.1 Definitions and goals

Definitions. Meteograms are the graphs, which combine model output (deterministic or ensemble) with form of **time evaluation graphics** of selected meteorological parameters. In case of ensemble forecasting ones are named Ensemble Prediction System meteograms (EPS-grammes). The information of this section relates to **the deterministic high-resolution (HR) model output. Goals and applications.** Meteograms permit to observe time evaluation of key meteorological parameters for selected vertical levels for concrete points. The 1-h (or less) time steps of presenting information (as a rule lesser than for forecasting charts) permits to notify a time of fronts passing, of star-end of weather phenomena, as well of daily temperature extrem time. Another application of meteograms (Fig. 24) is a very quick forecasters complication of meteorological data for big number of points for not large region to receive an information about spatial differences and uncertainties of some parameters. The analysis of NWP matters by forecasters can start by watching of meteograms, as well, it is useful to look at them after analysis of all forecasting maps, after understanding of forecasted synoptic and mesoscale processes. Fig. 24 shows the Meteograms design, which was realized as a result of feed-back from forecasters of Sochi / Hydrometcenter of Russia based on adaptation of DWD variant of COSMO software. The color and placing of picture for forecasts of different parameters are important.

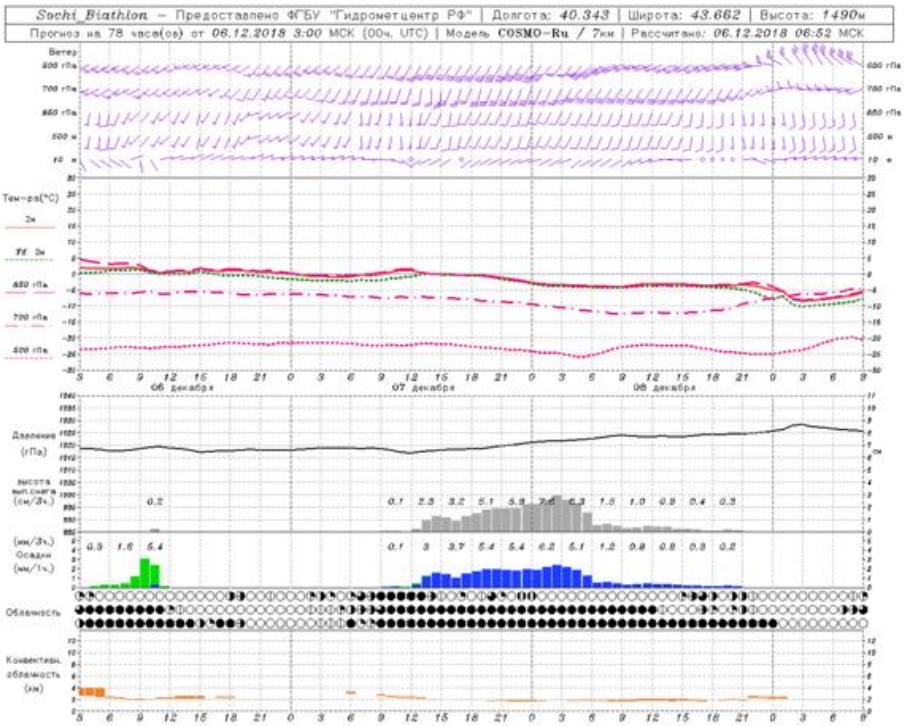


Figure 24: Example of deterministic meteogram for points of Sochi mountain.

6.5.2 Key principles for technology of meteogram forming

- **Meteograms are presented** in some sections of graphics for one point with unified time axe of selected elements adapted to the forecasters expert analysis, e.g. wind, temperature, clouds on several levels, precipitation, etc. The levels for pictures for different elements can be different. A feedback from forecasters for realizing the most efficient pictures design (icluding fast loading of pictures for big number of points on the monitor) is strongly recommended.

- **Meteograms technology has** to provide for quick forecasting analysis the pictures of few-days changes for nominated points of maximal number of important parameters with timestep no more than 1 hour.

- **A severe meteograms around nominated point or inside an area** (a city, a cluster of competitions, etc.) is recommended for more reliable forecasting of random precipitation and of probably hazards.

- **The volume of pictures should be minimal.** This requirement was set up: firstly, to necessity of quick forecasters analysis and comparison of large number of meteograms for different points for one region, secondly, by possible limitations of Internet channels available to forecasters outside on large forecaster centers.

- **Lists of points for meteogram visualization** should be prepared by forecasters/users with indication of Lat/Lon (as rules, there are points of meteostations, towns/cities, important objects, venues of competitions) in stage of forming of meteogram-technology. Systems of forming of meteograms of high resolution modeling such COSMO do not interpolate from the gridded model results to nominated points, and as rules,

a nearest model grid-point is automatically selected. In cases of high spatial variability of geographical properties grid- points have to be manually selected based an expert analysis of geographical properties. As an example, Fig. 25 shows grid-points of COSMO-Ru7 (blue) and COSMO-Ru2 (yellow). In the red are shown the points of venues / observing stations. COSMO-Ru2 grid- nodes nearest to the venues have a good concordance with the 2 nominated points (chance coincidence), but a most representative grid-point for the point Krasnaya Polyana should be chosen manually (which has a close high is preferable from 4 nearest grid-nodes).

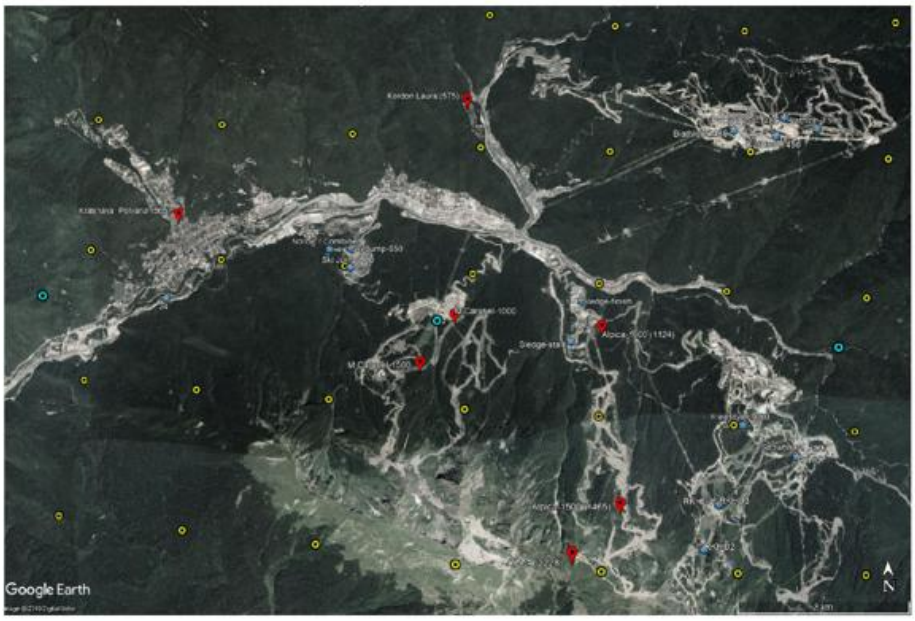


Figure 25: Grid-nodes of COSMO-Ru7 (blue circles) and COSMO-Ru2 (yellow circles) over Earth map for mountain cluster of Sochi region. Red balloons and blue snowflakes indicate the venues locations.

6.5.3 Forecasters analysis based on meteograms

Forecasters should take account that:

- Coordinates of nominated by forecasters points are not same as ones of meteograms (nearest corresponding model grid- points) (see above the previous section) Coordinate values of model meteograms points have be indicated at the top of the picture pages. Forecasters have to compare indicated values with coordinates of real nominated point. In cases of complicate geographical conditions it can lead to the completely wrong forecasts for selected points of local weather conditions (e.g. a land point can be automatically corresponded to a maritime nearest grid point, a point in the valley - to the point at the top of mountain, etc.). In the Fig. 26 grid-point coordinates longitude 40.2E, latitude=43.7N are indicated by red oval. The coordinates of nominated point are 40.1E, 43.6N).
- The real high of nominated point is not same as high of corresponding model grid point (important especially for the mountain cases) High of model grid points is indicated at the top of the picture pages (Fig. 26 at the green oval - 1544m). Forecasters have to

compare these values with ones of real nominated points and to analyze a difference. Some postprocessing technologies calculate the corrected values of T2m and of Td2m based on assumptions of temperature lapse rate. In our example, the real high is only 576m. The results of correction of T2m is shown on the meteogram by violet line, parallel to the red line, corresponding a T2m forecasts from direct model output.

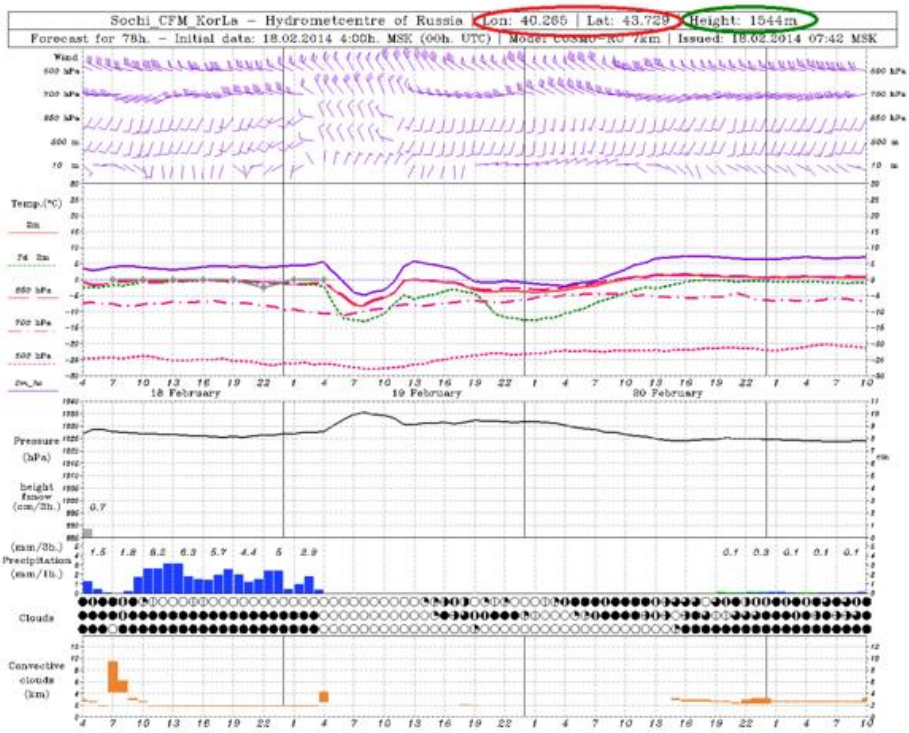


Figure 26: Example of meteogram for Cordon Laura. The coordinates and high of grid- box are circled in ovals (red and green).

There are some features of analysis, important for forecasters:

- *Pressure section:* pressure values and its tendencies, the time interval of minimum due to the rapid cyclone passage
- *Temperature section:*
  - Temperature values and their tendencies at 2, 850 hPa, 700 hPa and 500 hPa can be important for mountain area. Note the inversion state (e.g. if T2m less than T850, in mountains T850 less than T700). (Following special requests, the levels can be other).
  - T850 In mountains regions can be close to the T2m (or underground)
  - An additional T2m values as postprocessing result can be added. Be careful with its analysis.
  - The close and equal values of TD2m and of T2m can indicate the high probability of fog.
- *Precipitation section:*
  - Additional to the vertical columns (1-hour sums) the 3-h sums are written.

- If the T2m is corrected by postprocessing techniques, the additional control of phase of precipitation is useful. In our case (Fig. 26) after T2m lapse rate correction it was warmer than 0 degrees. So, the predicted snow should be not snow, but in case of continuous heavy rain, forecaster could make a decision himself.
- In case of short precipitation and/or precipitation of convective origin. It is useful to analyze meteograms for other close grid- points. The radius of probable precipitation is about 3-4 grid- cells!

- *Cloud section:*
  - Middle level clouds are the most important and indicate with high clear-sky or overcast conditions.
  - Low level clouds have a lowest forecasting skill. This is feasible to control based on synoptic knowledge.
  - Convection existing or not can help to understand the origin of clouds.
  - Maximum convection height (yellow columns at the bottom of the page) can indicate the dangerous convective situations in case of extremely high (more than 10 km) of convection level. In these cases the weather hazards of convective origin have a high probability not only for the point of meteogram, but also around this place.

- *Wind section:*
  - Wind direction and speed at 10 m, 500 m, 850, 700, 500 hPa levels are presented. For specialized forecasts the other levels can be required by users.
  - Sharp changes in wind direction at the lower levels can indicate the time of front passage (in our case- at the first hours of forecast and at 3-rd forecast day).
  - Wind speed more than 25 m/s at 500 m altitude can indicate as a threat of squall at the near-surface level.

6.6 Conclusion

In the current document we shoved the key positions of experience of trainings for forecasters for Sochi forecaster team in 2012-2014 years. This experience could be useful for further trainings from one hand, and from other hand should be developed in further.

7 Acknowledgements

This work was carried out within the COSMO PT CORSO-A and WWRP FDP/RDP FROST-2014. The authors are grateful to Tatiana Dmitrieva (Roshydromet) for providing the information on weather cases during the winter 2014 and to Tiziana Paccagnella (ARPAE) for supporting the work.

A Appendix

		Event Observed	
		YES	NO
Event Forecasted	YES	A	B
	NO	C	D

Table 8: 2x2 Contingency Table.

Threshold (mm/3h)	Forecast lead time (h)							
	3	6	9	12	15	18	21	24
	Domain 300 x 300 g.p.							
0.1	0.42	0.62	0.63	0.72	0.58	0.39	0.36	0.49
0.5	0.43	0.66	0.68	0.73	0.62	0.46	0.37	0.42
1	0.35	0.49	0.70	0.77	0.55	0.42	0.33	0.34
2	0.28	0.28	0.59	0.68	0.31	0.38	0.29	0.21
3		0.22	0.44	0.64	0.31	0.51	0.32	
5			0.32	0.55			0.53	
10			0.27	0.26			0.60	
	Domain 450 x 450 g.p.							
0.1	0.42	0.57	0.62	0.66	0.56	0.38	0.38	0.49
0.5	0.43	0.58	0.59	0.70	0.57	0.44	0.37	0.42
1	0.35	0.43	0.62	0.74	0.55	0.39	0.35	0.35
2	0.27	0.25	0.57	0.71	0.39	0.40	0.31	0.18
3		0.20	0.48	0.65	0.34	0.48	0.40	
5			0.32	0.55			0.47	
10			0.26	0.16			0.63	
	Domain 450x 650 g.p.							
0.1	0.42	0.57	0.62	0.66	0.56	0.38	0.38	0.49
0.5	0.43	0.58	0.59	0.70	0.57	0.44	0.37	0.42
1	0.35	0.43	0.62	0.74	0.55	0.39	0.35	0.35
2	0.27	0.25	0.57	0.71	0.39	0.40	0.31	0.18
3		0.20	0.48	0.65	0.34	0.48	0.40	
5			0.32	0.55			0.47	
10			0.26	0.16			0.63	

Table 9: CSI values.

Threshold (mm/3h)	Forecast lead time (h)							
	3	6	9	12	15	18	21	24
	Domain 300 x 300 g.p.							
0.1	0.28	0.51	0.53	0.64	0.50	0.29	0.25	0.38
0.5	0.34	0.59	0.61	0.67	0.56	0.40	0.29	0.33
1	0.29	0.42	0.64	0.72	0.49	0.37	0.27	0.27
2	0.25	0.23	0.53	0.62	0.27	0.35	0.25	0.17
3		0.19	0.39	0.60	0.29	0.49	0.29	
5			0.29	0.52			0.52	
10			0.25	0.24			0.59	
	Domain 450 x 450 g.p.							
0.1	0.29	0.45	0.51	0.58	0.47	0.27	0.27	0.38
0.5	0.34	0.51	0.50	0.63	0.51	0.37	0.29	0.34
1	0.29	0.36	0.55	0.68	0.50	0.33	0.30	0.28
2	0.24	0.21	0.51	0.67	0.36	0.37	0.27	0.14
3		0.17	0.43	0.61	0.32	0.46	0.38	
5			0.29	0.52			0.46	
10			0.25	0.15			0.63	
	Domain 450x 650 g.p.							
0.1	0.29	0.45	0.48	0.59	0.52	0.29	0.27	0.36
0.5	0.34	0.50	0.51	0.62	0.53	0.37	0.28	0.34
1	0.29	0.36	0.58	0.65	0.50	0.33	0.31	0.27
2	0.24	0.22	0.51	0.59	0.38	0.34	0.27	0.15
3		0.20	0.42	0.53	0.37	0.44	0.40	
5			0.28	0.55			0.52	
10			0.24	0.17			0.63	

Table 10: ETS values.

Threshold (mm/3h)	Forecast lead time (h)							
	3	6	9	12	15	18	21	24
	Domain 300 x 300 g.p.							
0.1	0.47	0.72	0.74	0.82	0.68	0.47	0.47	0.67
0.5	0.53	0.77	0.81	0.85	0.74	0.60	0.58	0.62
1	0.48	0.61	0.80	0.88	0.69	0.58	0.48	0.55
2	0.44	0.41	0.64	0.84	0.38	0.57	0.45	0.52
3		0.35	0.47	0.78	0.35	0.68	0.55	
5			0.37	0.73			0.74	
10			0.37	0.35			0.74	
	Domain 450 x 450 g.p.							
0.1	0.49	0.66	0.73	0.76	0.66	0.47	0.50	0.67
0.5	0.54	0.67	0.72	0.81	0.69	0.59	0.56	0.64
1	0.50	0.53	0.72	0.84	0.69	0.53	0.51	0.59
2	0.45	0.33	0.60	0.83	0.49	0.57	0.47	0.47
3		0.29	0.51	0.77	0.39	0.67	0.62	
5			0.37	0.69			0.65	
10			0.37	0.21			0.75	
	Domain 450x 650 g.p.							
0.1	0.49	0.64	0.69	0.77	0.73	0.49	0.51	0.63
0.5	0.52	0.66	0.72	0.80	0.74	0.58	0.54	0.64
1	0.49	0.53	0.75	0.82	0.73	0.54	0.53	0.56
2	0.45	0.35	0.60	0.81	0.52	0.56	0.47	0.49
3		0.32	0.50	0.73	0.46	0.65	0.64	
5			0.37	0.73			0.70	
10			0.37	0.24			0.75	

Table 11: TSS values.

Threshold (mm/3h)	Forecast lead time (h)							
	3	6	9	12	15	18	21	24
	Domain 300 x 300 g.p.							
0.1	0.43	0.68	0.69	0.78	0.67	0.44	0.40	0.55
0.5	0.51	0.74	0.76	0.80	0.72	0.57	0.45	0.49
1	0.45	0.59	0.78	0.84	0.66	0.54	0.42	0.42
2	0.40	0.38	0.69	0.77	0.42	0.51	0.40	0.29
3		0.32	0.56	0.75	0.45	0.66	0.45	
5			0.44	0.69			0.68	
10			0.41	0.39			0.74	
	Domain 450 x 450 g.p.							
0.1	0.45	0.62	0.68	0.73	0.64	0.43	0.43	0.55
0.5	0.51	0.67	0.67	0.77	0.67	0.54	0.45	0.51
1	0.45	0.53	0.71	0.81	0.66	0.49	0.46	0.44
2	0.39	0.35	0.68	0.80	0.53	0.54	0.43	0.25
3		0.29	0.60	0.76	0.48	0.63	0.55	
5			0.45	0.69			0.63	
10			0.40	0.25			0.77	
	Domain 450x 650 g.p.							
0.1	0.45	0.62	0.65	0.74	0.69	0.45	0.43	0.53
0.5	0.50	0.66	0.68	0.76	0.69	0.54	0.44	0.51
1	0.45	0.53	0.74	0.79	0.67	0.49	0.48	0.43
2	0.39	0.36	0.67	0.75	0.55	0.51	0.43	0.25
3		0.33	0.59	0.69	0.54	0.61	0.57	
5			0.44	0.71			0.68	
10			0.38	0.29			0.77	

Table 12: HSS values.

Threshold (mm/3h)	Forecast lead time (h)					
	6	9	12	15	18	21
	Domain 300 x 300 g.p.					
3	0.50	0.70	0.89	0.62	0.83	0.71
5		0.61	0.85			0.87
10		0.64	0.61			0.90
	Domain 450 x 450 g.p.					
3	0.49	0.72	0.88	0.65	0.83	0.78
5		0.62	0.83			0.83
10		0.64	0.48			0.90
	Domain 450x 650 g.p.					
3	0.53	0.71	0.84	0.69	0.81	0.80
5		0.60	0.86			0.89
10		0.63	0.52			0.90

Table 13: EDI values.

Threshold (mm/3h)	Time interval (h)							
	0-3	3-6	6-9	9-12	12-15	15-18	18-21	21-24
0.1	201	201	188	185	166	157	148	145
0.5	143	153	159	164	129	116	105	111
1	98	129	152	152	112	94	89	82
2	50	76	140	116	75	51	61	39
3	22	45	119	96	57	36	40	27
5	5	17	64	62	21	19	24	19
10	0	2	21	27	2	4	16	3

Table 14: Number of precipitation events of different thresholds for 3-hour intervals.

References

Astakhova, E. D., Montani, A., Alferov and Yu, D., 2015: Ensemble forecasts for the Sochi-2014 Olympic Games. *Russian meteorology and hydrology*, **40**, **8**, 531–539, DOI 10.3103/S1068373915080051

Kiktev, D. B., Astakhova, E. D., Zaripov, R. B., Muravev, A. V., Smirnov, A. V. and Tsyrulnikov, M. D., 2015a: FROST-2014 project and meteorological support of the Sochi-2014 Olympics. *Russian Meteorology and Hydrology*, **40**, **8**, 504–512, DOI 10.3103/S1068373915080026

Kiktev, D. B., Astakhova, E. D., Zaripov, R. B., Muravev, A. V, Smirnov, A. V. and Tsyrulnikov, M. D., 2015b: Erratum to "FROST-2014 project and meteorological support of the Sochi-2014 Olympics", *Russian Meteorology and Hydrology*, **40**, **12**, 844–845, DOI 10.3103/S1068373915120109

Montani, A., Cesari, D., Marsigli, C. and Paccagnella, T., 2011: Seven years of activity in the field of mesoscale ensemble forecasting by the COSMO-LEPS system: main achievements and open challenges. *Tellus A*, **63**, 605–624, DOI: 10.1111/j.1600-0870.2010.00499

Montani, A., Marsigli, C. and Paccagnella, T., 2013: Development of a COSMO-based limited-area ensemble system for the 2014 Winter Olympic Games. *COSMO Newsletter*, **13**, 93–99, available at http://cosmo-model.org/content/model/documentation/newsLetters/newsLetter13/cnl13_12.pdf

Montani, A., Alferov, D., Astakhova, E., Marsigli, C. and Paccagnella, T., 2014: Ensemble forecasting for Sochi-2014 Olympics: the COSMO-based ensemble prediction systems. *COSMO Newsletter*, **14**, 88–94, available at http://cosmo-model.org/content/model/documentation/newsLetters/newsLetter14/cnl14_10.pdf

Montani, A., Alferov, D., Astakhova, E., Marsigli, C. and Paccagnella, T., 2015: Performance of the COSMO-based ensemble systems during Sochi-2014 pre-Olympics. *COSMO Newsletter*, **15**, 77–82, available at http://cosmo-model.org/content/model/documentation/newsLetters/newsLetter15/cnl15_10.pdf

Paccagnella, T., Hacker, J., Marsigli, C., Montani, A., Pappenberger, F., Parsons, D., Swinbank, R. and Toth, Z., 2012: THORPEX Interactive Research Grand Global Ensemble - Limited Area Model Plan. *WMO publications*, **17**, available at http://www.wmo.int/pages/prog/arep/wwrp/new/wwrp_publications.html

Rivin, G. and Rozinkina, I., 2013: Priority Project CORSO: Consolidation of Operation and Research results for the Sochi Olympic Games, available at http://cosmo-model.org/content/tasks/priorityProjects/corso/default.htm

Schaefer, J. T., 1990: The critical success index as an indicator of waring skill. *Weather and forecasting*, **5**, 570–575

Schirmer, M. and B. Jamieson, 2015: Verification of forecasted winter precipitation in complex terrain. *The Cryosphere*, **3**, **9(2)**, 587–601, DOI 10.5194/tc-9-587

Shatunova, M. V., Rivin, G. S. and Rozinkina, I. A., 2015: Visibility forecasting for February 1618 2014 for the region of the Sochi-2014 Olympic Games using the high-resolution COSMO-Ru1 model. *Russian Meteorology and Hydrology*, **40**, **8**, 523–530, DOI 10.3103/S106837391508004X

List of COSMO Newsletters and Technical Reports

(available for download from the COSMO Website: www.cosmo-model.org)

COSMO Newsletters

No. 1: February 2001.

No. 2: February 2002.

No. 3: February 2003.

No. 4: February 2004.

No. 5: April 2005.

No. 6: July 2006.

No. 7: April 2008; Proceedings from the 8th COSMO General Meeting in Bucharest, 2006.

No. 8: September 2008; Proceedings from the 9th COSMO General Meeting in Athens, 2007.

No. 9: December 2008.

No. 10: March 2010.

No. 11: April 2011.

No. 12: April 2012.

No. 13: April 2013.

No. 14: April 2014.

No. 15: July 2015.

No. 16: July 2016.

No. 17: July 2017.

No. 18: November 2018.

COSMO Technical Reports

No. 1: Dmitrii Mironov and Matthias Raschendorfer (2001):
Evaluation of Empirical Parameters of the New LM Surface-Layer Parameterization Scheme. Results from Numerical Experiments Including the Soil Moisture Analysis.

No. 2: Reinhold Schrodin and Erdmann Heise (2001):
The Multi-Layer Version of the DWD Soil Model TERRA_LM.

No. 3: Günther Doms (2001):
A Scheme for Monotonic Numerical Diffusion in the LM.

No. 4: Hans-Joachim Herzog, Ursula Schubert, Gerd Vogel, Adelheid Fiedler and Roswitha Kirchner (2002):
LLM ¯ the High-Resolving Nonhydrostatic Simulation Model in the DWD-Project LITFASS.
Part I: Modelling Technique and Simulation Method.

No. 5: Jean-Marie Bettems (2002):
EUCOS Impact Study Using the Limited-Area Non-Hydrostatic NWP Model in Operational Use at MeteoSwiss.

No. 6: Heinz-Werner Bitzer and Jürgen Steppeler (2004):
Documentation of the Z-Coordinate Dynamical Core of LM.

No. 7: Hans-Joachim Herzog, Almut Gassmann (2005):
Lorenz- and Charney-Phillips vertical grid experimentation using a compressible nonhydrostatic toy-model relevant to the fast-mode part of the 'Lokal-Modell'.

No. 8: Chiara Marsigli, Andrea Montani, Tiziana Paccagnella, Davide Sacchetti, André Walser, Marco Arpagaus, Thomas Schumann (2005):
Evaluation of the Performance of the COSMO-LEPS System.

No. 9: Erdmann Heise, Bodo Ritter, Reinhold Schrodin (2006):
Operational Implementation of the Multilayer Soil Model.

No. 10: M.D. Tsyrulnikov (2007):
Is the particle filtering approach appropriate for meso-scale data assimilation ?

No. 11: Dmitrii V. Mironov (2008):
Parameterization of Lakes in Numerical Weather Prediction. Description of a Lake Model.

No. 12: Adriano Raspanti (2009):
COSMO Priority Project "VERification System Unified Survey" (VERSUS): Final Report.

No. 13: Chiara Marsigli (2009):
COSMO Priority Project "Short Range Ensemble Prediction System" (SREPS): Final Report.

No. 14: Michael Baldauf (2009):
COSMO Priority Project "Further Developments of the Runge-Kutta Time Integration Scheme" (RK): Final Report.

No. 15: Silke Dierer (2009):
COSMO Priority Project "Tackle deficiencies in quantitative precipitation forecast" (QPF): Final Report.

No. 16: Pierre Eckert (2009):
COSMO Priority Project "INTERP": Final Report.

No. 17: D. Leuenberger, M. Stoll and A. Roches (2010):
Description of some convective indices implemented in the COSMO model.

No. 18: Daniel Leuenberger (2010):
Statistical analysis of high-resolution COSMO Ensemble forecasts in view of Data Assimilation.

No. 19: A. Montani, D. Cesari, C. Marsigli, T. Paccagnella (2010):
Seven years of activity in the field of mesoscale ensemble forecasting by the COSMO–LEPS system: main achievements and open challenges.

No. 20: A. Roches, O. Fuhrer (2012):
Tracer module in the COSMO model.

No. 21: Michael Baldauf (2013):
A new fast-waves solver for the Runge-Kutta dynamical core.

No. 22: C. Marsigli, T. Diomede, A. Montani, T. Paccagnella, P. Louka, F. Gofa, A. Corigliano (2013):
The CONSENS Priority Project.

No. 23: M. Baldauf, O. Fuhrer, M. J. Kurowski, G. de Morsier, M. Müllner, Z. P. Piotrowski, B. Rosa, P. L. Vitagliano, D. Wójcik, M. Ziemiański (2013):
The COSMO Priority Project 'Conservative Dynamical Core' Final Report.

No. 24: A. K. Miltenberger, A. Roches, S. Pfahl, H. Wernli (2014):
Online Trajectory Module in COSMO: a short user guide.

No. 25: P. Khain, I. Carmona, A. Voudouri, E. Avgoustoglou, J.-M. Bettems, F. Grazzini (2015):
The Proof of the Parameters Calibration Method: CALMO Progress Report.

No. 26: D. Mironov, E. Machulskaya, B. Szintai, M. Raschendorfer, V. Perov, M. Chumakov, E. Avgoustoglou (2015):
The COSMO Priority Project 'UTCS' Final Report.

No. 27: J-M. Bettems (2015):
The COSMO Priority Project 'COLOBOC': Final Report.

No. 28: Ulrich Blahak (2016):
RADAR_MIE_LM and RADAR_MIELIB - Calculation of Radar Reflectivity from Model Output.

No. 29: M. Tsyrulnikov and D. Gayfulin (2016):
A Stochastic Pattern Generator for ensemble applications.

No. 30: D. Mironov and E. Machulskaya (2017):
A Turbulence Kinetic Energy – Scalar Variance Turbulence Parameterization Scheme.

No. 31: P. Khain, I. Carmona, A. Voudouri, E. Avgoustoglou, J.-M. Bettems, F. Grazzini, P. Kaufmann (2017):
CALMO - Progress Report.

No. 32: A. Voudouri, P. Khain, I. Carmona, E. Avgoustoglou, J.M. Bettems, F. Grazzini, O. Bellprat, P. Kaufmann and E. Bucchignani (2017):
Calibration of COSMO Model, Priority Project CALMO Final report

No. 33: N. Vela (2017):
VAST 2.0 - User Manual.

No. 34: C. Marsigli, D. Alferov, M. Arpagaus, E. Astakhova, R. Bonanno, G. Duniec, C. Gebhardt, W. Interewicz, N. Loglisci, A. Mazur, V. Maurer, A. Montani, A. Walser (2018):
COsmo Towards Ensembles at the Km-scale IN Our countries (COTEKINO), Priority Project final report.

No. 35: G. Rivin, I. Rozinkina, E. Astakhova, A. Montani, D. Alferov, M. Arpagaus, D. Blinov, A. Bundel, M. Chumakov, P. Eckert, A. Euripides, J. Förstner, J. Helmert, E. Kazakova, A. Kirsanov, V. Kopeikin, E. Kukanova, D. Majewski, C. Marsigli, G. de Morsier, A. Muravev, T. Paccagnella, U. Schättler, C. Schraff, M. Shatunova, A. Shcherbakov, P. Steiner, M. Zaichenko (2018):
The COSMO Priority Project CORSO Final Report.

No. 36: A. Raspanti, A. Celozzi, A. Troisi, A. Vocino, R. Bove, F. Batignani (2018):
The COSMO Priority Project VERSUS2 Final Report.

No. 37: A. Bundel, F. Gofa, D. Alferov, E. Astakhova, P. Baumann, D. Boucouvala, U. Damrath, P. Eckert, A. Kirsanov, X. Lapillonne, J. Linkowska, C. Marsigli, A. Montani, A. Muraviev, E. Oberto, M.S. Tesini, N. Vela, A. Wyszogrodzki, M. Zaichenko, A. Walser (2019):
The COSMO Priority Project INSPECT Final Report.

COSMO Technical Reports

Issues of the COSMO Technical Reports series are published by the *COnsortium for Small-scale MOdelling* at non-regular intervals. COSMO is a European group for numerical weather prediction with participating meteorological services from Germany (DWD, AWGeophys), Greece (HNMS), Italy (USAM, ARPA-SIMC, ARPA Piemonte), Switzerland (MeteoSwiss), Poland (IMGW), Romania (NMA) and Russia (RHM). The general goal is to develop, improve and maintain a non-hydrostatic limited area modelling system to be used for both operational and research applications by the members of COSMO. This system is initially based on the COSMO-Model (previously known as LM) of DWD with its corresponding data assimilation system.

The Technical Reports are intended

- for scientific contributions and a documentation of research activities,
- to present and discuss results obtained from the model system,
- to present and discuss verification results and interpretation methods,
- for a documentation of technical changes to the model system,
- to give an overview of new components of the model system.

The purpose of these reports is to communicate results, changes and progress related to the LM model system relatively fast within the COSMO consortium, and also to inform other NWP groups on our current research activities. In this way the discussion on a specific topic can be stimulated at an early stage. In order to publish a report very soon after the completion of the manuscript, we have decided to omit a thorough reviewing procedure and only a rough check is done by the editors and a third reviewer. We apologize for typographical and other errors or inconsistencies which may still be present.

At present, the Technical Reports are available for download from the COSMO web site (www.cosmo-model.org). If required, the member meteorological centres can produce hard-copies by their own for distribution within their service. All members of the consortium will be informed about new issues by email.

For any comments and questions, please contact the editor:

Massimo Milelli
Massimo.Milelli@arpa.piemonte.it

Consortium for Small-Scale Modelling

Technical Report No. 37

The COSMO Priority Project INSPECT Final Report

January 2019

DOI: 10.5676/DWD_pub/nwv/cosmo-tr_37

Deutscher Wetterdienst
MeteoSwiss
Ufficio Generale Spazio Aereo e Meteorologia
ΕΘΝΙΚΗ ΜΕΤΕΩΡΟΛΟΓΙΚΗ ΥΠΗΡΕΣΙΑ
Instytucie Meteorogii i Gospodarki Wodnej
Administratia Nationala de Meteorologie
ROSHYDROMET
Agenzia Regionale Protezione Ambiente Piemonte
Agenzia Regionale Prevenzione Ambiente Energia Emilia Romagna
Centro Italiano Ricerche Aerospaziali
Amt für GeoInformationswesen der Bundeswehr
Israel Meteorological Service

www.cosmo-model.org

Editor: Massimo Milelli, ARPA Piemonte

The COSMO Priority Project INSPECT

Final Report

Project participants:

A. Bundel[1]‡, ***F. Gofa***[2]‡, ***D. Alferov***[1], ***E. Astakhova***[1],

P. Baumann[3], ***D. Boucouvala***[2], ***U. Damrath***[4], ***P. Eckert***[3],

A. Kirsanov[1], ***X. Lapillonne***[3], ***J. Linkowska***[5], ***C. Marsigli***[6],

A. Montani[6], ***A. Muraviev***[1], ***E. Oberto***[7], ***M.S. Tesini***[6],

N. Vela[7], ***A. Wyszogrodzki***[5], ***M. Zaichenko***[1], ***A. Walser***[3]

‡ Project Coordinator

[1] RHM

[2] HNMS

[3] MCH

[4] DWD

[5] IMGV

[6] ARPAE

[7] ARPAP

Contents

1 Introduction **4**

2 The main outcomes of PP INSPECT Summary **5**

3 Filtering methods **7**

3.1 Neighbourhood Methods (Flora Gofa, HNMS) 7

3.1.1 Method applied (related to an INSPECT Task) and objectives 7

3.1.2 Short description of the dataset (forecast-observation data), adaptation required, software for the method application 7

3.1.3 Verification software 8

3.1.4 Main findings (plots and explanation) 9

3.1.5 Characteristics of the method applied) 11

3.2 Analysis of long time series of neighbourhood scores (in particular: FSS, upscaling with ETS and FBI) for precipitation. Further investigation into the most informative and compact representation of scores. 11

3.2.1 DWD experience (U. Damrath) 11

3.2.2 Evaluation of 4dVerif spatial verification visualization (X. Lapillonne, MeteoSwiss) 13

3.3 Wind verification with DIST method: preliminary results (M. S. Tesini, ARPAE-SIMC) 16

3.3.1 Motivation of the study 16

3.3.2 Representative value of the box for wind characteristics and verification setup 16

3.3.3 First results 16

3.3.4 Conclusions 19

3.4 Intensity-scale method (F. Gofa, HNMS) 19

3.4.1 Method applied (related to an INSPECT Task) and objectives 19

3.4.2 Short description of the dataset (forecast-observation data), adaptation required, software for the method application 21

3.4.3 Main findings (plots and explanation) 21

3.4.4 Characteristics of the method applied 23

4 Object-based methods **23**

4.1 SAL Method for deterministic and ensemble precipitation verification at HNMS (D. Boucouvala) 23

4.1.1 Description of the Method 23

4.1.2 SAL Calculation 24
4.1.3 EPS in terms of probability (a research topic) 31
4.2 MODE, CRA, SAL: IMGW-PIB experience 34
4.2.1 Method applied (related to an INSPECT Task) and objectives 34
4.2.2 Short description of the dataset (forecast-observation data), adaptation required, software for the method application 34
4.2.3 Main findings (plots and explanation) 34
4.2.4 Characteristics of the method applied 38
4.3 CRA experiments in Roshydromet for MesoVICT (A.Bundel and A. Muraviev)) 39
4.3.1 Deterministic study 39
4.3.2 An object-based approach to assess the MesoVICT ensemble data . . 49
4.3.3 Processing nowcasting forecasts using CRA at RHM (A. Muraviev) . . 50
4.4 SAL deterministic study in ARPAE-SIMC (M. S. Tesini and D. D'Alessandro) 52
4.4.1 Method applied (related to an INSPECT Task) and objectives 52
4.4.2 Short description of the dataset (forecast-observation data), adaptation required, software for the method application 53
4.4.3 Main findings (plots and explanation) 53
4.4.4 Characteristics of the method applied 54

5 Sensitivity of COSMO-LEPS forecast skill to the verification network: application to MesoVICT cases (A. Montani, C. Marsigli, T. Paccagnella, ARPAE-SIMC) 55
5.1 Overall aims 55
5.2 Verification datasets 55
5.3 Verification setup 56
5.4 Results 56
5.5 Conclusions 59
5.6 Future work 59

6 References 59

1 Introduction

As numerical weather prediction models began to increase considerably in resolution, it became clear that traditional grid-point-by-grid-point verification methods did not provide material information about forecast performance. Traditional verification scores often indicate poor performance because of the increased small-scale variability. Numerous methods have been proposed in order to assess the value of very-high-resolution forecasts, including spatial verification methods. Availability of radar and merged radar-station observations contributed to the growth of popularity of these methods. Furthermore, the plethora of spatial verification methods has led to the need to analyse how these methods relate to one another, how each method works, what information could be gleaned from each method, and whether any given method actually conveys any useful information or not. The ICP international project and its second phase MesoVICT (Mesoscale Verification Inter-Comparison over Complex Terrain) were initiated to study how these methods provide feedback about the forecast skill through well-structured experiments (http://www.ral.ucar.edu/projects/icp/). The main objectives of MesoVICT international project can be summarized as follows:

- To investigate the ability of existing and newly developed methods to verify fields other than deterministic precipitation forecasts
- To demonstrate the capability of spatial verification methods over complex terrain and gain an understanding of the issues that arise in such cases
- To encourage community participation in the improvement of spatial methods
- To provide the community with a test-bed with common datasets but also to provide assistance in developing and testing these methods

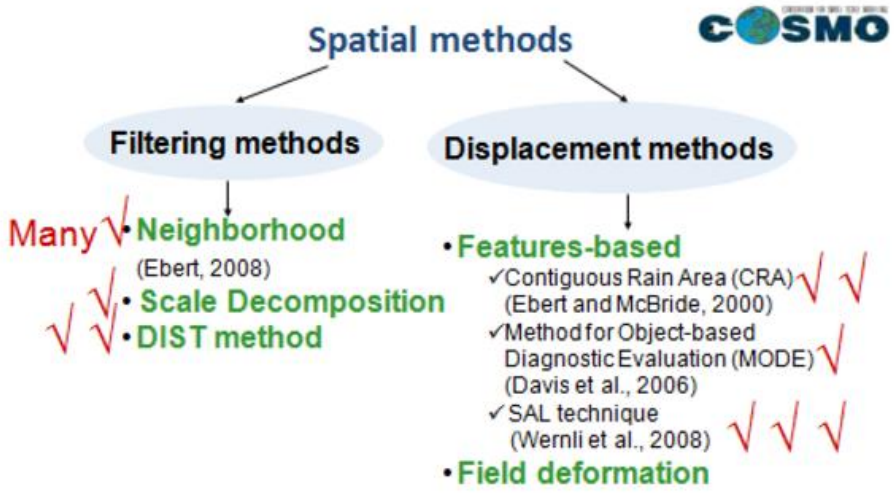


Figure 1: Classification of spatial verification methods and applications in COSMO within the INSPECT project (red signs).

The INSPECT project ran in parallel to MesoVICT to summarize the experience of applying spatial verification methods to COSMO forecast systems of very-high-resolution (1-3 km) compared to high-resolution models, providing criteria for deciding which methods are best suited to particular applications. In addition to targeting the goals of the MesoVICT project, PP-INSPECT provided COSMO users with more choice as to verification domains

and reference data, encouraging the participation of the COSMO community in the testing, development and improvement of spatial verification methods. Fig. 1 represents the classification of spatial verification methods and applications in COSMO within the INSPECT project indicated with red signs.

2 The main outcomes of PP INSPECT Summary

In this section, the main outcomes of the project are listed, while in the following paragraphs a detailed description will be given.

- A number of reruns of deterministic and ensemble forecast systems were performed for MesoVICT test cases (ARPAE-SIMC, MCH, RHM) (Table 1). All the reruns are interpolated into the same grid by M. Dorninger (Austria) in order to make easier the comparison, and are available by request at the MesoVICT site (http://www.ral.ucar.edu/projects/icp/).

- Scripts with examples for running neighbourhood, CRA, and SAL methods using free SpatialVx package are available at WG5 repository (HNMS, IMGW-PIB, RHM). Also examples of scripts to adapt radar and satellite data in a gridded format comparable with model output are available. For Neighbourhood (filtering) and SAL (object-based) methods, testing was performed by means of comparison of results from two independent software packages; bugs are reported to SpatialVx developer E. Gilleland (IMGW-PIB, HNMS). For Intensity Scale (IS) method (scale separation), MET software (NCAR) was also tested in addition to SpatialVx, but the graphical outputs of the packages were different and not comparable with those of SpatialVx. Further investigation is required for the differences in the application of the method.

- Several ways of compact visualization of neighbourhood, CRA and SAL methods were proposed (DWD, MCH, RHM). Especially for neighbourhood scores, such a cumulative framework can be implemented as part of the Common Verification activity.

- An object-based SAL (Structure-Amplitude-Location) method was found easier to implement than MODE and CRA methods as it does not require pair-wise matching of observed and forecast objects. The results however must be considered carefully as the method considers average characteristics over a domain. The accumulation precipitation range should not be small. It is recommended to calculate the SAL parameters with 6h precipitation range and higher, unless a highly convective case with significant precipitation amounts is tested. Object-based MODE and CRA methods provide more information compared to SAL about individual features of precipitation field, as they estimate matched pairs of observed and forecast objects. Smoothing of the fields can lead to the creation of bridges among different objects that are close to each other and unify them. This can significantly change the results of all object-based methods. On the other hand, smoothing can be undesirable for estimating objects with intense precipitation (or other variable of interest). The option to discard objects that are smaller than a certain size is found useful. When applied to observations, it eliminates small objects of any intensity that can be erroneous noise. Option for splitting objects is desirable sometimes. (HNMS, RHM, IMGW-PIB, ARPAE-SIMC).

- For MODE and CRA methods, it was found not feasible to identify one optimal universal matching function, in particular for high-resolution fields with objects of complex shape. For lower precipitation thresholds (and, consequently, wider features), more

Institution	Forecast system
MCH (P. Baumann)	COSMO-1 reruns for ALL MesoVICT cases are done and available at WG5 repository
ARPAE-SIMC (A. Montani)	ECMWF-IFS reruns (51 member) for cases 1 and 2 (8 initial dates)
MCH (A. Walser)	COSMO-E reruns (21 member) for cases 1 and 2 (8 initial dates)
RHM (D. Alferov and E. Astakhova)	COSMO-Ru2-EPS (51 member) for case 1 (1 initial date) and case 2 (1 initial date)

Table 1: Reruns of forecast system for MesoVICT cases.

reasonable results were obtained for a criterion based on matching observed and forecast objects if the distance between them is less than their average size. For higher thresholds, this criterion often does not allow for successful matches due to the small areas of features. A minimum boundary separation criterion seems more promising for intense events, but with a minimum boundary separation distance, beyond which, features should not be matched (RHM, IMGW-PIB).

- The IS scale separation method allows for the skill to be diagnosed as a function of the scale of the forecast error and intensity of the precipitation events. Results show that reduction of skill is mainly due to the small-scale misplacement of more intense (rare) precipitation events. Wavelet-based (Hier wavelets) scale-separation statistics are suitable for comparing models with different resolutions as the reference forecast accounts for the forecast variability. The method allows the analysis of precipitation instances, but it is not able to provide generalized information on the relative long term performance of a modelling system based on aggregated data.

- Applications of DIST, SAL and CRA methods to ensembles were made and new approaches on summarizing performance over various members and time accumulations were proposed.

- First results of experiments on introducing observation uncertainty into the spatial methods are given.

What was not completely fulfilled within the project and needs to be further studied:

- Introducing orography factor explicitly.

- Wind characteristics were only partially explored by M.S. Tesini (ARPAE-SIMC). The upscaling DIST method was applied, which analyses the statistical parameters of values in boxes of increasing size. For wind speed, the representative value of the box was defined as the median exceeding a predefined threshold; for wind direction, as the most populated category after having binned the direction in 8 categories. First results on DIST application to wind, were found not very satisfactory. The possible reasons were identified as follows:

  - possibly, the representative value of the box could be defined in another way;
  - the verification period was very short;
  - wind is too localized and the aggregation has benefit only if the boxes were chosen based on a different criteria that those of precipitation;
  - taking into consideration the orography (valley,) is required.

- Spatial applications to wind and other variables (e.g. Cloud cover) besides precipitation should be further developed.
- Only a limited number of applications to ensembles were performed. This direction of spatial method application is much demanded at present, and should be developed.
- Introducing observation uncertainty in the analyses was initiated by D. Boucouvala (HNMS) (see Sec. 4.1.3). This topic requires further study.
- Processing large amounts of data (for example nowcasting forecasts verification) will be of increased demand in the future. In Sec. 4.3.3, we describe an RHM experience of assessing the nowcasting scheme during the summer 2017 using the CRA method. The computational efficiency and the optimal organization of the data will be of utmost importance for processing large amounts of data.

Moreover, the PP INSPECT supported the efforts to increase COSMO visibility worldwide due to the active participation of COSMO members in the international project MesoVICT and its activities as well as in the WMO-JWGFVR workshops. Finally, it should be noted that the project was focused on the comparison of the spatial methods, and not on assessing the model performance, although some reflections to the advantages of different forecast systems were made.

3 Filtering methods

3.1 Neighbourhood Methods (Flora Gofa, HNMS)

3.1.1 Method applied (related to an INSPECT Task) and objectives

Neighbourhood verification is based on the principle of expanding the field of view to nearby (neighbours) data points in space, employing a spatial window around the forecast and observed points. In this way, the penalty for differences between modelled and observed values is relaxed. The size of this neighbourhood can be modified in order to verify model performance at several different scales, thus providing insight into the scales the model has the most skill at. Since the size of the neighbourhood can be varied, such approaches are well suited to verification of high-resolution models (Casati et al., 2008). In addition to neighbourhood size, the type and degree of filtering applied can also be modified. For example, extreme values may not be filtered out when examining severe weather events. Furthermore, in most cases, as in this research, the filter is applied to both the forecast and the observations. A more detailed review of neighbourhood approaches is available in Ebert (2008).

3.1.2 Short description of the dataset (forecast-observation data), adaptation required, software for the method application

The datasets used in the context of this study have been obtained from the Mesoscale Verication Inter-Comparison over Complex Terrain (MesoVICT) project. MesoVICT has been established in order to facilitate the application, capability and enhancement of spatial methods both for deterministic and ensemble forecasts (Dorninger, 2013). MesoVICT benefits from a huge data collection effort within the framework of the World Weather Research

Programme (WWRP) Project: Mesoscale Alpine Programme (MAP) D-PHASE over Central Europe in 2007. All six available test cases were analysed that cover a wide range of meteorological phenomena in and around the Alps. The example that is presented here is for the period 20-22 June 2007. With respect to the synoptic situation, the region of interest is ahead of a trough located over the British Isles, and warm moist air is being advected towards the Alpine Region. This leads to strong convective events on the evening of 20 June in the area north of the main mountain range. Subsequently, a cold front reaches the Alps from the west and moves to the east rather quickly while convective events are again observed ahead of the front (Fig. 2).

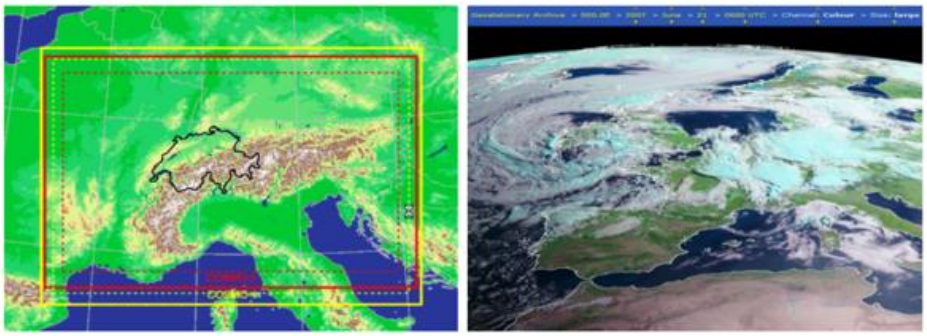


Figure 2: Left: COSMO-1 (dashed yellow), COSMO-2 (dashed red) integration domains, Right: Satellite image, cloudiness on 21.06.2007, 00UTC.

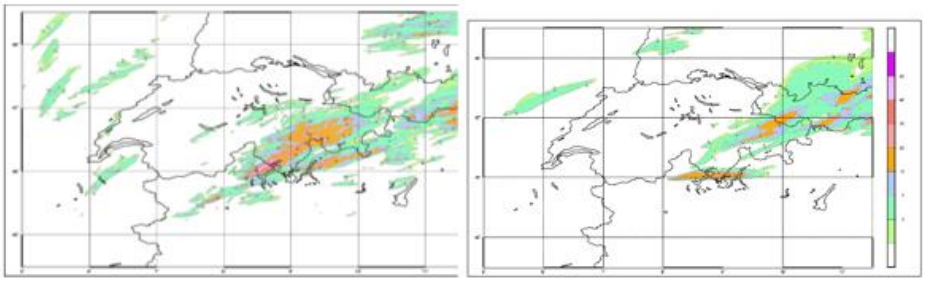


Figure 3: 12h accumulated precipitation at 21.06.08: 18UTC Left: COSMO-1, Right: COSMO-2.

From the multitude of NWP models with varying resolutions that are available through the MAP-D Phase, forecasts derived from COSMO-2 (2km res.) and COSMO-1 (1km res.) of the Swiss Meteorological Service were used. The domain of the COSMO model is shown in Fig. 3. Both models were nested on a coarser 7km COSMO model. Hourly precipitation forecasts from both models were upscaled prior to the application of neighbourhood methods in order to match the resolution of the observation fields in a final 8km grid spacing to match the observations.

3.1.3 Verification software

For the purposes of this research, the VAST (VERSUS Additional Statistical Techniques) software package, which was developed by the COSMO consortium and is based on Beth Eberts fuzzy verification IDL (Interface Design Language) code, was employed (Vela, 2017). VAST offers a number of neighbourhood verification tools, of which the following were tested

in the context of this research: upscaling, anywhere in the window, minimum coverage, fuzzy logic and joint probability. What distinguishes one method from another is the decision model, i.e. how strict or relaxed are the criterion that determine whether a forecast is successful or not. A large variety of methods and scores were calculated for a number of thresholds and window sizes, but only a selection of representative results are presented here.

3.1.4 Main findings (plots and explanation)

In this section, a short evaluation of the results of the application of some neighbourhood methods (Fig. 4) is given. Fractions skill score. The decision model is: "A forecast is useful if the frequency of forecast events is similar to the frequency of observed events", giving information on the spatial scales that the forecast resembles the observations, ranging from 0 to 1 (perfect). The score is most sensitive to rare events (e.g., small areas of precipitation); the useful scales are indicated in bold (Fig. 4). The FSS values for both COSMO forecasts are greater for light rain thresholds and larger scales, with useful skill displayed at spatial scales of around 130 km or larger for light rain and not at all for the heaviest rainfall rates. COSMO-1 forecasts exhibit similar behaviour with COSMO-2, being more useful for slightly smaller spatial scales (70km) for small to medium rainfall thresholds, while for higher thresholds COSMO-2 seems to be slightly more useful than COSMO-1.

Pragmatic approach. Instead of verifying the forecast probability within a neighbourhood against the observations within that same neighbourhood, the forecast is verified against the observed value in the central grid box. The decision model is that a useful forecast has a high probability of detecting events and non-events supported with the use of Brier skill score (BSS) to quantify the forecast success. The limited application of this method over the test case in Alps indicated that there is only minor improvement of the forecasts versus the reference, which is the sample climatology of the observations over the whole domain.

Upscaling method. It is the most widely used neighbourhood verification technique. Forecasts and observations are simply averaged to increasingly larger grid scales for comparison using a range of standard statistics. The decision model is that a good forecast has approximately the same mean rainfall amount as the observations. For this particular case, the ETS (equitable threat score) was calculated for each window size/threshold and, as shown, the scores generally improve with increasing scale and smaller rainfall thresholds, while the relative advantage of COSMO-1 forecasts is demonstrated.

Fuzzy logic approach. It is based on the fact that a forecast has a certain likelihood of being an event and a certain likelihood of being a non-event, and this is also the case for the observations. This likelihood is called the weight of support. This means that a forecast can be somewhat correct and somewhat incorrect at the same time (window). The decision model is, a forecast is useful if it is more correct than incorrect. From the categorical scores, BIAS is calculated in order to provide a more precise picture of the scales and thresholds that each model overestimates (BIAS > 1) or underestimates (BIAS < 1) hourly precipitation amounts. Other neighbourhood methods and scores for each method were calculated in an effort to explore the variability in the information that can be provided from their application to two different modelling systems which have not been included in this paper.

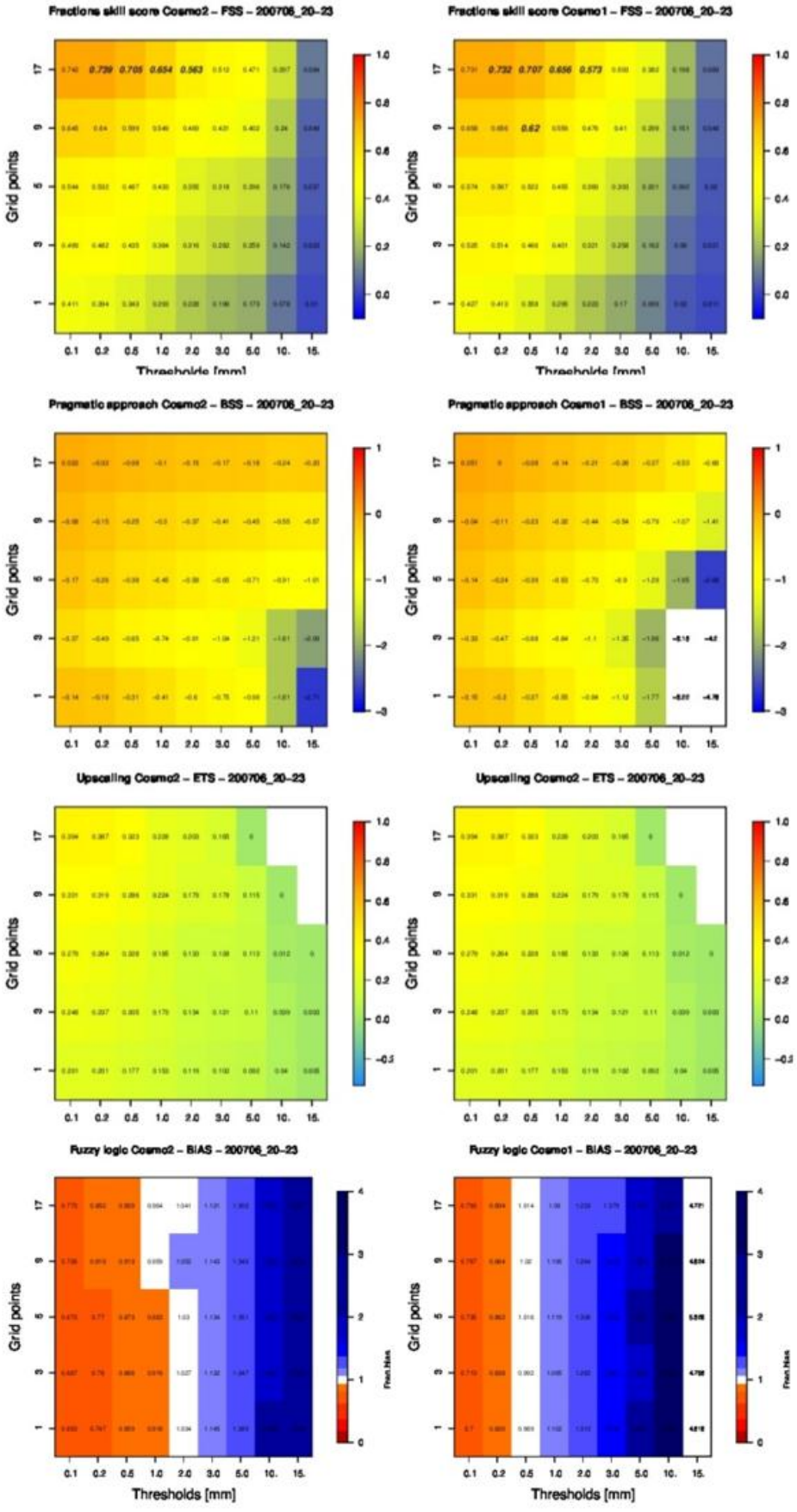


Figure 4: Fraction Skill Score (FSS) (first row), Pragmatic Approach (BSS) (second row), Upscaling (ETS) (third row), and Fuzzy Logic (BIAS) (fourth row) for COSMO-1 and COSMO-2.

3.1.5 Characteristics of the method applied)

- Efficiency in calculation time: the efficiency in time is quite satisfactory with respect to VAST. A significant effort is required to adapt the datasets and make them identical in size (grid dimension and resolution) prior to the application of VAST. If the user keeps the default amount of space windows (5) the calculation is rather fast, while it increases dramatically with the addition of even one additional space window. The adjustment of thresholds is easier and faster. No application was performed on time windows so far.

- Ability to deal with different density of observations: the method requires a complete set of gridded observations and forecasts with no gaps in the domain of verification. In case of inhomogeneous density of observations, the user has to adapt the dataset accordingly.

- Stability against observation errors: neighbourhood methods do not account for observation errors, as by relaxing the requirement of exact match in point and the use of averaged values over space windows for both forecast and observations, the weight of such errors on the verification results is eliminated.

- Ability to assess the added value of high-resolution models: neighbourhood methods provide a tool to compare modelling systems of various resolutions and are particularly valuable in the case of high resolution forecasts. However, before deciding on the methodology or score that is more suitable for a model evaluation, the first step in this approach involves carefully defining the attributes of a good forecast and subsequently identifying the specific methods and their associated decision models best suited to the particular application. Neighbourhood verification is particularly valuable in the case of high resolution forecasts, providing useful feedback on the scale and intensity for which each model configuration is advantageous. Precipitation events on different spatial scales are produced by different physical processes (e.g. large-scale frontal systems or small-scale convective events). Verification at different spatial scales provides greater insight into model performance to simulate these different processes.

Although the value of a neighbourhood verification framework has been demonstrated for this particular test case, its most sensible use is for evaluating sets of forecasts to determine typical forecast performance. For example, it can be used to monitor monthly or seasonal forecast performance in a region. It can also be used to evaluate updated versions of a model to identify at which scales and intensities, if any, skill has been improved (Gofa, 2017).

3.2 Analysis of long time series of neighbourhood scores (in particular: FSS, upscaling with ETS and FBI) for precipitation. Further investigation into the most informative and compact representation of scores.

3.2.1 DWD experience (U. Damrath)

At DWD, the spatial methods have been developed during many years. This section describes the analysis of long time series of the following scores: the Equitable Threat Score (ETS) for upscaling and the Fractions skill score (FSS). In (INTERP 2009), these scores were identified among the most useful. The analysis scheme is as follows:

- Getting the ETS for upscaling and FSS as monthly values from fuzzy verification

- No averaging over daily values is applied, but the calculation of scores from the contingency tables of the whole month is performed
- Calculation of running means of the results over one year
- Presentation of mean values and mean averages

Data sources that were used in this study:

- Precipitation forecasts of German COSMO-models and GME (with March 2015 ICON)
- Precipitation observations from radar data

Grid sizes and thresholds:

- Grid size from 0.025 (resolution of COSMO-DE) to 1.625 (65*resolution of COSMO-DE). For COSMO-EU the values are taken for the whole grid cell that is in this CDE-grid cell. Thus, there are about 9 points with equal values for the lowest window size
- Thresholds: 0.1, 0.2, 0.5, 1, 2, 5, 10, 20, 50 mm/12h or mm/24h

Fig. 5 gives an example of score visualization for the whole German territory. The red indicates that COSMO-EU is better, and the blue, that COSMO-DE. In this case, the higher resolution model advantage becomes evident only for the largest windows.

Overall, the results indicate that we are not able to make real forecasts for the lowest window size. A coarse value from the model with lower resolution has no double penalty.

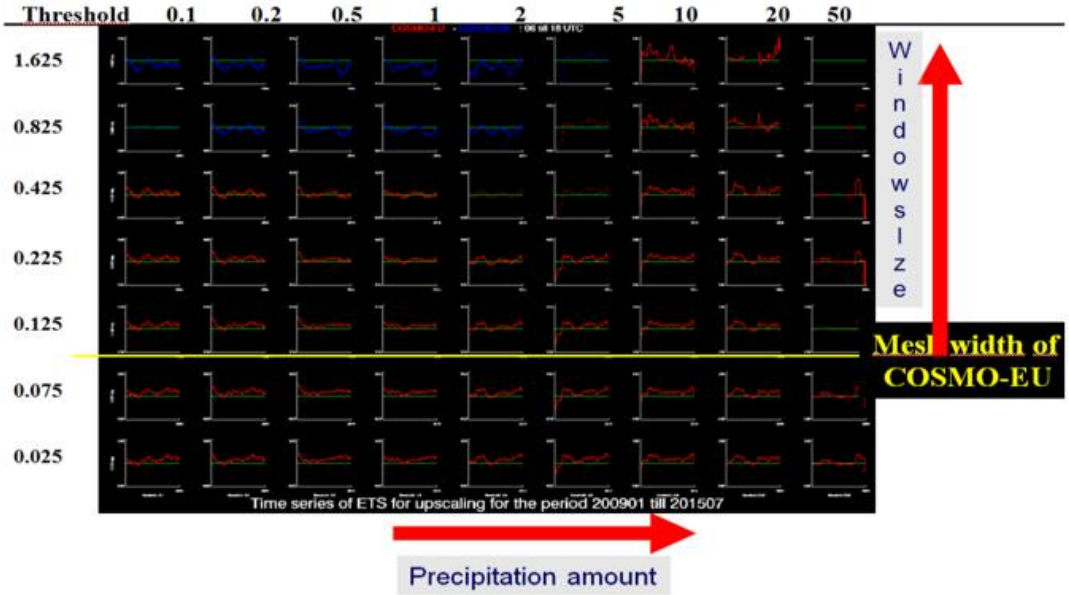


Figure 5: Comparison of COSMO-EU to COSMO-DE Differences of upscaling ETS. 06-18 UTC.

3.2.2 Evaluation of 4dVerif spatial verification visualization (X. Lapillonne, MeteoSwiss)

The use of spatial verification can bring new insight to the verification of model variables. It has a particular added value when it comes to verification of precipitation field since it can overcome the so called double penalty effect which occurs when a precipitation happen at a wrong geographical location in the model as compare to the observation. Because of its two dimensional structure it provides additional information as compared to stations based verification which needs to be visualized. In this report section we discuss some aspect of the visualization of these verification results and in particular how this information could be reduced so as to be easier to interpret.

Fraction skill score with 4dverif at Meteoswiss for precipitation verification

We focus here on the fraction skill score obtained with the 4dverif software run at MeteoSwiss. The fraction skill score (Roberts N.M., 2008) is one of possible available surface verification scheme. The basic idea of this score is to define an area or scale (here squares) and to count events in this region (fraction area) both in the model and in the observation. One then obtains a score for different scale see Fig. 6 and Fig. 7. A so called useful scale, see (Roberts N.M., 2008), is also defined above a certain score (in bold in Fig. 7).

The potential scale information introduces a new dimension in the verification parameter space, which is coming in addition to other existing parameters such as lead-time and initial forecast time. This provides potentially very detailed insight in the data which might be very useful for research purpose or to better understand the model but may be overwhelming for standard verification purpose, see Fig. 8.

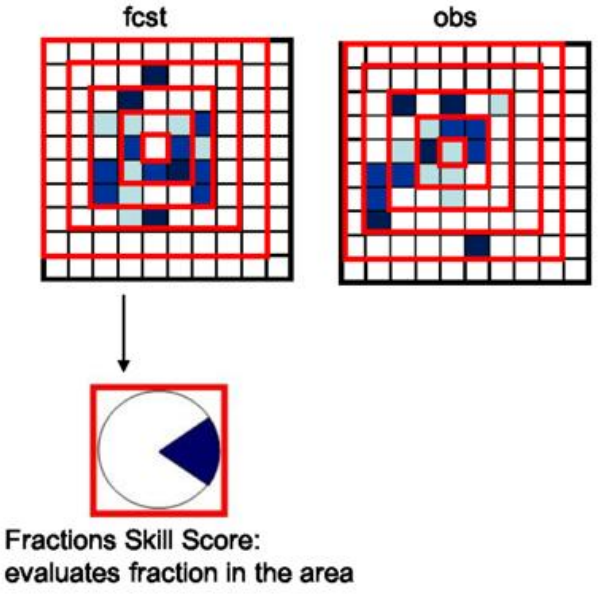


Figure 6: Surface evaluation area.

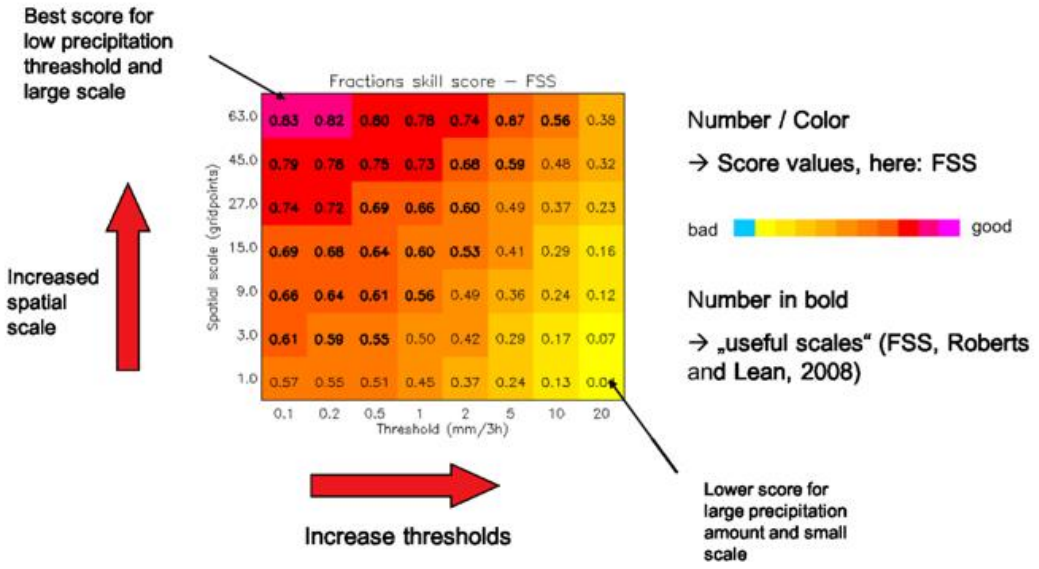


Figure 7: Fraction skill score (FSS).

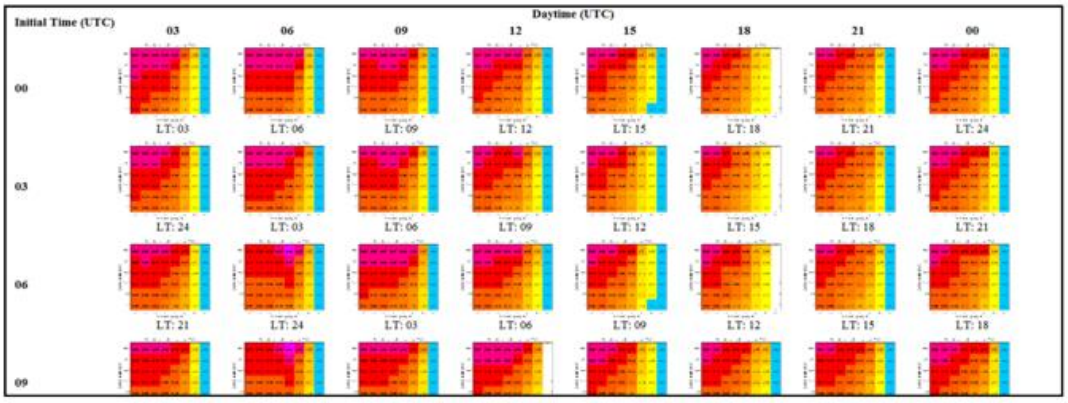


Figure 8: FSS for all lead times, initial time, scale and scores.

Simplified visualisation

It is suggested to reduce the available information by showing the most relevant part for standard verification on a one dimension plot which resembles usual station based verification or in a table. For the considered score and variable we propose for example 2 different cross sections of the data. The first one is to select a single meaningful scale and to show for selected threshold the score as a function of leadtime. In Fig. 9, we show the FSS for two models for the scale 19.6 km which roughly corresponds to the size of a warning region in Switzerland.

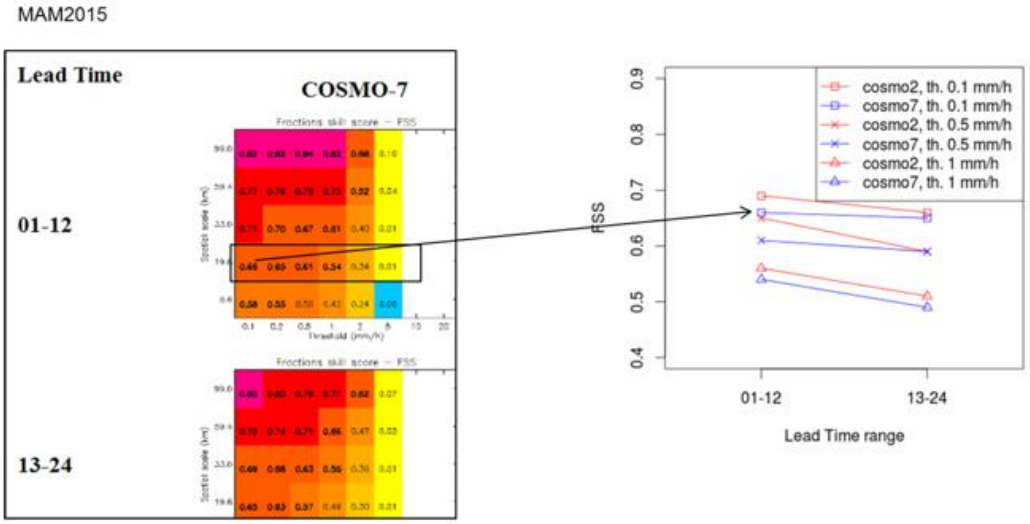
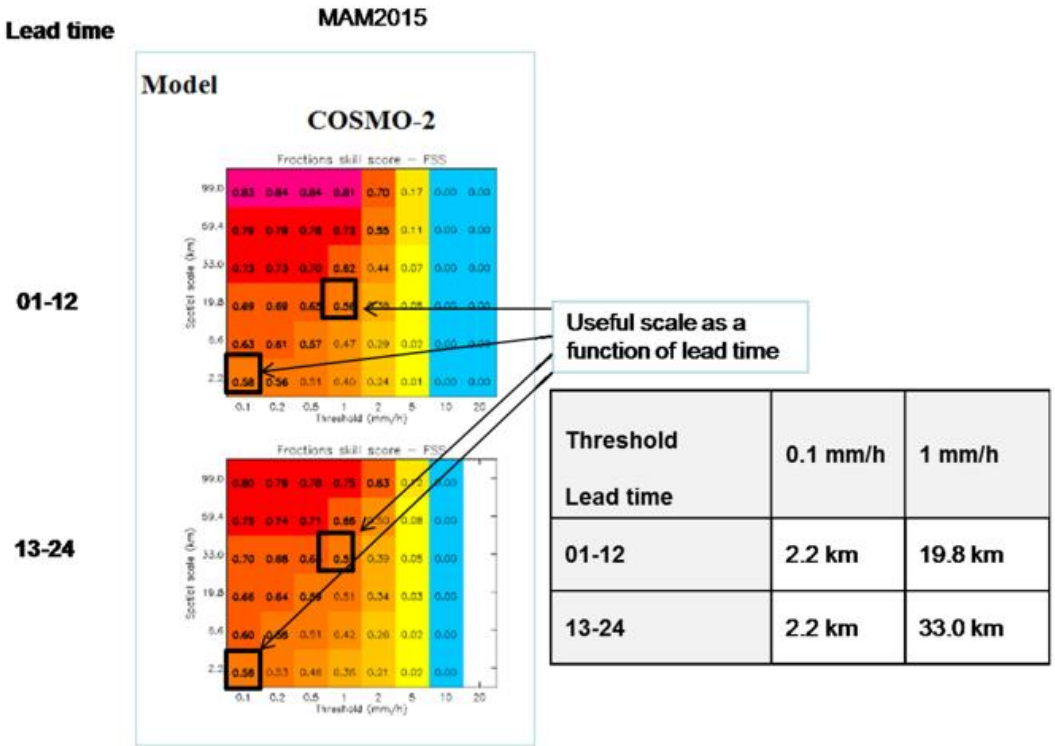


Figure 9: FSS for a selected spatial scale (19.6 km).

The second proposed way of displaying the data is to focus on the useful scale information. In Fig. 10, we show the useful scale as a function of lead time for different threshold. This could be interesting for example to help saying which model may be use for warning. Note that this information has a strong seasonal variability.



Threshold / Lead time	0.1 mm/h	1 mm/h
01-12	2.2 km	19.8 km
13-24	2.2 km	33.0 km

Figure 10: Useful scale as a function of lead time for different threshold.

Conclusions

The spatial verification provides new insight and information in comparison to standard station based verification. This additional information may be for some usage overwhelming and some reduction this information may be necessary. Here we propose for the fraction skill score two different potential ways of displaying the score. The first one is to look at the score for a given spatial scale while the other one focus on the so-called useful scale for a given lead-time and threshold.

3.3 Wind verification with DIST method: preliminary results (M. S. Tesini, ARPAE-SIMC)

3.3.1 Motivation of the study

Current wind forecast verification at ARPAE-SIMC is not completely satisfactory. It provides too local results difficult to summarize for a large number of stations. The DIST methodology (Marsigli et al., 2008) used operationally to verify precipitation has pointed out some advantages with interesting results. DIST provides the scores for different distribution parameters calculated for model and observed variables in boxes of increasing size. One of its main advantages is that it can be performed using both sparse point observations and gridded observation against gridded forecast (even if the grids are different). The size and even the shape of the box can be freely defined (e.g. alert areas for hydrological purposes). It provides simple information to forecaster or hydrologist about the performances of models in a single area of interest (e.g. Alert Area) or over the whole model domain aggregating the results of all boxes. The MesoVICT project encourages the investigation of the ability of existing or newly developed spatial verification methods to verify fields other than deterministic precipitation forecasts, e.g., wind forecasts.

3.3.2 Representative value of the box for wind characteristics and verification setup

It is important to define the representative value of the box for DIST application. Thinking to a more user-oriented verification we considered the median (e.g. the value below (or above) which 50% of the data may be found) and the 90th percentile (e.g. the value below which 90% of the data may be found, or above which 10% of data may be found) for wind speed. For wind direction, as a first step the values were binned into 8 category (N, NE, E, SE, S, SW,W,NW). Then the most populated category was taken as representative for the direction in the box. Since the direction for light wind may not be significant, another representative value has been evaluated considering only the direction for wind with intensity > 3 m/s. All the values of 3 consecutive hourly forecasts (and observations) that belong to the same area are put together to account for timing errors. The study was performed for all three MesoVICT cases (Dorninger, M.et al., 2013). The Swiss COSMO-2 and COSMO-1 model data were used. VERA gridded analysis was used as a reference data (Dorninger, M.et al., 2013).

3.3.3 First results

Fig. 11 represents three scores for events wind speed median exceeding a threshold. There is no clear increase of the forecast quality with increasing box size. In Fig. 12, the performance diagram is displayed for all three MesoVICT cases. In general, enlarging the box increases BIAS, but POD and FAR are slightly better. The scores move more or less linearly from 1

to 25 points in the box, but not from 100 to 400 pts. It is unclear if this behaviour depends on some scale of the considered phenomena or the data are not enough to produce consistent statistics. More investigation is needed to understand that. In Fig. 13, Wind speed threat score (TS) for COSMO-2 and COSMO-1 are given for boxes of increasing size. The event is defined here as 10% of points exceeding a predefined threshold. Scores (and trend of scores) considering boxes are nearly the same for the two models. COSMO-1 nearest grid point performs better than aggregation on 8 Km box. It is unclear if this can be explained with wind field characteristic or it is only an unlucky case. Maybe the choice of this percentile is not useful as was thought initially. Fig. 14 gives the PSS for wind direction for COSMO-2 and COSMO-1 for boxes of increasing size. The representative value is defined using all the data and considering only the direction for wind with intensity > 3 m/s. At larger scales, all the local information is filtered out. For boxes of smaller size, the information about local winds should be predominant. Another aspect is that it is not completely evident that VERA analysis is able to reproduce very local features.

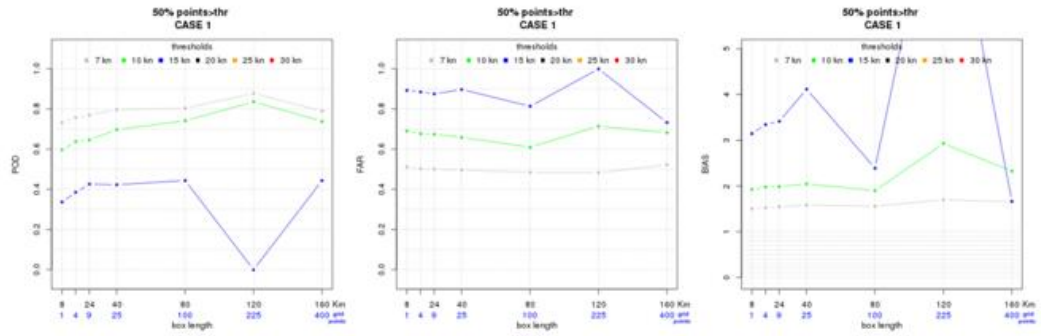


Figure 11: Probability of detection, False alarm rate, and frequency bias for wind speed (in knots), MesoVICT case 1, Cosmo-2 model. The event is defined as median exceeding a predefined threshold. The scores are plotted as a function of the box dimension.

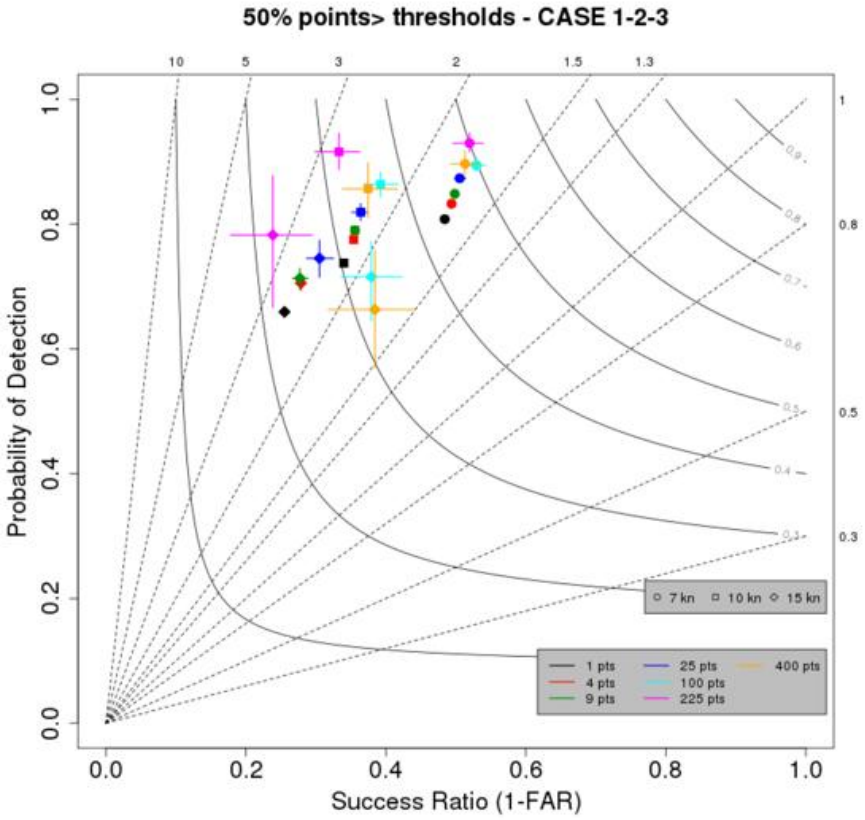


Figure 12: Performance diagram for wind speed (in knots), MesoVICT cases 1. 2. and 3, Cosmo-2 model. The event is defined as median exceeding a predefined threshold.

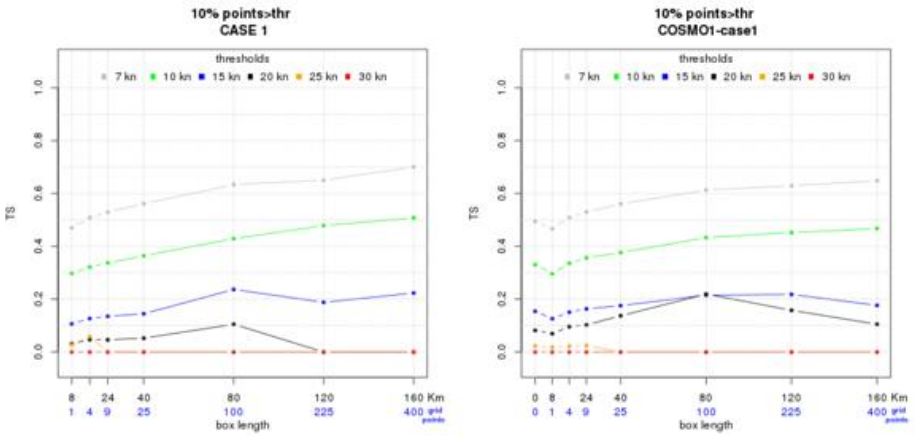


Figure 13: Wind speed threat score (TS) for COSMO-2 (a) and COSMO-1 (b) for boxes of increasing size. The event is 10% of points exceeding a predefined threshold.

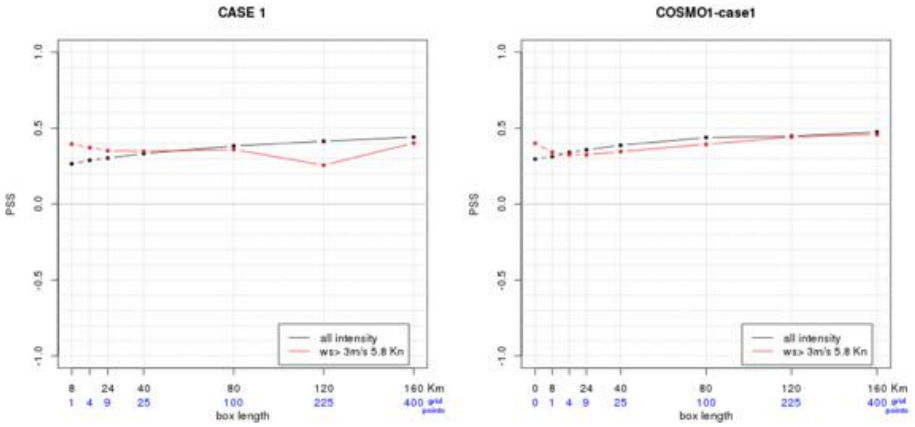


Figure 14: Wind direction, MesoVICT case 1, Cosmo-2 (a) and Cosmo-1 (b), PSS (Peirces skill score: What was the accuracy of the forecast in predicting the correct category, relative to that of random chance).

3.3.4 Conclusions

The first results on DIST application to wind were found not very satisfactory. The possible reasons were identified as follows:

- possibly, the representative value of the box could be defined in another way;
- the verification period was very short;
- wind is too local and the aggregation has is benefit only if the box were chosen differently;
- taking into account the orography (e.g., wind in valleys) is needed.

But before giving up tests are needed for other MesoVICT cases and using the JDC original observation (one of the main advantages of DIST was to deal with sparse point observations). It is also important to look at the geographical distribution of the scores.

3.4 Intensity-scale method (F. Gofa, HNMS)

3.4.1 Method applied (related to an INSPECT Task) and objectives

Scale Separation Methods: in general with these methods you decompose forecast and observation fields into the sum of spatial components on different scales by using spatial filters, and then you perform the verification on each scale component, separately. Verification on different scales can provide useful insight into NWP model representation of the different physical processes associated with phenomena on different scales. Scale-verification approaches aim to assess quality and skill of the forecasts for different spatial scales, analyse the scale-dependency of the forecast predictability (e.g. evaluate the no skill skill transition scale), and assess the forecast ability to reproduce scale spatial structure of observed precipitation fields. Precipitation fields are characterized by the presence of features on different spatial scales triggered by different physical phenomena. As an example, events such as

frontal systems are driven by the mesoscale dynamics of the atmosphere, whereas smaller scale events such as showers can be developed by local convective motions. Verification on different spatial scales can provide a deeper insight in the model performance at simulating different dynamics and give useful feedback for improvements. The intensity-scale technique for verifying spatial precipitation forecasts was tested in the framework of PP INSPECT. The technique provides a way of evaluating the forecast skill as a function of intensity of the precipitation rate and spatial scale of the error. The forecasts are assessed using the MSE skill score of binary images, obtained from the recalibrated forecasts and analyses by thresholding at different precipitation rate intensities. The skill score is decomposed on different spatial scales using a two-dimensional discrete Haar wavelet decomposition of the binary error images. Wavelets are functions characterized by a location and a scale (Daubechies, 1992). Similar to Fourier transforms, wavelets can be used to represent functions on different spatial scales, and so can be used to investigate scale properties of physical phenomena. Because of their local properties, wavelets are more suitable than Fourier series for representing spatially discontinuous fields such as precipitation. Moreover, because of their locality, wavelets are more efficient than Fourier components at representing sparse images containing few non-zero values. Different types of wavelets exist. Each wavelet type is defined by a mother and a father wavelet, characterized by different shapes and mathematical properties (e.g. smoothness, symmetry, etc.). In this study, Haar wavelets are used, because of their square shape which best captures the difference in binary variables. Fig. 15 shows the one- and two- dimensional Haar wavelets. Note that the two-dimensional wavelets are generated simply as the Cartesian product of the one dimensional wavelets.

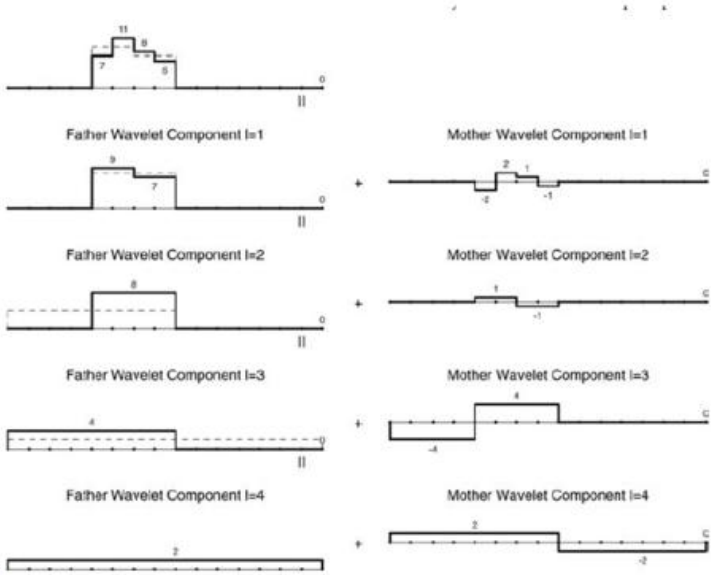


Figure 11. *Example of the one-dimensional discrete Haar wavelet filter applied to an example function (top left panel). At the first step the function is decomposed into the sum of a coarser* mean *function (the first father wavelet component) and a* variation-about-the-mean *function (the first mother wavelet component). At each step the Haar wavelet filter decomposes the father wavelet component obtained from the previous step into the sum of a coarser* mean *function (the l^{th} father wavelet component) and a* variation-about-the-mean *function (the l^{th} mother wavelet component). The l^{th} father wavelet component is obtained from the initial function by a spatial averaging over 2^l pixels. The process stops when the largest father wavelet component (mean over the whole domain) is found.*

Figure 15: One- and two- dimensional Haar wavelets.

Steps followed in Intensity Scale method application:

- Binary error decomposition: Thresholding is used to convert the forecast and analysis into binary images for each of the thresholds. Binary error is the difference of this:

$$Z = I_{y'} - I_x$$

- Binary error image is then expressed as the sum of components on different spatial scales by performing a 2-dimensional discrete Haer wavelet decomposition

$$Z = \sum_{l=1}^{L} Z_l$$

- Most substantial binary error image of the mother wavelet components are calculated for various spatial scales (l =1,..L=7 that corresponds to X km). The spatial scales refer to the spatial scale of the error and not that of the precipitation features or their displacement as it happens in the neighbourhood methods

- The MSE of the binary error image is calculated from:

$$MSE = \sum_{l=1}^{L} MSE_l \qquad MSE_l = \overline{Z_l{}^2}$$

  while for each threshold the skill score can be calculated from:

$$SS = \frac{MSE - MSE_{random}}{MSE_{best} - MSE_{random}}$$

  where and MSE_{random} is associated with a random forecast calculated from the bias and the base rate at each threshold

- Intensity scale verification technique is a spatial generalization of traditional binary verification (HSS, PSS).

3.4.2 Short description of the dataset (forecast-observation data), adaptation required, software for the method application

The datasets used in the context of this study have been obtained from the Mesoscale Verication Inter-Comparison over Complex Terrain (MesoVICT) project. All six available test cases were that analysed, cover a wide range of meteorological phenomena in and around the Alps. The example that is presented here is for the period 20-22 June 2007. From the multitude of NWP models with varying resolutions that are available through the MAP-D Phase, forecasts derived from COSMO-2 (2km res.) and COSMO-1 (1km res.) of the Swiss Meteorological Service were used. The domain of the COSMO model is shown in figure above. Both models were nested on a coarser 7km COSMO model. Hourly precipitation forecasts from both models were upscaled prior to the application in order to match the resolution of the observation fields in a final 8km grid spacing to match the observations. The software used was the R based SpatialVx and the waveIS routine. MET software (NCAR) was also tested but the graphical outputs of the methods were different and not comparable with those of SpatialVx. Further investigation is required for the differences in the application of the method.

3.4.3 Main findings (plots and explanation)

An example of the verification analysis is presented in Fig. 16 for 20070621-15UTC.

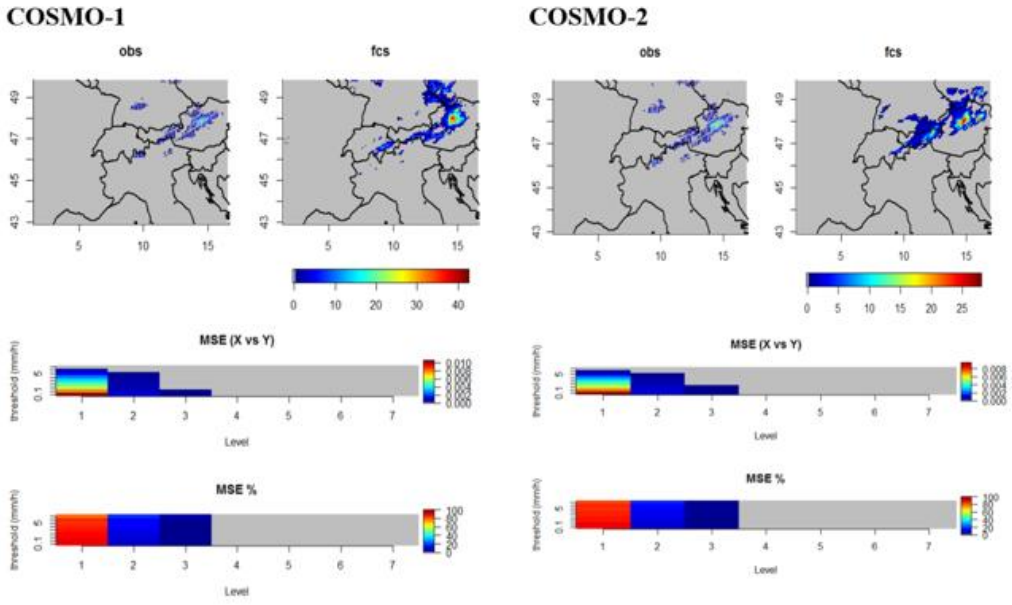


Figure 16: Example of the verification analysis for 20070621-15UTC.

From the analysis of this precipitation instant, it can be deducted that MSE almost disappears for error tiling of the order of 3x3 grid points. Comparing the two model performances, COSMO-1 shows slightly improved behaviour compared to COSMO-2. In Fig. 17, the results from the Skill score are given.

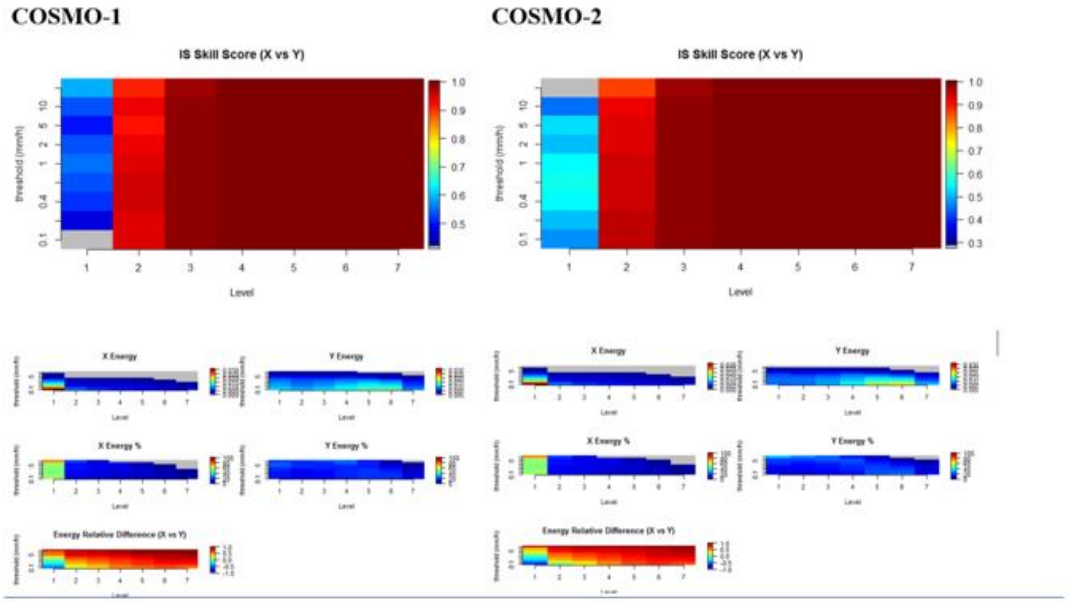


Figure 17: Results from the Skill score.

Small error scales (l=1) have skill close to zero as it is shown in the graphs, while slightly large scales exhibit large skill. COSMO1 ISS graphs exhibit that errors due to displacement of small spatial scale features are more important compared to those of COSMO-2. As a summary, both models have **small skills at the smallest scale** but skill improves when

considering larger spatial scales. ISS decreases as the precipitation threshold is increased and this is due to the **poor ability of the models to go beyond just the yes/no rain discrimination**.

3.4.4 Characteristics of the method applied

This filtering method allows the skill to be diagnosed as a function of the scale of the forecast error and intensity of the precipitation events. Results show that reduction of skill is mainly due to the small-scale misplacement of more intense (rare) precipitation events.

Wavelet-based scale-separation MSE skill score and scale-separation statistics are suitable for comparing models with different resolutions as the reference forecast accounts for the forecast variability. IS method constraints are related to the request to have precipitation analysis available for each grid point of the forecast field, and to the fact that Haar wavelet decomposition is designed for a square domain. Computationally, the method was easy to be applied and to derive numerical and graphical results, while their interpretation is not so straightforward and easy to comprehend from a non-experienced user.

The method allows the analysis of precipitation instances but it is not able to provide a generalized information on the relative long term performance of a modelling system based on aggregated data.

4 Object-based methods

4.1 SAL Method for deterministic and ensemble precipitation verification at HNMS (D. Boucouvala)

4.1.1 Description of the Method

SAL method (Wernli et. al 2008, 2009) is a spatial three component object- based quality measure which quantifies a precipitation forecast in terms of 3 parameters which correspond to a global field measure of Structure (S), Amplitude (A) and Location (L). An object is defined when it exceeds a fixed or statistically defined threshold value. The objects of the observed and forecast fields do not require one-to one matching and are identified separately. The fields are then transformed into binary representations of 1 (grids exceeding the threshold) or 0 (grids not exceeding the threshold).

The **A** component represents a normalized difference between the domain-averaged forecast D(R_{mod}) and observation fields D(R_{obs}) and it is the only one that **is independent of the identification of features** as it depends on the total precipitation amount. A positive value indicates overestimation of total precipitation, and negative indicates underestimation. The value of A is in the range of [-2,2], with 0 value corresponding to the perfect forecast for a system-averaged precipitation intensity. Values close to -2 show almost missed events and values close to 2 almost false alarms. A value of A=1 indicates an overestimation by a factor of 3.

$$A = \frac{D(R_{mod}) - D(R_{obs})}{0.5(D(R_{mod}) - D(R_{obs}))}$$

The **S** component compares the total of volumes of the normalized precipitation objects (scaled over the maximum value for each object), and provides information about their size

and shape. The range of S is [-2,2]. A positive value indicates that modelled precipitation objects are too large or too flat, and a negative value indicates that objects are too sharp and too small.

$$S = \frac{V(R_{mod}) - V(R_{obs})}{0.5(V(R_{mod}) - V(R_{obs}))}$$

The **L** component combines information about the distance of predicted and forecast mass centres and the error of a weighted average distance between the precipitation objects and centre of masses. It consists of two parts. $L = L_1 + L_2$. L_1 measures the normalized distance between the mass centres of the forecast x(R_{mod}) and observation fields x(R_{obs}), where d is the maximum distance found in the given domain between two boundary points. Its value range is [0,1]. The value of 0 indicates that the two fields mass centres are identical. However many different precipitation fields can have the same mass centres without being identical, therefore $L_1 = 0$ does not necessarily indicate a perfect forecast. L_1 **is independent of identification of features**.

$$L_1 = \frac{|x(R_{mod}) - x(R_{obs})|}{d}$$

L_2 is the difference of weighed mean normalized distance between the mass centre and the individual precipitation objects over observed r(R_{obs}) and forecast r(R_{mod}) fields and is a measure of difference of scattering of identified objects between the two fields. L_2 ranges between [0,1]. Therefore, L ranges between 0 and 2.

$$L_2 = 2\frac{|r(R_{mod}) - r(R_{obs})|}{d}$$

A perfect forecast is therefore characterized by zero values for all three SAL components. A **taSAL** index $=(|S| + |A| + |L|)$ is suggested by Lawson et al. (2016) (as an objective skill score in order to quantify the forecast quality by means of one only parameter. The bigger the index is the worse is the forecast.

4.1.2 SAL Calculation

Dataset

- In order to apply the method, precipitation objects need to be identified within a **gridded** verification domain which should be the same for both observed and forecast fields. In the case of MesoVICT data used for INSPECT project, gridded data in ASCII are already available. However, if the method is used for comparison with grib observations and bufr model data, a software for reading the files in such format should be available. A file with latitude and longitude of the gridded fields is also necessary.
- **The domain size is important**. It should be identical for both observed and forecast fields. It is not recommended to be too large as components from different precipitation regimes can override each other.
- **The accumulation precipitation range should not be small**. Hourly precipitation fields are often noisy, with not well defined objects. It is recommended to calculate the SAL parameters with 6h precipitation range and up, unless a specific case with significant precipitation amounts is tested.

Software required

In order to calculate the SAL components, after reading the input files, the following software are available:

- The original code (in Fortran) which can be provided by the authors.
- The libary SpatialVx (Gilleland, 2017) which is part of the free R language software with available documentation online. The advantage of this method is that by using featurefinder (function for defining objects) a the user can easily view objects and specify thresholds, smooth fields and discard small scale noise. The SAL parameters are then calculated by using the smaller function.

Object Identification Methodology and examples of SAL calculation

The selection of a threshold value for objects identification is required for this method and it can be critical if the fields contain objects with different local maxima. A small change in the threshold can lead to a different number and size of objects and therefore different L_2 and S values. The possibilities of setting a threshold R are the following:

- Constant fixed user defined threshold (e.g. 2 mm) for forecast and observed fields. (This method is more subjective)
- $R = f \cdot R^{max}$: threshold is a fraction of R^{max} (the maximum value of the field) and f is subjectively chosen factor with a value of 1/15 suggested by Wernli et al. (2008) as the most appropriate to identify objects. Higher values of f result in threshold increase
- $R = f \cdot R^{95}$: threshold is a fraction of the 95^{th} percentile of all gridpoint values in the domain which are larger than 0.1mm. (This is the method suggested by Wernli et al., 2009) and is used in the original code. This is sensitive to outliers. (eg. Single grid points with very intense precipitation)

Examples of SAL are given in Fig. 18, (calculated with method 3) where CMH S value is positive indicating that objects are flatter than observed (precipitation is more stratiform), and negative S for COSMO-2 means that modelled objects are sharper than observed. Positive (negative) values of A for CMH (COSMO-2) indicate overestimation (underestimation) of total domain precipitation. L values are slightly higher for COSMO-2 as there are fewer and more localized objects. TaSAL is lower for CMH, which indicates overall better forecast.

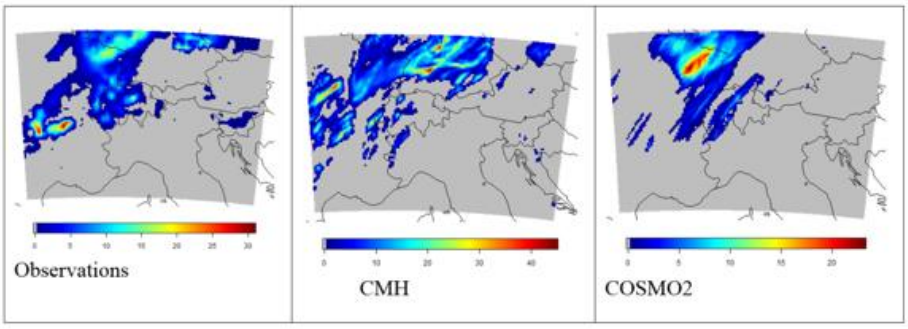


Figure 18: CMH and COSMO-2 forecasts versus Observations for MESOVICT case of 12 hourly Precipitation of 18h for 19/7/2007.

Model	S	A	L	taSAL
CMH	0.22	0.48	0.18	0.88
COSMO-2	-0.12	-0.55	0.25	0.92

Object Identification Options

- Smoothing: smoothing option is available on featurefinder function by setting do.smooth=TRUE and giving a value to smoothpar (which can also be different for observed and forecast fields). Specifically, by applying smoothing, the value at each grid is replaced by the mean value over a disk with a radius of a number of grid points given by the parameter smoothpar. The convolved data is **then** thresholded yielding a binary mask, so mostly affected are the object boundaries which are smoothed. Also small scale noise is filtered out. The selection of smoothing radius is not straightforward (Weniger et al., 2016) and it is not obvious how to select it for a given set of data. It is also relative to grid size. So, the same smoothpar can lead to light smoothing when applied to a grid of 1km but significant when applied to 7km. Smoothing for example can lead to bridges creation among different objects that are close to each other and unify them. If the selected smoothing factor affects one domain (forecast or observations) more than the other, then S and L_2 parameters may completely change with only a small smoothpar change. In general, the increase of smoothing radius does not necessarily improve the results of the parameters, as it may unify or separate objects depending on the threshold, therefore alter the number of objects. Examples of effects of smoothing for the case of Fig. 18 are shown in Fig. 19. The effects of smoothing on S in this example are apparent when moving from smoothpar=3 (Fig. 19b) to smoothpar=4 (Fig. 19d) as the unification of the objects in observed field results in a complete S change (even on sign). Flatter objects were predicted in Fig. 19b due to the larger modelled yellow object, while the observed objects unification in Fig. 19c resulted in slightly sharper objects now predicted by the model. The bigger smoothing in Fig. 19d resulted in unification of almost all objects and made small objects disappear.

- Omission of small objects: the min.size option of featurefinder (min.size=c(n_min_obs, nmin_fcs)) defines objects as cohesive threshold exceedances and objects with less than n.min are omitted. The interpretation of this parameter is more straightforward that smoothing (Weniger et al., 2016) and it is easier to foresee the consequences of a particular choice of a parameter value on the objects as it does not unify or separate objects. It does not affect shape of large objects. If the selection of factor removes small objects and affects object spread for one domain (forecast or observations) more than the other, the S and L_2 parameter may increase or decrease. Examples of effects of using min.size are shown in Fig. 20, where omitted modelled objects resulted in more widespread forecast precipitation with a slight and stable increase of S and L_2 values with min.size increase. User can visualize objects after using the function featurefinder in order to decide about the best threshold and smoothing selection, but this selection is more straightforward for one specific case and not for a series of data with different precipitation regimes, that will be plotted afterwards on a SAL Plot.

  Errors in observations (too big values) can be discarded in the calculations when threshold is a fraction of a percentile of all gridpoint values in the domain. Also, by applying the min.size option in the observed field, small objects of any intensity that can be erroneous noise vanish. However, erroneous values within normal range can lead to wrong observation objects and therefore SAL components.

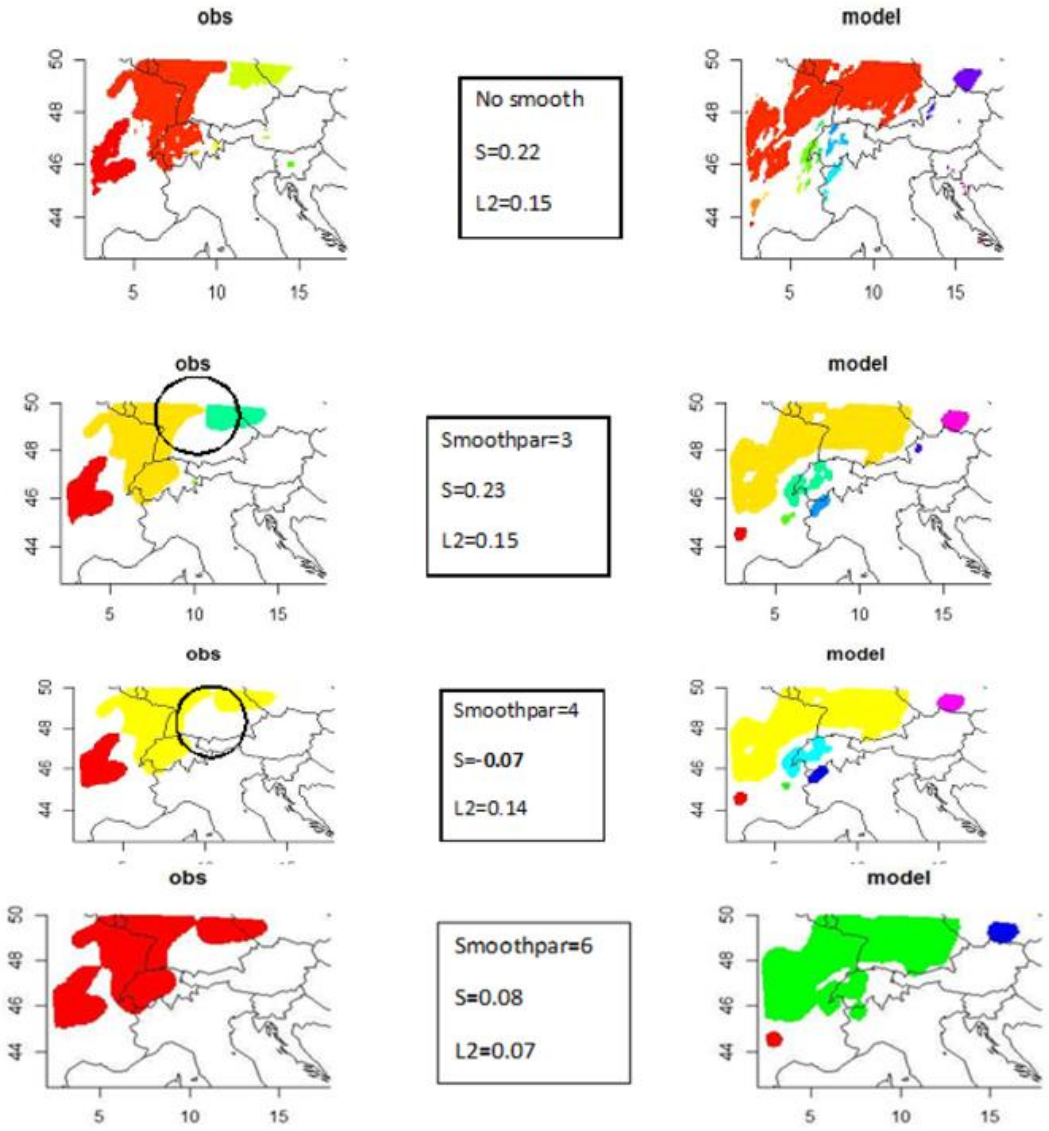


Figure 19: Examples of different smoothing factors and their impacts on objects and S / L_2 applied on the case of Fig. 18.

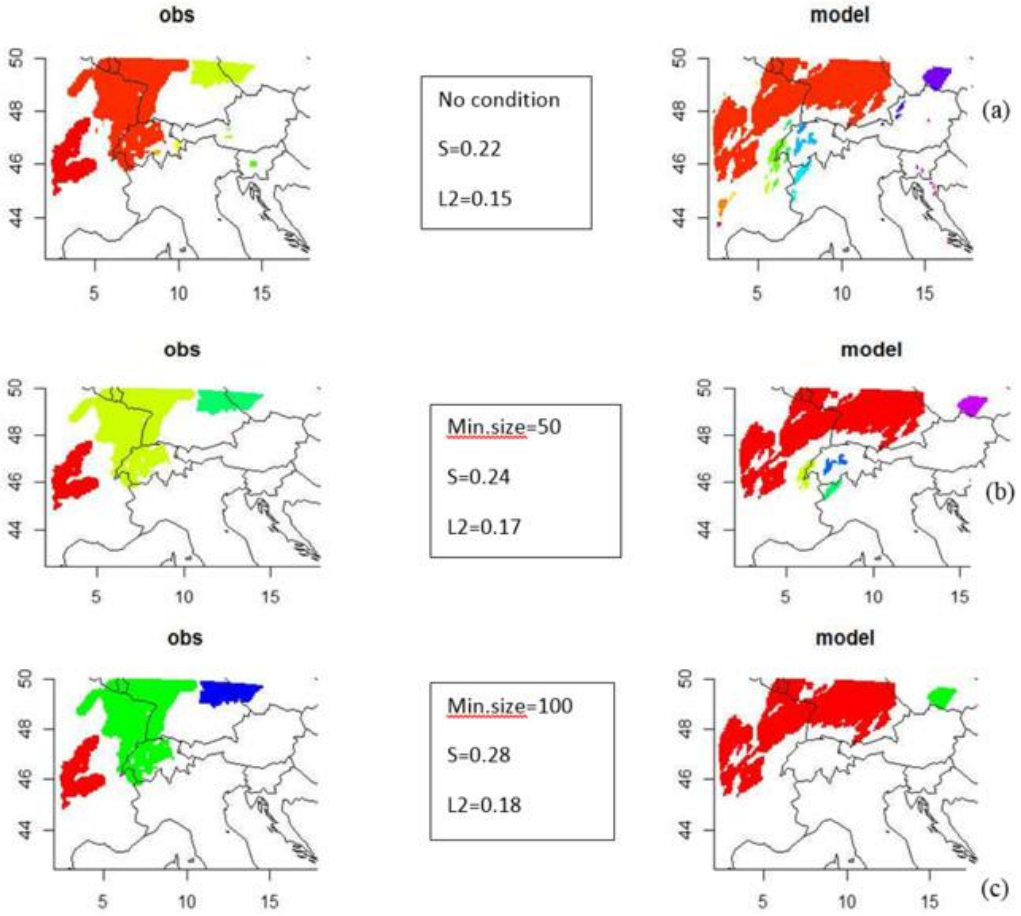


Figure 20: Examples of different min.size options and their impacts on objects and S / L_2 applied on the case of Fig. 18.

SAL Plots

The SAL method can be applied to a set of forecasts performed by the same model in order to define a general model tendency of predicting each of the three SAL components. This is done by the SAL diagram in which each point represents one case. The median value of S and A together with the 25^{th} to 75^{th} percentile box can also be plotted. The L component value for each point is depicted with a colour scale. Example of this plot is shown in Fig. 21.

Warning: if no features are found in either or both forecast and observed fields, the SAL values cannot be defined. In this case (no objects found by featurefinder in forecast, observed, or both fields), saller function cannot be executed and the case is defined as Miss, False Alarm, or Correct Negative respectively. The use of extreme values of SAL parameters (-2.2) in case of lack of objects is not recommended and cases are simply omitted.

Statistically Specified thresholds (with selection of appropriate scaling factor) can be used when dealing with a significant number of cases in one SAL plot, as the precipitation amounts are different for each one, and a fixed threshold can be too big for some cases of them and exclude them. However, for one particular case, or for a number of cases with similar situation (ex. only convective) or if only extreme events exceeding a specified threshold are studied, then a fixed threshold can be used. SAL parameters can also be used to test the performance

of an EPS ensemble by plotting the SAL values of each of the members on a SAL plot and get an estimate of the ensemble forecast for one particular time (Barrett et al, 2015).

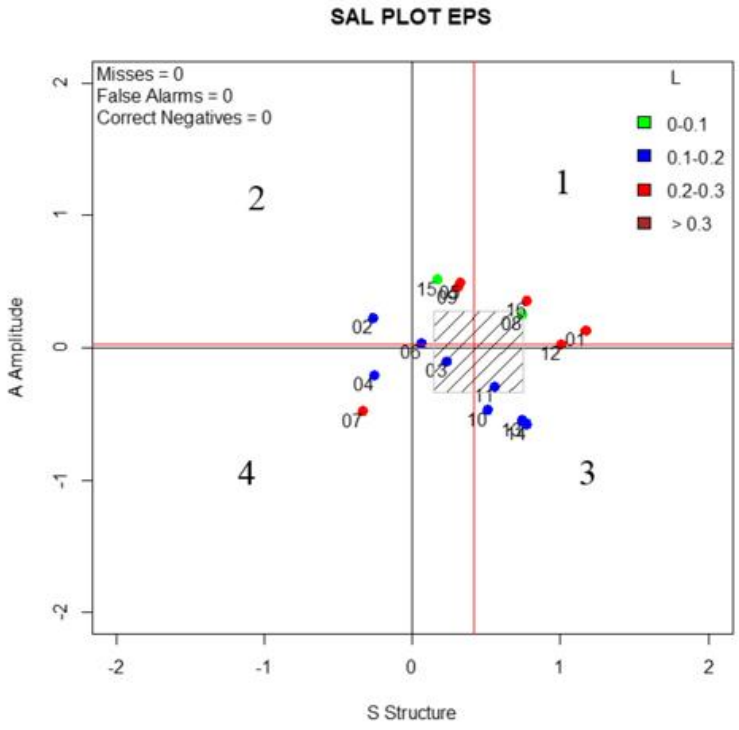


Figure 21: SAL diagram for COSMO-LEPS 3h precipitation for 21/6/2007 12UTC. The red lines denote the median values of A and L, the gray box is the area of 25^{th} to 75^{th} percentile.

In Fig. 21, an example of a SAL diagram with 16 members of COSMO-LEPS indicates that median S is positive, meaning that as an ensemble, predicted objects are flatter and larger than observed. The A median parameter is close to zero and slightly positive which means that amplitudes of observed and modelled fields are comparable. Members in quadrant 1 produce too much rain with too large or flat objects. L values are relatively low and less than 0.5. The forecast fields for each member may be significantly different. Therefore, fixed thresholds applied to a set of members may be too big for some of them, resulting in no object formation for some members, therefore S and L may be calculated with fewer of them. On the other side statistically specified thresholds for each member, imply a different threshold for each of them when compared to the observed field. It is up to the user and the specific case to select the appropriate method.

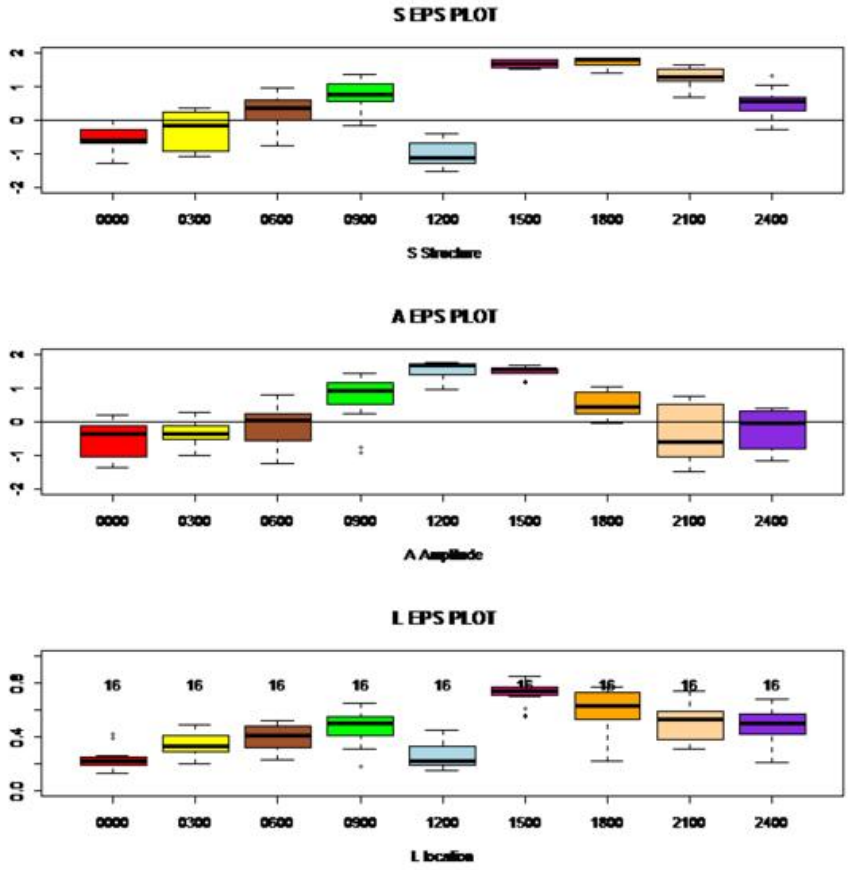


Figure 22: COSMO-LEPS hourly variation of ensemble SAL parameters (Statistically Specified threshold) for 20/6/07 with a Run beginning on 19/6/07.

EPS forecasts hourly variation can also be plotted as boxplots (each one representing the distribution of the members) of each parameter as a function of time lead (Fig. 22). The L parameter distribution is now also better represented than SAL Plots. The R SAL plot and boxplots are written in R language. The calculation time can be significant if the program reads a large number of files and plots many cases for one SAL Plot In order to perform a SAL plot over a set of many different forecasts of an EPS model, there are two possibilities:

- **Medians** of the SAL parameters over the members for each case are calculated and then plotted on a SAL plot. The number of points will be equal to the number of cases;
- **Medians** of the SAL parameters over all cases for each member are calculated and then plotted on a SAL plot. The number of points will be equal to the number of members.

Examples for MESOVICT COSMO-LEPS 3 hourly forecasts of the Run beginning on 18/07 12 UTC (from 20 to 22/7) with the two methods given in Fig. 23. The two methods give comparable A and S median values with different spreads, as expected.

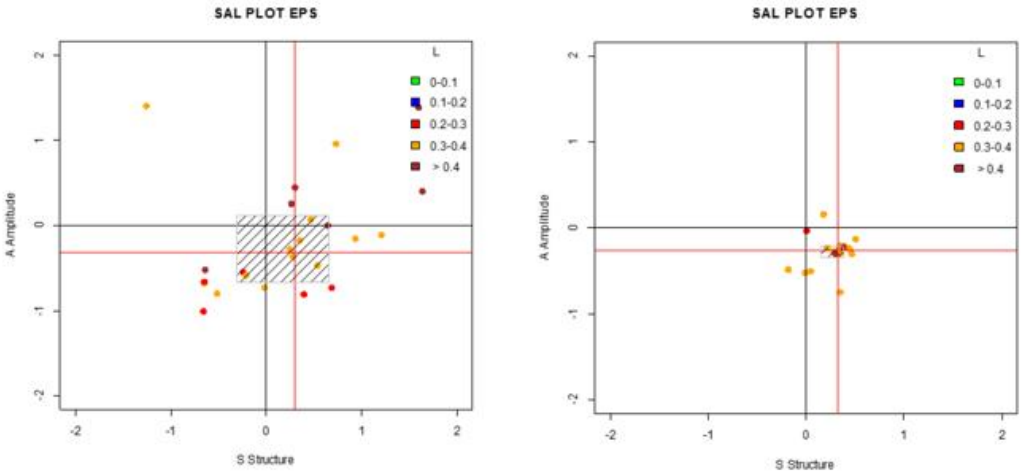


Figure 23: COSMO-LEPS SAL parameters for all 3-hourly forecasts from 20-22/7/07 with a run beginning on 18/6/07.

Further research on SAL applied to EPS models includes comparison of objects in fields of probability (Radanovics et al, 2015), and consideration of observation uncertainty.

4.1.3 EPS in terms of probability (a research topic)

Further research on SAL applied to EPS models includes comparison of objects in fields of probability (Radanovics et al, 2015) with consideration (if available) of observation uncertainty. In an effort to apply this concept to MESOVICT dataset the following ideas (which require further research) are presented in this document:

- *when the observation domain is constant and uncertainty is applied only for LEPS*

  First, the setting of precipitation threshold to be tested is needed (eg. 2mm). The fraction of the 16 LEPS members that predict precipitation above this specified threshold applied on every grid point consists the probability field in the model domain (range 0-1). In Fig. 24, different colours represent the different probabilities and the brown objects are of probability 1(all the 16 members predict precipitation above the threshold). When uncertainty is applied only to the model domain, these objects (in order for the comparison to be fair) can be compared to the observation objects which reflect the real conditions, and can also be represented by probability 1 (Fig. 24). In this case, A parameter will be only calculated for the 2 fields by taking into account only the objects with value 1 and setting to zero the remaining grid points for observed and modelled domains (because in the observations field the remaining grid points cannot be represented as probabilities) . Also, S parameter will reflect only their size and not sharpness. These objects are detected by the featurefinder function (Fig. 25) and the resulting SAL parameters will be a measure of how the objects over a specified threshold can be forecasted by all 16 members of EPS model. In this particular case S=1, A=0.38, L=0.3;

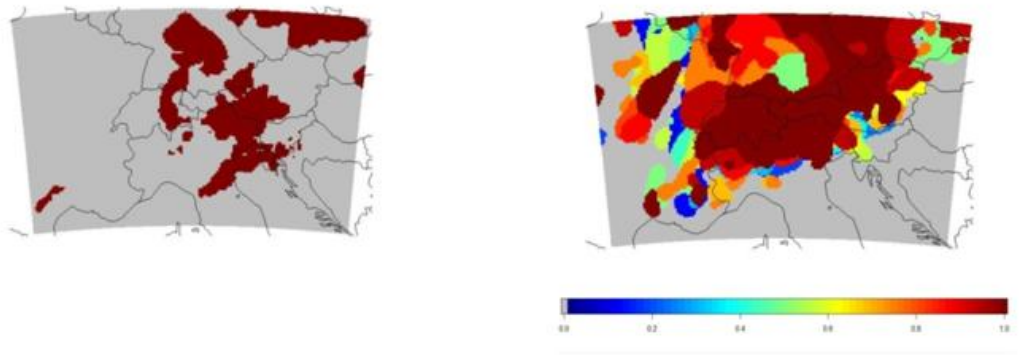


Figure 24: Probabilities of 3h precipitation threshold > 2mm for observations (left) and LEPS (right). 21/06 12UTC. The colour scale is the probability range.

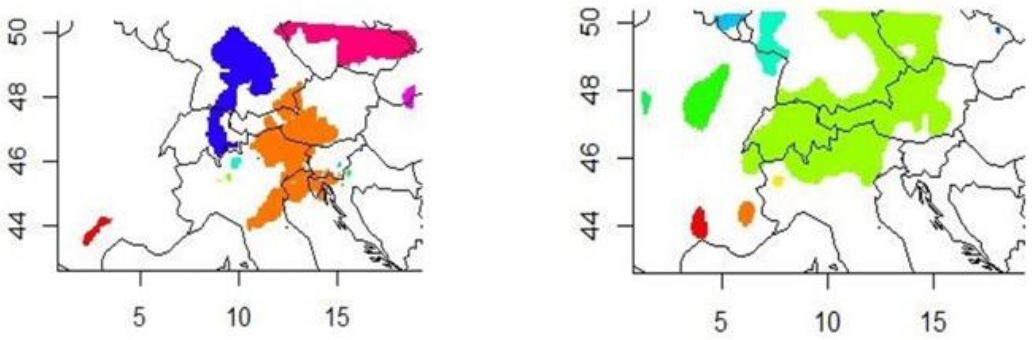


Figure 25: Objects of probability=1 as detected by the featurefinder function for observations (left) and model (right). Colours indicate different objects.

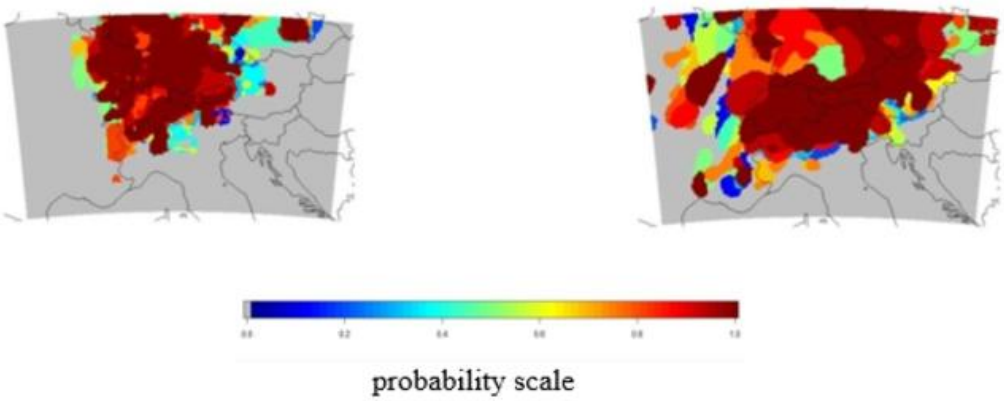
- *when uncertainty is applied also to observations (in this case 16 members of VERA ensemble)*

  When uncertainty is also applied to observations (Gorgas and Dorninger, 2012a), the concept of the fraction of the members exceeding the specified threshold can be applied in the same way to observed and LEPS domains, and fields of probability can now be created in both of them. In this case, probability thresholds of less than 1 can also be tested. For example, for precipitation threshold 2mm, the objects of each field created by the different probabilities exceeding it, are shown in Fig. 26a. In Fig. 26b, the objects of probability=1 (all members in observation and VERA fields predict precipitation above 2mm) detected by featurefinder in both domains are shown. In this case, S=0.37, A=0.6, L=0.1. The objects of probability threshold < 1 (0.5 in the case of Fig. 26b, which denote that at least half of members predict precipitation above the threshold) are bigger and include also higher probabilities can be compared with the SAL method for the two domains. In this case, S=0.65, A=0.5, L=0.05. Further research on LEPS SAL parameters includes the introduction of a SAL index (Radanovics, 2017a) for LEPS (Ensemble SAL) with average means over the members of the equation parameters for observed and model fields. This formulas that may be introduced in SpatialVx (Radanovics, 2017b), will be a more efficient way of SAL parameters estimation for Ensemble Forecasts.

$$L_1 = \frac{|\langle x(rr_{mod})\rangle - \langle x(rr_{obs})\rangle|}{d}$$

$$L_2 = 2 \times CRPS(P(\frac{r_{mod}}{d}), P(\frac{r_{obs}}{d}))$$

$$S = \frac{\langle V(mod)\rangle - \langle V(obs)\rangle}{0.5\langle V(mod)\rangle + \langle V(obs)\rangle}$$



a)



b)



c)

Figure 26: a) Probabilities of 3h precipitation threshold > 2mm for VERA ensemble (left) and LEPS (21/06 12h). b) Objects of probability threshold=1 as detected by the featurefinder function for VERA ensemble (left) and LEPS (right). Colours denote different objects. c) Same as b with probability threshold=0.5.

4.2 MODE, CRA, SAL: IMGW-PIB experience

The experience described in this section is unique in INSPECT, as IMGW-PIB applied three different object-based methods, which facilitated their intercomparison.

4.2.1 Method applied (related to an INSPECT Task) and objectives

MODE - Method for Object-Based Diagnostic Evaluation, its objective is to identify localized features of interest in scalar fields, merge and/or match features and compare features in two fields to identify which features best correspond to each other. CRA Contiguous Rain Area, identifies features of interest, uses pattern matching techniques to determine the location error, errors in area, mean and maximum intensity, and spatial pattern. The total MSE (Mean Square Error) is decomposed into components due to location, volume, and pattern error (MSE displacement, MSE volume, MSE pattern) (see also Chapter 4.3) SAL - Structure, Amplitude, and Location, requires a preselection of a domain of interest, a definition of a threshold to identify objects in the observational data and model forecast, one-to-one matching between the identified objects in the observed and forecasted fields is not required. A forecast is perfect if S = A = L = 0. (see also Sec. 4.1.1.)

4.2.2 Short description of the dataset (forecast-observation data), adaptation required, software for the method application

- Radar data
  - OPERA (Operational Programme for the Exchange of Weather Radar Information), 1 hour rainfall accumulation. The composites cover the entire Europe in a Lambert Equal Area projection. For the project data in HDF5 format was used. The HDF5 files are read directly in the R software by using "HDF5 interface to R". The data are adopted to geographical coordinates (latlon geographical projection) in terms of verification against COSMO PL data
  - Polish national RADAR (POLRAD network) data composite. The data are available in Rainbow binary XML format and can be processed with additional php5 tool available at IMGW-PIB to extract rainfall accumulation and geographical locations.

  Both data sets require a procedure of matching to COSMO PL model domain.
- Vienna Enhanced Resolution Analysis - VERA data
- Forecast data
  - COSMO-PL 7 km, COSMO-PL 2.8 km
  - COSMO-2 data - interpolated on the VERA grid.

4.2.3 Main findings (plots and explanation)

The all plots and statistics below were obtained using SpatialVx R-package developed at NCAR (Gilleland, 2015).

- MODE example. MODE graphical output shows matched objects (e.g. Hits) and unmatched objects (e.g. False alarm in forecast field, Misses in observation field), which are based on the interest value. The interest value is an overall measure of similarity between objects in the observed and forecast fields, ranges from 0 to 1. The value of 0.70 is used for objects to be considered matched. COSMO-PL7 precipitation model output was verified against OPERA radar data. The result of MODE method shows a good correspondence of the precipitation objects between COSMO-PL7 and radar data.

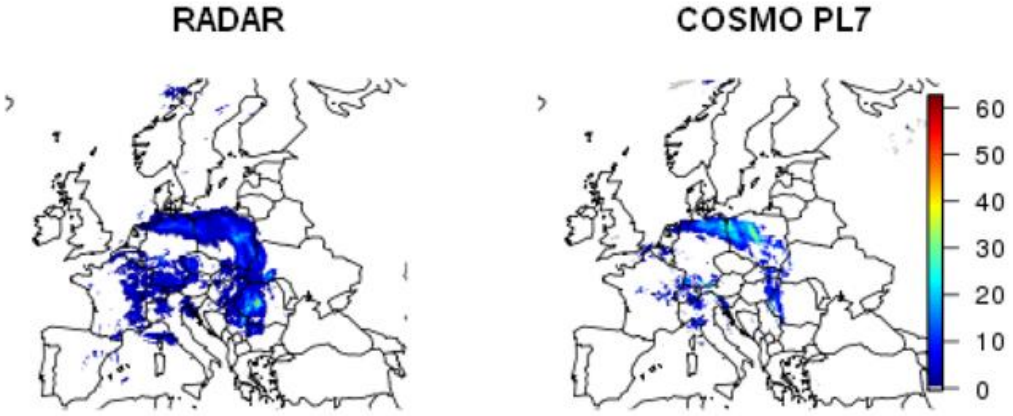


Figure 27: 24h QPF ending at 00 UTC on 05.05.2017.



Figure 28: Identified, matched objects, threshold 5mm, Matched objects are indicated in the same colour in both the observed and the forecast fields .Grey colour corresponds to unmatched objects.

- CRA example. CRA verification was used to verify forecast model COSMO-2 against VERA data. One of the cases was chosen for the verification. For object pairs 2 and 4 the total error is associated with the error in location, while for object pairs 1 and 3 the total error is associated with the fine scale structure.

Observation feature	Forecast feature	Total interest
1	1	0.85
2	2	0.7
2	1	0.46
1	2	0.42

Table 2: Ranking of feature pairings based on total interest.

	MSE.total	MSE.disp	MSE.volume	MSE.pattern
1	0.01222	0.00232	7.405e-05	0.00983
2	0.00173	0.00123	4.615e-07	0.0005
3	0.07752	0.01059	3.919e-03	0.06301
4	0.00166	0.00124	3.645e-07	0.00041

Table 3: Total MSE and its components.

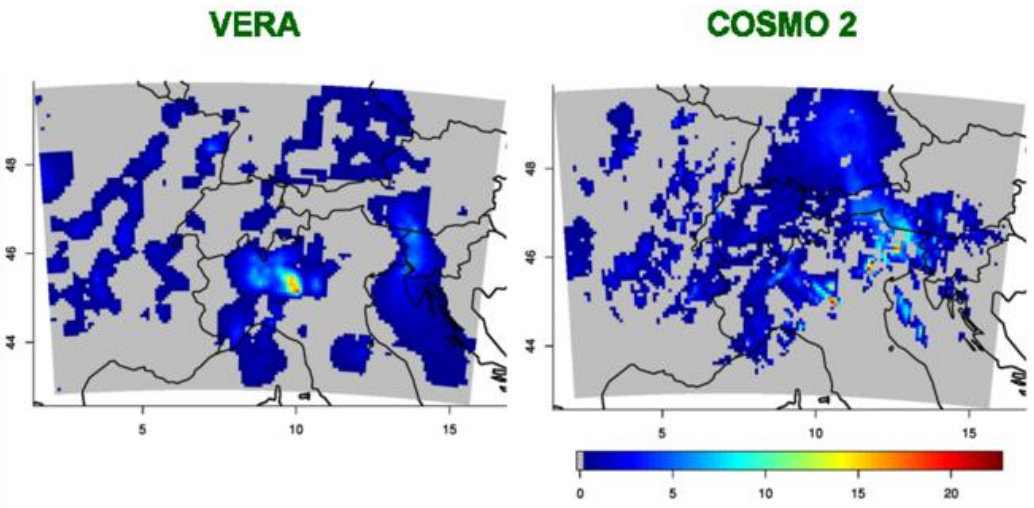


Figure 29: 1h accumulated precipitation 26.09.2007, 18UTC.

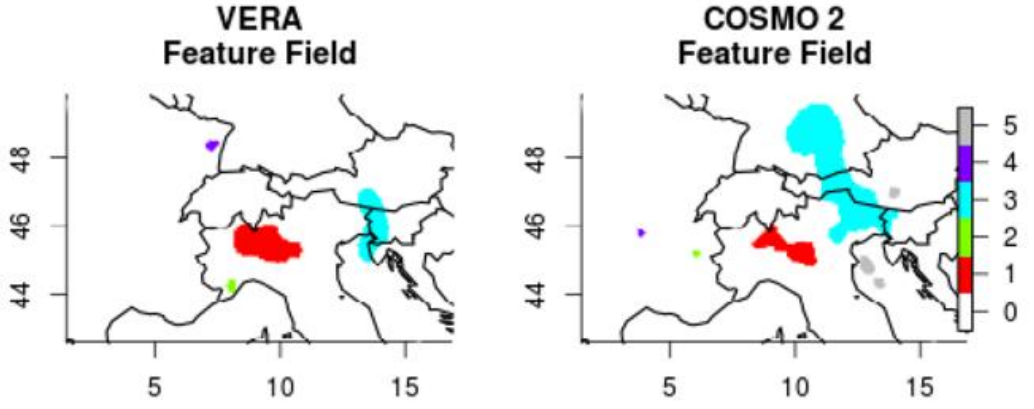


Figure 30: Objects, threshold 2 mm, 26.09.2007, 18 UTC.

main.tex

- SAL example. SAL verification was used to verify 1 hour accumulated precipitation output of forecast model COSMO 2.8 against radar data of POLRAD network. The verified period was from 05 18UTC to 07 06UTC August 2016. Almost all SAL entries are found in the top right quadrant of the diagram. The bottom right quadrant contains only a few of them. For all entries component S is positive which means that the predicted forecast objects are too large or widespread with respect to the observed objects. For most entries component A is positive which indicates an overestimation of the domain-averaged precipitation coming from the model. There are only a few entries when the model underestimates the precipitation (negative A component). No entries were found in top and bottom left quadrants.

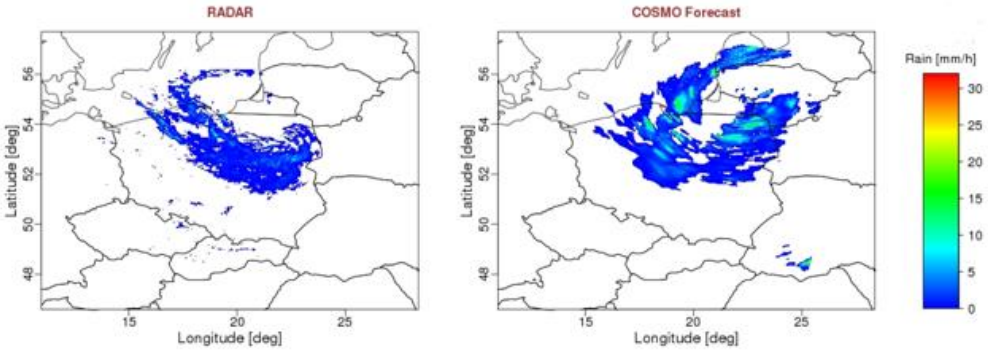


Figure 31: 1h accumulated precipitation, Radar data composite (POLRAD) against COSMO-PL 2.8, 06.07.2016, 20 UTC.

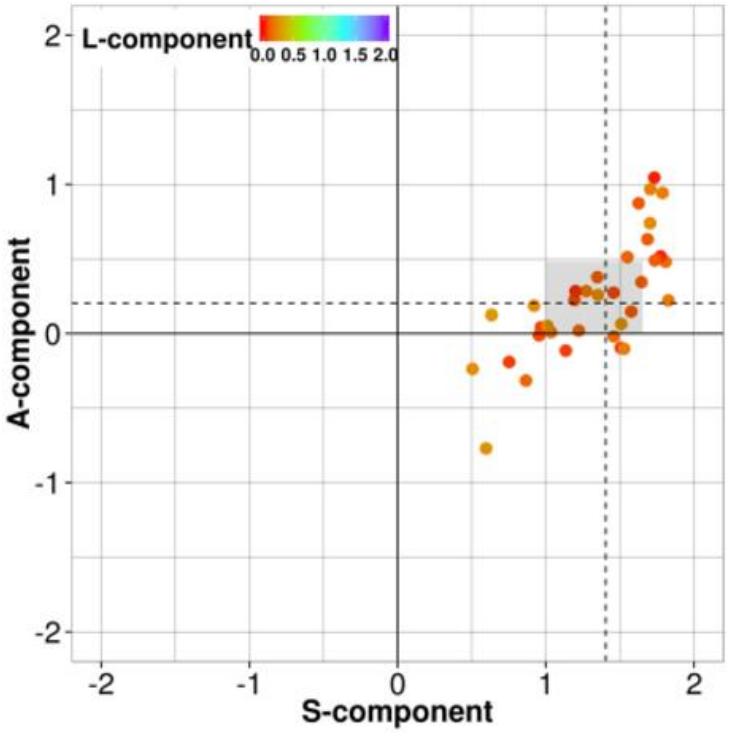


Figure 32: SAL verification, 1h accumulated precipitation, 05 18UTC 07 06UTC August 2016. Every dot shows the values of the three components of SAL for a particular forecast. L component is indicated by the colour of the dots. The grey area extends from the 25th to the 75th percentile of the distribution of S and A, respectively. The dashed lines depict the median values of S and A components.

4.2.4 Characteristics of the method applied

Identification in MODE is done separately in observation and forecast fields by using two parameters such as convolution radius and threshold. The method looks at characteristics of the objects such as intensity distribution, centroid location, area, curvature, orientation, and attempts to match objects in the forecast and observed field based on these characteristics. Objects nearby can be merged. CRA method gives useful information of the forecast errors. The total mean square error is decomposed due to location, pattern and intensity. The method depends on pattern matching. To find the optimal rigid transformation between two features can be difficult. SAL components correspond to aspect of amplitude, location and structure of precipitation field in a preselected area. All three methods MODE, CRA, SAL require identification features first. Applied method calculation time using SpatialVx library can depend on chosen merging/matching function, additionally all these methods are able to deal with different density of observation. Depending on the model resolution object features may have different pattern complexities and fine structures which further affects merging algorithm performance and computed scores.

4.3 CRA experiments in Roshydromet for MesoVICT (A.Bundel and A. Muraviev))

In the framework of MesoVICT (Mesoscale Verification Intercomparison over Complex Terrain, phase 2 of the ICP, https://ral.ucar.edu/projects/icp/), a set of cases is provided to compare various spatial verification methods. The object-based CRA (Contiguous Rain Area) method is used (Ebert, McBride, 2000). First, the objects are identified in observed and forecast fields. Then, the objects pairs are identified using some matching criterion based on the distance between the objects. Then, an optimal shift of the forecast object to the observed object is found by minimizing the error. Here also, different criteria can be used, such as the correlation coefficient and the mean squared error (MSE). In this study, the MSE criterion was used. Then, the difference is found between the initial MSE (represented as $MSE.total = MSE.displacement + MSE.volume + MSE.pattern$) and the MSE after the shift. This difference is the error due to forecast displacement: $MSE.displacement = MSE.total - MSE.shifted$. The MSE, which is left, consists of the squared difference between the mean precipitation volume in the forecast and observed object $MSE.volume = (\mathbf{F} - \mathbf{X})^2$ and of fine scale pattern discrepancies $MSE.pattern = MSE.shift - MSE.volume$. To calculate the CRA scores, free R SpatialVx package (https://cran.r-project.org/web/packages/SpatialVx/index.html) was used. It is developed by E. Gilleland contains most part of existing spatial methods, including identifying, matching, and merging features in observed and forecasted fields.

4.3.1 Deterministic study

Setup of experiments

- Mesovict core case: 20-22 June 2007;
- 1-h precipitation accumulations;
- Vienna Enhanced Resolution Analysis (VERA) observation analysis (Dorninger, M.et al., 2013) is used as reference data in this study;
- the Swiss COSMO-2 deterministic model is used as model data (2.2 km grid step).

Fig. 33 shows the time series of domain precipitation maximum during the MesoVICT core case. It can be seen that the absolute VERA maximum on 20 June 2007, 21h UTC, (49.84 mm/h) falls within the COSMO-2 domain. Most of other observed maximums were within the COSMO-2 domain. Overall, COSMO-2 reproduces well the time series of maximums, but gives the highest maximum 12 hours later, on 2007062020 much later, on 2007062108.

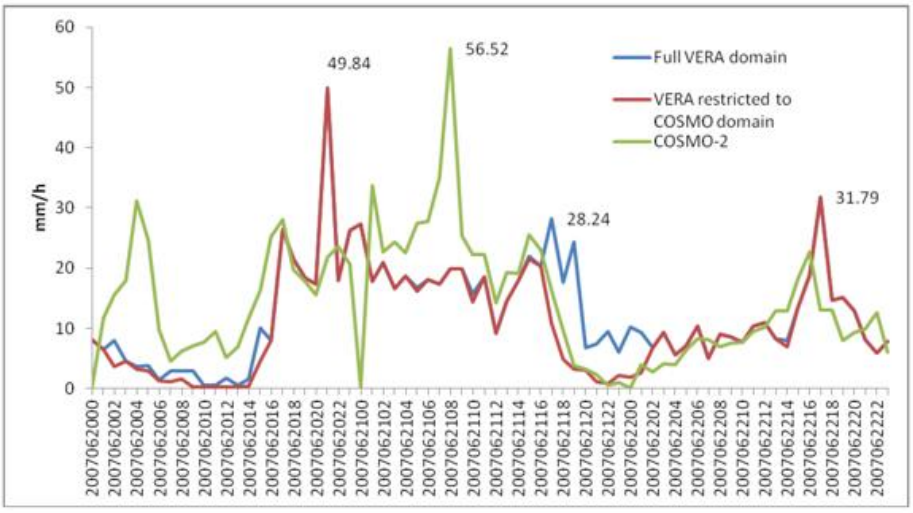


Figure 33: Time series of domain 1h precipitation maximums during the MesoVICT core case of 20-22 June 2007.

Identification of objects in R SpatialVx

Function FeatureFinder is used to identify objects in both observed and model fields. First, the field is smoothed using a convolution smoother, and then it is set to a binary image where everything above a given threshold is set to one (Davis et al, 2006). Features are identified by groups of contiguous events (or connected components in the computer vision/image analysis literature). Option min.size enables eliminating features with a size less than determined value from the analysis. Through a set of experiments, the reasonable value was determined as min.size = 20 grid points or ~36*36 km.

The effects of smoothing

By applying smoothing, the value at each grid is replaced by the mean value over a disk with a radius of a number of grid points given by the parameter smoothpar (see also Chapter 4.1 about the effects of smoothing). The FeatureFinder option uses disc kernel smoother from the R package smoothie.

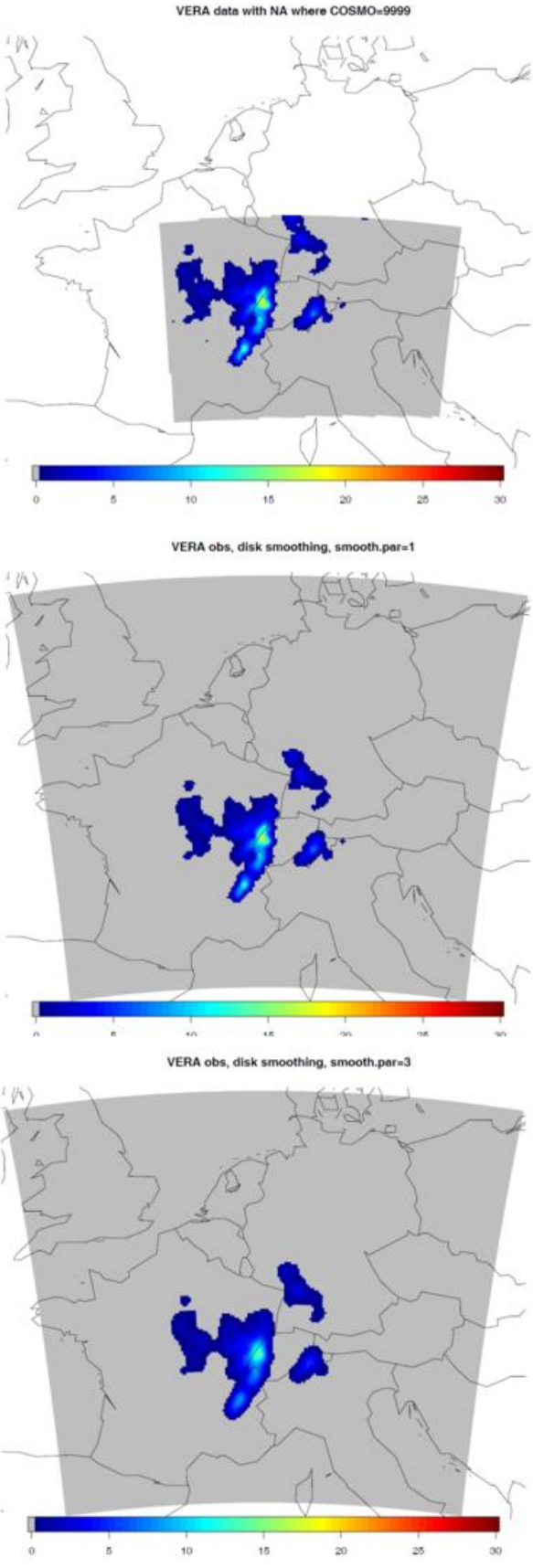


Figure 34: VERA gridded observation analysis on 2007062106: no smoothing (top), smoothing parameter =1 (middle), smoothing parameter = 3 (bottom).

Smoothing spreads the maximum over wider areas (Figure 4.3.1.2). Therefore, no or minimal degree of smoothing is needed in estimating intense precipitation areas. Smoothing parameter = 1 is chosen for the experiments described in this chapter. Functions for matching objects in R SpatialVx used in this study are as follows:

- Minboundmatch, the minimum boundary separation is calculated by first finding the distance map for every feature in the observed field, masking it by each feature in the forecast field, and then finding the minimum of the resulting masked distance map (Eric Gilleland, SpatialVx Manual). The distance map is found using distmap. The function distmap of point pattern computes the distance from each pixel to the nearest point in the given point pattern. If type is single, then the features are matched by the smallest minimum boundary separation per feature in each field. If type is multiple, then every feature is matched so long as their minimum boundary separation (measured in grid squares) is less than or equal to a specified value
- Centmatch is based on the method proposed by Davis et al. (2006a). It is possible for more than one object to be matched to the same object in another field. Objects are matched, if the centroid distance D is less than
  - the sum of the sizes of the two objects in question (size is the square root of the area of the object) (Centmatch 1)
  - the average size of the two objects in question (Centmatch 2)

  Centmatch does not merge objects explicitly, but determines possible merges applied if MergeForce function is run after centmatch (used in this study). The merging algorithm is described in (Eric Gilleland, SpatialVx Manual, deltamm and centmatch functions). It merges objects according to the minimum of distance metric between the objects.

Examples of CRA application

In Fig. 35 1h precipitation maps are given for 2007062021, VERA max precipitation during MesoVICT core case.

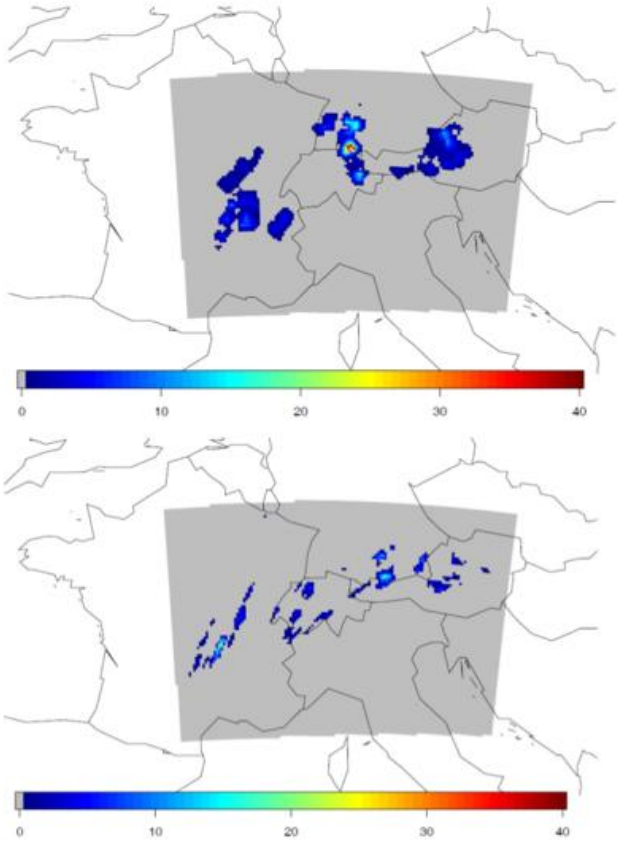


Figure 35: 1h precipitation maps from 2007062021 in mm/h: VERA observations (top), COSMO-2 (bottom).

Fig. 36 gives the matched features for a precipitation threshold 0.5 mm/h as an output of different matching functions for 2007062021.

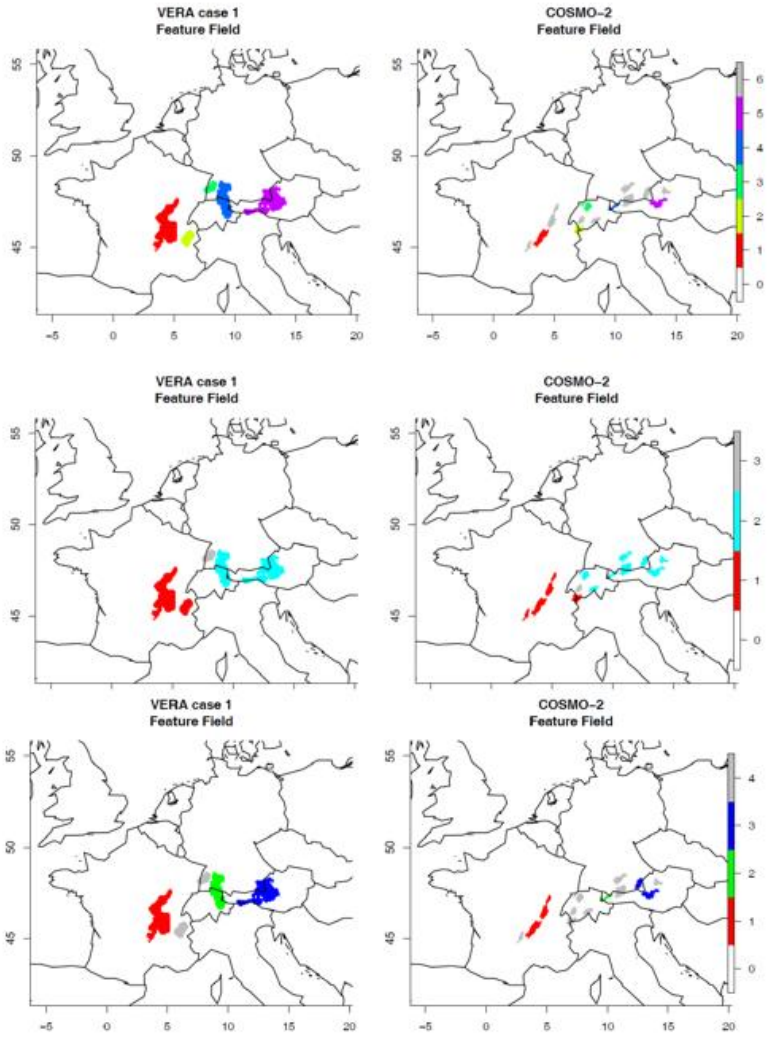


Figure 36: Matched objects pairs using (for precipitation > 0.5 mm/h) using different matching functions for 2007062021: Minboundmatch (top), Centmatch 1 (middle), Centmatch 2 (bottom). Same colours indicate paired objects.

It can be seen from Fig. 36 that it is difficult to objectively choose a best matching function. All methods are acceptable. The choice depends on the user preferences. Centmatch 1 makes implicit merging. In Fig. 37 the objects matched using minboundmatch are given for the same date, 2007062021, but for precipitation threshold > 5 mm/h. The functions Centmatch 1 and 2 do not make any matching in case of intense precipitation. Thus, these matching criteria are too strict for small features.

	displacement	volume	pattern
first pair	0.0006	0	0.0006
second pair	0.0007	0	0.0018

Table 4: CRA error components

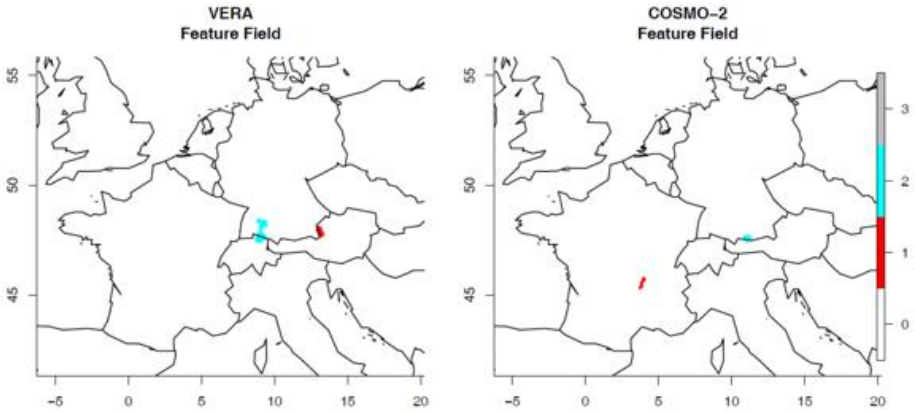


Figure 37: Matched objects pairs using minboundmatch, 2007062021, precipitation threshold > 5 mm/h.

The CRA scores (Table 4) show that the fine scale pattern error contributes most to the total mean squared error in this case. Let us consider another time slot from the MesoVICT case 1, 2007062115, when COSMO-2 made a good forecast (Fig. 38) with higher maximum intensities at the northeast of the domain. Fig. 39 for precipitation threshold 0.5 mm/h demonstrates that Centmatch 1 merges several features in the observed field to match them with one big precipitation object in the COSMO-2 field, while Centmatch 2 and Minboundmatch, which imply stricter distance criteria, do not merge separate objects. The CRA scores show that the fine scale pattern error is most important also in this case.

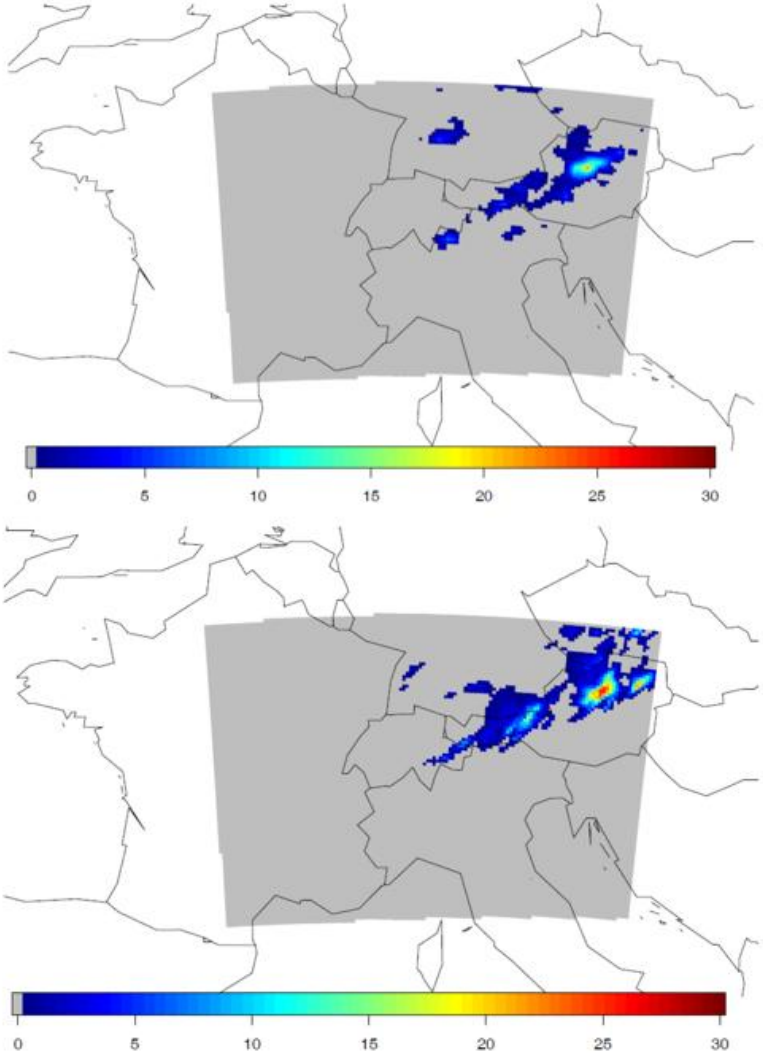


Figure 38: Matched objects pairs using (for precipitation > 0.5 mm/h) using different matching functions for 2007062021: Minboundmatch (top), Centmatch 1 (middle), Centmatch 2 (bottom). Same colours indicate paired objects.

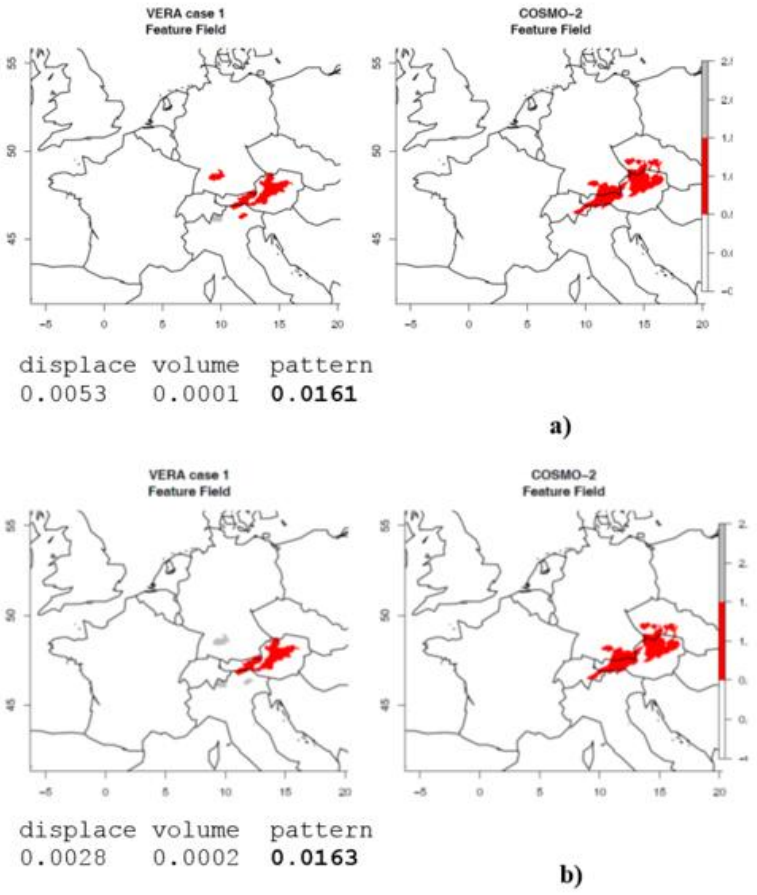
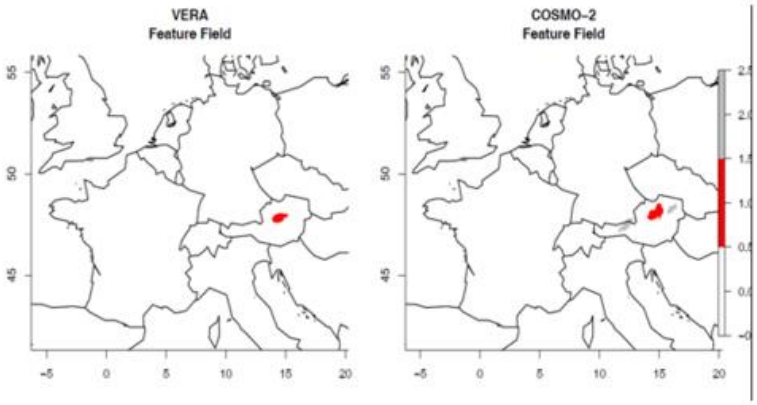


Figure 39: Matched objects pairs and corresponding CRA error components using (for precipitation > 0.5 mm/h) using different matching functions for 2007062115: a) Centmatch 1 b) Centmatch 2 and Minboundmatch (give same matches in this case), same colours indicate paired objects.

For higher precipitation threshold (Fig. 40), all matching functions give the same result. The best match is detected (the central object in COSMO-2 field with precipitation maximum). It should be noted that there were another two intense precipitation areas forecasted, which represent false alarms. In this method, the false alarms are discarded.



displace	volume	pattern
0.0009	0.0000	0.0008

Figure 40: Matched objects pairs and corresponding CRA error components (for precipitation > 5 mm/h) for 2007062115. All matching functions (Centmatch 1, Centmatch 2, and Minboundmatch) give the same matches in this case), same colors indicate paired objects.

Other time slots and synoptic situations were considered, which are not given here.

Conclusions

Smoothing can be undesirable for intense precipitation estimation, although it depends on the user requirements. Option for splitting objects is desirable sometimes. For lower precipitation thresholds and thus wider features, centmatch 2 gives more reasonable results overall. Centmatch 1 makes more merging. For higher thresholds, centmatch often leaves all the objects unmatched due to small areas of features. Minboundmatch seems more promising, but with a minimum boundary separation distance beyond which features should not be matched. According to CRA, most of the error usually comes from the fine structure of the fields (MSE.pattern) for lower precipitation thresholds. For higher thresholds, displacement error contribution increases. The optimal choice of matching procedure can be rather difficult. Each case should be considered before application of particular matching function. Aggregation of results is difficult. The SAL method seems easier to apply because it does not require pair-wise matching.

Ideas for future work

It seems useful to formalize the complexity of situations when the application of metrics is useless. Below is the list of possible approaches to that. It should be noted that it is only an idea at the present state:

- by the maximum number of different features in the field;
- by the complexity of their boundaries (fractals?);
- simple spatial dispersion of the field;
- by the number of holes in a feature (Betti number?);
- other criteria?

4.3.2 An object-based approach to assess the MesoVICT ensemble data

This chapter contains an exploratory study with a goal to transfer the object-based method to ensemble data. The results are preliminary. The starting point was the method proposed in (Johnson and Wang, 2012). The forecast probability is generated for each forecast object as the fraction of ensemble members forecasting the object of interest. In this case, the objects of interest are the observed objects unlike (Johnson and Wang, 2012) where one of the ensemble members was taken as reference to calculate object probabilities. In our approach, performance of the ensemble system could be assessed a posteriori, but the probabilities of objects defined in this way could not be forecasted in the real time, as the observations are not yet known at the time of the forecast. If we want to assess the real forecasts, we need to choose the objects of interest from the ensemble. Then, the member defining the forecast objects should be randomly chosen so that the results were not improved by attempts to select a "best" member. Then, the probability of each observed object can be estimated using the traditional probabilistic scores, the BSS, for example, but verification was not yet implemented. The setup of the experiments is as in Sec. 4.3.1, but COSMO-E ensemble of Swiss meteoservice is taken as model data. In Fig. 41, the upper map represents the VERA observed objects, and the pairs of maps below are the matched observed and model objects for the first six ensemble members from a 21st member ensemble. The colours indicate matched pairs. Then we can calculate the probability of predicting each of observed objects. For example, the VERA object painted in yellow colour in the upper map was matched to an object in 20 of 21 ensemble fields, thus, its probability is 20/21.

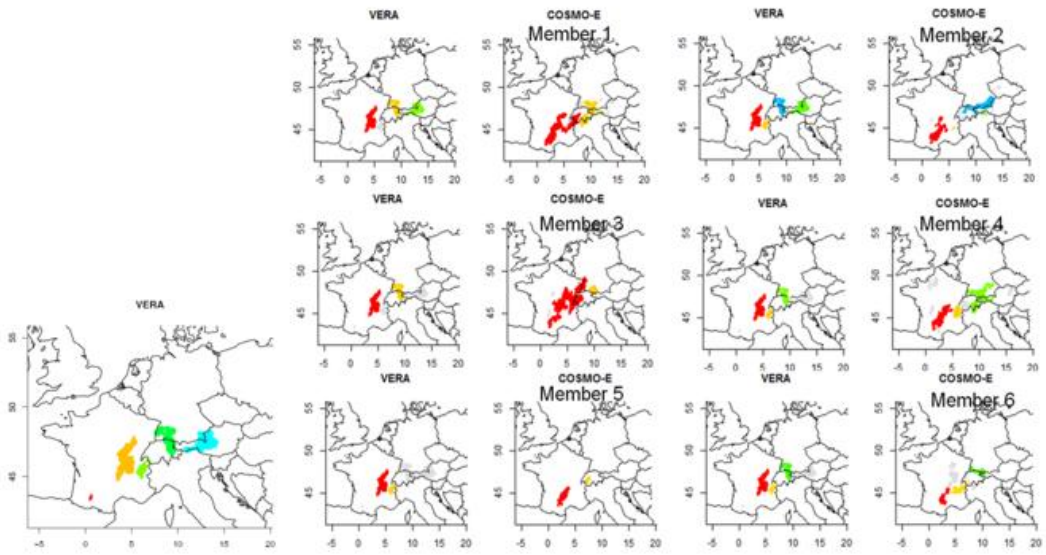


Figure 41: Minboundmatch: 2007062021, COSMO-E ensemble, first 6 of 21 members, precipitation threshold > 0.5 mm/1h. Probabilities of each of 5 observed objects: 1/21 20/21 10/21 19/21 14/21.

A deficiency of such an approach is that the CRA method itself cannot be applied, only the usual probabilistic measures, such as the BSS, can be calculated when a large number of forecasts is aggregated. Another drawback is that no merging of objects is possible as the list of observed objects must be the same for matching with all ensemble members, thus centmatch matching function, which produces merging, cannot be applied. To apply CRA, the possible approaches could be:

- to calculate location, volume, fine pattern errors for each ensemble member, and to average them;
- to identify objects using the probability threshold (Gallus, 2010).

An example of the second approach to object-based method is given in Sec. 4.1 (by D. Boucouvala).

4.3.3 Processing nowcasting forecasts using CRA at RHM (A. Muraviev)

The studies on test cases, such as MesoVICT cases, were conducted having in mind the main goal to verify operational forecasts, in particular, short-range and very-short-range forecasts. Below are the first results of verification of a nowcasting system implemented at the Hydrometcentre of Russia of Roshydromet (Muravev et al., 2018). The core of the system is the statistical STEPS scheme (Short Term Ensemble Prediction System) (Bowler N. et al., 2006) constructed as a multiplicative cascade model with an optical flow technology (the radar fields sequences are considered as an optical flow). Its motto is "seamless, stochastic, scaling, spectral, self-learning". STEPS can run in deterministic and ensemble modes. The results below are obtained with deterministic version. This chapter focuses on verification technology rather than on the scientific findings described in (Muravev et al., 2018).

Verification setup

Period: May 1, 2017 September 30, 2017(∼22000 forecasts). Nine radars over the Central Russia with a total area of about 1100x1300 km were used. For each radar, the area is 500*500 km was considered. The STEPS precipitation intensity forecast calculates fields up to 2.5 h lead time with 10-min time step (15 consequent fields for each forecast) with about 2km grid step. For verification, only 169 situations with intense precipitation were chosen by visual analysis. The SpatialVx package was used to identify objects and to calculate CRA scores. The objects with areas less than 1225=35*35 grid points (about 7070 km) and lager than 16384=128128 grid points (about 250250 km) were excluded from analysis using min.size and max.size option in FeatureFinder function. The radius of averaging for convolution smoothing was chosen empirically as 9 grid points (18 km).

Analysis

Let us consider a case from 17 May 2017. It can be seen from Fig. 42 that the nowcasting system forecasted well the rain object at the first lead time, but by the end of the forecast, the single object in the radar field splitted in two. In Fig. 43, it is reflected in the abrupt change in x_shift (shift in object mass centre in longitude) from positive to negative values at the last two lead times (14 and 15), because the system of object recognition and matching switched to a new object when the single object in the radar field (Fig. 42, lower right field) splitted in two. It follows from the CRA scores that the nowcast object is shifted eastward relative to the corresponding radar object. This case demonstrates the difficulties in matching objects during intense convection cases, as the objects appear and disappear chaotically and it is difficult to follow their history in both reference and forecast fields.

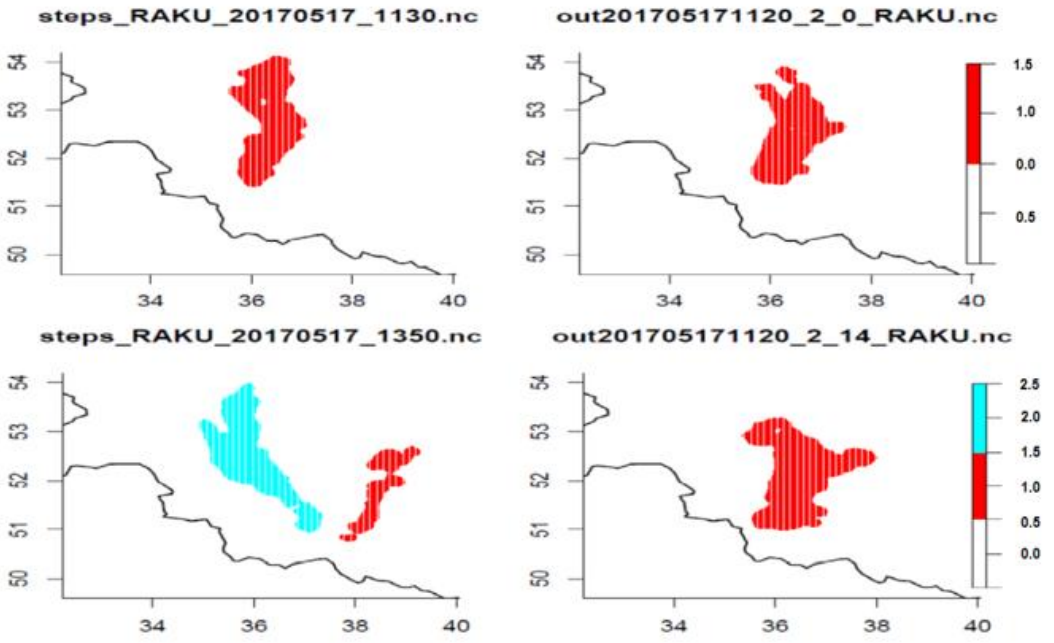


Figure 42: Objects matched using SpatialVx matching function Centmatch 1 (see Sec. 3.2.1) on 17 May 2017. Upper panel: the first nowcast time (11:30 UTC), lower panel: the penultimate nowcast time (13:50 UTC); on the left, the radar fields, on the right, the nowcast fields. Colours indicate matched pairs. Kursk (RAKU) radar.

R-SpatialVx craer output

ilead	x_shift	y_shift	MSE.total	.shift	.displ	.volume	.pattern
1	1.89	-10.49	0.4387	0.6986	-0.2599	0.0000	0.6986
2	2.83	-11.04	0.6058	1.0097	-0.4040	0.0002	1.0096
3	0.34	-10.44	0.7205	0.8957	-0.1753	0.0024	0.8933
4	-1.41	-13.42	1.2529	1.3553	-0.1024	0.0074	1.3479
5	-5.91	-12.93	1.7393	1.7697	-0.0304	0.0140	1.7557
6	4.20	-18.01	0.9870	1.2413	-0.2543	0.0044	1.2369
7	3.50	-13.52	0.9584	1.0873	-0.1288	0.0014	1.0859
8	2.36	-6.45	1.0874	1.0787	0.0087	0.0001	1.0787
9	3.24	-7.06	1.1609	1.1567	0.0042	0.0002	1.1565
10	5.49	-6.60	1.2815	1.2475	0.0340	0.0013	1.2463
11	6.65	-7.82	1.2953	1.2648	0.0305	0.0026	1.2622
12	10.41	-14.45	1.3093	1.1718	0.1375	0.0036	1.1682
13	11.33	-16.40	1.3937	1.2378	0.1559	0.0085	1.2293
14	-13.02	-12.33	2.3734	2.4361	-0.0627	0.0008	2.4353
15	-16.07	-14.96	2.6149	2.7596	-0.1446	0.0010	2.7586

Figure 43: CRA scores for the case of Fig. 42.

Aggregation of the scores and conclusions

To assess the forecast (or nowcast) system, we need to aggregate a large number of cases. The following method was proposed in this study: the distribution parameters of CRA scores were calculated: the mean, median, upper and lower quartiles, and minimum and maximum values. In Fig. 44, an example for the x_shift (longitudinal shift of the forecast object relative to the reference one) is given. A critical shift error value was introduced from the following

reasoning: the larger object areas intersect, the better. If the smallest object size is 35 by 35 grid points, the reasonable shift error in each of two horizontal axes could be chosen as 35 grid points (about 70 km in this case), that is the radius of round objects of 35 by 35 grid points. The green frame indicates that no less than 50% of object shifts do not exceed the critical value. The red frame indicates that all forecast object shifts do not exceed the critical value. It follows that not less than half of the objects are forecasted with an admissible shift in longitude (green frame) up to 90 min. In Fig. 44, the scores are displayed for one radar only (radar in the Kursk town, RAKU). The same aggregation was performed for nine radars in the Central region of Russia. This analysis enabled the following conclusions about the systematic object shift in longitude: the forecast objects are shifted westward (thus going too fast) for radars RAKU and RAVN and eastward (going too slow) for radars RUDK, RUDN, and RUWJ.

RAKU: CRA x_shift statistics OVER SITUATIONS

lead	min	q25	med	mean	q75	max
1	-15.280	-7.620	-2.680	-0.609	3.990	16.730
2	-23.480	-9.408	-2.505	-1.519	5.140	18.240
3	-25.920	-9.505	-5.345	-3.125	0.588	30.640
4	-33.920	-9.970	-0.940	-0.467	6.923	32.660
5	-50.030	-17.730	-5.530	-6.011	7.145	32.350
6	-43.530	-19.230	-4.490	-1.933	18.115	30.640
7	-44.900	-19.790	0.800	-2.318	13.760	41.780
8	-44.210	-13.613	-2.990	-2.133	10.455	41.160
9	-48.090	-12.640	-8.150	-5.302	10.428	27.000

Figure 44: Statistical parameters (mean, median (med), upper (q75) and lower (q25) quartiles, and minimum and maximum values) of CRA x_shift score (longitudinal shift of the forecast object relative to the reference one) calculated over the whole verification period May 1, 2017 September 30, 2017. The green frame indicates that no less than 50% of object shifts do not exceed the critical value, the red frame indicates that all forecast objects do not exceed the critical value. Kursk (RAKU) radar.

The same analysis for the latitudinal shift error showed that the systematic shift is to the north for all nine radars. This can be a feature of the optical flow organization in STEPS. The error does not exceed the empirical critical value of 35 km up to 90 minutes in both latitude and longitude for all the radars.

4.4 SAL deterministic study in ARPAE-SIMC (M. S. Tesini and D. D'Alessandro)

4.4.1 Method applied (related to an INSPECT Task) and objectives

The SAL method has been applied; it is an object-oriented method proposed by Wernli et al. in 2008 and provides information about structure (S), amplitude (A) and location (L) of a quantitative precipitation forecast (QPF) (See also Sec. 4.1.1) The definition of a threshold allow to identify the precipitation features inside the domain; a smooth parameter is used to filter small scale noise.

4.4.2 Short description of the dataset (forecast-observation data), adaptation required, software for the method application

The JDC dataset has been used as observations. This dataset consists of reports from more than 12.000 stations over Central Europe which results in a mean station distance of approximately 16 km. With the aim to interpolate irregularly distributed observations to a regular grid in mountainous terrain, the Vienna Enhanced Resolution Analysis (VERA) scheme has been used (horizontal grid resolution of 8 km). The forecast precipitation fields comes from the run 00 of COSMO-2 (horizontal grid resolution of 2.8 km). Due to the different resolutions, the forecast fields have been interpolated on the VERA grid. The COSMO domain extension has been adapted to the observational domain. The R software (SpatialVx package) has been used to apply the SAL method to six interesting cases occurred during the summer of 2017.

4.4.3 Main findings (plots and explanation)

The main result which comes out from the SAL application is that its verification ability is not constant but changes relatively to the considered configurations, in particular it seems to be higher with the decrease in the precipitation fields complexity. A single parameter to evaluate the structure, the amplitude or the location error in forecast is not enough in that cases in which the precipitation field complexity is too high; this becomes evident in Fig. 45: the precipitation intensity is overestimated in Germany and underestimated in France; these errors in forecast compensate each other and determine an amplitude value, referred to the total domain, which is approximately null.

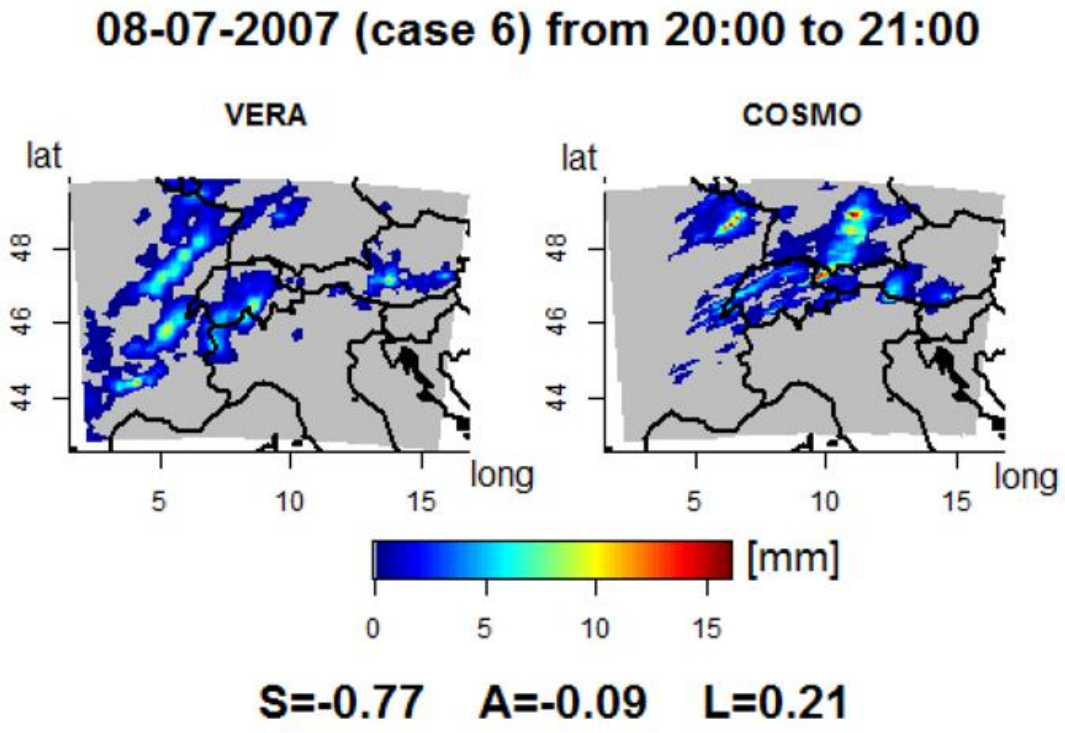


Figure 45: Precipitation intensity and SAL scores, MesoVICT case 6.

As evident from Fig. 46, the SAL scores derived from domains with reduced dimensions are more reliable because they refer to a restricted number of precipitation systems with similar characteristics, avoiding the problem of the loss of information over small scale due to the averaging over the complete domain. This suggests that the choice of the verification domain extension should be done taking it into account. It is clear that this kind of issue emerges for verification over limited accumulation period (1-3h); considering longer periods, the precipitation structures tend to be less fragmented and articulated, allowing the SAL to better evaluate the forecast.

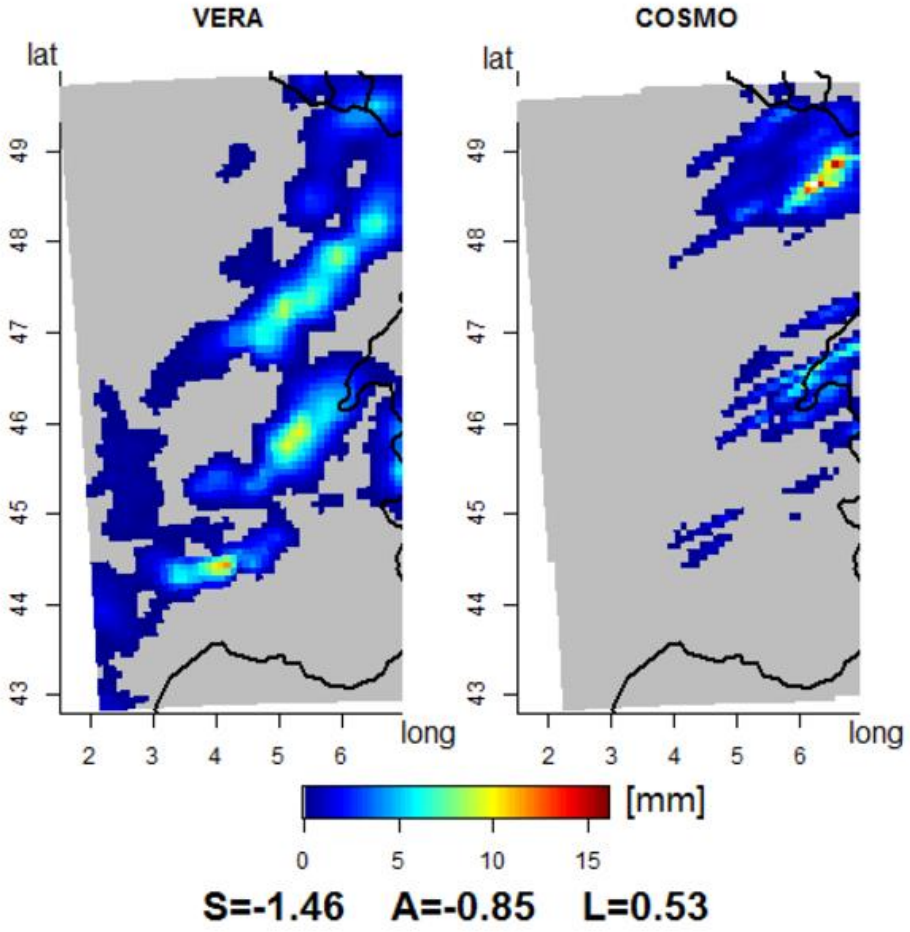


Figure 46: Precipitation intensity and SAL scores, MesoVICT case 6, smaller domain.

4.4.4 Characteristics of the method applied

The SAL has not required an excessive computational time for the verification of the considered cases.

The three scores provided by this method allow pointing out the characteristics of a high resolution model. For instance, the structure component S clearly emphasizes the ability of a high resolution model to predict more realistic precipitation features compared to coarser models. The threshold allows identification of the precipitation objects in the domains; the SAL is able to provide information about the location, amplitude and structure errors of these detected features. With respect to the location component L, this is provided as a sum of a L1 and L2 components; L1 gives a measure of the distance between the centres

of mass of the modelled and observed precipitation fields, while L2 takes into account the average distance between the centre of mass of the total precipitation fields and individual precipitation objects. Both L1 and L2 ranges from 0 to +1, so the final component L lies within the range [0,+2]. Based on this definition, different situations can yield the same value of L, in particular there is no sensibility to the rotation around the centre of mass. Furthermore the L value is strictly connected to the maximum dimension of the considered domain. In practical terms it means that, considering the same absolute displacement error, the smaller the domain dimensions, the bigger is L. The amplitude component A is defined as the difference of the domain-averaged precipitation values. The values of A are within [-2,+2] with A = 0 representing the best forecast. Although a zero value is desirable, it is important to remark that it does not necessarily represents a perfect forecast due to the infinity number of possible situations which can lead to identical values of the domain-averaged precipitation. A better indication is obtained integrating the structure component S. The threshold parameter can be a fixed value or a flexible one. The advantage of a fixed threshold is that verification can focus on a particular category, for instance, of intense events, and the statistical results are not blurred by weak events that might be of less interest. However, specification of a fixed threshold excludes poor forecasts from an object-oriented verification in situations in which the threshold is not exceeded in either the model (missed events) or the observations (false alarms).

5 Sensitivity of COSMO-LEPS forecast skill to the verification network: application to MesoVICT cases (A. Montani, C. Marsigli, T. Paccagnella, ARPAE-SIMC)

5.1 Overall aims

- To test the forecast skill of COSMO-LEPS in terms of total precipitation for different verification networks and different verification methods;
- to understand the meaning of the differences in the verification scores.

5.2 Verification datasets

Reference data are the verification networks available in 2007 (Fig. 47):

- **JDC** (**J**oint **D**Phase-**C**ops) dataset. About 12000 observations (mean station distance $\sim$ 12 km);
- **VERA** (**V**ienna **E**nhanced **R**esolution **A**nalysis), gridded analysis at the resolution of 8 km (Dorninger M. et al., 2013).

The model data come from the COSMO-LEPS suite available in 2007 at ECMWF (Montani et al., 2011).

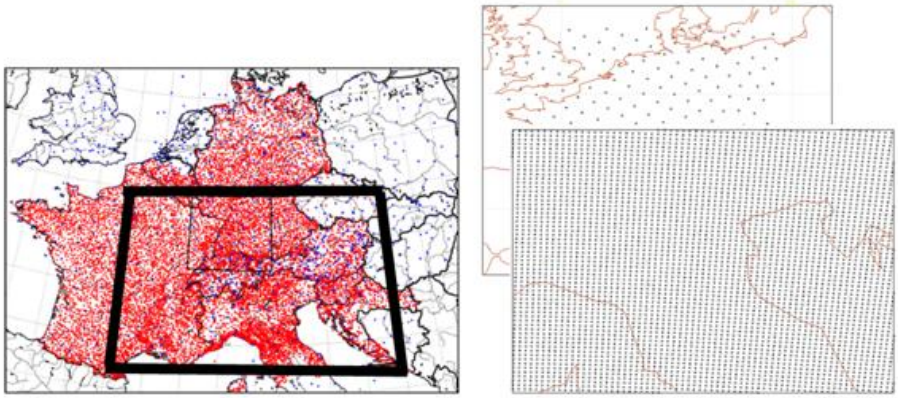


Figure 47: Verification area: DPHASE area (43-50N, 2-18E) (bold black frame).

5.3 Verification setup

- variable: 6h cumulated precipitation (0-6, ..., 18-24 UTC);
- period: all 6 mesoVICT cases (Jun Sep 2007);
- region: 43-50N, 2-18E (D-PHASE area);
- method: nearest grid point, bilinear interpolation, boxes of different sizes;
- forecast ranges: 0-6h, 6-12h, ..., 126-132h;
- thresholds: 1, 5, 10, 15, 25, 50 mm/6h;
- probabilistic scores: ROC area, RPS, Outliers.

5.4 Results

In Fig. 48, the precipitation ROC area scores are displayed for two interpolation methods using two different reference datasets (JDC and VERA). For precipitation threshold 1mm/6h (Fig. 48a), the system performance is similar with respect to the 2 verification networks. For precipitation threshold 10 mm/6h (Fig. 48b), higher skill is observed when COSMO-LEPS is verified against VERA gridded analysis. There is almost no impact of the verification technique (nearest grid point versus bilinear interpolation) for both thresholds.

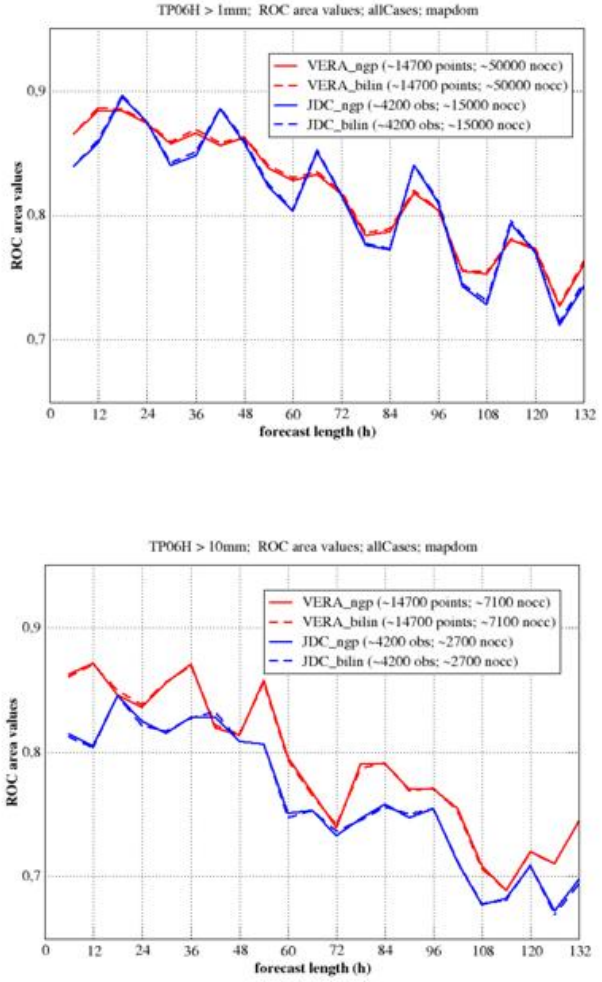


Figure 48: ROC area scores for two interpolation methods using two different reference datasets (JDC and VERA) for precipitation threshold 1mm/6h (top) and 10mm/6h (bottom).

In Fig. 49, a comparison is given between the probabilistic scores in DIST boxes of different size calculated using different reference datasets (JDC and VERA). DIST method is described in Sec. 3.3. It is seen that slightly higher skill is observed when COSMO-LEPS is verified against VERA gridded analysis. The skill increases with increasing box size. There is increasingly less dependence of the score on the verification network for larger boxes.

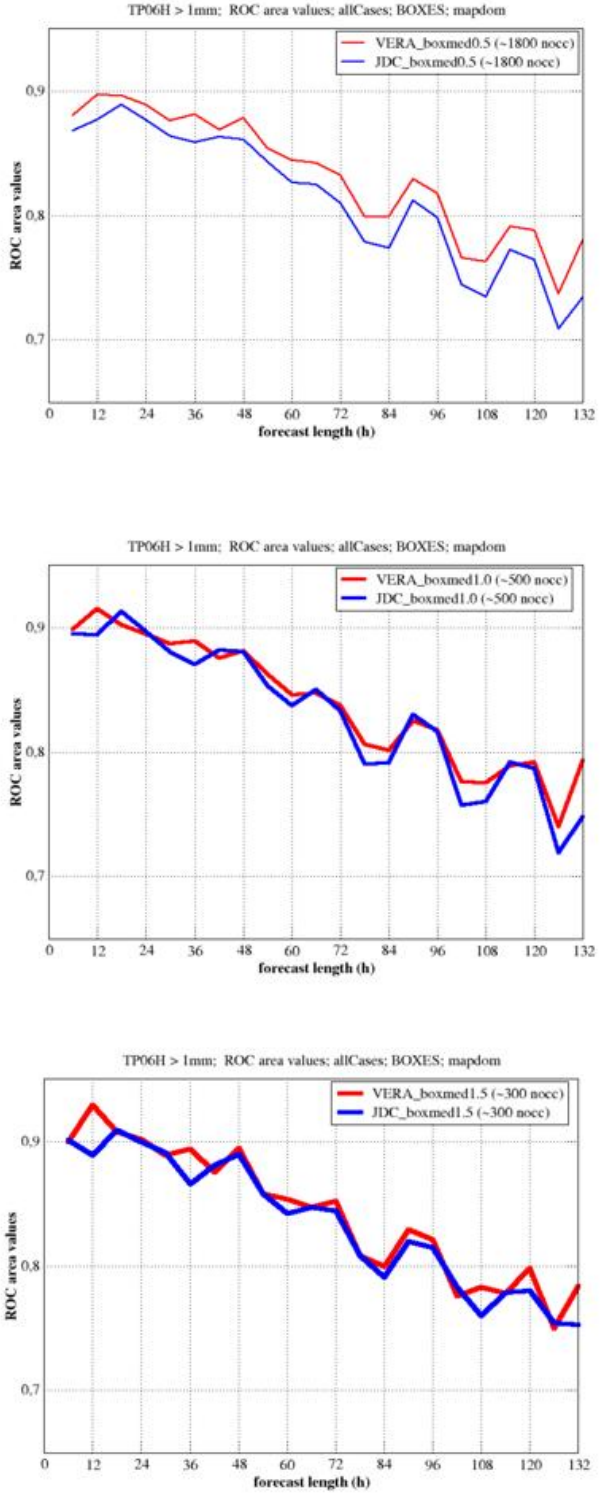


Figure 49: ROC area scores in DIST boxes of different size calculated using different reference datasets, JDC (blue) and VERA(red).

5.5 Conclusions

- For nearest grid point versus bilinear interpolation methods, the similar COSMO-LEPS forecast skill is observed using either gridded analysis or sparse observations (VERA or JDC) for verification network;
- for average precipitation in DIST boxes, there are similar scores for verification against gridded analysis or sparse obs for larger and larger boxes;
- as long as we "throw" everything in a box and compare average values (similar results considering the max values), the verification network does not make too much difference.

5.6 Future work

- To consider observation uncertainty: work with ensembles of VERA analysis and quantify scores variability;
- to work on higher-resolution ensembles (COSMO-E reruns).

6 References

Barrett, A. I., Gray, S. L., Kirshbaum, D. J., Roberts, N. M., Schultz, D. M. and Fairman, J. G., 2015: Synoptic versus orographic control on stationary convective banding. *Q.J.R. Meteorol. Soc.*, **141**, 1101–1113

Zied, B. B. and Theis, S. E., 2014: Spatial techniques applied to precipitation ensemble forecasts: from verification results to probabilistic products. *Meteorol. Appl.*, **21**, 4, 922–929

Bowler N., Pierce C., Seed A., 2006: STEPS: A probabilistic precipitation forecasting scheme which merges an extrapolation nowcast with downscaled NWP. *Q.J.R. Meteorol. Soc.*, **132**, 2127–2155

Casati B., Ross, G. and Stephenson, D. B., 2004: A New intensity-scale verification approach for the verification of spatial precipitation forecasts. *Meteorol. Appl.*, **11**, 141–154

Daubechies, I., 1992: Ten Lectures on Wavelets. *Society for Industrial and Applied Mathematics*, Philadelphia, PA, USA

Davis, C., Brown, B., and Bullock, R., 2006: Object-based verification of precipitation forecasts. Part I: Methodology and application to mesoscale rain areas. *Mon. Wea. Rev.*, **134**, 1772–1784

Dorninger, M., Mittermaier, M. P., Gilleland, E., Ebert, E. E., Brown, B. G. and Wilson, L. J., 2013: MesoVICT: Mesoscale Verification Inter-Comparison over Complex Terrain. NCAR Technical Note NCAR/TN-505+STR, 23 pp, doi:10.5065/D6416V21

Ebert, E. and McBride, J., 2000: Verification of precipitation in weather systems: Determination of systematic errors. *J. Hydrol.*, **239**, 179–202

Ebert, E., 2008: Fuzzy verification of high resolution gridded forecasts: A review and proposed framework. *Meteor. Appl.*, **15**, 51–64, doi:10.1002/met.25

Gallus, W. A. Jr., 2010: Application of Object-Based Verification Techniques to Ensemble Precipitation Forecasts. *Weather and Forecasting*, **25**, 144–158

Gilleland E., 2017: SpatialVx, https://cran.r-project.org/package=SpatialVx, R package Version 0.6-1

Gilleland E., Ahijevych, D. A., Brown, B. G. and Ebert, E. E., 2010: Verifying Forecasts Spatially. *Bull. Amer. Meteor. Soc.*, **91**, 1365–1373, doi: http://dx.doi.org/10.1175/2010BAMS2819.1

Gilleland,E., Ahijevych, D., Brown, B. G., Casati, B. and Ebert, E. E., 2009: Intercomparison of Spatial Forecast Verification Methods. *Weather and Forecasting*, **24**, 5, 1416–1430

Gofa F., Boucouvala, D., Louka, P. and Flocas, H. A., 2017: Spatial verification approaches as a tool to evaluate the performance of high resolution precipitation forecasts. *Atmospheric Research*, DOI:10.1016/j.atmosres.2017.09.021

Gorgas, T. and Dorninger, M., 2012: Concepts for a pattern-oriented analysis ensemble based on observational uncertainties. *Q.J.R. Meteorol. Soc.*, **138**, 664, 769–784

Johnson, A. and Wang, X., 2012: Verification and Calibration of Neighbourhood and Object-Based ProbabilisticPrecipitation Forecasts from a Multimodel Convection-Allowing Ensemble, *Monthly and Weather Review*, **140**, 3054–3077

Lawson, J. R. and Gallus, W. A., 2016: Adapting the SAL Method to evaluate reflectivity forecasts of summer precipitation in the Central United States. *Atmos. Sci. Let.*, **17**, 524–530

Duc, L., Saito, K. and Seko, H., 2013: Spatial-temporal fractions verification for high-resolution ensemble forecasts, *Tellus A*, **65**, 18171, http://dx.doi.org/10.3402/tellusa.v65i0.18171

Marsigli, C., Montani, A. and Paccangnella, T., 2008: A spatial verification method applied to the evaluation of high-resolution ensemble forecasts. *Met. Apps.*, **15**, 125–143, doi: 10.1002/met.65

Montani, A., Cesari, D., Marsigli, C. and Paccagnella, T., 2011: Seven years of activity in the field of mesoscale ensemble forecasting by the COSMO-LEPS system: main achievements and open challenges, *Tellus A*, **63**, 3, 605–624, DOI: 10.1111/j.1600-0870.2010.00499.x

Muravev A. V., Kiktev, D. B. and Smirnov, A. V., 2017: Operational precipitation nowcasting system based on radar data and verification results for the warm period of the year (May-September 2017), *Hydrometeorological Research and Forecasting*, **1**, 367 (In Russian)

Radanovics, S. (a), 2017: Using the SAL technique for Ensemble forecast Verification 7th International Verification Workshop, Berlin- Presentation

Radanovics, S. (b), 2017: Personal Communication

Radanovics, S., Vidal, J. P. and Sauquet, E., 2015: Probabilistic SAL: Evaluating the spatial properties of probabilistic precipitation simulations, 15th EMS Annual Meeting-Presentation

Steinacker, R., Ratheiser, M., Bica, B., Chimani, B., Dorninger, M., Gepp, W., Lotteraner, C., Schneider, S. and Tschannett, S., 2006: A mesoscale data analysis and downscaling method over complex terrain. *Monthly Weather Review*, **134**, 2758–2771

Eckert, P., 2009: COSMO Priority Project INTERP: Final Report. COSMO Technical Report No. 16, http://www.cosmo-model.org/content/model/documentation/techReports/default.htm

Weniger, M. and Friederichs, P., 2016: Using the SAL technique for spatial verification of cloud processes. *Atmospheric and Oceanic Physics*, 2091–2108

Wernli , H., Paulat, M., Hagen, M. and Frei, C., 2008: SAL - a novel quality measure for the verification of quantitative precipitation forecasts. *Mon. Wea. Rev.*, **136**, 4470–4487

Wernli, H., Hofmann, C. and Zimmer, M., 2009: Spatial Forecast Verification Methods Intercomparison Project: Application of the SAL Technique. *Wea. Forecasting*, **24**, 1472–1484

Weusthoff, T., Ament, F., Arpagaus, M., Rotach, M. W., 2010: Assessing the benefits of convective-permitting models by neighbourhood verification: examples form MAP D-PHASE. *Mon. Wea. Rev.*, **138**, 3418–3433

List of COSMO Newsletters and Technical Reports

(available for download from the COSMO Website: www.cosmo-model.org)

COSMO Newsletters

No. 1: February 2001.

No. 2: February 2002.

No. 3: February 2003.

No. 4: February 2004.

No. 5: April 2005.

No. 6: July 2006.

No. 7: April 2008; Proceedings from the 8th COSMO General Meeting in Bucharest, 2006.

No. 8: September 2008; Proceedings from the 9th COSMO General Meeting in Athens, 2007.

No. 9: December 2008.

No. 10: March 2010.

No. 11: April 2011.

No. 12: April 2012.

No. 13: April 2013.

No. 14: April 2014.

No. 15: July 2015.

No. 16: July 2016.

No. 17: July 2017.

No. 18: November 2018.

COSMO Technical Reports

No. 1: Dmitrii Mironov and Matthias Raschendorfer (2001):
Evaluation of Empirical Parameters of the New LM Surface-Layer Parameterization Scheme. Results from Numerical Experiments Including the Soil Moisture Analysis.

No. 2: Reinhold Schrodin and Erdmann Heise (2001):
The Multi-Layer Version of the DWD Soil Model TERRA_LM.

No. 3: Günther Doms (2001):
A Scheme for Monotonic Numerical Diffusion in the LM.

No. 4: Hans-Joachim Herzog, Ursula Schubert, Gerd Vogel, Adelheid Fiedler and Roswitha Kirchner (2002):
LLM ¯ the High-Resolving Nonhydrostatic Simulation Model in the DWD-Project LITFASS.
Part I: Modelling Technique and Simulation Method.

No. 5: Jean-Marie Bettems (2002):
EUCOS Impact Study Using the Limited-Area Non-Hydrostatic NWP Model in Operational Use at MeteoSwiss.

No. 6: Heinz-Werner Bitzer and Jürgen Steppeler (2004):
Documentation of the Z-Coordinate Dynamical Core of LM.

No. 7: Hans-Joachim Herzog, Almut Gassmann (2005):
Lorenz- and Charney-Phillips vertical grid experimentation using a compressible nonhydrostatic toy-model relevant to the fast-mode part of the 'Lokal-Modell'.

No. 8: Chiara Marsigli, Andrea Montani, Tiziana Paccagnella, Davide Sacchetti, André Walser, Marco Arpagaus, Thomas Schumann (2005):
Evaluation of the Performance of the COSMO-LEPS System.

No. 9: Erdmann Heise, Bodo Ritter, Reinhold Schrodin (2006):
Operational Implementation of the Multilayer Soil Model.

No. 10: M.D. Tsyrulnikov (2007):
Is the particle filtering approach appropriate for meso-scale data assimilation ?

No. 11: Dmitrii V. Mironov (2008):
Parameterization of Lakes in Numerical Weather Prediction. Description of a Lake Model.

No. 12: Adriano Raspanti (2009):
COSMO Priority Project "VERification System Unified Survey" (VERSUS): Final Report.

No. 13: Chiara Marsigli (2009):
COSMO Priority Project "Short Range Ensemble Prediction System" (SREPS): Final Report.

No. 14: Michael Baldauf (2009):
COSMO Priority Project "Further Developments of the Runge-Kutta Time Integration Scheme" (RK): Final Report.

No. 15: Silke Dierer (2009):
COSMO Priority Project "Tackle deficiencies in quantitative precipitation forecast" (QPF): Final Report.

No. 16: Pierre Eckert (2009):
COSMO Priority Project "INTERP": Final Report.

No. 17: D. Leuenberger, M. Stoll and A. Roches (2010):
Description of some convective indices implemented in the COSMO model.

No. 18: Daniel Leuenberger (2010):
Statistical analysis of high-resolution COSMO Ensemble forecasts in view of Data Assimilation.

No. 19: A. Montani, D. Cesari, C. Marsigli, T. Paccagnella (2010):
Seven years of activity in the field of mesoscale ensemble forecasting by the COSMO–LEPS system: main achievements and open challenges.

No. 20: A. Roches, O. Fuhrer (2012):
Tracer module in the COSMO model.

No. 21: Michael Baldauf (2013):
A new fast-waves solver for the Runge-Kutta dynamical core.

No. 22: C. Marsigli, T. Diomede, A. Montani, T. Paccagnella, P. Louka, F. Gofa, A. Corigliano (2013):
The CONSENS Priority Project.

No. 23: M. Baldauf, O. Fuhrer, M. J. Kurowski, G. de Morsier, M. Müllner, Z. P. Piotrowski, B. Rosa, P. L. Vitagliano, D. Wójcik, M. Ziemiański (2013):
The COSMO Priority Project 'Conservative Dynamical Core' Final Report.

No. 24: A. K. Miltenberger, A. Roches, S. Pfahl, H. Wernli (2014):
Online Trajectory Module in COSMO: a short user guide.

No. 25: P. Khain, I. Carmona, A. Voudouri, E. Avgoustoglou, J.-M. Bettems, F. Grazzini (2015):
The Proof of the Parameters Calibration Method: CALMO Progress Report.

No. 26: D. Mironov, E. Machulskaya, B. Szintai, M. Raschendorfer, V. Perov, M. Chumakov, E. Avgoustoglou (2015):
The COSMO Priority Project 'UTCS' Final Report.

No. 27: J-M. Bettems (2015):
The COSMO Priority Project 'COLOBOC': Final Report.

No. 28: Ulrich Blahak (2016):
RADAR_MIE_LM and RADAR_MIELIB - Calculation of Radar Reflectivity from Model Output.

No. 29: M. Tsyrulnikov and D. Gayfulin (2016):
A Stochastic Pattern Generator for ensemble applications.

No. 30: D. Mironov and E. Machulskaya (2017):
A Turbulence Kinetic Energy – Scalar Variance Turbulence Parameterization Scheme.

No. 31: P. Khain, I. Carmona, A. Voudouri, E. Avgoustoglou, J.-M. Bettems, F. Grazzini, P. Kaufmann (2017):
CALMO - Progress Report.

No. 32: A. Voudouri, P. Khain, I. Carmona, E. Avgoustoglou, J.M. Bettems, F. Grazzini, O. Bellprat, P. Kaufmann and E. Bucchignani (2017):
Calibration of COSMO Model, Priority Project CALMO Final report

No. 33: N. Vela (2017):
VAST 2.0 - User Manual.

No. 34: C. Marsigli, D. Alferov, M. Arpagaus, E. Astakhova, R. Bonanno, G. Duniec, C. Gebhardt, W. Interewicz, N. Loglisci, A. Mazur, V. Maurer, A. Montani, A. Walser (2018):
COsmo Towards Ensembles at the Km-scale IN Our countries (COTEKINO), Priority Project final report.

No. 35: G. Rivin, I. Rozinkina, E. Astakhova, A. Montani, D. Alferov, M. Arpagaus, D. Blinov, A. Bundel, M. Chumakov, P. Eckert, A. Euripides, J. Förstner, J. Helmert, E. Kazakova, A. Kirsanov, V. Kopeikin, E. Kukanova, D. Majewski, C. Marsigli, G. de Morsier, A. Muravev, T. Paccagnella, U. Schättler, C. Schraff, M. Shatunova, A. Shcherbakov, P. Steiner, M. Zaichenko (2018):
The COSMO Priority Project CORSO Final Report.

No. 36: A. Raspanti, A. Celozzi, A. Troisi, A. Vocino, R. Bove, F. Batignani (2018):
The COSMO Priority Project VERSUS2 Final Report.

COSMO Technical Reports

Issues of the COSMO Technical Reports series are published by the *COnsortium for Small-scale MOdelling* at non-regular intervals. COSMO is a European group for numerical weather prediction with participating meteorological services from Germany (DWD, AWGeophys), Greece (HNMS), Italy (USAM, ARPA-SIMC, ARPA Piemonte), Switzerland (MeteoSwiss), Poland (IMGW), Romania (NMA) and Russia (RHM). The general goal is to develop, improve and maintain a non-hydrostatic limited area modelling system to be used for both operational and research applications by the members of COSMO. This system is initially based on the COSMO-Model (previously known as LM) of DWD with its corresponding data assimilation system.

The Technical Reports are intended

- for scientific contributions and a documentation of research activities,
- to present and discuss results obtained from the model system,
- to present and discuss verification results and interpretation methods,
- for a documentation of technical changes to the model system,
- to give an overview of new components of the model system.

The purpose of these reports is to communicate results, changes and progress related to the LM model system relatively fast within the COSMO consortium, and also to inform other NWP groups on our current research activities. In this way the discussion on a specific topic can be stimulated at an early stage. In order to publish a report very soon after the completion of the manuscript, we have decided to omit a thorough reviewing procedure and only a rough check is done by the editors and a third reviewer. We apologize for typographical and other errors or inconsistencies which may still be present.

At present, the Technical Reports are available for download from the COSMO web site (www.cosmo-model.org). If required, the member meteorological centres can produce hard-copies by their own for distribution within their service. All members of the consortium will be informed about new issues by email.

For any comments and questions, please contact the editor:

Massimo Milelli
Massimo.Milelli@arpa.piemonte.it

Consortium

for

Small-Scale Modelling

Technical Report No. 43

The COSMO Priority Project $T^2(RC)^2$: Testing and Tuning of Revised Cloud Radiation Coupling, Final Report

April 2021

DOI: 10.5676/DWD_pub/nwv/cosmo-tr_43

Deutscher Wetterdienst
MeteoSwiss
Ufficio Generale Spazio Aereo e Meteorologia
ΕΘΝΙΚΗ ΜΕΤΕΩΡΟΛΟΓΙΚΗ ΥΠΗΡΕΣΙΑ
Instytucie Meteorogii i Gospodarki Wodnej
Administratia Nationala de Meteorologie
ROSHYDROMET
Agenzia Regionale Protezione Ambiente Piemonte
Agenzia Regionale Prevenzione Ambiente Energia Emilia Romagna
Centro Italiano Ricerche Aerospaziali
Amt für GeoInformationswesen der Bundeswehr
Israel Meteorological Service

www.cosmo-model.org

Editor: Massimo Milelli, ARPA Piemonte

The COSMO Priority Project $T^2(RC)^2$:

Testing and Tuning of Revised

Cloud Radiation Coupling, Final Report

Project participants:

***H. Muskatel*[1]‡, *U. Blahak*[2], *P. Khain*[1],**

***A. Shtivelman*[1], *M. Raschendorfer*[2], *M. Kohler*[2],**

***D. Rieger*[2], *O. Fuhrer*[3], *X. Lapillonne*[3],**

***G. Rivin*[4], *N. Chubarova*[4], *M. Shatunova*[4], *A. Poliukhov*[4],**

***A. Kirsanov*[4], *T. Andreadis*[5], *S. Gruber*[6]**

‡ Project Coordinator

[1] Israel Meteorological Service - IMS

[2] Deutscher Wetterdienst - DWD

[3] MeteoSwiss - MCH

[4] HydroMetCenter of Russia - RHM

[5] Hellenic National Meteorological Service - HNMS

[6] Karlsruhe Institute of Technology - KIT

Contents

1 Introduction **5**

2 Tasks and achievements **6**

3 New optical properties for water droplets and ice particles in COSMO model **7**

3.1 Introduction 7

3.2 Ice Particles 8

3.3 Water droplets 11

3.4 Sensitivity Experiments 12

3.5 Conclusions and recommendations 16

4 Monte-Carlo Spectral Integration **17**

4.1 Radiation scheme call-time temporal resolution 17

4.2 The Monte-Carlo Spectral Integration method 19

4.3 Conclusions and recommendations 22

5 New parametrization for vertical microphysical profiles in shallow cumulus **22**

5.1 Overview 22

5.2 Theoretical background 22

5.2.1 Calculation of shallow cumulus LWC and R_e in NWP models 22

5.2.2 Utilization of LES for simulation of small Cu 23

5.3 LES set-up 23

5.4 Results 26

5.5 Parametrization of microphysical parameters of cloud ensembles 29

5.6 Implementation of the parametrization in the COSMO model 32

6 New shallow convection shutdown scheme **33**

6.1 Overview 33

6.2 COSMO shallow convection parametrization 33

6.3 The effect of shallow convection parametrization on model forecast 35

6.4 The entrainment rate parameter $\boldsymbol{entr_{sc}}$ 40

6.5 Evaluation of forecast quality 41

6.5.1 Precipitation verification score $\boldsymbol{\Delta FSS}$ 41

6.5.2 Temperature and relative humidity score $\boldsymbol{T_RH_PROF}$ 42

6.6 Tuning the shallow convection scheme 42
6.7 Discussion and conclusions 45

7 Implementation of CAMS forecasted aerosols in COSMO radiation and microphysics schemes 48

7.1 Introduction 48
7.2 CAMS aerosols forecasting system 48
7.3 CAMS aerosols direct effect on radiation 49
7.3.1 CAMS aerosols optical properties 49
7.3.2 Testing the direct effect of CAMS aerosols on COSMO radiation . . . 50
7.4 CAMS aerosols indirect effect on radiation 54
7.4.1 Water droplets number concentration and effective radius 54
7.4.2 Water droplets activation using Segal and Khain (2006) scheme 55
7.4.3 Using Segal and Khain (2006) scheme in the 1-moment microphysics . 57
7.4.4 Case study - April 25-27, 2018 57
7.4.5 Ice nucleation scheme model inter-comparison using a case study . . . 64
7.4.6 DeMott (2015) ice nucleation scheme results vs. observational data . . 69

8 Implementation of ICON-ART forecasted dust in COSMO radiation scheme 70

8.1 Introduction 70
8.2 ICON-ART dust aerosols direct effect on radiation 71

9 Verifications of the new COSMO radiation scheme in clear skies and cloudy skies conditions 77

9.1 New MACv2 aerosol climatology and its verification in clear sky conditions . 77
9.1.1 MACv2 aerosol climatology 77
9.1.2 Comparison with Tegen climatology and in-situ observations 78
9.1.3 Radiation fluxes assessment 79
9.1.4 Temperature sensitivity to the changes in aerosol characteristics . . . 80
9.1.5 Temperature forecast sensitivity to aerosols 81
9.2 Verifications in Cloudy skies conditions 82
9.2.1 Assessment of water vapour, liquid and ice water content in radiative scheme 82
9.2.2 Global radiation sensitivity to aerosol content 82
9.2.3 T2m forecast sensitivity 84
9.3 Conclusions 85

9.3.1 Clear sky case 85
9.3.2 Cloudy case 85

10 Testing and tuning of the new cloud-radiation scheme 85

10.1 Overview 85
10.2 Global Radiation sensitivity 86
10.3 Calibration method 88
10.4 Calibration results 89

11 Acknowledgements 89

12 References 90

1 Introduction

Radiation transfer schemes are critical part of numerical weather prediction (NWP) models since solar energy is the engine for atmospheric dynamics. The seasonal and diurnal cycles are governed by attenuations in sunshine duration and intensity. The first and most important factor which determines the solar irradiance is the solar zenith angle. This angle is defined by the location on earth and the time and can be accurately calculated from deterministic equations. The second most important effect is the cloud cover, and not less important, the cloud optical thickness. The radiation-clouds are coupled in a two-way manner. The hitting of land and sea surfaces causes the thermodynamic instability that is needed for cloud formation and precipitation but also creates a mask that prevents solar fluxes to penetrate the atmosphere hence reducing the instability. Other constituents that impact the atmosphere opacity are the gasses, mainly H_2O, O_3 and CO_2, and aerosols.

The radiation scheme is a computationally expensive part of most NWP models although many simplifications are considered. Some of the simplifying assumptions used are the reduction of the dimension of the problem from 3D to a 1D problem namely the two-stream approximation in which only upward/downward fluxes are calculated. Another generalization is the use of only few spectral intervals (bands), in COSMO only 8, to describe the entire shortwave (SW) incoming solar radiation and the outgoing long wave (LW) radiation. This is a rough approximation especially for the description of the gasses absorption spectra which is rapidly changing as a function of wavelength. In COSMO radiation scheme the k-distribution method is applied to solve this problem and will be described later in section 4. As for clouds, parametrizations are used to describe the radiation-cloud interaction. First, the bulk cloud properties such as effective size and number concentration are defined from ice and water contents and assumptions about the size distribution functions. Second are the optical properties of the hydrometeors which are parametrized as a function of the effective size. In this project both steps were re-visited. The water droplets and ice particles number concentrations were calculated by more realistic schemes using forecasted aerosols contents to better define the effective size. The optical properties parametrizations of water droplets and ice particles were recalculated using sophisticated spectral integration with an elegant formulation that covers a very wide particles size range therefor allowing the inclusion of both rain and snow in the radiative transfer scheme. In addition, for the first time, the asymmetry factor for which defines the amount of forward vs. backwards scattering, was evaluated as a function of aspect ratio of the ice particles instead of their effective size (the reasoning for this is discussed by Fu, 2007).

In this project we also experimented a new approach for the aerosols input for the radiation. Usually NWP models either use climatology i.e. by Tanre (1983), or by Tegen (1997) which is a computationally cheap choice, or running a fully coupled aerosols-chemistry-atmosphere modules such as COSMO-ART, ICON-ART which are very costly. Here we proposed and realized a quasi-forecasted aerosols scheme. The forecasted aerosols by the full coupled models (in our case CAMS or ICON-ART) are interpolated in space and time into COSMO boundary files by *Int2lm* and are used by the radiation scheme. Of course that in cases of disagreement between COSMO and the aerosols model dynamics, the aerosols input is not ideal, i.e. when washout is present. Nevertheless, the performance is equal or better compared with monthly climatology option with only small computational price.

2 Tasks and achievements

This project was constructed of 12 tasks:

1. Testing and tuning of the new cloud-radiation scheme performance
2. Analysis/Revision of SGS cloudiness in the radiation scheme including LES simulations of cumulus clouds
3. Implementation of CAMS forecasted aerosols in the radiation scheme
4. Adapting switchable single/double precision to the radiation scheme
5. Implementation and testing of the MCSI method
6. Testing the radiation scheme against experimental datasets and benchmark models for clear/cloudy sky conditions
7. Implementation of new ice and water droplets optical properties in ICON-RRTM radiation scheme
8. Implementation and testing of ICON-ART forecasted aerosols in COSMO radiation scheme
9. Implementation and testing of CAMS forecasted aerosols in COSMO microphysical scheme
10. SAM LES utilization for parametrization of sub-grid scale shallow cumulus cloud cover and its testing
11. Updating the COSMO latest version - block structure and GPU compatible
12. Summary and documentations including web-app for cloud optics in COSMO webpage: http://www.cosmo-model.org/content/tasks/operational/ims/cloudOptics/.

The project lasted 4.5 years from September 2015 to March 2020. With the total amount of 10.77 FTEs in human resources coming from 5 institutions. The main achievements in this project are:

1. New optical properties for water and ice hydrometeors. The extinction coefficient, single scattering albedo and asymmetry factors were parametrized following Fu (1996, 1998) and Hu and Stamnes (1993). Extension of the effective size range allowing the inclusion of snow, graupel and rain. For the first time the asymmetry factor is defined as function of aspect ratio. The new parametrizations were applied in both COSMO and ICON models. Results published in Muskatel et al. (2021).
2. The Monte-Carlo Spectral Integration (MCSI) was realized in COSMO. A wise sampling technique that allows a reduction of calculations in the spectral space as an alternative to the usual time or space resolution reduction of the radiation scheme.
3. Implementation of CAMS forecasted aerosols as an input for the radiation (direct effect) and the microphysical processes (indirect effect). These aerosols fields can be used as input for droplet activation applying Segal and Khain (2006) scheme. Ice heterogeneous nucleation of these aerosols can be parametrized using Phillips (2008) or DeMott (2015) ice nucleation schemes.

4. Implementation of ICON-ART forecasted dust as an input for the radiation scheme. Global ICON-ART dust forecast runs semi-operationally twice a day in DWD. Now these 3 aerosols dust species can be used as an input for COSMO radiation scheme while other species of aerosols are taken from Tegen climatology.

5. Implementation of Kinne (2013) aerosols climatology as an input for radiation. This state-of-the-art climatology is based on observational data with finer resolution compared to the previous Tegen (1997) climatology.

6. A new parametrization of effective radius of shallow cumulus clouds using an adiabatic parcel model. As a result, a new sub-grid scale clouds LWC calculation is also applied.

7. A tuning procedure of the new radiation scheme. Around 30 new parameters were introduced in both $(RC)^2$ priority task and the following $T^2(RC)^2$ priority project. These parameters and switches were reduced to only 8 by a sensitivity analysis using the CALMO methodology and the IDEAL COSMO framework. These 8 parameters were fine-tuned by performing repeated 4-months period runs with many different name lists applying the CALMO method. A set of recommended default values is now available.

8. Massive testing of the new radiation scheme in Israel, Russia, Germany and Switzerland performed by IMS, RHM and MCH in many different atmospheric situations. All the mentioned new featured were tested against ground base measurements as well as benchmark models. Different aerosols inputs were compared and evaluated. In IMS the new scheme is semi-operational for two years.

9. The new radiation scheme, CLOUDRAD, with all its features is now available in the official COSMO release and is single/double precision as well as GPU compatible.

10. A web application for cloud optics is available for the public in COSMO webpage. It is suitable for any cloud-radiation modelling scheme in which the user can define the wavelengths intervals and calculate the optical properties parametrizations for both liquid and ice hydrometeors including dynamical graphics and text outputs.

3 New optical properties for water droplets and ice particles in COSMO model

(H. Muskatel, U. Blahak P. Khain)

3.1 Introduction

Radiation transfer through clouds is a key factor in earth's energy cycle and greatly effects the dynamics in the atmosphere. The numerical weather prediction model needs to forecast the amount of clouds, their thickness (LWC, IWC), the hydrometeors concentration and their effective size in order to calculate the amount of radiation transferred, absorbed and scattered by clouds. Having these parameters correctly described, the radiation module can calculate the clouds interaction with the radiation using three optical properties: the extinction coefficient, the single scattering albedo and the asymmetry factor (β_{ext}, ϖ, g). These properties needs to be defines for each hydrometeor separately (ice, liquid and aerosols) but also for each wavelength interval and each particle effective size. In this project we introduced a practical parametrization of both liquid droplets and ice particles optical properties

based on the single wavelength data of Fu (1996, 1998) and Hu and Stamnes (1993). We used an ensemble of 7500 particle size distributions (PSD) which enabled the effective size range to be extended to include larger hydrometeor categories such as rain, snow and graupel.

3.2 Ice Particles

The default COSMO optical properties parametrizations for ice hydrometeors, is based on IWC only. In more advanced models the effective size R_{eff} is used. We adopted the generalized effective size, $\mathrm{D_{ge}}$. It quantities the ratio between the volume and the statistically averaged projected area ($\overline{\mathrm{A}}$) of a randomly oriented needle particle (Fu, 1996):

$$\mathrm{D_{ge}}=\frac{\int_{\mathrm{Lmin}}^{\mathrm{Lmax}}\mathrm{DDL}\cdot\mathrm{n(L)dL}}{\int_{\mathrm{Lmin}}^{\mathrm{Lmax}}\left[\mathrm{DL}+\frac{\sqrt{3}}{4}\mathrm{D}^2\right]\mathrm{n\,(L)\,dL}}=\frac{2\int_{\mathrm{Lmin}}^{\mathrm{Lmax}}\mathrm{V(L)}\cdot\mathrm{n(L)dL}}{\sqrt{3}\int_{\mathrm{Lmin}}^{\mathrm{Lmax}}\overline{\mathrm{A}}\mathrm{(L)}\cdot\mathrm{n(L)dL}} \tag{1}$$

Where D and L are the width and length of the particle, n(L) is the particles size distribution (PSD). In our case we used an ensemble of particles which is assumed to follow a four-parameter modified gamma distribution (MGD):

$$\mathrm{N(L)}=\mathrm{N_0}L^{\mu}e^{-\lambda L^{\nu}} \tag{2}$$

$$M_i=\int_0^{\infty}L^iN\left(L\right)dL=\frac{N_0}{\nu}\frac{\Gamma(\frac{\mu+i+1}{\nu})}{\lambda^{\frac{\mu+i+1}{\nu}}} \tag{3}$$

$$\overline{L}=\frac{M_1}{M_0}=\frac{\Gamma(\frac{\mu+2}{\nu})}{\Gamma(\frac{\mu+1}{\nu})}\lambda^{\frac{-1}{\nu}} \tag{4}$$

where No is the scale parameter and μ, ν, λ control the shape of the distribution, M_i is the size distribution ith moment, and $\overline{L}$ is the mean particle length. A simpler gamma distribution is obtained by setting $\nu = 1$ hence:

$$\overline{L}=\frac{\mu+1}{\lambda} \tag{5}$$

We compose 7500 PSD ensemble by a systematic variation of the PSD parameters within a wide range. We change $\overline{L}$ in the range of 5-3000 μm in 500 logarithmically equidistant steps, while μ is changed from 0 to 14 which resulted $\mathrm{D_{ge}}$ to be in the range of 5-600 μm.

The asymmetry factor, as proved from ray scattering simulations for many types of ice crystals, dependents less on size and shape rather on the particle's effective aspect ratio (Fu, 2007):

$$\mathrm{AR}=\int_{\mathrm{Lmin}}^{\mathrm{Lmax}}(\frac{\mathrm{D}}{\mathrm{L}})\cdot\overline{\mathrm{A}}\cdot\mathrm{n(L)}/\int_{\mathrm{Lmin}}^{\mathrm{Lmax}}\overline{\mathrm{A}}\cdot\mathrm{n\,(L)\,dL} \tag{6}$$

The optical properties can be parametrized as a function of D_{ge} and IWC which for hexagonal particles is:

$$\mathrm{IWC}=\frac{3\sqrt{3}}{8}\rho_{\mathrm{ice}}\int_{\mathrm{Lmin}}^{\mathrm{Lmax}}\mathrm{D}\cdot\mathrm{D}\cdot\mathrm{L}\cdot\mathrm{n(L)dL} \tag{7}$$

ρ_{ice} is the bulk ice density ($0.917\ g\cdot cm^{-3}$). $\mathrm{D_{ge}}$ and AR can be evaluated from the mass-size relation used by the cloud microphysics scheme, for example, $m{=}aL^b$ where m is the particle mass. The raw data for the single particle extinction and scattering cross sections (σ_{ext}, σ_{sca}), asymmetry factor (g_p) and the forward scattering δ-function peak (f_δ) were taken from Fu (1996) and Fu et al. (1998).

The technique of spectral averaging over wide bands depends on the parameter one desires to compute the spectral integration technique is explained in details in Muskatel et al. (2021).

We parametrize $\overline{\beta'_{ext}}, \overline{\omega}, \overline{g}, \overline{f_d}$ as function of D_{ge} and AR by fitting rational functions division in the Padé approximation form:

$$f_{(x)}=\frac{\sum_i^N a_i x^i}{\sum_i^M b_i x^i} \tag{8}$$

Where x can be D_{ge} or AR and a_i, b_i are fitting coefficients. This requires a non-linear fitting algorithm like Levenberg-Marquardt, but it is very flexible and can reproduce nearly any asymptotic behaviour if N, M are chosen adequately. If $N= M$, an asymptotic convergence to a constant for $x\to\infty$ results. If $N< M$, the function converges to 0. For $\beta'_{ext}(D_{ge})$ we chose $N= 2$; $M= 3$, for $\omega(D_{ge})$ and $f_d(AR)$ we defined $N= 3;M= 3$ while for $g(AR)$ we put $N= 3;M= 2$. An example for the parametrization fit can be seen in Fig. 1 The asymmetry factor presented in Fig. 1 was calculated for particles with smooth surfaces, where the forward scattered peak (delta fraction f_d) is large because of the plane-parallel surfaces of the ice particles. However, real particles might have rough surfaces, where the forward scattering is smaller. The asymmetry factor for rough surfaces can be defined as (Fu 2007):

$$g_r=\frac{g-f_d}{1-f_d} \tag{9}$$

An example for f_d and g_r parametrization fit can be seen in Fig. 2.

In the original RG92-formulation, the scattering phase function is approximated by the so-called δup-Eddington approximation, which is a sum of a general two-term Legendre-polynomial expansion of the phase function plus a delta-forward peak, weighted by the forward scattered fraction f (Joseph et al. 1976). This approximation is "tuned" to the original phase function by matching of g, which is the first moment of the phase function, and by requiring that $f=g^2$, which follows from the matching of the second moment of the phase function with that of the Henvey-Greenstein function.

For ice particles in the visible spectral range, we now allow the formulation in a way that f is an independent free parameter (Fu 2007):

$$f_{rough}=\frac{1}{2\omega(D_{ge})} \qquad and \qquad f_{smooth}=\frac{1}{2\omega(D_{ge})}+f_d \tag{10}$$

where f is limited so that it cannot be larger than g^2.

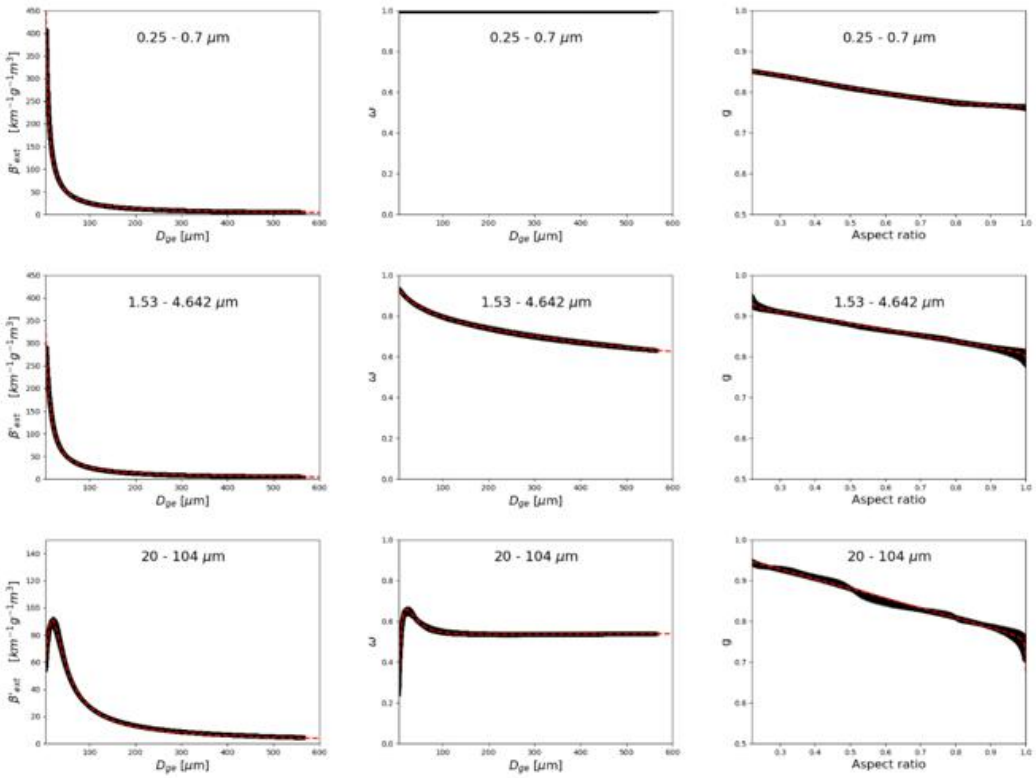


Figure 1: Parametrizations for β'_{ext} (volume extinction coefficient divided by IWC, i.e., mass extinction coefficient) (left column), single scattering albedo (centre column) and asymmetry factor (right column). The upper, middle and lower rows refers to wavelengths of 0.25-0.7 μm, 1.53-4.64 μm and 20-104 μm COSMO intervals respectively. The black line is composed of 7500 individual points, each represents a different PSD, and the red dashed line denotes the parametrization fit model.

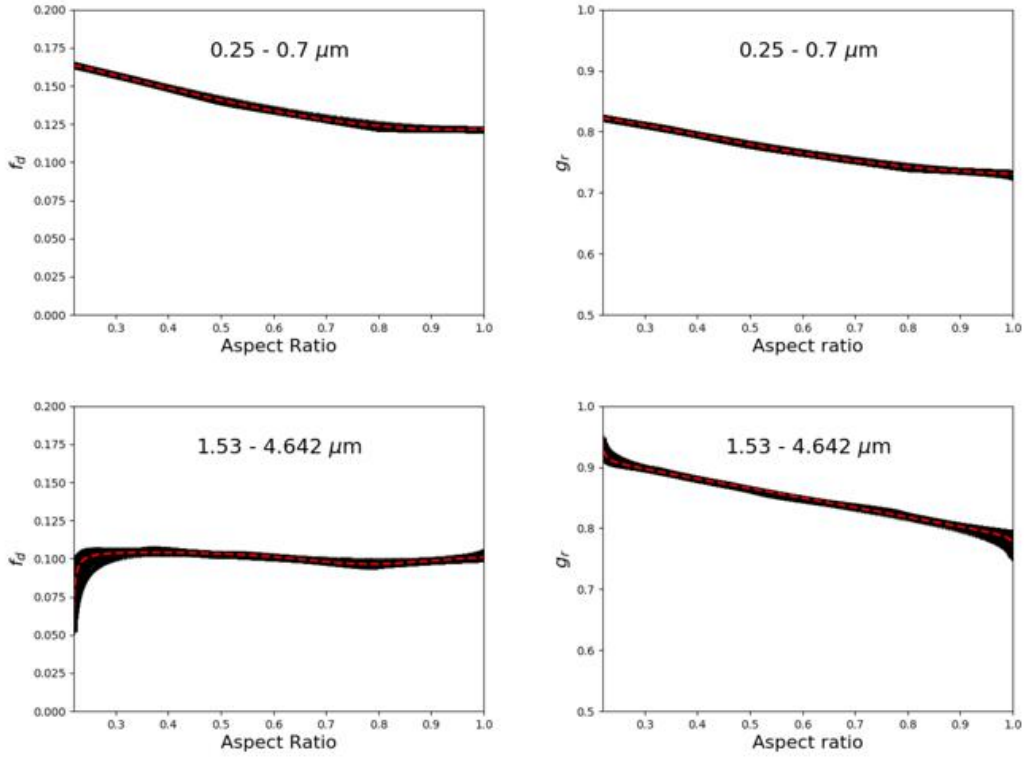


Figure 2: Parametrizations for delta fraction (left) and rough surface particle asymmetry factor (right). The upper and lower rows refers to wavelengths of 0.25-0.7 μm and 1.53-4.64 μm intervals respectively.

3.3 Water droplets

The default COSMO optical properties parametrizations are based on Mie calculations by Stephens (1989) and the parametrizations proposed by Slingo and Schrecker (1982) for water clouds. The effective radius for the quasi-spherical water droplets is define as:

$$R_e = \frac{1}{2} \int_0^\infty D^3 N(D)\, dD / \int_0^\infty D^2 N(D)\, dD = M_3/(2M_2) \tag{11}$$

This definition is motivated by the large-size limit where β'_{ext} is directly proportional to R_e^{-1}:

$$\lim_{D/\lambda \to \infty} \frac{\sigma_{ext}}{A_{geo}} \; ; \quad A_{geo} = \frac{\pi}{4} D^2 \tag{12}$$

$$\beta'_{ext} \equiv \frac{\beta_{ext}}{LWC} = \frac{2\frac{\pi}{4} M_2}{\frac{\pi}{6} \rho_w M_3} = \frac{3}{2\rho_w R_e} \tag{13}$$

$$R_e = \frac{1}{2} \frac{M_3}{M_2} = c_1 \left(\frac{LWC}{n_w} \right)^{c_2} \tag{14}$$

Where A_{geo} is the geometric cross section of a spherical droplet, LWC is the liquid water content, n_w, ρ_w are the number concentration and bulk density of water, respectively. The constant coefficients c_1, c_2 depend on the constant mass-size-relation parameters and on the size distribution parameters. Based on Mie calculations performed by Hu and Stamnes (1993) (HS93) and using the spectral averaging technique described in the previous section,

we applied the calculation to the 8 COSMO wavelength intervals. The same choices for $\rho_{w,max}= 1\ gm^{-3}$, $\Delta z_{min}= 100\ m$ and $\Delta z_{max}= 600\ m$ as was chosen for ice, are used here. We used the same fitting formula as for ice but with $N= 3$; $M= 4$, for $\beta'_{ext}(R_e)$ while for $\omega(R_e)$ and $g(R_e)$ we defined $N= 3; M= 3$. The three size sub-ranges of fitting used by HS93 where replaced with one formula that fits all ranges and is valid in the range $2.5\ \mu m \rightarrow \infty$. An example for the parametrization fit can be seen in Fig. 3.

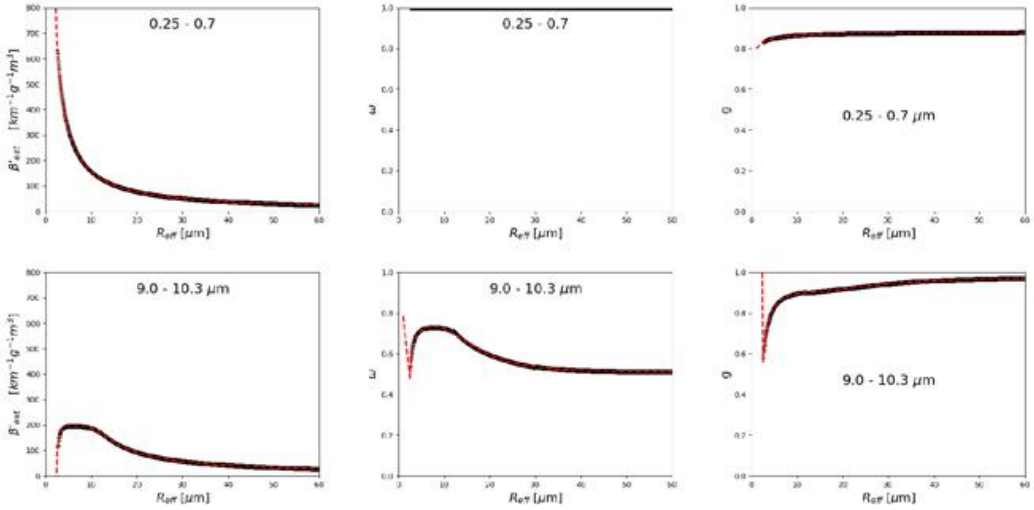


Figure 3: Parametrizations for volume extinction coefficient divided by LWC (left), single scattering albedo (centre) and asymmetry factor (right). The upper and lower rows refers to wavelengths of 0.25-0.7 μm and 9.0 - 10.3 μm intervals respectively. The black line is composed of HS93 original data spectrally averaged for our wavelength intervals and the red dashed line denotes the parametrization fit model. As can be seen from the plots, the fit is invalid for effective radius smaller than 2.5 μm. These fits showed asymptotic behaviour up to 7000 μm (not shown here).

3.4 Sensitivity Experiments

We examined the impact of the new optical properties parametrizations on the radiation transfer, and compare it with the default COSMO radiation scheme (RG92 thereafter) under different cloudiness situations. For that purpose, we have utilized the idealized version of the COSMO model to simulate radiation transfer through two types of clouds: warm stratus and cirrus. The characteristics of the simulated clouds are summarized in Table 1.

The implementation of new parametrizations generally influences the global radiation both directly and indirectly. The change in radiative heating leads to different evolution of the simulated cloud, which in turn influences the radiation transfer. For simplification, we ignored this feedback mechanism, namely removed the radiative heating term in the equation for temperature tendency. All the idealized COSMO simulations were performed between 10:00 and 16:00 UTC, while the zenith angle was fixed to 30°. The domain was chosen to be 100x100 km^2 around 30° N, with periodic boundary conditions and horizontal resolution of 0.025° (~2.5 km). Both deep and shallow convection Tiedtke-type schemes were switched off. Each simulation was initiated with vertical profiles of temperature and humidity suitable for stratiform cloud formation at the chosen heights. During the run period the simulated clouds slightly changed due to evaporation, particles sedimentation, and other processes.

Experiment	Warm stratus	Cirrus
1	2.2-2.7km, 279.2-281.4K	9.5-10.75km, 230.8-218.8K
2	2.0-2.7km, 280.0-281.4K	7.5-10.75km, 250.0-218.8K
3	2.0-3.3km, 280.0-279.0K	7.5-12.20km, 250.0-214.8K
4	1.7-3.3km, 280.4-278.2K	
5	1.5-3.3km, 282.0-279.0K	
6	1.2-3.3km, 284.4-280.2K	
7	1.0-3.3km, 286.0-281.0K	

Table 1: Characteristics of the simulated clouds in sensitivity tests using ideal COSMO framework.

However, they continuously covered the entire simulation domain homogeneously. For each simulation, the output fields (global radiation, total water path, etc.) at 5 min steps were averaged over the domain. Ignoring the first 50 min stabilization period, we obtained 51 values for each field for each simulation. Fig. 4 compares the global radiation of default RG92 and new parametrization for the 7 experiments of warm stratus. The global radiation is shown versus liquid water path. Obviously, the global radiation is smaller for thicker clouds. One can see that in the new version the clouds are optically thinner than in RG92. The global radiation difference is larger for thicker clouds, reaching 20%.

As explained in Section 3, the new scheme parametrizes the effect of cloud water number concentration on the effective radius, which influences the optical properties and the global radiation. Thus, for warm stratus of experiment 5, six more runs were performed with various number concentrations. Fig. 4b shows the effect of cloud water number concentration on the global radiation in the new scheme. In contrast to RG92 where the effective radius was not dependent on number concentration, the new scheme shows significant effect of number concentration and effective radius on the global radiation. Having the same liquid water path, a pristine cloud (number concentration of 10 cm^{-3}) may double the global radiation compared to a polluted one (1000 cm^{-3}).

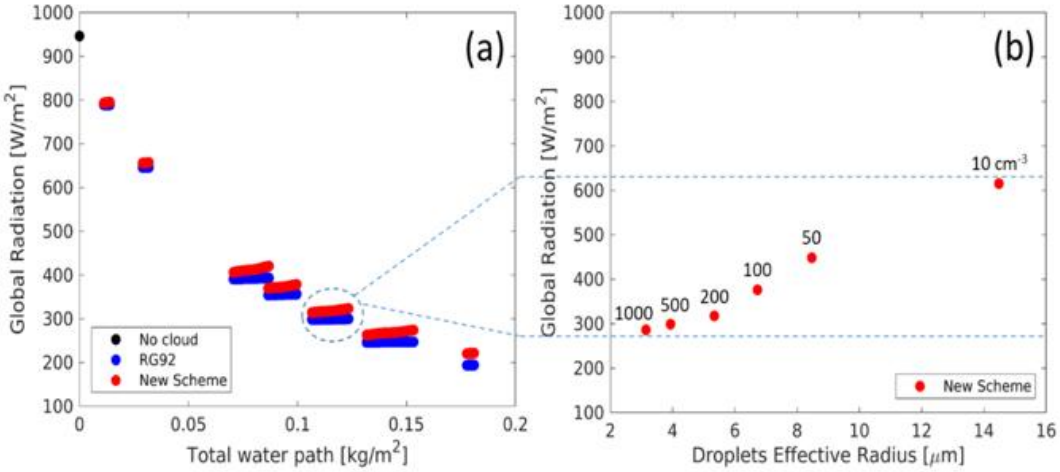


Figure 4: (a) Global radiation versus liquid water path for 7 experiments of warm stratus assuming cloud water number concentration of 500 cm-3. The clear sky reference is marked by black dot. The default COSMO radiation scheme RG92 (blue dots) and the new scheme (red dots) are presented. (b) Global radiation (red dots) in the new scheme versus cloud-averaged droplets effective radius for experiment 5 of warm stratus (see Table 1) marked by dashed circle. The red dots from left to right correspond to cloud water number concentrations of 1000, 500, 200, 100, 50, 10 cm^{-3}. The range of variation in global radiation due to change in effective radius is marked by dashed lines.

Similarly to warm stratus presented in Fig. 4a, Fig. 5a shows the global radiation versus ice water path for the 3 experiments of cirrus (see Table 1). In addition to the default RG92 (blue dots), four more versions of the new parametrization are presented (see Section 2 for details): First assumes rough ice particles surfaces (red dots), the second is similar to the first but adding snow particles into consideration (lime green), the third is similar to the second but assuming smooth surfaces (magenta) and the last is similar to the previous but using the forward scattered fraction approximation of $f = g^2$ instead of the Fu (2007) formulas (cyan). Obviously the global radiation is smaller for thicker clouds. In contrast to warm stratus, the cirrus cloud in the new versions is optically thicker than in RG92. The largest difference from RG92 occurs when assuming rough ice particles and considering snow effect on radiation, where the effect on the global radiation reaches 15% (for thick cirrus - experiment 3). Note that considering snow significantly reduces the global radiation (from red to lime green). Note also that assumption of smooth surfaces makes the clouds optically thinner (from lime green to magenta and cyan), and that there is no significant effect of the different assumptions for forward scattered fraction f (cyan and magenta).

As mentioned, D_{ge} is calculated in the model from ice water content and number concentration which is a function of temperature. In order to highlight the sensitivity of global radiation to D_{ge}, we artificially determine a constant D_{ge} value at all cloudy grid points. Thus, for cirrus of experiment 2, six more runs were performed with various D_{ge} values between 5 and 200 micron. The new version with the assumption of rough needles ignoring snow effect (red dots in Fig. 5a) was chosen for these runs. Fig. 5b shows the influence of D_{ge} on the global radiation in the new scheme. In contrast to RG92 where D_{ge} was not even introduced, the new scheme shows significant effect of D_{ge} on the global radiation. Having the same ice water path, a cirrus cloud with large particles (effective diameter of 200 micron) may yield 10% higher global radiation than an identical cloud with small particles (effective diameter of 5 micron).

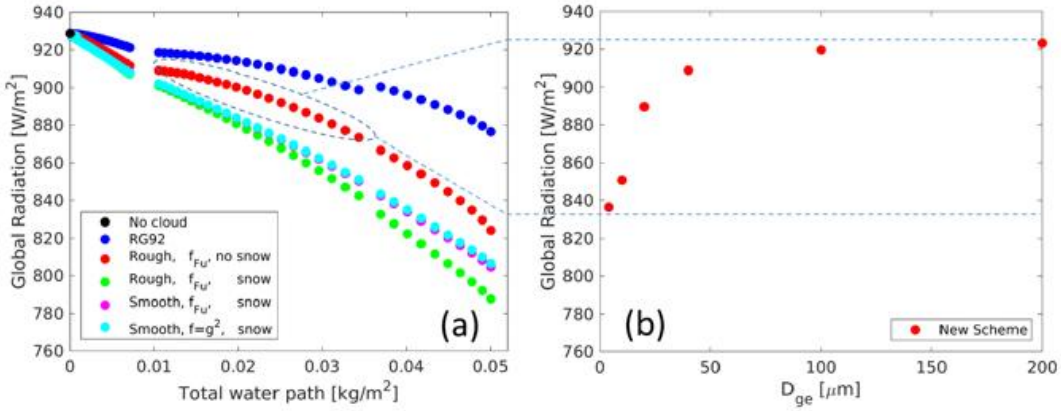


Figure 5: (a) Global radiation versus liquid water path for 3 experiments of cirrus. The clear sky reference is marked by black dot. In blue dots - the default COSMO radiation scheme RG92, red dots represents simulation which assumes rough ice particles surfaces and ignoring snow particles, lime grin dots is the result when snow particles are considered, the same but assuming smooth surfaces are in magenta and the last, in cyan, is similar to the previous but using the forward scattered fraction approximation of $f=g^2$ instead of the Fu (2007) formulas. (b) Global radiation in the Third version of the new scheme (red dots) versus cloud-averaged ice particles effective diameter for experiment 2 of cirrus (see Table 1) marked by dashed circle. The range of variation in global radiation due to change in ice particles effective diameter is marked by dashed lines.

The important quantity for climate applications is the net heating/cooling effect of the clouds. Usually during the day time the SW incoming radiation heats the atmosphere, which is then cooled down via LW outgoing radiation during night time. We cannot discuss this quantity here since our 6 hour long simulations. However, we can check the effect of the new scheme on the net radiation at top-of-atmosphere (incoming minus outgoing). Fig. 6 presents net top-of-atmosphere radiation difference between the new scheme and RG92 versus liquid water path for 7 experiments of warm stratus (Fig. 6a) and versus liquid water path for 3 experiments of cirrus (Fig. 6b). Positive (negative) values indicate warming (cooling) effect by the new scheme with respect to RG92. In Fig. 6b the differences (with respect to RG92) are calculated for the same 4 versions of the new scheme as described in Fig. 5. One can see that the new scheme has warming effect with respect to RG92 for warm stratus, and cooling effect for cirrus. Generally these effects are enhanced (in absolute values) for optically thicker clouds. Note that the assumptions regarding the roughness of the needles surfaces are of low importance for the net radiation (compare cyan, magenta and red dots on Fig. 6b). It is nicely seen that the consideration of snow enhances the net cooling, which can be explained by increase of the cloud albedo.

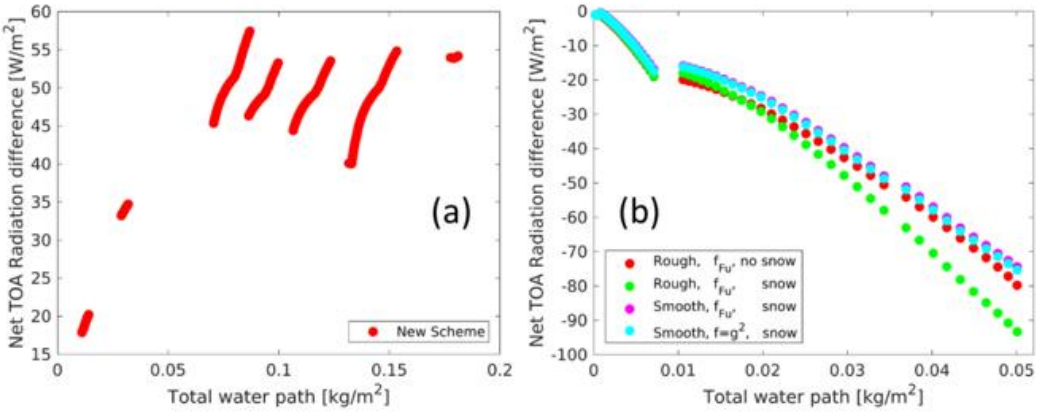


Figure 6: (a) Net (incoming minus outgoing) top-of-atmosphere radiation difference between the new scheme and RG92, versus liquid water path for 7 experiments of warm stratus. Positive values indicate warming effect by the new scheme with respect to RG92. (b) Net top-of-atmosphere radiation difference between the 4 versions of the new scheme and RG92, versus liquid water path for 3 experiments of cirrus (colours details are in the legend of Fig. 5a). Negative values indicate cooling effect by the new scheme with respect to RG92.

3.5 Conclusions and recommendations

The new cloud optics were tested not only in the ideal setup, as detailed in the previous section, but also tested in numerous test cases which will be described in the following sections. We recommend applying the new optics by using iradpar_cloud = 4 with minimal risk. We also recommend choosing lrad_ice_smooth_surfaces = .false. which means that the ice particles will be treated as having rough surfaces. The reasoning behind this recommendation is that rough surfaces ice particles better represents the shape variability. The net radiation on ground will be reduced by few percent having large amounts of ice and snow due to the reduction of forward scattering.

Other recommendation for the new cloud-optics would be: lrad_ice_fd_is_gsquared = .false. which means calculating the forward scattering peak using Fu (2007) formula, lrad_incl_qrqsqg=.true. to include rain, snow and graupel in the radiation scheme and using the large-size approximation by choosing lrad_use_largesizeapprox=.true. Other namelist recommendations can be seen in the appendix of section 3 (upper Air) in COSMO Newsletter No. 19 (October 2019).

A web application for ice and liquid hydrometeors optical properties parametrizations based on this work was created and available for the use of radiation models developers in COSMO webpage. In this web application (www.cosmo-model.org/content/tasks/operational/ims/cloudOptics) developers can insert model spectral integrals and produce parametrizations for ice and liquid hydrometeors including editable graphics.

4 Monte-Carlo Spectral Integration

(H. Muskatel)

4.1 Radiation scheme call-time temporal resolution

Radiation transfer schemes are one of the most computational expensive components in numerical weather prediction (NWP) models. In COSMO model, with only eight spectral intervals, a full radiation calculation costs as much as eight times the cost of the entire COSMO model run. Most of NWP models compromise on the spatial and/or temporal resolution of the radiation scheme. In the operational setup of COSMO-2.8 km, with a full spatial resolution and with a temporal resolution of 15 minutes, the computational cost of radiation is only 3% of the entire model (see Fig. 7).

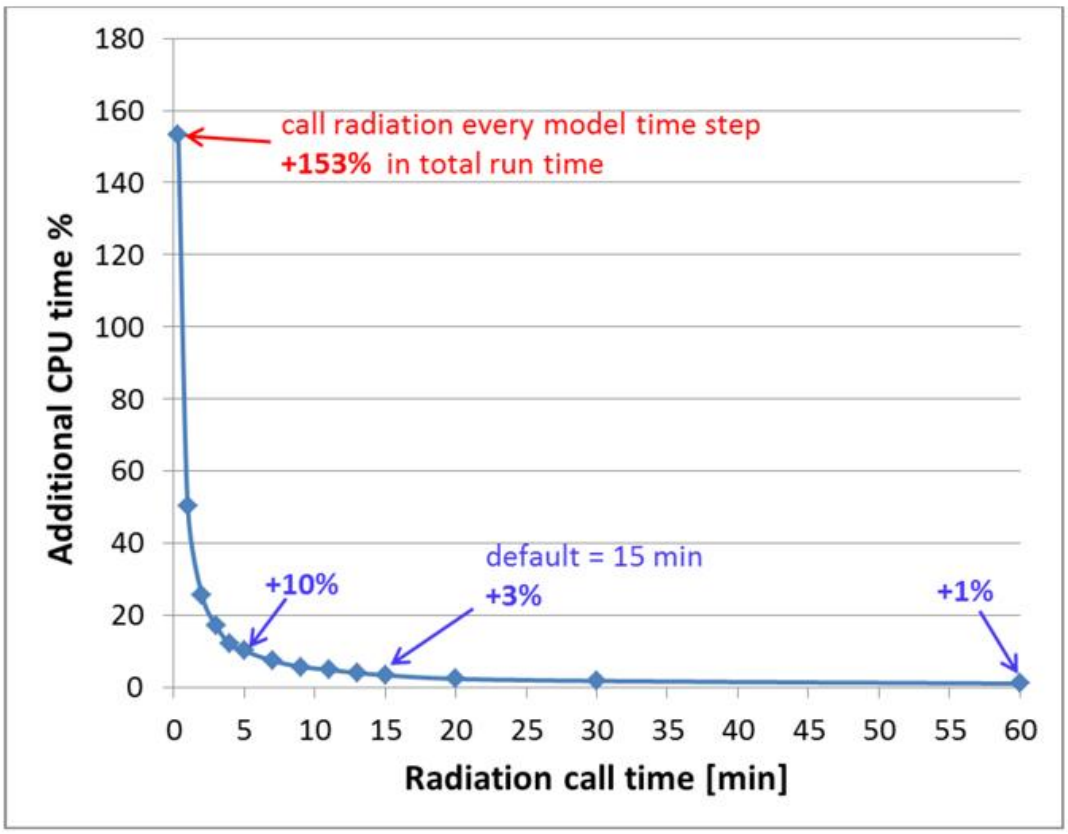


Figure 7: The additional COSMO-2.8km model runtime as function of radiation scheme call temporal resolution. I.e. calling the radiation scheme every 60 minutes adds 1% to total runtime, default resolution of 15 minutes costs 3% increase and calling evry model time step will result more than a double runtime compared with running COSMO with no radiation calculation.

This compromise can lead to local biases in net downward radiation and surface temperatures. To evaluate the magnitude of this effect we chose the 23-25 of April 2015 test case in the IMS-COSMO-2.8km domain. At this period, partial cloudiness and high wind speeds were experienced. The multiple model runs were performed with different radiation temporal resolutions from every model time step (20 seconds) up to 60 minutes. We treat the model

highest temporal resolution as the control run. The model's net downward radiation (global radiation) and 2m temperatures biases for three temporal resolutions: 60, 15, 5 minutes are displayed in Fig. 8. It is clear that the biases appears in the presence of clouds. Also, the biases grow larger in area and magnitudes when the radiation calls separation is larger. In Fig. 9 a domain average of the same experiment are presented. The three lines represents different lead time. It is shown here that there is almost a linear dependency of radiation (left panel) and temperature (right panel) biases as function of temporal resolution and that the biases grow larger for longer runtime. Notice that the line for the 34 hours lead time (blue) is almost flat meaning that there is very weak dependency on temporal resolution at this time. The reason is the clear skies conditions in the second day compared with the cloudiness in the first and third day of the simulation.

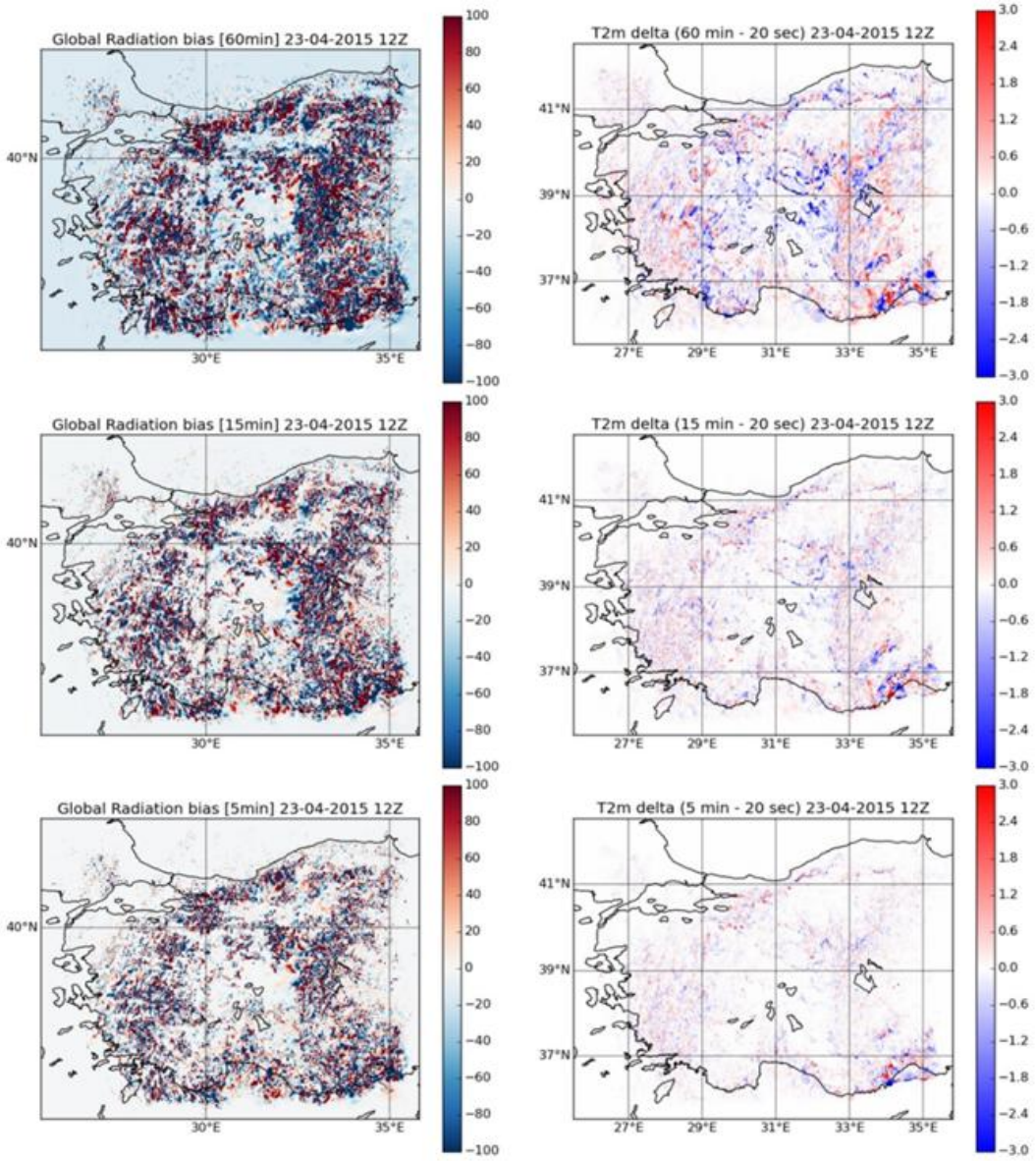


Figure 8: Global radiation (left panels) and 2m Temperature biases (right panels) for three different radiation scheme temporal resolutions 60 min. (upper), 15 min. (middle) and 5 min. (lower) compared with a full temporal resolution (every model time step of 20 seconds). A three days simulation of COSMO-2.8km in IMS domain 23-25 April 2015.

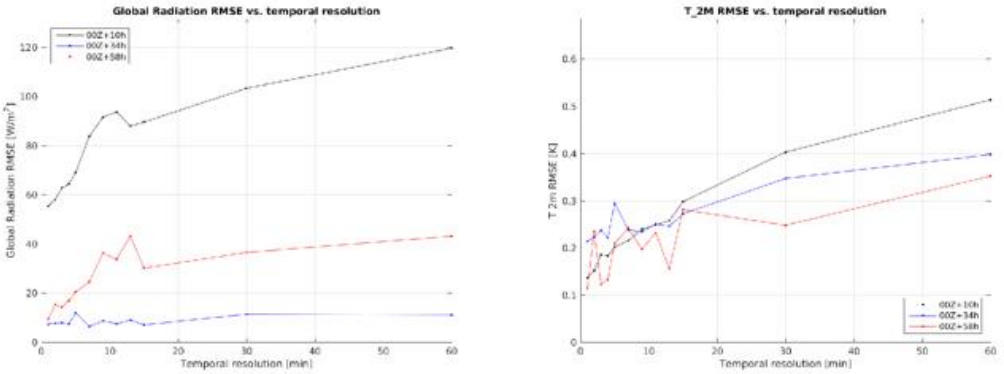


Figure 9: Domain average global radiation (left panel) and 2m temperature (right panel) biases (compared with a control run of full temporal resolution). Three lead times are presented: 10 hours (black), 34 hours (blue) and 58 hours (red). Results plotted as function of radiation call time temporal resolution. The black line represents the lead time with cloudy conditions and the blue line for clear skies conditions. The red line is intermediate conditions.

4.2 The Monte-Carlo Spectral Integration method

In an attempt to both reduce errors and to decrease the run-time we implemented a different approach which is to decrease the spectral resolution by a wise sampling technique, a method known as Monte Carlo Spectral Integration (MCSI). Many radiative transfer schemes and also COSMO RG92 scheme, uses the k-distribution method for the gases-radiation interaction calculations (Fu & Liou 1992). In this method the spectrum is transferred from wavelength space to cumulative probability space. This space is divided to intervals named *g-points*. In COSMO for each gas and for each spectral interval there are between two to eight g-points. In the operational mode of COSMO the Fast Exponential Sum Fitting Technique (FESFT) is used to fully calculate all of the mentioned g-points (Ritter & Geleyn 1992). In MCSI only one g-point is calculated in each time step according to its probability. In COSMO we used a softer version of MCSI where a g-point is selected in each of the spectral intervals which increases the computational cos but does neglect either of the spectral intervals in every time step. In the basic most expensive COSMO radiation scheme, the Exponential Sum Fitting Technique (ESFT), the fluxes calculation subroutines are called for each g-point which belong to the 8 COSMO bands and each of their combinations at each time step, a total of 301 times. In the FESFT, these subroutines are being called only 87 times for each of the g-points in the COSMO radiation scheme. This only are supposed to reduce the CPU effort by a factor of 3. If the radiation scheme is called every 15 minutes only (45 20-seconds time steps) as in the default setup, the runtime for radiation is ∼45 times faster. If the soft-MCSI method is used, only one g-point is selected for each spectral interval at each time step meaning only 8 times ($\sim$ 37 times faster). But using this method needs much frequent call time than the default 15-minutes temporal resolution. Since the radiation is by definition miscalculated at each time step, but the frequent call to the radiation scheme cancels out the errors on the long run since the g-point selection was based on their probability weights. We found out the using the MCSI with full temporal resolution (calling the radiation scheme every time step) in COSMO-2.8km setup can increase runtime by 33% with only slight reduction of global radiation and 2-meter temperature biases compared to FESFT. But using MCSI with a 100 seconds temporal resolution (every 5 time steps) can give the same benefits but

with only 4% increase in runtime. In the upper panel of Fig. 10, the 2m Temperature RMSE of different setups for the same experiment as explained for Figs. 8 and 9 are plotted against the model runtime divided by the model runtime for the default scheme (FESFT with 15 minutes temporal resolution). The RMSE is calculated against a full radiation scheme calculation (ESFT for every model time step) which serves as the control run. We see that the RMSE decreases for the MCSI method (red dots) when the temporal resolution is increased but with the price of CPU runtime. One can clearly see that the default setup (magenta) gives law RMSE values but with minimum model runtime compared with other methods and temporal resolutions seems like the ideal setup as was correctly assumed by previous COSMO model experts. Using the default setup but with a course resolution spatial resolution gives a slightly larger RMSE and slightly reduced model runtime. The lower panel of Fig. 10 shows the T2m bias as function of model runtime differences. As expected the bias is very small for all MSCI experiments and steady even for lower temporal resolutions. Nevertheless, the default setup is at least comparable to the best MCSI set up with 100 seconds resolution but with better runtime.

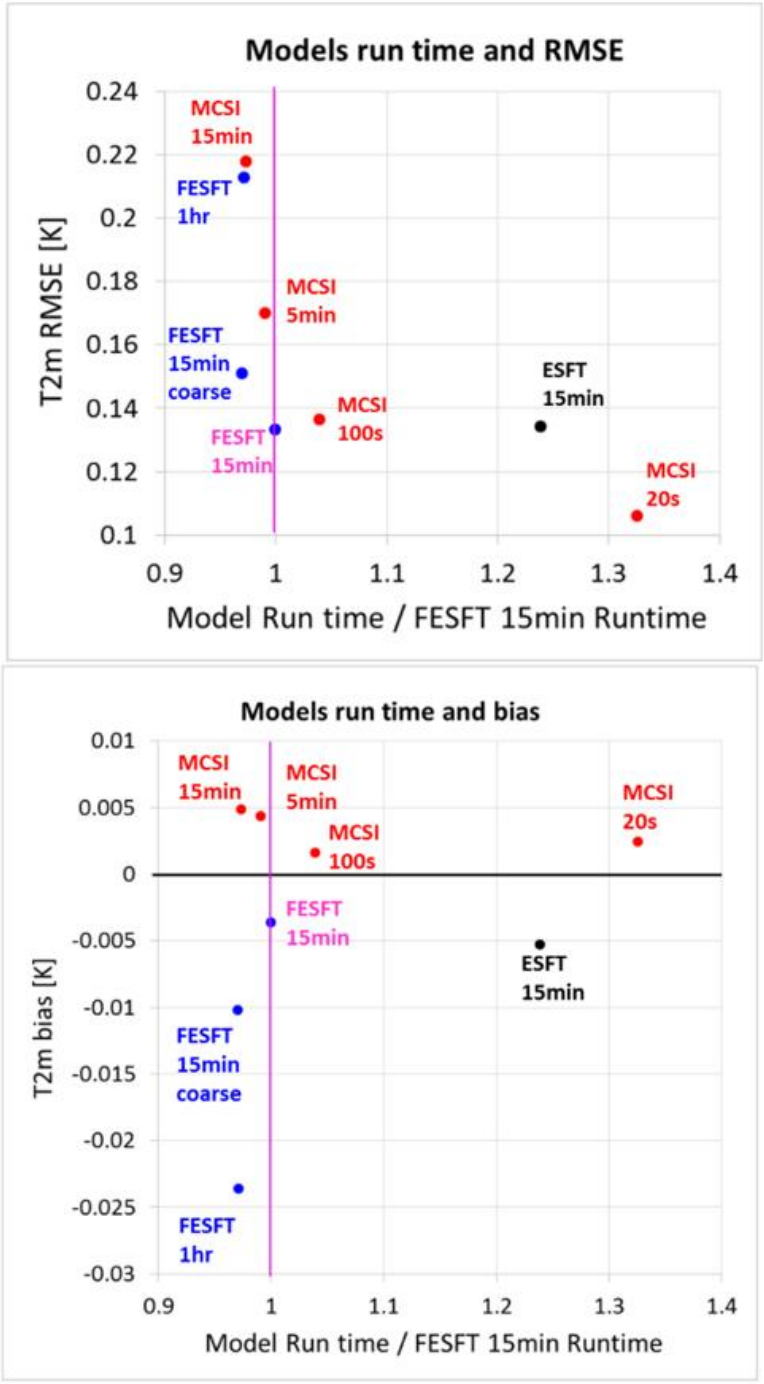


Figure 10: 2m-temperature domain average RMSE (upper panel) and bias (lower panel) compared with a control run of full temporal resolution using ESFT method (see text). The x-axis represents the model runtime compared with the default setup runtime (FESFT method with 15 minutes temporal resolution). Red dots is associated with MSCI method runs with different temporal resolutions, Blue dots represents the FESFT method run and black dot stands for the ESFT method.

4.3 Conclusions and recommendations

A new radiation solver for the scattering and absorption of the radiation by gases (H_2O, CO_2, O_3) was implemented. The new solver based on a soft version of the Monte-Carlo Spectral Integration, that was originally written by Bodo Ritter in a private version, is now fully implemented and tested in the official release of COSMO. To use it one should choose the name list parameter itype_mcsi = 1 with a recommended radiation temporal resolution of 100 seconds (i.e. for a model time step of 20 seconds one should set nincrad = 5). Still, the default scheme using itype_mcsi = 0 with a 15 minutes temporal resolution (nincrad = 45 for the previous example) is still the recommend setup for an ideal combination between performance and runtime. This recommendation is valid for the COSMO-2.8km setup. It is recommended to evaluate the MSCI option for different spatial resolutions (i.e. LES) or different applications like climate models.

5 New parametrization for vertical microphysical profiles in shallow cumulus

(P. Khain, H. Muskatel, U. Blahak)

5.1 Overview

Shallow convection is a sub-grid process in cloud-resolving models for which their grid-box is larger than the size of small cumulus clouds (Cu). At the same time such Cu substantially affect radiation properties and thermodynamic parameters of the low atmosphere. The main microphysical parameters used for calculation of radiative properties of Cu in cloud resolving models are liquid water content (LWC), effective droplet radius (r_e) and cloud fraction (CF). In this study, these parameters of fields of small warm Cu are calculated using large-eddy-simulations (LES). We performed it using the System for Atmospheric Modelling (SAM) with spectral bin microphysics. Despite the complexity of microphysical processes, two fundamental properties of Cu were found. First, is that despite of the high variability of LWC and droplet concentration (N_d) within clouds and between different clouds, the volume mean and effective radii per specific level vary only slightly; Second is that the values of r_e are close to those forming during adiabatic ascent of air parcels from cloud base. These findings allow characterizing a cloud field by a specific vertical profiles of r_e and of mean LWC, which can be calculated using the theoretical profile of adiabatic LWC and N_d at cloud base. Using the results of these LES, a simple parametrization of cloud-field averaged vertical profiles of r_e and of LWC is proposed for different aerosol and thermodynamic conditions. These profiles parametrization is implemented in COSMO to be used for calculation of radiation properties of subgrid Cu fields. For more details, the reader is referred to (Khain et al., 2019).

5.2 Theoretical background

5.2.1 Calculation of shallow cumulus LWC and R_e in NWP models

Large–scale models with grid spacing of tens of kilometres do not resolve clouds and require the use of convective parametrization schemes. The values of r_e and LWC that are usually prescribed in such models, inevitably leads to errors in calculation of related quantities.

The treatment of clouds in meso-scale cloud-resolving models (CRM) with grid spacing of a few kilometres is complicated since only the largest, grid scale, clouds are resolved in such models. Small clouds and especially shallow warm Cu, with a typical size smaller or similar to the grid spacing of CRM remain a sub-grid phenomena.

In CRM calculations of effective drop radii at resolvable scales are performed when the relative humidity (RH) in the grid point exceeds 100%. When the grid spacing is larger than the size of shallow Cu, the conditions for small clouds formation can be suitable even when the calculated mean grid relative humidity (RH) is lower than 100%. These clouds may, however, affect the radiative budget substantially, and the knowledge on r_e, LWC and CF values is necessary for such calculations.

In the limited area NWP r_e of unresolved clouds is a tuning parameter. For instance, in COSMO r_e=5 μm by default. Since on average over the grid box there is sub-saturation, the LWC in these shallow cumuli is crudely parametrized as a function of temperature (reduces with a decrease in temperature), mimicking the reduction of available water vapour for condensation with height. Recently, a new cloud radiation scheme was developed for COSMO (Blahak and Ritter, 2013), and is currently under evaluation. Among other developments, r_e of unresolved clouds is calculated in this scheme from the ratio of LWC and N_d. While LWC is evaluated using the parametrization described above, N_d is determined using the assumed aerosol concentration and the effective (unresolved) vertical velocity at cloud base. The large uncertainty in LWC causes r_e to be highly uncertain as well. As a result, such parametrizations may lead to significant errors in evaluation of effects of shallow convection on radiation and on other thermodynamic atmospheric properties.

5.2.2 Utilization of LES for simulation of small Cu

Large Eddy Simulations (LES) is an efficient method to simulate fields of small Cu and investigate Cu dynamics and microphysics, or to develop new parametrizations for those. To simulate cloud microphysical processes we use the detailed microphysical approach of the bin microphysics, which solves the microphysical equations for determining the droplet size distributions (DSD). In LES simulations the bin-microphysical approach is often used for investigation of thermodynamic factors and aerosols on the parameters of droplet size distributions, drizzle formation and on cloud dynamics (e.g., Jiang et al., 2008). Such parameters as LWC, N_d and $\mathrm{r_e}$ are determined directly from the calculated DSD. In addition to simulation of cloud fields, LES are used to develop parametrization schemes for the large scale models. In the present study we use LES results to investigate the behaviour of microphysical properties of non-precipitating and slightly precipitating shallow Cu fields under different aerosol conditions. The goal of the study is twofold. First, we will check the variability of $\mathrm{r_e}$ in clouds of different sizes and the robustness of utilization of one mean vertical profile of $\overline{r_e}(z)$ to characterize all the clouds within the field. We explore the reasons for the comparatively low horizontal variability of $\mathrm{r_e}$ despite of the high variability of LWC both within each cloud and between different clouds. Second, using the results of the LES we propose a simple parametrization of the mean vertical profiles of $\mathrm{r_e}$ and LWC that uses adiabatic LWC profile and N_d at cloud base. This parametrization is implemented in COSMO model to be used for calculation of radiation properties of subgrid Cu fields.

5.3 LES set-up

In this study LES were performed using System for Atmospheric Modelling (SAM) (Khairoutdinov and Randall, 2003) with Spectral Bin Microphysics (SBM, Khain at al. 2004, 2013) (for

details see: http://rossby.msrc.sunysb.edu/~marat/SAM.html). SAM is a non-hydrostatic, inelastic model with cyclic boundary conditions in the horizontal direction. The SBM is based on solving kinetic equations for size distribution functions of water drops and Aerosol Particles (AP). Aerosols and droplet size distribution functions are defined on the doubling mass grids containing 33 bins. The drops radii range between 2 μm and 3.2 mm. The size of AP serving as cloud condensation nuclei (CCN) ranges between 0.005 μm and 2 μm. Using the values of supersaturation with respect to water, the critical CCN radius is calculated (using the Köhler theory) and APs larger than the critical size are nucleated to droplets as described by Khain et. al (2000). The rest of APs are advected with air motion. Diffusional growth and evaporation of droplets are calculated basing on the changes in the supersaturation during a model time step. The time steps are chosen to be smaller than drop relaxation time. This is the physical condition of accurate calculation of diffusion growth/evaporation. Collision-coalescence is solved by the stochastic collision equation using the accurate method of Bott (1998). The collision kernels were calculated using an exact method described by Pinsky et al. (2001). Drop sedimentation is calculated using fall velocities determined by Beard (1976). Fields of small trade Cu were simulated within a domain of 12.8 km x 12.8 km x 5.1 km using horizontal resolution of 100 m, and vertical resolution of 40 m with a dynamical time step of 1 s. As a case study, small Cu observed during BOMEX were chosen for simulation (Siebesma et al., 2003). The vertical profiles of temperature and dew point used in simulations are shown in Fig. 11. The original BOMEX profile is that with the inversion at 1500m, the other two profiles with the inversions at 1000 m and 2000 m were used for analysing the effect of the inversion height on the microphysical properties of simulated cloud fields.

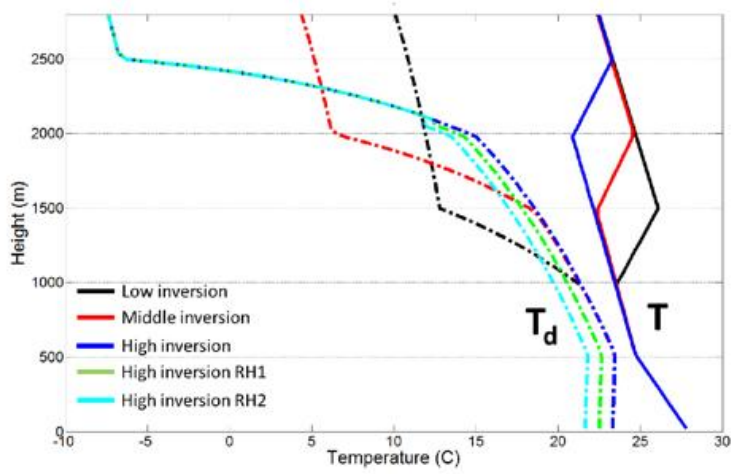


Figure 11: Initial vertical profiles of temperature (solid) and dew point (dashed) used in simulations: low inversion at 1000 m (black), high inversion at 2000 m (blue), middle inversion at 1500 m (red- the original BOMEX profile). Green and cyan profiles denote sensitivity tests with decreased relative humidity (by 5% and 10%, respectively) with respect to high inversion profile.

In the simulations we used concentrations of CN within the range from 500 cm^{-3} to 5000 cm^{-3} which lead to mean N_d at cloud base of $\sim 50\ cm^{-3}$ to $\sim 500\ cm^{-3}$. According to the accepted definition, this range of N_d includes three cloud types: clean (maritime), intermediate (clean continental) and polluted (continental) (Ghan et al. 2011). Note that comparatively small mean cloud N_d at cloud base at such CN concentration is determined by low vertical velocities at cloud base and by prescribed initial CN size distributions containing large fraction of

small CN, which cannot be activated at such vertical velocities. We do not consider clouds developing in the extremely clean atmosphere, and producing drizzle immediately after their formation. We will refer the simulations according to the CN concentration and inversion height: H-high, M-medium and L-low, e.g. E5000H, where E denotes "experiment" and 5000 shows CCN concentration. The list of simulations is presented in Table 2.

Name of experiment	Height of inversion (m)	Aerosol concentration (cm^{-3})	Main results				
			total CF (%)	STD of total CF (%)	<N_d> (cm^{-3})	<CWC> max (gm^{-3})	<r_e> max (μm)
E5000L	1000	5000	20.1	1.8	403	0.52	7.7
E5000M	1500	5000	17.9	1.0	371	0.54	8.2
E5000H	2000	5000	19.7	1.6	372	0.47	8.4
E3000L	1000	3000	20.5	1.6	248	0.58	9.4
E3000M	1500	3000	18.7	1.7	222	0.52	9.8
E3000H	2000	3000	20.4	1.7	221	0.47	10.2
E2000L	1000	2000	20.8	1.1	164	0.58	10.7
E2000M	1500	2000	18.8	1.1	149	0.51	11.3
E2000H	2000	2000	20.6	1.5	148	0.48	12
E1000L	1000	1000	21.9	1.0	81	0.55	13.6
E1000M	1500	1000	19.4	1.3	82	0.49	14.9
E1000H	2000	1000	21.7	1.6	83	0.42	15.5
E500L	1000	500	24.2	1.8	47	0.43	16.7
E500M	1500	500	21.5	1.3	49	0.37	18.2
E500H	2000	500	23.1	1.8	48	0.32	18.3

Table 2: List of simulations. Notations: "total CF" – time averaged total cloud fraction, "STD of total CF" – standard deviation of total CF, "<N_d>" – time and space averaged N_d, "<CWC> max" – maximum (over height) value of the mean profile of CWC, "<r_e> max" – maximum (over height) value of the mean profile of r_e.

In addition to simulations listed in Table 2 three supplemental simulations were performed. The simulation E2000H-50 is similar to E2000H but has horizontal grid spacing of 50 m. It was performed to analyse effects of model resolution on cloud thermodynamics and microphysics. Two other simulations E2000H-RH1 and E2000H-RH2 have air relative humidity within the layer from the surface to the inversion base by 5% and 10% lower than in E2000H, respectively. The profiles of Td(z) in these simulations are shown in Fig. 11. These simulations aim to investigate effects of environment humidity on cloud properties and to check universality of the parametrization proposed (see below) under different thermodynamic characteristics of the boundary layer. Convection is triggered by random temperature perturbations at the beginning of the simulations. For isolating the aerosol effect on the thermodynamic conditions, the radiative effects (as included in the large scale forcing) as well as the surface fluxes were prescribed in all simulations (see Dagan et al., 2016 for detail). The surface fluxes and the large scale forcing of BOMEX have been used for this study following Siebesma et al. (2003). All simulations were performed for 8.3 hours.

5.4 Results

In order to give an idea of how the cloud field simulated by SAM looks like which can simplify further interpretation of the results, we present in Fig. 12 3D snapshots of the LWC, Nd and r_e in E5000H. In this particular case rain water content is negligible, so LWC is equal to cloud water content (CWC), determined by cloud droplets with radii below 25 μm. This is the approximate maximum drop radius that can be reached by diffusion growth and non-intense collisions between small cloud droplets (Pinsky and Khain, 2002). The cloud field consists of clouds of different sizes and shapes. The smallest clouds rapidly evaporate by mixing with surrounding, while few largest clouds penetrate the inversion layer. The largest clouds contain cores with high CWC. As expected, the CWC increases with height, reaching its maximum near the cloud top, while Nd is nearly constant with height. Hence, the drop size r_e is increasing with height, as can be seen in Fig. 12c. It is possible to see that r_e changes in horizontal direction within the range 9-11 μm in the upper parts of clouds, i.e. the relative changes of r_e are much lower than those of CWC and N_d.

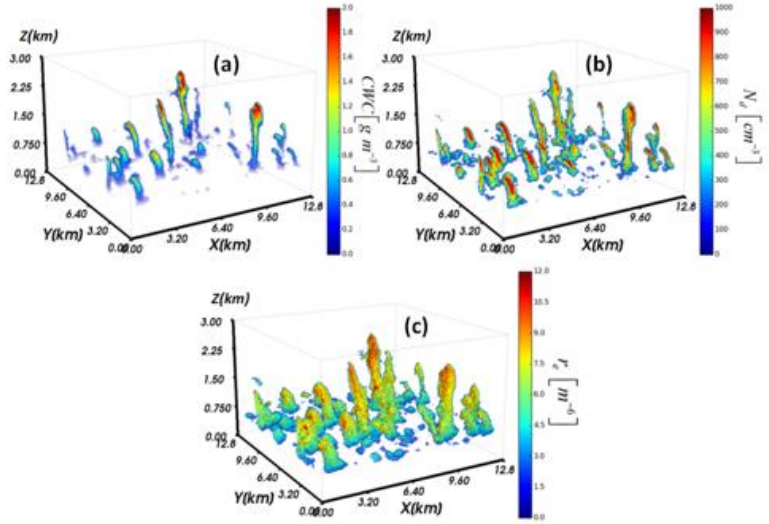


Figure 12: A snapshot of (a) CWC, (b) N_d, and (c) r_e fields for E5000H experiment: inversion is at 2 km, the CN concentration is 5000 cm^{-3}, t = 208 min. The impression of "noodle" shape clouds and not the usual "cotton balls" shape, are just due to the difference between the horizontal and vertical scales.

For more details regarding the performed simulation results the reader is referred to Khain et al., 2019. Here we continue with analysing r_e profile. The volume mean (r_v) and effective droplet (r_e) radii are among the most important microphysical characteristics of clouds. In several studies the mean volume and effective radii are related as $r_e \approx k r_v$. According to our simulations $k \approx 1.15 - 1.17$. The lowest values of coefficient k take place for polluted clouds in which DSD are the narrowest. Accordingly, the largest values of k take place for clean clouds, where DSD width is largest, and the existence of large cloud droplets increases r_e. Main properties of r_e in cloud field of small Cu can be derived from Fig. 13 showing height vs. re scattering diagrams for selected simulations with different inversion layer heights and different aerosol concentrations. These simulations reflect the basic properties of r_e. Purple lines in Fig. 13 denote the profiles of "adiabatic" effective radius of cloud droplets r_{e_ad}, which could be observed in adiabatically ascending cloud volume with droplet concentration N_{d_ad} calculated at cloud base. In Fig. 13 r_{e_ad} is calculated as:

$$r_{e_ad}(z) = 1.15 \cdot r_v = 1.15 \cdot \left(\frac{LWC_{ad}(z)}{\frac{4}{3}\pi \rho_w N_{d_ad}} \right)^{1/3} \tag{15}$$

where $LWC_{ad}(z)$ is adiabatic LWC that can be calculated as described, for example, by Pontikis (1996) or Pinsky et al. (2012). The adiabatic cloud number concentration N_{d_ad} is the concentration in an adiabatic cloud core. The cloud cores are adiabatic only at the first few hundreds of meters above the cloud base. Hence, in these levels $r_e(z)$ in the cloud cores should be equal to $r_{e_ad}(z)$. We have chosen N_{d_ad} so that $r_{e_ad}(z)$ will nearly coincide with $r_e(z)$ in the cloud cores. N_{d_ad} can be calculated in large scale models using, for instance, lookup tables as a function of aerosol concentration and cloud base vertical velocities (Segal and Khain, 2006) as it is done in COSMO, theoretical formulas (Pinsky et al. 2012) or other approaches (Ghan et al. 2011). The cloud base vertical velocities in the COSMO model are calculated as a sum of gridscale updraft, vertical component of turbulent fluctuations using turbulent kinetic energy (with isotropy assumption), radiative cooling effect (Khvorostyanov and Curry, 1999), and the convective velocity scale (Deardorff, 1970). Because of some uncertainties in evaluation of N_{d_ad}, we will refer r_{e_ad} to as "modelled" adiabatic effective radius. Although the Nd and LWC in cloud cores become smaller with height compared to N_{d_ad} and LWC_{ad}, but r_{e_ad} still represents well the effective radius in cloud cores. The advantage of r_{e_ad} is that it can be calculated in any model knowing the LCL (together with the cloud base temperature and pressure) and N_d at cloud base.

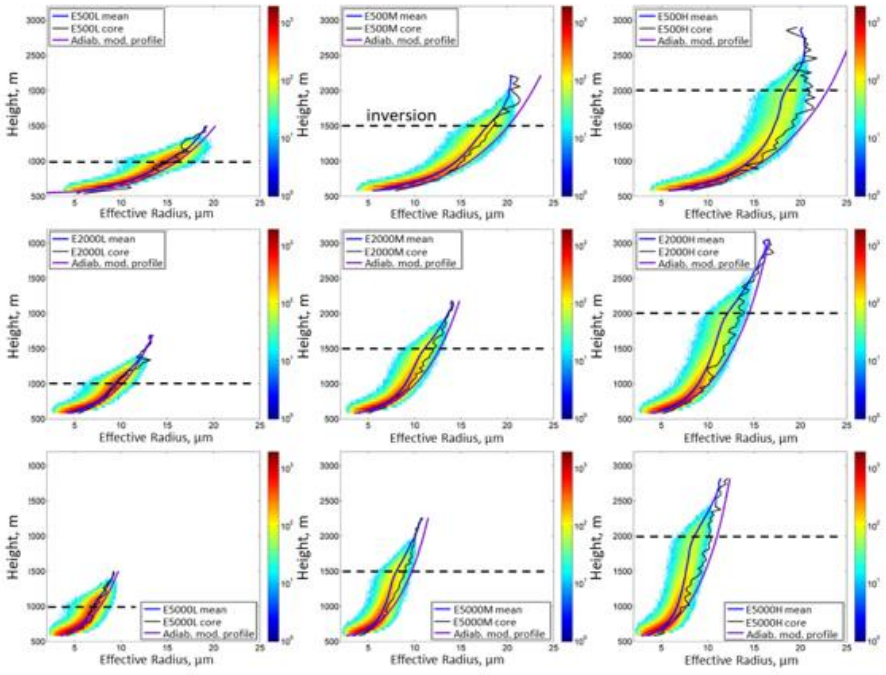


Figure 13: The height-r_e scattering diagrams for simulations with different CN concentrations. Left, middle and right columns show the cases with low (base at 1000m), middle (base at 1500m) and high (base at 2000m) inversion, respectively. Notations: The colour-scale reflects the number of cloudy grid points with specific r_e in logarithmic scale; black curves denote effective radii in clouds cores; purple curves denote the modelled approximation to adiabatic r_e profiles; blue curves denote profiles of horizontally averaged r_e; black dashed lines denote the inversion base heights.

An analysis of Fig. 13 shows several important features of r_e in clouds forming in cloud fields:

a. Strong effect of aerosols

A well-known effect is the faster r_e growth with height in case of low CCN concentrations. In case of clean environment, N_d is small, therefore the fewer droplets that form near cloud base have little competition on the available supersaturation (S_W) (Pinsky et al. 2012, 2014; Dagan et al. 2016). As a result, S_W remains relatively high and the droplets grow rapidly with height. At CN concentration of 5000 cm^{-3}, the maximum of the r_e remains below 13-15 μm, so these clouds do not produce neither raindrops nor drizzle. At CN concentration of 2000 cm^{-3}, the maximum r_e reaches 14-15 μm at z = 2000 m and light drizzle arises above this level (not shown here). In E500 the maximum of r_e exceeds 15 μm and raindrops arise (not shown here).

b. Low horizontal variability of effective radius

A fundamental property of r_e is low horizontal variability. This variability is much lower than that of LWC. Generally, the averaged (over all heights) relative variability varies between 10-15%. Our results show low variability of r_e. We partially attribute this insensitivity to the following. The mean volume radius is proportional to $(LWC/N_d)^{1/3}$. As the incloud nucleation leads to the formation of the smallest droplets, the LWC is defined by the first mode of droplets activated at cloud base. Because of the 1/3 power, the in-cloud nucleation cannot change N_d strongly enough to significantly affect the mean volume radius (as well as r_e). Low variability of r_e indicates that cloud field can be characterized by robust vertical profile of r_e that is close to the adiabatic one and depends on the aerosol loading.

c. The maximum effective radius is in cloud interior

The important feature is that the r_e is maximal in cloud interior (black lines), where LWC are maximum. In cloud cores the profiles of $r_e(z)$ almost coincide with the adiabatic values (purple lines) calculated according Eq. 15. This fact shows that cloud droplets reach maximum size in cloud cores, together with the maximum LWC and the maximum N_d.

d. Limiting value in case of raindrop formation

As seen in Fig. 13, r_e in cloud core in simulations with $CN = 500\ cm^{-3}$ is maximum in cloud cores and close to the adiabatic value. Formation of raindrops is seen by termination of the r_e growth with height. In case of rain drop formation, r_e determined within the range of cloud droplet radii ($< 25\ \mu m$) does not exceed about 22 μm and remains height independent (Figure 5.3, E500H). Such regime is known as rainout (Rosenfeld and Lensky, 1998). The reason of low dependence of r_e on height in case of raindrop formation is that raindrops collect cloud droplets of all sizes that leads to decrease in N_d, but does not change r_e of the cloud droplet mode.

According to the results, in case of rain formation, the maximum r_e of cloud droplets can be calculated as:

$$r_{e_{max}} = \min(22\mu m, r_{e_ad}) \tag{16}$$

Because of low variability of r_e, the values of r_e are concentrated around $\overline{r_e}$ which is slightly smaller than r_{e_ad}. The physical reasons of low variability of r_e were analysed by Pinsky et al. (2016b), Pinsky and Khain (2018a) and by Magaritz-Ronen et al. (2016b). Relative humidity in cloudy volumes, even well diluted ones, remains high which does not allow r_e to decrease anyhow significantly. Small decrease in r_e reflects the contribution of air volumes

newly penetrating clouds and located near cloud edges. In such volumes partial evaporation of drops penetrating from cloudy volumes leads to formation of DSD with lower effective radii. Rapid increase of relative humidity in such volumes with time leads to termination of evaporation of largest droplets penetrating from the cloudy volumes. As a result, the r_e in the volumes penetrating clouds rapidly reaches values typical of cloudy volumes, while LWC and N_d remain much lower than in the cloud core. The mixing with humid air, which entrains clouds, does not cause strong changes in drop sizes near cloud edge.

5.5 Parametrization of microphysical parameters of cloud ensembles

For practical goals, it is desirable to characterize cloud field by some mean vertical profile $\overline{r_e}(z)$. Analysis of results presented in Fig. 13 shows that $\overline{r_e}(z)$ is smaller than the maximum value $r_{e_ad}(z)$ only by ∼10-15%. The difference between $\overline{r_e}(z)$ and $r_{e_ad}(z)$ reaches its maximum at the inversion base level. This increase is related to the fact that cloud ensemble contains clouds of different size and clouds of lower width experience stronger effects of mixing because the interface zone affected by mixing in such clouds occupies a significant fraction of the cloud volume. Above the base of inversion the difference $r_{e_ad}(z)$-$\overline{r_e}(z)$ decreases again, since only largest clouds remain. This behaviour retards a simple approximation of $\overline{r_e}(z)$ via $r_{e_ad}(z)$. We will approximate dependence between these two quantities (as well as other approximation of averaged values) ignoring the upper part of clouds within inversion layer, for which the contribution to the optical depth of cloud layer is less than 5% (not shown). Within the layer below inversion base the cloud averaged r_e can be approximated as

$$\overline{r_e}\,(z) = \alpha(z) r_{e_ad}(z) \tag{17}$$

$$\alpha\,(z) = \ 0.95 - 1.2 \cdot 10^{-4}(z - z_{cb}) \tag{18}$$

Where z is in meters, z_{cb} is the cloud base level, determined by the minimal distance from the surface where supersaturation for the first time becomes positive and droplet nucleation takes place. In order to take into account the effect of raindrops, the values of $r_{e_{ad}}\,(z)$ in Eq. 17 were replaced by $r_{e,max}(z)$ calculated using Eq. 16. Vertical profiles of the cloud averaged r_e are calculated directly from LES and parametrized using Eqs. 15-17 are shown in Fig. 14.

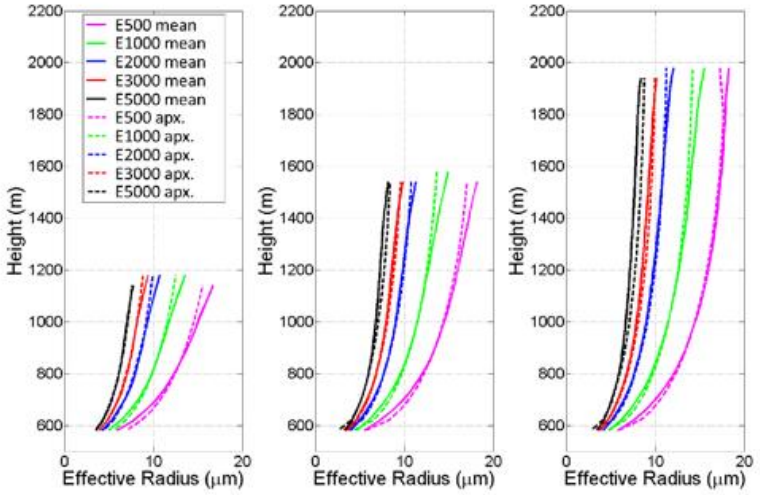


Figure 14: Vertical profiles of the cloud averaged r_e calculated directly from LES (solid lines) and parametrized using Eqs. 15-17 (dashed lines). Each panel is plotted for different inversion base height: low, medium and high, respectively.

One can see a good agreement of parametrized $\overline{r_e}(z)$ with those calculated directly in the LES within entire range of aerosol loadings and different levels of the inversion. The standard deviation is of 0.39 μm.

The next step is the parametrization of the mean droplet concentration as a function of N_d at cloud base. N_d, as was mentioned above, can be determined using different approaches in different kinds of atmospheric models, including NWP models. The concentration at cloud base can be referred to as adiabatic concentration N_{d_ad}, which being formed at cloud base does not change with height within ascending adiabatic parcels. In small Cu the changes of air density with height are small. Profiles of $\overline{N_d}(z)$ depend on whether clouds produce raindrops or not. In case of non-precipitating clouds $\overline{N_d}(z)$ and N_{d_ad} are equal to the maximum value N_{d_max}, which can be considered as constant with height. Analysis (not shown here) shows that the maximum N_d in clouds producing raindrops can be approximated as a constant till the level at which $r_{e_ad} = 12\ \mu m$ and linearly decreasing above this level. Statistical analysis shows that the profile of maximal N_d can be written in the form

$$N_{d_max}(z) = \begin{cases} N_{d_ad}, & z < z_{12}\ , \textit{where } r_{e_ad} = 12\ \mu m \\ N_{d_ad}\left[1-\gamma\,(z-z_{12})\right], & z > z_{12} \end{cases} \tag{19}$$

where $\gamma = 0.45 m^{-1}$ and z is in meters.

$$\overline{N_d}(z) \approx \beta N_{d_max}(z) \tag{20}$$

where on average (over all heights and simulations) $\beta = 0.38$ with standard deviation of 0.03. The parameters in expressions 17-19 are obtained minimizing the root mean square over all the simulations. Expressions 18 and 19 allow to calculate the averaged concentration profiles using N_d at cloud base and the height of the level where $r_{e_{ad}}$ reaches the precipitating threshold. Fig. 15 shows profiles of cloud averaged N_d obtained in LES and using expressions 19 and 20. One can see a good agreement between the approximations and profiles directly calculated using LES.

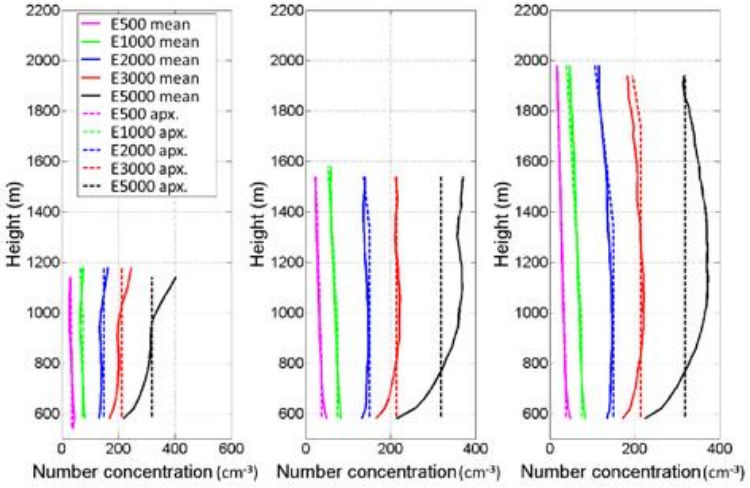


Figure 15: Profiles of cloud averaged N_d obtained in LES (solid lines) and using expressions 18 and 19 (dashed lines). Each panel is plotted for different inversion base height: low, medium and high, respectively.

In addition to $\overline{r_e}(z)$, the parametrizations of radiation transfer through unresolved cloudiness in many NWP and climatic models require a prognostic calculation of $\overline{LWC}(z)$. As mentioned in the introduction, the $\overline{LWC}(z)$ of unresolved clouds in the default version of the COSMO model is crudely parametrized as a function of the temperature. Now, using the parametrization of $\overline{r_e}(z)$ and $\overline{N_d}(z)$ as mentioned above, we are able to parametrize $\overline{LWC}(z)$ as well. Strictly speaking, the practically required values of $\overline{LWC}(z)$ should be determined as:

$$\overline{LWC}\,(z) = \overline{\frac{4}{3}\pi\rho_w N_d(z) {r_v}^3(z)} = \overline{\frac{4}{3}\pi\rho_w N_d(z)\left(\frac{r_e(z)}{1.15}\right)^3} \tag{21}$$

However, since variability of r_e is low, the last equality can be rewritten as:

$$\overline{LWC}\,(z) \approx \frac{4}{3}\pi\rho_w \overline{N_d}(z)\left(\frac{\overline{r_e}(z)}{1.15}\right)^3 \tag{22}$$

which is substantially simpler than Eq. 21. Fig. 16 presents the vertical profiles of $\overline{LWC}(z)$ calculated directly from the results of the LES simulations and the profiles of $\overline{LWC}(z)$ calculated using Eq. 22.

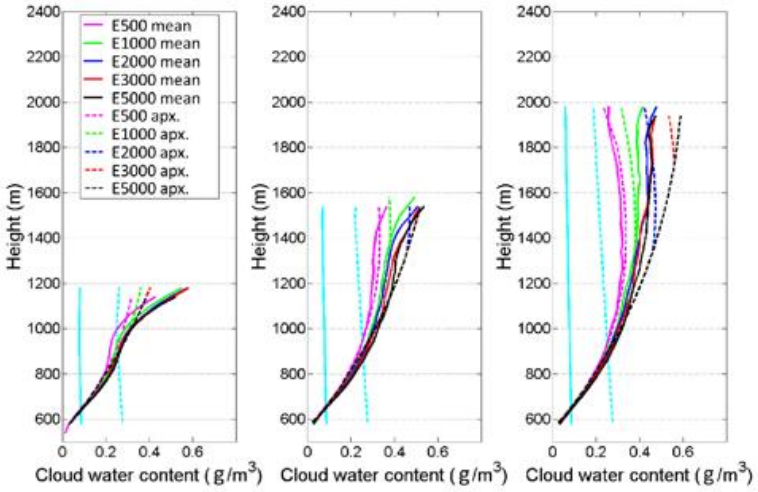


Figure 16: Vertical profiles of the cloud averaged CWC calculated directly from LES (solid lines) and approximation (Eq. 22) (dashed lines) for different aerosol loadings and for different inversion levels: low (left), medium (middle) and high (right). Cyan solid and dashed lines indicate the profiles obtained using different options within the default parametrization in COSMO.

One can see that Eq. 22 allows reproducing the LES profiles of $\overline{CWC}(z)$ quite accurately, especially in comparison with COSMO approximations (cyan solid and dashed lines). Deviations of CWC calculated using Eq. 22 from that calculated directly in LES seen at higher levels are not of high importance for calculation of radiation fluxes because CF of these clouds at such altitudes are low.

5.6 Implementation of the parametrization in the COSMO model

The new parametrization for $\overline{LWC}(z)$ and $\overline{r_e}(z)$ was implemented in COSMO for calculation of the optical properties of subgrid shallow cumulus. The main logical switch for activating the parametrization is luse_qc_adiab_for_reffc_sgs. Additional logical switch luse_qc_con_sgs allows calculating the subgrid scale LWC of shallow cumulus using either $\overline{LWC}(z)$ parametrization or the LWC(z) derived from the shallow convection parametrization (lconv = T). alpha1_adiab_rad and alpha1_adiab_rad parameters describe $\overline{r_e}(z)$ above cloud base z_{cb} according: $alpha1_{adiab_{rad}} - alpha2_{adiab_{rad}} * (z - z_{cb})$. The parameter beta_adiab_rad describes the ratio of cloud-average N_d of SGS shallow convection with respect to the cloud core value obtained by the Segal-Khain parametrization. The parameter gamma_adiab_rad describes the linear deviation with height ($r_e > 12$ μm level) of SGS shallow convection LWC from the "pseudo-adiabatic" value. The list of parameters of the new parametrization is presented in Fig. 17. It includes the meaning of each parameter, its type, default value, available range and recommended value.

Parameter	Meaning	Type	Def	Range	Recom
luse_qc_adiab_for_reffc_sgs	Use "adiabatic" parametrization for SGS shallow convection effective radius	LOG	F	T/F	T
luse_qc_con_sgs	Effective if luse_qc_adiab_for_reffc_sgs=F. F: use "adiabatic" parametrization for SGS shallow convection LWC. T: use LWC from shallow convection parametrization (if lconv=T)	LOG	F	T/F	T
alpha1_adiab_rad	Linear deviation with height (above cloud base) of SGS shallow convection effective radius from the adiabatic value alpha1_adiab_rad-alpha2_adiab_rad*(z-zcb). [-]	REAL	0.95	[0.7-1]	0.95
alpha2_adiab_rad	Linear deviation with height (above cloud base) of SGS shallow convection effective radius from the adiabatic value alpha1_adiab_rad-alpha2_adiab_rad*(z-zcb). [1/m]	REAL	1.2 E-4	[1-2] E-4	1.2 E-4
beta_adiab_rad	Ratio of cloud-average number concentration (of SGS shallow convection) with respect to the cloud core value (obtained from Segal-Khain)	REAL	0.38	[0.2-1]	0.38
gamma_adiab_rad	Linear deviation with height (above reff=12micron level) of SGS shallow conv. qc from the "pseudo-adiabatic" value. [1/km]	REAL	0.45	[0.2-0.7]	0.45

Figure 17: List of parameters of the new adiabatic parametrization for LWC and r_e in shallow cumulus. The Table includes the meaning of each parameter, its type, default value, available range and recommended value.

6 New shallow convection shutdown scheme

(P. Khain)

6.1 Overview

Global Numerical Weather Prediction (NWP) models use convection parametrization to describe both deep and shallow convection. Convection permitting models with grid spacing below ∼4 km usually describe deep convection on grid scale, but still parametrize the shallow convection, being sub-grid scale process. Many of these parametrizations are based on the mass-flux approach. The artificial combination of resolved and parametrized convection often negatively influences the model forecast skill and particularly precipitation. In this task we used COSMO 2.5 km resolution over the Eastern Mediterranean region to analyse the effect of the mass-flux shallow convection parametrization (SCP) on model forecasts. We show that SCP entrainment rate as well as restrictions on the shallow convection development height and maximum updraft speed have crucial effect on the forecasts of precipitation, temperature and moisture. Physically motivated tuning of these parameters can improve the model forecasts significantly. Finally, we estimate the climatic zones and seasons where SCP is expected to be particularly important for NWP.

6.2 COSMO shallow convection parametrization

COSMO mass flux Tiedtke type SCP (Tiedtke, 1989) calculates the grid scale feedback of subgrid-scale vertical fluxes of mass, heat, moisture and momentum in updrafts. The convective-scale eddy transports of dry static energy, moisture and momentum from cumulus updrafts are not described in terms of contributions from the individual ensemble components, but are represented by their average values using a one dimensional bulk cloud

model after Yanai et al. (1973). The updraft of the cloud ensemble is assumed to be in steady state, and the budget equations for mass, heat, moisture and momentum for the ascending air (the "updraft equations") are integrated. For their integration the possibility for shallow convection at a grid point is diagnosed. At the first model level above the surface an air parcel is defined with the grid-scale values of temperature (plus a small excess value representing subgrid scale perturbation), specific humidity and horizontal momentum. Lifting the parcel adiabatically allows to compute its condensation level. This level defines the cloud base or the level of free convection, if the parcel becomes buoyant with respect to the environment. The parcels values of temperature, mixing ratio, water content, and horizontal wind components at cloud base are then used as boundary conditions to integrate the updraft equations. In the updraft, entrainment is assumed to occur via turbulent exchange of mass and is parametrized as proportional to the updraft mass flux with a proportionality constant entr_{sc}. This constant is treated as a tuning parameter in the model with a default value of 0.0003 m^{-1}. The vertical integration of the updraft equations from cloud base to cloud top, where the parcel is no more buoyant, yields the values of the variables within the updraft. These values are then used to calculate the convective tendencies in the prognostic equations for the grid-scale variables of dry static energy (related to temperature), specific humidity and the horizontal wind components. During the ascent, the supersaturated parcel is assumed to condensate all the excess water vapour immediately. Since it is assumed that SCP should not produce precipitation, the resulting liquid water content is neglected by the model in autoconversion and other microphysical processes. This assumption may lead to an underestimation of light precipitation in the model. Besides, subgrid-scale vertical mixing by SCP tends to stabilize the CBL and thus to postpone or even cancel potential grid scale updrafts which produce precipitation. These drawbacks led to the necessity to limit the SCP in the model by turning it off. I.e. cancelling the subgrid-scale vertical mixing, in cases when the test parcel described above remains buoyant and rises too high in the atmosphere. Therefore, a second tuning parameter $thick_{sc}$ was introduced with a default value is 25000 Pa. This is the maximal pressure difference between the top and the bottom of the convection, and for higher values the scheme is turned off.

Fig. 18 schematically shows the typical options occurring at the model time step in SCP in case the test parcel is buoyant at the cloud base. In case 1 the entrainment entr_{sc} is chosen to be high, causing the parcel to stop being buoyant (top of the convection) already at level k2. In case 2 entr_{sc} is chosen to be lower, and the convection top occurs at level k3. In case 3 the parcel remains buoyant till the level k4 and the resulting convection vertical extent exceeds the threshold $thick_{sc}$. At that time step the SCP is turned off in the entire grid column, keeping the unstable profile unmixed and allowing grid scale updrafts to develop. In case 4 the SCP is turned off while the grid scale updrafts lead to grid scale supersaturation and activation of in-cloud microphysical processes and precipitation. This schematic picture shows that $thick_{sc}$ may have an influence in weakly unstable conditions, or unstable ones topped by an inversion. On contrast, during the peaks of the cyclones passage, the instability usually extends up to height of several kilometres. In these situations SCP is turned off and one would not expect any influence of $thick_{sc}$.

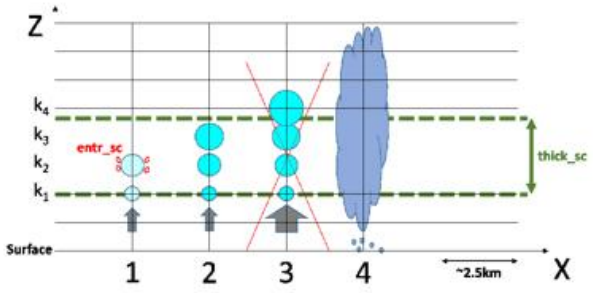


Figure 18: Schematic description of COSMO SCP. Case 1: $entr_{sc}$ is high, the top of the convection is at level k2. Case 2: $entr_{sc}$ is lower, the convection top occurs at level k3. Case 3: the convection vertical extent exceeds the threshold $thick_{sc}$. At that time step the SCP is turned off in the entire grid column. Case 4: the SCP is turned off, grid scale updrafts lead to grid scale supersaturation and activation of in-cloud microphysical processes and precipitation.

6.3 The effect of shallow convection parametrization on model forecast

At this section, cyclonic test case is used to explain the influence of the SCP on forecasts of precipitation. The selected test case occurred between December 30, 2015 and 2^{nd} of January, 2016. Fig. 19 presents the synoptic situation over the EM during these days using mean sea level pressure (MSLP) and geopotential height at 500 hPa from IFS analyses. One can see that the 500 hPa geopotential height over central Israel gradually drops from ∼5600 to ∼5500 m and then climbs back towards ∼5580 m.

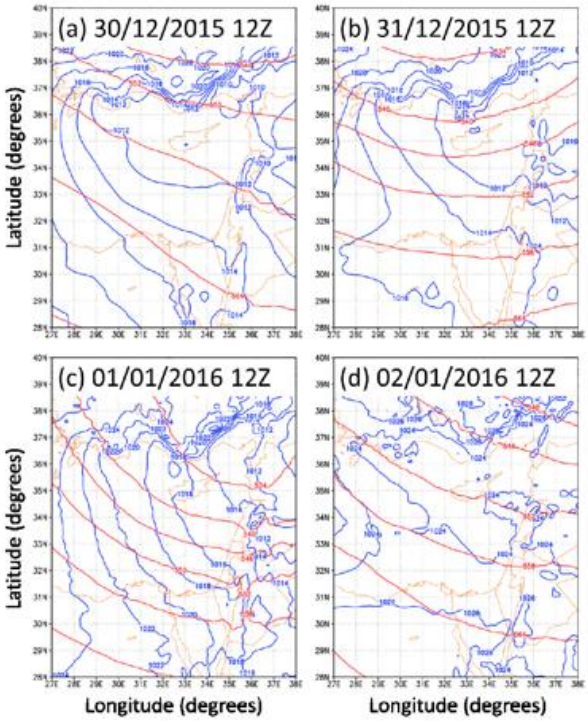


Figure 19: Cyclonic test case occurred during 30/12/2015-02/01/2016. The panels a-d show the IFS analyses of the mean sea-level pressure contours (blue lines) and the geopotential height (divided by 10) contours (red lines) for noon times (12Z) during the period.

It is a typical example of extratropical cyclones - the Cyprus Lows, which are responsible for most of the annual rainfall over the EM (Sharon and Kutiel, 1986; Alpert et al., 1990; Shay-El and Alpert, 1991; Ziv et al., 2006). The rain is formed within cold air masses of European origin that enter the region from the north-west. While moving over warmer Mediterranean waters, the air masses gain moisture and become conditionally unstable. The dynamics associated with the cyclone itself, together with that implied by the intersection of the westerly flow with the shoreline and, later on, with the mountain ridges, results in intensive rainfall over the Levant (Sharon and Kutiel, 1986). The concurrent upper-level system consists of a pronounced trough extending toward south-western Turkey. The upper trough over the EM induces cold advection aloft into the Cyprus Low region. Fig. 20 presents the initial (left panels) and the decay (right panels) stages of the cyclone evolution over the EM. The presented COSMO simulations were initiated on 30/12/2015 00 UTC (left panel) and on 01/01/2016 00 UTC (right panel).

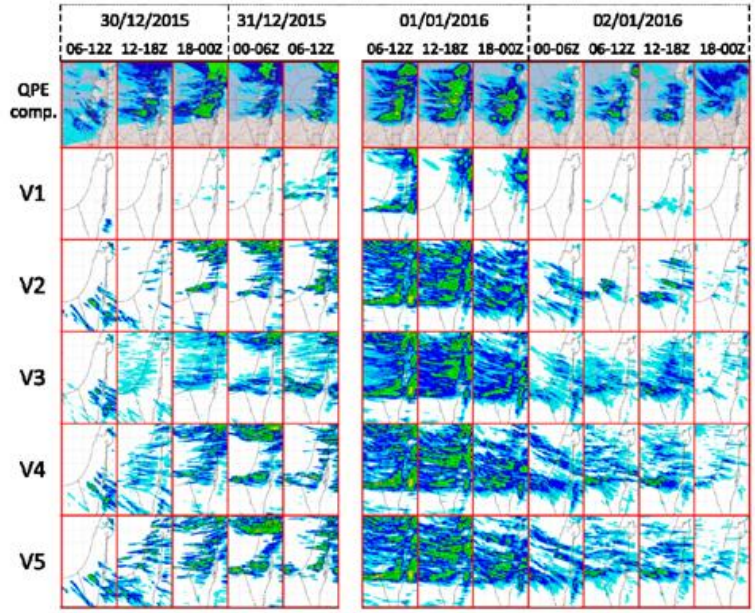


Figure 20: Initial (left panels) and the decay (right panels) stages of the Cyprus Low evolution over the EM (30/12/2015-02/01/2016). The QPE composite (first row) and five different COSMO SCP versions (see Table 3) forecasts are shown in 6hAP frames (rows 2-6). The peak of the cyclone evolution lasted for 18 hours during 31/12/2015 12Z – 01/01/2016 06Z and is not shown.

As explained in the previous section, the forecast for the peak of the cyclone evolution is not influenced by the SCP significantly. In this test case it lasted for 18 hours during 31/12/2015 12Z – 01/01/2016 06Z and is not shown. Fig. 20 (first row) presents the Quantitative Precipitation Estimation (QPE) composite evolution divided into 6 hourly accumulation periods (6hAPs). This QPE composite is compiled operationally at IMS using data from C-Band Doppler radar located in Bet Dagan and automatic rain gauges as described in Khain et al. (2020). The next five rows in Fig. 20 present 6hAP forecasts of the five COSMO versions (Table 3).

Version	$\boldsymbol{thick_{sc}}$ **[hPa]**	$\mathbf{entr_{sc}}$ **[m^{-1}]**	$\mathbf{W_{max}}$ **[m/s]**	**Rain strength**	**Rain Cover**
V1 (default)	25000	0.0003	-	Low	Low
V2	10000	0.0003	-	High	Low
V3	10000	0.003	-	Low	High
V4	10000	0.003	0.1	High	High
V4a	10000	0.003	0.3		
V4b	10000	0.003	0.15		
V4c	10000	0.003	0.05		
V5	SCP off	SCP off	SCP off	High	High

Table 3: Details of the five analysed versions of the COSMO SCP.

We begin the analysis of the five COSMO versions from comparing the "edge" versions V1 and V5, namely with very "active" SCP versus SCP turned off, respectively. Fig. 21 shows

the occurrence frequency of maximal over grid column wind speed and Convective Available Potential Energy (CAPE). The occurrence frequency was calculated for the period presented in Fig. 20 (30/12/2015-02/01/2016 without the 18 hours of the peak) over the sub domain 32-37E/29-34N.

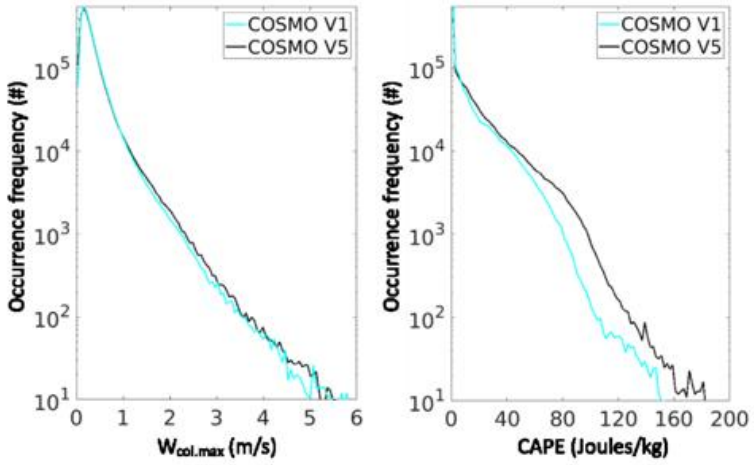


Figure 21: Occurrence frequency of (a) maximal over grid column wind speed and (b) CAPE. COSMO V1 (cyan) and V5 (black) are presented (see Table 3). The occurrence frequency was calculated for the period presented in Fig. 20 (30/12/2015-02/01/2016 without the 18 hours of the peak) over the sub domain 32-37E/29-34N. Note the logarithmic scale of y-axis.

As explained in the previous section, active SCP often weakens (or prevents) the evolution of grid scale convection and precipitation. Fig. 21 nicely shows that when the SCP is turned off, the updrafts are generally stronger and there are significantly more occurrences of high CAPE. As described in the previous section, COSMO SCP includes two tuning parameters. The first, $thick_{sc}$ (default value 25000 Pa), is the maximal vertical extent of the convection or the pressure difference between the top and the bottom, above which the scheme is automatically turned off. The second entr_{sc} (default value 3×10^{-4} m^{-1}) is the entrainment rate, which defines the mixing intensity of the rising parcel with the surrounding. As will be reasoned below, we added a third parameter, W_{max} (default value 0.1 m/s) which is the maximal grid scale updraft speed in a grid column above which the SCP is automatically turned off. Using the selected test case (see Fig. 6.3) we analyse five versions of the COSMO SCP (Table 3). Versions 1-3 differ by the values of $thick_{sc}$ and entr_{sc} parameters, while the effect of W_{max} is turned off. In version 4 we added changes in W_{max}. In version 5 we switch off the SCP so that convection may occur at grid scale only.

Spatial analysis of 6hAP precipitation which is presented in Fig. 20 (at the area covered by the radar) for QPE composite and precipitation forecast of various COSMO SCP versions yields the occurrence distributions (Fig. 22). The occurrence at each distribution bin, having width of 0.33 mm, reflects the average (over twelve 6hAP frames shown on Fig. 20) number of grid points which experienced 6hAP precipitation falling into that bin.

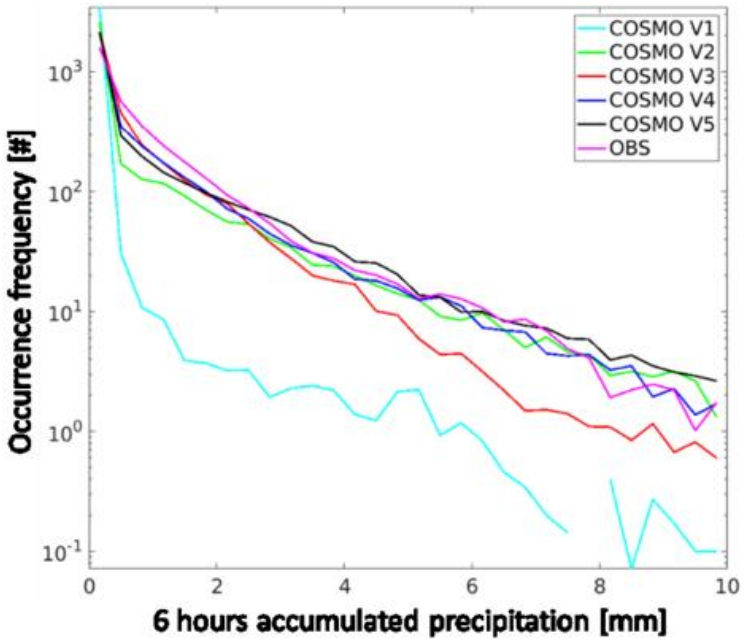


Figure 22: Occurrence distributions of precipitation over EM during a passage of Cyprus Low (30/12/2015-02/01/2016). The QPE composite (magenta) and five different COSMO SCP versions (see Table 3) forecasts are shown, respectively.

As can be seen from Fig. 20 and Fig. 22 (cyan compared to magenta), version 1 (see Table 3) strongly underestimates precipitation intensity and area. Having nearly adiabatic parcels and high permitted vertical extension (low entr_{sc} and high $thick_{sc}$, respectively), the SCP strongly mixes the lower atmosphere in vertical. This mixing ascends the water vapour from near the CBL top upwards into the free troposphere above the CBL. With less water vapour the grid-scale motions have lower potential producing grid-scale updrafts and precipitation.

Version 2 (V2) (green compared to magenta), performs better than V1, producing sufficiently strong precipitation. However, these strong precipitation spots are localized. Large areas still suffer from underestimation of weak precipitation. V2 differs from V1 by lower permitted vertical extension $thick_{sc}$. In strongly unstable areas the nearly adiabatic parcels (low entr_{sc}) can develop far above $thick_{sc}$. In these areas the SCP is turned off yielding proper grid scale updrafts and precipitation. In contrast, in weakly unstable areas the nearly adiabatic parcels do not reach the limit of $thick_{sc}$, the SCP is not turned off yielding strong vertical mixing and suppression of potential weak grid scale precipitation.

Version 3 (V3 - red compared to magenta), also shows positive results compared with V1, producing sufficiently wide precipitation cover. However it still suffers from underestimation of strong precipitation spots. V3 differs from V1 by lower permitted vertical extension $thick_{sc}$ and higher entrainment of the ascending parcels entr_{sc}. The physical motivation for increasing entr_{sc} and the choice of its value are explained in the next section. Similarly to V2, in weakly unstable areas the diluted parcels (high entr_{sc}) do not reach the limit of $thick_{sc}$ and the SCP is not turned off. However, here the vertical mixing is weak and the potential weak grid scale precipitation is not suppressed. Since SCP is rarely turned off, in strongly unstable areas these diluted parcels still cause significant vertical mixing partially suppressing potentially strong grid scale updrafts and precipitation.

Hence, in the framework of COSMO mass-flux SCP having two parameters for maximal

permitted vertical extension and the entrainment rate it seems impossible to reproduce the precipitation spatial distribution (magenta in Fig. 22) correctly. There is underestimation of either the cover by weak precipitation (version 2) or the strong precipitation values (version 3). Following the physical motivation behind version 3 (see Appendix), this version is chosen for further improvement. As mentioned above, in this version the SCP is rarely turned off even in strongly unstable situations. To solve this issue we added a third parameter (W_{max}, default value 0.1 m/s) which is the maximal grid scale updraft speed in a grid column above which the scheme is automatically turned off (version 4). The physical motivation is obvious – in grid column with sufficiently strong updraft, there is a potential for initiation of grid scale convection. In such column, switching off subgrid scale mixing by the SCP allows further CAPE development, followed by grid scale convection and precipitation. As can be seen from Fig. 20 (V4) and from Fig. 22 (blue compared to magenta), version 4 (Table 3) shows better results than versions 1-3, producing not only sufficiently wide precipitation cover but also sufficiently strong precipitation spots. The optimal value for W_{max} will be chosen following the tuning over ten test-cases (see next section).

A question arises, whether SCP is essential to the model, or it can be continuously turned off over the entire model domain. This test is conducted in version 5 (Table 3). As can be seen from Fig. 20 (V5) and from Fig. 22 (black compared to magenta), version 5 is of similar quality to version 4 producing sufficiently wide precipitation cover and sufficiently strong precipitation spots. However, SCP is essential in slightly unstable areas not covered by precipitation. In such areas lack of vertical mixing, which does occur at nature, may yield to concentration of heat and moisture at lower levels, causing wrong vertical profiles of temperature and humidity.

6.4 The entrainment rate parameter $entr_{sc}$

As explained in Sec. 6.2, the entrainment parameter entr_{sc} plays an important role in the SCP. Higher entr_{sc} values reduce both the intensity and the vertical extent of the mixing by the SCP. During the ascent, a parcel becomes saturated, yielding a condensation of water vapour to cloud water, resulting a profile of liquid water content LWC(z). This profile is closely related to entr_{sc}. For higher entr_{sc} values, the ascending parcel saturation is postponed, yielding smaller values of LWC. For entr_{sc}= 0 the parcel is raised adiabatically resulting in the highest possible value of LWC (hereafter, $\mathrm{LWC}_{ad}(z)$). Both $\mathrm{LWC}_{ad}(z)$ and the expected vertical profile of LWC in shallow Cu (hereafter, $\mathrm{LWC}_{cu}(z)$) are discussed in Khain et al., 2019. Obviously, COSMO mass flux SCP cannot reproduce the exact $\mathrm{LWC}_{cu}(z)$ produced by large-eddy-simulations and compared with observations. Still, comparison of LWC(z) with $\mathrm{LWC}_{cu}(z)$ may help setting up the correct value of entr_{sc}. For that purpose, we define LWC normalized adiabatic ratio averaged over height (z) above cloud base:

$$\mathrm{LWC}_{\mathrm{ratio}}=\overline{\frac{LWC\,(z)-LWC_{cu}(z)}{LWC_{ad}(z)-LWC_{cu}(z)}} \tag{23}$$

Positive (negative) values of $\mathrm{LWC}_{\mathrm{ratio}}$ indicate too large (small) LWC(z) and too small (large) entr_{sc}. The optimal value of entr_{sc} is obtained for $\mathrm{LWC}_{\mathrm{ratio}}\approx 0$. In order to estimate the optimal entr_{sc}, several values were selected: $3\cdot 10^{-6}$, $3\cdot 10^{-4}$, 10^{-3}, $3\cdot 10^{-3}$ and 10^{-2}. For each of these values, we have performed COSMO forecasts for two events, one in winter and one in summer, dominated by shallow convection. The first COSMO forecast was initiated on 23/02/2018 00 UTC, and the second – on 03/06/2018 00 UTC. For each 78 hours range forecast, all the grid columns with active shallow convection were analysed and the LWC(z) was plotted versus height above cloud base. Fig. 6.6 presents the vertically, horizontally and

time-averaged $\mathrm{LWC_{ratio}}$ versus entr_{sc} for winter case (red) and summer case (blue). One can see, that for negligible value of $\mathrm{entr}_{sc}=3\times10^{-6}\ m^{-1}$ $\mathrm{LWC_{ratio}}$ is close to one, meaning that COSMO shallow convection scheme describes adiabatically ascending parcels. For default COSMO value of $\mathrm{entr}_{sc}=3\times10^{-4}\ m^{-1}$, $\mathrm{LWC_{ratio}}$ is around 0.5, meaning strong overestimation of vertical mixing by the SCP. Note that for $\mathrm{entr}_{sc}=3\times10^{-3}\ m^{-1}$, $\mathrm{LWC_{ratio}}\approx0$, and therefore this value was chosen for further tuning of the SCP in Sec. 6.6.

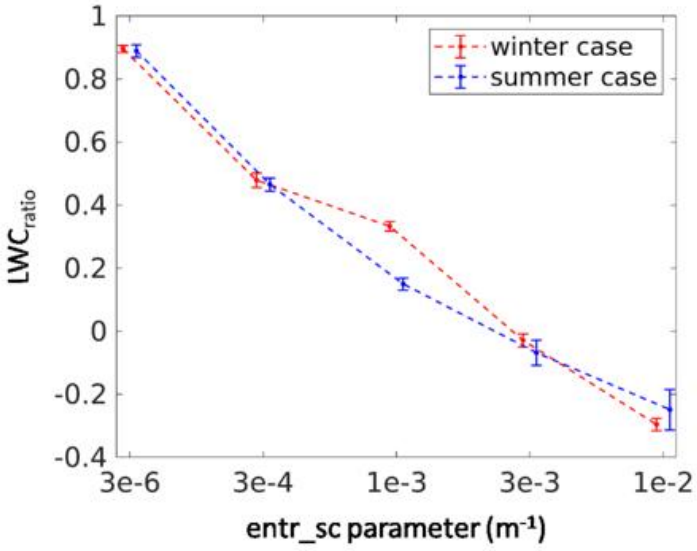


Figure 23: Vertically, horizontally and time-averaged LWC_{ratio} versus $entr_{sc}$ for winter case (23/2/2018 00 UTC run - red) and summer case (03/06/2018 00 UTC run - blue).

6.5 Evaluation of forecast quality

In order to analyse the forecasts quality two scores were chosen: precipitation verification score ΔFSS and temperature and humidity verification score T_RH_PROF.

6.5.1 Precipitation verification score ΔFSS

Due to the high variability of precipitation in space and time, it is common to verify it using Neighbourhood Methods. Here we use the Fractional Skill Score (FSS) (Roberts and Lean, 2008; Ebert, 2009; Mittermaier and Roberts, 2010). Besides FSS, additional neighbourhood methods of verification exist in the literature. These include extension of FSS to time dimension (Duc et al., 2013), scale-separation, object-based, and field deformation approaches (Davis et al. 2006a,b; Davis et al. 2009; Gilleland et al., 2009, 2010; Ben Bouallègue and Theis, 2014; Schwartz and Sobash, 2017). For each 6hAP forecasted and observed map, FSS was calculated for 30 km smoothing radius (see Khain et al. 2019 for the motivation) and for the thresholds of 0.01, 0.1, 0.5, 1, 2, 5, 10, 20 mm per 6h. The resulting FSSs were averaged over these thresholds, assuming double weight for the thresholds 0.5, 1, 2, 5 mm per 6h. The last are usually more important for the public than the negligible 0.01 and 0.1 mm per 6h and occur much more often than 10 and 20 mm per 6h. These averaged FSS were calculated both for COSMO and IFS and denoted as FSS_{COS} and FSS_{IFS}, respectively. Finally the precipitation verification score ΔFSS for each COSMO run was defined as:

$$\Delta FSS=\overline{FSS_{COS}-FSS_{IFS}} \tag{24}$$

where the average is over forecast ranges from +6h till +60h. ΔFSS varies in the range [-1,1], where ΔFSS>0 (ΔFSS<0) means COSMO precipitation forecasts are better (worse) than of IFS. As can be seen, IFS forecasts are of similar quality to those of COSMO, and it is convenient to use it as a reference.

6.5.2 Temperature and relative humidity score *T_RH_PROF*

The SCP is intended to vertically mix the CBL, and as such has a major influence on the temperature and relative humidity in the BL. In order to tune the scheme, we introduce the T_RH_PROF score which combines the verification of 2m-temperature and relative humidity versus stations measurements with the verification of the vertical profiles of temperature and mixing ratio versus radio-sounding data.

For each forecast initialized at 00 UTC the forecast ranges of +12h till +72h were verified at 12 hour steps. For 2-meter variables each forecast was verified versus 81 IMS stations over Israel, yielding RMSE for 2m-temperature and relative humidity (RMSET2m and RMSERH2m, respectively). For profiles verification we used the radio-sounding launched from Bet-Dagan (34.814E/32.007N) twice daily (at 00 and 12 UTC). Each model profile was interpolated on the radio-sounding measurements heights, and the RMSE was calculated giving five times larger weight to heights below 2 km above surface. The resulting RMSEs were averaged over the various forecast ranges yielding verification score for temperature profile (RMSETprof) and mixing ratio profile (RMSEQprof). These four scores were calculated for each COSMO (RMSET2m_cos, RMSERH2m_cos, RMSETprof_cos, RMSEQprof_cos) and IFS (RMSET2m_ifs, RMSERH2m_ifs, RMSETprof_ifs, RMSEQprof_ifs) forecast. Similarly to precipitation score described above, we normalize COSMO scores with respect to IFS and define $Skill_{field} \equiv 1-\frac{RMSE_{field_cos}}{RMSE_{field_ifs}}$, where $field$ can be T2m, TH2m, Tprof or Qprof. Finally, temperature and relative humidity verification score T_RH_PROF for each COSMO run is defined as:

$$T_RH_PROF=\frac{1}{4}\left(Skill_{T2m}+Skill_{RH2m}+Skill_{Tprof}+Skill_{Qprof}\right) \tag{25}$$

T_RH_PROF varies in the range $[-\infty,1]$, where $T_RH_{PROF} > 0$ ($T_RH_{PROF} < 0$) means COSMO precipitation forecasts are better (worse) than of IFS.

6.6 Tuning the shallow convection scheme

At this section we use ten typical rainy events first to show that turning off the SCP in cases of too strong grid scale updrafts (larger than W_{max}) improves the forecast, and second, to define the optimal W_{max}. Brief characteristics of the chosen events are summarized in Table 4. The chosen events are typical to rain season over EM. Usually during these 3-days long events significant parts of the simulation domain and the verification area are characterized by fair weather alongside unstable cyclonic areas. Therefore the following verification is not limited to rainy areas.

For each of the COSMO versions V1-V5 (see Table 3) a simulation was performed over the 10 chosen events (Table 4). In order to reveal the optimal W_{max}, three additional simulations V4a, V4b, V4c were performed using W_{max} values of 0.3, 0.15, 0.05 m/s, respectively. For

Chosen rainy events	**Model initiation time**	**Max. accum. precipit. (mm)**	**Peak time Bet-Dagan sounding**	**m.s.l pressure (hPa)**	**850 hPa temp. (C)**	**500 hPa geopot. height (m)**	**500 hPa temp. (C)**
12-14/ 12/2016	12/12 00 UTC	116	14/12 12UTC	1007	1.6	5510	-18.3
23-25/ 12/2016	23/12 00 UTC	76	25/12 00UTC	1011	1.6	5540	-19.3
11-13/ 02/2017	11/02 00 UTC	44	13/02 12UTC	1010	2.4	5530	-26.1
14-16/ 02/2017	14/02 00 UTC	68	16/02 00UTC	1112	0.0	5520	-21.9
12-14/ 04/2017	12/04 00 UTC	27	14/04 00UTC	1007	7.6	5650	-17.3
20-22/ 11/2017	20/11 00 UTC	47	22/11 00UTC	1011	4.6	5610	-18.9
05-07/ 12/2017	05/12 00 UTC	30	06/12 12UTC	1010	4.6	5600	-16.5
05-07/ 01/2018	05/01 00 UTC	66	05/01 12UTC	1001	3.6	5510	-22.3
18-20/ 01/2018	18/01 00 UTC	49	19/01 00UTC	1001	2.0	5420	-27.3
16-18/ 02/2018	16/02 00 UTC	66	17/02 12UTC	1007	3.0	5500	-25.3

Table 4: Characteristics of 10 selected rain events over EM. The columns from left to right represent: dates of each event; initiation time of COSMO run; maximum accumulated precipitation during the entire event at specific location; the time of sounding representing the peak of the event; Mean-sea-level pressure from the sounding; 850 hPa temperature from the sounding; 500 hPa geopotential height from the sounding; 500 hPa temperature from the sounding.

each simulation, the T-RH-PROF and ΔFSS scores were calculated. Fig. 24 presents ΔFSS (red dots) and T_RH_PROF (blue dots) for the various versions, calculated for the 10 chosen events. The dots were connected by straight lines to make the comparison of different versions more convenient.

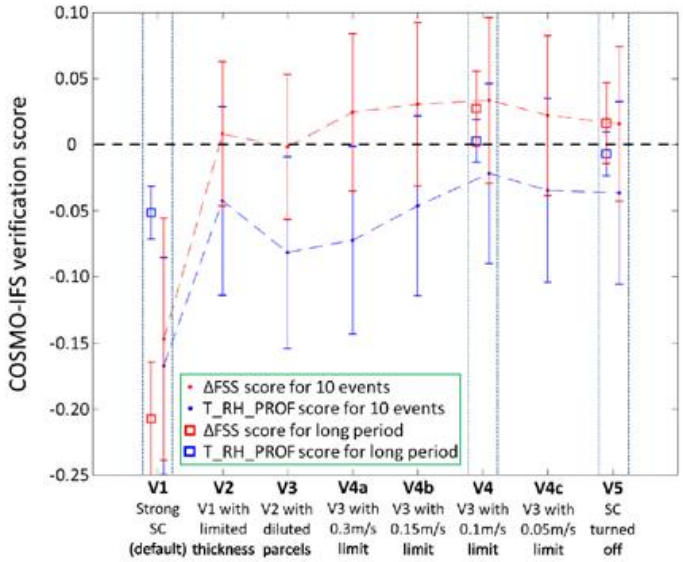


Figure 24: ΔFSS (red dots) and T_RH_PROF (blue dots) verification scores for the various versions (Table 3), calculated for the 10 chosen rain events (Table 4). The dots were connected by straight lines to make the comparison of different versions more convenient. The verification scores ΔFSS and T_RH_PROF for the entire winter season 01/11/2017-31/03/2018 are presented by red and blue squares, respectively.

One can see that reduction of the maximum allowed thickness for the shallow convection ($thick_{sc}$ parameter) significantly improves the forecast (V2 vs. V1). As mentioned above, this limitation is crucial as it allows the grid scale convection to develop. The increase of the entrainment rate (entr_{sc} parameter), which is physically motivated in the appendix, slightly worsens the forecast (V3 vs. V2). As discusses in the previous section (Figs. 20 and 22), V3 improves the weak precipitation coverage at the expense of deterioration of strong precipitation. Introduction of maximum allowed updraft (W_{max} parameter) for the shallow convection further improves the forecast. One can see a pronounced optimum at W_{max}= 0.1 m/s (version V4). At first glance, such low value seems too weak for realistic shallow convection. However, this grid scale value represents an averaged updraft over the model grid box of about $(2.5\ km)^2$. For higher horizontal resolutions W_{max} has to be retuned, and higher values are expected. Back to the current resolution, reduction of W_{max} towards 0.05 m/s (version V4c) slightly worsens the forecast. In this configuration the SCP switches off too frequently even in fair weather conditions, and is not replaced by grid scale vertical mixing. Such configuration mistakenly keeps the lower atmosphere unmixed, yielding in slight degradation of the verification scores. Finally, continuous switching off the SCP over the entire domain (V5) shows additional slight degradation of the performance.

At last, we show that the above tuning based on 10 rainy events indeed improves the wintertime forecasts over the EM. Versions V1 (default – strong SCP), V4 (optimum) and V5 (no SCP) were used to perform simulations over an entire winter season 01/11/2017-31/03/2018 (in total 151 72h-long simulations for each version). The verification scores T_RH_PROF

and ΔFSS were calculated for the entire period and are presented on Fig. 24 designated by blue and red squares, respectively. One can see that V4 is indeed optimal. However, the advantage over V5 (no SCP) is not significant. In rainy days switching off SCP might indeed be as good as V4 version, and definitely much better than activating the default SCP (version V1). On contrast, in fair weather days switching off SCP deteriorates the forecast. To prove it we performed similar analysis over all the fair weather forecasts, total of 75 cases, during the period 01/11/2017-31/03/2018. To isolate the main effect of the SCP, we focused on temperature verification part of 25 i.e. $T_PROF_T = \frac{1}{2}(Skill_{T2m} + Skill_{Tprof})$ during day times of each forecast (three 12 UTC values). It turns out that $\mathrm{T_{PROF_T}} = -0.0001 \pm 0.0204$ for version V4 (optimal) which is significantly better than $\mathrm{T_{PROF_T}} = -0.0472 \pm 0.0227$ for V5 (no SCP).

6.7 Discussion and conclusions

NWP models in convection permitting resolution often resolve deep convection but parametrize the shallow convection. This combination may have negative effect significantly influencing the model forecast. Majority of SCPs used in NWP convection permitting models are based on the mass-flux approach. In this work we analysed the effect of the widely used mass-flux SCP on COSMO model forecasts in convection permitting resolution of 2.5 km. On one side, the default configuration of the SCP turns out to be too active, causing decay of precipitation. On the other side, in fair weather without SCP the vertical mixing in the PBL is underestimated yielding degradation of temperature profiles. It turns out that even within the framework of regular mass-flux SCP, one can still find a delicate compromise by limiting the SCP activity. This compromise can be achieved by limiting the vertical extent, the entrainment rate and the updraft speed of the parametrized SC. The effect of each of the limitations thoroughly analysed using a test case of cyclone passage over the eastern Mediterranean (EM). Physically motivated tuning of the related parameters was performed using ten rainy events showing significant forecast improvement, which was validated based on entire rain season over the EM.

We now address the question whether SCP is important in other climatic zones except of EM. Although this question can be a topic of a different study, we provide a rough estimate below. As was shown, SCP significantly influences the forecast in unstable stratifications topped by an inversion around 800 to 500 hPa, as well as in weakly unstable situations. It is, however, not influencing severe situations with strongly unstable stratification reaching the upper troposphere. It is also not playing role in stable stratification dominated by stratiform precipitation. Although there are exceptions related to local climate, generally the central European climate is characterized by stratiform precipitation during wintertime and strongly convective during summertime. The Mediterranean climate is generally characterized by moderate convective precipitation during wintertime, strong convective events during autumn and spring, and dry summer. These weather types can be reasonably distinguished by CAPE values. In order to demonstrate these characteristics, we analysed the CAPE climatology in 8 sounding locations (Table 5) - 4 characterized by Mediterranean climate (hereafter “Mediterranean”) and 4 more characterized by central European climate (hereafter “European”).

For each location, twice daily (00 and 12 UTC) sounding data was retrieved for 20 years period 1/1/2000-31/12/2019 (www.weather.uwyo.edu/upperair/sounding.html). At each location at least 6000 available records exist allowing calculation of CAPE. Moreover, each of these stations provides 6 hourly precipitation measurements. In order to focus on rainy events, we selected only those CAPE values where there was non zero precipitation during

Sounding station	**Station number**	**Location**	**Latitude** (deg.)	**Longitude** (deg.)	**Climate**
Bet-Dagan	40179	Bet-Dagan (central Israel)	32.00	34.81	"Mediterranean"
LIRE Pratica di Mare	16245	Rome (central Italy)	41.65	12.43	"Mediterranean"
LIBR Brindisi	16320	Brindisi (south east Italy)	40.65	17.95	"Mediterranean"
LFKJ Ajaccio	07761	Ajaccio (Corsica, France)	41.91	8.80	"Mediterranean"
Praha-Libus	11520	Prague (Czech Republic)	50.00	14.45	"European"
EHDB De Bilt	06260	De Bilt (Netherlands)	52.10	5.18	"European"
LSMP Payerne	06610	Payerne (Switzerland)	46.81	6.95	"European"
LIML Milano	16080	Milan (North Italy)	45.43	9.28	"European"

Table 5: Sounding stations selected for CAPE analysis.

the last 6 hours. Fig. 25 shows the 90th percentile of monthly CAPE values at 4 "Mediterranean" locations (solid lines) and 4 "European" locations (dashed lines). Monthly CAPE values based on sample sizes below 30 were neglected.

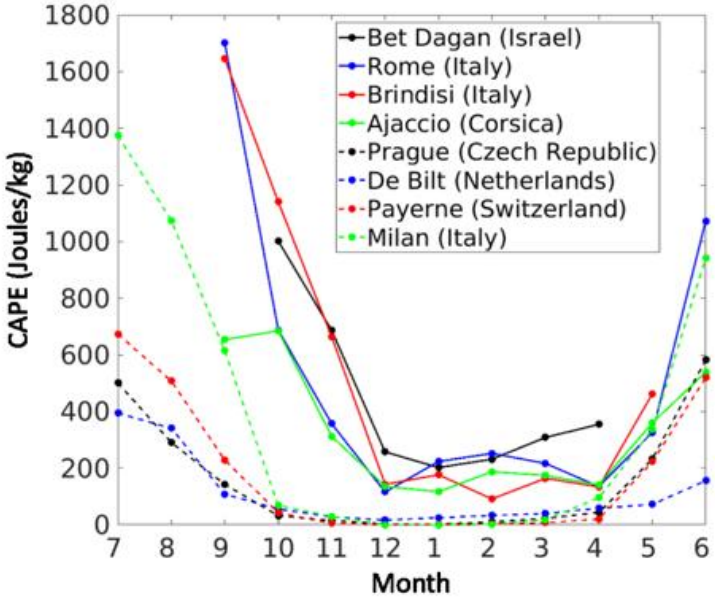


Figure 25: 90th percentile of monthly CAPE values at 4 "Mediterranean" locations (solid lines) and 4 "European" locations (dashed lines). The sample contains twice daily (00 and 12 UTC) sounding data for the period 1/1/2000-31/12/2019. Only CAPE values with non-zero precipitation during the last 6 hours were selected. Monthly CAPE values based on sample sizes below 30 were neglected.

As expected, during wintertime the "Mediterranean" locations are characterized by moderate CAPE around 100-300 J/kg. These are the values where SCP is expected to play an important role. However, wintertime at "European" locations is characterized by stratiform precipitation and hence negligible CAPE (below 50 J/kg). Consequently, we do not expect SCP to play an important role during European winter. Generally, the autumn and spring at the "Mediterranean" locations and summertime at the "European" locations are characterized by strong convective precipitation with high values of CAPE (300-1700 J/kg). SCP is automatically turned off in these cases and is not expected to influence the forecast. We do expect the SCP to influence the forecast during European autumn and spring where the CAPE values are moderate. The above statements are general and there are many exceptions. For example, De Bilt (Netherlands) shows moderate CAPE also during summer, so that SCP might be important there as well. Hence, in order to estimate whether and during which seasons the SCP is an important factor in NWP, one has to look at local climatology of CAPE.

To conclude, nowadays many weather forecasting centres run convection permitting NWP models, and often face difficulties obtaining satisfactory forecasts, particularly of precipitation. As mentioned, majority of these models resolve deep convection and use mass-flux approach to parametrize the shallow convection. This study shows that SCP configuration might be of crucial importance to the model forecasts. We believe that it sheds light on the numerical processes through which SCP affects the model forecasts, and most importantly, it provides a recipe to improve them.

7 Implementation of CAMS forecasted aerosols in COSMO radiation and microphysics schemes

(H. Muskatel, U. Blahak, P. Khain)

7.1 Introduction

Operational NWP models requires assessment of aerosols loads for both radiation transfer calculations (direct effect) and for microphysical parametrizations of liquid droplets activation and ice particles heterogeneous nucleation processes (indirect effect). Two approaches are often chosen for aerosols evaluation. First is using climatology values where yearly fixed values are chosen for each aerosol species as in Tanre climatology (Tanre et al., 1984, itype_aerosol = 1) or monthly means as in Tegen (Tegen et al., 1997, itype_aerosol = 2) and MACv2 (Kinne et al. 2013, itype_aerosol = 3) climatologies. All the three options mentioned above are available in the latest COSMO-CLOUDRAD version. In this approach the computational effort is minimal but air pollution events are neglected and sometimes severely degrade forecast skills (i.e. in dust outbreaks or volcanic eruptions events). The second approach is online-coupling of NWP models with aerosols and reactive trace gasses forecast. In these models (i.e. COSMO-ART and ICON-ART) the aerosols are treated as additional tracers and processes like emissions, wet and dry deposition, sedimentation and transport need to be explicitly calculated. This approach is usually expensive in terms of CPU consumption. As a result, it is operationally used as parallel modules to operational run with lower spatial resolution (i.e. ICON-ART-dust runs in DWD) or non-operationally upon demand (i.e. COSMO-ART). In this project we offered a third approach where the offline low resolution fully-coupled aerosols models forecast outputs are used as an input for the operational non-coupled LAM model. In this chapter we describe the use of CAMS-ECMWF forecasted aerosols as input for COSMO radiation and microphysics schemes while in chapter 8 we will discuss the use of ICON-ART-dust forecast. In this new approach the advantages compared to aerosols climatology is obvious since synoptic scale events including aerosols are included while being neglected in aerosols climatology approach. Since COSMO boundary and initial conditions are taken from global models (i.e. IFS or ICON), using the forecasted global aerosols based on these forecasting systems is a natural choice. The difference between interpolating atmospheric fields such as temperature and pressure from the driving model to the use of aerosols fields is that the data is updated in time, as for boundary conditions data, but for applied to the entire domain. The values of aerosols mixing ratios in 3D between two snapshots of aerosols fields are interpolated in space and time by INT2LM. The computational cost during runtime is minimal, since most calculations are performed in the pre-processing stage. Technically, INT2LM needs double run: once for the regular driving model and once for the aerosols. The initial and boundary files are later combined. The disadvantage of such method is that the aerosols are not coupled with COSMO dynamics but being advected, washed-out etc., only by the offline global aerosols model (i.e. CAMS). Differences in dynamics between the aerosols model and COSMO may lead to errors. Nevertheless, in the everlasting conflict between model realism and computational cost, we show that this is a fair compromise for operational NWP applications.

7.2 CAMS aerosols forecasting system

The Copernicus Atmosphere Monitoring Service (CAMS, formerly series of MACC projects) is an ECMWF project that provides near-real-time analysis and forecast of atmospheric

composition: aerosols, reactive gases, greenhouse gases, ozone, UV radiation and more. The aerosols 5-days ahead forecast is available twice a day with a 1-hour resolution. CAMS is based on IFS model with additional prognostic aerosols which are interactive with the dynamics and physics of the parent model (Morcrette et al. 2009). The processes treated are: emissions sources (some are updated in near-real-time), horizontal and vertical advection, dry and deposition, sedimentation and hygroscopicity. CAMS includes aerosols data assimilation using MODIS Terra and Aqua aerosols optical depth (AOD) and verified against AERONET AOD. The forecasted aerosols are mineral dust (MD) divided to three size bins, sea salt (SS) also with three size bins, black carbon (BC) and organic matter (OM) which both includes hydrophilic and hydrophobic species and Sulfate (SU). In Fig. 26 CAMS aerosols size limits, mode radius r_{mode} and geometric standard deviation σ of the log-normal distributions used to describe particle size distribution are presented. The mean volume particle masses of each species was numerically calculated using the formula:

Aerosol type	Size limits [μm]	r_{mode} [μm]	σ	modes weights	ρ [kg/m^3]	Particle mean mass [kg] at RH=80%	Soluble fraction
Sea salt	[0.03, 0.5]	0.1992, 1.992	1.9, 2.0	0.959, 0.041	1153	$7.80 \cdot 10^{-17}$	1
Sea salt	[0.5, 5]	0.1992, 1.992	1.9, 2.0	0.958, 0.042	1153	$3.33 \cdot 10^{-15}$	1
Sea salt	[5, 20]	0.1992, 1.992	1.9, 2.0	0.957, 0.043	1153	$9.34 \cdot 10^{-15}$	1
Dust	[0.03, 0.55]	0.29	2.00	1	2610	$2.87 \cdot 10^{-16}$	0.1
Dust	[0.55, 0.9]	0.29	2.00	1	2610	$4.73 \cdot 10^{-16}$	0.1
Dust	[0.9, 20]	0.29	2.00	1	2610	$1.56 \cdot 10^{-15}$	0.1
OM Hydrophilic	[0.005, 20]	0.0212	2.24	1	1800	$4.00 \cdot 10^{-18}$	0.59
OM Hydrophobic	[0.005, 20]	0.471, 0.0118	2.51, 2.0	$4.8 \cdot 10^{-6}$, 0.999952	2000, 1000	$4.91 \cdot 10^{-19}$	0
BC Hydrophilic	[0.005, 5]	0.0118	2.00	1	1000	$1.78 \cdot 10^{-19}$	1
BC Hydrophobic	[0.005, 5]	0.0118	2.00	1	1000	$5.98 \cdot 10^{-20}$	0
Sulfate	[0.005, 20]	0.0355	2.00	1	1760	$9.38 \cdot 10^{-18}$	1

Figure 26: CAMS aerosols size limits, mode radius r_{mode} and geometric standard deviation σ of the log-normal distributions used for particle size distribution. Sea salt and hydrophobic organic matter are described by a bimodal log-normal distributions with mode weights given in the third column from the right. ρ is the particle density. The particles mean masses were numerically calculated using Eq. 26.

$$\overline{m_v} = \frac{4\pi}{3}\rho \int_{r_{min}}^{r_{max}} r^3 \frac{1}{\sqrt{2\pi} ln\sigma \cdot r} \exp\left\{-\frac{1}{2}\left[\frac{\ln(r/r_{mode})}{ln\sigma}\right]^2\right\} dr \tag{26}$$

7.3 CAMS aerosols direct effect on radiation

7.3.1 CAMS aerosols optical properties

CAMS aerosols optical properties namely the extinction coefficient, the asymmetry factor and single scattering albedo, were originally calculated for IFS radiation RRTM scheme. This model has 16 wavelength intervals in the long-wave range (LW) and 14 intervals in the short wave (SW) range (A. Bozzo, private communication, 2016). In COSMO RG92 scheme there are only 5 intervals for LW and 3 intervals in the SW. Therefore, a special spectral averaging similar to the averaging procedure performed for ice particle as explained in Muskatel et al. (2021), was used to transfer the IFS high spectral resolution data to COSMO radiation scheme. The calculation includes weighting of the solar irradiance intensity at each wavelength according to Planck's function and layer thickness. The optical properties of the sea salt, sulfate and hydrophilic organic matter depend on relative humidity (RH) due to their growth factor in presence of water vapour. Larger RH usually results in

larger single-scattering albedo, extinction coefficient and asymmetry factor but these properties also depend on wavelength. An example for sea salt asymmetry factor for different RH for four COSMO spectral intervals are shown in Fig. 27. For the first time in COSMO radiation scheme, the optical properties of aerosols at each grid point is RH dependent.

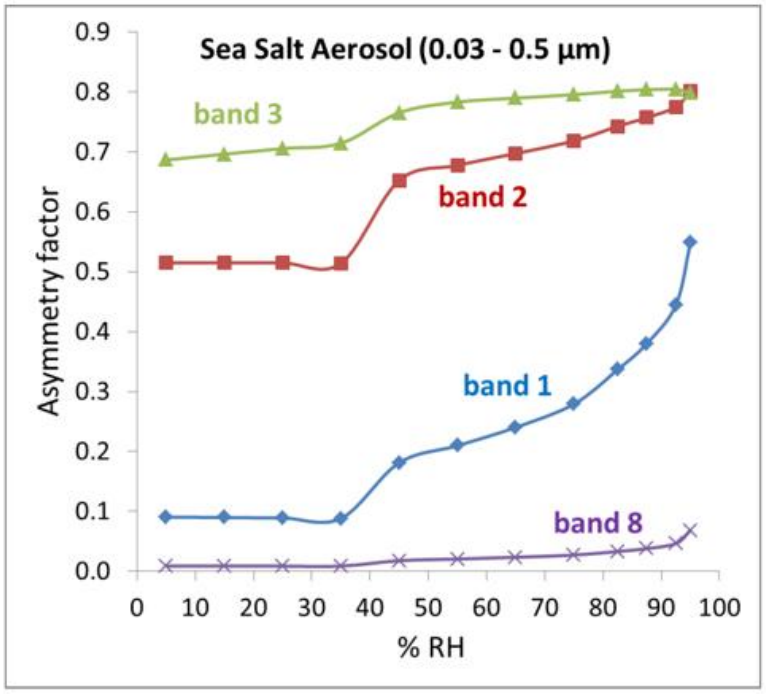


Figure 27: An example for CAMS aerosols asymmetry factor values of sea salt as function of relative humidity for COSMO bands 1 ($1.53\ \mu m - 4.64\ \mu m$), 2 ($0.7\ \mu m - 1.53\ \mu m$), 3 ($0.25\ \mu m - 0.7\ \mu m$), 8 ($4.64\ \mu m - 8.33\ \mu m$) data adapted from IFS RRTM radiation scheme (A. Bozzo, private communication, 2016) to COSMO RG92.

7.3.2 Testing the direct effect of CAMS aerosols on COSMO radiation

Direct effect of CAMS aerosols load in COSMO radiation scheme compared to other aerosols inputs were tested in several frameworks. The first is a using data from 10 selected radiation stations in Israel and two AERONET stations AOD measurements in Sede-Boker and Technion (see Fig. 28).

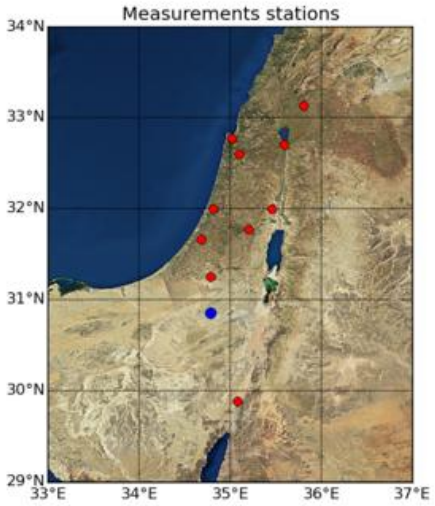


Figure 28: Israel satellite image with the locations of 10 IMS radiation (red dots) and 2 AERONET (blue dots) measurements stations. The data sets from these stations were used for the verification of COSMO aerosols inputs scenarios.

In the first verification, 29 selected test cases for mixed weather situations in the years 2015-2016 were chosen. The forecast range was either 30 or 42 hours using COSMO 5.0 version with spatial resolution of 2.8 km on IMS domain (see Fig. 37). Four versions were compared: the operational COSMO version with Tanre climatology, the new CLOUDRAD scheme with Tanre climatology, Tegen climatology and CAMS forecasted aerosols. The observational AOD data was taken from the AERONET station in Sede-Boker. In Fig. 29 one can see the models setup results for clear skies conditions. The cloudiness was defined by the model cloud cover. The points from all stations and hours of the day appear in one plot, model vs. observation. The 1:1 (black) line represents the ideal forecast. One can see that in both operational and the new CLOUDRAD versions, if Tanre climatology is used, the radiation is underestimated, which indicates an AOD overestimation. The negative bias almost disappears when using the new CLOUDRAD with both Tegen climatology or CAMS forecasted aerosols due to smaller error in AOD estimation (see Fig. 30). The AOD and global radiation bias and RMSE of climatology/model against 10 radiation stations and AERONET measurements in Sede-Boker for 7 test cases are presented in Fig. 30. The average RMSE and bias for these 7 clear skies cases and another 22 cloudy skies days are summarized in Fig. 26. The advantage of Tegen and CAMS over Tanre seems to vanish in cloudy skies condition probably due to the model tuning which was adapted to the operational setup.

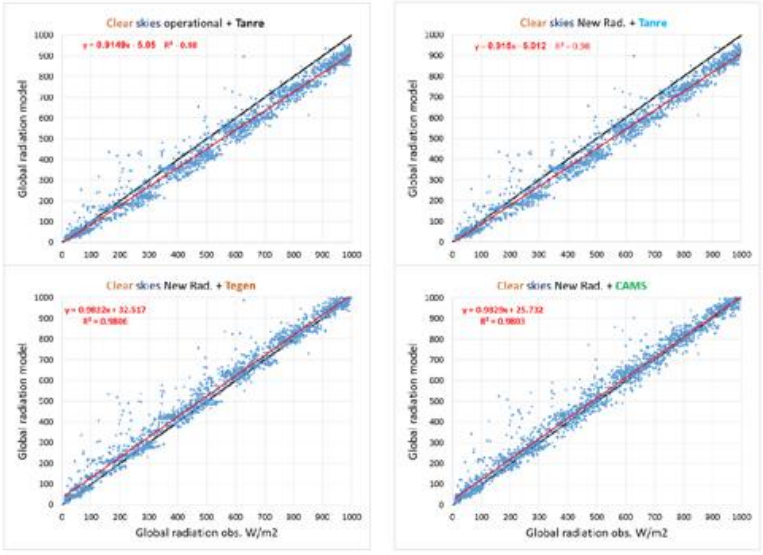


Figure 29: Clear skies conditions results for four radiation setups: operational COSMO version with Tanre climatology (upper left), new CLOUDRAD scheme with Tanre climatology (upper right), new CLOUDRAD with Tegen climatology (lower left) and new CLOUDRAD with CAMS forecasted aerosols (lower right) against measurements from 10 radiation stations in Israel. The 1:1 black line is the ideal match and red line is the linear fit between model and observation.

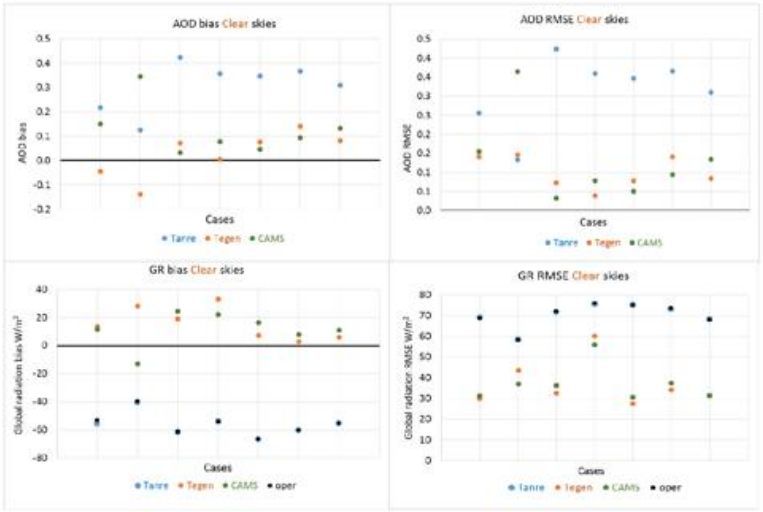


Figure 30: Clear skies conditions results for 7 test cases (17-18 May 2015, 14 and 26 February 2016, 18 April 2016, 19 and 24 June 2016) for four radiation setups: operational COSMO version with Tanre climatology (black), new CLOUDRAD scheme with Tanre climatology (Azure), new CLOUDRAD with Tegen climatology (orange) and new CLOUDRAD with CAMS forecasted aerosols (green). Upper panels show the AOD bias (left) and RMSE (right) climatology vs. measurement in AERONET station in Sede-Boker. Lower panels display the bias and RMSE of global radiation against measurements in 10 radiation stations in Israel.

Model	Clear skies (7 test cases)				Cloudy skies (22 test cases)			
	AOD		Global Radiation W/m^2		AOD		Global Radiation W/m^2	
	bias	RMSE	bias	RMSE	bias	RMSE	bias	RMSE
Tanre	0.31	0.31	-56.2	70.1	0.20	0.28	-11.1	131.5
Tegen	0.03	0.10	15.6	37.0	-0.12	0.17	54.2	140.5
CAMS	0.12	0.13	11.4	37.1	0.11	0.14	40.7	140.4

Figure 31: Clear skies (7 test cases) and cloudy (22 test cases) conditions results for three aerosols models input for COSMO-CLOUDRAD radiation scheme. AOD bias and RMSE calculated against AERONET data in Sede-Boker. Global radiation bias and RMSE are against measurements in 10 radiation stations in Israel (see Fig. 28).

Proper tuning of the CLOUDRAD version improves the scores even for cloudy skies conditions as can be seen in Fig. 32. In this Fig. the global radiation results for three models are presented: ECMWF-IFS with CAMS climatology (red), COSMO operational scheme with Tanre climatology and CLOUDRAD with CAMS forecasted aerosols. The period is July-August 2019 in IMS operational domain and verified against 17 ground based stations. Cloudy/clear skies definition was made by using CMSAF cloud cover product (https://www.cmsaf.eu) where clear/cloudy skies situations are defined when all models and satellite observation CLC is lower/larger than 5/95 % respectively. The RMSE for CLOUDRAD-CAMS version is the lowest compared to IFS and operational COSMO-Tanre version which has the largest RMSE for the entire period (Fig. 32 Upper-left). In the upper-right panel of Fig. 32 we see that the occurrences of errors larger than 50 W/m^2 (fiascos) in global radiation forecast is smallest in CLOUDRAD-CAMS compared to other models. Nevertheless, the mean bias of CLOUDRAD-CAMS is comparable to IFS in cloudy conditions (lower-left) and slightly higher than IFS. The bias of operational COSMO-Tanre is in the order of $\sim$50 W/m^2 in both cloudy and clear skies. COUDRAD-CAMS improved the bias also in cloudy skies conditions, indicates that the tuning procedure (see Sec. 10) significantly improved model skill.

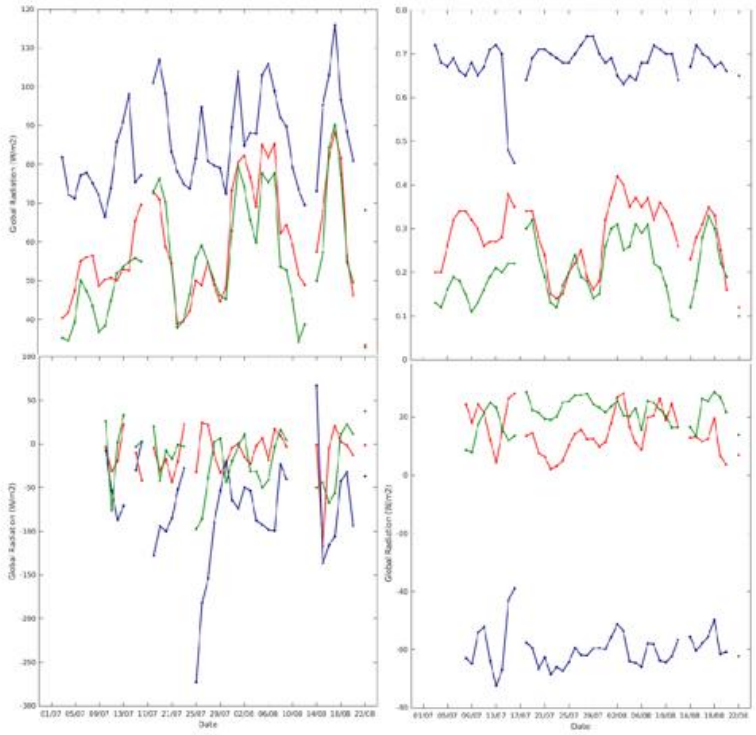


Figure 32: Global radiation results for three models: ECMWF-IFS with CAMS climatology (red), COSMO operational scheme with Tanre climatology (blue) and CLOUDRAD with CAMS forecasted aerosols (green). For the period July-August 2019 in IMS operational domain and is verified against 17 ground based stations in Israel. Upper left: global radiation RMSE [W/m^2], upper right: occurrences of fiascos where model error was larger than 50 W/m^2, lower left/right: cloudy/clear skies global radiation bias [W/m^2].

7.4 CAMS aerosols indirect effect on radiation

7.4.1 Water droplets number concentration and effective radius

The effective size and number concentration of water droplets significantly affect the cloud optical thickness. Fig. 4a shows that for the same total water path, changing droplets number concentration (tuning parameter cloud_num_rad) from 500 cm^{-3} ($R_{eff} \approx 4\ \mu m$) to 50 cm^{-3} ($R_{eff} \approx 9\ \mu m$) can change the global radiation on the surface from ~300 W/m^2 to ~450 W/m^2. In the operational radiation scheme (iradpar_cloud = 1) the effective size is defined by the formula: $\mathrm{R}_{eff} = \mathrm{c}_7 + \mathrm{c}_8 LWC$ (Ritter and Geleyn 1992) without an explicit dependency on number concentration. The effective radius in the new CLOUDRAD scheme (iradpar_cloud = 4) is calculated from the number concentration following the formula:

$$\mathrm{R}_{eff} = \mathrm{c}_1 \left(\frac{LWC}{\mathrm{n}_c} \right)^{\mathrm{c}_2} \tag{27}$$

Where n_c is the cloud droplets number concentration and $\mathrm{c}_{1,2}$ are coefficients related to the particle size distribution used by the microphysical scheme.

Formula 27 is used for grid scale clouds. For sub-grid scale (SGS) clouds, LWC is by definition zero. In the default radiation scheme, a tuning parameter (luse_reff_ini_x_as_reffx_sgs) is used

to define a fixed effective radius for SGS clouds and the tuning parameter for this background effective radius is reff_ini_c (default 5 μm). In the new CLOUDRAD scheme we added the option of calculating SGS effective radius in the same way done by grid scale clouds by setting luse_reff_ini_x_as_reffx_sgs=.FALSE.. In this case, formula 27 will be used with a special treatment to LWC as was discussed in Sec. 5.

Unlike the default radiation scheme where the chosen value for cloud_num_rad is effective at each cloudy grid box (default value 200 cm^{-3}), the new CLOUDRAD scheme (iradpar_cloud = 4, cloud_num_type_rad = 1) the number concentration is defined by setting cloud_num_rad as the value for cloud base and decreasing according to the vertical profile formula:

$$\mathrm{n}_c = \mathrm{n}_{c0} \cdot exp\left(-\frac{z - z_0}{\Delta z_{1/e}}\right) \tag{28}$$

Where z_0 is the cloud base height (tuning parameter zref_cloud_num_rad, default value 2000 m) and $1/\Delta z_{1/e}$ is the rate constant (tuning parameter dz_oe_cloud_num_rad , default 6000 m). n_{c0} is defined by the tuning parameter cloud_num_rad.

7.4.2 Water droplets activation using Segal and Khain (2006) scheme

In numerous studies it was shown that cloud droplets number concentration depends on aerosols concentrations (Segal and Khain, 2006, SK2006 hereafter) since the aerosols serve as condensation nuclei according to Kohler theory. In pristine atmosphere (i.e. in the Pacific Ocean) the aerosols number concentration is relatively small hence the cloud droplets number concentration is small and the cloud droplets effective radius is large. In a polluted atmosphere, cloud number concentration is higher. The limited humidity is spread on more particles resulting smaller droplets and optically thicker clouds. Using a simplistic estimations of cloud number concentrations based on fixed values at cloud base is unrealistic in most cases. In the new CLOUDRAD scheme we added the SK2006 activation scheme for cloud formation parametrization even in the 1-moment microphysical scheme (cloud_num_type_rad = 2). Segal and Khain (2006) used LES simulations with 2000-bin microphysics to parametrize cloud number concentrations as function of both vertical velocity at cloud base and aerosols size distribution. SK2006 is suitable for both stratiform and cumulus clouds in maritime, continental or extreme continental environments. They showed that the aerosols soluble concentration is the dominant factor in the resulted CCN concentrations. the realization of SK2006 in COSMO is by using 4D LUT to define n_c at cloud base using 4 parameters:

$$\mathrm{n}_{c,CB} = \mathrm{f}(\mathrm{N}_{CN,CB},\ log\sigma_{CN},\ r_{CN},\ w_{CB}^{eff}) \tag{29}$$

where σ_{CN} and r_{CN} are the geometric standard deviation and mode radius of the aerosols lognormal distribution (see Eq. 26), N_{CN} is the aerosols number concentration at cloud base which can be taken from CAMS (itype_aerosol = 4) or Tegen climatology (itype_aerosol = 2). w_{CB}^{eff} is the effective updraft speed for nucleation at cloud base.

When Tegen aerosols are used, the lognormal distribution parameters are fixed to the values $\sigma_{CN} = 0.3$ and $r_{CN} = 0.0335\ \mu m$. Aerosols number concentration for each of the species in Tegen climatology (dust, organic matter, sulfate and sea salt) are computed from optical depth assuming vertical exponential profile confined in the space between COSMO topography and 12 km height (the original Tegen topography is unavailable). The total N_{CN} is a summation over all species but with the soluble fraction consideration where dust soluble fraction is 0.9 and organic matter 0.9. Sulfate and sea salt are considered 100% soluble.

If CAMS aerosols are chosen as input for SK2006 activation scheme (cloud_num_type_rad = 2; itype_aerosol = 4), effective parameters for the lognormal distributions for the mixture of aerosols need to be calculated at each grid point. Weighted soluble particles number concentration $\overline{N}$, effective mode radius $\overline{r}$ and standard deviation $\overline{\sigma_g}$ are calculated according the formulas:

$$\overline{N_{CN}} = \sum_i N_i s_i \tag{30}$$

$$\overline{r} = \frac{1}{\overline{N}} \sum_i N_i s_i r_i \tag{31}$$

$$\overline{\sigma_g} = \sqrt{\frac{1}{\overline{N}} \sum_i N_i s_i \left[\sigma_{g,i}^2 + (r_i/\overline{r})^2\right]} \tag{32}$$

where r_i, $\sigma_{g,i}$, s_i are the mode radius, geometric standard deviation and the soluble fraction of each aerosol specie i detailed in Table 26. N_i are the number concentrations at each grid point for each species which are calculated from the 3D mixing ratios, $w_{a,i}$ $[kg{\cdot}kg^{-1}]$, provided by CAMS for each time step and each grid point:

$$(7.8) N_i(x,y,z) = w_{a,i}(x,y,z) \cdot \rho_{air}(x,y,z)/\overline{m_{v,i}}$$

where $\overline{m_{v,i}}$ are the mean (volume) particle masses of each aerosol tracer (see Eq. 26 and Table 26).

The appropriate vertical velocity for aerosol activation should be representative of adiabatic and diabatic cooling within updraft regions to parametrize supersaturation build-up during cloud condensation:

$$w_{eff} = \overline{w} + 0.7\sqrt{\frac{2TKE}{6}} - \frac{c_p}{g}\frac{\partial T}{\partial t} \tag{33}$$

Where $\overline{w}$ is the vertical velocity at cloud base, the middle term is the turbulence term and the third is the equivalent adiabatic updraft speed from radiative cooling.

For convective clouds, the option for imposing surface-based convective velocity scale as a lower limit diagnosed from convective cloud cover and theta-profile is implemented (name list parameter lincl_wstar_in_weff = .true.):

$$w_{CB}^{eff} = \max(\mathrm{w}_{eff}, \quad w^*) \tag{34}$$

$$w^* = \left(-g z_{topcon} \frac{\overline{w'\Theta'_{v,s}}}{\overline{\Theta'_{v,s}}}\right)^{1/3} \tag{35}$$

where z_{topcon} is the upper boundary of the convective PBL, Θ is the virtual potential temperature at PBL height (Deardorff, 1970).

As mentioned before, the cloud droplets number concentration is calculated at cloud base height which is diagnosed by scanning each column from bottom to top for first grid box with positive LWC or positive convective cloud cover. From this point and higher an exponential

profile decay is imposed using formula 28. If the effective updraft above cloud base is larger than the updraft calculated at cloud base (not a common situation), in-cloud nucleation is considered and the procedure detailed above is repeated but imposing the profile from half height between the cloud base and the actual height.

7.4.3 Using Segal and Khain (2006) scheme in the 1-moment microphysics

So far we discussed the direct and indirect effects of aerosols on radiation. In reality, the first and most important impact of aerosols is on cloud nucleation and dynamics. Clouds are the first factor effecting the radiation fluxes in the atmosphere covering roughly half of earth's surface. On the other hand, the very existence of clouds depends on the presence of aerosols. In pristine environments the cloud number concentration is usually low and the droplets are large. This will allow precipitation in the early stages of the cloud life which may suppress further development of the clouds to sever thunderstorms. In such situations, stratiform precipitation is expected and in cold temperatures, snow. In polluted environments higher cloud number concentrations are expected. In a humid environment, the droplets will grow slowly and can delay cloud formation and allow energy build up with stronger updrafts at later stages of cloud life (Rosenfeld et al., 2008). As a result, thunderstorms can develop with liquid and ice (graupel and hail) precipitation is possible. Nevertheless, extremely polluted environments results very high cloud number concentrations results in very small droplets which evaporate hence cloud formation is prevented (Rosenfeld et al., 2008).

In COSMO 1-moment microphysical scheme a size distribution is assumed and the mass fraction q^x can be predicted. The microphysical processes are determined by q^x. Cloud number concentration n_c is explicitly used only in the autoconversion rate parametrization (Seifert and Beheng ,2001)

$$S_{au} = \alpha \cdot q_c^4 / n_c^2 \tag{36}$$

$$\alpha = \frac{k_c}{20x^*} \frac{(\nu+2)(\nu+4)}{(k_c+1)^2} \tag{37}$$

Where S_{au} is the transfer rate due to autoconversion of cloud water, x^* is the separating mass between cloud and rain, k_c is the kernel coefficient for autoconversion and ν is the gamma exponent for cloud distribution. In the default COSMO 1-moment scheme n_c is a constant tuning parameter (default cloud_num = 500 cm^{-3}). In the new CLOUDRAD scheme n_c can be calculated as was described in details for the radiation in the previous section using the name list parameter icloud_num_type_gscp = 2. Here again, n_c will be calculated with SK2006 parametrization with Tegen climatology (itype_aerosol = 2) or CAMS forecasted aerosols (itype_aerosol = 4) as input aerosols for SK2006.

7.4.4 Case study - April 25-27, 2018

We examined the new CLOUDRAD radiation and microphysical scheme with CAMS aerosols and Segal & Khain droplet activation scheme using the event of 25-27/04/2018. In these three days of stormy weather in Israel, massive storm cells developed causing flush floods which caused the death of 14 people. Among them, 10 teenage hikers in the Eastern Negev on April 26, 2018. A low pressure system evolved in the Sinai Peninsula moving east (see

Fig. 33). Hot and humid air in lower layers along with cold air in the upper atmosphere caused extreme unstable atmosphere.

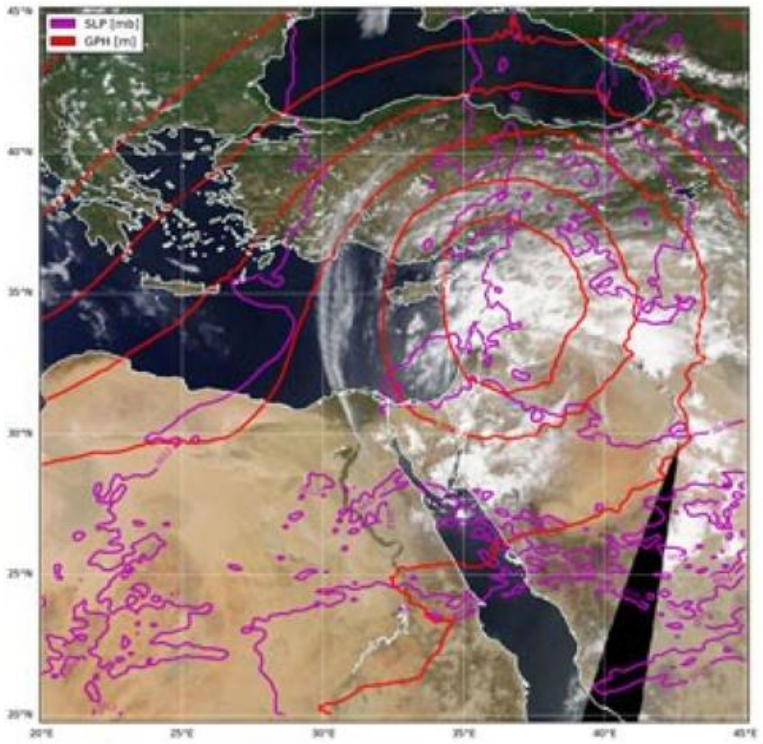


Figure 33: Synoptic analysis 26 April 2018 at 12:00 UTC, MODIS True Color RGB over Eastern Mediterranean. Red lines represents ECMWF analysis. Courtesy of Elyakom Vadislavsky.

The examination of CAMS aerosols cross sections for this highly convective event, reveals a diurnal cycle. The aerosols in all three days of the event are drifted upward by the convection at noon and descend at nights in a breath-like motion. A single snapshot of the event at April 25, at 14:00 UTC will be analysed here. Fig. 34 shows a cross section at 32N from 34E to 36 E from the Mediterranean Sea near Tel-Aviv to Amman in Jordan. The total hydrophobic aerosols concentration at cloud base heights (1000 m - 2000 m) reached 15000 cm^{-3} (Fig. 34 upper left panel) which is a typical number for polluted continental areas (Hess et al. 1998) especially in highly convective weather. Most of these hydrophobic aerosols are sulfate particles (lower right panel).

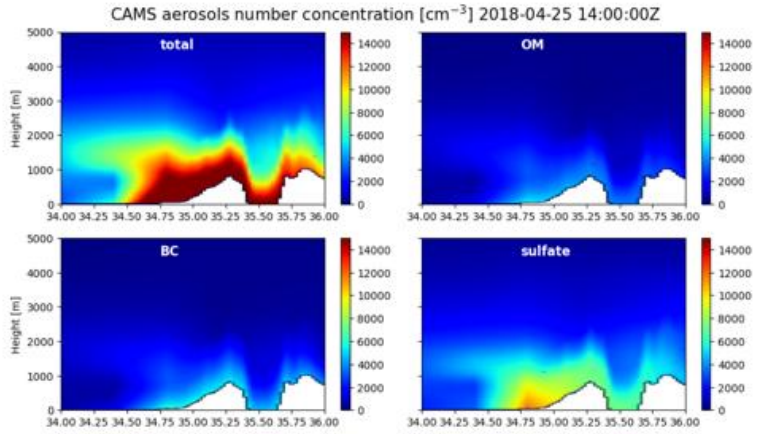


Figure 34: CAMS forecast for the 25^{th} of April 2018 at 14:00 UTC. A cross-section at 32N going from 34E to 36E. Top left: total hydrophilic CAMS aerosols number concentrations, top right: organic matter, bottom left: black carbon and bottom right: sulfate concentrations.

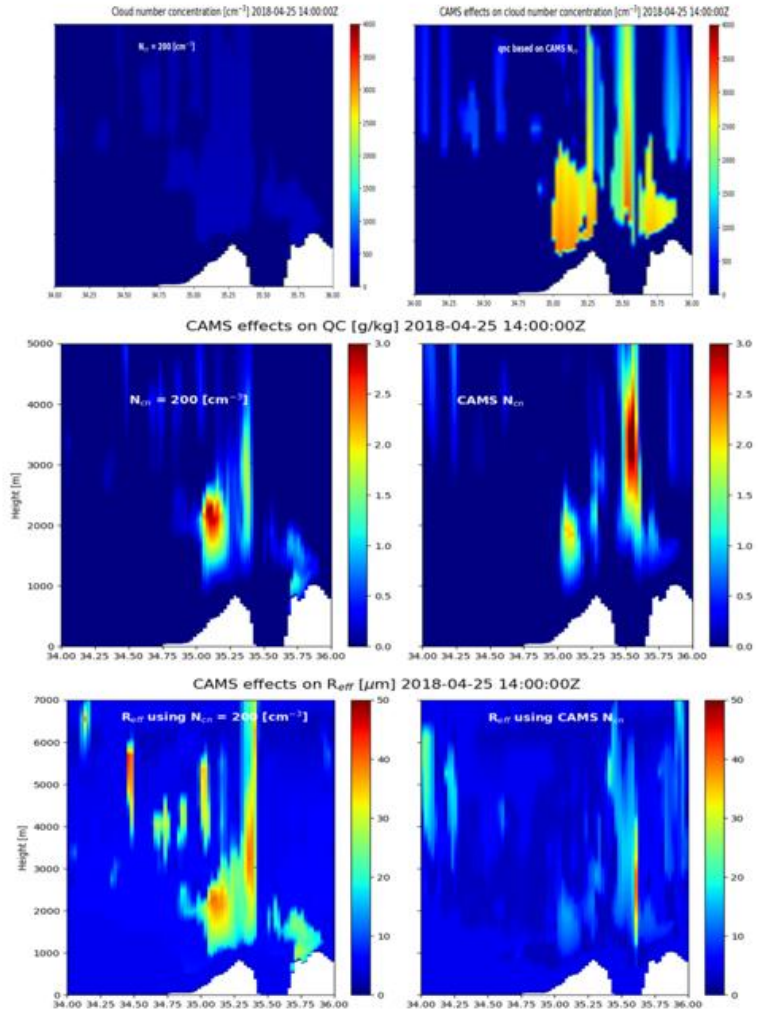


Figure 35: profiles for the 25^{th} of April 2018 at 14:00 UTC. Left panels: cloud number concentration using fixed value (cloud_num_rad = 2.0E+08) at cloud base and an assumed vertical profile. Right panels: CAMS forecast aerosols as input for Segal & Khain 2006 cloud activations scheme. Upper row: cloud number concentration profile $[cm^{-3}]$, midle row: LWC $[g/kg]$, lower row: droplets effective radius $[\mu m]$. The "noodle" shape of cloud is a result of the horizontal and vertical scales.

Fig. 35 shows the results for two model setups. The left panels represents the fixed number concentration at cloud base of 200 cm^{-3} and using a profile as described in formula 28 (cloud_num_type_rad = 1, cloud_num_rad = 2.0E+08). On the right panels SK2006 droplets activation scheme with CAMS aerosols are displayed (cloud_num_type_rad = 2; itype_aerosol = 4). The upper panels display cloud number concentrations profiles. One can see that the number concentrations of cloud droplets above Judea and Jordan mountains when using prognostic aerosols and SK2006 activation scheme are significantly higher than other areas and also compared to the default scheme (left panel). It is a result of both high aerosols densities at this hour and large updraft speeds due to deep convection and high instability of the atmosphere. The cloud number concentrations are diagnostic and are effective only at grid boxes with positive LWC. The middle panels of Fig. 35 show the LWC profiles for these two models. The clouds location and water load are significantly different. For example, the massive clouds above the Dead Sea at 36E are not present in the default scheme and can cause extreme flash floods in this area. Lower panels show results for the effective radius.

The prognostic scheme results in much smaller droplets.

The lower panels of Fig. 35 explain the immense effect of using forecasted aerosols and realistic cloud activation on the radiation. The clouds droplets are much smaller and with much larger densities which lead to a significant increase in cloud optical thickness (see Fig. 4). In Fig. 36 the results for the entire domain is presented. The colours indicates the points occurrences in the domain. The first row shown the cloud number concentration as a function of aerosols concentrations when SK2006 scheme is used in all grid points (left) and at cloud base (right). The cloud number concentrations can reach numbers as high as $3000\ cm^{-3}$ which may seem too large. Nevertheless, close inspection reveals that most points at cloud base have cloud number densities less than $1000\ cm^{-3}$ with an average of $621\ cm^{-3}$, a reasonable value for highly convective and polluted environments. As expected, the high $n_{c,CB}$ numbers are achieved when effective updraft speeds w_{nuc} are high as can be seen in the middle row of Fig. 36. The effective vertical wind speeds at cloud base can reach $\sim 3m/s$ (middle row right figure) while in the rest of the domain, at higher altitudes, the updraft can climb to much higher values (middle row, left panel).

The first two rows of Fig. 36 associate only with the CAMS and SK2006 configuration while the third raw shows the results of the two models setups described in Fig. 35. The effective radius as function of LWC is plotted enlightening the conclusion drafted from the lower panels of Fig. 35. We can clearly see that using forecasted aerosols combined with parametrized droplets activation can lead to more realistic droplet sizes of $\sim 7\mu m$ for continental clouds (see i.e. Fig. 6 in Reid et al. 1999) while using a fixed cloud number concentrations can cause large mistakes in cloud effective size and as a result, large errors in cloud optical thickness.

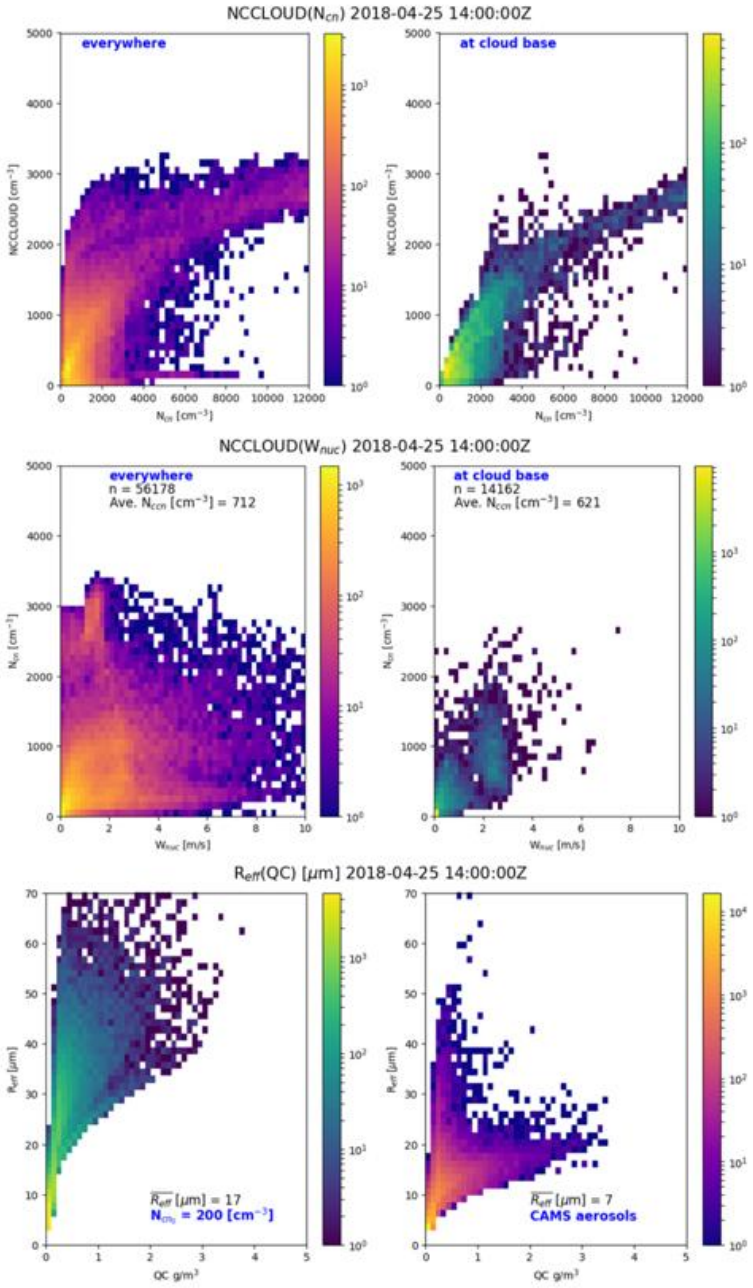


Figure 36: Upper row: droplet concentration as a function of aerosols number concentration $[cm^{-3}]$, middle row: droplet concentration as a function of effective updraft speed for nucleation $[m/s]$ (left: all points, right: at cloud base). Lower row: droplets effective radius $[\mu m]$ as a function of LWC [g/kg] (left: fixed droplet number concentration at cloud base, right: SK2006 activation scheme with CAMS forecasted aerosols.

In the previous sections we discussed the direct and indirect effects of the new SK2006 activation scheme radiation. While in Sec. 7.4.3 we discussed the influence of aerosols on the 1-moment microphysics scheme (on the auto-conversion rate). It can be done by using the name-list parameters icloud_num_type_rad/gscp in which setting each to the value of 2 will turn on the SK2006 activation scheme with the chosen aerosols input (Tegen or CAMS). The sensitivity of the model to each of these effects is presented in Fig. 37. For all four model configurations shown here, the aerosols input was CAMS (itype_aerosol =

4). The same test case was chosen but now the 11:00 UTC snapshot is taken to examine the effects on the maximum radiation at noon time. The upper four figures show incoming shortwave downward radiation on surface (global radiation) while the lower four show the 2m-Temperature. In each of these pair of four figures the upper left is for the new radiation scheme using fixed droplet number concentration (cloud_num_rad = 200 cm^{-3}) at cloud base icloud_num_type_rad/gscp = 1. In this configuration only the direct aerosols effect is activated. This setup will serve as a control run for which the absolute values are visualized. The other three figures shows the biases to the control run when we activate the indirect effects. Upper right panel represent the resulted bias due to turning SK2006 on but effective only in radiation (icloud_num_type_rad = 2). Lower left panel is the same but effective only in the microphysics (icloud_num_type_gscp = 2) and results when both effects are turned on icloud_num_type_rad/gscp = 2 are shown in lower right panel. The numbers on each of the three models are calculated over all model surface grid points compared to the control run in Wm^{-2} for the upper figures and K in the lower figures.

Analysis of these figures show that the indirect effect cloud droplets activation scheme on both radiation and microphysical schemes is significant. The biases of radiation/temperature can be as large as 300 Wm^{-2} / 3 K respectively. Although the RMSE and bias numbers appearing in each Fig. are a result of the average on all grid points where most of them are cloudless, these averages are unneglectable (bias ~ -7 Wm^{-2}, -0.04 K , RMSE $\sim$ 70 Wm^{-2}, 0.35 K). As expected, the use of CAMS aerosols which have larger number concentrations in this test case, reduced the droplet effective radius compared to the default scheme which in turns reduced the radiation on surface and the 2m-temperature. Surprisingly, the use of realistic aerosols and cloud activation scheme effected the microphysics (auto-conversion rate) in a way that caused significant changes in radiation but with smaller absolute values (RMSE $\sim$ 40 Wm^{-2}, 0.2 K). In this case, the radiation and temperature bias is almost zero since the effective radius of droplets was unaffected.

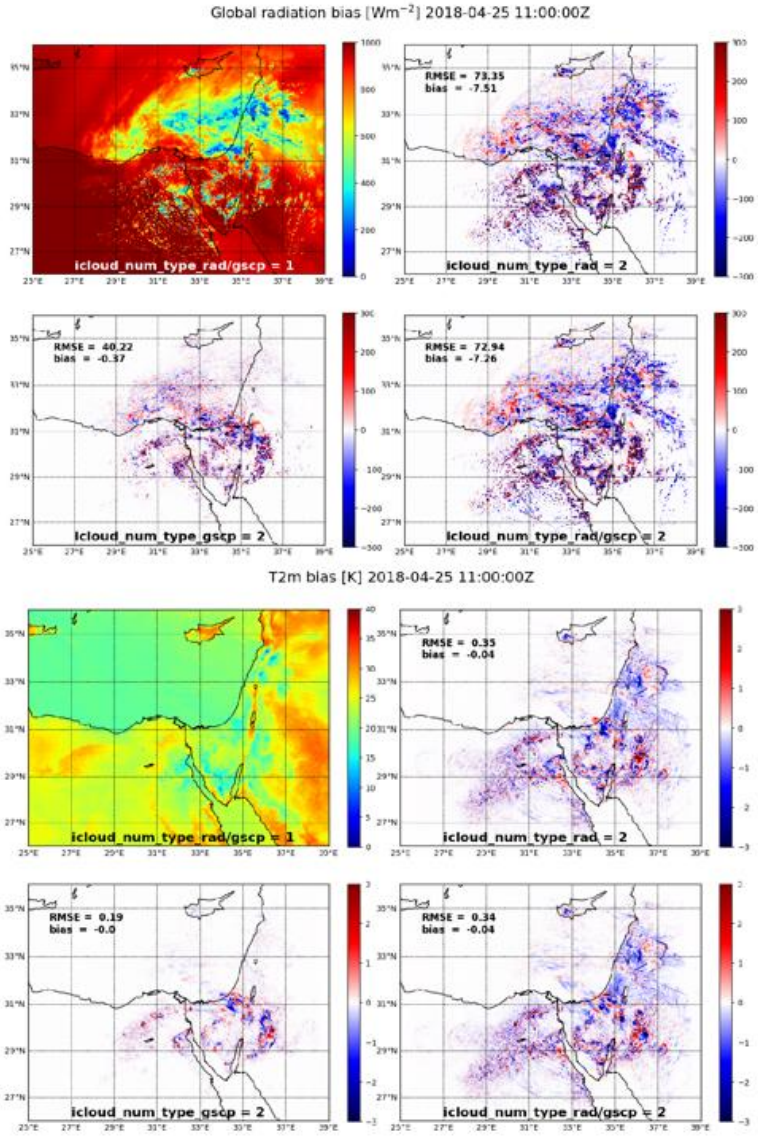


Figure 37: Global radiation (upper four figures) and Temperature (lower four figures) biases as a result of the indirect effects of SK2006 cloud activation scheme using CAMS forecasted aerosols. See text for details.

7.4.5 Ice nucleation scheme model inter-comparison using a case study

In Sec. 7.4.4, we showed the model results for the case study of 25-27-April-2020. In this chapter we will show the model sensitivity to the ice nucleation scenarios. The four models described in the previous section: the 1-moment scheme using Cooper (1986) parametrization (default), 1-moment microphysics using DeMott (2015) parametrization with CAMS dust forecasted fields, 2-moment microphysics with Phillips (2008) parametrization using fixed aerosols number concentrations and 2-moment scheme using CAMS 3D forecasted aerosols input. An example result of an atmospheric cross-section of IN concentrations for the 25-Apr-2020 14:00 UTC is presented in Fig. 38. We can see that the default Cooper (1986) scheme (upper left panel) underestimates IN concentrations compared with other models having no aerosols data as input. Fig. 39 presents the dust aerosols cross section for the same snapshot. The dust number concentration at ice cloud heights can reach a few tens

of dust particles per litter. As a result, high IN umber concentration can be seen in the DeMott (2015) parametrization (upper right) – the highest amongst all models. Since both ice supersaturation and the updraft speeds are not taken into account, high concentrations of ice cannot be seen in the cumulonimbus cloud formed at longitude 35°E. The 2-moment microphysics with Phillips (2008) ice nucleation scheme did simulate the formation of ice in this cloud at heights 4000-8000 meters where high vertical speeds and supersaturation values were found. Smaller number concentration were achieved using fixed aerosols concentration (lower left) compared to the forecasted CAMS input (lower right). The Phillips (2008) scheme also underestimated the IN concentration at cold temperatures (< 240K) compared to DeMott (2015) scheme. Fig. 40 displays the four models output of IN as a function of temperature for the same hour where brighter colours means higher occurrences in the domain for grid points with LWC $> 0.03\ g/m^3$. The numbers inserts are the domain averages. The DeMott parametrization result at this snapshot has an average IN concentration of 401 $[1/L]$ which is a factor of 4 larger than the default Cooper scheme and a factor of 7-10 larger than the averages of the Phillips (2008) nucleation scheme. The effect of the IN concentrations on the effective ice particle size can be seen in Fig. 41 where the average ice particle size for the DeMott scheme is $18\mu m$ while the default 1-mom scheme using Cooper is $24\mu m$, Phillips (2008) default 2-mom scheme resulted averaged size of $74\mu m$ and the same scheme using CAMS aerosols average is $56\mu m$. The effects on the IWC itself can be seen in Fig. 42.

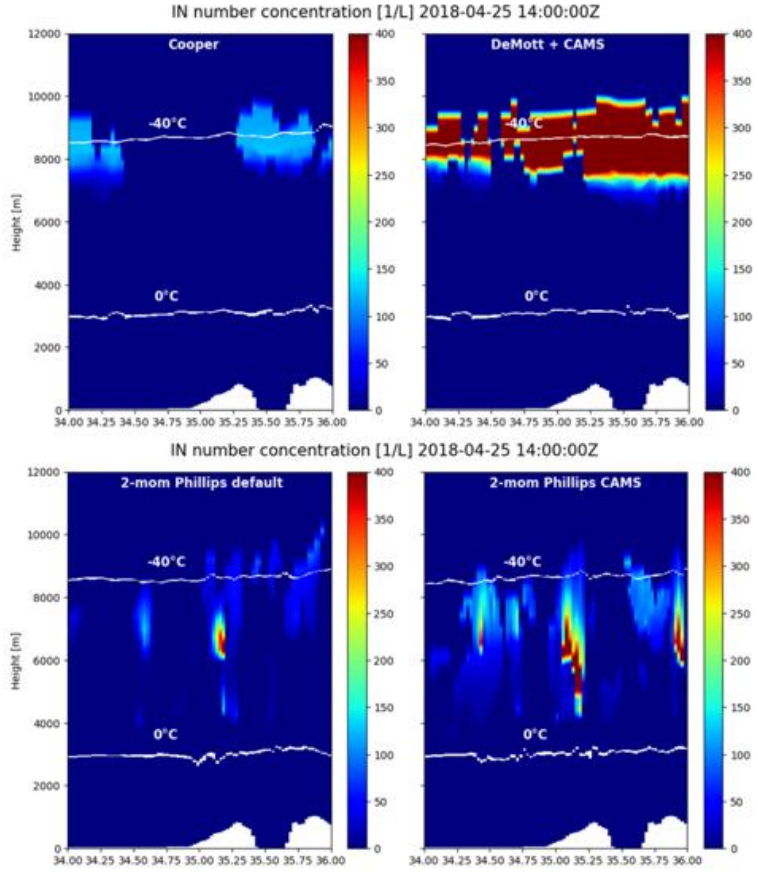


Figure 38: IN profiles in $[1/L]$ units for 1-moment microphysics using Cooper (1986) nucleation parametrization (upper left), 1-moment scheme using DeMott (2015) formulation using CAMS dust forecasted aerosols (upper right), 2-moment scheme using Phillips (2008) using default fixed aerosols number concentrations (lower left) and the same scheme using the 3D CAMS forecasted insoluble aerosols as input (lower right). The two white lines are the ice melting level and (roughly) the ice spontaneous freezing levels.

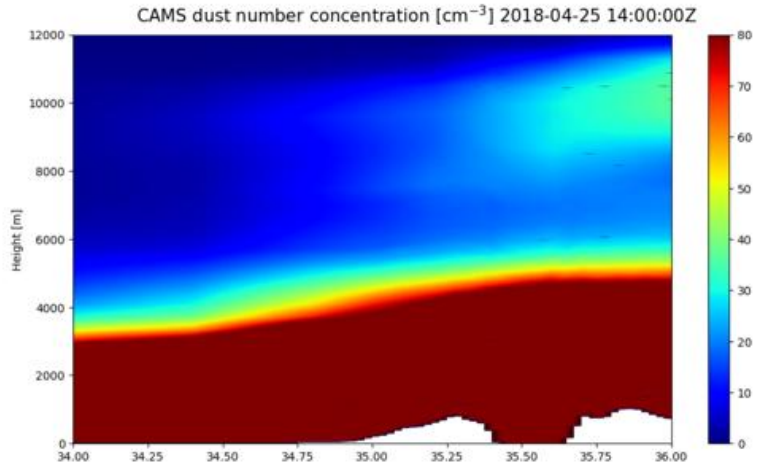


Figure 39: CAMS dust number concentration profiles forecasted for 25-04-2018 at 14:00. The scale was changed to emphasize the values at ice clouds heights (5000 m-10,000 m).

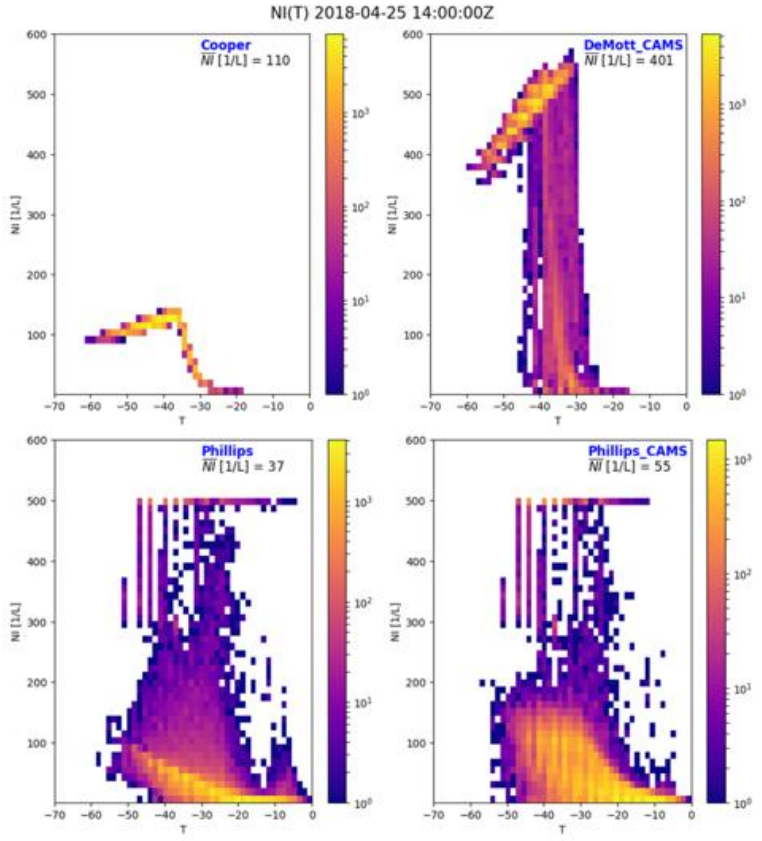


Figure 40: Occurrences plot for the IN concentration $[1/L]$ as a function of temperature for the same models described in Fig. 38. The number inside each panel represents the entire domain averages for grid point having non-zero ice content.

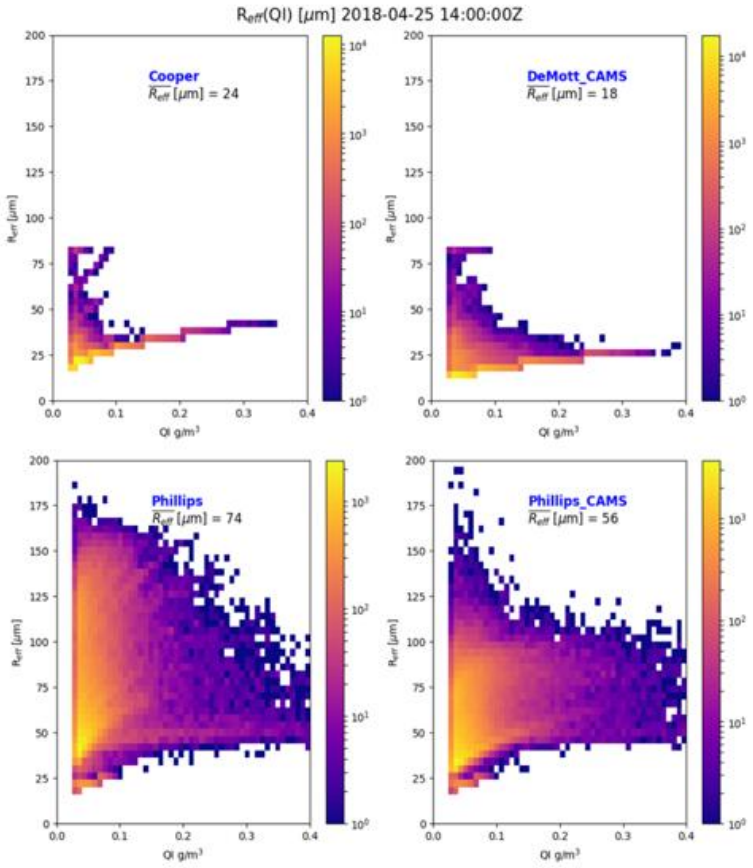


Figure 41: Occurrences plot for the IN concentration $[1/L]$ as a function of temperature for the same models described in Fig. 38. The number inside each panel represents the entire domain averages for grid point having non-zero ice content.

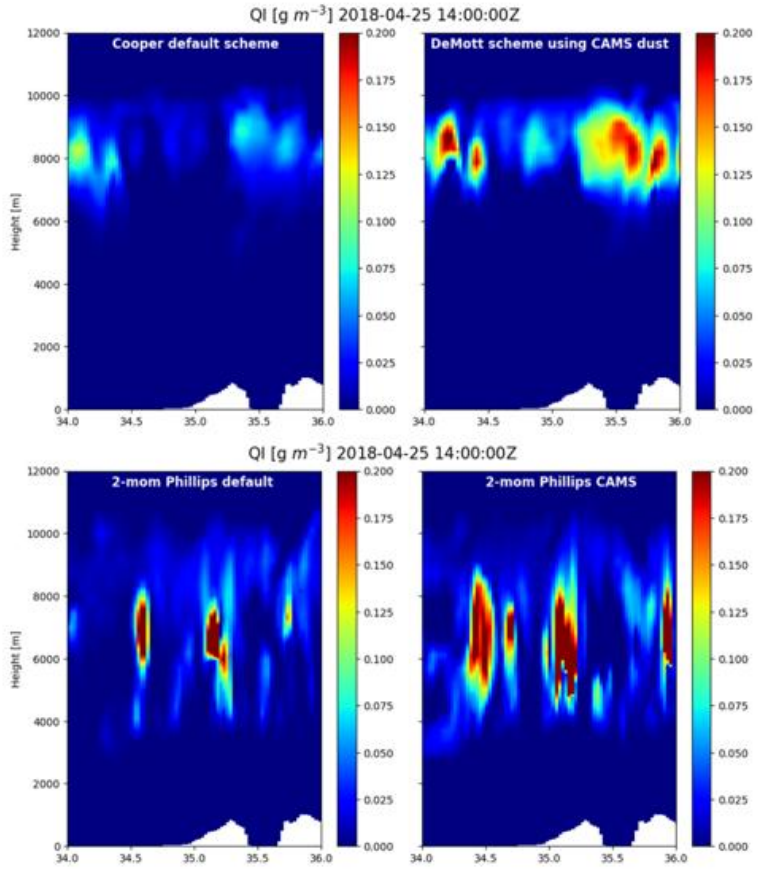


Figure 42: LWC profiles in [g/m^3] units for the same models described in Fig. 38.

7.4.6 DeMott (2015) ice nucleation scheme results vs. observational data

In order to statistically test the new DeMott (2015) ice nucleation scheme in COSMO using the CAMS forecasted dust field we performed 45 test cases runs in the IMS domain. The period chosen was in the October-November period and produced a 66-million points NI(T) plots as can be seen in Fig. 43. The upper left panel is for the default 1-moment COSMO microphysics using Cooper 1986 formula. In this plot of course, all points and the average (lime line) overlap. In the upper right panel the new DeMott & CAMS scheme results are presented. The scatter of points is due to the large divergence of dust particles densities. The averaged IN concentration for each temperature is in lime while point's colours visualize the occurrences in the domain. The same lime average line can be seen in the lower left panel but in a logarithmic vertical scale. The (schematic) blue line on this curve is copied on top of the plot in the lower right panel taken from Vergara-Temprado et al. (2018, with permission) which includes observational data from different locations around the globe. This shows that the new scheme implemented in COSMO fits the scattered points observed in terrestrial locations (red points).

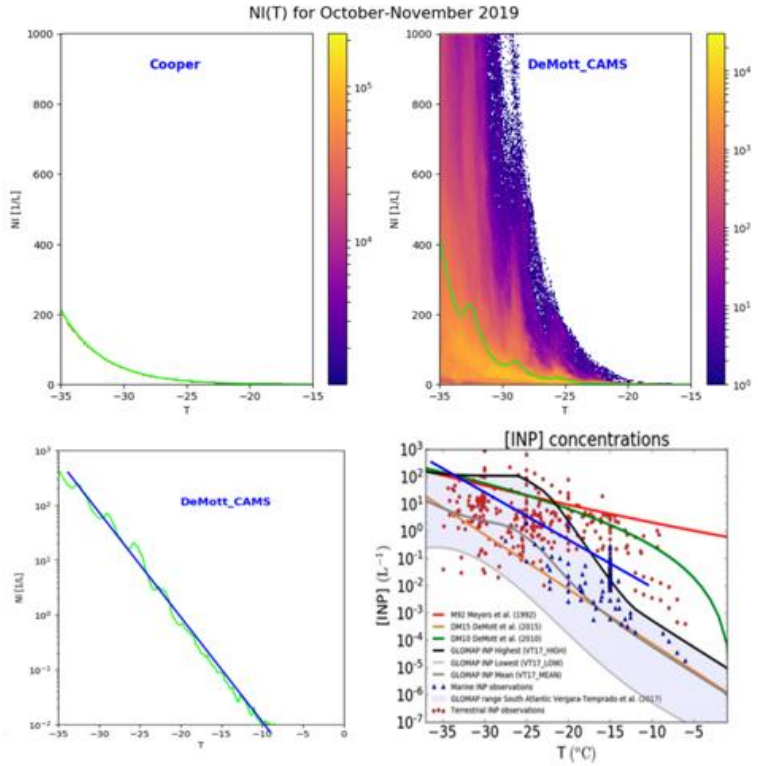


Figure 43: IN concentrations $[1/L]$ as a function of temperature for 45 test cases in the period of October-November 2019. Upper left: COSMO default ice nucleation scheme (Cooper, 1986), Upper right: COSMO new ice nucleation scheme using DeMott (2015) parametrization and CAMS forecasted dust concentrations, Lower left: the same but on a logarithmic scale, Lower right: observational data plot taken from Vergara-Temprado et al. (2018, with permission). See text for details.

8 Implementation of ICON-ART forecasted dust in COSMO radiation scheme

(H. Muskatel, D. Rieger, A. Shtivelman)

8.1 Introduction

ICON-ART is a global model system which online couples between ICON model (Zängl et al., 2015) and the ART modules for aerosols and reactive trace gases developed in KIT. The concentrations of the selected particles are calculated in every time step and synchronized with the NWP model dynamics.

COSMO model new CLOUDRAD radiation scheme has five options for aerosols input: Tanre climatology (Tanre et al., 1984, itype_aerosol = 1), Tegen climatology (Tegen et al., 1997, itype_aerosol = 2), MACv2 climatology (Kinne et al. 2013, itype_aerosol = 3), CAMS forecasted aerosols (Morcrette et al. 2009, itype_aerosol = 4) and now also ICON-ART-dust forecasted aerosols (itype_aerosol = 5). The details on ICON-ART model and especially dust forecast are discussed in Zängl et al. (2015), Schröter et al. (2018) and Gasch et al. (2017).

This semi-operational model, runs twice a day on global scale in DWD, currently including only three dust tracers but more aerosols species are planned for the future. As explained in the previous chapter regarding CAMS forecasted aerosols, the aerosols densities from the global aerosols model for every hour are interpolated in space and time by INT2LM over the whole domain. Since only dust forecast is available on a daily basis in ICON-ART, other four species of aerosols for the ICON-ART-dust option (itype_aerosol = 5) are taken from Tegen climatology (sea salt, organic matter, black carbon and sulfate).

8.2 ICON-ART dust aerosols direct effect on radiation

The direct effect of ICON-ART dust forecast on COSMO radiation was verified against ground-based measurements stations as detailed in Sec. 7 (see Fig. 28) and also 4 AERONET stations in Technion (Israel Institute of Technology in Haifa), Wiezmann Institute of Science (Rehovot), Sede-Boker and Elat. The time period selected was October-November 2018 and April-May 2019. These autumn and spring seasons in Israel region are very active in terms of dust outbreaks. The three COSMO-CLOUDRAD models aerosols inputs versions were: Tegen (1997) climatology, CAMS forecasted aerosols and ICON-ART-dust forecasted dust. The two variables which were evaluated were the downward shortwave radiation (global radiation) and the aerosols optical depth (AOD) at 500 nm. The global radiation in all skies conditions in all stations combined are presented in Fig. 44. The black 1:1 line represents the ideal model-observation match. The red/green lines are the linear fit to the model-observation scatter plot. Points located far from the black line means fiascos of radiation forecast and usually are due to cloud cover or cloud optical depth errors. Fig 45 is similar to Fig. 44 but for clear skies conditions. The clearness of the skies were defined as points for which all three models agreed on cloud cover less than 10%.

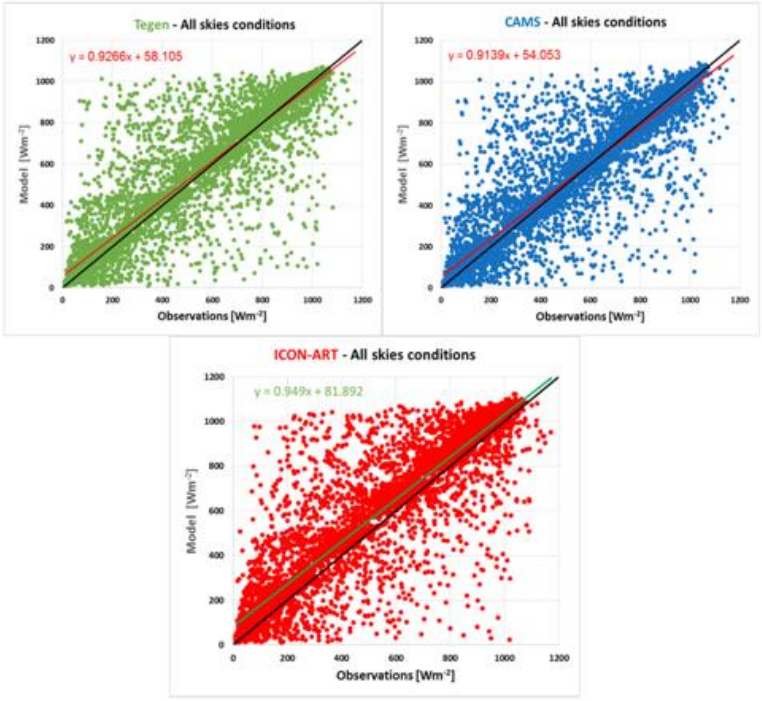


Figure 44: Global radiation model vs. observation for 10 ground based stations in Israel. For the period Oct-Nov-2018 & May-Apr-2019. All skies conditions at all grid-points and hourly snapshot time steps. Upper-left: CLOUDRAD scheme using Tegen climatology, upper right: CAMS forecasted aerosols, lower panel: ICON-ART-dust. Black line: 1:1 ideal match, red/green line: linear fit of the model-observation couples.

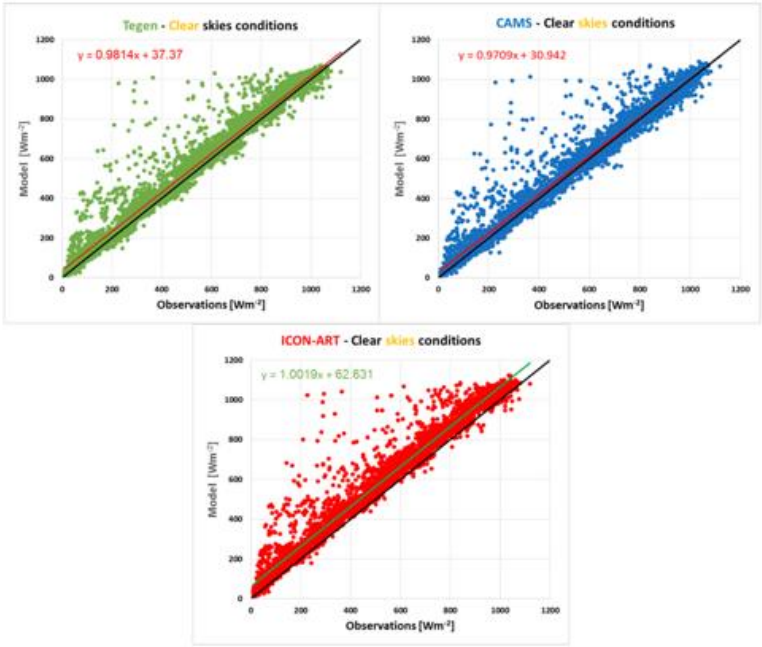


Figure 45: Same as in Fig. 44. For clear skies conditions defined for grid points in space and time for which at all models the total cloud cover was less than 10%.

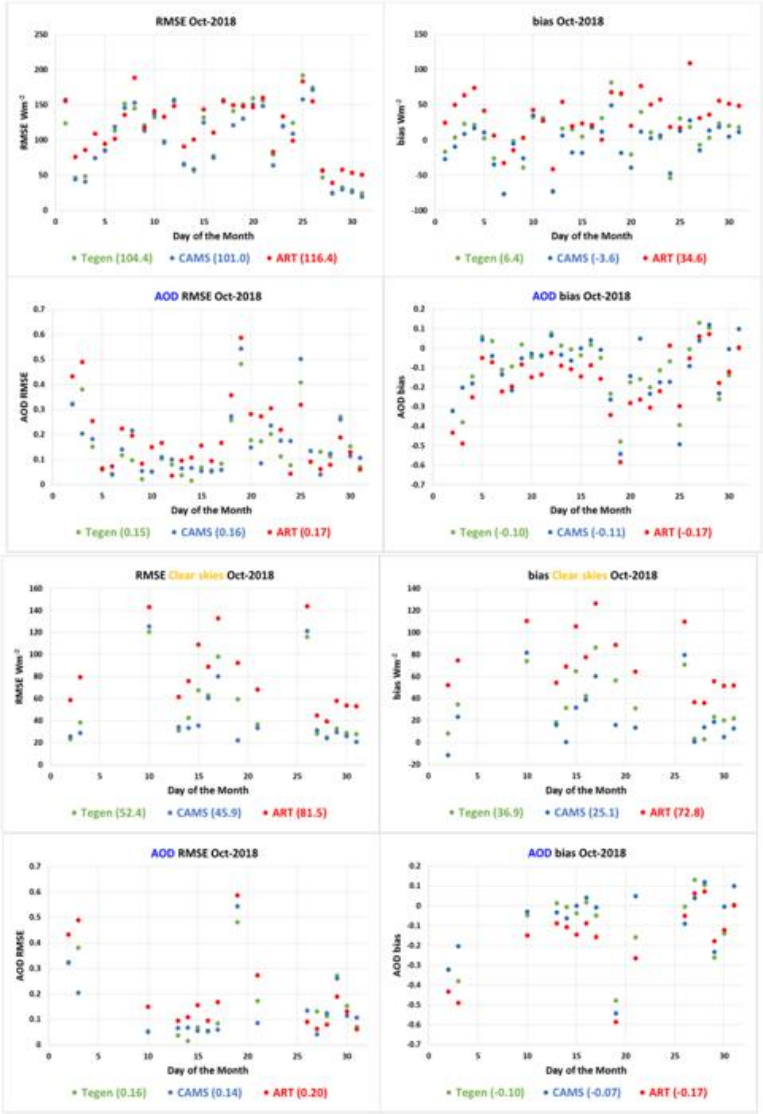


Figure 46: See text for details.

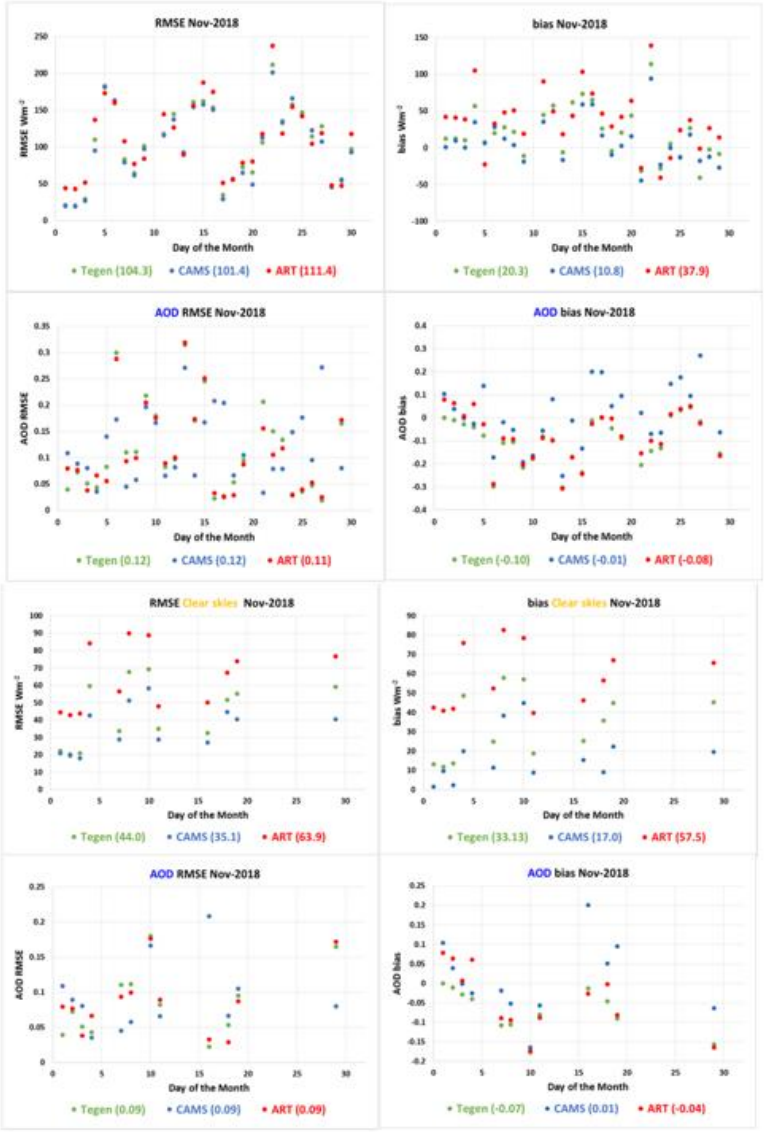


Figure 47: See text for details.

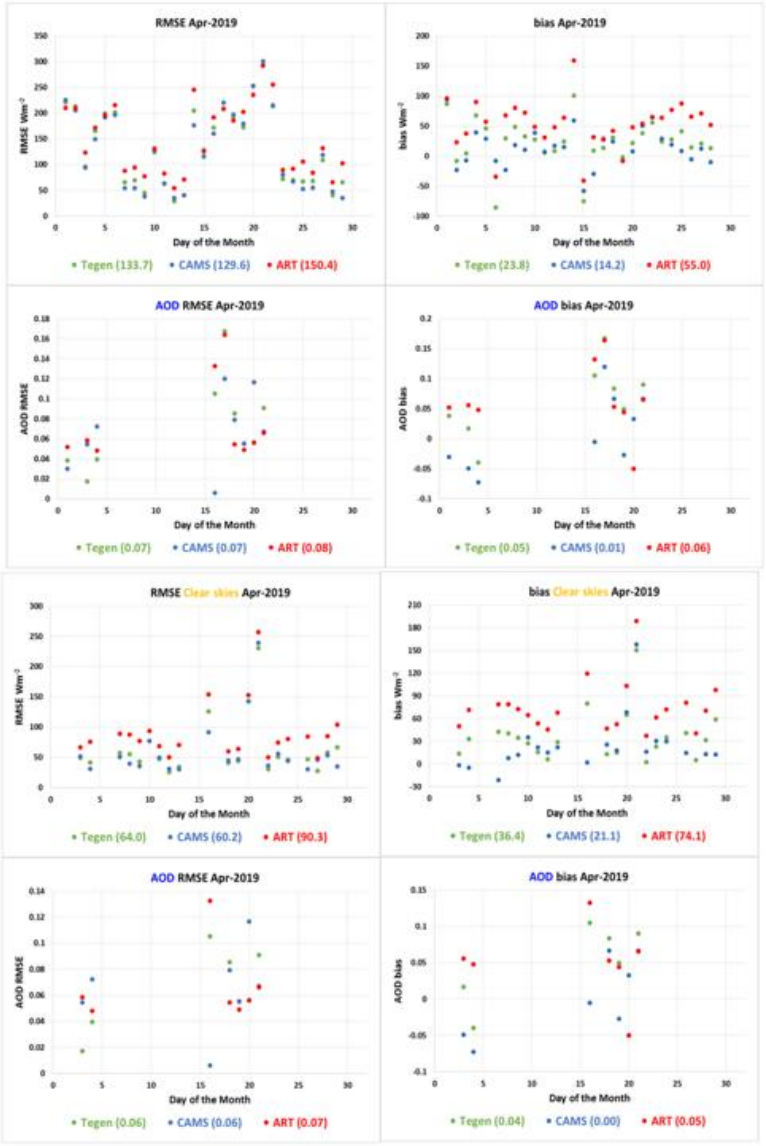


Figure 48: See text for details.

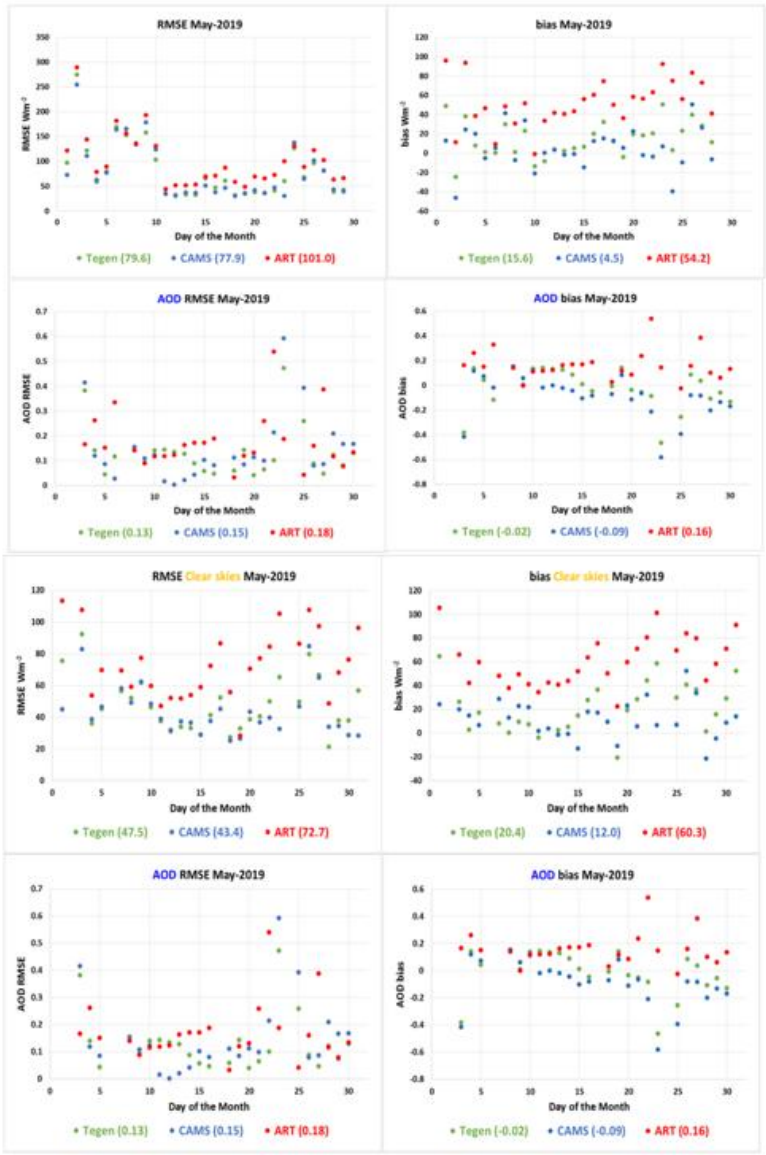


Figure 49: See text for details.

The results shown in Fig. 44 reveals the difficulty to forecast radiation fluxes without first having an accurate cloud cover estimation. Nevertheless, when observing the errors in 2-meter temperatures (not presented here) we see that usually the effect on surface temperature is in the order of 0.1 K. This is due to the fact that even when the cloud cover at a specific time step/grid point is wrong, the averaged fluxes over few minutes/hours are usually accurate when the overall synoptic situation is correctly forecasted. The clear-sky condition results shown in Fig. 45 reveals systematic errors in the models (apart from the outliers above the black line which are associated with clouded points not forecasted by the model). We can see that COSMO using Tegen climatology has a small radiative positive bias (negative AOD bias) which is more significant in the mornings and afternoons. CAMS forecasted aerosols linear fit red line almost overlaps the black line which means that the bias is very small during the whole day. On the other hand, ICON-ART-dust (with Tegen four other aerosols species) shows the poorest results with fixed positive bias which means that there is a negative bias in dust optical depth throughout the day. That may point to a systematic error in the dust forecast that may be a regional issue. Israel is in the midpoint between

two of the most significant dust emissions sources in the world – the Sahara Desert and the Arabian Peninsula. A systematic error due to a calculation error (code bug) is also a possibility which is being investigated.

Figs. 8.3 are subdivided into 4 pages, each page relates to a different month. In each page, the four upper plots represents the all-skies condition results and the four lower panels represents the clear-skies conditions points. Each point is a daily average value (over all stations and time steps of that day). For each 4-panels group, the upper-left/upper-right panels are the global radiation RMSE/bias averages and the lower-left/lower-right panels are for the AOD RMSE/biases. The monthly average values appear as coloured numbers under each plot. In October and November 2018, All models have a small negative AOD bias. Both radiation and AOD scores are very similar for both Tegen and CAMS forecast. CAMS results are slightly better with almost zero AOD bias in clear skies conditions. Unfortunately, the RMSE and bias is worsen when using ICON-ART-dust forecast. Although having similar AOD biases with Tegen, ICON-ART-dust has still much larger positive fluxes biases ($\sim$ 30 W/m^2) which needs further code investigation. In April 2019 all models showed an averaged positive AOD but still a positive radiation fluxes compared to the observations while in May 2019 only ICON-ART-dust showed a positive AOD bias. For these months as well, CAMS forecast had the best scores, second is Tegen climatology and third comes ICON-ART. The radiation RMSE are, as expected, larger for all-skies conditions ($\sim$100 W/m^2) compared with clear skies condition ($\sim$50 W/m^2) due to cloudiness but with much higher values for ICON-ART-dust compared with other models. This gap can be associated with the fixed positive bias in radiation when using the ICON-ART-dust aerosols. The RMSE for CAMS model is on the average $\sim$10-15 W/m^2 smaller compared to Tegen climatology RMSE due to the data assimilation and dynamical forecast of aerosols compared with the monthly mean values taken from Tegen (1997). We believe that in the future, such forecasted aerosols from ICON-ART or CAMS systems can be used also in the ICON model in both LAM or global modes of operations.

9 Verifications of the new COSMO radiation scheme in clear skies and cloudy skies conditions

(N. Chubarova, M. Shatunova, A. Poliukhov, A. Kirsanov, G. Rivin)

9.1 New MACv2 aerosol climatology and its verification in clear sky conditions

9.1.1 MACv2 aerosol climatology

The MACv2 climatology (Kinne, 2019) takes into account recent developments in aerosol modelling and experimental data and is a combination of the model ensemble data and ground-based aerosol measurements from AERONET dataset. It provides all necessary aerosol input parameters for the radiative computations in different spectral intervals for fine and coarse aerosol modes. It is also possible to retrieve an anthropogenic aerosol mode from this climatology. MACv2 aerosol climatology has monthly temporal resolution and provides 1°x1° spatial fields for wavelengths of 0.29, 0.32, 0.55, 0.87, 1.47, 2.0, and 2.6 μm in the solar spectrum and wavelengths 7, 8.85,9.75, 11.2 and 30 μm in the longwave range. An averaging procedure was performed to fit these wavelengths to COSMO 8-band radiative transfer model.

To include this aerosol climatology into the COSMO system we made the changes for the following blocks: EXTPAR, INT2LM and COSMO model. Unlike Tegen climatology (Tegen et al., 1997), receiving of all aerosol optical and radiation properties goes through EXTPAR, when using MACv2 climatology. Aerosol optical thickness (AOT), single scattering albedo (SSA) and asymmetry factor (ASI) values were normalized to the corresponding values at 550 nm and recorded in four-dimensional arrays: longitude, latitude, month and spectral interval.

9.1.2 Comparison with Tegen climatology and in-situ observations

We compared aerosol optical thickness (AOT), single scattering albedo (SSA) and asymmetry parameter (ASI) from the new MACv2 climatology as well from Tegen climatology with long-term measurements of AERONET at the Meteorological Observatory of the Moscow State University (further MSU MO or Moscow site) and AERONET/PFR data at the Lindenberg Observatory.

We used radiative measurements by Kipp & Zonen CNR-4 net radiometer at Moscow and by the BSRN (Baseline Surface Radiation Network) type of radiative instruments at Lindenberg. We focused mainly on the measurements of global solar irradiance. However, for obtaining surface albedo we also used reflected shortwave irradiance. Water vapour retrievals were also obtained using AERONET algorithm at 940 nm channel. In addition, we used upper – air soundings (temperature, water vapour) at both sites as well as Ozonesonde dataset - at Lindenberg. At Moscow air temperature measurements at 2 meters were analysed using routine observations and Vaisala automatic weather station. At Lindenberg the data from the automatic weather station were used. In order to reveal clear sky situations we used hourly visual observations at both sites.

AOT550 time series according to long-term measurements at the MSU MO (Abakumova et al., 2008, Chubarova et al., 2016) and MACv2 dataset are presented on Fig. 50. While AERONET data for Moscow site are available from 2002, AOT restored values from direct shortwave irradiance allowed to make comparison for the 30 years period. Increasing in AOT values are corresponded to eruptions of El-Chichon in 1982 and Pinatubo in 1991 and forest wildfires in 2002 and 2010. It is obvious that climatology does not take into account sharp random changes in AOT or other optical parameters. However, MACv2 data is in good agreement with point observations and demonstrates the same tendency in AOT decreasing during last 30 years.

MACv2 and Tegen climatologies overestimate AOT during most months at the both sites. SSA values from Tegen climatology practically do not vary throughout a year, while MACv2 SSA variations are closer to the observed values except winter when one can see noticeable overestimation for MACv2 data. Detailed comparison of MACv2, Tegen climatology data with in-situ observations for Moscow and Lindenberg sites presented in Chubarova et al., 2018 and Poliukhov et al., 2018.

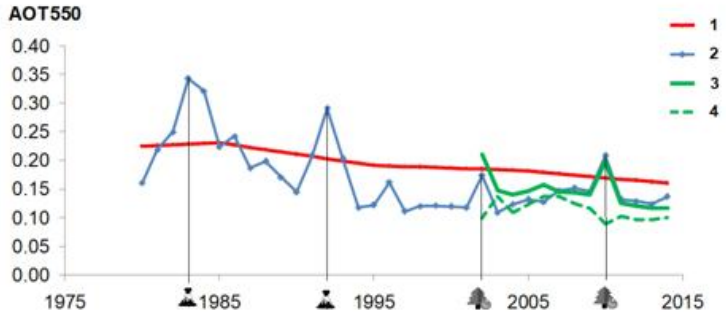


Figure 50: Comparison of aerosol optical thickness at 550 km from MACv2 climatology (1) with restored values from direct shortwave irradiance (2) and AERONET data mean (3) and median (4) values for MO MSU, Moscow.

In addition, the comparison for aerosol properties from Tegen and MACv2 climatologies against ground-based measurements over Israel in Eilat site with prevailing mineral type of aerosol, and over Arctic at the Tiksi Observatory in Russia have been performed. The results are described in Poliukhov et al., 2019.

9.1.3 Radiation fluxes assessment

To account the changes in all the aerosol properties (AOT, SSA, ASI) we chose global shortwave irradiance at ground as an aggregated characteristic. The comparisons between simulated and observed global solar irradiance datasets were fulfilled for different aerosol conditions and solar zenith angles for clear sky condition using accurate model simulations which were compared with solar measurements.

Using the obtained aerosol parameters from the climatologies and the observations we calculated global solar irradiance (Q) at ground and the corresponding difference $\Delta Q = Q_{climatology} - Q_{obs}$ (see Fig. 51). Radiative simulations were fulfilled using a modified CLIRAD radiative transfer code (Tarasova and Fomin, 2005) for noon conditions at the central day of a month. Results for Moscow (Fig. 51a) shows that Tegen climatology Q values were underestimated with a negative bias of 11-26 W/m^2 while for MACv2 Q bias varies from -23 to +4 W/m^2. The annual mean bias for the MACv2 climatology, -10.8 W/m^2, is closer to the observations compared with Tegen climatology having bias of -17.3 W/m^2. For Lindenberg site, both climatologies provide underestimation of global solar irradiance of about -10 W/m^2 for annual means compared with the Q values simulated with the aerosol input parameters taken from observations. Both of them have lower solar irradiance for almost all months mainly due to the overestimated AOT. At the same time, for the Tegen climatology in April and November in conditions with only small AOT overestimation (ΔAOT = 0.01-0.02) we observe even positive bias in solar irradiance (1-2 W/m^2) due to the large difference in SSA. For these months Tegen climatology provides much higher SSA values (0.92) compared with the observations (0.85). For Tegen climatology, 10-20 % of aerosol optical thickness over Europe relates to black carbon aerosol, which should significantly increase the absorption especially in visible spectrum. However, this is not enough to explain the lower SSA values observed at Moscow site, which probably occur due to smaller aerosol size.

A positive bias of AOT results in the underestimation by 2-3 % in global solar irradiance simulated by COSMO radiative algorithm for Moscow and Lindenberg sites (Chubarova et al., 2018; Poliukhov et al., 2018). Nevertheless, for some polluted cases the situation

may differ (Fig. 51). A sharp increase in the concentration of pollutants observed on 21 November 2014 in Moscow resulted in the difference between observed and simulated global radiation. AOT550 AERONET values reached 0.17-0.20, AOT055 according Tegen and MACv2 climatologies was similar – 0.17. However, there was a high concentration of NO2 (Fig. 51c) and possible additional absorption in visible region of spectrum due to this gas. In this case radiative transfer simulations made with Tegen and MACv2 data show large overestimation compare to observations. It is interesting that simulations with the former Tanre climatology (Tanre et al., 1984) show the best agreement with observations in this particular case.

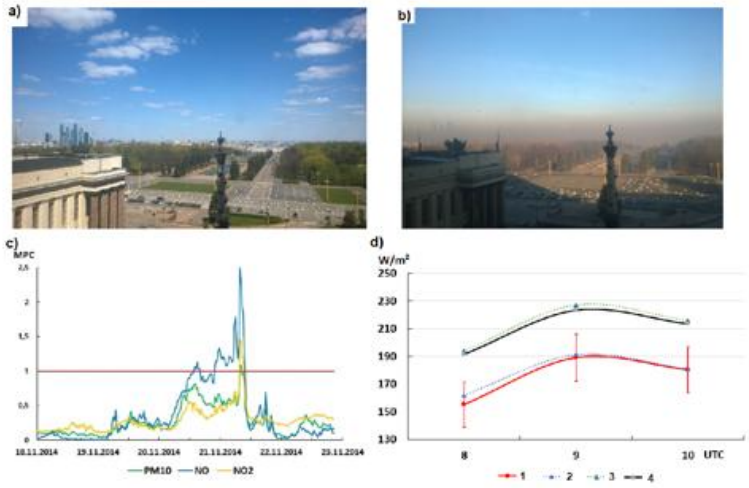


Figure 51: An example of polluted case: view over Moscow city on a) 17 November 2014 and b) 21 November 2014; c) observed level of pollutant concentration; d) observed (1) and simulated global radiation with Tanre (2), Tegen (3) and MACv2 (4) climatology data.

9.1.4 Temperature sensitivity to the changes in aerosol characteristics

The instant temperature effects of aerosol were analysed using different COSMO model runs with different aerosol climatologies and with zero aerosol conditions for the same clear sky days which are used in the analysis. Since aerosols over continental Europe are characterized by weak absorption in visible spectral range, it should provide the negative effect on temperature at ground level. To account the changes in all the aerosol properties (AOT, SSA and asymmetry factor) we chose net shortwave irradiance at ground as an aggregated characteristic. Net shortwave radiation is the difference in downwelling and upwelling shortwave irradiance and it also accounts for surface albedo effects, which play, however, minor role in our snow-less conditions. We analysed the dependence of difference in air temperature at 2 meters (ΔT) simulated in conditions with and without aerosols to the corresponding difference in net radiation (ΔB) to estimate the temperature sensitivity to aerosol. The negative values in net radiation at ground level due to aerosol provide negative effects on temperature difference. The difference in temperature should reach zero when ΔB=0 in conditions with zero AOT.

For Moscow and Lindenberg we obtained a pronounced statistically significant dependence which provides similar aerosol temperature effects. For Moscow, the effect is 0.8 $\pm$ 0.2 K per 100 W/m^2, which is in agreement with our previous estimates (Poliukhov et al. 2017). For Lindenberg the value is 1.0 $\pm$ 0.3 K per 100 W/m^2 with correlation coefficients r = 0.5,

0.6 respectively. The observed deviations may occur due to some slight variations in other parameters (water vapour, differences in profiles, etc.) in COSMO model runs.

Another testing was made using similar approach using comparisons with observations. In this case we should have much more deviations due to the influence of the uncertainty in actual atmospheric parameters which may differ from the simulated ones. We obtained the same tendency with the increase of positive temperature shift with positive bias in net radiation, which is mainly a function of aerosol loading. The gradients are similar to those obtained in the previous pure model experiment. These results confirm the pronounced temperature sensitivity to aerosol loading via its influence on net radiation at ground.

For estimating typical aerosol temperature effects for Moscow and Lindenberg, the changes in net radiation due to the changes in corresponding aerosol properties against aerosol–free conditions should be used. These temperature effects comprise about -0.2 K to -0.3 K for typical aerosol loads over these sites.

9.1.5 Temperature forecast sensitivity to aerosols

To estimate aerosol temperature effects we made simulation using COSMO for large domain (Europe – North Asia) with 13.3 km grid spacing for the central months of the seasons – January, April, July and October 2017. We performed simulations with Tanre climatology as a reference. Monthly averaged differences in T2m for July 2017 for simulations with Tegen and MACv2 aerosol climatologies as well as with CAMS reanalysis (see 7) are presented in Fig. 52.

T2m difference reaches 0.5 K (mostly on the regions with high probability of dust aerosol - North Africa, Meddle East, Central Asia) between simulations with old Tanre aerosol climatology and new one (MACv2) or CAMS. Significant positive T2m response up to 1 K appears in the North Africa and southern Europe in the case of MACv2 (Fig. 52b).

The assessment of temperature forecast considering MACv2 climatology and forecasted aerosol from CAMS compared to simulations with Tanre aerosol data was fulfilled using SYNOP and upper air sounding data. Simulation results with of MACv2 and CAMS show T2m RMSE decreases in southern Europe on 0.2-0.4 K (Fig. 53a,b). An effect of the new aerosol data implementation is neutral for the upper atmosphere.

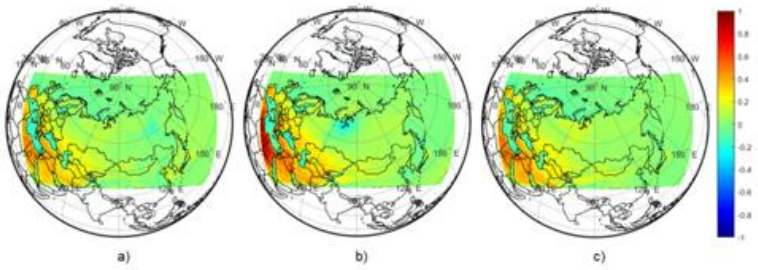


Figure 52: Monthly averaged differences in T2m for July 2017 for simulation with different aerosol setting compare to simulation with Tanre climatology: a) CAMS, b) MACv2, c) Tegen.

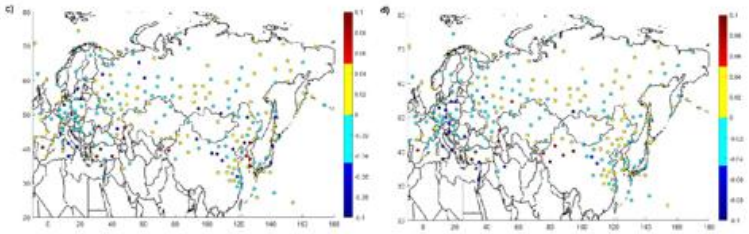


Figure 53: RMSE difference for T2m (a,b), T850 (c,d), T500 (e,f) forecasts between simulations with Tanre data and CAMS data (a,c,e) or MACv2 data (b,d,f).

9.2 Verifications in Cloudy skies conditions

9.2.1 Assessment of water vapour, liquid and ice water content in radiative scheme

To understand COSMO model behaviour in forecasting of the humidity characteristics we verified atmospheric water vapour content, cloud water and ice content, their vertical distribution and vertically integrated values using observations at Lindenberg observatory for the period March – October 2016. Appendix A contains the description of the experimental dataset.

All simulations were made with operational version of the model with 2.2 km grid spacing and 60 vertical levels for 550 x 600 km domain.

Results showed a correlation between errors in ice water content (QI) and water vapour content (QV) in the upper layers (6-12 km) (see Chubarova et al., 2018; Shatunova et al., 2019). An overestimation of QV values (see Fig. 2 in Chubarova et al., 2018) leads to overestimation of QI (Fig. 3 in Shatunova et al., 2019). In general, the model tends to overestimate total ice content. Model overestimate total water content (TQC) for rather small absolute values and underestimates TQC when its value is greater 0.1 kg/m^2.

9.2.2 Global radiation sensitivity to aerosol content

To investigate an impact of different aerosol setting on cloud optics and global radiation we made simulations with different set of concentration of cloud nuclei (CCN): fixed value characterized pure maritime, pollutant continental and intermediate clouds, and CCN calculated from Tegen aerosol climatology. Control runs were made with the default version of COSMO model without activation of the new COSMO radiation scheme (CLOUDRAD).

Simulations were performed with COSMO configuration with grid spacing 2.2 km for a domain covering Central Federal Region with Moscow located in the center of the domain for the warm period (April – October) of 2018. The data on global and direct radiation observed at the Meteorological observatory of Moscow State University were used to assess the quality of the obtained results.

Cloud optical thickness (OT) variation due to different CCN setting was investigated for the days with low cloud liquid water content. Cloud OT relative difference compare to control runs are presented in Fig. 54. Decreasing of cloud optical thickness within the lower 1.5

km layer of the atmosphere varies from 15% to 35 %. Smaller number concentration means larger water droplets and smaller OT (more transparent clouds).

The model setups tested (Figs 54, 55) were: the default radiation scheme (iradpar_cloud=1) as a control run, CCN calculated using SK2006 with Tegen aerosols as input (iradpar_cloud=4, cloud_num_type_rad = 2; itype_aerosol = 2), three setups with fixed number concentration at cloud base with exponential decay (iradpar_cloud=4, cloud_num_type_rad=1; itype_aerosol= 2, cloud_num_rad=100, 400, 1700) see Sec. 7 for details.

Comparison of global radiation simulated with default and CLOUDRAD schemes against observations is presented on Fig. 55. For the cases with optically thick clouds when the observed global radiation was less than 100 W/m^2 the errors of the predicted values do not exceed 50 W/m^2 and the old scheme showed here the best agreement. When observed global radiation is more than 250 W/m^2 which we can consider as optically thin cloud case, errors increase and difference between schemes become more evident. In overall, the results obtained with the new CLOUDRAD scheme have better agreement with observations (for details see Chubarova et al., 2018; Khlestova et al., 2019).

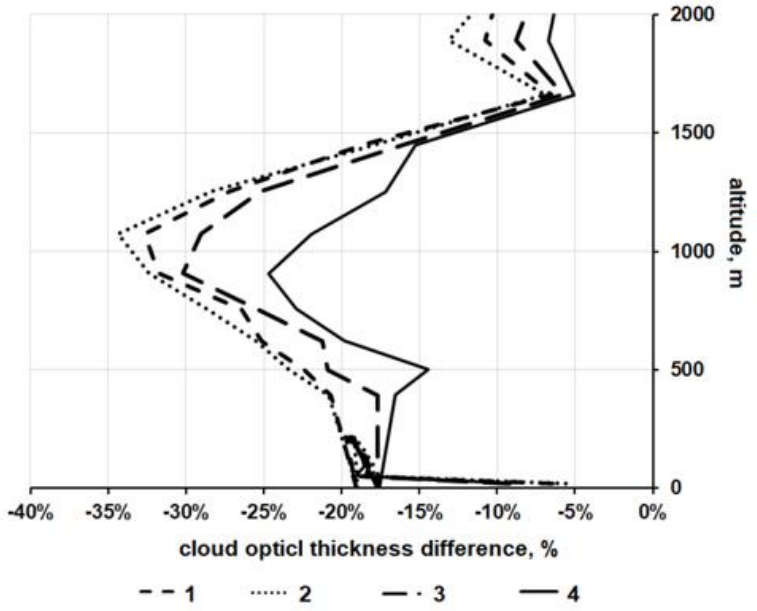


Figure 54: Cloud optical thickness relatively difference in dependence of CCN setting calculated with CLOUDRAD scheme compare to model version without CLOUDRAD. 1 – CCN from Tegen aerosol climatology, 2 – CCN = 100 cm^{-3}, 3 – CCN = 400 cm^{-3}, 4 – CCN = 1700 cm^{-3} see text for details of the setups.

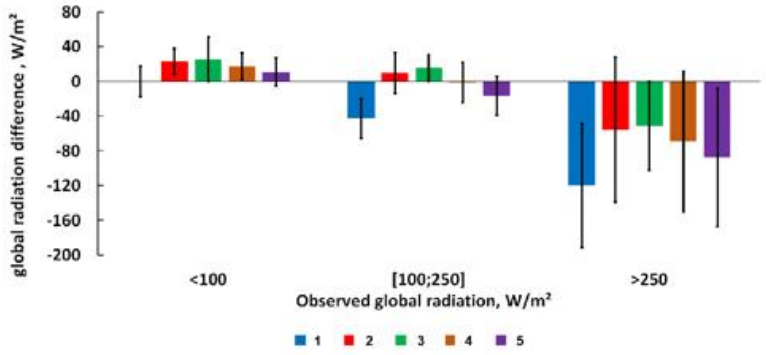


Figure 55: Verification of global radiation simulated with the old scheme (1) and the CLOUDRAD scheme with different aerosol setting (2 – CCN from Tegen aerosol climatology, 3 – CCN = 100 cm^{-3}, 4 – CCN = 400 cm^{-3}, 5 – CCN = 1700 cm^{-3}) against observations at Moscow State university observatory.

9.2.3 T2m forecast sensitivity

Taking into account the microphysical parameters of the cloud for evaluating its optical properties provide the increase in accuracy of both simulated global radiation, and air temperature forecast for the daytime. T2m forecast was verified against SYNOP observations (147 stations) for the period April-October 2018 for the Moscow region. Assessment shows that for the operational version (old scheme) RMSE equals 2.23 K and for the CLOUDRAD scheme RMSE is 2.04 K. The comparison of the scores for the two schemes is presented on Fig. 56. We should note that advantages of the old scheme within the first forecast hours is due to data assimilation system that was not applied for the simulations with CLOUDRAD.

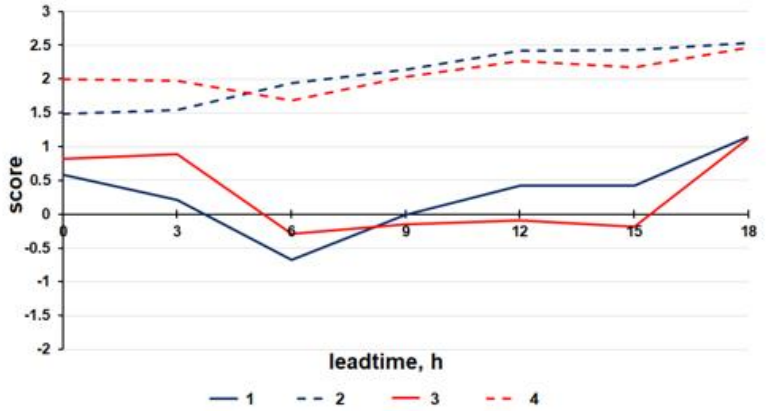


Figure 56: T2m forecast verification. Old scheme: 1 – Mean Error, 2 – RMSE; CLOUDRAD scheme: 3 –Mean Error, 4 – RMSE.

9.3 Conclusions

9.3.1 Clear sky case

MACv2 climatology provide better agreement with aerosol parameters for Moscow and Israel sites than Tegen climatology. The instant temperature sensitivity effects to aerosol loading is about 0.8-1.0 ±0.2°C per 100 W/m^2 in net radiation at ground. The application of a new MACv2 aerosol climatology provides a significant positive temperature (T2m) response of up to 1 K over Northern Africa and southern Europe in case of MACv2 compared with the results with the Tanre climatology application. Simulated results with MACv2 and CAMS demonstrate the T2m RMSE decrease in southern Europe on 0.2-0.4 K.

9.3.2 Cloudy case

Verification of COSMO model against ground-based measurements was made using the standard and CLOUDRAD cloud-radiation schemes with 2.2 km grid and 60 vertical levels for 550 x 600 km domain with start time at 00 UTC. In days with low cloud liquid water content, with solar irradiance above 250 W/m^2 we obtained a pronounced decrease in cloud optical thickness of 15-35%, when a new CLOUDRAD scheme was used. This change provides the increase in global irradiance at ground, which, in turn, leads to a better agreement with the observed global irradiance. In situations with optically thick cloudiness (with solar irradiance less 100 W/m^2) there is no difference between the two schemes.

Temperature T2m forecast sensitivity using the new CLOUDRAD scheme has been verified against SYNOP observations over Moscow region. The results demonstrated better agreement with the new CLOUDRAD scheme with decrease in RMSE from 2.23 (for the standard scheme) to 2.04 (CLOUDRAD scheme).

10 Testing and tuning of the new cloud-radiation scheme

(P. Khain)

10.1 Overview

The new cloud-radiation-coupling scheme includes revised sub-grid scale clouds effect on radiation, detailed optical properties for liquid and frozen particles of different sizes, more accurate representation of aerosol effects on cloud microphysics, etc. From algorithmical point of view, the new scheme contains many cloud-radiation dependencies which contribution is described by about thirty parameters. Besides, different options are activated using ten logical switches. This makes the tuning of the scheme a difficult problem. The idealized COSMO framework was previously used to determine the parameters having particularly high influence on the radiative fluxes in the model (Khain et al., 2016). Here we utilize an "objective" parameters tuning (Voudouri et al., 2017; Khain et al., 2017) via comparison of real model forecasts against global radiation from CM-SAF satellite data (Müller et al., 2015). The experiments were performed for several month during 2016 over COSMO-DE domain. We present parameters values of four subversions of COSMO-cloudrad, which optimize the global radiation over Offenbach, Lindenberg and Munich regions.

10.2 Calibrated COSMO-CLOUDRAD versions

The main features of the four calibrated versions, and the list of tuned parameters for each version are summarized in table 101. The four versions are: "Basic" version – Tegen aerosol climatology is assumed as well as constant cloud droplets number concentration and effective radius; "CAMS" version – Similar to "Basic" but assuming interpolated in time and space CAMS aerosol background; "SK basic" version – Tegen aerosol climatology is assumed, Segal-Khain parametrization is used for estimation of droplets number concentration and effective radius; "SK-SAM" version – similar to "SK basic" version with the use of "adiabatic" parametrization for droplets microphysics in convective SGS clouds (see chapter 5).

Key switches Tuned continuous parameters **Calibrated versions**

Parameter meaning	Parameter	Basic version	CAMS version	SK basic version	SK-SAM version
Tegen/CAMS CCN	itype_aerosol	2	4	2	2
Use Segal Khain parametrization for the droplets number concentration	icloud_num_type_rad	1	1	2	2
Use constant SGS droplets effective radius	luse_reff_ini_c_as_reffc_sgs	TRUE	TRUE	FALSE	FALSE
Use adiabatic profiles for droplets microphysics in convective SGS clouds	luse_qc_adiab_for_reffc_sgs	FALSE	FALSE	FALSE	TRUE
LWC reduction due to SGS variability	radqcfact [0.4 0.5 0.9]	X	X	X	X
IWC reduction due to SGS variability	radqifact [0.4 0.5 0.9]	X	X	X	X
SGS droplets effective radius	reff_ini_c [3 5 20]·10^{-6}	X	X		
SGS LWC scale factor	qvsatfact_sgscl_rad [0.005 0.01 0.02]	X	X	X	X
Droplets number concentration for radiation	cloud_num_rad [0.5 2 5]·10^{8}	X	X		
SGS droplets effective radius scale of adiabatic profile	reff_avg_fact [0.5 0.9 1]				X
SGS droplets concentration scale of adiabatic profile (clouds dilution)	qnc_avg_fact [0.1 0.38 1]				X

Figure 57: The main features of the four calibrated COSMO-cloudrad versions, and the list of tuned parameters for each version.

10.2 Global Radiation sensitivity

Before performing the calibration, we analyse the sensitivity of the global radiation to the change in the parameters (see Fig. 58). For every version and every parameter (X in Fig. 57) the averaged modelled (solid line) global radiation for 12Z is plotted against the parameter value (keeping other parameters in their default value) and is compared to the averaged observed value (dashed line).

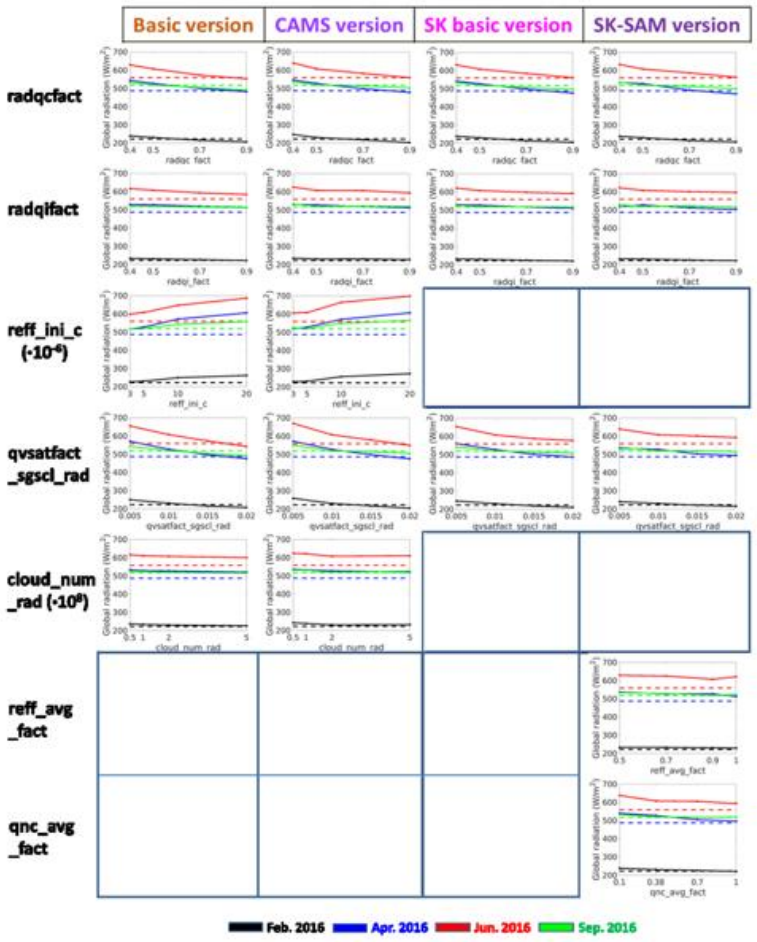


Figure 58: Sensitivity of the global radiation to the change in the parameters. For every version and every parameter (X in Fig. 57) the averaged modelled (solid line) global radiation (shortwave downward radiation on surface) for 12Z is plotted against the parameter value (keeping the other parameters default) and is compared to the averaged observed value (dashed line). February, April, June and September 2016 are denoted by black, blue, red and green lines, respectively.

Intermediate insights from Fig. 58:

1. Increase in radqcfact strongly reduces the global radiation due to increase grid scale and sub-grid scale clouds LWC.
2. radqifact, related to cloud ice water content, has weaker effect.
3. Increase in reff_ini_c, meaning higher SGS effective radius i.e. larger droplets, strongly increases the global radiation.
4. Larger qvsatfact_sgscl_rad, or larger SGS LWC, strongly reduces the global radiation.
5. Increasing cloud_num_rad (higher water droplets number concentration) slightly reduces the global radiation.
6. reff_avg_fact has two contradicting effects. A larger value increases the size of droplets in SGS cumulus making them more transparent. On the other hand, it increases clouds LWC which enlarge their optical depth.

7. Larger qnc_avg_fact slightly reduces the global radiation (because lower dilution leads to larger SGS LWC in cumulus. This parameter is more significant in convective seasons (i.e. April and June).

10.3 Calibration method

We have calibrated four COSMO-DE 2.8km 5.1 CLOUDRAD versions (Fig. 57) driven by ICON-EU analyses. For each version several continuous parameters are tuned (cyan in Fig. 57). The simulation and calibration domains are presented in Fig. 59.

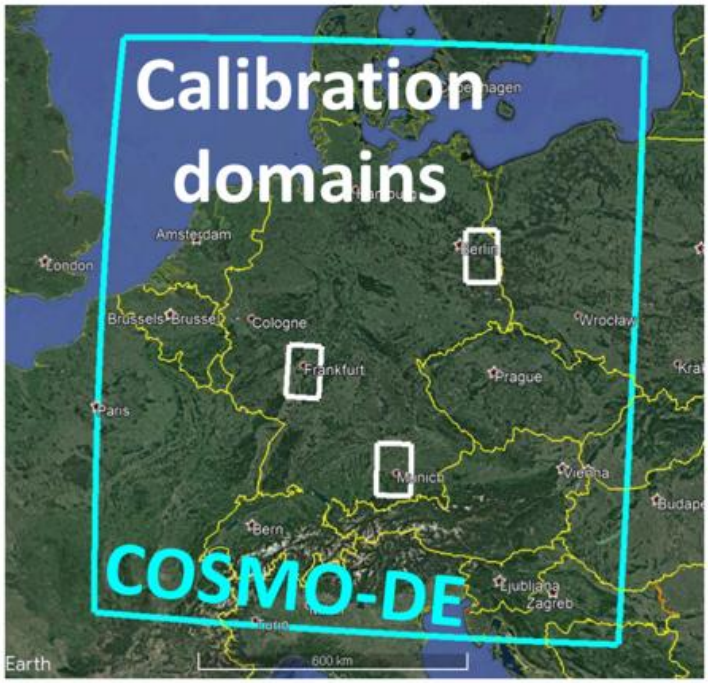


Figure 59: Simulation domain of COSMO-DE (cyan) and calibration domains (three white areas).

The calibration method is the following. First, several parameters combinations are chosen according to specific design (Voudouri et al. 2017). For each combination, COSMO runs are performed for February, April, June and September 2016. For every hour at every grid point, the forecast of global radiation is then interpolated in parameters space using 2^{nd} order polynomial with interaction terms. These interpolations yield a guess for the global radiation for any chosen parameters combination (Meta-Model). For optimization, the parameters space is then sampled by large number of parameter combinations. For each combination the Meta-Model is verified against CM-SAF hourly global radiation at 5km resolution. We look for the optimal parameters combination using a convergence algorithm (Khain et al. 2017). Finally the parameters combination which yields the optimal Meta-Model guess is defined.

10.4 Calibration results

	Basic version	CAMS version	SK basic version	SK-SAM version
radqcfact	0.547 (34.5%) 0.55 (17%) 0.503 (4.1%) 0.571 (19.6%)	0.507 (13.3%) 0.555 (13%) 0.492 (1.8%) 0.532 (22.8%)	0.496 (5.4%) 0.573 (24.2%) 0.468 (9.4%) 0.495 (5.9%)	0.483 (8.4%) 0.613 (42.7%) 0.496 (3.2%) 0.495 (7.3%)
radqifact	0.509 (14%) 0.493 (6.2%) 0.491 (1.1%) 0.486 (8.2%)	0.476 (8.6%) 0.485 (4.9%) 0.508 (6.5%) 0.487 (1.4%)	0.711 (89.4%) 0.581 (77.3%) 0.497 (8%) 0.487 (5.6%)	0.481 (10.5%) 0.48 (6%) 0.503 (2.9%) 0.493 (9.5%)
reff_ini_c ($\cdot 10^{-6}$)	5.85 (7%) 5.785 (1.2%) 5.87 (1.2%) 5.838 (8%)	5.965 (7.8%) 5.67 (3.3%) 5.461 (3.3%) 5.672 (4.9%)		
qvsatfact _sgscl_rad	0.012 (72.2%) 0.01 (50.7%) 0.014 (44.1%) 0.009 (26.2%)	0.014 (47.1%) 0.01 (25.1%) 0.012 (30%) 0.01 (36.4%)	0.011 (71.2%) 0.008 (22.5%) 0.017 (15.1%) 0.011 (76.6%)	0.012 (62.5%) 0.008 (16.2%) 0.01 (3.6%) 0.009 (26.3%)
cloud_num _rad ($\cdot 10^8$)	1.216 (11.2%) 1.281 (1.3%) 1.331 (15%) 1.3 (6.7%)	1.673 (11.2%) 1.274 (2.5%) 1.288 (5.6%) 1.536 (12.8%)		
reff_avg _fact				0.933 (2.9%) 0.923 (1.2%) 0.94 (1%) 0.933 (3.4%)
qnc_avg _fact				0.513 (70.8%) 0.32 (4.9%) 0.898 (2.4%) 0.685 (52.4%)

Figure 60: Optimal parameters values for February, April, June and September 2016 (black, blue, red and green, respectively) averaged over the 3 regions. In parenthesis – uncertainty with respect to parameter range.

Fig. 60 presents the optimal parameters values for the four calibrated COSMO-cloudrad versions for each of the four selected month.

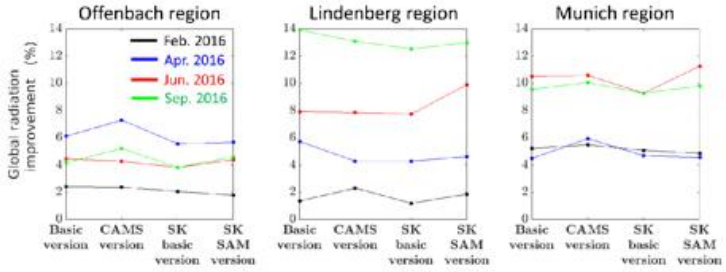


Figure 61: Global radiation estimated improvement (%) when using the optimal parameter combinations.

One can see that the global radiation forecast improvement by various COSMO-CLOUDRAD versions is similar. In summertime it reaches ∼10%. CAMS version has little effect with respect to the "Basic" because in that version the prognostic CCN plays role in the clear sky conditions only. The "SK-SAM" version improves the "SK basic" in summertime due to larger role of SGS cumulus clouds over Germany. Larger improvement from SK parametrization is expected when prognostic CCN is used for droplets activation but this experiment was not performed in this study.

11 Acknowledgements

We thank the following people: Qiang Fu for providing his codes for ice optics and for his many advices, Bodo Ritter for his original MCSI code, Paul J. DeMott for his advice on ice

nucleation processes, Alessio Bozzo for numerous discussions and for providing the aerosols optical properties data set used in ECMWF, Alexander Khain for fruitful discussions on cloud formation and aerosols and Theodore Andreadis for creating the COSMO cloud optics web-app.

12 References

Abakumova G., Gorbarenko, E., 2008. Transparency of the atmosphere in Moscow over the last 50 years and its changes in Russia. *LKI Publishing House (in Russian)*, p. 192

Alpert P., Neeman B.U., Shay-El Y., 1990. Climatological analysis of Mediterranean cyclones using ECMWF data. *Tellus*, **42A**, 65-77

Baldauf M., Seifert A., Förstner J., Majewski D., Raschendorfer M., Reinhardt T., 2011. Operational convective-scale numerical weather prediction with the COSMO model: description and sensitivities. *Mon. Weather Rev.* **139**, 3887–3905, https://doi.org/10.1175/MWR?D?10?05013.1

Baum, B.A., A.J. Heymsfield, P. Yang, and S.T. Bedka, 2005. Bulk Scattering Properties for the Remote Sensing of Ice Clouds. Part I: Microphysical Data and Models. *J. Appl. Meteor.*, **44**, 1885–1895

Baum, B.A., P. Yang, A.J. Heymsfield, C.G. Schmitt, Y. Xie, A. Bansemer, Y. Hu, and Z. Zhang, 2011. Improvements in Shortwave Bulk Scattering and Absorption Models for the Remote Sensing of Ice Clouds. *J. Appl. Meteor. Climatol.*, **50**, 1037–1056

Beard, K.V., 1976. Terminal velocity and shape of cloud and precipitation drops aloft. *J. Atmos. Sci.*, **33**, 852–864

Ben Bouallègue Z, Theis SE. 2014. Spatial techniques applied to precipitation ensemble forecasts: from verification results to probabilistic products. *Met. Apps*, **21**, 922–929. doi:10.1002/met.1435

Blahak, U., 2015. Simulating idealized cases with the cosmo-model. http://www.cosmo-model.org/content/model/documentation/core/artif_docu.pdf

Blahak, U. and Ritter, B., 2013. Towards revised cloud radiation coupling for the COSMO Model, COSMO/CLM User Seminar, 5-8 March, Offenbach, Germany

Bott, A., 1998. A flux method for the numerical solution of the stochastic collection equation. *J. Atmos. Sci.*, **55**, 2284–2293, doi:10.1175/1520-0469(1998)055<2284:AFMFTN>2.0.CO;2

Chubarova N. Y., Poliukhov A. A., and Gorlova I. D., 2016. Long-term variability of aerosol optical thickness in Eastern Europe over 2001–2014 according to the measurements at the Moscow MSU MO AERONET site with additional cloud and NO 2 correction. *Atmospheric Measurement Techniques*, **9**(2), pp. 313–334

Chubarova N. , J. Khlestova, M. Shatunova, V. Platonov, G. Rivin, U. Görsdorf, and R. Becker, 2018. Cloud characteristics and cloud radiative effects according to cosmo mesoscale model and measurements. Proc. SPIE 10833, 24th International Symposium on Atmospheric and Ocean Optics: Atmospheric Physics, 10833:108331N–1–108331N–8

Chubarova Natalia, Poliukhov Aleksei, Shatunova Marina, Rivin Gdaliy, Becker Ralf, and Kinne Stefan, 2018. Clear-sky radiative and temperature effects of different aerosol climatologies in the cosmo model. *Geography, Environment, Sustainability*, **11**(1), 74–84

Chubarova, N., Khlestova, J., Shatunova, M., Platonov, V., Rivin, G., Görsdorf, U., &

Becker, R., 2018a. Cloud characteristics and cloud radiative effects according to COSMO mesoscale model and measurements. Proc. SPIE 10833, 24th International Symposium on Atmospheric and Ocean Optics: Atmospheric Physics, 108331N (13 December 2018); https://doi.org/10.1117/12.2504340

Chubarova, N., Poliukhov, A., Shatunova, M., Rivin, G., Becker, R., & Kinne, S., 2018b. Clear-Sky Radiative And Temperature Effects Of Different Aerosol Climatologies In The Cosmo Model. *Geography, Environment, Sustainability*, **11**(1), 74–84. DOI: 10.24057/2071-9388-2018-11-1-74-84

Cooper, W. A., 1986. Ice initiation in natural clouds. Precipitation Enhancement: A Scientific Challenge. *Meteor. Monogr. Amer. Meteor. Soc.*, **43**, 29–32

Dagan G., I. Koren, O. Altaratz, and RH. Heiblum, 2016. Aerosol effect on the evolution of the thermodynamic properties of warm convective cloud fields. *Sci. Rep.*, **6**, 38769, doi:10.1038/srep38769

Davis C. A., Brown B. G., and Bullock R. G., 2006a. Object-based verification of precipitation forecasts. Part I: Methodology and application to mesoscale rain areas. *Mon. Wea. Rev.*, **134**, 1785–1795

Davis C. A., Brown B. G., and Bullock R. G. 2006b. Object-based verification of precipitation forecasts. Part II: Application to convective rain systems. *Mon. Wea. Rev.*, **134**, 1785–1795

Davis C. A., Brown B. G., Bullock R. G. and Halley-Gotway J., 2009. The method for object-based diagnostic evaluation (MODE) applied to numerical forecasts from the 2005 NSSL/SPC Spring Program. *Wea. Forecasting*, **24**, 1252–1267

Deardorff, W. J., 1970. Preliminary results from numerical integrations of the unstable boundary layer. *J. Atmos. Sci.*, **27**, 1209–1231

DeMott, P.J., Prenni, A.J., McMeeking, G.R., Sullivan, R.C., Petters, M.D., Tobo, Y., Niemand, M., Möhler, O., Snider, J.R., Wang, Z., Kreidenweis, S.M., 2015. Integrating laboratory and field data to quantify the immersion freezing ice nucleation activity of mineral dust particles. *Atmos. Chem. Phys.*, **15**, 393–409

Doms G, Foerstner J, Heise E, Herzog HJ, Mironov D, Raschendorfer M, Reinhardt T, Ritter B, Schrodin R, Schulz JP, Vogel G. 2011. A Description of the Nonhydrostatic Regional COSMO Model, part 2: Physical Parameterization. (Available at: http://www.cosmo-model.org)

Duc L, Saito K, H. Seko H. 2013. Spatial-temporal fractions verification for high-resolution ensemble forecasts, *Tellus A: Dynamic Meteorology and Oceanography*, **65**(1), DOI: 10.3402/tellusa.v65i0.18171

Ebert E., 2009. Neighbourhood Verification: A Strategy for Rewarding Close Forecasts. *Wea. Forecasting*, *24*, 1498–1510, https://doi.org/10.1175/2009WAF2222251.1

Field, P.R., Hogan, R.J., Brown, P.R.A., Illingworth, A.J., Choularton, T.W. and Cotton, R.J., 2005. Parametrization of ice-particle size distributions for mid-latitude stratiform cloud. *Q.J.R. Meteorol. Soc.*, **131**, 1997–2017, doi:10.1256/qj.04.134

Fu, Q. and K.N. Liou, 1993. Parameterization of the Radiative Properties of Cirrus Clouds. *J. Atmos. Sci.*, **50**, 2008–2025

Fu, Q., 1996. An Accurate Parameterization of the Solar Radiative Properties of Cirrus Clouds for Climate Models. *J. Climate*, **9**, 2058–2082

Fu, Q., 2007. A New Parameterization of an Asymmetry Factor of Cirrus Clouds for Climate Models. *J. Atmos. Sci.*, **64**, 4140–4150

Fu, Q., Yang, P., & Sun, W., 1998. An Accurate Parameterization of the Infrared Radiative Properties of Cirrus Clouds for Climate Models. *Journal of Climate*, **11**(9), 2223–2237

Gasch, P., Rieger, D., Walter, C., Khain, P., Levi, Y., Knippertz, P., and Vogel, B., 2017. Revealing the meteorological drivers of the September 2015 severe dust event in the Eastern Mediterranean. *Atmos. Chem. Phys.*, **17**, 13573–13604, https://doi.org/10.5194/acp-17-13573-2017

Gasparini, B., and Lohmann, U., 2016. Why cirrus cloud seeding cannot substantially cool the planet. *J. Geophys. Res. Atmos.*, **121**, 4877– 4893

Ghan, S. J., Hayder Abdul-Razzak, A. Nenes, Yi Ming, Xiaohong Liu, M. Ovchinnikov, Ben Shipway, N. Meskhidze, Jun Xu, and X. Shi, 2011. Droplet nucleation: Physically-based parameterizations and comparative evaluation. *J. Adv. Model. Earth Syst.*, **3**, M10001, 33 pp. DOI:10.1029/2011MS000074

Gilleland, E., D. Ahijevych, B.G. Brown, B. Casati, and E.E. Ebert, 2009. Intercomparison of Spatial Forecast Verification Methods. *Wea. Forecasting*, **24**, 1416–1430

Gilleland, E., D.A. Ahijevych, B.G. Brown, and E.E. Ebert, 2010. Verifying Forecasts Spatially. *Bull. Amer. Meteor. Soc.*, **91**, 1365–1376, https://doi.org/10.1175/2010BAMS2819.1

Giorgetta, M. A., Brokopf, R., Crueger, T., Esch, M., Fiedler, S., Helmert, J., 2018. ICON-A, the atmosphere component of the ICON Earth system model: I. Model description. *Journal of Advances in Modeling Earth Systems*, **10**, 1613–1637, https://doi.org/10.1029/2017MS001242

Gruber, S., Blahak, U., Haenel, F., Kottmeier, C., Leisner, T., Muskatel, H., et al., 2019. A process study on thinning of Arctic winter cirrus clouds with high-resolution ICON-ART simulations. *Journal of Geophysical Research: Atmospheres*, **124**

Hess M., Koepke P. and Schult I., 1998. Optical Properties of Aerosols and Clouds: The Sofware Package OPAC, *Bulletin of the American Meteorological Society*, p. 831

Hogan R., Mittermaier M., Illingworth A., 2006. The retrieval of Ice Water Content from Radar Reflectivity Factor and Temperature and Its Use in Evaluating A Mesoscale Model, *American Meteorological Society*

Hogan R.J., Illingworth A.J., 2003. Parameterizing ice cloud inhomogeneity and the overlap of inhomogeneities using cloud radar data, *J. Atmos. Sci.*, **60**, 756–767

Hu, Y.X. and K. Stamnes, 1993. An Accurate Parameterization of the Radiative Properties of Water Clouds Suitable for Use in Climate Models. *J. Climate*, **6**, 728–742

Illingworth A.J. et.al., 2007. Cloudnet – Evaluation of Cloud Profiles in Seven Operational Models Using Ground-Based Observations, *Bull. Amer. Met. Soc.*, **88**, 883–898

Jiang, H., G. Feingold, H. H. Jonsson, M.-L. Lu, P. Y. Chuang, R. C. Flagan, and J. H. Seinfeld, 2008. Statistical comparison of properties of simulated and observed cumulus clouds in the vicinity of Houston during the Gulf of Mexico Atmospheric Composition and Climate Study (GoMACCS), *J. Geophys. Res.*, **113**, D13205, doi:10.1029/2007JD009304

Joseph, J.H., W.J. Wiscombe, and J.A. Weinman, 1976. The Delta-Eddington Approximation for Radiative Flux Transfer. *J. Atmos. Sci.*, **33**, 2452–2459, https://doi.org/10.1175/1520-0469(1976)033<2452:TDEAFR>2.0.CO;2

Key, J. R., Yang, P., Baum, B. A., and Nasiri, S. L., 2002. Parameterization of short-

wave ice cloud optical properties for various particle habits, *J. Geophys. Res.*, **107**(D13), doi:10.1029/2001JD000742

Khain P., H. Muskatel and U. Blahak, 2016. Priority Project T2RC2: Determination of governing parameters in the new radiation scheme. COSMO User Seminar 2016

Khain P., I. Carmona, A. Voudouri, E. Avgoustoglou, J-M. Bettems, F. Grazzini, P. Kaufmann, 2017. CALMO - Progress Report. COSMO technical report 31, available at www.cosmo-model.org, DOI: 10.5676/DWDpub/nwv/cosmo-tr31

Khain, A. P., A. Pokrovsky, M. Pinsky, A. Seifert, and V. Philips, 2004. Simulation of effects of atmospheric aerosols on deep turbulent convective clouds by using a spectral microphysics mixed-phase cumulus cloud model. Part I: Model description and possible applications. *J. Atmos. Sci*, **61**, 2963–2982

Khain, A. P., and M. Pinsky, 2018. Physical Processes in Clouds and Cloud Modeling. *Cambridge University Press*, 642 pp.

Khain, A. P., M. Ovchinnikov, M. Pinsky, A. Pokrovsky, and H. Krugliak, 2000. Notes on the state-of-the-art numerical modeling of cloud microphysics, *Atmos. Res.*, **55**, 159–224

Khain, A., T. V. Prabha, N. Benmoshe, G. Pandithurai, and M. Ovchinnikov, 2013. The mechanism of first raindrops formation in deep convective clouds, *J. Geophys. Res. Atmos.*, **118**, 9123–9140, doi:10.1002/jgrd.50641

Khain, P., R. Heiblum, U. Blahak, Y. Levi, H. Muskatel, E. Vadislavsky, O. Altaratz, I. Koren, G. Dagan, J. Shpund, and A. Khain, 2019. Parameterization of Vertical Profiles of Governing Microphysical Parameters of Shallow Cumulus Cloud Ensembles Using LES with Bin Microphysics. *J. Atmos. Sci.*, **76**, 533–560, https://doi.org/10.1175/JAS-D-18-0046.1

Khairoutdinov, M. F., and D. A. Randall, 2003. Cloud resolving modeling of the ARM summer 1997 IOP: Model formulation, results, uncertainties, and sensitivities, *J. Atmos. Sci.*, **60**(4), 607–625, doi:10.1175/1520-0469

Khlestova J., Chubarova N., Shatunova M., 2019. Radiative and temperature effects of clouds based on the results of numerical experiments of the COSMO mesoscale model and measurement data. Proceedings of SPIE (The International Society for Optical Engineering), *25th International Symposium on Atmospheric and Ocean Optics: Atmospheric Physics*, **11208**

Khvorostyanov, V.I. and J.A. Curry, 1999. Toward the Theory of Stochastic Condensation in Clouds. Part I: A General Kinetic Equation. *J. Atmos. Sci.*, **56**, 3985–3996, https://doi.org/10.1175/1520-0469

Kinne S., 2019. The Macv2 aerosol climatology. *Tellus B Chem. Phys. Meteorol.*, **71**, 1–21

Kunz M., Blahak U., Handwerker J., Schmidberger M., Punge H.J., Mohr S., Fluck E., Bedka K.M., 2018. The severe hailstorm in southwest Germany on 28 July 2013: characteristics, impacts and meteorological conditions. *Q.J.R. Meteorol. Soc.*, **144**, 231-250, doi:10.1002/qj.3197

Lindner, T.H. and J. Li, 2000. Parameterization of the Optical Properties for Water Clouds in the Infrared. *J. Climate*, **13**, 1797–1805

Lohnert U., Meijgaard E., Baltinck H., Grob S., Boers R., 2007. Accuracy assessment of an integrated profiling technique for operationally deriving profiles of temperature, humidity and cloud liquid water. *Jour. Of Geoph. Res.*, **112**, D04205, doi:10.1029/2006JD007379

Lu, M. and J.H. Seinfeld, 2005. Study of the Aerosol Indirect Effect by Large-Eddy Simulation of Marine Stratocumulus. *J. Atmos. Sci.*, **62**, 3909–3932, https://doi.org/10.1175/JAS3584.1

Müller R., Pfeifroth U., Träger-Chatterjee C., Cremer R., Trentmann, J., Hollmann R., 2015. Surface Solar Radiation Data Set - Heliosat (SARAH) - Edition 1, *Satellite Application Facility on Climate Monitoring*, DOI:10.5676/EUM_SAF_CM/SARAH/V001

Macke, A., J. Mueller, and E. Raschke, 1996. Single Scattering Properties of Atmospheric Ice Crystals. *J. Atmos. Sci.*, **53**, 2813–2825

Magaritz-Ronen, L., A. Khain, and M. Pinsky, 2016b. About the horizontal variability of effective radius in stratocumulus clouds, *J. Geophys. Res. Atmos.*, **121**, 9640–9660, doi:10.1002/2016JD024977

Mittermaier M., Roberts N. 2010. Intercomparison of Spatial Forecast Verification Methods: Identifying Skillful Spatial Scales Using the Fractions Skill Score. *Wea. Forecasting*, **25**, 343–354, https://doi.org/10.1175/2009WAF2222260.1

Morcrette, J., et al., 2009. Aerosol analysis and forecast in the European Centre for Medium-Range Weather Forecasts Integrated Forecast System: Forward modeling. *J. Geophys. Res.*, **114**, D06206, doi:10.1029/2008JD011235

Muskatel, H.B., Blahak, U., Khain, P., Levi, Y., Fu, Q., 2021. Parametrizations of Liquid and Ice Clouds Optical Properties in Operational Numerical Weather Prediction Models. *Atmosphere*, **12**, 89, https://doi.org/10.3390/atmos12010089

Nickovic, S., Cvetkovic, B., Madonna, F., Rosoldi, M., Pejanovic,G., Petkovic, S., and Nikolic, J., 2016. Cloud ice caused by atmospheric mineral dust – Part 1: Parameterization of ice nuclei concentration in the NMME-DREAM model. *Atmos. Chem. Phys.*, **16**, 11367–11378, doi:10.5194/acp-16-11367-2016

Petty, G. W. and Huang W., 2011. The Modified Gamma Size Distribution Applied to Inhomogeneous and Non-spherical Particles: Key Relationships and Conversions. *Journal of the Atmospheric Sciences*, **68**(7), 1460–1473

Phillips, V. T. J., P. J. DeMott, and C. Andronache, 2008. An Empirical Parameterization of Heterogeneous Ice Nucleation for Multiple Chemical Species of Aerosol. *J. Atmos. Sci.*, **65**, 2757–2783, https://doi.org/10.1175/2007JAS2546.1

Pinsky, M. and A. Khain, 2018a. Theoretical Analysis of the Entrainment-Mixing Process at Cloud Boundaries. Part I: Droplet Size Distributions and Humidity within the Interface Zone. *J. Atmos. Sci.*, **75**, 2049–2064

Pinsky, M. and A. P. Khain, 2002. Effects of in-cloud nucleation and turbulence on droplet spectrum formation in cumulus clouds. *Quart. J. Roy. Meteorol. Soc.*, **128**, 1–33

Pinsky, M., A. Khain, I. Mazin, and A. Korolev, 2012. Analytical estimation of droplet concentration at cloud base. *J. Geophy. Res.*, **117**, D18211, doi:10.1029/2012JD017753

Pinsky, M., I. Mazin, A. Korolev and A. Khain, 2014. Supersaturation and diffusional droplet growth in liquid clouds: Polydisperse spectra. *J. Geophys Res.*, **119**, 12872–12887

Pinsky, M., Khain, A. P., and M. Shapiro, 2001. Collision efficiency of drops in a wide range of Reynolds numbers: Effects of pressure on spectrum evolution. *J. Atmos. Sci.*, **58**, 742–764

Pinsky, M., Khain, A., and Korolev, A. 2016b. Theoretical analysis of mixing in liquid clouds – Part 3: Inhomogeneous mixing. *Atmos. Chem. Phys.*, **16**, 9273-9297. www.atmos-chem-

phys.net/16/9273/2016/doi:10.5194/acp-16-9273-2016

Poliukhov A. A., N. E. Chubarova, D. V. Blinov, T. A. Tarasova, A. P. Makshtas, and H. Muskatel, 2019. Radiation effects of different types of aerosol in Eurasia according to observations and model calculations. *Russian Meteorology and Hydrology*, **44**(9), 579–587

Poliukhov, A. A., Chubarova, H. E., Shatunova, M. V., Rivin, G. S., Tarasova, T. A., Makshtas, A. P., Muskatel, H., 2018. Radiative effect of different aerosol types in clear sky conditions according to COSMO-Ru model. In 24th International Symposium on Atmospheric and Ocean Optics: Atmospheric Physics (**10833**, p. 1083308). International Society for Optics and Photonics. DOI: 10.1117/12.2504299

Poliukhov, A., Chubarova, N., Kinne, S., Rivin, G., Shatunova, M., & Tarasova, T., 2017. Comparison between calculations of shortwave radiation with different aerosol datasets and measured data at the MSU MO (Russia). In AIP Conference Proceedings (**1810**, 1, p. 100006). AIP Publishing. DOI: 10.1063/1.4975561

Pontikis, C. A., 1996. Parameterization of the droplet effective radius of warm layer clouds. *Geophys. Res. Lett.*, **23**(19), 2629–2632

Reid, J. S., Hobbs, P. V., Rangno, A. L., and Hegg, D. A., 1999. Relationships between cloud droplet effective radius, liquid water content, and droplet concentration for warm clouds in Brazil embedded in biomass smoke. *J. Geophys. Res.*, **104**(D6), 6145–6153, doi:10.1029/1998JD200119

Ritter, B. and J. Geleyn, 1992. A Comprehensive Radiation Scheme for Numerical Weather Prediction Models with Potential Applications in Climate Simulations. *Mon. Wea. Rev.*, **120**, 303–325

Roberts N.M., Lean H.W. 2008. Scale-Selective Verification of Rainfall Accumulations from High-Resolution Forecasts of Convective Events. *Mon. Wea. Rev.*, **136**, 78–97, https://doi.org/10.1175/2007MWR2123.1

Rosenfeld D., 2006. Aerosol-Cloud Interactions Control of Earth Radiation and Latent Heat Release Budgets. *Space Sci. Rev.*, **125**, 149–157, doi:10.1007/s11214-006-9053-6

Rosenfeld, D., I. M. Lensky, 1998. Satellite-Based Insights into Precipitation Formation Processes in Continental and Maritime Convective Clouds, *Bull. Am. Meteorol. Soc.*, **79**, 2457–2476, doi:10.1175/1520-0477

Rosenfeld, D., Lohmann, U., Raga, G. B., O'Dowd, C. D., Markku, M., Fuzzi, S., Reissell, A. and Andreae, M. O., 2008. Flood or Drought: How Do Aerosols Affect Precipitation? *Science*, 1309–1313

Rossow, W.B., and R.A. Schiffer, 1999. Advances in understanding clouds from ISCCP. *Bull. Amer. Meteorol. Soc.*, **80**, 2261–2288

Sassen, K., Wang, Z., and Liu, D., 2008. Global distribution of cirrus clouds from CloudSat/Cloud-Aerosol Lidar and Infrared Pathfinder Satellite Observations (CALIPSO) measurements. *J. Geophys. Res.*, **113**

Schröter, J., Rieger, D., Stassen, C., Vogel, H., Weimer, M., Werchner, S., Förstner, J., Prill, F., Reinert, D., Zängl, G., Giorgetta, M., Ruhnke, R., Vogel, B., and Braesicke, P., 2018. ICON-ART 2.1: a flexible tracer framework and its application for composition studies in numerical weather forecasting and climate simulations, *Geosci. Model Dev.*, **11**, 4043–4068, https://doi.org/10.5194/gmd-11-4043-2018

Schwartz, C.S., R.A. Sobash, 2017. Generating Probabilistic Forecasts from Convection-

Allowing Ensembles Using Neighborhood Approaches: A Review and Recommendations. *Mon. Wea. Rev.*, **145**, 3397–3418, https://doi.org/10.1175/MWR-D-16-0400.1

Segal Y., A. P. Khain, 2006. Dependence of droplet concentration on aerosol conditions in different cloud types: application to droplet concentration parameterization of aerosol conditions, *J. Geophys. Res.*, **111**, D15204, doi:10.1029/2005JD006561

Sharon D, Kutiel H. 1986. The distribution of rainfall intensity in Israel, its regional and seasonal variations and its climatological evaluation. *International Journal of Climatology.* **6**, 277–291

Shatunova, M.V., Khlestova, Y.O., Chubarova, N.E., 2020. Forecast of Microphysical and Optical Characteristics of Large-Scale Cloud Cover and Its Radiative Effect Using the COSMO Mesoscale Weather Prediction Model. *Atmos. Ocean Opt.*, **33**, 154–160, https://doi.org/10.1134/S1024856020020098

Shay-El Y, Alpert P. 1991. A diagnostic study of winter diabetic heating in the Mediterranean in relation to cyclones. *Quarterly Journal of the Royal Meteorological Society*, **117**, 715–747

Siebesma, A.P., Bretherton, C.S., Brown, A., Chlond, A., Cuxart, J., Duynkerke, P.G., Jiang, H., Khairoutdinov, M., Lewellen, D., Moeng, C.H. and Sanchez, E., 2003. A large eddy simulation intercomparison study of shallow cumulus convection. *Journal of the Atmospheric Sciences*, **60**(10), 1201–1219

Slingo, A., Schrecker, H. M., 1982. On the shortwave radiative properties of stratiform water clouds. *Q.J.R. Meteorol. Soc.*, **108**, 407–426

Slingo, A., 1989. A GCM Parameterization for the Shortwave Radiative Properties of Water Clouds. *J. Atmos. Sci.*, **46**, 1419–1427

Steinke, I., Hoose, C., Möhler, O., Connolly, P., and Leisner, T., 2015. A new temperature- and humidity-dependent surface site density approach for deposition ice nucleation, *Atmos. Chem. Phys.*, **15**, 3703–3717, https://doi.org/10.5194/acp-15-3703-2015

Stephens, G. L., 1979. Optical properties of eight water cloud types. CSIRO: Division of Atmospheric Physics, Tech. report 36

Stephens, G.L., 1984. The Parameterization of Radiation for Numerical Weather Prediction and Climate Models. *Mon. Wea. Rev.*, **112**, 826–867

Steppeler J., Doms G., Schattler U., Bitzer H.W., Gassmann A., Damrath U., Gregoric G., 2003. Meso gamma scale forecasts by non-hydrostatic model LM. *Meteorological Atmospheric Physics*, **82**, 75–96

Takano, Y., K. Liou, 1989. Solar Radiative Transfer in Cirrus Clouds. Part I: Single-Scattering and Optical Properties of Hexagonal Ice Crystals. *J. Atmos. Sci.*, **46**, 3–19

Tanre D., Geleyn J. F., and Slingo J. M., 1984. First results of the introduction of an advanced aerosol-radiation interaction in the ECMWF low resolution global model. *Aerosols and their climatic effects*, 133–177

Tarasova, Yarkho, 1991. Determination of aerosol optical thickness according to ground-based measurements of integral solar irradiance. *Russian Meteorology and Hydrology*, Planeta Publishing House, **12**, 66–71

Tegen, I., Hollrig, P., Chin, M., Fung, I., Jacob, D., and Penner, J., 1997. Contribution of different aerosol species to the global aerosol extinction optical thickness: Estimates from

model results. *Journal of Geophysical Research: Atmospheres*, **102**(D20), 23895–23915

Vergara-Temprado J., Miltenberger A.K., Furtado K., Grosvenor D.P., Shipway B.J., Hill A.A., Wilkinson J.M., Field P.R., Murray B.J., Carslaw K.S., 2018. Strong control of Southern Ocean cloud reflectivity by ice-nucleating particles. *Proceedings of the National Academy of Sciences of the United States of America*, **115**, 2687–2692

Voudouri A., Khain P., Carmona I., Bellprat O., Grazzini F., Avgoustoglou E. , Bettems J-M. and Kaufmann P., 2017. Objective calibration of numerical weather prediction models. *Atm. Res.*, **190**, 128–140

Ware R., Carpenter R., Guldner J., Liljegren J., Nehrkorn T., Solheim F., Vandenberghe F., 2003. A multichannel radiometric profiler of temperature, humidity and cloud liquid, *RADIO SCIENCE*, **38**, 4, 8079, doi:10.1029/2002RS002856

Wiscombe, W. J., 1977. The Delta-Eddington Approximation for a Vertically Inhomogeneous Atmosphere. NCAR Technical Note NCAR/TN-121+STR

Yanai, M., Esbensen, S., and Chu, J.-H., 1973. Determination of bulk properties of tropical cloud clusters from large-scale heat and moisture budgets. *J. Atmos. Sci.*, **30**, 611–627

Yang, P. and K. N. Liou, 1995. Light scattering by hexagonal ice crystals: comparison of finite-difference time domain and geometric optics models. *J. Opt. Soc. Am. A*, **12**, 162–176

Yang, P. and K. N. Liou, 1996. Finite-difference time domain method for light scattering by small ice crystals in three-dimensional space. *J. Opt. Soc. Am. A*, **13**, 2072–2085

Yang, P., L. Bi, B.A. Baum, K. Liou, G.W. Kattawar, M.I. Mishchenko, and B. Cole, 2013. Spectrally Consistent Scattering, Absorption, and Polarization Properties of Atmospheric Ice Crystals at Wavelengths from 0.2 to 100 μm. *J. Atmos. Sci.*, **70**, 330–347

Yang, P., Liou, K. N., Wyser, K., and Mitchell, D., 2000. Parameterization of the scattering and absorption properties of individual ice crystals, *J. Geophys. Res.*, **105**(D4), 4699–4718

Zängl, G., D. Reinert, P. Ripodas, and M. Baldauf, 2015. The ICON (ICOsahedral Non-hydrostatic) modelling framework of DWD and MPI-M: Description of the non-hydrostatic dynamical core. *Q.J.R. Meteorol. Soc.*, **141**, 563–579

Ziv B, Dayan U, Kushnir Y, Roth C, Enzel Y. 2006. Regional and global atmospheric patterns governing rainfall in the southern Levant. *International Journal of Climatology*, **26**(1), 55–73

List of COSMO Newsletters and Technical Reports

(available for download from the COSMO Website: www.cosmo-model.org)

COSMO Newsletters

No. 1: February 2001.

No. 2: February 2002.

No. 3: February 2003.

No. 4: February 2004.

No. 5: April 2005.

No. 6: July 2006.

No. 7: April 2008; Proceedings from the 8th COSMO General Meeting in Bucharest, 2006.

No. 8: September 2008; Proceedings from the 9th COSMO General Meeting in Athens, 2007.

No. 9: December 2008.

No. 10: March 2010.

No. 11: April 2011.

No. 12: April 2012.

No. 13: April 2013.

No. 14: April 2014.

No. 15: July 2015.

No. 16: July 2016.

No. 17: July 2017.

No. 18: November 2018.

No. 19: October 2019.

No. 20: December 2020.

COSMO Technical Reports

No. 1: Dmitrii Mironov and Matthias Raschendorfer (2001):
Evaluation of Empirical Parameters of the New LM Surface-Layer Parameterization Scheme. Results from Numerical Experiments Including the Soil Moisture Analysis.
DOI: 10.5676/DWD_pub/nwv/cosmo-tr_1

No. 2: Reinhold Schrodin and Erdmann Heise (2001):
The Multi-Layer Version of the DWD Soil Model TERRA_LM.
DOI: 10.5676/DWD_pub/nwv/cosmo-tr_2

No. 3: Günther Doms (2001):
A Scheme for Monotonic Numerical Diffusion in the LM.
DOI: 10.5676/DWD_pub/nwv/cosmo-tr_3

No. 4: Hans-Joachim Herzog, Ursula Schubert, Gerd Vogel, Adelheid Fiedler and Roswitha Kirchner (2002):
LLM ¯ the High-Resolving Nonhydrostatic Simulation Model in the DWD-Project LITFASS. Part I: Modelling Technique and Simulation Method.
DOI: 10.5676/DWD_pub/nwv/cosmo-tr_4

No. 5: Jean-Marie Bettems (2002):
EUCOS Impact Study Using the Limited-Area Non-Hydrostatic NWP Model in Operational Use at MeteoSwiss.
DOI: 10.5676/DWD_pub/nwv/cosmo-tr_5

No. 6: Heinz-Werner Bitzer and Jürgen Steppeler (2004):
Documentation of the Z-Coordinate Dynamical Core of LM.
DOI: 10.5676/DWD_pub/nwv/cosmo-tr_6

No. 7: Hans-Joachim Herzog, Almut Gassmann (2005):
Lorenz- and Charney-Phillips vertical grid experimentation using a compressible nonhydrostatic toy-model relevant to the fast-mode part of the 'Lokal-Modell'.
DOI: 10.5676/DWD_pub/nwv/cosmo-tr_7

No. 8: Chiara Marsigli, Andrea Montani, Tiziana Paccagnella, Davide Sacchetti, André Walser, Marco Arpagaus, Thomas Schumann (2005):
Evaluation of the Performance of the COSMO-LEPS System.
DOI: 10.5676/DWD_pub/nwv/cosmo-tr_8

No. 9: Erdmann Heise, Bodo Ritter, Reinhold Schrodin (2006):
Operational Implementation of the Multilayer Soil Model.
DOI: 10.5676/DWD_pub/nwv/cosmo-tr_9

No. 10: M.D. Tsyrulnikov (2007):
Is the particle filtering approach appropriate for meso-scale data assimilation ?
DOI: 10.5676/DWD_pub/nwv/cosmo-tr_10

No. 11: Dmitrii V. Mironov (2008):
Parameterization of Lakes in Numerical Weather Prediction. Description of a Lake Model.
DOI: 10.5676/DWD_pub/nwv/cosmo-tr_11

No. 12: Adriano Raspanti (2009):
COSMO Priority Project "VERification System Unified Survey" (VERSUS): Final Report.
DOI: 10.5676/DWD_pub/nwv/cosmo-tr_12

No. 13: Chiara Marsigli (2009):
COSMO Priority Project "Short Range Ensemble Prediction System" (SREPS): Final Report.
DOI: 10.5676/DWD_pub/nwv/cosmo-tr_13

No. 14: Michael Baldauf (2009):
COSMO Priority Project "Further Developments of the Runge-Kutta Time Integration Scheme" (RK): Final Report.
DOI: 10.5676/DWD_pub/nwv/cosmo-tr_14

No. 15: Silke Dierer (2009):
COSMO Priority Project "Tackle deficiencies in quantitative precipitation forecast" (QPF): Final Report.
DOI: 10.5676/DWD_pub/nwv/cosmo-tr_15

No. 16: Pierre Eckert (2009):
COSMO Priority Project "INTERP": Final Report.
DOI: 10.5676/DWD_pub/nwv/cosmo-tr_16

No. 17: D. Leuenberger, M. Stoll and A. Roches (2010):
Description of some convective indices implemented in the COSMO model.
DOI: 10.5676/DWD_pub/nwv/cosmo-tr_17

No. 18: Daniel Leuenberger (2010):
Statistical analysis of high-resolution COSMO Ensemble forecasts in view of Data Assimilation.
DOI: 10.5676/DWD_pub/nwv/cosmo-tr_18

No. 19: A. Montani, D. Cesari, C. Marsigli, T. Paccagnella (2010):
Seven years of activity in the field of mesoscale ensemble forecasting by the COSMO–LEPS system: main achievements and open challenges.
DOI: 10.5676/DWD_pub/nwv/cosmo-tr_19

No. 20: A. Roches, O. Fuhrer (2012):
Tracer module in the COSMO model.
DOI: 10.5676/DWD_pub/nwv/cosmo-tr_20

No. 21: Michael Baldauf (2013):
A new fast-waves solver for the Runge-Kutta dynamical core.
DOI: 10.5676/DWD_pub/nwv/cosmo-tr_21

No. 22: C. Marsigli, T. Diomede, A. Montani, T. Paccagnella, P. Louka, F. Gofa, A. Corigliano (2013):
The CONSENS Priority Project.
DOI: 10.5676/DWD_pub/nwv/cosmo-tr_22

No. 23: M. Baldauf, O. Fuhrer, M. J. Kurowski, G. de Morsier, M. Müllner, Z. P. Piotrowski, B. Rosa, P. L. Vitagliano, D. Wójcik, M. Ziemiański (2013):
The COSMO Priority Project 'Conservative Dynamical Core' Final Report.
DOI: 10.5676/DWD_pub/nwv/cosmo-tr_23

No. 24: A. K. Miltenberger, A. Roches, S. Pfahl, H. Wernli (2014):
Online Trajectory Module in COSMO: a short user guide.
DOI: 10.5676/DWD_pub/nwv/cosmo-tr_24

No. 25: P. Khain, I. Carmona, A. Voudouri, E. Avgoustoglou, J.-M. Bettems, F. Grazzini (2015):
The Proof of the Parameters Calibration Method: CALMO Progress Report.
DOI: 10.5676/DWD_pub/nwv/cosmo-tr_25

No. 26: D. Mironov, E. Machulskaya, B. Szintai, M. Raschendorfer, V. Perov, M. Chumakov, E. Avgoustoglou (2015):
The COSMO Priority Project 'UTCS' Final Report.
DOI: 10.5676/DWD_pub/nwv/cosmo-tr_26

No. 27: J-M. Bettems (2015):
The COSMO Priority Project 'COLOBOC': Final Report.
DOI: 10.5676/DWD_pub/nwv/cosmo-tr_27

No. 28: Ulrich Blahak (2016):
RADAR_MIE_LM and RADAR_MIELIB - Calculation of Radar Reflectivity from Model Output.
DOI: 10.5676/DWD_pub/nwv/cosmo-tr_28

No. 29: M. Tsyrulnikov and D. Gayfulin (2016):
A Stochastic Pattern Generator for ensemble applications.
DOI: 10.5676/DWD_pub/nwv/cosmo-tr_29

No. 30: D. Mironov and E. Machulskaya (2017):
A Turbulence Kinetic Energy – Scalar Variance Turbulence Parameterization Scheme.
DOI: 10.5676/DWD_pub/nwv/cosmo-tr_30

No. 31: P. Khain, I. Carmona, A. Voudouri, E. Avgoustoglou, J.-M. Bettems, F. Grazzini, P. Kaufmann (2017):
CALMO - Progress Report.
DOI: 10.5676/DWD_pub/nwv/cosmo-tr_31

No. 32: A. Voudouri, P. Khain, I. Carmona, E. Avgoustoglou, J.M. Bettems, F. Grazzini, O. Bellprat, P. Kaufmann and E. Bucchignani (2017):
Calibration of COSMO Model, Priority Project CALMO Final report.
DOI: 10.5676/DWD_pub/nwv/cosmo-tr_32

No. 33: N. Vela (2017):
VAST 2.0 - User Manual.
DOI: 10.5676/DWD_pub/nwv/cosmo-tr_33

No. 34: C. Marsigli, D. Alferov, M. Arpagaus, E. Astakhova, R. Bonanno, G. Duniec, C. Gebhardt, W. Interewicz, N. Loglisci, A. Mazur, V. Maurer, A. Montani, A. Walser (2018):
COsmo Towards Ensembles at the Km-scale IN Our countries" (COTEKINO), Priority Project final report.
DOI: 10.5676/DWD_pub/nwv/cosmo-tr_34

No. 35: G. Rivin, I. Rozinkina, E. Astakhova, A. Montani, D. Alferov, M. Arpagaus, D. Blinov, A. Bundel, M. Chumakov, P. Eckert, A. Euripides, J. Förstner, J. Helmert, E. Kazakova, A. Kirsanov, V. Kopeikin, E. Kukanova, D. Majewski, C. Marsigli, G. de Morsier, A. Muravev, T. Paccagnella, U. Schättler, C. Schraff, M. Shatunova, A. Shcherbakov, P. Steiner, M. Zaichenko (2018):
The COSMO Priority Project CORSO Final Report.
DOI: 10.5676/DWD_pub/nwv/cosmo-tr_35

No. 36: A. Raspanti, A. Celozzi, A. Troisi, A. Vocino, R. Bove, F. Batignani (2018):
The COSMO Priority Project VERSUS2 Final Report.
DOI: 10.5676/DWD_pub/nwv/cosmo-tr_36

No. 37: A. Bundel, F. Gofa, D. Alferov, E. Astakhova, P. Baumann, D. Boucouvala, U. Damrath, P. Eckert, A. Kirsanov, X. Lapillonne, J. Linkowska, C. Marsigli, A. Montani, A. Muraviev, E. Oberto, M.S. Tesini, N. Vela, A. Wyszogrodzki, M. Zaichenko, A. Walser (2019):
The COSMO Priority Project INSPECT Final Report.
DOI: 10.5676/DWD_pub/nwv/cosmo-tr_37

No. 38: G. Rivin, I. Rozinkina, E. Astakhova, A. Montani, J-M. Bettems, D. Alferov, D. Blinov, P. Eckert, A. Euripides, J. Helmert, M.Shatunova (2019):
The COSMO Priority Project CORSO-A Final Report.
DOI: 10.5676/DWD_pub/nwv/cosmo-tr_38

No. 39: C. Marsigli, D. Alferov, E. Astakhova, G. Duniec, D. Gayfulin, C. Gebhardt, W. Interewicz, N. Loglisci, F. Marcucci, A. Mazur, A. Montani, M. Tsyrulnikov, A. Walser (2019):
Studying perturbations for the representation of modeling uncertainties in Ensemble development (SPRED Priority Project): Final Report.
DOI: 10.5676/DWD_pub/nwv/cosmo-tr_39

No. 40: E. Bucchignani, P. Mercogliano, V. Garbero, M. Milelli, M. Varentsov, I. Rozinkina, G. Rivin, D. Blinov, A. Kirsanov, H. Wouters, J.-P. Schulz, U. Schättler (2019):
Analysis and Evaluation of TERRA_URB Scheme: PT AEVUS Final Report.
DOI: 10.5676/DWD_pub/nwv/cosmo-tr_40

No. 41: X. Lapillonne, O. Fuhrer (2020):
Performance On Massively Parallel Architectures (POMPA): Final report.
DOI: 10.5676/DWD_pub/nwv/cosmo-tr_41

No. 42: E. Avgoustoglou, A. Voudouri, I Carmona, E. Bucchignani, Y. Levy, J. -M. Bettems (2020):
A methodology towards the hierarchy of COSMO parameter calibration tests via the domain sensitivity over the Mediterranean area.
DOI: 10.5676/DWD_pub/nwv/cosmo-tr_42

COSMO Technical Reports

Issues of the COSMO Technical Reports series are published by the *COnsortium for Small-scale MOdelling* at non-regular intervals. COSMO is a European group for numerical weather prediction with participating meteorological services from Germany (DWD, AWGeophys), Greece (HNMS), Italy (USAM, ARPA-SIMC, ARPA Piemonte), Switzerland (MeteoSwiss), Poland (IMGW), Romania (NMA) and Russia (RHM). The general goal is to develop, improve and maintain a non-hydrostatic limited area modelling system to be used for both operational and research applications by the members of COSMO. This system is initially based on the COSMO-Model (previously known as LM) of DWD with its corresponding data assimilation system.

The Technical Reports are intended

- for scientific contributions and a documentation of research activities,
- to present and discuss results obtained from the model system,
- to present and discuss verification results and interpretation methods,
- for a documentation of technical changes to the model system,
- to give an overview of new components of the model system.

The purpose of these reports is to communicate results, changes and progress related to the LM model system relatively fast within the COSMO consortium, and also to inform other NWP groups on our current research activities. In this way the discussion on a specific topic can be stimulated at an early stage. In order to publish a report very soon after the completion of the manuscript, we have decided to omit a thorough reviewing procedure and only a rough check is done by the editors and a third reviewer. We apologize for typographical and other errors or inconsistencies which may still be present.

At present, the Technical Reports are available for download from the COSMO web site (www.cosmo-model.org). If required, the member meteorological centres can produce hard-copies by their own for distribution within their service. All members of the consortium will be informed about new issues by email.

For any comments and questions, please contact the editor:

Massimo Milelli
Massimo.Milelli@arpa.piemonte.it

Consortium for Small-Scale Modelling

Technical Report No. 36

The COSMO Priority Project VERSUS2 Final Report

November 2018

DOI: 10.5676/DWD_pub/nwv/cosmo-tr_36

Deutscher Wetterdienst
MeteoSwiss
Ufficio Generale Spazio Aereo e Meteorologia
ΕΘΝΙΚΗ ΜΕΤΕΩΡΟΛΟΓΙΚΗ ΥΠΗΡΕΣΙΑ
Instytucie Meteorogii i Gospodarki Wodnej
Administratia Nationala de Meteorologie
ROSHYDROMET
Agenzia Regionale Protezione Ambiente Piemonte
Agenzia Regionale Prevenzione Ambiente Energia Emilia Romagna
Centro Italiano Ricerche Aerospaziali
Amt für GeoInformationswesen der Bundeswehr
Israel Meteorological Service

www.cosmo-model.org

Editor: Massimo Milelli, ARPA Piemonte

The COSMO Priority Project VERSUS2

Final Report

Project participants:

***A. Raspanti*[1]‡, *A. Celozzi*[1]‡, *A. Troisi*[1], *A. Vocino*[1]‡,**

***R. Bove*[1]‡, *F. Batignani*[1]**

[1] Italian Air Force Meteorological Service

‡ Project Coordinator

Contents

1 Introduction **3**

1.1 Overview 3

1.2 Motivations 3

2 Tasks and achievements **5**

2.1 Project presentation 5

2.2 Project phases and tasks 5

2.2.1 Phase 1. COSMO year 2009 5

2.2.2 Phase 2. COSMO year 2010 5

2.2.3 Phase 3. COSMO year 2011 6

2.2.4 Phase 4. COSMO year 2012 6

2.2.5 Phase 5. COSMO year 2013 6

2.2.6 Phase 6. COSMO year 2013-4 7

2.2.7 Phase 7. COSMO year 2014-5 7

2.2.8 Phase 8 / Extension Phase COSMO year 2015-2016 8

3 Further developments **8**

4 Conclusions **9**

5 Meetings **9**

6 User and technical Manual **10**

7 References **10**

1 Introduction

1.1 Overview

The development, implementation and operational use of the original VERSUS package (2006-2009 PP project) satisfied most of the needs for traditional verification, but the constant increasing model resolution as well as the current and planned ensemble systems asked for more suitable information from verification activities. At the same time users of model forecasts asked for more information about the real quality of their model: this means a step towards user-specific verification information.

The extension of the VERSUS package to VERSUS2 has covered these items and has provided the COSMO community with a "state of the art" verification tool. The "System Architecture Design" (SAD) specification document was released in May 2009 and updated in January 2010 (www.cosmo-model.org/content/tasks/pastProjects/versus2/docs/versus2-SAD.pdf).

1.2 Motivations

The aim of the VERSUS-1 Priority Project, started at the end of 2006 and concluded in February 2009, with the official delivery of the package, was the development of a common and unified verification 'library' including a Conditional Verification (CV) tool. This library has been included in the public COSMO Software along with the new software from Priority Project VERSUS2. The package and all its main features have been planned and realised with the intention to be a useful and friendly tool for the entire COSMO community for operational as well as research activities to perform traditional and conditional verification (CV), based on conventional methods. As the typical approach to CV consist of a selection of one or several forecast products and one or several mask variables or conditions, which is used to define thresholds for the product verification, the flexible way to perform such a selection is to use an 'ad hoc database', planned and designed for this purpose. In this case the masks or filters can be simple or complex SQL statements. After the selection of the desired conditions, a classical verification tool to turn out statistical indexes can be used, along with a graphics package to plot the scores. The general VERSUS architecture is basically composed of a set of integrated tools:

- **Relational Data Base Management System** (RDBMS), to store observations (OBS) and forecast (FCS) data, Station Data, Configuration data to perform verification, Verification results, Scores and plots, and User permissions; the chosen data base is MySQL in case of the initial VERSUS version;
- **Front End loader** (FE), a "daemon" process to load data from different sources into the RDBMS (File system or another DB); among FE functionalities, and very useful for CV, it is possible to use a loader dedicated to the SRNWP Data Exchange Programme observations, consisting in good quality operational data from a limited set of well instrumented and high quality observation sites in Europe, in particular providing soil, surface and boundary layer data;
- **A process performing verifications** through specific requests (Integration into the "R" statistics package);
- **A web-based user interface** (server-client architecture).

The VERSUS1 project was divided into 10 tasks and most of them has been completed. The delivery of the complete package occurred during a Workshop/Tutorial in February 2009. In the course of the first VERSUS project development, most of the COSMO members moved towards higher resolution models as well as ensemble forecasting systems. The increasing resolution has, in general, the impact that objective scores for weather parameters can be worse for high resolution models than for low resolution models. Increased resolution, in fact, generally produces better defined mesoscale structures, greater amplitude features, and larger gradients, and inevitably leads to space and time errors. This is known as the "double penalty" problem. Nevertheless such a model can provide very useful information. The need for verification techniques that allow for some tolerance to reasonably small space and time errors is then clear, retaining the main feature to be capable to test the real quality of information provided by the high-resolution model and the possible connections between forecast deficiencies and specific weaknesses in the model formulation. At the same time, as COSMO model future plans were in the probabilistic and ensemble forecast direction, suitable verification methods had to be applied. In general there are three methods to evaluate this kind of forecasts (Casati et al., 2008):

- Verification of an ensemble distribution: methods used to verify ensemble distributions are rank histograms (Talagrand histograms), Continuous rank probability score and its related skill score (a measure for the difference between the cumulative distribution function of the forecasts and observation), and minimum spanning tree (a sort of multidimensional rank histogram, not so widely used);

- Verification measures for the probability density function (pdf) of a generic probability forecast: methods used are "linear probability" and the "ignorance score". Both the methods are local, evaluating the pdf at the observation value, and both rewards sharp distributions which are also accurate;

- Verification of the probability of an event: methods used are Brier Score (BS) and its decomposition, Brier Skill Score (BSS), reliability diagrams, ROC and the Rank Probability Score (RPS). It is useful to add to these methods also bootstrap confidence intervals to generalize score estimates over different sample sizes.

All the above verification techniques, and others specialised for extreme events and user needs, had been analysed and then included in the VERSUS package to have a common "state-of-the-art" tool for verification for the entire COSMO community. VERSUS is routinely used for the calculation of seasonal statistics over a common area according to the guidelines (http://www.cosmo-model.org/content/tasks/verification.priv) derived on an annual basis from WG5 for each participating model of COSMO consortium (Common Plots). VERSUS is also used in the framework of the NWP Test Suite, which is the software environment to perform carefully-controlled and rigorous testing with calculation of verification statistics for any COSMO model test version. For this aim VERSUS software has been also installed at the ECMWF on a dedicated virtual machine (an innovative solution for that time). The NWP Test Suite has been used over the years as benchmark for the major changes of the new COSMO model versions. These activities have been important for the software debug and continuous COSMO model development.

2 Tasks and achievements

2.1 Project presentation

The PP VERSUS2 has been approved in September 2009 during the 24th STC Meeting (07-08/09/2009) that took place in Offenbach, Germany and has been declared closed in September 2016, during the 38th STC Meeting (05-06/09/2016), in Offenbach as well, with the release of VERSUS 5.1 and VAST 1.4 packages (June-July 2016), which form the COSMO Common Verification Software (CVS). Further developments on the system have been carried out from the end of the project up to October 2018 and then reported here for completeness. VERSUS maintenance has been assured by the Italian Air Force Meteorological Service up to December 2018.

In a first phase (COSMO year 2009), a "User Requirements Specification" had been compiled, and has been implemented during the following phases of the project itself (COSMO years 2010-2016). Most of the single phases has been concluded in one COSMO year. Every year, based on the real deliverables produced, the plan has been updated accordingly to a quick review of the requirements of the next phase, and the new phase to be developed has been fully described (see COSMO GM presentations for details).

A concise account of the tasks and achievements developed during the project is thus chronologically presented in the next section.

2.2 Project phases and tasks

2.2.1 Phase 1. COSMO year 2009

It has been completed as planned in Cosmo year 2009 , with the delivery of System Design Overview Document (SDO, updated in July 2009 as requested by the STC) and System Architecture Design (SAD, approved by the STC). During this phase of the project the main activity consisted in the implementation of VERSUS system at every service within COSMO consortium, in particular through the realization of a multi-platform RDBMS version of the software and consequently the installation of multi-platform DB version of VERSUS at every service.

2.2.2 Phase 2. COSMO year 2010

This phase was composed of many different tasks: at level 0 the main goal was to provide assistance to all VERSUS users inside the consortium, through the Help Desk service, bugs fixing activities and the following VERSUS update patch release. The implementation of COSI (global Score Cosmo Index) was then carried out, through both the initial preparation of the technical reference document and the factual index implementation. Another important step was to implement the software features concerning conditional verification: VERSUS software modules and related web GUI updates were developed for the implementation of weather type dependent verification and conditional verification (WDV, CV). During this phase a detailed documentation of Fuzzy verification toolbox, necessary in order to perform verification on high resolution models, was produced, with the implementation realised via the VAST software. Another important achievement was the introduction of Feedback Files (FF from now) as input for the system, with the realisation of new loader modules to be integrated in VERSUS_FE; this type of file was useful for the management of

new observation data such as Airep, Amdar, Windprofiler, TEMP (non standard pressure level) and Radar wind data.

2.2.3 Phase 3. COSMO year 2011

In this phase continued the activity of Help Desk, bug-fixing and release of VERSUS updates, and in parallel was carried out the improvement of VERSUS security and "plug&play" installation and web pages: in detail new installation/patch update procedures and back-up functionalities for the DB were developed, as well as a review of web GUI search pages for improved functionality. The work for the final implementation of the Feedback Files capability was carried on, with the implementation of a loader module, the creation of new web GUI, conditional verification for data from FF and a stand-alone tool for FF creation for all partners ,with the related documentation. A dedicated test phase for FF tool implementation and FF functionalities in VERSUS was then realised. The attention of the developers was also focused in the improving of the probabilistic scores, necessary to the EPS verification, with the implementation of "R" package in VERSUS with the creation of new web pages for GUI and the production of the related documentation.

2.2.4 Phase 4. COSMO year 2012

In this year the aim of developers was focused on software usability: an improvement of the batch execution functionality, even with the possibility of using it for cross verification, and of the suspect observation menu were realised, as well as the addition of a data permanence process, able to delete observation and forecast older than a configurable time presence. The work on the FF processing modules, started the former year, continued. The use of Feedback Files (FF) was important to improve upper air verification and Conditional Verification activities, where large amounts of data must be manipulated. A feasibility study on how to proceed with the implementation of FF was created by the Project Leader (PL) team, reviewed by DWD in July 2010, and the new Database Structure for FF was then created. At the same time the importance of updating the system, according with the evolution of the standard meteorological message formats, was taken into account by the implementation of new BUFR format, for observation, and GRIB2, for forecast. The adoption by WMO of a new template for BUFR was the main reason for this task as well as the foreseen use of GRIB2 as output of COSMO models. The process consisted in updating the system for the upload functionality of new BUFR template and merge (in space and time) with the old format. The use of the new template has made verification more flexible for the cumulated precipitation. A document describing the activity was delivered and approved. The updating of the system for the treatment of produced forecasts coded in GRIB2 format was then carried out with the related documentation. At the same time continued the user support activity, the implementation of the FF modules and probabilistic scores within the R package.

2.2.5 Phase 5. COSMO year 2013

The goal of the year was to complete the most crucial developments define by participants of the last VERSUS user meeting that took place in Rome in April 2012. Concerning the Help Desk/bug-fixing activities and release of VERSUS updates new practices were introduced: a forum web page dedicated to help desk activity for the users was created and was stated that any new development of the software was followed by a documentation update

(User Manual and Technical Manual). Regarding the release process for the new patches, each new patch assumed the creation of a packet instalment. The patches were delivered to the users through the Italian Air Force Meteorological Service ftp server. Moreover the test of each new VERSUS release was followed by the related test procedure. Automation of processes/GUI adjustment were also carried out. In this task some generic improvements on GUI and VERSUS functionalities were carried on in order to improve friendliness and the operational use of the system; among these are cronjobs for running php scripts to compile verifications, automatic storage of figures with reasonable names for unambiguous identification, replication function for similar verification activities and inclusion of performance diagrams in VERSUS plots: an activity not connected to the automation, but with the need to include more statistical indexes for precipitation verification, in one graph. Inside the Probabilistic Scores area during this year the PL team finished the calculation and visualization of the ensemble and probabilistic scores in VERSUS, using as a reference the EPS documents edited by F. Gofa and A. Bundel. In the same year continued the implementation of the WMO BUFR standard for observations, with the creation of test procedures and following test phase, as well as the implementation of 1 and 3 hours period for cumulated precipitation and wind gusts.

2.2.6 Phase 6. COSMO year 2013-4

The purpose of this year was to complete some of the existing requirements and ensure the stability of the system. Beside the normal help desk and support activity this year the first VERSUS Course for Developers took place in Pratica di Mare (May 2013) for 3 days, with the aim to familiarize potential developers with the software architecture. Regarding the refinement of the system was realized a code adjustment for DB Partitioning and a definition of standard coding for precipitation parameter was set, thanks to the TAG and SCA collaboration and specification of WG5 requirements on the measures and verification activities to be performed with such data. The activity for the use of FF in Versus continued through the implementation of a dedicated loader module, a new web GUI and a specific test phase for FF tool implementation and FF functionalities. In the EPS products verification sector was carried on and concluded the development of the statistical indexes CRPS/CRPSS (Continuous Ranked Probabilistic Score/Skill Score) and the realization of the Spread/Skill relation plots. This allowed the beginning of the pre-operational phase, consisting in a series of test over a period of 2-3 months with a following comparison of VERSUS results with current operational EPS verification.

2.2.7 Phase 7. COSMO year 2014-5

This year the help desk activity was divided in two different support levels: the first one being managed by Russian colleagues for the basic requests. They involved the PL team in case of more technical problems and bug fixing. In addition VERSUS User Seminar was organized: it took place in Turin (May 2015) for 3 days with the aim to introduce the new functionalities; among these the concurrent use of VERSUS by more than one user: the system could now be used by more than one user simultaneously. The implementation of Feedback Files use in VERSUS was completed, with the development of a new versus library to read the Feedback File in NETCDF, the definitive implementation of Loader module for FF, the new web GUI and the improvement of the graphics for upper air verification. Another important step was executed in the process of implementation of VERSUS functionality to ingest and manage GRIB2. This process involved multiple tasks as the analysis and creation of new DB area, adjustment and upgrade of the Phoenix code, creation of new FE

in VERSUS, code/GUI adjustment and following functionalities test phase. The same year, with the aim of introducing additional statistical techniques compatible with VERSUS, a new activity was stated. This activity dealt with the introduction of new statistical techniques for high resolution forecast and observation data (neighbourhood methods). The COSMO Verification Community considered the use and adaptation of external packages or libraries for pre-processing of data for verification as one of its main priorities. For this reason the main goal of the activity was the integration or adaptation of pre-existing packages (e.g. Beth Ebert Fuzzy Verification Toolbox). Moreover this work was extended to the use of gridded precipitation data from composite sources (e.g. radar, raingauges) while a pre-processing tool capable of reading GRIB files (for forecast and/or observation) and producing data in suitable format for the VERSUS system itself was developed. To this purpose the PL coordinated the execution of the Project VAST, project funded by COSMO, started in June 2014 and ended in May 2015. The software allowed to produce spatial verification of the precipitation field (main goal), wind speed and total cloud cover. The argument is treated in detail in the COSMO Technical Report 33 (Vela, 2017).

2.2.8 Phase 8 / Extension Phase COSMO year 2015-2016

The phase 8 (or Extension Phase) has brought the project VERSUS2 to the final refinements. In particular with the release of patch 5.0 Version (December 2015) and 5.1 Version (July 2016) was solved the problem of loading multisteps files and implemented the total cloud cover verification. Regarding the software functionalities, for the GRIB2 ingest new front end were created, with update of VERSUS code and GUI, as well as the implementation of the connection with existing GRIB1 tables and following tests. After these processes various refinements activities have been carried out, such as a control on EPS score accuracy, a test phase on the XML file format ingestion and a report of the loading performances. In the end final tests on all system functionalities have been performed.

3 Further developments

In addition to the achievements of the VERSUS2 Priority Project other improvements have been developed during the period September 2016 - October 2018. We will present in this section a brief overview of the main innovations.

Patch 5.1.1: implementation of correct precipitation Performance Diagrams for ECMWF and COSMO 12UTC run.

Patch 5.1.2: problems with graphs of cumulative 24h precipitation 12UTC run solved; problems in the creation of cron directory for new VERSUS installations solved; upgrade of GUI menu list (problems with the former patch, RH was not visualised any more); improvement of batch execution menu (verifications already performed now have the label execution $\rightarrow$ yes).

Patch 5.1.3: Improvement of upper air verifications (creation of values at all levels); adjustment of the progressive verification number.

Patch 5.1.4: Included in 5.1.5 .

Patch 5.1.5: Management of a new buoy BUFR template which introduces a new descriptor for the buoy identifier; correct visualization of cross verification graphics.

Patch 5.1.6: Management of the new synop messages BUFR template, concerning cumulated/averaged fields defined by the time period descriptor (windgust, precipitation, etc).

4 Conclusions

The VERSUS2 Priority Project, as is visible looking at the chronology reported here, has brought a constant improvement of the original VERSUS software, in order to keep the pace with the development of new technologies and verification methods. Many innovations has been carried out in multiple fields: for example, in the direction of having a valid tool to verify the Ensemble Probabilistic System (EPS), a set of new statistical scores has been implemented (R package for EPS verification) as well as the new interface functionalities to manage it (GUI improvement); the database performances have also been improved in order to decrease the verifications execution time. Another fundamental activity inside the project has been the help desk support for all the Cosmo consortium members, consisting in solving practical issues and fixing the reported bugs with the relative releases of VERSUS software upgrades (patch). The team has also realised the implementation of Weather Type Dependent Verification and the improvement of Conditional Verification, the introduction in the system of the possibility to ingest new kind of data both in terms of type (Airep, Amdar, Windprofiler, TEMP and many more through the use of Feedback Files (FF)) and format (GRIB1 to GRIB2 management, ingestion of XML files of post-processed forecasts) and has worked over time to refine every aspect of the over-mentioned tasks.

5 Meetings

- CVS Meeting, 20 November 2006, Pratica di Mare, Italy
- VERSUS2 meeting, 12 March 2009, Langen, Germany
- VERSUS tutorial, 16-18 February 2009, Pratica di Mare, Italy
- VERSUS2 meeting, 15-16 December 2009, Pratica di Mare, Italy
- VERSUS2 meeting, 4 March 2010, Langen, Germany
- WG5-VERSUS2 common meeting (minutes), 2-4 April 2012, Pratica di Mare, Italy
- WG5-VERSUS2 common meeting (minutes), 8-10 May 2013, Pratica di Mare, Italy
- WG5-VERSUS2 common meeting (minutes), 24-25 June 2014, Bologna, Italy
- WG5-VERSUS2 common meeting (minutes), 8 September 2014, Eretria, Greece
- WG5-VERSUS2 common meeting (minutes), 27-29 May 2015, Torino, Italy
- 11th COSMO General Meeting, 7-11 September 2009, Offenbach, Germany
- 12th COSMO General Meeting, 6-10 September 2010, Moscow, Russia
- 13th COSMO General Meeting, 5-9 September 2011, Rome, Italy
- 14th COSMO General Meeting, 10-14 September 2012, Lugano, Switzerland
- 15th COSMO General Meeting, 2-5 September 2013, Sibiu, Romania

- 16th COSMO General Meeting, 8-11 September 2014, Eretria, Greece
- 17th COSMO General Meeting, 7-10 September 2015, Wrocław, Poland
- 18th COSMO General Meeting, 5-8 September 2016, Offenbach, Germany
- COSMO/CLM User Seminar, 5-7 March 2013
- COSMO/CLM/ART User Seminar, 17-19 March 2014
- COSMO/CLM/ART User Seminar, 2-6 March 2015
- COSMO/CLM/ART User Seminar, 7-9 March 2016
- COSMO/CLM/ART User Seminar, 6-8 March 2017
- COSMO/CLM/ART User Seminar, 12-16 March 2018

6 User and technical Manual

The pdf version of the updated user manual is available at the following link:

http://www.cosmo-model.org/content/model/documentation/core/user_manual_5.1.6_05-10-2018.pdf

The pdf version of the updated technical manual is available at the following link:

www.cosmo-model.org/content/model/documentation/core/technical_manual.pdf

7 References

Casati, B., Wilson, L. J., Stephenson, D. B., Nurmi, P. , Ghelli, A. , Pocernich, M. , Damrath, U. , Ebert, E. E., Brown, B. G. and Mason, S., 2008: Forecast verification: current status and future directions. *Met. Apps*, **15**, 3–18, doi:10.1002/met.52

Vela, N., 2017: V.A.S.T. (Versus Additional Statistical Techniques) User Manual (v2.0). www.cosmo-model.org/content/model/documentation/techReports/docs/techReport33.pdf

List of COSMO Newsletters and Technical Reports

(available for download from the COSMO Website: www.cosmo-model.org)

COSMO Newsletters

No. 1: February 2001.

No. 2: February 2002.

No. 3: February 2003.

No. 4: February 2004.

No. 5: April 2005.

No. 6: July 2006.

No. 7: April 2008; Proceedings from the 8th COSMO General Meeting in Bucharest, 2006.

No. 8: September 2008; Proceedings from the 9th COSMO General Meeting in Athens, 2007.

No. 9: December 2008.

No. 10: March 2010.

No. 11: April 2011.

No. 12: April 2012.

No. 13: April 2013.

No. 14: April 2014.

No. 15: July 2015.

No. 16: July 2016.

No. 17: July 2017.

No. 18: November 2018.

COSMO Technical Reports

No. 1: Dmitrii Mironov and Matthias Raschendorfer (2001):
Evaluation of Empirical Parameters of the New LM Surface-Layer Parameterization Scheme. Results from Numerical Experiments Including the Soil Moisture Analysis.

No. 2: Reinhold Schrodin and Erdmann Heise (2001):
The Multi-Layer Version of the DWD Soil Model TERRA_LM.

No. 3: Günther Doms (2001):
A Scheme for Monotonic Numerical Diffusion in the LM.

No. 4: Hans-Joachim Herzog, Ursula Schubert, Gerd Vogel, Adelheid Fiedler and Roswitha Kirchner (2002):
LLM ¯ the High-Resolving Nonhydrostatic Simulation Model in the DWD-Project LITFASS.
Part I: Modelling Technique and Simulation Method.

No. 5: Jean-Marie Bettems (2002):
EUCOS Impact Study Using the Limited-Area Non-Hydrostatic NWP Model in Operational Use at MeteoSwiss.

No. 6: Heinz-Werner Bitzer and Jürgen Steppeler (2004):
Documentation of the Z-Coordinate Dynamical Core of LM.

No. 7: Hans-Joachim Herzog, Almut Gassmann (2005):
Lorenz- and Charney-Phillips vertical grid experimentation using a compressible nonhydrostatic toy-model relevant to the fast-mode part of the 'Lokal-Modell'.

No. 8: Chiara Marsigli, Andrea Montani, Tiziana Paccagnella, Davide Sacchetti, André Walser, Marco Arpagaus, Thomas Schumann (2005):
Evaluation of the Performance of the COSMO-LEPS System.

No. 9: Erdmann Heise, Bodo Ritter, Reinhold Schrodin (2006):
Operational Implementation of the Multilayer Soil Model.

No. 10: M.D. Tsyrulnikov (2007):
Is the particle filtering approach appropriate for meso-scale data assimilation ?

No. 11: Dmitrii V. Mironov (2008):
Parameterization of Lakes in Numerical Weather Prediction. Description of a Lake Model.

No. 12: Adriano Raspanti (2009):
COSMO Priority Project "VERification System Unified Survey" (VERSUS): Final Report.

No. 13: Chiara Marsigli (2009):
COSMO Priority Project "Short Range Ensemble Prediction System" (SREPS): Final Report.

No. 14: Michael Baldauf (2009):
COSMO Priority Project "Further Developments of the Runge-Kutta Time Integration Scheme" (RK): Final Report.

No. 15: Silke Dierer (2009):
COSMO Priority Project "Tackle deficiencies in quantitative precipitation forecast" (QPF): Final Report.

No. 16: Pierre Eckert (2009):
COSMO Priority Project "INTERP": Final Report.

No. 17: D. Leuenberger, M. Stoll and A. Roches (2010):
Description of some convective indices implemented in the COSMO model.

No. 18: Daniel Leuenberger (2010):
Statistical analysis of high-resolution COSMO Ensemble forecasts in view of Data Assimilation.

No. 19: A. Montani, D. Cesari, C. Marsigli, T. Paccagnella (2010):
Seven years of activity in the field of mesoscale ensemble forecasting by the COSMO–LEPS system: main achievements and open challenges.

No. 20: A. Roches, O. Fuhrer (2012):
Tracer module in the COSMO model.

No. 21: Michael Baldauf (2013):
A new fast-waves solver for the Runge-Kutta dynamical core.

No. 22: C. Marsigli, T. Diomede, A. Montani, T. Paccagnella, P. Louka, F. Gofa, A. Corigliano (2013):
The CONSENS Priority Project.

No. 23: M. Baldauf, O. Fuhrer, M. J. Kurowski, G. de Morsier, M. Müllner, Z. P. Piotrowski, B. Rosa, P. L. Vitagliano, D. Wójcik, M. Ziemiański (2013):
The COSMO Priority Project 'Conservative Dynamical Core' Final Report.

No. 24: A. K. Miltenberger, A. Roches, S. Pfahl, H. Wernli (2014):
Online Trajectory Module in COSMO: a short user guide.

No. 25: P. Khain, I. Carmona, A. Voudouri, E. Avgoustoglou, J.-M. Bettems, F. Grazzini (2015):
The Proof of the Parameters Calibration Method: CALMO Progress Report.

No. 26: D. Mironov, E. Machulskaya, B. Szintai, M. Raschendorfer, V. Perov, M. Chumakov, E. Avgoustoglou (2015):
The COSMO Priority Project 'UTCS' Final Report.

No. 27: J-M. Bettems (2015):
The COSMO Priority Project 'COLOBOC': Final Report.

No. 28: Ulrich Blahak (2016):
RADAR_MIE_LM and RADAR_MIELIB - Calculation of Radar Reflectivity from Model Output.

No. 29: M. Tsyrulnikov and D. Gayfulin (2016):
A Stochastic Pattern Generator for ensemble applications.

No. 30: D. Mironov and E. Machulskaya (2017):
A Turbulence Kinetic Energy – Scalar Variance Turbulence Parameterization Scheme.

No. 31: P. Khain, I. Carmona, A. Voudouri, E. Avgoustoglou, J.-M. Bettems, F. Grazzini, P. Kaufmann (2017):
CALMO - Progress Report.

No. 32: A. Voudouri, P. Khain, I. Carmona, E. Avgoustoglou, J.M. Bettems, F. Grazzini, O. Bellprat, P. Kaufmann and E. Bucchignani (2017):
Calibration of COSMO Model, Priority Project CALMO Final report

No. 33: N. Vela (2017):
VAST 2.0 - User Manual.

No. 34: C. Marsigli, D. Alferov, M. Arpagaus, E. Astakhova, R. Bonanno, G. Duniec, C. Gebhardt, W. Interewicz, N. Loglisci, A. Mazur, V. Maurer, A. Montani, A. Walser (2018):
COsmo Towards Ensembles at the Km-scale IN Our countries (COTEKINO), Priority Project final report.

No. 35: G. Rivin, I. Rozinkina, E. Astakhova, A. Montani, D. Alferov, M. Arpagaus, D. Blinov, A. Bundel, M. Chumakov, P. Eckert, A. Euripides, J. Förstner, J. Helmert, E. Kazakova, A. Kirsanov, V. Kopeikin, E. Kukanova, D. Majewski, C. Marsigli, G. de Morsier, A. Muravev, T. Paccagnella, U. Schättler, C. Schraff, M. Shatunova, A. Shcherbakov, P. Steiner, M. Zaichenko (2018):
The COSMO Priority Project CORSO Final Report.

COSMO Technical Reports

Issues of the COSMO Technical Reports series are published by the *COnsortium for Small-scale MOdelling* at non-regular intervals. COSMO is a European group for numerical weather prediction with participating meteorological services from Germany (DWD, AWGeophys), Greece (HNMS), Italy (USAM, ARPA-SIMC, ARPA Piemonte), Switzerland (MeteoSwiss), Poland (IMGW), Romania (NMA) and Russia (RHM). The general goal is to develop, improve and maintain a non-hydrostatic limited area modelling system to be used for both operational and research applications by the members of COSMO. This system is initially based on the COSMO-Model (previously known as LM) of DWD with its corresponding data assimilation system.

The Technical Reports are intended

- for scientific contributions and a documentation of research activities,
- to present and discuss results obtained from the model system,
- to present and discuss verification results and interpretation methods,
- for a documentation of technical changes to the model system,
- to give an overview of new components of the model system.

The purpose of these reports is to communicate results, changes and progress related to the LM model system relatively fast within the COSMO consortium, and also to inform other NWP groups on our current research activities. In this way the discussion on a specific topic can be stimulated at an early stage. In order to publish a report very soon after the completion of the manuscript, we have decided to omit a thorough reviewing procedure and only a rough check is done by the editors and a third reviewer. We apologize for typographical and other errors or inconsistencies which may still be present.

At present, the Technical Reports are available for download from the COSMO web site (www.cosmo-model.org). If required, the member meteorological centres can produce hard-copies by their own for distribution within their service. All members of the consortium will be informed about new issues by email.

For any comments and questions, please contact the editor:

Massimo Milelli
Massimo.Milelli@arpa.piemonte.it

Consortium

for

Small-Scale Modelling

Technical Report No. 2

The Multi-Layer Version of the DWD Soil Model TERRA_LM

by

R. Schrodin and E. Heise

September 2001

DOI: 10.5676/DWD_pub/nwv/cosmo-tr_2

Deutscher Wetterdienst

MeteoSwiss

Ufficio Generale per la Meteorologia

Hellenic National Meteorological Service

Amt für Wehrgeophysik

Il Servicio Meteorologico Regionale di ARPA

www.cosmo-model.org

Editors: G. Doms and U. Schättler, Deutscher Wetterdienst, P.O. Box 100465, 63004 Offenbach, Germany
Printed at Deutscher Wetterdienst, Offenbach am Main

The Multi-Layer Version of the DWD Soil Model TERRA_LM

Reinhold Schrodin and Erdmann Heise

Deutscher Wetterdienst, Abteilung Meteorologische Analyse und Modellierung,
Frankfurter Str. 135, D-63067 Offenbach am Main, Germany
reinhold.schrodin@dwd.de, erdmann.heise@dwd.de

Abstract

For the calculation of soil surface temperatures and temperature profiles inside the soil a multi-layer version TERRA_LM shall replace the 'Extended Force Restore'(EFR) method. The multi-layer version is based on the numerical solution of the heat conduction equation (HCE method). The EFR method uses two soil layers only, however with soil-type dependent thicknesses. In the HCE method, the number of the layers as well as their thicknesses can be specified as the case requires.

The advantages of the HCE method over the EFR method are

(a) physical improvement:

As a consequence of the rather thick upper soil layer in the EFR method the treatment of freezing/melting of soil water/ice was not successful. Therefore, the freezing/melting process was not implemented in the operational soil routine TERRA. This process will be included in the updated version TERRA_LM.

(b) organisational simplifications:

In the thermal part of the soil model the thicknesses of the soil layers are no longer dependent on soil type.

The soil layers for the treatment of the soil water transport in the hydrological part of the soil model can be chosen identical to the soil layers for the heat transport.

In an additional chapter, a simplified version of the numerical treatment of melting of a snow cover is presented.

1. Background

The following short description of the 'Extended Force-Restore' method (EFR method) refers to Jacobsen and Heise (1982).

The method is based on the solution of two coupled linear differential equations for the mean temperatures T_1 and T_2 of two layers,

$$T_1 = \tfrac{1}{2}(T_s + T_m) \;, \qquad T_2 = \tfrac{1}{2}(T_m + T_u) \;,$$

where T_s is the soil surface temperature, T_m is the temperature at the lower boundary of the upper soil layer whose thickness is Δz_1, and T_u is the constant temperature (climate value) at the lower boundary of the second soil layer whose thickness is Δz_2.

The prognostic equations for the mean temperatures are

$$\frac{(\rho c \Delta z_1)}{2} \frac{\partial}{\partial t} T_1 \;=\; -(G_s - G_m) \;, \tag{1}$$

$$\frac{(\rho c \Delta z_2)}{2} \frac{\partial}{\partial t} T_2 \;=\; -(G_m - G_u) \;. \tag{2}$$

G_s is the soil heat flux at the surface represented by the atmospheric forcing (the sum of radiative fluxes and turbulent sensible and latent heat fluxes), G_m and G_u are the heat fluxes at the lower boundary of the first and the second soil layer, respectively, ρ is the density, and c is the specific heat which accounts for a constant mean water content (mean of air dryness point and pore volume). The thickness of the soil layers depends on the thermal characteristics of the soil. For the soil types used in LM/GME, the thickness of the upper layer Δz_1 varies for a rather dry soil between 0.07 m and 0.11 m, the thickness of the lower layer, Δz_2, varies between 0.25 m and 0.37 m. The thickness of the layers also depends on the water content that is time dependent. However, in operational implementation of the EFR method, the layer thicknesses are determined using a constant value of the water content that is used for the determination of c.

The hydrological part of the soil model is formulated as a multi-layer model already, the soil layer thicknesses being independent of soil type. Operationally we use two active layers with thicknesses of 0.1 m (upper layer) and 0.9 m (lower layer), which are different from those of the thermal part. Therefore, a simple treatment of the interaction between hydrological and thermal processes in the actual soil model TERRA is not possible.

This deficiency can be avoided by using the HCE method for the calculation of soil surface temperatures and temperature profiles in the soil.

The heat conduction equation reads

$$\frac{\partial T}{\partial t} \;=\; \frac{1}{(\rho c)} \frac{\partial}{\partial z} \left(\lambda \frac{\partial T}{\partial z} \right) \;. \tag{3}$$

At the upper boundary, the soil heat flux $G_s = -(\lambda \partial T/\partial z)_s$ is specified. At the lower boundary, a constant value T_u (climate value) is used. The volumetric heat capacity ρc is determined depending on the soil type and the actual water and ice contents. The heat conductivity λ is dependent on soil type and on soil water content.

For the solution of Eq. (3) the implicit finite differencing scheme is used which reads for the time index n

$$\frac{{T_k}^{n+1} - {T_k}^n}{\Delta t} = \frac{1}{(\rho c)_k} \frac{\partial}{\partial z} \left(\lambda \frac{\partial {T_k}^{n+1}}{\partial z} \right)_k . \tag{4}$$

The vertical discretisation at grid levels z_k results in a three-diagonal linear system

$$A_k \, T_{k-1}^{n+1} + B_k \, T_k^{n+1} + C_k \, T_{k+1}^{n+1} = D_k \tag{5}$$

which can be solved by an economic numerical procedure. To prevent high frequency oscillations the mean temperature of the uppermost soil layer is presently used as the soil surface temperature.

2. Comparison of EFR and HCE method

In this section, the reaction of the soil surface temperature on different forcing is shown for both the EFR and the HCE method. The results presented have been obtained by time integration to quasi-stationarity.

For harmonic forcing G_s, the temperatures T_s and T_m predicted by the EFR method agree with the respective analytical solution of the HCE. For this idealised condition of harmonic forcing, *Figure 1* shows the diurnal variation of soil surface temperature by the EFR method (t_EFR) in comparison to the analytical solution of the HCE equation (t_ANA) and to the two numerical solutions with the following vertical grid structures:

a) 100 layers of constant thickness of 0.005 m (t_100L),

b) 5 (active) layers with thicknesses 0.02, 0.02, 0.04, 0.08, 0.16 m (t_5L).

Figure 1 demonstrates that for the special case of harmonic forcing the differences in the results are small. The deviations between all temperature curves shown do not ecxeed 1 K at any time step. Apart from very small under- and overshooting, even the five layer version results (t_5L) cannot be distinguished from the other ones. These results confirm that for the case of harmonic forcing the numerical results of the EFR method and of the HCE method are equivalent.

As the next step, both methods are supplied with a modified forcing: harmonic forcing in the first half of the diurnal period, corresponding to the mean diurnal variation between 6 a.m. and 18 p.m. local time, and in the second half a constant forcing corresponding approximately to the mean situation between 18 p.m. and 6 a.m. To simulate more complex and realistic situations, this forcing is superimposed by a high frequency noise to test the

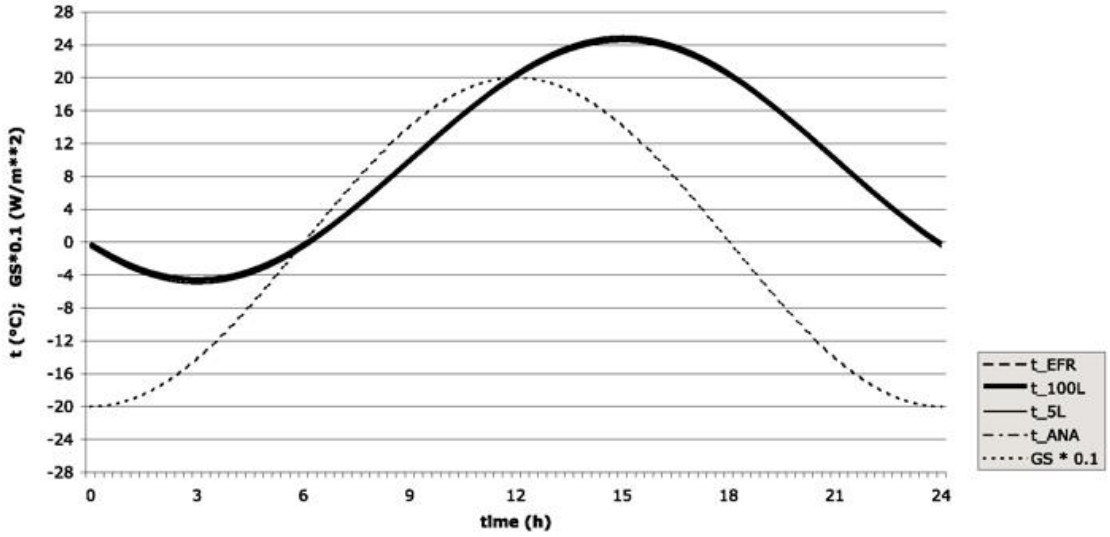


Figure 1: *Soil surface temperature using the EFR method (t_EFR) and the HCE method (t_XL) compared with the analytical HCE solution t_ANA (X=100: 100 layers, Δz = 0.005m; X = 5: 5 layers whose thicknesses increase with depth).*

ability of the different methods to provide a quick feedback in soil surface temperature. As no analytical solution is available now, the results of the HCE method with 100 layers are used as a reference. In *Figure 2*, the high frequency reaction to this type of forcing is shown. The results with the 5 layer version agree well with those of the 100 layer version.

This fast feedback of the soil surface temperature in the HCE method is caused by the choice of layers of small thickness close to the soil surface. On the contrary, the EFR method uses a thickness of the upper layer of about 0.1 m which results in a smooth feedback in the mean temperature of this layer and therefore also in the soil surface temperature. Again the EFR method agrees reasonably well with the 'true' simulation of the HCE method with 100 levels.

In a further test both methods are driven by a low frequency forcing with abrupt changes in three hour intervals to test the influence of a sudden but persistent change in solar radiation at the soil surface, caused for example by convective clouds. *Figure 3* shows that the EFR method simulates the temperature feedback with some delay especially at the points of extreme changes in the forcing at 9 a.m. and at 12 a.m. However, the results do not significantly differ in comparison to the results of the HCE method.

In summary these results demonstrate the quality of the EFR method operationally used in the DWD model suite. Indeed, if no freezing or melting processes inside the soil are considered, the EFR method is the most economic procedure to simulate the diurnal temperature variation with high quality.

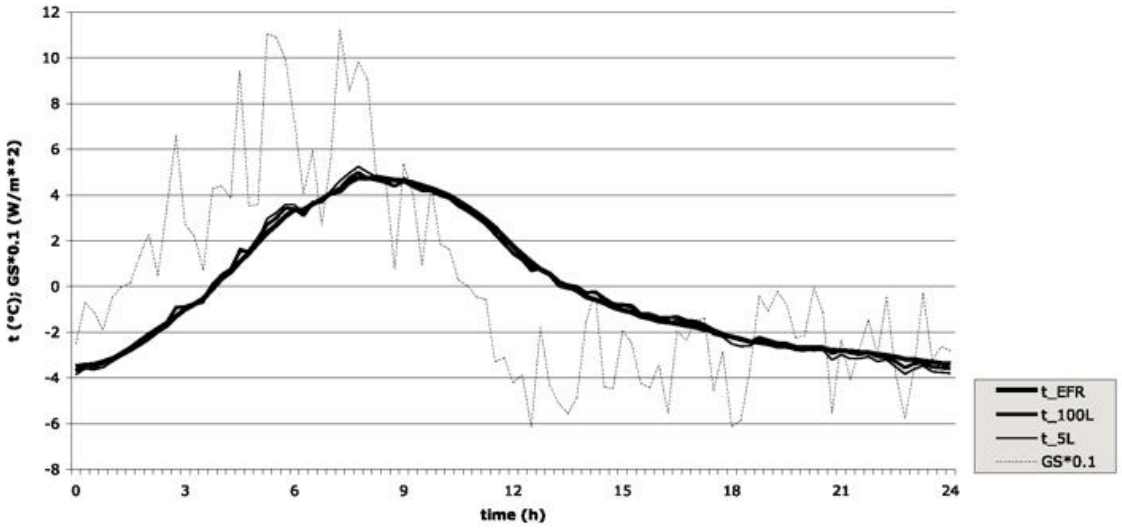


Figure 2: *Soil surface temperature calculated with the EFR method (t_EFR) and the HCE method(t_XL) for high frequent forcing GS (X=100: 100 layers, Δz = 0.005m; X= 4: 4 layers whose thicknesses increase with depth).*

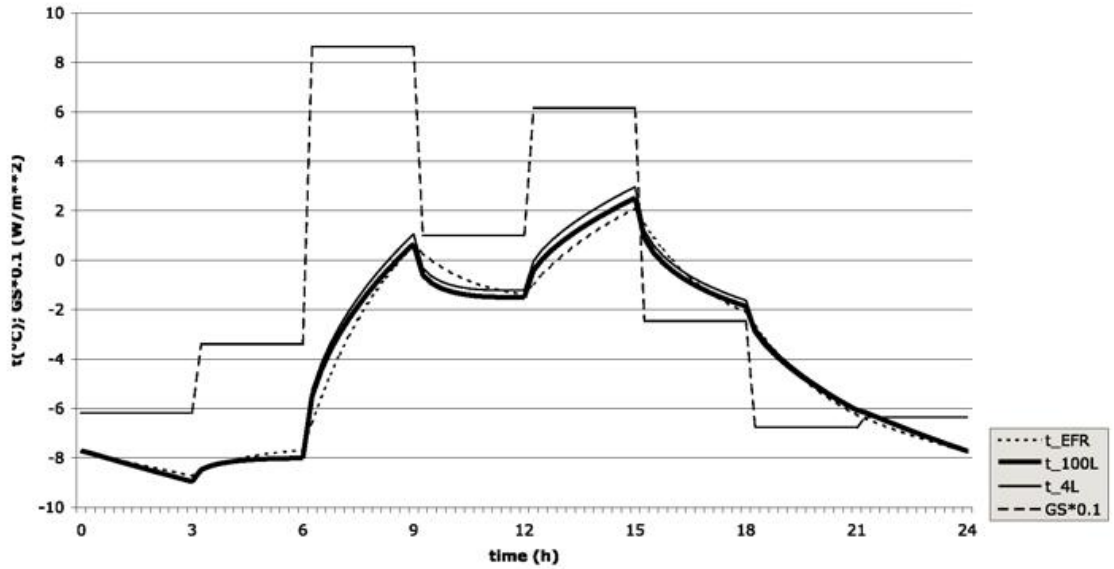


Figure 3: *Soil surface temperature calculated with the EFR method (t_EFR) and the HCE method(T_XL) for low frequent forcing GS (X=100: 100 layers, Δz = 0.005m; X= 4: 4 layers whose thicknesses increase with depth).*

3. The influence of freezing/melting of soil water/ice on soil surface temperatures

The process of freezing/melting of soil water/ice inside the soil is frontal in nature. Treating this process in discrete model layers results in averaging the front over the respective layer thickness. In the present operational models of DWD the upper layer in the hydrological part has a thickness of 0.1 m. The large amount of water/ice available in such a thick layer results in a remarkable suppression of temperature changes if phase transitions occur. In the worst case the diurnal cycle of the temperature can be totally suppressed for a period of several days.

This was the case for the Europa-Modell after it had become operational. Therefore, the freezing/melting process was switched off in that model. In the 4th generation model suite GME/LM the respective code was not included.

The neglection of freezing/melting processes also results in systematic errors. When crossing the melting point $t_0 = 273.15K$ the soil temperatures decrease/increase too rapidly. This leads to temperatures beeing too cold/warm for a considerable time.

Using the HCE method, the freezing/melting process can be included, and the deficiencies can be reduced by the use of high grid resolution, especially close to the soil surface. It will be shown, however, that for some short periods the temporal behaviour of soil temperature significantly depends on the grid resolution.

In section 3.1, the diurnal variation of the soil surface temperature is shown including freezing/melting of soil water/ice at t_0. A second approach (section 3.2) replaces t_0 by taking into account the influence of soil texture on the melting/freezing temperature as a function of soil water content.

3.1 The influence of the freezing/melting process at 273.15 K on the soil surface temperature

If the temperature T_{pre} resulting from the solution of the heat conduction equation (3) is crossing t_0 in any soil layer, a part of the existing soil water/ice will freeze/melt. The available energy for this phase change process is

$$\Delta E \;=\; (\rho c)\Delta z(T_{pre} - t_0)\;, \tag{6}$$

where $\Delta E < 0$ for freezing and $\Delta E > 0$ for melting.

The maximum possible change of liquid water $W_{l,max}$ and of ice $W_{i,max}$, respectively, can be calculated from

$$\Delta W_{l,max} \;=\; -\Delta W_{i,max} \;=\; \frac{\Delta E}{L_f \rho_w}\;. \tag{7}$$

L_f is the heat of fusion, ρ_w is the density of water. The actual change of ice content ΔW_i is given by

$$\Delta W_i = -MIN\{-\Delta W_{i,max}\ ; \quad W_i\} \quad if \ \Delta W_{i,max} < 0 \quad ,$$

$$\Delta W_i = \ MIN\{\ \Delta W_{i,max}\ ; W - W_i\} \quad if \ \Delta W_{i,max} > 0 \quad ,$$

where W is the actual total water content (sum of liquid water and ice) and W_i the ice content at the previous time step.

The effect on the temperature is included by using

$$T = t_0 + (\Delta W_i - \Delta W_{i,max})\frac{(L_f \rho_w)}{(\rho c \Delta z)} \tag{8}$$

to compute the final temperature T at the current time step.

For the whole period of melting or freezing inside a soil layer this procedure causes a final layer mean temperature of t_0 at the end of each time step. Additionally Eq. (8) considers the case that no phase transition occurs. In this case $\Delta W_i = 0$, and the energy ΔE will be completely used to change the soil temperature T.

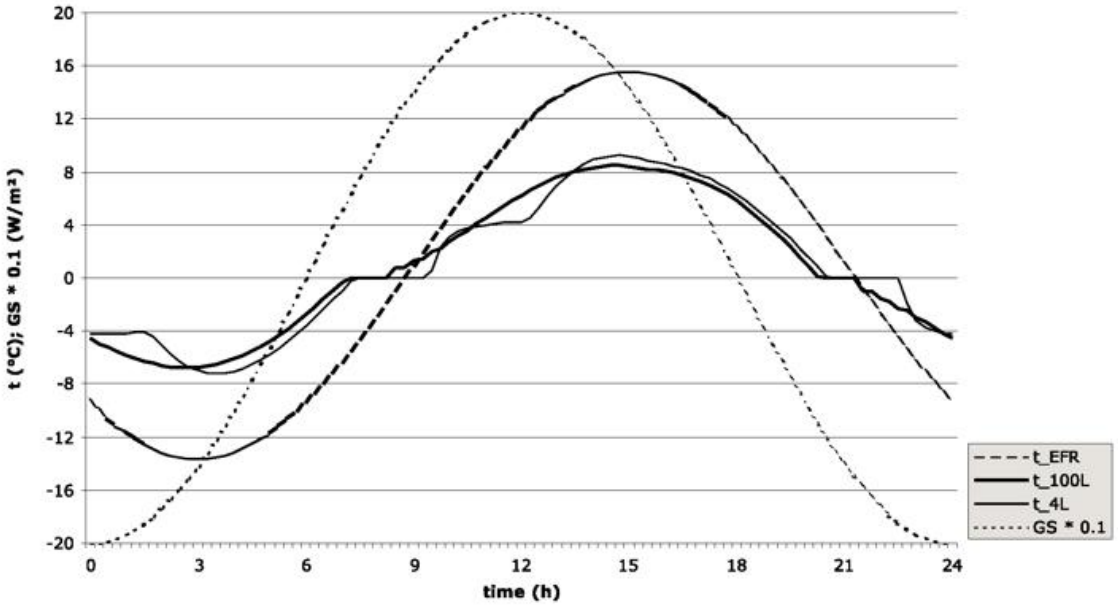


Figure 4: *Influence of soil freezing/melting at 273.15 K in the HCE method (t_XL) on the diurnal variation of soil surface temperature compared to the EFR method (t_EFR) without freezing/melting for harmonic forcing GS (X=100: 100 layers, Δz = 0.005m; X= 4: 4 layers whose thicknesses increase with depth).*

Figure 4 shows an example of the soil surface temperature behaviour with due regard for freezing/melting using the HCE method for two different grid resolutions. A comparison is made with the results using the EFR method, which, as already mentioned, is formulated with no regard for freezing/melting. Again the numerical solution of the 100-layer version of the heat conduction equation with constant layer thickness of 0.005 m is used as reference. Compared to the EFR method, the diurnal variation of the soil surface temperature is significantly damped. The extent of the effect is proportional to the amount of liquid water/ice available for freezing/melting.

The soil surface temperature behaviour for a version with only 4 active layers (layer thicknesses 0.02, 0.04, 0.08, 0.16 m) is also shown in *Figure 4*. Because of their greater thicknesses these four layers need more time to freeze/melt than the 0.005m layers of the 100-layer version. This is the reason for the pronounced step-like curve of the soil surface temperature in the 4-layer version compared to the 100 layer version. This effect can be minimized by using high grid resolution close to the soil surface. On the other hand, the lower limit of layer thickness is a function of the time step and has to take into account economic demands.

3.2 The soil type dependent melting/freezing and its influence on the soil surface temperature

Warrach (2000) uses a relation for the maximum of the volumetric water content $W_{l,max}$ in the soil based on a suggestion by Flerchinger and Saxton (1989). This relation reads

$$W_{l,max} = W_s \left[\frac{L_f (T - t_0)}{T g \Psi_s} \right]^{-1/b} . \tag{9}$$

W_s is the pore volume, T is the temperature, g is the gravitational acceleration, Ψ_s is the air entry potential at saturation, and b is the pore-size distribution index (Brooks and Corey, 1966).

After Cosby et al. (1984) the air entry potential Ψ_s and the pore-size distribution index b are determined by the soil type,

$$\Psi_s = \Psi_0 \cdot 10^{1.88 - 1.3 f_s} , \tag{10}$$

$$b = 2.91 + 15.9 f_c . \tag{11}$$

Ψ_0 is -0.01 m, and f_s and f_c are the fractions of sand and of clay in the soil, respectively. The following table shows for the soil types of the LM the fractions f_s and f_c (the remaining part of the soil fractions is assumed to be silt), the air entry potential Ψ_s calculated with Eq. (10) and the pore-size distribution index b calculated with Eq. (11).

	f_c	f_s	$\Psi_s(m)$	b
sand	0.90	0.05	- 0.0513	3.705
sandy loam	0.65	0.10	- 0.1084	4.50
loam	0.40	0.20	- 0.2291	6.09
loamy clay	0.35	0.35	- 0.2661	8.47
clay	0.15	0.70	- 0.4842	14.04

Eq. (9) can be transformed to calculate a freezing point temperature as function of the water content $W_{l,max}$ of the previous time step,

$$T_* \;=\; t_0 \left[1 - \frac{g\Psi_s}{L_f} \left(\frac{W_s}{W_{l,max}} \right)^b \right]^{-1} . \tag{12}$$

The temperature T_* is the equilibrium temperature where no freezing/melting is observed. If this equilibrium temperature in any soil layer is crossed by the solution T_{pre} of the HCE, freezing or melting occurs. As in section 3.1, the energy difference, that is proportional to the temperature difference T_{pre} - T_*, is used to melt ice or to freeze liquid water, that is

$$\Delta E \;=\; (\rho c)\Delta z (T_{pre} - T_*) \; . \tag{13}$$

Using modified formulations for ΔW_i,

$$\Delta W_i = -MIN\{-\Delta W_{i,max}; MIN(-(W - W_{l,max} - W_i), W_i)\} \quad if \;\; \Delta W_{i,max} < 0 \quad ,$$

$$\Delta W_i = \quad MIN\{\;\Delta W_{i,max}; MAX(\;(W - W_{l,max} - W_i),\; 0.)\} \quad if \;\; \Delta W_{i,max} > 0 \quad ,$$

the final temperature T can be calculated through the relation

$$T \;=\; T_* + (\Delta W_i - \Delta W_{i,max}) \frac{(L_f \rho_w)}{(\rho c \Delta z)} \tag{14}$$

that is analogous to Eq. (8).

The concept of a water content and soil type dependent freezing/melting temperature accounts for a more continuous behaviour of the soil temperature during freezing/melting. This is demonstrated in *Figure 5.* For the soil types (a) sand, (b) loam and (c) clay the quasi-stationary diurnal variation of the soil surface temperature (driven by a periodic harmonic forcing) for water content dependent freezing/melting (solid curve) is compared to freezing/melting at constant temperatures t_0 (dashed curve). The calculations are performed with a multi-layer version with layer thicknesses of 0.01, 0.03, 0.06, 0.12, 0.24, 0.48 m.

The total water content was set to 50% of the pore volume in each layer. For the soil type sand (a) the differences in the behaviour of temperatures are the smallest. With decreasing soil particle sizes lower temperatures are necessary to initiate freezing. Furthermore, for the soil type clay (c) even a water content of 50% of pore volume is not sufficient to allow any freezing at temperatures between 0°C and −10.5°C.

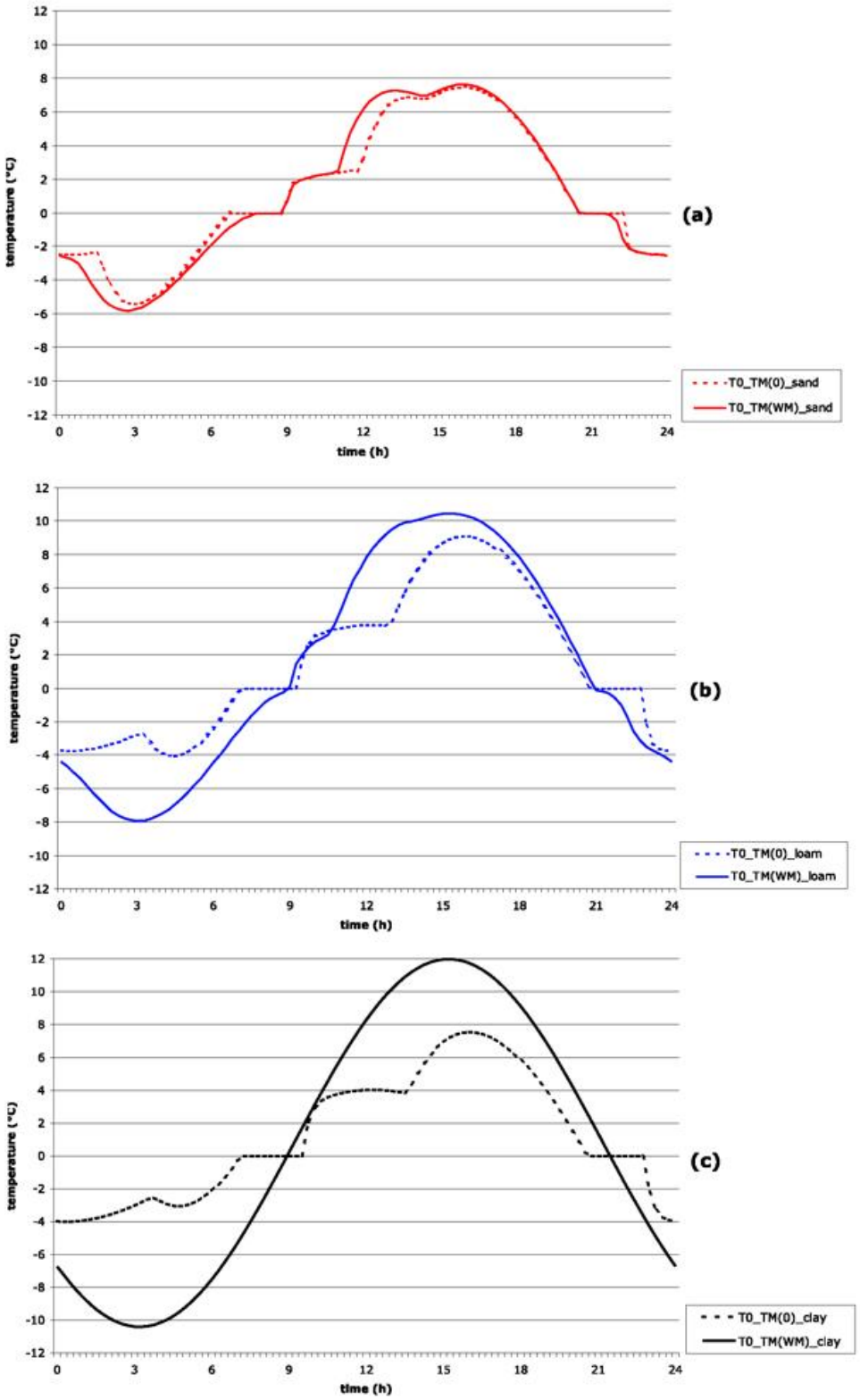


Figure 5: *Diurnal variation of the soil surface temperature for soil types (a) sand, (b) loam and (c) clay. Total water content: 50% of pore volume. $TO_TM(0)$: freezing/melting at $0°C$, $TO_TM(WM)$: freezing/melting as function of liquid water content.*

The local minimum of the soil surface temperature for the soil type sand in *Figure 5a* at 3 p.m. occurs because melting takes place in the layer between 4 and 10 cm which is supported by a downward directed heat flux causing a reduction of the soil surface temperature. However, when ice is completely melted the temperature in this layer can increase. This significantly reduces the downward directed flux and allows the soil surface temperature to increase again.

The method of simulation of the freezing/melting temperature described above produces results between the extrema of 'no freezing/melting', as in the EFR method, and of 'freezing/melting at t_0', as described in section 3.1.

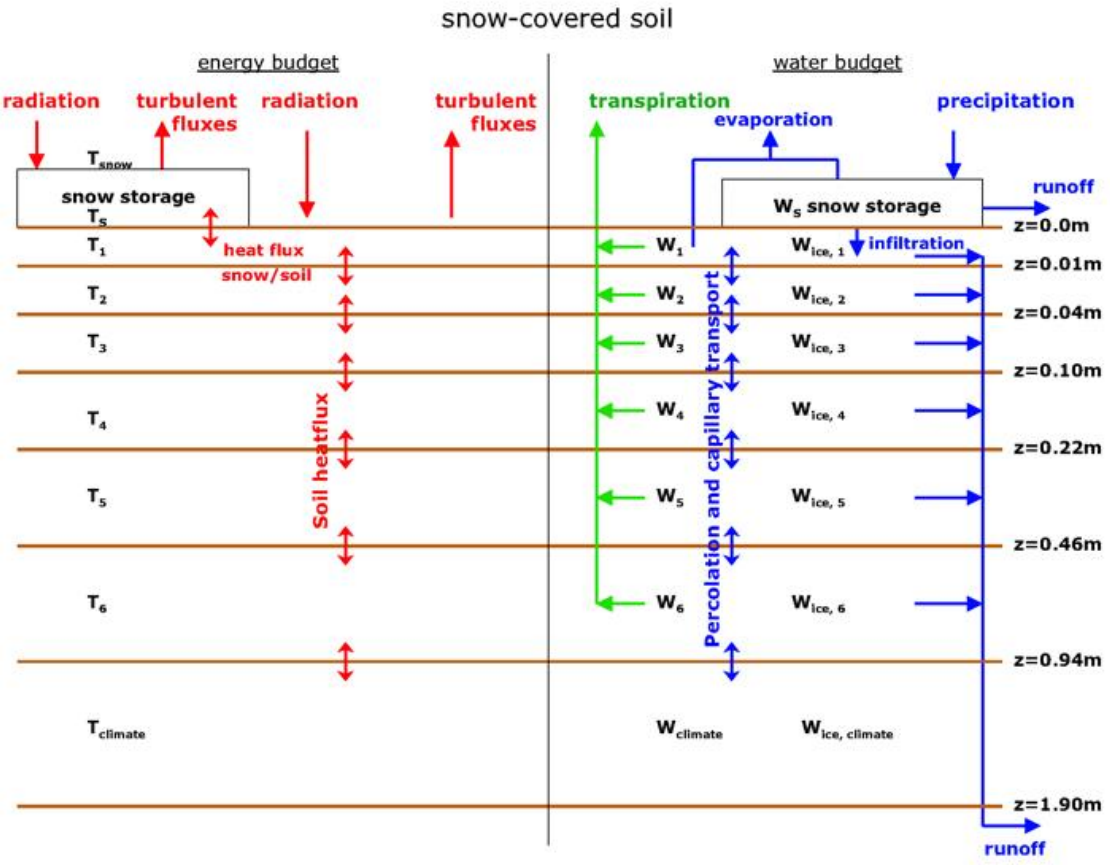


Figure 6: *The multi-layer grid of the soil model TERRA_LM: General structure and physical processes considered in case of a snow covered soil.*

4. A suggestion for fixing the vertical soil layer grid for the multi-layer HCE method

Because of computational limits, a maximum of six active soil layers can be afforded at present in the operational model LM. Experiments with different vertical layer distributions have shown that the uppermost layer should be of thickness of 0.01 m. Furthermore, the LM is nested in the Global Model GME with the lower boundary of the second hydrological layer in 1.0 m. For this reason, the following distribution of layer boundaries (layer bottom,

so-called half levels) for the thermal as well as for the hydrological part, is suggested:

$$z_k \;=\; 0.01\,,\; 0.04\,,\; 0.10\,,\; 0.22\,,\; 0.46\,,\; 0.94\,,\; 1.90\,m\,.$$

This distribution is built up by the formula

$$z_{k+1} \;=\; z_k + 0.03 \cdot 2^{(k-1)} \qquad \text{with} \qquad z_1 \;=\; 0.01\,m.$$

The layer limited by the half levels at 0.94 m and 1.90 m is the so called 'climate layer' with the values of temperature, liquid water content and ice content kept constant during a model run. Figure 6 shows an updated version of the layer structure published in COSMO Newsletter No. 1 (Doms and Schättler, 2001) for a snow covered soil.

Numerical experiments have shown that six active layers are sufficient for numerical weather prediction models. The results become useless if the the number of active layers in this distribution is reduced to less than four. Therefore, six soil layers are sufficient also for simulations over longer time periods with temperature waves penetrating deeper into the ground. Further experiments have shown that with additional layers close to the soil surface the results are not different remarkably, even if freezing and melting occurs.

5. An updated version for computation of melting of snow cover

The operational version for the treatment of melting snow required a rather complicated programming. In order to simplify this part of the model, the method was changed slightly (Heise and Schrodin, 2001). Now only two cases are distinguished:

Case (a)

The soil model calculates a preliminary temperature of the snow cover $T_{snow,p} > t_0$ and a preliminary soil surface temperature $T_{s,p} < t_0$. The reduction of $T_{snow,p}$ to $T_{snow} = t_0$ is simulated by redistribution of the heat content between the snowpack and the uppermost soil layer according to

$$\frac{T_{snow}+T_s}{2}(\rho c\Delta z)_{snow} + T_{so}(\rho c\Delta z)_{so} \;=\; \frac{T_{snow,p}+T_{s,p}}{2}(\rho c\Delta z)_{snow} + T_{so,p}(\rho c\Delta z)_{so} \qquad (15)$$

with $T_{snow} = t_0$ and the unknown temperatures T_s and T_{so}.

Additionally we assume

$$T_{so} - T_{so,p} \;=\; T_s - T_{s,p} \;=\; \Delta T_s\,. \qquad (16)$$

Combining (15) and (16) results in

$$\Delta T_s \;=\; [T_{snow,p} - t_0]\left[1 + \frac{2\cdot(\rho c\Delta z)_{so}}{(\rho c\Delta z)_{snow}}\right]^{-1}.$$

If T_s exceeds t_0, possible melting is postponed to the next time step.

Case (b)

If the preliminary temperature $T_{so,p}$ in the uppermost soil layer exceeds t_0, the redistribution of energy is simulated, now reducing T_{so} to t_0. Then Eq. (16) becomes

$$T_s \;=\; T_{s,p} - T_{so,p} + t_0 \;. \tag{17}$$

Replacing T_s in the budget equation (15) with T_s given by (17) results in

$$T_{snow} \;=\; T_{s,p} \,+\, T_{snow,p} \,-\, t_0 \,+\, 2[T_{s,p} - t_0]\frac{(\rho c \Delta z)_{so}}{(\rho c \Delta z)_{snow}} \;.$$

If $T_{snow} > t_o$, a melting step is performed. The energy available for melting is

$$E_{avail} \;=\; \frac{T_{snow} - t_o}{2}(\rho c \Delta z)_{snow} \;,$$

and the energy required for melting the whole snowpack is

$$E_{total} \;=\; L_f \rho_w W_s \;,$$

where W_s is the snow water equivalent. If $E_{avail} < E_{total}$, the melted fraction of snow ΔM_s is

$$\Delta M_s \;=\; \frac{E_{avail}}{E_{total}} W_s \;.$$

In case more energy is available than is required for melting the whole snowpack, we have $\Delta M_s = W_s$, and the soil surface temperature has to be recomputed through

$$T_s' \;=\; T_s \,+\, \frac{E_{avail} - E_{total}}{(\rho c \Delta z)_{so}} \;. \tag{18}$$

6. Conclusions and Outlook

Preliminary tests have shown that the HCE method is superior to EFR method if in the current soil model the freezing/melting process is to be included. The additional computational cost seems comperatively small. Furthermore, the HCE method can rapidly react to high frequency changes of the atmospheric forcing. A great advantage of the multi-layer version is the formulation of hydrological and thermal processes with exactly the same layer distribution. This simplifies the formulation of feedback processes between the thermal and hydrological parts as soil temperature and soil water interpolations are unnecessary.

The new multi-layer version of the soil model is currently implemented into the LM and a corresponding interface is written for the interpolation program GME2LM. Details on the implementation and on the evaluation of the scheme for real data cases will be published in a forthcomming issue. The new version is planned to become operational in winter/spring 2002.

References:

Brooks, R.H. and A.T. Corey, 1966: Properties of porous media affecting fluid flow. Journal of the Irrigation and Drainage Division. ASCE. 72, 61-88.

Cosby, B.J., Hornberger, G.M., Clapp, R.B. and Gin, T.R., 1984: A statistical exploration of the relationships of soil moisture characteristics to the physical properties of soils. Water Resour. Res., 20, 6, 682-690.

Doms, G. and U. Schättler (Eds.), 2001: COSMO Newsletter No. 1, available from the COSMO Website www.cosmo-model.org.

Jacobsen I. and E. Heise, 1982: A new economic method for the computation of the surface temperature in numerical models. Beitr. Phys. Atm., 55, 128-141.

Flerchinger, G.N. and Saxton, K.E., 1989: Simultaneous heat and water model of freezing snow-residue-soil system. I. Theory and development. Transactions of the ASEA, 32, 2, 565 - 571.

Heise, E. and Schrodin R., 2001: Aspects of snow and soil modelling in the operational short range weather prediction models of the German Weather Service. In preparation.

Warrach, K., 2000: Gefrorener Boden und Schneebedeckung unter besonderer Berücksichtigung des hydrologischen Verhaltens der Landoberfläche, Dissertation, GKSS, 125 pp.

List of COSMO Newsletters and Technical Reports

(available for download from the COSMO Website: www.cosmo-model.org)

COSMO Newsletters

Newsletter No.1, February 2001.

COSMO Technical Reports

No. 1, Dmitrii Mironov and Matthias Raschendorfer (2001): *Evaluation of Empirical Parameters of the New LM Surface-Layer Parameterization Scheme. Results from Numerical Experiments Including the Soil Moisture Analysis.*

No. 2, Reinhold Schrodin and Erdmann Heise (2001): *The Multi-Layer Version of the DWD Soil Model TERRA_LM.*

COSMO Technical Reports

Issues of the COSMO Technical Reports series are published by the *Consortium for Small-Scale Modelling* at non-regular intervals. COSMO is a European group for numerical weather prediction with participating meteorological services from Germany (DWD, AWGeophys), Greece (HNMS), Italy (UGM, ARPA-SMR) and Switzerland (MeteoSwiss). The general goal is to develop, improve and maintain a non-hydrostatic limited area modelling system to be used for both operational and research applications by the members of COSMO. This system is initially based on the Lokal-Modell (LM) of DWD with its corresponding data assimilation system.

The Technical Reports are intended

- for scientific contributions and a documentation of research activities,
- to present and discuss results obtained from the model system,
- to present and discuss verification results and interpretation methods,
- for a documentation of technical changes to the model system,
- to give an overview of new components of the model system.

The purpose of these reports is to communicate results, changes and progress related to the LM model system relatively fast within the COSMO consortium, and also to inform other NWP groups on our current research activities. In this way the discussion on a specific topic can be stimulated at an early stage. In order to publish a report very soon after the completition of the manuscript, we have decided to omit a thorough reviewing procedure and only a rough check is done by the editors and a third reviewer. We apologize for typographical and other errors or inconsistencies which may still be present.

The report series is also open for contributions from external users of the LM system at various universities and research institutes.

At present, the Technical Reports are available for download from the COSMO web site (www.cosmo-model.org). If required, the member meteorological centres can produce hard-copies by their own for distribution within their service. All members of the consortium will be informed about new issues by email.

For any comments and questions, please contact the editors:

Günther Doms
guenther.doms@dwd.de

Ulrich Schättler
ulrich.schaettler@dwd.de

Consortium for Small-Scale Modelling

Technical Report No. 25

The Proof of the Parameters Calibration Method: CALMO Progress Report

May 2015

DOI: 10.5676/DWD_pub/nwv/cosmo-tr_25

Deutscher Wetterdienst
MeteoSwiss
Ufficio Generale Spazio Aereo e Meteorologia
ΕΘΝΙΚΗ ΜΕΤΕΩΡΟΛΟΓΙΚΗ ΥΠΗΡΕΣΙΑ
Instytucie Meteorogii i Gospodarki Wodnej
Administratia Nationala de Meteorologie
ROSHYDROMET
Agenzia Regionale per la Protezione Ambientale del Piemonte
Agenzia Regionale per la Protezione Ambientale dell'Emilia-Romagna
Centro Italiano Ricerche Aerospaziali
Amt für GeoInformationswesen der Bundeswehr



www.cosmo-model.org

Editor: Massimo Milelli, ARPA Piemonte

The Proof of the Parameters Calibration Method: CALMO Progress Report

by

***P. Khain**[*], **I. Carmona**[*], **A. Voudouri**[**],*

***E. Avgoustoglou**[**], **J.-M. Bettems**[***], **F. Grazzini**[****]*

[*]IMS

[**]HNMS

[***]MeteoSwiss

[****]ARPA-SIMC

1 Introduction **3**

2 The physically expected sensitivity to the tested parameters **4**

2.1 tur_len 4

2.2 tkhmin 5

2.3 rlam_heat 7

2.4 rat_sea 8

3 The actual sensitivity to the tested parameters **11**

3.1 Division of Switzerland into three climatically unique areas 11

3.2 Maximum 2m-temperature (Tmax) sensitivity 11

3.3 Minimum 2m-temperature (Tmin) sensitivity 15

3.4 24h accumulated precipitation (Pr) sensitivity 17

4 The Meta-Model **20**

4.1 The Meta-Model: solution to the parabola problem 21

4.2 The Meta-Model: solution to the noise problem 22

4.3 The Meta-Model: additional constrain simulations 23

5 Performance score **24**

5.1 Normalization 25

5.2 Combined score for Tmax, Tmin and Precipitation 25

6 Results of parameters calibration **26**

7 Conclusions and considerations towards the next stage of CALMO project **32**

8 The Terra standalone (TSA) soil scheme for the CALMO project **34**

9 Appendix A: Transform of the 2m-temperature observations to the model grid **35**

10 Appendix B: Examples of stable and unstable conditions over Switzerland **37**

11 Appendix C: MCH verification results for the optimal parameters simulation **39**

1 Introduction

This report summarizes the work performed so far by Pavel Khain and Itzhak Carmona under the guidance of Antigoni Voudouri (head of the project) and Jean-Marie Bettems, and in collaboration with Euripides Avgoustoglou and Federico Grazzini. The CALMO project is based on the objective calibration method which was developed and implemented in regional climate model by Omar Bellprat and Christoph Schär (ETH). The purpose of the CALMO project is to implement the calibration method of (Bellprat et al., 2012) to NWP model COSMO. This report describes the implementation of the calibration method to COSMO-7km. In summary, the calibration method is the following:

a Define the parameters for calibration and their allowed ranges. In this work:

$$rlam_heat \in [0.1\ \mathbf{1}\ 10] \tag{1}$$

$$tkhmin \in [0\ \mathbf{1}\ 2] \tag{2}$$

$$tur_len \in [100\ \mathbf{500}\ 10000] \tag{3}$$

$$rat_sea \in [1\ \mathbf{20}\ 100] \tag{4}$$

b Define the forecast fields to be verified (in this work: maximum and minimum 2m-temperatures, 24h accumulated precipitation);

c Define the time periods for calibration (in this work: 3-20.01.2008 and 2-20.06.2008);

d Define the parameters (combinations) values for performing the COSMO simulations. In this work the combinations are: the default, maximum and minimum allowed values for each of the parameters (keeping the other 3 default), at least 1 pairwise interaction for every 2 parameters (for example maximum rlam_heat and minimum tur_len, keeping the other 2 default). The minimum number of simulations to be performed is $2N + 0.5N(N-1)+1$, where N is the number of calibrated parameters. **The simulations design, including initial and boundary conditions designs, the extensive scripting environment, and the simulations themselves were performed by Antigoni Voudouri.**

e After the simulations are performed, the Meta-Model is constructed (see Section 4), i.e. the forecasted fields are interpolated in parameters space via N-dimensional quadratic polynomial (for each field, for each region and each day, separately). These interpolation formulas (the Meta-Models) allow estimating the forecasted field value for arbitrary parameter values (for each region and each day) without performing real COSMO simulation.

f At the next stage, the parameters space is filled by a large number (in this work 10000) of parameters combinations. For each parameter combination, a forecast field time series is produced (using the Meta-Model), compared with the observations, and evaluated using a performance score (see Section 5).

g Finally, the parameters combination which obtained the best score is selected (see Sections 6 and 7).

h In principle, it is reasonable to perform a real COSMO simulation with the selected parameters combination, and verify whether the forecasts are indeed better (than with default parameters combination).

In order the calibration method to work, one first has to select the parameters which are the **most significant for the verified fields**. For example, for the maximum 2m-temperature we may need to focus on soil and radiation schemes parameters, while for precipitation, we may need to consider also microphysical parameters, etc. Therefore, in Sections 2 and 3 we first analyze the sensitivity of the verified fields to the chosen parameters. Generally, the sensitivity was found to be relatively small, meaning that at the next stage of the CALMO project we will have to extend the set of calibrated parameters and verified fields. In Sections 4-7 we will present the calibration procedure, following the steps e-g above.

As part of the next stage of the CALMO project, it is planned to calibrate parameters from the COSMO soil scheme Terra, for example the hydraulic soil conductivity. The plan is to run the Terra "standalone" (TSA) program (for the default soil parameters, and for any change of soil parameters) prior to running the COSMO model. Section 8 summarizes the work performed so far by the IMS team with the Terra "standalone".

2 The physically expected sensitivity to the tested parameters

2.1 tur_len

tur_len $[m]$ is l_∞ in Blackadar formula (Blackadar, 1962) for the turbulence length, which is present in the equations for the turbulent coefficients as described, for example, in the COSMO document part II §3.4 (see below).

"...in the present scheme we stipulate the following relation between horizontal and vertical diffusion coefficients in accordance with Schlünzen (1988) and Dunst (1980). The horizontal coefficients are determined from the vertical coefficients by use of an anisotropy factor considering the aspect ratio between horizontal and vertical mesh width:

$$K^H_{m,h} = r\frac{\sqrt{(a\cos\varphi\Delta\lambda)^2 + (a\Delta\varphi)^2}}{\Delta z}K^V_{m,h} \approx r\frac{\sqrt{2}\Delta}{\Delta z}K^V_{m,h} \tag{5}$$

Tentatively, we assume $r = 0.1$, and $\Delta \approx 2.8km$. In particular, we have assumed the ratio between horizontal and vertical coefficients to be independent of stability. To determine the horizontal from the vertical coefficients from this relation the vertical coefficient is specified after Prandtl and Kolmogorov as follows:

$$K^V_m = \phi_m l(\bar{e})^{1/2}, K^V_h = \phi_h l(\bar{e})^{1/2} \tag{6}$$

Here, the length scale l is adopted from Blackadar (1962) as a height-dependent scale of turbulence

$$l = \frac{\kappa z}{(1 + \frac{\kappa z}{l_\infty})} \tag{7}$$

Apart from the still undetermined factors ϕ_m and ϕ_h, which are thought to be stability-dependent, we need the determination of TKE

$$\bar{e} = \frac{1}{2}(\overline{u_i' u_i'}) \tag{8}$$

..."

Meaning: the higher is tur_len, the higher are the turbulent coefficients (both vertical and horizontal) in the middle-upper atmospheric levels, and consequently the higher are the turbulent fluxes (mixing) for all the variables and tracers. **Precipitation**: as a result of increasing tur_len, the low level mixing ratio (moisture) is transported upward, increasing mixing ratio on the upper levels, leading to larger cloud development and to the increase of precipitation (see for example Helmert et al. (2008)). We expect this precipitation enhancement to be pronounced mainly in **convective** conditions (typical in **summertime** over Switzerland and inland Europe), where increased tur_len will lead to increase of convective clouds development. In contrast, in stratiform conditions (more typical in **wintertime** over Switzerland and inland Europe), we expect this effect to be less pronounced. Important to mention, that in coastal areas, for example over Italy (close to relatively warm Mediterranean Sea), since the precipitation is highly convective in winter, we expect high precipitation sensitivity to tur_len also in wintertime (and not only in summertime, as in Switzerland). **Max/Min 2m-temperature**: since higher tur_len increases the middle-upper levels vertical mixing (of conservative variables, such as virtual temperature) as well as increases the convective circulation, the temperature profile tends to dry-adiabata, leading to **adiabatic heating in the lower atmosphere**, which in turn, is leading to the increase of 2m-temperature, both at day and night. **Important to note**:

a We would expect the mixing ratio (which is also conservative) to tend to be uniform with height (when increasing tur_len), i.e. increasing mixing ratio at upper levels, and decreasing them near surface. As part of the next stage of CALMO project, it is important to verify mixing ratio and the temperature profiles against **sounding** observations. That will prevent choosing wrong tur_len values which yield unrealistic profiles, although if improving 2m-temperature forecasts.

b Under stable conditions, for example during stable nights (fogs, frost on the ground, etc.), we expect that increasing tur_len will decrease the stability and eliminate these events.

2.2 tkhmin

Meaning: tkhmin $[m^2/s]$ and tkmmin $[m^2/s]$ determine the minimum limits for the turbulence coefficients. tkhmin presence is evident when the turbulent diffusion coefficients (then the mixing) are small, which occurs in **stable conditions**, at night near the surface, as well as at cold days near the surface (with snow cover for example). Increasing tkhmin will keep alive the turbulent kinetic energy at these stable conditions, increasing the mixing and **eliminating the strong inversions**. The expected effect at **stable nights**: increasing the 2m-temperature, i.e. the minimum temperature Tmin, as well as increasing the small convective cloudiness during these nights. Important to mention, that in order to increase the 2m-humidity during stable night and obtain fog, one should decrease tkhmin. The expected effect at **cold days near the surface**: slightly increasing the 2m-temperature, i.e. the maximum temperature Tmax (the last effect should be seen over Swiss plateau but not over Italy, because the proximity to the warm sea eliminates stable conditions during days). **Topography**: we expect this effect to be pronounced mainly in valleys and flat areas. It should not be important in mountains because the wind shears keep the turbulence alive (and the conditions are never very stable). **Season**: on **winter**, the stable conditions over Swiss plateau are common at nights but also during day time, so we expect the heating effect of tkhmin to be important. In contrast, during **summer**, the days are often unstable, and even the nights are not very stable, so we expect that heating effect of tkhmin is only slightly important (and only at nights). Fig. 1 (Cerenzia et al., 2014) presents an example

of the evolution of the near surface turbulent coefficient during a period of several days. One can see that it tends to drop below 1 m^2/s at nights and mornings. During these periods, tkhmin and tkmmin should play an important role.

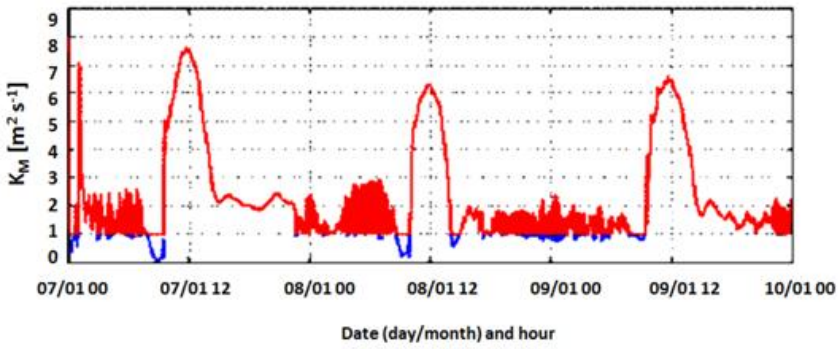


Figure 1: Time series of momentum diffusion coefficient at the lowest model level. Blue segments are the coefficients below the limit $K_M = 1m^2/s$.

Below we present a citation from Cerenzia et al. (2014) which describes tkhmin effect.

"...Nevertheless, some security limitations are active in order to prevent turbulence to decay. The most documented ones are the minimum limits for the vertical diffusion coefficients of momentum and scalars (namelist parameters tkmmin and tkhmin, see also COSMO User's Guide (2014)). In principle, they force the system to continue mixing also when the diffusion coefficients would drop below the prescribed minimum values. In the shear driven SBL case study simulated with COSMO Single-Column by Buzzi, the detrimental effect of this measure on the simulation of the SBL structures has been already underlined (Buzzi, 2008). In the same case study, it appears that the largest minimum limit of the diffusion coefficients not altering the SBL representation is $K_{min} = 0.1m^2/s$*, while in current operational setting it is* $K_{min} = 1m^2/s$ *(or* $0.4m^2/s$ *as recently suggested by DWD in order to avoid the detrimental effect on boundary layer clouds previously mentioned). In weak wind SBL, one can expect an even worse effect on the simulation, given that a stronger stratification should be established. In the case study considered here, the limitation to* $K_{min} = 1m^2/s$ *is frequently occurring (Fig. 1)..." "Another constraint acts on the sum of buoyancy and wind shear forcings in the TKE equation when the Richardson flux number (*$Ri_f = -f_h/f_m$ *) exceeds the critical value* Ri_c *(equal to 0.19 in operational setting), i.e. in very stable stratification. Essentially in this case the buoyancy term is excluded from the TKE calculation, so that the forcing sum depends only on mechanical forcing (positive definite), then the sum is prevented to become negative. Therefore, states of the system beyond* Ri_c *are not described by the TKE equation and are brought back to less stable conditions..." "According to our experience, these limits strongly effect the simulation of the very SBL..."*

Note: the parameter **pat_len**, which is *keeping turbulence alive* parameter (of the thermal circulation term fc in the equation for TKE), which takes into account the effects of turbulence forcing due to subgrid coherent circulations (like large eddies/convection), has the same effect as tkhmin: increase pat_len is equivalent to increase of tkhmin. pat_len parameter is highly uncertain, because of the lack of knowledge of this effect. For more information regarding turbulence closure models for SBL see Zilitinkevich S. et al. (2012).

2.3 rlam_heat

Meaning: rlam_heat [no units] is the parameter which linearly determines **the heat resistance length of laminar layer**; so that the higher is rlam_heat the higher is the resistance of laminar layer for heat transfer, and consequently, the lower is the heat transfer between the surface and the lower atmosphere. The vertical description of the transfer layer is illustrated in the following Fig. 2 (Buzzi, 2008):

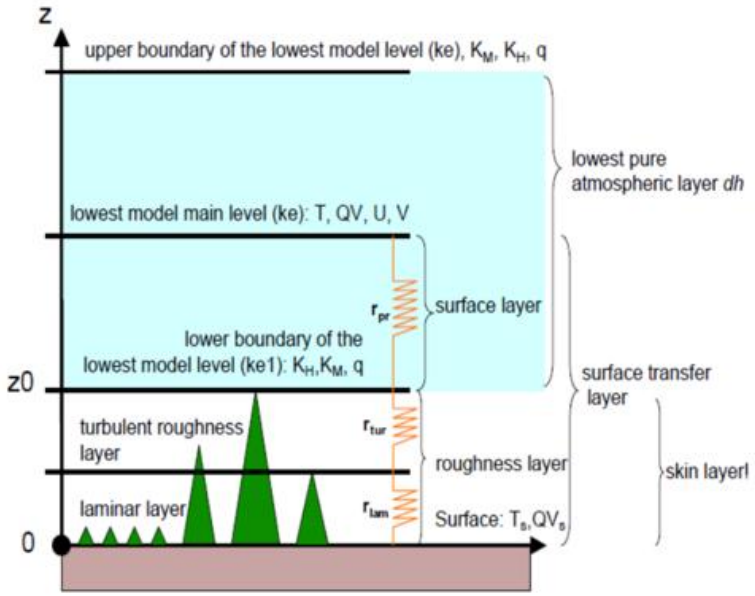


Figure 2: The surface transfer layer and its sub-layers: the surface layer (or Prandtl layer), the turbulent roughness layer and the laminar layer. For each sub-layer transport resistances for vector and scalar quantities are computed. The surface layer extends from the height corresponding to the roughness length Z_0 (level with the index ke1) to the lowest atmospheric main level (level with index ke), where the turbulent diffusion coefficients and all the model variables are known. At the bottom of the surface layer only the turbulence related variables as the diffusion coefficients are known. The roughness layer is placed below the height equal to the roughness length and is treated as a skin layer.

The formula for the heat resistance length of the laminar layer is below (Cerenzia, 2013):

"...momentum and heat resistance lengths for laminar layer are calculated according to:

$$dz_{sg,m} = r_{lam,m}\frac{z_0}{SAI} \tag{9}$$

$$dz_{sg,h} = r_{lam,h}\frac{z_0}{SAI} fakt \frac{K_h con_m}{K_m con_h} \tag{10}$$

where:

- $r_{lam,m}$ *and* $r_{lam,h}$ *are scaling factors set by default respectively to 0 and 1 and modifiable in the namelist,*
- z_0 *is the roughness length,*
- SAI *is the Surface Area Index that includes both the transpirant and the non-transpirant surfaces,*

- *fakt is a factor that increases the laminar resistance length in case the gridbox is over water:*

$$fakt = 1 + (1 - NINT(fr_{land}))(rat_sea - 1) \tag{11}$$

with fr_{land} the ratio between land and water surfaces in the gridbox and rat_sea a parameter sets to 20 and modifiable by namelist,

- *con_m and con_h are respectively the kinematic viscosity and conductivity.*

..."

Expected effect: During days with **unstable** conditions and warm surface, typical to summertime days in Switzerland (but also to warm unstable wintertime days, for example in Italy), we expect that increasing rlam_heat will decrease the heat fluxes upward from the warm surface, leading to less effective heating of the lower atmospheric layers, i.e. lower 2m-temperature and **lower Tmax (in summertime)**. In addition, that should cause to slight decrease of instability, which may lead to **decrease in convective precipitation (in summertime)**. During **stable** conditions, with cold surface, typical to wintertime nights, but also to wintertime cold days near the surface, and sometimes to summertime nights, we expect that increasing rlam_heat will decrease the heat runoff from the warm atmosphere to the surface, leading to heating of the lower atmospheric layers, i.e. higher 2m-temperature. That will **increase Tmin at wintertime nights, increase Tmax at wintertime cold-surface days, and sometimes increase Tmin at stable summertime nights.**

2.4 rat_sea

Meaning: rat_sea [no units], has the same effect as rlam_heat, but over sea. In equation 10 (Cerenzia, 2013) for the **heat resistance length of laminar layer**, *fakt* parameter is rat_sea in case of pure sea grid point (according equation 11).

We expect that the effect of rat_sea will be pronounced only over the sea or near sea regions, like Italy, but not over Switzerland. Generally, **the effect of rat_sea over Switzerland should be noisy**. In near coast areas (like in Italy), at wintertime, when the sea is relatively warm, the increase of rat_sea should decrease the temperature and humidity fluxes from the sea, leading to **decrease of precipitation**. In cyclonic situations, these fluxes decrease, may significantly flatten the cyclones. In near coast areas (like in Italy), at summertime, the precipitation is more often developed over the land, so the effect of rat_sea should be less pronounced. **Note**: in near coast areas (like in Italy), the effect of changes in rlam_heat and rat_sea is the same! For example, increasing rlam_heat from 1 to 5 will have the same effect as increasing rat_sea from 20 to 100.

Example for rat_sea effect over the sea (Eastern Mediterranean): In order to check, whether rat_sea parameter is important in regions which are affected by the Mediterranean Sea, a simple experiment was performed for the heavy rain event over the Eastern Mediterranean during 10-14.12.2013.

Fig. 3 shows the 24h accumulated precipitation over Israel for rat_sea=100 and Fig. 4 for rat_sea=1.

Fig. 5 presents the mean-sea-level pressure (for 11.12.2013 12UTC) over the Eastern Mediterranean for rat_sea=100 and Fig. 6 for rat_sea=1.

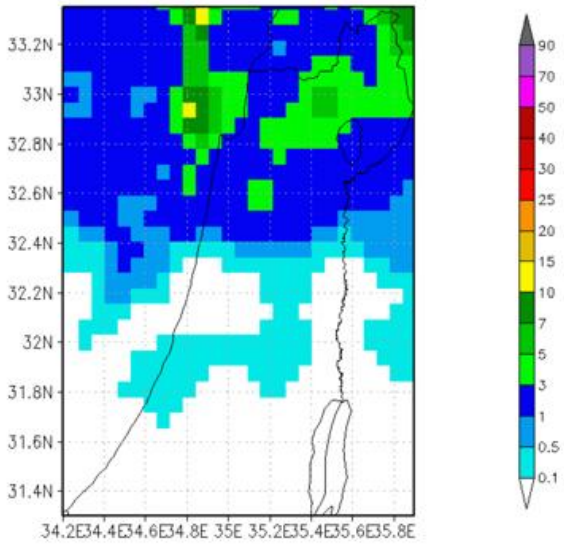


Figure 3: 24h accumulated precipitation over Israel 10.12.2013 for rat_sea=100.

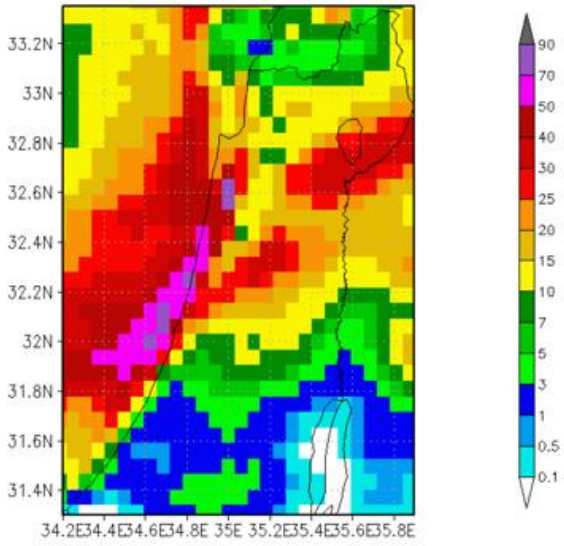


Figure 4: 24h accumulated precipitation over Israel 10.12.2013 for rat_sea=1.

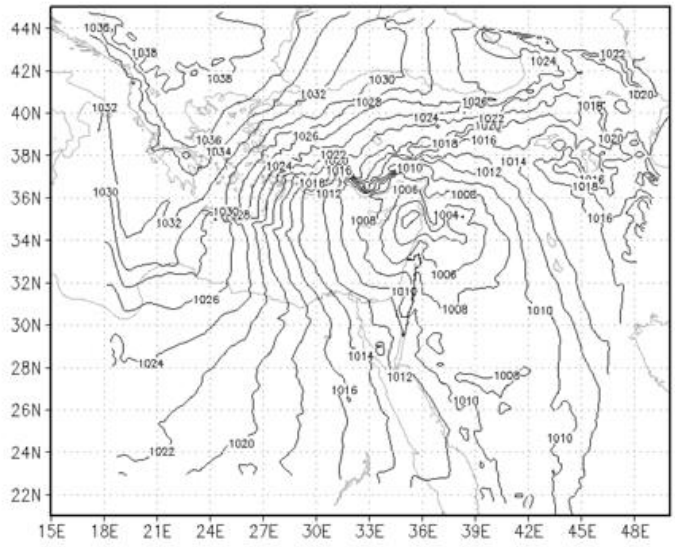


Figure 5: Mean sea level pressure (for 11.12.2013 12UTC) over the Eastern Mediterranean for rat_sea=100.

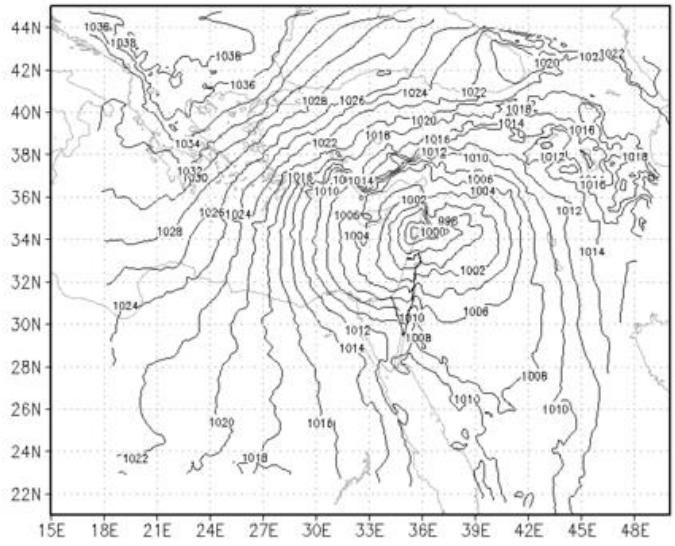


Figure 6: Mean sea level pressure (for 11.12.2013 12UTC) over the Eastern Mediterranean for rat_sea=1.

One can see that in case of rat_sea=1 the cyclone is much deeper and the accumulated precipitation is 10-20 times (!) larger than for rat_sea=100. **Conclusion: in coastal areas the rat_sea parameter might be highly important.**

3 The actual sensitivity to the tested parameters

3.1 Division of Switzerland into three climatically unique areas

In order to identify the general sensitivity of the COSMO forecasts to the parameters variations, there was a need to divide Switzerland area into a small number of climatically unique areas. Previously, Switzerland area was divided into 152 regions, yielding noisy effect of the parameters variations on the COSMO forecast, especially on the precipitation field. Therefore, we have divided Switzerland area into three climatically unique areas, according to Frei (2013), as presented in Fig. 7. The areas were defined as following:

- North - the area to the north of the Alpine crest, mostly coincides with the Swiss Plateau.
- Alps - the area of Alpine crest.
- South - the area to the south of the Alpine crest, mostly coincides with Ticino region.

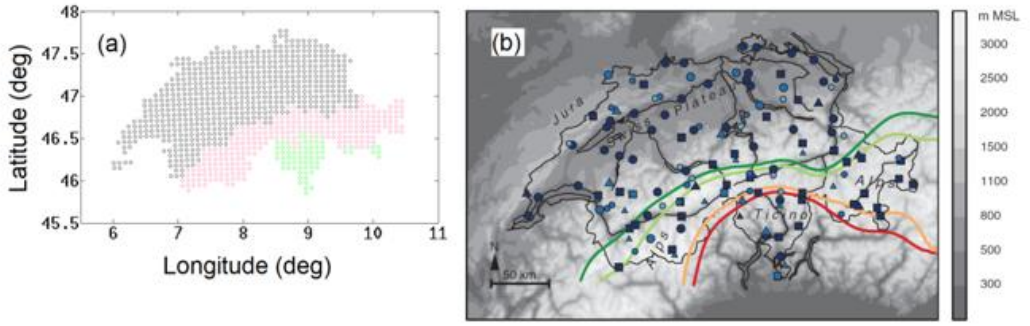


Figure 7: Division of Switzerland into three climatically unique areas, according to Frei (2013). (a) The three areas mapped to the COSMO 7km grid. (b) The original Frei (2013) topographical map. The green and the red lines were used for the areas definition.

3.2 Maximum 2m-temperature (Tmax) sensitivity

For identifying the general sensitivity of Tmax to the parameters variations, for each of the 4 parameters, we present 2 time series: for its minimum and maximum allowed values, respectively, while keeping the other parameters at their default values:

- rlam_heat: COSMO simulations LRLAM and HRLAM
- tkhmin: COSMO simulations LTKH and HTKH
- rat_sea: COSMO simulations LRATS and HRATS
- tur_len: COSMO simulations LTURL and HTURL

In addition, we present the time series of REF COSMO simulation (red), where all the 4 parameters keep their default values, and the observations time series OBS (black). As described in the Introduction, we have performed separate analysis for January and June 2008. Figs 8 and 9 present the 10 Tmax time series (described above) for January and June 2008, respectively.

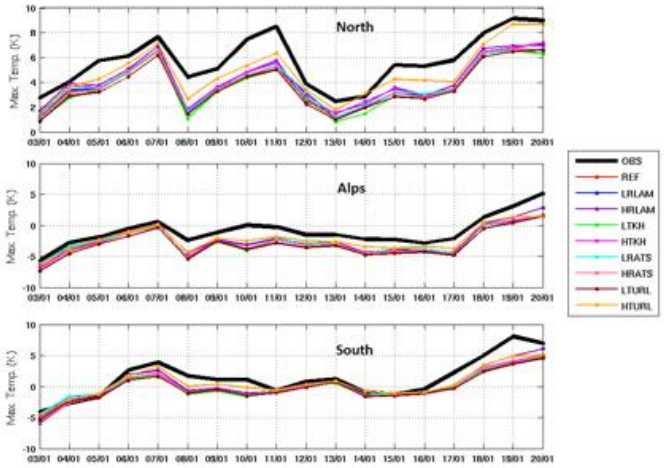


Figure 8: Tmax time series for January 2008, for the observations (black) and nine selected COSMO-7km simulations (colored).

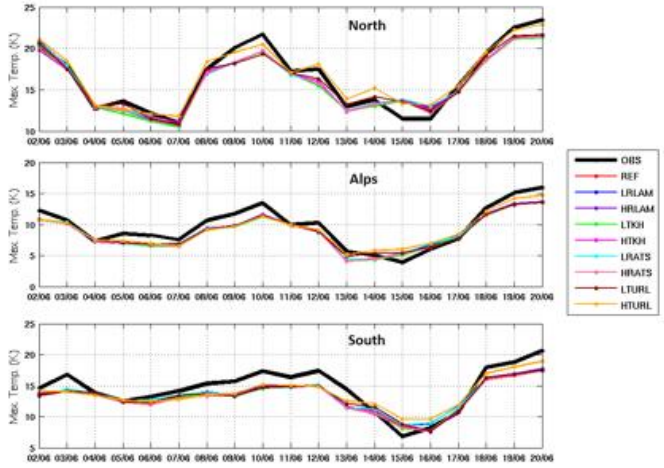


Figure 9: Tmax time series for June 2008, for the observations (black) and nine selected COSMO-7km simulations (colored).

Subtracting the observed Tmax from the simulated, we have constructed Tmax error distributions. Fig. 10 presents the Tmax error distributions for January (a) and June (b) 2008, respectively, for the nine selected COSMO-7km simulations.

In the following, we present typical examples for Tmax sensitivity for the North region

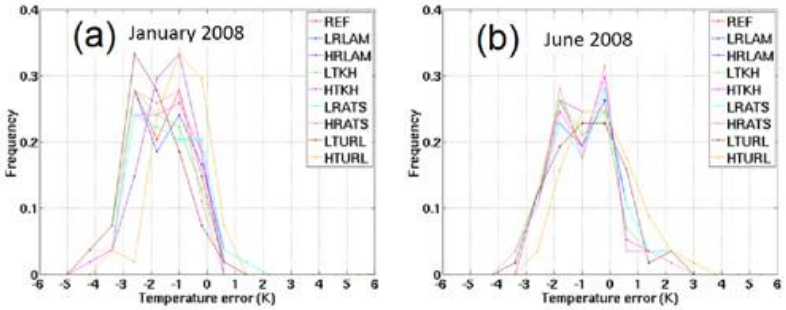


Figure 10: Tmax error distributions for January (a) and June (b) 2008, for the nine selected COSMO-7km simulations.

during different days for the 3 parameters separately (tur_len, rlam_heat and tkhmin; no tests for rat_sea due to technical problems). Several additional simulations for intermediate values of each of the parameters were performed. Fig. 11 presents Tmax sensitivity on tur_len parameter for 12.01.2008, typical for wintertime (a), and for 10.06.2008, typical for summertime (b), respectively. Fig. 12 presents Tmax sensitivity on rlam_heat parameter for 11.01.2008, typical for wintertime (a), and for 03.06.2008, typical for summertime (b), respectively. Fig. 13 presents Tmax sensitivity on tkhmin parameter for 11.01.2008, typical for wintertime (a), and for 03.06.2008, typical for summertime (b), respectively.

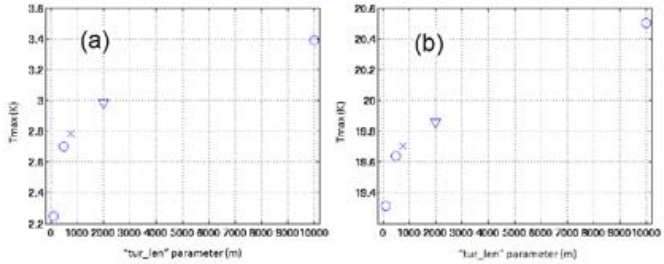


Figure 11: Tmax sensitivity on tur_len parameter for region North on 12.01.2008, typical for wintertime (a), and for 10.06.2008, typical for summertime (b), respectively.

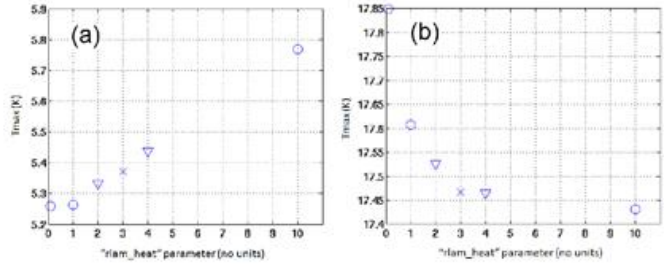


Figure 12: Tmax sensitivity on rlam_heat parameter for region North on 11.01.2008, typical for wintertime (a), and for 03.06.2008, typical for summertime (b), respectively.

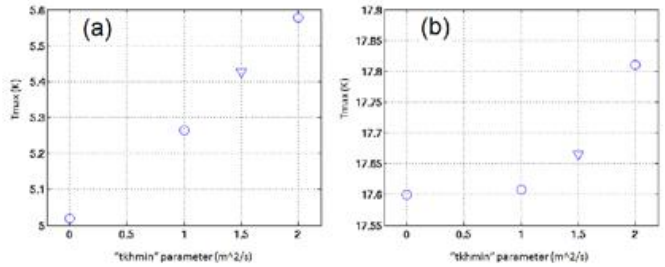


Figure 13: Tmax sensitivity on tkhmin parameter for region North on 11.01.2008, typical for wintertime (a), and for 03.06.2008, typical for summertime (b), respectively.

Conclusions regarding Tmax sensitivity to the 4 parameters variations

- The COSMO simulations of Tmax are generally colder than the observed values (as will be seen from analyzing Tmin in the next Section, the COSMO 2m-temperature day-night amplitude is too low). On January the COSMO underestimation is around 2K and on June around 1K (Figs. 8, 9, 10)
- **Generally, none of the COSMO simulations is warm enough (Figs. 8, 9). Therefore, the CALMO method will not solve the problem of Tmax underestimation using the 4 tested parameters, but only slightly improve the Tmax forecast. In order to solve the Tmax underestimation problem, one should calibrate different COSMO parameters (like soil scheme parameters, radiation scheme parameters, etc.)**
- As expected from the physical meaning of tur_len (see Section 2.1), the higher is tur_len the higher is the 2m-temperature (Figs. 10, 11). The sensitivity is very clear (about 1K) and the noise is low.
- As expected from the physical meaning of rlam_heat (see Section 2.3), the sensitivity of Tmax on rlam_heat depends on the stability conditions at specific day. On cold winter days, the stratification is often stable, so the increase of rlam_heat prevents the heat run-off from the lower atmosphere to the soil, leading to increase of Tmax. That is exactly the case on Fig. 12a. The stable stratification on that day is presented in Fig. 39 in Section 10. On summer days, the profile is often unstable, so the increase of rlam_heat prevents the warm soil to heat the lower atmosphere, leading to decrease of Tmax. That is exactly the case on Fig. 12b. The unstable stratification on that day is presented in Fig. 40 in Section 10.
- As expected from the physical meaning of tkhmin (see Section 2.2), the sensitivity of Tmax on tkhmin depends on the stability conditions at specific day. On cold winter days, the stratification is often stable, then the increase of tkhmin keeps the turbulence alive, leading to increase of Tmax. That is exactly the case on Fig. 13a. The stable stratification on that day is presented in Fig. 39 in Section 10. On summer days, the profile is often unstable, then tkhmin does not play any role, and its effect on Tmax is noisy. That is exactly the case in Fig. 13b. The unstable stratification on that day is presented in Fig. 40 in Section 10.
- It is expected that the effect of rat_sea over Switzerland is noisy. However, for technical reasons the sensitivity checks were not yet performed.

3.3 Minimum 2m-temperature (Tmin) sensitivity

For identifying the general sensitivity of Tmin to the parameters variations, for each of the 4 parameters, we present the same 10 time series, as in Section 3.2 above, both for January and June 2008. Figs. 14 and 15 present the 10 Tmin time series for January and June 2008, respectively.

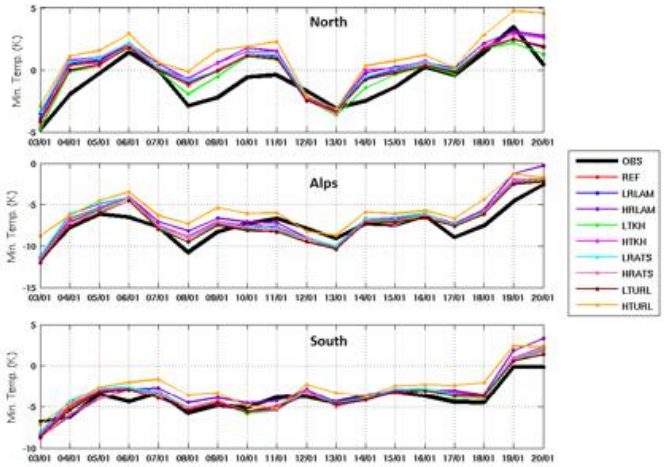


Figure 14: Tmin time series for January 2008, for the observations (black) and nine selected COSMO-7km simulations (colored).

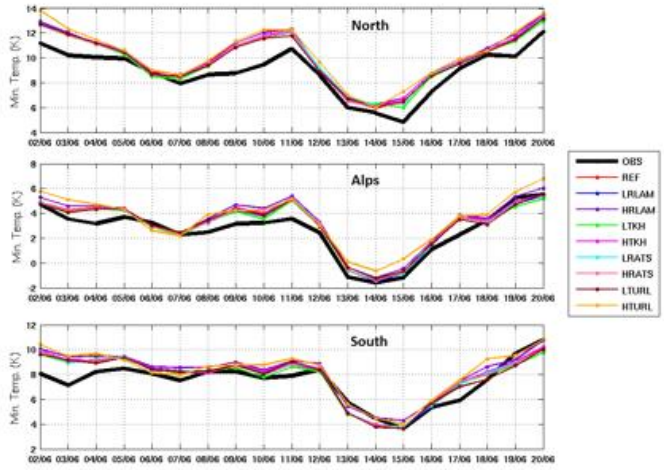


Figure 15: Tmin time series for June 2008, for the observations (black) and nine selected COSMO-7km simulations (colored).

Subtracting the observed Tmin from the simulated, we have constructed Tmin error distributions. Fig. 16 presents the Tmin error distributions for January (a) and June (b) 2008, respectively, for the nine selected COSMO-7km simulations.

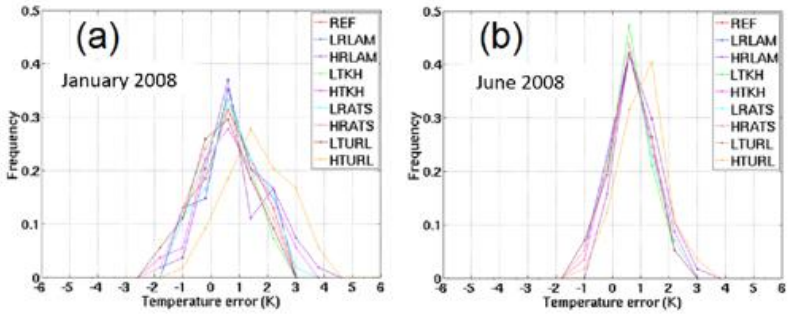


Figure 16: Tmin error distributions for January (a) and June (b) 2008, for the nine selected COSMO-7km simulations.

In the following, we present typical examples for Tmin sensitivity for the North region during different days for the 3 parameters separately (tur_len, rlam_heat and tkhmin; no tests for rat_sea due to technical problems). Fig. 17 presents Tmin sensitivity on tur_len parameter for 11.01.2008, typical for wintertime (a), and for 10.06.2008, typical for summertime (b), respectively. Fig. 18 presents Tmin sensitivity on rlam_heat parameter for 11.01.2008, typical for wintertime (a), and for 10.06.2008, typical for summertime (b), respectively. Fig. 19 presents Tmin sensitivity on tkhmin parameter for 11.01.2008, typical for wintertime (a), and for 10.06.2008, typical for summertime (b), respectively.

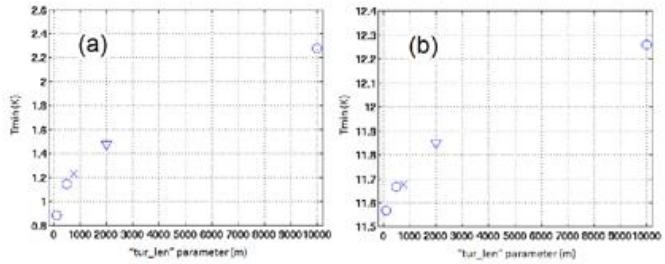


Figure 17: Tmin sensitivity on tur_len parameter for region North on 11.01.2008, typical for wintertime (a), and for 10.06.2008, typical for summertime (b), respectively.

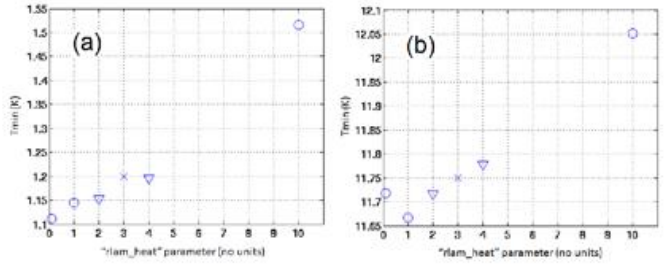


Figure 18: Tmin sensitivity on rlam_heat parameter for region North on 11.01.2008, typical for wintertime (a), and for 10.06.2008, typical for summertime (b), respectively.

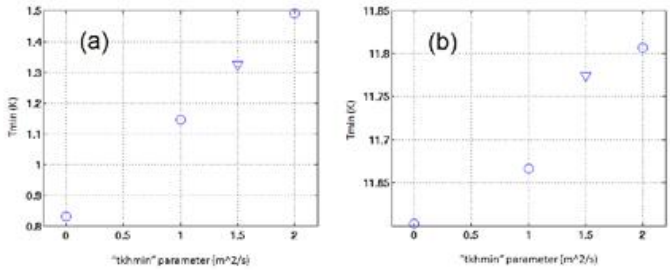


Figure 19: Tmin sensitivity on tkhmin parameter for region North on 11.01.2008, typical for wintertime (a), and for 10.06.2008, typical for summertime (b), respectively.

Conclusions regarding Tmin sensitivity to the 4 parameters variations

- The COSMO simulations of Tmin are generally warmer than the observed values (the COSMO 2m-temperature diurnal amplitude is too low). The COSMO overestimation is around 0.5-1K (Figs. 14, 15, 16).
- **Generally, none of the COSMO simulations is cold enough (Figs. 14, 15). Therefore, the CALMO method will not solve the problem of Tmin overestimation using the 4 tested parameters, but only slightly improve the Tmin forecast. In order to solve the Tmin overestimation problem, one should calibrate different COSMO parameters (like soil scheme parameters, etc.).**
- As expected from the physical meaning of tur_len (see Section 2.1), the higher is tur_len the higher is the 2m-temperature (Figs. 16, 17). The sensitivity is very clear (about 1K) and the noise is low.
- As expected from the physical meaning of rlam_heat (see Section 2.3), the sensitivity of Tmin on rlam_heat depends on the stability conditions at specific night. Generally, on nights the stratification is often stable, so the increase of rlam_heat prevents the heat run-off from the lower atmosphere to the soil, leading to increase of Tmin. That is exactly the case on Figs. 18a, 18b. The stable stratification on these nights is presented in Figs. 39 and 41 in 10, respectively.
- As expected from the physical meaning of tkhmin (see Section 2.2), the sensitivity of Tmin on tkhmin depends on the stability conditions at specific night. Generally, on nights the stratification is often stable, then the increase of tkhmin keeps the turbulence alive, leading to increase of Tmin. That is exactly the case on Figs. 19a, 19b. The stratification on winter night is generally much more stable than on summer night, leading to much larger effect of Tmin on tkhmin (Fig. 19a). The stable stratification on these nights is presented in Figs. 39 and 41 in 10, respectively.
- It is expected that the effect of rat_sea over Switzerland is noisy. However, for technical reasons the sensitivity checks were not yet performed.

3.4 24h accumulated precipitation (Pr) sensitivity

For identifying the general sensitivity of Pr to the parameters variations, for each of the 4 parameters, we present the same 10 time series, as in sections 3.2 and 3.3 above, both for January and June 2008. Figs. 20, 21 present the 10 Pr time series for January and June 2008, respectively.

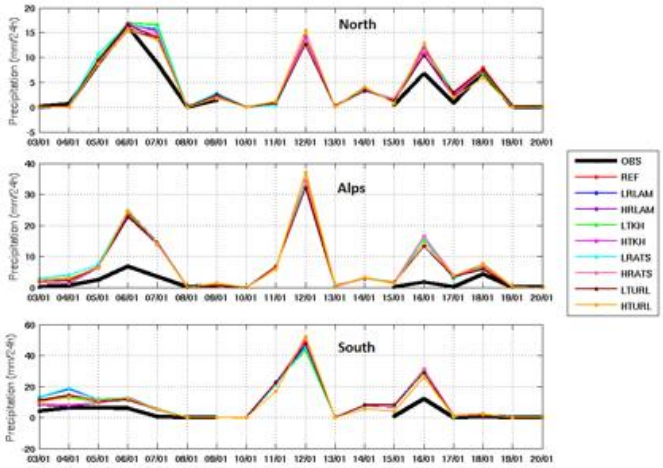


Figure 20: Pr time series for January 2008, for the radar measurements (black) and nine selected COSMO-7km simulations (colored). The period 10.01-14.01 is missing from the radar data.

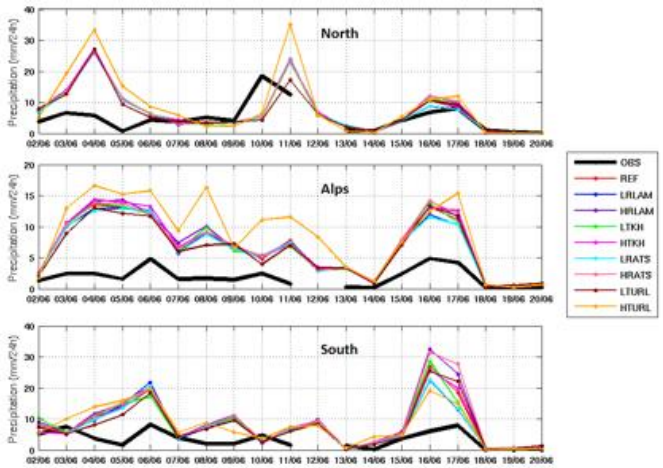


Figure 21: Pr time series for June 2008, for the radar measurements (black) and nine selected COSMO-7km simulations (colored). The day 12.06 is missing from the radar data.

Subtracting the measured Pr from the simulated, we have constructed Pr error distributions. Fig. 22 presents the Pr error distributions for January (a) and June (b) 2008, respectively, for the nine selected COSMO-7km simulations.

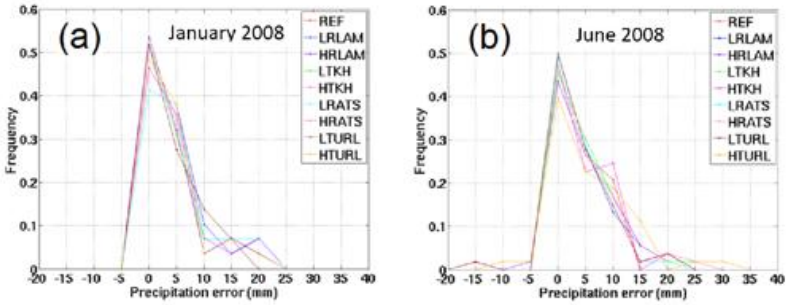


Figure 22: Pr error distributions for January (a) and June (b) 2008, for the nine selected COSMO-7km simulations.

In the following, we present typical examples for Pr sensitivity for the North region during different days for the 3 parameters separately (tur_len, rlam_heat and tkhmin; no tests for rat_sea due to technical problems).

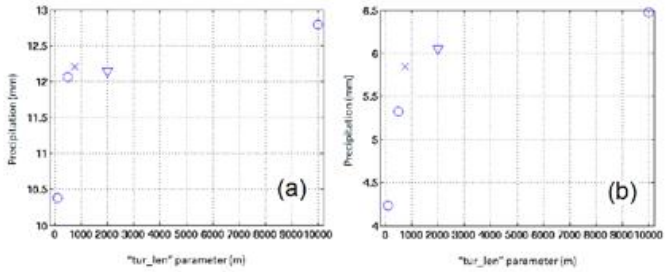


Figure 23: Pr sensitivity on tur_len parameter for region North on 16.01.2008, typical for wintertime (a), and for 10.06.2008, typical for summertime (b), respectively.

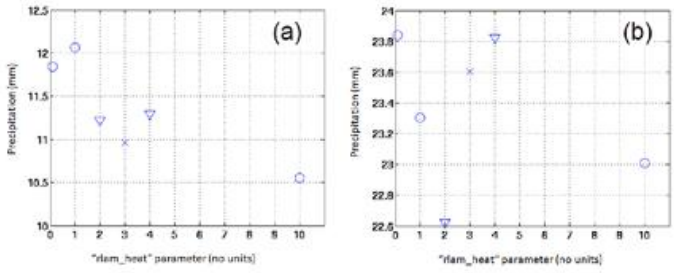


Figure 24: Pr sensitivity on rlam_heat parameter for region North on 16.01.2008, typical for wintertime (a), and for 11.06.2008, typical for summertime (b), respectively.

Fig. 23 presents Pr sensitivity on tur_len parameter for 16.01.2008, typical for wintertime (a), and for 10.06.2008, typical for summertime (b), respectively. Fig. 24 presents Pr sensitivity on rlam_heat parameter for 16.01.2008, typical for wintertime (a), and for 11.06.2008, typical for summertime (b), respectively. Fig. 25 presents Pr sensitivity on tkhmin parameter for 16.01.2008, typical for wintertime (a), and for 11.06.2008, typical for summertime (b), respectively.

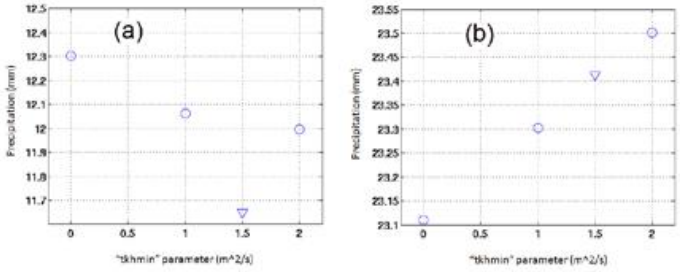


Figure 25: Pr sensitivity on tkhmin parameter for region North on 16.01.2008, typical for wintertime (a), and for 11.06.2008, typical for summertime (b), respectively.

Conclusions about 24h accumulated precipitation sensitivity to the 4 parameters variation

- The COSMO simulations generally overestimate the observed precipitation, especially on summertime (Figs. 20, 21, 22).
- **Generally, none of the COSMO simulations is dry enough (Figs. 20, 21). Therefore, the CALMO method will not solve the problem of precipitation overestimation using the 4 tested parameters, but only slightly improve the precipitation forecast. In order to solve the precipitation overestimation problem, one should calibrate different COSMO parameters (like microphysics scheme parameters, etc.).**
- As expected from the physical meaning of tur_len (see Section 2.1), the higher is tur_len the higher is the convective precipitation (Figs. 21, 22b, 23b). This sensitivity is very clear (up to 30%). However, the stratiform precipitation, more typical to wintertime (over Switzerland) generally exhibits little and noisy effect as function of tur_len (Figs. 20, 22a, 23a).
- As expected from the physical meaning of rlam_heat (see Section 2.3), the sensitivity of precipitation on rlam_heat is generally noisy (Fig. 24). On warm days with convective precipitation, we would expect that increase of rlam_heat will slightly decrease precipitation, but this effect is not presented at the examples above.
- As expected from the physical meaning of tkhmin (see Section 2.2), the sensitivity of precipitation on tkhmin (which is important in very stable conditions) is noisy.
- It is expected that the effect of rat_sea over Switzerland is noisy (in coastal areas like Italy, the effect should be very significant). However, for technical reasons the sensitivity checks were not yet performed.

4 The Meta-Model

In the following, we will focus on the 3 parameters rlam_heat, tkhmin and tur_len (rat_sea will not be used in the Meta-Model due to technical problems). Following the theory of Meta-Model construction (Neelin et al., 2010 and Bellprat et al., 2012), for any parameters combination [rlam_heat, tkhmin, tur_len], for a given day i and a region r, the COSMO field F (in our case Tmax, Tmin or Pr) may be approximated by 3-dimensional polynomial of order 2:

$$F_{i,r} \cong F_{i,r}^{d} + c_{i,r} + a_{i,r}^{(1)} x_1 + B_{i,r}^{(1,1)} x_1^2 + a_{i,r}^{(2)} x_2 + B_{i,r}^{(2,2)} x_2^2 + a_{i,r}^{(3)} x_3 + B_{i,r}^{(3,3)} x_3^2 + \\ + B_{i,r}^{(1,2)} x_1 x_2 + B_{i,r}^{(1,3)} x_1 x_3 + B_{i,r}^{(2,3)} x_2 x_3 \quad (12)$$

Where:

$$x_1 = \frac{rlam_heat - rlam_heat_d}{rlam_heat_{max} - rlam_heat_{min}}; x_2 = \frac{tkhmin - tkhmin_d}{tkhmin_{max} - tkhmin_{min}}; \quad (13)$$

$$x_3 = \frac{tur_len - tur_len_d}{tur_len_{max} - tur_len_{min}}$$

The index d stands for default. For default values of the 3 parameters, i.e. $[x_1 = 0, x_2 = 0, x_3 = 0]$, the approximated field should be close to $F_{i,r}^{d}$. The constants $c_{i,r}, a_{i,r}^{(1,2,3)}, B_{i,r}^{(1,2,3\times 1,2,3)}$ are obtained using several COSMO simulations, as described in the following. Each simulation (for given parameters values) yields $F_{i,r}$. When sufficient number of simulations is performed, one can interpolate the different known values of $F_{i,r}$ as function of $[x_1, x_2, x_3]$ using the 3D polynomial in eq. (12) above. The sufficient number is $2N + 0.5N(N-1) + 1$, so that for N=3 the sufficient number of simulations to be performed is 10.

Now the question arises: what is the quality of such interpolation? The following factors are important for the interpolation to be realistic (to be able to replace the COSMO simulations):

- The choice of parameters values (combinations) for COSMO simulations should be specific. In this work the **design** is chosen according to Bellprat (2012).
- The default values of the parameters should be located close to the **center of their allowed ranges**. Otherwise, in the empty parameter regions, the parabolic fit will reach very high (or very low) unrealistic peaks. The problem is, that the default values of rlam_heat and tur_len are significantly shifted from the centers of their allowed ranges: for rlam_heat: [0.1 1 10], and for tur_len: [100 500 10000]. That problem will be discussed and solved in section 4.1 below.
- The simulated COSMO field $F_{i,r}$ should **not be noisy** as function of the parameters $[x_1, x_2, x_3]$. In other words, the sensitivity of $F_{i,r}$ on $[x_1, x_2, x_3]$ should be higher than the noise level. However, various COSMO fields are noisy for various parameters. That issue will be discussed and solved in section 4.2 below.
- Use as many as possible additional constrain simulations (for additional parameters combinations). The added value of these simulations is discussed in section 4.3 below.

4.1 The Meta-Model: solution to the parabola problem

As mentioned, the default values of the parameters should be located close to the **center of their allowed ranges**. Otherwise, in the empty parameter regions, the parabolic fit will reach very high (or very low) unrealistic peaks. For example, we focus on the Tmax dependence on tur_len parameter for the North region on 12.01.2008. Fig. 26 presents the parabolic fit (blue dashed line) for 3 tur_len values (a) and 4 tur_len values (b). One can see that in the empty tur_len regions, the parabolic fit reaches very high unrealistic peaks. When adding one more tur_len value (b), the fit improves, but still exhibits unrealistically high peak. Our solution to that problem is **fitting the parabola to logarithm of the**

parameter, or more precisely: parabolic fit to $log(tur_len/100)$ (instead of to tur_len), and parabolic fit to $log(rlam_heat+1)$ (instead of to rlam_heat). In simple words, logarithm of a parameter brings the far away parameter values closer to the others, eliminating the empty parameter regions, and causing the parabolic fit to be more monotonic. Fig. 26 presents these fits by red solid lines. One can see that these fits are much more reasonable.

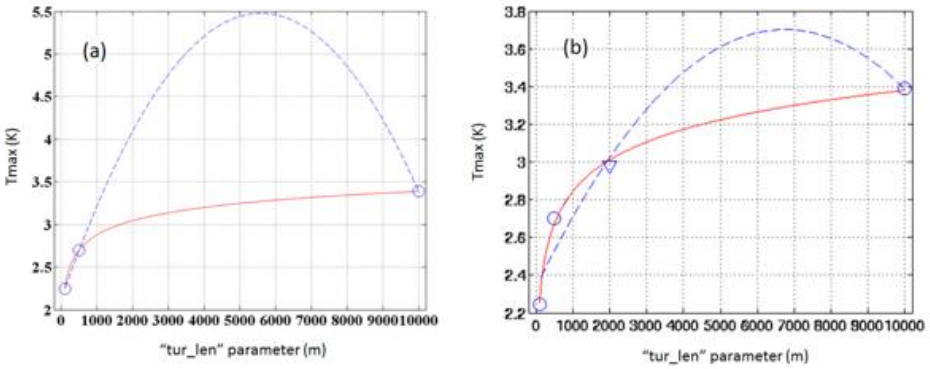


Figure 26: Tmax dependence on tur_len parameter for the North region on 12.01.2008. The parabolic fit (blue dashed line) and the parabola of logarithm fit (red solid line) are shown, for 3 tur_len values (a) and 4 tur_len values (b).

Important to mention:

- The exact dependence of the COSMO forecasts on its parameters is generally very complicated and not parabolic. Therefore, the parameter original definition, its logarithm or any other function of the parameter, all have the same "right to exist". So, generally, one may choose any function of the parameter which makes the parabolic fit more reasonable.
- For all the examples presented in Section 3, the parabolic fit to logarithm of the parameter yields much better results (not shown here).
- We do not use logarithm of tkhmin because its default value is located at the center of its allowed range [0 1 2].

4.2 The Meta-Model: solution to the noise problem

The simulated COSMO field $F_{i,r}$ should not be noisy as function of the parameters $[x_1, x_2, x_3]$. In other words, the sensitivity of $F_{i,r}$ on $[x_1, x_2, x_3]$ should be higher than the noise level. However, various COSMO fields are noisy for various parameters as was presented in Sections 2 and 3 above. As mentioned, for a given COSMO field $F_{i,r}$ one has to construct the 3D polynomial interpolation (12) as function of the parameters $[x_1, x_2, x_3]$. However, in case when one (or some) of the parameters yields noisy effect on $F_{i,r}$, for example x_1, the fit (12) will be problematic for 2 reasons:

- The fit (12) will not represent the true COSMO behavior in x_1 direction.
- The fit is performed using least mean squares method. The attempt to get the best fit in x_1 direction (which is noisy), may spoil the fit quality in the other directions (x_2, x_3), which are not noisy.

Therefore, we have implemented a new approach, which automatically detects the noisy parameter(s) for a given field/day/region, and neglects it (them) in the fitting formula (12).

The following steps are performed automatically:

- For a given field/day/region, a simple parabolic fit is performed (and the correlation R^2 is calculated) to each of the parameters separately.
- In case that R^2 is too low (we chose the threshold of 0.7), the noisy parameter is neglected in the fitting formula (12). For example, if for a given field/day/region, the parabolic fit for x_1 yields $R^2 = 0.4$, the fitting polynomial (12) will be reduced to:

$$F_{i,r} \cong F^d_{i,r} + c_{i,r} + a^{(2)}_{i,r} x_2 + B^{(2,2)}_{i,r} x_2^2 + a^{(3)}_{i,r} x_3 + B^{(3,3)}_{i,r} x_3^2 + B^{(2,3)}_{i,r} x_2 x_3 \qquad (14)$$

Consequently, the best possible fit will be constructed for each field/day/region. However, it is important to mention, that the effect of neglecting the noisy parameter plays an important role only in case when the response to the parameter variation is high (but noisy). However, usually when the response is high it is not noisy, and vice versa when the response is noisy, it is usually low. Therefore the procedure presented above, will usually play not significant role, but in some rare cases be, in contrast, very important.

4.3 The Meta-Model: additional constrain simulations

As was mentioned previously, the sufficient number of simulations for constructing the Meta-Model using formula (12) is $2N + 0.5N(N-1) + 1$, so that for N=3 the sufficient number of simulations to be performed is 10. However, it is obvious that adding more simulations, i.e. more parameter combinations, will better define the Meta-Model fit (12). According the theory for the parameters combinations design (Neelin et al., 2010 and Bellprat et al., 2012), it is important to perform **more than one interaction simulation** (simulation when 2 parameters are shifted to their minimum or maximum allowed values). For the 3 parameters *rlam_heat* $\in$ [0.1 1 10] , *tkhmin* $\in$ [0 1 2] , *tur_len* $\in$ [100 500 10000] the sufficient simulations are: [1 1 500], [0.1 1 500], [10 1 500], [1 0 500], [1 2 500], [1 1 100], [1 1 10000]; and 3 interaction simulations: [0.1 0 500], [0.1 1 100], [1 0 100].

In order to demonstrate the importance of additional simulations for the Meta-Model fit quality, Antigoni Voudouri (HNMS) performed also the following simulations:

- 7 additional interaction simulations: [10 2 500], [10 1 10000], [1 2 10000], [0.1 2 500], [10 0 500], [0.1 1 10000], [10 1 100]
- and 4 constrain simulations (changing the value of 1 parameter each time): [2 1 500], [4 1 500], [1 1.5 500], [1 1 2000].

From the simulations above, 2 Meta-Models were constructed. In order to verify their quality, additional test simulation was performed [3 0.5 750], which was not used for the Meta-Model fits. Fig. 27 shows a scatter plot for simulated precipitation (as an example), where each point represents one region at one day for the period 3-20.1.2008. The y-axis shows the Meta-Model estimation minus the reference (simulation with default parameters values), and the x-axis shows the COSMO simulation results minus the reference. In Fig. 27a the Meta-Model was constructed using the minimum number of simulations, while in Fig. 27b, the

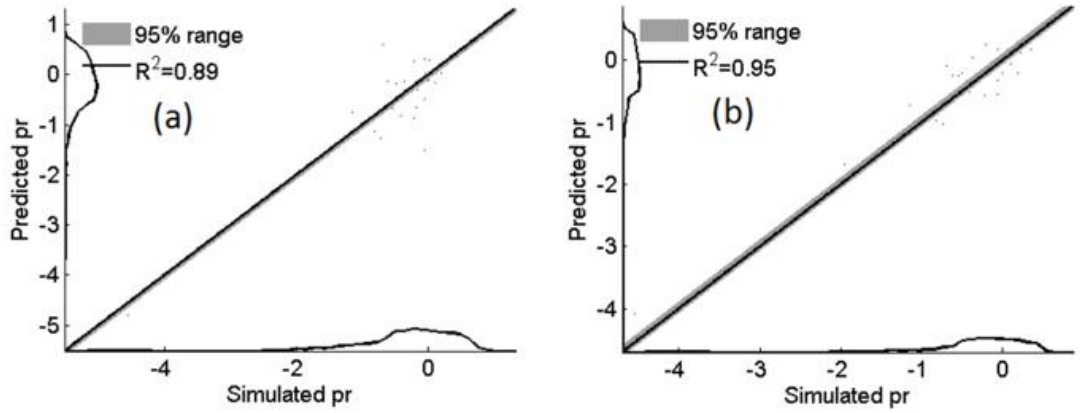


Figure 27: Estimating the Meta-Model quality for reproducing the precipitation field by comparing it with a test COSMO simulation for the period 3-20.1.2008. (a) The Meta-Model was constructed using the minimum number of simulations; (b) the Meta-Model was constructed using additional interaction and constrain simulations. In both axes, the REF simulation values were subtracted.

Meta-Model was constructed using additional simulations, as described above. Comparing the correlations ($R^2 = 0.89$ for case (a) and $R^2 = 0.95$ for case (b)), one can see a clear benefit for the Meta-Model quality when using additional simulations.

5 Performance score

After the Meta-Model is constructed, one has an estimation for the COSMO field $F_{i,r}$ for any day i and region r for any combination of the parameters [rlam_heat, tkhmin, tur_len]. The next step is to find the best parameters combination, i.e. the combination which yields $F_{i,r}$ forecasts which are the closest to the observations. In case only one field is verified, for example Tmax only, the general method is the following:

- Chose one combination of the parameters (here we define the combination index as p).
- Using the Meta-Model, calculate the forecast $F_{i,r}$ for every day and every region.
- Collect the observations $O_{i,r}$ for every day and every region.
- Calculate the RMSE for the given parameters combination:

$$(RMSE)_p = \sqrt{\frac{1}{N_{regs} N_{days}} \sum_{regions} \sum_{days} (F_{p,i,r} - O_{i,r})^2} \tag{15}$$

  Where: N_{regs} is the number of regions and N_{days} is the number of days.

- Calculate $(RMSE)_p$ for large number of parameters combinations (10000 in this report).
- Among all $(RMSE)_p$, find the parameters [rlam_heat, tkhmin, tur_len] combination which yields the minimal $(RMSE)_p$.

5.1 Normalization

The calculation presented above is not normalized, and therefore does not tell the whole story. The quality of COSMO forecast strongly depends on the region and the season. For example, the forecast with Tmax error of 5K in the Alps at winter may be actually better than with error of 3K in the Swiss Plateau at summer. Therefore one needs to normalize the forecast errors by a value which reflects the forecast complexity for a given day and region. However this value should not be dependent on any parameters combination, so normalization by typical forecast error is not appropriate. Therefore, we propose to normalize the forecast errors by the observations standard deviation σ_r at a given region r over a period of about a month (the period should not be too short in order to contain large enough sample, but not too long in order to represent the variability of a specific season):

$$\sigma_r = \sqrt{\frac{1}{N_{days}} \sum_{days} (O_{i,r} - \overline{O}_{i,r})^2} \tag{16}$$

Internal COSMO variability

There is an option to normalize also by internal COSMO variability adding it to σ_r (eq. 16 above). The COSMO forecast depends on the initial conditions, so that in principle, slightly different initial conditions may slightly change the forecast. Since the initial conditions are not perfectly defined, there is a hidden internal variability in the COSMO forecasts. This internal variability could be revealed by disturbing the initial conditions and calculating the forecasts standard deviation. However, currently this option is not available and is not used in this report.

5.2 Combined score for Tmax, Tmin and Precipitation

The final purpose of the CALMO project is to be able to find the parameters combination which improves the overall COSMO forecast. Therefore, the performance score should combine as many atmospheric fields as possible. Otherwise, there is a danger of choosing parameters combination which improves, for example, Tmax forecasts but spoil other important forecast fields. The first option is to use the following combination:

$$(RMSE)_{p,tot} = \sqrt{\frac{1}{N_{regs} N_{days}} \sum_{regions} \sum_{days} \left[\frac{(F_{Tmax,p,i,r} - O_{Tmax,i,r})^2}{\sigma^2_{Tmax,r}} + \frac{(F_{Tmin,p,i,r} - O_{Tmin,i,r})^2}{\sigma^2_{Tmin,r}} + \frac{(F_{Pr,p,i,r} - O_{Pr,i,r})^2}{\sigma^2_{Pr,r}} \right]} \tag{17}$$

The normalization by σ_r as presented above will cause the Tmax, Tmin and Pr terms to be dimensionless. However, these terms generally will have different weights. Here, there is a possibility for the user, to define these weights, i.e. to define which fields are more important to him to predict correctly. In this report we define the same weights for the 3 fields Tmax, Tmin and Pr. To do so, we normalize each term by its value averaged over all the parameters combinations, i.e.

$$W_F = \frac{1}{N_{comb}} \sum_{p} \left[\frac{1}{N_{regs} N_{days}} \sum_{regions} \sum_{days} \frac{(F_{p,i,r} - O_{i,r})^2}{\sigma^2_r} \right] \tag{18}$$

where: N_{comb} is the number of parameter combinations (10000 in this report).

Consequently, the final score used in this report is:

$$S_p = \sqrt{\frac{1}{N_{regs}N_{days}} \sum_{regions} \sum_{days} \left[\frac{(F_{Tmax,p,i,r} - O_{Tmax,i,r})^2}{W_{Tmax}\sigma^2_{Tmax,r}} + \frac{(F_{Tmin,p,i,r} - O_{Tmin,i,r})^2}{W_{Tmin}\sigma^2_{Tmin,r}} + \frac{(F_{Pr,p,i,r} - O_{Pr,i,r})^2}{W_{Tmin}\sigma^2_{Pr,r}} \right]} \tag{19}$$

which yields the same weights for the 3 fields Tmax, Tmin and Pr. For convenience, we define additional scores for each of the 3 fields separately:

$$S_{Tmax,p} = \sqrt{\frac{1}{N_{regs}N_{days}} \sum_{regions} \sum_{days} \frac{(F_{Tmax,p,i,r} - O_{Tmax,i,r})^2}{W_{Tmax}\sigma^2_{Tmax,r}}} \tag{20}$$

$$S_{Tmin,p} = \sqrt{\frac{1}{N_{regs}N_{days}} \sum_{regions} \sum_{days} \frac{(F_{Tmin,p,i,r} - O_{Tmin,i,r})^2}{W_{Tmin}\sigma^2_{Tmin,r}}} \tag{21}$$

$$S_{Pr,p} = \sqrt{\frac{1}{N_{regs}N_{days}} \sum_{regions} \sum_{days} \frac{(F_{Pr,p,i,r} - O_{Pr,i,r})^2}{W_{Pr}\sigma^2_{Pr,r}}} \tag{22}$$

The scores 20, 21, 22 will be used in Figs. 33 and 34 in Section 6 below.

At the next stage of the CALMO project we have to reconsider the score for precipitation, since RMSE type score is not optimal for that field. The general direction should be introducing a precipitation scores based of precipitation thresholds, like Fractions Brier Score. In addition, when the additional verified fields will be defined, such as sounding temperature and humidity profiles, we will have to formulate appropriate scores for these fields.

6 Results of parameters calibration

Following the discussion in Section 4, the Meta-Model was constructed for 3 COSMO fields Tmax, Tmin and Pr as function of the parameters [rlam_heat, tkhmin, tur_len], for the periods of 3-20.01.2008 and 2-20.06.2008, separately. In order to verify their quality, additional test simulation was performed [3 0.5 750], which was not used for the Meta-Model fits. Figs. 28 and 29 show scatter plots for simulated Tmax (left panels), Tmin (centered panels) and Pr (right panels), where each point represents one region at one day, for the periods of 3-20.01.2008 and 2-20.06.2008, respectively. The y-axes show the Meta-Model estimation minus the reference (simulation with default parameters values), and the x-axes show the COSMO simulation results minus the reference. For the tested parameter combination, the correlations R^2 between the COSMO forecasts and the Meta-Model estimations are generally high. Consequently, the overall method seems to prove itself: one can use the Meta-Model to reproduce COSMO forecasts for various parameters combinations.

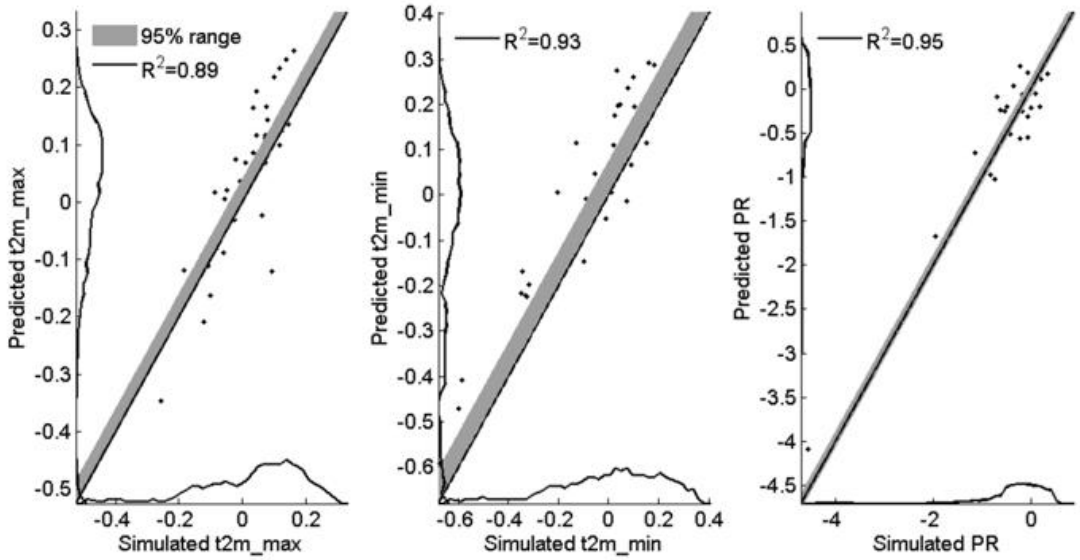


Figure 28: Estimating the Meta-Model quality for reproducing Tmax (left panel), Tmin (centered panel) and Precipitation (right panel) fields, by comparing them with a test COSMO simulation for the period 3-20.1.2008. In both axes, the REF simulation values were subtracted.

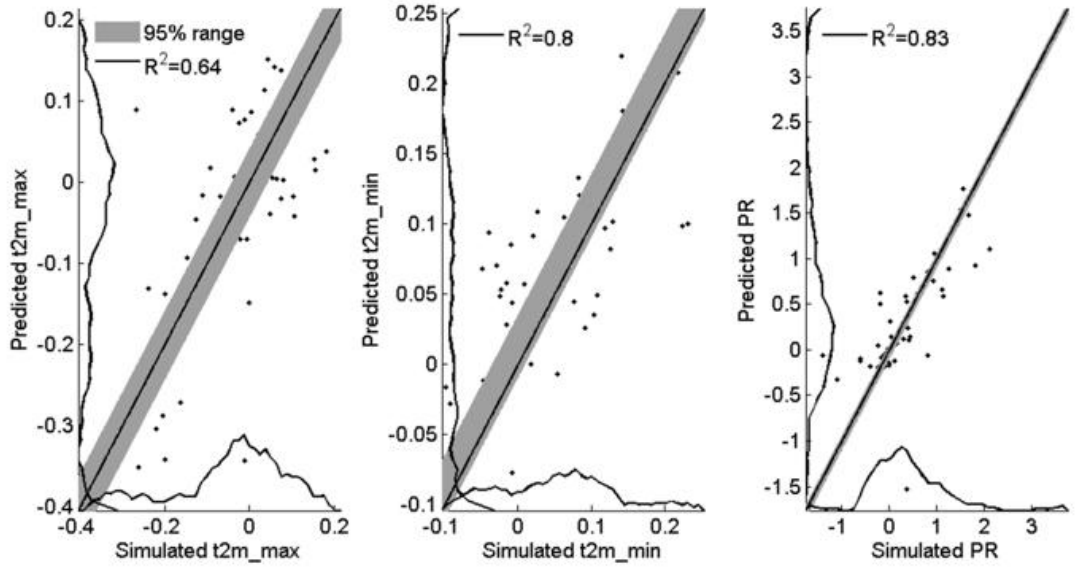


Figure 29: Estimating the Meta-Model quality for reproducing Tmax (left panel), Tmin (centered panel) and Precipitation (right panel) fields, by comparing them with a test COSMO simulation for the period 2-20.6.2008. In both axes, the REF simulation values were subtracted.

In order to analyze the general contributions of the various parameters to the constructed Meta-Model, we have calculated the normalized (by their standard deviation) and averaged (over fields, days and regions) linear, quadratic and interaction coefficients in the formula 12. These contributions are presented in Fig. 30 for the periods 3-20.01.2008 (left panel) and 2-20.06.2008 (right panel), respectively. One can see that generally tur_len and rlam_heat are more dominant in the Meta-Model than tkhmin. This result is physically expected, since in contrast to the other parameters, tkhmin plays a significant role only in highly stable atmospheric conditions, and therefore is important mainly for Tmin but not Tmax and precipitation.

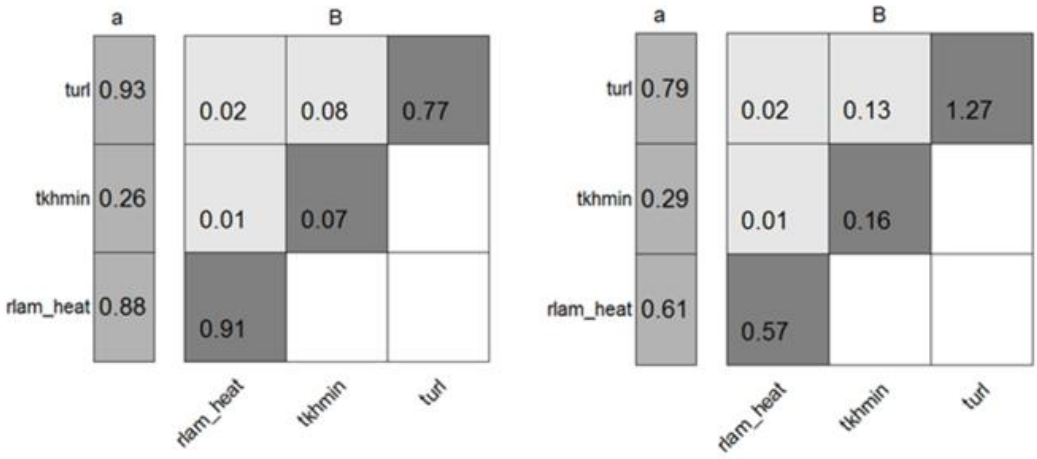


Figure 30: Contributions of the various parameters to the constructed Meta-Model. The presented linear, quadratic and interaction coefficients in the formula 12 were normalized (by their standard deviation) and averaged (over fields, days and regions). These contributions are presented for the periods 3-20.01.2008 (left panel) and 2-20.06.2008 (right panel), respectively.

Following the discussion in Section 5, we have used the Meta-Model to calculate the overall score S_p (see eq. 5.2) for any given parameters combination. Figs. 31 and 32 present the contours of S_p deviation, i.e. $S_p - \overline{S}_p$, for pairwise parameters combinations only, for the periods of 3-20.01.2008 and 2-20.06.2008, respectively. The upper panels represent rlam_heat and tkhmin combinations (while keeping tur_len default); the centered panels represent rlam_heat and tur_len combinations (while keeping tkhmin default); the lower panels represent tur_len and tkhmin combinations (while keeping rlam_heat default). The lower is the S_p deviation value, the better is the score, and the better is the specific parameters combination for the forecast quality. One can see, that for improving the forecast during January 2008 (Fig. 31), the tur_len has to be relatively high, rlam_heat as high as possible, and tkhmin as low as possible. On June 2008 (Fig. 32), all the 3 parameters should be as low as possible.

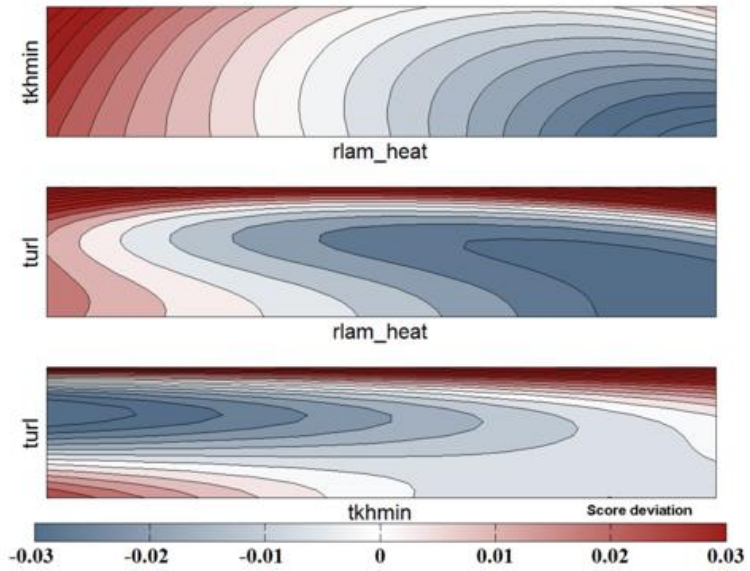


Figure 31: Contours of S_p (see eq. 5.2) deviation, i.e. $S_p - \overline{S}_p$, for pairwise parameters combinations only, for the period of 3-20.01.2008. The upper panel represents rlam_heat and tkhmin combinations (while keeping tur_len default); the centered panel represents rlam_heat and tur_len combinations (while keeping tkhmin default); the lower panel represents tur_len and tkhmin combinations (while keeping rlam_heat default). The lower is the S_p deviation value, the better is the score, and the better is the specific parameters combination.

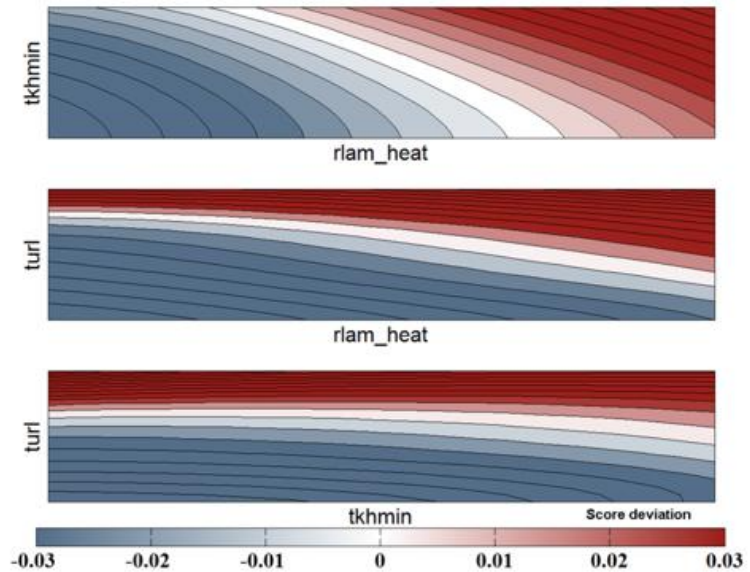


Figure 32: Same as Fig. 31 but for the period of 2-20.06.2008.

In order to analyze the origin of these results, we present similar plots for the 3 fields Tmax, Tmin and Pr, separately, using the scores 20, 21, 22 on Fig. 33 for 3-20.01.2008 and on Fig. 34 for 2-20.06.2008. Starting with the wintertime (3-20.01.2008) presented in Fig. 33, one can see the expected parameters dependencies:

a As discussed in Section 3.2, COSMO forecasts generally underestimate Tmax, so we expect the scores to be better for higher Tmax forecasts. As discussed in Section 2, higher tur_len, higher tkhmin and higher rlam_heat (on wintertime stable conditions), all lead to higher Tmax forecasts. That explains the results of the left panels on Fig. 33.

b As discussed in Section 3.3, COSMO forecasts generally overestimate Tmin, so we expect the scores to be better for lower Tmin forecasts, i.e. exactly the opposite of Tmax case. Consequently, lower tur_len, lower tkhmin and lower rlam_heat should lead to better Tmin forecasts. That explains the results of the centered panels on Fig. 33.

c As discussed in Section 3.4, COSMO forecasts generally overestimate precipitation, so we expect the scores to be better for lower precipitation forecasts. As discussed in Section 2, lower tur_len should decrease precipitation, tkhmin should be not significant, and higher rlam_heat may decrease precipitation (spoiling wintertime stable conditions). That explains the results of the right panels on Fig. 33, where we clearly see the advantage of low tur_len and high rlam_heat.

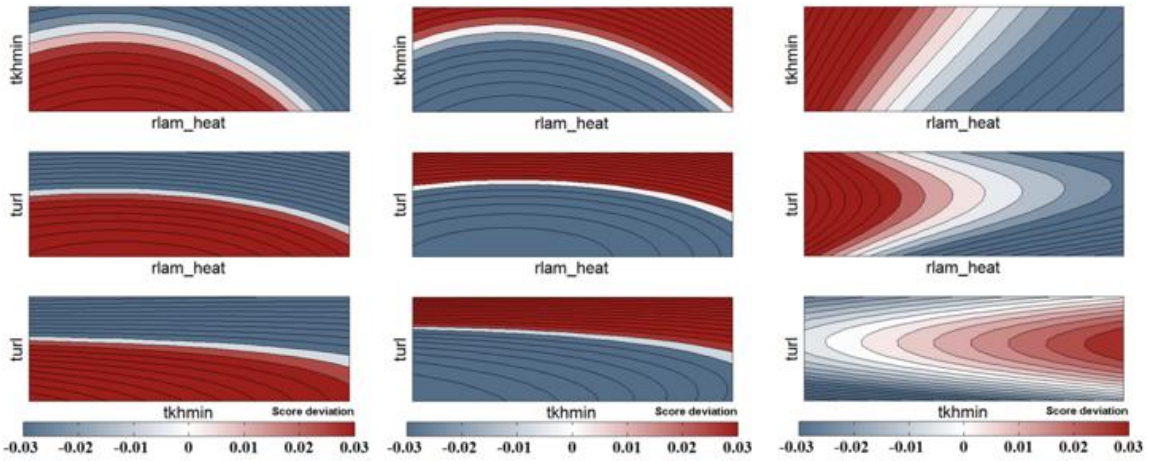


Figure 33: Contours of $S_{Tmax,p}$ (see eq. 20) deviation (left panels), $S_{Tmin,p}$ (see eq. 21) deviation (centered panels), and $S_{Pr,p}$ (see eq. 22) deviation (right panels), for pairwise parameters combinations, for the period of 3-20.01.2008. The upper panels represent rlam_heat and tkhmin combinations (while keeping tur_len default); the centered panels represent rlam_heat and tur_len combinations (while keeping tkhmin default); the lower panels represent tur_len and tkhmin combinations (while keeping rlam_heat default). The lower are the scores deviation values, the better is the specific parameters combination for the forecast quality.

For the summertime (2-20.06.2008) presented in Fig. 34, one can again see the expected parameters dependencies:

d Regarding Tmax and Tmin, the results are generally similar to the wintertime. However, the increase of rlam_heat at summer day, may reduce the low levels heating (by

the warm soil), leading to unwanted decrease in Tmax. That explains the slight difference of the Tmax dependence on rlam_heat between the wintertime (Fig. 33 left panels) and the summertime (Fig. 34 left panels).

e As discussed in Section 3.4, COSMO summertime forecasts highly overestimate precipitation, so we expect the scores to be better for lower precipitation forecasts. As discussed in Section 2, lower tur_len should highly decrease convective precipitation (typical to summertime), and tkhmin should be not significant. That exactly explains the results of the right panels on Fig. 34, where we clearly see the advantage of low tur_len. However, the low rlam_heat preference, as can be seen on Fig. 34 right panels, is not understood at this stage.

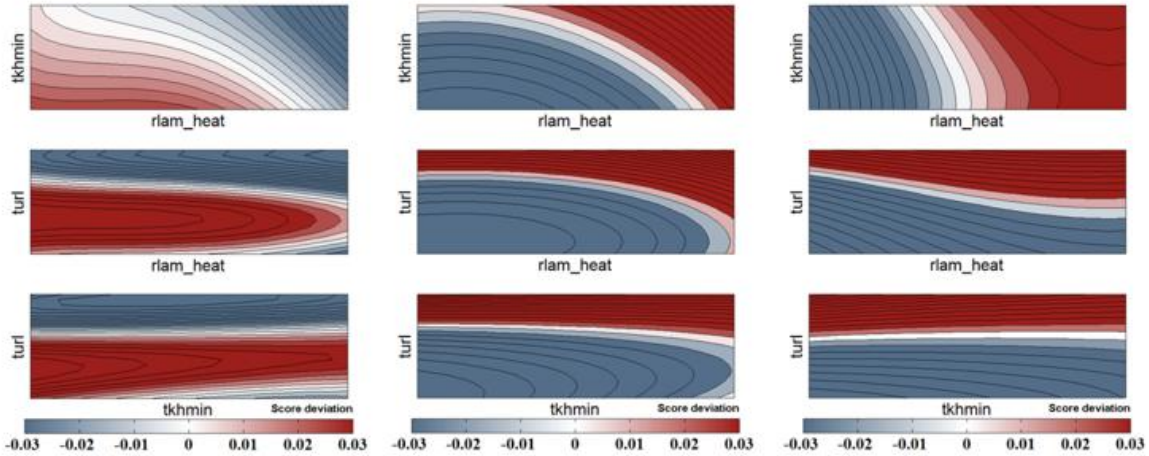


Figure 34: Same as Fig. 33 but for the period of 2-20.06.2008.

At the next stage of the calibration procedure, the S_p scores were calculated for 10000 parameters combinations, filling the parameters space in a Latin Hypercube design (Bellprat et al., 2012). Figs. 35a (for 3-20.01.2008) and 35b (for 2-20.06.2008) present S_p scores distributions, together with the score of the reference (REF) simulation (obtained using default values for all the parameters). For convenience, the distributions are presented as function of $\widetilde{S_p} = 1 - (S_p/S_{p,ref})$, so that:

- $\widetilde{S_p} < 0$ means that the score is worse than of the REF simulation;
- $\widetilde{S_p} = 0$ means that the score is equal to the REF simulation;
- $0 < \widetilde{S_p} < 1$ means that the score is better than of the REF simulation (1 is the best possible score).

One can see that definitely there are parameters combinations which should yield better forecasts than the current default parameter values (REF simulation). On summertime (Fig. 35b), the default parameters combination seems to be already well chosen (on the tail of the scores distribution), so by choosing different parameters combination, we can improve the forecast only slightly. However, on wintertime (Fig. 35a), there is a big range of parameter combinations which would significantly improve the forecast.

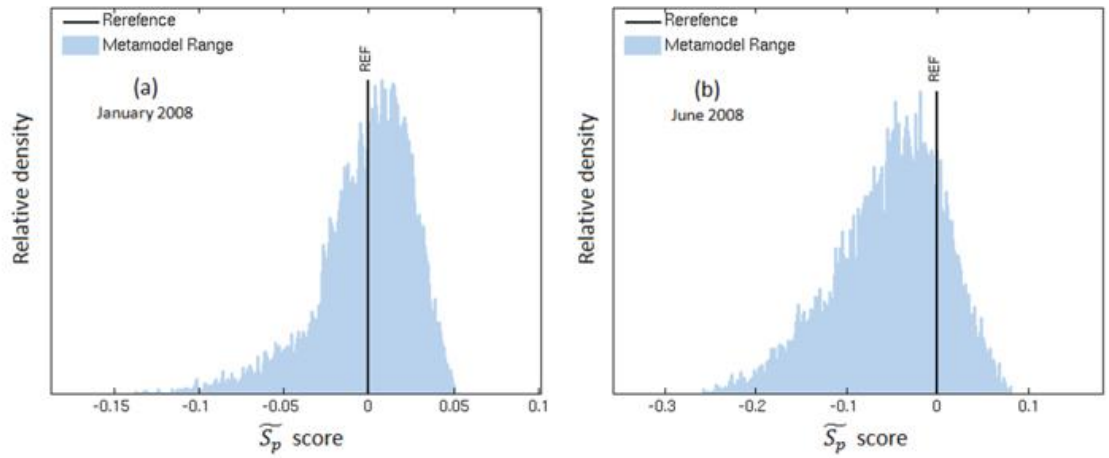


Figure 35: S_p scores distributions (for 10000 parameter combinations), together with the score of the reference (REF) simulation, for the period 3-20.01.2008 (a) and 2-20.06.2008 (b). For convenience, the distributions are presented as function of $\widetilde{S_p} = 1 - (S_p/S_{p,ref})$, so that the higher is $\widetilde{S_p} > 0$ means that the score is better than of the REF simulation.

7 Conclusions and considerations towards the next stage of CALMO project

Finally, the optimal parameters combinations for January and June 2008 were defined, and are presented in Table 1:

	rlam_heat [0.1 **1** 10]	tkhmin [0 **1** 2]	tur_len [100 **500** 10000]
January 2008	8.22	0.02	1037
June 2008	0.17	0.02	102

Table 1: Optimal parameters combinations for January and June 2008.

Antigoni Voudouri performed COSMO simulations with the optimal parameters combinations for January and June 2008. Figs. 36a (for 3-20.01.2008) and 36b (for 2-20.06.2008) present S_p scores distributions, together with the scores of the reference (REF) simulation and of the optimal parameters (Best) simulation.

From Fig. 36, one can see that the Best simulation indeed improved the forecasts comparing to the REF simulation! **This result is very encouraging, showing that the Meta-Model is able to reproduce the COSMO simulations in parameters space, and therefore can be used to calibrate the COSMO model.** It is also interesting, that the COSMO simulation score for the Best simulation is indeed very close to the Best possible score estimated by the Meta-Model. Pirmin Kaufmann (MeteoSwiss) performed the verifications of the optimal parameters simulation in comparison with the REF simulation, using the official MCH procedure. Generally, these verifications also show the advantage of the Best COSMO simulation over the REF simulation. Highlights of these verifications are presented in Section 11.

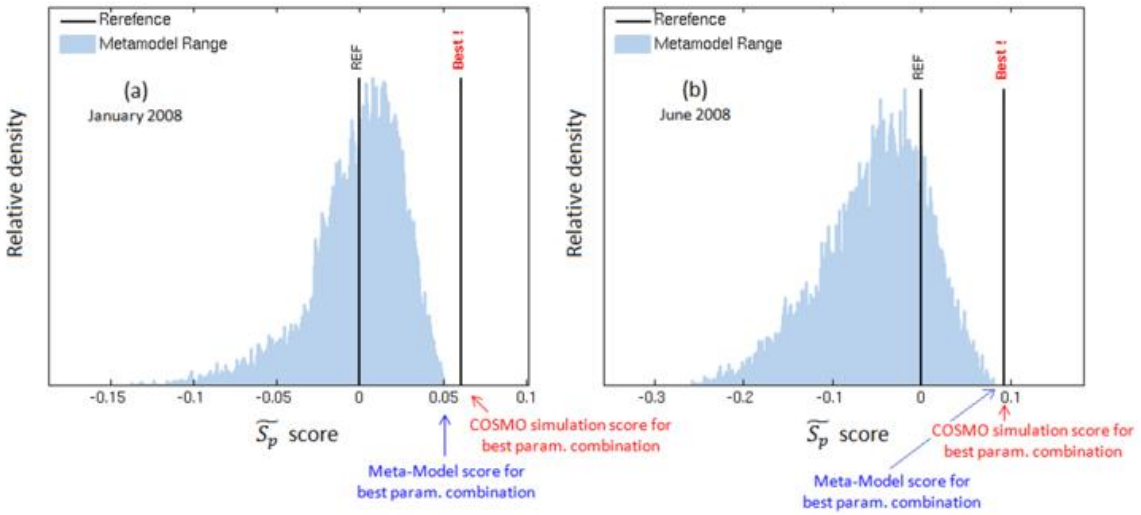


Figure 36: S_p scores distributions (for 10000 parameter combinations), together with the score of the reference (REF) simulation, and the optimal parameters (Best) simulation, for the period 3-20.01.2008 (a) and 2-20.06.2008 (b). For convenience, the distributions are presented as function of $\widetilde{S_p} = 1 - (S_p/S_{p,ref})$, so that the higher is $\widetilde{S_p} > 0$ means that the score is better than of the REF simulation. Best simulation indeed improved the forecasts comparing to the REF simulation!

Considerations towards the next stage of CALMO project

The optimal parameters combinations are very different between January and June 2008, which is generally unwanted. The following actions may improve the results and make them more reliable:

- For each of the verified fields, we have to choose (to calibrate) the **specific parameters which are the most significant for these fields**. For Tmax we may need to focus on soil and radiation schemes parameters, while for precipitation, we may need to consider also microphysical parameters, etc.
- It is important to **extend the set of verified fields** to include sounding profiles of temperature and humidity, integrated water vapor, etc. Otherwise, there is a danger of choosing parameters combination which improves, for example, Tmax forecasts but spoil other important forecast fields.
- It is important to **extend the tested periods** for at least several months. Currently the periods were definitely too short, which makes the results less reliable.
- Presumably, different parameters combinations should improve the COSMO forecast at different seasons (as shown above). Therefore, one could think of possibility to automatically modify the operational COSMO parameters on different seasons (and even for different parts of the domain), however these ideas stand beyond the scope of the CALMO project.

It is however important to mention, that even without performing the steps above, **we showed that the calibration method works and the Meta-Model is generally able to reproduce the COSMO forecasts**. In principle, it is reasonable to perform the COSMO simulation with the selected parameters combination for different periods

(which were not used to construct the Meta-Model), for example January and June but at a different year. That would be a final approval whether the forecasts are indeed better (than with default parameters combination).

8 The Terra standalone (TSA) soil scheme for the CALMO project

As part of the next stage of the CALMO project, it is planned to calibrate parameters from the COSMO soil scheme Terra, for example the hydraulic soil conductivity. In contrast to the regular COSMO parameters, the change in Terra parameters affects the COSMO forecasts with a significant delay (up to several years) via slow adaptation of the soil temperature and moisture profiles. Therefore, in order to calibrate the Terra parameters for specific year (2013 for example), one has to make the parameter changes several years earlier, and run the COSMO model in a cycle, slowly adapting the soil profiles to the parameter change. Moreover, errors in soil profiles caused by interpolation of soil fields from a coarse model disappear slowly, also on the scale of several years. Therefore, in order to obtain appropriate initial conditions in the soil (without interpolation errors), one again has to make the interpolation of soil fields several years earlier, and run the COSMO model in a cycle, slowly "forgetting" the interpolation errors. However, performing several years pre-run of the COSMO model (in a cycle mode) is computationally expensive. Instead, it is decided to use the Terra "standalone" (TSA) program driven by COSMO atmospheric analyses (from MeteoSwiss archive). The method is to initialize soil profiles from a coarse model interpolation, change the parameters of TSA (if needed), and run it for several years (prior to the tested year). Then, the obtained soil profiles will be installed as initial soil conditions for the COSMO model runs (for the tested year). With the great support from Jean-Marie Bettems (MeteoSwiss), Guy de Morsier (MeteoSwiss) and Julian Todter (Frankfurt University), we have run TSA for 3 years (2010-2012) with resolutions of 2.2 and 1.1 km (currently for the default soil parameters configuration), and prepared the soil initial conditions for the COSMO runs at the next stage of the CALMO project.

9 Appendix A: Transform of the 2m-temperature observations to the model grid

The 2m-temperature daily-mean, maximum and minimum observations data over Switzerland was originally transformed to a 2km-grid by C. Frei (MeteoSwiss), following the method described in Frei (2012). This 2km-grid (original grid) has a real (not smoothed) topography. In order to compare the 7km COSMO model results with the observations, one had first to transform the 2m-temperature observations data to the 7km **smoothed** topography grid of the COSMO model (target grid). Following the recommendation of C. Frei, the chosen method was the following:

a For every grid point in the target grid (red dot on Fig. 37) find the nearest 9 neighbors on the original grid (blue dots on Fig. 37).

b Plot the 2m-temperature values of these neighbors vs. their altitude (blue and red X on Fig. 38).

c Perform a linear fit of the data, which will be the local 2m-temperature profile.

d Having the altitude of the target grid point use the obtained linear regression to calculate its 2m-temperature.

e Perform this operation (a-d) for every target grid point, for every day.

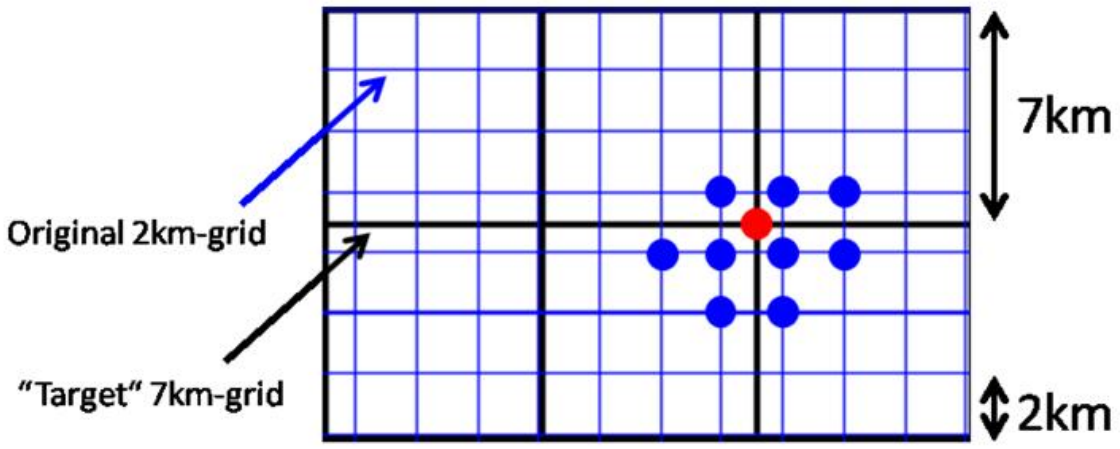


Figure 37: Transform of 2m-temperature observations from the original 2km-grid with the real topography to a target 7km-grid with a smoothed topography.

An example for the calculation of the measured 2m-temperature at a target grid point (Lat=46.07°/Lon=7.49°) on 10.01.2008 is presented on Fig. 38.

This example shows the following:

- The correction to the measured temperature (from the old method of interpolation used before to the new one) is important, of the order of several degrees Kelvin (-2K in this example).
- The local 2m-temperature profile is indeed linear (the results are similar for other regions and other days).

- The local 2m-temperature vertical gradient is unique (-5.8K/km in this example) for a given grid point area for a given day.

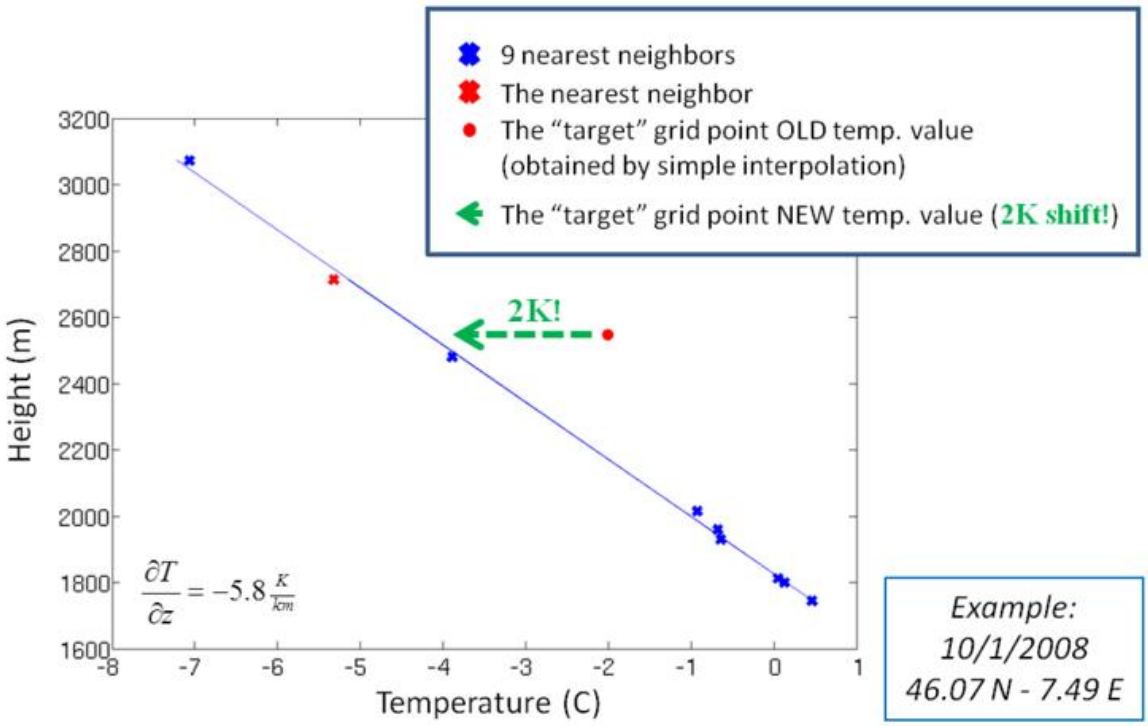


Figure 38: An example for the calculation of the measured 2m-temperature at a target grid point (Lat=46.07°/Lon=7.49°) on 10.01.2008.

10 Appendix B: Examples of stable and unstable conditions over Switzerland

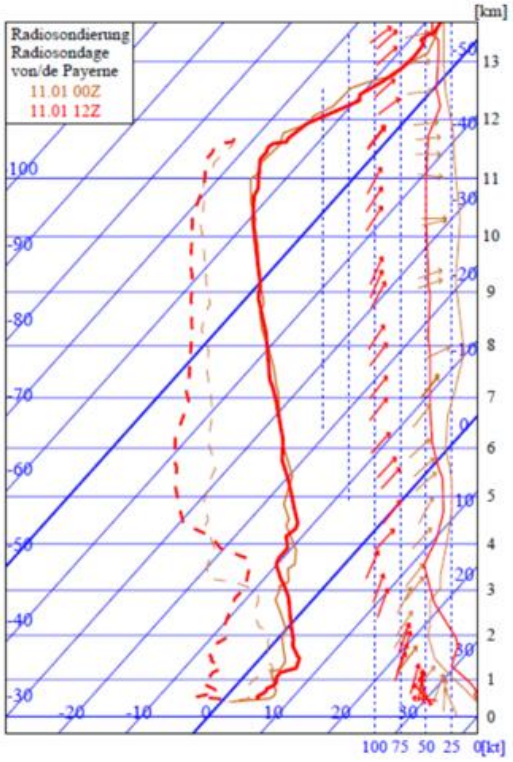


Figure 39: The stable low level stratification on 11.01.2008 (reference from Section 3). MeteoSwiss radiosounding site at Payerne, Switzerland.

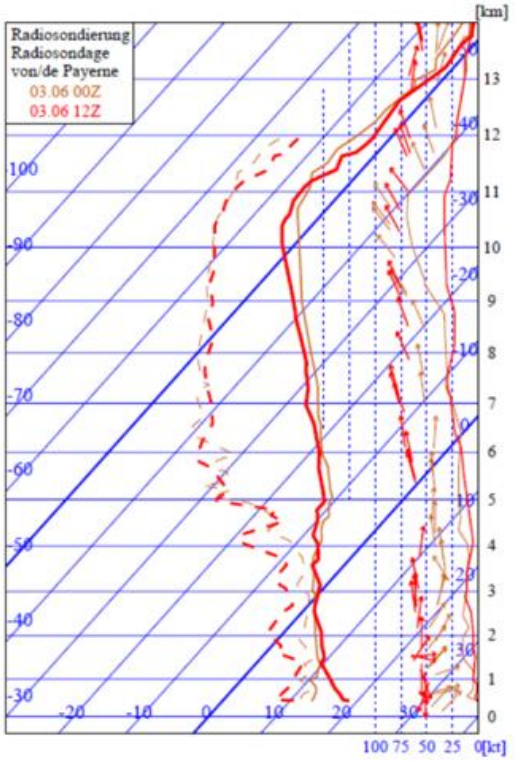


Figure 40: The unstable low level stratification on 03.06.2008 (reference from Section 3). MeteoSwiss radiosounding site at Payerne, Switzerland.

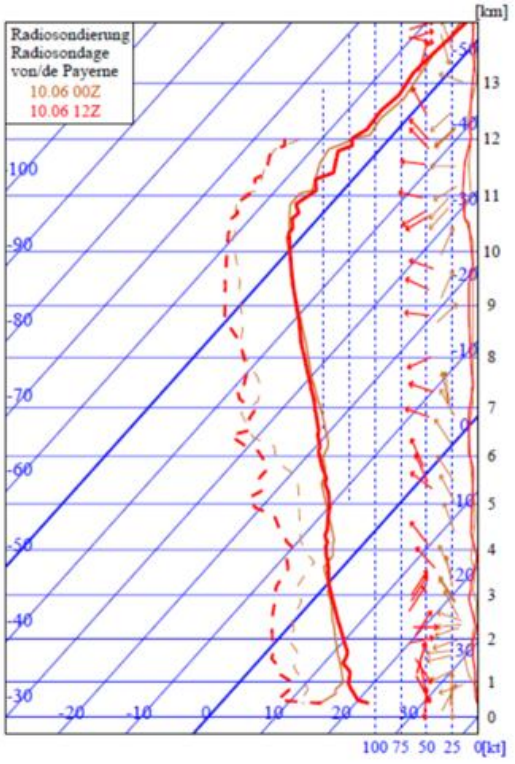


Figure 41: The stable low level stratification during night of 10.06.2008 (reference from Section 3). MeteoSwiss radiosounding site at Payerne, Switzerland.

11 Appendix C: MCH verification results for the optimal parameters simulation

Pirmin Kaufmann (MeteoSwiss) performed the verifications of the optimal parameters Best simulation in comparison with the REF simulation, using the official MCH procedure, for the periods of 2-20/1/2008 and 2-20/6/2008. Generally, these verifications show the advantage of the Best COSMO simulation over the REF simulation. Several highlights of these verifications are presented below, for the following verification domain (Fig. 42):

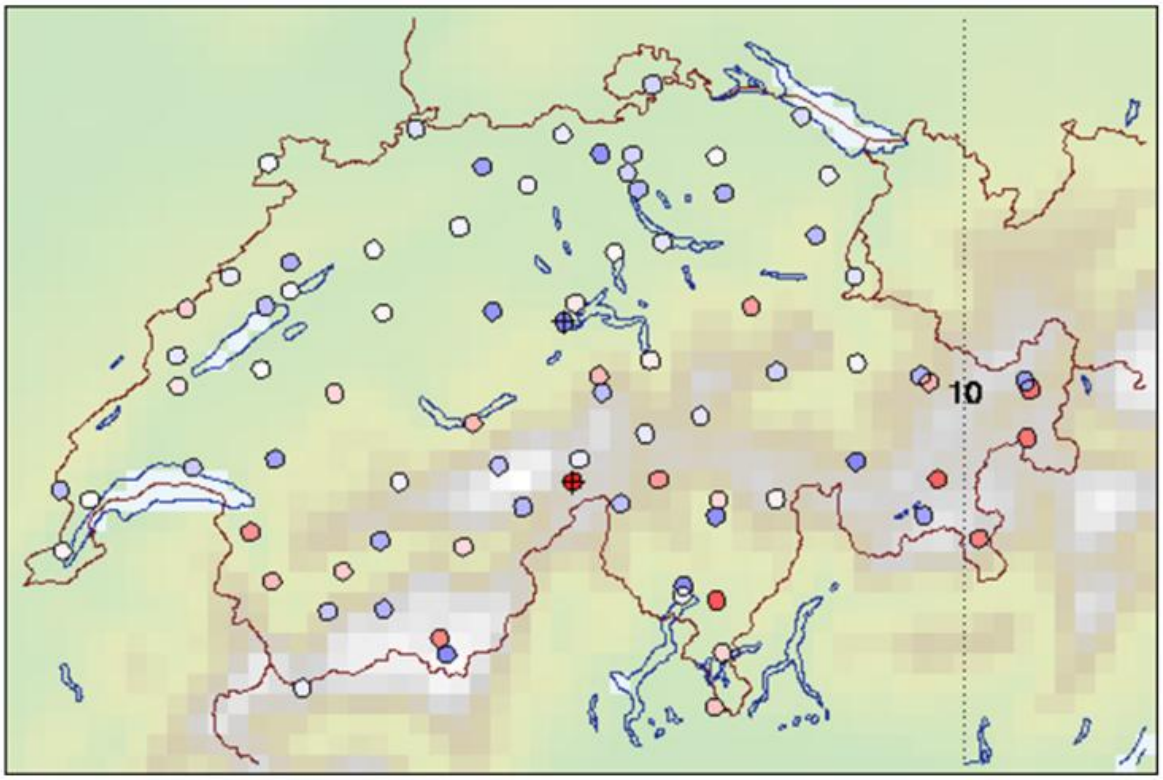


Figure 42: Verification domain.

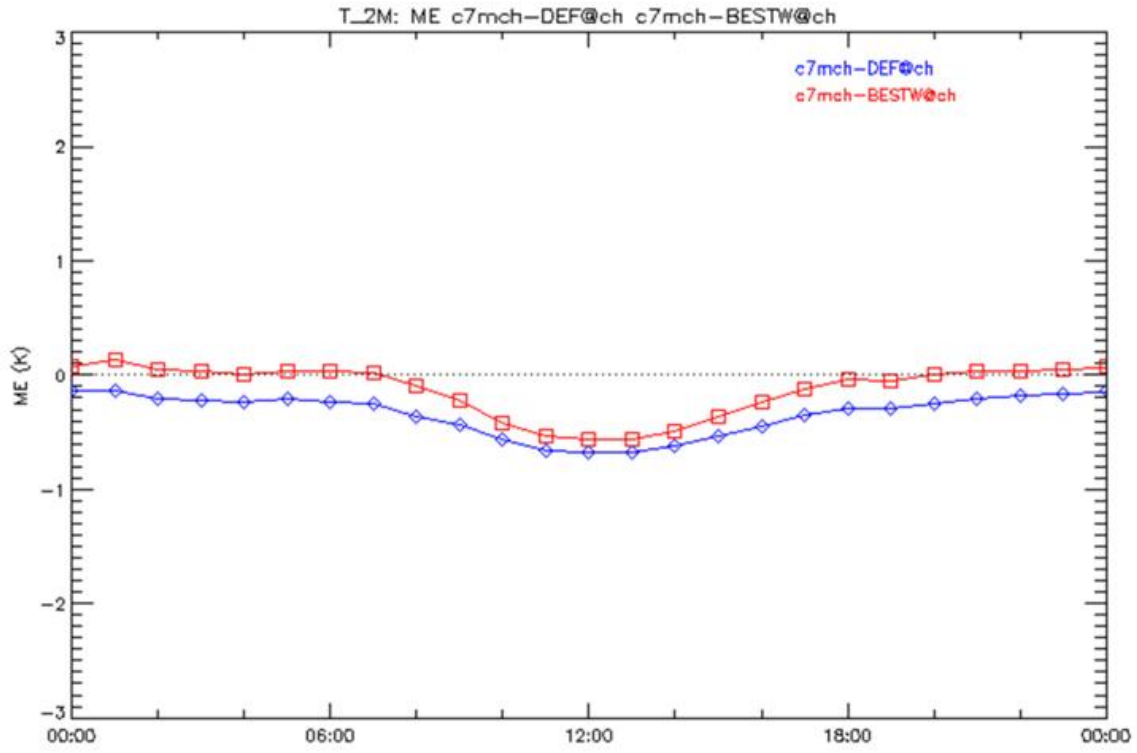


Figure 43: 2m-temperature diurnal cycle mean error for the REF (blue) and the Best (red) simulations, for the period 2-20/1/2008. The Best simulation is clearly better than REF simulation.

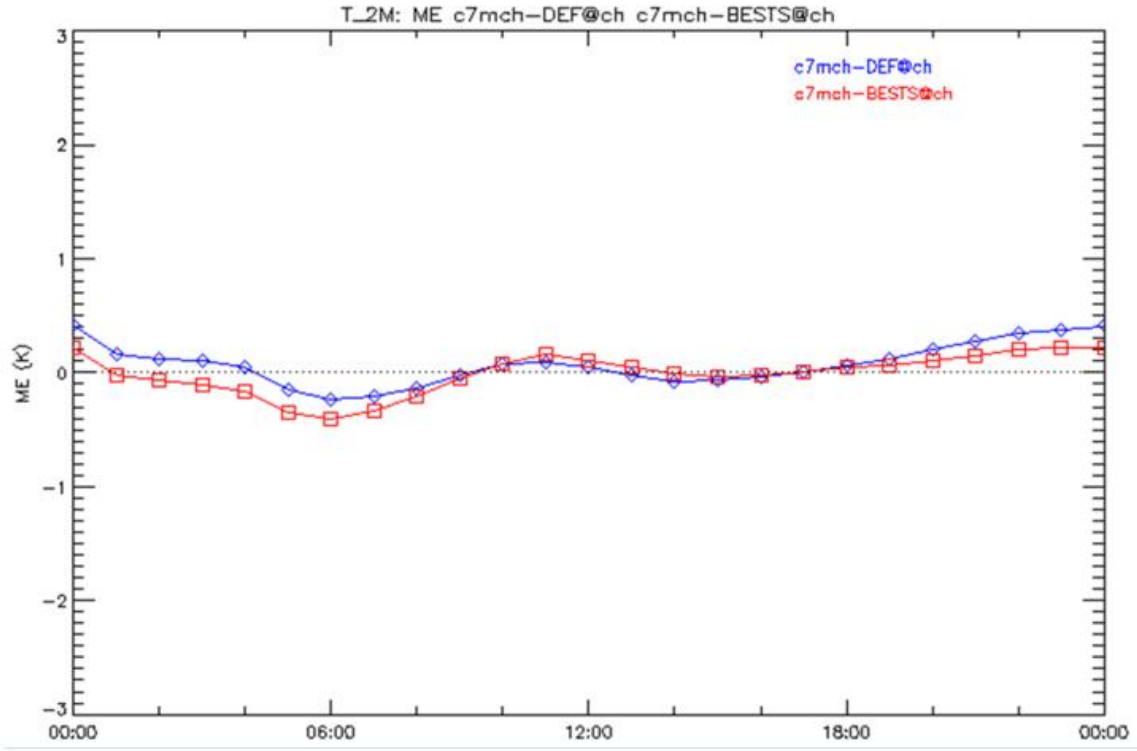


Figure 44: 2m-temperature diurnal cycle mean error for the REF (blue) and the Best (red) simulations, for the period 2-20/6/2008. The Best and REF simulations are of similar quality.

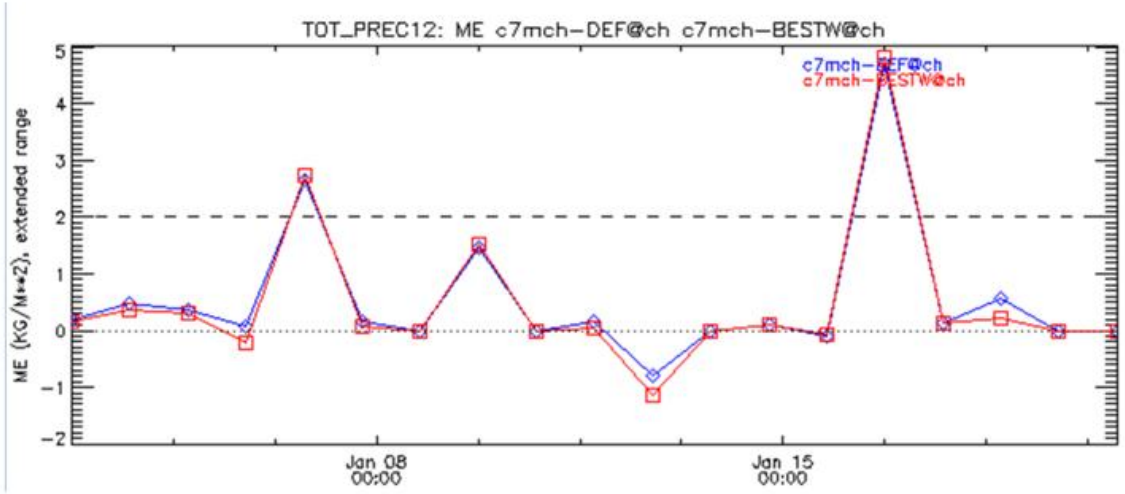


Figure 45: Mean error time series of the 12h accumulated precipitation for the REF (blue) and the Best (red) simulations, for the period 2-20/1/2008. The Best and REF simulations are of similar quality.

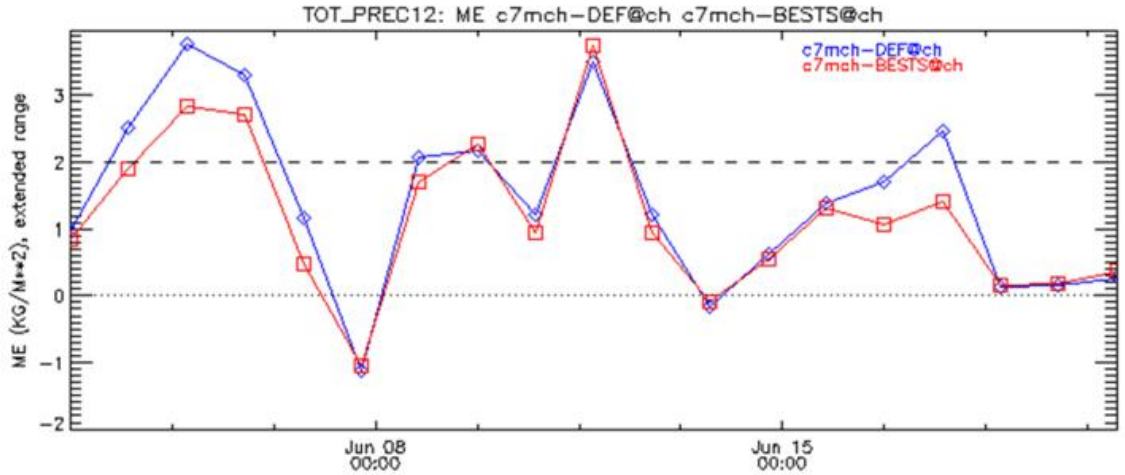


Figure 46: Mean error time series of the 12h accumulated precipitation for the REF (blue) and the Best (red) simulations, for the period 2-20/6/2008. The Best simulation is clearly better than REF simulation.

Acknowledgments

The CALMO project is based on the objective calibration method which was developed and implemented in regional climate model by Omar Bellprat and Christoph Schär (ETH). Special thanks to Omar Bellprat for providing the calibration code framework. The figures in Section 6 are based on the plots of Bellprat (2012). We are grateful for the support from and valuable discussions with Yoav Levi (head of R&D at IMS), Alon Shtivelman (IMS), Yitzhak Yosef (IMS), Simon Krichak (TAU), Guy de Morsier (MeteoSwiss), Oliver Fuhrer (MeteoSwiss), Marco Arpagaus (MeteoSwiss), Julian Tödter (GUF), and Ines Cerenzia (ARPA-EMR). We are thankful to Pirmin Kaufmann (MeteoSwiss) for performing the verifications of the optimal parameters simulation using the official MCH procedure and to Massimo Milelli (ARPA Piemonte) for the work he performed editing this report.

References

COSMO document part II, 2011.
Available online at: *http://www.cosmo-model.org/content/model/documentation/core/cosmoPhysParamtr.pdf*

Dunst M., 1980: Ergebnisse von Modellrechnungen zur Ausbreitung von Stoffbeimengungen in der planetarischen Grenzschicht, *Z. f. Meteorol.*, **30**, 47-59.

Schlünzen K.H., 1988: Das mesoskalige Transport- und Strömungsmodell METRAS Grundlagen, Validierung, Anwendung, *Hamb. Geophys. Einzelschr*, **88**, 139 pp. (in German with abstract in English)

Helmert J. et al., 2008: Single Column Simulations of COSMO for the GCSS RICO Precipitating Shallow Cumulus Case, 18th Symposium on Boundary Layers and Turbulence.
Available online at: *https://ams.confex.com/ams/pdfpapers/140006.pdf*

Zilitinkevich S. et al., 2012: A Hierarchy of Energy- and Flux-Budget (EFB) Turbulence Closure Models for Stably-Stratified Geophysical Flows, *Boundary-Layer Meteorology*, **146**, 3, 341-373.

COSMO document part VII, 2014.
Available online at: *http://www.cosmo-model.org/content/model/documentation/core/cosmo_userguide_5.01.pdf*

Cerenzia I. et al., 2014: Diagnosis of Turbulence Schema in Stable Atmospheric Conditions and Sensitivity Tests, *14th COSMO Newsletter.*
Available online at: *http://www.cosmo-model.org/content/model/documentation/newsLetters/newsLetter14/cnl14_04.pdf*

Cerenzia I. et al., 2013: Internal Report no. 2: Improvement of the PBL parameterization in COSMO model.

Bellprat O. et al., 2012: Objective calibration of regional climate models, *Journal of Geophysical Research*, **117**, D23.

Blackadar A. K., 1962: The Vertical Distribution of Wind and Turbulent Exchange in a Neutral Atmosphere, *J. Geophys. Res.*, **67**, 3095-3102.

Buzzi M., 2008: Challenges in Operational Numerical Weather prediction at High Resolution in Complex Terrain. *PhD thesis.*

Available online at: *http://www.meteoschweiz.admin.ch/web/de/forschung/publikationen/alle_publikationen/veroeff-80.Par.0001.DownloadFile.tmp/veroeff80.pdf*

Frei C., 2014: Interpolation of temperature in a mountainous region using non-linear profiles and non-euclidean distances, *Int. J. Climatol.*, **34**, 5, 1585-1605.

Neelin J. D. et al., 2010: Considerations for parameter optimization and sensitivity in climate models, *Proc. of the National Academy of Sciences of the United States of America*, **107**, 21349-21354.

List of COSMO Newsletters and Technical Reports

(available for download from the COSMO Website: www.cosmo-model.org)

COSMO Newsletters

No. 1: February 2001.

No. 2: February 2002.

No. 3: February 2003.

No. 4: February 2004.

No. 5: April 2005.

No. 6: July 2006.

No. 7: April 2008; Proceedings from the 8th COSMO General Meeting in Bucharest, 2006.

No. 8: September 2008; Proceedings from the 9th COSMO General Meeting in Athens, 2007.

No. 9: December 2008.

No. 10: March 2010.

No. 11: April 2011.

No. 12: April 2012.

No. 13: April 2013.

No. 14: April 2014.

COSMO Technical Reports

No. 1: Dmitrii Mironov and Matthias Raschendorfer (2001):
Evaluation of Empirical Parameters of the New LM Surface-Layer Parameterization Scheme. Results from Numerical Experiments Including the Soil Moisture Analysis.

No. 2: Reinhold Schrodin and Erdmann Heise (2001):
The Multi-Layer Version of the DWD Soil Model TERRA_LM.

No. 3: Günther Doms (2001):
A Scheme for Monotonic Numerical Diffusion in the LM.

No. 4: Hans-Joachim Herzog, Ursula Schubert, Gerd Vogel, Adelheid Fiedler and Roswitha Kirchner (2002):
LLM ¯ the High-Resolving Nonhydrostatic Simulation Model in the DWD-Project LITFASS.
Part I: Modelling Technique and Simulation Method.

No. 5: Jean-Marie Bettems (2002):
EUCOS Impact Study Using the Limited-Area Non-Hydrostatic NWP Model in Operational Use at MeteoSwiss.

No. 6: Heinz-Werner Bitzer and Jürgen Steppeler (2004):
Documentation of the Z-Coordinate Dynamical Core of LM.

No. 7: Hans-Joachim Herzog, Almut Gassmann (2005):
Lorenz- and Charney-Phillips vertical grid experimentation using a compressible nonhydrostatic toy-model relevant to the fast-mode part of the 'Lokal-Modell'.

No. 8: Chiara Marsigli, Andrea Montani, Tiziana Paccagnella, Davide Sacchetti, André Walser, Marco Arpagaus, Thomas Schumann (2005):
Evaluation of the Performance of the COSMO-LEPS System.

No. 9: Erdmann Heise, Bodo Ritter, Reinhold Schrodin (2006):
Operational Implementation of the Multilayer Soil Model.

No. 10: M.D. Tsyrulnikov (2007):
Is the particle filtering approach appropriate for meso-scale data assimilation ?

No. 11: Dmitrii V. Mironov (2008):
Parameterization of Lakes in Numerical Weather Prediction. Description of a Lake Model.

No. 12: Adriano Raspanti (2009):
COSMO Priority Project "VERification System Unified Survey" (VERSUS): Final Report.

No. 13: Chiara Marsigli (2009):
COSMO Priority Project "Short Range Ensemble Prediction System" (SREPS): Final Report.

No. 14: Michael Baldauf (2009):
COSMO Priority Project "Further Developments of the Runge-Kutta Time Integration Scheme" (RK): Final Report.

No. 15: Silke Dierer (2009):
COSMO Priority Project "Tackle deficiencies in quantitative precipitation forecast" (QPF): Final Report.

No. 16: Pierre Eckert (2009):
COSMO Priority Project "INTERP": Final Report.

No. 17: D. Leuenberger, M. Stoll and A. Roches (2010):
Description of some convective indices implemented in the COSMO model.

No. 18: Daniel Leuenberger (2010):
Statistical analysis of high-resolution COSMO Ensemble forecasts in view of Data Assimilation.

No. 19: A. Montani, D. Cesari, C. Marsigli, T. Paccagnella (2010):
Seven years of activity in the field of mesoscale ensemble forecasting by the COSMO–LEPS system: main achievements and open challenges.

No. 20: A. Roches, O. Fuhrer (2012):
Tracer module in the COSMO model.

No. 21: Michael Baldauf (2013):
A new fast-waves solver for the Runge-Kutta dynamical core.

No. 22: C. Marsigli, T. Diomede, A. Montani, T. Paccagnella, P. Louka, F. Gofa, A. Corigliano (2013):
The CONSENS Priority Project.

No. 23: M. Baldauf, O. Fuhrer, M. J. Kurowski, G. de Morsier, M. Müllner, Z. P. Piotrowski, B. Rosa, P. L. Vitagliano, D. Wójcik, M. Ziemiański (2013):
The COSMO Priority Project 'Conservative Dynamical Core' Final Report.

No. 24: A. K. Miltenberger, A. Roches, S. Pfahl, H. Wernli (2014):
Online Trajectory Module in COSMO: a short user guide.

COSMO Technical Reports

Issues of the COSMO Technical Reports series are published by the *COnsortium for Small-scale MOdelling* at non-regular intervals. COSMO is a European group for numerical weather prediction with participating meteorological services from Germany (DWD, AWGeophys), Greece (HNMS), Italy (USAM, ARPA-SIMC, ARPA Piemonte), Switzerland (MeteoSwiss), Poland (IMGW) and Romania (NMA). The general goal is to develop, improve and maintain a non-hydrostatic limited area modelling system to be used for both operational and research applications by the members of COSMO. This system is initially based on the COSMO-Model (previously known as LM) of DWD with its corresponding data assimilation system.

The Technical Reports are intended

- for scientific contributions and a documentation of research activities,
- to present and discuss results obtained from the model system,
- to present and discuss verification results and interpretation methods,
- for a documentation of technical changes to the model system,
- to give an overview of new components of the model system.

The purpose of these reports is to communicate results, changes and progress related to the LM model system relatively fast within the COSMO consortium, and also to inform other NWP groups on our current research activities. In this way the discussion on a specific topic can be stimulated at an early stage. In order to publish a report very soon after the completion of the manuscript, we have decided to omit a thorough reviewing procedure and only a rough check is done by the editors and a third reviewer. We apologize for typographical and other errors or inconsistencies which may still be present.

At present, the Technical Reports are available for download from the COSMO web site (www.cosmo-model.org). If required, the member meteorological centres can produce hard-copies by their own for distribution within their service. All members of the consortium will be informed about new issues by email.

For any comments and questions, please contact the editors:

Massimo Milelli
Massimo.Milelli@arpa.piemonte.it

Consortium for Small-Scale Modelling

Technical Report No. 20

Tracer module in the COSMO model

December 2012

DOI: 10.5676/DWD_pub/nwv/cosmo-tr_20

Deutscher Wetterdienst
MeteoSwiss
Ufficio Generale Spazio Aereo e Meteorologia
ΕΘΝΙΚΗ ΜΕΤΕΩΡΟΛΟΓΙΚΗ ΥΠΗΡΕΣΙΑ
Instytucie Meteorogii i Gospodarki Wodnej
Administratia Nationala de Meteorologie
ROSHYDROMET
Agenzia Regionale per la Protezione Ambientale del Piemonte
Agenzia Regionale per la Protezione Ambientale dell'Emilia-Romagna
Centro Italiano Ricerche Aerospaziali
Amt für GeoInformationswesen der Bundeswehr



www.cosmo-model.org

Editor: Massimo Milelli, ARPA Piemonte

Tracer module in the COSMO model

Anne Roches* *and Oliver Fuhrer*****

*C2SM
Universitätstrasse 16
Zürich
Switzerland

**MeteoSwiss
Krähbühlstrasse 58
Zürich
Switzerland

Revision	Modifications	Date	Author
1.0	Initial Release	December 2012	Anne Roches (C2SM) Oliver Fuhrer (MeteoSwiss)

Contents

1 Introduction **5**

2 Description of the tracer module **6**

2.1 Assumptions 8

2.2 Functionalities of the tracer module 8

2.2.1 Tracer definition and memory management 10

2.2.2 I/O methods 10

2.2.3 Advection (`T_ADV_ID`) 10

2.2.4 Horizontal hyperdiffusion (`T_DIFF_ID`) 11

2.2.5 Turbulent mixing (`T_TURB_ID`) 11

2.2.6 Passive convective transport (`T_CONV_ID`) 12

2.2.7 Lateral boundary conditions (`T_LBC_ID`) 12

2.2.8 Initial condition (`T_INI_ID`) 13

2.2.9 Boundary relaxation (`T_RELAX_ID`) 13

2.2.10 Rayleigh damping (`T_DAMP_ID`) 13

2.2.11 Clipping (`T_CLP_ID`) 14

2.2.12 COSMO options not implemented 14

2.3 The tracer module API 14

2.3.1 Methods for tracer handling 15

2.3.2 Methods for metadata handling 18

2.3.3 Infrastructure methods 20

3 A short user's guide **21**

3.1 The microphysics example 21

3.1.1 The generic code parts 21

3.1.2 The specific code parts 22

3.1.3 The microphysics specificities in generic code parts 23

3.1.4 Treating the surface field 25

3.2 How to introduce a new tracer? 26

3.2.1 Define the tracer and its metadata 26

3.2.2 Retrieve the tracer and its metadata 27

4 Implementation details **27**

4.1 Data structures 27
4.2 Workflow 28
4.3 Metadata module 29
4.4 Performance considerations 29

5 Results **30**

6 Issues and needs for further refinements **31**

7 Conclusions **32**

Abstract

A tracer module is implemented in the COSMO model in version 5.0 and higher. This model component offers a set of functionalities commonly required for the treatment of new prognostic variables (tracers) like memory management, input and output support or the computation of advective transport. It allows for a simplified introduction of tracers into the COSMO code, for a coherent treatment of tracers and for a well-structured code without redundancies. Application of this module may range from the tracing of air masses to the handling of microphysics species or aerosols.

1 Introduction

Water in all phases and various isotopic forms, volatile chemical compounds, radionuclides or aerosols are all important components of our atmosphere. The adequate representation of these tracers is thus a crucial theme for atmospheric modeling.
We use the term *tracer* to designate any substance present in the atmosphere as a trace constituent and which can be transported passively, i.e. without influencing the flow (except if the user chooses to implement a coupling term).

A consistent and flexible treatment of tracers in atmospheric models becomes increasingly important as the complexity of these models augments by the introduction of new submodules describing additional processes and implying the consideration of additional species and even including other environmental compartments. A clear trend in the extension of atmospheric models towards Earth's system models has been observed in the past decades. All atmospheric models which have made important steps into this direction handle tracers in general modules providing basic functionalities like memory management or advective transport to the submodules (hereafter called tracer clients) (e.g. Rast, 2009). Example of tracer clients are the microphysics, atmospheric chemistry modules, etc.

Traditionally, adding a new tracer variable into COSMO required extensive and tedious code modifications, since all tracers were treated as individual variables. The result was abundant code redundancy, bugs and inconsistencies in the treatment of the individual tracers. The general tracer module described here should facilitate extensions of the COSMO model by providing a comprehensive API (Application Programming Interface) to the tracer client. Consistency in the tracer treatment is promoted through the unity of the code describing a given process (e.g. advection). This also simplifies code maintenance and introduction of new features.

In this technical report a general description of the new tracer module can be found in section 2. A short user's guide explains how to use the tracer module by showing concrete examples (section 3) whereas section 4 provides some technical details on the implementation for model developers. Section 5 presents the results obtained with the tracer enabled version. Issues that might arise with this version are discussed in section 6 and conclusions are drawn in section 7.

2 Description of the tracer module

The tracer module consists in four new source code files, `src_tracer.f90`, `data_tracer.f90`, `src_tracer_metadata.f90`, `data_tracer_metadata.f90`. Extensive modifications to the existing COSMO source code files had to be performed as well, changing the programming paradigm based on individual variables for an automated treatment of the species (by looping over all tracers). in order to bring the required functionalities (see section 2.2) in an automated form for the tracers.

The tracer API is a collection of few subroutines and functions that can be called by the tracer client from any part of the COSMO code. They serve to define and retrieve tracers as well as their corresponding metadata (attributes storing information about the tracers). All subroutines and functions which can be called by the tracer client are located in the source file `src_tracer.f90` and are described in detail in section 2.3. Useful named constants are made available in the `data_tracer.f90` module. The source code files `src_tracer_metadata.f90` and `data_tracer_metadata.f90` contain low-level functions for handling metadata and are not called directly by the tracer client.

Basic information about the tracer (metadata) such as its name or the operations it has to undergo (e.g. advection, turbulent mixing, etc.) has to be passed to the tracer module upon definition of a new tracer. This is the so-called set of standard metadata. A short description of the mandatory standard metadata and of the optional standard metadata is provided in table 1 and table 2 respectively. No default value is provided for the mandatory metadata whereas the default value is used for the optional standard metadata if the user provides no specification of these items.

Table 1: Basic set of standard metadata: mandatory items

Identifier	**Type**	**Definition**	**Default value**
T_NAME_ID	CHAR	Tracer name	-
T_GRBPARAM_ID	INT	GRIB parameter number	-
T_GRBTABLE_ID	INT	GRIB table number	-
T_PARENT_ID	CHAR	Parent subroutine name (subroutine which defines the tracer)	-
T_UNITS_ID	CHAR	Units	-

Table 2: Basic set of standard metadata: optional items

Identifier	Type	Definition	Default value
T_NCSTDNAME_ID	CHAR	Standard name	"undefined"
T_NCLONGNAME_ID	CHAR	Long name	"undefined"
T_ADV_ID	INT	Do advection? Options: - T_ADV_OFF: no advection - T_ADV_ON: advection	T_ADV_OFF
T_DIFF_ID	INT	Do horizontal hyperdiffusion? Options: - T_DIFF_OFF: no horiz. hyperdiffusion - T_DIFF_ON: horiz. hyperdiffusion	T_DIFF_OFF
T_TURB_ID	INT	Do turbulent mixing? Options: - T_TURB_OFF: no turbulent mixing - T_TURB_1D: vertical turb. mixing - T_TURB_3D: 3-dimensional turb. mixing	T_TURB_OFF
T_CONV_ID	INT	Do passive convective transport? Options: - T_CONV_OFF: no passive convective transp. - T_CONV_ON: passive convective transp.	T_CONV_OFF
T_INI_ID	INT	Type of initial condition Options: - T_INI_ZERO: initialize to zero - T_INI_FILE: initialize using data from file	T_INI_ZERO
T_LBC_ID	INT	Type of lateral boundary condition Options: - T_LBC_ZERO: zero value - T_LBC_FILE: values read from file - T_LBC_CST: constant value - T_LBC_ZEROGRAD: zero-gradient condition	T_LBC_ZERO
T_BBC_ID	INT	Type of bottom boundary condition Options: - T_BBC_ZEROFLUX: zero flux condition - T_BBC_ZEROVAL: zero value condition - T_BBC_SURF_VAL: values provided in a surface field	T_BBC_ZEROFLUX
T_RELAX_ID	INT	Do boundary relaxation? Options: - T_RELAX_OFF: no relaxation - T_RELAX_FULL: relaxation at all boundaries - T_RELAX_INFLOW: relaxation at inflow boundary only	T_RELAX_FULL
T_DAMP_ID	INT	Do Rayleigh damping? Options: - T_DAMP_OFF: no damping - T_DAMP_ON: damping	T_DAMP_ON
T_CLP_ID	INT	Do clipping? Options: - T_CLP_OFF: no clipping - T_CLP_POSDEF: clipping	T_CLP_OFF

2.1 Assumptions

Some basic assumptions have been made about the tracers in order to keep a concise tracer API and ensure a uniform tracer treatment.

The tracers are scalar, 3-dimensional prognostic (i.e. time dependent) variables defined on the full model grid. They are defined along the three main spatial dimensions (rotated longitude `rlon`, rotated latitude `rlat`, model level `level`) of the COSMO grid. The tracers live at the mass-point (center of the grid box) collocated with temperature and pressure (`rlon, rlat, level`). It is not possible to have tracers on the staggered positions of the Arakawa-C/Lorenz COSMO grid (Schättler et al. 2011 or Doms 2011).

2.2 Functionalities of the tracer module

All basic functionalities which are common to all tracers as for example the allocation of the memory and transport by advection are provided. In a broad sense, the tracer module handles the infrastructure operations (related to the definition, the storage and the input/output of a variable) and the operations related to what is referred in COSMO as the "dynamics" (Schättler et al., 2011). It does not handle processes which are specific to a tracer or to a tracer class (basically the operations belonging to the "physics" according to the COSMO vocabulary or to additional submodules).

The prognostic equation for a tracer can be derived from the prognostic equation for water vapor (equation 3.148 in Doms, 2011):

$$\frac{\partial q^v}{\partial t} = \underbrace{-\left\{\frac{1}{a\cos\varphi}\left(u\frac{\partial q^v}{\partial \lambda} + v\cos\varphi\frac{\partial q^v}{\partial \varphi}\right)\right\} - \dot{\zeta}\frac{\partial q^v}{\partial \zeta}}_{ADV} \underbrace{- (S^l + S^f)}_{SRC/SINKS} \underbrace{+ M_{q^v}}_{MIX} \tag{1}$$

Expanding the third term (MIX) of equation (1) using its definition (equation 3.153 in Doms, 2011) and reordering the terms, we get:

$$\frac{\partial q^v}{\partial t} = \underbrace{ADV}_{A} + \underbrace{DIFF}_{B} + \underbrace{TURB}_{C} + \underbrace{CONV}_{D} + \underbrace{RELAX}_{E} + \underbrace{DAMP}_{F} + \underbrace{SRC/SINKS}_{G} \tag{2}$$

The terms in equation (2) are:

- A: horizontal and vertical advection (as described in chapters 4.4.2 and 4.4.3 of Doms, 2011)
- B: horizontal hyperdiffusion (or computational mixing) (as described in chapter 6.2 of Doms, 2011)
- C: turbulent mixing (as described in chapter 4.3.3 of Doms, 2011 and in chapter 3 of Doms et al., 2011)
- D: moist convection (as described in chapter 6 of Doms et al., 2011)
- E: boundary relaxation (as described in chapter 5.2 of Doms, 2011)
- F: Rayleigh damping (as described in chapter 6.4 of Doms, 2011)

- G: sources and sinks (in the case of qv, microphysical sources and sinks from/to the liquid and solid phases)

Written for an arbitrary tracer, equation (2) becomes:

$$\frac{\partial \psi}{\partial t} = \underbrace{ADV}_{A} + \underbrace{DIFF}_{B} + \underbrace{TURB}_{C} + \underbrace{CONV}_{D} + \underbrace{RELAX}_{E} + \underbrace{DAMP}_{F} + \underbrace{SRC/SINKS}_{G} \qquad (3)$$

Equation (3) is a general equation valid for any tracer ψ. The tracer module takes care of the 6 first terms (A to F). It means that these terms can be computed in an automated way by the tracer module. The tracer client simply has to set correctly the corresponding metadata (table 2). The 7th term, the sources and the sinks, is not computed by the tracer module, since this term is specific for each tracer. The tracer module simply makes available a tendency field that can be used to store the sources and the sinks. It is the responsibility of the tracer client to fill this term with the sources and the sinks appropriated for its tracer. Sources and sinks might be emissions, chemical transformations, phase changes or fluxes from/to the soil for instance.

We describe the functionalities of the tracer module in more details in the following subsections. If a standard metadata controls a functionality, it is added in brackets after the subsection title. The possible values for the standard metadata are listed in table 2.

2.2.1 Tracer definition and memory management

The definition of a new tracer is done by a call to the tracer API (described in section 2.3). Memory required by the tracer, its boundary values and its tendency field is handled internally by the tracer module. Pointers to these data fields can be retrieved by the tracer client by calling the tracer API.

2.2.2 I/O methods

In order to Input/Output (I/O) a field in COSMO, the variable has to have a corresponding entry in the `var` structure in the subroutine `setup_vartab`. The tracer module now automatically does this operation. An entry in the `var` structure is performed for the tracer and this tracer no longer appears explicitly in the code of the subroutine `setup_vartab`.

Any tracer can thus be read from and/or written out to file. However, associated fields like the tendency or a possible surface field cannot be read or written out in an automated way for the moment. This is further discussed in section 6.

The tracers can either be read/written in GRIB format or in NetCDF format like any other field in COSMO. Output is possible on model levels (`ml`), levels of constant pressure (`pl`) or levels of constant height (`zl`).

The relevant configuration switches are the following ones (namelist `INPUT_IO`):

- `yform_read`: determines the input format (GRIB or NetCDF)
- `yform_write`: determines the output format (GRIB or NetCDF)

- `yvarml`, `yvarpl`, `yvarzl`: determines the list of variables to output on the model levels, pressure levels and height levels, respectively

In order to write a tracer out, it must simply be added to the corresponding output list (`yvarml`, `yvarpl`, `yvarzl`). In order to read a tracer from file (as initial or/and as boundary condition), the metadata `T_INI_ID` and `T_LBC_ID` have to be set to `T_INI_FILE` and `T_LBC_FILE`, respectively. The model then automatically searches for the corresponding fields in the initial and boundary condition files and stops execution should they be missing.

2.2.3 Advection (`T_ADV_ID`)

The type of advection used for scalar quantities depends on the dynamical core selected by the user and on namelist switches that further refine the choice of a specific algorithm used for advection. The tracer module currently implements all major existing options and additionally offers the possibility to turn off advective transport for each tracer separately (e.g. for idealized cases or sensitivity studies).

For the Leapfrog core, the standard advection scheme for tracers is a second-order centered difference scheme in the horizontal and an implicit scheme in the vertical. Although certain species are transported using alternative advection schemes (e.g. semi-Lagrangian advection for precipitating microphysics species), the tracer module only implements the standard advection scheme (second order centered difference) for the tracers.
In the Runge-Kutta dynamical core a namelist switch allows a global selection (valid for all tracers) of the advection scheme. A complete list of the schemes is given below and a description of these schemes is provided in Doms (2011).

The relevant configuration switches are the following ones (namelist `INPUT_DYN`):

- `l2tls`: determines if the Leapfrog dynamical core or the Runge-Kutta one should be used
- `y_scalar_advect`: determines which scheme should be used in case of the Runge-Kutta core (van Leer, PPM, Bott2, Bott4, Van Leer Strang, PPM Strang, Bott2 Strang, Bott 4 Strang, Semi-Lagrange 3 MF, Semi-Lagrange 3 SFD)

The tracer module reproduces the advection as it is coded in the original code. Bottom and lateral boundary conditions used in this code part may not be consistent with the choices made by the tracer client (`T_LBC_ID` and `T_BBC_ID`).

2.2.4 Horizontal hyperdiffusion (`T_DIFF_ID`)

Horizontal hyperdiffusion is an artificial diffusion (computational mixing) performed to smooth the solution of the thermodynamical equations obtained by numerical integration. Two different schemes are available in the COSMO model (Doms, 2011) and both have been implemented for the tracers. Horizontal diffusion can also be switched off globally or for each tracer separately (see table 2).

The tracer module reproduces the horizontal diffusion as it is coded in the original code. Lateral boundary conditions used in this code part may not be consistent with the choice

made by the tracer client (T_LBC_ID).

The relevant configuration switches are the following ones (namelist INPUT_DYN):

- lhordiff: determines globally if horizontal diffusion should be activated
- itype_hdiff: determines which scheme should be used (4th order linear or 4th order linear monotonic with orographic limiter)
- hd_corr_trcr_in: determines the correction factor for scalar (tracers) used for the diffusion in the domain
- hd_corr_trcr_bd: determines the correction factor for scalar (tracers) used for the diffusion at the boundaries

2.2.5 Turbulent mixing (T_TURB_ID)

Different options are available for the turbulent mixing of tracers. Most of them compute the diffusion only in the vertical direction while an option enables to compute additionally the horizontal diffusion. The tracer module only implements the widely used options (i.e. prognostic TKE-based scheme with an implicit treatment using either a Dirichlet or a Neumann boundary condition at the Earths surface) and also the new option to have a 3-dimensional turbulent mixing. The option to switch off turbulent mixing for each tracer individually is made available.

The relevant configuration switches are the following ones (namelist INPUT_PHY):

- ltur: determines globally if turbulent mixing should be activated
- itype_turb: determines the parameterization used for turbulent diffusion (only value 3 is accepted for the tracers)
- imode_turb: determines the mode (implicit vs. explicit) of turbulent diffusion (only value 0 or 1 are accepted for the tracers)
- l3dturb: determines if horizontal diffusion should be computed in addition

The type of lower boundary condition is relevant for the turbulent mixing. This condition can be set using the metadata T_BBC_ID (see table 2).

More information about the turbulent mixing in the COSMO model can be found in Doms et al. (2011) and Buzzi (2008).

2.2.6 Passive convective transport (T_CONV_ID)

Passive transport of scalar quantities by convection was previously not available in the COSMO model. For the tracers, passive transport by convection using the Tiedtke scheme is implemented. It is done in an analogous way as for the momentum components in COSMO and follows ECMWF (2011). Other convection schemes available in COSMO (Kain-Fritsch, Bechtold, shallow-convection based on Tiedtke) are not implemented for the tracers and thus

cannot be selected for the tracers. It is possible to activate passive transport by convection for each tracer individually.

The relevant configuration switches are the following ones (namelist `INPUT_PHY`):

- `lconv`: determines globally if subgrid-scale convection should be activated
- `itype_conv`: determines the parameterization used for subgrid-scale convection (only value 0 is accepted for the tracers)

2.2.7 Lateral boundary conditions (`T_LBC_ID`)

Different types of lateral boundary condition (BC) can be applied to the tracers (see table 2). If boundary data coming from a coarser model are available in an input file, these data can be used as boundary condition. If such data are lacking for a tracer, other values can be used at the boundaries. One can choose between a value of zero at all boundaries, a constant value (which has to be defined in the code by the user) or a zero-gradient method, in which the values of the first line of the computing domain are chosen as boundaries.

There is no relevant configuration switch (except for the microphysics species).

2.2.8 Initial condition (`T_INI_ID`)

Different types of initialization can be applied for the tracers (see table 2). If initialization data coming from a coarser model or from an analysis are available in an input file, these data can be used as initial condition (IC). If such data are lacking for a tracer, an initialization using a value of zero can be chosen.

There is no relevant configuration switch (except for the microphysics species).

2.2.9 Boundary relaxation (`T_RELAX_ID`)

Boundary relaxation is performed in the COSMO model to gradually blend the solution of the model with the boundary values and thus avoid abrupt transitions in the fields and possible contamination of the solution due to numerical noise created by reflection at the boundaries. The scheme used is described in Doms (2011).
Boundary relaxation for each tracer can either be switched off (e.g. in case of idealized studies), can be performed at all boundaries or only at the inflow boundaries (like it is often done for precipitation quantities in COSMO.

The relevant configuration switches are the following ones (namelist `INPUT_DYN`):

- `rlwidth`: specifies the width of the relaxation zone (must be greater than 0 to perform relaxation)

2.2.10 Rayleigh damping (T_DAMP_ID)

Rayleigh damping may be applied in the COSMO model to avoid the reflection of gravity waves, which might occur at the top of the model due to its formulation as a rigid lid. Two types of damping are available in COSMO and for the tracers: damping by relaxing against the boundary fields or by relaxing against the filtered forecast fields (Doms, 2011). Additionally damping can be activated/deactivated on an individual basis for each.

The relevant configuration switches are the following ones (namelist `INPUT_DYN`):

- `lspubc`: determines globally if Rayleigh damping should be performed in the upper layers
- `itype_spubc`: specifies the type of Rayleigh damping
- `rdheight`: specifies the height of the damping layer bottom in meters (must be smaller than the top of the model domain to perform damping)

2.2.11 Clipping (T_CLP_ID)

Several clippings are performed throughout the COSMO code to ensure positive values for positive definite variables. Clipping removes thus negative values in order to ensure positive definiteness. We also offer this functionality for the tracers. It is possible to switch on or off the clipping for each tracer independently.

There is no relevant configuration switch.

Remark: For some species, different types of clipping are used at different locations in the COSMO code. The tracer module does not use different clipping types but consistently use the same method across the whole code.

2.2.12 COSMO options not implemented

Some existing schemes/configurations available in the COSMO model are not implemented for the tracers. These schemes/configurations have been considered as not relevant, outdated or as a major violation of a coherent tracer treatment. It is the case of:

- Semi-Lagrange advection in the Leapfrog dynamical core
- Positive definite advection scheme using Euler time stepping in the Leapfrog dynamical core
- Turbulent mixing in case $itype_turb \neq 3$ and $imode_turb \leq 2$
- Convective tracer transport for schemes other than the Tiedtke scheme (Kain-Fritsch, shallow convection, Bechtold)
- Special clipping types (e.g. massflux correction scheme)

2.3 The tracer module API

The tracer module API consists of the subroutines and functions stored in the source file `src_tracer.f90` as well as some predefined constants in the source file `data_tracer.f90`.All tracer module subroutine names start with `trcr_`. They provide methods to the tracer client for handling a specific tracer and its associated metadata or for handling a metadata for all tracers, and also some facilities (e.g. memory management), which are not specific to one tracer client.

A general feature of the tracer module is the ability to access any tracer or metadata by either its name or its index. The second option is much faster since it does not imply string comparison and is also the method to use in loops over all tracers (or over a subset of them).

All tracer module subroutines return an error status code (`ierr`) as the first argument. Any non-zero value indicates an error. A function which translates this error code into a human readable string is provided (see `trcr_errorstr` below). It is the tracer clients responsibility to check the status code returned and handle the error gracefully.

2.3.1 Methods for tracer handling

The methods described in this section are the ones the tracer client will use in order to define, access, modify tracers from the client code.

trcr_new This subroutine serves to define a new tracer. It must be called by the tracer client each time a new tracer has to be added to the COSMO model. It should be called from a meaningful location in the code (generally from an `organize_xxx` subroutine). Once the memory has been allocated by the tracer module (see `trcr_alloc` below) no more tracers can be defined.

The subroutine arguments are summarized in table 3 (in the correct order). Mandatory arguments have to be specified in each call of `trcr_new`. The other arguments can be passed or not. If they are not passed, the default value of the corresponding metadata is used (see table 2). Many arguments directly correspond to a metadata of the new tracer. Where this is the case, the corresponding metadata identifier is given in parenthesis after the definition of the argument.

A unique short name for the tracer has to be provided. It serves to identify the tracer and, at the same time, is the variable name for the NetCDF format (Unidata, 2011). The units have to be specified and should follow the SI system (International System of Units) if possible. These are the units used for reading and writing out the tracer. A GRIB parameter number as well as a GRIB table number has to be given as well. For standard meteorological variables, a specific GRIB number is dedicated to a specific variable. For some tracers, it might be more complicated since the WMO (World Meteorological Organization) has not attributed a fixed number to them. In that case, a GRIB parameter number and GRIB table number which are not yet occupied has to be chosen. The owner (or parent) name, i.e. the name of module which is in charge of the tracer, has to be passed as well.

Table 3: Aguments for `trcr_new`

Argument	Definition	Type	Intent	Mandatory?
`ierr`	Error status	`INT`	`OUT`	Yes
`yshort_name`	Tracer short name (`T_NAME_ID`)	`CHAR`	`IN`	Yes
`iGRIBparam`	Tracer GRIB parameter number (`T_GRBPARAM_ID`)	`INT`	`IN`	Yes
`iGRIBtable`	Tracer GRIB table number (`T_GRBTABLE_ID`)	`INT`	`IN`	Yes
`yparent`	Name of tracer owner (`T_PARENT_ID`)	`CHAR`	`IN`	Yes
`yunits`	Tracer units (`T_UNITS_ID`)	`CHAR`	`IN`	Yes
`ystandard_name`	Tracer standard name (`T_NCSTDNAME_ID`)	`CHAR`	`IN`	No
`ylong_name`	Tracer long name (`T_NCLONGNAME_ID`)	`CHAR`	`IN`	No
`itype_adv`	Advection specification (`T_ADV_ID`)	`INT`	`IN`	No
`itype_diff`	Horizontal hyperdiffusion specification (`T_DIFF_ID`)	`INT`	`IN`	No
`itype_turbmix`	Turbulent mixing specification (`T_TURB_ID`)	`INT`	`IN`	No
`itype_passconv`	Passive transport by convection specification (`T_CONV_ID`)	`INT`	`IN`	No
`itype_ini`	IC specification (`T_INI_ID`)	`INT`	`IN`	No
`itype_lbc`	Lateral BC specification (`T_LBC_ID`)	`INT`	`IN`	No
`itype_bbc`	Bottom BC specification (`T_BBC_ID`)	`INT`	`IN`	No
`itype_relax`	Relaxation specification (`T_RELAX_ID`)	`INT`	`IN`	No
`itype_damp`	Rayleigh damping specification (`T_DAMP_ID`)	`INT`	`IN`	No
`itype_clip`	Clipping specification (`T_CLP_ID`)	`INT`	`IN`	No
`idx_trcr`	Tracer index	`INT`	`OUT`	No

It is also strongly recommended to specify a standard name and a long name for the tracer. This should be done with respect to the CF conventions (Eaton et al., 2011) and a table of possible standard names is available on the Lawrence Livermore National Laboratory web-page[1].

Optionally, it is also possible to get back a unique index which can be used to identify the tracer (as a replacement for the tracer name in the `trcr_get` subroutine).

We also encourage to specify all other optional arguments of `trcr_new` which determine the behavior of the tracer. The possible values for the arguments are summarized in table 2.

trcr_get This subroutine enables the tracer client to retrieve a pointer to the tracer in order to perform specific operations (e.g. microphysics, atmospheric chemistry, etc.). The subroutine has to be called in each module or each subroutine (usually once per module should be enough) for each tracer and each time level required.

The subroutine arguments are summarized in table 4 (in the correct order).

Table 4: Aguments for `trcr_get`

Argument	Definition	Type	Intent	Mandatory?
`ierr`	Error status	`INT`	`OUT`	Yes
`idx_trcr`	Tracer index	`INT`	`IN`	Yes
or				
`yname`	Tracer name	`CHAR`	`IN`	Yes
`ptr`	Pointer to the tracer data	`REAL, POINTER`	`OUT`	No
`ptr_bd`	Pointer to the tracer boundary data	`REAL, POINTER`	`OUT`	No
`ptr_tens`	Pointer to the tracer tendency data	`REAL, POINTER`	`OUT`	No
`ptr_surf`	Pointer to the tracer surface field	`REAL, POINTER`	`OUT`	No
`ptr_tlev`	Time level for the pointers	`INT`	`IN`	No

Either the name or the index of the tracer (which can be retrieved using the subroutine `trcr_get_index` or directly during the tracer definition with `trcr_new`) has to be passed as input argument.

Pointers to the following data can be retrieved:

- a 3-dimensional pointer `ptr(:,:,:)` to the tracer data for the time level `nnow` or for the time level specified by the optional argument `ptr_tlev`. The pointer is dimensioned with `(ie, je, ke)`.

[1] http://cf-pcmdi.llnl.gov/documents/cf-conventions/1.6/cf-conventions.pdf

- a 4-dimensional pointer `ptr_bd(:,:,:,:)` to the tracer boundary data. The pointer is dimensioned with `(ie, je, ke, 2)`.
- a 3-dimensional pointer `ptr_tens(:,:,:)` to the tracer tendency data. The pointer is dimensioned with `(ie, je, ke)`.
- a 2-dimensional pointer `ptr_surf(:,:)` to the tracer surface data for the time level `nnow` or for the time level specified by the argument `ptr_tlev`. The pointer is dimensioned with `(ie, je)`.

Care should be taken not to call this subroutine excessively (e.g. in loops over all gridpoints) due to performance reasons (especially if the tracer name is used to retrieve the data instead of the tracer index).

trcr_get_ntrcr This function returns the total number of tracers currently handled by the tracer module (table 5). It has no argument. This function is used to create the upper bound of the loops over all tracers for instance (e.g. `DO iztrcr= 1, trcr_get_ntrcr()`).

Table 5: Aguments for `trcr_get_ntrcr`

Argument	Definition	Type	Intent	Mandatory?
result	Number of tracers	INT	-	-

trcr_get_index This subroutine returns the unique index identifying the tracer given its name.
The subroutine arguments are summarized in table 6 (in the correct order).

Table 6: Aguments for `trcr_get_index`

Argument	Definition	Type	Intent	Mandatory?
ierr	Error status	INT	OUT	Yes
yname	Tracer name	CHAR	IN	Yes
idx	Tracer index	INT	OUT	Yes

trcr_errorstr This function returns a meaningful error message for any error code issued by the tracer module. The input argument is the error code (see table 7). This error number can come from any subroutine of the tracer API listed in this section.

Table 7: Aguments for `trcr_errorstr`

Argument	Definition	Type	Intent	Mandatory?
ierr	Error status	INT	IN	Yes
result	Error message	CHAR	-	-

2.3.2 Methods for metadata handling

A tracer metadata describes a property or determines a specific behavior of a tracer substance. Apart from the standard set of metadata every tracer has (see tables 1 and 2), the tracer module allows the tracer client to define, set and retrieve arbitrary metadata for each tracer substance. This section describes the API methods available to the tracer client for handling the metadata associated with its own tracers. A metadata can be a single `integer`, `real`, `double`, `character`, `logical` as well as a one-dimensional array of any of these types. The methods for handling metadata are overloaded and the tracer client has a single interface for all of the above types. The interfaces are described in more details below. For simplicity reasons, we do not mention `real` and `double` for each interface but only `real` in this documentation.

trcr_meta_define Define a new metadata and provide its default value. The subroutine arguments are summarized in table 8 (in the correct order).

Table 8: Aguments for `trcr_meta_def`

Argument	Definition	Type	Intent	Mandatory?
`ierr`	Error status	`INT`	`OUT`	Yes
`yname`	Metadata name	`CHAR`	`IN`	Yes
`ydefault`	Default metadata value	`INT`	`IN`	Yes
or				
"	"	`REAL`	"	"
or				
"	"	`DOUBLE`	"	"
or				
"	"	`CHAR`	"	"
or				
"	"	`LOGICAL`	"	"
`iidx`	Metadata index	`INT`	`OUT`	No
`protect`	Flag to protect the metadata from possible deletion	`LOGICAL`	`IN`	No

The name of the metadata has to be provided as well as a default value. The default value will be applied to the metadata for all tracers, except if another value is specified for a given tracer (using `trcr_meta_set`, see below). The type of the default value determines the type of the metadata.

Optionally, the index of the metadata in the metadata structure can be obtained for more efficient access and it is also possible to protect the metadata from deletion by another tracer client.

trcr_meta_set Store values for a given metadata (identified by its name or index) for a specific tracer or for all tracers at once. The subroutine arguments are summarized in table 9 (in the correct order).

Table 9: Aguments for `trcr_meta_set`

Argument	**Definition**	**Type**	**Intent**	**Mandatory?**
`ierr`	Error status	`INT`	`OUT`	Yes
`itrcr`	Tracer index	`INT`	`IN`	Yes
or				
`ytrcr`	Tracer name	`CHAR`	`IN`	Yes
or				
nothing				
`imeta`	Metadata index	`INT`	`IN`	Yes
or				
`ymeta`	Metadata name	`CHAR`	`IN`	Yes
`ydata`	Specified value	`INT`	`IN`	Yes
or				
"	"	`REAL`	"	"
or				
"	"	`CHAR`	"	"
or				
"	"	`LOGICAL`	"	"

The name or the index of the metadata to set has to be provided as well as the value to store. If a tracer name or a tracer index is specified, then the value given will be used only for this tracer. If the tracer name or index is omitted, it is assumed that the tracer client wants to store metadata for all tracers and the last dimension of the value array needs to correspond to the number of tracers. The type of the values has to be of the same type (`INT`, `REAL`, `CHAR`, `LOGICAL`) than the default value provided to `trcr_meta_define`.

trcr_meta_get Retrieve a given metadata for a specific tracer or for all tracers at once. The subroutine arguments are summarized in table 10 (in the correct order).

Table 10: Aguments for `trcr_meta_get`

Argument	Definition	Type	Intent	Mandatory?
`ierr`	Error status	`INT`	`OUT`	Yes
`itrcr`	Tracer index	`INT`	`IN`	Yes
or				
`ytrcr`	Tracer name	`CHAR`	`IN`	Yes
or				
nothing				
`imeta`	Metadata index	`INT`	`IN`	Yes
or				
`ymeta`	Metadata name	`CHAR`	`IN`	Yes
`ydata`	Specified value	`INT`	`OUT`	Yes
or				
"	"	`REAL`	"	"
or				
"	"	`CHAR`	"	"
or				
"	"	`LOGICAL`	"	"

The name or the index of the metadata has to be provided and its value will be returned. If a tracer name or a tracer index is specified, then the value is returned only for this tracer. But if the tracer name or index is omitted, the value of the specified metadata will be returned for all tracers. The value array needs to be dimensioned accordingly.

2.3.3 Infrastructure methods

These methods are low-level methods used to manipulate the data structures and the information related to the tracers and the metadata. These methods are called only once in the code and should not be called by the tracer client, as they are already implemented in the model code.

trcr_init This subroutine is called at the beginning of the initialization phase and defines and initializes the mandatory metadata with default values, initializes some indices and nullifies some pointers used in the tracer module.

trcr_alloc This subroutine allocates the memory for the data structures used to save the tracers, their tendency and boundary fields and initializes these structures. It is called only once during the allocation phase of the COSMO model. After a call to this routine, no more tracers can be defined and a call to `trcr_new` will result in an error.

trcr_setup_vartab This subroutine is called from `organize_data.f90` and mimics the COSMO subroutine `setup_vartab`. This is a necessary operation in order to do I/O with the tracers. Additionally, we also associate a pointer to the corresponding surface field if this is required.

trcr_print This subroutine is called only once from `lmorg.f90` after the allocation phase. This routine produces a summary of all tracers and the associated metadata in the standard output of the COSMO model. The standard output should be checked by all tracer clients to make sure that their tracers are correctly handled (i.e. that the values of the metadata have been set accordingly to their needs).

trcr_cleanup This subroutine deallocates the memory allocated in `trcr_alloc`. It is called only once at the end of the COSMO program. After a call to this routine, any tracer data is lost an all calls to `trcr_get` or `trcr_meta_get` will result in an error.

3 A short user's guide

In this section, we first show briefly how we replaced the existing microphysics variables by the tracer module. This example should help users who already have their tracers coupled to the COSMO model (e.g. COSMO-ART) in making use of the tracer module. In a second example, we outline the main steps to introduce a new tracer into the model.

3.1 The microphysics example

We have replaced the current treatment of all microphysics species (water vapor: `qv`, cloud water: `qc`, cloud ice: `qi`, rain: `qr`, snow: `qs`, graupel: `qg`) by the tracer module. The microphysics species are no longer handled as individual global variables but are now packed in the data structures related to the tracers and can only be defined, accessed and modified using the tracer methods.

3.1.1 The generic code parts

In all code parts where actions that can now be performed by the tracer module were executed, we could simply remove the code lines related to the microphysics species. This is for instance the case of the allocation (`src_allocation.f90`), the filling of the `var` structure (`src_setup_vartab.f90`) or the handling of the I/O for initial and boundary conditions (`organize_data.f90`). These actions are common to all tracers.
An example of a code section which is generic for all tracers can be found in Fig. 1. In this code section, the list of the variables that need initial conditions to be read from file is generated. On the left panel, the original code is shown. The generation of the variable list implied to add each variable explicitly (i.e. using its name). In the new version, shown on the right panel, the metadata `T_INI_ID` is tested for each tracer and if this metadata indicates that IC have to be read from file (`T_INI_FILE`) then the tracer name is added to the list.

3.1.2 The specific code parts

In code parts that are specific to the microphysics, the original code could be kept almost unchanged. The main change is the access to the data. In the original code, a `USE` statement of the module `data_fields.f90` is performed in order to get access to the microphysics variables (`qv`, `qc`, etc.) and these variables can then be used directly. In the new version, some `trcr_get` have to be performed instead to retrieve the microphysics variables. An

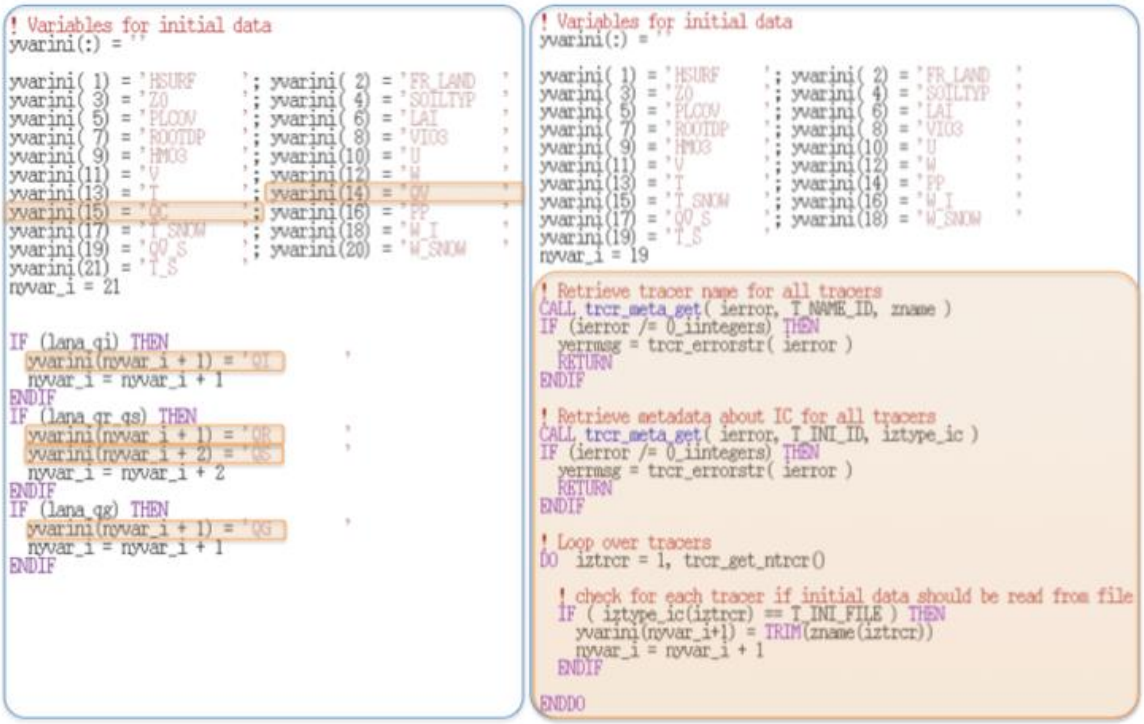


Figure 1: Replacement of the microphysics species in a generic code section
left panel: original code (without tracer); right panel: new code (with tracer)

example can be seen in Fig. 2. This code section is extracted from the subroutine `hydci_pp`, which computes the rate of change of temperature, cloud water, cloud ice, vapor, rain and snow due to microphysical processes related to the formation of grid scale precipitation. On the left panel (original code version), it becomes clear that each microphysics specie is accessed using the corresponding global variable defined in the source file `data_fields.f90` (`USE data_fields` statement). It is then used in the code at the time level `nx`. In the tracer version (shown on the right panel), local pointers are defined for each microphysical species for each required time level. Then the data are accessed using the statements `CALL trcr_get` for each variable at the required time level. These pointers are 3-dimensional pointers. The local pointers can then be used instead of the global variables in the parameterization.

It is crucial to notice that the tracer client now has to work with pointers instead of allocated fields. This implies for instance that all instances of `IF(ALLOCATED(my_var))` have to be replaced by `IF(ASSOCIATED(my_var))`. The validity of a pointer (which points on a given variable for a given time step) is not longer than one time step, whereas an allocated variable is valid throughout the whole simulation (thanks to the swapping of the time steps).

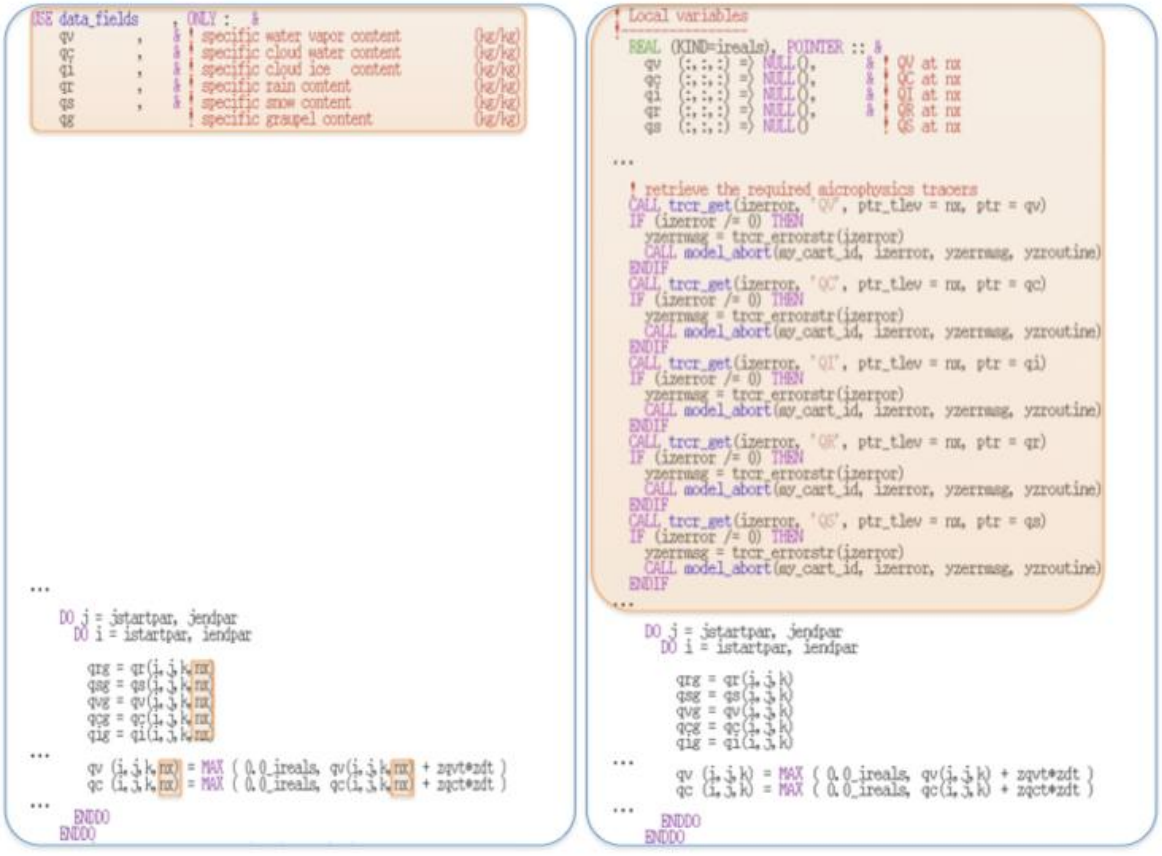


Figure 2: Replacement of the microphysics species in a specific code section
left panel: original code (without tracer); right panel: new code (with tracer)

3.1.3 The microphysics specificities in generic code parts

Major difficulties when replacing the existing treatment of the microphysics species by the tracer module methods arose in the code sections generic to all tracers. Indeed, numerous inconsistencies are present in the advection, in the turbulent mixing, in the treatment of the

lateral boundary conditions and in the time stepping for the microphysics species. Although these operations should usually be handled in a consistent way for all tracers, we could not harmonize the treatment of the microphysics species for backwards compatibility reasons. We had to find a solution to handle these specificities without altering the integrity of the tracer module. We made use of the metadata to distinguish these special cases. **The use of these special metadata is not recommended to other tracer clients and they will be removed from the code over time.**

We list below the metadata that we have defined to reproduce the original treatment of the microphysics species, the possible values and the default (i.e. the standard treatment for other tracers). We do not recommend using these metadata for other tracers without intensive testing. Indeed, it is not clear at all for most of them why the behavior they are activating is required for some microphysical species and if it would be meaningful for other species. Caution is thus required when manipulating these metadata.

CLP_10E-12 At the end of the turbulent mixing for the Leapfrog dynamical core, a clipping is performed to ensure that the positive definite quantities are not exhibiting negative values. In case of cloud ice (`qi`), another clipping method than the usual one is performed. Any value smaller than `10E-12` is set to zero instead of clipping only the negative values (i.e. smaller than `0`). The metadata `CLP_10E-12` is set to `FALSE` for all tracers except for `qi`. It means that we perform the usual clipping (clipping of the negative values only) for all tracers except for `qi` (for which we clip any value smaller than `10E-12`).

Remark: this metadata is only active for `qi` if the standard metadata `T_CLP_POSDEF` has been set to `TRUE`.

MASSFLX_CLP At the end of the turbulent mixing for the Leapfrog dynamical core and the Runge Kutta core, a clipping is performed to ensure that the positive definite quantities are not exhibiting negative values. In case of water vapor (`qv`) and cloud water (`qc`), a mass-flux correction scheme can be used instead of the usual clipping method. This is activated by a hard-coded internal switch (`lmassf_diffusion`) in the original code. The metadata `MASSFLX_CLP` is set to `FALSE` for all tracers except for `qv` and `qc`. It means that we perform the usual clipping for all tracers except for `qv` and `qc` (for which we redistribute the clipped mass).

Remark: this metadata is only active for `qv` and `qc` if the standard metadata `T_CLP_POSDEF` has been set to `TRUE`.

ADD_CLP_ADV When using the advection in the Runge-Kutta core not written in conservation form (`ltrcr_conserv_form=.FALSE.`), a clipping is performed at the end of the advection routine (`advection_pd`) but only for the precipitating species (`qr`, `qs`, `qg`). The metadata `ADD_CLP_ADV` is set to `TRUE` for these species whereas it is set to `FALSE` for any other tracer, thus activating this additional clipping only for the three species mentioned above. This metadata is of course only active if advection is performed (i.e. if the metadata `T_ADV_ID` has been set to `T_ADV_ON`).

BD_0GRAD_FORCED Several types of lateral boundary condition can be chosen using the metadata T_LBD_ID. This type is then used at several locations in the code, among others in the advection. A routine (lateral_boundaries_zerograd in the new code, western_boundary, eastern_boundary, southern_boundary and northern_boundary in the original code) in the advection part of the Runge Kutta core (subroutine advection_pd) sets the lateral boundaries in case of a zero-gradient boundary condition type. This routine should thus only be called if T_LBC_ID is set to T_LBC_ZEROGRAD. However this is done in any case for qi, qr, qs and qg in case the boundaries are not read from a file in the original code. We thus have to define a metadata which overwrites the boundary settings in the advection (for Runge Kutta) for these species except if the boundaries are read from file (T_LBC_FILE). BD_0GRAD_FORCED is thus set to FALSE for all tracers except for the above mentioned species. This metadata is of course only active if advection is performed (T_ADV_ON).

BD_SET_FORCED The type of lateral boundary condition is also used at the end of the dynamics computation (section 6.3.1 of lmorg.f90). At this location, the boundaries are set in case a zero-value (T_LBC_ZERO) or zero-gradient (T_LBC_ZEROGRAD) boundary condition has been chosen. For the precipitating species however, this boundary settings is done also if the boundaries have been read from file and the type (zero-value or zero-gradient) is defined according to the namelist switch itype_lbc_qrsg in the original code. In order to reproduce this behavior, the switch BD_SET_FORCED is introduced. It is set to zero for all species except for the precipitating species. For them, it is set to 1 or 2 according to the value of the namelist switch itype_lbc_qrsg. A value of 1 means a zero-gradient boundary condition whereas a value of 2 means a zero-value boundary condition.

SP_ADV_LF Advection in Leapfrog is normally done using centered differences and a Leapfrog time stepping scheme. The vertical advection is done implicitly. This default is applied to all tracers and to qv and qc. In the original code however, qi, qr, qs and qg are advected using others schemes. qi is advected using a positive definite scheme based on an Euler forward time stepping scheme. The vertical advection is also positive definite and is solved explicitly. For the precipitating species, a semi-Lagrange scheme with a Leapfrog time stepping is used. We use the metadata SP_ADV_LF to reproduce these various schemes. The default, SP_ADV_LF=1, is applied to all tracers except the species mentioned above; the normal Leapfrog scheme is used. For qi, the metadata SP_ADV_LF is set to 2, in order to make use of the Euler forward time stepping scheme. For the precipitating species, SP_ADV_LF is set to 3, inducing the use of the semi-Lagrange scheme.

Remark: A correct treatment of T_ADV_OFF is guaranteed only for the default Leapfrog scheme.

3.1.4 Treating the surface field

For any prognostic variable, there are possibly associated fields: the tendency fields, the boundary field, a surface field or an emission field for instance. In the current COSMO code, the only field that can be associated directly to a variable is the boundary field. This is dictated by the way COSMO defines a variable (i.e. by the composition of the var structure). It means that only the boundary field can be handled properly in an automated way.

However, in order to treat correctly the bottom boundary condition in case a surface field

should be used (`T_BBC_ID` set to `T_BBC_SURF_VAL`), we need an automated method to relate a surface field to the tracer. The method currently used is constrained by the variable handling in COSMO and is not very satisfying. The tracer client has to define the surface field (in `data_fields.f90`), to allocated it (in `src_allocation.f90`), to fill the `var` structure for it (in `src_setup_vartab`), to update it (in `lmorg.f90`) and to deallocate it (in `src_allocation.f90`) himself or herself. In the tracer routine `trcr_setup_vartab`, we search in the `var` structure for a field named like the tracer field but with an extension `_S` (`QV_S` for `QV` for instance). If such a field is found, the pointer `ptr_surf` in the tracer structure is associated to this field. We check that this pointer is associated in case `T_BBC_SURF_VAL` has been chosen for the tracer.

This method is inflexible; the name of the surface field must be constructed using the name of the tracer and the `_S` extension. And it is laborious, the tracer client having to perform lots of operations to handle this field. Care is required when a surface field should be used as bottom boundary condition.

3.2 How to introduce a new tracer?

The introduction of a new tracer is relatively straightforward using the tracer module.

The general workflow to introduce a new tracer can be summarized in:

- Defining the tracer: name, GRIB information, set of dynamics operation to undergo, type of initial and boundary conditions
- Defining associated metadata: determine if some information has to be attached to the tracer and if yes, define and set these metadata
- Defining initial and boundary conditions if needed (in case they are not read from file and should not have a zero value or a zero-gradient)
- Retrieving the tracer to perform various actions: computation of the source/sink terms of the tracer and update of the tracer, use of the tracer to compute derived quantities
- Adding the tracer to the output list in the namelist `INPUT_IO`

Each operation listed above has to take place in a meaningful location in the COSMO code. Some basic knowledge of the workflow in COSMO can help to use the tracer module correctly. We describe roughly the COSMO workflow in section 4.2.

3.2.1 Define the tracer and its metadata

The tracer client has to call `trcr_new` from an appropriate location. This appropriate location is usually `organize_physics` for the physical tracers, `src_artifdata` for artificial tracers and the "organizing" routine of associated modules (e.g. the "organizing" routine of the aerosol module in case of aerosols). This has to occur before the allocation phase but after the initialization of the tracer module (i.e. in section 2.1. of `lmorg.f90`). An example of an "organizing" routine can be found in Appendix A.

A crucial task for the tracer client is to choose the type of initial and boundary conditions for the tracer, to define which processes (advective transport, convective transport, etc.) it should undergo. In case of constant boundary conditions, the user has to retrieve the boundary field using the procedure `trcr_get` and assign a value to the corresponding pointer.

In some cases, it might be necessary to define additional metadata. It might be useful for instance to have the molar mass of some chemical tracers. These metadata can be defined at the same place using the procedures `trcr_meta_define` and `trcr_meta_set`.

3.2.2 Retrieve the tracer and its metadata

Wherever the tracer client needs to use its tracer (e.g. in parameterizations of physical or chemical processes), it has to retrieve it using `trcr_get`. The required time step has to be specified. It is also possible to retrieve the tendency, the surface field or the boundary data using the same procedure. An example can be found in Appendix B.

4 Implementation details

This section details some design choices made internally in the tracer module. It is important to note that this information is subject to change at any time and that the tracer client should not write code that assumes any of the information given here.

4.1 Data structures

The main data structures used to manage the tracers at a low level are allocatable arrays of type `REAL`:

- `trcr_data` is a 5-dimensional array dimensioned with `(ie, je, ke, n_trcr, n_tlev)` and contains the tracer fields.
- `trcr_data_bd` is a 5-dimensional array dimensioned with `(ie, je, ke, n_bd, 2)` and contains the boundary field for the tracers.
- `trcr_data_tens` is a 4-dimensional array dimensioned with `(ie, je, ke, n_trcr)` and contains the tendency field for the tracers.

The number of tracers, `n_trcr`, and the number of boundary fields for the tracers, `n_bd`, are updated by each call to `trcr_new`. The method `trcr_get` accesses these data structures and returns 3-dimensional pointers for the tracer data and the tracer tendency and a 4-dimensional pointer for the tracer boundaries.

4.2 Workflow

The COSMO workflow can be roughly described as follows:

1. Initialization phase
   (a) Initialization of the environment and domain decomposition

(b) Read of the namelist variables
(c) Initialization of the tracer module
(d) Definition of the tracers and of their metadata
(e) Allocation
(f) Print of the tracer list and metadata in the standard output
(g) Fill in of the `var` structure (I/O table)
(h) Definition of the variable list to read for IC, BC and for the restart
(i) Read (or computation) of the IC and of the two first BC sets
(j) Initialization of the output variable list
(k) Initialization of the various packages (dynamics, physics, assimilation,)
(l) (Model initialization by digital filtering)

2. Time stepping loop

(a) Time step initialization (read new BC data if needed and interpolate them in time, swap time levels, reset the tendencies to zero)
(b) Computation of the physical parameterizations (first set)
(c) Computation of the dynamics
(d) Setting of special boundaries
(e) Computation of the assimilation
(f) Computation of budgets
(g) Computation of the boundary relaxation
(h) Computation of the physical parameterizations (second set)
(i) Nullification of small values for the tracers
(j) Boundary exchanges
(k) Diagnostics computation
(l) Results output (if needed)

3. Finalization phase

(a) Deallocation of the memory
(b) Collection of the timings
(c) Finalization of the MPI environment

The operations on the tracers cannot be performed in any order but they have to fit into the COSMO workflow.

In order to check that the main tracer operations are done in the right sequence, the tracer module internally uses a status variable which is checked upon every call to the tracer module to ensure a legal calling sequence (state machine). This variable can take the value "start", "define", "alloc" or "finish". At the beginning of the code, the status is "start". `trcr_init` can only be called with this status. At the end of `trcr_init`, the status is changed to "define". `trcr_new` and `trcr_alloc` can only be called for the status "define". At the end of the allocation routine (`trcr_alloc`), the status is changed to "alloc". At this point, it is no longer allowed to define new tracers. The filling of the `var` structure (`trcr_setup_vartab`) and the printing of the tracer list and associated metadata in the standard output have to be

performed for the status "alloc". The subroutines which access the tracer structure, namely `trcr_get_index`, `trcr_check_index` and `trcr_get`, can be called for the status "define" or "alloc", depending on the arguments. `trcr_cleanup` has to be called with the status "alloc" and the status is changed to "finish" at the end of this subroutine.

4.3 Metadata module

The metadata management of the tracer module is handled by a general metadata backend in the source code files `src_tracer_metadata.f90` and `data_tracer_metadata.f90`. The tracer module defines a metadata container (of type `t_metadata`) and pipes all metadata requests from the methods `trcr_meta_define`, `trcr_meta_set` and `trcr_meta_get` to methods of the metadata backend. The metadata backend is not logically linked to the tracer module and can in principle be used for other metadata storage tasks.

Internally, all metadata is stored in a buffer of type `CHARACTER`. The different metadata are typecast using the Fortran `TRANSFER` intrinsic. Depending on the compiler dependent implementation, this allows for efficient access to metadata avoiding data copies.

Access to metadata can potentially be slow when done via name of the tracer and name of the metadata. This is especially the case, when a large number of tracers and metadata have been defined, implying a larger number of string comparisons. Accessing metadata in this way from within loops should be avoided at all costs. Access by tracer index and metadata index will be considerably more efficient. Further efficiency improvements can be achieved with metadata accesses for all tracers at once (omitting the tracer index or name in the metadata access methods, such as `trcr_meta_get`).

There are some internally hardcoded limits of the metadata module, such as the maximum length of the metadata name and the maximum length of strings that can be stored. If these limits are exceeded by any call to the metadata API, an appropriate error is issued. The user can then increase the limits and recompile.

4.4 Performance considerations

The performance has been tested on several platforms (Cray XT systems, Cray XE systems, NEC SX6, Mac OS). The performance of the model code is not changed significantly by our implementation on all tested platforms except for the NEC SX6, where a slowdown of about 10% has been observed. The main reason is vectorization issues. Some optimizations will be done in the future in order to achieve comparable runtime as with the original code. An improvement of the boundary exchange (bulk exchange instead of individual exchange for each tracer) is planned to prevent major performance issues when dealing with numerous tracers.

An experiment has been conducted to analyze the rise of the computing time by adding tracers successively, from zero additional tracers up to 100 additional tracers. For this experiment, COSMO-7 simulations of 24 hours forecast (as run operationally at MeteoSwiss but without any output) have been performed on a Cray XE6 system using 480 processing units. The resulting timings for a various number of tracers are illustrated in Fig. 3.
With zero additional tracers, one hour of simulation takes 21.45 seconds. Fitting a linear regression curve (least squares method) on the data, a slope of 0.7388 is obtained (equation: $time = 20.63 + 0.7388 * num_tracers$). It means that adding one tracer costs about 0.7388 seconds more (out of 21.45 seconds), i.e. an increase of 3.5% of the computing time per

additional tracer is observed. The computing time behaves extremely linearly with respect to the number of tracers.

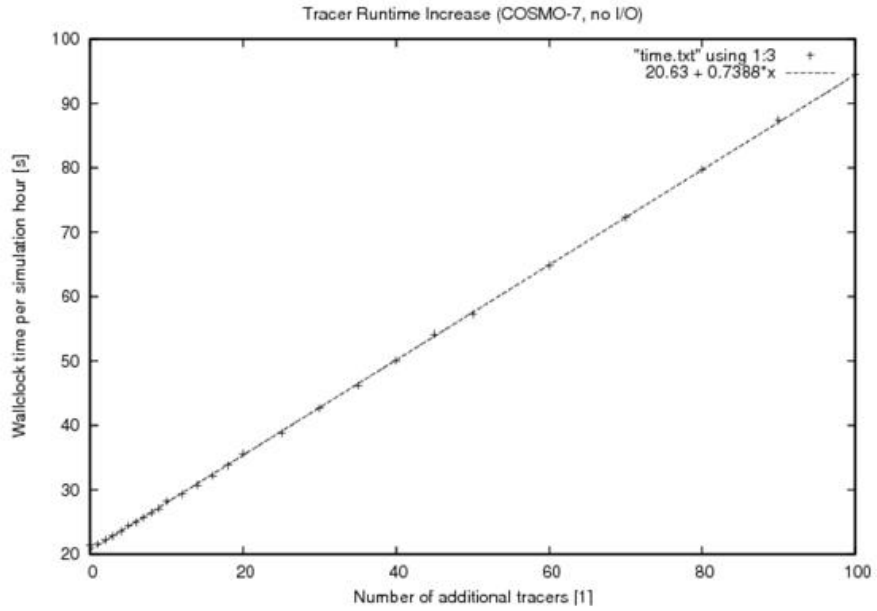


Figure 3: Runtime increase as a function of the tracer number

5 Results

The implementation of the tracer module is a purely technical change made to the code to improve its structure. It does not change the results.

After some code refactoring (mainly operation reordering), we could reproduce most of the results when handling the microphysics species with the tracer module. Some discrepancies have been observed and it turned out that these differences in the results were related to inconsistencies in the treatment of these species in the original code. Making use of the metadata mechanism, it has been possible to reproduce these specificities (inconsistencies) without degrading the integrity of the tracer module itself (see section 3.1.3).

The new code, including the handling of the microphysics species by the tracer module, has been extensively tested for several dozen of configurations. All tests have been successfully passed, i.e. bit-identical results have been obtained for all of them when comparing the original code and the tracer enabled code.

Parallelization has not been altered by our developments and the major configuration options of the original COSMO code are still available in combination with the tracer module.

6 Issues and needs for further refinements

The tracer module offers a facilitated tracer treatment. However it has been implemented in an existing code structure and only parts of this structure have been refactored. A larger effort would be needed to achieve more flexibility in the tracer definition and to reach a solution that could satisfy all tracer clients.

Technical and scientific aspects are still insufficiently well-handled for some tracer clients. From the scientific part, the main issue for a satisfying tracer treatment is related to conservation properties. Mass conservation is not guaranteed with the advection schemes implemented in COSMO. Other properties like the ratio between tracers are not conserved at all. This is not acceptable for several tracer clients.

From the technical side, the tracer module considers all tracers as being equal. We do not have a concept of tracer family for the moment. The possibility for differentiated treatment is left to the user, who can attach a new metadata, which controls a special behavior, to his set of tracers. In some cases, it might nevertheless be advantageous to have at least some "en bloc" methods to retrieve all aerosols in one call for instance. This kind of "en bloc" methods could easily be implemented in a future version.

Another technical limitation of the current COSMO code is related to the inflexible way of defining variables. Each field that has to be read/written has to appear in the `var` structure. This structure contains among others the GRIB number for the element but also some pointers to the variable itself and to the boundary field. This means that a boundary field can be associated to each variable but no other field can be attached to it. A more general way to define a field would help to handle associated fields for the tracers. Usually tracer clients want to have a surface field, an emission, a tendency a flux or other type of fields like a sedimentation velocity attached to their species. For the moment, only the boundary field is completely handled by the tracer module. The tendency field can also be considered as fully covered by the tracer module but cannot be written to output (which was also the case in the original COSMO version). A surface field can be attached to the tracer field if the user has chosen a surface value as bottom boundary condition but the tracer client still has to declare, allocate and define this surface field himself (see section 3.1.4). This solution is not satisfying in a long-term perspective. Emissions or other fields cannot be attached to the tracers in an easy way for the moment. Replacing the `var` structure by a more flexible datatype would alleviate this problem. In a prototype version, pointers can be saved into the metadata as well. This pointer support associated to a better definition of the fields in COSMO would enable to link variables in a convenient way.

Currently, metadata are defined within the code, requiring a new compilation each time a metadata is changed. Handling some of the metadata via namelists would eliminate the need for recompilation.

7 Conclusions

A major code modification has been implemented in the COSMO model for a better treatment of passive, scalar prognostic variables (tracers). The implementation of this tracer mod-

ule is a step towards an efficient, consistent and user-friendly tracer treatment in COSMO. The module has been successfully used for handling the microphysics species (of both the one-moment and the two-moment microphysics schemes) present in the model as well as for tracing air masses (work of Bojan Skerlak, ETH Zürich) and for the forecast of snow water content (Frick, 2012).

The mechanism to attach metadata to a tracer is a powerful functionality, which has been intensively used for the handling of the microphysics species. Indeed, the specificities (inconsistent treatment) present in some code parts for the microphysics species could be reproduced without attempting at the tracer module coherence and operating mode. Replacing the existing treatment of the microphysics species by the tracer module could therefore be done without altering the results.

Although the new module provides rather flexible methods for prognostic variables and convenient extension possibilities, the general definition of a field in COSMO remains inflexible. New methods for variable definition and additional support for pointer saving in the metadata would greatly improve the structure of the COSMO code and open new doors for future developments.

Acknowledgments

We would like to thank Ulrich Schättler, Ulrich Blahak, Michael Baldauf, Jochen Förstner, Matthias Raschendorfer, Axel Seifert, Heini Wernli, Bernhard and Heike Vogel, Daniel Reinert, Christoph Knote, Astrid Kerkweg and Pirmin Kaufmann for useful discussions, suggestions and support. We are grateful to Claudia Frick and Bojan Skerlak who volunteered to serve as guinea pigs!

References

Buzzi M., 2008: Challenges in Operational Numerical Weather Prediction at High Resolution in Complex Terrain.
Diss. ETH No. 17714
[Available online at: *http://e-collection.library.ethz.ch*].

Doms G., 2011: A description of the Nonhydrostatic Regional COSMO-Model.
Part I: Dynamics and Numerics. *Tech. Rep.*
[Available online at: *http://cosmo-model.org*].

Doms G. et al., 2011: A description of the Nonhydrostatic Regional COSMO-Model.
Part II: Physical Parameterization. *Tech. Rep.*
[Available online at: *http://cosmo-model.org*].

Eaton B. et al., 2011. NetCDF Climate and Forecast (CF) Metadata Conventions, version 1.6, 5 December, 2011.

ECMWF, 2011: IFS Documentation - Cy37r2, Operational implementation 18 May 2011.
Part IV: Physical Processes. *IFS Documentation*
[Available online at: *http://www.ecmwf.int*].

Frick C. 2012: The numerical modeling of wet snowfall events.
Diss. ETH No. 20624
[Available online at: *http://e-collection.library.ethz.ch*].

Rast S., 2009. Using and Programming ECHAM5 - a first introduction.
[Available online at: *www.mpimet.mpg.de/fileadmin/staff/rastsebastian/echam_5.5_lecture.pdf*]

Schättler U. et al., 2011: A description of the Nonhydrostatic Regional COSMO-Model.
Part VII: User's guide. *Tech. Rep.*
[Available online at: *http://cosmo-model.org*].

Unidata, 2011. NetCDF Users Guide. *http://www.unidata.ucar.edu/software/netcdf/docs/netcdf.html*

Appendix A: an organizing routine

```
!==============================================================================
!+ External procedure for organizing the calls to the xxx packages
!------------------------------------------------------------------------------

SUBROUTINE organize_xxx (yaction, ierror, yerrmsg)

!------------------------------------------------------------------------------
!
! Description:
!   This procedure is the driving routine for calling the xxx
!   parametrizations.
!
! Method:
!
! Current Code Owner:
!
! History:
! Version    Date       Name
! ---------- ---------- ----
! Code Description:
! Language: Fortran 90.
! Software Standards: "European Standards for Writing and
! Documenting Exchangeable Fortran 90 Code".
!==============================================================

USE ...

USE data_tracers,   ONLY:  T_ADV_ON      , T_DIFF_ON, T_TURB_OFF,  &
                           T_CONV_OFF    , T_INI_FILE, T_LBC_CST,  &
                           T_BBC_SURF_VAL, T_RELAX_FULL,           &
                           T_DAMP_ON     , T_CLP_POSDEF, T_ERR_NOTFOUND

USE src_tracers, ONLY: trcr_new, trcr_errorstr,                    &
                       trcr_meta_define, trcr_meta_set, trcr_get

!==============================================================

IMPLICIT NONE

!==============================================================

! Parameter list:
CHARACTER (LEN= *),       INTENT(IN)           ::                  &
  yaction      ! action to be performed

INTEGER (KIND=iintegers), INTENT(OUT)          ::                  &
  ierror       ! error status

CHARACTER (LEN= *),       INTENT(OUT)          ::                  &
  yerrmsg      ! error message

! Local variables:
INTEGER (KIND=iintegers)   ::   izerr

CHARACTER (LEN=25)         ::   yzroutine

! Tracer pointers
REAL (KIND=ireals), POINTER :: xcomp_bd(:,:,:,:) => NULL()
!------------------------------------------------------------------------------
!- End of header
```

```
!-------------------------------------------------------------------------------

!-------------------------------------------------------------------------------
!- Begin Subroutine organize_xxx
!-------------------------------------------------------------------------------
yzroutine = 'organize_xxx'
izerr     = 0_iintegers

...

!-------------------------------------------------------------------------------
! Section xxx: Tracer definition
!-------------------------------------------------------------------------------


IF (yaction == 'tracer') THEN

  ! init error value
  izerr = 0_iintegers

  ! Define all tracers required by the module xxx
  ! ---------------------------------------------

  ! define component X

  CALL trcr_new(                                          &
    ierr             = izerr,                             &
    yshort_name      = 'X_COMPONENT',                     &
    iGRIBparam       = 222,                               &
    iGRIBtable       = 6,                                 &
    yparent          = 'organize_xxx',                    &
    yunits           = 'kg kg-1',                         &
    ystandard_name   = 'x_component',                     &
    ylong_name       = 'specific content of component x', &
    itype_adv        = T_ADV_ON,                          &
    itype_diff       = T_DIFF_ON,                         &
    itype_turbmix    = T_TURB_OFF,                        &
    itype_passconv   = T_CONV_OFF,                        &
    itype_ini        = T_INI_FILE,                        &
    itype_lbc        = T_LBC_CST,                         &
    itype_bbc        = T_BBC_SURF_VAL,                    &
    itype_relax      = T_RELAX_FULL,                      &
    itype_damp       = T_DAMP_ON,                         &
    itype_clip       = T_CLP_POSDEF)

  IF (izerr /= 0_iintegers) THEN
    ierror  = izerr
    yerrmsg = trcr_errorstr(izerr)
    RETURN
  ENDIF


  ! Define and set all additional metadata required by the module xxx
  ! -----------------------------------------------------------------

  ! define metadata for molar mass [kg mol-1]
  CALL trcr_meta_define(izerr, 'MOL_MASS', -999_ireals)
  IF (izerr /= 0_iintegers) THEN
    ierror  = izerr
    yerrmsg = trcr_errorstr(izerr)
    RETURN
  ENDIF
```

```
  ! set molar mass for component X to 58.443 g mol-1
  CALL trcr_meta_set(izerr, 'X_COMPONENT', 'MOL_MASS', 58.443E-3)
  IF (izerr /= 0_iintegers) THEN
    ierror  = izerr
    yerrmsg = trcr_errorstr(izerr)
    RETURN
  ENDIF

!------------------------------------------------------------------------
! Section xxx: Other operations
!------------------------------------------------------------------------

ELSEIF (yaction == 'xxx') THEN

...
!------------------------------------------------------------------------
! Section xxx: Define the constant boundaries [kg kg-1]
!------------------------------------------------------------------------

ELSEIF (yaction == 'boundaries') THEN

  ! retrieve the boundaries of component X
  CALL trcr_get(izerr, 'X_COMPONENT', ptr_bd=xcomp_bd)
  IF (izerr/= 0) THEN
    ierror = izerr
    yerrmsg = trcr_errorstr(izerr)
    RETURN
  ENDIF

  ! set the constant boundaries of component X to 0.8 kg kg-1
  x_comp_bd(:,:,:,:) = 0.8_ireals

ENDIF


!------------------------------------------------------------------------
! End of module procedure organize_xxx
!------------------------------------------------------------------------

END SUBROUTINE organize_xxx
!******************************************************************************
```

Appendix B: Module using a tracer variable

```
!==============================================================
!+ Source module for the parameterization lambda
!------------------------------------------------------------------------------

MODULE src_lambda

!------------------------------------------------------------------------------
!
! Description:
!
! Current Code Owner:
!
! History:
!
! Code Description:
! Language: Fortran 90.
! Software Standards: "European Standards for Writing and
! Documenting Exchangeable Fortran 90 Code".
!==============================================================================
!
! Declarations:
!
! Modules used:
!
!
!------------------------------------------------------------------------------

USE ...

!------------------------------------------------------------------------------

USE src_tracers,      ONLY: trcr_get, trcr_errorstr, trcr_meta_get

!==============================================================================

IMPLICIT NONE

!==============================================================================
!
! Declarations
!
...
!
!==============================================================================

CONTAINS

!==============================================================================
!  Parameterization driver. Advances the process one time step ahead.
!------------------------------------------------------------------------------

SUBROUTINE lambda_driver

!------------------------------------------------------------------------------
!
! Description:
!
!
!
!==============================================================================
```

```
! Declarations

!  Local variables of type INTEGER

...

!  Local variables of type REAL

...

!  Tracer pointers
REAL (KIND=ireals), POINTER :: &
  xcomp  (:,:,:) => NULL() , &     ! component X at tlev=nx
  xtens  (:,:,:) => NULL()         ! tendency of component X

!  Metadata variables
REAL (KIND=ireals) :: molmass_x


CHARACTER(LEN=25) :: yzroutine = 'lambda_driver'

!==============================================================================
!  Start calculations
!------------------------------------------------------------------------------

IF(l2tls) THEN
  nx = nnew
ELSE
  nx = nnow
ENDIF

!------------------------------------------------------------------------------
! Retrieve pointer to required tracers
!------------------------------------------------------------------------------

CALL trcr_get(izerror, 'X_COMPONENT', ptr_tlev = nx, ptr = xcomp, ptr_tens=xtens)
IF (izerror /= 0) THEN
  yzerrmsg = trcr_errorstr(izerror)
  CALL model_abort(my_cart_id, izerror, yzerrmsg, yzroutine)
ENDIF

!------------------------------------------------------------------------------
!  Compute derived quantities using component X
!------------------------------------------------------------------------------

DO j = jstarts, jends
  DO i = istarts, iends
    lamba1(i,j) = xcomp(i,j,ke) * lambda2 + alpha
  ENDDO
ENDDO

...

!------------------------------------------------------------------------------
!  Use molar mass
!------------------------------------------------------------------------------

CALL trcr_meta_get(izerror, 'X_COMPONENT', 'MOL_MASS', molmass_x)
IF (izerror /= 0) THEN
  yzerrmsg = trcr_errorstr(izerror)
  CALL model_abort(my_cart_id, izerror, yzerrmsg, yzroutine)
ENDIF
```

```
DO j = jstarts, jends
  DO i = istarts, iends
    zeta(i,j,ke) = (xcomp(i,j,ke)/molmass_x)*rho(i,j,ke)
  ENDDO
ENDDO

...

!------------------------------------------------------------------------------
!  Update the tendency of component X
!------------------------------------------------------------------------------

DO k=1,ke
  DO j = jstarts, jends  ! DO loops over COSMO horizontal grid points
    DO i = istarts, iends
      xtens(i,j,k) = xtens(i,j,k) + (lambda3(i,j,k)-lambda1(i,j))*  &
                     (hhl(i,j,k)-hsurf(i,j))*beta^2
    END DO
  END DO
END DO

...
!------------------------------------------------------------------------------
!  Update component X
!------------------------------------------------------------------------------

xcomp(:,:,:) = xcomp(:,:,:) + xtens(:,:,:) * dt

!------------------------------------------------------------------------------
!  End calculations
!==============================================================================

END SUBROUTINE lambda_driver

!==============================================================================

END MODULE src_lambda
********************************************************************************
```

List of COSMO Newsletters and Technical Reports

(available for download from the COSMO Website: www.cosmo-model.org)

COSMO Newsletters

No. 1: February 2001.

No. 2: February 2002.

No. 3: February 2003.

No. 4: February 2004.

No. 5: April 2005.

No. 6: July 2006.

No. 7: April 2008; Proceedings from the 8th COSMO General Meeting in Bucharest, 2006.

No. 8: September 2008; Proceedings from the 9th COSMO General Meeting in Athens, 2007.

No. 9: December 2008.

No. 10: March 2010.

No. 11: April 2011.

No. 12: April 2012.

COSMO Technical Reports

No. 1: Dmitrii Mironov and Matthias Raschendorfer (2001):
Evaluation of Empirical Parameters of the New LM Surface-Layer Parameterization Scheme. Results from Numerical Experiments Including the Soil Moisture Analysis.

No. 2: Reinhold Schrodin and Erdmann Heise (2001):
The Multi-Layer Version of the DWD Soil Model TERRA_LM.

No. 3: Günther Doms (2001):
A Scheme for Monotonic Numerical Diffusion in the LM.

No. 4: Hans-Joachim Herzog, Ursula Schubert, Gerd Vogel, Adelheid Fiedler and Roswitha Kirchner (2002):
LLM ¯ the High-Resolving Nonhydrostatic Simulation Model in the DWD-Project LITFASS.
Part I: Modelling Technique and Simulation Method.

No. 5: Jean-Marie Bettems (2002):
EUCOS Impact Study Using the Limited-Area Non-Hydrostatic NWP Model in Operational Use at MeteoSwiss.

No. 6: Heinz-Werner Bitzer and Jürgen Steppeler (2004):
Documentation of the Z-Coordinate Dynamical Core of LM.

No. 7: Hans-Joachim Herzog, Almut Gassmann (2005):
Lorenz- and Charney-Phillips vertical grid experimentation using a compressible nonhydrostatic toy-model relevant to the fast-mode part of the 'Lokal-Modell'.

No. 8: Chiara Marsigli, Andrea Montani, Tiziana Paccagnella, Davide Sacchetti, André Walser, Marco Arpagaus, Thomas Schumann (2005):
Evaluation of the Performance of the COSMO-LEPS System.

No. 9: Erdmann Heise, Bodo Ritter, Reinhold Schrodin (2006):
Operational Implementation of the Multilayer Soil Model.

No. 10: M.D. Tsyrulnikov (2007):
Is the particle filtering approach appropriate for meso-scale data assimilation ?

No. 11: Dmitrii V. Mironov (2008):
Parameterization of Lakes in Numerical Weather Prediction. Description of a Lake Model.

No. 12: Adriano Raspanti (2009):
COSMO Priority Project "VERification System Unified Survey" (VERSUS): Final Report.

No. 13: Chiara Marsigli (2009):
COSMO Priority Project "Short Range Ensemble Prediction System" (SREPS): Final Report.

No. 14: Michael Baldauf (2009):
COSMO Priority Project "Further Developments of the Runge-Kutta Time Integration Scheme" (RK): Final Report.

No. 15: Silke Dierer (2009):
COSMO Priority Project "Tackle deficiencies in quantitative precipitation forecast" (QPF): Final Report.

No. 16: Pierre Eckert (2009):
COSMO Priority Project "INTERP": Final Report.

No. 17: D. Leuenberger, M. Stoll and A. Roches (2010):
Description of some convective indices implemented in the COSMO model.

No. 18: Daniel Leuenberger (2010):
Statistical analysis of high-resolution COSMO Ensemble forecasts in view of Data Assimilation.

No. 19: A. Montani, D. Cesari, C. Marsigli, T. Paccagnella (2010):
Seven years of activity in the field of mesoscale ensemble forecasting by the COSMO–LEPS system: main achievements and open challenges.

No. 20: A. Roches, O. Fuhrer (2012):
Tracer module in the COSMO model.

COSMO Technical Reports

Issues of the COSMO Technical Reports series are published by the *COnsortium for Small-scale MOdelling* at non-regular intervals. COSMO is a European group for numerical weather prediction with participating meteorological services from Germany (DWD, AWGeophys), Greece (HNMS), Italy (USAM, ARPA-SIMC, ARPA Piemonte), Switzerland (MeteoSwiss), Poland (IMGW), Romania (NMA) and Russia (RHM). The general goal is to develop, improve and maintain a non-hydrostatic limited area modelling system to be used for both operational and research applications by the members of COSMO. This system is initially based on the COSMO-Model (previously known as LM) of DWD with its corresponding data assimilation system.

The Technical Reports are intended

- for scientific contributions and a documentation of research activities,
- to present and discuss results obtained from the model system,
- to present and discuss verification results and interpretation methods,
- for a documentation of technical changes to the model system,
- to give an overview of new components of the model system.

The purpose of these reports is to communicate results, changes and progress related to the LM model system relatively fast within the COSMO consortium, and also to inform other NWP groups on our current research activities. In this way the discussion on a specific topic can be stimulated at an early stage. In order to publish a report very soon after the completion of the manuscript, we have decided to omit a thorough reviewing procedure and only a rough check is done by the editors and a third reviewer. We apologize for typographical and other errors or inconsistencies which may still be present.

At present, the Technical Reports are available for download from the COSMO web site (www.cosmo-model.org). If required, the member meteorological centres can produce hard-copies by their own for distribution within their service. All members of the consortium will be informed about new issues by email.

For any comments and questions, please contact the editor:

Massimo Milelli
Massimo.Milelli@arpa.piemonte.it

Consortium for Small-Scale Modelling

Technical Report No. 33

V.A.S.T.
(Versus Additional Statistical Techniques)
User Manual (v2.0)

September 2017

DOI: 10.5676/DWD_pub/nwv/cosmo-tr_33

Deutscher Wetterdienst
MeteoSwiss
Ufficio Generale Spazio Aereo e Meteorologia
ΕΘΝΙΚΗ ΜΕΤΕΩΡΟΛΟΓΙΚΗ ΥΠΗΡΕΣΙΑ
Instytucie Meteorogii i Gospodarki Wodnej
Administratia Nationala de Meteorologie
ROSHYDROMET
Agenzia Regionale Protezione Ambiente Piemonte
Agenzia Regionale Prevenzione Ambiente Energia Emilia Romagna
Centro Italiano Ricerche Aerospaziali
Amt für GeoInformationswesen der Bundeswehr
Israel Meteorological Service

www.cosmo-model.org

Editor: Massimo Milelli, ARPA Piemonte

V.A.S.T.

(Versus Additional Statistical Techniques)

User Manual (v2.0)

N. Vela [*]

[*] ARPA Piemonte, University of Turin

Contents

Contents

1 Introduction **4**

1.1 Fuzzy verification 4

2 Software description **4**

2.1 Components 4

2.2 Directories' structure 5

3 Installation and compilation **6**

3.1 NOTE FOR PEOPLE WHO HAVE ALREADY INSTALLED PREVIOUS VERSIONS OF VAST 7

3.2 NOTE for users working on a VERSUS machine 7

4 Activities performed by the software **7**

4.1 For LIBSIM users 7

4.1.1 The input files 8

4.1.2 The configuration files 9

4.1.3 input_libsim.conf 9

4.2 For all users 12

4.2.1 The input files 12

4.2.2 The configuration files 13

4.2.3 Performance of the verification 20

5 Use, recap for LIBSIM users **20**

5.1 Use, recap for non LIBSIM users only 21

5.2 Use, recap for both users 21

5.3 Perform the verification 22

6 Verification methods **23**

6.1 Upscaling (UP) 23

6.2 Anywhere in window (YN) 23

6.3 Minimum coverage (MC) 24

6.4 Fuzzy logic (FZ) 24

6.5 Joint probability (JP) 24

6.6 Multi-event contingency table (ME) 25
6.7 Brier Skill Score (Method=PG, Score=BSS) 25
6.8 Fractions Brier Skill Score (Method=FB, Score=FSS) 25
6.9 ETS ratio (Method=Practically Perfect Hindcast, Score=ETSr) 26
6.10 Area related root mean square error (Method= RM, Score=RMSE) 26

7 Output **26**
7.1 Methods that belong to type 1 26
7.2 Methods that belong to type 2 29
7.3 Methods that belong to type 3 29

8 Conclusions **30**

9 Acknowledgments **30**

10 References **30**

1 Introduction

This document explains how to use the VAST software provided by Naima Vela (Arpa Piemonte/University of Turin) developed according to VERSUS2 priority project, task 4: "Introduction of additional statistical techniques in VERSUS".
The software can perform the following tasks:

- Open and read txt files of forecast and observation produced by any external software following an example scheme
- Produce spatial verification of the precipitation field (main goal), wind speed and total cloud cover.
- If the user has the possibility to use the LIBSIM[1] software, VAST can produce its own input files starting from GRIB (observation and forecast) of BUFR (observation)

1.1 Fuzzy verification

Fuzzy verification answers the question:"Which is the link between spatial forecast and a combination of the intensity of the precipitation (or wind speed or total cloud cover) and the scale of the event?"

The scale decomposition methods allow us to diagnose the model errors and performances according to different scales. The scale-intensity approach links the traditional bi-dimensional verification categories: it returns the model skills according to different precipitation intensities (or wind speed or total cloud cover) and spatial scales. It verifies the model over the whole domain. It is useful in the spatial verification of discontinuous fields. It supplies information for both single case studies and forecast systems evaluated over a longer time. Using a neighbourhood verification method an exact correspondence between forecast and observation is not needed.

It is important to understand that this type of verification, for what concerns precipitation, gives better information when performed for case studies on limited areas, so that the patterns can be compared without being overhung by long time or large areas of no rain condition.

2 Software description

The architecture of the VAST software has been produced after a deep study of the IDL code of the Ebert software for fuzzy verification.

2.1 Components

The VAST software is composed by the following files:

- `install.sh`: Shell script that creates the directory tree and places the other scripts in the correct directory

[1]The "`extra software`" for VERSUS users

- `use_libsim.sh`[2]: Shell script that allows LIBSIM users to produce the VAST input files (txt) starting from GRIB and BUFR
- `vast.sh`[3]: Shell script containing all the instructions to execute the different parts of the procedure
- `input_libsim.conf`: Configuration file used by the shell script `use_libsim.sh` to set all the variables that point to directories and name of the files
- `directories.conf`: Configuration file used by the shell script `vast.sh` to set all the variables that point to directories and name of the files
- `input_csv2txt.nml`: Namelist read by `csv2txt.f90` Fortran code containing all the instructions regarding the directories, the name of the files, the internal variables and the parameters
- `input_fuzzy.nml`: namelist read by `read_txt.f90` and `fuzzy_verify.f90` Fortran codes containing all the instructions regarding the directories, the name of the files, the internal variables and the parameters
- `csv2txt.f90`: Fortran code that reads the output files from LIBSIM and transform them into txt files read by VAST
- `read_txt.f90`: Fortran code able to process the input TXT files (observation and forecast) and produce the input for the second and main Fortran code
- `fuzzy_verify.f90`: Fortran code that uses the outputs of the first one to perform the verification.

2.2 Directories' structure

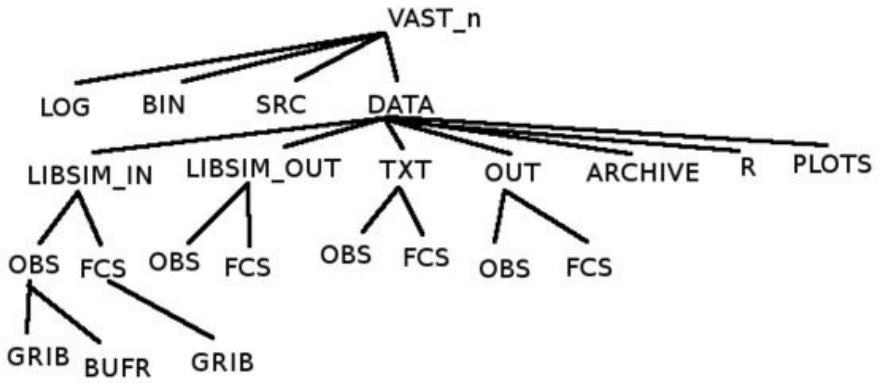


Figure 1: Default structure of the directories of the VAST software

[2]The file will contain numbers to identify the version of VAST to whom it belongs. i.e. `use_libsim_2_0.sh` will be referred to the VAST version 2.0

[3]The file will contain numbers to identify the version of VAST to whom it belongs. i.e. `vast_2_0.sh` will be referred to the VAST version 2.0

In Figure 1 it is possible to see the default structure of the directories in the software. If the presented structure conflicts with the users needs (particular displacement of the storage, or similar problems), it will be necessary to modify the configuration files accordingly.This has been made particularly hard by the requirement of having a common path that leads to the subdirectories (reducing the degrees of freedom of the structure of the software). In particular the user should not modify the relative path that links the `VAST/src` and `VAST/bin` directories.
The shell scripts "`use_libsim.sh`" and "`vast.sh`" will be automatically inserted in the directory "`bin`". The configuration files, the namelists and the Fortran codes will be automatically inserted in the directory "`src`".
If these files need to be displaced differently, the user will have to modify the scripts accordingly.
An archive file containing all the contingency tables calculated by the main Fortran code (`fuzzy_verify.f90`) during the verification will be created every time a verification is performed. It can be found in the directory `VAST/data/ARCHIVE` and it can be recognized by the date and time of the launch of the verification (`vast.sh`).

3 Installation and compilation

The user needs to install the Fortran compiler `gfortran` to use the Fortran codes contained in the package.
The user needs to install `R Project for Statistical Computing` to produce the plots of the needed indexes. In particular, the following libraries (and all their dependencies) need to be installed:

- `fields`
- `gplots`

To install the R packages, the user needs to log in as root, download the packages in the extension `package.tar.gz` and type the following command line:

- `R CMD INSTALL package.tar.gz`

The user needs then to unpack and copy the folder `vast_install` into the desired location by using the command line:

- `tar -xzf vast_install.tar.gz`

The user then needs to move into the `vast_install` directory to change the permissions for the shell script `install.sh` by giving the following command:

- `chmod 777 install.sh`

(The numbers could be different if the user wants to keep a particular category from executing the script)
Then the user needs to run the executable by giving the following command:

- `./install.sh`

The script will create all the directories needed by the software and will copy the scripts in the correct place. If the user needs a different structure for the directories, than it will be necessary to manually modify them and the codes.

Once the directories have been created, the user needs to place the input files in the correct place. If the user is using LIBSIM to pre-process the input files, than they will be put in the `obs` (`GRIB` or `BUFR`) and `fcs/GRIB` folders contained in the directory `VAST/data/LIBSIM_in`. If the user has a different software to produce the input files for VAST, than the preprocessed files must be inserted in the `obs` and `fcs` folders contained in the directory `VAST/data/TXT`.

All the shell scripts (`use_libsim.sh` if needed and `vast.sh`) have to be converted into executable files to be correctly used to produce the verification. To do so the user needs to move to the directory containing the executable files (`bin`) and use the following instruction from command line:

- `chmod 777` *`your_script.sh`*

(The numbers could be different if the user wants to keep a particular category from executing the script)
The compilation of the Fortran codes is automatically performed while launching the executables (`vast.sh` and `use_libsim.sh`).

3.1 NOTE FOR PEOPLE WHO HAVE ALREADY INSTALLED PREVIOUS VERSIONS OF VAST

If the user doesn't want to delete and recreate the directory's structure of VAST, he/she will have to delete all the files contained in the folders `VAST/bin` and `VAST/src` and substitute them with the files contained in the folder `vast_install_2_0` (with the exception of `install.sh`).

3.2 NOTE for users working on a VERSUS machine

If the user is running VAST on a VERSUS machine, it is possible to find all the needed extra packages for R in the directory `vast_install/documentation/R_packages_versus`
It is mandatory to use the given packages to be installed on the VERSUS version of the R software. Nothing changes for the installation instruction.

4 Activities performed by the software

4.1 For LIBSIM users

The LIBSIM users have the possibility to perform their verification starting from standard input files (GRIB or BUFR for the observation, GRIB for the forecast).

4.1.1 The input files

Input observation files: The observation files must be BUFR or GRIB. For a better behaviour of the software (faster and less memory demanding), it would be better to use files (BUFR or GRIB) that only contain the total precipitation variable. The files must be placed in the folder `VAST/data/LIBSIM_in/obs/BUFR` or `GRIB`. Since the files will be collected together by the command "`cat`", it is important that the GRIB files have a `.grb` extension, the BUFR files must have a `.bfr` extension.
Example files can be found in the folder `vast_install/documentation/data/LIBSIM_in/obs`.

Input forecast files: The forecast files must be GRIB. For a better behaviour of the software (faster and less memory demanding), it would be better to use files that only contain the total precipitation variable. The files must be placed in the folder `VAST/data/LIBSIM_in/fcs/GRIB`. Since the files will be collected together by the command "`cat`", it is important that they have a `.grb` extension.
Example files can be found in the folder `vast_install/documentation/data/LIBSIM_in/fcs`.

The characteristics of the input files can be deduced by analysing the example GRIB and BUFR given as examples with the package. Such details can be investigated by using the following commands:

- For GRIB:
  - `wgrib -V filename.grb`
- or
  - `grib_dump filename.grb`
- For BUFR:
  - the user can upload an example file to the url `http://apps.ecmwf.int/codes/bufr/validator/`

In Figure 2 it is possible to read the output of `wgrib -V` *`your_file.grb`* command for an observation GRIB.

```
rec 1:0:date 2014101321 APCP kpds5=61 kpds6=1 kpds7=0 levels=(0,0) grid=255 sfc nudge ana 0hr: bitmap: 23606 undef
  APCP=Total precipitation [kg/m^2]
  timerange 13 P1 0 P2 1 TimeU 1  nx 526 ny 518 GDS grid 0 num_in_ave 0 missing 0
  center 200 subcenter 255 process 1 Table 2 scan: WE:SN winds(grid)
  latlon: lat  42.950000 to 46.667000 by 0.007000  nxny 272468
          long 6.008000 to 11.310000 by 0.010000, (526 x 518) scan 64 mode 136 bdsgrid 1
  min/max data -2.96906e-06 11.4665  num bits 16  BDS_Ref -2.96906e-06  DecScale 0 BinScale -12
```

Figure 2: Output of `wgrib -V filename.grib` for observation

The most important parameter is the `timeRangeIndicator` which must be set to **13**

In Figure 3 it is possible to read the output of `wgrib` command for a forecast GRIB.

```
rec 1:0:date 2014101400 APCP kpds5=61 kpds6=1 kpds7=0 levels=(0,0) grid=255 sfc 0-10hr acc:
  APCP=Total precipitation [kg/m^2]
  timerange 4 P1 0 P2 10 TimeU 1  nx 447 ny 532 GDS grid 10 num_in_ave 0 missing 0
  center 200 subcenter 255 process 58 Table 2 scan: WE:SN winds(N/S)
  rotated LatLon grid  lat -21.925000 to -8.650000  lon -3.500000 to 7.650000
    nxny 237804  (447 x 532)  dx 25 dy 25  scan 64  mode 128
    transform: south pole lat -32.500000 lon 10.000000  rot angle 0.000000
  min/max data 0 78.7188  num bits 16  BDS_Ref 0  DecScale 0 BinScale -9
```

Figure 3: Output of `wgrib -V filename.grib` for forecast

Regular output files coming from COSMO models fit to this standard.

Thanks to the LIBSIM capabilities, the software works both with GRIB1 and GRIB2 files.

It is important that the **BUFR** files contain **only the hourly cumulate of the precipitation, without any duplicate**.

4.1.2 The configuration files

The elaboration of the input files for LIBSIM is performed thanks to two files: `use_libsim.sh` (the executable) and `input_libsim.conf` (its configuration file).

4.1.3 input_libsim.conf

The first part of the configuration file (Figure 4) contains the list of the directories that must be set for the correct functioning of the software:

```
#DIRECTORIES
#If any change has been made to the structure of VAST, than modify with the actual path
#
#COMMON PATH (up to the directory containing VAST)
common_path='/versus/'
#
#INPUT FILES
#Observation:
#IMPORTANT: comment the path not needed
#If GRIB files (comment if not):
dir_in_obs='VAST/data/LIBSIM_in/obs/GRIB/'
#If BUFR files (comment if not):
#dir_in_obs='VAST/data/LIBSIM_in/obs/BUFR/'
#Forecast
dir_in_fcs='VAST/data/LIBSIM_in/fcs/GRIB/'
#OUTPUT FILES
#Observation
dir_out_obs='VAST/data/LIBSIM_out/obs/'
#Forecast
dir_out_fcs='VAST/data/LIBSIM_out/fcs/'
#Fortran code
dir_src='VAST/src/'
#Executable
dir_bin='VAST/bin/'
#Log
dir_log='VAST/log/'
#
#
#OBSERVATION FORMAT: 'grib' or 'bufr'
#
format='grib'
```

Figure 4: Directories to be set to make the `use_libsim.sh` script work

It is important to notice that the user needs to set the type of input for the observation in two different ways (both need to be done):

- by uncomment the corresponding input path (and commenting the other)
- by setting the variable `format` to grib or bufr

The "`common_path`" variable consists in the absolute path where the `VAST` directory has been located in your machine, and it will be used to complete all the other relative paths (that **should not be modified**).

The second part of the configuration file (Figure 5) is dedicated to the specification of the name of the verification (that will be used to chose the correct output files in the second part of the verification), to specify the run of the model to be verified, to (optionally) select the input files by the leading part of their name (up to 10 carachters) and to select the cumulation period for the verification. The user must be aware of the value of the cumulation time of the input files and set the variable `cum` accordingly (the value must be equal or multiple of the input cumulation time).
Example: If the user have hourly cumulation for the observed precipitation and wants to re-cumulate it on the intervals 0-6, 6-12, 12-18, 18-24 (`cum='00 06'`), the first GRIB must contain the cumulated rain for the hour **one** (which means from 0 to 1).
If the input files are BUFR files, they must contain all the hourly cumulate of the precipitation OR the precipitation already cumulated on the desired period and no other cumulation periods.

```
#NAME OF THE VERIFICATION (string with no gaps)
name='201606_decade1_7km_12h'
#
#RUN (for forecast only, use string like '00', '06', '12', etc)
use_run='00'
#
#
#Identification of the files ('y'/'n')
#If 'y' then add string
add_id='y'
id_file='LAMIN0063'
#
#
#CUMULATION TIME
#The cumulation time must be equal
#or bigger (ONLY for precipitation) than the one
#of the input data
#The cumulation time must be given as follows.
#Ex: '00 03' means three hours cumulation
cum='00 12'
```

Figure 5: Name and cumulate parameters needed by LIBSIM

The third part of the configuration file (Figure 6) is dedicated to the configuration of the grid on which the verification will be performed. It is necessary for the grid to have lower resolution and a smaller area if compared to the forecast input, so that no missing point appear in the final result. The user will be able to check if the forecast grid contains any "holes" by plotting and visualising the CSV (directory `VAST/data/LIBSIM_out`) resulting files (an easy and free way to do that is to use the QGIS software. The user needs to see a perfect LON/LAT regular grid).

```
#GRID PARAMETERS
#The grid borders must be strictly smaller than the original area.
#The grid step must be strictly bigger than the original grid step.
#If the obs and fcs output files don't have the same grid
#it can mean that the selected area is too close to the original one
#(obs or fcs) or that the grid step is too close to the original one
#(obs or fcs) and holes have been left in the new grid.
#If the problem is the area, the user needs to reduce it.
#If the problem is the grid step, the user needs to enlarge it.
#So try with different parameters untill at least the forecast grid
#is regular and contains no holes
#Grid limits
x_min='6.315'
x_max='9.987'
y_min='43.1'
y_max='46.585'
#Number of grid points in each direction (x=lon, y=lat)
nx='39'
ny='40'
```

Figure 6: Grid parameters needed by LIBSIM

The data can include more than one day of precipitation but the grib messages must NOT overlap (i.e. day 01/01/2016 from hour 01 to hour 24 and then day 02/01/2016 from hour 01. **NOT** day 01/01/2016 from hour 01 to hour 72 and then day 02/01/2016 from hour 01.). The author suggests to use the software to verify single case studies (few days) over limited areas (i.e. the Piedmont region), since this kind of verification performs best when precipitation patterns are present and occupy the most part of the verified area. It is important that in the forecast files every date and time appear only once. If more files contain the same date and time (i.e. overlapping forecast runs) the resulting CSV will be overwritten.
The last part of the configuration file (Figure 7) contains the names of the files involved in the preprocessing of the files. The names of the files should be left as default.

```
#
#FORTRAN PROGRAM (should be left as default)
csv2txt_f90='csv2txt.f90'
#EXECUTABLE
csv2txt_exe='csv2txt'
csv2txt_log='csv2txt.log'
csv2txt_stderr='csv2txt_stderr.log'
#
#LISTS (should be left as default)
list_obs='list_obs.dat'
list_fcs='list_fcs.dat'
#
#NAMELIST (should be left as default)
namelist='input_csv2txt.nml'
```

Figure 7: Names of the files used by the preprocessing part of the software with LIBSIM

When all the variables have been set, the script `use_libsim.sh` will perform the following tasks:

- Collect all the input forecast files with the "`.grb`" extention AND the given specifications (run and, if chosen, name of the file) into a single grib called `forecast.grib`
  - it is VERY IMPORTANT that none of the forecast input files are called "`forecast.grib`". If that happens the procedure will cause a conflict and abort the execution
- Use the LIBSIM functionality "`vg6d_transform`" to re-grid the input files
- Count the number of the input messages

- Produce CSV files and place them in the correct directory
- Create a copy of a re-gridded forecast message to use it as a template to re-grid the observation
- Proceed to repeat the same operation for the observation files (with the extention ".grb" or "`.bfr`")
  - in case of grib files, the produced total input file is called "`observation.grib`"
  - in case of bufr files, the produced total input file is called "`observation.bufr`"
  - it is VERY IMPORTANT that none of the observation input files have one of these names. If that happens the procedure will cause a conflict and abort the execution

When all the CSV files are ready and displaced in the correct directory, the script creates lists of these files, and proceeds to compile and run the Fortran code (default is `csv2txt.f90`) that transforms the output of LIBSIM (`.csv`) into the input for VAST (`.txt`). So, to execute this code, the user must **first** complete the namelist file called `input_csv2txt.nml`. The user needs to substitute the example paths with the actual path of the half processed files(this needs to be done before launching the `use_libsim.sh` executable). The patterns to be completed are shown in Figure 8

```
&directories
!Fill in with the actual path (up to the directory containing VAST)
common_path='/versus/'
!Directories of input and output for csv2txt.f90
!(to be modified only if the user made modifications to the structure of VAST)
dirin_obs='VAST/data/LIBSIM_out/obs/'
dirin_fcs='VAST/data/LIBSIM_out/fcs/'
dirout_obs='VAST/data/TXT/obs/'
dirout_fcs='VAST/data/TXT/fcs/'
dir_log='VAST/log/'
&end

&filenames
!Lists of csv files (should be left as default)
filelist_obs='list_obs.dat'
filelist_fcs='list_fcs.dat'
!Name of the verification with no gaps
ver_name='201606_decade1_7km_12h'
&end
```

Figure 8: Configuration file for the Fortran code `csv2txt.f90`

This ends the first part of the procedure, executed through the file `use_libsim.sh`, dedicated to the LIBSIM users only.

4.2 For all users

4.2.1 The input files

The VAST input files must be `txt` files. Their internal structure is very strict but simple to reproduce, as shown in Figure 7

Longitude	Latitude	Value
6.315	43.010	-999.000
6.352	43.010	-999.000
6.389	43.010	-999.000
6.426	43.010	-999.000
6.463	43.010	-999.000
6.500	43.010	-999.000
6.538	43.010	-999.000
6.575	43.010	-999.000
6.612	43.010	0.000
6.649	43.010	0.000
6.686	43.010	0.000
6.723	43.010	0.000
6.760	43.010	0.000
6.797	43.010	0.000
6.834	43.010	0.000
6.871	43.010	0.000
6.908	43.010	0.000
6.946	43.010	0.000
6.983	43.010	0.000
7.020	43.010	0.000
7.057	43.010	0.000
7.094	43.010	0.471
7.131	43.010	1.525
7.168	43.010	1.434
7.205	43.010	0.805

Figure 9: Structure of the `txt` input file (observation or forecast)

The file is composed by:

- One header line containing the **exact** string: " `Longitude Latitude Value`"
- One column containing the longitude values
- One column containing the latitude values
- One column containing the precipitation, wind speed or total cloud cover values (-999 if no data)

The order of the coordinates is important. The first couple of coordinates must be the lower left corner and the longitude is the parameter that increases first. The coordinate values must be the same for the forecast and the observation files. In case of missing data, the "value" column must contain the number -999.
Also the name of the files is important and must follow the scheme:

- `obs_YYYYMMDDHHmm_`*`NameOfTheVerification`*`.txt`
- `fcs_YYYYMMDDHHmm_`*`NameOfTheVerification`*`.txt`

where YYYY is the year, MM is the month, DD is the day, HH is the hour and mm is the minute. The "*NameOfTheVerification*" must be assigned to the variable `ver_name` in the file `input_fuzzy.nml`
From version *2.0* it is possible to verify three different variables with VAST (NOT starting from LIBSIM): precipitation (mm), total cloud cover (%), wind speed (m/s). Once the input files have been loaded the user should modify the "`input_fuzzy.nml`" configuration file.

4.2.2 The configuration files

Once the input files are placed in the correct directory (`VAST/date/TXT/obs` or `fcs`), all the activities will be driven by the executable file `vast.sh`. So, the software needs to read

in the configuration files all the specifications related to this part of the execution. The two configuration files governing this part of the software are `directories.conf` (read by `vast.sh`) and `input_fuzzy.nml` (read by `read_txt` and `fuzzy_verify`). Figure 10 and Figure 11 show the information required by the configuration file `directories.conf`

```
#DIRECTORIES
#
#COMMON PATH (up to the directory containing VAST)
common_path='/versus/'
#
#If any change has been made to the structure of VAST, than modify with the actual path
#
#INPUT TXT files
dirin_obs='VAST/data/TXT/obs/'
dirin_fcs='/VAST/data/TXT/fcs/'
#Files processed by read_txt.f90 and ready to be used by fuzzy_verify.f90
dirout_obs='VAST/data/OUT/obs/'
dirout_fcs='VAST/data/OUT/fcs/'
#Backup of input and output
dirin_obs_backup='VAST/data/TXT/obs/backup/'
dirin_fcs_backup='VAST/data/TXT/fcs/backup/'
dirout_obs_backup='VAST/data/OUT/obs/backup/'
dirout_fcs_backup='VAST/data/OUT/fcs/backup/'
#R scripts (output of fuzzy_verify.f90)
dirout_r='VAST/data/R/'
#Backup of R scripts
dirout_r_backup='VAST/data/R/backup/'
#Plots
dirout_plots='VAST/data/PLOTS/'
#Fortran codes
dir_src='VAST/src/'
#Executables
dir_bin='VAST/bin/'
#Log files
dir_log='VAST/log/'
#
```

Figure 10: Directories to be configured for the execution of `vast.sh`

```
#NAME OF THE VERIFICATION (string with no gaps)
name="201606_decade1_7km_12h"
#
#FILE NAMES (If the user doesn't have a particular reason for changing these names,
#they should be left in the default version)
#Fortran files
read_txt_f90='read_txt.f90'
fuzzy_f90='fuzzy_verify.f90'
#Executables
read_txt_exe='read_txt'
fuzzy_exe='fuzzy_verify'
#Configuration files
namelist='input_fuzzy.nml'
#Lists
input_obs_list='list_obs.dat'
input_fcs_list='list_fcs.dat'
output_obs_list='list_obs.txt'
output_fcs_list='list_fcs.txt'
r_list='list.r'
#Logs
txt_log='txt.log'
fuzzy_log='fuzzy.log'
txt_stderr='txt_stderr.log'
fuzzy_stderr='fuzzy_stderr.log'
out_txt_log='out_txt.log'
```

Figure 11: File names to be configured for the execution of `vast.sh` (should be left as default with the exception of "`name`")

It is very important for the user to set the variable "`name`" according to the naming of the input files, so that the `vast.sh` executable can chose the correct data to be verified.

Figure 12 and Figure 13 show the information contained in the file `input_fuzzy.nml` and needed by the executable `read_txt`.

```
&common_dir
!Fill in with the actual path (up to the directory containing VAST)
common_path='/versus/'
&end

&directories_txt
!Directories of input and output for txt files
dirin_obs='VAST/data/TXT/obs/'
dirin_fcs='VAST/data/TXT/fcs/'
dirout_obs='VAST/data/OUT/obs/'
dirout_fcs='VAST/data/OUT/fcs/'
dir_log='VAST/log/'
&end
```

Figure 12: Common path and directories to be configured for the execution of `read_txt`. Directories should be left as default.

```
!Names of the list of output of read_txt.f90
!(should be left as default)
&filenames_txt
filelist_obs='list_obs.dat'
filelist_fcs='list_fcs.dat'
&end
```

Figure 13: File names to be configured for the execution of `read_txt` (should be left as default)

Figure 14 and Figure 15 show the information contained in the file `input_fuzzy.nml` and needed by the executable `fuzzy_verify`. The `filenames` group in the `input_fuzzy.nml` namelist also contains information about the model, the grid and the period of the verification. All these last specifications are read as character strings. Since the period, grid and model variables are used to produce the name of the output files, **they must contain no blanks**.

```
&directories_fuzzy
!Directory observation
dirin_obs='VAST/data/OUT/obs/',
!Directory forecast
dirin_fcs='VAST/data/OUT/fcs/',
!Directory output R )
dir_out='VAST/data/R/',
!Directory output plots
dir_plot='VAST/data/PLOTS/',
!Directory log
dir_log='VAST/log/',
!Directory archive
dir_arch='VAST/data/ARCHIVE/'
&end
```

Figure 14: Directories to be configured for the execution of `fuzzy_verify` (should be left as default).

```
&filenames
!List obs (should be left as default)
list_obs='list_obs.txt',
!List fcs (should be left as default)
list_fcs='list_fcs.txt',
!Model
model='COSMO-I7',
!Grid
grid='COSMO-I7'
!Period
period='201606_1-10'
!File list R (should be left as default)
file_list='list.r'
&end
```

Figure 15: File names to be configured for the execution of `fuzzy_verify` (should be left as default).

In Figure 16 the variables relative to the spatial boxes and the thresholds are shown. The user can choose up to ten different thresholds on which the verification will be performed (the thresholds can be different from those shown in the example). If the user needs less thresholds, the value of the unused thresholds must be -999 (like thresh(10) in Figure 16). All the used thresholds must come before the unused ones (i.e. thresh(1)=0.2, thresh(2)=0.5, thresh(3)=1, thresh(4)=2, thresh(5)=5, thresh(6)=10, thresh(7)=-999, thresh(8)=-999, thresh(9)=-999,thresh(10)=-999. **NOT** thresh(1)=0.2, thresh(2)=-999, thresh(3)=1, thresh(4)=2, thresh(5)=-999, thresh(6)=10, thresh(7)=-999, thresh(8)=20 ,thresh(9)=-999, thresh(10)=-999.)
The user has to indicate the resolution of the grid (in Km) by modifying the variable "grid_step". This will be used to produce the plots (this will be not used if the user choses the "grid points" for the space scale in the plots).
From version *2.0* it is possible to verify 3D boxes of observation and forecast by introducing the **time** dimension. The user should set the variable `n_dimension=1` if a standard 2D verification is required (or whenever there are missing timesteps in observation and/or forecast). The user should use a variable greater than 1 to elaborate 3D boxes.
Example1: n_timesteps=3 $\Longrightarrow$ previous, current, following timestep will be used for the verification
Example2: n_timesteps=5 $\Longrightarrow$ previous two, current, following two timesteps.
Another new feature of version *2.0* is the possibility to verify three differnt variables with VAST (NOT using LIBSIM): the variable is chosen by assigning the value '`pre`' (precipitation, mm), '`tcc` (total cloud cover, %)' or '`win`' (wind speed, m/s) to the `variable` line.

```
&dimensions
!Number of windows (1,3,5,9,17,33,65,...,(2^n)+1)
n_windows=5,
!NEW! Number of different timesteps for 3D box
!Example: n_timesteps=3 => previous one, current, following one
!Example: n_timesteps=5 => previous two, current, following two
!ATTENTION: the higher the number, the slower the process
n_timesteps=3,
!Grid resolution (km) used in plot definition
grid_step=8
!Number of valid thresholds
n_thresh=10,
!Thresholds (array of size 10. Fill with -999 if needed)
thresh(1)=0.2,
thresh(2)=0.5,
thresh(3)=1.0,
thresh(4)=1.5,
thresh(5)=2.5,
thresh(6)=5.0,
thresh(7)=7.5,
thresh(8)=10.0,
thresh(9)=15.0,
thresh(10)=20.0,
!Indicate the variable the user wants to verify:
!'pre' for precipitation (mm)
!'tcc' for total cloud cover (%)
!'win' for wind (m/s)
variable='pre'
&end
```

Figure 16: Spatial box and thresholds to be configured for the execution of `fuzzy_verify`

Figure 17 shows all the details needed by the code regarding the actual verification: methods and scores.
For type one, the methods can be different or the same one repeated (up to six times). A score must be associated to each method (ie: `method1(1)='UP'`, `score1(1)='BIAS'`; `method1(2)='MC'`,`score1(2)='FAR'`. This means that the `BIAS` will be calculated using the `Upscaling` method, while the `FAR` will be calculated using the `Minimum Coverage` method). For type two instead, the score and the method are striclty associated (ie: if `method2(1)='FB'`, then `score2(1)='FSS'`; if `method2(2)='PG'`, then `score2(2)='BSS'`; if `method2(3)='PP'`, then `score2(3)='ETSr'`). Type three only contains one score. The number of the used methods for each type must be indicated through the variables `nm1`, `nm2` and `nm3`. The unused methods and scores must be commented (the indication of the methods and scores must follow the same principle of the threshold indication: unused methods and scores must be placed at the end of the array).

```
&methods_scores
!Number of methods of type 1 (max 6)
nm1=5,
!Methods
!Choose between: UP, MC, YN, FZ, JP, ME
method1(1)='UP',
method1(2)='MC',
method1(3)='YN',
method1(4)='FZ',
method1(5)='ME',
!Scores
!Chose between: BIAS, POD, FAR, ETS (if method=UP),
!               POD, FAR, ETS (if method=MC, YN, FZ, JP)
!               HK (if method=ME)
score1(1)='BIAS',
score1(2)='POD',
score1(3)='FAR',
score1(4)='ETS',
score1(5)='HK ',
!Number of methods of type 2 (max 3)
nm2=3,
!Methods
!These methods are strictly coupled with the scores
!The decision is to calculate them or not
!(comment the line and adjust vector numbers)
method2(1)='FB',
method2(2)='PG',
method2(3)='PP',
!Scores
score2(1)='FSS',
score2(2)='BSS',
score2(3)='ETSr',
!Number of methods of type 3
nm3=1,
!Methods
method3(1)='RM',
!Scores
score3(1)='RMSE'
&end
```

Figure 17: Verification methods to be configured for the execution of `fuzzy_verify`

Examples for method 1:

- The user wants to obtain the following scores: bias, pod, far
- The user wants to use the following method for all the scores: upscaling
- Result:
  - method1(1)='UP'
  - method1(2)='UP'
  - method1(3)='UP'
  - !method1(4)=*whatever, commented*
  - !method1(5)=*whatever, commented*
  - score1(1)='BIAS'
  - score1(2)='POD'
  - score1(3)='FAR'
  - !score1(4)=*whatever, comented*
  - !score1(5)=*whatever, commented*
- The user wants to obtain the following scores: bias, pod, far

- The user wants to use the following methods: upscaling for bias, minimum coverage for pod, yes/no for far
- Result:
  - method1(1)='UP'
  - method1(2)='MC'
  - method1(3)='YN'
  - !method1(4)=*whatever, commented*
  - !method1(5)=*whatever, commented*
  - score1(1)='BIAS'
  - score1(2)='POD'
  - score1(3)='FAR'
  - !score1(4)=*whatever, commented*
  - !score1(5)=*whatever, commented*
- The user wants to obtain the following score: far
- The user wants to calculate FAR with three different methods: upscaling, minimum coverage, yes/no
- Result:
  - method1(1)='UP'
  - method1(2)='MC'
  - method1(3)='YN'
  - !method1(4)=*whatever, commented*
  - !method1(5)=*whatever, commented*
  - score1(1)='FAR'
  - score1(2)='FAR'
  - score1(3)='FAR'
  - !score1(4)=*whatever, commented*
  - !score1(5)=*whatever, commented*

Figure 18 shows the last specifications needed by `fuzzy_verify` to chose the correct data (`ver_name`), set the spatial scale in the plots (`km_points`) and to chose the format of the output (`png_pdf`). The `png_pdf` option must be set to **pdf** if the user is working on a VERSUS machine or with old versions of software R. Version *2.0* asks the user to indicate if their R version is newer ('y') or older ('n') than 3.0.

```
&plot_format
!Is your R version >=3.0? (y/n)
r_version='n'
!'png' or 'pdf'
png_pdf='pdf',
!'km' for kilometers, 'gp' for grid points
km_points='gp',
!NAME OF THE VERIFICATION (string with no gaps)
ver_name='?????'
&end
```

Figure 18: Format information for the making of the plots. Used by `fuzzy_verify`

4.2.3 Performance of the verification

Once that the `vast.sh` executable has been launched, the software performs the verification. These are the main steps of the execution:

- The software uploads the information contained in the configuration file `directories.conf`
- Compiles the Fortran code `read_txt.f90`
- Compiles the Fortran code `fuzzy_verify.f90`
- Creates the list of the input TXT files (forecast and observation)
- Runs the executable `read_txt` using the information stored in the namelist `input_fuzzy.nml`
- Produces the half processed DAT files in the directories `VAST/data/OUT/fcs` and `obs`
- Produces the namelist `VAST/src/output_txt.nml` that contains the information related to the data grid dimensions
- Produces the list of the half processed files used by `fuzzy_verify`
- Runs the executable `fuzzy_verify` using the information stored in the namelists `input_fuzzy.nml` and `output_txt.nml` (that produces the R scripts containing the instructions to create the plots)
- Runs the R command that compiles all the scripts containing the instructions to plot the results
- Moves the half processed data files and the R scripts in the backup directories

At the end of the procedure, the user will find all the desired plots in the folder `VAST/data/PLOTS`. If the user needs to perform small changes in the plots (labels, title, colours, legend displacement, etc.), it will be possible to modify the R scripts (located in the `backup` folder inside the `VAST/data/R` directory) without rerunning the verification.

5 Use, recap for LIBSIM users

Input files: The user needs to place the input files in the correct folders. Observation can be bufr or grib, forecast must be grib.

Configuration file: The user needs to configure the file `input_libsim.conf` by completing all the directories' paths, by commenting the unused path for observation input (BUFR if using GRIB and vice versa), by choosing the type of the input files (BUFR or GRIB), by setting the grid parameters (limits and steps), by choosing the cumulation period (`cum`) and by assigning a name to the verification. The configuration file is contained in the directory `VAST/src/`

Namelist: The user needs to complete the directories' paths.

Executable file: The user can now run the executable file `use_libsim.sh` from the `bin` directory by typing:
`./use_libsim.sh`

The executable will now produce the TXT files needed by VAST and place them in the directories `VAST/data/TXT/obs` and `fcs`.

5.1 Use, recap for non LIBSIM users only

Input observation files: The observation files must be txt files with the same characteristics of the ones contained in the folder `vast_install/documentation/data/TXT/obs` and described before. Their naming must contain the date and the name of the verification, as shown before.
Input forecast files: The forecast files must be txt files with the same characteristics of the ones contained in the folder `vast_install/documentation/data/TXT/fcs` and described before. Their naming must contain the date and the name of the verification, as shown before.

The observation and forecast grid must be exactly the same. The coordinates start from the bottom-left corner of the area and proceed by letting the longitude grow first. It is important that the header corresponds exactly to the one shown in the example files.

5.2 Use, recap for both users

Configuration file `directories.conf`: Before the first use of the software, the user will find question marks in the directories common path to be set. The user should fill in the complete path corresponding to the real position of the directory. The information inside this configuration file need to be inserted in the following way (the part within the quotation marks):

```
Variable='my_variable_name'
Directory='my_directory_path'
```

The comment lines need to be inserted in the following way:

```
# Comment
```

Configuration file `input_fuzzy.nml`:

Before the first use of the software the user will find question marks in the directories common path to be set. The user should fill in the complete path corresponding to the real position of the directory. The information inside this configuration file need to be inserted in the following way (the part within the quotation marks):

```
Variable='my_variable_name'
Directory='my_directory_path'
```

The comment lines need to be inserted in the following way:

```
!  Comment line
```

The user needs then to decide the extension of the larger spatial scale needed for the verification to be performed to set the corresponding parameter. This decision must be related to the total dimension of the grid and the resolution of forecast and observation data. The user also needs to decide which type (types) of verification are the most correct to evaluate the situation to be verified.
The program will perform the verification by increasing the extent of the boxes (if the method requires it) starting from the single grid point up to the desired one following the sequence (1, 3, 5, 7, 9, 17, 33, ..). For each box and for each scale the software will calculate the required indexes.

`Dimensions`:

- `n_windows`: Number of window dimensions (up to 10)
- `n_thresh`: Number of valid thresholds (up to 10)
- `thresh`: Value of each threshold (10 values, blanks at the end to be filled with -999)

`Methods_scores`:

- `nm1`: Number of methods of type one (UP, MC, YN, FZ, JP, ME) (up to 6)
- `method1`: List of methods of type one
- `score1`: List of scores to be calculated associated to each method (BIAS, FAR, POD, POFD, ETS, HK)
- `nm2`: Number of methods of type two (FB, PG, PP) (up tp three)
- `method2`: List of methods of type two
- `score2`: List of scores to be calculated associated to each method (FSS, BSS, ETSr)
- `nm3`: Number of methods of type three (RM) (only one)
- `method3`: List of methods of type three
- `score3`: List of scores to be calculated associated to each method (RMSE)

In the namelist files advises are given on how to combine the different methods and scores for type one. Type two and type three are fixed, so for example if the user chooses `method2(1)` **FB**, the `score2(1)` must be **FSS** and so on.

5.3 Perform the verification

Once everything has been set, the user only has to move to the directory associated to the variable "`dir_bin`" in the file `directories.conf` (i.e. "`VAST/bin`") and type:

- `./vast.sh`

The elaboration of the files will start followed by the verification process.

At the end of the verification process all the files contained in the sub directories of TXT and OUT will be moved to their backup folder.

6 Verification methods

Upscaling, anywhere in window, minimum coverage, fuzzy logic, joint probability and multi-event contingency table belong to the verification methods of type 1 (use contingency table and subdivide by thresholds). Brier skill score, fraction skill score and practically perfect hindcast belong to the verification methods of type 2 (don't use contingency table, subdivide by thresholds). Area related root mean square error belongs to the verification methods of type 3 (doesn't use a contingency table and doesn't subdivide by thresholds).

6.1 Upscaling (UP)

- Gets average values in window
- Averaged observation (forecast) $\geq$ threshold $\Rightarrow$ Ob (Fc) array = 1
- Averaged observation (forecast) $<$ threshold $\Rightarrow$ Ob (Fc) array = 0
- Possible scores: BIAS, FAR, POD, POFD, ETS

Hit	Ob = 1	Fc = 1
Miss	Ob = 1	Fc = 0
False Alarm	Ob = 0	Fc = 1
Correct Negative	Ob = 0	Fc = 0

Figure 19: Contingency table for "Upscaling" method

6.2 Anywhere in window (YN)

- Event (threshold exceeding) occurs anywhere in the window
- The portion of window where the event occurs is calculated
- Po (Pf) = Portion observed (Portion forecast)
- Possible scores: FAR, POD, POFD, ETS

Hit	Po $>$ 0	Pf $>$ 0
Miss	Po $>$ 0	Pf = 0
False Alarm	Po = 0	Pf $>$ 0
Correct Negative	Po = 0	Pf = 0

Figure 20: Contingency table for "Anywhere in window" method

6.3 Minimum coverage (MC)

- The portion of window where the event occurs is calculated
- Po (Pf) = Portion observed (Portion forecast)
- Scoring using proportional decision rule (min. cov. = 0.1, Marsigli criterion for 90th percentile)
- Possible scores: FAR, POD, POFD, ETS

Hit	$\text{Po} \geq 0.1 \quad \text{Pf} \geq 0.1$
Miss	$\text{Po} \geq 0.1 \quad \text{Pf} < 0.1$
False Alarm	$\text{Po} < 0.1 \quad \text{Pf} \geq 0.1$
Correct Negative	$\text{Po} < 0.1 \quad \text{Pf} < 0.1$

Figure 21: Contingency table for "Minimum coverage" method

6.4 Fuzzy logic (FZ)

- The portion of window where the event occurs is calculated
- Po (Pf) = Portion observed (Portion forecast)
- Scoring using fuzzy logic
- Possible scores: FAR, POD, POFD, ETS

Hit	$\min(Po, Pf)$
Miss	$\min(Po, (1 - Pf))$
False Alarm	$\min((1 - Po), Pf)$
Correct Negative	$\min((1 - Po), (1 - Pf))$

Figure 22: Contingency table for "Fuzzy logic" method

6.5 Joint probability (JP)

- The portion of window where the event occurs is calculated
- Po (Pf) = Portion observed (Portion forecast)
- Scoring using joint probabilities
- Possible scores: FAR, POD, POFD, ETS

Hit	(Po $*$ Pf)
Miss	(Po $*$ (1-Pf))
False Alarm	((1-Po) $*$ Pf)
Correct Negative	((1-Po) $*$ (1-Pf))

Figure 23: Contingency table for "Joint probability" method

6.6 Multi-event contingency table (ME)

- Square windows are used instead of radii
- Observation occurrence is calculated for each point and for each threshold
- Observation exceeding threshold $\Rightarrow$ Oy = 1
- Observation NOT exceeding threshold $\Rightarrow$ Oy = 0
- The portion of window where the event occurs is calculated only for the forecast
- Pf = Portion forecast
- Hanssen and Kuipers (HK) score is calculated

Hit	Oy = 1	Pf > 0
Miss	Oy = 1	Pf = 0
False Alarm	Oy = 0	Pf > 0
Correct Negative	Oy = 0	Pf = 0

Figure 24: Contingency table for "Multi-event contingency table" method

6.7 Brier Skill Score (Method=PG, Score=BSS)

Pragmatic approach: single observation, neighbourhood forecast. BSS: Measures the improvement of the probabilistic forecast relative to a reference forecast (usually the long-term or sample climatology), thus taking climatological frequency into account. Not strictly proper. Unstable when applied to small data sets: the rarer the event, the larger the number of samples needed.
Answers the question: What is the magnitude of the probability forecast errors?

$$\textit{Brier skill score} - \quad BSS = \frac{BS - BS_{reference}}{0 - BS_{reference}} = 1 - \frac{BS}{BS_{reference}}$$

Figure 25: Brier Skill Score formulation

$$\textit{Brier score} - \quad BS = \frac{1}{N}\sum_{i=1}^{N}(p_i - o_i)^2 = \frac{1}{N}\sum_{k=1}^{K} n_k(p_k - \bar{o}_k)^2 - \frac{1}{N}\sum_{k=1}^{K} n_k(\bar{o}_k - \bar{o})^2 + \bar{o}(1-\bar{o})$$

Figure 26: Brier Score formulation

6.8 Fractions Brier Skill Score (Method=FB, Score=FSS)

The FSS ranges from 0 to 1. A score of 1 is attained for a perfect forecast and a score of 0 indicates no skill. As r expands and the number of grid boxes in the neighbourhood increases, the FSS improves as the observed and model probability fields are smoothed and overlap increases.

$$FSS = 1 - \frac{\frac{1}{N}\sum_N (P_f - P_o)^2}{\frac{1}{N}\left[\sum_N P_f^2 + \sum_N P_o^2\right]}$$

Figure 27: Fraction Skill Score formulation

Where Pf (Po) is the portion of spatial box of the forecast (observation) grid covered by rain exceeding a certain threshold and N is the number of boxes.

6.9 ETS ratio (Method=Practically Perfect Hindcast, Score=ETSr)

Useful forecast resembles one that would have been issued by a forecaster given perfect knowledge of the observations beforehand. Finds maximum ETS for practically perfect hindcast, which is based on the threshold probabilities, and the probability threshold at which it occurs.

6.10 Area related root mean square error (Method= RM, Score=RMSE)

The Root mean square error is calculated over each box. It is calculated for the ordered arrays.

$$RMSE = \sqrt{\left(\frac{1}{n}\right)\sum\left(f_i - o_i\right)^2}$$

Figure 28: Root Mean Square Error formulation

7 Output

7.1 Methods that belong to type 1

A list of the graphics produced by VAST software is given here. The pictures are examples of the possible outputs. The graphics produced for the verification of scores calculated through methods of type one are:

- Scale-intensity

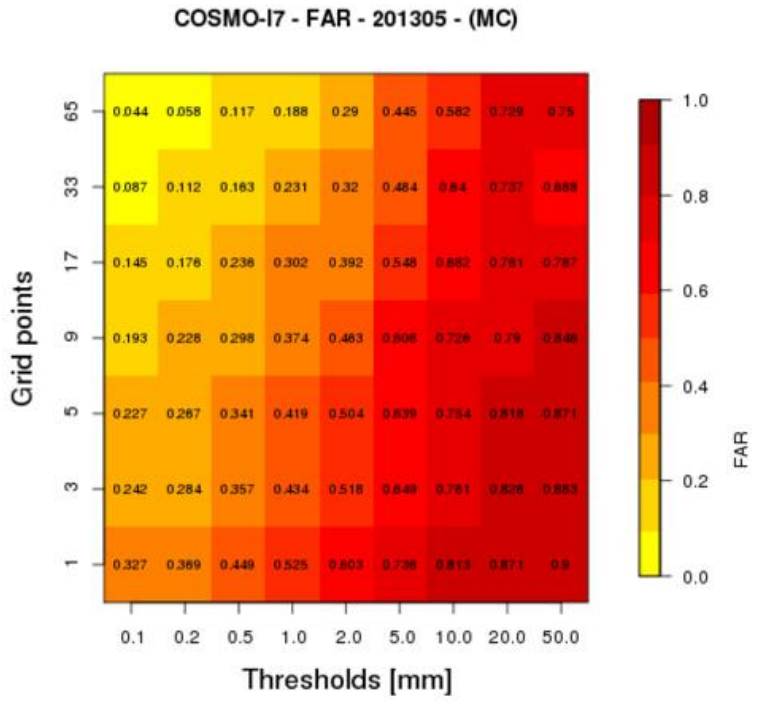


Figure 29: Example of a scale-intensity plot

- Score vs scale

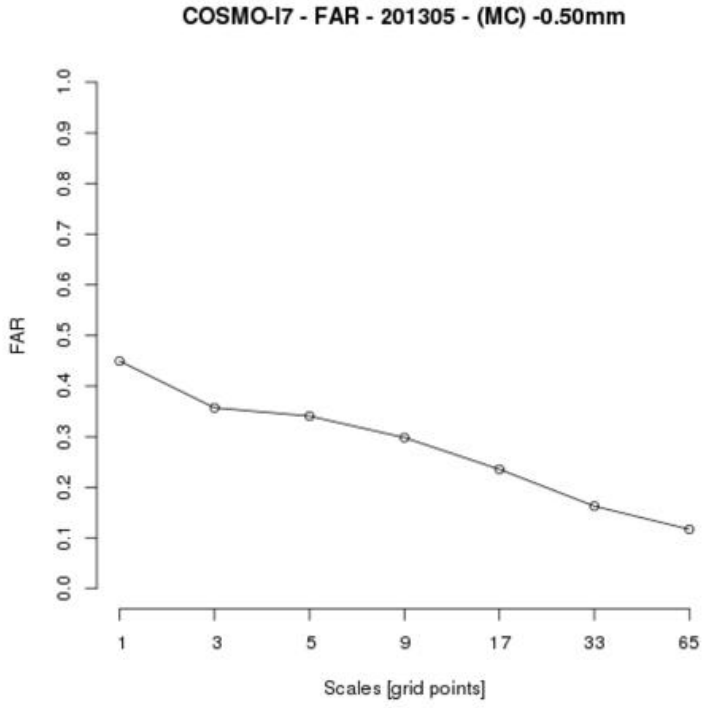


Figure 30: Example of a score vs scale plot

- Score vs scale (all together)

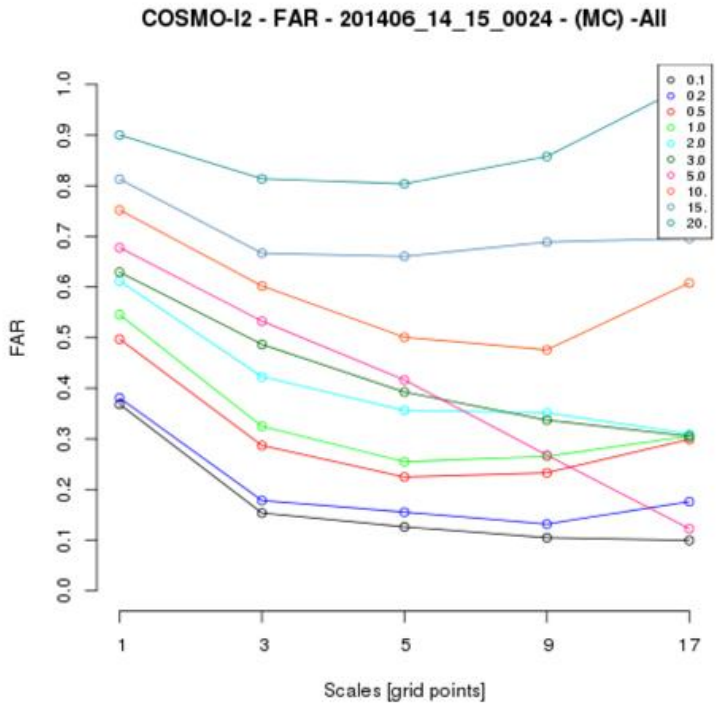


Figure 31: Example of a score vs scale plot (all together)

- Score vs intensity (at minimum scale)

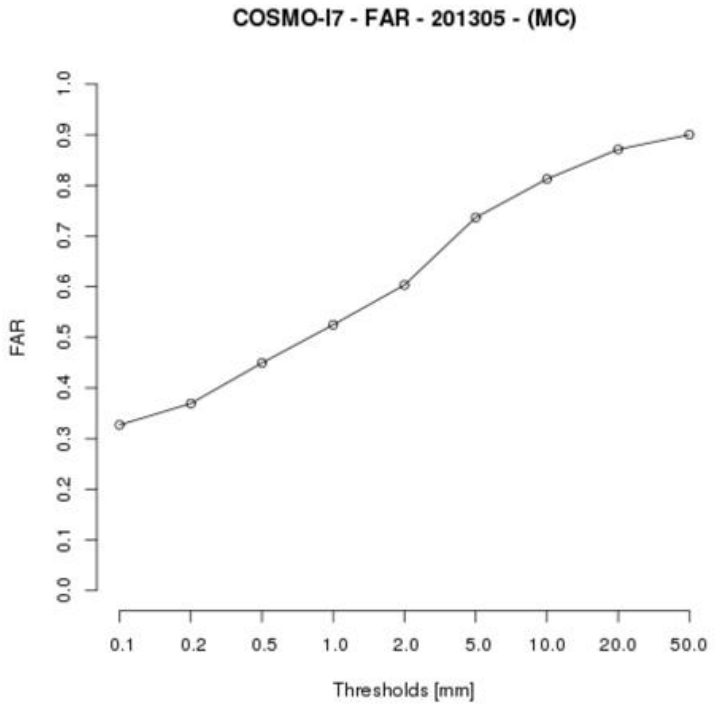


Figure 32: Example of a score vs intensity plot

7.2 Methods that belong to type 2

The graphics produced for the verification of scores calculated through methods of type one are:

- Scale-intensity

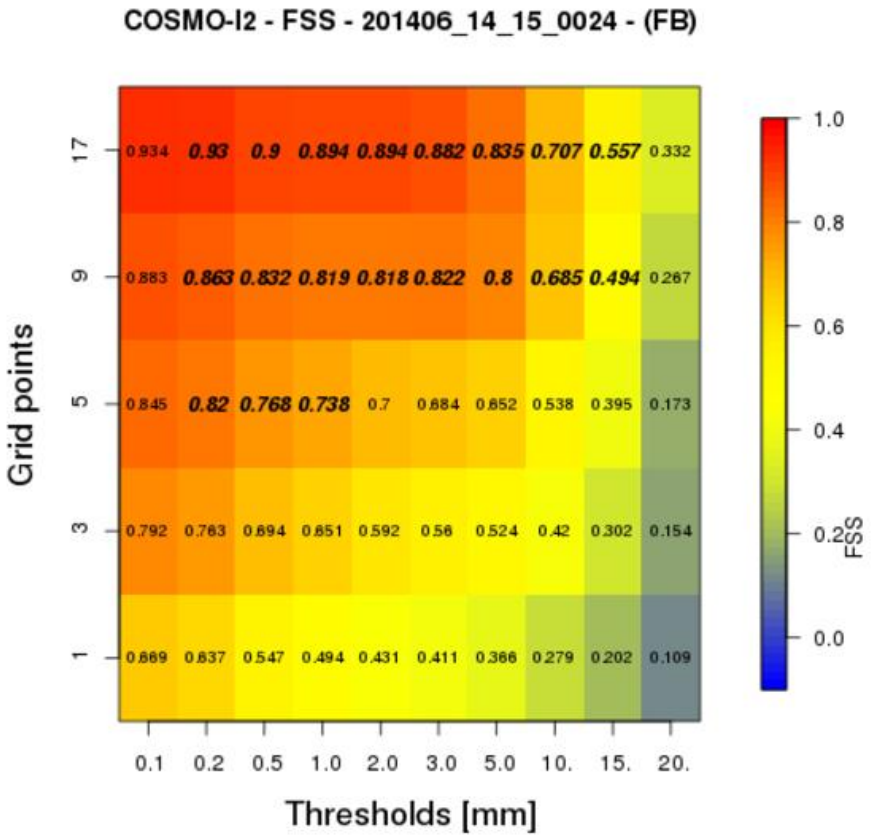


Figure 33: Example of a scale-intensity plot

7.3 Methods that belong to type 3

The graphics produced for the verification of scores calculated through methods of type one are:

- Score vs scale

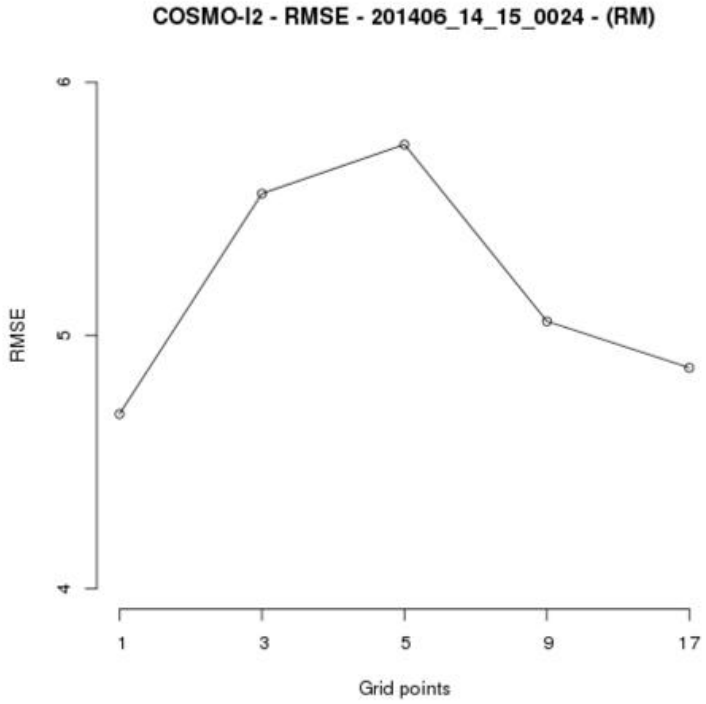


Figure 34: Example of a score vs scale plot

8 Conclusions

The software is designed to give the user the possibility to perform a wide range of spatial verification in a very handy way.
The LIBSIM users can perform their verification starting from GRIB (for both observation and forecast) and BUFR (for observation) files. The non-LIBSIM users must produce txt files according to the given instructions. In the future it might be useful to try to make VAST software independent from LIBSIM and able to use standard input files itself.

9 Acknowledgments

Thanks to all the Working Group 5 for the support.

10 References

Gilleland, E., Ahijevych, D.A., Brown, B.G. and Ebert, E.E., 2010. Verifying forecasts spatially. *Bull. Amer. Met. Soc.* **91**, 1365–1373.

Gilleland, E., Ahijevych, D., Brown, B.G., Casati, B. and Ebert, E.E., 2009. Inter-comparison of spatial verification methods. *Wea. Forecasting* **24**, 1416–1430.

Ahijevych, D.A., Gilleland, E., Brown, B.G. and Ebert, E.E., 2009. Application of spatial verification methods to gridded precipitation forecasts. *Wea. Forecasting* **24**, 1485–1497.

Ebert, E.E., 2009. Neighborhood verification of high resolution precipitation forecasts. *Wea. Forecasting* **24**, 1498–1510.

Casati, B., Wilson, L.J., Stephenson, D.B, Nurmi, P., Ghelli, A., Pocernich, M., Damrath, U., Ebert, E.E., Brown, B.G. and Mason, S., 2008. Forecast verification: current status and future directions. *Meteorol. Appl.*,**15**, 3–18.

Ebert, E.E., 2008. Fuzzy verification of high resolution gridded forecasts: A review and proposed framework. *Meteorol. Appl.*,**15**, 51–64.

Bowler, N.E., Arribas, A., Mylne, K.R., Robertson, K.B. and Beare, S.E., 2008. The MOGREPS short–range ensemble prediction system. *Q. J. Roy. Meteorol. Soc.* **134**, 703–722.

Buizza, R., Hollingsworth, A., Lalaurette, F. and Ghelli, A., 1999. Probabilistic predictions of precipitation using the ECMWF Ensemble Prediction System. *Wea. Forecasting* **14**, 168–189.

Buizza, R., 2005. The ECMWF Ensemble Prediction System. In: *Predictability of weather and climate,* (eds. T. Palmer and R. Hagedorn), Cambridge University Press, Cambridge, 459–488.

List of COSMO Newsletters and Technical Reports

(available for download from the COSMO Website: www.cosmo-model.org)

COSMO Newsletters

No. 1: February 2001.

No. 2: February 2002.

No. 3: February 2003.

No. 4: February 2004.

No. 5: April 2005.

No. 6: July 2006.

No. 7: April 2008; Proceedings from the 8th COSMO General Meeting in Bucharest, 2006.

No. 8: September 2008; Proceedings from the 9th COSMO General Meeting in Athens, 2007.

No. 9: December 2008.

No. 10: March 2010.

No. 11: April 2011.

No. 12: April 2012.

No. 13: April 2013.

No. 14: April 2014.

No. 15: July 2015.

No. 16: July 2016.

No. 17: July 2017.

COSMO Technical Reports

No. 1: Dmitrii Mironov and Matthias Raschendorfer (2001):
Evaluation of Empirical Parameters of the New LM Surface-Layer Parameterization Scheme. Results from Numerical Experiments Including the Soil Moisture Analysis.

No. 2: Reinhold Schrodin and Erdmann Heise (2001):
The Multi-Layer Version of the DWD Soil Model TERRA_LM.

No. 3: Günther Doms (2001):
A Scheme for Monotonic Numerical Diffusion in the LM.

No. 4: Hans-Joachim Herzog, Ursula Schubert, Gerd Vogel, Adelheid Fiedler and Roswitha Kirchner (2002):
LLM ¯ the High-Resolving Nonhydrostatic Simulation Model in the DWD-Project LITFASS.
Part I: Modelling Technique and Simulation Method.

No. 5: Jean-Marie Bettems (2002):
EUCOS Impact Study Using the Limited-Area Non-Hydrostatic NWP Model in Operational Use at MeteoSwiss.

No. 6: Heinz-Werner Bitzer and Jürgen Steppeler (2004):
Documentation of the Z-Coordinate Dynamical Core of LM.

No. 7: Hans-Joachim Herzog, Almut Gassmann (2005):
Lorenz- and Charney-Phillips vertical grid experimentation using a compressible nonhydrostatic toy-model relevant to the fast-mode part of the 'Lokal-Modell'.

No. 8: Chiara Marsigli, Andrea Montani, Tiziana Paccagnella, Davide Sacchetti, André Walser, Marco Arpagaus, Thomas Schumann (2005):
Evaluation of the Performance of the COSMO-LEPS System.

No. 9: Erdmann Heise, Bodo Ritter, Reinhold Schrodin (2006):
Operational Implementation of the Multilayer Soil Model.

No. 10: M.D. Tsyrulnikov (2007):
Is the particle filtering approach appropriate for meso-scale data assimilation ?

No. 11: Dmitrii V. Mironov (2008):
Parameterization of Lakes in Numerical Weather Prediction. Description of a Lake Model.

No. 12: Adriano Raspanti (2009):
COSMO Priority Project "VERification System Unified Survey" (VERSUS): Final Report.

No. 13: Chiara Marsigli (2009):
COSMO Priority Project "Short Range Ensemble Prediction System" (SREPS): Final Report.

No. 14: Michael Baldauf (2009):
COSMO Priority Project "Further Developments of the Runge-Kutta Time Integration Scheme" (RK): Final Report.

No. 15: Silke Dierer (2009):
COSMO Priority Project "Tackle deficiencies in quantitative precipitation forecast" (QPF): Final Report.

No. 16: Pierre Eckert (2009):
COSMO Priority Project "INTERP": Final Report.

No. 17: D. Leuenberger, M. Stoll and A. Roches (2010):
Description of some convective indices implemented in the COSMO model.

No. 18: Daniel Leuenberger (2010):
Statistical analysis of high-resolution COSMO Ensemble forecasts in view of Data Assimilation.

No. 19: A. Montani, D. Cesari, C. Marsigli, T. Paccagnella (2010):
Seven years of activity in the field of mesoscale ensemble forecasting by the COSMO–LEPS system: main achievements and open challenges.

No. 20: A. Roches, O. Fuhrer (2012):
Tracer module in the COSMO model.

No. 21: Michael Baldauf (2013):
A new fast-waves solver for the Runge-Kutta dynamical core.

No. 22: C. Marsigli, T. Diomede, A. Montani, T. Paccagnella, P. Louka, F. Gofa, A. Corigliano (2013):
The CONSENS Priority Project.

No. 23: M. Baldauf, O. Fuhrer, M. J. Kurowski, G. de Morsier, M. Müllner, Z. P. Piotrowski, B. Rosa, P. L. Vitagliano, D. Wójcik, M. Ziemiański (2013):
The COSMO Priority Project 'Conservative Dynamical Core' Final Report.

No. 24: A. K. Miltenberger, A. Roches, S. Pfahl, H. Wernli (2014):
Online Trajectory Module in COSMO: a short user guide.

No. 25: P. Khain, I. Carmona, A. Voudouri, E. Avgoustoglou, J.-M. Bettems, F. Grazzini (2015):
The Proof of the Parameters Calibration Method: CALMO Progress Report.

No. 26: D. Mironov, E. Machulskaya, B. Szintai, M. Raschendorfer, V. Perov, M. Chumakov, E. Avgoustoglou (2015):
The COSMO Priority Project 'UTCS' Final Report.

No. 27: J-M. Bettems (2015):
The COSMO Priority Project 'COLOBOC': Final Report.

No. 28: Ulrich Blahak (2016):
RADAR_MIE_LM and RADAR_MIELIB - Calculation of Radar Reflectivity from Model Output.

No. 29: M. Tsyrulnikov and D. Gayfulin (2016):
A Stochastic Pattern Generator for ensemble applications.

No. 30: D. Mironov and E. Machulskaya (2017):
A Turbulence Kinetic Energy – Scalar Variance Turbulence Parameterization Scheme.

No. 31: P. Khain, I. Carmona, A. Voudouri, E. Avgoustoglou, J.-M. Bettems, F. Grazzini, P. Kaufmann (2017):
CALMO - Progress Report.

No. 32: A. Voudouri, P. Khain, I. Carmona, E. Avgoustoglou, J.M. Bettems, F. Grazzini, O. Bellprat, P. Kaufmann and E. Bucchignani (2017):
Calibration of COSMO Model, Priority Project CALMO Final report.

COSMO Technical Reports

Issues of the COSMO Technical Reports series are published by the *COnsortium for Small-scale MOdelling* at non-regular intervals. COSMO is a European group for numerical weather prediction with participating meteorological services from Germany (DWD, AWGeophys), Greece (HNMS), Italy (USAM, ARPA-SIMC, ARPA Piemonte), Switzerland (MeteoSwiss), Poland (IMGW), Romania (NMA) and Russia (RHM). The general goal is to develop, improve and maintain a non-hydrostatic limited area modelling system to be used for both operational and research applications by the members of COSMO. This system is initially based on the COSMO-Model (previously known as LM) of DWD with its corresponding data assimilation system.

The Technical Reports are intended

- for scientific contributions and a documentation of research activities,
- to present and discuss results obtained from the model system,
- to present and discuss verification results and interpretation methods,
- for a documentation of technical changes to the model system,
- to give an overview of new components of the model system.

The purpose of these reports is to communicate results, changes and progress related to the LM model system relatively fast within the COSMO consortium, and also to inform other NWP groups on our current research activities. In this way the discussion on a specific topic can be stimulated at an early stage. In order to publish a report very soon after the completion of the manuscript, we have decided to omit a thorough reviewing procedure and only a rough check is done by the editors and a third reviewer. We apologize for typographical and other errors or inconsistencies which may still be present.

At present, the Technical Reports are available for download from the COSMO web site (www.cosmo-model.org). If required, the member meteorological centres can produce hard-copies by their own for distribution within their service. All members of the consortium will be informed about new issues by email.

For any comments and questions, please contact the editor:

Massimo Milelli
Massimo.Milelli@arpa.piemonte.it